



CERAI
Civil Engineering Research Association of Ireland
Promoting civil engineering research and practice in Ireland



OÉ Gaillimh
NUI Galway



PROCEEDINGS OF CIVIL ENGINEERING RESEARCH IN IRELAND CONFERENCE

29-30 AUGUST 2016

Editor: Jamie Goggins

*Assistant Editors: Ken Gavin, Annette Harte, Niall Holmes,
Shane Newll, Dermot O'Dwyer, Vikram Pakrashi & Niamh Power.*

Proceedings of

**Civil Engineering
Research in Ireland**

29-30 August 2016



Proudly presents
Civil Engineering Research in Ireland 2016 (CERI2016) Conference

Hosted by
National University of Ireland Galway



Editor:

Jamie Goggins

Assistant Editors:

Ken Gavin Annette Harte Niall Holmes Shane Newell Dermot O'Dwyer
Vikram Pakrashi Niamh Power

Published in 2016
ISBN 978-0-9573957-2-5

Published by
Civil Engineering Research Association of Ireland

© Copyright Declaration
All rights of papers in this publication rest with the authors.

This publication is part of the proceedings
of the Civil Engineering Research in
Ireland conference held at the National University of Ireland Galway,
Ireland on 29-30 August 2016

Copies of these proceedings are available from:

Dr Jamie Goggins
College of Engineering & Informatics
Engineering building
National University of Ireland Galway
Upper Newcastle
Galway H91 HX31
Ireland

Proceedings are also available via the conference portal; for access visit www.cerai.net

Website and conference engine by
Ex Ordo www.exordo.com

Organising Committee Members 2016

Civil Engineering Research Association of Ireland (CERAI) board members:

President:	Sreejith Nanukuttan (QUB)
Chair:	Jamie Goggins (NUI Galway)
Secretary:	Magdalena Hajdukiewicz (NUI Galway)
Treasurers:	Roger West (TCD) and Shane Newell (GMIT)
Ex Officio:	Des Walsh (CIT), Roger West (TCD), Sreejith Nanukuttan (QUB)
Other Members of CERAI	Bryan Magee (UU), Ken Gavin (TU Delft), Vikram Pakrashi (UCD), Paul Archbold (AIT), Giuseppina Amato (QUB), Niall Holmes (DIT)
CERI2016 Chairperson:	Jamie Goggins (NUI Galway)
CERI2016 Theme Leaders:	Vikram Pakrashi (UCD) - Bridges; Niall Holmes (DIT) - Concrete; Ken Gavin (TU Delft) - Geotechnical; Niamh Power (CIT) - Environmental; Shane Newell (GMIT) - Structures; Dermot O'Dwyer (TCD) - Teaching; Annette Harte (NUI Galway) - Timber & Other Civil Engineering Materials.

Scientific Committee Members 2016

The following are the scientific committee members for the CERI2016 conference:

First Name	Last Name	Affiliation
Giuseppina	Amato	Queens University Belfast
Paul	Archbold	Athlone Institute of Technology
Brian	Broderick	Trinity College Dublin
Aimee	Byrne	Dublin Institute of Technology
David	Cadogan	Cork Institute of Technology
Oscar	de la Torre	National University of Ireland, Galway
Peter	Deegan	Banagher Precast Concrete Ltd
Aidan	Duffy	Dublin Institute of Technology
Jack	English	Holmes Consulting Group, New Zealand
Bernard	Enright	Dublin Institute of Technology
Eric	Farrell	AGL Consulting
William	Finnegan	National University of Ireland, Galway
Breiffni	Fitzgerald	Dublin Institute of Technology
Attracta	Foley	Athlone Institute of Technology
Declan	Gavigan	Openhydro Ltd
Kenneth	Gavin	Delft University of Technology, Delft, Netherlands
David	Gill	AGL Consulting
Jamie	Goggins	National University of Ireland, Galway
Joe	Harrington	Cork Institute of Technology
Annette	Harte	National University of Ireland, Galway
David	Holleran	Oran Precast Ltd
Niall	Holmes	Dublin Institute of Technology
Oliver	Kinnane	Queens University Belfast
Bryan	Magee	Ulster University
Michal	Majka	Irish Rail
Martin	Mannion	Cork Institute of Technology
Bryan	McCabe	National University of Ireland, Galway
Brian	McCann	Institute of Technology, Sligo
Daniel	McCrum	Queens University Belfast
Cian	McGuinness	RPS Consulting Engineers
Michael	Minehane	RPS Consulting Engineers

John	Murphy	Cork Institute of Technology
Jimmy	Murphy	University College Cork
Sreejith	Nanukuttan	Queen's University Belfast
Stephen	Nash	National University of Ireland, Galway
Ahmed	Nasr	Dublin Institute of Technology
Shane	Newell	Galway-Mayo Institute of Technology
Eanna	Nolan	Irish Cement Limited
Dermot	O'Dwyer	Trinity College Dublin
Alan	O'Connor	Trinity College, University of Dublin
Padraic	O'Donoghue	National University of Ireland, Galway
Brian	O'Rourke	Cork Institute of Technology
Cormac	O'Suilleabhain	Cork County Council
Vikram	Pakrashi	University College Dublin
Sara	Pavia	Trinity College Dublin
Niamh	Power	Cork Institute of Technology
Luke	Prendergast	University College Dublin
Sarah	Pritchard	Buro Happold Ltd
Paul	Quigley	Gavin and Doherty Geosolutions
Gary	Raftery	The University of Auckland, New Zealand
John	Reddy	Ecocem Ireland
Kieran	Ruane	RPS Consulting Engineers, Cork
Paraic	Ryan	National University of Ireland, Galway
Donal	Ryan	University of the West of Scotland, UK
Suhaib	Salawdeh	National University of Ireland, Galway
Noel	Sheridan	ARUP
Brian	Solan	Ulster University
Mohammed	Sonebi	Queens University Belfast
Marios	Soutsos	Queens University Belfast
Des	Walsh	Cork Institute of Technology
Roger	West	Trinity College Dublin

This conference is kindly sponsored by the following organisations:

Gold Sponsors

Science Foundation Ireland



www.sfi.ie

ARUP

Roughan & O'Donovan Consulting Engineers



www.arup.ie



www.rod.ie

Cement Manufacturers Ireland

ECOCEM



www.cement.ie



www.ecocem.ie

Oran Pre-cast Ltd

Engineers Ireland West Region



www.oranprecast.ie



www.engineersireland.ie

CPD & Members discount provided by

Engineers Ireland



www.engineersireland.ie

Silver sponsors

Irish Concrete Society



Institution of Structural Engineers



Republic of Ireland Branch

www.istructe.ie

RPS Group



www.rpsgroup.com

Zwick



Testing Systems

www.zwick.co.uk

PMS Pavement Management Services



www.pms.ie

Irish Concrete Federation (ICF)



www.irishconcrete.ie

NETZSCH



www.netzsch.com

Student Prizes Sponsored by

L&M Keating



www.lmkeating.ie/

Tobins



www.tobinconsultingengineers.com/

Preface

On behalf of the Civil Engineering Research Association of Ireland (CERA), I am delighted to welcome you to the Civil Engineering Research in Ireland 2016 (CERI2016) conference and to the beautiful arty, bohemian city of Galway on the West coast of Ireland, which has officially been designated the European Capital of Culture 2020.

The Civil Engineering Research Association of Ireland (CERA) was formed in 2012 for the purpose of promoting civil engineering research and practice in Ireland, and its communication to academics and practitioners. The principal activity is the sponsoring and overseeing of the organisation of a conference series dedicated to this goal. The Civil Engineering Research in Ireland (CERI) conference series has grown initially from Concrete Research Ireland (CRI) and Bridge Research Ireland (BRI) symposiums, which subsequently held joint symposiums that became Bridge and Concrete Research Ireland (BCRI). Over the years, the themes of the conference broadened significantly, attracting submission from the titular areas, as well as from other areas in civil engineering. As the research needs broaden, and the range of submission widened correspondingly, the Organising Committee of BCRI 2012 recommended re-naming the conference series to Civil Engineering Research in Ireland (CERI). The first CERI conference was held in Queens University Belfast in 2014.

The CERI2016 conference is building on the enormous success of the histories of CRI, BRI, BCRI and CERI! 119 papers from a broad range of topics in civil engineering have been accepted for the CERI2016 conference, including bridge engineering, concrete technology, geotechnical engineering, environmental engineering, pedagogy in civil engineering, structural engineering and timber, as well as other civil engineering materials and technologies.

As you will see from the conference proceedings, there has been emphasis on applications, as well as theory, to maintain relevance to both industry and academia. Furthermore, we hope that the conference will nurture early-career researchers by making it accessible and offering opportunities wherever possible to grow them as the next generation of leaders in research and industry. To help achieve this aim, a number of initiatives have been undertaken, such as all student papers are entered into 'Best Student Paper' competitions from our main thematic areas and student bursaries have been awarded to contribute towards costs of students. Prizes for best paper will be allocated based on the innovative nature and originality of the work, potential impact of the research and its difficulty, as well as the overall quality of the written paper and oral presentation.

We are extremely grateful to Prof Enzo Siviero, Prof Corey Griffin, Prof W. John McCarter, Dr Annette Harte and Prof J. David Frost, who are our five eminent keynote speakers, for taking the time to share some of their knowledge and experience with us.

On your behalf, we also acknowledge and thank the members of the Scientific Committee, who have ensured quality and rigour in the conference proceedings by contributing their time and expertise in reviewing papers.

A core group of people, the Organising Committee, worked tirelessly over the last two years to bring this conference to you. More recently, so have many of my postgraduate students and researchers in coordinating this conference. On both mine and your behalf, I wish to thank them most sincerely.

We also acknowledge the dedication of Paul Killoran, Dermot Lally and the staff at Ex Ordo for making the conference organisation easier with their conference management software.

We are extremely grateful to the National University of Ireland Galway for facilitating the conference. Special thanks to Dr James Browne, President of the university, for opening the conference and to Prof Padraic O' Donoghue, Chair of Civil Engineering at National University of Ireland Galway and the Dean of Engineering & Informatics, Prof Gerry Lyons, for their support of the conference. I would like to wish Prof Lyons well on his imminent retirement. A Civil Engineering graduate from UCC, Prof Lyons became Professor of Information Technology in NUI Galway in 1991 and subsequently Dean of Engineering & Informatics at NUI Galway in 2010, which is just one example of the versatility of civil engineering graduates!

This conference would not be possible without the generous sponsorship we have received from the following companies and organisations, which we are most grateful: ARUP, Cement Manufacturers Ireland, ECOCEM, Engineers Ireland, Engineers Ireland West Region, Institution of Structural Engineers, Irish Concrete Federation (ICF), Irish Concrete Society, L&M Keating, NETZSCH, Oran Pre-cast Ltd, Pavement Management Services (PMS), Roughan & O'Donovan Consulting Engineers, RPS Group, Science Foundation Ireland, Tobins and Zwick. This sponsorship ensures that the association can deliver its promise to encourage and support young researchers.

Finally, we would like to thank all authors for their valuable contributions to this conference and adhering to the deadlines set. We hope that the proceedings will be of interest and use to all and a good reference to both researchers and practicing engineers.

Dr Jamie Goggins,
Chairperson, CER12016 conference

Table of Contents

Keynote Lectures

5th Joe O'Donovan Memorial Keynote Lecture - Bridges: Building Harmony With Bridges	<u>1</u>
<i>E. Siviero</i>	
Keynote Lecture - Environment: Multi-performance retrofits to existing buildings: Increasing resiliency and reducing the environmental impact of buildings through simultaneous structural and energy retrofits	<u>7</u>
<i>C. Griffin</i>	
Keynote Lecture - Concrete: Performance Monitoring for Sustainable Concrete Infrastructure	<u>15</u>
<i>W. J. McCarter</i>	
Keynote Lecture - Timber: Massive timber - the emergence of a modern construction material	<u>21</u>
<i>A. Harte</i>	
Keynote Lecture - Geotechnical: The Evolving Role of Materials in Infrastructure Systems	<u>31</u>
<i>J. D. Frost</i>	

Bridge I

Detection of train passages during forced vibration testing of bridge structure using energy harvesting technology	<u>37</u>
<i>P. Cahill, R. Karoumi, A. Mathewson, A. Andersson, V. Pakrashi</i>	
Effect of vehicle velocity on exciting the lateral dynamic response of two-span integral bridges	<u>43</u>
<i>L. Prendergast, K. Gavin, D. Hester</i>	
Drive-by Bridge Damage Detection Using Curvatures in Uncertain Environments	<u>49</u>
<i>D. Martinez Otero, E. OBrien, E. Sevillano Bravo</i>	
Drive-by inference of railway track longitudinal profile using accelerometer readings taken by in-service vehicles	<u>55</u>
<i>E. OBrien, C. Bowe, P. Quirke, D. Cantero</i>	
Evaluation of bridge safety based on Weigh-in-Motion data	<u>61</u>
<i>B. Heitner, E. OBrien, F. Schoefs, R. Décatoire, T. Yalamas, C. Leahy</i>	
Advancements of Vibration Based Damage Detection Techniques for Small to Medium Span Bridges	<u>67</u>
<i>J. Moughy, J. R. Casas</i>	
Monitoring and Maintenance of the Boyne Viaduct	<u>73</u>
<i>L. Connolly, A. O'Connor, C. Leahy, C. Bowe</i>	
Practical Applications of Weigh-in-Motion Data	<u>79</u>
<i>R. Corbally, A. O'Connor, F. Cahill</i>	

An Analysis of a Dataset of 1,400 Bridge Inspections in County Cork	<u>85</u>
<i>L. Dromey, K. Ruane, B. O'Rourke, J. Murphy</i>	

Environmental I

Building performance evaluation of domestic energy efficient retrofits in current and future climates	<u>91</u>
<i>T. McGrath, N. Campbell, S. Nanukuttan, D. Soban, M. Basheer</i>	
How accurate are Energy Performance Certificates indicated energy savings of building retrofits?	<u>97</u>
<i>P. Moran, M. Hadjukiewicz, J. Goggins</i>	
Monitoring the internal thermo-hygrometric environment of cathedrals in Ireland	<u>105</u>
<i>C. Shiell, R. West</i>	
Monitoring moisture in a historic brick wall following the application of internal thermal insulation	<u>111</u>
<i>R. Walker, S. Pavia</i>	
Design process to evaluate potential of wind noise at facade elements	<u>117</u>
<i>C. Paduano, R. Mac Réamoinn, J. Keenahan</i>	
Bi-phase methodology for sensitivity analysis of complex models, applied to the model of evaluating resilience in transport networks	<u>123</u>
<i>B. Martinez-Pastor, M. Nogal, A. J. O'Connor</i>	
Life cycle assessment of bio-SNG production via a nationwide system of gasification and methanation in Ireland	<u>129</u>
<i>A. Singlitico, J. Goggins, R. F. D. Monaghan</i>	
Is the development of a Net Zero Energy agricultural dairy farm possible in Ireland?	<u>135</u>
<i>L. Keane, N. Power</i>	
The impact of the Irish dairy processing industry on climate change	<u>141</u>
<i>W. Finnegan, J. Goggins, E. Clifford, X. Zhan</i>	

Materials I

Flexural response of bamboo-epoxy frames	<u>147</u>
<i>R. West, S. Bhalla, D. Bhagat</i>	
Dynamic analysis of the nonlinear response of high density fuel storage racks	<u>153</u>
<i>A. Gonzalez Merino, L. Costas De La Peña, A. González</i>	
The Shelbourne Hotel - Long Term Innovative Treatment of Corroding Steel Frame	<u>159</u>
<i>E. McKenna, B. McFarland, J. Kearney, D. Collier</i>	
Preliminary Investigation into the rate of carbonation of concrete blocks under normal production yard conditions	<u>165</u>
<i>A. Byrne, E. Nolan</i>	

Effect of waste ceramic powder on strength development characteristics of cement based mortars	<u>171</u>
<i>L. Ferrara, P. Deegan, A. Pattarini, M. Sonebi, S. Taylor, G. Kelly</i>	
Understanding the microstructure of alternative binder systems – banahCEM a metakaolin based geopolymer	<u>177</u>
<i>S. Lawther, A. McIntosh, S. Nanukuttan, J. Provis, M. Soutsos, D. Jose</i>	
The Potential Use of Ceramic Waste Sludge as a Supplementary Cementitious Material	<u>183</u>
<i>P. Archbold, M. Russell, C. Hoey</i>	
Developing braided FRP reinforcement for concrete structures	<u>189</u>
<i>S. Antonopoulou, C. McNally, G. Byrne</i>	
Characterisation and water aging of composite materials for tidal turbine blades	<u>195</u>
<i>D. Grogan, M. Flanagan, J. Goggins, C. Kennedy, A. Doyle, M. Walls, S. Leen</i>	

Bridge II

Monitoring of Bridges using Computer Vision Methods	<u>201</u>
<i>D. Lydon, S. Taylor, J. Martinez del Rincon, D. Hester, D. Robinson, M. Lydon</i>	
The Influence of Traffic Growth on Bridge Load Effect Forecasting	<u>207</u>
<i>C. Leahy, E. OBrien, A. O'Connor</i>	
Laboratory investigation of contactless displacement measurement using computer vision systems	<u>213</u>
<i>M. Lydon, D. Lydon, S. Taylor, D. Hester, D. Robinson</i>	
Rehabilitation of Haulbowline Bridges, Cork Harbour	<u>219</u>
<i>K. Ruane, M. Minehane, C. O'Suilleabhain</i>	
Rehabilitation of Steel Orthotropic Deck Bridges using High Strength Concrete Overlay renovation technique	<u>225</u>
<i>P. Moore, D. Tuinstra</i>	
Implementation of a drive-by monitoring system for transport infrastructure utilising GNSS	<u>231</u>
<i>P. McGetrick, D. Hester</i>	
Integrating multivariate techniques in bridge management systems for life-cycle prediction	<u>237</u>
<i>C. Hanley, J. Matos, D. Kelliher, V. Pakrashi</i>	
Abercorn Bridge – An Innovative Approach to Bridge Remediation	<u>243</u>
<i>C. O'Higgins, B. McFarland, P. Callender, S. Taylor, D. Gilmore</i>	
Arch Bridges under flood conditions, a study of the velocity distributions, and the resulting bed scour	<u>249</u>
<i>D. Ryan, G. Hamill, B. Solan, R. Ettema</i>	

Concrete I

Investigation of the Maturity and Engineering Performance of Self-Compacting Concrete for Pre-cast Elements	<u>255</u>
<i>P. Deegan, M. Sonebi, G. Kelly, S. Taylor, A. Pattarini</i>	
Effect of Steel Fibre Dosage on the Behaviour of Ultra High Performance Fibre Reinforced Concrete Beams and Slabs	<u>259</u>
<i>W. Wilson, T. O'Flaherty</i>	
Resistance of alkali activated slag concretes to chloride environments	<u>265</u>
<i>D. Bondar, D. Thompson, S. Nanukuttan, M. Soutsos, M. Basheer</i>	
The Influence of Basalt Fibres on the Mechanical Properties of Concrete	<u>271</u>
<i>P. Archbold, A. C. da Costa Santos, A. Loonam</i>	
An experimental study of the shear behaviour of Ultra-High Performance Fibre Reinforced Concrete	<u>277</u>
<i>S. English, J. F. Chen, M. Soutsos, D. Robinson</i>	
The Influence of Short Fibre Additions on the Pullout Behaviour of Reinforced Concrete	<u>283</u>
<i>J. Kenna, M. Mulheron, P. Archbold</i>	
Reducing the environmental impact of concrete products, while at the same time saving money	<u>289</u>
<i>J. Goggins, P. McGovern, K. McHugh, W. Finnegan</i>	
Development of resilient and environmentally responsible highway infrastructure solutions using geopolymer cement concrete	<u>293</u>
<i>A. Wilkinson, B. Magee, D. Woodward, S. Tretsiakova-mcnally</i>	

Technology I

Large Scale Structural Testing of Wind Turbine Blades Manufactured Using a One-Shot Out-Of-Autoclave Process	<u>299</u>
<i>M. Flanagan, F. Doyle, J. Goggins, E. Fagan, A. Doyle, T. Flanagan, P. Feerick, S. Leen</i>	
Risk assessment for an Italian road network due to an extreme earthquake hazard scenario and the associated landslide cascading effects	<u>305</u>
<i>J. Clarke, J. C. Lam, P. Gehl, K. Taalab, R. Corbally</i>	
Quantification of Multi Risk Scenarios Subjected to Extreme Weather Events	<u>311</u>
<i>D. Hajjalizadeh, C. Carey, E. O'Brien</i>	
Application of Image Processing to the Analysis of Congested Traffic	<u>317</u>
<i>E. A. Micu, E. O'Brien, E. Sevillano Bravo</i>	
A Simplified System for Assessing the Condition of Irish Regional and Local Roads	<u>321</u>
<i>B. Mulry, J. McCarthy</i>	
The Introduction and Implementation of Mobile Retroreflectivity Measurement of Pavement Markings in Ireland	<u>329</u>
<i>E. Greaney, A. Boyle</i>	

The Use of Average Least Dimension in Surface Dressing Design	<u>335</u>
--	-------------------

B. Mulry, K. Feighan, T. Casey

Assessing aerodynamic performance in cycling using computational fluid dynamics	<u>341</u>
--	-------------------

P. Mannion, E. Clifford, B. Blocken, M. Hajdukiewicz

Concrete II

Sustainable concrete with 95% recycled and natural components	<u>347</u>
--	-------------------

A. Alawais, R. West

Mechanical and thermal evaluation of different types of PCM-concrete composite panels	<u>353</u>
--	-------------------

D. Niall, O. Kinnane, R. West, S. McCormack

Using Photovoltaics to Power Electrochemical Chloride Extraction from Concrete	<u>359</u>
---	-------------------

S. Bond, L. O'Callaghan, N. Holmes, B. Norton

Pre-stressing using basalt fibre bars: An experimental investigation on a new frontier of precast concrete	<u>365</u>
---	-------------------

B. Dal Lago, P. Deegan, S. Taylor, P. Crossett, M. Sonebi, L. Ferrara, A. Pattarini

Evaluating a new CEM III/A cement for concretes exposed to harsh acid rich environments	<u>371</u>
--	-------------------

D. Thompson, N. Holmes, J. Reddy

Technology II

Potential applications for image-based systems in structural engineering	<u>377</u>
---	-------------------

O. D. L. Torre, S. Newell, M. Flanagan, J. Goggins

Evaluation of Camera Calibration Techniques for Quantifying Deterioration	<u>383</u>
--	-------------------

M. O'Byrne, V. Pakrashi, B. Ghosh, F. Schoefs

An overview of Arup Computational Fluid Dynamics Projects	<u>389</u>
--	-------------------

J. Keenahan, C. Paduano, R. Mac Réamoinn

Generating robust algorithms for energy efficient lighting as a performance aspect of the building operational energy optimisation framework	<u>395</u>
---	-------------------

T. Ganguly, M. Hajdukiewicz, M. Keane, J. Goggins

Diagnostics and intervention methods for façade retrofit of post-WWII non-domestic buildings in Europe for energy efficiency	<u>401</u>
---	-------------------

S. Zuhaib, M. Hajdukiewicz, M. Keane, J. Goggins

Teaching and Learning

A changing Civil Engineering curriculum at UCD	<u>407</u>
<i>P. Purcell</i>	
Teaching Engineering Design 1840s – Present	<u>413</u>
<i>D. O'Dwyer, R. Cox</i>	
Developing a deeper understanding of structural dynamics	<u>421</u>
<i>R. West, B. Basu, B. Broderick, G. McGranaghan</i>	
The Pedagogy of Building Information Modelling	<u>427</u>
<i>R. Eadie, B. Solan, B. Magee, M. Rice</i>	
Clacton and Holland on Sea Coastal Protection Case Study to assess the pros and cons of using BIM on coastal protection schemes	<u>433</u>
<i>D. D. Collery, A. McCloud, V. Deakin, J. Ennos</i>	

Geotechnics I

Some geotechnical characteristics of soft soil deposits along the Terryland River valley	<u>439</u>
<i>P. Quigley, B. McCabe, P. Hunt, M. Rodgers</i>	
Assessment of Ground Movement for a Deep Excavation in Soft Marine Clay	<u>445</u>
<i>S. Fallah, P. Casey, P. Sweeney</i>	
Heave-ho! A laboratory model of an underfloor environment incorporating pyritiferous fill	<u>451</u>
<i>E. McKeon, B. McCabe, B. Sexton, M. Cavalcante, J. L. Ibáñez, A. M. O'Connell</i>	
Performance testing of novel gravity-base foundation for offshore wind	<u>457</u>
<i>Y. Attari, L. Prendergast, K. Gavin</i>	
The geotechnical properties of the pulverised coal ash produced at Moneypoint Power Station	<u>463</u>
<i>C. Reilly, S. Rugero, P. Doherty</i>	
The behaviour of a novel dynamically installed anchor during deployment – insights from field tests	<u>469</u>
<i>S. Jalilvand, K. Gavin, P. Doherty, R. B. Gilbert, S. Vinayagamoothy, A. Bradshaw</i>	
Bearing Capacity beneath tapered blades of open dug caisson in sand	<u>473</u>
<i>R. Royston, B. Phillips, B. Sheil, B. Byrne</i>	
Landslide susceptibility assessment for engineered slopes using statistical and deterministic approaches	<u>479</u>
<i>K. Martinovic, K. Gavin, C. Reale</i>	

Structures

Comparative analysis of the probabilistic methods to estimate the probability of failure of offshore wind turbine towers	<u>485</u>
<i>R. Teixeira, A. J. O'Connor, M. Nogal</i>	
Experimental investigation and numerical modelling of domestic scale wind turbine blades	<u>491</u>
<i>E. Fagan, J. Goggins, S. Leen, O. D. L. Torre</i>	
The Four Courts, Dublin – Innovative Monitoring and Long Term Repair Techniques	<u>497</u>
<i>D. Gilmore, B. McFarland, E. McKenna, C. O'Higgins, J. Kearney</i>	
Large inelastic cyclic testing of the gusset-plate brace member assemblies in ultra-low cycle fatigue regime	<u>503</u>
<i>M. S. Hassan, J. English, J. Goggins, S. Salawdeh</i>	
Recommendations for Numerical Modelling of Concentrically Braced Steel Frames with Gusset Plate Connections subjected to Earthquake Ground Motion	<u>509</u>
<i>T. Ryan, B. Broderick, A. Hunt, J. Goggins, S. Salawdeh</i>	
Seismic Design and Performance of Non-structural Elements	<u>515</u>
<i>S. Salawdeh, J. Goggins</i>	
Stress analysis of welded steel catenary risers	<u>521</u>
<i>R. Devaney, P. O'Donoghue, S. Leen</i>	
Improving finite element implementation in topology optimisation	<u>527</u>
<i>S. Al-Sabah</i>	
Bridge Damage Detection using Moving Force Identification	<u>533</u>
<i>P. Fitzgerald, E. O'Brien, E. Sevillano Bravo</i>	

Timber

Distribution of stresses along the length of BFRP rods glued-in to Irish Sitka Spruce	<u>539</u>
<i>C. O'Neill, D. McPolin, S. Taylor, A. Harte</i>	
Viscoelastic Creep of FRP Reinforced Glulam	<u>545</u>
<i>C. O'Ceallaigh, K. Sikora, D. McPolin, A. Harte</i>	
The effects of planting density on the structural timber properties of 23-year-old Irish-grown Sitka spruce	<u>551</u>
<i>K. Simic, V. Gendvilas, C. O'Reilly, M. Nieuwenhuis, A. Harte</i>	
Mechanical characterization of green Sitka spruce logs	<u>557</u>
<i>L. Krajnc, N. Farrelly, A. Harte</i>	
Potential for Medium Rise Timber Structures in Ireland	<u>563</u>
<i>P. Glavin, A. Macilwraith, D. Coleman, T. McKenna</i>	

Timber/steel composite members in multi-storey buildings under standard fire test loadings	<u>569</u>
<i>M. Whelton, A. Macilwraith</i>	
A Review of the State of the Art of Timber Gridshell Design and Construction	<u>575</u>
<i>M. Collins, T. Cosgrove</i>	
Considerations for the Design of Bending Active Timber Gridshells	<u>581</u>
<i>M. Collins, T. Cosgrove</i>	
Probabilistic Climate Change Adaptation Analysis for Timber Power Pole Infrastructure	<u>587</u>
<i>P. Ryan, M. G. Stewart</i>	

Concrete III

An overview of the development of cement-based batteries for the cathodic protection of embedded steel in concrete	<u>593</u>
<i>N. Holmes, A. Byrne, B. Norton</i>	
Strength assessment of in-situ concrete for the evaluation of structural capacity: State of the art	<u>599</u>
<i>S. N. A. Sourav, S. Al-Sabah, C. McNally</i>	
Heat Activated Prestressing of Shape Memory Alloys for Active Confinement of Concrete Sections	<u>605</u>
<i>R. Suhail, G. Amato, J. F. Chen, D. McCrum</i>	
An Assessment of Reinforced Concrete Members in Tension Strengthened with Near Surface Mounted CFRP Strips	<u>611</u>
<i>A. Meehan, K. Ruane</i>	
Interface Shear Behavior of precast prestressed concrete beams with slender webs in beam and slab bridge construction	<u>617</u>
<i>M. Slevin, A. J. O'Connor</i>	
Behaviour of hybrid concrete lattice girder flat slab system using insitu structural health monitoring	<u>623</u>
<i>S. Newell, J. Goggins, M. Hajdukiewicz, D. Holleran</i>	

Environmental II

Sediment Transport Modelling on the River Bandon	<u>631</u>
<i>J. Harrington, J. Gamble</i>	
Low flow analysis of ungauged river catchments in Ireland	<u>637</u>
<i>P. Forde, L. O'Driscoll</i>	
Tidal Stream Energy Resource Assessment of the Shannon Estuary, Ireland	<u>643</u>
<i>A. Phoenix, S. Nash</i>	

Development of a 2D hydrodynamic model to assess the risk of flooding from wave overtopping and tidal inundation of a site in Co. Clare	<u>649</u>
<i>K. Barry, D. Walsh, J. Reilly, S. Lizondo, J. Ascoop, S. Lahiffe, T. Tiernan</i>	
Development of a high resolution wave model at AMETS using SWAN	<u>655</u>
<i>R. Atan, J. Goggins, S. Nash</i>	
Modelling the effects of Climate Change on historic maritime structures: Howth Harbour's East Pier (Ireland)	<u>661</u>
<i>S. Lizondo, J. Reilly, J. Ascoop, G. Connolly, J. Campbell</i>	
Evaluation of UV disinfection technologies for water reuse and rainwater harvesting in the Irish dairy industry	<u>667</u>
<i>K. Fitzhenry, N. Rowan, W. Finnegan, E. Tarpey, J. Goggins, X. Zhan, E. Clifford</i>	
Energy Benchmarking in Wastewater Collection and Treatment	<u>673</u>
<i>D. Cronin, N. Power</i>	
Effect of aeration rate on laboratory-scale IASBRs treating synthetic dairy processing wastewater	<u>679</u>
<i>E. Tarpey, W. Finnegan, K. Fitzhenry, X. Zhan</i>	

Geotechnics II

Numerical modelling of Cone Penetration Test in Clay using Coupled Eulerian Lagrangian Method	<u>685</u>
<i>S. Fallah, K. Gavin, S. Jalilvand</i>	
The treatment of karst features encountered during road construction in County Galway	<u>691</u>
<i>E. Madden, D. O'Hara</i>	
Performance of Road Embankments on Glacial Deposits in Ireland	<u>697</u>
<i>F. Buggy, P. Kissane, D. Rush, M. Long</i>	
Energy transfer ratio of hydraulic pile driving hammers	<u>703</u>
<i>K. Flynn, B. McCabe</i>	
Sheet-pile corrosion rates within an existing outfall channel in Dublin Port	<u>709</u>
<i>B. Sexton, D. Gill, C. O'Donnell</i>	
Author Index	<u>715</u>

BUILDING HARMONY WITH BRIDGES

Enzo Siviero¹

¹ Vice President of RMEI, Réseau Méditerranéen des Ecoles d'Ingénieurs
email: esiviero@esap.it, info@esap.it

ABSTRACT: The design of the bridge is, in the most classic consideration, a cultural act that has its roots in the ancient triad *firmitas, utilitas, venustas*, which Vitruvius himself coined, wherein structural form and function coincide. The theme of the bridge can also become thought and communicate its "being" as an object loaded with identity, with its own poetic intrinsic nature and means through which we can perceive and experience the place, a unique fact that, through the form exalted by the structure, confirms the true identity of a context, and can take on various different facets. This way, the aim of the paper is to investigate the approach to the work-context-landscape-suggestions "dialogue", which is fascinating not only in the research into the type as the founding moment for the structural design, but also as a basic assumption to encourage ongoing research into the formal potential that bridges offers in order to understand the meaning and the perception of the infrastructure in/of the landscape.

KEY WORDS: Bridges, Landscape, Harmony, Composition, Meaning, Perception

1 INTRODUCTION

It is interesting to notice how man, until prehistory, worked to modify nature through his intelligence and building of the first constructions. The primitives solved the problems of living using great technical and artistic ability. In the big hall of the Lascaux cave, France, or in the ceilings painted in the ravines of Altamira, Spain, are found signs of their work where darkness is perpetual. In a cavern, man has demonstrated he does not have to passively accept the space that nature offers to him: he takes possession, equips, decorates and modifies it, marking the distances and the limits which subdivide it. That's why the vault of the cavern of Altamira – with its representative designs, battles between animals and hunting scenes and abstract symbols - has been defined as the "Cappella Sistina" of prehistory. But it is with the passage from the Palaeolithic to the Neolithic that the first great revolution of human history occurred; that men so creating, are striven to construct, to complete and to modify what nature offered.

Exploring the landscape in which these men built the first "infrastructures", such as dams and deviations of the water course for cultivation of fields; and pushing themselves beyond this, they still had the problem of facilitating communications with other villages, without wading across rivers or avoiding obstacles: from this, the first footbridges and bridges were born. Sometimes these bridges were just fallen logs, sometimes they were made using ropes and wood, taking advantage of the elementary principles of the tensions, using structural solutions with stressed cables and suspension bridges, frequently in combination and, where possible, with wood trunks under a bridge. All of this occurred before the ancient invention of the arch was codified and made famous by the Romans. Structures that were in particular agreement with nature and landscape, not only for the materials or the

reduced dimensions, but also because they were signs of the landscape and not just residing in a landscape, as often happens today; works whose presence, like all the great ones, determines and creates a landscape, animating a nature not hostile, maternal, able to receive and not like a step-mother, sometimes seen with fear, like the bridges of the "Devil" in the ancient Medieval tales (Figure 1).



Figure 1. The Devil's bridge in Lucca (Italy)

Today, as in the past, bridges are therefore important elements, not only from the structural point of view, but also from the cultural one, in relation to their ability to create or modify important functional, social, economic relations in a place. If we put the associations among individuals, different communities, human beings and their environment as the true mechanism of the world, we can understand how important it is to build bridges not only to connect sites, but also to bring together people, cultures, nations and generations, as the motto "Bridging culture and sharing heart" declares. In this way, how can a small bridge be the "maker" of a place's transformation? What might be the reasons for a project, its meanings, and the consequences of the choices? When we talk

about the word "value" of a bridge, we mustn't refer exclusively to the economic significance of the thing.

Indeed, we should think about *value* as a result of a process of recognition of specific qualities of the infrastructure and the relationship between a work and its landscape. In general, a piece of infrastructure can create important relationships between man and landscape from perceptive, social, economic, and functional points of view. It can also generate negative or positive impacts, alterations or benefits to the urban landscape. It can become a symbol of the place or an important element of connection among different parts of territory from the social and economic points of view. This way, it is fundamental to think about bridges as infrastructures *of the* landscape, able to connect people and culture and that have been conceived and designed to become part of the culture and of the place and to connect people and culture. An emblematic example is the Bridge of Mostar, which was rebuilt after the Bosnia-Herzegovina war, and which represents a symbol of reconciliation, international cooperation and of the coexistence of diverse cultural, ethnic and religious communities.

2 THE THEME OF PERCEPTION

Reflecting on the social value of bridges, an important role is the perception of the theme that highlights the extent of the design. In fact, apart from a few rare examples, engineers and architects alike focus on the subject which, first designed and then given virtual form, becomes a physical object. Despite the land survey techniques, 3D modelling and photo inserts are able to give good results of the final outcome, the project subject remains the bridge which is what attention and creative forces tend to focus on. Thus, the result is generally the contextualised bridge. However, with this design approach not only is the landscape, a highly discussed topic in recent years with a general growing awareness, put in the background, but, no less important, the overall quality that should also be queried is how the bridge functions are realised, regarding the context of the strategic design, how many and which ties the bridge manages to create with its context (historic, economic, functional, local and network, perceptive, cultural and other points of significance).

Rather in operational terms, where the bridge is contextualised, there is still no idea of the transformed context, i.e. the outcome of a design process that considers the characteristics and vocations engaged in the location and the site for the project, where the continuous symbolic exchanges between the bridge and context can be recognised, until the bridge actually becomes the context, as if it had always been there and to which nothing can be added nor taken away. Consequently, by focusing design attention on the bridge and specifically investigating the context, there is the risk of altering the location, of not going beyond that fine conceptual dividing line of the passage from "Contextualised infrastructure", where the point of view of the infrastructure dominates, to the "transformed context" where the point of view is directed to the location, to the area overall that is used and affected by the relations. The result is that the bridge often is seen as an intruder, with the resulting public protests.

2.1 The quantity of perception

There are numerous variables that affect perception of bridges: the season, the type and quality of light during the day and night, when there may be artificial lighting, the light diffusion, and its intensity during the day and night, the orientation of the bridge with respect to its geographic position, any external observation points of the bridge, and the speed with which it is crossed. So, from how a bridge is sculptured by time, light and shade, we move on to "how much". How much of the bridge do we perceive? Obviously the answer is subjective to each single case, and even though it is complicated to theorise analysis models that are generally valid, we can at least identify those components that come into play in perception and which enable measuring it. One of the main aspects is proximity. Proximity is also affected by scale, based on the relative position between the plane where the visible surfaces of the bridge stand and the observer's plane.

This means that the view of the area from the bridge and of the bridge from the area, a continuing play of marquetry where perspectives and vanishing points are dominating factors. Elevation and central perspective dominate the scene we see if we observe a bridge in the distance on a scale with the landscape, which is amplified in the reflected image if there a river running beneath it. As we get closer to the bridge, foreshortenings and gradual progressive changes in form accompany us until we lose the perception of the structure beneath us and are able to see it in detail. But, if this path, this gradual change in scale, is read as continuity it is just as virtual as the 3D graphic models we mentioned previously. In fact, the problem of accessibility of perception arises. To understand this problem, it is sufficient to take one of the most glaring cases – the organization of the areas around the tallest bridge in the world: Millau in France. Downstream between the two riverbanks a small temporary bridge had been built to enable the heavy vehicles to work on the bridge piers. When the bridge was finally finished, the temporary bridge was not demolished but was included in the new landscape layout as a viewpoint to admire the surroundings which, in this case, is this monumental construction. Apart from the unusual view upwards, the small bridge also offers the chance of understanding the size of the tallest bridge in the world and to grasp its scale with respect to its surroundings.

This case leads us to reflect on the modulation of the ratio of the "quality of the work" / "number of viewpoints" to observe it. Theoretically, the poorer formal quality of the bridge, the more we attempt to deny its visibility, hiding it symmetrically and with attempts of camouflage, also considering the valorisation principles in our "Cultural Heritage Code" – the greater capacity of being a "cultural heritage" the greater accessibility to perception it should have. If we move from the landscape scale to the urban and architectural scale, the chance of getting a glimpse of the bridge is high, and from the perception of depth given by its width, which we previously saw, we now have the perception of depth given by its length up to the point where the bridge ends on the riverbank or embankment. The regular lines are distorted; the spaces between the horizontal lines of the planking and the arch holding the bridge become "triangle-

like". There is a change in range, a linguistic flexibility that should not be taken as a limitation but as expressive potential.

2.2 The Everyday Modellers: Shade and Time

Another aspect that comes into play in perceiving a bridge is shade, especially in Italy where there are not many bridges with large or very large spans, which impose the use of suspended bridges, here the majority are deck bridges or deck arch bridges, where the structural frame is all or partially beneath the deck. Consequently, for the greater part of the day we are only able to recognise the design of the bridge, or structural architecture holding it up, in the half-light or with difficult backlights. This means that shade is also a component that gives depth and substance, but also one that limits perception. Shade also helps to momentarily sculpture other elements in the context: the shade that the bridge throws when it is struck by sunlight, creating fascinating or invasive effects on the surrounding land. The perception time is another "gap" which has been little explored. It is fundamental in the perception of a bridge and has two main ranges of variables. One is of moments, a few seconds or a few minutes we need to catch a glimpse of the slenderness of the structural weave or the convergent lines of a parapet, which, with the deck, guide one's sight to other spaces and places. This is the time of the person who uses the bridge, who crosses over it. The other temporal range varies from days to a lifetime, and mainly concerns those who live close to the bridge and experience, or suffer it, as part of their everyday life (Figure 2).



Figure 2. E. Siviero, The Messina Bridge.
Study of the lighting in relation to the the perception of the bridge in the different hours of the day

3 BRIDGES, FOOTBRIDGES AND VIADUCTS BETWEEN ENGINEERING AND ARCHITECTURE

Today, as in the past, bridges are important elements, not only from the structural point of view, but also from the cultural one, in relation to their ability to create or modify important functional, social, economic relations in a place.

A bridge can create important relationships between man and landscape from perceptive, social, economic, and functional points of view. It can also generate negative or positive impacts, alterations or benefits to the urban landscape. It could be a symbol of the place or an important element of connection among different parts of territory from the social and economic points of view. This way, it is fundamental to think about bridges *as infrastructures of the*

landscape, able to connect people and culture and that have been conceived and designed to become part of the place.

During the aftermath to the second world war, Italian engineering drew international attention with a series of highly original structural works. The reconstruction of the thousands of bridges demolished has not yet been completed and the epic undertaking of the Autostrada del Sole (A1 motorway) is already underway. In this operative fervour, a real engineering school takes shape. The futuristic bridge over the Basento by Sergio Musmeci, the bridges by Riccardo Morandi and Silvano Zorzi are examples of *Italian* engineering in the forefront (Figure 3-4). In the Musmeci's bridge, the attempt to scientifically obtain the minimum form leads to one of the most original, effective symbols of the whole Italian experiment: a powerful, unprecedented plastic form in which the concrete surface becomes a specular image of the tensioned membrane (Figure 5).

Following, some examples of bridges in which the integration work - landscape - meaning is emblematic, are illustrated.



Figure 3-4. R.Morandi, the Fiumarella Viaduct, Catanzaro, 1958



Figure 5. S. Musmeci, The Basento Viaduct, 1967-1976

The bridge over the Battaglia Canal in the Province of Padua, Italy (Figure 6), is in a site of significant historical and architectural interest. In order to conserve the old view of the bridge, which has become a pedestrian bridge, and to improve the layout of the former road junction, the new bridge is 50 m away in the direction of Padua, and is characterised by a depressed single arch, which is monolithic with the foundations and the bridge deck above. The structural solution offers architectural and aesthetic improvements, given the slenderness of the individual elements, and the overall composition makes the entire work particularly streamlined. Statically, the bridge is configured as a closed frame, consisting of a horizontal deck joined to the abutments and made one with the arch in the middle. This type of arch bridge project is part of a new building philosophy that solves various road problems while respecting the environment and traditions. " *The modern arch recalls the ancient Roman tradition. It reflects in the water and creates an eye that is the heart, the mind, the way to express itself... so the bridge speaks, lives and makes us live...*" (Bridges suggestions. <http://www.uninettuno.tv/Canale.aspx?t=autore&a=Enzo%20Siviero>).



Figure 6. E. Siviero, The bridge over the Battaglia Canal in the Province of Padua.
The images show the real situation (a) and the virtual one (b), with the bridge overturned.
In both situations, the image of the bridge is the same, and the bridge creates a virtual eye looking at you

The bridge over the Santa Caterina Canal (Figure 7) was built in order to support the previous "Ponte della Passiva", which was totally inadequate for the current heavy road traffic. The design solution and the layout ensure the visual "lightness" of this work, and a respectful integration into the natural setting. The final visual effect is a striking reinterpretation of the arch which, by following the inclination of the riverbanks with respect to the road axis, creates a staggered succession of arches emphasizing the width of the deck and consequently the entire structure of the bridge.

The construction of the footbridge over the Bacchiglione River (Figure 8) to serve the new cycle-pedestrian lanes in the town of Ponte San Nicolò was completed in the spring of 1998. The project addressed the issue of building a reinforced concrete construction, almost entirely precast, using an arched girder type combined with classic elements of the building industry. After installing the arches, the deck was made by placing four prestressed concrete girders on each side between the thirds of the arch and the abutments of the bank, which form a reversed "T" section and spread over a 22.3 meter span. The final connection is given by an in-situ cast reinforced concrete slab onto the arch and girders. The choice of this building system, based on the prefabrication of the majority of the structural elements, meant the footbridge could be inaugurated without the use of temporary supports in the river bed and in a relatively short time, and in fact, with the exception of the foundation works, the entire construction was completed only in two weeks.

The bridge over the Sacco River, Rome (Figure 9), is part of a series of interventions in the new road network organization, due to building the new high speed railway line from Rome to Naples. The bridge has a transversal position with respect to the new railway line, with one of the two abutments very close to the railway embankment. Unfortunately however, the road has to pass under the railway line, which conditioned the planning research, which opted for a construction with a very low geometric profile, a depressed arch deck bridge that is independent of the railway line. The proximity of a historical multiple arch bridge to the small tower that remains of the ruins of an ancient convent, guided the careful planning to ensure the site and previous works were respected. The "permeability" of the structure is the distinctive feature of the bridge and achieves the aim both of overcoming the riverbed without interfering with its natural setting, and of reducing the interference with the water, increasing the rate of flow and reducing the transversal hydraulic thrust.



Figure 7. E. Siviero, The bridge over the Santa Caterina Canal.

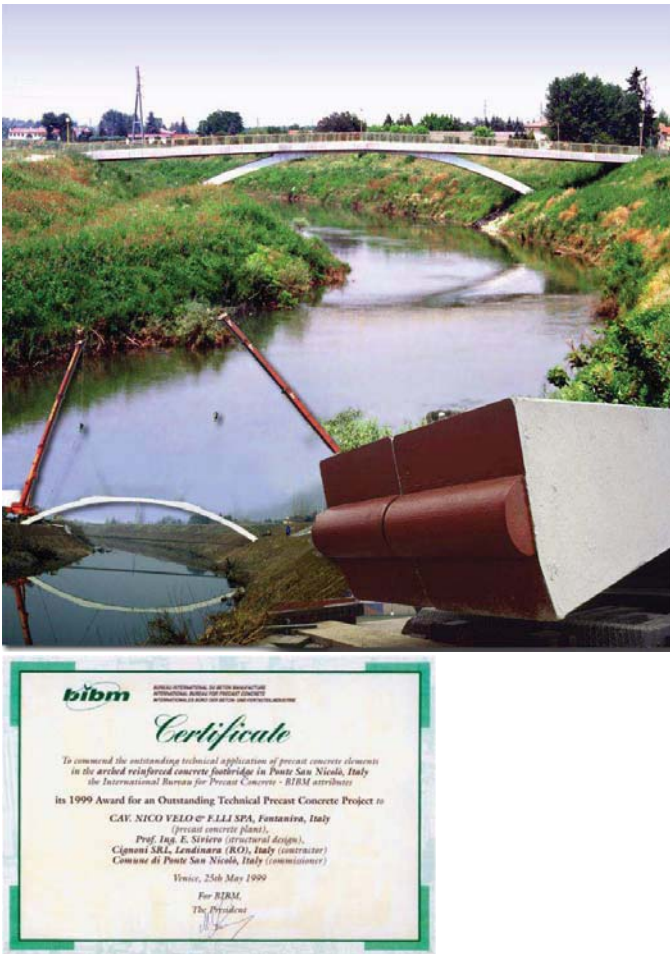


Figure 8. E. Siviero, footbridge over the Bacchiglione River, 1999, and the BIBM award (European Federation for Precast Concrete)



Figure 9. E. Siviero, The bridge over the Sacco River

The bridge in San Donà di Piave, Venice, (Figure 10) is part of a general road network project, which involved the construction of a new crossing over the River Piave. The site for the new bridge is characterized by the being very flat and with no vertical landscape features. For centuries farming was the main activity here. In Roman times, the farming land was “centurised”, i.e. divided into lots. The southern Piave area had Oderzo divided into “cardo” and “decumanus maximum”, alongside minor and parallel axes to create very precise geometries on the land. In recent decades, major changes related to the sprawl of urban and industrial areas have created an extensive infrastructure network that untidily overlaps the

original land design. Currently the landscape is flat, furrowed by a network of water collection and discharge canals that rigidly cut through the countryside. This context has a highly functional topographic layout that is repeated everywhere, without any substantial changes, and the bridge is a very unusual emerging structure. It extends for 500 meters with five arches, each one spanning from 90 to 100 meters, and a height of 7.30 meters. The horizon with no visible vertical elements and the flat squared, territory suggested creating a long continuous mark, as if giving thickness to the “century” signs. This continuity was a key factor, and therefore great attention was paid to joining the deck to the embankment, a very delicate problem that often is not resolved convincingly, and where there is still much room for research. The decision was taken that the pier abutment should literally rise from the ground and begin the horizontal extension of the bridge. The final appearance enhances the sculptural features, which are highlighted through the study of colour: the black and white fronts and the white insides give a very scenic effect. The formal outcome is of a landscape where this bridge, despite its size, has no beginning or end but disappears on the horizon, emphasizing the flatness of the land. It has become a place where the bridge is an infinite and independent sign, where the embankments are maintained and the perspective lines of the river are unaltered. Themes such as *landscape, history, identity*, found here their realization, and their meanings remain unchanged.

The LDV Kazan footbridge project in Istanbul (Figure 11) is placed in a new urban area, once upon a time abandoned, and now designed for new urban functionalities, as a park. The footbridge has been developed with the thinking that a connection is able to act as a crossing both physically and culturally. The footbridge is inclined in relation to the project park axis and it develops in a sinuous double curvature. By adopting Leonardo’s approach, the working team defined a generally stimulating design which allows the perception of the new place, wanted by inhabitants, in the urban daily living landscape.

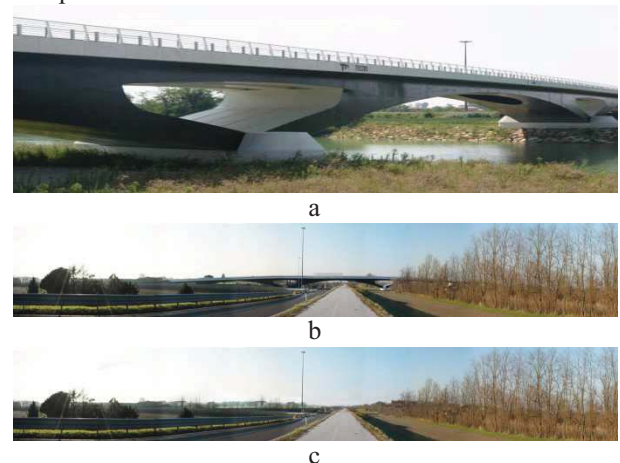


Figure 10. E. Siviero. The bridge in San Donà di Piave, Venice. Perception of the bridge from the road in relation to the distance of the observer (a, b). Perception of the road (c) without the bridge.



Figure 11. E. Siviero, the project of the LDV Kazan footbridge in Istanbul.

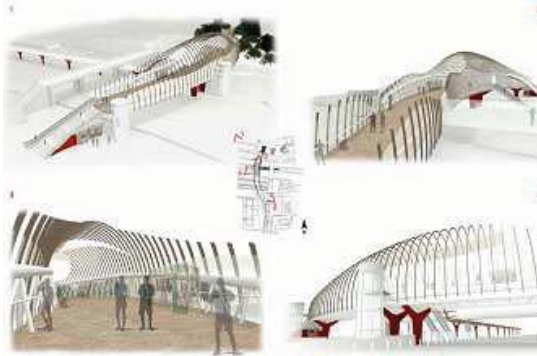


Figure 12. E. Siviero, the project of the Şirinevler footbridge in Istanbul.



Figure 13. E. Siviero, the project of the Gezi footbridge in Istanbul.

The *Şirinevler footbridge project* in Istanbul (Figure 12), placed in an urban context formed of different identities, has been developed thinking of not only a physical but also a cultural and perceptive connection. The design of the footbridge in Şirinevler, like those for the Istanbul Park in Kazan, is a design experience which combined an in-depth technological study with an anthropological approach.

The *Gezi footbridge project* (Figure 13) is expected very close to one of the main centres of life in Istanbul: Taksim Square. From this square, a major metropolitan hub, a significant flow of people reaches the important and nearby headquarters of Istanbul Technical University. The path between these two poles goes through the urban park designed by Prost. Even in the original design, in this context, there was a lack in the continuity of the park in correspondence with a two-lane street bearing heavy traffic placed below the plane of footpath. The two sides of the park were joined by the badly

scratched concrete structure, which showed different points of damage with partial loss of material. The structures crossed the total distance with three spans: main central one and two laterals. The piers were formed of a series of four concrete pillars, which supported the structure of the deck. In accordance with the city's transformation needs, the decision was taken to work on the valorisation of the cultural heritage of the urban texture by implementing a structure able to incorporate Prost's vision thus simultaneously including historic and natural issues as well as technological aspects. The first input project was to use materials very close to the Turkish culture. Wood was a material widely used in constructions in the core of Istanbul and the Wooden Houses are one of the most important examples. The predominant use of natural materials was also dictated by the presence of the characteristic stone water tower, standing as testimony of technological achievement. The slender shape of the segmental arch is made by a structural section of laminated wood reinforced with steel bars. The new footbridge was designed with the aim of giving a sign of tangible and intangible continuity to the connection between the historic past and the living present, using wood with the potentialities offered by current technology. In addition, from a functional standpoint, the footbridge offers two possibilities allowing the continuity of the footpath and the continuity of the park as a green area. The paving stones and vegetation accompany the people as they stroll through the park and do not stop at the footbridge, thus giving continuity. The central pair of arches, observed along the path, rises and opens up to the green grassy areas, until the arches reconverge on the deck to form a seat.

4 CONCLUSIONS

The bridge is the architectural work that best combines the shape rules with the structure and composition. In this sense, bridges have great plastic potential that must be seen as an opportunity to *design* on different scales: from the small element as part of the composition to create the bridge, as a composition element to modify the landscape.

Bridges are therefore important elements, not only from the structural point of view, but also from the cultural one, in relation to their ability to create or modify important functional, social, economic relations in a place.

This way, it is fundamental to think about bridges as *infrastructures of the landscape*, between Engineering and Architecture, able to connect people and culture and to recall the *genius loci*, as my motto "*Bridging cultures and sharing hearts*" declaims.

REFERENCES

- [1] Siviero E., Culatti M., Stocco A., Totaro A., Innovative Footbridges, In *Proceedings Of Iass Conference 2013, International Association For Shell And Spatial Structure*, Wroclaw (Poland) 23-27 September 2013, Pp. 183.
- [2] Siviero E., Ben Amara A., Guarascio M., Bella G., Adao Da Fonseca A., Slimi K., Zucconi M., *Timeit - Towards A Global World*, Proceedings Of The International Conference On Multi-Span Large Bridges, 1-3 July 2015, Porto, Portugal
- [3] Siviero E., *Concrete Arched Bridges: Harmony, Composition, Meanings, Perception*, Ukieri Concrete Congress Concrete Research Driving Profit And Sustainability 2 - 5 November 2015 Jalandhar Punjab India.

Multi-performance retrofits to existing buildings: Increasing resiliency and reducing the environmental impact of buildings through simultaneous structural and energy retrofits

Corey Griffin¹

¹School of Architecture, Portland State University, PO Box 751, Portland, Oregon, USA
email: cgriffin@pdx.edu

ABSTRACT: Existing buildings consume 40 percent of the primary energy in the US. While new zero-energy buildings can gradually reduce this energy use, the existing building stock must be improved through deep energy retrofits to make a significant impact in this sector. Current energy retrofits and research in the US focus primarily on upgrades of mechanical and lighting systems to maximize energy reduction for minimal investment. This incremental approach is effective but limited in the overall energy savings it can generate, as major transformations to the fundamental operation of a building are cost prohibitive. Due to their disruptive nature, structural retrofits offer the physical and economic opportunity to completely transform how a building operates in terms of heating, cooling and lighting – the largest sources of energy use. Consequently, this paper proposes replacing current incremental strategies prevalent in most energy efficiency retrofits with transforming existing buildings through a multi-performance retrofit that (1) improves the structural response to extreme-event loading, (2) maximizes daylight to replace electric lighting, (3) uses low-temperature radiant systems to replace HVAC units, (4) deploys climate-appropriate thermal mass and (5) upgrades the envelope to (6) effectively maximize passive thermal and bioclimatic strategies. This paper documents a database of 25 commercial buildings, primarily from the Pacific Northwest region of the US that have undergone different types of retrofits. Overall, multi-performance retrofits are more expensive than a stand-alone structural or energy retrofits but provide benefits that are not easily quantified. Three multi-performance retrofits are described in more detail to highlight the strategies used and benefits of this approach.

KEY WORDS: Multi-performance retrofit; Integrated design, Resilience.

1 INTRODUCTION

1.1 Environmental Impact of Buildings

Existing buildings consume 40 percent of the primary energy and contribute 40 percent of CO₂ emissions in the US [1]. These numbers exclude the significant environmental impact of manufacturing, transporting, installing, maintaining and eventually demolishing materials used in building construction [2]. While every other sector has been reducing energy use over the last 30 years, commercial buildings have increased their energy intensity (energy use per square foot) by over 8%. Furthermore, the total square footage of these buildings has increased by almost 60% over the same time period. Only the recent recession temporarily blunted what had been the continual growth in energy use by the building sector [1]. It is well documented that deficiencies in building performance are ubiquitous, and if addressed nationally in the US could contribute to over \$18 billion in savings annually [3]. Thus, to mitigate climate change, there should be no higher priority than ensuring that residential and commercial buildings are created, adapted and retrofit to minimize energy use, resource consumption, and cost. While new resilient, zero-energy buildings (ZEBs) can gradually reduce the environmental impact of this sector, the existing building stock must be improved through energy retrofits to make a significant impact. In the US, buildings built before the year 2000 make up 78 percent of the commercial building stock and account for 77 of total building fuel consumption [4].

1.2 Conventional Energy Retrofits

Current energy retrofits and research in the US focus primarily on upgrades or commissioning of mechanical and lighting systems to maximize energy reduction for minimal investment [5, 6, 7, 8]. This incremental approach is effective but limited in the overall energy savings it can generate. It should also be noted that the majority of studies in the US use computer modelling instead of monitoring buildings that have undergone energy retrofits. Unfortunately, there is little to no funding in the US to measure the performance of existing buildings to assess the relative merits of deployed retrofit tactics or for researchers to take an active part in the design, construction, commissioning or operations of a recently renovated building. Stakeholder behaviour will not be shifted from current patterns of incremental energy efficiency upgrades unless measured performance data from real buildings is presented to them [9].

Major transformations to the fundamental operation of a building that could reduce energy use intensity (EUI) to levels associated with ZEBs are deemed cost prohibitive and miss the opportunities to “tunnel through the cost barrier” [10]. These major transformations are also inhibited by a desire for buildings to remain operational during an energy retrofit to avoid displacing occupants [11]. Consequently, an analysis by the author of New Building Institute’s “Getting to Fifty” database - which houses details and measured data on buildings that have undergone what NBI calls “deep energy retrofits” that use 50 percent less energy than conventional

buildings - shows that these minimally invasive energy retrofits that focus solely on equipment upgrades still have a site energy use intensity (EUI) of at least 20 kWh/m²/yr (64 kBtu/sf/yr) [12], less than 20% better than the average US office building in 2012 [4]. While this level of energy savings is not insignificant, it is still over double the EUI of ZEBs.

1.3 Seismic context of the US Pacific Northwest

Episodic, greater than magnitude 9.0 earthquakes along the Cascadia Subduction zone were first discovered in the 1990s [13, 14, 15]. Consequently, building codes were updated throughout jurisdictions in the Pacific Northwest region of the United States – primarily in the states of Oregon and Washington – requiring new structures and existing buildings undergoing a change in occupancy to account for this new seismic risk. As the period between these earthquakes is hundreds of years with the last one occurring roughly 300 years ago [16], buildings constructed before 2001 lacked adequate structural capacity to deal with the ground acceleration from a Cascadia event. Consequently, unreinforced masonry (URM) structures make up a significant portion of the existing building stock in Oregon, particularly educational and apartment buildings. In a 2001 report that was recently updated, the City of Portland, Oregon identified over 1,750 URM buildings that are currently at risk during an earthquake [17]. These buildings also perform poorly in terms of energy use due to the lack of wall insulation and outdated mechanical and lighting systems, making them ideal targets for simultaneous energy and seismic retrofits. Modernist, steel framed buildings from the 1960s and 70s are also ideal candidates for similar reasons and have some of the highest EUIs compared to building of other eras [4]. Due to the simultaneous need to seismically upgrade and reduce energy use, a number of buildings in Oregon have undergone simultaneous retrofits yielding lower EUIs on average to conventional energy retrofits.

Outside of Oregon, existing buildings all along the west coast would benefit from these simultaneous energy and structural retrofits or *multi-performance retrofits*. As seismic hazards in other parts of the US and Europe are being re-evaluated in response to recent unusual seismic activity in the mid-west and east coast often related to hydraulic fracking [18], these strategies could be important as unforeseen structural retrofits are required while society strives to reduce energy use and carbon dioxide emissions.

1.4 Multi-performance Structures and Retrofits

In contemporary building construction, the selection of a structural system occurs early in the design process and is influenced by building codes, cost, scale of the project, and bay sizes required by the program [8]. Consequently, architects and engineers typically only consider structural performance in relationship to the cost of structure and the building program is considered. Selecting structural systems using a multi-performance set of criteria, including environmental impact, thermal mass, thermal conductance, increasing daylighting, acoustic transmission and fire-resistance, could offer considerable and largely untapped opportunities to reduce operational energy use and improve the indoor environmental quality of new and existing buildings while potentially lowering construction costs [19].

Preventative retrofits for earthquakes, hurricanes and other natural disasters also typically focus solely on improving the structural resilience of existing buildings. However, these retrofits could also radically reduce the energy use of existing buildings to the point where they could be transformed into ZEBs through an integrated design process [20]. Adapting strategies and technology used in the design and construction of new ZEBs to the retrofit of existing buildings is only possible when an event, such as a structural retrofit, allows for the significant disruption and alteration of the building's structure, enclosure, finishes and systems.

Unfortunately, there has been little research into the role the structural system or retrofit can have as part of an energy retrofit. A report on deep energy retrofits in the Pacific Northwest failed to list the structural engineer involved with the case studies highlighted even when a seismic retrofit was part of the renovation [11]. Consequently, the potential of using the existing structure and retrofit to improve other areas of performance, such as energy use, is neglected along with the economic advantages of leveraging funding for seismic retrofits. There is little existing research into the role of structural systems in energy retrofits with limited studies focused on housing in non-seismic zones, green roofs, and historic buildings [21, 22, 23, 24]. Only one paper could be found during a literature review that specifically looked at the environmental impact of seismic risk [25]. The paper concluded that structural retrofit of a non-building in a high seismic event is equally important to an energy retrofit in terms of environmental impact over the building's life cycle. However, the paper did not look at how the structural system or seismic retrofit might contribute to the proposed energy retrofit in the study.

This paper will investigate strategies for replacing current incremental structural and energy retrofits with radical transformations of existing buildings though multi-performance retrofits that:

- improves the structural response to extreme-event loading
- maximizes daylight to reduce electric lighting
- uses low-temperature radiant systems to replace conventional HVAC units
- deploys climate-appropriate thermal mass
- upgrades the envelope through increased insulation and airtightness
- effectively maximize passive thermal and bioclimatic strategies

Multi-performance retrofits by their nature focus on increasing the resiliency of existing buildings by increasing their lifespan and ensuring resources will not be lost in a natural disaster. At the same time, these building will be less resource dependent in terms of their operation, addressing the carbon dioxide emissions attributed to the building sector in the US that are a direct contribution to global warming and connected to the increased frequency of natural disasters [26]. The goal of a multi-performance retrofit is to not only regenerate existing buildings technically to reduce energy use and make it more resilient, but to regenerate the original spaces that are often badly compromised over time – to increase occupant comfort, ventilation, daylighting, and connections to the surrounding natural and built environment. Improving these architectural attributes is critical, as multiple

studies have shown a positive correlation between them and occupant health, productivity and satisfaction [27, 28, 29, 30, 31, 32].

2 METHODOLOGY

2.1 Overview

In order to better understand the advantages and potential disadvantages of multi-performance retrofits, a database of twenty-five buildings that had either a seismic, energy or multi-performance retrofit (simultaneous structural and energy retrofit) was developed by the author. This allows for comparisons of a number of performance criteria between the different types of retrofits. The three most promising examples of multi-performance retrofits were then researched in detail to provide case studies outlining lessons learned.

2.2 Building selection

As information on construction costs, measured energy use either before or after a retrofit, and details on specific retrofit tactics are seldom made public in the US, buildings were selected for this study based on the availability of detailed information about the retrofit. This study focuses on commercial buildings with total floor areas larger than 1,000 m² (roughly 11,000 ft²) up to 48,000 m² (roughly 515,000 ft²). Smaller buildings were excluded even though detailed information on the retrofits could be found as the systems and strategies used were not compatible with larger commercial buildings and were more comparable to residential retrofits. The buildings that had undergone an energy or multi-performance retrofit were selected primarily because measured EUI and construction cost data was publically available. 21 of the 25 buildings in the database are located in the US Pacific Northwest with 19 of those 21 in Oregon. The buildings in the database completed a retrofit between 2001 and 2013. These dates aligns with the change in seismic requirements for buildings due to a Cascadia subduction zone event. More recent retrofits are not included to allow at least one year of operations to collect EUI data.

2.3 Data collection

Data on each building was collected from a number of sources including public databases [12, 33, 34, 35] and white papers [11, 36, 37] on high performance buildings as well as datasets provided by the Oregon Department of Energy as part of the State Energy Efficiency Design (SEED) program that has been in operation since 1991 [38]. Data for projects that had only undergone a seismic structural retrofit were collected from published case studies as part of the State of Oregon's Seismic Rehabilitation Grant Program [39]. The following basic information was found for each building and its retrofit:

- location
- owner
- project team – architect, engineers, contractor
- type of retrofit – structural, energy or multi-performance
- year built and year retrofit was completed
- building type (occupancy)
- structural system
- floor area
- number of stories

- actual measured site EUI after retrofit (and before if available)
- construction cost (in 2013 US\$)

On top of this information, individual strategies used in each retrofit were documented and categorized, generating 24 strategies grouped into six major categories: structure, daylight and lighting, mechanical systems, thermal mass, envelope and passive strategies (natural ventilation, external shading devices, etc.).

2.4 Data limitations

There are several limitations to the data collected. Two of the most important pieces of information, EUI and overall construction cost, were self-reported by building owners to the various sources used here. Consequently EUI and cost data could have been calculated slightly differently introducing uncertainty in comparing one building's data to another. For example, many energy retrofits in the US qualify for grants, tax credits and other financial incentives that may or may not be accounted for in the construction cost data. Depending on the building, EUI data was collected during different years between 2005 and 2015, which is documented in the database. While some buildings offer multiple years of EUI, only one year of data was available for most of the buildings in the database. As weather can vary year to year, this makes comparing the EUI data between buildings more difficult. As is typical in the US, all EUI data is for energy used on site and does not account for losses at the source (i.e. electricity generation and transmission losses).

3 RESULTS AND ANALYSIS

3.1 Building characteristics

Due to the size and scope of the database generated for this paper, it is not possible to display it in its entirety. However, Tables 1 and 2 contain a brief summary of the buildings in the database.

Table 1. Characteristics of buildings in the database. EUI is site data post-retrofit.

Retrofit Type	No. of Buildings	Avg./Med. Cost (1,000,000 US\$)	Avg. EUI (kWh/m ²)
Structural	7	1.0/1.2	-
Energy	7	9.8/1.2	15
Multi.	11	26.8/13.1	13

As Table 1 highlights, 44% of the buildings in the database have undergone a multi-performance retrofit, with the remaining buildings split evenly between buildings that have either only had a structural or energy retrofit. The average and median costs for the multi-performance retrofits are significantly higher than those for individual structural and energy retrofits. The average EUI of the multi-performance retrofits is 20% lower than buildings that only underwent an energy retrofit. One reason the structural retrofits in this database are the least expensive is that on average they are smaller and shorter (Table 2). Another reason for the increased cost of the multi-performance retrofits is that on average they were originally built 30 years earlier and in many cases required more significant and expensive upgrades

to building systems, envelope and architectural finishes to bring these older buildings to same level of performance as the younger building set that only underwent energy retrofits.

Table 2. More characteristics of buildings in the database.

Retrofit Type	Avg. Stories	Avg. Floor Area (ft ²)	Avg. Year Built
Structural	1.7	50,000	1941
Energy	10.0	172,000	1954
Multi.	4.7	111,000	1924

In terms of ownership, 60% of the buildings in the database are publicly owned. Of the buildings that only underwent an energy retrofit, six out of the seven are privately owned. All but one of the public buildings in the database underwent a structural retrofit, either alone or as part of a multi-performance retrofit. This is a reflection of legislation providing funds for seismic retrofits in the State of Oregon as well as a lack of incentives for private building owners to provide seismic upgrades whereas there are financial incentives, often from utilities, for private buildings that undergo energy retrofits.

The structural systems of the buildings in the database (Figure 1) were representative of the commercial building stock in the Pacific Northwest where there are more light wood frame and timber structures in general. In cases of combined systems such as timber frame with exterior load bearing URM exterior walls, a single building would be recorded in both categories. As the structural retrofits in the database are smaller buildings, there are more light wood framed structures than the other types of retrofits. A little less than half of the multi-performance retrofits have URM.

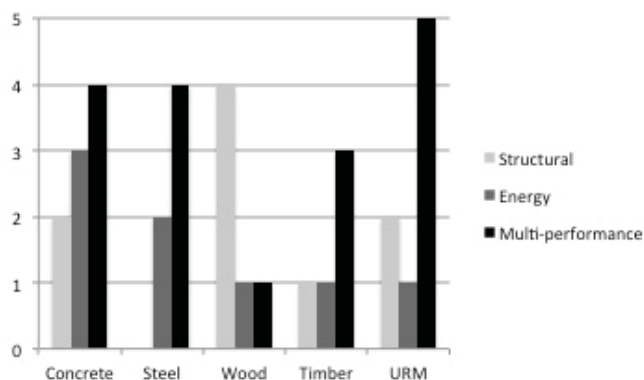


Figure 1. Types of structural systems represented in database buildings. Wood = light wood framing, URM = unreinforced masonry (load bearing)

3.2 Cost, size, EUI

To better understand the relationships between construction cost, building size and post-retrofit site EUI, Figures 2 and 3 show all of the buildings in the dataset grouped by retrofit type. The least expensive retrofits per unit of floor area were the structural retrofits – with all coming in under US\$50/ft². There is no correlation between lower EUI and higher cost as one might expect due to the need for more upgrades to reduce energy use – in fact the opposite is true for the buildings in the dataset that underwent just an energy retrofit. Without the EUI data before the retrofits occurred, it is difficult to understand

the relationship between cost and how much each building was improved, which would provide a more accurate picture of how effective each individual retrofit was.

Again, there is also no correlation between the size of building and cost per unit of floor area (Figure 2). At close to US\$500/ft², the most expensive retrofit is an outlier because that building was half multi-performance retrofit and half new construction. Other analyses comparing the age of the building before the retrofit to cost and the EUI to size of building also yielded no trends.

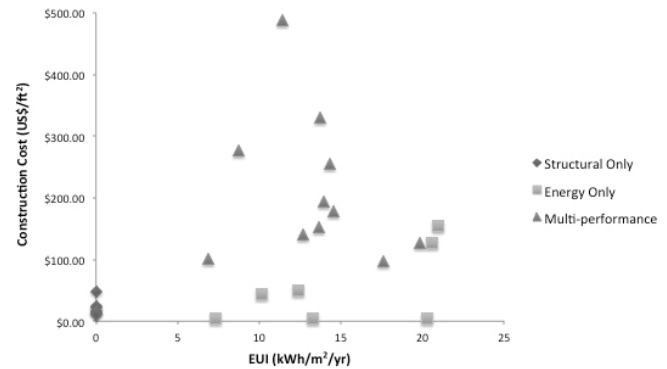


Figure 2. Post-retrofit site EUI versus construction cost per square foot of floor area.

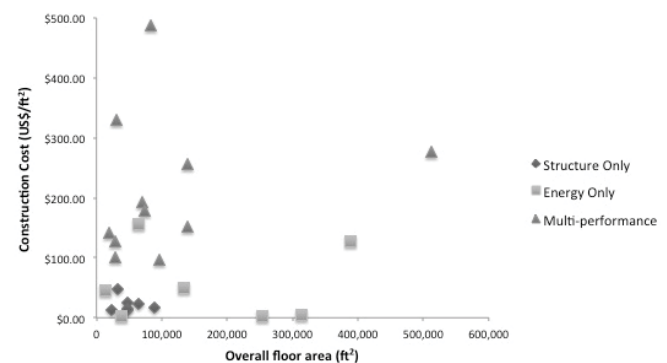


Figure 3. Building floor area versus construction cost per square foot of floor area.

3.3 Retrofit strategies deployed

An analysis of the strategies deployed in each type of retrofit yields more interesting results. In comparison to multi-performance retrofits, buildings that undergo just structural retrofits have three times as many structural strategies. As the entire budget is dedicated solely to improving structural performance in these retrofits, it is not surprising that more strategies would be deployed per building perhaps in a belt and suspenders approach. In contrast, simpler and more cost-effective structural strategies are required in a multi-performance retrofit when improving the structural response of the building is just one of many priorities.

Both the average energy and multi-performance retrofits focused approximately the same amount on mechanical and envelope strategies (Figure 4). Multi-performance retrofits showed a significant increase in daylighting strategies to complement new, more efficient lighting systems as well as deploying thermal mass and passive design strategies to reduce heating and cooling needs over energy retrofits. As

predicted, the ability for significant changes to be made to a building during a structural retrofit allowed for improved or new daylighting apertures and new thermal mass to be added. Almost half of the multi-performance retrofits also installed radiant systems for cooling or both heating and cooling. Overall, the average multi-performance retrofit deploys 8.7 strategies while a stand-alone energy retrofit only makes use of 4.9 strategies. The database doesn't account for improving the architectural quality through multi-performance retrofits that have additional benefits in terms of occupant health and productivity that extend beyond the first-cost of construction or energy savings studied here.

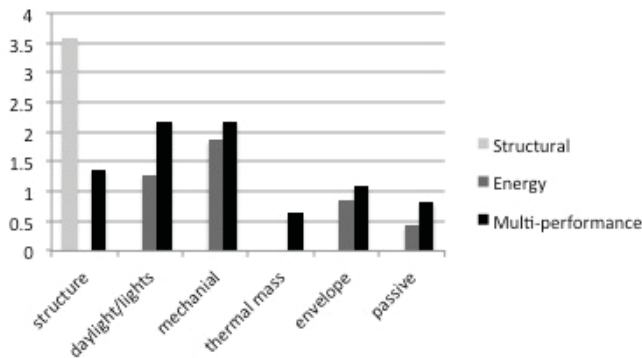


Figure 4. Average number of strategies deployed per type of retrofit.

4 CASE STUDIES

4.1 Shattuck Hall

Originally built in 1915 as an elementary school, Shattuck Hall is home to the School of Architecture at Portland State University (Figure 5). A multi-performance retrofit completed in 2008 included the addition of exposed concrete shear walls to the existing concrete column, joist and beam system.



Figure 5. Shattuck Hall Exterior, post-retrofit.

Many interior clay block non-load bearing walls and interior finishes were removed to create an open floor plan in spaces throughout the building and expose the concrete structure to serve as thermal mass (Figure 6). There was not enough height on the ground floor to increase the size of the ducts to meet current building code standard, so the existing duct system was used to provide ventilation air while heating and cooling is done by a new radiant panel system in the ceiling that also supports new lighting, fire suppression, ceiling fans and acoustic dampening. This decision turned out to be critical in significant reducing the energy used for thermal

comfort. Original lightwells that had been covered in previous renovations were restored and new skylights were added improving daylight in throughout the corridors and ground floor. Unfortunately, the existing uninsulated envelope was not upgraded.

- Post-retrofit EUI: 15 kWh/m²/yr (46 kBtu/ft²/yr)
- Floor area: 6830 m² (73,500 ft²)
- Construction cost per unit floor area: US\$178/ft²
- Total number of retrofit strategies: 10



Figure 6. Shattuck Hall studio interior, post-retrofit.

4.2 Lovejoy Building

The Lovejoy Building was originally built in 1910 as home to a hardware company and completed a multi-performance in 2004, one of the first in Oregon (Figure 7). The building is now office space for an architecture firm and retail/office tenants on the ground floor. The exterior walls were load bearing URM, and the interior structure was a timber frame with wood joists and decking for the diaphragm. The seismic retrofit consisted of applying shotcrete to the interior of the URM walls and adding a concrete slab on top of the existing wood floors. This new thermal mass was left exposed and radiant tubing was placed in the new concrete slabs to provide heating and cooling (Figure 8). Daylighting was significantly improved by increasing the height of window apertures and adding skylights. Operable windows and automated exterior sunshades allow the building to take advantage of outside air and sunlight when needed.

- Post-retrofit EUI: 13 kWh/m²/yr (40 kBtu/ft²/yr)
- Floor area: 1860 m² (20,000 ft²)
- Construction cost per unit floor area: US\$141/ft²
- Total number of retrofit strategies: 13



Figure 7. Lovejoy Building exterior, post-retrofit.



Figure 8. Lovejoy Building office interior, post-retrofit.

4.3 Edith Green Wendell Wyatt Federal Building

As the largest retrofit in the database, the Edith Green Wendell Wyatt Federal Building (EGWW) is one of the most unusual. Built in 1974, the office building for several federal offices was stripped back to its steel moment frame structure and given a completely new enclosure, mechanical and lighting systems (Figure 9). Removing the original precast concrete façade and replacing it with a significantly lighter curtain wall system significantly reduced the weight of the building so that additional strengthening of the lateral loading system was not required. The new envelope is optimised to provide maximum daylight while minimizing heat loss with insulated spandrel panels. The pattern of exterior shading devices are also optimised for each orientation to block unwanted solar gain. The new mechanical system is a combination of radiant ceiling panels for heating and cooling and a dedicated outdoor air system (DOAS) to provide ventilation – similar to Shattuck Hall. Daylighting was improved on the ground floor by removing portions of the structure in the lobby to create new double height spaces (Figure 10). In 2003, EGWW had an EUI of 20 kWh/ m²/yr (62 kBtu/ft²/yr) and the multi-performance retrofit reduced energy use by over 55%.

- Post-retrofit EUI: 9 kWh/m²/yr (28 kBtu/ft²/yr)
- Floor area: 47,600 m² (512,500 ft²)
- Construction cost per unit floor area: US\$276/ft²
- Total number of retrofit strategies: 14



Figure 9. EDWW exterior, before (left) and post-retrofit (right).



Figure 10. EDWW lobby interior, post-retrofit.

5 CONCLUSION

This paper has outlined the potential and need for more research into multi-performance retrofits that combine energy and structural retrofits to generate more benefits than either retrofit could accomplish alone. The initial database discussed in this paper is a starting point for more research into the advantages and potential disadvantages of multi-performance retrofits. Relying on publically available information has limited the sample size of the database and potentially made comparisons more uncertain. Funding will be required to expand it as the time required to find and collect the information is a significant burden.

As this research is continued, the author feels strongly that academics and professionals cannot abandon in-situ measurements of buildings before and after retrofits to better understand which types of retrofits and strategies are most effective. There is a need for pre- and post-retrofit EUI data, which is seldom collected in the US. There is a place for computer modelling, but the limitations inherent in most energy simulations cannot allow them to account for the types of synergies that can be found in a multi-performance retrofit.

Finally, this paper briefly touched on the architectural implications of multi-performance retrofits beyond structural and energy performance. In commercial buildings, occupant health and productivity is increasingly valued by employers as salaries are the single largest cost in a business. If improving the daylight and ventilation of a building increases productivity and that productivity can be quantified, the higher cost of a multi-performance retrofit in comparison to stand-alone structural or energy retrofits could more easily be justified.

ACKNOWLEDGMENTS

The author would like to acknowledge the contributions of graduate students Ben Denies and Julie McEvoy Baines to the early stages of this research. The author would also like to thank the Faculty Enhancement Grant program and Office of Research and Sponsored Projects, specifically former Vice President Jon Fink, at Portland State University for funding this research.

REFERENCES

- [1] US Department of Energy (DOE). (2011), *Buildings Energy Data Book*, US Department of Energy.

- [2] Ramesh, T., Prakash, R., Shukla, K.K., (2010). Life cycle energy analysis of buildings: An overview, *Energy and Buildings*, 42(10): 1592-1600.
- [3] Mills, E., Bourassa, N., Piette, M. A., Friedman, H., Haas, T., Powell, T., & Claridge, D. (2005, May). The cost-effectiveness of commissioning new and existing commercial buildings: Lessons from 224 buildings. In *National Conference on Building Commissioning: May* (Vol. 4, p. 6).
- [4] US Energy Information Administration (EIA). (2016), '2012 Commercial Buildings Energy Consumption Survey: Energy Usage Summary,' US Energy Information Administration.
- [5] Griffith, B., Long, N., Torcellini, P., Judkoff, R., Crawley, D. and Ryan, J. (2007) Assessment of the Technical Potential for Achieving Net Zero-Energy Buildings in the Commercial Sector. Technical Report TP-550-41957, NREL, Golden, CO.
- [6] Coffey, B., Borgeson, S., Selkowitz, S., Apte, J., Mathew, P., & Haves, P. (2009). Towards a very low-energy building stock: modelling the US commercial building sector to support policy and innovation planning. *Building Research & Information*, 37(5-6), 610-624.
- [7] Heo, Y., Choudhary, R., & Augenbroe, G. A. (2012). Calibration of building energy models for retrofit analysis under uncertainty. *Energy and Buildings*, 47, 550-560.
- [8] Mills, E. (2011). Building commissioning: a golden opportunity for reducing energy costs and greenhouse gas emissions in the United States. *Energy Efficiency*, 4(2), 145-173.
- [9] Griffin, C.T., Knowles, C., Theodoropoulos, C., & Allen, J. (2010), 'Barriers to the implementation of sustainable structural materials in green buildings', In: Cruz P, editor. *Structures and Architecture: Proceedings of the 1st International Conference on Structures & Architecture (ICSA2010)*. Guimarães, Portugal, 21-23 July 2010. 1315-1323.
- [10] Hawken, P., Lovins, A. B., & Lovins, L. H. (2013). *Natural capitalism: The next industrial revolution*. Routledge.
- [11] New Building Institute (NBI). (2011), 'A Search for Deep Energy Savings', white paper, Northwest Energy Efficiency Alliance, August 2011.
- [12] Data from New Building Institute (NBI). (n.d.), 'Getting to 50 – buildings database', accessed at <http://www.advancedbuildings.net/getting-50-buildings-database-0>
- [13] Adams, J. (1990). Paleoseismicity of the Cascadia subduction zone: Evidence from turbidites off the Oregon-Washington margin. *Tectonics*, 9(4), 569-583.
- [14] Satake, K., Shimazaki, K., Tsuji, Y., & Ueda, K. (1996). Time and size of a giant earthquake in Cascadia inferred from Japanese tsunami records of January 1700. *Nature*, 379(6562), 246-249.
- [15] Yamaguchi, D. K., Atwater, B. F., Bunker, D. E., Benson, B. E., & Reid, M. S. (1997). Tree-ring dating the 1700 Cascadia earthquake. *Nature*, 389(6654), 922-923.
- [16] Clague, J. J. (1997). Evidence for large earthquakes at the Cascadia subduction zone. *Reviews of Geophysics*, 35(4), 439-460.
- [17] Bureau of Development Services. (2016), 'Unreinforced Masonry (URM) Database', Report, City of Portland, Oregon, May 2, 2016.
- [18] Ellsworth, W. L. (2013), 'Injection-induced earthquakes', *Science*, 341(6142), 1225-1226.
- [19] Griffin, C.T., Douville, E., Thompson, B., & Hoffman, M. (2013), 'A multi-performance comparison of long-span structural systems', In *Proceedings of the 2nd International Conference on Structures & Architecture (ICSA2013)*. Guimarães, Portugal, 24-26 July 2013. pp. 1668-1676.
- [20] Moe, K. (2008). *Integrated design in contemporary architecture*. Princeton Architectural Press.
- [21] Vine, E. L., & Kazakevicius, E. (1999). Residential energy use in Lithuania: the prospects for energy efficiency. *Energy*, 24(7), 591-603.
- [22] Jaggs, M., & Palmer, J. (2000). Energy performance indoor environmental quality retrofit—a European diagnosis and decision making method for building refurbishment. *Energy and buildings*, 31(2), 97-101.
- [23] Castleton, H. F., Stovin, V., Beck, S. B. M., & Davison, J. B. (2010). Green roofs; building energy savings and the potential for retrofit. *Energy and buildings*, 42(10), 1582-1591.
- [24] Ascione, F., De Rossi, F., & Vanoli, G. P. (2011). Energy retrofit of historical buildings: theoretical and experimental investigations for the modelling of reliable performance scenarios. *Energy and buildings*, 43(8), 1925-1936.
- [25] Belleri, A., & Marini, A. (2016). Does seismic risk affect the environmental impact of existing buildings?. *Energy and Buildings*, 110, 149-158.
- [26] Rosenzweig, C., D. Karoly, M. Vicarelli, P. Neofotis, Q.G. Wu, G. Casassa, A. Menzel, T.L. Root, N. Estrella, B. Seguin, P. Tryjanowski, C.Z. Liu, S. Rawlins, & A. Imeson. (2008), 'Attributing Physical and Biological Impacts to Anthropogenic Climate Change', *Nature* 453(7193): 353-357.
- [27] Heerwagen, J.H. (2000), 'Green Buildings, Organizational success, and Occupant productivity.' *Building Research and Information*. 28(5): 353-367.
- [28] Heschong, L. (2003), 'Windows and Classrooms: A Study of Student Performance and the Indoor Environment,' Report, California Energy Commission: Pacific Gas and Electric Company. Fair Oaks, California.
- [29] Heschong, L. (2003), 'Windows and Offices: A Study of Office Worker Performance and the Indoor Environment,' Report, California Energy Commission: Pacific Gas and Electric Company. Fair Oaks, California.
- [30] Kellert, S. et al. *Biophilic Design*. Hoboken, New Jersey: John Wiley & Sons, Inc. 2008.
- [31] Ulrich, R. (1984), 'View through a window may influence recovery', *Science*, 224(4647), 224-225.
- [32] Seppänen, O., Fisk, W. J., & Lei, Q. H. (2006). Ventilation and performance in office work. *Indoor air*, 16(1), 28-36.
- [33] New Buildings Institute (NBI). (2015), 'Getting to zero database', website, <http://newbuildings.org/resource/getting-to-zero-database/>
- [34] US Department of Energy (DOE). (2016), 'High performance buildings database', website, <https://buildingdata.energy.gov/>
- [35] AIA Committee on the Environment (COTE). (2016), 'AIA Committee on the Environment Top Ten Projects', website, <http://www.aiatopten.org/>
- [36] Cassidy, R. (ed.). (2012), 'High-Performance Reconstructed Buildings: The 99% Solution', white paper, *Building Design + Construction*, 53(5), May 2012. Available at: http://www.bdcnetwork.com/sites/bdc/files/WP_BDC0512_low%20res_3.pdf
- [37] New Buildings Institute (NBI). (2011), 'A Case for Deep Savings', white paper, Northwest Energy Efficiency Alliance, September 2011. Available at: https://newbuildings.org/wp-content/uploads/2015/11/DeepSavings_11CaseStudies1.pdf
- [38] Oregon Department of Energy. (2016), 'State Energy Efficient Design (SEED) program', website, <http://www.oregon.gov/energy/CONS/SEED/Pages/index.aspx>
- [39] Summary of the Seismic Rehabilitation Grant Program can be found at: <http://www.ode.state.or.us/superintendent/priorities/june-20-seismic-rehabilitation-grant-program-overview.pdf>

Performance Monitoring for Sustainable Concrete Infrastructure

W. John McCarter

Heriot Watt University, School of Energy, Geoscience, Infrastructure and Society, Edinburgh, EH14 4AS, Scotland, U.K.
email: w.j.mccarter@hw.ac.uk

ABSTRACT: Satisfactory guidelines for ensuring adequate reinforced concrete durability can only be developed by monitoring concrete performance under a range of field exposure conditions over an extended period of time. Only then can there be a move from prescriptive durability specifications (minimum grade, maximum water-binder ratio, and minimum cement content) to performance-based methods. The situation is also made more complex by the range of cements now available - BS EN 197 defines a total of 27 products in the family of common cements. Implementation of both design for durability and performance-based standards and specifications are limited by the lack of rapid, simple, science-based test methods for characterizing the transport properties and deterioration resistance of concrete. This paper presents an overview of performance-based specification and developments in the application of electrical property measurements as a testing methodology in evaluating the relative performance of concrete mixes. The technique lends itself to in-situ monitoring thereby allowing measurements to be obtained on the as-placed concrete.

KEY WORDS: concrete, durability, performance, resistivity, formation factor, testing.

1 INTRODUCTION

It is an inescapable fact that our infrastructure deteriorates with time. A state of the nation report [1] graded the quality of the UK's infrastructure from B (fair) to D (poor) with an overall grading of C (average). The picture is the same in the US, where the ASCE (1998) Report on America's Infrastructure estimated a five-year total investment need of US\$1.3 trillion just to reinstate roads, bridges and other infrastructure systems to good serviceable life; in 2005, this investment need has risen to US\$1.6 trillion. Further to this, the average state of America's infrastructure was given a Grade D (Poor); as a specific example, in excess of 40% of 500,000 highway bridges are rated as structurally deficient or functionally obsolete and some US\$100 billion is the estimated requirement to eliminate the current backlog of bridge deficiencies and maintain repair levels [2].

Considering reinforced concrete structures, the initiation and propagation stages of deterioration result from a complex interaction of physical, chemical and electrochemical phenomena. The rate at which a particular structure deteriorates depends on many factors and evaluating the performance of reinforced concrete requires numerous data inputs, in particular, the response of the concrete to the changing micro-environment in the vicinity of a specific structural element or part of a structure. As it is the concrete cover-zone which protects the steel reinforcement - and therefore provides the first line of defence against the environment - it is understandable that considerable attention is directed towards assessing the performance of this zone [3]. The protective properties of the cover-zone are a major factor with regard to the in-service performance of the structure, likely deterioration rates for a particular exposure condition and compliance with specified design life. It is permeation processes such as diffusivity and sorptivity which are

important and there clearly exists a need to study and determine quantitatively those near-surface characteristics of concrete which promote the ingress of gases or liquids containing dissolved contaminants.

Regarding concrete durability, European Standard BS EN206 [4] deals with durability on the basis of a prescriptive, deem-to-satisfy approach by specifying minimum grade, minimum binder content and maximum water-binder ratio for a series of well-defined environmental classes. Interestingly, section 5.3.3 of this code allows for performance-related methods and defines concrete on the basis of an equivalent durability procedure (EDP); further detail on the EDP is presented in PD CEN/TR 16563 [5]. However, in order to fully implement a performance-based approach requires,

- i. long-term experience of local materials and practices and on a detailed knowledge of the local environment;
- ii. test methods based on approved and proven tests that are representative of actual conditions and have approved performance criteria; and,
- iii. analytical models that have been calibrated against test-data representative of actual conditions in practice.

2 PERFORMANCE TESTING

Although attempts have been made to introduce performance-based specifications, the lack of reliable, consistent and standardised test procedures for evaluating concrete performance has hindered its widespread implementation. Furthermore, there is also an intense need to evaluate the concrete as early as possible; the sooner information is obtained about the early-age properties of any given batch of concrete, the sooner adjustments can be made to the materials, proportions or processes for subsequent concrete placement,

and the sooner remedial measures can be initiated on the concrete already installed or construction practices altered (e.g. extended curing). Early-age testing is useful in this regard and, indeed, absolutely essential as the consequences of unsatisfactory concrete discovered at a later stage becomes expensive. The term *identity testing* is used in BS 8500-1:2015 [6] to describe testing to validate the identity of the mix. Identity testing attempts to verify some key characteristic of the concrete that relates to the desired performance and could take the form of a slump, flow, density, strength, water-content or some non-destructive or in-place method.

According to BS EN1990 [7], a reinforced concrete structure is designed in such a way that '*deterioration over its design working life does not impair the performance of the structure below that intended, having due regard to its environment and the anticipated level of maintenance*'. It is evident that consideration of a maintenance strategy forms an integral part of the structural design process. Implicit within this process is a consideration of adequate monitoring procedures, together with an appropriate level of inspection for the particular structure. As noted above, cover-zone transport mechanisms, their variation through the cover-zone, cyclic wetting/drying characteristics and temporal changes in properties all influence reinforced concrete performance and durability. In-situ monitoring of cover-zone concrete – in both the spatial and temporal domains – could thus assist in making realistic predictions as to the in-service performance of the structure; likely deterioration rates for a particular exposure condition, compliance with the specified design life and as an early warning indicator of incipient problems. Figure 1 highlights the usefulness of in-situ monitoring of concrete performance during the life of the structure which can be divided into three stages: an initial stage which represents the concrete response to the external environment, a second stage which represents the initiation of the deterioration process (corrosion in this instance) and a third stage where propagation of deterioration occurs.

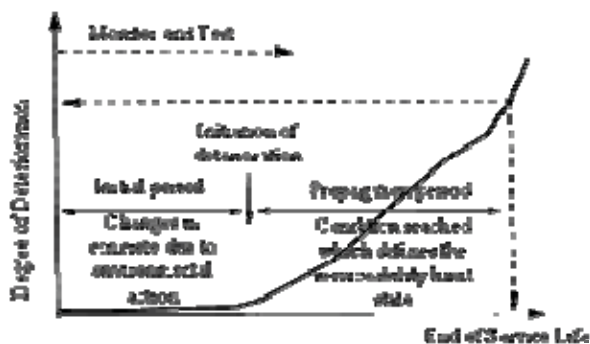


Figure 1. Components of service life.

The specification of the service-life/performance/durability of reinforced concrete by means a single parameter is the *holy grail* of the engineer and hence a subject of intense research interest. The challenges posed by a performance-based testing and specification approach to improve service life of concrete structures have been acknowledged for several years [8]. It is set against this background that this paper examines the use of the intrinsic electrical properties of cementitious materials (resistivity in

the current work) as a potential candidate testing methodology in assessing concrete performance. The resistivity of concrete is a relatively easy parameter to evaluate and the measurement technology also lends itself to remote monitoring and interrogation. The installation of a network of sensors, embedded at critical locations within a concrete structure, could provide continuous, real-time data on the response of the micro-environment within the cover-zone to changing ambient environmental conditions. Furthermore, as the resistivity of the concrete surrounding the rebar controls the magnitude of the corrosion current, it makes this parameter an important factor in the overall corrosion process.

3 ELECTRICAL PROPERTY MEASUREMENTS

From an electrical point of view, saturated concrete can be regarded as a composite comprising non-conductive aggregate particles embedded in an ionically conducting cementitious matrix, with conduction occurring primarily through the continuous pore-network. As a consequence, the electrical properties of concrete are directly related to pore tortuosity, pore connectivity and the degree of pore saturation, so its measurement could be of practical significance in assessing the durability of concrete structures. In addition, as the hydration process will alter the pore system beyond the standard curing period this will result in time-variant microstructural - hence electrical property - changes.

The electrical resistivity of a material is equal to the resistance, in ohms, between opposite faces of a unit cube of that material. If R is the bulk resistance of a prismatic sample of concrete placed between two electrodes of area A (cm^2), separated by a distance L (cm), then its bulk resistivity, ρ , is given by,

$$\rho = \left(\frac{RA}{L} \right) \text{ Ohm-cm } (\Omega\text{cm}) \quad (1)$$

Conventional treatment of resistivity data - saturated rocks in this instance - has been to utilise the formation factor F [9, 10] which is defined as the ratio of bulk resistivity, ρ , of the saturated rock to the resistivity of the saturating liquid, ρ_p . The formation factor is then related to the rock porosity, ϕ , through the relationship,

$$F = \frac{\rho}{\rho_p} = a\phi^{-m} \quad (2)$$

where the exponent m is the *cementation exponent*, and is related to the tortuosity and connectivity of the pore network within the rock and a is a correction factor which is valid over a particular range of porosities, ϕ . A wide range of values have been reported for m and a for different rock and sediment formations, with a , typically, in the range 0.4–2.5 and $m = 1.2$ –2.5 [11, 12]. Values of m and a are characteristic for a given porous rock formation and are determined empirically.

Provided that the solid phase can be regarded as an insulator in comparison to that of the interstitial aqueous phase, diffusion and resistivity of a saturated porous system

are connected through the Nernst-Einstein relationship [13, 14],

$$\frac{D}{D_o} = \frac{\rho_p}{\rho} = \frac{1}{F} \quad (3)$$

where D is the diffusion coefficient of the porous material, D_o the free solution diffusion coefficient of the ion.

The work outlined above shows that the electrical resistivity of concrete provides an indirect measure of the capillary pore network (continuity, tortuosity) which is a key property in a concrete's resistance to the penetration of a fluid. In order to fully exploit electrical property measurements in assessing the relative performance of different concrete mixes, the resistivity of the pore-fluid, ρ_p , is required or, at the very least, needs to be estimated. This is particularly relevant when supplementary cementitious materials (SCM) are used as these materials alter the concentrations of Na^+ , K^+ and OH^- within the interstitial aqueous phase in comparison to a plain Portland cement concrete. In order to evaluate the resistivity of the pore-fluid, pore expression techniques can be used; however, this is impractical for a variety of reasons, not least because it complicates the testing procedure. The pore-fluid resistivity could be estimated from the ionic concentrations predicted from the chemical composition of the binder. For example, the model of Taylor [15] predicts the concentration of various ionic species in the pore solution based on the cement composition and degree of hydration. From the estimated concentrations of the ions, it is then possible to evaluate the resistivity of the pore-fluid. In this work, the model developed by Snyder et al [16] and Bentz [17] is used to estimate the resistivity of the pore fluid.

4 EXPERIMENTAL DEVELOPMENTS

4.1 Cover-Zone Electrode Array

The Electrical measurements were obtained utilizing a multi-electrode array [18] which was embedded within the cover-zone at the time of casting. This arrangement allowed monitoring of the spatial distribution of both electrical resistance and temperature. In summary, the array comprises six electrode-pairs and four thermistors mounted on a PVC former, with the former being secured onto two, 15mm diameter steel bars; the cover-to-steel was 50mm. With this arrangement, the electrode-pairs were positioned at 10, 20, 30, 40, 50 and 75mm from the concrete surface. The electrical measurements obtained at 75mm are sufficiently remote from any effects at the concrete surface (e.g. drying, wetting) and will reflect cement hydration, pozzolanic reaction and microstructural development.

The resistivity of the concrete at each electrode-pair was evaluated by multiplying the measured resistance by a calibration factor, denoted k (i.e. equivalent to the geometrical factor A/L in equation (1) above). This was obtained by calibrating with the resistivity of 100mm cubes cast from the same batch as the slabs used in the experimental programme. The measured resistance, R (ohms), across the electrode-pairs were then converted to resistivity, ρ (in Ωcm), through the relationship,

$$\rho = kR \quad \Omega\text{cm} \quad (4)$$

For the electrode-array, k was obtained as 2.41cm.

4.2 Materials

The concrete mixes are presented in Table 1 with a crushed granite aggregate used throughout together with a mid-range water reducer (SikaPlast 15RM). Specimens were cast as 250×250×150mm (thick) slabs in steel formwork with the 250×250mm face cast against the formwork used as the working face. An electrode array described above was positioned at the plan centre of each slab; wiring from the embedded array was ducted out of the slab and terminated with a multipole D-connector. The 28-day and 180-day concrete compressive strengths (f_{28} and f_{180} , respectively) are presented in Table 1.

4.3 Testing Regime and Monitoring

On demoulding at approximately 24-hours, each specimen was wrapped in damp hessian and placed in a heavy-duty polythene bag which was then sealed. The specimens were then left in a laboratory at constant temperature ($20 \pm 1^\circ\text{C}$) for a period of 27-days. At this time, the four vertical faces and the as-cast face of the specimens were painted with two coats of a proprietary sealant and exposed to a laboratory environment $20 \pm 1^\circ\text{C}$, $55\% \pm 5\% \text{RH}$. After approximately 7-days, all samples were ponded with water for a period of 24-hours. This ensured the surface region of all specimens was in a similar saturated state. Samples were then allowed to dry for further 7-days before being subjected to a cyclic ponding regime comprising 1-day wetting followed by 6-days drying. Electrical resistance measurements were obtained by connecting the samples to a multiplexing system and an auto-ranging data logger. The resistance of the concrete between each electrode-pair was obtained a fixed frequency of 1kHz; the signal amplitude was 350mV with a measurement integration time of 1.0 second. Thermistor measurements were also acquired using the same system which were, subsequently, converted to temperature (in $^\circ\text{C}$). On demoulding at 24-hours, measurements on the array were then taken on a 12 hour cycle extending over periods extending up to 350 days.

5 RESULTS AND DISCUSSION

Only a selection of results are presented for illustrative purposes, with discussion focussing on the electrodes positioned at 75mm from the concrete surface.

5.1 Preliminaries

Figure 2 presents the resistivity, ρ , versus time response for the electrodes positioned at 10, 20, 30 and 75mm from the surface for the PC concrete mix ($w/b=0.65$) with data presented between 100 and 200 days after casting. (Note: for reasons of clarity, only every 5th measurement point is highlighted). The influence of the cyclic wetting/drying regime on the resistivity of the concrete is clearly evident for the electrode-pairs positioned 10mm and 20mm from the surface, with periods of wetting resulting in a decrease in

Table 1. Summary of concrete mixes (pl =plasticiser, w/b = water-binder ratio, FA = fly ash, GGBS = ground granulated blast-furnace slag).

Mix Designation	w/b	CEM I kg/m ³	GGBS kg/m ³	FA kg/m ³	20mm kg/m ³	10mm kg/m ³	Fine (<4mm) kg/m ³	pl l/m ³	f_{28} MPa	f_{180} MPa
PC	0.35	378	-	-	787	393	787	5.15	79	88
	0.65	263	-	-	790	395	790	-	39	46
GGBS/65	0.35	132	244	-	782	391	782	5.12	65	76
	0.65	92	170	-	786	393	786	-	31	40
FA/35	0.35	242	-	130	773	386	773	5.06	65	81
	0.65	169	-	91	780	390	780	-	24	38

resistivity and drying accompanied by an increase in resistivity. The electrode-pair positioned at 75mm, however, displays a continual increase and is not influenced by wetting/drying at the concrete surface. Similar responses were obtained for the other concrete mixes and it is for this reason that measurements from the electrode-pair positioned at 75mm from the exposed surface, and still within the near-surface region, are discussed below.

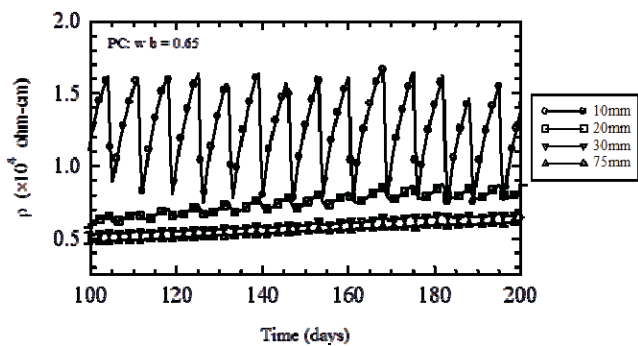


Figure 2. Variation in resistivity for electrode-pairs at 10, 20, 30 and 75mm from the concrete surface undergoing cyclic wetting (PC concrete, w/b=0.65).

5.2 Resistivity/Time response

Figure 3(a) presents the resistivity for concrete mixes with w/b=0.35 over the initial 4-weeks after demoulding. The resistivity of all mixes display a continual increase although the influence of the SCM's on resistivity is also evident. For periods <3 days, the PC concrete displays a higher resistivity than the FA/35 and GGBS/65 mixes and reflects the initial slower reaction of these systems. However, for periods >3-days, the resistivity of the GGBS/65 concrete achieves higher values than the PC concrete whereas for the FA/35 concrete, this effect does not occur until approximately 15 days. Similar trends are observed in Figure 3(b) for concrete mixes with w/b=0.65 although the resistivity of the FA/35 mix only achieves higher values than the PC mix at periods in excess of 28-days. It is also observed that an increase in the w/b ratio results in a decrease in resistivity. Figures. 4(a) and (b) display the resistivity at 75mm from the surface from 7-days up to approximately 350 days for 0.35 and 0.65 w/b ratios (Note: again, for clarity, only every 20th measurement point is highlighted on these curves). The influence of SCM's on the resistivity is clearly evident from these Figures; at the end of

the test period, the resistivity of the FA/35 and GGBS/65 mixes are almost an order of magnitude higher than the PC mix, at both w/b ratios. The increase in resistivity for both the GGBS and FA concretes reflects the on-going pozzolanic activity and pore structure refinement during the post-curing period. The increase in resistivity for the concretes presented in Figure 4 can be represented by the equation:

$$\rho = \rho_{ref} \left(\frac{t}{t_{ref}} \right)^n \quad (5)$$

where, ρ is the resistivity at time, t (in days); ρ_{ref} is the resistivity at a reference time, t_{ref} , and n could be regarded as an *aging* exponent which will be related to hydration and pozzolanic reaction. The reference time for the current work is taken as 28-days, hence $t_{ref} = 28$ -days and the respective resistivity at 28-days, ρ_{ref} , obtained from Figure 3. Best-fit curves to the data are plotted on Figure 4(a) and (b) (solid lines) through the measurement points with the fitting equations presented on these Figures. It is interesting to note that the aging exponent, n , would appear to be virtually independent of w/b ratio and is binder specific. This could be explained by the fact that the influence in of the w/b ratio is accounted for in the 28-day resistivity, ρ_{ref} .

Although the equations on these Figures were developed on the best-fit line to all the data points for a particular w/b ratio (i.e. over 700 measurement points), a curve could be evaluated from fewer measurements, which has obvious practical implications. For example, Figures. 5(a) and (b) present the best-fit curves (solid lines) based on resistivity measurements at 3 measurement points (7, 28 and 56 days) using the same reference time of 28-days. For comparative purposes, the best-fit curves based on all the measurement points on Figure 4 are also presented on Figure 5 (dashed lines).

5.3 Towards a Performance-Based Index

From the definition of formation factor (F) in equation (2) above, and its relationship with diffusivity through equation (3), the concretes could be ranked in terms of their resistance to ionic penetration using the parameter, F . However, the formation factor requires a knowledge of the pore-water resistivity. A straightforward procedure for estimating pore-water resistivity from the concentrations of Na^+ , K^+ and OH^- ions in the pore-water has been developed [16, 17].

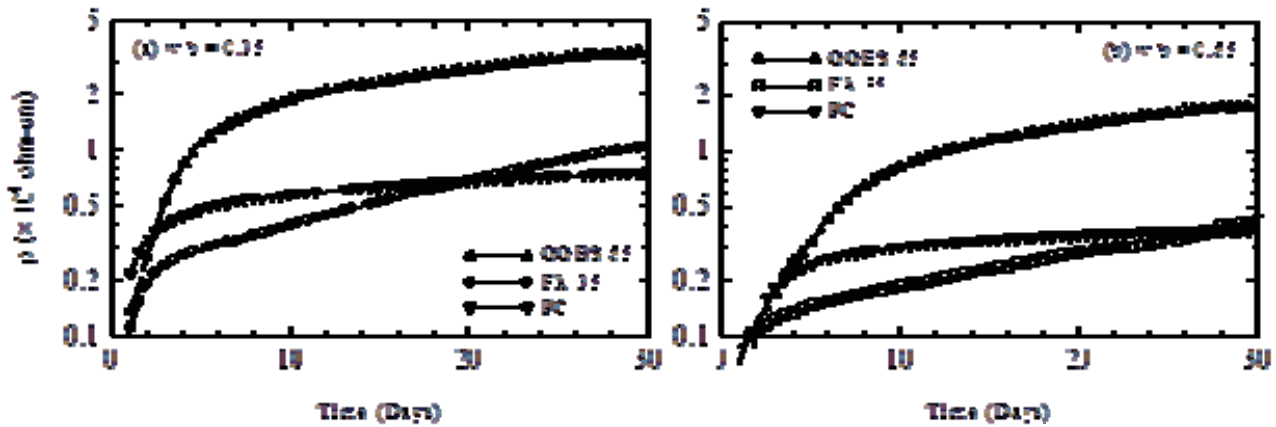


Figure 3. Increase in resistivity during initial 28-days after casting for (a) $w/b=0.35$ and (b) $w/b=0.65$.

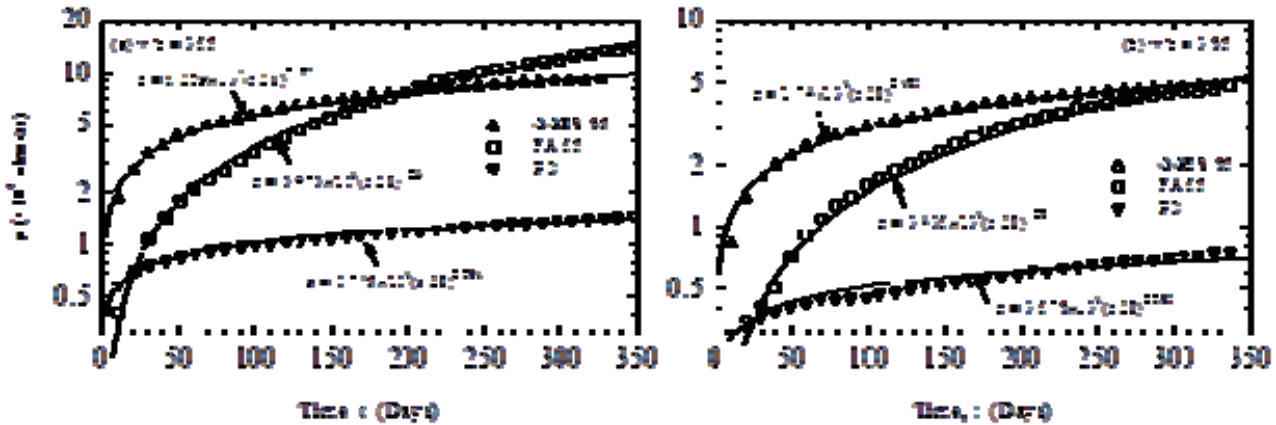


Figure 4. Increase in resistivity (at 75mm) over the period 7-350 days after casting for (a) $w/b = 0.35$ and (b) $w/b = 0.65$. Curve fits in the form of equation (5) are also presented.

In summary, for a particular degree of hydration, the concentrations of Na^+ and K^+ are computed from the binder composition (Table 2) and assuming that 75% of the Na_2O and K_2O will be released into the pore-water. The concentration of OH^- is then deduced from the electro-neutrality condition. Using the equivalent conductivity of each ion, these data are then used to compute the pore solution electrical resistivity, ρ_p .

Table 2. Oxide analysis of cementitious materials used in experimental programme.

% by weight	PC	FA	GGBS
SiO_2	20.68	51.0	34.33
Al_2O_3	4.83	27.4	12.60
Fe_2O_3	3.17	4.6	0.60
CaO	63.95	3.4	41.64
MgO	2.53	1.4	8.31
TiO_2	+	1.6	+
P_2O_5	+	0.3	+
SO_3	2.80	0.7	+
K_2O	0.54	1.0	0.47
Na_2O	0.08	0.2	0.25

Table 3 presents the computed F values for each concrete mix in Table 1 at both 28-days (F_{28}) and 56-days (F_{56}); in

calculating ρ_p , an average degree of hydration of 80% has been assumed throughout for each binder type. With reference to Table 3, decreasing the w/b ratio from 0.65 to 0.35 results in a fivefold (approximately) increase in F for each mix. Moreover, the beneficial effect of the FA and GGBS is clearly evident, particularly at longer time-scales; although these materials may not necessarily create concretes of lower porosity than their PC counterparts, it is of a more disconnected and tortuous in nature. It is interesting to note that whilst the GGBS/65 concrete displays the highest resistivity, when the resistivity of the pore-water is considered, it is out-ranked by the FA/35 concrete in the longer-term. From equation (3) above, the *instantaneous* diffusion coefficient, D , of a particular ionic species (e.g. Cl^-) could also be approximated from F (i.e. $D \approx D_0/F$) and the free-solution diffusion coefficient of that ion, D_0 (e.g. D_0 for the chloride ion is $1.84 \times 10^{-9} \text{ m}^2/\text{s}$ [19]).

6 CONCLUDING COMMENT

The work detailed has presented developments in the application of electrical resistivity measurements as a potential test method to rank the relative performance of a range of concrete mixes. The measurements were used in combination with the pore-fluid resistivity, the latter evaluated from the ionic concentration in the pore water. These values were then used to assess concrete performance in terms of Formation Factor (F). In general terms, the higher the F value for the concrete, the better its performance rating; however,

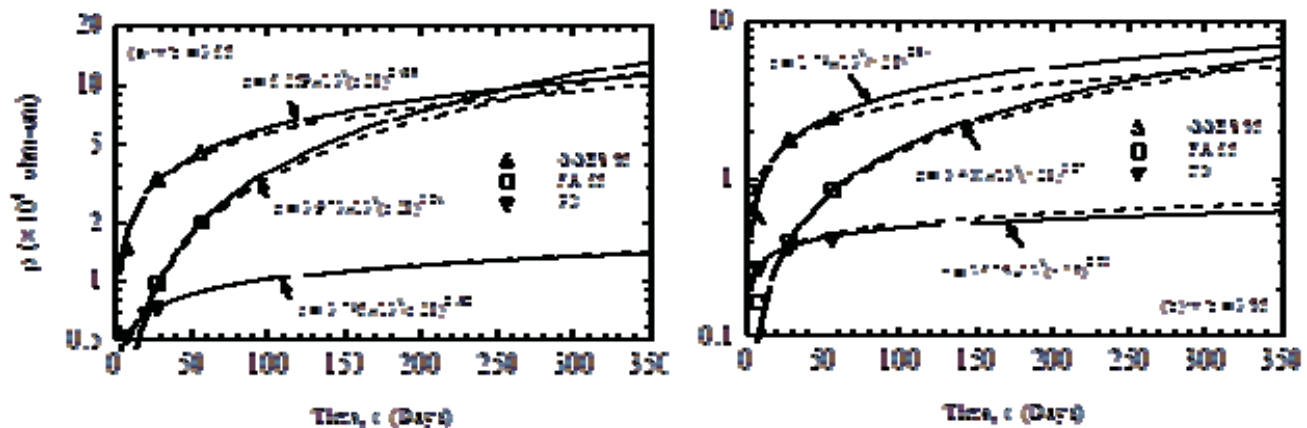


Figure 5. Curve-fits to resistivity measurements based on 3 (three) measurement points – 7, 28 and 56 days for (a) $w/b = 0.35$ and (b) $w/b = 0.65$.

Table 3. Formation factors (F) for the concrete mixes in Table 1 at 28-days (F_{28}) and 56-days (F_{56}).

Mix	w/b	$\rho_p (\Omega\text{cm})$	$\rho_{28} (\times 10^4 \Omega\text{cm})$	$\rho_{56} (\times 10^4 \Omega\text{cm})$	F_{28}	F_{56}
PC	0.35	10.7	0.725	0.865	677	808
	0.65	23.8	0.368	0.445	154	186
GGBS/65	0.35	27.9	3.23	4.46	1157	1598
	0.65	63.7	1.69	2.32	265	367
FA/35	0.35	8.31	0.952	2.01	1146	2418
	0.65	18.2	0.394	0.842	216	462

work is still required to obtain values, or range of values, for F for concrete classification purposes.

ACKNOWLEDGMENTS

The work presented formed part of the concrete durability programme into monitoring and improving the performance of structural concrete in bridges and in the development of performance-based testing procedures undertaken for Transport Scotland and the Engineering and Physical Sciences Research Council, UK. Funding from both organisations is gratefully acknowledged. The views expressed in this paper are those of the Author and not necessarily those of Transport Scotland.

REFERENCES

- [1] The state of the nation, *The New Civil Engineer*, 25th May, 2000, 15-17.
- [2] Swamy, R.N. Holistic Design: Key to Sustainability in Concrete Construction', *JSCE (Concrete Committee)*, Newsletter No. 13, April 2008.
- [3] Long, A.E., Henderson G.D. and Montgomery F.R., Why assess the properties of near-surface concrete. *Constr. Bldg. Matls.*, 15(2/3), 65-79, 2001.
- [4] British Standards Institution, BS EN206:2013 Concrete - Specification, performance, production and conformity, BSI, London.
- [5] British Standards Institution, PD CEN/TR 16563:2013 Principles of the equivalent durability procedure, BSI London, (ISBN 978-0-580-81434-1).
- [6] British Standards Institution, BS EN8500-1:2015+A1:2016 Concrete - Complementary British Standard to BS EN 206 Part 1: Method of specifying and guidance for the specifier, BSI, London.
- [7] British Standards Institution, BS EN1990 1990:2002+A1:2005 Eurocode – Basis of structural design, BSI, London.
- [8] Beushausen, H. and Fernandez-Luco L. (Eds), Performance-based specifications and control of concrete durability, *State-of-the-Art Report RILEM TC 230-PSC*, 2015 (ISBN 978-94-017-7309-6).
- [9] Archie, G.E., The electrical resistivity log as an aid in determining some reservoir characteristics, *Trans. of the Amer. Inst. of Mining and Metallurgical Engineers*, 147, 54-62, 1942.
- [10] Atkins, E.R. and Smith, G.H. The significance of particle shape in formation resistivity factor - porosity relationships, *Ibid*, 222, 285-291, 1961.
- [11] Worthington, P.F., The uses and abuses of the Archie equations, 1: the formation factor porosity relationship. *Jnl. App. Geophysics*, 30(3), 215-228, 1993.
- [12] Khalil, M.A. and Santos, F.A.M., Influence of degree of saturation in the electric resistivity hydraulic conductivity relationship. *Surv. in Geophys.*, 30, 601-615, 2009.
- [13] Atkinson, A. and Nickerson, A. K., The diffusion of ions through water-saturated cement, *Jnl. of Matls. Sci.*, 19, 1984, pp3068-3078.
- [14] Scherer G.W., Valenza J.J. and Simmons G., New methods to measure liquid permeability in porous materials, *Cem. Concr. Res.*, 37(3), 386-397, 2007.
- [15] Taylor, H.F.W. A method for predicting alkali ion concentrations in cement pore solutions', *Adv. Cem. Res.*, 1(1), 5-16, 1987.
- [16] Snyder, K.A., Feng, X., Keen, B.D. and Mason, T.O., Estimating the electrical conductivity of cement paste pore solutions from OH⁻, K⁺ and Na⁺ concentrations, *Cem. Concr. Res.*, 33(6), 793-798, 2003.
- [17] Bentz, D., A virtual rapid chloride permeability test, *Cem. Concr. Comp.*, 29(10), 723-731, 2007.
- [18] McCarter, W.J., Chrisp, T.M. and Starrs, G., A sensor apparatus and method for embedding in construction material, Patent No. GB2487691 and WO/2011048378, 2011.
- [19] Li, Y-H. and Gregory, S., Diffusion of ions in sea-water and deep-sea sediments, *Geochimica et Cosmochimica Acta*, 38, 703-714, 1974.

Massive timber - the emergence of a modern construction material

Annette.M.Harte^{1,2}

¹College of Engineering and Informatics, National University of Ireland, Galway, University Road, Galway

²Ryan Institute for Marine, Environmental and Energy Research, National University of Ireland, Galway
email: annette.harte@nuigalway.ie

ABSTRACT: In the move towards sustainable construction, timber and wood-based products are becoming increasingly important structural materials. The introduction of massive timber products with excellent load carrying characteristics allows timber to be used in larger, more complicated structures. Cross-laminated timber panel products have developed to the stage where they can be considered as economic and more sustainable alternatives to traditional materials. In this paper, the characteristics and design of CLT structures are described. Recent developments in mid- and high-rise CLT construction are reviewed and future opportunities identified. The potential to develop CLT from Irish timber is discussed.

KEY WORDS: Massive timber; Cross laminated timber; Tall timber buildings

1 INTRODUCTION

Massive timber is a term used to describe a family of engineered wood products of large section size that offers the construction industry an alternative to steel and concrete. The term is generally applied to thick panel products but can also include large section glued- or block-laminated linear elements. There has been a significant level of interest in these products and building systems due to their technical capabilities, cost-competitiveness and environmental properties.

The product that has received most attention in recent years is cross-laminated timber (CLT), sometimes referred to as X-lam [1]. CLT is a prefabricated multi-layer engineered panel wood product, manufactured from at least three layers of parallel boards by gluing their surfaces together with an adhesive under pressure (Figure 1). Alternate layers of boards are placed cross-wise to each other, which gives the product a high level of in-plane stability. The large thickness gives CLT panels their exceptional strength and stiffness.

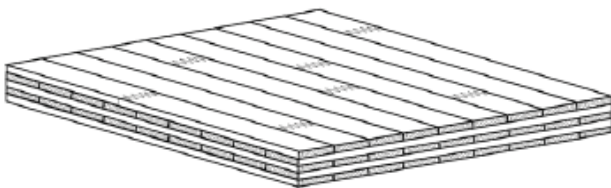


Figure 1. Five layer CLT panel [2].

Since its introduction in the 1990s, CLT has been the subject intensive research, which has enabled the development of product standards and design guidelines. According to the UNECE/FAO Forest Products Annual Market Review 2014-2015 [3], about 90% of CLT production worldwide is located in Europe, with a total production volume of 560,000 m³ in 2014, forecast to increase to about 630,000 m³ by the end of 2015. Plants have recently opened or are planned in Canada, the US, Japan, China and New Zealand [4].

Many buildings have been constructed using this technology across a range of building types mostly as low-rise construction. In the UK alone, over 100 educational buildings in CLT were constructed between 2003 and 2011 [5]. The use of CLT in mid-rise and high-rise buildings has received international media attention. To date, over 40 buildings between 5 and 14 stories tall have been completed and an 18-storey student residence is currently under construction in Canada [6] and taller buildings are planned.

In this paper, CLT as a construction material and system is examined, design approaches and some case study buildings are presented. In addition, the future for tall timber buildings, and current and future research needs are discussed.

2 CHARACTERISTICS AND DESIGN OF CLT STRUCTURES

2.1 Panel Manufacture

CLT panels are commonly manufactured to lengths, widths and thicknesses of up to 18 m, 5 m and 0.5 m, respectively. The number of layers forming a CLT panel is usually 3, 5 or 7. The European product standard for CLT, EN 16351 [7], permits layer thicknesses between 6 mm and 45mm; however, the standard layer thicknesses are 20, 30 and 40 mm. The recommended minimum board width is 4 times the thickness in order to reduce rolling shear failures. For the manufacture of the panels, structural grade timber is dried to about 12% and planed to the required thickness. Defects are cut out and boards are finger-jointed to produce the required lengths. Boards are laid side by side and may or may not be adhesively bonded along their narrow edges. Successive layers are added and the stack is face-bonded under pressure. Depending on the finish required further surface treatment may be required. Openings for doors, windows and services are made using CNC machinery to tight dimensional tolerances. The panels are stored in batches in accordance with the construction sequence and transported to site for erection as required. This sequence is illustrated in Figure 2.



Figure 2. Manufacture, transportation and erection of CLT panels [Images: KLH].

2.2 Characteristics of CLT

CLT provides opportunities to use timber products in a wider range of applications than was possible heretofore. Increased use of timber in building construction can positively contribute to sustainable building practices.

Timber is considered a natural, renewable resource, and extraction and manufacturing of timber products requires a very low amount of energy relative to more conventional structural materials used in construction. Prefabricated CLT building systems are easily erected in a low-dust, low-noise assembly with minimal site waste. Due to their low weight, there is reduced labour and craneage on site and rapid erection times. Ease of disassembly allows for reuse of the material and a more resource-efficient product life cycle. An important consideration is the fact that the timber buildings sequester carbon over their lifespan. Dry wood is about 50% carbon by weight and so massive timber buildings store considerable amounts of carbon. During the lifespan of the building, several forest rotations can take place with further carbon sequestration in the forest. Several studies have been carried out to quantify the environmental benefit of construction in timber using life cycle analysis procedures [8-9]. From an energy efficiency perspective, the use of CLT panels as part of the external building envelope makes it easier to achieve passive or net zero energy building standards as timber has a low coefficient of thermal conductivity and good air-tightness is achieved.

In addition to the sustainability benefits, one of the primary benefits of CLT panels is the use of offsite prefabrication allowing for high-quality certified production, independent of the weather. As holes and notches in panels can be pre-cut prior to arrival to site and assembling methods are straightforward, construction and project delivery times are improved and costs are reduced.

Cross-lamination gives CLT excellent in-plane and out-of-plane strength, rigidity, and stability characteristics [1]. The degree of anisotropy in properties and the influence of natural variations, such as knots, are reduced in comparison with construction timber, allowing for higher characteristic properties to be used in design. Due to the fact that timber is a low density material, overall building weight is reduced compared to other construction material, resulting in savings in foundation works when compared to other construction

materials. However, for tall CLT buildings the light weight may be a disadvantage when considering overturning effects due for example to wind loads, and additional measures such as tie-down rods may be required.

The use of CLT panels gives increased flexibility in architectural design as openings can be regular or irregular and placed at random. Where the panels are left exposed, building aesthetics are greatly enhanced as the exposed timber provides a warm sensation. Exposed timber in schools and healthcare buildings has been shown to have psychological benefits with heart rates and stress levels reduced, which resulted in higher levels of concentration in schoolchildren and faster recovery rates for patients [10-12].

2.3 CLT elements and building systems

CLT panels can be used as floors, walls and roofs and can be used in combination with other engineered wood products, concrete, steel and masonry. CLT panels can be vertically oriented as load-bearing walls and shear walls, or horizontally as load-bearing floors or roofs. CLT panels have been widely used in low-rise construction but are increasingly used for mid- and high-rise residential construction. Walls typically consist of three- to five-layer panels, whereas floors consist of five or more layers. For longer spans and unduly heavy loads timber-concrete composite floors provide an economic solution.

Table 1. Maximum economic span for different floor types

Floor construction	Max. span (m)
Timber studs	4
CLT – simply supported	5
CLT – continuous over supports	6
Ribbed timber slab – CLT + glulam	10
Timber-concrete composite	10

For low-rise buildings, platform construction is widely used. On each level, CLT walls are erected in a cellular arrangement and the floor is placed on top as seen in Figure 3. The floor then provides a platform for the next level. With increasing building height, the compressive force from the walls above acting on the floor below in the perpendicular to grain direction increases. To prevent excessive deflections, the force can be transferred to the wall or column below by means of self-tapping screws or other steel connectors. An alternative approach is to use balloon construction methods in which the walls are continuous from floor to floor and the floors are supported by steel brackets connected to the walls. In this way, the compressive loading perpendicular to grain issue is avoided but scaffolding may be required to support the floor.

For mid- and high-rise buildings, different arrangements of CLT elements in conjunction with glulam beams and columns have been used with the structural core constructed either from concrete or CLT. Some of these solutions are described in Section 3.

2.4 Structural design of CLT

Due to the lack of experience with CLT when Eurocode 5 [14] was developed, no specific design rules for CLT were included. In the intervening years, design rules have been

developed and are included as part of product-specific technical approvals and also in the National Annexes to Eurocode 5 in Austria and Germany. In Canada and the United States, CLT Handbooks [15-16] containing detailed design rules have been published. The CEN standardisation committee, CEN/TC 250/SC5, has established a working group to draft new design rules for inclusion in the next revisions to Eurocode 5. Recommendations for the design of CLT elements have been well documented in publications emanating from the European COST Actions [17-18].



Figure 3. Platform construction – Murray Grove [13].

For elements loaded out of plane, such as floors and roofs, the serviceability limit state deflections and vibrations limits generally govern the design. An important consideration that arises from the cross-lamination of members is the shear flexibility of the cross layers. Because of this, deflection calculations based on one of the following methods is used: the Gamma method, the shear analogy method and the Timoshenko shear flexible beam method. These methods generally give comparable results where the span-thickness ratio exceeds 15. For the calculation of the stresses, for simplicity only those layers oriented perpendicular to the axis of bending are assumed to contribute to load resistance. This is illustrated in Figure 4 for the case of bending stresses.

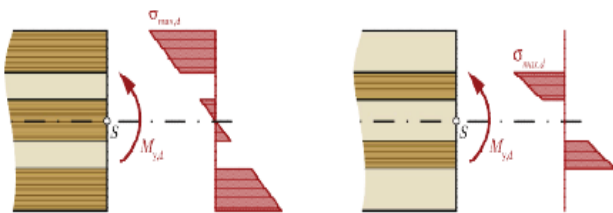


Figure 4. Bending stress distribution in CLT [17]

For elements loaded in-plane, the two main loading scenarios are compression and shear. For CLT walls carrying vertical loading, compressive stress and buckling checks are performed. For buckling, verification by either the equivalent beam method or using 2nd order theory is used. For CLT shear walls, a number of different failure mechanisms are possible depending on whether the narrow edges of the layers are bonded or unbonded [19]. For CLT panels with the narrow edge bonded, failure is in gross-shear, where shearing of all of the layers takes place. Where there is no edge bonding, failure can occur through net-shear failure by exceeding the shear resistance of the layers oriented in the weak direction or by

torsion failure of the glue-line between the layers. Further information on these and other design checks is detailed in [18].

2.5 Connections systems

Connections between the CLT elements is achieved via simple steel connectors and self-tapping screws. In Figure 5, some typical arrangements for panel-to-panel connections are illustrated. Arrangements for wall-floor connections are shown in Figures 6, 7 and 8. The design of these connections can be carried out in accordance with current Eurocode 5 procedures.

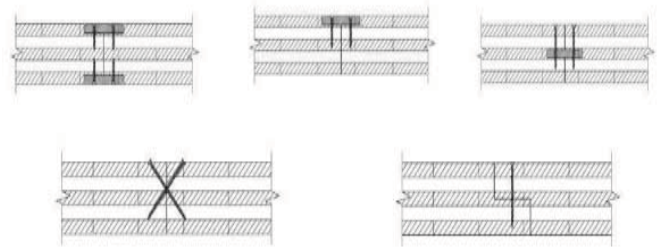


Figure 5. CLT panel-to-panel edge connections [20]

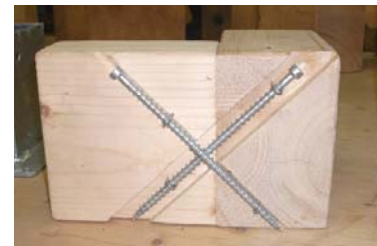


Figure 6. Self-tapping screws as connectors

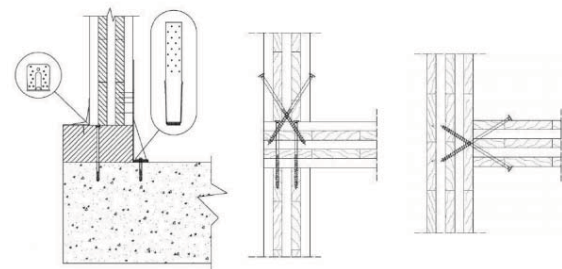


Figure 7. CLT wall-to-floor connections [20].



Figure 8. CLT wall floor connection – Murray Grove [13].

2.6 Fire Performance of CLT

Over the past couple of decades, research and testing has been performed to characterise the fire performance of timber structures so that safe fire design can be conducted [21-25]. It is well known that timber when ignited burns at a predictable rate with the formation of a charring layer. This charring layer forms a thermal barrier between the surface and the internal timber. During a fire incident, the cross-section of the timber element reduces at a predictable rate. Due to the large section size of massive timber members, they have an inherent fire resistance. Many studies have been undertaken to establish the charring rates for massive timber elements. In Figure 9, a CLT panel after a 1-hour fire test is shown. The exposed face of the panel shows the char formation while the unexposed face has shown no evidence of deterioration. In tests on CLT panels manufactured with temperature-sensitive adhesives [23], the charred layer delaminated during the tests resulting in increased charring rates, which can be characterised using a bi-linear charring model. For panel manufactured with less temperature-sensitive adhesives, the charred layers remained in place and continued to protect the layers underneath against increasing temperatures. This behaviour is the same as for solid panels and provides a constant charring rate throughout. In order to achieve a specific level of fire resistance, different measures are used. The CLT panel can be sized to ensure that the required resistance is met. The reduced section after the end of the fire duration must still have adequate capacity to carry the loads. Another approach is to encapsulate the panels with fire-rated gypsum boards. The combined resistance of the panels and gypsum boards provide the necessary fire rating. The next level of fire protection is to provide a sprinkler system.

Tests on several full-scale buildings have been conducted to investigate the influence of combustible surfaces on fire growth and fire spread inside and outside the room [22, 24]. As part of the SOFIE project [24], tests were carried out in Japan on a full-scale 3-storey CLT building under natural fire conditions to check the global performance and to find possible weaknesses of the timber structure. The walls and floors of the building comprised 85 mm thick and 142 mm thick CLT panels, respectively. They were encapsulated in either one or two layers of non-combustible gypsum board. The windows in the fire room were left open during the test. After the 1-hour fire test, all of the gypsum boards had completely fallen off and the measured charring depth varied between 5 mm and 10 mm. The tests confirmed that with pure structural measures it is possible to limit the fire spread to one room even for timber structures. There was no fire spread to adjacent rooms and in the room above the fire room, no elevated temperature or smoke were detected. Figure 10 shows the building under test 40 minutes after fire ignition.

As new timber technologies are developed and, in particular, connections that transfer loads between elements, it is important to consider the fire performance of these assemblies. As most connectors are manufactured from steel, it is essential as part of the fire design to account for the potential of the connectors to conduct heat into the core of the panels. In addition to connection behaviour in fire,

understanding penetration behaviour is critical to demonstrate that compartmentation is achieved.

In the current regulatory environment, testing is generally required to prove compliance for mid- and high-rise buildings. For recently constructed tall CLT buildings, the fire design has often been conservative. Sprinkler systems have been included even when compliance was deemed to have been achieved with encapsulation on the basis of the tests. Testing is also an important part of the ongoing fire engineering research that will underpin the development of standards.

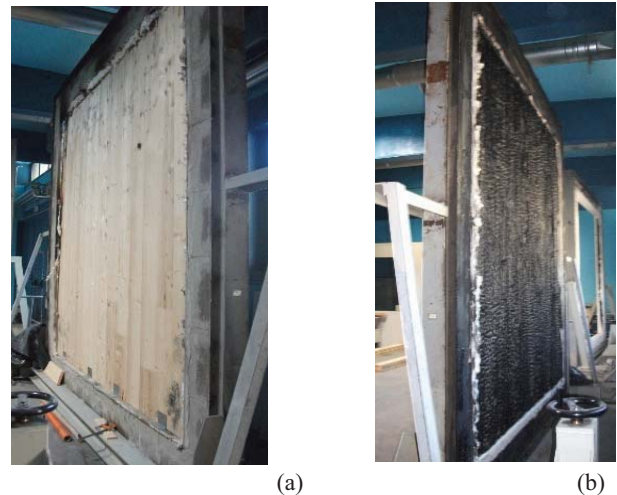


Figure 9. CLT panel after fire test (a) unexposed face (b) exposed face.



Figure 10. Fire test on 3-storey CLT building [24]

3 CLT BUILDINGS

In the last 20 years, many CLT buildings have been completed, mainly in Europe. The earlier projects were mainly single family dwellings but this quickly expanded to the multi-family residential, educational and commercial sectors. Due to the expertise developed with earlier projects and a significant level of research, the last 10 years have seen a significant move to using this technology in the mid- to high-rise construction sector. In Table 2, a list of all buildings of 5-storey and above completed since 2005 is given [6]. It

can be seen that over that period the number of projects and the height of the buildings has increased. The 14-storey TREET building in Norway is currently the tallest CLT building in the world but this record will be broken in 2017 when the 18-storey Brock Commons student residence is completed in Canada. A number of proposals for even taller buildings have been put forward and studies have shown that very tall buildings utilising CLT are feasible.

Table 2. Multi-storey CLT buildings completed 2005-2016.

Year	Building	Location	Use-No storeys
2005	<i>Svartamoen</i>	Trondheim, NO	<i>R</i> - 5
	<i>Fairmule House</i>	Hoxton, UK	<i>R</i> - 5
2006	<i>MFH Holzenhausen</i>	Steinhausen, CH	<i>R</i> - 6
2008	<i>E3</i>	Berlin, DE	<i>R</i> - 7
	<i>Lagerhuset</i>	Eslov, SE	<i>R</i> - 10
	<i>Limnologen</i>	Vaxjo, SE	<i>R</i> - 8
2009	<i>Murray Grove</i>	London, UK	<i>R</i> - 8
2010	<i>Edifice Fondation</i>	Quebec, Ca	<i>O</i> - 6
2011	<i>3xGrun</i>	Berlin, DE	<i>R</i> - 6
	<i>Bridport House</i>	London, UK	<i>R</i> - 8
	<i>H8</i>	Bad Aibling, DE	<i>R</i> - 8
2012	<i>PuuEra</i>	Heinola, FI	<i>R</i> - 5
	<i>Forte</i>	Melbourne, AU	<i>R</i> - 10
	<i>UBC Earth Sciences</i>	Vancouver, CA	<i>E</i> - 5
	<i>Lifecycle Tower</i>	Dornbirn, AU	<i>O</i> - 8
	<i>Whitmore Rd</i>	London, UK	<i>R</i> - 6
2013	<i>Wood Cube</i>	Hamburg, DE	<i>R</i> - 5
	<i>Tamedia</i>	Zurich, CH	<i>O</i> - 6
	<i>Via Cennia</i>	Milan, IT	<i>R</i> - 9
	<i>Maison de L'Inde</i>	Paris, FR	<i>R</i> - 7
	<i>Marina Verde</i>	Caorle, IT	<i>H</i> - 6
	<i>Bullitt Centre</i>	Seattle, US	<i>O</i> - 6
	<i>Wagramerstrasse</i>	Vienna, AT	<i>R</i> - 7
	<i>Panorama Giustinelli</i>	Trieste, IT	<i>R</i> - 7
	<i>District 03</i>	Quebec, CA	<i>R</i> - 6
	<i>Pentagon 2</i>	Oslo, NO	<i>R</i> - 8
2014	<i>UEA Student Res</i>	Norwich, UK	<i>R</i> - 7
	<i>Contralaminada</i>	Lleida, ES	<i>R</i> - 8
	<i>St Die-des-Vosges</i>	Vosges, FR	<i>R</i> - 8
	<i>Illwerke Zentrum</i>	Vandans, AT	<i>O</i> - 5
	<i>Rundeskogen</i>	Sandnes, NO	<i>R</i> - 8
	<i>Banyan Wharf</i>	London, UK	<i>R</i> - 10
	<i>Shaing-Yang Woodtek</i>	Taiwan	<i>M</i> - 5
	<i>Kingsgate House</i>	London, UK	<i>R</i> - 7
	<i>WIDC</i>	Pr George, CA	<i>E</i> - 6
2015	<i>Puukuokka</i>	Jyväskylä, FI	<i>R</i> - 8
	<i>Framework</i>	Portland, US	<i>O</i> - 5
	<i>Trafalgar Place</i>	London, UK	<i>R</i> - 10
	<i>Trentino-Quebec</i>	Trento, IT	<i>R</i> - 5
	<i>Cobalt Place</i>	London, UK	<i>R</i> - 6
	<i>Verde Living</i>	Adelaide, AU	<i>R</i> - 5
	<i>Curtain Place</i>	London, UK	<i>M</i> - 6
	<i>Treet</i>	Bergen, NO	<i>R</i> - 14
2016	<i>Nordic Lofts</i>	London, UK	<i>R</i> - 5

R- residential, *O* - office, *H* - hotel, *E* - education, *M* - mixed use

Many of the early adopters of CLT as a primary construction material were in regions or municipalities where 'Timber First' or sustainable policies were in place. The London borough of Hackney is the first local authority in

England to promote timber construction. Since it introduced a 'Timber First' policy in 2012, more than 18 multi-storey timber buildings have been built in the region. One of these buildings, the Stadthaus in Murray Grove, was the tallest timber building in the world when it was completed in 2009 and has received considerable international attention since that time. Vancouver aims to be the greenest city in the world by 2020 and is the site for what will be the highest CLT building when it is completed in 2017.

Three case study buildings are presented and future trends in high-rise construction are discussed.

3.1 Case Study Building 1: Limnologen apartment complex in Växjö, Sweden.

In the Välle Broar region in the municipality of Växjö in Sweden, a town planning strategy was developed in 2002 to increase the use of wood in construction. As part of this strategy, it stated that in the Välle Broar region, all construction must be based on the use of timber or wood based products.

As a result of an architecture competition, the Limnologen complex was born. It consists of four eight-storey apartment buildings, with seven timber storeys on a concrete foundation and concrete first floor (Figure 11).



Figure 11. Limnologen apartment buildings, Sweden.

The loadbearing structure is CLT, which is used in both the floors and walls. All exterior walls and some of the interior walls carry the vertical loads. The horizontal loads are transferred by the floors - acting as stiff plates - to the top of the walls. In some parts of the buildings, glulam columns and beams have supplemented the load bearing system in order to reduce the deformations. Typical internal and external wall and floor elements are shown in Figures 12 and 13. The load-bearing floor elements comprise 3-layer CLT panels acting compositely with tee-shaped glulam beams. Tension rods, anchored to the concrete at first floor level are required to carry the overturning forces due to wind loading. The tension rods were re-tightened after some time due to relaxation in the steel, creep deformations in the wood and due to possible drying of the wood.

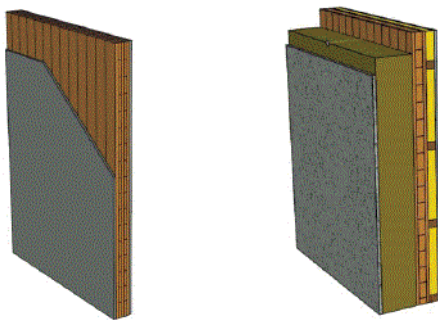


Figure 12. Typical internal (left) and external wall (right) details [26].

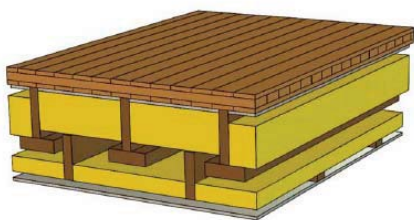


Figure 13. Typical floor-ceiling detail [26].

In order to minimise the risk of flanking transmission and impact sound transmission, the walls are not continuous across storeys, and a polyurethane sealant is used between the walls and the flange of the floor elements. Separation of the floor elements from the ceilings directly below forms part of the acoustic design as can be seen in Figure 13.

As these buildings were unique in Sweden, they were designated as research and educational buildings. Linneaus University and the SP Technical Research Institute have access to Broar Välle projects and both continue to monitor the buildings. Monitoring of vertical shortening, sway, sound transmission, and structural vibrations are ongoing.

3.2 Case study building 2: Mayfield School, Kent UK [27]

This project involved the expansion of an existing 1,000 pupil secondary school to accommodate an additional 800 pupils and 80 teachers, requiring an 8,000 m² expansion. The development had an 18-month timeframe in what was an active school site and had to achieve a BREEAM “excellent” target environmental performance rating.

Because of these constraints, the structural solution chosen was CLT together with glulam beams and columns. Steel beams were used in a small number cases for particularly long spans. The use of off-site manufacturing reduced the time on site and the superstructure was completed in 12 weeks. Figure 14 shows the buildings under construction. The lightweight timber significantly reduced the substructure works. Another key factor in achieving a shortened construction time was the use of an integrated building information modelling approach. Figure 15 shows the BIM model for the school developed by Ramboll UK, structural engineers on the project. Where possible, the timber was left exposed, due to its aesthetic appeal, to provide a warm interior, and to take advantage of beneficial effect on learning provided by timber interiors.



Figure 14. Mayfield school – construction phase [28].

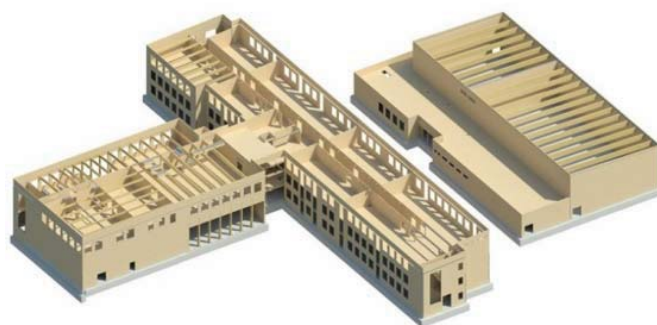


Figure 15. Ramboll BIM model of Mayfield school [28].

3.3 Case study building 3: UBC student residence [29]

The Brock Commons residence at the University of British Columbia (UBC) in Vancouver is currently under construction with an estimated completion date of August 2017. This 18-storey building will provide accommodation for over 400 students. The superstructure of the building comprises a reinforced concrete ground floor and two reinforced concrete cores while the remaining 17 floors will comprise CLT panels and glulam columns (Figures 16 - 17). On completion, it will be 53 m tall, with a floor area in excess of 14,500 m², and will be the tallest timber structure in the world. UBC aims to achieve LEED Gold certification for the building. In addition to its primary function as a student residence, the building will serve as a living laboratory for students and researchers, who will be able to study and monitor its operations.

The floor structure comprises 5-layer two-way spanning CLT panels supported on glulam columns on a 2.85 m x 4.0 m grid. The vertical loads are carried by the CLT floor structure and lateral stability is provided by the concrete cores and CLT diaphragms at each level. To prevent vertical load transfer through the CLT panels, steel connectors are used to transfer the columns loads directly to the column below, as seen in Figure 18.

The construction cost for this innovative building is estimated to be about 8% higher than comparable reinforced concrete building. This cost difference is expected to reduce as more CLT suppliers enter the marketplace and designers and builders become more familiar with massive timber

construction methods. Due to the uniqueness of this project, a conservative approach to the fire safety design was taken. The timber elements will be encapsulated in gypsum panels to give a 2-hour fire separation between compartments and an automatic sprinkler system with a back-up water supply will be installed.



Figure 16. Schematic of UBC student residence [29].



Figure 17. UBC student residence under construction



Figure 18. Floor column connector [29].

3.4 Tall timber buildings – the future

As can be seen from Table 2, timber buildings made from massive timber have been getting progressively taller. The tallest completed building is the 14-storey Treet building in Norway which is 49 m tall. In 2017, when completed the 18-storey Brock Commons student residence in Canada will be

53 m tall. The drive to develop tall buildings arises due to the demands for housing to cater for increasing global population and increased urbanisation. Tall buildings present unique challenges for structural designers. In order to investigate the technical and economic feasibility of using massive timber in tall buildings, to quantify the environmental benefit and to identify research needs, a number of international studies have been undertaken, including the *Case for Tall Wood Buildings* project, and the *Timber Tower Research* project. In these projects, different structural solutions for tall buildings are proposed, which use timber as the primary structural material but also incorporate steel and concrete elements.

In 2012, Vancouver-based Michael Green Architecture unveiled a conceptual design for 30-storey timber residential buildings in a report entitled *The Case for Tall Wood Buildings* [30]. The structural system, known as the FFTT system, is based on a ‘strong column-weak beam’ balloon frame approach. The system combines massive timber panels as the vertical structure, lateral shear walls and floors. The ‘weak beam’ component refers to steel beams, which are bolted to the timber panels, to provide ductility in the system under wind and seismic loading. Concrete is used for the foundations.

The FFTT system is applied to four case study buildings: Option 1 – 12-storey building with core only, Option 2 – 20-storey building with core and interior shear walls, Option 3 – 20-storey building with core and perimeter moment frames and Option 4 – 30-storey building with core and perimeter moment frames and interior walls. These options are illustrated in Figures 19 and 20. The gravity load-resisting system comprises CLT or CLT/concrete composite panels, designed to span one way over interior steel beams, which also act as link beams. The perimeter structure consists of glulam post and beam for Options 1 and 2, and moment frames of solid wood panels and steel link beams for Options 3 and 4. The lateral load resistance is provided by three lateral load resisting systems: the core, the perimeter moment frames, which would be integrated into the building facades, and interior partition walls used individually or in combination. Stiffness governs in most cases, and wind loading will govern for higher buildings even in higher seismic zones, as the building mass is relatively low.

A cost analysis was conducted for both 12-storey and 20-storey FFTT options, considering both the charring and the encapsulation approach to fire protection, and costs were compared to equivalent reinforced concrete frame structures. For both building heights, the costs for the FFTT structures with the charring option were the same as the concrete structures. Costs for the FFTT cases using the encapsulated approach were 2% higher. There is an expectation that as the design and development of FFTT building advances, there will be significant reduction in the construction costs.

Further research and development is required to validate the FFTT system including: advanced analysis of the lateral load resisting systems and connection options; testing of frame behaviour and typical connections; fire testing and modelling.



Figure 19. FFTT building frames: Options 1(12-storey) & 2 (20-storey) [30].



Figure 20. FFTT building frames: Options 3 (20-storey) & 4 (30-storey) [30].

The *Timber Tower Research* project [31] was undertaken by Skidmore, Owning and Merrill (SOM), designers of many tall buildings including the tallest building in the world, the Burj Khalifa in Dubai. The aim of the study was to develop a structural system for tall buildings using timber as the main structural elements and which minimises the carbon footprint of the building. The feasibility of a new structural mass timber system that can be designed to be competitive with reinforced concrete construction in buildings from 10 to 30 stories in height, while reducing the embodied carbon footprint by approximately 60% to 75%, was demonstrated. The design solution proposed includes a novel concrete-jointed timber frame. Massive timber is used for the primary members – floors, shear walls and columns and these are connected with steel reinforcing through concrete joints. The floor system and a typical concrete joint are illustrated in Figures 21 and 22.

The proposed structural system was applied to a prototype building based on an existing concrete building designed by SOM. The Dewitt-Chestnut apartment building, built in Chicago in 1966, is a 395' tall 42-storey concrete structure. This building was selected as the data was readily available and made very efficient use of materials, giving a lower-

bound for comparison. The timber design, utilising the concrete jointed timber frame is illustrated in Figure 23. The gravity load-resisting system comprises CLT floor panels that span between the timber shear walls at the centre of the building and the reinforced concrete spandrel beams and timber columns at the perimeter, as illustrated in Figure 22. The concrete beams stiffen the floor thereby enhancing the deflection and vibration characteristics, leading to a more efficient design. The beams transmit the floor loads via the columns and walls to the lower floor and eventually to the foundations. The lateral load-resisting system comprises CLT shear walls located near the core, designed to resist the wind loading in both directions and overall building torsion. Additional shear walls across the narrow building dimension are necessary to resist uplift due to wind loading on the wide faces of the building. The foundations and the lower two floor of the building are concrete. Overall, the building is 70% timber and 30% concrete.

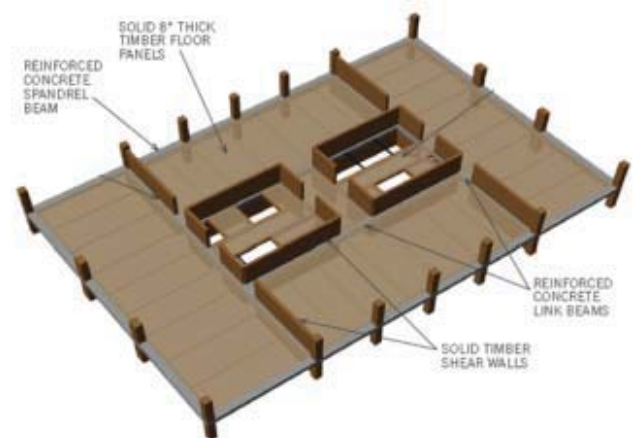


Figure 21. SOM concrete-jointed timber frame [31].

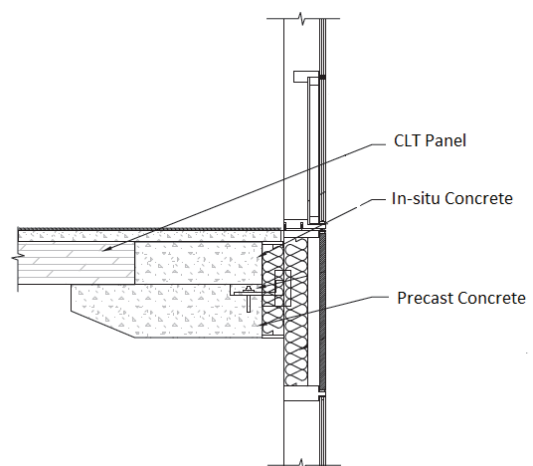


Figure 22. SOM concrete-joint detail [31].

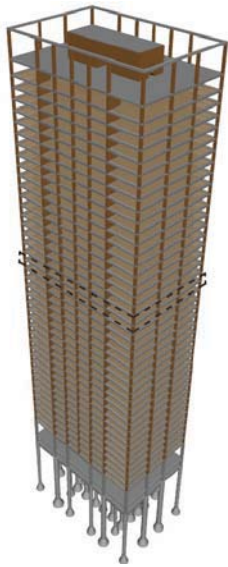


Figure 23. SOM 42-storey timber prototype [31].

A limited cradle-to-gate life cycle analysis was carried out to assess the relative environmental performance of the prototype and benchmark buildings. This included only the embodied carbon associated with the materials used and the energy used in the construction. Two scenarios were considered for the benchmark building: ‘standard materials’ and ‘sustainable materials’. The ‘sustainable materials’ option considers the use of cement replacement and air-drying of the wood. The carbon emission associated with construction were taken as the same for all cases. The embodied carbon footprint of the prototype building was found to be 60% than the benchmark building for the ‘sustainable materials’ option and 75% lower when considering the ‘standard materials’ options.

4 CLT IN IRELAND

Compared the UK, where over 600 CLT buildings have been constructed, this form of construction is relatively new to Ireland and until recently has been limited to single family dwellings. Two recently completed buildings in Dublin, the Ballyogen Environmental Management Centre and the Samuel Beckett Civic Campus have used CLT for walls, floors and roofs. In Figure 24, the Samuel Beckett building and a view of its interior are shown. There are plans for a number of low-rise public buildings. Given the success of this building system globally, it is expected that CLT construction will increase as with the construction industry grows over the coming years.

5 RESEARCH

In order to support the certification and wider use of this building system a considerable amount of research is underway across the globe including in Ireland. Areas of research which have been identified by COST Actions, Code Committees and feasibility studies, such as those described, include: technical properties, connection behaviour, vibration behaviour, fire, and sustainability. Two current COST actions, FP1402 and FP1404, bring together researchers on CLT in order to optimise the effectiveness of the individual efforts.

At NUI Galway, CLT research has been ongoing for over three years and two of the projects are outlined.



Figure 24. Samuel Beckett Civic Campus.

5.1 CLT from Irish timber

In a recently completed research project at NUI Galway, the viability of using Grade C16 Irish grown Sitka spruce to manufacture CLT panels was established. A suitable adhesive has been identified and optimum processing parameters have been established for CLT manufacture [33]. The in-plane and out-of-plane bending performance of Irish CLT panels has been established and rolling shear characteristics have been determined. The influence of layer thickness on the bending characteristics has been identified as an important factor in design [34]. CLT testing of a panel is shown in Figure 25 and rolling shear failure of the cross layer is seen in Figure 26. The flexural stiffness of the Irish panels compared well with commercial CLT panels manufactured from Central European Norway spruce. The development of a CLT manufacturing plant in Ireland presents an opportunity to add significant value to the output from Irish forests and to increase employment in rural areas.



Figure 25. Out-of-plane bending test on Irish CLT panel



Figure 26. Rolling shear failure of Irish CLT panel

5.2 Vibration characteristics of CLT floor systems

The serviceability limit state usually governs design of timber floor systems. The influence of connection systems and the influence of structural and non-structural concrete toppings on the dynamic performance of CLT floors is currently under

investigation in NUI Galway [35] with a view to optimising the serviceability design (Figure 27). Testing of different floor systems in the laboratory and in-situ in buildings is being undertaken together with finite element modelling. This work is ongoing.

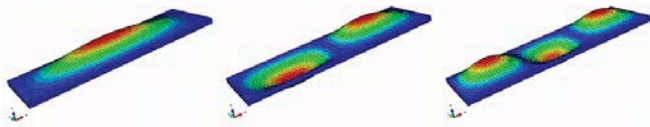


Figure 27. Mode-shapes of two-way spanning CLT panels.

6 CONCLUSIONS

The use of CLT in construction is growing and is being used in increasingly demanding applications. This trend is being driven by the challenge of sustainable construction and is being enabled by research and development across the globe that is driving the technology forward. In this paper, recent developments in CLT materials and construction trends have been reviewed and future opportunities and research needs identified. The potential to develop CLT from Irish timber has been demonstrated.

REFERENCES

- [1] Brandner, R., Flatscher, G., Ringhofer, A., Schickhofer, G., Thiel, A. (2016), 'Cross laminated timber (CLT): overview and development', *European Journal of Wood and Wood Products*, 74(3), 331-351.
- [2] EN1995-2:2004, *Eurocode 5: Design of timber structures - Part 2: Bridges*, CEN European Committee for Standardisation, Brussels, Belgium 2004.
- [3] UNECE/FAO, *Forest Products Annual Market Review 2014-2015*, 2015.
- [4] Schickhofer, G., Brandner, R., Bauer, H. (2016), 'Introduction to CLT, product properties, strength classes', *Proceedings of Conference of COST Actions FP1402 and FP1404*, Stockholm, Sweden.
- [5] Crawford D., Hairstans R., Smith R.E. (2013), 'Feasibility of cross-laminated timber production from UK Sitka spruce', *Proceedings of European Conference on Cross Laminated Timber*, Graz, Austria. 37-52.
- [6] <http://www.woodskyscrapers.com/>. Accessed: 050716.
- [7] EN16351:2015, *Timber structures - cross laminated timber-Requirements*, CEN European Committee for Standardisation, Brussels, Belgium.
- [8] Robertson, A.B., Lam, F.C., Cole, R.J. (2012), 'A comparative cradle-to-gate life cycle assessment of mid-rise office building construction alternatives: laminated timber or reinforced concrete', *Buildings*, 2, 245-270.
- [9] Dolan, D., Harte, A.M. (2014), 'A Comparison of the Embodied Energy and Embodied Carbon of a Timber Visitor Centre in Ireland with its Concrete Equivalent', *Proceedings of World Conference on Timber Engineering*, Quebec, Canada.
- [10] Fell, D. (2010), *Wood in the human environment : restorative properties of wood in the built indoor environment*, PhD thesis, University of British Columbia.
- [11] Sakarugawa, S., Miyazaki, Y., Kaneko, T., Makita, T., Influence of wood wall panels on physiological and psychological responses. *J of Wood Science*, 51:136-140, 2005.
- [12] Elias, M.J., Schools as a source of stress to children: an analysis of causal and ameliorative influences, *J of School Psychology* 27:393-407 1989.
- [13] <https://www.behance.net/gallery/12747107/Stadthaus-Murray-Grove-LondonUK>. Accessed 050716
- [14] EN1995-1-1:2004, *Eurocode 5: Design of timber structures - Part 1-1: General - Common rules and rules for buildings*, CEN European Committee for Standardisation, Brussels, Belgium, 2004.
- [15] Karacabeyli, E., Douglas, B., *CLT Handbook: cross-laminated timber, US Edition*, 2013.
- [16] Gagnon, S., Pirvi, C. (eds), *CLT Handbook: cross-laminated timber, Canadian Edition*, 2011.
- [17] Thiel, A., Brandner, R. (2015), 'ULS design of CLT elements - basics and some special topics', *Proceedings of Cross Laminated Timber - a competitive wood product for visionary and fire safe buildings: Joint Conference of COST Actions FP1402 and FP1404*, KTH, Stockholm, Sweden.
- [18] Harris, R., Ringhofer, A., Schickhofer, G. (2013), *Focus solid timber solutions - European conference on cross laminated timber (CLT)*, University of Bath, Bath, UK.
- [19] Brandner, R., Dietsch, P., Droscher, J., Schulte-Wrede, M., Kreuzinger, H., Sieder, M., Schickhofer, G., Winder, S. (2015), 'Shear properties of cross laminated timber (CLT) under in-plane load: test configuration and experimental study', *Proceedings of 2nd INTER Meeting*, Sibenik, Croatia
- [20] Tomasi, R. (2013), 'Seismic behaviour of connections for buildings in CLT', *Proceedings of European Conference on Cross Laminated Timber*, Graz, Austria. p. 37-52.
- [21] Gerard R., Barber D., Wolski A., *Fire safety challenges of tall wood buildings*. Arup North America, San Francisco, CA, and Fire Protection Research Foundation, Quincy, MA, USA, 2013.
- [22] Frangi, A., Fontana, M., Fire performance of timber structures under natural fire conditions, *Fire Safety Science* 8:275-290, 2005.
- [23] Frangi, A., Fontana, M., Hugi, E., Jobstl, R. (2009), 'Experimental analysis of cross-laminated timber panels in fire', *Fire Safety Journal* 44, 1078-1087.
- [24] Frangi, A., Boichichio, G., Ceccotti, A., Lauriola, M.P., (2008), 'Natural full-scale fire test on a 3 storey Xlam timber building', *Proceedings of 10th World Conference on Timber Engineering*, Miyazaki, Japan.
- [25] Brandon, D., Maluk, C., Ansell, M.P., Harris, R., Walker, P., Bisby, L., Bregulla, J. (2015), 'Fire performance of metal-free timber connections' *Proceedings of the ICE - Construction Materials*, 168(4), 173-186.
- [26] Serrano, E., *Documentation of the Limnologen project*, Report No 56, Vaxjo University, Sweden, 2009.
- [27] White, G., *Mayfield School*, <http://www.ramboll.com/projects/ruk/mayfield-school>, Accessed:050716.
- [28] Hartmann, K. (2015), 'Mayfield School. CLT + BIM = Added value', *Presentation to IITU Industry Seminar*, NUI Galway, Ireland.
- [29] Acton Ostry Architects Inc. (2016), *A tale of tall wood. Brock Commons student residence*, University of British Columbia, Vancouver, Canada.
- [30] Green, M. (2012). *The Case For Tall Wood Buildings*, mgb Architecture + Design, Vancouver, Canada, 2012.
- [31] Skidmore, Owings, and Merrill, LLP. 2013. *Timber Tower Research Project*. https://www.som.com/sites/default/files/20130506_SOM-Timber-Tower-Final-Report_1.pdf. Accessed January 14, 2014.
- [32] Wells, M. (2011), 'Tall timber buildings: applications of timber construction in multistorey buildings', *CTBUH Journal*, 2011(1), 24-27.
- [33] Sikora, K.S., McPolin, D.O., Harte, A.M. (2015), 'Shear strength and durability testing of adhesive bonds in cross-laminated timber', *J Adhesion*, 92(7-9), 758-777.
- [34] Sikora, K.S., McPolin, D.O., Harte, A.M. (2016), 'Effects of the thickness of cross-laminated timber (CLT) panels made from Irish Sitka Spruce on mechanical performance in bending and shear', *Construction and Building Materials*, 116, 141-150.
- [35] UiChulain, C., Sikora, K., Harte, A. (2016), 'Influence of connection systems on the serviceability response of CLT timber flooring', *Proceedings of World Conference on Timber Engineering (WCTE16)*, Vienna, Austria.

The Evolving Role of Materials in Infrastructure Systems

J. David Frost

School of Civil and Environmental Engineering, Georgia Institute of Technology, Atlanta, GA 30332, USA
email: david.frost@ce.gatech.edu

ABSTRACT: Materials have historically been one of the fundamental yet perhaps less appreciated building blocks of infrastructure systems. As increasing engineering challenges are placed on our systems due to the need to construct infrastructure in more challenging environments, the need to achieve higher performance standards due to the desire to increase maintenance intervals, the need to develop and adopt more sustainable materials and systems and the need to be prepared to meet unprecedented demands as a result of the need for increased resilience in the face of climate change and other unprecedented natural phenomena, materials are now at the core of some of the most innovative science and engineering based developments. This paper will illustrate through a few examples how approaches such as bio-inspired and multi-functional materials are emerging to play central roles in the next generation of infrastructure materials and systems. Specifically, the paper begins by presenting an example of the evolution, within human time-scale, of multi-functional geosynthetic materials. The paper shows how insights gleaned through the use of experimental and numerical micro-scale evaluation tools, in conjunction with new techniques such as 3-D printing, provide a robust basis for performance evaluation and prediction. The importance of innovating at field-scale is illustrated through the concept of inverted base pavements where again, new techniques and tools facilitate, unprecedented insights into system level performance. Finally, the paper concludes by showing how new materials and system innovations can be inspired by nature. The opportunity for humans to learn from and even mimic in many cases, the approach developed and evolved by nature over hundreds of thousands or even millions of years is potentially transformational.

KEY WORDS: Materials; Infrastructure; Sustainable; Resilient; Bio-inspiration; Bio-mimicry.

1 INTRODUCTION

Materials are a fundamental building block of all infrastructure systems. A common and long accepted base criteria used to assess both the material and system performance is to ensure that capacity exceeds demand throughout their life and this is at the core of all planning, design, construction and maintenance activities.

Notwithstanding their initial state, all infrastructure systems and the materials they are constructed from are subject to a set of evolving conditions that alter the initial capacity-demand relationship including reduction of operating capacity due to environmental induced deterioration, fatigue under repeated demand cycles, and the need to construct systems at less favourable sites than historically done, amongst others. At the same time, the initial capacity-demand relationship can also be affected by the demand being increased by the evolution of the transportation system components as well as natural and human-made hazards.

Apart from the engineering considerations noted above, an emerging set of constraints, many motivated by socio-economic and policy issues such as climate change, increased resilience expectations and the desire for sustainable solutions is further limiting our ability to identify efficient, cost-effective solutions. This has served as a catalyst for engineers to identify innovative solutions including smart, multi-functional, and bio-inspired materials amongst others.

This paper uses a number of examples at different temporal and spatial scales to illustrate how engineers have responded and can continue to do so to this ever-evolving societal

expectation to design and adopt new materials and systems that can meet the need to “do more with less” without compromising the future. The paper begins by presenting an example of the evolution of multi-functional geosynthetic materials. It continues by showing how insights gleaned through the use of micro-scale experimental and numerical evaluation tools provide a robust basis for performance evaluation and prediction. The importance of innovating at field-scale and not being constrained by historical precedent is illustrated through the concept of inverted base pavements. Finally, the paper concludes by showing how new materials and system innovations can be inspired by nature.

2 INNOVATIONS IN MATERIALS AND SYSTEMS

2.1 *Emergence of multi-functional materials*

Historically, when humans are faced with a challenge, they have typically developed a solution to address that issue and in many cases, have even used available materials and systems as part of that solution. Have you ever questioned why steel H-piles are sometimes used by geotechnical engineers for deep foundations? With few exceptions, it is not because this is an optimum shape for that purpose – it is merely due to the fact that this was a highly functional section developed and used by structural engineers and since it already existed, geotechnical engineers merely adopted it for their purposes, despite it not being optimum. Subsequent advances in pile foundation design as a function of subsurface stratigraphy and capacity issues as well as structural demand

led to the development of driven pipe piles and auger-cast concrete piles, amongst others. Accordingly, the section shape and material were evolving to yield a more optimum solution although it is noted that their role remained focused as a single function element – structural capacity.

While inclusions of different types have been used in soils for several thousands of years (Figure 1), the modern era of the field of geosynthetics has emerged and moved to a central role in infrastructure engineering over the past half century.



Figure 1. Ancient reinforced soil wall in China.

Initial focus of man-made inclusions in the modern era was to provide solutions for filtration and reinforcement. Products were developed to address specific functions including separation, reinforcement, filtration, drainage and containment. As new opportunities to develop products for these various challenges emerged, categories of products such as geotextiles, geogrids, geomembranes, geonets, geosynthetic clay liners, geofoams, geocells and geocomposites were developed. The latter represented a move towards developing products which could satisfy two or more functions noted above and heralded a maturing of the field from one-focused on single function to multi-function products. Today, this field continues to evolve with products such as a multi-functional wicking geotextiles (Figure 2) that can perform separation, filtration, drainage and reinforcement functions.

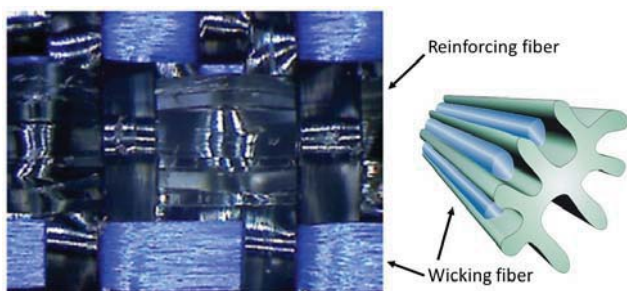


Figure 2. Multi-functional wicking geotextile.

2.2 Micro-scale material insights

The study of civil engineering materials has been predominantly conducted at the coupon or element scale. For example, understanding of the strength, deformation and hydraulic conductivity behaviour of soils has largely been based on laboratory tests performed on specimens (coupons) where the load, deformation and other properties are measured at the boundaries. Alternatively characterization and performance is evaluated using full scale field tests so that the influence of defects and other inhomogeneity's can be

correctly reflected in the interpreted behaviour. Similar perspectives can be concluded with respect to the simulation of material and system response using continuum based modelling approaches. All these coupon and full-scale approaches have served very well and allowed for rich insight into material behaviour to be gained.

At the same time, and catalysed in many cases by needs and developments in other fields, there has been an explosion in the availability of tools and techniques for studying material behaviour at micro and smaller scales and these are proving equally valuable in the study of civil infrastructure materials, particularly as the importance of multi-scale phenomena are being increasingly appreciated.

An example of this approach is illustrated for the interaction of aggregate particles and geogrids for pavement applications and the manner in which various newer experimental and numerical tools are being utilized. It is noted that this approach is not being proposed as a replacement for coupon and full-scale based approaches but as a complement to these proven methods that can provide insights at a different scale. Two different aggregate-geogrid combinations are shown in Figure 3. The image on the left shows an aggregate with nominal size 10% of the geogrid rib length while that on the right has nominal size 80% of the geogrid rib length. Of interest is what size aggregate within this range can yield optimal interaction and thus performance with the geogrid.

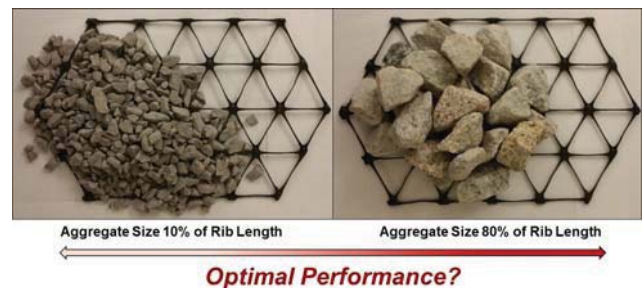


Figure 3. Different aggregate-geogrid combinations.

To evaluate this issue, a research study involving micro-scale tools and techniques is being conducted as follows:

- Micro-scale tensile testing of geogrid ribs is used to determine the geogrid tensile strength properties.
- The geogrid ribs are modelled using a Discrete Element Method (DEM) code (PFC3D) with particle clumps (Figure 4).

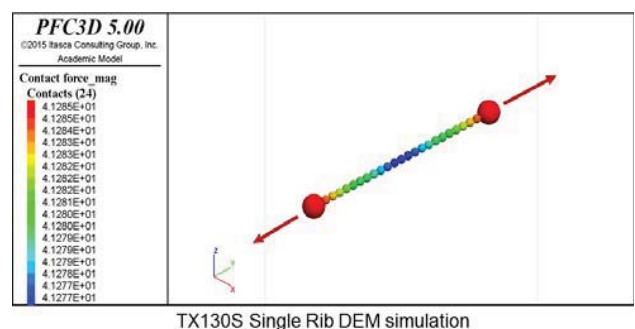


Figure 4. Geogrid numerical model calibration.

- Particles with pre-determined angularity indices are generated using a 3D printer (Figure 5) and then verified using an optical aggregate image analyser.

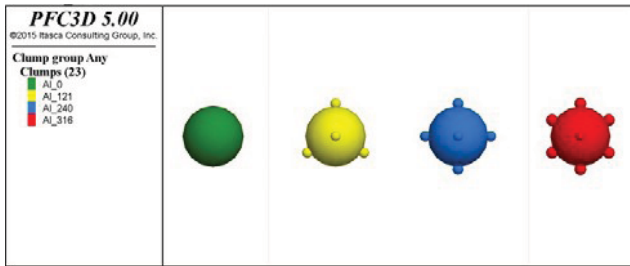


Figure 5. Images of 3D printed synthetic particles.

- Binary mixtures of 3D particles were generated for DEM simulations which included a subgrade layer, aggregate layers with a geogrid embedded in middle and a loading particle clump (Figure 6).

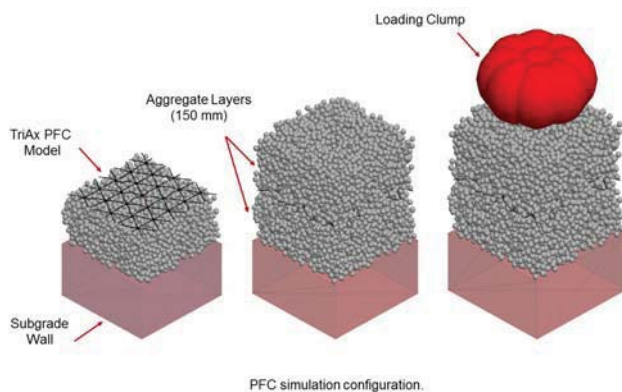


Figure 6. DEM model with subgrade, aggregate and geogrid.

Preliminary results from this study are enabling the relative contributions of particle interlocking, as measured by particle rotations and displacements in the simulations, to be determined. Numerical models with and without geogrids present show the beneficial contributions of this man-made material on the overall system behaviour [1].

2.3 Innovative pavement structures

The majority of paved roads worldwide are either built as either a flexible pavement (incorporate an unbound graded aggregate base, an asphalt base and an asphalt concrete surface layer) or a rigid pavement (incorporate an unbound graded aggregate base and a Portland cement concrete surface layer). While significant work has been achieved in studying the behaviour of the various layers and materials in these two different pavement systems, the underlying sequencing of layers has remained essentially unchanged and thus opportunities for further improvements in performance are diminishing. At the same time, desires for improved performance and/or longer intervals between maintenance, increased resilience in the presence of changing climate patterns and associated extreme events and more sustainable environmentally sensitive solutions along with depleted

funding for both new construction and maintenance are catalysing the need for new innovative designs that can lead to optimal use of materials. In an effort to address this, alternative pavement structures are thus becoming of interest. One such system is called an inverted base pavement (IBP). South Africa has developed and experience with using this approach for half a century. Despite this, limited usage has been made of this promising approach elsewhere in the world. At the core of this technique are two significant departures from conventional pavement designs and approaches.

Unlike conventional pavement structures, the layer stiffness profile does not decrease with depth. In contrast, a cement treated base (CTB) layer is placed above the compacted subgrade. The CTB is overlain by an unbound aggregate base layer which in turn is overlain by a relatively thin asphalt concrete layer. A comparison of a conventional flexible asphalt concrete pavement section and an inverted base pavement section is shown in Figure 7 [2].

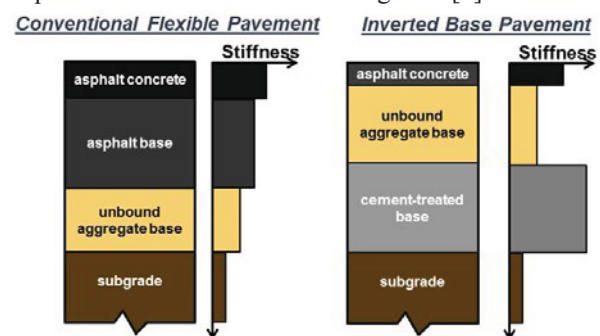


Figure 7. Comparison of stiffness profile for pavements.

The placement and densification of the unbound aggregate base layer in an IBP incorporates a technique called “slushing”. In contrast to conventional approaches for densification of aggregate layers which involve static or vibratory compaction of the placed material, the South African slushing technique involves sequences of over-watering, low impact smooth drum and rubber-tired compaction to increase the packing density in the unbound aggregate layer by removal of excess fines to achieve an optimum fine to coarse aggregate matrix. Water migrating to the surface by capillary action under the sequential compaction process carries excess fines to the surface where they are removed (Figure 8).

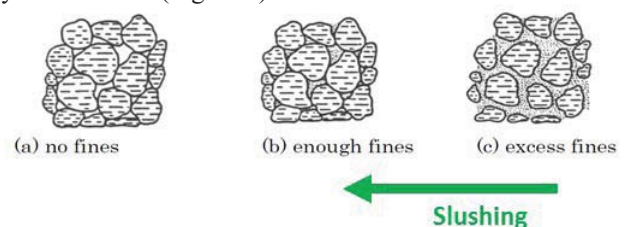


Figure 8. Slushing technique to remove excess fines.

A number of test sections have been constructed in the US in the past 15 years that are allowing for the performance of conventional and IBP's. Results of both falling weight deflectometer and pavement surface distress measurements made using a mobile imaging system (Figure 9) all confirm

superior long-term performance for inverted pavement sections.



Figure 9. Mobile pavement imaging system.

A comparison of the performance of conventional as well as two implementations of the IBP method are shown in Figure 10. The South African IBP section was constructed using the slushing compaction technique as described above while the Georgia IBP section used a modified version. Based on the measurements, it can be seen that both IBP techniques performed comparably and more importantly far exceeded the performance of the conventional section.

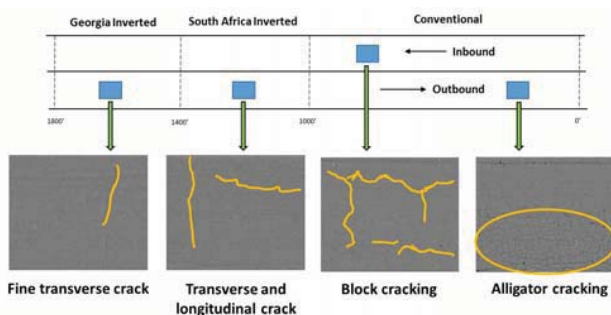


Figure 10. Performance comparison of pavement distress.

Based on the field performance measurements and numerical simulations of both conventional and IBP, it can be seen that the presence of the underlying CTB plays an important role in providing a rigid layer against which the compaction of the unbound aggregate base layer is achieved. Further, it appears that the slushing technique plays an important role in minimizing, if not fully eliminating, void space in the unbound aggregate layer so that pavement distress in the form of surface cracking and rutting is inhibited.

2.4 Bio-inspired innovations

With no more than a couple of thousand years of experience, humans have developed innovative techniques to leverage the subsurface for a variety of beneficial functions. In contrast, nature has had the benefit of several billion years to initially design and subsequently evolve the manner in which flora and fauna practice subsurface engineering. This paper presents

two examples of how nature has evolved its solutions in contrast to what humans have done and identifies enhancements that humans could better exploit, in the future, through a deliberate mimicking of what nature has done. In particular, a comparison of selected aspects of ant-soil interaction and root-soil interaction are used to illustrate where significant potential exists in the emerging field of bio-geotechnics. The paper describes some salient characteristics of the framework by which nature designs its technology, and in turn, how this approach can be used to augment how humans conceive and design new materials and processes.

As a measure of the interest in and potential for this approach, the US National Science Foundation funded four US universities (Arizona State University, Georgia Institute of Technology, New Mexico State University and the University of California Davis) through an \$18.5M cooperative agreement to establish the Center for Bio-mediated and Bio-inspired Geotechnics (CBBG) www.biogeotechnics.org to develop bio-geotechnical engineering processes and solutions inspired by nature to transform the design, construction, operation and maintenance of resilient and sustainable civil infrastructure and resource development systems.

While CBBG is the first civil infrastructure focused initiative of this scale, bio-inspiration and bio-mimicry have periodically emerged as sources of solutions to human challenges, particularly in the past few decades. Well known examples of bio-mimicry include “Velcro” or hook and loop which was inspired by how plant burrs attached to animal hair, the shape of the leading engines of high-speed “Bullet” trains which were inspired by the shape of the Kingfisher’s beak and the directional adhesive on the feet of Gecko’s which enables robots such as the “Stickybot” to climb vertical smooth surfaces. A comparison of the interface between a plant burr and a textile and the hook and loop structure of “Velcro” is shown in Figure 11.

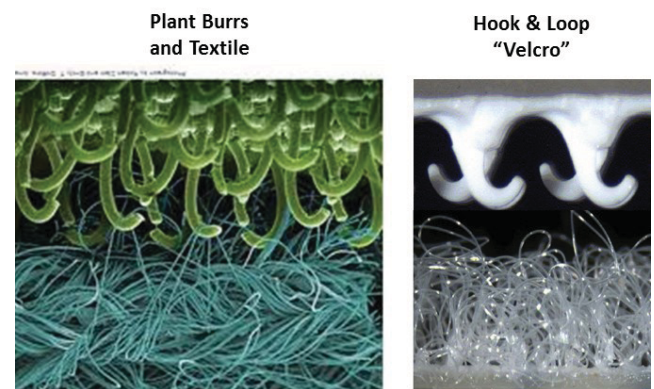


Figure 11. Comparison of plant burrs and “Velcro”.

Ants and soil mechanics: It has been estimated that ants use less than 0.1% of the energy that the most advanced human tunnelling machines do to excavate the same volume of soil. It is believed that ants are able to do so since they perform their tunnelling activities using a variety of approaches which seem to minimize the amount of energy expended at each step including tunnelling around obstacles, not removing particles that are deemed critical to supporting the surrounding soil particles (particles that are part of primary force chains) and creating clumps of several smaller particles as appropriate

before removing them from the tunnel. These insights have been gleaned from both observing their behaviour while tunnelling as well as studying the characteristics of castings of the ant hill structures they create. An image with a “harvester-ant” nest casting is shown in Figure 12.

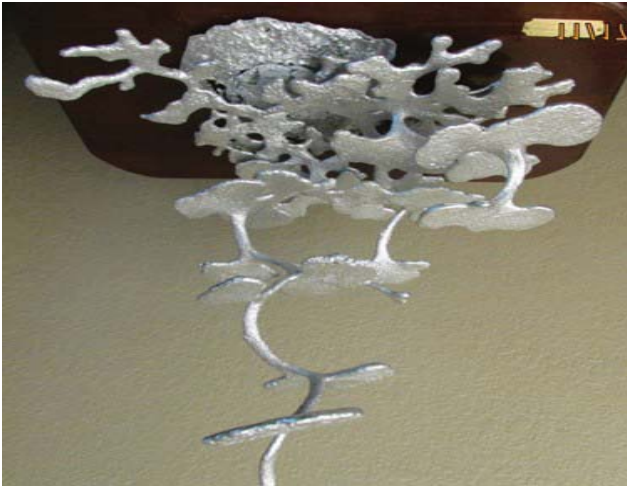


Figure 12. Harvester ant nest casting after removal of soil.

On-going studies are investigating the topology of the structure using DEM simulations and in particular, the geometrical configuration of the larger open structures which appear to be spaced apart by equal distances. Initial indications from the DEM simulations are that the presence of multiple cavities reduces the size of force chains in the vicinity of the openings and that more stable structures exist when multiple large cavities are present. A comparison of force chain plots for a single versus double cavity is shown in Figure 13 [3].

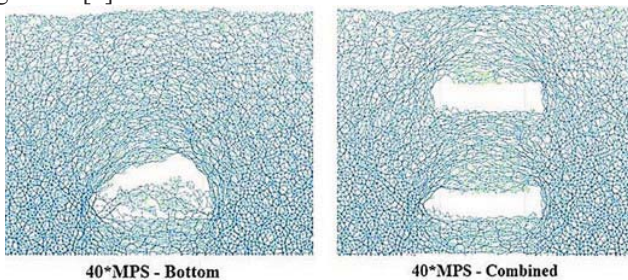


Figure 13. Force chains for single and double cavities.

Roots and soil mechanics: Plant roots accomplish multiple functions including provision of water (hydraulic function) and nutrients (chemical function) as well as providing anchorage (uplift and download) against external forces (wind). Other functions including regulating above ground-below ground heat balance under temperature extremes may also be an important function (thermal). As such, roots may be one of the most evolved multi-function systems in that all these functions are nominally accommodated in a single root system, albeit with different portions of the root system contributing to different degrees to these various functions. What is also noteworthy is that in many cases, the extent of the subsurface root system exceeds the size of the above ground tree branch system as can be seen in Figure 14. This is in contrast to many human constructed foundation systems

where the extent of the foundation is often limited to only a portion of the footprint of the superstructure.



Figure 14. Comparison of tree above and below ground.

To better understand the relationship between tree roots and the structural capacity of the roots as a foundation system, on-going studies are undertaking both experimental and numerical simulations using root analogues. The analogues being used included un-branched and branched wire cables that incorporate many of the characteristics of tap roots as well as 3D printed roots that incorporate many of the characteristics of fibrous roots. A selection of root analogues are shown in Figure 15.



Figure 15. Selection of tap and fibrous root analogues.

Results from experimental pull-out tests conducted on un-branched and branched tap roots with and without friction (achieved by coating outside of root fibres with sand) show significant differences in terms of both peak and large displacement root resistance. Typical results are shown in Figure 16 and indicate that branched tap roots reach a larger peak than un-branched ones and also exhibit significantly less post-peak reduction in resistance. Further, roots with textured surfaces (higher friction) typically indicate higher pull-out resistance compared to their smooth-surfaced (lower friction) counterpart as seen in Figure 16.

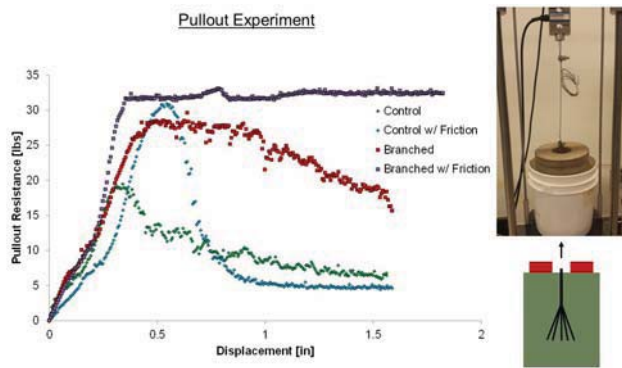


Figure 16. Pull-out resistance tests on tap root analogues.

Results from DEM numerical simulations of compression loading of fibrous root analogues further demonstrated differences between typical human-constructed and nature-constructed foundation systems. Figure 17 shows the force versus displacement response for different root analogues (straight, zig-zag, 15 degree splay and 30 degree splay). It can be seen that the common human implemented approach of using a straight shaft pile yields the lowest resistance while the large splay pile yields the largest resistance.

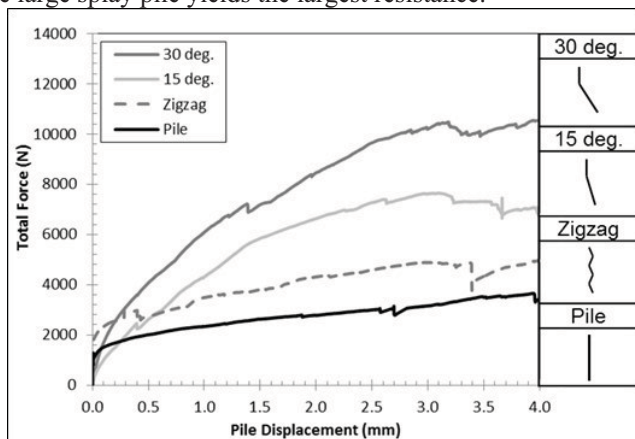


Figure 17. Compression of different root analogues.

This increase in compression resistance can be understood based on a review of the force chains associated with each simulation. As shown in Figure 18, as the pile configuration changes from straight shaft to 30 degree splay, the volume of soil that is subjected to compressive forces and thus larger force chains increases [3].

3 CONCLUSIONS

This paper has used a number of examples from recent and on-going research activities to illustrate both the evolving role of materials as a core driver for innovation in infrastructure systems as well as a key response mechanism to emerging demands in the face of climate change and other unprecedented natural phenomena.

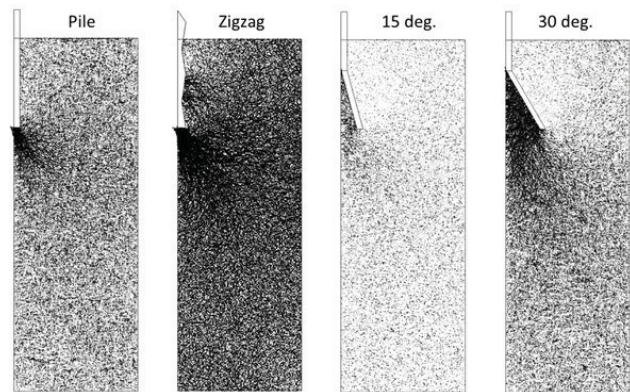


Figure 18. Force chains for different pile configurations.

The primary conclusions of the paper are:

- Designing new multi-functional materials will be critical to future performance enhancements.
- Study of materials at micro and smaller scales will be critical to truly understanding multi-scale response of infrastructure materials and systems.
- Pursuing innovative systems that yield transformational and not just incremental changes will be critical.
- Optimized designs can result from a willingness to relinquish vestiges from the past.
- Nature can be a great source of inspiration for next-generation materials and systems.

ACKNOWLEDGMENTS

The experimental and numerical research and associated field studies presented in this paper reflect the contributions of many individuals including Yi-Chang Tsai, Efthymios Papadopoulos, Seth Mallett, Andres Peralta, Alejandro Martinez and Mahdi Roozbahani. Their contributions are all gratefully acknowledged. The ongoing study on aggregate-geogrid interactions is supported in part by Tensar International. The ongoing study on inverted base pavements is supported by the Georgia Department of Transportation under Research Project RP 15-10. The bio-inspired studies presented in this paper are being undertaken by researchers in the NSF funded ERC on Bio-mediated and Bio-inspired Geotechnics (CBBG). The NSF support through PTE Federal Award No. EEC-1449501 is acknowledged.

REFERENCES

- [1] Peralta, A., Frost, J.D., Wayne, M., and Kwon, J., (2016), "Aggregate Morphology Considerations in Geogrid Stabilized Roadway Sub-Bases", *Proceedings of Geotechnical and Structural Engineering Congress*, Phoenix.
- [2] Papadopoulos, E. (2014). "Performance of Unbound Aggregate Bases and Implications for Inverted Base Pavements." *Ph.D thesis*, Georgia Institute of Technology, Atlanta.
- [3] Frost, J.D., Martinez, A., Mallett, S.D., Roozbahani, M.M., and DeJong, J.T., (2017), "The Intersection of Modern Soil mechanics with Ants and Roots", in review for possible publication in *Proceedings of ASCE Geo-Institute Geo-Frontiers Conference*, Orlando.

Detection of Train Passages during Forced Vibration Testing of Bridge Structure using Energy Harvesting Technology

Paul Cahill¹, Raid Karoumi², Alan Mathewson³, Andreas Andersson², Vikram Pakrashi⁴

¹ MaREI, Environmental Research Institute, University College Cork, Ireland and Dynamical Systems & Risk Laboratory, Civil, Structural and Environmental Engineering, School of Engineering, University College Cork, College Road, Cork, Ireland

² Division of Structural Engineering and Bridges, KTH Royal Institute of Technology, SE-100 44, Stockholm, Sweden

³ Heterogeneous Systems Integration Group, Microsystems Group, Tyndall National Institute, University College Cork, Cork, Ireland

⁴ Civil, Structural & Environmental Engineering, School of Engineering, University College Cork, Ireland and Dynamical Systems & Risk Laboratory, Civil, Structural and Environmental Engineering, School of Engineering, University College Cork, College Road, Cork, Ireland

Email: p.a.cahill@umail.ucc.ie, raid.karoumi@byv.kth, alan.mathewson@tyndall.ie, v.pakrashi@ucc.ie

ABSTRACT: Through integration with civil infrastructure, smart systems have the potential to provide real time health monitoring of the host structure. Such systems can be designed so as to be power independent whilst monitoring the structure using energy harvesting technology. The use of piezoelectric energy harvesters is particularly attractive for such applications, due to the dynamics of the host structure being reflected in the voltage and power outputs of such harvesters. It is therefore possible to identify not only the nature of the host, but also the loading to which it is being subjected through the output of the energy harvester. This paper investigates the detection of train passages over a host bridge structure during full scale forced vibration testing using piezoelectric energy harvesters. A shaker unit is utilised to subject the bridge to controlled forced vibrations and the deployment of an energy harvesting device to the bridge for such testing is completed. Its performance during the dynamic testing is analysed and the time domain power output from the harvester during testing is provided, with host characteristics identified. Incident based events were identified from the energy output and corresponds with train passages which occurred during the forced vibration testing. The potential use of energy harvesters to identify event based incidents is discussed and future applications identified. This paper further establishes the potential applications of energy harvesting technology with civil infrastructure through full scale experimental validation.

KEY WORDS: Energy harvesting; Piezoelectric; Smart sensors; Bridge dynamics; Train-Bridge interaction.

1 INTRODUCTION

The integration of smart technology with civil infrastructure is a topic which is receiving increased attention in recent years. Such technology has resulted in the creation of Wireless Sensor Networks (WSN's), through which key infrastructure can be monitored remotely [1]. WSN's have the capacity to monitor the full dynamic response of a structure and obtain information such as strain and acceleration responses during operational conditions [2]. It is therefore possible to remotely monitor critical infrastructure, with applications including bridges, underground railways and tower structures being successfully integrated with WSN's [3]. A drawback with such networks currently is, however, the reliance on external, finite power supplies such as batteries, which limits the lifetime of the network. Should WSN's be made power independent, achievable through the integration of energy harvesting technology, they have the potential to monitor a structure over its entire lifespan [4].

There are many types of energy harvesting technologies which have the potential to power small scale electronics, including vibration, thermal, solar and micro fluid flow [5]. Of these, for applications relating to the monitoring of the

dynamic response of civil infrastructure, vibration based energy harvesting is of particular interest and consists of three primary transduction methods, electromagnetic, electrostatic and piezoelectric [6]. Piezoelectric energy harvesting utilises materials which convert strain energy into electrical energy through the piezoelectric effect [7].

Research into the integration of piezoelectric energy harvesting technology with civil infrastructure has received some attention [8,9], however its full potential has yet to be realised. The problem of energy harvesting from bridge infrastructure has recently been formulated [10], with the use of different device configurations, namely a cantilever device and a surface-bonded patch device, being proposed [11]. Studies into the use of train loadings as a means of vibration excitation for both types of piezoelectric energy harvesters have also been conducted [12,13]. The validation of such harvesters with full scale infrastructure has not yet been fully achieved, with initial studies into the integration of the devices with a bridge structure being conducted [14]. Applications resulting from the energy harvested from structures have received limited attention, with the potential for damage detection [15] and weight-in-motion [16] being proposed. The use of piezoelectric energy harvesters with full

scale infrastructure undergoing forced vibration testing has not been studied to date, in part due to the difficulties associated with such testing.

The dynamic testing of bridge infrastructure provides major benefits for fields relating to bridge engineering. Such tests are important to determine key parameters of a bridge structure to be determined, including mode-shapes and damping ratios [17,18]. By experimentally obtaining such parameters, structural analysis of the bridge in question may be performed and allows for, amongst others applications, the [19]

- Enhancement of a database on the dynamical response of similar bridge structures, improving the prediction of the behaviour of new, similar structures.
- Ascertaining the condition of the bridge through the determining of critical parameters such as mass stiffness and damping.
- Theoretical modelling validation and updating.

The use of vehicle induced vibrations for structural analysis of bridge structures has been studied extensively, with the dynamic response of the bridge due to moving traffic loadings being monitored [20]. While such assessments are beneficial, issues do arise due to the presence of additional mass on the bridge structure in the form of the vehicle, which can influence the dynamical response of the bridge [21]. The use of ambient vibrations can resolve such issues [22], but it is through the use of external excitation devices that the most accurate experimental results can be ascertained [23].

Designs pertaining to external excitations devices utilised for the dynamical assessment of bridge infrastructure include vertical excitation using a dropped mass [24], an eccentric mass shaker for both horizontal [25] and vertical [26] excitation and a hydraulic shaker [27]. Such designs typically require the bridge to be closed to traffic for the duration of the testing process. It has therefore not been possible to date to detect both forced vibration loadings and traffic loadings simultaneously.

This paper investigates the detection of train passages using piezoelectric energy harvester integrated with a bridge structure undergoing dynamic testing. The theory of a cantilever based energy harvesting device is outlined, as is the design, construction and calibration of an experimental prototype. The application of the energy harvester to the host bridge structure is subsequently discussed and details of the excitation source for forced vibration testing provided. The results of the energy harvesters output during testing and the ability of the energy harvester to detect train events is determined. This paper illustrates further the potential applications that arise from the integration of smart technology with civil infrastructure.

2 PIEZOELECTRIC ENERGY HARVESTING DEVICE

2.1 Piezoelectric Energy Harvesting

When integrated with a host structure, the acceleration response of the host provides the base excitation for the piezoelectric device and the electromechanical behaviour of

the cantilever energy harvester is expressed by the coupled linear equations [10]

$$m_c \ddot{z} + c_c \dot{z} + k_c z - \theta V = -m_c \ddot{y}_b \quad (1)$$

$$\theta \dot{z} + C_p \dot{V} + \frac{1}{R_l} V = 0 \quad (2)$$

Where m_c , c_c and k_c are the mass, damping and stiffness of the energy harvester respectively and z is the relative displacement of m_c , with over-dots denoting differentiation with respect to time. The base acceleration of the host is given by y_b and θ is the electromechanical coupling coefficient, V is the voltage, with C_p and R_l being the capacitance and resistance respectively. For this study, the base acceleration is provided by the host bridge which is undergoing two loading mechanisms. The first, and primary, loading mechanism is a sinusoidal loading applied at constant magnitude with varying frequency. The second loading is due to the passage of a train over the bridge. The response of the energy harvester through the analysis of the voltage output due to such loadings is herein determined experimentally to establish energy harvesting applications arising from a structure undergoing multiple loadings.

2.2 Design and Construction of Piezoelectric Energy Harvesting Device

When considering a bridge whose natural frequency is unknown for the deployment of the energy harvester, it is not possible to create an optimised solution. Such a solution would require that its fundamental frequency match that of the host bridge structure. As a result, for this study a non-optimised device is considered. The design of the harvester was completed with a natural frequency of 15Hz being considered. As such the dimensions of the cantilever device, including its length, L_1 , width, w_1 , and thickness, t , along with the tip mass, m_1 , were determined so as to achieve this frequency. The cantilever was designed so as to be embedded within a rigid base, of length width and height L_B , w_B and h_B respectively, which is to be attached to the host bridge structure (Figure 1). Such a base is required to be of sufficient rigidity so as to prevent unwanted displacements and rotations at the base of the cantilever device. The active piezoelectric harvesting material is bonded onto a surface of the cantilever, with the cantilever substrate providing the necessary vibrations for energy harvesting.

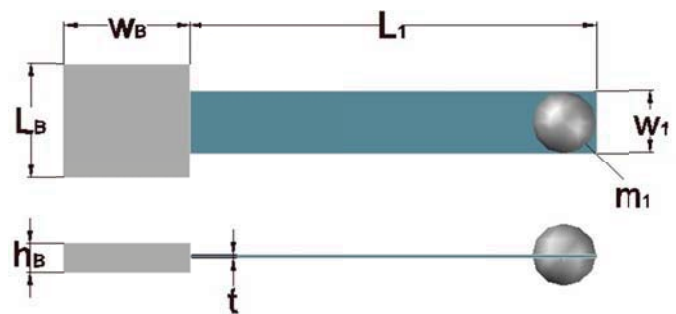


Figure 1. Illustration of cantilever energy harvester with embedment base

Following from the initial design of the energy harvester, the parameters of the experimental energy harvester were decided upon, with an aluminium substrate being chosen of thickness $0.0012m$, length $0.1775m$ and width of $0.025m$. Aluminium was chosen in part due to it being an electrical insulator and will therefore not influence the generated electrical energy. Onto the free end of the cantilever, a tip mass of $0.02kg$ was attached. The active piezoelectric material, in this case PolyVinylidene Fluoride (PVDF), was bonded to the upper surface of the cantilever, resulting in the completed experimental cantilever energy harvester (Figure 2). While other piezoelectric materials, such as Lead Zirconate Titanate (PZT), offer more efficient energy harvesting potential, the polymer nature of PVDF results in a material which has a high mechanical strength while retaining excellent flexibility resulting in a material which is adaptable and easy to work with experimentally [28]. Upon the creation of the harvesting device, experimental calibration was subsequently performed.



Figure 2. Experimental cantilever energy harvester with aluminium substrate and bonded PVDF energy harvester

2.3 Calibration of Energy Harvesting Device

For the experimental calibration of the energy harvester, the device was mounted onto an LDS Permanent Magnet Shaker (Figure 3), to which the input signal was supplied by a Diligent Inc. Analog Discovery waveform generator. Adjacent to the mounted energy harvester was placed a Microstrain G-Link LXRS wireless triaxial accelerometer, so as to provide a control for the applied vibration from the permanent magnet shaker.



Figure 3. Cantilever energy harvester attached to permanent magnet shaker for provision of controlled base excitation

For the experimental calibration of the energy harvester, two different types of excitation were applied to the harvester. The first consists of an impulse load, to determine the natural frequency of the device experimentally. The second type of loading involves the application of a sweep sine load of constant amplitude and increasing frequency.

For the pulse load of $1G$ in magnitude, the voltage response of the device was measured under open circuit conditions (Figure 4(a)). From this measured voltage response, the natural frequency of the device was obtained through a fast Fourier transform (FFT). It was found that the experimental natural frequency of the device was $15.57Hz$ (Figure 4(b)), in contrast to a theoretical calculation of $15Hz$. Following from the impulse response, the swept sine loading was subsequently applied to the energy harvesting device. A frequency range of between $1Hz$ and $40Hz$ was applied over a 120 second time period. While the ideal loading signal for this function would be a sine wave of varying frequency, this proved not to be possible using the Analog Discovery waveform generator. Instead, sinusoidal impulse loads were applied at increasing frequencies and a constant amplitude. It was for this reason

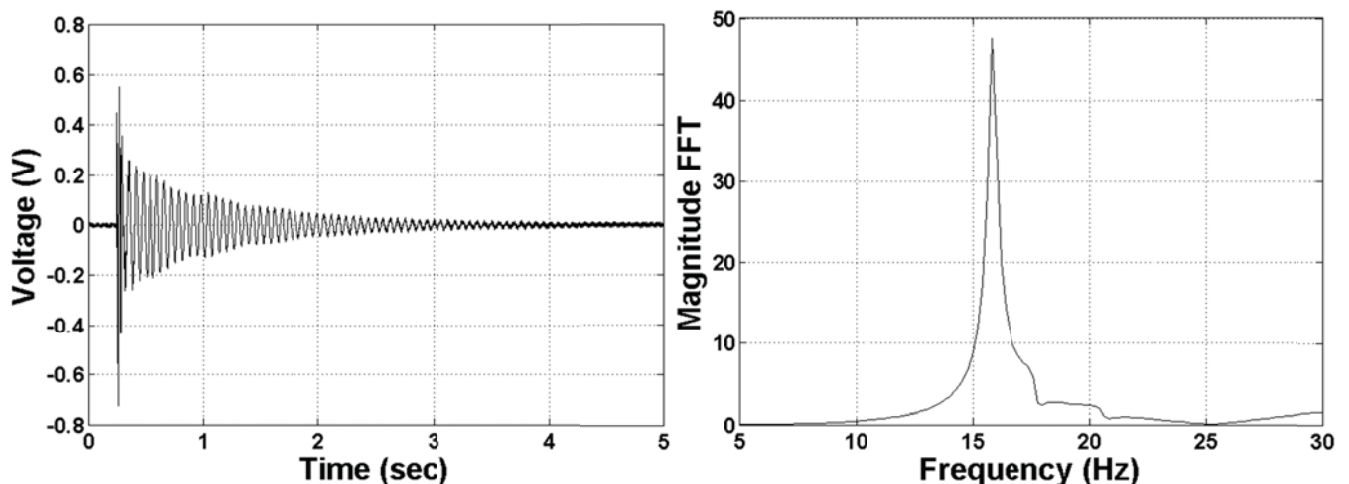


Figure 4. (a) Voltage response of energy harvesting device due to impulse load of magnitude $1G$ (b) Resultant FFT

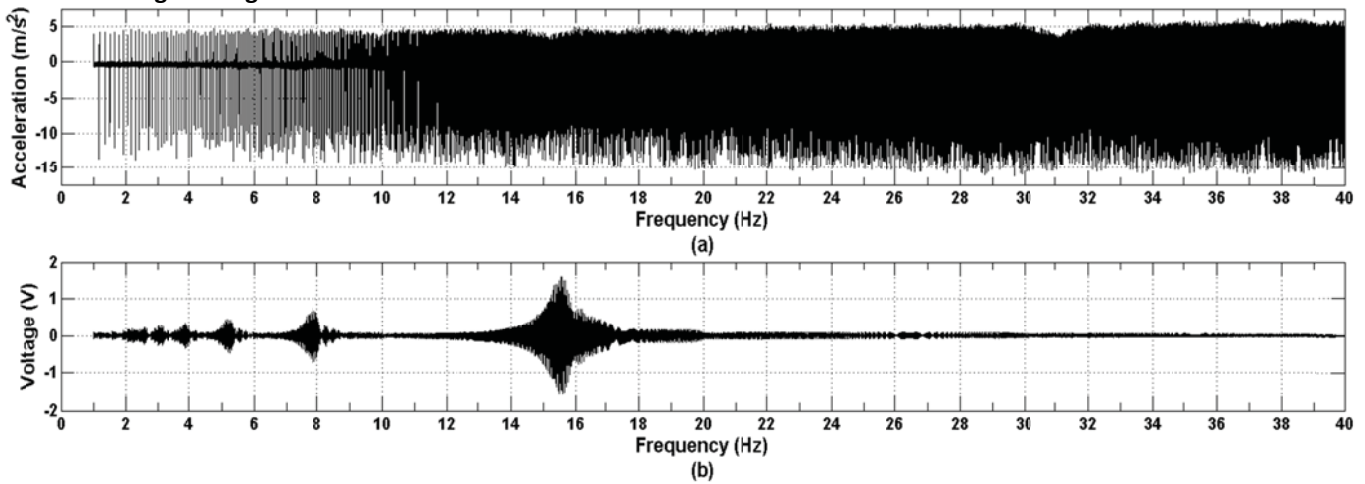


Figure 5. Swept sine loading of energy harvesting device including (a) Acceleration response with respect to loading frequency and (b) Measured voltage response of the energy harvesting device

that a short time period of 120 seconds was considered. Over a longer time period such impulses can be considered independent instead of being a continuous waveform, as achieved by the short time period chosen for this study. The magnitude of the loading was kept constant, with the wireless accelerometer being utilised for control, and the output voltage of the device was measured (Figure 5). The initial peak to peak loading magnitude at a frequency of 1Hz was measured at 18.7m/s^2 with a final loading magnitude of 21.2m/s^2 (Figure 5(a)). As can be seen in the voltage response of the energy harvesting device, such a drift has negligible impact on the energy harvesting output (Figure 5(b)). It is instead loading at the natural frequency of the device which has the most significant impact on the energy harvesting potential of the device, with a peak voltage of 1.59V being obtained at a loading frequency of 15.57Hz . Following the laboratory based calibrations of the energy harvesting device, the device was subsequently deployed with a bridge structure which was undergoing forced vibration testing while remaining open to traffic, presented in the following section.

3 DEPLOYMENT OF ENERGY HARVESTING ON BRIDGE STRUCTURE

3.1 Description of Host Bridge Structure

The bridge chosen for the deployment of the energy harvesters during forced vibrations was the Pershagen Bridge, Sweden. The bridge is a three span, 46.6m long, reinforced concrete slab bridge which carries two rail tracks. The central span is 18.8m in length and the two side spans both have lengths of 11.1m . An overhang exists between the side-spans and the abutments, which rest on backfill embankments. The structure is 11.9m width out to out and carries a 0.6m layer of ballast. Due to the existence of the overhangs and the backfill embankments, the structure is believed to exhibit some minor cantilever-like behaviour whilst undergoing the dynamic loadings from the train passages. It is therefore difficult to achieve a precise theoretical calculation of the natural frequencies and mode shapes, without key parameters being obtained during dynamic testing of the structure.

3.2 Assessment of Host Bridge under External Excitation

For the dynamic testing of the Pershagen Bridge, a hydraulic shaker designed by the Division of Structural Engineering and

Bridges, KTH Royal Institute of Technology Sweden was utilized. It consisted of a hydraulic cylinder with an attached strut connecting it to the bridge structure, between which was placed a load cell. This allowed for the force, frequency and displacement of the applied load to be constantly monitored and maintained [29]. The design of the shaker unit is such that it is positioned under the bridge structure and provides vertical excitation to the bridge deck while the bridge is operational. The train tracks carried by the bridge can therefore remain open during the dynamic testing and trains passages across the bridge unaffected. With the deployment of the energy harvesting device onto the bridge structure, it is therefore the primary aim of this paper to investigate the potential of using the devices to detect train passages whilst the dynamic testing is ongoing.

For the deployment of the energy harvesting device to the bridge structure, two primary considerations were taken into place. First, the device was to be mounted adjacent to an accelerometer, which would provide a base acceleration profile to which the device was subjected to during the testing. Secondly, the distance of the device from the location of the exciter was also considered, with the device being positioned adjacent to the exciter's location to allow for maximum response during the dynamic testing.

3.3 Details of Dynamic Load Testing of Pershagen Bridge

The device was affixed at the chosen location on the top edge beam of the bridge, with the cantilever overhanging the bridge to prevent the device coming into contact with the bridge deck or other fixtures. The device was subsequently connected to a data acquisition unit and the response monitored at 100Hz . The dynamic assessment of the structure was achieved with load amplitude of 5kN between a frequency range of 3 to 50Hz being applied by the shaker unit. An initial preload of 15kN was applied so as to ensure that connection between the bridge structure and the shaker was maintained at all times. The loading was applied at a rate of 0.05Hz per second. The response of the accelerometer at the location of deployment was monitored, as was the voltage response of the device. From the responses of both, the existence of events due to the passage of trains were investigated, and the ability of the energy harvesting device to detect such train passages was determined.

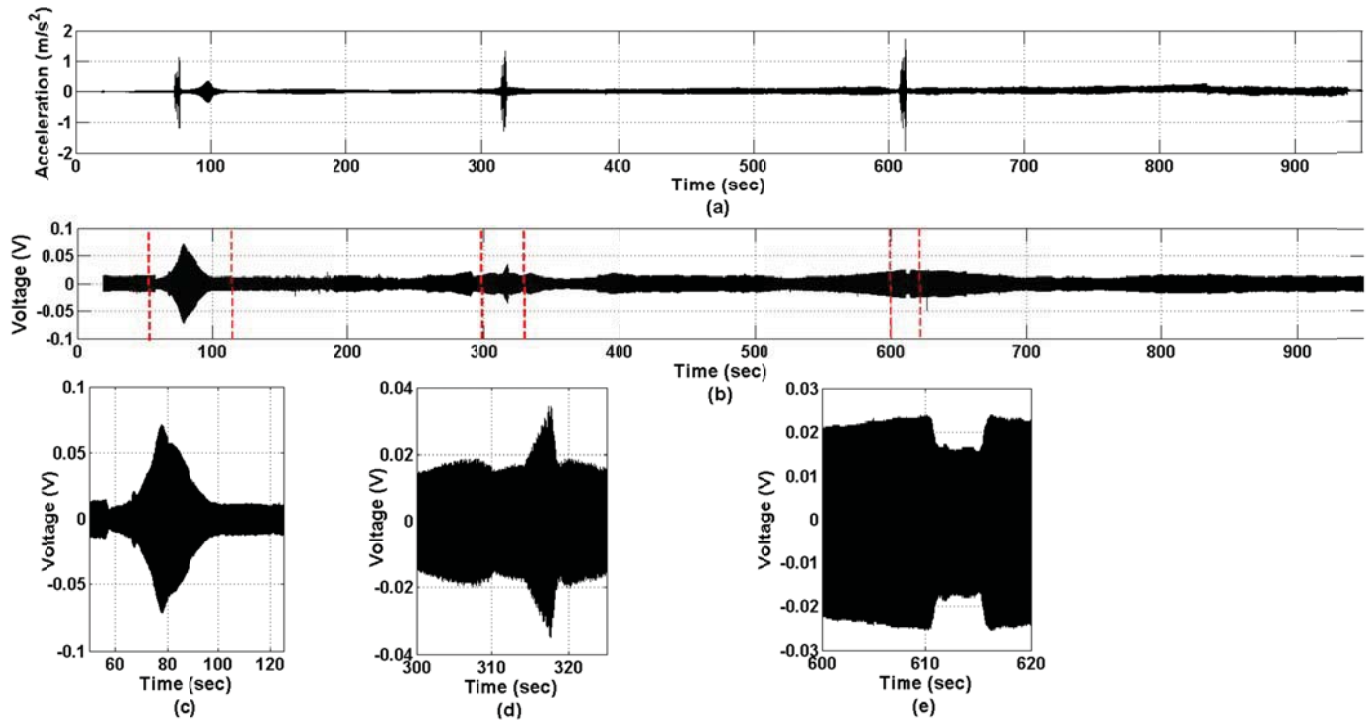


Figure 6. Response during dynamic testing of bridge structure with (a) Acceleration and (b) Measured resultant voltage of the energy harvesting device (c) Voltage response during Train 1 (d) Voltage response during Train 2 and (e) Voltage response during Train 3

4 EXPERIMENTAL ANALYSIS FROM ENERGY HARVESTING DEVICE FROM DYNAMICAL TESTING OF HOST BRIDGE STRUCTURE

The resultant acceleration and voltage output from the duration of the dynamic tests were obtained and compared (Figure 6). The testing occurred over a time period of over 15 minutes, during which time, three train passages were observed as having occurred. An examination of the acceleration response shows three distinct passages occurring at timestamps of 75 seconds, 314 seconds and 610 seconds (Figure 6(a)). A further acceleration incident is observed at the 95 second timestamp, which corresponds to the loading being applied at the fundamental frequency of the bridge, at 7.9Hz. An investigation of the voltage response of the cantilever energy harvesting device shows that the three train events do register a response (Figure 6(b)). The first train event occurs when the voltage response is at a maximum, due to the base excitation of the device being at a maximum harmonic loading condition. A closer inspection of the time at which the Train 1 passage occurs shows that the peak occurs during the voltage at time of 75 seconds (Figure 6(c)).

For the observed second train event, a more definitive train detection is observed from the voltage output of the energy harvesting device compared to that observed from Train 1 (Figure 6(d)). The comparison of the voltage and acceleration responses shows agreement in both the start time and the duration of passage of Train 2. When comparing the final passage, that of Train 3, the passage of the train is evident in once again in the acceleration response. The event registers for the energy harvester however, there is a decrease in the voltage output, with Train 3 acting as a damper on the energy harvesting device (Figure 6(e)). The duration and timestamp of the passage correspond for both the acceleration and

voltage responses. Of note is the influence of the environmental factors on the voltage output. It was noted that the wind conditions were blustery and influenced the results, with gust of winds causing the cantilever to vibrate and harvest energy. This is especially noticeable around the 600 second time period. The use of a wind shield would have prevented the wind from causing such interference.

As can be seen by the comparison of the acceleration and voltage response for the three identified train passages, the energy harvesting device has the potential to detect the passage of trains whilst the host structure undergoes external excitation. While more work is required so as to utilise such detections for applications such as weight in motion (WIM) and other applications, this paper illustrates the ability of energy harvesters to detect events whilst under different loading conditions. This is important when considering WIM and other applications, such as SHM, and should be further investigated as well as extended to other civil infrastructure applications.

5 CONCLUSIONS

This paper investigates the potential for utilising energy harvesting device for the detection of train loads whilst the host bridge structure undergoes dynamic testing. The design and fabrication of an energy harvesting device was presented. The use of impulse response testing and swept sine loadings to experimentally calibrate the energy harvesting device in a laboratory setting was investigated. The deployment of the device to a host bridge structure was outlined, as were details of the host, the external shaker and the dynamic testing procedure. The ability of the energy harvester to detect a train event during the forced vibration testing of the bridge was investigated. During such testing, three train passages were noted and were detected by both the accelerometer and by the

energy harvesting device. The events which were easily identifiable in the acceleration profile of the forced vibration testing were found to be present in the voltage output of the energy harvesting device. More research is required to obtain accurately correlations between the acceleration and voltage response and also for further applications arising from the integration of energy harvesting technology with civil infrastructure elements. This paper demonstrates that such applications are possible and further advance the range of applications that can be achieved through the integration of smart technology with civil infrastructure elements.

ACKNOWLEDGEMENTS

The authors would like to acknowledge the financial support from the Irish Research Council GOIPG/2013/482, Science Foundation Ireland TIDA Program and the FP7-PEOPLE-2013-IAPP-BridgeSMS Project.

REFERENCES

- [1] Kim, S., Pakzad, S., Culler, D., Demmel, J., Fenves, G., Glaser, S. and Turon, M. (2007), 'Health monitoring of civil infrastructure using wireless sensor networks', in *6th International Symposium on Information Processing in Sensor Networks*, IEEE, 254-263.
- [2] Gangone, M. V., Whelan, M. J. and Janoyan, K. D. (2011), 'Wireless monitoring of a multi-span bridge superstructure for diagnostic load testing and system identification' *Computer-Aided Civil and Infrastructure Engineering*, 26(7), 560-579.
- [3] Spencer, B.F. and Yun, C.-B. (2010), 'wireless sensor advances and applications for civil infrastructure monitoring', Technical report, Newmark Structural Engineering Laboratory. University of Illinois at Urbana-Champaign, Champaign, Illinois, USA.
- [4] Cahill, P., Jackson, N., Mathewson, A and Pakrashi, V. (2013), 'PolyVinylidene fluoride (PVDF) Material based energy harvesting from train and damaged bridge interaction', *Key Engineering Materials*, 569-570, 335-341.
- [5] Harb, A. (2011), 'Energy harvesting: state-of-the-art', *Renewable Energy*, 36(10), 2641-2654.
- [6] Beeby, S. P., Tudor, M. J. and White, N. M. (2006), 'Energy harvesting vibration sources for microsystems applications', *Measurement Science and Technology*, 17(12), R175-R195.
- [7] Priya, S. (2007), 'Advances in energy harvesting using low profile piezoelectric transducers', *Journal of Electroceramics*, 19(1), 167-184.
- [8] Xie, X. D., Wu, N., Yuen, K. V. and Wang, Q. (2013), 'Energy harvesting from high-rise buildings by a piezoelectric coupled cantilever with a proof mass', *International Journal of Engineering Science*, 72, 98-106.
- [9] Wischke, M., Masur, M., Kröner, M and Woias, P. (2011), 'Vibration harvesting in traffic tunnels to power wireless sensor nodes', *Smart Materials and Structures*, 20(8), 085014.
- [10] Ali, S. F., Friswell, M. I., and Adhikari, S. (2011) 'Analysis of energy harvesters for highway bridges' *Journal of Intelligent Material Systems and Structures*, 22(16), 1929 – 1938.
- [11] Erturk, A. (2011) 'Piezoelectric Energy Harvesting for Civil Infrastructure System Applications: Moving Loads and Surface Strain Fluctuations', *Journal of Intelligent Material Systems and Structures*, 22(17), 1959 – 1973.
- [12] Cahill, P. A., Nuallain, N. A., Jackson, N., Mathewson, A., Karoumi, R. and Pakrashi, V. (2014) 'Energy Harvesting from Train-Induced Response in Bridges.' *Journal of Bridge Engineering*, 10.1061/(ASCE)BE.1943-5592.0000608.
- [13] Cahill, P., Jackson, N., Mathewson, A. and Pakrashi, V. (2014), 'Comparison of piezoelectric materials for energy harvesting from civil infrastructure elements for use in health monitoring', in *'Life Cycles of Structural Systems: Design, Assessment, Maintenance and Management. Proceedings 4th International Symposium on Life-Cycle Civil Engineering*, 16-19 November 2014', CRC Press, Tokyo, 153–159.
- [14] Peigney, M., and Siegert, D. (2013) 'Piezoelectric energy harvesting from traffic-induced bridge vibrations', *Smart Materials and Structures*, 22(9), 095019.
- [15] Kaur, N. and Bhalla, S. (2015), 'Combined Energy Harvesting and Structural Health Monitoring Potential of Embedded Piezo-Concrete Vibration Sensors', *Journal of Energy Engineering* 141 (4) , 1–18.
- [16] Kołakowski, P., Szeląg, J., Sekuła, K., Swiercz, A., Mizerski, K. and Gutkiewicz, P. (2011), 'Structural health monitoring of a railway truss bridge using vibration-based and ultrasonic methods', *Smart Materials and Structures*, 20(3), 035016.
- [17] Salawu, O.S. and Williams, C. (1995), 'Bridge assessment using forced-vibration testing', *Journal of Structural Engineering*, 121(2), 161-173.
- [18] Morassi, A. and Tonon, S. (2008), 'Dynamical testing for structural identification of a bridge', *Journal of Bridge Engineering*, 13(6), 573-585.
- [19] Salawu, O.S. and Williams, C. (1995), 'Review of full-scale dynamic testing of bridge structures', *Engineering Structures*, 17(2), 113-121.
- [20] Kwark, J., Choi, E., Kim, Y., Kim, B. and Kim, S. (2004). 'Dynamic behaviour of two-span continuous concrete bridges under moving high-speed train', *Computer & Structures*, 82(4-5), 463-474.
- [21] Ülker-Kaustell, M. and Karoumi, R. (2011), 'Application of the continuous wavelet transform on the free vibrations of a steel-concrete composite railway bridge', *Engineering Structures*, 33(3), 911-919.
- [22] Farrar, C. and James, G. (1997), 'System identification from ambient vibration measurements on a bridge', *Journal of Sound and Vibrations*, 205(1), 1-18.
- [23] Cunha, A., Caetano, E., Magalhães, F. and Moutinho, C. (2013), 'Recent perspective in dynamical testing and monitoring of bridges', *Structural Control and Health Monitoring* 20(6), 853-877.
- [24] Peeters, B., Maeck, J and Roeck, G. D. (2001), 'Vibration-based damage detection in civil engineering: excitation sources and temperature effects' *Smart Materials and Structures* 10(3), 518-527.
- [25] Halling, M. W., Muhammad, I. and Womack, K. C. (2001), 'Dynamic field testing for condition assessment of bridge bents', *Journal of Structural Engineering*, 127(2), 161-167.
- [26] Maragakis, E., Douglas, B., Chen, Q. and Sandirasegaram, U. (1998), 'Full-scale tests of a railway bridge' *Transportation Research Record: Journal of the Transportation Research Board*, 1624(98), 140-147.
- [27] Farrar, C. R. and Jauregui, D. A. (1998), 'Comparative study of damage identification algorithms applied to a bridge: I. experiment', *Smart Materials and Structures*, 7(5), 704-719.
- [28] Vinogradov, A. and Holloway, F. (1999), "Electro-mechanical properties of the piezoelectric polymer PVDF.", *Ferroelectrics*, 226(1), 169-181.
- [29] Andersson, A., Ulker-Kaustell, M., Borg, R., Dymen, O., Carolin, A & Karoumi, R. (2015). "Pilot testing of a hydraulic bridge exciter", in *MATEC Web of Conferences*, 24, 02001.

Effect of vehicle velocity on exciting the lateral dynamic response of two-span integral bridges

Luke J Prendergast¹, Kenneth Gavin², David Hester³

¹Centre for Critical Infrastructure Research, School of Civil Engineering, University College Dublin, Belfield, Dublin 4, Éire

²Gavin and Doherty Geosolutions, Beech Hill Office Campus, Clonskeagh, Dublin 4, Éire

³School of Planning, Architecture and Civil Engineering, Queen's University Belfast, University Road, Belfast, BT7 1NN, Northern Ireland, United Kingdom

E-mail: luke.prendergast@ucd.ie, kgavin@gdgeo.com, d.hester@qub.ac.uk

ABSTRACT: Vibration-based Structural Health Monitoring (SHM) is an area of ongoing research and has received much attention from researchers in recent years. Online damage detection methods for bridges rely on placing sensors on the structure to detect anomalies in measured parameters such as acceleration, frequency or displacement among others. Changes in these parameters can be used to infer the presence of damage such as cracking in bridge beams, foundation scour etc. These methods mostly rely on using the signals arising on a bridge from ambient traffic or environmental loading. For foundation scour detection purposes, the lateral response of a bridge is of particular interest in that this has been shown to be particularly sensitive to the scour phenomenon. Vehicle-Bridge Interaction (VBI) effects can have a significant influence on the condition of output vibrations from a bridge element. In this paper, the effect of vehicle travelling velocity on the lateral response of a typical highway two-span integral bridge is investigated. In this context, the term lateral refers to the traffic direction. It is shown that depending on the velocity of the vehicle relative to the oscillatory period of the bridge it traverses, the bridge's dynamic response is either amplified or diminished by varying degrees. This phenomenon could influence the accuracy of a particular damage detection method relying on output system vibrations to infer damage.

KEY WORDS: Bridge Dynamics, Damage Detection, Vibration, SHM

1 INTRODUCTION

Structural Health Monitoring (SHM) is the art of monitoring the condition of a structure over its lifetime with a view to preventing excessive damage from accumulating. A very comprehensive overview of the topic is available in Farrar and Worden [1]. The motivation for asset owners (of bridges, in particular) for implementing technology of this nature is due to the potentially life-saving and economic benefits it can have by offsetting the cost (both in life and monetary terms) of excessive damage arising in the structure during its lifespan.

Online damage detection refers to detecting damage arising in a structure using sensors distributed on the structure. These sensors seek anomalies in the structural behavior during operation (by monitoring displacement, acceleration, frequency, mode shapes etc.). Dimarogonas [2] points out that this type of online damage detection began in the early 1970s when utility companies started looking at developing ways of identifying defects in rotating shafts while machinery was in use. To date, this is the most mature application of SHM in terms of being successful.

Vibration-based damage detection and health monitoring is an area of increased research interest in recent times [3–7]. The methods typically rely on the simple idea that damage arising in a structure will lead to changes in the structural stiffness at various locations, i.e. crack formation in a bridge beam leads to a local loss of bending stiffness. Since the modal properties of a dynamic system are inherently linked to its stiffness (and mass), damage will lead to changes in these properties.

Foundation scour is the term given to describe the process of soil erosion that can occur around bridge foundations due to adverse hydraulic action [6,8]. This is a very serious problem that is notoriously difficult to predict and detect [9]. Applying SHM techniques to scour detection has gained significant traction in recent years [5,10–16]. A common conclusion among researchers in this field is that the lateral response of a bridge sub-structural component (piles, pier) is the most sensitive to scour in terms of changes in modal properties [5,6,10,15,16]. It is therefore of interest to investigate phenomena that can affect the lateral dynamic response, or more specifically, impede the ability for a sensor located on the structure to effectively detect this response. The most practical way to excite a bridge (for vibration-based damage detection applications) is to use ambient traffic [17]. In this paper, the effect of vehicle travelling velocity as it traverses a bridge is investigated to highlight the significant effect that this can have via interaction with the bridge's own oscillatory motion (in the traffic direction). The type of bridge investigated is two-span integral bridges, due to their increasing popularity and prevalence.

2 NUMERICAL MODELLING

The issue relating to a vehicle travelling velocity across a two-span integral bridge is investigated using numerical modelling approaches. A mathematical model describing the dynamic system (the bridge) is developed in the MATLAB programming environment. Various aspects of the model are discussed in the following sub-sections. Section 2.1 briefly describes different types of integral bridges and section 2.2

describes the mathematical approach taken to model the bridge, the foundation soil and the vehicle load in this paper.

2.1 Types of Integral Bridge

Integral bridges are becoming increasingly popular as they do not require a conventional expansion joint and this can reduce maintenance costs significantly. There are four main types of integral bridge [5]: (1) Frame Abutment Type: In this type of bridge, the abutments form a portal frame with the bridge deck; (2) Bank Pad Abutment Type: In this type, an integral support exists between the bridge deck and bank pad end support; (3) Flexible Abutments: In this type, the abutments are formed as a series of piles or columns extending to the bank pad. These columns are not directly in contact with the soil but are placed in sleeves to allow better absorption of the bridge deck thermal movements; (4) Semi-Integral Abutment Type: In this type, there is an end screen wall which is integral with the bridge deck, however this wall does not directly support the bridge beams. The deck must be supported by some other mechanism. In this paper, type (3), a bridge with flexible support abutments, is modelled. A schematic of this type of bridge is shown in Figure 1.

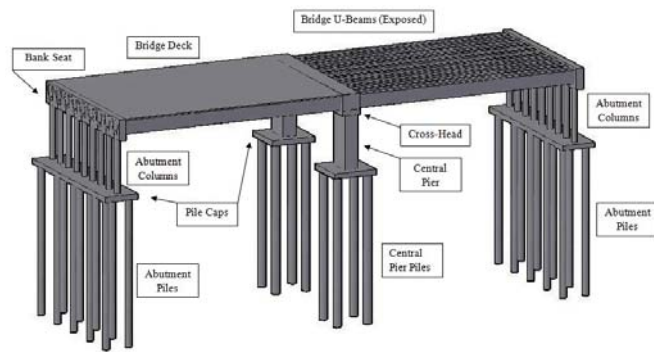


Figure 1. Schematic of Integral Bridge [5]

2.2 Mathematical Considerations

The bridge is modelled as a dynamic system. For ease of modeling, the integral bridge is treated as a 2D frame system and grouped geometric properties are used to model group behavior of the piles, abutments and piers as well as the individual deck beams. In short, lateral (into the page) and torsional behavior is omitted.

The individual bridge elements are modelled using 6-degree-of-freedom (6-DOF) Euler-Bernoulli frame elements [18], the mass $[\mathbf{M}_b]$ and stiffness $[\mathbf{K}_b]$ matrices as shown in (1). The foundation soil is modelled using a Winkler philosophy which models the continuous soil layers as discrete, mutually independent and closely spaced springs [19,20]. These spring elements have individual stiffness matrices $[\mathbf{K}_{s,i}]$ as shown in (2) and a null mass assumption.

$$[\mathbf{M}_b] = \frac{\rho AL}{420} \begin{bmatrix} 140 & 0 & 0 & 70 & 0 & 0 \\ \vdots & 156 & 22L & 0 & 54 & -13L \\ \vdots & \vdots & 4L^2 & 0 & 13L & -3L^2 \\ \vdots & \vdots & \vdots & 140 & 0 & 0 \\ \vdots & \vdots & \vdots & \vdots & 156 & -22L \\ \vdots & \vdots & \vdots & \vdots & \vdots & 4L^2 \end{bmatrix} \quad (1a)$$

$$[\mathbf{K}_b] = \begin{bmatrix} \frac{EA}{L} & 0 & 0 & -\frac{EA}{L} & 0 & 0 \\ \vdots & \frac{12EI}{L^3} & \frac{6EI}{L^2} & 0 & -\frac{12EI}{L^3} & \frac{6EI}{L^2} \\ \vdots & \vdots & \frac{4EI}{L} & 0 & -\frac{6EI}{L^2} & \frac{2EI}{L} \\ \vdots & \vdots & \vdots & \frac{EA}{L} & 0 & 0 \\ \vdots & \vdots & \vdots & \vdots & \frac{12EI}{L^3} & -\frac{6EI}{L^2} \\ \vdots & \vdots & \vdots & \vdots & \vdots & \frac{4EI}{L} \end{bmatrix} \quad (1b)$$

$$[\mathbf{K}_{s,i}] = k_{s,i} \begin{bmatrix} 1 & -1 \\ -1 & 1 \end{bmatrix}, \quad k_{s,i} \geq 0 \quad (2)$$

To model the bridge, knowledge of E (Young's modulus), I (moment of inertia), A (cross-sectional area) for each element is required as well as span lengths, column lengths etc. Standard properties are adopted to model the integral bridge in this paper and these properties are available in [5,6]. In summary, a two-span concrete bridge with each span being 25 m in length is modelled. A schematic showing the main model dimensions is produced in Figure 2. This figure also shows an inset of the individual bridge element degrees of freedom.

To model the foundation soil, the approach described by Prendergast et al. [5,11,21] is used. This approach considers each soil spring as a linear-elastic element (strain-independent $k_{s,i}$) and uses small-strain soil stiffness parameters (G_0 , E_0) to characterize the response. The approach was developed based on experimental work carried out to develop correlations between measurable geotechnical site data (Cone Penetration Tests, Multi-Channel Analysis of Surface Waves (MASW) [22]) and geotechnical stiffness parameters [10,23]. These approaches allow for soil spring stiffnesses to be specified that are capable of modeling a normally-consolidated loose, medium-dense or dense sand deposit. In this paper, the bridge is assumed to be founded in loose sand.

From the individual structural matrices shown previously, global mass $[\mathbf{M}_G]$ and stiffness $[\mathbf{K}_G]$ matrices are assembled for the full structure according to the procedure in Kwon & Bang [18]. The dynamic response of the bridge structure can be obtained by solving the second-order matrix differential equation shown in (3) using a numerical integration scheme. In this paper, the Wilson- θ integration scheme is used [24].

$$[\mathbf{M}_G] \begin{Bmatrix} \ddot{\mathbf{x}}_1(t) \\ \ddot{\mathbf{x}}_2(t) \\ \vdots \\ \ddot{\mathbf{x}}_N(t) \end{Bmatrix} + [\mathbf{C}_G] \begin{Bmatrix} \dot{\mathbf{x}}_1(t) \\ \dot{\mathbf{x}}_2(t) \\ \vdots \\ \dot{\mathbf{x}}_N(t) \end{Bmatrix} + [\mathbf{K}_G] \begin{Bmatrix} \mathbf{x}_1(t) \\ \mathbf{x}_2(t) \\ \vdots \\ \mathbf{x}_N(t) \end{Bmatrix} = \begin{Bmatrix} \mathbf{F}_1(t) \\ \mathbf{F}_2(t) \\ \vdots \\ \mathbf{F}_N(t) \end{Bmatrix} \quad (3)$$

where $[\mathbf{M}_G]$, $[\mathbf{C}_G]$ and $[\mathbf{K}_G]$ are the $(N \times N)$ global mass, damping and stiffness matrices for the model respectively and N is the total number of degrees of freedom in the system.

$\{\mathbf{x}(t)\}$, $\{\dot{\mathbf{x}}(t)\}$ and $\{\ddot{\mathbf{x}}(t)\}$ describe the displacement, velocity and acceleration of every degree of freedom for each time step in the analysis and $\{\mathbf{F}(t)\}$ describes the external forces acting on each of the degrees of freedom for a given time step. These external forces are determined by apportioning the vehicle load as forces and moments on adjacent bridge nodes as the load traverses the bridge, using Hermitian shape functions (interpolation functions). The damping matrix $[\mathbf{C}_G]$ is determined assuming a Rayleigh damping approach [25] and a damping ratio ($\xi_1 = \xi_2 = \xi$) of 2% is assumed.

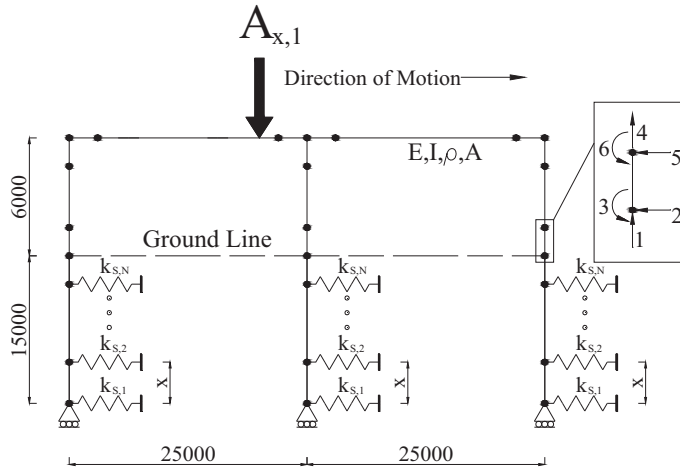


Figure 2. Model Schematic and Dimensional Data (mm)

3 VELOCITY EFFECTS

In this section, the interaction effects between a vehicle's travelling velocity over the bridge and the resulting impact on the bridge's own oscillatory motion (in the traffic direction) is investigated. Section 3.1 presents an analysis of the mode shape of the bridge pertaining to lateral sway motion and section 3.2 investigates the effect of a single vehicle load traversing the bridge.

3.1 Global mode shape of bridge

In order to extract the un-damped modal frequencies and mode shapes from the numerical model, it is necessary to conduct an eigenvalue analysis on the system matrix $[\mathbf{D}]$, specified as shown in (4).

$$[\mathbf{D}] = [\mathbf{M}_G]^{-1} [\mathbf{K}_G] \quad (4)$$

An eigenvalue analysis is conducted on $[\mathbf{D}]$ using MATLAB's in-built eigenvalue functionality. Extracting the system eigenvalues and eigenvectors corresponds to the un-damped frequencies and mode shapes of the model.

The fundamental mode shape of the integral bridge is a global lateral sway mode (in the traffic direction). For the given bridge properties assumed [5], the frequency of the fundamental mode is 1.5643 Hz with a corresponding period (T) of 0.639 seconds. The bridge modal shape at four vibration stages corresponding to $0.25 \times T$, $0.5 \times T$, $0.75 \times T$, and $1 \times T$ is shown in Figure 3.

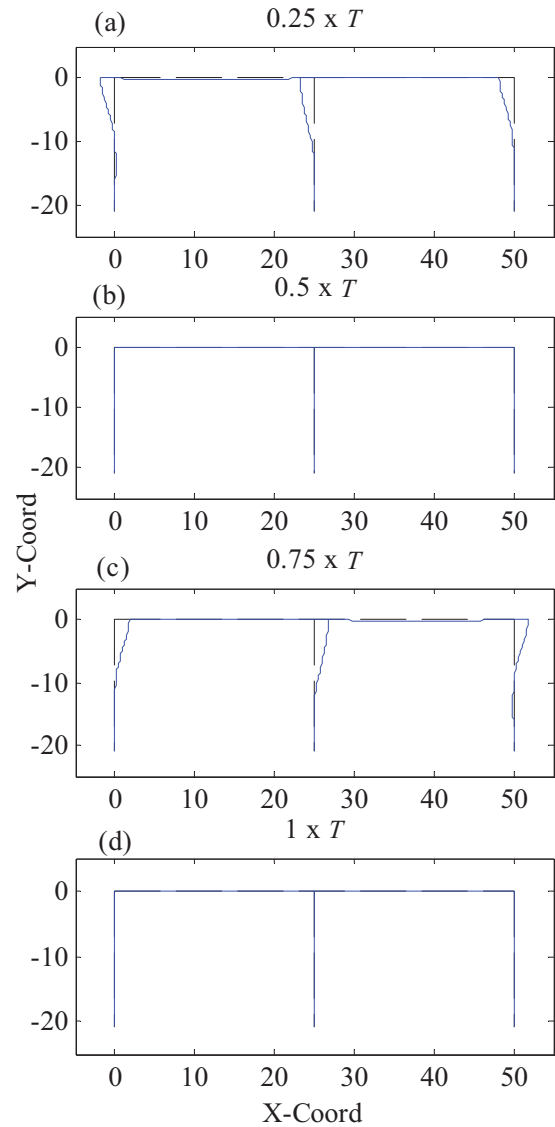


Figure 3. Four stages of first vibration mode – global sway

Figure 3 provides a pictorial view of the displaced shape of the given mode at a particular stage of vibration over one cycle. The time it takes for the given shape to arise and the direction of motion is displayed in Table 1.

Table 1. Bridge motion – direction and arrival times.

Fig 3 Image Ref	Arrival Time (s)	Motion Direction
(a)	$0.25 \times 0.639 = 0.16\text{s}$	Stationary (will move right)
(b)	$0.5 \times 0.639 = 0.32\text{s}$	Swaying to right
(c)	$0.75 \times 0.639 = 0.4795\text{s}$	Stationary (will move left)
(d)	$1 \times 0.639 = 0.639\text{s}$	Swaying to left

Interaction effects between the bridge's dynamic motion and the rate of load traversing are investigated in the next section.

3.2 Single traversing load

While the bridge undergoes global sway at the first natural frequency (see Figure 3), it first sways to the left (say) with span 1 deflecting downward, then sways right with span 2 deflecting downward. If we consider a single load traversing the bridge while it undergoes motion at its own natural frequency, the rate at which the load traverses will interact with the amplitude of the bridge's lateral motion. This will lead to differences in the magnitude of the free vibration response after the load (vehicle) has left the bridge. As the lateral bridge motion is the parameter of interest, a typical lateral displacement and acceleration response measured at the pier top due to a single load traversing is shown in Figure 4. For this analysis, the load of $V = 100$ kN traverses the bridge at 25 m/s and the signal contains 10 seconds of free vibration after the load departs.

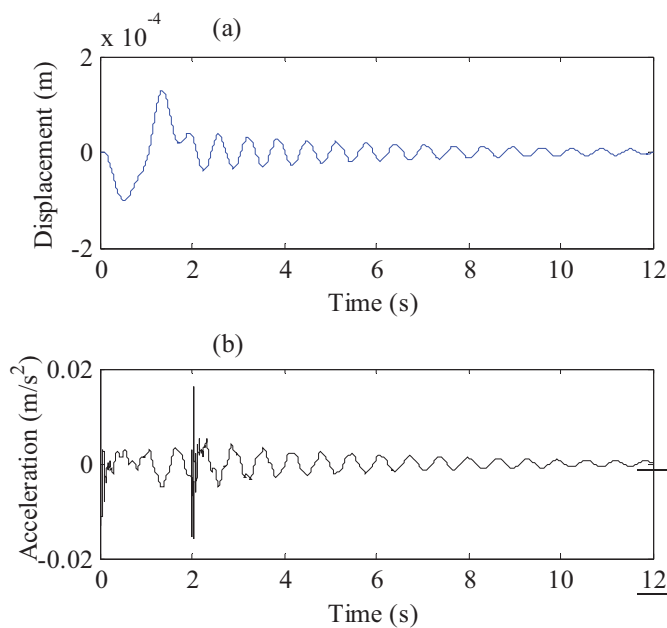


Figure 4. Pier top signals for load traversing at 25 m/s with 10 sec free vibration. (a) Lateral displacement. (b) Lateral acceleration.

The signals in Figure 4 are quite typical. The individual peaks as the load enters and leaves the bridge are evident in the acceleration plot in part (b). Once the load leaves the bridge, a logarithmic decay is evident in the free vibration of both displacement and acceleration. It is postulated in this paper that the rate at which the load traverses the bridge will affect the amplitude of the response signals due to interaction effects. More specifically, maximum amplification of the response should occur if the load traverses the first span in the time it takes for the bridge to undergo one half of its vibration cycle (i.e. reaching the pier when the bridge is in condition (b) of Figure 3). This means that the load will be on the left span when it naturally deflects downwards and on the right span when this naturally deflects downwards due to the bridge's periodic motion, thus amplifying this response. The opposite situation (maximum diminishing of signal) should occur if the load traverses span 1 in the time it takes for the bridge to undergo a full vibration cycle (i.e. condition (d) in Figure 3).

This is because in this case the load while on the left span for the first half of the vibration cycle will still be on the left span during the second half, where it will act against the bridge's natural motion, then it will pass onto the right span while the bridge is naturally pulling left for the first half of the next cycle, once more impeding the motion before finally working with the bridge for the second half of its second cycle.

To investigate this, an analysis is conducted herein. For the analysis in this paper, only the free vibration signal after the vehicle (load) leaves the bridge is produced. This is because as the load is on the bridge, it is more difficult to compare different responses due to the different times associated with the load leaving the bridge making direct comparisons difficult. A single load traverses the bridge with a velocity (v_s) such that it crosses the first bridge span (25 m) in a time that is a given ratio of the bridge's natural period. The ratios chosen are 0.25, 0.5, 0.75, 1, 1.25, 1.5, 1.75 and 2 times the bridge's natural period (T). The results of this analysis should confirm that a load traversing the bridge span 1 in a time that equates to half of the bridge's natural period is the most beneficial in terms of signal amplification (free vibration) while a load traversing the span 1 in a time equating to the full bridge period will impede the vibration the most. Establishing the effect at multiples of the bridge period (i.e. ratios > 1) is also undertaken to observe if the effect is any different and also to see how the system reacts with more realistic loading velocities. Table 2 outlines the crossing times and required velocities for the analysis. Note: for the analysis with ratios < 1 for crossing velocities, the vehicle (load) speeds are unrealistically high.

Table 2. Load velocities to traverse span 1.

Span (m)	T (s)	Time to cross Span 1 T_v (s)	Ratio T_v/T	Load v_s (m/s)
25	0.639	0.16	0.25	156.43
25	0.639	0.32	0.5	78.22
25	0.639	0.4794	0.75	52.14
25	0.639	0.639	1	39.11
25	0.639	0.799	1.25	31.29
25	0.639	0.959	1.5	26.07
25	0.639	1.118	1.75	22.36
25	0.639	1.278	2	19.56

The results for the analysis are shown in Figure 5 and 6. Figure 5(a) shows the lateral pier top displacement responses in free vibration for velocity ratios ≤ 1 . Figure 5(b) shows the lateral pier top acceleration responses in free vibration for velocity ratios ≤ 1 . Five seconds of free vibration is analysed. In Figure 5 it is evident that the maximum amplification of the free vibration response signals occurs for a load traversing the first span in the time it takes the bridge to undergo 0.5 times its vibration cycle. It is also shown that the lowest amplification of the signal occurs when the load traverses the first span in the time it takes the bridge to undergo a full cycle. The other ratios give intermediate results and the results are the same for both displacement and acceleration. This is sensible (and expected) as it indicates that when the load is completely in phase with the bridge motion (i.e. pushing down

on span 1 as it naturally deflects downwards due to periodic motion, then moving to span 2 as this naturally deflects downwards) we achieve maximum amplification. When the load acts to resist the bridge's own oscillatory motion, we achieve the lowest amplification.

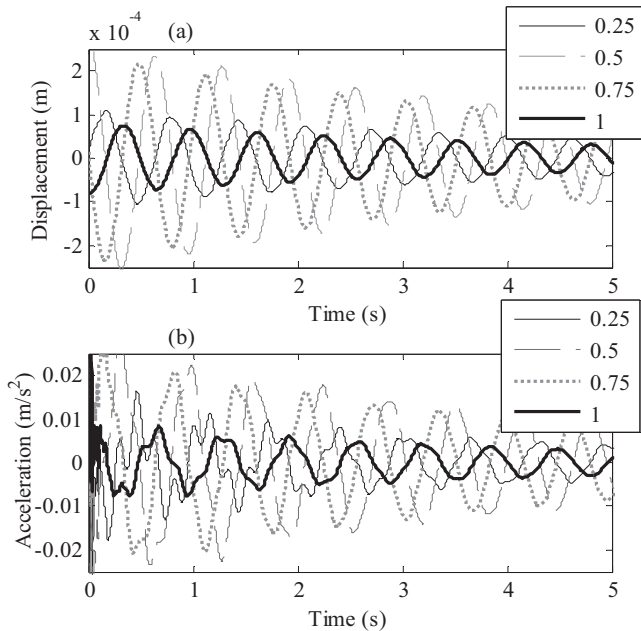


Figure 5. Lateral pier top signals for load traversing span 1 in specified ratio (0 to 1) of bridge period. (a) Displacement. (b) Acceleration.

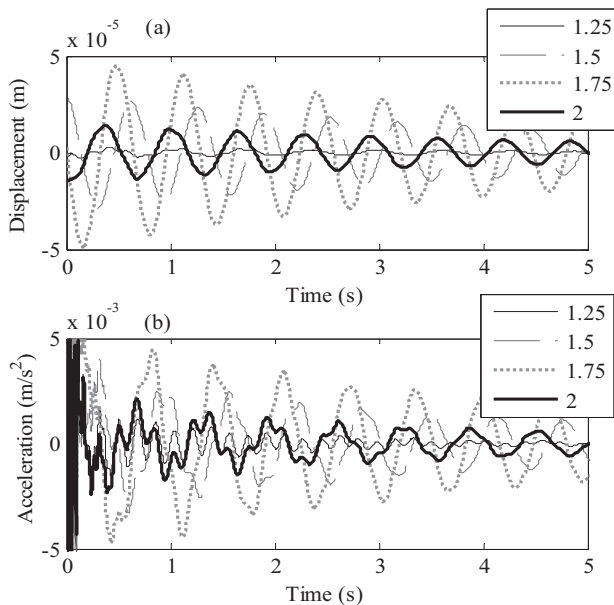


Figure 6. Lateral pier top signals for load traversing span 1 in specified ratio (1 to 2) of bridge period. (a) Displacement. (b) Acceleration.

Figure 6 shows the results for the load traversing span 1 in a time that is multiples of the bridge's natural period. The amplitude results in this case are almost an order of magnitude less pronounced (to be expected as there is an element of the load acting against the bridge movement for every case). The

results for Figure 6 indicate a different outcome than those in Figure 5. The maximum signal amplification occurs when the load reaches the end of span 1 in a time that is 1.75 times the bridge's period as opposed to 1.5 times which might have been expected from the first set of results. Also the lowest amplification occurs for the load traversing span 1 in 1.25 times the bridge period as opposed to 2 times, as might have been expected. The amplitude of the free vibration is a function of the bridge displacement, velocity and acceleration at the point when the load leaves the bridge and this can have a significant effect on the amplitude of the signal in free vibration. The results are less intuitive than when the load traverses in a specified ratio less than 1 of the bridge period as in this case it is easy to see when the load will act to impede the bridge motion. For ratios greater than 1, there is a trade-off effect in place as at some stage during the loading, the load will always be 'working against' the bridge motion to some degree. These results highlight the complicated interaction process at play in this problem and moreover show that using vehicle-induced vibration signals for bridge damage detection could potentially lead to issues with time-domain based SHM techniques.

4 CONCLUSION

Vibration-based Structural Health Monitoring is a growing research area. In this paper we describe the application of the approach to investigate reliable methods to detect damage arising in bridge structures using dynamic response measurements. For scour detection using vibration-based methods, the lateral response of a bridge sub-structural element has been shown to be most sensitive to scour. Obtaining dynamic signals from a bridge is mostly undertaken by monitoring its response to ambient traffic loading. Therefore, it is of interest to study potential effects that could arise from the interaction between the rate of loading a two-span integral bridge and the measured response.

In this paper, vehicle velocity effects were investigated in terms of how they can amplify or diminish the dynamic response of a bridge. The results show that the response magnitude in free vibration can vary significantly depending on how the load interacts with the bridge in terms of its own oscillatory motion. The results in many cases may not be intuitive and this study aims to highlight potential disparities that can arise.

This phenomenon could become an issue for time-domain related SHM techniques, as a diminished signal magnitude could become absorbed into the noise band of a standard sensor for example. Signal clarity can be a serious issue for many of these methodologies.

ACKNOWLEDGMENTS

The authors wish to acknowledge the support of the European Union H2020 project DESTination RAIL (Project No. 636285) and the Geological Survey of Ireland (GSI) Short-Call 2015 (Project No. 2015-SC-035).

REFERENCES

- [1] Farrar CR, Worden K. An introduction to structural health monitoring. *Philos Trans A Math Phys Eng Sci* 2007;365:303–15.
- [2] Dimarogonas AD. Vibration of cracked structures: A state of the art review. *Eng Fract Mech* 1996;55:831–57.

- [3] Hester D, González A. A wavelet-based damage detection algorithm based on bridge acceleration response to a vehicle. *Mech Syst Signal Process* 2012;28:145–66.
- [4] González A, Hester D. An investigation into the acceleration response of a damaged beam-type structure to a moving force. *J Sound Vib* 2013;332:3201–17.
- [5] Prendergast LJ, Hester D, Gavin K. Development of a Vehicle-Bridge-Soil Dynamic Interaction Model for Scour Damage Modelling. *Shock Vib* 2016;2016.
- [6] Prendergast LJ, Hester D, Gavin K. Determining the presence of scour around bridge foundations using vehicle-induced vibrations. *J Bridg Eng* 2016;In Press.
- [7] Prendergast LJ, Gavin K, Reale C. Sensitivity studies on scour detection using vibration-based systems. *Transp Res Procedia* 2016;14C:3982–9.
- [8] Hamill L. *Bridge Hydraulics*. London: E.& F.N. Spon; 1999.
- [9] Prendergast LJ, Gavin K. A review of bridge scour monitoring techniques. *J Rock Mech Geotech Eng* 2014;6:138–49.
- [10] Prendergast LJ, Hester D, Gavin K, O'Sullivan JJ. An investigation of the changes in the natural frequency of a pile affected by scour. *J Sound Vib* 2013;332:6685–702.
- [11] Prendergast LJ, Gavin K, Doherty P. An investigation into the effect of scour on the natural frequency of an offshore wind turbine. *Ocean Eng* 2015;101:1–11.
- [12] Ju SH. Determination of scoured bridge natural frequencies with soil–structure interaction. *Soil Dyn Earthq Eng* 2013;55:247–54.
- [13] Foti S, Sabia D. Influence of Foundation Scour on the Dynamic Response of an Existing Bridge. *J Bridg Eng* 2011;16:295–304.
- [14] Klinga J V., Alipour A. Assessment of structural integrity of bridges under extreme scour conditions. *Eng Struct* 2015;82:55–71.
- [15] Briaud JL, Hurllebaus S, Chang K, Yao C, Sharma H, Yu O, et al. *Realtime monitoring of bridge scour using remote monitoring technology*. vol. 7. Austin, TX: 2011.
- [16] Elsaid A, Seracino R. Rapid assessment of foundation scour using the dynamic features of bridge superstructure. *Constr Build Mater* 2014;50:42–9.
- [17] Farrar CR, Duffey TA, Cornwell PJ, Doebling SW. Excitation methods for bridge structures. *Proc. 17th Int. Modal Anal. Conf. Kissimmee*, vol. 7, Kissimmee, FL: 1999.
- [18] Kwon YW, Bang H. *The Finite Element Method using MATLAB*. Boca Raton, FL: CRC Press, Inc.; 2000.
- [19] Dutta SC, Roy R. A critical review on idealization and modeling for interaction among soil–foundation–structure system. *Comput Struct* 2002;80:1579–94.
- [20] Winkler E. *Theory of elasticity and strength*. Dominicus Prague: 1867.
- [21] Prendergast LJ, Gavin K. A comparison of initial stiffness formulations for small-strain soil – pile dynamic Winkler modelling. *Soil Dyn Earthq Eng* 2016;81:27–41.
- [22] Donohue S, Long M, Gavin K, O'Connor P. Shear Wave Stiffness of Irish Glacial Till. *Int. Conf. Site Characterisation I*, Porto, Portugal: 2004, p. 459–66.
- [23] Prendergast LJ, Gavin K, Igoe D. Dynamic soil-structure interaction modeling using stiffness derived from in-situ Cone Penetration Tests. *3rd Int. Symp. Cone Penetration Test.*, Las Vegas, NV: 2014.
- [24] Tedesco JW, McDougal WG, Allen Ross C. *Structural Dynamics: Theory and Applications*. 1999.
- [25] Yang Y, Yau J, Wu Y. *Vehicle-bridge interaction dynamics*. 2004.

Drive-by Bridge Damage Detection Using Curvatures in Uncertain Environments

D. Martinez¹, E.J. OBrien¹, E. Sevillano¹

¹School of Civil Engineering, University College of Dublin, Newstead, Dublin 4, Ireland
Email: daniel.martinezotero@ucd.ie, eugene.obrien@ucd.ie, enrique.sevillanobravo@ucd.ie

ABSTRACT: Considerable effort has been dedicated in recent years to the development of bridge damage detection techniques. Recently, drive-by monitoring has become popular as it allows the bridge to be monitored without installing sensors on it. In this work, the Traffic Speed Deflectometer (TSD), which incorporates a set of laser Doppler sensors on a straight beam to obtain the relative velocity between the vehicle and the pavement surface, is modelled to obtain deflections on the bridge as the vehicle drives. From these deflections it is possible to obtain the curvature of the bridge, from which inferences on damage can be made. However, most of the time, the measurements taken by drive-by sensors are subject to a set of uncertainties or noise that can lead the damage detection procedure to either give false positives or to miss damage. For that reason, an analysis is needed in order to determine if these methods can work properly in uncertain or noisy environments. Moreover, as the road surface roughness affects the dynamic interaction between the vehicle and the bridge, this may also have an effect on the damage predictions. Hence, the goal of this paper is to study the sensitivity of curvature measurements to both the presence of environmental noise and the effect of the road surface roughness.

KEY WORDS: Noise; Profile; Half-Car model; Drive-by monitoring; Curvature; Structural Health Monitoring; SHM; Traffic Speed Deflectometer; TSD.

1 INTRODUCTION

Many different Structural Health Monitoring (SHM) approaches can be found for bridge safety assessment purposes. Direct instrumentation of bridges has proven to be a successful solution for continuous monitoring applications with possible imminent failure [1], sometimes due to the presence of natural hazards [2].

Drive-by monitoring has been proposed as an alternative to direct instrumentation solutions, avoiding the need to use any sensor on the bridge as well as avoiding traffic interruptions when measuring [3]. In drive-by monitoring, sensors in the passing vehicle are used to monitor the structural response and hence the condition of the bridge. Therefore, drive-by is increasing in popularity, mainly for short and medium span bridges [4]. The Traffic Speed Deflectometer (TSD) has considerable potential in this context [5]. The TSD is a vehicle originally intended to measure pavement stiffness, but its level of accuracy when measuring deflection velocities can be used for SHM purposes. A constant velocity is assumed when obtaining the data.

The TSD can provide accurate measurements of deflection and it allows the calculation of curvature, which has been demonstrated to work well as a damage indicator [6]. However, in all drive-by monitoring applications there are at least two main sources of uncertainty: the noise present in the measured data and the effect of the road profile on the vehicle. Thus, it is necessary to determine the influence of these uncertainties when applying drive-by monitoring in order to develop an accurate damage detection procedure. Hence, the aim of this paper is to study if curvature can be used as a damage indicator when the uncertainties are considered in the damage prediction.

Four different situations are discussed in this paper: The results with no noise or road profile, the results with the added road profile but no noise, the results with an added random

noise but with smooth profile and the results including both sources of uncertainty.

2 CURVATURE AS DAMAGE INDICATOR

As is well known, curvature is defined as the second derivative of vertical displacements with respect to the distance at a given point in time:

$$\kappa(t) = \frac{\partial^2 y}{\partial x^2}(t) \quad (1)$$

Under a moving load, three measurements are required at each point in time to obtain curvature:

$$\kappa(t) = \frac{y(x - \partial x, t) - 2y(x, t) + y(x + \partial x, t)}{\Delta x^2} \quad (2)$$

Wahab et al [7] have demonstrated the potential of curvature to be used as a damage indicator. In their work, curvatures are calculated with the help of the Curvature Damage Factor (CDF) and successfully applied to the Z24 bridge in Switzerland. As an example of how curvature works, a static case is considered on a 20 m long simply supported beam with two loads of 100 kN each at 5 and 10 m from the left support. The beam has a stiffness of 44.1×10^6 kN/m² and a local stiffness reduction of 30% between 13 and 15 m. The corresponding curvature is illustrated in Figure 1. In this figure, damage can be easily detected between 13 and 15 metres from the left side of the bridge due to the local increase in curvature.

However, since it has been widely demonstrated that measured deflections are sensitive to the presence of different sources of uncertainty, it is obvious that the curvatures will also be sensitive to those uncertainties. There are two main

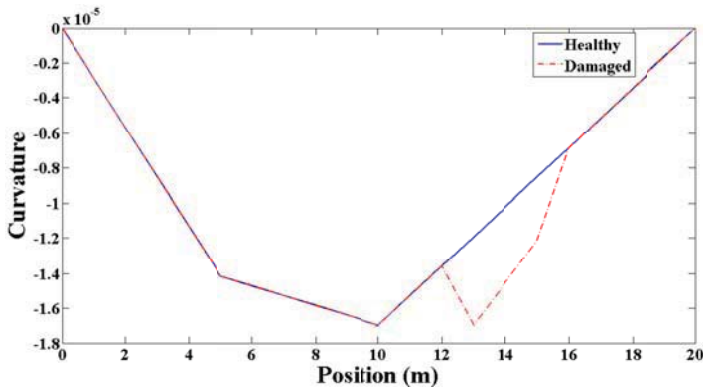


Figure 1. Curvature under two point loads

sources of uncertainty as outlined before: road profile and measurement noise. Vehicle-bridge interaction is affected during the measurement procedure by the road profile. A profile is simulated in this paper with a road class “A”, which changes in degree of roughness from 0 to 32 [8]. The noise is a random parameter that can also alter the measurements taken. Noise models have been formulated depending on the circumstances of the case study, but in [9] details of the two most typical ones can be found. The added random noise considered in this paper can be expressed as:

$$y_{noise} = y_{calc} + E_p \times N_{noise} \times y_{max} \quad (3)$$

where y_{noise} is the noise-polluted deflection, y_{calc} is the measured deflection, y_{max} is the maximum deflection, E_p is the noise level (1 for 100% noise) and N_{noise} is a random uniform distribution with zero mean and unit standard deviation. Simulating the noise in this way results in lower differences for polluted data when deflection is small.

3 NUMERICAL MODEL

A Half-Car model passing over an Euler-Bernoulli beam has been programed in MATLAB. This model has 4 degrees of freedom (DOFs): sprung mass bounce translation, sprung mass pitch rotation and two axle hop translations. It is illustrated in Figure 2.

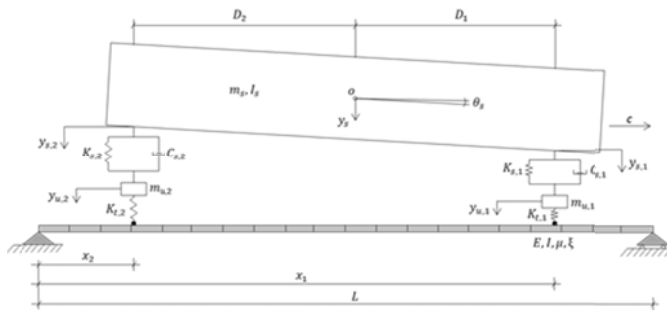


Figure 2. Diagram of the Half-Car model, adapted from [10].

The geometrical and mechanical properties considered for the vehicle are shown in Table 1, while those corresponding to the 1D elements of the Euler-Bernoulli beam are shown in Table 2.

A random noise of a 5% of the local deflection is introduced to the measured deflection signal and a class “A” roughness is introduced in the road profile. The parameters for the Half-Car model are given in Table 1.

Table 1. Geometrical and mechanical properties of the modelled vehicle

Half-Car Property	Notation	Value
Weight of the sprung mass	m_s	18 t
Unsprung mass axle 1	m_{u1}	1000 kg
Unsprung mass axle 2	m_{u2}	1000 kg
Length of the vehicle	L_v	11.25 m
Axle spacing	A_s	7.6 m
Tyre 1 stiffness	$K_{t,1}$	1.75×10^6 N/m
Tyre 2 stiffness	$K_{t,2}$	3.5×10^6 N/m
Damper 1 stiffness	$K_{s,1}$	4×10^5 N/m
Damper 2 stiffness	$K_{s,2}$	10^6 N/m
Damper 1 damping	$C_{s,1}$	10^3 Ns/m
Damper 2 damping	$C_{s,2}$	2×10^3 Ns/m
Centre of gravity distance from axle 1	D_1	3.8 m
Centre of gravity distance from axle 2	D_2	3.8 m
Height of the vehicle	h	3.76 m
Constant velocity	c	80 km/h (22.22 m/s)

Table 2. Geometrical and mechanical properties of the bridge

Bridge Property	Notation	Value
Number of elements	N	20
Frequency	f_s	1000 Hz
Length	L	20 m
Young's modulus	E	3.5×10^{10} N/m ²
2 nd moment of area	J	1.26 m ⁴
Mass per unit length	μ	37500 kg/m
Damping	ζ	3%
First natural frequency	f_1	4.26 Hz
Length of the approach	L_{app}	100 m

Details about the damage considered in this work are indicated in Table 3.

Table 3. Definition of damage

Damage Property	Value
Type of damage	Loss of stiffness (EI)
Quantity of damage	20% of EI
Extent of damage	2 m (10% of length)
Centred location of damage	7.5 m from left bearing

An approach of 100 m has been selected to ensure that the DOFs are in equilibrium when the vehicle arrives on the bridge. The number of elements has been chosen according to a simulated sensor gap of 1 m, which means that different sensors can measure the same point at different times

4 RESULTS AND DISCUSSION

Figure 3 shows the curvature under each moving axle for the healthy and damaged cases. The loss of stiffness causes a sudden curvature change in the damaged area that is particularly pronounced as the second axle crosses the damaged zone. The difference in curvature at 8 m, where the largest deviation of curvature is found when comparing the damaged curve with the healthy one, is 23% for the first axle and 26% for the second. Hence, the results clearly show that the use of curvature as a damage indicator is possible when no uncertainties are considered.

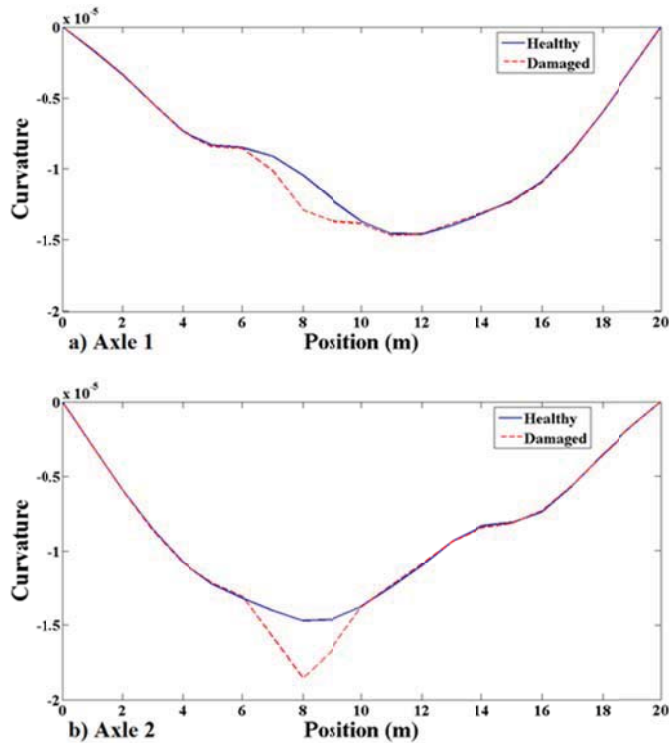


Figure 3. Curvature at moving reference for the healthy and damaged states under a) Axle 1 and b) Axle 2

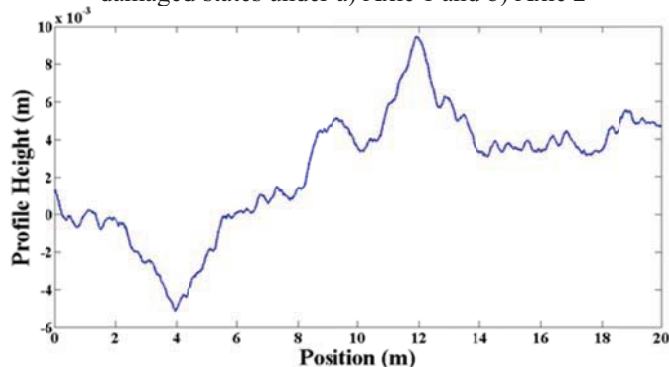


Figure 4. Bridge's road profile

Figure 4 shows a randomly generated road profile of class "A" roughness [8]. Figure 5 illustrates the curvatures calculated under the influence of the road profile. The graphs look very similar in shape compared to the smooth profile case. The largest difference between the healthy and the damaged situations is again at 8 metres from the left side of the bridge, with a deviation of 24% in the first axle and 26 %

in the second. This means that the effects of the road profile are negligible, at least for the case under study in this paper.

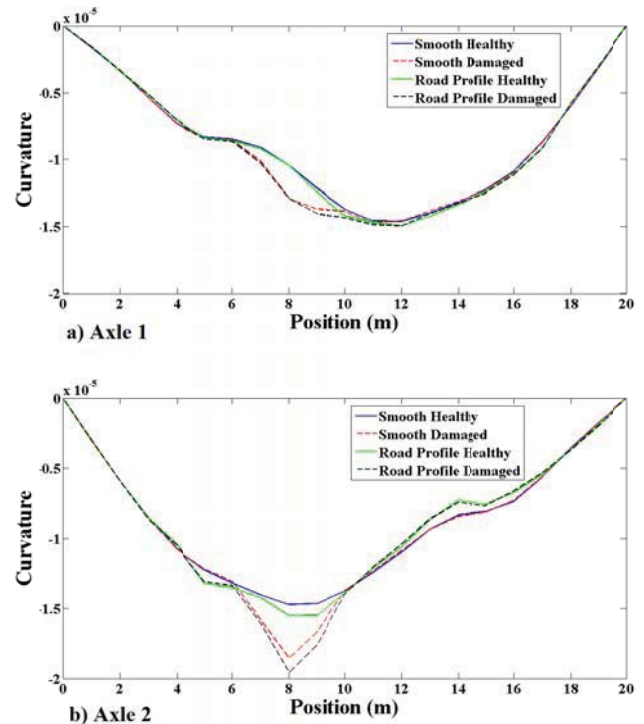


Figure 5. Curvature measurements influenced by the road profile in a) Axle 1 and b) Axle 2

Figure 6 shows the curvatures obtained when adding a random noise of 5% to the 'measured' deflections for a beam with a smooth profile considering that exactly the same situation of noise can be obtained. The graph does not match in shape with Figure 3, demonstrating that curvature is very sensitive to the presence of noise in the measurements. Nevertheless, the scales differ very little in absolute values between Figures 3 and 6, and the damaged case is still substantially different from the healthy one in all positions coincident with the location of damage. However, even though it is quiet easy to see that damage location is still well predicted, it is not possible to estimate accurately the magnitude of this damage, since the presence of noise noticeably reduce the difference between the healthy and the damaged lines.

Similar conclusions can be extracted from Figure 7, where the results presented correspond to those obtained with the same amount of noise and the same road profile as in Figure 4. Noise can be seen to have a greater influence than the profile, as the figure behaves in a similar way to the case with noise and smooth profile (Figure 6).

Therefore, from these two figures, it is clear that a method is needed in order to handle the presence of noise in these measurements. Even though the location of damage is quite clear, the severity of the damage cannot be predicted accurately, which can lead to dangerous scenarios in practical situations.

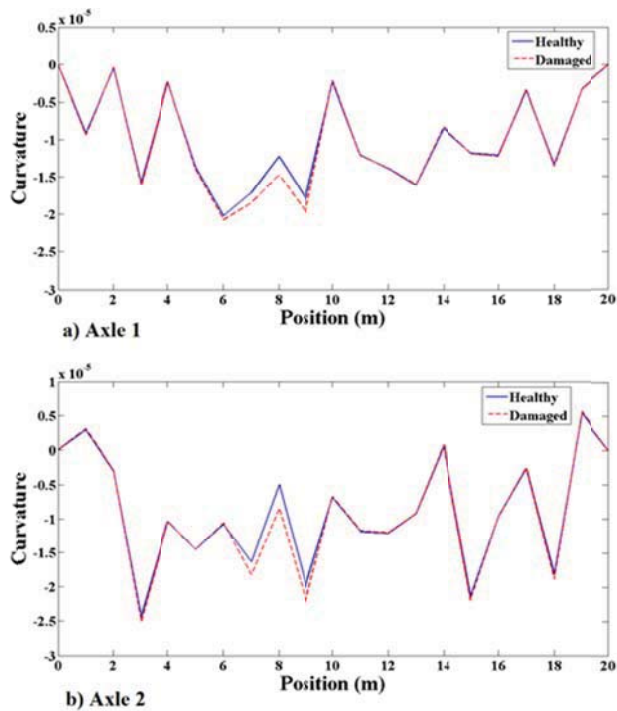


Figure 6. Curvature measurements with a random noise of 5% of deflection at a) Axle 1 and b) Axle 2

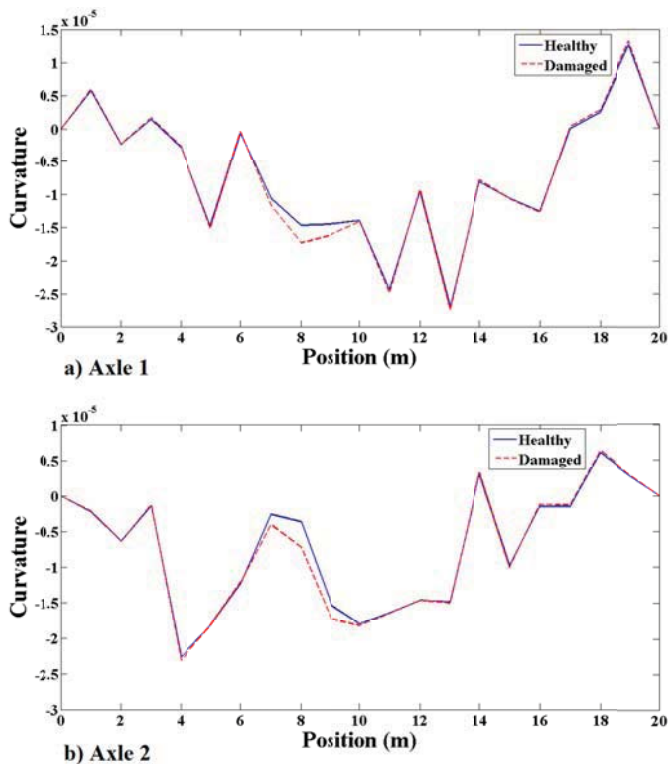


Figure 7. Curvature measurements with 5% random noise in deflection 'measurement' and a road profile for a) Axle 1 and b) Axle 2

5 CONCLUSIONS

The paper analyses the sensitivity of bridge curvature to a local loss of stiffness in a beam. The presence of noise in the

measurement is considered, as well as the effects of road profile. The curvature method works well when none of these sources of uncertainties are considered. When random noise is present in the measurements, it is more difficult to quantify the damage. However, when considering the effects of the road profile, the effect is small; a similar curvature change can be seen as for the smooth profile. In the case with the added noise, the curvature changes significantly, both for the damage and healthy cases. Fortunately, there is still a significant difference between healthy and damaged measurements, making it possible to at least detect the damage location, although no accurate severity predictions are possible given that the noise distorts a lot the shapes of the calculated curvatures. More investigation is required to handle the influence of random noise in the data in the damage detection procedure.

ACKNOWLEDGEMENTS



The authors acknowledge the support for the work reported in this paper from the European Union's Horizon 2020 Research and Innovation Programme under the Marie Skłodowska-Curie grant agreement No. 642453. Greenwood Engineering, designers of the TSD, are also acknowledged for their cooperation and support

REFERENCES

- [1] E.P. Carden, P. Fanning, Vibration based condition monitoring: a review, *Structural health monitoring* 3(4) (2004) 355-377.
- [2] Y. Fujino, D.M. Siringoringo, Bridge monitoring in Japan: the needs and strategies, *Structure and Infrastructure Engineering* 7(7-8) (2011) 597-611.
- [3] A. Malekjafarian, P.J. McGetrick, E.J. O'Brien, A Review of Indirect Bridge Monitoring Using Passing Vehicles, *Shock and Vibration* (2015) 16.
- [4] C.-W. Kim, R. Isemoto, T. Toshinami, M. Kawatani, P. McGetrick, E.J. O'Brien, Experimental investigation of drive-by bridge inspection, *5th International Conference on Structural Health Monitoring of Intelligent Infrastructure (SHMII-5)*, Cancun, Mexico, 11-15 December, 2011, Instituto de Ingeniería, UNAM, 2011.
- [5] G.R. Rada, S. Nazarian, B.A. Visintine, R.V. Siddharthan, N. Sivanesar, Use of High-Speed Deflection Devices in Network-Level PMS Applications: Are We Ready?, *9th International Conference on Managing Pavement Assets*, Alexandria, Virginia, USA, B. Diefenderfer & M. Katicha 2015 12.
- [6] F.N. Catbas, M. Gul, J.L. Burkett, Conceptual damage-sensitive features for structural health monitoring: laboratory and field demonstrations, *Mechanical Systems and Signal Processing* 22(7) (2008) 1650-1669.
- [7] M.A. Wahab, G. De Roeck, Damage detection in bridges using modal curvatures: application to a real damage scenario, *Journal of Sound and Vibration* 226(2) (1999) 217-235.

- [8] F. Tyan, Y.-F. Hong, S.-H. Tu, W.S. Jeng, Generation of random road profiles, *Journal of Advanced Engineering* 4(2) (2009) 1373-1378.
- [9] E. Simoen, G. De Roeck, G. Lombaert, Dealing with uncertainty in model updating for damage assessment: A review, *Mechanical Systems and Signal Processing*, 56 (2015) 123-149.
- [10] P. McGetrick, C.-W. Kim, A. González, Dynamic axle force and road profile identification using a moving vehicle, *International Journal of Architecture, Engineering and Construction* 2(1) 1-16 (2013).

Drive-by inference of railway track longitudinal profile using accelerometer readings taken by in-service vehicles

Eugene J. O'Brien¹, Cathal Bowe², Paraic Quirke^{1,2}, Daniel Cantero³

¹School of Civil Engineering, University College Dublin, Dublin 4, Ireland.

²Iarnród Éireann Irish Rail, Technical Department, Engineering & New Works, Inchicore, Dublin 8, Ireland.

³Department of Structural Engineering, Norwegian University of Science & Technology, Trondheim, Norway.
email: eugene.obrien@ucd.ie, cathal.bowe@irishrail.ie, paraic.quirke@irishrail.ie, daniel.cantero@ntnu.no

ABSTRACT: Accurate knowledge of the longitudinal profile of railway track is essential to support maintenance planning by track asset managers. The dynamic response of a train is largely dependent on the longitudinal profile of the railway track it crosses. This dynamic response can potentially be used to determine that profile. Cross Entropy optimisation is used to infer railway track longitudinal profile elevations through analysis of measured vehicle bogie accelerations with added uncertainty in vehicle and track properties. A numerical analysis is presented in this paper using a 2 dimensional half car vehicle and a finite element 3-layer track model implemented in Matlab. A population of track longitudinal profiles is generated through a random mechanism. A vehicle track interaction with randomly generated uncertainty in vehicle and track properties is carried out for each longitudinal profile in the population. The bogie acceleration signal produced for each profile is compared to the measured signal. The best fitting bogie accelerations are used to gather an elite set of rail longitudinal profiles. This elite set is used to generate an improved population of estimates for the next iteration. Once a convergence criterion is met the profile generating an acceleration signal that best fits the measured bogie acceleration signal is kept as the inferred longitudinal rail profile. This paper reports the results of the numerical simulations.

KEY WORDS: Railway; Track; Longitudinal Profile; Drive-by; Dynamics; Vehicle Track Dynamic Interaction; Maintenance.

1 INTRODUCTION

Research into using in-service railway vehicles to monitor track condition has gained considerable interest in recent years. 'Drive-by' Continuous Track Monitoring (CTM) techniques have the potential to inform track asset managers of track condition in 'real time' which improves maintenance forecasting [1]–[3].

Track longitudinal level is a standard measure of variation in elevation along a rail [4]. A longitudinal rail profile consists of consecutive measurements of longitudinal level and its variation is normally measured using a specialised Track Recording Vehicle (TRV) fitted with optical instruments. TRVs are expensive to operate and occupy the track, reducing the availability of the asset for revenue generating operations. Using in-service vehicles to monitor the track represents a potential cost-saving to track owners.

Variation in track longitudinal profile induces a vertical dynamic response in a vehicle crossing the profile [5]. This dynamic response has the potential to be used to determine that profile. Variations in track profile can then be monitored over time for maintenance purposes.

The Cross Entropy (CE) optimisation method is used in this paper to determine rail profiles from vehicle accelerations. A 2D planar car model and 2D finite element track model are used in the numerical method. The effect of added signal noise and uncertainty in vehicle and track properties is investigated. The sensitivity of the CE method is tested for two levels of randomly applied uncertainty in selected vehicle and track properties.

Using idealised numerical models to predict real-world behaviour of mechanical systems such as railway vehicles and track is dependent on the stability of the numerical method

and accuracy of the mechanical properties used [6]. Accurate measurement of mechanical properties for the purposes of model calibration is a challenge. Uncertainty in mechanical properties can occur through many sources including measurement, variation in material properties and non-linearities.

Any method using idealised numerical models to infer information from measured field data must display a tolerance to model parameter uncertainty. Uncertainty in mechanical properties is applied through a normal distribution function. In this paper the means of the model properties are taken from published values.

The main objectives of this paper are to find track longitudinal profile from measured vehicle acceleration through optimisation and, secondly, test the accuracy of the method due to uncertainty in selected vehicle and track properties.

2 NUMERICAL MODELS

2.1 Vehicle Model

Numerical models are used in this paper to characterise the dynamic interaction between a railway vehicle and the track. The vehicle, shown in Figure 1, is modelled as a 2D multi-body system consisting of 10 Degrees of Freedom (DOF) which is a common approach adopted by other researchers [7]–[9]. Rigid bars are used to represent the car body and two bogie frames. The wheels are represented as lumped masses. Spring and dashpot systems are used to connect the constituent parts of the vehicle and represent the primary and secondary suspension systems. Vehicle properties used in this study are listed in Table 1 and are taken from Zhai et al. [10].

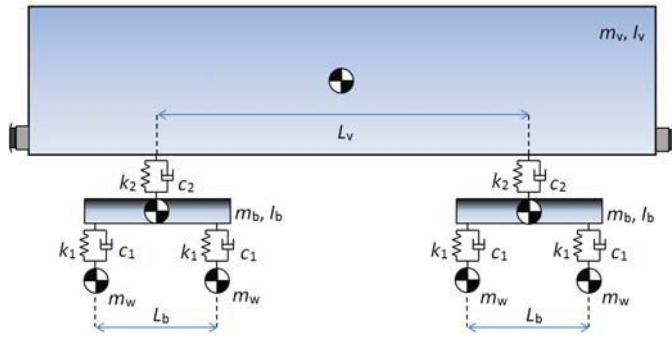


Figure 1. 2D car vehicle model – Car body and bogies represented by rigid bars connected by spring and damper systems representing vehicle suspension systems

Table 1. Properties of 2D car vehicle (Zhai *et al.* [10])

Property	Unit	Symbol	Value
Wheelset mass	kg	m_w	1 844
Bogie mass	kg	m_b	5 631
Main body mass	kg	m_v	59 364
Bogie moment of inertia	kg.m ²	I_b	9 487
Main body moment of inertia	kg.m ²	I_v	1.7×10^6
Primary suspension stiffness	N/m	k_1	4.8×10^6
Secondary suspension stiffness	Ns/m	k_2	1.8×10^6
Primary suspension damping	N/m	c_1	60×10^3
Secondary suspension damping	Ns/m	c_2	90×10^3
Distance between bogies	m	L_v	11.46
Distance between axles	m	L_b	3

2.2 Track Model

The finite element track model (Figure 2) consists of an Euler-Bernoulli beam (representing a UIC60 rail) resting on three layers of sprung mass systems set apart at regular intervals to represent the sleeper spacing. There is one beam element per sleeper spacing. Sleepers and ballast are modelled as lumped masses and are connected to the rail and each other by sets of spring and dashpot systems representing the visco-elastic behaviour of the rail pad, ballast and the sub-ballast. A similar track model is used throughout the literature [11]–[13]. Mechanical properties of the track are taken from Zhai *et al.* [14] and listed in Table 2.

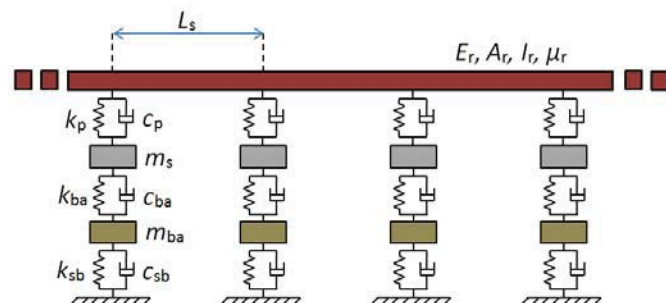


Figure 2. 3-layer track model representing rail, sleepers and ballast resting on rail pads, ballast and sub-ballast respectively

Random irregularities are added to the rail profile through the use of a Power Spectral Density (PSD) function. Definitions of PSD functions for the generation of rail

irregularities differ from country to country due to differences in measurement and evaluation techniques [15]. The American FRA rail classification system, described in [16], is applied here to generate the profiles used in the Vehicle Track Interactions (VTIs).

Table 2. Properties of 3-layer track (Zhai *et al.* [10])

Property	Unit	Symbol	Value
Rail elastic modulus	N/m ²	E_r	20.6×10^{10}
Rail cross-sectional area	m ²	A_r	7.7×10^{-3}
Rail second moment of area	m ⁴	I_r	32.2×10^{-6}
Rail mass per unit length	kg/m	μ_r	60.64
Rail pad stiffness	N/m	k_p	65×10^6
Rail pad damping	Ns/m	c_p	75×10^3
Sleeper mass	kg	m_s	251
Sleeper spacing	m	L_s	0.545
Ballast stiffness	N/m	k_{ba}	138×10^6
Ballast damping	Ns/m	c_{ba}	59×10^3
Ballast mass	kg	m_{ba}	531.4
Sub-ballast stiffness	N/m	k_{sb}	78×10^6
Sub-ballast damping	Ns/m	c_{sb}	31.1×10^3

2.3 Coupled Model

The vehicle and track models are coupled together by updating coupled terms of the equations of motion at each time step. It is assumed that the wheels remain in contact with the rail and that no decoupling occurs. A more complete description of the coupling and details on validation are available in [17].

The coupled equations of motion are solved in Matlab [18] using the Wilson- θ numerical integration scheme [19], [20]. A value of $\theta = 1.402815$ is used to ensure unconditional stability of the algorithm [21]. A time step of 0.002 s is used in all simulations corresponding to a sensor scan rate of 500 Hz.

A VTI analysis is carried out and the acceleration signal generated at the leading bogie sprung DOF, referred to as the reference acceleration signal, is used as input into the optimisation algorithm. The bogie acceleration signal is found to be most sensitive to vehicle primary stiffness, and both primary and secondary damping. For the track, sensitivity analysis finds that the four properties with the most influence on the vehicle bogie acceleration signal are the rail pad stiffness, ballast stiffness, sub-ballast stiffness and ballast mass. Randomly generated uncertainty is applied to these properties prior to initiating the optimisation method.

3 METHODOLOGY

Cross Entropy (CE) is the optimisation method used in this paper to find the rail longitudinal profiles. Detailed descriptions of the method can be found in [22]–[25]. CE optimisation is an iterative method in which a population of trial solutions (a population of longitudinal profiles in this case) is randomly generated. Using the 1st generation of trial solutions, an objective function is used to identify an ‘elite set’ of the best solutions. From the vector mean value of the elite set, a new generation of improved trial solutions is then generated. This process is repeated until convergence is achieved.

The objective function used in this study is shown in Equation 1. The squared differences between each value in the measured reference acceleration signal, \ddot{u}_{meas} and the vehicle acceleration calculated for a trial profile, \ddot{u}_{trial} is used. This differs from conventional CE in that each elevation in the profile is assessed in a sub-function, O_t :

$$O_t = (\ddot{u}_{trial,t} - \ddot{u}_{meas,t})^2 \quad (1)$$

where t is the scan number.

A schematic of the objective sub-function is shown in Figure 3. The population of estimates consists of k profiles consisting of m elevations in vector x . The optimisation sub-function O_t ranks each elevation in the population to form an elite set of values for each elevation. Each elite set is used to calculate the mean, μ , and standard deviation, σ , for the individual elevation values which are then combined to generate the next population of profile estimates.

As a result of the vehicle dynamic response to the profile, the rail elevation at a given location affects accelerations at many downstream times after the vehicle passes this point on the track. Mixing elevations from different profiles may therefore seem surprising. The approach is analogous to the Building Block hypothesis used in the Genetic Algorithm [26], i.e., the hypothesis that combining parts (building blocks) from different solutions with good features is likely to result in a good solution overall.

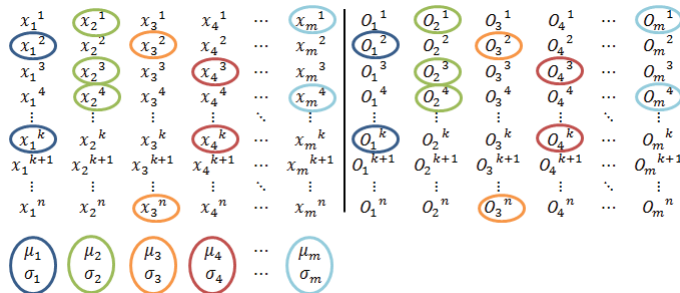


Figure 3. Cross Entropy optimisation sub function

The optimisation is split into phases where a small section of the track profile is inferred before stepping to the next phase. This reduces the number of unknowns in the problem. The phase windows are overlapped so that the results from the previous phase are used to ‘seed’ the first population of estimates for the subsequent phase. This windowing technique is described in more detail in Harris *et al.* [22].

4 RESULTS

The results of numerical tests using the CE method to determine rail longitudinal profiles are presented in this section. The sensitivity of the method to added signal noise and uncertainty in selected vehicle and track properties is tested. An FRA Class 4 rail profile, typical for conventional railway track, is randomly generated using its PSD function. The same rail profile is used throughout the paper so that comparisons can be made between the results. The 2D car vehicle traverses the track model at a constant velocity of 150 km/h. 3% Gaussian signal noise is added to the reference

acceleration signal prior to initialisation of the optimisation algorithm. The optimisation parameters used are presented in Table 3.

Table 3. Cross Entropy optimisation parameters

Property	Value
Length of profile inferred per phase	0.883m
Number of elevation unknowns, m , in each profile	10
Initial mean, μ	0
Initial standard deviation, σ	1
Size of each population of estimates, k	100
Size of elite set (percentage of k)	10
Convergence threshold	1e-13

A sum of squared differences per unit length measure of error is applied in this study to compare the elevations in the inferred profiles, $x_{inf,t}$ to the actual profile, x_{act} .

$$SSD\ Error = \sum_{t=1}^T (x_{act,t} - x_{inf,t})^2 / L \quad (2)$$

where L is the length of track inferred and T is the total number of scans in the signal.

Figure 5a shows inferred profiles resulting from 10 CE optimisations with no uncertainty in vehicle and track properties considered. A good estimation of rail profile is achieved in the presence of 3% added signal noise. There appears to be an accumulation of error in which manifests itself as a drift from the actual profile. Figure 4 shows SSD Error for results presented in Figure 5a. The variation in inferred profiles and accuracy is due to the added signal noise being different for each optimisation.

Figure 5b and 5c show the inferred profiles when 3% added signal noise and vehicle and track uncertainty of 5% and 10% are considered respectively, this time for 20 tests. Again, good approximations of the actual profile are given by the method with a level of drift similar to that shown for 0% uncertainty. This is confirmed by the similarity in SSD Error for all inferred profiles.

Figure 6 and Figure 7 show the randomly generated vehicle and track properties used in the optimisations for 5% and 10% uncertainty respectively. No clear relationship is found between the level of SSD Error and variation in any vehicle or track property tested. From these results it can be deduced that the method has a good tolerance to at least 10% uncertainty in the vehicle and track properties tested.

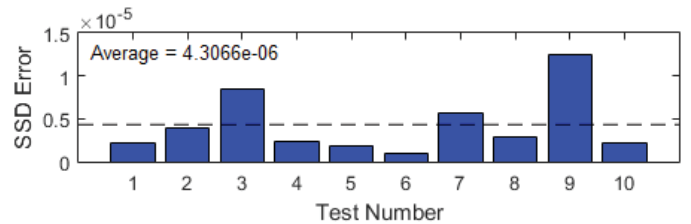


Figure 4. SSD Error between actual profile and inferred profiles presented in Figure 5a. (0% uncertainty in vehicle and track properties)

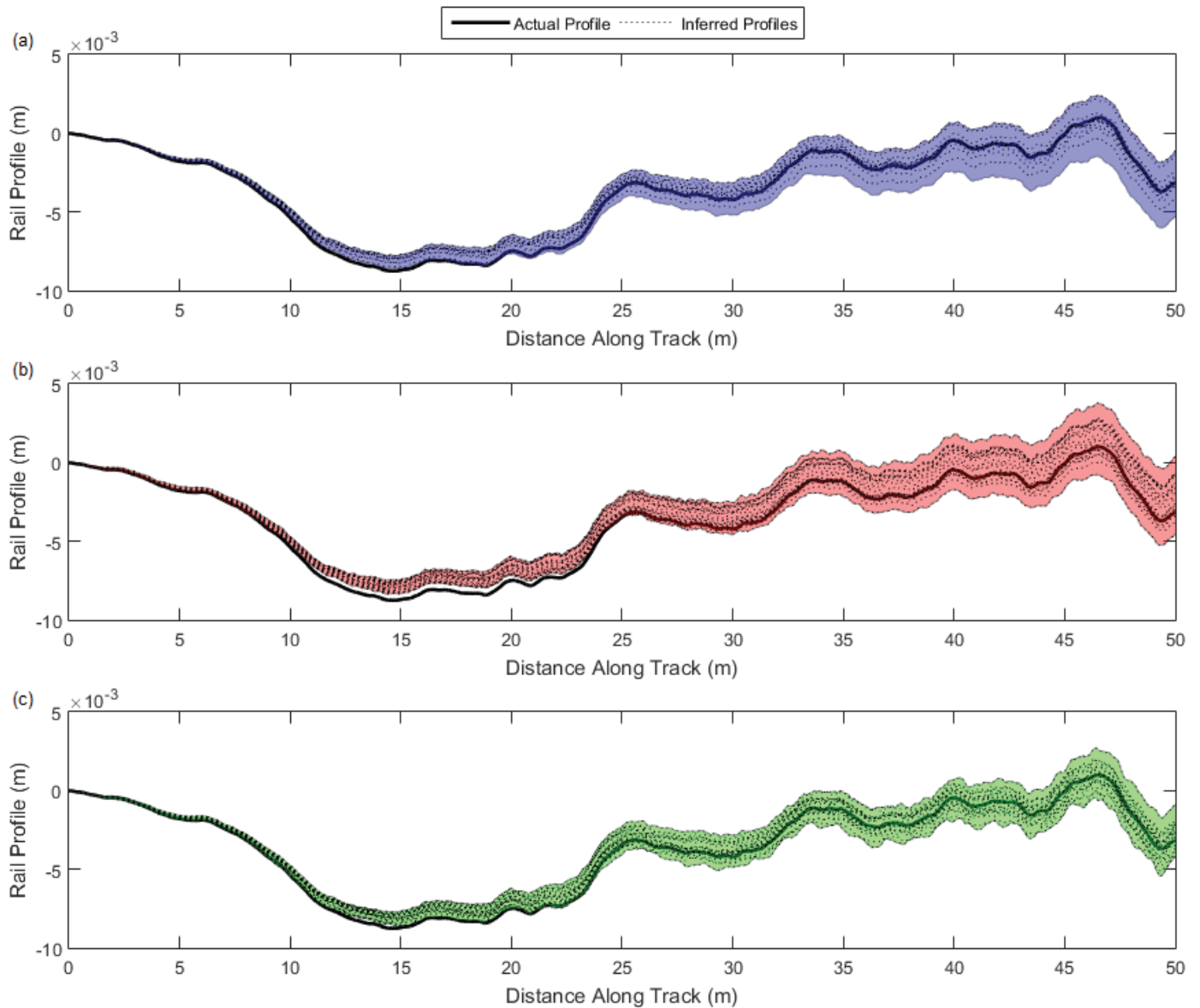


Figure 5. Actual and inferred profiles for FRA Class 4 rail profile with 3% added signal noise to bogie acceleration signal considering varying levels of uncertainty in vehicle and track properties a) 0% uncertainty (10 profiles); b) 5% uncertainty (20 profiles); c) 10% uncertainty (20 profiles). The shading represents the range of all inferred profiles

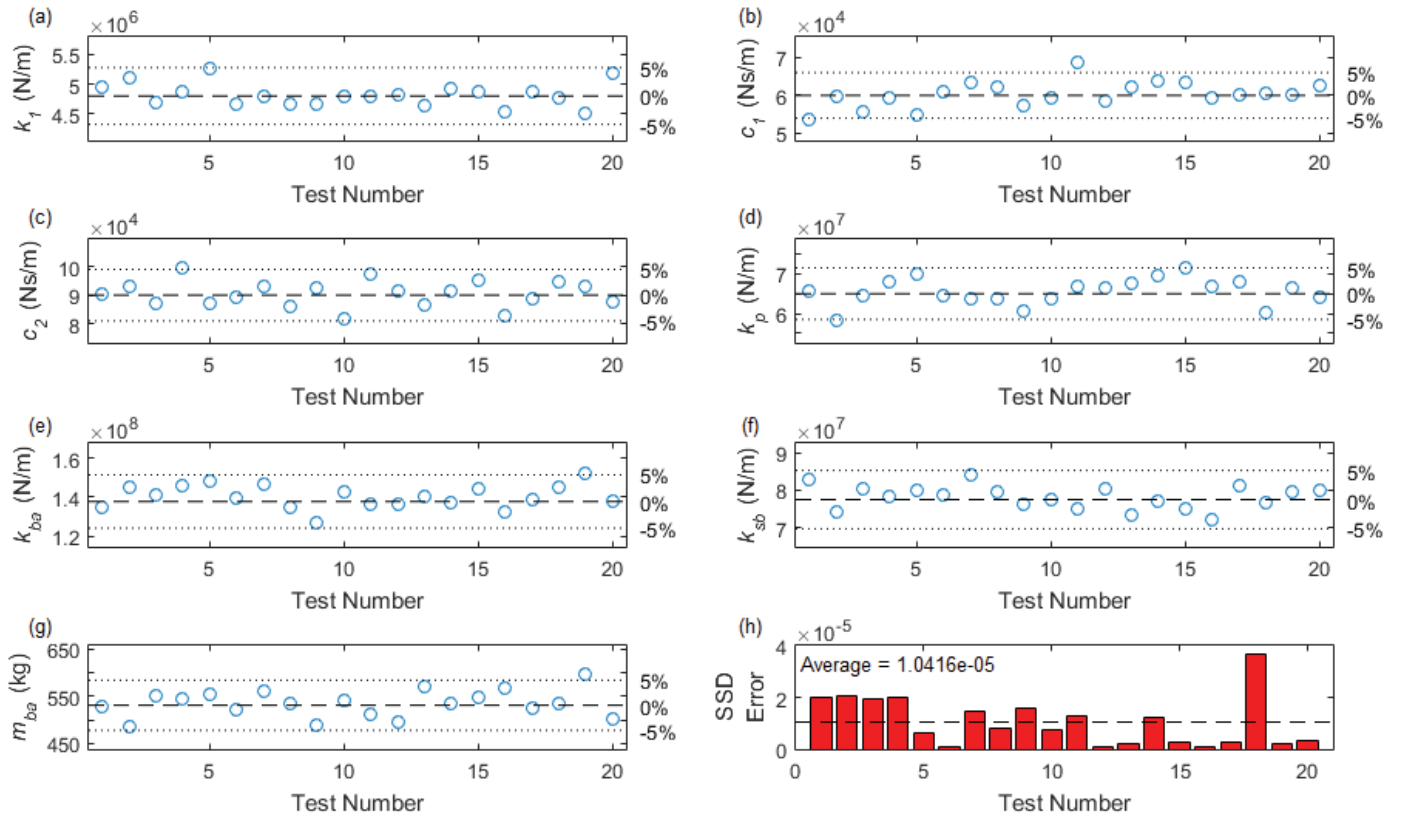


Figure 6. Vehicle and track property values used in optimisation vs. optimisation test number – 5% uncertainty; a) vehicle primary stiffness; b) vehicle primary damping; c) vehicle secondary damping; d) track rail pad stiffness; e) track ballast stiffness; f) track sub-ballast stiffness; g) track ballast mass; h) SSD Error between actual profile and inferred profiles

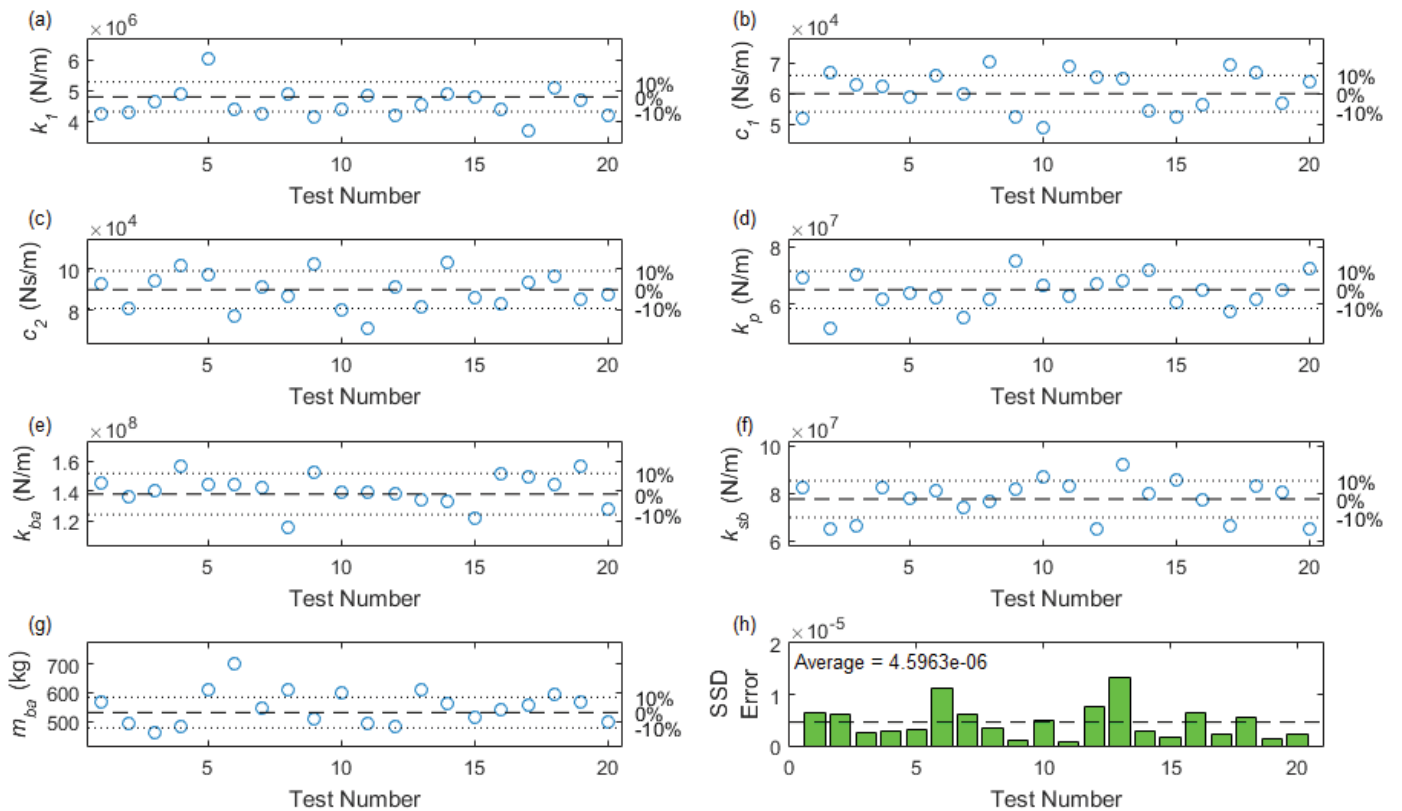


Figure 7. Vehicle and track property values used in optimisation vs. optimisation test number – 10% uncertainty; a) vehicle primary stiffness; b) vehicle primary damping; c) vehicle secondary damping; d) track rail pad stiffness; e) track ballast stiffness; f) track sub-ballast stiffness; g) track ballast mass; h) SSD Error between actual profile and inferred profiles

CONCLUSIONS

A method is presented for determining rail longitudinal profiles through inertial measurements of vehicle response. The sensitivity of the approach to uncertainty in vehicle and track properties is also tested. The results show that, considering added signal noise and no uncertainty in vehicle and track properties, the method returns good estimates of the actual track longitudinal profile albeit rarely providing an exact match. The 10 results presented vary slightly from each other and are prone to accumulation of small errors. This variation in results can be attributed to the method of evaluating each acceleration signal value individually, i.e. attempting to match to a noisy signal which is different for each optimisation. Due to the low level of error the method still has potential to detect local variations in profile which is useful information for maintenance planning.

The method retains a similar level of error when 5% and 10% uncertainty in the vehicle and track properties are considered. This tolerance to property uncertainty is critical to any real-world application of the method owing to the difficulty in accurately defining mechanical properties for rail vehicle and track models.

The method has the potential to be used with measurements taken from trains in regular service, thereby allowing them to be used as unattended track monitoring systems. Accurate knowledge of rail longitudinal profile allows asset managers make informed decisions on when and where to plan track maintenance.

ACKNOWLEDGEMENTS

The research presented in this paper was carried out as part of the Marie Curie Initial Training Network (ITN) action FP7-PEOPLE-2013-ITN. The project has received funding from the European Union's Seventh Framework Programme for research, technological development and demonstration under grant agreement number 607524. The authors are thankful for this support.

REFERENCES

- [1] P. Weston, C. Roberts, G. Yeo, and E. Stewart, Perspectives on railway track geometry condition monitoring from in-service railway vehicles, *Vehicle System Dynamics: International Journal of Vehicle Mechanics and Mobility*, vol. 53, no. 7, pp. 1063–1091, 2015.
- [2] H. Mori, H. Tsunashima, T. Kojima, A. Matsumoto, and T. Mizuma, Condition Monitoring of Railway Track Using In-service Vehicle, *Journal of Mechanical Systems for Transportation and Logistics*, vol. 3, pp. 154–165, 2010.
- [3] J. S. Lee, S. Choi, S. S. Kim, C. Park, and Y. G. Kim, A mixed filtering approach for track condition monitoring using accelerometers on the axle box and bogie, *IEEE Transactions on Instrumentation and Measurement*, vol. 61, no. 3, pp. 749–758, 2012.
- [4] IS EN 13848: Railway Applications - Track - Track Geometry Quality - CEN European Committee for Standardisation. .
- [5] S. D. Iwnicki, *Handbook of railway vehicle dynamics*. Taylor & Francis, 2006.
- [6] G. N. Absi and S. Mahadevan, Multi-fidelity approach to dynamics model calibration, *Mechanical Systems and Signal Processing*, no. 68–69, pp. 189–206, 2016.
- [7] X. Lei and N.-A. Noda, Analyses of dynamic response of vehicle and track coupling system with random irregularity of track vertical profile, *Journal of Sound and Vibration*, vol. 258, no. 1, pp. 147–165, 2002.
- [8] P. Lou and F. T. K. Au, Finite element formulae for internal forces of Bernoulli-Euler beams under moving vehicles, *Journal of Sound and Vibration*, vol. 332, pp. 1533–1552, 2013.
- [9] Y. Q. Sun and M. Dhanasekar, A dynamic model for the vertical interaction of the rail track and wagon system, *International Journal of Solids and Structures*, vol. 39, no. 5, pp. 1337–1359, 2002.
- [10] W. M. Zhai, K. Y. Wang, and C. Cai, Fundamentals of vehicle-track coupled dynamics, *Vehicle System Dynamics: International Journal of Vehicle Mechanics and Mobility*, vol. 47, no. 11, pp. 1349–1376, 2009.
- [11] K. Nguyen, J. M. Goicolea, and F. Galbadon, Comparison of dynamic effects of high-speed traffic load on ballasted track using simplified two-dimensional and full three-dimensional model, *Proceedings of the Institution of Mechanical Engineers, Part F: Journal of Rail and Rapid Transit*, vol. 228, pp. 128–142, 2014.
- [12] F. Lu, D. Kennedy, F. W. Williams, and J. H. Lin, Symplectic analysis of vertical random vibration for coupled vehicle-track systems, *Journal of Sound and Vibration*, vol. 317, no. 1–2, pp. 236–249, 2008.
- [13] X. Lei and B. Zhang, Influence of track stiffness distribution on vehicle and track interactions in track transition, *Proceedings of the Institution of Mechanical Engineers, Part F: Journal of Rail and Rapid Transit*, vol. 224, pp. 592–604, 2010.
- [14] W. M. Zhai, K. Y. Wang, and J. H. Lin, Modelling and experiment of railway ballast vibrations, *Journal of Sound and Vibration*, vol. 270, no. 4–5, pp. 673–683, 2004.
- [15] L. Fryba, *Dynamics of railway bridges*. London: Thomas Telford, 1996.
- [16] A. R. Berawi, Improving railway track maintenance using power spectral density, 2013.
- [17] D. Cantero, T. Arvidsson, E. O'Brien, and R. Karoumi, Train-track-bridge modelling and review of parameters, *Structure and Infrastructure Engineering*, vol. 2479, no. September, pp. 1–14, 2015.
- [18] MathWorks, Matlab. 2016.
- [19] K. J. Bathe and E. L. Wilson, *Numerical methods in finite element analysis*. Englewood Cliffs, UK: Prentice Hall, 1976.
- [20] J. W. Tedesco, W. G. McDougal, and C. A. Ross, *Structural dynamics, theory and applications*. California, USA: Addison Wesley Longman, 1999.
- [21] W. Weaver and P. R. Johnston, *Structural dynamics by finite elements*. Indiana, USA: Prentice Hall, 1987.
- [22] N. K. Harris, A. González, E. J. O'Brien, and P. J. McGetrick, Characterisation of pavement profile heights using accelerometer readings and a combinatorial optimisation technique, *Journal of Sound and Vibration*, vol. 329, no. 5, pp. 497–508, 2010.
- [23] J. Dowling, E. J. O'Brien, and A. González, Adaption of Cross Entropy optimisation to a dynamic bridge WIM calibration problem, *Engineering Structures*, vol. 44, no. 44, pp. 13–22, 2012.
- [24] P. Quirke, D. Cantero, E. J. O'Brien, and C. Bowe, Drive-by detection of railway track stiffness variation using in-service vehicles, *Proceedings of the Institution of Mechanical Engineers, Part F: Journal of Rail and Rapid Transit*, 2016.
- [25] E. J. O'Brien and J. Keenahan, Drive-by damage detection in bridges using the apparent profile, *Structural Control and Health Monitoring*, vol. 22, no. 5, pp. 813–825, 2014.
- [26] D. Goldberg, *Genetic Algorithms in Search, Optimisation and Machine Learning*. Reading, MA: Addison Wesley, 1989.

Evaluation of bridge safety based on Weigh-in-Motion data

Barbara Heitner^{1,2}, Eugene J. O'Brien^{2,4}, Franck Schoefs³, Thierry Yalamas¹, Rodrigue Décatoire¹, Cathal Leahy⁴

¹Phimeca Engineering, Cournon-d'Auvergne, France

²School of Civil Engineering, University College Dublin, Dublin, Ireland

³Research Institute of Civil Engineering and Mechanics, Université de Nantes, Nantes, France

⁴Roughan O'Donovan Innovative Solutions, Dublin, Ireland

email: heitner@phimeca.com, eugene.obrien@ucd.ie, franck.schoefs@univ-nantes.fr, yalamas@phimeca.com, decatoire@phimeca.com, cathal.leahy@rod.ie

ABSTRACT: This paper investigates various concerns, sensitivities of and correlation between the different parameters influencing the load on a bridge and its resistance to that load. The actual safety, i.e. the probability of failure, is calculated by combining the dead load, Weigh-in-Motion data based traffic load and resistance models. The usefulness of updating the developed bridge safety model using damage indicators from a Structural Health Monitoring system is also examined.

KEY WORDS: Reliability; Safety; Bridge; Probabilistic; Bayesian Updating.

1 INTRODUCTION

1.1 Motivation

Probabilistic assessment of bridges has been the subject of various studies in recent decades. It has been widely accepted that evaluating an existing bridge according to the standards and codes used for new structures can lead to unnecessary demolition or repair, and thus to high economic cost and an increase in the associated environmental impact.

In several studies in the literature, the authors developed a complete or partial bridge safety model based on probabilistic assessment of load and/or resistance. The main focus of these studies however varies widely. Rocha et al. [1] focus on the safety assessment of short span railway bridges for identifying critical train speeds and the associated probability of failure. Hajializadeh et al. [2] primarily study the effect of spatial correlation of both load and resistance on the probability of failure of concrete road bridges. The principal aim in Zhou et al. [3] is to quantify the effect of foreseen traffic growth on the time-dependent reliability of a reinforced concrete (RC) bridge, accounting for structural deterioration caused by chloride induced corrosion. Marsh & Frangopol [4] also concentrate on the deterioration model of an RC bridge deck but improve the model by incorporating corrosion rate sensor data.

These works can also be distinguished through the simplifications, idealizations and the applied levels of these. In the present work both load and resistance of a one-directional (single lane) bridge are modelled in a probabilistic context and the bridge safety is found by combining them and calculating the probability of load exceeding capacity. The structural model of the bridge is greatly simplified and loads other than dead and traffic loads are ignored, since the emphasis is placed on realistic traffic loading, the probabilistic assessments and the global methodology.

1.2 Bayesian updating

Bayesian updating is a powerful technique for combining a probabilistic model with a limited volume of information from measurement to achieve a more reliable model. It has already

been used for several different problems in the field of structural engineering, such as for estimating bridge characteristic load effects [5], for prediction of the effects of corrosion on RC beam bearing capacity [6] or for updating either fatigue reliability of steel structures [7] or degradation of RC structures [8] using non-destructive test data. In the framework of this paper a simple deflection-based damage indicator (DI) will be used as the measurement data for updating the bridge safety model and thus for obtaining a better measure of the actual condition of the studied RC bridge. It is acknowledged that more realistic damage indicators exist – deflection is used here simply to demonstrate the concept.

2 BRIDGE SAFETY MODEL

2.1 Resistance model

The resistance of the bridge is defined as the bending moment capacity of an RC deck cross-section. This resistance is calculated using both deterministic and random variables for the geometric, concrete and steel reinforcement properties. The incorporated random variables and their descriptions have been taken from the literature [9], [10], [11], [12]. The bridge is represented by a simplified 1D beam model. Spatial variability is not accounted for along the length of the beam as no deterioration process is considered.

2.2 Dead load model

As for the resistance model, the dead load model incorporates random variables that can be defined according to findings reported in the literature (e.g. after Akgül [13]). It accounts for the weight of concrete and the surface asphalt layer. Other bridge equipment is not taken into account as the corresponding load and its variation are relatively small. It can also be noted here that other loads, such as wind, thermal or seismic, are not considered in the current study.

2.3 Traffic load model

The traffic load model for this study is based on Weigh-in-Motion (WIM) data. The raw WIM data was cleaned and filtered for quality assurance purposes. There are different

techniques for cleaning WIM data [14], [15], [16] and the final result depends on individual subjective decisions. For the purpose of this study it is decided to focus on trucks that can travel without special permit on roads, i.e., standard vehicles.

Using this population of trucks, the bending moment can be calculated at each segment of the bridge induced by each vehicle at each instant in time. However it would not be efficient and useful to calculate and store all these load effects as the database may involve hundreds of thousands or even millions of heavy vehicles. Therefore it is decided to calculate daily maximum values in accordance with the Block Maximum approach as its efficiency is well known [17], [18], [3]. A drawback of this method is that only one load effect per day/block is considered, regardless of the heaviness of the actual day's traffic. In this way an inaccuracy is introduced through possibly ignoring some extreme trucks in the database. It is also to be noted that this study considers short span bridges. Hence the daily maximum load effects can be obtained from 1-truck loading events based on the assumption that these events are independent and identically distributed (iid).

There are several ways to approximate extreme data through the use of inferential statistics. For maximum bridge load effects, some of the most used tail fitting (and other) methods are studied in detail in Hajializadeh's work [19]. For bending moments induced by passing of the trucks of the database, the focus, in terms of safety, needs to be placed on the tail of this distribution, i.e., based on extreme value theory. This tail however can be defined in several ways. Some authors suggest the top $2\sqrt{n}$ data [20], where n is the number of blocks, some the top 30% [14] while Hajializadeh [19] uses the top 10% of the data as a compromise between the previous two definitions. In the current case it is decided to study both the top $2\sqrt{n}$ and 30% of data of the daily maximum bending moments for tail fitting. For fitting this block maximum data, the Generalized Extreme Value (GEV) distribution is chosen after Castillo [20]. GEV is a family of three distributions: Gumbel (type I), Fréchet (type II) and (negative) Weibull (type III), and is written as [21] :

$$G(x; \mu, \sigma, \xi) = \exp \left\{ - \left[1 + \xi \left(\frac{x - \mu}{\sigma} \right) \right]^{-1/\xi} \right\} \quad (1)$$

where μ is the location parameter, σ is the scale parameter and ξ is the shape parameter. Depending on the individual cases, any of the above three distribution can be confidently fit to the collection of extreme data, though some authors [20] argue that Fréchet is unsuitable for bridges given the natural limit on the space available and the capacity of axles.

2.4 Probability of failure

In the present study the failure of the bridge is defined as the failure of any of its segments (one or more at a time). There are several possible ways to obtain this general probability of failure. However due to the complexity of civil engineering structures, analytical solutions can rarely be derived. Hence, Monte Carlo simulation is widely preferred and its suitability has already been proven in several studies [22], [19], [4] for computing probabilities of structural failure. Assuming full

correlation between the segments, the results are independent from the discretisation of the bridge as shown in the following formulas:

$$Pf_{MC} = \frac{\sum_{j=1}^{N_{sim}} I_j}{N_{sim}} \quad (2)$$

where N_{sim} is the total number of simulations, j is the actual simulation and I_j can be expressed as:

$$I_j = \begin{cases} 1, & \text{if } G_j \leq 0 \\ 0, & \text{otherwise} \end{cases} \quad (3)$$

where the limit state function, G , of the j^{th} simulation is written as:

$$G_j = \min \left[C_{ij} - E d_{ij} - E t_{ij} \right] \quad (4)$$

where $i=1 \dots k$ and k is the number of segments in the bridge.

2.5 Bayesian updating

Until this point it has been assumed that the bridge is generally healthy, i.e. neither local damage nor a time-dependent deterioration process is assumed. However the aim of the methodology is to evaluate ageing bridges or bridges subject to impact where the occurrence of damage cannot be ignored. In most of the studies to date, damage of reinforced concrete bridges is accounted for through a corrosion process that decreases the area of the reinforcement and results in a time-dependent resistance model as presented by Enright & Frangopol [23]. Additionally, in many recent studies the spatial variability of resistance is also accounted for [24], [4], [22].

In the current paper it is proposed to apply Bayesian updating based on a damage indicator (DI). There are various damage indicators that can be used in the proposed model. The important point is to find a DI which is

- Relatively easy to measure;
- Gives relevant information about possible damage extent;
- And damage location in the bridge.

3 EXAMPLE APPLICATION

3.1 The bridge model

The simplified bridge model which is used in the example application is presented in Figure 1.

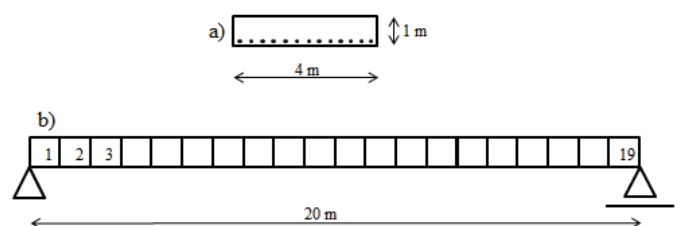


Figure 1. Example RC solid slab bridge's a) cross-section and b) longitudinal view.

3.2 Initial Weigh-in-motion (WIM) data

An extensive database of Weigh in Motion (WIM) data was available, courtesy of the Federal Highway Administration's Long Term Pavement Performance (LTPP) program [15]. For the purpose of this study one year (2011) of data from 19 sites in the USA are reviewed and after some preliminary investigation, a typical site is chosen: Illinois, I57. The total number of heavy vehicles in this database is 832,307 for 253 days (all working days in 2011) with an average daily truck traffic in the monitored lane of 3281. The main data of the trucks recorded can be seen in Table 1.

Table 1. The mean values and Confidence Intervals (CI) of the main parameters of WIM data.

	Unit	Mean	CI _{95%-}	CI _{95%+}
Speed	[km/h]	105.95	94.94	117.47
GVW	[tons]	22.93	3.81	35.88
Length	[m]	19.84	6.1	24.10
No. of axles	[-]	4.57	2	5
Wheel base	[m]	16.10	3.60	20.86
Gap behind	[sec]	37.00	1.41	106.6

The database had already been cleaned according to federal and state regulations [15] to give only the trucks travelling without a permit, assuming that the road/bridge owner is able to monitor and even to restrict the flow of permit trucks if needed. There are however some surprisingly heavy, long vehicles or vehicles having a surprisingly high number of axles. These may happen for one of two reasons. Firstly there had been no cleaning regarding the Gross Vehicle Weight (GVW) due to the inability to distinguish between permit and illegally over-loaded trucks. This can result in some suspiciously heavy vehicles passing through the filter that may be outliers or permit trucks. Secondly, there are so-called 'grandfather rights' and 'routine permit' trucks [25], which can have more specific axle-configurations and more than 8 axles in total but which however can travel regularly on the roads of the state.

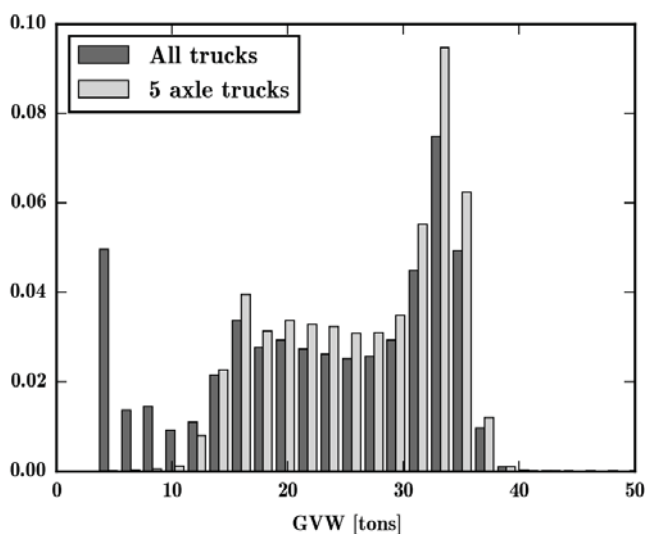


Figure 2. GVW histogram for all the trucks and for only 5-axle trucks at Illinois, I57 site.

The distribution of GVW for the trucks included in this study is shown in Figure 2. There are two major modes visible: one around 4 tons, which is caused mainly by 3 and 4 axle trucks and one around 35 tons, caused by fully loaded 5 and 6 axle trucks. In general, excluding the lightest vehicles, the histogram of the overall GVW strongly resembles the shape of the GVW histogram of the 5-axle trucks only (Figure 2). This is due to the fact that more than 75% of the total number of vehicles in the database are 5-axle trucks.

3.3 Data filtering

There are several ways of further cleaning/filtering WIM data, depending on the purpose of the study in question. The most common aspects and recommendations can be found in the study of Enright and OBrien [26]. However in the present work it is agreed to apply as few additional filters as possible in order not to exclude any truck that is realistic and can infer significant load effect in the bridge. After studying the population of trucks in detail, only one severe issue arose and led to further filtering of the database.

The 'gap behind' data show how far two consecutive trucks travel from each other. 0.2 sec can be set as a lower limit for a reasonable gap. Therefore trucks traveling closer than 0.2 sec (depending on the speed this can correspond to about 4-5 metres) are investigated further. These trucks can be divided into two groups: those with very similar speed and those with different speed. The trucks which travel very closely at around the same speed are assumed to actually be the same truck and are therefore merged into one vehicle. It is assumed that an error occurred in the measurements and the original truck happened to be split into two parts. On the other hand trucks traveling very close to each other but having different speed are simply excluded (filtered out) from further study.

3.4 Importance sampling of trucks

The primary aim of using WIM data is to calculate realistic bending moments in the bridge induced by the traffic load. To achieve this the bending moment induced during the vehicles' passing is calculated using the bridge's influence line. The Block Maximum method is applied to provide a time reference and to reduce the quantity of data.

To obtain the maximum bending moment per day for each segment (using the WIM data), Monte Carlo simulation could be used directly but it would reduce the computational advantage of the Block Maximum method. Therefore it is decided to use importance sampling to simulate only the trucks that are expected to have a critical effect on the bridge, i.e. that have a high chance to cause the daily maximum load effect. It is clear that the maximum bending moment per day will be triggered by trucks with either

1. high axle loads and/or GVW, or
2. small inter-axle spacings and/or wheelbase.

3.5 Daily maximum load effect

For each day of the year the trucks assumed to be the most critical are sampled from the population and the maximum bending moments they induce in each segment of the bridge during their passing are calculated. Afterwards the daily maximum values are chosen from the resulting data for each segment. The parameters used to condition the importance sampling (for identifying critical trucks) are as follows:

1. Trucks with the greatest GVW (top 20 trucks per day);
2. Trucks with the highest maximum individual axle loads (top 20 trucks per day);
3. Trucks with the highest tandem axle loads (top 20 trucks per day);
4. Trucks with the highest tridem axle loads (top 10 trucks per day);
5. Trucks having the highest density of weights, i.e. the highest GVW/wheelbase ratio (top 20 trucks per day).

This importance sampling process results in a maximum of 90 trucks (usually around 60 due to overlapping among the conditions) per day. The contribution of the sampling conditions regarding each segment of the bridge can be seen in Figure 3.

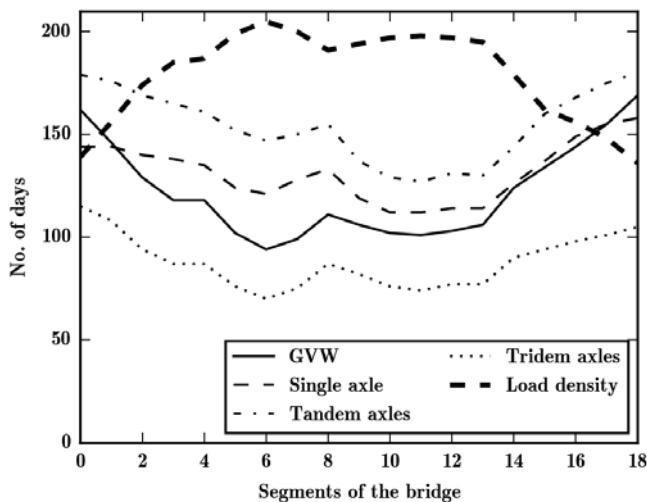


Figure 3. The contributions of the different importance sampling conditions to the daily maximum bending moment.

The absolute daily maximum load effects obtained through importance sampling are validated against the maximum daily values of the original WIM data of one week. Each graph shows from segments 0 to 18 (x axis) how many days out of the 253 (y axis) the condition is successful in sampling the truck causing the absolute maximum load effect. There is a clearly visible trend differentiating the segments closer to the middle of the bridge from those closer to the edges. Therefore it can be seen that a single criterion for the importance sampling cannot be used if the aim is to study all segments of the bridge. In addition, the maximum effectiveness, reached at the 6th segment by the 5th condition (load density), still does not exceed 85% (which would be 215 out of 253), which indicates once more the need of a multi-criteria system.

3.6 Final load effect distribution

In the original database there are more than 800 000 trucks. They are however still collected only for the time duration of one year, leading to 253 daily maximum values of load effect. To overcome this limitation, it is necessary to introduce inferential statistics. The ultimate goal is to find the

distribution of the most critical load effects the bridge may experience in the return period which may lead to its failure.

Using a Gumbel probability paper plot it is possible to obtain an idea about which GEV distribution the data follows most closely (see Figure 4). Applying the maximum likelihood method, both Gumbel and Weibull distributions are fitted for tail assumptions ($2\sqrt{n}$ and 30%). In most cases it is difficult to decide between the different fits by engineering judgement. Therefore the Kolmogorov-Smirnov test is applied and it provides two main conclusions. Both the Weibull and Gumbel distributions fit well to both types of tail data (all p-values, i.e. risks of incorrectly rejecting the proposed distributions, are much higher than the chosen significance level of 0.05). However as a decision is unavoidable, it is advised to make it segment-based (see some resulting p-values in Table 2) to obtain the most realistic tail distribution for each segment. After some investigations it is decided to use $2\sqrt{n}$ number of data (which gives higher p-values, i.e. closer fits, for the critical segments close to the midspan of the bridge) but to allow for both Weibull and Gumbel fits depending on the segment in question. For each segment, the GEV distribution fit with the higher p-value is chosen according to the Kolmogorov-Smirnov test results that can be found in Table 2.

Table 2. P-values of the Kolmogorov-Smirnov tests

Segment	Tail of $2\sqrt{n}$		Tail of 30%	
	Gumbel	Weibull	Gumbel	Weibull
6	0.644	0.614	0.667	0.432
7	0.785	0.717	0.654	0.648
8	0.899	0.760	0.651	0.755
9	0.903	0.946	0.706	0.776
10	0.963	0.856	0.410	0.609

As an example the Gumbel probability paper plot of daily maximum bending moment in the mid-segment of the bridge and its different tail fittings are shown in Figure 4.

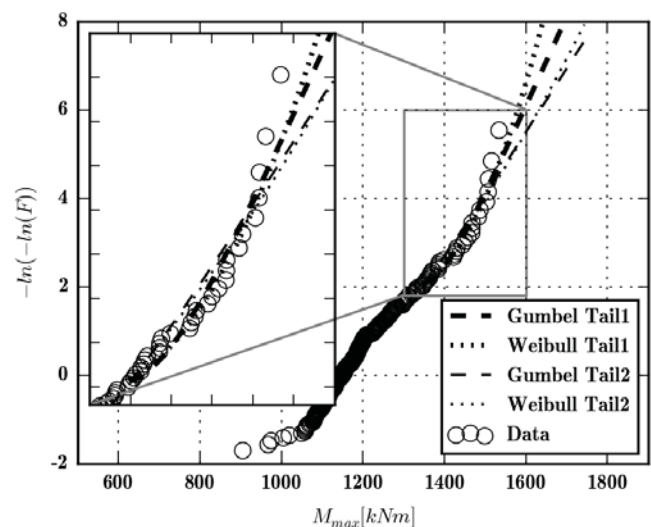


Figure 4. Gumbel probability paper plot of the daily maximum bending moment at the mid-segment of the bridge.

3.7 Resistance and dead load models

In this example the bridge is assumed to be a simply supported RC solid slab bridge, whose geometry is presented in Figure 1. To build the resistance and dead load models, several parameters are taken stochastically, using the descriptors found in the literature for defining their distributions (Table 3). All variables are considered to be normally distributed.

Table 3. Descriptors of the stochastic parameters.

Parameter	Nominal value	Unit	Mean value	Standard deviation
Slab depth	1000	[mm]	+ 0.8	3.6
Concrete cover	50	[mm]	+ 6	11.5
Concrete compressive strength	45	[N/mm ²]	+ 7.4	6
Steel yield strength	400	[N/mm ²]	+36	21.3
Unit weight of concrete	23.68	[kN/m ³]	x 1.05	x 0.11
Unit weight of asphalt	22.73	[kN/m ³]	x 1.0	x 0.25
Thickness of asphalt	80	[mm]	+ 0	40

Using Monte Carlo simulation, resistance is calculated given both deterministic and stochastic parameters. For the resulting data normal distribution is fitted and this distribution is identical for all the segments, since spatial variability of resistance is ignored at this point. The dead load is calculated similarly; however the induced bending moments are already spatially variable and so an empirical distribution of moments due to dead load is obtained for each segment separately. In the next step, a normal distribution is fitted to each of them.

3.8 Probability of failure

As described above, three distributions are obtained for each segment of the bridge. A normal distribution for the bending moment capacity, a normal distribution also for the dead load and finally a GEV distribution for the traffic load. The capacity distribution is taken here to be identical for all the segments, while the load distributions vary between segments. The probability of failure is obtained by Monte Carlo simulation according to the equations 2-4.

For the case of a healthy bridge, (without assuming any damage) it can be easily understood that for a simply supported bridge, the mid-segment represents the critical part, while the segments close to the supports can expect significantly lower probability of failure. However if accounting for damage this can change and it cannot be foreseen which segments will be the most critical. It is therefore necessary to consider all segments of the bridge when calculating the probability of failure.

It can also be observed that the greatest daily maximum bending moment does not always appear in the exact middle segment, but somewhere close to it. This slightly unusual result can be explained in two ways. At first, although a single

moving force would always induce the greatest bending moment in the mid-segment (in the case of the simply supported bridge under study), a moving truck load can behave differently thanks to the widely varying axle configurations (see Figure 5). It is also worth noting that the daily maximum bending moment at each segment is not necessarily caused by the same single truck. It is indeed more common to observe 3-4 different trucks per day that are responsible for the all the daily maximum bending moments on the bridge.

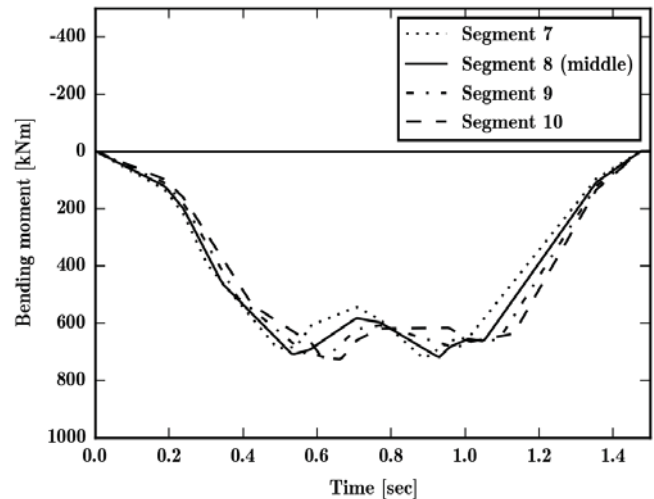


Figure 5. Truck induced bending moments in 4 different consecutive segments of the bridge due to a 5-axle truck passing

The probability of failure is calculated through equations 2-4 using Monte Carlo simulation with a sample size of 10^7 and accounting for full spatial correlation for both the moments due to dead load and traffic load along the bridge. This is on the basis that if one segment of the bridge experiences an extremely great induced bending moment, then it is very probable that all the others will do as well. However the probability of failure is calculated for each segment separately. The calculated general probability of failure of the studied bridge is 1.40×10^{-5} with a 95% confidence interval of $[1.17 \times 10^{-5}; 1.63 \times 10^{-5}]$. These values correspond to a bridge in a healthy state and this number should serve as a reference value when implementing damage in the model.

4 FUTURE WORK

Bayesian updating is briefly introduced in this paper; however the methodology is not yet implemented. The bridge safety model, that is explained and shown in this work, will be the subject of further studies that involve data from deflection-based damage indicators. The ultimate goal is to achieve a realistic general bridge safety model that is able to incorporate some new information on the damage state of the bridge that can be obtained easily, regularly and cost-effectively.

5 CONCLUSIONS

A general bridge safety model is presented in this paper. Three main parts of the model can be distinguished: moment capacity, moment induced by the dead load and moment

induced by the traffic load. The moment capacity and dead load models involve several stochastic variables based on the literature and are kept as simple as possible. On the other hand more attention is paid to the traffic load model and the calculation of the traffic-induced bending moment in the bridge. The traffic load model incorporates one year of WIM data obtained from a single site in Illinois, USA. The methodology particularly emphasizes how to build a realistic traffic load model and discusses several issues that may arise. The Block Maximum method and tail fitting are used to obtain realistic extreme bending moments in an efficient way. Throughout the work, Monte Carlo simulation is applied and importance sampling is used to keep this sometimes computationally expensive simulation method at a sustainable level. The main achievement of the present work is the relatively simple but reliable healthy bridge safety model that can be later used in a Bayesian updating framework (see in Section 4).

ACKNOWLEDGMENTS

The research has received funding from the European Union's Horizon 2020 research and innovation programme under the Marie Skłodowska-Curie grant agreement No. 642453. Federal Highway Administration (FHWA) is also thanked for providing access to their WIM database.

REFERENCES

- [1] Rocha, J.M., Henriques, A.A. and Calçada, R. (2014), 'Probabilistic safety assessment of a short span high-speed railway bridge', *Engineering Structures* 71: 99-111.
- [2] Hajializadeh, D., O'Brien, E.J. and Stewart, M.G. (2015), 'The sensitivity of bridge safety to spatial correlation of load and resistance', *Structures* 5:22-34.
- [3] Zhou, X.Y., Schmidt, F., Toutlemonde, F. and Jacob, B. (2014), 'Applying Weigh-in-motion traffic data to reliability based assessment of bridge structures', *ICOSSAR2013, 11th International Conference on Structural Safety & Reliability*, Jun 2013, New York.
- [4] Marsh, P.S. and Frangopol, D.M. (2007), 'Reinforced concrete bridge deck reliability model incorporating temporal and spatial variations of probabilistic corrosion rate sensor data', *Reliability Engineering & System Safety* 93:394-409.
- [5] Enright, B., Leahy, C. and O'Brien, E.J. (2014), 'A Bayesian approach for estimating characteristic bridge traffic load effects', *Civil Engineering Research in Ireland*, Belfast, UK, 28-29 August.
- [6] Ma, Y., Zhang, J., Wang, L. and Liu, Y. (2013), 'Probabilistic prediction with Bayesian updating for strength degradation of RC bridge beams', *Structural Safety* 44:102-109.
- [7] Zhang, R. and Mahadevan, S. (2000), 'Model uncertainty and Bayesian updating in reliability-based inspection', *Structural Safety* 22: 145-160.
- [8] Décatoire, R. (2015), *Optimisation of inspection plans for structures submitted to a stochastic degradation context: application on RC structures*, PhD Thesis. Université de Nantes, Faculté des Sciences et des Techniques.
- [9] Mirza, S.A. and MacGregor, J.G. (1979), 'Variations in dimensions of reinforced concrete members', *J Struct Div.* 105(4): 751-766.
- [10] McGee, R.W. (2001), *On the service life modelling of Tasmanian concrete bridge*, PhD Thesis, University of Tasmania, Hobart, Australia.
- [11] Attard, M.M. and Stewart, M.G. (1998), 'A two parameter stress block for high strength concrete', *ACI Structural Journal*. 95(3): 305-317.
- [12] Seo, D., Shin, S. and Han, B. (2010), 'Reliability-based structural safety evaluation of reinforced concrete members', *Journal of Asian architecture and building engineering* 9(2): 471-478.
- [13] Akgül, F. (2002), *Lifetime system reliability prediction for multiple structure types in a bridge network*, PhD thesis, University of Colorado, Boulder, Colorado.
- [14] Enright B. (2010), *Simulation of traffic loading on highway bridges*, PhD Thesis. College of Engineering, Mathematical and Physical Sciences, University College Dublin, Ireland.
- [15] Leahy, C. (2013), *Using weigh-in-motion data to predict extreme traffic loading on bridges*, PhD thesis, College of Engineering and Architecture, University College Dublin, Ireland.
- [16] Sivakumar, B., Ghosn M. and Moses F., *Protocols for collecting and using traffic data in bridge design*, NHCPR report 683, National Academy of Sciences, Washington, 2011.
- [17] Caprani, C.C., O'Brien, E.J. and McLachlan, G.J. (2007), Characteristic traffic load effects from a mixture of loading events on short to medium span bridge, *Structural Safety* 30: 394-404.
- [18] O'Brien, E.J., Bordallo-Ruiz, A. and Enright, B. (2014), 'Lifetime maximum load effects on short-span bridges subject to growing traffic volume's, *Structural Safety* 50: 113-122.
- [19] Hajializadeh, D. (2013), *Combined probabilistic modelling of load and resistance in bridges*, PhD thesis, College of Engineering, Mathematical and Physical Sciences, University College Dublin, Ireland.
- [20] Castillo, E., *Extreme value theory in engineering*, Academic Press, New York, 1988.
- [21] Coles, S., *An introduction to statistical modeling of extreme values*, Springer-Verlag, London, 2001.
- [22] Darmawan, M.S. and Stewart, M.G. (2007), 'Spatial time-dependent reliability analysis of corroding pretensioned prestressed concrete bridges', *Structural Safety* 29: 16-31.
- [23] Enright, M.P. and Frangopol, D.M. (1998), 'Probabilistic analysis of resistance degradation of reinforced concrete bridge beams under corrosion', *Engineering Structures* 20(11): 960-971.
- [24] Stewart, M.G. and Al-Harthy, A. (2008), 'Pitting corrosion and structural reliability of corroding RC structures: Experimental data and probabilistic analysis', *Structural Safety* (93): 373-382.
- [25] USDOT (2000), *Comprehensive truck size and weight study*. Washington DC: US Department of Transportation, FHWA-PL-00-029.
- [26] Enright, B. and O'Brien, E.J., *Cleaning Weigh-in-Motion data: Techniques and recommendations*, University College Dublin, 2011, available from: iswim.free.fr/doc/wim_data_cleaning_ie.pdf

Advancements of Vibration Based Damage Detection Techniques for Small to Medium Span Bridges

J.J. Moughty¹, J.R. Casas¹

¹Dept. of Civil and Environmental Engineering, Technical University of Catalonia-BarcelonaTech, Jordi Girona, 1-3, 08034 Barcelona, Spain

email: john.james.moughty@upc.edu, joan.ramon.casas@upc.edu

ABSTRACT: Overtime, the structural condition of bridges tends to decline due to a number of degradation processes, such as; creep, corrosion and cyclic loading, among others. Considerable research has been conducted over the years to assess and monitor the rate of such degradation with the aim of reducing structural uncertainty. Traditionally, vibration-based damage detection techniques in bridges have focused on monitoring changes to modal parameters and subsequently comparing them to numerical models. These traditional techniques are generally time consuming and can often mistake changing environmental and operational conditions as structural damage. Recent research has seen the emergence of more advanced computational techniques that not only allow the assessment of noisier and more complex data, but also allow research to veer away from monitoring changes in modal parameters alone. This paper presents a review of the current state-of-the-art developments in vibration based damage detection in small to medium span bridges with particular focus on the utilisation of advanced computational methods, such as machine learning, pattern recognition and advanced data normalisation algorithms.

KEY WORDS: Structural Health Monitoring; Damage Detection; Machine Learning;

1 INTRODUCTION

The identification of structural damage in bridges is a research topic that has generated significant attention in recent years. The primary reason for its surge in popularity is an aging road and rail infrastructure, which is subjected to traffic loading conditions that far surpass original design criteria. This unprecedented increase in loading accelerates structural fatigue, which in turn reduces service-life. Currently, non-destructive assessment methods entail visual inspections, impact echo tests and localised damage assessment methods. These methods, although useful and inexpensive, have numerous limitations; they are infrequent and dependent on the competence of inspectors and are confined to localised damage and external deterioration, while the true global bridge condition remains relatively unknown. Additionally, as bridge infrastructure continues to age and deteriorate, the frequency of inspection must increase to counteract the reduction in safety of these structures. This task is made more difficult due to its sheer enormity; recent figures show that Europe's highway bridge count is circa one million, and of Europe's half a million rail bridges, 35% are over 100 years old [1]. This has led to a considerable surge of research in how to efficiently manage their maintenance and upkeep [2]. Most prolific, however, is the study of vibration based damage detection and identification techniques. The present paper aims to separate the signal from the noise regarding the abundant recent developments of such techniques so that a more unified comprehension can be achieved.

2 DEVELOPMENT AND CHALLENGES OF VIBRATION BASED DAMAGE DETECTION TECHNIQUES

2.1 History of Damage Detection Techniques

The concept of using measured vibrations to discern damage in structures has been employed for some time. For instance, some early research by German engineers in the 1950's used

vibration intensities, attained from accelerations, as an empirical indicator of damage in buildings [3]. Since then, various modal parameters, such as natural frequency shifts [4], have been used for damage detection. An advantage of the frequency-based approach is its ease of application and the global nature of the identified frequencies; however, frequencies are sensitive to external conditions and cannot locate damage.

Apart from natural frequencies, other modal properties such as mode shapes, damping ratios and modal curvatures have been traditionally used to detect damage. For instance, cracking in a cross-section will increase internal friction and thus raise the value of the section's damping ratio; however, measuring damping ratios from vibration data produces large standard deviations, which impair their accuracy and effectiveness as a reliable damage indicator. Furthermore, damping ratios in bridges are heavily influenced by vibration amplitude and operational effects that further reduce their suitability as a damage indicator.

Mode shapes are quite an advantageous condition assessment tool as they are less influenced by environmental effects than natural frequencies [5] and also contain both local and global information, which can aid damage localization. Numerous mode shape monitoring techniques have been developed over the years, such as the Modal Assurance Criterion (MAC) [6], which measures mode shape changes over the entire structure by taking advantage of eigenvector orthogonality. Kim et al. [7] later advanced MAC in the development of the Coordinate Modal Assurance Criterion (COMAC) method, which monitors modal node displacement to detect and locate damage. Eq. (1) shows how COMAC can be applied to a node i , by measuring the normalised difference of mode shape vectors of the undamaged ($\phi_{i,j}^u$) and damaged ($\phi_{i,j}^d$) conditions. Application of MAC and COMAC in bridge structures found that the methods could detect most structural changes and locations, but also identified spurious

damage as well [8]. This was also observed when applied to beam structures, by Salgado [9], who showed that COMAC was prone to indicating false damage detections.

$$COMAC_{i,j} = \frac{[\sum_{j=1}^m \varphi_{i,j}^u \varphi_{i,j}^d]^2}{\sum_{j=1}^m (\varphi_{i,j}^u)^2 \sum_{j=1}^m (\varphi_{i,j}^d)^2} \quad (1)$$

Pandey et al. [10] expanded COMAC's theory to focus on the monitoring of mode shape curvatures, which are mode shapes' second derivative, in a technique known as the Modal Curvature Method (MCM). Its hypothesis is based on the relationship between modal curvature and flexural stiffness, as presented in Eq. (2) where modal curvature (φ'') is a function of cross-sectional bending moment (M) and cross-sectional flexural stiffness (EI). The premise of the MCM is that by using this relationship, one can monitor stiffness variations and detect damage, as cracks will reduce cross-sectional stiffness, resulting in a larger curvature value. Eq. (3) shows that the MCM simply uses the absolute difference between the damaged curvature ($\varphi''_{d,j}$) and undamaged curvature ($\varphi''_{u,j}$) values to detect damage. This can be conducted for single mode or for cumulative multi-mode, depending on application. This methodology demonstrated a high level of damage sensitivity and produced good results when tested [11]. The MCM has some drawbacks however; its results are dependent on the number of modes considered [12], inherent errors in curvature calculation from vibration data, usually through the central difference method, reduce the MCM's robustness. Furthermore, the MCM also requires a large quantity of sensors to ensure sufficient accuracy, particularly for higher modes, which thus reduces its practicality for mass application.

$$\varphi'' = \frac{M}{EI} \quad (2)$$

$$\Delta\varphi'' = \sum_{j=1}^m (\varphi''_{d,j} - \varphi''_{u,j}) \quad (3)$$

Modal curvatures have formed part of numerous damage detection methodologies since introduced. Most notable is the Damage Index Method (DIM) [13], which uses modal curvatures to calculate and monitor the modal strain energy between two adjacent nodes (Eq. (4)), where $\beta_{i,j}$ indicates a damage feature value for the i^{th} mode at location j , while $\varphi^{u''}$ and $\varphi^{d''}$ are the curvatures of the undamaged and damaged mode shapes, respectively, L is the element length, a and b are the limits of the evaluated element. As the DIM is based on modal curvatures, it therefore suffers from the same drawbacks as the MCM. This is particularly emphasized during the differentiation process, which amplifies high-frequency noise and can thus increase the variance of the subsequently extracted damage features.

$$\beta_{i,j} = \frac{[\int_a^b (\varphi^{d''})^2 dx + \int_0^L (\varphi^{d''})^2 dx]}{[\int_a^b (\varphi^{u''})^2 dx + \int_0^L (\varphi^{u''})^2 dx]} \cdot \frac{\int_0^L (\varphi^{u''}) dx}{\int_0^L (\varphi^{d''}) dx} \quad (4)$$

A comparative study of many of the aforementioned traditional, modal-based damage detection techniques was conducted by Talebinejad et al. [14]. The COMAC, MCM and DIM were all applied to a cable-stayed bridge FE model under varying vibration intensities and noise contamination levels. The study found that only high intensity damages were detectable through the application of these methods, that they were quite sensitive to noise contamination and that they identified numerous false damage events.

2.2 Common Challenges: Environmental and operational variability

A common challenge for many damage detection methodologies is insuring that detected damage events are truly damage and not benign system variations. Bridges are monitored over long periods of time and are subjected to large temperature fluctuations, harsh storms and numerous traffic scenarios. These varying conditions affect changes to a bridge's stiffness and mass in a non-linear manner, which in turn alters the bridge's modal properties. This is evident in Peeters & De Roeck's [15] assessment of the Z-24 Bridge in Switzerland, where significant variation in the bridge's natural frequency was observed when the ambient temperature dropped below freezing point (see Figure 1). The cause of this bi-linear behaviour was attributable to the newly solidified ice in the bridge deck contributing to its stiffness. Other authors have observed daily frequency shifts of 5% and seasonal shifts of well over 10% due to temperature fluctuations [16]. Operational variability also causes considerable frequency variation as increased mass due to traffic will reduce a bridge's natural frequency. Soyoz and Feng observed a 5% frequency reduction due to traffic while studying a bridge in California.

Small changes in natural frequency due to temperature variation can often be mistaken for structural damage and, in some cases, can also hide actual damage events, as Farrar [17] discovered when investigating the suitability of frequency variation for structural damage detection in bridges by incrementally introducing damage to a bridge girder. The expected results were that the induced damage would reduce the girder's stiffness and thus reduce its natural frequency. The actual results were quite different. Instead of the expected frequency drop, the girder's natural frequency rose for the first two damage scenarios before falling, as can be seen in Figure 2. It was subsequently revealed that the ambient temperature caused the initial increase in the girder's frequency.

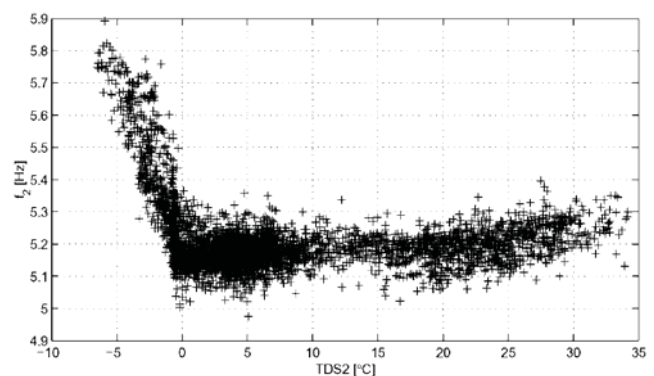


Figure 1 Z-24 Bridge - Frequency v Temperature - after [15]

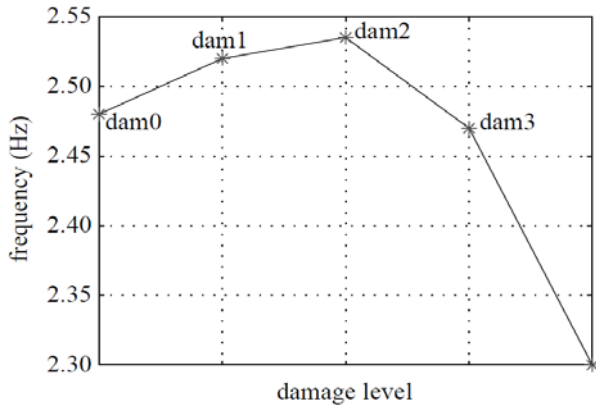


Figure 2 Frequency vs. Damage Sequence - after [17]

3 RECENT ADVANCEMENTS

3.1 Separating Environmental Variation from Damage

As mentioned in Section 2.2, environmental and operational variations have considerable influence on a bridge's dynamic behaviour which may be mistaken for damage. Data normalisation techniques help determine a bridge's baseline response under a range of normal environmental and operational conditions. Sohn [18] has previously covered numerous data normalisation methods used in SHM comprehensively. Generally, for data normalisation to be achieved, additional information is required relating to traffic and environmental conditions, usually temperature and wind speed. The process of data normalisation can be a challenge in itself due to the non-linear, multivariate nature of a bridge's behaviour and due to the quantity of data required.

Dervilis et al. [19] produced a study on the Tamar and Z24 Bridge to test a novel regression-based, multi-algorithm methodology for damage detection in changing environment and operational conditions. The algorithms used for the initial regression analysis and subsequent outlier detection in the vibration data were the Least Trimmed Squares (LTS) regression algorithm and the Minimum Covariance Determinant (MCD) estimator. The LTS regression algorithm is an adaptation on the popular least squares method of regression that minimises the sum of squared residual errors, however, instead of being applied to a full data set, it is applied to subsets, or clusters. This allows it to create a more robust fit to the data as it has a lower sensitivity overall to outliers when compared to many other regression techniques.

The MCD estimation method is applied to the LTS residual data. It is a multiple outlier detection method which expands on the classic Mahalanobis Squared Distance (MSD) method for outlier detection [20], where outliers are measured from the centre of a baseline data cluster, relative to the cluster size. The traditional MSD method has the disadvantage of potentially masking outliers, as the training data used to calculate the baseline cluster centre may already contain damage and erroneous data, resulting in an inaccurate baseline centre point. This would subsequently compromise the method's effectiveness for detecting future outliers. However, the advantage of the MCD estimation method is that it actively searches for and removes the inherent masking effect by identifying outliers in the training phase and ignoring them when calculating the cluster centre. This allows subsequent

outlier detections to be unaffected by the presence of erroneous data in the trained algorithm. It achieves this by finding the subset of data points (must be over half of total number) whose covariance matrix has the lowest possible determinant to that of the whole set. This process takes multiple iterations to be completed. The MCD baseline centre point is then computed from the final minimum covariance subset only.

Dervilis et al.'s main objective of the study is to explain that different forms of outliers give distinct and different characteristics with respect to environmental and operational variations and damage. This is achieved by plotting the LTS residuals against the MCD index and superimposing thresholds that define the change point in outlier characteristics, as presented in Figure 3 and explained in Table 1.

The Z24 Bridge vibration data was used to test the methodology's robustness in differentiating outlier differences. An example result plot of LTS residuals for temperature and first natural frequency versus MCD distance is presented in Figure 4. As can be seen, all six regions contain some data points. Region 3 contains normal behaviour data, while vertical regions 1 and 5 contain temperature induced outliers. Horizontal regions that cross the MCD threshold contain damage outliers. In the example presented the methodology was successfully able to discern the data points 1201-1500 as temperature induced variations and data points 2496-3932 as damage.

The benefit of employing this technique is that it clearly differentiates environmental induced variability from actual damage events.

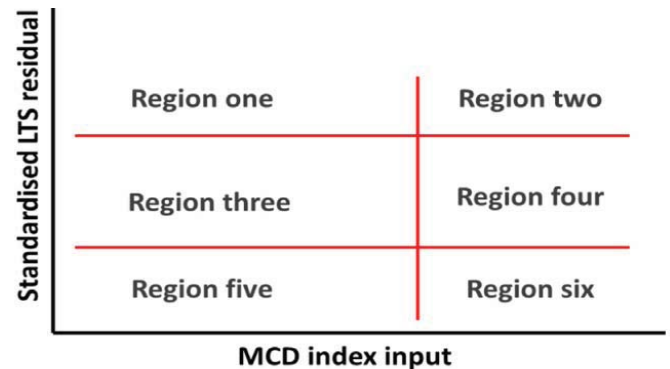


Figure 3 Residual outlier map - after [19]

Table 1 Residual outlier map description - after [19]

Region	Classification	Description
1	Vertical outlier	Outside horizontal thresholds but within vertical threshold
2	Bad leverage points	Outside horizontal thresholds and outside vertical threshold
3	Normal points	Within horizontal thresholds and vertical threshold
4	Horizontal outlier-good leverage points	Within horizontal thresholds but outside vertical threshold
5	Vertical outlier	Outside horizontal thresholds but within vertical threshold
6	Bad leverage points	Outside horizontal thresholds and outside vertical threshold

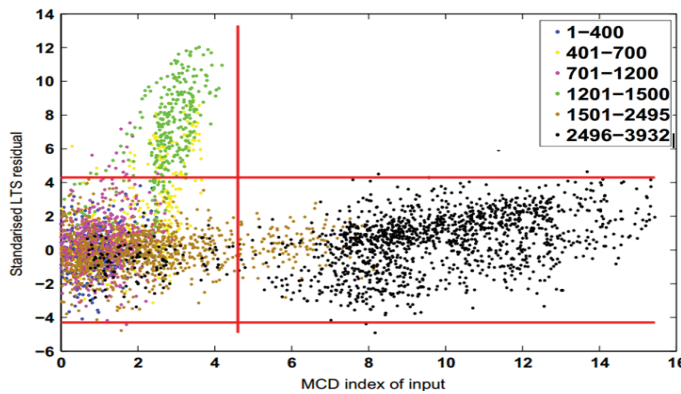


Figure 4 LTS residual vs. MCD distance - after [19]

Chatzi & Spiridonakos [21] proposed time-series based damage detection model that also attempts to infer a functional dependence between vibration data and environmental data through incorporation of a full numerical model of the structure in question. The method employed to achieve this is known as Polynomial Chaos Nonlinear AutoRegressive with eXogenous input (PC-NARX), as originally proposed in [22].

The PC-NARX model requires vibration data and temperature data as inputs so that the NARX portion of the methodology can fit a nonlinear relationship between the two in a training phase, which subsequently allows natural frequencies to be produced as an output. The Polynomial Chaos Expansion (PCE) allows parameters to be characterised as random variables, for example; acceleration time histories are represented by their PDF parameters so that measured vibration data can be handled as a set of random variables. This speeds up subsequent runtimes considerably, as large acceleration data sets can be reduced to a few representative values. Likewise, this methodology caters for the inclusion of structural uncertainty by allowing structural properties and dimensions to be included in the numerical model as PDF variables also. By having the structural properties and applied excitations, the PC-NARX can predict the dynamic response of a structure through a process called metamodeling. Chatzi & Spiridonakos demonstrate the efficiency of their proposed metamodeling of uncertain nonlinear systems subjected to stochastic excitation by comparing their predictions and simulation rates to that of a FE model. The results of which showed that the PC-NARX model achieved excellent accuracy, producing a normalised one-step-ahead prediction error of 0.0074%. Additionally, the PC-NARX based simulation rate was 100 times faster than that of the FE model. The ability of the PC-NARX methodology to accurately predict the dynamic response of a structure under varying environmental conditions implies that it should also be able to discern damage events by monitoring the magnitude of its prediction errors, as these are assumed to be normally distributed.

The PC-NARX was tested on the well known Z-24 bridge problem. Chatzi & Spiridonakos proposed a prediction error threshold of three standard deviations (99.7% confidence interval). Apart from isolated outliers, values of error outside this threshold will signify damage. The results of the Z-24 verification test showed that the PC-NARX was capable of

reliably discerning damage in a bridge subjected to varying temperature.

The PC-NARX methodology demonstrated great promise as it combines deterministic and probabilistic processes to produce an accurate and efficient tool for detecting abnormal changes in structural behaviour. However, the outputs can only be as precise as the inputs, so it is essential that the training phase includes a full seasonal cycle of environmental variables to allow the model to learn the structure's full spectrum of normal behaviour. This implies that application of the PC-NARX should be reserved for long-term monitoring purposes only.

3.2 Non-Modal Based Approaches to Damage Detection

As discussed in Section 2.1, modal based damage detection techniques contain a number of inherent drawbacks when applied to bridges. These drawbacks have led many researchers to investigate alternative procedures that circumvent the need for modal parameters. Dilella et al. [23] tested one such non-modal based technique, known as the Interpolation Damage Detection Method (IDDM), on a single span reinforced concrete bridge. The IDDM does not require a numerical model either; instead it defines a damage index in terms of deformed shapes to track changes in bridge condition. Reference deformed shapes are calculated from Frequency Response Functions (FRFs) of the undamaged structure and are used as a baseline condition for subsequent deformed shapes that are calculated during the testing and monitoring phase. By using deformed shapes as a damage indicator, one can take advantage of concentrated vibration amplitude irregularities to detect and locate damage [24]. Dilella et al. extends this base theory by incorporating a cubic polynomial spline interpolation function to the deformed shapes to extenuate behavioural variation without the need to calculate deformed shape curvatures. The detected abnormalities are denoted in IDDM by an interpolation error, which is simply the difference between the recorded and interpolated FRF profiles. Figure 5 presents a graphical explanation of the interpolation procedure conducted at a point Z_i along a beam axis Z . The term $E(z_i)$ denotes the interpolation error, calculated as the distance between the recorded signal ($H_g(z)$) and the spline interpolation value ($H_s(z)$).

Higher interpolation errors signify a higher likelihood of damage. In this way, the IDDM is a probabilistic method of damage detection whereby only interpolation errors that are greater than a pre-determined threshold value are deemed as probable damage events. This decision criterion means that there will be a certain amount of false damage and missed damage events due to some interpolation errors falling on the incorrect side of the threshold value. For this reason, the threshold value should be determined through an optimisation, or cost/benefit analysis to minimise false and missed detections. An example of the probabilities of false and missed damage events due to IDDM is portrayed in Figure 6, where E_T represents the location of the threshold value between the baseline/undamaged distribution ($P_{E,0}$) and in the possibly damaged distribution ($P_{E,d}$). The hatched areas P_m and P_f represent the probability of missed damage events and false damage events respectively. Note that threshold value is

determined from the mean of the undamaged distribution (μ_{E_0}) by the distance $v\sigma_{E_0}$, which is the variance of $P_{E,0}$ multiplied by a scaling factor (v).

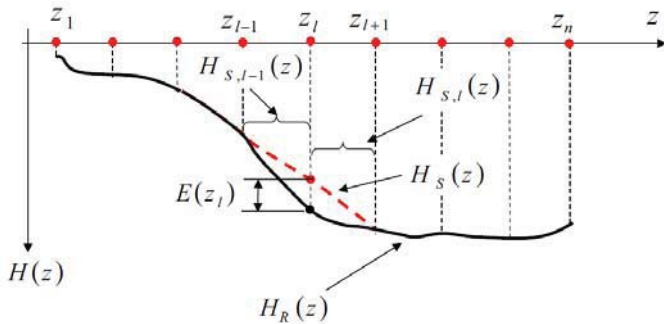


Figure 5 Spline interpolation of FRF - after [23]

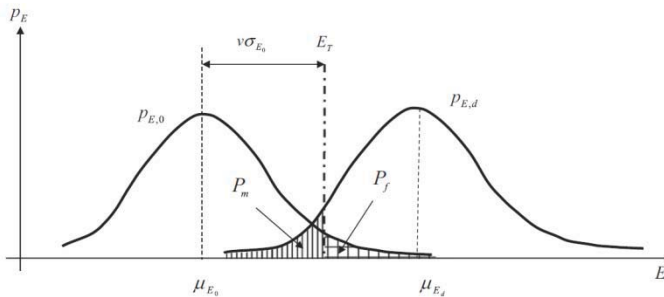


Figure 6 Threshold value and probabilities of false and missing damage events - after [23]

It should be noted that, accurate and detailed data is required for the undamaged state so that damage events can be confidently detected during the monitoring phase. However, if no data is available for the undamaged state then Dilena et al. propose a variation on the original method which will allow unsupervised damage detection to be conducted. It firstly assumes that, for an undamaged state, all sources of vibration will equally cause all locations to produce the same interpolation error variation. Conversely, if some locations produce significantly higher interpolation errors, then damage is confirmed at these locations. Again, to be deemed as damage, the interpolation error must surpass a predetermined threshold value. As the interpolation errors are assumed to be normally distributed for undamaged behaviour, the threshold value is thus calculated in terms of the average ($\mu_{\Delta E}$) and variance ($\sigma_{\Delta E}$) of the damage parameter $\Delta E(z_l)$. Eq. (15) shows how the threshold value is calculated using a variance multiplier (v), which can achieve false damage detection probabilities of 15%, 2% & 1% for $v = 1, 2, \& 3$, respectively, as normal distribution is assumed. Conversely, increasing the variance multiplier (v) will also increase the probability of missed damage events.

$$\Delta E(z_l) = \mu_{\Delta E} + v\sigma_{\Delta E} \quad (5)$$

Dilena et al. tested the performance of the IDDM on a single span RC bridge under forced harmonic vibration. Numerous damage events were introduced to the bridge in different locations during testing. The results of the IDDM were compared to those of the MCM, which was also tested. The results showed that the IDDM is capable of detecting and locating damage consistently; however, its performance is dependent on the threshold value chosen and on the geometry

of sensors. The experiment also showed that IDDM is capable of tracking the evolution of damage, which was tested by incrementally increasing the severity of the manually induced damage events. Damage localisation did not improve by increasing the number of vibration modes in the FRF range. When compared to the MCM results, the IDDM fairs quite well. The MCM demonstrated good sensitivity to damage for the first two vibration modes, but became less accurate thereafter. This is most probably due to the requirement of a denser array of sensors for accurate modal curvatures at higher modes. The IDDM requires fewer sensors than the MCM and, overall, has shown that the IDDM can reliably detect and locate damage without modal parameters as a damage indicator. A disadvantage of the IDDM is that its assumption that for an undamaged state, all sources of vibration will equally cause all locations to produce the same variation in interpolation error will not be suitable to all bridge applications.

Santos et al. [25] implemented a novel methodology to detect structural variation without the use of modal parameters. They proposed an output-only technique that possesses real-time capabilities. It uses cluster analysis to achieve baseline independence and it introduces the concept of symbolic data analysis (SDA) to reduce raw vibration or rotation data into much smaller representative sets of statistical quantities such as interquartile intervals or histograms. This process reduces data volume and increases processing speed considerably, without loss of information.

Santos et al. applied the technique to the Samora Machel Bridge. The assessment observed that symbolic objects based on interquartile intervals of measured rotations, which are able to accurately detect changes in bridge condition in a very short time. It achieves this by applying the dynamic cloud clustering algorithm, which is an adaptation of the popular k-means approach that converges to a solution quickly. This fast solution can cause issues however, as dynamic cloud clustering can converge to local minima. For this reason, cluster validation is conducted to results to enhance the methods robustness. This step is important for baseline free applications. It consists of computing a set of indices for all clusters. Each validity index describes each cluster's compactness and separation. The most accurate number of clusters identified is then compared to the indices obtained from each of the evaluated partitions to define the most truthful number of clusters.

Finally the novelty index is prepared by assessing the geometric weights of each cluster against each other. The objective of this phase is to create an automatic response index that can identify various magnitudes of damage in real-time. Figure 7 presents a comparison of two structural changes observed in the assessment of the Samora Machel Bridge. The index value is taken as the average squared distance between cluster centroids. It is evident that Figure 7 (b) has a larger distance between centroids, and thus indicates a greater structural change.

Due to its fast computation and low data storage requirements, Santos et al.'s symbolic data based approach offers the opportunity for real-time damage detection capabilities in bridges.

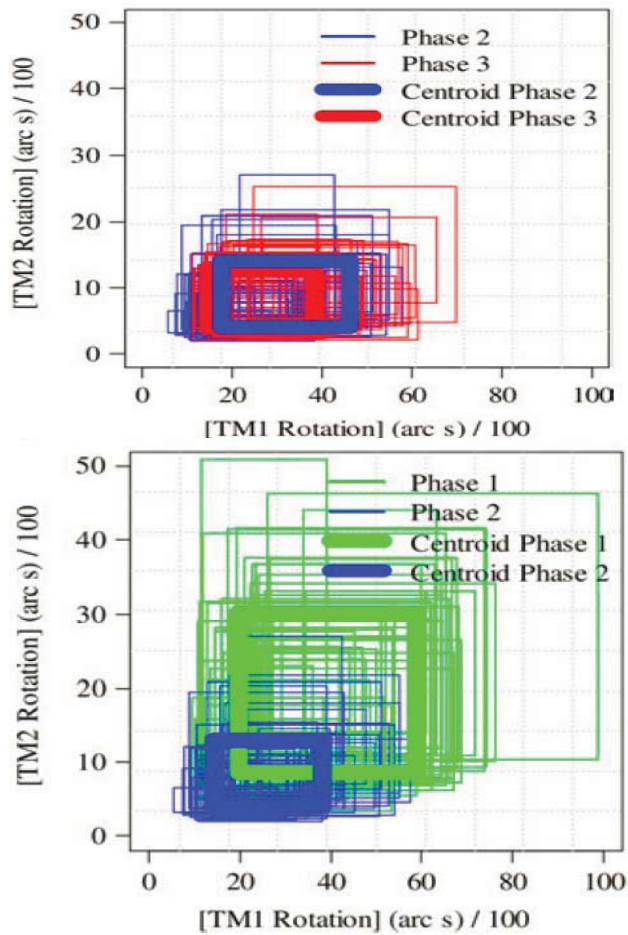


Figure 7 Comparison of cluster centroids defined for various behavioural variations [25]

CONCLUSIONS

Overall, it can be concluded that there is no outright consensus among researchers regarding which vibration based damage indicator or damage detection method is most suited to bridges structures. These structures do add an additional layer of complexity to the SHM conundrum, as each structure is unique in design and load, as opposed to aeronautical and mechanical applications. Therefore, conclusive conclusions can only be drawn when a methodology has shown consistent results on numerous bridge structures and under varying operational and environmental conditions. The best damage detection system shall not be the methodology that is most accurate in the lab, but the one that is most consistent in the field. An acceptable methodology must be robust enough to have a known error rate, so that uncertainty can be managed.

ACKNOWLEDGMENTS

This project has received funding from the European Union's Horizon 2020 research and innovation programme under the Marie Skłodowska-Curie grant agreement No. 642453.

REFERENCES

- [1] MAINLINE. Maintenance, renewal and improvement of rail transport infrastructure to reduce economic and environmental impacts. (2013) Deliverable D1.1: "Benchmark of new technologies to extend the life of elderly rail infrastructure" European Project. 7th Framework programme. European Commission.
- [2] Casas, J. R. (2010) "Assessment and monitoring of existing bridges to avoid unnecessary strengthening or replacement". A: International IABMAS Conference on Bridge Maintenance, Safety and Management. "V International IABMAS Conference on Bridge Maintenance, Safety and Management". Philadelphia: CRC Press, 2010, p. 2261-2269.
- [3] Koch, H.W. (1953). *Determining the effects of vibration in buildings*, V.D.I.Z., Vol. 25, N. 21, pp. 744-747
- [4] Adams R.D., Cawley P., Pye C.J., Stone B.J. (1978) "A vibration technique for non-destructively assessing the integrity of structures." *Journal of Mechanical Engineering Science*. 20: 93–100.
- [5] Farrar, C.R. & James, G.H. (1997). "System identification from ambient vibration measurements on a bridge". *J. of Sound and Vib*, 205, 1–18.
- [6] Allemang, R.J. and Brown, D.L. (1982), "A correlation coefficient for modal vector analysis", *Proceedings of the 1st SEM International Modal Analysis Conference*, Orlando, FL, November.
- [7] Kim, J.H., Jeon, H.S. & Lee, C.W. (1992) "Application of the modal assurance criteria for detecting and locating structural faults", *Proceedings of the 10th International Modal Analysis Conference*, San Diego, CA, pp. 536–540.
- [8] Salawu, O.S. and Williams, C. (1995), "Bridge assessment using forced-vibration testing", *J. Struct. Eng.*, 121(2), 161-173.
- [9] Salgado, R., Cruz, P. J. S., Ramos, L. F. & Lourenco, P.B. (2006), "Comparison between damage detection methods applied to beam structures", *Proceedings, IABMAS'06*, Porto, PT.
- [10] Pandey, A.K., Biswas, M. & Samman, M. (1991) "Damage detection from changes in curvature mode shapes", *J. of Sound & Vib* 145(2) 321–332.
- [11] Abdel Wahab, M. M. & De Roeck, G. (1999), "Damage detection in bridges using modal curvatures: Application to a real damage scenario", *Journal of Sound and Vibration*, 226(1), 217–35.
- [12] Farrar, C.R. and Worden, K. (2013). "Structural health monitoring - a machine learning perspective," 1st edn, John Wiley & Sons, Ltd. Chichester, West Sussex, UK
- [13] Stubbs, N., Kim, J.T. & Topole, K. (1992) "An efficient and robust algorithm for damage localization in offshore platforms", in *Proceedings ASCE 10th Structures Congress*, pp. 543-546.
- [14] Talebinejad, I., Fischer, C. & Ansari, F. (2011) "Numerical Evaluation of vibration-based methods for damage assessment of cable-stayed bridges" *Computer-aided civil and infrastructure eng.* 26, 239-251.
- [15] Peeters, B & Roeck, G.D. (2001) "One-year monitoring of the Z24-Bridge: environmental effects versus damage events". *Earthquake Engineering and Structural Dynamics*, 30, 149-171.
- [16] Xu YL, Chen B, Ng CL, Wong KY, Chan WY (2010) "Monitoring temperature effect on a long suspension bridge." *Structural Control and Health Monitoring*. 17: 632-653.
- [17] Farrar, C. R., Baker, W. E., Bell, T. M., Cone, K. M., Darling, T. W., Duffey, T. A., Eklund, A. & Migliori, A. (1994). "Dynamic characterization and damage detection in the I-40 bridge over the Rio Grande". Los Alamos National Laboratory Report: LA-12767-MS.
- [18] Sohn, H. (2007) "Effects of environmental and operational variability on structural health monitoring," *Philosophical Transactions of The Royal Society* 365, 539-560.
- [19] Dervilis, N., Worden, K., & Cross, E.J. (2015) "On robust regression analysis as a means of exploring environmental and operational conditions for SHM data" *Journal of Sound and Vibration* 347 279–296
- [20] Mahalanobis, P.C. (1936) "On the generalized distance in statistics", *Proc. Nat. Inst. Sci. India* 2 (1) 49–55.
- [21] Chatzi, E.N. & Spiridonakos, M.D. (2015) "Dealing with uncertainty in the monitoring of dynamically evolving systems" *Proceeding of the 7th International Conference on Structural Health Monitoring of Intelligent Infrastructure (SHMII)*. Torino, Italy, July 2015.
- [22] Spiridonakos, M.D. & Chatzi, E.N. (2015) "Metamodeling of structural systems with parametric uncertainty subject to stochastic dynamic excitation" *Int. J. For Earthquake Eng & Earthquake Effects on Structures*. 8(4), pp 915-934
- [23] Dilena, M., Limongelli, M.P. & Morassi A. (2015) "Damage localization in bridges via the FRF interpolation method" *Mechanical Systems and Signal Processing* 52-53, 162–180.
- [24] Zhang, Y., Lie, S.T. & Xiang, Z. (2013) "Damage detection method based on operating deflection shape curvature extracted from dynamic response of a passing vehicle", *Mech. Syst. Signal Process.* 35 238–254.
- [25] Santos, J.P., Orcesi, A.D., Cremona, C. & Silverira, P. (2013) "Baseline-free real-time assessment of structural changes". *Structure and Infrastructure Engineering: Maintenance, Management, Life-Cycle Design and Performance*, DOI: 10.1080/15732479.2013.858169.

Monitoring and Maintenance of the Boyne Viaduct

Lorcan Connolly¹, Alan O'Connor¹, Cathal Leahy¹, Cathal Bowe²,

¹Roughan & O'Donovan Innovative Solutions, Arena House, Arena Road, Sandyford, Dublin 18, Ireland

²Iarnród Éireann, Athenry Station, Co. Galway, Ireland

email: Lorcan.Connolly@rod.ie, Alan.O'Connor@rod.ie, Cathal.Leahy@rod.ie, Cathal.Bowe @irishrail.ie

ABSTRACT: The central steel span of the Boyne Viaduct in Drogheda, Co. Louth, was constructed in 1932. At the time of construction, the bridge was not expected to have a design life in excess of 76 years. It is therefore vital that the structure undergo a robust maintenance strategy in order to verify the ongoing performance in terms of reliability with respect to both the Ultimate Limit State (ULS) and the Fatigue Limit State (FLS). Global and localised 3D Finite Element modelling was used in conjunction with a reliability analysis of the structure in order to design a monitoring strategy. A combination of strain gauges and accelerometers were installed with the strain gauges being placed on the rail bearers and cross beams at sections which were expected to be critical both at ULS and FLS. Finite Element Model calibration from measurement allowed recalculation of the reliability index with lower uncertainties, resulting in a 48% increase in reliability. A reliability based fatigue analysis was also carried out at the sensor locations in order to calculate if sufficient reliability is provided on a yearly basis. The results showed that the most critical monitored section will have a minimum FLS reliability index of 9.3 after 150 years of service. The results of the analysis alleviate any safety concerns regarding the monitored locations of this iconic structure.

KEY WORDS: Reliability; Probabilistic Analysis; Truss; Bridge; Fatigue; Structural Health Monitoring; Maintenance.

1 INTRODUCTION

It is estimated that 30% of the European Railway bridge stock is over 100 years old [1]. Structural Health Monitoring (SHM) is an efficient method of obtaining real-time data on the condition for assessment of aging infrastructure. However, often these systems are installed on new and older structures without any specific targeting as to where/why/when to use the data.

In this paper, the results of a probabilistic Ultimate Limit State (ULS) assessment are used to inform an SHM plan for the Boyne Viaduct, located in Drogheda, Ireland (Figure 1). The Boyne viaduct has three steel spans, with only the central span being assessed as part of this research.



Figure 1. Aerial view: Central span of the Boyne Viaduct, Drogheda, Co. Louth, Ireland.

The data from the SHM system are employed first to calibrate a global Finite Element (FE) model. The failure probability at the critical ULS is then recalculated. Finally, the measured data is used to perform a probabilistic fatigue analysis including stochastic modelling of the load and resistance in terms of number of fatigue cycles to failure.

2 STRUCTURAL HEALTH MONITORING

In order to decide on appropriate sensor locations and types, it is important to consider the reason for instrumentation. Considering the age of this structure, the Fatigue Limit State (FLS) was expected to be significant. Therefore, strain gauge rosettes were selected as this would allow calculation of the principal stress for fatigue rain flow counting. In addition, this would allow direct comparison with results from the global FE model developed (Figure 2). The bridge was modelled in the commercially available MIDAS Civil software [2] using linear elastic beam elements with varying levels of fixity at the node points. The geometry was set up using as-built drawings and measurements on-site. The steel deck plate was modelled using plate elements. A young's modulus of $2.1 \times 10^8 \text{ kN/m}^2$ was assumed throughout. There is transverse wind bracing on the top of the structure and internal portal bracing. This was included in the model but is omitted from Figure 2 along with the track for clarity. A deterministic and probabilistic assessment was carried out on the structure. A full overview of the assessment is given in [3]. It was shown that yielding of the centre-span of the rail bearers in the central bay was the critical ULS load effect, with a reliability index of 4.4 [3]. Therefore, this section of the structure was instrumented with rosette strain gauges to measure internal stress at ULS and to assist in a fatigue analysis.

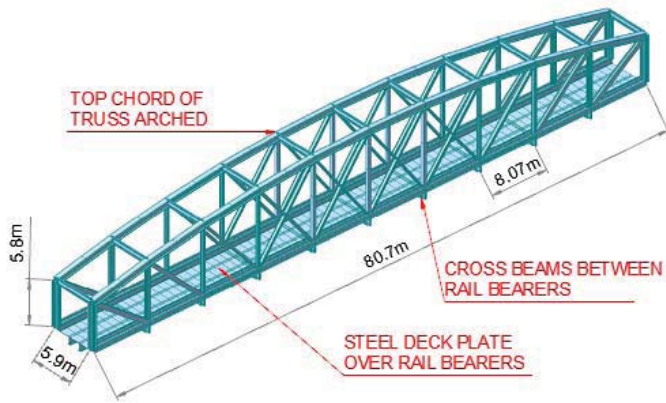


Figure 2. FE model of the Boyne Viaduct Central Span

During an inspection, significant section loss was noted due to corrosion at the flanges of the critical member identified. The section loss had occurred at the connection of the rail bearer to the cross beam, as shown in Figure 3. It was therefore considered appropriate that a strain gauge rosette be placed on each rail bearer at the central span to assess if the section loss identified is adversely affecting the structural performance.



Figure 3. Section loss for critical rail bearer

Past research has shown that the connections between rail bearers and cross beams are often critical for fatigue [4]. For this reason, the most critical cross-beam connection identified from the FE model was instrumented with a rosette strain gauge. This was found to be at the first cross beam from the southern support. Figure 4 shows an image of the strain gauge rosettes used, while Figure 5 shows the locations of the gauges on the cross beams and rail bearers. All gauges were placed on the bottom flange of the beams in order to monitor the worst Navier stress combination.

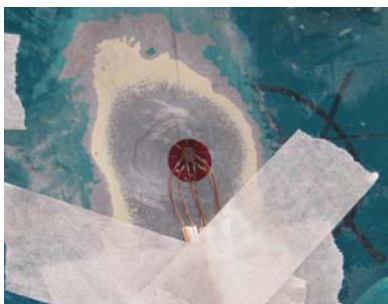


Figure 4. Strain gauges on rail bearers (5th bay)



Figure 5. Plan view at deck level showing strain gauge locations on deck elements

As part of recent repair works on the structure, a number of web stiffeners were replaced on the rail bearers. In terms of performing fatigue assessments from direct measurement, it is beneficial to instrument elements at the start of their fatigue life as this prohibits the requirement to back-calculate strain histories. In addition, a site visit indicated section loss at the “toe” of many of the existing stiffeners (Figure 6a). The authors were informed by the client that this is an issue on many bridges of this type. Therefore, one of the new stiffeners was instrumented with a rosette strain gauge both to perform a fatigue assessment and to assess if the section loss to the existing stiffeners should cause adverse safety concerns. 3D FE modelling was used to identify stress hot spots. Figure 7 shows the stress development in the stiffeners due to a moving knife edge load. It is clear that the location of highest stress is at the top of the stiffener. Therefore, the strain gauge was placed at the top of the stiffener as illustrated in Figure 6b.



Figure 6. Stiffeners on rail-bearers section loss (a) and strain gauge placement (b)

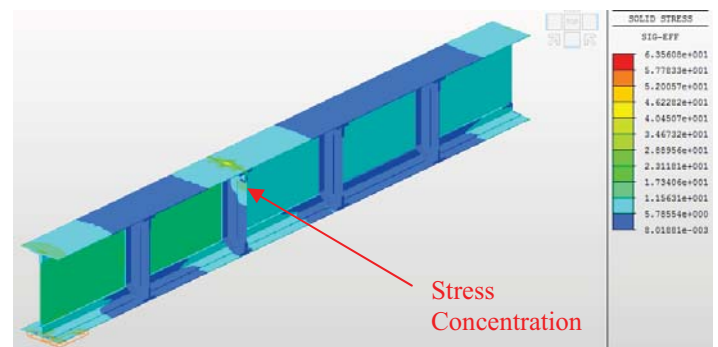


Figure 7. Stress contour on 3D FE model of rail bearer with stiffener

It should be noted that the stress levels identified in the stiffeners from the FE model were low in comparison with the load. Therefore, it was not expected that this section would be critical for fatigue. However, instrumentation at this location

was still deemed to be necessary in order to alleviate the concern associated with the corrosion illustrated in Figure 6a.

In total, 4 strain gauge rosettes were installed on the deck elements at the bottom flanges of the cross beams and rail bearers and also on one stiffener on the rail bearers. 3 accelerometers were also installed on the main truss elements in order to assist in a dynamic analysis, the details of which can be found in [5].

3 MODEL CALIBRATION

3.1 Train loading

Two main types of train configuration are present at the site, both of which carry passenger traffic only (no freight). The first a standard DMU carriage train with each carriage having the configuration and weights shown in Figure 8. The train may have 2-8 carriages.



Figure 8. Configuration of DMU carriages

The second type of train at the site is the Enterprise service, which has carriages broadly similar to that of the DMU trains, but has a class 201 locomotive at the front. The configuration of the class 201 locomotive is shown in Figure 9. A wagon spacing (bumper-to-bumper) of 0.5 m was used throughout.

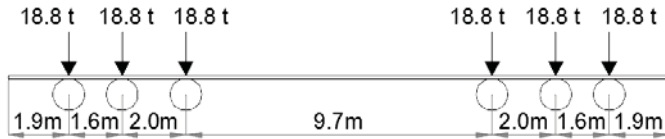


Figure 9. Configuration of locomotive class 201

3.2 Signal comparison

In order to generate stress signals from the FE model, influence lines for the sensor locations were exported to Matlab where code was developed to run specific axle loading configurations across them to generate the load effects. The influence lines extracted were related to the Navier stress combination given by:

$$i_{\sigma} = \frac{i_{mx}y}{I_x} + \frac{i_{my}x}{I_y} + \frac{i_{pz}}{A} \quad (1)$$

Where i_{σ} are the influence line ordinates for total stress, i_{mx} & i_{my} are the influence line ordinates for bending in each direction, i_{pz} are the influence line ordinates for axial force, y & x are the distances to the maximum point of stress in the member, I_x & I_y are the moments of inertia about each axis of bending and A is the cross sectional area. The stress considered to be comparable to the Navier stress from the model is the principal stress from the rosette strain gauges, calculated using Equation 2.

$$\frac{E}{2} \left(\frac{\varepsilon_1 + \varepsilon_2}{1 - \nu} \pm \frac{1}{1 + \nu} \sqrt{(\varepsilon_1 - \varepsilon_2)^2 + (\varepsilon_2 - \varepsilon_3)^2} \right) \quad (2)$$

Where E is the Young's Modulus, ν is the Poisson's ratio and ε_i is the strain reading on strain gauge i of the rosette. A critical input to the signal generation in Matlab is the speed of the train, which was not measured on-site. The speed of the train can be inferred from the signal itself given the knowledge of the carriage axle spacing. The speed of each train was calculated by dividing the spacing between each group of axles by the time increment between the peaks from the measured signal. The average speed on-site was found to be around 30 km/hr. This low value is to be expected, considering speed restrictions in-place across the viaduct. Trains were found to be accelerating as they moved north, and decelerating as they moved south. This is due to the location of a station on the south side of the bridge. This speed variation was taken into account when comparing the signals. Figure 10 shows a comparison of the stress signals at the bottom flange of the rail bearer due to the passage of a DMU train. While the signal shape is very similar, it is clear that the magnitude of stress from the FE model is 50% higher than that of the strain gauge.

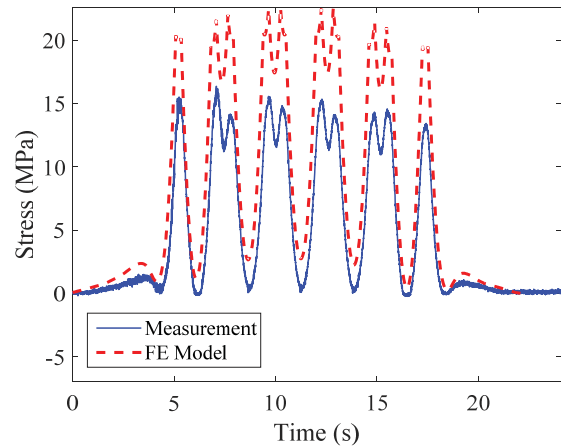


Figure 10. Stress response due to passage of DMU train

While it may be argued that the axle weights shown in Figure 8 may vary depending on passenger traffic, this would not explain the level of the discrepancy in Figure 10 as the axle weights of a full carriage would be expected to be only 1 tonne greater than that of an empty carriage. Figure 11 shows the stress comparison due to the passage of a train from the Enterprise service.

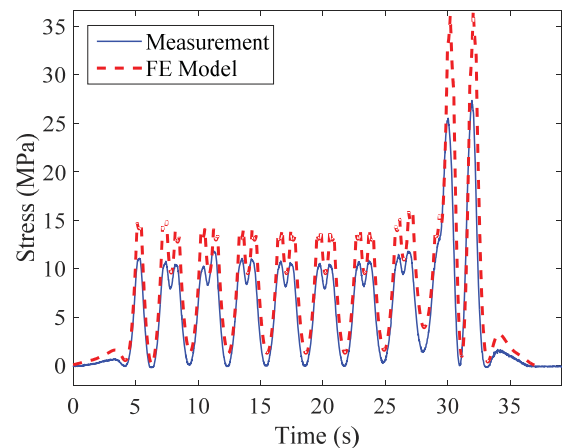


Figure 11. Stress response due to passage of Enterprise train

It is clear that for both train types, there is a discrepancy in magnitude of stress of 50%. In addition, the FE model generated sharper peaks than the measurement. This is most likely due to the ballast, which was not considered in the FE model. The results of comparison at the bottom flange of the cross beam showed the same result.

3.3 FE model adjustment

The truss bearings on the Boyne viaduct were articulated to allow translation in the longitudinal direction, as well as rotation at the bearings. This was verified with construction drawings and on site investigation. However, the bearings for the rail bearers could not be accessed on site. Therefore, the boundaries in the FE model were replaced with spring supports in order to restrict a portion of the main axis-bending. This was found to give a much better comparison between the measured and generated signals from the FE model. In addition, the sharp peaks identified in Figure 11 were removed by modelling the track more accurately, linking the rails and sleepers to the rail bearers with springs to model the effect of load distribution through the ballast. A vertical spring stiffness of 2.5MN/m was used to model the ballast. Finally, the model was refined by paying closer attention to eccentricities, beam end releases and reducing the mesh size for the deck plate, allowing a better model for composite action. Figure 12 shows a comparison of stress in the rail bearer for the same train as Figure 11 for the adjusted FE model. Figure 13 shows the same comparison at the cross beam. It is clear that both models show high correlation in response to that of the measurement. The average error in the peaks is 9.4% in Figure 12 and 2.0% in Figure 13. It was important to match the response at both locations in order to provide confidence that the response is similar throughout the structure. The remaining discrepancy between model and measurement may be attributed to discrepancies in the train weights and strain gauge error. In the following section, the ULS probabilistic assessment re-calculated using the adjusted model.

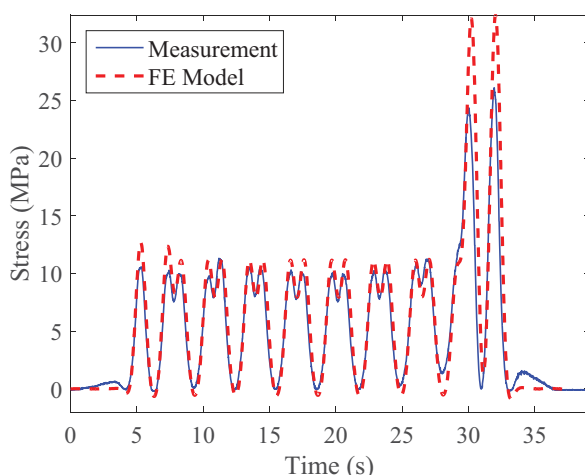


Figure 12. Stress response at rail bearer due to passage of Enterprise train (adjusted model)

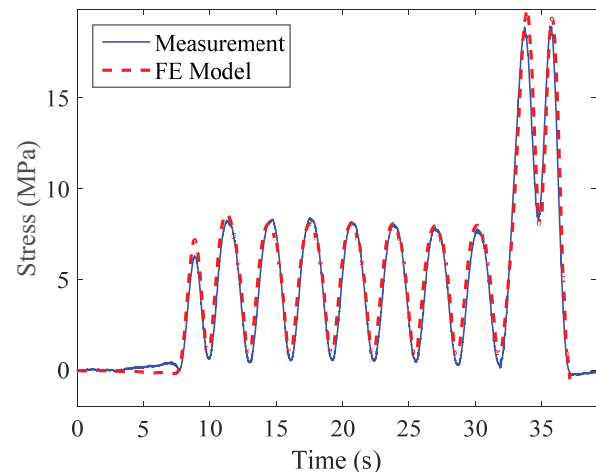


Figure 13. Stress response at cross beam due to passage of Enterprise train (adjusted model)

4 PROBABILISTIC ULS ASSESSMENT

4.1 Assessment from model

In the previous ULS assessment carried on the rail bearers the majority of the stochastic modeling was based on the guidelines of the Danish Roads Directorate (DRD) [6]. It is clear from the previous sections that the main result of the model calibration was to reduce the magnitude of the stresses at this location. Therefore, the rail bearer was reassessed as per [3], with the only difference being a reduction in the model uncertainty associated with the capacity. Due to the detailed model calibration, the coefficient of variation (CoV) of the model uncertainty associated with capacity is reduced from 10.4% to 6.6%. The combination of all these alterations to the assessment resulted in an increase in the β -value to 6.5. The disadvantage of the assessment performed is that in the absence of specific train weight data for the structure, the live load distribution was taken as the Eurocode LM71 [7] with a bias ratio of 0.66 and a CoV of 20%, for which the characteristic value represents the 98% fractile. It is therefore more appropriate to use the stress values from the measurement in the assessment.

4.2 Assessment from measurement

In order to perform a ULS assessment with consideration of the stresses from measurement, a histogram was plot of the maximum stresses for train passage events on the Boyne Viaduct. 35 days of measurement were available with varying numbers of train events per day. As expected, the distribution of stress is globally bimodal due to the presence of the two train types discussed in Section 3 above. A multimodal normal distribution was fitted to the data using Maximum Likelihood Estimation (MLE). The fit is shown in Figure 14.

The CDF distribution was found by cumulative integration of the PDF. Convolution was then used to allow calculation of maximum yearly value:

$$F_{\max}(x) = F(x)^N \quad (3)$$

Where $F_{max}(x)$ is the maximum yearly distribution and $F(x)$ is the daily distribution. N is the convolution constant, given here by the average number of trains per day (20) times the number of working days in a year (250).

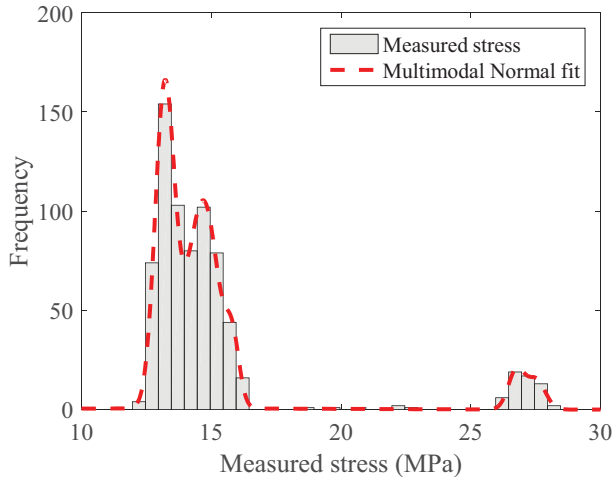


Figure 14. Bimodal GEV fit to maximum event stresses at rail bearer

For this method of probabilistic assessment, the consideration of model uncertainty for live loading is not applicable as the loading information is measured by the strain gauges. However, the stress distribution was multiplied by a random variable, e , to account for error in measurement. e was considered as a lognormal distributed variable with a mean value equal to 1.0 and a standard deviation of 0.03 after [8]. The principal stress signals represent total (static + dynamic) loading and as such, no allowance was required to account for dynamics. FORM analysis was used to calculate the reliability index, which converged to a value of 8.1. This value is considered to be significantly higher than any published recommendations for ULS at the highest consequence levels [9]. This value is not unexpected, considering that passenger loading forms the basis of the stress distribution, while the bridge was designed for freight traffic. It may be expected that the fatigue limit state will be more critical for the structure, considering that the structure is currently beyond its expected design life.

5 PROBABILISTIC FATIGUE ASSESSMENT

5.1 Assessment from measurement

The performance function considered for probabilistic fatigue assessment is given by:

$$g(x) \leq 0 \quad (4)$$

Where:

$$g(x) = D_{crit} - \sum_{i=1}^n \frac{n_{Ei}}{N_{Ri}} \quad (5)$$

Where n_{Ei} is the number of cycles associated with a specific stress range, $\Delta\sigma_i$; and N_{Ri} is the endurance (in cycles) related to a specific detail category under consideration at stress range $\Delta\sigma_i$. D_{crit} is defined here as the critical cumulative damage for

the detail under consideration. D_{crit} is modeled as a lognormal distributed variable with mean and standard deviation equal to 1.0 and 0.3 as recommended in the literature [8].

The procedure for determining a stochastic interpretation for the summation term is given in [9] and is illustrated in Figure 15. A rainflow counting algorithm is used to calculate the stress range histogram based on live load signals from measurement. This is then extended by multiplication of the model uncertainty for live load (or in the case of measured stresses, the error function, e , as discussed in section 4.1). It should be noted that stress ranges less than 1MPa were removed from the histogram as these were deemed to be due to noise rather than a specific train event. These low stress ranges do not have an effect on the fatigue life. The term n_{ei} is given by the count of each bin. A probabilistic S-N curve is then used to determine a stochastic representation of N_{Ri} for each stress range, $\Delta\sigma_i$. In the absence of existing research pertaining to probabilistic consideration of the Eurocode S-N curves, the DNV S-N curves [10] were used. The equation of the S-N curve line for a specific detail category is given as:

$$\log N = \log \bar{a} - m \log \Delta\sigma \quad (6)$$

Where m is the negative inverse slope and $\log(\bar{a})$ is intercept of $\log N$ -axis by the S-N curve, given by:

$$\log \bar{a} = \log a - 2s_{\log N} \quad (7)$$

Where $\log(a)$ is the Intercept of **mean** S-N curve with the $\log(N)$ axis and $s_{\log N}$ is the standard deviation of $\log(N)$, given as 0.2 in log space.

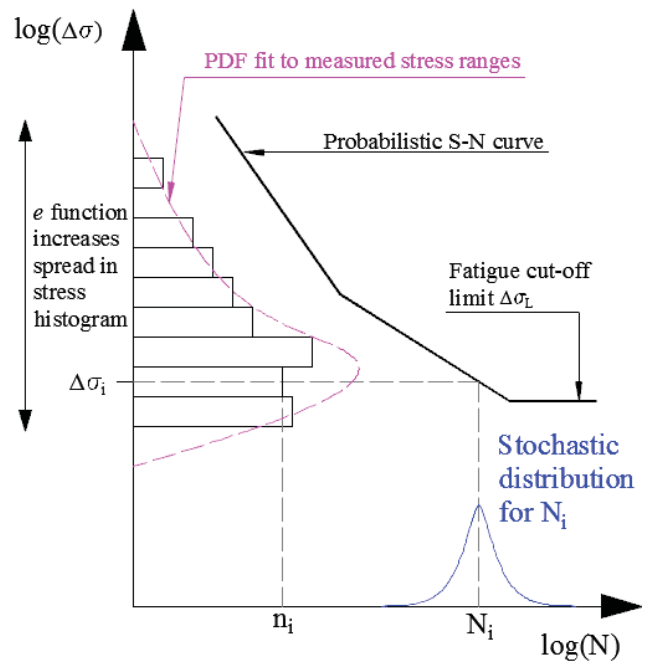


Figure 15. Probabilistic S-N curve approach

It was found that multi-modal behaviour was again evident in the stress range histogram. A multimodal Normal distribution was fitted to the data. Figure 16 shows the fit to the stress range data from one of the rail bearers.

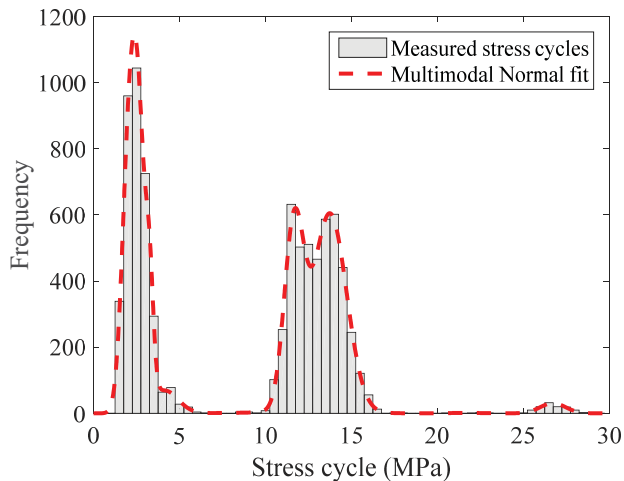


Figure 16. Multimodal normal fit to 1 month of measured stress cycles at rail bearer

A Matlab programme was written to perform the probabilistic fatigue assessment procedure outlined in Figure 15 at each monitored section of the Boyne Viaduct. The assessment was performed on a yearly basis; randomly sampling 1-year of stress range data from the fitted PDFs. Figure 17 shows the evolution of the reliability index for 150 years. The assessment is considered to start at the date of construction for all elements excluding the stiffener. The vertical dashed line shows the current age (84 years), which is the start of the fatigue life for the stiffener

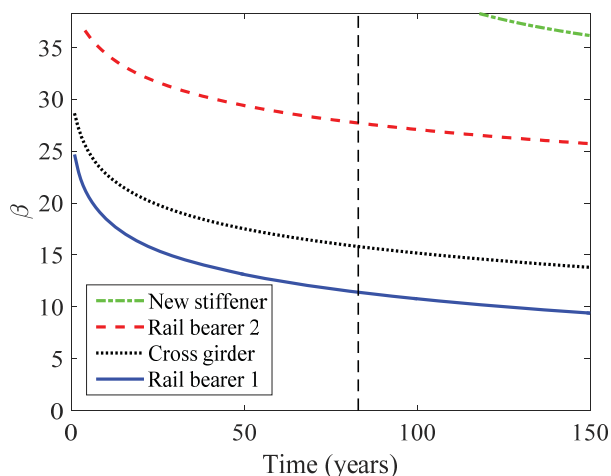


Figure 17. Evolution of reliability index at measured locations

It is clear that the rail bearer is the most critical section for fatigue, while the stiffener is not expected to show any signs of fatigue failure as expected. The FORM analysis did not converge on a design point for the stiffener until after 35 years. This implies that the probability of failure is zero for the first 35 years of service. The maximum value of $\beta = 9.3$ for the rail bearer after 150 years of service may be considered to be above the threshold limits defined in [9]. Again, the high levels of reliability are indicative of the low frequency and magnitude of live loading compared to the freight traffic for which the bridge was designed. It should be noted that the results shown are based on the assumption that the historic loading levels on the structure are similar to the current state.

6 CONCLUSIONS

A probabilistic ULS assessment was used to inform a Structural Health Monitoring (SHM) strategy for the Boyne viaduct. The results from measurement were used to calculate a more accurate interpretation of the reliability index at the critical locations monitored. Based on the assessment carried out it can be concluded that sufficient reliability is provided at ULS for the monitored locations.

A probabilistic fatigue assessment was also carried out using the measured strains which assumed that the loading history is consistent with the current level of loading. The results showed that the critical section of the rail bearers may not be expected to show signs of fatigue failure in the next 50 years. The measurements were also used to calibrate an FE model. This will allow an accurate fatigue assessment to be carried out on each element of the structure in the future. It is expected that this will include a more accurate consideration of the load history.

A long term monitoring plan is currently being designed for the structure using some of the sensors currently installed. This will allow statistical updating of the assessment herein on a regular basis, providing the infrastructure management with quantification of ongoing safety.

ACKNOWLEDGMENTS

The research leading to these results was part of the DESTINATION RAIL project, a project funded by the EU Horizon 2020 Programme under call H2020-MG-2014 Mobility for Growth. Grant agreement no: 636285. The authors also gratefully acknowledge Iarnród Éireann, for allowing the research associated with the Boyne Viaduct.

REFERENCES

- [1] SB1.2 (2004), European railway bridge demography, D1.2. Prepared by Sustainable Bridges - a project within EU FP6. Available from: www.sustainablebridges.net
- [2] Midas Information Technology Co., Ltd. Midas Civil Available at: <http://en.midasuser.com/product/civil/overview.asp> [Accessed 10 February 2016]
- [3] Connolly, L., O'Connor, A. And O'Brien, E.J. (2016), 'Probabilistic modelling and assessment of railway bridges', in *Proceedings of 8th International Conference on Bridge Maintenance, Safety and Management* (in press).
- [4] Al-Emrani, M. (2005), 'Fatigue Performance of Stringer-to-Floor-Beam Connections in Riveted Railway Bridges', *Journal of Bridge Engineering*, 10:179-185.
- [5] Connolly, L., Hajializadeh, D., Leahy, C., O'Connor, A., O'Brien, E.J., Bowe, C., (2016), 'Calculation of Dynamic Allowance for Railway Bridges from Direct Measurement' in *Proceedings of the Third International Conference on Railway Technology: Research, Development and Maintenance*, (in press).
- [6] Danish Roads Directorate (DRD) 2004, Report 291, Reliability-Based Classification of the Load Carrying Capacity of Existing Bridges, *Roads Directorate, Ministry of Transport, Denmark*, 2004.
- [7] EN 1991-2, 2003, Eurocode 1: Actions on structures – Part 2: Traffic loads on bridges, European Standard, CEN, Brussels, 2003.
- [8] Kwon, K. and Frangopol, D.M., (2010), Bridge fatigue reliability assessment using probability density functions of equivalent stress range based on field monitoring data, *International Journal of Fatigue*, 32: 1221-1232
- [9] JCSS, Joint Committee of Structural Safety, *Probabilistic Model Code I-III – Basis of Design*. 2000.
- [10] Veritas, Det Norske. "Fatigue design of offshore steel structures." No. DNV-RP-C203 (2010).

Practical Applications of Weigh-in-Motion Data

Robert Corbally¹, Alan O'Connor¹, Fergal Cahill²

¹Roughan & O'Donovan Innovative Solutions, Arena House, Arena Road, Sandymount, Dublin 18, Ireland

²Transport Infrastructure Ireland, Parkgate Business Centre, Parkgate St., Dublin 8, Ireland
email: robert.corbally@rod.ie, alan.oconnor@rod.ie, fergal.cahill@tii.ie

ABSTRACT: Weigh-In-Motion (WIM) systems provide an efficient means for collecting detailed information pertaining to everyday traffic usage and vehicle weights on a road network. Significant resources are required to carry out such large scale data collection operations, and it is therefore important that the collected data is used appropriately and efficiently and that the process represents value for money to the road authority. Transport Infrastructure Ireland (TII) recently upgraded their traffic monitoring system, which included the installation of six permanent WIM sites along the national primary network, with accurate data collection beginning in 2014. This paper presents an overview of a number of projects commissioned by TII and undertaken by Roughan & O'Donovan Innovative Solutions (ROD-IS), whereby WIM data was utilised to assist TII in decision making related to the regulation of vehicles permitted to use the Irish road network. One project examined the implications of abnormally loaded vehicles on bridges, and developed tools to assist in the permit issuing process. Others assessed the implications, for pavements and bridges, of changing particular Irish regulations for weight limits of various vehicle types. In addition, a study was carried out to examine the effects of a new truck configuration which was not covered by Irish regulations. All of these studies, which used WIM data from various sources, show practical applications of how WIM data can be, and has been, used to allow road authorities to better understand how their network is being impacted by vehicle loading. The results of these case studies provide substantial scientific evidence in relation to how traffic loading can impact the network, providing a solid basis for the decision making process involved in the management of a transport network.

KEY WORDS: Weigh-in-Motion; WIM; Traffic Loading; Bridge Loading; Vehicle Weight Limits.

1 INTRODUCTION

The efficient management of the Irish road network is of primary importance to ensure the ongoing functionality of our roads. With 5,300 km of national roads under its management [1], Transport Infrastructure Ireland (TII) is continually faced with challenging strategic decisions concerning the appropriate allocation of limited budgets. The level of traffic loading on pavements and structures is of major concern when considering the safety of structures and the deterioration of the road pavement.

The ability to monitor axle weights and gross weights of the vehicles using the network provides a useful insight into the actual traffic loading being experienced by bridges and pavements. This allows infrastructure managers to gain a deeper understanding of how the network is being used on a daily basis, ultimately facilitating more informed decision making in relation to the management of the network.

TII recently upgraded their traffic monitoring system, which included the installation of six permanent Weigh-in-Motion (WIM) sites along the national primary network, with accurate data collection beginning in 2014. In order to facilitate such large scale data collection significant resources are required to ensure continuous and accurate measurements. It is therefore important that the collected data is used appropriately and efficiently and that the process represents value for money.

This paper presents an overview of a number of projects commissioned by TII (formerly the National Roads Authority, NRA, prior to 2015) and undertaken by Roughan & O'Donovan Innovative Solutions (ROD-IS), whereby WIM

data was utilised to assist TII in understanding the effects of traffic loading on the network and the associated implications for bridges and pavements. TII have used the results of these studies to make recommendations on various regulations and procedures which govern allowable vehicle weights and dimensions on the Irish road network.

2 WEIGH-IN-MOTION

2.1 What is WIM?

The term 'Weigh-in-Motion' (WIM) refers collectively to the various technologies which can be used to calculate the axle-weights and gross-weights of trucks while they are travelling at traffic speed. While there are a number of different types of WIM system, typical installations consist of one or more sensors embedded in the road surface (e.g. Figure 1) which measure the weight of each axle as a vehicle drives over. In addition, axle-configurations and vehicle speeds are also calculated as the vehicles drive over the WIM sensors.

WIM technology provides a feasible means of monitoring and collecting traffic data on a large scale as there is no need to identify and stop individual vehicles for weighing. As all of the vehicles at a given site are weighed, a clear picture of trends in traffic loading and composition on a given section of the road network can be obtained without any disruption to traffic flow during measurements.

The availability of such information provides road managers with an accurate representation of the traffic using the network and ultimately allows more informed decisions to

be made in relation to the design, assessment and operation of the road network and associated infrastructure.



Figure 1. Installation of WIM Sensor.

2.2 WIM in Ireland

The six WIM sites which have been installed in Ireland are located on routes leading in and out of Dublin and their locations are shown in Figure 2.

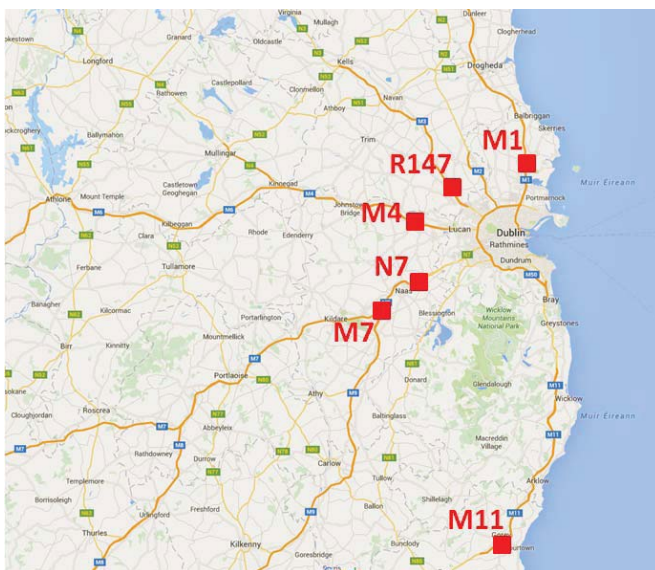


Figure 2. Location of Six WIM Sites in Ireland.

The WIM installations at each site consist of two piezo-polymer WIM sensors and one induction loop in every lane in each direction. The lane configuration details for each site are outlined in Table 1.

2.3 Making use of WIM Data

In order to justify the collection of WIM data it is important to ensure that the process represents value for money and that the road manager can utilise the collected data to improve

their ability to manage the road network and the associated infrastructure.

Table 1. WIM Site Details.

Site	Road Type	Lane Configuration
M1	Primary – Motorway	2 + 2
R147	Regional – Previously a primary route (N3). M3 motorway has now replaced this route.	2 + 2*
M4	Primary – Motorway	2 + 2
M7	Primary – Motorway	2 + 2
M11	Primary – Motorway	2 + 2
N7	Primary – Dual Carriageway	3 + 3

* Includes bus lane in each direction.

Typically, WIM systems record a wide array of information for each vehicle which passes over the sensor, including; date, time, lane, direction, vehicle class, speed, axle-weights, gross-weight, axle-spacings etc. Many WIM systems also incorporate cameras, allowing vehicles of interest to be visually examined on an individual basis. WIM data, if used correctly can be of great benefit to road managers with some of the potential uses listed below:

- Bridge design, assessment and load control;
- Improved understanding of pavement performance (truck axle weights are a leading factor in pavement damage);
- Assessing overload on the network and the indirect cost of any lack of enforcement of legal limits;
- Improving road safety;
- Statistical studies of freight movement and resulting implications for planning;
- Development of national codes and standards.

The following sections outline a number of studies commissioned by the NRA/TII and carried out by ROD-IS, in which WIM data was utilised to examine the implications of various aspects of traffic loading on the bridges and pavements on the road network.

3 ASSESSING IMPLICATIONS OF TRAFFIC LOADING

The level of freight being transported on the roads is continually increasing over time [2]. Increasing economic activity can be directly linked to freight transport [2] which can lead to increased rates of deterioration or damage to the pavements and bridges on the road network. In Ireland, legislation governs the maximum allowable weights and dimensions for vehicles which are legally allowed to travel on Irish roads [3]. The weight limits specified within the legislation have been prescribed for a number of reasons, including road safety, pavement construction/maintenance costs along with bridge safety. However, external forces have typically been the main driving force behind changes in motor vehicle size and weight regulations. Improvements in highways and freight vehicles and the resultant changes in size and weight limits, together with innovations in the management of freight and logistics, have been important sources of productivity growth. As long as these external driving forces persist, the regulations are likely to continue to

change through the political process. Planning for change affords the authorities responsible for the highway system an opportunity to manage this process rather than risk haphazard development [4].

ROD-IS has carried out a number of projects, commissioned by the NRA/TII, which aimed to assess the implications of various changes to the weight limits specified within the regulations. These studies utilised WIM data to quantify the effects the traffic has on bridges and pavements and to predict the expected effects that result from the proposed changes. In general, the work carried out within these projects consisted of analysis in three different areas; (i) general road bridges, (ii) masonry arch bridges and (iii) pavement damage. The traffic databases were utilised to compare the characteristic loading scenarios, for various bridges, to those induced by the design and assessment codes in use at the time of the study.

This section provides a brief summary of four projects which utilised WIM data to assist in the decision making process related to the management of the Irish road network. It is noted that accurate data collection at the Irish WIM sites only commenced in 2014, and as such, the studies which were carried out prior to this utilised suitable WIM databases from different countries as described in the following sections.

3.1 Weight Limits for 5-axle and 6-axle trucks in Ireland







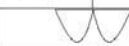

In 2011 the maximum allowable load for 5-axle trucks was 42 t. This weight limit represented a temporary 2 t derogation from the actual weight limit for 5-axle trucks, which was set at 40 t. In addition, the maximum weight allowable for 6-axle trucks at the time was 44 t. The NRA commissioned a study to examine the implications of increasing the weight limit for 6-axle trucks from 44 t to 46 t and of making the 5-axle 42 t derogation permanent. ROD-IS carried out this study on behalf of the NRA, with the work being carried out in two phases as detailed hereafter.

3.1.1 Phase 1: Preliminary Analysis

At the outset of Phase 1 an extensive WIM database containing one month of truck data from the Netherlands was employed. In order to classify typical truck configurations, a detailed statistical analysis was carried out of the 5-axle (40 t & 42 t) and 6-axle (44 t & 46 t) trucks contained in the database. This provided a vehicle template for the axle-configurations and axle-weights for 5-axle and 6-axle trucks which were subsequently used in the analysis.

In order to quantify the effects on general road bridges a number of influence lines were defined (Figure 3), which were deemed suitable to represent the critical global load effects for typical structures on the road network. These influence lines, which formed the basis of the re-calibration of the Eurocode LM1 load model [5], were analysed for bridge lengths ranging from 7.5 m to 200 m.

The preliminary analysis involved running convoys of fully loaded 5-axle and 6-axle trucks across each of the influence lines to identify the critical load effects. The analysis considered 'jammed' (5 m gap between trucks) and 'free-flowing' (25 m gap) scenarios. For the jammed scenarios, no allowance for dynamic amplification was included whereas the free-flowing scenarios included a dynamic amplification factor applied to each of the axles.

Influence Line Number	Representation	Description of the Influence Line
10		Total load.
11, 12		Maximum bending moment of a simply supported and double fixed ¹ span, respectively.
13		Maximum bending moment at the support of the former double fixed beam ¹ .
14, 15		Shear force at the ends of simply supported bridge (assuming traffic flowing left to right).
16		Moment at centre of central span in 3-span bridge with span ratios 0.7L:1.0L:0.7L (16a) and 0.4L:1.0L:0.4L (16b).
17, 18		Minimum and maximum bending moment at mid-span of the first of two spans of a two span continuous beam.
19		Continuous support moment of the former two span beam.
110		Continuous support reaction of the former two span beam.





¹with an inertia strongly varying between the mid-span and the ends

Figure 3. Influence Lines Representing General Road Bridges.

Once the critical load effects had been identified for each of the influence lines, these were then compared to the load effects induced by the following codified load models:

- HA design loading as per BD37/01 [6];
- LM1 design loading as per Eurocode 1 [7];
- HA assessment loading as per BD21/01 [8].

The ratios between the critical load effects induced by the truck convoys and the load effects resulting from these codified load models were calculated for each influence line (a ratio greater than 1.0 indicates that the design/assessment load effects are exceeded). Examining these load effect ratios highlighted a number of critical influence lines which demonstrated high load effect ratios. Based on these load effect ratios and the structural forms of particular interest to the NRA, the influence lines outlined in Figure 4 were chosen for further analysis in Phase 2.

Influence Line Number	Representation	Description of the Influence Line
10		Total load.
13		Maximum bending moment at the support of the former double fixed beam ¹ .
14, 15		Shear force at the ends of simply supported bridge (assuming traffic flowing left to right).
19		Continuous support moment of the former two span beam.

¹with an inertia strongly varying between the mid-span and the ends

Figure 4. Influence Lines for Detailed Analysis.

In addition to the analysis of general road bridges, Phase 1 also examined a variety of masonry arch geometries. Due to the geometric nature of arch bridges, a combination of axial and bending forces governs stability, making influence lines unsuitable for analysing them. As such, Archie-M software was used to carry out the analysis for masonry arches. The Phase 1 analysis of masonry arch bridges involved an assessment of the effect of the proposed increase in allowable vehicle load for 5 and 6- axle trucks, which was determined with respect to the ratio of maximum live load factor achievable at the ultimate limit state under each of the four truck silhouettes identified at the outset (5-axle 40/42 t & 6-axle 44/46 t) vs. that under the codified load model. It is noted that the only code load model analysed, and used for the purpose of comparison, relates to the assessment loading model prescribed by BD 21/01 since it alone allows application of single and group axle loads for the assessment of arch bridges. In total, twenty masonry arch configurations were considered, with the geometries being based on

particular structures on the Irish network. Single-span arches of 5, 10, 15 and 20 m were considered for five different geometric configurations:

- Circular arches (2 No.);
- Elliptical arches (2 No.);
- Three-centred arch (1 No.).

The results of this analysis showed that it would be more appropriate to calculate the characteristic tridem weight for 5-axle and 6-axle trucks and to compare this to the characteristic tridem weight specified within BD21/01. As such, arch bridges were considered within the detailed analysis that was carried out in Phase 2.

3.1.2 Phase 2: Detailed Analysis

While the Phase 1 analysis was useful for identifying critical structural forms to be examined it is noted that the absence of cars in the generated traffic mix could result in overly-conservative loading scenarios. Phase 2 involved more detailed and appropriate simulations for the influence lines outlined in Figure 4. This analysis required another WIM database to be employed, this time from Poland, which had the significant advantage of containing both trucks and cars. Again, jammed and free-flowing scenarios were considered and the maximum daily load effects induced by the traffic calculated for each of the influence lines outlined in Figure 4. Five different analyses were carried out in order to replicate the likely effects of the proposed changes to the regulations:

1. No modification to data: traffic used to calculate characteristic load effects;
2. Permit trucks removed and no change to trucks with 6 or less axles;
3. Permit trucks removed and any 5-axle truck deemed to be fully loaded, i.e., with weight in the range 36 t to 42 t is increased to 42 t;
4. Permit trucks removed and any 5-axle or 6-axle truck with weight in the range 36 t to 44 t is replaced with a 6-axle truck with weight 44 t.
5. Permit trucks removed and any 5- or 6-axle truck with weight in the range 36 t to 46 t is replaced with a 6-axle 46 t truck.

Based on the maximum daily load effects calculated for each influence line, a statistical extrapolation was carried out to calculate the 1000-year characteristic load effect. This extrapolation used a Weibull distribution which was fitted to the maximum daily load effects and extrapolated to provide the 1 in 1000 year load effect, which could then be compared to the characteristic load effects induced by the code load models. Figure 5 shows a plot, on Gumbel probability paper, of daily maximum load effects with a Weibull distribution fitted to the data to extrapolate to find the load effect corresponding to a 1000-year return period.

The results of the analysis showed that congested traffic governed on the longer bridges (over 50m) while for short/medium-span bridges the free-flowing scenarios were generally more critical. In addition, the results for general road bridges showed that the currently used design/assessment codes were adequate to encompass the likely effects resulting from the proposed changes to the regulations.

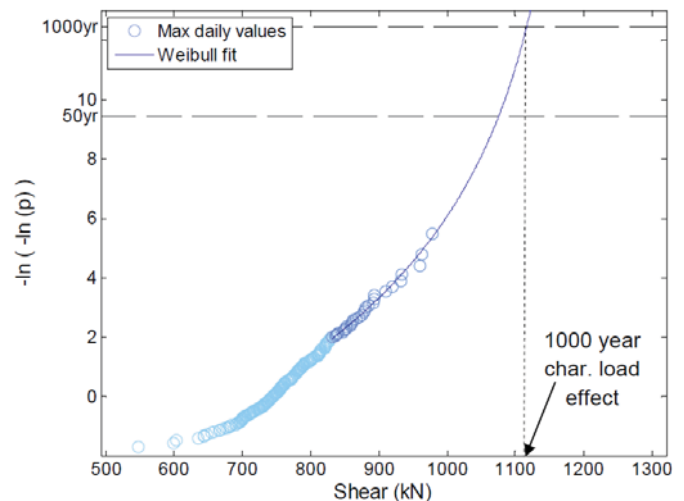


Figure 5. Characteristic Load Effect Calculation

The analysis of masonry arches involved a similar procedure, however in this case, rather than extrapolating to find the characteristic load effect, it was more appropriate to carry out a probabilistic extrapolation to find the characteristic tridem weight for 5-axle and 6-axle trucks as the tridem weight was shown to be the critical factor governing the stability of the masonry arches. These characteristic tridems were then used to compare the live load factor achievable at ULS to that achievable using the characteristic tridem weight of BD21/01 for the twenty arch configurations examined in Phase 1. Results showed that the proposed changes were unlikely to be critical for masonry arches.

Finally, in order to consider the potential implications for pavement damage, a reasonably simple calculation was carried out to estimate the likely increase in pavement damage associated with the proposed weight limit increases. The fourth power law, often used to approximate pavement damage, was used in this calculation as per Eq. 1.

$$PWDF = \sum_{i=0}^n ESAL_i^4 \quad (1)$$

Where $PWDF$ is the Pavement Wear Damage Factor, n is the number of axles on the vehicle and $ESAL_i$ is the Equivalent Standard Axle Weight of axle i which can be calculated by dividing the weight of the axle being considered by a standard axle-weight 8 t (e.g. an axle-weight of 8 t has an $ESAL = 1.0$). In order to assess the implications for pavement damage, the $PWDF$ was calculated for 1,000,000 t of freight using 40 t 5-axle vehicles, 42 t 5-axle vehicles or 46 t 6-axle vehicles. Carrying out this calculation showed that the derogation for 5-axle trucks, allowing a gross vehicle weight (GVW) of 42 t instead of 40 t, results in an increase of 11% in pavement damage, whereas carrying 46 t on 6-axes demonstrates 29% less damage than the 42 t 5-axle trucks. The overall results implied that increases in pavement damage were likely to be more significant than implications for bridges, and that a move towards 6-axle vehicles could reduce levels of pavement wear.

3.2 Administration of Abnormal Vehicles

In 2012 ROD-IS carried out a study, commissioned by the NRA, which aimed to develop tools to assist in the decision making process for issuing permits for abnormally loaded vehicles while considering their effects on bridges on the Major Inter-Urban (MIU) routes [9]. Again, the work was carried out in two phases as outlined in the following sections.

3.2.1 Phase 1

Phase 1 of the project involved carrying out initial research and defining the appropriate assumptions which would be used within any analysis carried out in the project. A detailed review of the Eirspan bridge database was carried out to identify the types of bridges present on the MIU network. It was found that influence lines used in the previous study (Figure 3) were suitable to represent the majority of structures on the MIU network. Some additional influence lines were also generated and included in the analysis to represent certain structures which weren't considered to be appropriately represented by those in Figure 3.

The next step was to identify and categorise typical vehicles being used to transport abnormal loads. Initially, records of permits previously granted by various local authorities were examined; however there was insufficient detail to accurately quantify the characteristics of the vehicles transporting abnormal loads. As such, a WIM database from the UK, containing approximately 2.8 million trucks was employed to examine abnormal vehicle characteristics. Eight weight classes were defined (50, 60, 70, 80, 90, 100, 125 and 150 t) and a detailed statistical analysis of the vehicles found within each weight class was carried out. On the basis of this analysis the most common vehicle configuration in each weight class was extracted and used to develop a set of abnormal vehicle silhouettes. The axle weight distribution on these silhouettes was derived using an optimisation which aimed to ensure that the silhouettes, while representing actual vehicles, would induce greater load effects than any other vehicle of the same configuration. These silhouettes, Figure 6, represented the primary output of Phase 1.

3.2.2 Phase 2

The second phase of the project focused primarily on the development of a basic software tool which could be used to consider the likely effects on bridges for an abnormal vehicle wishing to travel on the MIU network. This tool could be used by permit issuing authorities as part of their decision making process for granting permits. This tool was developed within Microsoft Excel, with computer code hidden in the background to carry out the analysis based on user inputs. Using a number of assumptions defined during Phase 1, the tool calculates load effects induced by a particular abnormal vehicle in each of the 391 influence lines considered. These load effects are then compared to the design load effects for abnormal vehicles as defined within, BD37/01 [6] and EC1 [7]. More details on the developed tool can be found in [9].

In addition to this software tool, Phase 2 also aimed to provide a load rating for the MIU network. This involved using the representative silhouettes developed in Phase 1 (Figure 6) and analysing their effects using the software tool. It was found that the so-called 'Green Motorway Network' was rated at

100 t indicating that typical abnormal vehicles (i.e. those represented by the silhouettes in Figure 6) are likely to be granted permits based on the analysis.

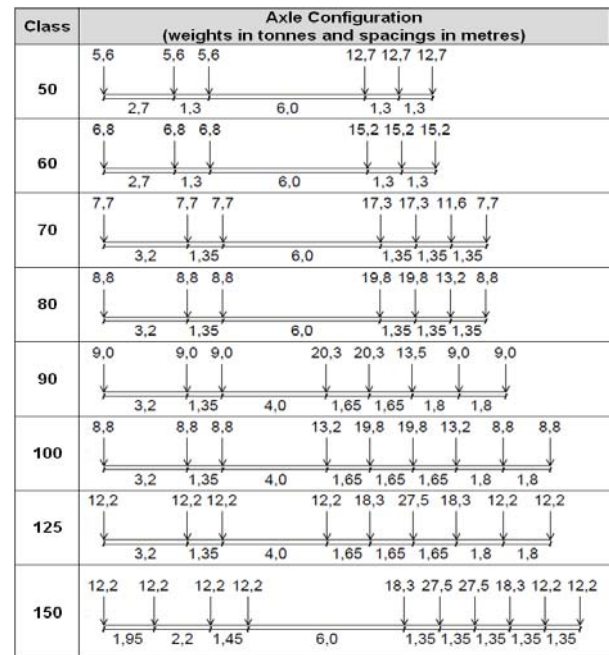


Figure 6. Representative Abnormal Vehicle Silhouettes [9]

3.3 Examining Weight Limits for Heavy Goods Vehicles.

In 2013, the NRA commissioned a study, undertaken by ROD-IS, to examine the potential of increasing weight limits across the different vehicle classes using Irish roads. Again, general road bridges, masonry arches and pavement damage were all considered within the analysis. The UK WIM database containing 2.8 million trucks was employed in this study, which was carried out in two phases in a similar manner to the previous projects. During the first phase, a preliminary screening exercise was carried out which considered convoys of trucks in jammed and free-flowing traffic scenarios in order to identify the critical influence lines which were to be analysed in more detail. Based on the results of the preliminary analysis, along with consideration of the structures which were of particular interest to the NRA, ten cases were considered for the detailed analysis in Phase 2.

For the Phase 2 analysis, the WIM data was used to carry out long-run simulations of traffic flow to examine the impact of traffic on the bridges on the network. These long run simulations use the measured WIM data to fit probabilistic distributions to various characteristics observed in the traffic, e.g. frequencies of different vehicle classes, axle-weights, axle-configurations, inter-vehicle gaps, velocities etc. Using these probabilistic distributions, further traffic, beyond that contained in the WIM database, can be generated and used to identify loading scenarios which may be more critical than any which occur within the measured traffic. Applying this approach, ten years of traffic measurements were generated and the maximum daily load effects calculated for each of the influence lines considered. A statistical extrapolation was then carried out to calculate the characteristic (50 and 1000-year) load effects which were then compared to the load effects generated by the design and assessment load models specified within the codes. This type of long-run simulation analysis

was carried out for various increases to weight limits in order to examine the sensitivity of the bridges to such increases. In addition, a similar approach to that described in Section 3.1.2 was used to calculate the characteristic axle, tandem or tridem-weights for different vehicle classes. The effects of these characteristic loads on masonry arches were then compared to the effects generated by the BD21/01 assessment loading in order to identify the implications for various increases to weight limits.

Again, a basic calculation was carried out using the fourth-power law to examine potential implications for pavement damage. As expected, increasing weight limits was shown to increase levels of damage, with the level of the increase varying depending on which vehicle type was being considered. The overall findings of the study, considering general road bridges, masonry arches and pavement damage, showed that based on the current design and assessment codes, any increase in weight limits for the vast majority of vehicle classes was likely to have adverse effects for the road network in one way or another with only minor increases being possible for a limited number of vehicle types.

3.4 Weight Limits for non-Regulated Vehicles

In 2015, after the collection of a year of WIM data from the six Irish sites, TII commissioned a project which aimed to identify suitable weight limits for five-axle rigid vehicles along with 6-axle truck-trailer combinations of 4+2 & 3+3 axle configurations. The 5-axle rigid trucks had previously not been covered by Irish regulations and as such a suitable GVW limit was required. The two 6-axle configurations were examined to identify the impact of increasing their allowable GVW limit. This project represented the first application of measured WIM data from Ireland, providing a realistic insight into the impacts of Irish traffic on road infrastructure. Prior to the analysis, extensive checking and cleaning of the data was carried out to ensure that the results of the analysis would be as accurate as possible. One full year of records measured at the M4 WIM site was used to carry out the analysis, which involved carrying out long-run traffic simulations for varying levels of truck weights. Due to the fact that the proposed 5-axle rigid configurations had not been used in Ireland, Dutch WIM data was employed to examine the characteristics of these types of vehicles.

As with the previous projects, a preliminary simplified analysis was used to identify critical influence lines for general road bridges, for which the long run simulations were subsequently carried out. In addition, assessments of the effects on masonry arches and pavements were also carried out using the same approach as described for previous projects.

The results of the simulations showed that the characteristic load effects induced by the current Irish traffic, without considering any changes to weight limits were unexpectedly high. It was found that there was a high level of overloading of vehicles on the Irish network; a problem which if not addressed could have major implications for the condition of our bridges and pavements.

In order to identify a suitable GVW for 5-axle rigid trucks, a similar approach was taken, with the WIM data being modified to introduce these new truck types into the traffic

mix, while considering different potential weight limits. It was found that a maximum GVW of 36 t was acceptable. In addition, for the 6-axle truck configurations examined it was found that the limit on 3+3 axle-configuration could be increased by 2 t without resulting in any significant implications for bridges or pavements. Unfortunately, a scarcity of 4+2 type vehicles in the WIM data meant that no major conclusions could be drawn in relation to an appropriate weight limit for these trucks. The most significant finding of the study related to the high levels of overloading on the Irish road network, indicating that without improved enforcement procedures for vehicle weight limits, the effects of the traffic on our bridges and pavements are likely to be in excess of what had previously been assumed before WIM data collection had commenced in Ireland.

4 CONCLUSION

Central to the efficient management of any road network is a comprehensive understanding of the factors influencing the usage and degradation of the infrastructure elements on the network. This paper outlines some of the benefits of utilising WIM technology to monitor traffic weights and provides an overview of the WIM sites which have recently been installed by TII in Ireland. In order to demonstrate some of the benefits of collecting WIM data this paper provides a brief summary of four projects which have used WIM data to assess various implications of traffic loading on the Irish road network. The results of these studies have provided TII with a better understanding of the impacts of traffic loading and have been used to inform a number of amendments to vehicle weight limit regulations in Ireland.

ACKNOWLEDGMENTS

The authors would like to gratefully acknowledge Transport Infrastructure Ireland, the U.K. Department for Transport, Rijkswaterstaat (Dutch Ministry of Transport and Waterworks) and IBDIM (Polish Road and Bridge Research Institute) for the provision of the Weigh-in-Motion data.

REFERENCES

- [1] NRA (2014) *National Route Lengths 2013*, Available at: http://www.tii.ie/tii-library/Network_Management/National%20Route%20Lengths/NationalRouteLengths2013_Final.pdf [Accessed 24 March 2016].
- [2] Eurostat (2009) *Panorama of Transport*, Office for Official Publications of the European Communities, Luxembourg.
- [3] Statutory Instrument No. 5 of 2003, 'Road traffic (construction and use of vehicles) regulations 2003', as amended.
- [4] O'Brien, E.J., O'Connor, A.J., Cahill, F. and Arrigan, J.E. (2012), 'Increasing Truck Weight Limits: Implications for Bridges'. *Procedia-Social and Behavioral Sciences*, 48, pp.2071-2080.
- [5] O'Connor, A., Jacob, B., O'Brien E. and Prat, M. (2001), 'Report of current studies performed on normal load model of EC1-traffic loads on bridges', *Revue Française de Génie Civil (RFGC)*, *Hermes Science Publications*, 5 (4), 411-434.
- [6] BD 37/01, 'Loads for highway bridges', *Design Manual for Roads and Bridges*, volume 1, section 3 part 14. Highways Agency, UK.
- [7] IS EN 1991-2 NA (2003), 'Eurocode 1: Actions on structures – part 2: traffic loads on bridges', NSAI.
- [8] BD 21/01, 'The assessment of highway bridges and structures', *Design Manual for Roads and Bridges*, volume 1, section 3 part 4. Highways Agency, UK.
- [9] Corbally, R., O'Connor, A., Cahill, F. and Daly, A. (2014) 'Administration of Abnormal Vehicles in Ireland' In *Civil Engineering Research in Ireland*, Belfast, UK, 28-29 August 2014.

An Analysis of a Data Set of 1,400 Bridge Inspections in County Cork.

Liam Dromey^{1,2}, John J. Murphy², Brian O'Rourke², Kieran Ruane^{2,3}

¹Cork County Council, County Hall, Cork, Ireland

²Department of Civil, Structural and Environmental Engineering, Cork Institute of Technology, Bishopstown, Cork, Ireland

³RPS Group, Innishmore, Ballincollig, Co. Cork, Ireland

email: liam.dromey@corkcoco.ie, johnjustin.murphy@cit.ie, brian.orourke@cit.ie, kieran.ruane@rpsgroup.com

ABSTRACT: A recent project by Cork County Council has allowed the compilation and analysis of detailed inventory and inspection data of 1,400 bridges on its regional and local road network. Each bridge and its constituent components or elements have been visually inspected and their structural condition rated based on a defined scale of deterioration and damage. This paper presents data on bridge structure type and geometry as well as condition ratings for each bridge component. The worst performing bridge components and the most recurrent damage types are identified. Conclusions are drawn on the overall condition of the bridge stock, the critical structural components and the deterioration mechanisms that impact upon them.

KEY WORDS: Bridge management systems; Structural inspection; Bridge defects; Data analysis.

1 INTRODUCTION

The National Roads Authority (now Transport Infrastructure Ireland) has developed Eirspan as the Irish bridge management system [1]. Between 2012 and 2014, Cork County Council undertook a survey of bridges on regional and strategic local roads. The survey process comprised two distinct stages:

- (i). Bridge inventory collection where the name, location, type and geometry of the bridge stock are recorded and collated. For each structure, up to 58 separate parameters were recorded.
- (ii). Principal inspection where the damage type is recorded and a condition rating value is assigned to the constituent components and the overall bridge structure. For each structure, up to 21 separate parameters were recorded.

The survey has thus yielded an extensive and detailed database of over 100,000 separate pieces of empirical information. To date, no analysis of bridge typology and physical condition based on this quantity of data has been undertaken on a regional Irish bridge stock. The available data set of inventory and principal inspection records provides an opportunity to undertake such an exploratory analysis.

This paper describes the findings of the analysis and how the findings improve the understanding of the performance of the bridge stock. The scope of the study consists of data integration, summary and descriptive statistics, and the interpretation of results. The objectives of this study are to compile and consolidate the available data set into a usable tabular format and extract information to discover previously unknown patterns, trends and relationships within the data.

The study has established the characteristics of the bridge stock in terms of geometry and condition ratings. The bridge components most susceptible to damage have been identified and a Pareto analysis has determined the most frequent types of damage that have impacted upon the bridges and their

constituent elements. The cost of rehabilitation in terms of components and condition ratings has been determined.

2 METHODOLOGY

The data set of the bridge survey observations has been generated by the Eirspan system in 'Notepad' format. Notepad is a plain text (i.e. data) editor for Microsoft Windows and is a basic text editing program that enables the creation of documents. The Notepad data files were imported into a Microsoft Excel spreadsheet where the data were sorted and checked for errors and inconsistencies. The Microsoft Excel spreadsheet provides a computer application for the organisation, analysis and storage of the data in tabular format.

The dataset, now in tabular spreadsheet format, has been manipulated and analysed and the results of queries undertaken form the basis for this paper.

3 BRIDGE TYPOLOGY

The database has records of 1,367 bridges, of which 435 were on regional roads and 932 were on strategic local roads.

3.1 Geometry

Of the surveyed bridges, 1,244 (91%) have three spans or less as shown in Figure 1.

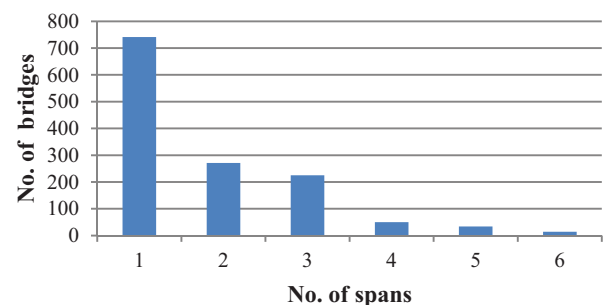


Figure1. Number of spans of surveyed bridges.

With respect to span lengths, 1,094 (80%) of bridges have span lengths no greater than 6m as shown in Figure 2.

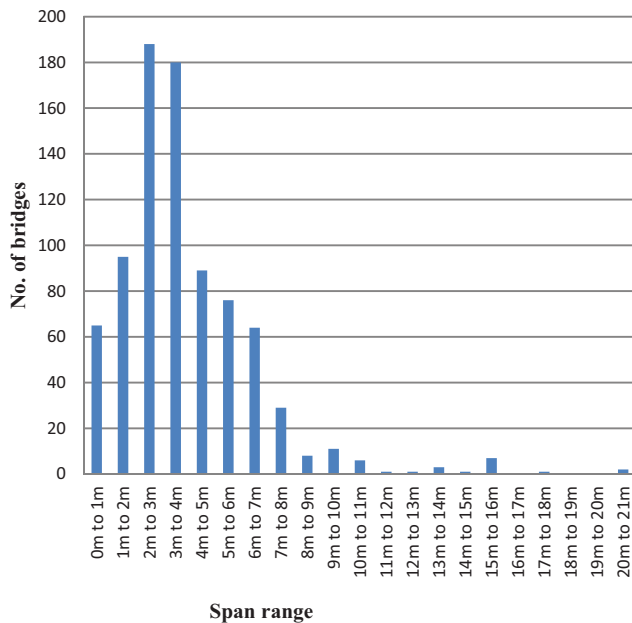


Figure 2. Range of span lengths of surveyed bridges.

The bridge out-to-out width, which is defined as the total width of the superstructure, is measured perpendicular to the bridge span [2]. Given that the surveyed bridges are on predominantly two-lane roadways, 1,148 (84%) have measured out-to-out width values less than 10m as shown in Figure 3.

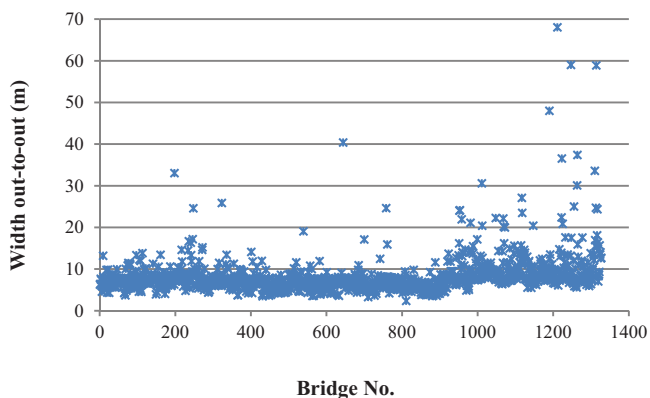


Figure 3. Out-to-out widths of surveyed bridges.

3.2 Superstructure types

The Eirspan system records the superstructure parameters by using a standard list of element descriptions. These records have been analysed and assessed to provide a fuller interpretation of the data set.

The parameter 'design of elevation of superstructure' describes the elevation, or longitudinal layout, of the superstructure. The most common types of superstructure elevation identified are the 827 (60.5%) 'arches of one or more spans' bridges and the 410 (30%) 'simple span, constant cross-section' bridges as shown in Figure 4. These two main

types have been further investigated in terms of construction material. In the case of arches, 783 (94.7%) are of stone masonry (Figure 5), while for simple spans of constant cross-section, 223 (54.4%) are of in-situ reinforced concrete and 97 (23.7%) are of stone masonry (Figure 6). This masonry material may be explained by the presence of 'clapper' bridges, which are large flat stone slabs supported on piers and abutments. In the data set, these bridges have a span range between 0.5m to 2.1m, with an average span of 0.9m. An example is shown in Figure 7.

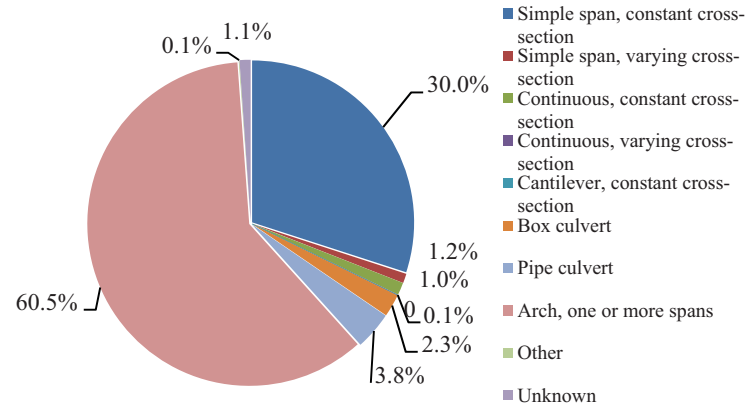


Figure 4. Design of elevation of superstructure.

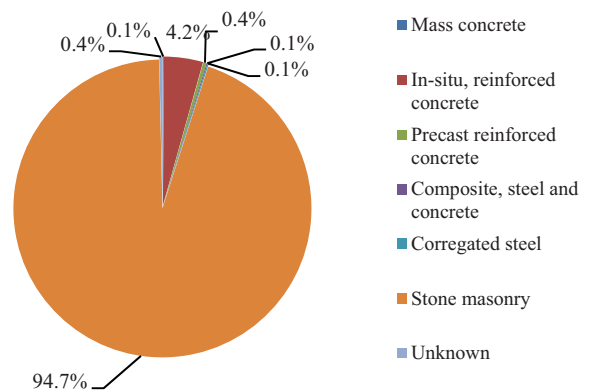


Figure 5. Construction materials of arches.

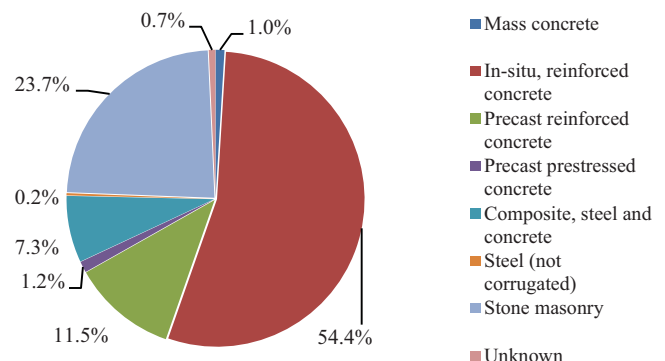


Figure 6. Construction materials of simple spans of constant section.



Figure 7. Typical 'clapper' bridge deck arrangement.

3.3 Substructure types

As in the case of the bridge superstructure, Eirspan records the substructure parameters by using a standard list of descriptions. The results of the analysis of the data for abutment type and material are presented in Figures 8 and 9.

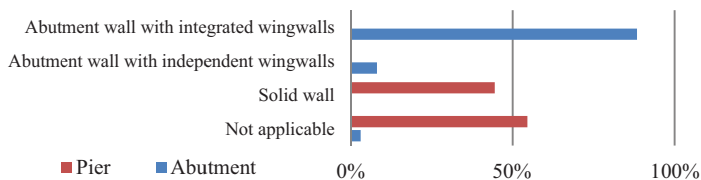


Figure 8. Abutment and pier type.

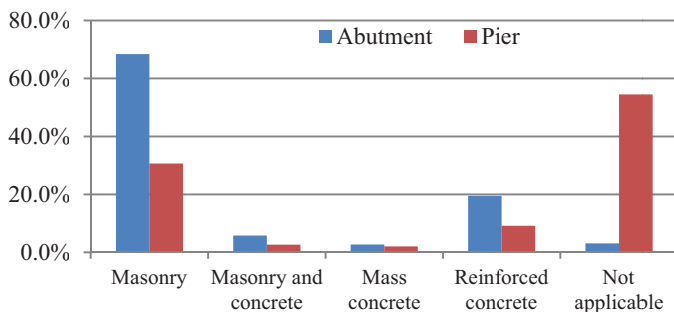


Figure 9. Abutment and pier material.

4 BRIDGE COMPONENT AND OVERALL STRUCTURE CONDITION RATINGS.

The Eirspan system [3] describes the inspection process as:

“a systematic visual check of all accessible parts of the structure.....these purposes are fulfilled by:

- *a condition rating of the structure and each of its components.*
- *registering the type and extent of any significant damage”.*

The condition rating for both the bridge components and the overall structure is a value between ‘0’ and ‘5’ (as well as ‘?’ and ‘-’). These rating values are defined in Table 1.

Table 1. Eirspan condition ratings.

Condition Rating	Definition
0	No or insignificant damage.
1	Minor damage but no need of repair.
2	Some damage, repair needed.
3	Significant damage.
4	Damage is critical.
5	Ultimate damage.
?	Unknown.

Eirspan [3] defines a total of 13 bridge components and the condition rating of the overall structure is determined by the individual ratings of five ‘critical’ components, which have been defined as ‘Abutments’, ‘Piers’, ‘Bearings’, ‘Deck/Slab’ and ‘Beams/Girders/Transverse beams’.

4.1 Overall structure ratings of surveyed bridges

From the analysis of the data, the percentage of bridges in terms of overall condition rating has been derived and is presented in Figure 10. In descending order they are 732 (53.5%) rated Condition 2, 272 (19.9%) rated Condition 3, 181 (13.2%) rated Condition 1, 81 (5.9%) rated Condition 5, 34 (2.5%) rated Condition 0 and 30 (2.2%) rated Condition 5.

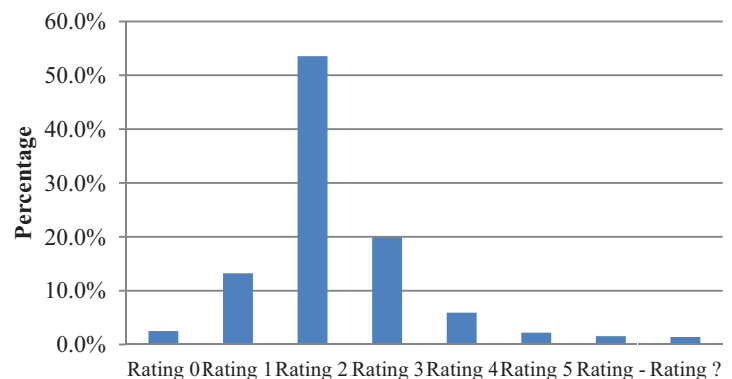


Figure 10. Overall structure ratings of bridge stock.

4.2 Critical component condition ratings

The component rating data have been analysed to identify the critical components, which determine the overall structure ratings; these are shown in Figure 11 for overall structure ratings ‘5’ to ‘2’.

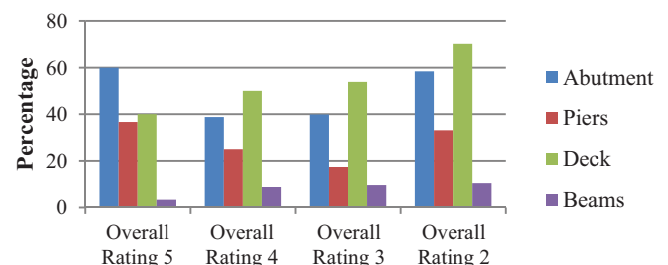


Figure 11. Percentage of critical component ratings at overall structural rating.

5 DAMAGE TYPES

The Eirspan system records damage type by using a standard list of descriptions [3]. These records have been analysed and the results assessed.

In the consideration of damage types or defects within systems or processes, Montgomery [4] describes the Pareto analysis methodology, which consists of identifying quality issues by category or by type of defector nonconformity. This analysis is based on the ‘Pareto Principle’, also known as the 80/20 Rule, which is a method of identifying issues that impact upon process performance and quality control [5]. It is attributed to the work of Italian economist Vilfredo Pareto, who observed that in the early 20th Century, 80% of the wealth in his country was owned by 20% of the population. It has been generalised to mean that approximately 80% of any given effect can be attributed to 20% of the possible causes. Conversely, the remaining 80% of causes account for only 20% of the effects.

The output from this analysis may be presented in a Pareto chart, which is a frequency distribution of attribute data arranged by category. For the recorded bridge data, the damage types for each component have been analysed in Pareto chart format for each of the critical components in Figures 12-15 and the ‘80% damage types’ for each component are presented in Table 2.

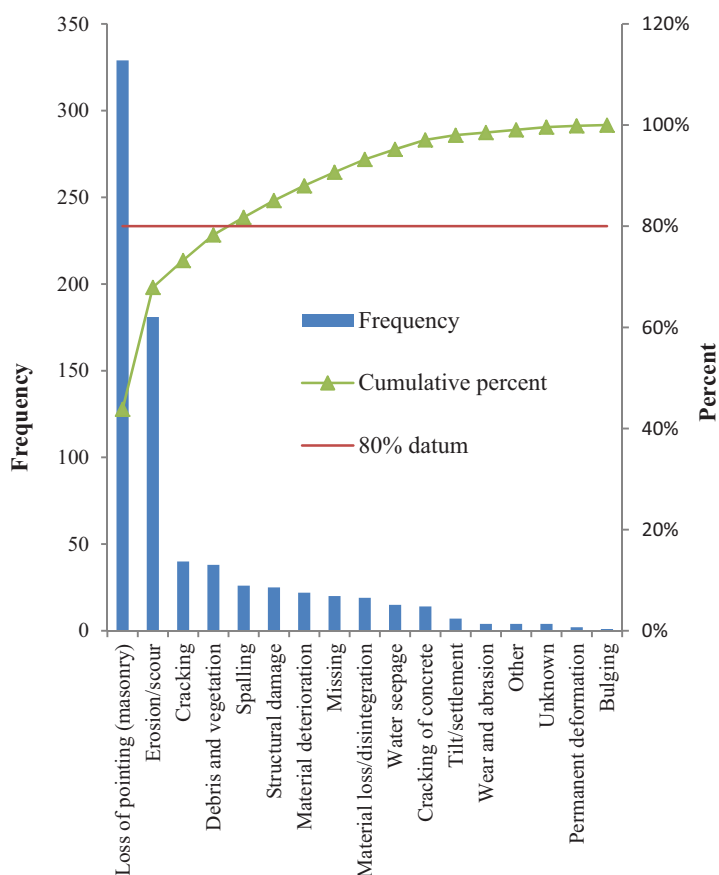


Figure 12. Pareto chart for damage to abutments.

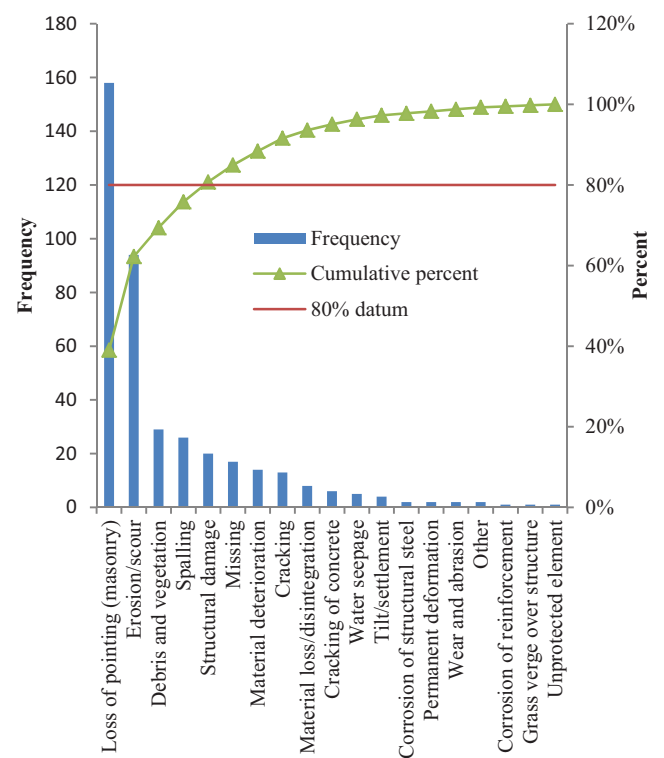


Figure 13. Pareto chart for damage to piers.

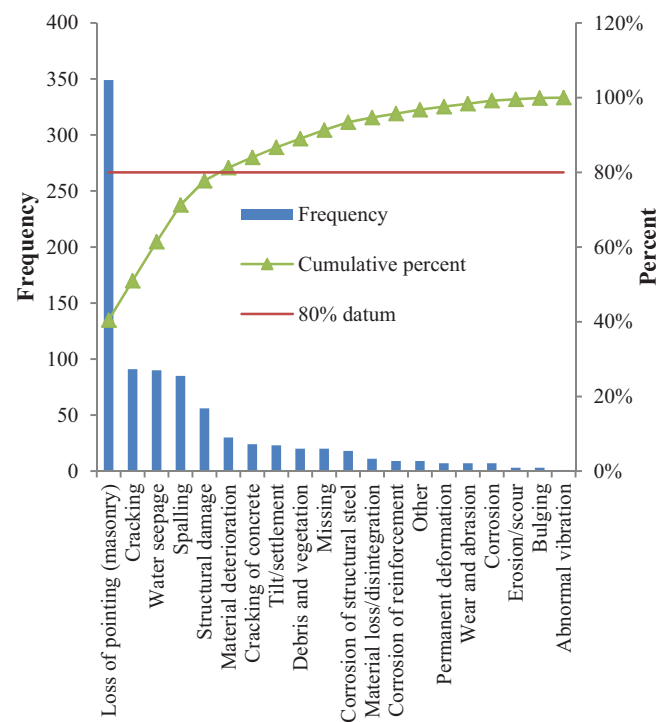


Figure 14. Pareto chart for damage to deck/slab.

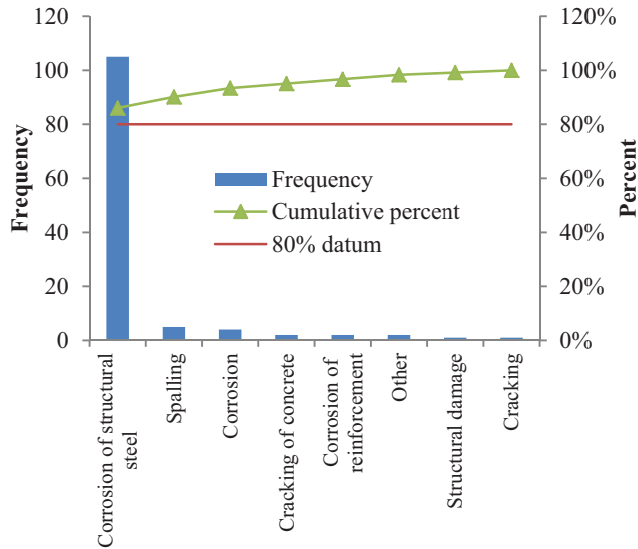


Figure 15. Pareto chart for damage to beams/girders/transverse beams.

Table 2. Most frequent types of damage.

Component Name	Most frequent types of damage
Abutments	<ul style="list-style-type: none"> Loss of pointing (masonry) Erosion/scour Cracking Debris and vegetation
Piers	<ul style="list-style-type: none"> Loss of pointing (masonry) Erosion/scour Debris and vegetation Spalling
Deck/slab	<ul style="list-style-type: none"> Loss of pointing (masonry) Cracking Water seepage Spalling Structural damage
Beams/girders/transverse beams	<ul style="list-style-type: none"> Corrosion of structural steel

Examples of component condition ratings from the data set are shown in Figures 16-18.



Figure 16. Intermediate pier component rated condition '5' in a structure with an overall condition rating of '5'.



Figure 17. Deck (arch barrel) component rated condition '5' in a structure with an overall condition rating of '5'.



Figure 18. Abutment component rated condition '5' in a structure with an overall condition rating of '5'.

6 BRIDGE STOCK REHABILITATION COST

Analysis of the data set shows that the total cost for the rehabilitation of the bridge stock is €24.4 million. This has been further investigated as shown in Figures 19 and 20. In terms of bridge components, bridge surfaces at €4.9 million are the largest cost followed by bridge decks at €4.7 million. With regard to condition ratings, Condition 2 rated bridges at €16.4 million are the largest cost followed by Condition 3 rated structures at €3.9 million.

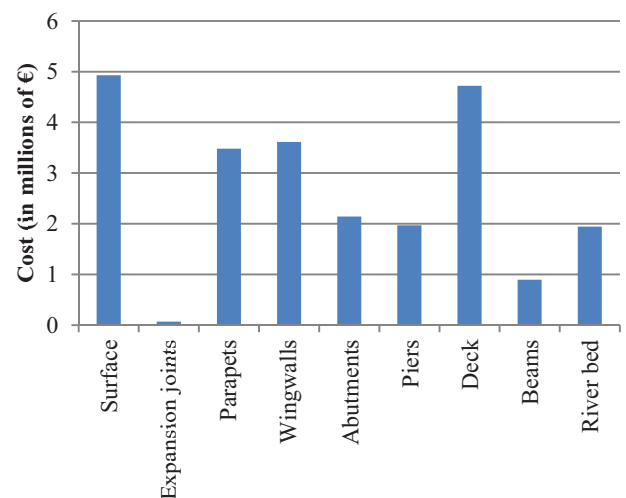


Figure 19. Rehabilitation costs in terms of bridge components.

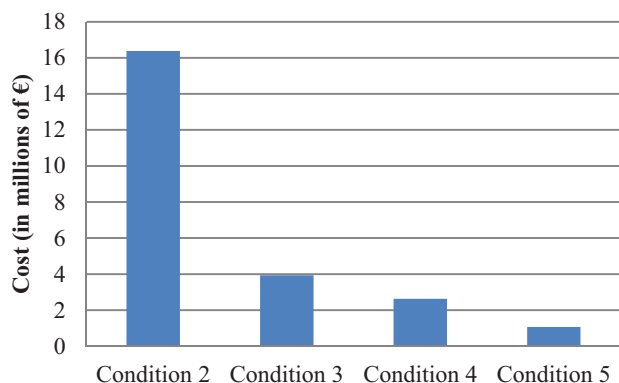


Figure 20. Rehabilitation costs in terms of overall bridge condition ratings.

7 SUMMARY

Research thus far has determined that the surveyed bridge stock may be described as being predominantly of structures having less than three spans with the majority of span lengths being less than 6m and with the out-to-out widths of the structures being predominantly less than 10m.

In terms of bridge superstructure cross-section and material, in excess of 60% of the structures are arches of one or more spans, followed by simple span bridges of constant cross-section at 30%. The arch bridges are overwhelmingly of masonry construction while the simple span arrangements are mainly of either in-situ reinforced concrete or masonry. For the bridge substructures, abutments primarily consist of masonry walls with integrated wingwalls. Intermediate pier information is not as complete as that available for abutments.

With regard to the overall condition of the surveyed bridge stock, 28% have suffered at least significant damage while 81% have suffered at least some damage.

The worst performing components for structures with an overall condition rating of '5' to '2' have been found to be the abutments and deck.

As part of the investigation of the data, a Pareto analysis of the reported damage types has been undertaken for the 'critical' components. For the abutments, the most frequent types of damage are loss of pointing (masonry), erosion/scour, cracking and debris/vegetation. In the case of piers, the most frequent are the loss of pointing (masonry), erosion/scour, debris/vegetation and spalling. For the deck/slab component, the most frequent are the loss of pointing (masonry), cracking, water seepage, spalling, and structural damage, while for the beams/girders/transverse beams component, the main damage types are corrosion of structural steel.

With respect to cost, the overall rehabilitation cost for the surveyed bridge stock is €24.4 million. In terms of bridge components, bridge surfaces are the largest cost followed by bridge decks. In the case of condition ratings, Condition 2 rated bridges form the largest cost followed by Condition 3 rated structures.

The approach taken in this study has shown that the data set is a valuable resource of empirical data, the analysis of which leads to a better understanding of the characteristics and

performance of the bridge stock. The critical bridge components have been verified and an analysis of the damage types has established that a small number of physical processes are responsible for the majority of bridge component deteriorations. The consideration of rehabilitation costs provides an insight into the scale of the task of managing the bridge stock.

The results of this study allow a better understanding of the deterioration factors impacting upon the bridge stock and thus improve the prediction of future bridge conditions and enhance decision making with respect to the allocation of resources.

8 FURTHER RESEARCH

The intended outcome of future research is the development of an integrated bridge prioritisation index as a decision making aid in the targeted allocation of resources for the rehabilitation of bridges on a regional road network. The research will build upon the work of Valenzuela et al. [6] on bridges on the Chilean road network. The proposed index will consider the structural condition, hydraulic vulnerability, repair cost and strategic importance of individual bridges on the network. It is proposed that the index will be calibrated by a review of bridge rehabilitation projects already undertaken in County Cork, by a survey of experts in the fields of bridge design and construction, bridge maintenance and bridge inspection; and by further in-depth statistical analysis of the data.

ACKNOWLEDGMENTS

The authors would like to thank Cork County Council for granting the authors access to the Eirspan data used in this paper.

REFERENCES

- [1] Duffy, L. (2004). 'Development of Eirspan: Ireland's bridge management system'. *Proceedings of Institution of Civil Engineers - Bridge Engineering*, ICE, September, 157, 139-146.
- [2] National Roads Authority, *EIRSPAN The Irish Structure Management System, System Manual No. 2, Inventory*, Rev. C, Dublin, 2008.
- [3] National Roads Authority, *EIRSPAN The Irish Structure Management System, System Manual No. 3, Principal Inspection*, Rev. C, Dublin, 2008.
- [4] Montgomery, D., *Introduction to Statistical Quality Control*, John Wiley & Sons, Hoboken, NJ, sixth edition, 2009.
- [5] Scott, C., Applying the Pareto Principle to Information Security Management, 2015.[Online]. Available: www.sans.edu.[Accessed 08 November 2015].
- [6] Valenzuela, S., de Solminiach, H., and Echaveguren, T. (2010). 'Proposal for an Integrated Index for Prioritization of Bridge Maintenance', *Journal of Bridge Engineering*, ASCE, May, 15, 337-343.

Building performance evaluation of domestic energy efficient retrofits in current and future climates

McGrath, T.E.¹, Campbell, N.¹, Nanukuttan, S.V.¹, Soban, D.², Basheer, P.A.M.³

¹School of Planning, Architecture & Civil Engineering, Queen's University Belfast, BT9 5AG, Northern Ireland

²School of Mechanical & Aerospace Engineering, Queen's University Belfast, BT9 5AG, Northern Ireland

³School of Civil Engineering, University of Leeds, England, LS2 9JT, UK

email: tmcgrath03@qub.ac.uk

ABSTRACT: Approximately half of the houses in Northern Ireland were built before any form of minimum thermal specification or energy efficiency standard was enforced. Furthermore, 44% of households are categorised as being in fuel poverty; spending more than 10% of the household income to heat the house to bring it to an acceptable level of thermal comfort. To bring existing housing stock up to an acceptable standard, retrofitting for improving the energy efficiency is essential and it is also necessary to study the effectiveness of such improvements in future climate scenarios. This paper presents the results from a year-long performance monitoring of two houses that have undergone retrofits to improve energy efficiency. Using wireless sensor technology internal temperature, humidity, external weather, household gas and electricity usage were monitored for a year. Simulations using IES-VE dynamic building modelling software were calibrated using the monitoring data to ASHARE Guideline 14 standards. The energy performance and the internal environment of the houses were then assessed for current and future climate scenarios and the results show that there is a need for a holistic balanced strategy for retrofitting.

KEY WORDS: Building performance evaluation, energy efficiency, climate change, retrofit.

1 INTRODUCTION

The UK Climate Change Act (2008) requires an 80% reduction of greenhouse gas emissions on 1990 levels by 2050 [1]. Approximately a quarter of carbon emissions come from domestic buildings [2]. The Standard Assessment Procedure (SAP) is the UK methodology for rating domestic energy efficiency. Domestic buildings in Northern Ireland are considered inefficient with an average SAP rating of D [3]. Approximately half of the stock was built before any minimum thermal standard, enforced in 1973 [4]. To achieve the ambitious reduction target significant measures to improve the energy efficiency and achieve an average SAP rating of B will be required [2]. Housing stock turnover is low with estimates that between 60-80% of the stock in 2050 is already standing today [5]. Whilst the energy efficiency of some of the stock can be improved with relatively non-invasive measures such as cavity fill, loft insulation and window upgrades some properties are categorised as “hard-to-treat”, where cost effective energy improvement measures are more difficult. There are 6.5 million solid wall houses in the UK, single skinned 215mm thick red brick construction with U-value of 2.0 W/m²K, which are categorised as “hard-to-treat” [6]. There are 87,600 pre-1919 houses of which 95.3% have SAP rating lower than C in Northern Ireland. Of domestic buildings that fall within the lowest SAP bands of F and G, pre-1919 properties represent 52.1% [3].

Another significant driver to improve the energy efficiency of domestic buildings in Northern Ireland is the issue of fuel poverty. A household is defined as being fuel poor if it needs to spend more than 10% of its income to heat the house adequately. The rate of fuel poverty in Northern Ireland is amongst the worst in Northern Europe with 42% of households classed as being fuel poor [3]. There have been 1,890 excess winter deaths over the last decade have been

directly attributable to people living in damp and cold homes [7]. In pre-1919 properties 68.7% of occupants are classified as being fuel power, the highest rate for all dwelling age brackets [3].

Given the significant legislative and social drivers the improvement of building energy performance via retrofitting of insulation materials and the inclusion of more efficient heating systems is unavoidable. This change is being lead primarily by the social housing sector who have a responsibility to provide affordable housing.

Due to the predicted changes in global weather patterns the sensitivity of retrofit measures to future climate conditions needs to be considered. Global average temperatures are predicted to rise between 1 to 5°C by 2100. Climate change will result in an increased frequency of extreme weather events with heatwaves and drought during summer months and warmer and wetter winter months. Current retrofit measures are designed considering past weather patterns and the hierarchy of reducing energy focuses on the minimisation of winter space heating. As a consequence of a warming climate there will be additional pressures on the built environment with over-heating and increased need for the use mechanical cooling in domestic housing becoming a possibility [8]. By computer simulation of building performance within future climate scenarios potential issues such as overheating can be identified early, as discussed by [9], [10]. The need for active ventilation systems can be considered as well as gained a deeper understanding of the full building life cycle performance. Generally as energy efficient retrofit measures often prioritise the reduction of winter time space heating there is the potential to exacerbate summer overheating issues in the future. It is important to design any retrofit measures considering the implications of a changing climate.

2 CASE STUDY PROPERTIES

2.1 Retrofit actions taken

The case study properties are owned by a social housing landlord in Belfast, Northern Ireland. The terraced houses were built between 1901 and 1908 and both are solid wall redbrick construction. They are located within a designated special area of conservation zone and alterations to the external façade are restricted. They have undergone significant retrofit measures to improve energy efficiency. House 1 consists of two terraced houses which have been joined together to make a large house suitable for a modern family. It has also had a small extension added to the rear of the property in the 1970s. In 2010, internal wall insulation was applied: 100mm sheep wool, 50mm polyisocyanurate board and 6mm magnesium board. House 2 is a detached property and had 60mm wood fibre insulation board and 9mm magnesium board applied internally, also in 2010. In an effort to reduce thermal bridging at the junction of the internal insulation and the 1st floor level 300mm of sheep wool insulation was added next to the external wall in each house. In the roof space of both properties, 200mm of glass mineral wool insulation was laid down between floor joists. The underside of the roof space had a further 30mm PIR insulation and 6mm magnesium board fixed in to the underside of the ceiling joists. Argon filled double glazing has been fitted in timber sash windows. Suspended timber floors were replaced with insulated solid floors with expanded polystyrene insulation and concrete screed.

Domestic hot water and space heating is provided by Worcester Greenstar 30 CDi gas condensing boilers with a SEDBUK certified efficiency of 89.8% [11]. To reduce infiltration, open fire places were sealed in both properties and efforts made to improve air-tightness. Mechanical ventilation heat recovery units were also installed to ensure good air quality using a Brookvent Aircycle system with a heat recovery efficiency of 78.2% [11].

A number of short term performance tests were carried out including air pressurisation tests, thermal imaging surveys and smoke pen tests. Air-tightness test results found that despite the retrofit measures the building envelope was not effectively sealed as results fall outside current minimum building regulation standards of 10 m³/hr.m².

3 MONITORING OF CASE STUDY PROPERTIES

Monitoring data for a year period between 1st August 2014 and 31st July 2015 are presented in this paper. Temperature and relative humidity measurements were gathered in three locations in each property; living room, bedroom and bathroom. Measurements were taken at five minute intervals with battery powered units using a TMP36 temperature sensor and HIH5030 humidity sensor. Gas was measured via a Metrix UG-G4 submeter with pulse outputs at 0.01m³ intervals. Electricity consumption was measured using a newly developed circuit monitor which sampled both voltage and current wave forms over approximately 2% accuracy in trials completed. Domestic hot water was measured with an ACWA meter with a pulse generated at 1 litre intervals. Data was communicated via a digital mesh network with the information gathered in a powered central unit. Information

was then transmitted via broadband connection to the cloud. During the monitoring period over 2 million readings were recorded across the case study properties.

3.1 Internal conditions – temperature and relative humidity measurements

Relative humidity levels between 40 and 70% are considered good as prolonged periods exceeding 70% will increase the potential for the development of dust mites, airborne fungi and bacteria as well as initiating chemical and biological degradation of building materials [12]. The monthly averages show consistent and low relative humidity over the monitoring period. In both properties the relative humidity never exceeded 70% in the living room or bedroom and only exceeded the guideline limit 0.4% and 0.8% of the time in the bathroom in House 1 and 2, respectively.

For thermal comfort, CIBSE recommends internal temperature range of 17-25°C [12]. Prolonged exposure to low temperatures is linked to a detrimental impact on the health of occupants, respiratory issues at temperatures below 16°C and cardiovascular issues at temperatures below 12°C [13]. During the monitoring period in House 1 the bedroom was recorded at below 17°C for 2.9% of the time whilst the living room was below 17°C for 1% of the time. In House 2 the bedroom was below 17 for 13.6% of the time and the living room for 38.3% of the time. CIBSE also provide overheating criterion, bedrooms and living rooms should not exceed 26°C and 28°C respectively for more than 1% of occupied time. The CIBSE criteria, whilst sometimes criticised for overly simplifying the complex relationship between temperature and thermal comfort [14], are considered an indicative datum for assessing potential over heating issues in properties. Overheating has the largest impact on vulnerable occupiers, elderly and young children, with the UK 2003 summer heat wave associated with 2,000 additional deaths [15]. Bedroom temperatures above the guideline were recorded for 0.4% and 0.2% of time in House 1 and House 2 respectively. Living room temperatures did not exceed the CIBSE limits during the monitoring period in either property. Average monthly temperature and relative humidity measurements for the living room case study properties are shown in Table 1.

Table 1. Monthly average temperature and relative humidity.

	House 1 Living Room		House 2 Living Room	
	Temp (Deg°C)	RH (%)	Temp (Deg°C)	RH (%)
Aug-14	22.4	39.8	19.4	49.0
Sept-14	21.9	41.8	20.6	49.8
Oct-14	21.1	39.6	18.3	53.5
Nov-14	20.6	37.2	19.6	51.7
Dec-14	19.6	31.6	18.3	47.2
Jan-15	19.4	29.7	15.5	44.6
Feb-15	19.1	28.9	15.6	42.5
Mar-15	20.2	28.1	18.9	41.2
Apr-15	20.8	29.6	18.1	43.2
May-15	20.8	32.0	*	*
Jun-15	21.7	33.9	17.5	41.3
July-15	21.9	38.2	18.6	45.2

*Data was lost during the month of May as central data device was disconnected.

3.2 Electricity consumption

To analyse the actual electricity usage of the houses a number of literature sources were used to establish typical electricity consumption patterns and benchmarks. A report completed for the Energy Saving Trust which presented the findings of a survey of electrical energy consumption in 251 households is used as a comparison [16]. The study found that average electricity consumption in households without electric heating was found to be 3638 kWh/year which when expressed in terms of average house floor area resulted in 65kWh/m²/year. Another study of 27 households in Northern Ireland [17] found that annual electricity consumption had a strong relationship with the floor area of the building with the correlation equation presented:

$$49 \times \text{Floor Area in m}^2 + 233 = \text{electricity consumption in kWh (1)}$$

The actual electricity consumption of the two monitored houses is presented alongside benchmark annual electricity consumption from previous literature [16], [17] in Table 2.

Table 2. Annual electricity consumption (kWh).

Electricity (kWh)	House 1	House 2
Actual	3094	3056
Zimmermann et al [16]	6685	3783
Yohanis et al [17]	5272	3085

House 1 consumes significantly less than benchmarks which may be explained by under occupancy. There are two occupants, one of whom is elderly and infirmed and the other a caregiver. Electricity usage in House 2 is in line with predictions.

Whilst the amount of electricity consumed is significant when it is consumed is also of importance, particularly for demand side management applications. Figure 1 shows the average daily electricity profile in the two houses compared with the UK profile from the Energy Saving Trust [16]. The profile for House 2 appears to be relatively high overnight which could be explained by occupiers working shift patterns. The load profile for House 1 is lower than literature sources again possibly explained by under occupancy.

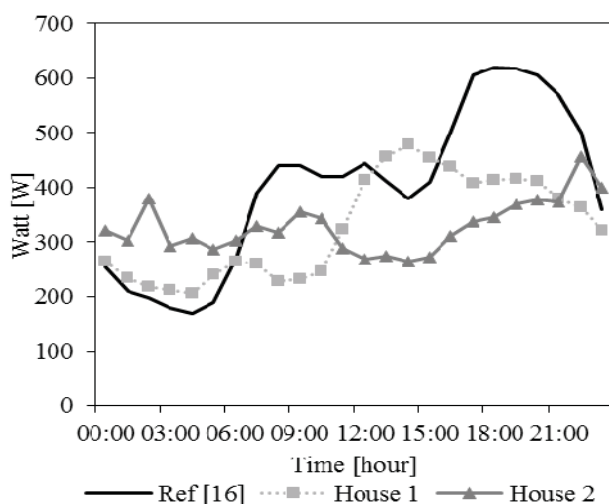


Figure 1. Average daily electricity profile of both properties compared to the UK profile obtained from [16].

3.3 Gas consumption – space heating and domestic hot water

Space heating and domestic hot water is supplied to both properties by a gas condensing boiler. The average daily domestic hot water usage was 99 litres and 216 litres for House 1 and 2 respectively. Average domestic hot water usage in a UK study of a 124 homes has been previously reported as 121 litres. The significant difference between this UK average and house 2 is being investigated further. Monthly gas consumption for the two properties are shown in Table 3.

Table 3. Monthly gas consumption.

Gas (kWh)	House 1	House 2
Aug-14	489.3	158.7
Sep-14	263.3	415.1
Oct-14	1184.0	552.7
Nov-14	1820.5	1150.6
Dec-14	2768.6	1701.2
Jan-15	3290.0	1386.5
Feb-15	2720.2	988.7
Mar-15	2437.7	907.9
Apr-15	1244.8	583.0
May-15	1136.4	49.1*
Jun-15	361.2	61.4*
Jul-15	252.7	284.5
Total	17968.8	8239.2

*Data was lost during the month of May and start of June as central data device was disconnected

4 MODELLING OF CASE STUDY PROPERTIES

Integrated Environment Solutions Virtual Environment (IES-VE) is a dynamic energy simulation modelling tool. It has been validated for a number of national and international standards such as ASHRAE 140:2007, CIBSE TM33 and ISO7730 [18] and has been found to have energy predictions in line with other dynamic simulation tools in standard scenarios. AutoCad drawings of the two houses were converted to DXF file formats and imported into IES-VE and traced to create the geometry of the building as shown in Figure 2.

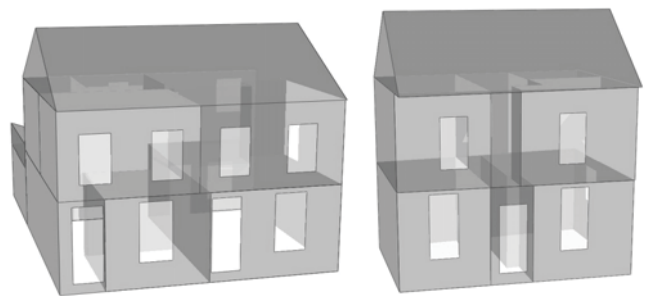


Figure 2. Case study properties geometry modelled in IES-VE. House 1 shown on the left and house 2 is on the right.

Thermal properties of the building envelope, heating profiles, infiltration/ventilation rates and temperature set points were included and are detailed in Table 4.

Table 4. House summary & IES-VE model inputs.

Description	Unit	1	2
Roof U-value	W/m ² K	0.16	0.16
Floor U-value	W/m ² K	0.22	0.22
Wall U-value	W/m ² K	0.22	0.45
Window U-value	W/m ² K	3.10	3.10
Door U-value	W/m ² K	2.2	2.2
Air-tightness	m ³ /hr.m ² at 50 Pa	15.04	10.52
Floor area	m ²	102.9	58.2
Occupants	No.	2	2
Occupancy type		24 hours	Shift workers
DHW average daily consumption	Litres	99	216
Set point temperatures	°C	19	18
Heating profile		6am – 10pm	6am – 8am & 6pm- 10pm

4.1 Model calibration

Until relatively recently calibration of models to measured results often relied on a trial and error approach, highly dependent on user knowledge, experience and statistical expertise [19]. Modelled and measured data were often compared using simple methods such as percentage error. These methods however could result in a compensation effect with overestimations cancelling out underestimations [19]. Two dimensionless error indices are recommended by a number of guidelines [19-21] to calibrate a building energy model: Mean Bias Error (MBE) (%) and Co-efficient of Variation of Root Mean Square Error (CVRMSE) (%). Models may be calibrated on a monthly or hourly basis. Mean bias error calculates the mean difference between measured and simulated data and is considered a good indicator of model bias. However this index allows for a cancellation effect of negative bias cancelling out positive bias and therefore an additional method of error measurement is required. Root mean square error (RMSE) (%) measures the variability of the data. It is the calculated difference between measured and simulated data points which is then squared. The squared errors are summed for a period and divided by the number of values taken. A square root is then taken of this result. By investigating the co-efficient of variation of root mean square error the accumulated magnitude of error of a model can be established. The CVRMSE does not suffer from the same cancellation effect as MBE, and is overall a better measure of the prediction accuracy of the model. A summary criteria for calibration on a monthly basis as recommended by three guidance documents is provided in Table 5.

Table 5. Monthly calibration criteria recommended by literature.

Monthly criteria (±%)	MBE	CVRMSE
ASHARE 14 [20]	5	15
IPMVP [22]	20	
FEMP [21]	5	15

The short-comings of these criteria have been detailed by [19], but they do not consider any inaccuracy associated with input parameters and consider energy consumption only, ignoring the simulation of internal conditions such as temperature and humidity. Given the relatively wide acceptance criteria range it is possible that numerous models of the same building could be considered calibrated.

In this paper calibration of gas consumption, for space heating and domestic hot water, was carried out on a monthly basis. Electrical energy consumption was not included in this paper as it currently only represents approximately 15% of total household energy use and can be highly occupant dependent [23].

Gas consumption measured and modelled for House 1 had an MBE and CVRMSE 0.6% and 12.0% of respectively. Gas consumption measured and modelled for house 2 had an MBE of 0.4% and CVRMSE of 14.9%. Figure 4 shows the modelled and measured gas consumption on a monthly basis for House 1 and 2.

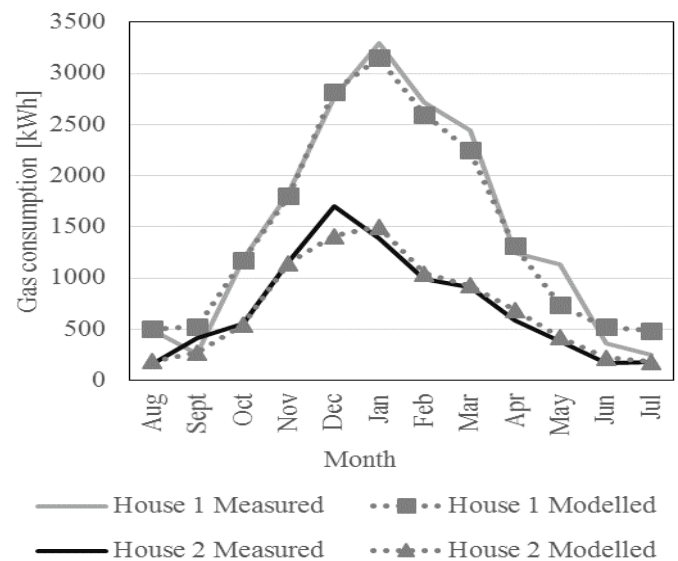


Figure 3. Monthly measured and modelled gas consumption for case study properties.

Whilst weather data was gathered at a local weather station during the monitoring period a weather file for central Belfast from the Prometheus project [24] was used. Using the local weather data may have allowed for better model calibration with improved MBE and CVRMSE values however the use of previously agreed reference files also allows easier cross referencing by other researchers.

4.2 Climate change projections

Climate projections in the UK have been funded by Department for Environment, Food and Rural Affairs

(DEFRA) and produced by the Met Office with all information made available on the UK Climate Projections (UKCP09) website. In UKCP09 the climate change projections may be generated from three different emissions scenarios and are available for three different years: 2030, 2050 and 2080. The three emissions scenarios are those developed in Special Report on Emissions Scenarios (SRES) produced by the IPCC Intergovernmental Panel on Climate Change in 2000. The scenarios are based on different rates of economic and social change covering items such as population change, economic growth, technologies and energy intensity of the 21st century. There is a high (SRES A1F1), medium (SRES A1B) and low (SRES B1) emissions scenario. Given the current trend of emissions, only the high emissions (A1F1) scenario has been included in this paper. It should be noted that other scenario will have less of an impact of overheating and therefore A1F1 provides the worst case position to judge the suitability/effectiveness of retrofit design.

To take into account the natural variability and uncertainty associated with climate results of whichever emission scenario or year selected, UKCP09 presents the projections with the probabilities of a range of possible outcomes. The climate data is issued as a probability density function resulting in a range of percentiles; 10, 33, 50, 66 & 90. It is important to note as explained by [25] that these probabilities are subjective having been estimated from the strength of existing information and are not objective estimates that account for all possible results. Whilst modelling should be completed for the range of risk as per previous studies outlined in [14], only the 90 percentile is used in this paper to establish the maximum potential risk and impact.

Using the information generated by UKCP09, the Prometheus project [24] have created weather files in the Energy Plus format that can be imported and used in most building simulation software. Weather files for forty five locations have so far been created, of which two are in Northern Ireland; Belfast and Derry/Londonderry. The files are available for three future time periods 2030, 2050 & 2080 with three emissions scenarios. Two weather file types are available from the Prometheus project, as discussed by [24], Test Reference Years and Design Summer Years. Test Reference Year (TRY) weather files are made up of months from different years and do not contain extreme heat-waves therefore are considered unsuitable for overheating risk assessment. Design Summer Years (DSY) are used for summer overheating assessment only and are based on average temperature of the summer months at the centre of the upper quartile of rankings obtained from approximately 20 individual years. Design summer year (DSY) weather files will be used to examine risk of overheating whilst test reference years will be used to examine any shifting pattern of energy loads for space heating with the properties. Internal set point temperatures and average domestic hot water consumption were assumed to remain at current levels in future climate scenarios.

4.3 Overheating in case study properties – current and future climates

Using the design summer year weather files for the high emissions scenario (A1F1) and the 90 percentile, overheating in the bedroom and living room was assessed for current and future climate scenarios. Only natural ventilation was included within the model as during site visits it was found that the installed MVHR systems were not active. The CIBSE criteria [12] for summer overheating were used as guidance with results summarised in the Table 6.

There is a difference between the measured and modelled internal temperatures in House 1; notably the measured internal temperatures in the bedroom only exceed 26°C for 0.4% of the time during monitoring period whereas the model reported 6.1% exceedance. Further model calibration including any adaptive behaviour taken by occupants and local weather file may reduce this difference. The measured and modelled results align better in the case of House 2.

Table 6. Percentage of hours of overheating in bedroom and living room - measured and modelled.

% time temperature exceeded	Bedroom exceeds 26°C		Living room exceeds 28°C	
	House 1	House 2	House 1	House 2
Measured	0.4	0.2	0	0
Current	6.1	0.1	0	0
modelled				
2030	30.4	1.7	1.3	0
2050	36.7	6.2	7.3	0.2
2080	43.9	21.5	16.2	8.3

As external summer temperatures increase as per changing climate scenarios in 2030, 2050 and 2080, there is an increase in the amount of time internal temperatures exceed the 1% guidance. House 1 appears to be at a higher risk of overheating in future climate scenarios with living room and bedroom temperatures exceeding guidance criteria 16.2% and 43.9% of the time. Given the high rates of overheating it is likely that House 1 would require mechanical cooling or significant physical interventions such as solar shading to ensure comfortable internal temperatures.

It should be noted that these figures do not account for any adaptive behaviours that occupants are likely to employ. Occupants are not passive and will make adjustments to window/blinds and clothing levels, which would be influential in alleviating overheating.

4.4 Gas consumption in case study properties – current and future climates

Annual gas consumption for space heating and domestic hot water measured and modelled in current and future climates for both case studies is shown in Figure 4. Test reference year weather files were used within the models. As the climate changes, with winters becoming milder, the need for space heating dramatically declines with House 1 consuming 44%

less gas in 2080 than in 2015 and House 2 consuming 47% less gas in 2080 than in 2015.

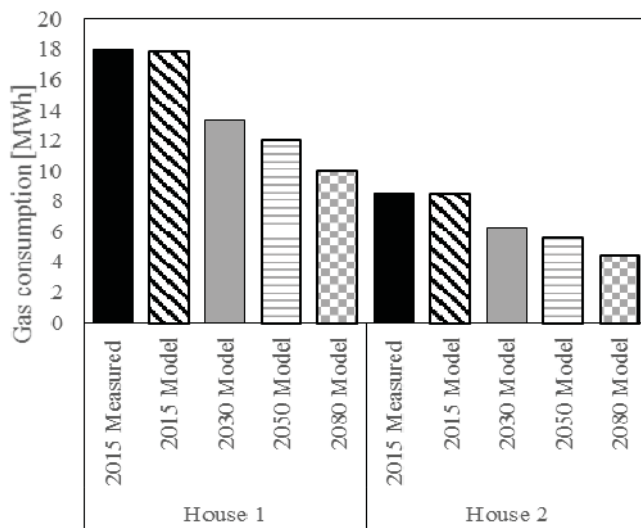


Figure 4. Gas consumption in House 1 and 2 - measured and modelled for current and future climate scenarios.

4.5 Cooling energy demand in future climate scenarios

Under the modelled scenario House 1 is likely to require mechanical cooling. To investigate the effect of implementing mechanical cooling House 1 was modelled for 2080 with a set point of 25°C. This resulted in a cooling demand of 2.81 MWh.

5 CONCLUSIONS

Modelling the retrofitted case study properties for future climate in 2030, 2050 and 2080 has shown a significant reduction in gas consumption and increased levels of summer overheating.

The need for cooling, a significant source of carbon emissions, must be considered in any retrofit strategy. Whilst emphasis should be placed on reducing heat demand during winter months the consequences of ignoring the changing climate would be significant. The study shows that such short term measures would result in future interventions that will be both costly and environmentally damaging. The future climate scenarios modelled were based on the high emissions scenario at the 90th percentile, this is the worst case scenario. Further iterations of the model should be undertaken at the lower percentiles to understand the range of risk. Further work will be undertaken to establish what effect reasonable interventions such as addition of solar shading and occupancy behavioural change will have on internal summer temperatures.

ACKNOWLEDGMENTS

The authors express their thanks to the sponsorship by Engineering and Physical Sciences Research Council (EP/M506709/1), Universities Ireland & ESB scholarship programme and internal funds provided by Queen's University Belfast. Sincere thanks are also provided to Hearth Housing Association for supporting this work.

REFERENCES

- [1] Parliament of the United Kingdom, "Climate Change Act 2008," 2008.
- [2] Energy Saving Trust, "Sustainable Refurbishment CE309," pp. 1–53, 2010.
- [3] Northern Ireland Housing Executive, "Northern Ireland House Condition Survey 2011 - Main Report," 2013.
- [4] Energy Saving Trust, "Energy Efficiency Best Practice in Housing Northern Ireland: assessing U-values of existing housing," 2005.
- [5] B. Boardman, "Homes Truths: A Low-Carbon Strategy to Reduce UK Housing Emissions by 80% by 2050," Oxford, 2008.
- [6] BRE, "A study of Hard to Treat Homes using the English House Condition Survey," 2008. [Online]. Available: https://www.bre.co.uk/filelibrary/pdf/rpts/Hard_to_Treat_Homes_Part_I.pdf.
- [7] Committee for Social Development, "Report on Fuel Poverty," Belfast, 2012.
- [8] P. de Wilde and D. Coley, "The implications of a changing climate for buildings," *Build. Environ.*, vol. 55, pp. 1–7, Sep. 2012.
- [9] J. Hacker and M. Holmes, "Thermal comfort: climate change and the environmental design of buildings in the United Kingdom," *Built Environ.*, 2007.
- [10] L. Collins, S. Natarajan, and G. Levermore, "Climate change and future energy consumption in UK housing stock," *Build. Serv. Eng. Res. Technol.*, vol. 31, no. 1, pp. 75–90, Jan. 2010.
- [11] BRE, "Product Characteristics Database (PCDB)," 2016. [Online]. Available: <http://www.ncm-pcdb.org.uk/sap/>.
- [12] Chartered Institution of Building Services Engineers, *Environmental Design Guide A*, 7th Edition. Norwich: CIBSE Publications, 2006.
- [13] J. Hills, "Getting the measure of fuel poverty: final report of the Fuel Poverty Review," 2012.
- [14] O. Kinnane, T. Grey, and M. Dyer, "Adaptable housing design for climate change adaption," *Engineering Sustainability*, vol. Ahead of p. 2016.
- [15] NHBC, "Understanding overheating – where to start: An introduction for house builders and designers," NHBC Foundation, 2012.
- [16] J.-P. Zimmermann, M. Evans, T. Lineham, J. Griggs, G. Surveys, L. Harding, N. King, and P. Roberts, "Household Electricity Survey A study of domestic electrical product usage," 2012.
- [17] Y. G. Yohanis, J. D. Mondol, A. Wright, and B. Norton, "Real-life energy use in the UK: How occupancy and dwelling characteristics affect domestic electricity use," *Energy Build.*, vol. 40, pp. 1053–1059, 2008.
- [18] Integrated Environmental Solutions, "IES," *Software validation and approval*, 2014. [Online]. Available: <http://www.iesve.com/software/software-validation>.
- [19] D. Coakley, P. Raftery, and M. Keane, "A review of methods to match building energy simulation models to measured data," *Renew. Sustain. Energy Rev.*, vol. 37, pp. 123–141, 2014.
- [20] ASHRAE, *Measurement of Energy and Demand Savings*, vol. 8400. 2002.
- [21] US Department of Energy, "M & V Guidelines: Measurement and Verification for Performance-Based Contracts - Version 4.0," 2015.
- [22] Efficiency Valuation Organization, "International performance measurement and verification protocol," 2012.
- [23] Department of Energy & Climate Change, "Energy consumption in the UK - Chapter 3: Domestic factsheet," 2015. [Online]. Available: <https://www.gov.uk/government/statistics/energy-consumption-in-the-uk>. [Accessed: 01-Oct-2014].
- [24] M. Eames, T. Kershaw, and D. Coley, "On the creation of future probabilistic design weather years from UKCP09," *Build. Serv. Eng. Res. Technol.*, vol. 32, no. 2, pp. 127–142, Oct. 2010.
- [25] UK Climate Projections, "UK Climate Impacts Programme UKCP09," *What is meant by probability in the UKCP09 probabilistic projections?*, 2012. [Online]. Available: <http://ukclimateprojections.metoffice.gov.uk/21680>.

How accurate are Energy Performance Certificates indicated energy savings of building retrofits?

P. Moran^{1, 2, 3}, M. Hadjukiewicz^{1, 2, 3}, J. Goggins^{1, 2, 3, 4}

¹College of Engineering & Informatics, National University of Ireland, Galway,

²Ryan Institute for Environmental, Marine and Energy Research, National University of Ireland, Galway, Ireland.

³Informatics Research Unit for Sustainable Engineering (IRUSE), Department of Civil Engineering, National University of Ireland, Galway, Ireland.

⁴Marine Renewable Energy Ireland (MaREI) centre, Galway, Ireland

email: p.moran3@nuigalway.ie, madga.hadjukiewicz@nuigalway.ie, jamie.goggins@nuigalway.ie

ABSTRACT: With the impending nearly zero energy building (NZEB) regulations for residential new builds and retrofits for the European Union (EU) housing stock and the percentage of new buildings relative to existing buildings is increasing at a rate of only 1% per year, retrofitting is recognised as the most immediate, pressing and cost effective mechanism to reduce energy consumption and carbon emissions in the building and construction sector. Currently, an Irish residential building Energy Performance Certificates (EPC) indicates the estimation of a buildings' annual energy usage that is assessed by the Dwelling Energy Assessment Procedure (DEAP). DEAP is the standard method for assessing the energy savings that are made by a residential building through retrofitting its technical characteristics to greater energy efficiency standards. This paper presents the pre-retrofit DEAP results of a sample set of urban social houses in Ireland and compares them to the actual energy usage of the houses highlighting the limitations of DEAP in estimating the pre-retrofit energy usage of the sample set of urban social housing. As many Irish government policies promoting the uptake in residential buildings base their energy savings on DEAP, the need for a more robust assessment procedure for determining the impacts retrofitting a building to a higher energy standard is discussed in addition to the need for engineers to start understanding the behaviour and attitudes towards energy consumption of the people living inside them in order to develop a holistic retrofit design that incorporates both technical and behavioural interventions.

KEYWORDS: Energy performance, Energy Performance Certificate, energy demand, occupant behaviour

1 INTRODUCTION

The Energy Performance Building Directive (EPBD) introduced legislation whereby all EU member states were required to introduce a standard assessment procedure for the energy performance certification of new and existing buildings in their respective countries [1]. The assessment procedure generally includes an analysis of the buildings (i) form, (ii) thermal, solar and daylight properties of the building envelope, (iii) air permeability, (iv) space, water heating and ventilation systems, (v) fixed lighting and (vi) fuel and renewable energy sources. These variables are assessed under standard occupancy and climatic conditions of the respective country [2]. As such, the assessment procedure does not capture the impact of human behaviour, including the consumption of household appliances.

The Energy Performance Certificates (EPCs) are seen as a tool for providing clear and reliable information to homeowners and tenants to compare and assess the energy performance of buildings [3], encourage owners to invest in improving the energy efficiency of the building through the provision of cost effective retrofit measures [3] and assist governments in developing policies to achieve national energy reduction targets in the building sector [2].

The Sustainable Energy Authority of Ireland (SEAI) maintains a register of Irish residential building EPCs, termed BERs [4]. The energy performance of a building is rated on a simple scale of A1 to G. An A1 rated dwelling equates to the most operational energy efficient building. The primary energy consumption in a building of A1 and G ratings are 25

kWh/m²/year and 450 kWh/m²/year, respectively. In total 633,972 BER's have been completed on Ireland's residential building stock [5]. The most common BER rating of Irish residential houses is a D1 for which the energy usage requirement ranges from 200 to 225 kWh/m²/year. The Dwelling Energy Assessment Procedure (DEAP) software is used to produce a BER [4]. DEAP is based on the European Standard IS EN 13790:2004 [6] and draws heavily on the UK's Standard Assessment Procedure (SAP) [7]. Further details can be found in [4].

The accuracy of EPCs for indicating the energy usage of residential buildings has been questioned in several studies in EU countries [8]–[13]. A Greek study found there to be on average a 44% lower energy usage in 8500 residential buildings compared to the theoretical energy usage according to these buildings EPCs [8]. A Dutch study of around 200,000 dwellings comparing the theoretical energy usage of their EPCs and actual energy usage found houses with higher energy performance ratings to be more accurate compared to houses with lower ratings for estimating their space and water heating requirements [10]. The houses with the poorest energy rating (G) used theoretically twice as much energy compared to what they actually consumed.

Similar to the findings of the Dutch study [10], an Irish study on the oil consumption of 142 houses pre-retrofit found that houses with a lower EPC were poorer predictors of the households oil consumption. This study found the houses on average to use 41% less energy compared to the theoretical usage estimated by the buildings DEAP [12]. Based upon the

post-retrofit data collected in this study, some of the main reasons for this difference is believed to be due to the estimated internal temperatures of the houses using DEAP compared to the actual temperatures and the underestimation on the usage of the secondary heating systems in the households.

With the impending nearly zero energy building (NZEB) regulations for residential new builds and retrofits for the European Union (EU) housing stock [14] and the percentage of new buildings relative to existing buildings is increasing at a rate of only 1% per year [15], retrofitting is recognised as the most immediate, pressing and cost effective mechanism to reduce energy consumption and carbon emissions in the building and construction sector [16].

There are currently many Irish governmental policies/schemes focused on promoting the uptake in residential building retrofits [17]. Currently DEAP, which produces a BER, is the standard method for assessing the energy savings that are made by a residential building through retrofitting its technical characteristics to greater energy efficiency standards and forms the basis for assessing the savings of various Irish government policies/schemes for promoting the uptake in residential building retrofits [17].

One of these schemes is known as Better Energy Homes. The scheme provides householders who want to make their homes more energy-efficient by providing incentives for the installation of energy efficiency measures [17]. An analysis on the effectiveness of 256 houses who received a grant through this scheme showed an estimated 21% reduction in their gas demand. However, the results estimate a shortfall of between 28-44% in the actual energy savings compared to the theoretical results based on their BER information [13].

As current policies are aimed at promoting the upgrade of houses for the most vulnerable (low-income households, social housing tenants, old people) [17], this paper aims to assess how accurate is DEAP for estimating the energy usage of urban social housing. This paper presents the pre-retrofit DEAP results of a sample set of urban social houses in Dublin and compares them to the actual energy usage of the houses. The limitations of DEAP in estimating the pre-retrofit energy usage of the sample set of social housing and the need for a more robust assessment procedure for determining the impacts retrofitting a building to a higher energy standard are discussed in addition to the need for engineers to start understanding the behaviour and attitudes towards energy consumption of the people living inside them in order to develop a holistic retrofit design that incorporates both technical and behavioural interventions.

This forms part of a research study whereby the temperature, relative humidity and energy usage profiles of 23 social houses in Dublin are being monitored pre- and post-retrofit using data logging instrumentation at high resolution in addition to examining the demonstrator buildings tenant (1) demographic profiles, (2) socio-economic status, (3) behaviour and attitudes towards energy consumption, energy conservation, the environment, environmental responsibility, thermal comfort, (4) views of quality of life and (5) what they consider to be a luxury and necessity in their life.

2 METHODOLOGY

The aim of this research project is to monitor the actual energy usage and greenhouse gas emissions of residential retrofit projects pre- and post- retrofitting works using data logging instrumentation for the temperature, relative humidity and energy usage profiles to determine the actual improvements achieved by retrofit works. Furthermore, information in relation to the behaviour and attitude of the building's habitants towards energy and greenhouse gas emissions, quality of life and thermal comfort within their homes is collected through face-to-face qualitative interviews and a questionnaire survey. Combining the data collected on energy consumption, temperature profiles of individual rooms, thermal comfort surveys and findings from occupant surveys will allow the most effective measures to be identified that consider the profiles of both the physical building and its occupants.

2.1 Survey Design

The questionnaire survey used in this study built on an existing lifestyle survey developed by researchers as part of the CONSENSUS Project [18]. CONSENSUS (Consumption, Environment and Sustainability) was a seven-year collaboration (2009-2015) between the National University of Ireland, Galway and Trinity College Dublin that investigated behaviours and attitudes in four key areas of household consumption (transport, energy, water and food). The CONSENSUS Lifestyle Survey, a key element of CONSENSUS, involved the collection and analysis of data from 1,500 households in Counties Derry/Londonderry, Dublin and Galway. To ensure maximum comparability with CONSENSUS data, questions from the CONSENSUS Lifestyle Survey are being used again in this project.

2.2 Data Instrumentation

In order to monitor the influence retrofitting works have on the energy use and thermal comfort of the residents, temperature and relative humidity data logging instrumentation is installed in each of the participating buildings. There are four/five temperature and relative humidity data loggers installed in each house with data recorded at 15 minute intervals. One data logger is installed in the kitchen and living areas and in two/three separate bedrooms. Electricity usage profiles are monitored using data logging instrumentation with data recorded at 1-60 minute intervals. Oil usage profiles are monitored using data logging instrumentation with data recorded at 60 minute intervals. Household electricity and gas meters are read once a month in addition to oil levels in oil tanks. Tenants are also asked to keep a diary record of their solid fuel usage.

2.3 BER Survey

Information is gathered with regards to the building's dimensions, orientation, thermal envelope characteristics, space, water heating and ventilation systems, internal lighting, renewable energy sources and fuel sources. Using the DEAP software [4], this information is used to determine a BER rating for a residential building under standard occupancy conditions and typical Irish climate conditions to estimate the

annual energy consumption and carbon emissions required to operate the building.

3 CASE STUDY

The social housing estate in Dublin involved in the study is located in a suburb area of Dublin, Ireland. The estate was constructed in two phases. The first phase in 1994 which consisted of 16 end-terraced (ET) houses, 16 mid-terraced (MT) houses and 14 apartments. The ET and MT houses are two-storey buildings with a total of six rooms in each of the buildings. These six rooms are divided into three bedrooms and individual kitchen, living and bathroom spaces. The apartments are not involved in the study.

An additional 30 residences – 12 ET houses, 12 MT houses and 6 semi-detached (SD) houses were constructed in 2000. Each building has two storeys with a total of seven rooms: three bedrooms, two bathrooms and individual kitchen and living spaces. 23 of the 62 households contacted in the estate agreed to participate in the study. Each of the different house construction types encountered in the Dublin study are shown in Figure 1(a)-(c).



Figure 1(a) MT and ET houses constructed in 1994, Figure 1(b) MT and ET houses constructed in 2000 and Figure 1(c) SD houses constructed in 2000

In the houses constructed in 1994, the walls of the buildings were mainly solid walls constructed using cavity blocks with interior timber battens and dry-lining plasterboard (u-value: $1.28 \text{ W/m}^2\text{K}$). A section of the exterior wall on the ground floor adjacent to the living room was constructed with cavity wall construction. This cavity was empty (u-value: $1.65 \text{ W/m}^2\text{K}$). The windows of the houses were PVC framed (u-value: $3.1 \text{ W/m}^2\text{K}$) with mineral wool insulation in between the joists of the attic (u-value: $0.4 \text{ W/m}^2\text{K}$).

The exterior walls of the houses constructed in 2000 were built using cavity wall construction with an exterior façade of either red brick or blockwork, plaster and paint. The cavity of these houses was partially filled with 60mm expanded polystyrene insulation (u-value: $0.45\text{-}0.46 \text{ W/m}^2\text{K}$). The windows of the houses were wooden framed (u-value: $3.1 \text{ W/m}^2\text{K}$) with mineral wool insulation in between the joists of the attic (u-value: $0.4 \text{ W/m}^2\text{K}$).

Table 1 details the year of construction, house type and u-values of the building elements assumed in the DEAP analysis of the participating residences in the study. The u-values of the wall construction types were determined using the wall u-value calculation method given in the current Irish building

regulations with the typical u-values of the materials taken from the current Irish building regulations [19] and DEAP [4]. The default u-values from DEAP for double glazed PVC and wooden frame windows are used for the windows. The default u-values for the floor and roof (100mm of mineral wool) are also taken from DEAP.

Table 1 Breakdown of the houses involved in terms of their year of construction, house type and u-values of the building elements assumed in the DEAP analysis

Construct ion Year	House Type	U-Value ($\text{W/m}^2\text{K}$)					Total
		Wall	Wall	Wind ow	Roof	Floor	
1994	MT	1.28	1.65	3.1	0.4	0.44	4
	ET	1.28	1.65	3.1	0.4	0.44	7
2000	MT	0.46	0.45	3.1	0.4	0.44	4
	ET	0.46	0.45	3.1	0.4	0.44	5
	SD	0.46	0.45	3.1	0.4	0.44	3

The main space heating systems in all the Dublin residences comprised of a gas-fired boiler as a central heating system with radiators in each of the rooms of the house. The boiler types in the households varied as some of the original boilers installed had been replaced over time. The efficiency of the different gas boiler types (main space heating) are given in Table 2 for the different construction types examined in this analysis. Also included in Table 2 are the efficiencies of the different secondary space heating systems employed in the buildings. Either a solid fuel open fire (30% efficiency), solid fuel stove (65% efficiency), gas fire (76% efficiency) or electric fire (100% efficiency) acted as a secondary heating system in the living room. The efficiencies of the secondary heating system are the default values used in DEAP.

Table 2 Efficiencies of the different main space heating (gas boiler types) and secondary space heating systems for the different house types examined in the DEAP analysis.

Space Heating Efficiency (%)		House Type					
Main	Secondary	MT 1994	ET 1994	MT 2000	ET 2000	SD 2000	Total
77	30	0	0	2	1	0	3
77	65	0	0	0	0	1	1
77	76	0	0	1	0	0	1
77	100	0	0	1	1	1	3
78.8	0	1	0	0	0	0	1
78.8	30	1	0	0	0	0	1
78.8	76	1	1	0	0	0	2
78.8	100	1	1	0	0	0	2
90.3	30	0	2	0	0	1	3
91.3	100	0	0	0	1	0	1
Total		4	4	4	3	3	18

The gas-fired boiler was also the main system used for providing hot water heating in the houses. The hot water was stored in a hot water tank after being heated by the gas-fired

boiler. There is also an electrical immersion available to heat the water in the hot water tank. The study in Dublin is currently on-going with the monitoring of the buildings beginning in February 2015. The buildings underwent retrofitting works to improve their thermal envelopes and heating systems. The works were complete in October 2015.

3.1 DEAP Scenarios

DEAP assessments of each of the houses involved in the study were carried out before and after the retrofitting upgrade works. Two different pre-retrofit DEAP scenarios are evaluated for 18 of the houses in this analysis. The first scenario is where each house is evaluated as if it were being evaluated as standard. Thus in this scenario, the solid fuel and gas secondary space heating systems are assumed to account for 10% of the houses space heating requirements and the electrical secondary space heating systems are assumed to account for 20% of the houses space heating requirements, as assumed in DEAP. The gas-fired boiler acts as the primary space and water heating system and is assumed to provide the remaining space and water heating requirements for the building. The second scenario takes into account the actions of the people living inside the buildings. Therefore, if the residents reported in the survey carried out that they never use their secondary space heating system, it is assumed to account for 0% of the space heating requirement of the building. If it was reported that they use their secondary space heating system, the same percentages for the different heating systems as described for scenario one are applied. Also, if they reported that they use their electrical immersion for water heating, it is assumed that 33% of the energy required to provide hot water was provided by the immersion, as assumed in DEAP. The gas-fired boiler acts as the primary space and water heating system and is assumed to provide the remaining space and water heating requirements for the building.

3.2 Gas and Electricity Meter Data and Estimations

As there is only data available from February 2015 to July 2015 of the houses electricity and gas usage pre-retrofit, estimations are made based on this data in order to compare to the results of the DEAP evaluations.

The gas and electricity meter readings were recorded at seven different intervals from the 12th of February to the 22nd July at least once a month. As the main space and water heating system of the houses use gas, the gas usage of the houses is assumed to be related to the external temperature. The average daily gas usages between the dates the meters were read are normalized using the average external daily temperatures recorded at Dublin Airport [20] (located with 11km of the estate) between the meter read dates. Linear interpolation is then used to estimate the average daily gas usage for each of the 12 months of the year based on the average external daily temperature recorded at Dublin Airport during each of the months. Using the number of days each month of the year has together with the estimated average daily usages for each of the months, the total yearly gas usages of the houses are calculated.

Unlike the gas usage of the houses, the electricity usage cannot be linked to the average daily temperature for the months with unknown data. Apart from February, each of the

intervals the electricity meter readings were taken at accounted for at least two thirds of the month's electricity usage. Thus, the average daily electricity usage during these intervals, including February, is assumed for the entire month and multiplied by the number of days of each month to give the total electricity consumption. For the remaining days of the year with no electricity usage data (1st January to the 31st January and 1st August to the 31st December), the average daily usage of the respective houses from the 12th February to the 22nd of July is determined and used as the electricity consumption for the remaining days of the year with no available data.

4 RESULTS AND DISCUSSION

The total annual primary energy consumption results of the two DEAP scenarios evaluated and BER rating for the 18 different houses are given in Table 3 together with the total primary energy consumption based on the collected meter data from the houses and the estimations made based on this data as described in section 3.2. The average of the two DEAP scenarios are within 9% of the estimates based on the gas and electricity meter readings for the MT and ET houses constructed in 1994 and 2000. The DEAP assessments of the SD houses are on average the least accurate in comparison to the meter data and estimates data. The standard deviation of the total consumption for each of the house types is larger for the meter readings and estimates compared to the two DEAP scenarios. This highlights the variability that the behaviour of the people in the households can have on the energy consumption that DEAP does not account for.

The house with the highest energy consumption difference between the DEAP scenarios and the meter readings and estimates is a SD house constructed in 2000. Based on the one on one surveys conducted within each of the households, there is a couple and three children (two under 14 years old and one between 18-25 years old) who live in this house and have the second highest annual income of the houses involved. This house also has the overall highest energy consumption based on the meter readings and estimates. This is despite having one of the most efficient gas boilers of all the houses (90.3%) and achieving the sixth best DEAP result in DEAP scenario one and two. Based on the measured annual consumption of this household (384 kWh/m²/yr.), it would achieve a BER of F which is the second worst rating a house can achieve. This however includes the impact that household appliances have on the energy consumption of the house which is not included in a DEAP.

The house with the lowest energy consumption based on the meter readings and estimates is a house with a single mother and one child who live in an ET house constructed in 2000 and have the lowest annual income of the houses involved in the study. This is despite achieving the tenth and seventh best DEAP result in DEAP scenario one and two. Based on the measured annual consumption of this household (157 kWh/m²/yr.), it would need to reduce its energy consumption by only 7 kWh/m²/yr. to be considered a NZEB building for existing buildings even before it has been retrofitted [21].

On average, the second DEAP analysis is more accurate in estimating the overall energy consumption of the houses constructed in 1994 compared to the meter data whereas the

Table 3 Total annual primary energy consumption results and BER ratings of DEAP scenario one and two and the collected meter data and estimations made for the 18 houses

House Type	DEAP Assessment (Scenario 1)		DEAP Assessment (Scenario 2)		Meter Data and Estimations
	Total (kWh/m ² /yr.)	BER Rating	Total (kWh/m ² /yr.)	BER Rating	Total (kWh/m ² /yr.)
Mid Terrace 1994					
	239	D1	239	D1	247
	266	D2	247	D1	200
	237	D1	237	D1	271
	257	D1	246	D1	311
Avg.	249		242		257
Std Dev.	14		5		46
End Terrace 1994					
	287	D2	253	D1	193
	292	D2	259	D1	320
	303	E1	288	D2	363
	282	D2	282	D2	222
Avg.	291		270		274
Std Dev.	9		17		80
Mid Terrace 2000					
	198	C2	198	C2	172
	187	C2	192	C2	170
	208	C3	208	C3	257
	198	C2	183	C2	258
Avg.	198		195		214
Std Dev.	8		10		50
End Terrace 2000					
	195	C2	179	C2	340
	225	D1	207	C3	157
	222	C3	214	C3	198
Avg.	214		200		232
Std Dev.	17		19		96
Semi-Detached 2000					
	202	C3	202	C3	384
	197	C3	202	C3	208
	223	C3	210	C3	175
Avg.	207		205		256
Std Dev.	13		5		112
All Houses					
Avg.	234		225		247
Std Dev.	38		33		71

first DEAP analysis is more efficient in estimating the overall energy consumption of the houses constructed in 2000 compared consumption to the meter data.

Based on the average energy consumption of all the houses, one could say that DEAP is accurate in estimating the annual energy consumption of the houses. However, when examining the estimated gas, electricity and solid fuel usage of the households in both the DEAP scenarios in comparison to the meter data and estimations, one can see that this statement does not hold true. The over estimation of DEAP in relation to the gas usage of the buildings compensates for its underestimation in electricity usage by not accounting for the appliance usage by the households and assuming standard electricity requirements for the building's lighting, heating system pumps and ventilation fans.

In terms of gas usage, the house type which has the smallest difference between the two DEAP scenarios and the meter data is the SD households. On average, DEAP scenario one uses 28% more gas per annum compared to what the house type actually uses. This however increases to 41% when comparing it to scenario two. The least accurate of the house types analysed are the MT houses constructed in 1994. DEAP scenario one and two estimates the house type uses 69% and 70% more gas per annum compared to the meter data and estimations annual usage. Based on the averages of all the houses, DEAP scenario one and two estimates the house types use 41% and 45% more gas per annum, respectively, compared to the meter data and estimations annual usage. Both houses with the highest and lowest total yearly energy consumption based on the meter data also have the highest and lowest total yearly gas consumption.

As expected the total electricity consumption based on the meter data is significantly larger compared to what both the DEAP scenarios estimate as a DEAP does not account for the energy consumption of household appliances. The house type with the largest difference is the SD houses constructed in 2000. DEAP scenario one and two estimate the houses use 25% and 21% of what the houses actually use according to the meter readings and estimations, respectively. The house with the lowest electricity consumption is an ET house constructed in 1994. A retired couple lives in this household. Both DEAP scenario one and two estimate 21% of what the house actually uses based on the meter data.

Based on the averages of all the houses, DEAP scenario one and two estimates the house types use 31% and 28% of the electricity that the houses actually use according to the meter data and estimations, respectively. Thus, assuming that the electricity accounted for by DEAP for the building's lighting, heating system pumps and ventilation fans is accurate, a DEAP may not account for up to 72% of its electricity use which is more than twice the 30% which has been previously estimated [12].

However, as stated only 6 months of monitored electricity data is available in this analysis. For the remaining days of the year with no electricity usage data (1st January-31st January and 1st August-31st December), the average daily usage of the respective houses from the 12th February to the 22nd of July is determined and used as the electricity consumption for the remaining days of the year with no available data. There are obvious limits associated with this method as electricity usage habits of people generally alter between the winter and summer months. Internal lighting is used more during the winter months due to less daylight. Also during the summer

Table 4 Average and standard deviation gas, electricity and solid fuel primary energy usage of the house types for DEAP scenario one and two and the meter data and estimations

House Type	DEAP Scenario 1 (kWh/yr.)				DEAP Scenario 2 (kWh/yr.)				Meter Data and Estimations (kWh/yr.)			
	Gas	Electricity	Solid Fuel	Total	Gas	Electricity	Solid Fuel	Total	Gas	Electricity	Solid Fuel	Total
Mid Terrace 1994												
Avg.	15339	2608	734	18680	15471	2671	0	18143	9050	10236	0	19286
Std Dev.	1179	1889	1467	1054	923	1314	0	394	1893	1880	0	3459
End Terrace 1994												
Avg.	17174	2688	1945	21806	18237	2026	0	20263	12502	8055	0	20557
Std Dev.	1831	1999	2246	581	1158	876	0	1107	3276	3450	0	6027
Mid Terrace 2000												
Avg.	13248	2762	1139	17149	12893	3430	589	16911	9366	9199	0	18565
Std Dev.	794	1424	1317	727	1045	1719	1179	901	2594	2182	0	4314
End Terrace 2000												
Avg.	13418	4238	881	18536	14610	2721	0	17331	10527	9543	0	20070
Std Dev.	1625	1768	1525	1442	1143	1006	0	1616	4901	3527	0	8313
Semi-Detached 2000												
Avg.	13760	2889	1321	17969	13971	2452	1321	17744	10698	11471	0	22168
Std Dev.	805	2100	1389	1169	1982	899	1389	431	8718	1405	0	9731
All Houses												
Avg.	14699	2978	1215	18892	15119	2668	351	18138	10408	9611	0	20019
Std Dev.	1953	1777	1510	6281	2226	1210	855	6719	4150	2564	0	5516

months, certain appliances which use a large amount of electricity, for example a tumble dryer, may be used less due to the warmer weather.

With regards to DEAPs underestimation of the building gas requirements, one has to account for the limitations associated with some of the assumptions used in the DEAP analysis. Default values for the building's window, floor, and roof u-values and secondary space heating systems are taken from DEAP. The airtightness of the buildings involved in the analysis are assessed using the DEAP software and may not reflect the real air tightness of each of the buildings analysed. A default thermal bridging factor of 0.15 W/m²k is also assumed in the analysis. These assumptions can have a large impact on the space heating requirements of a building with some recommending the revision of current default u-values for better accuracy [22]. These are also common assumptions taken when evaluating an existing building's BER due to the unavailability of information on the buildings technical characteristics. The standard occupancy of a household is assumed to be 2.27 in the DEAP analysis. The average occupancy of the 18 houses is 3.94 with only five of the 18 houses containing three people or less. Due to the small sample size, it is not possible to determine whether having less people in the household effects the actual energy usage of the household.

5 CONCLUSIONS

The DEAP assessed as standard (scenario 1) and DEAP taking into account occupant actions (scenario 2) for a sample set of

urban social housing in Dublin on average underestimates the gas usage of the houses by 41% and 45%, respectively, compared to actual gas consumption. Currently DEAP, which produces an Irish residential EPC that indicates an estimation of a residential buildings' annual energy usage, is the standard method for assessing the energy savings that can be made by a residential building through retrofitting its technical characteristics to greater energy standards. DEAP forms the basis for assessing the savings of various Irish government policies/schemes for promoting the uptake in residential building retrofits [17]. While current retrofits schemes for low-income households assume a 70% take back for comfort/rebound effect [17], the inaccuracies of DEAP in estimating energy usage of pre-retrofit social housing highlighted in this paper and the inaccuracies of EPCs in indicating the actual energy savings highlighted in other studies discussed, suggests estimated energy savings made by Irish government policies using DEAP may not come to pass and also prohibit homeowners from investing in more energy efficiency measures.

Thus, there is an urgent need to develop a more robust standard assessment procedure for assessing the energy savings that can be made through retrofitting the technical characteristics of a residential building to greater energy standards. However, monitoring the energy usage profiles of a household pre- and post-retrofit is not sufficient in determining the overall improvements that have been made.

For instance, based on the currently limited available post retrofit gas usage data of the Dublin social housing, no energy

savings were made in the household with the lowest gas usage. This house had temperatures of 18°C or less during February and March of 2015 before the retrofitting works. As the tenants were living in poor thermal conditions, they probably experienced a benefit of improved thermal conditions rather than energy reductions. This phenomenon, known as the rebound effect, has been estimated to offset energy savings by 30% [23].

With the number of retrofit measures homeowners have applied for grant aid in Ireland falling steadily since 2009 [24], homeowners may be more enticed to invest in retrofit measures if given more of a net benefit feedback on how their homes have improved due to a retrofit upgrade. This net benefit feedback could include information on not only the energy cost savings made by their retrofit upgrade but also the improvements to their internal environment and health benefits associated with these improvements.

The high variability of actual energy consumption, based on the collected readings from the electricity and gas meters, highlights the influence the people living in households have on energy consumption. Engineers need to start understanding the behaviour and attitudes towards energy consumption of the people living inside them. Once the main social norms and energy practices influencing their energy consumption behaviour, such as what people perceive to be a comfortable internal environment, typical indoor choice of clothing, people's attitudes regarding luxuries and necessities of housing items/appliances are understood, the feedback given to the tenants on the net benefits the technical interventions have can be complimented by behavioural interventions which focus on negating the impact the tenant's behavioural consumption habits are having on their energy consumption

ACKNOWLEDGMENTS

The authors wish to acknowledge the financial support from Science Foundation Ireland (SFI) for this research (Grant No. RSF1295). The authors would also like to thank the National University of Ireland Galway and particularly the Department of Civil Engineering in the College of Engineering and Informatics for the help with the project

REFERENCES

- [1] European Commission, "Directive 2002/91/EC of the European Parliament and of the Council of 16 December 2002 on the energy performance of buildings," *Off. J. Eur. Communities*, pp. 65–71, 2002.
- [2] IEA, "Energy Performance Certification of Buildings - A Policy Tool to Improve Energy Efficiency," International Energy Agency, 2010.
- [3] Bio Intelligence Service, R. Lyons, and IEEP, "Energy performance certificates in buildings and their impact on transaction prices and rents in selected EU countries," Final report prepared for European Commission (DG Energy), 2013.
- [4] SEAI, "Dwelling Energy Assessment Procedure (DEAP)-Irish Official Method for Calculating and Rating the Energy Performance of Dwellings," Sustainable Energy Authority of Ireland, 2012.
- [5] SEAI, "BER Statistics," 2016. [Online]. Available: http://www.seai.ie/Your_Building/BER/BER_FAQ/FAQ_BER/General/BER_Statistics.html. [Accessed: 10-Jul-2016].
- [6] NSAI, "I.S. EN ISO 13790:2004 Thermal Performance of Buildings-Calculation of Energy Use for Space Heating," National Standards Authority of Ireland, 2004.
- [7] U. Department of Energy & Climate Change, "Standard Assessment Procedure," 22 January 2013, 2013. [Online]. Available: <https://www.gov.uk/guidance/standard-assessment-procedure>. [Accessed: 10-Jul-2016].
- [8] C. A. Balaras, E. G. Dascalaki, K. G. Droutsas, and S. Kontoyiannidis, "Empirical assessment of calculated and actual heating energy use in Hellenic residential buildings," *Appl. Energy*, vol. 164, pp. 115–132, 2016.
- [9] P. A. Fokaides, C. N. Maxoulis, G. P. Panayiotou, M. K. A. Neophytou, and S. A. Kalogirou, "Comparison between measured and calculated energy performance for dwellings in a summer dominant environment," *Energy Build.*, vol. 43, no. 11, pp. 3099–3105, 2011.
- [10] D. Majcen, L. C. M. Itard, and H. Visscher, "Theoretical vs. actual energy consumption of labelled dwellings in the Netherlands: Discrepancies and policy implications," *Energy Policy*, vol. 54, pp. 125–136, 2013.
- [11] S. Kelly, D. Crawford-Brown, and M. G. Pollitt, "Building performance evaluation and certification in the UK: Is SAP fit for purpose?," *Renew. Sustain. Energy Rev.*, vol. 16, no. 9, pp. 6861–6878, 2012.
- [12] K. Petersen, H. Flick, P. Kenny, M. Bell, and M. PJ, "SERVE Energy Monitoring Project – Report on Implementation and Analysis," Sustainable Energy for the Rural Village Environment, 2012.
- [13] J. Scheer, M. Clancy, and S. N. Hógáin, "Quantification of energy savings from Ireland's Home Energy Saving scheme: An ex post billing analysis," *Energy Effic.*, vol. 6, no. 1, pp. 35–48, 2013.
- [14] European Commission, "Directive 2031/EC of the European Parliament and of the Council of 19 May 2010 on the energy performance of buildings (recast)," *Off. J. Eur. Communities*, pp. 13–35, 2010.
- [15] BPIE, "Europe's Buildings Under the Microscope A Country-by Country Review of the Energy Performance of Buildings," Buildings Performance Institute Europe, 2011.
- [16] E2APT, "The Fundamental Importance of Buildings in Future EU Energy Saving Policies," 2010.
- [17] DCENR, "National Energy Efficiency Action Plan 2014," Department of Communications, Energy and Natural Resources, Dublin, Ireland, 2013.
- [18] Lavelle & Fahy, "Consensus Lifestyle Survey: Background and methodology," Consumption, Environment and Sustainability, 2012.
- [19] DECLG, "Building Regulations 2011 - Technical Guidance Document L - Conservation of Fuel and Energy - Dwellings," Department of Environment Community and Local Government, Dublin, Ireland, 2011.
- [20] Met Éireann, "Met Éireann Dublin Airport Monthly Weather Data," 2016. [Online]. Available: <http://www.met.ie/climate/monthly-data.asp?Num=532>. [Accessed: 06-Apr-2016].
- [21] DECLG, "Towards Nearly Zero Energy Buildings In Ireland Planning For 2020 and Beyond," Department of Environment Community and Local Government, Dublin, Ireland, 2012.
- [22] C. Ahern, B. Norton, and B. Enright, "The statistical relevance and effect of assuming pessimistic default overall thermal transmittance coefficients on dwelling energy performance certification quality in Ireland," *Energy Build.*, vol. 127, pp. 268–278, 2016.
- [23] S. Sorrell, J. Dimitropoulos, and M. Sommerville, "Empirical estimates of the direct rebound effect: A review," *Energy Policy*, vol. 37, no. 4, pp. 1356–1371, 2009.
- [24] M. Collins and J. Curtis, "An examination of energy efficiency retrofit depth in Ireland," *Energy Build.*, vol. 127, no. December 2015, pp. 170–182, 2016.

Monitoring the internal thermo-hygrometric environment in cathedrals in Ireland

Christopher Shiell and Roger P. West

Department of Civil, Structural and Environmental Engineering, Museum Building, Trinity College,
The University of Dublin, Dublin 2.
Email: shiellc@tcd.ie, rwest@tcd.ie

ABSTRACT: Research has been carried out into the often conflicting concepts of thermal comfort, conservation of artefacts and preservation of the 57 active cathedral buildings on the island of Ireland. A body of research exists in this area for heritage type buildings, including churches, in both the United Kingdom and mainland Europe. However, a review concluded that no such research had been carried out in Ireland where a number of factors are unique such as history, climate, size of the buildings, the number of buildings and the artefacts contained within them. Uniquely cathedrals in Ireland were largely built for purpose and not as status symbols for their sponsors and also a relatively large number were built within a short period. The research for this paper enabled firm parameters to be identified in order to keep the investigation at a practical level whilst at the same time achieving academic objectives. The main results to date indicate that thermal comfort and cost are the two most important parameters for the owners and managers of these building and conservation and preservation are not considerations which are taken into account when operating or choosing the heating systems. Research has also shown that there is a general lack of knowledge about how the heating systems should be set up and operated. Many systems are poorly maintained, due to cost constraints, even though this adds to cost due to inefficient operation of the systems. There is a general lack of knowledge about the buildings themselves evidenced by the fact that many managers of these building do not know how these buildings are constructed and if there is any type of insulation installed. Research further suggests that there is little knowledge sharing between the owners and managers of the buildings.

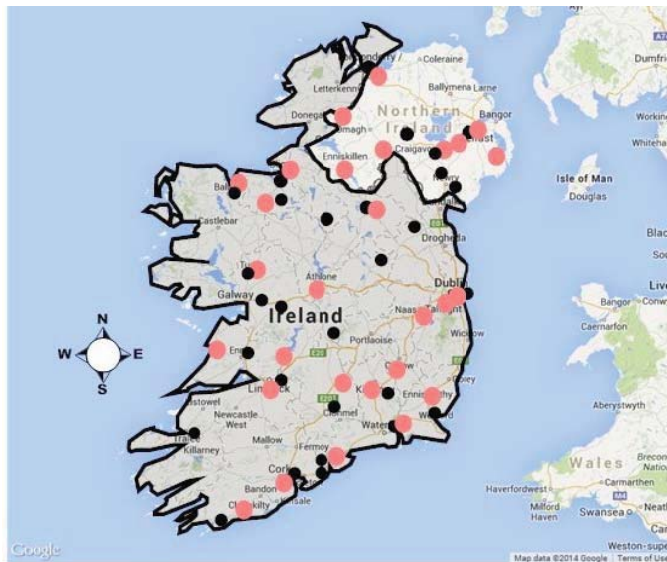
KEY WORDS: Cathedrals, Heating, Ireland, Conservation, Preservation, Thermal comfort.

1 INTRODUCTION

Cathedrals are irreplaceable buildings which are an important part of the heritage of a country [1]. Not only are the buildings themselves of great cultural and intrinsic value but they contain many artefacts of great monetary and cultural value and significance [2]. They are unique buildings for many reasons one being that they are largely still used for the purposes for which they were built, namely the holding of religious services and events. However whilst the uses to which the buildings are put has not greatly changed over the centuries, what people who use the buildings perceive to be an acceptable level of thermal comfort has changed [3]. Many of these buildings were built with no heating of any sort [4] and none was envisioned by their architects and builders but all of the still active cathedrals have now been fitted with some kind of heating system. These systems have almost exclusively been installed with only thermal comfort as a consideration and with little thought, or perhaps knowledge, as to the effects such systems have on the preservation of the buildings and the conservation of their artefacts [5]. Many of these systems were put in when the cost of fossil fuels was low and the owners and managers of the buildings are now struggling to cope with ever increasing heating costs caused by inefficient and sometimes inappropriate heating systems. The environmental impact of burning fossil fuels has only become an issue in relatively recent times and whereas religious buildings are largely exempt from environmental legislation, there is no guarantee that they will remain so.

Irish cathedrals, whilst being modest in size, are of a reasonably uniform construction. The walls are generally solid stone, with some being plastered on the inside. Windows are uniformly single glazed, some being stained glass and some plain glass. A number of cathedrals have storm glazing fitted externally. Floors tend to be a mixture of stone, tiles and wood. Roofs are almost exclusively tiled with an exception being a copper roof on a cathedral in Limerick. Ceilings on the other hand can be stone, which is usually found in older cathedrals, plastered and wood, either painted or plain. It is often not possible to distinguish, from ground level, the size of the space between the ceiling and the roof, if any. Many cathedrals contain very valuable pipe organs and some other artefacts which are particularly susceptible to changes in the environment, such as flags and books. The majority of internal fittings tend to be made of wood, such as pews and Confessionals and flooring. The oldest Irish cathedrals have been substantially altered over the centuries but the method and materials of their construction have not changed substantially. Attempts have been made, often with the addition of internal lobbies, to mitigate against drafts and the influx of cold air from the exterior. Most Roman Catholic cathedrals in Ireland were substantially revised internally as a result of the Second Vatican Council in 1962. The extent and effect of these changes varied from cathedral to cathedral.

Figure 1 shows the locations of the 57 active cathedrals on the island of Ireland which does not include schools and ancillary buildings such as offices.



● Roman Catholic ● Church of Ireland

Figure 1. Location of active cathedrals on the island of Ireland

There are in addition almost 3,900 active churches on the island of Ireland (www.thecatholicdirectory.com), (www.ireland.anglican.org), (www.presbyterianireland.org), (www.irishmethodist.org) which is a sizeable property portfolio. Even if regulation is not imposed, there is perhaps a moral obligation on the owners of these buildings to be seen to be trying to ensure that they are sustainable from an energy consumption point of view. Aesthetics are an important issue with heritage type buildings but with very large south facing roofs areas, it would be surprising if these could not be used to generate heat and power at some stage in the future.

Establishing the dates of the various cathedrals is an issue since so many have been substantially rebuilt and renovated over the centuries. Figure 2 shows the large number of Roman Catholic (RC) cathedrals which were built between 1799 and 1900. This was a building feat not equalled anywhere else in the world with a total of 23 cathedrals being built within a one hundred year span. This was the result of a relaxation of the penal laws which had applied to that Christian tradition. Considering that this building programme took place during a period of great turmoil in Ireland, which included the famine between 1845 and 1852, this makes the achievement and commitment even more remarkable. Events such as the famine often meant that building times were extended, sometime over a number of decades. St. Anne's cathedral in Belfast for instance was started in 1903 and largely for financial reasons was not completed until 1981. St. Patrick's Church of Ireland (CoI) cathedral in Armagh is reputed to have been destroyed and rebuilt no less than 16 times during its turbulent history which makes establishing the date of the building difficult. The date of first consecration was taken to provide consistency.

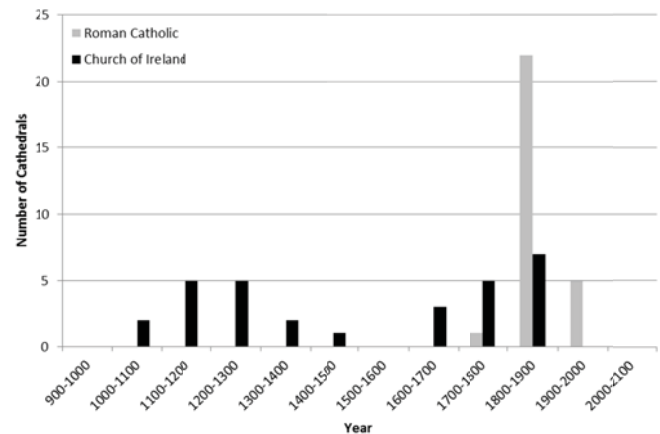


Figure 2. Age profile of cathedrals in Ireland by first consecration date.

2 HEATING CHARACTERISTICS

Of the 38 cathedrals which have been surveyed to date, the following is the breakdown of the fuels used:

Gas (both mains and tanked)	19
Oil	16
Electricity	3

The same 38 cathedrals have the following types of heating systems:

Underfloor	5
LPHW (Low Pressure Hot Water)	20
Radiant (only) gas	1
Combination	9
HVAC (Heating, ventilation and Air conditioning)	1
Under pew	1
Hot air only (oil fired)	1

One cathedral is part of a district heating system and draws its heat from a nearby civic office complex which is itself powered by gas. No cathedral surveyed to date has any type of renewable system in the form of either photovoltaic or solar thermal panels for the production of heat or power. The combination systems are usually a combination of underfloor heating with an LPHW system to back it up. Nearly all cathedrals use the heating intermittently which means that the buildings are constantly being heated up and cooled down with possible consequential adverse effects for both the buildings and the contents.

2.1 Heating and cooling profiles

Figure 3 is an example of a cathedral which has a gas LPHW system which is used intermittently. The boiler in this building was replaced in 2006 but the pipework was last replaced in 1914. The building contains a number of valuable artefacts including a pipe organ. The organ is situated within its own environmentally controlled space. Such high levels of relative humidity (RH) and substantial changes in temperature

(T) will have a long term detrimental effect on both the building and its contents. Figure 3 shows the readings taken from one of the data loggers during this period. Clearly heating is only on for certain days and for certain periods during the day and the temperature during the events is also determined by the ambient temperature when heating is switched on. As the cathedral cools during dormant periods, there are slight diurnal variations depending on outside conditions and, when analysing further, the natural thermal lag of the interior temperature compared to the exterior can be established for the building from cooling and heating responses in the absence of mechanical heating. These characteristics are being examined for every cathedral to identify patterns of behaviour and exemplars of good practice. The RH variations, which equilibrate quickly internally, are also being examined.

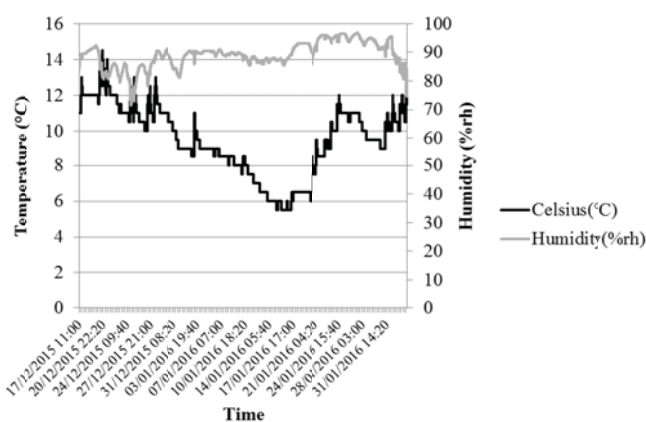


Figure 3. An example of a cathedral with intermittent heating

Figure 4 clearly illustrates the effect of intermittent heating where the building heats up very rapidly and then, because of thermal lag, cools down during the week before being heated up again on the following Sunday. This particular cathedral has a number of high value artefacts inside the building and the relatively high RH figures (65 to 85%) are not conducive to the preservation of these artefacts.

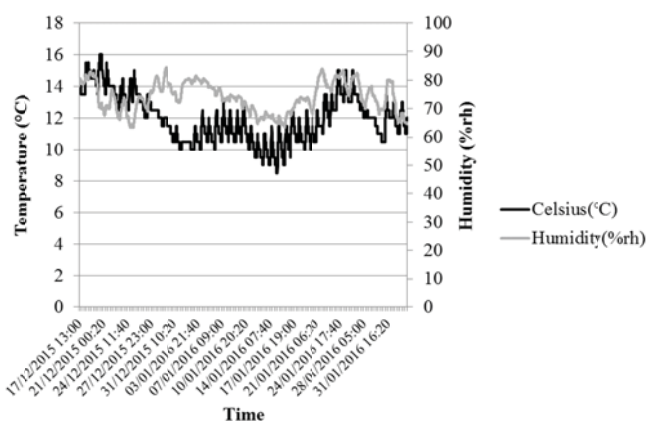


Figure 4. Another example of an intermittently heated cathedral.

Figure 5 shows how, by using the thermal mass of the building, cathedrals should be able to smooth out the presently

sharp differences between peak temperatures and consequently of RH. The way in which many cathedrals in Ireland are using their heating systems prevents them from benefiting from the large thermal mass of most of the buildings. Figure 3, for example, shows how the building's walls are reheated over periods of sustained heating, where, for high occupancy, a low level of regular heat may prove to be more economic and better for the cathedral's fabric.

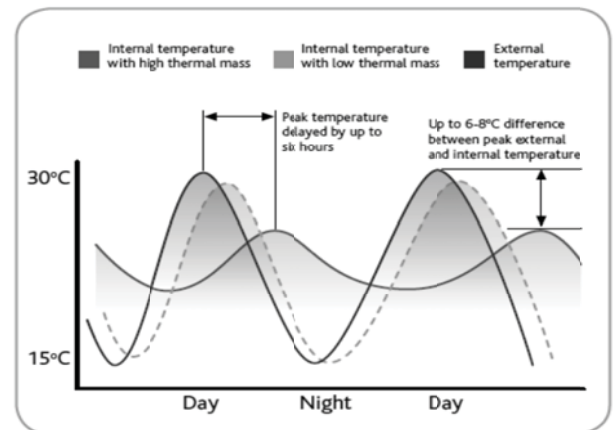


Figure 5. Stabilising effects of thermal mass on internal temperatures [6]

Further examinations need to be made of all cathedrals to discover the rate of heating of the building based on the boiler capacities and the number and output of the radiators. This will give an indication of the heat loss through the fabric, depending on the size of the building and may enable a cost to be established if the internal temperature T was raised by say 1°C (Figure 6). Note in this figure the stable nature of the temperature during the night and the slow natural heat loss when the heating is switched off. Similarly, natural cooling rates need to be understood for the different cathedral types.

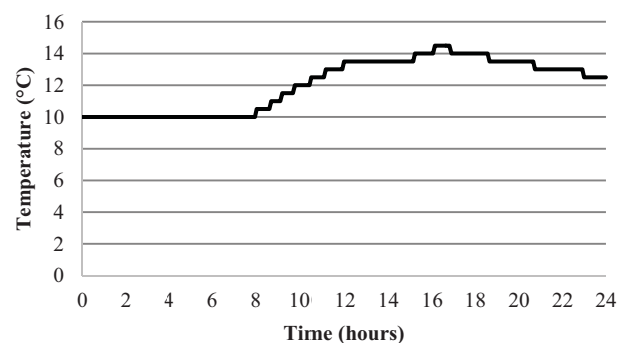


Figure 6. An example of a snapshot of temperature history used to evaluate the rates of temperature increase and decrease over a 24 period

2.2 Energy consumption

Many cathedrals in Ireland do not have accurate costings for their power consumption figures, often because the figures for a number of churches are amalgamated. Table 1 shows the difference, in the UK, between good practice for ecclesiastical

buildings and typical operation [7]. In other words typical operation is almost twice as bad as best practice. There is no reason to assume that the same will not apply in Ireland and this is being examined in this project.

Table 1. Best practice and typical operations in the UK [6]

	<u>Good Practice</u>	<u>Typical Operation</u>
Fossil fuel	80 KWh/m ²	150 KWh/m ²
Electricity	10 KWh/m ²	20 KWh/m ²

3 THERMAL COMFORT

Thermal comfort is a concept about which much has been and is being written and researched. The first effort to try to describe what is both subjective and personal, was made by Houghton in 1923 and this was to describe thermal comfort in terms of 'the environmental variables of ambient air temperature and relative humidity' [8]. ANSI/ASHRAE Standard 55 states that thermal comfort is 'that condition of mind that expresses satisfaction with the thermal environment' [9].

Cathedrals in Ireland and in general have a particular problem with the concept of thermal comfort which is caused by the perception that they are cold and by the changing uses to which the buildings are put. If the buildings are in constant use and the operators have the resources to do so, then keeping the building at a relatively low level of conservation heating of between 12° to 15°C and then raising the temperature for a relatively short period for a service, would seem to be the best policy [5]. As Schellen points out, it was not until the 1960s that it was realised that heating churches to acceptable thermal comfort levels would have detrimental effects on the buildings and their contents [5]. A stable environmental envelope is what serves these buildings best. The European funded Friendly Heating Project which was undertaken between 2002 and 2005 [10] specifically sought to protect and preserve the cultural heritage within monumental churches. However the general recommendation that it is better to heat the people in the church rather than the church itself, is not always practicable due to the changing uses to which these buildings are put which often necessitate changing the position of the seats. Most cathedrals in Ireland cannot, for financial reasons, afford to keep the heat running constantly, even at conservation levels. Consequently intermittent heating is normally used.

Ireland has an ageing cathedral congregation population profile and it would be reasonable to think that older people were more susceptible to thermal comfort levels. However research suggest that this is not the case since the lower metabolism of older people is compensated for by lower evaporation rates [11].

For over 40 years the standard way of calculating thermal comfort was to use Fanger's Predicted Mean Vote (PMV) model [12]. This system was developed by Fanger and was based on college aged students in temperate climates and in air conditioned buildings [13]. This is not entirely relevant to cathedral in Ireland and a more useful approach is known as

the adaptive approach which is based on field studies rather than laboratory results.

Figure 7 is the ASHRAE graph which shows the temperatures which people find acceptable in naturally conditioned buildings, such as cathedrals. It should be noted that the outside temperature is shown in C° while the inside temperatures are shown in F°. The advantage of the adaptive approach is that as well as taking into account the environmental factors of air temperature, radiant temperature, air velocity and humidity, it also includes the personal factors of clothing insulation and metabolic heat [14]. The general concept of adaptive thermal comfort is that people will adapt or change their own environment until they reach a state of comfort. People coming to a cathedral may expect to be colder than they would like and will therefore put on another layer of clothing, or keep their coats on in winter, for instance. Oleson and Parsons [15] showed that people were able to accept a wider range of temperatures in naturally ventilated buildings, such as cathedrals than was the case in buildings with a centralised HVAC system.

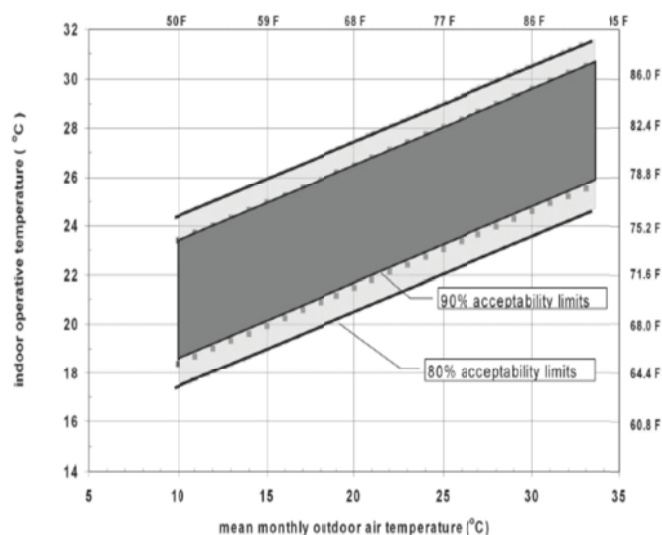


Figure 7. Acceptable operative temperature ranges for naturally conditioned buildings [9]

3.1 Climate change

This research spans two different jurisdictions namely Northern Ireland (NI) and the Republic of Ireland (ROI). In NI responsibility for the environment is handled by the Department of the Environment (www.doeni.gov.ni) and they have set specific targets for greenhouse gas emissions of a 60% reduction in CO₂ by 2050 with a 20% reduction by 2020 with a minimum 45% reduction by 2035, all against a baseline of 1990. In the ROI it is the Environmental Protection Agency (EPA) which sets targets for greenhouse gas emissions and they have set a target of an 80% reduction of greenhouse gas emissions by 2050 compared with 1990 levels. To date, religious buildings, in both jurisdictions, have been exempted from these targets but there is no guarantee that this will continue to be the case.

4 RESEARCH METHODOLOGY

Research suggests that no work has been undertaken to understand better the relationship between thermal comfort, conservation and preservation, at an acceptable cost, in cathedrals in Ireland. Empirical evidence also suggests that environmental issues are not being addressed by the owners and managers of these buildings. Accordingly it was decided to address these issues in a number of different ways. It was first necessary to draw up a list of the active cathedrals in Ireland. A number of books have been written about the cathedrals, including those in ruins, such as Galloway's book on the cathedrals of Ireland [16], but this research is only interested in those cathedrals which are still in use. Next it was decided to compile a questionnaire which would be used during site visits which would therefore be completed by the researcher and thus a response rate of 100% could be expected. Then it was deemed appropriate to use a cross-sectional case study of a representative sample of the cathedrals and to install equipment in, and monitor for a month during the heating season, some 20 cathedrals. This data would then be examined to see if it was possible to group various types of cathedrals together, depending on their age, construction, use and location, to establish if an optimal heating solution could be suggested, based on best practice.

Since these buildings are listed it was not possible or desirable to attach equipment to them since this would have inevitably adversely affected the fabric of the buildings. This limited the type of monitoring equipment which could be used. It was also important that the equipment was not visible, that it could not be moved or removed and yet that it could take the necessary readings. Accordingly the outside T and RH readings were recorded using a Tinytag TGP-4510 which is a rugged outdoor temperature and humidity monitor which measures T between -40°C to $+85^{\circ}\text{C}$ and measures RH between 0% and 100% [17]. Finding suitable places to place this equipment on the outside of the cathedrals proved especially challenging with the most suitable place being found to be inside the belfry, where one existed. Belfries are nearly always fitted with louvres which allow the loggers to be fully exposed to the outside environment without exposing them directly to the elements of direct sunlight and rainfall. The inside T and RH were recorded every five minutes using data loggers (OM-EL-USB-2, [18]) which are small, light and easy to place. Again finding suitable places for these loggers where they would not be seen or removed and still be at the ideal height of 2 meters, was particularly challenging. Data from these pieces of equipment were downloaded onto an Excel spreadsheet for analysis. The cathedral staff are given copies of the readings, without formal comment, in the hope that they might be of use to them in understanding and better controlling internal temperatures.

5 RESEARCH TO BE COMPLETED

During the summer months the remaining cathedrals which have not yet been surveyed, will be, although all of the largest cathedral have been surveyed to date. It may be deemed necessary to monitor certain additional cathedrals during the next heating season to improve the data available. During the summer months some of the already monitored cathedrals will be monitored again, in the absence of heating, to find out the

rate of natural environmental change within the building depending on the external T and RH. This will prove valuable information concerning the properties of thermal mass and lag and will allow the cathedral managers to adapt and perhaps shorten their heating cycles which will assist both in controlling cost and addressing environmental issues.

A number of clear trends have been established to date. There is a marked difference between the uses to which C of I and RC cathedrals are put. RC cathedrals have more religious services but many less other events such as concerts, dinners, graduation ceremonies and so on, than C of I cathedrals. The use to which the buildings are put has a very direct effect on the amount of energy which the building uses. Secondly, research suggests that the main factors concerning the managers and owners of these buildings are thermal comfort and cost. Conservation, preservation and environmental factors are not mentioned when answering questions during the site visits. Many of the systems are poorly maintained, often as a result of cost and when they are replaced this can be without due regard to current and possible future usage of the buildings. Poor maintenance of the existing systems will result in increased costs as the systems are not operating efficiently. There is a lack of knowledge concerning the operation and capabilities of the heating systems which may result in inappropriate use which will again result in increased costs and increased environmental damage. There is also a lack of knowledge about how the buildings are constructed amongst those responsible for them. Few managers of the buildings know for instance if the buildings have any type of insulation. Lack of insulation in appropriate roofs may result in a loss of over 35% of the heat generated. There is a considerable amount of work to be done in informing those responsible for the heating systems in Irish cathedrals as to how these systems should be set up, in accordance with best practice, taking into account the needs of the users as well as the type and location of the buildings.

6 CONCLUSIONS

The owners and managers of these cathedrals do not have sufficient data available to them to make informed choices about how to best use the heating systems which are installed in their buildings. The existing systems are often not the most suitable for the current uses to which the buildings are being put. Even when the existing system would appear to be suitable, it is not usually being operated most efficiently. For instance, a cathedral with underfloor heating, supplemented with an LPHW system, had a recorded floor temperature of 40°C . This overheating of the inside of the building was causing severe salt crystallisation on the surface of the outside walls.

There is insufficient expertise available, on site, concerning the operation of the systems installed and systems are often inadequately maintained, usually due to cost constraints, which results in poor performance and ultimately increased costs both financially and to the environment.

Systems are replaced without taking account a holistic approach to the whole building, which would include provision of insulation and air movements. Current usage is not always considered before expensive work is being undertaken. There can be a lack of communication with the

operators of the buildings and those specifying the equipment to be used. Finally there is a lack of collective bargaining when it comes to purchasing fuel and maintaining the equipment, given the sector's buying potential. Further research work will allow best practice recommendations to be made to assist cathedral owners and managers to make informed decisions on energy provision on an on-going basis.

REFERENCES

1. Bordass, W and Bemrose, C, (1996), *Heating your Church*, London, Church House Publishing.
2. Makrodimitri, M, Campbell, JWP and Steemers, K, (2011), Sustainability and heritage conservation: Assessment of environmental performance and energy management for historic churches, *3rd International Conference on Sustainability in Energy and Buildings, SEB` 11*, Marseilles, France, Springer.
3. Fanger, PO, (1973), Assessment of man's thermal comfort in practice, *British Journal of Industrial Medicine*, 30, 313-324.
4. Camuffo, D, Pagan, E, Rissan, S, Bratasz, L, Kozlowski, R, Camuffo, M and Della Valle, A, (2010), An advanced church heating system favourable to artworks: A contribution to European standardisation, *Journal of Cultural Heritage*, 11, 205-209.
5. Schellen, HL, (2002), *Heating Monumental Churches*. PhD, Technical University of Eindhoven.
6. CIBSE, (2010), *The Building Regulations 2010*. Approved document L2A, Conservation of fuel and power in new buildings other than dwellings, National Building Specifications Ltd, London.
7. De Saulles, TP, (2012), Thermal Mass Explained. In: *THE CONCRETE CENTRE (ed.)*, Camberley, Surrey.
8. Gagge, AP, Stolwijk, JAJ and Hardy, JD, (1967), Comfort and thermal sensations and associated physiological responses at various ambient temperatures, *Environmental Research*, 1, 1-20.
9. ASHRAE, (2004), Thermal Environmental Conditions for Human Occupancy. Atlanta, Ga. *American Society of Heating, Refrigeration and Air Conditioning Engineers (ASHRAE)*, ANSI/ASHRAE Standard 55-2004.
10. Camuffo, D and Della Valle, A, (2007), Church Heating: A balance between Conservation and Thermal comfort, *Sustainable Climate Management Strategies*. Tenerife, Spain, The Getty Conservation Institute.
11. Collins, K J and Hoinville, E, (1980), Temperature requirements in old age, *Building Services Engineering Research & Technology*, 1, 165.
12. Fanger, PO, (1970), *Thermal Comfort*. Danish Technical Press.
13. Van Hoof, J, (2008), Forty years of Fanger's model of thermal comfort: comfort for all?, *Indoor Air*, 18, 182-201.
14. Nicol, JF and Humphreys, MA, (2002), Adaptive thermal comfort and sustainable thermal standards for buildings, *Energy and Buildings*, 34, 563-572.
15. Oleson, BW and Parsons, KC, (2002), Introduction to thermal comfort standards and to the proposed new version on EN ISO 7730, *Energy and Buildings*, 34(6), 537-548.
16. Galloway, P, (1992), *The cathedrals of Ireland*, The Institute of Irish Studies, The Queen's University of Belfast.
17. Gemini Data Loggers, www.geminidataloggers.com. Accessed 21 September 2015.
18. OM-EL-USB-2, www.omega.co.uk.loggers, Accessed 21 December 2015.

Monitoring moisture in a historic brick wall following the application of internal thermal insulation

Walker_R, Pavia_S

Department of Civil, Structural and Environmental Engineering, Trinity College, Dublin 2, Ireland
email: walkerro@tcd.ie, paviass@tcd.ie

ABSTRACT: This paper monitors the in-situ moisture performance of a solid brick wall following the application of internal insulation using the timber dowel technique. Six internal insulations including thermal paint on lime plaster, aerogel (AG), cork-lime (CL), hemp-lime (HL), calcium silicate board (CSB) and PIR were applied to wall sections.

Improving the thermal performance of buildings reduces building operational energy and its associated negative impact on the environment. However, thermal insulation may increase moisture accumulation in walls undermining their long term durability and lowering their thermal efficiency. Currently, there is a lack of knowledge on the performance of traditional solid walls with respect to heat and moisture and the impact of internal insulation on their hygrothermal behaviour.

The changes in moisture recorded using timber dowels agreed with the moisture recorded using a commercial relative humidity (RH) probes. All the wall sections showed a reduction in moisture content over time as the construction moisture dried. The nature of the insulation significantly determined the wall moisture: after one year, the least vapour permeable and capillary active insulation (PIR, aerogel and paint) had higher moisture contents than the lime based insulation (LP, CL and HL). Moisture gradient across the wall (from the internal surface to wall mid-point) indicate that the lime based materials allow the dissipation of moisture towards the interior surface which is retarded by the low moisture permeability of the paint surface, aerogel and PIR.

KEY WORDS: brick wall; internal insulation; moisture behaviour.

1 INTRODUCTION

Retrofitting insulation to existing buildings can lower energy requirements for heating and cooling reducing both emissions and energy consumption. This has been recognised by the EU and several legislative initiatives have been introduced for building renovation and improving the energy performance of buildings. The building sector is one of the key consumers of energy in Europe using approximately 450Mtoe per annum of which space heating accounts for around 70% of the total energy use [1]. Minimising building energy use has the potential to reduce the adverse environmental impact of the building sector on the environment. Approximately 40% of the existing EU building stock was built prior to 1960 and the introduction of energy specific requirements [1].

External insulation is often the preferred method for upgrading walls however, this approach is not usually appropriate for historic building on account of the architectural and historic significance of their facades. Internal insulation can also impact on the historic character of a building but is commonly considered a preferable alternative. However, there are risks associated with this option, primarily the accumulation of moisture within the wall and consequent structural and material decay. The Sustainable Traditional Buildings Alliance's (STBA) report on the responsible retrofit of buildings notes that there are knowledge gaps on the hygrothermal performance of insulated walls [2].

This paper addresses the moisture risk posed by internal insulation by investigating the in-situ moisture behaviour of a solid brick wall following the application of a range of insulations. When thermally upgrading a wall, the thermal

performance of an insulation is a critical factor however, the insulation's effect on moisture accumulation within the wall is even more important as this can undermine the long term durability of the structure. Therefore, it is essential to achieve the optimum balance between energy saving and hygrothermal risk. In some cases, it may be necessary to limit thermal improvement in order to minimise the risk of moisture build-up.

Water is widely regarded as the most prevalent cause of decay in historic buildings. The most important principle is that moisture must not accumulate in a wall over time. Modern buildings are typically constructed using hard impervious materials intended to prevent moisture from entering the building. However, traditional and historic buildings (predating c.1940), function under a different premise, as their breathable fabrics of brick/stone and mortar allow moisture to dry from the wall (both internally and externally) preventing moisture accumulation over time. As a result, traditional and historic constructions are usually more vulnerable to moisture loads than modern buildings [3].

The risk of moisture accumulation in a particular wall is dependent on multiple factors including weather conditions (exposure to driving rain, sunlight, wind) and orientation. Different orientations have different hygrothermal performance depending on direction of prevailing wind and trajectory of the sun [4]. The wall thickness, the properties of constituent materials and the presence of insulation as well as the level of occupancy and the behaviour of occupants conducting water generating tasks such as drying clothes and showering, also determine moisture accumulation in walls.

The application of insulation on the interior of a traditional wall changes the hygrothermal behaviour of the wall and can result in moisture accumulation [5].

Insulation can increase the likelihood of moisture accumulation on account of two primary reasons. First, the reduced permeability of an insulation can impede the wall drying towards the interior. In addition, insulation lowers the wall temperature which reduces the drying capacity of the wall and increases moisture condensation. Consequently, Kunzel and Kiebl (1996) observe that there is no risk free solution to avoid water accumulation [6].

There is no agreement on the most appropriate method to accommodate water when internally insulating solid walls. Two approaches are commonly used when insulating historic structures to avoid moisture accumulation: vapour tight system which prevent moisture entering the wall from the interior and capillary active/vapour open insulation systems that facilitate drying of the wall moisture.

In the vapour tight system, a vapour retarder is installed on the interior side of the insulation to prevent moisture entering the wall. However, vapour tight systems prevent drying towards the interior, do not allow moisture buffering of room humidity and perforations can result in substantial underperformance. The popularity of this type of system is likely on account of the limited selection of insulation materials available over the past number of years [7].

In contrast, capillary active insulation works on the premise that wall moisture can be transported towards the interior by capillarity and the wall allowed to dry.

The moisture behaviour of vapour tight and capillary active insulation systems reported by different authors in traditional structures are inconsistent probably due to the wide variety of insulation materials, walls, sources of moisture ingress and individual circumstances.

A suitable internal insulation system must be tailored to individual specific building requirements taking into account the multiple variables that influence moisture accumulation. As noted by Nielsen et al. (2012), the same refurbishment method might have different outcomes when applied to different buildings [8].

This paper informs on the moisture performance of a number of internal insulation systems (for over 1 year following application) by monitoring their in-situ performance, when applied onto a solid brick wall. Moisture was introduced into the wall in a levelling lime plaster and within the wet insulation materials applied. Authors have both identified that construction moisture can cause long periods of high RH in walls with the associated risks [7, 9,]. A long-term monitoring program is in place to investigate the moisture behaviour of the walls over a longer time period.

2 METHODS

2.1 The building

The brick walls monitored belong to the Adjutant General's Building in the Royal Hospital Kilmainham, Dublin (Figures 1 and 2). The building was designed by the internationally renowned architect Francis Johnson (1760-1829) and constructed in 1805. It consists of 770mm brick walls (400mm beneath the windows). The approximate dimensions of the fired-clay bricks are 220*70*95 mm (length*height*

width) and the mortar joints are between 25 and 30mm. The exact structure of the walls is unknown however, the wall under the windows is probably a solid, two-brick thick wall in English bond while the remaining wall, also showing English bond on internal elevation, may hold some infill as the wall thickness does not correspond to the brick dimensions. The exterior is a roughcast lime render that was re-rendered in c.2005. The interior plaster was removed approximately 30 years ago and the building treated for timber decay at this time.



Figure 1. Adjutant General's Building in the Royal Hospital, Kilmainham, Dublin.



Figure 2. Interior of building prior to the application of insulation.

2.2 The insulation materials

Insulation was applied in three rooms to the north and west elevations of the first floor as shown in figures 3 and 4. Each insulated wall section had an approximate area of 10m² and comprised of three wall parts: above, below and to one side of the window (Figure 3). Six insulation and two lime plaster (control) sections were installed over a 3 month period as set out in table 1. The walls were levelled using lime plaster (table 1) before the application of the insulation. Timber fibre board was also applied but an exterior system was mistakenly used so its moisture behaviour is not included in this paper.

A thermal and moisture survey was undertaken prior to the application of the insulation. The insulation was applied between December 2013 and April 2014. During monitoring, the rooms were heated using oil filled radiators (average internal temperature c.18°C). The west and central rooms were heated from September 2014 until April 2015 while the east room was heated for a longer period (June 2014-April 2015).

The moisture storage and transfer properties of the insulation materials were measured in the laboratory and are included in a paper by the authors [10].

Table 1. Details of lime plaster and insulation materials.

Material	Coat/thickness	Composition weight
Plaster to level all walls	Scud coat c.5-6mm	2.5:1:0.63 sand:NHL5:water
	Scratch coat 25-75mm to make wall plumb	2.3:1:0.67 sand:NHL3.5:water
Lime plaster (control LP)	Floating coat c.12mm	3:1:0.6 sand:NHL3.5:water
	Skim coat 3mm	1:1:0.5 sand:NHL2:water
Paint on control lime plaster (P)	As above with 3 coats of paint	Emulsion with ceramic additives
Aerogel (AG)	Aerogel and plasterboard w/ foil 19.5mm Gypsum skim coat 3mm	Mechanical fixings manufacturer spec
Cork Lime (CL)	2*20mm layers	2.15:1 cork/lime:water
Hemp Lime (HL)	2*20mm layers	1:2.9:3.5 hemp:NHL2:water
Calcium silicate board (CSB)	30mm	Adhesive as per manufacturer spec
	Proprietary skim coat c.6-7mm	Base and finish coat
Thin PIR with foil (PIR)	37.5mm Gypsum skim coat c.3mm	fixings as per manufacturer spec

NHL –Natural Hydraulic Lime.

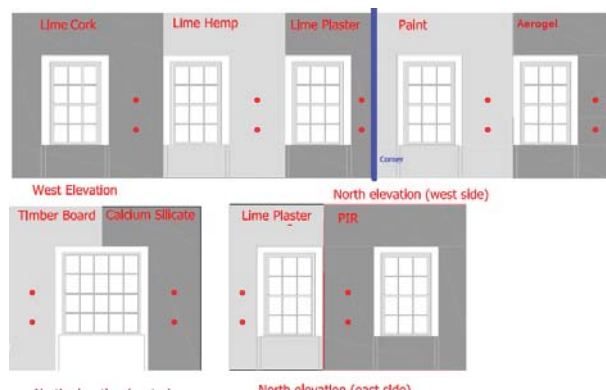


Figure 3. Layout of insulation on west and north elevations.

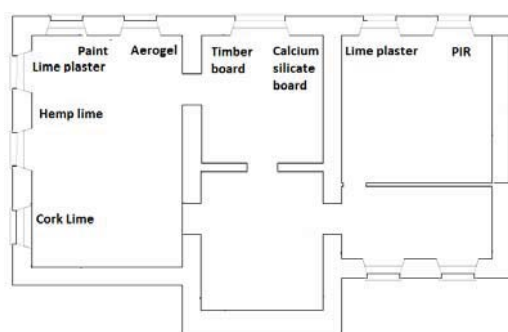


Figure 4. Building plan with location of insulation.

2.3 In-situ measured moisture properties

The insulation is present on two elevations (north and west) which are exposed to different meteorological conditions which will affect moisture behaviour in the wall. The prevailing wind direction in Ireland is south-westerly. Consequently, the west elevation will be exposed to higher quantities of wind-driven rain however, it will also undergo further drying from wind and the latter day sun. In contrast, the north elevation will face less wind-driven rain and little direct sunlight.

Moisture measurements were taken one month prior to the application of insulation. Insulation was applied, between December 2013 (M1) and April 2015 (M5), in the following sequence: cork lime, hemp lime, lime plaster, paint on lime plaster, aerogel, PIR and calcium silicate board. Moisture readings were resumed at month 8 (M8) with additional readings at months 11, 13, 15 and 17 so that M17 is one year after completion of the insulation application. The largest initial moisture content was present in the cork lime, hemp lime and to a lesser extent lime plaster owing to their wet application.

2.4 Measuring of wall moisture using timber dowels

Relative changes in moisture content were measured using timber dowels inserted in the wall and removed at regular intervals. The moisture content of the timber dowel was measured using a resistance moisture meter (Tramex PTM 6005). Changes in the moisture content of the dowel reflected changes in the moisture content of the wall. The dowel gives a good indication of changes in relative wetness [11]

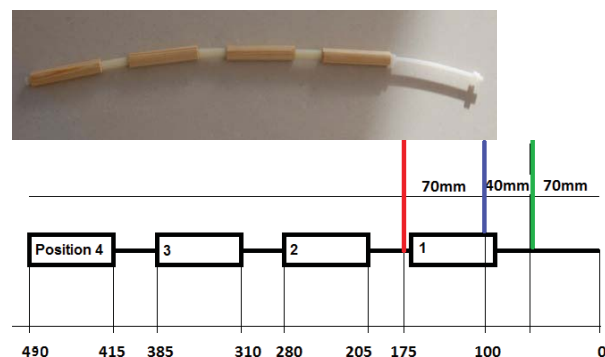


Figure 5. Rod of dowels used to measure the moisture content at different depths in the wall and schematic of rod with dimensions (mm). Green- surface of insulation (wall surface), blue – levelling plaster surface, red – original wall surface.

Rods of dowels were inserted in 14mm diameter cores drilled approximately 420mm into the wall (figure 5). The location of the rods is mapped in figure 3 as red dots. The rod comprised of four sections of pine dowel (length 75mm and diameter 12mm) separated by nylon spacers (length 30mm). This allowed measurement of the moisture content at different depths in the wall. The wall is approximately 840mm thick (770mm external render and brick and c. 70mm levelling lime plaster) with c.40mm of insulation. Dowel position 1 relates to the insulation-plaster interface and positions into the wall 2, 3 and 4 relate to depths of 135-210mm, 240-315mm and 345-

420mm. The timber rods are inserted approximately 320mm into the original wall so position 4 is nearly at the mid-point of the original wall. The position slightly varies depending on the thickness of the insulation and levelling plaster. The hole was plugged at the end to minimise ambient conditions in the room influencing the moisture content readings. The rod was inserted in the wall for 1 month, removed for the application of the insulations and subsequently reinserted 2 months later.

It is likely that the room environment and probe itself influence the measurement of the wall moisture. Consequently, moisture measurements are relative changes in moisture rather than quantitative values.

2.5 Monitoring of wall RH with probes

The wall temperature and RH were monitored using Lascar EL-USB 2+ temperature and humidity probes inserted into holes drilled in the wall and sealed with tape. The hole depth was c.130mm, extending through the insulation (c.40mm) and levelling plaster (c.70mm) to the interior surface of the brick wall. The RH readings are shown over a 1 month period and show the response of the walls to changing moisture conditions.

3 RESULTS

3.1 Measuring moisture using the timber dowel technique and comparison with commercial RH probes

As discussed in the introduction, the timber dowel technique involves inserting a section of timber dowel snugly in a wall until equilibrium moisture content is achieved between the wall substrate and the timber dowel. The dowel is then removed at intervals and its moisture content measured using an electrical resistance based moisture metre. Previous research by the authors found that the timber dowel does not measure actual wall moisture content but satisfactorily shows relative changes in the wall moisture content [11]

As part of this research, the average readings of the timber dowel were compared to commercial RH probes with the results in table 2. The timber dowel method measures the timber moisture content while the commercial probe measures the RH of the ambient air in a hole in which the probe is inserted.

The average readings of the timber rods at positions 1 and 2 (Figure 5) at month 17 were compared to RH probes inserted into 130mm cores (approximately positioned at the levelling plaster- insulation interface) for one month (M16-M17), 12 months after the application of the insulation. The RH measured depends on moisture conditions but also on the wall temperature as RH increases with decreasing temperature. Therefore, low thermal conductivity insulation results in higher RH as it reduces the wall temperature to a greater extent. For this reason, the relative humidity was converted to absolute humidity (using a formula derived from the ideal gas law) that measures the total moisture present irrespective of wall temperature.

The best agreement between the dowel and RH probe is the PIR board that shows both very high RH for the probe (c.89%) and moisture content in the dowel (13.2%). The remaining probe results are within a small range of relative humidity ((56.5%-63.5%) however both the dowel and probe measurements largely agree on the relative moisture levels.

For example, they show that CL and HL have low moisture values compared to the other insulation materials. Additionally, the paint and CSB have the highest moisture readings for both measurement techniques. Despite the small RH range (56.5%-63.5%), the similarity in the trend of moisture content of the insulations using the two measurement techniques provides confidence of a satisfactory level of accuracy on the moisture behaviour.

Table 2. Moisture reading of timber dowel and RH probe

Mesh size	Average timber dowel % (M17)	RH %	Temp °C	Absolute humidity (kg/m ³)
LP	11.18	56.5	16.3	0.00786
P	11.39	63.5	16.5	0.00894
AG	11.00	62.9	15.3	0.00824
CL	10.94	58.5	15.3	0.00753
HL	10.24	58.9	16.1	0.00809
CSB	11.41	60.8	16.2	0.00841
PIR	13.17	89.2	13.9	0.01072
Room			17.5	

In addition, previous research by the authors investigated moisture content in the timber dowels in varying RH environments in the laboratory [11]. The results (converted to absolute humidity) are plotted in figure 6 (blue). In this figure, the RHK wall humidity values measured with the probe and timber dowels are shown in red; and the black curves show the typical relationship between environmental relative humidity and timber moisture content (timber pine sorption isotherm - extract from 12- black). The RHK readings (red) overlaid in a position near the sorption isotherm suggests good agreement in the readings of the probe and timber dowels. The timber moisture readings in the dowel in the walls of the RHK are what would be expected based on the RH measured by the probes in holes in the wall.

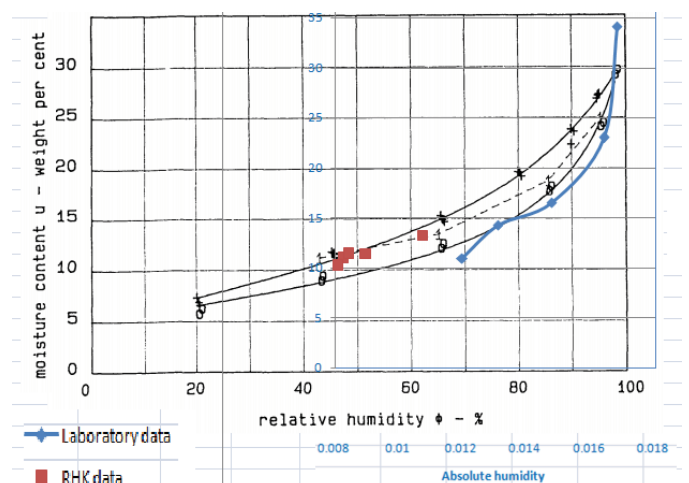


Figure 6. Comparing moisture content in timber dowel and the RH measured using the probe in the RHK wall, with previous laboratory results and timber sorption isotherm.

3.2 Overall trend of moisture in the wall

As discussed in the introduction, moisture movement in the wall is exceptionally complex, with several interactions simultaneously occurring at varying drying, wetting and cooling cycles.

In the case study, significant moisture was introduced into the wall in the levelling plaster and the wet application of insulation. The overall trend of falling moisture content, between M8-M17 (July to April) reflects the drying of this construction moisture. The initial construction moisture content in the wall varied, for each insulated section, on account of moisture introduced by the levelling plaster and/or wet insulation and the sequence of construction. The moisture content at the final stage (at M17) ranged between 10.24-11.39% (except for PIR) which is slightly above the average wall moisture content recorded prior to the application of the insulation (10.3% ranging between 9-11.9%). This suggests that most construction moisture had dried by this time.

The small increase in wall moisture between M11 and M13 however indicates that other sources of moisture are also contributing to the total wall moisture content. Moisture vapour (diffusion and air movement) and rainfall are also contributing to the total moisture content in the wall although likely to a lesser extent than construction moisture.

The effect of the hygric properties of the insulation are evident at months 13, 15 and 17 (M13, M15 and M17), as the least vapour permeable and capillary active materials (PIR, AG and paint) on average show higher moisture contents than the lime based materials (LP, CL and HL).

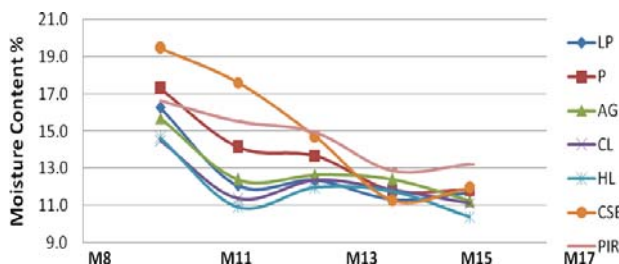


Figure 7. Relative changes in wall moisture content over time, (between month 8 and 17) measured with the dowel method.

In relation to drying, all the walls lost significant moisture between months 8 and 11. It is difficult to compare the drying rate for the walls on account of the varying initial moisture content at M8. However, it is evident that the PIR has the slowest drying rate. The aerogel and paint have similar drying rates to the lime based insulations despite their higher initial moisture content.

The aerogel and paint have similar drying rates to the lime based insulations despite their higher initial moisture content. Typically, drying rates are proportional to the quantity of moisture present so wetter materials will dry at faster rates. The slow drying rate (considering higher initial moisture content) of the least permeable materials (aerogel and paint) is likely inhibited by this characteristic while the good drying rate of the lime based materials (cork-lime and hemp-lime) is benefited by their high water vapour diffusion and capillary activity. The CSB has a much slower drying rate than expected, although at later ages, particularly between M15-

M17 (figure 7), the drying rate is much faster. It is likely that the sensitivity of the CSB to changing environmental conditions may have influenced the moisture content readings.

3.3 Moisture gradient in the wall over time

The moisture profile of the rods in the wall should indicate the direction of moisture transfer in the wall with moisture moving from areas of higher concentration.

The moisture profile of the insulated walls (from the interior to approximately mid-point into the wall) was monitored at 8,11,13,15 and 17 months with timber dowels. As aforementioned, the rods have four sections of timber dowel that are separated from each other by a nylon spacer. Each section of timber dowel indicates moisture content at a different depth in the wall (position 1 relates to the insulation/levelling-plaster interface and positions 2, 3 and 4 relate to depths of 135-210mm, 240-315mm and 345-420mm into the wall respectively- Figure 5). The beginning of the curves in figures 8-10 below relate to position 1 and the end to the midpoint of the wall (position 4).

Two rods were located in each insulated wall. The moisture content of each rod was plotted to give an indication of the moisture profile in the wall. A straight profile refers to less than 1.5% moisture variation at the four positions of the two rods. The angled profile relates to a constant gradient for both rod measurements with a greater than 1.5% difference between position 1 and 4 for at least one of the two rod measurements. The humped profile means that the moisture at the centre points is greater than that at either end by at least 1.5% for both rod measurements. When two distinctly differing profiles were evident for the two rods, both are shown. N/d refers to an undefined profile where the gradient differs for the two rods are inconsistent.

These graphs represent the moisture distribution across the wall rather than the actual moisture content which is not comparable due to varying initial moisture contents.

During application of the levelling plaster and wet insulation, moisture is introduced at the interior side of the wall (dowel position 1 – left hand side (LHS) of curve) and drawn deeper into the brick wall. As moisture dries in both directions, there should be a reduction in moisture content and an equilibrium of water distribution through the wall. If the internal insulation is impermeable, moisture will be forced to dry towards the exterior. Figure 8 shows a simplified visual approximation of the moisture profiles in the wall on account of water introduced during construction.

It is considered that construction moisture makes the greatest contribution towards the total wall moisture at early ages. However other sources of moisture also influence the profiles with rainfall raising moisture from the interior wall position (rod position 4) and internal room humidity transferring moisture from the room side (rod position 1).

Profile	Initial	Construction moisture introduced	Drying Insulation allowing moisture transfer to the interior	Insulation inhibiting moisture transfer to the interior	Construction moisture dried
	—	↘	↗	↘	—

Figure 8. Simplified moisture profiles in the wall considering construction moisture. The beginning of the curves (left hand side) relate to position 1 and the end (right hand side) to the midpoint of the wall (position 4).

The average moisture content (of months 8,11,13,15 and 17) at each position is shown in figure 9 and a visual representation of the moisture profile at each month is shown in figure 10.

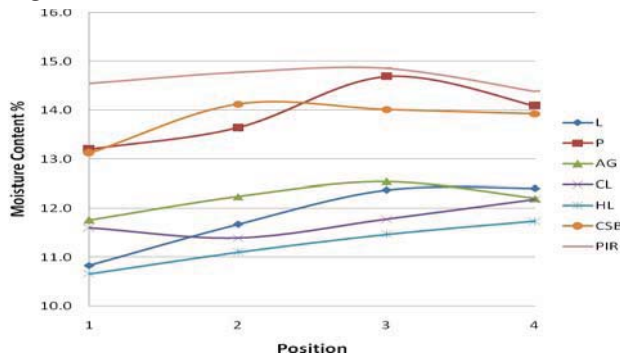


Figure 9. Average moisture content (month 8, 11,13,15 and 17) at the different dowel positions (fig 5)

	LP	P	AG	CL	HL	CSB	PIR
M8	n/d	—	n/d	—	—	—	—
M11	—	—	n/d	—	—	—	—
M13	—	—	n/d	—	—	—	—
M15	—	—	—	—	—	—	—
M17	—	—	—	—	—	—	—

Figure 10. Visual representation of moisture profiles across the wall measured using rods

The lime plaster moisture profiles in figures 9 and 10 indicate that drying is consistently occurring towards the interior which is consistent with its vapour permeable nature. The lime plaster with paint profiles reveal that moisture is moving towards the interior, although its higher moisture content and the small difference in average moisture content between positions 1 and 2 (figure 9) suggest that drying is inhibited at the wall surface by the paint.

All the moisture profiles of the cork-lime and hemp-lime (CL and HL) reflect the good liquid water capillary transfer of these materials: moisture is distributed across the wall on account of the moisture wicking ability of the materials allowing drying towards the interior.

The moisture profiles of the PIR (and aerogel to a lesser extent) largely suggest an inability for moisture to dissipate towards the interior with an accumulation of water near the surface of the original brick wall (humped profile) or evidence of moisture moving towards the exterior. This is attributed to the low capillary transfer and moisture barriers at the internal surface of these insulations.

The CSB has a higher moisture content at the time of measurement (due to construction sequencing it was applied last). The profiles of the CSB at M8 and M11 suggest that construction water is still in the wall and the following measurements (at M13 and M15) indicate that drying is occurring towards the interior facilitated by its highly capillary active nature.

ACKNOWLEDGMENTS

The authors wish to thank the Irish Research Council and Office of Public Works for funding this research. The authors

also thank the OPW in particular Ben Fay, George Whelan and Colin McAlloram for the installation of the internal insulation in the Adjutant General's Building. Laboratory work and site support was provided by the Dept. of Civil Engineering, Trinity College Dublin and the authors thank Dr. Kevin Ryan for facilitating the experimental work.

4 CONCLUSION

This paper monitors the in-situ moisture performance of a solid brick wall following the application of internal insulation including thermal paint on lime plaster, aerogel (AG), cork-lime (CL), hemp-lime (HL), calcium silicate board (CSB) and PIR.

Timber dowel and commercial relative humidity (RH) probes provided good agreement of relative changes of moisture content in the wall.

The moisture content of the walls reduced over time as the construction moisture dried. The moisture properties of the insulation influenced this drying. At one year, the least vapour permeable and capillary active insulation (PIR, aerogel and paint) had higher moisture contents than the lime based insulation (LP, CL and HL). The moisture profiles across the wall (from the internal surface to wall mid-point) further illustrated their moisture behaviour with the lime based materials allowing the dissipation of moisture towards the interior while, in contrast, this is retarded by the low moisture permeability of the paint surface, aerogel and PIR.

REFERENCES

- [1] Buildings Performance Institute Europe, *Europe's buildings under the microscope, A country-by-country review of the energy performance of buildings*, BPIE, 2011.
- [2] Browne, D. *The SPAB Hygrothermal Modelling: Interim Report*, The SPAB Research Report 3, London, October 2012.
- [3] Künzle H. M. and Holm A.H. *Moisture Control and Problem Analysis of Heritage Constructions*, IBP, Fraunhofer Institute, Stuttgart, 2009.
- [4] Marincioni, V. and Altamirano, H. (2014), 'Effect of orientation on the hygrothermal behaviour of a capillary active internal wall insulation system', *Proceedings of the 10th Nordic Symposium of Building Physics*, Lund, Sweden.
- [5] Vereecken, E. and Roels, S. (2014), 'A comparison of the hygric performance of interior insulation systems: A hot box-cold box experiment', *Energy and Buildings*, 80, 37-40.
- [6] Kunzel, H.M. and KieBl, K. *Drying of brick walls after impregnation*. Bauinstandsetzen 2, 1996, 87-100.
- [7] Toman, J. Vimmrova, A. and Cerny, R. (2009), 'Long-term on-site assessment of hygrothermal performance of interior thermal insulation system without water vapour barrier', *Energy and Buildings*, 241, 51-55.
- [8] Nielsen, A. Møller, E.B. Rasmussen, T.V. and Hansen, E.JdP. (2012), 'Use of sensitivity analysis to evaluate hygrothermal conditions in solid brick walls with interior insulation', *Proceedings of the 5th International Building Physics Conference*, Kyoto, Japan, 377-384.
- [9] Klöschke, P. Arumägi, E. and Kalamees, T. (2015), 'Hygrothermal performance of internally insulated brick wall in cold climate: field measurement and model calibration', *Journal of Building Physics*, 38(5), 444-464.
- [10] Walker, R. and Pavia, S. (2015) 'Thermal and hygric properties of insulation materials suitable for historic fabrics', *Proceedings of COINVEDI III International Congress on Construction and Building Research*, Universidad Politécnica de Madrid, Madrid.
- [11] Walker, R., Pavia, S. and Dalton, M. (2015) 'Measurement of moisture content in solid brick walls using timber dowel'. *Materials and Structures*, DOI 10.1617/s11527-015-0667-6.
- [12] Hansen, K.K. *Sorption Isotherms: A catalogue. Technical Report 162/86*, Building Materials Laboratory, The Technical University of Denmark, 1986.

Design process to evaluate potential of wind noise at façade elements

Dr.Cristina Paduano¹, Dr.Jennifer Keenahan¹, Réamonn Mac Réamoinn¹

¹Arup, 50 Ringsend Road, Dublin 4, Ireland

email: cristina.paduano@arup.com, jennifer.keenahan@arup.com, reamonn.macreamoinn@arup.com

ABSTRACT: Wind noise generation from a solar shading façade is a design concern of engineers. A shading façade consists typically of a series of fins which repeat sequentially and that is mounted at a certain distance from the building surface, forming with it the sides of a duct where the wind can pass through. The flow instability created by the vortex detachment from the fins can excite the acoustic mode of the duct and instigate a phenomenon of aero-acoustic resonance which manifests with the generation of tonal noise. No design tools are currently available to assess the likelihood of tonal noise to occur in similar façade. Existing guidance notes have been used by Arup Acoustics for the last 20 years and have never been fully tested in the built environment to confirm their validity. A numerical methodology is presented here which aims to predict, through the CFD modelling of the aero-acoustic resonant system, if the coupling of ducted flow and vortex shedding around the fins element of a façade could lead to tonal noise generation.

KEY WORDS: Façade noise, Wind noise, Aeroacoustic resonance.

1 INTRODUCTION

Some level of flow-induced noise is likely to develop around any structure/building or part of it exposed to the wind. The characteristics of that noise and the conditions under which it occurs will influence whether or not noise from a particular structure is likely to cause annoyance. Under certain conditions, wind flow across structures and gaps within the building facade can adopt tonal characteristics, which, if sufficiently loud and frequent, can cause disturbance. This is due to the fact that this noise can sound as a ‘whistling noise’ propagating through the façade structure and may disturb the activities within and outside the building.

Tonal noise from a building facade can be the indicator of a physical phenomenon known as “aero-acoustic resonance” which typically occurs when, in a ducted flow, a periodic vortex shedding develops having frequencies which are close enough to one of the acoustic mode of the duct itself.

In order to assess the likelihood of the wind generated noise to occur, existing guidance notes have been used by Arup Acoustics for the last 20 years and had never been fully tested or studied extensively in the built environment to confirm their necessity, and/or further optimisation. For years they have been more of a “catch-all” approach that is too often deemed impractical and unreasonable from an aesthetic and façade engineering standpoint (see Table I).

Table I: Existing guidance notes [1, 2].

Elements-aperture	Dimension	Comments
Unsealed slots, apertures and exposed elements within façade cladding	>100mm	For exposed elements introduction of vibration damping treatments needed. For cavities and apertures it is recommended to close all openings and apertures to avoid the creation of resonant cavities.
Wires, circular cables, tubular elements or hollow sections	>50mm	If a bigger dimension than 50mm is not possible to be included then provide special damping treatment.
Array elements	>100mm	In case of regular array of elements, smaller dimension of apertures should be avoided or provide special damping.
Constructions	>100mm	Irregular constructions should be used to break-up vortex street formations.

Recently, in light of the higher demand and use of solar shading, there has been the need for the existing guidance to be reviewed and further studied. A list of Arup Acoustics projects have been selected falling within two categories:

1. Projects analysed only through a desktop study and/or a CFD modelling study of vortex shedding at fins elements (without any on-site measurements or wind tunnel tests) – the façade elements are studied with the

likelihood of disturbance generated by the elements in terms of 'low, medium, high level'. The desktop study has been based on the evaluation of the Reynolds Number using as reference length the fins one (see figure 1 and figure 2).

- Projects analysed with on-site measurements or wind tunnel tests – in this case, the likelihood of disturbance generated by the façade elements is also provided and confirmed in terms of tonal noise frequency.

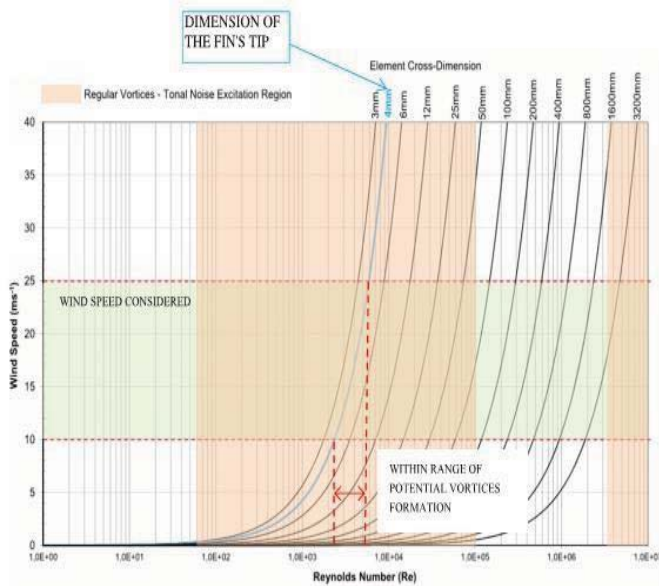


Figure 1: Relationship between wind speed and Reynolds Number with varying cross-dimension of the façade fin [1].

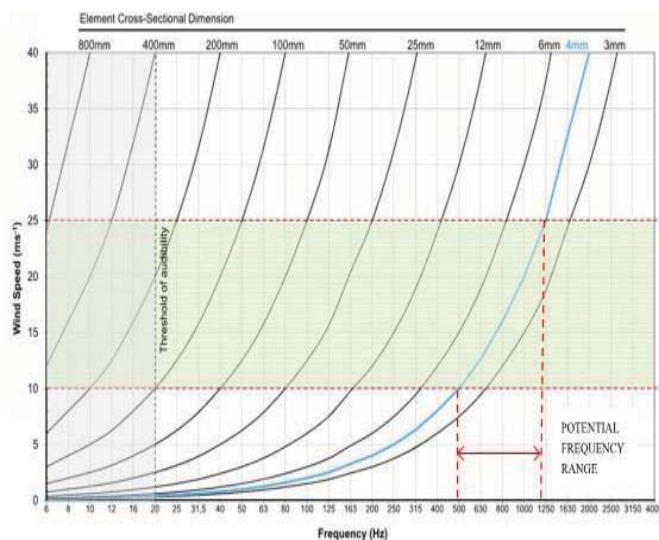


Figure 2: Relationship between wind speed and Reynolds Number with varying cross-dimension of the façade fin [1].

In light of the limitations offered and discovered by the existing acoustic guidance (see Table II), a design process

has been implemented for evaluating, using analytical methods, the shape and layout of façade element in order to avoid the instigation of aero-acoustic resonance.

Table II: Analysis of Arup projects with existing guidance notes [1].

Assessed Projects	Exhibits Noise or predicted > Low Risk (i.e. Med or High)	How it contradicts the Guidelines
Project 1) Desktop study undertaken	✓	Unsealed slots, apertures and exposed elements within façade cladding should be > 100mm
Project 2) Site measurements undertaken	✓	Unsealed slots, apertures and exposed elements within façade cladding should be > 100mm – louvre blades are 150mm but tonal noise was measured. However a regular construction with array of elements was installed.
Project 3) Desktop study undertaken + wind tunnel tests	✓	When arrays of elements are presented in the façade it is recommended the spacing to be >100mm - The spacing between façade tube elements is designed to be 10mm but no tonal noise was found in the wind tunnel
Project 4) CFD + wind tunnel tests	✓	Unsealed slots, apertures and exposed elements within façade cladding should be > 100mm - The perforation dimension (rectangular) is 20mm width and 90-305mm height but no tonal noise was measured in the wind tunnel facility.

2 AERO-ACOUSTIC BEHAVIOR OF A SHADING FACADE

Aeroacoustic resonance is experienced when a ducted flow is interested by a periodic vortex shedding. The frequency of vortex shedding approaches the acoustic frequency of the duct a flow is interested by a periodic vortex shedding and exhibits frequencies coincidence or close enough to the transverse acoustic mode of the duct itself[3].

As the flow passes the body, vortices are shed periodically at a frequency that increases linearly with the flow velocity. This relationship is characterised by a constant Strouhal number. During aero-acoustic resonance, the acoustic field modifies the hydrodynamic field so that the vortex shedding frequency coincidences with the acoustic resonant frequency not at a single flow velocity, but over a range of flow velocities. This is called *lock-in* [3, 4].

During lock-in the shedding frequencies remain constant as flow velocity is increased until resonance subsides and the vortex shedding process reverts to the frequency indicated by the Strouhal number. This behaviour is shown schematically in figure 3.

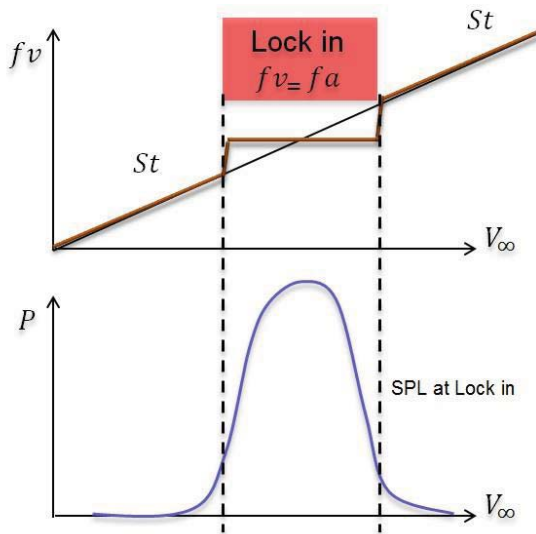


Figure 3: Scheme of frequency synchronisation and related sound pressure level (SPL) during lock-in condition [3]

In a shading façade this can occur when the flow instability created by the vortex detachment from the fins can generate unsteadiness in the flow passing through the duct formed between the shading façade and the building surface. This can excite the acoustic mode of the duct and instigate aero-acoustic resonance that manifests with tonal noise.

3 PROPOSED METHODOLOGY

The proposed methodology aims to investigate the potential of a shading façade to generate tonal noise as a consequence of *lock-in* being instigated between the fins of the façade and the ducted flow configuration which they form with the building surface behind them. This involves evaluating if the following conditions are occurring when a typical section of the façade is exposed to wind flows:

- The fins are generating a vortex shedding phenomena at considered wind flows conditions and,
- The flow within the duct behind assumes an oscillatory nature due to vortex shedding such to excite the acoustic mode of the duct and,
- The acoustic mode of the duct trigger in *lock-in* range the vortex shedding frequencies of the fins.

In case that the above conditions are verified and therefore aero-acoustic resonance is likely to occur for the façade, then the methodology could guide the engineers

toward the selection of more appropriate combination of fins – ducted flow which follow within the *off-resonance* range.

4 USE OF AN HYDRODYNAMIC ANALOGY TO SIMULATE AERO-ACOUSTIC RESONANCE

The frequency of the transverse acoustic mode of a rectangular section duct can be calculated using the following formula [3]:

$$f_a = nc/2w \quad (1)$$

Where c is the sound speed (340 m/s), w the width of the duct and n the number of transverse acoustic modes in the duct. The primary flow induced acoustic mode in a rectangular section duct consists of a transverse standing wave (i.e. normal to flow direction).

Tan *et al.* [4] proposed an hydrodynamic analogy in which the acoustic field is represented as an oscillating cross flow velocity boundary condition applied to an incompressible flow. A sinusoidal velocity of the form $A \sin(2\pi f_a t)$ is applied perpendicularly to the flow direction as shown in figure 5; A represents the acoustic particles velocity amplitude. The analogy is well known in literature as it has been applied successfully for the modelling of aero-acoustic resonance of bluff bodies ducted flows [4].

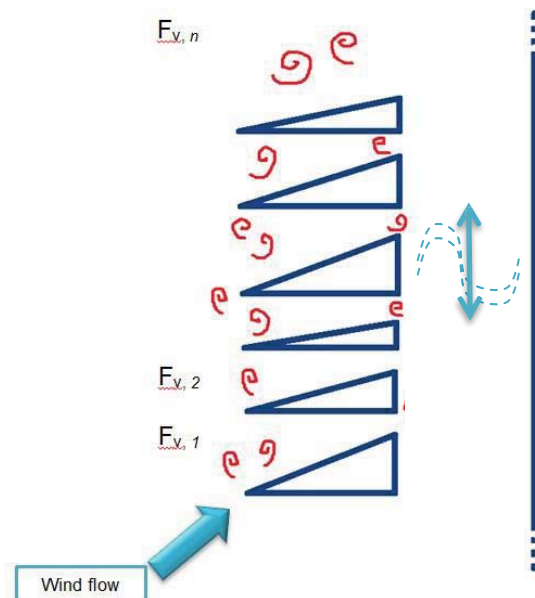


Figure 4: Vortex shedding and propagation of first transverse acoustic mode.

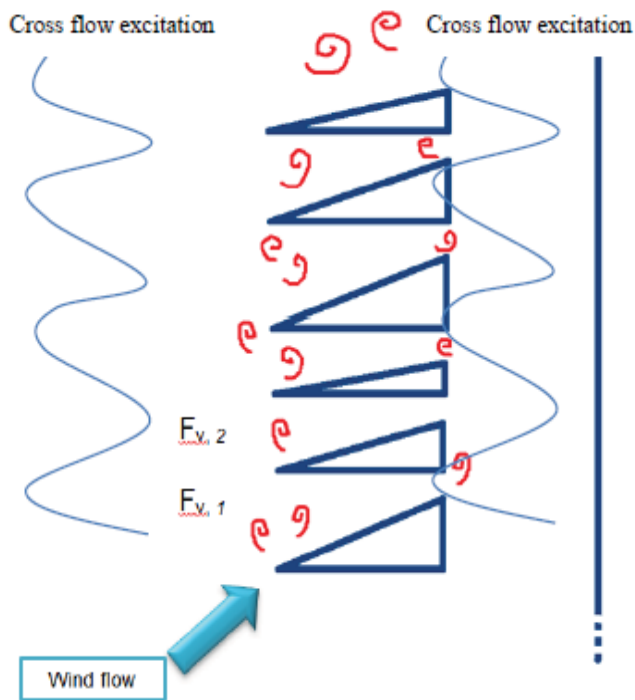


Figure 5: Scheme of cross flow oscillating velocity condition to model the acoustic excitation.

5 METHODOLOGY APPLICATION TO A SHADING FAÇADE LAYOUT

A series of CFD simulations are performed to solve the flow around a typical sequence of fin elements of a shading façade and the spacing behind it, this at a range of wind conditions. In order to verify the risk of tonal noise being generated by the analysed configuration, the following steps are implemented:

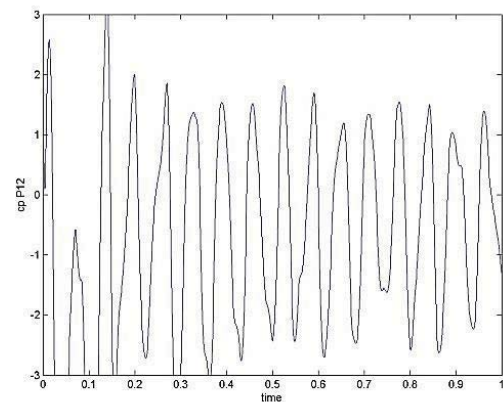
6 EVALUATION OF VORTEX SHEDDING AT THE FAÇADE FINS

The objective of this phase of the methodology is to verify if a periodic vortex shedding may form, under the considered wind flow conditions, from the fins.

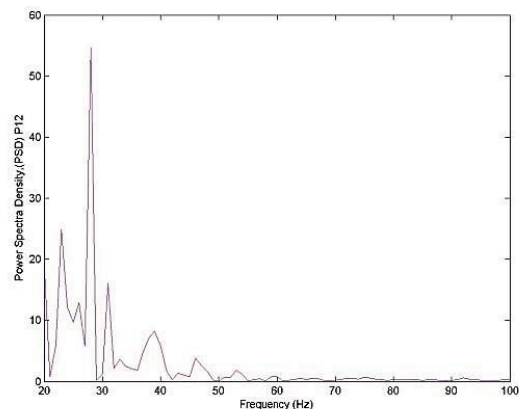
A 2D model of a typical section of the façade is prepared. The façade is exposed to 4 different cross flows at 10 m/s, 15 m/s, 20 m/s, 25 m/s and also 4 incidence angles for each flow magnitude (0°, 22°, 45°, 67°). The presence of possible vortex shedding structures is at first investigated by observing the contour plots of the vorticity fields obtained for each of the cases simulated.

During these analysis the time trace of the coefficient of pressure (c_p) is collected for each of the fins and a probe is inserted at the center of the spacing formed by the shading façade and the building surface to record time variations of the velocity magnitude of the flow passing through it. A FFT (Fast Fourier Transformation) of the time signal of the above quantities (c_p and V_{duct}) is produced in order to investigate their spectra frequencies content. In case of periodic vortex shedding, a clear spike at a single frequency

is visible in correspondence of the natural vortex shedding frequency [4].



(a)



(b)

Figure 6 (a) Time trace of the c_p collected at the downstream fin. (b) FFT of the oscillating c_p .

7 VERIFICATION OF RISK OF AERO-ACOUSTIC RESONANCE DUE TO FREQUENCIES COINCIDENCE ($f_v = f_a$)

The first transverse acoustic mode (f_a) of the duct is calculated using the empirical formula applicable to ducted flow. At first comparison is considered to verify if the frequency of vortex shedding obtained around the fins is similar to the acoustic frequency which could be instigated within the spacing behind. For the façade configuration analysed the acoustic frequency has been found to be $f_a = 212$ Hz.

This correspond to a frequency ratio $f_a / f_v \sim 4$.

However, the lack of coincidence between the frequencies above does not ensure the lack of tonal noise being emitted from the façade. The lock-in phenomena in fact can trigger resonance in a large range of frequency ratio and therefore this possibility must be considered by the study.

8 VERIFICATION OF RISK OF AERO-ACOUSTIC RESONANCE DUE TO LOCK-IN PHENOMENA

During this step the method focuses on investigating the possible extents of the lock-in range. In particular it is evaluated if the frequencies of vortex shedding, obtained at the previous steps could be driven in a lock-in mechanism by the excited acoustic frequency and which is the amplitude of acoustic necessary for this to occur.

Acoustic excitation is therefore introduced in the model as a flow boundary condition. This is in the form of an oscillating velocity representing the flow oscillation that the acoustic wave causes once instigated. The oscillating velocity is a sinusoidal wave of frequency (excitation frequency f_{exc}) equal to a ratio of f_a , in the range of 0.5 to 1.5 and, with an amplitude

A equal to 10% and 5% of the incoming wind flow. The c_p is collected from the simulations run with excitation and the frequency spectras plotted. In the case of lock-in, the frequency spectra shows a shifting of the vortex shedding frequency in correspondence of the frequency of acoustic (see figure 7) otherwise, if the system remain in *off-resonance* conditions then the two frequencies (vortex shedding and acoustic) are both appearing in the spectra, this indicating that the two periodic phenomena are co-existing but the acoustic wave is not able to enhance itself and self-sustain by triggering vortex shedding into a resonance phenomenon.

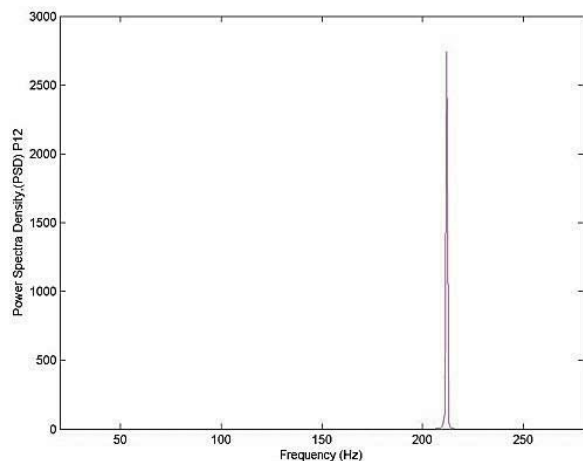


Figure 7: Scheme of frequency synchronisation and related sound pressure level (SPL) during lock-in condition (ref).

9 CFD MODEL DESCRIPTION AND SIMULATION ASSUMPTIONS

In the 2D model built to represent a typical section of the façade the fins have a reference length (L) of 300 mm and a pitch ratio measured at the fins edge (L/d) going from 2 to 5.

The width (w) of the spacing behind the fins is of 800 mm. The computational domain consists of an upstream and downstream of 5 times the total length of a fin. The side boundary of the domain are kept at a distance of 6 times the width w .

The flow is assumed to be incompressible standard air with $\rho=1.225 \text{ Kg/m}^3$ and $\mu=1.78 \times 10^{-5} \text{ kg/m} \cdot \text{s}$. The lower inlet boundary has a constant velocity. The upper and outlet boundary is defined with a constant static reference pressure (0 Pa). The right and left side boundaries are maintained as no slip walls for the simulations where no acoustic excitation is provided.

When the acoustic excitation is imposed, these boundaries are velocity inlets/outlet with an instantaneous spatially invariant velocity which is temporally periodic and with a zero mean.

The transient flow is solved using URANS. All modelling steps are prepared using the commercial CFD code ANSYS Fluent 14.5[6].

10 SIMULATION RESULTS

10.1 NATURAL VORTEX SHEDDING FREQUENCY OF THE FINS

The first set of simulations is executed with no acoustic excitation to reproduce the vortex shedding phenomena for each wind flow considered.

The contours of vorticity showed a clear and strong vortex street for each simulations. The frequency of vortex shedding is obtained from the FFT of the pressure coefficient collected at each of the fins. Almost all pressure coefficients of the fins demonstrated a periodic behaviour for each of the wind speed and incidence angle considered. For the flow velocities simulated the frequency of vortex shedding were in the range of 40-30Hz.

In addition, the oscillation of velocities were collected within the ducted flow, this displayed the same flow periodicity that was achieved by the flow around the fins.

Figure 8(a) that follows, shows the vorticity plot obtained when the wind flow applied is 25 m/s and the wind incidence angle 67° .

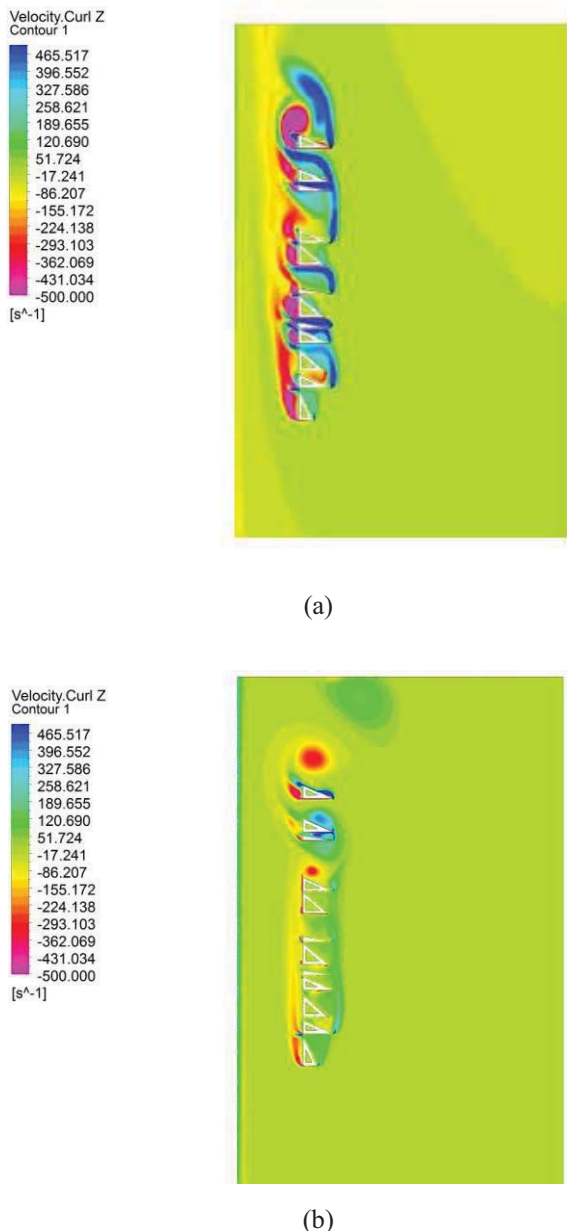


Figure 8: (a) Vorticity field at 25m/s and incidence angle of 67° without excitation applied. (b) Vorticity field at 25m/s and incidence angle of 67° with excitation of $A=10\%$ of V_{wind} and $f_{exc}=212$ Hz.

10.2 EXCITED VORTEX SHEDDING FREQUENCY OF THE FINS

The second set of simulations is executed with acoustic excitation, this for each wind flow considered. The contours of vorticity, in the case that have seen lock-in, have showed a reduction of the vorticity content. Figure 8(b) shows the vorticity plot obtained for the wind flow applied of 25 m/s and for an incidence angle of 67° and with the applied excitation frequency of 212Hz and $A=10\%$ V_{wind} .

Table III: Summary of spectra analysis results.

	25 m/s - $\theta=67^\circ$ NO excitation		With excitation $A=10\%$ v_{wind} - $f_a=212$ Hz	
	C_p	f_v (Hz)	C_p	f_v (Hz)
Fin1	No periodic	—	No periodic	—
Fin2	Periodic	~ 25	Periodic	Lock in
Fin3	Periodic	~ 35	Periodic	Lock in
Fin4	Periodic	~ 42	Periodic	Lock in
Fin5	Periodic	~ 35	Periodic	Lock in
Fin6	Periodic	~ 39	Periodic	Lock in
Fin7	Periodic	~ 40	Periodic	Lock in
Fin8	Periodic	~ 23	Periodic	Lock in
Fin9	Periodic	~ 25	Periodic	Lock in
Fin10	Periodic	~ 55	Periodic	Lock in
Fin11	Periodic	~ 25	Periodic	Lock in
Fin12	Periodic	~ 25	Periodic	Lock in

11 CONCLUSIONS

The simulation have shown that at all the wind flow velocities above the 20m/s the vortex shedding from the fins can be triggered into *lock-in* by the excited acoustic frequency as can be seen in table III which report the response of vortex shedding of each fins for the analysis carried out with wind flow speed of 25 m/s and incidence angle of 67° . The methodology illustrated in this paper can be used to verify if a combination of fins of a solar shading façade and the spacing formed by the façade and the building surface could lead to tonal noise, this as consequence of aero-acoustic resonance being instigated. The methodology could be further validated to verify which façade features lead to an *off-resonance* condition.

REFERENCES

- [1] Coppa, F, Wind Noise on External Facade Elements. Arup Acoustics 2014.
- [2] Coppa, F, Wind Noise Assessment on the facade fins - new building in Italy. Arup Acoustics 2013.
- [3] Howe, M.S., Theory of vortex sound, Cambridge University Press, 2003.
- [4] Tan, B.T, Hourigan, K., Sources of acoustic resonance generated by the flow around a long rectangular plate in a duct, Journal of Fluids and Structures, 2003, 18: p. 729-740.
- [5] Paduano, C., Meskell, C., Reynolds number effect of aeroacoustic resonance of two tandem cylinder in ducted flow, AIAA Conference, Colorado Spring 2012.
- [6] ANSYS Workbench, ANSYS Inc., Canonsboug, PA.

Bi-phase methodology for sensitivity analysis of complex models, applied to the model of evaluating resilience in transport networks.

Beatriz Martinez-Pastor¹, Maria Nogal¹ and Alan O'Connor¹

¹Department of Civil, Structural and Environmental Engineering, Trinity College Dublin, Ireland
email: bmartine@tcd.ie, nogalm@tcd.ie, oconnoaj@tcd.ie

ABSTRACT: Sensitivity analyses identify the importance of the model parameters and variables, providing a profound knowledge of the model. Most of the sensitivity analysis implies a local evaluation of the variability of the parameters. However, in those cases where the model involves a large number of degrees of freedom, these studies become highly time consuming and incapable of obtaining conclusive solutions. This paper presents a bi-phase approach, by integrating a local into a global sensitivity method. This methodology is recommended in those multidimensional models that make other approaches inefficient. The global phase is based on the statistical distribution of the variables, providing a robust and reliable solution, with low computational costs. With the aim of showing the potential of this approach, the method is applied to a complex existing model. This model aims to evaluate the resilience in transport networks when affected by an extreme weather event. As expected, this sensitivity analysis shows the large influence of the hazard intensity, but also shows how other variables, as the size of the area affected by the hazard and the role that the users play, can modify the values of the sensitivity analysis significantly.

KEY WORDS: Sensitivity analysis; Resilience; Hazards; Extreme Weather; Latin Hypercube; On-At-a-Time; Local Sensitivity; Global Sensitivity; Vulnerability.

1 INTRODUCTION

A variety of extreme weather events, including river floods, rain induced landslides, droughts, winter storms, wildfire, and hurricanes, have threatened and damaged many different regions worldwide. These events have a devastating impact on critical infrastructure systems resulting in high social, economic and environmental costs. For this reason, it is imperative to develop a mathematical tool that is able to measure systematically the impacts of extreme weather events on infrastructures.

Once the model for assessing the impacts of climatological hazards is developed, a sensitivity analysis should be carried out. A sensitivity analysis identifies the influence of each parameter on the outputs of the model, permitting a profound knowledge of its behaviour. In addition, the definition of the inputs will be more efficient after studying how these parameters modify and influence the model.

Different methodologies to address a sensitivity analysis have been developed previously. These methods can be differentiated between local methods and global methods, the former focuses on estimating the local impact of a parameter on the model outputs.

Global techniques are based on sampling methods which scan, in a random or systematic way, the complete range of the parameters involved in the model. Selection of the sampling strategy is crucial to the sensitivity analysis.

This paper presents a bi-phase sensitivity analysis, by integrating a local into a global sensitivity method. This methodology is recommended in those multidimensional models that make other approaches inefficient. Especially, in those cases where the model involves numerous degrees of freedom, since other methodologies become highly time consuming and incapable to obtain conclusive solutions.

The paper is organized as follows; Section 2 describes different methodologies to develop a sensitivity analysis. Section 3 introduces the proposed bi-phase sensitivity analysis; in Section 4, the model to evaluate resilience, used to apply the sensitivity analysis, is briefly explained, and in Section 5, a case of study is developed. Finally, in Section 6 some conclusions and future research lines are drawn.

2 SENSITIVITY ANALYSIS

A sensitivity analysis can be defined as “the study of how uncertainty in the output of a model (numerical or otherwise) can be apportioned to different sources of uncertainty in the model input” [1].

Some of the main reasons to develop a sensitivity analysis are highlighted:

- The model parameters require additional research for strengthening the knowledge base, thereby the output uncertainty is reduced.

- Some model parameters might have a negligible contribution, therefore they can be eliminated from the final model. This would result in a reduction of the required computational time.
- Bigger effort should be made in defining those variables and parameters with larger contribution into the model. The sensitivity analysis allows the identification of those important variables and parameters.
- The consequences in the results can be determined when changing a given input parameter or variable.

Different methodologies to analyse the sensitivity have been developed previously.

An initial classification can differentiate between global and local methodologies, based on two different levels to carry out a sensitivity analysis.

2.1 Local methodologies

A local sensitivity analysis evaluates sensitivity at one point in the parameter hyperspace. The local techniques aim to estimate the local impact of a parameter on the model output. A sensitivity coefficient is obtained, which is basically the ratio of the change in output to the change in input while all other parameters remain constant [2].

Some methodologies to develop a local analysis are, (a) differential sensitivity analysis, based on partial differentiation of the model in aggregated form; (b) one-at-a-time measures, which is one of the simplest method to develop a sensitivity analysis, is based on repeatedly varying one parameter at a time while holding the others fixed and (c) the sensitivity index, which calculates the output percentage difference when varying one input parameter from its minimum value to its maximum value.

2.2 Global methodologies

Global sampling methods scan in a random or systematic way the entire range of possible parameter values and possible parameter sets. These techniques analyze the whole parameter space at once. Some methodologies to develop a global analysis are, (a) simple random sampling, using Monte-Carlo analysis. This method works by generating a random value of the variable analysed and scaling this one to the target variable via its probability distribution. (b) Stratified sampling, which represents an improvement over simple random sampling by forcing the sample to conform to the whole distribution being analysed.

Any reduction in the number of simulations required for a Monte-Carlo analysis will result in a reduction in computational effort, for that reason, some techniques have evolved and can outperform the simple random sampling.

As an example, (c) the Latin-Hypercube simulation is a method of sampling that can be used to produce input values for estimation of expectations of functions of output variables

[3]. The method works by dividing the input into strata and then generating samples so that the value generated for each parameter comes from a different stratum [4].

3 METHODOLOGY

The applied methodology is an integration of two phases, a local into a global sensitivity method. This paper presents a combination of One-At-a-Time (OAT) for the local sensitivity and Latin Hypercube (LH) sampling for a global approach, [5].

3.1 Upper level approach

In order to address the first phase of this sensitivity methodology, a sampling strategy is carried out.

The selected global sampling procedure is the LH that allows the reduction of the sample size. Due to the importance of the pairing procedure, the method Translational Propagation algorithm proposed by [6] has been implemented in this analysis. The main advantage of this methodology is that it requires virtually no computational time. When the sample is obtained, the local sensitivity analysis can be accomplished as follows. Considering that the total space is covered and the sample is a reliable and robust representation of the entire space, the model is evaluated for each point of the sample, using a local sensitivity analysis.

3.2 Lower level approach

On the other hand, the second phase of this methodology is based on a local technique to evaluate the sensitivity.

According to the OAT technique, the analysis is performed by modifying every variable in each sample point in a percentage to calculate the corresponding model response in that close point. It is important to modify only one variable each time to identify the behaviour of the modified variable. Measuring the variation, according to the OAT methodology, the sensitivity in each point is captured.

This local method is as simple as efficient, however this process can become quite intensive with larger models. Then, instead of applying it in a large number of points to cover the entire range of the parameters, a global methodology has been chosen to obtain a sample of points that represents the different variables.

The formulation to assess the sensitivity is based on the concept of derivative, that is

$$\xi = \frac{R_d^+(x, Y) - R(Z)}{d}, \quad x, Y \in Z, \quad (1)$$

where Z is the set of variables involved in the model, x , is the modified variable and Y , the subset of variables which remain constant. R is model response calculated for the initial parameter set Z and R_d^+ is the model response when one parameter has been increased by a percentage, d . Sensitivity, denoted by ξ , is a dimensionless parameter.

The percentage, d , is also a critical point, as small values can show the instabilities of the model, being this behavior not

according with the tendency of the model. However, if this value is too large, the derivative loses its meaning.

4 MODEL

This methodology to develop a sensitivity analysis, is implemented for a complex model. In this case, the model evaluates the behaviour of a traffic network when an extreme weather event takes place, determining the resilience of the transport network ([7]).

The most common definition of resilience was given by [6], as “the capacity to absorb shocks gracefully”, and a further description of this can be found in [10].

With the aim of quantifying the resilience, [7] propose a “Dynamic Equilibrium-Restricted Assignment Model” (DERAM), which allows the simulation of the network behaviour when a disruptive event occurs. This approach permits the inclusion of the stress level of the system together with the extra cost generated by the hazard. This model proposes that the network behaviour is restricted by a system impedance, α .

The perturbation resilience is defined between (0, 100), 100% being the optimum value. Moreover, a cost threshold is included to assume the system break-down. This value restricts the perturbation resilience and is the limit-state associated with the failure of the travel cost network due to the extreme overcost generated by a strong perturbation. Although the system could theoretically recover, it would imply an unacceptable effort by the system.

With the goal of improving the resilience of a network when affected by a hazard and having a better understanding of the effects of extreme weather events, the weaknesses of the system should be identified. Therefore, the resilience of a network can be enhanced with the improvement of the most influential variables of the model. With this aim, a sensitivity analysis is carried out.

5 STUDY CASE

This methodology is applied in a simple traffic network to analyze the sensitivity of a set of variables.

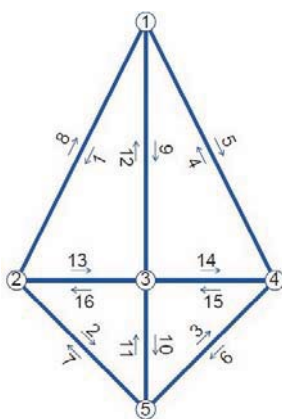


Figure 1. Network.

This traffic network consists of 5 nodes (cities), 16 links (roads) and 10 routes, (see Table 2).

The set of variables used for the sensitivity analysis together with its characteristics are shown in Table 1.

Table 1. Statistical distributions of the parameters

Links	Parameters	Distribution	Distribution parameters
Affected	$h(t)$	Beta	$\alpha=1.2, \beta=3$
No-affected	$h(t)$	Deterministic	0.001
Affected	p_a	Beta	$\alpha=1.2, \beta=2.5$
No-affected	p_a	Deterministic	0.001
All links	α	Beta	$\alpha=1.2, \beta=1.2$
Affected	β_a	Gamma	$k=2.9, \theta=0.5$
No-affected	β_a	Deterministic	0.83
Affected	γ_a	Gamma	$k=7, \theta=0.37$
No-affected	γ_a	Deterministic	4

Where β_a and γ_a are parameters related to the traffic characteristics; $h(t)$ is the hazard intensity whose range is (0,1), and p_a is the specific sensitivity of each link to a given hazard. For instance, in the case of pluvial flooding, p_a depends on the catchment area, slope of the road, type of pavement, existence of element of protection, etc. Subscript a implies association with link a .

For the following examples, the variables analysed will be the ones related with the hazard, i.e., $h(t)$, p_a and α . The sample size selected has been 25 points and the percentages of variation, d , are 1, 5, 10%. Figures 3-6 show the results associated with the percentage of 10%, since the results for the other percentages follow a similar tendency, excluding the case of the 1%, where some numerical instabilities of the model were identified.

For a detailed study of the rest of the parameters, see [9].

The sensitivity analysis is carried out by presenting different scenarios, to figure out the influence of the climatological parameters in the system. Moreover, a second goal is to demonstrate that the sensitivity depends on other factors as the area affected by the hazard, or the different possibilities that the users have to avoid the hazard (redundancy of the network).

In order to reach this goal, two sections are presented, (a) depending on the area affected by the hazard and (b) depending on the redundancy of the network.

5.1 Considering different affected areas.

To increase the knowledge and the understanding of the effect of the intensity of the hazard, three cases has been developed, since the influence of this parameter is crucial.

To that end, each of the cases has a different area damaged by the hazard, see Figure 2. First case (green area in Figure 2), only the links between the node 2 and node 3 are exposed to the climatological event. Second case (red area in Figure 2), half of the network is altered by the perturbation and, finally, in the third case, the entire network is affected.

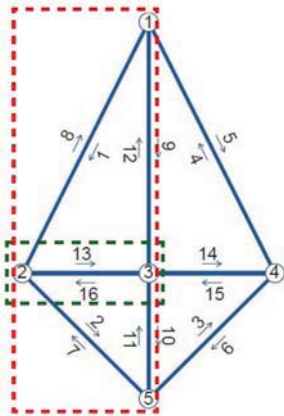


Figure 2. Areas affected by the hazard.

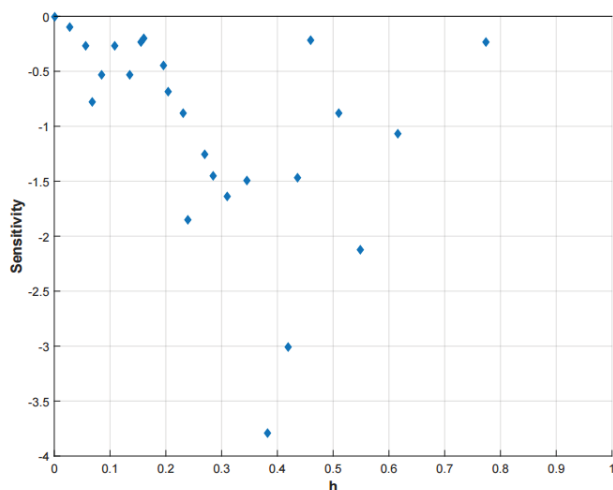


Figure 3. Sensitivity of h, links damaged 13-16.

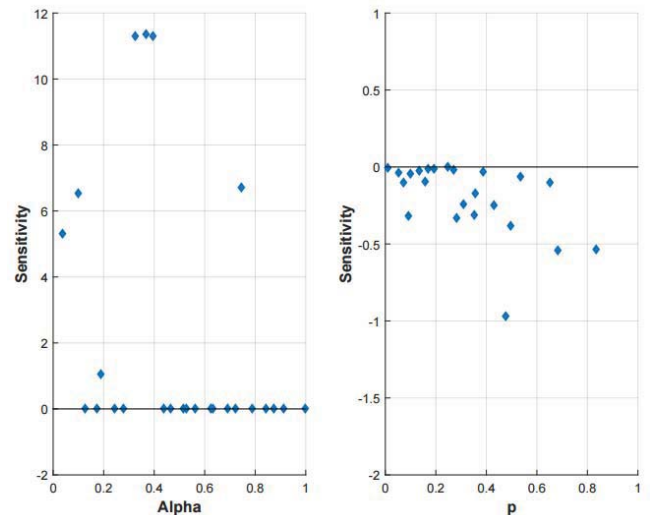


Figure 4. Sensitivity of alpha and p_a , links damaged 13-16.

Analyzing the first case, where only the links 13-16 are affected by the hazard, it is evident that the intensity of the hazard, $h(t)$ (Figure 3) has a larger sensitivity than p_a (Figure 4). In Figure 3, most of the points are within the range of 0 to -2. Some of them can reach higher values from -2 to -4. On the other hand, the sensitivity values of p_a do not go over -1, remaining a high proportion below -0.5.

It is noted that an increment in the values of $h(t)$ and p_a implies a reduction of the resilience, as evidenced by the negative sensitivity of these parameters.

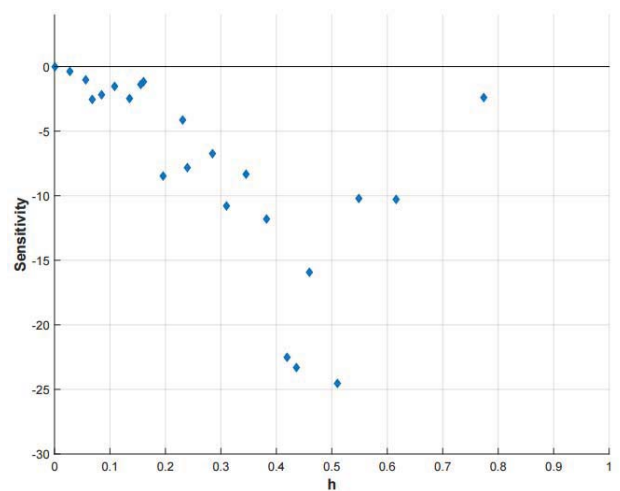
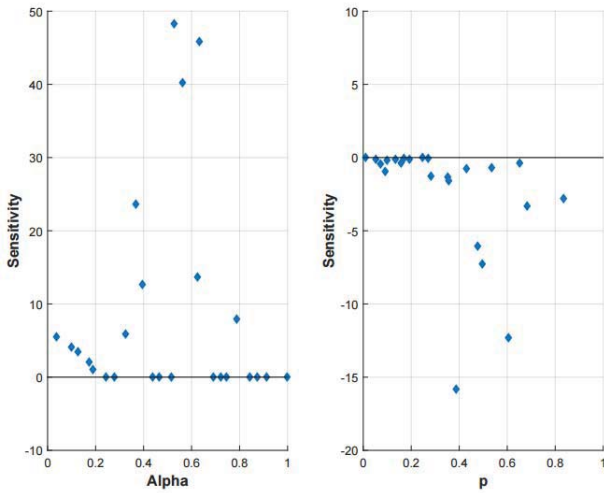
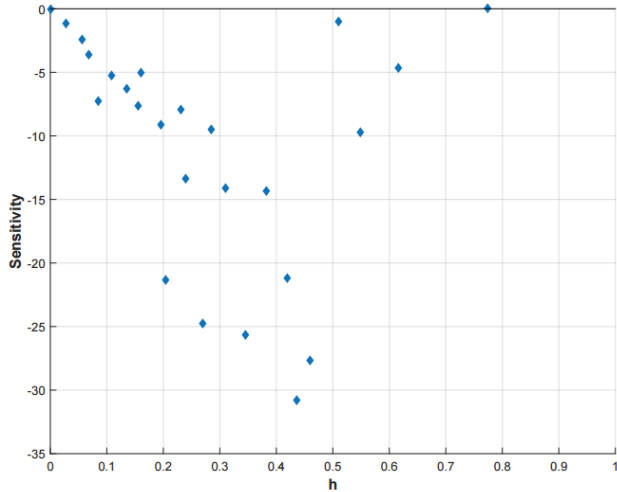
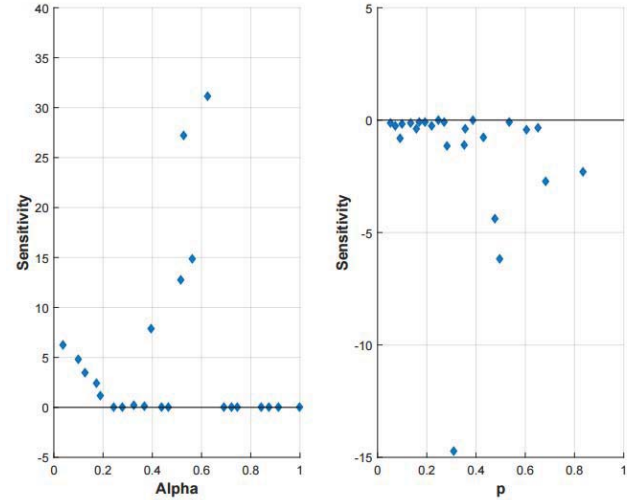


Figure 5. Sensitivity of h, half network damaged.

Figure 6. Sensitivity of alpha and p_a , half network damaged.

In the second case, Figures 5 and 6 show the sensitivity of the three parameters, i.e. $h(t)$, α and p_a when half of the network is exposed to the hazard. As can be noted from the Figures, the sensitivity of all the parameters related to the hazard increases substantially. When compared with the previous example, the values are approximately 10 times larger for $h(t)$ and p_a and five times for α . This happens because the area damaged by the hazard is larger for the second case. In addition, the greater sensitivity of $h(t)$ is corroborated with this example.

Figure 7. Sensitivity of h , all links damaged.Figure 8. Sensitivity alpha and p_a , all links damaged.

Finally, the third case, shown in Figures 7 and 8, confirms that the values for the sensitivity of $h(t)$ are even larger, since that the whole network is damaged by the hazard. Furthermore, the values of p_a continue to be smaller than $h(t)$.

5.2 Considering the redundancy.

In the previous cases, the focus was mainly in two parameters, $h(t)$ and p . However, the parameter alpha, the system impedance, reaches the highest values, becoming a very relevant variable. It is noted that an increment of α implies an increment of the resilience.

The influence of alpha on the resilience index is larger when users play an active role, that is, when they can improve their situation by changing their routes.

Therefore, the sensitivity of this parameter is going to depend mainly in the options that the users have to change, that is, the redundancy of the system.

Table 2. Routes, defined by the links.

Routes	Example 1	Example 2
1-13-14	✓	✓
9-10-3	✓	✓
2-11-12	✓	✓
13-2	✓	✓
3-4	✓	✓
7-8	✓	✓
5-15-16	✓	✓
5-6-7	✓	✓
9-10	✓	
1-2	✓	

To prove the considerable variability of this parameter, a second example has been introduced. For this new case, the number of routes has been reduced, as shown in table 2, using the case where half of the network is affected. Consequently, the change options of the users have been reduced and the active role that they can play has been decreased.

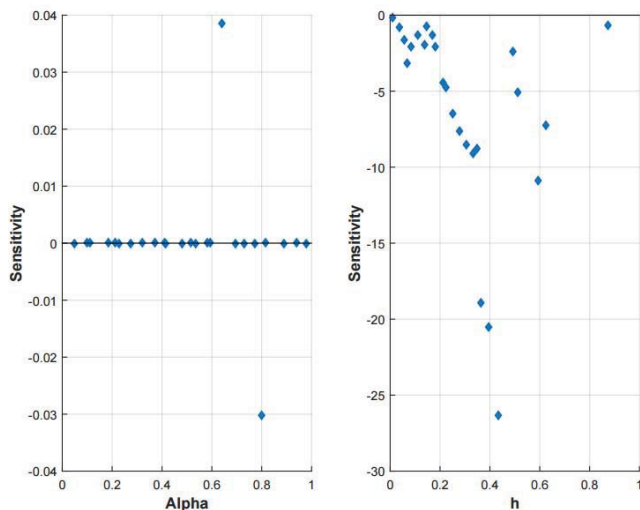


Figure 9. Sensitivity alpha and h , example 2.

In Figure 9 is shown that when the change possibilities are reduced, the sensitivity of alpha decrease largely. In this case, example 2, the sensitivity of alpha is negligible, when in all the previous examples (see Figures 3-8), alpha is the most sensitive parameter.

6 CONCLUSIONS

The selection of an adequate methodology to analyse the sensitivity of the parameters should include a statistical approach to reduce the computational times and the number of chosen points to cover the entire range of the parameters.

For that reason, a mixed methodology to analyse the sensitivity is proposed, which include local (One-At-a-Time) and global techniques (Latin Hypercube). This kind of methodology is justified when a large number of variables are involved, because local methods are very efficient but they do not cover the entire space; whereas, global methods provide a robust and reliable approach but the computational cost could be too high in complex models.

In addition, the following aspects can be highlighted:

- The pairing procedure known as the Translational Propagation algorithm, has been implemented, which requires minimal computational times.
- The sensitivity analysis shows the important role of the hazard intensity.
- The area affected by the hazard modifies the sensitivity of the hazard intensity substantially. Therefore, when the zone exposed to the hazard

increases, the values of the sensitivity of this parameter rise.

- The analysis reflects the significant influence of the system impedance, with the option of becoming as important as the hazards intensity. However, this only happens when users play an active role, that is, when they can improve their situation by changing their routes. If the users do not have route options and the redundancy of the network is insignificant, it is demonstrated that the parameter is not relevant in the sensitivity analysis.

Future research will provide an extension of this methodology, including aspects such as the topology of the network, the road capacity and the traffic demand.

ACKNOWLEDGMENTS

RAIN project has received funding from the European Union's Seventh Framework Programme for research, technological development and demonstration under grant agreement no 608166.

REFERENCES

- [1] Saltelli, A., Tarantola, S., Campolongo, F., & Ratto, M. (2004). Sensitivity analysis in practice: a guide to assessing scientific models. John Wiley & Sons.
- [2] Krieger, T.J., Durston, C., and Albright, D.C.: 1977. 'Statistical Determination of Effective Variables in Sensitivity Analysis', Trans. Am. Nuc. Soc. 28, 515-516.
- [3] McKay, M. D., Conover, W. J., and Beckman, R. J. (1979), "A Comparison of Three Methods for Selecting Values of Input Variables in the Analysis of Output From a Computer Code," Technometrics, 21, 239-245.
- [4] Helton J.C. and Davis F.J. 2003. "Latin hypercube sampling and the propagation of uncertainty in analyses of complex systems", Reliability Engineering and System Safety (81), pages 23-69, Elsevier.
- [5] Van Griensven, A., Meixner, T., Grunwald, S., Bishop, T., Diluzio, M., & Srinivasan, R. (2006). A global sensitivity analysis tool for the parameters of multi-variable catchment models. Journal of hydrology, 324(1), 10-23.
- [6] Viana, F. A., Venter, G., & Balabanov, V. (2010). An algorithm for fast optimal Latin hypercube design of experiments. International journal for numerical methods in engineering, 82(2), 135-156.
- [7] Nogal, M., O'Connor, A., Caulfield, B., and Martinez-Pastor, B. (2015a). Resilience of Traffic Networks: From the Perturbation to Recovery via a Dynamic Restricted Equilibrium Model. Reliability Engineering & System Safety, Submitted.
- [8] Foster, Harold D. 1993. Resilience Theory and System Evaluation. In Verification and Validation of Complex Systems: Human Factors Issues, Vol. 110 of NATO ASI Series edited by J. A. Wise, David V. Hopkin, and P. Stager. 35-60. Springer Berlin Heidelberg.
- [9] Martinez-Pastor, B., Nogal, M., O'Connor, A., & Caulfield, B. (2016). A Sensitivity Analysis of a Dynamic Restricted Equilibrium Model to Evaluate the Traffic Network Resilience. In Transportation Research Board 95th Annual Meeting (No. 16-3456).
- [10] Martinez-Pastor, B., Nogal, M., O'Connor, A., & Caulfield, B. Evaluation of Resilience in Traffic Networks: Model and Characteristics. ITRN Conference 2015.

Resources available for bio-SNG produced via a nationwide system of gasification and methanation in Ireland

Alessandro Singlitico^{1,2,3}, Jamie Goggins^{2,3,4}, Rory F. D. Monaghan^{1,2,3}

¹ Mechanical Engineering, National University of Ireland Galway, Galway, Ireland

² Ryan Institute for Environmental, Marine and Energy Research, Ireland

³ Centre for Marine and Renewable Energy (MaREI), Galway, Ireland

⁴ Civil Engineering, National University of Ireland Galway, Galway, Ireland

Email: a.singlitico1@nuigalway.ie

ABSTRACT: Ireland's most recent Energy White Paper proposes the guidelines for a radical transformation in the energy sector in Ireland and an enormous reduction of CO₂ emissions from 2015 to 2050. Biomass-derived synthetic natural gas (bio-SNG) via gasification and methanation (GaM) represents a potential route to decarbonise the use of natural gas. This work presents the initial assessments of suitable resource availability and performs GIS-based (Geographic Information System) mapping of them. The ultimate goal of the work is to design a GaM-based bio-SNG production and distribution network that is environmentally and economically sustainable. Results show that the energy potential of the feedstock for GaM has the potential to be 300% of current bioenergy use, utilising wastes, residues and energy crops grown exclusively on low-value marginal land. The potential key role of energy crops on marginal land is highlighted for further study. Future steps of the work will involve uncertainty quantification, full life cycle assessment and techno-economic analysis of the proposed system.

KEY WORDS: Bio-SNG; Synthetic Natural Gas; Gasification; Methanation; Renewable Energy; Life cycle Assessment; GIS.

1 INTRODUCTION

Natural gas (NG) accounts for 29% of total primary energy requirement (TPER) in Ireland, providing 15% of final energy use and 48% of fuels used for electricity generation. 96% of the NG used in Ireland in 2013 was imported [1]. In the same year the overall renewable energy contribution to total primary energy supply was 6.8%. Biomass is the second largest renewable energy resource, with a TPER of 279 ktoe (kilotonnes of oil equivalent), 31% of the total renewable share. 49 ktoe are generated from renewable wastes and 58 ktoe from non-renewable ones [2]. The Sustainable Energy Authority of Ireland (SEAI) forecast a large availability and variety of biomass resources suitable for combustion (i.e. thermochemical conversion) in Ireland, from waste products to energy crops [3]. Gasification and methanation (GaM) is a higher value energy conversion route than combustion, due to the fact its product, Bio-SNG (biomass-derived synthetic natural gas), can be injected into the gas grid [4]. This takes advantage of the existing NG infrastructure and NG's role as a fuel of systemic economic importance that can be used for heating, transport fuel and electricity generation.

Life cycle assessment can be used to study and optimise an overall energy system based on GaM technology, minimizing emissions and proposed overall cost, to make it environmentally sustainable and commercially viable. The objectives of this work is to evaluate the energy potential of possible feedstock categories including agriculture and forestry residues, municipal solid waste (MSW), digestate from anaerobic digestion (AD) facilities, and dedicated energy crops grown on currently under-utilised marginal land.

The first part of this work consists of reviews of literature and national reports in order to obtain a preliminary quantification of available bioenergy resources in the

Republic of Ireland (ROI) to design a nationwide bioenergy system. The resources identified in this assessment include indigenous second generation biofuels, which can be used as feedstock for thermochemical conversion to bio-SNG through the GaM processes. In the second part of the work the spatial distributions of the resources in the territory of ROI is presented with ArcGIS. Knowing the exact location of possible highly intense bioenergy areas is important information for siting and sizing of future GaM plants. In this study there are a large number of uncertain parameters that affect the energy recoverable from each feedstock and that can impact on the design of a bioenergy system.

2 RESOURCE ASSESSMENT

This study focuses on second generation biofuels, which do not compete for land use with agri-food or other industries. The resources studied are: agricultural residues, energy crops represented by Miscanthus in this case, forestry residues, dry mixed non-recyclable MSW, and digestate from AD facilities. The first three categories, which are lignocellulosic materials, are widely recognized as feedstock for gasification [5], while MSW and digestate are considered possibilities for waste-to-energy solutions [6] [7], which address waste management as well as energy challenges. The global energy potential (E) from the studied resources is given by:

$$E = E_{ag} + E_{EC} + E_{for} + E_{MSW} + E_{dig} \quad (1)$$

Where E_{ag} , E_{EC} , E_{for} , E_{MSW} and E_{dig} are the energy potentials in units of kilotonnes of oil equivalent of agricultural residues, energy crops product, forest residues, MSW and digestate respectively.

Table 1. Energy potential physically available from agricultural residues.

Reference	[8]	[9]	Teagasc [10]			SEAI [11]		
Straw source i	LHV_i [GJ/t]	A_i [kha]	Y_i [t/ha]	m_i [kt]	E_i [ktoe]	Y_i [t/ha]	m_i [kt]	E_i [ktoe]
Winter Wheat	16.25	65.1	4.2	273.0	106.1	8.0	520.8	202.1
Spring Wheat	16.25	6.5	3.0	19.5	7.6	6.0	39.0	15.1
Winter Oats	15.00	10.1	4.7	47.5	17.0	7.0	70.7	25.3
Spring Oats	15.00	8.5	3.9	33.1	11.9	5.6	47.6	17.1
Winter Barley	14.45	60.1	4.2	252.4	87.1	5.0	300.5	103.7
Spring Barley	14.45	155.6	3.6	560.2	193.3	4.0	622.4	214.8
Totals								
Theoretical		305.9		1,186.1	422.9		1,601.0	578.1
Physically available (5%)				593	21.1		80.05	28.9

2.1 Agricultural Residues

In the cases of agricultural residues and energy crops, the available annual energy potential (E_i) of a feedstock i (in units of ktoe) is calculated using equations (2) and (3):

$$E_i = m_i \cdot LHV_i \quad (2)$$

$$m_i = A_i \cdot Y_i \quad (3)$$

Where m_i is the available annual quantity in tonnes of feedstock, LHV_i is its lower heating value (LHV) in kilotonnes of oil equivalent per tonne. In the case of residues, the quantity available is proportional to the area covered by that crop in hectares (A_i) and the yield of residues per hectare in tonnes per hectare (Y_i). In case of agricultural residues, ranges of yield of residues at 15% of MC values from Teagasc [10] and the SEAI [11] [3], and LHV at 15% of MC in kilotonnes per hectare from the ECN Phyllis2 database [8] give a theoretical energy potential of 420-580 ktoe, which is summarised in Table 1. However only 5% of this quantity is available for energy production, as around 95% is used for animal bedding and mushroom compost [3]. Thus the final energy availability from agriculture residues (E_{ag}) is estimated at around 20-30 ktoe. Note values of A_i , m_i and LHV are given in units of kilo-hectares (kha), kilotonnes (kt) and GJ per tonnes (GJ/t).

2.2 Energy Crops

In this work only energy crops that do not compete with existing industries have been considered, which therefore rules out existing methods of energy crop production in Ireland, including rape seed oil. This implies that only energy crops grown on unutilised or under-utilised land should be considered. Rough grazing areas can be repurposed to energy crop cultivation without impinging on existing activities. From the last Census of Agriculture (2010), 436,000 ha are devoted to rough grazing [12]. Part of this area includes Special Areas of Conservation (SACs), inaccessible, rocky or acid soil areas. Excluding this areas, the available rough grazing area is reduced to 140,130 ha. The yield of Miscanthus at dry matter is considered to be 10 t_{DM}/ha from Teagasc [13], considering a reasonable average-low yield for marginal lands, and its LHV is 18 GJ/t from the ECN Phyllis2

database [8]. From equations (2) and (3) it results 602.33 ktoe of energy potential (E_{ec}).

2.3 Forestry Residues

Forests cover 731,650 ha, 10.5% of land area of ROI, of which 54.1% is owned by Coillte [14]. According to the Irish afforestation program, the land covered by forest is set to increase by 10,000 ha every year until 2035 [15]. Due to a lack of data at present, forestry residues energy potential (E_{for}) is assumed to be 89 ktoe [3]. This figure is currently undergoing detailed assessment and will be presented in future publications.

2.4 Municipal Solid Waste

Irish Municipal Solid Waste management is predominantly based on landfill. 1,000,000 t of waste is landfilled annually, which represents 41% of the total MSW managed in 2012 [16].

Table 2. Energy potential available from MSW.

Reference	[17]			
Waste composition k	LHV_k [GJ/t]	$m_{H,k}$ [kt]	$m_{NH,k}$ [kt]	E_k [ktoe]
Plastic	20.44	80.2	47.3	61
Organic waste	1.912	141.6	184.7	15
Paper and cardboard	6.44	94.9	129.1	34
Textiles	11.79	43.1	21.5	18
Wood	9.31	7.8	1.7	2
Fines	2.584	69.0	4.4	5
Total		435.9	388.7	135

The recyclable component of MSW is recycled, the organic fraction is digested/composted, and the remaining dry mixed residues are landfilled or incinerated. The landfilled portion of MSW contains a combination of plastic, wood, organic matter, paper, wood textiles which can be processed by gasification. Equation (4) is used to calculate the potential from dry mixed waste (E_{MSW}):

$$E_{MSW} = \sum_k [(x_{k,H} \cdot m_H) + (x_{k,NH} \cdot m_{NH})] \cdot LHV_k \quad (4)$$

Where $x_{k,H}$ and $x_{k,NH}$ are the mass fractions of material k in the overall household and non-household landfilled waste mass, m_H and m_{NH} respectively in tonnes, and LHV_k is the LHV of each material k from the World Bank database [17] in kilotonnes of oil equivalent per tonnes. Table 2 summarises the energy potential of MSW. Note that values of m_i and LHV are given in units of kilotonnes (kt) and GJ per tonnes (GJ/t).

2.5 Digestate from AD Facilities

Digestate from AD facilities is another potential energy resource. In 2013 only 11 ktOE was derived from biogas [2], while most of the energy content is left in the digestate. Equation (5) and (6) are used to calculate the energy potential (E_{dig}):

$$m_{dig} = m_{in} \cdot (1 - y) \quad (5)$$

$$E_{dig} = LHV_{dig} \cdot m_{dig} \quad (6)$$

Where m_{in} is the input mass entering the digester according to the Environmental Protection Agency (EPA) [18] in units of tonnes, y is the organic matter reduction factor, m_{dig} is the output digestate in tonnes, and LHV_{dig} is the LHV in units of kilotonnes of oil equivalent per tonne. Two limiting scenarios are considered, assuming organic matter reduction (OMR) due to AD of 40 and 60%. Table 3 shows the results of these scenarios. Note that values of m_i and LHV are given in units of kilotonnes (kt) and GJ per tonnes (GJ/t).

Table 3. Energy potential available from digestate.

Reference	[8]	[18]			
	LHV_{dig} [GJ/t]	y	m_{in} [kt]	m_{dig} [kt]	E_{dig} [ktOE]
Low OMR	11.17	0.4	270.6	162.4	43
High OMR	11.17	0.6	270.6	108.2	29

2.6 Total Potential Resource

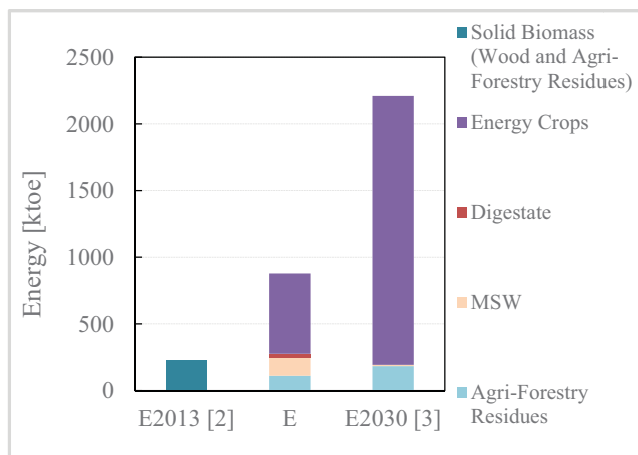


Figure 1. Comparison of calculated total potential bio-SNG resource (E) with current thermochemical use of biomass (E_{2013}), and the maximum forecast thermochemical bioenergy use in 2030 (E_{2030}).

Adding the resource estimates described above gives a total potential bio-SNG resource (E) of 1,762-1,783 ktOE. Figure 1 compares this lower value of E to the current thermochemical use (i.e. direct combustion) of biomass in Ireland (E_{2013}) [2], and the maximum forecast thermochemical bioenergy use in 2030 (E_{2030}) [3].

3 SPATIAL DISTRIBUTION

Knowledge of resource spatial distribution is crucial for life cycle assessment of large scale production of bio-SNG, which can be used to identify areas of high resource intensity (hot spots) and to optimise the supply chain. ArcGIS software is used to visualise spatial data and to create layers for each resource. Figure 2 to Figure 6 show the intensity of cereal crops, private forests, state forests and rough grazing areas, from which residues and energy crops can be harvested. The intensity of these resource locations is visualised for every electoral division (ED) in Ireland and is calculated by Equation (7).

$$I_{j,l} = \frac{A_{j,l}}{A_{ED,l}} \quad (7)$$

Where $A_{j,l}$ is the area covered by the specific source of biomass j (cereal crops, forest or rough grazing land) in the electoral division l , and $A_{ED,l}$ is the total area of the electoral division l , all in units of hectares, and I is the intensity of the source in each ED.

There are 3,409 EDs in Ireland. All the data for each ED are considered uniformly distributed. All the maps are in the projected coordinate systems IREN95 Irish Transverse Mercator. The distribution of production of MSW destined for landfill, as well as the locations of current landfill and AD facilities in Ireland are shown in Figure 7.

Data for cereal agriculture is presented in two ways Figure 2 and Figure 3. Figure 2 shows the total cereal crop intensity distribution (data from CSO via personal communication) while Figure 3 shows the proportion of each type of cereal (winter and spring barley, oats, wheat and other cereals) in each county [12]. The two figures are used because data on individual cereal crop area per ED is not available. What is evident from the maps is that cereals cultivation is focused in the South and East, with abundant spring barley.

Forestry activity, both state-operated and private is shown to be dispersed throughout the ROI (Figure 4 and Figure 5). These maps are obtained from Coillte and the Forest07 dataset from the Department of Agriculture, Food and the Marine via personal communication. With the Afforestation Scheme, the private forest area will expand until 2035 [15]. Residues from clear felling and thinning, which are too small for the timber industry, can be collected from the areas identified in the figures.

The total rough grazing area is estimated to be 436,377 ha in the Census of Agriculture 2010 [12]. This includes mountains and rocky land on which the livestock have grazed during that year, including SACs. Overlaying the SAC boundaries [19], areas the areas with slope greater than 15% and altitude greater than 1000 m [20], rocky areas [21] and acid soil areas (pH lower than 5) [22], the amount of available rough grazing area in non-protected land is 140,130 ha (Figure 6). This equates to 2% of ROI land area. Rough

grazing area can be evaluated for the cultivation of energy crops such as Miscanthus, which is highly adaptive to different kind of soils [23].

Figure 7 shows the distribution of the production of MSW destined for landfill, assuming uniform per capita production. It also shows the landfill facilities in the ROI in which MSW is managed. AD facilities are also included in the map for the use of digestate as GaM feedstock.

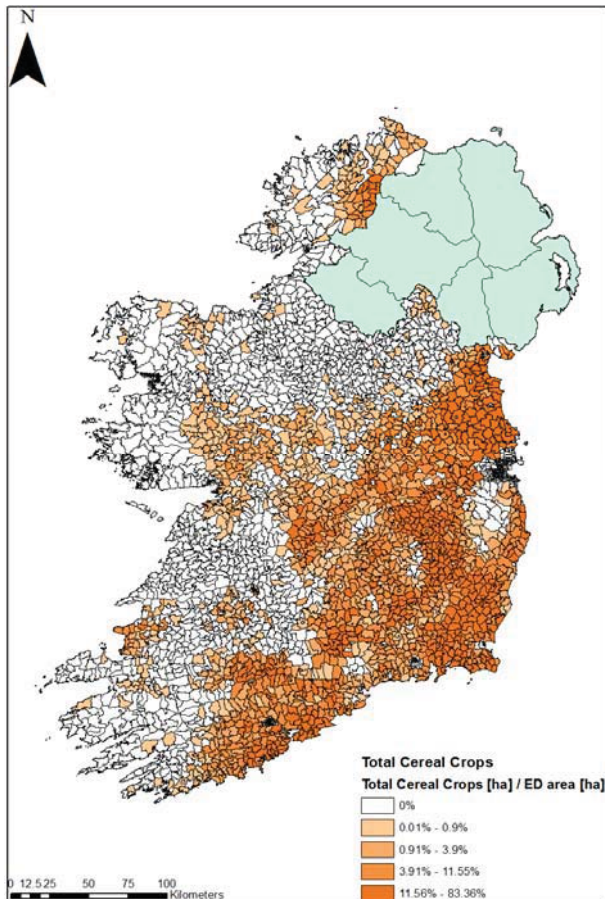


Figure 2. Total cereal crops intensity distribution by ED.

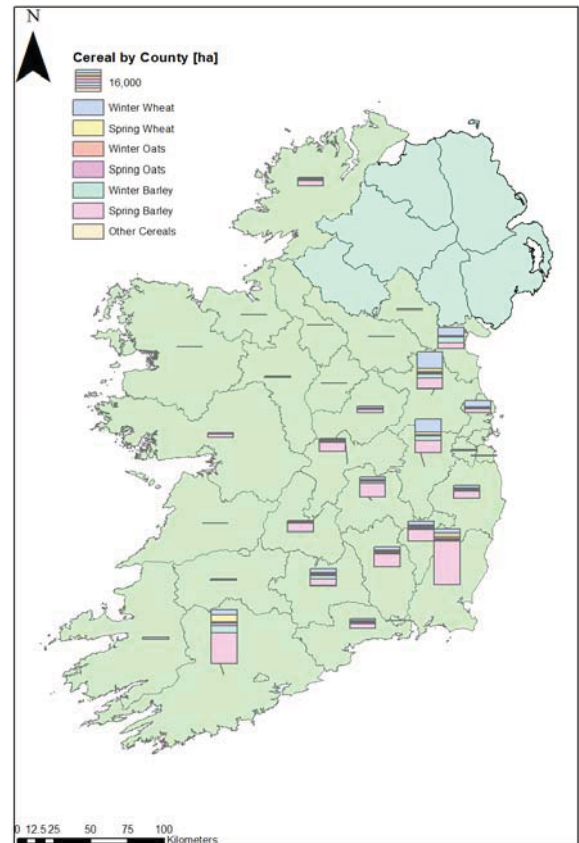


Figure 3. Breakdown of cereal type production by county.

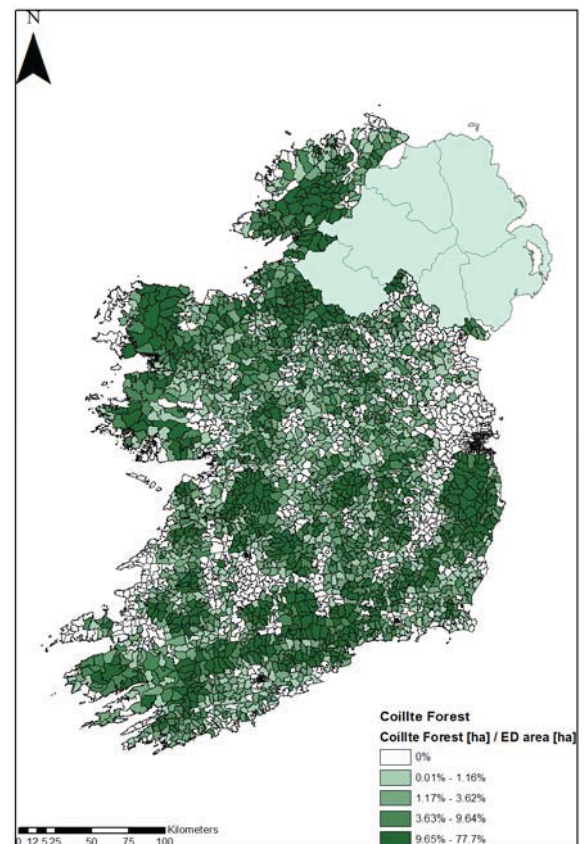


Figure 4. Coillte state-operated forestry intensity by ED.

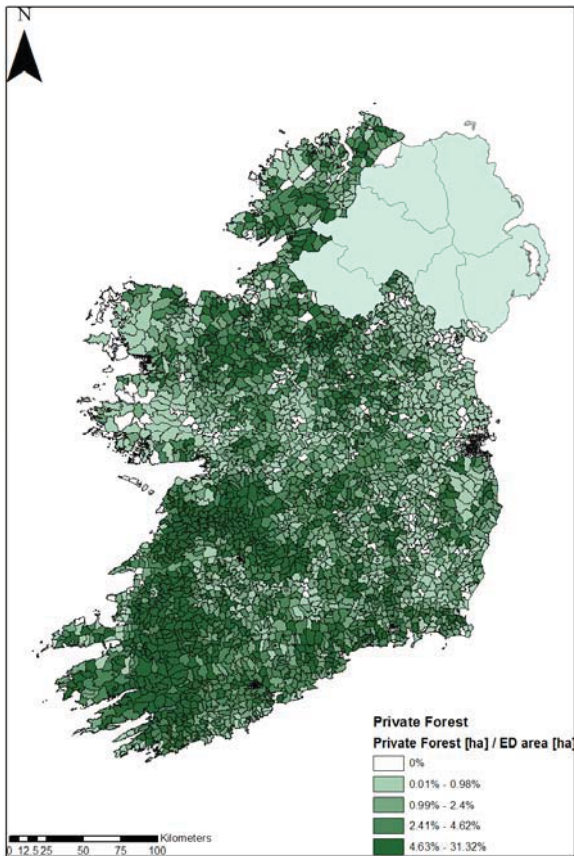


Figure 5. Private forestry intensity by ED.

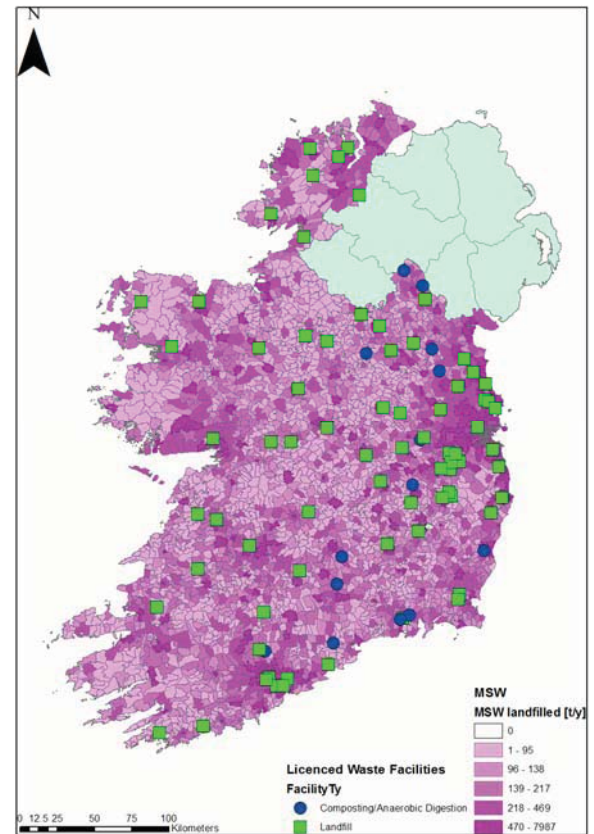


Figure 7. Production of MSW destined for landfill, and locations of landfill and AD facilities.

4 DISCUSSION OF RESULTS

This study shows the approximate potential of resources for producing bio-SNG through gasification and methanation in Ireland. Waste and residues could cover the current share of solid biomass in the TPER by producing higher-value bio-SNG through GaM, when compared to traditional biomass combustion. This work also shows the potential key role of energy crops, such as *Miscanthus*, which can be cultivated on low-value marginal land and can lead to an immense expansion of bioenergy potential, while bringing local economic benefits. With the introduction of energy crops such as *Miscanthus*, 880 ktoe would be available annually, 300% the current biomass energy supply.

The use of waste and residues can lead to more sustainable waste management and positive side-effects. Recovering MSW could reduce the practice of landfilling. Using digestate from AD facilities as feedstock for gasification could extract part of the energy potential left in the solid matter after digestion. Moreover typical gasification fly ashes are unattractive as fertilizer, because of their high carbon content. They can however be reused as fuel, in an indirect gasifier, which is suitable for bio-SNG production [24], producing low-carbon ashes, whose mineral content (K, Mg, Ca, Na, S) make them a suitable raw material for fertilizer production [25].

The spatial distribution of the resources is important information for the design of a nationwide bioenergy system, which will ultimately include pre-treatment, transport, storage,

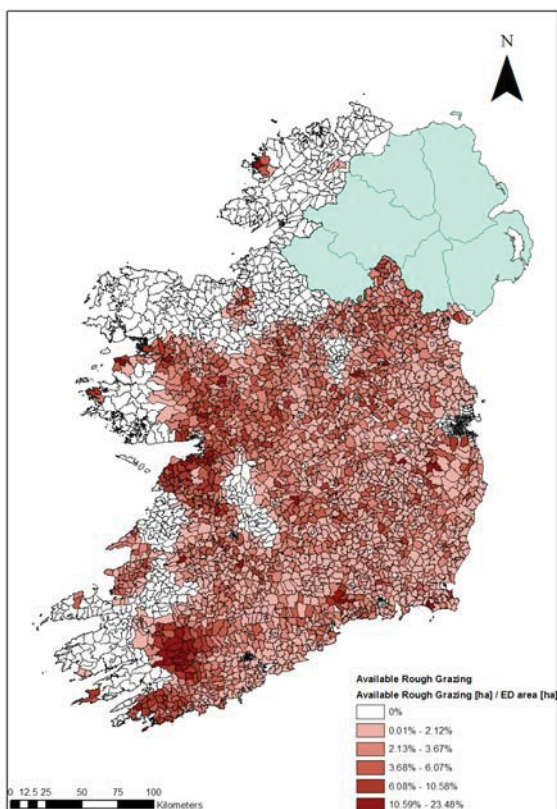


Figure 6. Available rough grazing area intensity by ED.

conversion and injection in the grid of the produced bio-SNG. This can inform the economic viability of the development of individual areas, siting and sizing for plants, the volume of resources involved and their transport and the distance travelled.

5 CONCLUSIONS AND FUTURE WORK

This resource assessment is the first stage of a larger research work which consists of a life cycle assessment production bio-SNG production via a nationwide system of gasification and methanation in Ireland. The resources considered include agricultural residues, forestry residues, energy crops, MSW and digestate from AD facilities. This study has identified the potentially crucial role to be played by energy crop cultivation on marginal low-value land. However, the uncertainties associated with these findings are unknown, and possibly very high. Therefore the next steps of this work are to carry out a detailed assessment of the key variables needed to calculate Miscanthus yield in poor quality soils. After this, the levels of uncertainty associated with the model will be studied and quantified. The quality of the primary data required by the model can be evaluated in a pedigree matrix [26] which will quantify the quality by five indexes: reliability, completeness, temporal correlation, geographical correlation, future technological correlation and sample size. Flowcharts of data manipulation have already been drawn to track the flows of data and uncertainty propagation [27] and will be maintained as points of reference for each resource.

ACKNOWLEDGMENTS

This research is co-funded by Science Foundation Ireland and Gas Networks Ireland through the Marine and Renewable Energy Ireland (MaREI) Research Centre. The authors wish to thank Teagasc, Coillte, Department of Agriculture, Food and the Marine, and Central Statistics Office of Ireland for providing data for this work.

NOMENCLATURE

A	Area
AD	Anaerobic Digestion
Bio-SNG	Bio-Synthetic Natural Gas
E	Energy
ED	Electoral Division
GaM	Gasification and Methanation
GHG	Greenhouse Gases
GIS	Geographic Information System
LHV	Lower Heating Value
m	Mass
MC	Moisture Content
MSW	Municipal Solid Waste
NG	Natural Gas
OMR	Organic Matter Reduction
ROI	Republic of Ireland
SAC	Special Area of Conservation
TPER	Total Primary Energy Requirement
Y	Yield

REFERENCES

- [1] Sustainable Energy Authority of Ireland, "Energy in Ireland: Key Statistics 2014," 2014.

- [2] M. Howley, M. Holland, and K. O'Rourke, "Renewable Energy in Ireland 2013," no. February, p. 60, 2015.
- [3] J. Bates, N. Barker, O. Edberg, J. Fitzgerald, R. Narkeviciute, S. O'Brien, and B. Poole, "BioEnergy Supply Curves for Ireland: 2010 - 2030," p. 93, 2012.
- [4] S. Zinoviev, F. Müller-Langer, P. Das, N. Bertero, P. Fornasiero, M. Kaltschmitt, G. Centi, and S. Miertus, "Next-generation biofuels: Survey of emerging technologies and sustainability issues," *ChemSusChem*, vol. 3, no. 10, pp. 1106–1133, 2010.
- [5] J. Koornneef, P. van Breevoort, P. Niothout, C. Hendriks, uchien Luning, and A. Camps, "Global Potential for Biomethane Production with Carbon Capture, Transport and Storage up to 2050," *Energy Procedia*, vol. 37, pp. 6043–6052, 2013.
- [6] J. D. Murphy and E. McKeogh, "Technical, economic and environmental analysis of energy production from municipal solid waste," *Renew. Energy*, vol. 29, no. 7, pp. 1043–1057, 2004.
- [7] Pell Frischmann Consultants Ltd, "Enhancement and treatment of digestates from anaerobic digestion," 2012.
- [8] Energy Research Centre of The Netherlands, "Phyllis2, Database for Biomass and Waste," 2016. [Online]. Available: <https://www.ecn.nl/phyllis2>. [Accessed: 14-Apr-2016].
- [9] CSO Publishing Ireland, "Area, Yield and Production of Crops," 2014. [Online]. Available: <http://www.cso.ie/en/releasesandpublications/er/aypc/areayieldandp/productionofcrops2014/>. [Accessed: 08-Dec-2015].
- [10] B. Caslin and J. Finnan, "Straw for Energy: Tillage Specialist 2010," Teagasc, Oak Park, Carlow, 12, 2010.
- [11] SEI, "The Renewable Energy Resource Potential of Dry Agricultural Residues in Ireland," 2003.
- [12] CSO, *Census of Agriculture 2010 - Final Results*, no. December. Cork, 2012.
- [13] B. Caslin and J. Finnan, "Fact Sheet: Miscanthus Tillage Specialists 2010," 4, 2010.
- [14] Department of Agriculture Food and the Marine, "Ireland's Forests - Annual Statistics 2015," Dublin, 2015.
- [15] Department of Agriculture Food and the Marine, "Afforestation Grant and Premium Scheme 2014-2020," Dublin, 2015.
- [16] M. F. McCoole, D. I. Kurz, M. M. McDonagh, Dr. Jonathan Derham, and M. D. O'Neill, "National Waste Report 2012," 2012.
- [17] T. Rand, J. Haukohl, and U. Marxen, "Municipal Solid Waste Incineration," Washington D. C., 1999.
- [18] Environmental Protection Agency, "Bulletin 4: Compost and Anaerobic Digestion Statistics for 2013," 2013.
- [19] National Parks & Wildlife Services, "Special Areas of Conservation Boundaries," 2016. [Online]. Available: <http://www.npws.ie/maps-and-data/designated-site-data/download-boundary-data>. [Accessed: 12-Jan-2016].
- [20] European Environment Agency, "Digital Elevation Model over Europe (EU-DEM)," 2016. [Online]. Available: <http://www.eea.europa.eu/data-and-maps/data/eu-dem/#tab-original-data>. [Accessed: 12-Mar-2016].
- [21] Teagasc, "Irish Soil Map," 2014. [Online]. Available: <http://gis.teagasc.ie/soils/downloads.php>. [Accessed: 13-Mar-2016].
- [22] C. Fay, D. Zhang, "Secure Archive For Environmental Research Data," *Towards a National Soil Database, Environmental Protection Agency Ireland*, Jul-2007. [Online]. Available: <http://erc.epa.ie/safer/resource?id=c265bb3f-2cec-102a-b1da-b128b41032cc>. [Accessed: 12-Apr-2016].
- [23] D. Fay, D. McGrath, C. Zhang, C. Carrigg, V. O'Flaherty, G. Kramers, O. T. Carton, and E. Grennan, "Towards a national soil database," Ireland, 2006.
- [24] M. Gassner and F. Maréchal, "Thermo-economic optimisation of the polygeneration of synthetic natural gas (SNG), power and heat from lignocellulosic biomass by gasification and methanation," *Energy Environ. Sci.*, vol. 5, no. 2, p. 5768, 2012.
- [25] J. R. Pels and D. S. De Nie, "Utilization of Ashes from Biomass Combustion and Gasification," in *October*, 2005, no. 17–21 October.
- [26] B. Weidema and A. S. H. De Beaufort, "Framework for Modelling Data Uncertainty in Life Cycle Inventories," *Int. J.*, vol. 6, no. Lci, pp. 127–132, 2001.
- [27] P. J. G. Henriksson, J. B. Guinée, R. Heijungs, A. De Koning, and D. M. Green, "A protocol for horizontal averaging of unit process data - Including estimates for uncertainty," *Int. J. Life Cycle Assess.*, vol. 19, no. 2, pp. 429–436, 2014.

Is the development of a Net Zero Energy agricultural dairy farm possible in Ireland?

William Keane¹, Niamh Power¹

¹Department of Civil, Structural and Environmental Engineering, Cork Institute of Technology, Cork, Ireland
Email: w.keane@mycit.ie, niamh.power@cit.ie

ABSTRACT: The purpose of this work is to determine the possibility of developing a Net Zero Energy (NZE) dairy farm in Ireland from a net energy consumption versus net renewable energy generation viewpoint. This paper provides a unique viewpoint for an Irish dairy farm setting and promotes the use of renewable technologies within the agricultural industry. This analysis of NZE was assessed through a life cycle energy assessment methodology for one calendar year. From the analysis of the dairy farm, it was found that the net energy intensity was 0.62 MJ/L milk. The largest energy consumer was from the synthetic fertiliser used within the dairy farm accounting for approximately 63% of gross energy use and likewise accumulates the largest emissions of 99.7 tCO₂ for the year. Indirect energy consumption within the dairy farm was found to outweigh direct energy usage at a ratio of 8:1. A scenario basis was adopted to quantify the possibility of NZE dairy farm through analysing four different types of renewable technologies (solar, wind, biogas and biomass). It was established that the development of NZE dairy farm is possible from the study farm analysed. The implementation of the optimal renewable technology for the study dairy farm (AD through using cattle slurry and 10% of the dairy farm land area with maize silage) achieved a reduction in net energy of -1,611 GJ for the dairy farm. This indicates that this study dairy farm could become a net energy production facility rather than a net energy consuming facility, and more importantly become the first classified NZE dairy farm in Ireland. Through the implementation of the renewable technologies within the dairy farm, approximately 223.2 tCO₂/annum could be saved.

KEY WORDS: Energy; Dairy Farming; Net Zero Energy; Renewable Technologies; Sustainability.

1 INTRODUCTION

1.1 Background

The dairy farming sector is one of the most important and influential agricultural sectors in Ireland. Reducing energy and greenhouse gas emissions from the dairy farm industry provides the motivation for this research; along with future predictions from the Harvest 2020 report which foresees Irish milk production expanding dramatically by at least 50% by 2020 [1]. This dramatic increase will not come without drawbacks, as Irish agriculture already has the highest GHG emissions per sector accounting for 32.3% of the national greenhouse gas emissions [2]. Through increased milk production intensity, dairy farming in Ireland will become even more energy and emission intensive. Considering the above, Irish dairy farmers are already finding it increasingly challenging to operate sustainably in a cost effective manner.

Renewable technologies used within this report, namely, solar PV, micro-wind, anaerobic digestion and biomass are tried and tested technologies in many parts of Europe. However, the development of these technologies in Irish dairy farms has been significantly slower in comparison with its European counterparts.

1.2 Focus of paper

The Net Zero Energy (NZE) concept is relatively new and not widely defined, however, the US National Renewable Energy Laboratory has headed much of the work on net zero energy to date, which is predominately orientated to commercial and domestic buildings. The purpose of this paper is to determine the possibility of developing a NZE dairy farm in Ireland from a net energy consumption versus net renewable energy generation viewpoint. This provides a unique viewpoint for an Irish dairy farm setting and promotes the use of renewable technologies within the agricultural industry.

Upton et al [3] (Ireland) and *Wells et al* [4] (New Zealand) completed analysis on the gross energy consumption of the

dairy farm. However, the analysis of net energy consumption of dairy farms in Ireland is a unique focus of this paper.

The paper firstly outlines the net energy analysis completed for the study dairy farm, and secondly highlights the results of implementing the optimum renewable energy technology to the dairy farm with the aim to achieve NZE under technical and economic conditions taking a cradle to farm gate life cycle approach.

A NZE dairy farm is a farm that has a net zero energy balance over a set period of time, usually taken as one year. This is achieved through the generation of energy from renewable technologies and through an energy efficient dairy farm design. Through the development of NZE dairy farm, a more sustainable and environmentally friendly strategy for the dairy agricultural sector can be attained.

1.3 Objectives of paper

The key objectives of the paper are to:

- Investigate the net energy consumption of an Irish dairy farm;
- Appraise renewable and efficient technology investment strategies with associated costing analysis for the study dairy farm;
- Analyse the viability of a NZE dairy farm through the development of different scenarios.

2 METHODOLOGY

2.1 Data collection and processing

An 85 hectare dairy farm with 125 milking cows was investigated through detailed questionnaires and farm visits. Selection criteria of this dairy farm included the availability of financial information, data on herd size, and the ability and willingness of the farmer to collect and maintain accurate energy related data. All data was collected for the year 2014. All inputs and outputs necessary to compile the life cycle

energy assessment were recorded manually by the dairy farmer and compiled by the author.

The approach taken within this report was to perform a life-cycle analysis of the technical and environmental aspects of the dairy farms energy consumption, which examined direct, indirect, and gross energy from cradle to farm gate. Giving an indication of the net energy requirements of the dairy farm to produce milk.

This was followed by the technical analysis of four different renewable energy technologies that could be installed within the dairy farm, which would be used to help reduce the net energy requirements of the farm. The four different technologies and products analysed are shown in Figure 1.

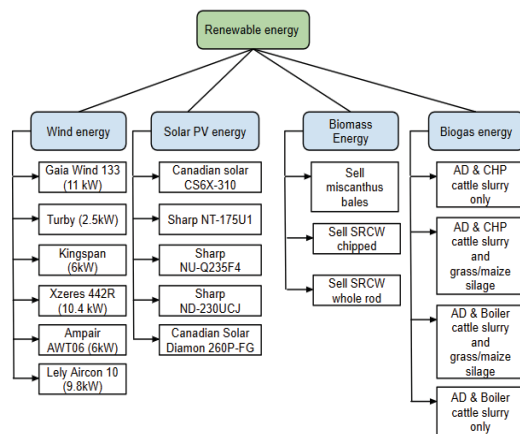


Figure 1: Model flow diagram of the relevant technologies used in the paper.

2.2 LCA Scope and boundaries

The first step in the model development was the establishment of an LCA framework (shown in Figure 2). This framework identifies connections between the different on farm operations and includes both direct and indirect energy consumption. Further to this, the model also includes a framework for the different renewable energy technologies.

This study includes the dairy production from field/cradle to farm gate, using a top down methodology to assess the energy requirements of the dairy farm and the potential renewable energy production of different renewable energy systems. The system boundary is defined from field to farm gate, which implies that energy use was quantified for all processes involved up to the moment that milk left the farm gate, including production and transport of diesel, concentrates, roughage, seeds, herbicides, and chemical fertilizers.

The energy required for milk transport offsite from the dairy farm is not considered. Calculations relating to on-farm activities, incorporates energy consumption and emissions from all agricultural operations on the dairy farm including external contractors work on the farm.

Indirect energy and GHG emissions calculations incorporate manufacturing and transport of fertilisers, seeds and chemicals; excluding embodied human input, the milk production process on-farm, capital inputs such as the energy embodied in machinery and sheds and the transport of certain feedstuffs, due to its variable nature from year to year on the dairy farm. Further to this, it does not take into account the environmental impacts and other factors to do with land use

change. And finally this research does not take into account the co-products such as cow meat.

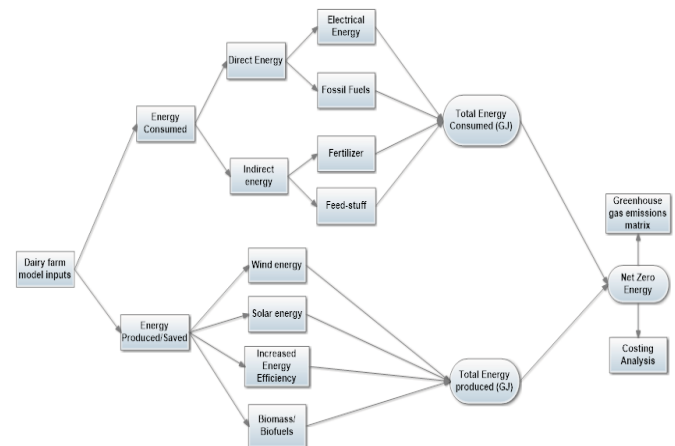


Figure 2: Flow diagram of the LCA framework of paper.

2.3 Functional units and reference units

It is beneficial to express the results in terms of energy content of the final delivered product. Therefore, the reference functional unit to characterise the NZE dairy farm is MJ/litre milk. Another functional unit namely, MJ is also used to analyse the net energy of the dairy farm. This helps to give a clear comparison between the significant results attained within this analysis and other studies in the area.

The accuracy of the energy consumption of the dairy farm within this model is compared to results from previous reports namely; *Upton et al* [3], and through a comparison with the different renewable energy models such as Retscreen, to help verify the results attained for the renewable energy production aspect of the model.

2.4 Dairy farm energy analysis methodology

The energy consumption calculation of the dairy farm follows the basic formula as shown in Equation 1.

$$E = \sum(I \times F) \quad \text{Equation 1}$$

Where: E = total energy consumption in MJ;

I = the amount of input or activity, expressed in a reference unit (such as litre);

F = the energy factor, expressed in MJ/reference unit.

In this equation, two types of data are used:

- The raw or primary data, expressing the amount of inputs from the dairy farm, such as diesel in litres or electricity in kWh;
- Background or secondary data, expressing the energy factors per unit of activity or input. In the case of diesel for example would be 36 MJ/L. Likewise, the GHG emissions calculations are calculated through the same methodology. The paper utilises a top down methodology in assessing the energy use of the dairy farms apart from hot water energy usage, which was analysed through a bottom up approach.

2.5 Energy balance

The net energy consumption of the dairy farm follows the formula as shown in

Equation 2. This formula is used to devise the net energy consumption, which will be later assessed through offsetting renewable energy generation.

$$\text{Net Energy (MJ)} = \text{Direct Energy} + \text{Indirect Energy} - \text{Embodied Energy in Milk}$$

Equation 2

2.6 Energy content in milk

The energy content of milk is calculated through Equation 3.

$$HHV_{\text{milk}} \left(\frac{\text{MJ}}{\text{kg}} \right) = 0.389 \times \text{fat}(\%) + 0.229 \times \text{protein}(\%) + 0.834$$

Equation 3 [5, 6]

This is equates to 3.14 MJ/kg or 3.25 MJ/L assuming a milk density of 1,035 kg/m³ [7].

The embodied energy in milk was included in this analysis to provide for both the energy inputs and energy outputs of the dairy farm. This approach allows assessing of the annual energy balance and the associated impacts with changes in milk production from the dairy farm.

2.7 Dairy farm energy analysis

This dairy farm is over double the size of an average Irish dairy farm of 60 cows, while this farm does not represent the typical Irish dairy farm, it does give an indication of the possibility of larger dairy farms achieving NZE in Ireland. Should the Irish dairy farm industry follow the New Zealand dairy cow number structure (376 cows/herd) in the lead up to the projected 50% increase in milk production in Ireland, the Irish typical dairy farm size will increase dramatically.

Table 1 present both gross and net energy used by the dairy farm. The direct energy inputs to produce a litre of milk on the dairy farm was 0.44 MJ/L milk. Diesel energy is the greatest direct energy consumer within the dairy farm with an energy input of 38% with electricity at 27%, shown in Figure 3.

Table 1: Net and gross energy consumption of the study farm

Description	Dairy Farm Characteristics
Number of cows	125
Milk production per year (L)	750,000
Gross energy (MJ)	2,904,451
Gross energy (MJ/L)	3.87
Energy in milk (MJ)	2,436,338
Net energy (MJ)	468,112
Net energy (MJ/L)	0.62

The indirect energy consumption of the study dairy farm was 3.43 MJ/L milk. Synthetic fertiliser is the most energy intensive at 71% of the overall indirect energy. Within the study of the dairy farm, the average gross energy required to produce 1 litre of milk was 3.87 MJ/L of which on average 89% was indirect energy and 11% direct energy consumed, a ratio of 8:1.

The calculated net energy input of the study dairy farm based on energy input and output amounted to 468.112 GJ. Table 1 also highlights that the net energy intensity of the dairy farm is 0.62 MJ/L milk.

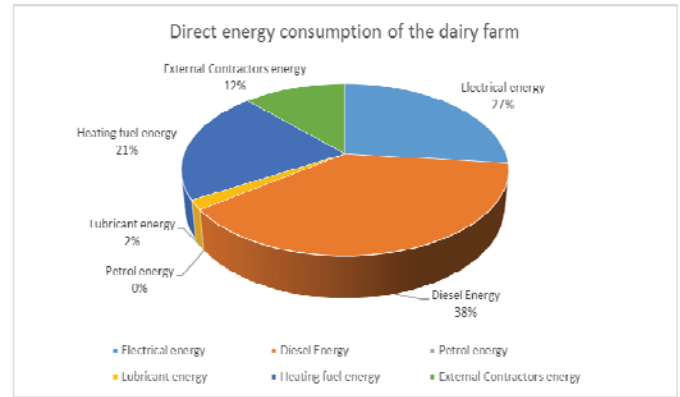


Figure 3: Direct energy use of the dairy farm.

2.7.1 Energy related emissions

The results showed that dairy farming energy related emissions from farm applications account for 192.26 tCO₂ or 0.26 kgCO₂/Litre milk. Figure 4 shows that purchased feedstuff and fertiliser are high contributors to the energy related emissions from the farm.

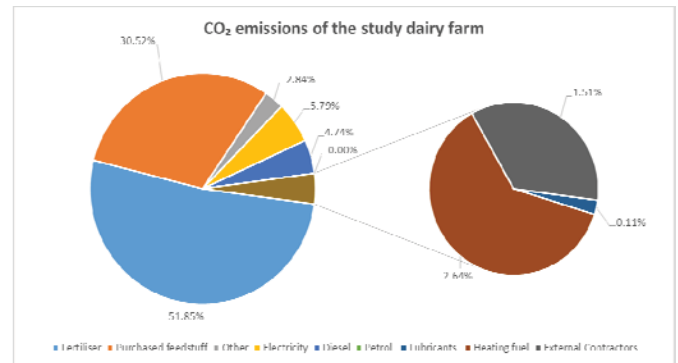


Figure 4: Breakup of emissions from the dairy farm.

3 RENEWABLE ENERGY GENERATION

3.1 Concept of analysis

The concept of the renewable energy analysis focus' on the technical and economic feasibility of the different renewable energy technologies. The comparison determination of the optimum technology is based on net energy production (MJ) and simple payback periods.

3.2 Wind energy technical analysis

To determine potential wind energy production on Irish dairy farms, analysis of wind speeds was required. This involved obtaining hourly wind climate data for a number of synoptic stations in close proximity to the study dairy farm (through MET Eireann [8]). These reference sites represent the wind climate present across the study dairy farm in the absence of onsite wind reading technology.

The procedure to obtain the predicted power output of the different micro-wind turbines on the dairy farm used two methods which analysed wind speeds namely; the Weibull distribution methodology and the MCP methodology.

3.2.1 Weibull Distribution

To develop the Weibull distribution, the averaged wind speed data for the different months of the year was obtained from

the synoptic stations. This averaged wind speed for specific months was analysed and a wind speed distribution was developed through the Weibull distribution equation as displayed in Equation 4 to give a representation of wind speed distribution over a period of time.

$$f(u) = \frac{k}{c} \left(\frac{u}{c}\right)^{k-1} \exp\left[-\left(\frac{u}{c}\right)^k\right] \quad \text{Equation 4}$$

Where: u = wind speed (m/s);
 $f(u)$ = Weibull probability (%);
 $c = 1.12\bar{u}$ (\bar{u} = average wind speed);
 $k = 2$

The Power Law was used to determine the difference in average wind speed at different heights, followed Equation 5.

$$\frac{U_z}{U_{zr}} = \left(\frac{z}{z_r}\right)^\alpha \quad \text{Equation 5}$$

Where: α = power law exponent (value given as 1/7);
 U_z = Wind speed at height Z (m/s);
 U_{zr} = Wind speed measured at a reference height Z_r .

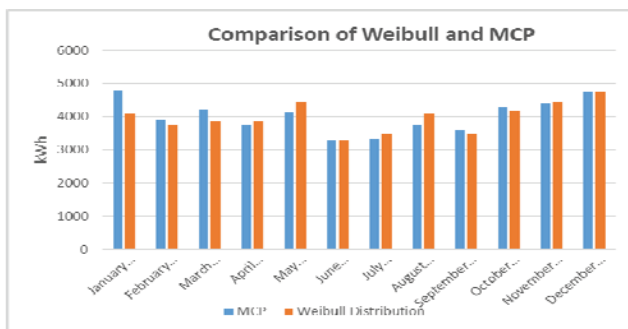


Figure 5: Comparison of Weibull distribution method and MCP method using Gaia 133 wind turbine with Roches Point synoptic data

3.2.2 Measure, correlate and predict (MCP)

The MCP methodology was the second means of wind speed data analysis. This included the analysis of hourly wind speed data from the synoptic sites for up to 10 years which included analysing up to 70,000 rows of data per synoptic station, and like the Weibull method is aimed to getting a representation of the amount of hours at a specific wind speed.

The MCP methodology is a more accurate technique in assessing wind data as actual hourly data is used instead of monthly averages for the Weibull distribution. The two methods are compared in Figure 5.

3.3 Solar energy technical analysis

Assessing the potential for solar technology on dairy farms required attaining solar radiation data from NASA [9]; this data is 12 monthly averaged daily solar radiation data that differs with location. The energy production from the PV array is highlighted in Equation 6.

$$E_{out} = A \times \eta \times H \times PE \quad \text{Equation 6}$$

Where: E_{out} = Energy (kWh);
 A = Total solar panel Area (m²);
 η = solar panel efficiency (%);
 H = Average solar radiation on panels (kW/m²/day);

PR = Performance ratio, coefficient for losses (range between 0.5 and 0.9, default value = 0.75).

This is followed by the total monthly of the alternating current energy generated by the PV system through Equation 7.

$$\sum_{i=1}^N E_{ac} \quad \text{Equation 7}$$

Where: N is the number of days in the month.

3.4 Biogas energy technical analysis

Anaerobic digestion (AD) of waste products is a tried and tested technology. As dairy farms produce large quantity of cattle slurry through the late autumn and winter months, there is a potential energy source not being availed of. For the purpose of this paper, the potential for biogas production from dairy farms in Ireland is analysed through the use of dairy cattle slurry and incorporates the option of either grass silage or maize silage as a supplementary feedstuff to the anaerobic digester with the addition of a boiler or CHP technology.

The model configuration is set up under wet process condition and is controlled under a mesophilic temperature range. The biogas can be used to generate both electrical energy and thermal energy using a combined heat and power generator (CHP).

The energy required to grow the crops will be deducted from the gross energy generated to achieve a net energy output of the potential energy attained from biogas. Biogas production was assessed through 0.953 m³/kg BS for grass silage, 0.862 m³/kg BS for maize silage and 0.3 m³/kg VS [10] for cattle slurry.

The mesophilic process requires the heating of the content within the digester to 35°C. Existing research through Murphy and McKeogh [11] take a thermal requirement of 30 kWh/t of input feedstock and the electrical demand of the digester is taken as 10 kWh/t of input feedstock [12].

Another item of note when operating an anaerobic digester is the biogas losses during digestion and processing, for the purpose of this paper it is taken as 2% of total biogas produced [13].

Table 2 outlines

the necessary details required to determine the energy yield from the anaerobic digester using the input of different waste products and crops such as cattle slurry, grass silage and maize silage. The dairy farm contributes 762,384 kg of slurry; this represents 125 dairy cows, 60 calves, 35 heifers and 2 bull being housed for 16 weeks, and 10 acres of maize silage and grass silage.

Table 2: Biogas - technical analysis.

	Cattle slurry	Grass silage	Maize silage
Area	-	10 acres	10 acres
Yield (kg)	762,384	270,281	265,830
TS (kg)	64,802.64	59,462	95,699
VS (kg)	55,082	53,516	91,871
BS (kg)	-	42,812	76,253
Biogas produced (m ³)	16,194	39,984	64,415
Gross energy (MJ)	340,078	839,671	1,352,724

For the purpose of the CHP and boiler units within the analysis, efficiencies of 35% electrical and 41% thermal for the CHP, while 80% thermal for the boiler were used.

When planning for an AD facility on a dairy farm, the financial feasibility of the plant is one of the key considerations. For the purpose of this paper the values provided by Aoife Ni Ruanaigh et al [14] are used. The model assumes a capital cost of €116 per tonne of influent matter into the digester and 8% operating costs arising from the initial capital investment. The operating costs include the heating and electrical costs associated with the AD.

The model for the biogas also looks upon the heating demand of the household and the dairy farm, and estimates the potential energy that could be produced by an anaerobic digester and biogas boiler onsite to fully meet both demands.

3.5 Biomass energy technical analysis

The two energy crops researched within this paper are:

- Miscanthus (sold as bales); and,
- Short rotation coppice willow (SRCW) (sold as chipped or whole rod).

Within the research, the average harvestable yield from 1 hectare of Miscanthus in Ireland is assumed to produce an average annualised crop yield of 11.7 t/ha [15] with a moisture content of 20% over a 16 year cycle. Likewise, Willow yields of 11 t/ha which accounts for two thirds productivity in the first three year cycle and 15% harvest and storage losses and also assumes a moisture content of 20% [15] over an annualised 23 year period. Calorific values of the energy crops were assumed as 13.7 MJ/kg for Miscanthus, and 12.3MJ/kg for SRCW.

The energy requirement for the production of Miscanthus and SRCW uses values from *Murphy et al* [16]. For the purpose of this paper however, the fertiliser requirement is assessed separately to account for the soil types within the dairy farm.

The fertiliser application rates for both crops were taken from the Miscanthus Best Practise Guide [17] and Short Rotation Coppice Willow Best Practice Guidelines [18] which are determined within the model by the soil type of the associated lands with the dairy farm.

For the purpose of this report, a maximum of 10% of the dairy farms total land area is provided for the growth of the energy crops, as over this percentage would be unrealistic and could reduce the output of the dairy farm for milk production.

3.6 Costing analysis

Within the model for assessing the payback of the renewable technologies, only a simple payback analysis is used. Simple payback uses only the capital costs and estimated first year savings of the technology. By dividing the capital cost by the first year's savings, a basic payback figure is calculated see Equation 8.

$$\text{Simple payback} = \text{Capital cost} / \text{First year saving} \quad \text{Equation 8}$$

The figure indicates clearly the amount of years it would take the investment to reach net cost zero, assuming there is no change in annual costs and that the present value of money is the same as it would be for the duration of the investments lifetime. It provides a quick and easy method to appraise the

different renewable technologies. The dairy farm's payback periods for the respective technologies are shown in Table 3.

Table 3: Payback of different renewable technologies.

Technology	Payback (Years)	First year savings	CAPEX & OPEX
Biomass energy (through selling 21 acres of Miscanthus)	2.94	€5,965	€17,555
Wind Energy (Gaia 133 11kW wind turbine)	11.23	€4,998	€56,100
Solar Energy (115.3m ² of solar panels)	11.37	€3,642	€41,420
Anaerobic Digestion (Cattle slurry and 21 acres of Maize)	3.54	€43,321	€153,193

Table 4: Details of renewable technologies applied to farm.

Technology	Biomass energy	Wind energy	Solar energy	Anaerobic Digestion
Optimum option	Sell Miscanthus bales	Gaia 133 (11kW)	Canadian Solar CS6X-310	Cattle slurry and maize silage
Details of RET	21 acres	18m hub height	115.13 m ² installed	21 acres maize
Net energy generated from RES	1,006 GJ	123 GJ	65 GJ	2,079 GJ
Emissions saved (tCO ₂ /a)	86.07	15.5	8.23	223.23
Initial Net energy intensity	0.62 MJ/L			
NZE	-538 GJ	344 GJ	403 GJ	-1,611 GJ
Net energy intensity after retrofit	-0.72 MJ/L	0.46 MJ/L	0.54 MJ/L	-2.15 MJ/L

4 MAIN RESULTS FOR NZE PERFORMANCE OF STUDY DAIRY FARM

The main results of implementing the optimal technology within the study dairy farm may be viewed in Table 4. From the analysis, it may be determined that both biomass and AD will ensure a NZE dairy farm. However, wind energy and solar energy on their own will not enable the farm to reach NZE status. AD using cattle slurry and 10% of dairy farm land area with maize silage, is the preferable technology on an energy basis, amounted to a reduction in net energy of -1,611 GJ or -2.15 MJ/L. This indicates that the study dairy farm could become net energy production facilities rather than net energy consuming facilities and more importantly become a NZE dairy farm.

5 DISCUSSION

5.1 Technical discussion

The net energy demand of this study dairy farm is 0.62MJ/L when the direct and indirect energy demand is balanced with the embodied energy in the milk. The indirect energy demand outweighs the direct energy demand 8:1. With the majority of this indirect demand coming from synthetic fertiliser. This demonstrates the importance of including this often hidden energy demand within the analysis.

On analysing the renewable energy technologies for the study dairy farm, it is highlighted that the development of NZE dairy farms is possible in Ireland. Dairy farmers have

two options that could significantly reduce their net energy consumption, namely, biomass (through Miscanthus and SRCW) and AD. Wind and solar energy, do not however, generate the same level of energy production and attain the same type of payback in comparison with the biomass and AD technologies.

It is highlighted that AD that intakes either maize or grass silage along with cattle slurry provides dairy farmers with the best option for reduced net energy consumption and reduced GHG emissions. And in the case of the dairy farm under investigation in this study can produce 1,611GJ of energy or 2.15MJ/L. Biomass, equally, provides a good alternative to dairy farmers should the high initial capital costs of AD present an issues.

5.2 Economic discussion

Under the stated conditions and selected commercially-available systems in the study, biomass is the preferable technology in terms of payback period, followed closely by AD (with cattle slurry and maize silage). Wind and solar energy are not as attractive from a payback viewpoint. The high capital costs and the lack of financial support are the two main disincentives for these energy options. However the biomass and AD systems also have high capital costs, which may be a burden to many farmers, along with the need to set aside land to grow the energy crop (e.g. miscanthus or maize).

Though the cost of manufacturing micro-renewable systems such as PV have been gradually decreasing in recent years, it is still not at an economical level to provide a viable option for Irish dairy farmers. Wind energy, as a result of the analysis within this study, becoming a more viable and realistic option that could provide increased renewable penetration within the Irish dairy farm industry. This is however, location dependant, as Roches point, for example, has the only wind resource among the five synoptic stations analysed that provides a viable option for the introduction of a micro-wind turbine within the dairy farm.

6 CONCLUSION

From the analysis of the dairy farm, it was found that the net energy intensity was 0.62 MJ/L milk. From the analysis the development of a NZE dairy farm is possible from the study farm analysed. The implementation of the optimal renewable technology for the study dairy farm (AD through using cattle slurry and 10% of the dairy farm land area with maize silage) achieved a reduction in net energy of -1,611 GJ for the dairy farm. This indicates that this study dairy farm could become a net energy production facility rather than a net energy consuming facility, and more importantly become the first classified NZE dairy farm in Ireland.

REFERENCES

1. Department of Agriculture, Food and the Marine, "Food Harvest 2020, Milestones to success", 2014. [Online]. Available: <http://www.agriculture.gov.ie/media/migration/agrifoodindustry/foodharvest2020/Milestones201415ArtFINALLayout1170914.pdf>. [Accessed 22 January 2015].
2. EPA, "Ireland's provisional greenhouse gas emissions in 2013", 2014. [Online]. Available: <http://www.epa.ie/pubs/reports/air/airemissions/GHGprov.pdf>. [Accessed 20 January 2015].
3. Upton J., "Strategies to reduce electricity consumption on dairy farms -An economic and environmental assessment", Phd Wageningen University, Wageningen, NL (2014), 2014
4. Wells C. , "Total Energy Indicators of Agricultural Sustainability: Dairy Farming Case Study", Phd, University of Otago, August 2001. [Online]. Available: <http://maxa.maf.govt.nz/mafnet/publications/techpapers/techpaper0103-dairy-farming-case-study.pdf>. [Accessed 17 February 2015].
5. NRC (National research council), "Nutrition requirements of dairy cattle", National Re-search Council, USA. Washington D. C, 2001. [Online]. Available: <http://profsite.um.ac.ir/~kalidari/software/NRC/HELP/NRC%202001.pdf>. [Accessed 28 July 2015].
6. M. Maysami, "Energy Efficiency in Dairy Cattle Farming and related Feed Production in Iran", 2013. [Online]. Available: <http://edoc.hu-berlin.de/dissertationen/maysami-mohammadali-2013-12-19/PDF/maysami.pdf>. [Accessed 28 July 2015].
7. Glenn Elert, "The Physics Factbook", [Online]. Available: <http://hypertextbook.com/facts/2002/AliciaNoelleJones.shtml>. [Accessed 15 August 2015].
8. MET Eireann, "Historical data of weather stations", 4 June 2015. [Online]. Available: <http://www.met.ie/climate-request/>. [Accessed 8 June 2015].
9. NASA, "Surface meteorology and Solar Energy", NASA, 2015. [Online]. Available: <https://eosweb.larc.nasa.gov/sse/RETScreen/>. [Accessed 17 July 2015].
10. Goulding D. & Power N., "Which is the preferable biogas utilisation technology for anaerobic digestion of agricultural crops in Ireland: Biogas to CHP or biomethane as a transport fuel", *Renewable Energy*, vol. 53, pp. 121-131, 2012.
11. E. McKeogh & J. Murphy, "Technical, economic and environmental analysis of energy production from municipal solid waste", *Renewable Energy*, 2004. [Online]. [Accessed 21 August 2015].
12. J. McCarthy & K. Murphy, "The optimum production of biogas for use as a transport fuel in Ireland", *Renewable Energy*, 2005. [Online]. [Accessed 21 August 2015].
13. C. Jury et al., "Life cycle assessment of biogas production by monofermentation of energy crops and injection into the national gas grid", *Biomass and Bioenergy*, 2010. [Online]. [Accessed 21 August 2015].
14. A. Ruanaigh & J. McGrory, "Developing Anaerobic Digestion Cooperatives in Ireland", 1 November 2011. [Online]. Available: <http://arrow.dit.ie/engscheleidis/3/>. [Accessed 6 August 2015].
15. D. Styles & M.B. Jones, "Energy crops in Ireland: Quantifying the potential life-cycle greenhouse gas reductions of energy-crop electricity", *Biomass & Energy*, 31 July 2007. [Online]. Available: <http://www.sciencedirect.com/science/article/pii/S096195340700089X>. [Accessed 5 August 2015].
16. F. Murphy et al, "Energy requirements and environmental impacts associated with the production of short rotation willow (*Salix sp.*) chip in Ireland", 2012. [Online]. Available: <http://researchrepository.ucd.ie/bitstream/handle/10197/5968/FM1.pdf?sequence=1>. [Accessed 31 July 2015].
17. Teagasc, "Miscanthus best practice guidelines", 2011. [Online]. Available:http://www.teagasc.ie/publications/view_publication.aspx?PublicationID=315. [Accessed 25 March 2015].
18. Teagasc, "Short Rotation Coppice Willow Best Practice Guidelines", February 2015. [Online]. Available: <http://www.agriculture.gov.ie/media/migration/ruralenvironment/environment/bioenergyscheme/TeagascCoppiceWillowGuidelines260315.pdf>. [Accessed 31 July 2015].

The impact of the Irish dairy processing industry on climate change

William Finnegan^{1,2}, Jamie Goggins^{1,2,3}, Eoghan Clifford^{1,2}, Xinmin Zhan^{1,2}

¹College of Engineering and Informatics, National University of Ireland, Galway, Ireland

²Ryan Institute for Environmental, Marine and Energy Research, National University of Ireland, Galway, Ireland

³Centre for Marine and Renewable Energy (MaREI), Galway, Ireland

email: william.finnegan@nuigalway.ie, jamie.goggins@nuigalway.ie, eoghan.clifford@nuigalway.ie, xinmin.zhan@nuigalway.ie

ABSTRACT: Last year, 2015, saw the abolition of the milk quota system that was in place in Europe, which instigated an immediate increase in milk production in many European countries. This increase will aid in addressing the world's ever growing demand for food but will incur increased stresses on the environmental impact and sustainability of the dairy industry. In this study, an environmental life cycle assessment (LCA) was performed in order to estimate the impact of the Irish dairy processing industry on climate change. The global warming potential (GWP), which is the measure of climate change, associated with a farm gate to processing factory gate analysis, which includes raw milk transportation to the processing factory, processing of raw milk into each product and packaging of the final product, is assessed in this study. In the analysis presented in this paper, the total average GWP for these life cycle stages is found to be 1.507, 0.469, 0.188, 0.187, 2.906, 0.48 and 2.381 kg CO₂eq kg⁻¹ product for milk powder, butter, fluid milk, cream, infant formula, cheese and whey powder, respectively. Additionally, an uncertainty analysis of the results is performed and a comparison of these results with international studies are included in this paper. The analysis presented in this paper helps to identify opportunities to reduce the GWP associated with post-farm processing of Irish dairy products.

KEY WORDS: climate change, dairy, global warming potential, Ireland, life cycle assessment, milk processing.

1 INTRODUCTION

At the end of 2015, climate change once again came to the fore as a topic of discussion in Ireland as world leaders negotiated the Paris Agreement at the 2015 United Nations Climate Change Conference (COP21). This global agreement outlines the methods and aims for the reduction of climate change. Currently, the Republic of Ireland is on the brink of a new era for the dairy industry as quotas, which restricted milk production since 1984, were abolished in March 2015. As a result, milk production is expected to increase by 50% by 2020, based on the reference years 2007 to 2009 [1], where Irish milk production is shown in Figure 1. Furthermore, if Ireland is to meet their climate and energy targets, as outlined in Food Harvest 2020, the efficient use of resources and fuels within the industry will need to be increased.

The primary aim of this study is to estimate the contribution of the Irish dairy processing sector to climate change and, consequently, highlight a number of areas where plans may be implemented in order to achieve more 'environmentally friendly' production of dairy products in Ireland. Life cycle assessment (LCA) provides a useful tool for estimating the environmental impact of the manufacture of dairy products. In addition, the main contributors to these emissions are highlighted within the analysis and its interpretation (for example, specific energy or resource consumption). LCA has been used in studies of many major manufacturing countries of dairy products in order to evaluate the environmental and socio-economic impacts of the industry and its products. These countries include the USA [2-5], Canada [6], New Zealand [7], Portugal [8-10], Spain [11, 12], Sweden [7, 13, 14] and a number of other European countries [15-23]. Previously, a macro-scale assessment of the global warming

potential (GWP) associated with the production of Irish dairy products using national data was performed [20]. The study presented in this paper is an extension of this initial or 'macro-scale' study.

In this paper, the impact of the Irish dairy processing industry on climate change is determined by assessing the GWP, which is the measure of climate change, associated with the manufacture of dairy products in the Republic of Ireland through life cycle assessment. A farm gate to processing factory gate analysis, which includes raw milk transportation to the processing factory, processing of raw milk into each product and packaging of the final product, is assessed in this study. A breakdown of the GWP between the life cycle stages analysed, along with a comparison the international studies, are included in this paper. Additionally, an uncertainty analysis of the results is performed in order to determine the variability of the life cycle inventory data and how it affects the reliability of the results using 1,000 Monte Carlo simulations.

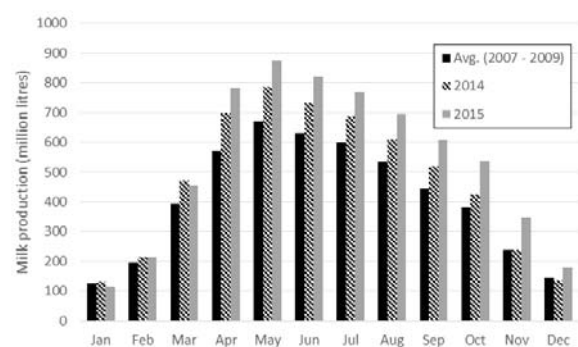


Figure 1: Monthly milk production in the Republic of Ireland. Data obtained from CSO [24].

2 MATERIALS AND METHODS

This study has been structured in accordance with the LCA guidelines of the International Organisation for Standardisation (ISO): ISO 14040 [25] and ISO 14044 [26]. Furthermore, particular attention was paid to the LCA methodology for the dairy industry published by the International Dairy Federation (FIL-IDF) [27]. The FIL-IDF LCA methodology encompasses a number of existing standards and guidelines, including ISO 14040 [25], ISO 14044 [26], PAS2050 [28] and the Intergovernmental Panel on Climate Change (IPCC) guidelines [29]. Data sets based on the ecoinvent database Version 3 [30] were used.

2.1 Goal and scope of the study

The primary goal of this study is to perform an environmental LCA of dairy product manufacture in the Republic of Ireland from farm gate to dairy processing factory gate. This assessment is performed in order to estimate the impact of the Irish dairy processing industry on climate change. The life cycle stages included within the system boundary of the study, are raw milk transportation, dairy processing and packaging, as shown in Figure 2. The life cycle impact assessment (LCIA) method used in this study is the IPCC 2013 GWP 100a, which has also been used in the study of Kim et al. [3] on cheese and whey production in the USA. The functional unit in this study was defined as one kilogram (kg) of product, as advised by FIL-IDF [27], and, therefore, the comparative environmental impact metric was defined as 1 kg CO₂eq kg⁻¹ product.

2.2 Life cycle inventory analysis

The life cycle inventory (LCI) for the manufacture of Irish dairy products was generated by surveying a number of dairy processing factories within the Republic of Ireland. Operational data was obtained from 11 dairy processing factories that produce a variety of dairy products. These factories processed approximately 49% of the total raw milk processed in the Republic of Ireland in 2013, which was 5.83 billion litres [24].

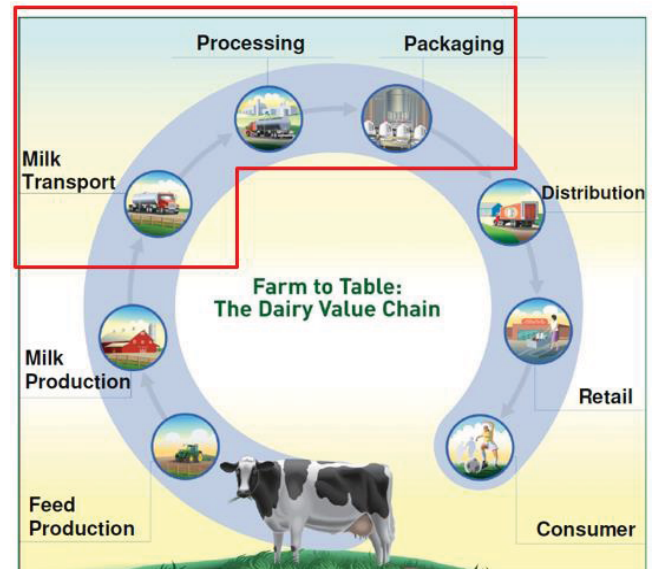


Figure 2: Life cycle of a dairy product and system boundaries. Adapted from [31].

The data requested from industry, which was constructed in accordance to FIL-IDF [27], was:

- Volume raw milk processed and other ingredients
- Raw milk transportation details
- Production statistics of the dairy processing factory
- Electrical and thermal energy consumption and breakdown between processes
- Water consumption and breakdown between processes
- Chemical usage, particular for cleaning
- Packaging details and raw materials used
- On-site wastewater treatment details
- Quantity of solid waste generated and amount recycled

Where aspects of the survey are not monitored on-site, engineering estimates or national averages were used. A summary of the LCI for the manufacture of dairy products in the Republic of Ireland in 2013 is presented in Table 1.

Table 1: Summary LCI for the manufacture of dairy products in the Republic of Ireland (average annual values per kg product obtained for each factory in 2013)

	Unit	Milk Powder	Butter	Fluid milk	Cream	Whey powder	Cheese	Infant formula
<i>Input:</i>								
Raw milk	L	7.34	6.05	0.99	2.56	8.77	5.45	5.95
Raw milk transportation	kg.km	1191	1102	199	557	1506	919	768
<i>Energy input:</i>								
Electrical energy	kWh	0.43	0.28	0.07	0.06	0.74	0.23	0.67
Thermal energy	kWh	3.39	0.36	0.16	0.01	4.79	0.46	2.59
Sodium hydroxide	g	14.4	8.4	1.5	1.3	17.8	11.1	21.6
Nitric acid	g	4.5	3	0.4	0.3	5.9	3.7	6.1
Water	L	10.2	5	1.3	1.3	13.2	14.9	13.9
Primary packaging	g	13.9	25.9	25	32.6	14	30	278.9
<i>Output:</i>								
Wastewater treated	L	11.4	7.8	1.4	1.3	14.4	7.1	11.4
Solid waste	g	50.4	27.2	1	-	25	16.2	82.8

2.2.1 Raw milk

The volumes of raw milk reported for the production of one kg of product are presented in Table 1. However, the environmental impact associated with raw milk production, along with other inputted ingredients, is not included in the current study. Nevertheless, raw milk transportation from the dairy farm to the dairy processing factory has been included within the study. Either the average distance per raw milk collection route or the total diesel used by the factory relating to raw milk transportation was specified within the survey. Where total diesel used was specified this was converted to distance per litre of diesel, which was assumed to be 2.84 km/litre diesel for a 50% laden milk lorry. Six of the Irish dairy processing factories surveyed in the project reported a value for raw milk transportation where the average distance per raw milk collection route was found to be 169 km. This value is much greater than the value specified by Quinlan [32] of 79 km. However, the value found in this study is far less than that found by Ulrich et al. [33] for the US dairy industry where the average round trip distance was 850 km.

2.2.2 On-site energy usage

The annual electrical and thermal energy consumption, along with a breakdown of energy usage within the factory, formed part of the survey of the dairy processing factories. For most products, the major consumers of energy are associated with the processing of the products. For example, evaporation and drying of milk powder consumed the majority of both the electrical and thermal energy. In many cases, the dairy processing factories reported the quantities of fuel types used (natural gas, fuel oil, coal, diesel, biogas, LPG, peat, etc.) rather than thermal energy. In these cases, calorific values were used to calculate the thermal energy, in kWh. Where combined heat and power (CHP) units were used, details of the annual quantity and type of fuel used, along with the resulting electrical and thermal energy, and details of any energy that was exported were specified.

2.2.3 Water and chemical consumption

In Ireland, water used in dairy processing has three main sources: groundwater, surface water or public supply. The quantity of water consumed on-site and details of its source was reported within the survey of the dairy processing factories. The average water consumption reported by the dairy processing detailed in this study was found to be 1.38 L L⁻¹ milk processed, which is significantly lower than the average water consumption for the Irish dairy processing industry in 2008 of 2.5 L L⁻¹ milk processed [34]. A breakdown between the main water users within the factory (e.g. CIP system, boiler feed, tanker wash etc.) was also requested but in many cases this was not available and, therefore, water statistics were reported on a whole-factory basis. The type of chemicals used (primarily sodium hydroxide and nitric acid in Ireland) and the quantity for the year was, also, reported on a whole-factory basis. The allocation of these resources between the various dairy products within each dairy processing factory is discussed in Section 2.3.

2.2.4 Packaging materials

The type of packaging used and the quantity of the individual finished packaged product were specified within the survey. These details were found to have a significant effect on the overall environmental impact of a product's manufacture.

2.2.5 Wastewater treatment

All of the dairy processing factories that were surveyed as part of this study had on-site wastewater treatment facilities. Therefore, operational wastewater treatment data was obtained in order to accurately model this process. Data relating to nutrient emissions to water, electrical energy consumption and chemical usage of the on-site wastewater treatment plant was detailed. This site specific data was incorporated into an ecoinvent database Version 3 [30] model for a wastewater treatment plant, class 2 and used in this study

2.2.6 Solid waste disposal

The annual quantity of solid waste sent off-site for disposal was surveyed. The solid waste was reported as either hazardous or non-hazardous waste and categorised according to four different methods of disposal: landfill; incineration; recycling; and other. For the purpose of this analysis, a conservative assumption, that all solid waste reported as 'other' was disposed at a landfill site, was taken.

2.3 Allocation of inputs and emissions within dairy processing

The energy usage breakdown is used to allocate energy usage between products manufactured at each dairy processing factory. Where processes are common to two or more products or energy usage is reported on a whole-factory basis, mass allocation, on a milk solids basis, is used to allocate energy between milk powder, butter and other dairy products in accordance with FIL-IDF [27]. In most cases, water consumption, chemical usage, wastewater and solid waste generation have been reported on a whole-factory basis. Water consumption, chemical usage and wastewater generation are allocated using the physico-chemical allocation matrix, which has been developed by Feitz et al. [35] specifically for the dairy industry and advised by FIL-IDF [36]. As solid waste generation is not included in the physico-chemical allocation matrix, it is allocated between products using mass allocation, on a milk solids basis.

3 RESULTS AND DISCUSSION

The operational data specified in the LCI (Section 2.2 and Table 1) is used to estimate the GWP associated with the manufacture of Irish dairy products. Both, direct (on-site) and indirect (off-site) environmental impacts are included in the analysis using emission factors based on the ecoinvent database Version 3 (Weidema et al., 2013), which is discussed in greater detail in Section 3.1. The results of the analysis are compared to international studies in order to benchmark the environmental performance of the Irish industry, which is presented in Section 3.2. Additionally, an uncertainty analysis using 1,000 Monte Carlo simulations was performed in order to derive the 95% confidence interval range for the GWP associated with each product, which is discussed in Section 3.3.

3.1 Global warming potential associated with dairy products

The average results of the GWP associated with each of the dairy products is presented in Table 2. In order to compare dairy products produced at the surveyed dairy processing factories, they were grouped into 7 groups:

- Milk powder: buttermilk powder; whole milk powder; skimmed milk powder; chocolate crumb
- Butter
- Fluid milk: whole milk; skimmed and semi-skimmed milk (Skim milk)
- Cream
- Infant formula: baby and infant powdered formula
- Cheese
- Whey powder: whey powders; proteins;

In this analysis, the dairy product with the highest GWP is infant formula at $2.906 \text{ kg CO}_2\text{eq kg}^{-1}$ product, where 60% of this total is associated with packaging materials. Powder products were found to have the next highest GWP, as a result of their high energy intensity required for evaporation and drying of raw materials, at $2.381 \text{ kg CO}_2\text{eq kg}^{-1}$ product and $1.507 \text{ kg CO}_2\text{eq kg}^{-1}$ product for whey powder and milk powder, respectively. Fresh dairy products, which require very little processing, were found to have the lowest GWP at $0.188 \text{ kg CO}_2\text{eq kg}^{-1}$ product and $0.187 \text{ kg CO}_2\text{eq kg}^{-1}$ product for fluid milk and cream, respectively.

Table 2. Average results of the GWP of Irish dairy products ($\text{kg CO}_2\text{eq kg}^{-1}$ product).

	RMT ¹	Processing	Packaging	Total
Milk Powder	0.126	1.353	0.028	1.507
Butter	0.117	0.320	0.032	0.469
Fluid milk	0.021	0.119	0.048	0.188
Cream	0.059	0.063	0.065	0.187
Infant formula	0.081	1.081	1.743	2.906
Cheese	0.097	0.346	0.037	0.480
Whey powder	0.159	2.193	0.029	2.381

¹RMT: raw milk transportation

For all of the dairy products, except Infant formula, the processing of raw milk into the final product is the life cycle stage which is the most significant contributor to GWP. Energy, both electrical and thermal, were the main contributors to GWP in the processing stage and, therefore, products that require higher energy intensity had a higher GWP for this life cycle stage. Hence why the GWP associated with processing of powder products (milk powder, infant formula and whey powder), which use high energy intensive evaporation and drying, are significantly higher than fresh dairy products (fluid milk and cream), which require low energy processes. The transportation of raw milk from the dairy farm to the dairy processing factory accounted for 3–31% of the GWP, depending on the product.

Since the majority of Irish dairy products are exported and are, therefore, bulk packaged, the contribution of packaging to GWP is less than 8% for milk powder, butter, cheese and whey powder. However, for products that are packaged into

their consumer packaging (i.e. fluid milk, cream and infant formula), packaging contributes more significantly to GWP at 25%, 35% and 60% of the total for fluid milk, cream and infant formula, respectively. A further breakdown of the contribution of the inputs and emissions to the total GWP associated with the manufacture of each dairy product assessed in this study is presented in Figure 3.

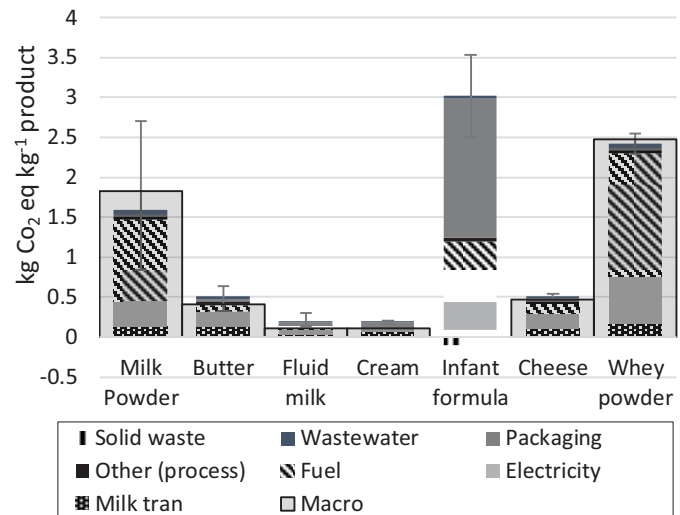


Figure 3. Contribution of the inputs and emissions to the total GWP associated with the manufacture of Irish dairy product.

The results of a similar macro-scale study [20] are also included as a comparison.

3.2 Comparison with previous Irish study

Previously, Finnegan et al. [20] estimated the global warming potential associated with the production of dairy products in the Republic of Ireland using country-level data. The analysis performed in this paper will build on this study by increasing accuracy, by using site specific data and including additional processes within the manufacture stage, as well as exploring additional environmental impacts of a number of post-farm dairy product life cycle stages.

A comparison to this previous macro-scale study [20] of the GWP of Irish dairy products are also included in Figure 3. The results of this detailed study show that the previous study provided a good estimate for the GWP of Irish dairy products as the two studies are in good agreement. The most significant discrepancy between the two studies is for milk powder. The processing of raw milk into milk powder found here to be $1.353 \text{ kg CO}_2\text{eq kg}^{-1}$ product is lower than a previous estimate of $1.824 \text{ kg CO}_2\text{eq kg}^{-1}$ product [20]. A possible reason for the difference is the allocation method [35] used in Finnegan et al. [20] and the results from a detailed survey of dairy processing factories was used in the current analysis to allocation between the two main products.

3.3 Comparison with international studies

In this section the results of the present study have been compared to selected international studies.

Kim et al. [3] found that the GWP for cheddar cheese in the US, for the life cycle stages used in the present study, which has an average of 63.2% dry solids, is $0.828 \text{ kg CO}_2\text{eq kg}^{-1}$ product. This is greater than the GWP of cheese (majority

cheddar cheese) in the present study which is found to be 0.48 kg CO₂eq kg⁻¹ product.

Thoma et al. [5] found that the GWP for fluid milk in the US, for the life cycle stages used in the present study, is 0.201 kg CO₂eq kg⁻¹ product. The GWP of fluid milk, found in the present study, is 0.188 kg CO₂eq kg⁻¹ product is marginally lower than the US study. This is mainly attributed to the GWP associated with the transportation of raw milk to the dairy processing factories.

Sheane et al. [22] reported, for the life cycle stages used in the present study, the GWP for fluid milk, cheese, cream and butter in Scotland, to be approximately 0.132, 0.555, 0.45, 0.27 kg CO₂eq kg⁻¹ product, respectively. The corresponding values in the present study for fluid milk, cheese, cream and butter, are 0.188, 0.48, 0.188, 0.469 kg CO₂eq kg⁻¹ product, respectively. The results for fluid milk and cheese are of a similar magnitude. However, the GWP associated with cream is significantly lower in the present study and the GWP associated with Butter is approximately 74% larger, compared to the Scottish study. The differences between the two studies may be as a result of a difference in product mix. For example, very little milk powder, which has a relatively environmental impact, is produced in Scotland compared to other products, which is a major product in Ireland. Additionally, differences in allocation methods between products within plants may have an impact on the results.

3.4 Uncertainty analysis

An uncertainty analysis was performed, as part of the impact assessment, to determine the variability of the LCI data and how it affects the reliability of the results of the LCIA. Each Monte Carlo simulation used randomly selected values for inputs, outputs and emissions according to a normal probability distribution. The standard deviation used in the normal distribution was estimated by analysing the data quality based on six criteria of the data: reliability, completeness, temporal correlation, geographic correlation, future technological correlation and sample size.

Table 3. Results of 1,000 Monte Carlo simulations for uncertainty analysis of various Irish dairy products (kg CO₂eq kg⁻¹ product).

	Mean	CV ¹ (%)	95% CI ²	
Milk Powder	1.513	38.2	0.380	2.646
Butter	0.469	33.5	0.161	0.777
Fluid milk	0.189	45.0	0.022	0.355
Cream	0.187	23.2	0.102	0.272
Infant formula	2.908	14.7	2.072	3.744
Cheese	0.480	21.7	0.276	0.684
Whey powder	2.383	19.5	1.473	3.293

¹CV: Coefficient of variation, ²CI: Confidence interval

The LCA results, presented in Section 3.1, are analysed using 1,000 Monte Carlo simulations and the results of these simulations are given in Table 3. The mean, coefficient of variation, 95% confidence interval ranges of the GWP associated with each dairy product from the uncertainty analysis has been presented. The most significant 95%

confidence interval ranges were 0.38-2.646 kg CO₂eq kg⁻¹ product for milk powder and 0.022-0.355 kg CO₂eq kg⁻¹ product for fluid milk. In both cases, this was the result of large variances in fuel and electricity usage reported by dairy processing factories that manufacture these products.

4 CONCLUSIONS

In this study, the GWP associated with the manufacture of a number of dairy products in the Republic of Ireland, from raw milk transportation to the processing factory, processing of raw milk into each product and packaging of the final product, is estimated through LCA. Therefore, this analysis can be used to identify opportunities to reduce the environmental impact of the Irish dairy industry.

Additionally, the results of this study will serve as a benchmark for the Irish dairy processing industry as individual processors can evaluate their performance in comparison. Based on the comparison presented in Section 3.3, overall, the Irish dairy processing industry is performing better than their US and Scottish counterparts. This is very encouraging as processors will aim to increase the length of their more efficient summer months as year-round milk production grows in the coming years.

As Ireland's agricultural and agri-food sector continues to grow, it has been suggested that a carbon tax on dairy processors, similar to the carbon tax paid by motorists for their cars and householders for their fuel bills, may be introduced as an incentive to reduce emissions [37]. It is evident in this study that energy consumption is the most significant contributor to GWP. Therefore, it is imperative that energy use within the plants is accurately determined in future studies and targeted measures to reduce energy consumption identified, as these will be key to reducing the GWP associated with dairy products. On the other hand, the use of renewable sources of energy in place of fossil fuels would also lead to reduction in the GWP of products.

ACKNOWLEDGMENTS

The authors would like to acknowledge the funding provided by the Department of Agriculture, Food and the Marine for the DairyWater project (Ref.: 13-F-507), for additional details: www.dairywater.ie.

REFERENCES

- [1] Farrelly, P., Crosse, S., O'Donoghue, P., Whyte, S., Farrelly, P.B., Burns, T., Byrne, D., Holmes, O., Maklin, R., McKearney, J.J., and Salley, F. (2014) *Environmental Analysis of Scenarios Related to the Implementation of Recommendations in Food Harvest 2020*. The Department of Agriculture, Food and the Marine.
- [2] Aguirre-Villegas, H.A., Milani, F.X., Kraatz, S., and Reinemann, D.J. (2012) 'Life Cycle Impact Assessment and Allocation Methods Development for Cheese and Whey Processing'. *Transactions of the ASABE*, 55(2): p. 15.
- [3] Kim, D., Thoma, G., Nutter, D., Milani, F., Ulrich, R., and Norris, G. (2013) 'Life cycle assessment of cheese and whey production in the USA'. *The International Journal of Life Cycle Assessment*, 18(5): p. 1019-1035.
- [4] Nutter, D.W., Kim, D.-S., Ulrich, R., and Thoma, G. (2013) 'Greenhouse gas emission analysis for USA fluid milk processing plants: Processing, packaging, and distribution'. *International Dairy Journal*, 31, Supplement 1(0): p. S57-S64.
- [5] Thoma, G., Popp, J., Nutter, D., Shonnard, D., Ulrich, R., Matlock, M., Kim, D.S., Neiderman, Z., Kemper, N., East, C., and Adom, F. (2013) 'Greenhouse gas emissions from milk production

- and consumption in the United States: A cradle-to-grave life cycle assessment circa 2008'. *International Dairy Journal*. 31, Supplement 1(0): p. S3-S14.
- [6] Vergé, X.P.C., Maxime, D., Dyer, J.A., Desjardins, R.L., Arcand, Y., and Vanderzaag, A. (2013) 'Carbon footprint of Canadian dairy products: Calculations and issues'. *Journal of dairy science*. 96(9): p. 6091-6104.
- [7] Flysjö, A. (2012) *Greenhouse gas emissions in milk and dairy product chains*, in *Department of Agroecology*. Aarhus University: Aalborg.
- [8] González-García, S., Castanheira, A., Dias, A.u., and Arroja, L. (2013d) 'Environmental life cycle assessment of a dairy product: the yoghurt'. *The International Journal of Life Cycle Assessment*. 18(4): p. 796-811.
- [9] González-García, S., Castanheira, E.G., Dias, A.C., and Arroja, L. (2013c) 'Environmental performance of a Portuguese mature cheese-making dairy mill'. *Journal of Cleaner Production*. 41: p. 65-73.
- [10] González-García, S., Castanheira, T.G., Dias, A.C., and Arroja, L. (2013b) 'Using Life Cycle Assessment methodology to assess UHT milk production in Portugal'. *Science of the Total Environment*. 442: p. 225-234.
- [11] González-García, S., Hospido, A., Moreira, M.T., Feijoo, G., and Arroja, L. (2013a) 'Environmental Life Cycle Assessment of a Galician cheese: San Simon da Costa'. *Journal of Cleaner Production*. 52: p. 253-262.
- [12] Hospido, A., Moreira, M.T., and Feijoo, G. (2003) 'Simplified life cycle assessment of galician milk production'. *International Dairy Journal*. 13(10): p. 783-796.
- [13] Berlin, J. (2002) 'Environmental life cycle assessment (LCA) of Swedish semi-hard cheese'. *International Dairy Journal*. 12(11): p. 939-953.
- [14] Flysjö, A., Thrane, M., and Hermansen, J.E. (2014) 'Method to assess the carbon footprint at product level in the dairy industry'. *International Dairy Journal*. 34(1): p. 86-92.
- [15] Broekema, R. and Kramer, G. (2014) *LCA of Dutch semi-skimmed milk and semi-mature cheese*. Blonk Consultants: Netherlands.
- [16] Djekic, I., Miocinovic, J., Tomasevic, I., Smigic, N., and Tomic, N. (2014) 'Environmental life-cycle assessment of various dairy products'. *Journal of Cleaner Production*. 68: p. 64-72.
- [17] Doublet, G., Jungbluth, N., Stucki, M., and Schori, S. (2013) *Life cycle assessment of Romanian beef and dairy products*, in *Harmonised Environmental Sustainability in the European food and drink chain (SENSE)*.
- [18] Eide, M. (2002) 'Life cycle assessment (LCA) of industrial milk production'. *The International Journal of Life Cycle Assessment*. 7(2): p. 115-126.
- [19] Fantin, V., Buttol, P., Pergreffi, R., and Masoni, P. (2012) 'Life cycle assessment of Italian high quality milk production. A comparison with an EPD study'. *Journal of Cleaner Production*. 28(0): p. 150-159.
- [20] Finnegan, W., Goggins, J., Clifford, E., and Zhan, X. (2015) 'Global warming potential associated with dairy products in the Republic of Ireland'. *Journal of Cleaner Production*. DOI: 10.1016/j.jclepro.2015.08.025.
- [21] Nilsson, K., Flysjö, A., Davis, J., Sim, S., Unger, N., and Bell, S. (2010) 'Comparative life cycle assessment of margarine and butter consumed in the UK, Germany and France'. *The International Journal of Life Cycle Assessment*. 15(9): p. 916-926.
- [22] Sheane, R., Lewis, K., Hall, P., Holmes-Ling, P., Kerr, A., Stewart, K., and Webb, D. (2011) *Identifying opportunities to reduce the carbon footprint associated with the Scottish dairy supply chain - Main report*. Scottish Government: Edinburgh.
- [23] van Middelaar, C.E., Berentsen, P.B.M., Dolman, M.A., and de Boer, I.J.M. (2011) 'Eco-efficiency in the production chain of Dutch semi-hard cheese'. *Livestock Science*. 139(1-2): p. 91-99.
- [24] CSO. *Statistical Product - Milk Production*. 2016 [cited 2016 11th February]; Available from: <http://www.cso.ie>.
- [25] ISO (2006a) *ISO 14040: Environmental Management - Life Cycle Assessment - Principles and Framework*. International Organization for Standardization.
- [26] ISO (2006b) *ISO 14044: Environmental Management - Life Cycle Assessment - Requirements and Guidelines*. International Organization for Standardization.
- [27] FIL-IDF (2015) *A common carbon footprint approach for the dairy sector. The IDF guide to standard life cycle assessment methodology*, in *Bulletin of the International Dairy Federation*. International Dairy Federation. p. 70.
- [28] BSI (2011) *PAS 2050: Specification for the assessment of the life cycle greenhouse gas emissions of goods and services*. British Standards Institute: London, UK.
- [29] IPCC (2007) *Climate Change 2007: The Physical Science Basis. Contribution of Working Group I to the Fourth Assessment Report of the Intergovernmental Panel on Climate Change* [Solomon, S., D. Qin, M. Manning, Z. Chen, M. Marquis, K.B. Averyt, M. Tignor and H.L. Miller (eds.)]. Intergovernmental Panel on Climate Change. p. 996.
- [30] Weidema, B.P., Bauer, C., Hirschier, R., Mutel, C., Nemecek, T., Reinhard, J., Vadenbo, C.O., and Wernet, G. (2013) *The ecoinvent database: Overview and methodology, Data quality guideline for the ecoinvent database version 3*, www.ecoinvent.org.
- [31] Wang, Y. (2011) *U.S. Dairy Life Cycle Assessment: From Grass to Glass*. Innovation Center for US Dairy.
- [32] Quinlan, C. (2013) *Optimisation of the Food Dairy Coop Supply Chain*, in *Business and Development*. National University of Ireland, Cork: Ireland.
- [33] Ulrich, R., Thoma, G., Nutter, D., and Wilson, J. (2013) 'Tailpipe greenhouse gas emissions from tank trucks transporting raw milk from farms to processing plants'. *International Dairy Journal*. 31, Supplement 1: p. S50-S56.
- [34] Geraghty, R. (2011) *Resource efficiency in Ireland's dairy processing sector*. Enterprise Ireland.
- [35] Feitz, A.J., Lundie, S., Dennien, G., Morain, M., and Jones, M. (2007) 'Generation of an industry-specific physico-chemical allocation matrix'. *Int. J. Life Cycle Assess.* 12: p. 109-117.
- [36] FIL-IDF (2010) *A common carbon footprint approach for dairy, a guide to standard life cycle assessment methodology for the dairy sector*, in *Bulletin of the International Dairy Federation* (No. 445). International Dairy Federation.
- [37] Melia, P. (2015) *Scientist backs tax on Ireland's food processors*, in *Irish Independent*, 12/12/2015: Dublin, Ireland.

Flexible Response of Bamboo-Epoxy Frames

Roger P West¹, Suresh Bhalla² and Diwakar Bhagat²

¹Department of Civil Engineering, Trinity College, University of Dublin, Ireland

²Department of Civil Engineering, Indian Institute of Technology, Hauz Khas, Delhi, India

email: rwest@tcd.ie, sbhalla@civil.iitd.ac.in, atul210012@gmail.com

ABSTRACT: This paper describes some of the very extensive outcomes of a structural load test on a full scale bamboo-epoxy composite frame. A bundle of 20 small diameter thick walled bamboo culms was bonded using epoxy-fibre resin to form a structural beam or column element which were connected at the beam/column joints using rebar and a novel epoxy sand composite. The frame was heavily instrumented with over 90 strain gauges to establish the location of any delaminations or hinge formations during inelastic behaviour under load. The frame and the gauges were assembled in India and shipped to Ireland for testing. In Trinity, the frame was supported by steel shoes bolted to a 3000kN internal reaction rig, with additional passive lateral support in case of instability during loading. This paper describes the load-displacement response under combined horizontal and vertical loading, together with an explanation of the frame's non-linear behaviour using the evidence provided by the strain gauges, including secondary moments due to the frame's flexibility. The load capacity of the frame was evident whereupon significant inelastic deformations occurred as the actuator heads continued to distort the frame under constant load.

KEY WORDS: Bamboo; Composites; Epoxy; Inelastic behaviour; Portal frames.

1 INTRODUCTION

Bamboo is a highly sustainable and renewable material and is popular in housing in developing and developed countries although this is normally restricted to at most two storey dwellings [1, 2]. Many species of bamboo are well known for their high tensile strength and good specific weight as well as their highly sustainable nature, making bamboo an eco-friendly building product [3]. Indeed, although some bamboos are known to have suitable tensile and compressive strengths for structural use [4], their high variability, low stiffness and joint connections create real engineering design challenges which mitigate against their use in medium density housing, which is currently a restriction on bamboo use in heavily populated cities in practice. As a composite, much has been published on its use in reinforced concrete as a sustainable steel reinforcement substitute [5, 6]. However, little has been done with bamboo-only frames due principally to the problems with jointing [7, 8]. The complex behaviour of a bamboo-epoxy frame is described in full in this paper leading to a good understanding as to how such a composite might have the potential to alleviate the housing problems in those parts of the world which have abundant indigenous bamboo.

2 TEST FRAME

To overcome these deficiencies, a series of three full scale bamboo-epoxy Portal frames has been manufactured in India and tested in Ireland. Each section comprised a mixed bundle of small diameter *Dendrocalamus Strictus* bamboo bound by an epoxy-fibre composite glue. A bundle of 20 small (38-43 mm diameter) thick walled bamboo culms was bonded using epoxy-fibre resin, making up a section which was approximately 230 mm x 270 mm in outer dimensions (Figure 1). The bundle averages out much of the well-known natural

variability in individual culms, yet providing considerable load carrying capacity and enhanced stiffness due to composite action. The elements are connected at the beam/column joints using 12 mm diameter L-shaped rebar embedded and bonded into each hollow culm and a novel epoxy-sand composite is cast to create a semi-rigid joint. The bases of the columns are assumed to be rigid because purpose-made steel shoes, which were transported with the bamboo frames, were bolted to the steel internal reaction rig and the base of the frames epoxied in-situ, with enhanced fixing using clamping down bolts.

As the loading regimes and structural responses are complex, several load patterns were applied to the different frames to failure but only one test frame result will be discussed here, that due to combined peak horizontal and vertical loads applied in series. From prior flexural tests on simply supported beams in India, the plastic moment capacity of the beam-column cross-section could be estimated and so theoretical failure loads could be calculated, assuming that the beam-column joints could sustain the required moments. This enabled the test regime to be planned in advance.

For the test described here, two loading jacks and load cells were placed on the frame, one horizontally at the top of the left hand column and one vertically at the centre of the beam. Load was applied by hand-pumping the jacks, firstly horizontally, then vertically. However, as the frame is flexible, it was necessary to continue pumping the horizontal jack when the vertical load was being applied because the horizontal initial deflections at the top of the columns, due to the horizontal loads, caused secondary moments when the vertical load was applied. Were this not the case and the horizontal jack was locked off at peak horizontal load, then the horizontal load would have reduced as the additional

lateral deflections caused by the secondary moments were in the same sense as those due to the initial horizontal loading. Additional passive lateral supports were provided out-of-plane in case of any lateral instability during loading, especially as the properties (strength and stiffness) of the bamboo section were not uniform in this direction.



Figure 1: View of cross section of typical bamboo-epoxy beam

2.1 Instrumentation

In total 90 strain gauges were embedded in or placed on the surface of the frame, but only 60 selected ones of these were attached to the data loggers during experimentation, as shown in Figure 2. Displacement transducers were added prior to loading, placed horizontally at the loading point at the top of the left hand column and underneath the vertical load at mid span on the beam. The test frame, placed inside the internal reaction rig, is shown immediately prior to loading in Figure 3.

2.2 Load application

Initially a horizontal load of 50 kN was applied gradually, followed by a vertical load of 91 kN. As may be observed in Figure 4 (from point A to point B), there was noticeable fluctuation in the horizontal load as the vertical load was being applied due to the secondary moments previously

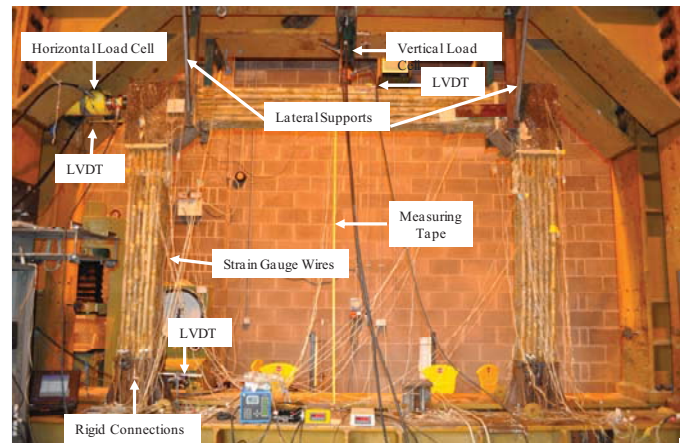


Figure 3: Setup of bamboo-epoxy frame prior to loading

described, as an attempt was made to maintain the horizontal load by pumping that jack. At point B in Figure 4, no matter how much the two jacks were pumped such that both jack heads extended, no further load resistance was offered by the frame. As may be observed, both loads fluctuated and non-linear displacement occurred, as will be described presently, to point C. At point C, the horizontal jack was locked off and the vertical load was removed gradually. Consequently, as the secondary moments reduced, the frame attempted to sway back to the left but was prevented from doing so by the now rigid horizontal jack head and thus the horizontal load can be seen to increase, even though the jack head did not move during the phase (until point D). Thereafter, the vertical load was removed entirely to point E, to zero load.

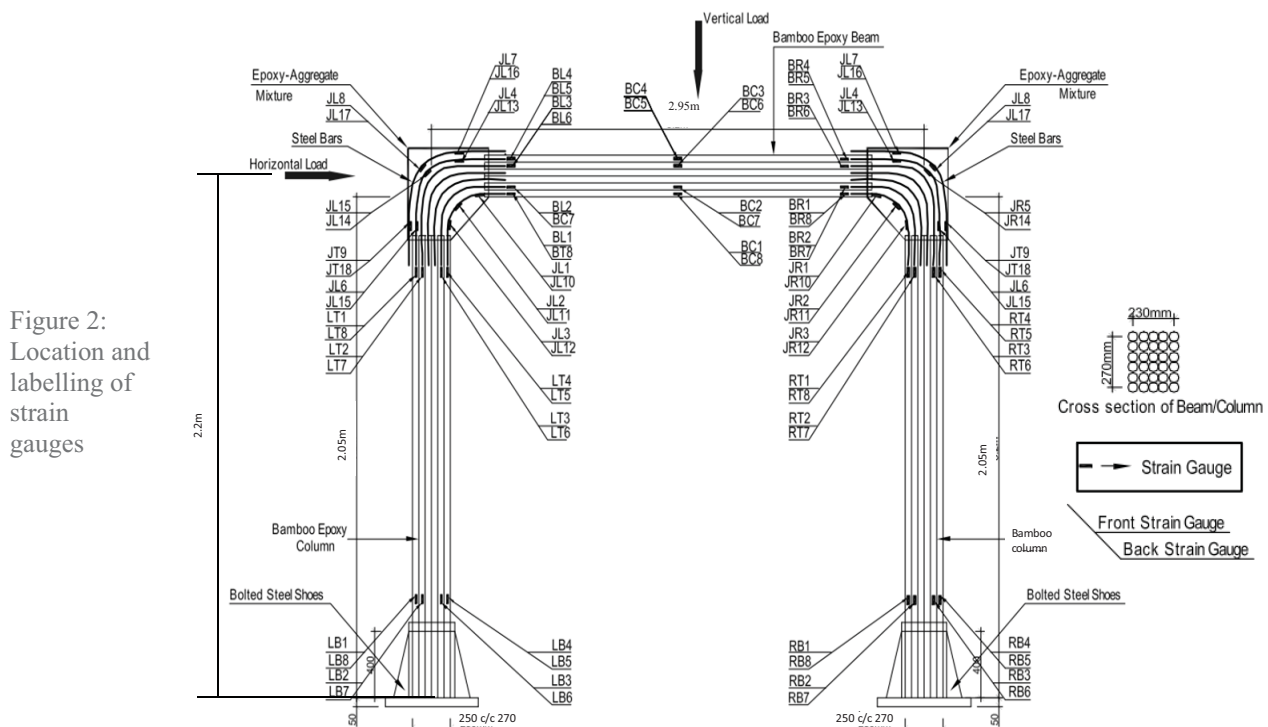


Figure 2: Location and labelling of strain gauges

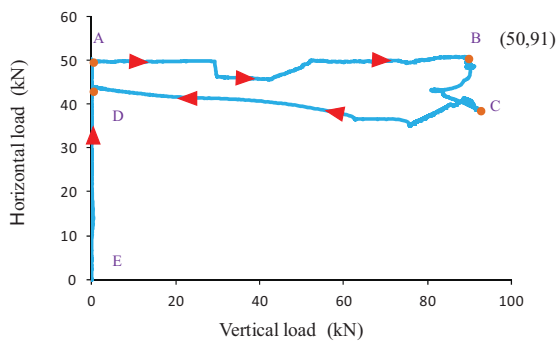


Figure 4: Plot of horizontal versus vertical load application

3 LOAD DISPLACEMENT RESULTS

When a vertical load is applied after a horizontal load has caused lateral displacements at the column heads due to the bamboo's flexibility, then considerable secondary moments in the columns occur. Ultimately, the inability to increase the load further is caused by a loss in stiffness due to the delamination of the epoxy in shear at particular locations, but without catastrophic failure of the bamboo. The presence of 60 strain gauges throughout each frame enables stress reversal and load transfer to be clearly observed during the flexural response. The bending moment diagrams and strain responses confirm the causes of this non-linear behaviour, as shall be illustrated here. The resilience of the frame during the plastic phase is such that there is only a slight load drop off and considerable recovery is noted to occur on unloading.

Specifically, it is instructive to examine the horizontal/vertical load-displacement plots to identify the phases of behaviour. In Figure 5(a), it may be seen that the development of horizontal displacement with horizontal load to point A is not entirely linear. The extent of the increase in the horizontal displacement with the increase in the horizontal load and moving horizontal jack head, can be seen between points A and B. Inelastic behaviour (B to C) due to some form of mechanism, to be described presently, can be observed as the horizontal displacement increased as the jack was being pumped in an attempt to maintain the load, which proved impossible. Finally, the slight increase in horizontal load as the vertical load was removed (C to D) is evident and subsequently removal of the horizontal load under an apparently reduced stiffness regime occurs to point E. Here there is a permanent displacement of the order of 22 mm due primarily to the inelastic behaviour in the frame in phase B to C.

A similarly instructive study of Figure 5(b) reveals no vertical displacement as the horizontal load is being applied (O to A), as expected at the centre of the beam under a sway loading, and relatively linear elastic behaviour to point B, up to maximum vertical load. There follows a phase of inelastic vertical displacement, as before, from B to C as the vertical jack chases the load under increasing extension of the head of the jack. Release of the loads in turn (C to D and D to E) confirms that there is also residual displacement vertically, at point E.

A similar examination of Figures 5(c) and (d), completes the understanding of the load-displacement plots. In particular in the former plot, the minor increased horizontal displacement under increasing vertical load between A and B is evident, as is the increase in horizontal load under reducing vertical load between C and D in the latter. The near zero vertical displacement at the centre of the beam under a 50 kN horizontal load (O to A) is confirmed in Figure 5(d).

The photograph of the deflected frame in Figure 6 at peak displacement reveals the flexibility of the frame generally, both in column sway and in beam flexure, but also the ability of the bamboo joints to resist substantial moments without visible distress is a major achievement - the joints are usually the most problematic aspect of bamboo construction.

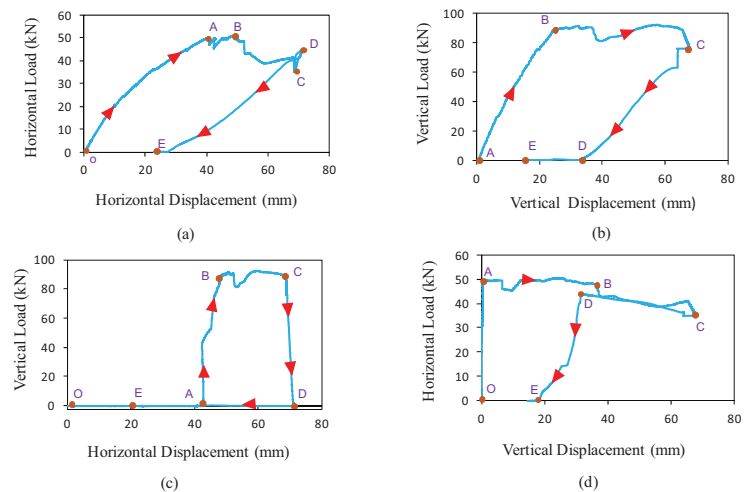


Figure 5: Plots of horizontal and vertical loads against horizontal and vertical displacements



Figure 6: Photograph of deflected frame during non-linear phase

4 LOAD-STRAIN RESULTS

In order to understand the variations in strain which occur in the various parts of the beam, not only does the inelastic behaviour play a part, but so also do the elastic bending

moments which pertain during the various stages of loading. Figure 7 shows the theoretical elastic bending moment diagrams at stages A and B in the load path. Here it should be observed that strains which arise during the application of vertical load are subtractive from horizontal load strains at the left hand column but additive at the right hand column. This leads to strain reversals in some strain gauges as the vertical load begins to be applied.

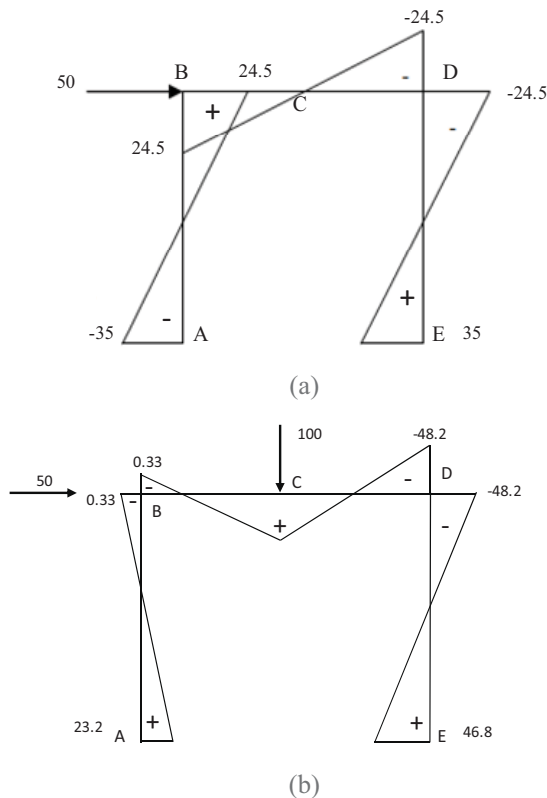


Figure 7: Theoretical elastic bending moment diagram under (a) horizontal and (b) combined loading

Considering selected horizontal load against strain plots first, gauge LT1 (see Figure 2) is the outermost gauge on the outside of the section at the top of the left hand column. The strain from O to A is negative (compressive, Figure 8(a)) as the column sags (that is, with positive moment) at this point, according to Figure 7(a). However, as vertical load is applied (A to B in Figure 8(a)), the moment direction is reversed and the strain is almost zero when the peak loads are applied, at B. At B, the moments here in the column are indeed small (Figure 7 (b)), confirming this low strain value. The continued application of horizontal (about 20 mm, from Figure 5(a)) and vertical displacement (about 40 mm from Figure 5(b)) in an attempt to increase the load further causes increased tension of the external bamboo culm, as evidenced from B to C in Figure 8(a). This suggests that this gauge is actively involved in monitoring the inelastic behaviour at this location in the frame. Load removal to almost zero strain at E indicates the complete relief of stress at this point.

This behaviour is in contrast to that at the inside face of the bottom of the right hand column (RB1, see Figures 2 and 8(b)). Here, according to Figure 7, moments are additive in

the two phases of loading, as may be seen by the positive strain from O to A being added to by strains from A to B as horizontal then vertical loads are applied (Figure 4).

In gauge BC1, at the underside of the centre of the beam, there is practically no strain until substantial horizontal load is applied (see the zero moment at this location in Figure 7(a)), then significant positive strain (on the tension side, in sagging) as the vertical load is applied (A to B). Interestingly, under the substantial inelastic displacements mentioned earlier between B and C, there is practically no strain increase between B and C in this figure, indicating this gauge is not actively involved in the inelastic behaviour.

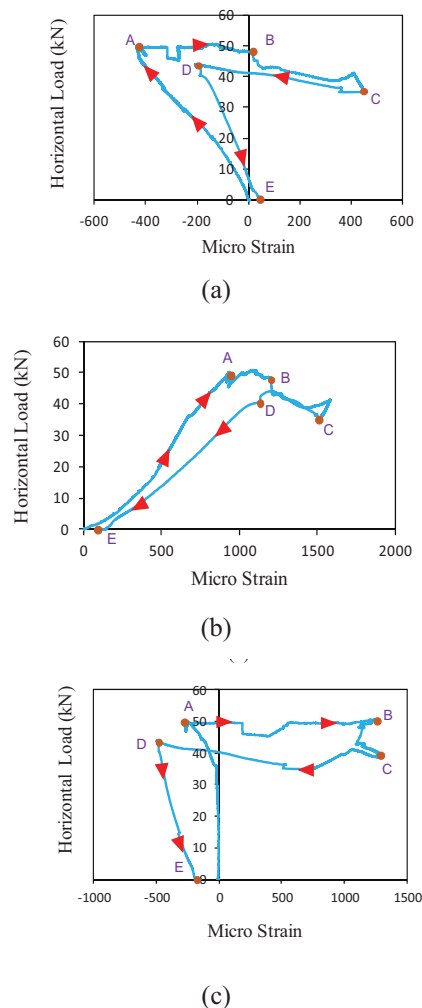


Figure 8: Horizontal load versus strain at locations (a) LT1 (b) RB1 (c) BC1

Similarly, when considering vertical load against strains, deeper insights can be obtained. For example, gauge LB1, at the outside bottom of the left hand column, positive strain occurs to point A under a sway load (Figure 9(a)), as expected from the hogging (that is, negative) moment here. When the vertical load is then applied, strain reversal occurs (A to B), as noted previously, due to the change in incremental bending moment here. However, strain reversal occurs yet again (B to C) under inelastic movement, where this is not just a relief of

strain to zero— it becomes positive again (to C) due to the continued horizontal movement at the top of the column stretching this gauge at this point – a double reversal under a monotonic load!

This phenomenon is not just confined to this case. Consider the case of BR4 (Figure 2), at the top surface of the right hand side of the beam. Here, strains are additive O to A to B (Figure 9(b)), as predicted by the additive nature of the bending moment diagrams here. However, when the inelastic behaviour occurs, strain reversal is significant (B to C) as the ongoing sway to the right under constant load causes a local compressive strain to C. Despite this, there is, as usual, almost zero residual strain under a significant residual horizontal displacement at zero load.

Finally, consideration of BC1 in Figure 9(c) shows that not only is there strain reversal here during the inelastic phase, as noted previously, but the stiffness as the vertical load is reduced is very similar to that when the load was applied at this gauge location, showing good elastic recovery.

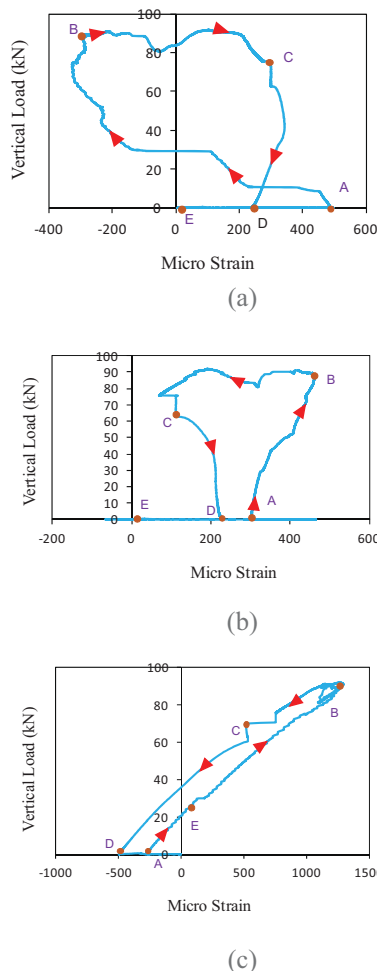


Figure 9: Vertical load versus strain at locations (a) LB1 (b) BR4 (c) BC1

5 DISCUSSION

While there are many more gauges which could be examined, these few examples indicate the degree of understanding that can be developed by a careful and

correlative examination of the load-displacement plots, bending moment diagrams and an array of load-strain plots. The frame is initially elastic and flexible; significant secondary moments arise due to this flexibility as vertical loads are subsequently applied; there is a well-defined load point at which no further load can be applied; the frame can be considered to be behaving inelastically and non-linearly and active locations in the plastic behaviour can be determined by the strain gauge responses. Despite this, on load removal, the frame is quite resilient with small residual strains and measurable deflections. The strain reversal patterns can be explained by the bending moment diagrams, the secondary moments which occur and the sense of the distortions which occur during non-linear behaviour.

The nature of the cause of the loss in stiffness due to the non-linear behaviour is not explored here but, suffice to say, conventional plastic hinges are not observed to occur – buckling or tensile tearing of the outside/inside culms did not occur. Indeed, based on the changes to the patterns of the strains through the depth of a section which is active in the non-linear phase, it would appear that shear delamination of the epoxy resin occurred, causing a stiffness reduction and load shedding. This is outside the scope of this paper.

6 CONCLUSIONS

This paper describes the results for the flexural testing of a bamboo-epoxy composite frame under horizontal and vertical loading. It has demonstrated the complex interacting effects which can occur when a flexible structure experiences secondary moments and load shedding. It also shows how an understanding of structural behaviour can be built up when load, displacement and strain data are combined to explain the response to the various phases of loading. In particular, it was described how bending moment diagrams can explain some strain reversals while others are explained by the nature of the frame mechanism which evolved during post-peak loading.

REFERENCES

- [1] Lugt, P., Dobbels, A. A. J. F. and Janssen, J. J. A. (2005), "An environmental, economic and practical assessment of bamboo as a building material for supporting structures", *Construction and Building Materials*, 9, 648-656.
- [2] Deshmukh, P. and Attar, A.C. (2013), Development and construction of Bamboo Roofing system- An Eco-friendly system", *International Journal of Scientific & Engineering Research*, 4, 8, 1262-1268.
- [3] Ghavami, K., (2007), "Low cost energy saving construction materials", *Proc. International conference on Modern Bamboo Structures*, 28-30 October, Changsha, China, 5-21.
- [4] NBC (2005), "Bureau of Indian Standards", *Building Construction Practices Including Painting, Varnishing and Allied Finishes Sectional Committee, CED 13*.
- [5] Sabbir, A., Ashfaul Hoq, S.M., and Fancy, S.F., (2011), "Determination of Tensile Property of Bamboo for Using as Potential Reinforcement in the Concrete", *International Journal of Civil & Environmental Engineering*, 11, 5 47-5.
- [6] Sakaray, H., Vamsi Krishna Togati, N.V. and Ramana Reddy, I.V. (2012), "Investigation of properties of bamboo as

reinforcing materials in concrete”, *International Journal of Engineering*, 2, 1, 77-83.

[7] Bureau of Indian Standards (BIS), *CED 13/T-103*, Manak Bhavan, New Delhi.

[8] Gupta, M., Bhalla, S., Bhagat, D., West, R. P. and Nagpal, A. (2014), “Pre-Engineered Construction Using Bamboo Portal Frame”, *Proceedings of 9th Biennial Conference on Structural Engineering Convention (SEC 2014)*, New Delhi, pp. 371.

Dynamic analysis of the nonlinear response of high density fuel storage racks

Alberto Gonzalez Merino^{1,2}, Luis Costas de la Peña¹ Arturo Gonzalez²

¹ Department of analysis and design, Equipos Nucleares, Avda. Juan Carlos I, 8 Maliaño, 39600, Spain

² School of Civil Engineering, University College Belfield, Dublin 4, Ireland
email: gonzalez.alberto@ensa.es, costas@ensa.es, arturo.gonzalez@ucd.ie

ABSTRACT: High Density Spent Fuel Storage racks are steel structures designed to hold nuclear spent fuel assemblies removed from the nuclear power reactor. Weighing around 60 tons, they are 5m high free-standing structures resting on the floor of a 12 m depth pool and separated by only a few centimetres. Their underwater seismic response is a troubling safety issue, especially after Fukushima nuclear disaster. However, only limited basic guidelines have been provided as regulatory design criteria to date. The racks' design deals with a very highly nonlinear behaviour, a transient dynamic response and a fluid-structure interaction problem. Industry is currently using available computer-aided finite element analysis software to solve the design problem in a cost-effective manner but some dispersion of results still exists. Hence, the nuclear regulatory authorities are requiring an evaluation of the current uncertainty associated to the assessment of rack displacements, rocking and maximum forces on supports. This paper discusses the main difficulties faced during the seismic analysis and presents an ad-hoc analysis methodology based on the hydrodynamic mass concept which takes advantage of a simplifying thermal analogy. The methodology, implemented in ANSYS FE Mechanical is hereby described for a reduced scale 2-rack model where the coupling effect of water in the dynamic motion of immersed racks is quantified and displacements and forces are provided. Finally, methodology assumptions are discussed and lessons learnt about the behaviour trends are summarized.

KEY WORDS: racks, free-standing; FEM; dynamic analysis; nonlinear; fluid-structure interaction; hydrodynamic mass.

1 INTRODUCTION

High Density Spent Fuel Storage (HDSFS) racks are used in the first step of the nuclear waste management process, during the wet storage of the irradiated assemblies. As shown in Figure 1, there may be numerous free-standing racks nestled in the depths of the spent fuel pool. They are designed to maximize the storage capacity of an existing pool, so the space between units is reduced as much as possible (i.e. in the order of a few centimetres).

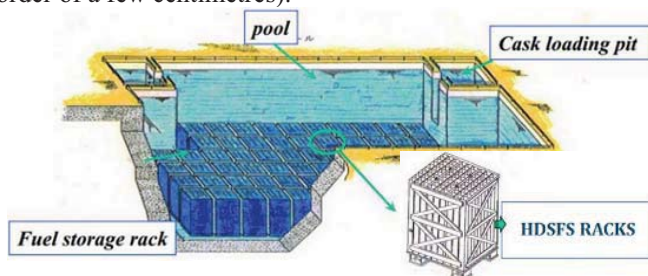


Figure 1. Location of racks in the fuel storage pool

The rack slenderness ratio determinates its seismic behaviour by taking side for either a rocking or sliding movement. The distinct geometries combined with a large spectrum of fuel distributions, types and earthquake accelerogram convert the design of racks into a singular engineering problem.

Equipos Nucleares, S.A. (ENSA) is a worldwide expert in racks design, manufacture and installation (Figure 2) [1][2][3] and has recently launched a research project to improve the understanding of the rack response and to reduce the existing uncertainty in analysis.

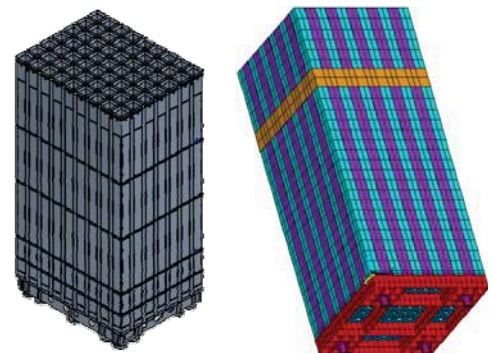


Figure 2. Sketch of a HDSFS rack manufactured by ENSA and its detailed 3D FE model

2 CONTEXT AND DIFFICULTIES

The typical features that characterize HDSFS racks are summarized hereafter:

- unique and singular structure,
- tailored dimensions adapted to the spent fuel pool geometry,
- made of structural stainless steel and neutron-absorbing materials,
- installation in radioactive ambient with restricted access preventing from any ground fixation,
- free-standing structure just resting on the pool depths,
- multi-body analysis combining several racks with multiple fuel assemblies rattling inside its storage cells,
- submerged conditions (under 12 m water head),
- nuclear regulation imposing the highest seismic requirements.

3 DESCRIPTION OF THE DYNAMIC PROBLEM

The design of the rack system for seismic loading faces the three main challenges: a nonlinear response, a transient dynamic problem and a Fluid-Structure Interaction (FSI). These phenomena are reviewed next.

3.1 Nonlinear response

It has been shown that the vibrating frequency of the free-standing rack decreases when the excitation increases due to the combination of rocking and sliding motions [4]. This feature is the best example of the high nonlinear behaviour of racks under seismic loads. Racks units suffer deformations and large amplitude displacements (e.g. sliding, rocking and lift-off) which constantly change the boundary conditions and alter the initial thickness of water gaps between racks. They may also cause the impact of fuel assemblies on the storage cell as well as between racks units.

These contacts represent the main source of nonlinearities as they create changing-status singularities affecting the stiffness of the system whether parts are touching or separated. Initial contact points can be cleared (e.g. uplifted support feet), and new ones can appear at each instant (e.g. physical contact between nearby racks or between a rack and the pool walls). After the non-interpenetration contact event, the two solids may slide relative to each other along the interface. New forces appear in the surface of contact in agreement with new boundary conditions: a normal reaction and a frictional force opposite to the movement. The value of these forces is uncertain and depends on the surface material stiffness and its friction coefficient.

As a result of these nonlinearities, the successive finite displacements are not commutable. Hence, unless the 3D seismic components are applied simultaneously, nonlinear displacements are not accurately predicted. This issue is overcome through a transient analysis along the whole duration of the seism where the outputs at the end of a calculus step are taken as initial conditions for the next step.

3.2 Transient dynamic problem

The seismic analysis requires the resolution of a system of equations which involve time-dependent variables. Due to the nonlinearities inherent to the racks system, the response of the rack system does not satisfy the superposition principle and the equation of motion must be solved by direct numerical integration. Direct integration methods attempt to satisfy equilibrium with finite precision at discrete points in space and time. In other words, individual numerical calculations have to be computed to solve the ordinary differential equation of motion at a series of discrete points in time which are small relative to loading duration.

It is therefore necessary to implement an iterative numerical method to solve the Finite Element (FE) equations of motion at multiple time steps. The basic equation of motion is given by Equation 1:

$$[M]\{\ddot{u}(t)\} + [C]\{\dot{u}(t)\} + [K]\{u(t)\} = \{F(t)\} \quad (1)$$

where $[M]$, $[C]$ and $[K]$ are the mass, damping and stiffness matrices of the structural system respectively and $\{u(t)\}$, $\{\dot{u}(t) = du(t)/dt\}$ and $\{\ddot{u}(t) = d^2u(t)/dt^2\}$ are vectors containing the translational and rotational degrees of freedom of the structure and their respective velocities and accelerations. $\{F(t)\}$ is the time-dependent vector of forces applied at each of the degrees of freedom.

The literature proposes a huge number of well-developed step by step iterative algorithms. Their accuracy and stability directly depend on the time step parameter and on the order of the derivate. However, the higher accuracy of the simulation, the lower becomes the stability field [5]. Due to the nonlinear behaviour of racks, only single-step, implicit, unconditional stable methods are suited to the rack seismic analysis.

3.3 Fluid-Structure interaction (FSI)

Besides the buoyancy vertical force, the presence of water determines the dynamic response of the racks and fuel assemblies. During a seismic event, the ground acceleration is transmitted from the pool to the racks by friction on feet and by compression throughout the water volume. In particular, the inertial effects derived from this water acceleration lead to coupling forces between the racks, and between the racks and the pool walls. It is noted that this FSI has to be considered for every submerged element, including the fuel assemblies inside their cells and for the racks themselves inside the spent fuel pool.

The magnitude of the FSI phenomena can be explained by the geometrical relationships inside the pool. Racks have a prismatic shape with large faces (the area of a rack face is in the order of 10 m^2) separated by relatively small water gaps (in the order of 50 mm). As a result, the motion of a rack boosts the fluid pressure within the water gaps and alters the balance of the complete system. This effect has an important impact on the dynamic behaviour, particularly on the natural frequencies.

The previous hydrodynamic pressure should be ideally calculated through Navier-Stokes equation for the 3D turbulent flow, but this is difficult and computationally expensive even in simple cases. Cost-effective analyses assume some simplification in water behaviour, ignore fluid damping and sloshing effects, and use the hydrodynamic mass approach. The concept of hydrodynamic mass is defined as the equivalent mass of water vibrating with the rack and it represents the dynamic external effect of the surrounding water volume [6]. In brief, the fluid is treated as a virtual extension of the structure changing its effective mass. Thus, Equation 1 becomes:

$$[M + m_{hydro}]\{\ddot{u}(t)\} + [C]\{\dot{u}(t)\} + [K]\{u(t)\} = \{F(t)\} \quad (2)$$

where the added matrix $[m_{hydro}]$ is referred to as hydrodynamic mass and represents the added masses associated to each rack itself (diagonal terms) and the inertial coupling among the multibody system (off-diagonal terms). Since this matrix multiplies the acceleration vector $\{\ddot{u}(t)\}$, it assigns a proper weight to each rack acceleration.

4 APPLICATION AND COMPUTATION OF RESULTS

The challenges introduced in Section 3, have been overcome by the use of an ad-hoc methodology specifically developed for ANSYS FE mechanical. This cost-effective approach to consider the FSI is based on the aforementioned hydrodynamic mass concept and takes advantage of a thermal analogy to perform the ensemble of calculations in unique software.

Both hydrodynamic masses and transient displacements are assessed here for a reduced scale 2-rack model. This illustrative application is aimed to validate the accuracy of the numerical results with experimental data from a future physical model test [7]. The general features of the mock-up shown in Figures 3 and 4 are summarized in Table 1.

Table 1. Description of the testing racks

Racks	2	units
Clearance	40	mm
Length	1919	mm
Width	696	mm
Height	1774	mm
Weight	2300	Kg

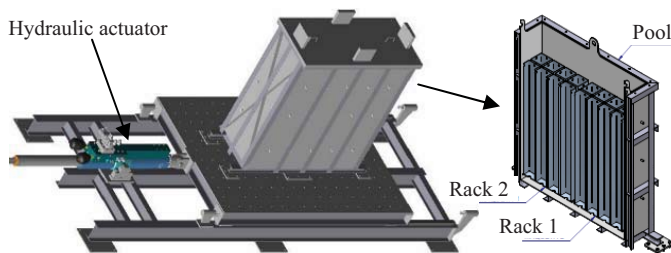


Figure 3. Sketch of the pool screwed to the vibration table.

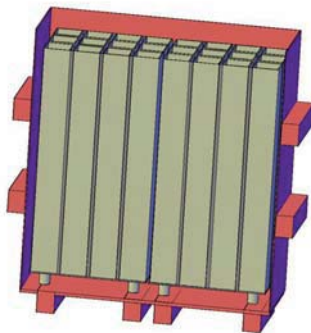


Figure 4. Detail of the 2 free-standing racks juxtaposed inside the pool.

4.1 Computation of the hydrodynamic masses through a thermal approach

In a first approach, the terms of the hydrodynamic mass matrix could be directly obtained by accelerating a rack and assessing the resulting hydrodynamic pressures over the racks faces and the pool walls. This scheme is easy to understand but difficult to implement due to the complex fluid behavior.

Alternatively, some cost-effective simplifications can be undertaken. If free surface sloshing is neglected and the water is assumed as inviscid and irrotational, the relationship

between the acceleration of the rack and the associated hydrodynamic pressure can be defined via the potential flow theory. In addition, if also the fluid compressibility is neglected, the velocity potential function Φ satisfies the Laplace equation ($\nabla^2 \Phi = 0$) and the pressure field can be determined via the Bernoulli equation. Boundary conditions are given by the acceleration of the in-water structures so the fluid acceleration is therefore equal to the normal acceleration of the wet interface, and zero in the free surface (no sloshing assumption). This mathematical problem has been solved for simple configurations so analytical formulations are currently available for small relative oscillation amplitudes of two coaxial cylinders in 2D [8], two coaxial squares in 2D [9], and two coaxial rectangles in 3D [10]. However, for more complex geometries, a Computational Fluid Dynamics (CFD) model of the enclosed fluid domain remains necessary.

At this point, it is of utmost importance to realise that the potential fluid flow shows a complete analogy with the steady-state heat conduction phenomena. In other words, the previous CFD problem is similar to a thermal problem governed by identical equations but other variables: hydrodynamic pressure is equivalent to temperature, acceleration is equivalent to heat flux, and fluid density is equivalent to the inverse of the heat conductivity. Thus, evaluate hydrodynamic pressures over faces and walls turns into getting a temperature distribution. For a given problem, the thermal approach offers a high accuracy and a computational time economy.

Consequently, the associated hydrodynamic masses can be assessed through the thermal FE model presented in Figure 5. Such a model allows to take into account the 3D fluid motion (i.e. heat flux under and above the rack body). The pool and racks external faces are assumed to be non-deformable. The clearance volume around racks is discretised in heat conduction ANSYS elements type SOLID 70.

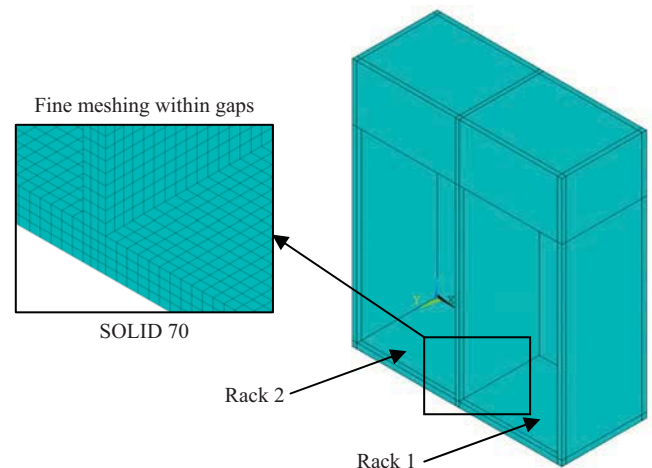


Figure 5. Equivalent thermal ANSYS FE model for the computation of the hydrodynamic masses

The thermal approach is described next. A couple of thermal sources are placed on two opposite rack's faces (positive in one side and negative in the other) like a virtual displacement. Then, the resulting temperature distribution is assessed and integrated along the faces of the racks affected by the

interaction. The procedure is repeated for each rack unit, in a manner that the added hydrodynamic mass ($M_{i,j}$), in the direction 'i' corresponding to a specific rack acceleration in the direction 'j' (\ddot{u}_j) is computed as the surface integral through the i-normal face of the temperature produced by a heat flux emitted from the j-normal faces.

According to the concept, a symmetrical system should lead to a symmetrical hydrodynamic mass matrix. This can be verified in Table 2 which presents the hydrodynamic masses in the x-direction added to each structure under a unitary acceleration in the x-direction of each structure. The hydrodynamic masses in other directions could be also assessed using the same procedure.

Table 2. Hydrodynamic mass matrix in x-direction

	$M_{xx, rack1}$	$M_{xx, rack2}$	$M_{xx, pool}$
$\ddot{u}_{x, rack1}$	6435	-1591	-5965
$\ddot{u}_{x, rack2}$	-1591	6435	-5965
$\ddot{u}_{x, pool}$	-5965	-5965	15302

where " $\ddot{u}_{x, index}$ " refers to structure where the unitary x-acceleration is applied (in m/s^2) and " $M_{xx, index}$ " represents the x-component (in kg) of the hydrodynamic mass corresponding to such an x-acceleration. For example, when the rack1 is accelerated in the x-direction ($\ddot{u}_{x, rack1} = 1 m/s^2$), the water induces a x-force over this rack 1 equivalent to increasing its mass ($M_{xx, rack1} = 6435$ kg).

It should be noted that the terms of the hydrodynamic mass matrix are affected by any relative displacement of racks. The variation throughout time in the thickness of the water gaps around the racks changes the geometrical relationships and therefore the hydrodynamic pressures field. The implemented methodology assumes that the water coupling forces limits the relative displacement between racks, so hydrodynamic mass matrix is assessed only once and just for the initial configuration. The numerical results will show that racks moves nearly in phase, so it seems acceptable to keep the hydrodynamic masses constant during the whole transient analysis.

4.2 Transient dynamic analysis of the seism

Once the hydrodynamic masses associated to each rack have been evaluated, they are entered into the dynamic FE model of Figure 6. Due to the complexity of the transitory analysis and the computation cost, the model should be as simple as possible: the cellular structure is represented through a unique beam, the fuel assemblies are grouped in a vertical rigid body, the base plate is shaped as a rigid shell and the total mass is discretised in 7 lumped points. Nevertheless, a reliable model has to maintain the original dynamic properties (i.e. natural vibration frequencies), so the stiffness of different elements must be carefully adapted. In addition, it should be built in 3D in order to reproduce the real spatial motion which cannot be approached by a 2D superposition principle as the behaviour is highly nonlinear.

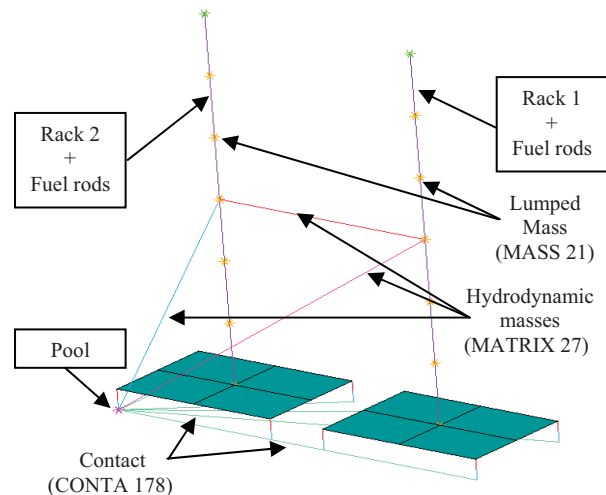


Figure 6. Dynamic FE model of the 2-racks system and the FSI coupling elements

It should be noted that the pool structure is considered as an infinitely rigid solid and therefore modelled by a unique node which is connected to the racks by the following ANSYS elements:

- CONTA 178, to model the free-standing condition: elastic contacts and Coulomb model of friction (coefficient = 0.50)
- MATRIX 27 with forced-distributed-surface contact (MPC), to add the coupling hydrodynamic masses and spread the hydrodynamic pressure over the entire rack faces.

As outlined in Section 3.2, a transitory analysis with full direct integration becomes necessary to accurately solve Equation (2) throughout the entire seismic event. Hence, a generalized α -method, available in ANSYS as 'HTT' algorithm, has been used to analyse the nonlinear behaviour of the racks under the 12 sec duration design earthquake shown in Figure 7, which reaches peaks of acceleration up to $8.75 m/s^2$.

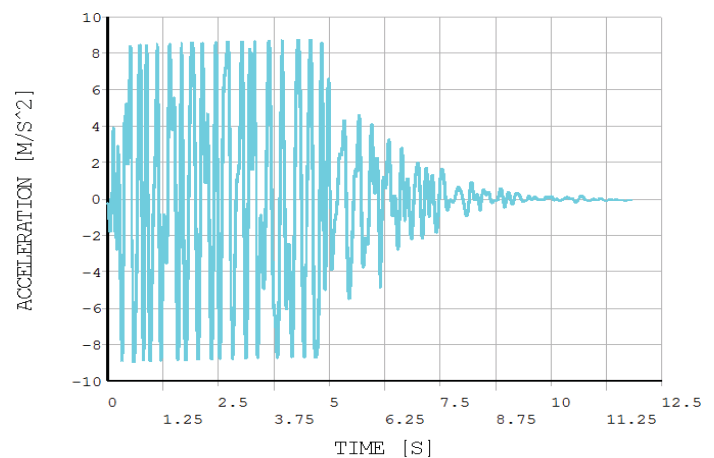


Figure 7. Design earthquake time-history

4.3 Numerical results: displacements and forces

This section provides the most relevant results characterizing the racks behavior in terms of base and top displacements (Figure 8), relative displacements (Figure 9 and Figure 10), vertical lifting of a foot (Figure 11) and reaction force on a foot (Figure 12).

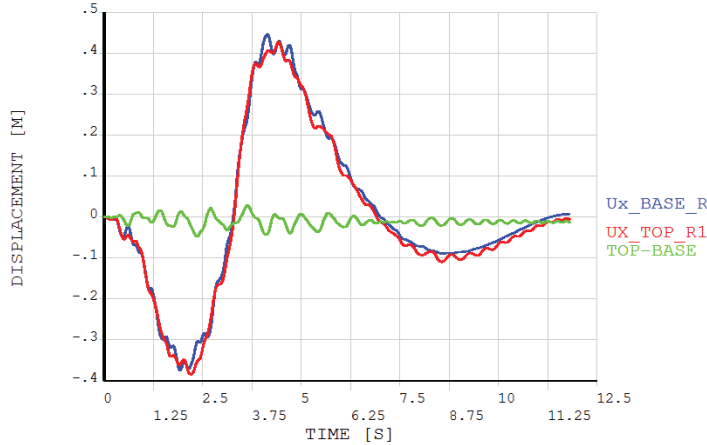


Figure 8. Top and base absolute and differential displacements in X of rack1

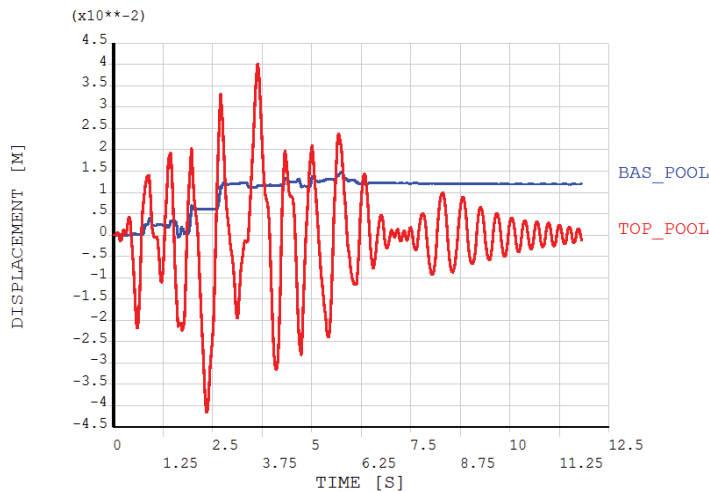


Figure 9. Top and base relative displacements in X between rack1 and pool

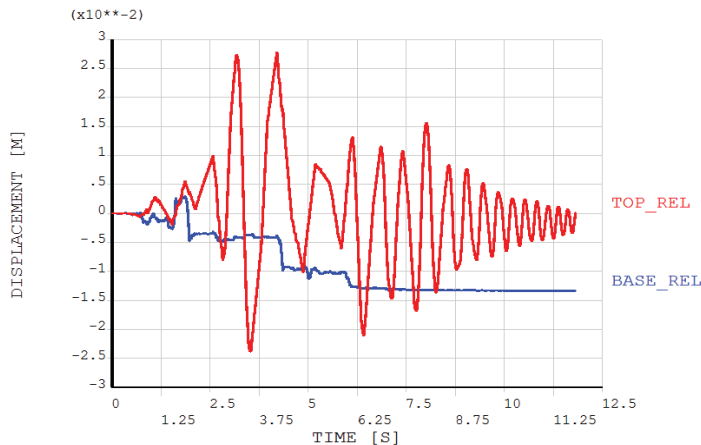


Figure 10. Top and base relative displacements in X between rack1 and rack2

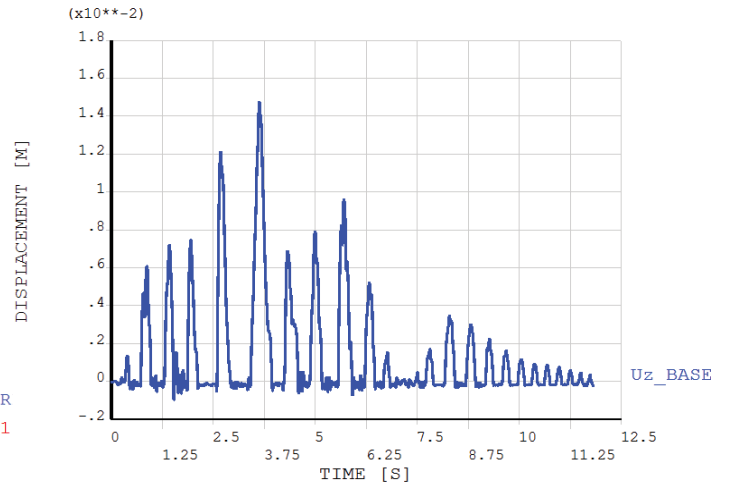


Figure 11. Vertical lifting of a Rack1 foot

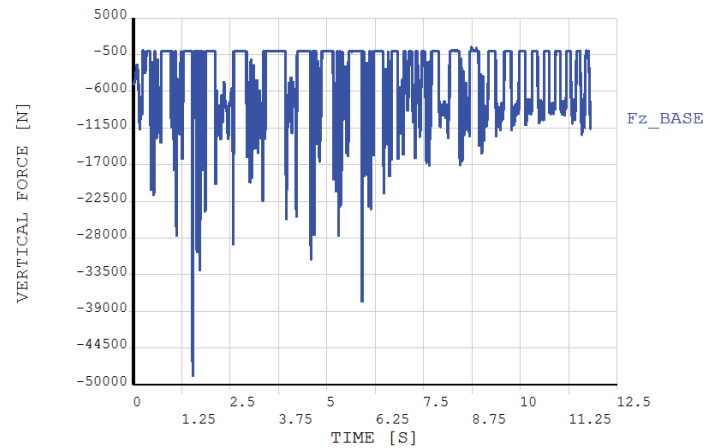


Figure 12. Vertical force in a Rack1 foot

Racks follow, in some way, the pattern of the ground motion which explain the big displacements as far as 40 cm, are shown in Figure 8. However, as per Figure 9 the relative displacement between a rack and the pool remains in the order of some centimetres for both top and base levels. The same comment can be drawn from Figure 10 regarding the relative displacement between the 2 racks. Nonetheless it should be noted that the relative displacements at the top level are much more instable with higher amplitudes than at the base level. It is the evidence of a non-negligible rocking behaviour around their axis. These oscillations are also visible for a single rack in the differential displacement of the top with respect of the base green line (labelled 'TOP-BASE') in Figure 8.

It is noted that both types of relative displacements remain below the initial gap, so no horizontal collision is expected to occur. Indeed, as far as the racks get closer, the clearance becomes lower and the hydrodynamic masses should be updated as outlined in Section 4.1, which should exponentially increase the coupling forces and further reduce the predicted displacements.

Regarding the vertical behaviour, Figure 11 shows multiple uplifting events of a singular foot up to 15 mm. For the given earthquake and case study, they are produced by the already

mentioned rocking behaviour. Even if the rack did not completely take off, the return movement cause strong impacts of 50 kN as seen in Figure 12.

5 CONCLUSIONS AND FUTURE WORK

This paper has pointed out the main difficulties involved in the design of high density spent fuel storage racks. In order to address the latter, a successful analysis methodology based on a few simplification assumptions has been proposed to determine their seismic behaviour when immersed in water. Main results regarding the transient displacements and impact forces have been given for a specific geometry. The following conclusions can be drawn for predesign purposes:

- Reduced clearance leads to an important coupling effect between racks which are otherwise independent.
- The terms of the hydrodynamic mass matrix explicitly show how the coupling forces are established between racks and between racks and pool.
- In particular, the relationship between the area of the face and the thickness of the water gaps is key in the importance of the fluid-structure coupling.
- For the study case, these values reach up to 300% of the rack self-weight. It means that the submerged racks behave as if they weighed 6435 kg extra when they are accelerated.
- The fluid-structure coupling becomes stronger when the gaps between racks become lower. Such a effect pushes the ensemble towards a rigid solid motion where both racks move nearly in phase.
- Small relative displacements would allow the use of a constant hydrodynamic mass matrix throughout the transient analysis which can save much computation time.
- The rack slenderness ratio determinates its rocking or sliding behaviour for a given configuration, seismic time-history and friction coefficient.

Further steps seek to assess the accuracy of the outlined analysis methodology and refine the current settings if possible. For this purpose, a physical model test will follow to validate the correlation between the computed results and the experimental data, and to evaluate the uncertainties inherent to the water assumptions, to the FE modelling and to the numerical time-integration algorithm. Multiple testing configurations are planned aiming at performing a sensitivity analysis of the governing parameters as well as quantifying the influence of changes in variables such as the initial clearance, the friction coefficients, the seismic time-history features, the fuel load distributions, etc. on the response.

In a final stage, a statistical analysis will be performed and guidelines for a probabilistic design provided. The ultimate goal is to be able to predict the behaviour patterns of any kind of racks configurations, with stochastic features, under different loading conditions through low cost analysis and with a bounded error.

ACKNOWLEDGMENTS



The main author would like to express his sincere gratitude to Equipos Nucleares S.A. (ENSA) for the opportunity to join their team as a research engineer and all authors thank the European Union's Horizon 2020 research and innovation programme funding this project under the Marie Skłodowska-Curie grant agreement No. 642453 (<http://trussitn.eu>).

REFERENCES

- [1] L. Costas, E. Gomez, 'Radwaste Management Spent fuel racks up', *Nuclear engineering international*, Global Trade Media, 2004.
- [2] L. Costas, J. Tovar Albillos, 'Rack to store fuels from nuclear reactors', *Patent US 20030174801 A1*, 2003.
- [3] L. Costas, J. Tovar Albillos, 'Segmented lattice rack to store fuels coming from nuclear reactors', *Patent US 6674827 B2*, 2004.
- [4] R. Moudrik, J.C. Queval, F. Gantenbein, 'Test and calculations on a scale one spent fuel storage rack', *International Conference on Structural Mechanics SMiRT*, Porto Alegre, 1995.
- [5] R. Andujar, J. Roset, V. Kilar, Interdisciplinary approach to numerical methods for structural dynamics, *World Applied Sciences journal*, Vol. 14, No. 8, 2011.
- [6] H. Chung, S. Chen, 'Hydrodynamic mass, CONF-840647—9, United States Government, 1984.
- [7] Gobierno de España, IHcantabria, ENSA, 'ANSTER - Almacenamiento Nuclear Seguro Ante TERremotos', <http://anster.ihcantabria.es/>
- [8] R. J. Fritz, 'Effect of liquids on the Dynamic Motions of immersed solids', *Journal of engineering for industry*, Trans, 167-173, 1972.
- [9] A. I. Soler, K.O. Singh, 'Dynamic coupling in a closely spaced two-body system vibrating in a liquid medium: the case of fuel racks', *3rd Keswick International conference in nuclear plants*, Keswick, 1982.
- [10] J. Stabel, M. Ren, H. Swelim, 'Calculation of seismic loads on fuel storage racks under consideration of fluid-structure interaction', *12th International conference on SMiRT*, 61-66 Stuttgart, 1993.

The Shelbourne Hotel – Long Term Innovative Treatment of Corroding Steel Frame

Enda McKenna¹, Brian McFarland², Jason Kearney³, Dermot Collier⁴

¹²³McFarland Associates Ltd, Unit A3, Sydenham Business Park, Harbour Court, 5 Heron Road, Belfast, BT3 9HB

⁴ACOL Ltd, Merrywell, Drumree, Co. Meath

email: ¹enda.mckenna@mcfassoc.com, ²brian.mcfarland@mcfassoc.com; ³jason.kearney@mcfassoc.com, ⁴dermot@acol.ie

ABSTRACT: The Shelbourne Hotel, Dublin first opened in 1824 and is without doubt one of the most prestigious and well known hotels in Ireland. Throughout the building's history, numerous structural alterations have occurred, one of which was the addition of an extra floor, believed to have been undertaken in 1901-1902. Structural steelwork was installed at a high level which was subsequently encased in concrete. During the recent remedial works to the external façade of the hotel, this steelwork was observed to be corroding with the expansive accumulation of rust product causing the encased concrete to crack. Steel frame corrosion (also known as 'Regents Street Disease') is becoming more problematic as these structures start to show their age and its early detection and correct diagnosis is vital for the future serviceability of the structure. Non-Destructive Testing (NDT) was undertaken on the concrete and an innovative cathodic protection treatment was installed using Hybrid Sacrificial Anodes to re-passivate the steel/concrete interface and provide long-term galvanic protection. A remote monitoring system was also installed to provide continuous feedback on the system's performance and trigger values have been set as early warnings to detect any adverse changes. This paper will look at Regents Street Disease in more detail including its: causes; detection; and possible repair scenarios based on the authors' experiences.

KEY WORDS: Steel Frame Corrosion, Regents Street Disease, Cathodic Protection, Anodes, Restoration

1 BACKGROUND

The cracking, displacement and spalling of stone and masonry due to the corrosion of steelwork is becoming increasingly common in steel-framed buildings constructed during the first half of the 20th Century [1]. This corrosion not only causes unsightly defects on our heritage structures, more worryingly, it can pose a serious health and safety risk to building users and the general public through the potential for falling debris and possible element/structural failure. To the untrained eye, it can be very difficult to accurately assess the causes of seemingly random cracking on façades that are attributed to steel frame corrosion. Furthermore, undertaking traditional remedial works such as removal of the cladding and treatment of the steelwork can be extremely disruptive and expensive.

The term 'Regents Street Disease' was first coined in the 1970s after the famous London address in which many of its buildings were displaying this form of deterioration. Corrosion of buildings and civil structures, many of which are now surviving beyond their intended design lives, is becoming a more serious and costly problem to deal with for asset owners, architects and engineers. Maintaining and extending the serviceable lives of our ageing infrastructure is now becoming a priority.

According to the National Association of Corrosion Engineers (NACE), one of the world's leading authorities on corrosion engineering and control, the annual cost of corrosion to the UK in 2008 was \$70.6 billion representing 3.1% of GDP [2]. It has also been suggested by others that on average, one ton of steel is lost every ninety seconds in the UK as a direct consequence of corrosion [3].

2 INTRODUCTION

Prior to the mid 1800's, much of our built heritage in larger towns and cities utilised timber, stone and masonry. It was not until the invention of the Bessemer steelmaking process in 1856, as well as the open hearth processes of 1868, that the first use of steel in buildings started to take off [1]. The construction of the Home Insurance Building, Chicago, in 1884-5, marked the development of steel frame construction techniques and the modern era of multi storey buildings.

Unfortunately, during the construction of these buildings, engineers and architects of the time did not take into consideration the potential defects that would later appear



Figure 1. Cracking on Masonry Façade Attributed to Steel Corrosion. Often Wrongly Identified as Structural Movement of Foundations etc

due to inappropriate detailing. Early 20th century steel framed structures were built with their stone/masonry façade tightly constructed around the steelwork. Any cavities tended to be filled with ‘builder’s rubble’ or other porous materials. It was assumed that the masonry surrounding the steelwork would offer sufficient protection from moisture ingress and thus protect the steel.



Figure 2. Corroding Steel Frame Filled with Porous ‘Builders Rubble’ on an Irish Heritage Structure. Note Vertical Cracking on Brickwork Façade over Steelwork

3 THE CORROSION PROCESS

Steel corrodes as it is not a naturally occurring material and constantly tries to return to its basic iron ore state. Most metals will eventually corrode in contact with their surroundings with exceptions from those which are found and used in their original state, such as gold and platinum.

Steelwork (and reinforcement) cast in concrete is protected from corrosion initially due to the high alkalinity of the freshly placed concrete surrounding it. The steel becomes passive due to the formation of a stable oxide film on its surface. The onset of corrosion can occur once this passive layer breaks down. This can occur due to the presence of aggressive substances such as chloride ions or through a process known as carbonation. Carbonation occurs in concrete when atmospheric carbon dioxide reacts with concrete and reduces its alkalinity. As moisture and oxygen enter the concrete matrix at cracks or through diffusion, corrosion can begin. The corrosion reaction will depend on various factors such as: oxygen availability; moisture availability; presence of chlorides or sulphates; and temperature. In order to halt this corrosion reaction, the environment or the reaction must be changed.

In the presence of moisture and oxygen, expansive corrosion products accumulate on the steel surface which can be upwards of ten times the size of the original consumed metal. For example, for every 1mm of steel that corrodes, 10mm of expansive corrosion product can be produced. This accumulation of rust product displaces the materials abutting the steel which in turn can cause cracking and open joints

further. As corrosion continues, cracks and joints open further allowing greater access for moisture and as such accelerates the problem. Today, steelwork is coated and more modern structures incorporate a cavity which prevents moisture build up around the steel frame. The risk of displacing and cracking on cladding materials is thus greatly reduced. However, the detection of any corrosion is almost impossible as there can be limited evidence of distress on the façade.

4 DETECTION AND ASSESSMENT METHODS

4.1 Visual Inspection

A detailed visual inspection is generally the first method of detection and assessment on any structure. Plotting elevational defects on detailed drawings of the façade not only indicates possible links between the causes and effects of corrosion but may also indicate the extent of corrosion progression. Gaining an appreciation of the structural makeup through historic drawings and surveys can lead to an indication of the source of the defects observed on the façades.

In conjunction with visual surveys, it is beneficial to supplement this data with information on crack widths. Opportunities may also arise where cracks or joints are large enough to insert optical probes or cameras to enable a visible inspection of any concealed voids.



Figure 3. Section from a Visual Survey Drawing of an Early 1900s Office Building in Belfast [7]. Note Majority of Cracking between Windows with Structural Steelwork Behind.

Ineffective detailing as well as a general lack of maintenance of gutters and other rainwater goods are probably the single biggest sources of corrosion on steel framed buildings and as such should be given due regard during visual inspections.

4.2 Non-Destructive Testing (NDT)

The majority of NDT options available for reinforced concrete are also applicable for most early 20th century steel framed structures due to the presence of the mortar in-fill around the

steelwork. Care must be taken when interpreting the results from these test methods as variations in mortar infill quality and presence can lead to inaccurate readings.

The most important tests to be undertaken include the removal of concrete/mortar samples for *laboratory analysis* and *carbonation depth testing*. Laboratory analysis includes the determination and level of potentially deleterious contents such as chlorides and sulphates. Carbonation tests can be taken on site and the results viewed instantaneously through the use of a pH indicator solution such as phenolphthalein. *Half-cell potential surveys* indicate the likelihood and location of any corrosion cells occurring on the steel. In some instances, moistening of the test surface may be required to aid in the collection of data. The findings from this survey can help locate areas of potential concern for further intrusive investigations. *Linear Polarisation Resistance (LPR) Corrosion Rate measurements* can provide an indication of the actual corrosion rates on the steel and can be used to aid in the calculation of the section loss on the steel. *Electrical resistivity measurements* are related to corrosion rate measurements as the resistivity and moisture content of the medium in contact with the steel can give an indication of the severity of corrosion if it were occurring.

A wealth of other test methods including: infrared; ultrasonic; and electromagnetic techniques are also available which can aid in the interpretation of detailing the structure.

However, taking the various assessment methods into consideration, one of the most effective methods of assessment to verify the findings from the various forms of NDT, is the localised removal of the façade to inspect the steelwork behind. Although semi-disruptive, and difficult to gain approval on listed heritage structures, it can provide a wealth of information such as: construction details; member sizes; and the ability to visually inspect. This exercise also allows the engineer to undertake steel thickness measurements to determine actual loss of section and therefore determine if there are any potential structural implications.

5 TRADITIONAL REPAIR OPTIONS

A failure to understand the inherent problems with these structures inevitably leads to wrong and insufficient remedial repairs being undertaken. Such short term repairs include: cracks sealed and repaired over; new coatings provided; brickwork replaced; and mortar beds raked out and filled in. The trouble with these repairs, although at times temporarily sufficient as they may reduce oxygen and moisture availability, is the fact that they do not deal with the source of the problem i.e. the corrosion of the steelwork behind, and they can be extremely expensive and disruptive to undertake.

A more medium term repair would involve the localised removal of the façade to gain access to the steelwork. Once the cladding has been removed, traditional repair methods can include:



Figure 3. Inappropriate Repair of Masonry Façade on Historic Structure in Belfast displaying Steel Frame Corrosion using Sand Cement

- Removal of the corrosion product build up through mechanical means, such as grit blasting or needle gunning, leaving the steel clean and bright;
- Application of a zinc rich coating on the surfaces to offer protection from further corrosion;
- Repair, upgrade and installation of new water management and moisture control methods such as broken downpipes and the inclusion of new DPCs; and
- Replacement of cladding with the inclusion of a void between the steelwork and cladding.

The above can be an effective repair which may last upwards of 10 to 15 years depending on various factors such as: quality of materials used; quality of workmanship; and regular maintenance. However, the removal of the defective cladding and treatment of the steel behind is highly disruptive and expensive. Areas of the structure not showing distress at the repair stage are usually not attended to and as such will inevitably corrode at a later date.

The long term repair option would include the use of cathodic protection to arrest the corrosion process. Cathodic protection provides protection to steel through the passage of a small D.C. current through the electrolyte (concrete) from an anode and onto the steel surface. Cathodic protection of steel is a well-documented approach to the long term protection of steel against corrosion. There are typically three types of systems:

1. Galvanic Anode Cathodic Protection (GACP);
2. Impressed Current Cathodic Protection (ICCP); and
3. Hybrid Protection (combination of both above systems).

GACP is based on the principal of dissimilar metal corrosion and the relative position of specific metals in the galvanic series. The current generated from a sacrificial anode is

directly related to the environment within which it is placed. Anodes are directly connected to the steel. As the anode material (such as zinc) would be higher in the galvanic corrosion chart in comparison with the steel, if corrosion was to occur, the anode would be consumed preferentially thus protecting the steel.

ICCP systems utilise an inert anode material (such as Mixed Metal Oxide (MMO), titanium etc.) which is used to induce a current onto the reinforcement under the passage of a constant current. A Transformer Rectifier (TR) is used to power the system and converts Alternating Current A.C. to D.C. One of the main benefits of an ICCP system is the ability of the rectifier to adjust and control the current being passed to the reinforcement. However, whilst alkalinity is generated at the reinforcement, acidity is produced at the anode.

The 'Hybrid' system operates by utilising the main functions of both GACP and ICCP. Once the anodes have been installed, a current is passed from a temporary power supply for circa one week to arrest any corrosion occurring at the reinforcement and to build up a passive layer around the steel (just like ICCP). Following this, the anodes are then attached to the reinforcement for long term protection (just like GACP). Although the first week of current passage would consume some of the anode, they would typically last a lot longer than a GACP system due to the protection offered at the outset. Long term acid generation at the anode is not a function of a 'Hybrid' system.

6 THE SHELBOURNE HOTEL

6.1 Background

McFarland Associates Ltd's first involvement with the Shelbourne Hotel restoration came about following the observation of a long horizontal crack at a high level on the Kildare Street elevation during the façade restoration works in May 2015. No one suspected the magnitude of the underlying problems until the main contractor, ACOL Ltd, commenced localised breaking out to begin repairs. Subsequent investigations revealed the presence of 2no. 220mm by 75mm 'C' sections, arranged back to back, within a concrete medium. The observed cracking was attributed to the corrosion of the outside member. The design team faced a difficult decision. Firstly, they considered the removal of the members in question. However, due to the extremely tight time constraints, as well as the practicalities of structural support during replacement, it quickly became evident that the structural steelwork had to stay. To meet design requirements of 100 years, cleaning the steel, coating it and reinstating concrete cover over would not have dealt with the underlying problem and as such was not regarded as a long term repair. McFarland Associates Ltd were commissioned to investigate the extent of the corrosion and to provide a long term repair option to ensure the continued structural integrity of the steelwork to meet the design requirements.



Figure 4. Subsequent Breakouts around the Horizontal Cracking Revealed the Presence of a Corroding Steel Member

6.2 Observations and findings

Initial observations revealed that the concrete medium surrounding the steelwork was made of clinker due to its dark colour and extensive voids. Light weight concretes manufactured with coke breeze aggregates were commonly used during the early 20th century. Corrosion problems can occur from the date of initial construction due to the acidic nature of some of the aggregates and the porosity of the concrete. The rate at which corrosion can occur is directly related to the water content of the concrete, with moist concrete surrounding steelwork giving high rates of corrosion.

For the most part, the steel appeared to be in a reasonable condition with only minor loss of section having occurred. The greatest area of section loss occurred at the location of a central downpipe where moisture had penetrated in the past. However, even at this location, the section loss was not of concern to the structural engineers. On site testing involved the: extraction of concrete samples for subsequent chloride, cement and sulphate contents by a UKAS accredited laboratory; half-cell potential measurements; concrete resistivity measurements; LPR Corrosion rate measurements; and concrete carbonation measurements. Chloride and cement contents were regarded as low and sulphate contents were above recommended limits. Half-cell potential readings indicated variations in corrosion activity with resistivity and LPR corrosion rate readings indicating a high possibility of corrosion occurring. All corrosion rate readings were above 2mA/m², at and below which would be regarded as the threshold for passive steel [4]. The concrete was also found to be fully carbonated to the level of steel meaning it was offering no protection against corrosion. It was quite evident, both visually and through the on-site testing, that corrosion had initiated and was occurring at varying rates across the elevation. One further elevation within the central courtyard of the hotel was also displaying steelwork corrosion with similar test results observed.

6.3 Solution

The only feasible option for a long term repair was to undertake some form of cathodic protection to switch off and control any future corrosion which may occur. An ICCP system was considered by the client. However, due to the: high cost; lead and installation time; a need for a constant power supply; and a requirement for regular maintenance of the system to ensure ongoing operation, this was discounted.

A Hybrid Cathodic Protection system was recommended by McFarland Associates Ltd as an alternative. The system utilises a dual technology anode based on the use of a sacrificial metal in both an impressed current role and a sacrificial anode role (Figure 5). Initially, an impressed current is driven from the installed anodes using a temporary 12V power supply. During this process, the steel is rendered passive inhibiting further corrosion activity. This occurs because the treatment generates inhibitive hydroxide ions at the steel and aggressive inclusions such as chloride ions are drawn from the concrete to the installed anode. At the end of the brief impressed current treatment, the power supply is removed and the installed anodes are connected directly to the steel to act as a sacrificial anode in a long term (galvanic) preventative role.

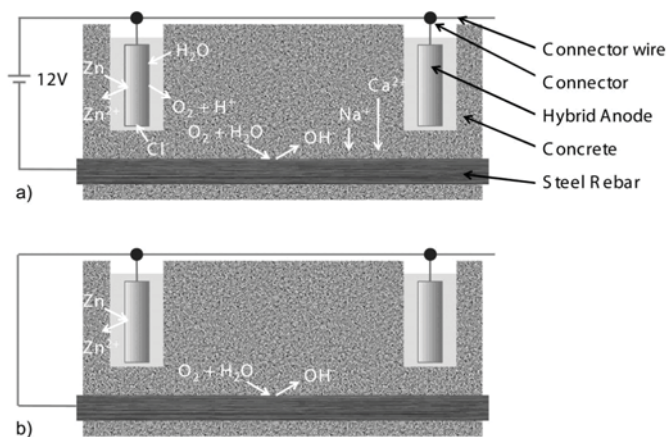


Figure 5. The Two Phases of the Hybrid Electrochemical Treatment [5]

It was deemed prudent to undertake a localised trial of the system at the Shelbourne Hotel prior to full system installation to ensure its: effectiveness; compatibility with the clinker/steelwork arrangement; and to collect site data to aid with the system design. One anode was installed within the clinker concrete. A temporary 12V D.C. voltage was applied to the hybrid anode through a shunt resistor and the steel was connected as the cathode. The applied current was measured after 10 minutes. A steel half-cell potential was measured at intervals away from the anode to determine polarisation of the steel. The D.C. voltage was removed and allowed to depolarise for 10 minutes. The hybrid anode was connected to the steel in galvanic mode through a calibrated multimeter and the current from the anode measured. The driving voltage from the anode was recorded as 1.15V. A current of 47mA was recorded when the hybrid anode was in impressed current mode and the galvanic current was measured as 0.5mA. This trial verified that: during the impressed current phase, the

clinker concrete would allow current to pass between the anode and steel; the driving voltage of the installed anode to the steel indicated that the galvanic current output during phase two of the treatment would be effective at maintaining steel passivity; and the influence of polarisation from the hybrid anode was within typical limits and that a spacing of 300mm between installed anodes would be effective at steel corrosion mitigation.



Figure 6. Hybrid Anodes in Preparation for Installation along the Kildare Street Elevation

6.4 System installation and verification

Following verification of on-site trial results, a full hybrid cathodic protection system was designed to the current international standard [6] taking into consideration: the surface area of the steel to be protected; anode sizing, quantities and distribution; and the required design life.

The system was divided into a series of independent anode treatment zones. A total of nineteen zones were installed on both the Kildare Street elevation as well as the internal courtyard elevation. All zones in both locations were terminated back to a central point. On the Kildare Street elevation, a number of zones were chosen for continued monitoring using independent manganese dioxide reference electrodes. Continuous monitoring is undertaken through the use of a remotely accessed datalogger installed on the roof of the building and powered via an attached solar panel. Trigger values have been set on the system to inform McFarland Associates Ltd engineers of any potential future problems such as an increase in corrosion rate or current output from the anodes which may be attributable to a problem on the structure such as a localised leak.

Measurements collected from the installed datalogger for the Kildare Street elevation zones over the first 210 days post installation are summarised in the graphs below. There is a clear responsive behaviour between temperature and anode galvanic current output, which is expected (Figure 7). An increase in temperature will typically increase corrosion rates. An increase in the anode galvanic currents in this instance

indicates a responsive behaviour from the installed anodes to initiate protection to the steel. As the structure dries out following refurbishment, the galvanic current reduces with time as it is not needed but will increase again if moisture levels increase – similar to temperature variations (Figure 8). Steel potentials more positive than -100mV represent passive steel. It can be seen that the steel potential values are generally increasing following the powerful polarisation from the hybrid electrochemical treatment (Figure 9).

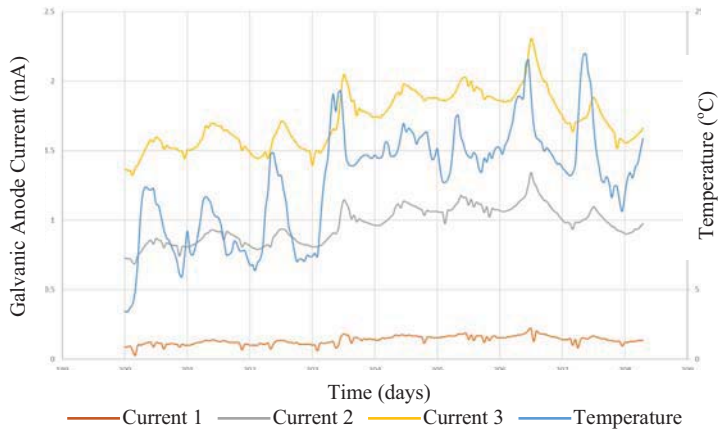


Figure 7. Comparison of Daily Temperature and Current from Installed Anodes on Kildare Street Elevation

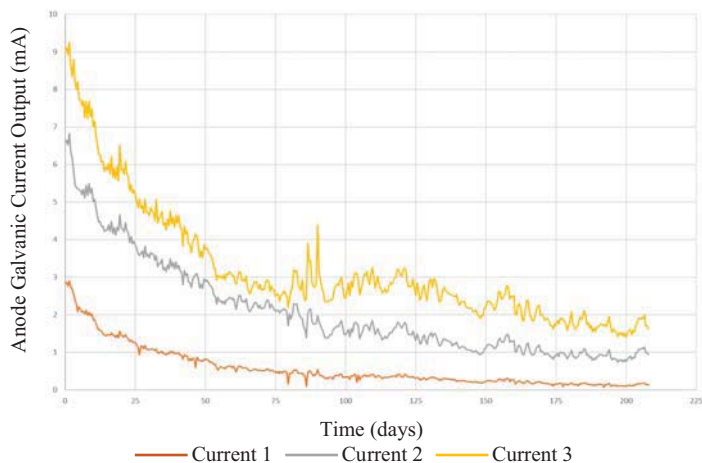


Figure 8. Galvanic Current of Installed Anodes on Kildare Street Elevation over Time

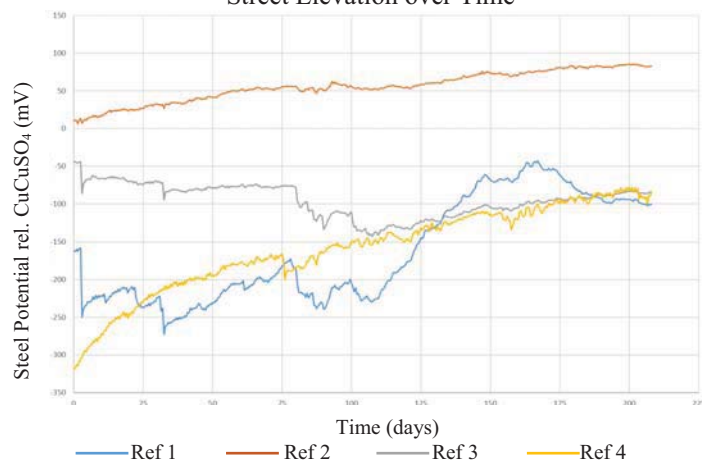


Figure 9. Steel Potentials Over Time



Figure 10. Finished Surface Following Installation of Cathodic Protection System. Note no Evidence of Anodes or Cabling which was Imperative for this Listed Structure.

7 CONCLUSION

As discussed, the corrosion of early 20th century steel framed structures is becoming more problematic for asset owners, architects and engineers to deal with. Traditional methods of repair can be a costly and disruptive process with only short to medium term results expected. An innovative approach to the treatment of corroding steel within heritage buildings has been outlined as an alternative. This treatment can be undertaken locally to where problems are determined to be occurring through on site specialist testing and analysis. It is seen as the favourable repair of choice for managers of heritage assets due to its long term effects and minimally intrusive nature which is vital for our listed structures (Figure 10).

REFERENCES

- [1] Historic Scotland, TAN 20: *Corrosion in Masonry Clad Early 20th Century Steel Framed Buildings*, 2000
- [2] 'Corrosion Costs and Preventive Strategies in the United States,' Report FHWA-RD-01-156
- [3] Lambert, P., 'Cathodic Protection Solutions for Steel-Framed Heritage Buildings' Concrete Repair Bulletin, September/October 2004
- [4] Concrete Society Technical Report 60, Electrochemical Tests for Reinforcement Corrosion, 2004, p.21).
- [5] Concrete Preservation Technologies (CPT) Product Brochure (<http://cpt-tech.co.uk/cpt-brochure/>)
- [6] BS EN ISO 12696:2012 – Cathodic Protection of Steel in Concrete
- [7] McFarland, B., McKenna, E. & Phillips, E. (2014) *Glendinning House Inspection and Testing*. McFarland Associates Limited.

Preliminary investigation into the rate of carbonation of concrete blocks under normal production yard conditions

Dr. Aimee Byrne¹, Dr. Eanna Nolan²

¹School of Civil & Structural Engineering, Dublin Institute of Technology, Bolton Street, Dublin 1, Ireland

²Irish Cement Ltd., Head Office, Platin, Drogheda, Co. Louth, Ireland

email: aimee.byrne@dit.ie, enolan@irishcement.ie

ABSTRACT: The release of CO₂ from calcination during the manufacture of cement can be partially or fully offset by the CO₂ it naturally absorbs during its lifetime. This paper reports results from a preliminary investigation into the rate of carbonation in concrete blocks stacked in a production yard over a period of 6 months. The blocks were stacked in a normal manner under natural exposure conditions. Carbonation progress was determined by splitting the blocks and spraying the freshly exposed surface with a phenolphthalein solution at intervals over the test period. It was found that the rate of the carbonation front progression differed depending on the exposure face and the type of block. Carbonation fronts on exposed front (FF) or side faces (SF) were seen to advance at rates of well over 1 mm per week for the initial 6 months of exposure. Exposed top faces (TF) of blocks showed a slower rate of carbonation; just over 0.6 mm per week. The speed of the advance of the carbonation front into concrete slowed over time, however, it was noted that slower progression occurred during the second half of testing over the wetter winter period. Rates of carbonation and estimates of carbon sequestration were calculated using the measurements taken in the investigation. The findings suggest that carbonation should be included in the manufacturing stage of life cycle assessments for open textured concrete products such as blocks. This research identifies parameters that should be included in future testing as well as areas where the test methodology would benefit from development.

KEY WORDS: Carbonation; Concrete blocks; Carbon Dioxide Sequestering; Phenolphthalein.

1 INTRODUCTION

The release of CO₂ from calcination during the manufacture of cement can be partially or fully offset by natural sequestration of carbon dioxide over the lifetime of cementitious products [1,2,3]. The effect is also detailed in the current CEN Product Category Rules of concrete and concrete elements, which was under enquiry at the time of writing [4].

The CO₂ attributed to cementitious products in life cycle assessments should be adjusted to take account of natural sequestration in order to accurately reflect its true environmental impact. International research has shown that the amount of CO₂ absorbed by concrete can account for up to 17% of all CO₂ emitted during cement manufacture in a given year (calcination and fuel) [1]. In Ireland this effect was conservatively estimated to result in a net reduction of 75 kg of CO₂/tonne cement [3]. Failure to take account of this sequestration of CO₂ into concrete can lead to misinformed policy formulation on global and regional climate change strategies.

Carbonation (or CO₂ sequestering) is the reaction between the hydrated calcium compounds in the building element and atmospheric carbon dioxide. These chemicals dissolve in the pore water of concrete which enters through the exposed surface via the pore network. The reaction results in the precipitation of calcium carbonate in the capillary pore system and a reduction in the pH of the concrete. Concrete design usually aims to reduce the depth of carbonation due to the potential risk of corrosion when the carbonation front reaches the level of embedded steel reinforcement. Consequently, the

main focus of research into carbonation in concrete to date has been on efforts to predict and limit the depth of carbonation. Despite this, and depending on the in-service use and exposure conditions, reinforced concrete is known to absorb significant amounts of carbon dioxide which are currently unaccounted for in most estimates of environmental impact.

The rate of carbonation in dense concrete is typically modelled mathematically in the general form shown in Equation 1 [5]:

$$x = k\sqrt{t} \quad (1)$$

Where x is the depth of carbonation, k is a carbonation coefficient (or 'k-factor') dependent on material properties, t is time. Numerous variables are known to affect the rate of carbonation and are included in a wide range of different formulae which can be grouped into three main categories: factors inherent to concrete (cement, additions, w/c ratio, strength etc.), curing and moulding conditions and exposure (environmental) conditions [6].

In unreinforced concrete there is no reason to limit carbonation and there is the opportunity for designers and manufacturers to actively encourage carbonation in service. The subject of carbonation of open textured concrete products (Concrete blocks, roof tiles etc.) is considerably less well researched than dense concrete although the mechanisms are identical.

In dense concrete it is normally assumed that high levels of carbonation are attained only after recycling at the end of life, particularly in a predominantly humid Irish environment and in higher grades of concrete [3]. In more open-textured

products it could be expected that full carbonation would normally occur during the service life of the building or structure (if exposed to air). During preliminary work for this project, old blocks (of unknown age but perhaps decades old) in the storage yard were found to be fully carbonated.

This study examined whether the carbonation of blocks in a production yard prior to dispatch to customers was of a significant level to include in environmental footprints for products manufacturing phase. A full life-cycle assessment of concrete blocks would also require an examination of the carbonation of blocks in service. This longer term in-service testing fell outside the scope of this initial study.

2 METHODOLOGY

The project sought to use a series of measurements on concrete blocks stored in a block manufacturers' yard (Figures 1a and 1b) to confirm the potential of cement-based non-reinforced construction materials to sequester atmospheric carbon dioxide (CO₂) and to understand how much of this may occur prior to their incorporation into structures or buildings.

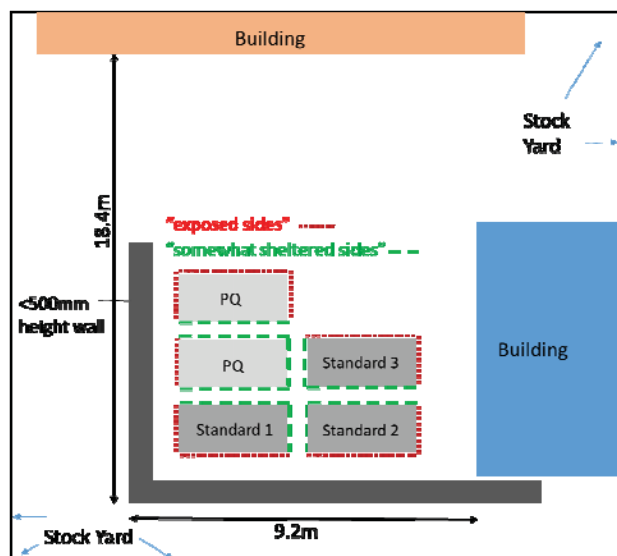


Figure 1a. Layout of stacks.



Figure 1b. Block stacks on site.

2.1 Experimental Variables

Concrete block type:

Two concrete block types were used to examine the effect of block properties on carbonation. The first type was a "standard" solid concrete block (Standard Block) and the second type was a more dense block manufactured to have

enhanced air tightness, acoustic, visual and painting properties* (PQ Block).

Block position in stack:

After manufacture it is common practice to arrange blocks in "rings" of single block height which are then placed on top of each other to make a "stack" in the yard. Five stacks in total were placed on site as shown in Figure 1a.

Figure 2 illustrates the typical block arrangement in a stack. The block position was anticipated as being a significant variable, therefore, four types of block exposure were identified:

- Top Face (TF) and Front Face (FF) of block exposed with other faces sheltered by adjacent blocks in the stack.
- TF, Side Face (SF) and FF exposed.
- FF exposed.
- FF and SF exposed.

Two type "a" blocks, one from an "exposed side" (see Figure 1a) and one from a "somewhat sheltered side", and one of each type "b", "c" and "d" were taken from each standard block stack, making 15 standard blocks sampled for each date of measurement. 5 blocks were taken from the PQ stacks. Care was taken to extract blocks from the stack without disturbing adjacent units. Units were not tested if their exposure conditions were altered by the removal of blocks from the stack previously.

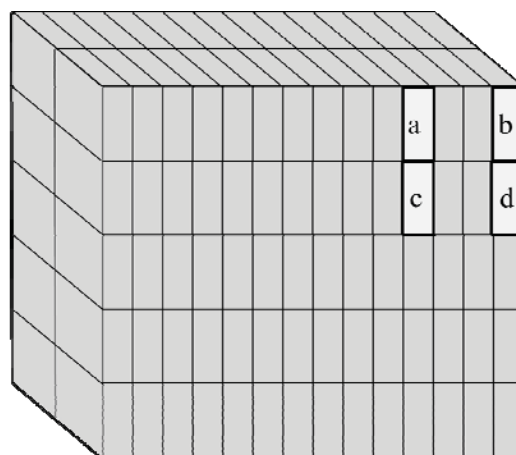


Figure 2. Stack shape showing 4 block types.

Exposure Time:

Concrete blocks are commonly retained in a production storage yard for at least 4 weeks before dispatch to site. The actual time spent in the production yard is likely to be heavily influenced by market conditions. Therefore, blocks were tested after approximately 0, 4, 8, 16 and 24 weeks after manufacture.

2.2 Tests

In dense concrete the depth of carbonation can be determined by spraying a freshly exposed surface (by splitting) of the

* Standard 7.5N Block and PQ Block (Aristocrat Range 10N) produced by Roadstone Ltd. All units 440x210x100mm.

concrete with a 1% phenolphthalein in ethanol solution [5]. The solution is made by dissolving 1gm of phenolphthalein in 90 cc of ethanol and made up to 100 cc by adding distilled water. The phenolphthalein solution is an indicator of pH with materials of lower than roughly pH 9 showing no colour change (assumed to be fully carbonated concrete –see section 1) and materials of higher pH than 9 showing pink/purple (uncarbonated concrete) [7].

Following spraying with phenolphthalein solution the depth of the carbonation (the uncoloured layer), as shown in Figure 3, from the external surface is measured to the nearest 0.5mm at different positions, and the average taken.

The feasibility of using this standard dense concrete carbonation test method for open textured material (cement blocks) was unknown at the outset of the project, however, the method produced clearly defined colour changes indicating carbonation depth during early stage testing. The method was therefore deemed an appropriate one to use for the duration of the test series.



Figure 3. Measuring depth of carbonation.

2.3 Testing Methodology

Samples were marked on exposed surfaces and transported to the test laboratory where they were split as shown in Figure 3 using an Avery Denison 100kN capacity 7123 traverse unit with the single point flexure setup. Break 1 split the block in half along the long face, and Break 2 split the FF in half producing two quarter blocks.

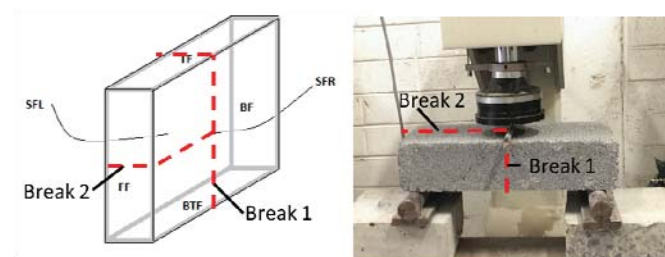


Figure 4. Splitting of the concrete blocks.

The freshly broken surfaces were immediately cleared of any dust and loose material before being sprayed, photographed and the depth of clear colour measured using a measuring tape or ruler as shown in Figure 3. It should be noted that findings from this study are deduced using these cut positions as a snapshot of carbonation within the block. The determination of interactions between exposure sides, for example at the exposed corner in block type “b”, is not possible using this method.

Average monthly meteorological data [6] for the test period was obtained from the Met Éireann Casement Aerodrome

station (Figure 5), which is roughly 3km away from the block exposure site.

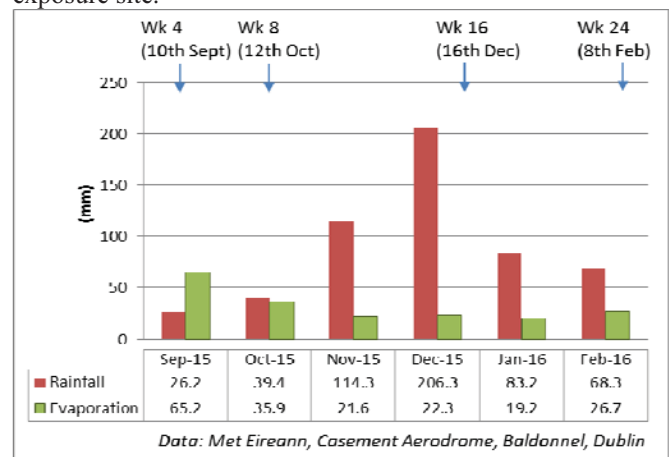


Figure 5. Rainfall and evaporation data for test period

3 RESULTS

When the substrate has a pH of below 9 the phenolphthalein indicator remains clear and it is assumed that the concrete is fully carbonated. On a substrate with a pH above 9 the indicator turns purple and the concrete is deemed uncarbonated (Phenolphthalein indicator turns purple).

3.1 Block type

The greatest carbonation depth was recorded on the exposed FF for both block types examined in this study. Figure 5 shows the average depths of carbonation on the FF of all Standard (15 blocks) and PQ Block (5 blocks) types over the test period. At 24 weeks the depth of ingress was on average 79% lower on the PQ blocks. This effect was particularly evident in the first 4 to 8 weeks of exposure whereby carbonation progressed much more rapidly in Standard Block types (Figure 6).

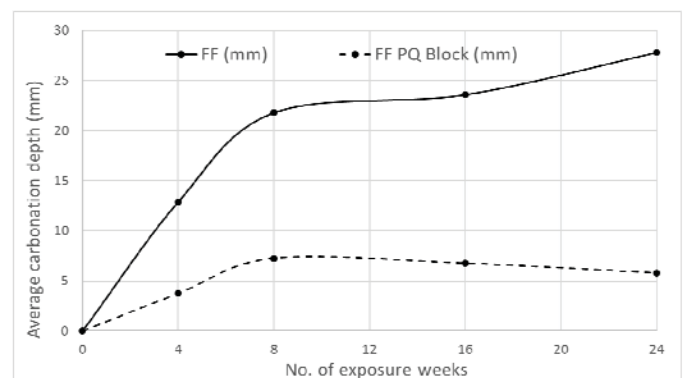


Figure 6. Depth of carbonation on Front Faces of Normal and PQ blocks.

Given that all blocks were exposed to the same weather conditions (Figure 5), it can be concluded that the difference in carbonation behavior between Standard and PQ blocks was due to their differing compositions and structure. The reason for this differential is very likely to be related to the reduced air permeability of PQ Blocks, which are designed to be more suitable for airtight buildings.

3.2 Block Stack Exposure

Standard Block stacks 1, 2 and 3 had one “exposed side” and one “somewhat sheltered side”, sheltered by neighbouring stacks (< 300mm adjacent) as defined in Figure 1a and photographed in Figure 1b. The “exposed sides” as indicated in Figure 1a generally experienced higher levels of carbonation as shown in Figure 7, which uses the example of “a” type block FF’s carbonation depth as recorded in week 16 to highlight this observation.

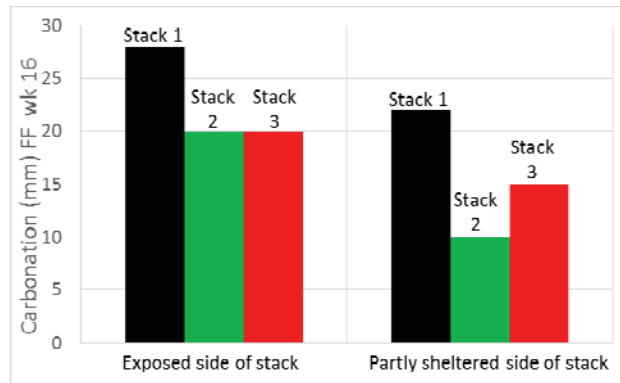


Figure 7. Comparison of “exposed sides” and “somewhat sheltered sides” week 16 data.

The general trend that more exposed sides of the stack experienced higher depths of carbonation was identified. However, no definitive pattern emerged and the degree of shelter offered by neighbouring objects and buildings was not taken into account when comparing sides. For future testing, more rigid measurement of sheltering combined with prevailing wind conditions and weather monitoring would be required to clearly define any relationship between sheltering and carbonation.

3.3 Pattern

Initial weeks showed a clearly defined line between coloured and uncoloured parts of blocks when sprayed with phenolphthalein solution. The findings for weeks 16 and 24 tended to have scattered mixes of coloured and uncoloured portions as well as more clearly defined lines. A comparison is shown in Figure 8 whereby (i) and (ii) show clearer borders between coloured and uncoloured portions, while later tests show less clear boundaries (iii) and (iv).

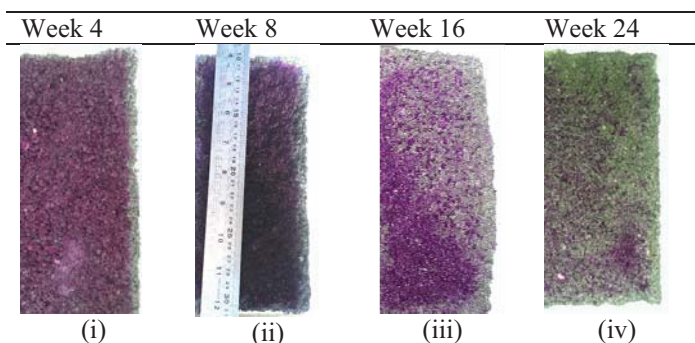


Figure 8. Comparison of ingress patterns in “b” blocks from the same stack in week 4, week 8, week 16 and week 24.

For the purposes of this study “scattered” areas were deemed to be uncarbonated concrete and measured accordingly. Particularly heavy rainfall was experienced during the months of November to January, which encompassed all post-week 8 readings (Figure 5) and is thought to be a possible reason for the dispersed pattern.

3.4 Exposure Faces

Although the highest carbonation was recorded on FFs (in both Standard and PQ Blocks) other exposed faces also showed varying significant depths of carbonation.

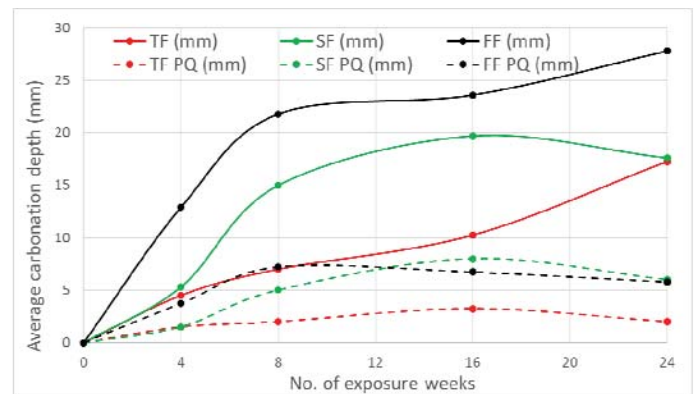


Figure 9. Relationship between exposed face position and carbonation front ingress by week.

Figure 9 displays that carbonation was significantly higher on FFs (all 15 blocks had exposed FF) compared to other exposed faces for Standard Blocks. Standard deviations increased as the weeks progressed, advancing from 1.9mm for week 4 recordings to 22.7mm for week 24. Generally, TFs showed the lowest carbonation depths (9 blocks had exposed TF) and a lower standard deviation of 1.2mm in week 4. The cause of this lower carbonation rate was not immediately evident. In week 24 the TF average increased steeply to the same depth of ingress as the SF average (6 blocks had exposed SF). Individual block values for TFs ranged between 10mm and 15mm, however, one “b” type corner block showed 40mm carbonation depth, which considerably increased the average. Removing this anomaly would reduce the average TF value to 12mm in week 24 which would maintain the identified trend. However, due to the low number of blocks used for the study no carbonation depth results were omitted from the data set.

In PQ blocks the differential between exposure faces was less pronounced. Similar to Standard Blocks, TFs of PQ blocks also exhibited the lowest level of carbonation.

Figure 9 shows the SF of Standard Blocks (and to a lesser extent PQ blocks) having an unexpected reduction in carbonation at week 24. Carbonation is an irreversible process and these measurements appear to show the degree of specimen to specimen variation in the results rather than a real effect as standard deviations increased from 0.5mm in week 4 to 12.7mm in week 24.

There is evidence that some degree of carbonation also occurred on internal faces of the blocks tested. Figure 10 provides an example of a “c” type block after 24 weeks of exposure. Only the FF is externally exposed, all other faces were sheltered by adjacent blocks in the stack, however, a

scattered purple and clear pattern was seen to ingress from the surface on those covered sides. Carbonation on the internal faces of blocks were not the focus of this testing series, however, all blocks were photographed at time of test which allows general observations to be made. All internal faces tended to show some carbonation, though the depths varied from 0-10mm in week 24. It is thought that the variation may have been due to the gap widths between adjacent blocks in the same stack.

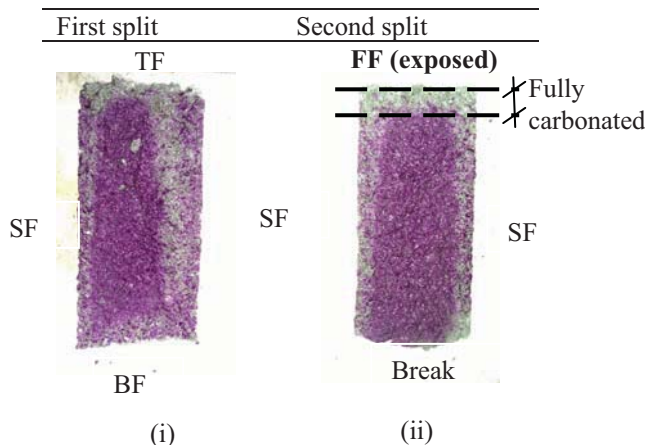


Figure 10. Example of “c” type Standard Block. (i) Break 1: all faces shown are internal. (ii) Break 2: only the FF is external.

3.5 Rate of carbonation

The general trend of rapid initial carbonation, which slows over time, was observed and displayed in Figure 11. The exception to this trend is noted for TF data point in week 24 as discussed in section 3.4. In normal dense concrete this can be explained by the time - carbonation depth relationship (Equation 1). This, however, may not completely explain the apparent fall off in carbonation rates in open textured blocks such as those examined for this study. Figure 5 clearly shows that the initial 8 weeks (taken Sept-Oct) were reasonably dry with the following weeks substantially wetter and with lower evaporation rates (Nov-Feb). It is speculated that this influenced carbonation rates significantly.

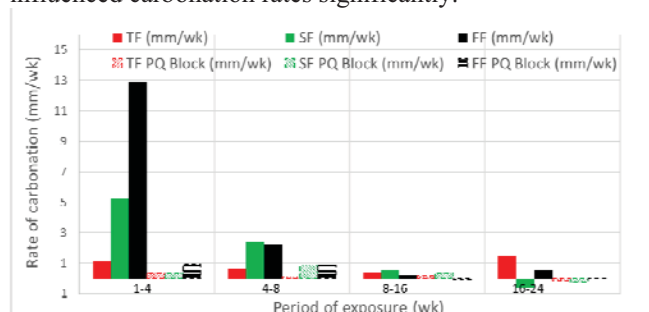


Figure 11. Relationship between exposed face position and rate of carbonation front progression in mm per week.

The “negative” rate of carbonation recorded in Figure 11 illustrates specimen to specimen variation (introduced in section 3.4) as carbonation of concrete is not process that can be reversed.

3.6 Estimate of sequestered carbon

Using the carbonation measurements recorded in this investigation (plotted in Figure 9) an estimate of the sequestered carbon in an average Standard Block can be made.

Table 1 – Percentage of blocks carbonated

block type	exposed faces	week 4	week 8
		% of block carbonated	% of block carbonated
type (a)	FF, TF	3.7	6.1
type (b)	FF, TF, SF	9.0	21.1
type (c)	FF	2.8	4.7
type (d)	FF,SF	8.1	19.7

Each tonne of CEM II/A cement is estimated to result in roughly 428kg of calcined CO₂ (not total CO₂) [3]. The exact quantity of cement in each block is considered commercially sensitive information and not publicly available. The estimate that one standard 440x215x100mm block typically contains 1kg of cement was used to estimate the quantity of sequestered carbon dioxide.

Using the results in table 1 for type “d” blocks it can be estimated that each type “d” block has immobilised 0.031kg of CO₂ by week 4 and 0.076 kg by week 8 (assuming a degree of carbonation of 0.9 [1]).

The limitations of this calculation are explicitly acknowledged. The rate of carbonation was found to be highly variable, with weather in particular being an influencing factor. The carbonation depths used in the calculation relate only to measurements in this initial study and cannot be generalised to represent typical or expected performance.

4 DISCUSSION AND CONCLUSION

This study has found that significant amounts of carbonation in concrete blocks can occur in an Irish production storage yard in relatively short periods. Peak rates of carbonation of up to 13 mm/week over 4 weeks were recorded in this study on exposed faces.

The study found that the positioning of block stacks and the position of individual blocks in a stack influenced the amount of carbonation that occurred. The results also show that weather and rainfall could have a very significant effect on the rate of carbonation. A notable finding from this initial study is the lack of information on the general nature of the rate of carbonation of open textured concrete products. A straightforward laboratory study is recommended to assist in providing the required insight into the general nature of carbonation of open textured blocks.

In life cycle analysis the impact of materials is divided into different life stages, therefore, this study relates only to the manufacture stage. The results of the study indicate that action by a manufacturer (e.g. covering or uncovering stacks during storage, adjusting the spacing of stacks) could be used to maximise recarbonation during storage and hence reduce the environmental footprint of their product.

Measurements from this study were used to estimate the amount of carbonation (carbon sequestration) occurring in a normal block in a particular location in the block stack. The estimates indicate that significant quantities of calcinated CO₂ arising from cement used in standard blocks was reabsorbed in the first 8 weeks of storage. This suggests that there is potentially a significant reduction in environmental impact of concrete blocks if carbonation is taken into account in lifecycle analysis. It is clear from this work that the recarbonation of standard open textured concrete should be considered in the manufacturing or product stage of life cycle assessments. Significantly less carbonation was seen to occur in more closed textured concrete blocks (PQ Blocks).

The test series was effective in highlighting variables that would benefit from more extensive monitoring and/or controlling in any future research on this topic. This includes the degree of stack sheltering, the measurement of gaps between blocks in each stack as well as a more detailed investigation of the degree of carbonation within the portion of blocks which indicated in a “scattered” weak indication of carbonation. Inter-specimen variation was evident in the results and should be kept in mind when designing further investigations.

Research into carbonation of open textured concrete products should also be extended to include carbonation in-service. The aim of such research would be to confirm that carbon sequestration continues after installation in most construction types.

ACKNOWLEDGEMENTS

The authors gratefully acknowledge the donation of product and practical assistance from Roadstone Ltd.

REFERENCES

- [1] Andersson, R., Fridh, K., Stripple, H., Häglund, M. 2013. Calculating CO₂ uptake for existing concrete structures during and after service life. *Environmental Science and Technology*, 47(20), 11626-11633
- [2] Engelsen, C.J., Henning Sæther, D., Mehus, J. Pade, C. 2005. Carbon dioxide uptake in demolished and crushed concrete. Nordic Innovation Centre. Project report 395. ISSN 0801-6461 ISBN 82-536-0900-0
- [3] Fitzpatrick, D, Nolan, É, Richardson, M, 2015 Sequestration of carbon dioxide by concrete Infrastructure: A preliminary Investigation in Ireland, *Journal of Sustainable Architecture and Civil Engineering*, Vol 1, No. 10, 66-77
- [4] prEN 16757:2015(E) Sustainability of construction works – Environmental product declarations – Product Category Rules for concrete and concrete elements. CEN/TC229 56 pp
- [5] A.M. Neville, *The properties of Concrete*, 5th Edition, 2011, Pearson. pp 846. ISBN 978-0-273-75580-7
- [6] Silva, A., Neves, R. de Brito J, 2014. Statistical modelling of carbonation in reinforced concrete. *Cement Concrete Composites*, 50, 73-81.
- [7] CPC-18 Measurement of hardened concrete carbonation depth, RILEM
- [8] Met Eireann 2016, Monthly data, accessed 7/4/16, www.met.ie/climate/monthly-data.asp

EFFECT OF WASTE CERAMIC POWDER ON STRENGTH DEVELOPMENT CHARACTERISTICS OF CEMENT BASED MORTARS

Liberato Ferrara¹, Peter Deegan², Gavin Kelly², Andrea Pattarini³, Mohammed Sonebi⁴ and Sue Taylor⁴

¹Department of Civil and Environmental Engineering, Politecnico di Milano, Milano, Italy

²Banager Precast Ltd., Banager, Ireland

³Azichem Ltd., Goito, Italy

⁴ School of Planning, Architecture and Civil Engineering, Queen's University of Belfast, Belfast, Northern Ireland, UK
email: liberato.ferrara@polimi.it, PeterD@bancrete.com, m.sonebi@qub.ac.uk

ABSTRACT: This study presents the results of a preliminary study aiming at assessing the feasibility of using waste ceramic powder as a partial replacement of cement in cement based mortars. The aim is to improve the sustainability footprint of concrete and cement based construction materials in the precast industry. Two different ceramic powders have been employed, one from crushed bathroom fixtures and dental prosthesis waste and a second one from foundry industry residuals. Two different cement replacement volume percentages have been considered for each powder type, equal to 10% and 30%. Effects of the replacement on the workability, shrinkage behaviour and on the compressive and flexural strength have been considered, up to curing periods as long as three months. This is aimed at establishing if there is any potential for pozzolanic activity. The study is prodromal to investigating durability characteristics, including exposure to severe environmental conditions. The results of the study provide an interesting insight into the possibility of using this kind of wastes as a concrete constituent, thus reducing the demand for raw cement and the burden on the landfills for disposing of such kind of invading waste.

KEY WORDS: ceramic waste powder, mechanical properties, sustainability.

1 INTRODUCTION

As concrete is the second largest used material worldwide, after water, the “concrete community” can significantly contribute to increasing the sustainability signature of our current “life-style” and, in particular, the construction sector as a whole. This actually continues to represent, despite the well-known negative economic trends, a significant share of the gross domestic product in both developed and emerging countries. At the same time, Construction and Demolition (C&D) activities are, according to recent estimates, 75% of the waste due to all human activities.

It has been claimed that one of the most significant environmental burdens of the whole life cycle of concrete is represented by the production of Portland cement. This is mainly due to the depletion of natural resources (limestone, clay etc.) and the high energy necessary for the production of clinker. It is thus evident that any effect to reduce the demand for cement or towards a clinker-free cement or alternative binders, such as geo-polymers, has a high sustainability value.

With reference to the first concept, the use of cement substitutes, with mere “inert filler” function or featuring either pozzolanic and/or cementitious additions (fly ashes, silica fume, ground granulated slag etc.) is now a well consolidated practice in the cement and concrete industry. This is well documented noting the benefits in terms of improved performance, fresh state behaviour, matrix compactness, strength, and durability.

The aforementioned cement substitutes are by-products or waste materials from activities other than construction “proprie dicta”, ranging from quarrying to electric power to steel production. Such advances invite novel research activities aimed at assessing the feasibility of using such materials as cement replacement or substitutes. There is a tremendously wide variety of waste products available from a

wide range of human activities. Examples ranging from agriculture to C&D wastes (recycled concrete aggregates for the production of recycled aggregate concrete). These are gaining wider and wider popularity and acceptance in standards and structural design codes worldwide.

In this framework, it is worth remarking that a conspicuous share of the C&D waste (54% according to recent estimates) is represented by ceramic materials (blocks, tiles, electrical insulation, bathroom fixtures), to which waste from the medical sector (anatomical and dental prostheses) and the ceramic production sector (up to 2% of the total production, depending on the degree of automation and quality control) have to be added. It would be of the foremost interest and importance to assess the feasibility of employing such a waste in a suitable form as a replacement/substitute either for cement and/or of natural aggregates in the production of concrete and cementitious composites [1].

Using ceramic waste in concrete production has been increasingly attracting researchers and practitioners in the last decade, both as replacement of cement [2-4] and as a raw material for the production of alternative clinkers [5-7]. Pozzolanic activity of the waste has been confirmed, which has led to setting some upper bounds on the ceramic-to-cement replacement ratios (35%), in order to limit the negative effects on strength development. This is due to both later hydration of the pozzolana as well as to the lower availability of calcium hydroxide necessary to activate the same pozzolanic reaction. Incorporation of the waste into cement and concrete was also effective in limiting the leaching of toxic substances such as zinc, boron and zirconium, normally employed for surface glazing of tiles and ceramic artifacts. Coarser ceramic waste particles were also used as a replacement of natural fine aggregates in the concrete, highlighting their potential as internal curing agents [8-10].

Moreover, because of the generally higher fineness that both waste ceramic powder and fine aggregates may feature with respect to cement and river sand, higher matrix compactness could be achieved, with reduced pore sizes. This also resulted in improved durability vs., e.g., chloride attack.

In this study, the feasibility has been investigated of partially replacing cement with ceramic powder originating from waste bathroom fixings/dental prosthesis and from foundry industry residuals. In the interest of simplicity, reference has been made to cement pastes and mortars, formulated from Self Compacting Concrete (SCC) mixes, in which up to 30% by volume of cement has been replaced with ceramic powder. Since the mere replacement of cement with ceramic powder results in a modification of the actual w/c ratio, an alternative mix-design strategy has also been adopted, in which fixed w/c and ceramic-to-cement replacement ratios have been input as the optimization variables. Results, with reference to shrinkage behaviour as well as to compressive and flexural strength of the investigated pastes and mortars, seem to confirm that ceramic powder can be effectively incorporated into concrete without detriment on the mechanical properties.

Table 1. Mix. Composition of investigated cement pastes and mortars (dosages in g/dm³).

Mix-code	PCER-ref	PCER-10	PCER-30	PCER-30wc
Cement	1632	1468	1142	1325
Ceramic		105	316	367
Water	461	461	461	374
Superplasticizer	14.2	14.2	14.2	23.3

Table 2. Mix. Composition of investigated cement pastes and mortars (dosages in g/dm³).

Mix-code	MCEM-ref	MCER-10	MCER-30	MCER-30wc
Cement	875	788	613	689
Ceramic		57	170	190
Water	247	247	247	194
Superplasticizer	7.3	7.3	7.3	26.7
Sand	1205	1205	1205	1205

Table 3. Slump-flow diameters of investigated mortars (12 data for each mix) – 1st ceramic powder

Mix-code	MCEM-ref	MCER-10	MCER-30	MCER-30wc
Av. diam. (mm)	298	333	322	297
Std. dev. (mm)	36	17	14	10

Table 4. Slump-flow diameters of investigated mortars (12 data for each mix) – 2nd ceramic powder

Mix-code	MCEM-ref	MCER-10	MCER-30	MCER-30wc
Av. diam. (mm)	295	330	305	311
Std. dev. (mm)	50	10	25	10

2 EXPERIMENTAL PROGRAM: MATERIALS AND TESTS

The two different employed ceramic waste powders comes from disposed bathroom fixtures/dental prosthesis (identified as 1st ceramic powder henceforth) and from residues of foundry industry (referred to as 2nd ceramic powder in the forthcoming paragraphs). Their composition, analysed by means of XRD, is shown in Figure 1, highlighting that they consists of silica and alumina. Particle size analysis with laser diffraction method was also performed for both powders (Figures 2a-b). The first powder has a significant fraction of sub-micron (nano)-sized particles; moreover, more than 90% of the particles have a diameter lower than 10 µm. This would result in increased matrix compactness. On the other hand the second powder is much coarser, with more than 90% of the particles larger than 100 µm, hence coarser than cement grains and somewhat comparable to the sand employed in mortar casting.

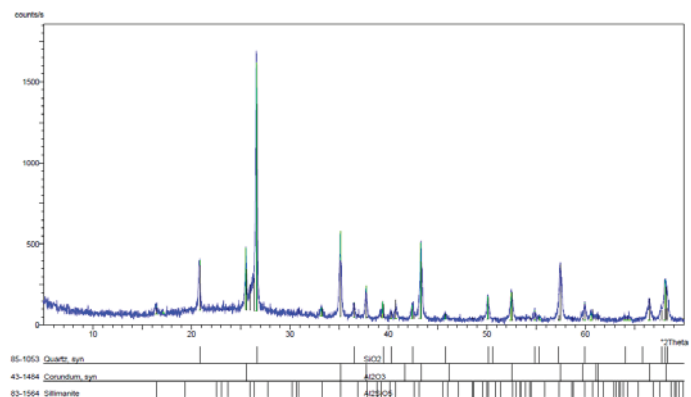
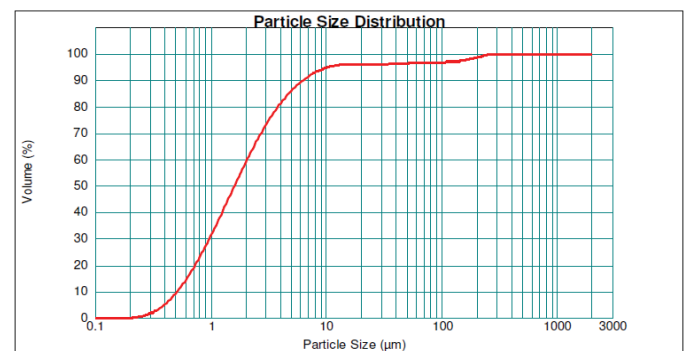
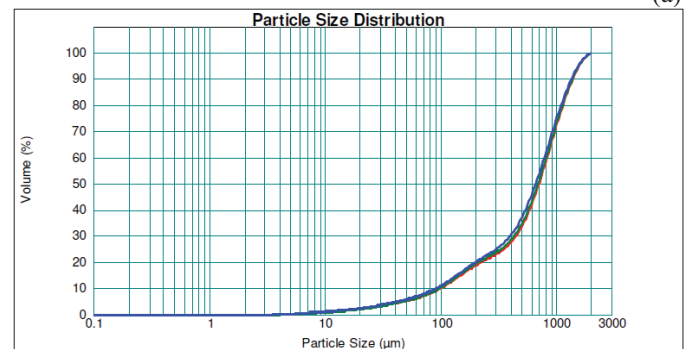


Figure 1. XRD analysis.



(a)



(b)

Figure 2. Cumulative particle size distribution for 1st (a) and 2nd (b) employed ceramic powders.

Their effects as cement replacement has been investigated with reference to cement pastes and mortars, formulated from SCCs, the composition of which is listed in Tables 1 and 2. Two different volume percentage replacements have been investigated, equal to 10% and 30%. For the latter, an “alternative” composition has been also proposed, which also keeps the w/c weight ratio unaltered, by suitable scaling of the dosage of all constituents.

Fresh state performance has been the first to be investigated by means of slump flow tests.

With each mix, prism specimens 40x40x160 mm have been cast, these are tested in bending and compression according to EN 196-1. Tests have been performed at 1, 3, 7, 28, 56 and 84 days, also to assess potential pozzolanic activity, if any. Until testing, specimens were cured in a moist room at 20°C and 95% RH. For each testing age three specimens were cast; the data-base will hence consist of three flexural strength and six compressive strength values for each mix at each testing age (a compression test is performed on each beam-half, after breaking the specimen in bending). Similar specimens have been also employed to test the development of total and autogenous shrinkage, for all the investigated pastes and mortars. Mercure Intrusion Porosimetry (MIP) tests have been performed on 28 d mortar samples.

3 EXPERIMENTAL PROGRAM: RESULTS AND DISCUSSION

Results of mini-slump flow tests on mortars (pastes have excessive flow and therefore the test is not significant), shown in Tables 3-4, this highlights that the substitution of cement with ceramic powder slightly affects, or better moderately improves, the mortar flowability, provided the water/powder ratio was kept constant. For the mixture obtained by scaling the dosage of constituents in order to keep the w/c ratio constant, similar flowability could be obtained only by increasing the dosage of superplasticizer in tandem. Because of its smaller particle size, the first waste ceramic powder is able to provide a lubricant effect to the cement, as is common for extra-finely ground cement substitutes. Interestingly, the addition of ceramic powder also seems to result into slightly less dispersed values of the mini-slump flow diameter, most likely because of the higher particle fineness and hence higher specific surface. This favours absorption of some extra water contributing to the increase in the mixture robustness. Despite is lower fineness, the second ceramic powder provides similar fresh state performance as the former, most likely the sub-10µm fractions being enough for the aforementioned lubrication effects.

In Figures 3 a-b and 4 a-b the time evolution of compressive and flexural strength of pastes and mortars made with the first ceramic powder are plotted. It can be observed that for low ceramic to cement replacement volume ratios, the likely pozzolanic activity of the former is able to compensate at quite later ages, the effects of cement reduction and proportional increase of the w/c ratio. For higher ceramic to cement replacement ratios, the aforementioned negative effects could only be overcome, by keeping constant the w/c ratio. The sole pozzolanic activity of the ceramic is not able to provide a compensation, probably also due to the likely lower availability of the cement hydration products (portlandite), necessary for its activation. In the case of

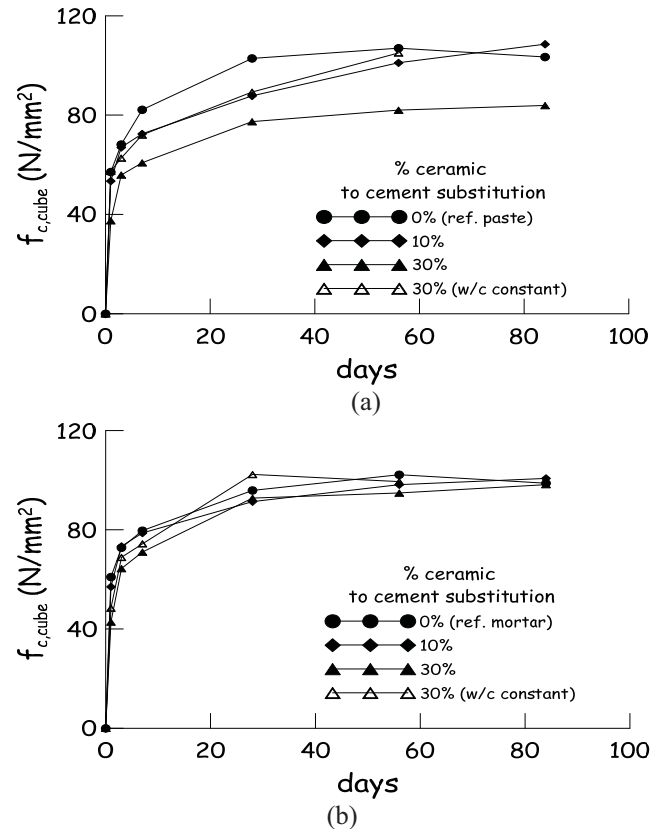


Figure 3. Time evolution of compressive strength for cement pastes (a) and mortars (b) made with 1st powder.

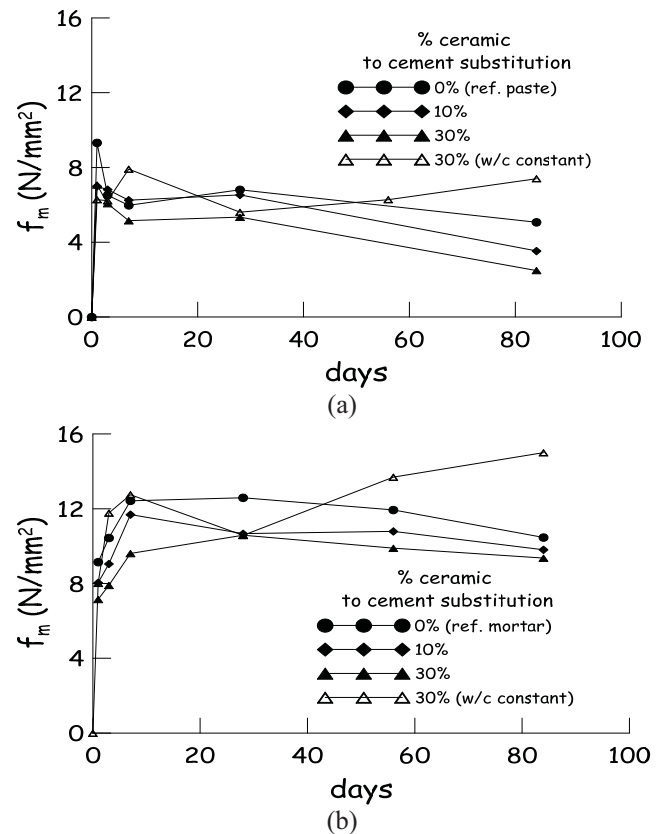


Figure 4. Time evolution of flexural strength for cement pastes (a) and mortars (b) made with 1st ceramic powder.

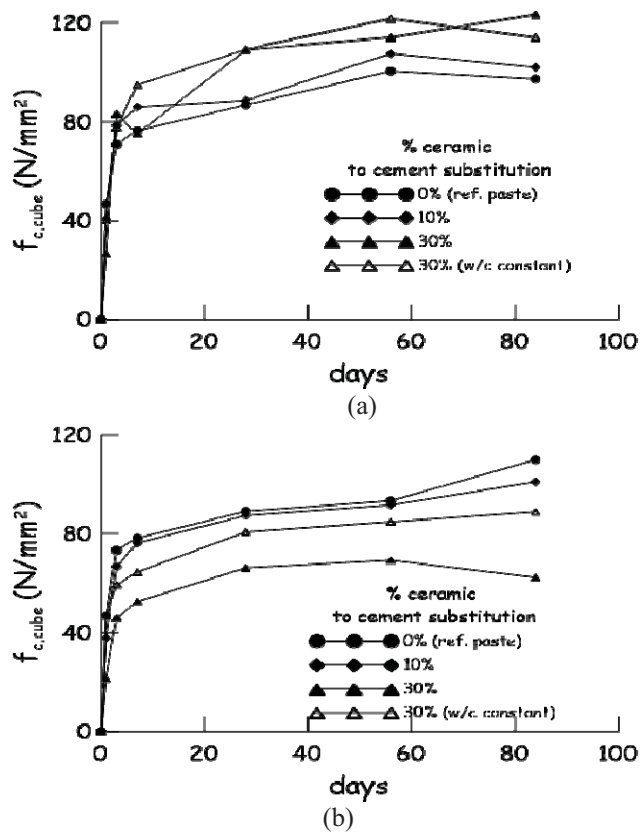


Figure 5. Time evolution of compressive strength for cement pastes (a) and mortars (b) made with 2nd powder.

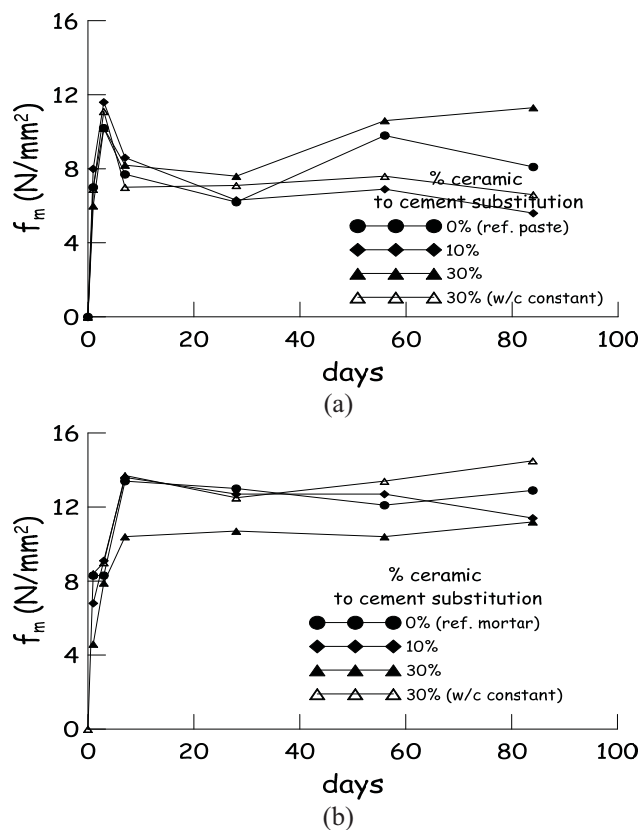


Figure 6. Time evolution of flexural strength for cement pastes (a) and mortars (b) made with 2nd ceramic powder.

mortars, these negative effects are strongly reduced, also because of the “stabilizing” effect provided by the fine aggregate. This accounting for about 46% of the mortar volume fraction, and thus leading to hypothesize that this effect could be even less evident in a concrete mix, if the paste volume fraction becomes even lower.

The same statements hold firm with reference to flexural strength (Figure 4 a-b). Quite surprisingly, after an almost constant trend for intermediate ages, the flexural strength seems to decrease for longer age, always more dramatically for cement pastes than for mortars. This could be partially explained with progressive stiffening and embrittlement of the composites with aging. This makes it more difficult for the sectional redistribution of bending stresses, which is a distinctive feature of the test.

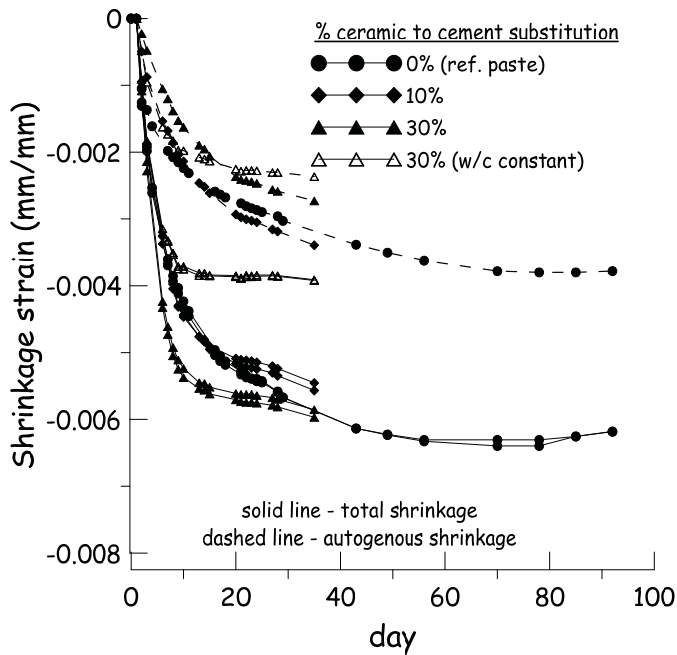
MIP test results (Table 5) show, at a first glance, that the total porosity is scantily affected by the replacement of cement with ceramic powder. A deeper analysis of the results shows that the ceramic powder, thanks to its fineness and despite its slower reaction and the lower availability of cement is able to guarantee not only an unaltered total porosity but also lower average and median pore radii. The increase in W/C is also unaffected. This would all contribute towards an improved durability, the potential hazard vs. aggressive substances being correlated to the pore radius.

In the case of the second ceramic powder the aforementioned negative effects in cement pastes (Figure 5a) are evident only at very early ages, differences between the different investigated replacement ratios being lower than in the previous case and, from 7 days curing onward, pastes containing ceramic always performing better than the reference one. It can be reasonably claimed that the coarser ceramic grains make the paste to behave more like a mortar than a paste, thus smoothing, also thanks to the presence of harder grains, the effects of a reducing cementitious activity. The reliability of holding constant the w/c ratio to guarantee the performance is confirmed also in this case. In the case of cement mortars cast with the second ceramic powder (Figure 5b), the negative effects of cement substitution with cement reappear, with the same ratio as discussed above with reference to first ceramic powder. It can be argued that the particle size distribution of the ceramic powder and of the sand may negatively interact, not having been jointly optimized for compactness, since the sole cement-to-ceramic volume replacement criterion has been followed. Anyway also in this case, the mortar with 30% cement-ceramic replacement and constant w/c ratio provides the best performance.

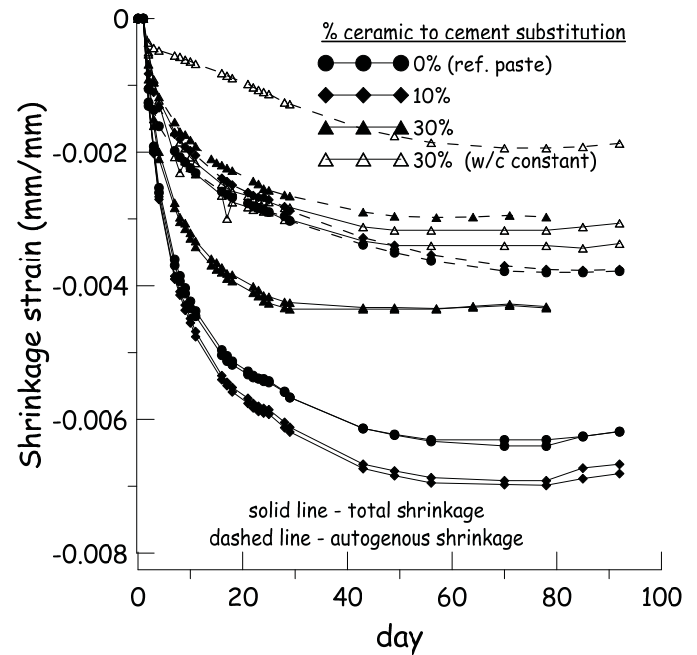
With reference to the flexural strength of pastes and mortars cast with the second ceramic powder, the same statements hold as exposed above to mixes cast with the first.

Table 4. MIP test results on mortars made with 1st powder.

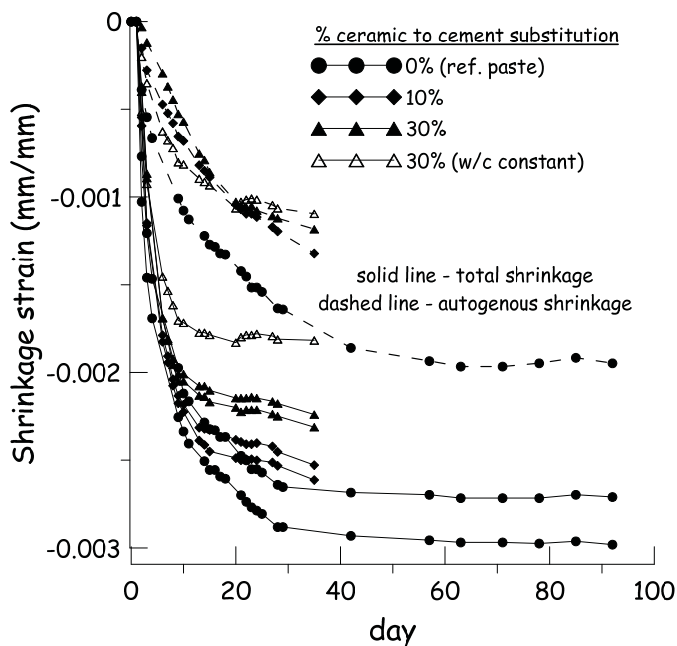
Mix-code	MCER-ref	MCER-10	MCER-30	MCER-30wc
Total porosity %	21.59	20.88	23.26	
Av. pore radius (μm)	0.0184	0.0143	0.0109	
Median pore radius (μm)	0.0264	0.0201	0.0142	



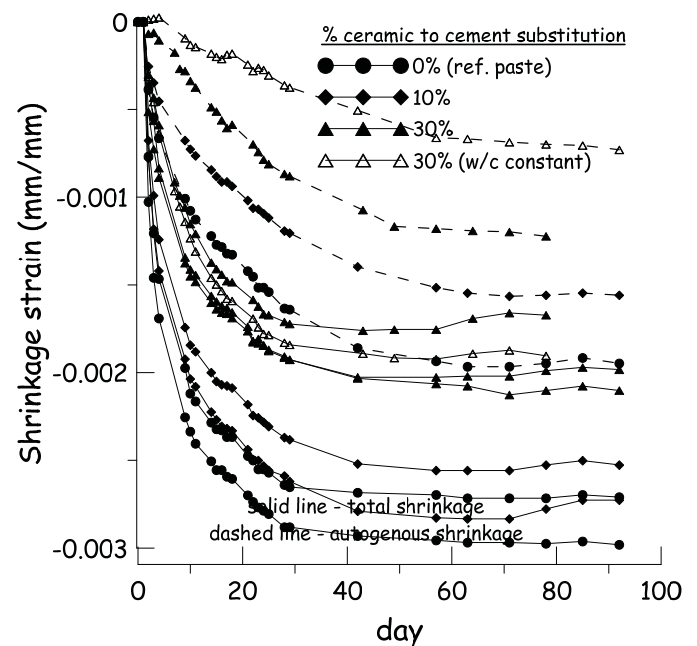
(a)



(a)



(b)



(b)

Figure 7. Time evolution of total free and autogenous shrinkage strain for cement pastes (a) and mortars (b) made with 1st ceramic powder.

Figure 8. Time evolution of total free and autogenous shrinkage strain for cement pastes (a) and mortars (b) made with 2nd ceramic powder.

Results of shrinkage test measurements (Figures 7-8), confirm the effectiveness of cement to ceramic replacement also in reducing this kind of deformation, generally the higher the volume percentage replacement the higher the measured reduction of shrinkage deformation. This cast positive shadows also with reference to the overall durability of cementitious composites obtained with the investigated cement replacements. Effects are more visible in the case of total shrinkage, most likely because of the alterations in w/c ratios yielded by a mere volume replacement of cement with

ceramic. As a matter of fact if the w/c ratio is kept constant, improvements also in the case of autogenous shrinkage are fairly evident. The second ceramic powder likely provides better performance than the former, probably because of a somewhat higher solid skeleton stability due to its coarse grains. As a matter of fact, improvement in mortar performance is always fairly better than that of corresponding pastes. The worse performance of pastes with 10% ceramic to cement replacement could be due a somewhat higher porosity cause by the coarser ceramic grains.

4 CONCLUSIONS

In this study a preliminary assessment has been performed of the feasibility of replacing cement with waste ceramic powders, obtained from disposed bathroom fixture/dental prostheses and from foundry industry residuals, in cement pastes and mortars.

Results have confirmed that the decrease of strength due to the reduction of cement content can be partially overcome at later ages by the likely pozzolanic activity of the ceramic, but can also be effectively tempered designing the mix composition so to keep constant the water to cement ratio. The fineness of the ceramic powder also plays an important role, also with reference to the interaction with the grain particle size distribution of the other powders and aggregates.

Improvements have been detected also with reference to the total and autogenous shrinkage deformation developments. This also paved the way to produce concrete with reduced early age cracking potential and hence higher durability, even with low w/c ratios, where the autogenous shrinkage deformation may be substantial, because of the positive mitigation effects yielded by the cement to ceramic replacement.

Negative effects on the fresh state performance can be easily overcome by suitably adjusting the SP dosage. Stabilizing effects of fine aggregates in mortars have been also highlighted, which leads to hypothesize that good results are going to be obtained with reference to concrete mixtures, with the further presence of coarse aggregates.

This prodromal study, which seems to confirm literature findings about the upper bound for cement replacement ratio, is going to be completed with durability investigation, in order to pave the way for the use of sustainable concrete incorporating waste ceramic powder for building engineering applications.

ACKNOWLEDGMENTS

The authors wish to acknowledge the financial support and funding received from the European Union, as this research is part of the FP7-PEOPLE-2012-IAPP project "EuroCrete: Development of sustainable, lower carbon, pre-cast concrete infrastructure". This work actually represents the summary of the activity performed by the authors during reciprocal secondments. The authors also acknowledge the cooperation of Mr. Eduardo Ballesteros Ribera, Mr. Héctor David Méndez Figueroa, Mr. Alex Pellegrini and Mr. Lorenzo Sgubbi in performing the experimental tests and reducing the data, in partial fulfilment of the requirements for the respective achievement of their MEng and BEng in Civil Engineering at Politecnico di Milano.

REFERENCES

- [1] Zimbili, O., Salim W. and Ndambuki, M. (2014). 'A review on the usage of ceramic wastes in concrete production', *International Journal of Civil, Environmental, Structural, Construction and Architectural Engineering*, 8, 91-95.
- [2] Amorin, L.V., Lira, H.L. and Ferreira, H.C. (2003). 'Use of residential construction waste and residues from red ceramic industry in alternative mortars', *ASCE Journal of Environmental Engineering*, 129, 916-920.
- [3] Vejmelová, E., Kulovaná, T., Keppert, M., Konvalinka, P., Ondráček, M., Sedlmajer, M. and Černý, R. (2012). 'Application of waste ceramics as active pozzolana in concrete production', *Proceedings IACSIT Coimbatore Conferences*, IACSIT Press, Singapore, 132-136.
- [4] Raval, A.D., Patel, I.N. and Pitroda, J. (2013). 'Ceramic waste: effective replacement of cement for establishing sustainable concrete', *International Journal of Engineering Trends and Technology*, 4, 2324-2329.
- [5] Ay, N. and Ünal, M. (2000). 'The use of waste ceramic tile in cement production', *Cement and Concrete Research* 30, 497-499.
- [6] Puertas, F., García-Díaz, I., Barba, A., Gazulla, M.F., Palacios, M., Gomez, M.P., and Martínez-Ramírez, S. (2008). 'Ceramic wastes as alternative raw materials for Portland cement clinker production', *Cement and Concrete Composites*, 30, 798-805.
- [7] Puertas, F., García-Díaz, I., Palacios, M., Gazulla, M.F., Gomez, M.P. and Orduña, M. (2010). 'Clinkers and cements obtained from raw mix containing ceramic waste as a raw material. Characterization, hydration and leaching studies', *Cement and Concrete Composites*, 32, 175-186.
- [8] Senthamarai, R.M. and Devadas Manoharan, P. (2005). 'Concrete with ceramic waste aggregate', *Cement and Concrete Composites*, 27, 910-913.
- [9] Sato, R., Shigematsu, A., Nukushina, T. and Kimura, M. (2011). 'Improvement of properties of Portland blast furnace cement type B concrete by internal curing using ceramic roof material waste', *ASCE Journal of Materials in Civil Engineering*, 23, 777-782.
- [10] Higashiyama, H., Yagishita, F., Sano, M. and Takahashi, O. (2012). 'Compressive strength and resistance to chloride penetration of mortars using ceramic waste as fine aggregate', *Construction and Building Materials*, 26, 96-101.
- [11] Gonzalez-Corominas, A. and Exteberria, M., (2014). 'Properties of high performance concrete made with recycled fine ceramic and coarse mixed aggregates', *Construction and Building Materials*, 68, 618-626.

Understanding the microstructure of alternative binder systems – banahCEM, a metakaolin based geopolymer

S. E. M. Lawther^{1&2}, J. A. McIntosh^{1&2}, S. Nanukuttan¹, J. L. Provis³, M. N. Soutsos¹, D. Jose²

¹School of Planning, Architecture and Civil Engineering, Queen's University Belfast, David Keir Building, Stranmillis Road, Belfast BT9 5AG, Northern Ireland

²banah UK Ltd, 1b Letterloan Road, Macosquin, Coleraine BT51 4PP, Northern Ireland

³Department of Materials Science and Engineering, University of Sheffield, Sheffield, S1 3JD, United Kingdom

email : susan.l@banahuk.co.uk, andrew@banahuk.co.uk, s.nanukuttan@qub.ac.uk, j.provis@sheffield.ac.uk

ABSTRACT: Geopolymer binders have emerged as an alternative to Portland Cement systems for specialist applications due to their improved durability and environmental impact. Geopolymer binders can be made by combining alkali activators with precursor materials including high purity dehydroxylated kaolin (metakaolin) or pulverised fuel ash. Although the technical and engineering properties of these materials can now be controlled to a high degree of precision, there is still much to be learnt about the underlying chemical reactions and the microstructure of the material. banahCEM is a geopolymer binder made from a calcined iron-rich kaolinitic clay. To aid in the understanding of the geopolymer system a SEM microstructural analysis of banahCEM has been carried out in comparison to high-purity metakaolin based geopolymer. Results indicate that there are several visible phases in the banahCEM geopolymer: 1) Geopolymer (alkali aluminosilicate) binder gel, 2) Partially reacted/relic metakaolin particles, 3) Reacted metakaolin particles, and 4) Impurities. Geopolymer produced from high-purity metakaolin is also composed of a geopolymer binder and relic metakaolin particles (phases 1 & 2). However, the size, proportion and distribution of the phases differ. By better understanding the microstructure of the geopolymer system, we in turn can learn how the mix proportions affect the properties and microstructure. However, and more importantly, we can manipulate the geopolymer system to suit a specific area of application, for example, increase the capacity to resist acid and chemical attacks.

KEY WORDS: Geopolymer, metakaolin, microstructure

1 INTRODUCTION

Environmental issues are currently a global concern in many areas of industry with low-carbon alternatives being sought where possible. Within the construction industry the production of Portland cement is a significant contributor to global carbon dioxide emissions which in turn has implications for global warming [1], [2]. Due to pressure to obtain commercially viable, low-carbon alternatives to Portland cement [3], novel cements are a high-priority area of research because of the potential environmental benefits. Metakaolin-based geopolymers (among others) have gained worldwide attention in the past 40 years [4] and are considered as a green alternative to Portland cement [5]. Geopolymer cement is typically produced by reacting an aluminosilicate-rich powder (the precursor/metakaolin) with an alkali hydroxide or alkali silicate solution [6] and results in the formation of a hardened material that has a three dimensional, X-ray amorphous structure [5].

The precursor, metakaolin, is a thermally treated product from kaolinite; a naturally occurring mineral. Kaolin is a group of kaolinitic clays. The clays are sheet silicates with what is often referred to as a 1:1 structure with one tetrahedral sheet and one octahedral sheet [7]. Currently metakaolin is typically acquired from high quality, high-purity kaolin sources [4] which in turn makes it an expensive precursor. Thus, there is a need to find a commercially viable precursor for metakaolin-based geopolymers.

Kaolinite can be formed in several different geological settings but typically forms as a result of weathering of the parent rock [8] which is often of volcanic origin. Depending on whether the parent rock was granitic or basaltic there are aluminium- and iron-rich varieties of kaolinitic rock

respectively. The parent rock and/or mode of formation of the kaolin can therefore affect the mineralogy, chemistry, morphology and grade of the kaolinite deposit [4], [9], thus geological knowledge of the source of kaolinite is crucial.

Commercial grade kaolin is distinguished by its whiteness, and fine, controllable particle size and high-quality deposits are often associated with granitic rocks [9]. In Northern Ireland, a kaolinite and iron-rich rock known as lithomarge (derived from basaltic rocks) is in abundance [6]. It primarily occurs as a unit within the Interbasaltic Formation (IBF) and is found throughout Co. Antrim and Londonderry. It is red/purple in colour, composed primarily of kaolinite and several impurities including Fe-Ti oxides [10], thus due to its colour and the impurities this source would be considered as an impure kaolinite source. However, due to its high kaolinite content it can be used as a commercially viable aluminosilicate precursor for geopolymer binders [6].

Lithomarge from Northern Ireland does contain impurities which may have an effect on the geopolymer properties. Tchakoute et al [11] tested several impure kaolinite sources and showed that increased proportions of gibbsite could be related to lower strength of the binder. However, it is unknown whether the association of smectite and iron oxide minerals with kaolinite will affect the chemistry and durability of the geopolymer concrete [12].

In this study two kaolinite precursors were used to make geopolymer binder: a commercial grade high-purity kaolin; and an iron-rich kaolinite precursor (lithomarge) from Northern Ireland. The binders are compared in terms of their microstructure. Results are used to present a microstructural model for metakaolin-based geopolymers and the influence of the grade/source of the kaolin on this microstructure.

2 MATERIALS AND METHODOLOGY

2.1 Precursor materials

Two sources of kaolinite were used to produce geopolymer binders. MetaMax white metakaolin was purchased from BASF. Metamax is a high reactivity metakaolin produced from high purity kaolin. It is a white mineral admixture that meets or exceeds all of the specifications of ASTM C-618 Class N pozzolans and also meets the strength activity index as per ASTM C-1240. It is a thermally treated kaolin (i.e. metakaolin) with particle size distribution d_{50} of $1.3\mu\text{m}$.

A sample of iron-rich lithomarge was collected from a quarry in Ballymena, Co. Antrim. The lithomarge was milled and flash calcined ($\sim 750^\circ\text{C}$) at Demeter Technologies, Fumel, France, and ball milled at banah UK Ltd. The lithomarge is coarser than the MetaMax. It was milled to have a coarser particle size distribution to comply with the proprietary banah specification and has a d_{50} of $<50\mu\text{m}$.

A sample of high-purity white kaolin purchased from Sigma-Aldrich was also analysed by XRD purely to show the differences between the high-purity and iron-rich kaolin. This material was not used to make any geopolymer binder, thus its properties will not be discussed in detail.

2.2 Methods

The mineralogy of the samples was characterised using X-ray diffraction (XRD) and particle size distribution analysed using a Malvern Mastersizer. XRD analysis was carried out using a PANalytical X-ray diffractometer (X'Pert³ Powder) using the PANalytical X'Pert Highscore software with the ICDD Powder Diffraction File database for semi-quantitative mineral identification. Microstructurally analysis was carried out using a Sigma SEM with integrated Oxford Instruments EDX detector and AZtec microanalysis computer software at Queens University Belfast. Images were typically captured using backscattered electron imaging (BSE) and X-ray mapping.

2.3 Mix design

Paste samples were cast for the high-purity and iron-rich metakaolin precursors using a formulation that has been developed from preliminary work on the metakaolin (lithomarge)-based geopolymer at banah UK Ltd. All samples were cured at 20°C for 28 days before being prepared for SEM analysis.

3 RESULTS

3.1 Mineralogy

High-purity kaolin was analysed by XRD and results confirm it to be composed of kaolinite and anatase (Figure 1). 'High-purity' kaolin typically implies approximately 99% kaolinite, thus the anatase is only present in trace amounts. MetaMax is a thermally treated kaolin. As a result of thermal treatment the kaolinite is dehydroxylated (-OH groups removed). The product of dehydroxylation is metakaolin and this material is X-ray amorphous [13]. As a result of this XRD analysis does not identify distinct peaks for kaolinite but an 'amorphous hump' at approximately the 22° 2θ position. Any trace minerals present will be identified by their unique peak profile. Figure 2 shows the XRD trace of the metakaolin

product MetaMax and there is an 'amorphous hump' at the 22° 2θ peak position as expected. The XRD trace of MetaMax does have several peaks and analysis indicates that these peaks are due to trace amounts of anatase within the sample (Figure 2). Due to the amorphous nature of the Metamax, semi-quantitative analysis cannot be carried out on the powder as only the trace minerals are assigned by the software. However, as mentioned, 'high-purity' typically implies approximately 99% kaolinite.

The iron-rich lithomarge from Co. Antrim was analysed in its raw form to enable semi-quantitative analysis to be carried out prior to dehydroxylation of the kaolinite (Figure 1). XRD highscore analysis indicates that the material is composed of 70.1% kaolinite, 24.3% goethite, 3.6% anatase and 2.1% magnetite. After calcining the iron-rich lithomarge, XRD analysis shows the characteristic 'amorphous hump' for kaolinite at the 22° 2θ position. Other peaks occur in this material and these have been identified as hematite (Figure 2). Goethite and magnetite undergo phase transformations on heating. Both minerals convert to hematite, thus only hematite is observed in the calcined iron-rich lithomarge (Figure 2).

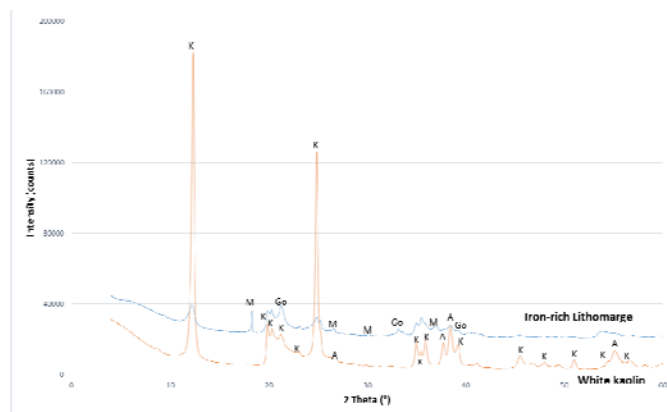


Figure 1. XRD analysis of white kaolin and iron-rich lithomarge. K=kaolinite, M=magnetite, Go=goethite, A=anatase.

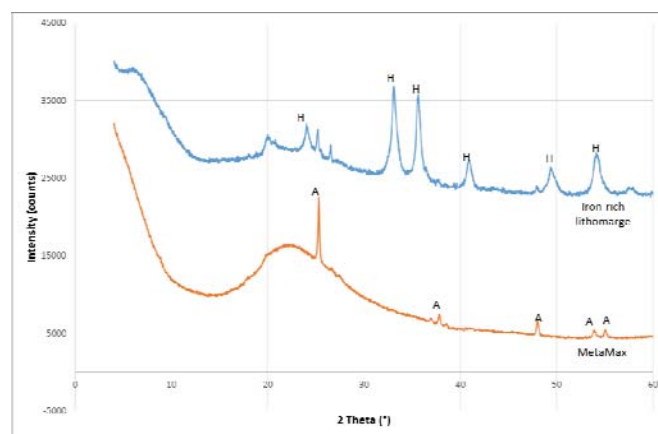


Figure 2. XRD analysis of MetaMax and calcined iron-rich lithomarge. H = hematite Note the 'amorphous hump' at 22° 2θ .

3.2 Microstructure

SEM analysis was carried out on the raw lithomarge and the geopolymer pastes made from iron-rich kaolin (lithomarge) and from the high-purity kaolin (MetaMax). The raw lithomarge was analysed to confirm the presence of kaolinite. X-ray spot analysis can be used to estimate the chemical formula of a mineral/phase. Spot analysis of the dominant phase in the lithomarge indicates that the Si:Al ratio is approximately 1:1 (Table 1). This is in agreement with the known chemical formula of kaolinite and SEM observations confirm it to be the dominant phase in the raw material thus corroborating the XRD results of the lithomarge.

Table 1. AZtec X-ray spot analysis of raw kaolinite in the lithomarge (top) and of the different phases found within the geopolymer paste. Values are in weight %. Approximate Si:Al ratio also indicated for the various phases.

Phase	Si	Al	K	Fe	Si:Al
Kaolinite	22.1	21.8			1:1
Partially reacted metakaolin	21.9	18.4	4.3	1.8	1:1
Reacted metakaolin	22.8	12.7	10		2:1
Fe-rich geopolymer binder	22	11.7	11.2	4.5	2:1
Impurities				43.4	
High-purity binder	23.2	12.3	11.9		2:1

In the geopolymer paste made from iron-rich kaolin four different phases were identified: 1) the geopolymer binder 2) partially reacted/relic metakaolin 3) reacted metakaolin and 4) impurities (Figure 3). X-ray spot analysis was used to chemically identify/distinguish the different phases (Table 1) and X-ray mapping was carried out to confirm the distribution of the elements within the system (Figure 4).

The geopolymer binder (1 in Figure 3) is the main phase within the paste and makes up the matrix of the system. It is fine grained with no apparent structure within it and is rich in potassium (K), aluminium (Al) and silica (Si) (Figure 4). Spot analysis provides evidence about the composition and based on peak intensities, the Si:Al ratio in the binder is approximately 2:1. The partially reacted/relic metakaolin particles (2 in Figure 3) are randomly distributed throughout the matrix, are irregular in shape, ~10-50 μm in size, are highlighted by a dark grey 'reaction' rim around the particle (Figure 3) and have a Si:Al ratio of ~1:1, similar to that of raw kaolinite (Table 1). However, the Al concentration in the partially reacted metakaolin is slightly reduced compared to kaolinite (Table 1) and the partially reacted metakaolin also contains K within its structure (Figure 4). X-ray mapping indicates that the partially reacted metakaolins are enriched in Si and Al compared to the geopolymer binder but depleted in K (Figure 4). This is confirmed by spot analysis of the binder, the 'reaction' rim and the relic metakaolin (Figure 5). The 'reaction' rim is more akin to the binder but has reduced

amounts of K (Figure 5). The reaction rim also has less Si than the relic metakaolin. Due to the similarities and differences between metakaolin and the relic metakaolin, these particles have thus been described as 'partially reacted' metakaolin. The reacted metakaolin particles are dark grey in SEM-BSE (Figure 3), they are randomly distributed throughout the matrix, irregularly shaped and are typically less than 10 μm in size. The reacted particles are similar in colour to the 'reaction' rims (Figure 3) and spot analysis indicates they are almost identical in composition to the binder (Table 1 and Figure 5). Therefore, this phase is essentially a 'reaction' rim around a partially reacted/relic metakaolin. The relic metakaolin is no longer visible, hence these particles are classified as reacted metakaolin particles. Impurities (4 in Figure 3) within the matrix are typically Fe-rich (Table 1 & Figure 4) and are bright white in SEM-BSE (Figure 3). They range from <1 to ~70 μm in size but the majority are <5 μm . As a result of the dominantly fine grain size and the impurities being widely distributed, Fe appears to occur throughout the entire system when analysed using X-ray mapping, with high concentrations coinciding with the larger particles (Figure 4).

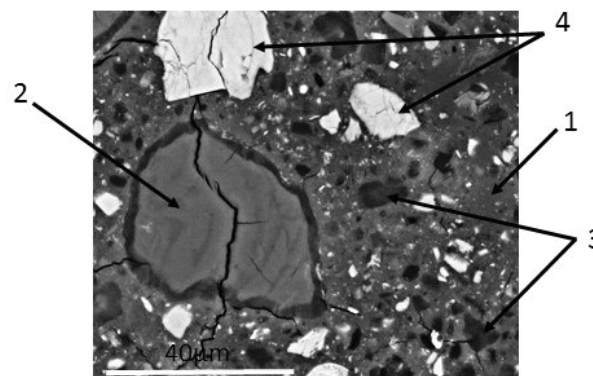


Figure 3. SEM-BSE image of the geopolymer paste made from iron-rich kaolin. The four identified phases are arrowed – see text for description.

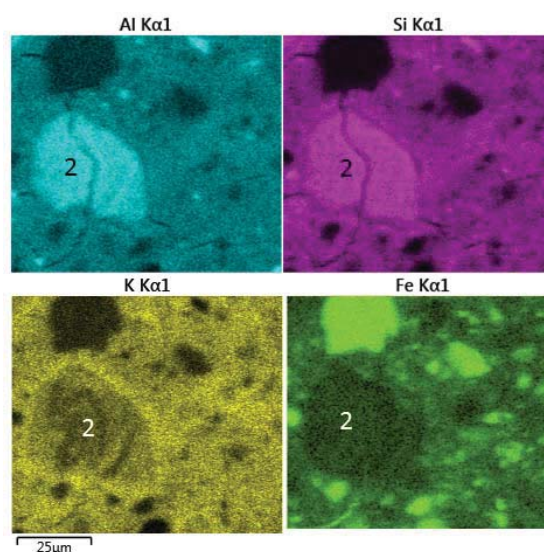


Figure 4. SEM-X-ray map of the geopolymer paste made from iron-rich kaolin. The relic metakaolin phase (2) identified by SEM-BSE is labelled.

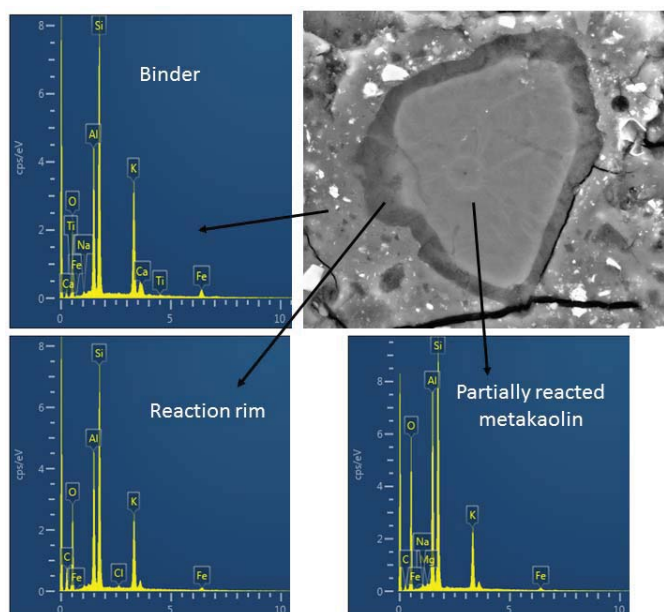


Figure 5. SEM-BSE image of partially reacted metakaolin and spot analysis of the metakaolin, the reaction rim and the geopolymer binder. Al and Si increases from binder to metakaolin whereas K decreases.

The geopolymer paste made from high-purity metakaolin is homogenous with no apparent features present when viewed at moderate magnification (Figure 6). Small pits are visible indicating the existence of a micro-porosity within the binder (Figure 6). When magnification is increased tenfold it is apparent that there are two main phases present 1) the geopolymer binder and 2) relic metakaolin particles (Figure 6). Trace amounts of titanium-rich (Ti-rich) impurities are also present but are sub-micron in size and sparse (Figure 6). The spot size for X-ray analysis is $\sim 20\ \mu\text{m}$. Therefore, due to the fine grained nature of the MetaMax (d_{50} of $1.3\ \mu\text{m}$) and its close relationship with the newly formed geopolymer binder, X-ray spot analysis cannot be utilised to distinguish the two phases apart. However, based on the purity of the metakaolin we can assume that anything other than binder is relic metakaolin as there are no other known phases present in the system. Image analysis can be used to estimate the proportions of the two main phases and analysis of the paste indicates the proportion of binder to relic metakaolin is $\sim 70:30$.

Spot analysis can be carried out on the geopolymer binder to ascertain its approximate composition as it is the dominant phase. Results indicate that Si:Al ratio is $\sim 2:1$ (Table 1) which is as expected and is similar to that found in the iron-rich metakaolin based geopolymer binder.

4 DISCUSSION AND MICROSTRUCTURAL MODEL

Observations of the geopolymer binders made from high-purity and iron-rich kaolinite precursors has shown that there are two phases which are common to both systems: 1) geopolymer binder and 2) partially reacted/relic metakaolin (Figure 3 and Figure 6). Spot analysis has shown that the basic composition of the two geopolymer binders are essentially the same regardless of kaolinite source, with both binders having a Si:Al ratio of approximately 2:1 (Table 1).

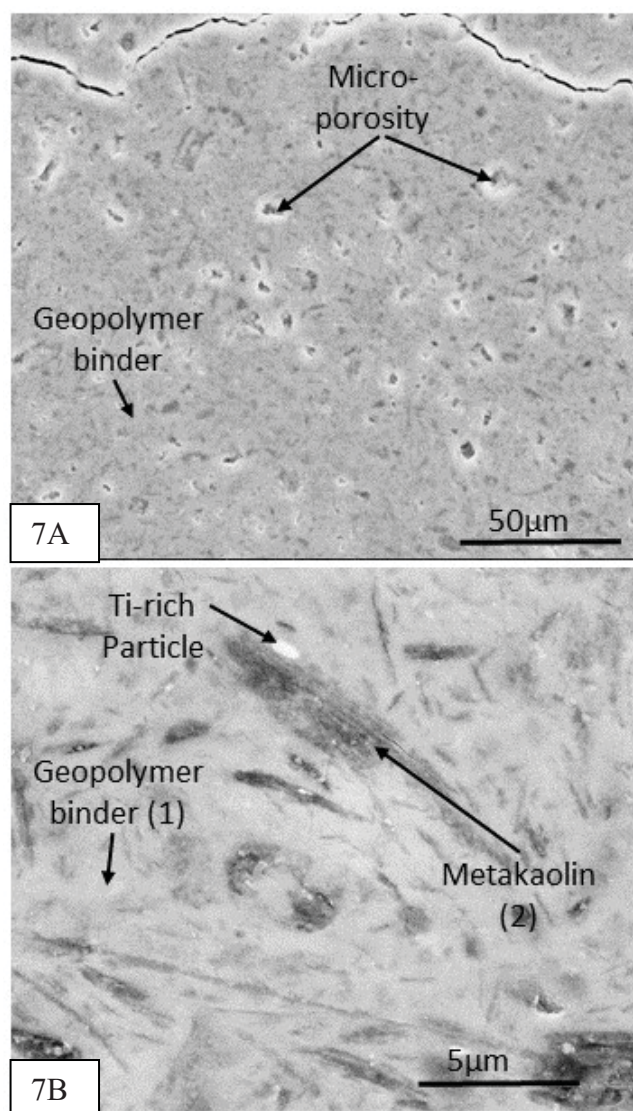


Figure 6. SEM -BSE images of geopolymer paste made from high-purity MetaMax. A) shows homogenous binder with micro-porosity throughout. B) shows zoom of binder revealing relic metakaolins and a Ti-rich particle.

The main differences between the two binders are: the presence of reacted metakaolin particles, impurities, and the larger grain size of the relic metakaolins in the iron-rich kaolin geopolymer. Also, in the high-purity kaolin geopolymer a micro-porosity has developed which is not apparent in the iron-rich kaolin geopolymer.

Both the high-purity and iron-rich based geopolymers have partially reacted/relic metakaolin but of different size. The variation in size of the relic metakaolins is a direct result of the different sizes of the precursor material. MetaMax has a d_{50} of $1.3\ \mu\text{m}$ whereas the iron-rich kaolin has a d_{50} of $<50\ \mu\text{m}$, thus the relic material will vary in size accordingly. However, the fact that metakaolin remains indicates that the geopolymer reaction has not gone to completion i.e. not all of the reactants (activator and/or metakaolin) were consumed. This could be due to several reasons however, to confirm why this has occurred further work will need to be carried out.

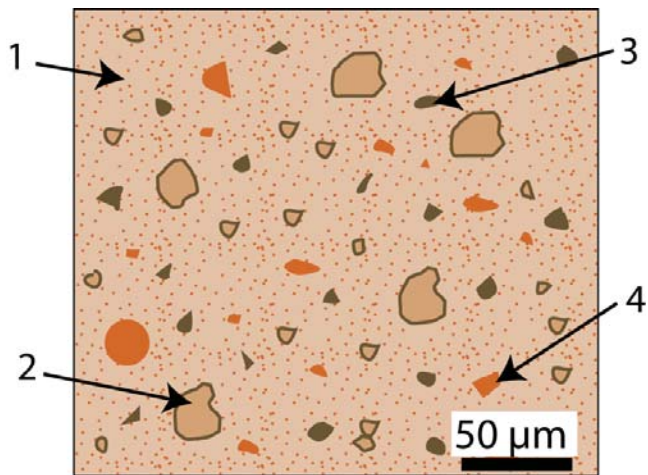


Figure 7. Microstructural model of iron-rich kaolin geopolymer at 'low' magnification. Phases 1-4 as described in text are labelled.

The partially reacted metakaolin particles in the iron-rich kaolin geopolymer are infused with K (Figure 4). From analysis of the raw kaolinite we know that K is not present in the kaolinite structure thus, it must be as a result of the geopolymerisation process. In the original kaolinite structure it is difficult to penetrate alkali or alkali earth cations [15]. However, after dehydroxylation the metakaolin is accessible to cations for adsorption [15]. Therefore, during the geopolymerisation process if there is excess K available in the system, the K will be able to penetrate into the structure of the relic metakaolin particles. It is likely that this process also occurred in the high-grade kaolin geopolymer but due to the finer grain size of the MetaMax (1.3 μm) and the EDX spot size (20 μm) on the SEM, analysis of the individual particles could not be carried out accurately.

Reacted particles have only been identified in the iron-rich kaolin geopolymer. Due to the fine grain size of the MetaMax, if these phases occur in the high-purity kaolin geopolymer they are expected to be <1 μm in size. Particles of such a small size are unlikely to be detected by this SEM due to power limitations. However, a higher powered microscope may reveal that this phase does also occur in the high-purity kaolin geopolymer.

Impurities do occur in both the iron-rich and high-purity kaolin geopolymers but it is a question of proportion and size. The iron-rich kaolin has approximately 30 % impurities (anything other than kaolinite is considered as an impurity) that range from <1 to 70 μm in size, whereas high-purity kaolin has ~1 % impurities that are <1 μm in size.

The results from this study have been used to create a microstructural model for geopolymers made from iron-rich and high-purity kaolin precursors (Figure 7 & Figure 8). The microstructural models show the main phases present in both of the geopolymer systems. In the iron-rich kaolin geopolymer the 4 phases are indicated 1) Geopolymer binder 2) partially reacted metakaolin 3) reacted metakaolin and 4) impurities. In the high-purity kaolin geopolymer the model shows the differences observed at different magnifications. At 'low' magnification the geopolymer binder (phase 1) is homogenous with only micro-pores visible. However, at 'high' magnification the relic metakaolin particles are also visible.

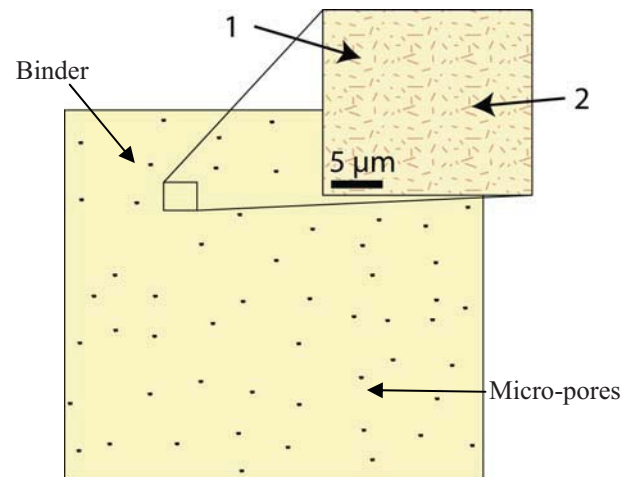


Figure 8. Microstructural model of high-purity kaolin geopolymer. Large image shows the geopolymer binder at 'low magnification' and inset shows 'high' magnification phases. Labelled phases are described in the text.

The models highlight how distinctly different the microstructure is at 'low' magnification for the geopolymer formed from two different sources and different purities of kaolin. Chemically the kaolinite and the geopolymer produced in both systems are essentially the same but yet microstructurally they are very different. The overall quality of cement binder and concrete is usually evaluated by its strength which is directly dependent upon the microstructure [16]. Therefore, if the microstructure is dissimilar, it is likely that the properties of the cement will also vary. However, work to date on the iron-rich kaolin geopolymer indicates that the compressive strength is not affected by the impurities and/or the different microstructure with 1 and 7 day strengths of 58 MPa and 89 MPa being recorded for paste samples [6]. An accelerated aging comparison of iron-rich and high-purity kaolin geopolymers has also been carried out with no significant differences in 28 day ambient or > 90 day accelerated aging mortar strengths [17]. Variations in strength have been recorded as a result of coarser grain size in the iron-rich kaolin geopolymer [17]. This variation in the precursor likely affected the proportions of the different phases, thus affecting final strength. It is likely that there is an optimum grain size to strength developed relationship, as with other cements - raw material preparation, binder formulation and mix design all play a significant role in the stability of a geopolymer concrete.

In conclusion, the main components of kaolin based geopolymer cement are the geopolymer binder and relic metakaolin. Depending on the purity of the kaolin source, reacted particles and impurities may also be present. The proportions will depend on the composition of the source and the microstructure observed will be a result of precursor composition and preparation technique. By understanding the basic microstructure of the kaolin-based geopolymer cement we can start to adjust the binder formulation to ascertain how it affects the microstructure. More importantly, we can manipulate the geopolymer system to suit a specific area of application, for example, increase the capacity to resist acid and chemical attacks

ACKNOWLEDGEMENTS

Thanks goes to Mark Russell and Trevor Sewell at Queens University Belfast for technical assistance.

REFERENCES

- [1] J.S.J. van Deventer, J. L. Provis, P. Duxson, and D. G. Brice, "Chemical research and climate change as drivers in the commercial adoption of alkali activated materials," *Waste and biomass valorization*, vol. 1, no. 1, pp. 145–155, 2010.
- [2] J. L. Provis and J. S. J. van Deventer, *Geopolymers structure, processing, properties and industrial applications*, 1st ed. Cambridge: Woodhead Publishing Ltd, 2009.
- [3] J. Davidovits, "World-wide increase in geopolymer research," 2010. [Online]. Available: <http://www.geopolymer.org/science/world-wide-increase--in-geopolymer-research>. [Accessed: 12-Apr-2016].
- [4] Z. H. Zhang, H. J. Zhu, C. H. Zhou, and H. Wang, "Geopolymer from kaolin in China: An overview," *Appl. Clay Sci.*, vol. 119, pp. 31–41, 2016.
- [5] P. Duxson, A. Fernandez-Jimenez, J. L. Provis, G. C. Lukey, A. Palomo, and J. S. J. Van Deventer, "Geopolymer technology: The current state of the art," *J. Mater. Sci.*, vol. 42, no. 9, pp. 2917–2933, 2007.
- [6] A. McIntosh, S. E. M. Lawther, J. Kwasny, M. N. Soutsos, D. Cleland, and S. Nanukuttan, "Selection and characterisation of geological materials for use as geopolymer precursors," *Adv. Appl. Ceram.*, vol. 114, no. 7, pp. 378–385, 2015.
- [7] H.-R. Wenk and A. Bulakh, *Minerals: their constitution and origin*, 1st ed. Cambridge: Cambridge University Press, 2004.
- [8] C. S. Exley, "Reconnaissance survey of some bauxitic clays in Co Antrim," *The British Ceramic Research Association, Res Paper no. 362*, 1957.
- [9] A. J. Bloodworth, D. E. Highley, and C. J. Mitchell, "Kaolin," p. 75, 1993.
- [10] I. G. Hill, R. H. Worden, and I. G. Meighan, "Geochemical evolution of a palaeolaterite: The Interbasaltic formation, Northern Ireland," *Chem. Geol.*, vol. 166, no. 1–2, pp. 65–84, 2000.
- [11] H. K. Tchakoute, C. H. Rscher, J. N. Y. Djobo, B. B. D. Kenne, and D. Njopwouo, "Influence of gibbsite and quartz in kaolin on the properties of metakaolin-based geopolymer cements," *Appl. Clay Sci.*, vol. 107, pp. 188–194, 2015.
- [12] J. Davidovits, *Geopolymer chemistry and applications*, 3rd ed. Institute Geopolymere, 2011.
- [13] G. W. Brindley and M. Nakahira, "The kaolinite-mullite reaction series: I. A survey of outstanding problems," *J. Am. Ceram. Soc.*, vol. 42, pp. 311–314, 1959.
- [14] J. E. Welton, *SEM petrology atlas*, no. 4. 2003.
- [15] A. K. Chakraborty, "Crystallization studies of preheated metakaolinite," in *Phase transformation of kaolinite clay*, A. K. Chakraborty, Ed. Springer India, 2014, p. 112.
- [16] S. Caliskan, "Aggregate/mortar interface: Influence of silica fume at the micro- and macro-level," *Cem. Concr. Compos.*, vol. 25, no. 4–5 SPEC, pp. 557–564, 2003.
- [17] J. A. McIntosh, D. Jose, S. E.M Lawther, and M. N. Soutsos, "Accelerated Aging Studies of a Calcined Clay-Based Geopolymer Binder," *The 9th International Concrete Conference, Dundee*, 2016.

The Potential Use of Ceramic Waste Sludge as a Supplementary Cementitious Material

Paul Archbold¹, Mark Russell², Colm Hoey²,

¹School of Engineering & Materials Research Institute, Athlone Institute of Technology, Dublin Road, Athlone Co. Westmeath, Ireland

²School of Planning, Architecture and Civil Engineering, Queen's University Belfast, David keir Building, Stranmillis Road, Belfast, BT9 5AG, Northern Ireland
email: parchbold@ait.ie

ABSTRACT: Cement based materials (CBM) are among the most common construction materials in the world. The most common form of CBM is concrete. One advantage of the material is that it can be produced locally, reducing transportation and energy costs. However, the use of raw materials in the production of both cement and aggregates carries an environmental cost. Due to its prominence in use, design and construction of concrete structures is governed by a plethora of codes of practice and design guides. These codes of practice generally classify CBM according to their strength class only and are restrictive on the CBM constituents. However, there is increasing desire to supplement or replace some of the raw materials used in producing CBM, while jointly reducing the amount of waste material being sent to landfill.

In this context, the authors have examined the potential use of ceramic waste sludge (CWS) as a supplementary cementitious material. CWS is a waste product, generated in the pharmaceutical industry, which at present is sent to landfill or exported for recycling in continental Europe. However, the constituents of the ceramic material suggest that it may possess pozzolanic properties, which could be of benefit in replacing Portland cement in concrete.

This paper presents the results of a series of characterisation tests to determine any pozzolanic or other pertinent properties of the material. Results show that use of the CWS as a partial cement replacement in certain applications may be possible and that pozzolanic reactions may occur at later stages, with other effects on the hydration process evident in earlier parts of the curing process.

KEY WORDS: Pozzolan; cement based materials, Concrete, ceramic waste

1 INTRODUCTION

1.1 *Environmental Impact of Cement Production*

Concrete is the most common construction material in the world and its primary components are aggregates, water and cement. Traditional aggregates are crushed rock and sand, which are extracted as raw materials in energy-intensive extraction processes. Worldwide cement production reached 3.6 billion tonnes in 2012 [1] and it is projected to grow by up to 1.2% per year, reaching between 3700 and 4400 megatonnes in 2050[2]. The environmental impact of this magnitude of cement production, owing primarily to the degradation of raw materials and the required use of fossil fuels in the production process, is receiving significant attention. For example, Stafford et al [3] recently carried out a life-cycle assessment on a cement processing plant in Southern Europe and concluded that the intensive consumption of raw materials and fossil fuels was the aspect that most affects the abiotic depletion potential.

1.2 *Environmental Impact of Ceramic Waste*

Ceramic products are made from natural materials which contain a high proportion of clay minerals. These are then "fired" in kilns at temperatures of up to 1000°C. These materials again involve the extraction of raw materials and significant consumption of fossil fuels in their production. Further, they are generally sent to landfill after their use as they generally cannot be processed or recycled. Research into possible re-use of ceramic materials is ongoing. One potential

avenue for this re-use may be in the replacement of some of the raw materials in concrete or cement-bound materials (CBM's).

1.3 *Use of Ceramic Waste as an Aggregate replacement in Concrete*

Many authors have researched the possibility of using waste ceramic materials as replacements for either the coarse or fine aggregates in concrete.

Ceramic waste has been shown to be a suitable replacement for coarse aggregates, however their increased porosity and water absorption require them to be pre-saturated prior to use [4], [5].

Similarly, foundry sand, a ceramic waste material, has been shown to be an effective replacement for natural fine aggregates. However, the use of ceramic sand may be limited to 30% replacement of the fine aggregates due to the high percentage of fine material [6]. As with the coarse aggregates, foundry sand has been reported to have a higher absorption rate than natural sand and a higher void ratio. Further, it is reported that the increased addition of waste foundry sand as a fine aggregate replacement reduced the slump of concrete [7], [8], [9]. Halicka et al [10] also noted a slight reduction in compressive strength, but interestingly reported an improved performance of the ceramic concrete in high temperatures.

1.4 Use of Ceramic Waste as a Supplementary Cementitious Material (SCM)

The production process for ceramic material involving the use of natural clays being treated at high temperatures has been shown to activate these clays, yielding pozzolanic materials. Ay & Unal [11] investigated the use of waste ceramic tiles in cement production, concluding that the waste material did possess pozzolanic properties. More recent studies have supported these assertions with Puertas et al [12] claiming that use of ceramic waste as a partial replacement for Portland cement produced viable mixes, with potentially higher reactivity and burnability as long as the particle size was maintained below 90 μm . Heidari et al [13] found that the replacement of Portland cement by up to 20% ceramic waste yielded no reduction in compressive strength of concrete specimens but did improve the water absorption of the concrete, suggesting improved durability performance. The addition of nano SiO_2 at low levels helped to improve both parameters.

Kenna & Archbold [14] examined the use of ceramic waste as a cement replacement and noted that its use led to reduced workability, but improved cohesion of fresh concrete, together with a lighter, more uniform finished colour and reduced 7-day compressive strengths but 28-day compressive strength was comparable to ordinary CEM I control mixes.

This paper reports on a continuation of the work of Kenna and Archbold [14] and specifically measures the pozzolanic nature of the waste ceramic material.

2 METHODOLOGY

2.1 Materials

The following materials were used in the manufacture of cement based materials:

Ceramic Waste Sludge (CWS)

The ceramic material utilized in the study was waste sludge derived from mass finishing processes. Mass finishing is a wet process which produces a ground ceramic sludge with moisture content up to and above 50%.

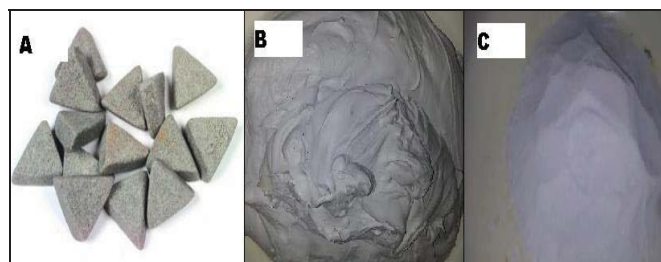


Figure 1: CWS production process (A) ceramic media prior to mass finishing process (B) ceramic waste sludge (C) dry milled CWS

In order to produce a dry powdered CWS, the ceramic sludge was dried at $T=105^\circ\text{C}$ for a period of 48 hours. The dried sludge forms a cake like solid in static drying conditions. This ceramic cake was subsequently milled until a ceramic powder was created with a particle diameter passing a 150 μm sieve.

The production process of CWS from orthopedic mass finishing media can be seen in Figure 1 [14].

The chemical and mineral composition and particle size information of CWS are detailed in Table 1, Figure 2 and Figure 3 respectively.

Table 1. Chemical composition of materials: results by XRF

Oxides (%)	PC	CWS
SiO_2	22.48	51.04
TiO_2	0.38	0.86
Al_2O_3	5.92	43.42
Fe_2O_3	2.78	0.52
CaO	62.98	0.18
MgO	2.13	0.19
SO_3	3.16	0.05
Na_2O	0.23	0.33
K_2O	0.59	2.96
P_2O_5	0.15	0.15
LOI*	1.54	1.73

*loss on ignition

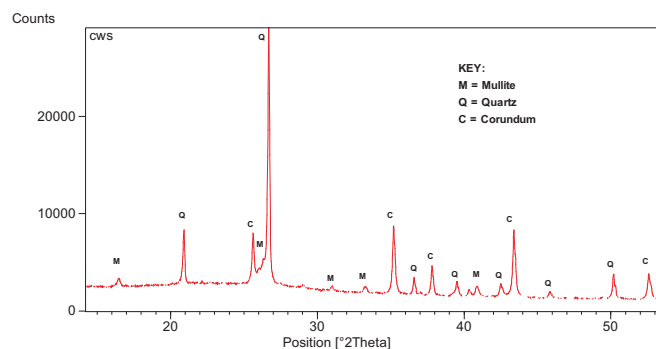


Figure 2: XRD trace of CWS highlighting mineralogy

Results indicate the chemical composition of CWS to be primarily SiO_2 and Al_2O_3 . Previous research [14] had indicated that this composition may reflect the presence of pozzolanic amorphous aluminosilicates within CWS. However, as Figure 2 indicates the mineralogy of CWS is predominately crystalline with minerals of mullite ($\text{Al}_6\text{Si}_2\text{O}_{13}$), quartz (SiO_2) and corundum (Al_2O_3). As shown in Figure 3, particle size analysis of CWS indicates it to be considerably finer than Portland cement with over 80% of its particles less than 10 μm .

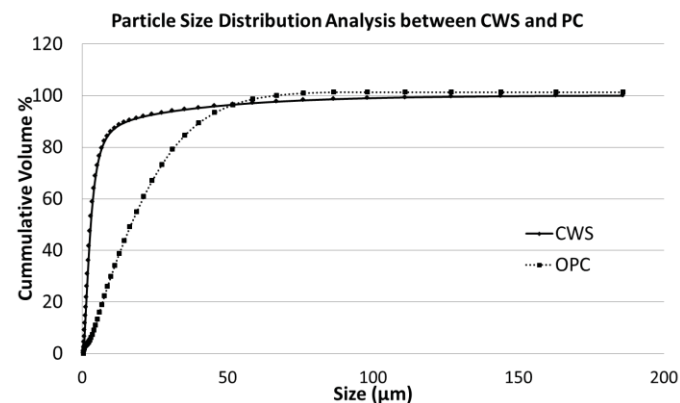


Figure 3: Particle size analysis of CWS and PC

Portland Cement (PC)

The PC used was class 42.5N Portland cement [15], supplied by a local cement manufacturer. The chemical composition and particle size information of PC are reported in Table 1 and Figure 3. As previously mentioned the particle size of Portland cement is greater than CWS.

2.2 Sample Preparation

The type of blends and their notations are given in Table 2. PC and PC/PFA blends (with 0.4 water to cementitious materials ratio) were manufactured using a mechanical mixer and placed in 50 mm size cube moulds. The samples were then tamped with a metal rod until the air bubbles stopped appearing at the surface. The samples were used to assess compressive strength of the various blends as well as their hydration and mineralogical changes.

Table 2. Mix proportions of cement blends investigated

Notation	PC	CWS
PC-100	100	0
CWS-15	85	15
CWS-20	80	20
CWS-30	70	30
CWS-40	60	40

2.3 Curing Regime

Immediately after casting, the blends were covered with a damp hessian cloth and placed in a constant temperature condition ($20^{\circ}\text{C} \pm 1^{\circ}\text{C}$) for 24 hours. After this period the samples were demoulded and placed in a constant temperature ($20^{\circ}\text{C} \pm 1^{\circ}\text{C}$) water bath until age of testing at 7, 28, 90 and 120 days.

2.4 Test Methods

The effect of the CWS on the PC paste mixes was determined from compressive strength, heat of hydration and mineralogical data. The mineralogical information was ascertained by the thermogravimetric (TGA) technique. At the specified ages three samples of each mix were tested for their compressive strength. Powder samples were obtained from each of the crushed cubes for TGA.

For TGA the paste samples (~20 mg) were placed in an alumina crucible and heated in Netzsch's STA 449C at $10^{\circ}\text{C}/\text{min}$ up to 1000°C . An inert nitrogen atmosphere was used and results were plotted on the TG curve, with weight against temperature. The amount of calcium silicate hydrates (C-S-H) and portlandite (CH), which gives an indication of the degree of hydration, was calculated as mass loss on the TG curve in the respective temperature range of $200\text{--}400^{\circ}\text{C}$ and $450\text{--}520^{\circ}\text{C}$ respectively.

The heat of hydration test was carried out over a seven day period by using the isothermal calorimetry method (TAM Air; TA Instruments). Samples were prepared by mixing 50g of water in a beaker ($w/c=0.4$). After thorough mixing, lasting 2-3 minutes, approximately 5 g of the paste was transferred to a plastic ampoule, which was in turn transferred to the calorimeter. The calorimeter temperature was set at 20°C . The successful monitoring of the heat evolved as a function of

time gave an indication of how hydration progressed in PC with the addition of CWS.

3 RESULTS AND DISCUSSION

3.1 Compressive Strength

The compressive strength of each paste sample is illustrated in Figure 4. Although the replacement of Portland cement by CWS resulted in a reduction in strength there are still some interesting results within this data that require clarification.

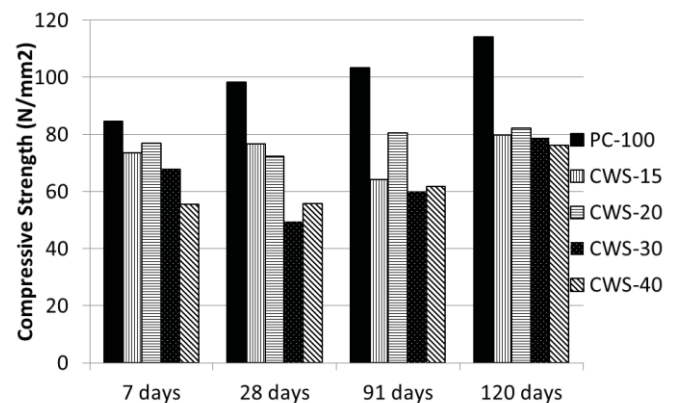


Figure 4. Compressive strength of pastes from 7 to 120 days

Firstly, when CWS is blended with PC, early age strength (e.g. 7 days) is higher than what would be expected if the strength was purely associated with Portland cement hydration. For example, CWS-20 exhibits 90% of the strength of the PC-100 sample after 7 days, even though it only contains 80% the cement content. It is unlikely that the increase in strength is related to pozzolanic activity as pozzolanic reactions are usually slow and take at least 28 days after hydration to occur. Rather, the strength of early age blends containing CWS could be attributed to the fine grained nature of CWS (see Figure 3) providing nucleation sites for accelerated cement hydration. It is also likely that the fine grained nature of CWS provides particle packing improvements whereby finer CWS particles fill the voids between cement grains and thereby enhance the hydrated cements mechanical strength.

Secondly, regardless of the amount of CWS added (15 to 40%) in the various PC blends, the late stage (120 day) strength of each blend is low compared to PC-100 – see Figure 4. This is at variance with what was anticipated by previous work carried out by McKenna and Archbold [14]. In this paper the authors assumed that, based on the suspected pozzolanicity of CWS, the long term strength of blends containing CWS would exceed that of pure PC. However, as shown in Figure 4, this is not the case. Therefore, based on the strength results alone it can be assumed that if the pozzolanic reaction anticipated by McKenna and Archbold [14] has occurred it is sufficiently small with no obvious benefit to long term strength development.

3.2 Paste Heat of Hydration

Given that early strength development (7 days) seems to have been enhanced in blends containing CWS, it was necessary to

investigate how the addition of CWS affects the hydration of PC with time. Results, shown in Figure 5 and Figure 6, begin after 45 minutes and do not include the exothermic reaction that results from the rapid initial dissolution of the cement compounds.

As highlighted in Figure 5 there are several stages of cement hydration. Results indicate that the induction period lasts longer in blends where increasing amounts of CWS have been added. The end of the induction period marks the start of the acceleration period, a period which is associated with the production of C-S-H. It is clear with increasing amounts of CWS the onset of the acceleration period (the main hydration phase) is delayed.

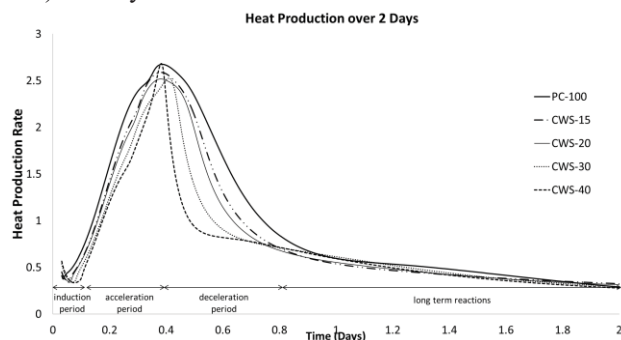


Figure 5. Rate of heat production: heat of hydration (mWg^{-1}) for first 2 days of hydration

The total heat (cumulative heat) from hydration of the various blends is shown in Figure 6. As expected, due to its greater amount of PC, the 100% PC sample (PC-100) exhibits greater amount of total heat compared to the blends incorporating CWS. If CWS didn't affect PC hydration then the total heat output from the blended mixes should be proportionate to the amount of PC within the blend. However, as Figure 7 shows, this is not the case. Figure 7 presents the total heat of each mix expressed in terms of heat per gram of Portland cement. Results indicate that the heat of hydration from Portland cement is accelerated in blended mixes compared to PC-100.

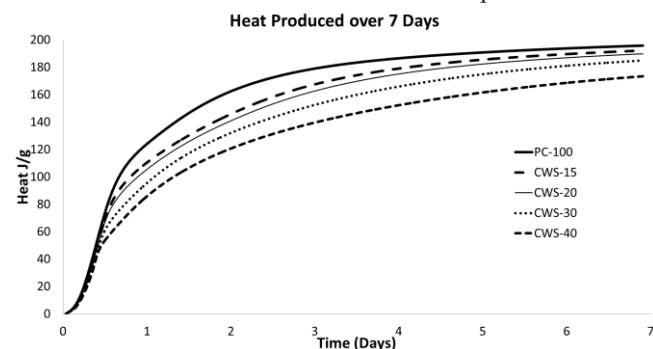


Figure 6. Total heat: heat of hydration (J g^{-1}) for first 7 days of hydration

Therefore, the addition of CWS has a positive role in accelerating early age hydration. Previous research has indicated that the presence of fine grained supplementary cementitious materials would result in an occurrence called the filler effect that provides additional nucleation sites for Portland cement hydration to occur [16]. Indeed, such an effect would therefore explain the compressive strength trends highlighted in the previous section.

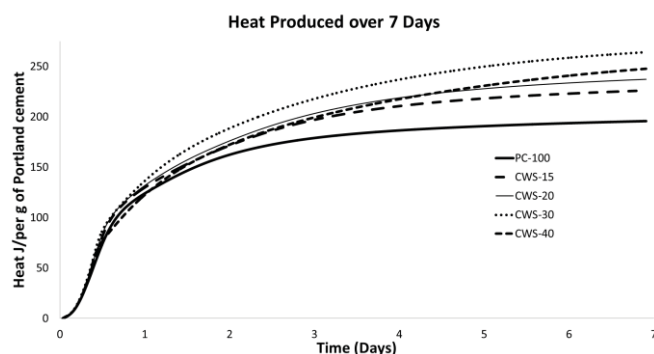


Figure 7. Total heat: heat of hydration (J g^{-1}) per gram of Portland cement in binder

3.3 Assessment of Pozzolan Reaction

Calcium Hydroxide (CH)

Quantification of calcium hydroxide (CH) content permitted an assessment of potential pozzolanic reactions within the various blended cements. The determination of the amount of CH is important when discussing both the degree of cement hydration, as well as the development of the pozzolanic reaction. During cement hydration the CH values increase; whereas during pozzolanic activity the CH will be consumed in a reaction that forms C-S-H gel. Thermogravimetry (TGA), coupled with its derivative (DTG), was used to quantify CH content of the hydrated pastes at 7, 28, 90 and 120 days. During heating CH will dehydroxylise at approximately 450°C . This reaction, which results in a mass loss within the sample, can be accurately determined from TGA curves over the temperature range identified by the DTG trace. The mass loss determined by TGA, which relates to H_2O , can then be used to calculate the quantity of CH in each sample. Figure 8 presents CH values calculated from TGA traces from each sample at all ages.

Results indicate that CH values of paste with no CWS (PC-100) continuously increasing during hydration; whereas slightly different trends were noted in samples containing CWS. It is possible that these results can be explained by a pozzolanic reaction consuming CH and forming additional calcium silicate hydrates and/or calcium aluminate hydrates. A reduction of CH values is noted in all blended samples between the ages 90 and 120 days hydration, with reduction in CH also evident in CWS-40 between 7 and 28 days hydration. Based on this result it seems likely that a form of pozzolanic reaction has occurred in all blends at later ages, especially in mixes with greater amounts of CWS, although as previously demonstrated this seems to have had little impact on long term strength development.

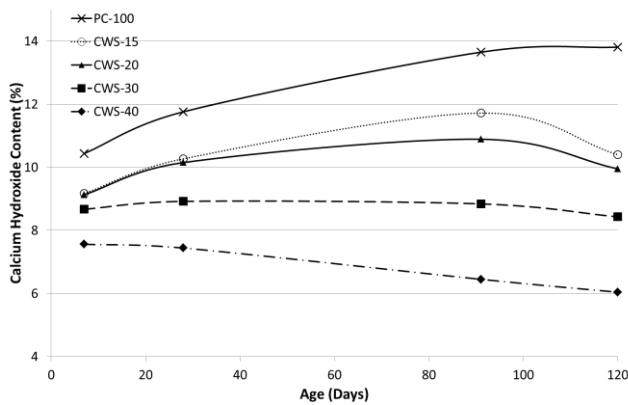


Figure 8. CH values (%) of Pastes from 7 to 120 days

Calcium Silicate Hydrate (C-S-H)

C-S-H makes up approximately 50-60% of a fully hydrated cement paste [17] and is principally responsible for the strength forming properties of that material. The presence of C-S-H in cementitious materials can be explained by two separate processes: hydration of calcium silicates in Portland cement and reaction of pozzolanic materials with calcium hydroxide in Portland cement. In this section TGA was used to give an indication of the relative amount C-S-H in each paste by determining the amount of water released during TGA experiment in the temperature range 200 to 400°C.

Results in Figure 9 indicate that PC-100 (100% PC) exhibits the greatest degree of C-S-H formation at later ages. This was to be expected given that all other pastes contain 60, 70, 80 or 85% PC. The enhanced production of C-S-H at early ages in blends containing CWS is most likely explained by the accelerated hydration of Portland cement as indicated in previous sections.

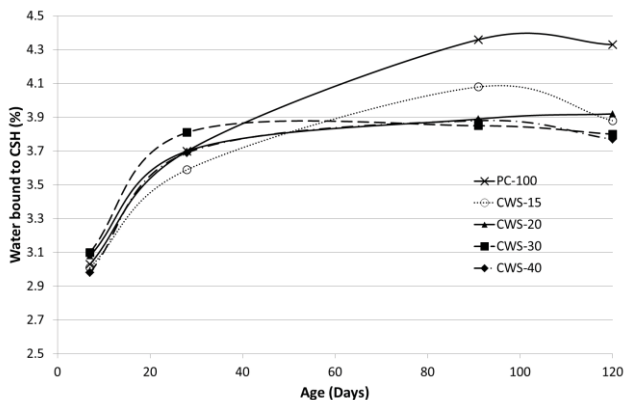


Figure 9. Amount of water bound to C-S-H (7-120 days) as determined by mass loss in TGA trace between 200-400°C

The results highlighted in Figure 9 are somewhat opposed to what was expected given the CH values reported previously. It was assumed that due to depleting CH values in blends containing CWS, that the development of C-S-H at later ages would be greater. As shown in Figure 9, with the exception of CWS-15, the blends incorporating CWS showed a negligible increase in the development of C-S-H between 28 and 120 days hydration.

The apparent contradiction in the CH and C-S-H results may indicate that the pozzolanic reaction may not be occurring and that the decrease in CH values over time may be due to some other factor. It is clear further study is required to decipher these issues.

4 CONCLUSIONS

Based on the results in the paper the following conclusions have been reached:

- Compressive strength development is initially accelerated in blends containing CWS; however, long term strength development is hindered. The hindering of long term strength would negate the idea of CWS exhibiting pozzolanic potential.
- Results, as evidenced by heat of hydration and TGA analysis, indicate that the addition of CWS in blended cements accelerates the initial hydration of Portland cement. It is thought that the fine grained nature of CWS provides additional nucleation sites for Portland cement hydration to occur. It is also thought this effect would explain the enhanced early age strength development in the CWS blends.
- The depletion of CH in blends containing CWS would suggest that a pozzolanic reaction is occurring. However, these results are somewhat in conflict with C-S-H results which show the development of C-S-H values from 28 to 90 days as negligible.

Finally, it has been demonstrated that accelerated early Portland cement hydration occurs in blends that contain CWS. This is clearly a physical impact based on the particle size of CWS. Regarding the pozzolanic potential, the results are less clear with some pointing toward CWS having pozzolanic potential whilst other results pointing in the opposite direction. Accordingly, a greater understanding of these issues would be necessary to allow a better understanding of the benefits of CWS as a supplementary cementitious material.

ACKNOWLEDGMENTS

The authors would like to thank Gannon Eco for providing the ceramic material.

REFERENCES

- [1] CEMBUREAU, Activity Report e the Cement Sector: a Strategic Contribute to Europe's Future, 2012.
- [2] WBCSD, Roadmap Timeline of Carbon Emissions Reductions, 2009.
- [3] Stafford, Ana C. Dias b , Luís Arroja b , Joao A. Labrincha ~ c , Dachamir Hotza, Life cycle assessment of the production of Portland cement: a Southern Europe case study, Journal of Cleaner Production Vol. 126 159 – 165, 2016.
- [4] Hagy, F.H., 'Structural Materials and Engineering', Nova Science Publishers, New York. 2009.
- [5] Anderson, T., Smith, S. & Au, F., Mechanical properties of concrete utilising waste ceramic as coarse aggregate, Construction and Building Materials No. 117 pp, 20–28, 2016.
- [6] Naik, T.R. & Kumar, R., 'Recycled materials in concrete industry', University of Wisconsin, Milwaukee 2003.
- [7] Guney, Y., Sari Y.D., Yalcin, M., Tuncan, A. & Donmez, S., 'Re-usage of waste foundry sand in high strength concrete', Waste Management, Vol. 30. 2010
- [8] Mansur, M.A., Wee T.H. & Cheran L.S., 'Crushed bricks as coarse aggregate for concrete', Construction and Building Materials, Vol. 96 1999.

- [9] Khatib, J.M., 'Properties of concrete incorporating fine recycled aggregate', *Cement and Concrete Research*, Vol. 35. 2005.
- [10] Halicka, A., Ogrodnik, P. & Zegardlo, B., Using ceramic sanitary ware waste as concrete aggregate, *Construction and Building Materials* 48 295–305, 2013.
- [11] Ay, N. & Unal, N., The use of waste ceramic tile in cement production, *Cement and Concrete Research* 30 497 – 499, 2000.
- [12] Puertas, F., Garcia-Diaz, I., Barba, A., Gazulla, M.F., Palacios, M., Gomez, M.P. & Martinez-Ramirez, S., Ceramic wastes as alternative raw materials for Portland cement clinker production, *Cement & Concrete Composites* 30 798–805, 2008.
- [13] Heidari, A., & Tavakoli, D., A study of the mechanical properties of ground ceramic powder concrete incorporating nano-SiO₂ particles, *Construction and Building Materials*, Vol. 38 (2013).
- [14] Kenna, F. & Archbold, P., Ceramic Waste Sludge as a Partial Cement Replacement, *Proceedings of Civil Engineering Research in Ireland*, Queens University Belfast, August 2014
- [15] British Standard EN 197-1, Cement- Part 1: Composition, specifications and conformity criteria for common cements, British Standard Institution (BSI), London, (2000)
- [16] Chindaprasit, P., Jaturapitakkul, C. & Sinsin, T., Effect of fly ash fineness on microstructure of bled cement paste, *Construction and Building Materials*, 21, pp 1534-1541 (2007)
- [17] Glasser, F.P., Fundamental aspects of cement solidification and stabilisation, *Journal of Hazardous Materials*, 52, pp 151-170 (1997)

Developing braided FRP reinforcement for concrete structures

S. Antonopoulou¹, C. McNally¹, G. Byrne²

¹School of Civil Engineering, University College Dublin, Newstead, Belfield, Dublin 4, Ireland

²Burgmann Packings Ltd, Tallaght, Dublin 24, Ireland

email: sofia.antonopoulou@ucd.ie, ciaran.mcnally@ucd.ie, greg.byrne@burgmannpackings.ie

ABSTRACT: In recent years, significant research has been conducted, by both industry and academia, into the optimum development and use of Fibre Reinforced Polymer composite materials in infrastructure. In particular, it is widely recognised that FRPs have the potential to replace conventional internal steel rebars in concrete reinforcement and offer performance benefits related to their advanced properties, such as corrosion resistance, high tensile strength etc.

A review of the available literature indicates that brittle behaviour of FRP can significantly decrease the expected ultimate load capacity and, thus have a negative effect on structure's long term durability. However, selecting braiding as manufacture technique and enhancing flexural capacity and shear strength through additional helical reinforcement, could provide structure with the additional ductility needed to prevent a brittle failure. Furthermore, the impact of deterioration mechanisms, focusing on the interaction between FRP and concrete in a structure, is an aspect for further investigation via laboratory testing and advanced analysis.

This study summarizes the results of research on structural design and manufacture methods of FRP composite materials by presenting new configuration and types of FRP reinforcement in order to encourage the use of these promising materials in construction industry.

KEY WORDS: Infrastructure; Concrete reinforcement; Fibre Reinforced Polymer; Basalt fibre; Braiding; FRP rebars.

1 INTRODUCTION

The long-term durability of steel reinforced concrete (RC) structures subjected to repeated loading and aggressive environmental factors has become a major concern in the civil engineering construction industry. Degradation of both mechanical properties and durability performance due to corrosion, severely affect service life and safety of steel RC elements and raises the need for their effective rehabilitation. [1, 2, 3, 4]

It is noteworthy that maintenance costs related to steel reinforcement corrosion are significant worldwide, with an estimated repair cost of over \$12.8 billion per annum for bridges in the United States alone. Not only do the corroded steel rebars lose tensile capacity, potentially requiring strengthening or replacement, but the surrounding concrete is damaged as well, as it cracks and spalls due to expansion of the steel. [5]

The use of fibre reinforced polymer (FRP) composite materials as a potential replacement for traditional steel in internal concrete reinforcement, has recently received a great deal of attention by civil engineering scientists, as well as industry. [1, 2] The advantages of FRP composite materials over steel include the excellent corrosion resistance, good fatigue properties, damage tolerance, low specific gravity, non-magnetic properties, light weight, low energy consumption during fabrication, and the potential real-time monitoring of their behavior. [6, 7] In addition, these innovative materials are considered to offer an overall more economical option for construction facilities. [3, 5]

Summarising, the optimum development of a reinforced concrete type in which the usual internal steel rebars are

replaced by FRP composite materials is considered to be an ongoing research topic worldwide, but the structural safety associated with this composite material is still not fully understood. [2, 4, 8]

The main objective of the experimental work presented in this paper, is the design and manufacture of BFRP rebars, using basalt fibres and a thermosetting polymer matrix - epoxy resin – manufactured by braiding technique and the evaluation of braiding parameters to rebar's properties as internal concrete reinforcement. It should be noted that these innovative braided BFRP rebars give a unique surface texture for better interfacial interactions with concrete, which are going to be investigated and analysed in detail during research's next phase.

Areas of future work within this project include the detailed investigation of FRP influence on structural reliability and an in-depth research on their strength, response & durability via laboratory testing, statistical analysis & reliability assessment of their long term performance as reinforcement in concrete structures.

2 LITERATURE REVIEW

2.1 Basalt fibre

Basalt fibre is an inorganic, natural fibre made from molten basalt rock. The production process, which is considered as energy efficient and environmentally friendly, includes the melting of quarried, crushed rocks at 1400 – 1500 °C and then, using the technology of continuous spinning, the extrusion of fibres at diameters ranging from 9 to 20 µm. [9, 10, 11, 12]

Basalt is primarily composed of plagioclase, pyroxene and olivine minerals, and the SiO_2 content is generally about 42 – 55 %, as shown in Table 1. [3, 4, 9]

Table 1. Typical chemical composition of basalt fibres.

Component	Content (wt %)
SiO_2	42 – 55
Al_2O_3	13 – 17
Fe_2O_3	7 – 13
CaO	9 – 12
MgO	6 – 9
Na_2O	2 – 4
TiO_2	1 – 2
K_2O	1 – 2

Due to their excellent properties, such as high tensile strength and modulus, wide range of thermal performance, good acid, salt and alkali resistance, high chemical stability, which are closely related to the origin and composition of raw material, basalt fibres have the potential to become an alternative, promising reinforcing material for FRP composites used in infrastructure applications. [3, 4, 10]

2.2 Braiding technique

Braiding technique has traditionally been used for the production of textile structures. The basic principle of braiding is the interlacing of yarns in a way that they cross each other in a diagonal direction. [7, 12] Braiding angle – the angle between braid yarns and axis of braid structure- is an important parameter that affects mechanical properties of braids and is usually adjusted by changing the take-up speed (cogs configuration) in braiding machine (Figure 1), obtaining a range between 20 and 85°. [12, 13]

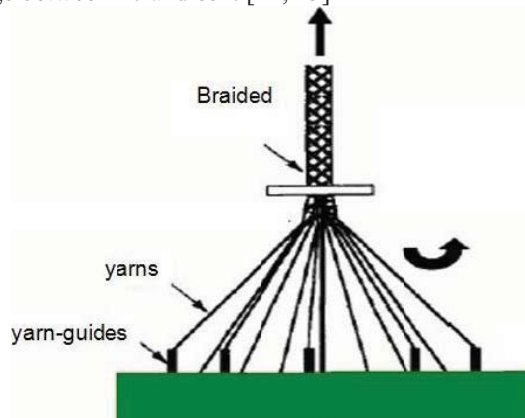


Figure 1. Braiding machine.

Recently, it is observed a increasing interest among researchers towards using braiding technique for FRP composite structures fabrication, aiming in enhanced final product properties. [13, 14]

To date most of the FRP reinforcement used in concrete has been manufactured by pultrusion, a low cost method providing composites with a constant cross section and a smooth surface. This well-known process for manufacturing composites consists of continuously pulling impregnated, formable fibre-reinforcing material through a shaping die where the material is heated and subsequently cured, giving a

final uniform cross-sectional shape. When FRP rebars are used as an internal reinforcement for concrete, the bond at the interface between FRP and concrete becomes critical, as it has a direct effect on structure's reliability. In case of pultrusion, a surface treatment is required to improve this bond and thus, ensure durability of the structure. [3, 12, 14]

On the other hand, braiding technique offers multiaxial orientation, conformability, excellent damage tolerance, improved mechanical properties, as well as allows the production of deformed rebars to enhance the bond on FRP – concrete interface. Moreover, braided FRP rebars could obtain higher flexural & shear strength, increased durability and improved crack resistance, compared to pultruded ones that exhibit low bending strength, mostly due to uni-directional structure. Although braiding method is less common as it is more expensive, it does present significant advantages in special civil engineering applications, mostly relating to the additional ductility provided and the increased bond between FRP and concrete, which has a direct influence on both the serviceability and the ultimate load-carrying capacity of the structure. [14, 15]

2.3 Fibre Reinforced Polymer for concrete reinforcement

According to the literature, FRP rebars have been introduced as a reinforcement for a variety of concrete structures subjected to aggressive environments. Using these non-corrosive rebars, can extend structure's service life and offer significant performance benefits, while reducing maintenance costs. In general, FRPs consist of high tensile fibres, such as carbon, glass, basalt, embedded in polymer matrices, thermosetting or thermoplastic ones, improving the mechanical properties of the system. [3, 5, 15]

Table 2. Properties of reinforcing fibres.

Fibre Type	Density (g/cm^3)	Failure stress (GPa)	Extension at failure (%)	Elasticity modulus (GPa)
Glass	2.4 – 2.5	2.8 – 3.0	4.7 – 5.6	74 - 95
Carbon	1.9 – 2.1	2.2 – 7.2	0.5 – 2.4	200 -700
Basalt	2.6 -2.8	1.9 - 2.6	3.5 – 4.5	70 - 90

It is broadly accepted that FRP composites can be a viable alternative for replacing steel as internal concrete reinforcement in a cost effective manner, as these materials may be competitive in terms of life-cycle costs. [16] In addition, they have several performance advantages namely the corrosion resistance, high tensile strength, low specific gravity, fatigue resistance, small creep deformations and many more. Other important advantages of these materials are the light weight that is one-third of the weight of steel, the thermal expansion coefficient that is very close to that of concrete, the high mechanical performance/price ratio. However, a direct substitution between FRP and steel reinforcing bars is not possible due to various differences in their physical and mechanical properties. The linear stress-strain behavior up to failure, the lack of ductility and energy absorbing capabilities are the main limitations that prevent the use of FRP rebars on a large scale. [6, 7, 16, 17]

If FRP reinforcement is to be used successfully and widely in concrete structures, it must be used to its full potential. This

means that it must be strained near to its breaking capacity under ultimate limit state conditions. [15, 16] When FRP bars are simply placed in concrete as a direct substitute for steel bars, it is impossible to achieve this aim, as the concrete tensile strain capacity is low (around 0.015%), while the unidirectional FRP tensile strain capacity is high (at least 1.5%). [6]

Therefore, developing FRP-reinforced structures that can meet strength, ductility, stiffness, as well as reliability demands, while minimizing cost, should be extensively investigated by researchers in the near future. [5] The apparent difficulty in design process, as the interaction of these various design requirements with FRP rebar manufacture parameters is complex, is considered as a challenge for the scientific community and should be addressed by careful selection of materials combined with integrated performance analysis. It is clearly understood that, only through the rational and efficient use of FRP composite materials, both construction industry and engineers, as well as manufacturers of these products, will gain the greatest benefit. [8, 17]

2.4 Design standards for FRP in construction

Due to the growing interest on the use of FRP composites in construction, a small number of design guidelines, codes and specifications for their efficient use in civil engineering applications were developed during the last decade.

Special publications by ACI - the ACI Guide for the Design and Construction of Structural Concrete Reinforced with FRP Bars, ACI-440.1R – and various other international standards, including the Japan Society of Civil Engineers, the British Standards Institution, the Canadian Standards Association International - CSA-S806-02 - that directly address the use of FRP, are available so far.

However, the use of FRP for reinforcement instead of steel is far from widely accepted in the conservative construction industry, mostly because of the lack of familiarity with this material, the high initial costs and the lack of structural ductility. Moreover, design codes are slowly developing for FRP rebars compared to the well-established ones for the use of steel bars in concrete members. [2, 3, 4, 5]

3 EXPERIMENTAL WORK

3.1 Materials

Different types of FRP bars are currently being used as internal reinforcement for concrete structures. In this study, basalt fibres will be the reinforcing material for the FRP composites manufactured by the process of braiding. Table 3 exhibits in detail the technical properties of the yarns used on the trials.

Table 3. Technical Datasheet for basalt yarns. (Basaltex)

Basalt roving type	Filament diameter (µm)	Linear density (TEX)	Tensile strength (MPa)	Elastic modulus (GPa)
300tex	13	300	2900 - 3600	87
600tex	17	600	2800 - 3200	88 - 90

Before braiding, basalt fibres are spooled in bobbins in order to be loaded in the braiding machine, as shown in Figure 2.

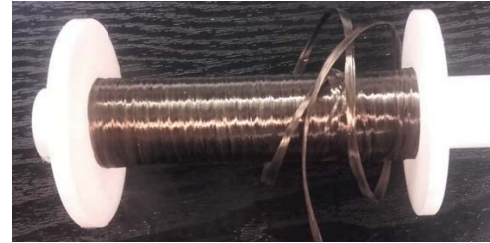


Figure 2. Spooled basalt yarn in bobbin.

3.2 Manufacturing process and design

The goal of this research activity is to develop an understanding of the mechanical behavior of braided composite bars and correlate it with textile processing conditions.

An important challenge, that needs special attention when designing textile composite materials, is the complex nature of the processing parameters, such as yarn size, number of carriers in the braiding machine, braid angle, in order to ensure optimum behavior of the final product and obtain the desired physical and mechanical properties for its end-use.

The development of a braided BFRP preform for use as rebar in concrete reinforcement after proper impregnation in epoxy resin and the influence of the braiding angle and the number of braiding layers are the main fields investigated within this study.

The objective of these trials is the production of a solid braid preform, consisted of a braided core (~ 3mm) and surrounded by two layers of PET material (Figures 3, 4), intended to aid resin flow, and an outer finishing braiding layer to complete the required dimensions. The target outer diameter of the braid sample is 5.0 mm. (Figure 5)

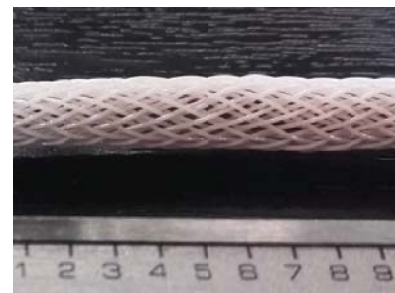


Figure 3. Two layers of PET flow mesh for resin impregnation.



Figure 4. Basalt core – PET mesh.

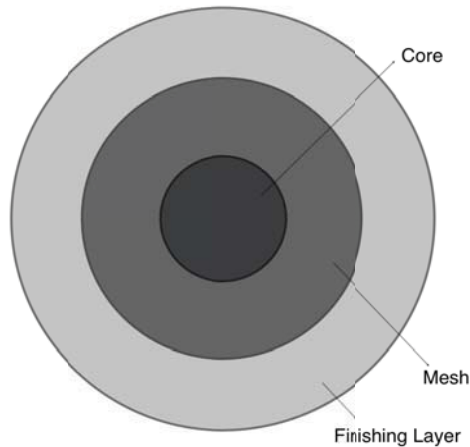


Figure 5. Cross-section of braided basalt preform.

3.3 Results

Braided BFRP rebar preforms were produced varying the number of layers and the parameters of braiding process, in order to achieve the desired structural geometry and meet the performance characteristics of existing rebar reinforcement.

The experimental work was divided into three distinct steps. Firstly, eleven samples of different core configurations were produced varying braiding parameters. The target was a solid braid of circular cross section, approximately 3 mm outer diameter (OD) and consisting of 1 - 2 layers. (Figure 6)



Figure 6. Braided core production trials.

Sample 1 was thicker than expected, with an OD of 3.7 mm, along with samples 2 (4.3 mm), 3 (3.6 mm) and 4 (3.5 mm), in which yarns were also popping out. In samples 5, 6 and 7, misshapen cores were noticed, while, in samples 9, 10 and 11, braiding angles were higher than expected, giving tight structures that would maybe present difficulty to infuse the epoxy resin at a later time. Sample 8, with an OD of 2.6 mm and a braiding angle of 15° , was chosen as the more suitable one. (Figure 7) Then, two layers of PET Monofilament braid were completed, followed by one finishing basalt layer to meet the size requirement.

A complete braided sample, made in Burgmann Packings, using basalt materials, is shown in Figure 8.

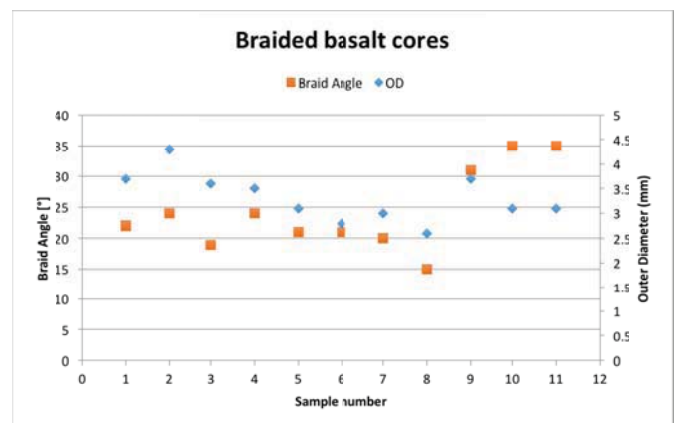


Figure 7. Relation between braid angle and outer diameter for core braids.



Figure 8. Braided BFRP rebar preform sample.

To sum up, the production of the core focused on two configurations, a single layer of 600 tex Basalt and a 2-layer version using 300 tex Basalt. Two approaches were also used for the PET flow mesh. The first approach was the production of a sleeve using 32 threads. The second approach was over braiding of the core using 16 or 24 threads. Both approaches worked and had different merits. The outer layers were produced using 600 tex basalt fibres with the target braid angle of $\pm 45^\circ$. Diameter, braid angle and weight were

measured for every layer of each sample, as shown in Tables 4, 5, 6.

Table 4. Technical details of sample braid 1.

Layer	Material (Yarns)	Machine (Thread)	OD (mm)	Angle (°)	Weight (g/m)
1	300 tex	8	1.6	11	2.4
2	300 tex	16	2.7	16	7.3
3	PET	32	3.5	9	10.6
4	PET	32	4.4	12	14.0
5	600 tex	16	5.1	45	28.0

Table 5. Technical details of sample braid 2.

Layer	Material (Yarns)	Machine (Thread)	OD (mm)	Angle (°)	Weight (g/m)
1	600 tex	8	2.5	13	5.0
2	PET	24	3.8	15	7.5
3	PET	24	4.0	15	10.0
4	600 tex	16	5.0	45	23.9

Table 6. Technical details of sample braid 3.

Layer	Material (Yarns)	Machine (Thread)	OD (mm)	Angle (°)	Weight (g/m)
1	600 tex	8	2.5	13	5.0
2	PET	32	3.8	11	8.2
3	PET	32	4.3	11	11.5
4	600 tex	16	5.0	45	25.2

Note: All values are an average of readings taken at several locations of manufactured sample braids; OD: Outer diameter; Braid yarns: Basalt (tex), PET Monofilament.

The braided preforms were produced in 16, 24 and 128 carriers braiding machines in Burgmann Packings Ltd laboratory in Dublin, Ireland, varying cogs configuration (35/35, 42/28, 40/30, 46/24, 100LL). The three selected braided samples that successfully meet the desired geometry requirements and are able to allow resin impregnation, as well as provide BFRP rebars with enhanced mechanical properties, are in the process of testing resin infusion in SuperTEX Austria. In a later stage, tests regarding their physical and mechanical properties, as well as ageing tests to evaluate their durability along with microstructural analysis, will take place at University College Dublin.

4 CONCLUSION

This paper describes the research that is currently in progress at University College Dublin concerning the development of braided BFRP bars for concrete reinforcement. The described preliminary work has been conducted to understand the behaviour of braided fabrics and the influence of geometrical factors and processing conditions on physical & mechanical properties of braided rebars. The results of this study can be considered as a fundamental step toward using braided BFRP rebars as internal reinforcement in concrete structures, replacing corrodible steel ones.

As this work is part of an ongoing project, a number of tasks towards an optimised design of flexible braided FRP

reinforcement along with the development of uncertainty models of loads and resistance are included in the short term research plan, in order to determine how this promising material can contribute to the overall structural behaviour & provide durable infrastructure.

ACKNOWLEDGMENTS

This project has received funding from the European Union's Horizon 2020 research and innovation programme under the Marie Skłodowska-Curie grant agreement No. 642453.

REFERENCES

- [1] Hollaway, L.C. (2010), 'A review of the present and future utilisation of FRP composites in the civil infrastructure with reference to their important in-service properties', *Construction and Building Materials*, 24 (12), 2419-2445.
- [2] Afifi, M.Z., Mohamed, H.M. and Benmokrane, B. (2015), 'Theoretical stress-strain model for circular concrete columns confined by GFRP spirals and hoops', *Engineering Structures*, 102, 202-213.
- [3] Fiore, V., et al. (2015), 'A review on basalt fibre and its composites', *Composites Part B: Engineering*, 74, 74-94.
- [4] Elgabbas, F., Ahmed, E.A. and Benmokrane, B. (2015), 'Physical and mechanical characteristics of new basalt-FRP bars for reinforcing concrete structures', *Construction and Building Materials*, 95, 623-635.
- [5] Behnam, B. and Eamon, C. (2013), 'Reliability-based design optimization of concrete flexural members reinforced with ductile FRP bars', *Construction and Building Materials*, 47, 942-950.
- [6] Portnov, G., et al. (2013), 'FRP Reinforcing bars - designs and methods of manufacture (Review of Patents)', *Mechanics of Composite Materials*, 49 (4), 381-400.
- [7] Pastore, C.M. and F. Ko, *Braided Hybrid Composites for Bridge Repair*, National Textile Center Annual Report, Drexel University, 1999.
- [8] Wang, H. and Belarbi, A. (2010), 'Static and Fatigue Bond Characteristics of FRP Rebars Embedded in Fiber-reinforced Concrete', *Journal of Composite Materials*, 44 (13), 1605-1622.
- [9] Parnas, R., M. Shaw and Q. Liu, *Basalt Fiber Reinforced Polymer Composites*, NETC 03-7, The New England Transportation Consortium, Institute of Materials Science, University of Connecticut, 2007.
- [10] Akhlaghi, F., Eslami-Farsani, R. and Sabet, S. (2012), 'Synthesis and characteristics of continuous basalt fiber reinforced aluminum matrix composites', *Journal of Composite Materials*, 47 (27), 3379-3388.
- [11] Banibayat, P. and Patnaik, A. (2014), 'Variability of mechanical properties of basalt fiber reinforced polymer bars manufactured by wet-layup method', *Materials & Design*, 56, 898-906.
- [12] Ahmadi, M.S., et al. (2009), 'An experimental study on mechanical properties of GFRP braid-pultruded composite rods', *EXPRESS Polymer Letters*, 3 (9), 560-568.
- [13] Branscomb, D., Beale, D., and Broughton, R. (2013), 'New Directions in Braiding', *Journal of Engineered Fibers and Fabrics*, 8 (2), 11-24.
- [14] Pereira, C.G., et al. (2008), 'Braided reinforced composite rods for the internal reinforcement of concrete', *Mechanics of Composite Materials*, 44 (3), 221-230.
- [15] Ashour, A.F. and Habeeb, M.N. (2008), 'Continuous concrete beams reinforced with CFRP bars', *Proceedings of the Institution of Civil Engineers*, 161 (6), 349-357.
- [16] Whitehead, P.A. and Ibell, T.J. (2005), 'Rational approach to shear design in fiber-reinforced polymer-prestressed concrete structures', *Journal of Composites for Construction*, 9 (1), 90-100.
- [17] Ibell, T., Darby, A. and Denton, S. (2009), 'Research issues related to the appropriate use of FRP in concrete structures', *Construction and Building Materials*, 23 (4), 1521-1528.

Characterisation and water aging of composite materials for tidal turbine blades

D. M. Grogan^{1,2,3}, M. H. Flanagan^{1,2,3,5}, J. Goggins^{1,2,3}, C. Kennedy^{1,2,3}, S.B. Leen^{2,3,4}, A. Doyle⁵, M. Walls¹

¹Civil Engineering, NUI Galway, Ireland

²Centre for Marine and Renewable Energy Ireland (MaREI), Galway, Ireland

³Ryan Institute, NUI Galway, Ireland

⁴Mechanical Engineering, NUI Galway, Ireland

⁵ÉireComposites Teo, Indreabhán, Galway, Ireland

email: david.grogan@nuigalway.ie, m.flanagan15@nuigalway.ie

ABSTRACT: It is widely acknowledged that Ireland has access to some of the richest tidal energy resources in the world. The technology required to efficiently and economically extract tidal energy is dependent on the current choice of tidal turbine blade construction materials, namely fibre reinforced polymer composites. The lifespan and economic viability of these devices is constrained, in part, by the degradation of the blade materials due to prolonged sub-sea immersion. To represent a worthwhile investment, it is expected that the turbines will remain operational for periods of time of up to 20 years. This work aims to investigate water ingress in four polymer composite materials commonly used to construct ocean energy devices. 3-D X-ray CT (computed tomography) is used to characterise the voids, resin-rich areas and other manufacturing defects present in each material. These defects are believed to significantly alter the rate of seawater diffusion, as well as the total uptake of seawater at saturation. The materials are then exposed to accelerated water aging in order to determine the rate of water uptake. Comparisons are then made between the materials based on the initial material characterisation and the results of the aging experiment. The material micro-structure, as well as the matrix material, are shown to strongly influence both the water uptake rate and total water uptake.

KEY WORDS: Polymer composites; Tidal turbine blade; Water aging; X-ray CT; Ocean energy.

1 INTRODUCTION

Tidal power has the potential to offer a reliable source of low carbon energy across many coastal regions of Ireland, the EU and other regions across the globe [1]. Current estimates project that tidal stream power will generate 148 MW by 2020 [2], and that ocean energy as a whole is to generate up to 188GW worldwide by 2050 [3]. Several prototype commercial turbines are in development, but in order to become commercially viable, these turbines must demonstrate long term reliability and reduce their cost per megawatt generated [1]. It is estimated that in order for tidal turbines to become commercially viable the capital expenditure per megawatt must be reduced to below €3 million [4]. The current capital cost per megawatt for prototype projects is much higher than this goal, with the MeyGen project having a gross capital expenditure per megawatt of circa €11 million [5]. Cost effective design, manufacture, and testing of tidal turbine blades remains a major challenge for the tidal turbine industry. The structure of tidal turbine blades is comparable to that of wind turbine blades; however tidal turbines must operate in much harsher environments, and withstand much higher loads [6]. Tidal turbine blades must withstand degradation due to immersion in seawater and be stiffer and stronger than wind turbine blades for a given power output [1]. These requirements have lead to research into alternative new materials and manufacturing methods for tidal turbine blade production (see, for example, [1, 7]). This paper first provides an overview of the current tidal energy market in order to provide a background for the research at hand. Subsequently, a detailed comparison of four composite materials proposed for use in tidal turbine blades is given, with a focus on moisture uptake due to accelerated water

aging. X-Ray Computed Tomography (CT) is used to characterise the microstructure of the as-manufactured materials and to provide an insight into the main mechanisms of moisture uptake for each material

2 MATERIALS

2.1 Overview of tidal turbine blade materials

Tidal turbine blades are likely to represent a significant proportion of the overall capital cost of commissioning a tidal turbine. As such, reducing the cost of the tidal turbine blades is an important step in reducing the overall cost per megawatt of tidal power. Due to their excellent mechanical properties and corrosion resistance Glass Fibre Reinforced Plastic (GFRP) and Carbon Fibre Reinforced Plastics (CFRP) are the most common materials used in both wind and tidal turbine blades [6]. For the majority of wind turbine blades the mechanical properties of GFRP meet the design requirements and GFRP is chosen over CFRP due to its lower cost. CFRP is generally only used in very large wind turbines [6], where the design requirements call for a material with higher specific strength and stiffness than GFRP. The larger loads experienced by tidal turbine blades will require much stiffer and stronger blades. This stiffness and strength increase may be achieved through the use of CFRP or by increasing the thickness of the composite layup. This paper looks at several materials and manufacturing methods suitable for use in tidal turbine blades and ocean energy devices.

2.2 CF & GF epoxy (powder)

Two powdered epoxy-based materials, one with glass fibres and the other with carbon fibres, manufactured at ÉireComposites Teo, were tested. Due to their low cost,

excellent material properties and ease of manufacture [8]. GF and CF powder epoxy materials are currently used in the wind turbine industry. The powder epoxy is a heat activated resin, which cures at 180°C. The dry glass or carbon is laid up on a flat metal plate and uncured powder epoxy is evenly distributed throughout the fibres. The entire lay-up is then covered in bagging material and sealed leaving only a connection for the vacuum pump. A vacuum is then applied and the part is heated to 180°C, which cures the part.

The use of powder epoxy is facilitated by the development of large integrally heated ceramic mold technology which can be used to process materials up to 200°C. Figure 1 shows a 13m GF powder epoxy wind turbine blade and the integrally heated ceramic mold used to cure the blade. This mold technology allows cost effective and scalable manufacturing of composites with heat activated powder epoxy materials. These powder epoxy materials offer several advantages over traditional resins. Firstly, there is no significant exothermic reaction during cure. This means that thick composite sections can be manufactured without having to control the cure process in order to avoid the tooling or part overheating. This in turn leads to quicker cycle times [8]. The material is solid at room temperature, has no special storage conditions and there are no Volatile Organic Compounds (VOC's) emitted during manufacture [8].



Figure 1 (Left) Integrally heated ceramic mold. (Right) 13m GF powder epoxy wind turbine blade [1].

Finally, composite parts can be formed into solid sub-assemblies without polymerisation. This means that for complex parts, such as tidal turbine blades, all parts can be formed into sub-assemblies off line using low temperature tooling. The solid parts may then be assembled on the integrally heated ceramic tooling for final polymerisation. This leads to a final part manufactured in a one-shot process without the need for gluing [1].

2.3 GF epoxy (Ampreg)

A Glass fibre composite, with Gurit's Ampreg epoxy resin [9], was manufactured at ÉireComposites Teo for testing. This epoxy system is designed for use in boat hulls, buildings and wind turbines. The GF Ampreg laminates are manufactured using Vacuum Assisted Resin Transfer (VART). The dry glass is laid up on a flat metal plate and covered in a distribution material which ensures that the vacuum is connected to the entire part and allows the resin to flow into the part. The entire layup is then covered in bagging material and sealed leaving only an inlet for the resin and a connection for the vacuum pump. A vacuum is applied to the part and degassed resin is allowed to flow into the part. Once the part has

been fully infused, the resin inlet is blocked to avoid air being drawn into the laminate. As the Ampreg epoxy cures, there is an exothermic reaction which generates heat in the laminate. For every 10°C rise in temperature, the reaction rate doubles, which, in turn, produces more heat [10]. For thin laminates, such as those manufactured for this work, this is not an issue as the heat quickly dissipates. However, for thick sections, this exotherm must be dealt with to avoid overheating. Overheating can cause a severe health and safety hazard, damage to the laminate itself or damage to the mold on which it is cured. To avoid overheating the reaction time has to be carefully controlled, which can lead to long cycle times. Currently, the majority of composite structures used in the renewable energy sector are manufactured using VART [1], as it is cost effective due to low material and tooling costs. In order to use this method to manufacture large complex parts, such as tidal or wind turbine blades, several parts are manufactured individually, then assembled and glued together to form the final part [1].

2.4 GF PEEK

A GF PEEK material, a thermoplastic glass fibre composite sourced from Rochling [11], was also tested. PEEK is a relatively expensive matrix material and is therefore unlikely to gain widespread use in larger ocean energy structures. However, due to the low water uptake of PEEK in comparison to other matrix materials, the material could find use in sub-sea turbine blade connection points. The composite material also differs from the other materials in this study in that it is a random-fibre composite with a fibre volume fraction of 30%, in comparison the epoxy-based uni-directional composites.

2.5 Overview of test specimens

Table 1 provides an overview of the square specimens used for material characterisation and water aging. The specimens were extracted from larger laminates using a diamond-tipped water-cooled saw in order to prevent damage to the specimen edges.

Table 1 Overview of the test specimens for each of the four composite materials used for material characterisation and water aging.

Material	GF epoxy (powder)	GF epoxy (Ampreg)	GF PEEK	CF epoxy (powder)
Dimensions (mm)	25 × 25	25 × 25	25 × 25	25 × 25
Lay-up	6-ply (45°/135°/0°) _s	8-ply (45°/135°/0°/90°) _s	N/A	4-ply (0°) ₄
Mean thickness (mm)	3.25	4.31	8.00	2.53
Mean weight (g)	3.95	4.97	7.75	2.42
No. of samples	6	6	6	6

3 MATERIAL CHARACTERISATION

A micro-structural analysis of each of the four materials was performed using 3-D X-ray CT at NUI Galway, prior to water aging. The scans were carried out using a 100kV Scanco

μ CT100 machine with a voxel resolution of 16 μ m. The technique allows the determination of material phases of varying density via the attenuation of X-rays as they pass through a specimen. This allowed quantitative characterisation of the void volume content of the specimens, as well as a qualitative investigation of fibre tows, stitching and resin rich areas. Three specimens of each material type were CT scanned.

3.1 GF epoxy (powder)

Scans of the GF powder epoxy specimens showed well-consolidated laminates. Large resin bands were visible in-between the glass fibre tows. The woven cross-stitching connecting the tows (perpendicular to main tow direction) were also visible as well as the fibre tow waviness. A void analysis of the specimens resulted in a 0% void volume fraction at the given scan resolution (16 μ m). No other manufacturing defects of note were observed in the specimens. Fig. 2 shows a plan and end view of a scanned GF powder epoxy specimen.

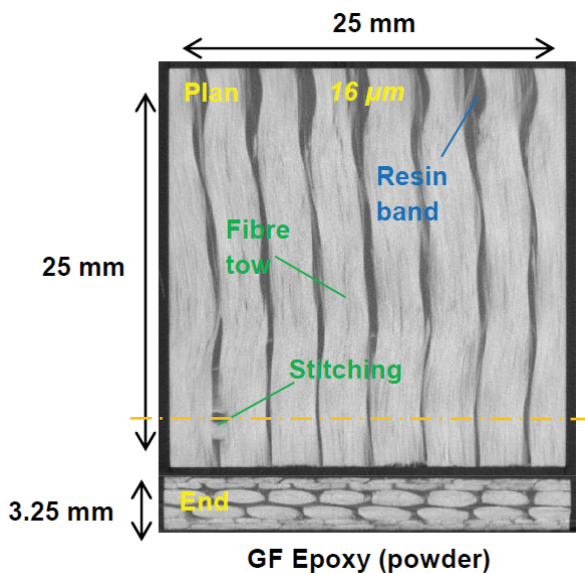


Figure 2 (Top) Plan view of a CT scan of GF powder epoxy specimen at a 0° ply. (Bottom) End view of the same scan along the indicated section line.

3.2 GF epoxy (Ampreg)

Like the powder epoxy specimens, the GF Ampreg epoxy specimen scans revealed well-consolidated laminates. Fibre tows, resin bands and tow stitching were detectable. A notable difference between the materials was the presence of a significant number of small and medium-sized voids in the Ampreg laminates. A void analysis of the three specimens resulted in an average void volume fraction of 0.25%. The majority of voids were located within the large resin bands between fibre tows. All specimens also showed a bias towards void formation near the bagging side of the laminate. On average, the specimen half nearest the bagging side had a void volume fraction of 0.35%, while the other half had a 0.15% void volume. No other manufacturing defects of note were observed in the specimens. Fig. 3 shows a plan and end view of a scanned GF Ampreg epoxy specimen.

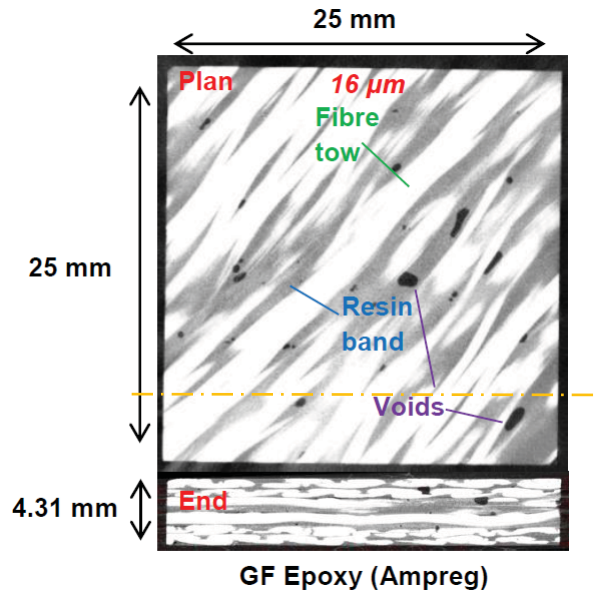


Figure 3 (Top) Plan view of a CT scan of GF Ampreg epoxy specimen at a 45° ply. (Bottom) End view of the same scan along the indicated section line.

3.3 GF PEEK

Given the random fibre distribution of the GF PEEK composite and the relatively small difference in density between glass fibre and PEEK, no discernible internal micro-structure was observed in the CT scans of the specimens at the given scan resolution. No voids or manufacturing defects were detected. Fig. 4 shows a plan and end view of a scanned GF PEEK specimen.

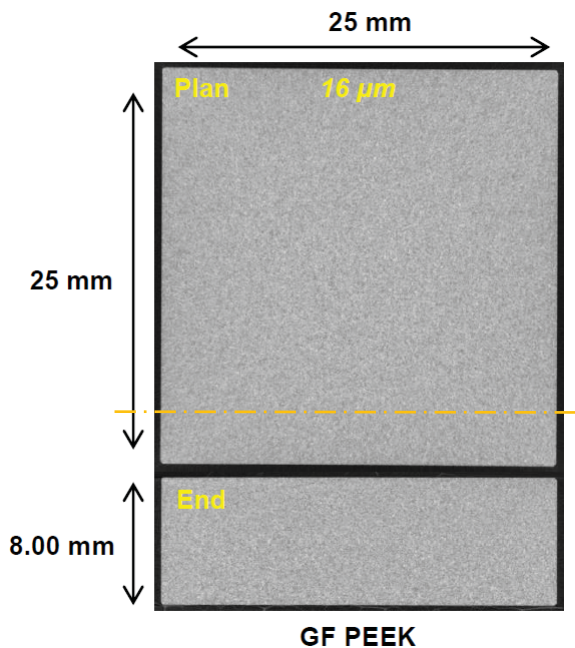


Figure 4 (Top) Plan view of a CT scan of GF PEEK specimen at the mid-plane. (Bottom) End view of the same scan along the indicated section line.

3.4 CF epoxy (powder)

Scans of the CF powder epoxy specimens showed well-consolidated unidirectional laminates. Resin bands were visible in-between the carbon fibre tows. Like the GF powder epoxy, woven cross-stitching connecting the tows is visible, this time with the stitching at an angle of approximately 60° to the main tow direction. The degree of fibre tow waviness can also be detected. A void analysis of the specimens resulted in a 0% void volume fraction at the given scan resolution. No other manufacturing defects of note were observed in the specimens. Fig. 5 shows a plan and end view of a scanned GF powder epoxy specimen.

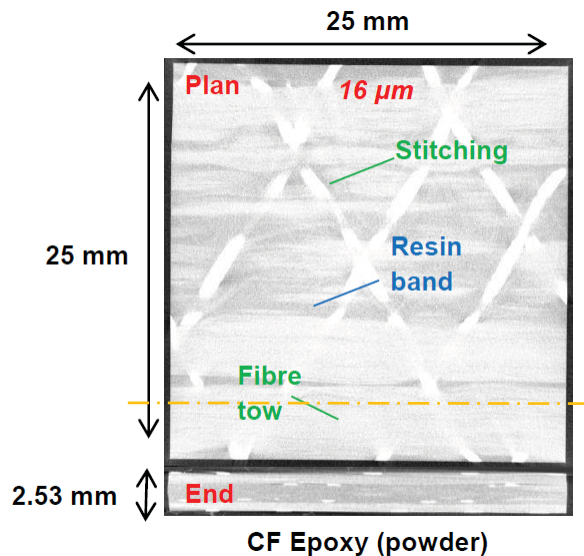


Figure 5 (Top) Plan view of a CT scan of CF powder epoxy specimen. (Bottom) End view of the same scan along the indicated section line.

4 ACCELERATED WATER AGING

Water aging was carried out in order to determine the level of moisture uptake for each of the materials due to prolonged sub-sea immersion. Epoxy resins have been shown to absorb moisture by up to 2.5% by weight [12]. Tests on epoxy composites have shown a dual absorption mechanism where a long term absorption and a Fickian diffusion process occur simultaneously [13]. The precise mechanisms of moisture uptake in composite materials are not fully understood, with manufacturing defects and micro-structural irregularities within laminates likely complicating the natural diffusion process.

4.1 Methodology

The ASTM standard for moisture absorption of polymer matrix composites (D5229/D5229M – 14) [14] was followed for the accelerated aging process. The specimens were dried in an oven at 50°C for 24 hours to remove any residual moisture before being weighed and measured. In order to accelerate the rate of moisture uptake, a water temperature of 50°C was chosen. Increasing the water temperature acts to increase the rate of diffusion without altering the saturation point of the specimens [15]. The specimens were removed from the aging bath and weighed once a week in order to track the rate of water uptake. Prior to weighing, the surface of the specimens was wiped with non-linting absorbent cloth. An

enclosed scales with an accuracy of $\pm 0.001\text{g}$ was used to weigh the specimens. The water bath used for testing is shown in Fig. 6.

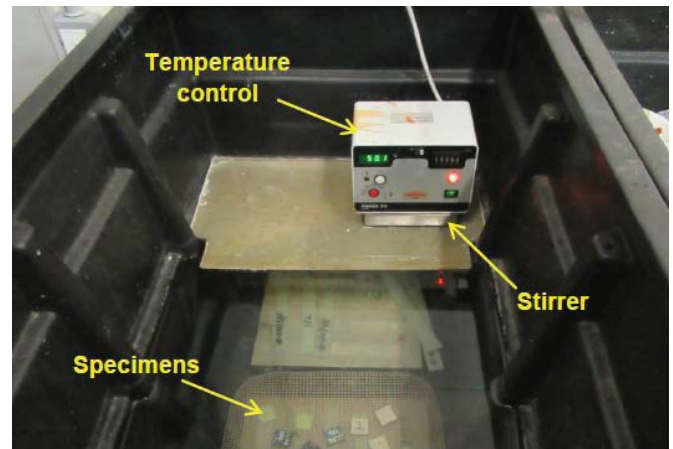


Figure 6 Water bath used for the accelerated aging of the test specimens. The temperature control is set to 50°C .

4.2 Results

The results of the water aging test for the four materials (6 specimens for each material) after 4 weeks immersion at 50°C are shown in Fig. 7.

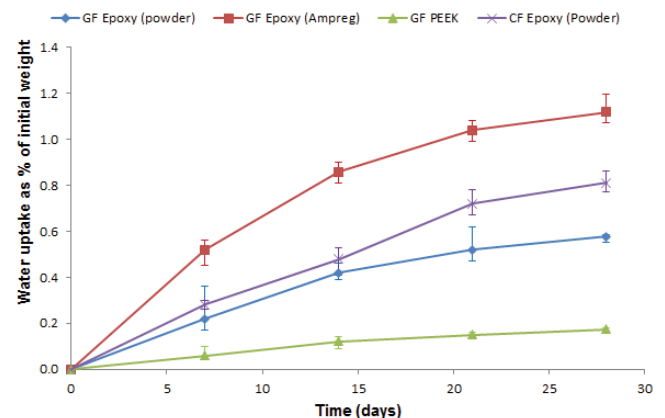


Figure 7 Water uptake weight for each of the four composite materials tested after accelerated aging in a water bath at 50°C for 4 weeks.

The GF Ampreg epoxy was found to absorb water at the highest rate, followed by the two powder epoxy composites. Given the relatively high void content of the Ampreg material as observed in the CT scans, it is likely that the voids act to increase the total weight of water that can be absorbed by a given laminate and allows the moisture to diffuse to the centre of the specimens at a faster rate. High levels of water uptake can have a detrimental effect on mechanical properties and the strength of composite materials [16]. The PEEK-based composite exhibits a significantly lower water uptake than the other epoxy-based materials, indicating that it would be highly resistant to the effects of water ingress due to prolonged sub-sea immersion. Apart from the CF epoxy specimens, the other materials appear to be approaching saturation after 4 weeks,

with the rate of water uptake decreasing noticeably after each measurement.

5 CONCLUSIONS AND FUTURE WORK

An overview of four prospective materials for use in tidal energy devices has been provided, including the associated manufacturing processes for large tidal or wind turbine blades. Accelerated water aging of the materials was carried out in order to determine their suitability for prolonged sub-sea immersion. Epoxy-based materials were found to absorb significantly more water than the PEEK-based material. The Ampreg epoxy material was also found to absorb more water, and at a faster rate, than the powder epoxy materials. Based on a micro-structural analysis of the materials using X-ray CT, it is proposed that the higher void content of the Ampreg laminates contributes to the increased water uptake but further work is needed to confirm this.

Future work will involve continued aging of the specimens until full saturation. Numerical modelling of the specimens is also envisaged, based on the existing CT scans. These models will be used to predict trends in void content and the rate of water uptake for immersed composite laminates.

ACKNOWLEDGMENTS

This research is funded by the Marine Renewable Energy Ireland (MaREI), the SFI Centre for Marine Renewable Energy Research – (12/RC/2302) and the Irish Research Council. The research was carried out in collaboration with ÉireComposites Teo. The authors would also like to express their gratitude to David Connolly for carrying out the X-ray CT scans at NUI Galway and OpenHydro Ltd. for providing additional materials.

REFERENCES

1. Flanagan T., Maguire J.M., Ó Brádaigh C.M., Mayorga P. & Doyle A.. Smart Affordable Composite Blades for Tidal Energy, EWTEC, Nantes, France, 2015.
2. Bloomberg New Energy Finance (2014). Tidal stream and wave power – a lot still to prove. Available: <http://about.bnef.com/press-releases/tidal-stream-wave-power-lot-still-prove/>. Last accessed 13th April 2016.
3. Rousseau N. Oceans of Energy-Europes Ocean Energy Roadmap 2010-2050, *ICOE*, Bilbao, 2010.
4. Ernst and Young. Cost of and financial support for wave, tidal stream and tidal range generation in the UK, 2010.
5. Meygen (2014). £51 million MeyGen Financial Close Completed. Available: <http://www.meygen.com/the-project/meygen-news/>. Last accessed 13th April 2016.
6. Grogan D.M., Leen S.B., Kennedy C. & Ó Brádaigh C. M. Design of Composite Tidal Turbine Blades, *Renewable energy*, 151-162, 2013.
7. Maguire J.M., Ó Brádaigh C.M., Doyle D., Logan M. & Ananda R. Resin Characterisation for Numerical Modelling of Through-Thickness Resin Flow During OOA Processing of Thick-Section Wind or Tidal Turbine Blades, *20th International Conference on Composite Materials*, Copenhagen, Denmark, 2015.
8. Ó Brádaigh C.M., Feerick P.J., Doyle A. & Doyle D. One-Shot Wind Turbine Blade Manufacturing using Powder-Epoxy and Electrically-Heated Ceramic Composite Tooling, CFK Valley Stade Convention, Stade, Germany, 2013.
9. Gurit (2016). *Ampreg 22 - Epoxy Wet Laminating System*. Available: <http://www.gurit.com/ampreg-22-1.aspx>. Last accessed 13th April 2016.
10. Gurit (2016). Exothermic Reactions. Available: <http://www.gurit.com/exothermic-reactions.aspx>. Last accessed 13th April 2016.
11. Rochling (2012) Sustapeek. Available: <http://www.roechling-plastics.us/en/products/high-performance-materials-specialty-products/sustapeek.html>. Last accessed 13th April 2016
12. ASTM Standard D 5229/D 5229M 14, Standard Test Method for Moisture Absorption Properties of Polymer Matrix Composite Materials, West Conshohocken, Philadelphia, USA, 1992.
13. P. Davies, F. MazEas, and P. Casari, 'Sea Water Aging of Glass Reinforced Composites: Shear Behaviour and Damage Modelling', *Journal of Composite Materials*, vol. 35, no. 15, pp. 1343–1372, Aug. 2001.
14. C. Arnold, F. Korkees, and S. Alston, 'The Long-Term Water Absorption and Desorption Behaviour of Carbon-Fibre / Epoxy Composites', *Proceeding of ECCM 15*, 2012.
15. Vodicka R. Accelerated Environmental Testign of Composite Material, Melbourne, Australia, 1997.
16. Segovia F., Salvador M.D, Sahuquillo O. & Vicente A. Effects of Long-term Exposure on E-glass Composite Material Subjected to Stress Corrosion in a Saline Medium, *Journal of Composite Materials*, 2119-2128, 2007.

Monitoring of Bridges using Computer Vision Methods

D. Lydon¹, S.E Taylor¹, J. Martinez-Del-Rincon², D. Robinson¹, M. Lydon¹, D. Hester¹

¹School of Planning Architecture and Civil Engineering, Queens University Belfast, BT9 5AG, Northern Ireland

²School of Electronics, Electrical Engineering and Computer Science, Queens University Belfast, BT9 5BN, Northern Ireland

email: dlydon01@qub.ac.uk, s.e.taylor@qub.ac.uk, j.martinez-del-rincon@qub.ac.uk, des.robinson@qub.ac.uk, m.lydon@qub.ac.uk, d.hester@qub.ac.uk.

ABSTRACT: This paper is an overview of the development and application of Computer Vision for the Structural Health Monitoring (SHM) of Bridges. A brief explanation of SHM is provided, followed by a breakdown of the stages of computer vision techniques separated into laboratory and field trials. Qualitative evaluations and comparison of these methods have been provided along with the proposal of guidelines for new vision-based SHM systems.

KEY WORDS: Computer Vision; Bridge Monitoring, Structural Health Monitoring.

1 INTRODUCTION

Existing Civil infrastructure is under an increasing level of stress from loading/environmental effects. These effects can be detrimental to the integrity of the bridges, and must be monitored in order to avoid dangerous incidents and insure public safety.

Visual inspections remain to be the most common method of bridge inspection worldwide. This method is used as a means of detecting obvious damage to structures such as cracks/shifting of components and is carried out by following a set of established guidelines according to bridge type. This method has many limitations which affect its reliability and is extremely sensitive to human error, particularly since a visual inspection is rarely carried out by a senior engineer. A survey of the reliability of visual inspections has detailed the high level of variability in this assessment method [1].

In recent years Structural Health Monitoring (SHM) systems have been developed to try to overcome these limitations. SHM can provide an unbiased means of determining the true state of our aging infrastructure. Sensor systems are used to monitor bridge deterioration and provide real information on the capacity of individual structures, hence extending bridge life and improving safety. Changes in stiffness is usually measured using strain sensors, but recent research has indicated that measuring displacement changes from calibrating vehicles can be used as a method of detecting bridge condition[2]. The deflection readings are gathered with respect to vehicles of known weight passing over the structure. If pre-weighed calibration trucks are not available for testing, vehicle weights can be either gathered from a database in order to gain approximate readings, or by using a weigh-in-motion system to gain precise information on vehicle weights.

Traditionally displacement is measured using transducers or accelerometers which are attached to fixed points on the structure. The transducers, such as linear variable differential transformers (LVDT), give a direct reading of displacement but generally require an independent frame for mounting, which for most bridges make them impractical for use in the field. On the other hand, accelerometers can be attached

directly to the structures (i.e. do not need a fixed reference) but post processing of the data is required to convert acceleration to displacement, as shown in Figure 1.

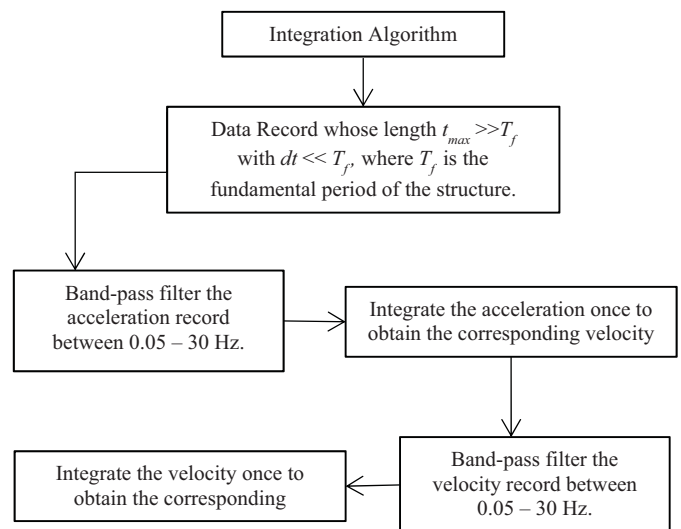


Figure 1. Integration Algorithm for Converting Accelerometer Data to Displacement [3]

While these readings can, under certain circumstances, provide a reasonably accurate estimate of deflection, there are several related problems with the method, such as:

- 1) Durability as the sensors can be damaged easily.
- 2) Equipment is expensive to purchase and time consuming to set up on site.
- 3) Measurement noise in the acceleration signal can result in errors in the calculated displacement signal.

In recent years, new methods have been investigated to address these issues, such as GPS readers, Laser Vibrometers and Computer vision techniques. GPS readers have been proved to be a reliable method of detecting deflection but

require satellite connectivity to function, which may not be feasible at all sites, and they are susceptible to high electromagnetic noise[4] they are also not ideal for short span bridges where movement ranges are modest. Laser vibrometers are comparable in effectiveness with transducers [5], but they are costly and difficult to set up/operate. On the contrary, video cameras are cheap, reasonably easy to use and can inspect a structure from a distance. They also mimic human visual inspection. The main drawback in their use as part of an SHM system is that the captured images require complex and intelligent data processing and analysis through computer vision algorithms.

This paper aims to provide a background on the evolution, application and practicality of Computer Vision techniques in SHM along with recommendations for future work in this area.

2 COMPUTER VISION IN SHM EVOLUTION

Computer vision is becoming a more widespread method of SHM. It operates by recording motion pictures of a target area on a civil structure. Early applications of Computer Vision to SHM involved the development of a hybrid system composed of traditional sensors paired with cameras in order to produce the output (Figure 2). Zuarin et al. [6] proposed a system where the cameras would replace the systems used for attaining vehicle weights, and be paired with sensors for measuring displacement/acceleration. A camera monitors traffic on a bridge in order to determine the amount of traffic passing over it, while a transducer is affixed to the bottom of the bridge to measure deflection.

More recently computer vision has been also applied as a replacement of transducers and accelerometers on measuring the bridge displacement. In these systems, the basic principle involves taking an image of the bridge to establish reference points, this is then compared to subsequent images to determine displacement. This process is known as registration [6]. There are several methods of processing the images gathered, which will be discussed in the following section.

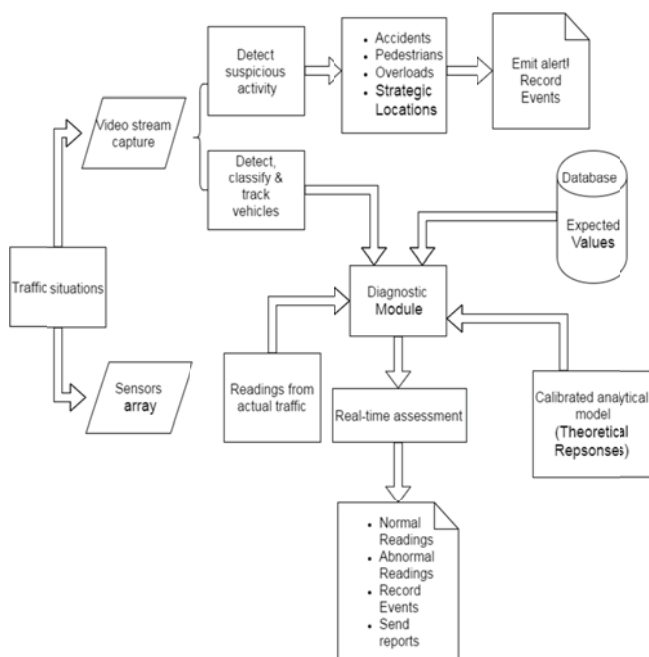


Figure 2 Hybrid Camera-Sensor System proposed by Zuarin et al[7]

2.1 Traffic detection

A method for detecting and tracking traffic is detailed in [8]. The model uses a background subtraction method, wherein a reference image of the empty bridge is taken, and any images featuring traffic is compared to this image, and any new objects are assigned to the foreground. These objects are treated as “blobs” tracked through the video. While this method tracks vehicles well in optimum conditions, it is not capable of handling invariant natural conditions such as low light/ rain and fog which makes it impractical for long-term monitoring on site. In addition, this approach is not suitable in congested traffic, as multiple small vehicles could be misread as one large object or large vehicles could block smaller ones from the camera. Those are two common problems in the current state of the art in computer vision.

A superior method is laid out in [9] where the authors extract vehicle features and use these features to track the vehicle, as shown in Figure 3. The system is not sensitive to the effects of changing lighting due to weather because only the most prominent features are tracked through frames and then grouped by motion to give a reading of vehicle location. This method is less susceptible to the occlusion problems that occurred in the previous approach because the system groups features that move together, so the only time that multiple vehicles could be grouped together is if they were extremely close to each other in the same lane and moving at identical speeds, which would be unlikely due to safety constraints.



Figure 3 Features of Vehicles tracked [10]

A comprehensive survey of video processing for traffic applications has been carried out by Kastrinaki et al[11].

2.2 Hybrid Camera-Sensor Approach

Once the traffic can be tracked and classified, the gross vehicle weights can be determined from a reference database. This information can then be used to determine the expected deflection that will be read by the attached sensors in a Hybrid approach.

2.2.1 Laboratory Work

A hybrid sensor camera system for classifying vehicles was developed in [12]. In this paper, the authors laid out a system for grouping vehicles into 7 different classes depending on the readings from strain gauges that were time synchronised with video images of the vehicles passing over a test bed setup. A

neural network was developed to classify the vehicles based on the application of a Bayesian filter to the collected strain gauge readings. The main purpose of the video images was to establish the location of the vehicles on the deck. However it was suggested that they could also be used to give gross weights of vehicles by assigning weights based on classes that were determined by an image based neural network.

A lab trial of another camera-sensor method was carried out in [7]. The computer vision algorithms were primarily used to determine the type of vehicle crossing their model bridge. Additionally the position of the vehicle at certain times was logged in order to build the Unit Influence Line (UIL) using the data obtained from the transducers placed on the underside of the model bridge at the times determined by the video. The proposed system provided promising results, particularly in detecting changes to deflection based on various damage scenarios, but it could not be immediately transposed to the field because it does not deal with an inherent issue in sensor-camera systems: time synchronisation. The data logger and USB camera in this study are linked to the same computer and can be synchronised to the same clock, but this approach would not be feasible in the field as a USB camera would not have the required pixel resolution to detect deflection from a distance. Moreover, the vision based system can only differentiate between 3 types of pre-determined vehicles, while a larger database is needed in order to create a viable real solution.

2.2.2 Field Work

Fraser et al detailed a system for combining camera input with sensor data in [13]. This system involved the combination of accelerometers and strain gauges with cameras for detecting and classifying vehicles. The data acquisition for the sensors/cameras was managed by the use of a wireless cloud which accessed a wired network in a nearby building. While this method is suitable in a built up area, it may not be possible in rural locations. The LabVIEW code used to synchronise the sensors also controlled the traffic-facing camera and captured images at a rate of 3 frames per second and a resolution of 640x480 pixels. It has not been specified if the code is efficient enough to improve this rate of capture and resolution, which will hamper its application to real time measurement of displacement as the scanning rate is insufficient for real time dynamic analysis. Critically a method for correcting camera movement due to wind/vibration has not been specified, an issue detailed in [14].

Another hybrid-camera sensor method trialled in the field was [15]. This method delivers an improved reading of bridge condition due to the correlation of the class-based vehicle loads with recorded bridge responses. This allows the system to give an approximate indication of where damage has occurred on the bridge. These systems have served as a precursor to camera-camera setups as they have proved the viability of replacing sensors for determining vehicle loads on bridges. In order to achieve a camera-only SHM approach, the next step is the replacement of sensors with cameras for reading displacement on bridges, which is analysed in section 2.3.

2.3 Video Registration for SHM

2.3.1 Target Based

The initial applications for Computer Vision as registration for SHM involved the use of target-based approaches. This involved affixing premade targets or markers such as LEDs, speckle or other randomised patterns to the bridge which are used as stable easily identifiable features to be tracked through a video, as shown in Figure 4.



Figure 4 Speckled pattern applied for field test [16]

2.3.1.a Laboratory Work

The readings obtained from camera-only systems are compared to readings from traditional sensors in order to determine their suitability for replacing these sensors in the future. The study detailed in [17] involves applying a Digital Image Correlation (DIC) technique to video of a shake table test carried out in the lab. The DIC readings were compared to verified measurements from accelerometers, which were attached to the test specimen. The method used a correlation approach [18], where an image was divided into sub-images, and the position of sub-image *A* in the reference image is compared to its position in further images in order to plot a translation matrix and determine displacement of the target point. The method has comparable results to accelerometer readings, but again does not cater for camera movement/vibration or differing light levels since it is run in a lab controlled environment. No information has been provided to clarify how the pixel units were converted to engineering ones for comparison with accelerometer readings, therefore the accuracy of their results cannot be verified.

A lab trial carried out in [19] describes an accurate (within 0.09mm of LVDT at monitoring distance of 2m) method for calculating displacement based on movement of white points on a black background inside a region of interest. This point tracking method is similar to an optical flow methodology proposed by [20], where key-point features are selected based on relative light intensity to the neighbouring pixels [21][22]. The features are then tracked through the subsequent frames and a plot of their movement can be created. The trial also used a region of interest in the image based on expected displacement and camera zoom capabilities, which reduces the image size that needs to be processed and enhances the processing time of the algorithm to within 1/30s and makes real-time measurement possible. This system also incorporates a method for synchronization of multiple cameras using a master-slave setup where PCs are linked over a wireless network in order to track multiple points of displacement simultaneously. This method proved to be quite effective in solving the issue of time synchronization in the lab, the issue of setting up a wireless network in the field could still be a factor however, as explained before. There is also no consideration given to overcoming the difficulties of

movement of the camera or environmental light changes during monitoring. The calibration of the camera to ensure accurate pixel-engineering units is an important step, and a valid method is laid out in [23], where the authors use the extrinsic parameters of the camera to obtain the conversion factor for that particular camera, which removes the need for a calibration target to be attached to the structure and made visible in the images recorded.

Correlation and optical flow approaches are merged in [24] in an attempt to gain sub-pixel accuracy of object displacement. The authors used computer-generated random patterned images and applied rotation and transformation effects to them. Their method did deliver the desired accuracy (maximum mean bias error of 0.03 pixels for 0.5 pixel displacement) and could potentially be modified for use on real images as it is accurate and computationally efficient.

2.3.1.b Field work

Recently, the replacement of sensors by camera systems has been trialed in the field. In [16] a pattern is applied to a bridge and displacement readings from a pre-weighted truck performing passes is verified against LVDT readings and a predictive model developed in the lab. The results are not used as a method of detecting damage, merely to verify the accuracy of their predictive model. The accuracy obtained is reasonable ($\pm 0.15\text{mm}$ compared to the model), but the monitoring difficulties of environmental change/ vibration of camera in the field are briefly discussed without any proposed solution.

Further work was carried out by Lee et al in [25] where the feasibility of a vision system for use on a long-span bridge was discussed. A key point raised from this paper is the treatment of the angular orientation of the camera with respect to the target; this issue is particularly relevant to bridges as the ideal scenario of the camera being placed 90° from the target is not always possible. This paper also discusses the possibility of monitoring the bridge during the night hours using artificial light to ensure constant light levels, a promising solution to the problem of differing environmental light. However it must be considered that traffic patterns could vary largely at night and so the data collected may not be representative of the daily conditions.

2.3.2 Feature Based

The application of targets to the bridge is a limiting factor in camera based monitoring due to the location of some monitoring points on long-span or otherwise remote locations. To address this issue, the next generation in SHM for bridges involves the use of non-target “contactless” approaches that only use the natural patterns created by concrete pour, bolts or environmental effects as points of reference to extract and track features.

2.3.2.a Laboratory Work

Many of the studies detailed previously used either a correlation approach, an optical flow or a combination of both these approaches. The study carried out in [26] proposed a new method of tracking displacement where images are subject to down-sampling and intensity interpolation in order to generate moiré fringes, which are then put through a phase-shifting process to determine displacement distribution. It is

stated in this paper that sub-millimetre deflection readings can be obtained, but they do not publish a full set of results for verification. Running times for the algorithm have also not been detailed in the paper so it cannot be compared to that of existing algorithms, but it is declared in that the comparison is favourable.

The lab study carried out in [27] did not use intensity of pixels for determining features to be tracked, but rather a process known as orientation-code matching (OCM), which performs well against effects such as lighting changes [28] and incorporates a subpixel method to reduce measurement errors (maximum error vs LVDT of feature tracking was 4.82% at a monitoring distance of 9.15m). This error percentage increases in proportion to monitoring distance, which is a common occurrence in field work with computer vision in SHM. Another system which catered for lighting changes was detailed in [29]. This method proposed the usage of a normalized correlation metric in order to account for changing lighting conditions, the results are shown in figure 5. This system had issues with very small displacements, which would make it unsuitable for use on short span bridges.

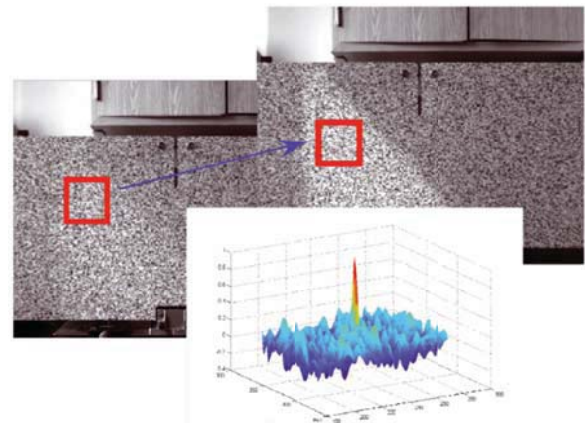


Figure 5 Results of Correlation metric applied to subsets of an image with changes of light [30]

2.3.2.b Field Work

A successful study into measuring displacements of a bridge was carried out by Feng et al in [31]. Their method involved determining an approximate value for displacement using a correlation/template matching approach to find the correlation peak of the sub-image. This sub-image is then upsampled in order to find sub-pixel displacement of the target area. This method worked well compared to LVDT readings, but two challenges which were not overcome were the effect of camera vibration and a heat haze which occurred when the air was non-uniformly heated by ambient temperatures. The heat haze problem is an issue in locations with high average temperatures, therefore it has not been mentioned in other publications but would definitely need to be overcome if computer vision is to be a viable solution worldwide.

A multi-point optical flow system was trialled by Kim et al in [32] with satisfactory results (less than 2% error due to displacement responses), but they had issues with image noise from smoke affecting accuracy of their captured images and low pixel resolution of the camera used in the test was also a factor in obtaining less than perfect accuracy in their readings.

The use of a higher resolution camera could make their solution more practical for widespread use in the field.

An advanced method for detecting displacements and vibrations in a structure is outlined in [33], as shown in Figure 6. A new framework for detecting and tracking key points (FREAK) is developed and integrated with a calibration method for converting pixel-based units to engineering units. This and similar methods differ from other optical flow or correlation-based methods on the use of a small set of sparse key-points rather than a dense correspondence of pixels.

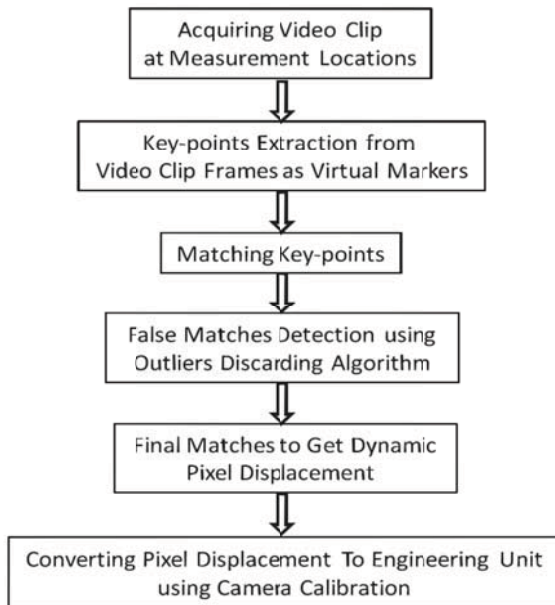


Figure 6 Algorithm Design [33]

This method provided accurate results under various lighting conditions and is useful for detecting both displacement and acceleration. While this method does have a high level of accuracy compared to LVDT ($\pm 0.01\text{mm}$ at a measurement distance of 3m, $\pm 0.04\text{mm}$ at 13m) it does not cater for camera movement as it is trialled in an indoor environment (football stadium) so it cannot be definitively stated that this method is suitable for immediate field usage.

Finally, a system which combines the traffic detection methods detailed above with camera-based displacement detection is [2]. This system measures axle spacing and position of vehicles crossing the bridge and synchronises their position with deflection readings taken by a second camera placed at a perpendicular angle to the bridge soffit. The videos are synchronised by the use of two LEDs which simultaneously flash through usage of an interval timer. The authors catered for the issue of camera vibration by creating a custom tripod system to smooth out vibrations and provide a sturdy base for the camera.

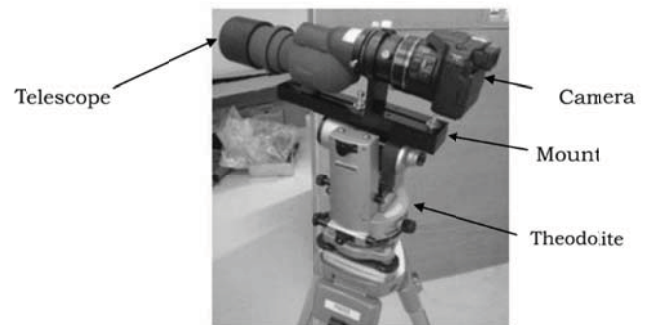


Figure 7 Camera setup from [2]

The accuracy of this system did not extend to sub-millimetre levels, primarily due to the resolution of the images provided by the camera. With a superior camera or usage of post-processing algorithms, it is possible that sub-pixel accuracy could be obtained.

CONCLUSIONS

The area of Computer vision in SHM is still a relatively new one, but the methods detailed above represent significant progress in recent times. It is believed by the authors that the methods proposed in [26], [27], [30], [33] present viable solutions for detecting bridge displacement or strains if adopted properly. If some/all of these methods could be combined with a calibration process similar to [34], a method for compensating for camera movement detailed in [35] and time-synchronization of cameras using a method akin to the one detailed in [36] it is possible that an efficient and accurate solution could be developed and put into practice in the near future and the authors are currently working on a solution that incorporates these elements.

ACKNOWLEDGMENTS

The Department for Employment and Learning Northern Ireland, Invest Northern Ireland, the National Science Foundation, and Science Foundation Ireland are gratefully acknowledged for their financial support.

REFERENCES

- [1] Baystate Roads Program, "Tech Notes Reliability of Visual

- Inspection for Highway Bridges,” 2003.
- [2] T. Ojio, Carey, E. J. O'Brien, Doherty C, and Taylor, “Contactless Bridge Weigh-in-Motion,” *ASCE Journal of Bridge Engineering*, pp. 1-27, 2015.
 - [3] A. M. Wahbeh, J. P. Caffrey, and S. F. Masri, “A vision-based approach for the direct measurement of displacements in vibrating systems,” *Smart Mater. Struct.*, vol. 12, no. 5, pp. 785–794, Oct. 2003.
 - [4] M. Meo, G. Zumpano, X. Meng, E. Cosser, G. Roberts, and A. Dodson, “Measurements of dynamic properties of a medium span suspension bridge by using the wavelet transforms,” *Mech. Syst. Signal Process.*, vol. 20, no. 5, pp. 1112–1133, Jul. 2006.
 - [5] H. H. Nassif, M. Gindy, and J. Davis, “Comparison of laser Doppler vibrometer with contact sensors for monitoring bridge deflection and vibration,” *NDT E Int.*, vol. 38, no. 3, pp. 213–218, Apr. 2005.
 - [6] L. G. Brown, “A survey of image registration techniques,” *ACM Comput. Surv.*, vol. 24, no. 4, pp. 325–376, Dec. 1992.
 - [7] R. Zaurin and F. Necati Catbas, “Structural health monitoring using video stream, influence lines, and statistical analysis,” *Struct. Heal. Monit.*, vol. 10, no. 3, pp. 309–332, May 2011.
 - [8] D. R. Magee, “Tracking multiple vehicles using foreground, background and motion models,” *Image Vis. Comput.*, vol. 22, no. 2, pp. 143–155, Feb. 2004.
 - [9] B. Coifman, D. Beymer, P. McLauchlan, and J. Malik, “A real-time computer vision system for vehicle tracking and traffic surveillance,” *Transp. Res. Part C Emerg. Technol.*, vol. 6, no. 4, pp. 271–288, Aug. 1998.
 - [10] B. Coifman, D. Beymer, P. McLauchlan, and J. Malik, “A real-time computer vision system for vehicle tracking and traffic surveillance,” *Transp. Res. Part C Emerg. Technol.*, vol. 6, no. 4, pp. 271–288, Aug. 1998.
 - [11] V. Kastrinaki, M. Zervakis, and K. Kalaitzakis, “A survey of video processing techniques for traffic applications,” *Image Vis. Comput.*, vol. 21, no. 4, pp. 359–381, Apr. 2003.
 - [12] L. Yan, M. Fraser, A. Elgamal, T. Fountain, and K. Oliver, “Neural Networks and Principal Components Analysis for Strain-Based Vehicle Classification,” *J. Comput. Civ. Eng.*, vol. 22, no. 2, pp. 123–132, Mar. 2008.
 - [13] M. Fraser, A. Elgamal, X. He, and J. P. Conte, “Sensor Network for Structural Health Monitoring of a Highway Bridge,” *J. Comput. Civ. Eng.*, vol. 24, no. 1, pp. 11–24, Jan. 2010.
 - [14] R. Gamache and E. Santini-Bell, “Non-intrusive Digital Optical Means to Develop Bridge Performance Information,” in *Non-Destructive Testing in Civil Engineering*, 2009, pp. 1–6.
 - [15] R. Zaurin, T. Khuc, F. N. Catbas, and F. Asce, “Hybrid Sensor-Camera Monitoring for Damage Detection: Case Study of a Real Bridge.”
 - [16] E. Santini-Bell, P. A. Brogan, P. J. Lefebvre, B. Brenner, and M. Sanayei, “Digital Imaging for Bridge Deflection Measurement of a Steel Girder Composite Bridge,” 2010.
 - [17] M.-H. Shih and W.-P. Sung, “Developing Dynamic Digital Image Techniques with Continuous Parameters to Detect Structural Damage.”
 - [18] J. P. Lewis, “Fast Template Matching,” *Vision Interface 95*, 1995. [Online]. Available: http://www.scribblethink.org/Work/nvisionInterface/vi95_lewis.pdf. [Accessed: 06-Apr-2016].
 - [19] Y. Fukuda, M. Q. Feng, and M. Shinozuka, “Cost-effective vision-based system for monitoring dynamic response of civil engineering structures,” *Struct. Control Heal. Monit.*, vol. 17, no. 8, pp. 918–936, Dec. 2010.
 - [20] C. Tomasi and T. Kanade, “Detection and Tracking of Point Features,” *Carnegie Mellon University Technical Report*, 1991. [Online]. Available: <http://www.lira.dist.unige.it/teaching/SINA/slides-current/tomasi-kanade-techreport-1991.pdf>. [Accessed: 06-Apr-2016].
 - [21] C. Harris and M. Stephens, “A combined corner and edge detector,” *Proceedings of the 4th Alvey Vision Conference*, 1988. [Online]. Available: <http://citeseerx.ist.psu.edu/viewdoc/download?doi=10.1.1.434.4816&rep=rep1&type=pdf>. [Accessed: 06-Apr-2016].
 - [22] E. Rosten and T. Drummond, “Fusing Points and Lines for High Performance Tracking,” *Proc. IEEE Int. Conf. Comput. Vis.*, vol. 2, no. October, pp. 1508–1511, 2005.
 - [23] S. Kim, H. Kim, C. Lee, and S. Kim, “A Vision System for Identifying Structural Vibration in Civil Engineering Constructions,” in *2006 SICE-ICASE International Joint Conference*, 2006, pp. 5813–5818.
 - [24] V. M. J. Sousa, A.M.R.; Xavier, J.; Vaz, M.; Morais, J.J.L.; Filipe, “Measurement of Displacement Fields With Sub-Pixel Accuracy By Combining Cross-Correlation and Optical Flow,” *8^o Congr. Nac. Mecânica Exp.*, no. Dic, pp. 21–23, 2010.
 - [25] J. J. Lee and M. Shinozuka, “Real-Time Displacement Measurement of a Flexible Bridge Using Digital Image Processing Techniques,” *Exp. Mech.*, vol. 46, no. 1, pp. 105–114, Feb. 2006.
 - [26] S. Ri and H. Tsuda, “Measuring small deformations of large structures using a digital camera | SPIE Homepage: SPIE.” [Online]. Available: <http://spie.org/newsroom/technical-articles/4877-measuring-small-deformations-of-large-structures-using-a-digital-camera?ArticleID=x94042>. [Accessed: 21-Jan-2016].
 - [27] M. Q. Feng, Y. Fukuda, D. Feng, and M. Mizuta, “Nontarget Vision Sensor for Remote Measurement of Bridge Dynamic Response,” *J. Bridge. Eng.*, vol. 20, no. 12, p. 04015023, Dec. 2015.
 - [28] F. ULLAH, S. KANEKO, and S. IGARASHI, “Orientation Code Matching for Robust Object Search,” *IEICE TRANSACTIONS on Information and Systems*, vol. E84-D, no. 8. The Institute of Electronics, Information and Communication Engineers, pp. 999–1006, 01-Aug-2001.
 - [29] M. Malesa, D. Szczepanek, M. Kujawińska, A. Świercz, and P. Kołakowski, “Monitoring of civil engineering structures using Digital Image Correlation technique,” in *EPJ Web of Conferences*, 2010, vol. 6, p. 31014.
 - [30] M. Malesa, D. Szczepanek, M. Kujawińska, A. Świercz, and P. Kołakowski, “Monitoring of civil engineering structures using Digital Image Correlation technique,” in *EPJ Web of Conferences*, 2010, vol. 6, p. 31014.
 - [31] D. Feng, M. Q. Feng, E. Ozer, and Y. Fukuda, “A Vision-Based Sensor for Noncontact Structural Displacement Measurement,” *Sensors (Basel)*, vol. 15, no. 7, pp. 16557–75, Jan. 2015.
 - [32] S.-W. Kim and N.-S. Kim, “Multi-point Displacement Response Measurement of Civil Infrastructures Using Digital Image Processing,” *Procedia Eng.*, vol. 14, pp. 195–203, 2011.
 - [33] T. Khuc and F. N. Catbas, “Completely Contactless Structural Health Monitoring of Real- life Structures using Cameras and Computer Vision.”
 - [34] C. A. Santos, C. O. Costa, and J. P. Batista, “Calibration methodology of a vision system for measuring the displacements of long-deck suspension bridges,” *Struct. Control Heal. Monit.*, vol. 19, no. 3, pp. 385–404, Apr. 2012.
 - [35] S. Yoneyama and H. Ueda, “Bridge Deflection Measurement Using Digital Image Correlation with Camera Movement Correction.”
 - [36] Y. Fukuda, M. Q. Feng, and M. Shinozuka, “Cost-effective vision-based system for monitoring dynamic response of civil engineering structures,” *Struct. Control Heal. Monit.*, vol. 17, no. 8, pp. 918–936, Dec. 2010.

The Influence of Traffic Growth on Bridge Load Effect Forecasting

Cathal Leahy¹, Eugene J O'Brien¹, Alan J O'Connor¹

¹Roughan & O'Donovan Innovative Solutions, Arena House, Arena Road, Sandymount, Dublin 18, Ireland
email: cathal.leahy@rod.ie, alan.o'connor@rod.ie, eugene.obrien@ucd.ie

ABSTRACT: Freight traffic in Europe is expected to grow by 1.8% per annum until at least 2030. Current approaches for assessing traffic loading on bridges do not generally allow for such growth. This paper presents a methodology which can model growth in both truck flows and weights when assessing traffic loading on bridges. As an example, the proposed approach is applied to Weigh-in-Motion (WIM) traffic data from a motorway in the Netherlands. Long-run scenario modelling based simulations are used to model different load effects on various bridge lengths. Different levels of growth in both truck weights and frequency are simulated. Time-varying Generalised Extreme Value distributions are then fitted to the resulting load effects to model changes with time. These distributions allow the characteristic 1000-year load effects and corresponding Eurocode alpha factors to be calculated. It is found that growth significantly affects the α -factors for all bridge lengths and load effects examined. Growth in weight has a much more significant effect than growth in flow, with a 1% annual growth in flow causing an average increase in characteristic load effects of 6% for the 40-year service life examined. In comparison, a 1% annual growth in truck weight results in a corresponding increase of 43%. However, there is more uncertainty associated with growth in weight as it is dependent on changes to legal limits and the level of enforcement. The results highlight the need for traffic growth to be considered in the design and assessment of bridges. This will allow the more efficient management of road networks with obvious economic and environmental benefits for road owners.

KEY WORDS: Bridge; Traffic; Loading; Growth; Simulation; Generalised Extreme Value Distribution; Eurocode; Load Model.

1 INTRODUCTION

The Eurocode load model for normal traffic, Load Model 1 (LM1), is applicable for the design of new bridges [1]. A scaled down version of LM1 may be suitable for the assessment of existing bridges and this scaling is generally done by applying α -factors to the original model. The Eurocode model can be scaled by estimating the characteristic maximum load effects and comparing the results to LM1.

Characteristic maximum load effects can be calculated in a number of ways. A popular approach is to use Weigh-In-Motion (WIM) technology to measure the weight of trucks as they travel along a road in normal traffic. Extrapolation from this measured WIM data to estimate the characteristic lifetime bridge load effects is an established procedure and has been used in many studies, both for site-specific assessment [2], [3] and for the development of bridge design codes [1], [4]. One commonly-used approach is to extrapolate using a statistical distribution fitted directly to the measured data. The Normal distribution has often been used for extrapolation, with the measured data being plotted on Normal probability paper [4]. The Generalized Extreme Value (GEV) distribution has also been used by many authors, both for site-specific assessment [2], [3] and for the development of bridge design codes [1], [4]. This family of distributions contains the Gumbel (type I), Fréchet (type II) and Weibull (type III) distributions. With this extreme value approach the distribution is fitted to block maxima, e.g., maximum daily or maximum weekly values. Other extrapolation approaches have also been used and the accuracy of different extrapolation approaches is compared in [5].

As an alternative to direct extrapolation from measured data, Monte Carlo simulation can be used [6], [7]. This involves fitting suitable distributions to the various measured parameters – axle weights, axle spacings, inter-vehicle gaps, traffic flow rates, etc. These distributions may be parametric, semi-parametric, or empirical [8]. Characteristic values can then be extrapolated from a number of years of simulated traffic, or long-run simulations representing thousands of years of traffic can be used to avoid the need for extrapolation [6].

These previously mentioned studies [6]–[8] generally assume that the characteristics of the traffic (i.e. truck weights, number of axles, flow, etc) are stationary and that future traffic will have the same characteristics as the currently measured traffic. However, road freight transport in the European Union is expected to grow by about 1.8% until 2030 due to economic growth and an increased flow of freight traffic between member states [9]. This is expected to result in an increase in both the weight and frequency of trucks. Consequently, in order to obtain an accurate estimate of maximum lifetime characteristic load effects, it is important to consider future traffic conditions.

This paper describes work which was performed as part of the Re-Gen research project (www.re-gen.net) to examine the effect of traffic growth on Eurocode alpha factors. The traffic modelling approach proposed by O'Brien et al. [10] is used to predict the characteristic load effects on two-lane same-direction bridges while allowing for traffic growth. WIM data from a road in the Netherlands is used as the basis for the simulations.

2 WIM DATA

The WIM data used in this study was collected between February and June 2005 on the A12 near Woerden in the Netherlands. This data was used as it contained two-lane same-direction traffic with time stamp records to an accuracy of one hundredth of a second for each vehicle. This time stamp accuracy is required in order to accurately determine the exact relative location of trucks on the bridge [11].

It should be noted that there is very heavy loading at this site. It has a large average flow rate of 6600 trucks per day and recent studies, which compared this site to other sites in Europe, showed the loading to be significantly greater than at the other European locations [6], [12]. As a result, the alpha factors calculated for this site will not be typical of sites across Europe. However, it is believed that the increases in alpha factors with traffic growth should be comparable with other sites.

All WIM databases contain a certain amount of erroneous data. This data must be identified and removed before any meaningful analysis can be performed. Erroneous data can be as a result of gross errors while weighing certain individual trucks. However, it can also be as a result of calibration drift or loss of calibration of the system which affects all records over a certain period. The cause of individual errors is not always known but can sometimes be caused by a vehicle straddling two lanes or by a long vehicle being recorded as two separate vehicles. Rules based on those proposed by Enright and OBrien [13] are used here to filter erroneous records. These rules examine the recorded axle spacings and weights to identify and remove suspicious configurations.

Once the erroneous records have been removed, the remaining truck records are then filtered to remove permit trucks. Permit trucks are removed from the WIM analysis as permits trucks are covered by Load Model 3 [1] which is outside the scope of this work. These trucks are removed using filtering rules proposed by Enright et al. [14].

In addition, the database includes weekends and bank holiday traffic which is significantly lighter in volume and average Gross Vehicle Weight (GVW), in comparison to normal weekday traffic. Due to these different statistical properties, the weekend and bank holiday data is removed so the analysis can be applied to a homogeneous dataset.

3 METHODOLOGY

3.1 Traffic simulation model

A Scenario Modelling approach [15] is used to perform long run traffic simulations of two-lane same-direction traffic. With two-lane same-direction traffic, there are many important correlations between truck weights and inter-truck spacing which influence the results. These correlations must be considered in order to accurately simulate the traffic. With the Scenario Modelling approach, the measured traffic in the WIM data is perturbed to create new traffic. The modelling approach is concerned only with the trucks in the WIM data; the cars are ignored as they are considered insignificant for loading on the bridge lengths considered here (15 – 45 m).

The measured data is divided into a series of scenarios which are then randomly selected and joined together to simulate a stream of traffic. During this process the selected

scenarios are perturbed using a smoothed bootstrap approach to generate new traffic [15]. This approach varies the GVW, the in-lane gaps and the inter-lane headway – see Figure 1.

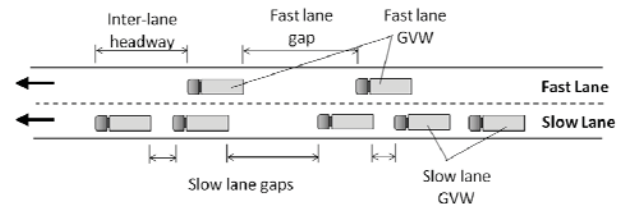


Figure 1. Sample scenario showing the properties which are varied in Scenario Modelling.

A 40-year simulation of traffic at the Netherlands WIM site with no traffic growth is shown in Figure 2. The simulated maximum daily load effects for hogging moment on a two-span continuous bridge of 45 m length are plotted alongside those of the measured WIM data. It can be seen that the simulated load effects are a good fit to those of the WIM data and that the trend in the measured data is effectively extrapolated.

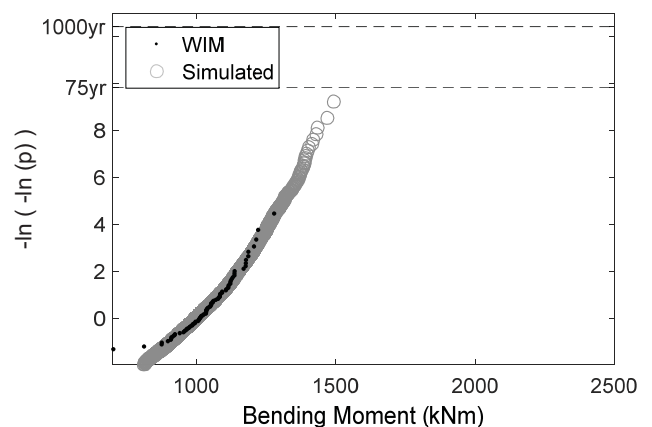


Figure 2. Maximum daily hogging moment on a two-span continuous bridge of 45 m length for a 40-year traffic simulation with the corresponding values from the WIM data.

3.2 Influence Line Analysis

The simulated traffic is passed over influence lines to examine the following three load effects for bridge lengths of 15, 30 and 45 m:

- **LE1:** Midspan bending moment on a simply supported bridge.
- **LE2:** Shear at the support of a simply supported bridge.
- **LE3:** Negative bending moment over the central support of a two span continuous bridge.

It should be noted that for LE3, a 15 m two span (2×7.5 m) continuous bridges is not a common configuration and is not examined in this work.

When calculating load effects in two-lane same-direction traffic, each lane is analysed using a simple influence line. The transverse stiffness of the bridge is allowed for by using lane factors [6]. The primary lane contributes all of its calculated load effect whereas the contribution of the

secondary lane is multiplied by a lane factor. The lane factors used are shown in Table 2 and are those which were found by Enright & OBrien [6] to represent stiff bridges where there is relatively large transverse distribution of load.

Table 2. Lane Factors for overtaking lane with high transverse stiffness.

Load Effect	Lane Factor
LE1: Mid-span bending moment, simply supported	1.0
LE2: Support shear, simply supported	0.45
LE3: Central support hogging moment, 2-span continuous	1.0

3.3 Modelling traffic growth

Increased freight transport can be divided into both a growth in flow and growth in the weights of trucks. As noted previously, an annual growth rate of 1.8% until 2030 has been predicted by the European Commission. This growth is likely to result in increases in both the frequency and weight of trucks. However, it is not known what proportion of each parameter will contribute to the total growth. Increases in weight are somewhat restricted by legal weight limits and the enforcement of these limits, whereas increases in truck flow do not have such restrictions. As a result, a number of different growth rates and combinations of growth rates are examined for the flow and weight of trucks – see Table 1.

Table 1. Combinations of growth rates examined.

		Annual Weight Growth		
		0%	0.5%	1.0%
Annual	0%	✓ ¹	✓	✓
Flow	1%	✓	✓	✓
Growth	2%	✓	✓	✓

¹The reference dataset with which the cases with growth will be compared.

The increase in flow is modelled by assessing each hour of the day independently. This is done to preserve the variations in flow by time of day. This variation can be seen in Figure 3. Increased flow with time is modelled by first determining the flow associated with the hour of the day and the year being simulated. Scenarios are then randomly selected from scenarios with this flow rate. This results in a gradual increase in flow rate over the simulation period. The measured hourly flow is illustrated in Figure 3 along with the flow rate at the end of a 40-year simulation period with an annual traffic growth rate in flow of 1%.

Increases in the weight of trucks with time are also modelled. To realistically increase truck weights, the axle configurations must also change as it is not realistic to just increase axle weights as axle configurations are largely dependent on the load capacity, and hence weight, of the truck. To increase truck weights, the measured traffic is first separated into two tonne weight bands – see Figure 4. For each weight band we have a distribution for the number of axles, with examples shown in Figure 5. It can be seen as the

weight of the truck increases, the distribution for the number of axles changes. To increase the weight of a truck in a scenario, it is replaced with another truck randomly selected from the appropriate higher weight band. In general, the new truck will be expected to have the same or more axles than the truck it replaces.

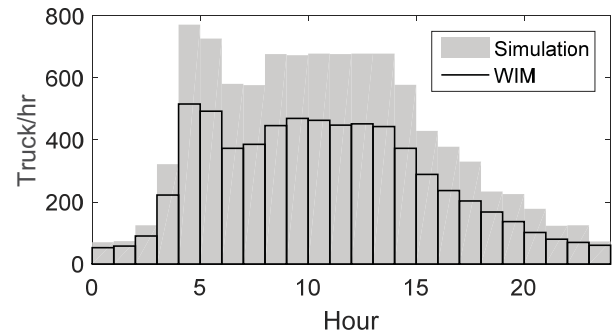


Figure 3. Flow variation at the WIM site and simulated flow rates at the end of 40-year simulation period with 1% yearly flow growth.

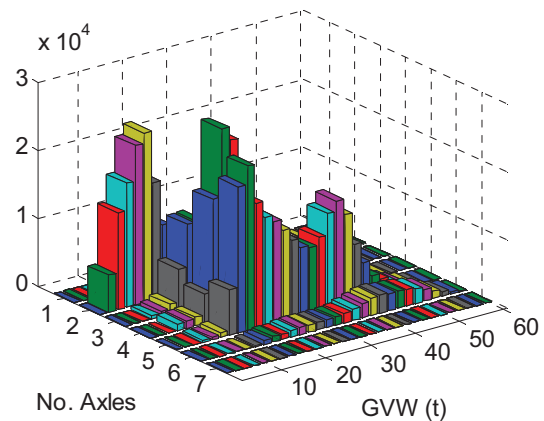


Figure 4. 3D histogram showing the number of axles on the measured trucks, in 2 t weight bands.

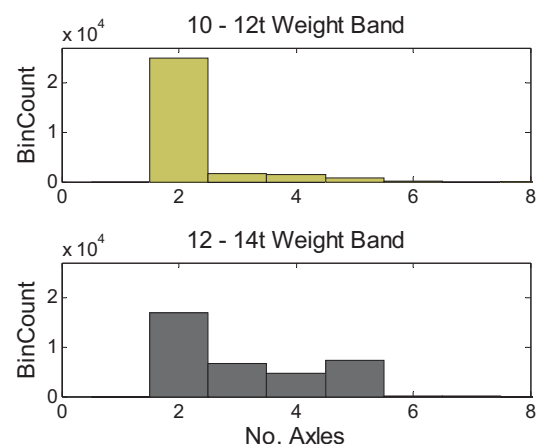


Figure 5. Histogram of the number of axles in the 10-12 t and 12-14 t weight bands.

In the simulation, measured trucks can only be replaced by heavier trucks from the WIM data up to a certain weight limit. Above a certain threshold, there will not be any heavier trucks

in the WIM data to randomly select to replace the measured truck – see right hand tail of Figure 6. This is particularly relevant towards the end of the simulation period where it may be required to simulate large increases in truck weight. As a result, it was decided that the random selection process for simulating heavier trucks would only be applied to trucks with a measured GVW of less than 50 t. This ensures that there is always a range of heavier trucks to randomly select. Above 50 t, the original axle configuration is kept and the weights on the axles are increased to simulate growth in weights. However, it is not realistic to continue to increase the weight on an axle without imposing an upper limit. After examination of the trends in axle weights in the WIM data it was decided to impose an upper limit of 20 t, above which the axle weights could not be increased. It should be noted that there were a small number of measured axles which exceeded 20 t and these were allowed to remain in the data.

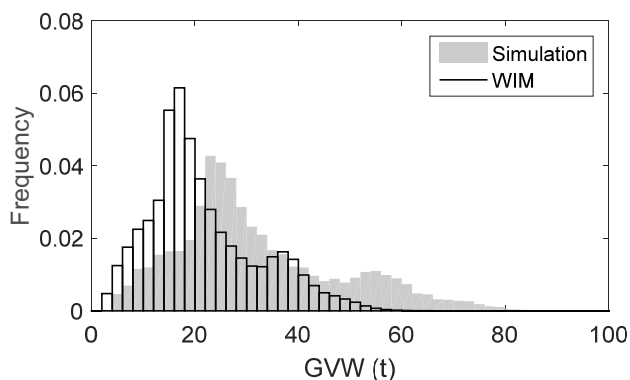


Figure 6. GVW histograms for the measured trucks and for the simulated traffic at the end of the 40-year simulation period with 1.0% yearly growth.

Figure 7 shows a 40-year simulation with the maximum growth rate examined (annual increases of 2.0 % in flow and 1.0 % in weights). When compared with the equivalent simulation with no growth in Figure 2, the effect of traffic growth on the load effects shown is clear.

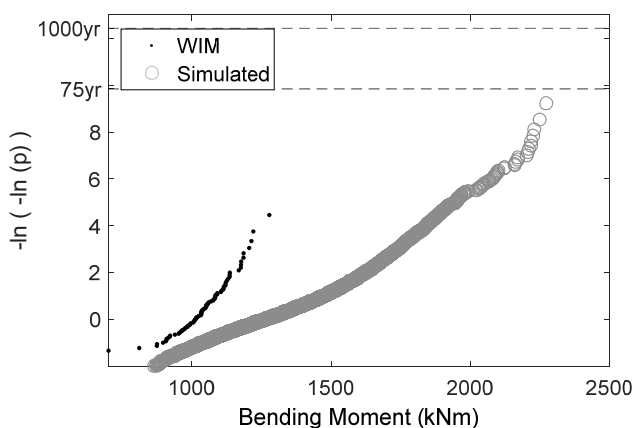


Figure 7. Maximum daily hogging moment on a two-span continuous bridge of 45 m length for a 40-year traffic simulation with annual growth of 1% in weight and 2% in flow.

3.4 Non-Stationary GEV Method for Estimating Characteristic Load Effects

To calculate characteristic load effects while allowing for traffic growth, O'Brien et al. (2014) proposed a non-stationary GEV approach. With this method, the parameters of the distribution are time dependent which allows the distribution to increase with traffic growth – see Figure 8.

To calculate the characteristic load effects for a bridge at the WIM site, a 40-year traffic simulation is performed for each annual growth rate for weight and flow. 40 years represents the remaining service life being assessed. The non-stationary GEV distribution is then fitted to the maximum 25-day load effects using maximum likelihood estimation. The 1000-year return period load effect can then be calculated. It is important to differentiate between the service life and return period. Service life is the period over which the traffic growth is occurring while return period is a level of safety.

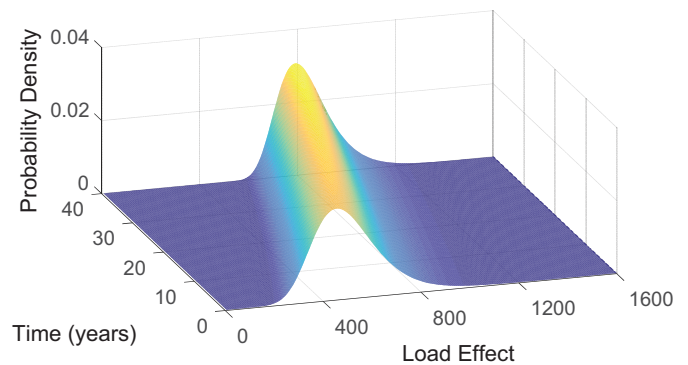
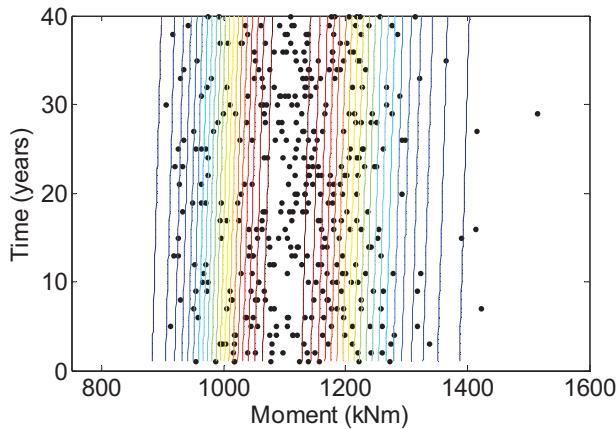
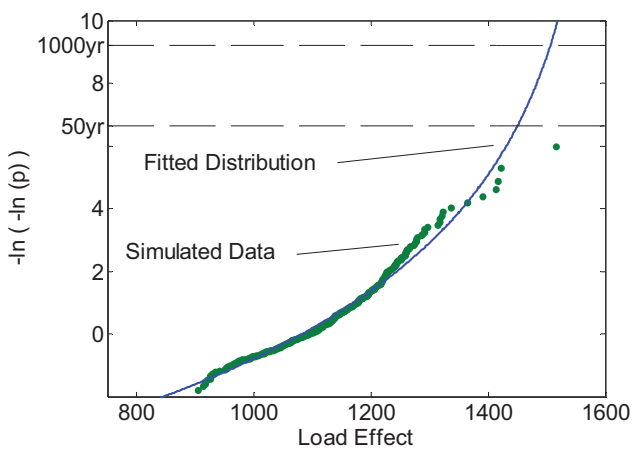


Figure 8. Non-stationary GEV distribution.

Figure 9 (a) shows the simulated maximum 25-day load effects increasing with time and a contour plot of the fitted non-stationary GEV distribution. Figure 9 (b) shows a Gumbel probability paper plot of the same data and the fitted distribution. The plot is effectively a cumulative distribution function (CDF) with the y-axis values plotted on a double log scale to allow the tail of the distribution to be easily examined. It shows that the fitted distribution is a good fit to the measured data and is effective in extrapolating the measured trend. It should be noted that Figure 9 plots the maximum 25-day load effects used in the analysis, unlike Figure 2 which shows maximum daily load effects.



(a) Non-stationary GEV distribution.



(b) Probability paper plot.

Figure 9. Non-stationary GEV distribution fitted to 25-day maximum load effects for IL3 on a 30 m bridge for a 40-year simulation with 1% flow and 1% weight growth.

A 1000-year return period was used in the calibration of the Eurocode LM1. This is predominantly used for the design of new bridges. For the assessment of existing bridges, the remaining service life is generally less than the design life and it may be more appropriate to use a shorter return period, i.e., a lower level of safety. The 75-year return period is shown on some of the plots as an example of a smaller return period. A return period of 75 years is used in bridge design in the United States but a smaller return period can be used for assessment [16].

3.5 Determining α -Factors

The simulated 1000-year load effects are compared with those given by the basic Eurocode Load Model 1 [1]. This ratio is referred to here as the α -factor and is given in Equation (1).

$$\alpha_{\text{factor}} = \frac{\text{Simulated 1000yr load effect}}{\text{Basic LM1 load effect}} \quad (1)$$

4 RESULTS

4.1 No growth

Table 3 shows the α -factors for the simulations with no annual traffic growth, i.e. traffic conditions as measured on site.

Table 3. α -factors with no traffic growth.

Bridge Length	IL 1	IL 2	IL 3
15 m	0.58	0.66	n/a
30 m	0.61	0.67	0.60
45 m	0.57	0.60	0.54

4.2 With annual growth in freight traffic

Table 4 shows the increase in the α -factor for the simulation with maximum annual growth (2.0% flow growth and 1.0% weight growth). This produced an average increase in alpha-factor of 48% with a maximum increase of 64% occurring for hogging moment on a 45 m bridge. Hogging moment appears to be the most sensitive of the load effects to traffic growth.

Table 4. Percentage increase in α -factor with 2% flow + 1% weight annual traffic growth.

Bridge Length	IL 1	IL 2	IL 3
15 m	36%	45%	n/a
30 m	44%	49%	52%
45 m	46%	49%	64%

It can also be seen that greater increases are evident for the longer bridge lengths. This is likely due to multiple truck presence events being more critical on longer spans. Increases in flow will have more influence on these events than on the single truck loading events which tend to govern for short bridge lengths.

Shear at the support (IL2), varies less than the other load effects with bridge length. IL2 has a lower lane factor as only a small proportion of the load in one lane causes shear at the support of the adjacent lane. The critical event in that case is more likely caused by a single truck loading event rather than side-by-side events. As a result, shear may be more dependent on individual axle weights rather than growth in overall vehicle weight. As axle weights were not allowed to increase above 20 t during simulation, there is an upper limit to axle weights but not to gross weight. This could explain the reduced influence of growth on shear (IL2).

Table 5 shows the average increase in alpha factor across all influence lines examined for each combinations of growth rate examined.

Table 5. Average α -factor increase for each combination of growth.

		Annual Weight Growth		
		0%	0.5%	1.0%
Annual Flow Growth	0%	-	19%	43%
	1%	6%	27%	51%
	2%	9%	31%	48%

It should be noted that there is a certain degree of random variation in simulations such as these which are based on random number generation. This is apparent in Table 5 for the results for an annual weight growth rate of 1%. The result for 1% growth in flow (51%) is greater than for 2% growth in flow (48%). Ideally, the simulations would be repeated a number of times to average out this random variation but this is not feasible in this case as the simulations are quite time consuming. To simulate each combination of weight and flow growth, an overnight simulation is required.

5 CONCLUSION

As freight traffic is expected to grow significantly until at least 2030, traffic growth needs to be allowed for when modelling traffic loading on bridges. A scenario modelling traffic simulation approach is used to model traffic growth in data measured at a Netherlands WIM site. A time-varying GEV distribution is fitted to the simulation results in order to determine characteristic load effects and corresponding α -factors. Different traffic growth rates are assumed over a 40-year service life.

The traffic at the Netherlands WIM site used is considered aggressive for bridge loading as truck weights and flows are high. For the measured traffic conditions (without growth), α -factors were in the range of 0.54 to 0.67. It is expected that α -factors at other sites would not generally be as high as this site for the load effects examined. However, the increases in α -factors with traffic growth are considered representative of what would occur elsewhere.

The simulations show that growth significantly affects the α -factors for all bridge lengths and influence lines examined. Growth in weight has a much more significant effect than growth in flow, with a 1% annual growth in flow causing an average increase in α -factors of 6% for a 40-year service life. In comparison, a 1% annual growth in truck weight results in an average increase in α -factors of 43%. However, it should be noted that growth in truck weights may be less likely as it is dependent on truck weight regulations and the level of enforcement of these regulations.

The results highlight the need to consider traffic growth when assessing site-specific traffic loading on an existing bridge. It also identifies the need for road owners to consider traffic growth when developing traffic load models for bridge design/assessment. Consideration of traffic growth in these situations will allow the more efficient management of road networks which has significant environmental and economic benefits.

ACKNOWLEDGMENTS

The research presented in this paper was carried out as part of the CEDR Transnational Road Research Programme Call 2013. The funding for the research was provided by the national road administrations of Denmark, Germany, Ireland, Netherlands, UK and Slovenia. The Ministry of Infrastructure and the Environment of the Netherlands (Rijkswaterstaat) are gratefully acknowledged for providing the WIM data used.

REFERENCES

[1] EC1, *Eurocode 1: Actions on structures, Part 2:*

- Traffic loads on bridges. European Standard EN 1991-1-2:2002.* Brussels: European Committee for Standardization, 2009.
- [2] T. J. Miao and T. H. T. Chan, "Bridge live load models from WIM data," *Eng. Struct.*, vol. 24, no. 8, pp. 1071–1084, 2002.
- [3] A. Getachew and E. J. OBrien, "Simplified site-specific traffic load models for bridge assessment," *Struct. Infrastruct. Eng.*, vol. 3, no. 4, pp. 303–311, 2007.
- [4] A. Nowak, "Live load model for highway bridges," *Struct. Saf.*, vol. 13, no. 1–2, pp. 53–66, 1993.
- [5] E. J. OBrien, F. Schmidt, D. Hajializadeh, X.-Y. Zhou, B. Enright, C. C. Caprani, S. Wilson, and E. Sheils, "A Review of Probabilistic Methods of Assessment of Load Effects in Bridges," *Struct. Saf.*, vol. 53, pp. 44–56, 2015.
- [6] B. Enright and E. J. OBrien, "Monte Carlo simulation of extreme traffic loading on short and medium span bridges," *Struct. Infrastruct. Eng.*, vol. 9, no. 12, pp. 1267–1282, 2013.
- [7] E. J. OBrien, B. Enright, and C. Leahy, "The Effect of Truck Permitting Policy on US Bridge Loading," in *11th International Conference on Structural Safety & Reliability*, 2013.
- [8] E. J. OBrien, B. Enright, and A. Getachew, "Importance of the tail in truck weight modelling for bridge assessment," *ASCE J. Bridg. Eng.*, vol. 15, no. 2, pp. 210–213, 2010.
- [9] P. Capros, L. Mantzos, V. Papandreou, and N. Tasios, "European energy and transport—trends to 2030—update 2007," *Eur. Comm. Energy Transp.*, 2008.
- [10] E. J. OBrien, A. Bordallo-Ruiz, and B. Enright, "Lifetime maximum load effects on short-span bridges subject to growing traffic volumes," *Struct. Saf.*, vol. 50, pp. 113–122, 2014.
- [11] A. Žnidarič, M. Kreslin, C. Leahy, E. J. OBrien, F. Schmidt, and C. Pederson, *Guidelines on collecting WIM data and forecasting of traffic load effects on bridges*. Technical report for the Re-Gen project, 2015.
- [12] E. J. OBrien and B. Enright, "Using Weigh-In-Motion Data to Determine Aggressiveness of Traffic for Bridge Loading," *J. Bridg. Eng. ASCE*, vol. 18, no. 3, pp. 232–239, 2012.
- [13] B. Enright and E. J. OBrien, *Cleaning Weigh-in-Motion Data: Techniques and Recommendations*. University College Dublin & Dublin Institute of Technology, 2011.
- [14] B. Enright, E. J. OBrien, and C. Leahy, "Identifying and modelling permit trucks for bridge loading," *Publ. online ahead print Proc. ICE - Bridg. Eng.*, 2015.
- [15] E. J. OBrien and B. Enright, "Modeling same-direction two-lane traffic for bridge loading," *Struct. Saf.*, vol. 33, no. 4, pp. 296–304, 2011.
- [16] C. Minervino, B. Sivakumar, F. Moses, D. Mertz, and W. Edberg, "New AASHTO guide manual for load and resistance factor rating of highway bridges," *J. Bridg. Eng.*, vol. 9, no. 1, pp. 43–54, 2003.

Laboratory investigation of contactless displacement measurement using computer vision systems

M. Lydon¹, D. Lydon¹, S.E Taylor¹, D. Hester¹, D. Robinson¹

¹School of Planning Architecture and Civil Engineering, Queens University Belfast, BT9 5AG, Northern Ireland

Email: m.lydon@qub.ac.uk, dlydon01@qub.ac.uk, s.e.taylor@qub.ac.uk, d.hester@qub.ac.uk, des.robinson@qub.ac.uk,

ABSTRACT: Much of the bridge stock on major transport links in North America and Europe was constructed in the 1950's and 1960's and has since deteriorated or is carrying loads far in excess of the original design loads. Structural Health Monitoring Systems (SHM) can provide valuable information on the bridge capacity but the application of such systems is currently limited by access and system cost. This paper investigates the development of a low cost portable SHM system using commercially available cameras and computer vision techniques. A series of laboratory tests have been carried out to test the accuracy of displacement measurements using contactless methods. The results from each of the tests have been validated with established measurement methods, such as linear variable differential transformers (LVDTs). A video image of each test was processed using two different digital image correlation programs. The results obtained from the digital image correlation methods provided an accurate comparison with the validation measurements. The calculated displacements agree within 4% of the verified measurements LVDT measurements in most cases confirming the suitability full camera based SHM systems.

KEY WORDS: Structural health monitoring, camera based monitoring, digital image correlation.

1 INTRODUCTION

Despite limitations, the most common method of bridge assessment is still visual inspections. However, bridge assessments are often overly conservative which can lead to costly and sometimes unnecessary repair or replacements. At the design stage the cost of conservatism is relatively small. However when the same degree of conservatism is applied to bridge assessments, some bridge structures may be deemed unfit for purpose when they are in fact safe. Structural Health Monitoring (SHM) Systems can provide valuable information on the bridge capacity and objectively identify the structural condition. SHM systems use advance sensing technologies to capture the critical responses of the structure but the application of such systems is currently limited by access and bridge type. This paper investigates the use of computer vision systems for SHM. In the long term, monitoring with cameras is expected to be more broadly utilised for structural engineering purposes because of its potential for inexpensive deployment in real life bridges. While advancing the knowledge by integrating multidisciplinary concepts from theory to application, this research will have direct benefits as civil infrastructure (and particularly ageing bridges) has become a critical societal concern from safety and cost perspectives. The engineering challenge is significant as structural assets across the country reach the end of their intended operational life, placing an enormous degree of responsibility on structural engineers. Due to strict planning regulations and environmental protection policies it is not possible to monitor the condition of these structures using conventional monitoring methods. Therefore the true state of their structural integrity is unknown particularly when these structures are continuously subjected to increased loading.

An initial set of laboratory trials were carried out to determine the level of accuracy in deflection measurement using a non-contact camera monitoring system. A digital camera was set up to monitor two sets of laboratory experiments. Video images of the tests were recorded at varying frame rates and the images were post-processed to calculate displacements. In each of the techniques used for post processing the displacement was extracted by tracking the movement of a textured pattern on the surface between successive frames. The results were validated using conventional displacement measurement techniques, such as linear variable displacement transformers (LVDT). Computer vision techniques and image processing algorithms, such as kanade-lucas [1] optical flow will be implemented to determine movement of the laboratory. In future similar procedures could potentially be used to monitor structural changes in existing buildings and monuments without the need for physical contact. This novel technique provides simplicity in deployment compared to traditional structural assessment methods which require access and sensor installation. This method is more cost-effective as the response will be measured without any need for sensors attached to the structure overcoming access problems.

2 THEORETICAL BACKGROUND

In recent years camera based monitoring has been introduced to SHM systems, in early applications displacement of several centimetres have been accurately measured by monitoring targets fixed to the bridge [2]. Previous research has highlighted the potential for the integration of imaging devices with traditional SHM

technology [3]. Many other SHM applications exist whereby camera based technology is used in conjunction with other sensor types [4], [5], [3], [6]. Challenges relating to surface damage of structures have also been addressed using vision based methods [7]–[9]. Computer vision involves analysing images to determine changing properties of their content. Digital image correlation (DIC) was first proposed by Chu et al. [10] and is now increasing in popularity across science and engineering disciplines. With dramatic improvements in commercially available digital cameras it is becoming a versatile and cost effective analysis method. DIC enables non-contact full field measurements of displacements, hence overcoming the access limitations of existing SHM systems. Other non-contact SHM methods based on microwave interferometry can provide an accurate solution for monitoring structures where access is an issue [11]. There have been considerable advances in both SHM and image processing techniques unfortunately these systems are not heavily utilized in practice. The most significant limiting factors are cost and complex system installation requirements. The objective of this research is to develop a low cost non-contact SHM system using commercially available cameras. The data collected can then be post-processed to determine structural displacement which will in turn will be used as a damage indicator for the structure. A series of laboratory trials have been carried out to develop the system prior to field applications. This paper describes the experiential studies carried out whereby two DIC methods are tested against contact measurements determined by LVDT.

The two methods used were the Optical flow algorithm and the Normalised Cross-Correlation approach. The images from each of the experiments were processed using both methods and the results were then compared.

2.1 Optical flow

The Optical flow (OF) technique is used to calculate an approximation of a motion field using spatiotemporal patterns of images [12]. The surface deflection is extracted by identifying features on the test specimen then tracking them through successive image frames. A region of interest (ROI) is specified within the full image for a more efficient computational time for field usage. Features are then extracted from the ROI which are tracked through the image frames. The two methods used for feature extraction in this experiential series were Harris Features [13] and Features from accelerated segment test (FAST) features [14]. Harris features method is one of the earliest methods of feature detection. This method uses a combination of edge and corner features to determine points of interest. It measures changes in pixel intensity across an image using an autocorrelation function, and determines the quality and number of edge-corner features in an image. Essentially the contrast between a number of neighbouring pixels allows for identification of a feature which can then be tracked. FAST feature is a more computationally efficient corner detection method first published in 2005. This system prioritizes the detection of corners over edges as the strong 2D intensity change allows for quicker distinction between neighbouring pixels.

The Kanade-Lucas-Tomasi (KLT) algorithm takes the features extracted by the above approaches and constructs a window (W) based on the points. It then compares each image in a sequence, and tracks the displacement of W through these images and maps it to an affine transformation T. This transformation can then be plotted using Matlab and the displacement of our ROI determined [15].

2.2 Normalised Cross Correlation

For this approach, the ROI was defined and then treated as a sub image of the principal image in the sequence. This method is a coarse fine approach to obtain a pixel level displacement. It is performed by mapping the reference sub image on the deformed sub-image. The normalised cross correlation matrix of the two images is then calculated by the use of the `normxcorr2` [16] function in Matlab. The peak of this matrix occurs where the sub images are best correlated, as determined by the following formula:

$$c(u, v) = \sum_{x,y} f(x, y) t(x - u, y - v) \quad (1)$$

This is a measure of similarity between the image f and the feature t . If there is a difference in peak locations, the ROI has been displaced and a graph tracking this change can be plotted.

3 EXPERIMENTAL STUDIES

This section describes the methodology employed to experimentally assess the performance, i.e. the sensitivity and accuracy, of optical methods in measuring deflection. The purpose of the experiments was to compare a known displacement with the one calculated by vision processing techniques described in the previous section. The results were validated with verified measurements using rulers or contact measurement using a linear variable differential transformer (LVDT).

3.1 Test 1: Ruler Test

This test was found to provide a good introduction to DIC methods, the simplicity of test set up eliminated common illumination and data synchronisation issues. Additionally it enables accurate calibration of the algorithm to convert pixel to mm movement on a single plane. This initial trial was set up in an area with controlled lighting and environmental conditions. Each of the techniques are sensitive to changing light conditions therefore this test provided data without changes in ambient conditions across the image sequence. The test set up is shown in Figure 1, a 1m long steel ruler was secured to a white background and a movable target was attached to the ruler. A green marker was attached to the top on the marker and pattern was printed on the remainder of the marker. The measurement readings on the ruler were used to scale pixels to millimetres. An additional scale reference was marked on the wall in line with the ruler.

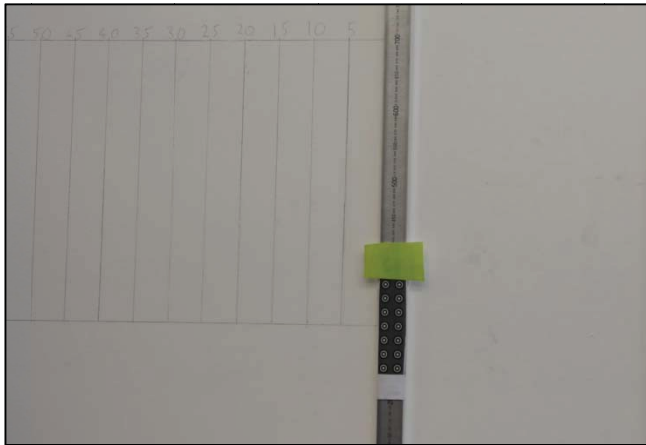


Figure 1 Ruler test – initial position

A standard DSLR camera was set up perpendicular to the wall and the test was recorded at a rate of 25 frames per second (fps). The full test involved moving the marker from the initial position at a reading 200mm, to the deformed position at a reading of 500mm on the ruler as shown in Figure 2 (maximum displacement 300mm). The marker was moved in increments of 100mm, the marker was subsequently returned back to its original position in increments of 50mm. The aim of the experiment was to provide proof of concept but an accurate comparison of the calculated and measured displacement cannot be presented since the measured displacement was recorded by taking visual readings on the ruler.

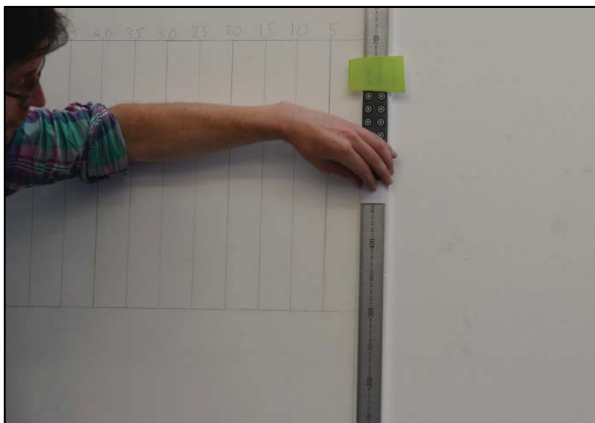


Figure 2 Ruler test - position of maximum displacement

3.1.1 Ruler Test: Results

The video file from the experiment was imported to Matlab for post processing. Firstly the optical flow method was applied. The KLT feature tracking algorithm was used to track the patterned section of the movable target. The image shown in Figure 1 was set at the initial video frame and the ROI was defined. In this case the ROI was a zone on the patterned part of the paper slider on the ruler. The Harris Features function was used to obtain the initial tracking points. The point tracker KLT uses image pyramids; each level of the image pyramid is reduced in resolution by a factor of two from the previous

level. The algorithm can handle larger displacements between frames by increasing the number of pyramid levels, as the number of levels increases the computation effort also increases. Each point is tracked in the lowest resolution and is refined with each level until convergence (Figure 3).

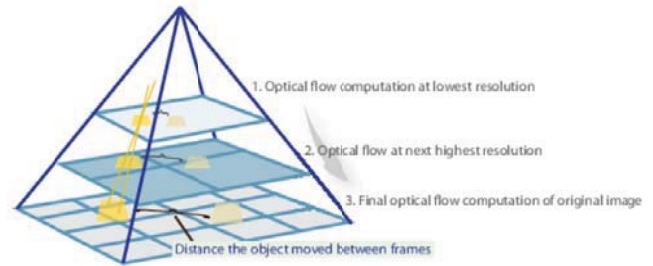


Figure 3 Number of Pyramid levels properties [17]

The video file was then separately post processed using the Cross Correlation method. This method gives a measure of degree of similarity between an image and a template [18]. Again the patterned section of the movable target was selected as the ROI, so in effect it is treated as the template image within the larger image. The cross correlation method computes the sum of the differences squared between the template and the picture at each location of the template. The results for both methods are shown in Figure 4, the graph shows that in stable lighting conditions both methods perform well in calculating the displacement of the patterned section of the movable target.

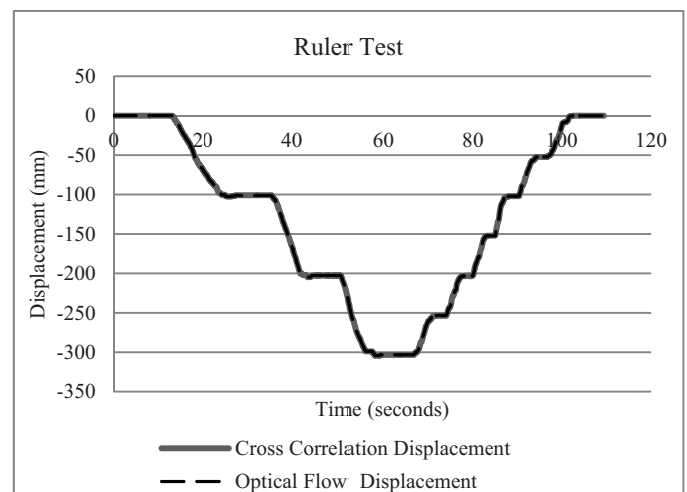


Figure 4 Ruler test – calculated displacements

3.2 Test 2: Timber beam bending

In this experiment a timber beam was simply supported under 600kN capacity hydraulic actuator as shown in Figure 5. The timber beam had a cross section of 47mm x 23mm and a clear span of 2300mm.



Figure 5 Timber beam test set up

The load was applied to the beam by displacement control; the maximum displacement for each test was selected and applied at a rate of 0.2mm/s. The load was applied at the mid span of the beam and the displacement was verified with the LVDT. Each test was recorded using two cameras, a standard DSLR at 25fps and a high speed camera. The maximum frame rate of the high speed camera is 3000fps but this requires high level lighting. As low lighting is more representative of site conditions this limited the frame rate to 60fps. The purpose of the test was to determine the accuracy of both image processing methods to deflection measurement and to determine sensitivity of frame rate on the results. To allow subsequent calculation of the pixel size in millimetres a reference measurement was attached to the face of the timber beam as shown in Figure 6.

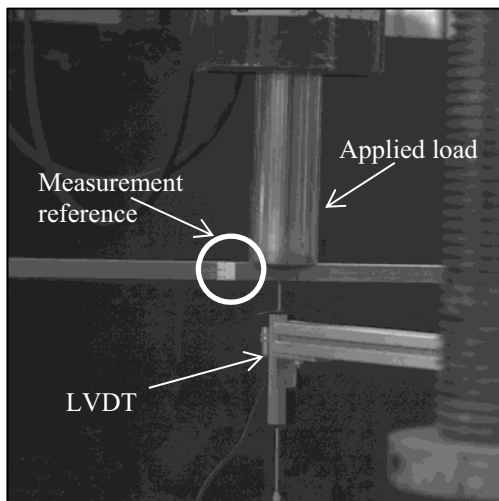


Figure 6 Timber beam – initial reading

3.2.1 Timber beam test: Results

The image processing methods described in the previous sections were used in calculating the deflection measurements in the following test series. Initially the test rig was set to a maximum deflection of 10mm. Figures 7 and 8 respectively

show the deflections calculated from the DSLR camera (25fps) and the high speed camera (60 fps).

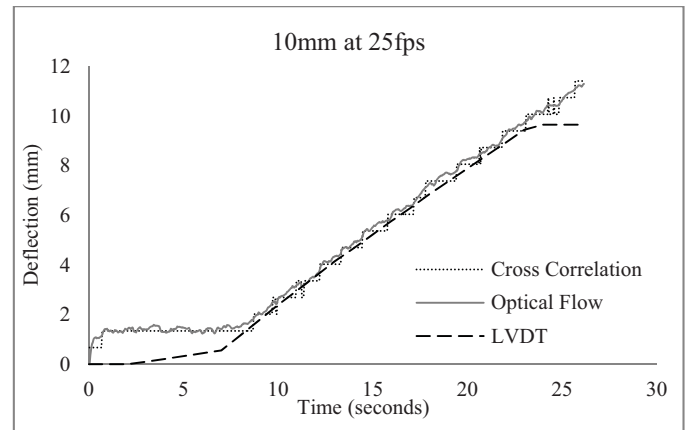


Figure 7 Measured and calculated deflections at 25fps

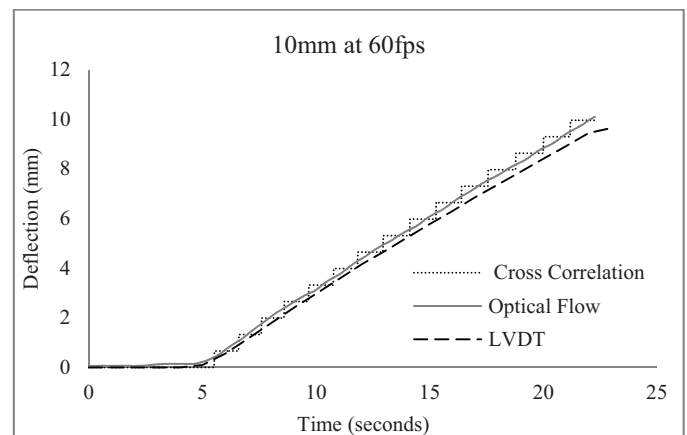


Figure 8 Measured and calculated deflections at 60fps

The test was then repeated with the test rig set to a maximum deflection of 3mm, Figures 9 and 10 respectively show the deflections calculated from the DSLR camera (25fps) and the high speed camera (60 fps).

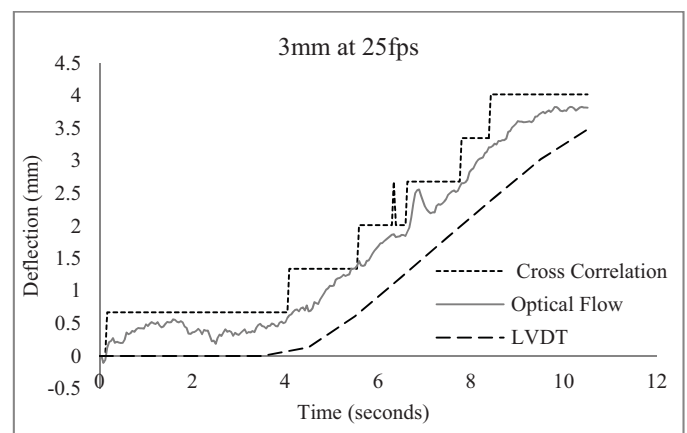


Figure 9 Measured and calculated deflections at 25fps

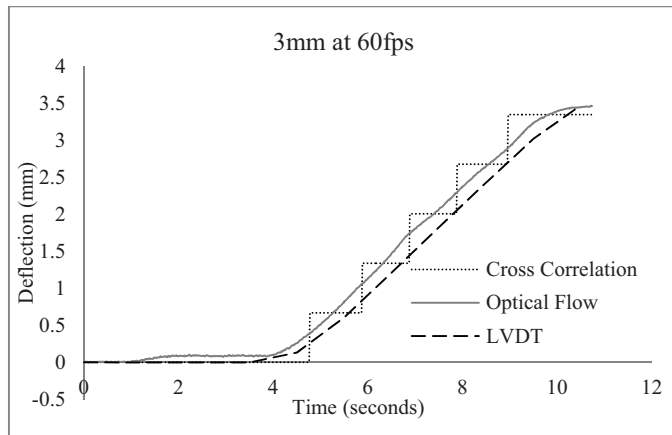


Figure 10 Measured and calculated deflections at 60fps

If a comparison of frame rate is made on the two tests, it is evident that a frame rate of 60fps provides a smoother plot in both cases, particularly with the optical flow algorithm.

A false deflection can be seen at the initial readings from the DSLR camera (Figures 7 and 9); this was caused by manually starting record mode on the camera. This is not seen in the results from the high speed camera as recording was triggered through a software program on a laptop. Therefore it was determined that for future testing it is critical that the camera can be triggered or recording is started prior to the test so the initial frames can be discarded.

In figures 7-10 the results from the cross correlation algorithm show the peak of the correlation coefficient moves in steps rather than an average of the distance, this is an inherent property of the algorithm. The agreement between the calculated and verified measured displacements can be seen in Table 1.

Table 1 Accuracy of calculated displacements

10mm deflection test					
Frame rate (fps)	LVDT (mm)	Cross correlation (mm)	Accuracy	Optical flow (mm)	Accuracy
25	9.66	11.4	-18%	11.29	-17%
60	9.66	10.0	-3%	10.07	-4%
3mm deflection test					
25	3.47	4.02	-16%	3.81	-10%
60	3.47	3.35	4%	3.47	0%

A frame rate of 60fps was found to provide more accurate results in both tests and it was found that the maximum error on calculated deflections was within 4% of the verified measured displacement. At a frame rate of 25fps the error is increased to a maximum of 18% although from Figures 7 and 9 it is evident that this increased error is mainly due to the false deflection caused by initiating recording at the beginning of the test. The optical flow was 1% less accurate than the

cross correlation method in the 10mm at 60fps test but was more accurate in every other test.

Overall the purpose of this research is to assess the potential for camera based monitoring of structures using deflection as a damage indicator. A final test was carried out to determine the suitability of deflection for damage detection. As with the previous two tests, the timber beam was set up under the testing rig. However, for this test the load was applied using stroke control, a maximum load of 0.5kN was applied to the midspan of the timber beam at a rate of 0.1kN/s. A 5mm deep saw cut was then made on the underside of the midspan of the beam and the test was repeated.

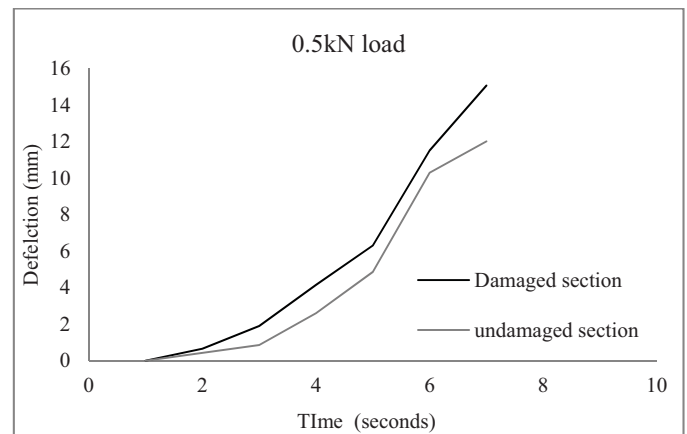


Figure 11 Optical flow calculated deflection to detect damage

The results in Figure 11 show the deflections calculated using the optical flow algorithm. The damage was equivalent to a 23% reduction in section at the midspan of the beam this resulted in a 25% increase in deflection, confirming that in this case deflection could be used as a damage indicator. As previously stated trials of existing camera based damage detection systems obtain the most accurate data through the use of hybrid camera-sensor systems [19], this research suggests that accurate deflections can be measured using a low cost camera only system. The sensitivity of deflection to damage allows this parameter to act as a damage indicator for existing structures through the use of a fully portable system.

CONCLUSIONS

This paper has detailed an experimental program carried out to assess the accuracy of camera based deflection measurements. The findings indicate that, in a laboratory environment, the optical flow algorithm can provide deflection calculations which correspond well with verified measurements from and LVDT. The findings of the final test suggest that deflection measurements could potentially act as a damage indicator in the long term monitoring of structures. After further development in the lab this system has been selected to monitor an existing bridge which is due for repair. Monitoring will take place pre and post repairs to confirm the suitability of this system for damage detection in the field.

ACKNOWLEDGMENTS

The Department for Employment and Learning Northern Ireland, Invest Northern Ireland, the National Science Foundation, and Science Foundation Ireland are gratefully acknowledged for their financial support.

REFERENCES

- [1] B. D. Lucas and T. Kanade, "An iterative image registration technique with an application to stereo vision.," in *International Joint Conference on Artificial Intelligence*, 1981, pp. 674–679.
- [2] J. J. Lee and M. Shinozuka, "Real-Time Displacement Measurement of a Flexible Bridge Using Digital Image Processing Techniques," *Experimental Mechanics*, vol. 46, no. 1, pp. 105–114, Feb. 2006.
- [3] R. Zaurin and F. Catbas, "Integration of computer imaging and sensor data for structural health monitoring," *Smart Materials and Structures*, vol. 19, no. 1, 2010.
- [4] D. González-aguilera and J. Gómez-lahoz, "Dimensional Analysis of Bridges from a Single Image," *Journal of Computing in Civil Engineering*, vol. 23, no. December, pp. 319–329, 2009.
- [5] C. C. Chang and X. H. Xiao, "Three-Dimensional Structural Translation and Rotation Measurement Using Monocular Videogrammetry," *Journal of Engineering Mechanics*, vol. 136, no. 7, pp. 840–848, 2010.
- [6] J. Ye, G. Fu, and U. P. Poudel, "Edge-Based Close-Range Digital Photogrammetry for Structural Deformation Measurement," *Journal of Engineering Mechanics*, vol. 137, no. 7, pp. 475–483, 2011.
- [7] S. Kabir, P. Rivard, D.-C. He, and P. Thivierge, "Damage assessment for concrete structure using image processing techniques on acoustic borehole imagery," *Construction and Building Materials*, vol. 23, no. 10, pp. 3166–3174, 2009.
- [8] T. Yamaguchi and S. Hashimoto, "Fast crack detection method for large-size concrete surface images using percolation-based image processing," *Machine Vision and Applications*, vol. 21, no. 5, pp. 797–809, 2010.
- [9] Z. Yin, C. Wu, and G. Chen, "Concrete crack detection through full-field displacement and curvature measurements by visual mark tracking: A proof-of-concept study," *Structural Health Monitoring*, vol. 13, pp. 205–218, 2014.
- [10] T. C. Chu, W. F. Ranson, and M. A. Sutton, "Applications of digital-image-correlation techniques to experimental mechanics," *Experimental Mechanics*, vol. 25, no. 3, pp. 232–244, 1985.
- [11] "www.idscorporation.com/georadar." .
- [12] V. M. J. Sousa, A.M.R.; Xavier, J.; Vaz, M. ; Morais, J.J.L.; Filipe, "Measurement of Displacement Fields With Sub-Pixel Accuracy By Combining Cross-Correlation and Optical Flow," *8^o Congresso Nacional de Mecânica Experimental*, no. Dic, pp. 21–23, 2010.
- [13] C. Harris and M. Stephens, "A combined corner and edge detector.," *Proceedings of the 4th Alvey Vision Conference*, 1988. [Online]. Available: <http://citeseerx.ist.psu.edu/viewdoc/download?doi=10.1.1.434.4816&rep=rep1&type=pdf>. [Accessed: 06-Apr-2016].
- [14] E. Rosten and T. Drummond, "Fusing Points and Lines for High Performance Tracking," *Proceedings of the IEEE International Conference on Computer Vision*, vol. 2, no. October, pp. 1508–1511, 2005.
- [15] C. Tomasi and T. Kanade, "Detection and Tracking of Point Features," *Carnegie Mellon University Technical Report*, 1991. [Online]. Available: <http://www.lira.dist.unige.it/teaching/SINA/slides-current/tomasi-kanade-techreport-1991.pdf>. [Accessed: 06-Apr-2016].
- [16] J. P. (Industrial L. & M. Lewis, "Fast Normalized Cross-Correlation Template Matching by Cross-," *Vision Interface*, vol. 1995, no. 1, pp. 1–7, 1995.
- [17] Mathworks, "uk.mathworks.com," 2016. .
- [18] L. G. Brown, "A survey of image registration techniques," *ACM Computing Surveys*, vol. 24, no. 4, pp. 325–376, Dec. 1992.
- [19] R. Zaurin, T. Khuc, F. N. Catbas, and F. Asce, "Hybrid Sensor-Camera Monitoring for Damage Detection: Case Study of a Real Bridge," *Journal of Bridge Engineering*, vol. 21, no. 6, 2016.

Rehabilitation of Haulbowline Bridges, Cork Harbour

Kieran Ruane¹, Michael Minehane¹, Cormac O' Suilleabhain²

¹ RPS Group Ltd., Innishmore, Ballincollig, Cork, Ireland

² Cork County Council, Environment Directorate, Inniscarra, Cork, Ireland

email: kieran.ruane@rpsgroup.com, michael.minehane@rpsgroup.com, cormac.osuilleabhain@corkcoco.ie,

ABSTRACT: This paper describes the complex rehabilitation of two large post-tensioned concrete bridges in Cork Harbour using non-linear finite element modelling to optimise the remediation works. The works were designed and delivered within budget in a short time period to allow the environmental rehabilitation of Haulbowline Island to proceed. The bridges have a combined length of 353m over 17 spans. The superstructure is a mixture of post-tensioned concrete elements and conventional reinforced concrete elements. A key feature of the bridges is that 7 of the spans are suspended from half joints which are post-tensioned transversely. A full scale assessment of the structures which included a Post-tensioning Special Inspection (PTSI) was conducted. Early stage load assessment models indicated that strengthening works would be required and that such works would be complex and long in duration. Subsequent non-linear finite element models of the bridge half-joints indicated that a reconfiguration of the bearing arrangement on the half-joints would improve the force distribution at these critical elements. This analysis allowed a strengthening scheme to be developed which could be implemented in a reasonably short timescale while keeping the bridges open to traffic. The strengthening scheme included the lifting of 7 suspended bridge spans, each weighing 200 tonnes, for bearing replacement. The scheme also included significant reinforced concrete repair works, the replacement of bridge joints, deck waterproofing, the reorganisation and renewal of several significant services on the bridge, the addition of a new deck edge beams with a modern bridge parapet system and the provision of enhanced public lighting.

KEY WORDS: Bridge inspection; Bridge rehabilitation; Bridge assessment; Finite element analysis.

1 INTRODUCTION

1.1 Background and History

Haulbowline bridges (Figure 1) are located to the east of Ringaskiddy in Cork Harbour. The southern channel bridge, comprising 9 spans and measuring 207m long, connects Paddy's Point to Rocky Island. The northern channel bridge, comprising 8 spans and measuring 146m long, connects Rocky Island to Haulbowline Island. The bridges serve as the sole road link to Rocky Island, where a crematorium is located, and Haulbowline Island, headquarters of the Irish Naval Service. Haulbowline Island was also the location of Ireland's only steelworks which operated between 1939 and 2001. From the early 1960's, waste from the steel production process was deposited on an area of reclaimed foreshore to the east of the island which became known as the 'East Tip'.



Figure 1. Haulbowline bridges.

As part of the proposed scheme to environmentally remediate the East Tip and transform it into a public recreational amenity, construction will require the transportation of a significant amount of imported earthworks/capping over the bridges. Accordingly, RPS was commissioned in 2012 by Cork County Council, on behalf of the Department of Agriculture, Food and the Marine, to undertake an inspection and assessment of Haulbowline Bridges.

1.2 Description of Structure

The bridges comprise a mix of reinforced concrete and post-tensioned concrete elements. The superstructure generally consists of post-tensioned spans with cantilevered ends to support reinforced concrete suspended spans on half-joints. The diaphragms at the ends of post-tensioned spans are also post-tensioned transversely. The substructure comprises reinforced concrete abutments founded on rock and reinforced concrete piers supported on driven precast concrete piled foundations. The superstructure is not integral with the substructure. Elastomeric bearing pads are provided at all support points and half-joints. Deck movements are accommodated at movement joints provided at each half-joint and at abutment locations. The bridges were opened in October 1966. They were commissioned by Irish Steel Holdings of Haulbowline Island, designed by O'Connell and Harley Consulting Engineers of Cork and constructed by Ascon Ltd. A photograph of the original construction of the southern channel bridge is given in Figure 2.

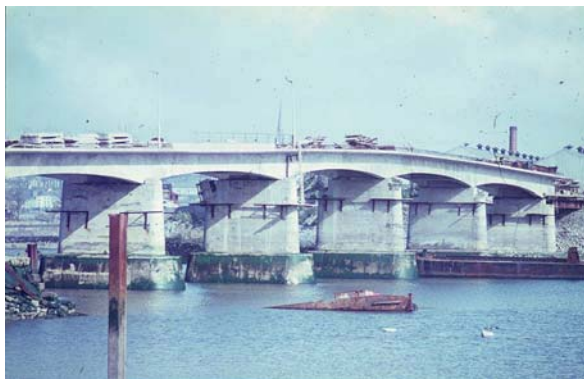


Figure 2. Southern channel bridge during construction.

2 HALF-JOINTS

Half-joints were introduced into bridge decks as a means of simplifying design and construction. This form of joint has little redundancy and is vulnerable to deterioration in the event of deck expansion joint failure, where chloride rich seepage through the joint can cause concrete deterioration and corrosion of the reinforcement. Loss of reinforcement section through corrosion can significantly reduce the safety margins expected of serviceable structures. Half-joints are a particular concern because they are not easily accessible for inspection or maintenance and they are mostly located over, or under, live traffic lanes. Utilising half-joints on new bridges is no longer common and current Irish and UK requirements explicitly preclude their use on highway structures.

There are numerous case studies of half joint deterioration in concrete bridges. On 30th September 2006, the failure of a half-joint on the Lavan Highway, Montreal, Canada resulted in a suspended span falling and crushing two cars and killing five people. The collapse was ultimately judged to be a result of substandard design, construction, inspection and maintenance. In current times, bridge owners and inspectors pay particular attention to the inspection, maintenance and rehabilitation of half joints on existing bridges to ensure the continuing safe use of such bridges.

There are twelve half-joints present on Haulbowline Bridges which are located in a harsh marine environment meaning they are particularly susceptible to deterioration.

3 INSPECTION AND TESTING

3.1 Inspection

A thorough inspection of the entire northern and southern channel bridges was undertaken in December 2012. An underbridge unit was used to access the bridge soffit. The inspection highlighted numerous serious defects summarised as follows:

- Significant cracking at the re-entrant corner at half-joints (Figure 3);
- Failure of deck expansion joints and consequent seepage to the half-joints;
- Considerable spalling of cover layer concrete due to expansive corrosion of the reinforcement throughout the bridges (Figure 4).

It is recognised that for half-joints, cracking is considered as structurally significant if the measured crack width exceeds

0.2mm [1, 2]. Measured crack widths at Haulbowline Bridges were typically in the range of 0.2mm-0.45mm. The maximum observed crack width was 1.5mm.



Figure 3. Typical inclined crack from the re-entrant corner at half-joints.



Figure 4. Typical concrete spall with exposed and corroded reinforcement.

3.2 Concrete Testing

A full suite of concrete tests were undertaken on each bridge. Up to eight test areas were set out on each bridge. At these test areas the following tests were undertaken:

- Cover meter survey to BS 1881-204:1988;
- Breakout areas for identification of reinforcement size and condition (150mm x 150mm area on soffit, 1000mm x 1000mm area on deck);
- Concrete Core removal (100mm diameter, 100mm long) and subsequent compression testing to BS EN 13791 or equivalent standard;
- Gathering of dust samples at 25mm depth, 50mm depth, 75mm depth, 100mm depth and 125mm depth for subsequent chloride content analysis to BRE 21/86;
- Depth of carbonation by phenolphthalein testing to BRE 21/86;
- Schmidt hammer tests to BS EN 12504-2 for concrete consistency;
- Half-cell Potential to TRL Application Guide AG9 or ASTM C876-91 (grid size 0.5m by 0.5m).

Generally, the concrete cover was shown to be in excess of 40mm and at some test panels it was in the range 40mm to 60mm. At all locations where concrete was broken out to expose reinforcement the bars were noted to be corrosion free. Half-cell potential testing provides an indication whether

active reinforcement corrosion is taking place at the time of testing. At all test locations, the test results indicated a low probability (<10%) of active reinforcement corrosion. The test results correlated to reinforcement samples exposed during concrete breakouts. Carbonation depths were in the range 0 to 5mm. Chloride ingress profiles were measured at 22 locations throughout the bridge. These profiles present the chloride ion content by percentage of mass of cement at intervals of 25mm from the surface of the concrete member. A chloride content of 0.2% is seen a threshold for the commencement of chloride-induced corrosion of reinforcement. At many locations, and at the reinforcement level, chloride contents were in excess of 1%. These would be considered high results. There are a number of localised areas on both structures where corrosion staining is present on the surface. This may be attributed to chloride-induced corrosion. All of the chloride ingress profiles showed decreasing chloride contents as the distance from the exposed surface increased. This is indicative of the ingress of chlorides from external sources (the marine environment) rather than chlorides present at the time of construction (e.g. use of Calcium Chloride as a concrete mix accelerator). Cores were removed from the structures at 10 locations. Concrete strengths were found to be high. The average strength of concrete observed in bridge piers was 85.4 MPa. The average strength of concrete observed in the bridge decks was 70.3 MPa. The lowest strength of concrete recorded in the deck was 55.9 MPa and the highest recorded strength was 88.6 MPa.

In summary, the concrete in the structures was found to be of a high quality. Concrete strengths were in excess of target strengths noted on construction drawings. Cover was found to be high throughout. Carbonation was very low. Chloride content was high and this was expected given the location of the structures in a marine environment. Though there is localised corrosion staining on the structure, the probability of active corrosion was low at the tested locations. Chloride-induced corrosion activity will increase in future years as chloride levels increase at reinforcement locations.

3.3 Post-Tensioning Special Inspection

A Post-Tensioning Special Inspection (PTSI) was undertaken in accordance with Document BA50/93. A total of 51 tendons were examined by drilling entry holes and using an endoscope. At all locations, no moisture was found trapped in the tendon duct. Of the 51 tendons investigated, 38 tendons were found to be fully grouted (Figure 5). The grout at these locations was found to be hard and glass-like. Thirteen tendons were found to be fully or partially voided. At these locations, the strands were either corrosion free or surface-rusted with no loss of strand section. Grout samples were retrieved from 36 tendons. Chloride content for these samples was found to be low. The range of results was 0.03 to 0.14%. Two longitudinal post-tensioning anchors and four transverse post-tensioning anchors were broken out. The anchors and strands matched the original construction drawing. Both the strands and the anchor plates were found to be corrosion free and anchor pocket material was found to be dense and fully grouted.

In summary, of 51 tendons opened, approximately 25% were found to contain full or partial voids. The strands in these voids were found to be in good condition and no moisture was encountered in the ducts. The grout in the non-voided tendons was found to be of a high quality and low chloride content was observed in test results. Anchors in the main post-tensioned spans were found to be in good condition.



Figure 6. Image from the PTSI showing Tendon T47 fully grouted and corrosion free.

3.4 Scour Inspection

An underwater inspection was carried out by the Irish Naval Service Diving Section (NSDS) in conjunction with RPS. The divers incorporated the following methodology in assessing the bridge foundations for scour:

- Any notable changes in seabed elevation at each foundation (undermining of footings/precast concrete aprons, exposure of piles etc.) were recorded;
- Any changes in seabed cross-section at the bridge, including location and depth of any scour holes were noted. Any depressions around piers and abutments were noted and measured;
- The soil surrounding each abutment/pier was probed using a rod. The soil type (colour), consistency and stiffness were noted.
- Any structural damage to the foundations (cracking, spalling of concrete, exposed reinforcement, movement) were recorded;
- Approach flow conditions and any unusual or turbulent flow conditions near or at the foundations were noted.

From the divers' observations/measurements and video feeds to the RPS team it was concluded that scouring in the Northern and Southern Channel was insignificant. Local depressions/scour holes were not observed at any bridge pier. No significant changes in the overall seabed cross-section in the Northern or Southern Channels were observed. The top 1m of soil was described as soft grey silt/alluvium. A thin, dense crust of mussel shells was observed across the entire seabed at the bridges and was considered to provide a protective layer against the effects of scour. There were no significant structural damage/defects to the bridge foundations observed during the underwater inspection. The only noted defect was minor spalling to a pile on the Northern Channel Bridge.

4 STRUCTURAL ASSESSMENT

A structural assessment was conducted to the requirements of BD 21/01, BD 44/95 and BA 39/93. The assessment was based on material strengths specified on record drawings and from the material testing undertaken on the bridge. With the exception of the half-joints (suspended spans), the bridges were determined to be capable of supporting 40t Assessment Live Loading and 45 units of HB. The capacity of the half-joints was limited to 26t Assessment Live Loading. It was considered that the deterioration and distress observed at the half-joints has been exacerbated by the following factors:

1. The presence of flexible bearings at half-joints. High rotations in the bearings can result in concentrated loading at the edge of the half-joint. Record drawings confirmed the presence of flexible bearings.
2. The record drawings show that there was no inclined reinforcement at the re-entrant corner of the half-joints. (Figure 7). It is recognised that the arrangement and detailing of reinforcement is an important factor in the performance of a half-joint [3]. Inclined reinforcement crossing the re-entrant corner intersects and limits the width/extent of cracking extending from the corner under service loading.
3. Expansion joint failure at all half-joint locations leading to leakage and ponding of chloride rich water on the half-joints.
4. Localised level differences/ surfacing undulations at expansion joints causing dynamic amplification of axle loads on the suspended span half-joints.

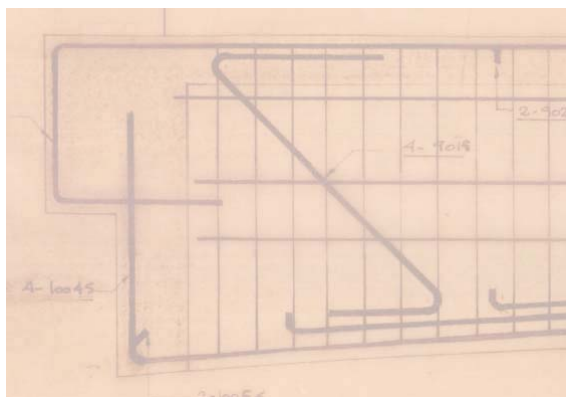


Figure 7. Half-joint reinforcement detail.

The structural assessment determined that the assessed capacity of the bridges was dictated by the capacity and condition of the half-joints. Accordingly, given the findings of the structural assessment and the serious nature of the cracking at the half-joints, it was recommended that works be undertaken, as a matter of urgency, to address the defects observed and strengthen/rehabilitate the bridge. A load restriction of 26t was placed on the bridges for the interim period until repair/strengthening works were completed. Two distinct options were recommended following the structural assessment to remediate the bridge half-joints:

1. Option 1 – Removal of half-joints. This option comprised the full removal of the half-joints and the introduction of reinforced concrete stitch diaphragms at half-joint

locations. This would require careful design as the structural system of the bridge would be changed from a statically-determinate, cantilever system to an indeterminate, structurally continuous system. Areas of the bridge deck adjacent to the stitch diaphragms would require additional reinforcement to cater for the moments and forces arising from the altered structural system. The works required for this Option would be substantial. The bridges would need to be closed to traffic for the duration of the works and a temporary bridge would be required to maintain access to both Haulbowline and Rocky Islands.

2. Option 2 – Remediation of half-joints. A scheme to change the bearing arrangement at the half-joints from discrete end bearings at each edge beam on the half joint bearing shelf to strip bearings or multiple bearings running the full length of the deck diaphragm to achieve a better load distribution across the entire half joint bearing shelf. This method would require the development of a complex, non-linear finite element model of the current and revised arrangement to substantiate the design. However, preliminary work in this area by RPS indicated that such a method would be viable. The high concrete strengths recorded in the material testing of the structures provide the basis for this proposal. While the works for this option would be complex, the bridges could remain open to traffic for the duration of the works.

5 NON-LINEAR FINITE ELEMENT ANALYSIS

RPS was appointed in 2013 to undertake the detailed design of the rehabilitation works to Haulbowline Bridges. The form of rehabilitation works adopted were as per Option 2 described in Section 4 i.e. remediation of the half-joints incorporating a new bearing arrangement and the use of non-linear finite element modelling to determine the ultimate resistance of the half-joints. The objective of the finite element (FE) modelling was to reproduce the behaviour that could be expected from a 'real' half-joint geometry and to investigate if the half-joints possessed capacities in excess of those predicted in the assessment using BD44 and BA39. Guidance regarding the use of computers in engineering calculations and the specific use of FE for concrete structures, is given by the Institution of Structural Engineers [4], Rombach [5] and FIB Bulletin 45 [6]. The principles laid out in these texts were adhered to in the finite element study.

5.1 Model Description

The non-linear finite element analysis (NLFEA) was undertaken using Lusas version 14.5. The geometry of the suspended span half-joint was approximated with a 2D idealisation. The concrete was represented by a non-linear plastic-damage-contact model with a capability to predict cracking, crushing, aggregate interlock and strain softening. Two dimensional plane stress quadrilateral elements with a quadratic interpolation order were used for the concrete matrix. The reinforcement at the half-joint was modelled as embedded bar elements, sandwiched between the concrete continuum elements, with a perfect bond assumed. The 2D idealisation adopted does not allow for variations in resistance to loading and varying stresses across the width of the joints.

However, it was considered that, at ULS, this smearing of resistance to failure was acceptable.

The onset and rate of propagation of cracking in the half-joint is dependent on the mesh density of the FE model. This mesh dependency is a function of the concrete cracking model and means that a convergence study is inappropriate. The re-entrant corner forms a stress concentration and the criterion for crack propagation is when the specified tensile stress is reached. The smaller the elements in the vicinity of a stress concentration, the higher the calculated stress levels become and the earlier a crack will propagate. The mesh density was therefore selected to provide the optimum balance between computational effort and agreement with experimental observations. Accordingly, a maximum element size of 25mm was adopted. A view of the FE model, including the mesh discretisation and reinforcement arrangement, is given in Figure 8.

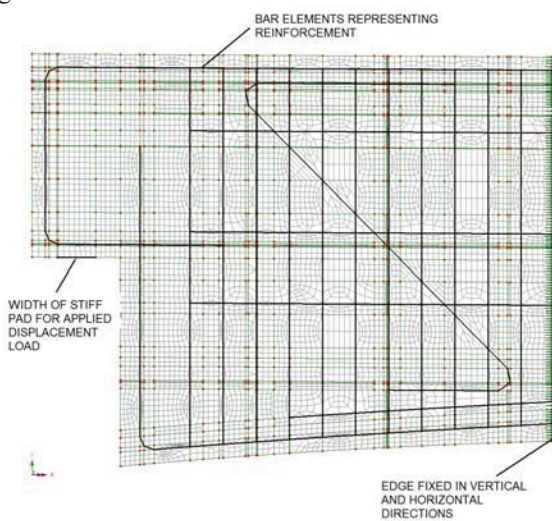


Figure 8. 2D plane stress model and mesh discretisation.

5.2 Boundary Conditions and Loading

The FE model was restrained both horizontally and vertically on one edge as shown in Figure 8. Loading was applied incrementally as a prescribed displacement via a stiff pad. Prescribing the displacement loading at a central point on the pad allows the nib to rotate freely. The stiff pad replicates the new bridge bearings and its presence in the model prevents localised stress concentration and failure of the concrete at the point of load application. Displacement-controlled loading stabilises the numerical analysis, preventing ‘cliff-edge’ behaviour in the model.

5.3 Material Properties

Analyses were undertaken with two sets of material properties – best estimate values and BD44 compliant values. The material properties are given in Table 1. The majority of the values were obtained from BD44. The material partial safety factor, γ_m , is included in the BD44 compliant values, but not in the best estimate values. Best-estimate properties were used to calibrate the FE model against experimental results, whereas the BD44 compliant values were used for arriving at an assessment resistance. The best-estimate material properties were selected based upon the results of the material testing outlined in Section 2.2.

Table 1. Material properties.

Parameter	Best-estimate value	BD44 compliant value
Poisson's ratio, concrete	0.2	0.2
Young's modulus, concrete (kN/mm ²)	39	39
Tensile strength, concrete (MPa)	4.7	3.8
Strain softening, concrete	0.006	0.006
Poisson's ratio, reinforcement	0.3	0.3
Young's modulus, reinforcement (kN/mm ²)	200	200
Yield strength, reinforcement (MPa)	250	217
Strain hardening, reinforcement (MPa)	85	85

5.4 Calibration of FE Analysis

The FE analysis was initially calibrated using a database of 23 half-joints tested by the Transport and Road Research Laboratory (TRRL) [7]. FE models were developed for four of the test beams and the failure loads obtained were consistently under-estimated/conservative compared to the test resistances. Enhanced capacities could be achieved by elevating concrete tensile strengths, increasing the strain softening parameters or altering the mesh density. However, this was not investigated due to the disparity in size and geometry between the TRRL geometries and the half-joints at Haulbowline Bridges. On the basis of the calibration study, it was concluded that the FE models provided conservative ULS capacities of half-joint geometries similar to the TRRL geometries using the best-estimate material properties.

5.5 Results

The assessed capacity of the suspended span half-joints, incorporating the new bearing provisions is given Table 2. The half-joint capacity determined from the NLFEA, incorporating BD44 compliant properties given in Table 1, were above the ULS applied loads with a utilisation factor of 0.79. The NLFEA capacity is also significantly greater than the assessed capacity using calculation models given in BD44 & BA39 for the Haulbowline Bridge geometries (factor of 1.78). This finding is consistent to that observed by Boothman et al. [8] who carried out NLFEA on half-joints on the Kingston Bridge in Glasgow, and obtained FE resistances ranging from 1.51-1.94 times higher than assessed capacities to BD44 & BA39.

Table 2. Half-joint capacity results.

Half-Joint	Applied ULS load (40T ALL + 45 HB), kN	Assessed capacity to BD44 & BA39, kN	FE result with BD44 compliant properties, kN
Suspended span	1747	1245(1.40)	2218(0.79)

(Utilisation factors in parentheses)

A deformed contour of reinforcement stress at SLS from the FE model is given in Figure 9 and the predicted cracking/crushing at failure is given in Figure 10. It is worth noting that some level of cracking from the re-entrant corner was observed from relatively low levels of live loading in the FE model, which is representative of the cracking observed

during the inspection and is deemed to be a result of a lack of inclined reinforcement crossing the re-entrant corner.

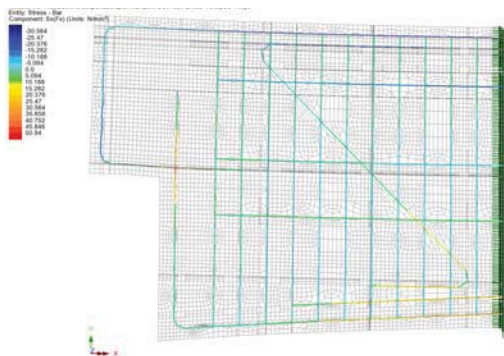


Figure 9. Deformed contour of reinforcement stress at SLS.

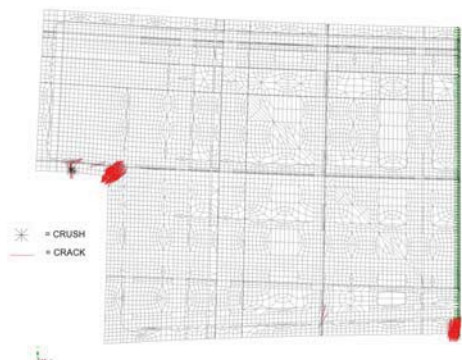


Figure 10. Predicted cracking/crushing at failure.

6 REHABILITATION WORKS

The Works included, inter alia, replacement of surfacing, street lighting, drainage, safety barriers, parapets and expansion joints, bridge deck waterproofing, temporary relocation and permanent reinstatement of existing utilities, provision of new services, provision of new bridge bearings requiring the jacking of bridge spans and making entry through reinforced concrete curtain walls, extensive concrete repair, and ancillary work associated with road and bridge construction.

A significant element of the Works was the extensive concrete repair required to each span of both bridges. To prepare the Works Requirements drawings, RPS conducted an extensive concrete repair inspection of every element of the bridge and scheduled repairs in tabular form on a drawing for each span with bespoke specifications and bill of quantity items. This was necessary to ensure the Works were described as completely as possible prior to tender in keeping with the requirements of the Public Works Contracts which are generally lump-sum in nature. Detailed and bespoke specifications were produced for bridge deck jacking and localised hydro-demolition to create pockets through curtain walls below deck diaphragms for bearing removal and replacement. RPS envisaged that temporary jacking platforms would be supported from the bridge piers to allow the suspended spans to be jacked. The form of contract was the Public Works Contract for Minor Building and Civil Engineering Works Designed by the Employer and the parent specification and Method of Measurement were from the

NRA Manual of Contract Documents for Road Works. Following a public procurement process the Contract was awarded to L & M Keating Ltd. (LMK) who commenced the Works in May 2014.

LMK utilised an alternative bridge deck jacking method which allowed the 200t suspended deck sections to be jacked from the topside using a pivot beam arrangement in conjunction with anchor bars attached to the deck. Deck jacking, the removal of the original bearings and the installation of new bearings in a revised arrangement were successfully completed during a series of overnight bridge closures. The overall scheme was completed in April 2015 on programme and within budget (€2m).

7 CONCLUSIONS

The delivery of a complex bridge rehabilitation scheme in such a short time frame from the point of discovery of significant structural defects was made possible by the use of modern analysis techniques. Major environmental works will be commencing on the island in 2016 and the bridge works were delivered without impacting the overall programme for these critical works. The completion of the bridge works which substantially improved the appearance of the bridges has been warmly received by the people of Cork who see the bridges project as a tangible starting point for the exciting plans to develop a public park on the island. A view of the completed southern channel bridge is given in Figure 11.



Figure 11. View of completed southern channel bridge.

REFERENCES

- [1] Highways Agency, *Interim Advice Note 53: Concrete Half-Joint Deck Structures*, Highways Agency, London, UK, 2004.
- [2] Transport Scotland, *TS Interim Amendment No. 20 – Concrete Half-Joint Deck Structures*, Glasgow, UK, 2006.
- [3] Mitchell, D., Cook, W., and Peng, T. (2010), 'The Importance of Reinforcement Detailing', *American Concrete Institute Special Publication 273*, pp. 1-16.
- [4] Institution of Structural Engineers, (2002). *Guidelines for the Use of Computers for Engineering Calculations*, IStructE, London.
- [5] Rombach, G., (2011). *Finite-Element Design of Concrete Structures – Practical Problems and their Solutions 2nd Ed.*, Institution of Civil Engineers, London, UK.
- [6] Fédération Internationale du Béton (FIB), *FIB Bulletin 45 Practitioners' Guide to Finite Element Modelling of Reinforced Concrete Structures*, Lausanne, Switzerland, 2008, 349 pp.
- [7] Clark, L., and Thorogood, P. (1987), 'Serviceability Behaviour of Reinforced Concrete Half-Joints', Transport and Road Research Laboratory, Wokingham, Contractor Report 70.
- [8] Boothman, D., Leckie, S., MacGregor, I., and Brodie, A., (2008), 'Assessment of Concrete Half-Joints Using Non-Linear Analysis', *Bridge Engineering*, Vol 161, Issue BE3, London, UK, pp. 141-150.

Rehabilitation of Steel Orthotropic Deck Bridges using High Strength Concrete Overlay renovation technique

Pat Moore¹, Dimitri Tuinstra²

¹Arup, 50 Ringsend Road, Dublin 4, Ireland

²Arup, Naritaweg 118, 1043 CA Amsterdam, the Netherlands
email: pat.moore@arup.com, dimitri.tuinstra@arup.com

ABSTRACT: Several large steel bridges in the Netherlands have been given an extended service life by the application of a thin layer of reinforced high strength concrete to the surface of the steel orthotropic deck. This innovative renovation technique has been subject to ongoing development since 2000, and there is now a growing body of experience with regard to the design, construction and maintenance aspects associated with this product.

At the end of 1990's the Dutch highway authority (RWS) were faced with an increasing asset maintenance demand due to fatigue damage in a number of important bridges on the road network. A renovation solution to address the issue has been developed from concept stage to implementation on some of its most critical bridges.

This paper provides an overview of the development of this strengthening method. The design principles of the system are presented and the important characteristics discussed. Some of the experiences from an ongoing major renovation programme is shared, in terms of ongoing developments in the design, specification, and execution of this product.

KEY WORDS: Steel Orthotropic Bridge; Steel Fatigue; High Strength Concrete Overlay; Rehabilitation.

1 INTRODUCTION

Within the current bridge stock on the Dutch highway network, there are a number of steel orthotropic deck bridges which are found to be subject to steel fatigue damage. The bridge owner, Rijkswaterstaat (RWS) is addressing this issue using an innovative renovation technique.

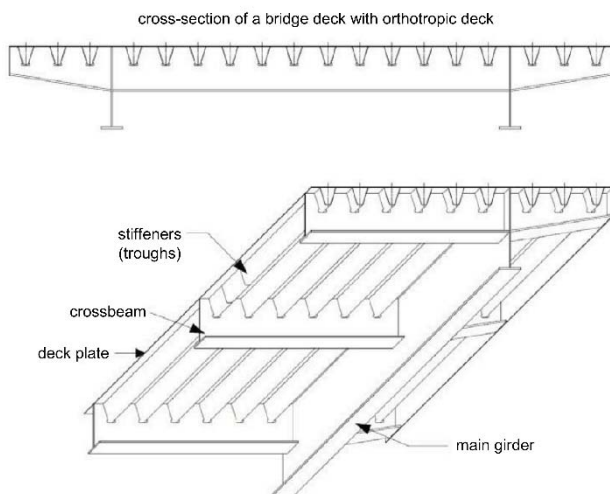


Figure 1 Typical orthotropic steel bridge deck

The bridges in question are generally found on large river and canal crossings, and most of them were built during the motorway construction boom in the 1960's and 1970's.

The orthotropic steel decks have a thin steel deck plate below the road surface, which is locally stiffened in the direction of the traffic, and in turn supported by a systems of transverse and longitudinal girders, as indicated in Figure 1.

This form of construction allows a relatively lightweight and structurally efficient deck system to be achieved, which is important for long span bridges. In addition, due to their light weight nature, this deck type is commonly found in moveable bridges.

However, since the 1990's many of these bridges, particularly on the busiest roads, have displayed evidence of fatigue damage in the deck. The fatigue damage results in cracks forming in the orthotropic deck, culminating in degradation to both the wearing surface (see Figure 2 below) and the steel structure itself.



Figure 2 Damage to asphalt surfacing

Fatigue damage typically occurs at locations of stress concentrations such as at welds, attachments and abrupt changes in geometry. Locally, the stresses at these locations are significantly higher than the stresses in the surrounding steelwork, and under repetitive load cycles, crack growth can

occur. The classic fatigue crack location is through the deck plate at the intersection of the trough leg and cross-girder, as indicated in Figure 3.

Consequently, the asset owner needs to implement a regime of regular inspections and repeated maintenance activities in order to keep the bridges fully operational, with temporary hindrance to road users where repairs are necessary. Repairing the asphalt and the steelwork on a regular basis is not a sustainable maintenance strategy as the frequency and severity of the damage increases with time, and the remediation works become more and more intrusive for both the bridge structure and the road users. Also, the damaged asphalt can pose a safety risk for the road users and often requires immediate action. Due to the location of the bridges in the congested highway network, the costly repairs are usually undertaken at night or during weekends. Without fundamental rehabilitation, the bridge will reach the end of its useful life earlier than intended.

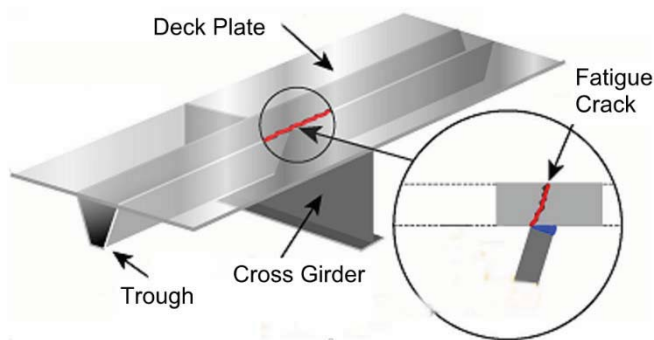


Figure 3 Fatigue crack in orthotropic steel bridge deck

To address this issue, RWS have developed a solution of applying a concrete overlay to the surface of the steel deck. This repair method is designed to address the fatigue damage that can occur in the deck plate and in the stiffening troughs connected to the deck plate. The overlay prolongs the life of the steel deck and extends the service life of the wearing surface. The solution has been developed since 2000 and has now been applied to a number of large bridges throughout the highway network.

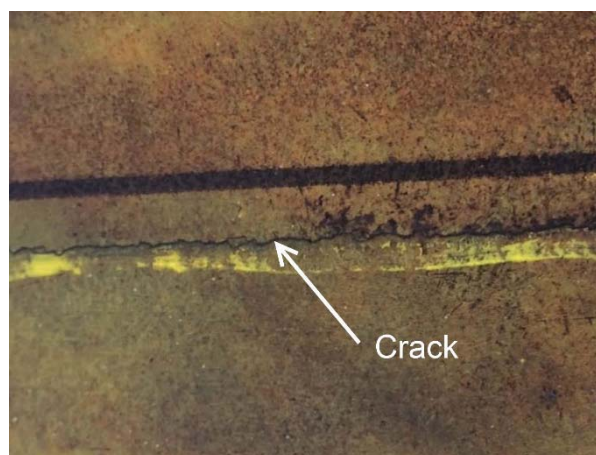


Figure 4 Crack in steel deck plate

2 BACKGROUND

In 1998, only 7 years after commissioning the second bridge at Van Brieneoord, which carries the A16 over the Nieuwe Maas in Rotterdam, the moveable bridge had suffered from severe fatigue damage that resulted in the need to replace the steel deck. This marked the start of the process to find a technically robust solution which could extend the operational life of these bridges and which could be implemented with an acceptable level of disturbance to the traveling public.

2.1 Research

The first phase in the process was to determine the likely scale of the problem in terms of which bridge structures within the main highway network were likely to experience fatigue damage leading to an escalation of inspection and maintenance in the future to ensure safe and continued use of the bridge. This led to a cataloguing and risk analysis of the key bridges within the road network which would require intervention in the coming years.

In parallel, research commenced into the cause of the fatigue damage with a view to better quantifying the fundamental reasons for the issues that were occurring on some of the bridges. The research included both theoretical and experimental studies to study the structural behaviour which results in the formation of cracks in the steel plates and the welds joining the steel plates [1], [2].

The outcome from the research was that there were two fundamental causes of the fatigue damage. Firstly, the structural detailing executed at the orthotropic deck was inappropriate for the locally high stresses that can occur in the deck. The steel deck plate is typically 10mm to 12mm thick at these bridges, which for static capacity is sufficient, but the stresses generated under repetitive loading from vehicles are sufficiently high to cause fatigue damage. In many cases, some of the detailing used to connect the deck plate to the longitudinal and transverse stiffeners were of a low fatigue performance category which results in high local stresses, and subsequently fatigue damage occurring over time.

Secondly, the number and weight of the vehicles has increased significantly since the construction of many of these bridges, in particular with respect to the more heavily loaded trucks. The increasing use of single tyres instead of dual tyres result in the vehicle load being transmitted to the deck in a more concentrated area and thus the steel deck is subject to a higher local pressure. Both the increased frequency and higher loads are leading to a shorter time before fatigue damage occurs at susceptible bridges.

For the bridges which have been identified as being at risk of fatigue damage, a programme of regular inspections, and where necessary repairs, is implemented (Rijdek Inspectie Stalen Kunstwerken). This inspection and maintenance programme enabled the network asset owner to continually assess and manage the maintenance needs of these bridges. The results from the inspection programme are used as part of the design development of the renovation technique.

2.2 Pilot Projects

After establishing the primary causes and mechanisms which underlie the fatigue damage, attention then turned to the development of solutions that could extend the useful life of

these bridges. Reducing the number or weight of vehicles passing over the bridges was not a feasible solution, given that many of the bridges in question were located on transport routes of national strategic importance. In terms of loading, attention was focused to better quantify the truck numbers and weight distribution which the bridges were subject to, in the past, the present and what could be expected in the future. This information is necessary to undertake an accurate assessment of the fatigue damage that had occurred to date, and what damage could be expected in the future. The traffic information becomes a key parameter in the performance specification of any solution and what design life can be reasonably expected. Ultimately the traffic measurement have been used as the basis for formulating a traffic load model which is considered in the fatigue assessment calculations.

To address the structural aspects, the solutions focused on increasing the structural strength and improving the detailing at the welded connections. Both these approaches reduce the stresses which occur in the steel plate under traffic loading and thus help to prolong the lifetime before damaging cracks occur in the steel plates and welds.

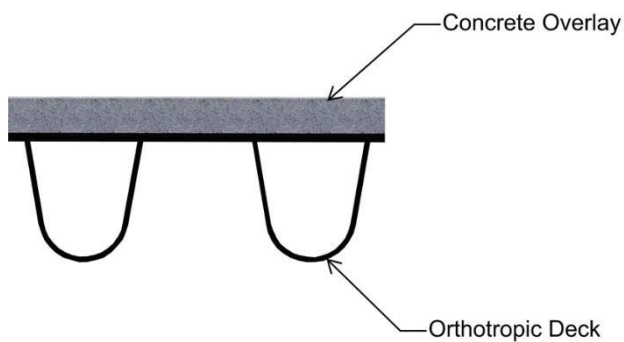


Figure 5 Concrete overlay on orthotropic steel bridge deck

It should be noted that the fatigue damage which occurs in and near the deck plate is primarily due to a local load effect, rather than a problem for the global supporting system. The high concentrated loads imposed at the wheels of heavy trucks results in high stresses in the steelwork near the point of application. Thus, options to increase the structural strength are focused on the local strength at and near the deck plate, and not necessarily the global superstructure system. The strength of the deck can be increased by adding extra structural elements to the deck plate, for example, in the form of additional steel plates or by the addition of structural concrete. The addition of steel plates has been developed and implemented at moveable bridges, where the extra weight and height due to a layer of structural concrete is prohibitive for the operation of the moveable bridge. However, for fixed bridges (non-moveable), the additional weight of concrete can, in many cases, be accommodated by the existing structure, with no or moderate modifications to the global support system. This renovation system is known as high strength concrete (HSC) overlay (see Figure 5).

At the location of poor fatigue details, depending on the effectiveness of the structural strengthening, the fatigue issue can be addressed by replacing the existing detail with an improved performance detail; albeit with the associated time and cost of undertaking this activity. It is generally found that such measures are only needed for details remote from the deck plate where deck plate strengthening using the HSC system is less effective.

Three bridges were identified as suitable candidate demonstration sites for the concrete overlay system which had been developed during the research stage of the process. Namely, Caland Bridge, Hagestein Bridge, and Moerdijk Bridge. At these bridges, the concrete overlay product has been installed. The purpose of the pilot bridges was to implement the application of the concrete product on active bridges. The works were undertaken between 2003 and 2007. Each bridge location presented its own specific challenges and were extremely valuable in the development of both the design and execution aspects of the overlay product. The knowledge developed and lessons learned were captured and fed back into the market by RWS and the collaborators [3].

The most valuable conclusions from the pilot bridges was that this product was shown to be an effective method of reducing the local stresses which could cause fatigue damage in the deck, and that the successful installation of the product required a high standard of workmanship and necessitated specialised construction methods.

2.3 Steel Bridge Renovation Programme (Project Renovatie Bruggen)

After the completion of the pilot bridges, the subsequent stage was the implementation of the Steel Bridge Renovation Programme (Project Renovatie Bruggen). This ambitious programme sought to renovate eight large fixed bridges and six moveable bridges in a period of 9 years, from 2009 to 2018. The concrete overlay product is only considered at the fixed bridges. The locations of these bridges is shown in Figure 6.



Figure 6 Location of fixed bridges (The Netherlands)

These eight (fixed) bridges were identified as being priority bridges within the highway network, which were suitable candidates for remediation using the concrete overlay. One of the fundamental objectives of the programme was to use a series of bridges as a method of developing and progressing the design and the construction aspects of the renovation process from one bridge to the next. With this in mind, the construction contract was formulated as a framework contract, whereby 3 main contractors were pre-selected, and the procurement of each of the bridge specific construction works was awarded using a mini-tender procedure per bridge. Each of the three contractors collaborated with the client (RWS) in capturing and creating knowledge relating to the construction and application of the concrete overlay. In this way, there has been an evolution of best practice in terms of construction methods.

Similar to the construction contract, a single engineering contract was formulated to facilitate the evolution of a centre of excellence with regard to the best practice for the engineering design aspects associated with the renovation of bridges. The engineering design contract was awarded to a single entity, the Managing Contractor. The Managing Contractor (Arup and Royal HaskoningDHV joint venture) is responsible for the assessment, design, procurement and construction supervision of the works.

To date, the renovation has been successfully implemented at 5 of the 8 bridges, namely Muidenbrug, Scharbergbrug, Brug Beek, Kreekrakbruggen and Galecopperbrug, with one bridge currently being renovated (Ewijkbrug). The two remaining bridges are Suurhoffbrug and the 2nd Arch Bridge at van Brienenoord.

At most of these bridges, the application of the concrete overlay is only a portion of the renovation works undertaken, and in some instances significant global strengthening has been necessary. The steel bridges typically have an asphalt layer with a thickness of about 50mm. Due to the greater density of HSC compared to asphalt and also due to the average overlay thickness of about 85mm, it is often necessary to strengthen the main structural elements of the superstructure. Occasionally strengthening of the substructure is also necessary. In addition, strengthening measures are sometimes necessary to account for future traffic loading.

More detail with regard to these works can be found in various publications [4], [5], [6], [7], [8], [9].

2.4 Life Cycle Aspects

Broadly speaking, for steel orthotropic deck bridges with fatigue damage, the bridge owner has the following options.

- Continue to inspect and repair, with increasing frequency and extent of intervention.
- Replace the bridge deck
- Strengthen the bridge deck
- Change the use of the bridge

There are multiple aspects which need to be considered during the evaluation of the options including:

- Costs (life cycle)
- Hindrance and asset availability
- Impact on Stakeholders, Image, Environment, Health & Safety

RWS have adopted an intended design life of 30 years from time of renovation for the purposes of the assessment and design of the renovation works. The assessment of the options concluded that the choice to strengthen the bridge deck (using concrete overlay) was the preferred choice.

At a number of bridges, as the renovation design progressed and a better understanding of the condition of the existing bridge and the implications of the renovation works on the existing structure, a more detailed assessment of deck replacement versus deck strengthening proved necessary, in order to justify and support the selected option. This was undertaken at Galecopper Bridge and Ewijk Bridge. At both these bridges, the detailed evaluation concluded that renovation was preferred compared to replacement. At Suurhoff Bridge, during the assessment and renovation design process, the preferred option was revised from the strengthening of the existing bridge to replacement of the bridge deck.

3 PRODUCT DEVELOPMENT

Over the past two decades the concrete overlay has developed from a concept to a standard solution. In 2000, this technique was highly innovative and as with many innovations, a period of time is needed to successfully validate and optimise the product, in order to ensure that the best potential is achieved. A brief overview of the product itself and some of the development aspects over this period is presented in the following paragraphs.

3.1 Design Principles

The steel orthotropic deck is strengthened with a layer of concrete, to improve the local fatigue performance of the steelwork and thus extend the functional life of the bridge. The concrete layer needs to be as light as possible, as the application of the concrete layer results in additional weight which must be carried by the existing bridge. In order to reduce the additional weight the thickness of the concrete layer kept as thin as possible, but must have sufficient thickness to provide the necessary structural strengthening and also needs to allow for the expected construction tolerances and deviations that may occur. The concrete layer needs to be durable and with minimal maintenance needs. The required thickness of concrete overlay depends on the specifics of the bridge, as the fatigue performance is dependent on the structural configuration, the historic traffic use and the predicted traffic use in the future. In order to keep the thickness to a minimum, concrete with a high compression strength is adopted.

The fatigue life of the steelwork is dependent both of the number and magnitude of stresses that it has experienced to date and the future stresses it is expected to be subjected to in the future. Where there is existing fatigue cracks in the steel deck and welds of a certain magnitude, it is necessary to repair these cracks prior to applying the concrete overlay, otherwise the thin overlay is unable to ensure the necessary extension of the design life.

3.2 State of the Art

The concrete overlay product has developed over a period of time. Currently main characteristics of the overlay as implemented within the Bridge Renovation Programme in 2016, are summarised below.

3.2.1 Concrete Material

The concrete has a design compressive (cylinder) strength of 90N/mm^2 (C90/105), and a design bending strength of 10N/mm^2 . The autogeneous shrinkage and drying shrinkage characteristics are important in order to minimise the shrinkage effects within the concrete layer itself and the imposed effects on the steel structure. The design limits are 0.3‰ and 0.45‰ after 90 days, respectively. On the bridge, all cracks with a width greater than 0.1mm measured 4 days after pouring the concrete are repaired (injected) for durability reasons.

3.2.2 Reinforcement

The concrete layer is reinforced using one layer of 12mm diameter B500B reinforcement bars at 75mm centres in both the longitudinal and the transverse directions. The minimum design cover is 20mm and the minimum distance from the top of the transverse reinforcement to the top of the steel deck is 50mm. The transverse reinforcement is the upper reinforcement layer.

Steel fibre reinforcement with a diameter of 0.4mm and a dosage of 75kg per cubic metre of concrete is provided.

3.2.3 Steel substrate preparation

Cracks in the deck plate which are found to be 3mm or more in depth are repaired. The steel surface is grit blasted to a SA2.5 profile finish prior to application of the epoxy bonding layer. Locations of pit corrosion and/or geometric irregularities are treated prior to application of the bonding layer.

3.2.4 Bonding layer

A 2-3mm layer of epoxy resin is applied to the prepared steel deck and scattered with calcined refractory bauxite aggregate (3-6mm size). The important design characteristic of the bonding layer is the shear strength which can be achieved both, between the bonding layer and the steelwork, and between the bonding layer and the concrete. The required shear strength for this connection varies depending on the bridge configuration and loading situation. Typically a shear strength of approximately 6MPa is required. During construction, measurement of the shear strength is not tested directly; instead the shear strength of the bond is indirectly verified by measuring the pull-off (tensile) strength. The typical construction requirements are that the bonding layer needs to attain a design pull off strength of 7.0N/mm^2 between the steel deck and the epoxy; and 3.5N/mm^2 between the bauxite aggregate/epoxy resin and the concrete overlay.

3.2.5 Wearing surface

The wearing surface varies per bridge location, and consists of either a thin wearing course of epoxy resin with embedded calcined refractory bauxite aggregate similar to the bonding layer system, or an asphalt surfacing system. The typical total thickness of the epoxy and bauxite wearing course is approximately 8mm. The top of the wearing course should be at the same height as the top of the expansion joint, which often necessitates modification or replacement of the expansion joints.

3.3 Analysis and verification

The early research focused on developing an understanding of the structural behaviour of an orthotropic steel deck subject to local wheel loading. In particular the distribution and magnitude of stresses in the steel plates and welds was investigated, and the fatigue performance that could be expected. This study was necessary to allow the development of analytical tools which could model the existing bridge deck behaviour and to model the effectiveness of any local strengthening measures.

The function of the high strength concrete overlay is to act compositely with the steel deck and thereby increasing the fatigue performance of the steel deck. The concrete is attached to the steelwork via the bonding layer. Thus, the analysis needs to capture the structural behaviour of the steelwork, bonding layer and concrete. In order to do so detailed finite element (FE) numerical models are utilised. These models are benchmarked against experimental models in order to validate the output from the numerical models. Shell elements are used to model the steel plates, and solid elements for the bonding layer and the concrete layer. The FE modelling typically include local zones of small mesh size (circa 10mm), to accurately capture the stresses at the local details where the fatigue damage can occur in the steel plates and welds, as shown in Figure 7.

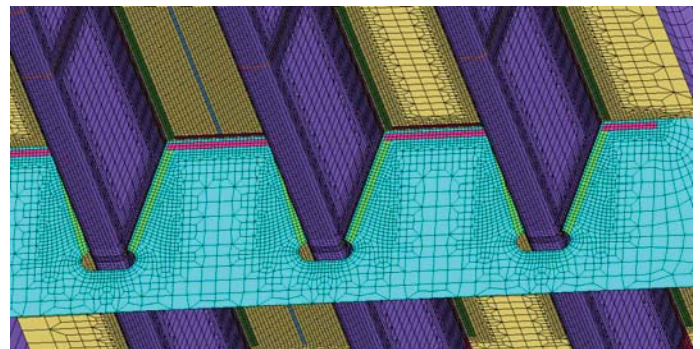


Figure 7 Typical FE model mesh

The fatigue analysis is based on the Palmgren-Miner cumulative damage method. In this approach, for a given fatigue detail, the stress history spectrum is determined. The stress spectrum utilises a project specific fatigue load model which describes a distribution of vehicle types and frequency, since the bridge was opened for traffic and the predicted traffic in the future. For the renovation program a fatigue load

model representing actual traffic data from the past and a prediction for the future as been formulated.

The design verification of the high strength concrete overlay is that, for a given detail, the calculated fatigue damage should be less than 1.0, at the intended design life. Where this is not demonstrated, alternate forms of renovation are implemented such as replacing the detail with a detail of improved fatigue performance. In some cases, verification is undertaken using crack propagation prediction techniques (fracture mechanics), however this often results in the need for periodic (future) inspections to validate the behaviour assumed in the crack growth calculations.

3.4 Design Development

Since the initial application of HSC on the steel orthotropic deck bridges, a number of design changes have occurred.

The development of the analysis from the earlier bridges has found that it is typically necessary to increase the required thickness from a value of approximately 60mm to approximately 75mm. This is a minimum design value, and in order to ensure the necessary construction tolerances are accommodated, the average applied thickness is usually found around 85 to 95mm.

For the bridges currently being renovated, the depth of the permitted unrepaired crack in the deck plate has reduced from 6mm at the earlier bridges to 3mm.

The reinforcement at the pilot bridges consisted of three layers of reinforcement mats, 8mm diameter at 50mm centres. Due to the congestion of reinforcement in combination with the low workability of the concrete mix, the reinforcement has been modified to two layers of 12mm diameter bars at 75mm centres, with the top layer of reinforcement in the transverse direction. In addition, the concrete cover has been increased from 20-25mm to 20-60mm. The cover tolerance of 20 to 25mm was found in practice to be difficult to achieve. This often resulted in reduced concrete cover which had implications for the durability of the reinforcement and the necessary anchorage lengths of the reinforcement bars.

4 FUTURE

The future development of the concrete overlay renovation technique can be classified into developments of the product itself and evolutions to the processes of its implementation.

4.1 Product Development

The use of stronger concrete materials, such as ultra-high performance concrete (UHPC), could permit the application of thinner layers of overlay while still providing the necessary structural strengthening to extend the design life of the bridge. This would reduce the global effects due to the additional weight imposed by the concrete overlay.

Thus far, efforts have been made in the development of fibre-only reinforced concrete and ultra high performance concrete (UHPC) solutions. The use of precast and prestressed systems have also been investigated. The implementation of these solutions are still in the early stages of development but are considered to be potential alternatives to the cast in-situ high strength concrete system currently in use.

4.2 Process Development

As the implementation of the high strength concrete system on steel orthotropic decks become more commonplace, there will be opportunities to adopt alternative procurement methods such as Design and Build and also Design, Build, Finance and Operate models. This would place more incentive in the construction market to further develop and optimise this method of strengthening orthotropic steel decks.

In addition, a more systematic way of prioritising and coordinating the maintenance programme of the bridge stock using life cycle analysis within the asset management process can be adopted as the performance of this system continues to be demonstrated in the field.

ACKNOWLEDGEMENT

RWS appointed the Managing Contractor to undertake the assessment, inspections, engineering, procurement, stakeholder management and construction supervision of eight bridges. The joint venture Managing Contractor consists of two parties: Arup and Royal HaskoningDHV.

The authors wish to acknowledge the support of the client, RWS, and for their permission to publish this paper.

A number of the figures are taken from the construction works at Kreekrakbrug, where the main contractor was Heijmans. (Fig 4, 8, 9, 11, 12, 13 & 14).

REFERENCES

- [1] Kolstein, M.H. 2007. *Fatigue Classification of Welded Joints in Orthotropic Steel Bridge Decks*.
- [2] De Jong, F.B.P. 2006. *Renovation Techniques for Fatigue Cracked Orthotropic Steel Bridge Decks*.
- [3] Adviesbureau ir. J.G. Hageman B.V. 2009. *HSB-Betonoverlagingen op Stalen Bruggen*, Rapport 6721-1-5.
- [4] Gration, D., Dooren van F., Nagtegaal G., Ashurst D., Kunst P. & den Blanken S. 2010. *Orthotropic Deck Fatigue: Renovation of 8 Bridges in the Netherlands*, Structural Faults + Repair Symposium, Edinburgh, 2010.
- [5] den Blanken, S. Nagtegaal, G. & Tuinstra, D. 2012. *Strengthening Solutions for the Extended Service Life of the Galecopperbridge in the Netherlands*, 18th IABSE Congress, Seoul, Korea.
- [6] Darlow, M & Karagiannis, D. 2013. *Assessment and Strengthening of the Kreekrakbrug, Assessment, Upgrading and Refurbishment of Infrastructure*, Proc. IABSE, Rotterdam, 6-8 May 2013.
- [7] Tuinstra, D., Breider J. & Nagtegaal G. 2013. *Fatigue assessment of steel bridge superstructures, Assessment, Upgrading and Refurbishment of Infrastructure*, Proc. IABSE, Rotterdam, 6-8 May 2013.
- [8] Moore, P., Lavery, C., Vonk, E. & Nagtegaal G. 2013. *Replacement of the Cable Stays at Ewijk Bridge, the Netherlands*, Assessment, Upgrading and Refurbishment of Infrastructure, Proc. IABSE, Rotterdam, 6-8 May 2013.
- [9] Vonk E., Flint, M. & Nagtegaal, G. 2013. *Renovation design of the Bridge at Ewijk in The Netherlands*, Assessment, Upgrading and Refurbishment of Infrastructure, Proc. IABSE, Rotterdam, 6-8 May 2013.

Implementation of a drive-by monitoring system for transport infrastructure utilising GNSS

McGetrick, P.J.¹, Hester, D.²

¹School of Planning, Architecture, and Civil Engineering, David Keir Building, Queen's University Belfast, BT9 5AG, Northern Ireland

email: p.mcgetrick@qub.ac.uk, d.hester@qub.ac.uk

ABSTRACT: Ageing and deterioration of infrastructure is a challenge facing transport authorities. In particular, there is a need for increased bridge monitoring in order to provide adequate maintenance, prioritise allocation of funds and guarantee acceptable levels of transport safety. Existing bridge structural health monitoring (SHM) techniques typically involve direct instrumentation of the bridge with sensors and equipment for the measurement of properties such as frequencies of vibration. These techniques are important as they can indicate the deterioration of the bridge condition. However, they can be labour intensive and expensive due to the requirement for on-site installations. In recent years, alternative low-cost indirect vibration-based SHM approaches have been proposed which utilise the dynamic response of a vehicle to carry out “drive-by” pavement and/or bridge monitoring. The vehicle is fitted with sensors on its axles thus reducing the need for on-site installations. This paper investigates the use of low-cost sensors incorporating global navigation satellite systems (GNSS) for implementation of the drive-by system in practice, via field trials with an instrumented vehicle. The potential of smartphone technology to be harnessed for drive by monitoring is established, while smartphone GNSS tracking applications are found to compare favourably in terms of accuracy, cost and ease of use to professional GNSS devices.

KEY WORDS: Acceleration; Bridge health monitoring; Drive-by; Global navigation satellite systems; Vehicle sensors.

1 INTRODUCTION

Bridges and pavements form an integral part of transport infrastructure worldwide. Over their lifetime, their condition will deteriorate due to factors such as environmental conditions, ageing and increased loading. In countries such as the U.S., Korea, Japan and across the E.U., a majority of bridge structures are now over 50 years old [1,2]. This leads to the requirement for increased monitoring and maintenance in order to prioritise allocation of funds and guarantee acceptable levels of transport safety, particularly where rehabilitation and life extension of bridge structures is necessary.

As traditional visual inspection methods for bridges can be highly variable, relying on visible signs of deterioration, bridge management systems (BMSs) are now more commonly integrating structural health monitoring (SHM) methods, involving direct instrumentation of bridge structures with sensors and data acquisition equipment, which target identification of damage from dynamic structural responses [3,4]. However, these methods can be labour intensive and expensive due to the requirement for on-site installations, which may require dense sensor networks. This has restricted widespread implementation of SHM for short and medium span bridges, which form the greatest proportion of bridges in service. Therefore, a more efficient alternative is required which can provide information about a bridge's condition.

Road pavement profile measurements are typically obtained using an inertial profilometer, which consists of a vehicle equipped with a height sensing device, such as a laser, which measures pavement elevations at regular intervals [5] with the effects of vehicle dynamics removed from the elevation measurements via accelerometer(s) and gyroscopes. The vehicle can travel at highway speeds and the method provides

accurate, high resolution profile measurements but a drawback is the expense associated with laser-based technology.

In recent years, alternative low-cost indirect vibration-based SHM approaches have been proposed by a number of researchers which utilise the dynamic response of a vehicle to carry out “drive-by” monitoring of bridges [6,7] and/or pavements [8]. The vehicle is fitted with sensors, such as accelerometers, on its axles to monitor vibration thus reducing the need for on-site installations and expensive laser-based sensors. However, these methods, summarised by Malekjafarian et al. [7], lack comprehensive experimental verification, with very few field trials reported in the literature. Based on existing research [7], three main challenges for drive-by monitoring have been identified as the road profile, the limited vehicle-bridge interaction (VBI) time (speed-dependent) and environmental effects, while also acknowledging practical issues such as ongoing traffic on a bridge and variation in speed of the instrumented vehicle.

Malekjafarian et al. [7] suggest that a potential solution to challenges related to limited VBI time and environmental effects is the use of instrumented vehicles that repeatedly pass over the same bridge, or pavement. This could be implemented by instrumenting a fleet of vehicles with sensors, e.g. public vehicles such as the public bus monitoring system investigated in Japan [9] which drive along the same route multiple times per day. An alternative lower-cost possibility is proposed in this paper; the use of smartphone technology and sensors. Due to the current prevalence of such technology, drive-by vehicle monitoring systems could potentially move beyond the limitation to unique instrumented vehicles, or localised instrumented vehicle fleets.

This paper is motivated by the aforementioned lack of field testing and thus investigates the implementation of such drive-by monitoring systems in practice via field trials. For this purpose, a two-axle vehicle is instrumented with accelerometers and global navigation satellite system (GNSS) receivers and is driven along predetermined routes in the Belfast road network. Aiming to take advantage of existing low-cost technologies, in addition to accelerometers designed for structural applications and a Leica GNSS receiver, smartphone accelerometers and global position tracking applications are also utilised during field trials. Measurements obtained from all sensors and receivers are compared in terms of accuracy, cost and ease of use in order to evaluate the effectiveness and feasibility of this monitoring system.

2 METHODOLOGY

For this field investigation, the instrumented vehicle was a Ford Transit van (Figure 1), weighing 1600 kg and fitted with accelerometers to measure vibration and GNSS receivers to record the vehicle position in the road network. A digital camera was also used to record video footage of each vehicle test run while the average vehicle speed during testing was 30 mph (48 km/h). The details of instrumentation and setup are outlined in the following sections.



Figure 1. Instrumented Vehicle.

2.1 Acceleration measurement setup

The overall setup of accelerometers in the vehicle is illustrated in Figure 2, consisting of 4 accelerometers measuring vertical vibration.

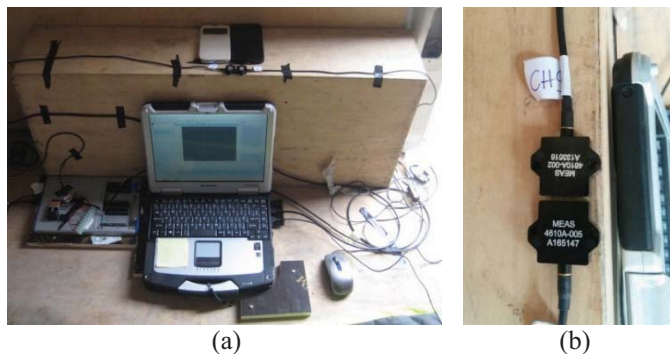


Figure 2. (a) Accelerometer instrumentation setup (b) uniaxial accelerometers.

2.1.1 Wired accelerometers

Two wired uniaxial accelerometers were installed at the same location in the body of the vehicle, adhesively mounted over the left rear wheel. The installed accelerometers were ultra-low noise signal conditioned model 4610A-002 ($\pm 2g$) and

4610A-005 ($\pm 5g$) units by Measurement SpecialtiesTM, shown in Figure 2(b), which provide low-pass filtered output. Excitation voltage was provided by a 9V battery during testing. Both $\pm 2g$ and $\pm 5g$ rated accelerometers were tested, for comparison with smartphone sensors and to ensure any large magnitude accelerations greater than $2g$ were recorded, respectively. The sampling frequency was 1000 Hz, which allows identification of any features with frequency components higher than 100 Hz, which would be undetected by the smartphone sensors.

2.1.2 Smartphone sensors

The built in accelerometers of an LG Nexus 5 and a Samsung Galaxy S4 were used for vertical smartphone acceleration measurements; both devices were mounted over the left rear wheel with adhesive (Figure 2(a)). The LG Nexus 5, retailing at €290 approximately, contains a 6-axis MPU-6515 chip with integrated triaxial MEMS Gyroscope and triaxial MEMS accelerometer by InvenSense Inc., built into the device motherboard. The maximum measurement range during testing was $\pm 19.61 \text{ m/s}^2$, equivalent to $\pm 2g$, although this can be increased. As vehicle body and bridge vibration magnitudes are generally less than $2g$, this range is suitable for bridge monitoring applications. The smartphone sampling frequency was set at a maximum of 200 Hz, which is also adequate for drive-by monitoring.

The Samsung S4, retailing at €220 approximately, uses a K330 triaxial accelerometer by STMicroelectronics. The maximum measurement range was $\pm 19.61 \text{ m/s}^2$ ($\pm 2g$), however, the maximum allowable sampling frequency on the Samsung S4 was 100 Hz during testing.

Accelerations were logged to the internal SD card of each device via the freely available Android smartphone application 'Vibration Alarm' by Mobile Tools. In terms of sampling consistency, it was observed that that for around 3% of the total number of recorded samples, the sample interval varied by $\pm 0.001 \text{ s}$ for both devices. Each accelerometer was powered by the internal lithium-ion batteries of their respective smartphones; the Nexus 5 by a 3.8 V, 2300 mAh battery and the S4 by a 3.8 V, 2600 mAh battery. An external 5200 mAh capacity portable power supply (costing €16) was also used as backup for the LG Nexus 5.

2.2 GNSS setup

In addition to recording acceleration measurements, accurately monitoring the position of the instrumented vehicle during its passage along a road network is valuable for a number of reasons. Firstly, if anomalous results or large peaks are observed in the acceleration record, they can be tagged with a location via GNSS tracking, allowing the engineer to rapidly pinpoint areas with potential pavement damage e.g. potholes or cracking. This type of approach has already been investigated for pothole detection in pavements using custom built devices combining accelerometers and GPS receivers [10], further incorporating video to enable screenshots of areas of interest [11], and smartphone applications integrating crowdsourcing [12]. Secondly, for bridge monitoring, it would enable identification of bridge crossings by the vehicle, allowing specific portions of the acceleration signal to be extracted and analysed using one of the many methods proposed in the literature [7].

2.2.1 Leica GNSS smart antenna

To serve as a reference for the vehicle position recorded by the Nexus 5 during testing, a Leica Geosystems Viva GS14 GNSS smart rover antenna was used to manually log the vehicle location coordinates to a removable SD card throughout testing, incorporating Network Real-Time Kinematic (RTK) corrections [13] obtained via mobile network. The antenna was mounted magnetically on the roof of the van and operated using a Leica Geosystems CS15 controller (see Figure 3). This system can achieve horizontal and vertical accuracies of 8 mm and 15 mm respectively for static measurements, although this is dependent upon various factors such as the number of satellites tracked, constellation geometry and observation time. Accuracy was expected to vary during testing, particularly in urban or wooded areas where satellite visibility or signal strength can be restricted, and due to the movement of the vehicle.

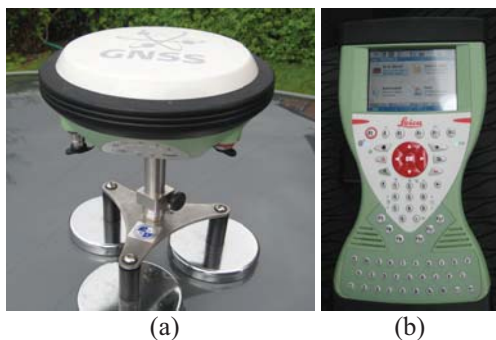


Figure 3. (a) Leica GS14 smart antenna (b) Leica CS15 controller.

2.2.2 Smartphone application

The vehicle location was also tracked during testing using a freely available Android smartphone application installed on the LG Nexus 5, namely 'GPSEssentials' by M. Schollmeyer [14]. This application utilises the smartphone's GPS transceiver (a Qualcomm WTR1605L) which also supports assisted GPS, to record the track followed by the vehicle. This particular application was selected as it provides average speed and elevation, allows the vehicle coordinates to be recorded and timestamped every second and can plot the resulting tracks in real time, or export them in .kml format for viewing on Google Earth.

2.3 Data acquisition

A National Instruments (NI) multifunction USB-6353 X-Series data acquisition (DAQ) device was used to log wired accelerometer measurements, at a sampling frequency of 1000 Hz, to a Panasonic Toughbook running NI Signal Express. Power to the DAQ device was provided by a 12V car battery placed in the rear of the vehicle, with the required output of 230Vac provided by an inverter. The total cost of this DAQ setup is approximately €7000.

2.4 Test Routes

Two test routes in the Belfast area of Northern Ireland were selected for testing, shown in Figures 9-11. Each route passes through urban and wooded areas, in addition to encompassing bridge crossings. Route 1 was 1.8 miles (2.9 km) long while

Route 2 was 12 miles (18 km) but included repeat bridge crossings over the M1 motorway. Both routes as tracked using GNSS systems are shown in Section 3.2.

3 IDENTIFICATION OF FEATURES

3.1 Acceleration Measurements

Figure 4 shows the full time history of acceleration measurements obtained from all accelerometers in the instrumented vehicle for route 1, while Figure 5 shows the corresponding spectra. It can be seen that despite the difference in sampling frequency, the smartphone acceleration time histories compare relatively well to the corresponding measurements from the wired 2g accelerometer, however, the Samsung S4 sensor (Figure 4(d)) is not as sensitive to the vibration magnitude as the Nexus 5, in many cases registering less than half the peak acceleration magnitude, which is influenced by its 100 Hz sampling frequency limitation. This is also reflected in the spectra (Figure 5). Although all sensors identify the dominant body bounce vibration mode of the vehicle at 2.3 Hz, the smartphone peak magnitude is 5 times less than that recorded by the wired sensor, indicating lower sensitivity; however, this magnitude difference is reflected across the whole spectrum.

Figure 4(a) shows the wired 5g accelerometer measurements for comparative purposes of positive accelerations; the sharp peaks at the beginning and end of the signals were used to confirm accurate synchronisation while the vehicle was motionless. During movement i.e. from 140 – 860 seconds, only four peaks exceeded +2g, marked in Figure 4 with arrows. However, the maximum peak magnitudes measured by the wired accelerometers were not obtained by the smartphones due to their range limit. The magnitudes and times for these four peak locations are given in Tables 1 and 2 respectively. From Table 1, it can be seen that in terms of smartphone measurements, the Nexus 5 accelerometer is more sensitive overall, reaching its range limit of 19.24 m/s^2 consistently for peaks exceeding 2g, suggesting that it may be a more suitable device for drive-by monitoring purposes. Also, this accelerometer has the potential to have its dynamic range increased by the user. It should be noted however that this range limit is slightly less than specified ($\pm 19.61 \text{ m/s}^2$), indicating that sensor calibration may be necessary.

From Table 2, the times corresponding to peaks in the acceleration signals with (left to right numbering) can be used to inspect video footage and timestamped vehicle location coordinates. Figure 6 shows video screenshots corresponding to each peak, highlighting that unique features are present at these locations. Peaks 1 and 2 were caused by speed ramps, while Peaks 3 and 4 were caused by manhole covers.

An example of the acceleration responses of the wired 2g uniaxial accelerometer and the Nexus 5 accelerometer for test route 2 are shown in Figure 8 for a west-east crossing of the skew-bridge (Figure 7) over the M1 motorway on Dunmurry Lane, which has a total length of approximately 38 m. This response was extracted based on the recorded position of the vehicle (Section 3.2) and inspection of video footage for test route 2. Similar responses were observed for repeated crossings. Firstly, it can be observed that the Nexus 5 accelerometer displays a noisier response, which is expected; the uniaxial accelerometer has been designed and constructed

for applications requiring low levels of output signal noise thus some higher frequency components have been removed from its response. However, both accelerometers display three periodic low frequency disturbances.

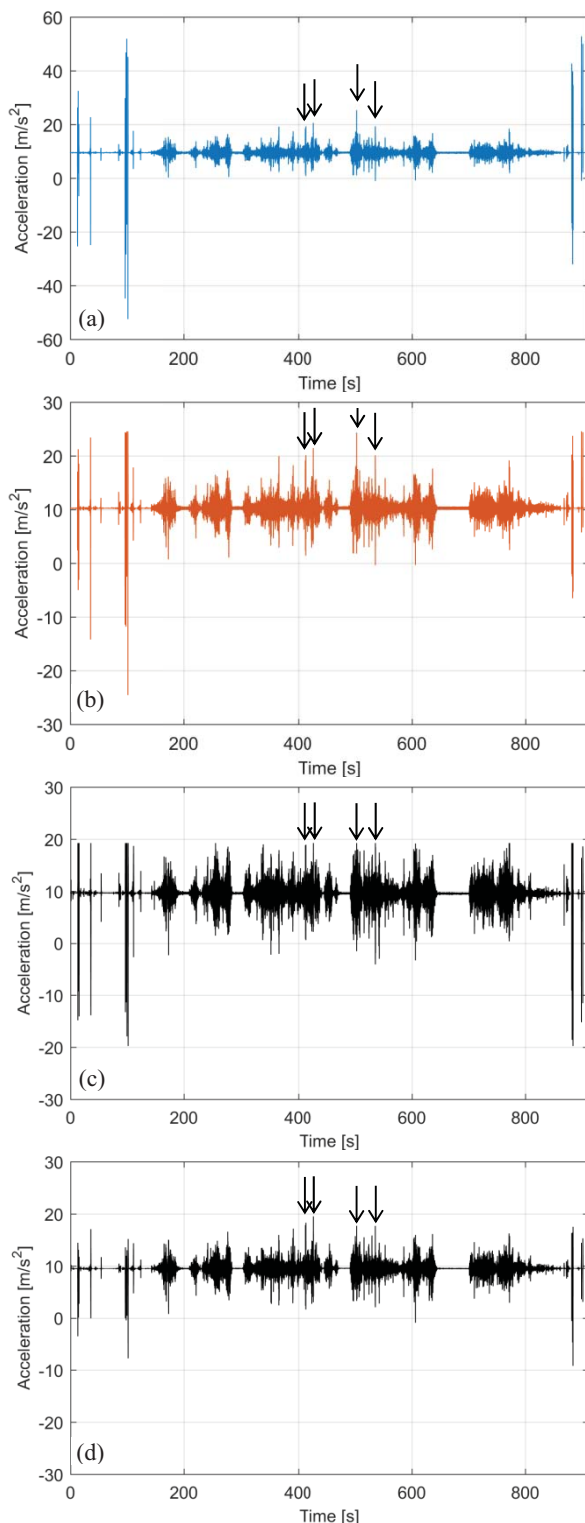


Figure 4. Acceleration measurements for test route 1 (a) 5g uniaxial (b) 2g uniaxial (c) Nexus 5 MPU-6515 (d) S4 K330.

On inspection of video footage, it can be confirmed that these correspond to the three expansion joints on the bridge, indicating that the drive-by monitoring system, at a minimum,

has potential to monitor deterioration of the expansion joint covering and/or the joint itself through analysis of the vehicle's dynamic response. Further analysis of these responses is necessary to investigate the effectiveness of other indirect drive-by monitoring methods and algorithms, including those developed by the authors.

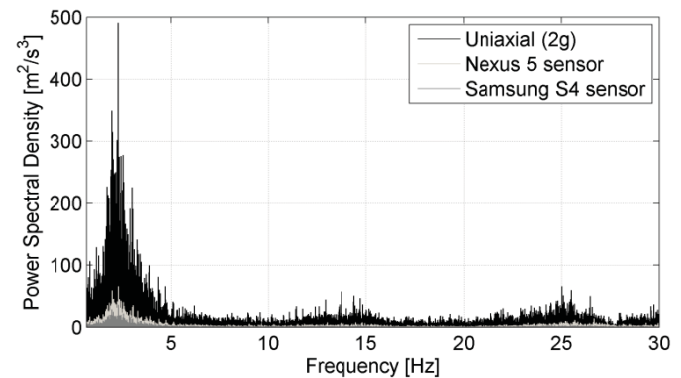


Figure 5. Acceleration spectra for test route 1.

Table 1. Magnitudes in (m/s^2) of peaks exceeding 2g on test route 1.

Accelerometer	Peak 1	Peak 2	Peak 3	Peak 4
5g uniaxial	19.31	20.6	25.31	19.3
2g uniaxial	20.13	21.42	24.31	20.09
Nexus 5 MPU-6515	18.92	19.24	19.24	19.24
S4 K330	18.27	19.5	17.69	17.67

Table 2. Times of peaks exceeding 2g on test route 1.

	Peak 1	Peak 2	Peak 3	Peak 4
Time from start [s]	413	428	504	536
Real time [hh:mm:ss]	15:56:49	15:57:04	15:58:20	15:58:52

3.2 GNSS tracking measurements

Figure 9 shows the vehicle location coordinates logged and timestamped during test route 1 by the Leica GS14 smart antenna. The four peaks identified from the acceleration time histories are indicated by white icons having a black dot, highlighting that where video or imagery are unavailable in practice, the location of specific points of interest can be identified via GNSS. These coordinates were logged manually as static points, thus accuracy varied due to the movement of the vehicle. The coordinate quality ranged from 0.01 m in relatively open areas to 8 m in wooded areas. The largest causes of error were trees or wooded areas lining the road which restricted a clear view of the sky for the antenna.

The vehicle position coordinates logged by the Leica GS14 during test route 2 are shown in Figure 10, where icons with black dots indicate two separate bridge crossings. The coordinate quality ranged 0.01 m to 5.7 m, averaging at 0.4 m. A gap in recorded coordinates can be seen at the bottom left of Figure 10; this was caused by a temporary crash of the CS15 controller operating system. This can be overcome by automatically logging raw data to the GS14's internal

memory, rather than manually as in this test. Overall, similar issues affecting accuracy were experienced as for route 1. In particular, at the M1 motorway bridge crossing (see Figure 10 inset), overhanging trees restricted recording of location at the western entrance to the bridge (Figure 7). In addition to raw data logging, this problem can be alleviated for GNSS systems by carrying out testing in winter rather than summer, when trees have shed their foliage. Other possible solutions include inertial navigation systems (INS), which incorporate accelerometers, gyroscopes, magnetometers and GNSS receivers, but an equivalent system for accurate vehicle tracking can be relatively expensive.

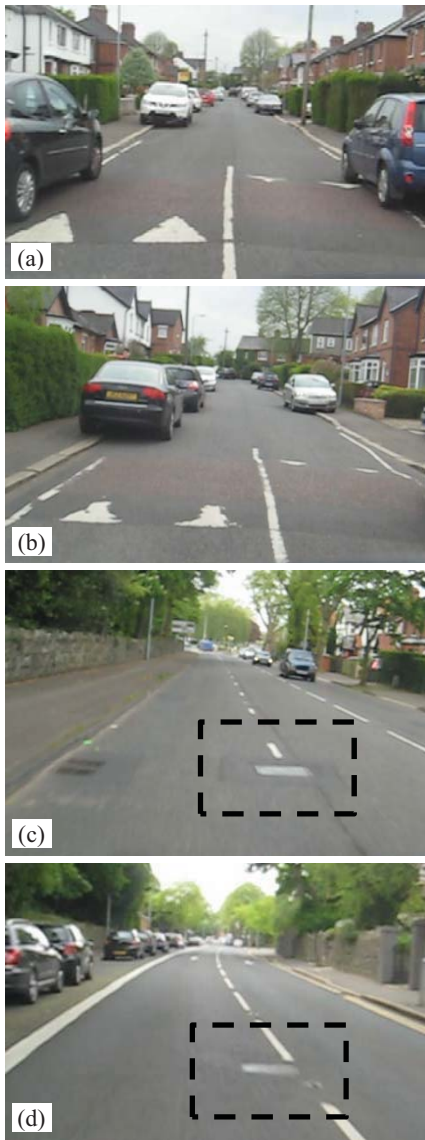


Figure 6. Video screenshots of peak locations for test route 1 (a) Peak 1 (b) Peak 2 (c) Peak 3 (d) Peak 4.

Figure 11 illustrates the vehicle position recorded by GPSEssentials during test route 2. The rapid update of position and accuracy in the region of the M1 bridge crossing is particularly of note – for this application its performance has at least equalled and possibly surpassed the Leica system. Therefore, there is a trade-off between optimum location for each application, unless an external antenna is used for the

smartphone. Despite this, overall it was observed that the smartphone accuracy was sufficient to identify when the vehicle was on the bridge. In terms of post-processing and visualising coordinates, GPSEssentials was very straightforward due to the output of a .kml format file; the Leica system required more user post-processing time to achieve the same output.



Figure 7. West entrance to bridge crossing over M1 motorway on Dunmurry Lane on test route 2.

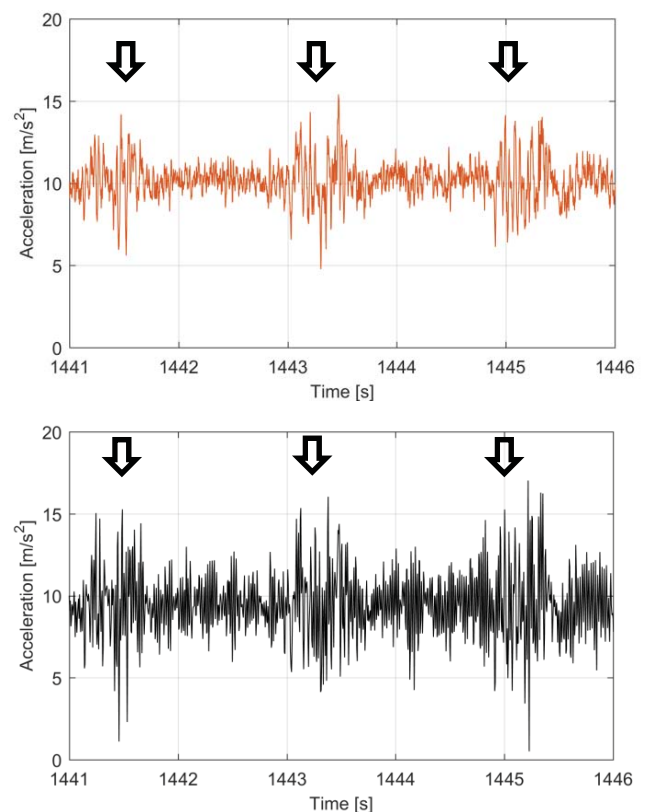


Figure 8. Acceleration measurements on bridge crossing over M1 motorway (a) 2g uniaxial (b) Nexus 5 MPU-6515.

4 CONCLUSIONS

For the drive-by monitoring system, comparing the smartphone sensors versus the wired accelerometers and Leica GS14 smart antenna in term of cost is straightforward; the wired accelerometers and DAQ system cost in the region of €8000 in total, while the Leica GS14 smart antenna system can retail from €18000 - €28000, giving an overall system cost of at least €26000. The equivalent cost of a smartphone is a factor of 100 less than this, giving a clear advantage to smartphone devices in terms of cost savings; 100 vehicles in a

fleet could easily be used as monitoring vehicles for the same instrumentation cost as one specialized instrumented vehicle.

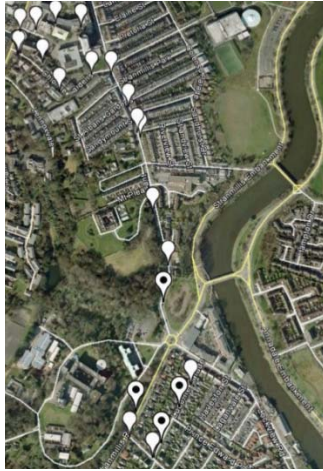


Figure 9. Vehicle position coordinates logged using Leica GS14 for test route 1.

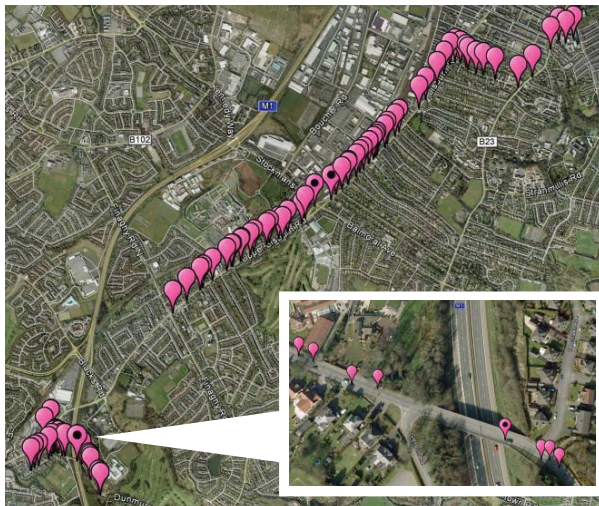


Figure 10. Vehicle position coordinates logged using Leica GS14 for test route 2.

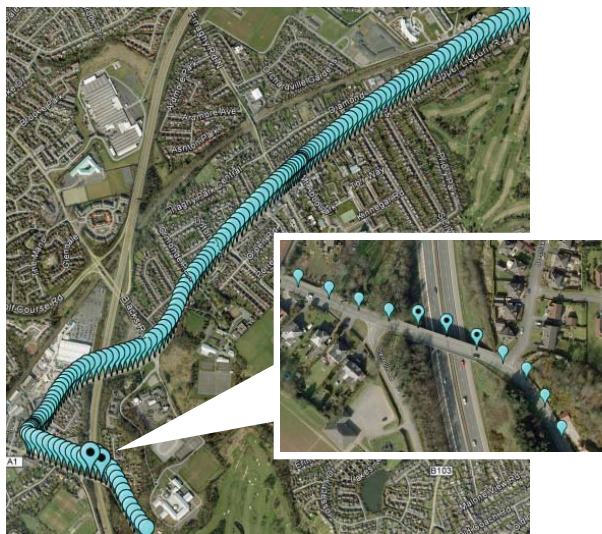


Figure 11. Vehicle position coordinates logged using GPSEssentials smartphone application for test route 2.

The smartphone applications were convenient, easy to use and involved less effort for post-processing vehicle location coordinates, reducing the need for any specialist training. Furthermore, the general level of accuracy illustrated by the smartphone acceleration measurements based on the tested sampling frequency and range indicates that it should be feasible to use these signals for drive-by monitoring approaches, although the levels of noise observed in this investigation must be considered. Further analysis of the acceleration signals and corresponding spectra magnitude is required to establish their suitability for bridge dynamic parameter and damage detection algorithms.

ACKNOWLEDGMENTS

The authors wish to express their gratitude for the technical support received by Mr. Kenny McDonald, Mr. Jamie Laing, and Mr. Conor Graham of Queen's University Belfast during the course of this investigation.

REFERENCES

- [1] Fujino, Y. and Siringoringo, D. M. (2011), 'Bridge monitoring in Japan: the needs and strategies', *Structure and Infrastructure Engineering: Maintenance, Management, Life-Cycle Design and Performance*, 7:7-8, 597-611.
- [2] Chupanit, P. and Phromsorn, C. (2012), 'The Importance of Bridge Health Monitoring', *International Science Index*, 6: 135-8.
- [3] Rytter, A. (1993), *Vibration based inspection of civil engineering structures*, Aalborg University, Denmark.
- [4] Carden, E.P. and Fanning, P. (2004), 'Vibration based condition monitoring: A review', *Structural Health Monitoring*, 3: 355-77.
- [5] Sayers, M.W. and Karamihas, S.M. (1998), *The little book of profiling*, University of Michigan Transportation Research Institute, UMTRI-96-19.
- [6] Lin, C.W. and Yang, Y.B. (2005), 'Use of a passing vehicle to scan the fundamental bridge frequencies: An experimental verification', *Engineering Structures*, 27: 1865-78.
- [7] Malekjafarian, A., McGetrick, P.J. and O'Brien, E.J. (2015), 'A review of indirect bridge monitoring using passing vehicles', *Shock and Vibration*, Volume 2015, Article ID 286139, <http://dx.doi.org/10.1155/2015/286139>.
- [8] McGetrick, P.J., Kim, C.W., González, A. and O'Brien, E.J. (2013), 'Dynamic axle force and road profile identification using a moving vehicle', *International Journal of Architecture, Engineering and Construction*, 2(1): 1-16.
- [9] Miyamoto, A. and Yabe A. (2012), 'Development of practical health monitoring system for short- and medium-span bridges based on vibration responses of city bus', *Journal of Civil Structural Health Monitoring*, 2: 47-63.
- [10] Stedman II, C. and DeMarco, A. (2007), *Automated GPS Mapping of Road Roughness*, Worcester Polytechnic Institute.
- [11] Poncela, A., de Diego, V., Lorenzana, A., and de Sebastian J. (2011), 'Automatic Portable system for fault detection in the pavement of roads using wireless sensors and GPS', *Proceedings of the 5th International Conference on Structural Health Monitoring of Intelligent Infrastructure (SHMII-5)*, 11-15 December 2011, Cancún, Mexico.
- [12] Carrera, F., Guerin, S. and Thorp, B.J. (2013), 'By The People, For The People: The Crowdsourcing Of "Streetbump", An Automatic Pothole Mapping App', *International Archives of the Photogrammetry, Remote Sensing and Spatial Information Sciences, Volume XL-4/W1, 29th Urban Data Management Symposium (UDMS 2013)*, 29 – 31 May, 2013, London, United Kingdom.
- [13] Takac, F. and Lienhart, W., (2008), 'SmartRTK: A Novel Method Of Processing Standardised RTCM Network RTK Information For High Precision Positioning', *Proceedings of ENC GNSS 2008*, 22-25 April 2008, Toulouse, France.
- [14] Schollmeyer, M. (2015), *GPS Essentials Manual*, <http://www.gpsessentials.com>.

Integrating multivariate techniques in bridge management systems for life-cycle prediction

Ciarán Hanley¹, José Matos², Denis Kelliher³, & Vikram Pakrashi¹

¹Dynamical Systems & Risk Laboratory (DSRL), School of Engineering, University College Cork, Ireland

²Department of Civil Engineering, University of Minho, Guimarães, Portugal

³Research Unit for Structures & Optimisation (RUSO), School of Engineering, University College Cork, Ireland
email: c.m.hanley@umail.ucc.ie, jmatos@civil.uminho.pt, d.kelliher@ucc.ie, v.pakrashi@ucc.ie

ABSTRACT: The use of bridge management systems (BMS) by infrastructure stakeholders has led to the collection and retention of large quantities of data concerning the condition states of bridges throughout national and regional networks. The database for the BMS is often populated by the results of routine visual inspections, based on a prescribed scale for defining the condition state of the bridge's individual elements, and of the bridge structure as a whole. The populating of the database also leads to the storage of large quantities of so-called metadata; which can describe the physical parameters of the bridge. The availability of this data allows the assessment of the BMS using multivariate techniques to enhance the life-cycle assessment of bridge networks, through advanced descriptive and predictive techniques applied to deteriorating network assets. Multivariate techniques such as principal component analysis have been demonstrated by the authors to be effectively applied as a descriptive tool to an existing BMS, and the results of a case study of a large dataset of bridges indicate its viability to be integrated into data-based approaches to infrastructural asset management.

KEY WORDS: bridge management systems; multivariate analysis; asset management; condition assessment.

1 INTRODUCTION

The preservation of a functional national and regional road infrastructure is dependent on the performance of road networks and, within them, vital network links in the form of bridge structures. Due to the societal and economic risk of their failure, it is important for infrastructural asset managers and stakeholders to implement appropriate management systems to ensure adequate mitigation of this risk under different, and often conflicting, performance criteria [1]. As such, many authorities have implemented bridge management systems (BMS) to monitor the state of their existing bridge stock [2,3], which allow for asset managers to better plan maintenance activities for their asset base using various assessment methods and criteria [4]. Often, these BMS's rely heavily on the use of visual inspections to establish condition ratings for the structures; the results of which often guide further assessment and, eventually, intervention, [5,6]. These inspections typically consist of inspecting individual components or elements of the bridges and assigning each element a condition rating based on a well-defined scale of damage present. The bridge is then assigned an overall condition rating, usually being not lower than the worst condition rating of the primary structural elements of the bridge. Thus, the overall condition rating of the bridge, often being the primary decision criteria, is significantly tied to the condition of a single element. This results in a scenario where similar bridges of vastly different states of deterioration can possess equal condition ratings. When a small number of these bridges are compared against each other, it is simple to discern which is in the worst state. However, in BMS's that contain thousands of bridges, such a comparison becomes cumbersome and infeasible.

This results in the potential to exploit modern computational methods and perform so-called 'big data analysis', which

allows the extraction of information from a large dataset for descriptive and predictive purposes, using advanced statistical techniques [7]. This paper investigates the use and applicability of multivariate analysis methods on condition rating data in BMS's, and how these techniques can be integrated in such systems so as to provide asset managers with additional and powerful computational tools for use in decision making processes for intervention activities. The multivariate analysis techniques highlighted are principal component analysis (PCA) and exploratory factor analysis (EFA); both data reduction techniques with interpretation similarities but are distinct in their assumption on the underlying structure of the data.

A dataset of 3,036 bridges was analysed and the potential for the integration of multivariate methods into existing BMS's is shown through a case-study of condition ratings for reinforced concrete and masonry bridges. The benefits of such techniques are shown to include a more accurate description of the deteriorated state of network assets and its impact into assessing the current health of a national or regional bridge stock, and improves an organisation's attempts to combat the so-called "asset time bomb" [8].

2 MULTIVARIATE ANALYSIS OF BMS

2.1 Description of BMS Dataset

A Portuguese BMS, managed by *Infraestruturas de Portugal*, containing 3,036 bridges was investigated for this analysis; where primary data, in the form of element and overall condition ratings, and meta-data was available for each bridge. This meta-data was in the form of crossing type, span information, structural form, and construction material. For the primary data, condition ratings were obtained through visual inspection of a number of prescribed elements present

on each bridge and evaluating their current condition. The condition of each element is graded on a scale of 0-5, where a condition rating of 0 indicates no damage, and a condition rating of 5 indicates total or ultimate damage (Table 1).

Table 1. Description of condition ratings in BMS

Condition Rating	Description
0	No damage
1	Minor damage
2	Some damage
3	Significant damage
4	Critical damage
5	Ultimate damage

The elements to be inspected on each bridge included structural elements such as the deck, abutments, piers, retaining/wing walls, and non-structural elements such as parapets, traffic barriers, bridge surface, waterproofing, etc. The various states of damage for each of these elements are usually well defined and so elemental condition ratings are typically reliable.

2.2 Assessment Methods

In order to appropriately assess and process the received data, a number of multivariate data techniques were investigated; namely principal component analysis (PCA) and exploratory factor analysis (EFA). In PCA, the primary purpose of the method is to reduce the dimensionality of a set of data, and redefine the input variables as principal components; being a linear combination of the original variables, but having a magnitude less than the original dataset while preserving most of the information [9].

Factor analysis is a technique similar to PCA in that its goal is to describe variability in a dataset of observed variables with a lower number of unobserved variables, or factors [10]. It varies from PCA in regard to the fact that it assumes correlation in the observed variables [11,12]. In the realm of factor analysis, EFA is a procedure to explore the underlying factor structure in a set of variables. A large difference in PCA and EFA is that principal components account for maximal amount of variance, whereas factors account for common variance.

Each of these methods demonstrates significant applicability for BMS's, and their use can be subject to how appropriate each is for specific analysis goals. For BMS's, there has been success in applying PCA with an attempt to identifying bridges based on common states of disrepair within the Irish bridge network [13]. As PCA does not assume an underlying data construct or causal relationship within the data, it was chosen as the more appropriate method for the assessment of this dataset. By conducting a PCA, it is possible to reduce the dimensionality of a large dataset and to redefine the input variables as principal components (PC), being a linear combination of the original variables, but having a magnitude less than the original dataset, while retaining most of the variance [14]. This is accomplished by highlighting the variables that demonstrate the most variance in the data set. The first principal component Y_1 is defined as:

$$Y_1 = \mathbf{a}'_1 \mathbf{x} = \alpha_{11}x_1 + \alpha_{12}x_2 + \dots + \alpha_{1p}x_p = \sum_{j=1}^p \alpha_{1j}x_j \quad (1)$$

Where $\mathbf{a}'_1 \mathbf{x}$ is a linear function of the elements \mathbf{x} having maximum variance, and \mathbf{a} is a vector of p coefficients α . The first principal component is the direction along which the data set shows the largest variation [15], and the second component is determined under the constraint of being orthogonal to the first component and to have the largest variance [16]. The second principal component $Y_2 = \mathbf{a}'_2 \mathbf{x}$ is found in a similar manner to the first principal component, and so on for the subsequent principal components, up to p PCs.

The sum of the square of the PC coefficients α_i is equal to unity, and thus the influence of any coefficient on the analysis is apparent in comparison to each other.

$$\sum_{i=1}^p \alpha_i^2 = \mathbf{a}' \mathbf{a} = 1 \quad (2)$$

3 RESULTS

The PCA was conducted on the two most common bridge types in the BMS dataset; 1667 reinforced concrete bridges and 713 masonry arch bridges. Within these data-subsets, the problem of 'missing data' needed to be accounted for. In multivariate analysis, it is often possible to use the existing structure of the data to estimate the missing data and complete a dataset. However, in the case of BMS's, an absent condition rating for a specified element is typically due to this element not being present on the bridge, and therefore it is neither appropriate or accurate to use algorithms to complete the dataset. This issue arises due to the necessity of creating a generic BMS that can be applicable to all bridge types.

In order to account for this, the PCA was conducted on the specified bridges, but was limited only to the primary elements that are to be expected on these bridges. The primary elements can be said to be structural and non-structural. Structural elements are typically the deck, abutments, walls, and piers. Primary non-structural elements are usually parapets/guardrails, embankments, surfaces, and bearings. As these bridges were single-span bridges, there was no necessity for the elements piers. Additionally, there was little information available on the condition of the bearings, and so the analysis was conducted for: abutments, parapets, walls, surface, deck, and embankments. For a comparison between reinforced concrete and masonry arch bridges, the element 'parapets' have been replaced by the more generic term of 'barriers', to account for guardrails and vehicular barriers. The exclusion of the other elements does not compromise the PCA, unlike EFA, as a PCA does not look for hidden correlation in the variables, but for highest variation in the presented variables.

3.1 Number of Principal Components

The number of important components can be visualised with a scree plot of the eigenvalues [17]. This can be a useful tool for determining what PC's are important and what PC's can be discarded from the data set. As the slope of the scree plot begins to flatten, the components become less important as

they have retained less variance than the previous components. From Figure 1 and Figure 2, it can be seen that the PC at which the plot begins to flatten out, or the elbow, occurs for both bridge types at the third PC, Y_3 . The first three PC's for the reinforced concrete and masonry arch bridges account for 74% and 71% of the variation in the data, respectively. Including the fourth PC results in retaining 84% and 82% of the variation, but is typically discounted based on the established scree plot criteria.

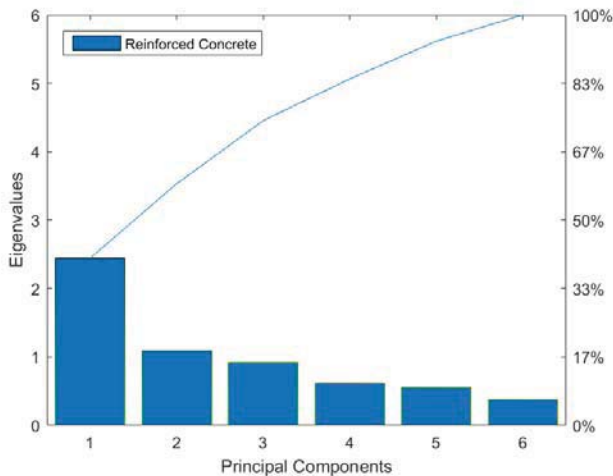


Figure 1. Scree plot of principal components for reinforced concrete bridges.

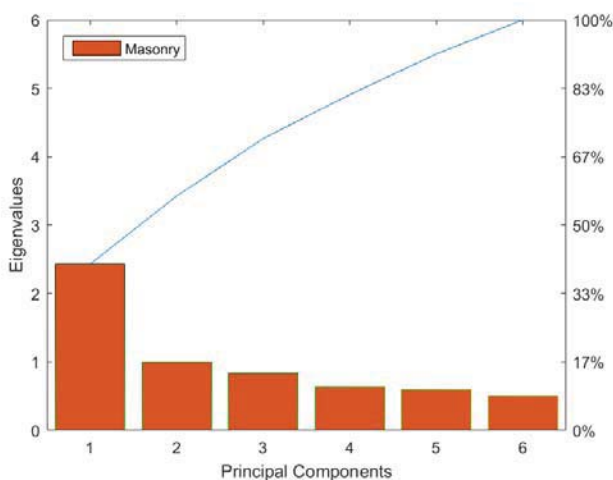


Figure 2. Scree plot of principal components for masonry arch bridges.

From these scree plots, it is clearly evident that the first PC Y_1 retains the most significant amount of variation; accounting for 41% of the variation in both bridge types, and is thus the primary PC.

3.2 Principal Component Coefficients

The PC coefficients α_j indicate the relationship between the bridge elements and Y_j . In the case of this BMS, where low condition ratings correspond to low damage and high condition ratings correspond to advanced damage, positive values of α_j indicates deterioration, and bridges that score highly in Y_j will be seen to have advanced deterioration in these elements. Conversely, α_j with negative values that score

highly will indicate elements that are in good condition. This relationship is also seen where low negative scores indicate the opposite to what high positive scores indicate. For Y_1 , it can be seen that each element has a positive value for α_1 , and it can also be seen that there is some correlation between the two datasets (Figure 3).

As each α_1 is positive, it can be said that Y_1 describes the general state of deterioration of a bridge in the datasets, where a high positive score indicates advanced damage for all the elements in the bridge, and a low negative score indicates bridges where these elements are in favourable conditions. In fact, as the largest coefficients are for the primary structural elements, Y_1 can further be described as a measure of the structural condition of the bridge.

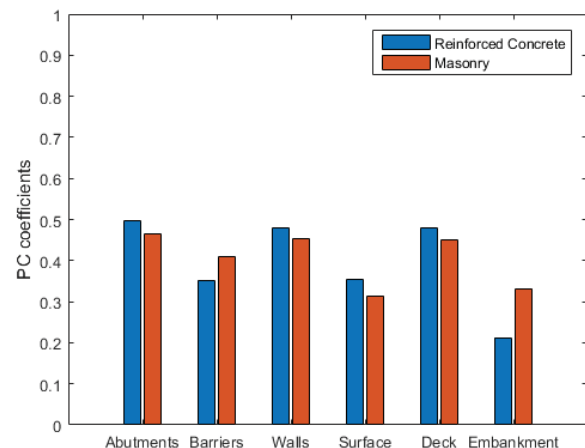


Figure 3. PC coefficients for the first PC, Y_1 .

Notably, it can also be seen that there is some correlation between the two datasets, despite bridges having different structural forms and being constructed with different materials. It can be seen that the greatest deviation occurs for the embankment, where α_1 for this element is less influential in the reinforced concrete bridges than in the masonry arch bridges. This demonstrates, in a way to be expected, that while many elements will behave in a similar way regardless of the bridge type, there remains a number of elements that are specific to certain bridge types, and exercise their own degree of influence on the PCA accordingly. This suggests that the PCA method needs to be applied in a more targeted fashion, and cannot be inappropriately applied to an entire dataset of a BMS, if the population of bridges is non-uniform. This provides opportunities to cluster or bunch the data based on associated meta-data, and establish defined signatures for various bridge types.

Unlike Y_1 , it can be seen that Y_2 describes a situation where there is a discrepancy between the condition ratings of the parapets, surface, and embankment, and the ratings for abutments, walls, and deck, or, simply, Y_2 can be said to describe bridges where there is a disparity between the condition ratings of the structural and non-structural elements (Figure 4). This would suggest that there are a greater proportion of bridges in both datasets that have structural elements in good conditions where non-structural elements had exhibited damage. This is often typical of asset-management strategies for bridges where the structural

elements are subject to a greater repair priority than the non-structural elements.

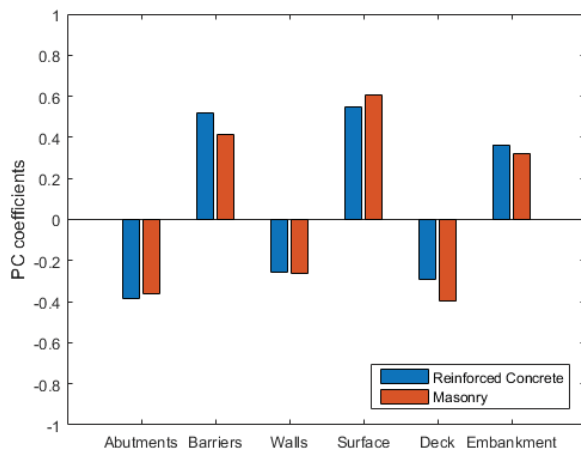


Figure 4. PC coefficients for the first PC, Y_2 .

The third PC Y_3 mostly describes bridges that have a discrepancy between the condition ratings of the embankments and surface of the bridge (Figure 5). The small PC coefficients α_3 for abutments, walls, and deck show that these elements aren't very influential in this PC, and thus it can be said that this PC primarily is a measure of the condition of the embankment and its relationship to the condition of the surface. Here, however, we see some deviation based on bridge types, where for masonry arch bridges the surface is the second most influential element, whereas for reinforced concrete bridges this influence is attributed to the barriers and thirdly the surface. This can be explained by how reinforced concrete bridges are likely to be more modern than masonry arch bridges, and are thus more likely to have traffic barriers installed, in addition to the parapets. The structural elements of abutments, walls, and deck account for little influence in this PC.

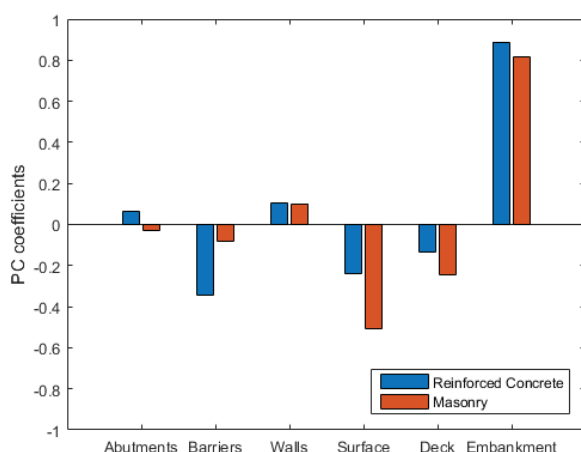


Figure 5. PC coefficients for the first PC, Y_3 .

3.3 Principal Component Scores

The principal component analysis creates new variables (ratings) for each of the observations (bridges) called *factor scores*, or *PC scores* [16]. These scores define the extent that

each bridge's condition ratings correlate to the PC's. It has been shown that Y_1 is a measure of the overall condition of the bridges, being the deteriorated state of each element. Thus, bridges that have high positive scores for Y_1 are expected to have damage present in each element, and bridges with low scores should generally be in a favourable state. This was confirmed by investigating the original datasets, which showed that the bridges with the lowest scores had condition ratings of 0 for each element, and the bridges with the highest score had condition ratings typically showed damage present in each element, with advanced condition ratings for each element typically between 3 and 5.

Now, as Y_1 shows the overall damage of the bridge, by way of the amount of damage in each element, these scores can be compared to the overall condition rating for each dataset. However, it can be seen that there does not exist a high correlation between these overall condition ratings and the PC scores. This can be seen for the reinforced concrete bridges in the dataset (Figure 6) and the masonry arch bridges in the dataset (Figure 7). For both these datasets, the coefficient of determination (R-squared) is approximately 0.6.

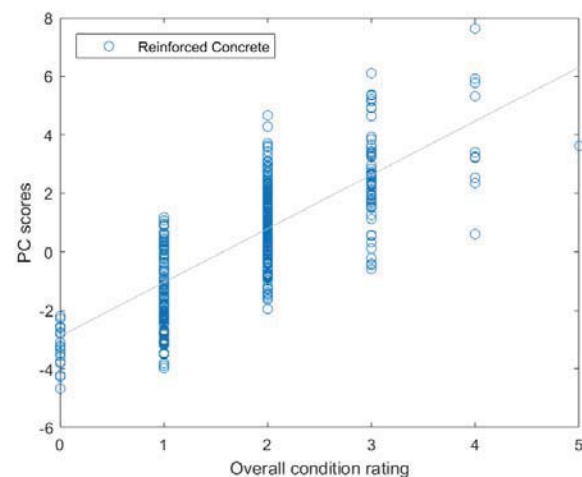


Figure 6. Correlation between PC scores for Y_1 and the overall condition rating (reinforced concrete).

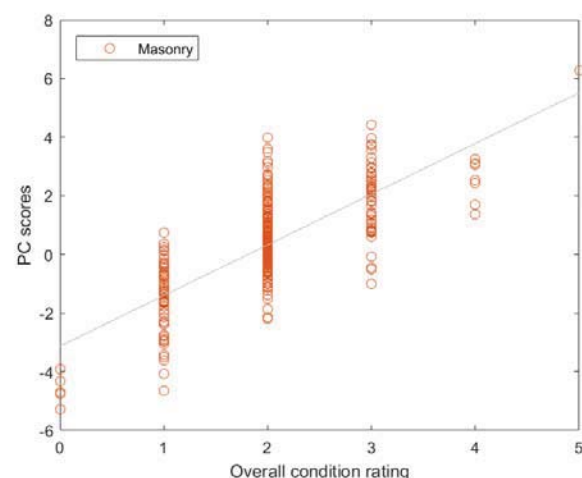


Figure 7. Correlation between PC scores for Y_1 and the overall condition rating (masonry arch).

From these figures, it is obvious that there is a significant discrepancy between this overall condition rating and Y_1 , which appears to represent the overall state of the structure. There exists an overlap of condition ratings for the same scores, with some bridges on the same score having condition ratings of 1, 2, and 3, for example, when there elements are largely in the same condition.

4 INTEGRATION TO EXISTING BMS

From Section 3.3, it is clear that there is scope for an improved form of the overall condition rating, in the guise of a linear combination of the condition ratings of the bridge's individual elements. However, as some elements are more important to the structural condition, an equal weighting should not be applied to each rating. In regard to equation 2, it is seen that the sum of the square of the PC coefficients α_i equal unity, and thus α_i^2 for each variable quantify it's relative influence and importance in the PC score. As the score for Y_1 has been shown to be a good descriptor of the overall condition of the bridge, the weighting factors can be derived from the squared coefficients α_i^2 as a first step. In this regard, the revised weighted condition rating ζ of the overall structure can be defined as:

$$\zeta = \sum_{j=1}^p \lambda_j x_j, \quad \lambda_j = \alpha_{1,j}^2 \quad (3)$$

Where ζ is a linear combination of the new weighting factors λ_j and the original condition ratings x_j for the individual elements. The new weighting factors λ_j for each element for both bridge types can be seen in Table 2.

Table 2. Weighting factors, λ

Element	Reinforced concrete	Masonry
Abutments	0.2466	0.2166
Barriers	0.1238	0.1669
Walls	0.2290	0.2043
Surface	0.1255	0.0989
Deck	0.2300	0.2033
Embankment	0.0451	0.1099
Σ	1.0000	1.0000

From this, it is clear that ζ is weighted further towards the structural elements than the non-structural elements, and would align with typical positions adopted by asset managers.

The approach of using weighting factors to determine a more realistic interpretation of the overall state of the bridge stock allows for a simple integration into an existing BMS, and does not require formalising a multivariate procedure into an existing framework. This is demonstrated for the presented datasets, whereby equation 3 was applied to the original condition rating data and compared the PC scores for Y_1 . It can be seen for the reinforced concrete (Figure 8) and masonry arch (Figure 9) bridges that there is high correlation between the PC scores and the revised weighted condition rating ζ . Additionally, ζ is presented in the same condition rating range as the original dataset, which allows for the simple comparison between ζ and the existing overall condition rating. While the current overall condition rating is

useful in determining the need for intervention, as an overall rating above a defined threshold triggers action, its use in describing the state of the complete asset base can result in a significantly misleading assessment. Additionally, the proposed weighted condition rating can be used in conjunction with the existing overall condition rating, whereby when presented with a high number of bridges which call for immediate intervention, ζ can be used to prioritise which bridges are most in danger structurally. This provides an extra decision tool that can be used, in addition to such aspects as the bridges importance to the road network, as well as cost of intervention activity.

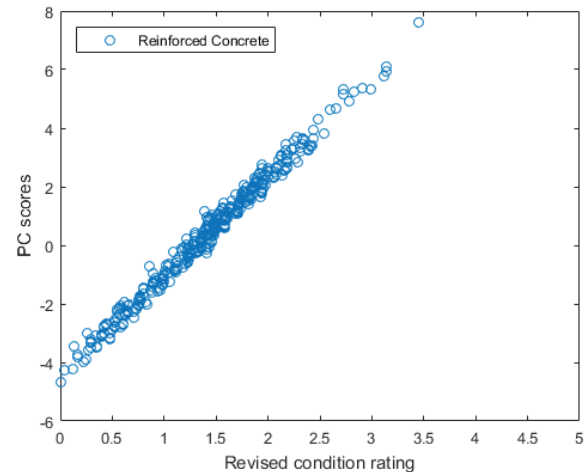


Figure 8. Revised weighted condition rating against Y_1 for reinforced concrete bridges.

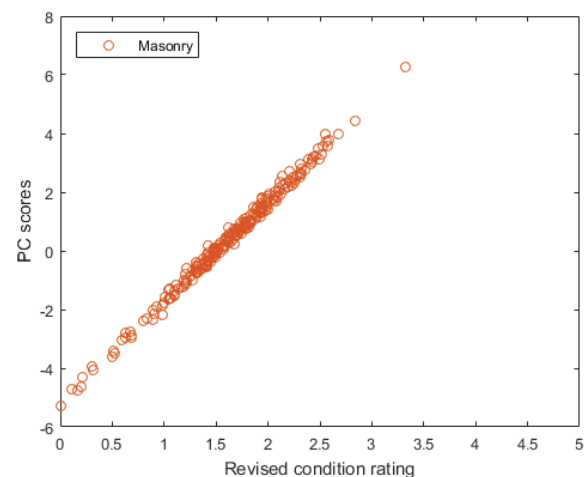


Figure 9. Revised weighted condition rating against Y_1 for masonry arch bridges.

5 CONCLUSIONS

The use of multivariate techniques for the purposes of improving the utility of BMS's was investigated, with a view to improving the descriptive nature of these systems. A PCA was conducted on a dataset of 3,036 bridges, with a focus on reinforced concrete and masonry arch bridges. It was seen that there was a good degree of correlation between the two bridge types for different elements, with only few variances, suggesting a commonality in behaviour of individual

elements, independent of the physical nature of the bridges. However, these variances are enough to caution against using a method such as PCA on an entire asset-base, and is much better utilised when the analysis is conducted in a targeted fashion.

It was observed that the first PC Y_1 provided an indicator of the overall condition of the bridge based on the conditions of the individual elements, and it was notable that when plotted against the overall condition ratings of the bridges, there was little correlation observed with the recorded values in the dataset. It was seen that there were bridges that had similar PC scores, indicating a similar condition rating breakdown in the elements, having vastly different overall condition ratings. Examples include some bridges with the same PC score having overall ratings of between 1 and 4. Similarly, there was significant variance within each condition rating, with some bridges having the same condition rating having very high and low PC scores. Referring back to the original dataset and ranking the bridges according to their scores for Y_1 , it was seen that bridges with the lowest scores had elements with condition ratings of 0, while the bridges with the highest score showed advanced damage in each element.

Further to this, it has been seen that there is a need to incorporate the overall state of the structure in complimentary way to existing overall condition ratings. From this analysis, it was seen that the PC coefficients represented a good starting point where to establish weighting factors λ_j to existing condition ratings, to create a revised weighted condition rating ζ . As a first point, these weighting factors can be presented to asset-managers for their input, and determine if these factors can be refined based off the experience of asset-managers and their decision making tools. In order to present these first point weighting factors, it will be necessary to investigate further bridge types, in order to see if generic weighting factors are applicable, or if it is necessary to have bespoke factors based on the structural form and location of the bridge. Gaining access to more datasets of national bridge stock is a priority in this regard. The implementation of these weighting factors into an existing BMS will be explored, as will guidance on how asset-managers can fully utilise and integrate these new tools into their decision making procedures.

ACKNOWLEDGEMENTS

The authors would like to gratefully acknowledge to support of TU1406 – *Quality specifications for roadway bridges, standardization at a European level* (BridgeSpec), a COST Action supported by EU Framework Programme Horizon 2020, as well as the financial support of the Irish Research Council *Government of Ireland Postgraduate Scholarship Scheme*.

REFERENCES

- [1] Mueller J, Stewart MG. The Price is Not Right. *Playboy* 2011;58:149–50.
- [2] Hearn G. Condition Data and Bridge Management Systems. *Struct Eng Int* 1998;8:221–5.
- [3] Lauridsen J, Bjerrum J, Andersen NH, Lassen B. Creating a Bridge Management System. *Struct Eng Int* 1998;8:216–20.
- [4] Matos JC, Casas JR, Figueiras JA. A new methodology for damage assessment of bridges through instrumentation: application to the Sorraia River Bridge. *Struct Infrastruct Eng* 2005;1:239–52.
- [5] Das PC. New Developments in Bridge Management Methodology. *Struct Eng Int J Int Assoc Bridge Struct Eng* 1998;8:299–302.
- [6] Estes AC, Frangopol DM. Updating Bridge Reliability Based on Bridge Management Systems Visual Inspection Results. *J Bridge Eng* 2003;8:374–82.
- [7] Manyika J, Chui M, Brown B, Bughin J, Dobbs R, Roxburgh C, et al. Big data: The next frontier for innovation, competition, and productivity. 2011.
- [8] Thurlby R. Managing the asset time bomb: a system dynamics approach. *Proc Inst Civ Eng - Forensic Eng* 2013;166:134–42.
- [9] Jolliffe IT. *Principal Component Analysis*. 2nd ed. Springer; 2002.
- [10] Child D. *The Essentials of Factor Analysis*. 3rd ed. Continuum International; 2006.
- [11] Suhr DD. Principal component analysis vs. exploratory factor analysis. In: Nelson GS, editor. *SUGI 30 Proc.*, Philadelphia, PA: 2005, p. 1–11.
- [12] Suhr DD. Exploratory or confirmatory factor analysis? In: LeBouton KJ, editor. *SUGI 31 Proc.*, San Francisco, CA: 2006, p. 1–17.
- [13] Hanley C, Kelliher D, Pakrashi V. Principal Component Analysis for Condition Monitoring of a Network of Bridge Structures. *J Phys Conf Ser* 2015;628:012060.
- [14] Jackson JE. *A User's Guide to Principal Components*. Wiley; 2003.
- [15] Ringnér M. What is principal component analysis? *Nat Biotechnol* 2008;26:303–4.
- [16] Abdi H, Williams LJ. *Principal component analysis*. Wiley Interdiscip Rev Comput Stat 2010;2:433–59.
- [17] Cattell RB. The Scree Test For The Number Of Factors. *Multivariate Behav Res* 1966;1:245–76.

Abercorn Bridge – An Innovative Approach to Bridge Remediation

Connor O'Higgins¹, Brian McFarland¹, Paul Callender¹, Prof. Su Taylor², Darren Gilmore¹

¹ McFarland Associates Ltd, Unit A3, Harbour Court, 5 Heron Road, Belfast, BT3 9HB, Northern Ireland

² School of Planning, Architecture and Civil Engineering, Queen's University, Belfast BT9 5AG, Northern Ireland

email: connor.ohiggins@mcfassoc.com; brian.mcfarland@mcfassoc.com; paul@callenderconsulting.com; s.e.taylor@qub.ac.uk; darren.gilmore@mcfassoc.com

ABSTRACT: Abercorn Bridge was built in 1932. It is located in Newtownstewart, Northern Ireland and is a 'Hennebique Ferro' integral reinforced concrete 4 span viaduct. The structure, being of the order of 84 years old, was showing signs of significant deterioration, so much so that one span was recommended for demolition due to its particularly poor condition. However, an alternative solution was proposed which offered to: retain all four spans; retain the overall aesthetics of the bridge; restore additional load capacity; preserve the bridge for at least a further 25 years; and reduce refurbishment costs. The alternative solution was adopted. Detailed inspection and testing of the bridge provided an accurate view of the bridge's condition thus allowing a concrete repair scheme, incorporating cathodic protection, to be designed. A finite element analysis (FEA) model was created to allow the bridge to be more rigorously analysed, particularly comparing its as-built, deteriorated state and refurbished conditions. Importantly, the FEA model indicated that the repair scheme on its own was not sufficient to restore the required load capacity and an innovative, lightweight, structural over-slab was incorporated. This "bespoke" over-slab was among the first such projects to use a combination of basalt reinforcement and lightweight aggregate concrete to create a strong yet lightweight slab. To increase the confidence of the alternative, innovative solution, Fibre Bragg Grating (FBG) sensors were used to: monitor the bridge during repairs; ensure the structural behaviour was consistent with the FEA model; and confirm that the over-slab was working integrally with the bridge deck beneath. A final load test was undertaken on completion of the Works to ensure that the required load capacity had been achieved. This paper describes in more detail the remediation process.

KEY WORDS: Abercorn Bridge; Bridge Remediation; Concrete Repair; Cathodic Protection; Finite Element Analysis (FEA); Basalt Reinforcement; and Lightweight Aggregate Concrete.

1 INTRODUCTION

Abercorn Bridge (Figure 1) was built in 1932 and is located in Newtownstewart, Northern Ireland. The bridge, being of the order of 84 years old, was showing signs of significant deterioration and had a weight restriction of 3 tonne Gross Vehicle Weight (GVW). Due to the extent of the deterioration, the scope of works within the tender for repair included for the demolition and reconstruction of span 4 as well as concrete repairs to the remaining 3 spans. An alternative proposal was submitted by McFarland Associates Ltd, in conjunction with Graham Structural Solutions, using novel technologies and materials, in which span 4 was retained while still meeting all the required targets with regards to strength and life span. This paper gives an overview of the restoration project with a focus on the innovative approaches which have differentiated it from most other bridge remediation projects.

2 DESCRIPTION OF STRUCTURE

The structure is a 'Hennebique Ferro' integral reinforced concrete 4 span viaduct. The Hennebique system was among the first methods used to construct reinforced concrete structures in the UK [1]. The bridge spans the river Strule with a 30° skew. Spans 1 to 3 are positioned over the river and are supported on reinforced concrete piers which are in turn supported on a series of piles. Span 4 is located over the

south west river bank and is supported by reinforced concrete piers and three lines of reinforced concrete columns supporting the



Figure 1. Abercorn Bridge.

three transverse deck beams. Spans 3 and 4 are effectively independent of each other with a buried expansion joint running the full width of the bridge structure and through the adjoining piers.

The bridge is constructed from seven key elements:

- A 178mm thick reinforced concrete deck slab;
- Longitudinal reinforced concrete beams;
- Transverse reinforced concrete beams;
- Reinforced concrete parapet edge beams;
- Large reinforced concrete piers;
- Reinforced concrete columns; and
- Integral reinforced concrete abutments.

An inspection of the bridge, undertaken in November 2006, identified shear cracking of the span 4 southern edge beam. This prompted a structural check to be carried out on the bridge structure, the findings of which indicated insufficient shear capacity with the cracked edge beam element. As a result a single lane restriction and 3 tonne GVW limit was imposed upon the structure.

3 INSPECTION AND TESTING

Various phases of inspection and testing works had been carried out over the years and the following extracts from inspection reports [2] indicate the condition of the key elements of the bridge:

3.1 Deck Slab

The majority of the deck slab soffit was in poor condition. This was evident in the extensive amount of spalling that revealed heavily corroded reinforcement. The main sources for this deterioration was the extensive areas of low concrete cover to reinforcement coupled with the ingress of chloride (de-icing) laden water from the road above. Electrode potentials were generally highly negative suggesting corrosion cells were initiated, particularly in the southern third of the 3-span bridge.

3.2 Pier Beams

The condition of the pier beams varied across the structure. One of the pier beams was in a very poor condition, largely due to a defective movement joint over. This pier beam had a crack running through its center measuring 15 mm at soffit level which penetrated the full depth of the beam. Other pier beams in the structure were in a more reasonable condition with only localised defects, most notably at the southern ends, where corrosion cells appeared to have been initiated.

3.3 Transverse Beams

Concrete had spalled on a number of the transverse beams and overall, their condition ranged from reasonable to poor. Corrosion cells appeared to have initiated in some of the beams but these were contained to localised areas.

3.4 Secondary Longitudinal Beams

The condition of the secondary longitudinal beams varied throughout the structure from reasonable to poor. A number of corrosion cells appeared to be active, the majority of which were concentrated on beams at the southern half of the structure.

3.5 Half-Cell Potential Survey

To give a more complete view of the condition of the bridge, prior to any repair works being undertaken, a half-cell potential survey was undertaken on any elements not previously tested. The half-cell technique measures the potential of steel reinforcing bars in the concrete in comparison with the known electrode potential of a reference electrode (half-cell). This potential of steel in concrete is an indicator of corrosion activity. When presented in the form of equi-potential contour plots, the half-cell potential survey proved a great tool for indicating where active corrosion was taking place and was thus the basis for the cathodic protection design.

4 FINITE ELEMENT ANALYSIS

For the purpose of aiding design and for validation of design concepts, a finite element analysis (FEA) model of Abercorn Bridge was produced.

The analysis software “LUSAS” version 14.7 was used to create the FEA model. The bridge model was created using “Thick Beam” and “Thick Shell” elements for the concrete beams and slab respectively. Figure 2 shows a section of the FEA model.

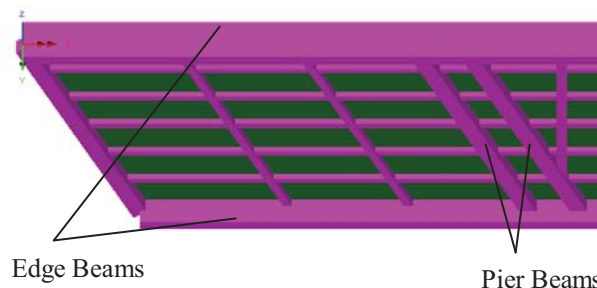


Figure 2. Geometry of Bridge (Span 4).

The FEA was undertaken using the original “as built” drawings for geometry and steel reinforcing arrays. Geometry was then confirmed during a series of site visits. Material properties were determined from various concrete cores and steel samples obtained from the bridge and tested in UKAS accredited laboratories. Areas of greatest interest were given a finer mesh, allowing for more comprehensive results to be obtained in these areas whilst minimising the amount of computation time required to analyse the FEA model. Analysis of the FEA model was undertaken using the single axle and single wheel load cases outlined within tables 5.3.1 and 5.3.2 of BD21/01 [3].

Initially, the FEA was used to check the capacity of the bridge in its deteriorated state. From this assessment, it was determined that span 4, even if fully repaired, would be unable to take the increased load specified, namely 10 tonne GVW. The FEA was then used to verify various design concepts for strengthening of the bridge.

To ensure that the FEA was accurately modelling the behaviour of the bridge, a “calibration” load test was carried out. For this load test, the bridge was subjected to a known load which was also modelled through FEA. The actual stresses measured could then be compared with the theoretical computations. Figure 3 shows the stress distribution in the concrete slab as a result of the load imparted onto the bridge.

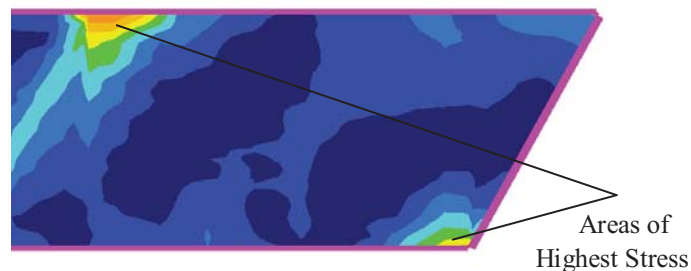


Figure 3. Stress Distribution in Concrete Slab.

The validated FEA model was then used for the design of various elements throughout the project, notably, the effects

of a substantial access scaffold being “hung” from the bridge. It was also possible to model various scenarios at any stage of the project timeline to determine the impact not only to the bridge as a whole but to individual structural elements also. For example, during the resurfacing of the bridge, the strains caused by the required plant were determined and confirmed to be within acceptable limits before the work could commence.

The FEA allowed efficient and confident decisions to be made throughout all stages of the project and was a vital tool in the success of the refurbishment.

5 DESIGN

The follow section outlines the significant design aspects of the Abercorn Bridge project.

5.1 Structural slab

To allow span 4 to be repaired, rather than demolished, a strengthening scheme was required to facilitate the extra loading required on the bridge. Using a combination of the FEA and traditional structural assessment methods, it was determined that a traditional over slab method would increase the self-weight to a point where the over-slab would be more of a detriment than a benefit. To counteract this, the structural slab was designed, in accordance with Eurocodes, to increase the load carrying capacity while minimising the increase in dead load of the bridge.

With this in mind, two lightweight materials were chosen for the structural slab: lightweight aggregate concrete; and basalt fibre reinforced polymer (BFRP).

Lightweight aggregate concrete has a number of advantages over traditional concrete, the most important being the reduced self-weight. The placed density of traditional concrete can vary from 2800 to 3100 kg/m³ and has an average dry density of 2400 kg/m³. Lightweight aggregate concrete, however, has a typical placed density of 2200 to 2400 kg/m³ and a dry density of 1800 kg/m³. Therefore, the use of lightweight concrete represents a reduction in self-weight of 33% placed and 25% cured compared to traditional concrete. Other benefits include a higher cement content than traditional concrete and a lower water cement ratio making it less permeable. The higher water absorption of the aggregate also ensures a better hydration of the cement. With this in mind, it is worth noting that the aggregate must be pre-soaked prior to mixing. Lightweight aggregate concrete also has a 33% reduction in thermal expansion coefficient, compared with traditional concrete, thus reducing the potential for cracks.

Basalt fibre is a high performance non-metallic fibre made from basalt rock melted at high temperature. The manufacture of basalt fibre requires the melting of the quarried basalt rock at about 1,400 °C. The molten rock is then extruded through small nozzles to produce continuous filaments of basalt fibre. The basalt fibre is then woven into a mat or pultruded with epoxy resin into reinforcement bars.

BFRP's main properties that make it a suitable replacement for steel reinforcing are its: high strength; low weight; high resistance to corrosion; and high tensile modulus. BFRP has 2.2 times higher tensile strength than steel, of the same diameter. This in combination with the fact that Basalt is 3.7

times lighter than steel makes it ideal when trying to reduce the dead load in a design. [4] As stated previously, basalt has a high resistance to corrosion as it does not rust or absorb water. This allows for a significant reduction in concrete cover thus allowing for thinner, lighter sections and more flexibility in design.

Commercially, lightweight aggregate concrete costs versus traditional concrete are generally comparable. BFRP reinforcement has higher initial costs versus steel, however, savings will be realised early on in the project due to the reduction in haulage costs, reduction in craneage/hoist costs and increased efficiency on site. Further savings are also realised during the lifetime of the structure through reduced maintenance costs and the removal of the risk of corrosion or degradation through chloride ingress or other contaminants.

One additional measure in the construction of the over slab was the placement of T12 shear pins at 2m centres along the longitudinal beams. This ensured that the existing deck and over-slab performed integrally. Prior to the installation of the overslab and the shear pins, the deck was milled to create a roughened surface. This imparted a degree of cohesion between the existing deck and the new over-slab. However, the design intent accounted for the shear pins as the sole mechanism for longitudinal shear resistance.

Once installed, the lightweight structural slab provided greater load dispersion than the original asphalt on its own and enabled the load carrying capacity of the bridge to be increased from 3 tonne GVW to 18 tonne GVW, a value that was significantly above what was thought possible (10 tonne GVW). Furthermore, the lightweight slab also increased the effective depth to tension steel thus increasing the deck flexural resistance.

The design of the integral over slab was undertaken using both “traditional” calculations and FEA modelling. Figure 4 shows the placement of the BFRP mesh prior to the pouring of the lightweight aggregate concrete.



Figure 4. placement of the BFRP mesh prior to the pouring of the lightweight aggregate concrete

5.2 Repair works

Concrete repairs were undertaken to all cracked, delaminated and spalled concrete as identified through a visual and “sounding” survey. Hydrodemolition (ultra high pressure water) was the chosen means of removal of defective concrete. This method of concrete removal has several benefits over “traditional” removal of concrete using breakers

as the process: maintains the structural integrity of the reinforcing steel; cleans the steel of surface corrosion, washes off any surface contaminants and cleans out pits; and avoids fracturing the parent concrete behind which forms the repair face. In addition, no dust is produced and in the case of this project, the water was captured after the operation to eliminate any risk of contamination of the river.

In the context of applying a cathodic protection (CP) system as part of the concrete repairs, the extent of concrete removal could be limited to the concrete that was identified as being defective. There was no need to extend the length of breakouts beyond that which was already delaminated or spalled save to provide a mechanical key behind the reinforcement. This meant that large areas of concrete, where reinforcement corrosion had been identified through the half-celling, could be retained. Another benefit of applying CP is the removal of the need to apply a steel primer, saving both time and money. Concrete reinstatement was through traditional means with hand placed concrete repair materials being used for small repairs and sprayed concrete repair materials for the larger areas, which was the case for the majority of repairs on this project.

After the repair of the concrete elements of the bridge and the installation of the CP system (Section 4.3) a “levelling” mortar was applied prior to the application of a uniform, anti-carbonation coating. Figures 5 and 6 show the concrete elements prior to and after repairs had been undertaken.



Figure 5. Concrete Elements Prior to Repair.



Figure 6. Concrete Elements After Repair.

Other repair works included resin injection of concrete cracks and the replacement of a buried expansion joint between spans 3 and 4.

5.3 Cathodic Protection

Corrosion is an electrochemical process involving both anodes and cathodes. Metal is lost (corroded) at the anode and this in turn protects surrounding areas (cathodes). It is the expansion of the metal at the anode, through corrosion, that cracks, delaminates and ultimately spalls cover concrete. Various electrochemical treatments exist for the prevention of corrosion and these involve the passage of a current, either temporarily or permanently, thus making reinforcement completely cathodic. One such electrochemical process, using hybrid anodes, incorporates the early short term passage of an electrical current with a longer sacrificial phase of protection. Hybrid anodes have provided a cost effective remediation solution for a wide variety of structures around the world. [5]

The cathodic protection system for Abercorn Bridge was designed with simplicity of installation, uniform current delivery, cost and robustness in mind. There are various stages that are considered in the design process, first of which is determining the most appropriate generic anode system.

DuoGuard Hybrid Anodes were used for the cathodic protection of the bridge. This system consists of an anode, encapsulated in a mortar, buried in drilled holes in the reinforced concrete structure. The DuoGuard hybrid anode is a dual technology anode based on the use of a sacrificial metal in both an impressed current and sacrificial anode role.

The system is designed to deliver a short-term, high, impressed current treatment to rapidly arrest the steel corrosion process. This impressed current phase usually lasts about 7 days and minimises further corrosion induced damage [5]. After a week the system then delivers a low current sustained treatment to ensure durability with low maintenance requirements. The DuoGuard system also retains the facility to re-apply further charge at any point in the future.

For aesthetic reasons, a discrete embedded method of installation was carried out. The size of anodes is part determined by design considerations such as lifespan and reinforcement content and part by practicality of installation. Figure 7 shows the installation of a typical anode.



Figure 7. Partially Installed Anode.

Anodes were installed within: the soffits of each of the four bridge spans; the concrete beams; and the parapet walls of the

structure. In addition, four monitoring zones were installed on the transverse pier beam between Spans 3 and 4 in accordance with BS EN ISO 12696:2012 [6] using buried manganese dioxide reference electrodes. These zones were chosen following the detailed half-cell survey and corrosion rate readings to identify the locations most at risk of future corrosion activity and should therefore be representative of the installed system as a whole. The monitored zones were connected to dedicated monitoring equipment installed on the edge beam of the bridge. This monitoring equipment was designed to record potentials and currents of the system which could then be used to verify the operation of the anode system and predict its future life.

5.4 Temporary works

Scaffold was required to provide access to the entire deck soffit as well as the outside faces of both parapets. The works area was required to be encapsulated to ensure no contamination of the river beneath. The scaffold was used at all stages throughout the project and as such had to be designed for a range of purposes. As assessment, using the FEA model, was undertaken to determine the impact of the scaffold which was designed to hang from the parapet walls. It was established from the assessment that the parapets provided a core strength to the structure and did not require enhancement. Figure 8 shows the installed scaffold supported from the parapet walls.



Figure 8. Installed Scaffold.

6 LOAD TEST

Four load tests were undertaken at various stages of the project:

- Initial validation of the FEA model which was to be used to aid design;
- To accurately measure the shear stresses experienced under live traffic loading and identify any inherent defects in the beams not identified through inspection;
- To confirm the load paths through the structure;
- To confirm the structural adequacy of the individual elements of the structure;
- Once the repairs were carried out and the structural overslab was cast, the load test confirmed the composite action is as per the design between the existing slab and the new overslab; and

- Confirm the new load carrying capacity of the entire structure.

For each of the load tests, fibre optic strain sensors were used to monitor the elements of the bridge while the required load was applied. The sensors used during load tests were Fibre Bragg Grating (FBG) sensors.

FBG sensors are made by laterally exposing the core of a single-mode, fibre to a periodic pattern of intense ultraviolet light. The exposure produces a permanent change in the refraction index of the fibre's core, creating a fixed index modulation according to the exposure pattern. This fixed index modulation is called a grating. When this grating is stretched or compressed by the change in length of the sensor, the reflexive properties of the grating are altered causing the wavelength of the reflected light to change. It is this measured change which allows calculation of the strain. At each periodic refraction change, a small amount of light is reflected but the majority propagates through the grating with negligible attenuation or signal variation allowing the light to travel very long distances.

The sensors can be multiplexed on a single fibre optic cable that can be extended for very long distances, whilst only requiring one monitoring unit. Armoured and protected cable, which provides protection from mechanical damage, can be used in demanding outdoor applications such as Abercorn Bridge. Moreover, the fibre optic cable can undertake large strains of up to 2% elongation meaning significant movements can be monitored at early critical stages. The optic fibre conveys optical signal and not an electric one, this is greatly advantageous as there's no electromagnetic interference and the presence of water poses no risk. Figure 9 shows the installed FBG sensors prior to load test.



Figure 9. Installed FBG Sensors.

The final load test was used to verify the load carrying capacity of the repaired and strengthened bridge. The load test was undertaken using a 6 axle calibrated lorry with a fully laden GVW of 44,000 kg. The load was applied in increasing increments of weight with the lorry travelling across Abercorn Bridge at 10 mph from north to south and when the lorry was returning over the bridge (south to north) it stopped directly over the sensors for a short period of time. This subjected the bridge to both a static and dynamic load. Several passes of the bridge were undertaken for each of the load increments to ensure consistent results were achieved. 2no. load tests were carried out to monitor all of the desired elements of the bridge. After the first load test was concluded, the sensors were removed and placed on further elements of the bridge for the second test.

To monitor the bridge elements while the lorry was travelling at 10 mph, a dynamic fibre optic interrogator was used to collect the readings. This interrogator is capable of taking 100 readings a second from each of the installed sensors. Figure 10 shows one of the graphs produced during one of the passes of the 44 tonne lorry. The first section of the graph shows the initial pass of the lorry at 10 mph and the second shows the lorry in a stationary position over the sensors.

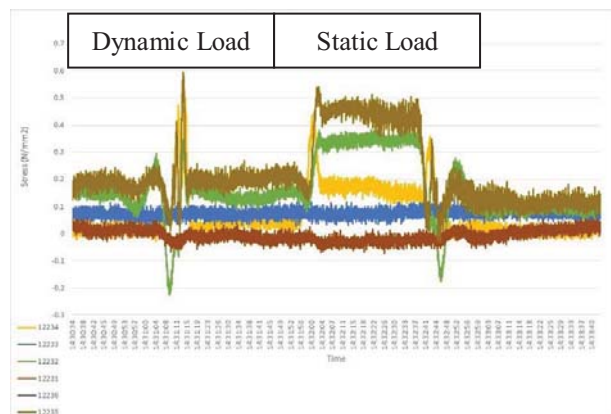


Figure 10. Strain During 44 Tonne Load Test.

After each increment of the load test, the maximum strain was determined from the results obtained. These maximum strains were then compared to the theoretical strains from the FEA model confirming as to whether the bridge was performing as expected at every stage of the load test. The results at every stage corresponded with the FEA model and so the maximum load of 44,000 kg was reached during the load test. This final load test confirmed that the required load carrying capacity was reached.

7 CONCLUSIONS

Through the use of novel technology and materials it was possible to prevent the partial demolition of the Client's asset while increasing load carrying capacity and fully meeting the Client's brief. These methods will hopefully be used in the future as a basis for sustainable asset management.

The finite element analysis was produced in the early stages of the project enabling design concepts to be efficiently checked with regards to their suitability. This meant that more time could be spent detailing the chosen design and this ultimately saved on the design costs.

Fibre optic sensors were used to validate the FEA model. These highly accurate sensors could not only determine the behaviour of the individual elements of the bridge but when used in series could evaluate the behaviour of the bridge holistically. By using the fibre optic sensors in this way the FEA model's accuracy was confirmed and it could be used with confidence to aid the design process.

Abercorn Bridge was among the first projects in Northern Ireland to use a combination of lightweight aggregate concrete and BFRP reinforcement. The use of these material, over traditional materials, allowed for the strengthening of span 4 as opposed to its replacement.

Along with the strengthening of the bridge, concrete repairs were carried out on all four spans. The installation of a

cathodic protection system on all elements of the structure ensured that the repairs will last for the required life span of the bridge as well as arresting any corrosion that may have initiated elsewhere.

Through the use of load tests, it was confirmed that the designed load carrying capacity of the repaired and strengthened bridge was achieved.

Although the load test, which had been undertaken to 44 tonnes, had confirmed the increased load carrying capacity of the bridge, it was recommended that an 18 tonne GVW weight restriction be imposed. This recommendation was due to the age, location of the structure and the real potential for the unknown historic overloading of the structure. Fatigue is a concern when reassigning a bridge's weight restriction and is very difficult to account for with an unknown history of loading. This and a combination of the bridge's intended remaining life lead to the weight restriction recommendation. The bridge was reopened (Figure 11) with a weight restriction of 18 tonne GVW after the completion of the works.



Figure 11. Reopened Abercorn Bridge after Works Completion

ACKNOWLEDGMENTS

The following acknowledgments are made in relations to the Abercorn Bridge Project: TransportNI – John McRobert, Graham Structural Solutions – Robert Nesbitt.

REFERENCES

- [1] Cusack, P (1987), Agents of Change: Hennebique, Mouchel and ferroconcrete, *Consmtion History*, Vol. 3, 1987, 61 – 74.
- [2] Amey, (2013), *Abercorn Bridge, Newtownstewart, No. 61835, Special Inspection Report*.
- [3] Department of Transport (2001) BD21/01. *The Assessment of Highway Bridges and Structures*.
- [4] PPC, Basalt Reab, Proven Performance Chemical, Bogart
- [5] Davison, N., Glass, G., Roberts, A., hybrid electrochemical treatment applied to corrosion damaged concrete structures, Presented at the Transportation Research Board, 87th Annual Meeting, Washington DC, 2008
- [6] British Standards Institution, BS EN ISO 12696:2012, Cathodic protection of steel in concrete, London, 2012

Arch Bridges under flood conditions, a study of the velocity distributions, and the resulting bed scour.

Donal Ryan¹, Gerard Hamill², Brian Solan³, Robert Ettema⁴

¹School of Engineering & Computing, University of the West of Scotland.

²Department of Civil Engineering, Queen's University Belfast, Northern Ireland.

³School of the Built Environment, Ulster University, Northern Ireland.

⁴Department of Civil Engineering, Colorado State University, United States of America.

email: donal.ryan@uws.ac.uk, g.a.hamill@qub.ac.uk, b.solan@ulster.ac.uk, rettema@engr.colostate.edu

ABSTRACT: In recent years, the increased frequency of extreme rainfall events has led to many bridge failures throughout the UK and Ireland. Particularly vulnerable are short span bridges, which typically include arch structures, where abutments and piers are quickly scoured at their foundations. Several bridges have collapsed under flood conditions and, recently, such events have occurred in Northern England during the floods during the latter part of 2015. This paper is the result of an on-going experimental investigation, funded by The Royal Society, where arch bridge scale models are subjected to pressurised flow. Results demonstrate the nature of the upstream and downstream velocity distributions, and resulting scour profiles. The study provides an insight into the significance of pressurised flow on the depth and extent of scour when compared to normal open channel conditions. Measurements of velocities were taken using Acoustic Doppler Velocimeter (ADV), where significant increases in bed velocities are experienced as the flow passes under the arch. Scour depth was measured using a 3D laser scanner, which verified the shape of the resulting scour hole. The outcome of this paper is the demonstration of the severity of scour within the vicinity of an inundated arch bridge structure. It highlights the likely risks to long term stability, identifying depth locations to consider in relation to protection against local scour.

KEY WORDS: Bridge; Flooding; Scour.

1 INTRODUCTION

There is now significant evidence, which suggests that climate change is having a major impact on infrastructure both presently and in the near future (Committee on Climate Change, [1]). These impacts include combination of social, economic and environmental. As the climate changes, weather patterns are becoming less predictable, and with more extreme events taking place e.g. rain and snow falls, it is increasingly difficult for infrastructure engineers to design structures to cope with these extreme occurrences. These extreme weather cycles create more rain, which causes rivers to flood. This has a large impact on the existing structures in the river and one aspect, which is not fully understood, despite extensive research, is hydraulic scour, as reported by the UK Roads Liaison Group. This is also not helped by the limited UK/Ireland standards applied within the Design Manual for Roads and Bridges (DMRB) in relation to designing for hydraulic action [2]. This has not been revised since 1994. However, current standards for inspection have been updated to take into account a risk based assessment procedure within DMRB [3]. The failure of these bridges may be because of the complex interplay of mankind and the environment, which is particularly hard to understand and model, hence the need for further work.

CIRIA C742 [4] states 'scouring is the removal of sediment primarily caused by fast moving water that lifts the material and transports it downstream'. It is potentially catastrophic when bridges, which have shallow foundations, are then undermined, thus severely reducing the structural integrity of the bridge. Ryan et al, [5] noted that in November 2009, the UK and Ireland were subjected to extraordinarily severe weather conditions for several days. The rainfall was logged

as amongst the highest levels of rainfall ever recorded within the UK and, as a direct consequence, unprecedented flooding occurred. In Cumbria, this flooding led to the loss of one life and the collapse of three road bridges, which were generally 19th century masonry arch bridges, with relatively shallow foundations.

As stated previously, Highways Agency published a revision to BA 74/06 "Assessment of Scour at Highway Bridges" in 2012. The new revision (i.e. BD 97/12) [3] advises on how to determine the level of risk associated with scour effects. Highways Agency also still refers to BA59/94 "The Design of Highway Bridges for Hydraulic Action" [2] provides design guidance based on references from publications prior to 1994. The significance of these reference dates is that the reference material cited does not take into account the current situation in relation to climate change.

In the UK, the above standards clarify that the recommended design guidance documentation for highway bridges does not provide advice on predicting/designing to reduce scour under pressurized flow conditions. Hence, the rationale behind this paper towards considering the effects of flood flows/inundation on existing structures, with particular emphasis on structures with limited spans. The impact of this research will become significant to stakeholders and designers, where the finding will inform maintenance guidance and provide design advice to engineers responsible for maintaining the life-span of this critical infrastructure by gaining full knowledge of the bridge behaviour under pressurized conditions.

2 BACKGROUND RESEARCH

2.1 Bridge Hydraulics and Scour

Several authors have investigated the hydraulics of flow in the vicinity of an arch bridge. The majority of this work was carried out for normal flow conditions, where arch inundation was not considered. Previous authors were also interested in the prediction of afflux and discharge through the bridge structure. However, when the soffit of a bridge is submerged there were two specific conditions (1) Sluice Flow and (2) Drowned Orifice flow. Equation 1 is proposed for sluice flow and equations 2 & 3 are proposed for drowned orifice flow. These equations have been previously reported in the FHWA publication of the Hydraulic Design of Safe Bridges [6]:

$$Q = C_d a_w \left[2g \left(Y_u - \frac{Z}{2} + \frac{\alpha_u v_u^2}{2g} \right) \right]^{1/2} \quad (1)$$

$$Q = C_d a_w (2g \Delta H)^{1/2} \quad (2)$$

where C_d (= 0.35 to 0.6) is the discharge coefficient, a_w is the total area of the opening flowing full (m^2), Y_u is the upstream depth (m) and Z is distance between the soffit and the bed level (m). Equation 3 defines ΔH as:

$$\Delta H = \left[\left(Y_u - \frac{Z}{2} + \frac{\alpha_u v_u^2}{2g} \right) - \left(Y_d - \frac{Z}{2} + \frac{\alpha_d v_d^2}{2g} \right) \right] \quad (3)$$

The subscripts u and d denote upstream and downstream respectively. The above equations have never been tested for Arch Bridges, and the only equation for predicting discharge was proposed by Biery & Delleur [7] as:

$$Q = C_d \sqrt{2g} \frac{17}{24} y_1^{3/2} b \left[\begin{array}{l} 1 - 0.1294 \left(\frac{y_1}{r} \right)^2 \\ - 0.0177 \left(\frac{y_1}{r} \right)^4 \end{array} \right] \quad (4)$$

where y_1 is the depth of flow at the section of maximum backwater (m), b is the span width at the spring line of the arch (m) and r is the radius of curvature of the arch (m). The limitation of Equation 4 is that the C_d value must be determined from Tables within the publication itself, and the same equation determines discharge for both sluice and orifice conditions, where no clear evidence from tests is demonstrated within the publication.

The above equations have been widely used to predict bridge afflux and have also been utilised to determine the flow through the bridge constriction and hence the average flow velocity through the same. As the velocity increases within a bridge constriction, formulae were developed to determine scour depth as a function of the relationship between upstream average velocity (v_u) and the average velocity through the constriction (v_a). A value for v_a is determined from Equation 4 for an arch bridge.

With knowledge on how to determine the y_1 upstream depth value, it was possible to determine the depth of scour by applying the Arneson & Abt [8] equation:

$$\frac{y_s}{y_1} = -5.08 + 1.27 \left(\frac{y_1}{H_b} \right) + 4.44 \left(\frac{H_b}{y_1} \right) + 0.19 \left(\frac{v_a}{v_c} \right) \quad (5)$$

where v_c is the critical velocity for incipient motion (m/s), H_b is the distance from the soffit of the bridge to the initial bed level (m) and y_1 is another term for the upstream bed level (m). This equation has previously been widely utilized and has become known as the HEC-18 equation, as published by Richardson & Davis [9]. However, Lyn [10] had identified that there were problems with the validity of equation 5 and proposed an alternative predictive relationship where y_s is the final depth of scour (m):

$$\frac{y_s}{y_1} = \min \left\{ 0.105 \left(\frac{v_a}{v_c} \right)^{2.95}, 0.5 \right\} \quad (6)$$

These revised equations have been widely used to predict pressurized scour in the USA to date.

2.2 Experimental Set-up & Data Acquisition.

Previous authors, including Arneson & Abt [8], Richardson & Davis [9] and Gou [11] carried out extensive physical modelling on sediment scouring. However, there was no evidence of attempting to understand the flow velocities within the vicinity of the bridges. Each author cited the work of early authors such as Laursen [12] and in relation to examining critical velocity of sediment (v_c), but made little attempt to carry out any work in establishing a relationship between scour depth and velocity within the vicinity of the bridge, under pressurised flow. There seems to be an emphasis on upstream average critical velocity and the average velocity through the bridge. These are averaged, based on continuity equation, and using Equations 1-4, depending on the physical conditions.

The present investigation considers the magnitude of these velocities through an arch bridge, in order to gain a better understanding of the nature of flow through a pressurised arch. Velocity measurements are taken by using a SonTEK 2D Acoustic Doppler Velocimeter (ADV), with a sampling frequency of 50 Hz. Measurements were taken for an initially flat bed, stabilized by using an Epoxy Resin treatment. Following this, the scour holes were allowed to fully develop to an approximate equilibrium stage of erosion (approx. 120 mins), and measurements taken for the purposes of making comparisons with the flat bed condition. A grid system is used both upstream and downstream of the arch models, where the grid density for velocity measurement (ADV probe) was increased within the vicinity of the higher velocities to that of a 20 x 20mm grid. Outside the confines of the arch, the grid was increased to a density of 50 x 50 mm.

Velocity measurements were taken on the XY plane at six positions (1) 1000 mm upstream of the flow entering the bridge arch, (2) at 500 mm upstream of the flow entering the bridge arch, (3), 50 mm upstream of the flow entering the arch, (4) 50 mm downstream of the flow exiting the arch, (5) 500 mm downstream of the flow exiting the bridge arch and (6) 1000 mm downstream of the flow exiting the bridge arch.

The data was then analyzed qualitatively to determine how the velocity profiles varied with distance through the arch.

All of the uPVC model bridge experiments have been carried out within a 10-metre long Perspex channel of dimensions 760 mm × 250 mm. The overall depth at the recess section was 480 mm. Water is supplied via a reservoir and 2 No. impeller pumps and is capable of supplying 100 l/s to the upstream supply reservoir.

For scour tests, a recess was constructed within the channel for the purposes of these experiments to a total depth of 230 mm. A bridge model structure was inserted half way down the channel. The abutment length (i.e. model road width) is 280 mm for these experiments. The width is 750 mm with a 365 mm span. This is reported in Ryan et al [3].

3 EXPERIMENTAL RESULTS & DISCUSSION

3.1 Velocity profiles in the vicinity of the arch bridge.

Equations 1-4 provide methods for determining discharges and average velocities. However, the average velocities are not representative of the near bed conditions, where high levels of turbulence and an upstream head (due to backwater effects) produces sluice conditions.

Figure 1(a) shows the upstream end of an experiment on a 365 mm arch, with 45° wing walls at a flow of 40 l/s. For this experiment there is a total of 60 mm head above the barrel of the arch.



Figure 1(a): Upstream conditions for bridge experiment.

Figure 1(b) show the downstream condition, where the flow velocities are much more rapid and depths are supercritical. It can be clearly shown that there is a considerable likelihood that excessive damage to the channel bed is likely in these conditions, especially with the likes of a masonry arch, where mortar joints can also experience wash-out.

Figure 2 shows the increase in channel centreline velocity versus distance upstream/downstream of a model arch for one

of the experiments. These experiments are taken for a flat/fixed bed scenario to provide some understanding of the bridge hydraulics.

The velocity profiles are taken on the upstream side (U/S) at a maximum depth of 200 mm from the bed. This is 20 mm below the water surface to allow full submergence of the ADV. On the downstream (D/S) side, velocity measurements are taken from 150 mm above the bed. This is due to the fact that the difference in level between upstream and downstream is 50 mm.

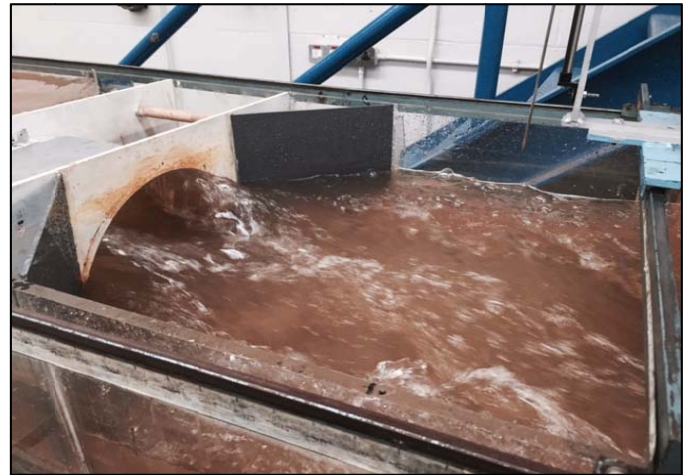


Figure 1(b): Downstream conditions for bridge experiment.

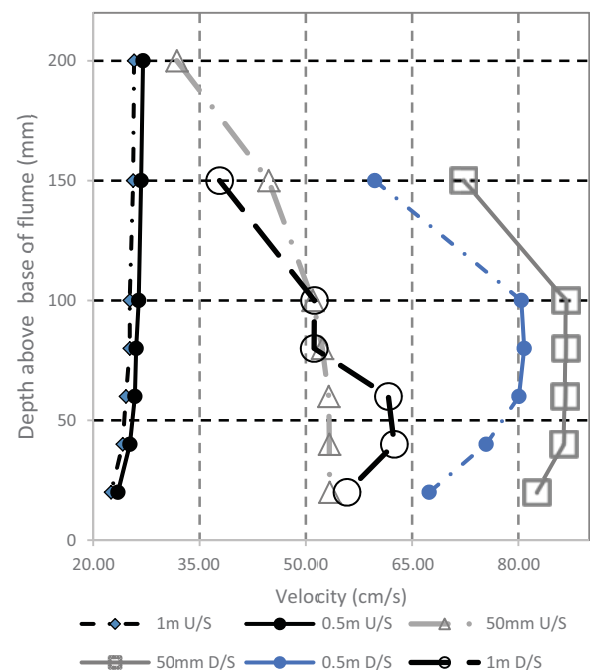


Figure 2: Centreline velocity distributions upstream and downstream of the model arch bridge.

At 1000 mm (1 m) and 500 mm (0.5 m) upstream of the bridge, it is clear that the effect of the bridge and wing walls is

almost negligible when considering the velocities at the centreline of the channel. The increase becomes appreciable when it reaches a point up to 50 mm upstream of the bridge opening. Velocity increases are demonstrated from 200 mm upstream and this is approximately where local scour commences. At 50 mm upstream, the maximum velocity has increased from 28 cm/s (0.28 m/s) to 62 cm/s (0.62 m/s), and has moved from near surface to approximately 40mm above the bed. Near bed velocities are at approximately 0.55m/s, which is easily in excess of the critical velocity for sediment transport. As the experiment moves downstream the maximum velocities approach 0.9 m/s and then gradually decrease to 0.55 m/s at 1 m downstream.

3.2 Scour Profiles.

Scour depth tests have been carried out with several combinations of arch barrel sizes, wing wall configurations and sediment sizes. Depending on the experimental conditions, the scour profiles slightly differ. In Ryan et al [5] it was reported in the absence of wing walls that the maximum depth of scour occurred at the upstream face of the abutment. When considering the presence of wing walls, there were slightly lower upstream depth results. The improved conveyance of flow inhibited the upstream turbulence (eddies) and led to a slightly different scouring pattern. The upstream scour is shown in Figure 3.



Figure 3: Scour hole for 40 l/s with 22.5° wing walls (2 mm d_{50} sediment).

It can be seen that the scouring has occurred but with some evidence of the abutment stone backfill slipping into the area where material is dislodged. This then has protects the existing foundation but encourages more constriction scour, especially as an additional flood wave passes.

The dotted line shows the extent of upstream scouring. Figure 4 shows the effect of wing wall placement on the overall depth of scour along the line of maximum scour. The bridge upstream face is located at the position of 500 mm, whereas the downstream face is at 800 mm. These are shown as dotted lines.

It is clear that the maximum depth of scour is less encouraged underneath the bridge in the presence of wing walls. However, further studies will determine the additional risk to other

locations around the structure to determine scour depths relative to the maximum depth of scour.

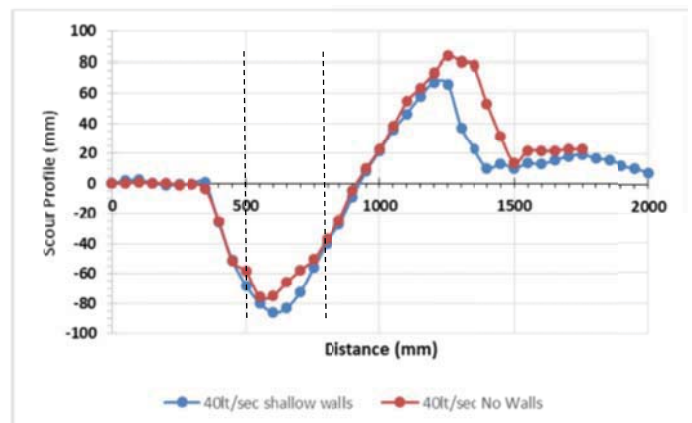


Figure 4: Longitudinal profile of scour hole along the line of maximum scour (40 l/s with 2 mm d_{50} sediment).

3.3. Current Scour prediction theories.

It was reported earlier in this paper that Lyn [10] revised equation 5 to proposed equation 6 as a means of determining scour depth under pressurised flow conditions. When the predictions from the HEC-18 equation are plotted against the current experimental data in Figure 5 it is clear that the scour depth from data produced for tests within the current study is reasonably close to the HEC-18 equation at the lowest discharge, but rapidly begins to move well above these predicted values as the discharge is increased. However, it is a concern that the HEC-18 equation predicts that the depth of scour decreases with a rise in discharge/velocity. When considering the same, a non-dimensionalised variable appears twice within the HEC-18 equation. It has been cited by Lyn [10] that there were issues with the same, and that unsatisfactory features were evident within the equation.

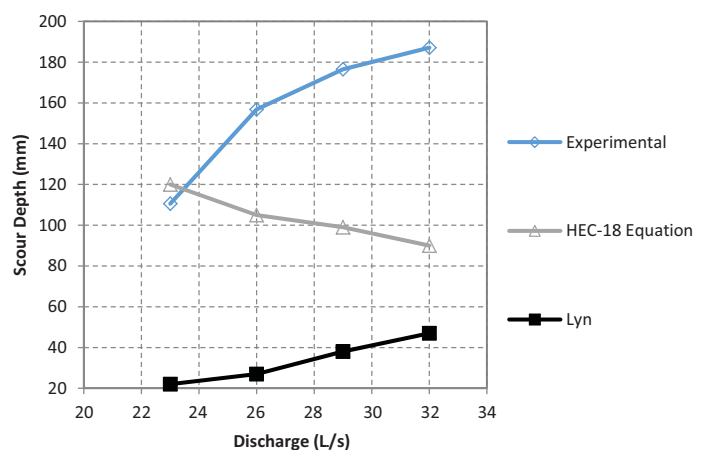


Figure 5: Comparison of experimental scour depths with existing equations (1.1 d_{50} sediment).

It is worth noting that the test results from Figure 5 relate to 1.1 mm d_{50} sediment. As the current study acquires further data, these observations will be further explored.

In relation to Lyn's [10] equation 6, there is an under-prediction of scour depth with discharge, therefore the present investigation will require the development of its own set of predictive equations. This is due to the three-dimensional nature of the scour development, where the flow is constricted in both vertical and horizontal directions. Previous authors on pressurised flow only considered vertical constriction.

4 CONCLUSIONS

The experimental observations from this study have shown that there is an appreciable rise in the magnitude of flow velocities within the vicinity of the bridge structure under pressurised flow. These velocities give rise to enhanced scour depths that are demonstrating a degree of under-prediction by current standards. These current standards are based on US Federal Highways Agency Guidelines and UK DMRB guidelines. They do not take into account the combined horizontal and vertical constrictions experienced by arch bridges. Further work is therefore being carried out to make a more informed prediction of scour within the vicinity of arch bridge structures subjected to pressurized conditions.

REFERENCES

- [1] Committee on Climate Change, "Tackling Climate Change", [Online], available from <https://www.theccc.org.uk/tackling-climate-change/>. [Accessed 12/09/2015].
- [2] Design Manual for Roads & Bridges, "The Design of Highway Bridges for Hydraulic Action", BA59/94 (1994). Department for Transport (UK).
- [3] Design Manual for Roads & Bridges, "The Assessment of Scour and Other Hydraulic Actions at Highway Structures", BD 97/12 (2012). Department for Transport (UK).
- [4] Kirby, A. M., Roca, M., Kitchen, A., Escameia, M., Chesterton, O. J. "Manual on scour at bridges and other hydraulic structures, second edition (C742)". April 2015, CIRIA.
- [5] Ryan, D., Hamill, G.A., McRobert, J., Smyth, W. "The hydraulics and resulting bed scour within the vicinity of submerged single span arch bridges". Proceedings of the Civil Engineering Research Association of Ireland, Belfast, 2014.
- [6] Federal Highway Administration (USA), "Hydraulic Design of Safe Bridges, Publication No: FHWA-HIF-12-018, Department of Transport. April 2012.
- [7] Biery P. F. and Delleur. W. Hydraulics of single-span arch bridge constrictions. Proc. Am. Soc. Civ. Engrs, J. Hydraulics Div, 1962, 88, HY2, March, 75-108.
- [8] Arneson, L.A. and Abt, S.R., (1998). "Vertical contraction scour at bridges with water flowing under pressure conditions." Transportation Research Record. 1647, 10-17.
- [9] Richardson, E.V., Davis, S.R., (2001) Evaluating Scour at Bridges, HEC-18, FHWA-NH-01-001, 4th Edition. US. D.O.T. Washington. DC.
- [10] Lyn, D.A., (2008) "Pressure-Flow Scour: A Re-examination of the HEC-18 Equation". Journal of Hydraulic Engineering. 2008.134. pp 1015-1020.
- [11] Guo, J., Kerenyi, K., Paga-Ortiz, J.E. "Bridge Pressure Scour for Clear Water Conditions". (2009) Report No: FHWA-HRT-09-041. U.S. Department of Transportation, Federal Highway Administration (FHWA).
- [12] Laursen, E.M., 1960, "Scour at bridge crossings" Journal Hydraulic Division, American Society of Civil Engineering, v. 89, no. HY3.

Investigation of the Maturity and Engineering Performance of Self-Compacting Concrete for Pre-cast Elements

P. Deegan¹, M. Sonebi², G. Kelly¹, S. Taylor², L. Ferrara³, A. Pattarini⁴

¹Banagher Precast Concrete Ltd., Co. Offaly (Republic of Ireland)

²Queen's University of Belfast, BT9 5AG Belfast (Northern Ireland)

³Politecnico di Milano, Milan (Italy)

⁴Azichem Ltd, Goito, Mantova, (Italy)

email: PeterD@bancrete.com, m.sonebi@qub.ac.uk, s.e.taylor@qub.ac.uk, liberato.ferrara@polimi.it, brunoalberto.dallago@polimi.it, a.pattarini@azichem.it

ABSTRACT: The prediction of concrete strength at an early age is very important in the concrete industry. This will help in accelerating the construction process, determining the safe time for de-tensioning of pre-stressed concrete and for stripping of formwork or the proper time to conduct any construction activity. The maturity method is a technique to account for the combined effects of time and temperature on the strength development of concrete. The method provides a relatively simple approach for making reliable estimates of in-place strength during construction. The maturity concept has gained increasing interest as a scientific way to evaluate in-situ strength of concrete in a very accurate way. In tandem with this the use of self-compacting concrete in precast concrete has grown substantially, worldwide in recent years.

This paper reports on an investigation of the effect of water-to-binder ratio (w/b) and the percentage of ground-granulated blast furnace slag on fresh properties, the hardened properties and the maturity of mixes to be used in pre-stressed structural elements. The filling ability, flowability and passing ability of SCC mixes were measured using slump flow and J ring. The compressive strength 1, 3, 7 and 28 days were determined. The maturity index was measured using maturity box apparatus at Banagher precast concrete. The results of this investigation show that w/b and the replacement of cement by GGBS had a significant effect on the maturity index. As expected, the reduction of w/b from 0.45 to 0.40 led to an improvement of compressive strength and the increase in percentage of GGBS resulted in a reduction of compressive strength. The Relationship between the maturity index and compressive strength has been established for several SCC mixes used by Banagher precast for releasing the pre-stressed tendons used in precast elements.

KEY WORDS: compressive strength; ground granulated blastfurnace slag; maturity; self-compacting concrete; w/b.

1 INTRODUCTION

Self-compacting concrete (SCC) is a concrete type that meets a unique combination of performance and uniformity requirements [1-4], it flows under its own weight, maintaining its homogeneity without any vibration. The filling ability of SCC (unconfined flowability) can be described by the ability of the concrete to flow into and to fill all spaces of the formwork under its own weight.

SCC has a low water-to-binder ratio, incorporating high quantities of fillers (cement and mineral additives such as ground granulated blast furnace slag (GGBS), fly ash (FA), limestone powder (LSP), an effective superplasticiser (SP), increasing the sand-to-aggregate ratio, and if needed, using a stabilising agent [1-4]. The use of SP can disperse cement grains, reduces inter-particle friction and enables the reduction in water content while maintaining the required levels of flowability [1-4].

These are more sensitive to temperature than those made only with Portland cement. This investigation focused on establishing whether maturity functions could be used to monitor early age strength development for precast elements. These could be used to control the temperature of the casting bed to obtain the early age strengths needed for lifting the units and also to be used for quality control assurance ensuring the strengths required are achieved to release the pre-stressed tendons in W-beams, slabs, etc.

The concept of estimating concrete strength in terms of curing time and temperature has been well developed, and a maturity function has been proposed by Saul and Nurse [5]. The Saul–Nurse maturity function took the following simple form.

$$M = \sum_0^t (T - T_0) \Delta t \quad (1)$$

where M is the maturity value at age t, T_0 is the datum temperature ($= -10^\circ\text{C}$), and T is the average curing temperature of the concrete during the interval Δt

The simplicity of using the Saul–Nurse maturity equation is shown. It has received much attention and found wide use in engineering practice as a proper method for in-situ strength determination in concrete structures. Freiesleben Hansen and Pendersen [6, 7] proposed a new expression for the maturity function based on the well-known Arrhenius equation, as follows:

$$M = \sum_0^t k(T) \Delta t \quad (2)$$

where $k(T)$ is the rate constant of hydration at temperature T.

The rate constant of hydration, $k(T)$, can be calculated using the Arrhenius equation as:

$$k(T) = Ae^{-E/RT} \quad (3)$$

where A is a proportionality constant (day^{-1}), R is the gas constant (8314 J/mol K), E is the activation energy (J/mol) and T is the absolute temperature (K).

The objective of this study is to investigate the relationship between the maturity index and the compressive strength of various SCC mixes.

2 EXPERIMENTAL PROGRAMME

2.1 Materials

Cement class CEMI 42.5R and GGBS were used as constituents of the binder. The average particle size of the GGBS was 13.8 microns. Limestone powder (LSP) was also used as a filler, with an average particle size was 9.1 microns. The chemical composition of these materials is shown in Table 1. A polycarboxylate ether-based superplasticiser (SP) was used, its specific density being 1.06 and with a water content of 65%. In addition to the sand, two coarse aggregates with different maximum size (8 and 14 mm) were used, all of them crushed.

Table 1. Chemical composition of cement, LSP and GGBS.

	Cement	LSP	GGBS
SiO ₂	19.61	1.74	35.65
TiO ₂	0.336	0.011	0.735
Al ₂ O ₃	5.02	0.09	11.53
Fe ₂ O ₃	3.14	0.11	0.96
MnO	0.097	0.048	0.210
MgO	2.67	0.54	7.22
CaO	63.79	55.24	41.26
Na ₂ O	0.22	<0.003	0.26
K ₂ O	0.469	0.026	0.396
P ₂ O ₅	0.077	0.132	0.008
SO ₃	3.04	<0.002	2.33
L.O.I.	2.40	42.71	-0.86

2.2 Mix compositions

Five different mixes were considered, differing in terms of their water-to-binder (w/b) ratio and their GGBS content and reference mix. Binder is cement and GGBS. They are summarized in Table 2. The w/b ratio was considered at the levels of 0.40 and 0.45. In all cases, the total binder content (total weight of cement and GGBS) was kept constant at 450 kg/m^3 . The relative amount of GGBS was considered at two different dosages: either 25% or 50% of the total binder weight. Ref mix was made with 100% cement and w/c is 0.42. The SP dosage was adjusted in each case after some trial mixes to achieve a maximum spread between 570-770 mm in the slump flow test. Fuller's theoretical curve was assumed when proportioning the aggregates, seeking the relative volumes that optimised the fit between the actual and the theoretical curve. The total aggregates content was 1600 kg/m^3 or 1650 kg/m^3 for the mixes with w/b of 0.45 and 0.40 respectively. The sand/coarse ratio was kept to 1.0 in all cases in order to ensure a reasonably good degree of cohesion. The LSP content was kept constant at 150 kg/m^3 in all cases.

Table 2. Mix compositions of all mixes tested.

Mix	Ref	SSC-A25	SCC-A50	SSC-B25	SSC-B50
w/b	0.42	0.40	0.40	0.45	0.45
C	475	337	225	337	225
LSP	--	150	150	150	150
GGBS	--	112	225	112	225
W	190	180	180	202	202
Sand	841	825	825	800	800
AG4/8	--	611	611	592	592
AG8/14	900	400	215	215	208
SP	3	2.2	2.9	2.5	2.5
SR	4	5			1.7

2.3 Maturity index test

The computer measured the temperature and time through the four thermo-coupling leads placed into the concrete product and connected to the computer (Fig. 1). The information contained within the computer prior to testing are:

- The C-value (constant related to type of cement)
- Test period
- Time/Date settings

The test period specified how long the test will run for. The test was carried out for a long period of time in order to get good results and readings. The computer linked to apparatus was set for a period of 75 hours which enabled us to take a reading every 10 minutes. The maximum period of time possible for testing is 1800 hours (75 days). The maturity apparatus measured temperature between -10°C to 110°C with a measurement accuracy of 0.5° .

The thermocouple leads supplied with the computer are 25 metres in length and are sacrificial meaning we cut the lead flush with the surface of the concrete when the test is complete. The leads require a rubber cap to be fitted to the exposed thermocouple wires. This cap is applied with a heat gun.



Fig. 1- Apparatus of maturity used at Banagher Precast Concrete

According to the supplier of the equipment, several cubes were made and cured at 20°C, 35°C and 65°C and tested.

The formula according to CIMEJ is given by equation (4):

$$R_g = \sum t \cdot T \cdot C^n \quad (4)$$

R_g: the weighted maturity (°Ch)

t: temperature (°C)

T: time in hours

C-value is taken 1.3 (with cement 42.5R used by Banagher)

n: numbers of test specimens.

The slump flow and V-funnel tests were used to evaluate the filling ability and deformability of SCC, respectively. The passing ability of SCC mixes was assessed by J ring test. Standard 100-mm cubes were demoulded one day after casting and covered with wet burlap and plastic sheeting. Specimens were then cured in lime water at 20 ± 2 °C until testing at ages of 1d, 3d, 7d, and 28d.

3 RESULTS AND DISCUSSION

3.1 Fresh properties

The experimental results obtained for the slump flow, J ring spread and V-funnel are plotted in Figures 2 and 3. According to SCC guidelines [8], all SCC mixes can be classified for slump flow SF2 (660-750 mm) except SCC-B50. As expected, the values of J ring spread were lower than the slump flow. It can be seen that most J ring spread values were more than 600 mm a part mix SCC-B50 which the initial slump flow was the lowest one (570 mm). This is due to the lower dosage of SP (SP = 1.7 L/m³). All results of V-funnel values showed that SCC mixes were classified as VF2 (V-funnel time between 9 to 25 s). The V-funnel time less than 15 scan be considered as a good flow-ability and deformability of SCC. In this case, SCC-A25 had the highest V-funnel time (21 s). This may due to the high dosage of SP of 2.9 L/m³ used in this mix, which can lead to more inter-friction between aggregates at the orifice, thus resulted in a high flow time.

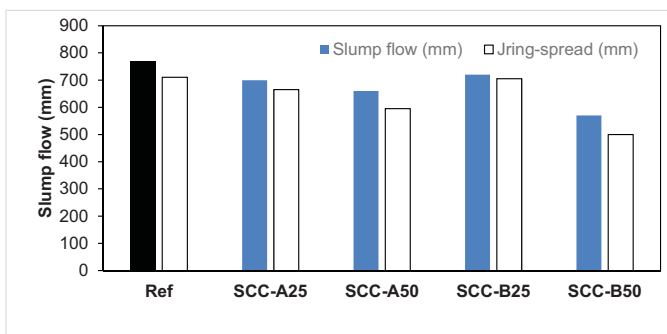


Figure 2. Variation of slump flow and Jring spread of all mixes.

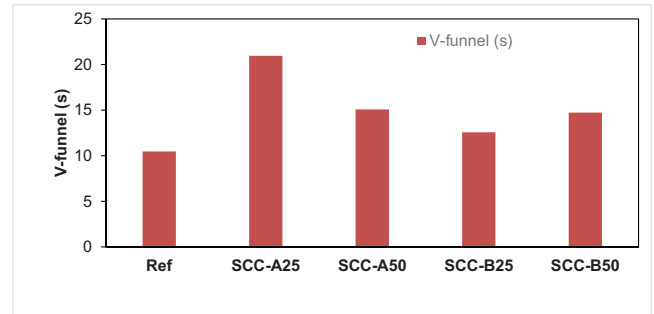


Figure 3. Variation of V-funnel time.

3.2 Compressive strength

The results of compressive strength at 1d, 3d, 7d and 28d are presented in Figure 4. The replacement of cement by 25% or 50% GGBS for both w/b ratio 0.40 and 0.45 led to lower results of compressive strength at 1d and 7d compared to reference mix containing only cement. However, the compressive strength results at 7d and 28 d of SCC-A25, SCC-A50, SCC-B25 and SCC-B50 were higher than those of ref mix particularly at 28 d with SCC mixes incorporating only 25% GGBS. As expected, the increase of w/b from 0.40 to 0.45 resulted in a reduction of compressive strength at all ages. Additionally, the increase of GGBS from 25% to 50% led a reduction on compressive strengths at 1d, 3d, 7d and 28 d.

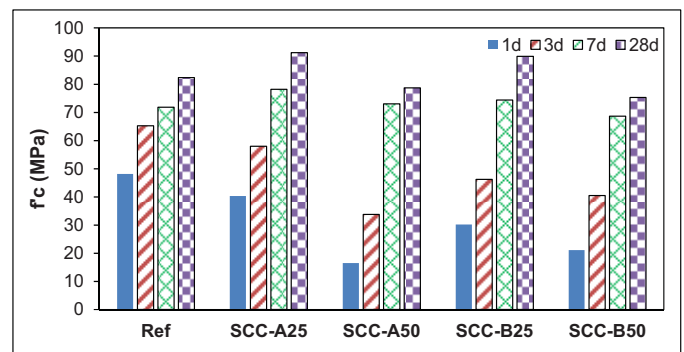


Figure 4. Development of compressive strength of all mixes.

3.3 Maturity index

Figure 5 presents the variation of compressive strength with maturity index. It can be observed that the maturity index increased with the increase in compressive strength. For any given maturity index, the reduction of percentage of GGBS from 50% to 25% led to an increase of compressive strength for both w/b ratios of 0.40 and 0.45. For any fixed maturity index, the reduction of w/b from 0.45 to 0.40 resulted in an increase of compressive strength. Additionally, for any given maturity, the ref mix demonstrated the highest compressive strength.

For example, at fixed maturity index of 1000 °Ch and w/b of 0.40, the increase in GGBS percentage from 25 to 50% led to a marked reduction of the compressive strength from 38 to 23 MPa (Figure 5). Similarly, in case of w/b of 0.45, the

reduction of compressive strength was from 48 to 30 MPa. This attributed to the change in w/b and percentage of GGBS. With ref mix without GGBS and w/b of 0.42 and cement content of 425 kg/m³, for similar maturity index of 1000 °Ch, the predicted compressive strength was 57 MPa.

Figure 5 can be used also to determine the maturity index for any fixed compressive strength. This figure is very useful for Banagher for releasing pre-stressing cables when the maturity is measured, the early compressive strength can be estimated for these curves in Figure 5. For example, for a compressive strength of 20 MPa, SCC mix made with w/b of 0.45 and 50% GGBS had a maturity index of 540 Ch which is lower than 840 °Ch for similar made with 0.40. Therefore, the reduction of w/b led to an increase in maturity index.

For a target compressive strength of 30 MPa, the maturity index was 640 Ch. There were two options either increasing w/b to 0.45 or increasing GGBS to 50%. In these cases, the maturity index was 1000 °Ch for mix made with w/b = 0.45 and 50% GGBS and 1490 °Ch for made lower w/b of 0.40 and incorporating 50% GGBS.

For w/b of 0.45 and fixed a compressive strength of 40 MPa, the maturity index was almost tripled increasing from 740 to 1910 °Ch. For similar compressive strength, the maturity index was lower for ref mix (w/b = 0.42 and C = 475 kg/m³) having value of 500 Ch.

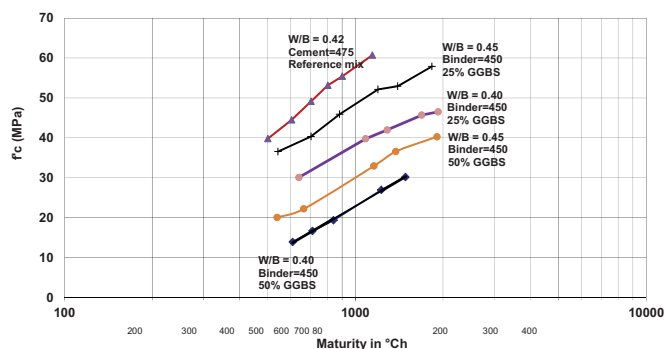


Figure 5. Variation of maturity index.

4 CONCLUSIONS

The effects of binder type and content (GGBS) and w/b on the filling ability, passing ability, the concrete compressive strength at 1 d, 7 d, 3d and 28 d and maturity index were investigated in this study. Based on the results, the following findings can be stated:

- In general, all SCC mixes demonstrated a good filling ability and passing ability. They were classified as SF1 for SCC-B50 and SF2 for other SCC mixes. SCC-A25 was classified VF2 for V-funnel time, and other SCC mixes were VF1.
- Increase in w/b and GGBS led to a reduction of compressive strength at all ages.
- The increase in w/b significantly affects the maturity index. For any given compressive

strength, the reduction in w/b led to an increase in maturity index for a similar percentage of GGBS.

- The increase of GGBS from 25 to 50% caused a significant increase in the maturity index.
- The relationship between maturity index and the predicted compressive strength is very useful for Banagher in order to establishing detensioning times for pre-stressing cables in precast elements.

ACKNOWLEDGMENTS

The authors wish to acknowledge the financial support and funding received from the European Union, as this research is part of the FP7-PEOPLE-2012-IAPP project "EuroCrete: Development of sustainable, lower carbon, pre-cast concrete infrastructure". This work actually represents the summary of the activity performed by the authors during reciprocal secondments.

REFERENCES

- [1] Sonebi, M., Khayat, K.H., (1999), 'Effect of Water Velocity on Performance of Self-Consolidating Underwater-cast Concrete', *ACI Materials Journal*, 96, 519-528.
- [2] Sonebi, M., Bartos, P.J.M., 'Hardened SCC and its Bond with Reinforcement', *Proceedings of the First International RILEM Symposium on Self-Compacting Concrete*, Stockholm, Sept. 1999, pp. 275-289.
- [3] Sonebi, M. (2004), 'Medium strength self-compacting concrete containing fly ash : modelling using factorial experimental plans', *Cement and Concrete Research* 2004; 34(7):1199-1208.
- [4] Sonebi, M., Tamimi, A., Bartos, P.J.M. 'Performance and cracking behaviour of reinforced beams cast with self-compacting concrete', *ACI Materials Journal* 2003; 100(6):492-500.
- [5] Saul, A. G. A., (1951) 'Principles Underlying the Steam Curing of Concrete at Atmospheric Pressure,' *Magazine of Concrete Research*, Vol. 2, No. 6, March, pp. 127-140.
- [6] Carino, N.J. and Tank, R.C. (1992) 'Maturity Functions for Concrete Made with Various Cements and Admixtures', *ACI Materials Journal*, Vol. 89, No. 2, March-April, pp. 188- 196.
- [7] Freiesleben Hansen, P. and Pedersen J., (1977) 'Maturity Computer for Controlled Curing and Hardening of Concrete', *Nordisk Betong*, 1, pp. 19-34.
- [8] EFNARC (2005), "The European Guidelines for Self-Compacting Concrete Specification, Production and Use".

Effect of Steel Fibre Dosage on the Behaviour of Ultra High Performance Fibre Reinforced Concrete Beams and Slabs

William Wilson¹, Tomas O'Flaherty¹

¹Department of Civil Engineering & Construction, Institute of Technology, Ash Lane, Sligo, Ireland
email: william.wilson@mail.itsligo.ie, oflaherty.tomas@itsligo.ie

ABSTRACT: Ultra High Performance Fibre Reinforced Concrete (UHPFRC) is a relatively new form of concrete that exhibits enhanced strength, ductility and durability properties in comparison to conventional fibre reinforced and high performance concretes. Use of UHPFRC reduces the section sizes that can be used in a structure, which in turn reduces the structure's self-weight and the volume of concrete and raw aggregates used in its construction. However, a disadvantage of UHPFRC is that it results in a significant rise in material costs over normal and even high performance concretes. Therefore, the sustainability of this material must be improved to make UHPFRC a viable option for the construction industry. Costs are significantly higher in Ireland as certain constituents are not readily available. In this research a UHPFRC mix that uses locally sourced materials, where possible, has been developed to produce a more sustainably viable material for the Irish construction industry. The research reported here is focused on results from experimental tests on small scale UHPFRC beams and flat slabs with varying fibre dosages and cross sections, which were tested using a four point bending test and punching shear test respectively. Results from additional tests on specimens that included conventional steel bar reinforcement are also presented for comparison. The results obtained give an insight into the requirements for secondary reinforcement in UHPFRC structures, which is currently somewhat inconsistently defined in UHPFRC design guidelines and recommendations. The conclusions from this research will be applied to UHPFRC numerical modelling problems and aid in the development of design codes and guidelines.

KEY WORDS: fibre reinforced concrete, infrastructure, sustainable construction, ultra high performance fibre reinforced concrete

1 INTRODUCTION

Ultra high performance fibre reinforced concrete (UHPFRC) is characterised by significantly improved mechanical performance, extremely low permeability and tensile strain hardening [1]. The addition of steel fibres improves tensile strength, and also makes it possible to achieve required levels of ductility [2]. UHPFRCs are likely to have a compressive strength of 130 to 230 MPa while the flexural strength is usually between 25 and 60 MPa depending on the early age curing methods used [3].

UHPFRC appears to be an encouraging new material not only due to its enhanced strength and ductility but also because mixing and casting procedures are comparable to existing practices for normal strength concretes [4]. However, UHPFRC gives rise to a substantial increase in cost above that of normal concrete and even high performance concrete (HPC) and it is therefore appropriate to determine applications that fully utilize UHPFRC's mechanical properties and performance characteristics. While the use of UHPFRC has grown in recent years across developed countries; it is unexploited in Ireland. This is mainly because the Irish concrete industry views the high cost of producing UHPFRC as an inhibitor but this view does not consider the whole life cycle benefits associated with UHPFRC. By clearly establishing and demonstrating the advantages of this material, sustainability in the Irish construction industry can be greatly enhanced as demonstrated in studies in other countries [5].

Two types of UHPFRCs that are sustainably viable options for use in the Irish construction industry, one using a coarse sand and one using fine sand have been developed, with results indicating the fine sand mix is the superior of the two. This paper discusses the experimental work undertaken to determine the influence of steel fibre volume on the structural performance of the fine sand mix. The effect of 0%, 1% and 2% fibre volumes were investigated on beams with varying cross-section and slabs with varying depth. Tests were also conducted on specimens with and without secondary steel bar reinforcement to investigate the need for conventional steel bar reinforcement in UHPFRC structures.

1.1 Beam Testing

To date most experimental studies on UHPFRC reported in the literature have concentrated on obtaining the characteristic strengths of a single UHPFRC mix. In addition, limited experimental results are available on the structural behaviour of beams in bending and in shear. For the flexural design of conventional concrete all concrete structures can be analysed once the concrete compressive and steel yielding strengths are known. Unfortunately this concept cannot be applied to UHPFRC structures as the behaviour is different from that of conventional concrete [6]. Recommendations have been proposed by AFGC [7] and the JSCE [8] to predict the flexural and shear strength of UHPC and UHPFRC beams although these methods deal with only one mix strength and fibre dosage and cannot be applied to a range of strengths or fibre dosages. Tests on UHPFRC I-beams illustrated that the

inclusion of stirrups increases the shear capacity of prestressed and reinforced UHPFRC beams [9]. The study also highlighted that before yielding secondary steel shear reinforcement can help to control crack opening in the beams. Bunjie and Fehling [10] investigated the shear behaviour of UHPC beams with and without fibres and showed that beams with no fibre reinforcement exhibited a sudden shear failure, while beams with fibre reinforcement experienced a bending failure, which illustrates that fibres increase the shear carrying capacity of UHPFRC beams. Other experimental studies that have been conducted on small-scale UHPFRC beams have shown that the placing method has an effect on the flow of concrete and resulting orientation and dispersion of the steel fibres, which in turn have a major impact on both the flexure and shear strength of UHPFRC beams [6], [11]. The majority of research previously undertaken considers only one beam size and one fibre dosage. The tests conducted in this research investigate the effect of varying fibre dosage on UHPFRC beam strengths and also the effect of changing the beam height to build on previous work described above.

1.2 Slab Testing

The highest stresses in concrete flat slabs will occur at the slab-column connection and thinner slabs are susceptible to punching shear failure. A punching shear failure is defined by the formation of a cone shaped crack around the column perimeter before the steel reinforcement reaches yielding. Design codes for normal concrete have reasonably simplified procedures and equations for the analysis and design for punching shear resistance. These guidelines were developed using results from a wide range of experimental and analytical investigations. These procedures are restricted to conventional concrete design and in general are not suitable for use with UHPFRC. The limited number of tests conducted on UHPFRC slabs have reported challenges in determining the punching shear capacity for two reasons. Firstly, in tests conducted without the use of secondary steel, a flexural failure occurred as the flexural strength was lower than the punching shear strength [12], [13]. Secondly, while other tests conducted with secondary steel generally produce a punching shear failure it is unclear in UHPFRC how much the secondary steel contributed to the strength which means these tests cannot predict the punching shear strength of UHPFRC without secondary reinforcement [14]. A novel testing method was developed in which notches were cut at various perimeters around the column head to induce a punching shear failure at that location [15]. Results found that in UHPFRC the basic control perimeter is reduced in comparison to normal strength plain concrete and is in agreement with past studies on fibre reinforced concrete slabs [16].

2 THE UHPFRC MIX DESIGN

2.1 Development of the UHPFRC Mix

Particle size distribution (PSD) curves in conjunction with the modified Andreasen and Andersen model [17] were used to design the UHPFRC mix. The final mix design for each plain and fibrous mix is presented in Table 1. Mix quantities were determined by varying the percentage of each constituent that would add up to give a volume of one cubic metre and give a composed PSD curve that best matches the target curve

determined using the modified Andreasen and Andersen model. Each concrete batch, in Table 1 is denoted in two parts, the first part, UHPC or UHPFRC, highlights if the mix is plain or fibrous respectively. This is followed by a number to illustrate the percentage of steel fibres used and the letter F to show it was a fine sand mix e.g. UHPFRC-2F is ultra high performance mix with 2% fibres.

2.2 Materials

Rapid Hardening Portland Cement (RHPC) CEM I Class 42.5R was used as it achieves a higher rate of strength development in comparison to normal cement. Elkem 920D was used as the Microsilica as it improves the early age and final strengths, density and durability of the concrete. A fine sand with a PSD in the range of 10 μ m - 550 μ m was used. Sika ViscoCrete Premier was selected as the accelerating high range water reducing/superplasticiser admixture. This admixture is specifically used in concrete with high early strength development, high water reductions and excellent flowability. The steel fibres used in this research are Dramix OL 13/20 with a length of 13mm, a diameter of 0.20mm, and a tensile strength of 2600MPa.

Table 1. Material quantities in each mix

Material	UHPC-F (kg/m ³)	UHPFRC-1F (kg/m ³)	UHPFRC-2F (kg/m ³)
Cement	810	810	810
Microsilica	203	203	203
Fine Sand	1022	1022	1022
Superplasticiser	42	42	42
Water	178	178	178
Steel Fibres	0	77.5	155

3 EXPERIMENTAL PROGRAM

A total of 12 beams and 9 slabs were cast as part of the experimental program. Compression and flexure/in-direct tensile tests were conducted using 3 cylinders and 3 prisms respectively to obtain the characteristic strengths of each fibre dosage with the average result of each test being reported here.

3.1 UHPFRC Mixing and Curing Procedure

The mixing time and procedure of UHPC and UHPFRC can vary depending on the type and speed of mixer used with typical values ranging from 10 – 25 minutes. In this research mixing was conducted using a Creteangle Multiflow 56 litre horizontal pan mixer. Firstly, the sand and silica fume is dry mixed for 3 minutes. The cement was then added and the dry particles were mixed for a further 5 minutes until a uniform dry powder mix was achieved. Over a period of 2 minutes the water and superplasticiser, which were previously mixed together, were added to the dry mix. After a further 4-5 minutes a significant change from a dry to wet consistency of the mix occurred, known as “the turn”. After a further 3 minutes a wet paste concrete was achieved. At this point the plain UHPC mixes were ready and specimens were then cast into the various moulds and placed on a vibrating table for compaction. For the UHPFRC mixes, the steel fibres were added by hand to mix over a period of 1 minute and mixing

occurred for a further 3 minutes until a uniform fibre distribution was obtained. UHPFRC specimens were cast and vibrated in a similar fashion to the UHPC specimens. Total mixing time was approximately 18 and 22 minutes for the UHPC and UHPFRC, respectively. All specimens were covered with a damp hessian cloth and polythene sheets and kept at a constant temperature of 20°C for 24 hours at which time demoulding occurred. All specimens were then placed in a curing tank at 20°C ± 2°C until testing at 28 days.

3.2 Compressive and Tensile Strength Tests

The compressive strength and associated stress-strain curve was determined using cylindrical specimens with a diameter of 100mm and a height of 200mm. If the standard procedure of load control to determine cylinder strength of conventional concrete was used when testing UHPC and UHPFRC specimens the quick release of energy at peak load would not facilitate recording of the post-peak behaviour or the post peak stress-strain curve. The three specimens are loaded using load control at a rate of 0.5MPa/s to 85% of the expected failure load which was pre-determined using a sample cylinder tested to failure using load control. At this point the load control was switched to displacement controlled loading using three linear variable displacement transducers (LVDT's) equally spaced around the cylinder and attached to the machine and loading continued at a rate of 1µm/s. Therefore, when peak load was reached the sudden failure of the UHPFRC specimens was prevented and the post-peak behaviour was accurately recorded. The plain ultra high performance specimens still exhibited an explosive failure but using displacement controlled loading this behaviour was precisely recorded. The elastic modulus for each batch was then calculated from the stress-strain curves.

The standard prism flexure test is an indirect tensile test and a four point test method was selected for this research. Specimens had a span of 300mm and a breadth and height of 100mm. The purpose of this test was not just to determine peak tension stress but to also find the residual strength given by the fibres after first cracking occurred. The test was initially conducted at a speed of 2µm/s with servo feedback from the average of two deflection LVDT's placed on either side of the specimen at midspan. The test speed was increased to 8µm/s when peak strength was obtained.

3.3 Beam and Slab Specimen Details

A total of 12 beams were cast as part of the experimental program as shown in Table 2. Three ultra high performance concrete strengths with 0%, 1% and 2% fibre volume were tested to investigate the effect of fibre volume on the structural behaviour. Two different beam sizes were selected to determine if size effects existed in UHPC and UHPFRC in a comparable manner to conventional concrete. Due to testing machine limitations the maximum beam height was selected as 150mm and to ensure beams would not stress under their own self-weight the minimum beam height was selected as 120mm. All beams had a span of 1500mm and a height to width ratio of 1.5 which is the ratio typically used in UHPFRC beams [6]. The selected beam dimensions give span to depth ratios of 10 and 12.5 respectively which along with the aspect ratio of 1.5 are typical values for full scale concrete beams. Figure 1 illustrates the reinforcement arrangement within the cross

section of the two beam sizes. During casting of the UHPC and UHPFRC beams the concrete was placed at one end of the form and allowed to flow to the other end until the form was full to ensure uniform fibre distribution. All specimens were compacted using a vibrating poker. The nomenclature for the beam specimens presented in Table 2 consists of four parts. As outlined in section 2.1, the first part, UHPC or UHPFRC highlights if the mix is plain or fibrous. This is followed by a number to illustrate the percentage of steel fibres used and the letter F to show if it was a fine sand mix. Next the beam height is given, 120mm or 150mm, and lastly an R denotes secondary steel reinforcement is present. e.g. a beam denoted UHPFRC-1F-120-R is an ultra high performance fibre reinforced concrete mix with 1% fibres, 120mm deep and has secondary steel reinforcement.

Table 2. Beam specimen details

Beam Name	Fibre Volume (%)	Beam Height (mm)	Secondary Rebar Ratio (%)
UHPC-F-120	0	120	0
UHPC-F-120-R	0	120	1.3
UHPC-F-150	0	150	0
UHPC-F-150-R	0	150	1.3
UHPFRC-1F-120	1	120	0
UHPFRC-1F-120-R	1	120	1.3
UHPFRC-1F-150	1	150	0
UHPFRC-1F-150-R	1	150	1.3
UHPFRC-2F-120	2	120	0
UHPFRC-2F-120-R	2	120	1.3
UHPFRC-2F-150	2	150	0
UHPFRC-2F-150-R	2	150	1.3

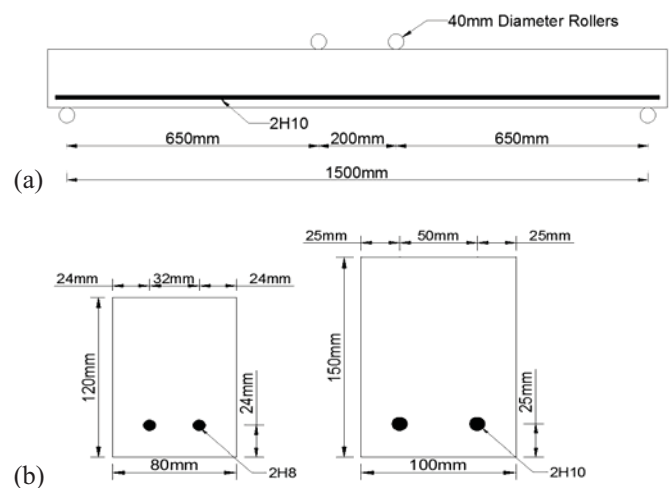


Figure 1. (a) 150mm beam longitudinal arrangement including loading and support locations and (b) Beam cross-section reinforcement arrangement.

Three slabs were tested for each of the ultra high performance concrete strengths. The specimen details are presented in Table 3 and are labelled in a similar manner to the beam specimens with the concrete strength and fibre volume followed by the slab thickness, and if secondary reinforcement was used it is denoted by the letter R. e.g. a slab denoted UHPFRC-1F-50 is an ultra high performance fibre reinforced concrete mix with 1% fibres, 50mm thick and has no

secondary steel reinforcement. The secondary reinforcement arrangement in the 50mm slabs is shown in Figure 2. The ultra high performance concrete mixes were placed by filling from the centre of the slab and allowing the concrete to flow to the edges of the formwork. Vibration of all specimens took place in a similar fashion to the beams.

Table 3. Slab specimen details

Slab Name	Fibre Volume (%)	Slab Height (mm)	Secondary Rebar Ratio (%)
UHPC-F-30	0	30	0
UHPC-F-50	0	50	0
UHPC-F-50-R	0	50	1.4
UHPFRC-1F-30	1	30	0
UHPFRC-1F-50	1	50	0
UHPFRC-1F-50-R	1	50	1.4
UHPFRC-2F-30	2	30	0
UHPFRC-2F-50	2	50	0
UHPFRC-2F-50-R	2	50	1.4

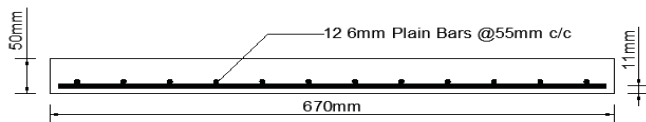


Figure 2. Slab reinforcement arrangement.

3.4 Test Arrangements for Beam and Slabs

All specimens were tested on a flexural frame with a 100kN capacity. Beam tests were conducted in a similar manner to the prism flexure tests described previously except the loading points were located only 200mm apart and the distance from each support to loading point was 650mm. Loading rate was controlled by displacement using two LVDTs which were attached to the loading frame and measured deflection at the beams midpoint as shown in Figure 3. It was determined from the literature that the 120mm and 150mm deep beams should be displaced at a rate of 3 μ m/s and 5 μ m/s respectively.



Figure 3. Beam flexural test setup.

Slabs were simply supported along each side at a distance of 20mm from the slab edge and loaded at the centre point using a square steel block with sides of 62.5mm to represent a punching load, as illustrated in Figure 4. The supports were located at the point of contra-flexure to encompass the hogging moment at the loading point. The 30mm and 50mm slabs were loaded using displacement loading at a rate 3 μ m/s and 5 μ m/s respectively.



Figure 4. Slab punching load test setup.

4 RESULTS AND DISCUSSION

4.1 Compressive and Tensile Strengths

The material properties of each mix type are given in Table 4. The values presented for the elastic modulus of each mix were calculated using the compression stress-strain curves shown in Figure 5. The results indicate how increasing the fibre dosage increases the values of all three strength properties investigated and how the addition of fibres dramatically changes the behaviour in the post-peak region of the compression stress-strain curve.

Table 4. Strength properties of each mix

Material Property	UHPC-F	UHPFRC-1F	UHPFRC-2F
Compression Strength (MPa)	126.4	130.1	146.7
Elastic Modulus (GPa)	44.12	45.00	46.15
Flexural Strength (MPa)	15.09	20.72	26.48

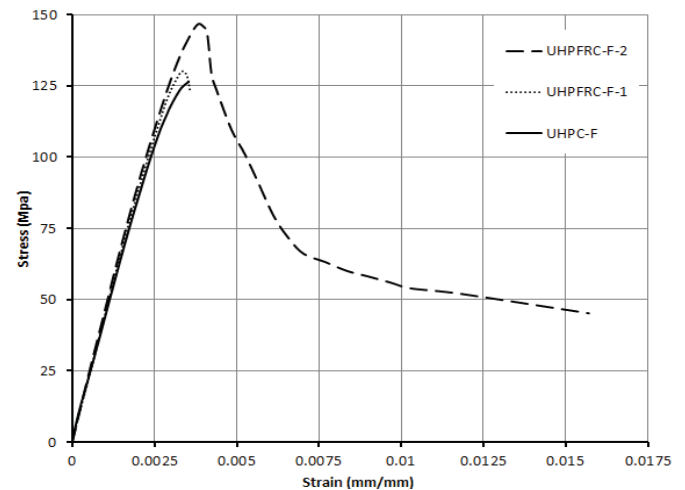


Figure 5. Compression stress-strain curves

4.2 Beam Peak Loads

The initial cracking loads and peak loads for each beam along with the failure mode is presented in Table 5 in four groups classified by beam size and inclusion or exclusion of secondary steel reinforcement. Firstly, by using the flexural strength of each mix presented in Table 4 to predict the peak load of the six beams without secondary reinforcement it was determined that the peak load was overestimated by 3% for

the UHPC-F beams, overestimated by 6% for the UHPFRC-1F beams and finally overestimated by 8% for the UHPFRC-2F beams. These results appear to indicate that size effects do exist in UHPC and UHPFRC and increase with fibre dosage. Comparison of results from the six beams with secondary steel demonstrate that the UHPC beams have the lowest peak load, as expected, and this value is increased for the UHPFRC beams with the 2% fibres given the highest peak loads. Furthermore, the results indicate that the two UHPFRC beams with 2% fibres and no secondary reinforcement, obtained peak loads approximately 30% lower than that of the UHPC beams with secondary reinforcement. This illustrates that by using UHPFRC in comparison to plain UHPC the requirements for secondary steel reinforcement are reduced.

Table 5. Beam initial cracking and ultimate loads

Specimen	Initial Cracking Load (kN)	Peak Load (kN)	Failure Mode
UHPC-F-120	-	8.82	Flexure
UHPFRC-1F-120	9.17	11.44	Flexure
UHPFRC-2F-120	8.47	14.89	Flexure
UHPC-F-150	-	16.53	Flexure
UHPFRC-1F-150	16.61	22.55	Flexure
UHPFRC-2F-150	14.55	30.10	Flexure
UHPC-F-120-R	7.09	22.74	Shear
UHPFRC-1F-120-R	8.12	28.17	Flexure
UHPFRC-2F-120-R	8.81	33.75	Flexure
UHPC-F-150-R	14.85	40.03	Shear
UHPFRC-1F-150-R	15.82	55.90	Flexure
UHPFRC-2F-150-R	16.84	64.66	Flexure

4.3 Beam Crack and Failure Patterns

The 120mm and 150mm deep beams exhibited similar failure patterns. For the two plain beams, with no fibres or secondary reinforcement failure occurred due to one single flexure crack at midspan, which propagated upwards from the bottom face of each beam. The four beams with fibre reinforcement but no secondary reinforcement initially cracked in a similar location to the plain beams. It is clear that the steel fibres bridged the initial crack and allowed the beams to carry additional load. As loading continued and the beam deflection increased these cracks increased in size and further micro-cracks appeared. The micro cracks did not appear to open significantly but continued to propagate to the beam's top face. Failure occurred due to one crack eventually opening up and fibre pullout occurring at midspan. This illustrates that the fibres in UHPFRC beams bridge the cracks and as a result redistribute stress across the cracks through the fibres. Therefore, the beams can undergo multiple cracking before fibre pullout and ultimate failure occurs.

Figure 6 presents the failure patterns for two of the 150mm deep beams with secondary steel reinforcement. For the UHPC beams with secondary reinforcement initial cracking occurred on the bottom face of the beam near midspan, as expected. However, a sudden shear failure was noted with a crack developing at the support location running along the rebar and then diagonally towards the loading point as shown in Figure 6 (a). Although no shear reinforcement was

provided in the beams preliminary calculations using EC2 illustrated that all beams should have failed due to flexure. This change in behaviour from the predicted results can be attributed to the significantly increased tensile and compressive stress capacity of UHPC, which changed the failure mode from a flexural failure to a shear failure. The benefits of adding steel fibres to the UHPC mix is clearly visible in Figure 6 (b), with the failure mode changing from a shear failure to a flexure failure. This demonstrates how steel fibres in ultra high performance concretes can be used in place of conventional shear links to prevent a sudden shear failure and thereby obtain quicker construction times.



Figure 6. Failure patterns for beams (a) UHPC-F-150-R failed in shear and (b) UHPFRC-2F-150-R failed in flexure.

4.4 Slab Peak Loads

Table 6 presents the initial cracking and ultimate loads of the slabs along with their respective failure modes. Failure modes are presented as failures due to flexure, punching shear or a combination of both in which the prominent failure mode is specified first. By comparing the UHPC and UHPFRC 50mm deep slabs with and without secondary reinforcement it is clear that the secondary reinforcement provided the greatest strength increase for the plain UHPC mix. The UHPFRC mixes with secondary reinforcement also portrayed an increase in strength over their unreinforced counterparts to a lesser extent. Consideration of the 30mm and 50mm slabs with no secondary reinforcement indicates that fibres contribute more to the load carrying capacity of thinner slabs. In a similar manner to the beam tests it is demonstrated that the UHPFRC-2F-50 slab obtained a higher failure load than the UHPC-F-50-R slab with secondary reinforcement. This also shows how fibre reinforcement in UHPFRC can be used as a substitute for conventional reinforcement.

Table 6. Slab initial cracking and ultimate loads

Slab	Initial Cracking Load (kN)	Ultimate Load (kN)	Failure Mode
UHPC-F-30	-	5.26	Flexure
UHPFRC-1F-30	5.81	16.52	Flexure
UHPFRC-2F-30	6.07	25.46	Shear-Flexure
UHPC-F-50	-	21.93	Flexure
UHPFRC-1F-50	25.74	36.52	Flexure
UHPFRC-2F-50	23.62	56.86	Flexure-Shear
UHPC-F-50-R	25.03	50.24	Shear
UHPFRC-1F-50-R	25.40	78.59	Shear-Flexure
UHPFRC-2F-50-R	26.10	86.96	Flexure-Shear

4.5 Slab Crack and Failure Patterns

The failure modes given in Table 6 highlight that the inclusion of fibres affects the slabs behaviour significantly. If

the three 30mm thick slabs are firstly considered it is shown that the failure mode is changed from flexure for the plain specimen to a shear-flexure for the 2% fibre mix. This illustrates for thin slabs, fibres increase the flexural strength to such an extent that the failure mode is changed to a punching shear failure. The same can be said for the 50mm slabs with no secondary reinforcement although the flexural strength increase is not as great as the failure mode in the UHPFRC-2F-50 slab is prominently flexure with shear also visible.

The UHPC-F-50-R slab failed due to punching shear as shown in Figure 7 (a) in which a punching shear perimeter is clearly visible. This type of failure was expected for the plain specimen due to the lack of shear reinforcement. By adding 1% fibres to this slab type the failure mode was changed to shear-flexure and furthermore by adding 2% fibres the failure mode became flexure-shear as shown in Figure 7 (b) where a large amount of flexure cracks are shown propagating from the slab centre with a small punching shear perimeter scarcely visible. This demonstrates that by adding fibres to secondary steel reinforced flat slabs the shear strength can be increased beyond the flexural strength to avoid a sudden shear failure.

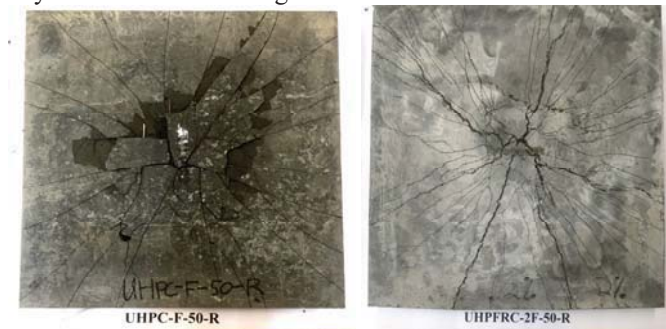


Figure 7. Failure patterns for slabs (a) UHPC-F-50-R fails in shear and (b) UHPFRC-2F-50-R fails in flexure-shear.

It was determined that the inclusion of steel fibres reduces the critical shear perimeter which is in agreement with previous studies. The average distance of the perimeter for the UHPC slab was $2.9d$ from the face of the loading point and this value reduced to $2.7d$ and $2.3d$ for the UHPFRC mixes with 1% and 2% fibres respectively.

5 CONCLUSIONS

Based on the results presented on the effects of fibre dosage on the behaviour of ultra high performance concrete the following conclusions can be drawn:

- UHPC beams with secondary longitudinal steel bar reinforcement exhibit a sudden shear failure although Eurocode equations predicted a flexure failure.
- UHPFRC beams with and without secondary reinforcement failed in flexure, which illustrates that steel fibres prevent shear failure occurring and could be considered as a substitute for conventional shear web reinforcement.
- UHPFRC with 2% fibres and no secondary steel can obtain similar strengths to UHPC beams and slabs with secondary reinforcement illustrating how fibres can be used instead of conventional reinforcement.
- The results from both the beam and slabs specimens demonstrate how UHPFRC has the ability to redistribute

stress and undergo multiple cracking before fibre pullout and failure occurs.

- The addition of fibres to slabs with secondary reinforcement reduces the punching shear perimeter.

ACKNOWLEDGEMENTS

The authors appreciatively acknowledge the following companies for sponsoring the materials for this research, Banagher Precast Concrete, Bekaert, Kerrigan's Quarry, Irish Cement and Sika Ireland. The research is funded under the Institute of Technology, Sligo President's Bursary Award.

REFERENCES

- [1] M. F. M. Zain, H. B. Mahmud, A. Ilham, and M. Faizal, "Prediction of splitting tensile strength of high-performance concrete," *Cem. Concr. Res.*, vol. 32, no. 8, pp. 1251–1258, 2002.
- [2] D. J. Kim, S. H. Park, G. S. Ryu, and K. T. Koh, "Comparative flexural behavior of Hybrid Ultra High Performance Fiber Reinforced Concrete with different macro fibers," *Constr. Build. Mater.*, vol. 25, no. 11, pp. 4144–4155, 2011.
- [3] C. Tam and V. W. Tam, "Microstructural behaviour of reactive powder concrete under different heating regimes," *Mag. Concr. Res.*, vol. 64, no. 3, pp. 259–267, 2012.
- [4] C. Wang, C. Yang, F. Liu, C. Wan, and X. Pu, "Preparation of Ultra-High Performance Concrete with common technology and materials," *Cem. Concr. Compos.*, vol. 34, no. 4, pp. 538–544, 2012.
- [5] F. Breu, S. Guggenbichler, and J. Wollmann, "Ultra-High Strength Concrete Mixtures Using Local Materials," *Vasa*, no. 575, pp. 1–13, 2008.
- [6] I. H. Yang, C. Joh, and B.-S. Kim, "Structural behavior of ultra high performance concrete beams subjected to bending," *Eng. Struct.*, vol. 32, no. 11, pp. 3478–3487, 2010.
- [7] Association Française de Génie Civil, "Ultra High Performance Fibre-Reinforced Concretes," p. 98, 2002.
- [8] Y. Uchida, J. Niwa, Y. Tanaka, and M. Katagiri, "Outlines of 'Recommendations for design and construction of ultra high strength fiber reinforced concrete structures' by JSCE," *Int. RILEM Work. High Perform. Fiber Reinf. Cem. Compos. Struct. Appl.*, vol. 4, no. March 2003, pp. 343–351, 2006.
- [9] F. Baby, J. Billo, J. Renaud, and C. Massotte, "Shear resistance of ultra high performance fibre-reinforced concrete I-beams," *Fract. Mech. Concr. Concr. Struct.*, 2010.
- [10] K. Bunjie and E. Fehling, "About shear force and punching shear resistance of structural elements of Ultra High Performance Concrete," in *Proceedings of the International Symposium on Ultra High Performance Concrete*, 2004, pp. 401–411.
- [11] N. V. Tue and S. Henze, "Determination of the distribution and orientation of fibres in steel fibre reinforced UHPC by photographic method," in *Proceedings of the second international symposium on ultra high performance concrete, Kassel*, 2008, pp. 505–12.
- [12] L. Moreillon, J. Nseir, and R. Suter, "Shear and flexural strength of thin UHPC slabs," *Proceeding Hipermat 2012. Third Int. Symp. UHPC Nanotechnol. High Perform. Constr. Mater.*, pp. 749–756, 2012.
- [13] D. K. Harris and C. Roberts-wollmann, "Characterization of punching shear capacity of thin ultra-high performance concrete slabs," in *Proceedings of the second international symposium on ultra high performance concrete, Kassel*, 2008, no. December, pp. 727–34.
- [14] H. A. A. Al-Quraishi, "Punching Shear Behavior of UHPC Flat Slabs," Kassel, 2014.
- [15] A. M. T. Hassan, G. H. Mahmud, S. W. Jones, and C. Whitford, "A new test method for investigating punching shear strength in Ultra High Performance Fibre Reinforced Concrete (UHPFRC) slabs," *Compos. Struct.*, vol. 131, pp. 832–841, 2015.
- [16] R. Narayanan and I. Y. S. Darwish, "Punching shear tests on steel-fibre-reinforced micro-concrete slabs," *Mag. Concr. Res.*, vol. 39, no. 138, pp. 42–50, 1987.
- [17] A. H. Andreasen and J. Andersen, "Ueber die Beziehungen zwischen Kornabstufungen und Zwischenraum in Produkten aus losen Körnern (mit einigen Experimenten)," *Kolloid-Zeitschrift*, vol. 50, no. 3, pp. 217–228, 1930.

Resistance of alkali activated slag concretes to chloride environments

Dali Bondar¹, Douglas Thompson², Sreejith Nanukuttan³, Marios Soutsos⁴ and P.A. Muhammed Basheer⁵

¹Research Fellow in School of Planning, Architectural and Civil Engineering, Queen's University Belfast, BT9 5AG

²Master Student in School of Planning, Architectural and Civil Engineering, Queen's University Belfast, BT9 5AG

³Senior Lecturer in School of Planning, Architectural and Civil Engineering, Queen's University Belfast, BT9 5AG

⁴Professor in School of Planning, Architectural and Civil Engineering, Queen's University Belfast, BT9 5AG

⁵Professor and Head of School of Civil Engineering, Leeds University, LS2 9JT

email: D.Bondar@qub.ac.uk; dthompson45@qub.ac.uk; s.nanukuttan@qub.ac.uk; m.soutsos@qub.ac.uk; P.A.M.Basheer@leeds.ac.uk

ABSTRACT: Researchers are focusing their attention on alternative binder systems using 100% supplementary cementitious materials as it allows better control over the microstructure formation and low to moderate environmental footprint. One such system being considered is alkali activated slag concretes (AASC), made by adding alkalis such as sodium hydroxide and sodium silicate to ground granulated blast furnace slag (GGBS). Whilst they have a similar behaviour as that of traditional cement systems in terms of strength and structural behaviour, AASC are reported to exhibit superior performance in terms of abrasion, acid resistance and fire protection.

In this article, the authors investigate chloride ingress into different grades of AASC. The mix variables in AASC included water to binder, and binder to aggregate ratio, percentage of alkali and the $\text{SiO}_2/\text{Na}_2\text{O}$ ratio (silica modulus, Ms). The first challenge was to develop mixes for different range of workability (with slump values from 40mm to 240mm) and reasonable early age and long term compressive strength. Further chloride ingress into those mixes were assessed and compared with the data from normal concretes based on literature. Findings show that compared to the PC concretes, the AAS concretes have lower rate of chloride ingress.

KEY WORDS: Alkali activated slag concretes; Cement less binders; Workability optimisation; Chloride environments; Chloride resistance.

1 INTRODUCTION

Alkali Activated Materials (AAM's) have been under consideration as an alternative binder system since 1908 [1]. However, despite having been aware of this materials potential for over a century, there is still relatively little known about the durability of AAM, especially the resistance to chloride ingress. Concrete is the foundation of modern civilisation, and cement is the component that contributes the most to carbon footprint of concrete. With an increasing concern over global warming, lower carbon emission is becoming a key factor in all areas of society. AAM's in general has lower embodied carbon dioxide than cement whilst offering similar strength characteristics, and depending on the mix this can be less than half the CO_2 cement produces per ton [2] while according to MPA new CEM I emissions are 640kg/ton. The CO_2 emission of the best mix in this study has been evaluated and is 40% of the mix produced with 100% CEM I. Another factor contributing to the renewed interest is that AAM's use industrial by-products as precursor, and so the potential for reducing material going to landfill and also using up the stockpile of ash and other by-products is also appealing.

There are three main types of AAM, each based on the precursor used, Metakaolin, Pulverised Fly Ash (PFA) and Ground Granulated Blast furnace Slag (GGBS). GGBS appears to be closest to conventional cement, and does not require curing at elevated temperature. In general, GGBS based AAM requires less activator than other AAMs, to start the reaction and to form the binder [3-5]. There is limited data available on resistance to chloride ingress in AASC. However, the findings reported by Torgal et al. suggest that the steady

state diffusion of chlorides in AAS binder is about $1.0 \times 10^{-14} \text{ m}^2/\text{s}$, which is much lower than in Ordinary Portland Cement binders ($1.4 \times 10^{-13} \text{ m}^2/\text{s}$) [6].

The workability of AASC using crushed aggregates is an area of concern as often excess water is required to enhance the workability. As the water evaporates out of the final product, larger pores are formed and this will increase the chloride ingress. Therefore, an experimental programme was developed to study the workability, strength development and resistance to chloride ingress for a range of AASC mixes. Workability ranging from S2 to S5 were (S2~40mm to S5>220mm) were targeted by changing the water to binder ratio, binder content, percentage of alkali and the silica modulus ($\text{SiO}_2/\text{Na}_2\text{O}$ ratio, Ms). Further the fresh properties, compressive strength at different ages, surface electrical resistivity (SR), bulk resistivity and non-steady state chloride migration were determined and reported for these various AAS concretes.

2 EXPERIMENTAL DETAIL

2.1 Materials

The primary raw material used in this study is a granulated blast furnace slag which was provided by ECOCCEM - Ireland. The chemical and physical properties are presented in Table 1 and 2.

Table 1: Oxide composition of GGBS

precursor	Component (mas% as oxide)					
	SiO_2	Al_2O_3	CaO	Fe_2O_3	MgO	LOI
GGBS	35.7	11.2	43.9	0.3	6.5	0.31

Table 2: Physical properties of GGBS

ECOCCEM GGBS	
Fineness $\geq 45\mu$	7.74%
Particle density	2.86
Water absorption	35.14%

Sodium hydroxide (NaOH) powders (or pellets) were dissolved in water to produce the alkaline solutions. The chemical composition of the sodium silicate solution was 15.5% sodium oxide (Na_2O), 30.5% silicon oxide (SiO_2) and 54% water. In this study, NaOH% was selected 4, 6, and 8% of slag weight and silicate modulus was selected 0.45 and 1.0.

The aggregates used in this study was crushed basalts from local sources in Northern Ireland and comprised 16.5mm and 10mm crushed coarse and fine aggregates and 4mm sand. These were combined in a ratio of 48:12:40 to get the maximum packing density in AASC mixes. Properties of both the aggregates are reported in Table 3. Potable tap water (i.e. drinking quality water) was used to make the concrete mixes.

Table 3: Physical properties of aggregates

Aggregates	Bulk specific gravity	Bulk SSD Specific gravity	Water Absorption (%)
Sand(0-4mm)	2.72	2.73	0.75
Fine Crushed Agg. (5-10mm)	2.67	2.75	3.14
Coarse Crushed Agg.(10-16mm)	2.60	2.67	2.60

2.2 Mixing

All the concrete mixtures were mixed in a laboratory pan-mixer. Crushed basalts aggregates and sand were dry mixed together for a minute and after adding the GGBS powder, mixing continued for 2 minutes and then the sodium hydroxide solution was added and after 2 minute further mixing, sodium silicate solution was added and mixing continued for a minute. The details of the different mixtures and their essential properties are presented in Table 4.

2.3 Measuring fresh properties

The slump test and flow test of each mix was carried out and the air content of mixes was measured in accordance with BS EN 12350 [7-8].

2.4 Casting and curing of the specimens

From each concrete mix, nine 100x100mm cubes, three 100x200mm cylinders and one 250x250x150 mm block were cast for the determination of compressive strength[9], 4-point Wenner probe electrical resistivity, bulk resistivity and chloride diffusivity[10]. The concrete specimens were cast in three layers and compacted on vibrating table. After casting, all the moulded specimens were covered with plastic sheets and left in the casting room for 24h. They were then demoulded and the block was wrapped in three layers of plastic wrap and other samples kept in a sealed plastic zip bag until test date.

2.5 Test preparations and procedures

In order to determine chloride diffusivity of AAS concretes three cores of diameter 100 mm per mix were cored from the 250x250x150 mm concrete block at age of 42 days. A slice with a thickness of 50 mm was cut off from each core after removing 5mm from top finishing surface. The vacuum saturation regime was used to precondition the slices so that the chloride flow is predominantly diffusive and initial sorption or capillary forces do not dominate. The vacuum was applied to remove air for three hours duration and released afterwards. Samples were wrapped in hessian saturated in deionised water to prevent leaching of ions from them and placed in the container. The weight of the sample was noted after an hour for weight (W_1) and then apply vacuum followed by further saturation. Weight was checked again (W_2). Usually after 6 hour, when $W_i - W_{(i-1)}$ was less than 0.1%, i.e., <1g of change for a 1kg, the samples were considered fully saturated. After conditioning to a surface-dry condition, an epoxy resin (Sika Gard-680S) was applied onto the surfaces of the specimens in three layers except the two test surfaces (cut surface). Chloride penetration depth and non-steady state migration coefficient of these concretes were determined by carrying out the test as outlined by NT BUILD 492 [10].

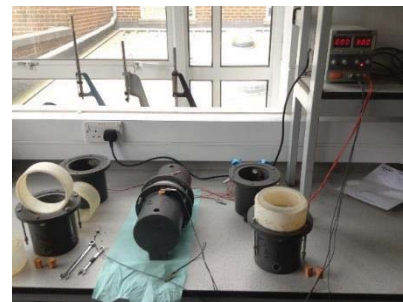


Figure 1 Cells for performing non-steady state migration test as per NT Build 492 [10].

Bulk resistivity measurement was performed on the same samples before and after the NT BUILD 492 test. Test set-up for measuring resistivity is shown in Figure 2.



Figure 2 Bulk resistivity test equipment and sample

The surface resistivity was determined using the Wenner four-probe on 100x200mm cylinders. The top face of cylinder was marked at the 0, 90, 180, and 270 degree points and four-probe SR meter was placed on the longitudinal surface of the concrete ensuring that all four probes were in contact with the concrete surface at each degree, see Figure 3. The resistivity measurement was recorded (two values at each degree) and

the average of eight measurements was taken as the surface resistivity.

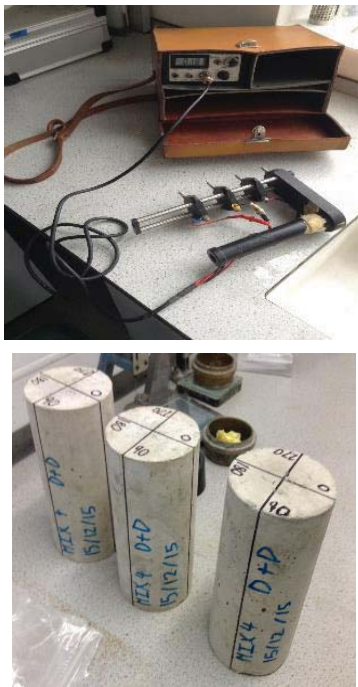


Figure 3 Surface resistivity test equipment and samples

3 RESULTS AND DISCUSSIONS

3.1 Fresh properties and compressive strength

The slump value of the concretes show that all the mixes had a slump greater than 40 mm. The mix design for the AAS concretes consisted of using various water to binder ratio, binder content, percentage of alkali and the $\text{SiO}_2/\text{Na}_2\text{O}$ ratio (silica modulus, Ms) to get different grade of AAS concretes with different classes of workability (Table 4).

Table 4: The details of the different mixtures and their properties

Mix No.	Slag (kg/m ³)	Ms (=SiO ₂ /Na ₂ O)	NaOH (%)	W/B	Slump (mm)	2days Comp. St.	28days Comp. St.	Concrete Grades
1	300	0.45	4	0.6	40	15.3	27.1	M25
2	360	0.45	4	0.7	225	11.1	21.5	M20
3	400	0.45	4	0.6	215	15.3	26.4	M25
4	400	0.45	4	0.55	108	17.8	30.0	M30
5	400	0.45	6	0.6	215	21.2	35.8	M35
6	400	0.45	6	0.55	135	24.7	44.0	M40
7	400	0.45	8	0.55	225	38.4	53.6	M50
8	400	1.0	4	0.55	160	25.8	47.8	M45
9	400	1.0	6	0.55	203	33.9	62.7	M60
10	400	1.0	8	0.55	240	33.7	64.4	M60

In all the mixes, the W/B (given in Table 4) included the total water in the mix including the water from water glass. All mixes met the minimum slump and compressive strength

requirement for their use in chloride environments, such as S2 and C20/25 specified in BS8500-1:2015 for XS (marine) environments. However, mixes 1 to 3 and 5 do not meet the maximum water-cement ratio stipulated by the standard. The mixes with 300 Kg/m³ and 400 Kg/m³ were used to study the effect of binder content on properties investigated. 300 Kg/m³ cement content was in accordance with binder contents suggested by BS8500-1:2015 [11] for XD1 (other than sea water) environments. Comparing mix 1 and 3 shows that increasing the binder content increases the paste which is helpful in increasing the workability from 40mm to 215mm. It also decreased the air content in fresh concrete from 2.5% to 0.4% however it had no major effect on strength. This is to be expected as the mix design was done based on a particle packing optimisation and therefore, the paste is filling in the voids and strength might have been optimised by the aggregate fraction and paste strength. Thus the strength of mixes with same chemical activators contents and different slag contents does not show significant differences. Increasing 10% water doubled the workability (comparing mix 4 to mix 3), while decreasing the strength by 14%.

Literature shows that increasing the sodium oxide content results in increased workability, reduced setting times and higher compressive strength. But high concentrations resulted in loose structure in sodium hydroxide activated samples [12-15]. The slump and flow results of the concretes are presented in Figure 4 and 5. Except mix no 7, all mixes flow value follow the same trend as Slump results. For the same water to binder ratio (0.55), comparing mix no. 4, 6 and 7 and mix no. 8, 9 and 10 with two different Ms ratio shows that the slump values of the AAS concretes with same Ms ratio increased with the increase of NaOH%. While the flow values decreases in the first group with lower Ms ratio and increases in the second group with higher Ms ratio. The slump and flow values also increased with the increase of Ms which can be seen by comparing mix no. 4 to 8, 6 to 9 and 7 to 10 in three different groups with three different NaOH%. In lower NaOH%, with the increase of Ms, the increase of slump is more pronounced. An increase in modulus Ms for mixes with higher alkali content, means more silicates are present, this whilst increasing the viscosity will reduce slump.

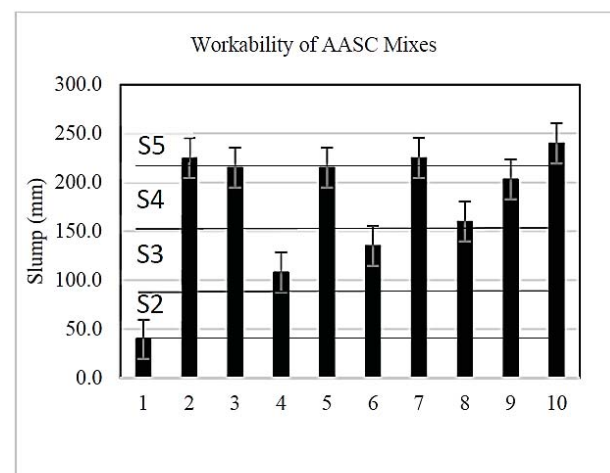


Figure 4 Slump results of AAS concretes

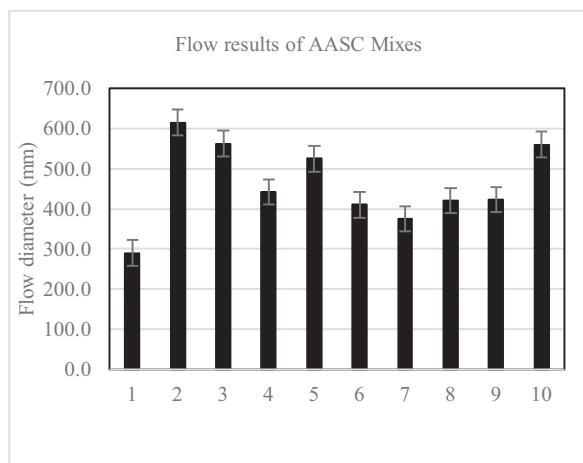


Figure 5 Flow results of AAS concretes

The air content of fresh mixes of AAS concretes is presented in Figure 6. It can be seen that in mixes made with higher alkaline percentage the air content is lower (comparing mix no. 4 to 6 and 7 and mix no. 8 to 9 and 10) and using higher silica content has had no major effect especially for mixes with lower alkaline content (comparing mix no. 4 to 8).

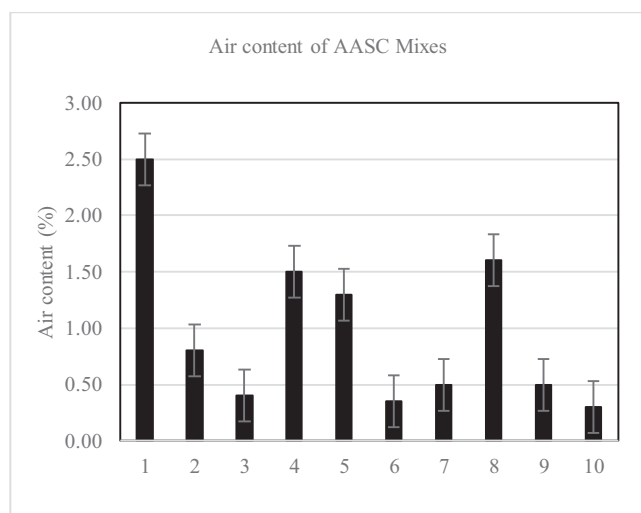


Figure 6 Air content in fresh mixes of AAS concretes

Figure 7 shows the compressive strength of AAS concretes mixes at 2, 7 and 28 days. The increase of NaOH% and Ms generally increases the compressive strength of AAS concretes, which is in agreement with the results reported by the others. This can be because of more N-A-S-H (sodium aluminosilicate hydrate) reacted product generated based on the increase of NaOH% and more C-A-S-H (calcium aluminosilicate hydrate) reacted product produced based on the increase of SiO₂ content. From the 28 day compressive strength (Table 4) it can be seen that mix no. 9 and 10 achieved the required strength for the exposure classes XS3, XD3. It is worth noting that for mix 10 setting time was around half an hour. Mixes no. 6, 7 and 8 seems to met the strength requirement for the exposure classes XS1, XD1 and XD2.

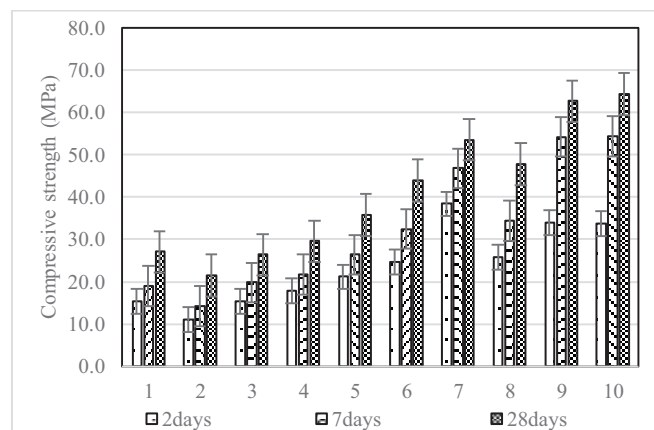


Figure 7 Compressive strength of AAS concretes mixes at 2, 7 and 28 days

3.2 Resistivity and Diffusivity

Figure 8 depicts the bulk/ surface electrical resistivity for different AAS concrete mixtures, respectively. Average values of bulk and surface resistivity data (from the three replicates) for all mixtures show the resistance to flow. Therefore higher resistivity could be attributed to denser structure with low connected porosity and/or less conductivity of the binder matrix and such mixes will be expected to be superior in resisting ionic (chloride) flow. They show that higher binder content in AAS concretes resulted in higher bulk resistivity but no such effect is visible on surface resistivity, indicating the lack of sensitivity of surface resistivity for assessing the whole concrete. While higher water to binder ratio (~10%) shows higher surface resistivity with no changes in bulk resistivity. Furthermore bulk electrical resistivity decreases for mixes made with higher silica modulus but surface electrical resistivity increases. This can show inhomogeneity of AAS concretes in conducting electricity from the surface layers and cross section. For mixes with same silica modulus, the surface resistivity decreases with increasing of sodium oxide percentage which is more regular in mixes with Ms=1. Whereas the bulk resistivity seems to have an extrema point which is at NaOH=6%. This may be related to the alkali content which is required to produce maximum reacted products.

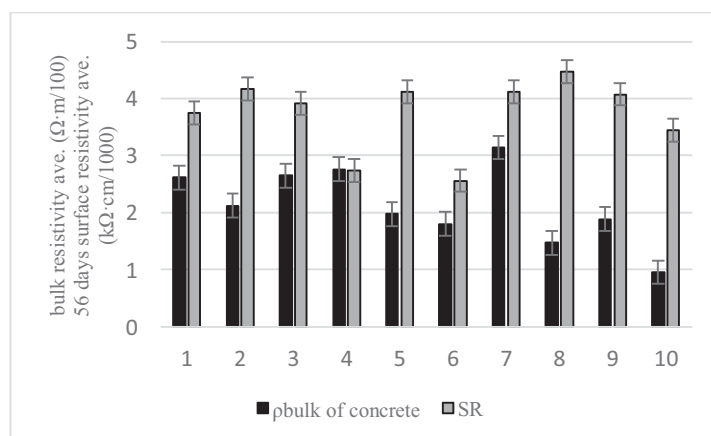


Figure 8 pbulk and SR of the AAS concrete mixes

Figure 9 shows the bulk resistivity before and after the samples for each mix underwent chloride penetration from NT BUILD 492. These results show that the resistivity after this test is relatively close to the resistance before, and it would seem this means that the voltage used in this test does not cause damage to the specimens, and therefore influence the results. Damage to the samples from high voltage tests has been of concern with other accelerated tests [1]. More importantly, the test seems to have not altered the ionic nature of the sample and therefore the chloride penetration will be marginal as shown in Figure 11.

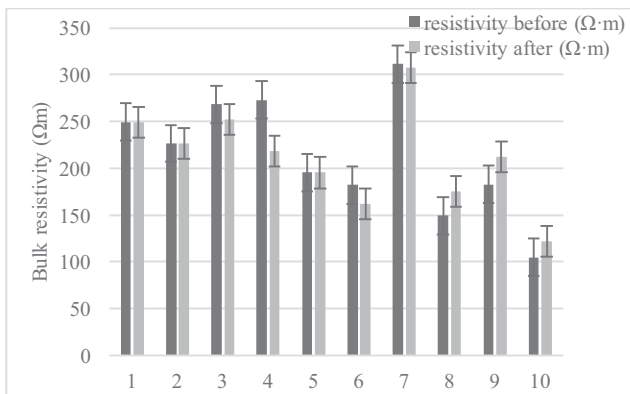


Figure 9 Bulk resistivity before and after NT BUILD 492

3.3 Chloride penetration depth

The Chloride penetration depths of samples were measured by caliper based on colour change boundary resulted after splitting the NT 492 test samples and spraying with AgNO_3 which is shown in Figure 10.



Figure 10 Splitted sample slices sprayed with Silver Nitrate

Figure 11 presents the chloride penetration depth in AAS concrete mixes and their non-steady state chloride migration coefficient calculated based on the penetration depth. The test voltage was considered to meet the maximum current limits in the standard between 20V and 35V and the test duration was 48hours for all the mixes which is twice of the duration suggested in standard for normal concretes. Although the pore solution conductivity of AAS concrete is higher than normal concrete, the final current passed through samples was between 10 and 30mA for different mixes which was still smaller than that passed through OPC concrete (~50mA for 30V[16]) and confirms the superior pore structure of this type

of concrete. As shown in Figure 11, the chloride penetration depth of AAS concretes was between 6mm to 10.5mm for different mixes and the non-steady state migration coefficient for these concretes varied from 1.12 to $2.24 \times 10^{-12} \text{ m}^2/\text{s}$ (except mix 10 which was $3.4 \times 10^{-12} \text{ m}^2/\text{s}$). These are much lower than the depth and D_{nssm} reported for OPC concrete [16-17] (the chloride penetration depth of OPC concrete sample was 41.5mm and the non-steady state migration coefficient was $3.36 \times 10^{-12} \text{ m}^2/\text{s}$ for the same test voltage and half test duration).

The above non-steady state migration coefficients were calculated using the chloride ion concentration, C_d , provided in the standard. The value, 0.07N, is the chloride concentration at which the silver nitrate produces a white precipitate. This value is for OPC concretes, and would not necessarily apply to the binders used in this study, however other research has shown that this figure is acceptable, and possibly even more accurate for binders such as GGBS [18-19]. This would indicate that the test is suitable for AAS, but to get a representative chloride depth, a higher voltage or longer duration is necessary as stated elsewhere [16].

The non-steady state migration coefficient, D_{nssm} , of the AAS concretes was found to be influenced by both NaOH% and Ms. For Ms equal to 0.45, an increase in NaOH% from 4 to 8 resulted in a decrease in D_{nssm} while the lowest D_{nssm} resulted when NaOH% is 8%. Ms of 0.45 and NaOH% of 8%, proved to be the optimum to give the lowest D_{nssm} .

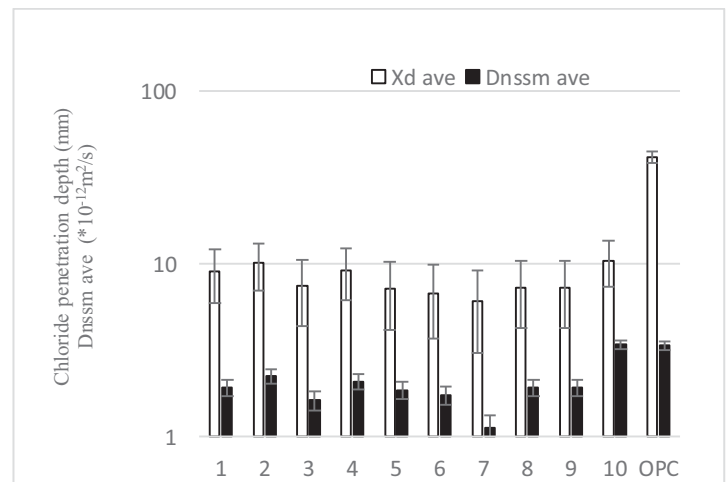


Figure 11 Chloride penetration depth and D_{nssm} of the ASSC mixes resulted from non-steady state chloride migration test

3.4 Correlation chloride migration coefficient and electrical resistivity

The results show that chloride ingress in AAS concretes can hardly be predicted by electrical resistivity because the resistivity of these concretes relies on pore structure and pore solution conductivity. It can be found that the non-steady state migration coefficient, D_{nssm} , of the AAS concretes is more related to their bulk resistivity as shown in Figure 12.

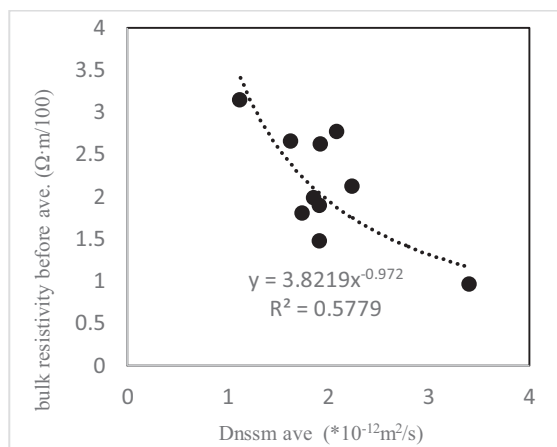


Figure 12 Correlation of Dnssm and bulk resistivity of AASC

4 Conclusion

- The work shows that AAS concretes can be designed for different class of workability and grades of concrete which are suitable for chloride environment.
- Typically AAS concretes require a water/binder ratio of 0.55, which is close to the maximum acceptable limit, and is the limit for XD3 and XS3 chloride exposure classes.
- A modulus, M_s of 0.45 and NaOH% of 8%, proved to be the optimum to give the lowest Dnssm and minimum chloride penetration depth.
- The chloride penetration depth and the non-steady state migration coefficient of AAS concretes are much more lower than OPC concretes and comparable to PC blended concretes.

REFERENCES

- [1] J.L. Provis, J.S.J. van Deventer, Eds., *Alkali-Activated Materials: State-of-the-Art Report*, RILEM TC 224-AAM, Springer/RILEM, Dordrecht, 2014, ISBN 978-94-007-7672-2
- [2] Provis, J.L., Palomo, A., Shi, C. (2015) 'Advances in Understanding Alkali-Activated Materials', *Cement and Concrete Research*, 78, 110–125
- [3] Li, C., Sun, H., Li, L. (2010) 'A Review: The Comparison between Alkali-Activated Slag (Si+Ca) and Metakaolin (Si+Al) Cements', *Cement and Concrete Research*, 40, 1341–1349
- [4] White, C. E., Daemen, L. L., Hartl, M., Page, K. (2015) 'Intrinsic differences in atomic ordering of calcium (aluminosilicate) hydrates in conventional and alkali-activated cements', *Cement and Concrete Research*, 67, 66–73
- [5] Lecomte, I., Henrist, C., Li'egeois, M., Maseri, F., Rulmont, A., Cloots, R. (2006) '(Micro)-structural comparison between geopolymers, alkali-activated slag cement and Portland cement', *Journal of the European Ceramic Society*
- [6] F. Pacheco-Torgal, J.A. Labrincha, C. Leonelli, A. Palomo, P. Chindaprasirt, *Handbook of Alkali-Activated Cements, Mortars and Concretes*, Woodhead Publishing, 2015, ISBN 978-1-78242-276-1
- [7] BS 1881-125 (2013) Testing concrete-Part 125: Methods for mixing and sampling fresh concrete in the laboratory, BSI, ISBN 978 0580 77923 7
- [8] BS EN 12350-2, 5&7 (2009) Testing fresh concrete-Part 2, 5&7: Slump test and Flow test and Air content measurement, BSI, ISBN 978 0 580 58789 4
- [9] BS EN 12390-3 (2009) Testing hardened concrete-Part 3: Compressive strength of test specimens, BSI, ISBN 978 0 580 76658 9
- [10] NT BUILD 492 (1999) Concrete, mortar and cement-based repair materials: chloride migration coefficient from non-steady-state migration experiments, Published by NORDTEST, ISSN 0283-7153
- [11] BS 8500-1 (2015) Concrete—complementary British Standard to BS EN 206-1—part 1: method of specifying and guidance for the specifier, BSI, ISBN 0 580 48251 0
- [12] Bondar, D., Lynsdale, C.J., Milestone, N.B., Hassani, N., Ramezaniapour, A.A. (2011) 'Effect of type, form, and dosage of activators on strength of alkali-activated natural pozzolans', *Cement and Concrete Composites*, 33, 251–260
- [13] Chi, M. (2012) 'Effects of dosage of alkali-activated solution and curing conditions on the properties and durability of alkali-activated slag concrete', *Construction Building Material*, 35, 240–245
- [14] Cihangir, F., Ercikdi, B., Kesimal, A., Deveci, H., Erdemir, F., (2015) 'Paste backfill of high-sulphide mill tailings using alkali-activated blast furnace slag: Effect of activator nature, concentration and slag properties', *Minerals Engineering*, 83, 117–127
- [15] Ma, Q., Nanukuttan, S.V., Basheer, P.A.M., Bai, Y., Yang, C. (2015) 'Chloride transport and the resulting corrosion of steel bars in alkali activated slag concretes', *Materials and Structures*, DOI 10.1617/s11527-015-0747-7
- [16] Ma, Q. (2013), *Chloride transport and chloride induced corrosion of steel reinforcement in sodium silicate solution activated slag concrete*, PhD Thesis, Queens University of Belfast, Northern Ireland, UK.
- [17] Nanukuttan, S.V., Basheer, P.A.M., McCarter, W.J., Tang, L., Holmes, N., Chrisp, T.M., Starrs, G., Magee, B., (2015), 'The performance of concrete exposed to marine environments: Predictive modelling and use of laboratory/on site test methods', *Construction and Building Material*, Article in press
- [18] Elfmarkova, V., Spiesz, P., Brouwers, H.J.H. (2015) 'Determination of the chloride diffusion coefficient in blended cement mortars', *Cement and Concrete Research*, 78, 190–199
- [19] Iyoda, T., Harasawa, Y., Hosokawa, Y. (2013) 'STUDY ON THE CHLORIDE DIFFUSION COEFFICIENT CALCULATED FROM A SIMPLE ACCELERATED CHLORIDE PENETRATION TEST USING ELECTRICITY', Proceedings of the Thirteenth East Asia-Pacific Conference on Structural Engineering and Construction (EASEC-13), Sapporo, Japan, C-6-6, <http://hdl.handle.net/2115/54302>

The Influence of Basalt Fibres on the Mechanical Properties of Concrete

Paul Archbold¹, Ana Caroline da Costa Santos², Adam Loonam¹

¹Faculty of Engineering & Informatics, Athlone Institute of Technology, Dublin Road, Athlone, Co. Westmeath, Ireland

²Universidade Tecnológica Federal do Paraná. Departamento Acadêmico de Construção Civil, Brazil.

email: parchbold@ait.ie

ABSTRACT: Fibre-reinforced concrete is commonly used in both structural and non-structural applications, particularly in precast concrete members. Traditionally, the fibres are either steel or (more recently) polypropylene.

The addition of fibres to the concrete matrix has been reported to offer improved post-crack performance and to enhance the concrete's toughness, which is important when transporting and handling smaller precast elements. The influence of fibres on mechanical properties such as compressive and tensile strength is less well established, with conflicting reports in the literature. Alternatives to both steel and polypropylene fibres have been suggested, with recent research turning to the use of basalt fibres. This paper reports on the influence of basalt fibres on the mechanical properties of both fresh and hardened concrete. A range of fibre additions have been examined and a series of tests to determine the rheological properties of fresh concrete, along with the compressive and tensile strengths of the hardened material. The results of these tests are benchmarked against published values and against control mixes and are presented here.

KEY WORDS: Basalt, FRC, compressive strength, flexural strength, workability, fibre

1 INTRODUCTION

Modern precast concrete manufacturers favour the use of fibre reinforced concrete (FRC) for a number of reasons, including the increased toughness of thin concrete sections, which makes them less vulnerable to damage during lifting and transport operations. Fibres also serve to limit crack propagation and improve post-cracking performance of concrete structures. While steel is the most common type of reinforcing fibre, more recently other materials have begun to gain widespread use. These include polypropylene and glass fibres. Indeed, the use of glass fibres to reinforce concrete has been promoted since early in the 20th century, with large-scale industrial production of glass fibre reinforced concrete (GFRC) taking hold in the 1970's [1].

Even more recently, researchers have begun to look at alternative materials, including natural fibres and engineered fibres such as carbon and basalt. Basalt fibres offer advantages over steel and glass in certain applications such as their performance in fire, due to their higher melting point [2] and their improved resistance to alkali environmental attack [3].

1.1 Workability of Basalt Fibre Reinforced Concrete (BFRC)

Similar to the use of other fibre types, the use of basalt fibres tends to significantly reduce the workability of the fresh concrete. Many authors report this reduction in slump values with increasing fibre content. Ma [4] suggests that this is due to two factors: firstly, there is increased friction between the constituent materials due to the presence of the fibres and secondly, unless the fibres have been pre-soaked, they will absorb water, leaving less free water in the concrete mix.

1.2 Compressive Strength of BFRC

Several authors have reported that the addition of low volume (<1% by volume) inclusion of basalt fibres has a positive effect on the compressive strength of the concrete [4], [5], [6], with increases in the 28-day strength of up to 24% with just 0.5% by volume of fibres [4]. Many of these also report an optimum fibre inclusion of approximately 0.2% to 0.4% by volume. Conversely, some researchers have reported a negative impact, with the use of fibres actually reducing the compressive strength [7], [8], with Dias & Thurmaturgo [7] recording a decrease in compressive strength of almost 28% for 0.5% vol of fibres. Interestingly in the case of Dias & Thurmaturgo, the fibre length was 45mm, while most researcher have employed shorter fibres in the length range of 12mm to 22mm. Palchik et al [9] compared the effects of short and long fibres and found that the longer fibres yielded smaller gains in compressive strength. Figure 1 shows a summary of reported values from the literature.

1.3 Flexural Strength of BFRC

The flexural strength of BFRC has proven to be more consistent with the introduction of basalt fibres. From the literature available, it appears that the flexural strength of samples consistently increases with increasing basalt fibre content [4], [5], [7]. Of interest is the fact that, similar to the compressive strength, there appears to be an optimum value for the fibre dosage, which is in the same region as the compressive strength values, lying between 0.2% and 0.4% by volume of concrete.

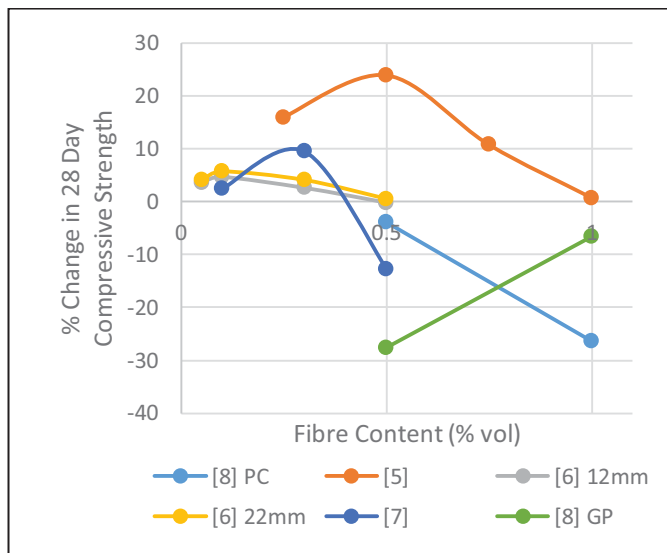


Figure 1. Reported Influence of Basalt Fibres on the 28-Day Compressive Strength of Concrete

Notwithstanding the evidence reported above, there is very little literature available to definitively establish robust relationships between the workability, compressive strength and flexural strength respectively of basalt fibre reinforced concrete. The aim of this study, therefore, is to examine these relationships and to add to the body of knowledge in this regard.

2 EXPERIMENTAL PROGRAMME

The authors carried out a series of tests to examine any relationships between the above mechanical properties and the dosage of fibres in BFRC.

2.1 Materials

The reference mix used in the study was a CEM I concrete, using ordinary Portland cement, with crushed aggregates. The monofilament diameter of the advanced basalt fibres used is 13µm, the cut length 12.7mm, density 2.7g/cm³ and was sourced from a supplier in the UK and originally from Dubna, Moscow Region, Russia. The fibres were delivered in a mat formation, so it was necessary to manually separate them prior to use. Figure 2 shows the fibres used in this experimental programme, prior to final separation.



Figure 2. Basalt fibres partially separated

2.2 Trial Mixes

In order to examine the relationship between the fibre dosage and compressive strength, two series of blind tests were carried out. In one trial, using a 30N design mix (denoted A0), fibre concentrations of 0.1% (A0.1), 0.3% (A0.3), 0.5% (A0.5) and 0.7% (A0.7) were used. A second trial mix, again with a nominal design value of 30N (B0) was used, incorporating fibre concentrations of 0.25% (B0.25), 0.5% (B0.5), 0.75% (B0.75) and 1% (B1.0). Samples from the first trial mix were also used to assess the workability and the flexural strength of the concrete. In this second mix, the fibres were not separated as much, leaving some of the fibres bundled together in the mix.

Table 1 lists the trial mixes employed, along with their respective fibre dosages.

Table 1. Trial Mixes

Mix	A0	A0.1	A0.3	A0.5	A0.7	B0	B0.25	B0.5	B0.75	B1.0
Fibre Content (%vol)	0	0.1	0.3	0.5	0.7	0	0.25	0.5	0.75	1.01

For each property being examined and for each variation of the composition, three tests were carried out.

2.3 Rheology Testing

The workability of the fresh concrete was determined using the slump test, carried out in accordance with IS EN 12350-2 [11]. This was carried out on the fresh concrete, prior to making samples for the compressive and flexural tests.

2.4 Compressive Strength Testing

The compressive strength was assessed using the cube test in accordance with IS EN 12390-3. [12]. 150mm cubes were cast and cured. Mix A was tested at both 7 days and 28 days. Mix B was tested at 7 days only. A total of 45 cube compression tests were carried out.

2.5 Flexural Strength

The flexural strength of Mix A samples was determined at 28 days in accordance with IS EN 12390-5 [13]. The specimens were 150mm x 150mm x 400mm, allowing a clear span of 385mm when subjected to the four-point bending test. 15 samples were subjected to the flexural test. The flexural strength, F_{cf} , was calculated as:

$$F_{cf} = F \times L / d_1 \times d_2^2 \quad (1)$$

where:

F = Applied force at failure

L = span of test sample

d_1, d_2 = lateral dimensions of test sample

There was an error in the procedure for testing the samples from Mix A0.7 i.e. the mix with 0.7% vol fibre content so those results have been omitted from this study.

3 RESULTS

The results from each of the tests are presented in Table 2. In this table, the average values from the 3 samples for each respective test are shown.

Table 2. Results from Experimental Programme

Mix Reference	Workability	Compressive Strength		Flexural Strength (N/mm ²)
	Slump (mm)	7 days (N/mm ²)	28 days (N/mm ²)	
A0	35	28.65	38.32	4.27
A0.1	40	29.76	40.57	4.48
A0.3	30	33.74	43.17	4.67
A0.5	15	31.51	42.46	4.67
A0.7	10	29.66	40.73	
B0		36.35		
B0.25		31.22		
B0.5		31.99		
B0.75		26.16		
B1.0		26.63		

The results from the workability tests, compressive strength tests and the flexural strength tests are represented graphically in Figure 3 to Figure 5 respectively.

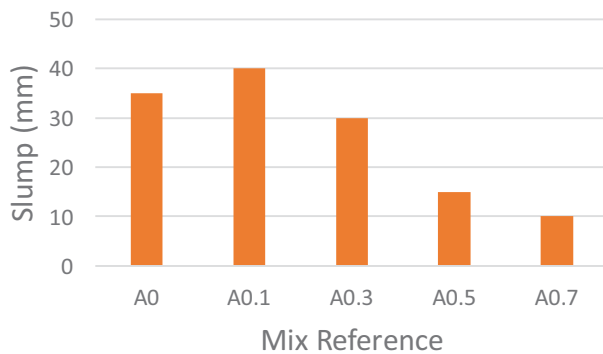


Figure 3. Results from Workability (Slump) Test

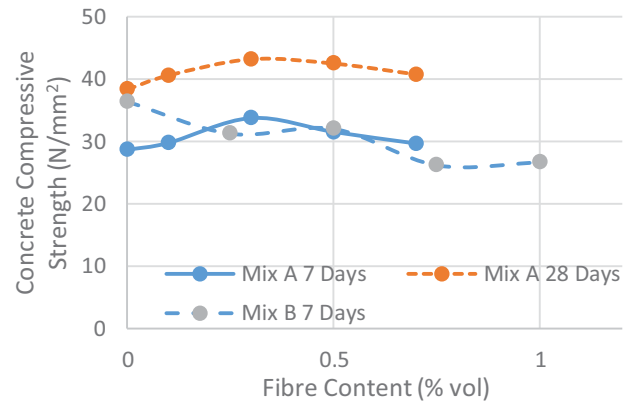


Figure 4. Results from Compressive Strength Tests

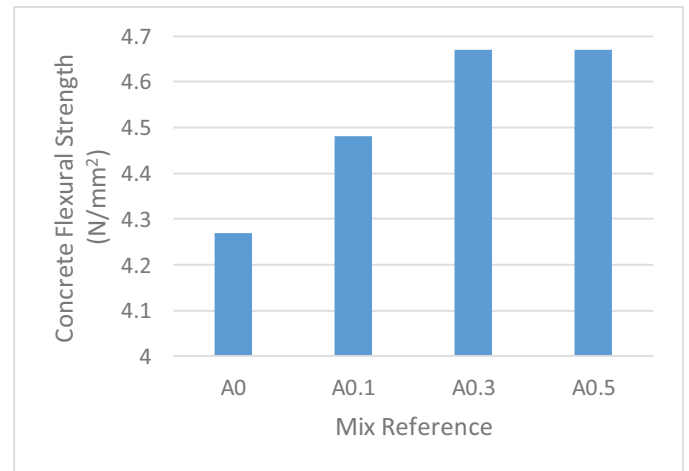


Figure 5. Results from Flexural Strength Tests

From the compressive strength testing, the influence of the fibres on the post-cracking behavior of the concrete could be visually observed. Figure 6 shows a cube from Mix B0 (i.e. no fibres present). This represents the traditional apple-core type compressive failure, indicating failure of the concrete matrix rather than aggregates failure.



Figure 6. Post-cracking cube from Mix B0

On the other hand, Figure 7 shows a cube from Mix B0.75 (0.75% vol fibre content). While the cracks are evident on the lateral surfaces of the cube and the compressive test results clearly showed a peak compressive load had been reached, the presence of the fibres served to hold the surface together.

Figure 8 shows a detail of another failed cube from Mix B0.75. It is interesting to note the presence of some fine aggregate and cement, which does not appear to have hydrated properly. This phenomenon in the presence of fibres has been observed by other researchers. This was not observed in the cubes from Mix A.



Figure 7. Post-cracking cube from Mix B0.75

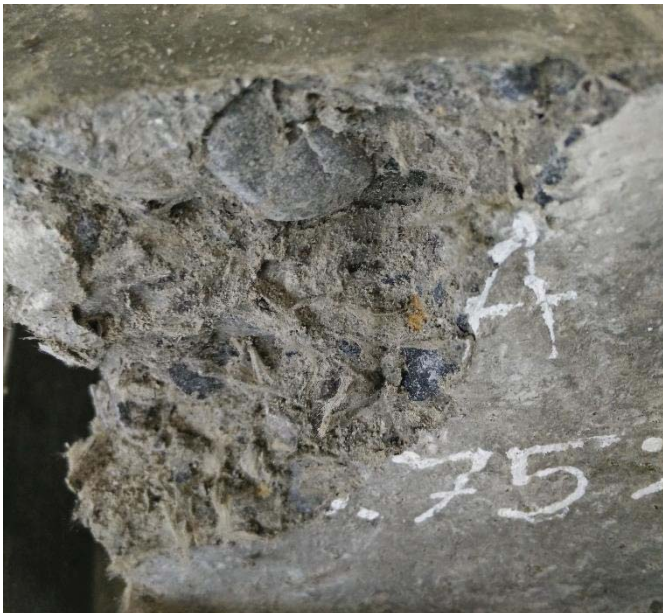


Figure 8. Detail from cube failure from Mix B0.75

4 DISCUSSION

4.1 Workability

In terms of the workability, the results showed a decrease in slump, with increasing fibre content. This is as expected and as reported in the literature for both basalt and other fibre types. The only exception to this was for Mix A0.1 (with 0.1% vol addition of fibres). As mentioned earlier, theories for this decrease relate to increased friction between the constituent materials and less available water due to the fact that unsoaked fibres will absorb some of the water in the mix. In this programme of study, the slump decreased by 75% with the inclusion of 0.7% vol. fibres.

4.2 Compressive Strength

The compressive strength test results from the two mixes yielded conflicting results. Mix A showed an increase in compressive strength at both 7 days and 28 days with increasing fibre content. In both case, there appeared to be an optimum fibre content at approximately 0.3%, which provided increases of 17.8% (7 days) and 12.7% (28 days) over the control samples. This is in broad agreement with some of the published data, where optimum fibre content of between 0.2% and 0.4% was observed [5], [6], [7].

In contrast, the results from Mix B showed a general decrease in compressive strength with increasing fibre content. This correlates with some further published data on the topic [7], [8] and highlights the need for much more detailed analysis of this particular relationship. In this study, the compressive strength reduced by a maximum of 28% for 0.75% vol. fibre content. The data from this study – although presenting two different views of the relationship between fibre content and compressive strength – does fit with various other published results. This is illustrated in Figure 9, where the results from this programme are plotted against the envelope of results from other researchers. It can be seen that these results all lie within this envelope of reported values.

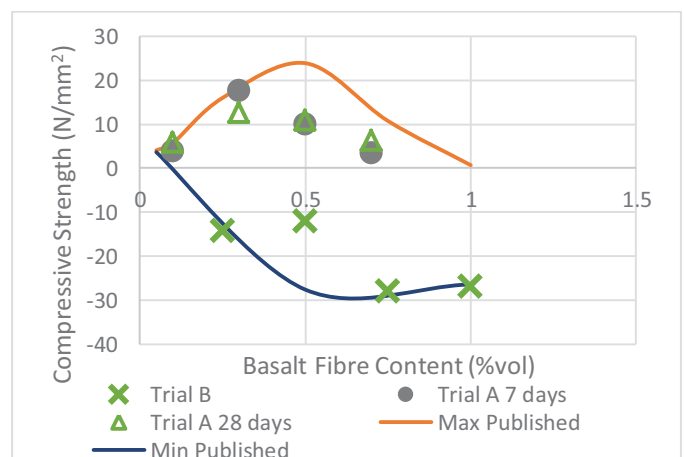


Figure 9. Compressive Strength Results from this Experimental Programme and Previously Published Data

In analyzing the contrasting responses from two nominally similar mixes, a number of points are worth noting as they merit further investigation: Firstly, in Trial Mix A, the fibres

were individually separated, while in Mix B, they were partially separated, leaving some of them “bundled” in the mix. This may be the key consideration as it has implications for some of the other points of note. Secondly, in Mix B, when the failed cube was visually inspected, some fine aggregates and some unhydrated cement was observed. This, together with the decrease in workability of the mixes with the introduction of the fibres appears to support the assertion by Ma [4] that the fibres may be absorbing considerable amounts of the water, leaving less free water in the mix, which prevents the cement from hydrating fully, leaving a weakened final product. On the other hand, in Mix A, this unhydrated cement was not observed. This may be because the concrete was mixed more thoroughly, ensuring full hydration of the compound. If this were to happen while the fibres absorbed some of the water present, the water-cement ratio would be reduced, leading to a higher compressive strength. Further, this bundling of fibres may increase the effective fibre length. This has shown to reduce the compressive strength of concrete. Therefore, it is essential that fibres should be separated individually and care must be taken during the mixing process in order not to detrimentally affect the performance of the final concrete. Further, pre-soaking the fibres may eliminate some of these issues.

4.3 Flexural Strength

The flexural strength results from the samples tested showed an increase in flexural strength with increasing fibre content. This is similar to published data. Figure 10 shows these flexural strength test results in the context of values reported by other researchers.

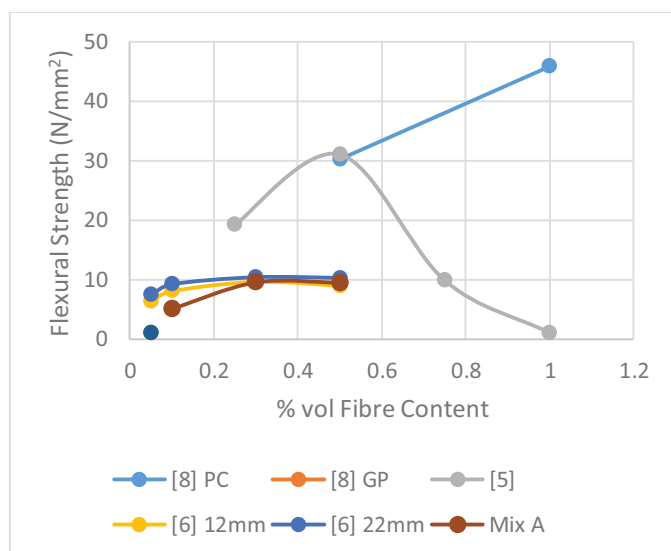


Figure 10. Flexural Strength Test Results Compared to Previously Published Values

It can be seen that the results are in line with those published elsewhere. Of note is the fact that there appears to be an optimum fibre content of approximately 0.3% from these experiments, which not only fits with values from elsewhere, but also equates to the optimum value for improving the compressive strength of this same mix.

5 ACKNOWLEDGEMENTS

Part of this work was generously funded through the Science Without Borders programme, provided by CAPES Foundation, Ministry of Education of Brazil, Brasilia – DF, Zip Code 70.040-020.

6 CONCLUSIONS

An experimental programme was carried out to investigate the relationships between basalt fibre content and the workability, compressive strength and flexural strength respectively of concrete mixes. The workability and flexural strength results were consistent with values published by other authors. They showed a decrease in workability and an increase in flexural strength with increasing fibre content. The two trials yielded contrasting values in terms of compressive strength, with one mix showing an increase in compressive strength with increasing fibre content, while the second mix showed the opposite. This is not completely surprising, given the mixed relationships reported in published data. These differences may be caused by the pre-treatment of the fibres. Further studies are being carried out to investigate the sensitivity of the results to the pre-treatment of the fibres, including the level of fibre separation and also the influence of pre-soaking the fibres.

A point of note is that in relation to Mix A, the optimum fibre content for improved compressive strength also gave the best flexural strength results. This was in the region of 0.3% by volume of basalt fibre inclusion.

REFERENCES

- [1] Ferreira JPJG, Branco FAB. The use of glass fiber-reinforced concrete as a structural material. *Exp Tech* 2007;31(3):64e73.
- [2] Ipbüker C, Nulk H, Gulik V, Biland A, Tkaczyk AH. Radiation shielding properties of a novel cement/basalt mixture for nuclear energy applications. *Nucl Eng Des* 2015;284:27e37.
- [3] Wei B, Cao H, Song S. Environmental resistance and mechanical performance of basalt and glass fibers. *Mater Sci Eng A Struct* 2010;527:4708e15.
- [4] Ma, J. 2010, Experimental Research on the Fundamental Mechanical Properties of Presoaked Basalt Fiber Concrete, CICE 2010 - The 5th International Conference on FRP Composites in Civil Engineering, September 27-29, 2010 Beijing, China, PP 1-4, available from http://www.iifc-hq.org/proceedings/CICE_2010
- [5] Patil, K. & Kulkarni, D. Comparative Study Of Effect Of Basalt, Glass And Steel Fiber On Compressive And Flexural Strength Of Concrete, *International Journal of Research in Engineering and Technology*, Volume: 03 Issue: 06, June 2014
- [6] Jiang, C., Fan, K., Wu, F., Cheng, D. Experimental study on the mechanical properties and microstructure of chopped basalt fibre reinforced concrete, *Materials and Design* 58 (2014) 187–193
- [7] Borhan, T. Properties of glass concrete reinforced with short basalt fibre, *Materials and Design* 42 (2012) 265–271
- [8] Palchik P.P. 2011, Kyiv National University of Construction and Architecture Protocol No 64-1-11, on control testing of fiber-concrete samples to determine their compression and tensile strength at bending
- [9] Palchik P.P. 2011, Kyiv National University of Construction and Architecture Protocol No 64-1-11, on control testing of fiber-concrete samples to determine their compression and tensile strength at bending.
- [10] Elshafie, S. & Whittleston, G., A Review Of The Effect Of Basalt Fibre Lengths And Proportions On The Mechanical Properties Of Concrete, *International Journal of Research in Engineering and Technology*, Vol. 4 (1) January 2015
- [11] National Standards Authority of Ireland, IS EN 12350-2, Testing fresh concrete - Part 2: Slump-test, 2009
- [12] National Standards Authority of Ireland, IS EN 12390-3, Testing hardened concrete - Part 3: Compressive strength of test specimens, 2009.

[13] National Standards Authority of Ireland, IS EN 12390-5, Testing hardened concrete - Part 5: Flexural strength of test specimens, 2009.

An experimental study of the shear behaviour of Ultra-High Performance Fibre Reinforced Concrete

Mr. Samuel English¹, Prof. Jian Fei Chen¹, Prof. Marios Soutsos¹, Dr. Desmond Robinson¹

¹School of Planning, Architecture and Civil Engineering, Queens University Belfast, Stranmillis Road, Belfast, United Kingdom

Email : senglish04@qub.ac.uk, j.chen@qub.ac.uk, m.soutsos@qub.ac.uk, d.robinson@qub.ac.uk

ABSTRACT: Ultra-High Performance Concretes (UHPC) have shown great promise in recent years especially in mechanical performance, however, little attention has been paid to the shear friction behaviour of these materials. According to current design standards, there is a limit on the shear capacity of concrete related to a compressive strength limit. This limit resulted from research showing that increased compressive strength does not give the same increase in shear strength. This is not the case with Ultra-High Performance Fibre Reinforced Concrete (UHPFRC), as the fibre reinforcement can provide a higher shear capacity. The aim of this study is to investigate the shear behaviour of UHPC with different fibre contents and steel reinforcement ratios. Specimens with different amounts of steel fibres ranging from 0.55 % to 2.20 % by volume, and with different amounts of standard reinforcement were tested. The test results show that the shear failure of unreinforced UHPC is very brittle and sudden. Standard reinforcement has very little effect on the shear capacity of UHPC; however, fibre reinforcement significantly increases the shear capacity of UHPC.

KEY WORDS: UHPFRC, Shear Friction, Fibre Reinforcement.

1 INTRODUCTION

The modern trend of increasing concrete strength has called for significant research to be carried out on many different aspects of concrete design. It is well documented that the shear strength of concrete does not increase significantly with concrete compressive strength due to the fracture surface becoming smoother [1–3]. It is, therefore, the reinforcement that provides the required shear capacity. The failure mechanism of concrete in shear is very brittle with reinforcement used as a method to provide ductility. Research has shown that the use of fibre reinforcement can significantly improve the shear performance of concrete [4,5]. It is in high strength concrete, however, that the true enhancement can be realised. This is mainly due to the increased bond strength between fibre and matrix [6] along with the increase in surface roughness.

This study aims to understand the degree of contribution that fibres have to the shear resistance of UHPFRC. This is accomplished through the comparison of conventional reinforced UHPC specimens with UHPFRC specimens. This paper also describes the specimen design and test method used to obtain the shear stress-slip curve of UHPC reinforced with fibres and conventional steel bars. The results obtained from this experimental programme are given and discussed. The results are also used to compare with available shear friction strength models from literature.

2 EXPERIMENTAL PROGRAM

This study involved testing a total of 21 un-cracked push-off specimens. The variables investigated were the reinforcement parameter and fibre content. It consists of seven series of specimens. A total of 9 fibre reinforced specimens consisting of 0.55%, 1.10% and 2.20% fibre

content, 9 conventional reinforced specimens consisting of 0.25%, 0.50% and 1.00% reinforcement content and one unreinforced specimen. Each specimen was designated by the letter R followed by the reinforcement content and then the letter F followed by the fibre content (see Figure 1).

2.1 Test specimens

The dimensions and reinforcement details of the test specimens are shown in Figure 1. The transverse reinforcement consists of one T12 bar (12 mm diameter deformed bars). Mild steel smooth bars, 6 mm in diameter (R6; $f_y = 250$ MPa) were employed as ties for all standard reinforced specimens

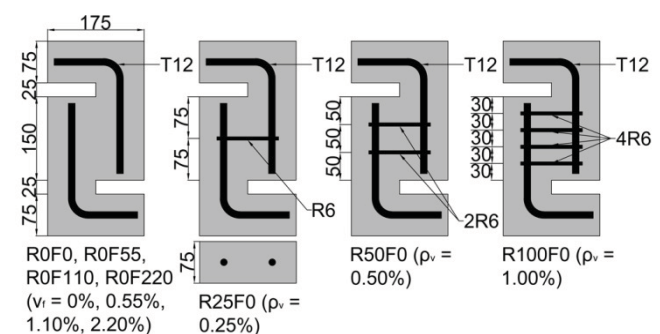


Figure 1: Specimen geometry and reinforcement layout (dimensions in mm)

The mix proportions and material details used in this study are given in Table 1. For each batch of concrete, three specimens were cast along with three cubes, three cylinders and three direct tensile specimens. All specimens were prepared and cured in the same way. The mixing procedure used was as follows;

1. Mix the dry materials for approximately 5 minutes, checking to see if mixed properly
2. Add in the water and superplasticiser and mix for approximately a further 2 minutes
3. After this add micro-silica slurry and mix for approximately 10 minutes, checking for proper mixing
4. Once a good consistency is achieved add the fibres (if applicable) and allow to mix until the fibres have combined with the mix

Table 1: Mix proportions for shear push-off specimens

Constituent	R0F0, R25F0, R50F0, R100F0	R0F55	R0F110	R0F220
Cement (CEM1)	0.209	0.209	0.209	0.209
GBS	0.144	0.144	0.144	0.144
Microsilica slurry	0.176	0.176	0.176	0.176
Silica sand	0.386	0.386	0.386	0.386
Superplasticiser	0.048	0.048	0.048	0.048
Water	0.075	0.075	0.075	0.075
Steel fibres (OL13/.16)	0.000	0.0055	0.011	0.022
Compressive strength (MPa)	127	146	159	164

During casting, the workability of the mix was obtained from flow test. All mixes obtained a similar flow of 180 mm. The specimens were stored at room temperature under damp hessian for 48 hours. Once de-moulded, they were placed in a 90°C water tank for a further 48 hours. The specimens were then removed from the tank and placed in a cooling box. The cooling box was used to reduce the likelihood of thermal shock. It consisted of an insulated box that had a small portion of the 90°C water placed in it. This allowed the specimens to cool down over a longer period than just placing at room temperature straight from the curing tank. The specimens were then removed from the cooling box and placed in a constant temperature and humidity room until the day of testing.

2.2 Test Setup, Instrumentation and Test Procedure

At 28 days after casting the un-cracked test specimens were tested using a servo-controlled hydraulic actuator with a capacity of 600 kN. The load was applied through the central portion using a spherical seat and knife edge loading plate located at the top (Figure 2). The specimens were supported by a steel plate of 100x100 mm resting on a set of rollers and plates. This also allowed loading to be concentrated through the central portion of the specimen as well as allowing crack dilation. Specific care was taken to ensure each specimen was placed centrally in the loading arrangement. The deformation of each specimen was measured using six displacement transducers positioned on the specimen as shown in figure 2. Four transducers were used for the vertical displacement and two were used for the horizontal displacement.

Each specimen was subjected to settling loads. This consisted of applying a crosshead displacement of 0.8 mm to the specimen at a rate of 0.01 mm/s and then returning the crosshead to its initial position at the same rate. The crosshead position was moved to account for any settlement in the test setup. During the test, the specimen was loaded at a crosshead displacement rate of 0.002 mm/s. Once the specimen failed, the loading rate was increased to 0.01 mm/s. Displacements were captured at a rate of 10 s⁻¹.

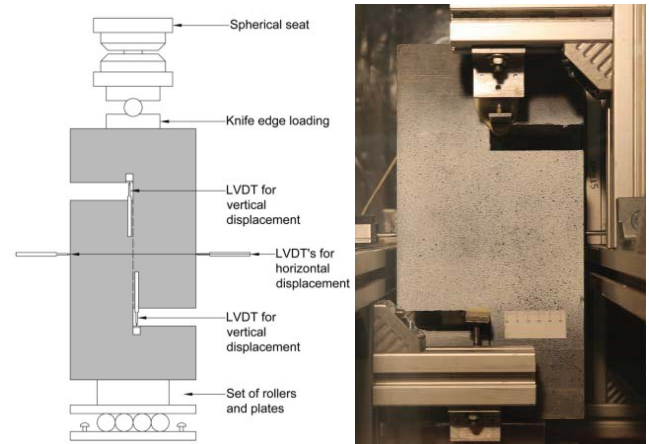


Figure 2: Loading arrangement

3 TEST RESULTS AND DISCUSSION

3.1 General behavior

Figure 3 displays the average shear stress-slip and shear stress-dilation curves obtained for all series of tests apart from the unreinforced specimens. The unreinforced specimens performed linearly up to peak load at which point there was an explosive failure. The failure was sudden with no prior warning. All of the reinforced specimens performed linearly up to the formation of tensile cracks at the notches. There was then the initiation and propagation of a shear crack within the shear plane of the specimen. The fibre reinforced specimens displayed ductile behaviour at peak load as there was a slight hardening response observed. Upon reaching the peak load all of the specimens failed with a sudden bang and a large drop in load occurred. An increase in load was observed after sudden failure. At this point, the reinforcement was engaged and started to carry further load. The reinforcement continued to carry this load until its failure or the test was stopped due to geometric constraints.

Specimen R100F0-2 and specimen R0F220-3 were an exception to this. In test specimen R100F0-2 there was a tensile crack located at the bottom notch, which propagated after peak load. With specimen R0F220-3 the shear planes rotated causing ductile failure to occur throughout the post-peak region. The apparent reason for specimen R0F220-3 failing in this manner seemed to be due to fibres distributing closer to the bottom face of the mould. During the test, it was visible that the shear crack formed firstly on one face (the cast face as this is where there was a lack of fibres) and then propagated towards the other face. This caused the specimen to perform ductile throughout the whole loading scheme.

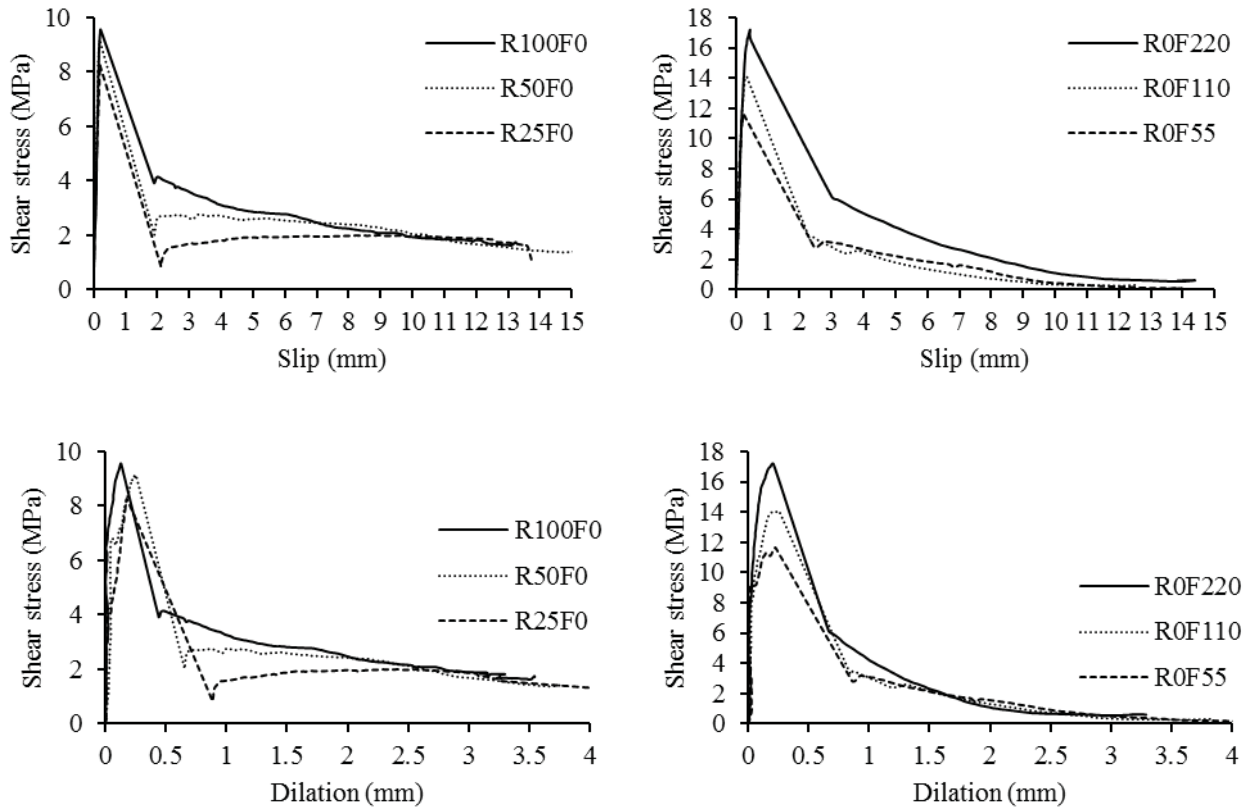


Figure 3: Shear stress-slip curves and shear stress-dilation curves for standard reinforced specimens and fibre reinforced UHPC specimens

3.2 Stiffness

Stiffness of the initial portion is affected by the reinforcement content present in the specimens. For instance, specimens R0F0, R25F0, R50F0 and R100F0 have stiffness's 47, 42, 48 and 50 N/mm³ respectively. This shows that with increasing standard steel reinforcement there is a slight increase in stiffness of the specimens. The fibre reinforced specimens, R0F55, R0F110 and R0F220 have stiffness's 70, 73 and 65 N/mm³ respectively. In these specimens, the fibre reinforcement significantly increases the shear stiffness, displaying an increase of 33% between R0F0 and R0F55. The specimens with 2.20% fibre content do not give the same increase in stiffness as the 0.55% and 1.10%.

3.3 Pre-crack shear strength

The pre-crack shear strength in the entire standard reinforced specimens occur around 6 MPa. Specimens R0F55 cracked at 9 MPa, R0F110 at 11 MPa and R0F220 at 7 MPa. This is an increase in pre-crack shear strength of 50%, 83% and 17% respectively over the peak stress achieved by unreinforced specimens. This is an indication that fibre content can improve the pre-crack shear strength of UHPC, however, there is a reduction in pre-crack shear strength in specimens R0F220. These specimens performed more ductile than the other fibre reinforced specimens at pre-crack shear strength. This was evident by no drop in load at pre-crack shear strength, as was observed in all the other specimens.

3.4 Peak shear stress

Specimens R0F0, R25F0, R50F0 and R100F0 reached a peak shear stress of 7.5 MPa, 8.5 MPa, 9.5 MPa and 9.5 MPa respectively. This shows that an increase in standard steel reinforcement does not significantly increase the peak shear stress of UHPC. This is evident from the medium and high standard reinforced specimens as there was no difference in the peak load achieved. The fibre reinforced specimens, R0F55, R0F110 and R0F220 gave an increase in peak shear stress equating to 35%, 46% and 56% above the peak stress achieved for the unreinforced specimens. The peak shear stress values for the fibre reinforced specimens are 11.5 MPa, 14 MPa and 17 MPa respectively. It is evident therefore that an increase in standard reinforcement does not have the same effect as an increase in fibre reinforcement does on the shear strength of UHPC. This would indicate that steel fibre reinforcement can be a viable method of effectively increasing the shear strength of UHPC.

3.5 Failure process and surface

Specimens R0F0 failed very suddenly and explosively with no warning of eminent failure. The unreinforced specimens developed two shear planes. The shear plane for the unreinforced and standard reinforced specimens was very smooth with very little surface asperities. This was not the case with the fibre reinforced specimens as the fibres

bridged the crack, therefore holding the shear planes together while also providing surface asperities.

3.6 Post-peak stress

The post-peak stress for R25F0, R50F0, R100F0, R0F55, R0F110 and R0F220 is 0.86 MPa, 2.02 MPa, 3.91 MPa, 2.83 MPa, 3.30 MPa and 6.15 MPa respectively. This shows that the amount of reinforcement present across the shear crack increases post-peak stress. In the standard reinforced specimens, a doubling of reinforcement generally doubled the post-peak load. More specifically an increase of 57% was achieved between R25F0 and R50F0 and 48% between R50F0 and R100F0. This is not the case with the fibre reinforced specimens, in which there was an increase in the post-peak load of 16% between R0F55 and R0F110 and 46% between R0F110 and R0F220. A doubling in fibre content does not necessarily have the same effect on post-peak stress as it does in the standard reinforced specimens, however, it is achieved in the specimens with the highest fibre content. It can also be noted that the fibre reinforced specimens achieve a higher post-peak stress than the standard reinforced specimens.

3.7 Post-peak behaviour

The post-crack behaviour of conventionally reinforced and fibre reinforced concrete is significantly different. In conventionally reinforced concrete the post-peak behaviour is characterised by an initial increase in shear stress as the reinforcement is engaged, after which there is a gradual

increase in shear strength where it plateaus and continues until sudden failure of the steel reinforcement. In fibre reinforced specimens there is also an initial increase in shear stress after failure. There is then a softening response observed as the fibres pull-out of the matrix.

3.8 Dilation

Dilation, as shown in Figure 3 is greatly reduced by higher standard reinforcement content. This is evident from the dilation curve for R100F0 which has a significantly reduced dilation at peak stress over the other standard reinforced specimens. Standard reinforcement also reduces the dilation after peak stress as shown by the gradual increase in post-peak dilation. This, however, does not seem to be the case for the fibre reinforced specimens. Fibre content does not decrease the dilation experienced at peak stress, although, the response is more ductile. It also does not have a significant effect on the post-peak dilation. A reason for this may be the clamping force that steel reinforcement can provide. The steel reinforcement bars were clamped to the transverse reinforcement, therefore providing a resistance to crack dilation. This is not the case for the fibre reinforced specimens as there is no physical tie between the transverse reinforcement. At crack propagation, the fibres are pulling out of the matrix and therefore dilation is related to the fibre pullout process. This is why an increase in fibre content does not seem to reduce the dilation across a crack.

Table 2: Equations available for shear transfer strength of concrete [20]

Researchers	Equation and description	Limitations
Birkeland and Birkeland (1966)[21]	$v_u = \rho f_y \tan \varphi = \rho f_y \mu$	$\rho \leq 1.5\%$ $v_u \leq 5.52 \text{ MPa}$ $f_c \leq 27.58 \text{ MPa}$
Mattock and Hawkins (1972)[22]	$v_u = 1.38 + 0.8(\rho f_y + \sigma_n)$	$v_u \leq 0.3f_c \leq 10.34 \text{ MPa}$
Mattock (1974)[23]	$v_u = 2.76 + 0.8(\rho f_y + \sigma_n)$	Clamping stresses higher than 1.38 MPa $v_u \leq 0.3f_c \leq 10.34 \text{ MPa}$
Hermansen and Cowan (1972)[24]	$v_u = 4 + 0.8\rho f_y$	Clamping stresses higher than 1.38 MPa
Loov (1978)[25]	$\frac{v_u}{f_c} = k \sqrt{\frac{\rho f_y + \sigma_n}{f_c}}$	
Walraven, Frenay and Pruijsser (1987)[26]	$v_u = C_1 (\rho f_y)^{C_2}$ $C_1 = 0.822 f_c^{0.406}$ $C_2 = 0.159 f_c^{0.303}$	
Mattock (1988)[14]	$v_u = 0.467 f_c^{0.545} + 0.8(\rho f_y + \sigma_n)$	$v_u \leq 0.3f_c$
Mau and Hsu (1988)[15]	$v_u = k \left(\sqrt{\frac{\rho f_y}{f_c}} \right)^\alpha$	$v_u \leq 0.3f_c$
Lin and Chen (1989)[27]	$v_u = \mu_e (\rho f_y + \sigma_n)$ $\mu_e = \left(\frac{1.75 \sqrt{f_c}}{\rho f_y + \sigma_n} \right)^{0.5} \leq 0.8 f_c^{0.25}$	$v_u \leq 0.3f_c \leq 12.46 \text{ MPa}$

Loov and Patnaik (1994)[12]	$v_u = k\lambda\sqrt{(0.1 + \rho f_y)f_c}$	$v_u \leq 0.25f_c$
Mattock (1994)[13]	$v_u = \frac{\sqrt{\rho f_y f_c^{0.73}}}{4.536}$	$v_u \leq 0.3f_c$
Kahn and Mitchell (2002)[11]	$v_u = 0.05f_c + 1.4\rho f_y$	$v_u \leq 0.2f_c$

4 COMPARISON WITH PUBLISHED EQUATIONS

The equations available for the shear friction response of concrete are shown in Table 2. Plotted in Figure 4 are the test results obtained from this study against the shear transfer strength equations from four different researchers [11–15]. Standard reinforced specimens are represented by the clear circles and fibre reinforced specimens are represented by the filled circles. Clamping stress for the standard reinforced specimens is obtained from the following expression ; ρf_y . The clamping stress for the fibre reinforced specimens is acquired from the following equations taken from the following reference [16];

$$v_{fib} = 0.83N_{fib}F_p \quad (1)$$

$$N_{fib} = \frac{v_f}{A_f} \alpha \eta \quad (2)$$

$$F_p = \tau_{bond} \pi d_f \frac{L_f}{2} \quad (3)$$

v_{fib} – clamping stress provided by the fibres (MPa), N_{fib} – number of fibres across an area (1/mm), v_f – volume fraction of fibres in the mix, A_f – Area of a fibre (mm^2), α – orientation factor (3/8), η – distribution factor, F_p – clamping force of single fibre (N), τ_{bond} – bond shear strength between fibre and matrix (MPa), d_f – diameter of fibre (0.16 mm), L_f – length of fibre (13 mm).

Once the clamping stress is obtained from equation (1) it is used in the shear transfer strength equation as usual.

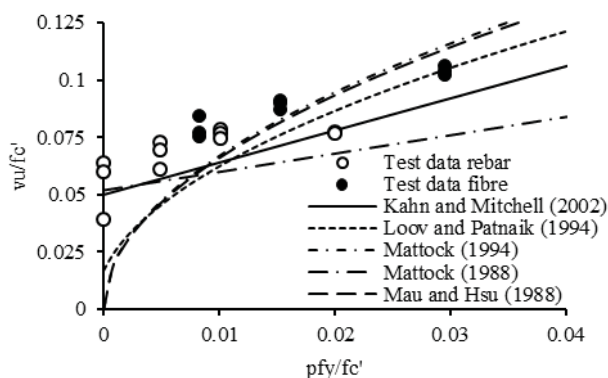


Figure 4: Normalised shear strength against normalised clamping stress

Shown in Table 4 and 5, are the performances of the four shear transfer strength equations at predicting the shear strength of both standard reinforced UHPC and fibre

reinforced UHPC. It is noted that the unreinforced specimens are not included in Tables 4 and 5.

Generally, the equations perform well at predicting the shear strength of the specimens, however, for the standard reinforced specimens, there are two equations that stand out. These are the equations developed by Mattock (1988) and Khan and Mitchell (2002). Mattock (1988) underestimates the shear strength by 21% with a COV of 6.76%, while Khan and Mitchell (2002) underestimate the shear strength by 14% with a COV of 9.71%. Furthermore, it is evident from Figure 4 that Kahn and Mitchell (2002) overestimates the shear strength of standard reinforced specimens at higher confinements.

For the fibre reinforced specimens, the equation developed by Kahn and Mitchell (2002) provides a good estimate of shear strength. On average it underestimates the shear strength specimens by 23% with a COV of 6.37%. The equation performs quite consistently throughout all three confinements as indicated by the low COV and Figure 4.

Table 3: Standard reinforced specimens: Average ratio of shear strength from test against shear strength from equations and their coefficient of variance

Researcher	Average v_u/v_{eq}	COV (%)
Mau and Hsu (1988)	1.18	22.95
Mattock (1988)	1.21	6.76
Mattock (1994)	1.17	22.82
Loov and Patnaik (1994)	1.20	20.62
Kahn and Mitchell (2002)	1.14	9.71

Table 4: Fibre reinforced specimens: Average ratio of shear strength from test against shear strength from equations and their coefficient of variance

Researcher	Average v_u/v_{eq}	COV (%)
Mau and Hsu (1988)	1.11	16.02
Mattock (1988)	1.49	4.11
Mattock (1994)	1.04	17.02
Loov and Patnaik (1994)	1.19	14.75
Kahn and Mitchell (2002)	1.23	6.37

CONCLUSIONS

The following conclusions can be drawn from this study;

1. Shear stiffness is increased with reinforcement clamping stress, however, the greatest increase was achieved by 1.10 % of steel fibres
2. Pre-crack strength increased significantly for fibre reinforced specimens, again 1.10 % of steel fibres achieving the highest
3. Peak load was increased by fibre reinforcement, with 2.20 % of fibres increasing the peak load by 56 % over the unreinforced specimen
4. Post-peak load was increased with reinforcement clamping stress, the greatest increase from 2.20 % of steel fibres
5. Ductility prior to failure and softening after failure were observed from the fibre reinforced specimens
6. Crack dilation is not reduced by an increase in fibre content, however, specimens perform more ductile, with the crack opening being controlled more effectively
7. The shear friction equation by Kahn and Mitchell (2002) predicts well the shear strength of standard and fibre reinforced UHPC

ACKNOWLEDGMENTS

The micro-silica and superplasticizer used in this study were provided by ELKEM and Fosroc respectively.

REFERENCES

- [1] Tuan HN, Otsuka H, Ishikawa Y, Takeshita E. A study on shear strength of concrete. JCI Annu ... 2006;1.
- [2] Khan LF, Mitchell AD. Shear Friction Tests with High-Strength Concrete. ACI Struct J 2002;99:98–103.
- [3] Sagaseta J, Vollum R. Influence of aggregate fracture on shear transfer through cracks in reinforced concrete 2011;63.
- [4] Valle M, Buyukozturk O. Behaviour of Fiber Reinforced High-Strength Concrete under Direct Shear. ACI Mater J 1993;90:122–33.
- [5] Tan K, Mansur M. Shear transfer in reinforced fiber concrete. J Mater Civ Eng 1990;2:202–14.
- [6] Valle M, Büyüköztürk O. Behavior of Fiber Reinforced High-Strength Concrete under Direct Shear. ACI Mater J 1993;90:122–33.
- [7] Xiao J, Xie H, Yang Z. Shear transfer across a crack in recycled aggregate concrete. Cem Concr Res 2012;42:700–9.
- [8] Constantinescu H, Magureanu C. Study of Shear Behaviour of High Performance Concrete Using Push-Off Tests 2011;1:77–82.
- [9] Crane C. Shear and shear friction of ultra-high performance concrete bridge girders. 2010.
- [10] Mansur M, Vinayagam T, Tan K. Shear transfer across a crack in reinforced high-strength concrete. J Mater Civ Eng 2008:294–302.
- [11] Kahn L, Mitchell A. Shear friction tests with high-strength concrete. ACI Struct J 2002;99:98–103.
- [12] Loov R, Patnaik A. Horizontal shear strength of composite concrete beams with a rough interface. PCI J 1994;39:48–69.
- [13] Mattock A. Reader comments of paper “Horizontal shear strength of composite concrete beams with a rough interface” published in PCI Journal, January-February 1994;39(1):48-69, by Loov RE, Patnaik AK. PCI J 1994;39:106–8.
- [14] Mattock A. Reader comments of paper “Influence of concrete strength and load history on the shear friction capacity of concrete members” published in PCI Journal, January-February 1987;32(1):66-84, by Walraven J, Frenay J, Puijssers A. PCI J 1988;33:165–6.
- [15] Mau S, Hsu T. Reader comments of paper “Influence of concrete strength and load history on the shear friction capacity of concrete members” published in PCI Journal, January-February 1987;32(1):66-84, by Walraven J, Frenay J, Puijssers A. PCI J 1988;33:165–8.
- [16] Aoude H, Belghiti M, Cook WD, Mitchell D. Response of steel fiber-reinforced concrete beams with and without stirrups. ACI Struct J 2012;109:359–67.
- [17] Wong RCK, Ma SKY, Wong RHC, Chau KT. Shear strength components of concrete under direct shearing. Cem Concr Res 2007;37:1248–56.
- [18] Bažant Z, Pfeiffer P. Shear fracture tests of concrete. Mater Struct 1986;19:111–21.
- [19] Khanlou A, MacRae G, Scott A, Hicks S, Clifton G. Shear performance of steel fibre-reinforced concrete. Australas. Struct. Eng. Conf., Perth, Australia: 2012.
- [20] Santos PMD, Júlio ENBS. A state-of-the-art review on shear-friction. Eng Struct 2012;45:435–48.
- [21] Birkeland P, Birkeland H. Connections in precast concrete construction. ACI J 1966.
- [22] Mattock A, Hawkins N. Shear Transfer in Reinforced Concrete-Recent Research. PCI J 1972;17:55–75.
- [23] Mattock A. Shear transfer in concrete having reinforcement at an angle to the shear plane. Am Concr Inst 1974;42:17–42.
- [24] Hermansen B, Cowan J. Modified shear-friction theory for bracket design. Am Concr Inst 1974;72:55–60.
- [25] Loov R. Design of precast connections 1978.
- [26] Walraven J, Frenay J, Puijssers A. Influence of Concrete Strength and Load History on the Shear Friction Capacity of Concrete Members. PCI J 1987;32:66–84.
- [27] Lin I, Chen Y. Shear transfer across a crack in reinforced high strength concrete. 2nd East Asia-Pacific Conf. Struct. Eng. Constr., Chiang Mai, Thailand: 1989, p. 505–10.

The Influence of Short Fibre Additions on the Pullout Behaviour of Reinforced Concrete

Mr John Kenna¹, Dr Mike Mulheron², Dr Paul Archbold³

¹Banagher Precast Concrete, Queen Street, Banagher, Co Offaly

²Department of Civil and Environmental Engineering, University of Surrey, Guildford, UK

³Materials Research Institute, Athlone Institute of Technology, Athlone, Co Westmeath

Email: JohnK@bancrete.com, m.mulheron@surrey.ac.uk, parchbold@AIT.IE

ABSTRACT: One of the principal factors affecting the bond between reinforcement and concrete is the anchorage length of the rebar embedded in the concrete. Requirements for minimum anchorage lengths prescribed in design codes can lead to congestion in the reinforcement and complications in detailing. The addition of short fibre to reinforced concrete can control the formation and growth of micro-cracks which begin to form in concrete under tension. Not only can this make the unit more ductile, but of interest here is the fact that this can increase the peak bond stress between rebar and concrete, and as a consequence reduce the required anchorage length of rebar in embedded concrete. This study compares the pull-out behaviour of ribbed rebar cast into specimens of plain concrete and samples reinforced with steel, polypropylene and glass short fibres respectively. Testing constituted a pull-out test employing displacement control to determine peak bond stress and post-peak behaviour. Standard compression tests were used to determine the compressive strengths of the concrete mixes. Results obtained were compared by analysing peak bond stress and post-peak pull-out behaviour of the ribbed rebar from the concrete specimens. The results showed that the peak bond stress of the control mix reinforced with the addition of short steel fibres demonstrated an increase in bond strength of 18%. In contrast to this, the addition of short polypropylene fibres reduced the peak bond stress while the addition of short glass fibres had a negligible impact on the peak bond strength. All short fibre additions improved the post-peak behaviour of the samples when compared to the control mix. These results are consistent with the findings of previous research.

KEY WORDS: Fibre-reinforced concrete, pullout behaviour, anchorage, polypropylene, glass, steel, bond.

1 INTRODUCTION

Reinforced concrete is one of the most widely used materials in the construction industry today. The functional capacity of reinforced concrete as a building material has evolved over the years with continued improvement in structural design and increased options for reinforcing elements. Reinforced concrete comprises concrete and reinforcing materials, employed to improve the concrete's structural properties [1].

In order for a reinforced concrete element to function correctly, it must be able to transfer the loads that it experiences from the concrete to the steel. This load transfer is achieved through the bond of the reinforcing steel bar f (rebar) to the concrete. As the load is increased on the reinforced concrete unit, so too does the bond stress between the rebar and the concrete [2]. Bond stress between rebar and concrete is defined as the force of adhesion per unit area of contact between the rebar and the concrete. When the load increases to a point that the stress on the rebar is higher than the maximum bond stress achievable between the rebar and the concrete, the bar will experience slip and pull-out from the concrete unit. The bond between the rebar and the concrete and the bond stress are therefore fundamental properties in reinforced concrete design.

Short fibres can comprise of different materials and are utilised in concrete for a range of purposes. For example, steel

fibres are used to improve the tensile capacity and flexural resistance of reinforced concrete elements, polypropylene fibres are used for improved crack control and glass fibres are used in permanent formwork. These are only some of the types and applications of fibre reinforcement available to designers.

In addition to the above mentioned functions, it has been noted that the presence of fibres in a concrete mix can also have an effect on the pull-out behaviour of rebar [3].

1.1 Bond-slip Behaviour

The bond mechanism is the interaction between the reinforcement and concrete [4]. For optimal reinforced concrete design, efficient and reliable force transfer between reinforcement and concrete is required [5]. The ACI states that the transfer of forces from the reinforcement to the surrounding concrete occurs for a ribbed bar by chemical adhesion between the bar and concrete, friction forces arising from the roughness of the interface and mechanical anchorage or bearing of the ribs against the concrete surface. The main factors, therefore which influence the bond between rebar and concrete are bar spacing, development and splice length, concrete cover and the use of confining transverse reinforcement. Bond strength also increases with increasing concrete compressive strength [5].

A model for bond stress-slip behavior has been proposed by Huang et al [6], which identifies four key parameters in the relationship. Firstly, the slip increases with increasing bond stress, up to a maximum value for the stress (slip = S1). This is followed by a plateau during which slip is increasing for constant bond stress (slip = S2), after which bond stress starts to decrease (slip = S3) for increasing slip values. Finally a constant residual bond strength is reached which is due to pure friction between the reinforcing bar with the cracked concrete lugs and the surrounding concrete (slip = S4).

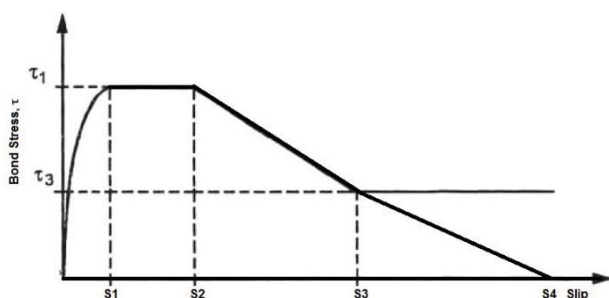


Figure 1. Simplified Bond Stress-Slip Relationship (after Huang et al [6])

1.2 Influence of Fibres on Bond-Slip Behaviour

There are conflicting results reported for the influence of short fibres on the bond-slip behavior during pullout tests. For steel fibres, for example, Yazici and Arel [13] reported an increase in pullout load due to the presence of fibres. Ganesan, however, reports a slight reduction in peak load caused by the presence of steel fibres [11]. The same authors also report a reduction in peak load when polypropylene fibres are added.

The purpose of this study is to examine how the presence of the different short fibre types listed above effect the pull-out behaviour of rebar from concrete. If the addition of short fibres can improve the bond-slip behaviour, this may allow for more lenient anchorage lengths to be provided in congested reinforced concrete sections.

2 METHODS

2.1 Experimental Programme

The bond stress-slip behaviour of the ribbed bar was analysed and compared for variance in test specimen with particular attention on the post-peak region. The aim of the analysis was to see if the expected improved crack control and pseudo-ductility of the concrete, modified from the inclusion of the fibres, translates into a significant modification of the bond stress-slip relationship. The pull-out behaviour was measured by observing the fluctuation in bond stress as a function of bar displacement of the reinforcement embedded in concrete specimens. A compression test was carried out on cubes to accurately determine their strength at the time of testing. All measurements were made under displacement control. Displacement control increases measurement sensitivity and allows the ongoing failure processes i.e. post-peak load displacement, to be monitored.

2.2 Testing Apparatus

The testing apparatus used was the Instron industrial series DX300 model which has a maximum load capacity of 300 kN. This apparatus is designed for high-capacity tension, compression, bend/flex and shear testing. During the pull-out test, the behaviour of the rebar under displacement was measured using extensometers.

2.3 Test Samples

The test sample consisted of a 200 x 200 x 200mm concrete cube with a B16 ribbed rebar cast in centrally and debonded to allow an anchorage length of 75mm. This provided a depth of cover to bar ratio of 5.75. This is above the minimum value recommended by Torre-Casanova et al. [7] to avoid failure through concrete splitting. The rebar extended out of the concrete by approximately 600mm to allow for gripping in the tensile testing machine. The rebar had an effective rib spacing of approximately 10.5mm.

In addition to the pullout test samples, 150mm cubes were cast to determine the compressive strength of the samples at testing.

There were four sample types in total – each using the same concrete mix but with the addition of different fibre types.

- Sample Type 1 – plain concrete mix
- Sample Type 2 – concrete mix containing steel fibres
- Sample Type 3 – concrete mix containing polypropylene fibres
- Sample Type 4 – concrete mix containing glass fibres.

Twelve castings of each sample were created and tested giving a total of 48 test samples. Of the 48 samples, 24 were used for pull-out tests with the remaining 24 used for compressive tests. The tests were completed when the concrete reached an age of 28 days. Sample blocks, number of samples per block and description of testing conditions are described in Table 1. EN 1992-1-1, 2005 Section 3.1.2 (2) states that the strength classes of concrete used in the code are based on the characteristic cylinder strength f_{ck} determined at 28 days.

Concrete was mixed in the Banagher Precast Concrete (BPC) works under controlled factory conditions. This resulted in the most consistent mixes of concrete due to the precise nature of the fully automated equipment and the quality of the mixer employed. In order to ensure that the concrete mix was consistent, a sample of the sand and aggregates that were used in the mix were tested for moisture content prior to testing occurred. The amount of water present determined the amount of free water that was to be added to the mix to ensure that a consistent water cement ratio was achieved. A total volume of 0.2m³ of concrete was batched which was the minimum amount required in order to achieve a consistent mix.

All samples were cast in the same manner. Concrete was fully mixed before the fibres were added. They were then added to the mixer and mixed for 5 minutes, prior to casting of the test sample. Timber moulds were manufactured to allow 6 samples be cast simultaneously. The concrete was manually placed and compacted into the moulds using a vibrating poker

to ensure the removal of entrapped air and assist the concrete to flow and to wet the surface of the steel bar.

Figure 2 shows samples being cast, with rebar protruding, while Table 1 lists the sample types, the type and dosage of fibres and the sample identification codes.



Figure 2. Concrete samples being cast

Table 1. Composition of Samples

Sample Type	Sample ID Code	Description	Fibre Type & Dosage
Type 1 Plain (Control)	1.1 – 1.6	Plain concrete with rebar for pullout test	N/A
	1.1 – 1.6	Plain concrete cubes for compressive test	
Type 2 SFRC	2.1 – 2.6	Steel FRC with rebar for pull-out test	NOVOCON® HE05535 steel fibres 30 kg/m ³ .
	2.1 – 2.6	Steel FRC cubes for compressive test	
Type 3 PFRC	3.1 – 3.6	Polypropylene FRC with rebar for pull-out test	Fibremesh®300-e3 micro-synthetic polypropylene fibres 0.9 kg/m ³ .
	3.1 – 3.6	Polypropylene FRC cubes for compressive test	
Type 4 GFRC	4.1 – 4.6	Glass FRC with rebar for pull-out	ANTI-CRAK® HP12 glass

		test	fibres 0.9kg/m ³
		Glass FRC cubes for compressive test	

2.4 Data Analysis

The pull-out behaviour of the rebar was examined under displacement control during the testing procedure. The rebar was pulled out of the sample at a constant displacement rate with the load applied to the bar from the testing apparatus increasing as required in order to maintain the predetermined displacement rate. As the test progressed, the bond stress on the rebar, and therefore the applied load, increased gradually until a peak bond stress was reached. After this point in the test, the bond stress on the rebar began to reduce. The load required to maintain the displacement rate reduced accordingly also. The section of the curve after the peak bond stress is the post-peak failure section. The bond stress did not reduce linearly in this section of the curve. Instead it experienced slight increases in bond stress with further displacement before reducing further as the test continued. The data received from the DX300 allowed the bond stress of the rebar to be plotted against the displacement of the rebar. A typical plot is shown in Figure 3. The y-axis represents the bond stress. The x-axis represents the displacement of the rebar based on cross head displacement output from the testing rig.

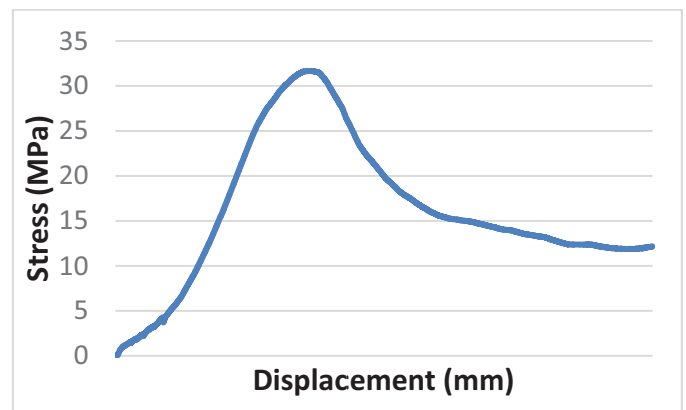


Figure 3. Typical Bond Stress vs. Displacement Curve.

3 RESULTS

Table 2 presents the mean compressive strength and the mean maximum failure pullout stress values from each sample type.

Table 2. Mean Compressive Strengths and Maximum Pullout Failure Strengths.

	Mean Compressive Strength (N/mm ²)	Mean Pullout Failure Stress (N/mm ²)
Plain (Control)	64	14.9
SFRC	65.9	18.2
PFRC	40.7	10.7

GFRC	62.3	14.9
------	------	------

Normalised curves for peak failure and post-peak behaviour for sample types 1 to 4 are shown in Figure 4 to Figure 7 respectively. Data on post-peak behaviour is missing from samples 2.1, 2.2 and 2.3 due to erroneous premature termination of the test.

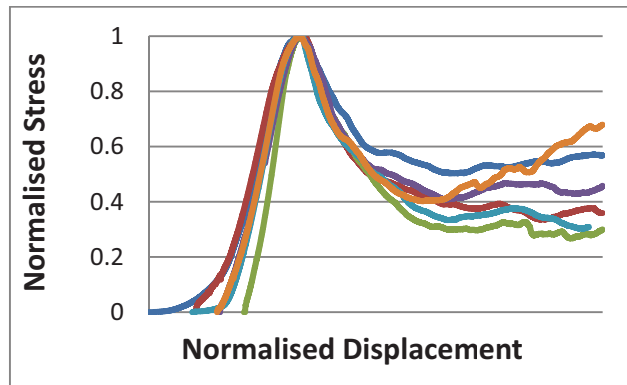


Figure 4. Control sample normalised bond stress vs. normalised cross head displacement curves.

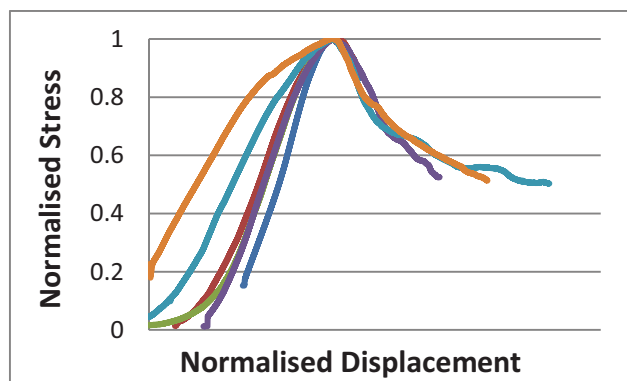


Figure 5. (SFRC) sample normalised bond stress vs. normalised cross head displacement curves.

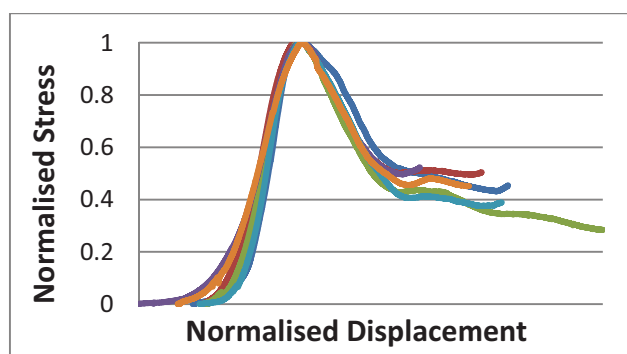


Figure 6. (PFRC) sample normalised bond stress vs. normalised cross head displacement curves.

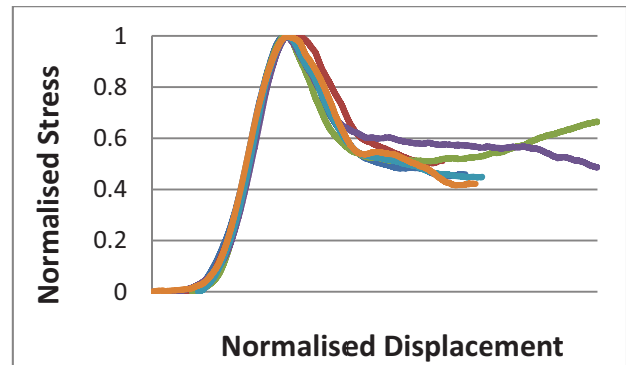


Figure 7. (GFRC) sample normalised bond stress vs. normalised cross head displacement curves.

4. DISCUSSION

Previous work undertaken on bond stress vs. displacement of rebar in pull-out tests using displacement control testing have shown that the stress-slip curve can demonstrate distinctive, cyclic peaks in the measured bond stresses as the bar pulls out of the sample [8]. In such cases, the stress-slip curve shows an initial peak, peak 1, which is representative of the maximum bond stress followed by a decrease in bond stress as the displacement continues (Figure 8). There are also typically two subsequent peaks, peak 2 and peak 3 where after the initial decrease in bond stress, there is a measurable increase in bond stress, followed by a further decrease, as displacement continues. These peak stress points have been associated with the rib pattern and spacing on the rebar which effects the pull-out stress and displacements of the rebar as the testing progresses [8].

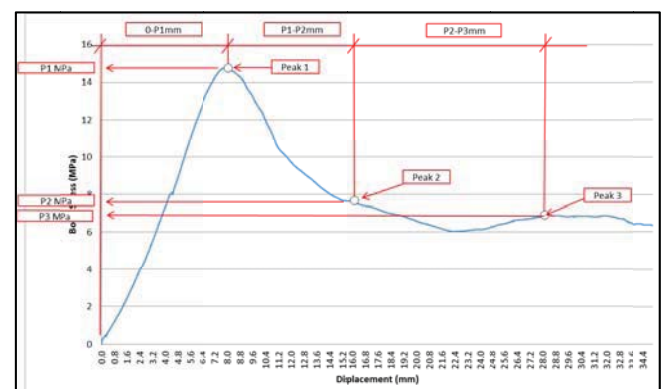


Figure 8. Graph showing location of peaks on stress-slip curves.

The post-peak behaviour of the results obtained in this study were analysed by comparing the values of maximum bond stress at these 3 peak values P1, P2 and P3. The bar displacement at each of these values was also measured in order to determine how much slip has occurred between the peak value intervals. The results presented in this study demonstrate that the pull-out curves obtained for the baseline sample of control concrete show both the expected initial shape and form. This shape is a cyclical curve which shows the bond stress decreasing between peaks as the displacement increases.

For the baseline samples tested here, the measured displacement at P1 is considerably higher than expected. The average measured displacement at first peak is 9.7 mm. Huang et al, demonstrated that the displacement at maximum bond stress should be between 1 mm and 3 mm [6]. This is in agreement with the results of Lee and Mulheron, [8] who measured a displacement at maximum bond stress is in the region of 2 mm [4]. *fib* Model code 2010 reports similar values of between 1 mm and 3.6 mm [9]. In the current study, it is likely that the larger measured value of displacement is due to the overall stiffness of the test equipment used and in the method of measuring the displacement, i.e. relying on cross-head displacement rather than any direct measurement of bar load-slip or extension. The samples were tested and measured using a rigid load frame. The load frame moves under displacement control and is linked electronically to an extensometer which records both the load and the cross-head displacement. Due to the significant loads applied during testing, the load frame inevitably experiences some deflection resulting in the measured displacement being an inaccurate measurement of the true displacement experienced by the bar. In addition, the rebar being pulled out of the test sample would experience some elastic extension due to the applied load during the testing. At the same time, due to the loading arrangement, the concrete cube in which the rebar is embedded would also undergo some elastic shortening. An analysis of the pull-out data obtained from the testing of the control samples confirms that the distances between peak bond stresses is comparable to the rib spacing of 10.5mm. The large initial displacements recorded here are worthy of further investigation, but are consistent across all samples.

Figure 4 demonstrates that the resulting curves from the control sample testing are consistent with each other up until the post-peak point where the concrete experiences fractious cracking due to rebar pull-out. This establishes the reliability and consistency of the testing procedure. The consistency of the pre-peak behaviour is expected. As the rebar approaches the peak bond stress, the chemical adhesion between the bar and concrete and the friction forces arising from the roughness of the interface no longer become sufficient to bond the rebar to the concrete. At the peak bond stress, the final bond mechanism of mechanical anchorage or bearing of the ribs against the concrete restrains the rebar and cracking begins to occur. This cracking is apparent in the post-peak behaviour and occurs at approximately 1 rib spacing from peak 1. The variable post-peak behaviour of the control sample due to cracking occurs because there is no control over the opening of the tensile cracks that form in the concrete failure surface as the ribbed rebar debonds from and pulls out through the concrete sample.

The addition of steel fibres to the concrete mix has increased the peak bond stress experienced in the samples by an average of 18%. This may be compared with the measured average of 2% increase in compressive strength of the concrete mix itself. It is therefore unlikely that the observed increase in bond strength occurs solely as a result of the change in the strength of the concrete mix. Instead, it suggests that the

interaction of the rebar and the concrete has been directly influenced by the presence of the steel fibres. This is the expected behaviour of the concrete sample when steel fibres have been added, e.g. as demonstrated by Baran et al. who found that concrete reinforced using steel fibres with dosages of between 15 and 60 kg/m³ increased the measured bond strength between 1 – 32% when compared to unreinforced concrete samples [10].

The pre-peak behaviour of the SFRC samples (Figure 5) is more varied than control samples (Figure 4). It is expected that the post-peak behaviour of the samples would be consistent as the sample is in the early stages of loading and the effect that the addition of the fibres has on the mix would not become apparent until the chemical adhesion between the bar and concrete and the friction forces arising from the roughness of the interface are no longer sufficient to bond the rebar to the concrete. It is not expected that the addition of fibres effect these initial bond mechanisms. The final bond mechanism is the mechanical anchorage or bearing of the ribs against the concrete surface. This is where the addition of fibres is expected to effect the mix as they will bridge across cracks forming on the failure surface between ribbed rebar and concrete leading to a more ductile unit and controlled post-peak behaviour. This suggests that the presence of the steel fibres retains crack opening so therefore the pull-out loads are higher and more consistent.

The addition of the polypropylene fibres to the concrete mix reduced the peak bond stress by 28% and reduced the compressive strength of the mix by 37%. These findings are in agreement with several other reported values, where the inclusion of polypropylene fibres has caused a reduction in compressive strength of the FRC [14], [15]. It is acknowledged that other authors have identified an increase in compressive strength with the introduction of fibres, so this area demands further study. The pre-peak behaviour of the polypropylene fibres is consistent and is similar to the control sample mix (Figure 6), suggesting that the presence of the polypropylene fibres retains crack opening. A similar study by Ganesan et al reported that the concrete samples reinforced with polypropylene fibres demonstrated an ultimate load and bond stress value of 5% lower than that demonstrated by a baseline sample which contained no polypropylene fibres [11]. The compressive strength of the fibre reinforced sample demonstrated a marginal increase of 1% than that of the baseline sample. The reduction in peak bond stress with a reduced compressive strength is typical of polypropylene reinforced fibres. This is in line with the theoretical values of bond stress calculations where the value of ultimate bond resistance is directly related to the compressive strength of the concrete sample.

The addition of glass fibres to the control mix has no clear effect on the peak bond stress of the mix but reduced the compressive strength by 3.1%. The results suggest that the addition of glass fibres to the control mix have not had any effect on the interaction between the concrete and the rebar. Deshmukh et al. showed that the increase in compressive strength of the mix is shown to be 8.81% with the addition of

0.03% glass fibres [12]. The dosage of glass fibres used in this study is 0.03% also so this behaviour is unexpected. The post-peak behaviour demonstrated by the glass fibre reinforced sample (Figure 7) is similar to the post-peak behaviour demonstrated by the steel and polypropylene fibre reinforced samples and suggests that the presence of the glass fibres retains crack opening.

In the structural design of reinforced concrete, the improved bond strength resulting from the addition of steel fibres to a concrete mix can be advantageous in reducing the required anchorage lengths of rebar in concrete and also increasing the effective anchorage length in any given design. The reduced variability and increased bond stress in post-peak regions could contribute to improved overall robustness at large displacements which (in some cases) could add to the safety of occupants. There is less potential for the addition of polypropylene and glass fibres to the concrete mix to fulfil this role.

It is clear that the addition of steel fibres can play a beneficial role in improving structural design and robustness but overall compatibility must be considered. The use of steel fibres carry a cost and also a risk of incorrect application if the correct volume fractions and mixing methods are not adhered to. It is rare in structural design that when a problem is encountered, there is only one solution. All solutions, including the solution where fibres can be added to the concrete mix where applicable, carry their own particular cost and risk. The solution chosen will depend on how much money the contractor or client has at their disposal and the level of risk that they are willing to apply. While there are limitations to applying the principle of short fibre steel reinforcement in practice, it should be considered as a viable option in reinforced concrete design.

5. CONCLUSIONS

The results of this study are consistent with the findings of previous research and demonstrate that the addition of short steel fibres improves the structural properties and ductility of reinforced concrete and are more efficient than either glass or polypropylene fibres addition. This has the potential to reduce the required anchorage length of main rebar in steel fibre reinforced concrete mixes by 10-15%. This would be advantageous to structural designers when detailing reinforced concrete in areas where anchorage space was limited due to rebar congestion. Short steel fibre reinforcement could therefore be considered as a viable solution to improve bond stress between ribbed rebar and concrete in structural design.

ACKNOWLEDGMENTS

The authors acknowledge the following staff at Banagher Precast Concrete; Peter Deegan, Sean Burke and Alan Kelly.

REFERENCES

1. Mosley, W.H., J.H. Bungey, and R. Hulse, *Reinforced Concrete Design*. 5th Edition ed. 1999, Houndmills, Basingstoke, Hashire RG21 6XS and 175 Fifth Avenue, New York, N.Y. 10010: PALGRAVE.
2. Wilby, C.B., *Concrete Materials and Structures*. 2nd Edition ed. 1991: The Press Syndicate of the University of Cambridge.
3. The Concrete Society, *Technical Report No. 65 Guidance on the use of Macro-synthetic-fibre-reinforced Concrete*. 2007, The Concrete Society Camberley, Surrey GU17 9AB.
4. Lundgren K. 2007. Effect of corrosion on the bond between steel and concrete: an overview. *Magazine of Concrete Research*, 59, 447-461.
5. American Concrete Institute (ACI) Committee, 2003. Bond and Development of Straight Reinforcing Bars in Tension Reported by ACI Committee 408.
6. Huang, Z., B. Engstrom, and J. Magnusson, *Experimental Investigation of the Bond and Anchorage Behaviour of deformed Bars in High Strength Concrete*. Chalmers University of Technology Report, 1996. **95**(4).
7. Torre-Casanova, A., Jason, L., Davenne, L. & Pinelli, X. 2013. Confinement effects on the steel-concrete bond strength and pull-out failure. *Engineering Fracture Mechanics*, 97, 92-104.
8. Lee, B. and M. Mulheron, *Fluctuation of bond stress-slip behaviour of deformed bar under displacement control*. *Magazine of Concrete Research*, 2012. **64**(10): p. 863-875.
9. fib, *fib Model Code 2010*. 2012.
10. Baran, E., T. Akis, and S. Yesilmen, *Pull-out behavior of prestressing strands in steel fiber reinforced concrete*. *Construction and Building Materials*, 2012. **28**: p. 362-371.
11. Ganesan, N., P.V. Indira, and M.V. Sabeena, *Bond stress slip response of bars embedded in hybrid fibre reinforced high performance concrete*. *Construction and Building Materials*, 2014. **50**: p. 108-15.
12. Deshmukh, S.H., J.P. Bhusari, and A.M. Zende, *Effect of Glass Fibres on Ordinary Portland Cement Concrete*. *IOSR Journal of Engineering*, 2012. **2**(6): p. 1308-1312.
13. Yazici, S. & Arel, H. S. 2013. The effect of steel fiber on the bond between concrete and deformed steel bar in SFRCs. *Construction and Building Materials*, 40, 299-305.
14. Waheeb, A. L. K., "Mechanical Properties and Time Dependent Deformations of Polypropylene Fibre Reinforced Concrete," *J King Saud Univ.*, Vol. 7, Eng.Sci. (1) (1993), pp. 67-76.
15. Choi, Y., Yuan, R.L., "Experimental Relationship between Splitting Tensile Strength and Compressive Strength of GFRC and PFRC", *Cement and Concrete Research*, Vol. 35 (2005) pp.1587-1591

Reducing the environmental impact of concrete products, while at the same time saving money

Jamie Goggins^{1,2,3}, Paddy McGovern⁴, Kieran McHugh⁴, William Finnegan^{1,2}

¹College of Engineering and Informatics, National University of Ireland, Galway, Ireland

²Ryan Institute for Environmental, Marine and Energy Research, National University of Ireland, Galway, Ireland

³Centre for Marine and Renewable Energy (MaREI), Galway, Ireland

⁴Tracey Concrete Limited, Enniskillen, Co. Fermanagh, Northern Ireland

email: jamie.goggins@nuigalway.ie, PaddyMc@traceyconcrete.com, william.finnegan@nuigalway.ie,

ABSTRACT: In this paper, the global warming potential and embodied energy associated with the manufacture of concrete precast products in Northern Ireland is assessed through life cycle assessment. This analysis is to form part of the environmental product declaration for precast concrete products manufactured at the factory. A cradle-to-gate analysis is performed, which includes raw material supply, transport to the manufacturer and manufacturing. The total global warming potential (GWP) and embodied energy (EE) for precast concrete products manufactured at Tracey Concrete Ltd in Northern Ireland were found to be 476.3 kg CO₂eq/m³ (or 202.7 kg CO₂eq/tonne) and 3243.9 MJ/m³ (or 1380.4 MJ/tonne), respectively. The impacts associated with the production of cement was, by far, the most significant contributor to the total impacts, as it accounted for approximately 71% and 48% of the total GWP and EE, respectively. The results of the study are presented and compared to an international study. A strategy for reducing the environmental impact of the manufacturing stage, in terms of embodied energy and global warming potential, is discussed and the monetary cost savings are presented. A strategy for reducing the environmental impact (GWP and EE) of the factory by installing an LED lighting system to improve the efficiency of on-site energy usage is proposed. This system would incur a reduction of 16,399 kg CO₂eq per annum, while saving approximately £16,827 per annum. This illustrates how reducing the negative environmental impact can also save money.

KEY WORDS: Concrete products; Embodied energy; Global warming potential; Life cycle assessment.

1 INTRODUCTION

The effect of human activity on the environment is an ever growing issue in society. When manufacturing any product, there is an impact on the environment as a result of inputs from the techno-sphere and emissions to air, soil and water. In order to quantify the environmental impact of a product, an environmental product declaration (EPD) may be used.

An EPD is based on life cycle assessment and should be produced in accordance to ISO 14025 [1]. In Europe, the European Committee for Standardization has published EN 15804 [2], a common Product Category Rules (PCR) for EPD development in the construction sector. Since its introduction, there has been a number of EPD's compiled for the production of cement (for example, Average UK Portland Cement [3]), GGBS (for example, produced by ECOCEM in Ireland [4]) and a number of precast concrete products [5-7]. EPDs can then be used to complete life cycle assessment of buildings and infrastructure. The first author, with co-authors, has highlighted the importance of choice of materials in construction projects (see, for example, [8-11]).

Tracey Concrete Ltd was originally founded in 1974 and is located in Enniskillen, Co. Fermanagh. They are one of the largest manufacturers of precast concrete products in the UK & Ireland and have supplied numerous major projects throughout Ireland, UK, Europe and Canada. Renowned for their consistent quality, efficient delivery and outstanding customer service.

In this paper, the global warming potential and embodied energy associated with the manufacture of concrete products by Tracey Concrete Ltd in Northern Ireland is assessed through life cycle assessment. This analysis is to form part of the EPD

for precast concrete products manufactured at the factory. The stages assessed are raw material supply (A1), transport to the manufacturer (A2) and manufacturing (A3), as per EN 15804. The results of the study are presented and compared to a similar study for precast concrete products in North America [5-7]. A strategy for reducing the environmental impact of the manufacturing stage, in terms of embodied energy and global warming potential, is discussed and the monetary cost savings are presented.



Figure 1. A photograph of the Tracey Concrete site, a precast concrete products manufacturer (traceyconcrete.com)

2 METHODS AND MATERIALS

This study has been structured in accordance with the LCA guidelines of the International Organisation for

Standardisation (ISO), ISO 14025 [1], ISO 14040 [12] and ISO 14044 [13], and EN 15804 [2]. The data sets used were based on operational data obtained from a concrete products manufacturer, product EPDs [3, 14], ICE [15], DEFRA [16] and the ecoinvent database Version 3 [17].

2.1 Goal and scope of the study

The primary goal of this study is to perform an environmental LCA of concrete products in Ireland from cradle-to-factory-gate. This assessment is performed in order to estimate the global warming potential and embodied energy associated with the manufacture of concrete products. The life cycle stages included within the system boundary of the study are raw material supply (A1), transport to the manufacturer (A2) and manufacturing (A3), as shown in Figure 2. There are two functional units in this study, which are defined as one metre cubed (m^3) of product and one tonne of product, and the comparative environmental impact metrics are defined as 1 kg CO_2 eq and 1 MJ. In this analysis, we are treating the process within the manufacturing stage on a whole factory basis and, therefore, there is no allocation between products required.

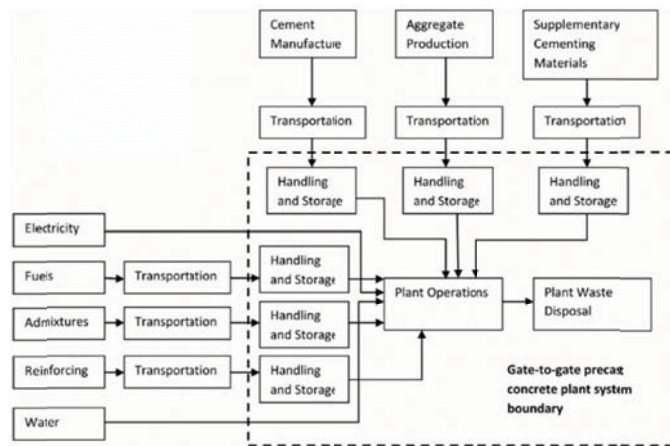


Figure 2. Product stage system boundary used in this study [6]

2.2 Life cycle inventory analysis

The life cycle inventory (LCI) for the manufacture of concrete products was generated by surveying one concrete product manufacturer, Tracey Concrete Ltd. The data obtained from the manufacturer was for one year from 1st August 2014 to 31st July 2015. In order to generate the LCI, the following daily data records for the year were obtained:

- Quantity and details of products produced
- Quantity and details of raw materials used: concrete, aggregates, steel reinforcement, lime, admixtures etc.
- Transportation details (km travelled etc.) of raw materials to the manufacturer
- Daily electricity usage
- Daily on-site fuel (diesel) consumption
- Details for onsite manufacturing equipment

A summary of the LCI for the manufacture of concrete precast products in Ireland (including both the annual total and normalised, per m^3 of product) is presented in Table 1.

Table 1. Life cycle inventory for the manufacture of concrete precast products (per m^3 and per tonne of product)

	Unit	per m^3	per tonne*
Cement**	kg	399	170
Transport distance	km	21.1	
Water	L	163	69.5
<i>Aggregates:</i>			
14mm Stone	kg	344.3	147
10mm Stone	kg	382.7	163
Course Sand	kg	667	284
Fine Sand	kg	297	126
Transport distance	km	87.7	
Lime Dust	kg	35.6	15.1
Additives	kg	0.15	0.1
Reinforcement	kg	29	12.3
Anchors	kg	0.24	0.1
Lubricating oil	L	0.43	0.2
<i>Energy:</i>			
Electricity	kWh	28.4	12.1
Diesel	L	4.59	2

*Assumption: density of concrete = 2,350 kg/m^3

** Includes 3.3% waste during manufacture

3 RESULTS AND DISCUSSION

The operational data specified in the LCI (Section 2.2 and Table 1) is used to estimate the GWP and EE associated with the manufacture of concrete precast products, which is presented and discussed in Section 3.1. These impacts are then compared to the results of a similar analysis conducted in North America [5-7] in Section 3.2. A strategy for improving the on-site energy efficiency is discussed in Section 3.3.

3.1 Global warming potential and embodied energy

The results of the analysis, which estimates the GWP and EE associated with the manufacture of concrete precast products in an Irish factory, are presented in Table 2. The total GWP and EE were found to be 476.3 kg CO_2 eq/ m^3 (or 202.7 kg CO_2 eq/tonne) and 3243.9 MJ/ m^3 (or 1380.4 MJ/tonne), respectively, where the density of concrete is assumed to be 2,350 kg/m^3 . For both impacts, the greatest contributor to the total was associated with the supply of raw materials, which accounted for approximately 88% and 76% of the total GWP and EE, respectively. The annual total GWP and EE associated with the concrete products manufacturer was found to be 12,640,610 kg CO_2 eq and 86,095,872 MJ, respectively.

The total GWP and EE has been broken down further than the analysis shown in Table 2 by analysing the contribution of inputs and emissions included in the study as outlined in Figure 3. This breakdown is presented in Figure 3. The impacts associated with the production of cement was, by far, the most significant contributor to the total impacts, as it accounted for approximately 71% and 48% of the total GWP and EE, respectively. The production of the steel used as reinforcement, the transportation of raw materials to the

factory and on-site energy usage were the other main contributors to the total impact.

Table 2. The global warming potential and embodied energy associated with the manufacture of concrete products in an Irish factory

	GWP (kg CO ₂ eq)		EE (MJ)	
	per m ³	per tonne	per m ³	per tonne
Raw material supply	417	177.5	2479.9	1055.3
Transport	38.9	16.5	469.7	199.9
Manufacture	20.4	8.7	294.3	125.2
Total	476.3	202.7	3243.9	1380.4

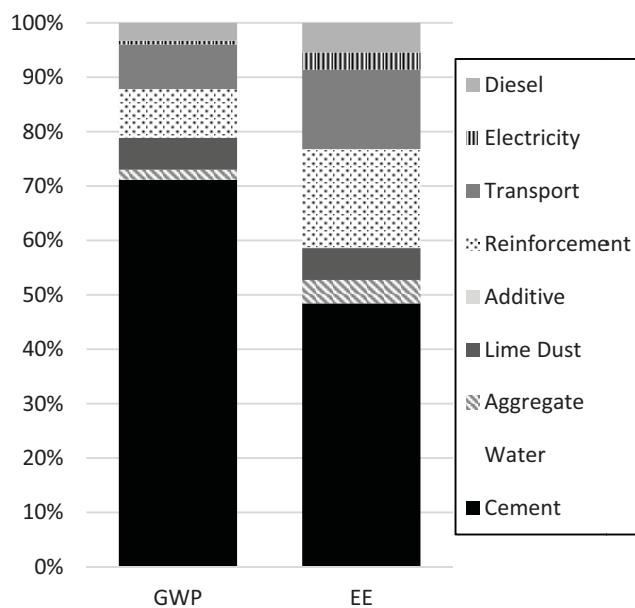


Figure 3. Breakdown of the contribution of inputs and emissions to the total GWP and EE

3.2 Comparison with international studies

In this section, the results of the present study have been compared to a study of precast concrete products conducted in Canada and USA. The results of a survey of 99 plants was reported. The study divided their products into four main groups: Structural precast concrete [6]; Underground precast concrete [7]; Architectural precast concrete [5]; and Insulated precast concrete [5].

The total GWP in the present study (202.7 kg CO₂ eq/tonne) is between 27-41% lower than the products in the North American study. This is as a result of impact of the supply of raw materials (177.5 kg CO₂ eq/tonne) and manufacturing (8.7 kg CO₂ eq/tonne) being significantly lower than the stages in the North American study. One of the contributors for the environmental impact of the supply of raw materials being lower is there is greater usage of additives in North America compared to the factory used in this study. With respect to manufacturing, the lower impact may be attributed to the natural curing process used in Ireland compared to more energy intensive curing processes in North America where heating or cooling may be required as a result of the climate.

However, the impact of transportation of raw materials to the plant (16.5 kg CO₂ eq/tonne) was found to be slightly higher in the present study compared to the North American study.

These results suggest that there would be an advantage, from an environmental standpoint, to sell produced in Northern Ireland to North American customers. If we take structural precast concrete as an example. On average, the GWP associated with producing it in North America is 307.8 kg CO₂ eq/tonne [6], which is 105.1 kg CO₂ eq/tonne higher than producing it in Northern Ireland. Since the GWP associated with shipping a tonne of product the approximate 5000 km from Ireland to North America is approximately 80 kg CO₂ eq/tonne (average cargo ship: 0.016 kg CO₂ eq/tonne.km [8]), it would still have a lower environmental impact.

Table 3. Comparison between the GWP (in kg CO₂ eq/tonne) for concrete products manufactured in a factory in Northern Ireland and the average GWP of a similar analysis conducted in Canada and USA

Product type	A1	A2	A3	Total
Structural precast concrete [6]	265.1	12.9	29.8	307.8
Underground precast concrete [7]	217.9	11.4	29.8	259.1
Architectural precast concrete [5]	265.2	12.7	29.8	307.7
Insulated precast concrete [5]	279	12.6	29.8	321.4
<i>Present study</i>	<i>177.5</i>	<i>16.5</i>	<i>8.7</i>	<i>202.7</i>

Table 4. Comparison between the EE (in MJ/tonne) for concrete products manufactured in a factory in Northern Ireland and the average total primary energy used of a similar analysis conducted in Canada and USA

Product type	A1	A2	A3	Total
Structural precast concrete [6]	1900.4	189.6	530.2	2620.2
Underground precast concrete [7]	1679.7	163.6	530.2	2373.5
Architectural precast concrete [5]	2091.1	193.1	530.2	2814.4
Insulated precast concrete [5]	2116.4	183.7	530.2	2830.3
<i>Present study</i>	<i>1055.3</i>	<i>199.9</i>	<i>125.2</i>	<i>1380.4</i>

3.3 Improving on-site energy efficiency

A possible strategy to aid in reducing the environmental impact (in terms of GWP and EE) of the factory is to improve the efficiency of on-site energy usage. Although, on-site energy usage is not the most significant contributor to environmental impact (2% of the total GWP), it is an area that management's decisions can directly affect (unlike GWP associated with the production of concrete, which is controlled by an external company, unless an alternative cementitious material is utilised in production, such as GGBS). An analysis of the on-site energy usage was performed in order to identify key areas where energy efficiency can be improved quickly

and affordably. The area that was identified was lighting within the factory.

The total annual on-site energy usage is 752,543 kWh (Table 1) and lighting accounts for approximately 30% of this at 226,822 kWh, which is equivalent to 26,085 kg CO₂eq. This value is based on the electricity supplier 'Energia', which uses approximately 75% renewables and 25% natural gas to produce electricity with global warming potential of 0.115 kg CO₂eq/kWh. In order to reduce lighting energy use, a LED lighting system is proposed, which is a suitable alternative to the existing system. The new system would reduce the electricity usage to 84,224 kWh and in-turn the GWP would be reduced to 9,686 kg CO₂ eq, which is a saving of approximately 63%.

The proposed system would have a greater effect on a company which sources their electricity from another supplier as the All Ireland market and Great Britain market are approximately 0.452 kg CO₂eq/kWh and 0.42 kg CO₂eq/kWh, respectively. Therefore, the electricity saving of 142,598 kWh would incur a reduction in their GWP of approximately 64,454 kg CO₂eq, for the All Ireland market, and approximately 59,891 kg CO₂ eq, for the Great Britain market.

The proposed system would not only have an environmental saving (total of 16,399 kg CO₂eq per annum) but, also a money saving of £16,827 per annum, assuming the current cost of electricity at £0.118 per kWh. The company obtained a quote for the proposed upgrade, which estimates the total cost as £66,899. Consequently, the estimated payback period is just over 4 years at 48.95 months. Therefore, this proposed system, not only, reduces the environmental impact of the company but also will save money for the company after only 4 years, which reinforces the point that reducing your negative environmental impact can also save you money.

4 CONCLUSION

In this paper, the global warming potential and embodied energy associated with the manufacture of concrete precast products in Ireland is assessed through life cycle assessment. A cradle-to-gate analysis is performed, which includes raw material supply, transport to the manufacturer and manufacturing. The total global warming potential and embodied energy were found to be 476.3 kg CO₂ eq/m³ (or 202.7 kg CO₂ eq/tonne) and 3243.9 MJ/m³ (or 1380.4 MJ/tonne), respectively. A strategy for reducing the environmental impact (in terms of GWP and EE) of the factory by installing an LED lighting system to improve the efficiency of on-site energy usage is proposed. This system would incur a reduction of 16,399 kg CO₂ eq per annum, while saving approximately £16,827 per annum.

Over the next few years, it is expected that it will be a requirement to have an EPD for every product a company manufactures. Therefore, if an EPD is compiled now and compared to competitors, provisions and strategies may be put in place to reduce the products environmental impact, which will look favorable when tendering for jobs. However, in order to ensure the accuracy of these findings, EPDs are to be verified by a registered independent third party.

ACKNOWLEDGMENTS

The first author would like to acknowledge the support of Science Foundation Ireland through the Career Development Award programme (Grant No. 13/CDA/2200). The last author would like to acknowledge the funding provided by the Department of Agriculture, Food and the Marine for the DairyWater project (Ref.: 13-F-507).

REFERENCES

- [1] ISO (2006) *ISO 14025: Environmental labels and declarations - Type III environmental declarations - Principles and procedures*. International Organization for Standardization.
- [2] CEN (2013) *EN 15804: Sustainability of construction works - Environmental product declarations - Core rules for the product category of construction products*. European Committee for Standardization: Brussels, Belgium.
- [3] MPA (2014) *Environmental Product Declaration: Average UK Portland Cement*. Mineral Products Association (MPA) UK: United Kingdom.
- [4] ECOCEM (2013) *Environmental Product Declaration for Ecocem GGBS cement*. ECOCEM Ireland Ltd.: Dublin, Ireland.
- [5] CPCI, NPCA, and PCI (2015c) *Environmental product declaration (EPD) for precast concrete: Architectural & insulated wall panels*. Canadian Precast/Prestressed Concrete Institute, National Precast Concrete Association & Precast/Prestressed Concrete Institute.
- [6] CPCI, NPCA, and PCI (2015a) *Environmental product declaration (EPD) for precast concrete: Structural precast concrete*. Canadian Precast/Prestressed Concrete Institute, National Precast Concrete Association & Precast/Prestressed Concrete Institute.
- [7] CPCI, NPCA, and PCI (2015b) *Environmental product declaration (EPD) for precast concrete: Underground precast concrete*. Canadian Precast/Prestressed Concrete Institute, National Precast Concrete Association & Precast/Prestressed Concrete Institute.
- [8] Duggan, A.R., McCabe, B.A., Goggins, J., and Clifford, E. (2015) 'An embodied carbon and embodied energy appraisal of a section of Irish motorway constructed in peatlands'. *Construction and Building Materials*. 79: p. 402-419.
- [9] Goggins, J., Keane, T., and Kelly, A. (2010) 'The assessment of embodied energy in typical reinforced concrete building structures in Ireland'. *Energy and Buildings*. 42(5): p. 735-744.
- [10] Goggins, J., Moran, P., Armstrong, A., and Hajdukiewicz, M. (2016) 'Lifecycle environmental and economic performance of nearly zero energy buildings (NZEB) in Ireland'. *Energy and Buildings*. 116: p. 622-637.
- [11] Manton, R., Duggan, A., Goggins, J., and Clifford, E. (2014) 'Carbon costs and savings of Greenways: creating a balance sheet for the sustainable design and construction of cycling routes'. *International Journal of Environment and Sustainable Development* 7. 13(1): p. 3-19.
- [12] ISO (2006a) *ISO 14040: Environmental Management - Life Cycle Assessment - Principles and Framework*. International Organization for Standardization.
- [13] ISO (2006b) *ISO 14044: Environmental Management - Life Cycle Assessment - Requirements and Guidelines*. International Organization for Standardization.
- [14] EFCA (2015) *Environmental Product Declaration: Concrete admixtures - Plasticisers and Superplasticisers*. European Federation of Concrete Admixtures Associations Ltd.: Sweden.
- [15] Hammond, G. and Jones, C. (2011) *Inventory of carbon & energy Version 2.0 (ICE V2.0)*. Department of Mechanical Engineering, University of Bath: Bath, UK.
- [16] Hill, N., Walker, H., Choudrie, S., and James, K. (2012) *2012 Guidelines to Defra / DECC's GHG Conversion Factors for Company Reporting: Methodology Paper for Emission Factors*. Department for Environment, Food and Rural Affairs: London, UK.
- [17] Weidema, B.P., Bauer, C., Hischer, R., Mutel, C., et al. (2013) *The ecoinvent database: Overview and methodology, Data quality guideline for the ecoinvent database version 3*, www.ecoinvent.org.

Development of resilient and environmentally responsible highway infrastructure solutions using geopolymer cement concrete

Allistair Wilkinson¹, Bryan Magee¹, David Woodward¹, Svetlana Tretsiakova-McNally²

¹Studies Allied to Built Environment Research (SABER), Ulster University, Shore Road, Newtownabbey, Northern Ireland.

²Built Environment Research Institute, Ulster University, Shore Road, Newtownabbey, Northern Ireland.

Email : wilkinson-a6@email.ulster.ac.uk, b.magee@ulster.ac.uk, wdh.woodward@ulster.ac.uk, s.tretsiakova-mcnally@ulster.ac.uk

ABSTRACT: Despite local and national road authorities striving to provide motorists with a durable and safe infrastructure environment, one in six UK roads is currently classed as being in poor condition. In terms of safety, Department for Transport statistics continue to report high numbers of road fatalities; 1,780 in 2015, representing a 3% increase from the previous year. As such, research focussed on developing resilient and cost effective planned/preventative highway maintenance solutions remains highly topical. Reported in this paper is research aimed at developing high performance, low impact solutions for both highway repair and skid resistance enhancement. Based on a metakaolin/alkali silicate-based geopolymer cementitious material, a mix optimisation investigation is initially reported, providing key fresh and mechanical material properties such as setting time and compressive/flexural strength. Using optimum mix designs, the paper then presents an assessment of geopolymer cement concrete's suitability as a highway repair material. To this end, wear and skidding resistance characteristics of potholes repaired with geopolymer cement concrete is reported, with initial findings suggesting excellent performance levels. Finally, the paper examines the potential use of a geopolymer cement-based artificial aggregate as a cost effective alternative to calcined bauxite for high friction surfacing applications. Initial production trials of aggregate will be discussed, together with effects of accelerated trafficking on texture depth retention.

KEY WORDS: Geopolymer Cement; Novel Cements; Road Maintenance; Permanent Road Repair; High Friction Surfacing.

1 INTRODUCTION

Interest from the construction industry in sustainable alternatives to conventional Portland cement has grown in recent years. Geopolymer cement provides an attractive alternative, due to advantageous performance and environmental properties. It is claimed that geopolymer cement production can achieve up to 90% less CO₂ emissions when compared with Portland cement production [1, 2]. Mechanical properties such as high compressive and flexural strengths [3], acid and sulphate resistance [4] and freeze-thaw resistance [5] make geopolymer cement suitable for a wide range of potential applications. Despite the impressive mechanical properties, a lack of harmonised standards in the UK and Europe have created a barrier to the use of geopolymer cement, and other alkali-activated cementitious materials (AACM). However, a Publicly Available Specification (PAS) considering AACMs is to be released in 2016 [6]. This document will set performance based requirements for AACMs where an aluminosilicate material and an alkali activator are used to form a cementitious binder. While some researchers argue that AACMs and geopolymer cements are different materials, this PAS will include cementitious binder systems which are marketed as geopolymer cements.

Road pavement applications have been identified as potential areas which could take advantage of the impressive performance properties of geopolymer cement. Firstly, potholes are a common issue across the entire UK road network, with one in six roads regarded as being of a poor standard [7]. In excess of 2.5 million potholes were repaired in England and Wales in 2014, at an average cost of £57 per

pothole. Despite this significant cost, an estimated £12 billion is required to bring the UK road network back to a good standard. Geopolymer cement may provide a solution to this issue. Limited research has been carried out in this area, with a Thai study reporting the suitability of geopolymer cement, albeit based on compressive and bond strength, rather than durability testing [8].

A second potential use for geopolymer cement is as a high performance aggregate, used as an alternative to calcined bauxite in high friction surfacing systems. High friction surfaces play an important role in the reduction of road traffic collisions, reducing injuries and saving lives. In service studies have shown a reduction in collisions by more than 50% after the application of a high friction surface [9]. These systems use calcined bauxite, a highly durable and hard-wearing aggregate, to provide additional grip to an existing road surface. The aggregate is bonded to the surface using an epoxy resin. While high friction surfacing is proven to reduce injuries and deaths on public highways, when correctly placed, the cost and environmental impact of the calcined bauxite have meant that alternative materials are required. While bauxite is a locally available aggregate in Northern Ireland, material suitable for high friction surfacing applications can only be sourced from countries such as China and Guyana, due to differences in the chemical structures of the aggregates. Long transportation distances, combined with quarrying, crushing, grading and high temperature calcination mean that the environmental impact of calcined bauxite is significant. When the cost of these processes, in addition to the environmental impact of the material, are considered, a

suitable alternative would have a major impact on the high friction surfacing market.

This paper reports preliminary findings from a research programme focusing on the development of a geopolymer mortar mix design, the selection of a suitable mortar for use as a geopolymer pothole repair material, and a geopolymer aggregate formed from waste geopolymer mortar for use in a high friction surfacing system.

2 EXPERIMENTAL PROGRAMME

2.1 Materials

This study focuses on the application of a calcined clay-based geopolymer cement system. Kaolinitic clays, an exposed layer at existing basalt quarries in Northern Ireland, have been identified as suitable aluminosilicate materials for geopolymerisation. The clay is calcined at 750°C, then ground to a fine powder. When mixed with a potassium silicate solution (approximately 55-60 wt. % potassium solids), geopolymerisation occurs, forming a cementitious binder similar to that of an ordinary Portland cement and water binder. This system, BanahCEM, is commercially produced in Northern Ireland and was used throughout the study. Aggregate for the mortar was locally sourced concreting sand. Mortar was mixed using a table top mixer. The mixing process was carried out in accordance with supplier instructions due to the lack of harmonised standards regarding the mixing of geopolymeric materials.

2.2 Mixture Proportions

Three variables which can impact upon the mechanical properties of geopolymer mortar are metakaolin powder content, activator content, and water content. For this study, content ranges were set for each variable. Three points within these ranges were selected, giving an upper, middle and lower content levels. For each mix, the content level of one variable was changed, with the two other variables remaining at the middle content level, as shown in Table 1. In order to maintain a constant mix density of 2400 kg/m³ for each mix, the sand content was adjusted depending on the other variable contents.

Table 1. Mix proportions for geopolymer mortar strength testing.

Mix	Mix Proportions (kg/m ³)				Geopolymer Liquid/Solid ratio
	Banah CEM Powder	Banah CEM Activator	Sand	Water	
1	500	300	1545	55	0.264
2	500	350	1495	55	0.282
3	500	400	1445	55	0.299
4	450	350	1545	55	0.304
5	500	350	1495	55	0.282
6	550	350	1445	55	0.264
7	500	350	1500	50	0.275
8	500	350	1495	55	0.282
9	500	350	1490	60	0.289

2.3 Compressive and Flexural Strength

Compressive strength testing was carried out on geopolymer mortar cubes, measuring 50 x 50 x 50 mm. Flexural strength was tested on geopolymer mortar beams measuring 40 x 40 x 160 mm. Specimens were cast in steel moulds and wrapped with polythene sheet to retain moisture during the initial hardening and curing phase. After 24 hours, the specimens were demoulded and stored at an ambient temperature of 20 ± 2°C, until testing was carried out. Compressive and flexural strengths were determined according to BS EN 1015-11: 1999 [10].

2.4 Geopolymer Mortar Workability

The workability of a pothole repair material is an important factor when determining the suitability of a material for use as rapid and permanent road repair material. Two workability tests were carried out. Mortar flow was measured using a table top flow table, in accordance with BS EN 1015-3: 1999 [11]. Mortar setting time was measured using manual vicat apparatus, according to BS EN 196-3: 2005 [12]. The workability tests were carried out on the mix which was selected, based on the compressive and flexural strength results.

2.5 Pothole Repair Material

An asphalt slab, with dimensions of 275 x 275 x 40 mm, was produced. Using a hammer and chisel, material was manually removed to form a circular defect with irregular sloped sides, and an approximate volume of 0.001m³ (Figure 1). The irregular shape of the defect meant that the conditions in which the geopolymer mortar would have to bond to the asphalt were poor, meaning that there was a risk of the mortar popping out of the specimen. This provided a worst case scenario for which the geopolymer mortar may have to endure. The high strength geopolymer mortar was placed in the defect and compacted using a steel tamping rod, followed by 30 seconds on a compacting table. An excess of the material was removed using a hand trowel. No additional surface texturing was applied to the geopolymer mortar. The slab was wrapped in a polythene bag for 24 hours for moisture retention. After 24 hours, the polythene was removed, and the slab was stored at an ambient temperature of 20 ± 2 °C for 6 days prior to testing.



Figure 1. A simulated pothole for geopolymer repair material investigation.

2.6 High Friction Aggregate

The geopolymer high friction aggregate was produced using waste geopolymer mortar specimens from the initial geopolymer strength testing studies. After the specimens were tested for compressive and flexural strength, the mortar was crushed using a jaw crusher. This formed a recycled geopolymer mortar aggregate. The material was sieved, according to BS EN 1015-1: 1999 [13] to retain particles sized from 1 to 3 mm. A 1:1 ratio of two part epoxy resin was mixed, and a 2 mm layer applied to a 10mm stone mastic asphalt (SMA) slab with dimensions of 300 x 300 x 50 mm. The geopolymer aggregate was dispersed over the slab until the epoxy had been covered. After allowing the epoxy resin to cure for 24 hours, excess aggregate was removed using a wire brush. Figure 2 shows the geopolymer high friction surface slab, prior to testing. This production method was then repeated with a second 10 mm SMA slab, using conventional calcined bauxite aggregate with the epoxy resin binder. This slab was tested alongside the geopolymer slab as a control sample to provide a benchmark for the initial geopolymer aggregate investigation.

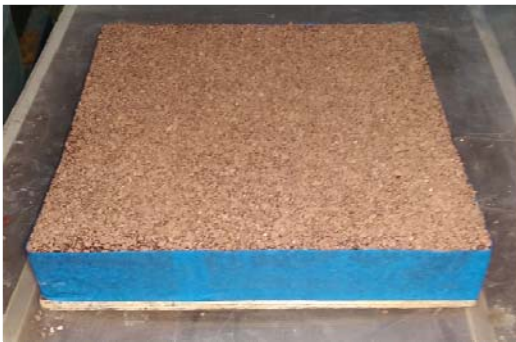


Figure 2. Crushed geopolymer mortar high friction surface test specimen.

2.7 Simulated Wearing and Skid Resistance

Accelerated wearing was carried out according to Appendix H of TRL Report 176 [14], using the Ulster University road test machine. The machine configuration involves loading 2 pneumatic tyres to 5 ± 0.2 kN. The tyres pass over the specimens at a rate of 10 revolutions per minute, and are free to move 160 ± 25 mm laterally across the specimens. This machine replicates low speed and high friction traffic loading, the harshest form of loading which a road surface can be subjected to. The pothole sample was subjected to 2000 wheel passes. The high friction surface slabs were subjected to 20,000 wheel passes.

As no surface texture was applied to the pothole sample, surface wearing was identified by a visual assessment. The surface texture changes of the high friction surfaces were quantified using the sand patch test method. This method measures the road surface macrotexture. The test, according to TRL Report 176 Appendix D [14], involved spreading a known quantity of silica sand in an even circle over the surface of the specimen. The diameter of the circle is measured and the textured depth is calculated using the equation:

$$\text{Texture Depth} = \frac{31420}{\pi^2} \text{ mm}$$

Skid resistance was measured according to RRL Road Note 27 [15]. The samples are saturated with water and pendulum apparatus is used to measure the resistance between the surface and a rubber slider which is attached to the pendulum. Skid resistance is measured in wet conditions, as a wet surface provides the lowest skid resistance value.

3 RESULTS AND DISCUSSION

3.1 Compressive and Flexural Strength

Table 2 shows the mean 7 day compressive strengths, and mean 28 day compressive and flexural strengths. As shown in the results, all specimens exhibited 7 day compressive strengths of at least 89% of the 28 day compressive strengths. Mixes 4 and 9 achieved the 28 day strength after 7 days, while mix 3 showed a slight reduction in compressive strength of around 3%, between 7 days and 28 days. As mix 3 had a higher activator content than the other mixes, this may suggest that the activator content exceeded the maximum content level of this component. Figure 3 illustrates the relationship between 7 day and 28 day compressive strengths. It was also found that the majority of 28 day flexural strength results were around 4% of the corresponding 28 day compressive strengths. This is a common trend when testing mortars using only fine aggregate. However, no trend between 28 day compressive strength and 28 day flexural strength was obvious from this investigation.

Table 2. Geopolymer mortar compressive and flexural strength results.

Mix no.	Compressive strength (N/mm ²)		Flexural strength (N/mm ²)
	7-day	28-day	28-day
1	59	62	2.7
2	66	67	2.4
3	61	59	2.7
4	54	54	2.7
5	66	67	1.7
6	69	77	2.3
7	69	76	3.1
8	66	67	2.7
9	58	58	2.4

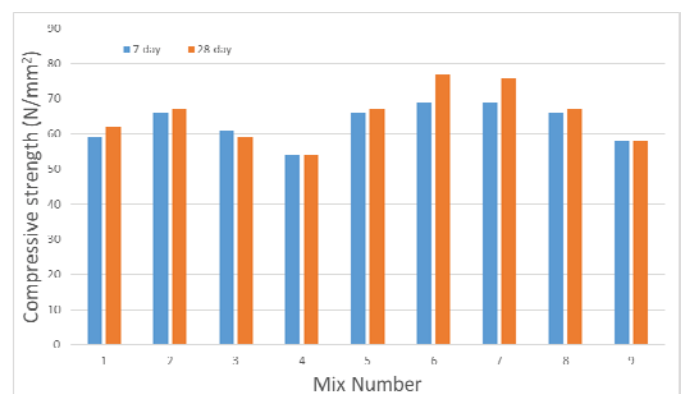


Figure 3. Relationship between 7 day and 28 day compressive strengths of geopolymer mortar mixes.

The ratio of geopolymer binder liquids to geopolymer binder solids is thought to play a role in the compressive strength of geopolymer mortar, much like the effect of water/cement ratio when using ordinary Portland cement. Figures 4 and 5 show the effect of geopolymer liquids to solids, for 7 day and 28 day compressive strengths respectively. As shown in figure 4, after 7 days, the general trend is that compressive strength decreases, as the geopolymer liquids to solids ratio increases ($R^2=0.35$). Figure 5 shows that this relationship becomes more apparent for 28 day compressive strength ($R^2=0.54$).

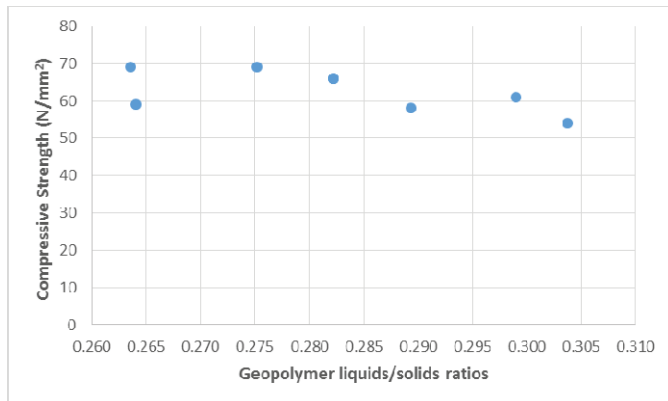


Figure 4. Effect of geopolymer liquids to geopolymer solids ratio on the 7 day compressive strength of geopolymer mortar.

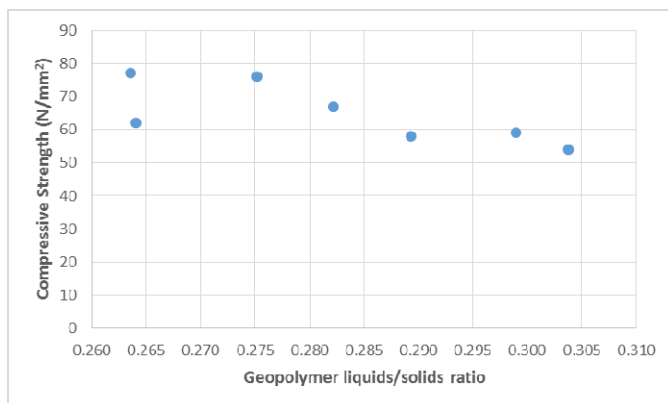


Figure 5. Effect of geopolymer liquids to geopolymer solids ratio on the 28 day compressive strength of geopolymer mortar.

The ratio of activator to powder also appears to play some role in the 28 day compressive strength of geopolymer mortar. This trend is shown in Figure 6, where $R^2=0.25$. However, some variance in the results would indicate that the geopolymer liquid to solids ratio plays a more important role in the geopolymer strength development.

The Specification for Highway Works Clause 1001 states that concrete for use as a surfacing material must be classed as CC37 [16]. This means that 7 day and 28 day compressive strengths of 32 N/mm² and 37 N/mm², respectively, are required for use as a surfacing material. This means that all mixes have exceeded the minimum compressive strength requirements. In addition, it has been proposed that a minimum 2 hour flexural strength of 2.4 N/mm² is required when testing repair materials under

laboratory conditions [17]. While seven of the mixes achieved this strength at 28 days, further testing will be required to determine the 2 hour flexural strength.

Mix 7 was selected for further workability testing, and for testing as a pothole repair material. This selection was based on the mix providing the highest flexural strength, along with high 7 day and 28 day compressive strengths.

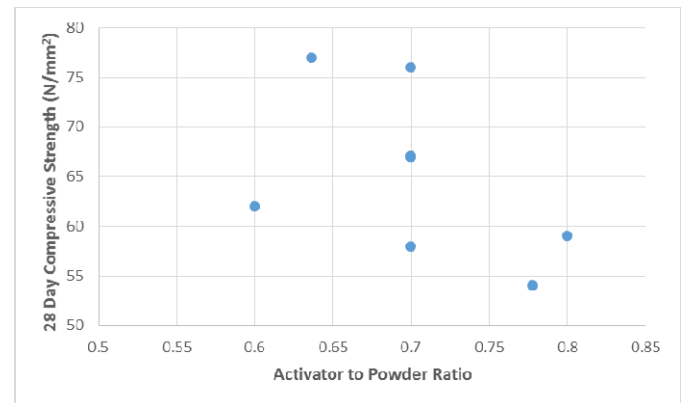


Figure 6. Effect of activator to powder ratio on 28 day compressive strength of geopolymer mortar.

3.2 Fresh pothole repair properties

The flow of the geopolymer mortar was recorded as 193 mm. According to BS EN 1015-6: 1991, this mortar can be classed as a plastic mortar, as it falls within the plastic mortar flow range of 140 to 200 mm [18]. The initial and final setting times were recorded as 150 minutes and 180 minutes, respectively.

The flow result of the mortar indicates a suitable level of workability for use as a repair material. The material is likely to require little compaction, and will be easy to spread into all areas of the defect to maximize bond adhesion. However, according to the Specification for Highway Works clause 946 [19], a pothole repair material should have cured sufficiently to withstand heavy vehicle trafficking after 30 minutes. With a final setting time of 180 minutes, the geopolymer mortar would require the setting times to be significantly reduced to be of use as a pothole repair material.

3.3 Pothole Repair Performance

After 20,000 wheel-passes, a visual assessment of the specimen was carried out. As geopolymer mortar is an untested material in this application, using this test method, it was expected that some performance issues would occur during the initial testing. Concerns about potential failure were due to the stiffness of hardened geopolymer cement mortar, and the possibility of the geopolymer mortar being incompatible with the existing asphalt surrounding the defect. However, after 2000 wheel passes, no surface defects were noticed (Figure 7). The visual assessment focused on surface cracking, delamination, de-bonding of the geopolymer from the asphalt, and material loss. The only indication of wear was some shining of the material surface. The skid resistance was measured before and after the accelerated wearing of the

sample. The skid resistance decreased slightly from 43 to 41 after wearing. While this was a positive initial test, the performance falls short of the requirements set out by RRL Road Note 27 [15]. The minimum skid resistance value for materials used on public roads is 45, with trunk roads and motorways requiring 55, and bends and roundabouts requiring 65. Therefore, further work involving surface texturing will be required to develop a geopolymer mortar which is suitable for road pavement use. Also, it is suggested that samples should be subjected to $100,000 \pm 1000$ wheel passes [14]. While initial durability results appear positive, a more extensive testing programme will be required to determine the performance of the repair material after much greater exposure to wearing conditions.



Figure 7. Geopolymer pothole repair material after simulated wearing.

3.4 High Friction Surfacing

The high friction surface slabs were subjected to 20,000 wheel passes, with texture depth and skid resistance measured prior to testing, and at various intervals during testing. Prior to testing, the texture depth of the geopolymer aggregate sample was recorded as 2.43 mm, with a skid resistance value of 80. The control slab had an initial texture depth of 2.58 mm, and a skid resistance value of 94. Figure 8 shows the changes in texture depth during testing. Figure 9 shows the changes in skid resistance during testing. After 20,000 wheel passes, the geopolymer slab retained a texture depth of 1.3 mm, and a skid resistance value of 55. This represented a 47% decrease in texture depth and a 31% decrease in skid resistance. This is compared with the calcined bauxite, which has a retained texture depth of 1.55 mm (40% texture loss) and a skid resistance value of 74 (21% skid resistance loss). Both slabs showed a significant decrease in texture depth after 1000 wheel passes. The geopolymer aggregate texture depth reduced by 39% after 1000 wheel passes, and the calcined bauxite texture depth reduced by 33%. After the initial 1000 wheel passes, the texture depth loss of the samples was more stable. While the retained texture depth of the geopolymer aggregate slab was significantly lower than the initial value, the 1.3 mm texture depth exceeds the minimum requirements for a road surface. The reference slab had a retained texture depth of 1.6 mm.

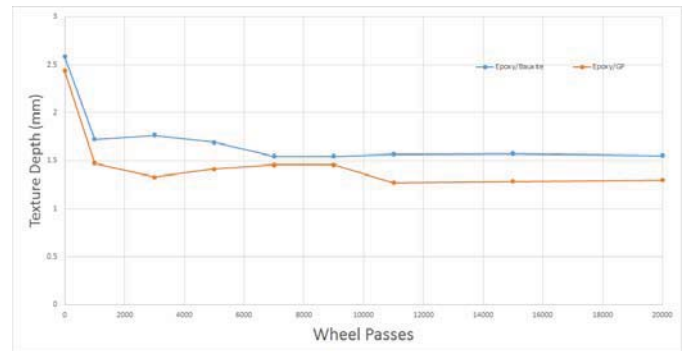


Figure 8. Effect of simulated wearing on surface texture depth.

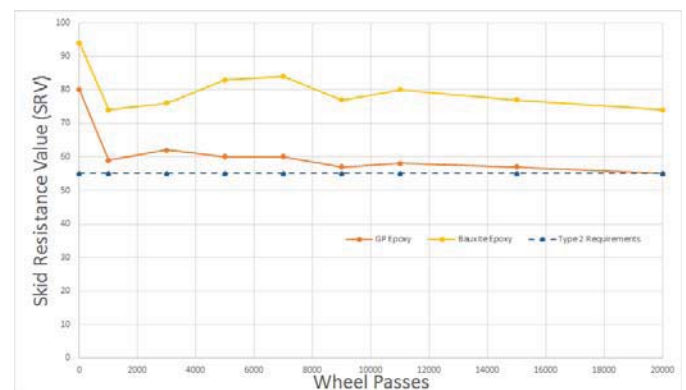


Figure 9. Effect of simulated wearing on skid resistance values.

The skid resistance value of the geopolymer aggregate slab can be classified as a Type 2 surface, according to RRL Road Note 27 [15], while the calcined bauxite slab achieved a Type 1 classification, as expected. This means that the geopolymer aggregate, without any further work or development, would be suitable for use in a type 2 application, such as trunk roads or motorways.

From the results, the skid resistance value differences between the samples may be attributed broadly to a difference in macrotexture depths. However, the results show that a decreasing texture depth doesn't directly compare with decreasing skid resistance values. This may suggest that factors other than macrotexture, such as aggregate shape and size may also have an effect on the skid resistance of a high friction surface. Also, some unexpected texture depth readings, such as the increase in geopolymer slab texture depth between 11,000 and 20,000 wheel passes, may be attributed to some aggregate being removed during testing. Further work is required in this area to better understand the factors which affect the skid resistance of high friction surfaces.

4 SUMMARY AND CONCLUSIONS

The first part of this investigation focused on the development of a geopolymer mortar mix design process, in order to produce a high strength geopolymer mortar. Mix designs were developed, based on the upper, middle and lower limits of content ranges which were considered for each variable in the mortar: powder, activator and water. Sand content was

adjusted only to maintain a constant mix density. Compressive strengths at 7 days ranged from 54 to 69 N/mm², while at 28 days, compressive strengths ranged from 58 to 77 N/mm². Flexural strengths, as expected, were significantly lower with 28 day strengths ranging from 1.7 to 3.1 N/mm². Based on these results, mix 7, with a mean 28 day compressive strength of 76 N/mm² and flexural strength of 3.1 N/mm² was selected for workability tests and as a pothole repair material. The crushed geopolymer mortar specimens were then crushed, using a jaw crusher, to form an aggregate suitable for use as a high friction surface aggregate.

The second part of this study involved the application of a geopolymer cement-based material in two road pavement applications: a pothole repair material and a high friction surface aggregate. These initial results indicated the potential usefulness of geopolymer cement-based materials in highway applications. As a pothole repair material, no surface deformations were noticed, other than some minor shining of the geopolymer surface. However, texture depth and skid resistance values were below minimum requirements. Also, a longer test period with the road test machine is required to gain a better understanding of the geopolymer performance over time. As a high friction aggregate, the impressive results achieved at a very early stage in the research provide a strong starting point in the further development of a suitable alternative to calcined bauxite in a high friction surfacing system. The potential to recycle geopolymeric materials for this application may also prove to be a positive when considering the whole life cycle of geopolymer cement. Overall, geopolymer cement has been identified as a material which can be adapted to perform well in differing road surface applications.

This study has identified three main areas for further consideration in the research programme.

1. Further research into the potential use of geopolymer mortar pothole repairs, to improve setting times and with surface texturing applied to satisfy texture depth and skid resistance value requirements.
2. Optimisation of geopolymer strength to create a durable, high performance aggregate for use as a high friction aggregate.
3. Investigation into factors affecting high friction surfaces, using conventional measurement techniques and new 3D photogrammetry techniques. This is to be followed by further optimisation of the geopolymer aggregate in terms of strength, shape and size.

ACKNOWLEDGMENTS

The financial and technical support for this research received from the Department for Employment and Learning, Northern Ireland and Banah UK Ltd., is gratefully acknowledged.

REFERENCES

- [1] McLellan, B.C., Williams, R.P., Lay, J., van Riessan, A. and Corder, G.D., 2011. *Costs and carbon emissions for geopolymer pastes in comparison to ordinary Portland cement*. Journal of Cleaner Production, 19 pp. 1080-1090.
- [2] Davidovits, J., 2013. *Geopolymer Cement: A Review*. Saint Quentin: Geopolymer Institute.
- [3] Banah UK, 2014. *Introduction to Geopolymer Binders*. Ballyclare: Banah UK.

- [4] Glasby, T., Day, J., Kemp, M. and Aldred, J., 2014. *Geopolymer Concrete for Durable Linings*. [Online] Available at: <http://www.tunneltalk.com/TunnelTECH-Jan2014> [Accessed 22 January 2016].
- [5] Abdulkareem, O.A., Al Bakri, A.M.M., Kamarudin, H. and Khairul Nizar, I., 2014. *Fire resistance evaluation of lightweight geopolymer concrete system exposed to elevated temperatures of 100-800°C*. Key Engineering Materials, 594-595 pp. 427-432.
- [6] British Standards Institution, 2016. *PAS 8820: 2016. Construction materials. Alkali-activated cementitious material and concrete. Specification*. Milton Keynes: BSI.
- [7] Asphalt Industry Alliance, 2015. *Why Asphalt?* [Online] Available at: <http://www.asphaltuk.org/mobile/index.asp?page=whyasphalt> [Accessed 26 May 2015].
- [8] Hawa, A., Tonnayopas, D., Prachasaree, W. and Taneerananon, P., 2013. *Development and Performance Evaluation of Very High Early Strength Geopolymer for Rapid Road Repair*. Advances in Materials Science and Engineering, 2013 pp. 1-9.
- [9] Robinson, H., 2013. *High Friction Surfacing*. Highways Magazine, [online]. Available at http://www.rsta-uk.org/downloads/High_Friction_Surfacing_in_Highways_Magazine_October_2013.pdf. [Accessed 1 February 2016].
- [10] British Standards Institute, 1999. *BS EN 1015-11: 1999. Methods of test for mortar for masonry. Determination of flexural and compressive strength of hardened mortar*. Milton Keynes: BSI.
- [11] British Standards Institute, 1999. *BS EN 1015-3: 1999. Determination of consistence of fresh mortar (by flow table)*. Milton Keynes: BSI.
- [12] British Standards Institute, 2005. *BS EN 196-3: 2005. Determination of setting times and soundness*. Milton Keynes: BSI.
- [13] British Standards Institute, 1999. *BS EN 1015-1: 1999. Methods of test for mortar for masonry. Determination of particle size distribution (by sieve analysis)*. Milton Keynes: BSI.
- [14] Transportation Research Laboratory, 1997. *Report 176 Laboratory Tests On High-Friction Surfaces For Highways*. Berkshire: TRL.
- [15] Road Research Laboratory, 1969. *Road Note 27 – Instructions for using the portable skid-resistance tester*. London: HMSO.
- [16] MCHW, 2016. *Manual of Contract Documents for Highway Works, Volume 1: Specification for Highway Works, Series 1000: Road Pavements – Concrete Materials*. London: Department for Transport.
- [17] McDaniel RS, Olek J, Magee BJ, Behnood A, and Pollock R, 2014. *NCHRP SYNTHESIS 463 - Pavement Patching Practices: A synthesis of Highway Practice*. Washington D.C.: Transportation Research Board
- [18] British Standards Institute, 1991. *BS EN 1015-6: 1991, Methods of test for mortar for masonry – Part 6: Determination of bulk density of fresh mortar*. Milton Keynes: BSI.
- [19] MCHW, 2005. *Manual of Contract Documents for Highway Works, Volume 1: Specification for Highway Works, Series 900: Road Pavements – Bituminous Bound Materials*. London: Department for Transport.

Large Scale Structural Testing of Wind Turbine Blades Manufactured Using a One-Shot Out-Of-Autoclave Process

M. H. Flanagan^{1,2,4}, F. Doyle¹, E. Fagan^{2,4}, J. Goggins^{2,4,5}, A. Doyle¹, T. Flanagan¹, P. J. Feerick¹, S.B. Leen^{3,4,5}

¹ ÉireComposites Teo, Indreabhán, Galway, Ireland

² Civil Engineering, NUI Galway, Ireland

³ Mechanical Engineering, NUI Galway, Ireland

⁴ Centre for Marine and Renewable Energy (MaREI), Galway, Ireland

⁵ Ryan Institute, Galway, NUI Galway, Ireland

email: m.flanagan15@nuigalway.ie, f.doyle@eirecomposites.com, jamie.goggins@nuigalway.ie

ABSTRACT: This paper gives details of large scale static testing carried out on 13m long wind turbine blades manufactured using powder epoxy glass fibre material, cured on integrally heated ceramic tooling in a novel one-shot process. In order to demonstrate the advantages of the one-shot process, details of the manufacturing process are given for comparison with traditional methods used to manufacture wind turbine blades. The preliminary test results are compared with Finite Element (FE) models and results of similar testing reported in literature. The results show that the blade performed as per the design intent and the powder epoxy material and the one-shot process offers a viable alternative to traditional materials and manufacturing methods used in the renewable energy sector.

KEY WORDS: Polymer composites; Glass fibre; Ceramic tooling; One-shot process.

1 INTRODUCTION

Conventional wind turbine blade manufacture involves manufacturing sub-assemblies and bonding them together to form the final blade. This process is used as it is cost effective, as well as tried and tested. However, there are several disadvantages to the process. For example, (i) the bondlines are inherently weaker than the composite surrounding them and, as such, represent a weak point in the overall structure of the blade, and (ii) the manufacture of thick sections is challenging, as the resins use exotherm and emit volatile organic compounds during cure.

This paper describes the development and testing of wind turbine blades manufactured in a one-shot process with no bondlines. The blades are manufactured using powder epoxy materials that have comparable strength to traditional epoxy glass fibres, but have several advantages [1,2]. Table 1 gives a comparison of powder epoxy composite material properties to Vacuum Assisted Resin Transfer Moulding (VARTM) composites and prepreg vacuum bag only manufacturing methods currently used in the manufacture of wind turbine blades [3].

Table 1 Material properties of competing material systems normalised for 53% glass fibre volume fraction.

Property	Powder Epoxy[1]	VARTM[1]	Prepreg[1]
Tensile strength (MPa)	957	821	952
Compressive strength (MPa)	666	511	687
Tensile Modulus (GPa)	39.2	37.8	42

Unlike traditional glass fibre epoxy manufacture where exotherm from the resin during cure must be controlled to avoid damage to the part, or a potential health and safety hazard [4], there is no significant exotherm during the

manufacture of powder epoxy glass composites [2]. The material is solid at room temperature and formable without polymerisation at low temperatures. This means that sub-structures can be formed off-line on low cost, low temperature tooling and assembled to form the final part, which is then polymerised in one-shot cure. This process enables the manufacture of large parts with complex internal structures without secondary bonding procedures. Furthermore, it enables joints with complex ply drop-offs and overlaps that would be difficult or impossible with traditional bonding techniques. The powder epoxy matrix bonds to metal during cure which allows metal inserts to be embedded in the layup during cure, eliminating the need to drill and glue inserts. The material can be stored at room temperature and has a very long shelf life when compared to traditional epoxy resins. There are no volatile organic compounds emitted during cure, which means that the manufacturing process is in line with the tightest European manufacturing regulations [5]. The material is supplied in a semi-pre-impregnated form, where the glass is uniformly coated in powder epoxy. This means that during cure the powder epoxy only has to travel through the thickness of one ply in order to ensure that the fibres are fully wet-out and that there is uniform fibre volume throughout the entire structure.

One obstacle to the use of powder epoxy in the manufacture of large composite parts in the renewable sector is that the cure is heat activated at circa 180°C. This means that low cost tooling, capable of a high number of cycles between room temperature and 180°C, with a thermal expansion close to that of the manufactured part, and a heating system capable of efficiently heating the part are needed in order to manufacture using the powder epoxy material. ÉireComposites has developed ceramic composite tooling with integrated electrical heating that meets the above criteria [2,6]. This tooling has been used to manufacture 13m long commercial wind turbine blades for the Vestas V-27 wind turbine using powder epoxy glass fibre material.

This paper gives details of the steps involved in manufacturing the 13m long blade using the one-shot Out-Of-Autoclave (OOA) process with integrally heated composite ceramic tooling and compares it to traditional manufacturing methods. Following this, the results of testing embedded metal inserts and full-scale testing of 13m long wind turbine blades are presented. The results of the testing are compared to results from literature and to a FE model.

2 MANUFACTURING

2.1 Introduction

This section provides a comparison of a traditional OOA manufacturing process for the Vestas V-27 blades and ÉireComposites one-shot OOA manufacturing process. Both blades have the same box section internal structural concept common in wind turbine blades [3].

2.2 Conventional manufacturing process

The original Vestas V-27 blades were manufactured in several parts, which were assembled together and glued to form the final blade. The blade is comprised of 10 main parts, shown in Figure 1, and several smaller bond-line re-enforcement parts, which are all manufactured separately using individual tools. Parts 1 to 4 are the root insert anchors, which transfer the loads from the metal inserts to the composite structure. Parts 5 and 6 are the spars comprised mainly of uni-directional fibres, which give the part bending stiffness. Parts 7 and 8 are the webs comprised mainly of tri-axial material for torsional stiffness. Parts 9 and 10 are the aerodynamic shell comprised mainly of tri-axial fibres and a balsa core for stiffness.

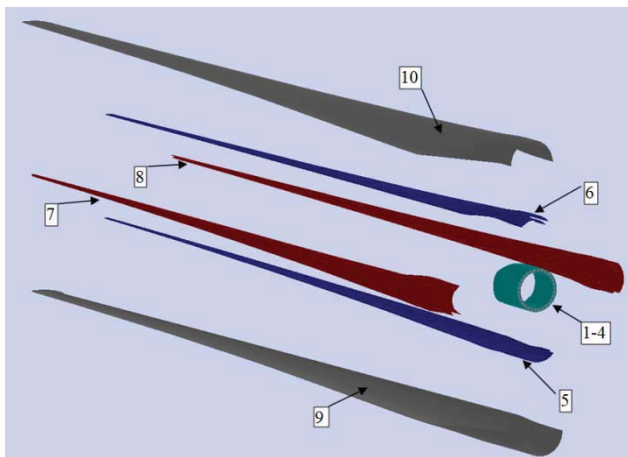


Figure 1 Sub-assemblies of a conventional Vestas V-27 wind turbine blade, showing the four root anchors (parts 1-4) in light green, the upper and lower spars (parts 5 and 6) in blue, the webs (parts 7 and 8) in red and the shells (parts 9 and 10) in grey.

Table 2 gives an overview of the individual processes involved in the manufacture of each blade. All individual parts are manufactured using traditional processes such as wet layup, or vacuum assisted resin transfer on low cost tooling. All the parts are glued together in several stages to form the final assembly. Once the final blade is bonded together, holes

are drilled at the root of the blades and metal inserts are glued into the root in order to facilitate attachment of the blade to the hub. Figure 2 shows a section of a decommissioned blade showing the internal box structure and the bond-lines.

Table 2 List of the main processes in the manufacture and assembly of a Vestas V-27 wind turbine blade manufactured using traditional bonding techniques.

Process	Sub assembly parts (as per Figure 1)	Sub-assembly
Part Manufacture	All parts manufactured individually	NA
Bonding	Part 1, part 5	Spar 2 assembly
Bonding	Part 2, part 6	Spar 1 assembly
Bonding	Part 3, part 7	Web 2 assembly
Bonding	Part 4, part 8	Web 1 assembly
Bonding	Spar 1 assembly, Web 1 assembly, Spar 2 assembly, Web 2 assembly.	Box section assembly
Bonding	Box section assembly, Part 9, Part 10	Composite blade
Drilling & Bonding	Composite blade, 30 metal inserts	Final blade

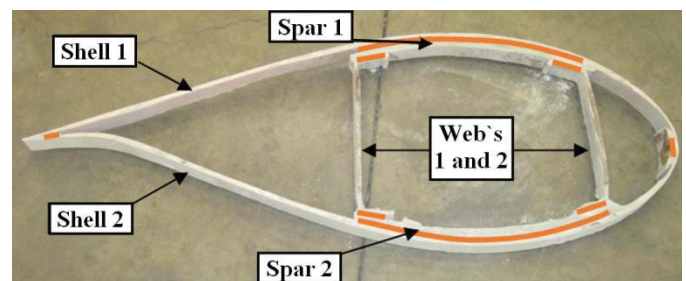


Figure 2 Section of Vestas V-27 wind turbine blade showing the internal box section with bond-lines highlighted in orange.

Due to the low cost of materials and tooling, this process is currently widely used in the manufacture of wind turbine blades. Based on the average thickness of the bond-lines of 5mm for the original V-27 blade, a surface area of the bonded areas of 8.2m² and taking the density of epoxy glue as 1342kg/m³, it is estimated that the glue adds 55kg or 9% of the overall weight of the blade. Gluing the rigid sub-assemblies into place to form the complex internal structure of the final blade is a difficult process, which requires tight geometric and process tolerances in order to avoid misalignments, voids and gaps in the bond-lines of the final structure. Figure 3 shows a section of the original blade where the lower spar is not correctly aligned or bonded to the skin of the blade. This section was the worst examined, but many of the bond-lines examined were of low quality with large gaps and voids. The original blade examined was a retired blade that had reached the end of its service life. Current state-of-the-art blades are likely to be manufactured to a higher standard. However, the same fundamental process of manufacturing sub-assemblies and gluing them together is still the predominant manufacturing method used in the wind industry today.



Figure 3 Section of Vestas V-27 blade showing the misalignment of central box structure with a large area of the lower spar not connected to the shell of the blade.

2.3 Éirecomposites one-shot manufacturing process

ÉireComposites have developed a manufacturing process that eliminates gluing by polymerising the entire structure, complete with embedded metal inserts, in one-shot. The process uses heat-activated powder epoxy material and has many advantages over traditional manufacturing techniques.

The ÉireComposites one-shot blade is comprised of 4 sub-assemblies, as shown in Figure 4. Each sub-assembly is formed and wet-out, but not polymerised, at low temperatures on low cost tooling. Metal inserts are embedded into the sub-assemblies during the initial forming stage. The solid sub-assemblies are designed with mating ply overlaps and drop to re-reinforce the mating join-lines.

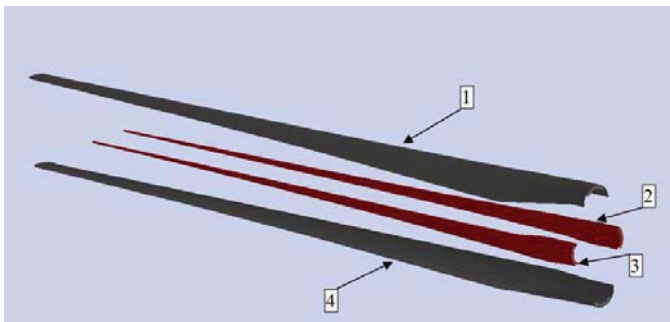


Figure 4 Sub-assemblies of a one-shot Vestas V-27 wind turbine blade, showing (i) the top skin, top root anchors, inserts, and top spar (part 1) in grey, (ii) the leading edge root anchors, inserts and leading edge web (part 2) in red, (iii) the trailing edge root anchors, inserts and trailing edge web (part 3) in red, and (iv) the bottom skin, bottom root anchors, inserts and bottom spar (part 4) in grey.

Table 3 gives an overview of the steps involved in the ÉireComposites one-shot process. Once the sub-assemblies are assembled together in the heated ceramic mould, a vacuum is applied and the whole part is polymerised in one-shot with the metal inserts already embedded. During polymerisation, the powder epoxy flows again. This allows the ply overlaps, which are rigid at room temperature, to melt into one another and form a glue-less structure with complex ply overlaps and no gaps, voids or misalignments. This type of joint would be very difficult to form with traditional gluing, as the plies are completely rigid during the gluing process so any gaps or misalignments will remain after bonding as shown in Figure 3.

Table 3 List of the main processes in the manufacture and assembly of a Vestas V-27 wind turbine blade manufactured using ÉireComposites one-shot process.

Process	Sub assembly parts (as per Figure 4)	Sub assembly
Sub assembly forming	Shell 1, spar 1, root anchor, and inserts	Part 1
Sub assembly forming	Leading edge root anchor, web 1, and inserts	Part 2
Sub assembly forming	Trailing edge root anchor, web 2, and inserts	Part 3
Sub assembly forming	Shell 2, spar 2 root anchor, and inserts	Part 4
Curing (180°C)	Part 1, Part 2, Part 3, Part 4.	Final blade

Figure 5 shows a finished 13m long commercial blade with embedded metal inserts and a complex internal structure that has been manufactured using powder epoxy material using an integrally heated ceramic mould in a one-shot OOA process. The blade is a derivative of the Vestas V-27 blade and uses the same layout and internal sub-structure as the original blade.



Figure 5 Commercial 13m long blade manufactured using a one-shot OOA process.

3 INSERT PULL-OUT TESTS

Wind turbine blades use metal inserts to connect the blade to the hub of the wind turbine. The original Vestas V-27 blades had 30 inserts drilled and bonded into the root of each blade. In order to compare ÉireComposites glue-less insert placement technique to traditional gluing techniques, pull-out tests were performed on inserts manufactured using each method. Figure 6a shows images of the drilled and bonded metal insert test samples on the left, and the ÉireComposites embedded samples on the right. The drilled and bonded inserts were taken from a decommissioned blade, which had not reached the end of its service life. Despite this, there may have been a reduction in load capacity due to its service history. Figure 6b shows the test fixture and a test sample, while Figure 6c shows the sample and test fixture installed in a 250kN test machine. Results of the pull-out tests performed on two glued inserts and one embedded insert showed that the embedded insert reached nearly twice the failure load of the glued inserts without any signs of failure. It should be noted that this is not a direct comparison of insert types, as the glued inserts were part of a decommissioned blade, whereas the embedded inserts were manufactured specially for the test.

Furthermore, the embedded inserts reached the maximum load of the test machine without failure. The test setup is currently being modified for use in the 500kN test machine in order to measure the failure load for the embedded insert test specimens.

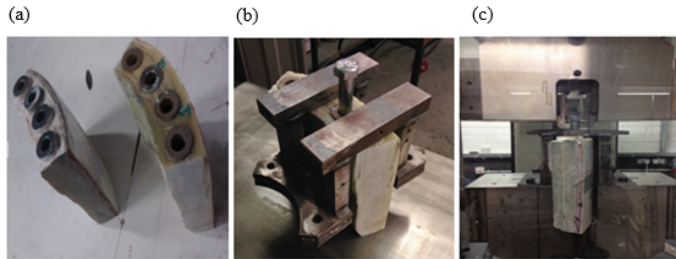


Figure 6 (a) Left: Drilled and bonded inserts from original blade, Right ÉireComposites embedded inserts (b) test fixture used to test insert pull-out strength (c) Test fixture and inserts installed in 250kN test machine.

4 FULL-SCALE BLADE TESTING

As part of the blade qualification process, large-scale static testing of the 13m long wind turbine blade manufactured in one-shot using the powder epoxy material was carried out. A test concept shown in Figure 7 was used to test the blades. Using this concept, the forces from each blade react the other, which meant that a test frame capable of reacting the test loads was not necessary. This provided a cost effective solution for the testing. The final test setup is shown in Figure 8. Load saddles were manufactured from C-channel steel sections that clamped around plywood inserts cut to the profile of the blade. Silicone sheeting was placed between the wooden profile and blade to avoid local damage to the blade from the clamping force. The load saddles were connected to each other with a block and chain in the centre, as shown in Figure 8. The weight of each blade was supported by a trolley positioned at 10m, which allowed the blades to deflect during testing.

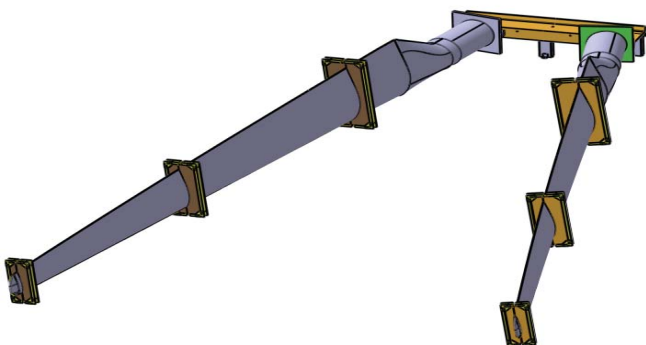


Figure 7 13m long blade test-concept showing the test frame, two blades installed and the 6 load saddles used to connect the block and chain to the blades.



Figure 8 Test setup used to test the blades.

Figure 9 shows a graph of the bending moment on the blade during testing. The test loads were calculated based on a wind speed of 50m/s with the blade chord perpendicular to the wind direction.

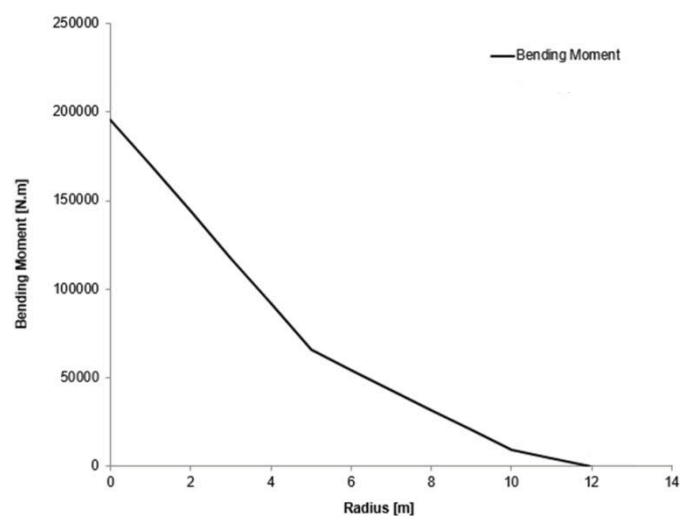


Figure 9 Bending moment on blade during max loading.

The blade was loaded using chain blocks and the load saddles shown in Figure 7 at 5m, 10m and 12m from the root of the blade. The load was continuously adjusted until the target load was reached at each station. Once the target loads were reached, the deflection at each blade station was recorded. The test setup meant that each blade was loaded in a different flap-wise direction. The deflection measurements of the left hand blade in Figure 8 at maximum loading are given in Figure 10, together with the results of an FE analysis of the blade and results from literature of testing carried out on a Vestas V-27 blade [7]. Although the material, manufacturing method, and internal structure of the blade from literature differs somewhat from the blade presented in the current study, the result from literature provides a useful comparison between the current design and the original design. During loading, the load deflections was linear for both blades. Monitoring the position of the test fixture showed that the whole test rig rotated during testing which may have affected the accuracy of the test results by up to $\pm 7\%$. The difference between the FE and the test results may be due to (i) variation fibre volume and layup which may occur in a production environment and is not captured in the FE, (ii) difference

between idealised loading and boundary conditions in FE and actual loading, and (iii) the plain stress elements do not accurately represent the root area of the blade. During loading there were no signs of any form of failure of the blade such as surface buckling, cracking, or acoustic emissions.

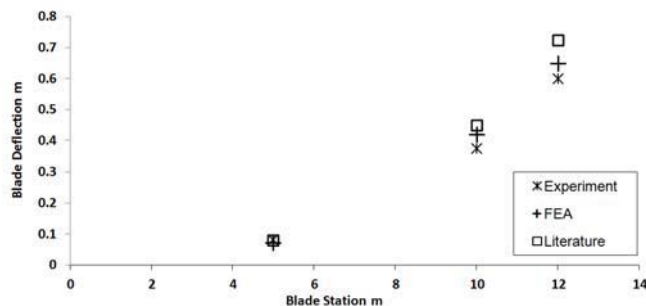


Figure 10 Comparison of deflections measured at 100% loading, calculated using FE and deflections reported in literature [7] of a similar Vestas V-27 blade.

5 CONCLUSIONS

The current work gives details of testing carried out on a 13m long wind turbine blade and metal inserts used to attach the blade to the wind turbine. The blade was manufactured using integrally heated ceramic tooling and heat-activated thermosetting epoxy powder material.

The results of static testing the 13m long blade show good agreement with the FE model. The FE model will be used as a baseline for a blade design optimisation study focused on reducing manufacturing costs and weight reduction.

The testing also confirms the suitability of the powder epoxy material and the one-shot process in manufacturing large composite structures with a typical internal structure and also the use of integrally heated composite tooling. Research into the powder-epoxy material is ongoing with current work investigating the use of powder epoxy glass fibre and carbon fibre in tidal turbines and other applications, as part of the EU MarinComp [8] and FloTec projects [9].

Integrally heated tooling has been used to manufacture carbon fibre aerospace demonstrators [6] and the tooling could provide cost effective solutions for large-scale OOA manufacturing in automotive and civil engineering applications.

The initial results of pull-out tests on metal inserts are promising but further work is needed to directly compare the imbedded insert manufacturing method to traditional insert bonding techniques. A follow up study will redesign the pull-out test rig in order to allow the inserts to be tested to failure and also manufacturing several inserts and glue them in place for a more accurate comparison between the powder-epoxy bonding process and current gluing processes used in the wind and tidal industries. Another potential area of interest is the complex bonds that could be manufactured using thermoplastics or heat-activated powder epoxy materials.

ACKNOWLEDGMENTS

The research was carried out as part of a collaboration between NUI Galway and ÉireComposites Teo, supported by the Irish Research Council and Science Foundation Ireland

under Grant No. 12/RC/2302 through MaREI, the national centre for Marine and Renewable Energy in Ireland.

REFERENCES

- 1 Flanagan T., Maguire J., Ó Brádaigh C.M., Mayorga P., Doyle A., Smart Affordable Composite Blades for Tidal Energy, EWTEC, Nantes France, 2015.
- 2 Ó Brádaigh C.M., Doyle A., Doyle D., Feerick P.J., One-Shot Wind Turbine Blade Manufacturing using Powder-Epoxy and Electrically-Heated Ceramic Composite Tooling, CFK Valley State Convention, Stade, Germany, 2013.
- 3 Gurit (2016). Wind Energy Handbook. Available: <http://www.gurit.com/wind-energy-handbook.aspx> . Last accessed 3rd May 2016.
- 4 Gurit (2016). Exothermic Reactions. Available: <http://www.gurit.com/exothermic-reactions.aspx> . Last accessed 13th April 2016.
- 5 Council of the European Union, VOC Solvent Emissions Directive, ID 1999/13/EC, 1999
- 6 J. Dolan J., Doyle A., Ó Brádaigh C.M., D. Jaredson D., Out-of-Autoclave Manufacture of Large Integrated Structures Using Thermoplastic Composite materials, ECCM15, Venice, Italy, 2012.
- 7 A. A. Mohamed A.A., "Modelling av NACA 63.200 vindturbinblad", Master's Thesis, University of Stavanger, Norway, 2011.
- 8 Marincomp (2015). Novel Composite Materials and Processes for Offshore Renewable Energy. Available <http://www.marincomp.eu/> .last accessed 3rd May 2016.
- 9 EireComposites (2016). ÉireComposites to Build Blades for 2MW Floating Tidal Device. Available: <http://www.eirecomposites.com/news/flo-tec-horizon-2020> . Last accessed 3rd May 2016.

Risk assessment for an Italian road network due to an extreme earthquake hazard scenario and the associated landslide cascading effects

Julie Clarke¹, Juan Carlos Lam², Pierre Gehl³, Khaled Taalab⁴, Robert Corbally¹

¹Roughan and O'Donovan Innovative Solutions, Dublin, Ireland

²ETH Zurich, Institute of Construction and Infrastructure Management, Zurich, Switzerland

³University College London, EPICentre, Dept. of Civil Engineering, London, UK

⁴University College London, SpaceTime Lab, Dept. of Civil, Environmental and Geomatic Engineering, London, UK
email: julie.clarke@rod.ie

ABSTRACT: Natural hazards, such as earthquakes, have the potential to cause damage to transport infrastructure networks and can lead to significant network disruption and associated losses. The INFRARISK project (*Novel Indicators for Identifying Critical INFRAstructure at RISK from Natural Hazards*) is developing methodologies to assess the impact of extreme natural hazard events on critical transport infrastructure networks. To demonstrate the systematic application of the proposed methodologies, a road network in Northern Italy is being assessed due to an extreme earthquake hazard scenario and the associated landslide cascading effects. The road network is distributed over an area of approximately 990km² and is located along the Scandinavian-Mediterranean corridor of the TEN-T network, which is considered a vital axis for the European economy. The vulnerability of the road network is assessed according to the seismic vulnerability of the 340 bridges and 30 tunnels located along the network, as well as the vulnerability of 870 km of roads to earthquake-triggered landslide hazards. This paper presents the initial results of the risk assessment, which evaluates the direct consequences to the road network due to an extreme seismic hazard scenario. The methodology also supports the quantification of indirect consequences for transport networks due to natural hazard scenarios, which is the subject of future work.

KEY WORDS: Transport networks; Risk assessment; Seismic hazard; Landslide hazard.

1 INTRODUCTION

Transport infrastructure is critical to the effective functioning of societies. However, extreme seismic events can cause severe disruption to infrastructure networks due to the physical damage that occurs, resulting in additional travel times for network users and associated economic losses. For example, the 6.8 magnitude Northridge earthquake in 1994 significantly impacted the regional transportation system in the area of Los Angeles, California, and generated a year's worth of highway repair work as a result of the single event [1]. In Europe, the magnitude 6.3 earthquake that occurred in L'Aquila, Italy in 2009 caused transport disruption due to bridge damage and road blockages [2].

The INFRARISK project (*Novel Indicators for Identifying Critical INFRAstructure at RISK from Natural Hazards*) is developing methodologies to assess the impact of extreme, low probability natural hazard events on critical transport infrastructure networks (<http://www.infrarisk-fp7.eu/>). The project is focused on the TEN-T road and rail networks, which comprise the core European transport network corridors, and are critical to the effective functioning of the European economy. The objective of the INFRARISK project is to enable infrastructure managers and owners to perform stress tests for critical networks to determine their resilience to low probability, extreme natural hazard events and, consequently, to assist in the decision making process with regard to the protection of critical infrastructure networks.

As part of the INFRARISK project, the developed methodologies are being applied to selected European case studies to demonstrate the systematic application and feasibility of the proposed methodologies [3]. This paper

presents one of the INFRARISK case studies, which assesses the risk of an extreme seismic hazard scenario and the associated cascading effects in terms of earthquake-triggered landslides for a road network in Northern Italy. Initial results are presented herein in terms of the cost associated with restoring the network to the level of service that existed prior to the natural hazard event, i.e. the direct consequences. The adopted methodology also considers the associated indirect consequences, relating to the additional travel times encountered by road users and the resulting economic losses, which is the subject of future work.

2 BACKGROUND

Seismic risk assessment for distributed transport networks generally involves the use of probabilistic methods to quantify the uncertainty associated with the ground motion intensities and the network structural damage [4] [5]. Furthermore, seismic loss estimation for distributed networks necessitates the consideration of spatially correlated ground motions for individual earthquake scenarios [6] [7].

Probabilistic methods have been employed to assess the seismic risk for highway networks, whereby the seismic vulnerability of the network bridges are characterised according to fragility curves [8] and the consequences were quantified in terms of network disruption [9]. Furthermore, the consequences of seismic hazard scenarios for road networks have been quantified in terms of the additional travel times encountered by road users [10] and the accessibility disruption for local communities [11].

The risk to distributed networks due to earthquake hazards has also been addressed in recent European-funded projects.

For example, the RISK-UE project described a general methodology to assess the seismic risk to lifeline systems and proposed mitigation strategies [12]. Likewise, the SYNER-G project assessed the seismic risk to infrastructure networks. The consequences were assessed in terms of the associated losses for critical facilities [13], and the interaction between damaged infrastructure networks and the damaged built environment was examined as part of the seismic risk analysis [14]. In this study, a probabilistic seismic risk assessment process is employed, which considers cascading effects in terms of earthquake-triggered landslides and is focused on low probability, extreme earthquake hazard scenarios.

3 ITALIAN ROAD NETWORK

To demonstrate the systematic application of the proposed INFRARISK methodology, a road network in the vicinity of the city of Bologna in Northern Italy was examined. The network forms part of the European TEN-T road network, specifically along the Scandinavian-Mediterranean corridor, which is considered a vital axis for the European economy. This road network is located in a seismically active region (Figure 1), which is also prone to landslides (Figure 2). Consequently, the impacts of an extreme earthquake hazard scenario and the associated cascading effects in terms of earthquake-triggered landslides were analysed for the selected road network.

4 METHODOLOGY

The proposed INFRARISK stress testing framework [17] requires an estimation of the risk to critical networks due to the associated hazards. To do so, a quantitative probabilistic risk assessment procedure was adopted for the selected Italian road network due to an extreme seismic hazard scenario and the associated landslide cascading effects.

4.1 Spatial Boundaries

The selected Italian road network is located in the Emilia Romagna region and is distributed over an area of approximately 990km² in the vicinity of the city of Bologna. Along this network, 340 bridges (excluding culverts) and 40 tunnels were identified. The geographical location of the bridges and tunnels was obtained from Open Street Map (<http://download.geofabrik.de/>), as illustrated in Figure 3.

4.2 Seismic Hazard Scenario

To consider a low probability earthquake hazard scenario, a Monte Carlo simulation (MCS) method was employed [18]. MCS is commonly adopted when dealing with low probability ground motions as it facilitates the identification of seismic events that contribute most to target amplitude levels, and provides a powerful and flexible means for considering the uncertainties associated with the prediction of seismic ground motions, providing a clear link with the probabilistic risk analysis [19].

Based on this approach, ground-motion scenarios in terms of peak ground acceleration (PGA) were developed for selected probability levels, and a specific extreme value threshold at a

reference site. These ground-motion scenarios were linked to a critical element along the road network, which was selected based on the network functionality. To identify the critical network element, a betweenness centrality method was adopted, which is used to identify the structural elements that would result in a substantial decrease in the serviceability of the network due to their failure [20].

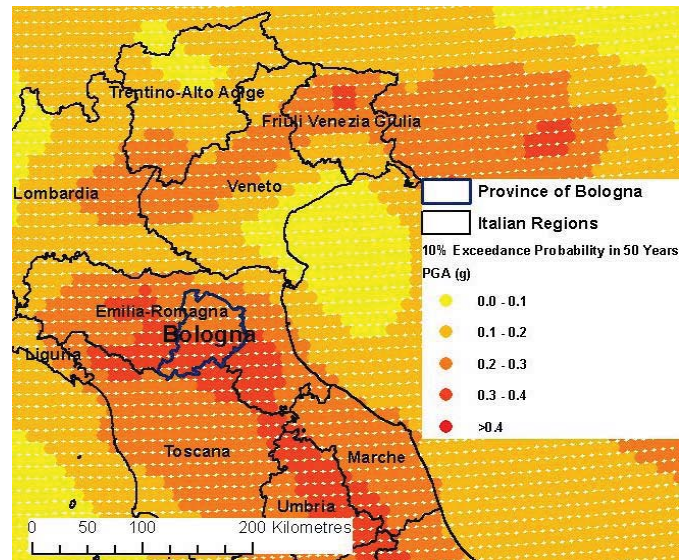


Figure 1. Peak ground acceleration (g) with a 10% exceedance probability in 50 years [15]

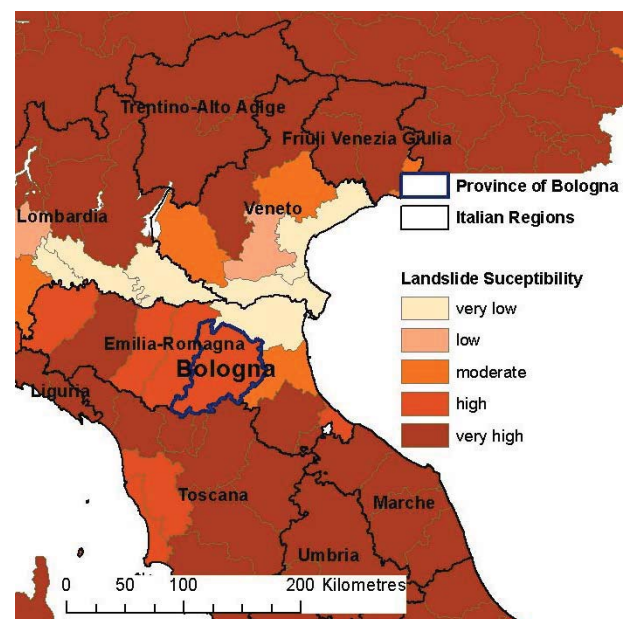


Figure 2. Susceptibility of Northern Italy to landslide hazards [16]

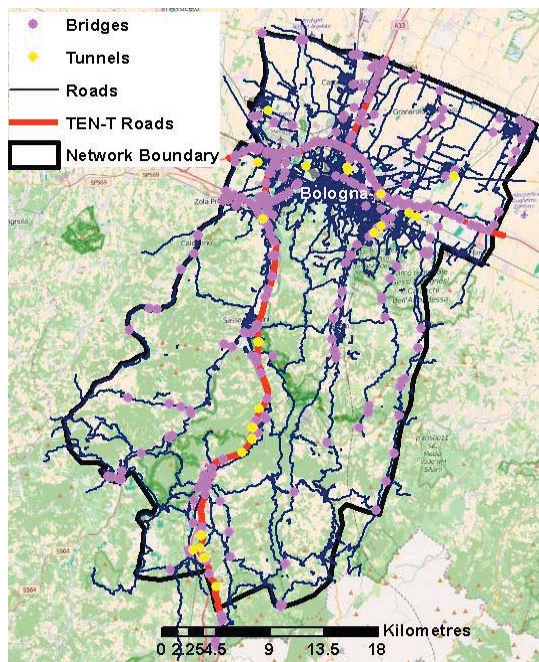


Figure 3. Italian road network

4.3 Landslide Susceptibility

The risk of the associated cascading effects in terms of earthquake-triggered landslides was also considered for the Italian road network. To assess the susceptibility of the network region to earthquake-triggered landslides, landslide yield acceleration values (k_y) were calculated, which indicate the horizontal acceleration that results in the initiation of sliding of the slope. Values of k_y were calculated for the case study region based on geological information and a 10m resolution Digital Elevation Model, according to a sliding block displacement approach [21] (Figure 4).

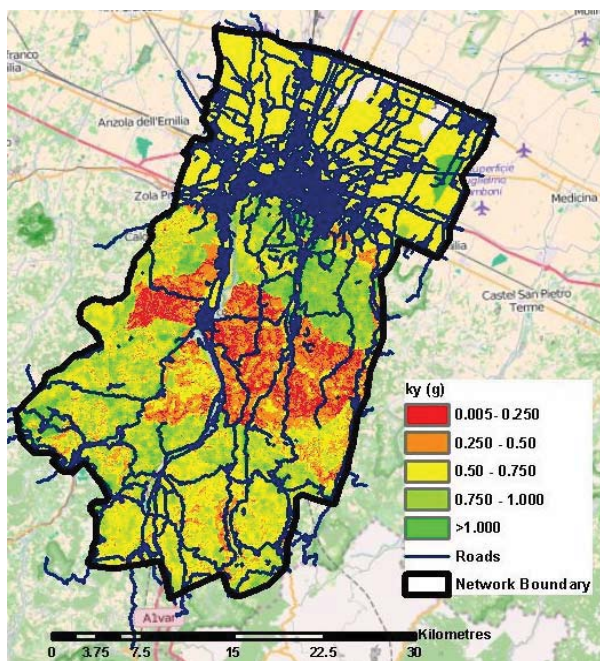


Figure 4. Landslide susceptibility

4.4 Structural Vulnerability

To estimate the seismic risk to the road network, the vulnerability of the network bridges and tunnels to seismic loading was assessed. Additionally, the vulnerability of individual road sections to earthquake-triggered landslides was assessed. To do so, fragility curves were assigned to the network elements (i.e. bridges, tunnels and road sections). Fragility curves provide the probability of reaching or exceeding specified damage states according to a measure of ground motion intensity and are represented according to Equation 1:

$$P(DS \geq ds | IM) = \phi \left(\frac{\log IM - \log \alpha}{\beta} \right) \quad (1)$$

where ds is a damage state threshold of interest for a particular structure, α and β are the mean and logarithmic standard deviation of the fragility curve respectively, and ϕ is a standard normal cumulative distribution function.

For large transport networks, it is not feasible to derive fragility curves for individual structures and, therefore, fragility curves were assigned based on structural features and defined typologies [21]. For each bridge along the road network, the following structural data was gathered according to a visual inspection using Google Earth: primary material, secondary material, type of deck, width and length of deck, deck structural system, pier to deck connection, type of pier to deck connection, number of piers per column, type of section of the pier, height of the pier, number and length of spans, type of connection to the abutments, skew angle, bridge configuration, foundation type and seismic design level. A database of bridge fragility curves [22] was subsequently used to assign fragility curves based on each of the bridge typologies, as determined according to taxonomy parameters. Where multiple fragilities curves were available for a given bridge typologies, median fragility curves were estimated along with their 16% and 84% confidence bounds to account for the associated epistemic uncertainties (Figure 5). A similar approach was adopted for the identified network tunnels based on the following structural information: construction method, shape, depth, geological conditions, supporting system, and a database of tunnel fragility curves [23]. For both bridges and tunnels, the fragility curves were defined in terms of four damage states (ds): 1) Slight, 2) Moderate, 3) Extensive, and 4) Complete.

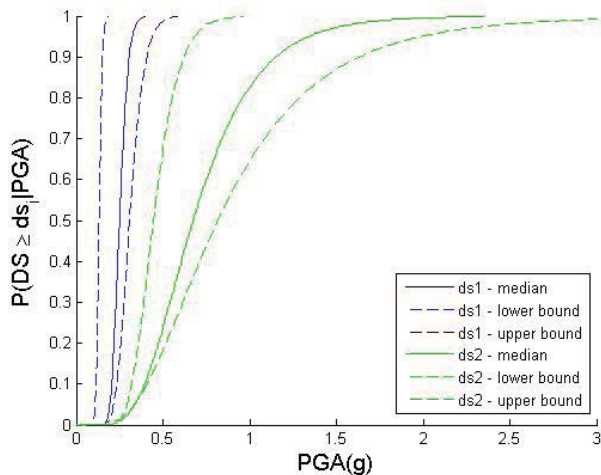


Figure 5. Example bridge fragility curves (ds1, ds2) for bridge type 1

Fragility curves were also assigned to road sections built on slopes of greater than 10 degrees to characterise the structural vulnerability of the road pavement to earthquake-triggered landslides. To do so, a methodology was adopted [24] that uses existing fragility curves for roads due to earthquake-triggered landslides [25] and represented in terms of PGA [26]. The fragility curves assigned to road sections were dependant on the road type (i.e. major or urban) and the associated k_y value, and were represented in terms of three damage states: 1) Slight, 2) Moderate and 3) Extensive (Figure 6).

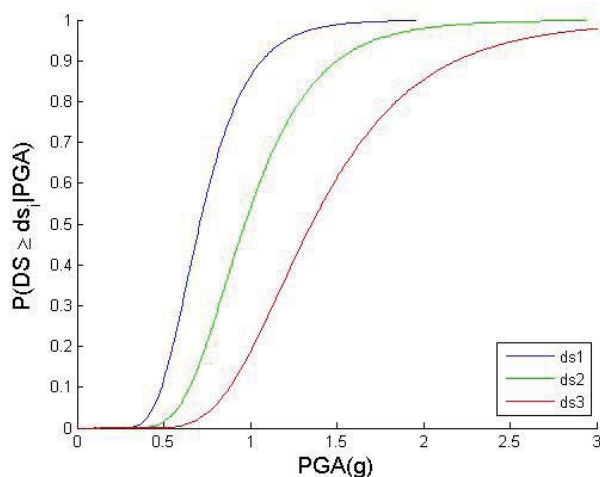


Figure 6. Example road fragility curves for urban roads ($k_y=0.2$)

The potential repair cost for the road network due to the associated hazards was estimated based on the individual network elements. To do so, the damage states defined for the network elements were directly related to a repair cost (Table 1) based on a survey that was distributed to infrastructure managers and experts within the INFRARISK consortium [21].

Table 1. Network direct consequences.

Damage State	Repair Costs (€1000s)		
	Bridges	Tunnels	Road Sections (per km)
Slight/Minor	100	150	50
Moderate	750	1000	100
Extensive	1000	3000	350
Complete	1000	10000	-

4.5 Risk Estimation

To estimate the risk to the road network due to the earthquake scenario considered, a probabilistic analysis was performed according to a MCS method using random sampling, for which 1000 simulation loops were performed. Figure 7 illustrates a single sample of damage to the road network. For each network damage sample, the direct consequences were evaluated according to the total repair cost for the network.

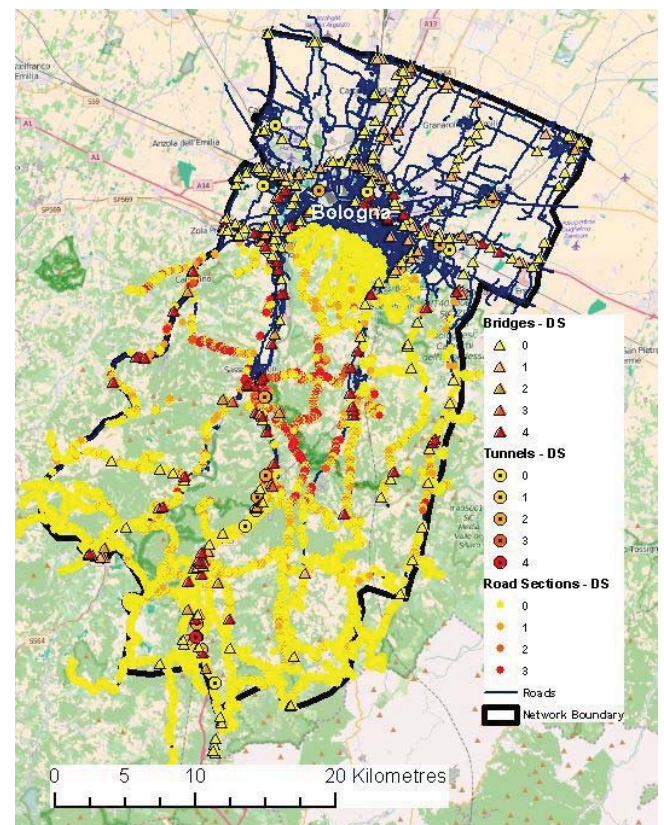


Figure 7. Network damage sample

5 RESULTS

To assess the convergence of the solution, the coefficient of variation (CoV) of the total repair cost was analysed according to the number of MCS loops, as illustrated in Figure 8. The solution converged to less than 1% after 200 simulation loops.

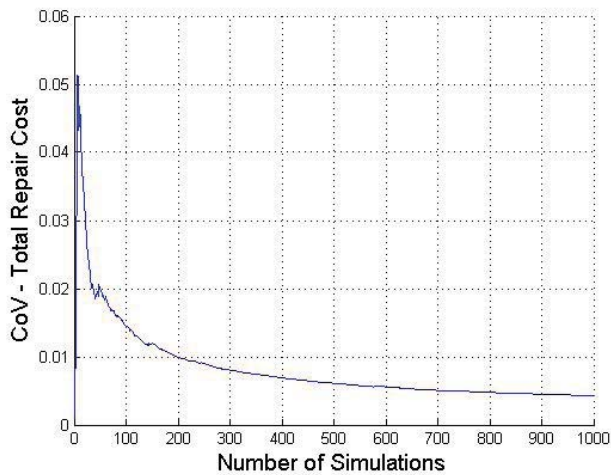
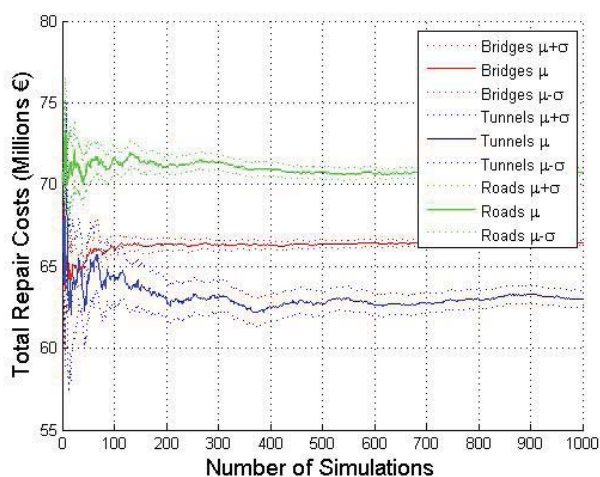


Figure 8. Convergence of solution

The evolution of the mean, μ , and the standard deviation, σ , for the network element repair costs (i.e. bridges, tunnels and roads) are illustrated in Figure 9. The potential damage to the network roads due to earthquake-triggered landslides contributed most significantly to the total potential repair costs for the network for the seismic hazard scenario considered.

Figure 9. Network element repair costs (μ and σ) according to number of simulation loops

The exceedance probability in terms of the total repair cost for the road network due to the low probability, extreme seismic hazard scenario considered is illustrated in Figure 10. The results demonstrate that the total repair costs for the road network will most certainly exceed €140million for the scenario considered and, furthermore, there is a 50% chance that the total repair costs will exceed €193million. In addition to the monetary losses presented herein, there are indirect consequences due to the hazard scenario resulting from the additional travel times encountered by road users as a result of the network disruption and the consequent economic losses. This is the subject of future work for the Italian road network presented herein.

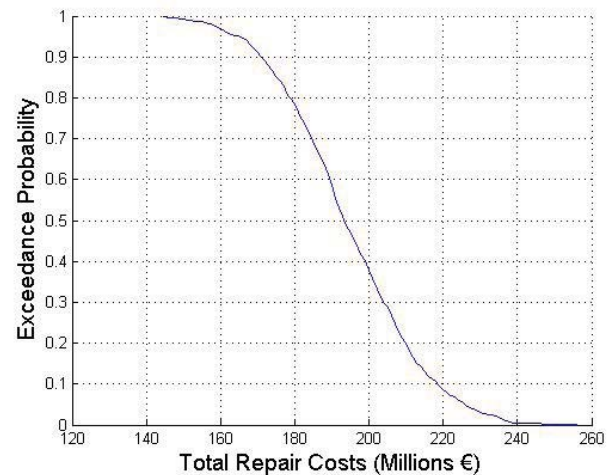


Figure 10. Total repair cost of network

6 CONCLUSION

This paper has presented the initial results of a risk assessment for a critical infrastructure road network due to an extreme seismic hazard scenario and the associated landslide cascading effects. The objective of the case study presented herein is to demonstrate the systematic application of the methodologies developed in the INFRARISK project.

Initial results have been presented for an Italian road network, which relate to the direct consequences associated with an extreme seismic hazard scenario. The associated repair costs are significant and this risk estimate may be considered as part of a broader stress testing framework for to determine whether or not the level of risk is acceptable and, furthermore, to assist in the decision making process with regard to the protection of this critical road network.

ACKNOWLEDGMENTS

INFRARISK is funded by the European Commission's FP7 programme, Grant Agreement No. 603960. Further information can be found at www.infrarisk-fp7.eu. The authors gratefully acknowledge the contributions of the other INFRARISK consortium partners: Swiss Federal Institute of Technology in Zurich, Dragados SA, Gavin and Doherty Geosolutions Ltd., Probabilistic Solutions Consult and Training BV, the Spanish National Research Council, University College London, PSJ, Stiftelsen SINTEF, Ritchey Consulting AB, and the University of Southampton.

REFERENCES

- [1] A. J. DeBlasio, A. Zamora, F. Mottley, R. Brodesky, M. E. Zirker and M. Crowder, "Effects of Catastrophic Events on Transportation System Management and Operations, Northridge Earthquake - January 17, 1994," U.S. Department of Transportation, 2002.
- [2] G. R. Miyamoto, "L'Aquila Italy M6.3 Earthquake, April 6, 2009," 2009.
- [3] M. Ni Choine and K. Martinovic, "Critical Infrastructure Case Studies, INFRARISK Deliverable D8.1," European Commission, 2014.
- [4] N. Jayaram and J. W. Baker, "Efficient sampling and data reduction techniques for probabilistic seismic lifeline risk assessment," *Earthquake Engineering and Structural Dynamics*, vol. 39, no. 10, pp.

- 1109-1131, 2010.
- [5] Y. Han and R. A. Davidson, "Probabilistic seismic hazard analysis for spatially distributed infrastructure," *Earthquake Engineering and Structural Dynamics*, vol. 41, no. 15, pp. 2141-2158, 2012.
 - [6] H. Crowley and J. J. Bommer, "Modelling seismic hazard in earthquake loss models with spatially distributed exposure," *Bulletin of Earthquake Engineering*, vol. 4, pp. 249-273, 2006.
 - [7] R. Lee and A. S. Kiremidjian, "Uncertainty and correlation for loss assessment of spatially distributed systems," vol. 23, no. 4, 2007.
 - [8] M. Shinozuka, M. Q. Feng, J. Lee and T. Naganuma, "Statistical analysis of fragility curves," no. 126, 2000.
 - [9] S. E. Chang, M. Shinozuka and J. E. Moore, "Probabilistic earthquake scenarios: extending risk analysis methodologies to spatially distributed systems," *Earthquake Spectra*, pp. 557-572, 2000.
 - [10] N. Shiraki, M. Shinozuka, J. E. Moore, S. E. Chang, H. Karneda and S. Tanaka, "System risk curves: probabilistic performance scenarios for highway networks subject to earthquake damage," *Journal of Infrastructure Systems*, vol. 13, no. 1, 13.
 - [11] M. Miller and J. W. Baker, "Coupling mode-destination accessibility with seismic risk assessment to identify at-risk communities," *Reliability Engineering and System Safety*, vol. 147, pp. 60-71, 2016.
 - [12] K. Pitilakis, M. Alexoudi, S. Argyroudis, O. Monge and C. Martin, "Earthquake risk assessment of lifelines," *Bulletin of Earthquake Engineering*, vol. 4, pp. 365-390, 2006.
 - [13] F. Cavalieri, P. Franchin, G. P. and B. Khazai, "Quantitative assessment of social losses based on physical damage and interaction with infrastructural systems," *Earthquake Engineering and Structural Dynamics*, vol. 41, no. 11, pp. 1579-1589, 2012.
 - [14] S. Argyroudis, J. Selva and P. Gehl, "Systematic seismic risk assessment of road networks considering interactions with the built environment," *Computer-Aided Civil and Infrastructure Engineering*, vol. 30, pp. 524-540, 2015.
 - [15] D. Giardini, J. Woessner, L. Danciu, H. Crowley, F. Cotton, G. Grunthal, R. Pinho and G. Valensise, "SHARE European Seismic Hazard Map for Peak Ground Acceleration, 10% Exceedance Probability in 50 years," 2013. [Online]. Available: <http://www.share-eu.org/node/90>.
 - [16] A. Gunther, M. Van den Eeckhaut, J. P. Malet and J. Hervás, "European Landslides Susceptibility Map (ELSUS1000), European Soil Portal," 2013. [Online]. Available: <http://esdac.jrc.ec.europa.eu/>.
 - [17] B. Adey, J. Hackl, J. C. Lam, P. van Gelder, P. Prak, N. van Erp, M. Heitzler, I. Iosifescu and L. Humi, "Ensuring acceptable levels of infrastructure related risks due to natural hazards with emphasis on conducting stress tests," in *International Symposium on Infrastructure Asset Management*, Kyoto, Japan, 2016.
 - [18] D. D'Ayala and P. Gehl, "Hazard Distribution Matix, INFRARISK Deliverable D3.1," European Commission, 2014.
 - [19] R. M. W. Musson, "PSHA validated by quasi observational means," *Seismological Research Letters*, vol. 83, no. 1, pp. 130-134, 2012.
 - [20] K. Taalab and F. Medda, "Infrastructure Platform, INFRARISK Deliverable D5.3," European Commission, 2016.
 - [21] D. D'Ayala and P. Gehl, "Fragility functions matrix, INFARISK Deliverable D3.2," European Commission, 2016.
 - [22] V. Silva, H. Crowley and M. Colombi, "Fragility function manager tool," in *SYNER-G: Typology Definition and Fragility Functions for Physical Elements at Seismic Risk*, 2014.
 - [23] S. Argyroudis and A. M. Kaynia, "Fragility functions of highway railway infrastructure," in *SYNER-G: Typology Definition and Fragility Functions for Physical Elements at Seismic Risk*, 2014.
 - [24] K. Pitilakis, S. Fotopoulou, S. Argyroudis, D. Pitilakis, J. Senetakis, K. Treulopoulos, K. Kakaderi and E. Riga, "Physical vulnerability of elements at risk to landslides: Methodology for evaluation of fragility curves and damage states for buildings and lifelines, SAFELAND Report D2.5," European Commission, 2011.
 - [25] NIBS, "HAZUS-MH MRIL Technical Manual," Federal Emergency Management Agency, Washington DC, 2004.
 - [26] J. D. Bray and F. Travarasrou, "Simplified procedure for estimating earthquake-induced deciatoric slope displacements," *Journal of Geotechnical and Geoenvironmental Engineering*, vol. 133, no. 4, pp. 381-392, 2007.

Quantification of Multi Risk Scenarios Subjected to Extreme Weather Events

Donya Hajjalizadeh¹, Ciaran Carey², Eugene OBrien^{2,3}

¹ Roughan & O'Donovan Innovative Solutions, Dublin, Ireland; now at Engineering and the Built Environment, Anglia Ruskin University, England

² Roughan & O'Donovan Innovative Solutions, Dublin, Ireland

³ Department Civil Engineering, University College Dublin, Dublin, Ireland
email: donya.alizadeh@anglia.ac.uk, ciaran.carey@rod.ie, eugene.obrien@ucd.ie

ABSTRACT: Changes in the likelihood and severity of extreme weather events and climate-related disasters can result in the failure of critical infrastructure (CI) elements and networks. A Quantitative risk assessment of such failures is a core part of risk management protocols. In the RAIN project, funded by 7th Framework Programme, a systematic risk analysis framework is being developed which quantifies risks due to extreme events by explicitly considering the impacts of extreme weather events on critical infrastructure. In this paper, an overview of developed advanced risk assessment procedure quantifying multi-mode risks and the techniques required to assess the interaction between different hazardous events and various critical infrastructure systems is provided. In this study it is assumed that multi-risk scenarios refer to two main components: a. multi-hazard (i.e. the potential for one or more secondary hazard triggered by a primary hazard event) and b. multi-vulnerability (i.e., potential for failure propagation in critical infrastructure network(s)) scenarios. Descriptions of various multi-hazard and multi-vulnerability scenarios are provided and the approach required to quantify risk arising from each scenario is outlined and the application is illustrated for flash flooding case study in North of Italy.

KEY WORDS: Multi-mode; risk assessment; extreme weather event.

1 GENERAL GUIDELINES

Extreme weather such as heavy and prolonged rainfall, floods, heavy snowfall, extreme heat or cold, weather are increasing and causing extensive damage to the European Union's (EU) transportation energy and telecommunication infrastructure. Previous experiences have shown that around 10% of all costs for road maintenance in the EU are devoted to repairing damage caused primarily by heavy rainfall and floods. Extreme weather events also have a strong impact on energy infrastructure, such as power grids, which when damaged, can lead to disruption to the entire generation and distribution system. Consequently, adopting adaptive measures to increase resilience is becoming more important as the severity of extreme weather events, and their effect on society, security and the economy, increases with climate change.

The RAIN (Risk Analysis of Infrastructure Networks in Response to Extreme Weather) project aims to provide an operational analysis framework to minimize the impact of major weather events on the EU. A holistic risk mitigation approach will be used to establish the key components of existing critical infrastructure network and to assess the sensitivity of these components to extreme weather. The authors' main contribution to this project is to quantify the risks and impacts of critical infrastructure failure within Work Package 6 (WP6) activities. The objective of WP6 of the RAIN project is twofold, namely a) to assess the societal, security and economic impacts of critical infrastructure (CI) failures based on single-mode and multi-mode failures and b) to identify the quantifiable benefits, from a societal security and economic standpoint, of providing resilient infrastructure.

This article describes the advanced risk assessment procedure developed to quantify multi-mode risks. This technique will be applied to preselected case studies to

benchmark the methodologies developed and to provide a measurable indicator of the benefits of providing resilient infrastructure.

2 REVIEW OF MULTI-RISK ASSESSMENT FRAMEWORK

The multi-risk concept refers to various combinations of hazards and various combinations of vulnerabilities so it requires a review of existing concepts of risk, hazard, exposure and vulnerability, within a multi-risk perspective. Therefore a multi-risk assessment should consider two main components: 1) a multi-hazard and 2) a multi-vulnerability component.

According to Deliverable D5.1 of the MATRIX project (Garcia-Aristizabal and Marzocchi, 2011) the multi-hazard concept may refer to (a) the fact that different hazard sources might threaten the same exposed elements (either at the same time or at different times), or (b) one hazardous event can trigger other hazardous events (cascade effects). On the other hand, the multi-vulnerability perspective may refer to (a) a variety of exposed sensitive targets (e.g. population, infrastructure, cultural heritage, etc.) with different degrees of vulnerability against the various hazards, or (b) time-dependent vulnerabilities, in which the vulnerability of a specific class of exposed elements may change with time as a consequence of different factors (e.g., the occurrence of other hazardous events, etc.).

In this report, a multi-hazard event refers to interactions in which the primary hazard triggers or increases the probability of secondary hazards occurring. The multi-vulnerability component represents the dependencies and interdependencies (i.e., potential failure propagation from one system to another system) in the infrastructure network. In contrast, single risk assessment concepts consider the risk of a particular hazard

occurring in a particular geographical area during a given period of time (Hajializadeh and Tucker, 2015) leading to failure of one or more CI(s) without considering the interactions between the risk components (i.e., Hazards and Vulnerabilities). Figure 1 illustrates the difference between single and multi-mode risk scenarios; with the interactions represented by the dashed line not present in single mode risk scenarios.

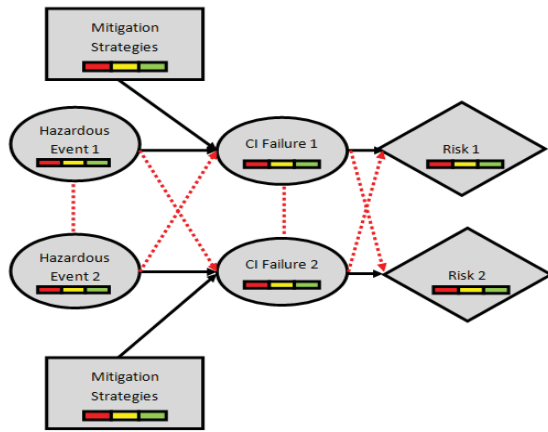


Figure 1. Single-risk and Multi-risk example for a system of two hazardous events and two critical infrastructures

In the following section, the general framework of the risk assessment technique being developed in WP5 of RAIN project is provided, explaining the implementation of the technique for multi-mode scenarios.

2.1 Bayesian probability method for multi-risk assessment

Based on the United Nations Office for Disaster Risk Reduction (UN-ISDR) definition, risk is the probability of harmful consequences, or expected losses from death, injuries, property, livelihoods, economic activity, disrupted security, or environment resulting from interactions between (natural, human-induced or man-made) hazards and vulnerable conditions (Van Westen et al. 2011). In short, risk is the probability of losses.

Based on this definition of risk, Risk Assessment is a methodology to determine the nature and extent of risk by analyzing potential hazards and evaluating existing conditions of vulnerability that could pose a potential threat or harm to people, livelihoods and the environment on which they depend. Risk assessment encompasses the identification, quantification, risk analysis (qualitative, semi-quantitative, and quantitative) and evaluation of risks associated with a given system. Overall, the risk assessment aims to support rational decision-making regarding risk-bearing activities (Apostolakis, 2004).

In WP5, details of a Bayesian probability theory based risk assessment framework are presented (van Erp and van Gelder, 2015). This framework is a probabilistic graphical model that represents hazardous events and the resulting infrastructure failure by means of a directed acyclic graph (DAG). It is worth noting that Bayesian Networks are a special instance of the more general Bayesian probability theory; as Bayesian probability theory (1) applies to both continuous and discrete probability distributions, (2) has a built-in model-selection

functionality, and (3) offers several approaches to translate states of uncertainty to probability distributions (van Erp and van Gelder, 2015).

In summary, the framework (Figure 2) starts with establishing the context. The system being analyzed is defined in terms of its elements and what constitutes normal operation to serve as a baseline reference point. In the next step, the risks are identified. The source of hazard will be identified and characterized and then the scenarios of risk are established and consequences and vulnerability elements will be defined. Mitigation measures will subsequently be introduced for each vulnerable element of interest. At the risk inference stage, the likelihood of the different scenarios and their attendant levels of damage will be estimated considering the level of mitigation actions. The scenarios according to damage level will be assembled and results will be presented into the appropriate risk curves and priorities. In the final step, risk evaluation, the results will be evaluated and interpreted to guide the risk manager or infrastructure owner on strategies to be adopted to reduce risk to an acceptable level. There are many intermediate steps in the five step process when assessing extreme weather risks but the principles are fundamental for implementing a general risk assessment framework. Detailed description of each step is given in Deliverable D5.1 (Van Gelder & Van Erp 2015) of the RAIN project.

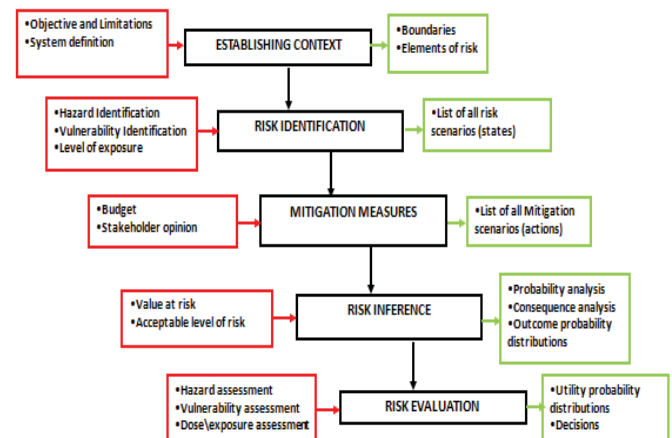


Figure 2. Bayesian Risk Analysis Framework

The initial inputs in a risk assessment framework are the various multi-mode scenarios which could potentially occur. The different hazard and vulnerability components are represented by nodes, with corresponding probability distributions. As explained in the previous section, each multi-mode scenario has two main components: the multi-hazard element, considering the interaction between hazardous events, and the multi-vulnerability component, which accounts for infrastructure typology and their corresponding functionality dependencies and interdependencies. In the multi-vulnerability component a “system” can refer to either an individual infrastructure with corresponding elements or a network of infrastructures as illustrated by Figure 3. Figure 4 illustrates an example of system interdependency between different networks.

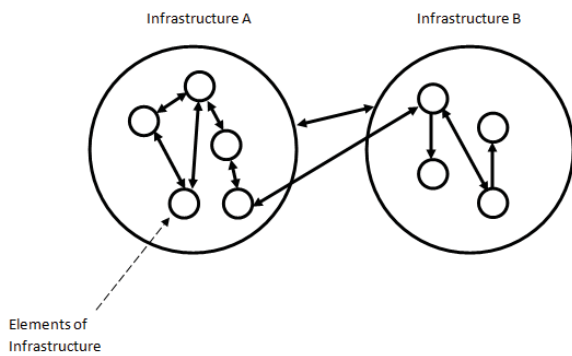


Figure 3. Dependencies and Interdependencies in Infrastructure system(s)

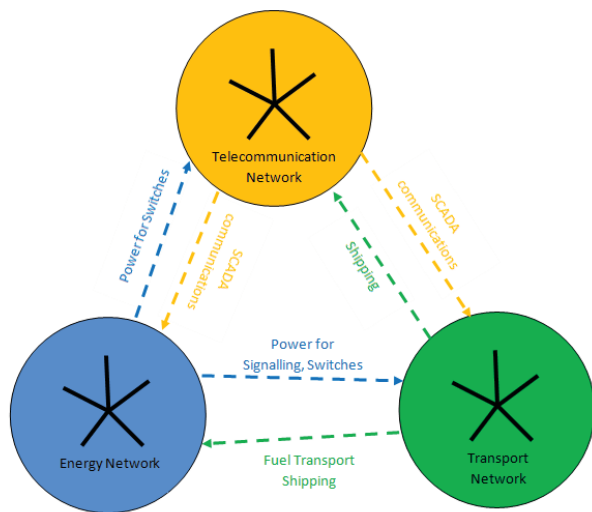


Figure 4. Interdependencies between networks

The current study provides an overview of each multi-risk scenario component, details on selected multi-hazard and multi-vulnerability scenarios, their implementation in the risk assessment framework and application for selected case studies.

3 MULTI RISK SCENARIOS

3.1 Multi Hazardous scenarios

Two or more hazards may affect the same region at the same time without any interaction and with their simultaneous occurrence happening purely by coincidence. Where interaction does take place the term ‘cascade’ or ‘domino’ is often used in the literature (Kumasaki et al. 2015). Kappes et al. (2012) gives an outline of terms used to describe the interaction between hazards and group ‘knock-on effect’ and ‘follow-on event’ as well as ‘triggering effect’ along with ‘cascade’ etc.

In this study, ‘interactions’ are considered to be those where a primary hazard triggers or increases the probability of secondary hazards occurring. In other words, primary hazards (those which occur first) interact with secondary hazards by (a) triggering the secondary hazards (b) increasing the probability of the secondary hazard or (c) both triggering and increasing the probability of the secondary hazard. Kappes et

al. (2012) note that in using the term ‘interaction’ the impression can be created that there is bidirectional influence between the hazards which may or may not be the case.

There are distinct and broad ranges, spatially and temporally, over which each of the different extreme weather events have an impact. Generally, the assessment of spatial and temporal scales does not consider interactions between different hazards, instead focusing on single hazards. Such approaches often treat hazards as isolated or independent phenomena. Such an assumption can lead to the distortion of management priorities, increased vulnerability to other spatially relevant hazards, or an underestimation of risk (Gill and Malamud, 2014).

In this study the interactions between hydrological, Atmospheric, biophysical groups from Gill and Malamud’s (2014) study are used as multi-hazardous scenarios which will be considered further in developing multi-mode scenarios. These multi-hazardous scenarios are summarised in Table 1 below. The table also outlines the forecasting potential of the location, timing and magnitude of each secondary hazard, given information about the primary hazard. Each forecasting factor is given a classification from N (value 0) to H (value 3) depending on what information is available to help constrain the factor. In this Table N refers to None, L to Low, M to Medium and H to High contributing factor. These three values are totalled to give a rating from 0-9, and colour coded in terms of the ability to characterise the secondary hazard, with poor (0-3, light shading), semi (4-6, medium shading) or excellent (7-9, dark shading).

Table 1. Ability to characterize triggered and increased probability secondary hazards given information from the primary hazard. (Gill and Malamud, 2014).

PRIMARY HAZARD	SECONDARY HAZARD	FORECASTING FACTORS			OVERALL RATING
		LOCATION	TIME	MAGNITUDE	
Landslide	Landslide	N-L-M-H	N-L-M-H	N-L-M-H	6/9
	Flood	N-L-M-H	N-L-M-H	N-L-M-H	6/9
Snow Avalanche	Landslide	N-L-M-H	N-L-M-H	N-L-M-H	5/9
	Snow Avalanche	N-L-M-H	N-L-M-H	N-L-M-H	5/9
	Flood	N-L-M-H	N-L-M-H	N-L-M-H	5/9
Flood	Landslide	N-L-M-H	N-L-M-H	N-L-M-H	5/9
Drought	Wildfire	N-L-M-H	N-L-M-H	N-L-M-H	3/9
	Landslide	N-L-M-H	N-L-M-H	N-L-M-H	7/9
Storms	Snow Avalanche	N-L-M-H	N-L-M-H	N-L-M-H	5/9
	Flood	N-L-M-H	N-L-M-H	N-L-M-H	7/9
	Tomado	N-L-M-H	N-L-M-H	N-L-M-H	3/9
	Lightning	N-L-M-H	N-L-M-H	N-L-M-H	4/9
Tornadoes	Lightning	N-L-M-H	N-L-M-H	N-L-M-H	4/9
	Landslide	N-L-M-H	N-L-M-H	N-L-M-H	6/9
Hailstorm	Snow Avalanche	N-L-M-H	N-L-M-H	N-L-M-H	5/9
	Flood	N-L-M-H	N-L-M-H	N-L-M-H	7/9
	Lightning	N-L-M-H	N-L-M-H	N-L-M-H	4/9
Snowstorm	Volcanic Eruption	N-L-M-H	N-L-M-H	N-L-M-H	3/9
	Landslide	N-L-M-H	N-L-M-H	N-L-M-H	6/9
	Snow Avalanche	N-L-M-H	N-L-M-H	N-L-M-H	5/9
	Flood	N-L-M-H	N-L-M-H	N-L-M-H	7/9
	Ground Collapse	N-L-M-H	N-L-M-H	N-L-M-H	3/9
	Ground Heave	N-L-M-H	N-L-M-H	N-L-M-H	6/9
Lightning	Wildfire	N-L-M-H	N-L-M-H	N-L-M-H	6/9
	Landslide	N-L-M-H	N-L-M-H	N-L-M-H	4/9
Extreme Temperature (Heat)	Snow Avalanche	N-L-M-H	N-L-M-H	N-L-M-H	4/9
	Flood	N-L-M-H	N-L-M-H	N-L-M-H	5/9
	Drought	N-L-M-H	N-L-M-H	N-L-M-H	5/9
	Storm	N-L-M-H	N-L-M-H	N-L-M-H	2/9
	Wildfire	N-L-M-H	N-L-M-H	N-L-M-H	3/9
Extreme Temperature (Cold)	Drought	N-L-M-H	N-L-M-H	N-L-M-H	5/9
	Hailstorm	N-L-M-H	N-L-M-H	N-L-M-H	6/9
	Snowstorm	N-L-M-H	N-L-M-H	N-L-M-H	6/9
	Landslide	N-L-M-H	N-L-M-H	N-L-M-H	5/9
Wildfires	Flood	N-L-M-H	N-L-M-H	N-L-M-H	5/9
	Wildfire	N-L-M-H	N-L-M-H	N-L-M-H	6/9
	Extreme Temp. (Heat)	N-L-M-H	N-L-M-H	N-L-M-H	6/9
	Extreme Temp. (Heat)	N-L-M-H	N-L-M-H	N-L-M-H	6/9

According to Gill and Malamud's (2014) study, there are four types of hazard interaction: 1) interactions where a hazard is triggered, 2) interaction where the probability of a hazard is increased, 3) interactions where the probability of a hazard is decreased, 4) events involving the spatial and temporal coincidence of natural hazards. Table 2 indicates the secondary hazardous events resulting from primary events and the type of interaction.

Table 2. Hazard interactions and their types (Gill and Malamud, 2014).

COLOUR CODE		NATURE OF SECONDARY HAZARD (FOLLOWING ONE OCCURRENCE OF PRIMARY HAZARD)											
		Potential for a small number of hazard events (individual or a few occurrences)											
		Potential for a large number of hazard events (multiple occurrences)											
SYMBOL		EXPLANATION											
		Hazard Triggers Secondary Hazard											
		Hazard Increases Probability of Secondary Hazard											
		Hazard Both Triggers and Increases the Probability of Secondary Hazard											

		Secondary Hazard											
		Landslides	Snow Avalanche	Flood	Drought	Storm	Tornado	Hailstorm	Snow Storm	Lightening	Extreme Temperature (Heat)	Extreme Temperature (Cold)	Wildfires
Primary Hazard	Landslide												
	Snow Avalanche												
	Flood												
	Drought												
	Storm												
	Tornado												
	Hailstorm												
	Snowstorm												
	Lightening												
	Extreme Temperature (Heat)												
	Extreme Temperature (Cold)												
	Wildfires												

In this study, hazard interaction is accounted for by considering an increase in the secondary hazard intensity and likelihood as a function of primary hazard intensity and probability of occurrence.

3.2 Multi vulnerability scenarios

Infrastructure networks do not exist in isolation. Rather they are interconnected to other infrastructure networks and, as technological development increases, so too does the linkage between networks (Wang, Hong, and Chen 2012). The term interdependency is used to describe the relationship between infrastructures (Rinaldi et al. 2001) where each infrastructure influences the other(s). This bidirectional relationship can increase the complexity in the system of systems significantly.

According to Zimmerman (2001), infrastructures can be interconnected functionally and spatially – an example of a functional interconnectedness failure between infrastructures would be a fault in power supply causing issues with train lines. An example of a spatial interconnectedness failure would be a burst water main flooding a road etc.

In general, infrastructure interdependencies can be categorized according to various dimensions in order to facilitate their identification, understanding and analysis. According to the literature (Rinaldi et al., 2001), there are typically six dimensions to characterise the interdependencies:

- The type of interdependencies (physical, cyber, geographic, and logical),
- The infrastructure environment (technical, business, political, legal, etc.),

- The couplings among the infrastructures and their effects on their response behaviour (loose or tight, inflexible or adaptive),
- The infrastructure characteristics (organisational, operational, temporal, spatial),
- The state of operation (normal, stressed, emergency, repair), the degree to which the infrastructures are coupled,
- The type of failure affecting the infrastructures (common-cause, cascading, escalating).

The interdependencies of a network of infrastructures depending on the scale of modelling can be established through either 1) Holistic Perspective – Infrastructure Level, where each infrastructure is viewed as a single, monolithic entity with well-defined boundaries and a (possibly reduced) set of functional properties; or 2) Reductionist Perspective – Component Level, which identifies “elementary” components within an infrastructure and then describes the evolution of the entire system based on the “aggregated” behaviour of these components. In the reductionist perspective, the boundaries of each infrastructure tend to fade, but the interactions between components can be detected.

The RAIN project is focused on three main infrastructure networks: (i) Land Transport Infrastructure, (ii) Energy Infrastructure and (iii) Telecommunications Infrastructure. In WP3 of the RAIN project a methodology was developed to identify critical components for land transport infrastructure. The details can be found in RAIN Deliverable D3.1 (Dvorak and Luskova, 2015) and are summarised in the first column of Table 3 below. Table 3 also shows the critical components for both the Energy and Telecommunications networks that were identified in RAIN WP4. Further details are provided in D4.1 (Marin and Halat, 2015).

Table 3. Critical Infrastructure Components

Land Transport Infrastructure	Energy Infrastructure	Telecommunication Infrastructure
<ul style="list-style-type: none"> • Roads; • Intersections; • Stations of public transport; • Bridges; • Tunnels; • Intersection control systems; • Railway tracks; • Railway stations; • Railway bridges; • Railway tunnels; • Terminals of intermodal transport; • ETCS (European Train Control System); • Electronic signal boxes; • Train control; • Remote operation management; • Security systems of railway crossings. 	<ul style="list-style-type: none"> • Generators and their auxiliary power systems; • Transmission lines (including HVDC links); • Transmission transformers (including feeders to distribution); • Switches and breakers; • Protection relays; • SCADA and associated Telecoms; • Other Voltage-management devices. 	<ul style="list-style-type: none"> • Outside Plant equipment; • The End Offices; • The Central Offices; • Aerial trunk lines; • Underground trunk lines; • RF link trunk lines. • Class 1, 2, and 3 centres; • Aerial backbone lines; • Underground and submarine backbone lines; • RF and Satellite Backbone lines; • Base Stations (BS); • Base Station Controllers (BSC); • Mobile Switching Centre (MSC); • Gateway MSC; • Home Location Register (HLR); • Visitor Location Register (VLR).

The full list of selected scenarios for multi-vulnerability component for all considered infrastructure networks is given in D6.2 (Hajializadeh et al. 2015). To implement the interdependencies of these multi-vulnerability scenarios, a comprehensive network modelling approach is used for modelling different components of vulnerable land, energy and telecommunication networks and their interaction with multi-hazardous events and its implementation into the risk

framework. This approach produces a mathematical formalisation of interdependent framework and hence provides a quantitative technique for multi-hazardous and multi-vulnerability risk modes. The outcome of the network modelling will be fed into the risk frameworks in the form of an updated inference network and associated probabilities. In this study, the methodology proposed in Pant et al. (2014) is used to not only model the interdependencies but also take account of system flow redistribution. According to this technique, the unconditional probability of failure of an individual asset can be calculated by integrating the product of fragility and probability distribution over different intensities of a hazardous event.

$$P[r] = \int_y L(r|y) f_Y(y) dy \quad (1)$$

where $f_Y(y)$, is the continuous probability distribution of a hazard, $L(r|y)$, is the fragility function of r , given a hazardous event of y , $(r|y)$, given as $L(r|y) = P[r = 0|y]$, r , representing the state of attributes assigned to an asset, a , which can be a set of attributes such as asset geometry or infrastructure type.

Assuming $D(r, a)$, as the consequence associated with asset failure, the risk is measured as the product of the failure probability of the asset and the consequence incurred due to failure, which is calculated by:

$$\begin{aligned} R(r) &= \int_y L(r|y) f_Y(y) D(r, a) dy \\ &= D(r, a) \int_y L(r|y) f_Y(y) dy \end{aligned} \quad (2)$$

The probability of the infrastructure system in a state of $r^j, j \in \{1, \dots, 2^b\}$, can then be calculated as:

$$\begin{aligned} P[r^j] &= \int_y P(r^j|y) f_Y(y) dy \\ &= \int_y P(r_1^j, \dots, r_b^j|y) f_Y(y) dy \end{aligned} \quad (3)$$

Where $P(r^j|y)$ is the conditional probability of state r^j given hazard y which captures the product of individual asset state conditional probabilities. Then the updated failure state given the interdependencies and corresponding probability will be fed into the risk assessment framework in the vulnerable nodes (critical infrastructure) to quantify the effect of interdependencies. A detailed description of the technique is explained in D6.2 (Hajjalizadeh et al. 2015).

This technique will be applied to preselected case studies to benchmark the methodologies developed and to provide a measurable indicator of the benefits of providing resilient infrastructure. The following section provides a summary of selected case studies.

4 CASE STUDY

The first case study is critical transport and operational tactical connections of the Loviisa nuclear reactor as a result of sudden flooding and rising seawaters at the Gulf of Finland (Figure 5). A severe gale in the Northern Baltic Sea took place on January 7th, 2005 when a violent storm formed over the British Isles and moved from East to Central Finland. Several countries were affected by the violent storm including the

United Kingdom, Norway, Denmark, Sweden and the Baltic countries. The highest winds occurred south of Finland and the biggest problem was the rise in sea level, which was as much as +197cm in Hamina. Waves reached heights of up to 8 metres and there was a significant sea level rise in the Gulf of Finland by the evening of 8th January.

Following the first early warning signals from the Finnish Institute of Marine Research (FIMR) to the Ministry of the Interior, the situation awareness of the Finnish emergency management agencies started to build on various assessments and predictions from the Finnish Meteorological Institute's and the FIMR's forecast machinery.

Water closed roads throughout the coastal region and traffic was cut off in many places in the Helsinki region. According to estimates, the storm caused €20 million in costs to the insurance company Sampo alone. Sampo estimates that in Finland its customers suffered damage worth €7 million.



Figure 5: Finnish Nuclear Station

The second case study is in the region of Friuli Venezia Giulia (Northern Italy) located in an Alpine area on the border with Austria and Slovenia, with 1036 inhabitants (Figure 6). This area is located in the Valcanale valley at the confluence of the Fella river and the streams of Rio Malborghetto and Rio Uque. On 29th of August 2003, a flash flood caused by a rain storm (Table 2) hit the region. A result of the rainfall and flood water (primary hazard) was landslides (Table 1). The debris flow reached a peak of 4 m in the centre of one of the hamlets of the municipality (the village of Ugovizza). The water transported sediments, stones, shrubbery and trees into the village and caused two casualties and extensive material damage. Approximately 600 residents were evacuated and the damage amounted to €190 million. Clearing away the mud from the streets took almost one month. Damage to the basic services (water, electrical power, road connections and telecommunication) led to problems for the local population, and rescue services alike. The first responders in the emergency phase were volunteers from Austria and Slovenia, since the road connection on the Italian side of the valley was blocked. The regional civil protection only reached the municipality two days later (i.e. the damage to the transport network affected the electricity network [Figure 4.]). Within the municipal system, the drainage and the electric lines had to be completely restored, while the aqueduct was blocked for several days. The recovery phase raised issues related to equity in the distribution of compensation payments, and

disagreements among local people about the reconstruction process.



Figure 6. Alpine Region Case study

The application of developed risk assessment technique and benchmarking process of the framework against case studies will be provided in the final deliverable of WP6, due in October 2016. The expected outcome of the work involved in this deliverable will give decision-makers an improved understanding of climate change risks in Europe and the uncertainty associated with its assessment. It will bring the best available evidence together using a consistent framework that describes the sensitivity, vulnerability and potential risks related to climate change. This will be one of the first European assessments of climate risks and goes further than previous reviews by drawing together different strands of evidence, comparing risks and providing a preliminary evaluation of the consequences of climate from social, economic and security perspectives.

ACKNOWLEDGMENTS

This project has received funding from the European Union's Seventh Programme for research, technological development and demonstration under grant agreement N° 608166. The contents of this presentation are the author's views and the European Union is not liable for any use that may be made of the information contained therein.

REFERENCES

- [1] Apostolakis, G.E. (2004). How useful is quantitative risk assessment? *Journal of Risk Analysis*, 24(3), pp: 515-520.
- [2] Dvorak, D. and Luskova, M. (2015). Report on the list of critical land transport infrastructure elements and the most probable threats to critical land transport. Deliverable D3.1, EU funded RAIN project (Risk Analysis of Infrastructure Networks in response to extreme weather), 2014 - 2017, GA no. 608166.
- [3] Garcia-Aristizabal, A. & Marzocchi, W. (2011). State-of-the-art in multi-risk assessment. Deliverable 5.1, EU funded MATRIX project (New Methodologies for Multi-Hazard and Multi-Risk Assessment Methods in Europe), 2010-2013, GA no. 265138.
- [4] Gill JC, Malamud BD. (2014) Reviewing and visualizing the interactions of natural hazards *Reviews of Geophysics* 52: 680-722
- [5] Hajializadeh, D. and Tucker, M. (2015). Quantification of single-mode risks and impacts. Deliverable D6.1, EU funded RAIN project (Risk Analysis of Infrastructure Networks in response to extreme weather), 2014 - 2017, GA no. 608166.
- [6] Hajializadeh, D., Carey, C.H. and Tucker, M. (2015). Quantification of multi-mode risks and impacts. Deliverable D6.2, EU funded RAIN project (Risk Analysis of Infrastructure Networks in response to extreme weather), 2014 - 2017, GA no. 608166.
- [7] Kappes, M.S., Keiler, M., von Elverfeldt, K. and Glade, T. (2012). Challenges of analysing multi-hazard risk: a review. *Natural Hazards*, 64(2), 1925-1958. <http://doi.org/10.1007/s11069-012-0294-2>
- [8] Kumasaki, M., King, M., Arai, M., and Yang, L. (2015). Anatomy of cascading natural disasters in Japan: main modes and linkages. *Natural Hazards*. <http://doi.org/10.1007/s11069-015-2028-8>
- [9] Marin, J and Halat, M. (2015). Report on energy and telecommunication infrastructure description and identification of critical energy and telecommunication infrastructures at a European Level. Deliverable D4.1, EU funded RAIN project (Risk Analysis of Infrastructure Networks in response to extreme weather), 2014 - 2017, GA no. 608166, pending publication
- [10] Pant, R., Hall, J., Thacker, S., Barr, S. and D. Alderson. (2009). National scale risk analysis of interdependent infrastructure network failure due to extreme hazards, Infrastructure Transitions Research Consortium, EPRS, Engineering and physical science Research Council.
- [11] Rinaldi, S., Peerenboom, J., and Kelly, T. (2001). Identifying, understanding, and analyzing critical infrastructure interdependencies. *Control Systems, IEEE*, 11-25. Retrieved from http://ieeexplore.ieee.org/xpls/abs_all.jsp?arnumber=969131
- [12] UNISDR (2009) UNISDR Terminology on Disaster Risk Reduction. Geneva, Switzerland: UNISDR. p24. 474 Available online: http://www.unisdr.org/files/7817_UNISDRTerminologyEnglish.pdf accessed 21 475 January 2015
- [13] Van Gelder, P & Erp, N. (2015). Report on risk analysis framework for single and multiple hazards. Deliverable D5.1, EU funded RAIN Project (Risk Analysis of Infrastructure Networks in response to extreme weather), 2014 - 2017, GA no. 608166 - pending publication
- [14] van Westen, C. J., Montoya, L., Boerboom, L., and Badilla Coto, E. (2002). Multi-Hazard Risk Assessment using GIS in urban Areas: A Case Study for the City of the Turrialba, Costa Rica.. *Hazard Mapping and Risk Assessment*, 53-72.
- [15] Wang, S., Hong, L., and Chen, X. (2012). Vulnerability analysis of interdependent infrastructure systems: A methodological framework. *Physica A: Statistical Mechanics and Its Applications*, 391(11), 3323-3335. <http://doi.org/10.1016/j.physa.2011.12.043>
- [16] Zimmerman, R. (2001). Social Implications of Infrastructure Network Interactions. *Journal of Urban Technology*, 8(3), 97-119. <http://doi.org/10.1080/106307301753430764>

Application of Image Processing to the Analysis of Congested Traffic

E. Alexandra. Micu¹, Eugene J. OBrien¹, Enrique Sevillano¹

¹School of Civil Engineering, University College Dublin, Newstead Building, Dublin 4, Ireland
email: elena.micu@ucd.ie, eugene.obrien@ucd.ie, enrique.sevillanobravo@ucd.ie

ABSTRACT: The aim of this paper is to explore the feasibility of using images to extract information about traffic such as gaps between vehicles, the car/truck mix and vehicle length. Congested conditions govern the safety of long-span bridges. Conventional vehicle sensing technologies such as weigh-in-motion or inductive loops are generally only accurate for free-flowing traffic. In this paper, image analysis is used to extract key parameters of congested traffic such as vehicle length, gaps between vehicles and car/truck mix. A high resolution camera will be used in this work to capture aerial images of congested traffic. These images will be processed automatically to distinguish vehicles as objects on the road, to identify the type of vehicle (regular cars or trucks, etc.) and to locate the edge of each vehicle. In order to achieve that result, an algorithm able to detect and count the vehicles on the road as separate objects will be firstly applied, enclosing each object within a rectangle.

KEY WORDS: Bridge; Congested traffic; High resolution camera; Image processing; Long span; Traffic monitoring.

1 INTRODUCTION

Traffic congestion has become an important problem in all developed countries, mainly due to the increasing number of vehicles. As a result of this increasing number of vehicles on the roads, bridges are often becoming bottlenecks in the network. This issue is important because many bridges are either approaching or have exceeded their expected design life [1]. The critical traffic loading condition for long-span bridges is congestion, when many heavy vehicles may be closely spaced on the bridge. The engineer assessing the bridge needs data on such loading conditions. Typically, car/truck mix and inter-vehicle gap data would be needed for some thousands of congestion events to allow a fit of load effect results to an Extreme Value statistical distribution. Traffic data, traditionally collected with inductive loop detectors, does not provide information about congested traffic situations because inductive loops are generally ineffective in stop-and-go conditions. Due to this shortcoming, a better solution is needed for traffic monitoring.

A bridge is assessed for a notional load model, deemed to represent the worst combination of trucks that can be reasonably expected to cross it in the return period. For long-span bridges, engineers often assume long convoys of trucks jammed on the bridge with no cars in between, which is not realistic. Weigh-In-Motion (WIM) systems are used to collect vast amounts of truck weight and traffic data that can be used to obtain site-specific and region-specific traffic load models for bridge design and load capacity evaluation [2]. However, given that many WIM technologies do not work well at low speeds, WIM data is collected in free-flowing conditions [3]. This makes it difficult to have weight information about congested traffic. Furthermore, WIM data often only includes truck data, so the gaps between trucks mean that the presence of cars is implicitly accounted for in free-flowing conditions. Hence, headways obtained from WIM data collected at high speed cannot be used to simulate a congestion situation model

because of the different gaps, cars and driving behaviours involved [4]. Traditional methods for gathering traffic information capture data through measuring stations based on induction loops [5]. However, induction loops cannot be used to gather data about traffic congestion on long span bridges since speeds are not constant. This is a drawback for congested traffic situations and this work proposes to use a camera based monitoring system that can overcome all those issues.

Image analysis can provide a means to extract and quantify objects and patterns in image data, consequently providing answers about the length of heavy trucks or the frequency of long platoons of trucks on the bridge. Thus, a high resolution camera is proposed for this work to capture aerial images of congested traffic. In order to achieve that result, colour images have been processed, taken by helicopter from 300 m altitude.

2 IMAGE PROCESSING

Image processing is a technique which uses mathematical operations to transform an image in order to extract meaningful features related to it. This works with input data which can be an image, a sequence of images, or a video and return as output data either an image or a group of characteristics or parameters [6].

A function $F(x,y)$ can describe an image and the pair (x,y) represents the coordinates for an image element. The intensity at that element is given by the value of F at that point [7]. Hence, an image is usually displayed as a wide matrix of distinct picture elements, or pixels, each of which has an intensity correlated with it:

$$F(x,y) = \begin{bmatrix} F(1,1) & \cdots & F(1,N) \\ \vdots & \ddots & \vdots \\ F(M,1) & \cdots & F(M,N) \end{bmatrix} \quad (1)$$

All pictures can be classified as colour images, grey-scale images or binary images as illustrated in Figure 1.

R: 254 G: 203 B: 203	R: 248 G: 150 B: 162	R: 231 G: 100 B: 119	R: 212 G: 77 B: 90	R: 194 G: 89 B: 97	R: 173 G: 112 B: 119	R: 157 G: 130 B: 136	R: 149 G: 138 B: 141
R: 254 G: 242 B: 244	R: 250 G: 184 B: 196	R: 234 G: 117 B: 141	R: 214 G: 87 B: 108	R: 195 G: 90 B: 102	R: 176 G: 112 B: 120	R: 159 G: 132 B: 136	R: 150 G: 141 B: 142
R: 254 G: 247 B: 248	R: 251 G: 199 B: 210	R: 236 G: 124 B: 152	R: 212 G: 86 B: 117	R: 196 G: 95 B: 110	R: 176 G: 115 B: 122	R: 161 G: 134 B: 137	R: 153 G: 143 B: 144
R: 254 G: 250 B: 250	R: 251 G: 193 B: 206	R: 230 G: 125 B: 157	R: 210 G: 91 B: 121	R: 194 G: 97 B: 110	R: 175 G: 118 B: 123	R: 161 G: 137 B: 140	R: 155 G: 147 B: 146

(a)

105	99	87	81	91
140	134	115	105	96
173	167	157	140	121
178	178	172	165	150

(b)

0	0	0	0	0	0	0	0
0	0	0	0	0	0	0	0
1	1	0	0	0	0	0	0
1	1	1	1	0	0	0	0
1	1	1	1	1	0	0	0
1	1	1	1	1	0	0	0

(c)

Figure 1: Three types of images showing intensities: (a) RGB (colour) image; (b) Grey-scale image; (c) Binary image

A colour image is composed of three basic two-dimensional matrices, the red (R), green (G) and blue (B), as can be seen in Figure 1(a). On the other hand, a grey-scale image, represented in Figure 1(b), is an image in which the intensity of pixels varies from 0 (black) at the lowest intensity to 255 (white) at the highest. Finally, only two colours are used to represent a binary image: black and white, where the white colour is used for the foreground (or objects) while the rest of the image is the background (Figure 1(c)). The images are considered as matrices and are processed using Matlab [8].

This research uses two main approaches to image processing: thresholding, which is the simplest technique of image segmentation, and morphological reconstruction. Image thresholding is a simple method of separating an image into foreground and background. It divides objects by transforming grey-scale images into binary images [9].

The values of pixels intensity lie in L grey levels, $[1, 2, \dots, L]$. The total number of pixels is:

$$N = n_1 + n_2 + \dots + n_L \quad (2)$$

where n_i represents the total number of pixels at level i . The grey-level intensity is normalized by the following equation and its values are in the range $[0, 1]$:

$$p_i = n_i / N \quad (3)$$

The pixels are separated into two groups, C_0 and C_1 , which represent the background and the objects, respectively, at a threshold level T . The group C_0 represents pixels in the range of levels $[1, \dots, T]$, and the group C_1 represents pixels in the range of levels $[T+1, \dots, L]$. The importance of this threshold,

T , is to divide images into two main groups of pixels: those remaining in the background and those belonging to the foreground. This can be done by calculating the minimum variances for each group of interest.

The group probabilities are given by:

$$q_1(T) = \sum_{i=1}^T p_i \quad (4)$$

$$q_2(T) = \sum_{i=T+1}^L p_i \quad (5)$$

The background mean is expressed as:

$$\mu_1(T) = \sum_{i=1}^T i p_i / q_1(T) \quad (6)$$

The mean of the objects can then be expressed as:

$$\mu_2(T) = \sum_{i=T+1}^L i p_i / q_2(T) \quad (7)$$

The variances in the background and foreground are calculated by:

$$\sigma_1^2(T) = \sum_{i=1}^T [i - \mu_1(T)]^2 \cdot \frac{p_i}{q_1(T)} \quad (8)$$

$$\sigma_2^2(T) = \sum_{i=T+1}^L [i - \mu_2(T)]^2 \cdot \frac{p_i}{q_2(T)} \quad (9)$$

Finally, the minimum group variance is estimated as:

$$\sigma_w^2(T) = q_1(T) \sigma_1^2(T) + q_2(T) \sigma_2^2(T) \quad (10)$$

When images are processed using the morphology technique, the procedure is then based on patterns. This procedure implements a structuring element in a binary image to create a new one without imperfections and with the same dimensions. Dilation and erosion are the essential morphological steps in image processing. Dilation attaches pixels to the edges of objects in an image, while erosion removes pixels that represent an imperfection. The structuring element is characterized by its dimensions and shape. Both of these are important in processing because they determine the number of pixels attached or removed.

3 APPLICATION OF IMAGE PROCESSING TO TRAFFIC MONITORING

The process begins by reading the image, checking its intensity and converting it into grey-scale as shown in Figure 3.



Figure 3. Grey-scale image.

The image undergoes an adjustment to its intensity values by means of a function that has an optional parameter of particular interest - the gamma value - which controls the exposure level. When gamma has a value equal to 1, there is no change. Otherwise, values less than 1 produce an image with brighter output values, and gamma values greater than 1 produce an image with darker output values. Figure 4 shows the result for a gamma value of 0.5.



Figure 4. Adjustment with gamma = 0.5.

The next step is to convert the image from grey-scale into binary. This can be performed by thresholding, illustrated in Figure 5.



Figure 5. Binary image.

At the same time, thresholding is useful to remove unnecessary detail from an image, such as road markings and to concentrate on essentials, such as vehicles.

The next stage involves the removal of small objects and smoothing the connected components. This is done by means of an analysis of the area of each connected object, where the area is in fact the actual number of pixels defining that object (Figure 6). Whenever the analysed area is greater than or equal to a given value (this value represents a value less than a vehicle's area), that area is retained. Otherwise, the object is removed from the image [10].



Figure 6. Binary image with small objects removed.

Another function based on morphological reconstruction is applied next [11]. This restores the shape of the objects that are retained by attaching or removing pixels. Hence, a connected component is created, which represents a group of pixels with the same value and connected with each other based on their neighbourhood. Then, this labels all the components in the binary image and returns the number of

components it finds in it [12]. The objects found in this way are shown in Figure 7 where 5 objects can be seen.



Figure 7. Defined objects.

The last step of this process is to check the shape of each object against the original input image. Thus for the objects in Figure 7, the perimeter of each area is calculated and drawn on the original image to compare the results. This is shown in Figure 8.

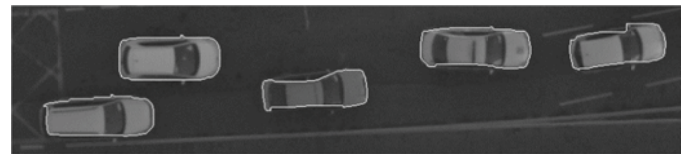


Figure 8. Original image with calculated perimeter.

Finally, each object is 'framed' with the rectangle that completely encloses it, as shown in Figure 9. The sides are always kept parallel to the axes in this process leading to inaccuracy if the vehicle is not travelling parallel to an axis – see the right-most vehicle in Figure 9. The properties of the bounding rectangle are important because they provide information about the object, such as length, and will be used to classify the object into different types [13].



Figure 9. Framing each object into a rectangle.

Figure 10 and Table 1 present the cars' lengths obtained through two methods: manual counting and the length of the framing rectangle of Figure 9.

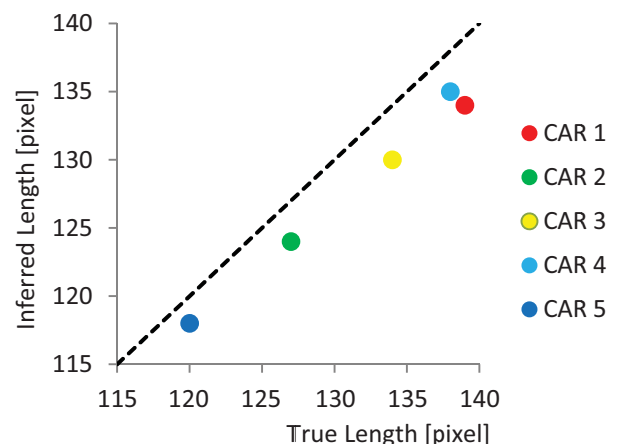


Figure 10. Inferred vehicle lengths.

Table 1. Vehicle lengths [pixels].

Car	Inferred length	Measured length
Car 1	134	139
Car 2	124	127
Car 3	130	134
Car 4	135	138
Car 5	118	120

4 CONCLUSIONS

This paper has examined the traffic on a road with an image processing algorithm. The process can detect and measure the outline dimensions of vehicles on the road. Figure 8 shows that the shapes of the obtained objects after processing are similar to the real shapes of the objects. Afterwards each object was identified and framed into an enclosing rectangle. Each rectangle provides information about the car's length and the area of the rectangles can be used to classify the objects into different types.

The results of this research indicate that good quality images have the potential to provide quality information about traffic such as vehicle class, length, and inter-vehicle gaps. These parameters are extremely valuable in assessing critical traffic loading conditions in long-span bridges. One of the more significant findings to emerge from this study is that image processing allows the analysis of traffic condition. The future goal is that this algorithm will be further improved and then applied to analyse traffic congestion on long-span bridges.

ACKNOWLEDGMENTS

The authors would like to thank Science Foundation Ireland for their support of this research under the US/Ireland programme. The authors are also grateful to Mr. Hamid Gharibi and Prof. Debra Laefer for providing images for this research.

REFERENCES

- [1] Catbas, F. N., Gul, M. and Burkett, J. (2008), *Damage Assessment Using Flexibility and Flexibility-based Curvature for Structural Health Monitoring*, Smart Materials and Structures, Vol. 17, No. 1, Article ID 015024, 12 pages.
- [2] F. Moses (1979), *Weigh-in-motion system using instrumented bridges*, Journal of Transportation Engineering 105(3) 233-249.
- [3] E.J. O'Brien, A. Lipari, C.C. Caprani (2015), *Micro-simulation of single-lane traffic to identify critical loading conditions for long-span bridges*, Engineering Structures 94, 137-148.
- [4] E.J. O'Brien, C.C. Caprani (2005), *Headway modelling for traffic load assessment of short to medium span bridges*, Institution of Structural Engineers, 83 (16): 33-36.
- [5] O'Brien, E. J., Lipari, A. & Caprani, C. (2011), *Estimation of Density and Gaps in Congested Traffic*, Proceedings of the Irish Transport Research Network, 31 August-1 September, Cork, 8 pages.
- [6] Gonzalez, R.C. Woods, R.E. & Eddins, S.L. (2009), *Digital Image Processing Using MATLAB*, Gatesmark Publishing, USA, 2nd Edition.
- [7] R.C. Gonzales, R.E. Woods, S.L. Eddins (2004), *Digital image processing using MATLAB*, Pearson Prentice Hall.
- [8] A. McAndrew (2004), *An introduction to digital image processing with matlab notes for scm2511 image processing*, School of Computer Science and Mathematics, Victoria University of Technology 1-264.
- [9] Otsu, N. (1979), *A Threshold Selection Method from Gray-Level Histograms*, IEEE Transactions on Systems, Man, and Cybernetics, Vol. 9, No. 1, pp. 62-66.
- [10] G. Shapiro (1992), *Computer and Robot Vision*, Volume I, Addison-Wesley.
- [11] P. Soille (2013), *Morphological image analysis: principles and applications*, Springer Science & Business Media.
- [12] Schalkoff, Robert J. (1989), *Digital image processing and computer vision*. Vol. 286. New York: Wiley.
- [13] S. Rege, R. Memane, M. Phatak, P. Agarwal (2013), *2D Geometric shape and color recognition using digital image processing*, International Journal of Advanced Research in Electrical, Electronics and Instrumentation Engineering 2(6) 2479-2487.

A Simplified System for Assessing the Condition of Irish Regional and Local Roads

Brian Mulry, BE, MEngSc, CEng, MIEI, MIAT ¹

John McCarthy, BA, BAI, MSc, CEng, MIEI ²

¹PMS Pavement Management Services Ltd., Raheen Industrial Estate, Athenry, Co. Galway

²Department of Transport Tourism & Sport, 44 Kildare Street, Dublin 2.

email: brianmulry@pms.ie, johnmccarthy@dtas.ie

ABSTRACT: The surface condition of road pavements is a vital element in pavement management to prioritise projects, select appropriate treatments and make the best use of available resources. To evaluate the condition of the Regional and Local Roads, a simplified pavement inspection methodology, the Pavement Surface Condition Index (PSCI) rating system, has been developed.

The PSCI system has been developed for Rural Flexible, Urban Flexible and Urban Concrete roads. Three separate manuals have been published by the Department of Transport, Tourism and Sport (DTTAS). The manuals describe the types of defects for Irish roads in each category and provide a simple 1 to 10 system based on pavement defects to visually rate pavement surface condition. The condition survey is carried out from a moving vehicle and the assigned PSCI rating is recorded and geo-referenced using an innovative tablet and App device. The results of the rating system are relatable to specified maintenance treatment measures for Irish roads.

The implementation of the 1 to 10 PSCI system involved the development of new IT solutions and the nationwide training of local authority personnel in 31 local authorities. The simplified system and App device are being used by local authorities to visually rate their rural and urban road networks with over 70,000 kilometres (c. 75%) of network rated to-date. The overall objective is to use the 1 to 10 rating data to establish the existing pavement condition, and the lengths of roadway requiring various types of remedial works, both nationally and at county level.

The PSCI rating is a key element of the DTTAS and Local Government Management Agency (LGMA) MapRoad pavement management system, and the DTTAS Regional and Local Road grant programmes are directly linked to the PSCI and associated treatment measures. Moreover, the PSCI is also a new key performance indicator for roads that is prescribed by the National Oversight and Audit Commission (NOAC) as part of its annual report on the Performance Indicators in Local Authorities.

This paper describes the development, implementation and use of the PSCI rating system including the use of an innovative tablet and App device for collecting the data on Irish roads. The paper will outline the findings from undertaking an extensive programme of training of local authority personnel, and will examine the survey results and experience to-date in the use of the system and data.

KEY WORDS: Regional and Local Roads; Pavement Condition; Local Authorities; Pavement Management; Performance Indicator.

1 ROAD NETWORK MANAGEMENT AND FINANCIAL BACKGROUND

The overall road network in Ireland comprises 99,008 kilometres and includes 5,415 kilometres of National Roads and 93,593 kilometres of Regional and Local Roads. The length of public road per 1000 population is 21.46 kilometres per 1000 which is over two and a half times the EU (European Union) average of 8.51 kilometres per 1000. The maintenance and upkeep of this network is thus very challenging, and in particular against a background of reducing funding and resources over recent years.

The National road network which includes the motorways, dual carriageways, national primary and secondary routes is less than 6% of the total public road length. The National network is managed by Transport Infrastructure Ireland (TII) formerly the National Roads Authority (NRA). The nature of Regional and Local roads is fundamentally different to the National road network. The Regional and Local roads, at

93,593 km, account for 94% of the total road network and carry around 55% of all road traffic. There are 13,121 km of Regional road and 80,472 km of Local roads. The Local road network is classified into three sub-groupings; local primary (LP - 24,373 km), local secondary (LS - 33,222 km) and local tertiary (LT - 22,878 km). Typical road widths by road classification are c. 6 metres for regional roads, c. 4.5 metres on local primary roads, c. 3.5 metres on local secondary roads and c. 2.5 metres on local tertiary roads. Most of the roads carry low volumes of traffic, less than 100 commercial vehicles per day, with many local roads providing cul-de-sac access to a few households [1]. Hence, the management of this network requires a different approach.

The 31 Local Authorities are responsible for the maintenance and upkeep of the Regional and Local roads network. Funding is provided through a combination of central government from the Department of Transport, Tourism and Sport (DTTAS), and locally generated funding by local authorities. In 2014, a total of €294 million was made

available by the DTTAS for expenditure on the Regional and Local roads network [2], with another c. €120 million of expenditure from local authority resources, yielding a total expenditure of around €414 million.

In 2011, a major pavement condition study was carried out on the entire Regional road network based principally around machine-based data (RSP, SCRIM) in conjunction with visual rating using a newly developed Pavement Surface Condition Index (PSCI) system for rural roads [3]. However, the cost of automated data collection as a proportion of the available maintenance budget, in particular, on the Local road network would be too high to be economically viable on a routine basis. A very high proportion of the roads is limited in width, has poor geometrics, poor surface condition and many are cul-de-sac roads making them unsuitable for machine surveys. In addition, it is uneconomical to perform a detailed manual distress survey on such lower class roads as the available budget per kilometre is at a low level, and the costs of data collection per kilometre would become excessively high as a percentage of the available budget. Accordingly, a simplified system for applying a condition rating index whereby greater lengths of road can be surveyed using a geo-referenced mobile application is obviously attractive for these road classes.

2 DEVELOPMENT OF THE PSCI RATING SYSTEM

The Rural Flexible roads manual for the PSCI system was developed in 2011/2012 to provide a simple condition rating index for the evaluation and rating of the surface condition of Irish rural roads at network level [4]. Since then, two further manuals have been developed for Urban Flexible and Urban Concrete roads [5, 6]. The three manuals, shown in Figure 1, outline the different types of pavement defects for Irish roads, and provide a simplified 1 to 10 system to visually rate pavement surface condition. The manuals provide detailed descriptions of the distress types, how to link them to the 1 to 10 rating scale, and include high resolution colour photographs of the distress types and of road pavements in each of the 1 to 10 rating categories. The manuals provide a standardised approach to rate pavement condition and to link the pavement distress to specified treatment measures for Irish Rural Flexible, Urban Flexible and Urban Concrete roads.

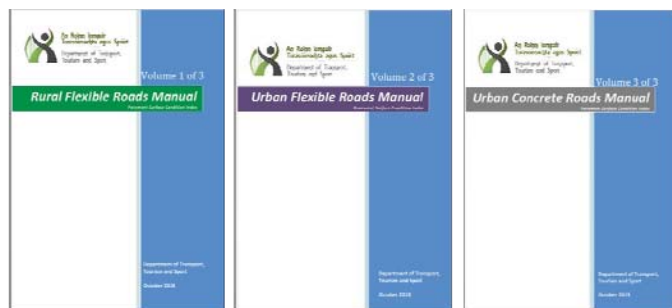


Figure 1. Rural Flexible, Urban Flexible and Urban Concrete Roads Manuals [4, 5, 6].

The manuals and software technologies were developed in collaboration with a Steering Group of the DTTAS including members from DTTAS, Local Government Management

Agency (LGMA) and Senior Engineers from South Tipperary, Carlow and Donegal County Councils. In developing the PSCI system, substantial use was made of the template provided by the PASER (Pavement Surface Evaluation and Rating) methodology originally developed by the Wisconsin Department of Transportation for local roads in the US [7]. The PASER system was significantly modified for Irish road conditions including pavement defects and remedial work types.

The remainder of this paper will mainly discuss the development, implementation and use of the rural flexible roads manual. While the range of defects, mapping of defects to the 1 to 10 rating, and the maintenance treatment categories are different in the Rural Flexible, Urban Flexible and Urban Concrete roads manuals, the underlying system, data collection methodology and technologies used are the same across all three manuals.

2.1 Rural Flexible Pavement Defects

Based on the results of very considerable research and field trials in Ireland [8, 9], there are 10 pavement distresses outlined in the Rural Flexible roads manual as they are by far the most common flexible road distresses encountered on Irish roads. The first half of the manual provides detailed descriptions and colour photographs of the ten distress types. The distresses are grouped into four categories as follows:

Surface Defects

Ravelling
Bleeding

Pavement Deformation

Rutting
Surface Distortion (shape problems, bumps, sags and depressions)

Cracks

Alligator Cracking
Edge Cracking/Breakup
Other Cracking (longitudinal, transverse, reflection, slippage)

Surface Openings

Patching
Potholes
Road Disintegration

The ten pavement defects can be re-classified into three causative groups, namely, surface-related, structural-related and other-related pavement defects. Surface defects comprise ravelling and bleeding; Structural defects (i.e. load-related) comprise rutting, alligator cracking, edge cracking/breakup, potholes, poor/failed patching and road disintegration; while Other Pavement defects include other cracking, good/fair patching and surface distortion. With an understanding of the surface defects, structural defects and other pavement defects categories, the PSCI 1 to 10 system can be used to evaluate and rate flexible pavement surfaces.

2.2 The PSCI Rating System

Figure 2 shows the PSCI rating system as outlined in Table 1 of the Rural Flexible manual. The PSCI provides a numerical

rating of road condition using a simplified 1 to 10 rating scale. The PSCI scale ranges from 10 for a pavement in excellent condition to 1 for a pavement in failed condition. For consistency of approach, the rating is assigned based on visible pavement defects only. The rating manual provides detailed descriptions on how to link the pavement defects to the 1 to 10 scale, and includes high resolution colour photographs of road pavements in each of the 1 to 10 rating categories. Figure 3 shows an extract of Rating 7 from the rural manual.

Overall PSCI Rating	Primary Rating Indicators*	Secondary Rating Indicators*
10	No Visible Defects.	Road surface in perfect condition.
9	Minor Surface Defects ¹ . Ravelling or Bleeding ≤10%.	Road surface in very good condition.
8	Moderate Surface Defects ¹ . Ravelling or Bleeding 10% to 30%.	Little or No Other defects.
7	Extensive Surface Defects ¹ . Ravelling or Bleeding ≥ 30%.	Little or No Other defects. Old surface with aged appearance.
6	Moderate Other Pavement Defects ² . Other Cracking ≤ 20%. Patching generally in Good condition. Surface Distortion requiring some reduction in speed.	Surface defects ¹ may be present. No structural distress ³ .
5	Significant Other Pavement Defects ² . Other Cracking ≥ 20%. Patching in Fair condition. Surface Distortion requiring reduction in speed.	Surface defects ¹ may be present. Very localised structural distress ³ (< 5 m ² or a few isolated potholes).
4	Structural Distress ³ Present. Rutting, Alligator Cracking or Poor Patching for 5% to 25%. Short lengths of Edge Breakup/Cracking. Frequent Potholes.	Other defects may be present.
3	Significant Areas of Structural Distress ³ . Rutting, Alligator Cracking or Poor Patching for 25% to 50%. Continuous lengths with Edge Breakup/Cracking. More frequent Potholes.	Other defects may be present.
2	Large Areas of Structural Distress ³ . Rutting, Alligator Cracking or Very Poor Patching for ≥ 50%. Severe Rutting (≥ 75mm). Extensive Very Poor Patching. Many Potholes.	Very difficult to drive on.
1	Extensive Structural Distress ³ . Road Disintegration of surface. Pavement Failure. Many large and deep Potholes. Extensive Failed Patching.	Severe Deterioration. Virtually undrivable.

* Individual pavements will not have all the types of distress listed for any particular rating. They may have only one or two types.

Note 1: Surface Defects = Ravelling or Bleeding.

Note 2: Other Pavement Defects = Other Cracking (longitudinal, transverse, reflection or slippage), Surface Distortion (Shape problems, depressions/sags, shoving, bumps, settlement or heave), Good/Fair Patching.

Note 3: Structural Distress = Load-related defects comprising Rutting, Alligator Cracking, Edge Breakup/Cracking, Poor/Failed Patching, Potholes or Road Disintegration.

Figure 2. The PSCI Rating System [4].

The 1 to 10 system is colour-coded with Ratings 1 to 4 coloured Red, Ratings 5 and 6 coloured Amber, Ratings 7 and 8 coloured Blue, and Ratings 9 and 10 coloured Green. This colour-coding follows throughout the manual, and is also used in the mobile survey App, and in mapping the PSCI ratings within the DTTAS MapRoad pavement management system.

As shown in Figure 2, the rating is assigned using Primary- and Secondary- rating indicators based only on visible pavement distress. A primary rating indicator is a defect that must be present on the road, a secondary rating indicator is a defect that may or may not be present in conjunction with the primary defect(s). The significance of the surface-related, structural-related and other-related pavement defects in the 1 to 10 rating system can also be seen from Figure 2, with surface-related defects mapping to ratings 7 & 8, other-related defects mapping to ratings 5 & 6, and structural-related defects mapping to ratings 1 to 4.

To rate pavement surface condition using the 1 to 10 system, one needs to understand the pavement distresses and become familiar with the photos and descriptions of the individual rating categories in the 1 to 10 rating scale. The impact of surface-related distresses, structural-related distresses and other defects should be identified. The purpose of the survey is to rate the overall condition of a roadway, rather than collect detailed distress data on individual short segments or isolated events.

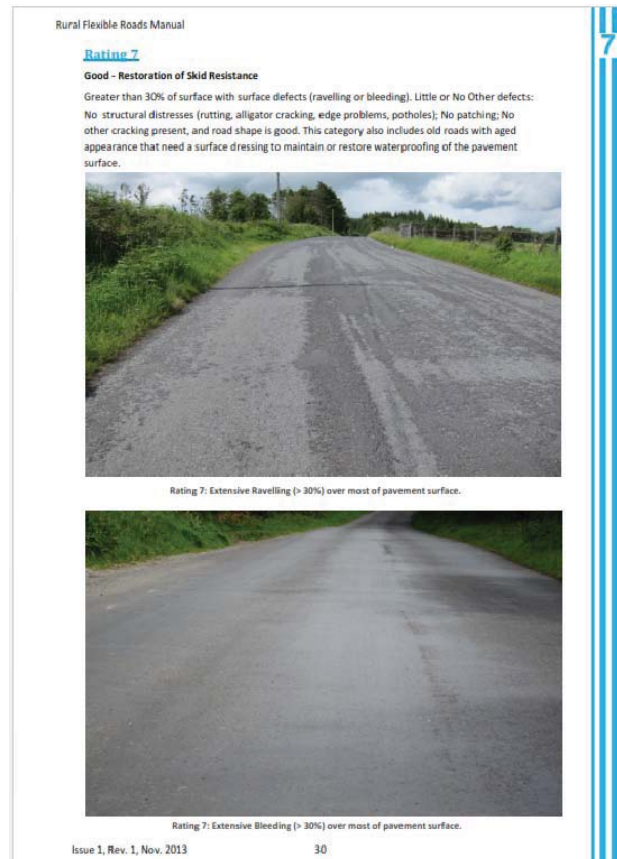


Figure 3. Sample Extract of Photos for Rating 7 in the Rural Flexible Manual [4].

2.3 Mapping Distress to Treatment Measures

The PSCI 1 to 10 ratings are directly linked to four maintenance treatment categories specified for use on Irish Regional and Local roads by the DTTAS. The four maintenance treatment categories are Routine Maintenance, Restoration of Skid Resistance, Surface Restoration and Road Reconstruction. Figure 4 shows the mapping of the 1 to 10 ratings to the different treatment measures as outlined in Table 2 of the Rural Flexible manual, where ratings 1 to 4 map to the Road Reconstruction category, 5 and 6 map to the Surface Restoration category, 7 and 8 map to the Restoration of Skidding Resistance category, and 9 and 10 map to the Routine Maintenance category.

Overall PSCI Rating	Treatment Measures	Surface	Structure
10	Routine Maintenance	Excellent	Good
9		Very Good	
8	Resealing & Restoration of Skid Resistance	Fair	Good
7		Poor	
6	Surface Restoration - Carry out localised repairs and treat with surface treatment or thin overlay.	Fair	Fair
5		Poor	
4	Structural Overlay - Required to strengthen road. Localised patching and repairs required prior to overlay.	Poor Overall	Poor Overall
3			
2	Road Reconstruction - Needs full depth reconstruction with extensive base repair.	Very Poor Overall	Failed Overall
1			

Figure 4. Mapping PSCI Rating to Treatment Measures [4].

2.4 Pilot Surveys

Several refinements were made in developing the Rural Flexible survey manual and PSCI condition rating system. A number of preliminary field trials on a variety of different roads were carried out in early 2011 by personnel with experience of pavement defects and condition rating manuals. Following these initial trials, the draft survey manual and 1 to 10 system was trialled by pilot survey for the first time with Local Authority road staff in Carlow County Council in October, 2011. The pilots involved discussions with senior road engineers and a field trial to assess the application of the manual and 1 to 10 rating system by 4 engineering staff (2 Executive Engineers, 1 Engineering Technician and 1 Area Supervisor). Prior to the field trials, two routes of Regional and Local roads with a range of road condition categories were identified. The pilot routes were 13.5 kilometres (Loop 1) and 16.2 kilometres (Loop 2) in length.

An instrumented van with GPS and Distance Measuring Instrument (DMI) connected to a forward view HD digital video camera and a laptop was provided for the trials. As the Tablet and Mobile App were still in development at this stage, the laptop was loaded with recording software which allowed continuous condition rating using the 1 to 9 keys on the laptop keyboard, with 0 representing condition rating 10. When the rater decided that a new condition rating was appropriate, the rater pressed the relevant numeric key. All four raters carried out a condition rating survey in the field on each of the loops.

Significant improvements were made to the manual and rating system based on the outcomes from the pilot surveys.

Overall, the pilots showed that the manual and continuous rating system were simple to understand, and had very good acceptance from the raters. The continuous rating hardware/software also worked well in the field. There was in general good agreement across the four raters in relation to identification of stretches with different ratings, and agreement that the 1 to 10 system was easy to use. The site trials indicated that a minimum length to justify a change in rating of c.200 metres was the most appropriate. The pilots also indicated that a training course would be needed to train learners in the use of the 1 to 10 rating system and Mobile App.

3 DATA COLLECTION USING THE MAPROAD MOBILE APP

A key objective of the system was to be able to record survey data electronically without the use of paper, and to be able to upload the data in the field directly to the DTTAS pavement management system. An innovative mobile survey App, called MapRoad Mobile, has been specifically developed to facilitate the visual condition rating of roads and the rapid capture of the PSCI data from a moving vehicle. The smart mobile solution operates on a Tablet device based on the Android operating system [10].

3.1 MapRoad Mobile PSCI App

The recommended tablet device for the MapRoad Mobile App is the Samsung Galaxy 10.1 tablet. The Mobile App uses the internal GPS device on the tablet and, when available, mobile data connection (3G) to acquire location and to capture and display data. Typical location accuracy with the internal GPS device on the tablet is 5 to 10 metres. An external Bluetooth GPS device can be used to improve this accuracy to 2 to 3 metres.

In the field, the assigned PSCI 1 to 10 ratings and associated GPS data are recorded in real-time using the underlying Local Authority Road Network Schedule (GIS Shapefile), the Tablet device and Mobile App. The PSCI and associated GPS data are automatically saved on the Tablet device and the data can be uploaded directly to the DTTAS MapRoad pavement management system by connecting to the internet using WiFi or mobile data connection (3G).

With the MapRoad Mobile App, the operator has the ability to select the survey type (Rural, Urban or Concrete), create a new project, upload a project, load a project, and check for updates. Once a new project has been created, MapRoad Mobile will display a ratings keypad on the right of the screen, with a map panel on the left showing the Local Authority Road Schedule as shown in Figure 5. The numbers on the keypad are colour-coded to match the 1 to 10 rating system of red (1 to 4), amber (5 & 6), blue (7 & 8) and green (9 & 10).

The PSCI condition rating survey is a continuous driven visual condition survey carried out from a moving vehicle by a two-person team, the driver and the rater. To start recording, or dropping points on the map, the rater chooses an initial rating (1 to 10), and then starts the survey. Once the driver starts driving, points will be dropped on the map approximately every 2.5 seconds or every 35 metres. The points dropped on the map are colour-coded to match the 1 to 10 rating system. For a PSCI rating of 3, red points will be

dropped on the map, if changed to 7 the points being dropped will change to blue and so on. The rating is applied to the full width of a road segment based on its overall condition and the defects present on the road. Moreover, the rater assesses the total length of a road section, there is no sampling involved. While the rating assigned and GPS coordinates are linked to the road schedule and recorded for every 35 metres, the visual rating is only changed once the condition of the road and defects observed change. Roughly a length of at least 200 metres is required to justify recording a change in the condition rating category. The operator can stop, pause or resume dropping and capturing points at any time.

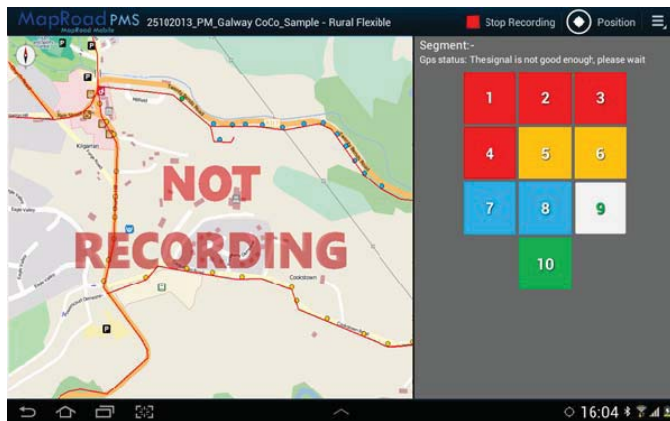


Figure 5. MapRoad Mobile App [10].

The PSCI survey is reasonably fast with a high daily output. Typically, the survey speed for rural roads can be in the range of 30 to 50 km/h depending on the condition of the roadway. From experience to-date, once the rater has become familiar with the photos and descriptions in the manual, and built up a “mental database” of the condition categories based on rating a number of roads, the speed of rating generally increases. The higher end of the speed range is suitable where visibility is clear and the road appears to be in good condition. As the condition of the road deteriorates, the survey speed should be reduced. Typically, 150 to 200 km of road can be surveyed per day in this speed range.

4 TRAINING OF LOCAL AUTHORITY STAFF

As the Rural Flexible roads manual, comprising the PSCI 1 to 10 rating system and Mobile App, was a completely new approach to visual condition surveys in Ireland, it would be necessary to train Local Authority roads staff nationally. In addition, the successful implementation of the new system relied heavily on achieving cooperation from Local Authority roads staff across the country and on ensuring an understanding of the role of the PSCI within the overall approach to pavement management both at local and national level.

4.1 Training Workshops

As part of the implementation of the system, National and Regional Workshops were held by the DTTAS as well as the development of a dedicated Training Course. The Regional workshops and training course were run through the five Road Service Training Group (RSTG) Regional Training Centres located in Roscrea, Cork, Dublin, Castlebar, and Stranorlar.

In May, 2012, the manual was launched at a one-day National Workshop in Dublin. The workshop was attended by over 90 senior engineering personnel with representatives from 29 Local Authorities, 5 City Councils, 2 Borough Councils and 4 Town Councils. In addition, prior to the roll out nationally of a full scale training course, four other 1-day regional workshops were held in November, 2012. Over the four days, the workshops were attended by 204 Local Authority roads staff who would be directly involved in the use of the PSCI manual and Mobile App.

4.2 Training Course

A separate training course has been developed for the Rural Flexible, Urban Flexible and Urban Concrete manuals, and a detailed course specification, entitled the ‘Road Pavement Condition Rating Surveyor’, has been published by the Local Authority Service National Training Group (LASNTG) for each manual [11, 12, 13]. The aim of the training courses is to train learners in the correct and safe methodology to carry out a PSCI condition rating survey.

The training course for each manual has been developed and modified since 2012 and now consists of a blended learning course with three parts:

- Part 1 is an Online module hosted on the Moodle open-source learning platform and consists of an introduction to the manual, the defects and a basic online assessment;
- Part 2 consists of 1-day of theory in the classroom including simulation rating on a desktop PC, training on how to use the tablet and App and a multiple-choice classroom assessment; and
- Part 3 consists of a subsequent site practical exam whereby the learner would rate a pre-approved sample road network using the tablet and mobile App device.

In the classroom training, the learners are trained using a simulation programme to demonstrate on a desktop computer the ability to properly rate road segments using the 1 to 10 rating system. The software programme presents a windshield survey to the learner using video clips of road segments in each of the 1 to 10 rating categories, and allows the learner to record the rating as per a live survey. A screen grab of the desktop interface for the simulation programme is shown in Figure 6. The training circuit video clips are pre-rated by experienced personnel to establish the standardised underlying condition rating for the training video clips. The learner desktop ratings are compared against the underlying ratings to measure learning in the classroom. The classroom module also includes training in how to use the tablet and Mobile App, and how to upload a completed project to MapRoad.

For the site practical exam, an assessment route is identified close to each of the five training centre locations with roads which had a range of conditions in the 1 to 10 rating categories. The assessment routes are firstly surveyed by experienced personnel using the tablet and App device to establish the underlying condition rating for subsequent comparison with the learner ratings. In addition, the condition of the assessment routes is recorded using high definition forward view digital video referenced to both chainage and GPS coordinate systems to maintain a permanent record of the road condition. In the site practical exam, each learner is

required to independently rate the assessment route using the tablet and App, and to upload the data. It is recommended that the site assessment should be undertaken within three weeks of completing Part 2 of the course. The learner ratings are compared against the underlying ratings to assess Pass/Referred standard.



Figure 6. Simulation Programme for Desktop Rating.

4.3 Outcomes From the Training Course

The rating system and training has been implemented since 2012 over a wide range of survey personnel as shown in Table 1. From 2012 to 2015, there were 36 training courses on the Rural Flexible manual delivered to 314 staff from 31 Local Authorities. Of the 314 learners trained, 274 (87%) have undertaken the site practical exam with 228 (83%) having passed the exam to become approved raters and 46 (17%) who were referred. Training has also been provided to 30 staff on the Urban Flexible manual and to 27 staff on the Urban Concrete manual in the Dublin and Cork urban districts.

Table 1. Range of Personnel on Rural Flexible Training.

Learner Type	Number of Learners
Senior Engineer	5
Senior Executive	33
Executive/Area Engineer	151
Assistant Engineer	47
Graduate Engineer	5
Engineering Technician	62
Area Manager/Supervisor	11
Total	314

5 ANALYSIS AND USE OF THE PSCI DATA NATIONALLY

The PSCI system has become well established across all local authorities and is a key element of the DTTAS MapRoad pavement management system [14]. The simplified system and Mobile App are being used by Local Authority personnel to visually rate their road networks and develop works programmes based on the condition data. Moreover, the PSCI is also a new key performance indicator for roads that is prescribed by the National Oversight and Audit Commission

(NOAC) as part of its annual report on the Performance Indicators in Local Authorities [15].

From an economic perspective, the implementation of the PSCI system provides technical data which allows the DTTAS and Local Authorities to demonstrate funding requirements and set programmes in line with available budgets. The Regional and Local Road grant programmes funded by the DTTAS are directly linked to the PSCI and the specified treatment measures. The PSCI data are used to prioritise sections and to create a Roads Programme for the grant applications and annual returns to the DTTAS. Since 2012, Local Authorities are required to submit 'Before' and 'After' PSCI condition ratings on all works schemes included in their annual works programme [16, 17]. In addition, since 2014 Local Authorities are required to implement a network level visual condition survey regime (100% coverage) using the PSCI every year on Regional, every 2 years on LP and LS, and every 5 years on LT roads.

Figure 7 shows the National picture of the PSCI ratings and a breakdown of the length in each rating category completed up to May 2015 with over 57,600 kilometres (62%) of the Regional and Local roads network having been rated by Local Authority road staff. Since May 2015, a further circa 12,500 kilometres have been surveyed giving an overall coverage of over 70,000 kilometres (c.75%) of the network.

The PSCI system was successfully used as part of a major pavement condition study in 2011 to survey the entire 13,121 km of the Regional Roads network [3, 18]. The visual rating was carried out from high definition forward view digital video of the road surface condition collected in the field.

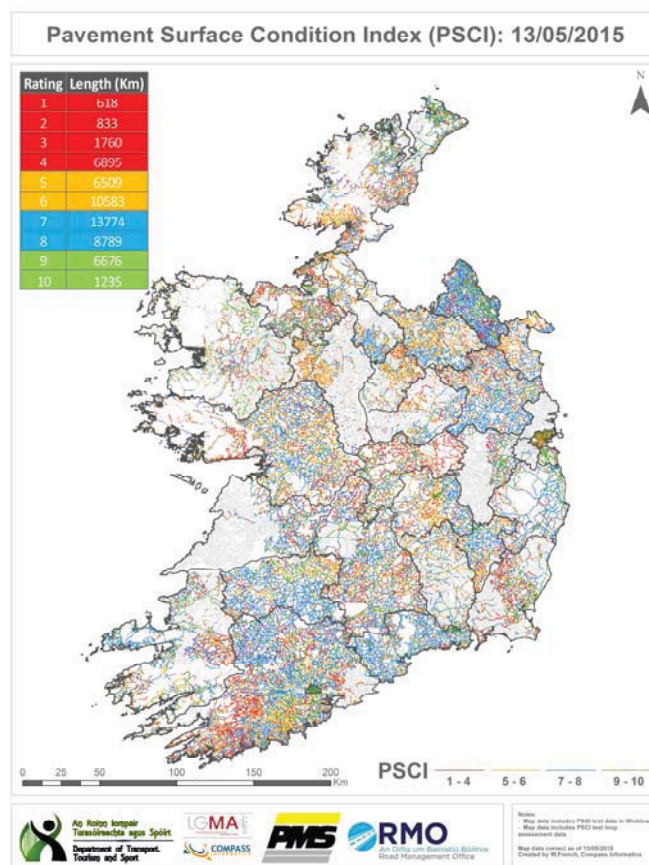


Figure 7. National Picture of PSCI Ratings - May 2015.

Table 2 shows the percentage length by PSCI rating and maintenance treatment for each road type that was surveyed by local authorities and recorded on the MapRoad system as at 31/12/2014 [15]. The output data from the 2011 Regional Road study are also shown in Table 2 for comparison [18]. The patterns in condition distribution by class are similar to those recorded in previous National surveys, with very good agreement between the visual rating data for the Regional roads from the 2011 and 2013/2014 surveys. The overall objective is to use the results of the 1 to 10 ratings for Regional and Local roads to establish the existing pavement condition at network level, and the lengths of roadway requiring various types of remedial works, both nationally and at county level.

Table 2. Maintenance Treatment Type By Road Category.

Road Class	% Length Surveyed	Year	PSCI Rating/Treatment Type Percentages			
			1 to 4	5 & 6	7 & 8	9 & 10
			Reconstruction	Surf. Rest.	Skid Resist.	Routine Maint.
Regional	100%	2011	10%	22%	43%	25%
Regional	30%	2013/2014	8%	24%	44%	24%
Local Primary	53%	2013/2014	11%	31%	43%	15%
Local Secondary	44%	2013/2014	17%	35%	36%	12%
Local Tertiary	31%	2013/2014	31%	30%	29%	10%

6 SUMMARY AND CONCLUSIONS

A simplified pavement inspection methodology, the Pavement Surface Condition Index (PSCI) rating system, has been developed in Ireland to evaluate the condition of the Regional and Local Roads network. The system is outlined in three manuals, the Rural Flexible roads manual, the Urban Flexible roads manual and the Urban Concrete roads manual, published by the Department of Transport, Tourism and Sport (DTTAS). The PSCI provides a rating using a simple 1 to 10 scale based on pavement defects to visually rate pavement surface condition. The results of the rating system are relatable to specified maintenance treatment measures for Irish roads.

The condition survey is a continuous driven survey carried out from a moving vehicle by a two-person team, the driver and the rater. The assigned PSCI rating is recorded and geo-referenced using a tablet and App device called MapRoad Mobile. Typically, the survey speed for rural roads can be in the range of 30 to 50 km/h depending on the condition of the roadway and 150 to 200 km of road can be surveyed per day.

The PSCI has become well established in all local authorities. The simplified system and Mobile App are being used by Local Authority personnel to visually rate their rural road networks and develop works programmes based on the condition data. Since its development, training on the PSCI system has been provided to over 360 roads staff from 31 Local Authorities, with over 70,000 kilometres (c.75%) of the Regional and Local roads network surveyed to-date.

The PSCI condition rating data are immediately available in the DTTAS MapRoad pavement management system, and can be used to prioritise projects, to choose the most cost effective treatments, and to demonstrate value for money and the need for increased investment. In order to provide current data, it is recommended to collect PSCI network-level data every year on Regional, every 2 years on Local Primary and Local

Secondary, and every 5 years on Local Tertiary roads. In addition, the PSCI is a new key performance indicator for roads that is used by the National Oversight and Audit Commission (NOAC) as part of its annual report on the Performance Indicators in Local Authorities.

ACKNOWLEDGMENTS

The authors would like to acknowledge and thank the members and participating organisations of the DTTAS Steering Group. In particular, Dominic Mullaney (DTTAS), Liam Fitzgerald (Carlow), John McLaughlin (Donegal), Paul Fox (LGMA), Kieran Feighan (PMS Ltd.) and Ken Dowling (Compass Informatics). The authors would like to acknowledge the very significant contribution of Mr. Peter Britton (R.I.P.), South Tipperary County Council, who died on July 27th, 2014 following a tragic accident in the French Alps.

REFERENCES

- [1] Pavement Management of Secondary Roads in Ireland, Dr. Kieran J. Feighan, 4th International Conference on Managing Pavements, Durban, South Africa, 1998.
- [2] Regional and Local Road Funding 2015, Dominic Mullaney, Department of Transport, Tourism and Sport, Local Authority Roads Conference - Reforms, Challenges and Safety, Ireland, May 2015.
- [3] Assessing the Condition of the Irish Regional Road Network 2011/2012, Dr. Kieran Feighan and Brian Mulry, PMS Pavement Management Services, Institution of Engineers of Ireland, November 2013.
- [4] Rural Flexible Roads Manual - Pavement Surface Condition Index, Vol. 1 of 3, Department of Transport, Tourism and Sport, October 2014.
- [5] Urban Flexible Roads Manual - Pavement Surface Condition Index, Vol. 2 of 3, Department of Transport, Tourism and Sport, October 2014.
- [6] Urban Concrete Roads Manual - Pavement Surface Condition Index, Vol. 3 of 3, Department of Transport, Tourism and Sport, October 2014.
- [7] PASER Asphalt Roads Manual, Wisconsin Transportation Information Center, University of Wisconsin-Madison, 2002.
- [8] A Windshield Survey Method for Pavement Condition Assessment, Brennan, Mulry and Feighan, 2nd International Symposium on Highway Surfacing, University of Ulster at Jordanstown, January 1994.
- [9] Non-National Road Pavement Condition Study, Distress Catalogue Descriptions and Rating Procedures, PMS Pavement Management Services Ltd. and Department of the Environment, Heritage and Local Government, Ireland, 2004.
- [10] Operational Method for MapRoad Mobile App for Android, Version 3.0, Compass Informatics Ltd., Ireland, August 2014.
- [11] Course Specification, Road Pavement Condition Rating Surveyor (Rural), Local Authority National Services Training Group (LASNTG), Roscrea, Ireland, 2016
- [12] Course Specification, Road Pavement Condition Rating Surveyor (Urban), Local Authority National Services Training Group (LASNTG), Roscrea, Ireland, 2016
- [13] Course Specification, Road Pavement Condition Rating Surveyor (Concrete), Local Authority National Services Training Group (LASNTG), Roscrea, Ireland, 2016
- [14] www.maproadpms.ie, MapRoad PMS Portal, Department of Transport, Tourism and Sport, Ireland, Accessed April 5, 2016
- [15] Performance Indicators in Local Authorities 2014, National Oversight and Audit Commission (NOAC) Report, December 2015.
- [16] Circular RW 3/2012, Department of Transport, Tourism and Sport, Ireland, April 2012
- [17] Circular RW 21/2014, Department of Transport, Tourism and Sport, Ireland, October 2014
- [18] Regional Road Network Pavement Condition Study Report by PMS Pavement Management Services Ltd., Department of Transport, Tourism and Sport (DTTAS)/National Roads Authority (NRA), May 2012.

The Introduction and Implementation of Mobile Retroreflectivity Measurement of Pavement Markings in Ireland

Mr Eoin Greaney, Mr Alan Boyle

Pavement Management Services Ltd, Raheen Industrial Estate, Athenry, Co. Galway.

email : eoingreaney@pms.ie, alanboyle@pms.ie

ABSTRACT

This paper describes research undertaken to investigate the suitability of mobile retroreflectivity equipment for the evaluation of pavement markings in Ireland. Having selected the LTL-M as a suitable mobile device, its repeatability and reproducibility as well as its correlation with a reference handheld device, the LTL-X was established using a control circuit. The research shows that the presence of moisture has a significant effect on the retroreflected luminance (RL) results, with unreliable data recorded on damp or wet line markings. Under dry conditions, it was established that the results are very repeatable and reproducible and there is excellent correlation between the mobile device and the reference handheld device. It can be concluded that the mobile retroreflectivity device, LTL-M, is suitable for reliable evaluation of pavement line markings in Ireland when operated in dry weather conditions.

KEY WORDS

LTL-M; LTL-X; Mobile Retroreflectometer; Handheld Retroreflectometer; Retroreflected luminance; EBCL; WBCL; Centreline; Pavement Marking; Line Marking; Eastbound; Westbound; Control Site; Reference data; Moisture.

1 INTRODUCTION

Pavement line markings delineate the roadway path and specify traffic lanes in a safe and efficient manner for road users. Retroreflectivity describes the ability of a pavement marking to reflect light back to its source and is critical in ensuring the safety of road users, especially in low-light conditions and at night. The retroreflectivity of pavement markings is achieved with the addition of glass beads to the markings, which are then illuminated by vehicle headlamps. It is assessed by measuring the coefficient of retroreflected luminance (RL), which is a measurement of the brightness of a pavement marking as seen by drivers of motorised vehicles in vehicle headlight illumination at night-time and is expressed in $\text{mcd}\cdot\text{m}^{-2}\cdot\text{lx}^{-1}$ (2).

Research was undertaken to investigate the suitability of mobile retroreflectivity equipment for the evaluation of pavement markings in Ireland and to identify if a mobile retroreflectometer would cope with the challenges posed by Irish road and climatic conditions. Equipment from various worldwide manufacturers were investigated and the LTL-M Retroreflectometer was identified as a suitable system and was acquired, initially for the purposes of this research.

Establishing if there was an accurate correlation between an established reference handheld retroreflectometer and the LTL-M was a priority of the research. In addition, investigating the repeatability of the mobile retroreflectometer from multiple runs on the same day and reproducibility over time (multiple runs over different days) was one of the main aims of the research project.

It is extremely difficult, to accurately assess the level of moisture present on the surface of a line marking and the possible impact different moisture levels would have on the RL results. To establish an accurate baseline for the test results, the reference data from the handheld device was collected under dry weather conditions on dry line markings.

2 CONTROL SITE DESCRIPTION

A suitable control site was identified and this was used to establish a reference set of data from the handheld device. The same control site was used for the collection of data using the LTL-M for the purposes of this research project. The control site used in the research is the centre line marking along a section of road, north of Athenry, Co. Galway. The section forms part of the R339 and extends west for 390 metres from the junction with the L3103. The same centreline marking was tested using the LTL-M in both the eastbound and westbound directions; throughout the remainder of this paper, testing of the centreline in the eastbound direction is referred to as EBCL and testing of the centreline in the westbound direction is referred to as WBCL. At the time of testing, the centreline marking was relatively new (it is estimated to have been laid in the previous 18 months). The control site consisted of approximately 100 metres of continuous white centreline and approximately 300 metres of broken white centreline.

3 RETROFLECTOMETER EQUIPMENT

3.1 Handheld Retroreflectometer (reference device)

Annex H of the UK DMRB (4) describes how variability can be found in the expected results from mobile retroreflectometer equipment when compared to a handheld device. It is widely accepted that handheld devices certified in accordance with relevant specifications and standards produce reliable and accurate RL data. Such a device was utilised to produce reference data for use in the assessment of the performance of the mobile retroreflectometer in this research.

The handheld retroreflectometer chosen was the LTL-X Retroreflectometer system designed by Delta in Denmark. The LTL-X measures the RL value with the road illuminated

at an angle of 1.24° and using an observation angle of 2.29° . These angles simulate a viewing distance from a driver's perspective of 30 metres in the direction of travel. The LTL-X system is controlled by multiple microprocessors. A keyboard located on the top of the LTL-X allows the operator to use the device. The LTL-X completes a measurement automatically by the push of the green button on the keyboard and presents the corresponding result on the visual display. The result is transferred automatically to the LTL-X's internal memory.

The LTL-X is certified in accordance with EN 1436:2007 + A1:2008. The calibration of the LTL-X Retroreflectorometer is traceable to NIST (National Institute of Standards and Technology, USA) and PTB (Physikalisch – Technische Bundesanstalt, Germany) ⁽³⁾. The LTL-X is factory calibrated; however, it is also calibrated against a calibration tile with a known RL prior to testing. The calibration tile has a typical calibration period of 2 years and the tile used during this research held a current calibration certificate ⁽³⁾.

3.2 Mobile Retroreflectorometer (trialled device)

The mobile retroreflectorometer used for this research project was the LTL-M Retroreflectorometer system designed by Delta in Denmark. The LTL-M retroreflectorometer is a mobile field instrument intended for measuring the retroreflection properties of pavement markings. The LTL-M has the ability to measure the RL value (coefficient of retroreflected luminance) and the DC (Daylight Contrast) as well as recording the presence of RPMs (Raised Pavement Markers also called road studs). RL is a measurement of the brightness of a pavement marking as seen by drivers of motorised vehicles in vehicle headlight illumination at night-time. The daylight contrast is the contrast between the road surface and the pavement marking as seen by the driver during the daytime. RPMs (often referred to as 'cat's eyes') are another means of guiding traffic during the night through small devices positioned on the road surface providing a strong retroreflection. For the purposes of this research, attention concentrated on the RL values obtained from the LTL-M.



Figure 1. Vehicle mounted LTL-M

The LTL-M Retroreflectorometer is mounted on a vehicle (in this case a van) as shown in Figure 1, allowing the surveying of pavement markings to be undertaken at normal traffic

speeds. The equipment specification indicates that the LTL-M will provide 100% coverage of the pavement markings at speeds of up to or equal to 90 km/hr but measurements at higher speeds are possible ⁽²⁾. At speeds of greater than 90 km/hr, the coverage will be less than 100%, the rate depending on the actual speed. As with the LTL-X, the instrument's illumination angle is 1.24° and the reflected light is measured at an angle of 2.29° , which corresponds to an observation distance of 30 metres. The LTL-M defines a pavement marking as an area of the road surface providing a retroreflection of a minimum of $40 \text{ mcd}\cdot\text{m}^{-2}\cdot\text{lx}^{-1}$. A pavement marking is recognised if it is a minimum one-metre long and a minimum five centre metres wide ⁽²⁾.

The LTL-M Retroreflectorometer is certified in accordance with EN1436 + A1:2008 (Road marking materials – Road marking performance for road users). The calibration of the LTL-M Retroreflectorometer is traceable to NIST (National Institute of Standards and Technology, USA) and PTB (Physikalisch – Technische Bundesanstalt, Germany). The LTL-M survey data was collected in accordance with the UK DMRB ⁽⁴⁾ and EN 1436:2007 + A1:2008 ⁽¹⁾.

4 DATA COLLECTION

4.1 LTL-X testing of the Control Site

The control site was tested using the LTL-X on the 21st February 2013 with the assistance of a traffic management mobile lane closure, to ensure the safety of the survey operators. The control site was tested in the eastbound direction using the LTL-X. The weather conditions during testing of the site were dry with no rain or frost on the previous day, the surface of the pavement was also dry. The handheld overall average RL result for the control site was $227 \text{ mcd}\cdot\text{m}^{-2}\cdot\text{lx}^{-1}$ (entire length on the EBCL). These RL results obtained from the centreline marking using the LTL-X in the eastbound direction were used as the reference baseline data for the research project.

4.2 LTL-M testing of the Control Site

The LTL-M was calibrated before each survey cycle as per the manufacturer's specifications. Immediately after each calibration, it was checked against a strip of retroreflective tape of known RL (approx. $170 \text{ mcd}\cdot\text{m}^{-2}\cdot\text{lx}^{-1}$). Typically, each survey cycle comprised of five survey runs in each direction, carried out a nominal test speed of 75 km/hr. The survey data was aggregated into reporting segments of 10 metres and overall section length.

The control site was tested using the LTL-M on 12 separate days, consisting of five days in February and seven days in May 2013. Overall, there were 95 survey runs carried out on the EBCL and 94 survey runs carried out on the WBCL. The majority of runs (75 no.) along the control site were completed in dry weather conditions, while 20 of the runs were completed when damp/wet line marking conditions existed.

The weather and centreline marking (dry/damp/wet) conditions during each of the survey days where recorded. Table 1 shows the dates that the LTL-M surveys were undertaken and summarises the climatic conditions on each day.

Table 1. Climatic Conditions on Control Site

Date	Max Temp (°C)	Min Temp (°C)	Rain (mm)	Weather	Surface
14/02/13	10.4	1.8	0.9	Light Rain	Wet
15/02/13	9.7	0.1	0.3	Light Rain	Wet
18/02/13	9.6	2.7	0	Cloudy	Dry
19/02/13	10.2	1.8	0	Cloudy	Dry
20/02/13	8.8	-0.9	0	Cloudy	Dry
15/05/13	11.6	3.0	1.5	Rain	Wet
16/05/13	12.5	5.3	5.5	Dry	Damp
17/05/13	15.7	5.4	0.1	Cloudy	Dry
21/05/13	16.9	8.4	0	Cloudy	Dry
22/05/13	14.6	7.1	0.1	Cloudy	Dry
23/05/13	13.3	3.8	0	Cloudy	Dry
29/05/13	19.5	5.4	0	Cloudy	Dry

5 DATA RESULTS

5.1 Daily LTL-M Results

The overall average RL values recorded for each run on the centerline marking in the eastbound (EBCL) and westbound (WBCL) directions for each day are shown in Tables 2A to 2D.

Table 2A. February EBCL daily average RL results.

Date	Run 1	Run 2	Run 3	Run 4	Run 5
14/02/2013	181	185	78	167	165
15/02/2013	163	177	159	169	180
18/02/2013	229	222	225	227	225
18/02/2013	220	220	220	227	221
19/02/2013	233	230	234	234	228
19/02/2013	228	232	231	223	221
20/02/2013	234	231	227		

Table 2B. May EBCL daily average RL results

Date	Run 1	Run 2	Run 3	Run 4	Run 5
15/05/2013	232	145			
15/05/2013	235	231	234	223	
16/05/2013	216	205	215	213	
16/05/2013	202	197	205	200	206
17/05/2013	233	223	226	224	
17/05/2013	233	234	229	227	231
21/05/2013	228	226	226	226	232
21/05/2013	232	227	224		
22/05/2013	234	234	233	234	232
22/05/2013	228	230	225	232	234
22/05/2013	234	233			
23/05/2013	220	220	223	230	228
23/05/2013	232	226	232		
29/05/2013	232	232	232	226	228
29/05/2013	226	232	231	228	223

Table 2C. February WBCL daily average RL results

Date	Run 1	Run 2	Run 3	Run 4	Run 5
14/02/2013	231	228	214	184	209
15/02/2013	218	208	218	195	212
18/02/2013	269	266	256	254	258
18/02/2013	254	255	255	259	256
19/02/2013	269	270	269	269	269
19/02/2013	257	256	266	265	265
20/02/2013	258	263			

Table 2D. May WBCL daily average RL results

Date	Run 1	Run 2	Run 3	Run 4	Run 5
15/05/2013	274	247			
15/05/2013	270	273	262		
16/05/2013	248	251	247	257	
16/05/2013	223	238	237	245	239
17/05/2013	265	258	260	257	258
17/05/2013	263	274	260	267	261
21/05/2013	259	266	274	272	269
21/05/2013	261	268	263		
22/05/2013	273	273	273	272	262
22/05/2013	262	258	261	262	272
22/05/2013	270	268			
23/05/2013	260	262	258	263	267
23/05/2013	267	266	265		
29/05/2013	265	265	266	265	259
29/05/2013	259	266	267	266	260

The data obtained from the LTL-M testing provided some interesting results. On initial observation, there seems to be quite a large range in the overall RL values, with maximum and minimum daily averages varying from 274 mcd·m⁻²·lx⁻¹ to 78 mcd·m⁻²·lx⁻¹, respectively. However, on cross referencing with the climatic conditions shown in Table 1, a pattern showing a large degree of variability when the centerline was damp or wet and much better consistency when the line marking was dry becomes apparent. Therefore, the results were split into two groups, with data collected when the pavement surface was dry in one group and data collected when the pavement surface was damp or wet in the second group. It was also observed that the overall section RL average values for the dry weather surveys were very consistent in each direction but, the values in the westbound direction were about 35 mcd·m⁻²·lx⁻¹ higher when compared to the eastbound direction. Therefore, the data was further split into subgroups; tested in eastbound and westbound directions.

6 DATA ANALYSIS

6.1 Overall Dry Weather EBCL Testing

Table 3A shows the average results from the LTL-M testing in the EBCL completed in dry conditions in February while Table 3B shows the corresponding May runs. In terms of overall average RL values collected on the EBCL in February and May, the mobile LTL-M device compares extremely favorably with the average RL value of 227 mcd·m⁻²·lx⁻¹ collected by the hand held LTL-X device in February.

Table 3A. Dry February EBCL RL results

Number of runs	23
Average RL Value	227
Standard Deviation	4.9
Max RL value	234
Min RL value	220

Table 3B. Dry May EBCL RL Results

Number of runs	52
Average RL Value	229
Standard Deviation	4.0
Max RL value	235
Min RL value	220

There were 75 runs completed in dry weather conditions on the EBCL in total. The average 10-metre LTL-M results from each day are plotted by chainage (distance in metres along the length of the section) against the LTL-X results as shown in Figure 2A. It is clear from Figure 2A that there is very good agreement in the profile shape and magnitude of the plotted results, across all of the LTL-M daily averages and when compared to the LTL-X results.

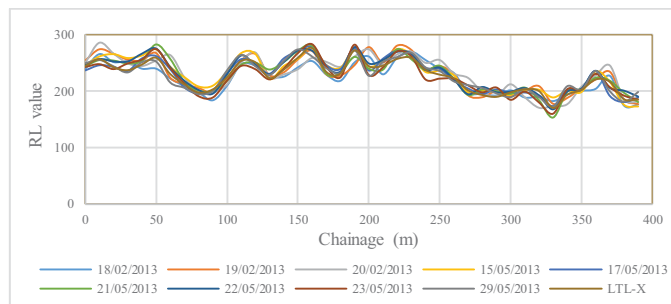


Figure 2A. Dry EBCL: LTL-M v LTL-X comparison

The comparison between the dry data collected along the length of the EBCL (10m averages) for each day, from the LTL-M and LTL-X, using linear regression analysis is shown in Table 3C. The LTL-M data was plotted on the X-axis with the LTL-X data on the Y-axis.

Table 3C. Dry EBCL Regression Analysis

	Weather Conditions	Surface Conditions	Regression Coefficient	Coefficient of Determination
18-Feb	Cloudy	Dry	1.01	0.82
19-Feb	Cloudy	Dry	0.98	0.83
20-Feb	Cloudy	Dry	0.98	0.93
17-May	Cloudy	Dry	0.97	0.91
21-May	Cloudy	Dry	0.98	0.87
22-May	Cloudy	Dry	0.97	0.93
23-May	Cloudy	Dry	1.00	0.87
29-May	Cloudy	Dry	0.99	0.88

In linear regression analysis setting the intercept equal to zero gives a slope, m , such that:

$$y = m.x$$

The regression coefficient (m) indicates that the mobile RL values range from 1% lower than the handheld values to 3% higher than the handheld values across the survey runs for each day. The coefficient of determination (R^2) for each day indicates that the regression line represents the data extremely well. In summary, the analysis of the EBCL data indicates that the mobile LTL-M device gives repeatable and reproducible RL results that are extremely consistent when compared to the handheld LTL-X RL values, in dry weather conditions.

In analysing the individual runs collected with the LTL-M in dry conditions on the same day, the results indicate that the conclusions made above analysis hold up. As an example, there were five runs completed on the February 18, 2013 in dry conditions. These are plotted by chainage against the LTL-X in Figure 2C. The profile and magnitude of the plotted LTL-M results again indicate excellent repeatability and correlation with the LTL-X data.

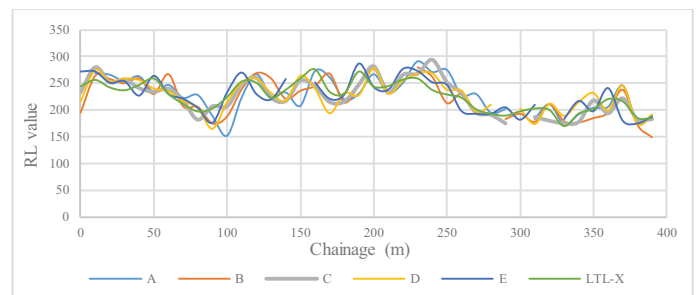


Figure 2C. Dry EBCL18/02/13: LTL-M v LTL-X RL comparison

6.2 Dry Weather WBCL Testing

Table 4A shows the average results from the LTL-M testing in the WBCL completed in dry conditions in February while Table 4B shows the corresponding May runs.

Table 4A. Dry February WBCL RL results

Number of runs	22
Average RL Value	262
Standard Deviation	6.0
Max RL value	270
Min RL value	254

Table 4B. Dry May WBCL RL Results

Number of runs	52
Average RL Value	265
Standard Deviation	5.2
Max RL value	274
Min RL value	256

The range between maximum and minimum values and the standard deviation for the dry May data are also very similar to the February data for the WBCL.

There were 74 LTL-M runs completed along the WBCL in dry weather conditions. The average 10-metre LTL-M results from each day are plotted by chainage in Figure 2A.

Examination of the profile and magnitude of the plotted results shown in Figure 3 along with the overall average results in Tables 4A and 4B again indicate a high level of repeatability and reproducibility in the LTL-M results

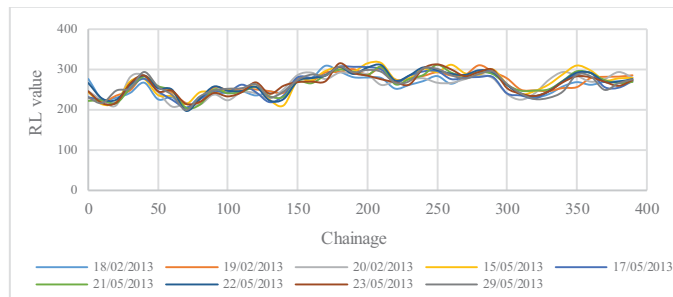


Figure 3. Dry WBCL: LTL-M comparison

The results from the LTL-M WBCL data are on average approximately $35 \text{ mcd}\cdot\text{m}^{-2}\cdot\text{lx}^{-1}$ higher than both the LTL-M and LTL-X EBCL data. The difference in the results between the EBCL and WBCL is highlighted as a curiosity rather than an indication of inconsistency in the results recorded by the equipment, as intuitively it is reasonable to assume that the direction in which the pavement marking is laid can influence the retroreflective properties of the pavement markings. Subsequent correspondence with the equipment manufacturer, Delta, confirmed that they have also observed this on other sites. Currently, the direction in which the centreline on the control site was laid is not known. Further research and analysis incorporating additional runs with the mobile and handheld devices in both directions along lines across multiple sites would be necessary in order to confirm that the direction in which the line is laid does influence the RL values and to determine if this effect can be accurately quantified.

6.3 Wet Weather Testing

It became clear after an initial analysis of the results that data collected when the centreline was wet or damp was very variable. The LTL-M identifies a pavement marking as an area of the road surface providing a retroreflection of a minimum of $40 \text{ mcd}\cdot\text{m}^{-2}\cdot\text{lx}^{-1}$. As the RL results tended to be significantly lower in wet conditions, it was concluded that this was the most likely reason for the device being unable to identify the pavement marking in extremely wet conditions. The analysis of results from successful runs completed in damp or wet conditions are presented as follows.

Table 5A shows the average results from the LTL-M testing in the EBCL completed in wet or damp conditions in February while Table 5B shows the corresponding May runs. Examination of this data shows that there is poor agreement in the average results across both months and the range of values and standard deviations indicate a much higher degree of variability when compared to the dry runs. Overall, the LTL-M reported an RL average value of $160 \text{ mcd}\cdot\text{m}^{-2}\cdot\text{lx}^{-1}$ for February, compared to an average of $200 \text{ mcd}\cdot\text{m}^{-2}\cdot\text{lx}^{-1}$ for May. The maximum and minimum average RL values across both months range significantly from $216 \text{ mcd}\cdot\text{m}^{-2}\cdot\text{lx}^{-1}$ to $78 \text{ mcd}\cdot\text{m}^{-2}\cdot\text{lx}^{-1}$.

Table 5A. Wet February EBCL RL results

Number of runs	10
Average RL Value	162
Standard Deviation	30.7
Max RL value	185
Min RL value	78

Table 5B. Wet May EBCL RL results

Number of runs	10
Average RL Value	200
Standard Deviation	20.6
Max RL value	216
Min RL value	145

Table 6A shows the average results from the LTL-M testing in the WBCL completed in wet or damp conditions in February while Table 6B shows the corresponding May runs. Again, the overall averages for each month, show poor consistency when compared to those carried out in dry weather. Again, the range of values and the standard deviations indicate much greater variability when compared to data collected in dry conditions.

Table 6A. Wet February WBCL RL results

Number of runs	10
Average RL Value	212
Standard Deviation	14.1
Max RL value	231
Min RL value	184

Table 6B. Wet May WBCL RL results

Number of runs	10
Average RL Value	243
Standard Deviation	9.3
Max RL value	257
Min RL value	223

There were 20 runs carried out with the LTL-M in damp or wet line marking conditions during February and May 2013 and a large degree of variability was identified in the results recorded. Further analysis of the data from runs carried out during each day, confirms that the same degree of variability exists in the data collected in damp line marking conditions in a single day. For example, Figure 6A shows data from five LTL-M runs carried out on February 14, 2013 also plotted against the data collected in dry conditions using the handheld LTL-X on February 21, 2013. As is clear from Figure 6A, while there is some agreement in the shape of the profiles, there is significant variance in the magnitude of the RL values recorded. The plots also highlight that the RL data recorded by the LTL-M is consistently lower by varying degrees, than the data recorded by the LTL-M and LTL-X in dry conditions. It is worth noting that based on visual inspections on that particular day; the line marking was observed to be at its wettest during survey run C. This in conjunction with the fact that no reliable data could be collected in extremely wet

conditions would indicate that RL values decrease as moisture levels increase.

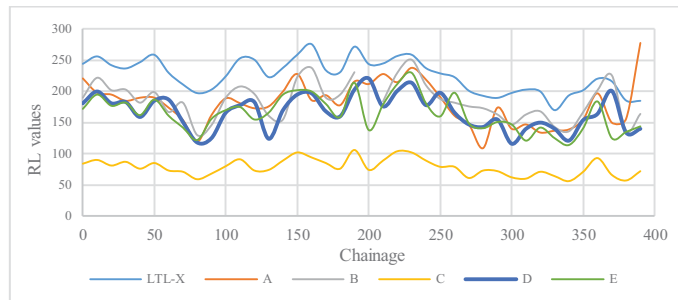


Figure 6A. Wet EBCL LTL-M on 14/02/13 v Dry LTL-X RL

The comparison between the wet data collected along the length of the EBCL (10m averages) for each day from the LTL-M and LTL-X, using linear regression analysis is shown in Table 6C. The LTL-M data was plotted on the X-axis with LTL-X data on the Y-axis.

Table 6C. Wet EBCL Regression Analysis

	Weather Conditions	Surface Conditions	Regression Coefficient	Coefficient of Determination
14-Feb	Raining	Wet	1.45	0.58
15-Feb	Raining	Wet	1.33	0.23
15-May	Raining	Wet	1.52	-0.22
16-May	Dry	Damp	1.09	0.86

In linear regression analysis setting the intercept equal to zero gives a slope, m , such that:

$$y = m.x$$

The regression coefficient (m) indicates that the mobile RL values range from 9% to 52% lower than the handheld values across the survey runs for each day. The coefficient of determination (R^2) for each day indicates that the regression line does not represent the data when the surface is wet, however as the surface dries out the regression line starts to better represent the data. In summary, the analysis of the EBCL data indicates that the more moisture that is present on the surface during testing the less accurate the results become.

The LTL-M completed 10 runs in both February and May in wet or damp weather conditions along the WBCL. Again, the overall averages for each month, as shown in Tables 6A and 6B show poor consistency when compared to those carried out in dry weather. Again, the range of values and the standard deviations indicate much greater variability when compared to data collected in dry conditions.

7 CONCLUSIONS

The Delta LTL-M mobile Retroreflector device was acquired in order to carry out research into its suitability as a device to be introduced and implemented for the measurement of pavement markings in Ireland. A bank of control site data was collected using the LTL-M during the trial period from February to May 2013. In addition, a reference set of data was established using data collected on the same control site using

a handheld LTL-X device. The results of the data analysis shows that the LTL-M displays excellent agreement with the LTL-X, in RL values recorded when the testing occurs in the same direction in dry pavement marking conditions. Evidence from the trials indicate that the direction of survey has some impact on the RL values collected on a pavement marking, possibly due to the direction in which the pavement marking is laid having an impact on its retroreflective properties. It has been established that the LTL-M shows excellent repeatability across multiple runs on the same day and excellent reproducibility in results over time (multiple runs over different days). The research also shows that the level of moisture on the pavement marking has a significant impact on the retroreflective properties of that pavement marking. The wetter the road surface is the more unreliable the RL values are, however as the pavement begins to dry the values get closer to dry surface condition values. More research could be completed to establish the relationship between the moisture level of the pavement surface and the corresponding RL results. However, this would involve the continuous measurement of moisture levels along the pavement surface during surveying as any increase or decrease in moisture levels on the pavement surface during surveying will lead to an increase or decrease in the RL values of the pavement marking. This would lead to an extremely slow and tedious surveying process being established. In addition, external factors such as moisture getting on the LTL-M camera lense while surveying during the rain or splash back from the pavement surface whilst wet can significantly reduce the RL values along the survey route. These factors significantly reduce the validity of the RL values of a pavement marking when surveyed during damp or wet conditions, as it is impossible to establish an accurate baseline to reference all RL values against. In conclusion, the research shows that the LTL-M device assessed in this research is suitable for accurate and reliable mobile retroreflectivity measurement of pavement markings in Ireland, when carried out in dry conditions.

REFERENCES

1. IS EN1436 – 2007 + A1:2008, Road marking materials – Road marking performance for road users, August 2007.
2. Delta, LTL-M Mobile Retroreflectometer User Manual – Version 1.05 English, Nov 2011.
3. Delta, LTL-X Retroreflectometer Manual – Rev. 15, August 2012.
4. Highways England, UK DMRB TD 26/07 Vol 8, Section 2, Part 2, Inspection and maintenance of road markings and road studs on motorways and all-purpose trunk roads, May 2007.

The Use of Average Least Dimension in Surface Dressing Design.

Brian Mulry, BE, MEngSc, CEng, MIEI, MIAT ¹

Dr. Kieran Feighan, BE, MSCE, Ph.D, CEng, FIEI ²

Tom Casey, BSc, MBA, CEng, FIEI ³

¹PMS Pavement Management Services Ltd., Raheen Industrial Estate, Athenry, Co. Galway

²PMS Pavement Management Services Ltd., Orion House, 53 Main Street, Rathfarnham, Dublin 14

³Transport Infrastructure Ireland, Parkgate Business Centre, Parkgate St, Dublin 8

ABSTRACT: Surface dressing is the application of a thin layer of bituminous binder and single-sized aggregate chippings to the surface of a road, in one or more layers. The technique has been widely used on Irish roads for many years to improve skid resistance, seal the road surface and to arrest deterioration. The procedure has become increasingly important since the introduction of standards for skidding resistance on National roads by Transport Infrastructure Ireland (TII). TII are currently developing a new analytical design approach for surface dressing on National roads.

Based on best practice in other countries, an essential parameter used in the analytical design of surface dressing is the Average Least Dimension (ALD) of the aggregates used. The ALD is used to determine the optimum rates of spray of binder and rates of spread of chippings for surface dressing. The purpose of this research study carried out in 2015 was to determine the most appropriate way of calculating the ALD using surface dressing aggregates from Irish quarry sources. A total of five different methods were examined, two direct measurement methods and three computational methods. The direct measurement methods used included the use of a new device developed in South Africa to automatically measure ALD. The data for the study was collected by sampling and testing four different aggregate sizes from eight quarry sources nationwide. The testing included the determination of particle size distribution and flakiness index for each sample, in addition to determining the ALD by each of the five methods.

This paper will outline the findings of the research study undertaken including an analysis of the range of ALD values obtained for Irish quarry sources, and a comparison of the three computational methods of estimating ALD against the direct measurement methods. In addition, the paper will recommend a method for calculating the ALD of Irish aggregates to be used in surface dressing.

KEY WORDS: Surface Dressing; Average Least Dimension; Irish Aggregates; Analytical Design Procedure, National Roads.

1 INTRODUCTION

Surface dressing has been used extensively in Ireland for many years for the upkeep and maintenance of road pavements including national routes. In addition, expenditure on surface dressing represents a significant proportion of the road maintenance budget each year. It is therefore essential that surface dressings are properly designed to ensure they are durable for their expected life, provide value for money and maximise the return on investment.

A surface dressing consists of the uniform application of a thin layer of bituminous binder and single-sized aggregate chippings to the surface of a road, in one or more layers. The technique has been widely used on Irish roads to improve skid resistance, seal the road surface and to arrest deterioration. The procedure has become increasingly important since the introduction of the HD28/11 "Management of Skid Resistance" standard for skidding resistance on National roads published by the Transport Infrastructure Ireland (TII), formerly the National Roads Authority (NRA) in 2011 [1]. In this regard, TII are developing a new analytical design approach for surface dressing on National roads. The approach will be incorporated in an upcoming revision of HD300/15 "Design of Bituminous Mixtures, Surface Treatments, and Miscellaneous Products and Processes" [2].

Based on research and best practice in other countries, an essential parameter used in the analytical design of surface dressing is the Average Least Dimension (ALD) of the aggregates used. The ALD is used to determine the optimum rates of spread of binder and chippings for surface dressing.

The purpose of the research study was to determine the most appropriate method of calculating the ALD for surface dressing aggregates from Irish quarry sources. A total of five different methods were examined, two direct measurement methods and three computational methods. The objectives of the research were to assess the range of ALD values for Irish quarry sources, to compare the three computational methods of estimating ALD against the direct measurement methods, and to recommend a computational method for calculating ALD. The data for the study was collected by sampling and testing 4 different aggregate sizes from 8 quarry sources nationwide. The testing included the determination of particle size distribution and flakiness index for each sample, in addition to determining the ALD by each of the five methods.

The paper will outline the findings of the research study undertaken including an analysis of the range of ALD values obtained for Irish quarry sources, and a comparison of the three computational methods of estimating ALD against the direct measurement methods. In addition, the paper will

recommend a method for calculating the ALD of Irish aggregates to be used in surface dressing.

The findings of the research have been used to carry out surface dressing trials at 12 sites in six local authorities. The outcomes of these trials will be used to finalise the Surface Dressing Analytical Design procedure which will be incorporated in an upcoming revision of HD300/15 [2].

2 BACKGROUND

Following an extensive literature review and study of best practice in other countries, it became clear that a key parameter used in the analytical design of surface dressing is the Average Least Dimension (ALD) [3, 4, 5, 6].

The surface dressing design methods used in Australia and New Zealand are based on work originally conducted by Hanson (1935) who developed an engineering approach to the selection of optimum rates of spread of binder and chippings for surface dressing [3, 4]. The procedure considered the volume of voids between the chippings after spreading and rolling, and the orientation the chippings adopt after trafficking. Hanson found that after construction and trafficking compaction, chippings will orient to the flattest direction and thereby adopt a position whereby their least dimension is vertical, hence giving rise to the concept of Average Least Dimension (ALD) as shown in Figure 1. To ensure that the aggregate chips are not submerged in binder during service, the average least dimension of the aggregates is used to determine an appropriate rate of spread of aggregate and binder [3].



Figure 1. Orientation of Chippings After Trafficking [7].

As shown in Figure 2, Hanson's main observations were that:

1. Chippings when initially placed loose on the binder had a percentage voids of approximately 50%, which reduced to around 30% after construction rolling, and further reduced to about 20% under traffic compaction. This resulted in a single layer of chippings that bedded in with shoulder-to-shoulder contact after trafficking.
2. The amount of binder to be used is related to the volume of voids in the covering aggregate. Sufficient binder should be added so that between 65 to 70% of the voids are filled with binder when the aggregate is fully compacted under traffic.
3. The average depth of the aggregate layer after construction and traffic compaction is approximately equal to the ALD of the aggregate chippings used.

The least dimension of an aggregate particle is the smallest perpendicular distance between two parallel plates through which the particle will just pass. The average least dimension is the arithmetic mean of all the measured least dimensions of the aggregate particles measured [5]. There is significant overlap with the flakiness index, used for many years as an aggregate characteristic in surface dressing design in Ireland, but international practice has shown that the flakiness index alone does not fully capture the shape properties required.

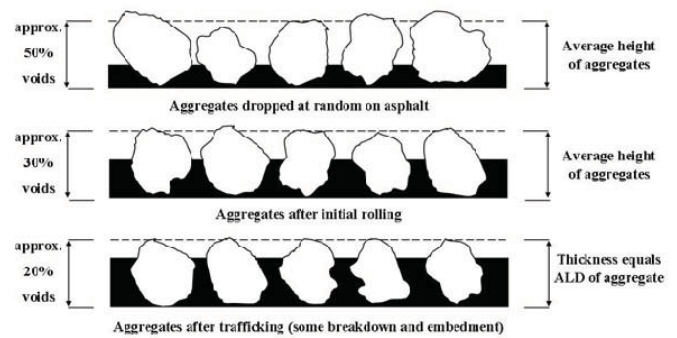


Figure 2. States of Embedment of Surface Dressing Chippings [2, 4].

Accordingly, it was decided to conduct research to determine the most appropriate way of calculating the ALD using surface dressing aggregates from Irish quarry sources.

3 METHODS USED FOR AVERAGE LEAST DIMENSION

A total of five different methods were examined, two direct measurement methods and three computational methods.

3.1 Direct Measurement Methods

In the two direct measurement methods, the ALD of an aggregate sample was determined by measuring the least dimension of every particle in a 200 chip representative sample of the overall sample, and dividing the total of the least dimensions by the number of particles measured. The direct measurement method was carried out in accordance with the test standard TMH1 Method B18(a) [5].

The first direct measurement method consisted of physical measurement whereby the least dimension of each of the 200 representative chippings was physically measured using a Vernier calipers. This method is extremely slow, tedious and time-consuming, and in reality provides a baseline with which other faster methods of ALD computation can be compared.

The second direct measurement method is a variation on the first, and consisted of machine measurement using a device developed in South Africa to automatically taking dimension measurements of the 200 representative chippings as shown in Figure 3. The machine is operated using a computer, software and a control unit with the ALD value automatically calculated. This machine method is significantly faster than the Vernier calipers measurement, and effectively provides a more efficient method of generating a baseline ALD for comparison with the computational methods, but it is still much too time-consuming for routine measurement of ALD.



Figure 3. ALD Machine.

3.2 Computational Methods

Three computational methods of estimating ALD were examined, and compared to the results obtained from the manual and mechanical measurements of ALD.

The first computational method uses a Nomograph as shown in Figure 4 [6, 7]. The Nomograph uses two key input parameters determined from routine laboratory testing, the median particle size and the flakiness index of aggregate in the sample. The median particle size is defined as the sieve size that 50% of the sample will pass through, and is determined by interpolation from a grading analysis using a full set of sieves.

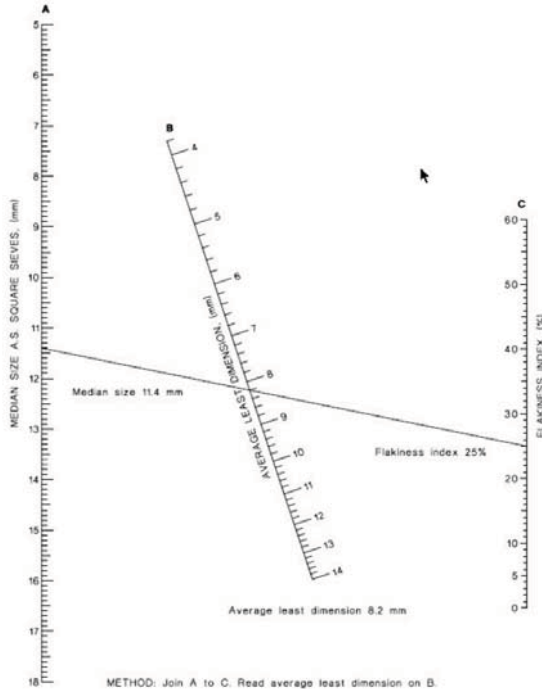


Figure 4. Shell Nomograph [6, 7].

A second computational approach investigated the use of an equation developed to replicate the results obtained from the Nomograph [3]. The key input parameters are again flakiness index and median particle size. The equation is

$$ALD = (M_e) / (1.139285 + (0.11506 \times FI)) \quad (1)$$

where:

M_e = Median Particle Size (mm)

FI = Flakiness Index (%)

Finally, a new and more complex computational approach developed by Dumas in South Africa was investigated [8]. In the cases of the Nomograph and Nomograph equation methods, the median particle size is the only variable which describes the particle size distribution of the aggregates. The underlying principle of the Dumas method is that the median on its own cannot fully reflect the characteristics of the particle size distribution. Hence, more information is required in addition to the median.

The approach taken in essence is to characterise the particle size distribution based on percentage passing and percentage

retained on five sieves, rather than the single interpolated sieve used to define median particle size. The Dumas approach is based on examination of the percentage retained (PR) from the gradation analysis for five different PR values, 10%, 25%, 50%, 75% and 90%. The PR values are used to determine the degree of peakiness (K-value) and degree of symmetry (S-value) which are used together with the median value (M_e), flakiness index (F_i) and fraction not measured (F_r) to calculate the ALD [8, 9]. The calculation process described by Dumas is quite complex, but has been developed in this research through a Microsoft Excel spreadsheet, with the calculated ALD values derived directly from the full gradation analysis results and the flakiness index. The full Dumas equation and values required for this computational method are outlined in the test standard TMH1 Method B18(b)T [9].

4 SAMPLING AND TESTING OF SURFACE DRESSING CHIPS

4.1 Sampling

Pavement Management Services Ltd. (PMS) was commissioned by TII to carry out sampling and laboratory testing of 6mm, 10mm, 14mm and 20mm nominal size chippings from eight quarry sources nationwide. The sampling was carried out from stockpiles in each quarry in accordance with IS EN 932 Part 1 [10]. The quarry sources are labelled A to H. The sources selected typically provide chippings of high polished stone value (PSV) for surface dressing on National routes. The samples were taken from stockpiles at each quarry in March 2015, with 29 quarry source/aggregate size samples taken in total. The samples were taken in 20kg sample size bags. Table 1 shows a summary of the number of 20kg samples by size taken at each quarry.

Table 1. Summary of Quantity Sampled.

Source	Number of Samples (20kg) Taken by Size			
	20mm	14mm	10mm	6mm
Quarry A	2	2	2	1
Quarry B	2	2	2	1
Quarry C	N/A	2	N/A	1
Quarry D	2	2	2	1
Quarry E	2	2	2	1
Quarry F	2	2	2	1
Quarry G	N/A	2	2	1
Quarry H	2	2	2	1
Total	12	16	14	8

N/A = Not Available

4.2 Sample Reduction

The bulk samples taken in the quarries for each nominal size of aggregate were reduced down to a workable quantity and to obtain a representative sample of chippings for the laboratory testing using a riffle box procedure in accordance with IS EN 933 Part 2 [11]. The various sizes of aggregate chippings were split down into the following approximate test sample quantities for each test:

Grading and Flakiness Index:

- 5.0kg samples for 20mm aggregate
- 2.5kg samples for 14mm aggregate
- 1.5kg samples for 10mm aggregate
- 0.5kg samples for 6mm aggregate

Average Least Dimension (ALD):

- 10kg of each aggregate size

4.3 Laboratory Testing

The grading analysis and flakiness index were carried out on the 6mm, 10mm, 14mm and 20mm aggregate samples from each quarry source. The grading analysis was carried out in accordance with IS EN 933 Part 1, and the flakiness index was determined in accordance with IS EN 933 Part 3 [12, 13].

The ALD was determined for the 10mm, 14mm and 20mm aggregate samples from each quarry source in accordance with the direct measurement method specified in TMH1 Method B18(a) [5]. The ALD was assessed by measuring the least dimension of every particle in a representative sample and dividing the total of the least dimensions by the number of particles measured. The measurements were recorded using the automated ALD machine shown in Figure 3 for all of the 10mm, 14mm and 20mm aggregate samples.

To obtain a representative sample of chippings for the ALD test, the test samples of aggregate were washed using a 2mm sieve and dried off. The test samples were then further split down using a riffler to such a size as to give at least 200 aggregate particles in each representative sample. The sample was then sieved through a sieve of aperture size that is half the nominal size of the aggregate to be tested and the particles passing through the sieve were discarded. Using the ALD device, the smallest dimension of each particle retained on that sieve is measured to the nearest 0.1mm and the measurements and number of particles measured is recorded.

The ALD is calculated to the nearest 0.01mm as follows

$$\text{Average least dimension (mm)} = A/B \quad (2)$$

where:

A = sum of the smallest dimension of all the particles (mm)

B = number of particles

The ALD value is reported to the first decimal place. The average least dimension was also determined by manual measurement, whereby the least dimension of each of the 200 representative chippings was physically measured using a Vernier calipers on four randomly selected test samples of aggregate for comparison with the ALD device results.

5 ANALYSIS OF RESULTS

5.1 Median Size and Flakiness Index Results

The median particle size (M_c) and flakiness index (FI) results for each aggregate sample are given in Table 2. The M_c and FI values were used to compute the ALD values for each sample using the Nomograph and the Nomograph equation. The M_c and FI values were also used together with the calculated PR, values to compute the ALD using the more complex Dumas equation [8, 9].

Table 2. Median Particle Size and Flakiness Index Values.

Quarry	Nominal Size (mm)	Median Size (mm)	Flakiness Index (%)
Quarry A	20	15.8	14.2%
	14	11.6	8.6%
	10	8.0	11.0%
	6	4.8	13.0%
Quarry B	20	15.2	11.7%
	14	12.1	17.5%
	10	7.8	23.0%
	6	4.3	21.9%
Quarry C	14	11.7	11.6%
	6	5.0	27.5%
Quarry D	20	15.8	9.9%
	14	11.7	30.0%
	10	7.8	13.2%
	6	3.9	15.7%
Quarry E	20	17.4	6.6%
	14	11.2	12.9%
	10	8.3	18.1%
	6	5.0	20.7%
Quarry F	20	16.7	8.9%
	14	12.0	13.4%
	10	7.6	20.7%
	6	5.1	16.7%
Quarry G	14	11.5	13.6%
	10	8.4	15.6%
	6	4.6	31.3%
Quarry H	20	16.0	15.6%
	14	11.4	16.4%
	10	7.8	14.5%
	6	4.7	32.4%

5.2 Comparison of Machine ALD and Manual ALD

The ALD values obtained for the four sets of measurements made using the automated ALD machine and the Vernier calipers are shown in Table 3. The results of the manual measurements compare very well with the results from the ALD machine. The marginal differences between the two sets are well within the typical variability in ALD measurement encountered in practice. As outlined earlier, the automated ALD approach is considerably faster than the manual measurement and accordingly, the automated measurement approach was used for the remainder of the baseline measurements.

Table 3. Machine versus Manual ALD measurements.

Quarry	Nominal Size (mm)	Machine ALD (mm)	Manual ALD (mm)
Quarry B	20	11.7	12.2
Quarry D	20	12.0	12.2
Quarry E	14	7.9	8.2
Quarry G	10	5.7	5.9

5.3 Analysis of ALD Results

The compiled results for the ALD direct measurement and computational methods undertaken as part of this research are given in Table 4. The ALD values obtained for the eight Irish quarry sources ranged from 3 mm to 14 mm. This range of values are in the range covered by the Nomograph shown in Figure 4, and are similar to values calculated and used in other countries including Australia, New Zealand and South Africa.

Linear regression was used to perform the statistical analysis of the data from the study [14]. The regression and statistical data analysis was carried out using Microsoft Excel, and MINITAB, a widely used statistical package.

Table 4. Summary of ALD Results.

Quarry	Nominal Size (mm)	Automated ALD (mm)	Nomograph ALD (mm)	Nomograph Equation ALD (mm)	Dumas Equation ALD (mm)
Quarry A	20	11.9	11.9	12.1	11.5
	14	8.8	9.4	9.4	8.9
	10	5.6	6.4	6.3	6.0
Quarry B	20	11.7	11.6	11.9	11.6
	14	7.8	9.0	9.0	8.6
	10	5.4	5.6	5.5	5.3
Quarry C	14	8.7	9.2	9.2	8.8
	20	12.0	12.4	12.6	11.9
Quarry D	14	8.5	7.8	7.9	7.4
	10	5.6	6.2	6.1	5.4
	20	12.5	N/A	14.3	13.4
Quarry E	14	7.9	8.7	8.7	8.2
	10	5.4	6.2	6.1	5.9
	20	12.9	13.0	13.5	12.6
Quarry F	14	9.3	9.2	9.3	8.9
	10	5.1	5.5	5.5	5.3
	20	12.9	13.0	13.5	12.6
Quarry G	14	8.1	8.9	8.9	8.4
	10	5.7	6.5	6.4	5.9
	20	11.2	11.8	12.1	11.7
Quarry H	14	8.4	8.5	8.6	8.1
	10	5.0	6.0	6.0	5.3
	20	11.2	11.8	12.1	11.7

5.4 Comparison of Nomograph ALD and Nomograph Equation ALD

The ALD data calculated from median particle size and flakiness index results for each sample using the Nomograph and the Nomograph equation are plotted in Figure 5. There was very good agreement between the ALD values from both methods with a very high R^2 of 99.7%. The regression equation without an intercept is given by:

$$\text{Nomograph Equation ALD} = 1.0097 \times \text{Nomograph ALD} \quad (3)$$

These results indicate that the Nomograph equation gives effectively identical results to the Nomograph. It is much quicker and more efficient to use the equation rather than the Nomograph, and hence it is recommended that the Nomograph equation be adopted for use in preference to the Nomograph.

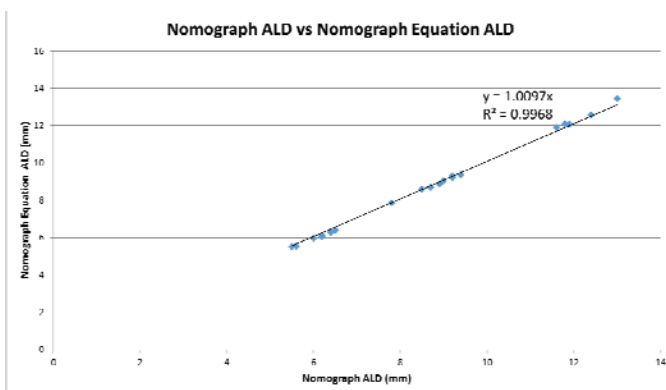


Figure 5. Plot of Nomograph ALD Versus Nomograph Equation ALD.

5.5 Comparison of Nomograph Equation ALD and Dumas Equation ALD with Automated Machine ALD

The main purpose of the research was to determine the most appropriate method of computation of ALD for Irish aggregates. The ALD values obtained using the automated ALD machine was used as the baseline data. Figure 6 shows a plot of the Automated ALD (X-axis) versus the ALD computed using the Nomograph equation and the Dumas equation. As can be seen, there is a strong linear relationship with both computed ALD values.

The Dumas approach yields a slightly higher R^2 at 97.4% versus 97.1% for the Nomograph equation. The two computational methods do give different results, with a clear separation in the trend lines visible in Figure 6.

Figure 7 shows the same data as Figure 6, but this time with a “forced” regression having a zero intercept. It is clear from Figure 7 that the Dumas computed ALD yields an almost exact 1:1 relationship with the automated ALD. The slope of the regression line is 1.0059, with a very high R^2 of 97.3%. The slope of the regression line between the Nomograph equation ALD and the automated ALD is significantly higher, at 1.063, and has a slightly lower R^2 value of 96.8%. There is still a very good correlation between the two sets of ALD results, but the Dumas relationship is preferable.

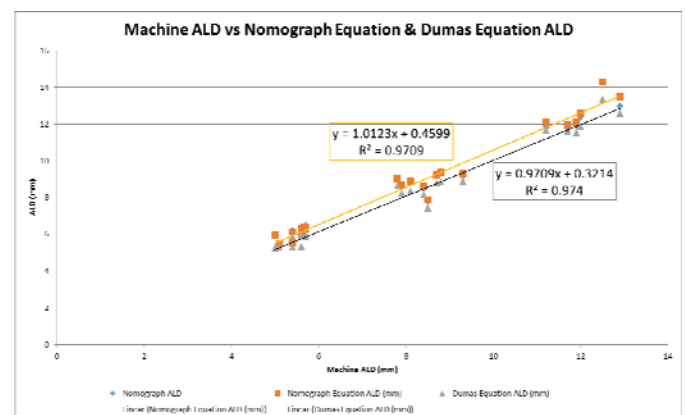


Figure 6. Plot of Machine ALD Versus Nomograph Equation and Dumas Equation ALD.

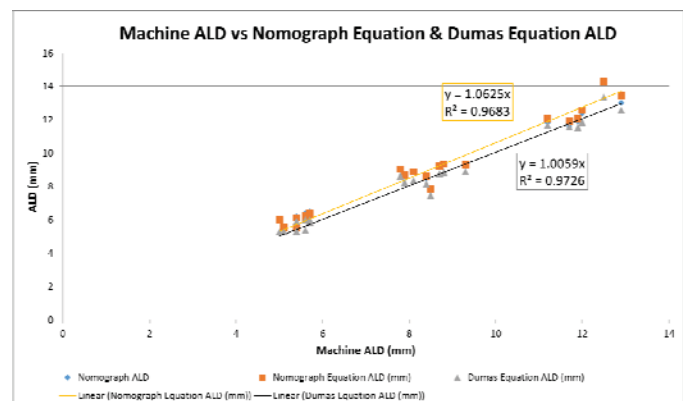


Figure 7. Plot of Machine ALD Versus Nomograph Equation and Dumas Equation ALD (no intercept).

The residual errors between the observed and the fitted values for the regression analysis of Machine ALD versus Dumas equation ALD are shown in Figure 8 with almost all of the residuals between -0.5mm and $+0.5\text{mm}$.

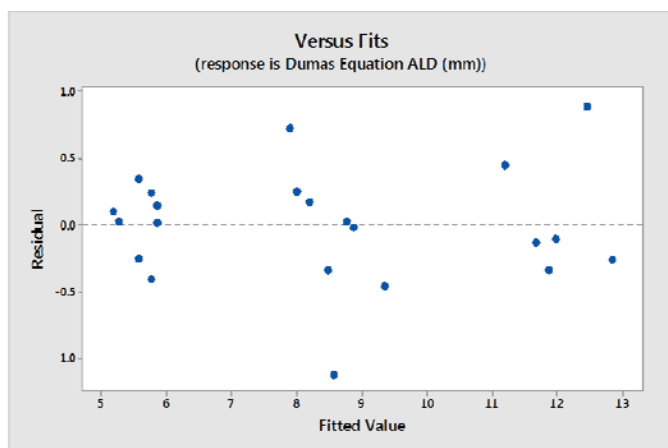


Figure 8. Residual Plots for Regression Analysis of Machine ALD Versus Dumas Equation ALD.

6 CONCLUSIONS

TII are developing a new analytical design approach for surface dressing on National roads which will be incorporated in an upcoming revision of HD300/15. The Average Least Dimension (ALD) of the chippings used is an essential parameter in the analytical design procedure.

A large scale research project was undertaken to investigate the use of the ALD parameter in analytical Surface Dressing design in Ireland and to determine the most appropriate way of calculating the ALD for Irish aggregates. A total of five different methods were examined, two direct measurement methods and three computational methods. The objectives of the research were to assess the range of ALD values for Irish quarry sources, to compare the three computational methods against the direct measurement methods, and to recommend a computational method for calculating ALD.

Testing was carried out on 10 mm, 14 mm and 20 mm aggregates sourced from eight Irish quarries that supply large volumes of aggregate to surface dressing operations. A new device developed in South Africa to automatically measure ALD was used in the study to provide the baseline data for comparison with the computational methods. The computed ALD values were obtained from the gradation and flakiness index results using a direct Nomograph approach, an equation approach based on the Nomograph, and a more complex computational approach developed by Dumas in South Africa.

The ALD values obtained for the eight quarry sources ranged from 3 mm to 14 mm which were in the range covered by the Shell Nomograph, and are similar to values seen in other countries including New Zealand, Australia and South Africa.

The analysis of the Irish results showed that the Nomograph equation gave virtually identical results to the direct Nomograph results. Accordingly, it is recommended that the

equation should be adopted in preference to the Nomograph as it is quicker to use and less subject to variation.

The Nomograph equation ALD and the Dumas equation ALD both showed good agreement with the machine measured ALD, with the Dumas equation showing a better overall relationship. Based on examination of regression results, it is recommended that the Dumas approach should be used to determine the computed ALD as it more fully reflects the characteristics of the particle size distribution of the aggregates, and it gives a better relationship to the actual measured ALD. Using the Dumas method, the ALD can be accurately calculated using results from standard gradation and flakiness index laboratory testing for surfacing dressing aggregates.

The findings of the research have been used to carry out surface dressing trials in August/September 2015 at 12 sites in six local authorities. The outcomes of these trials will be used to finalise the Surface Dressing Analytical Design procedure which will be incorporated in an upcoming revision of HD300/15 [2].

REFERENCES

- [1] NRA Design Manual for Roads and Bridges, Volume 7: Pavement Design and Maintenance, Management of Skid Resistance, Section 3, Part 1, NRA HD 28/11, National Roads Authority, Ireland, November 2011.
- [2] NRA Design Manual for Roads and Bridges, Volume 7: Pavement Design and Maintenance, Design of Bituminous Mixtures, Surface Treatments, and Miscellaneous Products and Processes, Section 2, Part 6, NRA HD 300/15, March 2015.
- [3] National Cooperative Highway Research Program (NCHRP) Report 680, Manual for Emulsion-Based Chip Seals for Pavement Preservation, Transportation Research Board, Washington DC, 2011.
- [4] Transit NZ, RCA, Roading NZ, Chipsealing in New Zealand, Transit New Zealand, Road Controlling Authorities, Roading New Zealand, Wellington, New Zealand, 2005.
- [5] TMH1 Method B18(a), The Determination of the Average Least Dimension of Aggregates by Direct Measurement, Standard Test Methods, Technical Methods for Highways, Pretoria, South Africa, 1986.
- [6] Jackson G. P., Surface Dressing. Bitumen Division, Shell International Petroleum Co. Ltd., London, 1963.
- [7] The Shell Bitumen Handbook (5th Ed.), D. Whiteoak, Shell Bitumen UK, July 1990, 281-292.
- [8] Dumas, B., Determination of the Average Least Dimension of Surfacing Aggregates by Computation, Proceedings of the 8th Conference on Asphalt Pavements for Southern Africa (CAPSA'04), Sun City, South Africa. September 2004.
- [9] TMH1 Method B18(b)T, Computational Method for the Determination of the Average Least Dimension of Surfacing Aggregates, Technical Methods for Highways, Pretoria, South Africa, 2001/03.
- [10] IS EN 932 Part 1: 1997; Test for General Properties of Aggregates – Part 1: Methods for Sampling, National Standards Authority of Ireland, 1997.
- [11] IS EN 932 Part 2: 1999; Test for General Properties of Aggregates – Part 2: Methods for Reducing Laboratory Samples, National Standards Authority of Ireland, 1999.
- [12] IS EN 933 Part 1: 2012; Test for Geometrical Properties of Aggregates – Part 1: Determination of Particle Size Distribution – Sieving Method, National Standards Authority of Ireland, 2012.
- [13] IS EN 933 Part 3: 2012; Test for Geometrical Properties of Aggregates – Part 3: Determination of Particle Shape - Flakiness Index, National Standards Authority of Ireland, 2012.
- [14] Applied Linear Statistical Models, Michael H. Kutner, John Neter, Christopher J. Nachtsheim, William Li, McGraw-Hill College, 5th Edition, November 2004.

Assessing aerodynamic performance in cycling using computational fluid dynamics

Paul Mannion¹², Eoghan Clifford¹², Bert Blocken³⁴, Magdalena Hajdukiewicz¹²

¹Department of Civil Engineering, National University of Ireland Galway, University Road, Galway, Ireland

²Informatics Research Unit for Sustainable Engineering (IRUSE), Ireland

³Department of the Built Environment, Eindhoven University of Technology, Eindhoven, The Netherlands

⁴Department of Civil Engineering, KU Leuven, Belgium

Email: p.mannion10@nuigalway.ie, eoghan.clifford@nuigalway.ie

ABSTRACT: Aerodynamic resistance is one of the leading challenges to overcome in elite cycling. To optimize cycling aerodynamics, estimates must first be made by means of wind tunnel testing, computational fluid dynamics or track testing. Computational fluid dynamics (CFD) is an emerging field in analysing cycling aerodynamics. Wind and urban physics create conditions difficult to model in a wind tunnel environment, and while physical track and/or velodrome testing occurs in actual cycling environments, it is difficult to control and quantify all influencing environmental factors. CFD allows for complete control over all model parameters. It also allows for controlled flow conditions to quantify small aerodynamic performance improvements through changes in athlete posture/equipment along with extensive measurement capabilities. Modelling cyclists and other vulnerable road users in urban environments can complement urban designs and strategies to enhance pedestrian/cyclist safety in high wind conditions. Additionally, modelling the aerodynamics of bluff body objects such as a cyclist's body follows a similar procedure to modelling the airflow over complex structures. This paper presents not only an in-depth survey of existing CFD research on cycling aerodynamics and its impact on the cycling community, but also highlights gaps in knowledge regarding cycling aerodynamics and suggests a methodology for future research to follow.

KEY WORDS: Urban Physics; Aerodynamics; Computational Fluid Dynamics; Wind tunnel; Cycling.

1 INTRODUCTION

There are several different resistive forces affecting the performance of cyclists; aerodynamic resistance, road gradient, rolling resistance, drive train and wheel bearing resistance. However, aerodynamic improvements, particularly on flat to rolling terrain, offer the greatest potential for improvements in cycling speed [1]. For example, at speeds in excess of 50 km/h the aerodynamic resistance is up to 90% of the total resistance experienced by the cyclist [2]. It is evident over the history of cycling, that significant performance gains have been made, primarily due to the advancement of technology and the understanding of the underlying physics. For example, a performance improvement index was developed by Haake [3], to allow for comparison between athletes, and for a comparison between sports; a higher index indicating a greater improvement in the sport. The results for cycling are impressive, with a 221% increase in the International Cycling Union (UCI) one-hour track cycling record over 111 years. Furthermore, the 4-km individual pursuit improved by 35% over 32 years.

Studying the flow field around a cyclist can be challenging. Performing smoke tests in a wind tunnel can shed some light on the complex flow interactions. However, wind tunnel testing often presents aerodynamic improvements solely through evaluating drag reduction, as detailed flow fields can be difficult to obtain [4]. Computational fluid dynamics (CFD) tools can be a useful asset to study whole flow field data. CFD provides the ability to analyse the wake flows of athletes; thus, identifying the causes of drag. The benefits of CFD are now being widely recognized within the cycling industry. The use of CFD tools is also well established within motorsport. Other elite sports such as swimming,

skiing, bobsleighs and to some extent running have also embraced its potential [5]–[8]. Olympic gold medals can be won by tenths of a second [7], and it is possible to use CFD to realise aerodynamic enhancements which lead to additional speed or time savings. Advances over the past two decades in computer hardware have had positive impacts on the utilisation of CFD for sports aerodynamics research, from motor sport applications to summer and winter Olympic sports [9]. A key aim of aerodynamic testing is discovering new cycling positions that conform to the UCI rules while providing aerodynamic benefits. Similar procedures have been found to be successful in other sports such as bobsleigh aerodynamics. Computational modelling in bobsleighs on the positioning of the internal crew members yielded significant aerodynamic benefits without breaching regulations [6].

2 CFD METHODOLOGY FOR CYCLING

CFD has become one of the greatest assets in understanding cycling aerodynamics in recent years. Detailed flow-field information can be attained along with drag force detail on individual components. Defraeye et al. [4] assessed the accuracy of CFD for cycling applications. A scale model of a cyclist was used to validate CFD models using wind tunnel experiments. In addition to three-component forces and moments, high-resolution surface pressure measurements were taken from the scale models surface at 115 locations, which provided detailed information on the flow field. The data provided from the wind tunnel tests are used to compare the performance of several Reynolds-Averaged Navier Stokes (RANS) turbulence modelling techniques, large-eddy simulations (LES), and low-Reynolds number modelling (LRNM) and wall functions for boundary layer modelling

techniques. The RANS shear-stress transport (SST) $k-\omega$ model provided the best overall performance, followed closely by LES. LES provides valuable transient information but at a high computational cost. Furthermore, the additional temporal sensitivity analysis that is required makes LES less attractive for practical calculations. LRNM held the best performance to model the boundary layer in comparison to wall functions. Only the rider was modelled in this research, with high resolution 3D scanning providing the geometrical information required.

Drawn on previous best practices, Figure 1 proposes a methodology for the aerodynamic analysis of sports equipment and athletes using CFD. This methodology also is applicable to various urban physics fluid related problems.

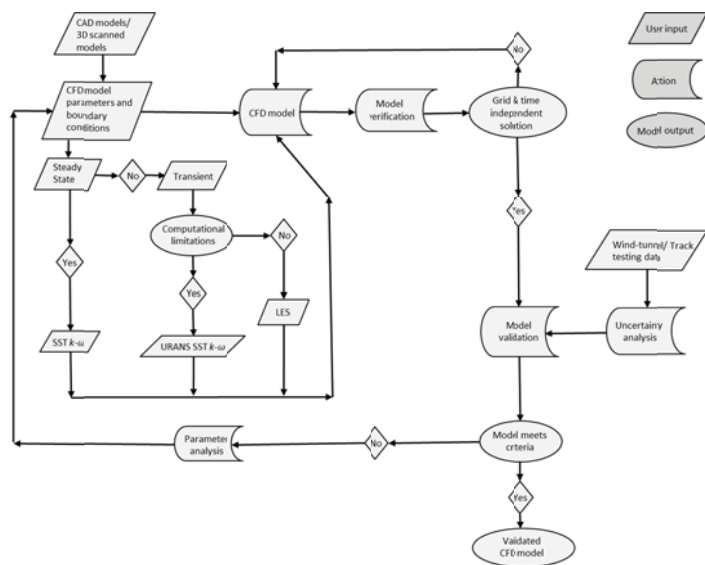


Figure 1. A proposed flowchart methodology for aerodynamics analysis of cycling using CFD.

3 WINDTUNNEL VALIDATION METHODS FOR CFD MODELS

Wind tunnel testing can provide aerodynamic drag and moment characteristics as well as providing opportunities for flow visualization. A multi-component force sensor is used to determine the drag and additional yaw forces and moments acting on the cyclists. Wind tunnel testing can be relatively expensive and requires further investment where flow visualization is required. Flow visualization techniques can yield information on why different cycling positions generate less drag, providing a means to further lower the drag profile of a cyclist. There are various methods available for flow visualization in wind tunnel testing, smoke tests being the most common. Oil and ink flow methods are also common. Crouch et al. [10] demonstrated how aerodynamic drag can be assessed from the perspective of the fluid through which the cyclist moves. Such techniques provide more information regarding how drag forces are generated. Crouch et al. [10] also studied the evolution of the wake around the crank cycle using a quasi-steady approach in wind tunnel experiments, discovering that the dominant mechanism affecting large variations in drag from the rider's legs is not the variation in the frontal surface area over the pedal stroke, but the large

change in the flow structure over the crank cycle [10], [11]. It was concluded that there is the potential to improve rider aerodynamics through a targeted approach at reducing the drag associated with the vortices flow structures developed from locations on the rider's body. This research utilized various wind tunnel flow visualization techniques such as a series of detailed time averaged velocity field wake surveys, skin friction flow visualizations, wool tuft flow visualizations, and time averaged surface pressure measurements for varying leg positions.

Chowdhury et al. [12], [13] developed one of the most recent full scale testing methodologies for the measurement of aerodynamic properties as a function of cyclist's body positions along with various cycling accessories under a range of air flow velocities. Both static and dynamic testing can be performed using this methodology in a suitable wind tunnel. A six-component force sensor under the platform provides force and moment measurements. Repeatable crosswind testing may be conducted with the aid of a camera system for consistent athlete posture positioning. A drawback of this methodology however is the lack of loaded rotors to provide a set resistance to the cyclist under dynamic testing conditions, along with the inability to transfer the rotation to the front wheel, which has been widely used elsewhere in the literature [14]–[16]. García-López et al. [17] addressed the sensitivity of aerodynamic drag in wind tunnel testing with recommendations for future research which is applicable to other researchers. These include pedalling at a race pace to adequately represent the mean power maintained over the course of the event. The front wheel should be allowed to rotate at the same pace as the rear wheel. The bicycle should be fixed to a valid power meter that allows lateral movement of the bicycle-cyclist system, and synchronization of the force balance and the bicycle's crank. The system used by Defraeye et al. [18] is presented in Figure 2. A methodology for wind tunnel testing is presented in Figure 3 which is also valid for other civil applications.

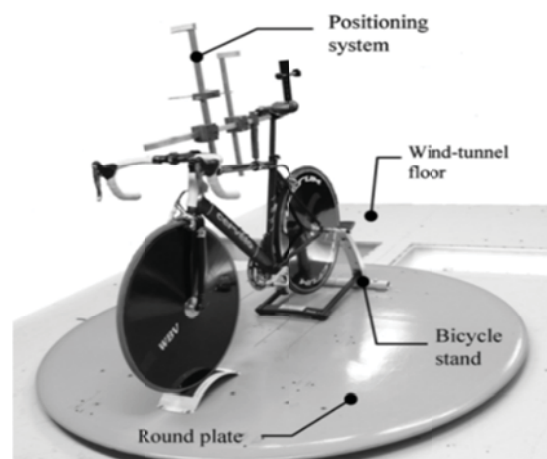


Figure 2. Cyclist and bicycle setup for wind tunnel experiments [18].

Corrections for blockage, due to the wind tunnel cross sectional area being too small relative to the frontal area of the test object, must be taken into account where required. Solid

blockage is an important parameter for the validity of wind tunnel data. The walls of the wind tunnel can compress the streamlines and increase the velocity of the fluid over the test object [19]. This local speed is thus higher than the reference wind tunnel speed causing inaccuracies with aerodynamic coefficient calculations. The blockage ratio in Equation 1 determines if blockage corrections are required. A_t is the frontal area of the test item, and A_{wt} is the cross sectional area of the wind tunnel test section. Typically correction is required if the blockage ratio is greater than 7.5-10%. A complete methodology for blockage correction is found by Mercker & Wiedemann [19]. The drag area ($C_D A$) is presented in Equation 2. This is the typical reference value used for comparison and drag reduction purposes [20]. F_D is the axial aerodynamic drag force, ρ is the air density, V is the air velocity, A is the frontal area, and C_D is the drag coefficient.

$$BR = \frac{A_t}{A_{wt}} \quad (1) [22]$$

$$C_D A = \frac{F_D}{\frac{1}{2} \rho V^2} \quad (2) [21]$$

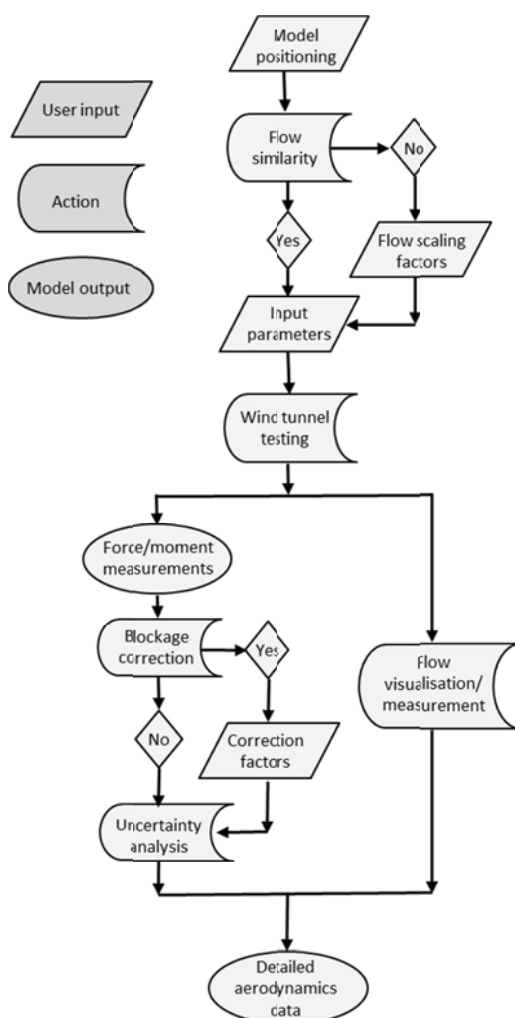


Figure 3. A proposed flowchart methodology for wind tunnel analysis of cyclists and bicycles.

4 CYCLIST AERODYNAMICS MODELLING WITH CFD

Fintelman et al. [23] used validated CFD models to investigate the flow field around a static cyclist at various yaw angles. RANS simulations (k- ϵ and SST) were used to analyse various yaw angles, while detached-eddy simulation (DES) and LES were used to analyse only a single yaw angle of 15° due to their increased computational expense. The bicycle was included in the simulation along with the rider, with simplified geometry with features such as the nose, lips, bicycle spokes and cables being neglected. A standard urban helmet was used instead of an aerodynamic TT helmet as this research is focused more at cycling safety than aerodynamic performance. Discrepancies between different CFD modelling techniques and the wind tunnel results were apparent with 17% difference in drag force between LES and experimental results at a yaw angle of 15°. Geometrical simplifications in the CFD along with interference drag from the wind tunnel test stand could be contributors to these discrepancies.

Defraeye et al. [18] studied three common cycling postures using CFD, those postures being standard upright position, dropped position, and time trial position. From the LES simulation of the cyclist alone without the bicycle, the drag area (m²) of each position was 0.219, 0.172 and 0.142 respectively. These results confirm that a reduction in the frontal area of cyclists significantly reduces their drag area. It is further proved that the aerodynamic drag of the cyclist is 60-70% of the total drag experienced by the rider and bicycle combined.

CFD has been used to yield new insights into the phenomena known as drafting in the cycling world. Blocken et al. [24] made several new observations regarding drafting in cycling with the first published CFD simulations of drafting supported by wind tunnel validation. These included that the presence of the trailing cyclist reduces the underpressure at the back of the leading cyclist, yielding a drag reduction for the leading cyclist. Two cyclists were used in both the wind tunnel and CFD testing. However, only the riders were modelled in the CFD tests with the drag area of the stand and bike being taken away from the wind tunnel test results for comparability. Interference drag was also neglected.

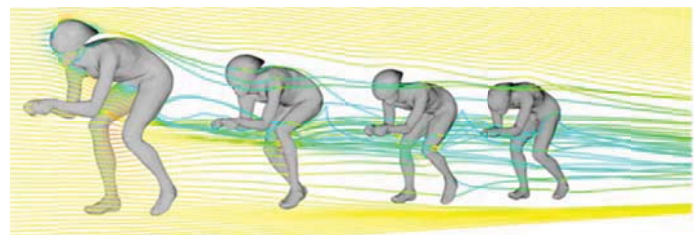


Figure 4. Streamlines of the airflow around four drafting cyclists [25].

Defraeye et al. [25] followed up on the research by Blocken et al. [24] further investigating the drafting phenomena using four individual cyclists, each 3D scanned and modelled in different racing positions. Thus team drafting was analysed with variations in individual positions, e.g. upright position for the leading cyclist and other variations.

Such research using numerical studies on cyclists in a pace line is extremely useful for determining an optimal cyclist sequence for time trial events both on the road and in velodromes. It was made clear that the drag of a cyclist is dependent on their position in the pace line. Second and subsequent positions experience drag reductions up to 40% in comparison to a single cyclist not partaking in drafting, with the second from last cyclist receiving the largest aerodynamic benefit from the formation.

Blocken & Toparlar studied other areas including the aerodynamic effects of a trailing car on the drag of a single cyclist (Figure 5) [26]. Both a static bicycle and rider were modelled in this simulation, but with some geometrical simplifications. A 3D scanned cyclist was physically modelled at a reduced scale for wind tunnel validation studies. The standard k- ϵ turbulence model was used with wall functions used instead of low Reynolds number modelling. The results show a 3.9 second impact on a 50 km time trial event. Thus following from the results of this research, Blocken & Toparlar recommend to the UCI that the 10 metre minimum distance rule should be altered to 30 metres to negate this aerodynamic benefit unknowingly availed of by some cyclists. It is noted that during actual races, the 10 metre limit is not strictly enforced and that there is at least one car, if not multiple, potentially influencing the drag of a cyclist.

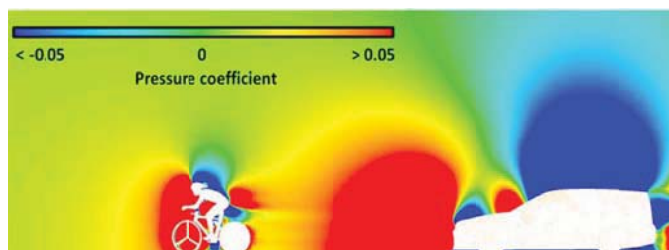


Figure 5. A pressure map of a trailing car on a cyclist [26].

The variation in drag force and associated downstream flow structure with crank angle was investigated numerically and experimentally by Griffith et al. [27]. CFD under-predicted drag measurements by 15% in comparison to wind tunnel experiments, however, the author put this partially down to the simplification of the geometry of the cyclists and bicycle. A good match of the downstream flow structure is found for the CFD and wind tunnel results. Minimum drag was observed at a crank angle of 15°, when the two thighs of the cyclist were aligned. The maximum drag is observed at a crank angle of 75°, when one leg is at full extension and the other leg is raised towards the rider's torso. The transient nature of the entire flow field was revealed by these CFD studies. Griffith et al. [27] concluded that the drag force experience by the rider depends on the surfaces to the rear and the downstream vortical flow structures associated with them. The strength of the vorticity structure can be linked to the drag force as shown by the alignment of either thigh perpendicular to the flow aggregating the power of downstream vortical structures. The author also indicates that caution should be exercised when modelling components isolated from the entire cycling geometry, as the positioning of the legs affected

not only the drag force on the legs, but the drag force on the rider's torso.

5 WHEEL AERODYNAMICS MODELLING WITH CFD

In addition to simulating cyclist's aerodynamic performance using CFD, it has also been used to model the aerodynamics characteristics of wheels. Godo performed comprehensive aerodynamics research on a commercial bicycle wheel using CFD [28]. He presented a methodology for rapid and consistent aerodynamics studies on a range of bicycle wheel geometries under a large range of flow conditions. Ten different yaw angles were modelled at two speeds of 32 km/h and 48 km/h using steady state RANS analysis using the one equation Spalart-Allmaras turbulence equation. In addition to this, transient analysis using delayed detach eddy simulation (DDES) was run for five of the yaw angles at the same two speeds. This research allowed for flow structures to be identified and compared for different yaw angles and for the observation of a unique transition from downwards to upwards acting force as the yaw angle is increased. Viscous drag was found to be less than 3% of the overall force with the remainder of the force computed a result of pressure drag. The spokes generate a comparable drag to the wheel hub, with the tyre and rim generating the majority of the drag force.

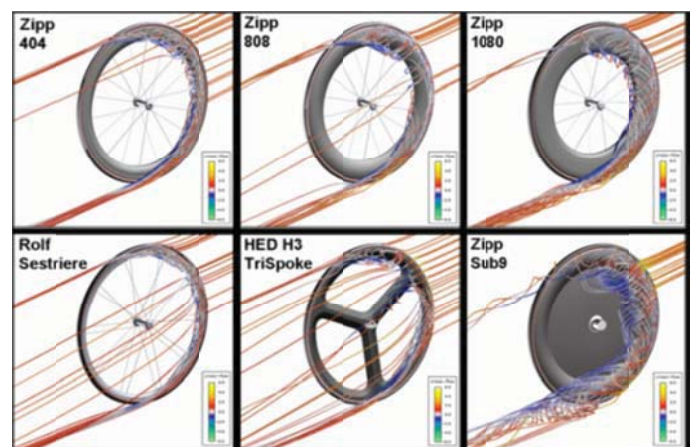


Figure 6. Streamlines at a yaw angle of 10° showing recirculation on the suction side of six different wheels [29].

Godo et al. [29] continued to build on their previous work using their methodology to analyse and compare six different wheels. Significant differences between the wheels were shown with deeper rim wheels offering a clear advantage under commonly experienced yaw angles (5-15°). Pogni et al. [30] also confirmed the satisfactory capability of CFD to describe the aerodynamic behaviour of bicycle wheels using steady state RANS simulations. Knup & Farmer further investigated the suitability of CFD for studying the aerodynamics of wheels [31]. Six different wheels were tested at varying yaw angles using steady state analysis with the k- ϵ turbulence model. The drag of a disc wheel was shown to decrease with increasing yaw angle, turning negative at 20°.

6 PARACYCLING AERODYNAMICS

While the racing bicycle for professional or casual use has experienced extensive development with regard to aerodynamics using CFD techniques, similar development has not occurred with regard to tandem cycles or hand-cycles that are used by elite para-cyclists. Hand-cycle design can be specific to the athlete involved due to variations in disability. Thus completely different positions can be used during the race depending on the cyclist, particularly in race phases such as a downward slope where the cyclist does not need to pedal and can adjust their position to minimize aerodynamic drag. Existing elite hand-cycles are a young technology with little aerodynamic research conducted to enhance their potential. The only available published literature to the best knowledge of this author is by Belloli et al. [15] who performed dynamic wind tunnel testing of two hand-cycle/rider combinations, an arm powered hand cycle, and an arm trunk powered hand cycle (Figure 7). A specialized system was built for the wind tunnel testing where the hand cycle is mounted on a support frame with each wheel placed on rollers with an adjustable resistance.

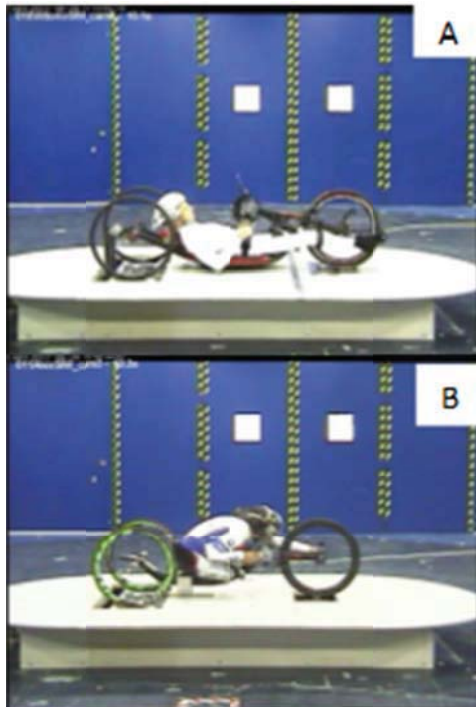


Figure 7. An arm powered hand-cycle (7a), and an arm trunk powered hand-cycle (7b), both in aerodynamic postures [15].

7 DISCUSSION/CONCLUSIONS

There are numerous gaps present in current knowledge of cycling. Firstly, bicycles and their riders are rarely modelled together using CFD due to the computational expense. Thus, interference drag between the rider and the bicycle is neglected if one or the other is left out [18, 24, 32]. When validating CFD simulations against wind tunnel data, the drag area of the bicycle is subtracted from the wind tunnel measurements to give comparable data to the CFD results. This further neglects interference drag however leading to

possible discrepancies within results. When athletes and their bicycles are modelled together, numerous simplifications are made to the model to reduce computational expense. For example, the spokes and cables on the bike are often neglected and the finer details of the cyclist such as facial features are also neglected [26]. A drawback of CFD is its current inability to model the varying roughness on riders TT suits. LRNM and wall functions have been used in the past to model the surface of the rider, with little or no difference between the skin, suit and helmet surface modelling [24, 26, 33]. Wall functions allow for some roughness to be taken into account; however they assume certain flow conditions without actually solving the viscous sub-layers at the surface geometry, as is the case with LRNM.

Dynamic simulations using CFD have not yet been utilized for cycling to the best knowledge of this author. Such instantaneous transient data of a pedalling cyclist would provide highly sought and valuable aerodynamics data to the cycling community. The ability to visualise the flow around a dynamic cyclist on the graphical platform CFD provides could prove invaluable. Some attempts have been made to graphically display flow patterns from a dynamic cyclist using experimental methods. Three dimensional flows around a full scale cyclist mannequin were investigated in pursuit of explaining the large variations in aerodynamic drag measured as the mannequins legs are positioned around the 360° crank cycle [10]. While this research provided a major leap forward in the current understanding of cycling aerodynamics, CFD analysis would supplement and extend research of this nature providing a broader and in-depth understanding of the complex dynamic flows on a platform readily accessible to most researchers. Hucho identified trailing streamwise vortices as a primary feature of vehicles wakes, having a large impact on the drag of a vehicle [34]. Crouch et al. found similar flow structures in the wake of cyclists and determined that future investigation into the wake of cyclists will have the largest impact on reducing the aerodynamic drag force [10].

The use of CFD in sport was reviewed by Hanna, covering a 20 year period, 1992 to 2012 [9]. While this paper focuses on motorsport and other sporting events, many of its conclusions and predictions are relevant for the cycling world. Virtual modelling of athletes in real time at competitive events is predicted, in an effort to gain competitive advantages on the day. Physically realistic CFD/multiphysics models of athletes are also predicted to virtually test new equipment or sports textile suited to individual athletes. A drawback of wind tunnel testing is the difficulty in obtaining whole flow field data. Wind tunnel studies commonly have investigated only the aerodynamic forces on the cyclist; however the research conducted by Blocken et al. [24, 26, 35] on cycling aerodynamics has utilised CFD to obtain whole flow field data, heavily validated by wind tunnel studies. This combination provides reliable aerodynamics results, yielding new insights into the wake flow of cyclists and the fundamental causes of aerodynamic drag. Some discrepancies remain between CFD simulations and their wind tunnel validation tests. Support structures are required for wind tunnel experiments of bicycles. These structures are not in place for the corresponding CFD studies. It is recommended by this author that CFD studies should initially mimic the

wind tunnel validation tests to the best extent, and upon validation, the support structures can be removed from the model to give a clearer indication of the flow field around a cyclist.

Some wind tunnel analysis has been conducted on competitive hand-cycles [15], however there is no current knowledge or understanding of the flow around hand cycles, recumbents and tandems, despite a general agreement in the cycling world that recumbent type cycles are more aerodynamic than their upright counterparts [36]. Tandem cycling is all but untested in cycling aerodynamics to the best knowledge of this author. Research in this area has begun in NUI Galway in the form of a 4 year structured PhD programme. This new research will investigate the aerodynamics of paracycling using CFD, with a focus on tandem cycling. The present author gratefully acknowledges the funding provided by the department of Engineering and Informatics.

REFERENCES

- [1] D. G. Wilson and J. Papadopoulos, *Bicycling Science*. MIT Press, 2004.
- [2] F. Grappe, R. Candau, A. Belli, and J. D. Rouillon, "Aerodynamic drag in field cycling with special reference to the Obree's position," *Ergonomics*, vol. 40, no. 12, pp. 1299–1311, 1997.
- [3] S. J. Haake, "The impact of technology on sporting performance in Olympic sports," *J. Sports Sci.*, vol. 27, no. 13, pp. 1421–1431, 2009.
- [4] T. Defraeye, B. Blocken, E. Koninckx, P. Hespel, and J. Carmeliet, "Computational fluid dynamics analysis of cyclist aerodynamics: Performance of different turbulence-modelling and boundary-layer modelling approaches," *J. Biomech.*, vol. 43, no. 12, pp. 2281–2287, 2010.
- [5] P. Gardano and P. Dabnichki, "On hydrodynamics of drag and lift of the human arm," *J. Biomech.*, vol. 39, no. 15, pp. 2767–2773, 2006.
- [6] P. Dabnichki and E. Avital, "Influence of the position of crew members on aerodynamics performance of two-man bobsleigh," *J. Biomech.*, vol. 39, no. 15, pp. 2733–2742, 2006.
- [7] J. H. Hart, "The use of CFD in the chase of Olympic gold," *Sport. Eng.*, pp. 1–11, 2006.
- [8] A. Rouboa, A. Silva, L. Leal, J. Rocha, and F. Alves, "The effect of swimmer's hand/forearm acceleration on propulsive forces generation using computational fluid dynamics," *J. Biomech.*, vol. 39, no. 7, pp. 1239–1248, 2006.
- [9] R. K. Hanna, "CFD in Sport - a Retrospective; 1992 - 2012," *Procedia Eng.*, vol. 34, pp. 622–627, 2012.
- [10] T. N. Crouch, D. Burton, N. a. T. Brown, M. C. Thompson, and J. Sheridan, "Flow topology in the wake of a cyclist and its effect on aerodynamic drag," *J. Fluid Mech.*, vol. 748, pp. 5–35, 2014.
- [11] T. Crouch, J. Sheridan, D. Burton, M. Thompson, and N. a. T. Brown, "A quasi-static investigation of the effect of leg position on cyclist aerodynamic drag," *Procedia Eng.*, vol. 34, pp. 3–8, 2012.
- [12] H. Chowdhury, F. Alam, and D. Mainwaring, "A full scale bicycle aerodynamics testing methodology," *Procedia Eng.*, vol. 13, pp. 94–99, 2011.
- [13] H. Chowdhury and F. Alam, "Bicycle aerodynamics: an experimental evaluation methodology," *Sport. Eng.*, vol. 15, no. 2, pp. 73–80, 2012.
- [14] N. Barry, D. Burton, J. Sheridan, M. Thompson, and N. a. T. Brown, "Aerodynamic drag interactions between cyclists in a team pursuit," *Sport. Eng.*, vol. 18, pp. 93–103, 2015.
- [15] M. Belloli, F. Cheli, I. Bayati, S. Giappino, and F. Robustelli, "Handbike Aerodynamics: Wind Tunnel Versus Track Tests," *Procedia Eng.*, vol. 72, pp. 750–755, 2014.
- [16] G. Gibertini, G. Campanardi, D. Grassi, and C. Macchi, "Aerodynamics of Biker Position," pp. 2–5, 2008.
- [17] J. García-López, J. A. Rodríguez-Marroyo, C.-E. Juneau, J. Peleteiro, A. C. Martínez, and J. G. Villa, "Reference values and improvement of aerodynamic drag in professional cyclists," *J. Sports Sci.*, vol. 26, no. 3, pp. 277–286, 2008.
- [18] T. Defraeye, B. Blocken, E. Koninckx, P. Hespel, and J. Carmeliet, "Aerodynamic study of different cyclist positions: CFD analysis and full-scale wind-tunnel tests," *J. Biomech.*, vol. 43, no. 7, pp. 1262–1268, 2010.
- [19] E. Mercker and J. Wiedemann, "On the Correction of Interference Effects in Open Jet Wind Tunnels," 1996.
- [20] L. Underwood and M. Jermy, "Optimal hand position for individual pursuit athletes," *Procedia Eng.*, vol. 2, no. 2, pp. 2425–2429, 2010.
- [21] F. M. White, "Fluid Mechanics," *Book*, vol. 17, no. 3, p. 864, 2009.
- [22] E. C. Maskell, "A Theory of Blockage Effects on Bulb Bodies and Stalled Wings in a Closed Wind Tunnel," *Her Majesty's Station. Off.*, pp. 1–27, 1965.
- [23] D. M. Fintelman, H. Hemida, M. Sterling, and F.-X. Li, "CFD simulations of the flow around a cyclist subjected to crosswinds," *J. Wind Eng. Ind. Aerodyn.*, vol. 144, pp. 31–41, 2015.
- [24] B. Blocken, T. Defraeye, E. Koninckx, J. Carmeliet, and P. Hespel, "CFD simulations of the aerodynamic drag of two drafting cyclists," *Comput. Fluids*, vol. 71, pp. 435–445, 2013.
- [25] T. Defraeye, B. Blocken, E. Koninckx, P. Hespel, P. Verboven, B. Nicolai, and J. Carmeliet, "Cyclist Drag in Team Pursuit: Influence of Cyclist Sequence, Stature, and Arm Spacing," *J. Biomech. Eng.*, vol. 136, no. 1, p. 011005, 2013.
- [26] B. Blocken and Y. Toparlar, "A following car influences cyclist drag: CFD simulations and wind tunnel measurements," *J. Wind Eng. Ind. Aerodyn.*, vol. 145, no. 0, pp. 178–186, 2015.
- [27] M. D. Griffith, T. Crouch, M. C. Thompson, D. Burton, and J. Sheridan, "Computational Fluid Dynamics Study of the Effect of Leg Position on Cyclist Aerodynamic Drag," vol. 136, no. October, pp. 1–9, 2014.
- [28] M. Godo, "An Aerodynamic Study of Bicycle Wheel Performance using CFD," *47th AIAA Aerosp. Sci. Annu. Meet.*, vol. 12065, pp. 1–21, 2009.
- [29] M. Godo, D. Corson, and S. Legensky, "A Comparative Aerodynamic Study of Commercial Bicycle Wheels using CFD," *Aiaa*, 2010.
- [30] M. Pogni, N. Petrone, M. Antonello, and P. Gobbato, "Comparison of the Aerodynamic Performance of Four Racing Bicycle Wheels by Means of CFD Calculations," *Procedia Eng.*, vol. 112, pp. 418–423, 2015.
- [31] J. Knupe and D. Farmer, "Aerodynamics of High Performance Race Bicycle Wheels," no. April 2009, pp. 1–15, 2009.
- [32] T. Defraeye, B. Blocken, E. Koninckx, P. Hespel, and J. Carmeliet, "Computational fluid dynamics analysis of cyclist aerodynamics: Performance of different turbulence-modelling and boundary-layer modelling approaches," *J. Biomech.*, vol. 43, no. 12, pp. 2281–2287, 2010.
- [33] T. Defraeye, B. Blocken, E. Koninckx, P. Hespel, and J. Carmeliet, "Computational fluid dynamics analysis of drag and convective heat transfer of individual body segments for different cyclist positions," *J. Biomech.*, vol. 44, no. 9, pp. 1695–1701, 2011.
- [34] I. Hucho, "Aerodynamics of Road Vehicles," *Annu. Rev. Fluid Mech.*, vol. 25, pp. 485–537, 1993.
- [35] B. Blocken, T. Defraeye, E. Koninckx, J. Carmeliet, and P. Hespel, "Surprises in cycling aerodynamics," *Europhys. News*, vol. 44, no. 1, pp. 20–23, 2013.
- [36] A. C. Gross, C. R. Kyle, and D. J. Malewicki, "The Aerodynamics of Human-Powered Land Vehicles," *Scientific American*, vol. 249, pp. 142–152, 1983.

Sustainable concrete with 95% recycled and natural components

Ahmed Alawais, Roger P West

Department of Civil Engineering, Trinity College, University of Dublin, Ireland

email: alawaisa@tcd.ie, rwest@tcd.ie

ABSTRACT: This paper describes an on-going research project which aims to use solely recycled materials as constituents to form concrete without adversely affecting its mechanical properties. This will require a pre-treatment of some constituents before using them to compensate for the strength loss because of their addition. This paper involves the study of the effect of using the recycled materials: ground granulated blast-furnace slag (GGBS), recycled aggregate (RA), recycled tyres in the form of crumb rubber and natural resources such as harvested rainwater and crushed hemp in order to minimise waste disposal and the embedded carbon. This will also reduce dependence on less sustainable materials, such as quarried aggregate, Portland cement and fresh water. This paper will describe the research approach to be taken in this project to achieve this aim.

KEY WORDS: GGBS, Hemp, Rain water harvesting, Recycled aggregates, Rubberized concrete

1 INTRODUCTION

Humans since ancient times have explored their surrounding materials through experiments and accumulated experience in the practice of construction, thereby recognising the characteristics of building materials which can most effectively meet their needs. In this context, concrete is one of the most important materials in human civilization, where it is used widely in construction, despite the fact that cement and aggregate production and transport cause the emission of large amounts of carbon dioxide. Therefore buildings are responsible for a substantial share of the energy consumed in developed countries; they are accountable for approximately one third of the total energy emissions and large quantities of carbon dioxide (CO₂) release. Such emissions consist of embodied CO₂ as well as the CO₂ generated from the different phases of the building's life cycle, starting from the production of the material to assembly, its operational life and ending with the disposal of the building and its materials [1-3].

Furthermore, the growing demand for concrete constituents is a threat to the environment and the sustainability of its resources into the future. According to a market study by The Freedonia Group, by 2017 the world demand for cement, shown in Table 1, will be 4.7 billion tonnes which means that more than 2 billion tonnes of water and more than 11 billion tonnes of aggregates, both of which are also scarce resources, will also be consumed [4]. In addition, it is estimated that the total quantity of construction and demolition waste collected in 2004 was approximately 11 million tonnes [5].

Table 1 World cement demand (million metric tons) [5]

Item / % Annual Growth	2007	2012	2017	2007 - 2012	2012 - 2017
Cement Demand	2727.0	3665.0	4745.0	6.1	5.3
North America	166.0	127.0	165.0	-5.2	5.4
Western Europe	223.0	138.0	171.0	-9.2	4.4
Asia/Pacific	1805.0	2715.0	3495.0	8.5	5.2
Central & South America	110.0	145.0	190.0	5.7	5.6
Eastern Europe	132.0	127.0	167.0	-0.8	5.6
Africa/Mideast	291.0	413.0	557.0	7.3	6.2

However, the usage of recycled materials, can compromise concrete strength and durability, and this will demand selected pre-treatment methods for these components to compensate for the natural strength losses due to their inclusion. This paper will discuss some of these alternatives, such as:

- Surface treating the crumb rubber, made from waste tyres, with NaOH [6].
- Add a chemical activator to GGBS to enhance strength development [7].
- Segregate high strength recycled concrete before surface treating and coating [8].
- Filter and treat harvested rainwater [9].
- Using hemp to bind the micro cracks in the cement matrix together [10].

Understandably, the green building materials market is rapidly expanding and the utilisation of these recycled materials has the potential to create a novel concrete with substantially enhanced sustainability. However, whether or not these complementary actions are feasible without significant loss in performance is not known and ascertaining this is the primary objective of this work.

2 RUBBER IN CONCRETE

Waste tyres are divided into two types, car and truck tyres, although researchers show more interest in car tyres due to their high production volume compared to truck tyres. However, there are few differences between them, especially in their natural and synthetic rubber contents. Table 2 shows a comparison between car and truck tyres constituents [11].

Table 2 Constituent materials of tyres [11]

Composition weight (%)	Car tyre	Truck tyre
Natural rubber	14	27
Synthetic rubber	27	14
Black carbon	28	28
Fabric, filler accelerators, and antiozonants	16-17	16-17
Steel	14-15	14-15

Ganjian et al. [11] also categorised waste tyres by sieve size:

- Shredded or chipped rubber to replace the aggregates
- Crumb rubber to replace sand
- Ground rubber to replace cement

The drop in strength was significant when rubber was used to replace conventional cement. Fig.1 shows results of 28-day compressive strength tests, comparing the replacement of normal aggregates and cement with rubber. Khatib and Bayomy [12] illustrated the impact of adding two types of rubber - crumb to replace the sand and shredded (at a size of 10–50mm) to replace the aggregates. Their study showed that concrete made with crumb rubber has a lower strength loss than concrete made with shredded rubber.

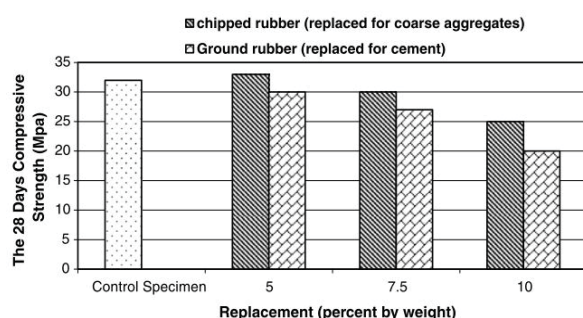


Fig.1 Comparison between the replacement of aggregates and cement with rubber after 28 days [11]

Segre and Joeke [6], in their study, surface treated the rubber particles with saturated NaOH for 20 min before using them. They concluded that rubber particles thus treated exhibit better cohesion with the cement, however it worked on smaller particles more effectively than larger particles regarding minimizing of the compressive strength reductions. Inevitably, the higher flexibility as much as the lower strength of the shredded rubber causes the cement matrix to have to take more loading under stress, where traditionally it is the reverse. Unless small percentages of substitution are used, it is not known how to maintain strength of rubberised concrete.

3 GGBS IN CONCRETE

GGBS production involves less energy compared with the energy required in the production process of Portland cement. Therefore, replacing cement with GGBS will lead to a substantial reduction of carbon dioxide gas emissions, even allowing for tyres as fuel in cement production, which means that GGBS is a more environmentally friendly construction material. Secondly, GGBS concrete can also soften the visual impact of structures, for above 50% replacement rate a noticeably whiter colour is seen in GGBS concrete and solar reflectance is improved. Furthermore, it is well known that setting time will be marginally extended and the concrete will remain workable for a longer period of time resulting in less risk of cold joints in large pours. However, not only can it be used to replace up to 70% of cement in a concrete mix in Ireland, but it potentially has a better water impermeability, slower diffusion rate and an improved resistance to sulphate and chloride attack, which can lead to a reduction in the maintenance cost and an improvement in the life span of the structure [13]. For higher than 70% blends, in these more

environmentally advantageous mixes, GGBS tends to act as a filler unless the hydration is stimulated by a chemical activator.

3.1 GGBS alkali activators

GGBS is a slow reacting cementitious material, which can achieve a higher compressive strength when adding an alkali activator to it. Kim [7] classified alkali activators into six groups:

- Caustic alkalis
- Non-silicate weak acid salts
- Silicates
- Aluminates
- Aluminosilicates
- Non-silicate strong acid salts

Of these activators, NaOH, Na₂CO₃, Na₂O·nSiO₂ and Na₂SO₄ are the most available and economical chemicals in the market. Although GGBS on its own does react with water without an activator, the hydration rate is very slow and impractical for site use in the absence of either Portland cement or a chemical activator.

3.2 Compensating for the loss of compressive strength with GGBS

GGBS is used to enhance geopolymer concrete properties [14]. In Salih et al.'s [15] study they illustrated the fabrication of a high strength alkali activated binder by alkali activation of a binary mix of palm oil fuel ash (POFA)¹ and GGBS, where POFA is a waste material in South East Asia. As can be seen in Fig. 2, the addition of GGBS increased the compressive strength, yet results indicate that the alkali activation of POFA on its own is comparatively slow and limited in strength capacity. The compressive strength is increased by replacing 50% POFA with GGBS. Furthermore, the compressive strength improvement was also observed when replacing up to 50% of class F Fly Ash and Metakaolin with GGBS [16,17].

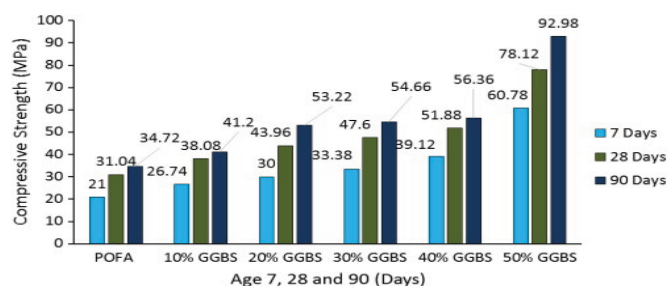


Fig.2 Compressive strength results POFA blended with GGBS as partial replacement by weight [15]

4 RECYCLED AGGREGATE

Demolishing old structures is creating many millions of tons of concrete waste annually, historically sent to landfills. Collapsed structures due to natural disasters, such as earthquakes and tsunamis, send more construction waste to

¹ The POFA is mainly consisted of SiO₂, CaO and low content of Al₂O₃

landfills. One viable solution for this vast amount of waste debris is to recycle it as new concrete aggregate, therefore it will partially contribute to decrease the demand on natural aggregate.

Recycled aggregate (RA) is composed of adhered mortar and original aggregates. The properties of recycled aggregate concrete (RAC) must be enhanced in order for it to work effectively in load-bearing structures [18]. However, one common approach, which involves strengthening the RA by pre-coating with Silica Fume [19,20], may cause new pollution or high cost. Therefore Wang [18] suggested that “a good durable RAC can be achieved by using pozzolanic materials as a replacement of cement”. Not only did he suggest the addition of materials, but he came out with a new mixing scheme where the “W3T4” method is illustrated in Fig.3.

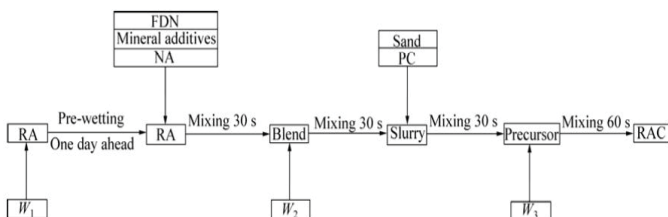


Fig.3 Procedure for “W3T4” method for producing RAC [18] where FDN = naphthalin-type super-plasticizer, NA = natural coarse aggregate, RA = recycled aggregate, PC = Portland cement, RAC = recycled aggregate concrete, W = water

His results showed an increase of about 25% in the compressive strength of RAC with 25% of RA replacement and 10% Phosphorous slag (PHS) +10% GGBS additives, despite a 64% decrease in the permeability and a lower elastic modulus than normal concrete.

5 RAIN WATER HARVESTING

With the increasing surface runoff flooding due to the vast urbanization contribution, rainwater harvesting is one of the best available methods for creating sustainable water cycles in urban developments [21]. Furthermore, Martin et al. [9] state that rainwater harvesting systems have two main elements:

- A catchment area to collect the rainfall
- A large vessel that holds the harvested rainwater until it's called upon

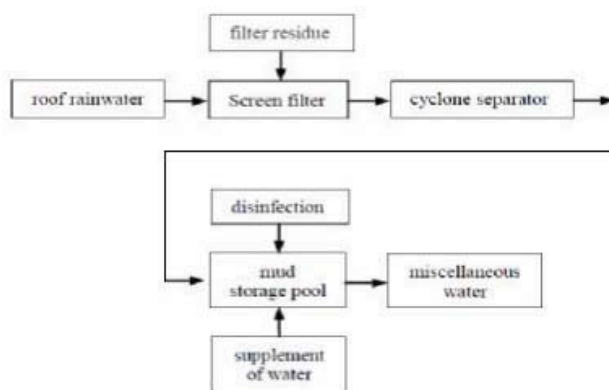


Fig.4 Suggested method of treating rainwater [23]

Since it's estimated that half of the total sealed surfaces in cities comprise roofs, they contribute most to the urban water runoff flow, therefore, they provide an excellent possibility for rain water harvesting surfaces [22]. Moreover, Zhen et al. [23] show that in an urbanized environment surfaces are covered with a waterproof membrane, thus blocking the diffusion of rainfall into the soil.

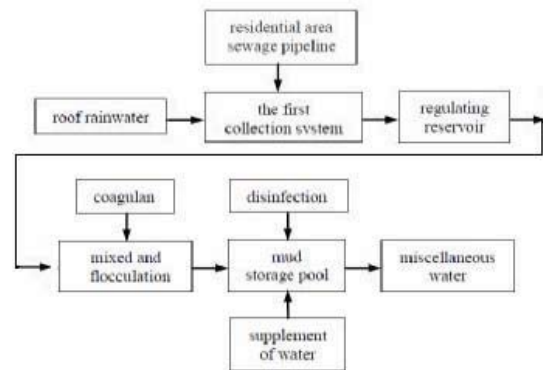


Fig.5 Alternative suggested method of treating rainwater [23]

Therefore, the urban hydrologic cycle is changed due to the rainwater going through pipelines instead of natural infiltration. They suggest treating rainwater depending on the regulations and the level of filtration needed. Figs. 4 and 5 represent two different ways of treating rainwater, although it is recognised that a more environmental approach is to filter rainwater through purification using natural green spaces in the residential areas due to its lower energy consumption, more convenient materials and lower construction cost. In dense urban environments, this is often not feasible.

6 HEMP IN CONCRETE

Since the beginning of the nineties, research has led to the further development of hemp mixed with a binder as a new building material. It enables one to build more sustainable buildings and this contributes to a significant reduction of the carbon footprint. It enables the “concrete” to store approximately 35 kg of CO₂/m² of wall built with a thickness of 25 cm over 100 years [10]. Another study concluded that a hemp concrete wall allows carbon sequestration up to 83 kg CO₂/m² of wall [24]. Hemp fibre has a strong tolerance in an alkaline environment and a moderate tensile strength and that makes it a feasible reinforcement material [25]. Furthermore, chemical treatments of hemp are considered in adjusting surface properties to enhance its adhesion with the matrix and in improving its mechanical properties [26]. On the other hand, plasmas surface modification stimulates adhesion and the action of coupling agents. It also causes rougher surfaces. In addition, surface modification helps to free radicals in the chemical structure. Moreover, the atmospheric plasma technique for surface modification of fibres does not affect the bulk properties. Yet, no solvent is used, and the duration times of treatment are short.

7 CURRENT WORK

A concrete mix was designed with 85% GGBS, recycled tyres in the form of crumb rubber, aggregates comprising waste quarry dust, recycled concrete, processed grit and quarry powder [28]. The four different designed mixes are illustrated in Table 3. Hemp was omitted in the demonstrator base pours, but will be included in later mixes.

Table 3 Details of the concrete mix [28]

Mix	Cement	Sand	10mm Aggt.	20mm Aggt.	GGBS	Crumb Rubber	Recycled concrete	Processed grit	Quarry powder	H ₂ O
1	395	590	400	800	200
2	55	590	400	800	340	200
3	55	590	340	365	200
4	55	340	225	280	280	25	200

The development of the compressive strength, shown in Fig. 6, was monitored over 56 days. In Mix 2, the high (85%) GGBS content caused a 30% drop in strength from 45 MPa to 32 MPa, suggesting that this is due to some of the GGBS not being hydrated without artificial stimulus and acts as an inert void filler.

In Mix 3, when all the aggregates were substituted with crumb rubber, the weight of aggregates after a volume mapping of limestone to rubber, reduced to 365 kg/m³. The strength dropped further by up to 90% of the base strength. This was predicted as the rubber is much more flexible than limestone and the cement paste had to take more of the load, which it was not designed to do. Also, the concrete was hard to compact and finish.

Finally, in Mix 4 when other constituents (recycled aggregate, grit and quarry dust) were substituted, there was no remarkable effect on the strength comparing to Mix 3, yet concrete was more compactable and finishable [28]. The RA contains weak adhered cement paste instead of virgin aggregate which explains the further drop in strength.

It is quite evident that to create a highly sustainable concrete using mostly recycled materials poses very serious technical challenges with regard to maintaining its mechanical properties and this is the subject of extensive further work.

8 CONCLUSION

Concrete mechanical properties are affected by using recycled materials as a substance, especially compressive strength and modulus of elasticity, yet the reduction in these properties when using these substances may be countered to some degree by:

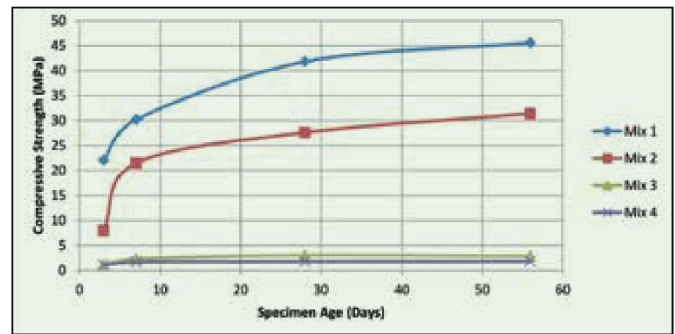


Fig.6 Strength development for concrete mixes [28]

- Soaking the rubber in NaOH
- Activating GGBS with alkaline activators
- Pre-treating the recycled aggregate
- Segregation of high strength RA for use
- Hemp fibres inclusion for crack control
- Treating harvested rainwater prior to use
- Selecting a natural rather than manufactured water reducer, leading to lower water/cement ratios

It is the objective of this on-going research project to continue to explore the range of options in an attempt to obviate the detrimental effects of the inclusion of these recycled materials on the strength and stiffness of concrete.

9 REFERENCES

- [1] Sadineni SB, Madala S, Boehm RF, (2011), Passive building energy savings: a review of building envelope components, *Renewable Sustainable Energy Rev*, 15, 3617–31.
- [2] Anastaselos D, Oxizidis S, Papadopoulos AM, (2011), Energy, environmental and economic optimization of thermal insulation solutions by means of an integrated decision support system, *Energy Build*, 43, 686–94.
- [3] Rakhshan K, Friess WA, Tajerzadeh S, (2013), Evaluating the sustainability impact of improved building insulation: a case study in the Dubai residential built environment, *Build Environ*, 67, 105–10.
- [4] Freedonia Group, World Cement. Freedonia Group, (2013), <http://www.freedoniagroup.com/industry-category/build/construction-building-products.htm>.
- [5] Environmental protection agency, (2004), National Waste Report <http://www.epa.ie/pubs/reports/waste/stats/nationalwastereport2004.htm#VvqOvNJ96U1>.
- [6] Segre N and Joeekes I, (2000), Use of tire rubber particles as addition to cement paste, *Cement and Concrete Research*, 30(9), 1421-1425.
- [7] Kim, HS, Park, JW, An, YJ, Bae, JS, and Han, C, (2011). Activation of ground granulated blast furnace slag cement by calcined alunite, *Materials transactions*, 52(2), 210-218.
- [8] Ajdukiewicz, A and Kliszczewicz, A, (2002), Influence of recycled aggregates on mechanical properties of HS/HPC, *Cement and Concrete Composites*, 24(2): 269-279.
- [9] Elisabeth M A., Buchberger, SG and Debaditya Chakraborty, D, (2015), Reliability of Harvested Rainfall as an Auxiliary Source of Non-potable Water, *Procedia Engineering*, 119, 1119-1128.
- [10] Arnaud, L, Gourlay, E, (2012), Experimental study of parameters influencing mechanical properties of hemp concretes, *Construction and Building Materials*, 28, 1, 50-56.
- [11] Ganjian, E, Morteza K, and Maghsoudi, A, (2009), Scrap-tyre-rubber replacement for aggregate and filler in concrete, *Construction and Building Materials*, 23(5), 1828-1836.
- [12] Khatib, Z K and Bayomy, FM (1999), Rubberized Portland cement concrete., 11(3), 206-213.

- [13] M.G.R., Chennai, Tamil Nadu, (2014), Sustainable Studies on Concrete with GGBS As a Replacement Material in Cement, *Jordan Journal of Civil Engineering*, 8(2).
- [14] Oh JE, Monteiro, Jun, SS, Choi, S, Clark, SM, (2010), The evolution of strength and crystalline phases for alkali-activated ground blast furnace slag and fly ash-based geopolymers, *Cement Concrete Research*, 40 (2), 189–196.
- [15] Salih, MA, Farzadnia, N, Ali, AAA and Demirboga, R, (2015). Development of high strength alkali activated binder using palm oil fuel ash and GGBS at ambient temperature, *Construction and Building Materials*, 93,289-300.
- [16] Nath, SK, Kumar, S, (2013), Influence of iron making slags on strength and microstructure of fly ash geopolymer, *Construction and Building Materials*, 38, 924–930.
- [17] Puligilla, S, Mondal, P, (2013), Role of slag in microstructural development and hardening of fly ash-slag geopolymer, *Cement and Concrete Research*, 43, 70–80.
- [18] Wang, HL, Wang, JJ, Sun, XY and Jin, WL, (2013), Improving performance of recycled aggregate concrete with superfine pozzolanic powders, *Journal of Central South University*
- [19] Tam, VWY, CM Tam and Le, KN, (2007), Removal of cement mortar remains from recycled aggregate using pre-soaking approaches, *Resources, Conservation and Recycling*, 50(1), 82-101.
- [20] Kiyoshi, E, Teranishi, K, Nakagome, A, i Kishimoto, H, Shinozaki, K and Narikawa, M, (2007), Application of recycled coarse aggregate by mixture to concrete construction, *Construction and Building Materials*, 21(7), 1542-1551.
- [21] Lee, JY, Bak, G, and Han, M, (2012), Quality of roof-harvested rainwater Comparison of different roofing materials, *Environmental Pollution*, 162,422-429.
- [22] Farreny, R, Morales-Pinzón, T, Guisasola, A, Tayà, C, Rieradevall, J, Gabarrell, X, (2011), Roof selection for rainwater harvesting: Quantity and quality assessments in Spain, *Water Research*, 45, 10, 3245-3254.
- [23] Zhen, S, Xun, Y, Xu, S and Zhou, Y, (2015), Analysis of Plans for Rainwater Reuse in a Residential Area in Jiangsu, China.
- [24] Pretot, S, Collet, F and Garnier, C, (2014), Life cycle assessment of a hemp concrete wall: Impact of thickness and coating, *Building and Environment*, 72, 223-231.
- [25] Li, Z, Wang, X, Wang, L, (2006), Properties of hemp fibre reinforced concrete composites, *Composites Part A: Applied Science and Manufacturing*, 37, 3, 497-505.
- [26] Sandrine, UB, Isabelle, V, Hoang, MT and Chadi, M, (2015), Influence of chemical modification on hemp–starch concrete, *Construction and Building Materials*, 81, 208-215.
- [27] Bozaci, E., Sever, K., Sarikanat, M., Seki, Y, Demir, A, Ozdogan, E and Tavman, I, (2013), Effects of the atmospheric plasma treatments on surface and mechanical properties of flax fiber and adhesion between fiber–matrix for composite materials, *Composites Part B:Engineering*, 45, 565-572.
- [28] West, RP, Alawais, A, Kwatra, N, (2015), Sustainable concrete as a platform for outreach, *2nd RN Raikar Memorail Intl. conference & Banthia-Basheer Intl. Symposium on Advances in Science & Technology of Concrete*.

Mechanical and thermal evaluation of different types of PCM-concrete composite panels

Dervilla Niall^{1,2}, Oliver Kinnane³, Roger P. West² and Sarah McCormack²

¹Dublin Institute of Technology, Ireland

²Trinity College, University of Dublin, Ireland

³Queens University Belfast, Northern Ireland

email: dervilla.niall@dit.ie, o.kinnane@qub.ac.uk

ABSTRACT: Thermal mass indicates the ability of a material to store and release heat and is a function of the heat storage capacity of a material. The thermal mass of construction materials can be used to reduce the energy required for heating and cooling buildings. The heat storage capacity of concrete can be increased by incorporating phase change materials (PCMs) into the concrete and hence providing additional latent heat storage capacity. Research was carried out to compare the thermal behaviour of two different types of PCM/concrete composite panels. The first type of panel was formed by adding microencapsulated paraffin to fresh concrete during the mixing process. The second panel was formed by vacuum impregnating butyl stearate into lightweight aggregate which was then included in the concrete mix. This study aimed to establish which type of PCM/concrete composite material was most effective at improving the thermal mass behaviour of the panel and also to evaluate the effect that the PCM had on the relevant properties of concrete. The panels were exposed to radiative heat energy in a controlled environment for a specified time period during which the surface and internal temperatures of the panel were recorded. The temperature data together with the measured density and thermal conductivity was used to evaluate and compare the thermal mass behaviour of each type of PCM/concrete composite material. The addition of PCM to the concrete significantly increased the overall thermal storage capacity of the concrete despite reducing the density and thermal conductivity of the concrete. It was determined that the concrete containing the lightweight aggregate/PCM was more effective at increasing the thermal storage capacity up to a depth of 100mm.

KEY WORDS: Phase change materials; PCM concrete; Thermal conductivity; Thermal diffusivity; Thermal storage

1 INTRODUCTION

The use of renewable energy sources is increasing due to the drive to reduce the threat of climate change and secure energy supply. Solar energy is a major renewable heat energy source however its intermittent nature means that its effectiveness is dependent on the inclusion of an efficient thermal energy storage system. Thermal storage systems can utilize sensible heat storage, latent heat storage or a combination of both. In sensible heat storage systems, energy is stored in a material by increasing its temperature. The capacity of a material to store energy depends on the amount of energy required to change the temperature of a unit amount of the material, ie the specific heat capacity of the material.

The mass of a building can be used to provide a sensible heat storage system and hence act as a *thermal mass*. For a material to provide good thermal mass it requires a high specific heat capacity, C_p (J/kgK), a high density, ρ (kg/m³) and an appropriate thermal conductivity, k (W/mK) that suits the required storage period. This study aimed to improve the thermal mass characteristics of concrete by adding latent heat capacity through the incorporation of phase change materials and hence increasing its overall heat storage capacity.

The latent heat capacity of a PCM is the heat energy absorbed by the PCM when it changes from one phase to another, ie from solid to liquid and from liquid to gas. For practical reasons it is only feasible to use the solid-liquid phase change of a material when incorporating a PCM into a building component. The temperature of the PCM remains constant during phase change. The heat capacity of a

PCM/concrete material is not constant as it varies in accordance with the state of the phase transition. For PCM composites the heat capacity is a combination of specific heat capacity and latent heat capacity. For this reason this paper will refer to the overall heat capacity of the PCM/concrete composites.

There are many different types of PCMs hence the selection of a phase change material for a given application requires consideration of the properties of the phase change materials and a weighing up of their particular advantages and disadvantages in order to reach an acceptable compromise. Primarily the selection of a PCM should ensure that the melt temperature range of the PCM is suitable for the intended application. For a space heating application in a building, only phase change materials with a melting temperature within the range of human comfort temperature (18-22°C) can be deemed suitable [1].

Paraffin is an organic PCM with melting temperatures ranging between 20°C and 70°C. A number of researchers ([2], [3] and [4]) have carried out thermal energy storage studies that combined paraffin with concrete. Generally from a review of studies that considered PCM/concrete composites, paraffin appears to be the most common choice of PCM as it is inactive in an alkaline medium, chemically stable and relatively inexpensive. However paraffin has a relatively low conductivity [5].

Butyl stearate is a fatty acid with melting temperatures similar to that of paraffin. It has also successfully been combined with concrete in previous research.

There are three main methods used for incorporating PCMs into concrete - immersion, vacuum impregnation and encapsulation. The immersion technique was used by a number of previous researchers ([6] and [7]). However the time required for the absorption of the PCM and evidence of leakage while in use were highlighted as problematic issues.

The vacuum impregnation method involves firstly evacuating the air from porous aggregates using a vacuum pump. The porous aggregates are then soaked in a liquid PCM under vacuum. Finally the PCM soaked aggregate is added to the concrete mix. Zhang et al. [8] studied the ability of different types of porous aggregate to absorb butyl stearate. For the vacuum impregnation method it was found that an immersion time of 30 minutes at a temperature of 30° C above the melting temperature of the PCM optimises the absorption of the PCM.

The most commonly used method for incorporating PCMs into construction materials is micro-encapsulation, where PCM particles (1µm to 1000µm) are encapsulated in a thin shell which is made from natural and synthetic polymers. These microcapsules are then added to the concrete during the mixing process. This method provides a large surface area of PCM throughout and hence it has the advantage of a high heat transfer rate per unit volume. Other advantages are that the capsules prevent leakage and resist volume change during phase change. However the microcapsules affect the mechanical properties of concrete [9].

For this study two methods of incorporating the PCMs with concrete were selected, a microencapsulated paraffin product which was available ready made and vacuum impregnated butyl stearate which was manufactured in the laboratory. The study aimed to establish the most effective method of incorporating phase change material into concrete and also an optimum depth of PCM to maximize the efficiency of the thermal storage behaviour of the phase change material.

2 METHODOLOGY

Based on the two different methods selected for combining PCMs and concrete, test groups of sample panels for the experimental design were selected, two of each type (one duplicate) and two control panels without PCMs.

A panel depth of 200mm was selected to reflect the typical thickness of a wall within a building hence the panels were constructed to be 200mm x 200mm x 200mm. Each panel had 3No. thermocouples cast internally into the concrete at equal depth intervals of 50mm. Thermocouples were also located on the front and rear faces. After casting the concrete panels were cured for 28 days. As moisture content can significantly influence the thermal conductivity of concrete the panels were allowed to dry out for a further 28 days during which moisture content was monitored. All panels had a moisture content less than 4% prior to conductivity tests being carried out.

The context of this research project was to study the potential thermal storage behaviour within a pcm-concrete internal leaf of a cladding panel. In this application the internal leaf would normally have a layer of insulation on the outer face hence transmission of heat through the panel is minimal. For this reason, international standards for determining the thermal transmission properties *through* materials (ISO 8990, ASTM C1363-05) were not used. To

confine the investigation to the transmission of heat into and within the pcm-concrete panel, the panels were surrounded with insulation on all but one face which was then exposed to a heat source. To exclude the environmental effects such as temperature variation in the test room, an insulated light box was designed and constructed as shown in Figure 1.

In previous research ([7], [11]) conduction and convection were used as mechanisms of heat transfer. In this study, in order to replicate a solar heat source radiation was chosen as the mechanism of heat transfer. To control the amount of heat energy that each panel is exposed to, a particular artificial light source (Follow 1200 pro lamp) was used with which it is possible to control the wavelength of the electromagnetic waves that are emitted.

Initial tests were carried out with the lamp to determine the light intensity (Lux) and spread of light that reaches a surface positioned at particular distances from the lamp. The heat energy reaching the surface was also measured in these tests using a pyrometer. The results of these tests enabled the dimensions of the light box to be optimised to ensure that the heat energy is uniformly applied to the surface of the concrete panels and that the intensity of the heat energy is sufficient to heat up the panels within the selected time frame of 12 hours.

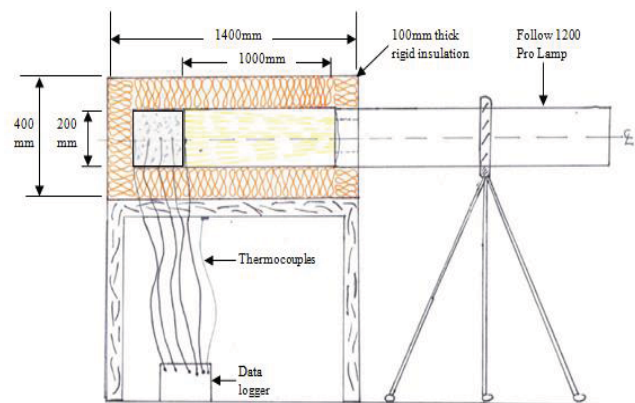


Figure 1. Schematic of the light box design

A microencapsulated PCM product called Micronal was used and came in powder form, (Figure 2). Previous research studies, ([2] and [4]) concluded that 5% by mass of concrete is the optimum quantity of Micronal to be used in a concrete mix application. Higher quantities of Micronal yielded impractically low concrete strengths and also caused significant reduction in the thermal conductivity and density which tended to counteract the increase in thermal storage capacity.



Figure 2. 1.44kg of Micronal DS 5040X

The lightweight aggregate/PCM composite was manufactured in the laboratory. Initial tests were carried out to establish the absorption capacity of three types of lightweight aggregate. It was established that an expanded clay aggregate called LECA possessed the highest absorption capacity. The LWA/PCM composite was made by vacuuming the exact required quantity of butyl stearate (PCM) into the LECA using a sealed dessicator, (Figure 3).



Figure 3. Manufacture of the aggregate/PCM composite

Differential Scanning Calorimetry tests were carried out on the PCMs to determine their actual latent heat capacity and melting temperature ranges. The summary results are shown in figure 4. The results of these tests enabled the amount of latent heat capacity added to the panels to be accurately determined and equalised for each type of panel.

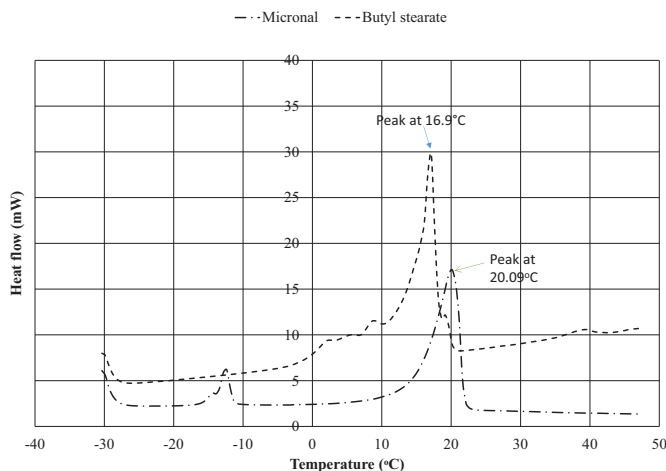


Figure 4. Heat flow V's temperature for PCMs

The thermal conductivity of each panel is a critical parameter for this study as once the heat is absorbed at the surface of the panel, the conductivity of the panel material will directly influence the heat flux through the sample and hence the thermal mass behaviour. An adjusted hot plate apparatus was used to determine the conductivity of the panels. The concrete panels were heated in the hot plate rig until a steady state condition was confirmed. The heat flux, q , (W/m^2) exiting the front face of the concrete panel was then measured by placing a heat flux pad of area A , on the surface of the concrete. The measurement is given in W/m^2 which is equivalent to $\text{Joules}/(\text{sec m}^2)$ ie q/At . The depth of the samples, d , is known and hence the conductivity can be calculated from:

$$k = \frac{q}{At} \cdot \frac{d}{(T_h - T_c)} \quad (\text{W/mK}) \quad (1)$$

The mass and density of each of the panels were also recorded.

Light box tests were carried out in which each panel was placed in the light box, one at a time and heated by the lamp for 12 hours. The temperatures of the front and rear surfaces and at equal intervals within the concrete panel were recorded during the heating and cooling periods. The recorded temperature data together with the measured densities and thermal conductivities were used to determine the thermal properties of each panel and to compare the thermal storage behaviour of the panels

3. RESULTS AND DISCUSSION

3.1 The effect of PCMs on the properties of concrete

A concrete mix was designed in accordance with Teyenne et al. [10]. It was noted during the trial mix that the addition of microencapsulated PCM reduced the workability of the fresh concrete significantly. The quantity of superplasticiser had to be increased to a level normally associated with self-compacting concrete in order to obtain a workable concrete.

During the manufacture of the panels containing the LWA/PCM composite particles, the 'stickiness' of the fresh concrete suggested that some of the PCM leaked during the hydration process. It is likely that the heat of hydration caused the PCM to melt and as the LWA/PCM particles were not yet sealed by the hardened cement matrix the PCM leaked into the cement matrix. The leaked PCM may inhibit the migration of water and hence interfere with the hydration process and adversely affect strength development. Evidence of leakage of the butyl stearate was observed on the surface of the panels after they set (Figure 5).



Figure 5. Leakage of PCM from the lightweight aggregate

The addition of both the microencapsulated PCM and the LWA/PCM composite had an adverse effect on the strength of the concrete panels. Both types of PCM panels only achieved strengths in the order of 25MPa after 28 days (Figure 6) compared to 50MPa for the control specimens. This aligns with results from previous research [2]. It is noted that two of the 56 day results are lower than the corresponding 28 day results which is unexpected however it is within the variability of the testing. One reason for the loss of strength is due to leaked PCM, or possibly as a result of damaged capsules, interfering with the hydration process and/or adversely

affecting the bond between the cement paste and the aggregate.

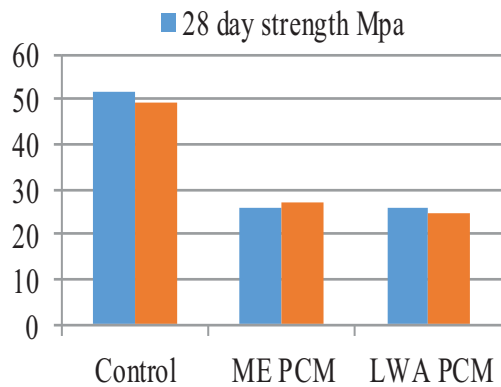


Figure 6. Concrete strengths achieved

The thermal conductivity results for the control panels were within the expected range for concrete. The addition of both types of PCM resulted in a reduction in thermal conductivity of the concrete. This is caused by the low conductivity of the PCM material. A reduced conductivity is not necessarily a problem as the desired conductivity depends on the required time frame within which the phase change must occur - 12 hours in this study. Notwithstanding this, it is important that the conductivity of the PCM/concrete composite is sufficient to ensure optimum effectiveness of the enhanced latent heat capacity provided by the PCM.

The density of both types of PCM/concrete composites was lower than the control concrete due to the lower density of the PCM relative to the density of cement paste. The conductivity and density of the materials (Table 1) influence the thermal behaviour however the effect that they have varies depending more on the ratio of conductivity to density of the material than on the absolute values of each.

Table 1. Conductivity and density of panels

Panel Type	Density (kg/m ³)	Conductivity (W/mK)
Control (C3)	2284	1.56
Control (C4)	2295	2.10
ME PCM 1	2075	1.20
ME PCM 2	2112	0.98
LWA/PCM 1	2076	0.82
LWA/PCM 2	2010	1.18

3.2 Heating behaviour

The specific heat capacity of a material is given by:

$$C_p = \frac{\Delta Q}{m \Delta T} \quad (\text{J/kgK}) \quad (2)$$

where:

ΔQ = quantity of heat energy transferred to material, (Joules).

ΔT = change in temperature of the material ($^{\circ}\text{C}$).
 m = mass of heat storage material.

For a PCM/concrete composite material the heat capacity varies during the phase transition therefore as proposed by [11], eq. (2) must be modified to include the temperature gradient over time:

$$C_p = \frac{A \cdot q}{m \frac{dT}{dt}} \quad (\text{J/kgK}). \quad (3)$$

where 'A' is the area of the sample (m^2), q is the heat energy supplied to the sample (W/m^2), m is the mass (kg), dT/dt = increase in sample temperature in a given time step ($^{\circ}\text{C/s}$).

During the light box tests each panel was exposed to equal amounts of heat energy from the lamp over an equal time period of 12 hours hence the 'q' value is the same for each panel. Also the area exposed to the light is the same for each panel at 0.04m^2 . Hence the overall thermal storage capacity of the panels can be compared by evaluating the mass x dT/dt value for each panel.

The heat flux, that is the rate of heat transfer through the material, varies throughout the depth of the material as the PCM changes phase. As a result the heat flux transferred to the surface of the sample is overestimated with respect to the internal temperature gradient over time which leads to an overestimate of the overall thermal storage capacity. To overcome this issue the applied heat flux 'q' is left in the equation as a constant and only the data from the three internal thermocouples at 50mm, 100mm and 150mm are considered.

The temperature data for each panel was analysed and dT/dt throughout the 12 hour period was determined. The dT/dt curve was then multiplied by the mass of the relevant panel and the reciprocal of the result was calculated, ie $1/(m(dT/dt))$ and plotted. The overall area under the resulting curves is indicative of the overall thermal capacity and a comparison of the thermal storage capacity of the panels was made.

Figure 7 shows a plot of the relative overall thermal storage, as recorded at 50mm depth throughout the 12 hour period. It can be noted that the panels containing PCM provide greater thermal storage capacity. Computing the area under each of the curves confirms that the panels containing the lightweight aggregate/PCM composite provide the highest overall thermal capacity at a depth of 50mm.

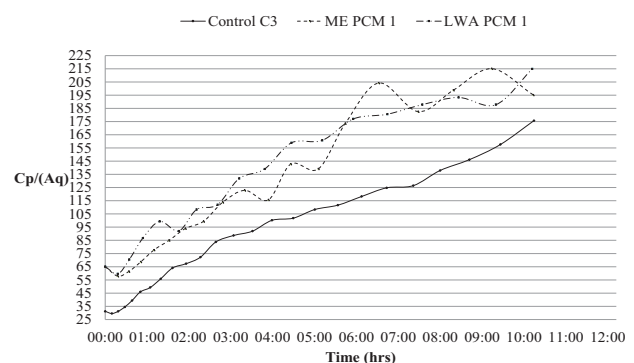


Figure 7. Curves showing relative overall thermal capacity at 50mm

The percentage of additional thermal storage and thermal mass provided by the PCM panels was determined and the results are shown in table 2. It is noted that the LWA/PCM panel provides the greatest increase in thermal storage of 61.7%. The panel with microencapsulated PCM (ME PCM) also provides a significant increase in thermal storage of 57.5%.

Table 2. Additional thermal storage provided by PCM panels at 50mm

Panel Type	ΔT in panel ($^{\circ}\text{C}$)	% Overall thermal storage relative to control panel
Control	25	100.0
ME PCM	19	157.5
LWA PCM	18	161.7

Tables 3 and 4 show the equivalent results computed from the data recorded at 100mm depth and 150mm depth.

Table 3. Additional thermal storage provided by PCM panels at 100mm

Panel Type	ΔT in panel ($^{\circ}\text{C}$)	% Overall thermal storage relative to control panel
Control	23	100.0
ME PCM	17	147.0
LWA PCM	15	143.0

Table 4. Additional thermal storage provided by PCM panels at 150mm

Panel Type	ΔT in panel ($^{\circ}\text{C}$)	% Overall thermal storage relative to control panel
Control	23	100.0
ME PCM	17	152.0
LWA PCM	15	147.0

At each thermocouple location the LWA/PCM panel displays the lowest change in temperature over the 12 hour period. It can be noted that the overall thermal storage of the PCM panels reduces with depth relative to the control panel. Part of the reason for this is that the overall thermal storage for the control panel increases. However another thermal property that contributes to this behaviour is thermal diffusivity, α which is the ratio of the conductivity of a material to its volumetric heat storage capacity.

$$\alpha = \frac{k}{\rho C_p} \quad (\text{m}^2/\text{s}) \quad (4)$$

Thermal diffusivity indicates the rate at which temperature changes occur in a material. The higher the value of thermal diffusivity the quicker the material will reach temperature equilibrium with its environment. The lower conductivity and higher heat storage capacity of the PCM panels resulted in reduced thermal diffusivity which in turn reduced the effectiveness of the PCM as depth increased as the heat took longer to reach the PCM. As shown in Figure 8, the LWA PCM panels displayed the lowest diffusivity. This means that

the heat took longer to penetrate 100mm in the LWA/PCM panels, so over the 12 hour period the overall heat reaching 100mm depth in the LWA/PCM panels is less than that in the control panel and also the ME PCM panels. Hence the PCM becomes less effective with increasing depth. In a real application the level of exposure to a heat source depends on both local climate and position of the concrete element within the building, ie exposure to daylight. So the effective depth of the PCM will depend on the proposed location of the composite material. In applications where the heat energy is reaching up to a depth of 100mm into the composite PCM material the LWA/PCM panels provide a greater thermal storage capacity.

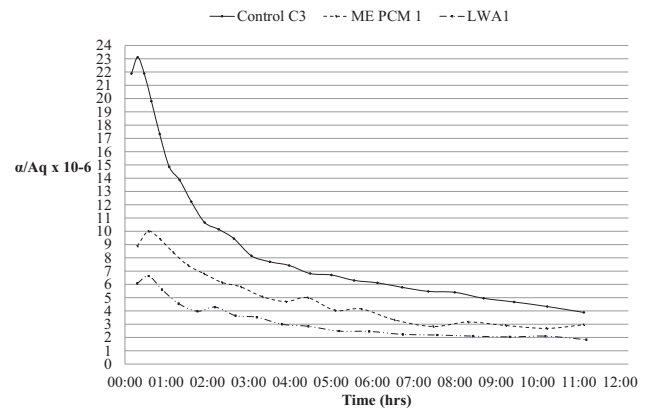


Figure 8. Relative thermal diffusivity recorded at 50mm

Another key property that influences thermal mass behaviour is the thermal inertia of a material denoted 'I' which is a measure of the responsiveness of a material to variations in temperature. Thermal inertia is given by the following equation: [12]:

$$I = \sqrt{\rho C_p k} \quad (\text{J}/(\text{m}^2 \text{K} \sqrt{\text{s}})) \quad (5)$$

where ρ is the density, k is the thermal conductivity and C_p is the specific heat. A high thermal inertia describes materials that characterise high thermal mass and high thermal conductivity. Such materials will display small changes in temperature throughout the diurnal cycle. Referring to equation (4) for thermal diffusivity, α , equation (5) can also be written as follows:

$$I = \frac{k}{\sqrt{\alpha}} \quad (\text{J}/(\text{m}^2 \text{K} \sqrt{\text{s}})) \quad (6)$$

It can be noted from equation (6) that the higher the thermal diffusivity of a material the lower the thermal inertia. Hence for a building material to provide good thermal mass it requires an appropriate balance between thermal diffusivity and thermal inertia.

Figure 9 shows the relative thermal inertia recorded at a depth of 50mm. It is noted that despite having the lowest thermal diffusivity, the LWA/PCM panel displays the lowest thermal inertia. This is caused by the low conductivity and density of the LWA/PCM panels.

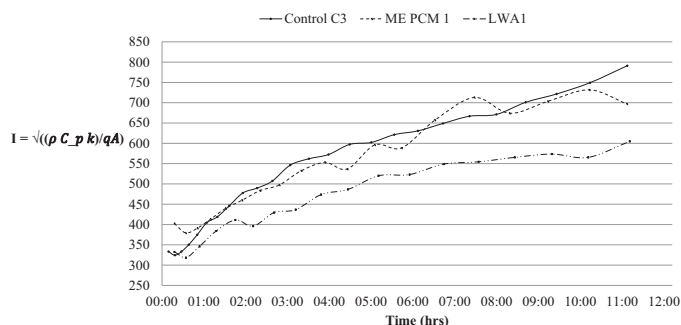


Figure 9. Relative thermal inertia recorded at 50mm

4. CONCLUSIONS

Based on the results of the analysis presented in this paper the following conclusions can be made:

- Up to a depth of 100mm the concrete panels containing the LWA/PCM composite provided the greatest increase in thermal storage capacity compared to the control panel.
- The LWA/PCM panel displayed the lowest increase in temperature throughout the 12 hour heating period.
- The addition of both types of PCM caused a reduction in thermal conductivity and density. This resulted in lower thermal diffusivity in the panels containing PCM.
- As depth increases the level of thermal storage provided by the ME PCM panel approaches the storage provided by the LWA/PCM panel and at a depth of 100mm the storage provided by the ME PCM panel was slightly greater than the LWA/PCM panel. Hence if the local conditions allow the heat energy to penetrate deeper than 100mm the ME PCM composite material will provide a greater increase in thermal storage capacity.
- The effectiveness of both types of PCM in increasing the overall thermal storage of the concrete panels relative to the control panel reduces with depth. This is due to the fact that the thermal diffusivity of the PCM panels is lower than the control panels hence the heat takes longer to reach a depth of 100mm in the LWA/PCM and ME PCM panels.
- As thermal diffusivity is the parameter that is hindering the effectiveness of the LWA/PCM composite, improving the conductivity of the LWA/PCM panels would further enhance the thermal performance of the material.

5. FURTHER RESEARCH

Further research is currently being carried out to investigate the influence of ground granulated blast furnace slag (GGBS) on the thermal properties of PCM/concrete. Methods of improving the thermal conductivity of concrete containing lightweight aggregate/PCM composite are also being explored.

ACKNOWLEDGMENTS

This work is part of the IMPRESS project¹ funded by the Horizon 2020 Framework Programme. The aims of the IMPRESS project are to develop innovative precast products for renovation of existing building stock thereby improving the performance and energy efficiency of European buildings.
¹<http://www.project-impres.eu>

REFERENCES

- [1] Pasupathy, a., Velraj, R. and Seeniraj, R.V., 2008. Phase change material-based building architecture for thermal management in residential and commercial establishments. *Renewable and Sustainable Energy Reviews*, 12(1), 39–64
- [2] Hunger, M., Entrop, A. G., Mandilaras, I., Brouwers H. J. H. and Founti, M., 2009. The behaviour of self-compacting concrete containing micro-encapsulated Phase Change Materials. *Cement and Concrete Composites*, 31(10), 731–743
- [3] Eddahak-Ouni, A., Drissi, S., Colin, J., Neji, J. and Care, S., 2014. Experimental and multi-scale analysis of the thermal properties of portland cement concretes embedded with microencapsulated Phase Change Materials (PCMs). *Applied Thermal Engineering*, 64(1-2), 32–39
- [4] Fenollera, M., Miguez, J. L., Goicoechea, I., Lorenzo, J. and Alvarez, M. A., 2013. The Influence of Phase Change Materials on the Properties of Self-Compacting Concrete. *Materials*, 6(8), 3530–3546
- [5] Ling, T.-C. and Poon, C.-S., 2013. Use of phase change materials for thermal energy storage in concrete: An overview. *Construction and Building Materials*, 46, 55–62
- [6] Hawes DW, Feldman D, 1992. Absorption of phase change materials in concrete. *Sol Energy Mater Sol Cell*; 91–101
- [7] Lee, T., Hawes, D. W., Banu, D. and Feldman, D., 2000. Control aspects of latent heat storage and recovery in concrete. *Solar Energy Materials and Solar Cells*, 62(3), 217–237
- [8] Zhang, D., Li, Z., Zhou, J. and Wu, K., 2004. Development of thermal energy storage concrete. *Cement and Concrete Research*, 34(6), 927–934
- [9] Memon, S.A., 2014. Phase change materials integrated in building walls: A state of the art review. *Renewable and Sustainable Energy Reviews*, 31, 870–906
- [10] Teychenne, D. C., Franklin, R. and Erntroy, H., 1997. *Design of normal concrete mixes*. BRE press
- [11] Pomianowski, M., Heiselberg, P., Jensen, R.L., Cheng, R. and Zhang, Y., 2014. A new experimental method to determine specific heat capacity of inhomogeneous concrete material with incorporated microencapsulated-PCM. *Cement and Concrete Research*, 55, 22–34
- [12] Pomianowski, M., Heiselberg, P. and Jensen, R.L., 2012. Dynamic heat storage and cooling capacity of a concrete deck with PCM and thermally activated building system. *Energy and Buildings*, 53, 96–107

Using Photovoltaics to Power Electrochemical Chloride Extraction from Concrete

Sean Bond¹, Lynette O Callaghan², Niall Holmes³, Brian Norton⁴

^{1,2}School of Civil & Structural Engineering, Dublin Institute of Technology, Bolton St, Dublin 1, Ireland

³School of Mechanical and Transport Engineering, Dublin Institute of Technology, Bolton St, Dublin 1, Ireland

⁴Dublin Energy Lab, Bolton Street, Dublin 1, Ireland

email: ¹seanbond2005@yahoo.ie, ²lynette.ocallaghan@dit.ie, ³niall.holmes@dit.ie, ⁴president@dit.ie

ABSTRACT: Corrosion of embedded steel in reinforced concrete (RC) is a world-wide problem, that reduces structural performance and lifespan. Chloride attack may be a result of seawater, de-icing salts or contaminated admixtures, brought on by ingress of chlorides into the concrete.

Electrochemical Chloride Extraction (ECE) is a non-destructive treatment for contaminated RC structures, that due to uncertainty of treatment times and applied current densities, is only 50% effective. It is often diesel powered has an environmental impact and often very costly due to the long treatment times.

To improve the efficiency of ECE the influences of concrete resistance, cement type and duration of treatment have been investigated in an experimental programme.

The use of Photovoltaic (PV) panels to improve the efficiency of ECE is presented which replace fossil fuels as a power source enabling a more environmentally sustainable treatment. These findings will increase the life span of vital infrastructure and reduce expensive ongoing repairs with decreased traffic congestion and inconveniences associated with bridge repairs.

KEY WORDS: Electrochemical Chloride Extraction; Efficiency; Concrete Resistance; Current density; Photovoltaics.

1 INTRODUCTION

Corrosion of RC structures is a worldwide problem resulting in a loss of structural performance. Since concrete is permeable, it is susceptible to the ingress of chloride ions. The source of these chlorides are a combination of de-icing salts, seawater and contaminated admixtures [1].

Electrochemical Chloride Extraction of Chloride ions, embedded in reinforced concrete structures, operates by creating an electrical circuit between the surface of the concrete and the steel reinforcement. This process is driven by a direct current (DC) electricity supply. Previously, diesel powered generators have powered this treatment, leading to an inefficient process due to the long durations over which ECE operates.

In terms of the electrical requirements of ECE, a steady voltage of 25 to 40V is normally used to produce a current density of between 1 and 5 A/m². The power requirements of the system depend on the internal resistance of the concrete. The current paths travel through the pore water solution towards the surface. The more ions in the pore water solution, the higher the current since ionic flow is the basis for ECE. As the chlorides are removed, the concrete's resistance increases thus requiring a lower current later on in the treatment [2].

A photovoltaic (PV) device directly converts light into electricity at an atomic level. When solar energy, in the form

of photons, is absorbed electrons are released from a PV material as shown in Figure 1. The operation of a photovoltaic array does not emit greenhouse gases nor particulates as is the case with a diesel generator.

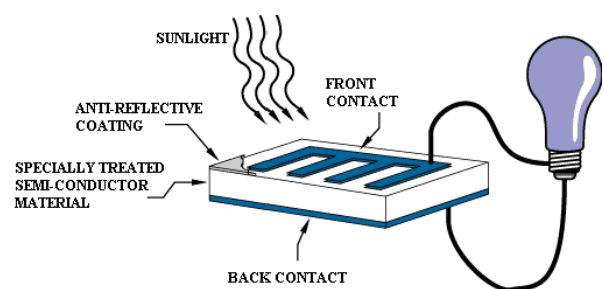


Figure 1 Operation of a Basic Photovoltaic Cell [7]

In order to size an appropriate PV array to replace traditional diesel generators, the electrical requirements must first be determined. Using RETScreen 4 [8], an appropriate panel array has been sized to meet the requirements of a system operating autonomously purely from PV.

2 BACKGROUND

2.1 How Electrochemical Chloride Extraction Works

A titanium mesh, submerged in an electrolyte, is used to create an anode at the concrete surface and connected to the positive terminal of the DC supply. The embedded steel reinforcement is then made cathodic by connecting it to the negative terminal of the DC supply. This arrangement is shown in Figure 2.

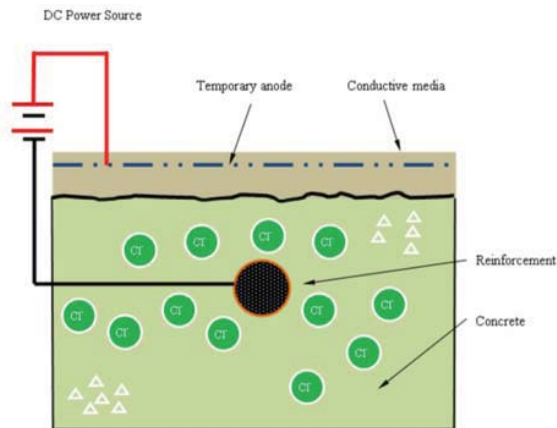


Figure 2 Setup of Electrochemical Chloride Extraction

In a conventional battery cell, the cathode is positive and the anode is negative. In an electrolytic cell, energy is repelled back through the negative terminal, provided externally, which makes the cathode negative and the anode positive. As electrons carry a negative charge, they are repelled from the negative terminal of the power supply and migrate towards the positive cathode. The circuit is completed through the pore water solution within the concrete. This system drives the negatively charged chloride ions towards the temporary anode as in Figure 3.

Hydroxyl ions will accumulate around the reinforcement surface to form a passive oxide film on the steel surface that helps fight against corrosion. The accumulation of these hydroxyl ions promotes regeneration of the steel surface, that may in turn repair this oxide film, previously damaged by corrosion.

By moving the chloride ions away from the reinforcing steel, further corrosion of the steel is prevented. Unfortunately, the return of the chlorides is inevitable but since a large proportion of the existing chlorides may be removed, the corrosion process is slowed down thus extending the useful life.

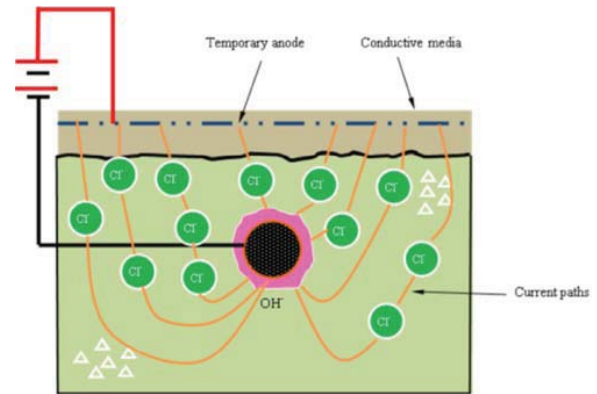


Figure 3 Complete Electrochemical Circuit

2.2 Treatment Times

Chlorides exist in the form of free, chemically bound and physically adsorbed ions. The free chloride ions exist in the pore water solution of the concrete from de-icing salts or from sea-water. Under the effect of an electric field, adsorbed chlorides are released, which leads to an increase in free chloride concentration in the pore solution. Due to ECE treatment, the free chlorides are removed quickly. When the current is switched off, the dissolution of chemically bound chlorides leads to re-establishing of the equilibrium between chemically bound and free chlorides. Part of the dissolved chloride will be physically adsorbed on the pore walls and equilibrium between free and adsorbed chlorides is re-established [5]. Thus by allowing a break in the treatment, the efficiency of chloride removal is increased. Work carried out by Elsener [5] explored breaking the treatment into on/off phases. This promoted the dissolution of bound chloride ions into the pore-water solution of the concrete. The length of treatment depends on the concentration of chlorides in the concrete. However, 8 weeks of treatment is usually applied for ECE as to limit the accumulated charge passing through the concrete [2-5].

2.3 Photovoltaics

The photovoltaic effect was first noted in 1839, when Becquerel observed that “electrical currents arose from certain light induced chemical reactions” [9]. Later on in 1905, Einstein described the photoelectric effect on which photovoltaic technology is based, for which he later won a Nobel prize in physics [7].

In order to investigate the feasibility of using a PV panel to power ECE, the system must be able to provide a steady voltage and include battery storage for night-time use.

While there are many photovoltaic technologies [10] most PV panels are made of crystalline silicon cells. The efficiency of these panels are between 14 – 20% and depends whether the panel is a mono or poly crystalline structure with the former being more efficient. Thus, with an average radiation level of 1000W/m^2 and an area of 1m^2 , one can expect 200W/m^2 with a panel rated at 20% efficient. At low irradiance levels (200W/m^2), the power output of such a panel would be 40W/m^2 .

A PV panel is controlled using a maximum power point tracker (MPPT) controller. This regulates the output voltage of the panel in order to gain the ideal current. Since the power is dependent on current, the maximum power point must be maintained as shown in Figure 4. As the amount of available sunlight decreases, the level of voltage drawn must be decreased in order to achieve the most efficient current.

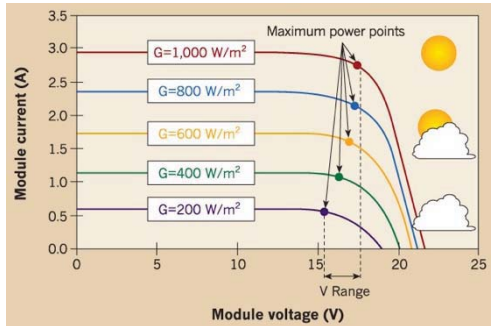


Figure 4 Typical maximum power point curve [11]

Once the PV panel and MPPT controller have been selected, the batteries can be sized. The panel cannot be directly connected to the steel since the voltage and current being delivered will not be steady which is a requirement of ECE. The batteries are charged by the PV panel, which are then used to power the treatment. In most cases, lead acid batteries are used. The system is illustrated in Figure 5.

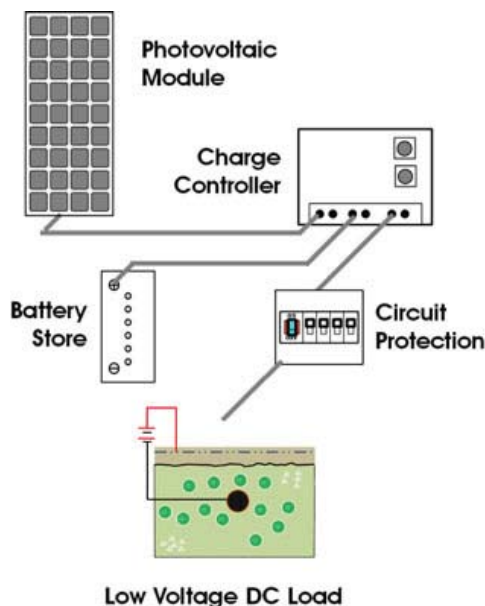


Figure 5 Block Diagram of DC PV system [12]

3 METHODOLOGY

3.1 Resistivity Measurements

By measuring the surface and internal resistivity of concrete, one may gain an insight into the electrical requirements of ECE and optimised for a more efficient process.

The resistivity of concrete increases rapidly during the first 20 days of moist storage, but after 30 days it becomes almost constant. Since conduction can be regarded as electrolytic in

nature, the initial increase in resistivity is probably due to the continued hydration of the concrete.

To investigate this, a concrete specimen was cast with CEM I cement. The aim was to obtain a weekly value of resistivity up to 8 weeks (56 days) which may be predicted using simple electrical formulae. This allows the resistivity of particular concretes to be accounted for in the system.



Figure 6 Resipod used for Resistivity Measurements

To measure the resistivity, a commercial 4-point Wenner probe Resipod [14] shown in 6 was used. The probe induces a current between the two outer probes, while measuring the potential difference between the inner probes. The resistance may be calculated once the resistivity is measured using equation 1, where s is the distance between each probe (5cm for Resipod), ρ is the measured resistivity of the concrete surface ($k\Omega \cdot cm$) and R is the resistance of the concrete (Ω).

$$\rho = R2\pi s \quad (1)$$

Assuming the resistance calculated using current and voltage measurements of a previous treatment [15], a prediction of the resistivity of the specimen is possible. This allows verification of the methodology used by experimentally testing. This system used a constant 30V DC with a measured current of 34.6mA and current density (σ_s), equal to $4.5A/m^2$ of the steel circumferential area (10mm diameter bar). Given the resistance of the circuit was 866Ω (using ohms law), and distance s from the rebar to the titanium mesh was 5cm, the resistivity (ρ) may be predicted using Equation 1 as $27.2k\Omega \cdot cm$. However, with different cement types, the resistance of the system may change.

4 EXPERIMENTAL WORK

The experimental work focused on attaining a resistivity value of concrete used in previous works [15]. The resistivity was of particular interest due to its variability in different cement types.

In order to measure the resistance of the concrete, a concrete slab (245mm wide x 245mm deep x 100mm thick) was cast along with 6 cubes for compressive strength testing at 7 and 28 days. The mix was designed for compressive strength of 35MPa using CEMI with a w/c of 0.5. The moisture content of the aggregate and sand was measured prior to casting in order to achieve the desired w/c ratio. The mix proportions are shown in Table 1.

The specimens were compacted using a vibration table to ensure no trapped air remained inside the mix. After curing for 24 hours in a sealed plastic bag, the concrete were placed

into a curing tank for 7 days until the first series of cubes were tested. The specimen was painted on five sides leaving the top free. The resistivity of the specimen was measured weekly up to 56 days.

Table 1: Concrete Composition kg/m³.

CEM I	Water	W/C	FA	CA	
				10mm	20mm
450	225	0.5	561	570	570

FA – Fine Aggregate, CA – Coarse Aggregate

4.1 Results

The average 7 and 28 day compressive strengths were 53 and 64.2MPa respectively. The results from the resistivity measurements are shown in 7. As expected the value of the resistivity gradually increased over the 8 week period.

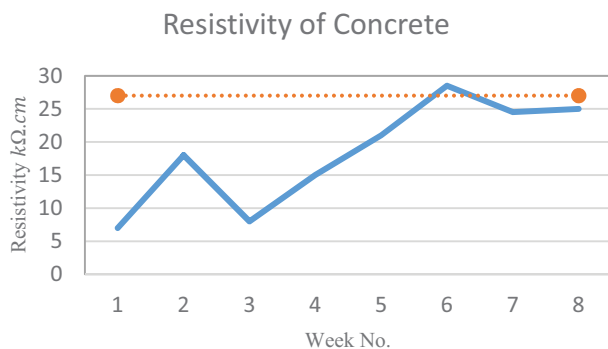


Figure 7 Resistivity Measurements

5 CASE STUDIES

5.1 ECE Treatment in Ottawa

Work carried out by Bennett and Fong [2] explored the trial application of ECE on a bridge deck in Ottawa. The deck had a surface area of 300m², of which half was treated and half left as a control. The start up current for both North and South spans was 48A with a total treatment area of 68m².

A 60kW diesel fuelled electricity generator was used to provide the three phase AC power for the system. Since ECE requires DC, an inverter was used. The requirements for the study are summarised in

Table 2.

Table 2 System Properties (Lab and Field)

	Unit	Field
Power, P	Watts, W	2304
Current, I	Amps, A	48.0
Voltage, V	Volts, V	48.0

5.2 ECE Treatment in Virginia

A field trial carried out by Clemeña and Jackson [4] on a highway overpass in Virginia used high currents for ECE treatment. With an area of 174m², the start-up current for ECE was around 160A, equating to around 4000A-hr. Therefore, it is clear that localising treatment to key structural elements in strategic locations, current requirements are lower. Focusing on regions of a structure more vulnerable to chloride ingress, for example piers of a bridge within the tidal zone or subject to ongoing sea spray, localisation of ECE may be achieved.

5.3 Cost of Diesel Generator

The cost of a diesel generator for an 8-week period ranges from around €10,000 to €15,000. For the field trial carried out by Bennett and Fong [2], the fuel consumption was 6000 litres of diesel equating to €6000. Therefore, the total expected cost of using a diesel generator (excluding fittings and wiring) would equate to over €25,000 including inverters @ €2000 each.

6 APPLICATION OF PV TO AN EXISTING STRUCTURE

Photovoltaic technology is always being improved with new efficient panels being brought to the market constantly. During the period of writing this paper, the most efficient commercially-available panel was made by Panasonic with an output at low (200W/m²) and normal (800W/m²) irradiance levels summarised in Table 3.

Table 3 Power Output at Low and Normal Irradiance Levels

Irradiance Level	Low 200W/m ²	Normal 800W/m ²
Max. power (Pmax) [W]	63.5	247.2
Max. power voltage (Vmp) [V]	56.2	54.2
Max. power current (Imp) [A]	1.13	4.58
Open circuit voltage (Voc) [V]	66.0	65.1
Short circuit current (Isc) [A]	1.21	4.91

Considering that running the system in during the warmer months would be a lot more feasible than in winter, the lowest average daily solar irradiation levels for Dublin, between April and September will be used in the sizing calculations.

6.1 Sizing of PV System

Using the treatment area for the Ottawa bridge, a current of 48A was used. This level of current is too high for PV to supply and it would take 100m² of PV to provide which is unfeasible. Instead, by localising the treatment the efficiency would be improved.

By means of an example, an analysis of the Firth Bridge in Dornoch, Scotland (Figure 8) was undertaken. The piers of this bridge are susceptible to chloride ingress due to the marine environment and rising tides. The tidal levels at the bridge site rise and fall by 2m every day. The piers are shaped like an octagon with each face 300mm wide. This gives an effective localised treatment area of 4.8m²/pier. Assuming the

start-up current for the treatment area may be scaled down from the case studies, the piers would require 3.4A each (6.8A for the pair) to power ECE equating to approximately 326.4W at a 48V daily load.



Figure 8 Firth Bridge Dornoch, Scotland [16]

By using a simplified design method by Markvart [17], the number of solar panels required to provide power to the system may be calculated given local climate data. The average daily hours of sunshine over the 6-month period is 15. Therefore, the batteries must provide power ~37.5% of the time (nighttime hours). The load must be increased by this value in order to account for this as calculated in eq 1-3. The efficiency of the battery, η_{bat} , is taken as 76%.

$$load \div \frac{\eta_{bat}}{1 - f(1 - \eta_{bat})} = 326.4 \div \frac{0.76}{1 - 0.375(1 - 0.76)} = 390.8W \quad (3)$$

$$Daily Load = 390.8 \times 24 = 9379.2 Wh$$

Intuitively, the number of panels required in series is one as the system voltage will never exceed 48V (a panels maximum rated output voltage is 58V).

The number of parallel panels is computed below, where I_L is the equivalent load current, E_L is the typical daily power requirements of the load, V_{DC} is the operating voltage of the system, I_{PV} is the nominal current of the PV array, PSH is numerically equal to the irradiation per day and I_{SC} is the short circuit current of the panel:

$$I_L = \frac{E_L}{24V_{DC}} = \frac{9379.2}{24 \times 48} = 8.14 A \quad (4)$$

$$I_{PV} = \frac{24I_L}{PSH} = \frac{24 \times 8.14}{2.78} = 70.27A \quad (5)$$

$$No. in Parallel = \frac{I_{PV}}{I_{SC}} = \frac{70.27}{7.44} = 9.45 \approx 10 \quad (6)$$

A similar analysis using RETScreen 4 was performed using the same criteria as above with the requirements calculated as 14 panels with a battery capacity of 710A-hr. Being

conservative, the higher number obtained from RETScreen will be used.

6.2 Batteries

A battery storage system with an output of 48V and 6.8A (for a pair) must then be developed in order to store and deliver the power. To validate the results from RETScreen, the battery system is sized numerically. Choosing two days of autonomy and a 60% depth of discharge, the daily capacity is equal to 9379.2 Wh/day. Assuming 97% wiring and distribution efficiency, the battery must be able to provide 9669.3 Wh/day. Dividing this by the voltage required, the daily amp-hour requirements is equal to 201.4 A-hr/day. The required system capacity is calculated below.

$$\frac{201.4 \times 2}{0.6} = 671.3 A \cdot hr \quad (7)$$

The battery system therefore must have a rated capacity of approximately 671.3 A-hr/day at 48V. Again, a conventional approach has been taken in the sizing, so RETScreen values will be used for the battery system (14 panels, 710A-hr battery bank).

6.3 Cost of System PV System

The PV system designed above would require 14 no. HIT330 panels @ €400 each (€5,600) and 16 no. L16RE-B 370 AH 6V Trojan batteries @ €307 each (€4912). Include a charge controller (~€2,000) giving a total cost of using a PV system as €12,512.

7 DISCUSSION

7.1 Resistivity Measurements

The methodology for the resistivity measurements was mainly concerned with validating the prediction made in section 3.1. By showing that the resistivity may be used to determine the internal resistance of concrete specimens, an accurate prediction on the current and voltage to be used for treatment can therefore be determined. Since only one specimen was used to validate this principle, the results may not reflect the true nature of the concrete. Despite this, it is a reasonable method of determining the electrical properties of an RC structure. It should also be noted that the internal resistivity of the concrete will be lower than that at the surface. Thus the prediction made here is conservative.

7.2 Photovoltaics

Based on the PC costing, it can save up to 50% of existing investment for employing ECE. Aside from reduced costs, PV is a clean source of energy making the treatment more economically friendly compared to traditional diesel generators.

8 CONCLUSIONS

The following conclusions have been drawn:

- ECE treatment on large areas of RC structures requires a very high current. This prevents PV from being employed to power ECE in large areas.
- Localising the treatment reduces the area by focusing on key structural elements enabling ECE to be powered solely using photovoltaics.
- Measuring the resistivity of concrete tailors the PV system for specific requirements.
- RETScreen 4 together with simplified design methodologies are effective tools for preliminary sizing of PV arrays.

ACKNOWLEDGMENTS

The author acknowledges the financial support from the PhD scholarship funded by the College of Engineering and Built Environment at DIT.

REFERENCES

- [1]. Al-Numan, B., & Cicek, V. (2011). *Corrosion Chemistry* (Vol. 1st Ed). New Jersey, Salam, Massachusetts: John Wiley & Sons. Scrivener Publishing LLC.
- [2]. Bennett, J., Fong, K., & Schue, T. (1993). *Electrochemical Chloride Removal and Protection of Concrete Bridge Components: Field Trials: Report No. SHRP-S-669*. Washington DC: National Research Council.
- [3]. Canadian Strategic Highway Research Program. (1995). *Electrochemical Chloride Extraction from Concrete Bridge Components*. Ottawa: Transport Association of Canada.
- [4]. Clemeña, G., & Jackson, D. (2000). *Trial Application of Electrochemical Chloride Extraction on Concrete Bridge Components in Virginia*. VTRC 00-R18, Virginia Department of Transportation and the University of Virginia, U.S. Department of Transportation Federal Highway Administration.
- [5]. Elsner, B., & Angst, U. (2007). Mechanism of electrochemical chloride removal. *Corrosion Science*, 49, 4504-4522.
- [6]. Yajun, L., & Xianming, S. (2009). Electrochemical Chloride Extraction and Electrochemical Injection of Corrosion Inhibitor in Concrete: State Of The Knowledge. *Corrosion Reviews*, 27 (1-2), 53-81.
- [7]. Knier, G. (2012). *How Do Photovoltaics Work?* Retrieved Jan 29, 2016, from NASA: <http://science.nasa.gov/science-news/science-at-nasa/2002/solarcells/>
- [8]. Natural Resources Canada. (2016, 4 1). *RETScreen*. Retrieved 4 7, 2016, from Natural Resources Canada: <http://www.nrcan.gc.ca/energy/software-tools/7465>
- [9]. Chapin, D., Fuller, C., & Pearson, G. (1954). A new p-n junction photocell for converting solar radiation into electrical power. *Journal of Applied Physics*, 25, 676-7.
- [10]. Chaara, L. E., Iamonta, L. A., & Zeinb, N. E. (2011). Review of photovoltaic technologies. *Renewable and Sustainable Energy Reviews*, 15, 2165-2175.
- [11]. Mayfield, R. (2012). *The Highs and Lows of Photovoltaic System Calculations*. Retrieved March 6, 2016, from Electrical Construction and Maintenance : <http://ecmweb.com/green-building/highs-and-lows-photovoltaic-system-calculations>
- [12]. windandsolar.co.uk. (2016). *Small Off Grid System*. Retrieved 03 26, 2016, from <http://www.windandsun.co.uk/information/types-of-system/small-off-grid-system.aspx#.Vv78nIRtLRt>
- [13]. Whittington, H. W., McCarter, J., & Forde, M. C. (1981). The conduction of electricity through concrete. *Magazine of Concrete Research*, 33 (114), 48-60.
- [14]. proceq.com. (2016). *REsipod Resistivity Meter*. Retrieved 03 21, 2016, from proceq.com: <http://www.proceq.com/nondestructivetestequipment/concrete-testing/moisture-corrosion-analysis/resipod.html>
- [15]. Bond, S., Osmani, C., Holmes, N., & Norton, B. (2016). *Influence of Cement Type on Electrochemical Chloride Extraction*. Dublin.
- [16]. David. (2011). *Dornoch Firth Bridge from the south shore, November*. Retrieved 04 6, 2016, from Flickr: https://www.flickr.com/photos/david_maclean/6319609846
- [17]. Markvart, T. (2000). *Solar Electricity*. Southampton.

Pre-stressing using BFRP bars: an experimental investigation on a new frontier of precast FRSCC

Bruno Dal Lago¹, Peter Deegan², Su E. Taylor³, Philip Crossett³, Mohammed Sonebi³, Liberato Ferrara¹, Andrea Pattarini⁴

¹Department of Civil and Environmental Engineering, Politecnico di Milano, P.za Leonardo da Vinci 32, Milan, Italy

²Banagher Precast Concrete, Queen Street, Banagher, Co. Offaly, Republic of Ireland

³School of Planning, Architecture and Civil Engineering, Queen's University, University Road, Belfast, BT7 1NN, Northern Ireland

⁴Azichem, via Gentile 16a, Goito, Mantova, Italy

email: brunoalberto.dallago@polimi.it, PeterD@bancrete.com, S.E.Taylor@qub.ac.uk, m.sonebi@qub.ac.uk, liberato.ferrara@polimi.it, a.pattarini@azichem.com

ABSTRACT: Basalt fibre reinforced polymer (BFRP) bars are proposed as a pre-stressed reinforcement for precast concrete elements because of their enhanced resistance to aggressive agents which makes them far more corrosion resistant than steel. Moreover, the lower elastic modulus enables a limit on the instantaneous and time-dependant losses and makes their application to pre-stressed precast concrete particularly promising. A full scale experimental investigation has been carried out in the framework of the EU funded research project Eirocrete at Banagher Precast Concrete Ltd on a precast concrete voided light-weight floor slab pre-stressed with basalt reinforced polymer bars and made with fibre reinforced self-compacting concrete (FRSCC). The experiment was aimed at verifying the correct functioning of the pre-stressing system, typically employed for steel tendons, the time-dependant behaviour of the beam during service loading and its resistance, allowing to obtain information about reliability and robustness of this technology.

KEY WORDS: Basalt Fibre Reinforced Polymer (BFRP) bars; Pre-stressing; Steel-free beams; fibre reinforced self-compacting concrete (FRSCC).

1 INTRODUCTION

Extensive research has been performed worldwide in the recent decades with the aim of providing solutions for the substitution of steel reinforcement in concrete members. The main reasons are durability and reduction of carbon emission. Composite materials have been successful in this quest. Among the composites, the production of basalt fibre reinforced polymer (BFRP) bars has been advanced (see Fiore et al. [1]) and its application to concrete has been experimented by Tharmarajah et al., Zhang et al. [2, 3] and applied in practice (Taylor et al. [4]). It has also been used pre-stressing in timber by McConnell et al. [5].

BFRP bars are characterised by a high tensile strength, ranging from 920 to 1650 MPa, and a relatively low elastic modulus, ranging from 45 to 59 GPa (Crossett et al. [6]). These particular features make their application in pre-stressed concrete promising, since their resistance is lower but comparable with that of traditional pre-stressing steel, while having an elastic modulus about four times smaller. This implies that both elastic and long-term pre-stressing losses occurring in pre-stressed concrete elements due to the shortening of the member will be relevantly reduced with the use of BFRP bars. The use of FRP bars in pre-stressed concrete has been studied by Dolan et al. and Zhou [7,8] and extended to BFRP bars by Stoll et al. and Crossett et al. [9,6]. Crossett et al. [10] also studied the BFRP-concrete load transfer mechanism with reference to sandblasted bars.

A challenge for the application of pre-stressing composite bars is the temporary mechanical anchorage prior to the release of the load. All fibre composite materials are characterised by orthotropic mechanical behaviour, with a

better performance when the load is applied in the direction of the fibres, while the strength is typically much lower when the load is applied orthogonally with respect to the fibres. The typical anchorage devices used for steel tendons are based on wedges that apply strong lateral pressures to the bars. Solutions to be applied to fibre composite bars have been proposed by Crossett et al., Al-Mayah et al., Carvelli et al. and Schmidt et al. [6, 11, 12, 13] with reference to FRP bars. This paper investigates the structural behaviour of a steel-free pre-stressed slab member designed and tested under the research project IAPP-Eirocrete funded by the European Commission within FP7. The 10m long fibre reinforced self-compacting concrete (FRSCC) slab member was pre-stressed with BFRP bars and had GFRP shear links. Polypropylene fibres were added at 4 kg/m³ of concrete to improve service performance. The design concept and the technical features of the element are presented. The manufacturing of the element is described in detail, highlighting the occurrence of some unexpected issues. The experimental results of a 3-point loading test on the element are reported. Comments about the reliability and robustness of BFRP pre-stressed concrete are finally provided with reference to both its structural behaviour and its technology challenges in an established industry using steel.

2 STRUCTURAL DESIGN OF THE SLAB MEMBER

A voided light-weight section was used due to its popularity in the UK market. Since the cross section, shown in Figure 1, is not symmetrical along the vertical axis, the positioning of the pre-stressing BFRP bars has been studied in such a way to minimise torsional effects. The element has been designed under the assumptions of its use as a roof element, for which

the additional dead loads other than self-weight, as coming from waterproofing and thermal insulation layers, may be considered negligible. The design condition adopted, without a particular reference to a snow load, is the serviceability limit state, in particular with the goal of having a positive evolution of camber, similar to traditional pre-stressed elements with steel tendons. This meant that the achievement of a pre-camber and a controlled rise in service over the time of the release is generally a design criterion to be pursued.

Due to the use of an innovative material in the beam, the simplified formulation for the estimation of pre-stressing losses provided by Eurocode 2 (EN 1992-1-1:2005) [14], based on the linearisation of the long-term interaction among the phenomena influencing deformability, including viscoelastic member shortening, concrete shrinkage and reinforcement relaxation, was not used. A novel semi-analytical procedure was developed based on the explicit interaction (as Equation 1) with de-coupling of the longitudinal and transversal deformation whilst taking into account the shortening evolution profile to assess the pre-stressing losses. The C45/55 concrete behaviour curves and mechanical properties provided in [14] were used. The average mechanical properties of BFRP (rupture stress $f_{u,b} = 900$ MPa and elastic modulus $E_{m,b} = 56$ GPa) have been considered as previously tested by [3 & 5]. In the design stage, relaxation of the BFRP bars has been neglected. Further details are given in the FP7 deliverable reports with EU Commission.

$$v(t, t_0) = v_e(t) + \int_{t_0}^t v_e(t) \dot{\phi}(t, t_0) dt \quad (1)$$

12 BFRP bars, placed at 40 mm from the soffit for bond stress distribution in the concrete, were designed for 500 MPa pre-stress, which corresponds to ~50% rupture stress. Figure 1(a) shows the layout including the design of the shear links.

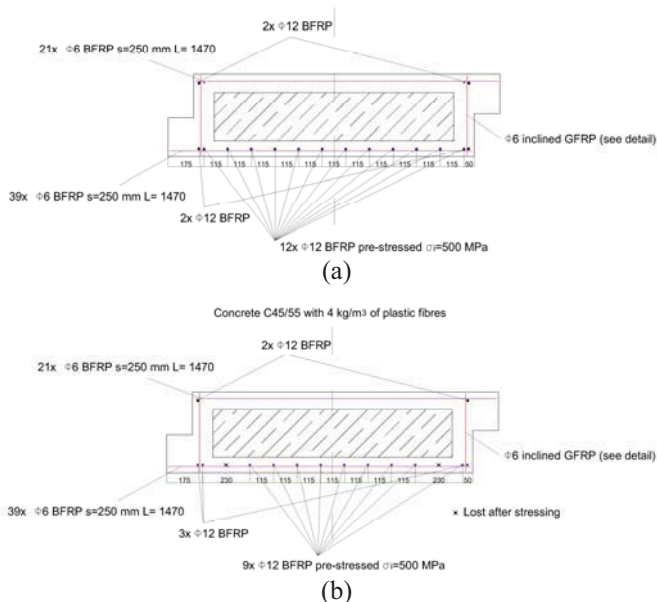


Figure 1. Slab beam cross section: (a) designed, (b) realised.

The maximum bending moment was calculated using mechanical non-linear moment-curvature relationship for this cross-section, including pre-stress losses at 58 days from release of the pre-stressing. BFRP bars were modelled with a linear elastic behaviour. The Sargin curve provided in the ModelCode 10 [15] was used for concrete. The effect of the polypropylene fibres was taken into account in the post-cracking residual tensile stress tests in accordance with EN14617 [16]. The calculated bending moment vs curvature relationship is shown in Figure 2. A maximum resistance equal to 550 kNm was predicted. The post-cracking field is characterised by a sudden load loss followed by a much softer branch which inclination is due to the elastic elongation of the pre-stressing bars. Failure of the BFRP bars in tension is expected. The post-failure residual bending strength of the diagram is due to the residual tensile contribution of the non-pre-stressed bars and the Polypropylene fibres. The design shear load has been calculated considering the contributions of the self-weight and of the predicted maximum mid-span point load to be applied during the test.

The shear reinforcement was 45° inclined 6 mm diameter straight GFRP bars. As they are corrosion resistant, there is no need to keep a minimum clear concrete cover so just a few millimetres cover was used. This also increased the anchorage, which was effective within less than 10 diameters due to the sandblasting surface treatment of the bars. Two shear reinforcement trusses have been designed to be inserted in the ribs. 4 BFRP bars with 12 mm of diameter were placed 2 at the bottom and 2 at the top of the section to fix the transverse bars. These bars were not pre-stressed. Their contribution is included in the moment-curvature diagram.

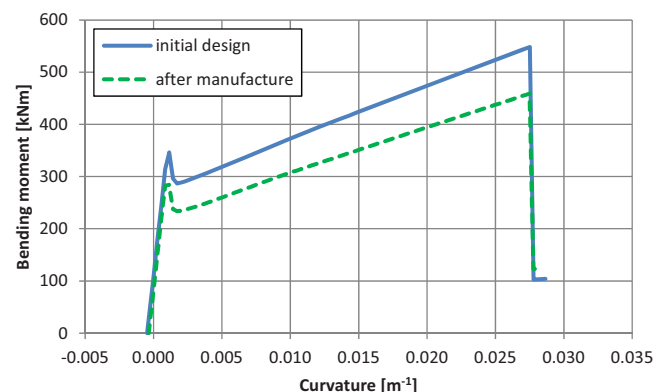


Figure 2. Non-linear bending moment vs curvature relationship.

Figure 3(a) shows details of the beam, including shear reinforcement. It can be observed that three transversal stiffening ribs at the quarter span, were detailed and formed by cutting the polystyrene blocks which formed the voids. The upper and lower slab have been provided with distributed transversal GFRP reinforcement with 6 mm diameter bars.

In order to investigate the experimental anchorage length of the BFRP bars, a series of optical sensors were fixed to 3 BFRP bars at locations shown in Figure 3(c). Details of the application of optical sensors are reported in Taylor et al. [17] and Mokhtar et al. [18].

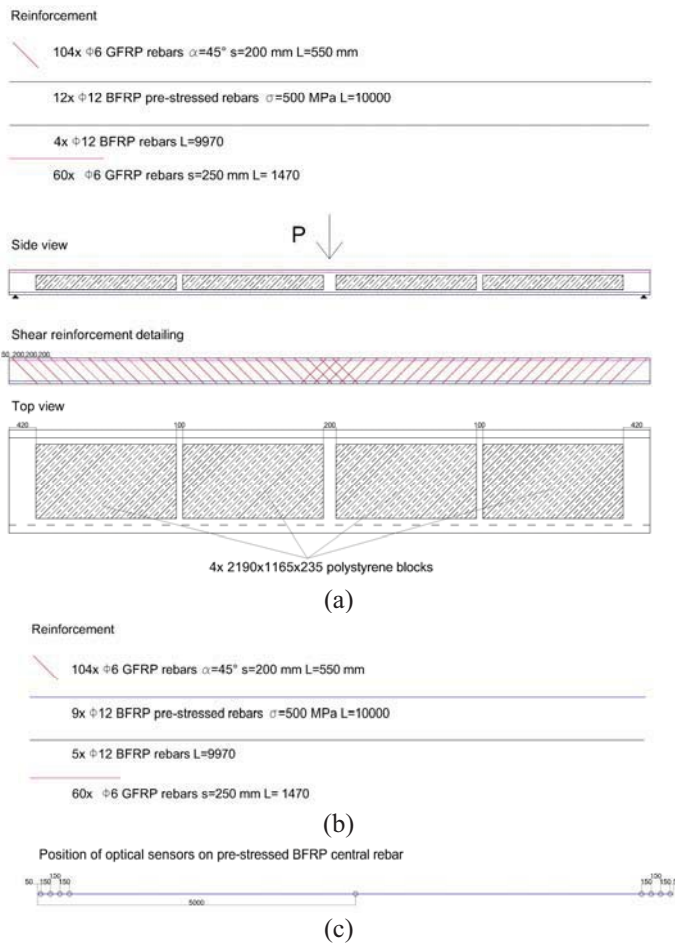


Figure 3. Slab beam views and reinforcement details: (a) designed, (b) reinforcement realised, (c) position of optical sensors on one central BFRP bar.

3 MANUFACTURING OF THE SPECIMEN

The beam element was cast at the factory of Banagher Precast Concrete. The whole process is illustrated in the following, highlighting the challenges that occurred.

The element was cast in a longer pre-stressing bed. Thus, an inner timber mould was built (Figure 4). The BFRP bars had been ordered with a length of 12 m. which was too short for this bed which had a length of 15 m. In order to solve this, steel couplers were applied externally with respect to the inner mould (Figure 5) and coupled bars of 18 m were used to accommodate the hydraulic jack for pre-stressing and enable anchoring with traditional steel tendons wedges on the opposite side.

Traditional wedges used for pre-stressing steel were chosen, despite the literature survey on the scarce efficiency of those retainers due to the strong concentration of transversal stress in the bars. Nevertheless, several pre-tests performed at Banagher were positive. The problems in literature mainly refer to testing equipment, associated with the objective to break the rebar, while in this study the temporary restraint was for a pre-stress level of 50% of the rupture strength. The optical sensors were installed prior to tensioning at positions calculated taking into account the expected elongation of the cables. Table 1 summarises the

mix composition of the FRSCC which has been developed from previous laboratory test [19] with w/b of 0.45 and containing polypropylene fibres (38 mm length) and self-healing admixture (SH). SCC was made with limestone powder (LSP) and ground granulated blast furnace slag (GGBS). The slump flow was 700 mm, Jring ring (Pj) was 18 mm and V-funnel time was 20 s.



Figure 4. View of the mould.

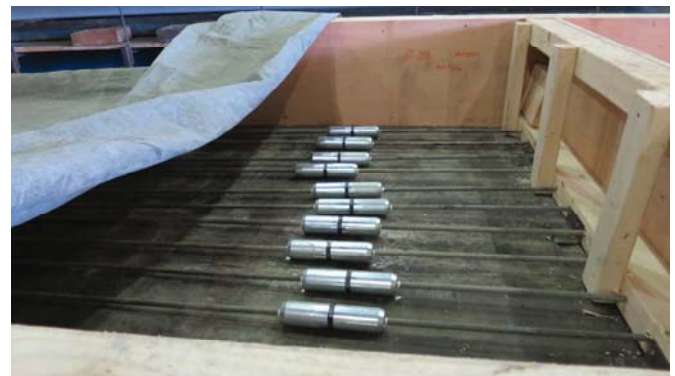


Figure 5. Mechanical couplers (external to the mould).

Table 1. SCC mix composition.

Mix	C	GGBS	LSP	Agg. 14mm	Agg. 8mm	Sand
kg/m ³	338	113	150	215	610	825
Additives	Fibres PP		SP		SH	
kg/m ³	4		2,9		3,6	

The BFRP rebars were stressed with a hollow core hydraulic jack with an automatic wedge pushing system, as used for steel tendons. Figure 6 shows the operator (Peter Deegan) stressing each of the bars which were pulled from the same side with an initial stress of 500 MPa. This corresponded to a load of 56.5 kN, and an elongation of 151 mm. The operation was successful and the elongation was checked for each cable and was as predicted. After about 15 minutes from stressing, the first tensile failure of one rebar occurred at the position of the wedge, due to the lateral pressure exerted by it. Within the following 30 minutes, two additional similar failures occurred. A detail of the delamination failure is shown in Figure 7. Figure 8 shows one bar after failure.



Figure 6. Tensioning operation with wedge blockage system.



Figure 7. Particular of a BFRP rebar broken after tensioning.



Figure 8. Tensile failure of one BFRP rebar broken after tensioning.

The first bar to fail was removed and replaced with a new bar. For safety reasons, the substituted rebar was not pre-tensioned. It appears that this failure was a result of the detail at the wedges as this had not occurred in the laboratory tests where a protective coat of resin was used between the bar and the wedges. It was decided to continue with the casting of the FRSCC, and accepting the loss of two pre-stressing bars and the failed stressing of one of them. Since removing the failed rebars was judged to be difficult, they were left in the casting.

The cast was successfully performed and uniform dispersion of fibres was obtained except for some isolated clots which were removed by hand or with the help of a rake.

After having poured the lower flange, the shear resisting trusses were inserted in correspondence of the ribs (Figure 9).

The moment-curvature diagram associated with the updated reinforcement layout is shown in Figure 2.



Figure 9. Positioning of shear resisting trusses in correspondence of the ribs.

4 TEST SETUP

The slab member (shown in Figure 10 after removal from the mould) was simply supported on top of concrete blocks placed at the edges. 10 mm thick timber slats have been placed between the member and the supporting blocks to distribute the load. The load was applied at mid-span by a +300 mm stroke mono-directional accurately calibrated hydraulic jack with a 50 T capacity used in a steel reaction frame. A steel box beam was placed between the jack and the slab. Figure 11 shows the test rig.

Three digital displacement transducers were placed at the soffit of the mid-span section, one at the centre and two near the beam side face edges. Two additional dial gauges were placed at about 800 mm from the support to measure any settlement at the support region. Load was applied incrementally and in cycles as described in the next section.



Figure 10. Steel-free pre-stressed beam moving to test rig.



Figure 11. Test setup.

5 EXPERIMENTAL RESULTS

The loading was applied in cycles repeated twice at increasing load amplitudes, in order to investigate the crack propagation effect at each load step. A first load amplitude of 25 kN (corresponding to a bending moment of 159 kNm including the contribution of the self-weight) was performed to investigate the pre-cracking behaviour, then the load was increased to first crack formation. The following load amplitudes were gradually increased up to failure.

Based on the updated section (Figure 1b) and on the mean material properties, a failure point load of 145 kN (460 kNm) was predicted. The test results are summarised in Figure 12. The load history (Figure 12a) shows that the beam has attained the expected load, and that it did not fail even at the maximum load reached during the last cycle, equal to 155 kN (484 kNm).

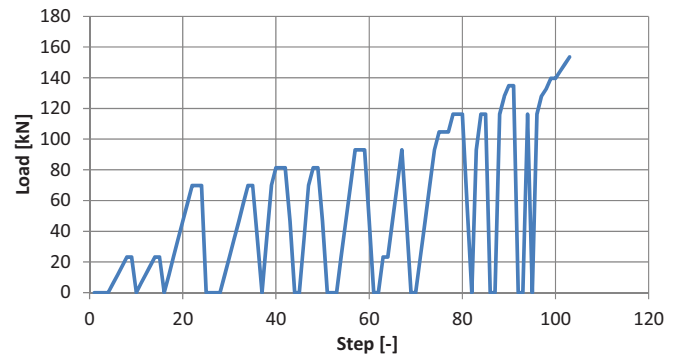
Load vs displacement results (Figure 12b) show that first cracking occurred at an applied load of 70 kN (272 kNm), which was aligned with what expected (280 kNm).

The initial stiffness was maintained up to ~25 kN, due to the effect of the pre-stressing force, after which the behaviour softens with a stiffness degradation depending on the extent of the cracks. Since the BFRP bars are fully elastic, the residual deflection, after large load cycles was very small.

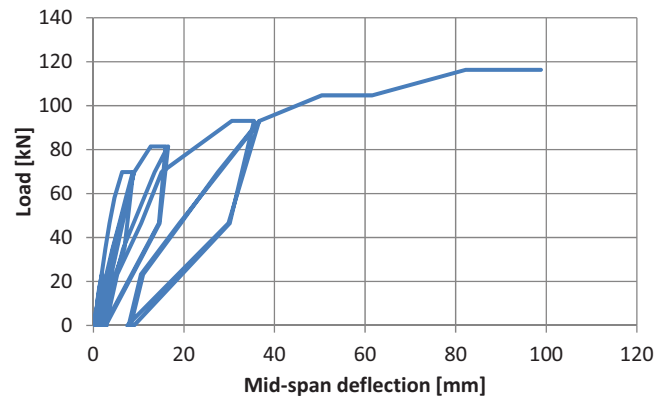
Displacement data from the last load cycle was not recorded as the transducers were removed for safety. An approximated deflection of 150 mm is estimated to have been attained.

The large deflection of the beam at the +120 kN cycle is observable in Figure 13. The crack pattern at the +120 kN cycle is reported in Figure 14. The numbers indicate the pressure level of the pump in bars at the formation of the crack. A factor of 2.33 was calibrated to convert to kN.

A good distribution of cracks allowed to keep the crack opening small. The formation of the cracks at each location typically occurred with a vertical major one with superposing cracks forming at a space equal to the fibre length and converging towards the vertical one.



(a)



(b)

Figure 12. Experimental results: (a) Load history, (b) load vs deflection diagram.

Polypropylene fibres strongly contributed to the distribution of cracks. The mid-span cracks propagated up to about 50 mm from the beam extrados, inclining towards the point load in the upper branch due to the strong shear action. Inclined shear cracks near the supports were not observed. After unloading at all load cycle amplitudes, all cracks closed due to the pre-stressing action.



Figure 13. Test beam subject to large deflection.



Figure 14. Marked crack pattern.

6 CONCLUSIONS

The manufacturing of a 10 m long steel-free pre-stressed beam with BFRP longitudinal bars, GFRP shear-resisting bars and fibre reinforced SCC showed an interesting technological solution for developing corrosion resistant pre-cast concrete elements even if the pre-stressing of the BFRP bars is limited to half of their rupture stress. Traditional wedging anchorage systems, used for steel, caused the failure of 25% of the bars due to breakage of the outer fibres. A novel anchorage device was developed in lab tests [6] which protects the fibres and allows better stress distribution.

The 3-point loading test showed a satisfactory performance of the element, with an efficient elastic performance of the pre-stressing reinforcement even at a load larger than the predicted resistance, corresponding to mid-span deflections of $\sim 1/70$ of the span at peak load. Negligible residual deflection and crack closing were observed after unloading. The element was not taken to failure due to the attainment of an unexpected over-resistance. It has been left under a sustained cracking load in order to investigate the self-healing performance.

The crack pattern of the member showed a very good capacity of crack distribution and corresponding low mean crack opening, which is mainly attributable to the polypropylene fibres.

The shear-resisting truss consisting of GFRP non-bent bars inclined at 45° behaved satisfactorily even in the post-cracking phase.

Based on the observed performance in the reported test, the authors believe that this technological solution is reliable and robust and its application to pre-stressed elements promising, provided that a suitable anchorage system of the BFRP bars during production is adopted.

ACKNOWLEDGEMENTS

The experimental activity has been performed within the objectives of the EiroCrete research project, funded by the European Commission within the FP7-PEOPLE-2012-IAPP - Marie Curie Action: "Industry-Academia Partnerships and Pathways". The technicians of Banagher Precast Concrete that contributed to the project are acknowledged, especially Gavin Kelly and Kevin Dalton. Dr. Myra Lydon and Darragh Lydon from the Queen's University of Belfast are also acknowledged for their assistance in the execution of the tests.

REFERENCES

- [1] Fiore, V., Scalici, T., Di Bella, G. and Valenza, A. (2015), 'A review on basalt fibres and its composites', *Composites Part B*, 74-94.
- [2] Tharmarajah, G., Taylor, S. E., Robinson, D. & Cleland, D. J. (2015) Corrosion resistant fibre reinforced polymer (FRP) reinforcement for bridge deck slabs, *Proceedings of the Institution of Civil Engineers: Bridge Engineering* Vol. 168 Iss 3, September, 2015, pp. 208-217
- [3] Zhang, L., Sun, Y. and Xiong, W. (2015), 'Experimental study on the flexural deflections of concrete beam reinforced with basalt FRP bars', *Materials and Structures*, 48, 3279-3293.
- [4] Taylor, S.E., Robinson, D. and Sonebi, M. (2011a), 'Basalt-fibre-reinforced polymer reinforcement', *Concrete*, April, 48-50.
- [5] McConnell, E., McPolin, D. & Taylor, S. (2015) Post-tensioning glulam timber beams with basalt FRP tendons *Proceedings of the Institution of Civil Engineers: - Construction Materials*. DOI:10.1680/coma.14.00032
- [6] High, C., Seliem, H.M., El-Safty, A. and Rizkalla, S.H. (2015), 'Use of basalt fibers for concrete structures', *Construction and Building Materials*, 96, 37-46.
- [6] Crossett, P., Taylor, S., Robinson, D., Sonebi, M., Garcia-Taengua, E., Deegan, P. and Ferrara, L. (2015a), 'The flexural behaviour of SCC beams pre-stressed with BFRP', *Advanced Composite in Constructions*, 62-67.
- [7] Dolan, C.W., Bakis, C.E. and Nanni, A. (2000), 'Design recommendations for concrete structures pre-stressed with FRP tendons', Report of the FHWA contract No. DTFH61-96-C-00019.
- [8] Zhou, P.X.W. (2003), 'Flexural behavior and deformability of fiber reinforced polymer prestressed concrete beams', *Journal of Composites for Construction*, ASCE, 7(4), 275-284.
- [9] Stoll, F., Saliba, J.E., Casper, L.E. (2000), 'Experimental study of CFRP-prestressed high-strength concrete bridge beams', *Composite Structures*, 49, 191-200.
- [10] Crossett, P., Taylor, S., Robinson, D., Sonebi, M. and Garcia-Taengua, E. (2015b), 'Monitoring the transfer length of pre-stressed BFRP SCC beams', *Proceedings of 7th International Conference on Structural Health Monitoring of Intelligent Infrastructure (SHMII-7)*, Torino, Italy, July 1st-3rd.
- [11] Al-Mayah, A., Soudki, K. and Plumtree, A. (2007), 'Novel anchor system for CFRP rod: finite-element and mathematical models', *Journal of Composites for Construction*, ASCE, September/October, 469-476.
- [12] Carvelli, V., Fava, G. and Pisani, M.A. (2009), 'Anchor system for tension testing of large diameter GFRP bars', *Journal of Composites for Construction*, ASCE, September/October, 344-349.
- [13] Schmidt, J.W., Bennitz, A., Taljsten, B. and Pedersen, H. (2010), 'Development of mechanical anchor for CFRP tendons using integrated sleeve', *Journal of Composites for Construction*, ASCE, July/August, 397-405.
- [14] EN 1992-1-1:2005 (2005), Eurocode 2: Design of concrete structures. Part 1-1: general rules and rules for buildings.
- [15] CEB-fib (2010), Model Code for Concrete Structures. Fédération Internationale du Béton / International Federation for Structural Concrete, Lausanne, Switzerland.
- [16] EN 14617-12:2012 (2012), Agglomerate stone. Test methods. Determination of dimensional stability.
- [17] Taylor, S.E., Grattan, S., Sonebi, M., Robinson, D., Sun, T. and Hughes, D. (2011b), 'Monitoring of Thompson's bridge BFRP reinforced deck with discrete optical sensors', *Proceedings of 5th International Conference on Structural Health Monitoring of Intelligent Infrastructure (SHMII-5)*, Cancun, Mexico, December 11th-15th, 65-72.
- [18] Mokhtar, et al. (2011), 'Fiber-optic strain sensor system with temperature compensation for arch bridge condition monitoring', *Sensors*, 5321.
- [19] Garcia-Taengua, E., Sonebi, M., Crossett, P., Taylor, S., Deegan, P., Ferrara, L. and Pattarini, A. (2016), 'Performance of sustainable SCC mixes with mineral additions for use in precast concrete industry', *Journal of Sustainable Cement-Based Materials*, 5(3), 157-175.

Evaluating a new CEM III/A cement for concretes exposed to harsh acid rich environments

David Thompson¹, Niall Holmes¹ & John Reddy²

¹School of Civil & Structural Engineering, Dublin Institute of Technology, Bolton Street, Dublin 1, Ireland

²Ecocem Ireland Ltd, F1 EastPoint Office Park, Dublin 3

Email : david.thompson@dit.ie; niall.holmes@dit.ie; john.reddy@ecocem.ie

ABSTRACT: The Irish Annex to the European specification, performance, production and conformity of concrete, IS EN 206, recommends CEM III/B cement for acid rich environments containing between 66 to 80% GGBS. However, BS 8500, the UK annex to EN 206 and the British Research Establishment (BRE) Special Digest 1, recommends CEM III/A cement with a GGBS range of 36-65%. This project investigated the performance of a new CEM III/A cement produced by Ecocem Ireland in concretes exposed to such environments using an extensive suite of laboratory tests.

In Ireland, up to €5.8bn will be invested to provide fresh drinking water and clean wastewater. Concrete deterioration in wastewater treatment systems is mostly caused by sulphates and sulphuric acids found in aggressive chemical additives used. Due to the constant operational nature of these facilities, poor concrete performance leads to shut-downs with serious environmental consequences. The Department of Agriculture requires that all farm based concrete complies with the Nitrates Directive and is certified to IS EN 206. This is only possible by using concrete mixes with adequate durability capable of withstanding the harsh environments found in farms, like silage pits, milking parlour floors, etc.

The results from this study show that the CEM III/A cement used performed as well, or better than, other commonly used cements for these environments. It performed particularly well in mass changes following exposure to sulphuric acid and sulphates with higher compressive strengths too.

KEY WORDS: Sulphate attack, sulphuric acid, concrete, mass loss, expansion, contraction.

1 INTRODUCTION

This project investigated whether CEM III/A cement is suitable to be used where harsh, acid rich, environments can be expected. CEM III/A is a blastfurnace cement containing between 36-65% ground blastfurnace slag (GGBS) and is an equivalent to sulphate resisting cement (S.R.C.). Concrete in wastewater systems are susceptible to different forms of attack including biologically produced sulphuric acid and sulphates. The addition of GGBS increases the resistance of concrete to these forms of attack [1, 2].

In such situations concrete sewer corrosion begins when the pH of the alkaline concrete surface is lowered by dissociation of hydrogen sulphide and by carbonation. There is then a build-up of neutrophilic sulphide oxidizing bacteria and fungi colonise on the concrete surface and contribute to a successive oxidation of reduced sulphur compounds to dissociated sulphuric acid. At this point the pH falls below 2 and the sulphuric acid is produced which in turn produces ettringite and gypsum on the concrete surface. The source of the sulphate is the groundwater which contains dissolved sulphate. These two processes occur at the same time and the concrete then begins to crack due to the expansive pressure caused by the growth of ettringite within the cement paste, [3, 4, 5]. This deterioration of concrete may lead to the loss of ability to transport sewerage, contamination of ground and groundwater, excessive ground settlements and cave-ins [6].

The Irish Annex to the European specification, performance, production and conformity of concrete (IS EN 206) recommends that a CEM III/B cement for acid rich environments (66 to 80% GGBS). However, BS 8500 (the UK annex to EN 206) and the British Research Establishment (BRE) Special Digest 1 recommends CEM III/A cement (36 to 65% GGBS).

The objective of the study is to determine if CEM III/A from Ecocem Ireland, (containing between 36-65% GGBS) can be recommended in Ireland to reduce the effect of sodium sulphate and sulphuric acid attack in concrete. The findings could form the basis of concrete design for water and wastewater treatment facilities and the agricultural market particularly those structures in contact with silage. A substantial suite of experimental work was undertaken which assessed the performance of the new cement in these environments and compared against other blended cements, particularly CEM II/A-L on the market.

2 METHODOLOGY

2.1 Mix proportions

Samples were cast for five different cement types. A summary of the mixes is shown in Table 1. The mix proportions are shown in Table 2.

Table 1. Summary of concrete cast

Mix ID	Description
1	CEM II A-L + 36% GGBS
2	CEM II A-L + 65% GGBS
3	CEM II A-L + 50% GGBS
4	CEM III/A (Ecocem blend)
5	Sulphate resisting cement (S.R.C)

Table 2. Mix Proportions

	Mix 1	Mix 2	Mix 3	Mix 4	Mix 5
CEM II	360	360	360	-	-
CEM III	-	-	-	360	-
S.R.C.	-	-	-	-	360
Fines	685	685	685	685	685
Coarse 10mm	405	405	405	405	405
Coarse 20mm	810	810	810	810	810
	(Above quantities in kg/m ³)				
W/C ratio	0.45	0.45	0.45	0.45	0.45
GGBS (%)	36	65	50	-	-

2.2 Sample preparation

The research work included casting 40 concrete prisms (285x75x75mm) for expansion and contraction tests and 70 concrete cubes (150x150x150mm) for change in mass and compression strength tests. The concretes were cast in a large pan mixer and compacted using a vibrating table. All samples were placed in a curing tank at 21°C after 24 hours for 28 days.

2.2.1 Sodium sulphate exposure

Four prisms used for expansion and contraction tests were placed into a polyethylene container, see Figure 1(a) and submerged in a sodium sulphate solution, ensuring the quantity was sufficient to cover the prisms by a minimum of 10mm. The solution contained 50g of sodium sulphate (Na₂SO₄) per litre of distilled water. The solution was replaced with a freshly made solution every two months.

2.2.2 Sulphuric acid exposure

Four prisms were cast for expansion and contraction tests in the sulphuric acid solution. Two prisms were placed in a polyethylene container and submerged in a 1% solution of sulphuric acid, ensuring the quantity was sufficient to cover the prisms by a minimum of 10mm. The two remaining prisms were used as a control for both and placed in water for the duration of the test programme. A sulphuric acid solution of 1% by volume, with a pH level of 1.5, is considered as representative of the acidity levels found in aggressive sewer environments [6, 7], and therefore adopted for the laboratory experiments. A pH level of 1.5 represents the most severe conditions to be expected in service but this level may vary in practice due to a number of environmental factors.

2.3 Expansion and contraction tests

Expansion and contraction readings were taken from the all samples. Readings were taken using a reference rod (A). The reference rod was then removed and the prism was then placed in the instrument and a reading recorded (B, see Figure 1(b)). The prism was then placed in the solution for 28 days at which point it was removed and measured (C). Finally the sample was placed into the instrument and a reading (D) was taken. The active deformation of the sample was calculated using the formula: $[(D - B) - (C - A)]$. Additional (C and D) readings were taken every 28 days for 6 months.

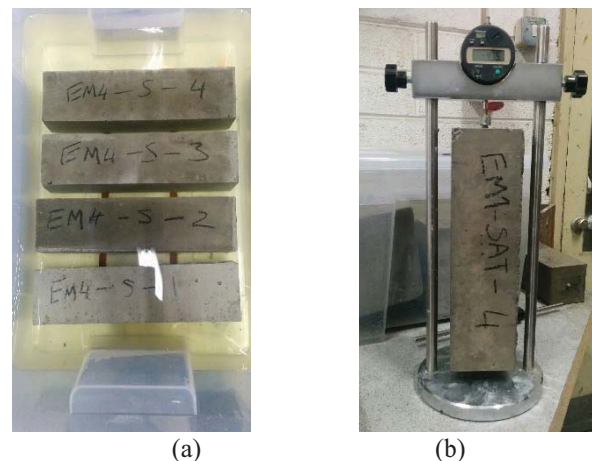


Figure 1. (a) Comparator reader with prism, (b) prisms submerged in sodium sulphate solution

2.4 Mass loss – sulphuric acid exposure

Twelve cubes were cast for each mix. 24 hours after casting, all cubes were placed in a curing tank for 28 days. Six cubes from each mix kept in water to act as the control. Six cubes from each mix were placed in a polyethylene container and filled with a 1%, by volume solution of sulphuric acid to cover the cubes by a minimum of 10mm.

After a further 28 days all cubes were removed from their containers and brushed with a wire brush under running water which resulted in milky white runoff (Figure 2). The samples were washed weighed to determine if any mass loss had occurred. Any loosely adhering corrosion products present on the cubes placed in acid were brushed away prior to recording the mass. Samples were then returned to their containers for a further 28 days. Readings were again taken at 28 day intervals for 6 months.

The acid was monitored throughout the testing in order to maintain a PH value of 1.5 \pm 0.3. Once the solution deviated from this value the whole solution was replaced. This occurred three times in the 6 month period.

2.5 Compressive strength

While mass change is the traditional method for measuring the attack in concrete to acids, compressive strength tests are also a reliable performance measure of the resistance of concrete to acid attack [6]. Strength test were carried out on both the control and exposed cubes at 28 days, see Figure 3

and again upon completion of the testing programme at 196 days.



Figure 2: Cube brushed under running water



Figure 3: Cube in compression testing machine at 28 days

3 RESULTS

3.1 Expansion and contraction tests

Figures 4 – 6 show the average change in length of the prism exposed to water, sulphuric acid and sodium sulphates respectively. As may be seen from Figure 4, the CEM III/A cement had the highest changes in length over the exposure time in comparison with the other cement types for exposure to water. Only CEM II A-L + 36% GGBS increased in length by the end of the testing programme.

Figure 5 shows that the CEM III/A cement had a slightly higher initial contraction than the others for the samples exposed to the sulphuric acid solution. However, the steel pins used to take the reading were damaged by the severity of the acid compromising the results from 3 months onwards. Each of the other mixes showed a consistent trend in terms of contraction at each monthly interval.

Figure 6 shows the change in length of all mixes reduced over time when exposed to the sodium sulphate solution, with the greatest change in length coming from the sulphate resisting cement mix.

3.2 Mass loss – sulphuric acid exposure

Figure 7 show the change in mass of the 150mm cubes exposed to sulphuric acid. Samples stored in water showed no

change in mass throughout the testing while all samples lost mass for the first two months with each mix then alternating between mass loss and gain for the remaining four months. The

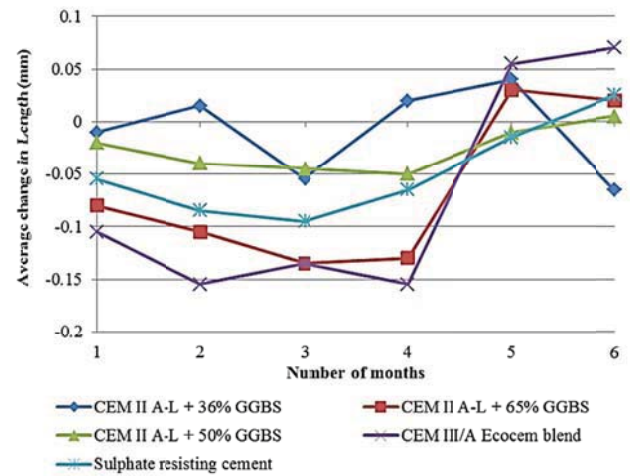


Figure 4. Average change in length – 280x75x75mm prisms exposed to water

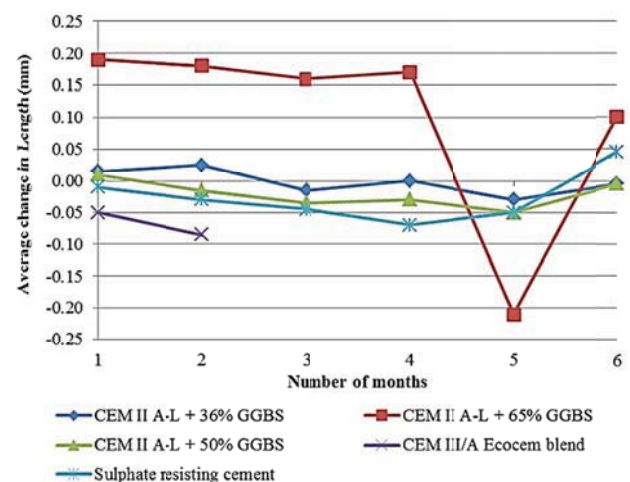


Figure 5. Average change in length – 280x75x75mm prisms exposed to sulphuric acid

CEM III/A showed the least variation in change of mass compared to the other mixes while the CEM II A-L + 65% GGBS showing the greatest variation.

3.3 Strength Test – Water and sulphuric acid exposure

Figures 8 show the average compressive strength of the cubes at 28 days and at 196 days for both exposed and control cubes. From this figure we can see that the CEM III/A mix had the highest strengths at each point in time. It can also be seen that the 196 day cubes immersed in the sulphuric acid solution were weaker than control samples at 196 days.

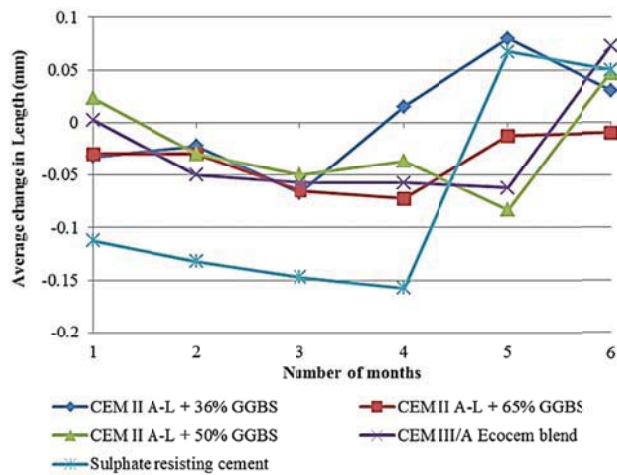


Figure 6. Average change in length - 280x75x75mm prisms exposed to sulphates

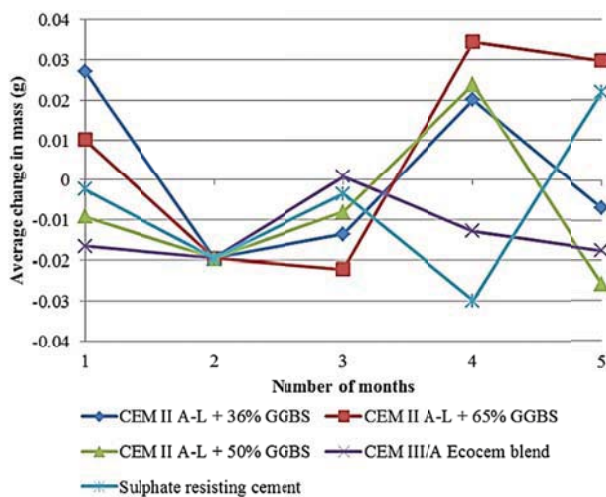


Figure 7. Change in mass - 150mm³ cubes exposed to sulphuric acid

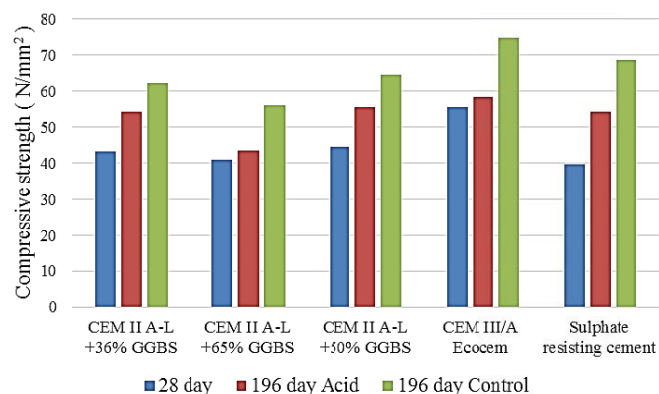


Figure 8: Compression test results

4 DISCUSSION

4.1 Experimental results

4.1.1 Expansion and contraction

All mixes showed a varying degree of expansion and contraction when exposed to sulphuric acid and sodium sulphate. The results show that samples kept in both solutions show a trend to contraction for 1-3 months with results towards the end of the testing programme showing expansion. The CEM III/A mix performed comparable to the other mixes in the sodium sulphate solution indicating that it is not negatively affected in these conditions.

4.1.2 Degradation of test specimens

Samples were also visually monitored throughout the testing programme in terms of surface degradation after brushing. Figure 9 shows a cube from mix 1, CEM II A-L + 36% GGBS which demonstrated the worst surface degradation that had occurred.

All samples showed signs of gypsum formation on the surface of the concrete which may have contributed to the surface degradation. Care was also taken to ensure that the amount of brushing carried out on each sample was consistent but some samples appeared to withstand this abrasion more than others. Degradation was observed to some degree in all samples after the initial brushing with the CEM III/A performing particularly well.



Figure 9: Surface degradation of cube from mix 1

4.1.3 Mass loss

Mass loss was recorded 28 days after initial exposure of the cubes to the sulphuric acid solution. All cubes lost mass initially after the first 28 day cycle with all mixes then alternating between gaining and losing mass over remaining time of testing. The variation in mass changed quite significantly over the testing period with months 4 and 5 showing a high range in mass change for all mixes except CEM III/A. The CEM III/A showed the least variation in mass change compared to the other mixes for the duration of the testing. Previous studies utilising a similar mass loss method have shown varying results including a gradual decrease in mass over exposure time, [9] while others have shown samples increasing in mass initially and then decreasing [10,

11]. The relatively consistent results from the CEM III/A mix indicate that it may better resist the acidic conditions it was exposed compared to the other CEM II mixes.

4.1.4 Compressive strength

The results of the compressive tests show that the control samples kept in water were stronger than those samples kept in solutions. The CEM III/A mix had the highest 28 and 198 day strengths. Previous studies have shown that concrete compressive strength decreases after prolonged exposure to acids, [6, 9, 10]. While each of these studies used different mix designs the trend shows compressive decreasing. However, this study found an increase in compressive strength for all samples immersed in acid compared to the 28 day test. However, over time, all cubes exposed to acid were weaker than those kept in water including the CEM III/A cubes which shows that the sulphuric acid did negatively affect the final compressive strength of the cubes.

4.2 Additional comments

According to the results of this study the CEM III/A (Ecocem blend) is able to withstand the effects of harsh acid environments simulated in these laboratory experiments. The average contraction and expansion of this mix was less than S.R.C. for samples exposed to the sodium sulphate solution. The mass loss for the samples exposed to sulphuric acid was also the lowest of each of all mixes and in terms of compressive strength, CEM III/A cubes performed better than all other mixes after exposure to sulphuric acid.

5 CONCLUSION

Overall this study showed that CEM III/A performed comparatively well or better compared to other the mixes in terms of expansion/contraction, mass loss and compressive strength compared to the CEM II A-L mixes with varying percentages of GGBS and S.R.C. This agrees with the recommendation in BS 8500, the UK annex to EN 206 and the British Research Establishment (BRE) Special Digest 1, which recommends CEM III/A cement with a GGBS range of 36-65% for use in harsh acid environments as the results here show that CEM III/A would be suitable for use in these harsh acidic conditions.

ACKNOWLEDGMENTS

The authors gratefully acknowledge the financial support provided by Enterprise Ireland through an Innovation Partnership Feasibility grant.

REFERENCES

- [1] Higgins, D. & Crammond, N., (2003), 'Resistance of concrete containing ggbs to the thaumasite form of sulphate attack', *Cement & Concrete composites* 25:921-929.
- [2] Attigobe, E. K., & Rizkallal, S. H., (1988), 'Response of concrete to sulphuric acid attack', *ACI Materials Journal*, 85(6):481-488.
- [3] Ešťoková, A., Harbuťáková, V.O., Luptáková, A., Številová, N., (2012), 'Study of the deterioration of concrete influenced by biogenic sulphate attack', 20th International Congress of Chemical and Process Engineering CHISA 2012 25 – 29 August 2012, Prague, Czech Republic
- [4] Vollertsen J, Nielsen AH, Jensen HS, Andersen TW, Jacobsen TH. (2008), 'Corrosion of concrete sewers -The kinetics of hydrogen sulfide oxidation', *Science of the Environment*, 394:162-170.
- [5] Okabe S, Odagiri M, Ito T, Satoh H. (2007), 'Succession of sulphur-oxidizing bacteria in the microbial community on corroding concrete in sewer system'. *Applied and Environmental Microbiology*, 73:971-80.
- [6] Chang, Z.-T., Song, X.-J., Munn, R., Marosszeky M. (2005) Using limestone aggregates and different cements for enhancing resistance of concrete to sulphuric acid attack. *Cement and Concrete Research*, 35:1486-1494.
- [7] Ariffin, M.A.M., Bhutta, M.A.R., Hussin, M.W., Mohd Tahir, M., Aziah, N. (2009), 'Sulphuric acid resistance of blended ash geopolymers concrete', *Construction and Building Materials*, 3:80-86.
- [8] O'Connell, M., McNally, C., Richardson, M.G. (2010) 'Biochemical attack on concrete in wastewater applications: a state of the art review'. *Cement and Concrete Composites*, 32:479-485
- [9] Gengying L, Guangjing, X., Yunhai, L., Yegao, Y., (2009), 'The physical and chemical effects of long-term sulphuric acid exposure on hybrid modified cement mortar', *Cement & Concrete Composites* 31:325-330
- [10] Hekala, E., Kishar, E., Mostafa, H., (2002), 'Magnesium sulfate attack on hardened blended cement pastes under different circumstances', *Cement and Concrete Research*, 32:1421-1427
- [11] Al-Moudi, O. S. B., (1995), 'Performance of 15 reinforced concrete mixtures in magnesium-sodium sulphate environments', *Construction and Building Materials*, 9:149-158.

Potential applications for image-based systems in structural engineering

O. De La Torre,^{1,3,4} S. Newell,^{1,2} M.H. Flanagan,^{1,5} J. Goggins,^{1,3,4}

¹Civil Engineering, National University of Ireland Galway, University Road, Galway, Ireland

²Galway-Mayo Institute of Technology, Old Dublin Road, Galway, Ireland

³Centre for Marine and Renewable Energy Ireland (MaREI), Galway, Ireland

⁴Ryan Institute, National University of Ireland, Galway, Ireland

⁵EireComposites Teo, Indreabhan, Galway, Ireland

emails: oscar.delatorre@nuigalway.ie, s.newell2@nuigalway.ie, m.flanagan15@nuigalway.ie, jamie.goggins@nuigalway.ie

ABSTRACT: This paper presents a series of examples where systems based on images have been used to quantify deformation and strain fields for different applications. The objective of this work is to highlight the strengths and weaknesses of these technologies compared to more traditional systems. In particular, two image-based technologies have been studied: a Digital Image Correlation (DIC) device and a high speed camera. The former has been used in three different static tests: a compression test, a 4 points bending test and a tensile test. The latter was employed in a vibration analysis where the DIC could not be used due to its particular camera specification. Both technologies potentially produce easy to interpret results, which with commonly used alternative technologies usually require a significant post process effort. On the other hand, for effective and reliable results, the image-based technologies can require a previous treatment of the sample and a very careful experimental setup. Moreover, the possibility of performing global measurements compared to more local ones carried out by conventional sensors make these systems very attractive for structural engineering.

KEY WORDS: Digital Image Correlation, High Speed Acquisition, Speckle

1 INTRODUCTION

Image based technologies have been extensively used in many fields of science for a long time now (for example, medicine, space, physics). In the recent years, the significant improvement in cameras performance (for example, resolution, rate, sensors) and reduction in cost has made these technologies accessible and suitable for monitoring a large variety of structural engineering applications. The aim of the present paper is to show different applications where image based technologies have been used and evaluate not only their results, but also the experimental setup and post process data flow required to obtain them.

Digital Image Correlation (DIC) is a non-contact optical method based on full field speckle images which can be used to measure displacement and/or strain [1]. It basically takes pictures at different stages of deformation or movement and by tracking subsets of pixels it can correlate the displacement and/or the strain between different images [2],[3]. Stereo images using two or more cameras can produce 2D and also 3D results.

High speed image acquisition works under exactly the same principle as normal acquisition, but by dramatically reducing the exposure time, frequencies of several thousands of frames per second are currently easily achieved [4]. Such high frequencies could be useful to observe sudden phenomena or high frequency vibration [5].

2 TESTED CASES

In order to gain knowledge of the strengths and weaknesses of these technologies, a variety of tests have been designed. Compression, bending and tensile tests have been performed with samples of very different shapes and materials. Specifically, DIC was employed in the following tests (i) a carbon fiber cylinder statically compressed to observe its

buckling performance, (ii) a 3.65 meters long precast concrete slab in a four points bending test to check its deflection and (iii) a glass fibre epoxy sample in a classic tension test. Also, a high speed camera has been used to characterise a modal test table in terms of its frequency-displacement performance.



Figure 1. Some of the tested objects: a carbon fibre cylinder (top left), shaker (top right) and concrete slab/plank (bottom)

2.1 DIC tests setup

An ARAMIS 5M (GOM ®) model has been used for this work. It is a stereo camera device (2448 x 2050 pixel resolution) with 12 mm focal length lens. Before proceeding with the actual test, in order to use DIC technology, the tested

sample should be prepared. The images used should be grey-scaled and with a high level of contrast. As explained above, DIC tracks subsets or facets between images at different levels of strain or displacement. These facets typically undergo displacement and deformation so any point of the facet could change its relative position to another from image to image. In order to be able to locate them among the images there should be a system to reference them. Assuming a very simple system where a single facet (center point A and generic point B) is displaced and deformed between time t and time $t+\delta t$, we should consider the quantities shown in Figure 2.

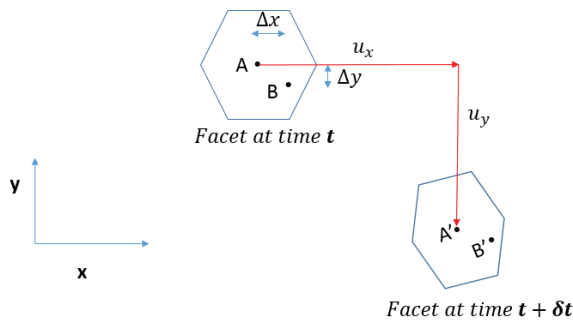


Figure 2. Facets movement and deformation.

As observed, the facet at time $t+\delta t$ has been displaced (the center of the facet has moved from A to A') and deformed (distance AB is different than distance A'B') with respect to time t . Equation (1) and (2) let us relate the centre location of the facet at both instants of time:

$$x' = x + u_x + \frac{\partial u_x}{\partial x} \Delta x + \frac{\partial u_x}{\partial y} \Delta y \quad (1)$$

$$y' = y + u_y + \frac{\partial u_y}{\partial x} \Delta x + \frac{\partial u_y}{\partial y} \Delta y \quad (2)$$

The displacement field is obtained from the A to A' movement and the strain field from the partial derivatives in the equations.

A speckle pattern is frequently applied on the sample's surface under study. In order to increase the contrast, a white paint layer is usually applied beforehand. Figure 3 shows the samples used in this work with their respective speckle pattern.

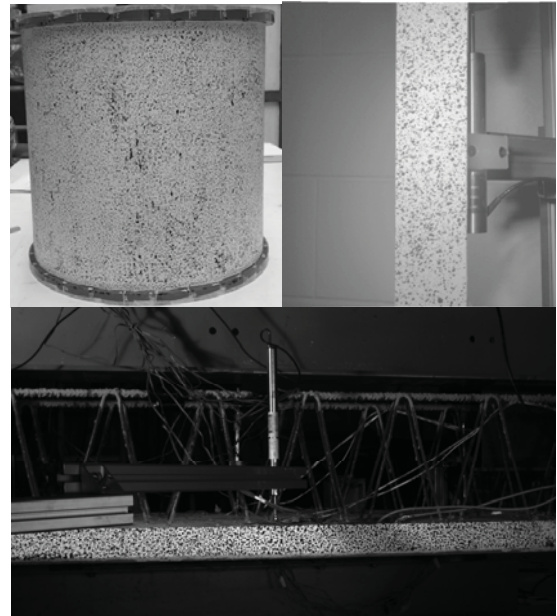


Figure 3. Speckle patterns on the tested samples. (a) Composite cylinder for compression test, (b) GRFP coupon for tensile test, and (c) precast concrete filigree slab for bending test

Equations (1) and (2) clearly address a major issue related to DIC: results depend on how well identified the points are in each image. This means that ultimately, the results are speckle dependant. There is a significant amount of literature studying the effects of pattern quality, type, speckle size and/or subset size on the obtained results, [6], [7], [8]. This leads to very careful and time consuming test setups going through an iterative process to evaluate the speckle pattern itself. In this work, three different field of views have been used for the DIC cameras: $300 \times 250 \text{ mm}^2$ for the tensile test, $750 \times 600 \text{ mm}^2$ for the cylinder test and $1000 \times 800 \text{ mm}^2$ for the concrete slab. Since the speckle size is related to the field of view two different methods have been used to produce the desired speckle patterns: a spray for the glass fibre test and a pattern brush for the bigger areas. It is important to mention that the accuracy of the results is obviously related to the chosen field of view (typically given as a % of the FOV) and, therefore should be previously taken into account.

2.2 Glass fiber sample tension test

A 50 mm wide and 340 mm long glass fibre reinforced composite sample has been tested. The layup of the glass was $[(+/-45)_0]_s$ and it was tested normal to the 0 fibres in order to observe as much strain as possible. A 5 mm/min displacement controlled loading rate has been used during the tensile test. A 1 Hz sampling frequency has been used for the DIC and a $300 \times 250 \text{ mm}^2$ field of view. In order to check the accuracy of the DIC capturing local strain effects, a strain gauge has been also installed. Figure 4 shows the sequence of the test.

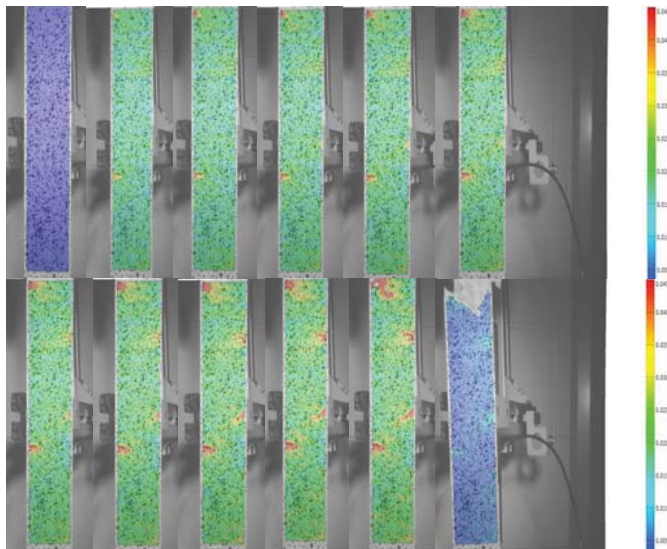


Figure 4. Strain field, in microstrain, within the sample during the test

The strain field within the sample can be considered as a rather homogenous field where very important local tensions develop. These strain concentrations indicate sub surface defects and, hence, DIC could be used as a non-destructive test technique for composites. Ultimately one of these local phenomena produces the failure, but these plots are extremely useful to conclude that there are other zones in the sample of high failure risk.

In order to analyse local strains a virtual area has been simulated on the sample's surface which approximately corresponds to the strain gauge location (on the opposite face), as shown in Figure 5.

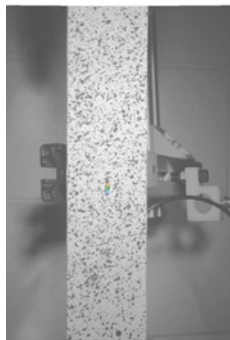


Figure 5. Strain Gauge analogous region.

The results comparison before failure are shown in Figure 6. The DIC seems to capture to a good agreement the behaviour of the strain gauge. The results in the virtual area have been averaged for all the images, which could explain the smoother profile of the DIC results.

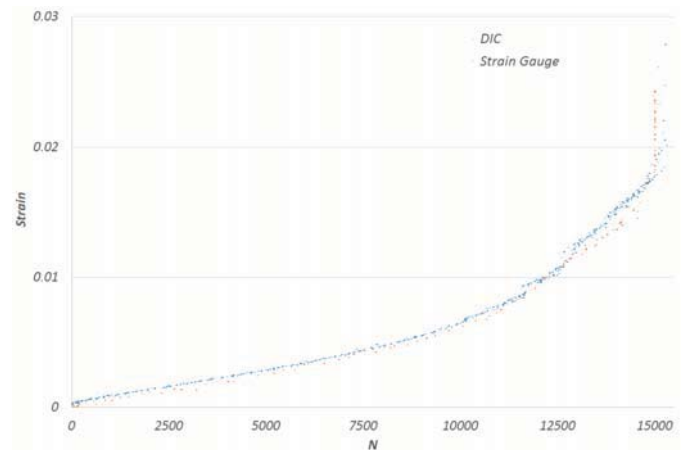


Figure 6. Averaged DIC strain results in the region (orange) and strain gauge results (blue) versus load for a standardised tensile coupon test

2.3 Cylinder buckling test

A 500 mm height cylinder has been compressed to analyse its buckling pattern. Its diameter tapers from 531.4 mm (top side) to 544.5 mm (bottom side) and it is made of carbon fiber. A 5kN loading step has been used and photographs have been taken in every step until failure. A 750 x 600 mm² field of view has been used, which effectively covered the whole height of the sample. Figure 7 shows the cylinder before and after failure within the test rig. In the rightmost image, a horizontal displacement field calculated by the DIC has been overlapped.

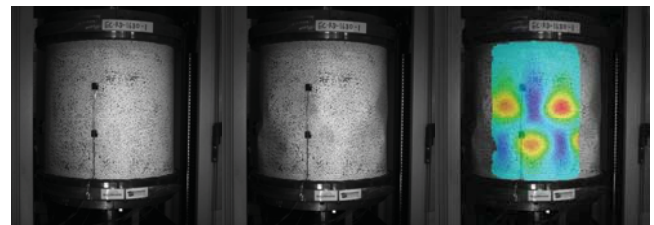


Figure 7. Before (left) and after (center) images of the tested cylinder. Resulting displacement field overlapped (right)

Even if, in this case, the buckling shape is clearly visible to the naked eye, given the resulting displacement levels, obtaining field results along an area could make further analysis easier. For instance, in this case 5 different sections have been defined equidistantly spaced and perpendicular to the cylinder axis as shown in Figure 8. Displacement along the different sections can be then plotted to better study the resulting diamond shape pattern.

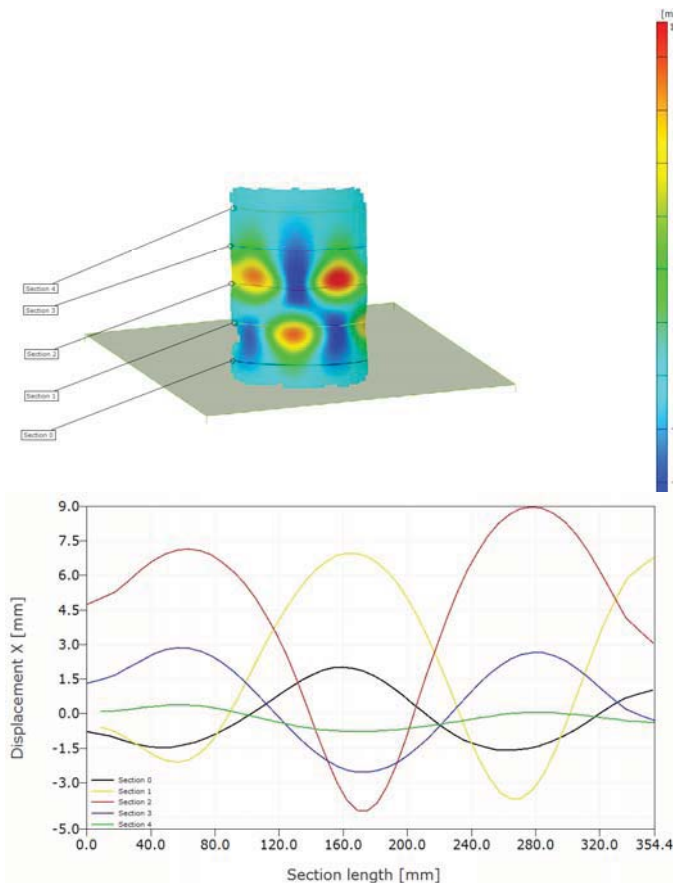


Figure 8. General 3D results (top) and displacement along the different sections (bottom)

2.4 Four points bending concrete slab

A 3.65m long x 0.55m wide x 0.065 m thick precast concrete lattice girder plank has been tested in a 4 points bending configuration (lower image Figure 1). The slab has been loaded by means of a hydraulic actuator, which was moving at a rate of 0.6 mm/min until failure. In order to observe the deflections between the two loading points, the DIC was positioned adjacent to the side of the plank with a 1000x800 mm² field of view such that the full thickness of the plank was observed. A Linear Variable Differential Transformer (LVDT) sensor has been located at mid-span which was also observable using the DIC (Figure 3). The LVDT measures in the vertical direction and has been used to compare with DIC results. A comparison of the vertical deflection measured by the DIC and LVDT is shown in Figure 9. Since the LVDT position can be clearly identified using the DIC, a virtual point has been located in the equivalent location. The recorded data from the LVDT is compared with this equivalent point in Figure 9.

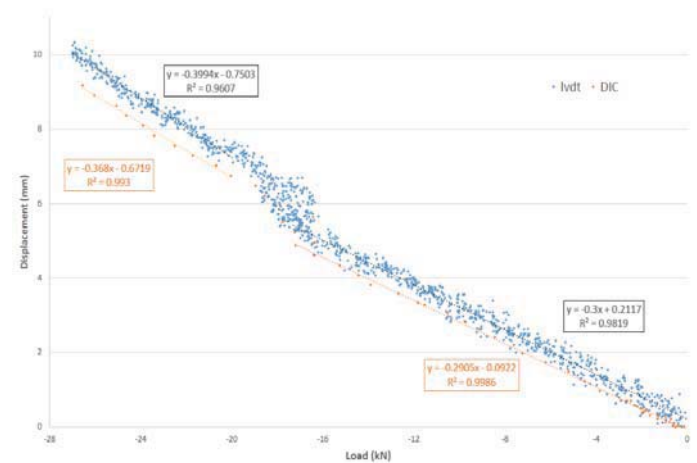


Figure 9. LVDT results (blue) and DIC results (orange) of the equivalent point

As observed in Figure 9, the DIC follows the trend shown by the LVDT's results. During the test, there was a sudden movement of the reaction frame where the actuator is attached and that is clearly visible in both results (around 17 kN). After this, the DIC results are well below the LVDT. Since the LVDT is a single-point contact sensor, it is very likely that after the sudden movement of the frame, the sensor is measuring a different point and given the surface roughness of the concrete sample the gap between the DIC and the LVDT results can increase as shown in the last part of the loading. This could also be the cause of the important dispersion of the LVDT's results. DIC seems, though, to typically predict lower displacements over the entire range of loading. The trend lines shown in Figure 9 for both 0 to 17 kN and 20 to 26 kN ranges highlight the difference.

When observing the field displacement along the whole measured area of the precast plank, the unsymmetrical deformation of the precast plank was noted. In Figure 10, the vertical displacement as recorded by the DIC is shown and highlights the deformation pattern of the plank at midspan. As observed, the load was not equally applied at both sections and, therefore, the slab was more deflected on one extreme (right side of the image) than the other (left side of the image).

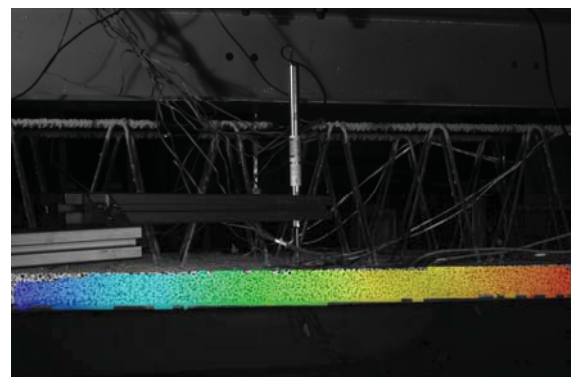


Figure 10. Vertical displacement field results indicating non-symmetrical deformation

2.5 High speed camera test setup

Due to the current specifications of the cameras in this DIC device, it is not possible to use it to analyze high frequency phenomena. Whenever the exposure time of the photograph is of the same order of magnitude as the time scale of the phenomenon to be captured, the results are not reliable. Therefore, to analyze the vibration performance of a shaker (Figure 1) in the 20-1000 Hz range a high speed camera has been used.

Since several thousands of frames per second (fps) are typically acquired with these cameras, it is necessary to use a good lighting system that allows the sensor capturing the sample. For this test, a Vision Research Phantom v310 camera has been used along with two Dedocool tungsten light heads. This camera can record at 3250 fps at a full resolution (1280 x 800), but higher rates can be achieved by decreasing the resolution.

2.6 Frequency-displacement performance test

The objective of this test is to study the peak to peak travel of the shaker at full power (± 5 V) for different frequencies. In order to compare the results obtained by analyzing the images, an accelerometer (ENDEVCO 752A12) has been located on the top of the M6 thread by means of a magnet (Figure 11). Six different frequencies have been studied. The camera has recorded at 5600 fps for all of the cases. The image resolution is 800 x 600.



Figure 11. ENDEVCO 752A12 accelerometer with a magnet base.

In order to postprocess, the images and accelerometer's data, a Labview programme developed in-house has been used. Figure 12 shows a Labview capture of the edge identification used to measure the effective displacement of the sample in the vertical direction.

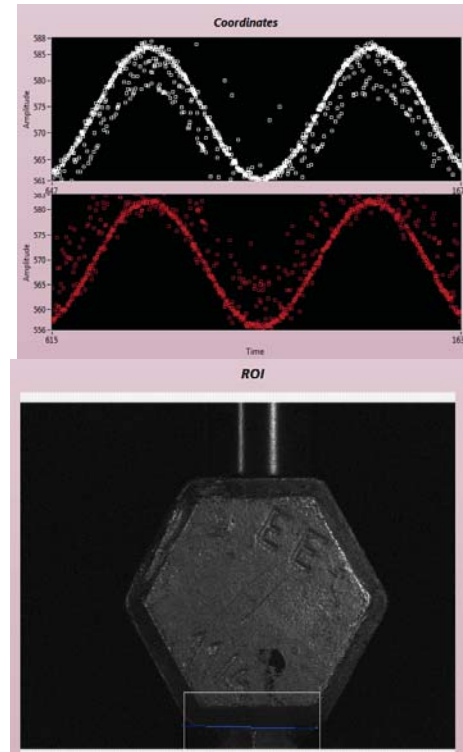


Figure 12. Postprocessing routine capture. Vertical coordinates plot (top) and Region of Interest under study (bottom)

In order to check the double integration procedure required to obtain the displacement from the accelerometer's output, a previous comparison between the accelerometer and a LVDT has been done at 10 Hz and 2V and at 20 Hz and 5V. When integrating, the low frequency band is amplified and a filter is necessary to avoid non desired frequencies. In this case, a highpass filter has been used with a cutoff frequency of 95% of the exciting frequency. Table 1 shows this comparison and the relative error, equation (3), where the LVDT result has been used as the reference value.

$$e = \left| \frac{x_i - x_{ref}}{x_{ref}} \right| \cdot 100 \quad (3)$$

where x_{ref} is the reference value.

Table 1. Peak to peak displacement (mm) comparison between the accelerometer and the LVDT

Frequency (Hz)	10	20
Voltage (V)	2	5
LVDT	2.3	5.4
	86	77
Accelerometer	2.3	5.3
	47	22
Error (%)	1.6	2.8

Table 2 summarises the obtained results both by double integrating the accelerometer's signal and by image identification for the six different tested frequencies

Table 2. Peak to peak displacement (mm) for the different tested frequencies

Frequency (Hz)	20	40	80	100	200	500
Accelerometer	5.32	5.68	1.4	0.7	0.1	0.0
	2	0	39	72	30	17
High Speed Camera	7.06	7.40	1.8	0.9	0.1	---
	8	0	14	82	23	
Error (%)	32.8	30.3	26.	27.	5.4	---
			1	2		

There is a significant level of noise in the coordinates detection (Figure 12), which suggests that a better focus of the edges of the surface should have been done. During the test, the focus has been manually adjusted for every case. A poor focus of the region of interest leads to higher errors as clearly shown in Table 2. Moreover, the images used give a ratio of approximately 0.123 mm/pixel, which is clearly insufficient to capture the vibration at 500 Hz.

3 CONCLUSIONS

Image based technologies can be a reliable solution for quantifying phenomenon of different structural problems, as shown in the present work. These systems output non-contact measurements and field (multiple points) measurements which can be of great value depending on the application. When compared to more traditional, local and contact sensors their results are in good agreement.

DIC on the other hand, requires a sample preparation which can be both challenging and very time consuming. Also, a certain level of expertise should be gained to avoid speckle dependent results.

High speed imagery postprocessing is not simple and even with flexible programming tools such as Labview, the workflow can be complex. However, as shown in this work, it is not only a tool to “see” phenomena, but also to measure up to a certain level of confidence. The experimental setup in this case does not involve a previous sample treatment, but also requires a good level of knowledge. Specifically, the use of external lighting, camera resolution and a correct focus of the region of interest are some of the variables which greatly determine the quality of the results, as shown in this work.

ACKNOWLEDGMENTS

The authors would like to acknowledge the support of the European Commission Horizon 2020 project Built2Spec (637221) and Science Foundation Ireland through the National Centre for Marine and Renewable Energy Ireland (MaREI) (Grant no. 12/RC/2302). The third author would also like to acknowledge the financial support of the Irish Research Council through a postgraduate fellowship. The last author would also like to acknowledge the support of Science Foundation Ireland through the Career Development Award programme (Grant no. 13/CDA/2200).

REFERENCES

- [1]- McCormick, N., Lord, J., 2010. *Digital Image Correlation*. Materials Today, vol 13, p 52-54.
- [2] Grant, B., Stone, H., Withers, P.J., Preuss, M., 2009. *High-temperature strain field measurement using digital image correlation*. Journal of Strain Analysis for Engineering Design, vol 44, p 263-271.
- [3] Wang, K., Carsley, J., He, B., Li, J., Zhang, L., 2014. *Measuring forming limit strains with digital image correlation analysis*. Journal of Materials Processing Technology, vol 214, p 1120-1130.
- [4] Obreschkow, D., Kobel, P., Dorsaz, N., de Bosset, A., Nicollier, C., Farhat, M., 2006. *Cavitation Bubble Dynamics inside Liquid Drops in Microgravity*. Physical Review Letters, PRL 97.
- [5] Kravtsova, A., Markovich, D.M., Pervunin, K.S., Timoshevsky, M.V., Hanjalic, K., 2013. *High-speed imaging of cavitation regimes on a round leading-edge flat plate and NACA0015 hydrofoil*. Journal of Visualization, vol 16:181-184.
- [6] Lecompte, D., Smits, A., Bossuyt, S., Sol, H., Vantomme, J., Van Hemelrijck, D., Habraken, A.M., 2006. *Quality assessment of speckle patterns for digital image correlation*. Optics and Lasers in Engineering, vol 44, p 1132-1145.
- [7] Crammond, G., Boyd, S.W., Dulieu-Barton, J.M., 2013. *Speckle pattern quality assessment for digital image correlation*. Optics and Lasers in Engineering, vol 51, p 1368-1378.
- [8] Sun Yaofeng, Pang, J., 2007. *Study of optimal subset size in digital image correlation of speckle pattern images*. Optics and lasers in engineering.

Evaluation of Camera Calibration Techniques for Quantifying Deterioration

Michael O'Byrne¹, Franck Schoefs², Bidisha Ghosh³, Vikram Pakrashi¹

¹ Department of Civil and Environmental Engineering, University College Cork; Cork, Ireland

² Université Bretagne-Loire, Université de Nantes, Research Institute of Civil Engineering and Mechanics (GeM)/Sea and Littoral Research Institute (IUML), CNRS UMR 6183/FR 3473, Nantes, France; IXEAD/CAPACITES, Nantes, France

³ Department of Civil, Structural and Environmental Engineering, Trinity College Dublin; Dublin, Ireland
E-mail: michael.obyrne@ucc.ie, bghosh@tcd.ie, franck.schoefs@univ-nantes.fr, v.pakrashi@ucc.ie

ABSTRACT: Imaging systems offer an efficient way of obtaining quantitative information on the health status of structural components. They hold particular value for underwater inspections as they can be easily adapted for underwater use and they enable physical information to be captured from a scene for the purpose of later analysis. In order to make the visual data a part of a quantitative assessment, it is necessary to calibrate the imaging systems so that photographed instances of damage can be expressed and measured in physically meaningful real world units, such as millimetres, which can then be used by engineers in subsequent analyses. The imaging system employed in this study is a stereo rig. It consists of two synchronised cameras that capture images of the scene from slightly different perspectives, thereby encoding depth information. This paper evaluates and compares two main approaches for calibrating such a stereo systems, namely, the classical checkerboard procedure and self-calibration based on Kruppa's equations. Conventional checkerboard calibration must be carried out on-site by photographing a planar checkerboard pattern that is held at multiple random poses, while self-calibration can be carried out after-the-fact and relies only on the static scene acting as a constraint on the camera parameters. The performance of each approach is assessed through a set of experiments performed on controlled real-world specimens as well as on synthetic data. Results indicate that checkerboard calibration is slightly more accurate than self-calibration; however, the practical advantages of using self-calibration may outweigh this reduction in accuracy. An understanding of the advantages and limitations associated with each camera calibration allows inspectors to rationalise the use of either approach as part of their inspection regime, and it helps them to fully capitalise on the benefits of image-based methods.

KEY WORDS: Imaging; Camera calibration; Self-calibration; Deterioration quantification; Structural Health Monitoring.

1 INTRODUCTION

Efficient monitoring strategies seek to collect and extract maximum useful information from structural performance data at a minimum cost and in a reliable manner, while limiting or supplementing the qualitative, subjective and unreliable aspects. An increasingly popular way of enhancing the quality of the data acquired from inspections relies on making more effective use of imaging devices. Imaging devices are capable of introducing a source of quantitative information that can offset some of the inherent limitations of conventional visual inspections.

Many marine structures are assessed visually either by trained divers or by Remotely Operated Vehicles (ROVs). Visual inspections carried out by divers almost always capture photographs to include in the inspection report, while ROVs are typically equipped with at least one camera/video system. In both cases, the acquired imagery is usually qualitatively reviewed and archived; however, it is rarely exploited to the fullest potential in a quantitative sense despite requiring only minimal effort to do so. The quantitative nature of the data obtained from image analysis is important and naturally lends itself to numerous applications, including for developing new damage models, or strengthening existing ones, which can be used to forecast the rate of propagation of damage as the structure continues to operate.

Methods of extracting quantitative information from images vary in terms of the level of sophistication. Naïve approaches entail placing an object of known dimensions in the scene,

such as a ruler, and then inferring the dimensions of nearby instances of damage by establishing a scale factor that relates pixel units to real world units, such as millimetres. More robust and advanced solutions can reconstruct the full 3D scene through the acquisition of multiple views. This is typically accomplished using either Structure-From-Motion (SFM) photogrammetry or stereo-based approaches, both of which require camera calibration to determine a relation between 2D image coordinates and the 3D world. Furthermore, capturing the 3D shape, instead of just a 2D projection as a standard camera does, opens the possibility of embracing a host of emerging technologies, such as virtual and augmented reality [1].

Structure-from-motion photogrammetry techniques are used to reconstruct a scene from a sequence of overlapping images acquired by a single moving camera [2]. The process is based on the automatic extraction of points of interest (a sparse set of features), the tracking of this sparse set of features across the image sequence, and the estimation of their 3D positions using multiple views [3]. Photogrammetry techniques have the advantage of being easy to implement on-site as they only require a diver to operate a single unconstrained camera and capture photographs as normal. However, they are limited insofar as the 3D reconstructions are scale ambiguous (i.e. the 3D scene can only be recovered up to an unknown scale factor), there is a requirement that the scene remains static, and the performance of the technique is heavily reliant on the successful tracking of features over time. Reliably tracking

features is difficult when operating in underwater conditions characterised by poor visibility [4]. Given these limitations, this paper focuses on calibration of stereo systems as it is felt that the effort and expense associated with underwater inspections warrants the use of more dependable solutions.

Stereo systems have been widely used for underwater inspections that have been carried out by divers [5] and ROVs [6]. These systems consist of two horizontally displaced digital cameras to simultaneously photograph a scene from slightly different perspectives, resulting in two images that are collectively referred to as a stereo pair. 3D information can be extracted by comparing information about the scene from the vantage point of the left camera with that of the right camera. The use of two cameras represents a good compromise between reliability and operational complexity as 3D shape information can be obtained from a single stereo pair once the stereo system has been calibrated, and unlike SFM, stereo systems can be used even if the scene does not remain static (i.e. it evolves over time) since both images in the stereo pair are captured simultaneously.

Camera calibration [2] is the process of finding the camera's extrinsic and intrinsic parameters. It must be carried out for each set of inspection conditions and for each stereo camera configuration. For a stereo system, the extrinsic parameters describe the rotation and a translation of the right camera with respect to the left camera, while the intrinsic parameters consist of the focal length, the optical centre, also known as the principal point, and the skew coefficient. Once the intrinsic and extrinsic camera parameters are known, and, taking into account of radial distortion, image pixels can be back-projected to 3D rays in space.

A well calibrated stereo system is essential for ensuring that the reconstructed 3D shape accurately reflects the true real-world shape. This paper evaluates and compares two main approaches for calibrating stereo systems, namely, the classical checkerboard procedure and self-calibration that is based on Kruppa's equations. This performance of each approach is assessed through a set of experiments performed on controlled real-world specimens as well as synthetic data. A measure of the accuracy of the estimated calibration parameters is found by comparing the sizes of the reconstructed shapes with the known sizes and by calculating the re-projection error. The contribution of this paper lies in the application of this study to the domain of underwater inspections where the usefulness of extracting quantitative information from visual data is greatly felt, as well as in the novel methodology that leverages the advantages of real world and virtual data.

The background of stereo-based 3D imaging is discussed in the following section. Section 3 presents the images that are analysed in this paper. Section 4 evaluates and compares the performance of each calibration procedure. Section 5 concludes the paper.

2 BACKGROUND

2.1 Camera Model

The most widely used camera model is the pinhole camera. In this model, the relationships between world coordinates \mathbf{X} and image (pixel) coordinates \mathbf{x} is modelled via the perspective transformation. Let $\mathbf{x} = (u, v, 1)$ be the

homogenous coordinates of a point in an image. The equation for relating these image points to real world points is:

$$s \begin{bmatrix} u \\ v \\ 1 \end{bmatrix} = \mathbf{P} \begin{bmatrix} X_s \\ Y_s \\ Z_s \\ 1 \end{bmatrix} \quad (1)$$

where s is a non-zero scale factor, $\mathbf{X} = (X_s, Y_s, Z_s, 1)$ are world coordinates, and \mathbf{P} is a 3×4 projection matrix that completely represents the mapping from the scene to the image. \mathbf{P} encapsulates both the extrinsic and intrinsic parameters of a camera. It is given by:

$$\mathbf{P} = \mathbf{K} [\mathbf{R} | \mathbf{T}] \quad (2)$$

where \mathbf{R} and \mathbf{T} are the extrinsic parameters - representing the rotation matrix and the translation of the camera in the 3D scene, respectively. Both the rotation matrix and the translation vector have three degrees of freedom. \mathbf{K} is an upper-triangular matrix that represents the intrinsic parameters. It has five degrees of freedom. The five intrinsic parameters correspond to the focal length in pixels for the horizontal and vertical axes, f_x , and f_y respectively, the skew parameter, sk , and the two principle points x_0 and y_0 , (the optical centre of the camera), as summarised in Equation 3.

$$\mathbf{K} = \begin{bmatrix} f_x & sk & x_0 \\ 0 & f_y & y_0 \\ 0 & 0 & 1 \end{bmatrix} \quad (3)$$

2.2 Stereo Imaging

Recovering depth from stereo images involves a number of sub-problems, including rectification, matching, and reconstruction. Rectification is the process of transforming the left and right images of a stereo pair, such that corresponding points in each image are separated only by a horizontal distance and not by a vertical distance. Rectification can be carried out either with calibration information using the essential matrix, or without it using the fundamental matrix. The essential matrix, \mathbf{E} , is a 3×3 matrix that depends only on the extrinsic parameters \mathbf{R} and \mathbf{T} . The fundamental matrix, \mathbf{F} , is a generalisation of the essential matrix. It relates corresponding points in the stereo images and may be estimated from seven or more point correspondences. The seven parameters represent the only geometric information about cameras that can be obtained through point correspondences alone. It does not require any knowledge of camera internal parameters.

All points in the rectified images should satisfy the epipolar geometry of a rectified image pair (i.e. that the images are aligned horizontally). This may be expressed as follows: if a point \mathbf{x}_l in the left image corresponds to a point \mathbf{x}_r in the right image then they should satisfy the constraints in Equation 4 and 5. These constraints are geometrically equivalent; the only difference being that Equation 4 is more general as it is based on the fundamental matrix, \mathbf{F} , while Equation 5 makes use of camera calibration information by including the calibration matrices for the left and right cameras, \mathbf{K} and \mathbf{K}' respectively,

as well as the relative position and orientation between the cameras which is captured by the essential matrix \mathbf{E} :

$$\mathbf{x}_i'^T \mathbf{F} \mathbf{x}_i = 0 \quad (4)$$

$$\mathbf{x}_i'^T \mathbf{K}^{-T} \mathbf{E} \mathbf{K}^{-1} \mathbf{x}_i = 0 \quad (5)$$

Rectification makes the task of matching pixels in the left and right image considerably faster as it confines the search to the horizontal direction only.

The second stage of the stereo process entails solving the stereo correspondence problem. Stereo correspondence is principally about finding matching points between the left and right stereo images, typically using some measure of similarity such as the Sum of Absolute Differences (SAD) or a correlation based metric. In this paper, a loopy Belief Propagation (BP) based technique is adopted, as described by Ho [7]. The output of this stage is a dense disparity map which represents the distance in pixels between corresponding points in the rectified images.

The final step uses this disparity map to reconstruct the 3D scene, as the disparities are proportional to the distance between the cameras and the 3D world points. If the camera's intrinsic and extrinsic parameters are known then a full metric 3D scene can be computed.

It is worth mentioning that each stage of the stereo imaging pipeline is dependent on the preceding stages. For instance, inaccurate rectification adversely impacts on the level of success that can be attained in subsequent stages. An image that is poorly rectified will likely lead to unreliable matching, and consequently, will result in a low quality 3D reconstruction. This underlines the value of having reliable calibration data to start off with.

2.3 Checkerboard Calibration

Checkerboard based calibration involves capturing stereo photographs of a checkerboard/chessboard, that is positioned at several unknown positions and orientations in the scene, as depicted in Figure 1. A checkerboard pattern is used as the black and white grid structure naturally produces a lot of high contrast corner points that can be easily detected and precisely located by the calibration algorithms.

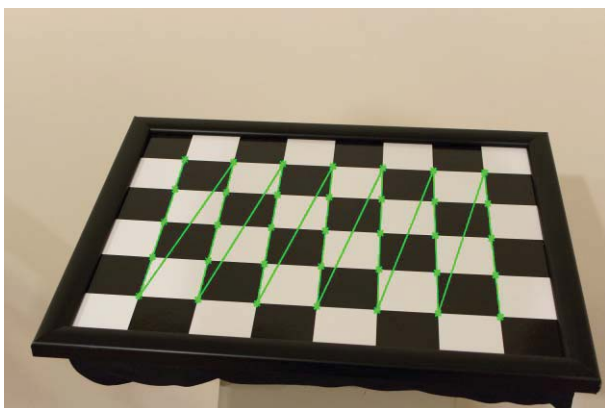


Figure 1. Checkerboard based calibration.

A seminal example of checkerboard calibration algorithm is given by Zhang [8]. Zhang's method calibrates cameras by solving a particular homogeneous linear system that captures

the homographic relationships between multiple perspective views of a checkerboard that is known to be planar. This calibration approach is popular as it is capable of achieving accurate results whilst being relatively easy to carry out on-site. Generally, it is advisable to capture more than ten photographs of the checkerboard under the same conditions that the inspection photographs will be captured under (i.e. same underwater medium, intrinsic camera settings, stereo-rig configuration etc.), in order to obtain reliable calibration parameters.

2.4 Self-Calibration

Self-calibration, also known as auto-calibration, is an attractive way of determining the intrinsic and extrinsic camera parameters as it does not require the diver/photographer to undertake any preliminary calibration procedures, nor does it require the assistance of a second diver or the use of additional props. Self-calibration refers to the process of obtaining a calibrated camera matrix using static scene as a constraint for the five degree-of-freedom pinhole camera model, as represented by the matrix \mathbf{K} in Equation 3. Theoretically, a minimum of three views is needed for full calibration assuming the intrinsic parameters remain constant between views (i.e. the focal length, or any other parameter, is not adjusted between views). In reality, however, the principle points, x_0 and y_0 , can usually be safely estimated to be at the image centre. Furthermore, most modern imaging sensors and optics provide further prior constraints such as zero skew and unity aspect ratio, which means that the horizontal and vertical focal length, f_x and f_y , can be regarded as having the same value. Integrating these priors will reduce the minimum number of views required to two. This paper adopts the approach described by Faugeras et al. [9], whereby two positions of the stereo system were analysed. Kruppa's equations provide an initial estimate of the focal lengths in the left and right camera matrices, \mathbf{K} and \mathbf{K}' respectively, and the principal points, x_0 and y_0 , are initially assumed to be located at the image centre, while the skew is taken as 0. The camera matrices are then refined through non-linear optimization.

The only additional information required is the baseline, which is the distance between the two cameras (measured in millimetres). It provides the single necessary piece of information for obtaining correctly scaled 3D reconstruction.

There are some inherent drawbacks associated with self-calibration. Firstly, real cameras are affected by radial and tangential lens distortion. While checkerboard calibration is capable of estimating the distortion parameters and undistorting the images, self-calibration methods are not well equipped to deal with this additional layer of complexity. This is especially problematic when dealing with wide-angle lenses as the level of distortion tends to be particularly severe.

Secondly, self-calibration requires the extraction of a sparse set of corresponding points from the left and right frames of the stereo pair, \mathbf{x} and \mathbf{x}' respectively, in order to set up the static scene constraint problem. However, if not enough corresponding points are found (a minimum of 5 is required), or if erroneous correspondences are present, then the essential matrix cannot be determined, or it will be poorly estimated. This issue is mitigated by using the robust, state-of-the-art SIFT (Scale Invariant Feature Transform) algorithm [10] for

extracting and matching points of interest in the left and right images in conjunction with bundle adjustment, which serves to reject outlier matches.

3 DATA ANALYSIS

3.1 Applications of 3D shape recovery for underwater inspections

Recovering quantitative shape information is a challenging but useful task, and has wide applicability in many areas of Structural Health Monitoring (SHM). This paper focuses on an application specific to marine structures; that is, measuring the marine growth accumulation. Marine growth colonisation has adverse effects on the hydrodynamic performance of marine structures. The two key parameters that are needed for structural reliability computation are the thickness and the roughness [11]. Both of these vary around and among structural components and require knowledge of the 3D shape of the marine growth to be computed.

The calibration procedures under consideration are evaluated on controlled shapes representative of marine growth, as well as on synthetic data that has been designed to reflect a realistic underwater scene whilst maintaining full control over the camera parameters and the 3D structure.

3.2 Real Data

The specimens were designed to represent the size and shape of typical hard fouling organisms such as barnacles and semi-rigid fouling organisms such as sea anemones. They are comprised of standard geometric shapes. The barnacles are represented by cones of height 25 mm, while the sea anemones are represented by hemi-spheres/protracted domes that come in three heights - ranging from 25 mm to 40 mm.

The stereo system consisted of two Canon EOS 600D DSLR cameras. Both cameras shared identical settings (e.g. aperture, ISO, shutter speed) and their focal lengths were 32 mm. The image resolution was 2282 x 1167 pixels. An example of an image taken by the left camera of the simulated barnacles and sea anemones is shown in Figure 2.



Figure 2. Simulated marine growth species taken by the left stereo camera.

3.3 Synthetic data

This study used synthetic data as it provided a way of imitating the texture and irregular shape of natural marine growth in a typical underwater inspection setting, whilst retaining complete control of the scene and the cameras. As a reference, a photograph of natural marine growth on a real world structure is presented in Figure 3. The synthetic data consisted of a virtual 3D model of a jacket-type platform that was colonised by marine growth, as shown in Figure 4. The 3D model was set in a physically accurate underwater environment, where the common issues that affect underwater optical imaging systems were present, such as scattering and colour absorption. Other factors that occur in real world scenes, such as luminous complexities (e.g. bright spots caused by the use artificial lighting, surface reflections and caustics) and marine snow (turbidity) were also accounted for.



Figure 3. Real world structure affected by marine growth.



Figure 4. Rendered image of marine growth colonised structure taken by the left camera of the virtual stereo system.

The checkerboard based calibration for the virtual stereo system was carried out in the same manner as the calibration for the real stereo system. It entailed capturing 14 images of a checkerboard pattern, held at various random locations and orientations, in the underwater scene as the calibration phase must be done under the same conditions as that of the main image acquisition phase. An example of an image taken by the left virtual camera of the checkerboard is shown in Figure 5.



Figure 5. Checkerboard calibration for the virtual scene.

4 RESULTS

This section presents the estimated camera calibration matrices based on the checkerboard calibration and self-calibration procedures. The results of the 3D shape recovery are also provided.

4.1 Results for Real Data

The calibration matrices for the left camera, \mathbf{K} , as estimated using checkerboard calibration and self-calibration are as follows:

$$\text{Checkerboard, } \mathbf{K} = \begin{bmatrix} 3686 & 0 & 1221 \\ 0 & 3717 & 817 \\ 0 & 0 & 1 \end{bmatrix}$$

$$\text{Self-calibration, } \mathbf{K} = \begin{bmatrix} 3649 & 0 & 1296 \\ 0 & 3624 & 864 \\ 0 & 0 & 1 \end{bmatrix}$$

The calibration matrices for the right cameras are similar; they are omitted due to space constraints. Using these calibration matrices, the scene was reconstructed and the height of the marine growth species was estimated. A view of the reconstructed scene using self-calibration is shown in Figure 6. The estimated height values corresponding to each calibration approach are presented in Table 1.

Table 1. Reconstruction Accuracy

Marine Growth Species	No. of cases	Actual Height	Root-Mean-Square Error	
			Checkerboard calibration	Self-calibration
Sea Anemones (small)	7	25 mm	3.9 mm	8.6 mm
Barnacles	7	25 mm	8.2 mm	7.7 mm
Sea Anemones (medium)	2	35 mm	4.4 mm	4.7 mm
Sea Anemones (large)	3	40 mm	3.4 mm	6.3 mm



Figure 6. Reconstructed scene using self-calibration

4.2 Results for Synthetic Data

The calibration matrices for the left camera, \mathbf{K} , as estimated using checkerboard calibration and self-calibration, along with the ground truth matrix (which is known and can be controlled since virtual cameras are being used), are as follows:

$$\text{Checkerboard, } \mathbf{K} = \begin{bmatrix} 1334 & 0 & 801 \\ 0 & 1334 & 601 \\ 0 & 0 & 1 \end{bmatrix}$$

$$\text{Self-calibration, } \mathbf{K} = \begin{bmatrix} 1340 & 0 & 804 \\ 0 & 1324 & 600 \\ 0 & 0 & 1 \end{bmatrix}$$

$$\text{Ground Truth, } \mathbf{K} = \begin{bmatrix} 1333 & 0 & 800 \\ 0 & 1333 & 600 \\ 0 & 0 & 1 \end{bmatrix}$$

Depth maps were generated using camera matrices based on the checkerboard calibration and self-calibration, as shown in Figure 7a and 7b respectively. Comparison with the ground truth depth map, which is illustrated in Figure 7c, reveals that the Root-Mean-Square Error (RMSE) for the checkerboard calibration was 22.9 cm, while the RMSE for the self-calibration was almost identical at 23 cm. These depth maps represent the actual distance of points in the scene from the camera. Only visible points on the structure were considered for the purpose of assessing the reconstruction error more effectively.

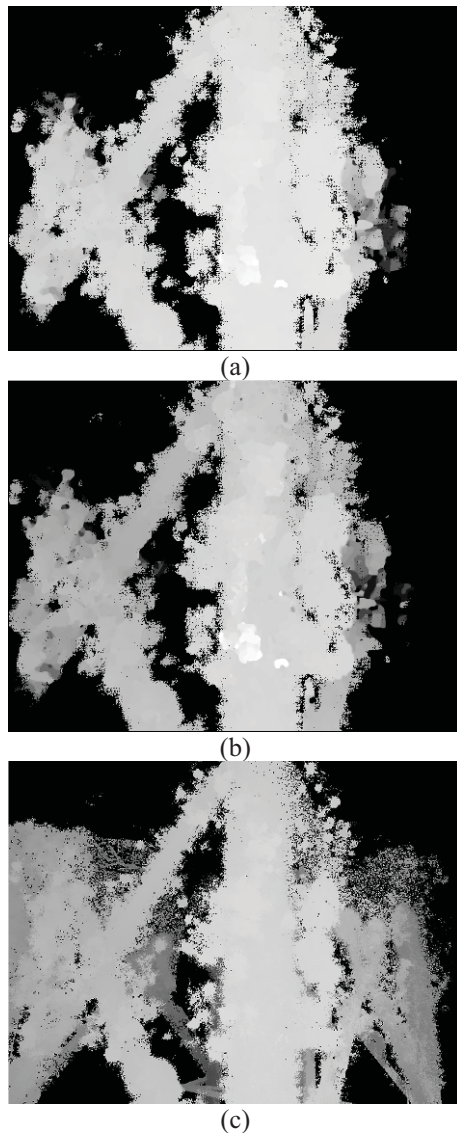


Figure 7. (a) Depth map from checkerboard calibration, (b) depth map from self-calibration, and (c) ground truth.

4.3 Discussion

For the real cameras, the focal lengths estimated through self-calibration and checkerboard calibration showed good agreement with each other. While there was a more notable difference between the estimated principal point values, this did not translate into a significantly errant reconstruction as both calibration methods produced good reconstructions, as evident from the generally low RMSE reported in Table 1. It is apparent though that the checkerboard calibration offers some accuracy improvements over self-calibration.

For the virtual cameras, the estimated camera matrices were very close to the ground truth values, although once again, the checkerboard calibration produced marginally better results. These findings suggest that checkerboard calibration should be undertaken to obtain the best results, however, self-calibration can be a good alternative if checkerboard calibration is not possible.

CONCLUSION

Cameras are a versatile tool capable of making visual data a part of quantitative assessment. In order to extract quantitative information from the visual data, it is necessary to perform camera calibration. This task is often overlooked despite being a crucial part of the imaging pipeline. With this in mind, it is of great practical importance that inspectors are aware of the various camera calibration approaches available and have knowledge about their respective advantages and limitations so that they can fully capitalise on the power of cameras as a quantitative assessment tool and integrate them into the inspection framework.

This paper presents a comparison between two of the most prominent classes of camera calibration techniques, namely, the classical checkerboard procedure and self-calibration. These calibration procedures are evaluated on controlled shapes that are representative of macro-scale marine growth, as well as on synthetic data which has been specifically designed to reflect some of the deleterious effects and phenomena encountered in underwater environments, such as luminous complexities, poor visibility, light attenuation and backscatter which diminish the ability of the camera, and calibration procedures, to effectively identify and quantify instances of deterioration. Results indicate that checkerboard calibration is noticeably more accurate than self-calibration; however, the practical advantages of using self-calibration may outweigh this reduction in accuracy.

ACKNOWLEDGMENTS

The authors wish to thank Science Foundation Ireland and Capacités SAS/IXEAD society for supporting this research.

REFERENCES

- [1] Marchi, L., A. Ceruti, et al. (2016). 'Augmented Reality Tools for Structural Health Monitoring Applications', *Applications in Electronics Pervading Industry, Environment and Society*, 115-121.
- [2] Hartley, R., A. Zisserman, *Multiple View Geometry in Computer Vision*, Cambridge University Press, 2003.
- [3] Cocito, S., Sgorbini, S., Peirano, A. & Valle, M. (2003). '3-D reconstruction of biological objects using underwater video and image processing', *Experimental Marine Biology and Ecology*, 297, 57-70.
- [4] O'Byrne, M., Pakrashi, V., Schoefs, F., and Ghosh, B. 'A Comparison of Image Based 3D Recovery Methods for Underwater Inspections'. *7th European Workshop on SHM*, 8-11 July, 2014, Nantes, France.
- [5] Negahdaripour, S., and Firoozfam, P. (2006) 'An ROV Stereovision System for Ship-Hull Inspection,' *IEEE Journal of Oceanic Engineering*, 31(3), 551-564.
- [6] Morales, R., and Pereira, D. (2006). 'Prototype of Stereoscopic Vision System to Improve the Image Quality in Turbid Waters during Underwater Inspections,' *OCEANS 2006*, Boston, MA, 1-4.
- [7] Ho, N. (2012). 'Loopy Belief Propagation, Markov Random Field, Stereo Vision'. Available: http://nghiaho.com/?page_id=1366. Accessed 25th Nov 2014.
- [8] Zhang, Z. (2000). 'A Flexible New Technique for Camera Calibration', *IEEE Transactions on Pattern Analysis and Machine Intelligence*, 22(11), 1330-1334.
- [9] Faugeras, O. D., Luong, Q. T., and Maybank, S. J. (1992). 'Camera Self-Calibration: Theory and Experiments', *Computer Vision — ECCV'92*, G. Sandini, ed., Springer Berlin Heidelberg, 321-334.
- [10] Lowe, D. G. (1999). 'Object Recognition from Local Scale-Invariant Features', *Proc. of the 7th IEEE International Conference on Computer Vision*, 20-27 Sept. 1999, Kerkira, Greece, 1150-1157.
- [11] Schoefs, F., & Boukinda, M.L. (2010), 'Sensitivity Approach for Modelling Stochastic Field of Keulegan Carpenter and Reynolds Number Through a Matrix Response Surface'. *Journal of Offshore Mechanics and Arctic Engineering (JOMAE)*, 132(1): 1-7.

An Overview of Arup Computational Fluid Dynamics Projects

Jennifer Keenahan¹, Cristina Paduano¹, Réamonn Mac Réamoinn¹

¹Arup, 50 Ringsend Road, Dublin 4, Ireland

email: jennifer.keenahan@arup.com, cristina.paduano@arup.com, reamonn.macreainn@arup.com

ABSTRACT: In recent years, end users have become more concerned with the human experience and the personal comfort of the individual is becoming more important in the design of the built environment. Computational Fluid Dynamics (CFD) is a tool that permits assessment of personal comfort. CFD is a stream of fluid mechanics that utilises numerical methods to analyse and solve problems involving fluid flows. The fundamental basis for these problems are the Navier-Stokes equations. While research applications of CFD are developing, as is the use of CFD in the aerospace industry, the use of CFD in Civil Engineering applications is currently at the cutting edge. Arup have recently developed a team to work on such projects and some of these will be presented in this paper. The paper will discuss the research question of each project, the methodology adopted in developing the models, the results of the simulations and some lessons learned going forward. Based on the projects done to date, it can be concluded that CFD has been shown to be a powerful tool that adds valuable information to fluid flow problems.

KEY WORDS: Computational Fluid Dynamics (CFD); Navier-Stokes; thermal comfort; pedestrian comfort.

1 INTRODUCTION

Computational Fluid Dynamics (CFD) is the use of computers and numerical methods to solve problems in fluid flow. It is a method for solving partial differential equations in continuum mechanics using numerical techniques. It involves breaking the problem down into a discrete number of volumes that can be analysed more easily [1]. Combining the solutions from these small volumes permits the generation of the complete solution. The equations governing fluid motion are based on the fundamental physical principles of the conservation of mass, momentum and energy. CFD has been successfully applied in many areas of fluid mechanics, including, heat and mass transfer [2], chemical reaction and combustion [3], aerodynamics of cars and aircrafts, and pumps and turbines. The use of CFD in civil engineering applications, although more recent, is currently at the cutting edge due to the direct practical applications. Applications of CFD to civil engineering include wind modelling and the dynamic response of structures [4], ventilation [5], fire, smoke flow and visibility [3], dispersion of pollutants and effluent [6], and heat transfer in buildings [7]. Traditionally, the interaction of these phenomena has been carried out experimentally, using scaled models and short calculations. However, it is rarely possible to accurately capture all phenomena guaranteeing repeatability. In the advent of improving computational power, and the development of numerical techniques such as Finite Element Analysis, CFD offers an opportunity to model many variations of the same problem at full scale, more efficiently, in a virtual environment.

As with any computer simulation, the quality of the results is dependent on the quality of the inputs, the assumptions, modelling characteristics employed and the equations used to represent the phenomena. There will inevitably be approximations, and a robust model validation process is

essential. A high level understanding of the modelling process and of the phenomena being modelled is necessary for the output to be of any practical use.

In order to capture the phenomena in sufficient detail, large finite volume models are necessary requiring significant processing power. These large models generate a great amount of data, which in turn needs to be stored and analysed. The advantages of CFD however, far out-weigh the disadvantages. It is a non-intrusive, virtual modelling technique with powerful visualisation capabilities. Results can be captured across the entire domain. There are also significant cost and time savings with CFD as there is opportunity to assess comparisons between alternative systems quickly and efficiently, without the disruption of making physical changes on site.

This paper will discuss some projects recently undertaken by the new CFD team at Arup, namely, a Dublin Docklands tall building wind study, a Hospital thermal comfort study, and a Dundrum Ventilation Shaft fire study. The research question of each project will be discussed, the methodology adopted in developing the models presented, and finally the results illustrated.

2 CFD MODELLING METHODOLOGY

Modelling in CFD comprises three main stages: pre-processing, simulation and post-processing.

Pre-processing firstly involves the construction of the geometric model for the flow domain of interest, and the subsequent division of this domain into small control volumes (cells), a process often called ‘meshing’. The flow field and the equations of motion are discretized, and the resulting system of algebraic equations is solved to give values at each node. Once the model and the mesh have been created, appropriate initial conditions and boundary conditions are then applied.

The Navier-Stokes equations, the governing equations for the behavior of fluid particles, are solved iteratively in each control volume within the computational domain until the solution converges. The field solutions of pressure, velocity, air temperature and other properties can be calculated for each control volume at cell centers and interpolated to outer points in order to render the flow field.

Post-processing involves graphing the results and viewing the predicted flow field in the CFD model at selected locations, surfaces, or planes of interest. The Navier-Stokes equations, used within the CFD analysis, apply a numerical representation to approximate the laws of physics to produce extremely accurate results, providing that the scenario modelled is representative of reality. In each of the following examples, Fire Dynamic Simulator Version 5.5.3 was used.

3 DUBLIN DOCKLANDS TALL BUILDING WIND STUDY

Computational Wind Engineering (CWE) is a branch of CFD concerned with behavior of wind. Similar to wind tunnel tests, it can be used to understand the wind flow through an urban environment and the effect of a proposed development on the local wind microclimate. Unlike boundary layer wind tunnel tests, a virtual topographical model can be constructed at full scale and therefore, avoids any similarity problems (i.e. Reynolds number violation). In addition, the wind speed profile, which is consistent with reality, can be specified directly in CWE rather than generated artificially in a wind tunnel using additional roughness elements.

The proposed development at the Dublin Docklands consists of the construction of an office building ranging in height from 8 to 17 storeys, known as the Dublin Docklands tall building. The construction of new buildings and the alteration of the existing landscape may alter the flow of the wind in the surrounding area [8]. The proposed development can generate a wind environment at ground level that is discomforting or even possibly dangerous to pedestrians. The assessment of discomfort and distress of pedestrians was carried out in accordance with the Lawson Comfort Criteria [9] (Table 1). The main source of pedestrian discomfort relates to the force of the wind felt on their body and their clothing, as additional effort is required to negotiate the wind. Even though the force acting on a person is related to the wind speed, the level of pedestrian discomfort depends on frequency of occurrence and the activity being undertaken as well as the wind speed.

Table 1. Lawson Comfort Criteria.

Wind effect	Threshold	Stationary	Strolling	Transit
Calm				
Felt on face				
Leaves move	4.0 m/s			
Dust raised	6.0 m/s			
Felt on body	8.0 m/s			
Hard to walk	10 m/s			
Trees moving				
Storm	15 m/s			
Dangerous	20 m/s			

A boundary layer wind tunnel study of the proposed development at the Dublin Docklands was previously

conducted by BMT Fluids to assess the impact of the proposed development on the wind microclimate. Arup were commissioned to conduct a further wind assessment to examine the locations identified as causing pedestrian discomfort or distress and to evaluate the effectiveness of the proposed mitigation measures.

The local wind climate was determined from historical meteorological data recorded at Dublin Airport. Two different datasets were analysed, namely; the data associated with the maximum daily wind speeds recorded over a 30 year period between 1985 and 2015, and the mean hourly wind speeds recorded over a 10 year period between 2005 and 2015. The wind speeds in the vicinity of the development will differ from the wind recorded in Dublin Airport. It is necessary to transform the wind speeds to take account of local conditions [10]. From this, a single wind speed profile was determined for each direction for both comfort and distress criteria, as illustrated in Figures 1 and 2.

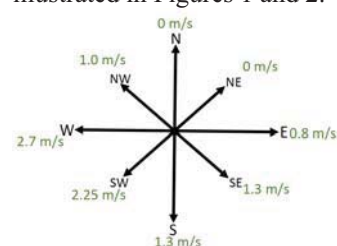


Figure 1. Comfort criteria

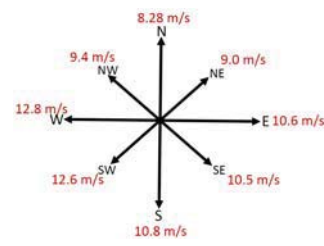


Figure 2. Distress criteria

The geometry for the CFD model was developed in 'Sketchup' drawing package using drawings received from the Client and Google Earth images of the surrounding area. The geometry was imported into 'Fire Dynamics Simulator' (FDS) software [11-12], used in the CFD modelling. A view from the East of the Dublin Docklands tall building is illustrated in Figures 3 and 4. The Dublin Docklands tall building was taken at the center of the computational domain which extended 550m in the North-South direction and 410 m in the East-West direction. The domain was modelled as 102.4 m in height.



Figure 3. Sketchup Geometry

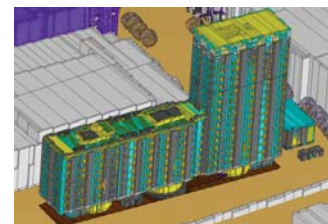


Figure 4. CFD model

As part of the computational process, the domain was divided into a total of 16million cells. The cells range in size from 0.4 m at the Dublin Docklands tall building to 3.2 m at the outer domain. Closed boundary conditions were applied on the bottom face of the domain, and open boundary conditions were modelled elsewhere. Data sampling locations were chosen to be as close as possible to the exact sensor locations used in the wind tunnel tests.

For the purposes of validation of the CFD modelling process, the conditions in the wind tunnel were modelled using CFD and comparisons were drawn. The results of this

validation showed good consistency with the original wind tunnel test results.

The assessment of the pedestrian comfort and distress in the pedestrian thoroughfare between the 3Arena and the Dublin Docklands tall building indicates that the main areas of concern are at the southern end. The equivalent wind speeds from the perspective of comfort and distress are 12m/s and 24 m/s respectively (Figure 5). These speeds arise when high westerly winds are directed to ground level by the building façade. These high winds cause discomfort and distress between the 3Arena and the Dublin Docklands tall building (Figure 6). Midway along the building, the equivalent hourly average gust wind speed from a comfort perspective is 8.3 m/s. At the northern end, the analysis reveals that the wind speeds are insufficient to cause either discomfort or distress.

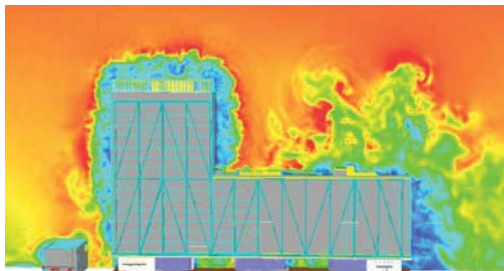


Figure 5. Distress Criteria, Wind from the West, Minimum values in blue (0m/s), Maximum values in red (20m/s)

In addition, it is possible that the winds from the south and north will cause distress to the general public. The equivalent hourly average gust speed is estimated at 15.4m/s and 16.3m/s from the North and Southwest, respectively. These wind speeds exceed the distress threshold for the general public of 15m/s.

The assessment of the pedestrian comfort and distress in the passageways between the Dublin Docklands tall building reveals that the wind conditions might be discomforting and distressing to pedestrian. However, the level of discomfort and distress is related to the wind direction. For instance, while westerly winds with an annual return period may produce conditions unsuitable for undertaking any activity within the undercroft, a slight shift in direction to the south results in an acceptable environment. It would appear that much of the pedestrian discomfort and distress is due to westerly winds. From the perspective of comfort, the equivalent hourly average gust speed in the undercroft passageways ranges between 10 m/s and 13.9 m/s for westerly winds, which is considered uncomfortable irrespective of the activity being undertaken. The main source of distress is due to westerly winds which range between 15m/s and 30m/s along the length of the building. These high wind speeds near ground level are due to the building funnelling high level winds downward. The wind speeds are further increased through the undercroft passageways as the wind is forced through narrower openings underneath the building (Figure 6). Although it might be expected that easterly winds might cause similar pedestrian discomfort and distress within the building undercroft, it is apparent from Figure 7 that this is not the case. The wall on the western boundary of Dublin Port acts to disturb the wind. The bluff nature of the wall causes the flow to separate and the formation of large vortex between

the wall and the Dublin Docklands tall building (Figure 8). The vortex acts to push much of the wind over the Dublin Docklands tall building. As a consequence there is less flow passing under the Dublin Docklands tall building.

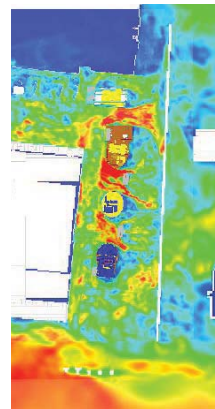


Figure 6. Distress Criteria, Wind from the West, Minimum values in blue (0m/s), Maximum values in red (20m/s)

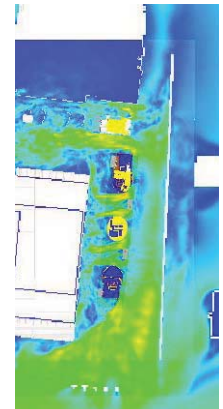


Figure 7. Distress Criteria, Wind from the East, Minimum values in blue (0m/s), Maximum values in red (20m/s)

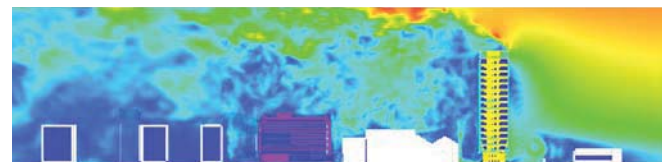


Figure 8. Distress Criteria, Wind from the East, Minimum values in blue (0m/s), Maximum values in red (20m/s)

The assessment of the Dublin Docklands tall building indicated that the southern extent of the pedestrian thoroughfare between the 3Arena and the Dublin Docklands tall building is prone to pedestrian discomfort and distress. Pedestrian discomfort and distress is also predicted in the undercroft of the Dublin Docklands tall building. The analysis reveals that high speed winds at ground level responsible for possible pedestrian discomfort were largely due to westerly winds, where the building acts to direct high level wind towards the ground. The provision of a 2.5 m wide canopy with a 0.45 m upstand for the full width of the western side of the building is proposed as a mitigation measure.

4 HOSPITAL THERMAL COMFORT STUDY

Arup was commissioned to conduct a thermal comfort analysis of a proposed new Hospital. An initial analysis of historical weather data was carried out to identify thermal conditions. Computational Fluid Dynamics (CFD) modelling was utilized in order to understand the internal flow field in the bedrooms and to identify zones of patient discomfort.

Thermal comfort is a subjective evaluation by humans of their satisfaction with the thermal environment. Maintaining a standard of thermal comfort for occupants of enclosures is an important goal of HVAC systems [13-14]. Owing to the global initiative to improve carbon footprints, many building owners are opting for naturally ventilated systems. A desired internal temperature of 22°C for patient comfort has been specified by the Design Team. The objective of this study is to

estimate whether an internal temperature of 22°C can be maintained:

- During winter conditions, with an ambient outside temperature of -4.5°C
- With the louvers in the open position
- Assuming the heating system of radiant panels prescribed by the Design Team is fully operational
- Assuming the geometry and layout of the rooms as received from the Design Team.

The temperature climate in the vicinity of the new hospital was estimated from almost 20 years of historic temperature data (December 1996 until December 2015) recorded at a local airport. Analysis of the data revealed that the most frequent minimum temperatures were between 4-8°C, however it was not uncommon to have temperatures as low as -4°C. On seven occasions in 20 years, the temperature fell below -8°C, and the minimum temperature recorded over the analysis period was -10°C which occurred twice (Figure 9).

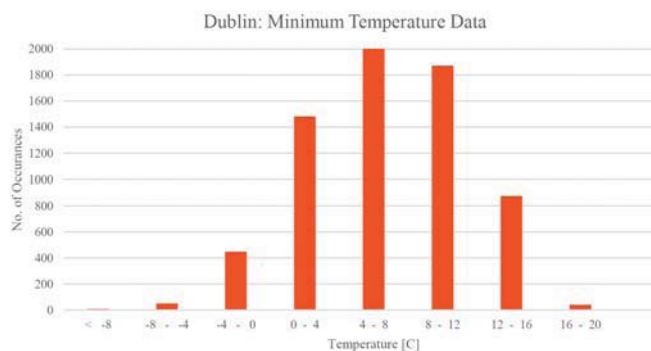


Figure 9. Frequency of Minimum Temperature Data

EN1991-1-5 provides information on ambient temperature for thermal modelling. The indicative outdoor temperature may be determined from Figure NA.1, Table 5.1 and Table 5.2. Taking into account the weather maps provided by the Eurocode, winter conditions, a light coloured façade surface, and a North-East facing orientation, a minimum air temperature of -9°C was determined.

The geometry for the CFD model was created using the Revit model previously developed for the project. A total of three top-floor bedrooms were modelled, each with a floor area of 23 m². The slab-to-slab height was taken as 4.0 m and a false ceiling was included at a height of 3.0 m above floor level. Radiant panels were modelled as surface mounted on the false ceiling, as illustrated in the plan view of the model (Figure 10). Each bedroom has three 3.0 m x 0.6 m panels, one 1.2 m x 0.6 m panel and one 1.8 m x 0.6 m panels giving a total area of radiant panels per bedroom of 7.2 m². Glazing units 2.5 m x 1.95 m and aluminum spandrel panels 2.5 m x 1.0 m and 2.5 m x 0.75 m were modelled, all of which can be seen in the elevation view of the model (Figure 11).

Extractor units with a diameter of 0.15 m were modelled in the vicinity of the shower in the ensuite of each room. A transfer filler of area 0.6 m x 0.6 m with 50% free area was modelled in the lower portion of the ensuite doors. A louver of 2.5 m wide and 0.3 m high was modelled in each room. The free area of these louvers was taken as 2.5 m x 0.2 m.

As specified by the Design Team, the heat flux of each 3 m x 0.6 m panel was taken as 1 kW/m². The heat flux of the

smaller panels were factored down by area. The extractor flow rate, also specified by the Design Team, was taken as 0.065 m³/s.

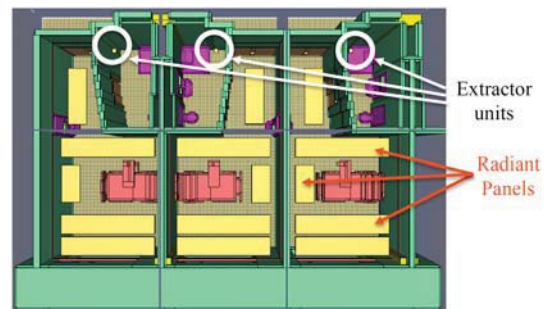


Figure 10. Plan view of bedroom

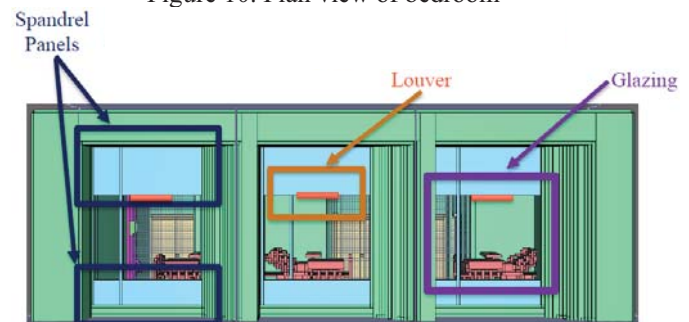


Figure 11. Elevation view of bedroom

The boundaries to the model at the floor, the ceiling, the back (along the internal corridor) and the sides (internal partitions with neighbouring bedrooms) were modelled as closed boundaries. The internal initial temperature was taken as 22°C. The front of the model (the side containing the windows) was modelled as an open boundary, with an applied external ambient temperature of -4.5°C. This is represented by the blue portion in Figure 12.

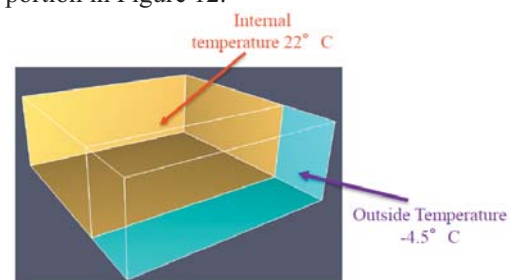


Figure 12. Initial conditions

The results from the CFD modelling at a height of 0.5m above the floor are illustrated below. Figure 13 presents the internal and external temperatures when the louver is in the open position and the external temperature is set at -4.5°C. Results indicated that the internal temperature at a height of 0.5 m above the floor reaches 17.2°C when the external temperature is 0°C and 18.4°C when the external temperature is +5°C.

The results from the CFD modelling at a height of 1.5 m above the floor were also captured when the louver is in the open position and the external temperature is set at -4.5°C, 0°C and +5.0°C respectively. Results indicated that the internal temperature at a height of 0.5 m above the floor

reaches 17.8°C when the external temperature is 0°C and 19.0°C when the external temperature is +5°C.

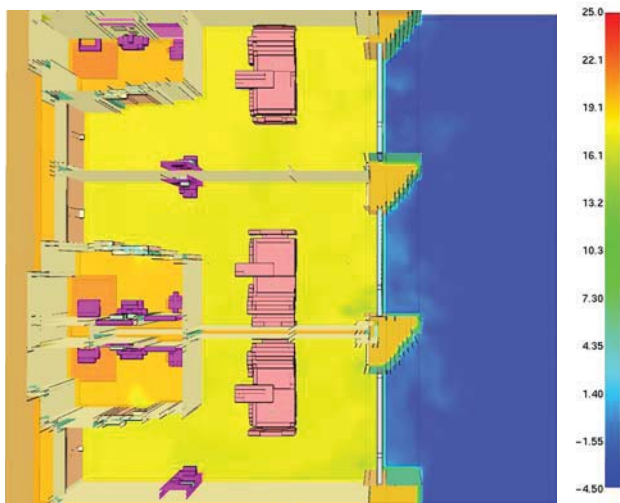


Figure 13. External Temperature -4.5°C

Figure 14 is an elevation view from outside the windows of the bedroom. It serves to highlight the contrast between the temperatures near the radiant panels and the temperatures in the vicinity of the bed when the external temperature was taken at -4.5°C. The results of the CFD modelling demonstrate that the heat flux produced by the prescribed radiant panels in each room are not capable of maintaining an ambient internal temperature of 22°C with either size louver, when they are in the open position and the external temperature is -4.5°C. Results also indicated that an ambient internal temperature of 22°C cannot be maintained with the larger louver and an external temperature of +5.0°C.



Figure 14. External Temperature -4.5°C

From the analysis of temperature data carried out for the local area, peak temperatures of +5.0°C occur approximately 5% of the time, average temperatures of +5.0°C occur approximately 16% of the time and minimum temperatures of +5.0°C occur approximately 34% of the time. Referring back to Figure 9, a temperature of +5.0°C occurs in the most frequent band. Given this, and the results of the CFD simulations – the proposed configuration of radiant panels and louvers will not deliver an ambient temperature of 22°C and will result in a thermally uncomfortable environment. Results from this work resulted in a revised consideration of the proposed ventilation system for the hospital.

5 DUNDRUM VENTILATION SHAFT FIRE STUDY

Smoke Management System Limited commissioned Arup to produce a CFD modelling analysis for the mechanical differential pressure shaft proposed for the Dundrum Apartment block, Dublin. The building is an existing 3 storey

high residential development with a basement car park. The height of the highest floor is 8.575 m above ground.

The proposed system (Figure 15) comprises a mechanical extract system of 2 m³/s, which is linked to the lobby area with a vent situated at high level close to the ceiling, and a naturally ventilated inlet shaft, which connects to the lobby area via a vent that is located at low level (i.e. with an inlet point close to the floor).

The system for the lobby area is composed of two extract fans (one in operation and one on standby) that are sized in order to not exceed a differential pressure of -50 Pa inside the lobby area. This is in order to avoid leakage of smoke into the staircase area while permitting the opening of the doors as the system continues to extract air smoke. The two extract fans are located on the roof. The fans are connected to each lobby through a shaft, which has an approximate area of 0.5 m², with a damper situated close to the ceiling in each lobby.

The replacement air supplied into the lobby is provided through a small inlet shaft. This shaft, which supplied the make-up air, is connected to each lobby through a low level louver or transfer grille. The purpose of the provision of make-up air is to prevent the pressure differential of -50 Pa being exceeded.

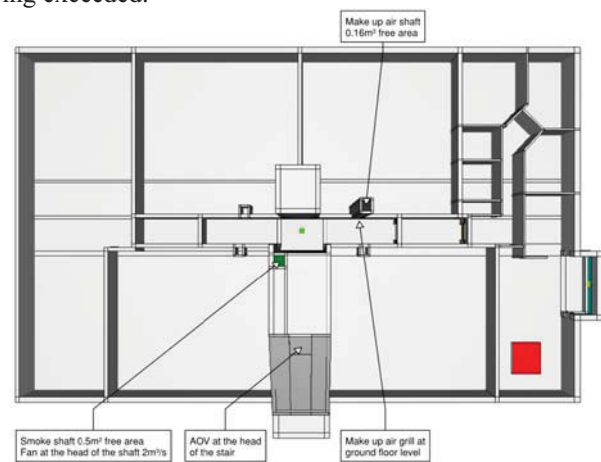


Figure 15. Proposed depressurisation system

The pressure is maintained by the imbalance between the extraction rate and the inlet rate of airflow. Upon detection of fire in any of the lobbies, the extraction fans come into operation. The smoke shaft damper opens on the level where the fire is detected, while the dampers on the other levels remain closed. Air from the make-up shaft will be drawn into the appropriate lobby area automatically by the extraction system. The system will extract continuously and it will be sized in order to not exceed the -50 Pa with the staircase door closed.

Through a CFD analysis, the capability of the depressurisation mechanical smoke system to achieve the following tenability criteria [15] for the lobby area is examined:

- Visibility: minimum 10m to light-reflecting signage (e.g. wall);
- Temperature: maximum 60°C at 1.8 m (head height) and below for occupants;
- Velocity: velocity 5 m/s at all locations on the egress route, except at the inlet/ extract vents. A velocity of 10

m/s is acceptable in close proximity to the inlet and extract vents;

- Pressure: a pressure difference of < 50 Pa should ensure that the door opening force does not exceed 100 N at the handle of a typical (0.8 m x 2.0 m) single leaf door. The pressure difference across the stair door (and doors to apartments other than that of fire origin) will be limited such that the force required to open the door(s) does not exceed 100 N.

Two models were developed for the purpose of this study:

- 1) Fire Model: this scenario aims to demonstrate that the proposed depressurization system is capable of preventing smoke entering the evacuation staircase in the event of a fire in one of the apartments.
- 2) Pressure assessment model: the aim of this scenario is to demonstrate that the proposed depressurization system is capable of maintaining a sufficient pressure differential (i.e. < 50 Pa) within the lobby so that doors can be opened and closed when the smoke extract system is operating.

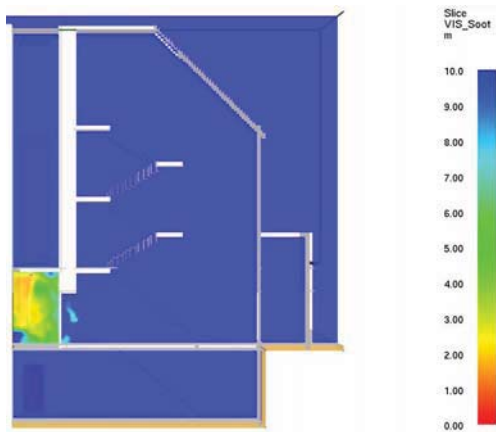


Figure 16. Visibility in the escape stair

The CFD results for the fire scenario have shown that smoke does not spread to the escape staircase. Tenable conditions for visibility (more than 10 m) and temperature (less than 60°C) are maintained at all times inside the escape staircase (Figure 16). Therefore, this indicates that the proposed depressurisation system is capable of preventing smoke entering the staircase. In addition, smoke spreading within the lobby is cleared at 210 s which corresponds to less than 120 s after the apartment door is closed. The time taken to clear the smoke inside the corridor is less than 2 minutes, which is deemed an acceptable performance of the smoke control system. In addition, the velocity levels are kept below 10 m/s except on the vicinity of the inlet grill which is considered acceptable.

The CFD results for the pressure assessment model have shown that the pressure levels are maintained between -12.5 and 7.5 Pa when the proposed depressurisation system is activated and reached steady state conditions. These pressure levels are within the range of -50 and 50 Pa which corresponds to the acceptance criteria so that occupants can open or close doors in the lobby. Therefore this indicates that the proposed depressurisation system is capable of maintaining a sufficient pressure differential within the

corridor so that doors can be opened and closed when the smoke extract system is operating.

6 CONCLUSION

This paper presented three projects recently completed by the Arup Ireland CFD team. These three examples serve to highlight the wide breadth of applications possible with CFD modeling, providing a depth of understanding and insight. In the case of the Dublin Docklands wind study, CFD had a role to play in informing design such to mitigate unpleasant wind conditions. Permission was granted by the planning authority placing CFD analysis as equivalent to wind tunnel testing. For the Hospital thermal comfort study, CFD modelling indicated that the initial design would result in uncomfortable conditions in the bedrooms, where they would be warm enough but without inflow of fresh air, or too cool but with inflow of fresh air. The outcome of the CFD study was to modify the design. For the smoke shaft in Dundrum, CFD modelling was able to show that the modified smoke shaft had the capacity to perform adequately and satisfy tenability criteria. In summary, CFD has the potential to improve quality of design, is of immediate practical use and has a significant role to play in consulting engineering in the future.

REFERENCES

- [1] J.H. Ferziger and M Peric, *Computational Methods for Fluid Dynamics*, Springer, third edition, 2002.
- [2] Lien, J. and Ahmed, N., (2012), 'Indoor air quality measurement with the installation of a rooftop turbine ventilator', *Journal of Environmental Protection*, 3, 1498-1508.
- [3] Senveli, A., Dizman, T. and Celen, A., (2014), 'CFD analysis of smoke and temperature control system of an indoor parking lot with jet fans', *Journal of Thermal Engineering*, 1(2), 116-130.
- [4] Montazeri, H and Blocken B., (2013), 'CFD simulation of wind-induced pressure coefficients on buildings with and without balconies: validation and sensitivity analysis', *Building and Environment*, 60, 137-149.
- [5] Meroney, R.N., (2009), 'CFD prediction of airflow in buildings for natural ventilation', in *Proceedings of the 11th Americas Conference on Wind Engineering*, San Juan, Puerto Rico.
- [6] Prasad, K., Li, K., Moore, E.F., Bryant, R.A., Johnson, A. and Whetstone, J.R., (2013), 'Greenhouse gas emissions and dispersion', *NIST special publication 1159*.
- [7] Kobayashi, N., and Chen, Q., (2003), 'Floor-Supply displacement ventilation in a small office', *Indoor and Built Environment*, 12(4), 281-292.
- [8] Penwarden, A.D., (1973), 'Acceptable wind speeds in towns', *Building Science*, 8, 259-267.
- [9] T.V. Lawson, *Building Aerodynamics*, Imperial College Press, London, UK, 2001.
- [10] E. Simiu, *The design of buildings for wind: a guide for ASCE 7-10 Standard users and designers for special structures*, second edition, John Wiley & Sons Inc, Hoboken, New Jersey, USA, 2001.
- [11] K. Mc Gratten et al., *Fire Dynamic Simulator (Version 6) User's Guide 2014: NIST Special Publication 1019*.
- [12] K. Mc Gratten et al., *Fire Dynamic Simulator (Version 6) Technical Reference Guide, NIST Special Publication 1018*.
- [13] Papakonstantinou, K.A., Kiranoudis, C.T., Markatos, N.C., (2000), 'Computational analysis of thermal comfort: the case of the archaeological museum of Athens', *Applied Mathematical Modelling*, 24, 477-494.
- [14] Webb, M., (2013), 'Building energy and CFD simulation to verify thermal comfort in under floor air distribution (UFAD) design', in *Proceedings of the 13th international building performance simulation association*, Chambéry, France,
- [15] PD 7974-6:2004 Applications of fire safety engineering principles to fire safety design of buildings. Human factors: Life safety strategies – occupant evacuation, behaviour and condition (sub-system 6).

Generating robust algorithms for energy efficient lighting as a performance aspect of the building operational energy optimisation framework

Turya Ganguly^{1,2,3}, Magdalena Hajdukiewicz^{1,2,3}, Marcus Keane^{1,2,3}, Jamie Goggins^{1,2,3,4}

¹Civil Engineering, College of Engineering and Informatics, National University of Ireland, Galway

²Ryan Institute, National University of Ireland, Galway

³Informatics Research Unit for Sustainable Engineering, National University of Ireland, Galway

⁴Marine Renewable Energy Ireland (MaREI) research centre, Galway, Ireland

Email: t.ganguly1@nuigalway.ie

ABSTRACT: This paper presents a part of the ongoing research in the [nZEB-Retrofit](#) project in the National University of Ireland, Galway. This research aims to optimise residential building performance by enhancing the key performance metrics of certain performance aspects. In this paper, one of these aspects (lighting) has been discussed, algorithms developed and tested on the living room of a semi-detached dwelling in Dublin. The main objective of the paper is to formulate algorithms to: 1) calculate the power required to illuminate a space up to standard CIBSE design illuminance, 2) calculate the energy consumption and costs per year for lighting that space, and 3) determine power loss and potential energy savings from lighting. For this purpose, key performance indicators (KPIs) that would facilitate the optimisation process have been selected from several national and international standards and guides. The key findings of this paper are that (1) the difference between the provided power of the light to the required power significantly affects the energy costs, and this should be a key consideration in the selection of light source and (2) the output effectiveness of a lighting source is largely dependent on various factors like lamp lumen depreciation (LLD), luminaire dirt depreciation (LDD) and optical and thermal losses. It is inversely related to energy consumption.

KEY WORDS: BIM, scenario modelling, building optimisation, national standards and guides, energy simulation.

1 BACKGROUND

This work is based on the scenario modelling framework developed by O'Donnell et al. [1]. This method used reproducible transformation leverage formulae to generate specific grades of information useful for building managers to understand. The usefulness of this method lies in the fact that a variety of performance aspects can be analysed to formulate data from different sources such as measured building data, predicted data from simulation model or utility provider data from dynamic tariffs. The class diagram representation of the scenario modelling method is given in Figure 1. In different scenarios, specific aspects are considered (see aspect list in Table 1) in building objects (zones/ spaces). They have specific objectives, which are driven by metrics. Once the datum sources for these metrics are quantified, the results are formulated. Each metric definition contains only one formula that may access raw data from any number (denoted as N) of predefined data streams.

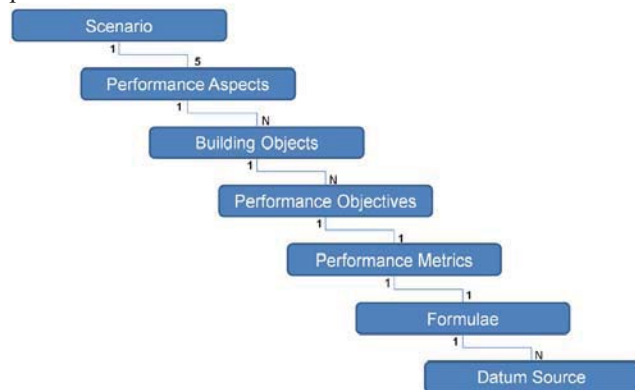


Figure 1 - Class diagram representation of the scenario-modelling method [1]

This mechanism helps in the comparison of measured and simulated data. O'Donnell et al. [1] have presented some hypothetical and real life examples in their work, such as reduction of zone temperature, evaluation of system heating performance and comparing indoor comfort and energy consumption. Each scenario deals with some performance aspects whose objectives involve enhancement of certain metrics. This is achieved by comparing measured and simulated data sources, which in turn facilitate the development of algorithms.

2 RESEARCH APPROACH

The approach taken is that which yields the greatest benefits for homeowners. Given the large number of owner occupied houses in Ireland, a mechanism of fulfilling the needs of the owners/ occupants is significant. The selection of the aspects has been made based on the literature review and it is possible to quantify these aspects into performance objectives with definitive performance metrics that will have a two-fold function – 1) achieving significant energy savings and enhancing Building Energy Performance (BEP), 2) influencing the decision of homeowners by demonstrating visible energy savings and aesthetic upgradation. Table 1 presents the performance aspects that have been selected for this research and their corresponding sources. This list is non-exhaustive nor final, being open for further editions. In this paper, only the performance aspect 'Lighting' has been analysed in detail, and studies on the other performance aspects will be the consequent parts of the research.

Table 1- Performance aspect selected for this research and corresponding sources

No.	Performance aspect	Source
1	Lighting	[2]–[9]
2	Visualisation	[10][11]
3	Interior comfort conditions	[2], [12]–[14]
4	Building acoustics	[15], [16]
5	Renovation scheduling	[17], [18]
6	Sustainability (LCA)	[10], [16], [19], [20]
7	Legislation	[2], [21], [22]
8	Health and safety	[23]–[25]
9	Retrofitting costs and payback	[10], [26]
10	Pro-environmental attitude (human)	[27], [28]

Building systems are complex. Most, if not all, of the performance aspects are linked in a certain way. Performance of one aspect more often than not, affects the performance of the other. Figure 2 presents an interdependency diagram, depicting the relationship between the performance aspects of a built environment.

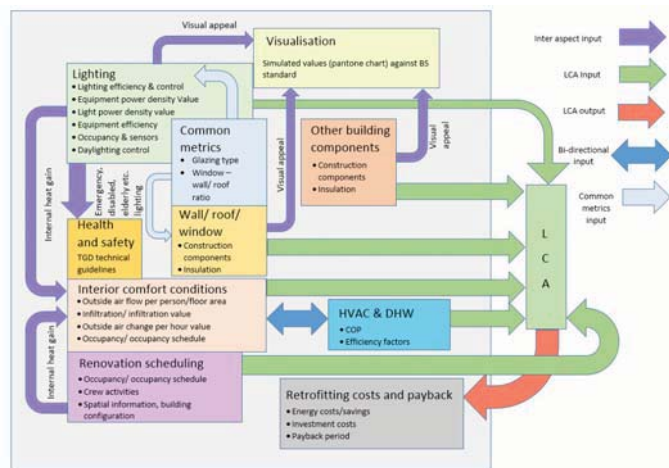


Figure 2 - Performance interdependency diagram

The diagram is under development and will be revised with further ongoing research. Some salient features of the diagram are given below:

- Lighting and wall/ roofs/ windows have common metrics (glazing type and window - wall/roof ratio) that drive the performance of these aspects.
- The lighting of the room generates internal heat gain, and there is also heat gain from the occupants as well, which affects the internal comfort conditions of the space indirectly.
- The characteristics of lighting and building components such walls, roofs, windows, doors indirectly affect the visual properties of the building.
- Interior comfort conditions depend directly on certain performance metrics with indirect inputs from wall/ roof/ window features and other building components.
- Renovation scheduling is directly dependent on the occupancy schedule of the tenants/ homeowners and the renovation crew as well as spatial info and building configuration.
- Life cycle assessment of a building can only be possible with information from lighting conditions, building

components, interior environment, HVAC and DHW and renovation scheduling.

- An accurate life cycle assessment helps retrofitting cost and payback analysis, which directly depends on performance metrics – energy cost/ savings, investment costs and payback period.

3 PERFORMANCE ASPECT - ENERGY EFFICIENT LIGHTING

The scenario-modelling method recognises conventional performance analysis contexts and categorises them as building objects. These building objects can be micro (zone) or macro (building site, building portfolio or simply building). Figure 4 presents the performance aspects of the building energy optimisation framework.

In this paper, only one performance aspect – lighting – has been analysed only. The relationship between the aspects and its performance objectives, metrics, algorithms and measurements have been presented in Table 4. The data sources have been identified and algorithms for artificial lighting of a space have been developed in section 4.

The lighting consideration for a whole building should be done zone or space wise, since the lighting requirement for each zone is different from the other. The performance objective is to optimise lighting, based on certain metrics provided in standard guides and technical documents [2]–[9]. The recommended lighting requirement for a dwelling has been provided by the Chartered Institution of Building Engineers [7], and presented in Table 2. The guide provides standard options in using light sources, energy efficient automatic lighting controls, maintenance, emergency lighting and luminaire types, among other aspects.

Table 2 – The CIBSE recommended lighting levels (developed from [7])

Building zone or space	Recommended illuminance (lux)
Entrances	200
Corridors	100 for daytime, 20 for night time
Stairs, stairwells, and lift lobbies	100 on the treads
Bathrooms and toilets	100 for toilets, 150 for bathrooms
Bedroom	100
Living room and kitchens	200
External lighting	10 for pathways and car parks, 20-30 for care homes with transition between interior and exterior areas

4 ALGORITHM DEVELOPMENT FOR ACHIEVING PERFORMANCE OBJECTIVES OF LIGHTING FRAMEWORK

4.1 Formulae for calculating power (W_{total}) required for lighting as per standard design illuminance (IL)

The first step of the algorithm development is to find the total power (W_{total}) required to light a space up to the CIBSE recommended illuminance levels [7] shown in Table 2. To do so, it is required to find out the lighting power density (LPD) of the light source, which is the ratio of the room illuminance (IL, measured in lux or lumens/m²) and the light output effectiveness (OE, measured in lumens/ watt). LPD is the

wattage of power required for each square meter of floor space

$$LPD = [IL/OE] (W/m^2) \quad (1)$$

Illuminance (IL) here is the lux level to which the lighting needs to be powered (say, 200 lux for the living room and kitchen, obtained from Table 2, which should be catered by both natural and artificial sources). Natural light contribution is described briefly in sub-section 7.1.

Output effectiveness (OE) is product of the luminous efficacy (LE, measured in lumens/ watt) with depreciation factors such as LLD (lamp lumen depreciation), LDD (luminaire dirt depreciation), CU (coefficient of utilisation), TC (thermal coefficient), all measured in percentages.

$$OE = [LE \times CU \times LLD \times LDD] (lm/W) \quad (2)$$

Light efficacy (LE) of a lighting source is the ratio of the light output (lm, measured in lumens) and the power (W, measured in watts), given by equation (3).

$$LE = [lm/W] (lm/W) \quad (3)$$

The coefficient of utilisation (CU) is a percentage that depends on the fixture used for the light source. It determines the optical efficiency of the secondary optical device, which is the fixture [6]. The LED luminaire design guide [6], developed by CREE Inc., suggests assuming a specific percentage for reflectivity and also the light hitting the reflector cup of the fixture. Equation (4) gives the formula for coefficient of utilisation.

$$CU = [(100\% \times UL) + (RF \times RL)] (\%) \quad (4)$$

Where, UL = un-reflected light/ incident light, RF = fixture reflectivity, RL = percentage of light hitting the reflector cup.

For all light sources besides LEDs, LLD is commonly calculated as the ratio of mean to initial lumens, where mean lumens are defined as the output at a certain percentage of rated life, based on the lumen depreciation curve for a specific product [5]. In contrast, when quantity of light is an important design consideration, the IES recommends using an LLD of not greater than 0.70 for LEDs, regardless of the rated lifetime or lumen depreciation characteristics of the product [8]. The default value of LLD for compact fluorescent lamps (CFLs) is given as 0.92 in the IES handbook [8].

The General Electric (GE) Company, in their product catalogues [29] use typical luminaire dirt depreciation (LDD) values extracted from the IES lighting handbook [8]. Table 3 presents those values, which have been used in the section 7, for analysing the light sources for the selecting the best option of lamps.

Table 3 - Typical luminaire dirt depreciation (LDD) value [29]

Typical luminaire dirt depreciation	Light	Medium	Heavy
Environment (dirt level)	0.94	0.86	0.77
Enclosed fixtures	0.97	0.93	0.88
Enclosed and filtered	0.94	0.84	0.74
Open and ventilated	0.94	0.86	0.77

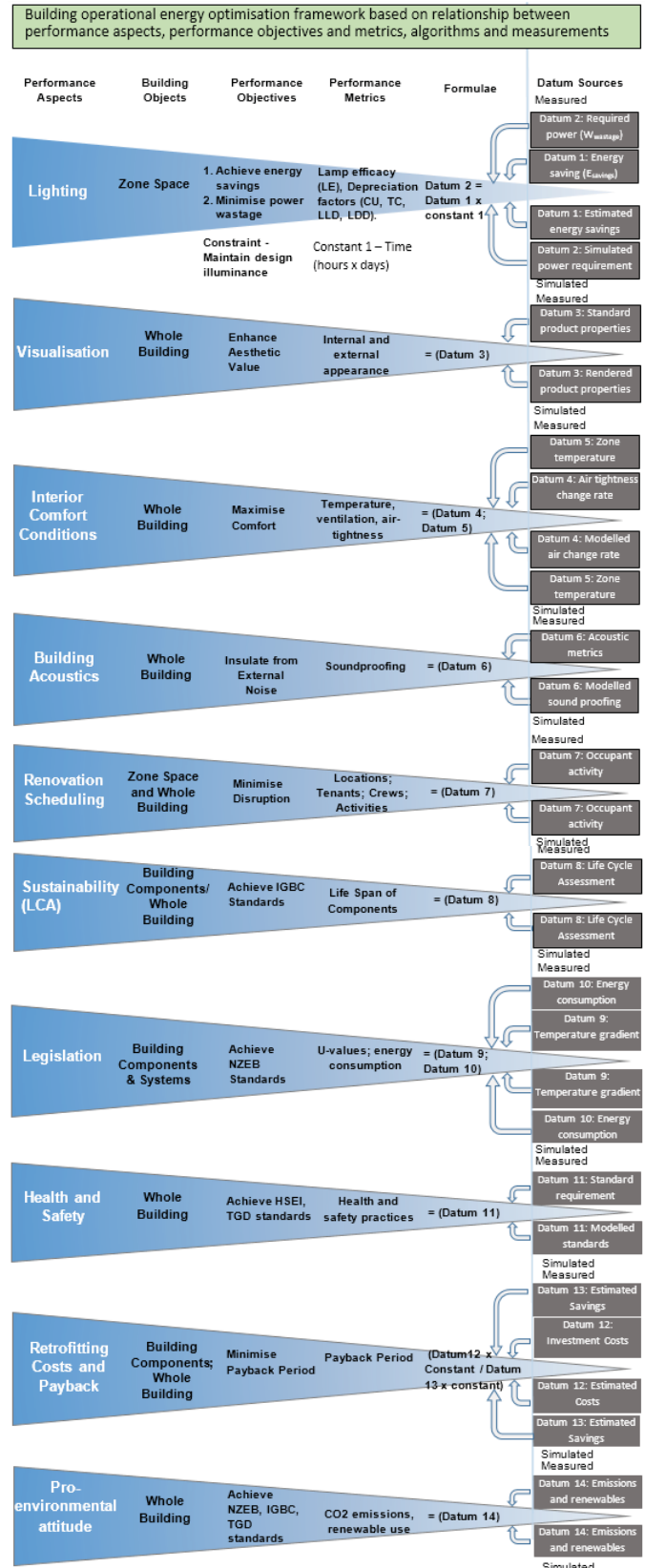


Figure 3- Building operational energy optimisation framework (lighting aspect described in detail in Table 1)

It has to be mentioned here that a constant ($C_{surface}$) should be taken into consideration to account the surface reflectivity, room surface dirt depreciation, colour and other similar factors. These factors affect the effectiveness of the incident

light. For example, a lighter coloured wall would decrease the LPD while dirt on the same would increase it. However, due to lack of datasets, this constant has not been considered in the case study calculations in section 7.

The LPD is the power required to light a square metre of space. So, to find the total power (W_{total} , measured in watts) to light up the whole space, LPD is multiplied with the total floor space (TFA, measured in m^2) it is supposed to light, given by equation (5).

$$W_{total} = [LPD \times TFA] (W) \quad (5)$$

Once the W_{total} is calculated, dividing it by the wattage of the light source (W_{source}) and rounding it up to the nearest whole number gives the number of light sources (N) required:

$$N = W_{total} / W_{source} \quad (6)$$

4.2 Formulae for calculating energy consumption and costs per annum

The second step of the algorithm development is to find the energy consumption for power required to light the space. Once the number of light sources are determined, the power delivered to the room can be found out by multiplying N with the power per lamp (W_{source}). The energy consumption for the space for a period of time (E) in kWh is calculated using: $E = [N \times W_{source} \times 3600 \times 2.8 \times 10^{-7} \times \text{hours} \times \text{days}]$ (7) (kWh)

According to the Dwelling Energy Assessment Procedure (DEAP) [2] issued by the Sustainable Energy Authority of Ireland (SEAI), winter months are from October to May (243 days) and summer is June to September (122 days). It is very important that the calculations for energy consumption for a year be done separately for winter and summer months, since the number of hours of lighting will be different. Energy costs for lighting for a given space is given by:

$$C_{year} = [(E_{winter} + E_{summer}) \times C_{kWh}] (€) \quad (8)$$

where C_{year} = annual energy costs, E_{winter} = energy consumption in winter months, E_{summer} = energy consumption in summer months, C_{kWh} = cost of electricity per unit of electricity.

4.3 Formulae for calculating power wastage and potential energy savings from lighting

The final step of the algorithm development is to calculate power wastage and formulate the potential energy savings per year. The product of N and W_{source} gives the total power of light delivered to the room (W_{prov}). The difference between W_{total} and W_{prov} provides the power wastage for the space (9). So, it is evident that there needs to be a proper selection of light sources, in order to reduce the power wastage.

$$W_{wastage} = [W_{prov} - W_{total}] (W) \quad (9)$$

Potential energy savings ($E_{savings}$) per year can then be calculated by the equation (10). As with the energy consumption (E), the potential energy savings calculation should be done separately for winter and summer months, for greater accuracy.

$$E_{savings} = [W_{wastage} \times 2.7 \times 10^{-7} \times \text{time}] (kWh/year) \quad (10)$$

5 ASSIGNING ALGORITHMS TO THE BUILDING OPERATIONAL ENERGY OPTIMISATION FRAMEWORK

Table 4 vividly presents of the performance objectives, metrics, formulae and datum sources of the performance aspect – lighting. The objectives of the lighting design are to achieve energy savings, minimise power wastage, while maintaining design lighting illuminance (constraint). The performance metrics on which these goals depend are the lamp efficacy, lamp depreciation factors and surface constant. The performance objectives are attained with the help of equation 10, while the other equations (1-9, 11-13) help construct the main formula. LPD, W_{total} , E, W_{prov} , W_{source} , C_{year} are the data sources used ascertaining the formulae. They together make up datum 1 - $W_{wastage}$ and datum 2 - $E_{savings}$. The simulated results for energy savings and lighting power requirement is done in the BIM of the zone space. However, this is outside the scope of the paper, whose objective is algorithm development for measuring data.

Table 4 – Relationship between performance objectives, performance metrics and algorithms for lighting

Performance objectives	Performance metrics	Formulae	Datum sources
1. Achieve energy savings ($E_{savings}$)	Lamp efficacy (LE), Lamp depreciation factors (CU, TC, LLD, LDD),	$E_{savings} = [W_{wastage} \times 2.7 \times 10^{-7} \times \text{time}]$ (kWh/year)	$E_{savings}$ and $W_{wastage}$ which include -
2. Minimise power wastage ($W_{wastage}$)	Surface constant ($C_{surface}$ - for reflectivity, room surface dirt depreciation, colour and similar)		LPD, W_{total} , E, W_{prov} , C_{year} , W_{source}

6 ALGORITHM FOR NATURAL LIGHTING

During daylight time, natural light is combined with artificial sources to achieve target illuminance in lux (lumens/ m^2). IL, mentioned in the previous sections, is illuminance that should be achieved only by artificial light. So, equation 11 shows the deduction for the part illuminated by natural light (IL_{nat}) is the difference of the total illuminance (IL_{total}) and the IL.

$$IL_{nat} = [IL_{total} - IL] (\text{lumens}/m^2) \quad (11)$$

Daylight factor (DF) is the ratio of the light level inside a space, which is IL_{nat} , to the light level outside the structure (IL_{ext}). So, IL_{nat} in terms of DF and light level outside the space (IL_{ext}) is given by:

$$IL_{nat} = [DF \times IL_{ext}] (\text{lumens}/m^2) \quad (12)$$

The daylight reaching any point inside a room is usually made up of three components: sky component (SC), externally reflected component (ERC), internally reflected component (IRC) [6]. If no external obstruction exists, the externally reflected component is omitted. In side-lit rooms, the maximum DF is near the windows, and it is mainly due to the sky component. Daylight factor is used to assess the adequacy of daylight, given by:

$$DF = (A_{win} \times T \times \theta) / (A_{intsurf} \times ((1-R^2))) (\%) \quad (13)$$

where A_{win} = window glazing area in m^2 , $A_{intsurf}$ = total area of internal surfaces in m^2 , T is the glass transmittance corrected for dirt, θ is visible sky angle in degrees from the centre of the window, R is the average reflectance of area $A_{intsurf}$.

7 APPLYING ALGORITHMS ON A CASE STUDY SPACE

An important part of any research is validation. The algorithms generated in section 4 and 6 have been tested on a case study space. The space is a living room area in a semi-detached house in Dublin. The area of the room is 12.51 sqm and is presently using incandescent lighting sources.

7.1 Contribution of natural lighting to design lux

Using the algorithms from section 6 for natural daylighting, on the case study living room having $A_{intsurf}$ of 60 sqm and glazing area of 1.6 sqm (62% of total window area), natural light incidence angle (θ) of 73° , average reflectance (R) as 0.6 (value given in BS-EN12464-2011 [30]) and transmittance of 0.6 (standard for double glazed glass), the average natural internal illuminance (IL_{nat}) comes to 20 lux. This calculation is done for an overcast day, the outdoor illuminance for 1075 lux [30]. This fraction is deducted from the design lux, and the rest is supplied by the artificial lighting design.

7.2 Selection of case study light sources

8 kinds of light sources (2 CFLs, 4 LEDs and 2 incandescent) have been analysed and tested on the sample area, based on the lighting consideration in table 3. The idea is to test these sources on a smaller space, and then use the same set of algorithms for a larger area or zone-groups.

Though the exact nature and characteristics of the actual lamps used in the room are unknown, the two types of incandescent sources selected in the analysis should provide a fair idea of the electricity consumption for lighting the spaces up to the required level of 180 (200 - 20) lux. All the bulbs used are samples from the GE lighting sources catalogue [29]. The different light sources selected show varying degree of efficacy. One may question why lamps with different illuminance is chosen. This is simply to analyse which is more efficient – less number of high illuminance sources or more lamps with lesser nominal lumens. The same fixture properties have been taken for all light sources, so as to maintain parity in analysis. It has been assumed that 60% of the light will hit the reflector cup and the reflectivity of the fixture is 85%, as per the CREE technical report [6]. The coefficient of utilisation (CU) then comes to 91% (calculating as per equation (4)). Thermal losses are taken as 15%, as per the IES lighting handbook [8], so $TC=85\%$.

7.3 Computation of critical properties of selected light sources

Table 5 presents the light sources and the calculated values of OE, LPD, W_{total} , W_{prov} , N , E , C_{year} . LE is the design luminous efficacy of the sources. The effect of the depreciation factors (CU, TC, LLD, LDD) is quite evident and the OE is approx. 60% for most of the sources. W_{prov} is the cumulative power provided by N lamps. For instance, the nominal power for CFL 1 provided by the manufacturer is 23. Therefore, 3 lamps are needed to provide more than 56W, which is the requirement of the room. $(69-56) = 13W$ is the

excess power. For N lamps, the annual energy consumption is denoted by E and C_{year} is the annual energy costs for lighting the space.

The primary factor that affects energy consumption of a lighting source is the efficacy (LE) of the lamp. Incandescent sources normally have extremely low LEs, and they tend to be relatively costly compared to CFL and LED sources. This is evident from the column representing E and C_{year} , for Incandescent 1 and Incandescent 2 lamps.

Table 5 – Computed critical properties of selected light sources

Light source	LE Lm/w	OE Lm/w	LPD W/m ²	W_{total} W	W_{prov} W	N No.	E kWh	C_{year} (€)
CFL 1	65	40	4.5	56	69	3	218	43
CFL 2	79	49	3.7	46	76	2	240	47
LED 1	77	47	3.8	48	52	4	164	32
LED 2	80	49	3.7	46	49	1	155	30
LED 3	78	48	3.8	47	50	10	157	31
LED 4	60	37	4.9	61	63	14	199	39
Incandescent 1	9	6	32.7	409	425	15	1344	262
Incandescent 2	13	8	22.1	277	300	3	949	185

7.4 Findings

Figure 4 shows a relationship graph between the output effectiveness (OE) and the annual lighting energy consumption for the room. Remarkably, though CFL 1 has a lower OE of 40 lumen/ watt, it only consumes 218 kWh in a year. Compared to that, CFL 2 has an OE of 49 lumens/ watt, but it needs 240 kwh/year of electricity to keep the area lighted at the recommended levels. The LED sources show pattern, with slight variance in the (E/OE) ratio. The performance of LED 4 in comparison is slightly worse than its other CFL and LED counterparts. The incandescent lights show extremely poor performance in comparison to the other light sources.

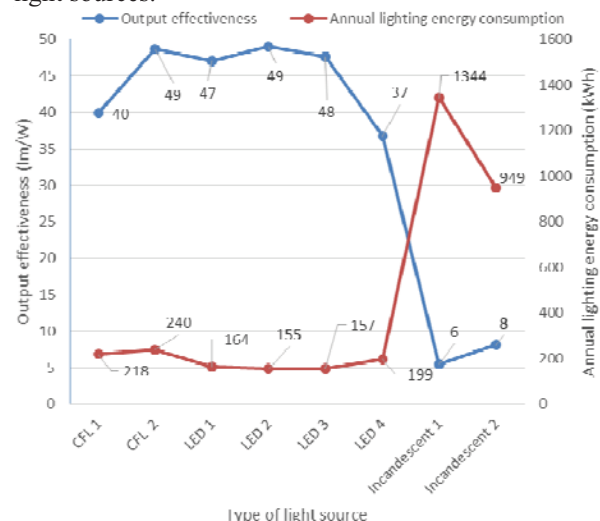


Figure 4 - Effect of output effectiveness (OE) on annual lighting energy consumption (E) of the room.

Figure 5 is a combination line chart that compares the annual energy costs for lighting of the room to the potential savings of the same. The two lines are far from symmetrical,

proving the importance of proper source selection for spaces. The ratio of the power required (W_{total}) to the area of the room (TFA) which gives the LPD (watt/m^2) is extremely important for the selection as well. The combination of powers of different bulb sources should be such that W_{wastage} is minimum. So, though efficacy (LE) is an important criterion for selection of the light sources, the pivotal one is the typology of selection.

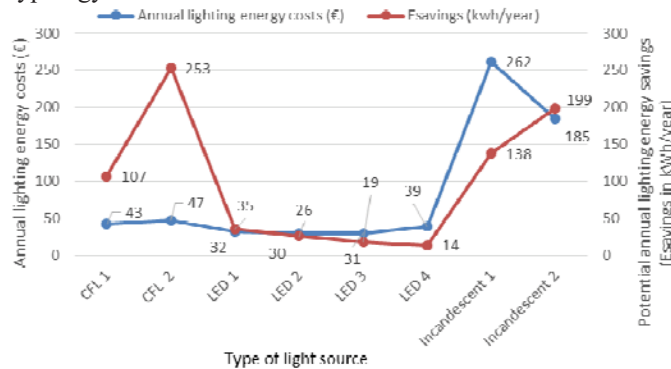


Figure 5 – Comparison of potential energy savings to annual energy lighting costs of the room space

8 LIMITATIONS

There are some limitations in this research:

- Thermal losses for all of the sources are taken as 15%. More research and test results for ascertaining a more accurate thermal coefficient (TC) is required.
- A proper selection of a lamp could only be possible after a thorough life cycle analysis of the sources. The author plans to test the algorithms on the whole house and check for the most feasible solution.
- Factors such as colour rendering and appearance, controls and light distribution will be researched in depth in the future. Such factors affect the visual aspect of the zone space and are intrinsic to energy efficient design of lighting.
- A constant (C_{surface}) to take into account the surface reflectivity, room surface dirt depreciation, colour and other similar factors should be considered. These factors affect the effectiveness of the incident light. However, due to lack of datasets, this constant has not been considered in the case study calculations.

9 CONCLUSION AND FUTURE WORK

It is evident from figure 5, that the LPD is an important criterion for the selection of light sources, and in turn for reducing power wastage and increasing energy savings. The greater the difference, the greater the wastage. A good option may be to use a combination of lamps to achieve W_{prov} as close as possible to W_{total} . The aim of the research is to reduce energy consumption, which promotes task lighting, parameters such as light angles, intelligent locations, reflectance and light range are crucial to the installation of the light sources. Although, the efficacy of a lamp is known to be the most important factor for lamp selection, it has to be kept in mind that a more efficient lamp will not necessarily translate into the most energy savings, as evident from the findings. Room size, reflective angles and characteristics of walls and other surfaces, focal points of sources, bends in

walls, location of furniture and controls are extremely important for proper space lighting. These factors will be studied in further research and their interdependencies will be identified in similar case studies. To fully implement this framework, the measured value from these algorithms will also be calibrated with the simulated results from the energy calculations of the BIM. The framework will then be tested on other different buildings.

ACKNOWLEDGMENTS

The authors would like to acknowledge the support of SFI through the CDA programme (Grant No. 13/CDA/2200).

REFERENCES

- [1] J. O'Donnell, M. Keane, E. Morrissey, and V. Bazjanac, "Scenario modelling: A holistic environmental and energy management method for building operation optimisation," *Energy Build.*, vol. 62, pp. 146–157, 2013.
- [2] C. and L. G. (Declg) Department of the Environment Government of Ireland, "Dwelling Energy Assessment Procedure (DEAP) 2012, Ver. 3.2.1," Dublin, 2012.
- [3] SEAI, "A Guide to Energy Efficient and Cost Effective Lighting," Dublin, 2010.
- [4] International Code Council, *International Energy Conservation Code*. USA, 2012, p. 177.
- [5] M. Royer, "Lumen Maintenance and Light Loss Factors: Consequences of Current Design Practices for LEDs," Oak Ridge, 2013.
- [6] CREE, "LED Luminaire Design Guide," New York, 2012.
- [7] CIBSE, "LG9 : Lighting Guide 9," London, 2013.
- [8] D. DiLaura, G. Steffy, R. Mistrick, and K. Houser, *The IES Lighting Handbook (Tenth Edition)*, 10th ed. New York: Illuminating Engineering Society.
- [9] W. F. (Bill) Blitzer, "Light in Design – An Application Guide (IES CP-2-10)," New York, 2003.
- [10] K. Park and K. Kim, "Essential BIM Input Data Study for Housing Refurbishment: Homeowners' Preferences in the UK," *Buildings*, vol. 4, no. 3, pp. 467–487, 2014.
- [11] N. Nisbet and B. Dinesen, "Constructing the Business Case: Building Information Modelling," *Br. Stand. Institution, London*, 2010.
- [12] ASHRAE, *Ventilation for acceptable indoor air quality*, vol. 84. USA, 2004.
- [13] Department of Environment Heritage and local government, "Technical Guidance Document Part-F Building Regulations," Dublin, 2009.
- [14] M. Vaughan, "Building Regulations Part L and Part J," 2013.
- [15] Department of Environment Heritage and local government, "Technical Guidance Document - Part E Building Regulations," Dublin.
- [16] K. Simpson, "Energy Efficiency Refurbishment in UK Owner-occupied Dwellings: The Occupant's Perspective," Loughborough, 2014.
- [17] P. Ho and M. Fischer, "An Examination of Current Practices in Identifying Occupant Interactions in Renovation Projects," California, 2009.
- [18] P. Yee, M. Fischer, and J. Haymaker, "Automated identification of occupant interactions in renovations of occupied buildings," *J. Inf. Technol. Constr.*, vol. 18, no. March 2012, pp. 182–213, 2013.
- [19] A. GÖKGÜR, "Current and future use of BIM in renovation projects," Chalmers University of Technology, 2015.
- [20] D. Di Mascio and X. Wang, "Building information modelling (BIM)-supported cooperative design in sustainable renovation projects benefits and limitations," *Lect. Notes Comput. Sci. (including Subser. Lect. Notes Artif. Intell. Lect. Notes Bioinformatics)*, vol. 8091 LNCS, pp. 205–212, 2013.
- [21] K. O' Rourke, "EPBD implementation in Ireland," Dublin, 2012.
- [22] Department of Environment Community and Local Government, "Towards Nearly Zero Energy Buildings In Ireland Planning For 2020 and Beyond," Dublin, 2012.
- [23] Health and Safety Authority of Ireland, *Statutory Instruments - Safety, Health and Welfare at Work (Construction) Regulations 2013*, no. 291. Ireland, 2013, p. 80.
- [24] Health and Safety Authority of Ireland, *Health, Safety and Welfare at Work (General Application) (Amendment) Regulations 2016*, no. 36. 2016, p. 31.
- [25] Department of Environment Heritage and local government, "Building Regulations 2006 Technical Guidance Document B Fire Safety," Dublin, 2006.
- [26] K. Simpson, "Energy Efficiency Refurbishment in UK Owner-occupied Dwellings: The Occupant's Perspective," no. January, 2014.
- [27] P. C. Stern, "Toward a Coherent Theory of Environmentally Significant Behavior," *J. Soc. Issues*, vol. 56, no. 3, pp. 407–424, 2000.
- [28] L. Christie, M. Donn, D. Walton, L. Christie, M. Donn, and D. Walton, "The 'apparent disconnect' towards the adoption of energy-efficient technologies," vol. 3218, no. May 2015, pp. 37–41, 2011.
- [29] GE Lighting, "GE lighting catalogue," Fairfield, 2011.
- [30] The British Standards Institution, "EN12464-1 : 2011 Light and lighting," London, 2011.

Diagnostics and intervention methods for façade retrofit of post-WWII non-domestic buildings in Europe for energy efficiency

Sheikh Zuhaib^{124*}, Magdalena Hajdukiewicz¹²⁴, Marcus Keane¹²⁴, Jamie Goggins¹²³⁴

¹Informatics Research Unit for Sustainable Engineering, College of Engineering and Informatics, National University of Ireland, Galway

²Civil Engineering, College of Engineering and Informatics, National University of Ireland, Galway, Ireland

³Marine Renewable Energy Ireland (MaREI) research centre, National University of Ireland, Galway, Ireland

⁴Ryan Institute, National University of Ireland, Galway, Ireland

Email : s.zuhaib1@nuigalway.ie

ABSTRACT: The growing demand of deep façade retrofits in refurbishment projects across Europe, is often accompanied by low-energy targets and architectural attributes. Factors like variability in context, material, environment and composite construction types and comfort requirements, often complicate the façade retrofits. It becomes difficult to generalise the method of retrofit for each building case. A proper understanding of the diagnostics and intervention principles improves the overall cognizance of retrofits with other systems and sub-systems. Passive retrofit strategies offer great potential to reduce the energy demand of non-domestic buildings. This paper presents a review of research and passive intervention methods that can act as guiding principles for modern façade retrofits for post-war non-domestic buildings and maintain the integrity of the building to provide higher human comfort levels and improved energy performance.

KEY WORDS: Retrofits, Energy efficiency, Passive design strategies

1 INTRODUCTION

The post-1945 economic boom almost doubled the building stocks in many European countries [1]. It was responsible for the growth of non-domestic buildings such as office, commercial, health and educational facilities. Approximately 37% of the non-domestic building stock (age between 31-50 yrs.) are likely to get retrofits in the next 20 years [2]. Buildings from this period are generally characterized with poor insulation, large single glazed façades, larger floor plates, high costs for energy, and carbon footprints. Non-domestic buildings in Europe account for 25% of the total stock and it is a well observed fact that they have greater energy consumption per unit of floor area compared to dwellings [3]. Occupants experience high thermal discomfort that further leads to a reduction in productivity levels in these buildings. It has been advised to prioritize the need for reducing energy demand through retrofitting [4]. Often in refurbishment projects, façade retrofits are undertaken to fix maintenance problems, translate into costly interventions especially for overcoming energy failure and architectural decay. This study highlights the importance of development of guidelines for retrofitting such buildings to meet the current energetic requirements. Planning the retrofits strategically with effective diagnosis of problems would result in huge reduction of capital costs, operational and embodied energy, improvement in indoor environment, air quality, thermal comfort and disruption caused in the building. These end benefits can potentially be reduced by deep retrofit of the existing façades.

1.1 Building stock

In the non-domestic sector of Europe, building refurbishments offer greater opportunities than building new energy efficient buildings to meet Europe's emission targets, as new buildings represent annually less than 1.5% of the total building stock [5]. The post-war non-domestic buildings are generally built

during the years 1945 to 1975 when the building regulations were not stringent and had little focus on energy conservation [6]. New technologies resulted in acceptance of the glass and metal curtain walls and realisation of machine made envelopes [7]. The implementation of poor building technology employed in these buildings and high-energy consumption are well-defined traits to identify them [3]. They followed an international, modernist and minimal style architecture, which is uniform across many of the non-domestic buildings from that period [8]. A prominent category of buildings from this period, have, either partially or fully glazed façades. After the energy crises in 1970's thermal energy efficiency of buildings gained importance in the legislations across Europe [3]. Therefore, this study focuses on these buildings, which are potentially promising to investigate the façade retrofit opportunities and energy savings.

1.2 Methodology

The aim of this study is to identify different technical diagnosis and passive (without active mechanical systems) intervention methods used to improve the energy efficiency and quality of building under the following aspects:

- Post-war glazed façades
- Passive environmental strategies
- Low- emission refurbishment

Further, a comprehensive literature review demonstrates the diagnosis of defects with the limitations of passive interventions in façade retrofits for achieving energy efficiency. Active systems and methods are out of scope of this paper.

2 BUILDING PHYSICS

2.1 Energy efficiency, thermal performance and moisture control

Energy efficient retrofit has become a focal point of construction activity in Europe after EU mandates [9,10]. There is an evident influence of façade retrofits on the total energy loads and internal environment conditions with respect to thermal and moisture balance. The infill panels, the frame construction, spandrel and other perimeter areas affects the thermal performance of glazing systems [11]. Better High performance insulating surfaces hold a direct reduction in the surface temperatures and the risk of radiant temperature asymmetry is minimised. It also blocks the downdraft of cold air descending through the glazed surfaces and heating systems influence on comfort is reduced [12]. Generally, large glazed surfaces are associated with the objectives of building physics, materials, components and climatic response of the building [13]. This can guide us further into taking down the information and evaluate them based on retrofitting objectives. Moisture protection is the main objective of glazing systems but poor systems can allow water to penetrate through gravity, kinetic energy, air pressure difference, surface tension, and capillary action [14].

2.2 Human comfort

One of the most important component of human comfort in retrofits is the perceived room temperature [15]. With large glazed façades, there is a high possibility of uneven surface temperatures [16]. Figure 1 indicates the comfortable temperature range for surrounding surfaces. A study conducted by Lyons et. al [17] which evaluated generic glazing systems from clear single panes to high performance glass for comfort impacts, concluded that direct solar load has major influence on comfort and draft effects are higher with large glazed façades.

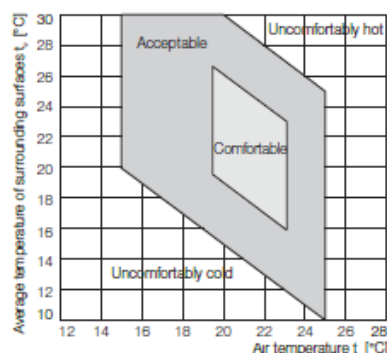


Figure 1: Comfort in relation to the interior air temperature and the temperature of the surroundings [12]

3 RETROFIT CONCEPTS

In an energy efficient refurbishment, the construction standards of the existing building are upgraded to comply with retrofit norms and regulations [18]. Possible construction upgrades for post-war non-domestic buildings include improving the thermal insulation, eliminating thermal bridges, renewal glazing or windows, and solar heat gain reduction by providing sunshades, or retrofitting of thermal mass in the form of latent storage media [12]. Providing weatherproof

windows and extractor fans can control the natural ventilation. Other ventilation measures such as ducts and atria can optimise the cross-ventilation of the building. In non-residential buildings, an even distribution of daylight as far into the building as possible is essential. Daylight optimisation measures with larger windows can improve the daylighting in the spaces [19]. However, large areas of glazing increase the thermal loads in the summer and the sunshades required to combat this can lessen the amount of daylight entering the building.

One of the most cost effective ways to improve the façade are the passive design strategies, which can deeply reduce the thermal loads of the building. Section 6 will elaborate more on passive interventions and their effects. Passive interventions are based on design strategies like: passive heating, passive, cooling, passive ventilation and daylighting [20].

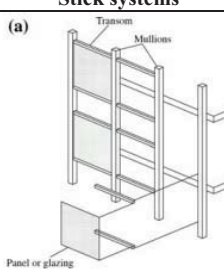
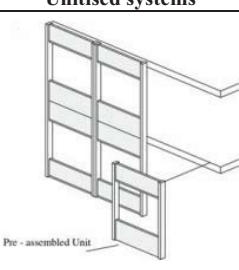
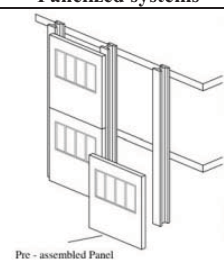
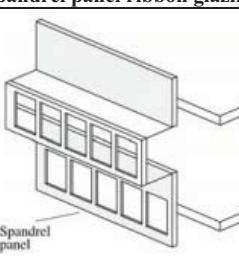
According to Rey [7], interventions on building façades are significant as they are linked to technical installations. There can be three types of strategies for retrofitting:

1. Stabilization strategy: Holds incremental interventions, that does not modify the appearance
2. Substitution strategy: Consists of complete replacement and transforms the appearance and substance
3. Double- skin façade strategy: Partially stabilises the façade and add a new glass skin, preserving the original state of the façade.

4 FAÇADE SYSTEMS

Flat sheets of polished cast mirror glass and drawn window glass were the most common types of glass used in buildings until the rise of double glazing (two panes of glass separated by strips of aluminium) in the post war period [21]. Some of the most common glazing systems observed in the post-war non-domestic buildings in Europe are shown in Table 1 [22].

Table 1: Common post-war glazing systems in Europe

Stick systems	Unitised systems
 <p>Transom Mullions Panel or glazing</p>	 <p>Pre - assembled Unit</p>
Panelized systems	Spandrel panel ribbon glazing
 <p>Pre - assembled Panel</p>	 <p>Spandrel panel</p>

Stick systems consist of vertical members (mullions) and horizontal members (transoms) anchored to the structural

frame. Glass or other panels are then fixed into the openings of the metal grid. Unitised systems are panels that are pre-assembled prior to installation in the field and then units are stacked to form mullions and transoms. Panelised systems utilise features of unitised and stick systems where prefabricated units are attached to already installed mullions. These systems later developed into more efficient curtain walling systems such as structural sealant glazing and point fixed structural glazing. They were constructed with timber sections, aluminium sections or rolled steel sections with a coating to prevent corrosion [23].

5 FAÇADE FAILURES

5.1 Driver of façade retrofits

To improve the serviceability and indoor environmental conditions majority of façade retrofits are planned for non-domestic buildings. The service life of a building is generally 60 years but building components have shorter duration. Table 2 gives an indication of the age of the components desired for retrofitting the façade [12].

Table 2: Life time expectancies of envelope components [12]

Component	Min. (yrs.)	Max. (yrs.)
Render, façades	30	60
Windows	25	40
Insulating glass units	20	35
Building envelope as a whole	20	60

Diagnosis would have been very simple if there was just one solution to the existing problems. Several defects or combinations of defects cause the façades to fail. The failures can be due to physical problems, material failure due to ageing, detailing failure, maintenance failure or outmoded and obsolete production of façade components [24]. These are the major drivers of façade retrofits and they are responsible for acceleration in deterioration [25]. Table 3 indicates the general problems with glazed façades, their probable cause and locations.

Marradi et al. [26] performed a process mapping with experts for glass façade renovations and found that the main issue while dealing with existing façades is the complexity in assessment of its current performance. The suggestion encompassed to evaluate the existing façade performance through sensor based monitoring or in-situ tests with regard to thermal and structural conditions.

5.2 Diagnosis of façade failures

5.2.1 Survey of existing structure

The cataloguing and description of damages including earlier repairs is a crucial step in retrofit planning. A differential analysis of the causes of damages is advised by Schittich [13] to address:

- Ageing, material fatigue and wear and tear
- Poor/non-existent maintenance and upkeep
- Inexpert repairs or renovations
- User behavior in terms of heating and cooling
- Status of building technology and standards of the time
- Planning and production errors

• Table 3: Problems in glazed façades

Problem	Causes	Location
Water penetration	Improper design Improper installation Glazing leaks Sealant failures Weather-stripping Thermal break shrinkage Improper repairs	Glazing pockets Internal gutter or flashings Glazing joints Property of sealant Operable windows Mullion system Drainage holes and joints
Air leakage and thermal discomfort	No air barrier and thermal breaks	Operable window vents, joints at mullions, defective sealant joints
Condensation	No insulation	Perimeter joints, mullions near spandrel
Acoustics	Loose infills, air leakage	Junctions and joints
Material failures	Electrolytic action	Frame joints with structure, coatings
Structure failure	Poor connections High wind loads	Frame

Visual inspection is necessary for primary qualitative data collection prior to detailed inspection about the building and it is effective if reflected in performance evaluation of the façade [12]. A number of surveys can integrate the concept of visual inspection, to check conformance to design documents, load and environmental conditions, external appearance, interior condition and supporting services [18].

5.2.2 Inspection and measurements

There are established standard practices for inspections and measurements which can positively be employed for identifying the performance issues [27]. ISO 12655:2013 governs the calculation of measured energy use in buildings. Air-tightness and air-infiltration testing is done through blower door test (ISO 9972:2015). Infiltration rates can be measured using tracer gas measurements (ISO 12569:2012). Thermal imaging aids in identification of thermal bridges, air and moisture penetration (ISO 6781:2015). For non-destructive tests, dielectric meters perform the surface scanning to quantify the presence of moisture. The Glaser or dew point method helps to study the occurrence of interstitial condensation for steady-state interior and exterior climate conditions, for assessment with respect damage to component (ISO 13788:2012). Figure 2 illustrates an example of the condensation point analysis in a wall assembly.

For in-situ, measurement of thermal resistance and thermal transmittance of opaque elements of the existing façade thermofluxometry is used (ISO 9869-1:2014). ISO 15099:2003 assists to assess the thermal performance of fenestrations and shading devices. Spectrometer can also be used to measure the glazing emissivity.

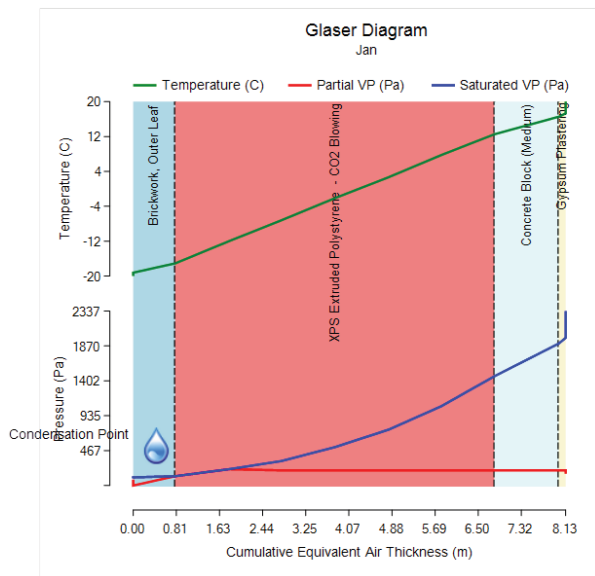


Figure 2 Example of condensation analysis in a wall assembly

5.2.3 Analysis and evaluation

A detailed analysis and evaluation of the collected information is very critical for broader decision-making before commencing retrofits based on uncertainties such as financial risks involved, time required, cost benefits and lifecycle scenarios [28]. The preparation of the diagnosis scenario can involve mapping the overall determination of façade condition and quantitative information about its energy performance. The methodologies must be developed according to a set of procedures with a logical sequence in order to adopt a proper solution, since many failures in interventions result from the inexistence or inadequacy of diagnosis [29]. Diagnosis or other expert systems can be utilised for logical diagnosis of defects using data banks, charts, fault tree tools or knowledge based systems [30]. Therefore, this study discusses the passive retrofit interventions for façades to ascertain their impact and benefits.

6 PASSIVE RETROFIT INTERVENTIONS

Considering the environmental approach, passive retrofitting strategies are ideal but the choice of passive system/s is difficult to adopt for existing buildings where the other systems and sub-systems are already in place. Therefore interventions can build upon four basic strategies build upon, 1) Heat loss in summer, 2) Overheating in summer, 3) Natural ventilation measures and 4) Daylight utilisation opportunities [31]. Passive retrofit strategies can have deep impact on thermal loads of post-war glazed façades with measures such as shading, fabric insulation, reduction in glazing area, and adaptive controls [5].

6.1 Passive design strategies

Passive design strategies can be an individual or a combination of passive design elements for the retrofit of façades. Table 4 lists common passive design elements

mapped against the actions and strategies from the analysis of literature. They can be utilised for their benefits towards the reduction in energy loads and improvement in indoor comfort levels for post-war non-domestic buildings.

Table 4: Passive design strategies and respective elements

Design elements	Application	Passive design strategies			
		H	C	V	D
Building shape	Extensions, sunspaces, balconies	◆	◆		◆
Buffer spaces	Ventilated, double skin, atriums, glazed balconies	◆		◆	◆
High performance glazing	Clear/ low-e/double/ triple glazing, aerogel glazing, vacuum glazing, switchable reflective, SPD film, fritting	◆			◆
Operable windows	Size, placement, low conductance frames			◆	◆
Solar shading (operable/ fixed)	external sunshades, louvres, blinds, overhangs, vertical fins	◆	◆		
Thermal Mass	PCM, aerated concrete	◆	◆		
Light colours	Colour of exterior finishes		◆		
High performance insulation	PCM, vacuum insulation panels	◆			
Air and moisture tightness	Caulking/sealing	◆			
Natural lighting improvement	Reflective blinds, light shelves, clerestories				◆
WWR (wall window ratio)	Low(N/E), high (S/W)	◆	◆		◆
Waste heat recovery	Mixed mode heat-recovery ventilation	◆		◆	

Note: H: heating, C: cooling, V: ventilation, D: daylighting

Research and case studies in literature suggest that passive methods for façades cannot only save significant energy but also improve comfort levels in the existing office and commercial buildings [32]. A study by RIBA investigated use of passive design strategies in refurbishment of an office building built in 1970's [5]. The reduction in primary energy consumption achieved was 64%. Hestnes et. al [33] studied retrofitting scenarios with passive design strategies on office buildings and was able to reduce the energy loads to <100kWh/m²/year. Façade interventions are fundamental to deep retrofits and aim to achieve efficiency of more than 50% in energy reduction [34]. Cellai et. al [35] simulated the effects of shading device typologies for energy efficient refurbishment of existing buildings and presented a comparative analysis that determined the effects on thermal and visual comfort. The effect of double layer glass façades was also studied for office buildings by Brunoro and Rinaldi [36] through several case studies where the energy performance before intervention was 250-270 kWh/m² that got reduced to about 30-40% after retrofit.

6.2 Scale and cost of interventions

The original structure undergoing refurbishment holds several perplexities of preservation and conservation. They require critical understanding before approaching for any refurbishment measures.

Six intervention approaches are discussed by Samuel [37] as shown in Table 5 below.

Table 5: Types of intervention methodologies (adapted)[37]

Approach	Activity	Cost	Action
Abstention	Do nothing	Directly proportional to risk (loss of property)	-
Mitigation	Around the façade	Inexpensive	Band aid-repairs, selective reconstruction
Reconstitution	On the façade	Inexpensive	Over cladding
Substitution	Direct replacement	Expensive	Recladding
Circumvention	Different than original	Expensive	New and different façade
Acceleration	Controlled demolition	Very expensive	Removal

Doing nothing is less costly than doing something initially, but ultimately it costs in terms of the loss of the components or building [38]. Mitigation involves treatment to selective portions of façade demanding attention and left untouched due to limitation of budgets or avoidance of disturbance. Mitigation is an inexpensive approach [39]. Reconstitution in a similar way is inexpensive, as the existing façade remains as it is and an additional layer is provided to meet the required objectives of energy and façade preservation [37]. Substitution requires complete replacement of façade and its components, such as re-cladding [38]. On the other hand, most expensive options include circumvention and acceleration that have high carbon footprint and are less desirable for energy efficient retrofits but may be unavoidable in some situations [37]. A recent study on cost of refurbishments evaluated that major causes of disparity in EU are market practices, maturity and quality and experience [40].

6.3 Life cycle impact of interventions

Façade retention for protected structures promotes sustainability and reduces the embodied and operational energy compared to new builds [41]. Boardman suggests that cheapest way to achieve zero carbon requirements is through refurbishment to higher standard [4]. Life cycle studies (LCA/LCCA) are among least included ones in planning stage of façade retrofits or in general, in the refurbishment projects [25]. On a general note, the overall impact of refurbishment will always be lesser than demolition or new builds due to the embodied energy contained in the materials [5].

Generally, building envelope repair and replacement costs contribute 20–30% of the overall building repair and maintenance life cycle costs [42]. An example of cold climate building upgrade using LCC is shown in Figure 3, where envelope only modifications contributed to up to 60% energy savings during the buildings' service life of 30 years [43]. This supports that passive interventions to façade retrofits can potentially reduce the energy consumption to a significant level.

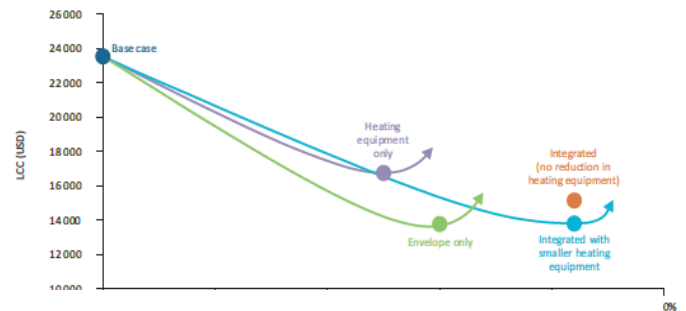


Figure 3: LCC curves in a moderate climate [43]

There exists a lack of regulations or protocols for evaluation of production energy requirements in retrofitting [44]. The use of regulated values for the production, maintenance and disposal of materials will lead to greater energy savings and measurable use of energy resources in retrofits [22]. Three façade variations in a hypothetical assessment in Figure 4 showed variations in embodied energy (surface area 50m²)- a) fully glazed- 515 kWh/a- 185%, b) partially glazed- 423 kWh/a- 152% and c) totally closed- 278 kWh/a- 100%. The diagnosis and interventions if planned strategically can reduce the environmental impact in terms of cumulative embodied energy and operational energy during buildings life cycle.

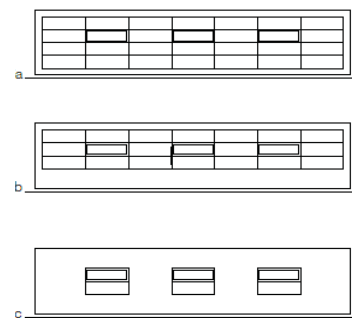


Figure 4: Glazing scenarios to evaluate embodied energy [31]

7 CONCLUSIONS

The complexities in retrofitting the post-war façades require greater collective understanding of the functional, economic and environmental requirements to meet the challenges of current regulations and EPBD targets. A logical sequence based on the knowledge systems that address various surveys, inspections and measurements according to standards and evaluation addressing risks and uncertainties, should lead to the selection of the appropriate diagnostic techniques. The

passive intervention opportunities offer higher energy savings and increased thermal comfort. Handling the issues of embodied and operational energy during the life cycle of building should involve careful consideration about the scale and cost of interventions. Well-established guidelines and protocols are needed to identify the optimum intervention levels for the retrofit of post-war glazed façades.

ACKNOWLEDGMENTS

This study is conducted during a PhD research on energy efficient of retrofitting existing façades carried by the author at National University of Ireland, Galway. The authors would like to acknowledge the support of Science Foundation Ireland through the Career Development Award programme (Grant No. 13/CDA/2200).

REFERENCES

- [1] N. Kohler, P. Steadman, and U. Hassler, 'Research on the building stock and its applications', *Build. Res. Inf.*, vol. 37, no. 5–6, pp. 449–454, 2009.
- [2] JRC European Commission, 'Development of European Ecolabel and Green Public Procurement for Office buildings JRC IPTS Draft Report - Economical and market analysis', no. June, 2011.
- [3] BPIE, *Europe's Buildings Under the Microscope: A country-by-country review of the energy performance of buildings*. Belgium, Brussels: Buildings Performance Institute Europe, 2011.
- [4] F. Stevenson, 'Reducing energy demand through retrofitting buildings', *Build. Res. Inf.*, vol. 41, no. October, pp. 605–608, 2013.
- [5] N. Baker, *The Handbook of Sustainable Refurbishment: Non-Domestic Buildings*. 2009.
- [6] Ö. Duran, S. C. Taylor, and K. J. Lomas, 'Evaluation of refurbishment strategies for post-war office buildings', *Build. Simul. Conf.*, no. Odpm 2012, pp. 138–145, 2015.
- [7] E. Rey, 'Office building retrofitting strategies: Multicriteria approach of an architectural and technical issue', *Energy Build.*, vol. 36, pp. 367–372, 2004.
- [8] N. Bullock, *Building the Post-war World: Modern Architecture and Reconstruction in Britain*. Psychology Press, 2002.
- [9] EU, 'Directive 2010/31/EU of the European Parliament and of the Council on the energy performance of buildings', *Off. J. Eur. Union*, pp. 13–35, 2010.
- [10] EU, 'Directive 2010/31/EU of the European Parliament and the Council of 19 May 2010 on the energy performance of buildings (recast)', *Off. J. Eur. Union*, pp. 13–35, 2010.
- [11] A. Gustavsen, S. Grynninga, D. Arasteh, B. P. Jelle, and H. Goudey, 'Key elements of and material performance targets for highly insulating window frames', *Energy Build.*, vol. 43, no. 10, pp. 2583–2594, 2011.
- [12] G. Fisch Krause, *Refurbishment Manual: Maintenance, Conversions, Extensions*, vol. 1. Munich: Birkhäuser, 2009.
- [13] C. Schittich, *Building in Existing Fabric: Refurbishment, Extensions, New Design*. Munich: Birkhäuser, 2003.
- [14] WBDG, 'Building Envelope Design Guide - Curtain Walls', 2012. [Online]. Available: https://www.wbdg.org/design/env_fenestration_cw.php. [Accessed: 10-Apr-2016].
- [15] M. Boduch and W. Fincher, 'Standards of Human Comfort', *Semin. Sustain. Archit.*, p. 12, 2009.
- [16] C. Schittich, G. Staib, D. Balkow, M. Schuler, and W. Sobek, *Glass Construction Manual*, 2nd ed. Walter de Gruyter, 2007, 2007.
- [17] P. R. Lyons, D. Arasteh, and C. Huizenga, 'Window performance for human thermal comfort', *Trans. - Am. Soc. Heating, Refrig. Air Cond. Eng.*, vol. 106, no. August 1999, pp. 594–604, 2000.
- [18] NSAI, *NSAI- Standard Recommendation S.R.54:2014- Code of practice for energy efficient retrofit of dwellings*. Dublin, Ireland: National Standards Authority of Ireland, 2014.
- [19] S. Burton, *Energy-efficient Office Refurbishment: Designing for Comfort*. Routledge, 2013.
- [20] PHA, 'Active for More Comfort: Passive House', p. 77, 2014.
- [21] D. Yeomans, 'Construction history', 1998, pp. 59–82.
- [22] R. Afghani Khoraskani, 'Advanced Connection Systems for Architectural Glazing', pp. 5–20, 2015.
- [23] S. Van de Voorde, I. Bertels, and I. Wouters, 'Post-war building materials', p. 460, 2015.
- [24] A. Cunningham, *Modern Movement Heritage*. Taylor & Francis Group, 2013.
- [25] A. Martinez, M. Patterson, A. Carlson, and D. Noble, 'Fundamentals in Façade Retrofit Practice', *Procedia Eng.*, vol. 118, no. AUGUST, pp. 934–941, 2015.
- [26] B. Marradi and M. Overend, 'Development of a process mapping for glass facade renovations', in *Challenging Glass 4 & COST Action TU0905 Final Conference*, 2014, pp. 177–187.
- [27] ISO, 'International Organisation for Standardization', 2016. [Online]. Available: <http://www.iso.org/iso/home.htm>. [Accessed: 10-Apr-2016].
- [28] P. Sanguinetti, 'Integrated Performance Framework To Guide Façade Retrofit', Georgia Institute of Technology, 2012.
- [29] R. Calejo, 'Design and diagnosis of building pathologies', in *4th meeting on civil constructions: maintenance and rehabilitation of buildings*, 1996.
- [30] I. Flores-Colen and J. De Brito, 'A systematic approach for maintenance budgeting of buildings facades based on predictive and preventive strategies', *Constr. Build. Mater.*, vol. 24, no. 9, pp. 1718–1729, 2010.
- [31] C. Richarz, C. Schulz, and F. Zeltler, *Energy-Efficiency upgrades: Principles, Details, Examples*. Munich: Birkhäuser, 2008.
- [32] L. Gelfand and C. Duncan, *Sustainable Renovation: Strategies for Commercial Building Systems and Envelope*. Wiley and Sons, 2011.
- [33] A. G. Hestnes and N. U. Kofoed, 'Effective retrofitting scenarios for energy efficiency and comfort: Results of the design and evaluation activities within the OFFICE project', *Build. Environ.*, vol. 37, no. 6, pp. 569–574, 2002.
- [34] Z. Hart, M. McClintock, V. Olgyay, A. Jackaway, and M. Bendewald, *Deep Energy Retrofits: An Emerging Opportunity*. Colorado, United States: Rocky Mountain Institute, 2013.
- [35] G. Cellai, C. Carletti, F. Sciurpi, and S. Secchi, *Building Refurbishment for Energy Performance, Green Energy and Technology*. Switzerland, 2014.
- [36] S. Brunoro and A. Rinaldi, 'Double layer glass façade in the refurbishment and architectural renewal of existing buildings in Italy', pp. 1898–1905, 2006.
- [37] S. Y. Harris, *Building Pathology: Deterioration, Diagnostics, and Intervention*. John Wiley & Sons, 2001.
- [38] S. Shah, *Sustainable Refurbishment*. John Wiley & Sons, 2012.
- [39] P. F. Gower, P. David, and A. Peacock, 'Reducing CO2 emissions through refurbishment of non-domestic UK buildings', in *In Proceedings of the 5th International Conference on Improving Energy Efficiency in Commercial Buildings.*, 2010, vol. 1, pp. 73–82.
- [40] M. F. Boneta, 'Cost of energy efficiency measures in buildings refurbishment : a summary report on target countries. D3.1 of WP3 from Entranze Project', no. August 2013, pp. 1–35, 2013.
- [41] R. Hartungi and J. O. E. Howe, 'Sustainable Conservation and facade retention developments in historic cities', pp. 1–15, 2010.
- [42] G. R. Genge, 'Repair of faults in building envelopes', *J. Build. Phys.*, vol. 18, no. 1, pp. 81–89, 1994.
- [43] IEA, 'Technology Roadmap "Energy efficient building envelopes"', France, 2014.
- [44] M. K. Dixit, J. L. Fernández-Solís, S. Lavy, and C. H. Culp, 'Need for an embodied energy measurement protocol for buildings: A review paper', *Renew. Sustain. Energy Rev.*, vol. 16, no. 6, pp. 3730–3743, 2012.

A changing Civil Engineering curriculum at UCD

Patrick J. Purcell¹

¹School of Civil Engineering, University College Dublin, Belfield, Dublin 4, Ireland
email: pj.purcell@ucd.ie

ABSTRACT: The paper describes some examples of innovative developments in the 4-year undergraduate Civil Engineering curriculum at UCD. The developments described were undertaken to stimulate active learning and higher order thinking. The paper focuses on innovations in what and how engineering students learn. In particular, the following examples of innovative teaching and learning strategies will be described in the paper:

- (a) The introduction of free elective modules for undergraduate engineering students;
- (b) The use of digital technology to facilitate online learning and the development of virtual laboratories;
- (c) The introduction of modules that stimulate student creativity and the use of teaching techniques such as peer-assisted mentoring to improve student engagement.

Anecdotal evidence and quantitative student feedback suggests that the foregoing initiatives have, in general, enhanced the student experience.

KEY WORDS: Civil Engineering education, Innovative teaching, Student engagement, University College Dublin.

1 INTRODUCTION

Civil Engineering is undergoing rapid changes, driven by growing population demands and environmental concerns, the information technology revolution and by scientific advances in fields such as biotechnology and materials science. Obviously, such changes demand that civil engineering curricula evolve to produce graduates capable of meeting these new challenges.

There have been numerous calls to broaden the education of engineers and thus prepare them to serve society with an awareness of and sensitivity to the cultural, political, economic and social dimensions of their work [1]. Jennings et al. [2] state that engineering students ‘need to be aware of the importance of human as well as technical factors in the work they do, and the need to appreciate that communication skills and the ability to work with others are vital’. For example, the Institution of Engineers of Ireland [3] requires that, in addition to the normal technical competence expected of a professional Engineer, graduates must be able to demonstrate:

- An understanding of the need for high ethical standards in the practice of engineering, including the responsibilities of the engineering profession towards people and the environment;
- The ability to work effectively as an individual, in teams and in multi-disciplinary settings together with the capacity to undertake lifelong learning;
- The ability to communicate effectively with the engineering community and with society at large.

The University College Dublin (UCD) Strategy for Education and Student Experience Framework document 2015-2020 [4] states that:

‘We strive to give our students a holistic education, instilling in them a desire to learn and create, to question and reason, to innovate and to contribute to society at all levels’.

This paper, as illustrated in Figure 1, will describe the changes in the Civil Engineering curriculum at UCD with the objectives of:

- (a) dovetailing into the overall University educational objective of creating innovative graduates;
- (b) meeting the accreditation criteria of Engineers Ireland;
- (c) using novel methods of engaging engineering students and making their educational experience more rewarding;
- (d) using information technology to deliver elements of the programme in a more innovative manner.

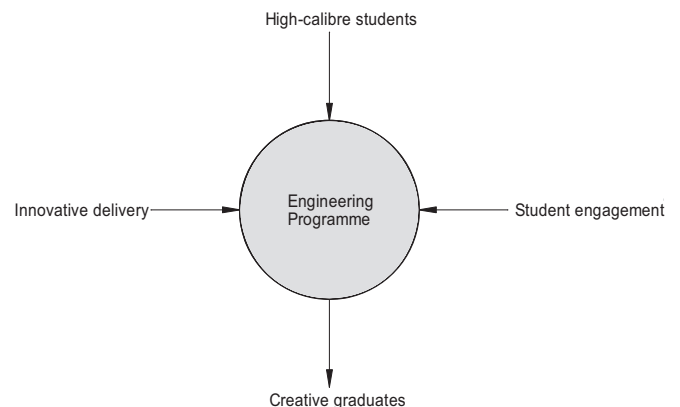


Figure 1. Schematic of educational objectives at UCD Civil Engineering.

2 CHANGES IN WHAT STUDENTS LEARN

There have been many innovations in recent years to make undergraduate education more student-centred, offering students greater flexibility and choice in **how** and **what** they study. The learner-centred approach facilitates students' different aptitudes, interests, backgrounds, educational objectives and allows students an appropriate degree of choice in managing their own studies [5]. It accommodates varying levels of progression and recognises different levels of attainment. This, in turn, opens new pathways and opportunities for non-traditional students, promoting wider access to, and participation in, higher education.

In relation to **what** students learn, most university curricula have gradually evolved into core curriculum as a specified or fixed course of study coupled with some element of student choice in selecting elective or optional modules. The free elective system has played a critical role in the development of the modern American university as we know it and is becoming more widespread in European institutions. The benefits of electives include:

- adding value to the degree, enabling specialisation in the chosen discipline or,
- facilitating students to pursue wider interests or explore an area that is new to the student.

The Civil Engineering programme at UCD was traditionally a 4-year bachelors degree. The introduction of the UCD Horizons initiative in 2005 resulted in the development of fully-modularised, semesterised and credit-based degree programmes; each academic year is worth 60 ECTS credits. Under the re-structured curriculum at UCD, in a given academic year, students choose *core* modules from their specific subject area, a number of *options* (if applicable) and *elective* modules, which can be chosen from within the student's programme of study (in-programme electives) or from any other programme across the entire University (non-programme or general electives). Table 1 summarises the modular structure at UCD. Students can select ten credits out of the sixty credits they take each year from any programme across the University. The philosophy underlying this curricular transformation is to give the freedom of choice to students to broaden their knowledge in different areas or deepen their knowledge in their chosen programme of study. Crucially, Horizons facilitates the formation of graduates that are 'intellectually flexible and globally engaged', central to UCD's Education Strategy.

Following the completion of a 3-year, 180 credit bachelor of engineering science programme, students can choose to either:

- (a) Complete a bachelors degree in one further year of study, or
- (b) Undertake a masters degree over a further two years meeting the educational requirements for Chartered Engineer status with Engineers Ireland.

Table 1. General modular structure at UCD.

Module	Comment
Core	Students are required to take these modules
Options	Students may be required to select a number of modules from a specified suite of modules
Electives (In-programme)	Students can select a maximum of 2 modules per year from a suite of modules offered by the programme
Electives (General)	Students can select a maximum of 2 modules per year from any programme across the University, subject to timetable and space restrictions

In line with Engineers Ireland and the Bologna requirements, undergraduate education at UCD is moving gradually to a two-cycle, five-year degree structure. Table 2 summarises the number of core, option and elective credits that students of the current four-year Civil Engineering programme take in each Stage (Year) of their studies. In respect of the elective choice, students can choose either:

- (c) ten credits in-programme electives which enable students to deepen their engineering knowledge,
- (d) ten credits non-programme (general) electives which allow students to widen their knowledge in modules of general interest to the student or
- (e) a five-credit in-programme elective combined with one five-credit general elective.

One of the key objectives of introducing general electives into the undergraduate engineering curriculum at UCD was to develop the non-technical attributes listed above in engineering students graduating from UCD.

Traditionally, students were primarily assessed by end-of year examinations, but with the introduction of semesterisation, twice-yearly, end-of-semester, 2-hour examinations are the norm. There is now more continuous assessment of students and mid-semester 1-hour examinations are increasingly common.

Table 2. Credits per Stage (year).

	Core	Option	Elective
Stage 1	45	5	10
Stage 2	50	0	10
Stage 3	50	0	10
Stage 4	45	15	0

In addition to the introduction of electives, there have been changes in the core curricular content. Students now undertake less physical laboratories and manual drafting than in the past (see Fig. 2). Instead, reflecting the IT revolution, there is more emphasis on computer-aided design (CAD), as illustrated in Figure 3. There are also more 'non-engineering' modules such as planning, law, environmental impact

assessment incorporated into the curriculum. As a result of the recommendations of employers and accreditation visiting panels, students are required to develop competence in 'soft-skills' such as an ability to work in group settings, to communicate effectively, to interface with other disciplines etc. With the aforementioned requirements of industry and the profession, are we, as engineering educators, trying to fit a quart into a pint pot [6]? In addition, the demands of industry for 'training' so that the graduate is ready to 'hit the ground running' must be balanced against the mission of the University to 'educate' the undergraduate in fundamental principles.

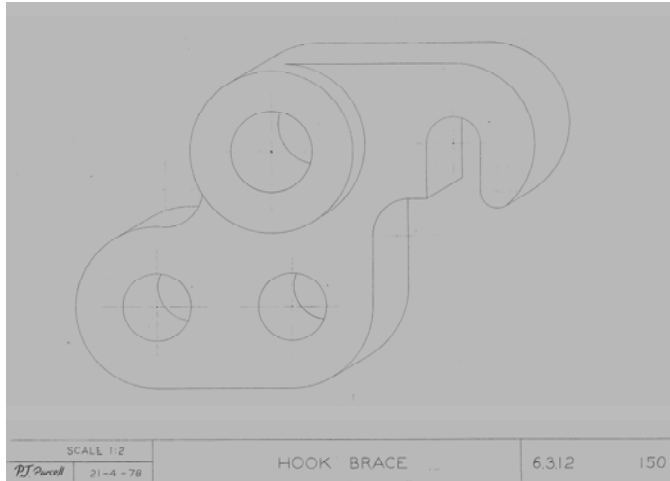


Figure 2. Manual drafting in UCD Civil Engineering 1978.

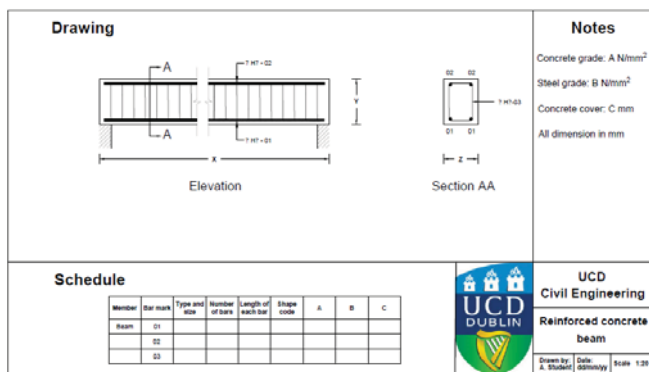


Figure 3. CAD in UCD Civil Engineering 2015.

3 CHANGES IN HOW STUDENTS LEARN

3.1 Active learning

In relation to **how** students learn, novel pedagogical techniques (other than sitting passively in a classroom) that make students take an active, task-orientated and self-directed approach to their own learning are increasingly common in higher education. Felder [7] defines active learning 'as anything course-related that all students in a class session are called upon to do other than simply watching, listening and taking notes. Learning approaches such as problem-based

learning (PBL) have the capacity to create vibrant and active learning environments in higher education. In such enquiry-based approaches to learning, 'students define their own learning issues, what they need to research and learn to work on the problem and are responsible themselves for searching appropriate sources of information' [8].

As part of an annual, one-week, UCD 'Experience Engineering' Programme for second-level students interested in pursuing Engineering as a career, a problem-based introductory session to the discipline of Civil Engineering for these students was developed, as described by Cosgrove et al. [9]. The purpose of this exercise, in which participating students undertake a Structural Design challenge, is to foster an interest amongst the participating students in Engineering as a career.

The objective of the Structural challenge is to design and construct an efficient truss structure, using limited material resources, to:

- to span a specified distance;
- to carry the maximum load at mid-span;
- to minimize mid-span deflection.

Students, as illustrated in Figure 4, are divided into groups of about 5-6 students per group. The exercise demonstrates the following attributes:

- Engagement by the students;
- Application of theory in context;
- Ingenuity by students;
- Competitiveness between groups;
- Teamwork building.



Figure 4. Structural Engineering challenge.

Student engagement entails adopting pedagogical approaches that stimulate active learning and higher order thinking. There are tried-and-trusted techniques to keep students active-learners:

- Interactive lectures;
- Active learning;
- Peer-assisted mentoring.

Interactive lectures are lectures interspersed with brief in-class activities that require students to use information or concepts presented in the lecture. Students learn by doing, not by watching and listening. Felder et al. [10] defines active learning as ‘anything course-related that all students in a class-session are called upon to do other than watching, listening and taking notes’. One technique for promoting student engagement is the use of peer-assisted mentoring, i.e. the use of students more advanced (e.g. post-graduate students) to mentor undergraduate students. Peer-assisted mentoring should not be confused with ‘normal’ tutoring of undergraduates, in which the tutors are financially compensated. In peer-assisted learning, there is an educational gain for both the mentoring students and the mentees and all students are awarded credit for their respective roles in the educational arrangement.

An example of active-learning facilitated by peer-assisted mentoring in the School of Civil Engineering at UCD is described below. The first-year undergraduate module in question is ‘Creativity in Design’ (CVEN10040) and the postgraduate module is ‘Innovation Leadership’ (CVEN40390). The ‘Creativity in Design’ module provides an active-learning engineering experience through which students develop their observation skills, problem solving skills and lateral thinking and teamwork abilities. Undergraduate students work in small groups, facilitated by a peer-assisted mentor (a post-graduate student enrolled on the Innovation and Leadership module). The undergraduate students (mentees) must suggest innovative solutions to real-world problems that are presented to them. In Stage 2 Civil Engineering, students, as part of the Construction Materials module (CVEN 20080), are required to construct a piece of home ‘furniture’ of their own choosing from a range of common Civil Engineering materials such as concrete and timber, as illustrated in Figure 5.



Figure 5. Stage 2 students presenting their home ‘furnishing’ creations.

3.2 Use of Information technology

The use of computer-based technology can be particularly useful in enhancing engagement, in delivering more effective assessment and in providing timely feedback. ‘Virtual’ laboratories can be used to supplement or even, in some instances, replace physical laboratories. The rationale for introducing virtual laboratories at UCD School of Civil Structural and Environmental Engineering is that, in a time of diminishing resources, virtual laboratories can go some way to bridging the gap between demand and capacity to deliver laboratory-based practicals.

Within the materials component of Highway Engineering (CVEN40710), Stage 4 Civil Engineering students have traditionally undertaken laboratory demonstrations in small groups. To improve the student experience, a video library of on-site activity and laboratory testing methods has been developed, facilitating students in appreciating and understanding the practical elements of their programme, as illustrated in Figure 6. Future development of this innovative method of delivery would be to link virtual laboratories with on-line MCQ assessment, as follows:

- How do students view virtual laboratories?
 - Upload onto Virtual Learning Environment;
 - Description of experiment;
 - View Video;
- Student assessment?
 - Assessment linked to learning;
 - Multiple Choice Questions on video clip;
 - Progression from one experiment to another.

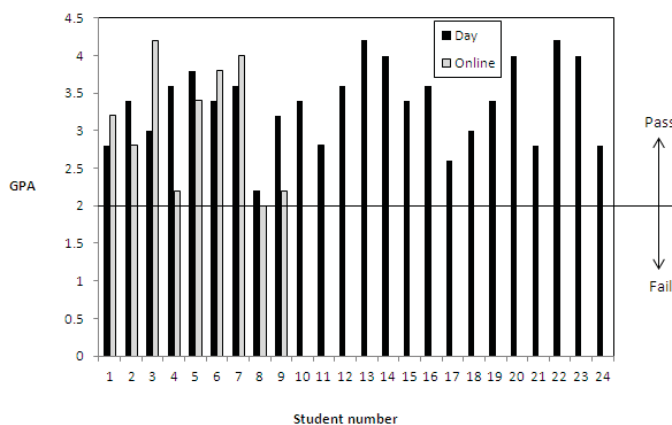


Figure 6. Developing virtual laboratories [11].

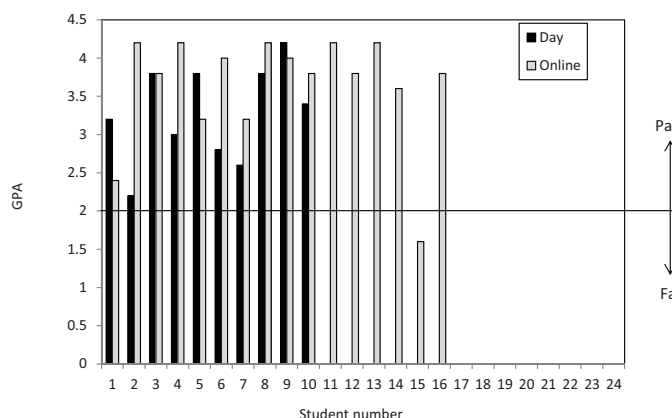
A second example of innovative delivery is the introduction in the academic year 2013-2014 of two online modules introducing water engineering to students pursuing a master of applied science degree ('online students'). The delivery of this material to students registered for these modules enables this cohort of students to take these modules remotely and at their own pace. The modules are also delivered in parallel to students who attend in person at the University ('day students'). The examination performance of these two groups of students in the case of one of the water resources engineering modules is shown in Figure 7 (a) for academic year 2013/2014 and in Figure 7 (b) for academic year 2014/2015. Examination of the figure shows that:

- For the 'day' students the average GPA was 3.4 in both academic years;
- For the 'online' students the average GPA was 3.1 in 2013/2014 increasing to 3.8 in 2014/2015.

In addition to the improved GPA of the online students from 2013/2014 to 2014/2015, examination of Figure 7 shows that there was increased interest in the student cohort undertaking the module online, as the delivery has become more established.



(a)



(b)

Figure 7. Comparative examination performance of 'day' and 'online' students (a) 2013/2014 (b) 2014/2015.

4 CONCLUSIONS

Some examples of innovative developments in the undergraduate Civil Engineering curriculum at UCD have been described. These initiatives have been introduced to stimulate undergraduate student engagement through the use of novel content and delivery methods. Anecdotal evidence and quantitative student feedback suggests that the foregoing initiatives have, in general, enhanced the student experience.

In relation to 'what' students study, analysis of the student registration data would suggest that engineering students, given the choice to pursue further 'depth' in their core area of study or 'breadth' outside their programme, generally opt for the latter option. In addition, there would appear to be far fewer non-engineering students opting for engineering modules than engineering students opting for non-engineering modules.

In relation to 'how' students study, innovative teaching methods such as peer-assisted tutoring have been introduced. In addition, novel learning methods such as the use of computer-based technology that enable students to undertake digital laboratories and to take modules remotely using online technology have been introduced and are gaining traction amongst the student body.

REFERENCES

- [1] Heidebrecht, A. (1999), 'Evolution of engineering education in Canada', A Report of the Canadian Academy of Engineering.
- [2] Jennings, A. and Mackinnion, P. (2000), 'Case for Undergraduate Study of Disasters', J. Perform. Constr. Facil., ASCE, 14:1(38).
- [3] Engineers Ireland Accreditation Criteria for Engineering Education Programmes, <http://www.engineersireland.ie/EngineersIreland/media/SiteMedia/services/accreditation/Accreditation-Criteria-for-Engineering-Education-Programmes-FINAL-amended-Mar-09.pdf>
- [4] UCD Education Strategy 2015 – 2020, <http://www.ucd.ie/strategy2015-2020/download/index.html>
- [5] Betts, M. and Smith, R. (1998), 'Developing the Credit-based Modular Curriculum in Higher Education', London: Falmer Press.
- [6] Barr, A. and Fordyce, D., (1993), 'A Quart in a Pint Pot', Proc. Innovation and Change in Civil Engineering Education, Queen's University of Belfast.
- [7] Felder, R. and Silverman, L. (1998), 'Learning and Teaching Styles in Engineering Education, Engineering Education', Vol. 78, No.7, pp. 674-681.
- [8] Barrett, T. and Moore, S. (2010), 'New Approaches to Problem-based Learning', Revitalising Your Practice in Higher Education, Routledge Press.
- [9] Cosgrove, T., Phillips, D. and Quilligan, M. (2010), 'Educating Engineers as if they were human: PBL in Civil Engineering at the University of Limerick', 3rd International Symposium for Engineering Education, University College Cork, Ireland.
- [10] Felder, R. (2009), 'Active learning: an introduction', *ASQ Higher Education Brief*, 2(4), August 2009.
- [11] UCD Teaching and Learning, Teaching Awards and Grants / Digital Seed Funding, <http://www.ucd.ie/teaching/awardsgrants/digitalseedfunding/>.

Civil Engineering Education in 19th Century Ireland

Dermot O'Dwyer¹, Ronald Cox²

^{1,2}Department of Civil, Structural and Environmental Engineering, Museum Building, Trinity College Dublin, Ireland
email: dwodwyer@tcd.ie, rcox@tcd.ie

ABSTRACT: This paper examines how Irish engineering education has changed since the time of the founding of the first Irish university engineering schools in the 1840s. The paper focuses on the early curricula and methods of instruction before comparing them with current engineering programmes and the programme outputs required by Engineers Ireland.

The paper identifies the material that was taught in the first Irish university engineering courses and details the texts that were available to these early students. The Trinity College Dublin 1843 final year examination in practical engineering is presented in an appendix to the paper and it and other examination papers are analysed to identify the knowledge that was considered necessary for civil engineering students. The Boyne Viaduct is mentioned briefly because this project involved some of the first Irish civil engineering professors and the first graduates from an Irish engineering programme.

The paper also considers the accreditation requirements that engineering programmes must achieve today and considers whether the core components of an engineering education have changed. Finally, the paper looks at how project work and case-based studies have been constant elements in fostering engineering design skills and briefly considers modern developments in teaching engineering design

KEYWORDS: CERI 2016; Engineering Teaching and Learning; History of Engineering Education.

1 INTRODUCTION

French engineering in the eighteenth and early nineteenth century was more technically advanced than civil engineering in Britain [1]. There were a number of reasons for this including a more enlightened approach to technical education. The French École des Ponts et Chaussées, established in 1746, is accepted as being the oldest engineering school. The English-speaking world lagged quite a bit behind and Trinity College Dublin (TCD), whose Engineering School was founded in 1841, was among the first English-speaking universities to offer courses in engineering [2]. The three Queen's Colleges at Cork, Galway and Belfast, which were established in the late 1840s, were also among the earlier colleges to have engineering programmes [3,4,5].

These early Irish university engineering programmes had predecessors. The establishment of engineering schools was perhaps also encouraged by the perceived need for more technical training and by the existence of commercial schools of engineering [2,4] and the efforts of other learned institutions to provide technical education [7].

The lack of engineering schools, professors of engineering and dedicated engineering programmes did not mean that engineering was completely neglected in the universities. Bartholomew Lloyd, Professor of Natural & Experimental Philosophy in TCD had lectured mechanics in an applied manner appropriate to engineers for many years prior to the establishment of the Engineering School. The first Professor

of Engineering in Galway, William Bindon Blood had been an undergraduate in TCD. In 1838 Blood obtained the College Gold Medal in Mathematics and Physics before graduating with a BA in 1839 [4]. Blood would have studied under Bartholomew Lloyd and his son Humphrey, whose courses in subjects such as mechanics were clearly addressing engineering. Blood also studied in Edinburgh where the university also had a long history of engineering related courses. John Robison, Professor of Natural Philosophy in the University of Edinburgh, was lecturing structural analysis to pupils, including John Rennie Senior in the 1800s [6]. Similarly, although Cambridge didn't have an engineering school at the time, Whewell, a college lecturer, had published *The Mechanics of Engineering, Intended for use in Universities, and in Colleges of Engineering*.

Interestingly, the engineering profession does not seem to have been a significant driver of the development of formal technical education at the time. This fact is perhaps best illustrated by the example of James Thompson, the first professor of Engineering at Queen's University Belfast and older brother of William Thompson (Lord Kelvin). James Thompson had received a full technical education at Glasgow and Edinburgh and yet his father had to pay £100 to have him apprenticed to Fairbairn [3]. However, this attitude to a university-based technical education rapidly changed as engineering became a more mathematical, scientific profession. That said, one could argue that the current requirement that an engineer cannot become chartered until he

or she has spent time in practice is in the same spirit as Thompson's apprenticeship to Fairbairn.

2 ENGINEERING IN TRINITY COLLEGE DUBLIN

Trinity College Dublin's Engineering School was the first University engineering school in Ireland. However, this paper's emphasis on Trinity's Engineering School is based on the lucky happenstance that some of the early engineering examination papers survive. In addition, the philosophy and practice of the engineering school were recorded at the time and this gives a valuable record of engineering education in the 1840s.

One other record of Irish engineering education in the 1840s from the commercial sector should be acknowledged. John Gregory, who was primarily a mathematician, was also the Resident Director of the College for Civil Engineering, Mining and Agriculture and a practicing civil engineer. In 1842 Gregory published a text book on Civil Engineering that is quite detailed, see Figure 1 [8].

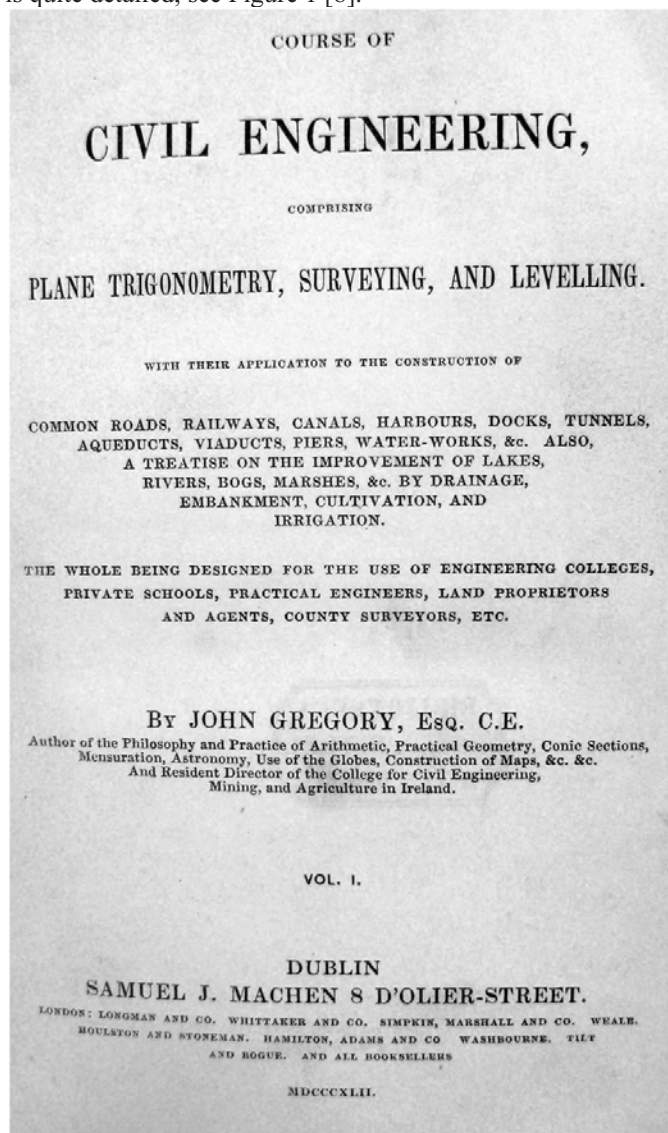


Figure 1. Title page of Volume I of Gregory's two volume *Course of Civil Engineering*.

In his book Gregory not only gives a state-of-the-art overview of some areas of civil engineering technology but gives some details of contemporary projects. The other key sources from this time are the books written by the lecturing staff within TCD [10-13]. In addition, the level of technical expertise of the early staff can be determined by the projects they were involved in, and in the case of John Macneill [14], the first Professor of Engineering in TCD, of the French texts he translated [15].

The foundation of the Engineering School was largely the work of Humphrey Lloyd, when Professor of Natural & Experimental Philosophy. However, the story of engineering in TCD really starts with Humphrey's father, Bartholomew Lloyd, who was one of the young professors in mathematics and physics who remodelled mathematics in TCD on the continental system [16,17]. When Humphrey Lloyd set up the engineering school it was hardly surprising that he visited France and later based the School curriculum on French practice [18].

2.1 Course Structure

The earliest students studied a range of subjects including chemistry, geology, physics, mathematics and mathematics. The Rev. Robert V. Dixon in his praelections on the Engineering School in 1849 and 1854 gives a good synopsis of the curriculum at that time [19,20].

However, before detailing the years of an engineering course it must be remembered that students attending Trinity College Dublin also took a BA and hence they had a very rounded education [2].

The first year of the engineering programme included courses in abstract mathematics, theoretical mechanics, hydrostatics and hydrodynamics, theoretical and applied chemistry, mineralogy and crystallography.

In the second year the student covered the principles and practice of: surveying and levelling, drawing, mapping and plotting, principles of experimental sciences, the theory of the application of steam as a motive power and in mechanics as applied to the construction of machines and great public works.

The third year of engineering study involved studying: actual details of construction, both theoretical and demonstrative geology, the mode of carrying out field work, the method of conducting office-work including the drawing up of plans and making out estimates. Dixon states that in order to test his (a valid pronoun at the time, the world's first woman engineering graduate was Alice Perry who graduated with a BE from Queen's University Galway in 1906[4]) proficiency in this branch of his studies, he is required to produce at his final examination for the diploma a project for a line of railway through a prescribed district, including all necessary plans, sections, elevations, and estimates.

A number of the examination papers for these subjects survive [21]. In one or two other cases, although the engineering examinations have not survived, the material that was covered can be inferred from the texts written for the students, the student note books [22] or from examinations that were taken by students from other disciplines. The Lloyd premium is a case in point. This examination was in the area

of mechanics and optics and a number of examination papers from around 1840 are recorded in the University Calendars. The questions on these papers are still relevant and would challenge today's students. For example, the question below is taken from Lloyd's mechanics premium examination of 1840.

8. Required the inclined plane along which a given force, acting parallel to the plane, shall draw up a given weight to a given height in the least time.

This question was included in the scholarship examinations in TCD this year (2016) when, happily, it was answered well.

2.2 Chemistry and Geology,

Dr. Apjohn's Chemistry and Geology examination from 1843 survives: the full list of 78 questions was printed in the following year's Calendar. Unfortunately the Calendar didn't specify how many questions were to be answered or how long the candidates had to complete their answers.

The first questions on the paper are concerned with pure Chemistry but many of these questions were selected for their relevance to construction or civil engineering. Thus, question seven below is an example of a theoretical but practical chemistry question

7. Describe how hydro-sulphuric acid and sulphuret of ammonium are made, and their uses in analysis.

Questions nineteen and fifty-two are typical of the chemical questions that are concerned with civil engineers' knowledge and use of materials.

19. What are the essential constituents of an hydraulic lime, and what the state of their existence in the stone before and after being burned?

52. What are the differences in chemical constitution between malleable iron, steel and pig iron?

The geology questions are a similar mix of theoretical and applied questions. The engineering related questions are not only related to the use of different stone in construction, as in sixty-five below,

65. What qualities should be possessed by a good stone for metalling roads? And what rocks are found to possess these in the highest degree?

2.3 Physics

The physics paper, which was set by Humphrey Lloyd and comprised 23 questions, starts with the statement that the students were also examined in mathematics and mechanics both practical and applied. This mix of the theoretical and applied was present in Lloyd's father's 1826 mechanics text [9], which made an effort to address the application of mechanics to practical problems.

The physics paper concentrates on a limited number of areas including: thermal expansion of materials, the properties of steam and the principles underlying the mechanical operation

of steam engines. In some cases the questions relate to the final application of the physical principle, for example, Question 8,

8. Principle and construction of the compensation rods used in the Trigonometrical Survey?

This question relates to Major General Colby's compensating bars which were used in the Ordnance Survey of Ireland, which was nearing completion at the time of the exam. In other cases the questions are theoretical but examine an area of theory directly related to practice.

16. Required, the expression for the density of steam, at any pressure and temperature, obtained by combining the laws of Mariotte and Dalton?

The questions examined the students on the very latest thinking. For example, question twenty-one is related to the effect of air resistance of trains. This form of resistance to motion had only recently been identified as significant. This is clear from the discussion of the topic by Dionysus Lardner in the seventh edition of his treatise on steam engines [23].

21. What is the effect of the air's resistance, as affecting railway gradients?

2.4 Practical Engineering

The questions in physics, chemistry and geology might have been anticipated by reading the texts available to the students. In addition to the texts written by their lecturers students had access to a number of international texts on a variety of civil engineering subjects [24-28]. J.M. Sganzin & M. Reibell, *Programme ou Résumé des Leçons Cours de Construction avec des applications tirées spécialement de l'art de l'ingénieur des Ponts et Chaussées* was one such book. It contains an atlas of construction details that must have been of great use to the students [29], see Figure 2.

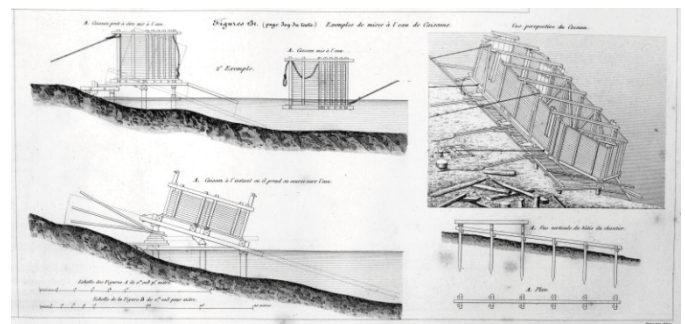


Figure 2: Showing the launching of a timber casson [29].

However, the most useful source of reference on practical engineering must have been their professor, John Macneill. Macneill, a protégée of Telford, was a particularly experienced engineer. His tables for calculating cut and fill volumes [30] were the industry standard.

The 1843 practical examination paper, which was taken in the final year, is contained in full in the appendix to this

paper. The paper contained two sections, the first were a series of seventy-one viva voce questions the second comprised eleven questions that required calculation.

Perhaps the most striking thing about the examination paper is how professionally relevant the questions were. This is in sharp contrast to the academic style of most contemporary texts on mechanics or mathematics, first year TCD students sat mathematics papers set in Latin. In contrast Macneill and his Assistant Renny's paper is very clearly focused on the details of day to day practice. For example, question three,

3. In a section of a turnpike road, what scales would you employ for the longitudinal distances and vertical heights? and what scales for a railway or canal?

seeks a key piece of information that must have been either learned through practice or memorised by rote. In a similar manner the questions relating to arches and retaining walls in the viva voce section of the exam show that the students were expected to know a range of appropriate rules of thumb. For example, questions 32, 33 and 54 required students to give suitable dimensions for arches and a retaining wall without calculation. However, such useful rules of thumb were not considered definitive because questions 5 and 6 from the calculation section of the exam, which also treat arches and retaining walls, clearly required solutions based on an analysis of the mechanics of each problem.

The practical examination gives a lot of information about the type of work that civil engineers might be engaged in. There are questions concerned with surveys, roads, canals, railways, bridges, sea and dock walls and tunnels. There are also a limited number of questions related to the behaviour of beams in bending but there are few references to general building. This is because constructing buildings was considered to be outside the general field of an engineer [20]. This attitude to building and indirectly to structural analysis of buildings is also apparent from the scant treatment of structural analysis by Gregory in his *Course of Civil Engineering* [8]. This attitude to building seems strange today but in the early 1840's the science of strength of materials was not fully developed and the structure of most buildings could be sized using scantlings or rules of thumb. Bridges were an exception but these exams date from before the collapse of Robert Stephenson's cast-iron bridge over the river Dee. This and other material failures led to a number of parliamentary investigations into the use of iron in bridges and led to a greater awareness of the need for rigorous analysis.

The questions on beam bending in the practical exam don't give a full picture of structural analysis within the Irish universities at this time. A study of the design and construction of the Boyne Railway Viaduct at Drogheda give a valuable insight. The design of the viaduct became mired in controversy, but this much is clear: the initial inspiration for the continuous three-span constant-depth high-level wrought-iron lattice girder was John Macneill's [31]. Much of the detailed design was apparently undertaken by James Barton, one of the first diplomates to graduate from the School of Engineering at TCD [32]. The method used to calculate the stresses in the continuous girder had been published by William Bindon Blood [33], a graduate of the University of

Dublin and Professor of Engineering in Galway and the complex calculations were cross-checked by Andrew Searle Hart, who lectured mechanics in TCD. Bindon Blood Stoney, another TCD alumnus, who would later write a book on the theory of strains in girders [34], was also involved in the construction and testing of the Boyne Viaduct [35].

Ultimately the positions of the locations of the points of contra flexure were found experimentally during the construction. This work was of international significance. Although Navier had analysed an indeterminate beam a decade or more earlier [36] and Moseley had subsequently presented a similar analysis in English a few years later [37]. Advances in this field were happening in practice rather than in universities, the analysis of Robert Stephenson's Britannia bridge being much more advanced than any mathematical treatment that had previously been published [38,39].

3 ENGINEERING IN THE QUEEN'S COLLEGES

Engineering in the three Queen's Colleges (Cork, Galway and Belfast) followed similar lines to TCD [7]. Galway's first full-time professor, William Bindon Blood, established a firm analytical base in the college, which was probably perfected during his period working for I.K. Brunel. Blood's analytical ability can be seen in his paper on the stresses in the diagonal members of lattice girders [33]. This was a significant paper dealing with statically indeterminate structures. Blood's analytical ability shows that universities were teaching courses of direct relevance to engineers in the years before formal engineering schools were established.

Queen's University Belfast had one of the most technically accomplished professors of engineering in James Thompson, its first professor [3]. In its earliest years Queen's Belfast had a programme similar to that in TCD but they established a structure where students studied a two year course in civil engineering after which the students were expected to spend three years in practice before returning to college to take a Diploma exam at the end of this five year period. The low numbers who returned to take the Diploma exam led to this initiative being discontinued. A number of examinations from the early years of the engineering course survive [3] but these give less insight into the level of attainment of the graduates than the TCD examination papers.

4 BOARD OF WORKS, RAILWAYS AND EMPIRE

The Irish Board of Works did not play a direct part in the establishment of the university engineering schools. However, the engineers of the Board of Works, particularly Colonel (Later Field Marshal Sir) John Fox-Burgoyne, were largely responsible for establishing the ICEI. Burgoyne, Harry Jones and Richard Griffith (who all headed the Board of Works at different times) clearly practiced a technically superior type of engineering. Perhaps the best evidence of this technical wealth is found in the Reports of the Irish Railway Commission, which was actively chaired by Thomas Drummond the Irish Under-Secretary [40]. The Board of Works were also responsible for commissioning engineering works. The establishment of County Surveyorships also added to the number of official posts that required technically trained engineers [4].

The railway also played a role not only in the rapid development of engineering technology but also in establishing a demand for engineers in the United Kingdom and further afield. The large scale growth of the British Empire also had an effect and many of the nineteenth century graduates from the Irish Universities spent their careers in India and other countries in the Empire.

These developments led to an increase in the demand for qualified engineers and to the requirement that engineers should be technically competent.

5 ENGINEERS IRELAND'S ACCREDITATION

In its early years The Institution of Civil Engineers of Ireland (ICEI) had close ties with the school of engineering in Trinity College Dublin and for many years it used the college's rooms to hold its lectures and meetings [41]. The link with Trinity was strong because both organisations were Dublin based. However, in the nineteenth century and for most of the twentieth century there was no formal relationship between the engineering schools and the ICEI. Thus the move from three year engineering degrees to four year degrees that took place in Ireland in the late fifties was not a requirement tied to accreditation.

In 1969 the ICEI and Cumann na nInnealtóirí merged [42] to form The Institution of Engineers of Ireland (IEI), known today as Engineers Ireland. In the early 1980s the relationship between the IEI and the engineering schools changed and the IEI became responsible for the accreditation of engineering courses in this country. The IEI in turn has been very active in ensuring that Irish engineering qualifications are recognised abroad. This has been achieved through international agreements such as the Washington and Sydney accords. The result of these moves has been for engineering schools to develop sets of programme outcomes for each level of engineering course. These programme outcomes are developed such that they are in agreement with the programme outcomes required by Engineers Ireland, hence they are also in harmony with programme outcomes in other countries.

In recent years these programme outcomes have evolved to be both specific in the type of programme outcomes that must be achieved while simultaneously allowing great freedom as regards the specific content of a course. This freedom regarding the content of engineering courses was the inevitable response to the increase in the range of topics that engineers study. In the 1840's the discipline of civil engineering encompassed mechanical and later electrical engineering before these separated to become recognised disciplines. Today the number of specialist engineering fields ranging from biomedical to computer engineering is constantly expanding. Civil engineering graduates may follow careers in environmental engineering, geotechnical engineering, energy engineering, coastal engineering or a host of other fields, all of which have their own specific technologies. It is not feasible for an engineering graduate to cover everything and an attempt to do so would limit the depth of their learning. Thus the focus is on developing core analysis and design skills. Engineering technology is changing so rapidly that continuing professional education is essential

and training engineers to continue to learn is a key part of a modern engineering education.

The programme outcomes for a level-nine course, the level required for Chartered Membership, requires graduates to have the advanced technical skills necessary to tackle very challenging problems and also requires them to have good communications skills and the ability to work well as part of a team.

These skills would have been just as important for our earliest engineering graduates as they are today. Therefore it is interesting to consider how well the early courses would fair in a modern accreditation. The first observation is that there are many similarities between the current and the original curricula. Both the original engineering programmes and the current programmes concentrate the early years of the degree on ensuring that graduates have a thorough grounding in mathematics and the sciences, with an emphasis on the application of those sciences to engineering. Both the old and the new programmes include final year projects. However, the purpose of the current final year theses, particularly since a level-nine qualification became necessary for chartered membership, is to ensure that graduates are able to undertake independent research. The original final year project was more concerned with showing that a graduate had a full knowledge of the process of surveying, designing, drawing and costing a major infrastructure project. That said, contemporary works such as the design of the Boyne Viaduct show how close to, or in advance of, the state-of-the-art some major projects were and it is clear from the participation of some of TCD's earliest graduates in this project that their college education must have prepared them well.

The current moves of some colleges to ensure that all graduates have a broad education is interesting when compared with the education of early graduates because the early TCD graduates were required to have completed the common first year, in which students studied mathematics, mechanics, Latin and Greek. There is an interesting letter from the Registrar of TCD written in 1903 and referred to in Robert Cochrane's Presidential Address to the ICEI in 1904 in which the Registrar comments that most students spend about five years in college [43]. This shows that the current five year engineering programmes are not completely at odds with the situation in the past.

6 CREATIVITY IN DESIGN

Teaching engineering design has been a fundamental part of engineering programmes from their inception. However, that is not to imply that the methods of teaching design and fostering engineering design creativity have not changed. One of the original pedagogical methods employed in the École des Ponts et Chaussées from its inception was to engage students in studying previous designs, this approach remains valid. Similarly, presenting students with a design objective and tasking them with developing detailed designs complete with drawings, specifications and costings is an approach that was used in Irish university engineering schools from their inception. This method is still widely used and remains very useful. However, what has changed is that Engineering educators are now applying engineering problem solving

skills to the task of education itself. This is most clearly seen by the development of a number of international peer-reviewed journals dealing with engineering education. This move in education is reflected in the emphasis on programme outcomes rather than a concentration of programme content. This move has been essential because many fields of engineering are advancing quickly and content that is technology specific can date quickly. The focus on programme outcomes has helped educators concentrate on core skills.

The treatment of creativity in Engineering is one interesting example of how engineering programmes have been developing. Whereas in the past a design module might have concentrated on developing particular low-level skills, such as RC detailing, a modern programme will also teach general problem solving and group working skills and may have formal lectures and workshops that explore strategies for encouraging creative design.

Many of the current design programmes in Trinity College use a CDIO (Conceive – Design – Implement – Operate) framework. Other exercises use a problem based learning paradigm. These new techniques have much in common with some of the earliest approaches because they are case-based. What is certainly changing is the range of different pedagogical models that the students are being exposed to. Students are also encountering a variety of assessment methods, which range from traditional examinations to interactive blogs, peer assessment, self-reflective diaries and other novel methods. These developments encourage students to develop a range of skills.

REFERENCES

- [1] S. B. Hamilton, 'The French Civil Engineers of the Eighteenth Century,' *Transactions of the Newcomen Society*, 1941; 22(1), pp. 149-159.
- [2] R.C. Cox, *Engineering at Trinity*, Dublin: School of Engineering, Trinity College Dublin, 1993.
- [3] M. Gould, *150 Years of Civil Engineering at Queen's 1849-99*, The School of Engineering, The Queen's University, Belfast 1999.
- [4] P. Duffy, 'Engineering', *From Queen's College to National University*, T. Foley (Ed), Four Courts Press Ltd., Dublin, 1999.
- [5] J.A. Murphy, *The College: A History of Queen's/University College Cork*, Cork University Press, Cork, 1995.
- [6] Birse, R.M. *Engineering at Edinburgh University: A short history 1673-1983*. School of Engineering, Edinburgh, University of Edinburgh.
- [7] W. Whewell, *The Mechanics of Engineering*, Intended for use in Universities, and in Colleges of Engineering, Cambridge: J. & J. Deighton, 1841.
- [8] J. Dooge, 'Engineering Training & Education', R. Cox (Ed.), *Engineering Ireland*, Cork, Collins Press, 2006, pp 36-54.
- [9] J. Gregory, *Course of civil engineering, comprising plane trigonometry, surveying and levelling*, London: Samuel J. Machen, 1846.
- [10] B. Lloyd, *An elementary treatise of mechanical philosophy: Written for the use of the under-graduate students of the University of Dublin*, Dublin: Richard Milliken, 1826.
- [11] J. Luby, *The Elements of Geometry in General terms ...etc.*, Dublin: J. J. Ekins, 1833.
- [12] A.S. Hart, *An elementary treatise on mechanics*, Dublin: William Curry, Jun., and Company, 1844.
- [13] A.S. Hart, *An elementary treatise on hydrostatics and hydrodynamics*, Dublin: William Curry, Jun., and Company, 1846.
- [14] P.J. Geraghty, 'Sir John Macneill (1793-1880): King of the Irish Railways', *Transactions of the Newcomen Society*, 2008, 78:2, 207-234
- [15] C. H. Navier, *On The Means Of Comparing The Respective Advantages Of Different Lines Of Railway; and on the use of locomotive engines*, translated from the French by John MacNeill, London: Roake & Varty, 1836.
- [16] T.D. Spearman, 'Humphrey Lloyd 1800-1881', *Hermathena*, 130, 1981, pp. 37-52.
- [17] R. Flood, 'Taking Root: Mathematics in Victorian Ireland', *Mathematics in Victorian Britain*, R. Flood, A. Rice and R. Wilson (Eds), Oxford: Oxford University Press, 2011.
- [18] H. Lloyd, *Praelection on the studies connected with the School of Engineering delivered on the occasion of the opening of the School*, the 15 November, 1841, Dublin: Milliken, 1841.
- [19] R.V. Dixon, *Praelection On the University System of Education: Delivered to the Students in the School of Engineering, Trinity College, Dublin*, Dublin, 1849.
- [20] R.V. Dixon, *Scientific Training for Practical Pursuits: A Farewell Address to the Students of the School of Engineering, Trinity College, Dublin*, Dublin: Hodges and Smith, 1854.
- [21] *University of Dublin Calendars (1840-1853)*, Dublin: Milliken and Son, 1840-53.
- [22] T.H. Going, *Student notebook*, Held in the School of Engineering Archive, Trinity College Dublin, 1849.
- [23] D. Lardner, *The steam engine explained and illustrated with an account of its invention and progressive improvement, and its application to navigation and railways etc.* 7th Ed., London: Taylor and Walton, 1840.
- [24] D. H. Mahan, *An Elementary Course in Civil Engineering*, edited by Professor Barlow, Glasgow: Archibald Fullarton & Co., 1838.
- [25] J.M. Sganzin, *An Elementary Course in Civil Engineering*, Boston: Hiliard, Gray and Company, 1837.
- [26] J. Millington, *Elements of Civil Engineering*. J.Dobson, Philadelphia: J. Dobson, 1839.
- [27] G. W. Buck, *A practical and theoretical essay on oblique bridges*, London: John Weale, 1839.
- [28] H. Parnell, *A treatise on roads: Wherein the principles on which roads should be made are explained and illustrated, by the plans, specifications, and contracts made use of by Thomas Telford, Esq. on the Holyhead Road*, London: Longman, Rees, Orme, Brown, Green & Longman, 1833.
- [29] J.M. Sganzin & M. Reibell, *Programme ou Résumé des Leçons Cours de Construction avec des applications tirées spécialement de l'art de l'ingénieur des Ponts et Chaussées*, Paris: Carilian – Goeury et Vor Dalmont, éditeurs, Library des Corps Royaux des Ponts et Chaussées et des Mines, 1839-1841.
- [30] J. Macneill, *Tables for Calculating the Cubic Quantity of Earth Work in the Cuttings and Embankments of Canals, Railways, and Turnpike Roads*, London: Roake and Varty, 1833.
- [31] R. Cox, 'Bridging the gap: the Boyne Viaduct 1855 – conception, design and construction', *Riocht na Midhe: Records of the Meath Archeological and Historical Society*, Vol. XVII, 2006, pp. 223-253.
- [32] J. Barton, 'On the economic distribution of material in the sides or vertical portion, of wrought-iron beams. (Including Plate)', *Minutes of the Proceedings of the Institution of Civil Engineers*, 1855 14:1855, pp. 443-458.
- [33] W. T. Doyne & W. B. Blood, 'An investigation of the strains upon the diagonals of lattice beams, with resulting formulae. (Including Appendix)', *Minutes of the Proceedings of the Institution of Civil Engineers*, 1852 11:1852, pp. 1-10.
- [34] B. B. Stoney, *The Theory of Strains in Girders and Similar Structures: With Observations On the Application of Theory to Practice and Tables of the Strength and Other Properties of Materials*. 2nd ed., London: Longmans, Green, and Co., 1869.
- [35] B. B. Stoney, 'Description of some experiments made at the Boyne Viaduct in 1854', *Transactions of the Institution of Civil Engineers of Ireland*, vol. 5, 1860, pp. 135-143.
- [36] C. Navier, *Résumé des Leçons Données sur L'Application de la mécanique a L'établissement des constructions et des machines*, 2nd Ed., Paris: Chez Carilian-Goeury, 1833.
- [37] H. Moseley, *The mechanical principles of engineering and architecture*, London: Longman, Brown, Green & Longmans, 1843.
- [38] E. Clark & R. Stephenson, *The Britannia and Conway tubular bridges: With general inquiries on beams and on the properties of materials used in construction*, London: Day and Son and John Weale, 1850.
- [39] T.M. Charlton, *A history of the theory of structures in the nineteenth century*. Cambridge: Cambridge U.P., 1982.
- [40] Irish Railway Commission. *First & Second Reports of the Commissioners Appointed to Inquire Into the Manner in Which Railway Communications Can Be Most Advantageously Promoted in Ireland*, London, Dublin: H.M.S.O., 1837-1838.
- [41] R. Cox and D. O'Dwyer, *Called to Serve*, Institution of Engineers of Ireland, Dublin, 2014
- [42] R. Cox and F. Callanan, 'The Irish Chartered Engineering Institution', R. Cox (Ed.), *Engineering Ireland*, Cork, Collins Press, 2006, pp55-86

- [43] R. Cochrane, 'President's Address', *Transactions of the Institution of Civil Engineers of Ireland*, vol. 32, 1907, pp. 26-81.

Appendix: 1843 TCD engineering examination paper

Practical Engineering,
Professor Macneill and Mr. Renny

1. How would you proceed to lay down a plan from a survey made by the chain alone? and how from a survey made by the chain and theodolite?
2. What scale do you consider the best for laying down a plan of an estate, a parish, a townland, a road, a railway, or a canal?
3. In a section of a turnpike road, what scales would you employ for the longitudinal distances and vertical heights? and what scales for a railway or canal?
4. How would you represent elevations of mountains, hills &c., on a plan?
5. How would you proceed to make a chart on Mercator's projection? and what is the use of this projection?
6. How would you proceed to survey a road actually constructed?
7. How would you proceed to survey a town?
8. How would you proceed to survey an estate or parish?
9. How would you calculate the superficial contents of such a survey, viz. of an estate or parish?
10. How do you determine the true meridian, so as to ascertain the magnetic variation?
11. How would you proceed to survey a bay or harbour?
12. What precautions would you take to ascertain the state of the tides at the moment of taking the soundings?
13. How do you adjust the Y level, Troughton's level, and Gravatts' level?
14. Where is it necessary to make allowance for the curvature of the earth—and what is the amount of such allowance?
15. How do you adjust the theodolite?
16. How do you take a section with the theodolite?
17. How do you take a section by the barometer?
18. How would you make a survey for a new line of road?
19. How would you make a survey for a railway?
20. What particular circumstances ought to be noticed, in making a survey for a canal?
21. How would you lay out a turnpike road, preparatory to commencing the work?
22. What dimensions would you allow for the carriage-way, the foot-path, side drains, and fences?
23. How would you form the roadway, before the materials were put on it?
24. What description of materials would you prefer for a turnpike road?
25. How would you distribute the materials, and what thickness of earth would you put on?
26. What precautions would you take to secure a good drainage?
27. What curve would you give to the surface of the carriage way?
28. How would you proceed to form a road through a bog?
29. What declivity would you consider desirable for a turn-pike road?
30. How would you determine the proper size of the culverts and bridges on a line of road?
31. What dimensions would you consider necessary for the cross-drains in a wet soil?
32. If you had to build a culvert of six feet span, having abutments five feet high, what rise would you give the arch? What thickness would you give the abutments and the arch, if the material to be employed were brick? And what would be the cost, if the bricks were 20s. per thousand, lime 1s. per barrel of thirty gallons, sand 2s. per cubic yard, bricklayers' wages 16s. per week, and labourers' 9s.?
33. If you had to build a bridge of rubble masonry of thirty feet span, the abutments of which are to be eight feet high, what thickness would you give to the abutments and to the arch, supposing it to be a circular segment rising one-third of the span?
34. If an embankment should be required on a line of road, what width would you give it at top, and what slopes according as the soil happened to be clay, loam, or sand? How would you fence it, and what precautions would you take in forming the embankment?
35. What slopes would you consider necessary in a clay cutting, and what in a bog?
36. How would you found a bridge or culvert in a bog?
37. What price, per cubic yard, should be allowed for cutting a road through lime-stone rock, and through green stone?
38. What precautions would you take to keep a road in repair, for a year after it was formed?
39. If a plan of an arch, with its piers and abutments, were given, how would you proceed to determine if it were in equilibrium or not?
40. How would you calculate the lateral thrust against the abutments?
41. What form of section do you consider best for a cast-iron girder of a bridge?
42. At what distance would you place cast-iron girders of a bridge from each other; and how would you fill the space between the girders?
43. How would you secure the cast-iron girders to the abutment?
44. If you had to construct a timber platform or road-way, meeting on stone piers, the space being thirty feet, what dimensions would you consider necessary for the main-beams, and how near to each other would you place them, the greatest weight to cross over the bridge being supposed to be ten tons? How thick would you make the sheeting?
45. What proportion of sand would you put to lime for rubble-work, in the abutments and piers of bridges, and what for the arch and inside work?
46. In what parts of the bridge would you introduce cement, and in what proportions would you mix sand with cement?
47. In making use of sand-stone and free-stone, what precautions would you take?
48. What are the different descriptions of brick in use in this country?
49. What bond would you employ in bridge-work, and in a retaining wall?
50. In what situations are timber bridges preferable to those of stone?
51. If you wished to put sheets under a beam of a bridge of fifty feet span, what length would you give to the sheets? at what angle from the face of the abutment would you place them? and how would you secure them to the abutments?
52. What description of timber would you prefer for a bridge, and what for piles and platforms?
53. In what situations are suspension bridges preferable to cast-iron bridges and stone bridges?
54. If you had to build a retaining wall of brick, twenty feet high, to support a bank of sand, how thick would you make it at the bottom and at the top, and what form would you give to it? If the wall were to be of rubble-masonry, what dimensions would you give it? and if you introduced counter-ports, what dimensions would you give them?
55. What form do you consider best for a tunnel through clay soil?
56. What thickness would you give to the side walls and arch of a brick-tunnel in clay, the width being thirty feet?
57. How would you proceed to lay out a line of railway, preparatory to commencing the work?
58. How would you lay down the curves on the ground?
59. How would you lay out the lines of the top of the slopes in cuttings, and the bottoms of the slopes in embankments?
60. What thickness of ballasting would you consider necessary?
61. How would you determine the velocity of a river – the inclination of the surface and form of the channel being given?
62. How would you calculate the time of filling a lock from the upper level?
63. What angle do you consider the best for lock-gates?
64. How would you calculate the pressure against a lock-gate?
65. What slope would you give to the embankment of a dam or reservoir?
66. How would you guard against the water of the basin overflowing the banks?
67. How would you protect the slopes of a reservoir?
68. What form of wall would you adopt for a sea-wall?
69. What form of wall would you adopt for a dock-wall?
70. What thickness would you give to a dock-wall thirty feet high, built in a soft clay or mud?
71. How would you secure a dock-wall, if built on a sandy foundation?

QUESTIONS FOR CALCULATION IN PRACTICAL ENGINEERING.

1. Given the angle taken by a sextant, in a boat at sea, between two points on shore, slightly elevated, = $60^{\circ} 40'$, also the angles of depression of the boat taken by theodolites from the points on shore = $\begin{Bmatrix} 1^{\circ} 10' \\ 0^{\circ} 50' \end{Bmatrix}$, required, the horizontal angle at the boat between the two points.
2. Having, by means of a theodolite, observed, on the 7th October, 1843, at 9 hours A. M., in latitude and longitude nearly of Dublin College Observatory, the elevation of the Sun's centre to be $20^{\circ} 7'$, the magnetic bearing of Sun's centre $159^{\circ} 24'$, also the magnetic bearing of a distant steeple $45^{\circ} 6'$. Required the bearings with true meridian of the Sun's centre, and of the distant steeple? also the variation of the compass?

3. Given $AC = 30$ miles, $\angle A = 60^\circ 4' 10''$, $\angle B = 49^\circ 46' 17''$, $\angle C = 70^\circ 9' 42''$; required the error of observation of angles, if any? Required also the length of sides AB and BC, calculated on geodetic principles?
4. Having observed with barometer,
 Height of mercury, top of hill, { Attached thermometer, 60° .
 = 28.924 inches { Detached thermometer, 54° .
 Height of mercury, top of hill, { Attached thermometer, 68° .
 = 30.630 inches { Detached thermometer, 60° .
 Required the height of the hill?
5. A segmental arch of 135° , having a span of 40 feet, thickness of masonry above the key stone 5 feet, depth of voussoirs 2 feet, the extrados a horizontal line, and height of abutments, 30 feet; required the thickness of abutment?
6. An embankment of earth of 24 feet height, having a natural slope of 45° , is to be supported by a retaining wall of masonry, having an inner batter of two feet: the specific gravity of masonry being to that of earth as 4:3, required the thickness of the wall?
7. The dimensions of a cutting are, base, 30 feet; slopes of sides, 2; base to 1, perpendicular; height of cutting at one end, 50 feet, at the other end 10 feet; the length of cutting 500 feet; required, the cubic yards of cutting, and verify the calculation by Mac Neil's table?
8. A cast iron beam, resting on two props 20 feet distant, has to sustain 15 tons without injury to its elasticity, the breadth of the beam is to be one-fourth of the depth; required the depth of the beam?
9. A beam of Riga fir 6 inches deep by 4 inches broad, projects 10 feet from a wall, and supports a weight at its extremity; required the greatest weight it can bear without breaking? also the ultimate angle of deflection?
10. The radius of curvature of the curved part of a rail-road being 5000 feet, the velocity of carriages being 30 miles per hour, and distance between rails being 5 feet; required the height of outer rail to obviate centrifugal force?
11. Having to lay down points for a curved portion of a rail-road, the radius of curvature being 6000 feet, and chord of curved part being 1200; required the ordinates for chords, subtending at the centre of the circle, angles of 2° and 4° ? Also, in employing Mr. Bourne's method, required the distance between the extremity of a chord 100 feet long, and the extremity of the adjacent chord produced to a distance of 100 feet?

Developing a deeper understanding of structural dynamics

Roger P. West, Biswajit Basu, Brian M. Broderick and Gerard McGranaghan
Department of Civil, Structural and Environmental Engineering,
Trinity College, University of Dublin, Dublin 2

email: rwest@tcd.ie, basub@tcd.ie, bbrodrck@tcd.ie, gmcgrana@tcd.ie

Abstract As a mathematically intensive subject, the teaching of structural dynamics to structural engineers can mean that mathematical manipulation dominates effort rather than developing an understanding of fundamental behaviour, especially as vibrational responses are not always intuitive. This paper will describe some techniques which have been used to encourage undergraduate and postgraduate students to develop a better appreciation of how the mathematics of the various problems reflects our observations of the real world. By de-emphasising the mathematical processes, which are treated as rehearsed pre-requisites, the focus during lectures lies in using physical models to observe behaviour, sometimes perforated by experiments conducted in a laboratory setting and demonstrably supported by the mathematical solutions. Furthermore, by allowing students to bring a list of self-assembled but pre-approved key equations into examinations, the nature of assessment becomes one of problem-solving using real data, backed up by a developed expectation of structural response. The process of assembling the list of the relevant equations, their form, units, typical values and expected outputs, means that students have to make a conscious effort to know when and how to use the equations correctly in the solution of a myriad of dynamic problems. To the engaged student this has resulted in a deeper understanding of this subject which has heretofore been an anathema to some.

Keywords: Deep learning; Dynamic models; Structural dynamics

1 BACKGROUND

The development of a deep understanding of structural dynamics by more senior undergraduate or postgraduate engineering students presents special challenges not encountered in many other modules. While other structural engineering subjects, such as those addressing the analysis of plates and shells or the finite element method, can be equally challenging mathematically, the lack of an instinct or intuition developed from real life experiences of the response of different structural and mechanical systems to time-varying loads presents an extra layer of difficulty in the application of analytical techniques to the solution of problems in structural dynamics. The resulting perception of structural dynamics as an abstract topic can be a key determinant in the impression that the subject should only be studied by students with advanced skills in engineering analysis and mathematics. In other cases, the apparent familiarity with the mathematical approach, so favoured by engineers, is an irresistible attraction when selecting module electives.

The more altruistic view, that of being aware that an understanding of structural dynamics is an essential skill in the engineering designer's toolbox, is seldom a driver in the choice of module. The subject is certainly unlikely to be identified as lying on the path of least resistance, even for those who are mathematically adept. When electives can be changed by students in the first few weeks of a module, often the decay in participant numbers in dynamics modules is rapid but asymptotic as fears concerning difficulty and complexity are realised as early lectures proceed. The risk is that some students may not immediately follow the complex concepts and notations and consequently zone out of the lecture. Smith et al. [1] point out that to deliver maximum benefit to the students especially during conceptually complex and content

dense materials (such as in this subject) lecturers should not allow students to become passive during the learning process. This paper describes the authors' collective experience of how the delivery and assessment of this conventionally difficult topic within a broader curriculum can be improved by concentrating on understanding the physical phenomena that influence dynamic response whilst deploying analytical approaches employing a variety of mathematical techniques with which students are or should be familiar.

2 SYLLABUS

The standard choice of topics for an introductory Masters course in structural dynamics comprises a surface-skimming array of simplified problems defined by familiar mathematical solutions. Formulaic adherence to techniques for identifying natural frequencies and dynamic responses of single (SDOF), multiple (MDOF) or infinite degree of freedom systems subjected to idealised harmonic, periodic, transient or impact time-varying loadings does little to excite students or motivate deep learning. However, an examination of resonance, response spectra and the consequences of damping in practice do bring some reality to the standard mathematical solutions. On the other hand, the introduction of ever more complex and analytically unwieldy methods, such as the use of Duhamel's integral to deal with general loading based on the superimposition of varying short-duration impacts or complex eigenmodes for non-classically damped systems, serves to compound the conceptual quagmire, especially for the unengaged or those with a different learning style. The specification of learning outcomes that emphasise the variety of application areas to which structural dynamics can be applied is useful in developing student's initial understanding of the essence of the subject. Avitabile [2] presents a similar

view, emphasising the need to solidify the learning of theory through practical examples.

3 PRE-REQUISITES

In order to concentrate on a deeper understanding of the physical phenomena being described, there should not be undue focus on the achievement of manipulating the multitude of mathematical equations and derivations that can arise in a formal treatment of the subject. The study of the structural dynamics does, nonetheless, require as a prerequisite competence in certain mathematical techniques, but if these are well-defined at the start of the course, and if supports are provided to enable students to refresh their skills to the level required, such prerequisites need not be a barrier to participation or success in the module. A suggested list of pre-requisites is given in Table 1, in which a mixture of numerical techniques or exact analytical solutions to second or fourth order differential equations (DE) are blended with algebraic know-how. An introduction to matrix inversion and the properties of eigenvalue problems should not be delivered within the syllabus of the structural dynamics module – these should have been signalled as necessary tools for structural engineering in prior studies within an undergraduate course.

Table 1: List of some mathematical and analytical pre-requisites

Topic	Application
De Moivre's theorem	To convert a complex exponentials into trigonometric functions
Roots of cubic equation	Solution of characteristic equations
Second order DE	Solve for natural frequencies of SDOF system
Fourth order DE	Solve for natural frequencies of infinite DOF system
Determinants	To invert a matrix of eigenfrequencies
Cramer's Rule	Invert matrix for eigenfrequencies
Simple harmonic motion	For natural frequency determination
Fourier series	To combine harmonics into a periodic response
Orthogonality of eigenvectors	To develop generalised co-ordinates to solve MDOF problems
Index laws	To separate the attenuating factor from the cyclic response
Matrix algebra	To prove orthogonality of mode shapes

4 TEACHING DELIVERY

Within any class, students can be sub classified into groups based on the ways in which they receive and process information [3] and accordingly various teaching style methods are recommended in order to address these learning styles. Inevitably, here, there will be a significant amount of

mathematical manipulation of the equations of dynamic equilibrium and their solutions. However, by providing suitable hand-outs and explanations of the theoretical developments, lecture time focus can be on the physical behaviours these describe, using in-class models, sketching the typical responses to imposed loads beforehand, then showing how the actual mathematical solutions produce equations which comply with one's intuition, if indeed it does, or why it does not.

For example, understanding the physical meaning of the circular natural frequency, with units of radians/second, can be achieved through plotting the vertical ordinate for a rotating mass on the end of a rod. By converting this concept of simple harmonic motion into that of a pendulum helps the student visualise the mathematics describe the motion of a common object. That can then be translated into that of a cantilever tip response after it has been given an initial displacement and released in free vibration. The mathematical analogue of the mechanical with the structural enables a visual examination of the key parameters involved, such as acceleration, velocity and displacement, through to natural frequencies, natural periods and damping.

In turn then, the mathematics, with the established pre-requisites ensuring comfortable treatment to the relevant equations, can yield, for example, something of the following form:

$$u(t) = e^{-\xi\omega_D t} (A \sin \omega_D t + B \cos \omega_D t) - \frac{1}{m\omega} \int_0^t P(\tau) e^{-\xi\omega(t-\tau)} \sin \omega_D \tau d\tau \quad (1)$$

in which the negative exponential component is clearly decremental (the attenuating factor, strongly dependent on the damping ratio, ξ). The trigonometric terms deliver the cyclic nature of the response and the Duhamel's integral (the latter part of Equation (1)) can provide the steady state solutions which can accommodate the diversity of loading, including stochastic loading if needed (using a numerical solution of the integral). An estimate of the nature of the response with time, (through sketching displacement-time plots) should be attempted, together with a comparison of the peak dynamic response with the static response, which allows the significance of the dynamic response of the structure to be realised. The idea that dynamic responses can be many multiples of the static response, often a surprise to students, confirms the need for this analysis, and offers a motivation for student's participation.

Furthermore, in a classroom setting, the live execution of computational examples by hand is invaluable to developing an understanding by the students of the solution and the process through which it is obtained.

5 USE OF TUTORIALS

Tutorial or self-learning questions in structural dynamics tend to be harder for lecturers to set, as different values of parameters have to be experimented with to produce a realistic solution. The students also need to expend considerable effort to solve these weekly problems to keep up with the lectures and this should be reflected in the proportion of the final marks given to the continuous assessments. As in the domain of statistics, it is essential that the learning of dynamical techniques and calculations is experiential. However, although

over the years lecturers inevitably develop a bank of tutorial questions that can be asked on each of the topics covered in the syllabus (otherwise, for reoccurring questions, previous solutions inevitably tend to circulate in the student community and subsequent high tutorial marks are not reflected in exam performances), a more recent successful approach has been to assign the students' registration numbers to the problem parameters and thus all solutions are effectively randomly different, though the principles are the same. For example, in establishing the response of a single degree of freedom system to a harmonic load, $P(t) = P_0 \sin \Omega t$, for a student with student registration number 14356802, the mass is assigned to be 14 tonnes, the stiffness 35kN/mm, the forcing function P_0 , 68kN and a forcing circular frequency, Ω , of 2 radians/second. Although this does make marking/correcting the exercise more time-consuming, the peak displacements can be plotted on a response spectrum and those students who do not get the right answer are easily identified as they lie off the predicted response curve (see Figure 1). The tutorial effectively becomes a parametric analysis on the response which engenders additional interest and discussion in the lectures. By informing the students of this in advance, more care is taken over obtaining the correct solutions. This approach is not always appropriate but it does appear to alter the tutorial and lecture dynamic for the better. The owners of errant solutions are not identified publicly.

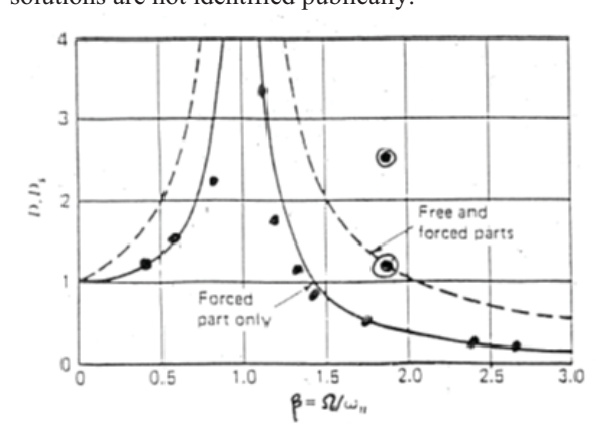


Figure 1: Student's tutorial solutions plotted on a response spectrum

6 USE OF MODELS

It is well known that many students gain and retain a great deal more from visual observation than from verbal information [4], especially from short demonstrations during lectures [5]. Generally, using small scale models in the lecture theatre to demonstrate dynamic behaviour and yield visual observations on the effect of parameter changes means that students can appreciate how the mathematics delivers on the expectations derived from observation. For example, a mass oscillating on the end of spring or a swinging pendulum of varying length, for which natural periods and frequencies of oscillations are coupled with patterns of acceleration, velocity and displacement, are directly analogous to an oscillating beam in free vibration, with all responses being governed by similar equations for simple harmonic motion. This approach is readily extended to system identification with instrumentation output, for example, from an accelerometer

on the tip of a cantilever beam, allowing model parameters to be calculated (Figure 2a). Similarly, the different responses of wooden, plastic and steel rulers to impact loading reveal the consequences of different damping characteristics. A more complex response with several modes being excited, occurs when a beam is subjected to a hammer impact (Figure 2b). Visually, a model of oscillating welding rods of differing lengths excited using a harmonic ground motion shows clearly and unforgettably the consequence of a resonant response (Figure 3). The timely use of these types of models in the lecture theatre provides evidence of how the mathematics supports the observations and not vice versa.

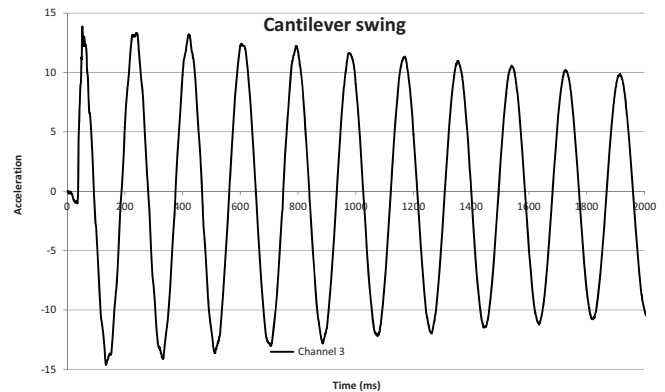


Figure 2a: Simple damped response of a beam in free vibration due to an initial displacement

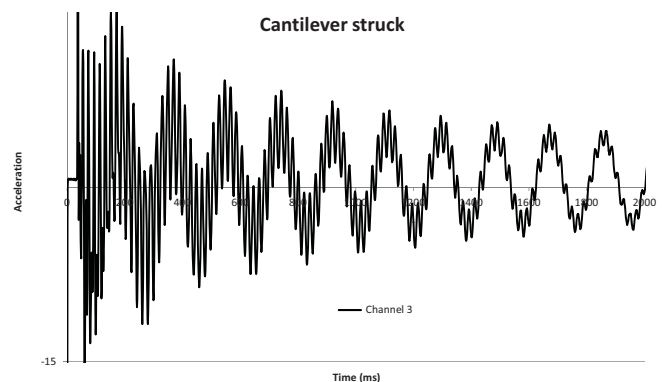


Figure 2b: Complex free response of a beam due to an impact load

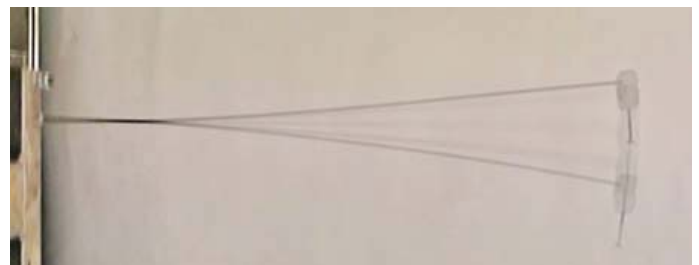


Figure 3: Photograph of a welding rod under harmonic ground motion resonating at its first mode of vibration

Hands-on laboratory experiments are an essential aid to student appreciation of the vibrational response of

mechanical and structural systems. For example, a two-storey frame can be analysed to calculate the expected natural frequencies, observed through varying harmonic input ground motion until resonance is observed to occur (Figure 4a). Explanations are sought for discrepancies between the theoretical and observed frequencies, by which process assumptions are tested for validity. For example, in Figure 4a, as predicted, the first mode of vibration of a shear frame is observed, where the use of a strobe with a light flashing at an integer multiple of the natural frequency can “freeze” the mode shape, as shown. Additionally, by using an eccentric mass on one of the floors, it may also be observed that the important first torsional mode (Figure 4b) lies between the first and second flexural modes, which will not be predicted using an analytical model that employs degrees of freedom chosen to represent only the transverse vibration response. This highlights to the student, indelibly, the risks inherent in assumptions in models, analytical or numerical. Clearly the mathematics still have a strong role to play in demonstrating this, but the extensive use of models to convey a deeper understanding of the sometimes unexpected and counter-intuitive nature of dynamic responses is later revealed by the mathematics in the lecture. Avitabile [2] describes this approach as providing students with the opportunity to see ‘theory in action’, emphasising the benefits offered by careful integration of analytical topics and experimental issues.

Analytical solutions to the vibration response of structures are often not feasible when the response becomes nonlinear, in which case numerical solution approaches are necessary. Depending on the nature of the nonlinearities influencing the response, it may not be practical to observe these using model experiments. In this case, the use of numerical simulations offers the opportunity for students to explore parametrically nonlinear response behaviour. The MATLAB software platform has been used as versatile platform to expose students to various aspects of numerical analysis. Other suitable software includes the software ANSYS for finite element analysis and the NONLIN and EQ-Tools applications developed by the US Federal Emergency Management Agency to support education in earthquake engineering [6].



Figure 4: (a) First flexural mode and (b) first torsional mode of a two-storey shear frame

7 EXAMINATION

Traditionally, due to the inherently intensive mathematical solutions required, the students are, on entering the examination hall, either in trepidation of memory loss of the principal equations and lengthy proofs, or the instructor setting the exam paper has had to reproduce for the student in the question the equations necessary to attempt the examination paper, which, of course, trivialises the answer. An alternative approach is to permit the students to bring in a single A4 sheet on which they have written the relevant key equations by hand, individually and this has been a successful latitude in recent years. No additional text, explanations, proofs, diagrams or worked examples are allowed on these sheets, only the equations themselves (see Figure 5). The sheets are pre-approved by the lecturer, and submitted with the student's answer script at the end of the exam. While this is somewhat different to the normal open book exam, it has several distinct advantages: the student is motivated to revise all aspects of the module and to not only decide on which are the key equations to include, but also when each applies, what the symbols represent, the units to be used and, most importantly, what outputs are obtained on application of the equation. There is real benefit in the student having to make decisions during revision about what they should include in the limited space available. Furthermore, the use of a “crib” sheet allows the lecturer to set more demanding and realistic exam questions and, on attempting a question, the students have to decide which equations to select before applying them. This raises the bar substantially on the quality of the exam paper and depth of the student's understanding of the dynamic problems presented. And, of course, it represents what happens in reality in a design office when hand calculations are needed.

$$\begin{aligned} \xi &= \frac{c}{2m\omega_n} \quad \omega_d = \omega_n \sqrt{1 - \xi^2} \\ U(t) &= e^{-\xi\omega_n t} \left[u_0 \cos \omega_d t + \left(\frac{\dot{u}_0 + \xi\omega_n u_0}{\omega_d} \right) \sin \omega_d t \right] \\ U(t) &= U_0 e^{-\xi\omega_n t} \cos(\omega_d t - \alpha) \\ U^2 &= u_0^2 + \left(\frac{\dot{u}_0 + \xi\omega_n u_0}{\omega_d} \right)^2 \quad \omega_0 = 2\pi f_0 \\ \alpha &= \tan^{-1} \left(\frac{\dot{u}_0 + \xi\omega_n u_0}{\omega_d u_0} \right) \quad T_0 = \frac{2\pi}{\omega_0} = \frac{1}{f_0} \\ C &= 2\xi\sqrt{Km} \quad \xi = \frac{1}{2\pi} \ln \left(\frac{u_0}{u_d} \right) \\ T &= \frac{2\pi}{\omega_n} \quad B = \frac{\beta}{\omega} \\ U(t) &= e^{-\xi\omega_n t} \left[A_1 \sin \omega_d t + A_2 \cos \omega_d t \right] + \frac{P_0}{K} \cdot \frac{1}{(1-B^2)^2 + (2\xi B)^2} \sqrt{(1-B^2)^2} \\ U(t) &= U_0 \cos(\omega_d t - \alpha) \quad \alpha = \tan^{-1} \left(\frac{2\xi B}{1-B^2} \right) \quad U = U_{max} = \frac{P_0}{K} \cdot \sqrt{1-B^2} \end{aligned}$$

Figure 5: Scan of individually “crib” sheet allowed in exams

8 CONCLUSIONS

A familiarity with vibrations and dynamics enables structural engineers to conceive creative solutions to a wider range of structural forms and systems. This paper has illustrated several unorthodox approaches to the teaching of structural

dynamics that can liberate students and engineers from the comfort (or trauma) of the formulaic mathematical solutions to problems into the realms of developing an intuition for what to expect in dynamic problems, including the unexpected. Through the use of models in lectures and laboratories, mathematical methods become enslaved by observations and their underlying assumptions are challenged. Assessment through either unique individualised tutorials, as described, or examinations in which recall of multiple complex equations plays no part, frees the student up to demonstrate an understanding of expected behaviour and make subsequent critical observations, accepting always that rigour in mathematical and calculation techniques are vital parts of solving all dynamic problems.

9 REFERENCES

1. Smith, KA, Sheppard, SD, Johnson, DW and Johnson, RT (2005), Pedagogies of engagement: Classroom-based practices, *Journal of Engineering Education*, 94(1), 87–101.
2. Avitabile, P, (2007), Teaching structural structural dynamic modelling techniques in the UMASS Lowell modal analysis program, *Proc Modal Analysis Conference IMAC-XXV*, Society for Experimental Mechanics, Orlando FL.
3. Felder, RM and Silverman, LK, (1998), Learning and teaching styles in engineering education, *Journal of Engineering Education*, 78(7), 674–681.
4. Felder, RM, (1993), Reaching the second tier: Learning and teaching styles in college science education, *Journal of College Science Teaching*, 23 (5), 286–290.
5. Edward, NS, (2002), The Role of Laboratory Work in Engineering Education: Student and Staff Perceptions, *International Journal of Electrical Engineering Education*, 39, 11-19.
6. FEMA (2013), *NEHRP Recommended Seismic Provisions: Training and Instructional Materials*, FEMA, pp 752.

The Pedagogy of Building Information Modelling

Robert Eadie¹, Brian Solan¹, Bryan Magee¹, Mark Rice²

¹School of the Built Environment, Ulster University, Jordanstown Campus, Newtownabbey, Northern Ireland

²Graham Construction, Dover, England.

email: r.eadie@ulster.ac.uk

ABSTRACT: Building Information Modelling (BIM) has been made mandatory for all UK Government contracts over the European threshold. This has led to its hurried adoption within Higher Education Institutions with many adopting similar pedagogies to those used for teaching CAD. This paper seeks the views of the BIM Academic Forum, set up to establish a common BIM curriculum in the UK and Ireland on the pedagogies that should be adopted in BIM teaching. It finds that as BIM is more than just a technology, and as such a different pedagogical approach to that used in CAD teaching should be taken. This approach while in the main constructivist, learning by doing, should also have components taught using didactic methods. The findings further indicate that educators need support from accreditation panels and industry in adopting this new technology which will continue to evolve over the next number of years.

KEY WORDS: Pedagogy; Civil Engineering; BIM; CAD.

1 BACKGROUND

Pedagogy is defined as an identified activity carried out by a person (normally a lecturer) planning to supplement learning development in another individual [1]. Bernstein (2000) goes further, defining pedagogy as a sustained process where an individual or group acquire new or develop existing forms of knowledge from somebody or something deemed to be an appropriate provider/evaluator [2].

In order to deliver necessary skills required by industry, Universities have been investing in software to deliver Computer Aided Design (CAD) and Building Information Modelling (BIM). Pedagogical practices need to be considered to include these new challenges and requirements from industry with regards to shifting stipulations of competency required from fresh graduates leaving tertiary education [3]. It cannot, however, be just the provision of hardware and software but must include the pedagogical base behind how the material is delivered. Active learning is where both the educator and learners cooperate to formulate and achieve a combined experience whereby the learner has an active role [4].

Emphasis is placed on a student centred learning environment which aids students in controlling their own learning. The active learning experience increases enthusiasm and motivation towards learning [5]. What has not been fully researched is application of different pedagogies to BIM teaching.

2 PEDAGOGICAL STRATEGIES

2.1 Pedagogical Strategies Spectrum

There are three relevant positions on the learning process; behavioural, cognitive, and constructivist [6]. These emanate from the two schools of Greek philosophy; Plato's work producing rationalism and Aristotle's work producing empiricism. Aristotle considered learning through how people

think or behave through imitation of particulars. Constructivism developed from this through the work of Paigent [7].

2.2 Constructivism

Hein (1991) indicated that constructivism considers: *that there is no knowledge independent of the meaning attributed to experience (constructed) by the learner, or community of learners* [8]. Plato is the opposite end of the didactic spectrum where a theoretical framework is constructed [9]. Constructivism therefore does not focus on an ontological reality but on a constructed reality. Cognitive theory, dealing with the learner, is the basis for the constructivist line of thought; the nature of the learner. Constructivism has been the approach suggested for software use by a number of organisations as participation is one of the best pedagogical approaches to teaching engineering courses [10, 11, 12]. From a technology standpoint, it has been suggested by many that technology can support the use of constructivist approaches to teaching and learning [13, 14]. Constructivism has led to the term 'problem-based learning' [15], which is ideal for the teaching of BIM. However, educators in traditional educational environments are not always positive regarding teaching aided by technology [16].

2.3 Behaviourism

A behaviourist approach to education differs, as behaviourists describe learning as a process of connecting stimuli and responses [17]. Conveyance of instructions, constant repetition of outcomes and previous experiences are deemed to be the most important objectives within teaching [18]. It is suggested that these activities produce modifications in a student's behaviour through these peripheral stimuli [17]. The learner is therefore reactive to conditions in the environment rather than discovering the environment for themselves [6]. So a behaviourist only looks at the final result

of learning and not the actual learning experience. Therefore, behaviourism has influenced traditional approaches to learning such as didactic education.

Critics suggest that an inactive learning environment for the student provides little motivation to learn and thus the learning is not as deeply embedded. However, according to Schaffer and Small (2004) [19], the integration of computers with small and large group didactic instruction allows optimal use of resources in addition to conforming to accepted theories of adult learning. This approach is well-accepted by students [19]. Traditionally education has focused on behaviourist pedagogies [20].

The fact that different parts of the same program should have more didactic content than others [21] raises the issue that the pedagogical approach to BIM needs to be examined. This paper will examine whether the more instructive behavioural approach is necessary to sit alongside the constructivist theory in relation to BIM-related teaching.

3 CAD AND BIM TEACHING

3.1 Differences between CAD and BIM

CAD has become an industry standard tool for the production of construction drawings across the architecture, engineering and construction (AEC) sectors. CAD was developed and became an industry standard around 30 years ago [22]. However, the capabilities and capacities of computers have moved on. Software packages have become more sophisticated. Drawing packages have the capability of effortlessly producing 3D models. This led to the development of BIM which allows users to include intelligent information about each entity within the 3D model. Van Nederveen et al. (2009) [23] acknowledges that BIM contains this information in the 3D model, stating BIM is about: *the building itself as well as its components and comprises information about properties such as function, shape, material and processes for the building life cycle*. Instead of models being created from line drawing through CAD, projects are constructed from virtual elements such as walls, foundations, windows, doors and roofs. The creation of models from elements is known as object-based modelling whereas CAD produced line-based models are known as entity-based models [24].

3.2 Teaching Pedagogy for CAD and BIM

The move from CAD to BIM is a paradigm shift creating many opportunities and challenges [25]. Macdonald (2011) [26] argues that there is little pedagogical difference in approach between manual draughting and 2D CAD. However, she argues that, due to its collaborative nature, BIM sits apart. As a result some suggest that BIM should be taught in cooperation with a studio or via small design challenges. They argue that similar to CAD, students are not attending to: *learn how to draw lines, arcs, circles, etc., but to comprehend the procedural nature of the building design process* [27]. Therefore, an amount of didactic teaching on the process is required prior to the problem-based learning approach to model building. Ibrahim (2007) [28] argues that: *training required for BIM based CAD should focus on the change in the work flow rather than the application interface and functionalities*. Therefore, it is very different than teaching CAD and less didactic in nature. As there is a disagreement on

the means of approach and the comparisons between CAD and BIM, this paper seeks to fill that knowledge gap by gathering quantitative and qualitative data from BIM academics regarding the preferred methods to be adopted.

4 METHOD

4.1 Survey sample

In 2011, the BIM Academic Forum (BAF) was founded to provide guidance and consistency in BIM adoption across Higher Education Institutions (HEIs). They were tasked with the provision of a framework to indicate the different aspects of BIM to be taught at each level [29]. The BAF incorporates academic representatives from across UK and Ireland. Currently it contains over 30 members from 60 different institutions [29]. After the telephone sift, 38 unique institutions were identified. A representative from each was then asked to participate and 24 agreed to do so. Responses from a structured on-line questionnaire were collated from BAF members willing to respond, as it was deemed these academics held the expert knowledge relating to BIM teaching. Their responses were both qualitative and quantitative in nature.

4.2 Survey software

Limesurvey™ software was used to supply the piloted structured on-line questionnaire and also the final version. Limesurvey™ generates unique tokens specific to each individual participant. These tokens ensure through the survey management tool that responses can only be submitted from the designated sample. Responses are stored on the software on-line database for analysis purposes. The quantitative responses were analysed automatically through the Limesurvey™ software. However, qualitative responses were exported from this software and analysed in NVIVO™, which provided a certain degree of quantitative analysis of the qualitative responses.

4.3 Survey response and validity

From the initial population size, 24 BAF members agreed to participate in the survey. Fifteen responses were submitted where the survey was completed in their entirety. Partially completed responses were ignored. On the basis of questionnaires that were completed in their entirety a 62.5% response rate was attained. The sample size was calculated using the Krejcie and Morgan (1970) [30] method which indicates that for such a small sample, all HEIs are required for validity. A minimum response rate of 50% is required for analysis purposes [31]. With 15 responses received (i.e. greater than the 12 required), subsequent analysis met this criterion.

4.4 Expertise of the participants in BIM

BIM expertise is measured by the UK Government via the Bew and Richards Triangle [31] on four levels, labelled 0-3. Level 0 is basically 2D CAD and level 3 is the single fully integrated model. The UK Government requires level 2 on all its contracts by 1st April 2016 [32]. The skill level of the academics teaching BIM and sitting on the academic forum should therefore be at or above this level.

Table 1. Academic Skill Level on Bew and Richards Triangle

On the Bew and Richards scale what level of BIM have you had experience working to?		
Answer	Count	Percentage
Level 0	0	0%
Level 1	1	7%
Level 2	9	60%
Level 3	5	33%
No answer	0	0%

It can be seen from Table 1 that the expected level of expertise existed in those who sat on the BAF. Sixty percent (60%) were already operating to the UK Government's required level, with an additional third operating above this level. Only a single response was obtained that did not meet this level equating to 7% of the sample. This indicates that the expertise of those responding to the questionnaire was to the correct level.

The results further provide evidence that HEIs are implementing BIM to a minimum of level 2 throughout their institutions. This is the level required in the UK Government Construction Strategy Report [32].

5 FINDINGS

5.1 Pedagogical Approach to teaching BIM

From the literature review at the commencement of this paper it was suggested that constructivism paradigm was the approach best suited to the teaching of BIM and CAD on engineering courses [10,11,12]. The results of the questionnaire confirm this. Indeed, Table 2 below indicates that all of the academics agreed that the constructivist approach should be adopted for BIM teaching.

Table 2. Constructivism and teaching BIM

Do you consider that the constructivist approach to BIM teaching is the correct way to approach BIM teaching?		
Answer	Count	Percentage
Yes	15	100%
No	0	0%
No answer	0	0%

This unanimous result was followed by a qualitative question probing the reason for the response shown in Table 2 and allowing comment on other approaches to BIM teaching. Eight of the fifteen responses (53.4%) suggested that while the constructivist approach was chosen, it could not be used in isolation. It was suggested that *a mix of methods, balanced or hybrid approach* was required. They further suggested that a *learning by doing approach* should be *filtered for the correct approaches* to ensure that a *change mentality* was adopted. They suggested the didactic element should include:

1. *Guidance on best practice;*
2. *Guidance on online etc. resources that can be accessed by individuals;*

3. *Guidance as elements can be omitted. Also the collaborative approach can be missed out, so exposure to current thinking is necessary;*
4. *Foundational aspect to learning mechanics of the application; once this is overcome constructivism principals will apply.*

However, the qualitative reasoning for the result in support of the constructivist approach centred on the fact that students need to learn BIM by *doing*. It was suggested that students need to have: *the same challenge as the construction industry faces now*. A similar approach can be taken in adopting problem-based learning where academics: *define outputs and let students explore best ways of achieving same*. Furthermore, independent learning by doing was suggested in the following response:

Students need to understand what the problem is and determine the appropriate process and tool. I believe if students appreciate that they need to improve communication between disciplines to ensure appropriate information is generated at the right time, then PAS 1192 et al. become part of their solution; they don't get it if we tell them!

Even more support was given to BIM being taught through project-based learning as *'chalk and talk' does not work in this context*. The collaborative nature of the BIM process was also provided as a reason for: *learning by doing*. *Students normally try to use their own established communication techniques e.g. physical data transfer. After a while they realise that BIM tools transfer the same data better*. The findings indicate, therefore, that while the constructivist pedagogical approach should be adopted, it should not be used exclusively and that the majority of academics consider a balanced approach of different pedagogies should be used.

5.2 Pedagogical approaches to CAD and BIM

While identification of specific content for BIM modules at Levels 4-7 is the primary objective of BAF, the worked discussed to this point shows that it is also extremely important to identify an optimal pedagogy. While there is limited research regarding optimal approaches to BIM-related pedagogy, there is a wealth of experience in CAD teaching. While the literature review concluded that the two systems are very different, results shown in Table 3 indicate that the majority of respondents (87%) consider that the conclusions of Ibrahim (2007) [28] were fully justified and a different approach should be taken to the teaching of BIM than that previously adopted for CAD.

Table 3. Pedagogical approach similarities - CAD and BIM

Do you consider that the same pedagogical principles that are used in the teaching of CAD should also be applied to the teaching of BIM?		
Answer	Count	Percentage
Yes	2	13%
No	13	87%
No answer	0	0%

A further qualitative-style question elicited the rationale behind this outcome. The breadth of material and the *wider scope* of BIM application were the main reason offered. It was stated that BIM is: *not just a technical solution, so it differs significantly from teaching CAD*. Furthermore: *the value network of BIM is far beyond that of CAD and this will reflect into the teaching and learning*. While two of the responses acknowledged some similarities between BIM and CAD teaching, nine of the fifteen responses (60%) identified the much wider aspect of BIM teaching with the following main differences provided:

1. *Procurement and 4 & 5D BIM are differing subject areas;*
2. *Collaboration/downstream use of information, standards and processes must be taught in conjunction with practical modelling skills;*
3. *Less reliance on 'software training' and more on the individual student learning the software and applying it through projects/cases;*
4. *BIM is more an integration of different design and planning skills. For example, it puts quantities into the middle of the design. Therefore, collaboration and communications are essential;*
5. *Drawing and graphical representation is fundamentally different to virtual modelling. The latter requires advanced knowledge of the discipline.*

Three of the responses concentrated on the need for *theory* in addition to *practice* in the teaching of BIM in order for it to be understood fully. There was also an acknowledgement that: *BIM can radically change the way students learn and think*. However, *there is not enough evidence or details about how this has changed*. Therefore, *our current way of delivery has just been incremental*. Radical change in HEIs takes time. We, as HEIs, are slow in responding. Therefore, there is a further need for those in HEIs to change the methods and practice of BIM teaching in a tertiary education context.

Providing a synthesis on respondents' views above, it can be seen that CAD teaching processes have limited application in regard to utilising them for teaching BIM. Didactic approaches need to be adopted for BIM so that in-depth theoretical knowledge is passed to students, in addition to the hands-on approach to teaching a software programme usually adopted when teaching CAD.

5.3 Qualitative comments on BIM teaching

Ten further qualitative responses were received regarding approaches that should be taken for BIM teaching and how the BAF can facilitate a best way forward for all HEIs.

The changing nature of the industry and also the requirements and capabilities of BIM have been highlighted by six of the ten responses. The fact that BAF is quite restrictive in its approach was highlighted but acknowledged as the best way forward existing at the minute. One response stated that: *BAF's approach is flawed as it is too limiting in what we can do. It is still best to allow for change to take place and the protocols are still in development and case studies are [sic] still needed to demonstrate best practices*.

Furthermore, the capacity changes of the software itself were identified in the comment: *what we do now may not be the right way to adopt and implement on site*.

The changing nature of the industry and the use of new platforms in the construction industry were also acknowledged in the comment: *we are in the situation of new platforms - mobile and tablet / cloud hosting - becoming more prevalent. This is changing how we build buildings*. However, the fact that not all in industry have adopted BIM-enabled approaches was also acknowledged: *BIM is a testing subject. We still need to promote its adoption*. Support from industry partners in the delivery of teaching was also supported and barriers caused by certain accreditation bodies: *HEIs need to thoroughly discuss the teaching of BIM and accreditation bodies need to be involved in this process. The fast evolving technology, policy and standards together with the lack of involvement by accreditation bodies and limited knowledge of lecturers are making this task really challenging. In the meantime, HE could adopt a practice-oriented approach and use industry lecturers to deliver some of the content*.

Further comments on the teaching provision suggested: *tutorials offered by Whitefrog as a very useful resource and a discrepancy in the approach to the content of modules with some suggesting a blended approach but also incorporated into individual modules whereas others suggested they were trying to embed BIM through the syllabus rather than having too many compartmented specific BIM taught modules, except in Architectural Technology which demands more hands on competency in 3D modelling*.

The collaboration and management aspects of BIM should not be restricted to a single platform bringing the interoperability of the software to the fore. *BIM should be considered as a main framework for managing construction projects effectively and should not be limited to training on software such as Revit and the delivery of a multi-platform data enables learners across the built environment to collaborate with cultural changes to adopt open BIM*. Student involvement across different disciplines and courses has been promoted as best practice.

Feedback was also touched on in relation to the design aspects of BIM with: *the visualisation of the design provides quick and enjoyable feedback and helps students to understand the construction technology involved*.

There still remains, however, some uncertainty around the approach taken with one respondent acknowledging: *whether we have the right approach is difficult to determine. Staff buy-in and coordination is necessary for the correct approach to teaching BIM to be adopted although it has been acknowledged that there are a few BIM champions in various areas*.

The general view of BAF members is, therefore, that practices in BIM teaching is still developing and it will take time to develop an optimum BIM teaching strategy from the specific content to be included at different levels. As such, the best way to teach BIM is still to be fully determined as BIM software capabilities are still developing.

6 CONCLUSIONS

This paper examined the pedagogical strategies involved in the teaching of CAD and BIM. It traced the two main pedagogical strategies used for their teaching: Constructivism and Behaviourism. From a BAF perspective it was concluded that the constructivist approach should be the one used in BIM teaching for the software elements. However, the group acknowledged that guidance through didactic teaching was also required.

Furthermore, this research showed that guidance on the best practice, location of online resources and foundational background to the application needs to be delivered in didactic style. Therefore, while the policy of the Joint Board of Moderators (JBM) [10] and others [11, 12] has been proved in the main to be correct, it needs to be widened to encompass the wider BIM remit. The respondents indicated that the 'problem based learning' approach of CDIO [12] is fully supported for the software elements of BIM. However, they also suggested that it should be supplemented with didactic instruction. This differs from the constructivist only approach in much of the documentation and should change the approach to BIM teaching in a HEI context. However, it was acknowledged that HEI's are slow to change and the practice of BIM teaching in a tertiary education context will have to adapt eventually.

The wider aspect of BIM in relation to CAD is also expressed in the findings, as a substantial majority do not consider the same pedagogical approach should be taken to teaching the two systems. BIM should have more didactic teaching elements than CAD due to it being more than a technical solution.

The elements covered by didactic teaching were proposed to be specific discipline knowledge, procurement, standards and processes such as PAS 1192 and quantity take-off. A mixture of styles should therefore be used to communicate BIM in order for it to be understood fully.

The fact that the BAF are trying to produce a method of BIM teaching that will meet the needs of all HEI's as far as content is concerned caused concern to some of the respondents. As BIM develops across platforms, cloud, tablet and mobile phone, the construction industry will change and in reality they are attempting to, as one respondent put it, *hit a moving target*. This will prove challenging for the pedagogical aspect of BIM as well. Teaching methods will also have to adapt to meet industry's needs.

In the interim some sections of the industry still need to be convinced as to the benefits of BIM and the findings show accreditation panels with little knowledge of BIM should incorporate members with BIM experience. This would give confidence to HEI's who are still unsure as to whether they have adopted the correct approach to BIM teaching and gain the staff buy-in for the adoption of a management system which will see increased use and evolve over the next number of years.

REFERENCES

- [1] P. Mortimore, (1999), *Understanding Pedagogy and its impact on learning*, Paul Chapman/Sage, London.
- [2] B. Bernstein, (2000), *Pedagogy, Symbolic Control, and Identity: Theory, Research, Critique*, Rowman & Littlefield, Oxford.
- [3] G. Attwell and J. Hughes (2010), *Pedagogic Approaches to Using Technology for Learning Literature Review*, Available on-line at <http://dera.ioc.ac.uk/2021/1/harnessing-technology-literature-review-january-111.pdf> [Accessed February 2016]
- [4] Leach, J. and Moon, B. (1999) 'Recreating pedagogy'. In Leach, J. and Moon, B. (eds) *Learners and Pedagogy*. London: Paul Chapman.
- [5] Department of Education and Skills (2006), *Learning Outside the Classroom MANIFESTO*, Available on-line at <http://www.lotc.org.uk/wp-content/uploads/2011/03/G1-LOtC-Manifesto.pdf> [Accessed February 2006].
- [6] P. Ertmer and T. Newby (2013) *Constructivism: Comparing Critical Features From an Instructional Design Perspective*, Performance Improvement Quarterly, Vol.26(2), 43-71, Available on-line at http://ocw.metu.edu.tr/pluginfile.php/3298/course/section/1174/peggy_2013_comparing_critical_features.pdf [Accessed February 2016]
- [7] M.Chapman (1988) *Constructive Evolution: Origins and Development of Piaget's Thought*, Cambridge University Press, Cambridge.
- [8] P. Boghossian (2006) Behaviourism, Constructivism and Socratic Pedagogy, Educational Philosophy and Theory, Vol. 38, No. 6, 2006
- [9] R. Stenberg (1999), *The Nature of Cognition*, MIT Press, USA.
- [10] JBM (2013), *Good Practice Guide – Digital Technologies in Degree Programmes*, Available on-line at http://www.jbm.org.uk/uploads/JBM115_GoodPracticeGuideDigitalTechnologiesV2.pdf [Accessed February 2016].
- [11] S. Collins, (2008). *Enhanced Student Learning Through Applied Constructivist Theory*. Transformative Dialogues: Teaching & Learning Journal, Vol. 2(2), Pg 1-9.
- [12] CDIO, (2015). *The CDIO INITIATIVE*. Available on-line at: <http://www.cdio.org/about> [Accessed February 2016].
- [13] A. Bork (1992). *Learning in the twenty-first century: Interactive multimedia technology*. In M. Giardina (Ed.), *Interactive multimedia learning environments: Human factors and technical considerations on design issues*. Heidelberg, Germany: Springer.
- [14] M. Linn, (1998). *Learning and instruction in science education: Taking advantage of technology*. In D. Tobin, & B.Frazer (Eds.), *International handbook of science education*. Dordrecht, The Netherlands: Kluwer.
- [15] J. Savery and T. Duffy, (1995). *Problem based learning: An instructional model and its constructivist framework*. Educational Technology, Vol. 35, pg. 31-38.
- [16] W. Kymmell, (2008). *Building Information Modeling : Planning and Managing Construction Projects with 4D CAD and Simulations*, United States : McGraw – Hill Construction Series
- [17] Committee on Developments in the Science of Learning (1999) *How People Learn Brain, Mind, Experience, and School*
- [18] Skillsyouneed(2016), *Learning Approaches*, Available on-line at <http://www.skillsyouneed.com/learn/learning-approaches.html> [Accessed February 2016].
- [19] K. Shaffer, and J. Small, (2004), *Blended learning in medical education: Use of an integrated approach with web-based small group modules and didactic instruction for teaching radiologic anatomy*, Academic Radiology, Vol.11,(9), September 2004, Pg 1059–1070.
- [20] M. Knowles, E. Holton III, and R Swanson (2014), *The Adult Learner: The Definitive Classic in Adult Education and Human Resource Development*, Routledge, Oxon.
- [21] P. Doolittle and W. Camp (1999), *Constructivism: The Career and Technical Education Perspective*, Journal of Career and Technical Education, Vol 16 (1), pg. 23-46
- [22] G. Aound, A. Lee, and A. Wu, (2005). *From 3D to nD Modelling*. Journal of Information Technology in Construction Vol. 10 Editorial pp 15-16. Available online at: http://www.itcon.org/data/works/att/2005_2.content.02825.pdf [Accessed February 2016].
- [23] S. Van Nederveen, R. Beheshti, and W. Gielingh, (2009). *Modeling Concepts for BIM*. In: Underwood, J., and Isikdag, U., eds., *Handbook of Research on Building Information Modeling and Construction Informatics: Concepts and Technologies*, Hershey, PA: Information Science Reference, 1-18
- [24] T. Liu, and T. Hsieh (2007) *nD modelling: industry uptake considerations*. Proceedings of the 28th ISARC, Seoul, Korea) .Pgs 758-763.
- [25] A. Denzer, and K. Hedges, (2008) *From CAD to BIM: Educational Strategies for the Coming Paradigm Shift*. AEI 2008: pp. 1-11
- [26] J.Macdonald (2011), *BIM – Adding value by assisting collaboration*, LSAA 2011 Conference, Novotel, Sydney Olympic Park, October 2011 in Proceedings of LSAA 2011 Conference, ed Kneen, P., Lightweight Structures Association Australia, Sydney.

- [27] F. Techel and K. Nassar (2007), *Teaching Building Information Modelling (BIM) From a Sustainability Design Perspective*, in proceedings of 3rd International Arab Society for Computer Aided Architectural Design ASCAAD Conference on Em'body'ing Virtual Architecture, ASCAAD-07, Alexandria, Egypt.
- [28] M. Ibrahim (2007), Teaching BIM, What is missing? in proceedings of 3rd International Arab Society for Computer Aided Architectural Design ASCAAD Conference on Em'body'ing Virtual Architecture, ASCAAD-07, Alexandria, Egypt.
- [29] BAF (2013), BIM Academic Forum, Available on-line at <http://www.bimtaskgroup.org/bim-academic-forum-uk/> [Accessed February 2016].
- [30] R. Krejcie, and D. Morgan (1970), *Determining Sample Size for Research Activities*, Educational and Psychological Measurement, Vol 30 (3), pg. 607-10.
- [31] A. Rubin, and E. Babbie, E. (2009) *Essential Research Methods for Social Work*, USA:Cengage Learning.
- [32] Efficiency and Reform Group, (2011) *Government Construction Strategy*, Cabinet Office, UK:London.

Clacton and Holland on Sea Coastal Protection Case Study to assess the pros and cons of using BIM on coastal protection schemes

Dr David Collery¹, Andrew McCloud², Victoria Deakin³, and James Ennos⁴,

¹Department of Building and Civil Engineering, Galway and Mayo Institute of Technology, Mott MacDonald Ltd

²Canham Consulting, Norwich, UK,

³ Mott MacDonald House, 8-10 Sydenham Road, Croydon, UK

⁴ Tendring District Council, Clacton, UK

email: David.Collery@gmit.ie,

AndrewMcCloud@canhamconsulting.co.uk,

Victoria.Deakin@mottmac.com

Jennos@tendringdc.gov.uk

ABSTRACT:

Building Information Modelling (BIM) is a topic that is high on the agenda within the construction industry, so much so, that it has central UK government backing, who have set a target to require “collaborative 3D BIM (with all project and asset information, documentation and data being electronic) on its projects by 2016” [1]. Yet there seems to be little impetus for implementation within local authorities, despite the opportunities for significant cost savings and efficiencies. BIM is the process of creating digital data sets formed of graphical and non-graphical information in a shared digital space called a common data environment. BIM incorporates all aspects of the building process from design concept, design, construction right through to the facilities management.

The Clacton and Holland-on-Sea Coastal Protection Scheme is one of the first coastal protection infrastructure projects in the UK, designed and implemented using BIM [2] making this first scheme very important in terms of setting a bench-mark for best practice in this area and is therefore considered to be an ideal case study to showcase this information.

Aim

The aim of this paper is to identify the extent to which BIM was used within the Clacton and Holland-on-Sea Coastal Protection Scheme, evaluate the benefits of its use through the project and to communicate these lessons to the potential implementation of BIM in the Irish Construction Industry.

In order to meet the primary aim of this paper, several ‘research objectives’ have been identified. They are:

- 1) To what extent was BIM used at Clacton?
- 2) What were the benefits of BIM being implemented on the Clacton project?
- 3) What lessons from the Clacton project could be applied to BIM implementation within the Irish Construction Industry?

KEY WORDS: BIM, Coastal Protection;

1 INTRODUCTION TO CASE STUDY

Clacton is a coastal tourist destination in Essex, UK, which has been protected from erosion by way of coastal protection since 1880. However, there has been a long term trend of lowering beach levels, which has resulted in a number of defence failures [3]

In addition to the increased risk of defence failure the low beach levels are expected to affect tourism in the area, which is a major concern to the local Councils. With approximately 4.5 million visitors per year, tourism in Clacton is key to the local economy and is valued at over £344 million per year across the district [3].

In 2013 Tendring District Council (TDC) successfully secured £36 million of funding to implement a coastal protection scheme. This enabled TDC to embark on the design of a sustainable coastal protection scheme. The design consultant “Mott MacDonald” worked with TDC and the local stakeholders to develop a coastal protection scheme that

provided a sustainable solution balancing the requirements for providing coastal protection with the beach user’s experience (tourism). The scheme comprised of 22 rock ‘fishtail’ groynes, one terminal rock groyne and almost a million cubic metres of beach recharge, which provides protection to 3,019 residential and commercial properties along a 5 kilometre stretch of coastline. With the use of a beach management plan the scheme will provide protection for the next 100 years as well as providing increased tourism benefits [2].

Following the appointment of Mott MacDonald, it was immediately highlighted the likely benefits that BIM could bring to such a complex project as identifying it as a good opportunity to trial BIM in previously untested environment [2]. It was agreed that the project would trial the implementation of BIM to achieve BIM level 2.

2 WHAT IS BIM

The UK Government, through the BIM Task Group, states that BIM is focussed on a collaborative approach through the whole life-cycle of an asset, utilising shared 3D models with structured data attached to them [1].

The concept of 'BIM levels' (and 'BIM level 2 compliance') has become the 'accepted' definition of what criteria are required to be deemed BIM-compliant, by seeing the adoption process as the next steps in a journey that has taken the construction industry from the drawing board to the computer and, ultimately, into the digital age. [4]

The purpose of devising an evolutionary process of Levels 0 - 3 is to categorise technical and collaborative working, enabling a concise description and understanding of the processes, tools and techniques to be used. The maturity levels are widely referred to in industry to the extent that the UK Government's phased implementation is based on these levels – it is required that all UK Government funded projects must be delivered to a BIM Level 2 after April 2016.

2.1 The Maturity Model

The BIM process due to the nature of technology develops a data management system. BIM has been split into a number of 'levels' showing the 'maturity' of the systems in place. The Maturity Model - also known as the iBIM model or the BIM Wedge - was developed by Mark Bew and Mervyn Richards in 2008. There are many versions of the base model with subtle differences (Figure 1).

The BIM maturity model includes four levels with stable (levels 0 and 1), stabilising (level 2), and yet to stabilise (level 3) definitions. BIM is being used at the moment at a number of different levels of sophistication, with UK Government requiring a Level 2 BIM to be implemented on construction projects.

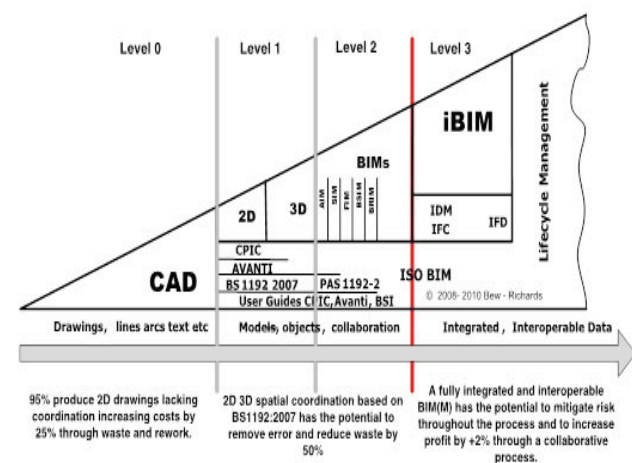


Figure 1 Bew and Richards BIM maturity model [1].

The BIM maturity levels concept has become widely accepted in the UK as the definition of the criteria that need to be met/implemented in order for an organisation to consider themselves to be BIM-compliant [4].

It should be noted that a different model is used in the USA to define BIM levels, known as 'Levels of Development' (LOD). However, this will not be discussed any further in this paper.

Level 0 BIM

In its simplest form, level 0 effectively means no collaboration. 2D CAD drafting only is utilised, mainly for Production Information. Output and distribution is through paper or electronic prints or a mixture of both. The majority of the industry is already well ahead of this now [4].

Level 1 BIM

Level 1 BIM is comprised of a mixture of 3D CAD for concept design, and 2D for drafting of statutory approval documentation. Drawing and CAD standards are managed to BS 1192:2007, and data is shared electronically by a common data environment (CDE). There is no collaboration between different disciplines – each group/partner publishes and maintains its own data [4].

Level 2 BIM

Level 1 – used as the foundation to move onto Level 2.

The Level 2 involves the production of additional standards and codes of practice in addition to Level 1, along with advisory documents, the Employers Information Requirement, and supports developing a BIM Execution Plan to meet these requirements. A single CDE must be provided with a clear set of standards and procedures for checking and approving data within the CDE [5].

Level 3 BIM

Moving from Level 2 to Level 3 represents the greatest BIM Challenge. It introduces the holy grail of the single project model – all members of the integrated team working from one design model. A fully integrated and collaborative real time project model that is likely to be facilitated by web service [6].

Currently seen as the holy-grail, this represents full collaboration between all disciplines by means of using a single, shared project model which is held in a centralized repository. All parties can access and modify that same model, and the benefit is that it removes the final layer of risk for conflicting information. This is known as 'Open BIM', and the UK government's target date for public-sector working is 2020 [4].

PAS1192-2 – Overview

PAS1192-2 is the specification for information management for the capital/delivery phase of construction projects using Building Information Modelling.

The purpose of the PAS1192-2 is to support the objective to achieve Building Information Modelling maturity Level 2 by specifying requirements for this level, setting out the framework for collaborative working on BIM enabled projects and providing specific guidance for the information management requirements associated with projects delivered using BIM.

The requirements within the PAS1192-2 build on the existing code of practice for the collaborative production of architectural, engineering and construction information, defined within BS 1192:2007. The PAS describes the shared use of individually authored models in a Common Data Environment (CDE), being a single source of information for any given project, used to collect, manage and disseminate all relevant approved project documents for multi-disciplinary teams.

The significance of these steps, in real terms, is that UK government has adopted this definition in its Construction Strategy, by requiring that all publicly-funded construction work be undertaken by using BMI to Level 2, from 2016. This mandate has been set as one measure to help in fulfilling their target of reducing waste in construction by 20%. It is considered that abortive work, discrepancies, mistakes, and inefficiencies in the information supply chain are major contributors to this waste; and that collaborative working can assist in their reduction [3].

In Ireland the Public Works Contracts (PWC) suites (2007) does not have requirement for BIM or electronic communications within the contracts. These suites of contract promote the traditional contractual relationship. It is advisable that PWC be updated to move towards the legal mandating of BIM. Currently these contracts are not set up to promote collaboration and effectively through the transfer of risk create a hostile environment. A collaborative approach should be achieved through the re-drafting of the PWC suite of contracts to include use of BIM technologies [7].

3 BIM WITHIN THE CLACTON SCHEME

This section is divided into three sections, design phase, tendering phase and construction phase of the scheme and how BIM was a fundamental part of all three.

3.1 Design Phase

At the start up meeting for the design phase of the works, BIM aspect of the project was discussed and the decision supported by Mott MacDonald consultant to deliver the design to BIM level 2, make the Clacton scheme the first coastal protection

project delivered to this level. An Employer Information Requirement (EIR) and BIM Execution Plan (BEP) were developed for the scheme, which set out the level of information that would be provided at different stages of the design. For the scheme to meet the BIM level 2 requirements, Bentley Projectwise was used as the projects common data environment (CDE). The CDE provided a checking and approving process internally which aligned to Mott MacDonald QA process. All data was made available once approved “Published” to all parties within the scheme (Figure 2).

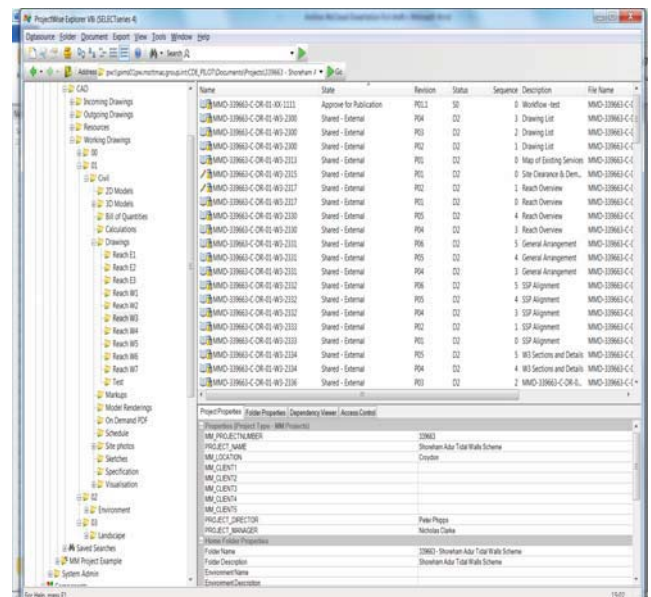


Figure 2 Screen shot from Projectwise - CDE

The single model was developed with the use of AutoCAD Civil 3D software. The use of AutoCAD Civil 3D to design the groynes and beach profile provide the project team greater understanding than even before of how the new rock groynes structure would interact within the existing environment. Bathymetric, topographical and geotechnical surveys provided the data for the modelling the foreshore which provided key parameters of the design.

Each groyne had to be sufficiently embedded into the London Clay strata, to prevent failure. The orientation of the structures was an important aspect of the design to try to normalise the coastline. Having a single model with each groyne structure linked into meant this could be accurately checked. The model allowed the design team work with more complex trigonometry and geometry, so rather than standardising the groynes, each groyne was bespoke. This provided an increased level of optimisation of the groyne structures. Figure 3 details a 3 dimensional view a groyne structure.

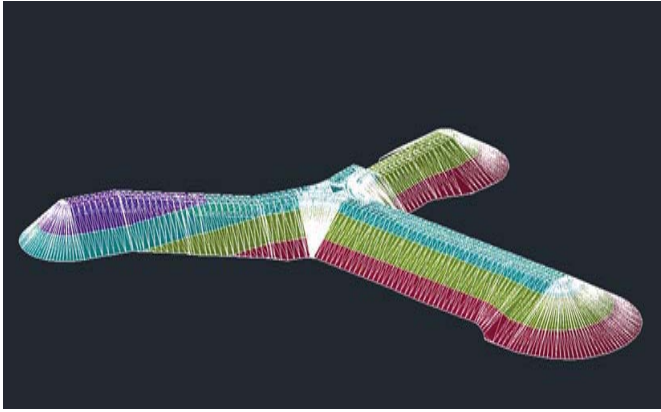


Figure 3 Three-Dimensional view of groyne structure

One of the key benefits of having the scheme designed within a 3D model was having confidence regarding material volumes required for the scheme. This allowed for preliminary costs of the scheme to be undertaken. Similarly, accommodating design changes within the model provided approximately 30% saving on design time and costs.

A visualisation model and 3D printout of the model was used for stakeholder engagement, which proved very positive, as different aspects of the scheme could be discussed in real-time at stakeholder engagement events.

3.2 Construction Tender Phase

All tendering contractors had access to the design model and it was communicated that the preferred bidder would have the use of the design model to construct the scheme. This allowed for accurate like for like tenders to be submitted and a reduction in tender queries. It was communicated by the tendering parties that the model reduced the time required to develop take-off and tender costs.

3.3 Construction Phase

On award of the construction contract to the preferred supplier “VBA consortium (VolkerStevin, Boskalis Westminster, Atkins)” the CDE was made available to view the live model. On site, the BIM model was imported into the site excavators and used to build the rock groyne, from excavation of the London clay under water for the groyne toe to rock placement. The Trimble equipment accurately plotted the excavators’ real time position using GPS onto the design model and provided the operator with levels of cut and fill and the imprint of the structure. Figure 4 present the operator screen within a rock placement excavator.

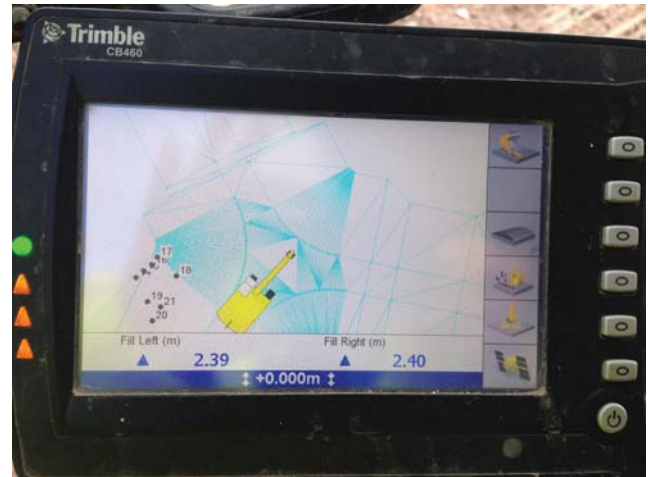


Figure 4 Site BIM model in use “Screen inside site excavator”

Surveying

The Contractor surveyed each section of the rock structures as sections were completed using the Trimble GPS equipment installed in the excavators. This method provided an accuracy of $\pm 12\text{mm}$. The method of recording the data and checking reduced the requirement for the surveyors and site supervisors to walk on the rock structures. This method reduced the health and safety risk to the site team in relation to this process. Figure 5 present a photograph of an excavator undertaking a survey of a rock groyne.

QA and As-Built model

The surveys were converted into BIM models that were overlaid onto the design models to identify instantly where any high or low spots were within the as built structure.



Figure 5 Excavator surveying section of rock groyne”

The primary advantages to this approach were three fold. Firstly the use of excavator mounted GPS equipment eliminated the need for surveyors to be placed in potentially

hazardous situations in order to carry out detailed topographic surveys of the as-built structures, which made the process considerably safer. Secondly, the process was made more efficient as the machine operator could survey the structure as it was built.

Finally, it increased the accuracy of the as-built survey approval procedure. With the two model layers combined, the checking process is very visual and errors can be determined quickly and easily. It is understood that this process could be automated by defining a set of rules and allowing the model to 'intelligently' compare the two surfaces and highlight areas that fall outside of the set parameters/placement tolerances. Figure 6 details an as-built model of a groyne and Figure 7 presents an as-built model being overlaid on the design model; checking the tolerances of the rock placement.



Figure 6 As-built survey of groyne structure

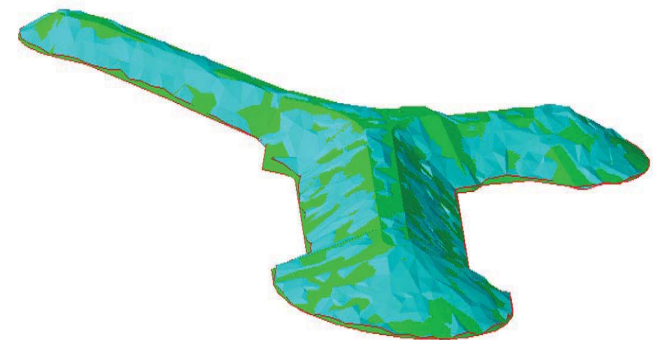


Figure 7 Design and survey models combined

Onsite Design Changes

A number of design changes were required due to variations in the London clay strata, which were discovered whilst the groynes were being constructed. Having the design model available on the CDE, the design changes could be undertaken within a number of hours and approved, greatly reducing programme delays and standing time.

4 LESSONS LEARNT

The lessons learnt are broken down into design and construction phases of the scheme as

4.1 Design Phase

The design team faced a number of hurdles, firstly Civil 3D was not originally developed for this type of infrastructure project and we were pushing the limits of the software. The design team recognised early on that we would struggle with our internal angles, so we had to configure the model carefully to deal with the geometry of the structures.

Secondly; becoming confident with the checking and approving system that we set up in accordance with PAS 1192-2 within Projectwise, require some time and took a number of training/refresher workshops were needed for the design team. A number of IT issues were encountered regarding the work-flows and approval system due to the software short-cuts reducing in delays.

4.2 Construction Phase

Arranging and allowing the Contractor access to the CDE, this took some time along with managing the Contractor's staff access requirements and team changed.

With the increased level of information provided to the excavator operators, we had one issue with rock placement. The excavator operators were trying to place all the rocks within surfaces of the model at the toe detail and not realising that first/toe rock was designed to be any oversize rock, which was allowed to be outside the rock placement tolerances. The model was updated to reflect this aspect.

5 CONCLUSION

This case study outlines the benefits and constraints that were encountered with the implementation of BIM within the scheme from design through to execution.

The lessons learnt from this scheme regarding implementing of BIM in a project/team for the first time regardless of the project type, are as follows;

- provide adequate training for all staff members that will be using the CDE from the very beginning of the project and allow time to become familiar with use of the system,
- name a CDE/BIM champion of the project that has capacity to assess other team members
- have CDE/BIM as an item on the month progress agenda – to allow items to be discussed and obtain buy-in by all parties

While the project team believes that overall the implementation of BIM was positive, the main benefits of implementing BIM within the scheme is the ongoing asset management of the scheme for the Employer (TDC). As beach profiles can and likely to vary after stormy periods,

surveys can be undertaken and imported into the model to assess if local recharge of beach material is required or likely additional recharge required in the near future. Therefore; the main benefit of implementing BIM in this scheme is to the Employer and ongoing asset management of the scheme.

REFERENCES

- [1] Building Information Modelling (BIM) Task Group (2013) *Frequently Asked Questions: What is Building Information Modelling (BIM)*. Available at: <http://www.bimtaskgroup.org/bim-faqs/> (Accessed: 12th December 2014)
- [2] Phipps. P, (2014) *New Civil Engineer –Flooding BIM*, January addition Thomas Telford, London, UK.
- [3] McCloud A (2015) BIM in Coastal Engineering- *Applying the lessons learned on the Clacton and Holland-on-Sea Coast- Protection Scheme to BIM implementation at North Norfolk District Council* Dissertation University of Canterbury
- [4] NBS, (2014). *RIBA Enterprises Ltd.* [Online] Available at: <https://www.thenbs.com/knowledge/bim-levels-explained> [Accessed 7 February 2016].
- [5] PAS 1192-2 (2013) Specification for information management for the capital/delivery phase of construction project using building information modelling. Published by BSI Standard limited.
- [6] Infrastructure and Project Authority (2016) UK Government Construction Strategy,
- [7] McAuley, B., Hore, A.V and West, R. (2012) Implementing Modelling in Public Works Projects, Proceedings of the 9th European Conference on Product and Process Modelling, Reykjavic, July 25 – 27 2012.

Some geotechnical characteristics of soft soil deposits along the Terryland River Valley, Galway

Paul Quigley¹, Bryan A. McCabe², Pat Hunt³ and Michael Rodgers⁴

¹Gavin and Doherty Geosolutions, Dublin

²College of Engineering and Informatics, National University of Ireland, Galway

³Westmeath County Council, Mullingar, Co. Westmeath

⁴formerly of College of Engineering and Informatics, National University of Ireland, Galway

email: pquigley@gdgeo.com, bryan.mccabe@nuigalway.ie, phunt@westmeathcoco.ie, michaelrodgers64@gmail.com

ABSTRACT: The ground conditions in the Terryland River Valley area present considerable site development challenges to geotechnical engineers. The soft soil formation consists of peat overlying very soft, highly compressible calcareous silt overlying slow draining organic silts and inorganic clays. These soil deposits are typical of those encountered in Limestone Basin regions throughout Ireland. NUI Galway has been involved in investigating these soils since the 1980s. The investigations at Terryland involved Cone Penetration Testing (CPT), shear vane and piston sampling plus laboratory testing. This paper summarises some previously unpublished data and places the results in the context of various published soil data from sites elsewhere in Ireland. The laboratory testing confirms that the design parameters for the soft soils in the Terryland River Valley are more onerous than for many other soft soil sites in Ireland.

KEY WORDS: calc tufa, marl, silt, clay, consolidation, compressibility

1 INTRODUCTION

The ground conditions along the Terryland River Valley, north of Galway City centre, have posed challenges for construction in the area over the last 30 years, as evidenced by the earthworks failure in Figure 1. The geotechnical characteristics of the Terryland River Valley deposits are presented in this paper with a view to providing a frame of reference for future developments on similar soft soil deposits. Particular emphasis is placed on 1-D compression behaviour.

The measurements presented are derived from adjacent ground investigations at Terryland for:

- (i) a section of the N6 dual carriageway east of the Quincentennial Bridge [1] (south zone and part of the north zone in Figure 2) and
- (ii) both a piled embankment research trial and the Dún na Coiribe residential development (part of north zone in Figure 2).



Figure 1 Earthworks failure along the Terryland River Valley

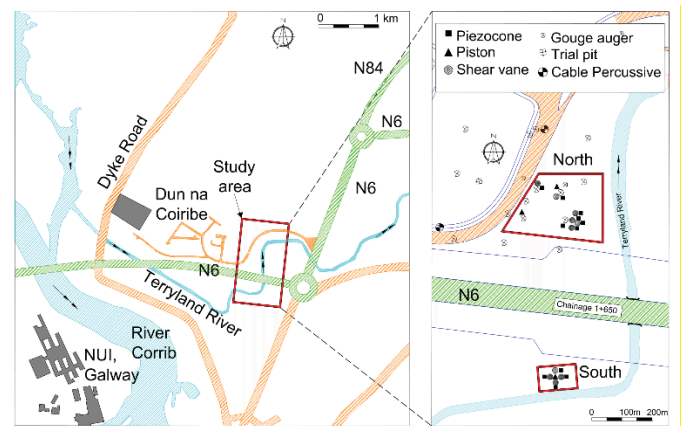


Figure 2 Terryland River Valley and investigation areas

2 GEOLOGY

2.1 Solid Geology

The bedrock at the test location is carboniferous limestone, generally pale to medium grey in colour, well-bedded, fossiliferous and medium-grained to coarse-grained. It is moderately strong to very strong with fractures which are closely-spaced to medium-spaced and at a low angle. The bedrock is part of the Visean Limestone formation of the Lower Carboniferous age which underlies much of Galway city and east Co. Galway [2].

2.2 Quaternary Geology

The Terryland River flows from the River Corrib (see Figure 2) and ultimately through a series of sinkholes into the sea, although the network of karst features between the sinkholes and the sea is not precisely known. During high tides, the direction of flow in the Terryland River can be reversed.

The soft soils in the Terryland River Valley are identified as alluvium or bogs on geological drift maps. A portion of the Terryland site was part of a lakebed until land reclamation works began in the 1850s. The lake was formed over glacial till, which was deposited over the limestone during the last Ice Age. The glacial till generally consists of well-graded sands, gravels and boulder clay [3].

The Quaternary geology comprises peat overlying calcareous soils, which in turn overlie lake deposits of silts. The top 0.2 m – 0.3 m of the peat is fibrous in nature, supporting the surface vegetation. The peat becomes more humified with depth, typically ranging from H5 to H7 on the Von Post [4] scale. During trial excavations, the peat below 0.3 m unusually had a yellowish colour (Figure 3) that turned black upon exposure to air. It is assumed that this peat was formed in anaerobic conditions implying that the water table did not fluctuate below this level.



Figure 3 Cream-yellow coloured peat excavated below 0.3m.

The calcareous soil was formed as a result of calcium carbonate (CaCO_3) coming out of solution from the groundwater. Water originating from lime-rich strata saturated with CaCO_3 flowed upwards under artesian conditions at discrete locations through the underlying lake deposits. In reduced pressure conditions, the CaCO_3 emerged from solution and formed the calcareous deposit known as calc tufa or marl. Numerous bands of shells were deposited in the calc tufa as the bed of the lake was raised during the deposition process.

The lake deposits overlying the glacial till consist of green-grey organic silt containing numerous reeds and other organic matter, overlying blue-purple-grey inorganic clay. The organic silt was generally more laminated than the inorganic clay. The deposition of the lake soils followed by the formation of the calc tufa raised the bed of the lake sufficiently high to support the growth of reeds. This in turn gave rise to reed peat being formed in the upper strata [5].

3 SITE INVESTIGATION AND IN SITU TESTING

The site investigations at Terryland followed procedures established by NUI Galway based on previous experience of investigations in soft soils. Initially, a gouge auger was used to determine the nature and extent of the soft soil deposits. Next, piezocone tests were performed as they were quicker and easier to complete than shear vane tests or piston sampling (the fieldwork pre-dated the use of piezoballs in Ireland). Shear vane tests and continuous piston sampling

were then carried out close to piezocone locations. Cable percussive boreholes were also carried out in the glacial layer. A description of the site investigation techniques and soil types encountered is provided.

3.1 Gouge auger

The gouge auger is a simple but very effective means of determining the stratification of soft soils. It consists of a 1 m long split tube, 30 mm in diameter, fitted with a detachable handle. It can sample soils to a depth of 15 m by adding a series of 1 m long extension bars. The stratification was determined by visual inspection of the recovered core. Portions of the core were removed for water content and Atterberg limit determinations.

3.2 Piezocone testing

The NUI Galway piezocone consists of a 60° cone with a cross-sectional area of 10cm^2 and the porous filter was located behind the cone tip. The piezocone was driven into the soil at a rate of 20mm/sec. The cone end resistance, pore water pressure and sleeve friction were recorded at 100mm intervals by a datalogger. The piezocone was held stationary at its maximum depth and the pore water pressure was recorded. In keeping with similar sites, the friction values recorded were very low and therefore are difficult to rely upon.

A representative variation of cone end resistance and pore water pressure with depth is shown in Figure 4. Uncorrected and corrected cone factors N_k and N_{kt} were typically found to lie in the range 5-12 and 6-12 respectively, with a small number of higher values [1]. A significant increase in pore water pressure is noted when the piezocone was held stationary, suggesting that a slightly artesian condition is present.

3.3 Shear vane testing

A Geonor H-10 (65mm x 130mm) shear vane was used at Terryland. The inferred profiles of undrained shear strength (c_u , without Bjerrum's correction for plasticity index) with depth are shown in Figure 4. The corresponding corrected undrained strength ratios (c_u/σ'_0 , where σ'_0 is the free-field vertical effective stress) are higher than might be expected based on the well-known Ladd *et al.* [6] correlation with OCR; this is attributed to drainage in the calc tufa during shear vane testing.

3.4 Continuous piston sampling

Continuous sampling was carried out using a Geonor piston sampler. Thin-walled aluminium sample tubes, 1.0 m in length and 101.6 mm in diameter, were driven into the soil using a tripod and winch reaction system. The leading edge of the tubes had a 30° cutting edge and the wall thickness was 1.75 mm, providing an area ratio of 7%. Once the sample tube had been extended fully, the operators waited approximately 15 minutes to allow any excess pore water pressures to dissipate before extracting the samples, which were up to 0.9 m long. The tubes were sealed on site with paraffin wax to prevent water loss. They were placed horizontally in a large box and carefully surrounded by polystyrene packaging to prevent excessive rocking that could disturb the microfabric of the very soft soils.

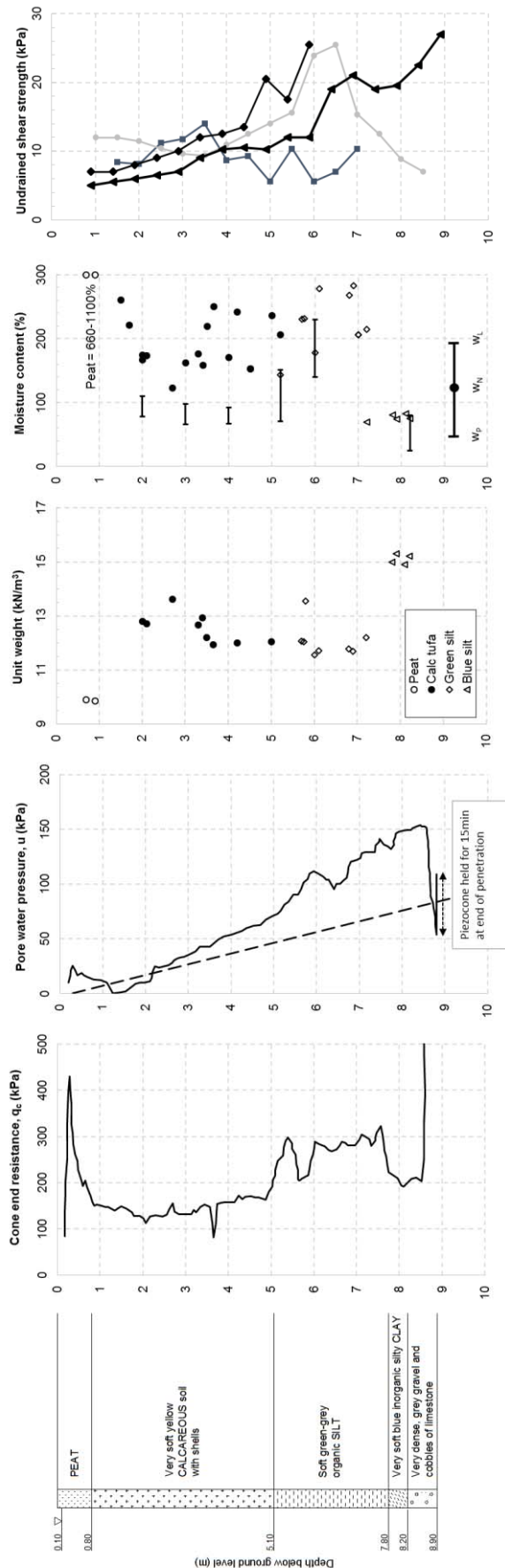


Figure 4 Typical geotechnical profile at the Terryland site.

Once in the laboratory, the samples were stored horizontally to minimise the loss of water. When the samples were extruded, a split pipe was placed at the open end of the tube to support the sample. The sample was cut off using a thin nylon line and the tube was resealed at both ends with paraffin wax.

3.5 Cable percussive boreholes

Irish Drilling Limited carried out cable percussive boreholes at Terryland. The cable percussive method is a crude method of sampling soft soils as mixing can occur. In this case, it was used to determine the nature and extent of the glacial deposits. It was possible to chisel into the gravel until refusal of the Standard Penetration Test (SPT) occurred. Refusal was dramatic, indicated by the SPT hammer 'bouncing', and no further penetration of the SPT cone possible [7].

4 BASIC MATERIAL PARAMETERS

4.1 Stratigraphy and groundwater

The stratification across the test site was reasonably uniform although some minor variations in the depth to the glacial till were established. The interpreted layering is shown on Figure 4. The groundwater was generally at or close to the ground surface.

4.2 Water content, index tests and bulk density

The distributions of bulk unit weight, water content and Atterberg limits with depth are shown on Figure 4. The unit weight of the soils was determined from the specimens used for consolidation tests.

The Atterberg chart (Figure 5) shows the calc tufa data plotting below the A-line as a silt of extremely high plasticity, whereas the green organic silt also plots below the A-line much further to the right. The blue inorganic clay plots just above the A-line as a high plasticity clay.

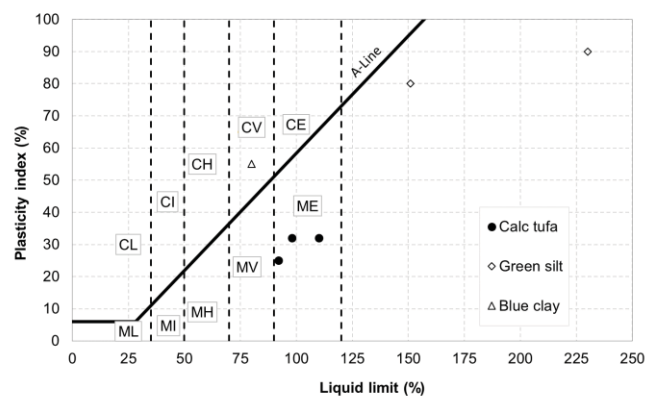


Figure 5 Atterberg chart

The natural water content of the peat varied from 660% to 1100%, while that of the calc tufa ranged from 120% to 260%. The green organic silt had water contents between 150% and 280% while the blue clay had a water content range of 70% to 80%. The plastic limit for the organic and inorganic soils was established using the rolling ball method. However, Baaker [8] suggested that the linear shrinkage method was more suitable for determining the plastic limit of calcareous soil so this method was preferred for the calc tufa. The liquid

limit was determined using the cone penetrometer test. The liquid limit results for the calcareous soils are typically about 100%, much lower than the natural *in situ* water content range. This is indicative of a structured or a slightly cemented silt. Sensitivity (the ratio of natural shear strength to remoulded shear strength) values ranging between 5 and 12 were found from fall cone tests carried out on undisturbed samples.

4.3 Sample Quality

The soft nature of the Terryland overburden soils meant that the recovery of quality samples was challenging. Sample disturbance was evaluated using methods proposed by Lunne *et al.* [9] and modified by Löfroth [10]. Lunne *et al.* [9] proposed that the volumetric strain required to recompress the specimen to the *in situ* vertical effective stress is a useful indicator of the degree of sample disturbance. Löfroth [10] carried out a study of sample disturbance effects for soft, Swedish soils and proposed a modified version to account for specimens with water contents up to approximately 150%. The boundaries between the sample quality classes have been extrapolated by the authors in Figure 6 to account for the higher water contents at Terryland; the figure indicates that the sampling was successful.

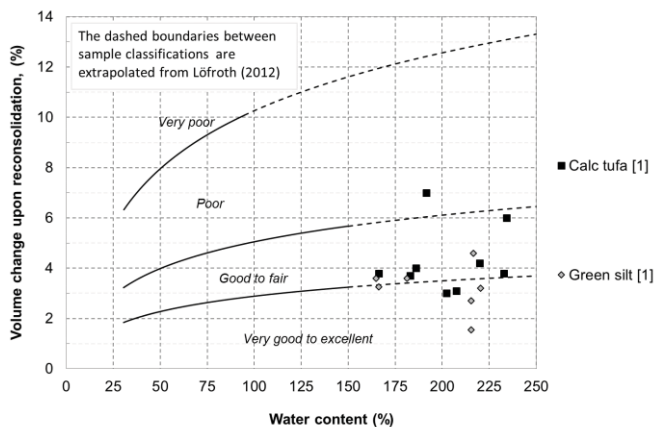


Figure 6 Sample quality at Terryland

5 ONE-DIMENSIONAL COMPRESSION BEHAVIOUR

A series of 75mm or 76mm diameter standard oedometer and constant rate of strain (CRS) oedometer tests were carried out on samples from Terryland. Plots of vertical effective stress against axial strain for standard oedometer tests are plotted in Figure 7 for the calc tufa and in Figure 8 for the organic silt. The typical loading sequence, following recommendations from Sandbaekken *et al.* [11], is 0.25, 0.5, 1.0, 1.5, 2.25, 4.5 and 9.0 times the free-field vertical effective stress σ'_0 .

5.1 Compression index

McCabe *et al.* [12] provided an empirical relationship between the compression index (C_c) and various indices for soft, compressible soils in Ireland in the water content range of 60 – 150%. The relationship between C_c and the natural water content (w_N) in eqn (1) was deemed to be the most reliable.

$$C_c = 0.014(w_N - 22.7) \dots \dots \dots (1)$$

McCabe *et al.* [13] examined data from Terryland and elsewhere in Ireland and found that eqn (1) was also reasonably valid for clays and silts having higher water contents than 150%. However, the relationship typically overpredicted the measured C_c values for calcareous soils. A tentative relationship is proposed for calcareous soils based on data from Terryland and other calcareous silt sites in Ireland for $125\% < w_N < 300\%$ (Figure 9).

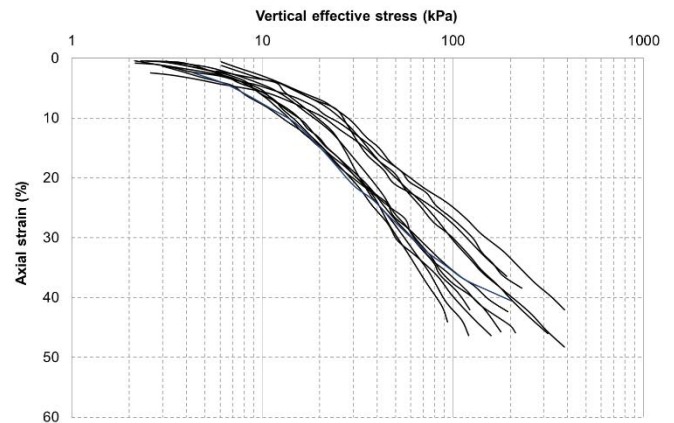


Figure 7 Oedometer results for calc tufa (3.5m-5.8m)

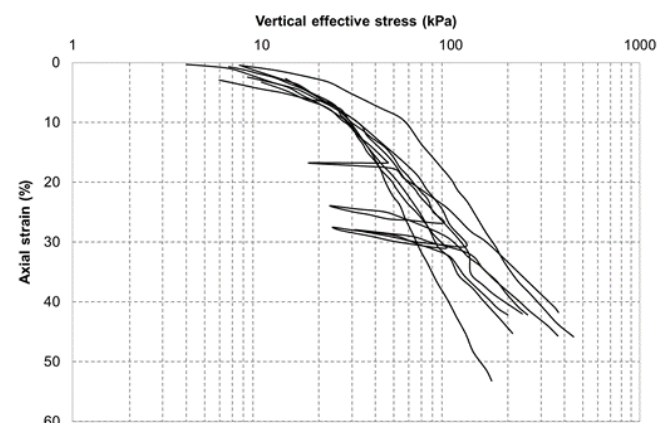


Figure 8 Oedometer results for organic silt (5.8m-8.1m)

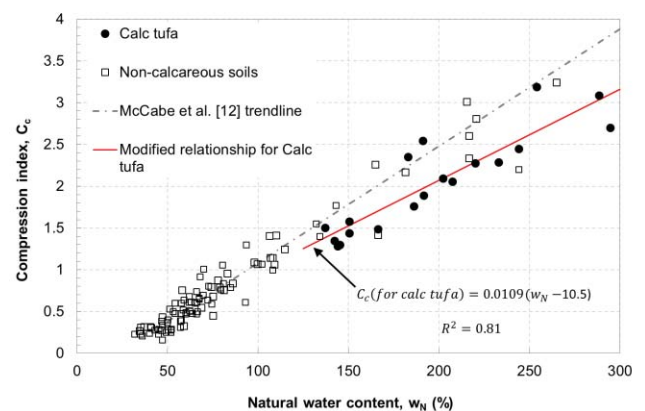


Figure 9 Relationships between natural water content and compression index (adapted from [13])

5.2 Yield stress and tangent modulus

The Casagrande graphical construction for estimating the yield stress can be difficult to implement for Irish soils as many log stress versus strain curves can be very rounded without an obvious point of maximum curvature. The Janbu [14] method has been used on a number of Irish sites, e.g. [15, 16] to overcome this issue. The tangent modulus (M) is estimated from:

$$M = \frac{\Delta \sigma'}{\Delta \varepsilon} \dots \dots \dots (2)$$

The yield stress (σ'_c) can be inferred from the relationship between M and the vertical effective stress σ' . There is a distinct break point as the soil structure is broken down before recompression of the soil occurs; this typically occurs at σ'_c . This is shown graphically in Figure 10. Some Swedish soils display a different relationship and the yield stress is determined in an alternative way. TK Geo [17] suggests that the soil deforms at a constant tangent modulus commencing at the yield stress before increasing at a stress σ'_L (Figure 11). This is most likely due to the degree of structure in the soils, particularly in the Gothenburg region.

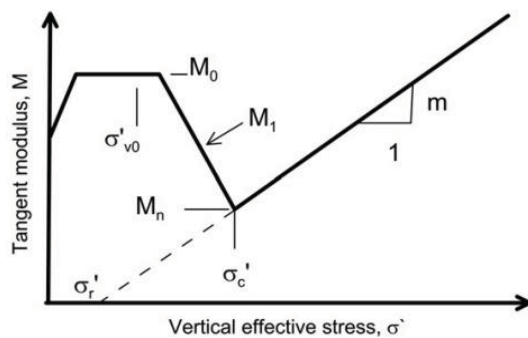


Figure 10 Classical Janbu tangent modulus versus stress model (image adapted from [14]).

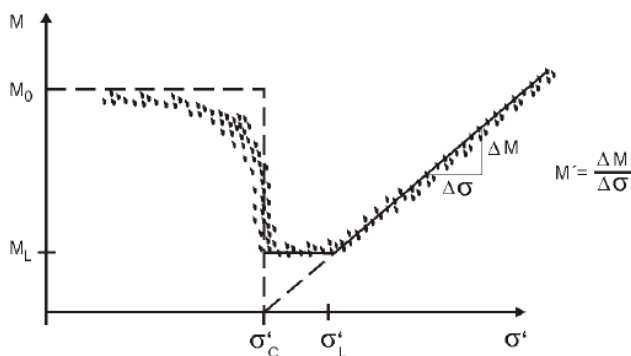


Figure 11 Relationship between the vertical effective stress (σ') and tangent modulus for Gothenburg clays [17]

The CRS tests carried out on the soils (Figure 12) have been analysed using the Janbu method (Figures 13 and 14). The data suggest that the initial tangent modulus M_0 is relatively low and it is difficult to determine the yield stress with this

method. However, there appears to be a stress range corresponding to the stress range σ'_c to σ'_L where the tangent modulus M is relatively constant, similar to the Swedish soils. Janbu [14] proposed that the constrained modulus could be characterised by a power function as follows:

$$M = m p_a \left(\frac{\sigma'}{p_a} \right)^{1-a} \dots \dots \dots (3)$$

where m is the modulus number, p_a is the reference stress usually taken as 100 kPa and a is a dimensionless stress exponent. The data from Terryland suggest that the modulus number m typically varies between 4 and 7 for both the calc tufa and the organic silts. These values are shown in the context of Long's [15] data for lower water content soils in Figure 15. The Terryland data indicate that the results are less sensitive to water content than the estuarine silts examined by Long [15]. The a parameter in eqn (3) was typically zero for calc tufa which is in line with suggestions for soft soils [14]. Long [15] found that the a parameter for many Irish soft soils was typically 0.25; the data for the green organic silt in Terryland are in keeping with these findings.

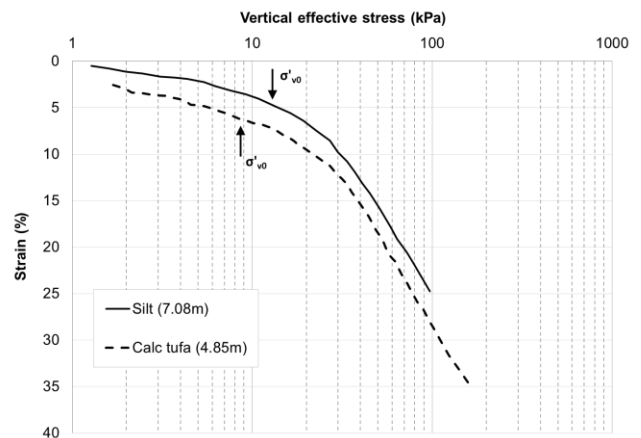


Figure 12 CRS data for calc tufa at 4.95m depth and green organic silt at 7.1m depth [1]

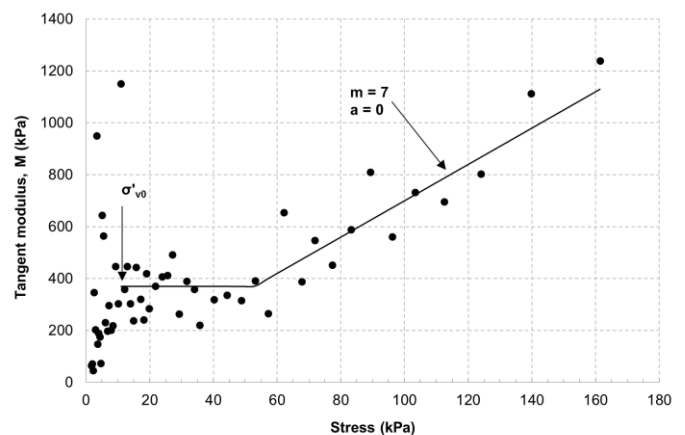


Figure 13 Plot of M versus stress with the Janbu [14] power relationship for calc tufa specimen taken at 4.95m

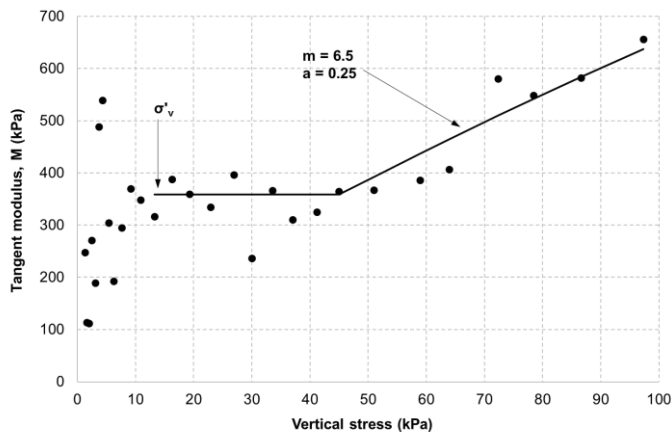


Figure 14 Plot of M versus stress with the Janbu power relationship for green organic silt specimen taken at 7.1m

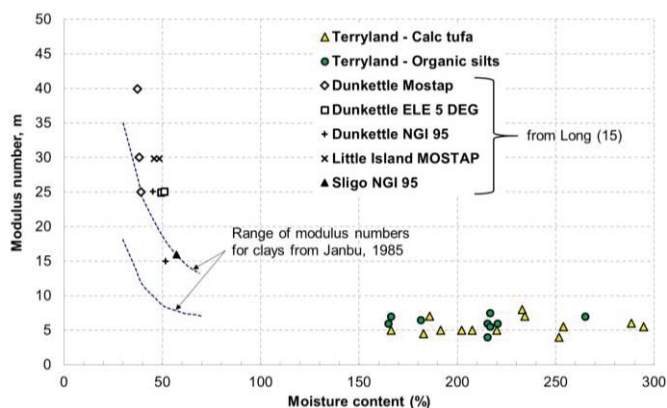


Figure 15 Range of modulus numbers for Terryland and data from sites elsewhere in Ireland from [15]

6 CONCLUSIONS

In this paper, some NUI Galway experience of the ground conditions present in the Terryland River Valley area of Galway City is presented, intended as a frame of reference for geotechnical engineers dealing with similar soils. The soft ground investigations at Terryland were found to be particularly challenging. Some of the main conclusions from the investigation are:

- (i) The geotechnical parameters for the calc tufa can vary significantly, as evidenced by the water content and Atterberg limit variation both with depth and across the site.
- (ii) The CPT end resistances are very low (typically less than 300 kPa) and therefore the soft soils may be more suitable for investigation with a piezoball to develop greater resistance and resolution.
- (iii) The soils are susceptible to sample disturbance, but good quality piston samples can be retrieved using well-maintained equipment used with sufficient care.
- (iv) The empirical relationship for C_c proposed by McCabe *et al.* [12] for soft Irish soils appears to be appropriate for the high moisture content silts and clays at Terryland, but overpredicts C_c for the calc tufa. An alternative relationship is proposed for calcareous soils.
- (v) The calc tufa is probably a weakly structured material with many similar characteristics to Swedish soils. The

CRS tests suggest that the Janbu [14] method for determining the yield stress is not appropriate, while the method proposed by TK Geo [17] appears to be more applicable. This facet of the calc tufa behaviour is worthy of further investigation.

ACKNOWLEDGMENTS

The authors would like to acknowledge COFORD, Coillte Teo., O'Malley Construction Ltd. and Galway County Council for their generous financial support, in addition to staff and postgraduate students at NUI Galway who helped with laboratory and field testing.

REFERENCES

- [1] Hunt, P. (1991). 'Analysis of soft soil deposits at a location on the Eastern Approach Road, Galway', M.Eng.Sc thesis, National University of Ireland, Galway.
- [2] MacDermot, C.V., McConnell, B. and Pracht, M. (2003). 'Bedrock Geology 1:100,000 Scale Map Series, Sheet 14, Galway Bay', Geological Survey of Ireland.
- [3] Soil Mechanics Associates Ltd. (1980). 'Galway Eastern Approach Road Site Investigation; Stage 2', Report to Galway Corporation, October 1980.
- [4] Von Post, L. (1922). Sveriges geologiska undersöknings torvinventering och några av dess hittills vunna resultat. Sv. Mosskulturfcir. Tidskr. I: | 21.
- [5] Long, M.M. and Rodgers, M. (1995). 'Geotechnical behaviour of very soft calcareous soils in Ireland', Proc. XI European Conference on Soil Mechanics and Geotechnical Engineering, Copenhagen, Vol. 8, pp. 103 to 108.
- [6] Ladd, C., Foot, R., Ishihara, K., Schlosser, F. and Poulos, H. (1977) Stress-deformation and strength characteristics, Proceedings of the 9th International Conference in Soil Mechanics and Foundation Engineering, Tokyo, Vol. 2, pp. 421-494.
- [7] Irish Drilling Limited (1997). 'Proposed residential development at Terryland, Galway – site investigation report', Unpublished report for O'Malley Construction Limited, September.
- [8] Baaker, L. (1987). 'Groundwater investigation of the Owenmore River catchment, Co. Sligo', Unpublished report submitted to Teagasc.
- [9] Lunne, T., Berre, T. & Strandvik, S. (1997). Sample disturbance effects in soft low plasticity Norwegian clay. Proc. Symposium on Recent Developments in Soil and Pavement Mechanics, 81-92, Balkema, Rio de Janeiro.
- [10] Löfroth, H. (2012). Sampling in normal and high sensitive clay – a comparison of results from specimens taken with the SGI large-diameter sampler and the standard piston sampler St II, Swedish Geotechnical Institute, Varia V637, Linköping.
- [11] Sandbaekken, G., Berre, T. and Lacasse, S. (1985). Oedometer testing at the Norwegian Geotechnical Institute, Report for ASTM Symposium on Consolidation of Soils Laboratory testing, Fort Lauderdale, Florida, USA.
- [12] McCabe, B.A., Sheil, B.B., Long, M.M., Buggy, F. and Farrell, E.R. (2014). Empirical correlations for the compression index of Irish soft soils. Proc. ICE Geotechnical Engineering, Vol. 167, Issue 6, December 2014, pp 510–517
- [13] McCabe, B.A., Sheil, B.B., Long, M.M., Buggy, F., Farrell, E.R. and Quigley, P. (2016). Discussion: Empirical correlations for the compression index of Irish soft soils. Proc. ICE Geotechnical Engineering, Vol. 169, Issue 1, February 2016, pp 90–92
- [14] Janbu, N. (1985). Soil models in offshore engineering (25th Rankine Lecture). Géotechnique, Vol. 35, Issue 3, pp 241–281.
- [15] Long, M. (2007). 'Engineering characterization of estuarine silts', Quarterly Journal of Engineering Geology and Hydrogeology, Vol. 40, pp 147–161.
- [16] Carroll, R. A. (2011). Use of CRS test to predict settlement in an Irish silt, Proc. 21st European Young Geotechnical Engineers' Conference, Rotterdam.
- [17] TK Geo (2011). Trafikverkets tekniska krav för geokonstruktioner, Publikationsnummer: 2011:047 ISBN: 978-91-7467-114-8 (in Swedish).

Assessment of Ground Movement for a Deep Excavation in Soft Marine Clay

Sogol Fallah, Patrick Casey, Paul Sweeney

Arup, 50 Ringsend Rd, Dublin 4, Ireland

email: sogol.fallah@arup.com, patrick.casey@arup.com, paul.sweeney@arup.com

ABSTRACT: This paper compares the results of finite element analysis of ground movements and measured ground movements during construction of an immersed tube tunnel. The tunnel consists of three immersed tunnel (IMT) elements. The entrances to the IMT sections will be formed initially by a trough structure and then two cut and cover tunnels on each side of the river. Along the tunnel alignment there is a relatively homogeneous soft clay overlying bedrock. The soil behaviour in finite element models were described using hardening soil model with small strain stiffness (HS-Small). The input parameters of HS-Small model were calibrated against laboratory tests such as triaxial compression, triaxial extension, oedometer and direct shear tests. Then, the calibrated parameters were used to predict the movements under loading and unloading of the soil during several construction phases. Displacement and pore water pressure changes were monitored during the construction. The measured values were compared to the predicted displacements by finite element analysis. The monitored data showed a reasonable match with predicted displacements.

KEY WORDS: soft marine clay; ground movement assessment; Immersed Tube Tunnel; FE analysis.

1 INTRODUCTION

The results of numerical methods such as Finite Element (FE) method, are strongly dependent on the constitutive models used to describe the soil behaviour and the assigned values to the input parameters of the model. Therefore, the calibration of the input parameters against laboratory test data is extremely important. The goal of the calibration process is to develop a set of input parameters that are representative of the soil properties.

Immersed tube tunnels are underwater structures and are commonly used for road and rail crossings of rivers and sea channels. They consist of immersed tunnel elements connected to a cut and cover tunnel at each side of the river. The elements are constructed at a dry pit at the side of the river, and then floated to the tunnel site to be sunk into place and then linked together. Figure 1 shows the schematic picture of the immersed tube tunnel alignment.

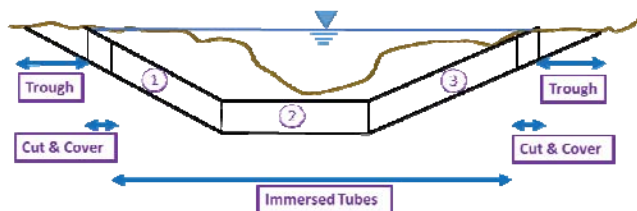


Figure 1. Schematic picture of an Immersed Tube Tunnel alignment

This paper provides the detailed process of the development of a material set that will be used in the finite element analyses of excavations as part of an Immersed Tube Tunnel construction. Due to confidentiality of the data, the name of the project and measured values are not reported in this paper.

A uniform distribution of material in depth was assumed on the project site. Since the material properties slightly changes with depth, it is very difficult or impossible to find a single parameter set that can perfectly predict the test results at all different depths. However, a reasonable match should be provided when comparing the laboratory test data at different depths.

Recent researches indicate that the Hardening Soil model with small strain stiffness, available in FE package PLAXIS 2D, replicates the behaviour of the soft clay reasonably well for normal construction (e.g. Ismail and Teshome (2011)). Therefore, the HS-Small model has been used for the ground movement assessment.

This paper briefly discusses the HS-Small soil model and the definitions of the input parameters. Then, the detailed process of the input parameter calibration is explained. Finally, the comparison of the predicted ground movement with the measured values during construction of an Immersed Tube Tunnel, using calibrated material set is presented.

2 HARDENING SOIL MODEL WITH SMALL STRAIN STIFFNESS (HS-SMALL)

Hardening soil model with small strain stiffness (HS-Small) is an advanced model available in PLAXIS which can be used for both soft soil and stiff soils. HS-Small uses Mohr-Coulomb failure surface and hardening plasticity in pre-failure stress state. Plastic strains are calculated by the multi-surface yield criteria, which defines the irreversible shear straining due to deviatoric loading and compression hardening yield surface defines the irreversible volumetric straining due to isotropic loading.

The yield surface in HS-Small model is not fixed in principal stress space as opposed to elastic perfectly plastic

models such as Mohr Coulomb. It can be expanded due to plastic straining caused by shear hardening and compression hardening. The stiffness of the soil is governed by triaxial loading stiffness, E_{50} , the oedometer loading stiffness, E_{oed} and the unloading-reloading stiffness, E_{ur} . The formulation of these stress dependent stiffnesses are as follows,

$$E_{50} = E_{50}^{ref} \left(\frac{c \cdot \cos \varphi - \sigma_3' \cdot \sin \varphi}{c \cdot \cos \varphi - p^{ref} \cdot \sin \varphi} \right)^m \quad (1)$$

$$E_{oed} = E_{oed}^{ref} \left(\frac{c \cdot \cos \varphi - \frac{\sigma_3'}{K_0^{NC}} \cdot \sin \varphi}{c \cdot \cos \varphi - p^{ref} \cdot \sin \varphi} \right)^m \quad (2)$$

$$E_{ur} = E_{ur}^{ref} \left(\frac{c \cdot \cos \varphi - \sigma_3' \cdot \sin \varphi}{c \cdot \cos \varphi - p^{ref} \cdot \sin \varphi} \right)^m \quad (3)$$

where p^{ref} is the reference stress for stiffnesses; E_{50}^{ref} is secant stiffness in standard drained triaxial test at p^{ref} ; E_{oed}^{ref} is tangent stiffness for primary oedometer loading p^{ref} ; E_{ur}^{ref} is Unloading/reloading stiffness p^{ref} ; m is the power for stress dependency of stiffness; c is (effective) cohesion; φ is (effective) angle of internal friction and K_0^{NC} is K_0 value for normal consolidation. Figure 2 demonstrates the definition of the stiffness parameters.

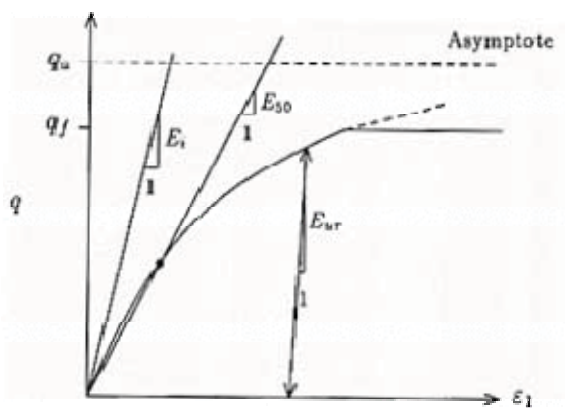


Figure 2. Hyperbolic stress-strain relation in primary loading for a standard drained triaxial test (after Schanz et al. 1999)

The E_{ur} stiffness is used in the HS-Small model to simulate the elastic behaviour of the soil in loading and unloading. However, the soil behaviour can be considered truly elastic in a very small strain range. The soil stiffness decays as the strain increases. The changes of the stiffness with strain is considered in the HS-Small model by considering two more parameters,

$$\frac{G_s}{G_0} = \frac{1}{1 + a \left| \frac{\gamma}{\gamma_{0.7}} \right|} \quad \text{where } a = 0.385 \quad (4)$$

where G_0 is the initial or very small-strain shear modulus and $\gamma_{0.7}$ the shear strain level at which the secant shear modulus G_s is reduced about 70% of G_0 . Further details on HS-Small can be found in Brinkgreve et al. (2014) and Schanz et al. (1999).

3 METHODOLOGY

The available laboratory tests were simulated using the PLAXIS test element and the results were compared to the laboratory test data. In this calibration exercise, the compression triaxial test at depth 30 m and oedometer test at 27 m (similar depths) were considered simultaneously and the input parameters of the HS-Small were varied until a good match was found between the laboratory test data and PLAXIS results for both tests. Then, the performance of the calibrated parameters in predicting the result of triaxial and oedometer tests at other depths were assessed.

4 RESULTS

4.1 Calibration

A flow process chart on development of Material set M2 is shown in Figure 3. The table of input parameters for each material set, comments and changes in each stage and comparison of the results to laboratory test data are depicted in this figure. Numerous simulations were performed in order to find a material set that is capable of replicating the soil response in different stress paths. The goal of this part of the study is to find a perfect match for both triaxial and oedometer tests at the same (or similar) depths. The undrained triaxial compression test at depth 30 m and one dimensional consolidation test at depth 27 m were selected accordingly.

Different studies existed in the literature in relation to the sites close to the site of this study. Material set A1 was selected based on the reported calibrated data in the mentioned studies on the project location and was used as an initial point in the calibration process. The results of simulation of the undrained triaxial compression test using Material set A1 were assessed in terms of stress-strain curve, stress path and pore pressure changes with strain. The results from test simulations were compared to the measured values in laboratory tests. As it can be seen in Figure 3 the predicted shear stress values by material set A1 are lower than the laboratory test data at strains less than 2% and higher at larger strains. The stress path partly matches the lab data but does not follow the curved shape. The predicted excess pore pressures are lower than the measured values. The oedometer test was also simulated and the comparison of the results show a reasonable match. However, the slope of the curve in the unloading reloading part is steeper than the lab data.

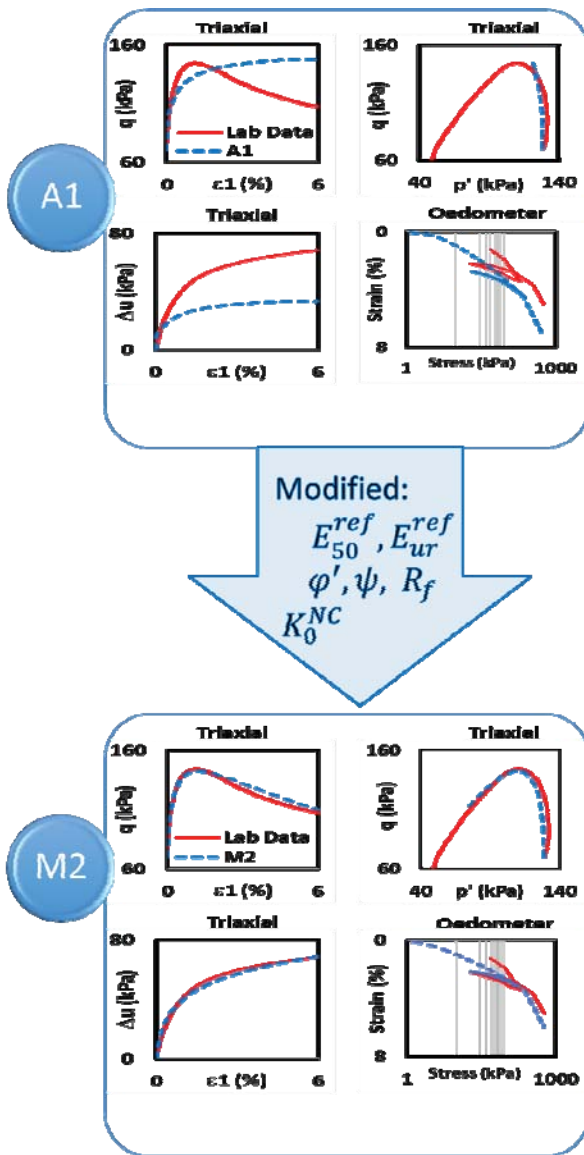


Figure 3. Flow process chart on development of Material set

A series of simulations were performed in order to improve the prediction of soil response in FE simulations of laboratory tests. The effect of each input parameter in conjugation with other parameters were explored and the parameters were varied until a perfect match was obtained for both the triaxial test at depth 30 m and the oedometer test at depth 27 m. This material set is referred to as the M2 set.

Material set M2 is stiffer compared to material set A1. The values of stiffness parameter E_{50}^{ref} and E_{ur}^{ref} , were increased in order to replicate the soil behaviour in the small strain range of the triaxial test and the unloading/reloading section of the oedometer test. The friction angle was also increased from 30 degrees to 38 degrees to capture the peak value of the stress strain curve. The post peak softening behaviour of the soil was simulated by considering a negative value of -8 degrees for the dilation angle. As a result, the stress-strain curve in triaxial test for both the pre-peak and post-peak segments were perfectly predicted by FE simulation. An excellent estimation of the pore pressure changes with strain was also obtained.

The stress path also shows a very good agreement with the lab test data and the curved shape of the stress path in the $q - p'$ space was predicted very well.

Although an excellent match was found for material set M2, it is very important to check the obtained parameters against the factual data and with the local experience in the region. There is little factual evidence to support the use of the friction angle equal to 38 degrees in design. Local practice is to use an upper bound of 30 degrees for the friction angle; hence, this value will be adopted here. The revised material set based on local experience, is called M4. There are a few more changes in material set M4 as explained in the following paragraphs.

Similar to friction angle value, there is little factual evidence to support a negative dilation angle for the clay and a dilation angle of zero was adopted in Material set M4.

The coefficient of lateral earth pressure in a normally consolidated stress state, K_0^{NC} , PLAXIS is automatically estimated from Jacky's formula as following,

$$K_0^{NC} \approx 1 - \sin \phi \quad (5)$$

Using friction angle of 38 degrees from material set M2, the K_0^{NC} was obtained 0.38. Local experience shows that the K_0^{NC} value is closer to 0.55 with the K_0 value equal to 0.625. K_0^{NC} and K_0 values were set to 0.55 and 0.625 in material set M4, respectively. Figure 4 and Figure 5 illustrate the comparison of the FE analyses results using material sets A1, M2 and M4 with laboratory test data of triaxial and oedometer tests.

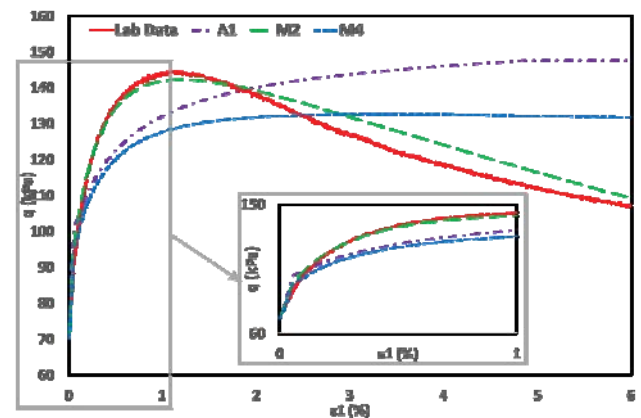


Figure 4. Comparison of PLAXIS triaxial test results using material sets A1, M2 and M4 to laboratory triaxial test results at 30 m

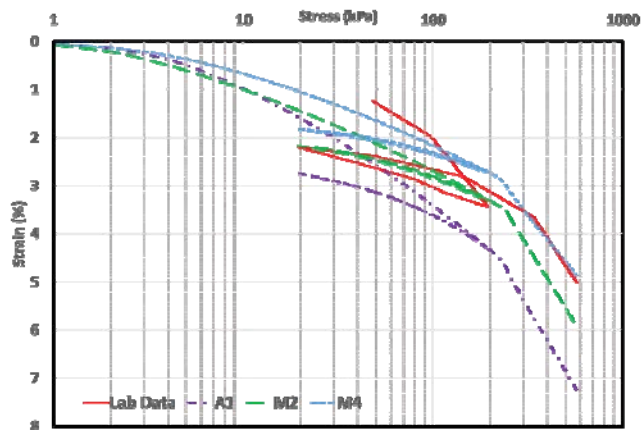


Figure 5. Comparison of PLAXIS oedometer test results using material sets A1, M2 and M4 to laboratory oedometer test results at 27 m

4.2 Validation of the parameter set M4 at other depths

The calibrated material set, M4, was checked against the triaxial test data at depth 42 m and oedometer test data at 17.7 m and 22 m. These tests were simulated using element test in PLAXIS and the results were compared to the laboratory test data.

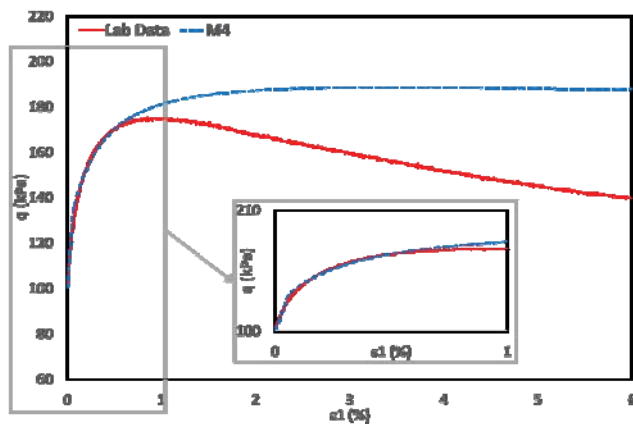


Figure 6. Comparison of PLAXIS triaxial test results using material sets A1, M2 and M4 to laboratory triaxial test results at 42 m

Figure 6 shows that a perfect match was found in the small strain range ($\epsilon_1 < 1\%$). The difference between the predicted stress-strain curve and the measured laboratory data grows as the strain increases. This is due to the softening behaviour of the soil for the strain range larger than 1 %. As mentioned before, the HS-Small can capture this behaviour by considering negative dilation angle. However, local experience shows that the dilation angle of zero can predict the clay response better. Furthermore, the strain range in the excavation is mostly in the small strain range in which a very good match has been obtained. The mobilised undrained shear strength of the soil should be monitored during the analyses, to make sure that it does not exceed the undrained shear strength of the soil obtained from lab and field tests.

An acceptable match was observed in the desired strain range, for oedometer test results at depth 17.7 m and 22 m (see Figure 7 and Figure 8).

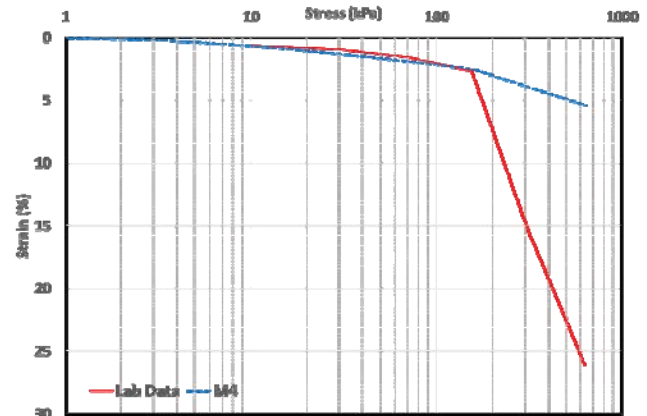


Figure 7. Comparison of PLAXIS oedometer test results using material sets M4 to laboratory oedometer test results at 22 m

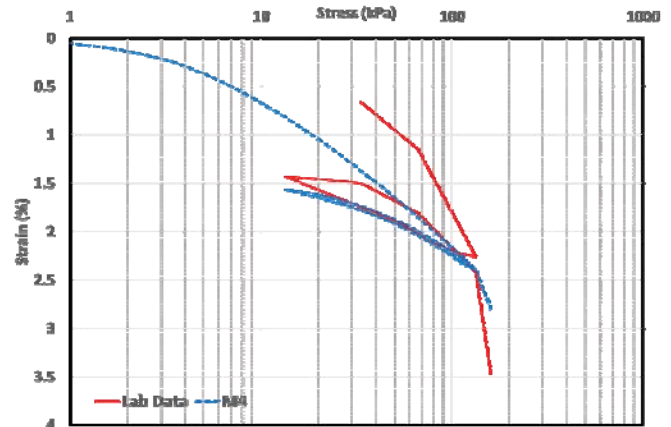


Figure 8. Comparison of PLAXIS oedometer test results using material set M4 to laboratory oedometer test results at 17.7 m

5 COMPARISON OF GROUND MOVEMENT WITH MONITORING DATA

The global movement assessment for the immersed tube tunnel is a complex calculation involving several different construction stages, extensive temporary works and varying soil properties arising from the different depths of excavation and stress unloading along the alignment. This section describes the predicted ground movements that will occur around the tunnel during construction and operation and compares the results with the measured data at site.

The cut and cover elements were designed as gravity structures with no tension piles. The output from the ground movement analyses, is in the form of time versus movement. This study illustrates movements at the interface between cut and cover and IMT sections.

Figure 9 illustrates FE model of the two dimensional cross section of the tunnel at the IMT element and the cut and cover tunnel intersection. Different soil layers were defined to consider the change of permeability with depth. The HS-small

model was used to describe the soft marine clay using the calibrated input parameters. Pipe-pile walls were defined as plate elements and the piles behind the walls were simulated using embedded pile row elements, which have some advantages over plate elements in modelling discrete piles.

The concept of an embedded pile was created in an attempt to include the interaction of the piles in an out-of-plane direction. This is done by employing interface elements that control the relative behaviour of the pile and soil elements. Furthermore, modelling piles as plate elements restricts the soil movement perpendicular to the pile. However, soil can move through the pile row in 3D models. Embedded pile row elements in the 2D model, addresses this concern and allows the soil to flow through the pile element by the indirect coupling of interfaces to soil elements. The properties of the piles elements were calibrated against the measured pile load test at the site of the project. The performance of the embedded pile row element has been reviewed in different researches (Engin (2009); Dao (2011); Engin et al. (2008); Tschuchnigg and Schweiger (2015)).

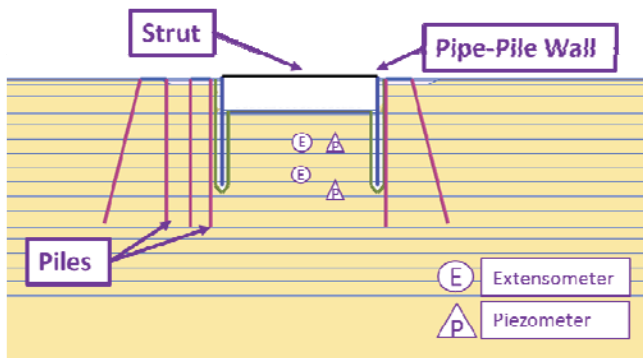


Figure 9. FE model of the two dimensional cross section of tunnel at the IMT element and the cut and cover tunnel intersection

The geo-monitoring program at the project site consisted of extensometers and piezometers at different depths. Different construction phases including installation of rig platform, crane piles, pipe-pile wall, waling beam & strut were simulated using PLAXIS. This was followed by the underwater excavation, drainage layer installation, underwater concrete installation, dewatering and ballast layer installation. The results of the FE model were stored at the locations where the geo-monitoring instruments were installed. Then, the variations of the displacements and pore pressure changes with time were compared to the monitored data.

Figure 10 and Figure 11 show the comparison of the measured pore pressure changes (normalised with the maximum predicted value from FE analysis) at levels equal to -20 mOD and -35.5 mOD. A very good agreement was observed between the two data series. The time series clearly matched the pattern of pore pressure change due to unloading and reloading sequences. As seen in Figure 10 and Figure 11, pore pressure reduces during the underwater excavation stage due to the unloading of soil weight. The decreased pore pressure partly recovers after installation of the drainage layer and UW concrete. Dewatering resulted a large reduction in the

pore pressure beneath the excavation base, which is demonstrated with a big jump in pore pressure changes plots.

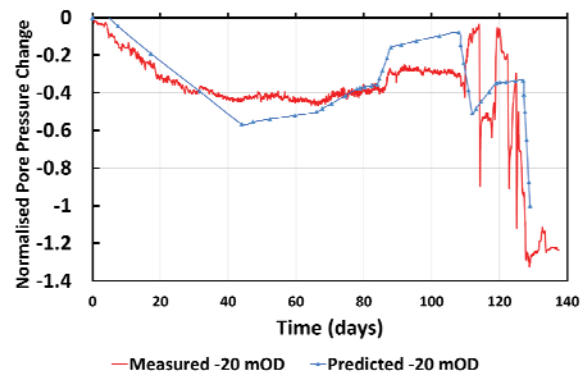


Figure 10. Comparison of the measured pore pressure changes to predicted values by FE analysis: level -20 mOD

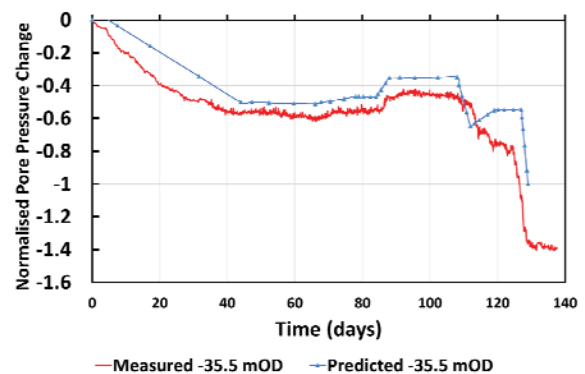


Figure 11. Comparison of the measured pore pressure changes to predicted values by FE analysis: level -35.5 mOD

Figure 12 and Figure 13 demonstrate the variation of vertical displacement (normalised with the maximum predicted value from FE analysis) with time at the base of excavation at levels of -19.5 mOD and -28.5 mOD. The trend of displacement changes predicted by PLAXIS matches the monitored data at both levels. A gap can be observed between the FE results and the measured data at level -28.5 mOD. However, the difference is deemed to be in the acceptable range considering the special variation of the sub soil layers, stiffness and strength soil properties, permeability, etc. and also inaccuracy in the construction timing. As depicted in Figure 12 and Figure 13, soil heaves during unloading stages of UW excavation and dewatering. The FE modelling of the excavation in soft marine clay using the HS-small model is a reliable approach to predict the pore pressure changes and the vertical displacements with a proper calibration of the input parameters.

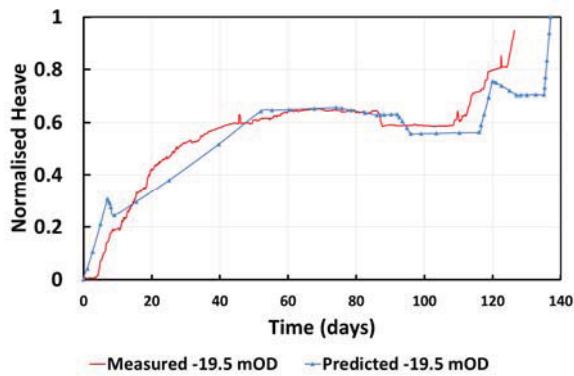


Figure 12. Comparison of the measured vertical displacements to predicted values by FE analysis: level -19.5 mOD

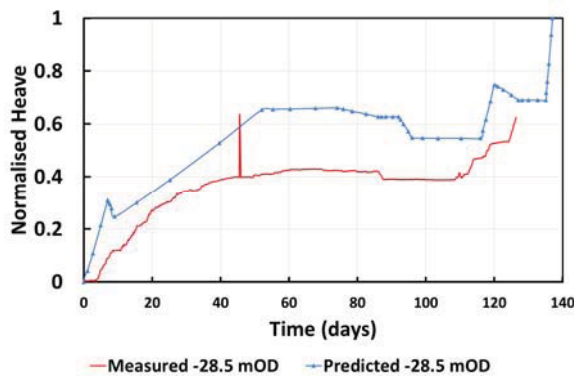


Figure 13. Comparison of the measured vertical displacements to predicted values by FE analysis: level -28.5 mOD

6 SUMMARY AND CONCLUSION

The process of the input parameters calibration for finite element analysis was presented in this paper. The HS-Small model was selected to perform the FE analysis. The input parameters of the model were varied until the results of the FE simulation of triaxial and oedometer test data at similar depths (30 m and 27 m) simultaneously matched the laboratory test data. Then the obtained parameters were modified based on local experience on the clay at project location. Finally, the calibrated material set was checked for available test results at different depth on site and an acceptable match was found between the results and laboratory test data.

A two dimensional cross section at the interface of the cut and cover structure and the IMT element was selected for ground movement analysis. The vertical displacements and pore pressure changes were monitored during the construction. The comparison of the predicted and measured values, demonstrated a very good agreement between the two series.

The results highlighted the importance of the calibration of the input parameters with different laboratory test data, to provide a reliable predictions. The findings also illustrated the good performance of the Hardening Soil with Small Strain Stiffness constitutive model, in predicting the behaviour of a soft marine clay during excavation.

REFERENCES

- [1] Brinkgreve, R. B. J., Engin, E., & Swolfs, W. M. (2014). PLAXIS Material Models Manual 2014, Plaxis bv
- [2] Dao, T. P. T. (2011). "Validation of PLAXIS embedded piles for lateral loading." TU Delft, Delft University of Technology.
- [3] Engin, H. K. (2009). "Modelling piled foundation by means of embedded piles."
- [4] Engin, H. K., Septanika, E. G., and Brinkgreve, R. B. J. (2008). "Estimation of Pile Group Behavior using Embedded Piles." *12th International Conference of International Association for Computer Methods and Advances in Geomechanics (IACMAG)*, 1–6.
- [5] Ismail, A., and Teshome, F. (2011). "Analysis of deformations in soft clay due to unloading." 74.
- [6] Schanz, T., Vermeer, P. A., and Bonnier, P. G. (1999). "The hardening soil model : Formulation and verification." *Proc., Plaxis Symp. "Beyond 2000 in Computational Geotechnics," Amsterdam, Balkema, The Netherlands*, 281–296.
- [7] Tschuchnigg, F., and Schweiger, H. F. (2015). "The embedded pile concept – Verification of an efficient tool for modelling complex deep foundations." *Computers and Geotechnics*, Elsevier Ltd, 63, 244–254.

Heave-ho! A laboratory model of an underfloor environment incorporating pyritiferous fill

McKeon, É.P.¹, McCabe, B.A.², Sexton, B.G.¹, Cavalcante, M.³, Ibañez-Valle, J.L.⁴, O'Connell A.M.⁵

¹formerly of College of Engineering and Informatics, National University of Ireland, Galway

² College of Engineering and Informatics, National University of Ireland, Galway

³Science Without Borders visiting student, College of Engineering and Informatics, National University of Ireland, Galway

⁴Visiting researcher, College of Engineering and Informatics, National University of Ireland, Galway

⁵Aidan O'Connell and Associates Limited, Portlaoise

email: bryan.mccabe@nuigalway.ie, aidan@aoconnellassoc.com

ABSTRACT: Damage to domestic dwellings in the greater Dublin area of Ireland caused by the expansion of underfloor fill material containing pyrite has become a high-profile national problem in recent years. In this paper, a novel experiment is described in which the succession of underfloor materials, with vertical dimensions at full scale, is reproduced. The study has enabled the amount/rate of expansion and pressures generated due to the expansion of the pyritiferous fill, with and without imposed loading on the concrete slab, to be ascertained over a period of 800 days. The rates of expansion are relatively consistent with those recorded from reference pipe experiments. These data form an important frame of reference for anticipating the time at which damage might begin to manifest itself in domestic dwellings.

KEY WORDS: pyrite; mudstone; expansion.

1 INTRODUCTION

The rapid economic growth experienced by the Republic of Ireland from the mid-1990s was influenced significantly by a buoyant construction industry. House-building was a major contributor, with the number of units completed in a calendar year peaking at 88,188 in 2006, compared to 30,575 in 1995 [1]. Tuohy *et al.* [2], quoting the Irish Concrete Federation, noted that the increased rate of building meant that 1200 quarries were in operation in the mid-2000s with some “*opportunistic supply of materials without the necessary technical knowledge at specifier, user or supplier level*”.

Some of the quarried fill material used in house foundations in the east of Ireland contained pyrite, a naturally-occurring mineral that oxidises to form products including sulphuric acid. Sulphuric acid reacts with calcite (another common mineral constituent of fill materials) to generate gypsum which can give rise to an increased fill volume compared to the original pyrite and calcite. The reaction process is detailed in Reid *et al.* [3]. Expansion of pyritiferous fill used in house foundations may result in heave of ground-bearing floor slabs and lateral displacement of foundation walls, leading in turn to significant damage to the superstructure, including cracking floors and walls, jamming doors, buckling of interior partition walls and movement of stairs. Czerewko and Cripps [4] provide a useful schematic of the process.

Experimental research has been carried out at NUI Galway since 2010 to identify the factors upon which pyritiferous expansion depends [5-7]. These studies used fill retrieved from beneath the floor slabs of dwellings in the greater Dublin area exhibiting structural distress. Samples were re-established in PVC pipes 229mm in diameter standing vertically in plastic basins with varied depths of water in the basins. Vertical movement of the fill was recorded using a dial gauge mounted on an independent frame. The use of smooth

pipes and the absence of vertical loading on the fill represented a deliberate attempt to encourage the maximum amount of expansion, although no attempt was made to accelerate the oxidation process.

Sutton *et al.* [5] prepared ten such pipes with constant density (approx. 2000 kg/m³) using a single fill source and varied the fill height (500 mm, 750 mm and 1000 mm) and the depth of water, i.e. submerged depth (30mm and 60mm). The pipes were situated in an unheated laboratory, so ambient temperatures closely tracked seasonal changes, generally increasing from 4°C to 15°C over 6 months. Significant expansion was manifest (which has not always been the case in unaccelerated studies elsewhere [e.g. 8]) and changes in the pH of the water in the basins were consistent with the generation of sulphuric acid. The magnitude of heave was proportional to the fill depth. However, the submerged depth was found to have little effect.

Using fill from a different source, McCabe *et al.* [6] reported on six further tests using the same apparatus with constant fill heights (500 mm), varied densities (nominally 1800 kg/m³, 2000 kg/m³ and 2200 kg/m³) and varied water depths (10 mm and 30 mm), situated in a temperature-controlled room with hold periods at 10°C, 15°C and 20°C over the duration of testing. Earlier heave onset times and/or greater heave magnitudes were observed in higher density fill. There was no long-term effect of temperature on the rate of heave over the temperature range considered once the effects of thermal expansion of the entire experimental system were accounted for.

From heave rates measured at NUI Galway and those reported by Maher *et al.* [9], McKeon [7] inferred that the rate of heave may be influenced by the proportion of mudstone in the fill material. This relationship is currently under systematic investigation at NUI Galway.

In this paper, a novel laboratory foundation model is described, which encapsulates a greater volume of fill than the pipe experiments and replicates more closely the underfloor conditions typical of an Irish dwelling. The block wall of the model represents the rising walls and encloses a vertical succession of materials from the *in situ* soil to the concrete floor slab, including some pyritiferous fill material. The heave of the slab was monitored, in addition to the relative humidity and pressure at points within the body of fill. A load was imposed on the slab after 17 months and the tests have been in progress for a period of 26 months at the time of writing. Three pipe experiments (of the type described in [5-7]), using fill from the same batch incorporated in the foundation model, were carried out in parallel for reference.

2 EXPERIMENTAL ARRANGEMENTS

2.1 Foundation Model Materials

The NUI Galway Pyrite Foundation Model (FM) comprises a masonry box structure with internal dimensions of 1.125 m × 1.125 m × 0.770 m (Figure 1). The blockwork walls were constructed on two adjacent precast concrete slabs, raised off the ground. The walls consist of seven courses of standard 4-in (100 mm) blocks built on the flat face giving a 210 mm-thick wall consistent with conventional rising wall construction in Ireland. The vertical succession of materials/finishes A-K and M is shown in Figure 2.



Figure 1. NUI Galway Pyrite Foundation Model, including imposed load of 3.4 kPa (inset: pipe experiments D2 and D3).

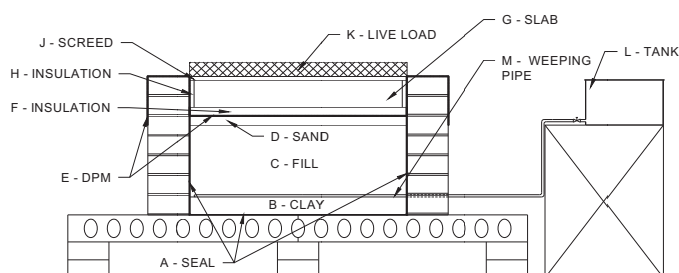


Figure 2. Section through NUI Galway Pyrite Foundation Model.

A: Bituminous seal:

The bituminous seal was applied internally to the base and to the sides up to the level of the underside of the concrete slab (i.e. 600mm above the base) with a view to inhibiting any moisture escape which would induce drying of the fill.

B: Compacted clay:

The clay was sourced from the foundation of a house undergoing remediation for heave damage in north Co. Dublin. The moisture content at the time of construction of the foundation model was found to be approximately 19%, while values of plastic limit and liquid limit were established as 17% and 35% respectively. These results are consistent with those of Upper Brown Dublin Boulder Clay as reported by Menkiti and Long [10]. The clay was spread evenly on the base of the model and compacted in one 100mm layer to approximately 2000 kg/m³ using a bespoke 15kg tamper.

C: Pyritiferous mudstone fill:

Fill thicknesses in practice are typically 400-600 mm; 400 mm was adopted for this experiment. The target density of the fill was approximately 1800 kg/m³, in keeping with values back-calculated by weighing the entirety of fill removed from beneath a floor slab and determining accurately the volume of space vacated. Compaction was achieved using the same tamping device that was used for the clay. The fill was placed and compacted in the model in 7 layers, each 55 mm – 60 mm deep, taking care that few fill particles were crushed during the compaction process. In Figure 3, the density achieved in each layer in the foundation model is plotted as a function of the height from the bottom of the fill to the midpoint of each layer (hollow symbols). Moisture contents (determined at 105°C) of samples taken 50 mm, 150 mm, 250 mm and 350 mm from the bottom of the fill are represented in Figure 4.

D: Blinding sand:

A 50mm thickness of blinding sand was laid at a density of 1600kg/m³. Given that the radon gas extraction system required by Irish Building Regulations would allow air to circulate to underfloor fill in practice, 5 no. 20mm dia. holes were drilled in each of the four side walls at a level corresponding to mid-depth in the sand. This facilitates the oxidation process through access to fresh air.

E: 1200 gauge Damp Proof Membrane (DPM):

This plastic DPM inhibits any moisture egress through the insulation or concrete slab above, as is standard construction practice (indicated by the dashed line in Figure 2). The DPM is continued upwards along the interior face of the model walls and is sealed on the outside of the model as can be seen in Figure 1, essentially ensuring a complete moisture barrier.

F: High density insulation:

Kingspan Kooltherm K3 Floorboard, 50mm thick, was used and cut to fit snugly on top of the DPM.

G: Concrete slab:

A precast hollowcore concrete slab (mass 303.9 kg) was placed on top of the insulation. The slab measured 1.075m ×

1.075m in plan by 150mm in thickness. Elements D, F and G imposed a combined stress of 3.4kPa on the fill.

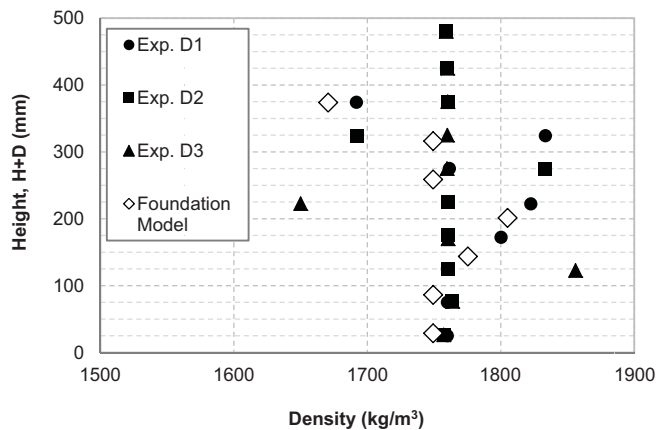


Figure 3. Initial density v height for FM and D1-D3.

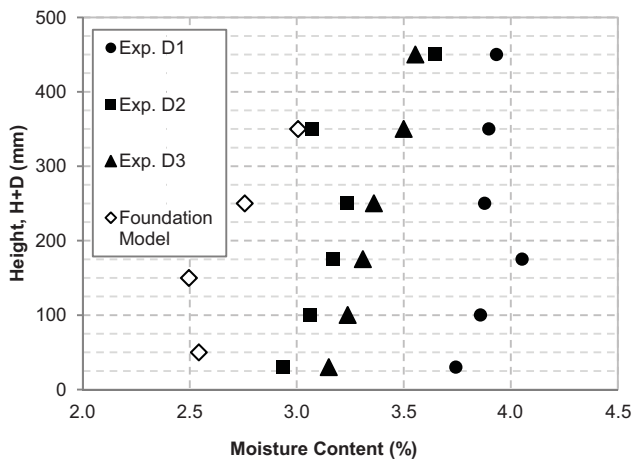


Figure 4. Initial moisture content v height for FM and D1-D3.

H: Insulation strips:

In the 25 mm surrounds between the walls of the model and the slab, cold-bridging insulation strips were fitted and any gaps were filled with expanding foam.

J: Screed:

A self-levelling screed was poured on top of the slab to give smooth contact points for the dial gauge tips.

K: Imposed load:

I.S. EN 1991-1-1:2002 [11] requires slabs in domestic dwellings to be designed for a live load of 1.5kPa. An external load was imposed approximately 17 months after commencement of the experiment using concrete blocks (soap bars) of nominal dimensions 95mm × 95mm × 445mm. A total of 50 soap bars (some split into two) provided an average loading of approximately 3.4kPa over the slab, i.e. doubling the stress already supported by the fill owing to the weights of D, F and G, and deliberately surpassing the 1.5kPa value to induce a clear response. As can be seen from Figure 1, the positions of the soap bars were dictated by the positions of both the dial gauges and the requirement of an unobstructed line-of-sight to them; the plan area coverage is approximately 71%.

A **water tank (L)** was also provided outside the model with its base 400mm above the top of the clay layer, which can be connected to a '**weeping pipe**' (**M**) irrigation facility at the interface between the clay and fill. This was intended to provide additional water to the fill which may be available from a thicker clay layer in the field. However, since the expansion rate did not show signs of abating after 800 days, this irrigation facility was not utilised.

2.2 Relative Humidity Probes

Relative humidity probes RH1-RH4 were used to assess the moisture content of the fill at two levels. All sensors were located 227mm from the side walls. Two probes RH1 and RH3 were positioned in diagonally-opposite locations 100 mm above the bottom of the fill while the other two diagonals were occupied by sensors RH2 and RH4, 300 mm above the bottom of the fill. The fill surrounding the probe housing was sieved and only particles larger than 5mm were placed within 50 mm. This ensured that little deleterious matter passed through the 5 mm dia. holes in the housing reducing the chance of probe clogging or damage. Each relative humidity cable was sealed in a rubber covering to avoid damage.

Small containers of fill were used to develop calibrations between relative humidity and moisture content for RH1-RH4 prior to their incorporation within the foundation model. The relationships were non-linear but repeatable, in keeping with research showing that the relationship between the relative humidity of an air pocket in a concrete cube sample and the moisture content was non-linear [12]. However, the relationships were only valid up to a moisture content of approximately 4%, after which the relative humidity remained at 90-95% irrespective of moisture content. Therefore inference of moisture content from the sensors would only be meaningful if the moisture content remained below 4%. A similar experience of limited useful range of humidity sensors has been reported at the University of Sheffield [13]. Each of the probes RH1-RH4 also recorded temperature.

2.3 Pressure Cells

Two single-sided and one double-sided circular vibrating wire pressure cells (supplied by ITM Soil Ltd., U.K.) were installed in the foundation model. The external diameters of the single-sided and the double-sided cells were 240mm and 200mm respectively, while the active face (i.e. the area measuring the pressure) was 176mm for both types. The range of all the pressure cells used was 0-1 MPa in allowance for the possible development of high stresses (damage to the Golder Swell Test [9] was calculated to have required a pressure of 600 kPa). Each cell also incorporated a thermistor.

One single-sided pressure cell (PC1) was placed vertically on the middle of the block wall, with active side facing the fill. The double-sided cell (PC2) was placed horizontally at the mid-height within the fill and centred in plan. The second single-sided cell (PC3) was placed vertically above PC2 with active side facing down at the interface between the sand layer and insulation. Only particles passing the 5 mm sieve were placed within 25 mm of the cells in keeping with the manufacturer's instructions. The proportion of the plan area of the fill occupied by the faces of cells PC2 and PC3 was 3.6% and 2.5% respectively and therefore their presence was not

believed to have interfered significantly with the expansion process. Each pressure cell also measured temperature.

2.4 Dial Gauges

The movement of the concrete slab was monitored by dial gauges, one in the centre of each quadrant of the slab (DG1-DG4) and a fifth near the centrepoint of the slab (DG5). DG5 was added 28 days after the other four in light of the early tilting observed. The dials were mounted on a frame independent of the walls and slab of the foundation model.

Soon before the load (K) was imposed, an additional dial gauge (DG6) was added to monitor potential outward movement of one side wall; this was positioned externally on the opposite side of the blockwork to PC1 and at the same level as its centrepoint.

2.5 Reference Pipe Experiments

In order to ascertain the relative performances of the foundation model and the pipe apparatus [5-7], 3 no. pipe experiments D1 to D3 were established using fill derived from the same batch and compacted to approximately the same average density as the foundation model. The first expansion readings from these pipes were taken 28 days after the first expansion readings from the foundation model. Test D1 was subject to a temperature of 20°C (for the vast majority of the testing period) in a temperature-controlled room. Replicate tests D2 and D3 were located in immediate proximity to the foundation model in the open laboratory (inset to Figure 1); and were therefore exposed to the same temperature and humidity variations. Variations of initial density and moisture content over the 500mm depth of fill are also shown in Figure 3 and 4 respectively (solid symbols), where they can be compared to those of the foundation model.

3 PYRITIFEROUS MUDSTONE FILL PROPERTIES

3.1 Introduction

The fill sample used in the foundation model and in the reference pipe tests D1-D3 was originally quarried in 2005. In 2013, it was extracted from the foundation of a house in Co. Dublin undergoing remediation for damage due to pyritiferous heave. Geological tests were carried out in 2012 by Sandberg LLP Laboratories, London, on samples of fill taken from the same house prior to the remediation process.

3.2 Moisture Content, Grading and Lithology

A single moisture content value of 4.6% (air dried at 38°C) was reported in 2012 [14], suggesting that the material may have dried slightly before the experiments were performed (see Figure 3). The fill is classified as a sandy GRAVEL and the grading largely conforms to National Roads Authority (NRA) Clause 804 bounds. A description of the main rock types was given for the sample as part of the geological report [14]; three distinct lithologies were identified: (i) Calcareous (silty, carbonaceous) mudstone, (ii) Typically strong, argillaceous (silty, carbonaceous) limestone and (iii) Typically strong limestone (carbonaceous and non-carbonaceous). The report also stated that the surfaces of the fill particles were covered in abundant calcareous and argillaceous dust that contained altered framboidal pyrite. Gypsum crystals were present on the surface of some particles.

3.3 Chemical Testing

Chemical test results are set out in Table 1; values in bold have been calculated based on equations set out in Reid *et al.* [3]. Electron microscope and X-Ray diffraction test results for the fill used in this research are shown in Table 2.

Table 1. Chemical test results

AS (SO ₄) (%)	WS (mg/l SO ₄) (%)	TS (S) (%)	OS (S) (%)	Original Pyrite (%)	Existing Pyrite (%)	Oxidised Pyrite (%)	% of Original Pyrite Oxidised
4.18	1886	2.00	0.61	3.74	1.13	2.61	69.7

Table 2. Electron Microscope and XRD test results

Total Mudstone (%)	Total Calcareous Mudstone. (%)	Total Non-Calcareous Mudstone (%)	Mudstone with gypsum- filled cracks (%)	Total Limestone (%)	Gypsum (%)	XRD Testing		
						Pyrite (%)	Calcite (%)	Gypsum (%)
71.3	15.2	43.9	12.2	15.8	1.2	2.1	13	11

4 RESULTS AND DISCUSSION

4.1 Temperature in laboratory and in fill

The ambient room temperature varied in the range 18°C-25°C over the duration of the experiment. The temperatures recorded by PC1-PC3 and RH1-RH4 typically fell 1.5°C and 2°C below the recorded ambient temperature respectively. The room temperature was used to estimate the thermal expansion of the reference frame and dial gauges while the temperature measurements from within the model were used to determine the thermal expansion of the internal materials.

The coefficient of thermal expansion of the fill was assumed equal to that measured for a pyrite-free Clause 804 fill material established in two additional pipes ($15 \times 10^{-6} / ^\circ\text{C}$) [7]. The effect of thermal expansion on the entire experimental system was found to be negligible.

4.2 Humidity in fill

RH3 failed to operate consistently once installed within the foundation model, so its results were excluded. The initial humidity readings for RH1, RH2 and RH4 taken once the foundation model was established (60-70%) indicated moisture contents that were broadly compatible with those shown for the foundation model in Figure 4. The subsequent variation with time can be summarised as follows:

- Sensor RH1 registered an increase in humidity to 92-93% within about 15 days and remained stable thereafter. The increased moisture content in the fill is evidently drawn from the clay 100mm below, but the actual value cannot be determined with certainty due to the upper limit of the calibration.
- Sensors RH2 and RH4, both 300mm above the clay layer, showed a more gradual increase in humidity to values in the range 80-85%. The inferred moisture

contents for RH1 and RH2 represent increases of the order of 0.25% from the initial values.

Given the stable output from the gauges, only intermittent readings were deemed necessary beyond the 270 day mark to confirm that the irrigation facility was not required.

4.3 Heave

4.3.1 Foundation Model

In Figure 5, the magnitudes of heave are normalised by the fill thickness of 400mm and zeroed at the 45 day mark, before which self-weight settlement and some tilting of the slab arose. The normalised heave registered by the centre gauge shows almost identical output to the average of gauges DG1-DG4. In the absence of imposed loading, the average normalised heave rate over a 470 day period is approximately 0.0021 mm/mm/yr or for the 400mm thickness of fill used, a heave rate of 0.86 mm/yr.

Upon application of the imposed load at day 520, all gauges (with the exception of DG2) registered an instantaneous settlement of 0.07-0.1 mm, with minimal additional movement over a 40 day period. Thereafter, heave movements re-established themselves at a reduced rate of approximately 0.0007 mm/mm/yr or 0.27 mm/yr (for 400mm). This reduced rate is in keeping with experience that more heavily loaded ground floor rooms such as utilities and kitchens experience lower rates of heave than in living rooms and hallways where similar fill is present.

The dial gauge mounted on the side wall DG6 registered no discernible movement over the period for which it was in place. Moreover, a visual inspection of the blockwork and joints showed no evidence of deterioration over time.

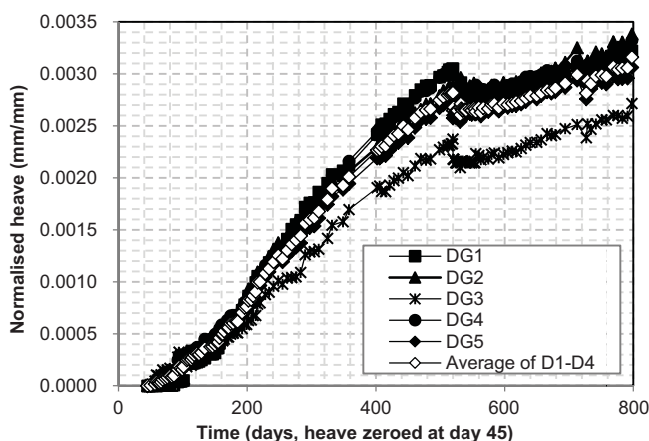


Figure 5. Normalised displacement v time for FM.

4.3.2 Pipe experiments

The movements registered by all pipes D1-D3, normalised by their fill heights of 500mm, are plotted on Figure 6 (the time origin on this graph corresponds to that on Figure 5). Replicates D2 and D3 exhibit very similar heave responses, demonstrating repeatability as found in other pipe experiments [7]. The curve for D1 is notably smoother than the others, probably on account of its constant temperature environment.

All pipes show a high initial rate of heave, which is greater for those pipes in the open laboratory. At the time of writing,

this is believed to be an 'establishment' effect which is a function of the experimental arrangement rather than the expansion process; the same phenomenon was also observed in expansion experiments in the University of Sheffield [15]. At approximately 70 days, the rates slow significantly and become steady thereafter in all cases, with a normalised heave rate of 0.0014 mm/mm/yr for D1 and 0.0016 mm/mm/yr for D2/D3 over a 470 day period. The average normalised heave rate for the Foundation model (prior to the imposed load) is also included in Figure 6 for comparison. In spite of the 3.4 kPa loading from the slab and sand, the foundation model heave rate is approximately 35% greater than that for D2 and D3. This may be due to unequal influences of friction at the model interfaces; while the pipe is smoother than the bitumen-coated blocks, the relative influence on the pipe walls on heave (pipe aspect ratio: height/diameter = 2.18) is greater than that of the foundation model walls (model aspect ratio: height/width = 0.36). In the foundation model, wall friction may have a relatively smaller effect on the body of fill.

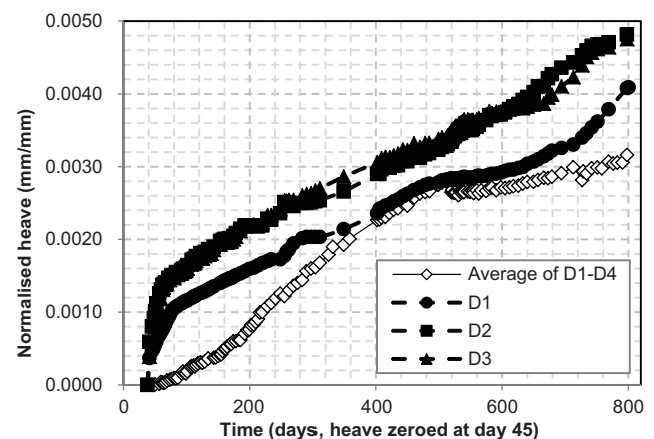


Figure 6. Normalised displacement v time for FM, D1-D3

4.4 Pressure

In Figure 7, the net pressure (zeroed at the 45 day mark to correspond with the observed heave, see Figure 5) is plotted against time. The following comments can be made about the pressure cell output over the course of the experiment:

- (i) The pressures are relatively low, consistent with an unrestrained slab that has been lifting steadily. In fact, the measured pressures are at the lower end of the 28-600 kPa range established by Maher and Gray (2014) from a literature review, although all of these have been estimated rather than measured directly. In any case, the levels of restraint of the slab will dictate the relative development of heave and fill pressures.
- (ii) The slight differences in heave rates up to 520 days identifiable in Figure 5 can be explained by subtle pressure change patterns in Figure 7, albeit the pressure changes are relatively minor. For example, the period of higher heave from days 160-300 corresponds to reducing pressures, whereas the reduced rate from days 300-520 corresponds to relatively constant pressures.
- (iii) The local fluctuations in pressure mirror the temperature variations, so therefore reflect the thermal expansion and

contraction of the materials within the Foundation Model. Cell PC2 is less sensitive to these effects, as might be expected due to compensating effects of its two active sides.

- (iv) The 3.4 kPa load applied on day 520 induced the expected step increases in PC2 and PC3 (annotated on Figure 7). The effect was less clear for PC1, as might be expected given its orientation.

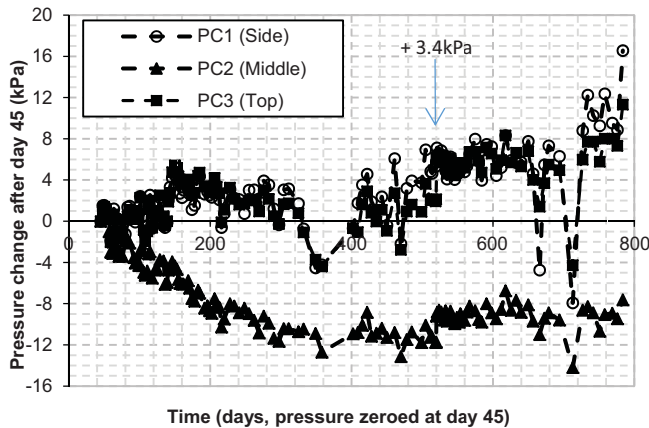


Figure 7. Net pressure v time.

4.5 Discussion

Adopting 500mm as the average fill thickness used in practice, the rates inferred for the fill material used in this study can be extrapolated from 400mm to 500mm (valid based on previous research [5]), becoming 1.05 mm/year (floor slab only) and 0.34 mm/year (floor slab plus 3.4 kPa imposed loading).

A key implication of these expansion rates is that they enable an estimate to be made of the likely duration to manifestation of damage arising from pyritiferous heave. This information is relevant to:

- homeowners with houses founded on pyrite-free fill material, wondering if the window for pyrite-induced damage has passed, and
- interested parties assessing whether damage claimed for has resulted from pyrite.

In developing IS 398 [17], the new Irish standard for pyrite, the threshold for damage has been adopted as 5mm differential movement over 1m across a floor slab. Therefore, in the 'floor slab only' case, the inferred time-to-damage is 4.8 years. Using the two rates quoted above and assuming that linear interpretation between them is valid, the estimated time-to-damage for a floor slab carrying 1.5 kPa (imposed live load requirement [11]) is 6.8 years. It should be noted that these times-to-damage should only be considered relevant to the material investigated in this research in the NUI Galway foundation model; further research is required to ascertain appropriate heave rates and times-to-damage for fill of alternative lithologies (such as different mudstone/limestone proportions and TS values).

5 CONCLUSION

In this paper, the expansion of pyritiferous fill has been investigated using a larger volume of material and more

representative experimental boundary conditions than have been considered heretofore.

Over a period of 800 days, the movement of a concrete slab (with and without an imposed load) arising from the expansion of 400mm thickness of fill has been monitored. The moisture content has been maintained constant and fill temperatures have varied between 16°C and 23°C. Relatively small pressures have been recorded within the fill, consistent with the free movement of the slab observed. Heave rates have been reported as 0.0021 mm/mm/yr (with load-free slab) and 0.0007 mm/mm/yr (with slab loaded to 3.4 kPa). These rates can be used to estimate the duration required for damage to occur assuming an appropriate damage threshold, such as the 5mm differential movement alluded to in IS398.

Further investigation is required to determine equivalent heave rates and times to damage for fill materials with alternative lithologies.

REFERENCES

- [1] Central Statistics Office CSO (2008). Construction and Housing in Ireland, 2008 edition, Pm A8/1862, Stationery Office, Dublin, Ireland.
- [2] Tuohy, B., Carroll, N. and Edger, M. (2012) Report of the Pyrite Panel, 174 pages <http://www.environ.ie/en/PyriteReport/>
- [3] Reid, J. M., Czerewko, M. A. and Cripps, J. C. (2005) Sulfate specification for structural backfills – TRL Report TRL447 Crowthorne, Transport Research Laboratory, 2nd Edition.
- [4] Czerewko, M.A. and Cripps, J.C. (2015) Investigation of destructive ground heave affecting
- [5] Sutton, D., McCabe, B.A., O'Connell, A. and Cripps, J.C. (2013) A laboratory study of the expansion of an Irish mudstone/siltstone fill material, *Engineering Geology (Elsevier)*, Vol. 152, pp. 194-201.
- [6] McCabe, B.A., McKeon, E.P., Virbukiene, R.J., Mannion, P.J. and O'Connell, A.M. (2015) Pyritiferous mudstone-siltstone: expansion rate measurement and prediction, *Quarterly Journal of Engineering Geology and Hydrogeology*, Vol. Vol. 48, pp. 41-54.
- [7] McKeon, E.P. (2015) An Investigation into the factors affecting the rates of heave of a pyritiferous mudstone fill, *MEngSc thesis*, NUI Galway.
- [8] Hoover, S.E., Greenawalt, W. and Tittmann, B. (2015) Experimental and theoretical modelling of expansion in pyritic shale, *Geotechnical Testing Journal*, Vol. 38, No. 2, pp. 166-178.
- [9] Maher M., Azzie, B., Gray, C. and Hunt, J. (2011) A large scale laboratory swell test to establish the susceptibility to expansion of crushed rock containing pyrite. *14th Pan-Am CGS Geotechnical Conference*, Toronto, Canada, Oct. 2-6.
- [10] Menkiti, C.O. and Long, M. (2007) Geotechnical properties of Dublin Boulder Clay. *Geotechnique*, Vol. 57, No. 7, pp. 595-611.
- [11] I.S. EN 1991-1-1 (2002) (English): Eurocode 1: Actions on structures - Part 1-1: General actions - Densities, self-weight, imposed loads for buildings [Authority: The European Union Per Regulation 305/2011, Directive 98/34/EC, Directive 2004/18/EC]
- [12] Jiang, J. and Yuan, Y. (2013) Relationship of moisture content with temperature and relative humidity in concrete, *Magazine of Concrete Research*, Vol. 65, No. 11, pp. 685-692.
- [13] Taylor, A.J., Cripps, J.C. and Clarke, S.D. (2013) An in-situ monitoring system for natural temperature and relative humidity. *Proceedings of Eurock 2013 - Rock Mechanics for Resources, Energy and Environment*, pp. 351-356
- [14] Sandberg LLP (2012) Report on the laboratory testing of a sample of fill for the potential to give rise to heave (project anonymised), 8 pages.
- [15] Taylor, A.J. (2015) The expansion of pyritic mudrocks: A consideration of the Irish problem, *PhD thesis, University of Sheffield*
- [16] Maher, M.L.J. and Gray, C. (2014) Aggregates prone to causing pyrite-induced heave: How they can be avoided. *Proceedings of the 17th Extractive Industry Geology Conference*, pp. 58-66.
- [17] National Standards Authority of Ireland (2013). IS 398:2013 Standard dealing with the inspection/testing (Part 1) and remediation (Part 2) of properties damaged by pyritic fill heave.

Performance Testing of a Novel Gravity Base Foundation for Offshore Wind

Attari, Y¹, Prendergast, L.J.², Gavin, K^{1,3}

¹Gavin & Doherty Geosolutions, Dublin, Ireland

²School of Civil Engineering, University College Dublin, Dublin, Ireland

³Geo Engineering, Faculty of Civil Engineering and Geosciences, Delft University of Technology, Delft, Netherlands

Email: ¹Yeganeh@gdgeo.com, ²Luke.prendergast@ucdconnect.ie, ³K.g.gavin@tudelft.nl

ABSTRACT: In recent years, the international demand to produce green energy has been growing to address the issues of energy security and climate change. To date, the wind sector has probably advanced the most due to high availability of wind resources. Erecting wind turbines offshore, however, presents significant new engineering challenges. Offshore foundations for these energy converters must be able to resist large overturning moments as well as numerous cycles of lateral loading caused by wave and wind. Thus, the need for an efficient cost-effective foundation to support the turbines is becoming more important. In this paper, a specific design of a gravity base foundation system developed for offshore wind turbines is considered. The foundation is a conical hollow concrete gravity type structure which rests on the seabed and utilises its self-weight to support the turbine. A scale-model of the proposed foundation has been experimentally tested at the University College Dublin test site in Blessington, Ireland. This paper presents the findings of this research.

KEY WORDS: Offshore Wind, Gravity Base Foundation, GBF.

1 INTRODUCTION

The current interest in greener sources of energy has arisen to address the issue of climate change that threatens to endanger the stability of the world's climate. The phenomenon of global warming is mainly caused by the emission of carbon dioxide (CO₂) from the combustion of fossil fuels. In order to tackle this environmental issue as well as to provide energy security, sustainable sources of energy such as wind, wave, solar, biomass and geothermal power are being substituted for fossil fuels [1]. Among these clean sources of energy; wind technology has been most frequently employed due to high availability of its resources [2].

Onshore wind farms provide green energy; however, they are inhibited by site availability restrictions and tend to cause some public objections due to aesthetic and noise-producing principles [3],[4]. Developers therefore have begun to investigate exploiting the offshore wind resource.

Erecting wind turbines in the ocean presents significant new engineering challenges. Offshore wind foundations must be able to resist large overturning moments as well as numerous cycles of lateral loading caused by waves and wind. Moreover, wind turbines are becoming larger with taller wind towers and rotor blades in greater diameters. This complicates the loads that are applied to the supporting structure and foundations [5]. The foundation for the new generation of offshore wind turbines should maintain its stiffness and satisfy its design objectives throughout its design life in harsh coastal environments. Thus, the need for an efficient cost-effective foundation to support the turbines is becoming more important.

Multiple solutions have been proposed to support offshore wind turbines, such as, monopiles, gravity base foundations, suction caissons and multi-pod support structures (namely tripods and jackets). Since almost 27 percent of the capital costs of the construction of a wind turbine offshore relate to

foundation costs, the cost of a foundation is a major factored to be considered [6]. This places more focus on the choice of foundation solution. For each wind farm, the foundation system is selected based on several factors such as the magnitude of design loads, seabed conditions, wave and current velocities, ice climate, water depths at the site and site geology [5] among other factors.

GBFs are suitable foundation options employed in the wind energy industry as well as oil and gas sector. Gravity foundations are less expensive to construct than monopiles, but the installation costs are higher, largely due to the need for dredging and subsurface preparation and the use of specialized heavy-lift vessels [7]. But certainly, a more effective design with suitable economic considerations and suitable geotechnical performance, will justify more frequent employment of GBFs in future offshore wind farms in deeper water.

In recent years, various designs have been proposed for gravity structures in order to develop a self-buoyant foundation that minimises the costs for marine operations [8]. The different designs aim to enhance the performance and stability of the foundation as well as to reduce the costs associated with its construction and deployment [8]. With the current interest in building wind farms in deeper water depths, the limitations associated with monopiles will limit their usage. Thus, gravity base structures with suitable specifications should be designed to fill an important niche for the deeper water depth regions. This paper presents an analysis of the geotechnical performance of a novel floating gravity base structure as a potential cost-effective foundation solution for future offshore wind farms.

2 LITERATURE REVIEW

The concept of gravity structures was first implemented in the oil and gas sector. Gravity base foundations are heavy

concrete structures utilising their self-weight to withstand overturning moments and sliding shear applied on them by means of wave and wind loading [9]. However, when the foundation is deployed in the sea, the buoyancy effect reduces its self-weight resulting in less resistance against overturning compared to those installed onshore [10]. Despite the fact that GBFs rely on their self-weight to resist service loads, their design should be optimised in a way that the overall material consumption, manufacture, transport and installation costs also stand within reasonable limits. GBFs are constructed as hollow concrete shells to facilitate transport and installation. In order to provide sufficient dead weight to support the turbine against lateral loads, the GBFs are ballasted, once in place [10]. Ballast material can be sand, rock and iron-ore which are all available at a relatively low cost [11]. Using concrete in manufacturing gravity base structures makes the foundation design less dependent on fluctuating steel prices and also reduces the need for piling [9].

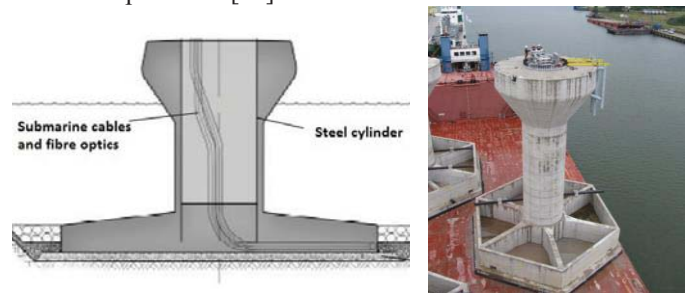
Gravity base foundations are usually built from reinforced concrete. Foundation slabs for onshore gravity structures can be poured in situ. However, this method cannot be applied to offshore wind turbines. This means that the foundation has to be constructed near the coast and be transported to the proposed location in the sea by special barges. The foundation is then lowered onto the seabed. The transportation issue puts a limit on the maximum weight of the offshore gravity structure; they are usually designed to be hollow [10]. When the structure is deployed in the water, it can be filled with ballast to increase the supporting weight. Gravity foundations are most likely to be used where piles cannot be driven [12] or in ice-prone regions [13]. Up to now, gravity foundations have been the second most widely used foundation after monopiles, currently covering 16% of the total operational offshore wind farms [14].

GBFs are suitable for deeper water (up to 60 metres) with low maintenance needs, since concrete is inherently durable in the marine environment [15]. Construction of gravity structures is fast and routine and usually cheaper than other foundation types since concrete is not subjected to high price fluctuations like steel [16], [17]. They do not need any piling operations and may also be repositioned [18], [19]. One of the plus points of GBFs is that the main parts of the structure are visible for inspection and further checks unlike monopiles and other deep embedded foundations [18]. However, Seabed preparation is necessary before deployment of these structures [15]. The welding details for self-buoyant structures might be time-consuming, and more importantly, their transportation and deployment need specific facilities and heavy-lift vessels that can resist the heavy weight of the structure [20], [17], [18].

GBFs are installed in several offshore wind farms, including Middelgrunden, Nysted, Thornton Bank, and Lillgrund. A more effective design with suitable economic considerations and suitable geotechnical performance may justify more frequent employment of GBFs in future offshore wind farms in deeper water. The design method for GBFs has originated from the conventional methods applied for the design of

shallow foundations. In recent years, novel self-buoyant GBF concepts have been proposed, that can be floated and towed to the specified location and ballasted to the seabed. Successful application of these alternative foundations can significantly limit the associated cost of transport and installation (BVG Associates 2013). Installation of gravity base foundations requires competent homogeneous seabed, comprised of dense sand, stiff clay or shallow bedrock, as the massive weight of the foundation can induce large settlements and bearing capacity issues in less competent soil types [9], [11].

The design configuration of GBFs has been altered over time. The first generation of GBFs were manufactured as reinforced concrete structures with an overall shape as illustrated in Figure 1.a. They were mainly constructed in dry docks that were later flooded when the foundation was ready to be floated-out [7]. The second generation of GBFs started with Nysted I project (see Figure 1.b.); their improved design comprised of a wide base, hollow pipe with thick walls and an ice cone at the top [7]. Aside from the novelty in manufacture, their installation was also improved by using floating pontoons or submersible barges as manufacturing platform [7]. This method reduces the occupation of large onshore space in ports or yards, and also eliminates the load-out and float-out operations [21].



(a) (b)
Figure 1. (a) First and (b) second generation of GBFs
(www.ontario-sea.org), (<http://www.gs-seacon.pl>)

The third type of GBFs were designed to have a thinner base, a conical hollow shaft (with thinner walls) instead of a pipe-shaped middle structure and a pipe at the top to attach to the turbine tower. Figure 2 shows a schematic view of this design. This approach was first introduced for the Thornton Bank offshore wind farm, located off the coast of Belgium [21].

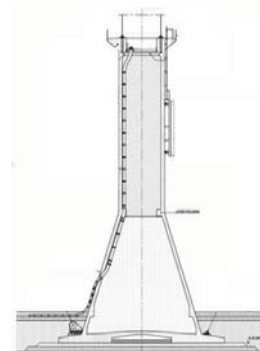


Figure 2. Third generation design of GBFs [22]

So far, gravity base foundations have been installed in shallow to moderate water, relatively close to the shore [9]. In order to justify the application of this foundation concept for deeper water, modifications in design, manufacture and installation are necessary. To address this issue, novel concepts in installation and design, such as, self-floating and crane-free GBFs are being introduced.

Optimisation of a gravity base foundation should be performed with a focus on minimising material consumption, reducing manufacture and design complexity and at the same time, maintaining the required lateral capacity against service loads. This study attempts to investigate the performance of a novel gravity based concept which is believed to significantly reduce the manufacturing efforts and hence, contribute to reducing the overall cost of the original foundation. In this paper, a proposed design for a GBF will be introduced and the test methodology followed for the experimental validation of the performance of this novel concept, as well as the implemented numerical simulation approach will be outlined.

3 EXPERIMENTAL METHOD

Understanding the behaviour of a foundation is essential in order to ensure suitable performance during its service life. Novel foundation concepts need to be carefully studied and tested in small or full-scale models before they can be deployed in industry. Evaluation of an offshore wind turbine foundation requires a thorough understanding of its load bearing mechanism. In this paper, in order to investigate the performance of the proposed concept, a 1:15 scaled model of the proposed GBF design was constructed and underwent a series of field tests. The experiments aimed at applying lateral loads to the scaled structure, in order to represent the actual wind and wave loads in the offshore site. The objective of the load tests is to analyse the load transfer process between the foundation and the underlying soil and to assess the lateral load bearing capacity of the foundation. Furthermore, the magnitude of displacements and rotations the structure experiences during these tests confirms if the foundation is capable of satisfying the limit states specified by the relevant design guidelines for offshore foundations. Accordingly, the results of the tests are carefully analysed to draw a conclusion on the soil behaviour, foundation capacity and viability of this concept.

The proposed foundation is a conical shaped concrete GBF. Its overall shape (Figure 3) resembles the third type of GBFs, similar to those used on the Thornton Bank Wind farm [23]. To study the viability of this foundation design, a concrete model of the proposed prototype was constructed by Bullivant Taranto and transported to UCD's research site located in Blessington, approximately 25 km south-west of Dublin. This structure was subjected to a set of planned tests to analyse its performance when it is subjected to lateral loads resembling the offshore wind and wave load effects. Load-testing the prototype indicates the failure mechanism as well as the magnitude of the lateral loads that can be applied before failure.

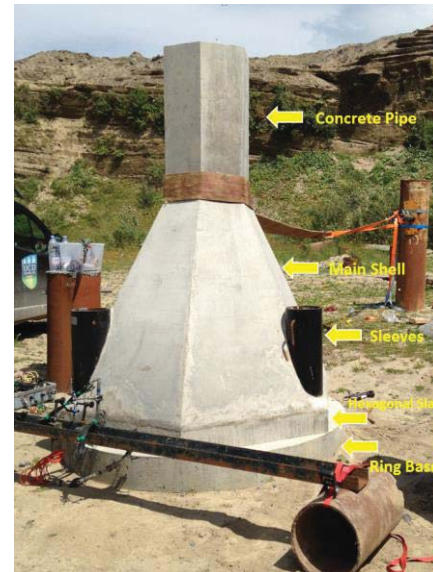


Figure 3. Overall shape and components of the GBF

A scale-model experiment for analysing the performance of the proposed foundation concept was performed on the scaled-structure at the University College Dublin (UCD) test site at Blessington, County Wicklow, Ireland. The Blessington test site has been developed over the last decade and has been used to test numerous prototypes and scale foundations [24], [25], [26], [27] and [28]. Therefore, several tests have already been performed with the geotechnical properties of the Blessington sand. The experiments show that the test site is made up of very dense, glacially derived sand with a relative density of approximately 100%, unit weight of 20 kN/m^3 and specific gravity of particles equal to 2.69 [24] and [29]. The main properties of the Blessington soil, according to the conducted tests by UCD geotechnical research group, are provided in Table 1.

Table 1. Properties of Blessington Sand [29]

Description	Value
Soil unit weight	20 kN m^{-3}
Soil specific gravity	2.69
Sand relative density	Approximately 100%
Ground water level	13 metres below ground level (bgl)
Degree of saturation above the water table	63% - 75%
D_{50}	0.1 - 0.15 mm
Percentage of coarse-grained particles (Particles with diameters less than 0.6 mm)	Less than 10%
Constant volume friction angle	37 degrees
Peak friction angle	42 – 57 degrees
Residual friction angle	39 to 31 degrees (with an average of 36)

The experimental method consisted of static and cyclic load tests with and without piles attached to the structure. In this section, information about the instrumentation, load test set-up and data acquisition method are presented.

A lateral load test was designed and conducted in Blessington, 25 kilometres south-west of Dublin, to evaluate the lateral response of the foundation. The aim is to provide a setup for pulling the structure laterally. The load test setting is shown in Figure 4. In order to reach a suitable layout for pulling the structure, firstly, a loading pile in the vicinity of the structure was chosen. A hydraulic jack was then horizontally fastened to the loading pile using ratcheting straps. A steel shaft connects the hydraulic jack to a load cell. The load cell was then bolted into a steel plate. This steel plate was attached to the main structure with a high strength ratcheting strap (see Figure 5). The other end of the ratcheting strap is attached to a strap which goes around the neck of the GBF to enable the load transfer. The monotonic loading of the structure is comprised of applying horizontal loads of 2 kN increments, while each load step was maintained for 2 minutes after the stabilisation (see Figure 6 for loading sequence).



Figure 4. Load test layout of the scale-model

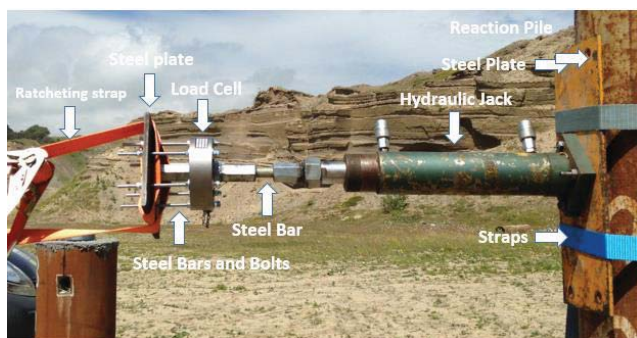


Figure 5. Setup of load cell and hydraulic jack

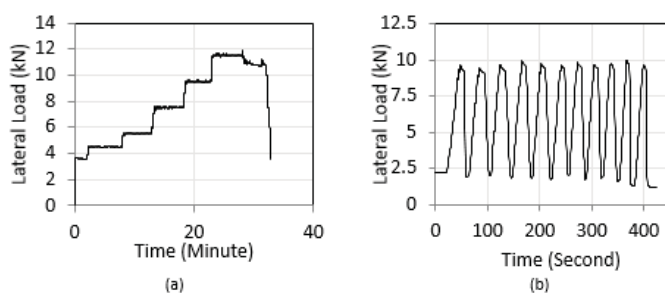


Figure 6 (a) Monotonic, (b) cyclic loading sequence of the structure

The graph of load versus horizontal displacement (See Figure 6.a) shows that the maximum horizontal load that the structure can sustain before reaching failure in the form of horizontal sliding is 11.7 kN. Once this load is achieved, the structure experiences a sudden failure; the horizontal displacements continue to increase at a constant horizontal load, until the foundation is unloaded. The stiffness of the foundation, which is defined as the slope of the load vs. displacement graph, is relatively constant during the loading process until it reaches the ultimate load, when the stiffness suddenly drops and the foundation slides on the soil surface. The maximum horizontal displacement of the scaled structure after failure, is approximately 35 millimetres.

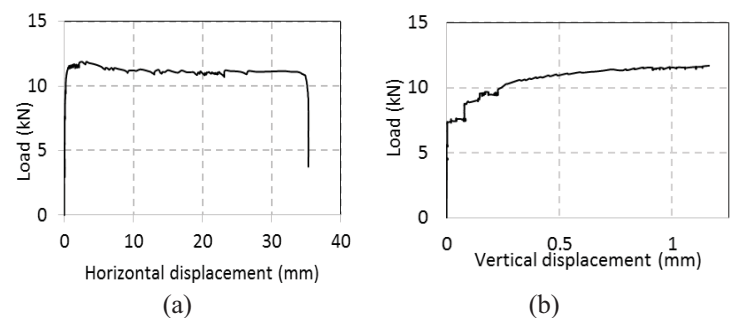


Figure 7. (a) Load-Horizontal displacement, (b) Load-Vertical displacement diagrams

Vertical displacement of the scaled foundation due to horizontal loading is also presented in Figure 6.b. The vertical displacement has progressed with a more gradual slope compared to the case of horizontal displacements. The graph shows the positive vertical displacements recorded at the toe of the foundation which is gradually rising from the soil surface due to the applied horizontal load. The maximum vertical displacement reached before the structure slides is 1.2 millimetres (at the ultimate load).

After the failure of the structure due to static loading, a set of load cycles were applied to the scaled foundation. This type of loading was aimed at replicating the cyclic effect of the sea waves and wind loads applied on the offshore wind turbine support structures in service. The reaction of the foundation due to cyclic loading is studied by interpreting the displacements and rotations generated in the structure during these load cycles. It shall be noted that the maximum loads applied in these cycles are less than the maximum load-bearing capacity of the foundation observed in the previous stage, in order to allow for multiple load cycles to be applied to the structure before sliding occurs.

Figure 7.a shows the accumulated vertical displacements of the foundation versus horizontal cyclic loading. Figure 7.a shows that after the cycles of loading, a maximum of 3.5 millimetres vertical displacement of the foundation is recorded. After the unloading of the structure in these cycles, the structure still has a residual vertical settlement of 0.5 millimetres vertical displacement. This graph also points that minimal vertical displacement occurs to the structure when loads up to 7 kN are applied. After this point, the slope of the

load-displacement graph changes and vertical displacements develop more rapidly.

The moments generated in the foundation during cyclic tests were calculated based on the recorded loads. Figure 7.b shows the rotations recorded in the structure due to the cycles of applied moments. The moments generate minimal rotations up to 12 kN-m, after which the rotations reach from 0.05 degrees to a maximum of 0.19 degrees with a steeper slope.

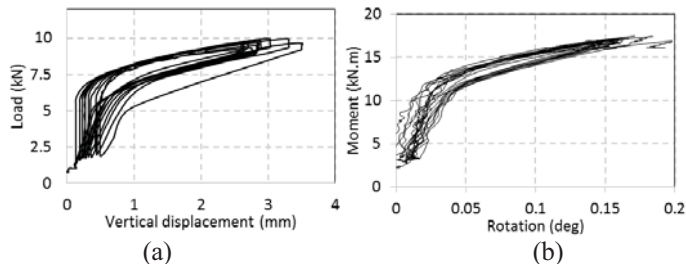


Figure 8. (a) Load-displacement graph, and (b) Moment-rotation graph for cyclic loading

The obtained graphs give an overview of the performance of the scaled gravity structure and provide a platform to calibrate the numerical models planned to be developed for the same tests.

4 CONCLUSION

This paper investigates the performance of a novel offshore gravity structure, which was developed with the aim of reducing the cost and the associated risks of installation of the offshore wind substructures. The proposed modifications are believed to improve the load-bearing capacity and efficiency of the foundation. A summary of the field tests and measurements that have been conducted to evaluate the performance of this novel foundation concept, known as the proposed structure were provided in this paper.

For the purpose of evaluating the foundation design, a scale-model of the proposed structure was constructed. The model was tested at the UCD test site in Blessington, where the soil profile resembles North Sea sand properties. A set of monotonic and cyclic lateral load tests were performed on the scaled foundation with the aim of assessing the potential load-bearing capacity of the foundation when subjected to simulated offshore wind and wave loads. Rotation and displacements of the structure were recorded during these load tests. These results represented the performance of the scaled structure and provided a basis for the development of a numerical model to replicate the foundation's behaviour. This model will be further employed to analyse the full-scale foundations and fully validate the novel design. The details of further analysis will be presented in future publications.

ACKNOWLEDGMENTS

We'd like to thank Enterprise Ireland who funded this research through the Commercialisation Fund. We would like to show our gratitude to Dr David Igoe for invaluable assistance with the experimental tests. We also thank Dr Paul

Doherty who provided support that greatly enhanced the research.

REFERENCES

- [1] F. Breu, S. Guggenbichler, and J. Wollmann, "Wind and Solar Power Systems: Design, Analysis, and Operation," *Vasa*, pp. 87–101, 2008.
- [2] R. Koekkoek, "Gravity Base Foundations for Offshore Wind Farms Gravity Base Foundations for Offshore Wind Farms," no. April, 2015.
- [3] P. Stuart, "What Are The Challenges Of Installing, Operating And Maintaining Wind Turbines Offshore." 2007.
- [4] B. W. Byrne and G. T. Houlsby, "Assessing novel foundation options for offshore wind turbines," *World Marit. Technol. Conf.*, pp. 1–10, 2006.
- [5] S. Malhotra, "Selection, Design and Construction of Offshore Wind Turbine Foundations, Wind Turbines," 2011. [Online]. Available: http://cdn.intechopen.com/pdfs/14804/InTech-Selection_design_and_construction_of_offshore_wind_turbine_foundations.pdf. [Accessed: 02-Oct-2015].
- [6] M. I. Blanco, "The economics of wind energy," *Renew. Sustain. Energy Rev.*, vol. 13, no. 6–7, pp. 1372–1382, 2009.
- [7] M. D. Esteban, B. Couñago, J. S. López-Gutiérrez, V. Negro, and F. Vellisco, "Gravity based support structures for offshore wind turbine generators: Review of the installation process," *Ocean Eng.*, vol. 110, pp. 281–291, 2015.
- [8] A. Attari, P. Doherty, E. Reig Amoros, and C. Paulotto, "Design drivers for buoyant gravity-based foundations," *Wind Energy*, p. n/a–n/a, 2015.
- [9] LEANWIND, "Logistic Efficiencies And Naval architecture for Wind Installations with Novel Developments WP Framework / Industry Challenges Report – construction , deployment and installation," no. 614020, 2014.
- [10] T. Burton, D. Sharpe, N. Jenkins, and E. Bossanyi, *Wind Energy Handbook*, vol. 25, no. 3. 2001.
- [11] Z. J. Westgate and J. T. Dejong, "Geotechnical Considerations for Offshore Wind Turbines," *Offshore (Conroe, TX)*, pp. 1–130, 2005.
- [12] P. Vølund, "Concrete is the Future for Offshore Foundations," *Wind Eng.*, vol. 29, no. 6, pp. 531–539, 2005.
- [13] H. Gravesen, S. L. Sørensen, P. Vølund, A. Barker, and G. Timco, "Ice loading on Danish wind turbines: Part 2. Analyses of dynamic model test results," *Cold Reg. Sci. Technol.*, vol. 41, no. 1, pp. 25–47, 2005.
- [14] European Wind Energy Association, *Deep water*, no. July. 2013.
- [15] Arup, "GRAVITY BASE," 2011.
- [16] A. Mieke, "Omae2012-8 Geotechnical Stability of Gravity Base Foundations for Offshore Wind Turbines," pp. 1–7, 2012.
- [17] M. J. Kaiser and B. F. Snyder, "Offshore Wind Energy Cost Modeling Chapter 2 Offshore Wind Energy System Components," *Offshore Wind Energy Cost Model.*, pp. 189–200, 2012.

- [18] Z. Saleem, "Technique for Noise Mitigation," no. April, pp. 1–68, 2011.
- [19] T. Feld, J. . Rasmussen, and P. H. Sørensen, "Aalborg Universitet Structural and Economic Optimization of Offshore Wind Turbine Support Structure and Foundation Feld , Tove ; Rasmussen , J . L ; Sørensen , P . H .," 1999.
- [20] I. Ruiz, "Gravity Base Foundations for Offshore Wind Farms Gravity Base Foundations for Offshore Wind Farms," 2013.
- [21] M. D. Esteban, J. J. Diez, J. S. López, and V. Negro, "Why offshore wind energy?," *Renew. Energy*, vol. 36, no. 2, pp. 444–450, 2006.
- [22] P. Van den Bergh and L. Ponnet, "Offshore Wind Farm THORNTON BANK PHASE I Presentation," vol. 2009, pp. 1–83, 2009.
- [23] K. Peire, H. Nonneman, and E. Bosschem, "GRAVITY BASE FOUNDATIONS FOR THE THORNTON BANK OFFSHORE WIND FARM," *Terra Aqua*, vol. 115, pp. 19–29, 2009.
- [24] K. G. Gavin and B. C. O. Kelly, "Effect of Friction Fatigue on Pile Capacity in Dense Sand," no. January, pp. 63–71, 2007.
- [25] K. Gavin and B. Lehane, "Base load – displacement response of piles in sand," vol. 1063, no. 2005, pp. 1053–1063, 2007.
- [26] D. J. P. Igoe, K. G. Gavin, and B. C. O. Kelly, "Shaft Capacity of Open-Ended Piles in Sand," *Am. Soc. Civil Eng.*, no. October, pp. 903–913, 2011.
- [27] A. Tolooiyan and K. Gavin, "Computers and Geotechnics Modelling the Cone Penetration Test in sand using Cavity Expansion and Arbitrary Lagrangian Eulerian Finite Element Methods," *Comput. Geotech.*, vol. 38, no. 4, pp. 482–490, 2011.
- [28] L. J. Prendergast, D. Hester, K. Gavin, and J. J. O. Sullivan, "An investigation of the changes in the natural frequency of a pile affected by scour," *J. Sound Vib.*, vol. 332, no. 25, pp. 6685–6702, 2013.
- [29] P. Doherty, L. Kirwan, K. Gavin, D. Igoe, S. Tyrrell, D. Ward, and B. O'Kelly, "Soil properties at the UCD geotechnical research site at Blessington," in *Proceedings of the Bridge and Concrete Research in Ireland Conference*, 2012, pp. 499–504.

The geotechnical properties of the pulverised coal ash produced at Moneypoint Power Station

Ciaran Reilly¹, Saul Rugero², Paul Doherty³

¹Ciaran Reilly & Associates, 46 Moyglare Abbey, Maynooth, Co. Kildare, Ireland

²ESB International, Stephen Court, 18-21 St. Stephen's Green, Dublin 2, Ireland

³Gavin and Doherty Geosolutions, Office 1B, Parkview House, Beech Hill Office Campus, Dublin 4, Ireland
email: ciaran@ciaranreilly.ie, saul.rugero@esbi.ie, pdoherty@gdgeo.com

ABSTRACT: Pulverised Fuel Ash (PFA) and Furnace Bottom Ash (FBA) are by-products from the combustion of coal at coal-burning power stations. This paper considers the geotechnical properties of the stockpiled PFA, FBA, and mixed Pulverised Coal Ash (PCA) produced and stored at Moneypoint Power Station in County Clare, Ireland. Moneypoint is Ireland's largest coal-burning power station and currently produces 162,000 tonnes of PFA and 18,000 tonnes of FBA per annum and houses a stockpile of 5,000,000 tonnes of mixed PCA. PFA and FBA are typically grey, weakly cemented, coarse-grained materials with particle size gradings similar to natural sands and gravels. PCAs have many uses as earthworks materials and engineering fills, although uptake is limited by a lack of knowledge of the properties of the materials, especially since the properties of a particular ash depend on the characteristics of the furnace and of the coal burned. The opportunity to carry out field and laboratory testing on the stockpiled PCA at Moneypoint arose during design work for the Moneypoint Wind Farm. The results of the field and laboratory testing carried out are presented in the paper, along with a brief discussion on the potential uses of the PCA from Moneypoint Power Station.

KEY WORDS: Pulverised Coal Ash; Pulverised Fuel Ash; Geotechnical Testing; Lightweight Fill; Material Properties.

1 INTRODUCTION

1.1 Pulverised Coal Ash

Pulverised Coal Ash (PCA) is the term given to a mixture of Pulverised Fuel Ash (PFA) and Furnace Bottom Ash (FBA), both by-products from the combustion of coal at coal-burning power stations. Of the total ash arising from the combustion of coal, approximately 10-15% is FBA.

Fresh PCA is typically a grey, fine-grained material with a particle size grading similar to a silt, however when stockpiled, pozzolanic reactions take place that cause clumps or agglomerations to form, growing and changing shape to become coarse-grained with time [1].

PCA has been widely used as an embankment fill material for roads, levees and cycle ways and as a backfill material for retaining walls [1,6,11]. In Ireland, uptake for these uses is limited by the geographic locations of producers of PCA and a lack of knowledge of the properties of the materials, especially since the properties of a particular ash depend on the characteristics of the furnace and of the coal burned. However, since the sources for PCAs are known and fixed, PCA from an individual source can be characterised and considered for use in a construction project just as a natural soil would be.

1.2 Moneypoint Power Station

Moneypoint Power Station is a large coal-fired power station owned and operated by ESB, the semi-state energy company, and located near Kilrush in County Clare. It is located on a large tract of land fronting onto the Shannon Estuary, where a coal-handling jetty has been established to supply coal to the power station. Moneypoint is one of Ireland's largest power stations with a total capacity of 915 MW. It is proposed to

construct a wind farm in the station grounds, Moneypoint Wind Farm, which will consist of five 3.45 MW wind turbine generators with a total output capacity of 17.25 MW.

1.3 PCA storage at Moneypoint Power Station

PCA is produced from the burning of pulverised coal at Moneypoint and, aside from sales to the cement manufacturing industry, a large proportion of the PCA produced is stored in the designated Ash Storage Area at the station. The location of the Ash Storage Area is shown in Figure 1. It covers approximately 25 hectares and is located in a natural depression within the Moneypoint Site, north of the N67 Kilrush to Killimer road.

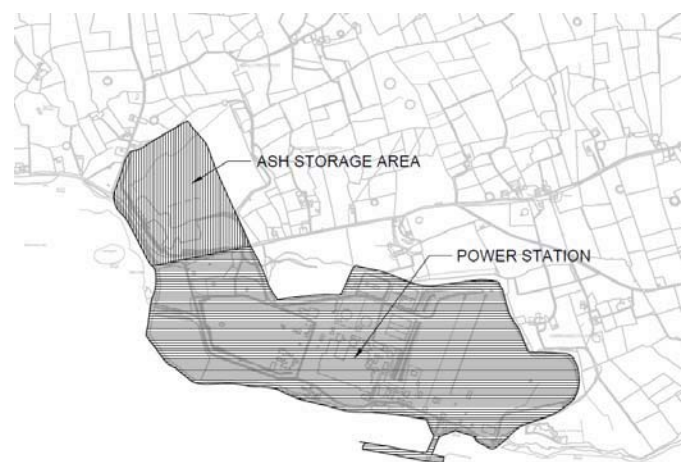


Figure 1. Ash storage area in Moneypoint Power Station.

One of the wind turbine generators that will make up Moneypoint Wind Farm, turbine G001, is sited within the Ash Storage Area.

Storage of ash commenced in 1985 and was implemented initially by placing alternate layers of PFA and FBA [2]. The ash is reportedly transported and placed at approximately 15% moisture content and compacted using a dozer. Current practice is to store PFA and FBA in separate areas with a view to future retrieval of the FBA for recycling.

At present, 5 million tonnes of PCA are deposited in the Ash Storage Area with an additional 300,000 tonnes to be potentially deposited by 2025 when operations at Moneypoint Power Station are expected to cease.

1.4 Reasons for study

The work reported in this paper was carried out during the execution of geotechnical design work for the construction of a wind turbine generator within the Ash Storage Area at Moneypoint Power Station. The work was commissioned by ESB International (ESBI) and carried out by Gavin & Doherty Geosolutions (GDG). Field and laboratory testing was carried out by Priority Geotechnical, Minerex Geophysics, National Materials Testing Laboratory (NMTL), and BHP.

2 LITERATURE REVIEW

2.1 Geotechnical properties of PCA

Fresh PCA is a grey, fine-grained material produced through precipitation from the flue gas of a coal furnace. Although the properties of the PCA from each source are unique [1], generally the chemical composition of PCA consists of oxides or dioxides of silicon, aluminium, calcium, iron, and magnesium, with smaller amounts of other elements including sulphur, sodium, potassium, vanadium, and titanium [3]. PCA is usually composed of particles which are small, hollow spheres [4] but with relatively high specific gravity due to the presence of iron [3].

The oxides of silica, alumina and ferric within PCA lead to significant pozzolanic reactivity within the material. In time, stockpiled PCA self-hardens due to these pozzolanic reactions, with the particles growing and changing shape, becoming coarse-grained [1].

Mass densities of PCA fills vary greatly, with values reported ranging from 0.994 to 1.8 Mg/m³, [4,5,6,7], while in the absence of reliable test results, commonly-used design guidance suggests consideration of loose and dense mass densities of 0.66 and 1.02 Mg/m³ respectively [8]. This range of values are presented in Table 1. **Error! Reference source not found.**

Table 1. Reported and recommended mass densities for PCA.

	Mass density (Mg/m ³)	
	Lower	Upper
Ireland [5]	1.4	1.8
Malaysia [4]	0.994	
UK [6]	1.1	1.45
UK [7]	1.54	1.66

BS 8002 [8]	0.66	1.02
-------------	------	------

2.2 Case histories

Over the last 50 years there have been numerous cases of the successful application of PCA as a fill material [1,6,11], with primary benefits being related to cost, ease of placement, the light weight of many PCAs, and the reduction in environmental impact brought about by reusing a waste material. However, it is suggested that PCA may be susceptible to frost and water damage and inundation collapse, so care is needed in the specification and use of the material for engineering purposes [1].

Benefitting in particular from the pozzolanic reactivity and potentially low mass density of PCA reported earlier, Nettleton et al. [9] describe the use of pulverised fuel ash fill for part of the A13 embankment at Dagenham, UK, which was constructed on an area of very soft organic silt dredged from the River Thames. The use of PCA reduced the calculated load on the foundation soils by some 25%. The earthworks solution involved placing a 100mm layer of ash followed by a 200mm layer of local silt dredgings. Quicklime was spread and mixed, acceptance tests were carried out and finally the layer was compacted to 95% maximum dry density. The material performed satisfactorily.

Limited use of PFA from Moneypoint as a lightweight fill was made during the construction of the 5km Bunratty Bypass, which was opened in 1992 [5]. Compaction trials carried out at the site showed that an in-situ mass density of 1.4 to 1.8 Mg/m³ was achieved, which is somewhat lower than the commonly considered-adopted design mass density of crushed rock fill of between 2.0 and 2.2 Mg/m³. In the case of the Bunratty Bypass, a locally available uniformly graded sand, which had an in-situ density of 1.8Mg/m³ and so very close to that of the Moneypoint PFA, proved to be more economical in use.

Arising from this, a consensus emerged in Ireland that the Moneypoint PFA was both heavy when compacted and commercially unviable for use in road construction at the time [10].

Taking account of local availability and cost advantages of the material, large volumes of local PCA have been successfully used as embankment fill for flood defence works and cycle ways in the Czech Republic [11], where the PCA has been used as a core material with the embankment side slopes protected from erosion and frost action by a layer of natural soil and topsoil. This also improves the aesthetics of the embankment.

The use of PCA as a fill for reinforced soil and as backfill to retaining walls has been described [1] and model specifications have been published [12,13].

3 FIELD WORK

3.1 Extent of field work

Due to the intention of siting a wind turbine generator within the Ash Storage Area, quite extensive field work was undertaken. Field work consisted of intrusive investigations and a geophysical survey. Intrusive investigations included three trial pits, two cable percussive boreholes, one rotary core borehole and three plate loading tests.

The geophysical survey consisted of the acquisition of two seismic refraction and Multi-Channel Analysis of Surface Waves (MASW) profiles and two electrical resistivity tomography (ERT) profiles.

3.2 Field observations

Field observations from trial pits and boreholes described the stockpiled ash deposits encountered as:

- Grey gravelly, very silty sand. Sand is fine to coarse.
- Grey, slightly gravelly sand. Gravel is fine to coarse, angular to subangular. Sand is fine to coarse.
- Grey, silty, very gravelly Sand with occasional lenses of grey Silt. Gravel is angular, fine to coarse. Sand is fine to coarse.
- Compacted ash deposits. Silty sandy gravel with high cobble content.
- Light grey, weakly cemented, silty sandy gravel.

The stockpiled ash deposit was found to be up to 6m thick at the site of wind turbine generator G001. A trial pit carried out by the Authors reached 2.5m below ground level, limited to this depth by the maximum reach of the excavator available. The material encountered was described as loose to medium dense, light grey, weakly cemented, silty sandy gravel. An image of this trial pit is shown in Figure 2. Ground water was not encountered within the ash deposit.



Figure 2. Image of trial pit to 2.5m in Ash Storage Area. Stability of sides shows the effect of observed weak cementation between particles.

3.3 Sampling

A number of samples, including bulk disturbed and small disturbed samples, were retrieved from cable percussive boreholes and trial pits. Additionally, the Authors retrieved a large bulk disturbed sample of PCA from 2.5m below ground level for shear strength testing at low normal stress at a specialist geotechnical laboratory.

3.4 SPT N

Given that no particular engineering requirements were followed when placing the PCA within the Ash Storage Area at Moneypoint, it is interesting to observe the effect of the

reportedly ad-hoc compaction using a tractor dozer on the in-situ density of the deposit. The SPT N values obtained from the borehole sunk at the location of G001 are plotted in Figure 3. The corrected values were calculated by assuming an energy ratio of 60% for the automatic trip hammer used.

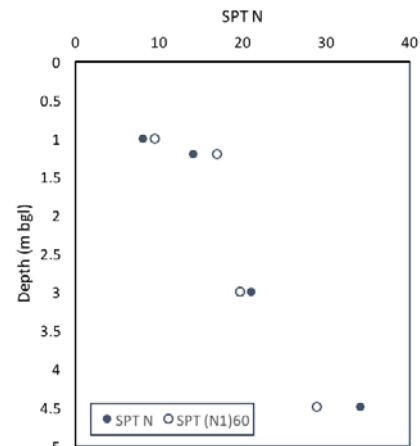


Figure 3. Uncorrected and corrected SPT N values for Moneypoint PCA.

As would be expected for a uniform deposit, the SPT N values increase approximately linearly with depth. The deposit is medium dense between 1m and 4.5m below ground level, becoming dense after 4.5m.

3.5 In-situ CBR testing

A number of in-situ California Bearing Ratio (CBR) tests were carried out just below the surface of the PCA deposit at Moneypoint. These tests were carried out to assist the design of access roads across the deposit.

As part of an investigation to support a previous design for a wind farm at the site, Geotech Specialists Ltd. carried out three plate loading tests at selected locations near the surface of the ash deposit. The results of these tests were CBR values of 9.4, 12.3, and 20.9%.

More recently, a number of CBR values were assessed based on correlations with the Transport Research Laboratory Dynamic Cone Penetrometer [14]. These tests allowed for CBR values to be obtained through correlations at depths from 0.30 to 0.92m below ground level. CBR values of 6, 7, 9, 10, and 40% were interpreted for the ash deposits between these depths.

Considering these two sets of results, it is clear that the PCA deposit at Moneypoint, although not placed with any great degree of engineering control, presents a relatively competent subgrade for access road construction. CBR values of 6 to 40% were interpreted near the surface.

4 LABORATORY TESTING

4.1 Classification

Samples of stockpiled PCA retrieved were described as slightly gravelly sand, silty very gravelly sand, and gravelly very silty sand. There was no determinable liquid limit and the samples were found to be non-plastic.

The in-situ moisture content of the PCA at Moneypoint was relatively high, ranging between 18.2% and 62%. Samples were taken over the top 2.5m of the deposit.

4.2 Dry density

The maximum dry density was found to range from 1.18 Mg/m³ to 1.20 Mg/m³ when determined in accordance with BS 1377:4 Section 3 using a 2.5 kg rammer, with an optimum moisture content ranging from 2 to 14%. This wide variation is attributed to the inhomogeneous nature of the deposit at Moneypoint, where the FBA and the PFA are interlayered. In addition, mechanical compaction may have broken up the grains and changed the particle size distribution of the test specimens. This difficulty in determining the optimum moisture content for the Moneypoint PCA could lead to difficulties in specifying acceptability criteria for earthworks built using the material. The minimum dry density of the ash, after gravel-sized particles had been broken down, was estimated in accordance with BS 1377:4 Section 4.4, where a specimen of known mass was placed in a glass measuring cylinder, inverted a number of times, and allowed to fall freely to rest, before the volume was measured. The dry mass density thus determined was 0.88 Mg/m³. The same glass measuring cylinder was then placed in a shaker and shaken until the minimum volume was obtained for the same mass of dry ash. This dry mass density was 1.22 Mg/m³ and was taken as the maximum dry density. The minimum and maximum dry densities thus measured are presented in Table 2.

Table 2. Minimum and maximum dry density of Moneypoint PCA determined using a glass measuring cylinder.

	Dry mass density (Mg/m ³)	
	Minimum	Maximum
Moneypoint PCA	0.88	1.22

4.3 Particle size

The particle size distribution curves for three samples of stockpiled PCA obtained from trial pits within the Ash Storage Area area at Moneypoint are shown in Figure 4.

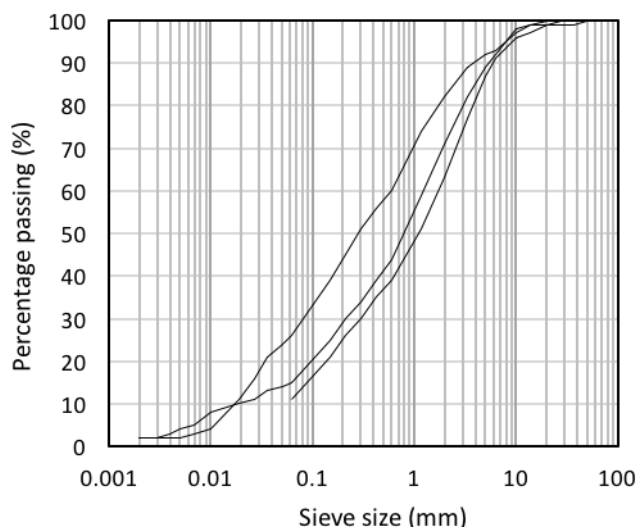


Figure 4. Particle size distribution curves for Moneypoint Power Station PCA

As noted previously [1], the fresh fine-grained ash tends to form clumps of sand- or gravel-sized particles during storage due to pozzolanic action. The stockpiled PCA at Moneypoint Power Station was found to be coarse-grained and well graded, with a D₅₀ particle size of 0.75mm. The coefficient of uniformity C_U was 29.4 and the coefficient of curvature C_C was 1.17.

4.4 Specific gravity

The specific gravity of the Moneypoint PCA was measured as 2.2. It is noted that the specific gravity of PCA particles can vary widely, with values from 1.46 to 2.94 reported in the literature [3].

4.5 Shear strength

Corrected SPT N values of between 9 and 29 were measured in the PCA deposit. Using published correlations [15], peak friction angles could be expected to range from 30.0 to 36.2°.

Further to this, five direct shear tests were carried out in the small (60mm x 60mm) shear box apparatus at low and medium normal stresses on samples placed loosely and subjected to Proctor compaction using a 2.5kg rammer.

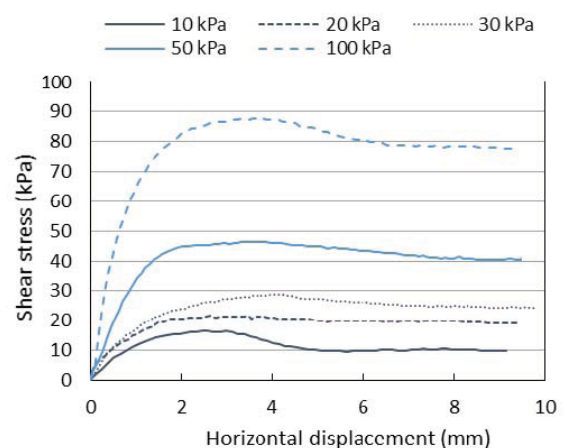


Figure 5. Shear stress against horizontal displacement in direct shear testing of Moneypoint PCA.

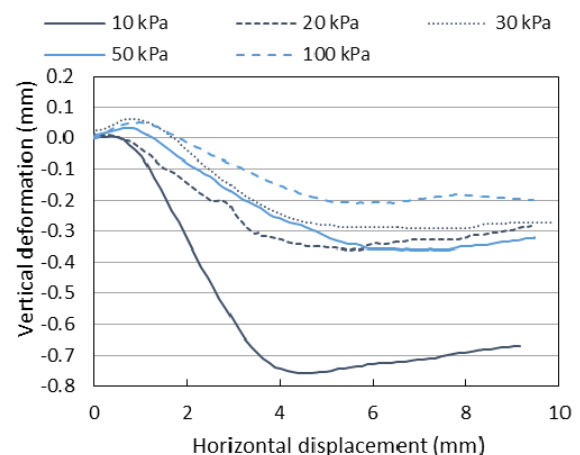


Figure 6. Vertical deformation against horizontal displacement in direct shear testing of Moneypoint PCA.

Figure 5 shows a plot of shear stress against horizontal displacement for the five direct shear tests carried out. All tests were carried out slowly enough to ensure drained conditions existed. The Figure shows that a peak shear stress develops after between 3mm and 4mm of travel or 5% and 6.7% shear strain before the shear stress reduces as the material near the shear surface approaches a constant volume condition. The vertical deformation during the tests are shown in Figure 6. After an initial volume increase, the material contracts towards a constant volume.

The maximum peak shear stress and the shear stress judged to represent constant volume conditions are plotted in Figure 7. Neglecting the small apparent effective cohesion intercepts, peak and constant volume angles of shearing resistance of 36.9° and 38.9° respectively were interpreted.

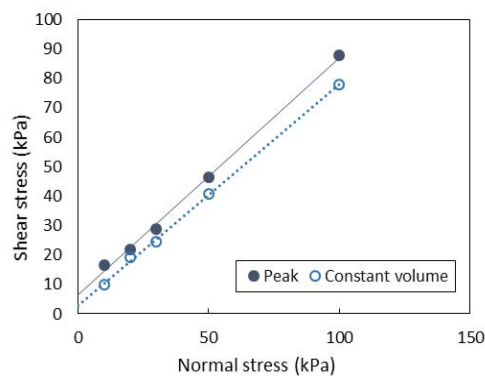


Figure 7. Shear stress against normal stress in direct shear testing of Moneypoint PCA.

It is recommended that constant volume rather than peak angles of shearing resistance are utilized for design in PCA [1]. Further testing is warranted to establish if particle breakage becomes a factor in shearing of stockpiled PCA at higher normal stresses.

4.6 Laboratory CBR testing

Laboratory CBR testing of PCA samples retrieved from 1m below ground level yielded laboratory CBR values ranging from 17.9 to 23.8% at moisture contents of 19% to 34%. The range of laboratory CBR values measured was within the range of in-situ CBR values obtained from correlations, which was 6 to 40%.

4.7 Chemical tests

Specimens from one sample were subjected to chemical testing. The pH was found to be 7.96, and water soluble sulphate as SO_4 as found to be 380 mg/L. These measurements do not cast the material as particularly aggressive to concrete or steel when measured against the guidance documents and design codes commonly used in engineering practice [16,17]. However, given the origins of the material, special consideration should be given to the protection of any structural elements planned for incorporation into a PCA fill.

4.8 Susceptibility to inundation collapse

Simple testing to determine the susceptibility of Moneypoint PCA to inundation collapse was carried out. Two remoulded

specimens were set up in 150mm diameter oedometer cells and loaded in effective stress increments up to 100 kPa, with one of the cells being flooded during the test. The specimens were set up at the parent sample's natural moisture content of 15% and an initial bulk mass density of 1.25 Mg/m^3 , this bulk mass density being judged to be the maximum density achievable using the 2.5kg rammer at the moisture content of the sample. The dry mass density was 1.09 Mg/m^3 , or 89% of the maximum dry density of Moneypoint PCA indicated in Table 2.

Each specimen was loaded in vertical effective stress increments of 10, 20, 40, 60, and 100 kPa with the corresponding void ratio being established for each increment. One of the cells was flooded between the application of the 40 kPa increment and the 60 kPa increment and that test was completed while the cell was flooded. The results of the two tests are shown in Figure 8.

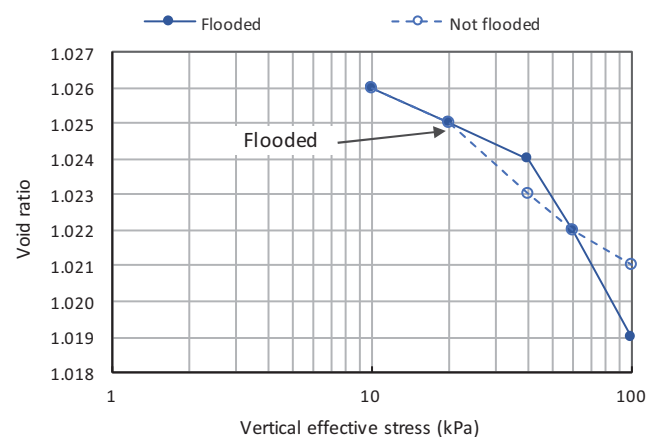


Figure 8. Results of tests to determine inundation collapse susceptibility of Moneypoint PCA.

Since the void ratio of the flooded specimen reduces more than that of the dry specimen during the increment immediately after flooding, it is suggested that the Moneypoint PCA may be susceptible to inundation collapse at dry densities less than 90% maximum dry density. However, further testing is required to verify this finding and to determine the susceptibility of the Moneypoint PCA to inundation collapse at higher dry densities which would be more commonly specified for engineered earthworks.

5 POTENTIAL ENGINEERING USES

5.1 Embankments and engineered fills.

While the UK Specification for Highway Works [13] contains provision and support for the use of coal ash in earthworks for road schemes, the equivalent Irish documents contain no such guidance, albeit that PCA may be assessed as Class 1 or Class 2 general fill under the Specification for Road Works [18].

Several studies have shown the suitability of PCA for embankments and engineered fills [1,9,11], once the proposed material's behaviour is understood adequately and acceptance criteria are thoughtfully set. Although the Moneypoint PCA is heavier than typical PCAs, and so the advantages of low mass density that other PCAs offer aren't present to the same

extent, the material still warrants consideration for the construction of embankments and engineered fills due to the environmental benefits of reusing a waste material.

5.2 Backfill to retaining structures

While UK engineering practice [12,13] allows the use of fresh PFA as backfill to retaining walls and abutments as Class 7B: "Selected conditioned pulverised fuel ash (PFA)", Irish practice has not facilitated this use to date. For example, the Specification for Road Works prescribes that fill to reinforced soil be of natural sand, gravel or rock or crushed concrete, whilst fill to structures must be crushed rock or crushed concrete [18].

The testing results presented above show that the stockpiled PCA at Moneypoint could be well suited as a backfill to a retaining structure, possessing as it does a relatively high constant volume friction angle and a relatively low mass density. The relatively low mass density of the Moneypoint PCA would reduce long term settlements in retaining walls or reinforced soil applications, thereby improving performance and reducing maintenance costs. When used as retaining wall backfill, the relatively low compacted density of PCA would potentially result in lower horizontal pressures on the wall, allowing for lighter, less expensive, wall sections. Further, the relatively low compacted density would reduce the settlement of underlying compressible soils and would increase the global stability of the wall.

5.3 Inundation collapse

The assessment of a fill such as PCA for inundation collapse requires careful lab testing or specialist in-situ test procedures [19]. Limited testing carried out during this study indicates that the Moneypoint PCA may be susceptible to inundation collapse at a dry density slightly less than 90% of the maximum dry density. Further testing in the laboratory and in-situ is recommended to verify this finding and establish the response of the PCA to inundation when compacted at a density in excess of 90% of the maximum dry density.

6 CONCLUSIONS

This paper has presented the results of a programme of field and laboratory testing carried out to characterise the stockpiled PCA deposit within the Ash Storage Area at Moneypoint Power Station.

This deposit extends to 5 million tonnes of stockpiled material that is available for reuse with another 300,000 tonnes of fresh material to be potentially available for use or deposited by 2025 when operations are expected to cease.

Several geotechnical properties of the material have been presented and clarified in a manner not available before.

Two promising uses of the material are put forward, as an engineered fill material benefitting from the low environmental impact of the material and as backfill to reinforced soil structures or retaining walls benefitting from the relatively low mass density and the low environmental impact of the material. Difficulties in the specification and use of the material were also discussed, including the high range of optimum moisture content values identified during laboratory testing, which may make the verification of the

acceptability of the material difficult, and the material's possible susceptibility to inundation collapse at lower densities.

Further testing would be required to support a specific usage of the material as an engineered fill or a backfill to a reinforced soil structure or retaining wall.

ACKNOWLEDGEMENTS

The Authors would like to acknowledge the contributions made by Billa Chana of NMTL, Brian Murphy of ESBI, and Paul Quigley of GDG towards this paper.

REFERENCES

- [1] Clarke, B.G. and Coombs, R. (1996). 'Specifying and using pulverised fuel ash as an engineered fill'. *Waste Management*, 16(1), pp.101-108.
- [2] ESB Energy International (2011), Moneypoint Generating Station IPPC Licence Review Form.
- [3] Goswami, R. K. (2004). *Geotechnical and environmental performance of residual lateritic soil stabilised with fly ash and lime*. PhD thesis, Indian Institute of Technology Guwahati, India.
- [4] Ismail, K.N., Hussin, K. and Idris, M.S. (2007), 'Physical, chemical & mineralogical properties of fly ash'. *Journal of Nuclear and Related Technology*, 4, pp.47-51.
- [5] Farrell, E., Davitt, S., and Connolly, C. (1997), 'Bunratty Embankment – Overview of Performance.' *Road Embankments on Soft Ground in Ireland*, Eds. Farrell, E., Lehan, B., Long, M. and Paul, T. The Institution of Engineers of Ireland, Dublin.
- [6] Sear, L.K.A. (2008), Using coal fly ash in road construction. *Proceedings of LJMU 2008 Annual International Conference*. Liverpool, UK.
- [7] Cousens, T.W. and Stewart, D.I. (2003), 'Behaviour of a trial embankment on hydraulically placed PFA'. *Engineering Geology*, 70 (3-4), pp. 293-303.
- [8] BSI. *BS 8002:1994+AC:2001. Code of Practice for Earth Retaining Structures*. 2001.
- [9] Nettleton, A., Robertson, I., Smith, J.H. (1996), 'Treatment of Silt Using Lime and PFA to form Embankment Fill For The New A13.' *Lime Stabilisation. Proceedings of the Seminar Held at Loughborough University*. J. H., Rogers, C. D. F., Glendinning, S., & Dixon, N., Eds. Thomas Telford, London, UK.
- [10] Farrell, E., Lehan, B., Long, M. and Paul, T., Eds., *Road Embankments on Soft Ground in Ireland Proceedings of a Seminar on Road Embankments on Soft Ground*. The Institution of Engineers of Ireland, Dublin, 1997.
- [11] Mráz, V., Havlice, M., Horváthová, T. (2015), 'Application of Coal Combustion By-Products in Levees'. *Proceedings of the international students' scientific conference RISEM 2015 - Research and Innovation of Secondary Materials with Focus on Civil Engineering*. Valentin, J., Suda J., Čížková Z., Nežerka V., Somr, M. Eds. CTU, Prague.
- [12] UK Government. (1995), BD 30/87. Backfilled Retaining Walls and Bridge Abutments. Design Manual for Roads and Bridges. Volume 2, Section 1.
- [13] UK Government. (2016), Specification for Highway Works. Series 600, Earthworks.
- [14] Kleyn K G and Savage, P. F. (1982), 'The application of the pavement DCP to determine the bearing properties and performance of Road Pavements'. *International Symposium on Bearing Capacity of Roads and Airfields*. Trondheim, Norway.
- [15] Peck, R.B., Hanson, W.E. and Thornburn, T.H. (1974). *Foundation Engineering*. Wiley, New York, second edition.
- [16] NSAI. *I.S. EN 206:2013. Concrete - Specification, performance, production and conformity*. Dublin, Ireland, 2013.
- [17] BRE. *Special Digest 1: 2005. Concrete in aggressive ground*. Watford, UK, 2005.
- [18] National Roads Authority. (2013), Specification for Road Works. Series 600, Earthworks.
- [19] Charles, J. A. and Watts, K. S. (1997). *Building on fill: collapse compression on inundation*. BRE Information Paper: IP 5/97. BRE, Watford, UK.

The behaviour of a novel dynamically installed anchor during deployment – insights from field tests

Soroosh Jalilvand¹, Kenneth Gavin², Paul Doherty³, Robert B. Gilbert⁴, Vinayagamoothy Sivakumar⁵, Aaron Bradshaw⁶

¹School of Civil, Structural and Environmental Engineering, University College Dublin, Dublin4, Ireland

²Faculty of Civil Engineering and Geosciences, TU Delft, Netherlands (formerly UCD)

³Gavin & Doherty Geosolutions, Dublin, Ireland (formerly UCD)

⁴Department of Civil, Architectural and Environmental Engineering, The University of Texas at Austin, Austin, TX 78712, United States

⁵School of Planning, Architecture and Civil Engineering, Queen's University Belfast, University Rd, Belfast, BT7 1NN, Northern Ireland

⁶Department of Civil & Environmental Engineering, University of Rhode Island, Kingston, RI 02881, United States

Emails: soroosh.jalilvand@ucdconnect.ie, k.g.gavin@tudelft.nl, pdoherty@gdgeo.com, bob_gilbert@mail.utexas.edu, v.sivakumar@qub.ac.uk, bradshaw@egr.uri.edu

ABSTRACT: Offshore wind developments are moving towards deep water where the energy is abundant and visual and sound interference is minimised. However, construction in deep water poses several challenges to developers, among which are the high cost of operation and material transport. The current study addresses the behaviour of a novel foundation system (pending US patent) that aims at minimising the cost of deployment for emerging offshore wind facilities. To this end, the preliminary results of an offshore field test on the small scale dynamically installed anchor are presented and the testing methodologies are briefly outlined. The results provide insights into the behaviour of the anchor as it is released into the water column, impacts with the seabed, and finally, achieves its maximum penetration depth. This is enabled through a detailed study of the data obtained from an accelerometer built into the anchor, which tracks the anchor motion over the course of its deployment. Overall, the findings in this research contribute to an enhanced understanding of the behaviour of dynamically installed anchors as perceived through field tests.

KEY WORDS: Dynamically installed anchor; Offshore test.

1 INTRODUCTION

A major challenge in developing offshore wind developments is the high cost and risk involved in the construction of platforms to host such facilities. Floating platforms are the most viable options for emerging offshore wind turbines in deep water (>60m). Therefore, the development of efficient foundation solutions to serve the next generation of offshore wind turbines is critical to the sustainable growth of wind energy sources. The Flying Wing Anchor (pending US patent) is a novel foundation concept in the form of a plate anchor that addresses this issue through its enhanced deployment technique and efficient functionality. The anchor has a fluke in the form of a steel plate that is hinged to a freely rotating shank. The shank is initially fixed to the fluke, allowing for the anchor to be installed dynamically under its own weight. This results in significant gains in terms of operational time and resource commitment, while contributing to the performance of the anchor by providing an initial embedment. Once the anchor settles into the seabed at the end of its free fall, the line attached to the anchor is loaded resulting in opening-up of the shank. From this point onward, the anchor behaves like a drag embedment anchor, meaning that it can build up penetration (and as a result, bearing capacity) with increased dragging. The dual performance of the Flying Wing Anchor enables quick installation and optimized bearing capacity, previously unattainable using the torpedo or drag embedment anchors alone.

To date, numerous investigations have been performed on the behaviour of dynamically installed anchors, among which are

the comprehensive studies conducted on torpedo anchors [1–4], Dynamically embedded plate anchors (DEPLAs) [5,6], and Omni-Max anchors [7–9]. Building upon this rich platform, a set of offshore anchor trials were conducted to assess the behaviour of the Flying Wing Anchor during deployment. The following sections provide a brief overview of the testing methodology and the quantitative findings obtained from the analysis of the anchor motion during the penetration phase of deployment.

2 METHODOLOGY

2.1 Vessel

The cruise was undertaken from 1st to 10th December 2015 on board the Irish Marine Institute's Celtic Voyager. The vessel accommodated a group of 13 crew members, technicians and scientists who participated in the various stages of anchor deployment and site investigation. Figure 1 shows a deck view of the Celtic Voyager, where the A-frame and the pulleys, together with the deck-mounted winches, were used to deploy the anchor and perform the site investigation operations.

2.2 Test site

The offshore testing program was performed in a relatively sheltered area off the coast of Scotland (see Figure 2) where the sediment has been broadly categorized as Muddy Sand [10] according to the BGS classification, which is a slight modification of the Folk classes [11]. The water depth at the location of the test is approximately 50m, which provided

adequate drop height for the investigations performed in these anchor trials. The target area was approximately 1500m x 500m and was chosen to provide close proximity to local ports while causing no interference with the underwater features and the marine traffic.



Figure 1. Anchor deployment on board the Marine Institute's Celtic Voyager.

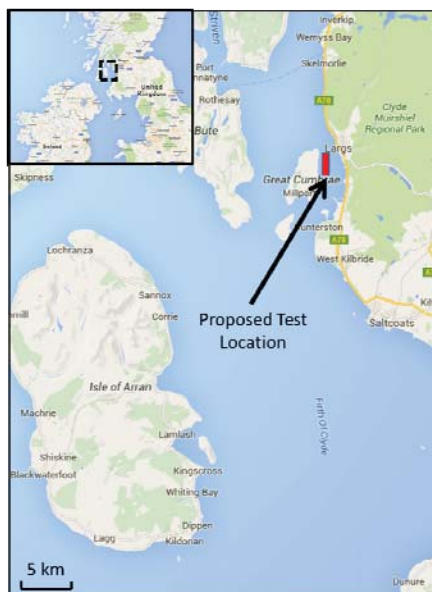


Figure 2. The test site was located in a relatively sheltered area off the coast of Scotland.

2.3 Model Anchor

The model scale anchor investigated in this study is a small scale Flying Wing Anchor with a characteristic size of 700mm that consists of two planar parts (flukes) connected using a central beam, which is hinged to a rotating shank (see Figure 3). The shank is initially restrained in position relative to the fluke, but it can open up once the anchor is loaded. This will cause the anchor to embed deeper into the seabed beyond the

penetration obtained as a result of the free fall. This behaviour is similar to conventional drag-in-plate systems [12]. The anchor continues embedment until the load in the mooring line reaches the anchor ultimate capacity. Further loading at this stage will not result in significant gains in either anchor embedment or anchor capacity.

2.4 Deployment strategy

The anchor deployment involved:

- attaching the mooring line (dashed-line in Figure 3) and the installation line (solid line in Figure 3) to the anchor,
- lowering the anchor using the installation line and a deck-mounted winch to the specified drop height
- releasing the anchor by triggering a quick release shackle on the deck, and
- loading the anchor using the installation line.

At the end of loading, the anchor was retrieved using the mooring line connected to the tail of the anchor. This would allow for the mobilization of minimum anchor capacity during the retrieval process.

2.5 Operational Challenges

The presence of multiple lines during the anchor deployment resulted in complication of the offshore operations. In addition, the bad weather condition and the relatively small size of the Celtic Voyager posed serious challenges to the station-keeping of the vessel, resulting in frequent cancellations of the operations. The deployment challenges were mostly overcome through a close collaboration and communication among the scientists on board and the experienced crew members of the research vessel.

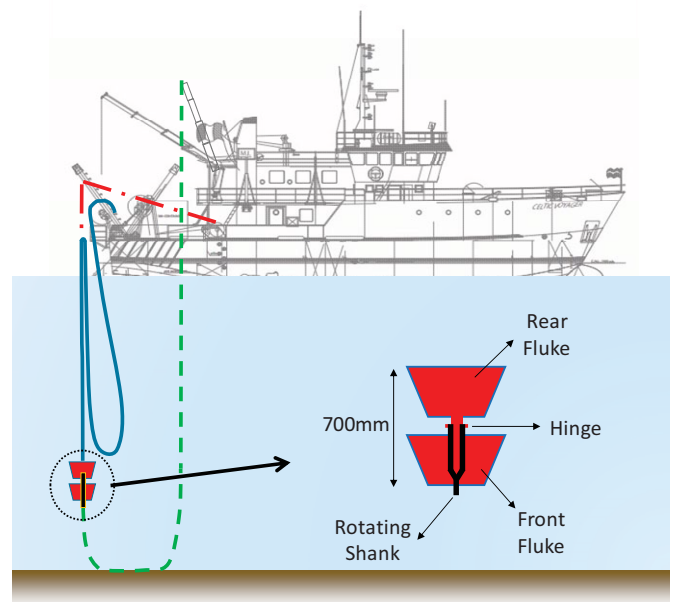


Figure 3. Schematic of the anchor deployment strategy.

3 RESULTS AND DISCUSSION

The anchor motion was monitored using an accelerometer that was packaged in a water-tight unit together with batteries and

a data logger, and mounted on the anchor. In order to obtain the anchor velocity and displacement during the free fall and penetration phases, numerical integration was performed on the data obtained from the accelerometer. In the following sections the results of the anchor monitoring during a typical deployment process are presented and the trends in displacement, velocity and acceleration are discussed.

3.1 Anchor velocity

Figure 4 shows the variation of anchor velocity with time from the point of release of the anchor to the end of penetration. It can be observed that the anchor builds up speed upon triggering of the quick release shackle. The velocity increases gradually until it reaches an upper limit known as the terminal velocity. At this point, the amount of drag resistance balances out the gravitational force applied on the anchor. The terminal velocity obtained by the anchor during the demonstrated drop was approximately 4 m/s, which is lower than the range of velocities required for successful penetration [6]. This hints at the need for further streamlining of the anchor for future trials.

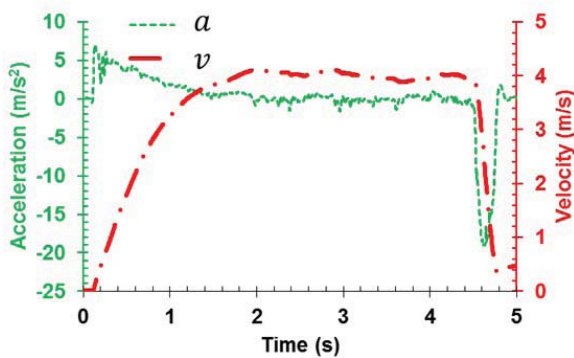


Figure 4. The variation in velocity and acceleration and of the anchor as it undergoes free fall and subsequently comes to a stop after impact with the seabed.

3.2 Anchor acceleration

The acceleration of the anchor along the vertical axis (direction of the anchor travel) for the sample trial is shown in Figure 4. As it can be observed, the anchor acceleration is zero at the initiation of the drop and it increases rapidly upon the release of the anchor. The peak acceleration reached by the anchor is 7.0 m/s^2 . The results of similar trials on torpedo anchors have reportedly demonstrated a peak velocity of 8.9 m/s^2 immediately after the release of the anchor [6]. As the anchor gradually builds up speed, the value of the drag force applied on the anchor increases and as a result the anchor acceleration diminishes. Starting at $t=2.2 \text{ sec}$, the resultant drag and gravitational forces converge to zero causing the anchor to experience a constant terminal velocity of 4 m/s , which corresponds to zero acceleration. The anchor continues to fall at the terminal velocity until it impacts with the seabed at 4.4 sec , resulting in a peak deceleration of -19 m/s^2 . The resulting deceleration, caused by the seabed bearing, viscosity and drag forces, brings the anchor to a complete rest within 0.5 sec .

3.3 Anchor displacement

The anchor displacement throughout the free-fall and penetration phase was derived by numerical double integration of the acceleration data. Figure 5 shows the displacement of the anchor during the sample trial. The drop height is approximately 15 m . The anchor penetration into the seabed as a result of the free fall is estimated as 660 mm , which is approximately one anchor length. The point of impact is obtained by the study of acceleration of the anchor where the impact time is associated with the initiation of a steep descent in acceleration values.

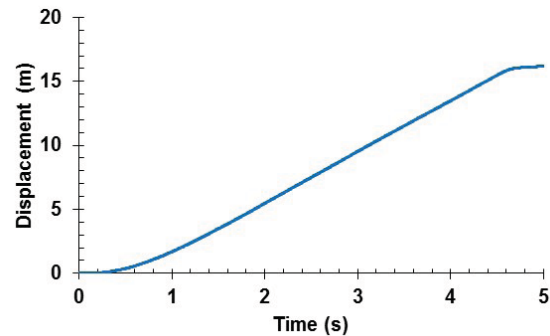


Figure 5. Anchor displacement calculated using accelerometer data.

3.4 Lateral stability

In order to assess the lateral stability of the anchor during free-fall and as a result of the impact with the seabed, the longitudinal (direction of anchor travel) and lateral accelerations of the anchor are investigated in Figure 6. According to the graph, the value of anchor lateral acceleration is negligible at the start of the free fall and throughout the anchors movement through the water column. As the anchor impacts the seabed, a sudden peak can be identified in both lateral and longitudinal accelerometer data. However, the surge in the former is considerably (about 90%) lower than the longitudinal acceleration peak, suggesting that the anchor was close to vertical at the time of release and maintained its orientation throughout the drop. Finally, the anchor landed almost vertically into the seabed. A closer examination of lateral stability can be performed by incorporating the data from gyroscopes in addition to accelerometer. This is beyond the scope of current study.

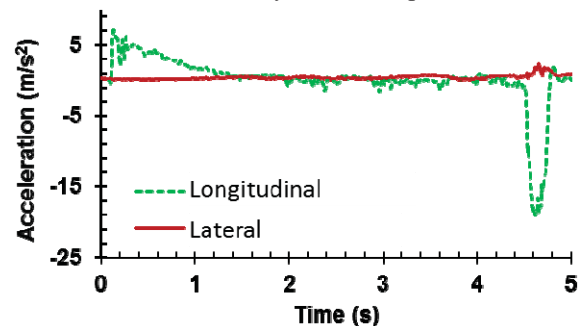


Figure 6. The lateral stability of the anchor under impact.

4 CONCLUSIONS

The current study presents the preliminary results from a set of offshore anchor trials that assessed the behaviour of a novel anchor system during deployment in the offshore environment. The anchor concept (Flying Wing Anchor) was designed to combine the best attributes of torpedo anchors and drag-in-plate anchors to provide an efficient installation technique and optimum capacity per material usage. The trials were conducted on board the Celtic Voyager in December 2015, where a group of 13 crew members, technicians and scientists worked together to accomplish the various tasks involved in the deployment of the anchor and relevant site investigations.

The deployment strategy involved (1) equipping the anchor with instrumentation package, a mooring line and an installation line, (1) lowering the anchor using the installation line to the required drop height, (2) dropping the anchor by triggering a quick release shackle, and (3) loading the anchor using the equipped mooring line. The deployment required simultaneous operation with both mooring and installation lines connected to the anchor, which resulted in operational difficulties.

Throughout the deployment process, the anchor motion was monitored using a built-in accelerometer. This enabled the tracking of the anchor as it underwent free fall in the water column and, subsequently, impacted with the seabed came to a complete halt. The performance of the anchor instrumentation is demonstrated through the results of a sample anchor trial, which is performed from a drop height of 15m. The results showed the variation of acceleration and velocity during the free fall and penetration. It was demonstrated that the anchor terminal velocity quickly mobilized upon the release of the anchor, pointing at the presence of a large drag resistance compared to the weight of the small scale anchor. The terminal velocity obtained by the anchor was approximately 4 m/s, which could be enhanced in future trials by further streamlining the anchor. Double integration of measured accelerations allowed for measurement of anchor displacement across the various phases of installation. The penetration depth was then calculated by extracting the amount of anchor displacement occurring between the time of impact and the time when the anchor velocity converged to zero. The time of impact was calculated with a close investigation of changes in anchor acceleration. The results showed a penetration depth of approximately one anchor length for the sample trial presented in this study. Finally, it was concluded that the anchor remained vertically stable throughout the free fall and impact with the seabed as no significant variation in the lateral acceleration of the anchor is observed during these stages.

ACKNOWLEDGMENTS

This research was conducted with the financial support of Science Foundation Ireland under the US-Ireland R&D Partnership Program Grant Number SFI/12/US/E2479. This research survey is supported by the Marine Institute, and is funded under the Marine Research Programme by the Irish Government

REFERENCES

- [1] M. S. Raie and J. L. Tassoulas, "Installation of torpedo anchors: Numerical modeling," *J. Geotech. Geoenvironmental Eng.*, vol. 135, no. 12, pp. 1805–1813, 2009.
- [2] M. S. Hossain, Y. Kim, and D. Wang, "Physical and Numerical Modelling of Installation and Pull-Out of Dynamically Penetrating Anchors in Clay and Silt," in *ASME 2013 32nd International Conference on Ocean, Offshore and Arctic Engineering*, 2013, pp. V006T10A019–V006T10A019.
- [3] C. D. O'Loughlin, M. D. Richardson, M. F. Randolph, and C. Gaudin, "Penetration of dynamically installed anchors in clay," *Geotechnique*, vol. 63, no. 11, pp. 909–919, 2013.
- [4] H. Sabetamal, M. Nazem, J. P. Carter, and S. W. Sloan, "Large deformation dynamic analysis of saturated porous media with applications to penetration problems," *Comput. Geotech.*, vol. 55, no. 0, pp. 117–131, Jan. 2014.
- [5] D. Wang and C. D. O'Loughlin, "Numerical study of pull-out capacities of dynamically embedded plate anchors," *Can. Geotech. J.*, vol. 51, no. 11, pp. 1263–1272, 2014.
- [6] A. P. Blake and C. O'Loughlin, "Installation of dynamically embedded plate anchors as assessed through field tests," *Can. Geotech. J.*, no. ja, 2015.
- [7] J. T. Shelton, "OMNI-Maxtrade anchor development and technology," in *OCEANS 2007*, 2007, pp. 1–10.
- [8] E. H. Zimmerman, M. Smith, and J. T. Shelton, "Efficient gravity installed anchor for deepwater mooring," in *Offshore Technology Conference*, 2009.
- [9] J. Liu, L. Lu, and Y. Hu, "Keying behavior of gravity installed plate anchor in clay," *Ocean Eng.*, vol. 114, pp. 10–24, 2016.
- [10] D. Evans, "Clyde (Sheet 55N 06W), Sea bed Sediment and Quaternary Geology,(1: 250,000 Offshore Map Series)," *Br. Geol. Surv.*, 1985.
- [11] S. J. Blott and K. Pye, "Particle size scales and classification of sediment types based on particle size distributions: Review and recommended procedures," *Sedimentology*, vol. 59, no. 7, pp. 2071–2096, 2012.
- [12] C. P. Aubeny and C. Chi, "Mechanics of Drag Embedment Anchors in a Soft Seabed," *J. Geotech. Geoenvironmental Eng.*, vol. 136, no. 1, pp. 57–68, Jan. 2010.

Bearing capacity beneath tapered blades of open dug caissons in sand

Ronan Royston^{1,2}, Bryn M. Phillips^{1,2}, Brian B. Sheil¹, Byron W. Byrne¹

¹ Department of Engineering Science, University of Oxford, UK

² Ward and Burke Construction, Kilcolgan, Co. Galway

Email: ronan.royston@eng.ox.ac.uk, bryn.phillips@hertford.ox.ac.uk, brian.sheil@eng.ox.ac.uk, byron.byrne@eng.ox.ac.uk

ABSTRACT: An open-dug caisson shaft is a form of top-down construction in which a concrete shaft is sunk into the ground using the weight of the shaft and additional kentledge, if required. Excavation at the base of the caisson shaft wall allows the structure to descend through the ground. A thorough understanding of the interaction between the caisson shaft and soil is essential to maintain controlled sinking of the caisson. In this paper, the failure mechanisms developed beneath caisson blades in sand are investigated. A series of laboratory tests were carried out at the University of Oxford to explore how varying blade angles affect the performance of the bearing capacity beneath the caisson. Cutting angles of 30°, 45°, 60°, 75° and 90° (flat) were penetrated into sand under plane strain conditions; forces were monitored using a Cambridge-type load cell while soil displacements were recorded using Particle Image Velocimetry (PIV) techniques. The aim of this study is to understand how the soil failure mechanism develops and to determine the optimum cutting angle. The results of the laboratory tests can be scaled to predict the likely behaviour in the field. Results show that the bearing capacity is significantly dependent on the cutting angle; in a dense sand a steep cutting angle may be used to aid sinking of the caisson.

KEY WORDS: Caisson; tapered blade; bearing capacity; laboratory testing.

1 INTRODUCTION

An open-dug caisson shaft is a form of top-down construction. They have many functions in industry such as launch and reception pits for tunnel boring machines and underground storage tanks for foul and storm water attenuation. Caissons can be sunk through various soil types including sand, clay and rock. It can be a very safe and efficient form of construction as the permanent structure is used to retain the soil and water during excavation as shown in Figure 1.



Figure 1 30 m diameter reinforced concrete caisson at Anchorsholme Park, Blackpool, constructed by Ward and Burke Construction

In order for a caisson to sink into the ground, both the skin friction that develops between the soil and the concrete shaft in addition to the bearing capacity of the soil beneath the shaft walls must be overcome. A common technique to aid the sinking process is the use of a tapered blade, or cutting edge,

beneath the wall of the shaft. The purpose of the cutting edge is to cut into the ground, anchor the caisson horizontally and maintain verticality. It mobilises the failure mechanism of the soil towards the centre of the shaft, so that the soil in this area can be easily excavated to allow the caisson to sink. In order to achieve controlled sinking of the shaft, a thorough understanding of the bearing failure that develops in different soils is therefore essential. It ensures operatives in the field know where to excavate to induce bearing failure beneath the shaft walls. Moreover, a reduction in the bearing capacity beneath the caisson blades means less kentledge will be required to get the shaft to formation level.

The bearing capacity of sloped caisson footing depends on the angle of the tapered blade, roughness of the interface, angle of friction of the soil, width of the footing and the unit weight of the soil. In this paper it is assumed that the caisson diameter is large, 2D plane strains will develop with minimal conical action. While some work has been undertaken on sloped conical footings [1-2], limited information is available on 2D plane strain conditions for tapered footings.

Tomlinson [3] recommends various tapered angles depending on the soil type; flatter cutting angles are recommended for sand compared to clay. Nonveiller [4] describes various potential rupture surfaces. As the caisson penetrates into the soil, the resisting forces increase until a new state of equilibrium is achieved.

A method for quantifying the bearing capacity factor, N_γ , using limit-equilibrium theory was proposed to quantify the bearing capacity of tapered footings beneath caissons [5-6]. According to this approach, the value of N_γ is less sensitive to the angle of friction compared to the blade angle and embedment depth of the wall. However, some important parameters are neglected in this method, such as the interface friction between the soil and sloped blade of the caisson.

The aim of this study is to explore the performance of various tapered angles in sand through a series of laboratory tests. Particle image velocimetry (PIV) analysis is employed to track the failure planes developed in the soil during testing. In addition, a number of tests were carried out to examine the influence of overburden pressure during sinking.

2 EXPERIMENTAL EQUIPMENT

A three degree of freedom loading rig, developed at the University of Oxford [7], was used for the laboratory testing in this study (see Figure 2 and 3). A Cambridge-type load cell, attached to the end of the loading arm, records vertical, horizontal and moment reaction.

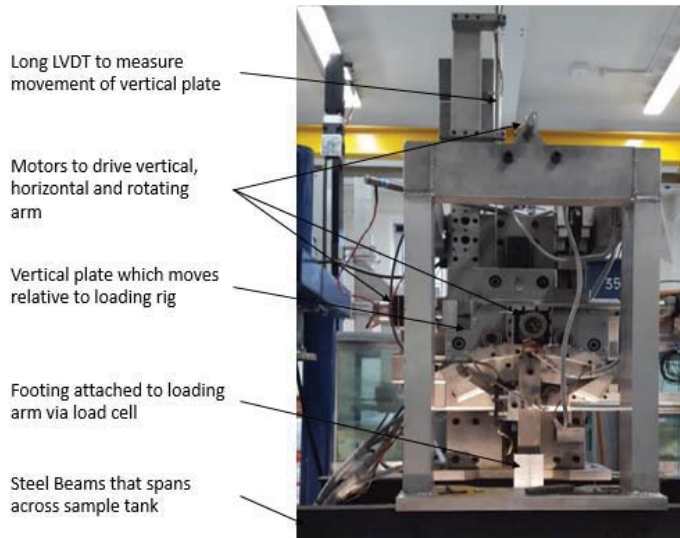


Figure 2 Three degree of freedom loading rig

The loading rig was located on top of a 600 mm x 300 mm x 95 mm testing tank which has a perspex front, which allows the sand movements to be recorded during testing, see Figure 4. A Nikon DS3200 camera located 700 mm from the front of the tank was used to capture images at a frequency of 1 Hz during testing. A downward penetration rate of 0.5 mm/sec was adopted for all tests; rate effects in sand are not expected to be significant. PIV analysis was carried out by processing the images using MATLAB module GeoPIV [8].

The experiments were conducted using a dry, yellow Leighton Buzzard DA30 silica sand, the properties of which are summarised in Table 1.

Table 1 Properties of Leighton Buzzard DA30 sand

Property	Value
$D_{10}, D_{30}, D_{50}, D_{60}, D_{90}$, (mm)	0.36, 0.45, 0.51, 0.54, 0.65
Specific Gravity, G_s	2.73
Minimum dry density, γ_{min} (kN/m ³)	14.5
Maximum dry density, γ_{max} (kN/m ³)	17.1
Critical state friction angle, ϕ'_{cs} (°)	32

Loose sand samples were prepared using a sand raining procedure in conjunction with a low drop height. Dense samples were prepared by vibrating the testing tank after sand

raining. To ensure a repeatable bulk density was achieved for each sample, the tank was filled using the same drop height for all tests.

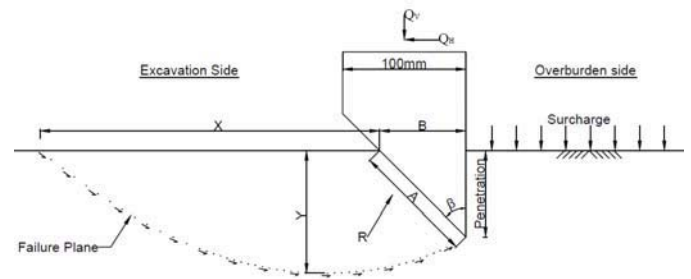


Figure 3 Test setup and soil failure wedge

A schematic of a typical cross section of a cutting edge and possible soil failure plane is provided in Figure 3, where B is the width at embedment, A is the length of the face, β is the tapered cutting angle, Q_v and Q_h are the vertical and horizontal reactions, R is the resultant reaction of the forces, and X and Y are the width and depth of the failure plane. It is worth noting that value of β generally used in industry is 45°, derived from on-site experience.

Aluminum pieces were created as the test pieces of varying cutting angles, β . In order to reduce the friction between the test pieces and the sides of the tank, 1 mm polytetrafluoroethylene (PTFE) sheets were placed either side of the piece with compressible foam placed in between the PTFE and the test piece. The test piece spanned the width of the test tank to ensure plane strain conditions.



Figure 4 Testing tank



Figure 5 Cone Penetration

3 VALIDATION OF TESTING PROCEDURES

Cone tests were performed, with an 8 mm diameter cone and a 60° cone angle, to examine the uniformity of the sample. The cone was penetrated 150 mm into soil samples prepared with three different relative densities, I_D , as per Equation (1), where γ is the density of the prepared sample. The cone was attached to the rig as shown in Figure 5 and penetrated through the sand at a rate of 1 mm/s. From the results presented in Figure 6, the cone penetration resistance appears consistent with depth thus indicating a uniform sample. Moreover, it is obvious that at higher relative densities, there is a commensurate increase in the cone resistance.

$$I_D = \frac{\gamma_{max}}{\gamma} \left(\frac{\gamma - \gamma_{min}}{\gamma_{max} - \gamma_{min}} \right) \quad (1)$$

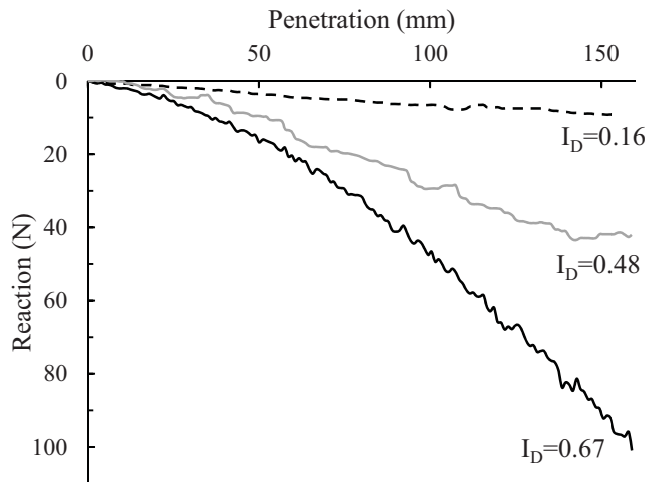


Figure 6 Cone penetration results

A series of preliminary tests were carried out to validate the present sand properties, sample preparation and experimental techniques. Careful consideration of the stress level is required in order to extrapolate model-scale laboratory testing to expected behavior in the field. At higher stress levels the dilatancy of soil is suppressed; relationships proposed by Bolton [9] are used to relate the critical state angle of friction to the peak angle of friction based on relative density and the stress state of the sand in the laboratory testing. Equations (2) and (3) are based on plane strain conditions for the relationship between critical and peak angles of friction based on the isotropic stress and density of the sample:

$$\phi'_{max} = 5I_R + \phi'_{cs} \quad (2)$$

$$I_R = I_D(10 - \ln p') - 1 \quad (3)$$

where ϕ'_{max} and ϕ'_{cs} are the peak and critical state friction angles, respectively, p' is the mean effective stress in the soil at failure and I_D is the relative density of the soil.

In order to validate the test results and sample preparation, a 90° piece (flat piece) was used to compare present measurements to published literature. The relative density of each test sample was calculated using the data presented in Table 1 which, in turn, was used to determine the value of ϕ'_{max} . Bearing failure was assumed to occur at 0.1B, neglecting soil cohesion and influence of overburden, the bearing capacity, q_{rd} , can therefore be defined as follows:

$$q_{rd} = \frac{1}{2} B N_\gamma \gamma' \quad (4)$$

where B is the width of the flat footing, N_γ is a bearing capacity factor and γ' is the effective unit weight of the soil.

Test results for the flat pieces are shown in Figure 7. Theoretical bearing loads are based on the approaches for calculating N_γ by Hansen [10] and Meyerhof [11]. Test results are consistent with theory and provide additional confidence in the experimental set up and the Bolton method [9].

Figure 8 shows an example of the incremental displacements in the soil obtained using PIV; the predicted failure plane according to Rankine theory, with a friction

angle of 32°, has also been superimposed on the image. The sample in Figure 8 is for a dense sample which has a peak angle of friction of 45° when applying Equations (2) and (3). This is not consistent with the 32° overlaid as the dilation of the sand is suppressed at higher densities.

The development of a triangular active wedge beneath the footing, in addition to the passive wedges, is obvious from this output.

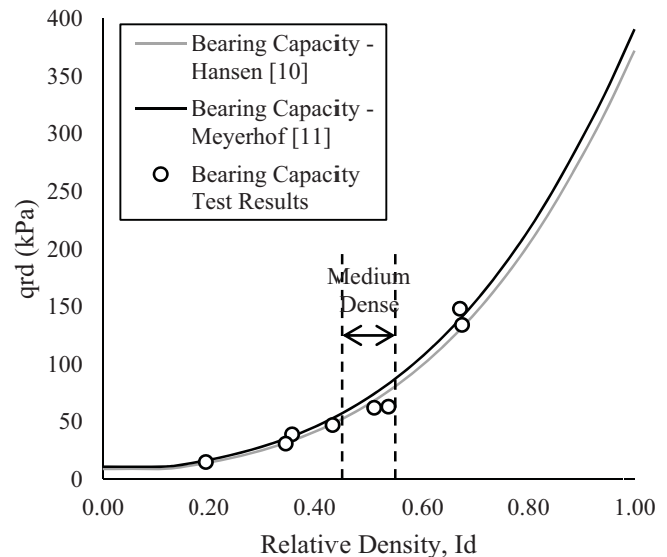


Figure 7 Theoretical and measured bearing capacities

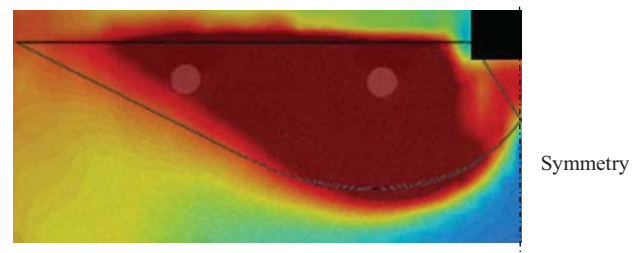


Figure 8 PIV of flat piece test

4 TESTING OF TAPERED ANGLE PIECES

A series of tests were carried out using cutting angles, β , of 30°, 45°, 60° and 75°. The test set-up for the cutting edges is shown in Figure 3. Each test was carried out on a medium-dense sample. The medium-dense tests have a relative density ranging between 0.44 and 0.54.

4.1 Influence of cutting angle, β

Figure 9 plots the influence of β on the variation of R with penetration. The resultant forces are higher for the shallower angles; this is attributable to the much greater bearing width of the flatter angles for the same penetration.

The influence of β on the relationship between Q_H and Q_V is examined in Figure 10 and Figure 11. The relationships presented in Figure 10 are remarkably linear where the steeper cutting angles reduce the vertical reaction. The ratio of horizontal to vertical force is shown in Figure 11 based on a best fit line to the results in Figure 10. In general, there appears to be a linear variation in Q_H/Q_V with β . It is worth noting that Q_H is as high as 0.9 Q_V for a 30° cutting angle

which could result in a large hoop tension force in the wall of the caisson.

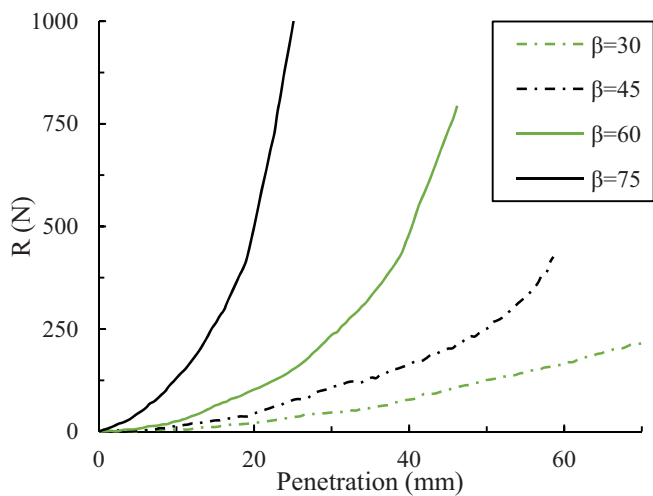


Figure 9 Resultant force of angle pieces

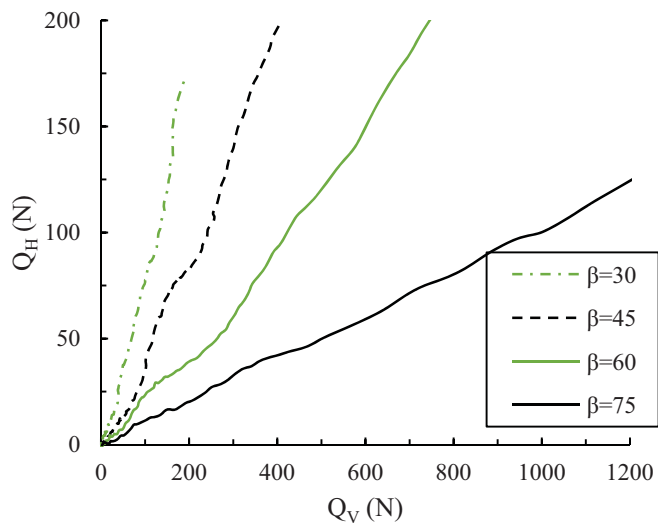


Figure 10 Horizontal against vertical forces

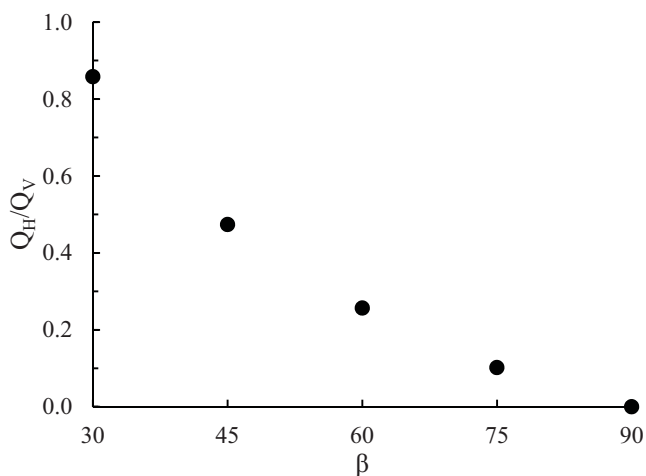


Figure 11 Ratio of Horizontal to vertical forces

Figure 12 shows the vertical bearing capacity of the footing, $q_{rd,v}$, against the embedment width. All angled footings

illustrate a similar increase in bearing capacity with embedded width. The theoretical vertical bearing capacity of a flat footing is also plotted for various values of B . The bearing capacity of the flat footing is approximately 1.4 times the bearing capacity of the angle piece at values of B less than 50 mm. As the bearing pressure increases, there is a change in the rate in the increase of the bearing capacity. This could be attributable to the stress-state of the soil as penetration progresses; additional numerical work is being conducted to explore this aspect.

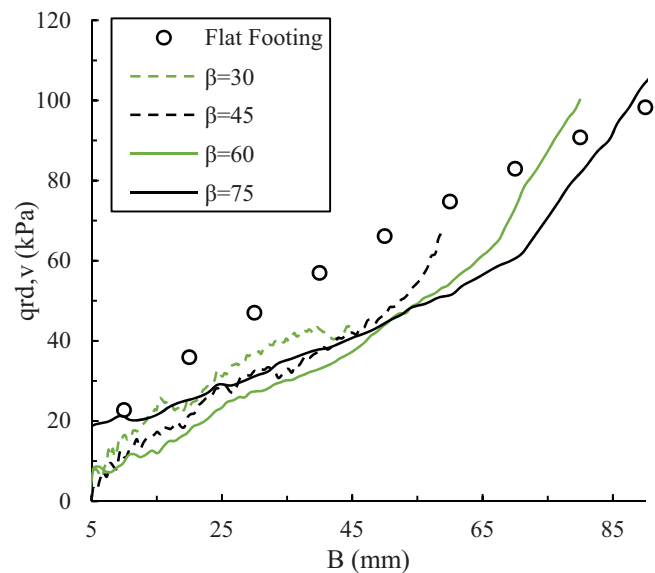


Figure 12 Effect of cutting angle on N_γ

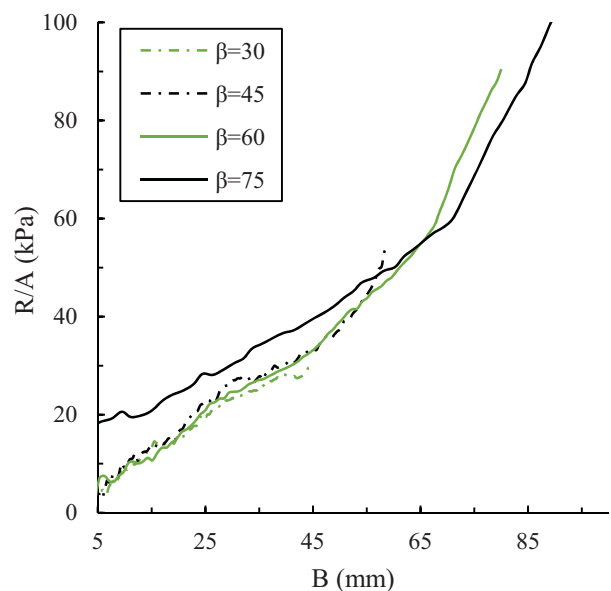


Figure 13 Average Face Pressure against footing width

In Figure 13, the variation of the pressure at the cutting face, R/A , is plotted against B . This framework appears to provide improved agreement between tests and appears to be relatively invariant to β . The slight differences in resultant pressures could be based on the slight differences in the relative densities and test discrepancies.

The failure mode for the different footing varies depending on the tapered angle, β . Figure 14 (a-d) shows the incremental total displacements of the soil; an embedment width of $B=40$ mm was chosen for these comparisons. At this stage of testing, the face pressures are similar (see Figure 13). The failure mechanism occurs towards the excavation side, as shown in Figure 14, as the tapered angles move into the active wedge of soil according to the Rankine theory for soil bearing failure. For the flatter angles, as the failure stresses in the soil develop, the soil begins to fail towards the excavation and overburden side, similar to a traditional flat footing.

Figure 15 shows how the zone of influence varies with β . The depth and width of the failure zone is much higher for the steeper tapered angles at $B=40$ mm.

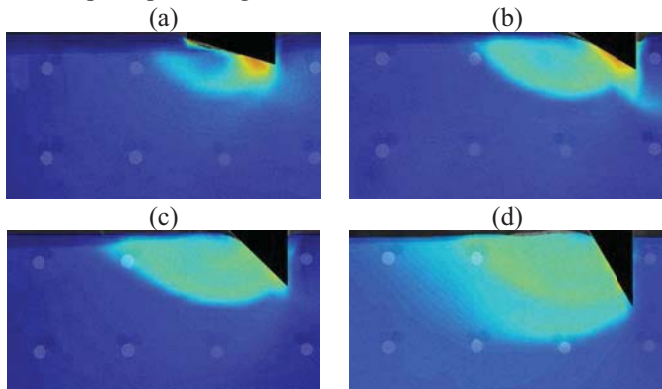


Figure 14 Resultant displacement at $B=40$ mm: (a) $\beta=75^\circ$, (b) $\beta=60^\circ$, (c) $\beta=45^\circ$, (d) $\beta=30^\circ$

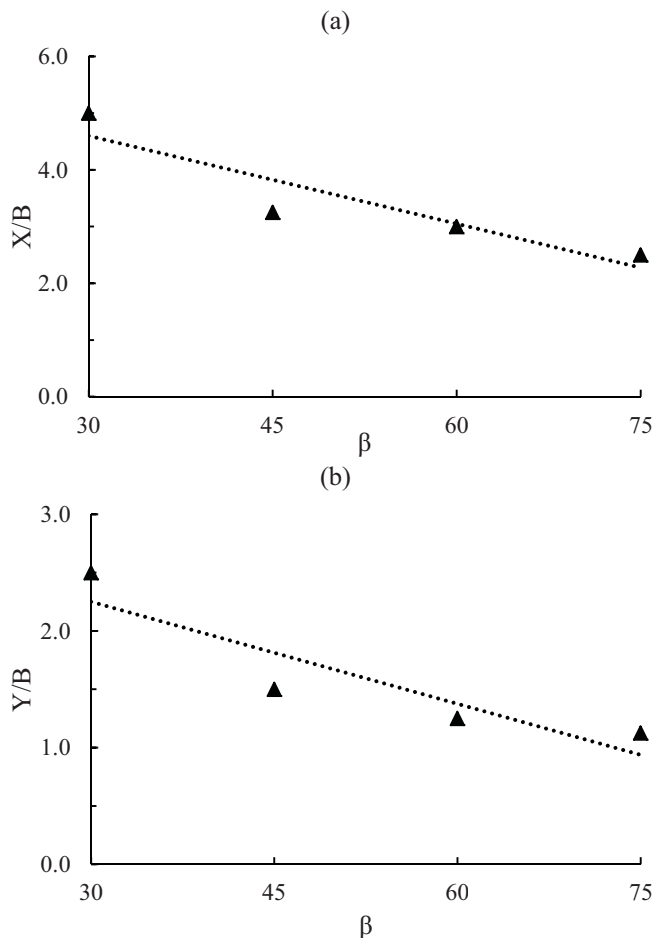


Figure 15 (a) Horizontal and (b) vertical zone of influence; $B=40$ mm

4.2 Influence of overburden on one side

In the field, there will always be a surcharge outside the caisson from the overburden soil as excavation and sinking of the shaft commences. This surcharge will increase as the caisson sinks further into the ground. A surcharge was applied by applying a weight on the overburden side (see Figure 3). Surcharges of 12.5kPa, 25kPa and 50kPa were considered.

The overburden has two effects on the soil and the resulting failure mechanism. Firstly it increases the initial stress in the soil and secondly, it will encourage failure of the soil towards the excavation side. Figure 16 and Figure 18 shows the effects of the overburden against the base case of a level surface.. It can be clearly seen that the overburden increases the bearing capacity of the soil beneath the footing.

The increase in bearing capacity is more sensitive to the shallower tapered angles, as the increase in resultant reaction is larger for β equal 75° compared to the β equal 45° test. The failure mechanism of the soil is shown in Figure 17 and Figure 19. For the higher surcharge pressures, the failure mechanism varies and is pushed towards the excavation side and the failure plane becomes larger.

The failure mechanism occurs towards the excavation side, as shown in Figure 14 for flatter angles (c-d), as the tapered angles move into the active wedge of soil according to the Rankine theory for soil failure. For the shallower tapered angles, as the failure stresses in the soil develop, the soil begins to fail towards the excavation and overburden side, similar to a traditional flat footing. This can be clearly seen in Figure 19 (g), as the soil failure mechanism develops on both sides of the 75° piece.

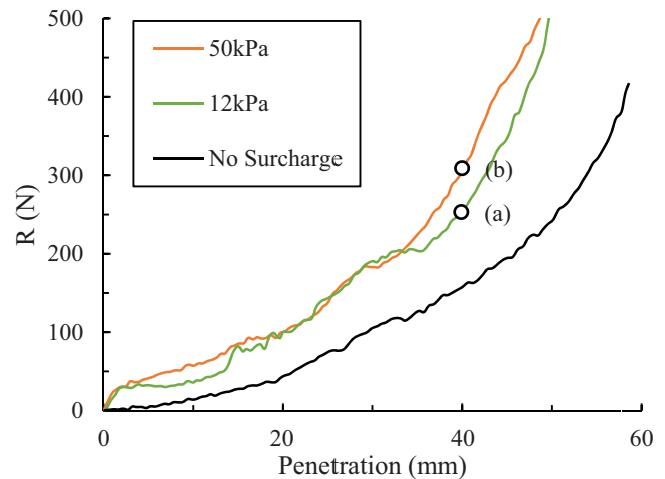


Figure 16 Influence of surcharge on resultant force; $\beta=45^\circ$,

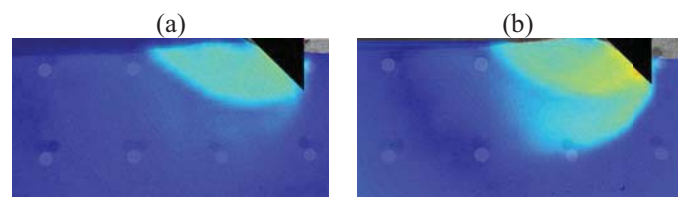


Figure 17 (a) 12kPa surcharge (b) 50kPa surcharge; $B=40$ mm, $\beta=45^\circ$, see Figure 16

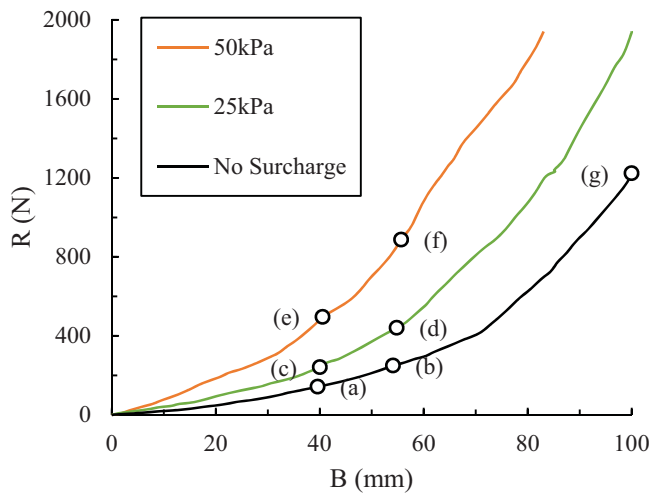


Figure 18 Influence of surcharge on resultant force; $\beta=75$,

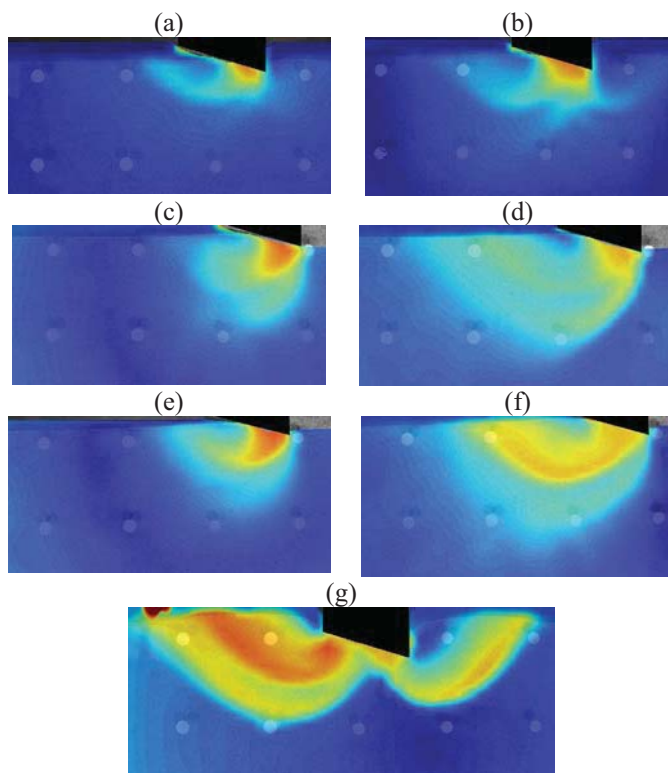


Figure 19 (a+b) No surcharge (c+d) 25kPa surcharge (e+f) 50kPa surcharge (g) No surcharge, $B=100\text{mm}$ and 35mm penetration; $\beta=75$, see Figure 18

5 CONCLUSIONS

In this paper, a suite of tests carried out on small-scale tapered footings in medium-dense sand has been presented. The authors have arrived at the following conclusions arising from this study:

- The forces that develop at the base of a caisson are largely dependent on the tapered angle of the footing. While steeper footings have a much reduced vertical resistance, at the same penetration, this is offset by an increase in the horizontal reaction. The bearing pressure on the face of the footing appears to be invariant to the

cutting angle of the test piece and varies linearly with the embedment width of the piece.

- Applying an overburden pressure on one side of the footing best models conditions in the field. The overburden has a greater influence on flatter cutting angles since failure wedges are developed on both sides of the cutter unlike steep angles where the failure wedge develops on the excavation side only. The overburden forces failure to occur on the excavation side, thereby increasing the bearing capacity.
- Output from the PIV analysis of the present tests can be used to guide excavation on site in order to induce failure of the soil beneath the caisson.
- Further work is being carried out at University of Oxford to extend these results and confirm the applicability to conditions in the field. In particular, further comparisons with full-scale measurements will be carried out to ensure that the proposed methods are reliable and valid.

ACKNOWLEDGMENTS

The authors gratefully acknowledge the financial support provided by Ward and Burke Construction Ltd.

REFERENCES

- M. J. Cassidy and G. T. Housby, "Vertical bearing capacity factors for conical footings on sand," *Geotechnique*, no. 52, pp. 687–692, 2002.
- G. T. Housby and C. M. Martin, "Undrained bearing capacity factors for conical footings on clay," *Geotechnique*, vol. 53, no. 5, pp. 513–520, 2003.
- M. J. Tomlinson, *Foundation Design and Construction*, 7 edition. Harlow, England; New York: Prentice Hall, 2001.
- E. Nonveiller, "Open caissons for deep foundations," *J. Geotech. Eng.*, vol. 113, no. 5, pp. 424–439, 1987.
- N. B. Solov'ev, "Use of limiting-equilibrium theory to determine the bearing capacity of soil beneath the blades of caissons," *Soil Mech. Found. Eng.*, vol. 45, no. 2, pp. 39–45, 2008.
- F. Y. Yan, Y. C. Guo, and S. Q. Liu, "The Bearing Capacity Analyses of Soil beneath the Blade of Circular Cassion," in *Advanced Materials Research*, 2011, vol. 250, pp. 1794–1797.
- C. M. Martin, "Physical and numerical modelling of offshore foundations under combined loads," University of Oxford, 1994.
- S. A. Stanier, J. Blaber, W. A. Take, and D. White, "Improved image-based deformation measurement for geotechnical applications," *Can. Geotech. J.*, no. ja, 2015.
- M. D. Bolton, "The strength and dilatancy of sands," *Geotechnique*, vol. 36, no. 1, pp. 65–78, 1986.
- J. Hansen, "A general formula for bearing capacity, Danish Geotechnical Institute Bulletin," *No.(11)*, 1961.
- G. G. Meyerhof, "Some recent research on the bearing capacity of foundations," *Can. Geotech. J.*, vol. 1, no. 1, pp. 16–26, 1963.

Landslide susceptibility assessment for engineered slopes using statistical and deterministic approaches

Karlo Martinović^{1,2}, Kenneth Gavin^{2,3}, Cormac Reale¹

¹School of Civil Engineering, University College Dublin, Newstead, Dublin, Ireland

²Gavin & Doherty Geosolutions Ltd., Beech Hill Office Campus, Dublin, Ireland

³Faculty of Civil Engineering and Geosciences, TU Delft, Stevinweg 1, 2628 CN Delft, Netherlands
email: kmartinovic@gdgeo.com, kgavin@gdgeo.com, cormac.reale@ucd.ie

ABSTRACT: Landslides cause hundreds of deaths and billions euros of damage to infrastructure and the environment each year. The field of landslide hazard and risk assessment has gone through a massive development in the last twenty years by introducing a wealth of statistical and geotechnical landslide susceptibility models. However, these efforts have been largely restricted to landslides occurring in natural terrain. Current risk assessment approaches for earthworks on large transportation networks still largely take form of subjective risk matrices with inputs gathered by visual walkover surveys. This paper shows the application of two distinctive objective landslide susceptibility approaches on a case study of Irish rail. The first is a 'statistical', or 'data-driven' approach, which uses logistic regression as a statistical tool to establish the influence of slope-describing variables that have led to landslide occurrence. In 'geotechnical' or 'deterministic' approach, geometrical and geotechnical properties of each slope are used to carry out probabilistic slope stability analysis, resulting in probability of failure for each slope. Both approaches result in susceptibility zoning for earthwork assets across the network, effectively ranking them in the criticality terms. This study compares the requirements, applicability and outcomes of each approach, and discusses the methods needed for developing each of them into hazard and risk assessments.

KEY WORDS: Landslide susceptibility; Engineered slopes; Risk assessment; Transport network.

1 INTRODUCTION

Landslides represent a serious geohazard across the world, resulting in hundreds of billions euros in damage and thousands of injuries and deaths each year [1]. To respond to this, much research over the past 20 years has gone into developing and enhancing the prediction of landslides' spatial and temporal distributions and consequences. All these procedures follow a general landslide risk assessment framework. Risk assessment is derived by combining hazard assessment (probability of occurrence of a landslide of certain size in a certain time period) and consequence assessment (impact of that landslide on elements at risk which can be people, structures, environment etc.) [2], outlined in Figure 1. Hazard assessment further consists of susceptibility analysis, obtaining the spatial distribution of landslide likelihood; and temporal analysis evaluating its frequency, often combined with consideration of landslide size (magnitude). Consequence assessment incorporates the identification of elements at risk and their vulnerability assessment.

A large variety of methods for calculating and mapping landslide susceptibility, hazard and risk have been developed and applied to different areas up to date [3], [4], [5]. Landslide susceptibility methods are usually subdivided into qualitative and quantitative methods. Qualitative methods are subjective as they are based on expert opinion and engineering judgment, either directly or indirectly through subjective determination of factor weightings. Examples of qualitative methods include geomorphological mapping, analytic hierarchy process and weighted linear combination.

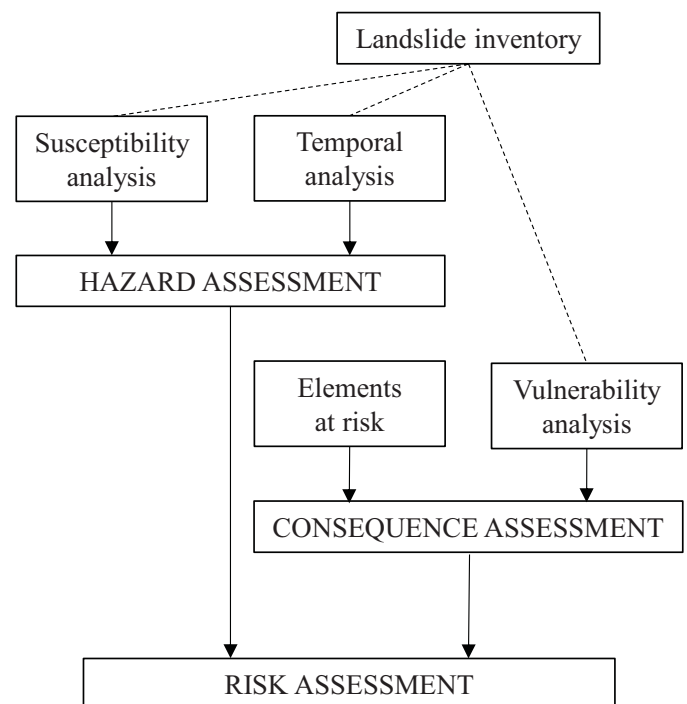


Figure 1. Risk assessment framework

Quantitative methods try to find a numerical correlation between study area's topographical, geotechnical and environmental attributes and landslide occurrence. These methods are generally considered more effective due to their reduced subjectivity, bypassing the need for expert opinion. Quantitative methods are usually carried out using either a deterministic (or 'geotechnical') or a statistical (or 'data-

driven') approach. The deterministic approach is based on geotechnical slope stability calculations, while statistical approach is based on statistical evaluation of the influence of slope attributes on landslide-affected slopes by examining past failure data using a variety of statistical techniques. Commonly used statistical methods include frequency ratio analysis, discriminant analysis and logistic regression analysis. Additionally, other data-driven methods such as artificial neural networks are also in use.

While numerous examples of these methods applied to case studies of natural hillslopes can be found, there is relatively little research focused on engineered slopes (cuttings and embankments) on transportation networks. That is somewhat surprising since, due to their location immediately adjacent to transport networks, these landslides can result in drastic consequences such as infrastructure damage, massive transport delays, injuries and even fatalities. Current state of the art of risk assessment methodologies used by asset managers is largely limited to simple subjective risk matrices with data stemming from visual walkover surveys. However, this can be improved by developing quantitative susceptibility, hazard and risk assessment methods that focus on engineered slope specifics.

2 GEOTECHNICAL APPROACH TO LANDSLIDE SUSCEPTIBILITY ANALYSIS FOR IRISH RAIL NETWORK EARTHWORKS

A landslide susceptibility model based on probabilistic slope calculations was developed for cutting and embankments assets on Irish Rail (IR) network as an initial step towards bespoke risk ranking model and decision support tool [6]. A first step included developing a structured database of geometrical, geotechnical and environmental slope characteristics for every asset. This database includes data such as asset location, type, height, slope angle, vegetation cover, soil type, drainage type, and other. Geometrical characteristics were collated following the processing of a detailed digital elevation model (DEM) obtained by aerial LiDAR survey. Soil type was assigned to each asset based on the Geological Survey of Ireland's soil cover maps using a GIS platform. Six main soil types characteristic for IR's assets and surrounding ground were identified: glacial till, granular material (glaciofluvial sands and gravels), soft clays, peat, rock and non-engineered fill. The accuracy of soil type assignment was validated using discrete borehole logs located on the rail network. For each soil type, a typical range of geotechnical parameters was identified from background literature and existing geotechnical reports. This was further complemented by a detailed site investigation for six assets representative of each major soil type.

As the Irish rail network stretches over hundreds of kilometres, large variability in geotechnical parameter values for each soil type can be expected. For that reason, all parameters are described using mean value and standard deviation. This enabled the performance of probabilistic slope stability calculations which give a more accurate representation of stability than standard deterministic approaches.

The 'Hasofer-Lind' first order reliability method (FORM) [7] was used to calculate the probability of failure associated with each asset and its coupled limit state. The 'Hasofer-Lind' approach is an invariant method for calculating the reliability index β , which can then be transformed into a probability of failure P_f .

The first step using this methodology is to transform all variables into normalised random variables. This is accomplished by means of equation (1).

$$\bar{x}_i = \frac{x_i - E[x_i]}{\sigma[x_i]} \quad (i = 1, 2, \dots, n) \quad (1)$$

After normalising the variables the next step is to express the limit state in terms of the reduced normal random variables, as in eqn. (2)

$$g(\bar{X}) = g(\bar{x}_1, \bar{x}_2, \dots, \bar{x}_n) \quad (2)$$

In this reduced variable space the limit state surface describes the boundary between stable and unstable zones. The Hasofer Lind reliability index is then expressed as the minimum distance between the origin (the mean value of the reduced limit state) and the failure zone. Assuming normal random variables, a probability of failure can then be obtained using the following equation (3).

$$p_f = p[g(\bar{X}) < 0] = 1 - \Phi(\beta) \quad (3)$$

Where $\Phi(\beta)$ is the standard normal cumulative distribution function.

Three limit states reflect the three failure types for which limit equilibrium slope stability calculations were carried out: (i) shallow translational, (ii) deep rotational slide, and (iii) rock wedge failure (for rock cuttings), see Figure 2.

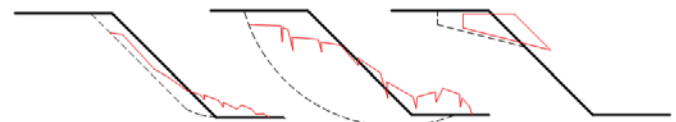


Figure 2. Three failure modes considered in slope stability analyses: (i) shallow translational, (ii) deep rotational slide, and (iii) rock wedge failure

The calculations result in baseline probabilities of failure for each asset. Since these calculations incorporate only simple geometrical and geotechnical data, detailed observations for each asset need to be included in order to account for small differences in landslide-triggering conditions between the assets, controlled by variables which cannot be easily included in limit equilibrium calculations. These variables include data that is usually recorded in a qualitative manner, such as type and condition of drainage, type and density of the vegetation, slope erosion and overall condition, etc. Twenty of these variables, named Degradation Factors (DF), were identified with the help of experienced Irish Rail site inspectors' engineering judgment. Each DF was given the weight based on experience and interrogation of past failures. The total product of DF weights gives the final DF adjustment factor which is combined with baseline reliability indices to obtain final reliability indices and final probabilities of failure. Flowchart of this process is presented in Figure 3. These final

probabilities of failure enable to effectively rank and compare all assets across the network.

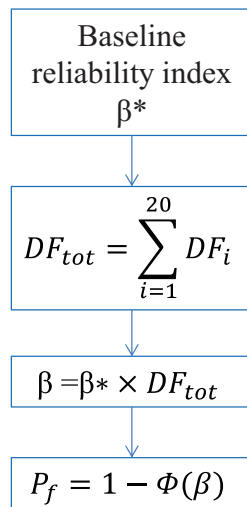


Figure 3. Flowchart of incorporation of degradation factors

3 STATISTICAL APPROACH TO LANDSLIDE SUSCEPTIBILITY ANALYSIS FOR IRISH RAIL NETWORK EARTHWORKS

Another landslide susceptibility analysis on the same network was carried out using a ‘statistical’ (or ‘data-driven’) approach. This approach aims to interrogate the usefulness of past failure records in obtaining conclusions on landslide distribution across the network. The logistic regression statistical technique uses the historical landslide data (some examples in Figure 4) to quantify the influence of topographical, geotechnical and environmental slope characteristics (factors) of slopes on which landslides were recorded. It then uses these results to assess the probability of landslides on all other assets in the network based on their own combinations of these factors.

This approach was tested on the case study area of Athlone Division, a north-western section of Irish Rail network comprising about a third of all earthwork assets (cuttings and embankments). The extent of Irish Rail network (thin lines) and Athlone Division (thick lines) is outlined in Figure 5. A database prepared for the geotechnical approach of susceptibility analysis (described in previous section) was used here to obtain the data on slope characteristics. Since different factors are responsible for initiating different landslide types, it is a common practice to carry out a susceptibility analysis for each landslide type separately [5]. In this example, susceptibility analysis was carried out for shallow translational slides, as they were found to be the most prevalent landslide type across the Irish rail network.



Figure 4. Examples of typical landslides on Irish rail network: a) on embankment, b) and c) on cutting

A selection of factors relevant to landslide initiation is a process that depends on landslide type and study area characteristics. Budimir et al. [7] carried out an extensive literature review on the topic of landslide susceptibility analysis using logistic regression, with the aim of determining the frequency and significance of factors used for susceptibility analysis. The review showed that there are no universal criteria established for selecting factors, resulting in the factors selected for analysis varying wildly between studies.

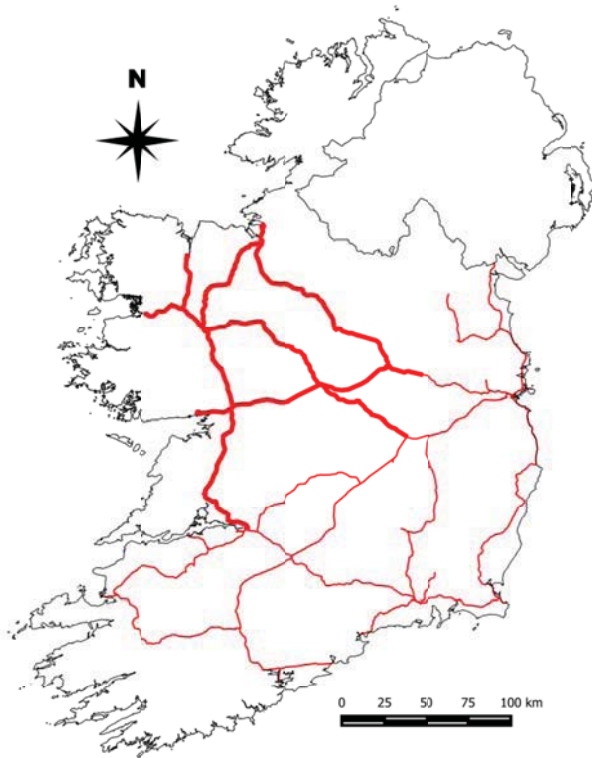


Figure 5. Irish Rail network with rail lines in Athlone divisions (thick lines)

In this study, nine factors describing the asset have been selected, each with a number of possible classes. Factors were selected based on background literature research and the reported causal factors from the available landslide register. The factors selected are slope height (scalar), slope angle (scalar), asset type (cutting or embankment), aspect (classes: N, NE, E, SE, S, SW, W, NW), vegetation type (bare ground, grass, shrubs, trees), adjacent slope (flat terrain, flow towards asset or flow from the asset), soil type (glacial till, granular material, soft clays), annual rainfall (800-1000 mm, 1000-1200 mm, 1200-1400 mm) and slope conditions (1, 2 or 3 based on inspector's observations). Some of these factors such as asset type or slope condition are specific to engineered slopes for transport networks and have not been used in landslide susceptibility studies before.

The goal of logistic regression is to find the best fit model that describes the combined relationship between these factors (independent variables) and the presence or absence of landslides (dependent variable) on all slopes. The final result of this model is a probability p of the landslide occurring, with values ranging from 0 to 1 for each asset, calculated by:

$$p = \frac{1}{1 + e^{-Z}} \quad (4)$$

where Z is generated by the coefficients depending on the input data for each factor, obtained by Equation (5):

$$Z = \beta_0 + \beta_1 X_1 + \beta_2 X_2 + \dots + \beta_n X_n \quad (5)$$

where $\beta_1, \beta_2, \dots, \beta_n$ are the regression coefficients that determine the contribution of the different input factors (independent variables X_1, X_2, \dots, X_n), obtained iteratively using maximum likelihood estimation. β_0 is the intercept value of the model.

The asset factor database was divided into training set (70 %) using which the model was set up and the validation set (30 %) against which the model results were verified. The logistic regression was then carried out on the training set. Regression coefficients obtained for each factor class are presented in the Table 1.

Table 1. Regression coefficients

Factor	Class	β
Object type	Embankment	0
	Cutting	1.327
Aspect	E	0
	N	0.312
	NE	-0.405
	NW	-0.236
	S	-0.540
	SE	0.832
	SW	-0.636
	W	1.110
Adjacent slope	-1	-0.797
	0	0
	1	1.704
	2	1.410
Asset height	Height [m]	0.135
Asset slope angle	Angle [°]	0.078
Vegetation type	Bare	1.383
	Grass	0.932
	Shrubs	0.394
	Trees	0
Soil type	Granular till	0
	Granular material	-0.542
	Soft clays	-21.393
Rainfall	800-1000 mm	0
	1000-1200 mm	0.239
	1200-1400 mm	0.959
Condition	1	0
	2	2.000
	3	3.284
Constant	β_0	-8.54

In general, results identified the slope angle as the most important driver for the shallow instability, complementing similar conclusions made for natural slopes [8]. Cuttings were found to be more susceptible to failure than embankments, attributed among other things to influence of groundwater level which was generally at shallower depth for cuttings. Slope condition was found to exert a significant influence on landslide occurrence, highlighting the role of small localized defects in landslide initiation.

These results were also used to infer quantitative comparison of the relative influence between classes of the same factors to landslides occurrence. Some of the results are graphically presented in the Figure 6. These results for example show that bare slopes are 4 times more likely to fail

than densely vegetated ones, and that west facing slopes are 3 times more likely to fail than the east facing ones.

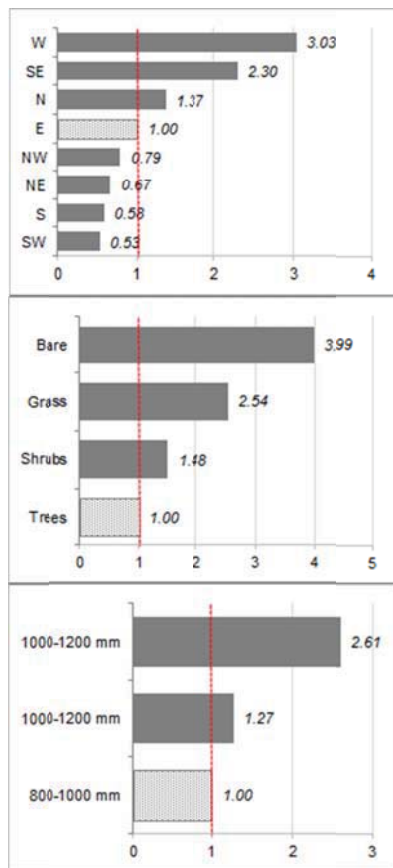


Figure 6. Odds-ratios for a) aspect, b) vegetation type and c) annual rainfall

The performance of the model was interrogated using several statistical measurements such as chi-square test and McFadden's and Nagelkerke's R^2 tests. These results indicated a very good fit of the model. The model was then validated using the validation dataset. Probabilities of failure of assets in validation dataset were obtained by applying regression coefficients acquired through training model. Assets with $p > 0.5$ were regarded to be predicting the landslides. They were then compared to the actual state of assets (presence/absence of landslides). Comparison was carried out with the help of confusion matrix [9], classifying assets into true positives, true negatives, false positives and false negatives. The confusion matrix showed the overall accuracy of the model to be 92.3%, but slightly overpredicting the absence of landslides. That was attributed to a small sample size of landslide-affected assets in both training and validation datasets. Model was additionally validated using Receiver Operating Curve (ROC), shown in Figure 7. The ROC curve presents the relationship between the model's sensitivity and specificity, expressions inferred from the values from the validation confusion matrices with varying cut-off levels. ROC confirmed a very good fit of the model, with area under curve (AUC) of 0.902 for validation dataset (AUC=0.5 representing a random fit and AUC=1 indicating a perfect fit).

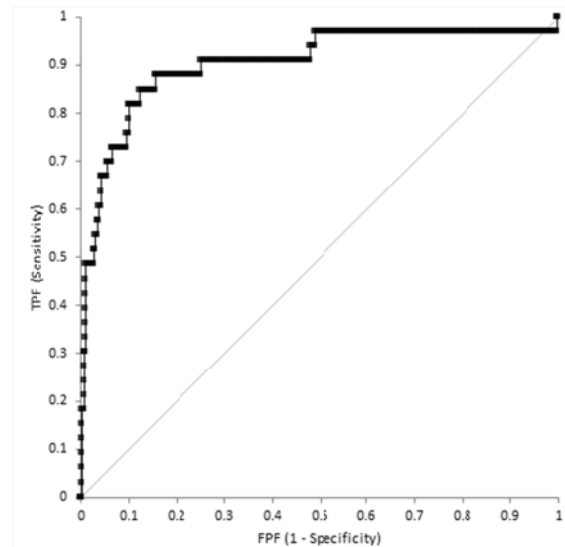


Figure 7. ROC curve for validation dataset

Using the calculated probabilities, assets were classified into five susceptibility classes: very low (79.4% of all assets), low (13.0%), moderate (3.9%), high (2.3%) and very high (1.4%); effectively identifying and ranking the top critical assets. A large percentage of assets in a 'very low' class is indicative of engineered slopes, which are designed to satisfy stability.

4 STEPS TO RISK ASSESSMENT

Landslide susceptibility analysis presents the spatial distribution of landslide occurrence likelihood. However it does not provide information on the frequency of occurrences or the impacts landslides can cause.

The temporal occurrence of landslide can be expressed in terms of frequency, return period, or exceedance probability. It is often obtained through statistical empirical analysis of past failures in the study area in a discrete time interval. For landslide hazard assessment on transport networks, it is common to look at joint temporal aspects of landslide event and traffic features, such as temporal probability that a vehicle (car or train) will be at the debris path. Similar approach can also be used to obtain magnitude-frequency curves, jointly assessing landslides' size and temporal aspect.

Another way of obtaining the temporal patterns of landslide occurrence is by analysing the frequencies and return periods of the triggering factors that initiate the landslides, rather than the landslides themselves. For rainfall triggered landslides, the influence of rainfall is typically interrogated using either physical model or rainfall thresholds. Physical models couple the hydrological and slope stability models to assess the response of the slopes in study area to the applied rainfall [10]. Rainfall thresholds represent the lower bound of a combination of some rainfall characteristics such as intensity, duration or accumulation necessary to induce landslides [11]. They are obtained in an analytical way by collating the data on rainfall characteristics in place during and before the known historical landslides.

Another major subcomponent of a risk assessment is the consequence assessment. Consequence assessment aims to quantify the impact that a specific landslide has on the

surrounding built and natural environment. The first step here is to define the elements at risk that can be potentially affected by landslides and for which risk assessment is being carried out. The examples of elements at risk are people, buildings, infrastructure, and other. The next step involves obtaining the vulnerability of each element at risk to the landslide. Vulnerability is defined as the degree of potential damage, or loss a given element may experience as a result of a landslide of a particular type and intensity [4]. The vulnerability of an element depends on the element at risk observed, the type of landslide, relative position of element at risk to the landslide, and the magnitude and run-out distance of the landslide. For example, vulnerability of people in vehicles to slow moving deep rotational landslide is extremely low, while the vulnerability of a road or rail element positioned at the crest or toe of the same landslide is extremely high. Conversely, vulnerability to shallow rapid moving debris flow is much higher for people than for reinforced concrete buildings or road/rail elements. Vulnerability is typically expressed using vulnerability factors with values ranging between 0 and 1, quantified through expert judgment or by using statistical methods to analyse the consequences of historical landslides. The alternative way of obtaining the vulnerability values is by developing the fragility curves, which express the conditional probability of exceedance of a pre-defined damage level for various values of landslide intensity [12].

The final risk value is obtained as a product of hazard and consequence assessment results. The last step in risk assessment typically involves evaluating the risk against existing risk criteria. Risk criteria depend on the perception of risk in the society exposed to hazard, and as a result they vary from country to country and between infrastructure management organisations. Further actions towards risk acceptance or mitigation are covered in detail through risk management frameworks.

5 CONCLUSIONS

Two approaches to landslide susceptibility assessment for engineered slopes on transport infrastructure are outlined in this study. Both approaches were applied on the earthworks on the rail network in Ireland. The first, 'geotechnical' approach is based on slope stability calculations for each of the cutting and embankment on the network. Slope stability calculations were carried out in a probabilistic fashion to accommodate the large uncertainty in soil parameter values expected across the network. The resulting probabilities of failure were then fine-tuned using engineering experience to include the detailed asset-specific observations. The second, 'statistical' approach is based on interrogating the past landslide records to quantify the influence of geotechnical and environmental attributes of those slopes on landslide occurrence. It was carried out using a statistical multivariate method of logistic regression. Statistical model was trained on the training dataset and resulted in probability of the landslide occurrence for all geotechnical assets in the study area.

While both approaches were proven to be highly useful for determining landslide susceptibility for engineered slopes, the approaches differ in some features. In comparison, statistical method requires less computing power and explicitly takes past experience into account. It also results in the quantitative

recommendations of influence of each factor class to failure occurrence. However, it is very sensitive to the completeness of past failure dataset and the variations in dataset size and training/validation ratios. It also needs to be carried out for every landslide type individually. Unlike statistical approach, the geotechnical approach takes account of soil mechanics principles and geotechnical characterisation of each asset. That makes results progressively more precise as the available asset data is being widened following site investigation across the network. It is also able to readily include the effect of any observation through the use of degradation factors.

Landslide susceptibility assessments like the two described in this study require temporal analysis and vulnerability assessment to be developed into the full risk assessment. This study finally gives a short overview of the typical methods used to carry out these steps.

ACKNOWLEDGMENTS

This work is partly funded by the Horizon 2020 DESTination RAIL Project (Decision Support Tool for Rail Infrastructure Managers) EU Project No. 636285. This research is supported by the Irish Research Council Employment Based Postgraduate Programme scholarship fund.

REFERENCES

- [1] Aleotti, P., & Chowdhury, R. (1999), 'Landslide hazard assessment: summary review and new perspectives', *Bulletin of Engineering Geology and the environment*, 58(1), 21-44.
- [2] Varnes, D. (1984) Landslide hazard zonation: a review of principles and practice. No. 3.
- [3] Guzzetti, F., Carrara, A., Cardinali, M., & Reichenbach, P. (1999), 'Landslide hazard evaluation: a review of current techniques and their application in a multi-scale study, Central Italy', *Geomorphology*, 31(1), 181-216.
- [4] Fell, R., Ken KS Ho, S. Lacasse, E. Leroi.(2005), 'A framework for landslide risk assessment and management', *Landslide risk management*, pp. 3-25.
- [5] Corominas, J., Van Westen, C., Frattini, P., Cascini, L., Malet, J. P., Fotopoulou, S., ... & Pitilakis, K. (2014), 'Recommendations for the quantitative analysis of landslide risk', *Bulletin of engineering geology and the environment*, 73(2), 209-263.
- [6] Doherty, P., Gavin K., Martinović K., and Reale, C. (2014), 'GEORISK-A Risk Model and Decision Support Tool for Rail and Road Slope Infrastructure', *Proceedings of the International Conference on Road and Rail Infrastructure CETRA2014*, pp 573-579
- [7] Budimir, M. E. A., Atkinson, P. M., & Lewis, H. G. (2015), 'A systematic review of landslide probability mapping using logistic regression', *Landslides*, 12(3), 419-436.
- [8] Dai, F. C., Lee, C. F., Li, J., & Xu, Z. W. (2001), 'Assessment of landslide susceptibility on the natural terrain of Lantau Island, Hong Kong', *Environmental Geology*, 40(3), 381-391.
- [9] Mancini, F., Ceppi, C., & Ritrovato, G. (2010) GIS and statistical analysis for landslide susceptibility mapping in the Daunia area, Italy. *Natural Hazards and Earth System Sciences*, 10(9), 1851-1864.
- [10] Godt, J. W., R. L. Baum, W. Z. Savage, D. Salciarini, W. H. Schulz, and E. L. Harp. (2008) 'Transient deterministic shallow landslide modeling: requirements for susceptibility and hazard assessments in a GIS framework', *Engineering Geology* 102, no. 3: 214-226.
- [11] Aleotti, P. (2004) 'A warning system for rainfall-induced shallow failures', *Engineering Geology* 73, no. 3: 247-265.
- [12] Fotopoulou, S. D., Pitilakis, K. D. (2013). 'Fragility curves for reinforced concrete buildings to seismically triggered slow-moving slides', *Soil Dynamics and Earthquake Engineering*, 48, 143-161.

Comparative Analysis of the Probabilistic Methods to Estimate the Probability of Failure of Offshore Wind Turbine Towers

Rui Teixeira¹, Alan O'Connor¹, and Maria Nogal¹

¹Department of Civil, Structural & Environmental Engineering, Trinity College Dublin, Ireland
email: rteixeir@tcd.ie, oconnoaj@tcd.ie, nogalm@tcd.ie

ABSTRACT: Offshore wind energy experienced an exponential growth in installed power since the beginning of the current century. While this growing trend is expected to continue, further growth of the sector imposes more demanding engineering methods. It is then envisaged that enhanced technical competitiveness can be achieved through a progressively less deterministic design process. Under the described context, a comparative study on the applicability of different probabilistic methods to estimate the probability of failure (P_f) of offshore wind turbine (OWT) towers under extreme events is presented here. Depending on the complexity introduced in the analysis of the OWT towers the applicability of different probabilistic approaches may be limited. FORM, SORM, Monte Carlo Simulation are examples of well-established methodologies to estimate P_f . Nevertheless, alternative methodologies such as the directional simulation can be an even more efficient solution for the problem. This preliminary assessment of the probabilistic approaches enables further developments in reliability methodologies for the specific case of OWT towers.

KEY WORDS: Offshore wind turbine; Probabilistic analysis; Reliability assessment; Extreme values; Support structures.

1 INTRODUCTION

Offshore wind energy experienced an exponential growth in installed power since the beginning of the current century. While this growing trend is expected to continue, further growth of the sector imposes more demanding, complex and accurate engineering methods. At the same time, improvement of the techniques applied in the sector is necessary to unlock new breakthroughs that will enable it to become progressively more competitive as a source for generating energy.

Addressing the subjacent uncertainty of the variables involved in the analysis of Offshore Wind Turbines (OWT) gives the designer a new dimension of analysis. Perception of the statistical deviations experienced by the design variables, enables a more complete understating of the risk associated with the operation of an OWT.

The probabilistic analysis of OWT is not a new practice. In fact, with a brief analysis of the standards for designing OWT (IEC 61400 class [1], [2]) or some recommended guidelines (e.g. [3]) it is possible to infer that assessing uncertainty is a recurrent process inside the design chain. Although, a significant challenge still exists in this field to progressively improve the established techniques, and to develop new methodologies that address topics where the subject, uncertainty, is not yet accounted for.

When working on a particular OWT project, some ambiguity can be identified in the standards that rule the process. It is frequent for these to require the designer to produce a reliable design, leaving to his/her consideration the methodology applied for the effect. Also, application of deterministic design processes or safety coefficients that account for subjacent uncertainties is still a recurrent practice that leads to structural over-design.

The ultimate goal of a probabilistic assessment is to estimate the risk of failure of a certain system. The criteria for failure is established by the designer, and shall be justified based on physical or other types of coherent constraints.

When a probabilistic approach is used the risk is given by the system's probability of experiencing or exceeding a certain occurrence that is defined as a failure and is given by the probability of failure (P_f). The Reliability Index (β) is one of the most common indicators to measure the reliability of a system and relates directly to P_f through equation (1).

$$P_f = \Phi(-\beta) \quad (1)$$

where Φ represents the standard normal cumulative distribution. The relation in equation (1) can be represented also as $P_f = 1 - \Phi(-\beta)$ that gives the probability of exceedance the threshold for which quantity β is representative.

Several studies summarized and discussed the way probabilistic methods are applied to wind turbines [4], [5]. Nevertheless, even considering the extensive work existing in the field, a similar reference discussion is still needed for the specific case of OWT support structures. Additionally, the mentioned ambiguity in the design guidelines motivates a comparative study between the techniques currently applied in the sector.

To address the proposed challenge an additional four sections were defined. Section 2 briefly explains the concept of reliability analysis, Section 3 presents some of the most relevant works on reliability when applied to OWT support structures and Section 4 identifies some of the relevant challenges in this field. Finally, the most relevant conclusions are presented in Section 5.

2 RELIABILITY ASSESSMENT

Two dimensions of analysis are set when approaching the reliability of a system. One is related to the fluctuation of the external conditions that excite the system and usually are called the load model (L); the other is related to the response of the system and how it varies, being frequently called the response model (R). When analysing a physical system the complexity considered in each of the two dimensions will dictate the complexity of the global problem.

To assess a system failure the designer needs to identify the modes on how it may fail. For this, a physical representation of the system is needed and for each failure mode one main equation, usually called limit-state function ($g(x)$, where x represents a set of random variables), is defined to evaluate the occurrence of failure. This equation compares the load model considered L with the respective resistance model R and failure may occur when the L surpasses R . This relation is usually expressed as $g(x) = R(x) - L(x)$, and failure occurs when $g(x) < 0$.

Through the previous overview of the reliability analysis process is possible to understand that the complexity of the overall approach will depend on the level of complexity implemented on each of the models selected to evaluate R and L . If the models are simple, no major limitations are found when applying a reliability methodology. But, in reality, this does not often occur. If we look to the specific case of OWT, it is straightforward to comprehend that, as a coupled system, the physics of it are quite complex. Therefore, fully addressing the probabilistic analysis of a system faces a significant challenge: if the analysis becomes too complex, the limit-state is highly non-linear and the methodologies applied to estimate its corresponding P_f are either very time consuming or inaccurate.

These two aspects are quite significant when the whole context of analysis goes through optimization problems and extensive analysis where the time and accuracy are the main rulers of the process.

Two major types of assessment regarding system's limit state analysis and failure can be identified: Serviceability Limit State (SLS) or Ultimate Limit State (ULS). The current paper focuses on the application of reliability methodologies for OWT towers and support structures considering ULS and extreme events.

3 RELIABILITY ANALYSIS OF OWT TOWERS

Working with ULS and extreme events means working with events that have a low probability of occurrence and are usually located in the tails of the statistical distribution where the probability density function is low. Eventually, statistical extrapolation is almost inevitable for practical purposes. Regarding the structural analysis and with particular emphasis on the support structures, several studies can be highlighted dealing with ULS and their inherent necessity to consider extrapolation methodologies.

In [6] the comparison between applying probabilistic analysis and deterministic analysis when dealing with extreme values theory is addressed. In this comparison three methods to determine the distribution of extreme response, global maximum, peak over threshold and the process model, are used to establish the response with a return level of 100 years. The flap moment at the blade root and the overturning

moment at the sea bottom were analysed. The second is of particular interest when analysing OWT towers and support structures.

The response based approach is then compared to the external conditions approach. The differentiating factor between these two approaches is related to the way that long term occurrences are evaluated. The first approach uses the short-term response of the system to extrapolate the long-term response, whereas with the second approach, the external conditions are extrapolated and then, the response of the system is calculated for the respective previously extrapolated conditions.

To set the long term distributions of loads, the practice recommended in [1] for power production and commonly considered as the standard for the extrapolation of long-term loads, is integrating the short-term maximum conditional response with the joint probability of external random variables. This is done through the integral in equation (2).

$$P(L > l_T) = \int_x P[L > l_T | X = x] f_X(x) dx \quad (2)$$

where $P(L > l_T)$ is the probability of exceedance associated with a load l_T . To evaluate the integral, the conditional short-term exceedance distribution of the extreme response when certain external conditions x are met $P[L > l_T | X = x]$ is multiplied by the joint probability density function $f_X(x)$ and integrated over its parameters.

This method requires to set the short term distribution over the domain of the environmental random variables X so that $P[L > l_T | X = x]$ can be defined. This is usually done by analysing a number of n extreme loads. The empirical load distribution function obtained is used to fit a parametric probability model.

Further, according to the standards it is usually assumed that the largest loads occur at widely separated times being thus statistically independent. The probability of the largest load L exceeding a given load l in the observation time T is given by Equation (3) [7].

$$Prob(L > l_T | X) = 1 - (F(l|X))^N \quad (3)$$

where N is the number of occurrences in the observation period T . Therefore, if an observation period of 1 year is considered $T = 1$ and $F(l|x)$ is the 10 minutes short term cumulative distribution of loads, N is the number of 10 minutes sea states that occur in a time interval of 1 year. With this assumption of independence, estimating the values for long return periods T_r becomes straightforward and the application of Equation (3) simpler. For instance, if an observation period of 1 year is considered, the load L associated with the cumulative value of 0.01 will have a T_r of 100 years.

With the R and L models defined, this methodology allows the analysis of $g(x)$ and its respective probability of being negative.

Compared with the external loads condition the response based approach covers the likely limitation caused when the extreme loads do not occur with the extreme environmental conditions. Here, all the domain of X is considered. On the other hand, the response based approach presents itself as very resource consuming and is only fully possible in the design phase when the OWT design parameters are established, being thus, inefficient in early-design stages.

To tackle some of the limitations identified [8] introduces a methodology to extrapolate loads based on limited field data measured on an OWT installed in Blyth, United Kingdom. To estimate the long term load exceedance probabilities, bootstrap techniques are applied and the uncertainty generated by extrapolating long term loads based on limited field data is addressed. The parameter used as reference for analysis is the Mudline Bending Moment, which is the moment generated in the tower at seabed level.

Apart from the methodologies to settle distributions of maxima referred before [8] addresses also the application of the Block Maxima method to set the extreme values distributions.

Additionally, [9] evaluates the application of inverse First Order Reliability Methods (FORM). These methods have the particularity of being, when compared with the extrapolation of loads based on the integration of the conditional distribution of loads and the joint probability function, of more efficient implementation but fluctuating accuracy. Implementing a FORM in fact is the same as, instead of dealing with the real limit-state function, assuming that a linear equation will be a reasonable approximation to describe it. The analysis procedure involves the search for the point in the failure surface closest to the origin, approximation of the failure surface by a linear surface and consequent definition of a region away from the origin constrained by the linearized surface. The method can be applied also to search for all the points associated with a certain occurrence probability. It is then straightforward to understand that in some complex cases this methodology, despite its efficiency of application, can introduce significant errors in the analysis.

The inverse variation of the FORM is related to the transformation that is applied to the variables to and from the normalized space, also known as Rosenblatt transformation [10]. In the inverse methodology, a transformation to the normalized space takes place to find the isoprobability lines, and then an inverse transformation is applied to the normal space where a more intuitive analysis is possible. One of the most well-known methods, which is also recommended in the IEC guidelines, is the Environmental Contour Method (EC) [11]. The EC method is applied to find sea states with similar probability of occurrence, e.g. 20 or 50 year return period, and search along the defined contour for the maximum load. All the occurrences in the contour will have the same long term probability of occurrence, Figure 1.

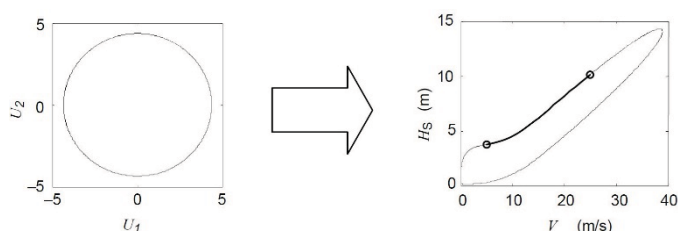


Figure 1 - Example of EC method applied to extrapolation of 50 years met-ocean conditions [2].

On the left side the normalized space is represented, where the contour of interest can be picked by using the value of the radius β . U_1 and U_2 are the variables of interest (significant wave height - H_s and wind velocity - V) in the normalized space. On the right side the EC is shown after the inverse

transformation. The method disregards the fluctuations of response of the OWT for given met-ocean parameters.

In [12] the results of the EC method for a OWT are compared with the full integration presented in Equation (3).

One of the alternatives to bypass the limitation of not considering the variability in the response is applied in [13] by using a three-dimensional inverse FORM analysis. By introducing the variability of the response a new variable is added and the analysis occurs in a three-dimensional space, Figure 2. This implies the added work of defining the full probability distribution of the turbine extreme loads through simulations. The problem, is then very similar to the one to be solved by the direct integration method, but, here estimating the probability of failure is achieved by searching in a 3-D space for the most likely point associated with the failure function and target P_f . On the left side is possible to see the normalized three-dimensional space of variables and on the right side the real space of variables after the inverse transformation. Instead of a single contour that averages the response, the result is a three-dimensional contour that accounts for its uncertainty.

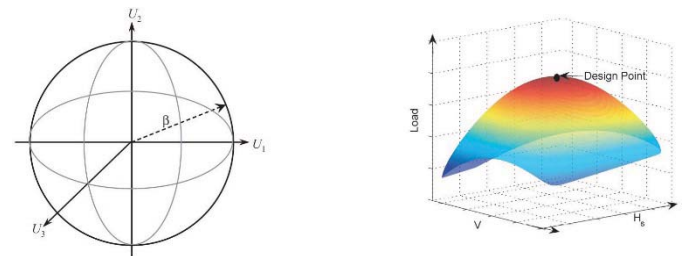


Figure 2 - 3D Inverse FORM methodology example [9].

Using a three-dimensional approach comes with obvious increased effort and complexity.

As an alternative for very complex $g(x)$ functions, a higher order function to approximate $g(x)$ can be applied. This is the case when the FORM approximation is increased by one order generating then a Second Order Reliability Method (SORM). Again, when applying the SORM methodology, a trade-off between the gains in accuracy and increase in the analysis and complexity needs to be carefully addressed.

Standing in between these two methodologies one can find EC methods with corrections to account for the variability of the loads. These seek to balance the efficiency and accuracy offered by the two methods. The limitation of the EC method was firstly discussed in [11], and, in the same paper the method is introduced, a suggestion for the implementation of an inflated contour that mitigates the influence of using a median load value is given. Later, in [14], this problem is further discussed and some quantities are derived to account for the response variability.

In [15] the concept of incremental wind-wave analysis (IWWA) for the analysis of OWT support structures under extreme loading is introduced. This methodology involves using static, non-linear analysis to define pushover curves that are function of a load factor γ . These curves are combined with previously defined i mean return periods of the external variables (e.g. $MRP_{wind,i}$) that when combined with the pushover curves previously defined, merge as a IWWA curve. The IWWA curve encloses information corresponding to the load pattern of every return period considered.

Recently, in [16] a work on reducing the number of simulations needed for analysing OWT supports structures under extreme ocean environmental loads is presented. To achieve this the analysis of the reliability was developed with basis on the formulation of a peak response factor (PRF). This PRF in addition with the static response of the system is used to normalize the peak response (R_p). The R_p is the variable used to evaluate $g(x)$ and is set as a function of the design variables X . This normalization intends to make the peak response independent of the design parameters, simplifying the application of reliability methodologies like the FORM.

Sampling methods are an efficient alternative to the analytical methods presented. Monte Carlo Simulation (MCS) is perhaps the most well-known sampling method. While sampling methods are exact as they estimate the real probability of failure, they can be, when searching for an occurrence that has very low probability, prohibitive in the time needed to achieve results.

Strategies to reduce the computational time used in MCS when applied to OWT are evaluated in [17]. In this case a Tension-Leg-Platform is examined and FORM is used to reduce the simulation time of the MCS.

It was highlighted before that the standards for the design of OWT present two major kinds of analysis: the ULS and SLS. This major division originated a standard definition of different design load cases (DLC) that cover the different expected circumstances experienced by OWT. A table resuming OWTs expected DLC can be found in [2].

When following the design standards and guidelines, applying probabilistic analysis to OWT and extrapolating long term loads, the response of the system is addressed and the process generally involves, due to the fact that one is addressing a complex system, the evaluation of different response variables ($F_x, M_x, F_y, M_y, \dots$, where F stands for load and M for moment with the respective Cartesian index x, y, z) for the different DLC. Analysis of the different OWT loads in an univariate way is a frequent practice and tends to overestimate the design of the OWT. But, in reality, it is very likely for the extreme responses of the cited variables to not occur simultaneously. According to [18] during the design process considering simultaneous extremes is still a practice that leads to over design of OWT for the specific case of ULS analysis. Based on it, a methodology based on Pareto-optimal loads is proposed there to tackle the conservative design resulting from the univariate maxima consideration.

4 NEW CHALLENGES ON RELIABILITY OF OWT SUPPORT STRUCTURES

The previous sections were focused on the extrapolation of short-term and long-term environmental averaged occurrences or short-term and long-term time responses based on random external conditions. Although, the codes to design OWT also stipulate the evaluation of individual extreme occurrences (e.g. wave heights in DLC1.6 or DLC6.1c). Defining the long term individual occurrences brings an additional order of complexity to the problem. It is recommended the usage of appropriate site measurements to set the long term individual occurrences. As result an extreme individual occurrence conditional on a known averaged occurrence is defined. The data needed to specifically address this issue is generally limited since it is not common for the monitoring equipment to record full time series when assessing long term

measurements. Again, this limitation is one of the causes of difficulty in inferring about the probability of simultaneous occurrence of individual events (e.g. extreme gust and extreme individual wave height combined). Evaluating the referred conditional probability can be difficult and time consuming, impelling the designer to use the deterministic design conditions given in the code for estimating the individual wave height or wind gust velocity. This results eventually in a potential contribution for the over-design of an OWT tower.

Most of the works in the probabilistic assessment of OWT towers were derived under the assumption that for a pitch controlled OWT the maximum loads occur in operating conditions. Application of alternative probabilistic techniques as the ones described still needs to be addressed for parked, start-up and shut-down states.

Moreover, when physical simulation is used to estimate long term loads in the offshore environment the theories used for the effect can be quite limiting in some aspects. One of these, that is of particular interest, is when the steepness of the waves gets so high that the common theory used to model waves becomes invalid to describe them. The effect of this higher order physical phenomena on the estimation of extreme response was evaluated before for the case of an OWT mono-pile foundation [9]. Considerations for breaking waves that may cause high loads in the support structure are given in the standards [2] [3]. Their effect in OWT towers was addressed before, an overview is given on [19].

Although some work was identified, the effect of wave theories up to 5th order and breaking waves on long term statistics and respective calculation of system failures for ULS needs to be further addressed in the future.

It is important to highlight that dissociating the analysis OWT towers from the support structure is not a correct approach. When looking at the towers, these need to be seen as a joint structure with the mono-pile, the jacket, the gravity base or in case of floating structures, the Spar, the Tension-Leg-Platform or the semi-submersible foundation.

Techniques applied in the past to address the probabilistic design of OWT towers were presented. Yet, alternative methodologies, whose applicability for OWT towers was not analysed, are available and are of interest to consider during future developments in this field of structural reliability analysis.

It is very difficult for alternative methodologies to compete with FORM and SORM when it comes to the accuracy-effort ratio. With the current trends of progress in the computational field it is expected for the gap in time requirements to complete a reliability analysis existing between methodologies that are highly accurate, sampling methodologies or directional simulation, and that calculate the results fast, like FORM, to decrease. It is very likely then for their application to widen, which may unlock new practices in the reliability analysis of OWT towers.

In [13] it is referred that the 3D inverse FORM is reliable when compared with the direct integration method, and that the additional effort needed to implement it when comparing with the 2D inverse FORM may be worth of the additional work needed. This assumption was derived based on the case study presented. Further studies should be considered to address the extents, as OWT become more complex, of the limitations caused by using a FORM approach.

Despite showing high potential and taking into account the response variability, it is expected for the first order approximation to introduce some errors in the results that grow progressively as the complexity of the analysis increases.

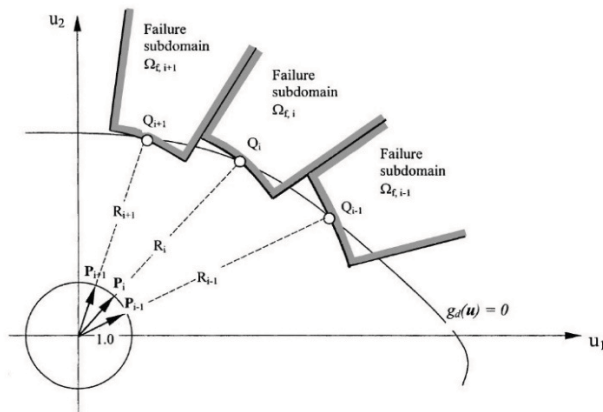


Figure 3 - Limit State $g(x)$ and its approximation with the Directional Integration Method [20].

A potential methodology that was not evaluated for OWT towers is the directional simulation. The directional simulation has the particularity of very accurately approximating the probability of surpassing a defined limit state by its real probability. This methodology identifies a series of directions for integration, which are integrated either by approximation or closed-form and evaluated to estimate P_f by a weighted average of the directional integrals, (see Figure 3). An example of directional integration for structural reliability analysis and estimation of the P_f can be identified in [20].

The directional simulation mitigates the recurrent limitation of dealing with very highly non-linear limit states, but its accuracy and efficiency are highly dependent on the procedure and directions used for integration [20].

When it comes to sampling techniques, MCS is probably the most widely applied sampling methodology, but, as mentioned, when P_f is very small its application can be prohibitive. The sampling analysis time can be cut off with hybrid techniques like the radial-based importance sampling (RBIS). As the name indicates, radial-based importance sampling consists in eliminating parts of the domain that are known, and focusing the analysis on the region of interest. This methodology, introduced in [21], is adapted and combined with directional methods to analyse structural reliability in [22]. A graphical example illustrating the method can be seen in Figure 4.

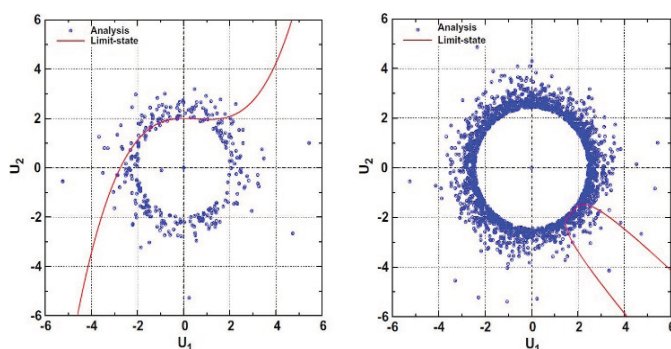


Figure 4 - Example of adaptive RBIS presented in [22].

The methodology is implemented by excluding the safe part of the domain from the sampling process. The sampling domain is reduced and therefore the computational time needed to calculate the probability of occurrence of a certain event, which in our case is the P_f .

The control actions applied to OWT are very likely to have a significant impact on the estimation of ULS and extreme loading. In particular, reliability based approach that accounts for variations of the extreme distribution tails as function of control actions are a field of particular growing interest.

Another field of growing interest is the optimization of OWT. In [23] an overview of the optimization processes for OWT is presented. Here, it is highlighted how the probabilistic optimization is an order of magnitude more complex than more common optimization methods which are extensively exploited in the article. In the recommendations, a strong emphasis is given to the optimization processes through reliability-based designs. Even considering that these are more difficult and time-consuming, they allow a clearer, better defined optimization problem and exploit eventual uncertainties that translate to the safety margins and block some of the potential for optimization.

An interesting question underlined is on how new computational methods (e.g. probability evolution algorithms or computational methods inspired by biological systems such as; genetic algorithms and evolutionary programming) may relate to the reliability based design.

Table 1 presents a comparative summary of the reliability analysis of OWT support structures. The main advantages and disadvantages of each methodology are summarized.

5 CONCLUSION

A detailed literature review has been carried out and some of the previous works developed to evaluate OWT support structures and their risk of failure were discussed in the present paper. Additionally, some methodologies to assess the structural reliability of OWT support structures analysed and discussed. It was inferred that the problem of designing OWTs is commonly divided into two big spheres of extreme values theory analysis: the loading and the response dimensions.

It was seen that until now direct integration and FORM were the methodologies more frequently applied to develop a reliable analysis of OWT under extreme occurrences. In the context of establishing a basis of work for further steps in the probabilistic assessment of OWT and support structures, alternative methodologies and challenges demanded by the sector were identified.

The present paper intends therefore to set a reference point for further assessment of the subject. Despite, as shown before, being a sector for which several recommendations and guidelines were developed there is still a shortage of an accepted well around best practice that takes the designer or researcher step-by-step in the process of probabilistically assessing OWT towers and support structures. The main strategic challenge for the probabilistic assessment of OWT support structures will be to converge and balance further research developments under the lack of a global accepted procedure so that an unified field of reliability based design is established and accepted.

Table 1 - Reliability Methods for OWT support structure analysis

METHODOLOGY	ADVANTAGES	DISADVANTAGES	APPLICATION TO OWT SUPPORT STRUCTURES
Direct Integration	Current standard methodology considered in the sector for extrapolation; Highly accurate; Non case-specific	Computationally expensive for practical application; Limited in early-stage design phase	[1] [2] [6] [9]
FORM			
Environmental Contour	Fast calculation method; Analysis is set in normal space of variables	Analysis occurs in the environmental space of variables, no load variability is considered; Linear approximation to $g(x)$ can make it inaccurate	[2] [12] [13] [24]
Environmental Contour with correction	Fast calculation method; Analysis is set in normal space of variables; Approximation of load variability by correction of the contour	Linear approximation to $g(x)$ can make it inaccurate	[12] [13] [24]
3D Inverse FORM	Relative fast calculation method when compared with other methodologies that consider the same number of variables	Linear approximation to $g(x)$ can make it inaccurate, application is case-specific; Limited in early-stage design phase	[13]
SORM	More accurate than FORM methods	Case-specific and dependent on $g(x)$ complexity; Slower due to increased order in approximating $g(x)$	e.g. non-OWT structures [25]
Sampling (e.g. MCS, Importance sampling)	Highly accurate and of universal application	The calculation time is usually highly and dependent on the probability computed	[26] [27] or non-OWT structures [22]
Directional Simulation	Accurate	Convergence is dependent on the procedure applied and directions picked for integration	Not applied. e.g non-OWT structures [20]
New methodologies: IWWA, Peak Response Factor(PRF) FORM	PRF FORM has low computational time	Less established methods; Limited range of evaluations were done so far; Depending on the complexity IWWA can get very time-consuming;	[15] [16]

ACKNOWLEDGMENTS

This project has received funding from the European Union Horizon 2020 research and innovation programme under the Marie Skłodowska-Curie grant agreement No. 642453.

REFERENCES

- IEC, "Wind turbines part 1: Design requirements," 2005.
- IEC, "Wind turbines part 3: Design requirements for offshore wind turbines," 2009.
- DNV, "Design of offshore wind turbine structures. Offshore Standard DNV-OS-J101," DNV GL AS, 2014.
- J. Wen, Y. Zheng, and F. Donghan, "A review on reliability assessment for wind power," *Renewable and Sustainable Energy Reviews*, no. 13(9):2485–2494, 2009.
- N. B. Negra, O. Holmström, B. Bak-Jensen, and P. Sorensen, "Aspects of relevance in offshore wind farm reliability assessment," *Energy Conversion, IEEE Transactions on*, no. 22(1):159–166, 2007.
- P. Cheng, G. J. W. van Bussel, G. A. M. van Kuik, and J. H. Vugts, "Reliability-based design methods to determine the extreme response distribution of offshore wind turbines," *Wind Energy*, no. 6(1):1–22, 2003.
- E. Gumbel, *Statistics Extremes*, Columbia Univ. Press, 1958.
- P. Agarwal and L. Manuel, "Extreme loads for an offshore wind turbine using statistical extrapolation from limited field data," *Wind Energy*, no. 11(1):673–684, 2008.
- P. Agarwal, *Structural reliability of offshore wind turbines*, PhD thesis, The University of Texas at Austin, 2008.
- Rosenblatt M., "Remarks on a multivariate transformation," *Annals of Mathematical Statistics*, no. 23(2):470–472, 1952.
- S. R. Winterstein, T. C. Ude, C. A. Cornell, P. Bjerager, and S. Haver, "Environmental parameters for extreme response: Inverse FORM with omission factors," in *In Proc. 6th Int. Conf. on Structural Safety and Reliability*, Innsbruck, Austria, 1993.
- K. Saranyasoontorn and M. Lance, "On assessing the accuracy of offshore wind turbine reliability-based design loads from the environmental contour," *International Journal of Offshore and Polar Engineering*, no. 15(02), 2005.
- P. Agarwal and L. Manuel, "Simulation of offshore wind turbine response for long-term extreme load prediction," *Engineering structures*, no. 31(10):2236–2246, 2009.
- S. R. Winterstein and K. Engebretsen, "Reliability-based prediction of design loads and responses for floating ocean structures," in *In 27th International Conference on Offshore Mechanics and Arctic Engineering*, Lisbon, Portugal, 1998.
- K. Wei, S. R. Arwade, and A. T. Myers, "Incremental wind-wave analysis of the structural capacity of offshore wind turbine support structures under extreme loading," *Engineering Structures*, no. 79:58–69, 2014.
- D. H. Kim and S. G. Lee, "Reliability analysis of offshore wind turbine support structures under extreme ocean environmental loads," *Renewable Energy*, no. 79:161–166, 2015.
- J. J. Jensen, A. S. Olsen, and A. E. Mansour, "Extreme wave and wind response predictions," *Ocean engineering*, no. 38(17):2244–2253, 2011.
- M. Muskulus, "Pareto-optimal evaluation of ultimate limit states in offshore wind turbine structural analysis," *Energies*, no. 8(12):14026–14039, 2015.
- M. A. Chella, A. Tørum, and D. Myrhaug, "An overview of wave impact forces on offshore wind turbine substructures," *Energy Procedia*, no. 20:217–226, 2012.
- J. Nie and B. R. Ellingwood, "Directional methods for structural reliability analysis," *Structural Safety*, no. 22(3):233–249, 2000.
- A. Harbitz, "An efficient sampling method for probability of failure calculation," *Structural safety*, no. 3(2):109–115, 1986.
- F. Grooteman, "Adaptive radial-based importance sampling method for structural reliability," *Structural Safety*, no. 30(6):533–542, 2008.
- M. Muskulus and S. Schafhirt, "Design optimization of wind turbine support structures - a review," *Journal of Ocean and Wind Energy*, no. 1(1):12–22, 2014.
- K. Saranyasoontorn and M. Lance, "Design loads for wind turbines using the environmental contour method," *Journal of Solar Energy Engineering*, no. 128(4):554–561, 2006.
- A. Der Kiureghian, H.Z. Lin, and S. J. Hwang, "Second-order reliability approximations," *Journal of Engineering Mechanics*, no. 113(8):1208–1225, 1987.
- A. Naess, O. Gaidai, and S. Haver, "Efficient estimation of extreme response of drag-dominated offshore structures by Monte Carlo simulation," *Ocean Engineering*, no. 34(16):2188–2197, 2007.
- N. Saha, Z. Gao, T. Moan, and A. Naess, "Short-term extreme response analysis of a jacket supporting an offshore wind turbine," *Wind Energy*, no. 17(1):87–104, 2014.

Experimental investigation and numerical modelling of domestic scale wind turbine blades

Edward M Fagan^{1,3,4}, Sean B Leen^{2,3,4}, Oscar de la Torre^{1,3,4}, Jamie Goggins^{1,3,4}

¹Civil Engineering, National University of Ireland, Galway, Ireland

²Mechanical Engineering, National University of Ireland, Galway, Ireland

³Ryan Institute, National University of Ireland, Galway, Ireland

⁴Marine Renewable Energy Ireland (MaREI) Research Centre, Galway, Ireland

email: e.fagan1@nuigalway.ie, sean.leen@nuigalway.ie, oscar.delatorre@nuigalway.ie, jamie.goggins@nuigalway.ie

ABSTRACT: Static testing of two domestic scale wind turbine blades is presented. One of the two blades consists solely of glass-fibre reinforced polypropylene, while the other includes additional carbon-fibre reinforcement in the spar caps. Static testing is performed with a Whiffle tree test rig to determine the structural response of the blades. The rig applies the load at eight contact points along the blade to mimic the bending moment profile experienced by a blade in operation. Modal testing was also performed on the two blades and the values of natural frequencies reported. The following objectives were undertaken: (i) evaluate and compare the static test results of the two wind turbine blades, (ii) use the results to validate finite element (FE) models of the blades and (iii) use the validated FE models in a design optimisation study. The FE models are generated using the Python programming language and are based on manufacturing specifications for the blades. The goal of the optimisation study is to improve the stiffness of the glass-fibre blade, without the addition of the more costly carbon-fibre plies. A genetic algorithm is used to determine the optimum section thickness along the length of the blade. The FE models showed close agreement with the experimental results. The result of the optimisation study was a blade 4% heavier than the original glass-fibre blade but with significant improvement in stiffness (30% decrease in tip deflection for the same load). The positive result from this initial design study will enable expansion of the design variables for future analyses.

KEY WORDS: Wind turbine blade, FRP composites, structural testing, optimisation, finite element modelling, genetic algorithm.

1 INTRODUCTION

Small-scale wind turbines are defined as having a rotor diameter from 0.5 to 10 m. At the upper end of this scale is the 3 to 10 m diameter turbines which typically have a standard power rating of between 1.4 and 16 kW [1]. The blades under investigation in this study are from a 15 kW turbine. This scale of device is aimed primarily at household power generation, focusing on farms and small businesses. These turbines present a useful power source but are dependent on two factors: (i) the initial costs, and (ii) the unit cost per kWh produced. A major component in the initial and subsequent maintenance costs is the blades of the turbine. Hence, minimising the blade production costs is important for both initial installation and for replacement due to the damage accumulated during operation. The efficiency of power generation is also of importance; from a mechanical perspective this represents the stiffness of the blades and, hence, their energy conversion efficacy.

The two blades tested in this study are constructed primarily from glass-fibre reinforced polypropylene. Additionally, one of the blades has carbon-fibre epoxy plies embedded in the spar caps to improve its stiffness. The addition of carbon-fibre plies dramatically increases the costs of production and also complicates the manufacturing process. Therefore, a balance is required between blade stiffness and the cost of materials. Other than the construction materials the blades are aerodynamically identical and are interchangeable in the 15 kW turbine.

Structural testing is performed to demonstrate to a reasonable level of certainty that the wind turbine blade possesses the strength and service life for its original design [2]. Often static testing is conducted before and after fatigue tests to provide a

measure of the residual strength and stiffness of the structure due to the accumulation of damage [3]. Static tests on wind turbine blades are often conducted by applying a number of weight loads along the length of the blade. The loads produce the equivalent bending moment distribution in the blade as from operational or extreme winds. Publicly reported studies tend to prioritise the medium to large scale blades (25 to 50 m in length) or, on the other end of the spectrum, the micro to mini scale (0.25 to 1.5 m). Little attention is paid to domestic scale blades. From a review of small scale wind turbines only one study was cited for the design and testing of a turbine blade similar to the scale presented here [4], [5]. One point noted by the review author was a lack of research on the optimisation of blade design for manufacturing and operational concerns. The majority of research instead focused on the aerodynamic performance characteristics for varying tip speed ratio, rotor speed, pitch angle, etc.

Optimisation techniques provide an invaluable tool for designers, enabling them to search through many hundreds of design iterations for the best solution. A number of researchers have applied optimisation techniques to the design of composite structures, including wind turbine blades [6] - [9]. The outcomes of these studies include mass reduction, blade stiffness improvements and optimisation of ply fibre angles. The technique used in the current study is a genetic algorithm. The method uses validated finite element (FE) models to determine an optimum structural design for the glass fibre blade to achieve the maximum stiffness with minimal increase in mass. The parametric shell element FE blade models are created from geometric data. A small number of design variables were chosen for this first optimisation study;

however, the moderate computational costs mean future studies will increase the size and scope of the design space.

2 METHODS

2.1 Experimental testing

Structural testing of wind turbine blades involves applying an equivalent mechanical load to match the aerodynamic loading the blade experiences during operation. In typical static testing the loads are applied via weights, cranes or hydraulic actuators connected to the blade at a number of load points [10]. The greater the number of load points the more accurately the bending moment distribution is reproduced. Figure 1 shows the Whiffle tree rig used in the experiments. The Whiffle tree splits the crane load between eight separate loading points. The eight points each apply a percentage of the total load to the surface of the blade via bars. This distribution has been determined from the operating conditions of the wind turbine. Table 1 shows the load percentages applied along the blade and the locations of the load points. The table also shows the locations of the four draw-wire displacement sensors used to measure the blade deflection. Modal tests were conducted using an impact hammer and a combination of accelerometers and strain gauges. The tests provided the natural frequencies for the first three bending mode shapes of the blades. The locations of the strain gauges and accelerometers are also shown in Table 1.



Figure 1. Whiffle tree rig applies the total load to the blade at eight locations distributed along its length.

Table 1. Loading distribution and blade instrumentation (SG = strain gauge, SP = string pot/draw-wire displacement sensor, A = accelerometer).

Location (r/R)	Load (% of total load)	Sensors
0.000	4	-
0.125	7	-
0.225	-	SG1, A1
0.250	9	SP1
0.375	11	SG2
0.475	-	SG3
0.500	14	SP2
0.555	-	SG4
0.600	-	SG5, A2
0.625	16	-
0.750	18	SP3
0.840	-	SG6, A3
0.875	21	SP4

The glass-fibre blade was instrumented with a combination of $120 \pm 0.4\%$ Ω (model Micro Measurements EA-06-060RZ-120) linear electrical resistance strain gauges and $120 \pm 0.3\%$ Ω (model CEA-06-240UZ-120) electrical resistance rosette strain gauges. Three draw-wire displacement sensors (model Micro-Epsilon WDS-500-P60-CR-P) with a measuring range of 500 mm (linearity $\pm 0.1\%$ FSO) and one draw-wire displacement sensor (model Micro-Epsilon WDS-1000-P60-BH-PB) with a measuring range of 1000 mm (linearity $\pm 0.02\%$ FSO) were used to measure the blade deflection. The load applied through the crane to the Whiffle tree was measured with a Sensotec 50000 lbs load cell (model 41/0573-01, linearity $\pm 0.1\%$ full scale). The modal tests required a Dytran model 5805A impulse sledge hammer with a one pound head (sensitivity 1 mV/lbf) and three accelerometers (model ENDEVCO 752A12) with a sensitivity of up to 5% in the amplitude response for the applied range.

The key measurements sought in the experiment are the distribution of strain along the blade, the deflection of the blade and the natural frequencies and mode shapes for comparison with the FE models. The strain gauges were located along the centre line of the spar cap on the compression side of the blade. From the initial FE models the highest strains in the blades were found on the compression side, this also helped to avoid the load application bars from damaging the gauges.

Table 2. Material properties of the composite plies used in the blade models [11].

	E_1 (GPa)	E_2 (GPa)	G_{12} (GPa)	ν_{12}
UD Twintex	21.5	6	1.00	0.20
UD Plytron	28	3.5	1.39	0.35
UD CF-epoxy	104.6	6.9	3.67	0.32

The blades were constructed primarily from laminates made from glass-fibre polypropylene (GFPP), with carbon-fibre epoxy used in the spar caps of the reinforced blade. Two types of GFPP were used, Twintex and Plytron. Table 2 shows the material properties for typical Twintex, Plytron [11] and carbon-fibre epoxy. Due to the proprietary nature of the blade a simplified version of the layups used in the blades is presented in Figure 2. The subscripts in the figure denote the number of plies of each orientation in the section, with the thickness of the layups varying along the length of the blade. The variables $x_1 - x_5$ refer to the design optimisation methodology, further discussion of which can be found in Section 2.3 below.

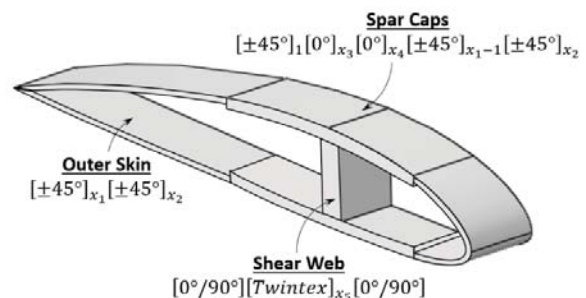


Figure 2. Layups for the three main regions of the blade.

The three main sections of the blade cross-section are the spar caps, the shear web and the outer skin. The spar caps and shear

web essentially form an I-beam which acts as the main structural component of the blade. Biaxial layers of Twintex orientated at $\pm 45^\circ$ to the longitudinal axis of the blade form the outer skin, the spar caps are comprised of layers of unidirectional Plytron plies orientated along the length of the blade and the shear web is constructed from a Plytron rib between biaxial Twintex layers.

2.2 Finite element modelling

A number of research groups have shown the applicability of a shell-based approach to modelling composite wind turbine blades [12], [13], [14]. A composite layup can be applied to shell elements in the FE program, allowing quick and accurate modelling of the behaviour of the blades. Computational efficiency is a key driver of the methodology due to the large number of models required for the optimisation study; typically, hundreds of models will need to be analysed before the optimal solution is found. The FE models are generated using a Python code developed in-house. The code requires input data including:

- Chord length distribution along the blade,
- Aerodynamic twist distribution along the blade,
- Location of the leading edge of the blade in the x- and y-directions,
- Distribution of airfoils along the blade, and the chord-normalised coordinates for each airfoil designation,
- Distribution of the location and width of the spar caps (normalised by the chord length),
- Distribution of the number and location of the shear webs,
- Material properties and layup sequences for each radial blade section,
- Flapwise and edgewise loads on the blade,
- Mesh and FE job analysis settings.

Once the required inputs have been set the code automatically generates the full FE model and performs the analysis. Post-processing of the results for evaluation of the optimisation procedure is also conducted using Python. The code has been previously used in the analysis of tidal turbine blades [15], [16] and is well suited for optimisation and parametric studies due to its automated nature.

The aerodynamic lift and drag forces experienced by a wind turbine blade can be resolved into the forces in the flapwise (perpendicular to the rotor plane) and edgewise (parallel to the rotor plane) directions. The edgewise forces contribute to the torque driving the turbine, while the flapwise forces comprise the thrust acting on the blade. The thrust is the most significant force acting on the blade for the static strength tests and the current set up with the Whiffle tree rig is restricted to testing the blade in the flapwise direction. Hence, further testing to account for the edgewise loading (and fatigue testing to monitor the effect of small amplitude cyclic loads for lifetime assessment) is necessary to fully analyse the response of the structure under all loading conditions.

In order to apply the out of plane loading to the blade eight partitions matching the loading locations (from Table 1) are created. The width of the partition matches the load application bars and the same load distribution is applied to the blades as shown in Table 1.

The loads are applied to the blade using a form of multi-point constraint (MPC). All of the nodes in the section where the load is applied are constrained to a single reference point onto which the force is applied as a point load in the y-direction. The coupling distributes the load between the reference point and the nodes in the section. The root of the blade is constrained in all six degrees of freedom. A schematic of the loading and boundary conditions on a typical blade model is shown in Figure 3.

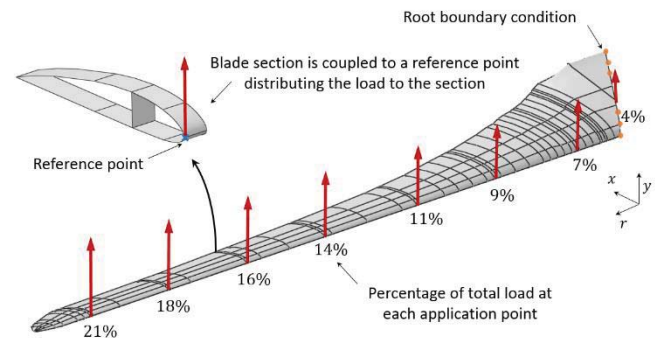


Figure 3. The finite element model of the blade indicating the loads and boundary conditions.

The FE models use S4R 4-noded, doubly curved, reduced integration elements. A mesh convergence study was performed in order to minimise the computational expense of each analysis. The results of the convergence study are shown in Figure 4. The total number of elements chosen for the model was approximately 8600, with an error of approximately 1.33% from the converged results for the blade tip deflection.

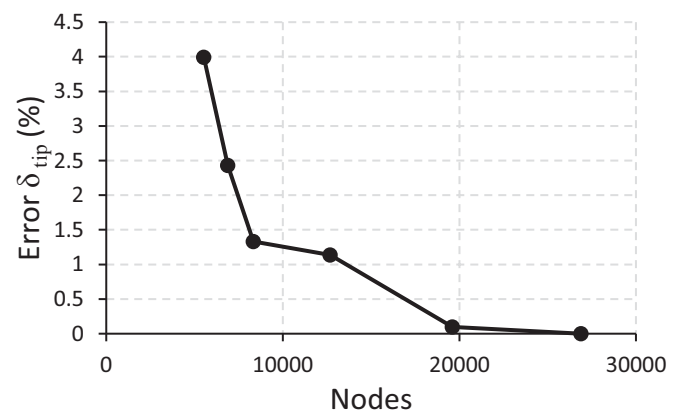


Figure 4. Mesh convergence study for the GFPP blade.

2.3 Design optimisation

The optimisation task is focused on improving the stiffness of the glass-fibre blade while also minimising the resultant blade mass, a multi-criteria optimisation. In order to simplify the task, it was decided to focus on the issue of blade stiffness while using a penalty function to limit the blade mass and, hence, solve a single criterion optimisation problem. For the present study only the thickness distribution of the laminates along the length of the blade was investigated, therefore, the blade geometry and material were not varied.

The objective function for the optimisation was the tip deflection of the blade, with a constraint on the blade mass also applied using a penalty function. The penalty was applied if the blade mass exceeded 125% of the original glass-fibre blade

mass. Large tip deflections imply inefficient energy transfer, can result in significant changes to the aerodynamics of the turbine and can result in the blade tip striking the tower (fouling) in extreme cases. The objective function is given by:

$$\min_{\mathbf{x} \in D} (f(\mathbf{x}) = \delta_{tip}(\mathbf{x}) p(\mathbf{x}))$$

where $\delta_{tip}(\mathbf{x})$ is the tip deflection of the blade, $p(\mathbf{x})$ is the penalty function, \mathbf{x} is the vector of design variables and D represents the design space containing all possible solutions. The penalty function is defined as:

$$p(\mathbf{x}) = \begin{cases} 1 & \text{if } \mathbf{x} \text{ is feasible} \\ \frac{M(\mathbf{x})}{1.25 M_{GF}} & \text{otherwise} \end{cases}$$

where $M(\mathbf{x})$ is the blade mass of the current model and M_{GF} is the mass of the original glass-fibre blade. The value of the objective function determines the fitness of any one set of design variables.

The vector \mathbf{x} consists of five design variables controlling the number of plies in the layups of several regions of the blade. The blade can be considered to consist of base layers of $\pm 45^\circ$ plies extending from the root to 95% of the blade length ($0.95R$). Within these biaxial layers the unidirectional (UD) spar caps are embedded. Hence, the layups in Figure 2 for the spar cap region indicate one biaxial layer followed by the UD layers, with the remaining biaxial layers completing the composite laminate. The model allows the inclusion of an additional number of biaxial and UD layers that extend from the root of the blade to $0.375R$ (see Figure 5). The remaining 5% of the blade at the tip is composed of a simple layup of two biaxial layers.

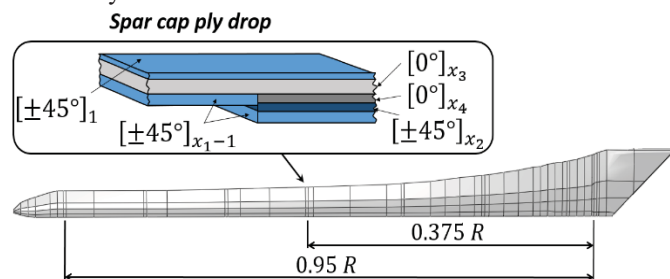


Figure 5. Ply drop locations in the blade model and diagram of the ply thicknesses due to the design variables [inset].

The number of $\pm 45^\circ$ plies in the base layer is controlled by the design variable x_1 , the number of extra $\pm 45^\circ$ plies is controlled by the variable x_2 , the number of 0° plies in the base layer is controlled by x_3 , the number of extra 0° plies is controlled by x_4 and the thickness of the shear web is controlled by x_5 . The first four design variables are integer numbers of plies, while the last variable is a real number. The design variables are shown in Table 3 alongside their respective maximum and minimum allowable values. Figure 5 shows a cross section of the spar cap laminate at the ply drop location. An initial check of the thickness of the laminates at this location determines the legality of each set of design variables. This is necessary to avoid the non-physical overlap of the top and bottom of the spar cap which is possible within the design space.

The optimisation methodology is outlined in the flowchart in Figure 6. The flowchart describes the steps in the genetic

algorithm and the incorporation of the FE models. The steps are as follows:

1. The design variables are randomly selected, within the design limits, for the population.
2. An FE model of the blade is generated for each set of variables and the success of each individual in the population is tested using a measure of “fitness”.
3. A percentage of the fittest candidates are retained.
4. A very small percentage of the retained candidates may undergo mutation of one of their (randomly selected) design variables.
5. Pairs of the retained candidates are crossed to create new candidates with qualities of both parents. The new candidates are produced to return the population to its original size.
6. The fitness of each member in the new population is evaluated.
7. If the stop criterion (total number of generations, for example) is met the optimisation is complete, otherwise the process is continued through another generation.

Table 3. Design variables, their limits and optimum values.

Variable	Description	min	max	Optimal
x_1	Base $\pm 45^\circ$ plies	2	6	2
x_2	Extra $\pm 45^\circ$ plies	0	5	0
x_3	Base 0° plies	1	20	11
x_4	Extra 0° plies	0	14	9
x_5	Web thickness	1.0	10.0	8.5

Additionally, in order to promote genetic diversity in the new population, a small percentage of the original population (that don't meet the cut off to be retained) are randomly added to the new population. The parameters for the genetic algorithm include: a total population of 40 members, a total of 15 generations, retention of the top 40% of the previous generation, random selection of 5% of the remaining original population and a probability of mutation of 1%.

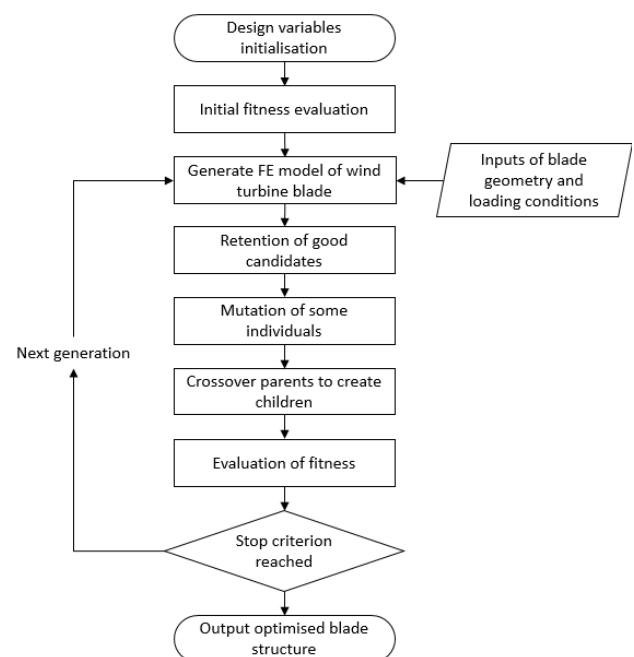


Figure 6. Optimisation flowchart for the genetic algorithm.

3 RESULTS AND DISCUSSION

3.1 Experimental results and FE comparison

Figure 7 shows the results of the static tests on the two blades along with the associated FE model results. The blade deflections are shown for the same load applied to both blades. The significant increase in stiffness due to the addition of the CF-epoxy plies is evident with a reduction in tip deflection of approximately 82%.

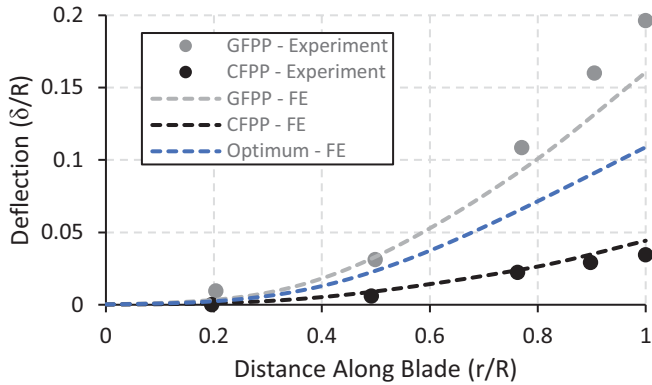


Figure 7. Blade deflections results from the experiments and FE models for the GFPP, CFPP and optimum blades.

Figure 8 shows the load-deflection curves for the two blades. The load values have been normalised by the maximum load experienced by the CF-epoxy reinforced blade. The significant increase in stiffness due to the carbon-fibre spar caps is again evident. The non-linearity in the load-deflection curve for the CF-epoxy blade is due to some slippage in the mechanical linkages of the rig during the test. Further assessment of the rig will be conducted before subsequent tests are carried out. The CF-epoxy blade was capable of considerably higher total load, approx. 170% of the GFPP blade, for the same tip deflection.

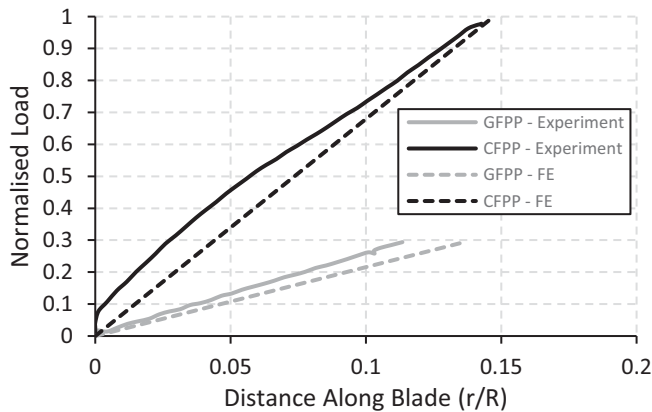


Figure 8. Load vs deflection curve for each blade with comparisons to their respective FE models.

Table 4 presents the results of the tests and FE models for the tip deflections and includes the percentage difference between each. Table 5 shows the comparison between the blade mass for test blades and FE models. A difference of 4% to 6% exists between the blade and the model masses; this is attributed to several factors, (i) additional glass-fibre material added during the manufacturing procedure but not accounted for in the original manufacturing documents, (ii) additional non-

structural material which was omitted from the FE models and (iii) a slight variability in material density and fibre volume content which are inherent in the production of composite structures.

Table 4. Tip deflection results from the experiments and finite element modelling (normalised by blade length).

	Experiment	FE	Diff. (%)
GFPP blade	0.196	0.161	-18
CF-epoxy blade	0.035	0.044	26
Optimised blade	-	0.109	-

Table 5. Experimental and FE blade mass values.

	Measured (kg)	FE (kg)	Diff. (%)
GFPP blade	19.10	18.3	-4.2
CF-epoxy blade	22.50	21.0	-6.7
Optimised blade	-	20.13	-

The increased stiffness has a noticeable effect on the natural frequencies of the CF-epoxy blade. Table 6 presents the first three natural frequencies of the GFPP, CF-epoxy reinforced and optimised blades from the FE models and experiments.

Table 6. Natural frequencies of the blades from the modal tests and FE models.

		Measured (Hz)	FE (Hz)
GFPP	ω_1	2.7	2.25
	ω_2	10.0	6.92
	ω_3	14.5	8.74
CF-epoxy	ω_1	2.5	3.65
	ω_2	5.3	8.71
	ω_3	21.3	12.6
Optimised	ω_1	-	2.0
	ω_2	-	5.0
	ω_3	-	9.5

The strain distribution along the length of the GFPP blade is shown in Figure 9, plotted alongside the results of the FE models. Peaks are evident in the FE results where ply drop offs occur. The major peak at approx. 0.8R is due to the loading point coinciding with the last ply drop, which does not occur in the actual test.

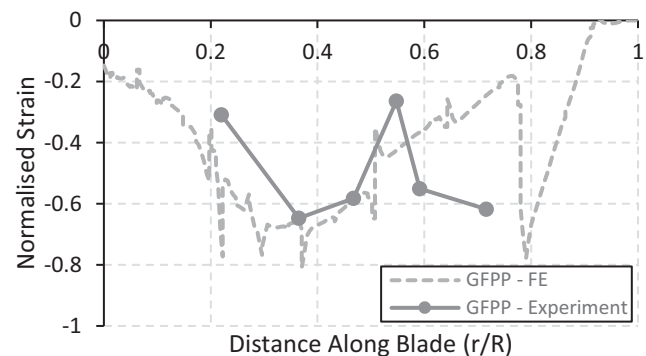


Figure 9. Comparison between experimental results and FE models of the strain in the GFPP blade.

3.2 Optimisation results

Table 3 shows the optimised values of the design variables after application of the genetic algorithm to the problem. The resultant blade has a tip deflection of approximately 0.11R and

a blade mass of 20.13 kg. Figure 10 shows the development of the fitness values (objective function) for each member of the population through each generation. The figure also plots the average value of the fitness for the entire population for each generation. The objective function is given a value of zero if the design variable set does not meet the legality constraint and these individuals are not carried on to the proceeding generation. The random mutations can lead to new illegal individuals as can be seen at generation 10. The objective function has converged to the optimum value after approximately 7 generations, however, the random mutations continue to explore the design space through the following generations. A comparison between the thickness of the spar cap laminates along the length of the blade in the initial GFPP blade, the CF-epoxy reinforced blade and the optimised blade is shown in Figure 11.

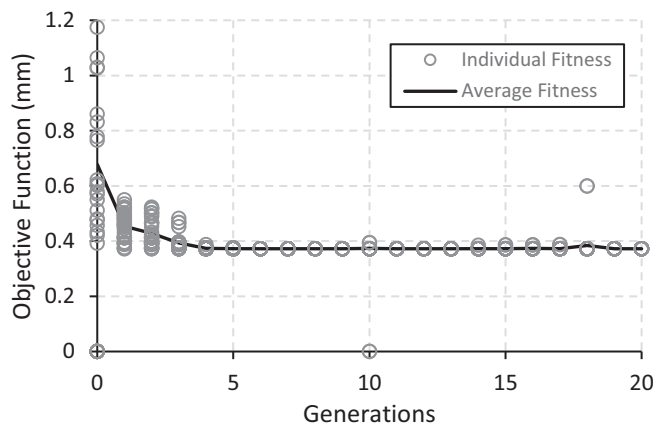


Figure 10. Results from the genetic algorithm optimisation.

All computations were conducted on an Intel core i7 desktop computer with 8 CPUs and 16 GB RAM. Each analysis took approximately one minute to run, with additional time required for model generation and post-processing. The total duration of computation for the genetic algorithm method was approximately 16 hours. A total of 800 models were generated and assessed for the study.

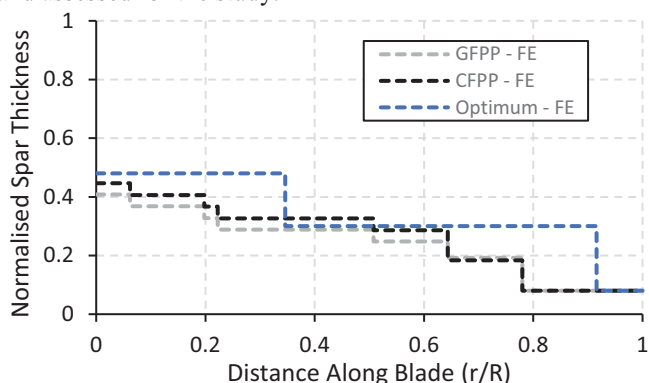


Figure 11. Thickness distribution of the three blades.

4 CONCLUSION

Two glass-fibre polypropylene domestic scale wind turbine blades, one with carbon-fibre epoxy reinforcement, were tested and the two blade designs were compared. Shell element finite element models were created and validated using the test results. The predicted mass and tip deflection results agreed

reasonably well with the corresponding experimental values, particularly in terms of relative values for the two blade types. The FE models were used in a design study utilising a genetic algorithm for search optimisation. The optimised blade represents a compromise on blade stiffness from the carbon-fibre reinforced blade but a significant improvement on the glass-fibre one. Since the removal of carbon-fibre from the blade represents a significant saving in manufacturing costs, the optimised blade is considered an improvement in design.

ACKNOWLEDGMENTS

This material is in part based upon works supported by the Science Foundation Ireland Marine Renewable Energy Ireland (MaREI) research centre under Grant No. 12/RC/2302. It was also funded by a fellowship from the College of Engineering and Informatics, NUI Galway, and was supported by an NUI Travelling Studentship, 2014. Additional thanks are given to the technical staff at NUI Galway and the group of mechanical engineering Masters students for their efforts on the testing of the wind turbine blades.

REFERENCES

- [1] Tummala A., Velamati R. K., Sinha D. K., Indraj V., and Krishna V. H. (2016), 'A review on small scale wind turbines', *Renewable and Sustainable Energy Reviews*, 56, 1351–1371.
- [2] D. S. I. E. C. Ts, "DS/IEC/TS 61400-23 Full-scale structural testing of rotor blades," 2002.
- [3] Lee H. G. and Park J. (2016), 'Static test until structural collapse after fatigue testing of a full-scale wind turbine blade', *Composite Structures*, 136, 251–257.
- [4] Habali S. M. and Saleh I. A. (2000), 'Local design, testing and manufacturing of small mixed airfoil wind turbine blades of glass fiber reinforced plastics', *Energy Conversion & Management*, 41, 249–280.
- [5] Habali S. M. and Saleh I. A. (2000), 'Local design, testing and manufacturing of small mixed airfoil wind turbine blades of glass fiber reinforced plastics', *Energy Conversion & Management*, 41, 281–298.
- [6] Paluch B., Grédiac M., and Faye A. (2008), 'Combining a finite element programme and a genetic algorithm to optimize composite structures with variable thickness', *Composite Structures*, 83, 284–294.
- [7] Lund E. and Stegmann J. (2005), 'On structural optimization of composite shell structures using a discrete constitutive parametrization', *Wind Energy*, 8, 109–124.
- [8] Chen J., Wang Q., Shen W. Z., Pang X., Li S., and Guo X. (2013), 'Structural optimization study of composite wind turbine blade', *Materials and Design*, 46, 247–255.
- [9] Jureczko M., Pawlak M., and Mężyk A. (2005), 'Optimisation of wind turbine blades', *Journal of Materials Processing Technology*, 167, 463–471.
- [10] Zhou H. F., Dou H. Y., Qin L. Z., Chen Y., Ni Y. Q., and Ko J. M. (2014), 'A review of full-scale structural testing of wind turbine blades', *Renewable and Sustainable Energy Reviews*, 33, 177–187.
- [11] A. C. Long, Ed., *Design and manufacture of textile composites*, Woodhead Publishing Limited, Cambridge, UK, first edition, 2005.
- [12] Kong C., Bang J., and Sugiyama Y. (2005), 'Structural investigation of composite wind turbine blade considering various load cases and fatigue life', *Energy*, 30, 2101–2114.
- [13] Jensen F. M., Falzon B. G., Ankersen J., and Stang H. (2006), 'Structural testing and numerical simulation of a 34m composite wind turbine blade', *Composite Structures*, 76, 52–61.
- [14] Yang J., Peng C., Xiao J., Zeng J., Xing S., Jin J., and Deng H. (2013), 'Structural investigation of composite wind turbine blade considering structural collapse in full-scale static tests', *Composite Structures*, 97, 15–29.
- [15] Fagan E. M., Yeung R. W., Leen S. B., and Goggins J. (2015), 'Structural and Hydrodynamic Modelling of Composite Tidal Turbine Blades', *11th European Wave and Tidal Energy Conference (EWTEC)*, Nantes, France.
- [16] Fagan E. M., Leen S. B., Kennedy C. R., and Goggins J. (2015), 'Finite element based damage assessment of composite tidal turbine blades', *11th International conference on the damage assessment of structures (DAMAS)*, Ghent, Belgium.

The Four Courts, Dublin – Innovative Monitoring and Long Term Repair Techniques

Darren Gilmore¹, Brian McFarland¹, Enda McKenna¹, Connor O'Higgins¹, Jason Kearney¹
¹McFarland Associates Ltd, Unit A3, Harbour Court, Sydenham Business Park, 5 Heron Road, Belfast, BT3 9HB
 email: darren.gilmore@mcfassoc.com, brian.mcfarland@mcfassoc.com, enda.mckenna@mcfassoc.com,
 connor.ohiggins@mcfassoc.com, jason.kearney@mcfassoc.com

ABSTRACT: The Four Courts, Ireland's main courts building, is situated adjacent to Dublin's River Liffey and was built between 1776 and 1796 making parts of the structure well over 200 years old. During the 1922 civil war, a large proportion of the dome and drum of the structure suffered extensive damage as a result of bombardment and fire. The dome, formerly constructed of timber, was rebuilt in reinforced concrete at the end of the 1920s. Some 85 years later, this iconic building is showing its age with the early onset of reinforcement corrosion and the continued deterioration of stonework. An innovative combination of testing, structural health monitoring and repair design were required to restore the structure's integrity, whilst minimising disruption to allow the courts to function unhindered. Inspection and Non-Destructive Testing (NDT) was undertaken to determine the nature, source, extent and significance of observed deterioration. The use of a cutting-edge, magnetic field, remote, crack monitoring system also provided insight into the movement of structural cracks. Analysis of the combined results including Finite Element Analysis (FEA) modelling gave a holistic view of the nature of deterioration within the structure. This allowed for bespoke remedial works to be designed including: two access scaffolds; a cathodic protection installation; and a composite Polyparaphenylene Benzobisoxazole (P.B.O) and mortar mesh strengthening system. This paper will look at the various aspects of the structural investigation and analysis and describe in more detail the remedial works proposed.

KEY WORDS: Remediation; Concrete; Dome; Non-Destructive Testing; Structural Health Monitoring; Finite Element Analysis; Cathodic Protection; Composite Materials.

1 INTRODUCTION

The Four Courts is situated within Inns Quay on the north side of the River Liffey. The earliest known works on the site began in 1776 and were based on the designs of Thomas Cooley. Cooley subsequently died in 1784 and James Gandon was appointed to add the courts to the original plan. "Gandon incorporated Cooley's building, adding two quadrangles and a central block" [1]. Whilst the Four Courts were occupied by the 1st Battalion of the Dublin Brigade during the 1916 Easter Rising, they largely survived unscathed. However, it was during the 1922 civil war, when occupied by anti-treaty forces, that the dome and drum suffered extensive fire damage. The uppermost dome, formerly constructed in timber, was rebuilt in reinforced concrete and reopened in 1932. The dome is believed to be the first reinforced concrete dome in Europe [1]. In addition, the Corinthian capitals were rotated to hide the damage that they had sustained.

It was in 2011, when part of a Corinthian capital fell onto the roof of the Four Courts below, that concerns were raised over the condition of the structure. An extensive and complex access scaffold was subsequently erected around the outside of the dome and this remains in place today.

McFarland Associates Ltd (MAL) were appointed in May 2015 as Engineering Consultants for the project. The Works to date have focused on the: inside surface of the upper dome; the upper reinforced concrete slab and truss supports directly beneath the upper dome; and the lower, ornate dome, suspended from the trusses. The Brief for any remedial works

was to provide a further 100 years' serviceable life. Current and future phases of the work will see the: repair and/or replacement of the Corinthian capitals; repair to the stonework above; re-waterproofing of the uppermost drainage channel; and cathodic protection or replacement of a steel support angle around the perimeter of the dome over the capitals.

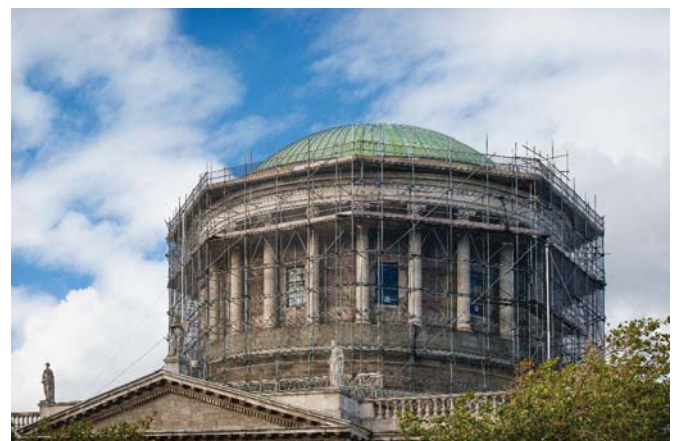


Figure 1. Scaffolding Erected to allow Access for Investigative Works Internally and Externally

2 A BRIEF DESCRIPTION OF THE STRUCTURE

As best described by the authors of a History of the City of Dublin [2] - "The whole edifice of the Law Courts and the

Law offices together form an oblong rectangle of 440 feet frontage to the river and 170 feet deep (to the rear). The centre pile, 140 feet square, divides off the law offices and forms two courtyards, one to the East and the other to the West, which courtyards are shut out from the street by handsome screen walls perforated by arches."

"The middle structure contains the Four Courts of Judicature, of the Chancery, King's Bench, Exchequer and Common Pleas, with all requisite conveniences for the proper discharge of the various business transacted."

At the centre of the Four Courts building is the Round Hall, a 20m diameter hub covered by a concrete dome structure which sits upon the rotunda main hall. This dome measures approximately 20m across its base and is constructed from reinforced concrete approximately 155mm in depth. It is understood that the reinforced concrete dome was formed from a single pour, by twenty men, over a thirty hour period with only one short interval. The outside roof of the dome is clad with copper sheets and steel reinforcing tension bars are located around the base of the dome to resist hoop stresses. Externally, a series of 24no. stone columns, with ornate stone capitals, support the base of the dome. A 1.2m oculus at the top of the dome is glazed.

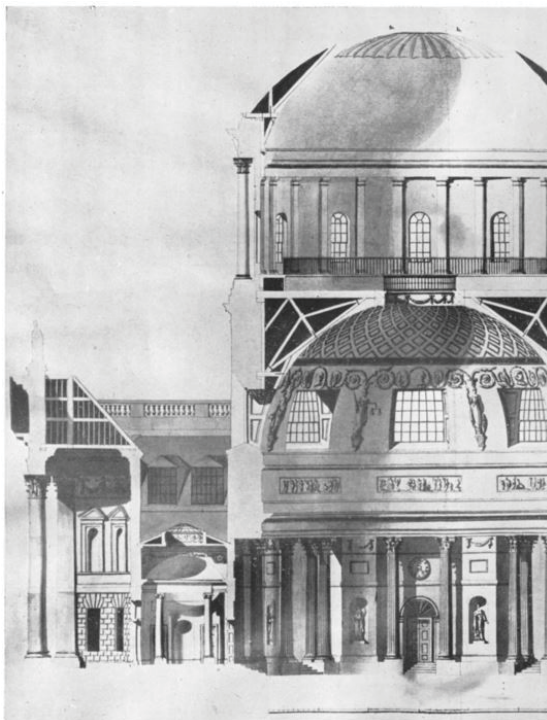


Figure 2. Historical Section through Rotunda. Note Upper Dome and Upper Floor both Originally Timber

Internally, below the upper main dome, there is a floor slab constructed from reinforced concrete. The floor slab varies in depth from 120mm to 168mm and has a circular opening in the centre which is approximately 4m in diameter.

This slab is supported on a series of 16no. steel trusses, which are also supporting an ornate plaster dome, hung from the underside of the steel trusses. The hall below is constructed with masonry walls and contains internal Corinthian columns.

3 STRUCTURAL INVESTIGATION

3.1 Visual Inspection

Various detailed inspections of the exterior and interior of the dome and drum highlighted a variety of issues.

Dome

Whilst being an excellent example of reinforced concrete of its era, there was nonetheless widespread areas of poor compaction, particularly around the lower circumference. Radial and circumferential cracks were also apparent and the inner surface retained a number of small wooden blocks which were originally used as reinforcement spacers. Nonetheless, the dome had remained largely dry over the years and the occurrences of delaminated and spalled concrete were few and far between. It was also apparent that the inner surface had been painted at least once, sometime in the past but this had largely worn away.

The copper on the exterior was removed locally to allow a cursory inspection of the underlying surface to be undertaken. An area of approximately 2m x 2m of copper was removed at the base of the dome, just above the drainage channel. At this location, the copper was found to be in good condition as was the concrete beneath. The copper had obviously provided good protection over the years and had not, in itself, suffered any great degradation. The location of the copper removal also allowed a breakout to be undertaken to examine the condition of the M8 bars that were included to resist the hoop stresses. Only two of the three bars were found, albeit they were not at positions indicated on drawings but their condition was excellent.

Upper Drum - External



Figure 3. Corrosion of the Steel Tension Band at the Base of the Dome and Associated Concrete Spalling

Perhaps the greatest amount of damage had occurred to the Corinthian column capitals and an encased steel angle above (Figure 3). This "tension band", a later strengthening addition, contained a 100mm x 100mm "L" shaped steel angle that was both recessed into the stone and over-rendered. Corrosion of the steel angle over the years had cracked and delaminated the render encasement and this posed a significant health and safety risk. The capitals, which had already been rotated, had continued to weather and deteriorate as had the various decorative, Portland stones above. Localised failure of these elements also posed a similar risk. We note that the repair and or replacement of the items

described above will constitute the next phase of the works and as such will not be detailed further in this paper.

Upper Floor

Directly beneath the upper dome is the upper floor. Now reinforced concrete, it was once timber and was used as the Record store for the Accountant-General. Whilst being in overall reasonable condition, radial, hairline cracking was noted above support positions. The supporting trusses beneath were observed to be in good condition albeit they were not fire protected.

Ornate Dome

The ornate dome, which is suspended from the trusses described above, had suffered localised failure in the past with a plaster rose falling to the hall beneath. This warranted a full cleaning and inspection to be undertaken of the upper surface of the dome and the supplementing of fixings. This work was undertaken under the guidance of Richard Ireland and will not be covered further in this paper.

Lower Drum – Internal

The Main Hall, the centre piece of the Four Courts, has been well maintained over the years. Nonetheless, a variety of cracks were observed in the stonework over openings on the north, east, south and west elevations.

3.2 Non-Destructive Testing (NDT)

In addition to the detailed visual inspection, a series of tests were undertaken on the dome and upper floor to establish the nature, source, extent and significance of any deterioration observed.

Testing included the removal of concrete samples for laboratory analysis and carbonation depth testing. Laboratory analysis included the determination and level of potentially deleterious contents such as chlorides and sulphates as well as an indication of cement contents. Carbonation tests involved the use of phenolphthalein, a pH indicator solution, to determine if the alkalinity of the concrete had been reduced. Half-cell potential surveys indicated the likelihood and location of any corrosion cells occurring on the reinforcement. The principle of the half-cell potential survey is to detect corrosion activity by delineating the cathodic and anodic zones within a reinforced concrete element. Corroding (anodic) and passive (cathodic) reinforcement in concrete exhibits a difference in electrical potential resulting in the formation of a macrocell [3]. Measuring the potential difference between the anodic and cathodic zones can be achieved with the use of a suitable reference electrode. The reference electrode is placed on the surface of the concrete whilst a separate electrical connection to the reinforcement is established. Connecting both the reference electrode and the reinforcement to a high impedance voltmeter enables the potential difference to be determined [4]. Electrical resistivity measurements gave an indication of the potential severity of corrosion if it were occurring. Linear Polarisation Resistance (LPR) Corrosion Rate measurements provided an indication of the actual corrosion rates on the reinforcement and was used to aid in the calculation of the section loss on the

reinforcement. In contrast to the measurement of potential difference using the half-cell technique, current flow at the corroding electrode is determined using the linear polarisation technique. Determining the corrosion current subsequently enables the corrosion rate to be calculated [5]. Through the use of the LPR equipment, the reinforcing steel is perturbed by a small, externally imposed, potential shift whilst the current decay is monitored over a fixed period thus enabling the corrosion current to be determined [6].

Dome - Internal

Concrete cover to reinforcement was found to be generally low throughout the dome and the quality of the concrete was found to be very variable. Moderate to low cement contents, combined with the variable concrete quality, had further resulted in varying degrees of carbonation and the situation, whereby, large amounts of reinforcement were no longer contained within a suitably alkaline environment. This was not surprising, particularly bearing in mind the age of the dome and the practices that would have been employed at the time of construction. Nonetheless, the compressive strength of the concrete was found to be reasonable and chlorides had not been included in the original mix.

In the absence of clear construction drawings and in order to assist with the structural assessment, a 3-D Ground Penetrating Radar (GPR) scan was undertaken, see Figure 4 below for a typical output.

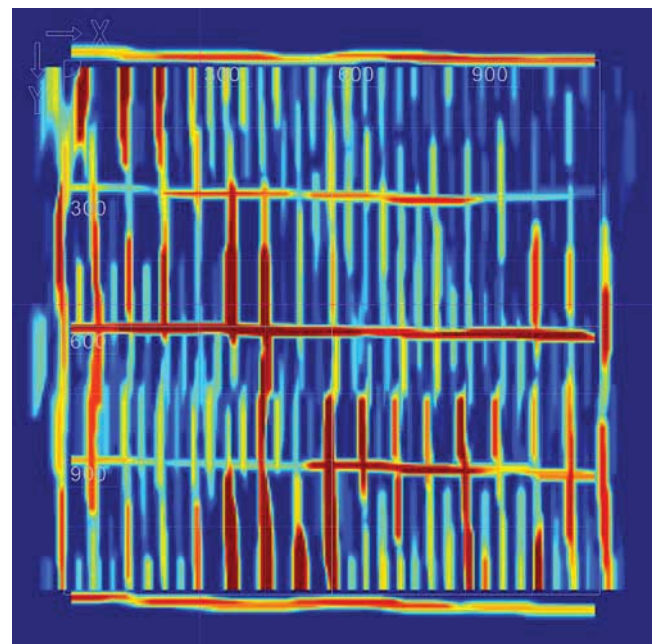


Figure 4. Ground Penetrating Radar Results Over a 1.2m² Area Showing Reinforcement – No Voids Noted

Importantly, the scan indicated the presence of a second layer of reinforcement at a depth of 160mm to 200mm, something that an electromagnetic covermeter had not detected. In addition, the scan appeared to confirm that poor compaction of concrete was limited to the surface only.

To try and determine the extent of any reinforcement corrosion, a half-cell survey was undertaken over the entire inner surface – see Figure 6 below.

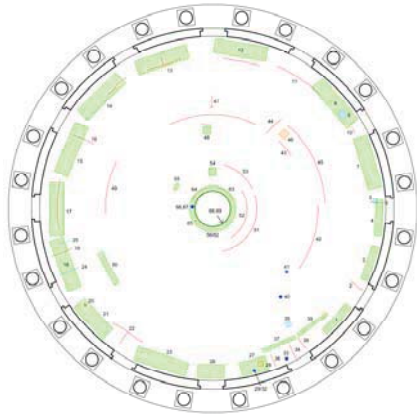


Figure 5: Visual Inspection Summary (Green: Honeycombed Concrete; Red: Cracking)

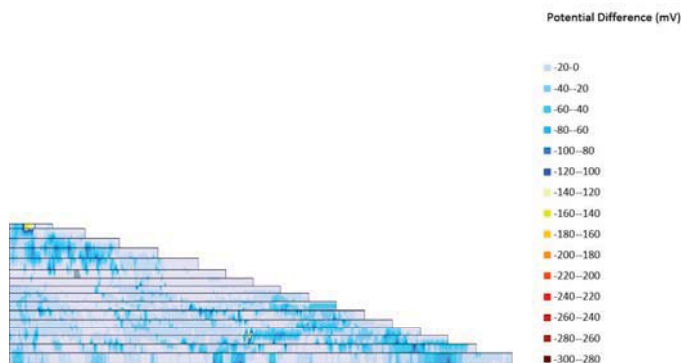


Figure 6. Half-Cell Survey of Internal Face of Dome on 'Folded-Out' Elevation

Whilst the half-cell potentials indicated that the probability of corrosion was uncertain, it is important to remember that the technique has limitations when trying to detect carbonation induced corrosion. Nonetheless, a more rigorous assessment of the results and in particular identifying change in potentials over short distances revealed that corrosion had been initiated at various location. Resistivity and corrosion rate measurements, however, both confirmed the rate of corrosion to be low. Of significance, however, the half-cell data correlated well with the visual survey (Figure 5) and highlighted the fact that corrosion had probably been initiated around the base of the dome.

Dome – External

The very limited testing on the outside surface of the dome did not reveal anything of any concern. The generally deeper cover to reinforcement, coupled with the good condition of the copper appeared to have maintained a dry, protective environment.

Upper Floor

Testing of the upper floor comprised confirmation of reinforcement detailing through GPR and electromagnetic

means. As is often the case, reinforcement was found to exist but not as indicated on the available drawings.

3.3 Proposed Works

With the expectation of a 100 years' extension in serviceable life, it was essential that repairs were undertaken to the reinforced concrete dome. Some form of cathodic protection would also be required to mitigate the effects of reinforcement corrosion that had been initiated but had not as yet caused extensive concrete cracking, delamination or spalling. Other considerations in the repair process included the provision of access to undertake the works and the removal of residual coatings on the internal surface.

4 STRUCTURAL INVESTIGATION AND ASSESSMENT

4.1 Structural Assessment

Three access scaffolds were required, namely: one from the main hall to the underside of the ornate dome; the second, to provide access from the trusses to the underside of the upper floor; and the third, from the upper floor to the underside of the upper dome.

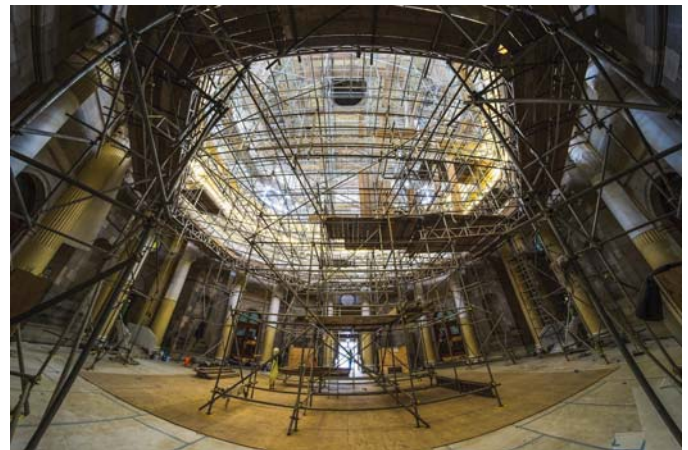


Figure 7. Scaffolding at Ground Floor Level

The first scaffold was required to give access to the entire underside of the ornate dome yet allow the relatively free movement of people within the Main Hall. This was accommodated through the provision of a fairly straight forward "birdcage" arrangement that allowed the weights to be taken through a central tower with secondary towers around the perimeter of the main hall. Weights were easily accommodated on the ground bearing floor slab. The second and third scaffolds were required to give access to the entire underside of the upper floor and dome yet be safely supported on the upper concrete floor and trusses beneath. This proved to be more complex and warranted the use of Finite Element Analysis (FEA).

The analysis software "LUSAS" version 14.7 was used to create the FEA model and a typical output can be seen in Figure 8.

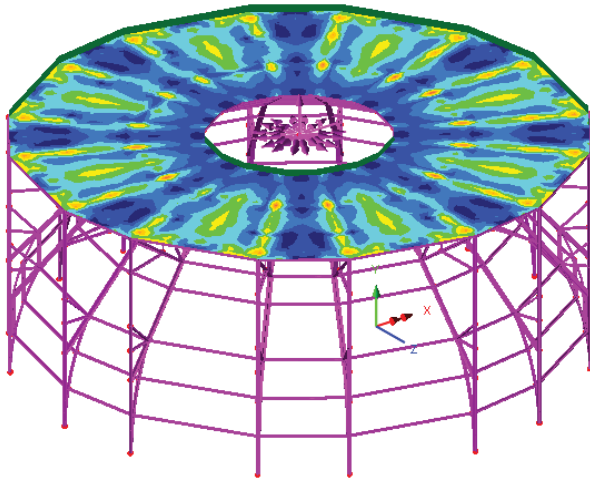


Figure 8. Finite Element Model of Upper Concrete Slab and Support Trusses

The FE model and analysis confirmed that the supporting trusses were actually quite clever and innovative in their design and were more than capable of supporting the proposed loads. The reinforced concrete slab, however, whilst being capable of supporting the intended scaffold loads was not sufficient for the proposed change of use to a public gallery. A structural check determined that the floor slab failed in bending at a loading of 3.52 kN/m^2 ; a 42% increase in bending moment capacity would be required to accommodate the loading associated with the change in use. In addition, cracks were visible in the top surface of the concrete slab, directly over the trusses, thus indicating the localised over-stressing. The variable nature of the reinforcement also caused concern over the shear capacity of the slab.

A design was subsequently produced for strengthening the underside of the slab using an open-weave polybenzoxazole (PBO) fibre fabric embedded in a specialised inorganic cementitious mortar. The benefits of this unique system include: breathability; inherent non-combustibility; non flaming characteristics; and their general performance in elevated service temperature environments. Although the system has not as yet been installed, it is expected to form part of the next phase of the works. It is further likely that a load test, monitored with fibre-optic sensor technology, will be undertaken to confirm the uplift in strength required.

4.2 Structural Health Monitoring

Bearing in mind the age and sensitivity of the structure and the intention of temporarily adding an additional 100 tonnes of access scaffold to the inside of the structure, it was decided to monitor the cracks that had been detected in the Main Hall. For this purpose, innovative Magnetic Crack Monitors (MCMs) were installed to record movements constantly as opposed to periodic measurements that is the case normally with either Tell-Tales or Demec Pips.

Four magnetic field crack sensors were installed over the four cracks at the compass points around the Main Hall. Information from these sensors was then passed remotely to a central telemetry base station which in turn was connected

wirelessly to an office computer. An external temperature sensor was also connected to the base station to allow for compensation for differential temperatures between the outside and inside of the structure.



Figure 9. Installation of a MCM on a Masonry Crack

Each remote MCM takes an hourly measurement of crack width movement in 2no. axis by noting the position of a magnet to which it is calibrated and located on the opposite side of the crack (see Figure 9).

Monthly monitoring from May 2015 to date showed a correlation between all three variables being measured, namely crack width, shear and temperature. Increases in external temperature were directly related to a decrease in crack width and vice versa. However, the shear width showed lesser movement than the crack width and the overall trend with regards to temperature was much less consistent over the period of monitoring.

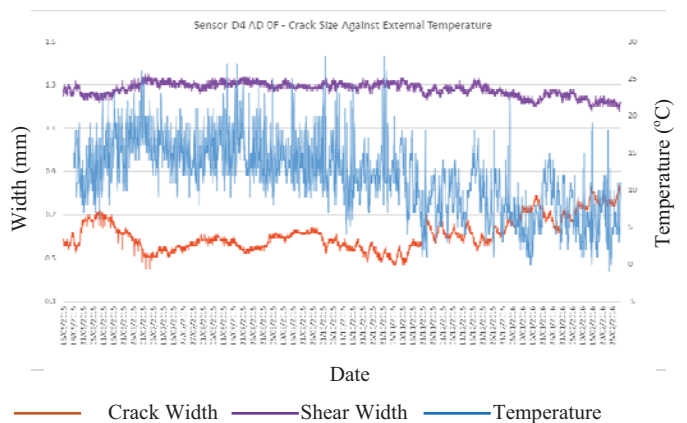


Figure 10. Typical Crack Movement Results from an MCM

The continuous nature of the information obtained from the MCMs added to our confidence that the additional loads imposed on the structure had no noticeable effect on cracks that were obviously historic. This level of detail and understanding would not have been possible using other existing methods (Figure 10).

5 REMEDIATION (PHASE 1 – UPPER DOME)

At this stage, the only remedial works completed have been the restoration of both domes. Note that this section only relates to the remediation of the upper dome.

The first part of the remediation process was to remove the existing coatings to expose the parent concrete. However, this had the potential to be both noisy and dusty and could release potential contaminants contained within the various layers of paint. A number of paint samples were therefore extracted and sent for laboratory analysis to determine their lead content, the results of which revealed negligible levels. Trials of various coating removal methods were undertaken, taking into consideration the concern of dust creation, which included: abrasive wheel; needle gunning; and the use of a poultice. A localised trial revealed that the use of a poultice, albeit the preferred option from a health and safety perspective, was not degrading the paintwork sufficiently enough to remove all the coatings and a number of applications would have been required in order to achieve a suitable finish. Subsequently, a combination of both needle gunning and abrasive wheel was used. The contractor proposed the use of a dust suppression system attached to the equipment which successfully eliminated the generation of dust at the source of removal. The abrasive wheel covered large areas quickly while needle gunning removed coatings at depth within localised areas of voiding.

A hybrid cathodic protection (CP) system was designed and installed at the base of the dome to provide ongoing protection from the effects of reinforcement corrosion. Half-cell testing revealed that the majority of active corrosion cells were occurring at the base of the dome. Further to this, the base of the dome was seen as the greatest area of long term concern from corrosion due to the presence of the drainage channel on the outside concrete surface. The hybrid CP system design determines the number and mass of anodes require to pass a charge of 50 kilocoulombs which is required to passivate the steel reinforcement. Following this initial period of active passivation (sustained by the application of direct current) the anodes must be designed such that they possess enough remaining mass to perform galvanically over their intended design life.

It was evident that a new protective coating system was required in order to reinstate suitable cover to the embedded reinforcement and to provide ongoing protection from the effects of carbonation. Pull-off tests were undertaken both on the exposed parent concrete, to determine bond suitability, as well as to a number of repair combinations. A re-profiling mortar was subsequently installed to both fill areas of honeycombing and 'blow holes' as well as providing additional cover. An anti-carbonation coating was then applied over the re-profiling mortar.

Historical records referenced the dome as originally having a finished surface resembling the night's sky, complete with stars. It was deemed appropriate that the original aesthetic surface should be reinstated and as such expert painter Don Knox was engaged to paint a series of gold leaf stars on a midnight blue background (Figure 11).

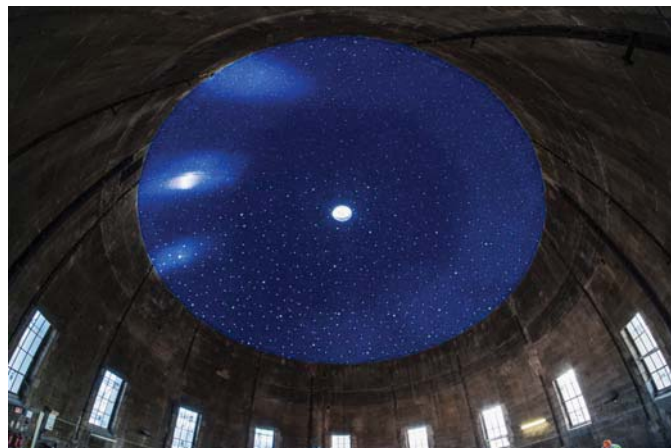


Figure 11. Finished Concrete Dome

6 CONCLUSIONS

The Four Courts in Dublin is arguably the most recognisable and iconic building in Dublin, if not Ireland. Its reinforced concrete upper dome, thought to be the oldest in Europe has performed well for many years but reinforcement corrosion has recently been initiated. This paper has highlighted how modern techniques can be used sensitively to preserve, conserve, restore and strengthen these historic structures providing significant extensions to their serviceable life. In addition, modern and innovative monitoring techniques can be employed to ensure that works are undertaken without causing any additional damage.

Whilst only the domes have been fully repaired to date, we welcome the challenges of the next phase of this exciting and important refurbishment project.

ACKNOWLEDGMENTS

Office of Public Works, P.J. Hegartys, ACOL Ltd, Structural Concrete Bonding, Richard Ireland, Don Knox

REFERENCES

- [1] Byrne, T. J., *Reconstruction Work at the Four Courts*, Office of Public Works, Dublin, Ireland, 1928.
- [2] Warburton, Whitelaw and Walsh, *'History of the City of Dublin'* London, 1818
- [3] Babaei, K. (1986) *Evaluation of half-cell corrosion deck test for concrete bridge decks*. Washington State Department of Transportation. Report number: WA-RD 95.1
- [4] Bertolini, L., Elsner, B., Pedferri, P. & Polder, R. (2004) *Corrosion of Steel in Concrete*. Weinheim, WILEY-VCH Verlag GmbH & Co. KGaA
- [5] Metal Samples Corrosion Monitoring Systems (n.d.) *Linear Polarisation Resistance Monitoring*. Available from: <http://www.alspi.com/lprintro.htm> [Accessed 5th January 2016]
- [6] Song, H. & Saraswathy, V. (2007) Corrosion monitoring of reinforced concrete structures- A review. *International journal of electrochemical science*. 2(2007), 1-28. Available from: www.electrochemsci.org [Accessed 1st March 2016]

Large inelastic cyclic testing of the gusset-plate brace member assemblies in ultra-low cycle fatigue regime

M.S. Hassan^{1,2}, J. English¹, J. Goggins^{1,2,3}, S. Salawdeh^{1,3}

¹Civil Engineering, College of Engineering & Informatics, National University of Ireland-Galway, Ireland

²Ryan Institute for Environmental Marine and Energy Research, National University of Ireland-Galway, Ireland

³Centre for Marine and Renewable Energy Ireland (MaREI), Galway, Ireland

Email: m.hassan3@nuigalway.ie, jack.english@live.ie, jamie.goggins@nuigalway.ie, suhaib.salawdeh@nuigalway.ie

ABSTRACT: In this paper, the test results of four gusset plate-brace member assemblies in the ultra-low cycle fatigue regime (less than 20 cycles) is presented. Square hollow sections (SHS) of four different cross sections (i.e. 60 x 60 x 4-2591mm, 80 x 80 x 4-2591mm, 80 x 80 x 4-2526mm, 100 x 100 x 4-2526mm) were employed as the brace members in conjunction with gusset plates that have two separate sizes (i.e. 200 x 300 x 5mm, 266 x 292 x 5mm). The test setup and details of the assembly are described, as well as the frontier areas important from the research aspect are addressed. The tests were carried out under the loading protocol recommended by the European Convention for Constructional Steelwork (ECCS) for the structural testing. The results show that the assembly tends to develop significant strength and stiffness (buckling in compression and yielding in tension) from the brace when end connections are rigid or substantially rigid. A stiff type connection tends to develop when the gusset plate is thicker and stockier than the brace member in the assembly; however, it does not imply that a large, thick, and highly stiff gusset plates should be employed in practice, as this may lead to uneconomical material costs and over-conservative member design. The global and local brace slenderness is found to be another factor that affects the response features of assemblies significantly.

KEY WORDS: cyclic testing; concentrically braced frames; steel hollow braces; gusset plate.

1 INTRODUCTION

Concentrically braced frames (CBFs), in which the bracing elements intersect the centre line of beam-column joint connections, forms one of the most competent earthquake resistant structures, that is, stiff, strong and economical, for providing lateral resistance in both low and high rise structures. They resist lateral inertia forces by a vertical concentric truss mechanism consisting of alternating compression and tension in the bracing members; however, the type of braces concerned herein are tension only, meaning that the tension brace resists the seismic demand. During seismic demand, these bracing members can be deformed hysteretically, which is characterized as buckling in compression, yielding in tension, and a U-shaped pinching effect in the locally buckled region. As a result of large inelastic excursions the braces experience a fracture related to ultra-low cycle fatigue.

CBF systems were developed with an aim of minimizing inter-story drift while confining inelastic deformations in the brace and assuring structural elements like beams, columns, etc., to remain elastic. The idea is simple to design, fabricate and allow the required strength and stiffness to be obtained at low cost by utilising the brace as a primary dissipating member. Consequently, extensive experimental research studies have been conducted over several decades with the intention to determine the factors that influence the cyclic behaviour and fatigue life of bracing members. In this context, the early work of Black et al [1] and Jain et al [2], which showed global slenderness has a significant effect on the cyclic behaviour, is one of a pioneering work that led to contribution in the development of analytical expressions for predicting the cyclic behaviour of braces. Tang and Goel [3]

later proposed an empirical equation for predicting the fatigue life of bracing members based on the aspect ratio, the local and the global slenderness of a brace section. The brace axial ductility capacity, which later drives the drift capacity of a CBF system, remains a frontier factor of the research. Later, Tremblay [4], Goggins et al [5] and Nip et al [6] proposed empirical equations for determining the ductility capacity considering the global and local slenderness of the brace. In light of these facts, the design code has imposed stringent guidelines onto the shape and geometry of the brace for consideration in their design, so that an adequate axial ductility can be obtained for the designed CBF without significant deterioration of brace stiffness and strength, including the connection strength.

Indeed, the CBF systems are acknowledged for their high stiffness and strength capacity due to diagonal bracing elements; however, they are not very attractive in terms of ductility. Consequently, their performance could be susceptible to near field earthquakes, which are usually accompanied by large amplitude pulses of motion and induced shocking wave effect. The past response of braced frames during earthquakes has been noted to be varied in behaviour, i.e., in some cases the stiff and serviceable performance during earthquake loading has resulted, but in other, obvious resistance and ductility were significantly smaller than expected when a failure in brace and connection occurred [4].

Concentric braces dissipate significant seismic energy from their periodic buckling and yielding behaviour, which reveal lateral stiffness and strength possessed by the CBF for restoring lateral drift. During brace buckling, braces significantly induce strain demands on the connection as a result of axial shortening and mid-length deformations. The

strain demand increases at both ends as buckling and yielding occur in the brace relative to the loading intensity. The end connections including the gusset plate, therefore, must be proportioned and detailed in a way so that they can permit brace elastic and inelastic rotation without failing in buckling, tearing and/or fracture.

Gusset plates are thick plate structural elements that connect lateral load resisting system (braces) to the gravity load-bearing system (beams and columns) by means of bolted, riveted and/or welded connections to form CBF. It is widely accepted that lack of confidence in knowledge related to the behaviour of gusset plate exists due to the number of reasons: (i) the behaviour of gusset plate is complex under cyclically subjected load, (ii) absence of sufficient data on the monotonic and cyclic inelastic behaviour and (iii) speculation of various method over design practice. One of the commonly employed methods, Whitmore width concept [5], has found an upper bound method for the seismic design of gusset plate [9]. Other existing methods, like The KISS method, parallel force method and the truss analogy method, were primarily developed in the context of truss framing systems subjected to quasi-static monotonic loading. Thus, the applicability of these methods to cyclically loaded gusset plates of various geometries has to be researched. In addition, the relative properties of gusset plate sensitive from the seismic design and their effect over the gusset plate-brace member configurations have to be addressed in order to highlight their impact on the CBF system overall.

It is until recently that the response of gusset plate to seismic loading has received significant attention and being addressed collectively with the braces in order to achieve the desired stiffness and strength demand from CBF economically. As such, the connection tearing and fracture of gusset plate is to be avoided.

Most of the existing research on the CBF system is mainly available in the design context of the American CBF's systems (referred as Special Concentrically Braced Frames, SCBFs) that provide an aid to revise, re-calibrate and re-assure the recommendations prescribed by the American standard. This standard allows the monitoring of system performance over the pre-defined damage thresholds, defined as Operational, Immediate Occupancy, Life Safety and Collapse Prevention. The early contributions that led toward the development of such system are Kahn, and Hanson [10], Astanah et al [11], and Lee and Goel [12]. They emphasized the effect of the premature failure of the connections and braces have on the SCBF and concluded that SCBF can yield much better response if failure is avoided. As a result of research, detailed connection design was documented in the AISC Seismic Design Provision [13] to have the satisfactory performance of the system under designed earthquake. However, these design rules to some extent resulted in the gusset plates that were relatively larger, uneconomical and impractical for the used in SCBF system, as mentioned previously. A concept that tries to balance the yielding mechanisms between the brace and gusset plate during the seismic action is introduced by utilising the capacity design approach (Roeder et al. [14]). This concept determined to yield thinner and more compact sections while improving the performance of the SCBF as a

whole to meet multi-objective performance defined by AISC 2002 [13] for the ductile designing of SCBF systems.

In order to consider these updates and its compatibility in the European design framework as well as the need to revise, recalibrate and re-assure the codified performance of CBF to a real system, a pilot research program 'BRACED' (Brace Response Assessment-Computation, Experiments, Design) was recently carried out under the Transnational Access Programme offered by the EU FP-7 network by the five academia; Trinity College Dublin, Commissariat à l'Énergie Atomique, Saclay, National University of Ireland, Galway, University of Ljubljana, and Imperial College London. The project primarily investigates the ultimate performance of the CBF's systems, using the largest European earthquake simulator, with realistic braces and connections, to real-time earthquake loading. The project particularly assesses the dynamics of the braces, gusset plate and brace connection relative to the performance codified as per the EC-8 standard [15]. The details and outcomes of the project documented in these publications [16, 17]. The work presented herein is a continuation of this project with similar objectives to those outlined above.

In this paper, the results of the four quasi-static cycling tests on the gusset plate-brace member assembly are presented. The testing arrangement and specimen assembly are detailed. The results in the form of hysteresis loops and failure modes are presented and discussed. The future direction of the work is also highlighted.

2 SPECIMENS AND TESTING SETUP

The purpose of the experimental testing is to (i) study the cyclic behaviour of gusset-plate brace member assembly in the ultra-low cycle fatigue regime, and (ii) then to use that data for the development of a finite element model. The main intention is to assess the ultimate behaviour of a CBF system comprised of the assemblies used herein during earthquakes. Specimens of cold formed carbon steel of Grade S235 JRH were employed in conjunction with hot-rolled, structural steel plate of Grade S275 J2 for the testing.

The monotonic tensile material properties of the braces and gusset plates are established from the nominal values prescribed as 235MPa and 275MPa, respectively, for the yield strength. The ultimate tensile strength is expected to lie between the values of 360-510MPa and 370-530MPa, respectively. These values are tentative, and require static monotonic tensile testing for their accurate description. Testing was carried out on four gusset plate-brace member assemblies comprised of SHS braces and rectangular or tapered gusset plates. The configuration of each assembly, comprising the brace and gusset plate section, is given in Table 1, for which the associated symbols are defined in Figure 1. In Table 1, the test ID is identified as specimen number (e.g., S1 or S2, etc.), followed by the dimension of brace (depth x width x thickness), specification of material (carbon steel, 'CS'), forming route (either cold forming, 'CF' or hot-rolling 'HR'), the dimensions of gusset plate (depth x width x thickness), the type of gusset (either rectangular or tapered), the brace length, L_b , the weld fillet length, L_w , and the angle, θ , that represents the inclination of brace relative to

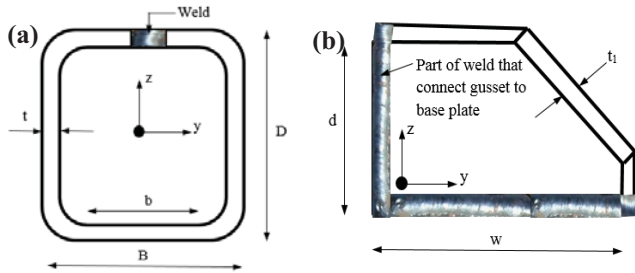


Figure 1. Schematic labelling convention of (a) brace cross-section, (b) gusset plate specimen.

The code has imposed an upper limit on the global slenderness $\bar{\lambda}$ for sections to be used as diagonal braces in CBFs, specified as 2.0. This limit is introduced to limit the stiffness and strength degradation from the slender braces so that the structural stability should not be affected. The expression for the global slenderness is given as:

$$\bar{\lambda} = \sqrt{\frac{f_y A}{N_{cr}}} \quad (1)$$

where f_y is the nominal yield strength, A is the cross-sectional area, N_{cr} is the elastic critical buckling load. When the high dissipative response from the system is expected, the Eurocode [18] suggests using Class-1 cross section to avoid resistance degradation. This class of cross-section tends to develop plastic hinges with the given rotation capacity without a reduction in their cross-sectional resistance. The local slenderness that determines the class of the section is given as b/t_e , where b is the flat width of the wider face of the section, t is the thickness of the section and $\epsilon = \sqrt{235/f_y}$.

Specimens involved in this study conform to the $\bar{\lambda} < 2.0$ as per the EC8 [15] specification. All cross sections herein are classified as Class 1 cross-section as per the Eurocode 3 Part 1-1 [18] standard.

Eurocode-8 [15] suggests the dissipative zones (braces) must yield before the yielding of non-dissipative zones (connections, beams, and columns, etc.) during an earthquake. One way to satisfy this condition is to use high yielded strength steel for the non-dissipative zones compared to the dissipative zones in the design practice. As such, the nominal yield strength of steel for non-dissipative zones and connections should exceed the actual maximum yield strength of the steel of dissipative zones. The actual maximum yield strength can be calculated as $f_{y,max} = 1.1 \gamma_{ov} f_y$, where γ_{ov} are the overstrength factor and its recommended value are 1.25 as per the Eurocode-8 [15], f_y is the nominal yield strength of a steel.

In this study, the gusset plate (non-dissipative member) used is fabricated of steel Grade S275 compared to the steel used to fabricate braces (dissipative member) of S235. Moreover, full penetration fillet welds of thickness 6mm (typical) were employed as joining mechanisms between the gusset plates and the brace members. The weld has a length equal to 104mm and 115mm for the braces that has a full length equal to 2526mm and 2591mm, respectively.

The fatigue testing of the braces was carried out under cyclic axial displacement in the internal reaction frame, as

the gusset plate. The measured dimension of brace and gusset plate members are given in Table 2.

shown in the Figure 2a, in the structure research laboratory at the NUI-Galway. The assembly is comprised of 500kN Instron hydraulic actuator mounted at a height of 2600mm at an angle 26.4° from the ground surface. The ends of the specimens were attached with hydraulic actuator and reaction end by using the bolted connections. These ends were restrained in all degrees of freedom except the loaded direction. A suitable number of transducers around the testing assembly were used to measure any relative movement during the tests, which could then be removed when the test data were processed. Strain gauges were placed at the centre of each flange and web at the mid-length of specimens in order to measure the strain distribution across the section during brace buckling and yielding. A suitable number of strain gauges were placed at the junction of the gusset-plate-brace member to the nearest distance of $2t_p$ and $8t_p$ in order to measure the distribution of strain in the confined region sensitive to a rotation due to brace buckling and yielding. Two wire-draw transducers were used at the mid-length to measure the lateral deformation of the brace in the horizontal and vertical direction. Additional details on the specimens, stiffeners, and end connection can be found in Figure 2 (b) to Figure 2 (d).

The cyclic protocol follows the recommendation of ECCS 1986 [19], i.e., one cycle at each level of 0.25, 0.5, 0.75, and $1.0 \delta_y$, followed by the three cycles at each level of 2, 4, 6, 8 δ_y etc., where, δ_y represents the estimated axial yield displacement. The displacements were applied at strain rates between $5 \times 10^{-4} \text{s}^{-1}$ to $5 \times 10^{-2} \text{s}^{-1}$ over a variable frequency. The strain rate is within the recommended range for quasi-static testing [20].

3 PRELIMINARY RESULTS

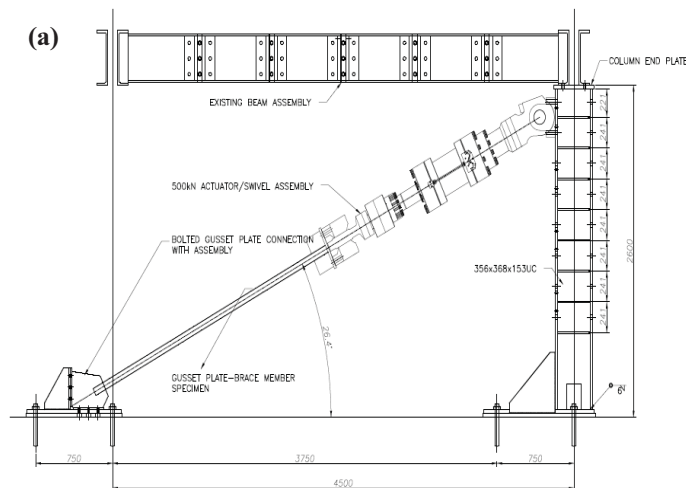
The performance of the assembly, comprised of the gusset plate-brace member, to ultra-low cycle fatigue is described. All the bracing elements remain essentially straight in the initial elastic cycles. The two specimens identified as S1 and S2 experienced buckling and yielding in compression and tension, respectively. Upon local buckling, plastic hinges formed at the compressive corners/web of the mid-length cross section, while significant rotation was developed on the gusset-plate brace member junction. Local buckling of the cross section occurred in the subsequent cycles in the hinged region, which resulted in a highly localized strain that led to the sudden fracture of the remaining cross-section. As expected, in the other two assemblies identified as S3 and S4, ineffective and premature buckling occurred in the brace, but significant buckling and yielding occurs at the gusset plate as such they were intentionally designed to acquire failure at the gusset connection. In particular, the failure occurred at the very end of braces primarily located in the gusset plates. In these cases, the inelastic energy resulted from buckling and yielding of the gusset plate rather than the brace buckling and yielding, which in practice is contrary to the design of CBF systems. This explains the crucial role of non-dissipative components such as gusset plates, in the strength and stiffness capacity of CBF system subjected to earthquake loading.

Table 1. Assembly's identification and details of the gusset plate-brace members associated with assembly.

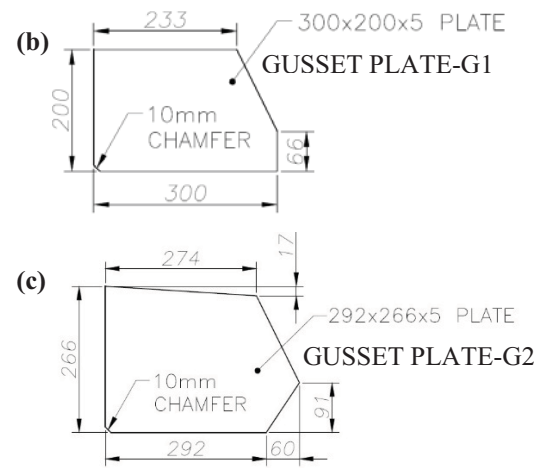
Test ID	Brace-gusset plate assembly		Type of Gusset plate	L _b	L _w	θ degree
	Brace cross-section	Gusset plate cross-section				
S1	60x60x4-CS-CF	200x300x5-CS-HR	Rectangular	2591	111	45°
S2	80x80x4-CS-CF	200x300x5-CS-HR	Rectangular	2591	111	45°
S3	80x80x4-CS-CF	266x292x5-CS-HR	Tapered	2526	104	45°
S4	100x100x4-CS-CF	266x292x5-CS-HR	Tapered	2526	104	45°

Table 2. Measured geometric dimensions of gusset plate and brace sections after testing.

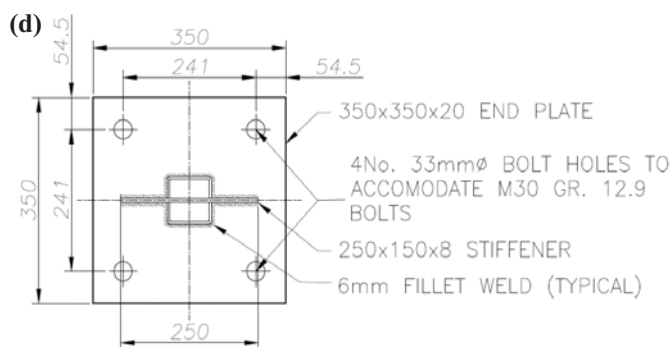
Test ID	Brace specification					Gusset plate specification		
	Depth (mm)	Width (mm)	Thickness (mm)	Length (mm)	Corner radius (mm)	Depth (mm)	Width (mm)	Thickness (mm)
S1	61.70	61.36	4.74	2591.00	11.73	200.00	298.80	5.71
S2	80.80	79.78	5.30	2591.00	13.23	200.30	298.00	6.15
S3	81.10	82.00	5.51	2530.00	13.25	258.00	295.00	6.10
S4	100.6	101.16	5.18	2526.00	16.52	260.00	290.00	6.40



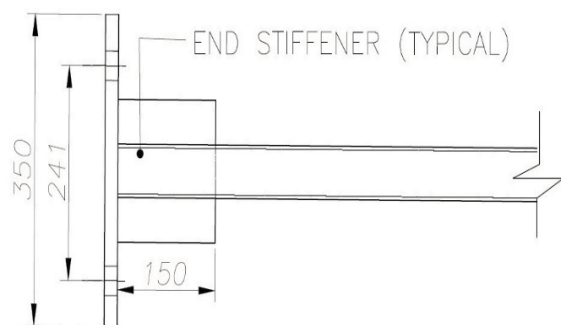
Reaction frame and assembly of cyclic testing (Elevation view).



Detailing of G1 and G2 gusset plate dimension (Elevation view).



Plan view



Elevation view

End connection details of the specimen.

Figure 2 (a)-(d): Schematic presentation of the testing setup and specimen, (a) Elevation view of the reaction frame and assembly, (b) Elevation view of the thick gusset plate-G1, (c) Elevation view of the thick gusset plate-G2, (d) Plan and elevation view of end connection details that were used for testing (dimensions in mm).

Specimen ID	$\bar{\lambda}$	b/t ϵ	F _c (KN)	F _{t,max} (KN)	W _{total} (KN/mm ²)	Number of cycles to			Displacement ductility Prediction/test	
						Global buckling	Local buckling	Fracture	Nip et al. [6]	Tremblay[4]
S1 ^F	0.61	7.14	147	339	36.27	11	14	20	0.64	0.70
S2 ^F	0.45	11.50	211	369	45.42	11	14	20	1.15	1.17
S3 ^{F,E}	0.44	11.38	217	355	43.62	-	-	20	0.56	0.57
S4 ^{F,E}	1.11	14.74	271	377	46.54	-	-	20	0.64	1.20

^F Tested to failure

^{F, E} Failure at end connection.

Table 3. Summary of test results.

Failure in the heat affected zone, referred as the welded area cycle at a ductility of 12, which can be characterized as ultra-

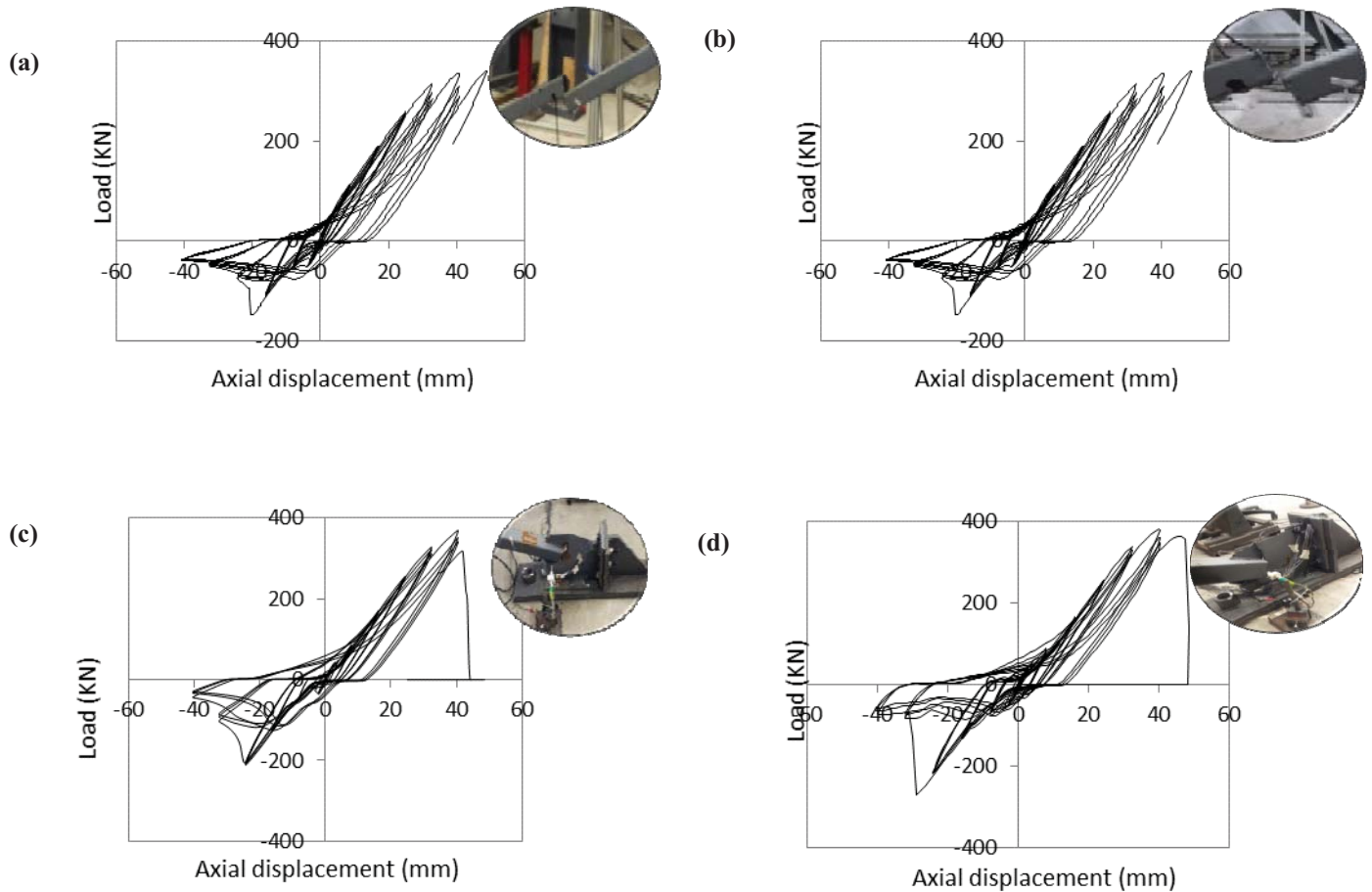


Figure 3 (a)-(d): Load displacement hysteresis loop for specimens (a) S1, (b) S2, (c) S3, (d) S4.

between the assembly parts, is not observed. The seismic code, recommends configuring connection of the former type (S1 and S2) so that the failure of the gusset plate should be avoided and the system ductility must obtain from the inelastic behaviour of the brace.

The test results in terms of the buckling load, F_c, maximum tensile force, F_{t,max}, energy dissipated, W_{total}, number of cycles to global and local buckling including the fracture, together with the displacement ductility from the two predictive models; Nip et al. [6] and Tremblay [4], given in Eqs. (2) and (3), respectively, is summarized in Table 3. In spite of two different failure modes, the four assemblies failed in the 20th

low cycle fatigue.

$$\mu_f = 6.45 + 2.28\bar{\lambda} - 0.11(b/t\epsilon) - 0.06(\bar{\lambda})(b/t\epsilon) \quad (2)$$

$$\mu_f = 2.3 + 8.3\bar{\lambda} \quad (3)$$

The global and local buckling occurred when the first cycle of a larger axial displacement demand is imposed, i.e., 11th and 14th cycle for the ductility level of 6 and 8, respectively. Although the assemblies are stockier in characteristic, as depicted from their slenderness ratios presented in Table 3, they have shown a good ductile performance in term of a number of cycles to failure and ductility capacity. The ductility predictive models proposed by Nip et al. [6] and Tremblay [4] underestimate capacity of specimens in terms of

their ductility. One reason could be the use of tentative values of yield strength in the models which has resulted uncertain results. In general, these models offer a satisfactory prediction of displacement ductility over the full slenderness range, as the input parameters of the model are representative of the physical quasi-static cyclic tests and hold all relevant factors that may influence the brace ductility. The full hysteresis loops and ultimate failure of the four assemblies are presented in Figure 3. In all specimens, the compressive strength degraded substantially after first buckling with the exception of the brace and gusset plate buckling. The compressive strength continues to degrade when larger axial displacement demand is imposed. The effect of the Baushinger effect (increase in yield strength resulting in a decrease in compressive yield strength) is widely pronounced in all the hysteresis loops presented. However, the response of the specimens in tension remains unstable at larger displacement demand. Failure in the assembly was assumed when fracture either at mid-length of braces or next to the connections occurred.

4 CONCLUSION

In this paper, four quasi-static cyclic test results of the gusset plate-brace member assembly subjected to ultra-low cycle fatigue is presented and described. The results show that the diagonal bracing assembly is able to develop desired stiffness and strength demand from the brace when the gusset plate is stiff and compatible with its brace member. But, when the gusset plate is incompatible to brace configuration, failure occurred at or near to the connection and the assembly ductility is driven by gusset plate. The design in which system ductility is governed by gusset plate performance is not allowed in practice. The two assemblies S2 and S3, which have the same global and local slenderness of the brace member, dissipated an equal amount of energy in spite of experiencing different failure modes. In general, all specimens failed in the 20th cycle and have shown adequate performance up to a ductility level of 12.

These test results will be used to develop robust and efficient Finite Element (FE) and Physical Theory (PT) based model using the state-of-the-art tools and techniques in ABAQUS 6.13 and OPENSEES, respectively. Fatigue testing on the coupons of structural steel in ultra-low cycle fatigue regime will be carried out to determine the cyclic properties of material. A material model capable of translating the kinematic shift and handling cyclic hardening of material in stress space will be used for FE simulation. Parametric studies employing a wide range of gusset plate geometry and configuration with varied global and local brace slenderness will also be studied. The study overall aims to improve the seismic design of CBF's systems.

ACKNOWLEDGMENTS

The first author would like to acknowledge College of Engineering & Informatics for providing PhD studentship. The authors gratefully acknowledge NUIG technicians for their technical input and expertise in organising the experimental setup for this project. The third author would like to acknowledge the support of Science Foundation

Ireland through the Career Development Award programme (Grant No. 13/CDA/2200).

REFERENCES

- [1] Black, R.G., Wenger, A.B, Popov, E.P, Inelastic Buckling of Steel Struts Under Cyclic Load Reversals. 1980: UCB/EERC-80/40.
- [2] Jain, A.K., Goel, S.C, Hanson, R.D Hysteretic cycles of axially loaded steel members. Journal of the Structural Division, ASCE, 1980. 106 p. 1777-1795.
- [3] Tang, X., Goel, S.C, Brace fractures and analysis of phase I structure. Journal of Structural Engineering, ASCE, 1989. 115: p. 1960-1976.
- [4] Tremblay, R., Inelastic seismic response of steel bracing members. Journal of Constructional Steel Research, 2002. 58: p. 665-701.
- [5] Goggins, J.M., Broderick, B.M, Elghazouli, A.Y, Lucas, A.S Behaviour of steel tubular members under cyclic axial loading. Journal of Constructional Steel Research, 2006. 62: p. 121-131
- [6] Nip, K.H., Gardner, L., Elghazouli A.Y, Cyclic testing and numerical modelling of carbon steel and stainless steel tubular bracing members 424-41. Engineering Structures, 2010. 32 p. 424-441.
- [7] Roeder, C.W., Lehman, D.E, Yoo, J.H, Performance -Based Seismic Design of Braced Frame Gusset Plate Connections. Connections in Steel Structures V-Amsterdam. (2004), 2004.
- [8] Whitmore, R.E., Experimental investigation of stresses in gusset plates. 1952: Bulletin No. 16, Engineering Experiment Station, University of Tennessee.
- [9] English, J.P., Goggins, J, Nonlinear Seismic Response of Concentrically Braced Frames using Frames using Finite Element Models. 15th World Conference on Earthquake Engineering, Lisbon, Portugal, 2012. 2012.
- [10] Kahn, L.F., Hanson, R.D, Inelastic Cycles of Axially Loaded Steel Members. Journal of Structural Division, ASCE, 1976. 102: p. 947-59.
- [11] Astaneh-Asl, A., Goel, S., Hanson, R.D., Cyclic Behaviour of Double Angle Bracing Members with End Gusset Plates, in Research Report UMEE 82R7. 1982: Department of Civil Engineering, University of Michigan, Ann Arbor, MI.
- [12] Lee, S., Goel, S.C., Seismic Behaviour of Hollow and Concrete Filled Square Tubular Bracing Members, in Research Report UMCE 87-11. 1987: Department of Civil Engineering, University of Michigan, Ann Arbor, MI.
- [13] American Institute of Steel Construction, A., Seismic Provisions for Structural Steel Buildings. 2002: Chicago, IL.
- [14] Roeder, C.W., Lumpkin, E. J, and Lehman, D. E, A balanced design procedure for special concentrically braced steel frame connections Journal of Constructional Steel Research, 2011. 67 (11): p. 1760-1772.
- [15] EN, -. B. Eurocode 8: Design of Structures for earthquake resistance Part 1: General rules, seismic actions, and rules for buildings. 2004.
- [16] Broderick, A.D.H.B.M., Quasi-Static Testing and Correlative Dynamic Analysis of Concentrically Braced Frames with Hollow Steel Braces and Gusset Plate Connections. 15th World Conference on Earthquake Engineering, Lisbon, Portugal, 2012. 2012.
- [17] B.M. Broderick, A.H., P. Mongabure, J.M. Goggins, S. Salawdeh, G. O'Reilly G, D. Beg, P. Maze, F. Sinur, and A.Y. Elghazouli., Assessment of the seismic response of concentrically braced steel frames and design (BRACED), in Experimental Research in Earthquake Engineering, Geotechnical, Geological and Earthquake Engineering, F. Taucer, Apostolska, Roberta, Editor. 2015: London.
- [18] Ireland, N.S.A., Eurocode 3: Design of Steel Structures - Part 1-1: General Rules and Rules for Buildings. 2005.
- [19] Technical Committee 1, E., Structural Safety and Loadings – Technical Working Group 1.3, Seismic design recommended the testing procedure for assessing the behaviour of structural steel elements under cyclic loads. 1986: Brussels.
- [20] BSI, Metallic materials- Constant amplitude strain controlled axial fatigue- method of test 2006.

Recommendations for Numerical Modelling of Concentrically Braced Steel Frames with Gusset Plate Connections subjected to Earthquake Ground Motion

Terence Ryan¹, Brian Broderick², Alan Hunt², Jamie Goggins³, Suhaib Salawdeh³

¹Department of Civil Engineering & Materials Science, University of Limerick, Limerick, Ireland

²Department of Civil Engineering, Trinity College Dublin, College Green, Dublin 2, Ireland

^{3,4}Department of Civil Engineering, National University of Ireland Galway, University Road, Galway, Ireland

email: terence.ryan@ul.ie, bbrodrck@tcd.ie, jamie.goggins@nuigalway.ie, suhaib.salawdeh@nuigalway.ie

ABSTRACT: In seismically active areas Concentrically Braced Steel Frames (CBFs) are commonly used in steel frame structures as an economic and effective means of both providing resistance to the lateral loading induced during earthquakes and limiting the associated displacements. Here, an integrated experimental and numerical approach is taken to investigate the performance of CBF's subjected to seismic action of varying intensity.

As part of the BRACED transnational research project funded by the European Commission's Seventh Framework Programme (FP7), a series of shake table experiments on full-scale single-storey CBFs recorded the response of test frames employing various combinations of bracing member sizes and gusset plate connection details to simulated ground motions. These simulated ground motions were scaled to produce elastic response, brace buckling/yielding and ultimately brace fracture.

This recorded experimental data is used to validate a three-dimensional numerical model developed using the OpenSees seismic analysis software. Results from the experimental and numerical models are compared under the key criteria of frame acceleration, lateral drift and brace axial force. The sensitivity of the model to variations in structural and model parameters is assessed and recommendations for future numerical modelling are presented. Results indicate that model performance is sensitive to the initial brace eccentricity applied, with a value of 1.0% of overall brace length providing a more realistic representation of global frame stiffness and drift response than the lower values recommended in literature, but an underestimate of the compression resistance of the brace.

KEY WORDS: Earthquake Engineering; Braced Frames; Gusset Plates; Time-history Analysis, Simulation.

1 INTRODUCTION

Bracing is commonly employed in steel framed buildings to provide lateral resistance and limit lateral displacements during seismic events. In most case, the design resistance of the brace is achieved through non-linear behaviour.

In concentrically braced frames (CBFs) the centre-line of the diagonal bracing coincides with the intersection of the beam and column members of the frame. CBFs provide a means of energy dissipation through the alternate cyclic yielding and post-buckling deformation of their braces, while the inherent stiffness of the structural form serves to minimise non-structural damage and residual deformations.

1.1 Diagonal Frames and V-Frames

CBFs can be subdivided into diagonal frames and v-frames. While both rely on non-linear behaviour of the brace to resist lateral loading, diagonal frames may be designed considering that the design lateral resistance is provided by the tension braces only, whereas in v-frames, the resistances of both the tension and compression members must be considered in seismic design analysis. This study investigates the seismic response of diagonal frames.

1.2 Gusset Plate Connections

In addition to bracing member stiffness, performance of CBFs subjected to strong ground motions is influenced by the connections between the brace and the rest of the frame, which is most commonly a gusset plate connection.

In conventional design, the diagonal bracing members are considered the dissipative elements of the frame, and are designed to yield before failure will occur at the connections. Gusset plate connections must therefore be designed to have tension and compression capacities much larger than the brace and are not considered to contribute to energy dissipation.

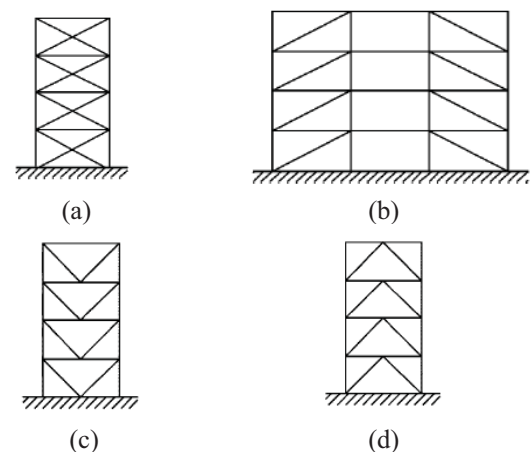


Figure 1. CBFs with diagonal bracings (a),(b) and v-bracing (c),(d) (from Eurocode 8 [1])

In such design, a standard linear clearance (SLC) is provided in the gusset plate. When in compression, global buckling of the brace must be accommodated through the formation of adequate plastic hinges in the gusset plates at either end of the brace to allow out-of-plane member end

rotation. Therefore, the gusset plate cannot be designed to remain elastic during earthquake response, since the plate must yield during the out-of-plane bending experienced during brace compression. The plate must also be sufficiently stiff not to buckle in compression, even in the presence of the plastic hinges, and it must possess sufficient strength not to yield over the Whitmore width [2] when the brace is in tension.

In practice, the requirement for the gusset plate to remain elastic in tension while stable (not buckling) but ductile (allowing the formation of plastic hinges due to out-of-plane bending) in compression so as to facilitate global buckling of the brace can lead to large gusset plates sizes. These stiff plates have been observed to result in local damage to the beam, column and braces in the areas adjacent to the gusset plates [3].

An alternative ‘balanced’ design approach is proposed [3] in which some limited tensile yielding of the gusset plate is allowed during strong ground motion. This is achieved through careful sizing and detailing of the plate, providing an elliptical clearance (EC) in the gusset plate as opposed to a SLC. This approach leads to smaller overall gusset plate dimensions, a shorter effective length and therefore increased plate buckling resistance. Gusset plates designed using both the SLC and EC approaches are considered in this study.

In addition to its out-of-plane and axial stiffness, the behaviour of the gusset plate is influenced by the form of its connection to the other members of the frame. The gusset may be connected to both the beam and the column (CA) or to the beam only (CB) as shown in Figure 2. When modelling CBFs for seismic design analysis, the beam-to-column connection is typically considered to have little or no rotational stiffness, however in the case of connection arrangement CA, the gusset plate can provide significant in-plane rotational resistance at this connection. Both arrangements are considered in this study.

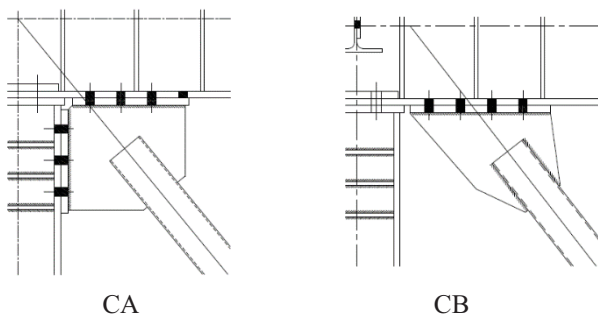


Figure 2. Common gusset plate connection arrangements

1.3 Modelling Approaches

As with all numerical models, when choosing an approach to model CBFs the required accuracy must be considered in the context of model complexity and computational cost.

Three-dimensional finite element models use shell or brick elements to represent the braces and calculate the hysteretic response of the brace using nonlinear material models and large deformation theory. While potentially accurate, these continuum models are not suitable for global time-history analysis of building frames due to large computational expense resulting from the model complexity.

Line-element models use beam-column elements and zero-length elements to model the brace and the gusset plate connections [4]. These models, which require significantly less computation time than continuum models, typically provide an accurate simulation of global behaviour and reasonable predication of many local behaviours.

This study uses the OpenSees seismic analysis software [5] to create a line element model in which the braces, beams and columns are modelled using force-based fibre beam-column elements. These elements are formulated to capture the material and geometric non-linearities experienced during large amplitude earthquake response. The gusset plate connections are represented using nonlinear rotational hinge elements, which assign a specified out-of-plane rotational stiffness to the end of each brace.

2 EXPERIMENTAL STUDY

The models developed in this study are validated against a set of experimental data from the BRACED project [6]. This project involved a series of twelve shake table experiments on a full scale CBF employing various combinations of bracing member cross-section size and gusset plate design configuration and thickness (t_{plate}), as shown in Table 1.

Table 1. Experimental Test Set-ups

Test	Brace	Type	Gusset Plate	
			t_{plate} (mm)	Design
1	80x80x3.0 SHS	CA	12	SLC
2	80x40x3.0 RHS	CA	8	SLC
3	60x60x3.0 SHS	CA	8	SLC
4	150x50x3.0 RHS	CA	12	SLC
5	80x80x3.0 SHS	CA	5	EC
6	150x50x3.0 RHS	CA	4	EC
7	80x40x3.0 RHS	CA	4	EC
8	80x80x3.0 SHS	CB	12	SLC
9	150x50x3.0 RHS	CB	12	SLC
10	60x60x3.0 SHS	CB	4	EC
11	150x50x3.0 RHS	CB	4	EC
12	80x40x3.0 RHS	CB	4	EC

The BRACED test frame was 2.955 m in height with a span of 4.9 m and a total seismic mass of 45 tons (Figure 3). Columns were HE 200 B sections with full in-plane rotation allowed at the base, while the beam was an IPE 400 O section. Tests 1 to 7 featured connection arrangement CA between the brace and the other frame members, with Tests 8 to 12 featured connection arrangement CB. At floor level, brace ends were connected to MTS swivels.

While commonly welded in practice, the gusset plates were bolted to the beam and column to facilitate replacement of the brace specimens between tests.

Each set-up was subjected to table excitation scaled to simulate equivalent earthquake ground motion corresponding to 50%, 10% and 2% chances of exceedance in a 50 year

period. The simulated ground motions were based on the El Centro ground motion record of the 1940 Imperial Valley earthquake. Applied table accelerations were unidirectional along the horizontal x-axis. A range of frame response quantities were recorded using high resolution instrumentation including accelerations, displacements, brace axial forces and strains [6].

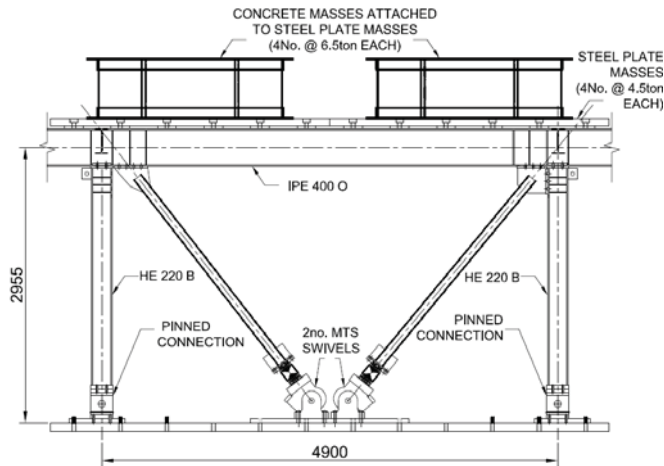


Figure 3. Experimental Set-up

3 OPENSEES REFERENCE MODEL

A reference OpenSees model of the CBF test frame shown in Figure 3 was created capable of representing all of the brace member and gusset plate combinations described in Section 2. This model was employed in nonlinear static pushover analysis and time-history simulations of the seismic response of the test frame. In time history analysis, the simulated ground motions applied to the model are the horizontal accelerations recorded on the shake table during the corresponding experimental test run.

3.1 Members

Braces are modelled using force-based beam-column fibre elements. Results from tensile tests of samples from the relevant brace specimens are used to specify brace yield strengths. Nominal external dimensions of brace cross-sections are used, while wall thicknesses are back-calculated from the measured mean cross-sectional areas of the tested sections.

Uriz, Filippou [7] noted that brace models with two inelastic elements and three integration points per element gave an accurate representation of inelastic buckling behaviour. Hunt [8] noted the effect of varying the number of elements was minimal when examining the monotonic compression and hysteretic performance of test models, but optimum curvature response was observed when using at least four elements per brace.

The reference model in this study has four elements per brace and uses five integration points per element. It was found that further increases to the number of elements and/or integration points resulted in increased processing times without any obvious improvement in model accuracy.

Force-based beam-column fibre elements are used to model the CBF beam and columns. The material properties applied are the nominal values provided by the steel supplier.

3.2 Boundary Conditions

An overview of the modelled test frame is shown in Figure 4. Nodes are numbered and given the prefix 'n'.

Table 2 describes the boundary conditions applied to the model for each degree-of-freedom, in which '1' indicates fully restrained and '0' no restraint for a given degree-of-freedom. The prefixes 'D' and 'R' indicate translation along and rotation about the relevant global axes respectively. Nodes at ground level (n1, n4, n5, n6) are restrained against translation in all directions and are free to rotate about the global y-axis.

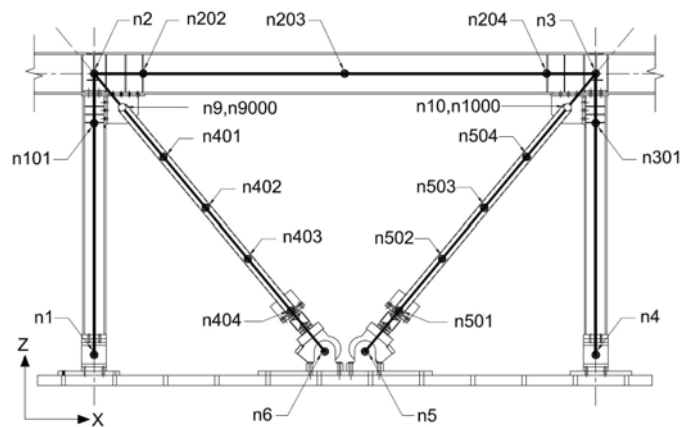


Figure 4. Node Locations, OpenSees Model

The MTS swivel bases at the ends of the braces have an angle range of -30° to $+90^\circ$ in plane from the vertical, and 7° tilt out-of-plane from the vertical. Therefore node n5 and n6 are also free to rotate about the global x-axis due to the swivel action at these locations. Restraint against rotation about the z-axis at the swivel supports is recommended by Hunt [8] and is provided in the reference model.

The nodes at the tops of the columns (n2, n3) are restrained against out-of-plane translation along the global y-axis to represent the ties provided at these locations to adjacent outrigger frames.

Table 2. Reference model boundary conditions

Nodes	Location	Dx	Dy	Dz	Rx	Ry	Rz
n1,4	Column (Base)	1	1	1	1	0	1
n2,3	Column (Top)	0	1	0	1	0	1
n5,6	Swivels	1	1	1	0	0	1

3.3 Beam to Column Connections

RigidLink elements are used between certain nodes at the connections to represent the increased member bending stiffness in these regions (bold elements, Figure 5).

For connection type CA, the beam to column connection is modelled as continuous due to the additional rotational stiffness provided by the gusset plate. For CB, a pinned connection allowing rotation about the global y-axis is provided at the beam-column interface by providing an appropriate 'zeroLength' element between n102 and n1020.

3.4 Initial Brace Eccentricity

Initial eccentricities in the range of 0.01 to 1% of overall brace length are typical of the practical recommendations to induce buckling in modelled compression members [7]. An initial eccentricity of 1.0% is provided at the midpoint of each brace in the reference model to both the global y- (out-of-plane) and z- axes (in-plane). Brace buckling and global frame behaviour was found to be very sensitive to the initial eccentricity applied.

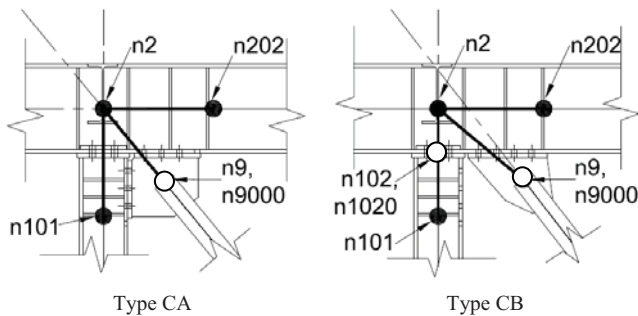


Figure 5. Model Beam to Column Connections CA and CB

3.5 Gusset Plate Connections

The gusset plate connections are modelled using rotational springs defined using “zero-length” elements. The out-of-plane rotational stiffness and plastic moment of resistance of each gusset plate arrangement were calculated from the relevant measured material and geometric properties using the recommendations of Hsiao, Lehman [9].

4 MODEL VALIDATION

Eigenvalue, pushover and time history analyses were performed on the reference model to assess its effectiveness in reflecting the behaviour of the physical test frame.

Table 3. Natural Periods

Test	Natural Period, T_n [s]	
	Experimental	Model
1	0.216	0.183
2	0.235	0.226
3	0.225	0.217
4	0.222	0.191
5	0.219	0.185
6	0.225	0.198
7	0.246	0.230
8	0.226	0.196
9	0.258	0.205
10	0.242	0.242
11	0.220	0.213
12	0.246	0.253

4.1 Structural Period

The structural period of the reference model was calculated for each test set-up using an eigenvalue analysis in OpenSees. The measured and modelled natural periods of each test frame are compared in Table 3. The periods obtained from the model were generally less than those recorded for the corresponding

experimental test. The greater stiffness of the model is likely to be a result of the idealisation of components and connections, which do not account for minor bolt slippage, member imperfections etc. present during experimental testing. The observation that the variation in the measured natural periods between tests is less than expected given the relative sizes of the brace members in different tests suggests that these secondary effects may have been significant. In contrast, the modelled values of T_n do reflect the different brace sizes in the different tests.

4.2 Pushover Analysis

Pushover analyses of the reference model were used to assess the maximum tension and compression forces the braces in the reference model could develop prior to failure. Increasing horizontal displacements under constant gravity loading were applied to the model at roof level in 1.0 mm increments and the brace member internal forces and base reactions generated were recorded. The design buckling and plastic resistances of the model braces could therefore be identified and compared with both the theoretical values calculated from Eurocode 3 [10] and the peak forces recorded during experimental testing.

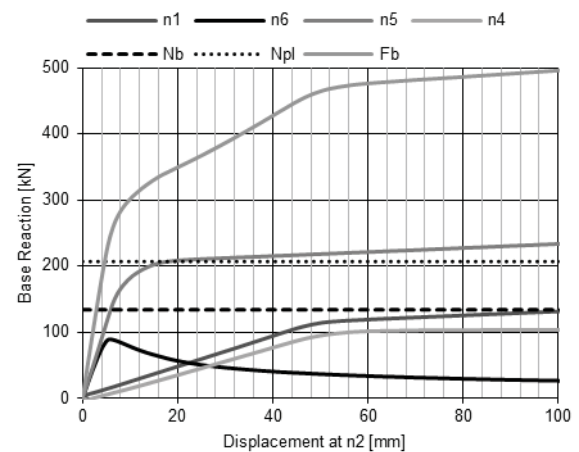


Figure 6. Pushover Analysis, Test 1 ($e = 0.01 L$)

Figure 6 presents the global lateral force-displacement behavior obtained from pushover analysis of the Test 1 frame arrangement with an initial brace eccentricity at the midpoint of each brace, e_{br} of 1.0% of the brace length, L .

The horizontal reactions at the column bases ($n1$, $n4$) and the swivels at the ends of the left and right braces ($n6$, $n5$ respectively) are plotted against the applied displacement at the top of the left column ($n2$). F_b is the recorded base shear, being the sum of the horizontal reactions at the base of the frame. The applied displacement is in the positive X-direction, therefore the left brace is in compression and the right brace is in tension. N_b is the horizontal reaction required at the base of the compression brace at its theoretical buckling resistance, calculated from its measured geometric and material properties using an effective length equal to the actual brace length. N_{pl} is the horizontal reaction at the base of the tension brace when it reaches its theoretical yield point.

In Test 1 the compression brace buckles before reaching its theoretical buckling resistance, while the tension brace reaches its plastic resistance before failure. The sensitivity of brace buckling behavior is discussed further in 5.1.

4.3 Time-History Analysis

Transient dynamic analysis of the reference model was carried out for each test run. The simulated ground motions applied were the horizontal shake-table accelerations recorded during the corresponding experimental run.

A time-step of 0.1953 seconds was specified for the transient analysis to match the rate at which experimental data was recorded. A total of 33 test runs were simulated across the ground motion intensities; 12 at 50%/50, 11 at 10%/50 and 10 at 2%/50. The relative accelerations, % drift at roof level and brace member internal forces were output from the reference model and compared to the experimentally recorded values.

Figure 7 compares OpenSees reference model responses with experimental data from extracts of a sample test run, showing good fidelity between the responses.

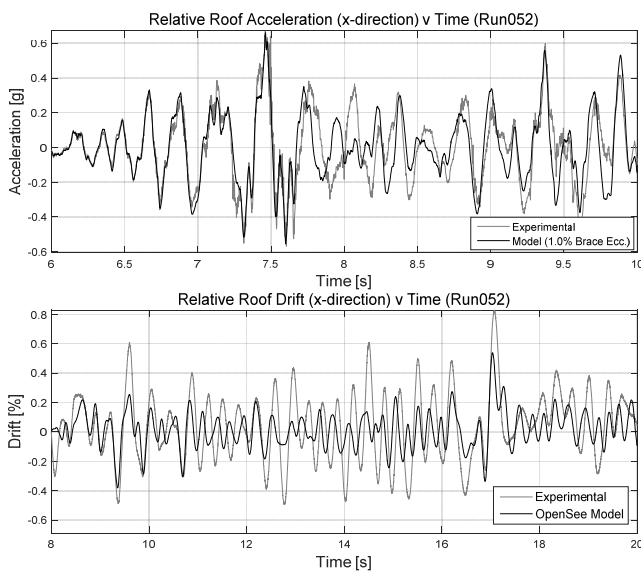


Figure 7. OpenSees and Experimental response comparison; Test3, Run052 (2%/50)

Peak model responses for each run were expressed as a percentage of the corresponding peak experimental values. These values were then compared by ground motion intensity and gusset connection type (Figures 8 to 11).

4.3.1 Relative Acceleration

Peak relative acceleration is more reliably estimated by the reference model in frames with connection type CA for all ground motion intensities. Scatter reduces considerably at the highest ground motion intensity where the response is governed by ultimate resistance of the frame to lateral loads.

4.3.2 % Drift

Peak experimental drift values are underestimated by 30-40% by the reference models for both connection types at ground motion intensities of 50%/50 and 10%/50 (Figure 9). At 2%/50 the % drift appears to be significantly over-estimated by the OpenSees model for frames with CB type connections, while those with CA are further underestimated.

4.3.3 Brace Axial Forces

The reference model underestimates brace peak axial compression forces for both connection types across all

ground motion intensities (Figure 10). Peak brace tension is more accurately represented in all cases (Figure 11). Scatter reduces in both sets of results as ground motion intensity increases for the reason outlined in 4.3.1.

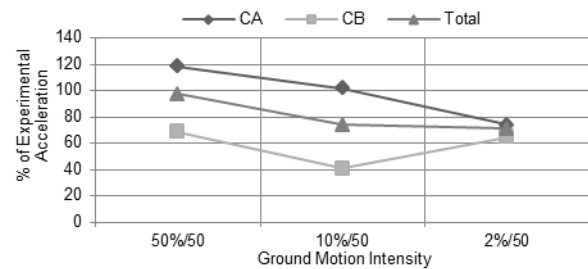


Figure 8. Peak Relative Acceleration Comparison

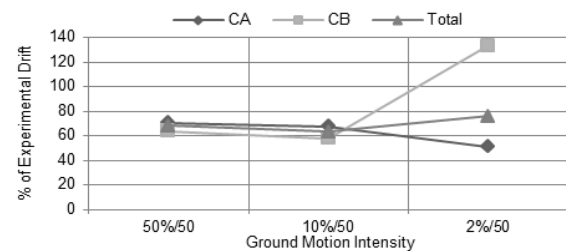


Figure 9. Peak % Drift Comparison

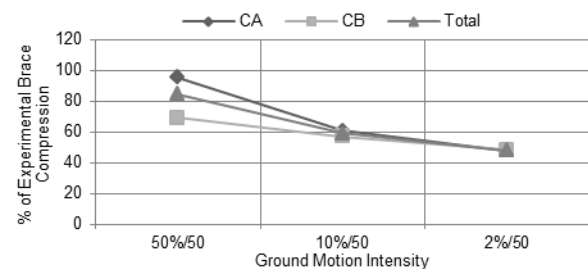


Figure 10. Peak Brace Compression Comparison

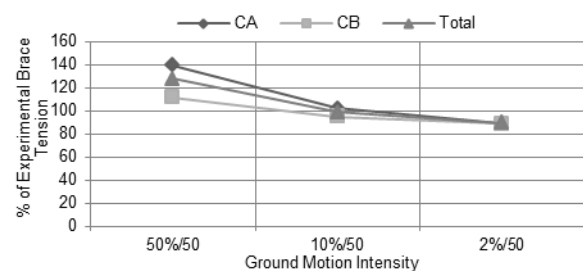


Figure 11. Peak Brace Tension Comparison

5 PARAMETRIC STUDY

5.1 Initial Brace Eccentricity

The sensitivity of the model to the initial eccentricity applied to the braces was considered. Pushover analyses of all twelve test set ups were carried out for eccentricities from 1.0% to 0.1% of the total brace length applied mid-span to both in-plane and out-of-plane directions (convergence failures were commonly observed for most test set-ups when the eccentricity was reduced below 0.1%).

Peak axial compression in the brace for each test set-up was obtained and compared to the theoretical buckling capacity of the member from Eurocode 3 assuming pinned connections at each end of the brace (Figure 12).

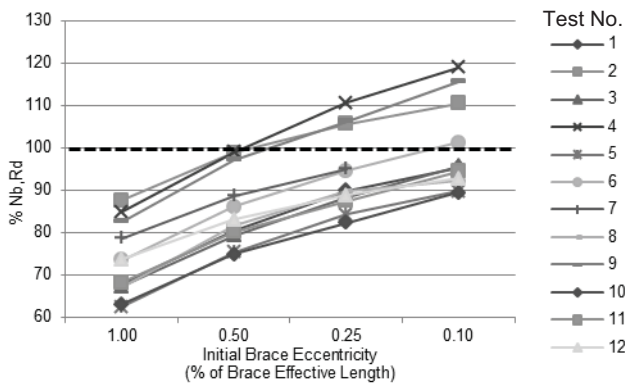


Figure 12 Percentage of theoretical buckling resistance realised v Initial model brace eccentricity

Reducing the eccentricity increased the compression generated in the modelled brace prior to buckling. An eccentricity of 0.1% achieved a mean peak compression force of 95% of the theoretical buckling capacity in the brace compared with 73% at an eccentricity of 1.0%.

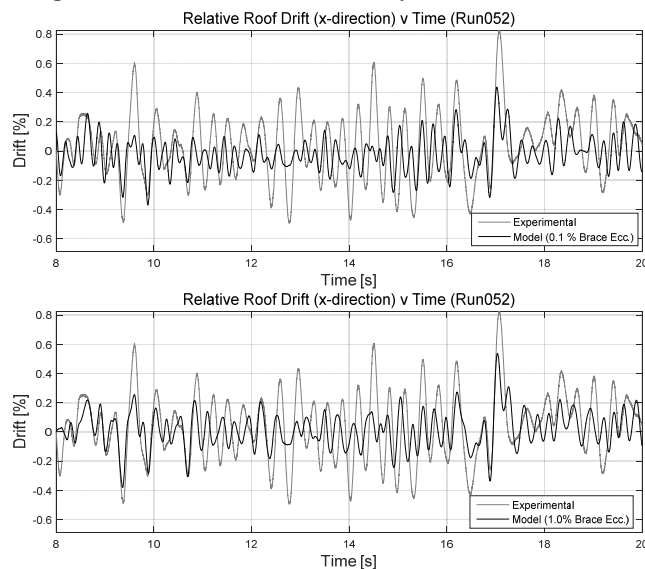


Figure 13 OpenSees drift responses compared for 1.0% and 0.1% initial brace eccentricities

Eigenvalue analyses confirmed that reducing the eccentricity also reduced the natural period of the modelled frame i.e. increased the stiffness. This reduction was more noticeable in frames with CA type connections.

Inspection of time-history analyses found that reducing the brace eccentricity to 0.1% lead to greater underestimation of drift (see Figure 13). Specifically, reducing brace eccentricity from 1.0% to 0.1% lead to the average under-estimation of peak drift values increasing from 21% to 32%.

Although pushover tests suggested minimal changes in behaviour when applying the eccentricity along the global y-axis (out-of-plane) only, subsequent transient analysis found that applying the eccentricity about one axis only also lead to greater underestimation of the drift response.

5.2 Gusset Plate Model

The impact of using a force-based element to represent the gusset plate connection was examined. It was found that this method provided similar global and local responses to the

rotational hinge used in the reference model. In addition, the reference model produced fewer convergence failures when the rotational hinge method was used.

6 CONCLUSIONS

The OpenSees modelled response of a test CBF was observed to be stiffer than the experimentally observed response, and the model appears to generally underestimate the experimental drift response. For CBFs where the brace is connected to both the beam and the column (CA connections) the modelled peak drift was 51 to 71 % of the experimentally observed value. For CB connections, modelled drift was 58 to 64 % of the experimental values at lower ground motion intensities but rose to 133 % at intensities of 2%/50. The lower drifts are consistent with the shorter natural period of the model.

The reference model appears significantly more accurate at predicting peak relative accelerations in CBFs with CA connections at lower ground motion intensities.

Peak brace compression was consistently underestimated by the reference model and was found to be sensitive to the initial eccentricity applied to the brace. Reducing initial brace eccentricity to 0.1% of the brace length improves prediction of peak brace compression forces but also increases frame stiffness leading to greater underestimation of drift.

Applying an eccentricity of 1% of the overall brace length appeared to best represent the combined drift and forces generated in the test frames.

Peak tension forces appear to be overestimated at lower ground-motion intensities but are typically within 10% of the experimentally recorded values for higher intensity ground motions.

REFERENCES

- [1] CEN, EN 1998-1:2004, Eurocode 8: Design of Structures for Earthquake Resistance-Part 1: General Rules, Seismic Actions and Rules for Buildings., European Committee of Standardisation: Brussels, 2004.
- [2] AISC, *Steel Construction Manual*. Chicago, Illinois: American Institute of Steel Construction, Inc. 14th Edition, 2011.
- [3] Roeder, C.W., E.J. Lumpkin, and D.E. Lehman (2011), 'A balanced design procedure for special concentrically braced frame connections'. *Journal of Constructional Steel Research*. 67(11): p. 1760-1772.
- [4] Uriz, P. and S.A. Mahin, *Toward Earthquake-Resistant Design of Concentrically Braced Steel-Frame Structures*, Pacific Earthquake Engineering Research Center (PEER): University of California, Berkeley, 2008.
- [5] OpenSees. *OpenSees Version 2.4.5*. 2008 [cited 2016 January]; <<http://opensees.berkeley.edu/OpenSees/user/download.php>>.
- [6] Hunt, A.D. and B.M. Broderick (2012), 'Seismic testing of concentrically braced frame models for the BRACED project'. *Stessa 2012: Proceedings of the 7th International Conference on Behaviour of Steel Structures in Seismic Areas*: p. 165-170.
- [7] Uriz, P., F.C. Filippou, and S.A. Mahin (2008), 'Model for cyclic inelastic buckling of steel braces'. *Journal of Structural Engineering-Asce*. 134(4): p. 619-628.
- [8] Hunt, A., (2013), *Design and Analysis of Concentrically Braced Steel Frames under Seismic Loading*, Thesis, Ph.D. Thesis, Department of Civil, Structural & Environmental Engineering, University of Dublin, Trinity College, Ireland.
- [9] Hsiao, P.-C., D.E. Lehman, and C.W. Roeder (2012), 'Improved analytical model for special concentrically braced frames'. *Journal of Constructional Steel Research*. 73(0): p. 80-94.
- [10] CEN, EN 1993-1-1:2005, Eurocode 3: Design of Steel Structures - Part 1.1: General Rules and Rules for Buildings European Committee of Standardisation: Brussels, 2005.

Seismic Design and Performance of Non-structural Elements

Suhaib Salawdeh^{1,2}, Jamie Goggins^{1,2,3}

¹*Civil Engineering, College of Engineering & Informatics, National University of Ireland, Galway, Ireland.*

²*Centre for Marine and Renewable Energy Ireland (MaREI), Galway, Ireland.*

³*Ryan Institute, Galway, Ireland*

email: suhaib.salawdeh@nuigalway.ie, jamie.goggins@nuigalway.ie

ABSTRACT: The non-structural components in buildings represent a high percentage of the construction cost and can reach up to 85% of the total capital cost. Performance of non-structural elements in past earthquakes have dramatically illustrated their vulnerabilities. Failure of these components in an earthquake can cause a very high economic cost, can disrupt the functionality of buildings and facilities and can pose a safety hazard to occupants from falling elements. Apart from falling hazards, it can obstruct the safe movement of occupants evacuating buildings and can hamper rescue efforts.

For the above reasons, building codes and standards organizations, owners and occupants, construction industry manufacturers and several design disciplines are focusing on this topic. In this paper, a literature review of the performance of non-structural components in recent earthquakes will be carried out. Then, the design philosophy and design provisions of non-structural elements in EC8 will be discussed and compared to several international seismic codes. Finally, the future extension plans of the reaction frames at the strong floor area in NUI Galway heavy structures research laboratory to perform cyclic tests on different types of claddings will be illustrated.

KEY WORDS: Non-structural elements, design codes, cladding systems, earthquake design.

1 INTRODUCTION

Non-structural elements are those components within the structure that are not part of the primary load bearing system. According to FEMA E-74 [1], non-structural components can be divided into three broad categories:

1. Architectural components which are built-in non-structural components that form part of the building, such as partitions, ceilings, storefronts, glazing, cladding, veneers, chimney, fences, and architectural ornamentation.
2. Mechanical, Electrical, and Plumbing (MEP) components which are built-in non-structural components that form part of the building, such as pumps, chillers, fans, air handling units, motor control centres, distribution panels, transformers, and distribution systems including piping, ductwork and conduit.
3. Building contents which are the non-structural components belonging to occupants of the building such as furniture, fixtures, equipment, and contents such as shelving and book cases, industrial storage racks, retail merchandise, books, medical records, computers and desktop equipment, wall and ceiling mounted TVs and monitors, file cabinets, kitchen, machine shop or other specialty equipment, industrial chemicals or hazardous materials, museum artifacts, and collectibles.

Whittaker and Soong [2] found that the structural components of a commercial building account for approximately 15-25% of the original construction cost, while the built-in non-structural (architectural and MEP) components account for the remaining 75-85% of the cost as illustrated in Figure 1.

Steinbrugge and Schader [3] carried out a survey of 25 damaged commercial buildings after the 1971 San Fernando Earthquake and found that the structural damage was limited to 3% of the total property losses, while MEP loss was 7%,

the interior finishes loss was 56% and the rest 34% of the total loss was due to exterior finishes damage.

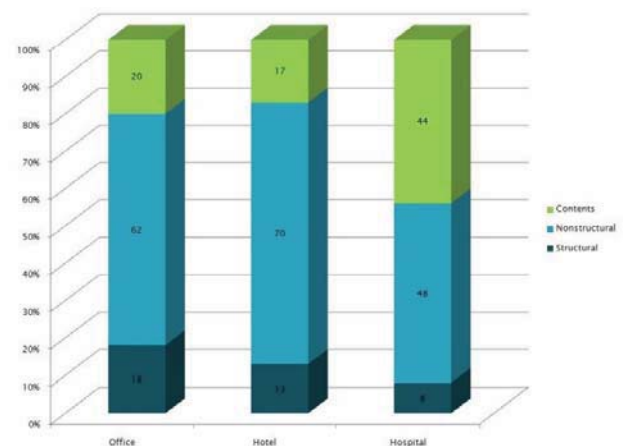


Figure 1: Typical investments in building construction [2].

2 CODE PROVISIONS

Many factors affecting the performance of a non-structural elements such as the response of its supporting building, ground motion, size and weight of the non-structural elements, their location in the building (for example, the first floor or roof), flexibility of the component and importance of the non-structural element.

Architectural components and the attachment of these components to the structure should be considered in the seismic design. For noncritical MEP systems and components, the design is limited to bracing and attachment to the structure without evaluating the capacity of the components or system

itself. Important components such as fire sprinkler piping systems, should be considered in the seismic design as they are expected to remain in place, sustain limited damage and function following an earthquake.

The equivalent lateral force method is the basis of most seismic codes provisions for non-structural element design. In this approach, the lateral seismic force is found as a fraction of the weight of the non-structural element.

2.1 Eurocode 8

2.1.1 Design seismic loads

EC8 [4] suggests that all non-structural elements of buildings that might, in case of failure, cause risks to persons or affect the main structure of the building or services of critical facilities, shall, together with their supports, be verified to resist the design seismic load, F_a , shown in Equation (1).

$$F_a = \frac{S_a \gamma_a}{q_a} W_a \quad (1)$$

where,

F_a is the horizontal seismic force, acting at the centre of mass of the non-structural element in the most unfavourable direction;

W_a is the weight of the element

γ_a is the importance factor of the element which ranges from 1.5 for important and/or hazardous elements to 1.0 for all other elements

q_a behaviour factor for non-structural elements equal to either 1.0 or 2.0.

- Behaviour factor of 1.0 is used for cantilever parapets or ornamentation, signs and billboards, chimneys, and tanks is assigned as 1.0
- Behaviour factor of 2.0 is used for exterior and interior walls, partitions and facades, anchorage elements for false ceilings and light fixtures.

S_a is the seismic coefficient applicable to non-structural elements shown in Equation (2)

$$S_a = \frac{a_g}{g} S \left[\frac{3 \left(1 + \frac{z}{H} \right)}{1 + \left(1 - \frac{T_a}{T_1} \right)^2} - 0.5 \right] \quad (2)$$

a_g/g is the ratio of the design ground acceleration on type A ground, a_g , to the acceleration of gravity g

S is the soil factor

T_a is the fundamental vibration period of the non-structural element

T_1 is the fundamental vibration period of the building in the relevant direction

Z is the height of the non-structural element above the level of application of the seismic action

H total height of the building

For a rigid non-structural element, ground storey ($z = 0.0$) input acceleration will be the same as the peak ground acceleration and for the non-structural element attached at the roof ($z = H$) the input acceleration is 2.5 times the ground acceleration.

For non-structural elements of irregular structure, great importance or of a particularly dangerous nature, the seismic analysis shall be based on a realistic model of the relevant structures and on the use of appropriate response spectra derived from the response of the supporting structural elements of the main seismic resisting system.

2.1.2 Drift demands

Due to horizontal loads induced by seismic activity, the structure will deflect horizontally. Codes call this lateral deflection as drift and limit it to requirements for the drift of one level (horizontal movement of one level with respect to the one above or below). A good seismic performance during earthquakes for external and internal non-structural walls can be ensured in two ways,

1. by limiting inter-storey drift of the supporting structure
2. by designing the elements to accommodate the expected lateral displacement without damage

The criteria chosen depend upon the importance of the building and how it is expected to perform during the earthquake.

For normal structures, connections should be designed to accommodate relative displacements due to design seismic loads. If linear analysis is performed, the displacements induced by the design seismic action shall be calculated on the basis of the elastic deformations of the structural system by means of the following simplified expression

$$d_s = q_d d_e \quad (3)$$

where

d_s is the displacement of a point of the structural system induced by the design seismic action.

q_d is the displacement behaviour factor, assumed equal to q unless otherwise specified

d_e is the displacement of the same point of the structural system, as determined by a linear analysis based on the design response spectrum in accordance EC8.

However, in absence of elastic analysis, storey drift can be considered as the basis to compute the relative displacement which can be computed from storey drift of the structure.

Second-order effects ($P-\Delta$ effects) need not be taken into account if the following condition is fulfilled in all storeys

$$\theta = \frac{P_{\text{tot}} \cdot d_r}{V_{\text{tot}} \cdot h} \leq 0.10 \quad (4)$$

where

θ is the inter-storey drift sensitivity coefficient

P_{tot} is the total gravity load at and above the storey considered in the seismic design situation

d_r is the design inter-storey drift, evaluated as the difference of the average lateral displacements ds at the top and bottom of the storey under consideration and calculated as shown in Equation (3)

V_{tot} is the total seismic storey shear; and

h is the inter-storey height

If $0.1 < \theta \leq 0.2$, the second-order effects may approximately be taken into account by multiplying the relevant seismic action effects by a factor equal to $1/(1 - \theta)$. The value of the coefficient θ shall not exceed 0.3.

EC8 limits the inter-storey drifts as follows:

- for buildings having non-structural elements of brittle materials attached to the structure: $d_r v \leq 0,005h$
- for buildings having ductile non-structural elements: $d_r v \leq 0,0075h$
- for buildings having non-structural elements fixed in a way so as not to interfere with structural deformations, or without non-structural elements: $d_r v \leq 0,010h$

where

d_r d_r is the design inter-storey drift action.

h h is the storey height

v is the reduction factor which takes into account the lower return period of the seismic action associated with the damage limitation requirement.

The value of the reduction factor v may also depend on the importance class of the building.

The values to be ascribed to v for use in a country may be found in its National Annex. Different values of v may be defined for the various seismic zones of a country, depending on the seismic hazard conditions and on the protection of property objective. The recommended values of v are 0.4 for importance classes III and IV and $v = 0.5$ for importance classes I and II.

2.2 International Building Code (IBC [5])

The horizontal seismic design force (F_a , called F_p in IBC) shall be applied at the component's centre of gravity and distributed relative to the component's mass distribution and shall be determined in accordance with Equation (5). For non-structural components IBC refers to Chapter 13 in ASCE 7 (2005).

$$F_p = \frac{0.4a_p S_{DS} W_p}{\left(\frac{R_p}{I_p}\right)} \left(1 + 2\frac{z}{h}\right) \quad (5)$$

$$0.3S_{DS}I_pW_p < F_p < 1.6S_{DS}I_pW_p$$

where

W_p is component operating weight.

S_{DS} is spectral acceleration for short period structures = $(2/3)S_{MS}$; $0.4S_{DS}$ represents the peak ground acceleration.

a_p is component's amplification factor which varies from 1 to 2.5. For example, for exterior non-structural wall elements and body of wall panel

connections a_p can be taken as 1.0 and for fasteners of the connecting system it can be taken as 1.25.

I_p is component's importance factor that varies from 1 for normal components to 1.5 for components containing hazardous substances.

R_p is component response modification factor that varies from 1 to 12. For exterior non-structural wall elements and body of wall panel connections R_p can be taken as 2.5 and for fasteners of the connecting system it can be taken as 1.0.

Equation (5) computing design seismic force assuming that input acceleration at the ground storey ($z = 0.0$) is equal to the peak ground acceleration similar to EC8. At the roof level ($z = H$), the input acceleration is equal to three times the peak ground acceleration while it is 2.5 times the ground acceleration in EC8.

A major difference in EC8 approach from IBC (IBC 2012) is that it accounts for ratio of period of element to that of structure as shown in Equation [2] which takes into account the relative flexibility of non-structural element as compared to that of its supporting structure.

Components must be anchored to the structure. For many components, the anchor bolt may be the yielding element in the load path. Anchors in concrete or masonry must be designed to have ductile behaviour or to provide a specified degree of excess strength.

2.2.1 Exterior Non-structural Wall Elements and Connections according to IBC 2012

Exterior non-structural wall panels or elements that are attached to or enclose the structure shall be designed to accommodate the seismic relative displacements provided in design codes and movements due to temperature changes. These elements shall be supported by means of positive and direct structural supports or by mechanical connections and fasteners in accordance with the following requirements taken from IBC 2012:

- Connections and panel joints shall allow for the storey drift caused by relative seismic displacements (D_p), or 13 mm, whichever is greatest.
- Connections to permit movement in the plane of the panel for storey drift shall be sliding connections using slotted or oversize holes, connections that permit movement by bending of steel, or other connections that provide equivalent sliding or ductile capacity.
- The connecting member itself (bodies of connectors) shall have sufficient ductility and rotation capacity to preclude fracture of the concrete or brittle failures at or near welds.
- All fasteners in the connecting system such as bolts, inserts, welds, and dowels and the body of the connectors shall be designed for the force (F_p) determined by Equation [3] with proper values of R_p , and a_p , and applied at the centre of mass of the panel.

- e. Where anchorage is achieved using flat straps embedded in concrete or masonry, such straps shall be attached to or hooked around reinforcing steel or otherwise terminated so as to effectively transfer forces to the reinforcing steel or to assure that pull-out of anchorage is not the initial failure mechanism.

2.2.2 Connections parameters

Six properties are the main parameters which characterize the seismic behaviour of the connection; they can be measured through monotonic and cyclic tests as follows:

- strength: the maximum force that can be resisted by the connection
- ductility: maximum plastic deformation divided by to the yielding deformation
- dissipation: energy dissipated through the load cycles related to the correspondent perfect elastic-plastic cycle
- deformation: ultimate deformation reached at failure
- decay: the loss of strength through the load cycles compared to the force level
- damage: residual deformation after unloading compared to the maximum displacement and/or details of failure or rupture

2.3 Limitations

There are significant deficiencies within the provisions of EC 8 and of other codes with regard to the design of non-structural components, Hoffmeister et. al.[6]:

- All codes assume the first fundamental period and linear shape for the seismic forces acting on non-structural components. This is not true for irregular structures. This concerns torsional effects as well as the contribution of higher lateral modes, in particular if their periods are close to the fundamental period of the component [7].
- The response of the supporting structure with regard to the elastic design response spectrum is not considered; only the peak ground acceleration and the soil factor are taken into account instead;
- There is currently no guidance on how to consider interactions between structural and non-structural systems. In many practical design situations, decoupled analyses are conducted using a “cascading” approach. In this approach, the dynamic properties and the floor responses of the primary structure are estimated without considering the interaction with the non-structural component. The structural response at the attachment level is then considered as the input motion for the estimation of the response of the non-structural component. One of the most popular of these cascading methods is the Floor Response Spectrum (FRS) method.

- The non-elastic response of the supporting structure is neglected in FRS method. It is to be expected that the non-linear response changes the FRS significantly;

To illustrate the FRS, the acceleration transmitted from supporting structure is governed by the elastic vibration modes and corresponding frequencies. The elastically responding structure acts like a band-pass filter, the acceleration on the structure can be determined by

- Linear time step analysis resulting in a time history of acceleration at any point within the structure; these time histories are then transformed into elastic response spectra, each valid for a particular floor level;
- Using filter functions to transform the ground acceleration response spectra into response spectra at different levels of the structure as shown in Figure 2.

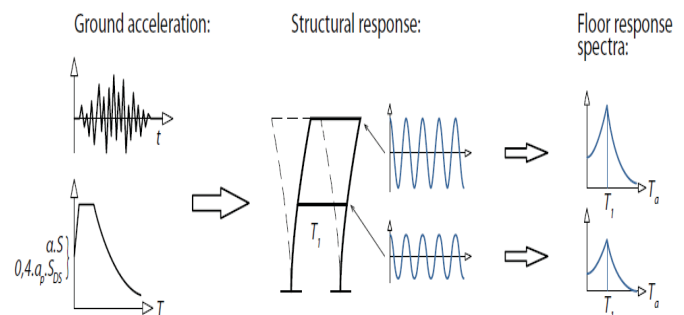


Figure 2: Principle of the determination of floor response spectra for elastically responding structures [6].

3 Cladding methods

For framed structures different cladding types can be used:

1. Heavy cladding systems consisting of precast concrete. Movement should be accommodated by sliding or ductile connections. In highly seismic areas ductile connections are commonly used.
2. Intermediate weight cladding systems consisting of glass fibre reinforced concrete (GFRC). Pre-cast concrete is approximately three to four times heavier than GFRC, so that seismic forces for GFRC are reduced when compared to precast panels. GFRC panels are installed in a similar way to pre-cast concrete. However, thermal movement of concrete is approximately half of GFRC material leading to limitation in size. GFRC thermal movement must be allowed for in fixing through the use of Teflon washers or other means. When this requirement is accommodated, it will be useful from a seismic viewpoint.
3. Lightweight cladding systems. They can consist of
 - a. Glazing and metal insulated panels alternating horizontally. Sometimes the whole elevation can be covered with Panels only. The panels normally are fabricated in factories. It is assembled and integrated from exterior facing, insulation and interior finish. They

can be as well a built on site spandrel wall from steel studs covered by metal facing.

- b. Curtain wall system consists of metal and glass. Same glazing is normally used for opaque and transparent areas, with dark or reflective glass backed-up by insulation.

Slip joints between adjacent panels can be provided in curtain walls to accommodate in-plane racking motions in seismic regions.

A common practice that curtain walls have framing rigidly attached to the structure framing system. When the earthquake forces cause the structure to drift, the metal frame may be impacted by the corners of the glass. Because of that adequate clearances should be maintained between frames and glass (these clearances can be estimated by analysis provided in the seismic codes). In this technique no need to provide connections that allows the movement of curtain walls independently from the main lateral resistance structure. Flexible gaskets can be used to retain glass within the frame and clearance between glass and metal frame can be achieved by inserting spacers such as small rubber blocks. The rubber spacers and flexible gaskets allow for this significant movement of the glass within the metal frame and the rubber blocks must be compressed before the impact between glass and the metal frame.

In-plane forces protection is primarily from seismic forces while out-of-plane protection is from wind effects.

Brueggman et. al. [8] conducted dynamic racking tests simulating seismic movements that could be imposed upon a curtain wall system as a result of inter-storey drifts coupled with air leakage tests. This investigation led to the development of an "Earthquake-Isolated Curtain Wall System (EICWS)". This system de-couples each storey level of the system structurally from adjacent floor levels. The response of the isolated curtain wall frames to a number of modes of vibration is shown in Figure 3. The seismic "decoupler" joint can accommodate relative inter-storey movements while maintaining a building envelope weather seal as shown in Figure 4.

4 Testing proposal at NUIG

Cyclic test of a non-structural wall cladding can be carried out at NUIG at the strong floor area and extended reaction frames in the heavy structures research laboratory. Cyclic tests are preferable more than monotonic tests, as the capacity degrades under back and forth movements (e.g., loadings from earthquakes). To understand the behaviour will do two monotonic push-over tests (one in each direction), followed by cyclic tests. Many cyclic loading protocols have been evolving to create a realistic seismic loading condition for laboratory testing of non-structural element systems. The loading rate is small enough to consider these protocols as

"static" or "quasi-static", while having complete reversal of load in a cyclic manner.

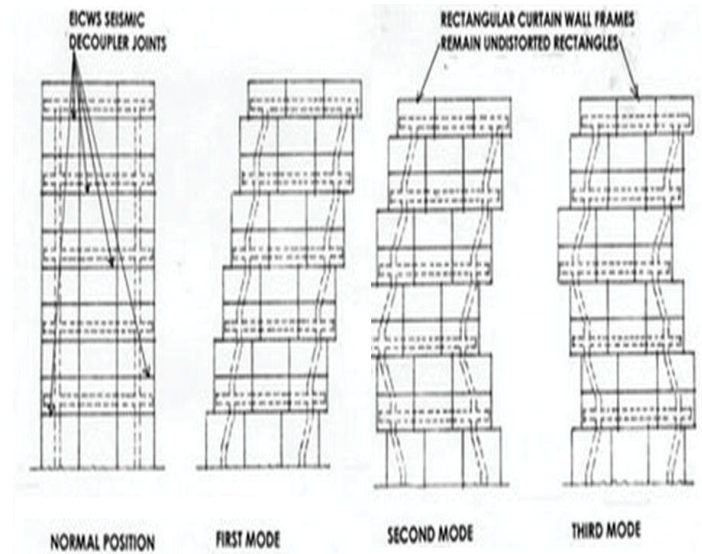


Figure 3: Diagrammatic response at first, second and third modes of vibration in earthquake-isolated curtain wall system schematic. [8]

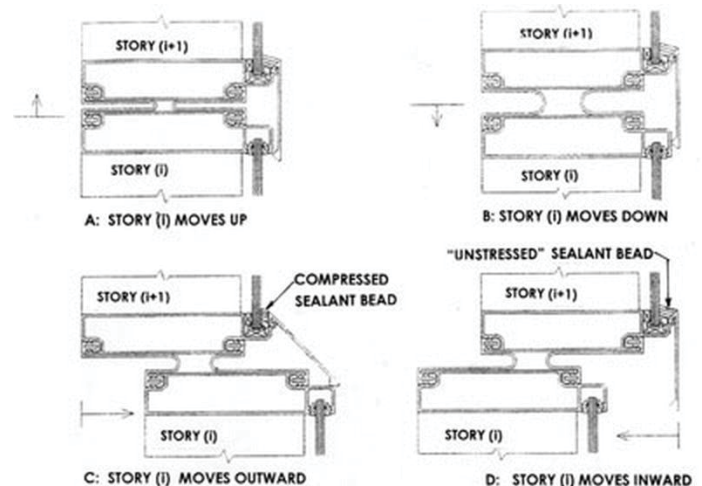


Figure 4: Decoupler joint details in The Earthquake-Isolated Curtain Wall System (EICWS). [8]

NUIG heavy structures laboratory can accommodate testing panels with a different lengths and widths and wide range of thicknesses.

To find how components behave during testing and support the development of models to predict the behaviour of systems, displacement, strain, and rotation sensors will be placed in a strategical manner to achieve the goals.

Two options are proposed by NUIG for testing:

Option 1: A schematic diagram for Option 1 testing at NUIG structures lab is shown in Figure 5. In this option the panels are placed vertically similar to the as-built situation. The test set-up can accommodate panels with a maximum length of 4.5 m and a width of 0.9 m. Up to three stacked panels of

dimensions of 4.5m x 0.9m can be tested. In this option, the panels are reduced-scaled to accommodate the testing frame. To quantify size effects numerical modelling for panels could be carried out using a finite element program, such as Abaqus [9] or Ansys [10]. Moreover, physical testing of individual components, such as connections, could also be carried out to assure that it is behaving as required and accommodate the lateral loads properly.

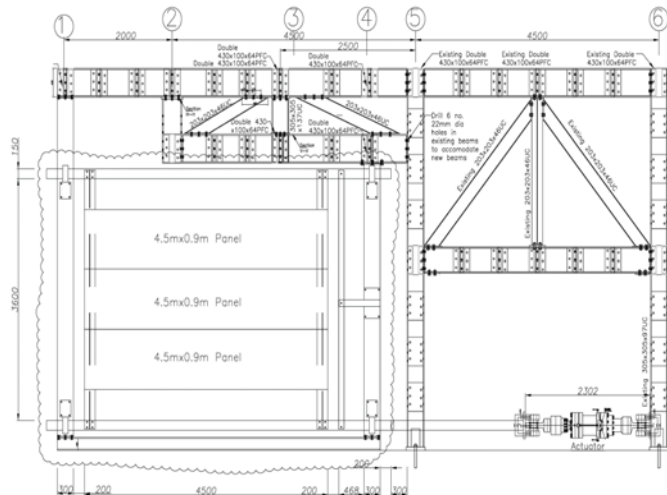


Figure 5: Test setup for the first option of proposed cladding testing frame at structure labs at NUIG.

Option 2: In the second option, which is shown at Figure 6, the panels are fixed to a frame lying flat to the ground and the panels are placed horizontally. This option can accommodate testing panels with a maximum length of 6 m and a width of 1.2 m. Up to three panels of dimensions of 6m x 1.2m can be tested simultaneously. An advantage of this option that we can accommodate larger panel sizes minimising size effects. A disadvantage is that the panels are laid horizontally and the gravity loads will not be taken it account properly while testing, unlike the as-built situation proposed in Option 1.

5 CONCLUSION

Safety hazards and economical costs for the performance of non-structural elements in earthquakes were mentioned. A comparison between the design philosophy and design provisions of non-structural elements in EC8 and IBC was carried out.

A brief illustration for the future extension plans of the reaction frames at NUI Galway heavy structures research laboratory to perform cyclic tests on different types of claddings was discussed.

ACKNOWLEDGMENTS

This material is in part based upon works supported by the Science Foundation Ireland Marine Renewable Energy Ireland (MaREI) research centre under Grant No. 12/RC/2302. The second author would like to acknowledge the support of Science Foundation Ireland through the Career Development Award programme (Grant No. 13/CDA/2200).

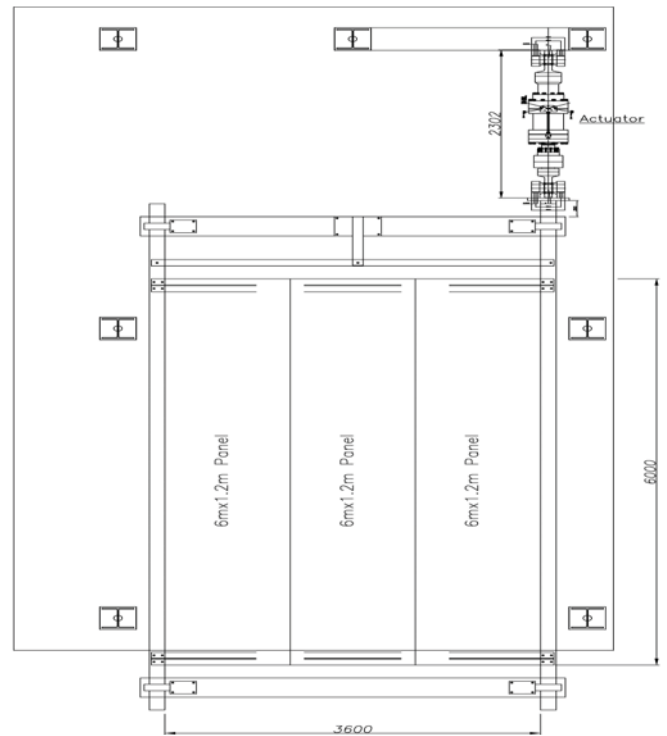


Figure 6: Test setup for option 2 cladding testing frame where the panels are laid (installed) horizontally.

REFERENCES

- [1]. FEMA E-74, *Reducing the Risks of Nonstructural Earthquake Damage, A Practical Guide*. Fourth Edition ed. 2012.
- [2]. Whittaker, A.S. and T.T. Soong. *An overview of nonstructural component research at three U.S. earthquake engineering research centers*. in *Seminar on Seismic Design, Performance, and Retrofit of Nonstructural Components in Critical Facilities*. 2003. Redwood City, California.: Applied Technology Council, ATC-29-2, pp. 271-280.
- [3]. Steinbrugge, K.V. and E.E. Schader, *Earthquake damage and related statistics In San Fernando, California, Earthquake of February 9, 1971*. U.S. Dept. of Commerce, National Oceanic and Atmospheric Administration, San Fernando, California, earthquake of February 9, 1971, 1973. 1A: p. pp. 709-710 and 713.
- [4]. CEN, *Eurocode 8, design of structures for earthquake resistance – Part 1: General rules, seismic actions and rules for buildings*. 1998, EN 1998.
- [5]. IBC, *2012 International Building Code*. 2012: Falls Church, VA, USA.
- [6]. Hoffmeister, M. Gündel, and M. Feldmann, *Floor Response Spectra for Dissipative Steel Supports of Industrial Equipment*, in *COMPDYN 2011 - 3rd International Conference on Computational Methods in Structural Dynamics & Earthquake Engineering*. 2011: Greece.
- [7]. Holschoppen B., *Contribution to the design of industrial plants on seismic load*, in *Department of Structural Mechanics*. 2009, Department of Structural Mechanics, RWTH Aachen University.
- [8]. Brueggeman, J.L., R.A. Behr, H. Wulfert, A.M. Memari, and P.A. Kremer, *Dynamic Racking Performance of an Earthquake-Isolated Curtain Wall System*. *Earthquake Spectra*, 2000. 16(4): p. 735-756.
- [9]. ABAQUS, *User manual, version 6.5*. Hibbitt, Karlsson and Sorensen Inc. 2006.
- [10]. ANSYS, *Version 6.1*, ANSYS Inc. 2002.

Stress analysis of welded steel catenary risers

Ronan J. Devaney¹, Padraic E. O'Donoghue^{2,3}, Sean B. Leen^{1,3}

¹Mechanical Engineering, College of Engineering and Informatics, NUI Galway, University Road, Galway, Ireland.

²Civil Engineering, College of Engineering and Informatics, NUI Galway, University Road, Galway, Ireland.

³Ryan Institute for Environmental, Marine and Energy Research, NUI Galway, University Road, Galway, Ireland.

ABSTRACT: The use of steel catenary risers in offshore oil and gas production has increased significantly in recent years due to their distinct advantages over flexible risers. The motivation for this paper is to develop a detailed assessment approach with respect to steel catenary risers, thus eliminating the requirement for overly conservative factors of safety. This paper presents a global-local finite element modelling approach, with the Flexcom dynamic analysis package used to determine the global load quantities for two ultra-deepwater free hanging steel catenary risers. These results then feed into a local model using Abaqus with the analysis focusing on the failure susceptible regions such as in the vicinity of a girth weld. The methodology accounts for the geometrical discontinuities of the weld and the different mechanical properties of the parent material, weld metal and heat affected zone, which result in fatigue hot-spots for dynamic structures such as steel catenary risers.

Material properties for two line pipe steels, a current generation X65 and a next generation X100 are investigated in the local analysis. Two pipe wall thicknesses are examined, with the weld geometry being different for each and it is shown that this weld detail can lead to significantly different stress concentrations. X100 is shown to be superior to X65 with respect to yielding for both geometries.

KEY WORDS: Weld; Finite element; Steel catenary riser; Energy; Structure; Offshore.

1 INTRODUCTION

1.1 Background

The specification of steel catenary risers (SCRs) for offshore oil and gas projects has increased significantly, due to their advantages in addressing the key challenges of deepwater riser design, namely, collapse capacity, weight limitations, corrosion and temperature resistance.

Fatigue performance is one of the main drivers in SCR design, where design codes ([1], [2]) recommend a factor of safety of 10 for riser service life, often equal to more than 250 years. To design the next generation SCR systems, a greater understanding of the conditions experienced at locations susceptible to fatigue failure is required. In particular, ensuring the integrity and consistency of the welds in a SCR is one of the primary obstacles to improving fatigue life. The geometrical discontinuity and material mismatch, resulting from the welding process, are typically the determining factors in SCR fatigue performance for a given design [3].

The motivation for this research is to develop a detailed assessment approach with respect to SCR welds, thus eliminating the requirement for over-conservative factors of safety. By implementing a more efficient design methodology for SCRs, it will be possible to further exploit the weight reduction and increased capacity facilitated by the development of next generation high strength steels.

The resulting SCR weight reductions have the potential to deliver significant cost savings by minimising the buoyant support required from floating production facilities and increasing pipe laying productivity. The improvement in the SCR design capacity will allow for economically viable access to new ultra-deepwater (greater than 1524 m) resources

by enabling the use of more conventional and cost effective riser technologies.

1.2 Modelling

Global-local modelling is an invaluable technique for detailed analysis of a region of interest on a large dynamic structure. This technique has previously been applied to SCRs by Hu and co-workers [4] to model in detail the seabed-riser interaction at the touchdown zone. A further advantage to global-local modelling is the potential for the application of complex fatigue failure criteria, such as that developed by Chaboche et al [5], to a local region of a large structure such as an SCR.

In the present work, global-local modelling is used to allow for accurate assessment of the resulting stress-strain history at a welded joint of a large scale SCR system due to in-service conditions. The detailed local girth model incorporates a weld geometry with separate material properties applied to the parent material (PM), heat affected zone (HAZ) and weld metal (WM), based on loading conditions obtained from a critical failure zone of the global SCR model.

2 MODELLING

2.1 Global riser model

Global dynamic analysis is conducted on two SCR models using Flexcom offshore engineering finite element (FE) software, developed by Wood Group Kenny [6]. The global model consists of a floating production storage and offloading vessel (FPSO) from which a free hanging SCR with a total length of 4298.5 m is suspended, with its end lying on the seabed at a depth of 3000 m as shown in Figure 1.

This sea depth is representative of the current frontier in ultra-deepwater oil and gas production. Shell's Perdido production platform in the Gulf of Mexico is currently the world's deepest at 2450 m, while Shell has also commenced development of the Stones field in the Gulf of Mexico at a depth of 2926 m, from which oil and gas will be conducted to a FPSO by means of lazy-wave SCRs and flexible risers.

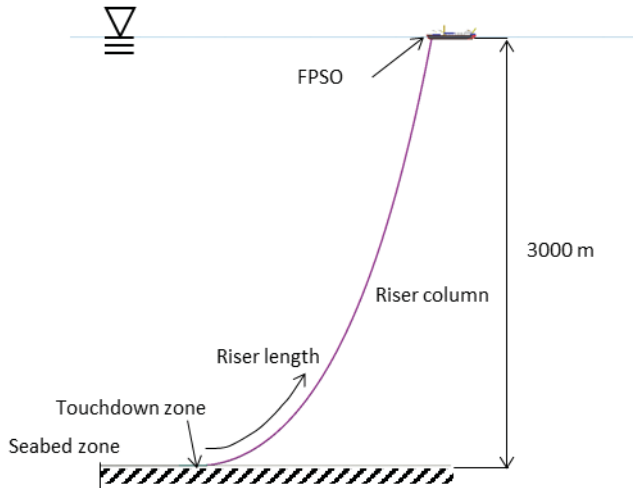


Figure 1. A schematic image of the global SCR model used during Flexcom analysis. The three critical zones with increased mesh refinement are labelled and highlighted.

The SCR is connected to the FPSO through a flex joint and an I-tube, while the seabed end of the SCR is fixed. The SCR configurations used during global analysis are plain pipes without weld profiles, with an outer diameter of 406.4 mm. Two different wall thicknesses (WT) 15 mm and 25 mm were considered. The elastic material properties and dimensions used for both global SCR models are shown in Table 1.

Table 1. Material properties and profiles of the global SCR models analysed.

Model	E (GPa)	ν	OD (mm)	WT (mm)
1	200	0.3	406.4	25
2	200	0.3	406.4	15

The SCRs are modelled using two-noded hybrid beam-column elements with 14 degrees of freedom, which were developed by O'Brien and McNamara [7] and are specifically designed to accommodate the low bending stiffness and arbitrarily large 3D non-linear displacements and rotations of flexible risers.

For element refinement purposes the SCR is subdivided into three zones, the seabed zone (550 m), the touchdown zone (200 m) and the riser column (3548.5 m) as shown in Figure 1. A total of 705 elements are used in the SCR model. Refined 1.5 m elements are used in the touchdown zone, while the element size is varied from 1.5 m to 7.5 m in the seabed zone and riser column.

For both SCR configurations the flex joint is modelled as a linear 0.5 m beam element with a mass of 102 kg and a rotational stiffness of 21.63 kN.m/degree, and the

final element connecting the SCR to the FPSO is modelled as a rigid I-tube.

The seabed is modelled as a beam on elastic foundation model, with a stiffness of 143.4 kN/m/m. Seabed friction coefficients of 0.2 and 0.4 with friction stiffnesses of 45N/m/m and 90N/m/m are assigned in the longitudinal and transverse directions respectively. Standard flex joint and seabed properties are used. In all analyses the SCR contains an internal fluid, which is modelled as crude oil with a density of 870 kg/m³ at a pressure of 18 MPa, while the seawater density is assumed to be 1025 kg/m³.

Analyses are conducted for both SCR geometries using regular Airy waves, at wave amplitudes ranging from 1 m to 10 m. The wide range of wave amplitudes analysed corresponds to a variety of loading conditions, from everyday wave loading to 100 year storms at offshore production zones throughout the globe. A piecewise linear, time independent model, is specified for the current in all analyses. A velocity of 0.3 m/s is specified up to a sea depth of 55 m, which decreases linearly to 0.15 m/s at a depth of 100 m and then remains constant to the seabed.

2.2 Local girth weld model

The local models are based on an axisymmetric assumption, including only axial stress and pressure loading components. Bending moment loading is not included in the local modelling, the justification for this is addressed in Section 3.3.

The output of the global SCR model acts as an input to the local girth weld model by providing the stress boundary conditions for the combined internal pressure, external pressure and axial stress loading. These are obtained at the critical failure location determined during global analysis. The axial stress is applied to the girth weld model as a uniform pressure acting in the longitudinal direction across the wall at one end, while the model is axially constrained at the opposite end. The internal pressure obtained from global analysis is applied along the inner surface of the local girth weld model, while the hydrostatic pressure is applied over the outer surface.

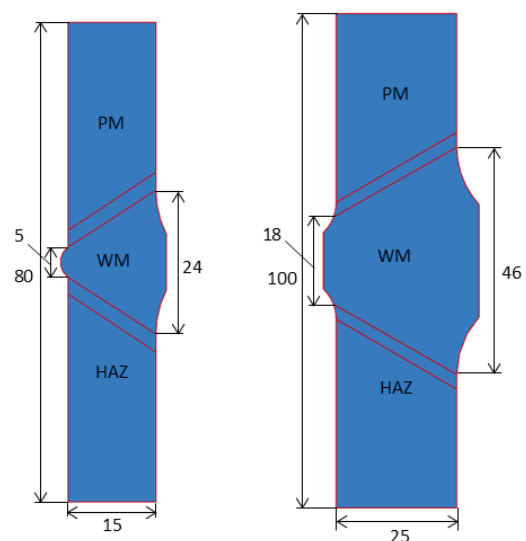


Figure 2. A dimensioned schematic image of the 15 mm and 25 mm WT girth weld models (All dimensions in mm).

Two line pipe steels are examined in the local analyses of the girth welds, X65 and X100 [8]. The elastic-perfectly plastic (EPP) material model is used, with separate material properties assigned to the three constituent weldment zones, PM, WM and HAZ, as labelled in Figure 2.

The material properties used during analysis of the local girth weld model are shown in Table 2. The X65 material properties used were experimentally determined by Netto et al [9]. The X100 material properties used for the PM and the WM are based on those measured by Kondo and co-workers [10], while the X100 HAZ material properties have been estimated based on the change in yield stress at the HAZ observed in the X65 material.

Table 2. The constituent material properties used during local girth weld analysis.

Material	Weldment zone	E (GPa)	σ_y (MPa)
X65	PM	199.69	500.2
	HAZ	195.85	440.1
	WM	202.4	500.1
X100	PM	199.69	719.5
	HAZ	195.85	681
	WM	202.4	826.5

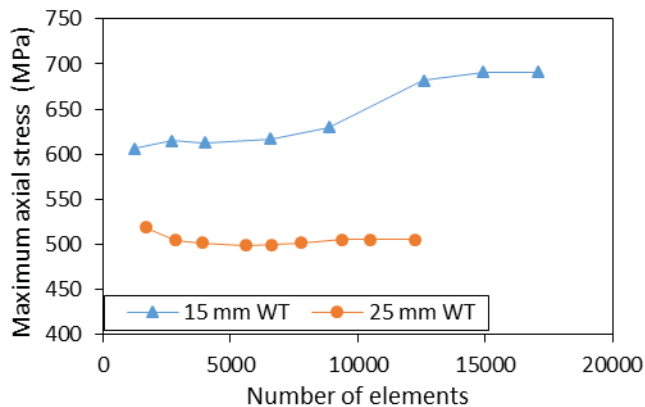


Figure 3. Results of the convergence study, conducted at a 2 m wave amplitude on X65 material.

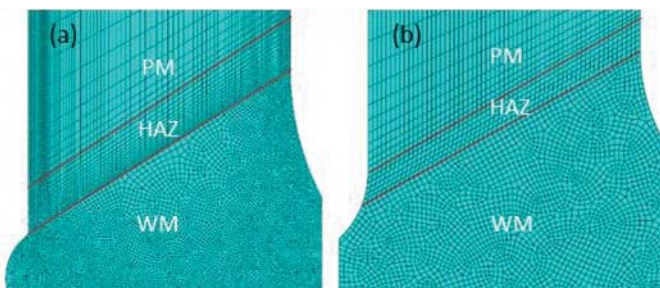


Figure 4. Detail view of the converged mesh for the (a) 15 mm WT model and (b) 25 mm WT model.

CAX8R axisymmetric eight node reduced integration quadratic elements are used for the local girth weld models. A suitable mesh for each model geometry was confirmed through mesh convergence studies with respect to the maximum axial stress predicted at a 2 m wave amplitude using X65 material properties. The results of the mesh

convergence study are shown in Figure 3. Convergence was achieved using a mesh of 7747 elements on the 25 mm WT girth weld geometry and 16740 elements on the 15 mm WT weld geometry.

As expected, elements are biased towards the notch regions at the junctions of the PM, HAZ and WM to accurately capture stress concentrations and the effect of inhomogeneous material properties as shown in Figure 4.

3 RESULTS

3.1 Global analysis

The global dynamic analysis of the SCR models predicted that the critical failure location was in the hang-off zone of the SCR just below the FPSO, at a distance of 4288 m along the SCR from the seabed end, as highlighted in Figure 5. For the local girth weld analysis, it is assumed that the weld is located in this critical failure location. This region experienced the highest levels of mean and alternating axial stress combined with a local increase in the alternating and mean resultant bending moment.

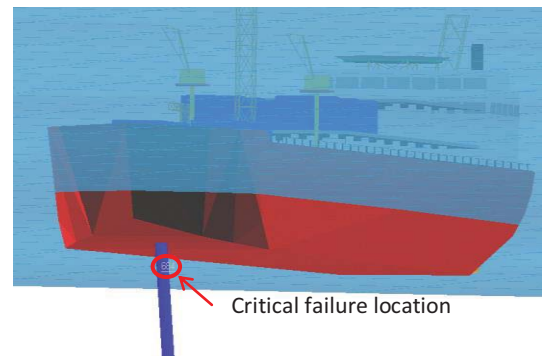


Figure 5. The critical failure location which was determined during global analyses.

The high mean axial stress in this location is due to the self-weight of the large SCR section which is suspended below. The heaving motion of the FPSO with the waves is the primary cause of the high alternating axial stress at this location as shown in Figure 6.

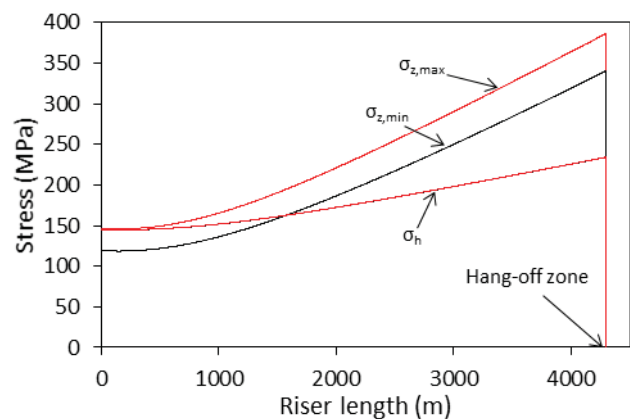


Figure 6. The envelopes of axial (σ_z) and hoop (σ_h) stress along the SCR length for the 15 mm WT model at a wave amplitude of 2 m.

The location of maximum bending moment is at the touchdown zone of the SCR; it then dramatically reduces

along the length of the SCR towards the FPSO, with a small increase at the hang-off zone. The increased bending moment at the hang-off zone shown in Figure 7, is a result of the discontinuity in stiffness at the transition between the SCR and the flex joint below the FPSO. The combined effect of the high axial and internal pressure loading with the increased bending moment at this location, results in the hang-off zone being the critical failure location for both SCR models. The dominant stress at this location is the axial stress which is much greater than the maximum stress due to bending.

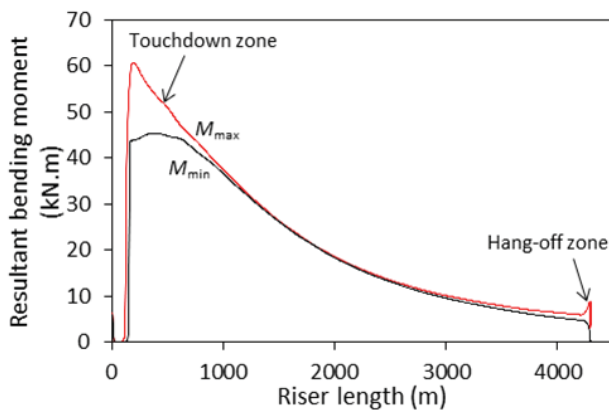


Figure 7. The envelope of resultant bending moment along the length of the SCR for the 15 mm WT model at a wave amplitude of 2 m.

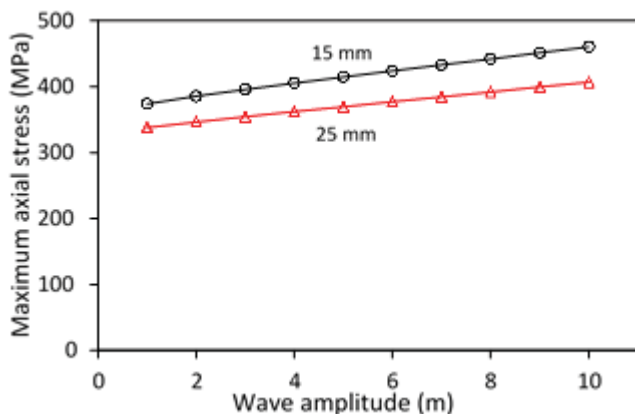


Figure 8. Plot of the maximum axial stress predicted at the failure critical element during global analyses.

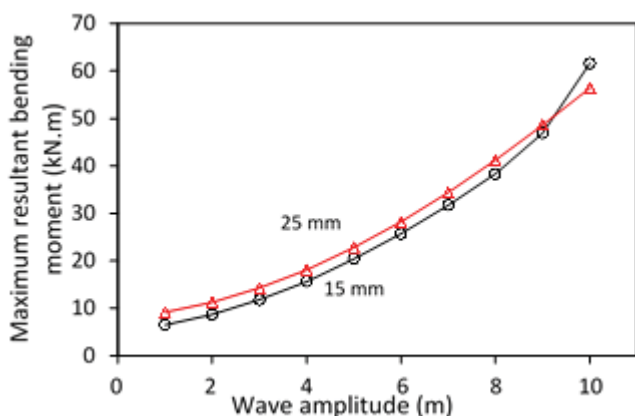


Figure 9. Plot of the maximum bending moment predicted at the failure critical element during global analyses.

There is an approximately linear increase with wave amplitude, in the maximum axial stress predicted in the failure critical element of both SCRs, as shown in Figure 8. The 25 mm WT model gives lower stress levels in all cases.

The bending moment at the failure critical element increases significantly with wave amplitude as shown in Figure 9. The bending moment is greater in the 25 mm WT model for lower wave amplitudes due to its increased stiffness relative to the 15 mm WT model, but is exceeded by the bending moment on the 15 mm WT model at high wave amplitudes due to dynamic effects.

3.2 Local analysis

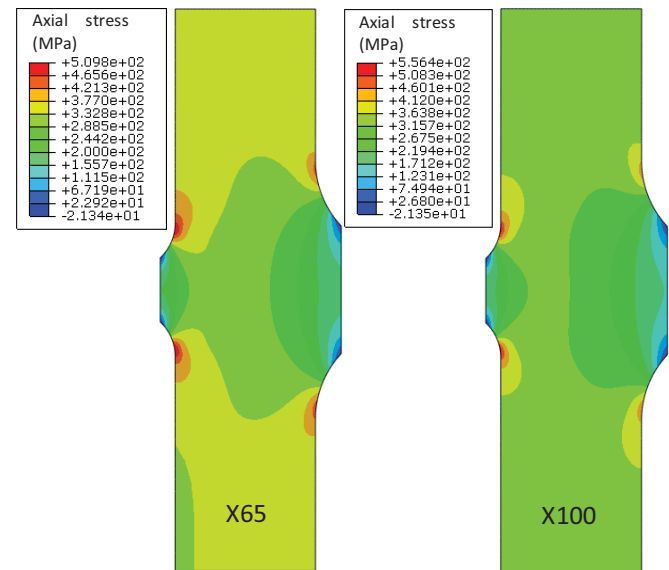


Figure 10. Contour plots of the maximum axial stress distribution at a 2 m wave amplitude on the 25 mm WT model.

Figure 10 presents contour plots of the maximum axial stress distribution for the 25mm WT model for both X65 and X100. It has been established that yielding occurs at the weld root in the HAZ for the X65 material, but no yielding is predicted at any of the analysed wave amplitudes for this model using X100 material properties. Thus, the X100 is effectively elastic and an axial stress concentration factor (SCF) of 1.61 is predicted for the 25 mm WT model from the results based on the ratio of the peak axial stress to the uniform axial stress away from the weld.

Contour plots of the maximum axial stress distribution for the 15 mm WT geometry are presented in Figure 11 for both the X65 and X100 materials. For both materials, HAZ yielding is predicted in the 15 mm WT model at all load cases. To compare with the SCF for the 25 mm WT model, an additional analysis was conducted on the 15 mm WT model, at an applied lower axial stress such that yielding did not occur. A significant axial SCF of 4.48 was predicted at the HAZ in the weld root of the 15 mm WT model. This higher SCF is very much influenced by the detail of the weld geometry (see Figure 2).

The critical location for the both girth weld models is the weld root, at the junction of the WM and the HAZ. This form of SCR girth weld is heavily penalised in fatigue design codes [11] due to the difficulty of ensuring a quality weld because of the lack of access to the weld root for inspection

and control, and the unbacked welding technique which is typically used.

This highlights the importance of a qualified, consistent welding procedure in improving the fatigue performance of SCR girth welds. The level of control required to obtain a consistent root pass is considerably more difficult to attain for welding conducted on an offshore floating facility. Reel-lay installation methods have an inherent advantage in this respect, with better control of the quality and consistency of the welds.

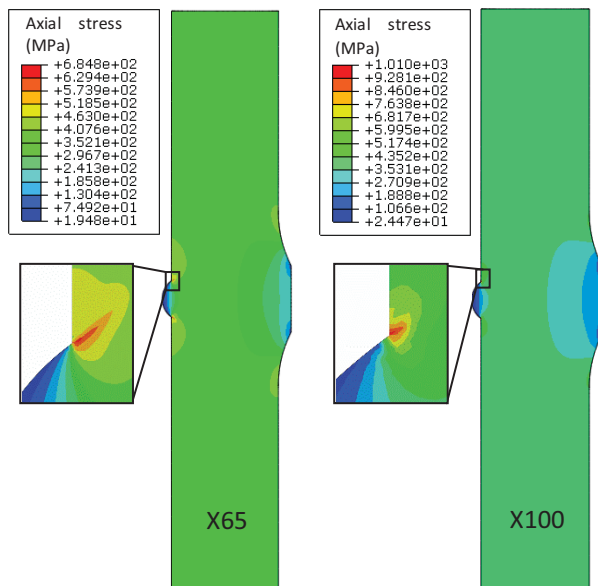


Figure 11. Contour plots of the maximum axial stress distribution for a 2 m wave amplitude on the 15 mm WT model.

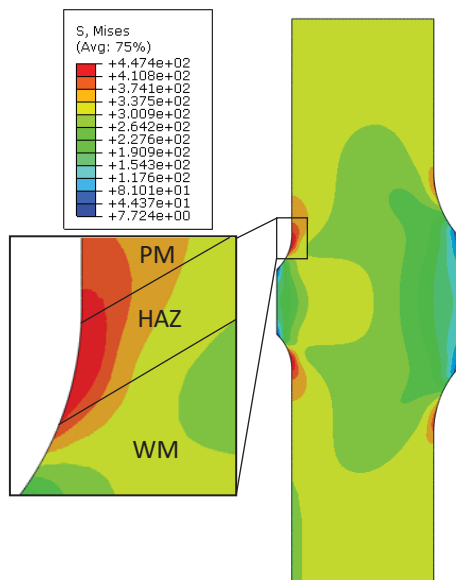


Figure 12. Contour plot of the maximum cyclic von Mises stress on the 25 mm WT X65 girth weld model a 2 m wave amplitude.

The effect of cyclic loading on the local girth weld models was examined by alternating the applied axial stress between the maximum and minimum values obtained during global analysis for a given wave amplitude. It was noted that

the localised plasticity predicted in the HAZ at the weld root did not increase in subsequent cycles after the initial loading to the maximum axial stress.

The hotspot location on the 25 mm WT model is located in the HAZ adjacent to the PM at the weld root as shown in Figure 12 for X65, with yielding occurring in the HAZ in this case. The cyclic axial stress-strain behaviour predicted at this location is shown in Figure 13. The stress increases approximately linearly with axial strain during the first loading cycle, where the internal pressure, external pressure and axial stress are applied to the model. During the subsequent cycling of the applied axial stress, the stress-strain response is altered due to elastic shakedown within one cycle.

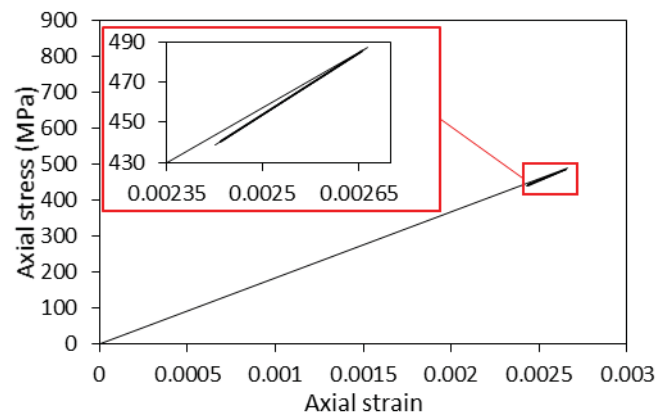


Figure 13. Plot of the axial stress-strain response over 250 cycles for the hotspot located in the HAZ at the weld root, for the 25 mm WT X65 model at a 2 m wave amplitude.

3.3 Bending moment effects

The axisymmetric girth weld modelling did not account for the effect of the bending moment loading on the SCR. It was determined that for the global SCR models analysed, the additional effect of the bending moment, shown in Figure 14, is almost negligible in comparison to the axial and hoop stress loading on the SCR.

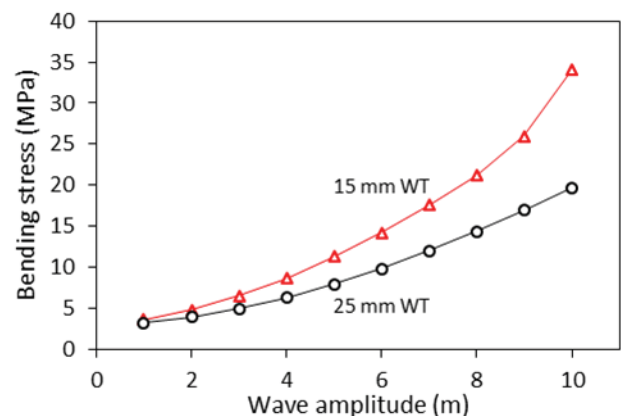


Figure 14. Plot of bending stress calculated at the critical region, based on the results shown in Figure 9.

The predicted bending stress contribution was calculated based on the results shown in Figure 9 using the bending equation. The maximum contribution to the direct

stress by the bending moment would be less than 8% of the nominal axial stress at a high wave amplitude.

4 CONCLUSIONS

Global dynamic analysis was conducted on two different SCR wall thickness geometries over a wide range of wave amplitudes. The results of the global analysis predicted a critical failure location in the hang-off zone of the global SCR models; a region known for its susceptibility to fatigue failure.

The axial stress was determined to be the dominant component of loading at this fatigue hotspot. The effect of bending moment loading in this region was negligible in comparison to the contributions of the other loading modes, allowing local axisymmetric modelling of the girth weld geometry in Abaqus.

The significant variation in the SCFs of the weld geometries analysed highlighted the importance of control over the weld geometry to improve fatigue performance, thus reducing the required factors of safety. Cyclic plasticity was predicted for both girth weld geometries. The X65 material was predicted to be susceptible to weld root plasticity for both SCR wall thickness models, whereas X100 was shown to be susceptible only for the thinner case. Geometrical attributes of the weld were shown to be important, concomitantly with differences in material properties caused by the welding process.

The localised plasticity at the hot spot located in the weld root, was predicted to undergo an elastic shakedown within one cycle, primarily attributed to the assumption of cyclic load control.

Future work on global modelling of SCRs will focus on the possible effects of different riser configurations such as a lazy wave design, on the stresses or damage in the riser. The effect of more complex non-linear 3D seabed properties may also be examined.

Future work on the local modelling of SCR girth welds will implement the J_2 plasticity model with multi-material properties, with a focus on the prediction of the localised fatigue damage accumulation in the weld.

ACKNOWLEDGMENTS

This publication has emanated from research conducted with the financial support of Science Foundation Ireland as part of the MECHANICS joint project between NUI Galway and University of Limerick under Grant Number SFI/14/IA/2604.

The authors would also like to thank Dr. Adrian Connaire of Wood Group Kenny for his advice and support in providing the Flexcom software used in this publication.

REFERENCES

- [1] Det Norske Veritas. DNV-RP-F204 riser fatigue; Oslo, 2010.
- [2] American Bureau of Shipping. Guide for Fatigue Assessment of Offshore Structures; Houston, 2014.
- [3] M. Abelanet, D. Karunakaran, R. Jones, S. Eyssautier, and P. White, "Deepwater steel catenary risers require attention to fatigue factors," *Offshore magazine*, no. 10, Oct-2013.
- [4] G. Hu, M. Campbell, and C. Huang, "Dynamic Plastic Deformation of Deepwater Steel Catenary Risers Under Extreme Cyclic Compressive Loading," in *Offshore Technology Conference*, 2014, pp. 73–79.
- [5] J. L. Chaboche and P. M. Lesne, "A non-linear continuous fatigue damage model," *Fatigue Fract. Eng. Mater. Struct.*, vol. 11, no. 1, pp. 1–17, 1988.
- [6] *Flexcom Version 8.4.1 software documentation*. Galway: Wood Group Kenny, 2015.
- [7] P. J. O'Brien, J. F. McNamara, and F. Grealish, "Extreme Bending and Torsional Responses of Flexible Pipelines," in *Proceedings of the 11th International Offshore Mechanics and Arctic Engineering Symposium*, 1991, pp. 319–324.
- [8] API Specification 5L and ISO 3183, "Specification for Line Pipe," 2008.
- [9] T. A. Netto, A. Botto, and M. I. Lourenc, "Fatigue performance of pre-strained pipes with girth weld defects: Local deformation mechanisms under bending," *Int. J. Fatigue*, vol. 30, pp. 1080–1091, 2008.
- [10] J. Kondo, J. Zhou, and D. Taylor, "Mass Production and Installation of X100 Linepipe for Strain-Based Design Application," in *Proceedings of IPC 2008*, 2008, pp. 1–7.
- [11] S. J. Maddox, J. B. Speck, G. R. Razmjoo, and G. Park, "An Investigation of the Fatigue Performance of Riser Girth Welds," *J. Offshore Mech. Arct. Eng.*, vol. 130, no. February, pp. 1–11, 2008.

Improving finite element implementation in topology optimisation

Salam Al-Sabah

Arup, 50 Ringsend Road, Dublin 4, Ireland, D04 T6X0

email: salam.al-sabah@arup.com

ABSTRACT: Structural optimisation has the potential of producing substantial design improvements and cost reductions when applied to whole structures or structural components. Of the many possible directions of structural optimisation, topology optimisation (TO) is the most challenging. On the other hand, TO has the most potential benefits in real-world applications as the whole structural layout and sizing are open to improvements, rather than member sizes only. With the development of new methods and availability of more powerful computers, TO progressed rapidly during the last 25 years. The initial difficulties encountered at the early stage of development are mostly resolved now. Many methods are currently available to carry out TO. Although there are many differences between different TO methods, they share one common aspect in the need to carry out structural analysis repeatedly. This part of TO is the most time consuming element and any improvement can produce significant efficiency improvements. Typically, finite element (FE) method is used to carry out that part of TO. FE is currently the most widely used general structural analysis method. However, its implementation in TO can be made more efficient. In this research, this task was achieved by improving the way in which the element stiffness matrix was related to TO. The particular properties of the four noded rectangular element, typically used in TO, were exploited to this end. Also, the way global stiffness matrix was handled during the repeated solution process. Different examples were solved to demonstrate the efficiency improvements. Results were compared with previously published ones and shown to be of similar accuracy.

KEY WORDS: CERI 2016; Topology optimisation; Finite element; BESO.

1 INTRODUCTION

Optimisation objective is to find the best possible solution that satisfies the overall aim within the limited available resources. It can be applied to a variety of disciplines such as economy, management, and design. For example, the best solution can be the one that increases profit, reduces material cost, or produces the lightest structure.

Structural optimisation aims to find the best structure that satisfies the objective function requirements within the solution domain and constraints. The optimum solution is also influenced by the limitations of the optimisation method.

The need for structural optimisation is driven by economic factors and the need to design more efficient structures that consume less materials and energy and have less environmental impact. The developments in structural optimisation resulted from the development of new optimisation methods, the availability of powerful computers at low cost, and the introduction of new manufacturing techniques such as additive manufacturing that allow the fabrication of more complex, optimised geometries.

2 TOPOLOGY OPTIMISATION

Structural optimisation can be grouped into three categories: size, shape, and topology optimisation (TO). The size optimisation is limited to finding the optimum member sizes without changing the initial structural arrangement. It requires an initial sizing of the members that will be improved through the optimisation process. Shape optimisation is achieved by modifying an initial shape defined by external and possibly internal boundaries that needs to be predefined. TO requires minimal initial information as the method allows for both shape and topology to the optimisation process. Only physical and geometric design space, load, and boundary conditions are required to start the optimisation process. TO opens the

structural design to more novel and efficient solutions, but is by far the most challenging technically [1].

The solution of TO problems progressed significantly since the landmark paper of Bendsoe and Kikuchi in 1988 [2]. Some of the main methods currently available are the Solid Isotropic Material with Penalisation (SIMP), level set method, Genetic Algorithms (GA), Homogenisation, and Evolutionary Algorithms (EA). The most widely used EA method is the Bi-directional Evolution Structural Optimisation (BESO) [1].

In spite of the major differences in the formulation of different TO methods, these methods share the need to carry out structural analysis repeatedly. The most widely used continuum structural analysis method is the finite element (FE) method.

In this research, FE method is implemented in a BESO method to carry out the TO.

2.1 BESO method

The BESO method was an improvement over the Evolutionary Structural Optimisation (ESO) method [1]. The main BESO solution steps can be summarised as following:

- i. The solution control parameters are defined. These are:
 - a. The constraint volume ratio (VR) which is the ratio of target volume (V^*) to the initial volume (V_0).
 - b. The evolutionary volume ratio (ER) which represents the percentage of volume decrease (or increase) in the following solution cycle.
 - c. The volume addition ratio limit (AR_{max}) which is the limit on volume increase (or decrease) between successive solution cycles once V^* is reached.

- d. The BESO filter radius (r_f) size is specified. The filter is used to calculate the averaged element sensitivity number and to guard against possible checkerboard pattern when low-order finite elements are used. The filter is also important in making the BESO method mesh-independent. The element sensitivity is its strain energy [3].
- ii. The design domain is discretised into a number of finite elements forming the FE mesh. Usually, the element size is constant.
- iii. Initially, all elements are assumed to exist with their initial property index set to 1. This value is changed to a small value close to zero when an element is removed.
- iv. A finite element analysis is carried out using the current state of structure. Sensitivity number of all elements is calculated.
- v. The element sensitivity is averaged over the current and previous solution cycle. This averaging is required to stabilise the solution process. The BESO filter is applied and averaged element sensitivity numbers are calculated.
- vi. Elements are removed and/or added based on their averaged sensitivity number. Elements that have low averaged sensitivity values are removed while removed elements with higher values are restored. This transition of element existence state is key to the BESO. Threshold sensitivity number for removing and adding elements is based on ordered element averaged sensitivity and the percentage volume to be removed and/or added.
- vii. Steps iv-vi are repeated until V^* is attained and the convergence criterion is satisfied. Usually, the convergence criterion is related to the change of total structure compliance over the last number of solution cycles.

Details on the BESO solution steps can be found in [1].

2.2 Finite element implementation

All TO algorithms require many solution cycles to converge to a stable solution. The number of cycles can vary from few tens to many hundreds. It is clear from the BESO solution steps described in section 2.1 above that one of the most time consuming part of the solution is step (iv), the FE analysis. Since this step is common to all different TO algorithms, any improvement in the efficiency of FE analysis can have substantial effect on the optimisation total analysis time.

In most implementations of FE analysis in TO algorithms, the following features are found [1], [4]:

- i. A low-order finite elements are used. In a 2D plane stress analysis, linear, C_0 , elements are usually used. These elements have linear shape function. Continuity of the unknown displacements is maintained at element boundaries, while unknown derivatives (rotations) are not continuous.
- ii. The solution domain is discretised into many rectangular elements of the same size. The reason is to use the same element stiffness matrix over the

design domain. More detailed results can be obtained when mesh is refined.

- iii. To reduce solution time, the element stiffness matrix is expressed in its final closed form, usually obtained with the help of symbolic mathematics software.
- iv. Structure stiffness matrix is assembled in a sparse form from all element stiffness matrices.
- v. A sparse equation solver is used to solve the FE stiffness equation.

In addition to the dedicated software packages that support TO, it is common to write development codes using a matrix manipulation programming language such as Matlab [5]. Some implementations are readily available and had improved over the last 15 years [4], [6].

3 PROPOSED FE IMPLEMENTATION IMPROVEMENTS

The following sections describe the proposed improvements to FE implementation in TO.

3.1 Incremental update of structure stiffness matrix

In a typical TO implementation of FE method, the structure stiffness matrix is assembled at each solution cycle. In BESO analysis elements are removed and added to the solution depending on their averaged sensitivity number. As presented in section 2.1 this step is applied at each solution cycle depending on the element sensitivity number relative to the threshold. Typically, the percentage of deleted (or added) elements at each solution cycle is small. This is necessitated by the need to avoid sudden changes in the structural stiffness that might lead to numerical instability.

In this research, it is proposed that the structure stiffness matrix is assembled only once at the first solution cycle. The matrix is kept current in memory. In the following solution cycles, elements with low averaged sensitivity number are identified for removal from the solution as per step (vi) in section 2.1. The element stiffness matrices of this list are subtracted from the current structure stiffness matrix. The opposite is performed for elements that are to be added to the solution.

3.2 Use of sub-element stiffness matrices

The single, most time-consuming part of the FE solution is the solution of stiffness equation. The solution involves the factorisation of the stiffness matrix and reduction of the load vector. For fully populated matrix, the number of operations required to factorise the stiffness matrix is related to n^3 , where n is the matrix size [7]. The increase in the number of operations becomes quite high when the finite element mesh is refined. For example when the element side length is reduced to half the original size, n increases by a factor of nearly 4. In this case, the number of operations, hence factorisation time, is increased by a factor of nearly 64. This level of increase becomes unacceptably high for fine FE meshes and alternative, more efficient factorisation methods are used instead.

It was recognised early in the development of FE method, that the structure stiffness matrix is sparse. It is not uncommon, particularly in 2D analysis, to have less than 1% nonzero elements in the structure stiffness matrix. Attempts to

use this feature resulted in the development of the more efficient skyline and frontal solvers [8], [9].

Currently, the most efficient methods are the sparse matrix solvers. For a sparse matrix, the number of operations is related to the range n^1 to n^3 depending on the degree of matrix sparsity and the location of non-zero elements in the matrix. In addition to the huge potential gain in solution time, there is a substantial reduction in the required storage space of the stiffness matrix. Both of these two advantages make sparse solvers the preferred option to be used in TO. Even so, refining a rectangular FE mesh by doubling the number of elements in each direction will result in a minimum time penalty factor of 4.

The improvement proposed in this research is based on the particular way used in the numerical integration of the element stiffness matrix. The FE formulation of linear quadrilateral plane stress elements usually involve a 2x2 numerical integration scheme [8]. Figure 1 shows a 2x2 Gaussian integration points expressed in natural coordinates for a linear quadrilateral element.

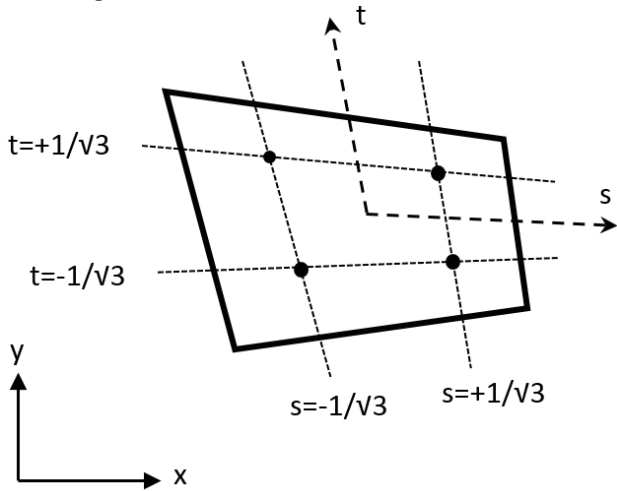


Figure 1. Gaussian integration points of linear element.

The total element stiffness matrix is assembled from the contribution at each of the four integration points, Equation 1.

$$[K] = \iint_A [B]^T [D] [B] dA = \int_{-1}^1 \int_{-1}^1 [B]^T [D] [B] |J| ds dt$$

$$= \sum_{i=1}^2 \sum_{j=1}^2 w_i w_j [B(s_i, t_j)]^T [D] [B(s_i, t_j)] |J(s_i, t_j)| ds dt \quad (1)$$

where $[D]$ is the material property matrix, $[B]$ is the strain-displacement matrix, $|J|$ is the determinant of the Jacobian matrix, A is the element area, w is the numerical integration weight, and s and t are the natural coordinates. Summations are made for the four integration points.

It can be argued that the quadrilateral linear element is made of four sub-elements. The properties of each sub-element are represented by the properties at the relevant integration point.

In this research, and taking this view, it is easy to conclude that it is possible to reduce the element size to one quarter the original size with no corresponding increase in the structure stiffness matrix size. The actual number of elements in the

base and modified models will remain the same during global analysis. The only additional overhead is the need to treat each element locally as an assembly of four sub-elements in the modified model. Each sub-element is treated as a full element with its own property index. The time penalty for this step is small relative to the benefits of reducing the effective structure stiffness matrix size as will be demonstrated in section 4.

The benefit of this approach is the ability to add or remove one quarter of each element independently, rather than the whole element in typical TO analysis. The results of this approach are more detailed than those of the base model and are comparable to those resulting from a model having nearly four times more elements.

4 NUMERICAL IMPLEMENTATION

The FE implementation improvements proposed in section 3 can be applied in a TO software using any programming language. In the current research, the improvements were implemented in a BESO TO software written in Matlab [5]. This choice was driven by the rapid software development allowed by Matlab and the ease of carrying out matrix operations efficiently. However, these advantages come with a cost when vectorisation is not used. In that case there is a substantial reduction in computational speed.

In the current Matlab code, all speed-critical operations were vectorised.

To test the performance improvements resulting from the proposed FE implementation, the software was used to solve two examples that were traditionally used in TO. A comparison was made with the unmodified method to demonstrate the accuracy of results and performance gains. All numerical tests were run on a computer with a 64 bit operating system. It had an Intel Xeon E31225 CPU having 4 cores running at 3.1 GHz and 8 GB RAM.

4.1 Short cantilever

The short cantilever shown in Figure 2 is 160 mm long and 100 mm deep. It is made from a 1 mm thick plate with a modulus of elasticity of 207 GPa and a Poisson's ratio of 0.3. A downward load is applied at mid-depth of the free end.

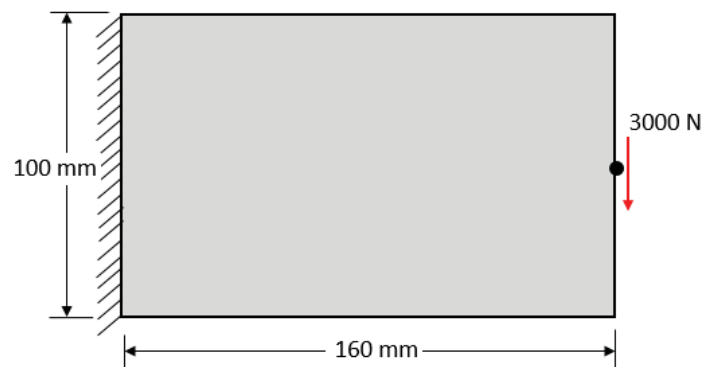


Figure 2. General arrangement of short cantilever example.

The example was solved for the following BESO control parameter values: VR=0.5, ER=1%, AR_{max}=1%, r_f=6 mm.

The base finite element mesh was made from 32x20 square elements. This mesh was refined by an integer refinement

factor N such that the mesh is made from $(32N \times 20N)$ square element. Value of N was varied from 1 to 8. Hence a mesh with $N=1$ has 640 elements while the one with $N=8$ has 40960 elements.

The results obtained from the base, unmodified, FE implementation in BESO TO are shown in Figure 3. These results were obtained for $N=1, 2, 4$, and 8 , respectively. Variations of the example were previously solved by other researchers [1], [10]–[12]. Current results are similar to those obtained previously.

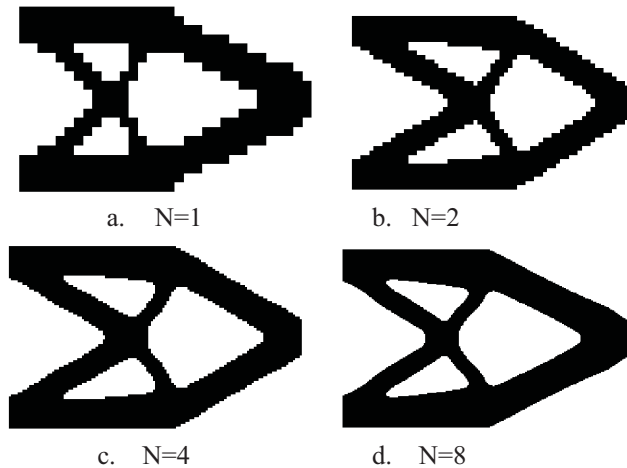


Figure 3. Base model final geometry for different mesh densities.

The analysis was repeated with a modified program that adopted the incremental update of structure stiffness matrix as described in section 3.1. The same results were obtained as those shown in Figure 3. However, there was a reduction of running time as shown in Table 1.

Table 1. Running time for different mesh densities.

Italic: base results

Bold: results with incremental stiffness

() : improvement factor

N	N^2	% nonzero elements	Time/cycle (sec)	
			[K] assemble	Total
1	1	<i>1.22%</i>	<i>0.00567</i> 0.00065 (8.7)	<i>0.01228</i> 0.00752 (1.6)
2	4	<i>0.33%</i>	<i>0.02437</i> 0.00118 (20.7)	<i>0.04743</i> 0.02415 (1.9)
4	16	<i>0.08%</i>	<i>0.1007</i> 0.00426 (23.6)	<i>0.21174</i> 0.1137 (1.9)
8	64	<i>0.02%</i>	<i>0.40157</i> 0.01497 (26.8)	<i>1.049</i> 0.70667 (1.5)

The table shows the time per cycle, averaged over all the solution cycles. The results were presented for the values of N^2 . This measure was used due to the fact that the number of elements (and approximately number of nodes) is related to this quantity. It is evident from these results that the

incremental update of structure stiffness matrix is more efficient than recalculating the matrix at each solution cycle. The proposed method is faster by a factor of 8.7 for $N^2=1$ increasing to a factor of 26.8 for $N^2=64$. These results indicate a continuous increase in the speed improvement factor with the increase of stiffness matrix size. This is related to the numerical overhead which is more apparent in small problems with small value of N . Ultimately, the limit for this improvement is twice the value of AR_{max} , which is related to the time for subtracting the stiffness matrices of the removed elements and the time for adding the stiffness matrices for the added elements.

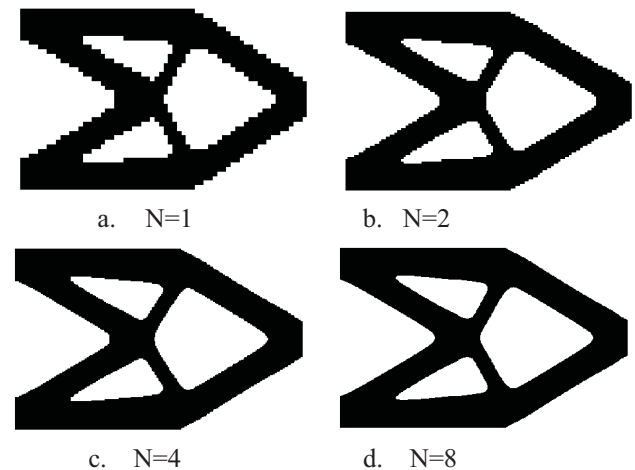


Figure 4. Improved model results from different mesh densities.

The final effect on total analysis cycle time varied from a time improvement factor of 1.5 to 1.9.

Table 1 also shows the percentage of nonzero elements in the structure stiffness matrix. This ratio varied from 1.22% for $N=1$ to 0.02% for $N=8$. These values indicate the huge reduction in storage requirements when using sparse matrices in FE analysis.

The analysis was repeated again, where in addition to the incremental updating of structure stiffness matrix, the improvement of using sub-elements as described in section 3.2 was added. In this case, each finite element was treated as being made from four sub-elements. The analysis was carried out for $N=1, 2, 4$, and 8 . The results are shown in Figure 4.

Solution progress for the base, unmodified, and the improved solutions for a mesh with $N=8$ for the base model and $N=4$ for the improved solution is shown in Figure 5.

Each element was treated as an assembly of 4 sub-elements, each of which can be independently deleted or added. In this case, results from $N=2, 4$, and 8 obtained from the base model can be compared to those obtained from $N=1, 2$, and 4 from the sub-element model, respectively. This is indicated by the double headed arrows of Figure 6. As a result, a new element refinement factor ($N^*=2N$) was used to indicate the doubling of sub-element numbers.

It is clear from these results that the solution progress and refinement is similar in both models.

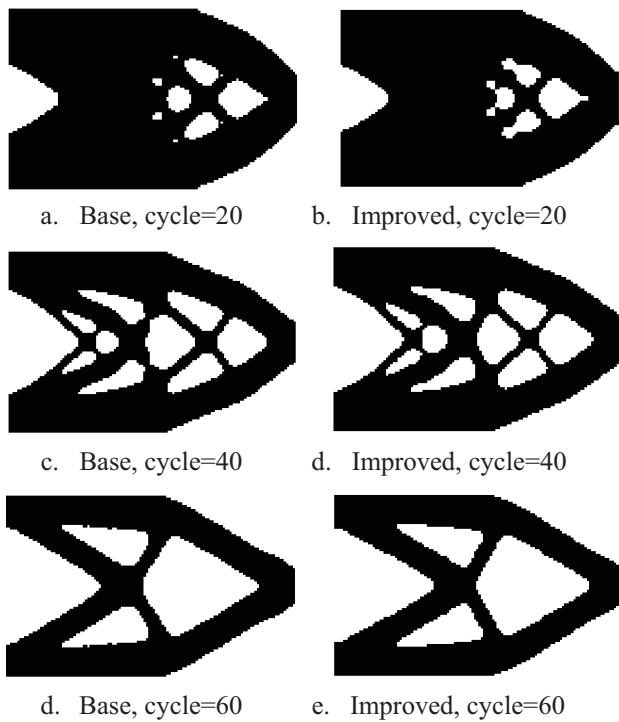


Figure 5. Short cantilever results at different analysis stages
N=8 for base model, N=4 for improved model.

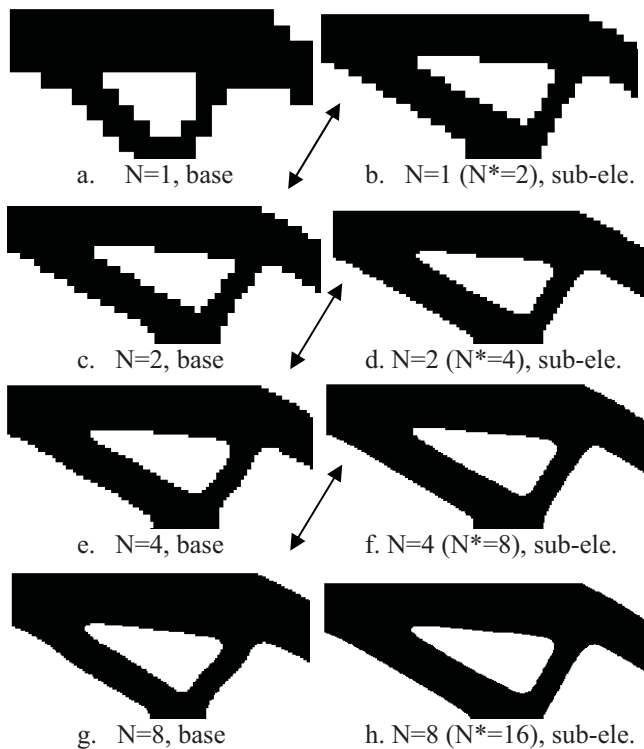


Figure 6. Base and improved results of short cantilever.

The main reason for the modifications proposed in this work was to improve the analysis performance. Table 2 presents the performance improvements in the assembly of the structure stiffness matrix, factorisation of the stiffness equation, and in total time for each analysis cycle. All times

were averaged over the solution cycles. The comparison was made between N values of 2, 4, and 8 for the base model and N=1, 2, and 4 ($N^* = 2, 4$, and 8) for the improved model, respectively. An improvement between 37.5 to 72.2 times was obtained in the matrix assembly. Improvement in factorisation was between 3.3 and 4.9 times. The improvement in total cycle time was between 3.7 to 5 times.

Table 2. Running time for different mesh densities.

Italic: base model

Bold: improved model

() : improvement factor

N, N*	N ² , N* ²	No of nodes	Time/cycle (sec)		
			[K] assemble	Factorisation	Total
2	4	2665 693	0.02437 0.00065 (37.5)	0.01459 0.00436 (3.3)	0.04743 0.00949 (5.0)
4	16	10449 2665	0.10070 0.00142 (70.9)	0.07943 0.01711 (4.6)	0.21174 0.03890 (5.4)
8	64	41377 10449	0.40157 0.00556 (72.2)	0.39324 0.07995 (4.9)	1.0490 0.28371 (3.7)

It can be concluded from these results that, by implementing the proposed changes, it is possible to achieve significant performance improvements without affecting results quality.

4.2 Simply supported beam

A simply supported beam, 240 mm long and 40 mm deep is shown in Figure 7. It is made from a 1 mm thick plate with a modulus of elasticity of 210 GPa and a Poisson's ratio of 0.3. A downward load is applied on the top face at mid-span.

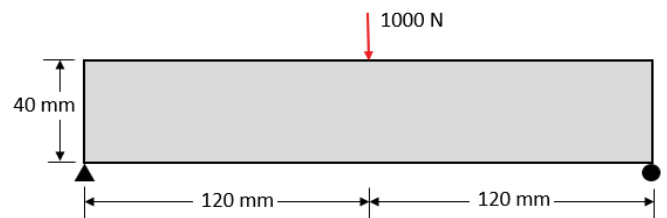


Figure 7. General arrangement of simply supported beam.

Due to symmetry of geometry, boundary conditions, and load only half the beam is modelled. The example was solved for the following BESO control parameter values: VR=0.5, ER=1%, $AR_{max}=1\%$, $r_f=4.7$ mm.

Variations of the example were previously solved by other researchers [1], [4], [13]. The current results are similar to those obtained previously.

The model was meshed with a $30N \times 10N$ mesh. This mesh was refined using refinement factors, N, of 2, 4, and 8. The analysis was repeated with a modified program that adopted the incremental update of structure stiffness matrix and using sub-elements as described in section 3. In this case, the analysis was carried out for a mesh refinement factor, $N^*=2N$, of 2, 4, and 8. Analysis results are shown in Figure 8.

Quality of results is shown to be similar for the base and improved versions.

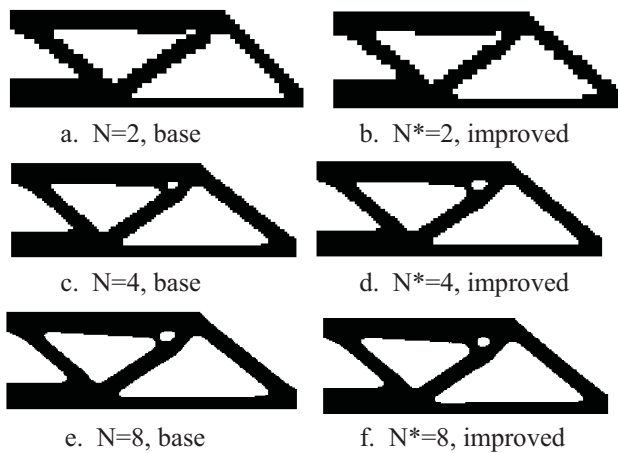


Figure 8. Simply supported beam results.

Table 3 presents the performance improvements in the assembly of the structure stiffness matrix, factorisation of the stiffness equation, and in total time for each analysis cycle. All times were averaged over the solution cycles. The comparison was made between N values of 2, 4, and 8 for the base model and $N^*=2, 4$, and 8 ($N = 1, 2$, and 4) for the improved model, respectively. An improvement between 23.3 to 55.0 times was obtained in the matrix assembly. Improvement in factorisation was between 4.1 and 5.5 times. The improvement in total cycle time was between 3.8 to 6.5 times. The performance improvements are similar to those obtained in the short cantilever example.

Table 3. Running time for different mesh densities.

Italic: base model

Bold : improved model

() : improvement factor

N, N*	N ² , N* ²	No of nodes	Time/cycle (sec)		
			[K] assemble	Factorisation	Total
2	4	1281	0.01210	0.00699	0.024500
		341	0.00046	0.00171	0.00376
			(26.2)	(4.1)	(6.5)
4	16	4961	0.04708	0.03287	0.09335
		1281	0.00202	0.00803	0.02233
			(23.3)	(4.1)	(4.2)
8	64	19521	0.19612	0.19173	0.50368
		4961	0.00358	0.03462	0.13374
			(55.0)	(5.5)	(3.8)

A note on the performance of the sparse solver is worth mentioning. By analysing the factorisation times shown in Tables 2 and 3 for different mesh densities, it can be concluded that the factorisation time is related to n^x , where x vary between 1.16 and 1.24. This is a huge improvement compared to full matrix solvers, where the value of x is 3.

5 CONCLUSIONS

Two modifications were proposed to improve the implementation of FE in TO. These were the continuous updating of structure stiffness matrix and the use of sub-elements. Two examples were solved to demonstrate the

accuracy and the performance increase resulting from the proposed improvements. Based on the example results, the stiffness matrix assembly time was found to be 23.3 to 72.2 times faster than the base results. Factorisation process was between 3.3 to 5.5 times faster. Overall total cycle analysis time was between 3.7 to 6.5 times faster than the base results. It was also found that the results were similar to those obtained from the base, unmodified, method.

Although these results were obtained using a BESO method, the proposed improvements can be applied to any other TO method. This is due to the usual use of FE method in all continuum TO methods. In addition, although the current software was written in Matlab, the proposed improvements can be applied using any other programming language.

Existing TO software can be modified to incorporate the proposed improvements without major difficulties.

The proposed improvements can provide simple and reliable way to enhance the performance of all TO methods without affecting the quality of results.

REFERENCES

- [1] X. Huang and M. Xie, *Evolutionary Topology Optimization of Continuum Structures: Methods and Applications*. John Wiley & Sons, 2010.
- [2] M. P. Bendsoe and N. Kikuchi, "Generating Optimal Topologies in Structural Design Using a Homogenization Method," *Comput. Methods Appl. Mech. Eng.*, vol. 71, no. 2, pp. 197–224, 1988.
- [3] D. N. Chu, Y. M. Xie, A. Hira, and G. P. Steven, "Evolutionary structural optimization for problems with stiffness constraints," *Finite Elem. Anal. Des.*, vol. 21, no. 4, pp. 239–251, Apr. 1996.
- [4] O. Sigmund, "A 99 line topology optimization code written in matlab," *Struct. Multidiscip. Optim.*, vol. 21, no. 2, pp. 120–127, 2001.
- [5] MathWorks-Inc., "MATLAB." 2010.
- [6] E. Andreassen, A. Clausen, M. Schevenels, B. S. Lazarov, and O. Sigmund, "Efficient topology optimization in MATLAB using 88 lines of code," *Struct. Multidiscip. Optim.*, vol. 43, no. 1, pp. 1–16, 2011.
- [7] G. H. Golub and C. F. Van Loan, *Matrix Computations*, 4th ed. Baltimore: JHU Press, 2012.
- [8] Klaus-Jürgen Bathe and E. L. Wilson, *Numerical methods in finite element analysis*. the University of Michigan: Prentice-Hall, 1976.
- [9] M. M. Irons, "A frontal solution program for finite element analysis," *Int. J. Num. Meth. Eng.*, vol. 2, pp. 5–32, 1970.
- [10] D. Nha Chu, Y. M. Xie, A. Hira, and G. P. Steven, "On various aspects of evolutionary structural optimization for problems with stiffness constraints," *Finite Elem. Anal. Des.*, vol. 24, no. 4, pp. 197–212, 1997.
- [11] T. E. Bruns, "A reevaluation of the SIMP method with filtering and an alternative formulation for solid-void topology optimization," *Struct. Multidiscip. Optim.*, vol. 30, no. 6, pp. 428–436, 2005.
- [12] S. M. Jebeli and M. S. Panahi, "Article information :," *Eng. Comput.*, vol. 32, no. 2, pp. pp.234–257, 2015.
- [13] K. Ghabraie, "An improvement technique for Bi-directional Evolutionary Structural optimisation (BESO) method," *Struct. Multidiscip. Optim.*, vol. 51, no. 3, pp. 799–800, 2015.

Bridge Damage Detection using Moving Force Identification

Paul C. Fitzgerald¹, Eugene J. OBrien¹, Enrique Sevillano¹

¹School of Civil Engineering, University College Dublin, Dublin, Ireland

email: paul.fitzgerald.3@ucdconnect.ie, eugene.obrien@ucd.ie, enrique.sevillanobravo@ucd.ie

ABSTRACT: Moving Force Identification (MFI) has been used previously for the purpose of bridge damage detection. The calculated forces from an MFI algorithm change in the event of there being a region of damage on a bridge. The governing equations of the MFI algorithm are ill-conditioned, necessitating the introduction of a regularisation technique. First order Tikhonov regularisation is used in the MFI algorithm being investigated in this paper. This requires an appropriate smoothing parameter to be found which is commonly acquired through the use of an L-Curve. The L-Curve is a log-log plot of the norm of the regularised solution versus the norm of the least squares solution for a range of smoothing parameters. It is recommended in literature to use the region of maximum curvature of the L-Curve as the basis of finding the optimal smoothing parameter. For the case of using MFI to calculate the axle forces on a healthy bridge, this may very well be the optimal basis for choosing the smoothing parameter. This paper investigates the sensitivity of a damage indicator to the choice of smoothing parameter. The sensitivity corresponding to the point of maximum curvature is of particular interest as it indicates if the point of maximum curvature is suitable for damage detection purposes. Preliminary results show that the damage indicator magnitude is sensitive to the choice of smoothing parameter. Furthermore, the point at which the damage indicator is least sensitive to the smoothing parameter does not correspond to the region of maximum curvature on the L-Curve.

KEY WORDS: Moving Force Identification; Damage Detection; Bridge.

1 INTRODUCTION

Visual inspections are the primary method of assessing bridge condition in the current era. Problems associated with this include an expensive labour cost and unreliability due to a lack of consistency and science in the approach. It is important to have a reliable bridge inspection method in order to prevent catastrophic occurrences like the Interstate 34 Bridge in Minneapolis in 2007 [1]. Unnecessary premature repair of bridges can also be prevented with an adequate bridge health monitoring scheme.

The relationship between changes in stiffness or mass and changes in natural frequency has led many in the field of damage detection to use natural frequency as an indicator of damage. Salawu et al. review the various methods of using changes in frequency as a damage indicator [2]. While these methods can be relatively cost efficient, they may prove inadequate for locating the area of damage. This is due to the fact that identical cracks in different locations may cause the same amount of frequency change.

Changes in mode shapes have also been used to provide information on damage location and severity. A high level of accuracy is required in these methods however, making it more difficult to detect damage from measurements [3]. While mode shape change methods are more beneficial in predicting the damage location than frequency based methods, a combination of these methods is more useful [4]. Damping may also be used as a damage indicator which has been shown to be more sensitive to changes in natural frequencies or mode shapes in many cases [5-7].

Sensor-based monitoring has increased in recent years as a result of the drawbacks associated with visual inspection

methods. The improvement in computational technology has facilitated this shift. Camera-based bridge monitoring is of particular interest in this paper. Cameras are continuously improving and becoming more affordable also. With an appropriate setup it is possible for a high resolution camera to be able to measure the deflections of a point or number of points along a bridge as vehicles pass over it. This deflection data may then be used for the purpose of damage detection.

An MFI algorithm is investigated in this paper as a means of detecting damage of a bridge. Bridge deflection data is used as an input to the algorithm. OBrien et al. have shown the calculated axle forces to be sensitive to damage [8]. The sum of the squared of the differences between the mean of the calculated axle force history of a large quantity of vehicles for a healthy case and a damaged case is used as a damage indicator. The damage indicator increases with an increase in damage but its ability to locate the area of damage is limited.

This paper investigates the effect that the choice of smoothing parameter has on the magnitude of the damage indicator. It is shown that the damage indicator magnitude changes with different choices of smoothing parameters. The sensitivity of the damage indicator corresponding to the region of maximum curvature on the L-Curve is also investigated. It is important to have a damage indicator that is sensitive to damage and not that sensitive to the choice of smoothing parameter. Interestingly, results suggest that the region of maximum curvature on the L-Curve does not correspond with the point that the damage indicator has minimal sensitivity to the smoothing parameter choice.

2 MOVING FORCE IDENTIFICATION THEORY

MFI calculates the force histories such that the difference between the measurements (deflection in this case) and what is calculated from the dynamic equations is minimised. Law et. al [9] were the first to propose this method. The MFI algorithm used in this paper is one proposed by Gonzalez et al. which is an improvement on the method created by Law et. al and utilises a first order regularisation process [10]. The algorithm is now explained in a summarised fashion where more detail may be sought in the references if desired. The matrix differential equation for structural dynamics is represented by

$$[M_g]\{\ddot{u}\} + [C_g]\{\dot{u}\} + [K_g]\{u\} = F(t) \quad (1)$$

where $\{u\}$ is a vector of displacements, $F(t)$ is a forcing function and M_g , C_g and K_g are the mass, damping and stiffness matrices respectively. A more appropriate representation for the purpose of calculating the unknown forces is

$$[M_g]\{\ddot{u}\} + [C_g]\{\dot{u}\} + [K_g]\{u\} = [L]\{g(t)\} \quad (2)$$

where $g(t)$ is a vector of time dependent force magnitudes which are distributed to the relevant degrees of freedom by the location matrix, $[L]$, which takes into account the applied force locations on the bridge at a particular time. By defining

$$\{v\} = \{\dot{u}\} \quad (3)$$

and

$$\{a\} = \{\dot{v}\} \quad (4)$$

it may easily be shown that

$$\begin{aligned} \{a\} = & -[M_g]^{-1}[C_g]\{v\} - [M_g]^{-1}[K_g]\{u\} \\ & + [M_g]^{-1}[L]\{g(t)\} \end{aligned} \quad (5)$$

Equations (3) to (5) may now be combined to give

$$\begin{aligned} \begin{Bmatrix} \dot{u} \\ \dot{v} \end{Bmatrix} = & \begin{bmatrix} 0 & I \\ -[M_g]^{-1}[K_g] & -[M_g]^{-1}[C_g] \end{bmatrix} \begin{Bmatrix} u \\ v \end{Bmatrix} \\ & + \begin{bmatrix} 0 \\ [M_g]^{-1}[L] \end{bmatrix} \{g(t)\} \end{aligned} \quad (6)$$

By defining a state vector, $\{X\}$, containing displacements and velocities, $\{u\}$ and $\{v\}$, equation (6) may be represented by

$$\{\dot{X}\} = [A]\{X\} + f(t) \quad (7)$$

where

$$[A] = \begin{bmatrix} 0 & I \\ -[M_g]^{-1}[K_g] & -[M_g]^{-1}[C_g] \end{bmatrix} \quad (8)$$

and

$$f(t) = \begin{bmatrix} 0 \\ [M_g]^{-1}[L] \end{bmatrix} \{g(t)\} \quad (9)$$

By using e^{At} as an integration factor on equation (7), followed by discretising and applying Padé approximations [11,12] to the result, equation (7) becomes

$$\{X\}_{j+1} = [M]\{X\}_j + [P]\{g\}_j \quad (10)$$

where

$$[P] = [M - I][A]^{-1} \begin{bmatrix} 0 \\ [M_g]^{-1}[L] \end{bmatrix} \quad (11)$$

and

$$M = e^{[A]h} \quad (12)$$

with h being the time step between two consecutive intervals.

The optimisation problem is to find the forcing function, $\{g\}$ that minimises the error, E , defined by

$$\begin{aligned} E(X_j, g_j) = & \sum_{j=1}^N ((QX_j - d_j), W(QX_j - d_j)) + (g_j, Bg_j) \end{aligned} \quad (13)$$

where N is the number of time-steps, d_j is a vector of measurements for the j^{th} interval, Q is a vector extracting the relevant state variables from the state vector, W is the identity matrix, and B is a regularisation parameter introduced due to the ill-conditioned nature of the problem. The notation (x,y) denotes the vector product in equation (13). The optimal smoothing parameter, B , is obtained from a method known as the L-Curve method [13] which seeks a trade-off between an acceptable least squares solution and ill-conditioning. Figure 4 later on in the paper displays an example of an L-Curve. The optimal regularisation parameter is located at the corner of the L-Curve, which corresponds to the point of maximum curvature [17].

A first order regularisation method is used in this paper which regularises the derivative of the forces as opposed to the forces themselves which would be the case in zeroth order regularisation. The minimisation process is solved by using dynamic programming [14] and Bellman's principle of optimality [15].

3 MOVING FORCE IDENTIFICATION AS A DAMAGE INDICATOR

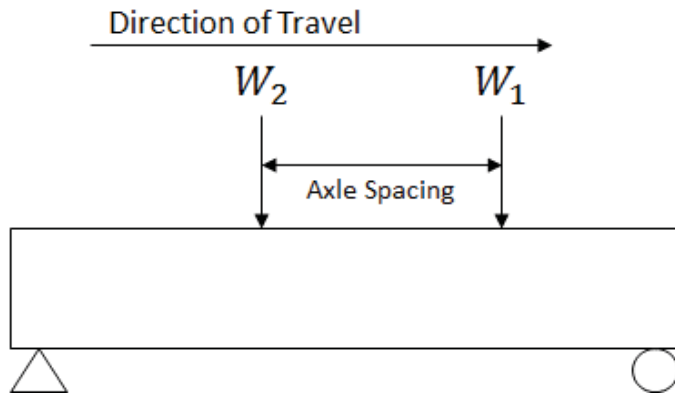


Figure 1. Two point loads traversing a 20 m simply supported beam

It has been shown previously by O'Brien et al. [8] that MFI can be used as a damage indicator. An example involving two point loads crossing a simply supported beam (at the same speed) is now demonstrated to show the effect of damage on the MFI algorithm results. Figure 1 shows the setup.

The first point load, W_1 , has a magnitude of 98.1 kN and is leading the second point load by 5 m. The second point load has a magnitude of 65 kN. The loads are travelling at a speed of 12 m/s on a beam with a cross sectional area, density, modulus of elasticity, length and second moment of area of 10 m^2 , 2446 kg/m^3 , $35 \times 10^9\text{ N/m}^2$, 20 m , and 1.15 m^4 respectively. The MFI algorithm is run for a healthy case and also for varying levels of damage. Damage is introduced as a percentage loss in stiffness along a one metre segment between a distance of seven and eight metres along the bridge.

Figure 2 shows the resulting calculated forces for W_1 for the healthy case and also for damaged cases. It can be seen that the damage cases have higher calculated forces and are further from the healthy case with increasing damage. The spike in the calculated forces in Figure 2 (at around the 0.2 s point) coincides with the arrival of W_2 on the beam at which point the problem is more ill-conditioned.

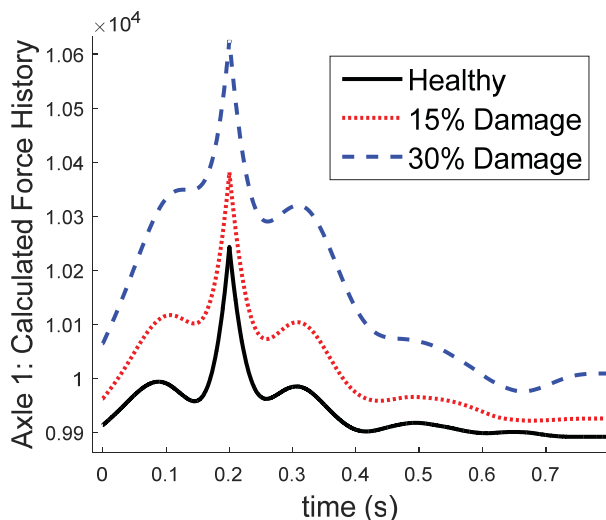


Figure 2. W_1 calculated force history for healthy and damaged cases

O'Brien et al. [8] apply the concept of statistical spatial repeatability to form a damage indicator based on the root mean squared difference between the mean of the calculated forces from a population of vehicles crossing a healthy bridge and a damaged bridge. A contour plot of damage indicator versus damage location and severity is obtained by varying the location and severity of damage. The results from O'Brien et al. lead to a damage indicator that is relatively good in predicting the extent of damage but is poor in predicting the location of the damaged based on any damage indicator value.

A similar analysis is performed in this work with the same problem arising. A finite element model of a beam is used in this analysis to generate deflection responses. A twenty metre beam is divided up into twenty elements. Noise is added to the deflection responses, d_{calc} , in order to create realistic measurements values, d_j , for each time step. Noise is introduced using the formula

$$d_j = d_{calc} + E_p d_{max} N_{noise} \quad (14)$$

where N_{noise} is a normally distributed vector with a mean of zero and a standard deviation of one, d_{max} is the maximum deflection at the centre of the bridge as the vehicle passes and E_p is the noise level which was chosen to be five per cent in this case.

Figure 3 shows the result obtained by using the first axle (point load in this case) as the basis of the damage indicator. Figure 3 is generated by repeating the process described above for a population of axle weights crossing the beam. The population of vehicle parameters is obtained from normal distributions using the mean and standard deviation values listed in Table 1. There are 500 vehicles used for each level of damage in the simulation.

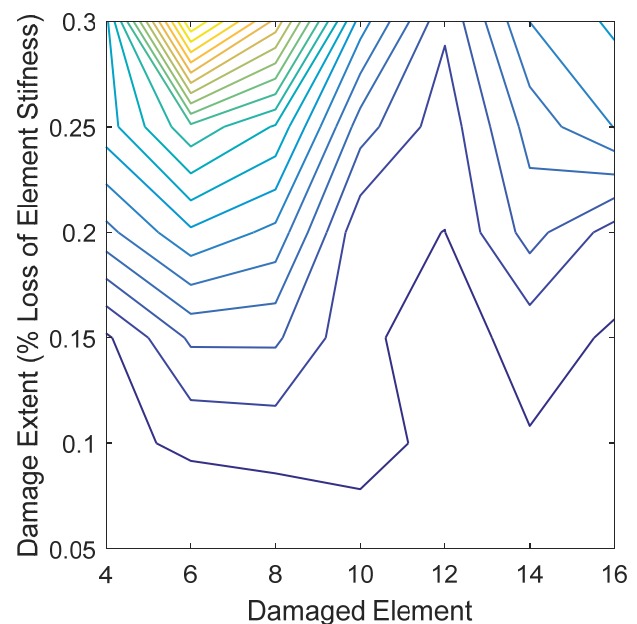


Figure 3. Contour plot of damage indicator

Table 1. Vehicle distribution parameters

Vehicle Parameter	Mean	Standard Deviation
GVW- Gross Vehicle Weight (kN)	120	12
Axle 1 (W_1) % of GVW	40	4
Axle 2 (W_2) % of GVW	60	6
Vehicle Velocity (m/s)	25	2.5
Axle Spacing (m)	5	0.5

4 INVESTIGATION INTO THE EFFECT OF SMOOTHING PARAMETER CHOICE ON DAMAGE INDICATOR MAGNITUDE

Table 2. Vehicle parameters

Vehicle Parameter	
GVW- Gross Vehicle Weight (kN)	120
Axle 1 Weight (kN)	65
Axle 2 Weight (kN)	98
Vehicle Velocity (m/s)	12
Axle Spacing (m)	5

The results depicted in Figure 3 are useful although somewhat limited for the reasons listed previously. The intention in this paper is to investigate the effect that the choice of smoothing parameter has on the value of the damage indicator.

The smoothing parameter that was used previously was the value correlating to the region of maximum curvature on the L-Curve. An L-Curve was plotted for each vehicle in the simulation process and the optimal parameter was found for each vehicle. This work investigates the sensitivity of the damage indicator to smoothing parameter and if in fact the region of maximum curvature is the most suitable basis for choosing this parameter. One case is used to simplify the analysis. The details of the loads are listed in Table 2. Damage is introduced as a thirty per cent reduction in stiffness in the seventh element. The beam details are the same that were used previously.

The first step involves plotting the L-Curve. The least squares norm versus the solution norm is plotted on a log-log plot for a range of smoothing parameters, 'lambda', increasing from zero. The least squares norm, L_{norm} is defined as

$$L_{norm} = \left(\sum_{j=1}^N ((QX_j - d_j), W(QX_j - d_j)) \right)^{1/2} \quad (15)$$

and the solution norm, S_{norm} , is defined as

$$S_{norm} = \left(\sum_{j=1}^N (g_j, g_j) \right)^{1/2} \quad (16)$$

where N is the number of intervals at which the axle force histories are calculated at. Figure 4 shows the resulting curve.

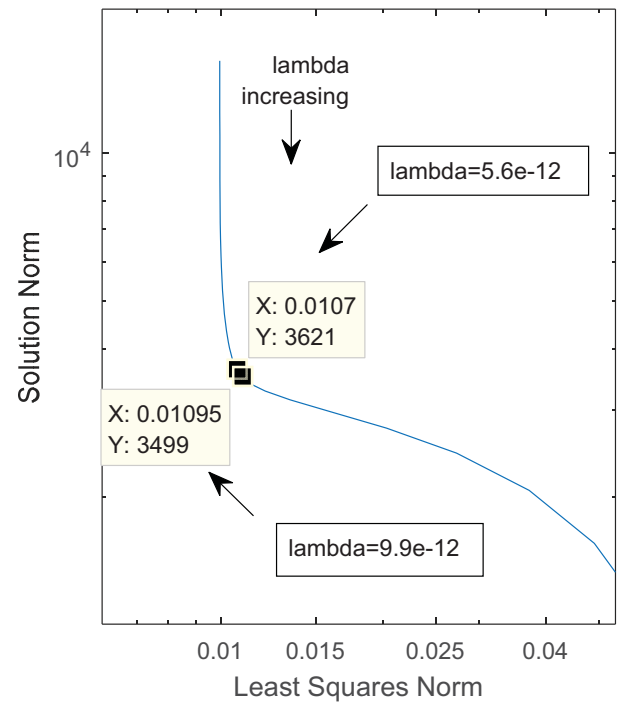


Figure 4. L-Curve

In order to achieve the exact point of maximum curvature, the range of smoothing parameters is refined in the general location where the point exists. In Figure 4, this point corresponds to the region between smoothing parameters 5.6×10^{-12} and 9.9×10^{-12} . It is not practical to locate this parameter manually so a more suitable method is to use a curvature plot [17]. A curvature plot is depicted in Figure 5 below for the region corresponding to smoothing parameters between 1×10^{-12} and 1×10^{-11} . The formula used to compute the curvature values of the L-curve here is taken from [17].

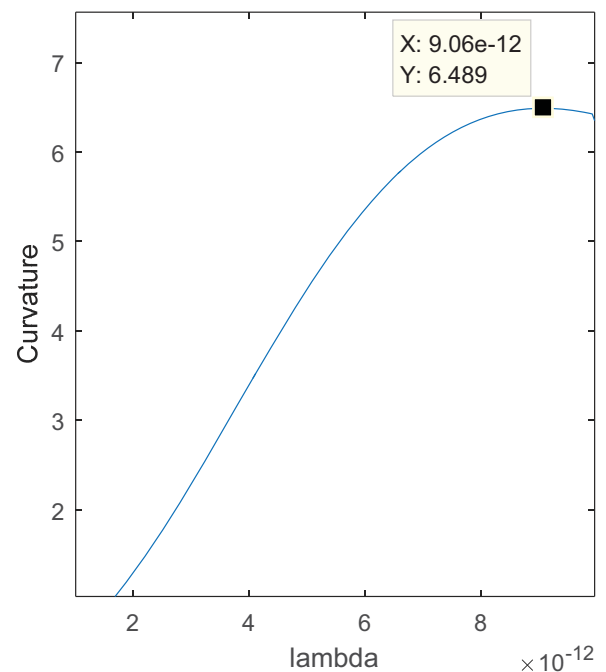


Figure 5. Curvature plot of L-Curve

From Figure 5, it is clear that the smoothing parameter corresponding to the region of maximum curvature is equal to 9.06×10^{-12} . This analysis examines the value of the damage indicator (from Axle 1 data) in this smoothing parameter range and it is compared to the curvature plot above. The damage indicator is again based on the root mean squared difference between the actual force and calculated force.

Ideally, the damage indicator should be sensitive to damage and not the choice of smoothing parameter. Examining Figure 6, it can be seen that at low curvatures the damage indicator is quite sensitive to the smoothing parameter. It then reaches a region where it is least sensitive to smoothing parameter. This is correlating to a value of 2.46×10^{-12} in Figure 6. The damage indicator increases in a linear fashion with smoothing parameter from that point on. An interesting point worth noting from Figure 6 is the fact that the maximum curvature point is not corresponding to the point where the damage indicator is least sensitive to the smoothing parameter choice. Another point worth noting is the fact that the damage indicator increases by a factor of 4.46 between the point where it is least sensitive to the smoothing parameter and the point of maximum curvature.

The damage indicator in Figure 6 compares the calculated forces for Axle 1 to the actual forces (which was constant at 65 kN). In reality, the actual force would be unknown. Therefore, it makes more sense to base the damage indicator on differences between calculated forces of the healthy and damaged case. This is also important because the calculated forces for the healthy case are inaccurate if the optimal smoothing parameter is not used. Figure 8 shows the result and there is a clear difference to Figure 7 but the decreasing and increasing trend of the damage indicator is still visible.

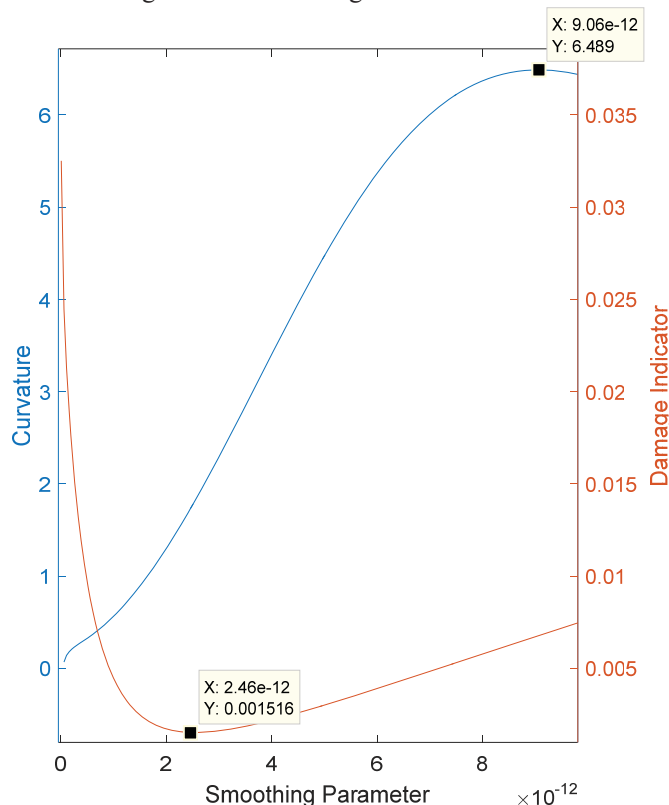


Figure 6. Curvature and smoothing parameter vs Damage Indicator

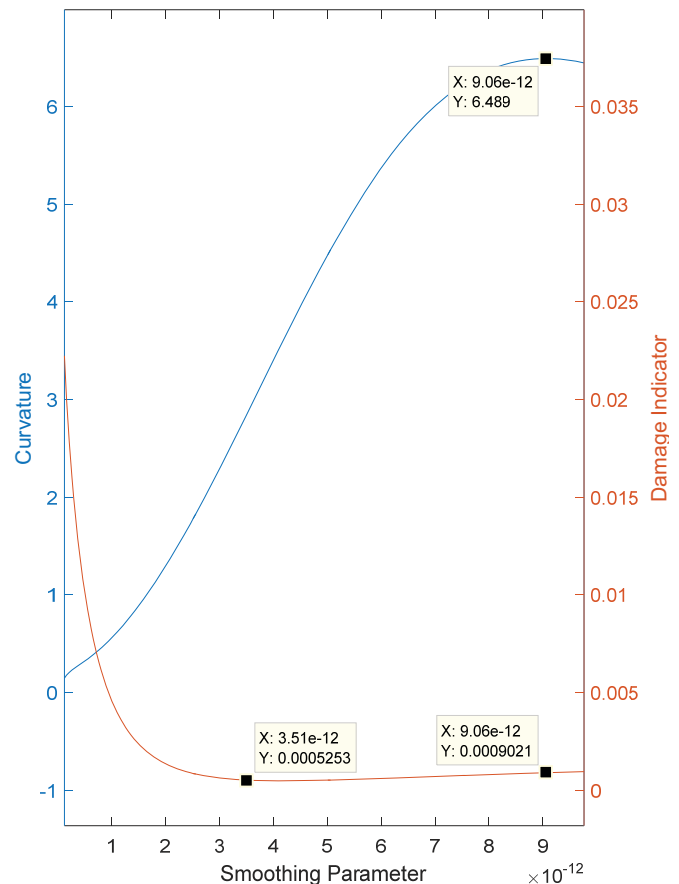


Figure 7. Damage indicator using calculated forces for healthy case

Figure 7 confirms that the region of maximum curvature is not corresponding to the point where the damage indicator is least sensitive to the choice of smoothing parameter. The damage indicator magnitude changes by a factor of 1.7 in this case between these two points. Finally, the last important observation is the fact that the damage indicator has far smaller values in Figure 7 than in Figure 6 suggesting that the source of inaccuracy in calculating the forces in a healthy case has a high effect on the damage indicator value. It is worth noting that the point of minimum sensitivity to smoothing parameter has seen the damage indicator reduce by a factor of 2.89 between the two cases in Figure 6 and Figure 7. Conversely, the point of maximum curvature has seen the damage indicator reduce by a factor of 7.49 between the two cases.

5 CONCLUSION

From the points discussed, there is a valid argument that the point of maximum curvature may not be the most suitable option for choosing the smoothing parameter for the purpose of damage detection. The investigations conducted here are quite limited however. Further investigation would be necessary for confirmation. There was also no investigation conducted into how the damage indicator varies with different damage locations and severities and how it behaves if this

point of minimum sensitivity to smoothing parameter is used instead. For this reason, further tests would be required to see if the MFI algorithm is improved by using the alternative smoothing parameter.

ACKNOWLEDGEMENTS

The authors wish to acknowledge the financial support received from Science Foundation Ireland under the US-Ireland Research Partnership Scheme towards this investigation.

REFERENCES

- [1] Azarbayejani M, El-Osery A, Reda Taha MM. Entropy-based optimal sensor networks for structural health monitoring of a cable-stayed bridge. *Smart Structure Systems* 2009; 5:369–379.
- [2] Salawu OS. Detection of structural damage through changes in frequency: a review. *Engineering Structures* 1997; 19(9):718–723.
- [3] Kim J, Stubbs N. Improved damage identification method based on modal information. *Journal of Sound and Vibration* 2002; 252(2):223–238.
- [4] Shih HW, Thambiratnam DP, Chan THT. Damage detection in slab-on-girder bridges using vibration characteristics. *Structural Control and Health Monitoring* 2013; 20:1271–1290.
- [5] Curadelli RO, Riera JD, Ambrosini D, Amani MG. Damage detection by means of structural damping identification. *Engineering Structures* 2008; 30(12):3497–3504.
- [6] González A, O'Brien E.J., McGetrick P.J.. Identification of damping in a bridge using a moving instrumented vehicle. *Journal of Sound and Vibration* 2012; 331(18):4115–4131.
- [7] Keenahan, J., O'Brien, E.J., McGetrick, P.J., González, A..The use of a dynamic truck-trailer drive-by system to monitor bridge damping. *Structural Health Monitoring* 2014; 13(2):143–157
- [8] O'Brien E, Carey C, Kennahan J. Bridge damage detection using ambient traffic and moving force identification. *Structural Control and Health Monitoring* 2015; 22(12): 1396–1407.
- [9] Law SS, Fang YL. Moving force identification: optimal state estimation approach. *Journal of Sound and Vibration* 2001; 239(2):233–254.
- [10] González A, Rowley C, O'Brien EJ. A general solution to the identification of moving vehicle forces on a bridge. *International Journal for Numerical Methods in Engineering* 2008; 75(3):335–354.
- [11] Bellman R. Introduction to matrix analysis, 2nd Edition. Philadelphia: SIAM, 1997; 176–177.
- [12] Trujillo DM. The direct numerical integration of linear matrix differential equations using padé approximations. *International Journal for Numerical Methods in Engineering* 1975; 9:259–270.
- [13] Hansen P. Analysis of discrete ill-posed problems by means of the L-curve. *SIAM Review* 1992; 34(4):561–580.
- [14] Trujillo DM. Application of dynamic programming to the general inverse problem. *International Journal for Numerical Methods in Engineering* 1978; 12:613–624.
- [15] Bellman R. Introduction to Mathematical Theory of Control Processes. Academic Press: New York, 1967.
- [16] O'Connor T, O'Brien EJ, Jacob B. An experimental investigation of spatial repeatability. *International Journal of Heavy Vehicle Systems* 2000; 7(1):64–81.
- [17] Hansen PC. The L-curve and its use in the numerical treatment of inverse problems. *Computational Inverse Problems in Electrocardiology* 2001; 119–142.

Distribution of stresses along the length of BFRP rods glued-in to Irish Sitka Spruce

Caoimhe O'Neill¹, Daniel McPolin¹, Su Taylor¹, Annette Harte²

¹School of Planning, Architecture and Civil Engineering, David Keir Building, Queen's University Belfast, Belfast, Co. Antrim, Northern Ireland, BT9 5AG

²College of Engineering and Informatics, Engineering Building, National University of Ireland, Galway, University Road, Galway, Co. Galway, Ireland.

email: coneill86@qub.ac.uk, d.mcpolin@qub.ac.uk, s.e.taylor@qub.ac.uk, annette.harte@nuigalway.ie

ABSTRACT: Glued-in rods (GiR) present a viable alternative to traditional steel moment connections in both new build and retrofit of timber structures. Limited research has been carried out on the distribution of stresses along the glued length of a rod under a load combination of axial force and bending moment. Previous research has found that under an axial-only load with short embedded lengths the entire length of the rod reaches peak stress at once and fails at a relatively low load with high peak stress. At longer embedded lengths failure is more gradual, with one end reaching peak stress before the other leading to a higher failure load and lower peak stress. This research aims to confirm that this holds for combined loading also; that stresses are not distributed evenly along the embedded length of a GiR and that failure arises at the loaded end due to a peak in stress concentration at this location. Electrical Resisting Strain gauges and Draw Tower Grating fibre optic sensors were used to capture the stress profile along the length of the GiR. Embedded length and edge distance were varied to investigate the effect of these variables on stress distribution. Specimens were tested under a pull-bending test set-up. Generally, a linear increase in strain was observed at each measured location until failure. In all specimens, failure was observed to occur with a stress peak towards the loaded end. In a number of specimens peak stress was observed to move away from the loaded end as the specimen approached failure, suggesting the bond at this end had failed.

KEY WORDS: Glued-in rods; Timber; Stress distribution; Composites.

1 INTRODUCTION

The development of lightweight, corrosion resistant and sustainable moment resistant timber connections using glued-in rods (GiR) would facilitate the adoption of timber elements in large construction projects.

Glued-in rods present a sustainable, aesthetically pleasing alternative to the cumbersome conventional steel moment connections that are often encountered in timber construction. Not only do connections with glued-in rods look better than conventional connections, they also have enhanced fire protection as the rods which transfer moment are embedded inside, and are therefore protected by, the timber.

Glued-in rods have significant potential in a wide range of both new build and restoration projects. Successful renovation has been carried out in roof and floor beams in buildings subject to decay [1], [2]. In new build, five areas were identified where glued-in rods may be used for connections: frame corner, beam-post connection, beam-beam joint, supports and hinged joints [3].

Since the late 1980s there have been many research projects commissioned on the use of bonded-in rods in timber construction e.g. GIROD and LICONs [4], [5]. In spite of this, no universal standard exists for their design. There had been an informative annex in the pre-standard PrBS ENV 1995-2:1997 which provided limited coverage of the design of bonded-in rods using steel bars however this document was replaced by BS EN 1995-2:2004 and no guidance is included in this current document.

While GiR are often steel some other rod types have been studied, namely Fibre Reinforced Polymers (FRPs). Earlier studies investigated the use of glass fibre reinforced polymer (GFRP) as an alternative to steel [6]–[8] while carbon fibre reinforced polymer (CFRP) has been used more recently [9]. Despite its significant cost effectiveness compared to CFRP and its greater tensile strength compared to GFRP, basalt fibre reinforced polymer (BFRP) has only been investigated in a very limited manner for use in glued-in technology [10]. BFRP has a modulus of elasticity closer to timber than the more commonly used material, steel. It is also a much lower cost material compared to the other FRPs. These advantages resulted in the selection of BFRP for use in this research.

The stress distribution along a GiR is generally considered to show a peak at the loaded end with dissipation of the stress occurring along the length of the rod as suggested by [11], [12] for axially loaded systems. At a fixed loading rate it appears that for short embedded lengths almost the entire length of the rod reaches peak stress at once and hence fails at a relatively low load and with high peak stress. At longer embedded lengths failure is more gradual, with one end reaching peak stress before the other leading to a higher failure load and lower peak stress.

Other research found that long embedded lengths resulted in minimal change in stress concentrations beyond the optimum embedded length and thus suggest that the bondline becomes inactive beyond the optimum length [13].

This research aims to determine if this assumption of stress distribution is valid for pull-bending mechanisms where the glued-in rod is under a combination loading; that stresses are not distributed evenly along the embedded length of a GiR and that failure arises at the loaded end due to a peak in stress concentration at this location.

2 TEST PROCEDURE

2.1 Background

Embedded length is one of the most influential variables on the strength of glued-in rods. A preliminary study was performed to assess how embedded length affected the pull-out strength of glued-in BFRP rods in Irish Sitka Spruce. As was anticipated, an increase in pull-out strength was observed with an increase in embedded length. It was observed that between the shortest embedded length of 80mm and the longest length of 600mm the pull-out capacity increased by a factor of 2.13. This was as expected since the larger interface area with each increase in embedded length provides additional resistance to the applied loading. Optimum embedded length was identified as $l_b=280\text{mm}$. At this point sufficient pull-out strength was achieved to resist loading that would be experienced in service.

Splitting was observed in several of the specimens of optimum embedded length. In these specimens failure strength was significantly lower than in specimens where no splitting was observed. In an attempt to alleviate this problem, a set of specimens were tested where embedded length remained at 280mm but edge distance increased in steps of one bar diameter. It was found that by increasing the edge distance by even a small amount instances of splitting could be reduced or eliminated, thus allowing specimens to reach their full potential capacity. The optimum edge distance was identified as $a=42\text{mm}$. This edge distance provided a good balance between a significant reduction in instances of splitting and a large enough lever arm to generate bending moment in the system.

2.2 Materials

Class C16 Irish Sitka Spruce (*Picea sitchensis*), sourced from Balcas Sawmill in Northern Ireland with a size of 75mm x 225mm sawn section was used. Material testing revealed that this timber had a 5th percentile bending strength $f_{m,k}=16.8\text{N/mm}^2$, shear strength $f_{v,k}=8.7\text{N/mm}^2$ and a density $\rho_k=381\text{kg/m}^3$.

Basalt Fibre Reinforced Polymer (BFRP) rods of 12mm diameter were used in this experimental programme. These rods were found to have a tensile strength of 920N/mm^2 under a low loading rate of 0.2kN/s [14]. Unlike steel or some other FRPs, no extensive cleaning of the rods was required prior to bonding as they are sand-coated which provides a good surface for adhesion.

In a number of studies it was determined that epoxy adhesives had higher strength than phenol resorcinol or polyurethane alternatives and that epoxies are most suitable for glued-in rod applications [15], [16]. A two-part thixotropic gap filling epoxy was used to ensure the bond had a higher shear strength

and stiffness than the timber being used. This adhesive only flows under shear so is ideal for GiR applications such as overhead beam repair or jointing overhead. The Rotafix epoxy used is comprised of a base which is an epoxy resin and a polyetheramine mixture hardener. The epoxy had a bond strength of $6\text{--}10\text{N/mm}^2$ after curing for a minimum of five days [17].

2.3 Test set-up

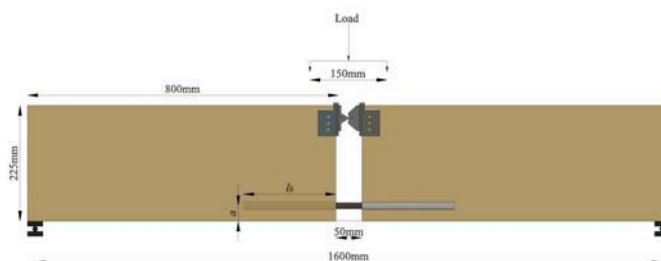


Figure 1. Configuration of Pull-bending test

Pull-out capacity can be used as a measure of the strength of a glued-in rod. The pull-out test system used was a pull-bending set-up, as pictured in Figure 1. The pull-bending system allows bending strength of the glued-in rod connection to be evaluated by removing the timber in the section being loaded so that the only resistance is from the BFRP bars glued-in to the timber.



Figure 2. a) ERS gauge, b) DTG fibre mounted on BFRP rod

Two methods were used to obtain the stress profile along the length of the GiR: Electrical Resisting Strain (ERS) gauges and Draw Tower Grating (DTG) fibre optic sensors. The sensors were attached directly on to the BFRP rod as per Figure 2 to assess the how stresses were distributed along the glued length under loading.

Electrical resisting strain (ERS) gauges relate small changes in length to a change in current, allowing measurement of microstrain. 30mm gauges were used. A noted disadvantage of their use is that they are relatively large and require wiring which may interfere with the bond in a GiR. DTG measure strain by detecting a change in wavelength of light reflected along a fibre optic sensor. This change in wavelength correlates to a change in strain. In the manufacture of DTGs the fibre is notched whilst being pulled resulting in a more

mechanically stable fibre than traditional fibre Bragg gratings. The fibre is reasonably simple to install as it is glued on to the sanded surface of the rod with a fast setting adhesive. The fibre is however relatively fragile therefore care must be taken during installation not to catch the fibre on a sharp edge or to bend the fibre excessively. Testing is slower when using DTGs as they measure strain within a fixed wavelength range. If the range is exceeded the test must be paused to allow recalibration of the wavelength range.

Stress distribution was assessed in a number of specimens to monitor how distribution changed with varying edge distance and with varying embedded length. For these tests optimum embedded length and edge distance had been identified through earlier testing.

A number of configurations were analysed using both strain acquisition methods. This allowed a comparison between both methods of measurement. The composition of the sample set is given in Table 1.

Table 1. Configuration of test specimens

	ID	l_b (mm)	a (mm)	Location of readings (mm from loaded end)
Edge Distance	ERS1	280	42	0, 70, 140, 210, 280
	ERS2	280	54	0, 70, 140, 210, 280
	ERS3	280	66	0, 70, 140, 210, 280
Embedded Length	ERS4	80	42	0, 20, 40, 60, 80
	ERS5	600	42	0, 150, 300, 450, 600
	DTG1	80	42	0, 20, 40, 60, 80
	DTG2	280	42	0, 20, 70, 140, 210, 280
	DTG3	600	42	0, 20, 150, 300, 450, 600

2.4 Specimen fabrication

Rods were cut to length and sanded local to the position of the ERS gauges. The gauges were then glued directly on to the rod. The double connection setup of the pull-bending test allowed that the ERS gauges could be staggered left and right to minimise interference with the glue line. Similarly, where DTGs were used the rod was sanded along the entire length and the fibre was glued directly on to the rod using superglue. Previous research has shown that attaching the DTG fibres in this manner has no negative effect on readings obtained.

2.5 Test procedure

Samples were loaded in 0.5kN increments to failure using a UKAS calibrated 600kN capacity hydraulic actuator. Deflection at mid-span and net horizontal movement of the bar as the sample was loaded and recorded with data acquisition connected to the transducer. Failure load was recorded when the sample could not take any additional load. The mode of failure was recorded also – percentage failure mode was then calculated for each bonded length. Each test

was repeated nine times due to the high variability of the timber used.

3 EXPERIMENTAL RESULTS

3.1 Failure mode

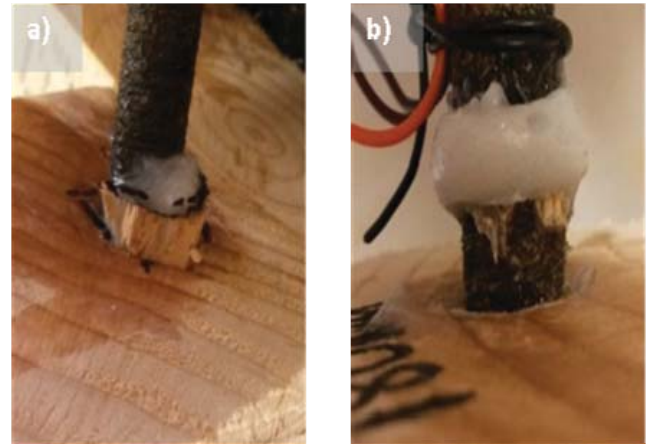


Figure 3. Failure modes observed: a) shear in timber, b) rod/adhesive failure

All specimens failed in a sudden, brittle manner. Two primary failure modes were identified and are pictured in Figure 3: a timber plug pull-out indicative of shear failure in the timber and a ‘clean’ pull-out signifying a failure of the rod/adhesive interface. In no cases was there failure within the adhesive or any rod failure.

The most prevalent failure mode observed was a pull-out failure in shear of the timber with a total of 67.6% of all samples failing in this manner. This was as expected due to the timber being the weakest element in the connection. Rod/adhesive failure was thought to have occurred due to the sand coating on the BFRP rod not adhering sufficiently well to the adhesive. The BFRP rod never failed since the force required for the rupture of the rod was never reached.

3.2 Suitability of test method

Strain data obtained from both methods of acquisition was reviewed and the most appropriate data set for each variable was chosen. It was established that for the majority of specimens using the ERS method proved to give the best data in terms of completeness.

With the shortest embedded length of $l_b=80\text{mm}$ using ERS gauges stress distribution was irregular at all load points. On inspection after failure it was observed that the adhesive had not formed a sufficient bond. It is suspected that this was due to the relatively large volume of wires prohibiting the formation of a good bond along the short embedded length. This was not a problem experienced with any of the larger embedded lengths.

A significant disadvantage highlighted with the use of the DTG fibre optic sensors was their fragility. In this case, on one of the specimens one sensor at the end of the fibre was damaged in the gluing process, leaving the data set incomplete.

3.3 Stress distribution along glued length

Generally, a linear increase in strain was observed at each measured location along the glued length until failure. In all specimens, the loaded end (0mm) recorded the maximum strain, proving the presumption that failure occurs primarily at the loaded end.

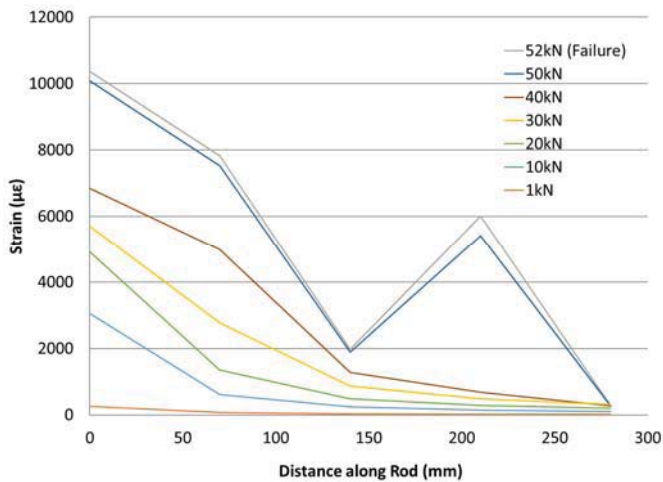


Figure 4. Stress distribution along glued length with increasing load ($l_b=280\text{mm}$, $a=42\text{mm}$)

Figure 4 illustrates the influence of increasing load on the stress distribution along the glued length. In a typical specimen stresses were distributed in a triangular fashion with the start of the glued length having the highest stress concentration and this dissipating along the glued length to a minimum concentration at the unloaded end. Further along the glued length it was observed that behaviour became more linear. This suggests that bending has less of influence on performance of the GiR further along the glued length than at the loaded end. As loading increased stresses increased at each measured location along the rod.

3.3.1 Influence of increasing edge distance, a

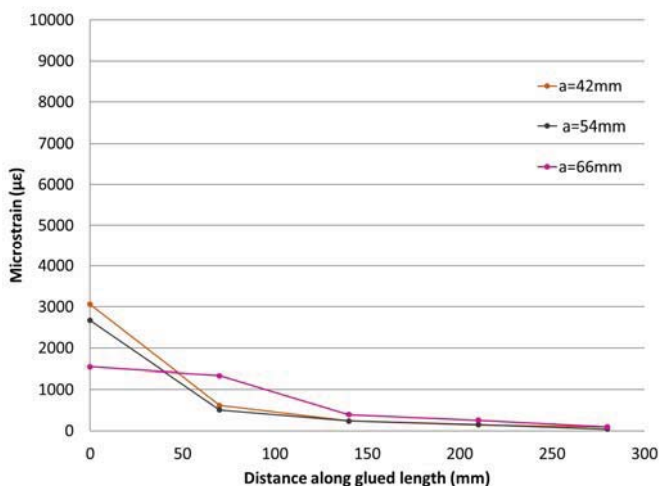


Figure 5. Stress distribution along glued length with increasing edge distance at a load of 10kN

Increasing edge distance tended to result in a reduction of stresses at each measured point along the bond length, as illustrated in Figure 5. When edge distance is increased the lever arm is reduced and hence the moment generated at the loaded end (0mm along rod) decreases.

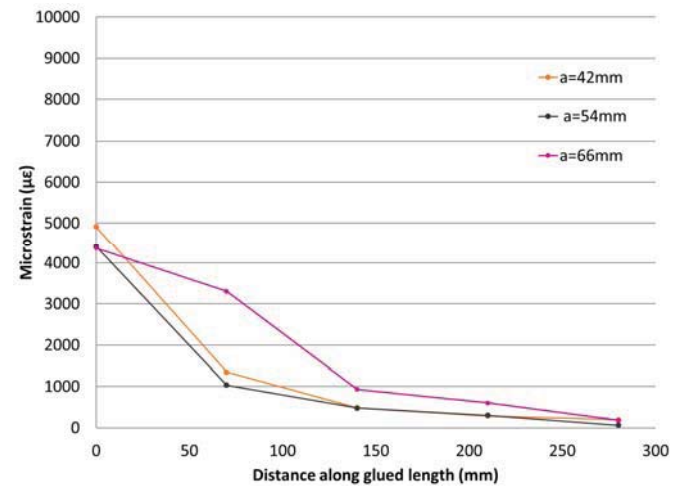


Figure 6. Stress distribution along glued length with increasing edge distance at a load of 20kN

With an increase in applied load the stress profile along the remained similar with an increase in stresses being observed at each measured location. Specimens with $a = 42\text{mm}$ and $a = 54\text{mm}$ failed at a similar ultimate load and both failed with a shear pull-out of the timber surrounding the bond. Specimen $a = 66\text{mm}$ failed at a lower load than the other two specimens and failure mode could not be visibly identified.

3.3.2 Influence of increasing embedded length, l_b

Increasing embedded length resulted in higher stresses being recorded at each measured location along the rod. Increased strain at the loaded end was observed with increasing embedded length. This is perhaps a result of a release of strain occurring in the shorter embedded lengths as the rod slips due to less anchorage in these specimens. However additional data must be collected to confirm this theory.

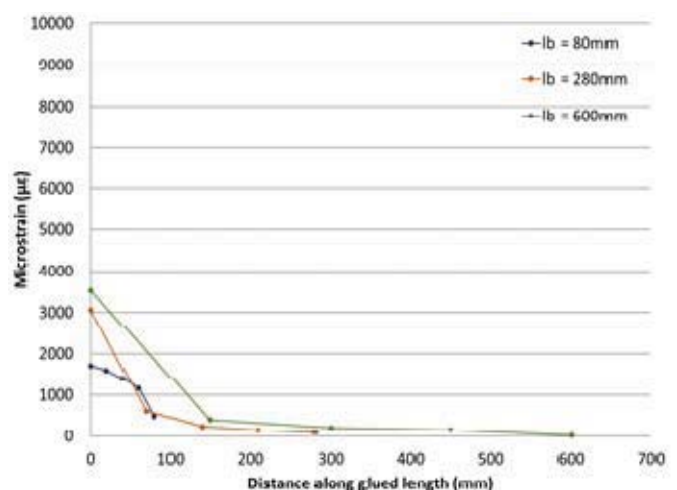


Figure 7. Stress distribution along glued length with increasing embedded length at a load of 10kN

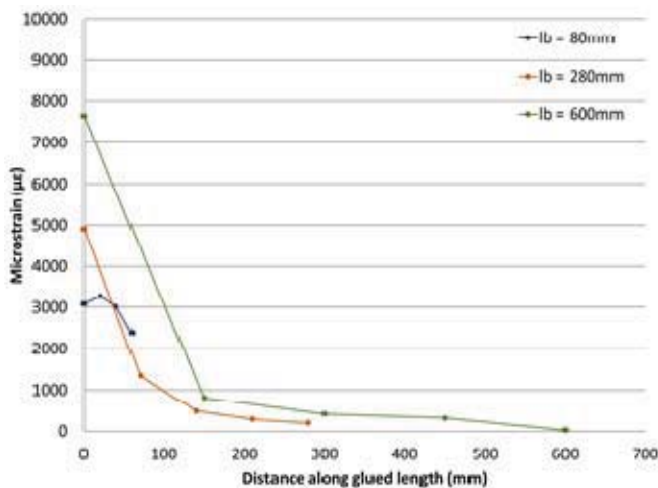


Figure 8. Stress distribution along glued length with increasing embedded length at a load of 20kN

As load increased, the distribution of stresses along the embedded length increased somewhat linearly, as seen in Figure 8. At a load of 20kN the shortest embedded length of $l_b = 80\text{mm}$ was nearing failure. With the sensors on this specimen spaced closer together than those on the other specimens an unzipping effect can be seen where failure propagates from the loaded end along the glued length. This is illustrated in Figure 8. It is not clear whether the other specimens evidenced this same movement of failure since the spacing between the first and second sensor on the glued length was considerably larger.

Although stresses did not increase as significantly at measured locations towards the anchored end than at the unloaded end it can be seen in Figure 7 and Figure 8 that there were some amount of stresses being carried towards the anchored end. This contradicts the findings of other researchers such as Yeboah [13] who suggested that the rod becomes inactive beyond an embedded length of 250mm and that no increase in strength is achievable beyond this length. As was observed in previous research by the authors, summarised in Section 2.1, the pull-out strength of the glued-in rods in this study continued to increase with increasing embedded length. This ability of the rod to carry stresses along the entire glued length explains how this increase in capacity is achieved. It is worth noting however that as the embedded length increases the stress capacity appears to be increasing at a lesser rate suggesting that a plateau in strength will be reached at some point.

4 CONCLUSIONS

- Experimental tests showed that the entire glued length of the glued-in rod connections contribute to resistance of the applied load, even in the longest embedded lengths.
- Stress distribution along the length of a glued-in rod under combined axial and bending force is not linear, with the loaded end reaching failure first and this then propagating along the glued length of the rod.

- Further work is suggested to assess the performance of such a connection method as a moment connection in a portal frame application.
- Higher loaded-end strains were observed for longer embedded lengths, further research should be undertaken to assess the slip behaviour with increasing embedded length.

ACKNOWLEDGMENTS

This research is funded by the Department of Agriculture, Food and the Marine of the Republic of Ireland under the FIRM/RSF/COFORD scheme as part of 'Innovation in Irish timber Usage' (project ref. 11/C/207). The authors would also like to thank the technical staff in QUB for their assistance in the lab.

REFERENCES

- [1] D. Smedley, P. Alam, and M. Ansell, "George Street, St. Albans, UK—a case study in the repair of historic timber structures using bonded-in pultruded plates," ... *9th World Conf. Timber* ..., no. 2006, 2006.
- [2] K. U. Schober and K. Rautenstrauch, "Experimental Investigations on Flexural Strengthening of Timber Structures with CFRP," in *Proceedings of the International Symposium on Bond Behaviour of FRP in Structures (BBFS 2005)*, 2005, pp. 457–464.
- [3] E. Gehri, "High Performing Jointing Technique Using Glued-in Rods," in *11th World Conference on Timber Engineering 2010, WCTE 2010*, 2010.
- [4] R. Bainbridge, C. Mettem, K. Harvey, and M. Ansell, "Bonded-in rod connections for timber structures—development of design methods and test observations," *Int. J. Adhes. Adhes.*, vol. 22, no. 1, pp. 47–59, 2002.
- [5] J. G. Broughton and A. R. Hutchinson, "LICONS Task 2-Sub task 2.2," 2004.
- [6] K. Harvey and M. P. Ansell, "Improved timber connections using bonded-in GFRP rods," in *Proceedings of 6th World Conference on Timber Engineering, Whistler, British Columbia*, 2000.
- [7] M. Madhoushi and M. P. Ansell, "Experimental study of static and fatigue strengths of pultruded GFRP rods bonded into LVL and glulam," *Int. J. Adhes. Adhes.*, vol. 24, no. 4, pp. 319–325, Aug. 2004.
- [8] M. Ansell and D. Smedley, "Briefing: Bonded-in technology for structural timber," *Proc. ICE-Construction* ..., vol. 160, no. 3, pp. 95–98, Jan. 2007.
- [9] L. F. P. F. P. Juvandes and R. M. T. Barbosa, "Bond Analysis of Timber Structures Strengthened with FRP Systems," *Strain*, vol. 48, no. 2, pp. 124–135, 2012.
- [10] D. Yeboah, S. Taylor, D. McPolin, R. Gilfillan, and S. Gilbert, "Behaviour of joints with bonded-in steel bars loaded parallel to the grain of timber elements," *Constr. Build. Mater.*, vol. 25, no. 5, pp. 2312–2317, 2011.
- [11] R. Steiger, E. Gehri, and R. Widmann, "Pull-out strength of axially loaded steel rods bonded in glulam parallel to the grain," *Mater. Struct.*, vol. 40, no. 8, p. p 69–78, Jan. 2006.
- [12] M. Jahreis, K.-U. Schober, W. Haedicke, and K. Rautenstrauch, "Non-destructive testing, measurement and numerical damage analysis of high demanding stress regions in FRP reinforced timber structures by," in *Composites 2010 American Composites Manufacturers Association*, 2010, pp. 1–6.
- [13] D. Yeboah, "Rigid Connections in Structural Timber Assemblies," Queen's University Belfast, 2012.
- [14] G. Tharmarajah, "Compressive Membrane Action in Fibre Reinforced Polymer (FRP) Reinforced Concrete Slabs," Queen's University Belfast, 2010.
- [15] E. Serrano, "Glued-in rods for timber structures * a 3D model and nite element parameter studies," vol. 21, pp. 115–127, 2001.
- [16] J. G. Broughton and A. R. Hutchinson, "Adhesive systems for structural connections in timber," *Int. J. Adhes. Adhes.*, vol. 21, no. 3, pp. 177–186, 2001.
- [17] Rotafix Ltd, "Rotafix Structural Adhesive (LM) - Epoxy Bonding Adhesive," 2015.

Viscoelastic Creep of FRP Reinforced Glulam

Conan O’Ceallaigh¹, Karol Sikora¹, Daniel McPolin², Annette M. Harte¹

¹ College of Engineering & Informatics, National University of Ireland, Galway, University Rd., Galway, Ireland

²School of Planning, Architecture and Civil Engineering, Queen’s University Belfast, University Road, Belfast BT7 1NN, UK
Email: conan.oceallaigh@nuigalway.ie, karol.sikora@nuigalway.ie, d.mcpolin@qub.ac.uk, annette.harte@nuigalway.ie

ABSTRACT: The reinforcement of timber using fibre reinforced polymer (FRP) rods or plates is widely accepted as an effective method of increasing the strength and stiffness of members, while at the same time reducing the variability in properties. The short-term behaviour of these reinforced members is relatively well understood, however, the long-term or creep behaviour of such members has received less attention. The objectives of the present work are to determine the durability of reinforced timber beams under sustained loading and constant climate conditions. Timber is a viscoelastic material so its deformation response is a combination of both elastic and viscous components. This viscous creep component is defined as a deformation with time at constant stress and at constant environmental conditions.

Sitka spruce is the most widely grown specie in Ireland and is the focus of this study. Glued Laminated (Glulam) beams were manufactured from Sitka spruce and a selected portion of them were reinforced with basalt-fibre reinforced polymer (BFRP) rods. The short-term flexural testing of these beams in their unreinforced and reinforced state demonstrated a significant increase in stiffness with a modest percentage reinforcement ratio. The long-term flexural testing required the design of a creep test frame to implement a constant stress of 8 MPa in the compression zone of an equal proportion of unreinforced and reinforced. The long-term strain and deflection results for the first 52 weeks of testing are presented. The reinforcement was found to have an insignificant impact on the creep deflection but the maximum tensile creep strain was significantly reduced.

KEY WORDS: BFRP, Irish Grown Sitka Spruce, Reinforced Timber, Viscoelastic Creep

1 INTRODUCTION

The mechanical and physical properties of softwood timber can vary considerably as a result of the age and rate of growth of the tree and other environmental factors which affect the wood cell density and strength [1]. Sitka spruce is characterised as a fast growing, low density timber which when subjected to flexural loading generally fails in tension due to the presence of knots [2]. In Ireland, this species has an average rotation length of 35 – 40 years [3]. This low density timber demonstrates limited capacity to carry substantial loads. However, when combined to create a composite element such as a glued laminated beam, the capacity of this softwood timber may be greatly increased.

The performance of glued laminated beams may also be enhanced with the addition of fibre reinforced polymer (FRP) composite reinforcement. It has been seen that the addition of modest reinforcement ratios can delay tension failure in glued laminated elements. The reinforcement utilises the additional capacity of the timber in the compression zone resulting in much more consistent behaviour as well as a significant increase in flexural stiffness [4, 5].

Long-term effects in these timber beams are of crucial importance to structural engineers when designing timber structures. These long-term effects, or creep effects, are commonly seen in timber elements when stressed under a load for long periods of time. Creep effects in timber can be divided into two primary categories, namely viscoelastic creep and mechano-sorptive creep. Timber is a viscoelastic material so its deformation response is a combination of elastic and viscous components. This viscoelastic creep component is defined as a

deformation with time at constant stress and at constant environmental conditions. Mechano-sorptive creep is a deformation due to an interaction between stress and moisture content change [5, 6] in variable environmental conditions. Mechano-sorptive creep is independent of time [8] and is directly related to the change in moisture content and mechanical stress.

These creep effects must be understood as excessive deflection will result in premature failure. The objective of this study is to examine the long-term deformation of FRP reinforced timber beams manufactured from fast grown Irish timber. This study focuses on the viscoelastic creep mechanisms in unreinforced and reinforced beams under constant load in constant environmental conditions.

2 LITERATURE REVIEW

Creep phenomena have been the subject of particular interest for the timber engineering research community. Under serviceability conditions, viscoelastic creep depends on the stress and temperature of the timber and although viscoelastic creep occurs under a constant climate conditions, it is important to note, the magnitude of viscoelastic creep also depends on the moisture content of the timber [8, 9]. In a study by Hering and Niemz [10], the viscoelastic behaviour of European beech timber subjected to four-point bending was investigated and the longitudinal creep compliance at three different moisture contents (8.14%, 15.48% and 23.2 %) was investigated. Each timber specimen was loaded to approximately 25% of the ultimate bending strength. As can be seen in Figure 1, a viscoelastic compliance function which increased linearly with

moisture content was successfully fitted to the data. This study was performed over a relatively short period of time (≈ 200 hr).

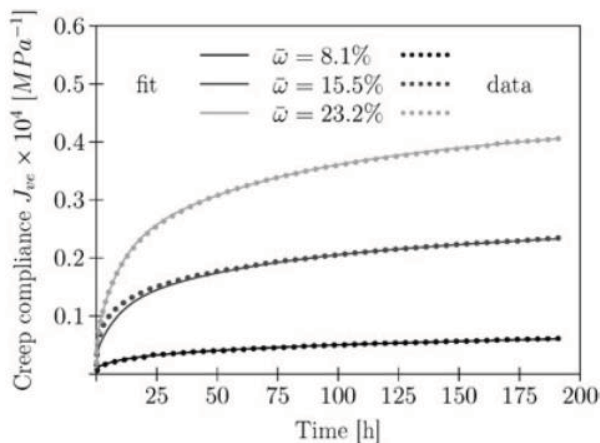


Figure 1. Creep data vs creep compliance function fit [10]

Another study designed to examine if the rate of creep eventually decreases towards a creep limit was performed by Hunt [11]. Experimental creep data on unreinforced timber was examined over a 13 week period. The conclusions from these tests were then applied to creep tests over a much longer period of time (8 years [12]). Creep functions were matched and extrapolated to estimate the long-term creep after 50 years under load. No evidence was found to suggest a viscoelastic creep limit in timber when stressed in a constant climate. There are no long-term creep tests results of a similar duration to disprove their findings. This shows the potential for timber elements to deform throughout their service life and demonstrates the importance of understanding its behaviour.

The long-term creep behaviour of timber elements has been shown to produce significant deformations with time and these are accounted for in design standards for various Service Class conditions. However, the long-term behaviour of timber elements that have been reinforced with the use of a FRP material has received little attention in previous research. The short-term behaviour of these reinforced elements demonstrate significant improvements in stiffness and ultimate moment carrying capacity. The long-term behaviour of reinforced timber elements have also primarily focused on creep effects in a variable climate and only a limited number of studies focus on viscoelastic creep effects within constant climate conditions.

Lu et al. [13] imposed a constant load on unreinforced and reinforced glued laminated beams under constant climate conditions. Ten beams were loaded in four-point bending. The 460 kg load applied corresponded to 30% of the ultimate strength of the glulam beam. The results allowed for the comparison of different reinforcement configurations (6mm rebar in compression zone, 6mm rebar in the tensile zone and 8mm rebar in the tensile zone) against the control (unreinforced) specimens as shown in Figure 2. Although a significant reduction in creep can be seen, the constant dead load on both unreinforced and reinforced beams leads to varying stress levels within each beam, a key contributor to the overall magnitude of viscoelastic creep.

Plevris and Triantafillou [15] performed long-term creep tests on reinforced beams. There was a relatively small sample

size of 3 beams, one unreinforced control beam and two reinforced beams with two different percentage area reinforcement ratios of 1.18% and 1.65% respectively. The tests were carried out under constant climate conditions. They determined from the experimental results, that the creep behaviour of the FRP-reinforced wood is primarily dominated by creep within the timber.

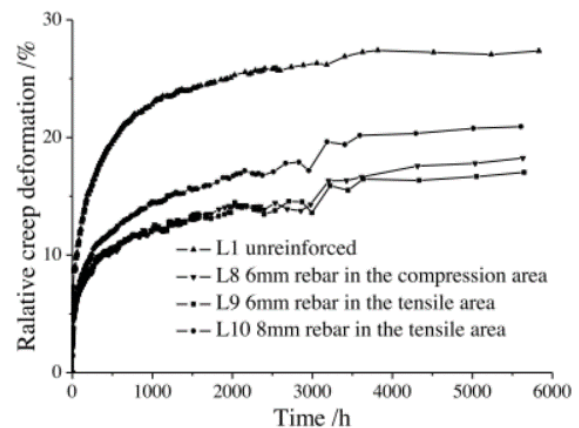


Figure 2. Relative creep results Lu et al. [14]

Therefore, in order to examine the influence of the reinforcement on the performance of reinforced beams, it is important to apply a common stress level in all unreinforced and reinforced timber beams.

3 EXPERIMENTAL PROGRAMME

3.1 Introduction

To examine the effect of rod reinforcement on the long-term performance of glued laminated beams in constant environment, the following experimental programme has been designed.

Irish grown Sitka spruce boards were conditioned to approximately 12% moisture content and strength graded using a mechanical grading machine. From the grading results, 40 glued laminated beams were designed and manufactured in the Timber Engineering Laboratory at the National University of Ireland, Galway. The beams comprise of four laminations, with each beam measuring 98 mm x 125 mm x 2300 mm. These beams were specifically designed to exhibit similar stiffness properties in each manufactured beam. This was successfully demonstrated in short-term flexural testing of each beam in its unreinforced state. Twenty of these beams were subsequently reinforced with two, 12 mm basalt fibre reinforced polymer (BFRP) rods adhered within two circular routed grooves in the bottom tensile laminate (Figure 3). This accumulated to a modest percentage reinforcement of 1.85%. Once reinforced, short-term flexural testing was repeated to examine the increase in bending stiffness as a result of the reinforcement. An equal proportion of the unreinforced and reinforced beams were then subjected to a constant dead load in a controlled climate chamber. The controlled climate chamber was set to a constant relative humidity of $65\% \pm 5\%$ and a constant temperature of $20^\circ\text{C} \pm 2^\circ\text{C}$ throughout the test.

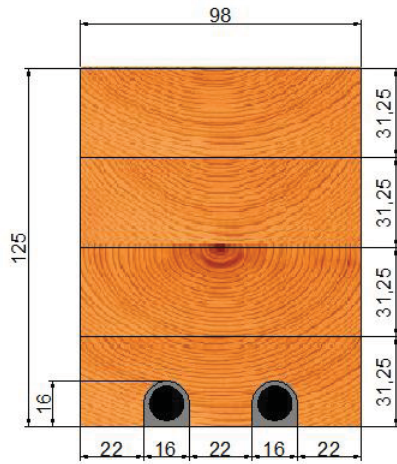


Figure 3. BFRP Reinforced Glulam

3.1.1 Test Frame Design and Instrumentation

There is no standard method for examining the creep behaviour of timber beam elements. As a result, different methods and test rigs have been designed and used to examine creep deflection. The majority of authors implement a four-point bending test setup, however, in some cases a three-point bending test set up [15] or an evenly distributed load across the whole length of the member have been used [16].

In this study the long-term creep test frame was designed to implement the same test configuration described in EN 408 [17] for short-term flexural tests (Figure 5). The test frame was designed to accommodate 18 beams simultaneously loaded to a constant bending stress to induce viscoelastic creep with time. The sustained load is applied through a lever arm as illustrated in Figure 4. The lever arm length is adjustable and loads (steel plates) can be added or removed as necessary. A total vertical load of approximately 6241 N and 5748 N was applied to the reinforced and unreinforced beams, respectively.

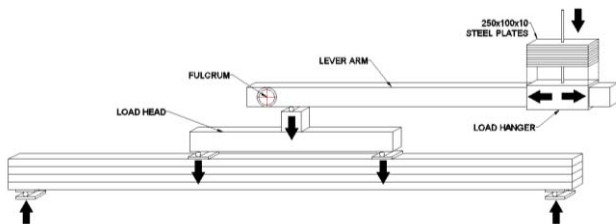


Figure 4. Creep test beam loaded using lever arm

The beam mid-span deflection is measured using a dial gauge and the longitudinal strain is measured using electrical resistance strain gauges on the tension and compression faces. A proportion of the beams are monitored with additional strain gauges on the side of the beams to observe the strain profile through the cross section. These long-term strain results are monitored using a Campbell Scientific data acquisition system, which initially recorded strains every 5 minutes during the early stages of the test, which is associated with relatively rapid creep deformations. This frequency was slowly reduced with time to its current frequency of 1 hour. The beams are tested in a climate chamber at a temperature of 20 ± 2 °C and at a relative

humidity of 65 ± 5 % throughout, which coincides with Service Class 1 as defined in Eurocode 5.

3.1.2 Loading Regime

The applied load chosen corresponds to approximately 25-30% of the ultimate load of the unreinforced glued laminated beam which will produce measurable deflections in a reasonable time scale without causing failure in the specimen. Each beam is loaded to achieve a stress of 8 MPa on the compression face. To achieve this stress level, different loads were required for each beam with greater loads required on the reinforced beams. Short term flexural test results provided stiffness values of each beam [18]. The measured mean modulus of elasticity of each beam was used in a transformed section analysis to determine the required load.



Figure 5. Loaded Creep Frame in Constant Climate

This method is implemented to examine the long-term effect of reinforcement when the timber is loaded to similar stress levels.

Each beam is loaded separately through individual lever arms. The initial elastic deformation is noted for each beam directly after loading and the deflection results are then recorded at regular intervals with time.

4 RESULTS

4.1 Short-term Test Results

The short-term test results for the twenty reinforced beams are presented in Table 1. The mean bending stiffness is presented for these beams in their unreinforced and reinforced states (Table 1). There is a significant increase in bending stiffness with an average increase of 16.30 % for a moderate percentage reinforcement of 1.85 %. This promotes fast-grown Irish Sitka spruce as a suitable donor material to reinforce with FRP material, due to the significant improvement in the short-term flexural performance. The percentage increase in stiffness is also presented.

Table 1: Short-term flexural stiffness

Stiffness (N/mm ²)	Unreinforced	Reinforced	Percentage Increase (%)
$EI_{Local} (x10^{11})$	1.46 (.120)*	1.69 (.119)	16.30 (3.66)

*Mean Values (Std. Deviation)

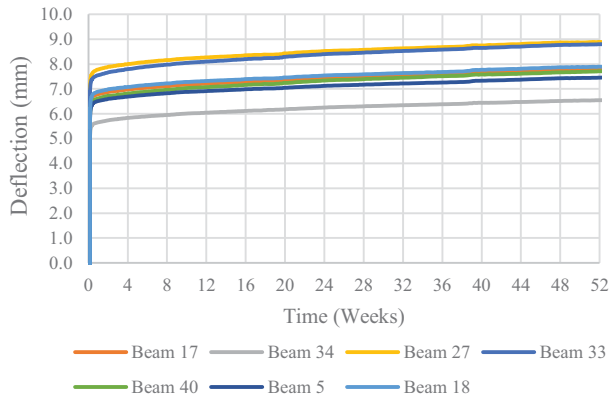


Figure 6. Unreinforced Deflection Results

4.2 Long-term Test Results

The test results for the first 52 weeks are presented. Eighteen beams (9 reinforced and 9 unreinforced) are tested under constant load in the constant climate. The long-term deflection test results are expressed as total deflection and relative creep (C_R) deflection, which is defined as the deflection at time t , expressed in terms of the initial elastic deflection as seen in Equation (1) [19].

$$C_R(t) = \frac{w(t)}{w_0} \quad (1)$$

Where:

C_R = Relative creep,
 w_0 = Initial deflection,
 $w(t)$ = deflection at time, t .

4.2.1 Long-Term Deflection Results

The long-term deflection of each beam under load in a constant climate condition is presented. The unreinforced beam group consists of nine unreinforced beams loaded to a bending stress of 8 MPa in four-point bending. Seven of these beams are monitored with vertical displacement dial gauges (Figure 6). Beam 27 (8.89mm) and Beam 34 (6.54mm) have the highest and lowest total deformation (initial elastic deformation and long term creep deflection) after 52 weeks, respectively. This is as expected as they have the lowest and highest bending stiffness, respectively, when measured during short-term flexural tests. The reinforced beam group consists of nine reinforced beams similarly loaded to a bending stress of 8 MPa in four-point bending. Seven of these beams are monitored with vertical displacement dial gauges (Figure 7). Beam 30 (7.88mm) and Beam 26 (5.97mm) have the highest and lowest total deflection after 52 weeks, respectively. The variability within timber can be seen in the total deflection results in Figure 6 and Figure 7. In order to compare the deflection results between the unreinforced group and reinforced group and observe the effect of reinforcement on long-term deflection, the average deflections of each beam group are shown in Figure 8. After 52 weeks, the mean total deflection in the unreinforced beam group (7.92mm) is 11% greater than the reinforced beams group (7.13mm).

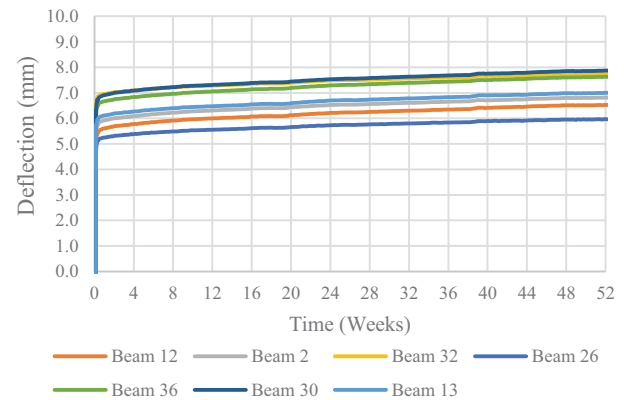


Figure 7. Reinforced Deflection Results

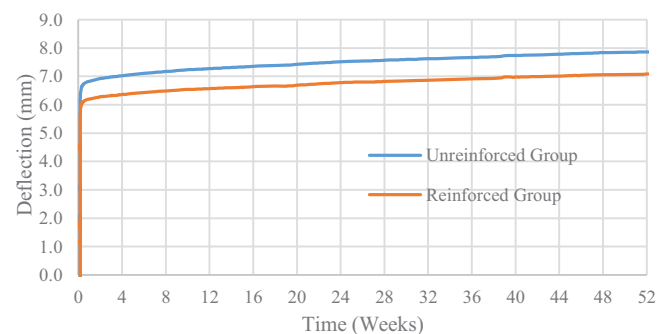


Figure 8. Average Group Deflection

To focus on the long-term deflection after the initial elastic deflection, the relative creep results are presented. Figure 9 presents the mean relative creep deflection results with time for the unreinforced beam group and the reinforced beam group beams in a constant climate. Although there is a reduction in the overall deflection in the reinforced beam group due to the FRP reinforcement, there is less than 1.5% difference between the measured relative creep deflections of both groups. A statistical analysis of the group means has shown no statistically significant reduction in viscoelastic creep due to the FRP reinforcement in a constant climate.

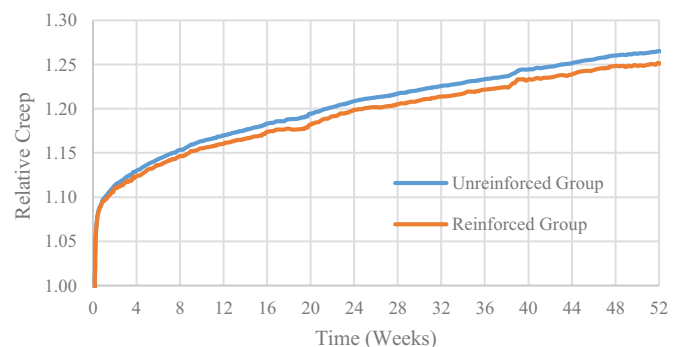


Figure 9. Mean relative creep deflection

4.2.2 Long-Term Strain Results

As previously mentioned, the strain results are measured using electrical resistance strain gauges designed for long-term use on timber. The strain gauge is adhered to the timber surface

of the beam situated between two routed grooves which house the BFRP rods (Figure 10). The longitudinal strain has been measured on the tension and compression face of 7 unreinforced and 7 reinforced beams. The mean total strain measurement from the tension and compression face of the unreinforced and reinforced beam groups are presented in Figure 11.

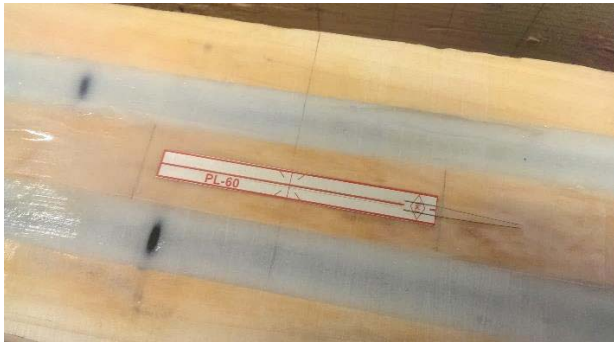


Figure 10. Strain Gauge Position on Reinforced Beam

The strain gauge measurements on the compression face are similar when both beam groups are compared with the reinforced beam group experiencing slightly less strain than the unreinforced beam group. In contrast, the difference between the strains measured on the tension face of each beam group is more significant. The reinforced beams experience 24.5% less strain on average after 52 weeks. This difference is as a result of the rod reinforcement and its position within the tensile laminate of each reinforced beam. The strains which would normally appear within the timber have been shared with the superior BFRP rod reinforcement resulting in the reduced strain within the timber.

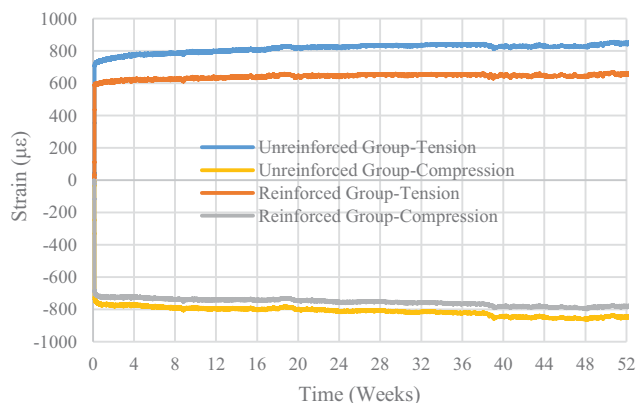


Figure 11. Mean Total Strain Measurement Results

To solely examine the viscoelastic strain, the mean strain results have been presented without the elastic strain component in Figure 12. Similar mean strains are observed in the compression face of both the unreinforced and reinforced beams groups indicating a similar stress and creep rate within both beam groups. In comparison, the mean strains on the tension face show larger strains within the unreinforced beam group. This is again as a result of the reinforcement within the reinforced beam group and its position within the tensile laminate.

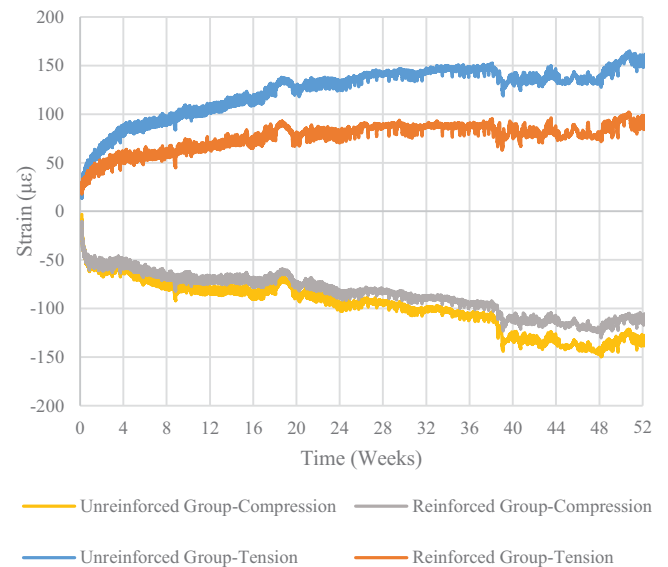


Figure 12. Mean Viscoelastic Strain Measurement Results

Representative results of strains measured through the cross section of the unreinforced (Beam 40) and reinforced (Beam 26) beams are presented in Figure 13 and Figure 14, respectively. It must be noted that these results are observed on singular beams and not an average value, hence the variability within timber must be considered when examining these beams. It can be seen that the unreinforced beam experiences greater strain in the tension zone than the reinforced beam. The rate of creep is seen to be higher in the unreinforced specimen. The measured strains in the compression zone are similar when comparing the unreinforced and reinforced beams and any difference is thought to be associated with the inherent variability within timber.

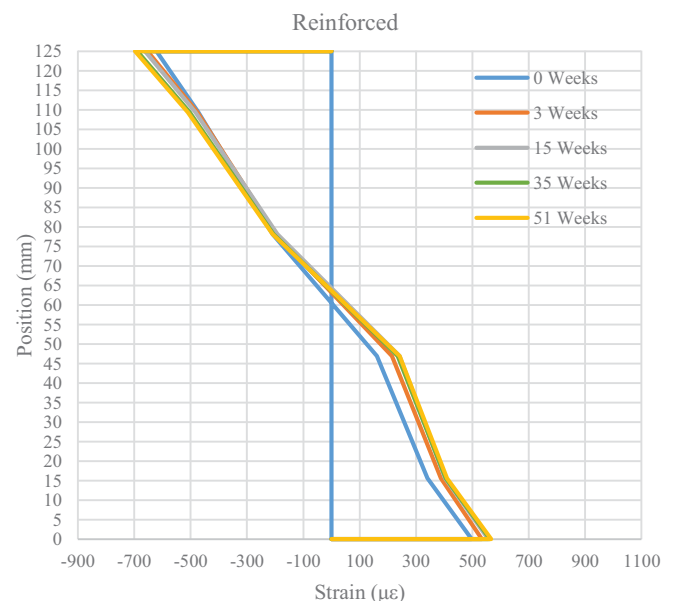


Figure 13. Cross section strain-Reinforced (Beam 26)

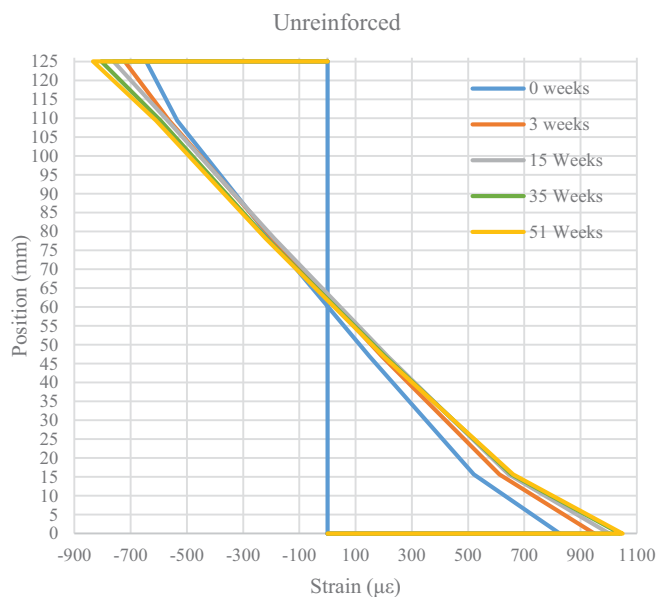


Figure 14. Cross section Strain-Unreinforced (Beam 40)

5 CONCLUSION

The long-term viscoelastic creep effects in unreinforced and reinforced timber and the experimental programme have been described. The short-term four-point bending tests demonstrated that the addition of BFRP rod reinforcement in modest quantities can greatly increase the short-term stiffness of glued laminated beams. An average increase in local bending stiffness of 16.3% was observed for a moderate percentage reinforcement of 1.85%.

The long-term deflection results have shown a beneficial overall decrease in the total deformation (initial elastic deformation and viscoelastic deformation) due to the reinforcement. The analysis of the relative creep results have shown no statistically significant reduction in viscoelastic creep deflection when comparing the mean relative creep results of both beam groups.

The measured strain results in the longitudinal direction and through the cross section of the beams with time have been presented. The long-term viscoelastic strain on the compression face has been shown to be quite similar in both beam groups indicating a similar bending stress has been subjected to each beam in the test programme. The results have also shown a significant reduction in strain on the tension face of the reinforced beam group as a result of the reinforcement. Examining the measured strains through the cross section of both the unreinforced and reinforced beams has also highlighted this reduced strain within the timber in the tension zone of the reinforced beam. Higher levels of creep strain were observed within the unreinforced beams. The reduced magnitude of the creep tensile strain observed within the reinforced beams is thought to be a result of the restraining effect of the FRP rod reinforcement.

ACKNOWLEDGMENTS

This work has been carried out as part of the project entitled 'Innovation in Irish timber Usage' (project ref. 11/C/207) funded by the Department of Agriculture, Food and the Marine of the Republic of Ireland under the FIRM/RSF/COFORD

scheme. The authors would also like to thank ECC Ltd. (Earrai Coillte Chonnacht Teoranta) for supplying all the timber used in this project.

REFERENCES

- [1] M. Treacy, J. Evertsen, and Á. N. Dhubháin, "A comparison of mechanical and physical wood properties of a range of Sitka spruce provenances," COFORD, National Council for Forest Research and Development, 2000.
- [2] J. R. Gilfillan, S. G. Gilbert, and G. R. H. Patrick, "The use of FRP composites in enhancing the structural behavior of timber beams," *J. Reinf. Plast. Compos.*, vol. 22, no. 15, pp. 1373–1388, 2003.
- [3] G. Raftery and A. Harte, "Material characterisation of fast-grown plantation spruce," *Structures Build.*, vol. 167, no. 6, pp. 380–386, 2014.
- [4] J. R. Gilfillan, S. G. Gilbert, and G. R. H. Patrick, "The Improved Performance of Home Grown Timber Glulam Beams Using Fibre Reinforcement," *J. Inst. Wood Sci.*, vol. 15, no. 6, pp. 307–317, 2001.
- [5] G. Raftery and A. Harte, "Low-grade glued laminated timber reinforced with FRP plate," *Compos. Part B Eng.*, vol. 42, no. 4, pp. 724–735, 2011.
- [6] L. D. Armstrong and R. S. Kingston, "Effect of moisture changes on creep in wood," *Nature, London*, vol. 185, no. 4716, pp. 862–863, 1960.
- [7] L. D. Armstrong and R. S. T. Kingston, "The effect of moisture content changes on the deformation of wood under stress," *Aust. J. Appl. Sci.*, vol. 13, no. 4, pp. 257–276, 1962.
- [8] L. D. Armstrong, "Deformation of wood in compression during moisture movement," *Wood Sci.*, vol. 5, no. 2, pp. 81–86, 1972.
- [9] D. G. Hunt, "A creep limit in wood?," *Cost 508 workshop on fundamental aspects of creep in wood*. Lund, Sweden, p. pp 1–19, 1991.
- [10] S. Hering and P. Niemz, "Moisture-dependent, viscoelastic creep of European beech wood in longitudinal direction," *Eur. J. Wood Wood Prod.*, vol. 70, no. 5, pp. 667–670, Feb. 2012.
- [11] D. G. Hunt, "The prediction of long-time viscoelastic creep from short-time data," *Wood Sci. Technol.*, vol. 38, no. 7, pp. 479–492, 2004.
- [12] P. Gressel, "Zur Vorhersage des langfristigen Formänderungsverhaltens aus Kurz-Kriechversuchen," *Holz als Roh- und Werkst.*, vol. 42, no. 8, pp. 293–301, 1984.
- [13] W. Lu, M. He, K. Yue, and W. Liu, "Experimental Study on Bending Creep Behaviour of Reinforced Glulam Beam," *World Conference on Timber Engineering 2012, WCTE 2012, July 15, 2012 - July 19, 2012*. Auckland New Zealand, 2012.
- [14] C. Gerhards, "Effect of Grade On Load Duration of Douglas-Fir Lumber In Bending," *Wood Fiber Sci.*, vol. 20, no. 1, pp. 146–161, 1988.
- [15] N. Plevris and T. Triantafyllou, "Creep Behavior of FRP-Reinforced Wood Members," *J. Struct. Eng.*, vol. 121, no. 2, pp. 174–186, 1995.
- [16] R. W. Runyen, D. W. Dinehart, S. P. Gross, and W. G. Dunn, "Creep behavior of wood I-joists with web openings exposed to normal and low relative humidity conditions," *11th World Conference on Timber Engineering 2010, WCTE 2010, June 20, 2010 - June 24, 2010*. Trento, Italy, 2010.
- [17] NSAI, "LS. EN 408," *Timber Structures - Structural Timber and Glued laminated timber - Determination of some physical and mechanical properties*. 2010.
- [18] C. O. Ceallaigh, A. Harte, K. Sikora, and D. McPolin, "Mechano-sorptive Creep of FRP Reinforced Laminated Timber Beams," *Civil Engineering Research in Ireland, CERi 2014*. Queen's University Belfast, 28-29 August 2014, 2014.
- [19] C. Bengtsson, "Mechanosorptive Creep in Wood - Experimental studies of the influence of material properties," Chalmers University of Technology, Goteborg, Sweden, 1999.

The effects of planting density on the structural timber properties of 23-year-old Irish-grown Sitka spruce

Karlo Simic¹, Vilius Gendvilas², Conor O'Reilly², Maarten Nieuwenhuis², Annette Harte¹

¹ College of Engineering & Informatics, National University of Ireland, Galway, University Rd., Galway, Ireland

² UCD Forestry, School of Agriculture and Food Science, University College Dublin, Belfield Dublin 4, Ireland

ABSTRACT: In Europe, with the move towards more sustainable construction, there is an increasing demand for structural timber. The purpose of this research is to explore new forestry management strategies, which will produce an optimum balance of the quantity and quality of structural timber over a minimum period of time. The focus is on timber from Sitka spruce which is the most important Irish commercial forest tree species.

Planting density is an important factor affecting both structural timber quantity and quality. Trees with wider spacing get more light and grow faster, which affects annual ring width and knot size. These, in turn, affect the bending strength, modulus of elasticity and density of timber, which are the grade determining properties according to the EN 338:2003 standard. The current standard planting density in Ireland is 2500 stems/ha and the timber produced meets the requirements for the C16 strength class. This study has two aims, first to explore the possibilities of improving the strength class by increasing the planting density and second, to explore the possibilities of keeping the same class while increasing the quantity of structural timber by reducing the planting density.

The effects of different planting densities, ranging from 1550 to 3700 stems per hectare, on the structural properties of Sitka spruce timber originated from a forest in County Leitrim are examined. Overall, 72 trees were felled and cut into logs. Logs were non-destructively tested using acoustic tools and subsequently processed into structural timber. The timber boards were then tested using two different types of strength graders in order to examine the difference in timber quality between different planting densities. The results showed statistically significant effects of different planting densities on the variation in timber modulus of elasticity and density.

KEY WORDS: structural timber performance, Irish grown Sitka spruce, planting density

1 INTRODUCTION

In plantation forestry, spacing between trees is a very important factor that influences tree growth [1]. For light demanding species such as Sitka spruce, which is the most important Irish commercial forest tree species, occupying 52.4% of the forest area [2], trees in stands with wider spacing get more light and grow faster which affects many timber characteristics, such as timber density, knot size and juvenile wood amount [3]. Although the influence of tree spacing on timber density has been widely studied [4]–[6], the effects of knot size and juvenile wood zone have more influence on properties of sawn timber products for structural application [3]. Spacing between trees is controlled by planting density (initial spacing at stand establishment) and thinning (re-spacing) before or near time of canopy closure depending on the silvicultural practice chosen. In Ireland, the standard planting density of Sitka spruce plantations is 2500 stems/ha and the current thinning practice involves the systematic removal of every seventh line and the selective thinning of the crop between the lines created [7]. The influence of different types of thinnings on structural timber properties was studied on timber from a Sitka spruce stand in Northern Ireland [8], [9]. Wind throw is a major issue in the management of Sitka spruce plantations in Ireland and it was estimated that the average annual volume wind thrown over the period 1948–1997 was 12.7% of the average annual volume sold [10]. One of the approaches that addresses this problem is to use a no

thin regime but there are concerns that higher proportions of juvenile wood can lead to a reduction in timber quality [11]. As Europe is moving towards the use of more sustainable construction materials, an increase in demand for structural timber can be expected. A shorter rotation length can be a solution for the growing market but there is also a risk of lower quality timber because of larger proportions of juvenile wood zone [12].

The aim of this study is to examine the effects of different initial planting densities of Sitka spruce stands on structural timber quantity and quality. Although basal area is often used in the literature as a measure of stand productivity, it is not the best indicator of structural timber quantity as most of the commercial sawmills in Ireland process only the logs that are larger than 14 cm in diameter. The yield of structural timber is related to factors influencing or affected by average tree size [13]. Therefore, in this study tree diameter at breast height (DBH) and individual tree volume were taken as a measure of structural timber quantity. Also, the tree stem straightness was examined as the yield of structural timber depends on it to a large extent. Timber for structural uses is classified to the strength classes which are defined by characteristic strength, characteristic density and mean value of modulus of elasticity (MOE) in bending in EN 338:2003 [14]. There is variety of different measurement techniques for determination of timber strength class properties. In this study, timber MOE was measured using non-destructive techniques such as longitudinal stress wave, X-ray and bending techniques [15].

As the study is in its early stages, only the results from the longitudinal stress wave and X-ray machines will be reported in this paper.

2 MATERIAL AND METHODS

2.1 Site

The study was conducted on Sitka spruce (*Picea sitchensis* [Bong.] Carr.) trees originated from Lisgillock Glebe forest (latitude 53.985104° N, longitude 7.772218° W, elevation 100 m) in County Leitrim, Republic of Ireland. The site was established in 1992 with the Queen Charlotte Island provenance with yield class 26, which corresponds to a maximum mean annual increment of 26 m³/ha. Due to the problems with the construction of forest roads, the site was kept unthinned until 2014 when about 40% of the trees were removed. As the experiment started in 2015, the influence of thinning on the timber properties was negligible.

In total, 12 plots with ten different planting densities, 1550, 1650, 1750, 1850, 2300, 2350, 2550(1), 2550(2), 3100(1), 3100(2), 3550 and 3700 stems per hectare were selected from the forest. In order to have better presentation of data, the main goal, during the selection of the plots, was to have three planting density groups with four plots in each group. Plots 1550, 1650, 1750 and 1850 were assigned to the low planting density group, plots 2300, 2350, 2550(1) and 2550(2) were assigned to the standard planting density group while plots 3100(1), 3100(2), 3550 and 3700 were assigned to the high planting density group. The plots were situated on the east facing slope ranging from 8 to 22% gradient and 100 m above sea level with surface water gley soil that was previously rough grazing land. Each plot was 8 m x 25 m (0.02 ha) in size with the longer side orientated in the slope direction and within the interior of the stand. Although the stand was thinned, determination of the planting densities in the forest was accomplished by counting trees and stumps.

2.2 Sampling

In 2015, when the stand was 23 years old, diameters at the breast height (1.3 m) were measured and stem straightness was assessed. From each plot six trees were selected for felling in accordance to dominance with respect to diameter: two dominant, two co-dominant and two sub-dominant trees were selected from each of 12 plots. All the trees within the plots larger than 15 cm in DBH were assessed visually for straightness of the bottom 6 m of the stem using a seven-point scoring system based on the UK Forestry Commission's Protocol [16] with modifications for the sample size and tree diameters at the time of felling. The scoring system signifies the maximum length of straight logs, with score 1 for no straight logs available and score 7 for at least 5 m of straight log available from the bottom 6 m of the stem. The trees with poor stem form were omitted from the selection. Overall, 72 trees were selected for felling. After the measurements on the felled tree, the 10-m-long log was cut starting from 25 cm

above the ground level and fundamental frequency was measured using the MTG instrument (Brookhuis Micro-Electronics, The Netherlands) on the forest ground. Then, 10-m-long log was cross cut into four 10 cm thick discs and three 3-m-long logs.

After the extraction from the forest, the fundamental frequencies of 213 pieces of 3-m-long logs were measured using the MTG instrument in the sawmill yard. Finally, the 198 3-m-long logs were processed using nine cutting patterns that maximised the boards output into 904 pieces of structural timber in two cross sectional dimensions, 100 x 44 mm and 75 x 35 mm (Table 1).

2.3 Testing

Tree volume was calculated over bark from ground to 7 cm diameter using the Tree Model software [17]. For selected trees, tree volume was calculated using DBH and height measured on each of the selected trees while average plot volume was calculated using average DBH of all the trees in a plot and average height of selected trees. Cutting efficiency for a planting density group was calculated as the timber board volume to log volume percentage ratio.

The dynamic modulus of elasticity of undried timber boards ($E_{dyn,undried}$) was calculated from the stress wave velocity ($v_{undried}$) and green density ($\rho_{undried}$) using the following equation (1) [15]:

$$E_{dyn,undried} = \rho_{undried} v_{undried}^2 \quad (1)$$

Stress wave velocity and density were measured, using the MTG timber grader with a balance connected, on 899 pieces of timber. Direct adjustment of dynamic MOE ($E_{dyn,12,adj}$) to 12% moisture content (M.C.) was applied using the equation (2) [18]:

$$E_{dyn,12,adj} = \frac{E_{dyn,undried}}{0.868} \cong 1.15 \cdot E_{dyn,undried} \quad (2)$$

After kiln drying to 18% ± 2% M.C., the boards were graded with the X-ray machine (Microtec Goldeneye, Italy) in the sawmill from which the data on timber density (ρ_{x-ray}) and MOE (E_{x-ray}) were obtained. Visual override rejection was not performed and 898 boards were graded.

2.4 Data analysis

Data were analysed in SPSS statistical software. Extreme outliers were removed according to [19]. Then, homogeneity of variances and normality were tested. Regression analysis with F-test at $\alpha = 0.05$ level of significance was used to investigate the effect of different planting densities on the variation in timber MOE and density.

Table 1 – Characteristics of planting density groups on stand, selected trees and boards level

	Planting density group		
	Low	Standard	High
Stand level			
Stand density range (trees/ha)	1550 – 1850	2300 – 2550	3100 – 3700
No. of trees measured	83	114	157
DBH (cm)	25.71 (4.24)	21.41 (3.40)	17.99 (3.93)
Average tree volume (m ³)	0.550	0.347	0.266
Stem straightness	6.17 (1.25)	5.63 (1.62)	5.49 (1.80)
Selected trees level			
Height to DBH (m/m)	78.38(8.47)	88.07 (8.65)	95.41 (10.39)
Selected tree volume (m ³)	0.621 (0.17)	0.420 (0.10)	0.343 (0.09)
Boards level			
Total number of boards cut	406	294	202
No. of 35 mm x75 mm boards	171	157	97
No. of 44 mm x100 mm boards	235	137	105
Cutting efficiency (%)	45.27	43.92	39.97

Standard deviations are shown in parentheses.

3 RESULTS

3.1 Timber quantity characteristics

There was a statistically significant explanation of variation in timber volume by different planting densities. Planting density explained 37.8 % in tree DBH variation (Figure 1). Tree DBH ranged from 7.6 to 37.0 cm, with mean values of 25.71, 21.41 and 17.99 cm for low, standard and high planting density groups, respectively.

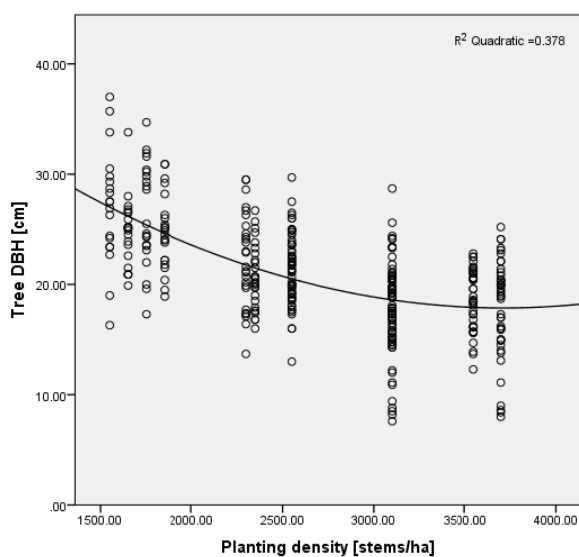


Figure 1 – Relationship between planting density and tree DBH

The volumes of selected trees ranged from 0.155 to 1.015 m³, with mean values of 0.621, 0.420 and 0.343 m³ for low, standard and high planting density groups, respectively (Figure 2). Values for average plot volume were 0.550, 0.374, 0.266 m³ for low, standard and high planting density groups, respectively.

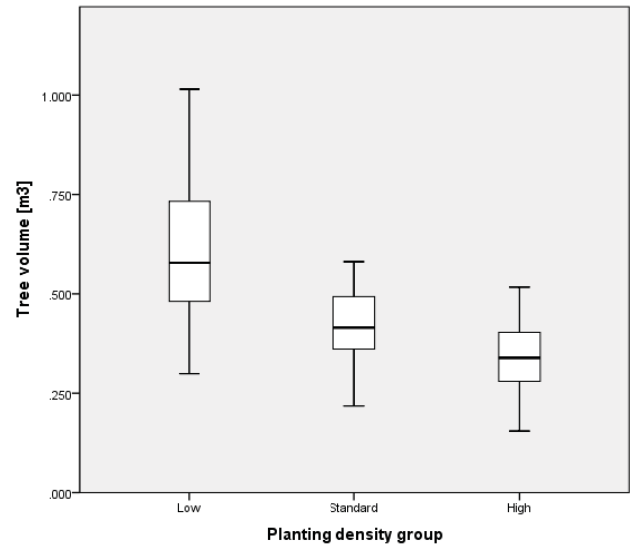


Figure 2 – Comparison of tree volume of selected trees between different planting density groups

There was a statistically significant explanation of variation in timber volume by different planting densities. The confidence intervals for tree volume from the three different planting density groups did not overlap. The mean value of tree volume from the low planting density group was 47.9 % higher than the mean value of tree volume from the standard density group, while the mean value of tree volume from the high planting density group was 18.3 % lower than the mean value of tree volume from the standard planting density group. Average stem straightness score ranged from 6.17 in the low planting density group to 5.49 in the high planting density group. Cutting efficiency was 45.27% for the low, 43.92% for the standard and 39.97% for the high planting density groups.

3.2 Timber quality properties

The $E_{\text{dyn,undried}}$ ranged from 4159 to 11168 MPa, with mean values of 7330, 7777 and 8149 MPa for low, standard and high planting density groups, respectively (Table 2). The mean values of $E_{\text{dyn,12,adj}}$ for low, standard and high planting density groups were 8458, 8969 and 9325 MPa, respectively. The confidence intervals for $E_{\text{dyn,undried}}$ and $E_{\text{dyn,12,adj}}$ between the three different planting density groups did not overlap. The explanation of variation in $E_{\text{dyn,undried}}$ and $E_{\text{dyn,12,adj}}$ by different planting densities was found to be statistically significant.

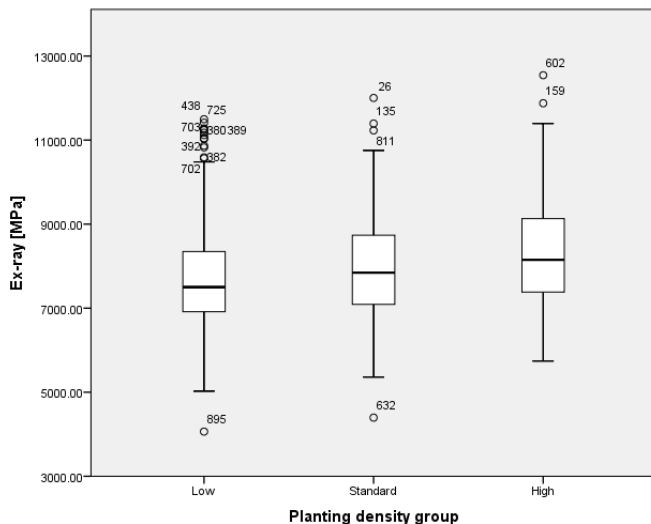


Figure 3 – Comparison of $E_{x\text{-ray}}$ between different planting density groups

Values for the $E_{x\text{-ray}}$ ranged from 4063 to 12544 MPa. The explanation of variation in $E_{x\text{-ray}}$ by different planting densities was found to be statistically significant. The mean values of $E_{x\text{-ray}}$ for low, standard and high planting density groups were 7679, 7910 and 8312 MPa, respectively (Figure 3). The confidence intervals for $E_{x\text{-ray}}$ between the three different planting density groups did not overlap. For all three planting density groups, the mean values of $E_{x\text{-ray}}$ exceed 7600 MPa which is one of the requirements for assigning timber population to C16 according to EN 338:2003 [14]. In total, 98.67% of boards attained C16 strength class.

There was a statistically significant explanation of variation in $\rho_{x\text{-ray}}$ by different planting densities. The $\rho_{x\text{-ray}}$ ranged from 292 to 647 kg/m³, with mean values of 408, 423 and 441 kg/m³ for low, standard and high planting density groups, respectively. The confidence intervals for $\rho_{x\text{-ray}}$ between the three different planting density groups did not overlap. The characteristic (5-percentile) values for $\rho_{x\text{-ray}}$ were 326, 340 and 351 kg/m³ for low, standard and high planting density groups, respectively.

Table 2 – Properties of sawn timber for different planting density groups

	Planting density group		
	Low	Standard	High
Total No. of boards tested	403	294	201
$E_{\text{dyn,undried}}$ (MPa)	7330 (1302)	7777 (1399)	8149 (1267)
Mean $E_{\text{dyn,12,adj}}$ (MPa)	8458 (1607)	8969 (1639)	9325 (1597)
Mean $E_{x\text{-ray}}$ (MPa)	7679 (1237)	7910 (1164)	8312 (1297)
Mean $\rho_{x\text{-ray}}$ (kg/m ³)	408 (58.8)	423 (54.7)	441 (65.0)
Characteristic $\rho_{x\text{-ray}}$ (kg/m ³)	326	340	351

Standard deviations are shown in parentheses.

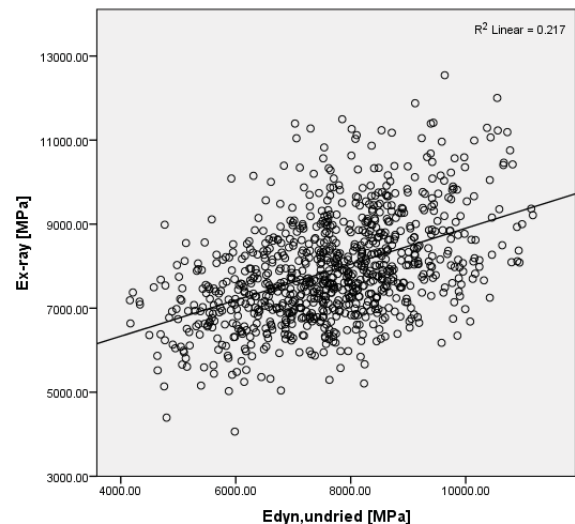


Figure 4 – Relationship between $E_{\text{dyn,undried}}$ and $E_{x\text{-ray}}$

For all three planting density groups, the characteristic values of $\rho_{x\text{-ray}}$ met the requirement for C16 strength class ($\rho_k \geq 310$ kg/m³) from the EN 338:2003 [14].

Moderately strong correlation was found between $E_{\text{dyn,undried}}$ and $E_{x\text{-ray}}$ ($r = 0.466$). $E_{\text{dyn,undried}}$ explained 21.5 % of variation in $E_{x\text{-ray}}$ ($R^2 = 0.217$) for all three planting density groups combined, while explanations of $E_{x\text{-ray}}$ by $E_{\text{dyn,undried}}$ for individual planting density groups was 10.7% for the low, 26.1% for the standard and 31.9% for the high planting density group (Figure 4).

4 DISCUSSION

The results from this study showed the increase in timber mechanical properties with increase of planting density. This is consistent with other studies that examined influence of planting density on structural timber properties [11], [13], [20], [21]. Results suggest better prediction of $E_{x\text{-ray}}$ by $E_{\text{dyn,undried}}$ with the increase of planting density.

In [13] structural timber yields of unthinned 28-year-old Sitka spruce stands in Northern Ireland were examined using the Cook Bolinders grading machine. Planting density ranged from 2403 to 4565 stems/ha. It was found that higher yields of structural timber were negatively related to the initial stocking (planting density). On average, 44.8% of timber boards attained SC4 (Strength class 4 according to BS 5268, equivalent to C24 according to EN 338), compared to 24% in the lowest planting density stand with 2403 stems/ha. Average tree volume was 0.21 m³, while in this study the results of high density group, which corresponded to the selected plots in [13], showed average tree volume of 0.266 m³.

In [11] it was found that planting density of Sitka spruce stands in the UK is an important factor affecting the structural performance of timber cut from crops that had remained

unthinned. However, the effect was not linear, with crops at both close (less than 1.5 m) and wide spacing (more than 3.0 m) affected less by change in planting distance than those established at spacings within this range. It was reported that planting density affects the number and size of large knots (≥ 25 mm in diameter) in the butt and second logs, from which, a negative effect of wider spacing on timber strength can be suggested. In the next phase of this study, the MOE measurements from a Cook Bolinders grading machine will be compared to the results of testing of timber from similar spacing and age plots from [11].

In [21], the influence of initial plant density on timber properties of 40-year-old Douglas fir in Bavaria, Germany was examined. Timber boards originated from three different planting densities: 1000 stems/ha, 2000 stems/ha and 4000 stems/ha were tested. It was found that high initial planting density results in lower knottiness, higher timber density and higher dynamic MOE and tensile strength. The early results from this study are consistent with these findings.

The results suggest that the timber from all three examined planting densities of 23-year-old Irish grown Sitka spruce meet the requirements for C16 strength class. However, in [22] it was reported that twist reduced the yield of structural timber by 25% from the 28-year-old Sitka spruce stand. Due to high proportion of juvenile wood, timber stability is affected and distortion seems to be a limiting factor for an increase in quantity of structural timber.

ACKNOWLEDGMENTS

We would like to thank Daryl Fahy, Conor Fahy, Tim Scarry, Mike Naughton, Fergal Duffy, Damien Cross and Niall Gavin from Earrai Coillte Chonnacht Teoranta (ECC Teo), Corr na Mona, Co. Galway for technical support, kiln drying and grading of timber boards in their sawmill. Darragh Little, from Forest Enterprises Limited, gave the access to the forest. Momme Reibisch organised the felling and extraction of the logs from the forest. Paul Reynolds from Drimeen Sawmills, Mohill, Co. Leitrim processed the logs into timber. Conan O'Ceallaigh and Luka Krajnc assisted with the fieldwork. Dr Franka Bruchert provided useful comments for the sampling methodology. This study is part of the FASTFORESTS project which is under the WoodWisdom Eranet+ research programme. The funding was provided by the Research Division of the Department of Agriculture, Food and the Marine and by the EU FP 7 programme.

REFERENCES

- [1] P. A. Wardle, "Spacing in Plantations," *Forestry*, vol. 40, pp. 47–69, 1967.
- [2] ROI Forest Service, "Ireland's forest - Annual Statistics," 2014.
- [3] E. Macdonald and J. Hubert, "A review of the effects of silviculture on timber quality of Sitka spruce," *Forestry*, vol. 75, no. 2, pp. 107–138, Feb. 2002.
- [4] D. Ward and J. J. Gardiner, "The influence of Spacing on Tracheid length and Density in Sitka spruce," *Irish Forestry*, vol. 33, no. 1, pp. 37–56, 1976.
- [5] J. J. Gardiner and P. O'Sullivan, "The Effect of Wide Espacement on Wood Density in Sitka Spruce," *Irish Forestry*, vol. 35, no. 1, pp. 45–51, 1978.
- [6] Z. Javadi, M. MacSiurtain, and J. J. Gardiner, "The effect of tree Espacement upon Wood Density in Sitka Spruce," *Irish Forestry*, vol. 40, no. 2, pp. 92–97, 1983.
- [7] P. M. Joyce and N. O'Carroll, *Sitka Spruce in Ireland*. Dublin: COFORD, 2002.
- [8] P. Savill and A. Sandels, "The Influence of Early Respacing on the Wood Density of Sitka Spruce," *Forestry*, vol. 56, no. 2, pp. 109–120, 1983.
- [9] J. Moore, A. Achim, A. Lyon, S. Mochan, and B. Gardiner, "Effects of early re-spacing on the physical and mechanical properties of Sitka spruce structural timber," *Forest Ecology and Management*, vol. 258, no. 7, pp. 1174–1180, Sep. 2009.
- [10] E. Hendrick, "The establishment, growth and stability of Sitka spruce (*Picea sitchensis* (Bong.) Carr.) in Ireland with particular reference to wet mineral soils," NUI Dublin, 1999.
- [11] J. D. Brazier and I. D. Mobbs, "The influence of planting distance on the structural wood yields of unthinned Sitka spruce," *Forestry*, vol. 66, no. 4, pp. 332–352, 1993.
- [12] A. N. Ni Dhubbáin, D. Magner, and M. Nieuwenhuis, "Juvenile wood in Irish grown Sitka spruce and the impact of rotation length," *Irish Forestry*, vol. 63, no. 1&2, pp. 26–36, 2006.
- [13] R. Schaible and L. J. Gawn, "Variation of timber strength of Fast Grown Unthinned Sitka Spruce in Northern Ireland," *Irish Forestry*, vol. 46, no. 1, pp. 43–50, 1989.
- [14] CEN, *EN 338:2003 - Structural timber - Strength classes*. 2003.
- [15] R. J. Ross, "Nondestructive evaluation of wood: second edition," *General Technical Report FPL-GTR-238*. Department of Agriculture, Forest Service, Forest Products Laboratory., Madison, WI, U.S., p. 169, 2015.
- [16] E. Macdonald, S. Mochan, T. Connolly, and O. F. Forest, "Protocol for Stem Straightness Assessment in Sitka Spruce," pp. 1–8.
- [17] COFORD and IFER, "TreeModel - Irish Stem Profile & Single Tree Volume Equations." 2013.
- [18] H. Unterwieser and G. Schickhofer, "Influence of moisture content of wood on sound velocity and dynamic MOE of natural frequency- and ultrasonic runtime measurement," *European Journal of Wood and Wood Products*, vol. 69, no. 2, pp. 171–181, 2011.
- [19] D. C. Hoaglin and B. Iglewicz, "Fine tuning some resistant rules for outlier labeling," *Journal of American Statistical Association*, vol. 82, pp. 1147–1149, 1987.
- [20] H. Simpson and M. Denne, "Variation of ring width and specific gravity within trees from unthinned Sitka spruce spacing trial in Clocaenog, North Wales," *Forestry*, 1997.
- [21] A. Rais, W. Poschenrieder, H. Pretzsch, and J.-W. G. van de Kuilen, "Influence of initial plant density on sawn timber properties for Douglas-fir (*Pseudotsuga menziesii* (Mirb.) Franco)," *Annals of Forest Science*, vol. 71, pp. 617–626, Feb. 2014.
- [22] E. Hendrick and G. Murphy, "The effect of fast growth on structural yields of SS - a study on a yield class 30 stand - Report No. 8/91." Coillte Research and Development, Bray, p. 20, 1991.

Mechanical characterization of green Sitka spruce logs

Luka Krajnc^{1,2}, Niall Farrelly², Annette M. Harte¹

¹ College of Engineering & Informatics, National University of Ireland, Galway, University Rd., Galway, Ireland

² Forestry Development Department, Teagasc, Athenry, Co. Galway, Ireland

Email: luka.krajnc@nuigalway.ie, Niall.Farrelly@teagasc.ie, annette.harte@nuigalway.ie

ABSTRACT: Timber is by its nature a very heterogeneous material. Many different factors impact its mechanical properties, from tree species to environment (climate, competition, soil...). While a number of studies in the past dealt with sawn timber and its mechanical properties, only a small number of them studied round logs. An even smaller number dealt with logs where moisture content is above fibre saturation point, e.g. green logs. The objective of this study is to investigate and describe the load-deflection response of green Sitka Spruce logs using a four point bending test. The trees for this study were felled at the age of 20 years and consequently the percentage of juvenile wood is relatively high.

Green logs behave differently when stressed in comparison to dry timber. The flexural stiffness is significantly lower and the load-deflection response is highly non-linear. The test results are useful for designing further green round log testing, especially when studying wind throw in standing trees, as they can give a clearer picture of the stresses that can be expected. There are significant differences in static and dynamic modulus of elasticity between bottom and top logs from the same tree. More logs will have to be tested to further characterize the nature of those differences.

KEY WORDS: round logs, Sitka spruce, structural properties, green logs

1 INTRODUCTION

Structural properties of timber are an important factor in design and construction of timber structures. As timber is by its nature a very heterogeneous material where many different factors interact with and/or impact its mechanical properties, a high confidence level when studying the relationships between them is relatively difficult to achieve.

While different sawn timber products such as kiln dried boards are often used in construction and as such have been a subject of many different studies, round logs are a less studied subject. The use of round logs in timber construction is relatively uncommon when compared to other timber products. The biggest potential markets were identified both in small buildings and large engineered structures, while small diameter round logs could also be utilised in footbridges, sound barriers and landscaping [5]. One could argue that the usage is scarce because not enough is known about the behaviour of the material itself. On the other hand scarcity of research might imply that there is no need on the market to know more about using round logs. While that might be true, predicting sawn timber properties from round wood measurements would be very helpful to sawmills, as it would enable the early classification of the logs regarding quality of the expected sawn timber.

This lack of research has had an impact on developed standards – for instance there are standards for testing sawn timber [1]-[3] and for round poles [4], but there are currently no standards for structural testing of logs. CEN standards

written for sawn timber are not directly applicable to round timber, especially to small diameter round timber. For example, a high proportion of juvenile wood would indicate that the strength could be lower when the diameter gets smaller – contrary to EN 384 size adjustments for sawn timber [5]. While there is no universally accepted definition of juvenile wood, it is typically described as the zone near the pith of the log. In Sitka spruce the transition between juvenile and mature wood appears to occur around the age of 12 to 13 years [19]. A proposal for testing round small round timber was developed as a part of a large EU Research project (FAIR CT 95-0091) [5], in which the large proportion of juvenile wood is taken into consideration. This has yet to be implemented in harmonised standards.

A small number of researchers has examined the behaviour of logs in different bending tests [6]-[16], mainly of dry round logs. Sample sizes ranged from 24 to 445 logs tested, while approximately half of the papers examined used a three point bending test and the other half a four point bending test. A cantilever test was used in only one of the papers examined [13]. Span to depth ratios varied from 18:1 to 29:1, while studies [10], [13] and [16] used a fixed specimen length rather than a fixed span to depth ratio. None of the studies found were performed on Sitka spruce logs (*Picea sitchensis* [Bong.] Carr.); the majority of the testing was done on specimens from different species across the *Pinus* genus. The diameters of the logs tested varied between 10 and 20 cm in most of the previous studies [6]-[16]. Studies [7], [8] and [13] tested green logs (moisture content above fibre saturation level) using three point bending tests or as a cantilever [13].

The focus of the present work is to establish the mechanical properties of roundwood from Irish Sitka spruce. In this paper, results from a test programme to establish the properties of green timber will be presented. Later studies will investigate the properties of dried logs. This information will inform the identification of possible end uses for the product, contribute to the understanding of the structural behaviour of standing trees and allow sawmillers to sort logs on the basis of structural capacity before processing.

2 MATERIAL AND METHODS

2.1 Material

A total of 37 logs of Sitka spruce (*Picea sitchensis* [Bong.] Carr.) was sourced from a forest plantation near Frenchpark, County Roscommon, Ireland. The trees were planted in 1995 and felled in November of 2015.

After felling, the logs were extracted from the forest and transported to the testing facilities at the National University of Ireland, Galway. All logs were 3000 mm in length.

2.2 Methods

Using a crane each log was weighed and the diameters at both ends and in the middle were measured using a diameter tape. The logs were not debarked before testing.

2.3 Non-destructive testing

Using a MTG Timber Grader (*Brookhuis Applied Technologies, Netherlands*) each log was tested to determine its fundamental frequency in the longitudinal direction in order to test the possible usage of the device on logs. Not all logs were measured using the MTG Timber Grader.

The volume of each individual log was calculated as the sum of two conical frustums using the three measured log diameters (both ends and middle). Density was then derived from the volume and weight. Moisture content was measured and was above fibre saturation point in all of the logs, as they were tested fresh, i.e. in green condition.

The dynamic modulus of elasticity was derived from the fundamental frequency (f), log length (l) and density (ρ) (Equation (1)) according to [5].

$$E_{dyn} = 4l^2 f^2 \rho \quad (1)$$

2.4 Destructive testing

After measuring the logs with the MTG Timber Grader, they were set up in the testing machine and prepared for a four point bending test (see Figure 1). As there are no standards for structural testing of round logs, the testing protocol used was based on the proposed standard of small diameter round log testing [5] and the standard for testing dry sawn timber [3].

As the middle diameters of the logs varied and the length was fixed, a constant span-to-depth ratio could not be achieved.

Instead a constant span of 2700 mm was chosen. The loading heads were 900 mm apart. After preliminary testing a loading rate of 0.3 mm/s was chosen to ensure the maximum load was achieved in 300s (± 120 s). The testing was stopped when no further log or testing head movement was possible due to size restraints of the testing rig. Displacement was measured at midspan using two string pots mounted at the base of the machine, they were attached to the upper side of the log using a steel plate. Both displacements and the force applied were recorded with the help of LabView software [17] with a sampling rate of one measurement per second.



Figure 1: Four point bending test setup

The static modulus of elasticity, determined using the linear portion of the load/displacement plot, was calculated from the load/displacement linear regression using Equation (2) - the square of the correlation coefficient was greater than 0.99 in all cases.

$$E_{static} = \frac{a(3l^2 - 4a^2)(F_2 - F_1)}{48I(w_2 - w_1)} \quad (2)$$

where

F_1 and F_2 are the loads corresponding to $0.1F_{max}$ and $0.4F_{max}$, w_1 and w_2 are the corresponding displacements, F_{max} is the maximum load recorded during the test, I is the mean second moment of area of the log section, a is the distance between the support and load head.

The bending strength was calculated using Equation (3) as per the round log testing standard proposal [5] using the diameter at the point of failure (d), the maximum load (F_{max}) and the distance between the support and load head (a).

$$f_m = \frac{16F_{max}a}{\pi d^3} \quad (3)$$

2.5 Data analysis

All data analysis was performed with the help of the statistical software IBM SPSS 22 [18]. Gathered data were checked for normality using Shapiro-Wilk's test and homogeneity of variances was tested using Levene's test. Correlations were

assessed using the Pearson correlation coefficient and Spearman's rank correlation coefficient.

3 RESULTS

Ten logs were the bottom logs and 27 were the top logs of the trees. A maximum of two logs per tree was sampled. Logs were randomly selected within trees at the time of extraction to ensure maximum statistical power of the experiment. The sampling groups are unequal, which was accounted for in later stage data analysis, where relevant.

The average tested log diameter was 18.01 cm (calculated as an average of the diameters at both ends and the middle), ranging from 14.1 to 23.7 cm with a standard deviation of 2.6 cm. Some characteristics of the measured variables are listed in Table 1.

Table 1 – Characteristics of the measured variables

	N	Min.	Max.	Mean	Std. Dev.
Volume [m ³]	37	0.05	0.13	0.08	0.02
Density [kg/m ³]	37	703.7	967.1	859.5	62.0
Fundamental frequency [Hz]	29	400.0	571.0	493.0	46.6
M [kg]	37	37.5	110.5	66.9	17.2
DBH [cm]	37	17.6	23.8	20.4	1.8
E _{dyn} [N/mm ²]	29	4882.2	10762.6	7599.4	1722.3
E _{stat} [N/mm ²]	37	1715.9	6875.3	4623.9	1502.6
F _{max} [N]	37	16219.7	74369.0	36691.3	12910.5
Bending strength [N/mm ²]	37	15.5	47.7	36.2	6.0

Some significant correlations were discovered between the measured and calculated variables. The static modulus of elasticity moderately to strongly correlates with all of the diameters measured, most strongly with the diameter at the thicker end of the log (Pearson's $\sigma = -0.872$, $p = 0.000$). It is also in correlation with the density (Pearson's $\sigma = 0.615$, $p = 0.000$) and fundamental frequency (Pearson's $\sigma = 0.790$, $p = 0.000$). Surprisingly, there is no correlation with the diameter at breast height (DBH) and either the static or dynamic MOE.

Significant correlations were also found between bending strength and (1) the diameter at the failure location (Pearson's $\sigma = -0.548$, $p < 0.000$), (2) the static modulus of elasticity (Pearson's $\sigma = 0.386$, $p = 0.019$) and (3) the dynamic modulus of elasticity (Pearson's $\sigma = 0.400$, $p = 0.031$). With the exception of the fundamental frequency, all of the correlations stated above have a higher Pearson's Rho when compared to

Spearman's Rho, which indicates a more linear type of relationship.

The static modulus of elasticity also significantly correlates with the dynamic modulus calculated from fundamental log frequency and log dimensions (Pearson's $\sigma = 0.790$, $p = 0.000$), which indicates that the MTG Timber Grader could also potentially be used on green logs. The same applies for any similar devices that can measure the fundamental frequency of the logs, which can then be used to calculate dynamic modulus of elasticity.

One-way ANOVA was performed on the data to study the impact of log position within the tree on the measured characteristics. The results show that there are significant differences ($p = 0.000$) between the bottom and top logs in density (ρ), bending strength, fundamental frequency, static modulus of elasticity (E_{stat}) and the dynamic modulus (E_{dyn}) derived from fundamental frequency. The static modulus of elasticity by log position is displayed in Figure 2.

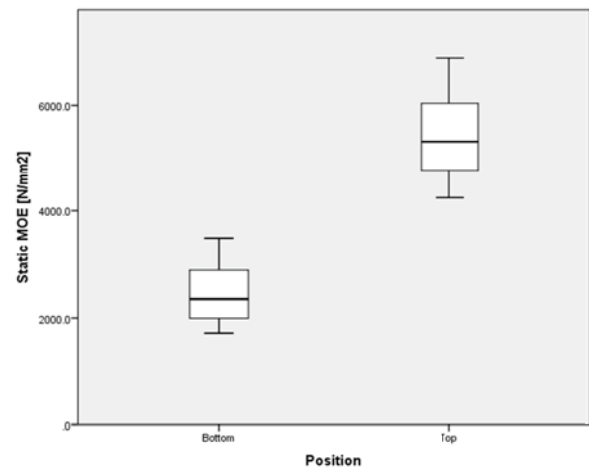


Figure 2: Static MOE distribution by log position

The measured bending strength values ranged between 15.5 N/mm² and 47.7 N/mm² for the 37 logs tested. This compares well with values reported for Irish Sitka spruce boards tested at 12% moisture content in tension and compression [20]. In that study, the tensile strength values of the dry boards ranged between 10 N/mm² and 45 N/mm² and the compressive strength values ranged between 25 N/mm² and 49 N/mm².

The tested green round logs have a mean static modulus of elasticity of 4624 N/mm², which is significantly lower than the typical value of 8000 N/mm² for Irish Sitka spruce dry sawn timber. The mean dynamic modulus of elasticity, on the other hand, is much higher and has an average value of 7600 N/mm². Further testing is required in order to develop an accurate relationship between the dynamic and static moduli of elasticity.

Another noticeable difference in the structural response is that the load-deflection behaviour is highly non-linear whereas dry sawn timber is typically more brittle and linear elastic to failure. Typical green log load-deflection curves are shown in Figures 3 and 4.

Post hoc analysis of the gathered data showed that the logs could be classified into two groups in relation to the typical shape of the load-deflection curve after reaching maximum stress. As shown in Figures 3 and 4 the fibres can either yield very quickly (54% of the logs tested, resulting in Figure 4 shaped peak) or slowly (46% of the logs tested, Figure 3 shaped peak).

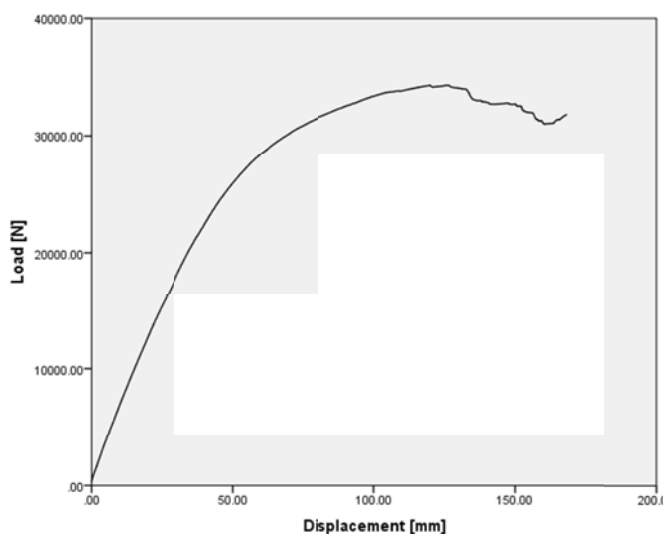


Figure 3: Typical load-deflection response (compressive failure)

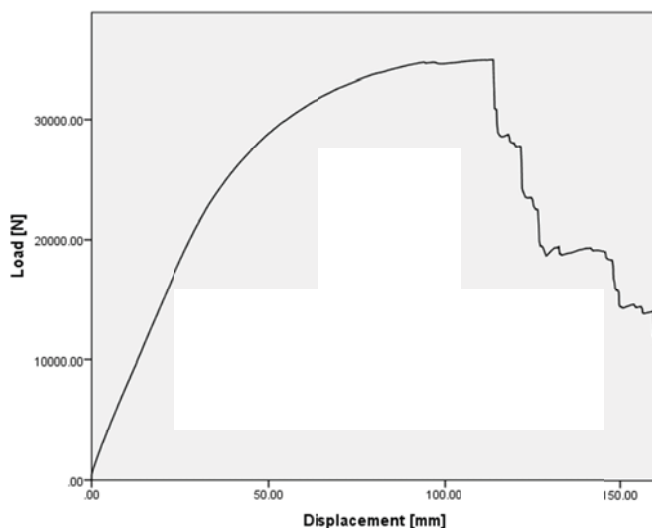


Figure 4: Typical load-deflection response (tensile failure)

The difference between the post peak load-deflection response demonstrated in Figures 3 and 4 is associated with the type of failure. The failure mode associated with the Figure 3 type

response is the result of compressive yielding of the top surface of the log. On the other hand the failure mode associated with the Figure 4 response is the result of tensile failure in the bottom half.

4 DISCUSSION

Testing of 37 green logs of Irish Sitka spruce was carried out to determine the mechanical behaviour. The measured strength values were comparable with measurements on dry boards. The static modulus of elasticity measured in a four-point bending test was however significantly lower than for dry boards. Dynamic modulus of elasticity measurements from the vibration tests were distinctly higher than those from static bending tests. Further investigation on the influence of the moisture content on the frequency measurement is required to explain this difference and a larger sample is required to develop a robust relationship between the dynamic and static moduli.

The discovered correlations between the static modulus of elasticity and various diameters are of interest to further studies regarding both using round logs in construction and when studying the load response in standing trees, for example in wind throw investigations.

The non-existent correlation between breast height diameter (DBH) of the tested trees and the static or dynamic MOE, while both of them correlate with the log diameters, shows that the log taper should not be disregarded when studying either round logs or standing trees of Sitka spruce.

The strong correlation between static and dynamic MOE shows that methods or devices based on the relationship between the fundamental frequency and its elasticity, such as MTG Timber Grader, have potential in grading green logs as well as dry boards. In industrial conditions the correlation coefficient would probably be lower, as the same relationship was observed on boards in several previous studies [5].

The comparison of different mechanical properties between top and bottom logs is interesting, as the results are counter intuitive. One would expect a higher density and higher static MOE in lower, thicker logs. On the other hand, the relationship between the thick end diameter and E_{stat} is negative when taking all log samples into account. To gather any definitive conclusions a more balanced sample is needed, as the statistics tests performed on bottom and top logs did not control for effect of log diameter on account of the small sample size of bottom logs.

Based on the results of this study, the testing protocol used was deemed to be successful and will be used in future structural testing of green round logs.

ACKNOWLEDGMENTS

The authors would like to thank Colm Walsh and Gonzalo González Fernández for their help with the testing. The first author would like to gratefully acknowledge the support from a Teagasc Walsh Fellowship in the conduct of this work.

REFERENCES

- [1] CEN, EN 338:2003 - *Structural timber - Strength classes*.
- [2] CEN, EN 384:2010 - *Structural timber - Determination of characteristic values of mechanical properties and density*.
- [3] CEN, EN 408:2010+A1:2012 - *Timber structures - Structural timber and glued laminated timber - Determination of some physical and mechanical properties*.
- [4] CEN, EN 14251:2003 - *Structural round timber – Test methods*.
- [5] Ranta-Maunus, A., 1999. Round small-diameter timber for construction: Final report of project FAIR CT 95-0091, VTT Publications.
- [6] Green, D. W., Gorman, T. M., Evans, J. W., Murphy, J.F., Hatfield, C. A. (2008), Grading and properties of small-diameter Douglas-fir and Ponderosa pine tapered logs. *Forest Products Journal* 58(11): 33-41.
- [7] Green, D.W., Gorman, T. M., Murphy, J. F., Wheeler, M. B. (2007), Moisture content and the properties of lodgepole pine logs in bending and compression parallel to the grain. Research Paper FPL-RP-639. Madison, WI: U.S. Department of Agriculture, Forest Service, Forest Products Laboratory. 11 p.
- [8] Larson, D., Mirth, R., & Wolfe, R. (2004), Evaluation of small-diameter Ponderosa pine logs in bending. *Forest Products Journal*, 54(12), 52-58.
- [9] Zangiácomo A.L., Christoforo A.L., Gonçalves D., Rocco Lahr F.A. (2014), Evaluation of the shear effect to determine the longitudinal modulus of elasticity in *Corymbia Citriodora* round timber beams, *International Journal of Materials Engineering*, Vol. 4 No. 1, pp. 37-40. doi: 10.5923/j.ijme.20140401.05.
- [10] Fernandez-Golfin JI, Diez-Barra MR, Hermoso E, Mier R. (2007), Mechanical characterization of visually classified, small-diameter Laricio pine round timber. *Span. J. Agric. Res.* 5(3): 304-311.
- [11] Morgado, T. M., Rodrigues, J., Machado, J. S., Dias, A. G., & Cruz, H. (2009). Bending and compression strength of Portuguese Maritime pine small-diameter poles. *Forest Products Journal*, 59(4), 23-28.
- [12] Morgado, T. F. M., et al. (2008), Grading and testing of Maritime pine and larch roundwood. Conference COST E. Vol. 53.
- [13] Cerda, G., Wolfe, R.W. (2003), Bending strength of Chilean Radiata pine poles. *Forest Products Journal*. Vol. 53, no. 4: 61-65
- [14] Høibø, O., & Vestøl, G. I. (2010), Modelling the variation in modulus of elasticity and modulus of rupture of Scots pine round timber. *Canadian Journal of Forest Research*, 40(4), 668-678. doi:10.1139/X10-021
- [15] Vestøl, G. I., & Høibø, O. (2010). Bending strength and modulus of elasticity of squares with wane as compared with round timber of Scots pine (*Pinus sylvestris*). *Forest Products Journal*, 60(1), 40-47.
- [16] Green, D. W., Gorman, T. M., Evans, J. W., & Murphy, J. F. (2006), Mechanical grading of round timber beams. *Journal of Materials in Civil Engineering*, 18(1), 1-10. doi:10.1061/(ASCE)0899-1561(2006)18:1(1)
- [17] LabView (Laboratory Virtual Instrument Engineering Workbench), (2014). National Instruments, Texas, USA.
- [18] IBM Corp. Released 2013. IBM SPSS Statistics for Windows, Version 22.0. Armonk, NY: IBM Corp.
- [19] Brazier J.D. and Mobbs I.D., (1993), The influence of planting distance on structural wood yields of unthinned Sitka spruce. *Forestry* 66: 333-352.
- [20] Raftery, G.M., Harte A.M., (2014), Material characterisation of fast-grown plantation spruce, *Structures and Buildings*, 167(SB6), 380-386, dx.doi.org/10.1680/stub.12.00052.

Potential for Medium Rise Timber Structures in Ireland

Paul Glavin¹, Andrew MacIlwraith^{2,3}, Donogh Coleman², Ted McKenna²

¹Glavloc Build Systems LTD, Middleton, Co. Cork, Ireland

²Department of Civil, Structural and Environmental Engineering, Cork Institute of Technology, Bishopstown, Cork, Ireland

³Fire & Building Control Department, Cork County Council, Ireland

email: paulg@glavloc.ie, Andrew.Macilwraith@cit.ie, donogh.coleman@cit.ie, ted.mckenna@cit.ie

ABSTRACT: Timber is one of the most sustainable materials available today when sourced from certified sustainable managed forests. It has excellent structural properties, with strength to weight ratios twice that of steel and greater again when compared to concrete. Contrary to popular belief, timber also has excellent fire resistance properties with limited negative characteristics. In Ireland, timber construction is typically limited to use in residential type buildings, and other traditional areas such as roofing, while it is rarely used on medium rise and commercial buildings. This is the case in Ireland for a myriad of reasons including, durability, fire performance, acoustic characteristics and availability of suitable indigenous structural timber. The key objective of this research was to examine the viability of using timber for medium rise commercial structures in Ireland. The design of a complex eight storey hybrid building was completed to investigate the potential for timber frame construction. The structure included glulam elements, cross laminated timber panels, and steel tension cabling. A number of software solutions were developed for the analysis and design of the various structural components. The solutions were then compared with outputs from proprietary software solutions (e.g. Dlubal, Tedds, and STAADpro). The results from the research successfully demonstrate a 30 to 40 percent capacity increase in components, by using this approach of post tensioned timber with steel cables, while also delivering other unforeseen benefits such as improved aesthetics, and increased thermal properties. This project demonstrates that engineered timber products used in a more innovative ways, combined with other traditional materials, could have a much greater role to play in our building industry. This approach could yield many benefits over traditional construction techniques, while also fulfilling sustainability obligations.

KEY WORDS: Glulam; CLT; Timber; Steel Cable.

1 INTRODUCTION

The use of timber, and timber based products in Ireland is generally limited to small domestic buildings, roofing in larger buildings, and a small number of non-structural niche areas. While this was understandable in the past due to the inherent issues with natural timber, it is very difficult to understand in today's environment where the range of timber based products is ever increasing, as are preservation and fire resistance technologies. The technology is available to construct larger structures from timber products. In 1995 the TF2000 project in Britain demonstrated this by constructing a full scale six storey timber framed building (Trada 2002). An extensive battery of tests was carried out, which included simulated earthquakes, fire, and disproportionate collapse amongst other tests. The results from this project, and these tests, verified the case for extending the use of timber to larger scale buildings, and laid the foundations for its acceptance as a viable alternative to steel and concrete. However, increased use of timber construction for such projects remains limited.

The research presented may be considered more design than research. However, to encourage the use of timber it was considered that pushing the boundaries of perception in terms of timber design might spark a realization and acceptance of the true potential of timber construction. To achieve such an exploration of the possibilities and technical capabilities of timber products, a complex eight storey building was designed as a case study. This approach required a comprehensive

review of timber as a structural material and allowed for experimentation with different design solutions to solve a variety of technical problems. The purpose of this paper is to understand the challenges of using timber as the primary structure in larger buildings, and to focus on how innovation and design, can overcome these challenges to enable its use as a mainstream material. This paper will demonstrate through the design of a medium rise building, how some of these challenges might be overcome, through new approaches in design, and the utilisation of modern timber products in conjunction with steel cable tensioning.

2 PROJECT EXAMPLE DESIGN

The concept building is a circular eight storey building approximately 55m tall. The façade of the building is made up of timber and glass pods. The structure is built around a glue laminated timber geodesic core structure. Each floor is partially suspended from this core with a network of steel tension cables. The central core extends uninterrupted from ground floor to roof, with suspended walkways around the inside of the core at each storey (*Figure 1*). The cables that run up through the core are emphasized as an architectural feature. Each of the eight floors of the building is supported by eight pairs of glue laminated beams, which are supported by the core of the building internally, and extend to the perimeter where they are suspended from steel cables. These glulam beams are also post-tensioned by steel cables to enable much larger spans (*Figure 2*).



Figure 1. Interior of Concept Building.

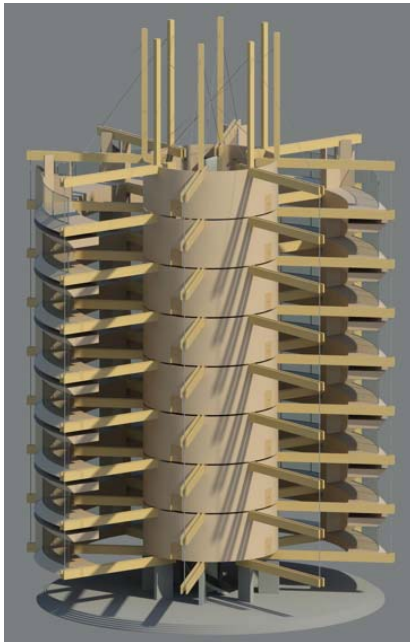


Figure 2. Building Mechanics.

In *Figure 3*, the elevation of the complete building can be seen with the beams suspended from the steel cable network, and the “pods” supported by the beams. The complete building facade can be seen in *Figure 4*. Note the cable masts on the roof from which the floors are effectively hung.



Figure 3. Pods Suspended from External Cables

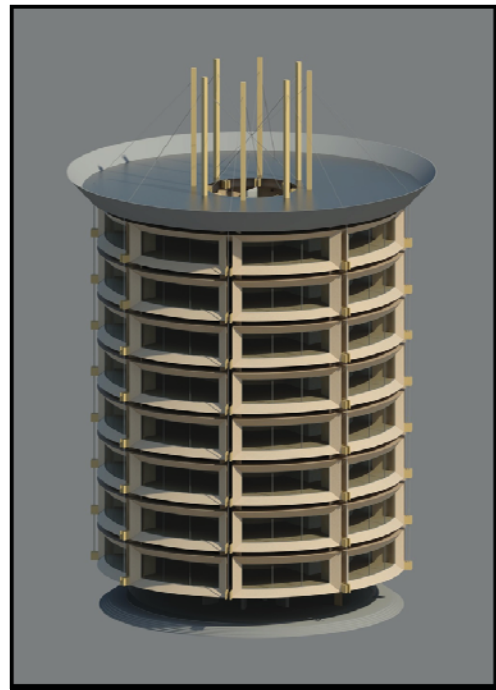


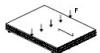
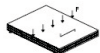
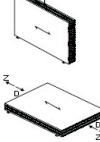
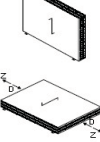
Figure 4. Concept Building.

3 STRUCTURAL DESIGN

3.1 CLT Floor Design

The methods of calculation selected for the design of the cross laminated timber (CLT) floors were the composite theory method and the theory of mechanically jointed beams approach. The composite theory method is commonly used for calculations involving various forms of plywood. It can also be used to design glue laminated panels where the span to depth ratio is equal to, or greater than 30. For designs less than this ratio, the theory of mechanically jointed beams is used. The composite theory method takes account of layers of the laminate that are loaded parallel to the grain, as well as the cross layers that are loaded perpendicular to the grain. The gross section properties are multiplied by a composition factor K that accounts for the different build-up laminates in the panel.

The theory of mechanically jointed beams uses the stiffness properties of the floor by calculating the effective stiffness (EI_{eff}). The floor is treated as a one metre wide beam for this method. The section properties determine the EI_{eff} value. The floor panel must be mechanically jointed for this method rather than just glued. To use this method, the floor must have a span to depth ratio less than 30 as previously mentioned. The K -value is calculated using the table in *Figure 5*. Floor panels are generally loaded perpendicular to the plane of the floor. The floors in the research case building were designed as single span only and are loaded parallel to the grain. As a result K_1 must be calculated with the first formula in the table (*Figure 5*) where E_{90} is the Mean Modulus of Elasticity perpendicular to the grain, and E_0 is Mean Modulus of Elasticity parallel to the grain. α is the thickness of the various cross laminations.

	k_i
	$k_1 = I - \left(I - \frac{E_{90}}{E_0} \right) \cdot \frac{a_{m-2}^2 - a_{m-4}^2 + \dots \pm a_1^2}{a_m^2}$
	$k_2 = \frac{E_{90}}{E_0} + \left(I - \frac{E_{90}}{E_0} \right) \cdot \frac{a_{m-2}^2 - a_{m-4}^2 + \dots \pm a_1^2}{a_m^2}$
	$k_3 = I - \left(I - \frac{E_{90}}{E_0} \right) \cdot \frac{a_{m-2}^2 - a_{m-4}^2 + \dots \pm a_1^2}{a_m^2}$
	$k_4 = \frac{E_{90}}{E_0} + \left(I - \frac{E_{90}}{E_0} \right) \cdot \frac{a_{m-2}^2 - a_{m-4}^2 + \dots \pm a_1^2}{a_m^2}$

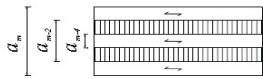


Figure 5. Composition factors K_i for solid wood panels with cross layers (Innovations 2011)

CLT floors come in lengths up to 15m. The design has assumed a double span over the secondary beams (Figure 6) with the ends being simply supported. In order to calculate these moments, multiple moment distribution matrixes were utilized and a Dlubal RFEM software analysis conducted (Figure 7).

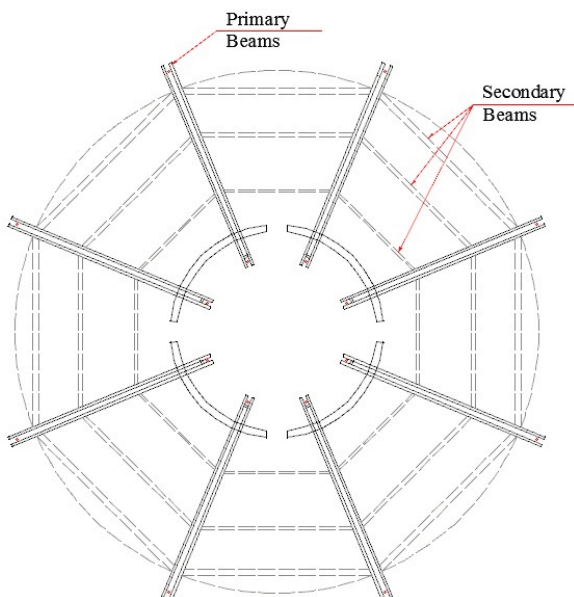


Figure 6. Primary and Secondary Beam Layout

One of the important design verifications for CLT floors relates to vibration. The *fundamental floor frequency* is determined, which enables the deflection due to vibration to be calculated. The *Unit Impulse Response* of the floor is also checked.

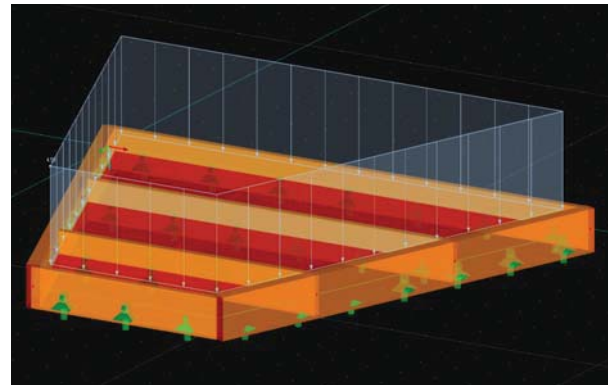


Figure 7. Dlubal RFEM Software Analysis of Floor Segment

4 PRIMARY BEAM DESIGN

The beam designs in this building are very complex due to the spans involved, and the inherent large sections that are associated with glue laminated timber beam design. One of the most significant challenges of this project is to optimize the spans of the beams and CLT floor, while at the same time maintaining reasonable section sizes. One of the design features of this building is the use of steel cabling. Steel cables extend up through the central core of the building, through the cable towers and down the outside of the building. The floors are effectively suspended from these external steel cables via steel connectors. The cables in the core are anchored into the foundations of the building to allow for post-tensioning of the primary beams, which extend into the core by over two metres. Figure 8 demonstrates the load transfer.

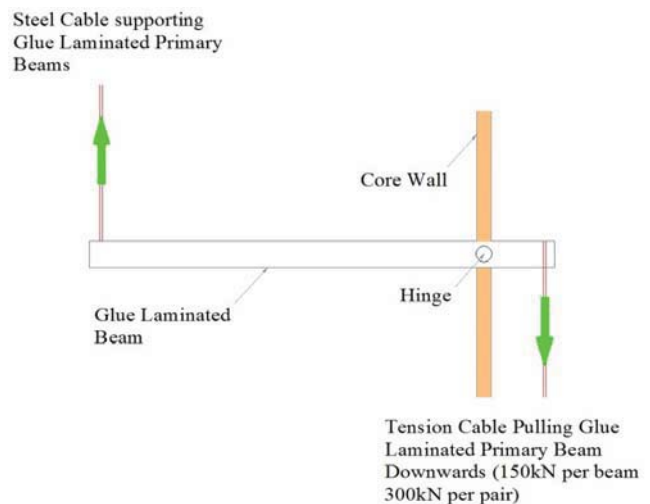


Figure 8. Tensioning of Primary Beams

By using this method it is possible to reduce the maximum moment in the primary beams by up to 40%, therefore making it possible to reduce the size of the beams. These beams may require timber spacers between floors in order to prevent deflections in the floor when they are not fully loaded. From Figure 9 it can be seen that the un-tensioned beam has a bending moment of 940 kNm whereas the tensioned beam has

a bending moment of 715 kNm. By using a process of trial and error it was found that the optimal force to exert on each beam, via the steel cables, was 150kN. If the tensioning force was increased beyond this magnitude it was found that the hogging moment became out of balance, leading to excessive moment differential. It should be noted that there is however a rise in the shear force in the beam, particularly where the beam is supported by the core walls. A Dlubal RFEM software analysis of the final beam design was conducted to verify the results from the Excel calculations.

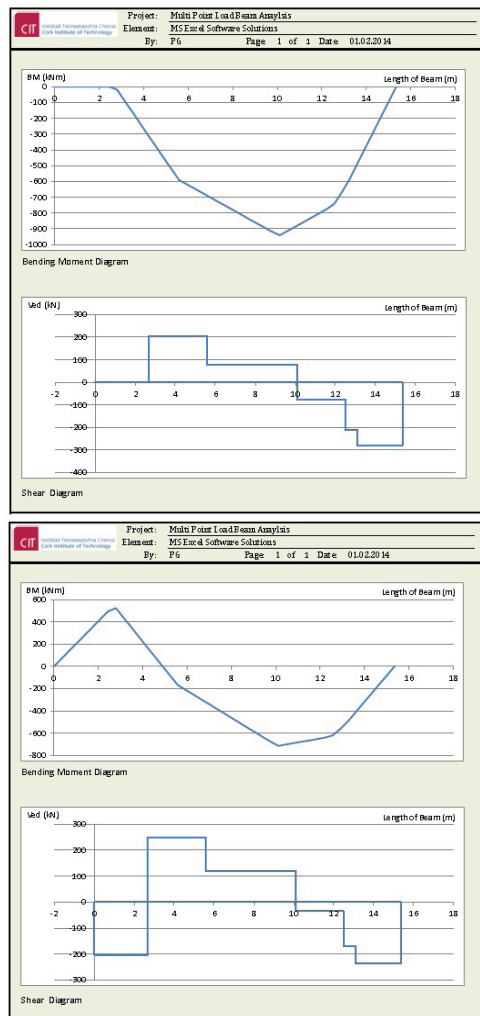


Figure 9. Comparisons of Tensioned and Un-tensioned beams

5 CABLING DESIGN

The primary beams are supported by a system of cables as shown in *Figure 10*. A steel connection attaches the end of the glue laminated beams to cable (A) externally on the building, while another steel connection attaches to cable (B) which is contained in the central atrium. *Figure 10* shows the load paths via the cable support structure. Cable (A) is anchored via a steel connection to the top of the glue laminated core and cable (B) is fixed into the concrete foundation in the atrium at the bottom of the core structure.

In order to design the various structural support components in the building such as the cables, beams, and cable towers the forces in each member were resolved. The forces in each of the structural elements were calculated to determine the maximum load in each element including permanent and variable loads. These loads were then factored as appropriate to ultimate limit state and the element designed.

The roof beams are identical to the other primary beams except that they have a very large compressive force in them due to the cables at roof level. The cables create nearly 3500kN of compressive force in each pair of primary beams. These beams also carry similar loads to the other primary beams as the roof is constructed using the same cross laminated panels as the floors. The only difference is that characteristic load for the roof is lower than that for an office.

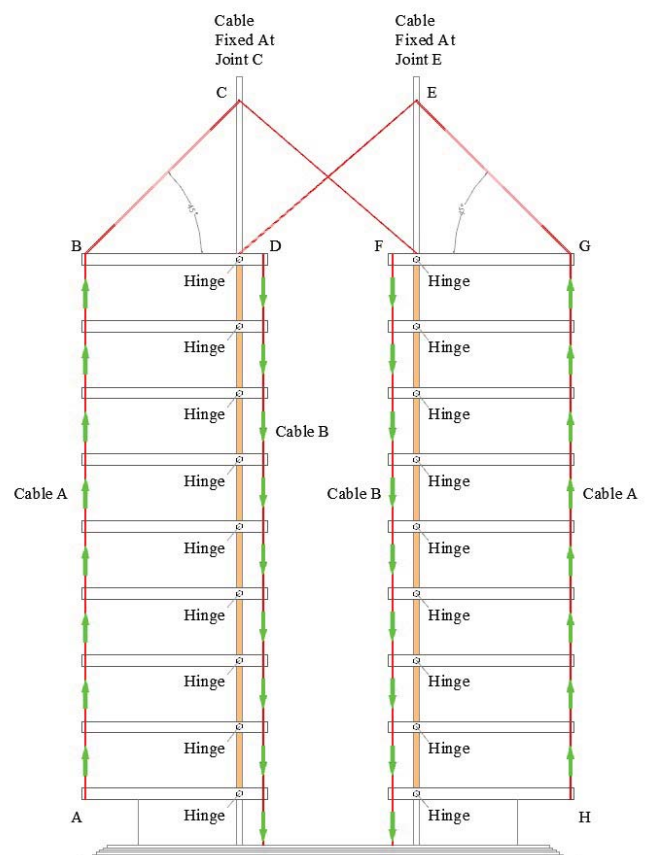


Figure 10. Diagram showing the load paths via the cable support structure

6 CORE DESIGN

The central core is the main structural element of the building. The purpose of the core is to resist both horizontal and vertical loads, and transmit these loads safely to the foundations. The core is required to provide shear, compressive, sliding and overturning resistance. The core geometry uses a hexagonal cell type pattern to reduce both the quantity of timber required in its construction, and the overall weight of the core element. This design approach should also facilitate an easier

construction process as the sections can be prefabricated in smaller units.

The forces in each cell of the core have been resolved by using steel cable reinforcement. There is a number of reasons for this design. If the core was constructed of solid glue laminated timber, it would only be possible to have the timber components spanning either horizontally or vertically. The problem with this is that timber has far better bearing characteristics when loaded parallel to the grain rather than perpendicular to the grain. The chosen geometry allows the loads to be transferred through the timber's stronger axis, substantially reducing the quantity of timber required in the cores construction. It is also a more interesting design, which showcases the timber superstructure while allowing light through from each floor via fire resisting glazing. Another advantage is the ability of the geodesic geometry to sustain damage without compromising structural integrity. This is an important advantage when designing to prevent disproportionate collapse.

In *Figure 11* the core has been “flattened out” in order to show the structural layout of the glue laminated members. The size of the members reduces at each storey level as the loading reduces.

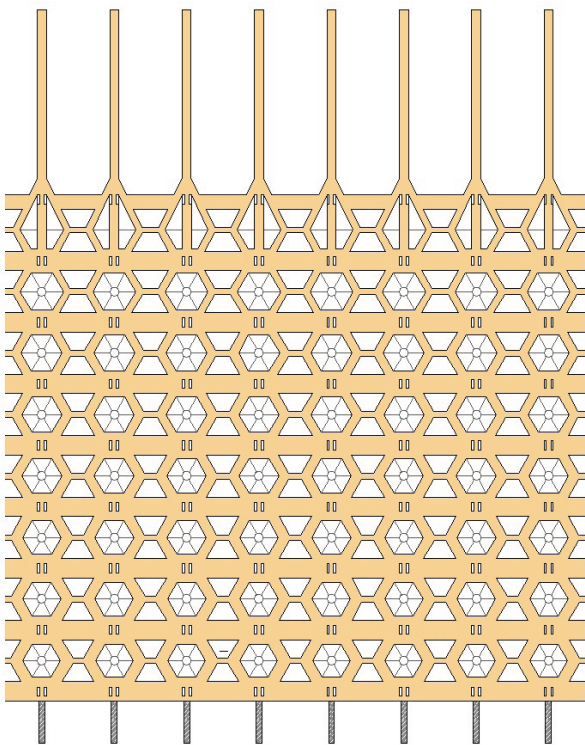


Figure 11. Core Geometrical Makeup (Flattened out for Clarity)

7 FIRE

Timber, contrary to popular belief, is quite a good material in a fire situation, when it has been designed and treated correctly. Timber burns at a predictable rate (depending on the

species), and temperature has little effect on its structural properties. The major weakness that is inherent in timber is its susceptibility to fire spread in its natural state. This can be alleviated through the use of an appropriate fire resisting liner (Such as fire board) or other timber treatments. The cables in the design example are the most vulnerable element of the building. It would be difficult to both protect them from fire damage for 120 minutes and maintain their aesthetics. For this reason and also for the requirements relating to disproportionate collapse, a number of cables can be removed without endangering the integrity of the building structure. As a secondary precaution a mist projection system was proposed to protect the internal cables from damage in a fire event. Details of how a mist system works is clearly explained in Building Research Technical Report 4/2005.

The timber elements in this building are all designed for a minimum 120 minute fire rating. In accordance with TGD B section 3.2.5.2 in buildings where there are floors over a height of 10 metres and a fire resistance rating of over 60 minutes, must use a non-combustible material in accordance with appendix A, Table A8 of TGD B. The code refers to tests specified in BS 476: Part 4: 1970 for materials that can be classified as non-combustible. The main elements of fire requirements from TGD B were also looked at in this case study to ensure the viability of the design. Escape distances were calculated, and a number of extra escape stairs were incorporated into the design (*Figure 12*).

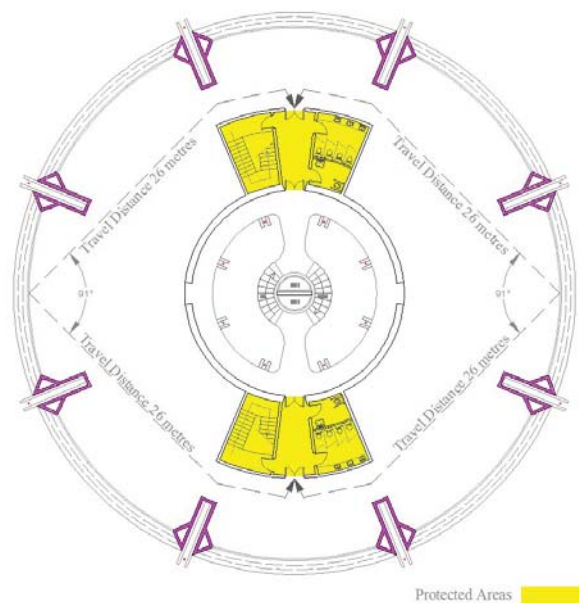


Figure 12. Escape Distances

8 DISPROPORTIONATE COLLAPSE

The general robustness of a building is very important, in particular to resist the disproportionate collapse of a building. Disproportionate collapse is when a single element failure due to an incident results in a full or partial collapse of the structure. All building have to comply with measures in TGD A and EN 1991-1-7 (2006) to prevent this situation occurring.

There are two approaches; the first is to design the building in such a way that there are no critical conditions. This means that any member such as a beam or column, or other structural element, can be removed while the remaining structure retains its integrity. The second method is to design all critical members to resist an accidental pressure of 34kN/m^2 . From TGD Diagram 15 the area of collapse must be limited to 15 per cent of the floor area of the storey and not extend beyond one floor above and below. The risk class of the building is established from TGD A Table 6. The design example is in the 2b upper risk group as it is greater than four storeys. From TGD Diagram 15 the area of collapse must be limited to 15 per cent of the floor area of the storey and not extend beyond one floor above and below.

The results from Dlubal indicate that the primary beam would remain structurally viable in the event of failure of the internal cables and indicates that the primary beam would be operating at 86% of its capacity, when resisting an accidental load due to internal cable failure. Deflection of 100mm in the primary beam would occur under this scenario (*Figure 13*).

The internal cables are not as critical as the external cables. Unlike the external cables which provide the main source of support to the floors suspended from them, the internal cables only provide a post-tensioning function. The main internal support for the primary beams is provided by the glue laminated core. The primary beam was modelled to find the reaction in the event of an internal cable failure. The beam was found to pass but with a deflection of 54.1mm.

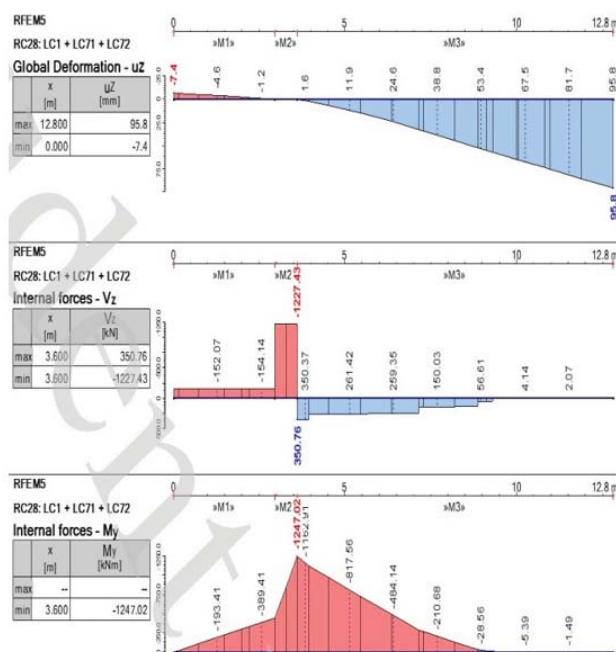


Figure 13. Modelling of External Beam Failure

9 CONCLUSION

The development of the design example has demonstrated that timber is a viable alternative to steel and concrete as a primary structural material in larger buildings. There are many advantages to using structural timber in larger buildings, sustainability being one of the major ones. Presently most European timber comes from sustainably managed forests, making timber one of the only truly sustainable materials available.

During the design process for the case study it was found that there are a number of difficulties with designing in accordance with the Eurocodes, in particular Eurocode 5. It is currently necessary to seek design guidance from alternative sources to EC5, such as the IStructE Manual for the design of timber structures, and other industry publications to find an appropriate design methodology. A dedicated Eurocode publication for the design of larger scale structures, utilising glue laminated timber, and other engineered timber products would be a welcome addition to Eurocode 5.

REFERENCES

- CEN (2010). Eurocode 1: Actions on structures - Part 1- 4: General actions - Wind actions (Including Irish National Annex). Dublin, NSAI.
- CEN (2010). Eurocode 5: Design of timber structures-Part 1-1: General - Common rules and rules for buildings Dublin, NSAI.
- CEN (2010). Eurocode 0: Basis of structural design (including Irish National Annex). Dublin, NSAI.
- Innovations, F. (2011). CLT HandBook. Canada, FP Innovations.
- Wallis, B. (2014). "Wellington Bomber." from <http://www.sirbarneswallis.com/Geodetics.htm>.
- BS (1997). BS 5588-11:1997. Fire precautions in the design, construction and use of buildings. BSI
- IStructE (2007). Manual for the design of timber buildings structures to Eurocode 5. London, Institute of Structural Engineers.
- Trada (2002). "TRADA Timber Industry Yearbook" <http://www.trada.co.uk/images/onlinebooks/44DEFBCA-5137-4A65-8A3B-B07EBD2E56A4/index.html#d0e24>
- DOE (2006). Technical Guidance Document A. Ireland.
- DOE (2006). Technical Guidance Document B. Ireland.
- CEN (2006) EN 1991-1-7 (English): Eurocode 1: Actions on structures - Part 1-7: General actions - Accidental actions [Authority: The European Union Per Regulation 305/2011, Directive 98/34/EC, Directive 2004/18/EC]

Timber/steel composite members in multi-storey buildings under fire test loadings

Matthew Whelton, Andrew Macilwraith

Department of Civil, Structural and Environmental Engineering, Cork Institute of Technology, Rossa Ave, Cork, Ireland
email: matthew.whelton@mycit.ie, andrew.macilwraith@cit.ie

ABSTRACT: This paper sets out to assess the potential benefits of incorporating steel sections into timber members used in tall beam and post structures. The investigation involved identifying the tensile capacity of the members, intended as tying members in an accidental event involving a standard fire. Three-dimensional, thermo-mechanicals models were developed to identify the time timber and the timber/steel composite members could sustain the required tensile load in a fire condition. The finite element software package ANSYS was used to model the members and the results obtained compared to experimental tests carried out. It was found that the duration the composite members sustained the tensile load was significantly longer than solid timber members, as well as incorporating ductility into the structural system.

KEY WORDS: Timber, Steel, Fire, Disproportionate Collapse

1 INTRODUCTION

Through the use of cross-laminated timber panelised structures, timber has proven to be a viable alternative to reinforced concrete and steel structures in tall residential buildings. However, to provide the unrestricted, open plan floor space required for modern commercial buildings, there may be a need to move towards beam and post structures.

In recent years, a number of these building structures have been constructed, however, literature and research in the area is limited. This paper investigates the adoption of the indirect method outlined in IS EN 1991-1-7 [1], to ensure a timber structure has sufficient robustness to prevent a disproportionate collapse in accidental situations.

2 RESEARCH PROPOSAL

The indirect method involves the provision of a minimum horizontal and vertical tying capacity to allow catenary action to support the remaining structure after an accidental event. However, due to the brittle nature of timber in tension, solid timber beam elements required to bridge a damaged part of the structure, rely primarily on their elastic bending capacity.

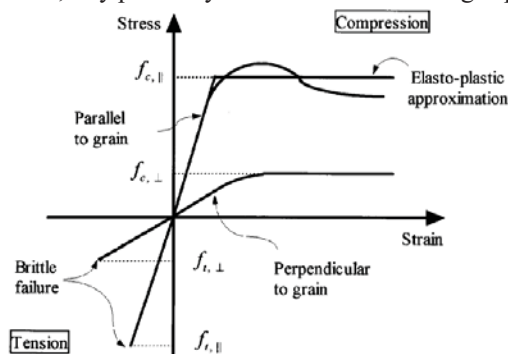


Figure 1: Stress-strain Relationship for Timber [2]

As a sudden failure would occur once the elastic limit has been exceeded, catenary action cannot be used to resist the accidental loading conditions as plastic hinges cannot form

[3]. The aim of this study was to investigate the incorporation of relatively small steel sections into the members to introduce ductility into the structural system. As is the case with reinforced concrete, the ductility introduced into the cross-section by steel will allow the required vertical deformations to develop a catenary [4].

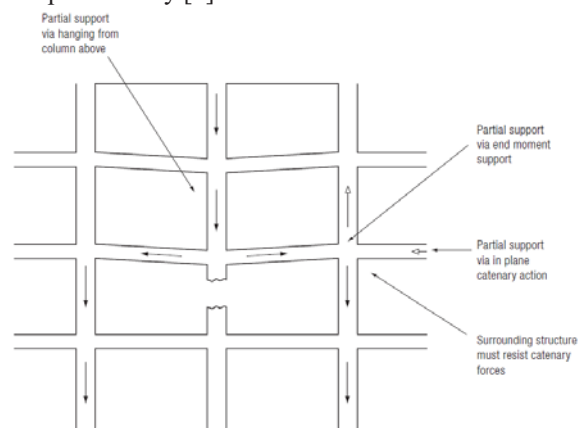


Figure 2: Floor Survival via Catenary and Hanger Action [5]

Furthermore, it was expected that the composite members would sustain the required tying forces for a more predictable and longer period of time in an accidental situation involving a fire.

The aim of this paper was to assess the thermal and mechanical behaviour of this type of member in tension, through, experimental and numerical analysis, particularly when subjected to the ISO 834 standard fire curve [6].

3 ROBUSTNESS AND ACCIDENTAL ACTIONS IN THE EUROCODES

Identifying and preventing every accidental action is unfeasible for a number of reasons. Therefore, to ensure a disproportionate collapse does not occur as a result of an unidentified accidental action, EN 1991-1-7 requires a building to have sufficient robustness. For tall commercial

buildings, with between four and fifteen storeys, the recommended strategy for an unspecified accidental situation is the indirect method, which involves the provision of horizontal and vertical tying. Equation 1, which has been extracted from EN 1991-1-7, forms the basis for the design tensile forces assessed.

$$T_i = 0.8(g_k + \psi q_k)sL \text{ or } 75\text{kN, whichever is greater (1)}$$

Where:

s is the spacing of ties,

L is the span of the tie,

Ψ is the relevant factor in the expression for combination of action effects in the accidental design situation (i.e. ψ_1 or ψ_2 in accordance with expression (6.11b) of EN 1990 [7]).

Vertical ties are required to resist a tensile force equal to the largest permanent and variable action applied to the column, calculated using expression 6.11 of EN 1990.

Limitations of the laboratory testing equipment required the members tested to be sized based on a 3m x 3m grid, supporting typical office loading. Under this loading arrangement it was found that the tying capacity required of horizontal members is 45kN. The purpose of the limiting value of 75kN in Equation 1 is to reduce the susceptibility of the members being dislodged as a consequence of an explosion [5]. Adhering to Equation 1, all tensile tests were conducted with a 75kN applied force.

4 MATERIAL PROPERTIES

The properties of the timber and steel at both ambient and elevated temperatures were identified through experimental testing and a review of existing literature.

4.1 Steel

The thermal and mechanical properties for grade S275 steel used in this research were based on the recommendations of EN 1993-1-1 [8] and EN 1993-1-2 [9]. The functions of the mechanical properties with respect to temperature are plotted in Figure 3 and the thermal properties illustrated in Figure 4.

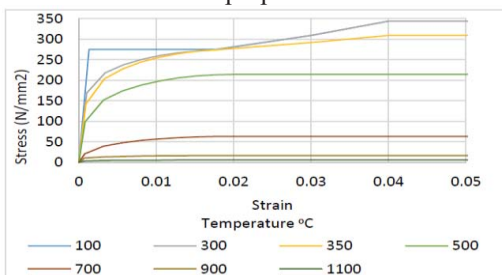


Figure 3: Stress-strain curves for carbon steel at elevated temperatures

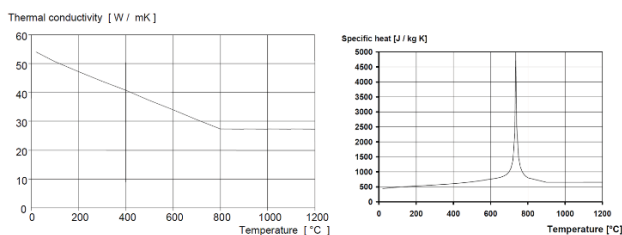


Figure 4: Thermal Conductivity and Specific heat of carbon steel as a function of temperature [9]

4.2 Timber

The timber used in this research was Irish grown Sitka Spruce, graded as C16. The thermal and mechanical properties were identified through a combination of laboratory testing and existing research.

4.2.1 Mechanical Properties

4.2.1.1 Elastic Properties

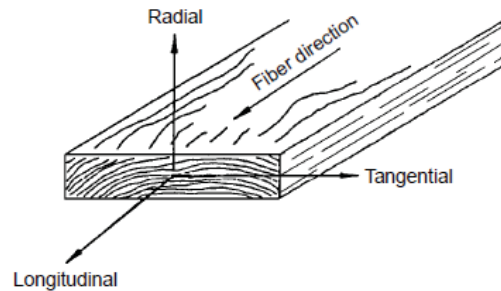


Figure 5: E-value Testing [10]

Timber is an orthotropic material, which requires nine properties to define the elastic behaviour; 3 elastic moduli, 3 Poisson's ratios and 3 shear moduli.

These values were obtained through tests outlined by IS EN 408:2010 [11] and supplemented with values obtained using the elastic ratios presented by Green et al. [10] for Sitka Spruce.



Figure 6: E-value Testing

Twenty-eight sample pieces were tested to measure the modulus of elasticity and shear modulus of the timber. As shown in Table 1 the values show reasonable agreement with those recommended in EN 338 [12].

Table 1: Overview of Mechanical Testing Results

Property	IS EN 338 (N/mm ²)	Measured (N/mm ²)
Mean Modulus of Elasticity Parallel to the Grain	8000	8184.99
5% Modulus of Elasticity Parallel to the Grain	5400	5528.6
Mean Shear Modulus	500	401.29

The ratios of these elastic properties measured also corresponded to the results presented by Green et al., justifying their use in identifying the remaining elastic properties.

The double line model proposed by König [13] was adopted to identify the mechanical properties at elevated temperatures.

Table 2: Identified Elastic Properties of Irish Grown Sitka Spruce Graded as C16

Temp °C	Elastic Ratio	E _L	E _T	E _R	G _{LR}	G _{LT}	G _{RT}
		N/mm ²					
20	1	8185	352	638	523	441	24
100	0.5	4092	176	319	261	221	12
300	0.05	40	1	3	2	2	0.1

Note: Values for intermediate temperatures are linearly interpolated

Although both König [13] and EN1995-1-2 assume the strength and stiffness of timber at 300°C is zero, an elastic ratio of 0.05 was used to model the timber. This allowed the mathematical models to remain stable at temperatures above 300°C.

4.2.1.2 Ultimate Tensile Stress

To identify the ultimate tensile stress ten small clear specimens of Irish grown Sitka Spruce graded as C16 were tested. The average result of these tests is presented in Table 2.



Figure 7: Tensile Test of a Tapered 700mm x 70mm x 10mm Test Pieces

Table 2: Overview of Mechanical Testing Results

Property	Raftery and Harte (N/mm ²)	Measured (N/mm ²)
Ultimate Tensile Stress Parallel to the Grain	67.3	50.27

In Raftery and Harte (2013) [14], tensile testing of 140 small clear specimens of Irish grown Sitka Spruce showed that the ultimate tensile stress ranged from 23N/mm² to 104N/mm², with a mean value of 67.3N/mm². This compares well to the values found in this research.

4.2.2 Thermal Properties of Timber

The *Advanced Calculation Method* presented in Annex B of IS EN 1995-1-2 [9] was adopted to define the thermal properties of timber. As illustrated in Figure 8 the thermal properties are temperature dependant.

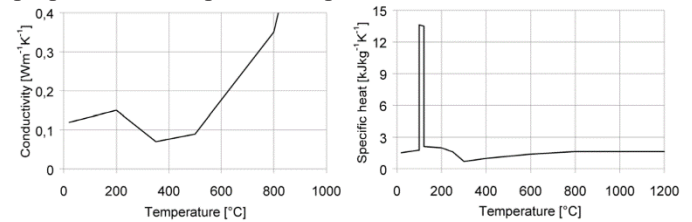


Figure 8: Thermal Conductivity and Specific Heat of Timber and Char Layer

5 COMPOSITE MEMBER DESIGN AND EXPERIMENTAL TESTING

Three cross-section arrangements were considered, two composite members consisting of timber and steel in addition to a solid timber cross-section used for comparison. Figure 9 outlines the general arrangements.

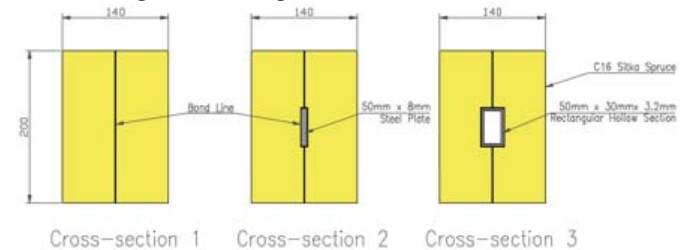


Figure 9: Timber and Timber/Steel Cross-sections

The elements were sized based on a 3m x 3m structural grid under typical office loading and were bonded using phenol-resorcinol resin. The reduced grid size was necessitated by the dimensions of the openings in the kiln.

5.1 Elevated Temperature Tensile Testing

Elevated temperature tensile testing of the cross-sections illustrated in Figure 9 were conducted to assess the length of time the members could sustain the 75kN tying force under standard fire conditions.

5.1.1 Test Arrangements

Five standard fire tests were conducted; one on the solid timber member, and two for each composite member. The composite members were tested with two different end connection configurations, either welded to the ends of the embedded steel element or bolted as shown in Figure 10 and Figure 11.

Table 3: Kiln Test Arrangements

Test No.	Cross-section Tested	Connection
1	Solid Timber	Bolted
2	Timber with a 50mm x 8mm steel plate	Bolted
3	Timber with a 50x30x3.2 RHS	Bolted
4	Timber with a 50mm x 8mm steel plate	Welded
5	Timber with a 50x30x3.2 RHS	Welded



Figure 10: Tensile Test Set-up

As illustrated in Figure 11 the test beams were placed in the kiln with one end restrained in the longitudinal direction, while a 75kN force was applied with the use of hydraulic jacks connected to the opposite end.



Figure 11: End Restraints for the Elevated Temperature Tensile Tests

5.1.2 Fire Curve

To simulate the fire conditions, the kiln was programmed to increase in temperature using the heating profile specified in ISO 834 [6].

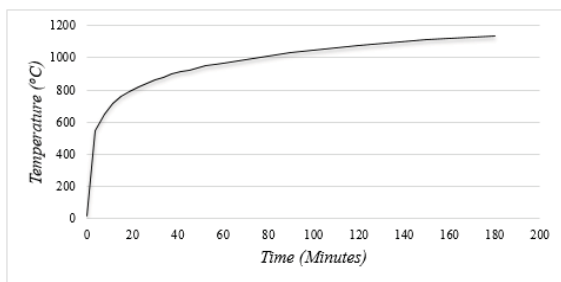


Figure 12: Programmed Time Temperature Curve

Thermocouples were positioned throughout the member to measure the temperature distribution within the cross-section.

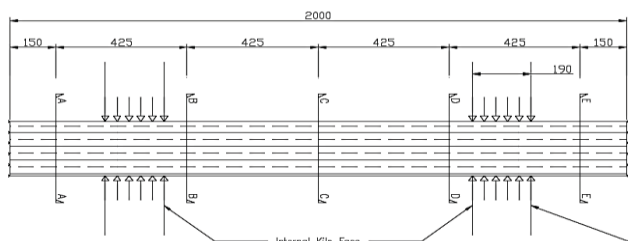
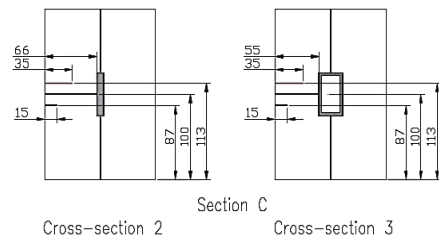
Figure 13A: Thermocouple Locations
(See below for related sections)

Figure 13B: Thermocouple Locations

5.1.3 Elevated Temperature Results

Each member was tested to assess the duration it could sustain the 75kN load. Table 4 outlines the results for each test and the percentage increase in time the composite members sustained the applied force with respect to the timber member.

Table 4: Tensile Test Results

Test Number	Time (minutes)	Increase in Time with embedded steel (%)
1	62.5	-
2	85.6	36.96
3	84.1	34.56
4	82.9	32.64
5	83.1	32.96

As shown, test numbers 2 - 5 sustained the tying force for between 20.4 minutes and 23.1 minutes longer than the solid timber test piece, representing an average increase of 34.28%. Furthermore, a ductile failure was observed for the composite members, compared to a sudden brittle failure for the solid timber member.

6 FINITE ELEMENT ANALYSIS

ANSYS finite element analysis software was used to simulate the standard fire testing conducted in the laboratory. A two-phase analysis procedure was required, first to identify the temperature profile of the model with respect to time and secondly, to conduct a non-linear mechanical analysis. The analysed length of the member was reduced to 0.15m, while maintaining the full cross-sectional dimensions, to reduce the significant processing time.

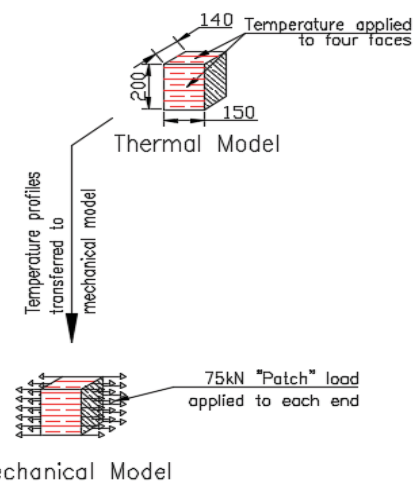


Figure 14: Finite Element Analysis Approach

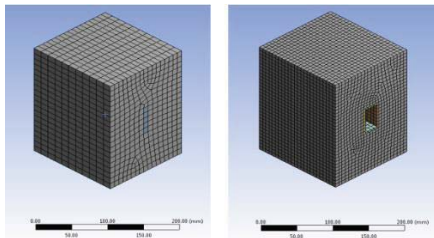


Figure 15: Meshed Models

The timber and steel portions of the cross-sections were defined using the mechanical and thermal properties outlined in Section 4.0.

6.1 Finite Element Analysis Results

6.1.1 Thermal Analysis Results

A non-linear time dependant temperature increase was applied to the four exposed faces of the models, to simulate the ISO 834 fire curve. Illustrations of the temperature distributions in cross-section 3 at various times are presented in Figure 16.

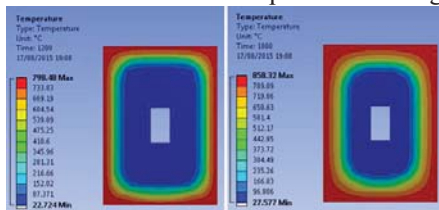


Figure 16: Temperature Distributions at 20 and 30 minutes

The time-temperature relationship at various depths within the timber and the steel sections are graphically presented in Figure 17.

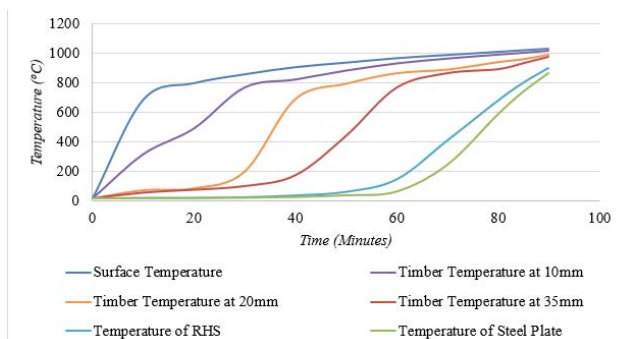


Figure 17: Time-Temperature Relationship at Various Depths

6.1.2 Mechanical Analysis Results

The temperature distributions obtained from the thermal analysis were transferred into the mechanical model where the resistance of the temperature dependant material properties were assessed.

The results of the finite element analysis for the tensile resistance of the composite members are shown in Figure 18, where the y-axis represents the factor of actual capacity vs the required capacity, or redundancy factor.

As shown, cross-section 2 sustained the 75kN tensile load approximately thirteen minutes longer than cross-section 3, despite the fact that at ambient temperatures cross-section 3 had a greater tensile capacity. This is attributed to the additional 11mm of timber cover to the steel in cross-section 2. The ultimate failure occurs with no mechanical contribution from the timber for both cross-section 2 and cross-section 3.

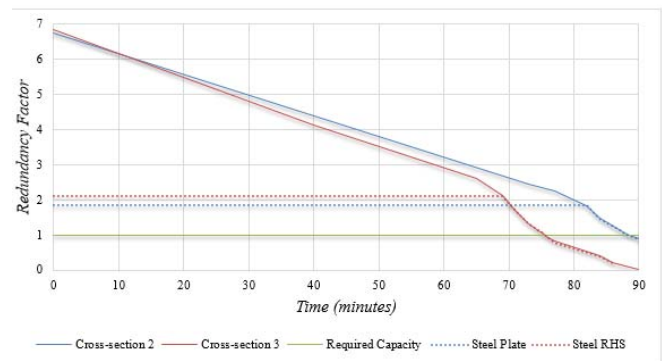


Figure 18: Redundancy Factor (Finite Element Analysis)

Using cross-section 3 as an example, it can be seen that the capacity of the member reduces at a steady rate for the first 69 minutes, simulating the reduction in stiffness and mechanical resistance of the timber portion of the member, as the section increases in temperature. At 69 minutes the entire timber portion of the cross-section is at temperatures above 300°C and no longer provides mechanical resistance. The increased rate in reduction of tensile capacity at 69 minutes corresponds to the steel portion of the cross-section increasing in temperatures above 400°C to 563.7°C at 75.4 minutes, where ultimate failure occurs.

To verify the above statement, the tensile models were reanalysed, assuming there was no mechanical bond between the timber and steel, with the tensile forces applied directly through the steel portion of the cross-section. The results of this analysis are illustrated by the blue and red “dotted” lines in Figure 18. As shown, without the contribution of the timber, the tensile capacity of the member is significant lower in the early stages of the analysis, however, the capacity remains constant up to 69 minutes due to the insulating properties of the timber. At 69 minutes the shape of the dotted line and corresponding solid lines in Figure 18 decrease at the same rates simulating the reducing yield strength of the steel as the temperature increases above 300°C. This demonstrates that the mechanical resistance of timber has no effect on the time the load is sustained.

7 COMPARISON OF LABORATORY MEASUREMENTS AND FINITE ELEMENT ANALYSIS RESULTS

Figure 19 illustrates the differences between the temperatures of the steel section measured in the laboratory and those identified through the finite element analysis. As can be seen, the rate of increase and magnitude of the temperature are similar in both cases, giving confidence in the thermal model adopted.

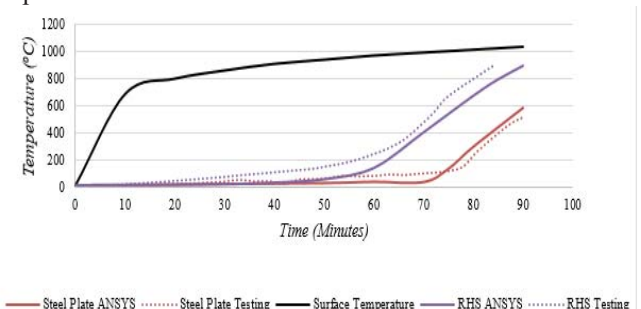


Figure 19: Comparison between the Thermal Analysis and Measured Readings

The small differences in failure times observed in the laboratory compared to those found using finite element analysis, highlight the accuracy of the models, particularly when the inconsistency of the material properties of timber are considered.

Table 5: Finite Element Analysis Results Compared to Laboratory Testing Results

Test No.	Cross-section	Time (Minutes)	Difference (Minutes)
1	1	62.5	+ 7.2
ANSYS	1	55.3	-
2	2	85.6	- 3.9
4	2	82.9	- 6.6
ANSYS	2	89.5	-
3	3	84.1	+ 8.7
5	3	83.1	+ 7.7
ANSYS	3	75.4	-

8 CONCLUSIONS

8.1 Mechanical Properties of Timber

The significant range of elastic moduli measured, further justifies the requirements of EN 1995-1-1 to use the lower 5th percentile of the elastic moduli test results in design. The EN 338 recommended values for grade C16 timber for the mean and 5th percentile Young's modulus correspond with those measured from the twenty-eight samples of Irish grown Sitka Spruce. The modulus of elasticity measured during ambient temperature tensile tests agrees with those measured through the bending approach prescribed in BS EN 408, further justifying the results.

The ratios of the elastic moduli to the shear moduli measured in the laboratory, largely agree with those presented in the work by Green et al., discussed in Section 4.0 of this document. Therefore, in the absence of more accurate and specific data it is recommended that these ratios are used to define the properties of Irish grown Sitka Spruce.

Composite Behavior at Ambient Temperatures

Tensile testing of the timber/steel cross-sections at ambient temperatures, demonstrate that these relatively small members remained composite under axially applied forces higher than the 75kN tying resistance required by EN1991-1-7 for situations where horizontal tying is used in design to limit disproportionate and progressive collapse.

8.3 Elevated Temperature Tensile Testing

The average temperatures measured at various depths within the timber and at the surface of the steel during the fire tests had good correlations between the results obtained from the thermal finite element analysis. This suggests that the expressions used to define thermal conductivity, specific heat and coefficients of thermal expansion recommended in Annex B, Advanced Calculation Methods, of EN 1995-1-2, are applicable to Irish grown Sitka Spruce.

The incorporation of the relatively small steel sections into the timber members increased the time they sustained the applied tensile force under the standard fire curve by an average of 34.28%.

8.4 Connections

The different types of connection used in the laboratory tensile tests did not have a significant bearing on the time the member sustained the tensile force. The finite element analysis results demonstrate, the ultimate failure occurs at a point where no mechanical resistance was provided by the timber portion of the cross-section. Therefore, provided the connection used allows the steel portion of the cross-section to transfer the required tensile force, the connection type will have no significant bearing on the length of time the member can sustain the tying force.

8.5 Failure Mode

The failure of the solid timber members at both ambient and elevated temperatures was an abrupt brittle failure. This sudden failure is likely to amplify the effects of an accidental event, however, with the incorporation of steel into the timber cross-sections the failure mode was ductile. The addition of ductility into the structural system allows the tying members to yield, encouraging further load distribution, delaying or possibly even preventing ultimate failure of the tying member.

REFERENCES

- [1] IS EN1991-1-7:2002. *Eurocode 1 - Actions on Structures - Part 1-7: General Actions - Actions on Structures Exposed to Fire*. s.l. : NSAI, 2002.
- [2] Peng Lei. *Performance of Heavy Timber Connections in Fire*. Ph.D Thesis. Ontario: Carleton University, 2010.
- [3] Sven Thelandersson and Daniel Honfi. *Behaviour and modelling of timber structures with reference to robustness*. Joint Workshop of COST Actions TU0601 and E55, Slovenia, 2009.
- [4] Yi Li, Xinzhen Lu, Hong Gao and Lieping Ye. *Improved Tie Force Method for Progressive Collapse Resistance Design of RC Frame*. Structures Engineering Structures, 33(10), pp.2931–2942, 2011.
- [5] A.G.J. Way. *Structural Robustness of Steel Framed Buildings*. s.l. : Steel Construction Institute, 2011. Vol. SCI Publication P391.
- [6] ISO 834. *Fire Resistance Tests - Elements of Building Construction, Part 1: General Requirements*. Switzerland : Organisation for Standardization, 1999.
- [7] NA to IS. EN1990:2002. *Irish National Annex to Eurocode 0 - Basis of Structural Design*. s.l. : NSAI, 2010.
- [8] IS EN1993-1-1:2005, *Design of Steel Structures – Part 1-1: General rules and rules for buildings*, NSAI, 2005.
- [9] IS EN1993-1-2:2005, *General Rules – Structural Fire Design*, NSAI 2005.
- [10] Green D W, Winady J G, and Kretschmann D E. *Mechanical Properties of Wood*. Chpt. 5. 2002.
- [11] BS EN 408:2010 + A1 2012, *Timber Structure. Structural Timber and Glue Laminated Timber. Determination of some physical and mechanical properties*, BSI 2011.
- [12] IS EN 338:2009, *Structural Timber – Strength Classes*, NSAI 2009
- [13] König, J. *Structural Fire Design according to Eurocode 5 - Rules and their Background*. s.l. : Fire and Materials, 2005. pp. 147-163.
- [14] Raftery, G. M., & Harte, A. M. (2013). Material characterisation of fast-grown plantation spruce. *Proceedings of the Institute of Civil Engineers: Structures and Buildings*, 167(6), 380-386. doi:10.1680/stbu.12.00052
- [15] IS EN1995-1-2:2004, *Design of timber structure. General rules, Structural Fire Design*, NSAI 2004.

A Review of the State of the Art of Timber Gridshell Design and Construction

Matt Collins¹, Prof. Tom Cosgrove¹

¹Department of Civil Engineering and Materials Science, University of Limerick, Castletroy, Limerick, Ireland
Email: matthew.collins@ul.ie, tom.cosgrove@ul.ie

ABSTRACT: Timber gridshells are lightweight doubly curved structures. They are generated by deforming a flat timber grid towards a curved shell-like target shape. The designer can achieve a best fit approximation to a pre-determined target shape by varying the grid, boundary geometry and member stiffness. Thus a wide variety of built forms can be created. Additionally timber is a renewable resource. Despite these advantages, few timber gridshells have been realised. Bending active gridshells are complex to analyse, design and construct. The research presented here is a comparative study of a number of existing timber gridshells in terms of approach to design and analysis, material selection and construction process. The joints, the number of layers, type of bracing and type of covering are also examined. Barriers to the more frequent adoption of timber gridshells in design are identified. Research currently underway at the University of Limerick is aimed at reducing these barriers.

KEY WORDS: Timber; Gridshells; Bending active; Free-Form Architecture; Precedents.

1 INTRODUCTION

Throughout history, building structures have been created using a wide variety of forms. Shell structures are particularly versatile in the variety of forms they can assume. Timber has been used throughout the Middle Ages, Early modern period, 19th century, 20th century and is still a very prominent material in the 21st century as a structural element in buildings. Gridshells are discrete shell structures. A gridshell, like a continuous shell, is a structure that gains its strength and stiffness through its double curvature configuration. Gridshells are made from elements that have one dimension considerably longer than its other two, which makes timber a suitable material. A timber gridshell enables doubly curved structures to be formed from a set of straight, prefabricated, identical components. The development of computer methods in modelling complex three-dimensional structures is a development that will increasingly facilitate designers in using this challenging structural form. Additionally, engineered materials further facilitate designers to achieve complex geometries.

Many types of curved structures exist today. Gridshells can be classified as either bending active or bending inactive. The term bending active means that the structural elements have to be deformed by bending to give the structure its final shape. A type of bending pre-stress is thus generated in the members during forming [1]. Alternatively, bending inactive describes a structure whereby the structural elements do not need to deform to give the structure its shape. A typical bending inactive structure would be a truss, portal frame or a geodesic dome such as the Eden project or the Quebec Biosphere. The majority of bending inactive gridshells have been constructed from steel. These structures are comprised of numerous

straight elements each inclined at a different angle to its adjacent element and joined at nodes usually by welding, if the geometry is irregular, to give the structure its curved shape. An example is the roof over the great court in the British Museum [2] and the courtyard roof in the Museum of Hamburg History [3]. In addition, a number of bending inactive timber gridshells have been constructed such as the University of Exeter Forum [4] and Centre Pompidou Metz [3]. The timber members for Centre Pompidou Metz are created by machining smaller curved timber sections out of initially straight glulam timber of large cross section. In contrast, bending active gridshells are not all that common, however a number of them have been constructed such as the Multihalle in Mannheim [5], the Weald and Downland Museum [6], and the Savill Garden centre [7].

In order to advance the knowledge base of gridshells, a detailed account of those gridshells that have already been constructed is required. Many aspects of gridshells can be personalised, giving each gridshell a completely different appeal. Six notable bending active gridshells are described here. The design context, computational modelling and analysis procedures, material selection and production, joint details and construction methods are described. Subsequently having described individually each gridshell, the development of gridshells over time is discussed with a final focus on how this research advances the topic of gridshells.

2 DEFINITION OF A GRIDSHELL

Bending active gridshells are lightweight doubly curved structures, creating open plan spaces that make efficient use of sustainable materials. Only a few of these elegant structures exist today. They are complex structures made by deforming

initially straight elements. The analysis and design of these structures is difficult and is centred on the form finding of the gridshell. An initially flat grid must be sufficiently flexible to be able to bend and twist towards a target shape. The exact target shape may not be an equilibrium form for the given materials, sections and geometry. Nonetheless a final shape can be achieved which approximates to the target shape.

A gridshell may be thought of as a shell whose material has been gathered as strips concentrated along lines or laths and intersecting at nodes. This new system is a lattice shell that can transmit forces in the direction of the laths and can also resist some out of plane bending. A lattice shell can be seen as a series of arches that are connected together creating a series of (usually) quadrilateral shapes. For this reason a lattice shell does not entirely conform to shell action by itself [8]. In order for the lattice shell to conform to shell action a means is necessary by which in-plane shear stresses can be distributed through the shell. This is done by applying some form of bracing to triangulate the quadrilaterals of the structure enabling in-plane shear stresses to be developed, resulting in a gridshell. A more detailed description of gridshell bracing systems can be found in section 3.3. By concentrating the shell into strips, openings are easily created. By adjusting the depth of the strips, the stiffness out of plane and thus the buckling capacity can be modified [6].

The benefit of bending active timber gridshells becomes apparent in the construction stage. Complex forms can be shaped relatively easy [6]. The way in which these forms are created is generally by laying a flat grid of continuous timber laths in two directions. The laths are then connected at their intersections (nodes) with a cylindrical joint. The cylindrical joints allow rotation for the individual laths to scissor relative to each other so that deformation can occur [9]. Once the required shape is reached, the perimeter nodes are constrained to the edge boundaries, all the nodes are tightened and the structure is stiffened by some form of bracing system (Figure 1). This construction method is suitable for a material that; is lightweight; can be bent without too much effort; and has sufficient capacity to resist the loads after construction. Timber satisfies these three criteria.



Figure 1: From a flat grid to a lattice shell to a gridshell

The way in which the gridshells in this study were constructed vary considerably from constructing them in-situ piece by piece, laying out the grid above and pulling it down, and laying out the grid on the ground and pushing it up.

3 GRIDSHELL COMPONENTS

3.1 Layers

There are practical and physical limitations on the tightness of curvature to which gridshell members of a particular cross-section can be bent. The depth of member required for a single layer gridshell to achieve relatively large spans may be too deep to permit bending of the flat lattices to a final shape with tight radii of curvature. The solution to this problem is to use multiple layers for the gridshell which have smaller section sizes [6]. The layers are initially un-coupled therefore they deform independently of each other and because of their small section size, they can form tight curvatures. Once the form has been found, the individual layers are connected together to create a composite structure which has greater out-of-plane bending strength enabling the gridshell to span longer distances.

A single layer gridshell (Figure 2a) has a single lath in each direction where as a double layer gridshell (Figure 2b) has two laths in each direction. A double layer gridshell is, in simple terms two single layer gridshells one placed on top of the other but locked together to create the composite action. This develops greater out-of-plane bending strength and stiffness. The parallel members are allowed to slide relative to each other during the formation process so that the flexural stiffness of the members is that of a single layer gridshell. A qualitative stress block for a single layer and a double layer (coupled and uncoupled) is given in Figure 3.

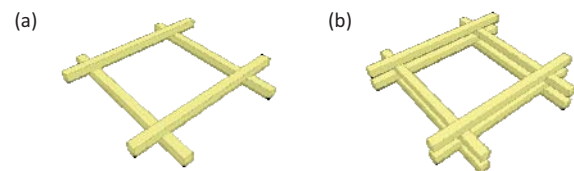


Figure 2: (a) a single layer gridshell and (b) a double layer gridshell

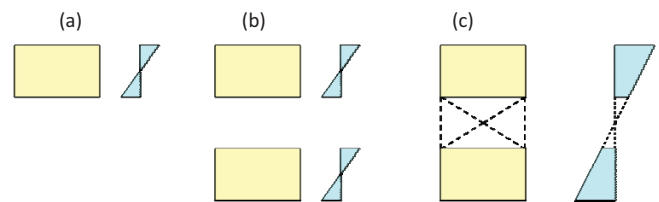


Figure 3: Qualitative allowable stress blocks of different gridshell layers, (a) single layer, (b) double layer (uncoupled), and (c) double layer (coupled).

When the double-layered gridshell approaches the target shape, the nodes are tightened and shear blocks in the form of wedges or solid blocks of timber are inserted between the layers, thereby ensuring composite action between the two layers. A double layer gridshell with a gap between the layers equal to the thickness of the members themselves has a flexural stiffness that is 26 times stiffer than that of a single layer of the same material (assuming full compatibility).

There is potential to further this type of system, multi-layered (>2) gridshells could be utilised to achieve larger spans. By adding more layers or increasing the depth of the shear block the out-of-plane bending strength and stiffness is further increased [10].

In addition, according to linear elastic beam bending theory, the local radius of curvature that a beam can achieve is directly proportional to the thickness. Assuming a constant strength and stiffness, the only difference between the double layer and geometric equivalent single layer is the magnitude of the thickness of the material. A single member in the double layer has a thickness that is at least three times smaller than the thickness of a geometrically equivalent single layer. Therefore, a radius of curvature can be achieved with the double layer that is three times smaller than would be possible with a geometrically equivalent single layer.

3.2 Crossover Joint

Gridshell structures have very large numbers of nodes and so the design of the crossover joint is essential to the success of the overall structure. The formation process of a gridshell has the most influence on the type of nodal joint adopted. During the typical formation of a bending active gridshell, the grid must allow rotation of the laths (scissoring) at the joints (Figure 4). Here, the lengths of the diagonals in (a) are equal but in order to form the lattice into the correct shape scissoring is required. Thus the lengths of diagonals in (b) are not equal ($L_{13} > L_{24}$) [6].

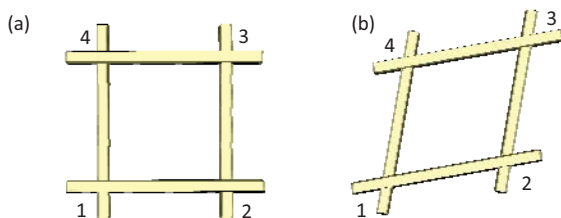


Figure 4: Scissoring of gridshell members, (a) before scissoring, and (b) after scissoring.

A wide variety of crossover joints were designed for different gridshells. For single layer gridshells, the joint detail is not too complex as relative sliding of the layers is not required. However, particular attention is required in a double layer gridshell to detail the joints in such a way as to permit sliding during forming.

Once the gridshell has been formed, the joints are tightened which prevents this independent sliding. The reason for allowing sliding between layers is to prevent the build-up of any unwanted stress in the laths during forming allowing tighter curvatures to be achieved. The required curvatures of the two laths are different due to their geometrical location in space. Thus, the distance between adjacent nodes on each lath is different. This phenomenon is displayed in Figure 5, showing a portion of a double-layered gridshell before and after being deformed. The distance L between Node 1 and Node 2 is the same for both laths before deformation. With sliding allowed, the gridshell is formed and now the distance

between both laths is not the same. The angle θ is the same for the arcs created by the neutral axis of both laths. $R_1 > R_2$ and $L = R\theta$. Therefore $L_1 > L_2$.

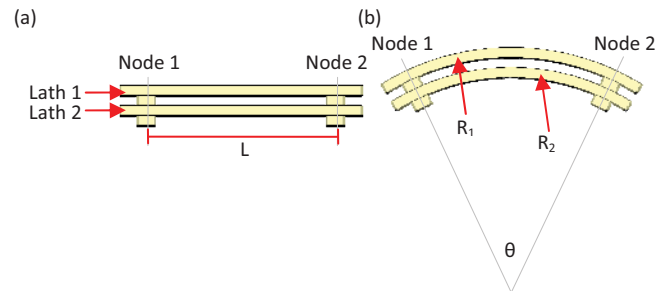


Figure 5: Relative sliding of layers, (a) as a flat grid, and (b) after deforming.

Gridshells are lightweight and undergo significant deformations due to snow and wind loadings as well as fluctuations in moisture content. Therefore, the joints need to be detailed appropriately to facilitate these movements.

3.3 Bracing

For three dimensional structural stability and for shell action [3] to be developed in a gridshell, a means is necessary by which the shear forces can be transmitted from one edge of the gridshell to the other. Therefore, a gridshell must have sufficient in-plane shear strength whereby the laths will efficiently distribute the applied forces and the gridshell will behave similar to a continuous shell. In-plane shear strength can be provided in several ways:

- Rigid joints
- Cross ties (tension only bracing)
- Rigid diagonal bracing
- A continuous membrane layer

The reason for the bracing system is to triangulate the structure to provide in-plane shear strength and stiffness (Figure 6). Quadrilaterals are inherently flexible because their geometry can change without a change in member length. However, this is not true for a triangle whereby the members themselves must deform for the entire structure to deform.

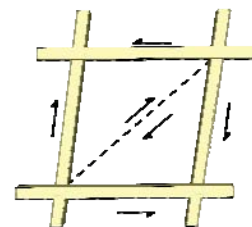


Figure 6: Gridshell element with diagonal bracing

The bracing is typically applied to the gridshell structure once the forming process has been completed and each end node is at its designated boundary. The internal supports remain in place until the bracing has been added. This is to ensure that the completed structure accurately represents the target shape. Without the bracing, the structure would be incomplete and

excessive deflections or even failure might result from the self-weight and construction loading.

Each of the bracing types has advantages and disadvantages. The rigid diagonal bracing offers advantages over cross-tie bracing. Steel cables can only act in tension and hence each quadrilateral would require two cables running orthogonally. However, timber can carry both tension and compression, meaning that it is only necessary to run a bracing lath in one direction across a given quadrilateral [6]. Rigid joints are poor at creating a stiff overall structure on their own and must be used in conjunction with another type of bracing. If rigid joints were to be used on their own, the size of the joint required to create full fixity may be too big and obtrusive.

The rigid bracing system can be formed using long lengths similar to the laths themselves (bending active bracing) or by short straight lengths (bending inactive bracing), one for each quadrilateral. For bending active bracing additional bending stress are introduced to the structure. This may cause a change in geometry of the overall structure due to additional out of plane forces being applied at the joints. An additional benefit of rigid bracing is that external facades such as cladding panels can be attached directly to the bracing thereby reducing the complexity of the connections.

Crosstie bracing does not add any additional out-of-plane forces to the structure. However, crosstie bracing is tensioned upon application and if this tensioning is not carried out in a controlled manner, unwanted changes in geometry may occur. In contrast, temporary crosstie bracing can be beneficial during the form finding process to force certain areas of the structure to scissor in a certain direction. Depending on the joint type and façade used, the crosstie bracing does not increase the overall depth of the structure unlike the rigid bracing. Moreover, an alternative to linear bracing elements is to use planar elements such as stressed skin panels [10].

3.4 Materials

Gridshells can be created by using materials such as timber, steel, Fibre Reinforced Plastics (FRPs) and even cardboard tubes. This versatility makes gridshells an ideal structure to design and create very efficient forms. A material with a high f_m/E_m ratio is most suited to gridshells [11]. This material should have a low elastic modulus to enable bending without too much force and a high bending strength to allow tight curvatures to be achieved. High slopes and curvatures are efficient in supporting the accumulation of vertical force that occurs close to a support in compression or tension.

The timber used for the Weald and Downland [6] gridshell and the Savill Garden [10] gridshell was improved by cutting out short grain and other irregularities such as knots and clusters of pin knots. The defects were cut out and the defect free sections of the laths were re-joined using finger joints. For these joints a liquid PUR glue was used which is suited to the gluing of finger joints with green timber. Long uninterrupted laths in a gridshell reduce the number of

structural components as well as simplifying the joint detail to a single repeatable joint across the structure.

Timber has an advantage over other materials when it comes to selection of a material for a gridshell, especially when it comes to multiple layers. Waste is reduced, the improved timber is used for the laths and the remaining timber can be used for the shear blocks and other non-critical components. Doubly curved gridshells offer a greater variety of curvatures than with other structures. However, the issues around defects and variability have to be dealt with when it comes to timber due to it being a natural material.

4 EXISTING GRIDSHELLS

The Multihalle gridshell in Mannheim Germany was the first large-scale bending active timber gridshell. Constructed from Western hemlock, it was designed by Frei Otto and built in 1975. The form was developed using physical models. Long lengths of timber were produced by finger jointing but many finger joints broke during the forming process. Lath breakages were repaired on site by adding splice pieces to the sides of the broken member. Steel cable bracing was used; the specific tension force in the cables set the stiffness of the overall gridshell. A fabric membrane was used as a weathering skin. The gridshell was assembled flat on the ground. It was then raised using movable platforms. Spreader beams were used at the tops of the platforms to distribute the forming forces.

Twenty-seven years would pass before the next large scale bending active double layer gridshell would be built, this time at the Weald and Downland Museum in Sussex. This gridshell had many notable improvements from its predecessor. Firstly, computer based form finding and structural analysis was used. Better material selection and processing using finger and scarf joints along with improved monitoring on site during forming significantly reduced the number of breakages. The material selected was green Oak, which had a high moisture content reducing its bending stiffness for form finding. The erection sequence was similar to that used at Mannheim except that the flat grid for the Downland gridshell was raised to a level equal to the finished level of the valleys. Then under gravity it was deformed downwards towards the target position. The formation of the gridshell was sequenced and was rigorously monitored to identify potential breakages and other complications before they became critical [6]. In addition, the bracing was made from the same material and also functioned as a mount for the cladding. The structure was clad in western red cedar boards, polycarbonate glazing to allow in light and a ribbon roof made from flexible polymer concrete. To connect the layers together without drilling slots and holes in the timber sections, a patented nodal connection was developed to clamp the layers together.

A different type of gridshell appeared in Helsinki in 2003. The members were manufactured pre-curved using four laminates of red fir. Additionally, steam bending was utilised to further bend the members into position on site. A simplified nodal connection using a single bolt was easily implemented as the gridshell was erected lath by lath and the boltholes were

drilled when the laths were in place. No deforming of a flat grid was carried out, which would have been difficult given the vertical orientation of this gridshell. This gridshell has no external façade so the timber was treated with an oil-based wood preservative with UV protection.

The largest bending active gridshell designed to date was opened as the visitor centre of the Savill Gardens in Windsor Great Park in 2006. This shallow double layer gridshell made from Larch had only two breakages during construction. This is due to the low curvatures and the knowledge that had been gained from previous gridshells. A greater strength and stiffness was achieved for this double layer gridshell by increasing the depth of the shear blocks beyond the depth of the gridshell members. A combination of the erection procedures that has gone before was used. Firstly, a single layer was formed by deforming a flat mat. Then, the shear blocks were screwed to this layer and lath by lath, the second layer was screwed to the shear blocks. The bracing system comprised of two layers of plywood that acted as a stressed skin membrane. Roof insulation and metal roof cladding is fixed to the plywood. Oak laths are then fixed to the cladding to complete the roof structure.

The Chiddingstone Orangery gridshell, although it is considerably smaller than the previously mentioned gridshells still represented an advance on previous Gridshells in some respects. This gridshell was made from locally sourced green chestnut. In addition, it is the first timber gridshell to accommodate a frameless glass roof, proving that these structures can be made stiff enough to support brittle finishes. However, this was only made possible, by further developing the patented node used in the Weald and Downland gridshell to accommodate the glass and cable bracing.

Advances in materials allowed gridshells to be designed using polymer composite materials [12]. The structural behaviours of these manmade materials are more predictable, having uniform linear elastic properties in the case of GFRP. Manufacturing GFRP tubes with standard dimensions allowed use of swivel scaffolding connectors. In addition, advances in computer technology since the Mannheim gridshell in 1975 allowed for the precise finished geometry of the gridshell to be predicted before erection. As a result, the fabric membrane was prefabricated off-site prior to completion of the gridshell structure, saving considerable time and money.

The timber gridshells presented here had high costs associated with them because a high amount of processing was required to obtain suitable defect free lengths of timber. Therefore, to increase the availability of the gridshell form to architects, engineers and clients a lower cost material would be required.

5 BARRIERS

As can be seen one of the most significant barriers to the development of gridshells is the availability of an appropriate material. High material selection and processing costs hinder the availability of gridshells as a viable structure. In addition, the analysis of bending active gridshells is complex given the non-linear geometries and organic shapes. Specialist computer software is required to firstly predict the geometry that a flat grid would take when formed towards a target shape and then predict the deformations and stresses that are developed due to self-weight and applied loads. Stress due to both forming and those throughout the structures design life need to be considered. An accurate prediction of the gridshell geometry is required in order to be able to design other elements of the building such as external finishes and boundary locations.

6 CONCLUSIONS

In summary, under the headings discussed for the six gridshells mentioned, six different materials were used (including five different timber species). Each gridshell took on a unique shape and size. Three different forms of bracing were developed as well as six different external finishes applied. This study shows that gridshells are very versatile to different architectural forms and finishes. A summary of key data on each gridshell is presented in Table 1 and Table 2. The historical timeline of each of these gridshells is presented in Figure 7 beginning with the Shukhov gridshell [13].

Timber gridshells are sustainable structures being constructed from a renewable resource. They are lightweight. They are structurally efficient being of shell-like form. The construction procedures and techniques are now relatively well developed. Current research at UL is investigating the potential of an engineered Irish timber product as an alternative to solid timber in bending active gridshells.

Table 1: Comparison of each gridshell presented in each study

Gridshell	Location	Plan size	Height	General Shape	Layers	Lath size	Material	Bracing
Multihalle Mannheim	Mannheim Germany	60m x 60m 40m x 40m	15.5m	Two principle domes connected with tunnels	2	50mm x 50mm at 0.5m	Western Hemlock	Twin 6mm cables at every 6th node
Helsinki Gridshell	Helsinki Zoo Finland	82m ²	10m	Vertical Bubble	1	60mm x 60mm	Laminated red fir	Timber Floor Diaphragm
Weald and Downland	Singleton UK	50m x 16m	7.35m 9.5m	Triple Bulb Hourglass	2	50mm x 35mm at 1m	Green Oak	Green Oak
Savill Garden	Windsor UK	90m x 25m	4m	Sinusoidal shape Three domes	2	80mm x 50mm at 1m	Larch	Plywood membrane
Chiddingstone Orangery	Chiddingstone UK	12m x 5m	~1m	Elliptical dome	2	40mm x 30mm	Green Chestnut	Steel Cables
Solidays' Festival	Paris	26m x 15m	7m	Unsymmetrical two domed	1	42mm Diameter 3.5mm Thickness	GFRP Tubes	GFRP Tubes

Table 2: Role of software for each gridshell presented in this study

Gridshell	Form Generation	Equilibrium Form Finding	Engineering Design (stress checks)
Multihalle, Mannheim	Wire mesh model Physical hanging chain model	Physical hanging chain model Mathematical Model	Experimental tests ARUP (buckling analysis)
Helsinki Gridshell	Scale models 3D Computer Model	None	LUSAS FEA Software
Weald and Downland	1:43 wire mesh model 1:30 wooden strips model	Dynamic Relaxation Physical models	STAAD Pro Dynamic Relaxation
Savill Garden	Mathematical Model	Dynamic Relaxation Physical models	FEA software
Chiddingstone Orangery	Mathematical Model	Buro-Happold Computer Modelling	Buro-Happold Computer Modelling
Solidays' Festival Gridshell	Mathematical Model	Dynamic Relaxation	Dynamic Relaxation

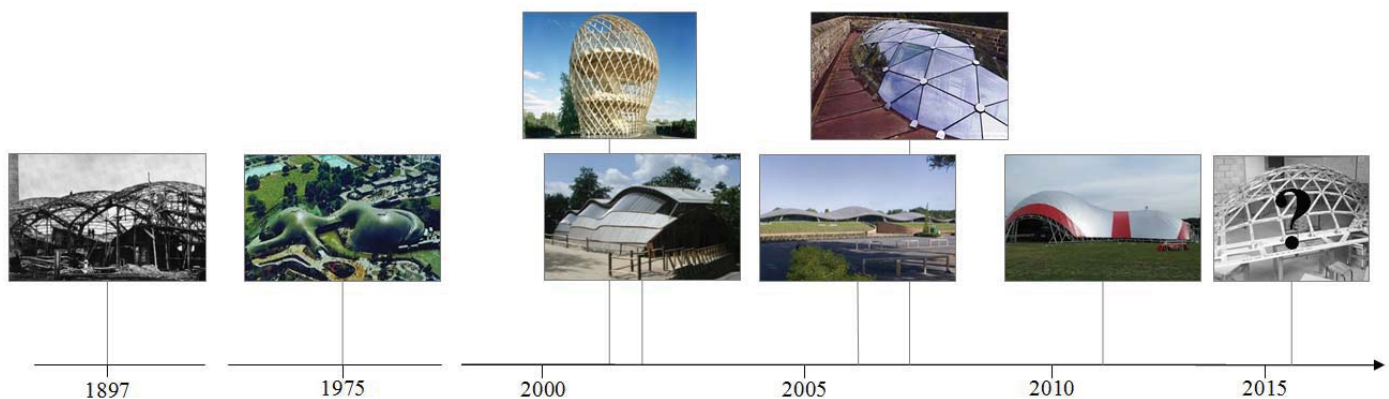


Figure 7: Historical timeline of bending active gridshells presented in this study

ACKNOWLEDGMENTS

This research has been funded by the Irish Research Council (IRC), EMBARK 2012.

REFERENCES

- [1] Lienhard J, Alpermann H, Gengnagel C, Knippers J. Active bending, a review on structures where bending is used as a self-formation process. *International Journal of Space Structures*. 2013;28(3-4):187-96.
- [2] Williams CJK. The analytic and numerical definition of the geometry of the British Museum Great Court Roof. *Digital tectonics*, Wiley-Academy, United Kingdom. 2001:78-85.
- [3] Adriaenssens S, Block P, Veenendaal D, Williams C. *Shell Structures for Architecture: Form Finding and Optimization*: Taylor & Francis; 2014.
- [4] Olsson J. Form finding and size optimization-Implementation of beam elements and size optimization in real time form finding using dynamic relaxation. 2012.
- [5] Happold E, Liddell W. Timber lattice roof for the Mannheim Bundesgartenschau. *The Structural Engineer*. 1975;53(3):99-135.
- [6] Harris R, Romer J, Kelly O, Johnson S. Design and construction of the Downland Gridshell. *Building Research & Information*. 2003;31(6):427-54.
- [7] Harris R, Haskins S, Roynon J. The Savill Garden gridshell: design and construction. *The Structural Engineer*. 2008;28.
- [8] Paoli CCA. Past and future of grid shell structures: Massachusetts Institute of Technology; 2007.
- [9] Otto F, Henniecke J, Matsushita K. Gitterschalen Grid shells. IL: Institut für Leichtere Flächentragwerke. 1974:340.
- [10] Harris R, Roynon J, Happold B. The savill garden gridshell: Design and construction. *The Structural Engineer*. 2008;86:27-34.
- [11] Lienhard J. Bending-active structures : form-finding strategies using elastic deformation in static and kinetic systems and the structural potentials therein. Stuttgart: Universitätsbibliothek der Universität Stuttgart; 2014.
- [12] Douthe C, Baverel O, Caron J. Form-finding of a grid shell in composite materials. *Journal-International association for shell and Spatial Structures*. 2006;150:53.
- [13] Beckh M, Barthel R. The first doubly curved gridshell structure-shukhovs buildings for the plate rolling workshop in vyksa. *Proceedings of the third international congress on construction history*2009. p. 159-66.

Considerations for the Design of Bending Active Timber Gridshells

Matt Collins¹, Prof. Tom Cosgrove¹

¹Department of Civil Engineering and Materials Science, University of Limerick, Castletroy, Limerick, Ireland
Email: matthew.collins@ul.ie, tom.cosgrove@ul.ie

ABSTRACT: Bending active gridshells are generated by deforming a flat timber grid towards a curved shell-like target shape. As a result of this deformation bending pre-stresses are developed during the forming of the structure. This is a condition virtually unique to this structural form. Additionally the forming process generates combined bending, torsion and axial stresses in curved members. Design rules for this complex condition are not yet included in current design standards. Various researchers have proposed limit state criteria for individual combined stress pairs. These are discussed in the light of EN 1995-1-1:2005 and a possible integrated approach is suggested. Some outstanding testing needs are identified. The impact of the construction process on the design and modelling process is also discussed.

KEY WORDS: Timber Gridshells; Design Criteria; Combined stress; Limiting stress conditions; Gridshell construction.

1 INTRODUCTION

Gridshells are doubly curved structures, constructed from initially straight elements that resemble shell structures. Shell structures are inherently effective in their structural performance leading to high span to thickness ratios. They derive their strength and stiffness from their three dimensional geometry and curvature. Large open plan spaces can be created with a minimal amount of material. Gridshells represent a state of the art in structural timber engineering, which are difficult to engineer. There are two principle categories of gridshells, classified as bending active and bending inactive gridshells. The term bending active means that the structural elements have to bend considerably to give the structure its shape, a type of bending pre-stress [1]. Alternatively, bending inactive describes a structure whereby the structural elements do not need to bend to give the structure its shape. A typical bending inactive structure would be a truss, portal frame and a geodesic dome.

The majority of bending inactive gridshells have been constructed from steel whereby the structure is comprised of numerous straight elements each inclined at a different angle to its adjacent element to give the structure its curved shape. Bending active gridshells on the other hand are not all that common, however a number of them have been constructed such as the Multihalle in Mannheim [2], the Weald and Downland Museum [3], and the Savill Garden centre [4] (Figure 1). Notably, the majority of bending active gridshells are constructed from solid timber.



Figure 1: Savill Garden Gridshell

The design of bending inactive gridshells is not too complex as the members are straight and do need to deform to give the structure its shape. Therefore, the members transfer loads primarily through axial forces. In contrast, during the forming of bending active gridshells, the members undergo bending and twisting. This results in a combination of bending, axial and shear stresses being developed in the members. Current timber design codes do not account for these combinations of stresses.

Large scale bending active gridshells are a relatively recent and uncommon building structure type. Current standards do not contain specific design guidance for bending active gridshells. This paper discusses gridshell design with reference to the current standards. Current design approaches to timber members are reviewed. The appropriateness of current approaches is discussed and suggestions appropriate for gridshells are outlined.

Design procedures are required for both members and joints (crossover and boundary joints). A limit state approach to the design of gridshell members is described in section 2. Additional criteria are required for bending active gridshells. An approach to the design of gridshell joints is described in section 3. Proposals for experimental tests are made to fill the knowledge gaps for the design of gridshell members and

joints. A two stage approach required for the design of gridshells is discussed in section 4. Finally, implications of typical construction methods for the modelling process are discussed in 5.

2 MEMBER DESIGN

Members may fail due to excessive bending, shear or axial stresses or due to a combination of these stresses. A combined stress failure criterion is required. In section 2.1, the equations used to determine the design bending stresses of the laths are set out. Section 2.2 sets out the equations that determine the design shear stress. Section 2.3 sets out the equations that determine the design axial stresses. Limiting criteria for each of these stresses are also discussed. In addition, limiting criteria for some combined stress conditions are outlined in section 2.4. Finally, the modification factors for the design of timber members are discussed in section 2.5 with details on how they affect gridshells. The possible forces and moments acting on the ends of a single gridshell member are shown in Figure 2.

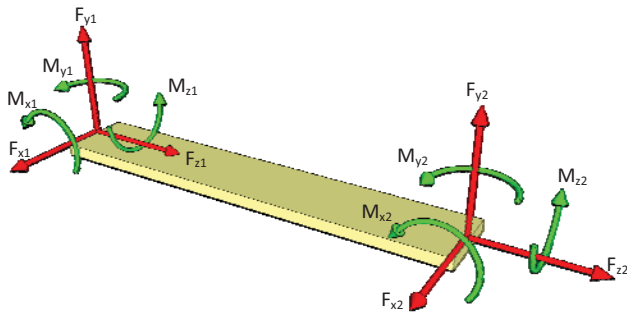


Figure 2: Forces and moments acting on a gridshell element

2.1 Bending

The members of the gridshell may be subject to two bending moments, about the local x- and y-axes. A linear stress distribution is assumed through the section. According to Eurocode 5, the bending stresses should satisfy the following criteria:

$$\sigma_{m,x,d} \leq f_{m,x,d} \quad (1)$$

$$\sigma_{m,y,d} \leq f_{m,y,d} \quad (2)$$

Following Euler-Bernoulli beam bending theory, the design bending stress about the local x- and y-axes are:

$$\sigma_{m,x,d} = \frac{M_{d,x}(\frac{h}{2})}{I_{xx}} \quad (3)$$

$$\sigma_{m,y,d} = \frac{M_{d,y}(\frac{b}{2})}{I_{yy}} \quad (4)$$

The profile of bending stresses with depth in curved beams (such as gridshell members) is not a straight line in accordance with Navier's theory and Hooke's law [5]. The maximum stress occurs at the inner fibre, σ_1 (Figure 3). The equations presented here are derived for use in curved and

tapered glulam beam design but can also be applied to curved gridshell elements. For design purposes, the maximum bending stress of a curved beam can be calculated approximately with simple bending theory by modifying the design bending stress equation with a shape factor k_L . This shape factor depends on the ratio between the thickness of the section d and the radius of curvature R .

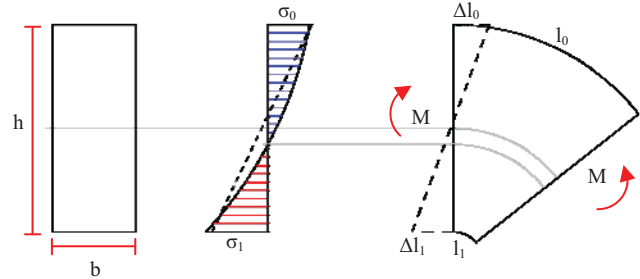


Figure 3: Distribution of bending stresses in a curved beam

The design bending stress in the apex zone of the curved beam can therefore be calculated in equation 5 and the correction factor k_L is calculated in equation 6 [5].

$$\sigma_{m,d} = k_L \frac{M_{ap,d}}{Z} \quad (5)$$

$$k_L = k_1 + k_2 \left(\frac{h_{ap}}{R} \right) + k_3 \left(\frac{h_{ap}}{R} \right)^2 + k_4 \left(\frac{h_{ap}}{R} \right)^3 \quad (6)$$

The factors k_1 to k_4 for a prismatic curved beam are:

$$k_1 = 1 + 1.4 \tan \alpha + 5.4 \tan^2 \alpha = 1$$

$$k_2 = 0.35 - 8 \tan \alpha = 0.35$$

$$k_3 = 0.6 + 8.3 \tan \alpha - 7.8 \tan^2 \alpha = 0.6$$

$$k_4 = 6 \tan^2 \alpha = 0$$

When $h_{ap} \ll R$, the influence of the curvature on the design bending strength becomes small, this is the case for bending active gridshells. Therefore, a linear stress distribution can be assumed. The design bending strength is obtained from equation 7:

$$f_{m,d} = \frac{k_h k_{crit} k_{sys} k_{mod} f_{m,k}}{\gamma_m} \quad (7)$$

In bending active gridshells, bending about both axes is common. According to Eurocode 5, a member subject to bending in two directions should satisfy the combined stress criteria given in equations 8 and 9.

$$k_m \frac{\sigma_{m,x,d}}{f_{m,x,d}} + \frac{\sigma_{m,y,d}}{f_{m,y,d}} \leq 1 \quad (8)$$

$$\frac{\sigma_{m,x,d}}{f_{m,x,d}} + k_m \frac{\sigma_{m,y,d}}{f_{m,y,d}} \leq 1 \quad (9)$$

Where, k_m is a combined bending strength factor, for rectangular sections, $\sigma_{m,x,d}$ is the design bending stress about the local x-axis, $\sigma_{m,y,d}$ is the design bending stress about the local y-axis, $f_{m,x,d}$ is the design bending strength about the local x-axis, and $f_{m,y,d}$ is the design bending strength about the local y-axis.

2.2 Shear and Torsion

Shear stresses are present in the gridshell members in the form of direct shear and torsion. Eurocode 5 provides no guidance for design torsional stresses. From linear elastic theory, the direct shear stress distribution through the cross section in accordance with elastic beam theory is parabolic with the maximum value at the neutral axis as shown in Figure 4a [5]. The torsional stress distribution through the cross section follows a membrane analogy [6]. The maximum torsion stresses occur in the middle of the edges of a member. For a rectangular section, these maximum stresses occur at the middle of the long edges as shown in Figure 4b. A member subject to simultaneous direct shear stress and torsion should satisfy the combined stress criteria given in equations 10 and 11.

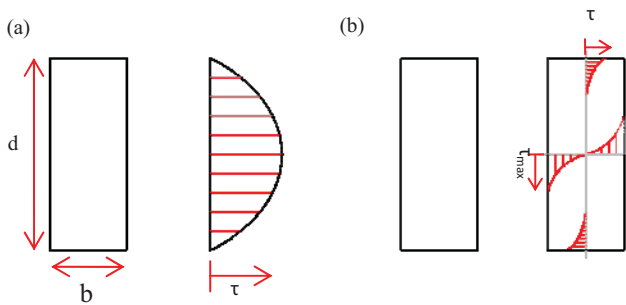


Figure 4: Shear stress distribution, a) direct shear and b) torsion

$$\tau_{v,d} \leq f_{v,d} \quad (10)$$

$$\tau_{tor,d} \leq f_{v,d} \quad (11)$$

The design stress for direct shear [7] and torsion [6] are determined from equations 12 and 13 respectively.

$$\tau_{x/y,d} = \frac{3F_{x/y,d}}{2A} \quad (12)$$

$$\tau_{tor,d} = \frac{3M_{z,d}}{bd^2} \left[1 + 0.6095 \frac{d}{b} + 0.8865 \left(\frac{d}{b} \right)^2 - 1.8023 \left(\frac{d}{b} \right)^3 + 0.9100 \left(\frac{d}{b} \right)^4 \right] \quad (13)$$

Where:

- $\tau_{x/y,d}$ is the design shear stress in the x and y directions
- $\tau_{tor,d}$ is the design torsion stress
- A is the shear area
- $F_{x/y,d}$ is the design shear force
- $M_{z,d}$ is the design torque about the local z-axis
- b and d are the section geometry ($d \geq b$)

In the context of gridshells, the direct shear force can occur in the local x-direction and the local y-direction of the member. The axial force will be in the local z-direction. Therefore, the shear force in each direction is calculated from the component of the global force V_d , acting parallel to the local x- and y-axes. Similarly, the torsion is determined from the moment T about the local z-axis. The design shear strength is obtained from equation 14. This equation is used for verification of both direct shear and torsion failure conditions.

$$f_{v,d} = \frac{k_{sys} k_{mod} f_{v,k}}{\gamma_m} \quad (14)$$

Combination of direct shear and torsion stresses can occur in gridshells. Möhler and Hemmer [8] have suggested the criterion given in equation 15. They highlighted a lack of torsion data and that the torsion design strength $f_{tor,d}$ is higher than the direct shear strength $f_{v,d}$. Thus, $f_{v,d}$ is suggested which is more conservative where no torsion test data is available.

$$\frac{\tau_{tor,d}}{f_{tor,d}} + \left(\frac{\tau_{xy,d}}{f_{v,d}} \right)^2 \leq 1 \quad (15)$$

Where, $\tau_{tor,d}$ is the design torsion stress, $f_{tor,d}$ is the design torsion strength, $\tau_{xy,d}$ is the design shear stress, and $f_{v,d}$ is the design shear strength.

2.3 Axial

Both tension forces and compression forces can be present in gridshell members. Compression forces are the most common axial forces under normal loading conditions. However, multidomed gridshells have valleys where members may be in tension even under gravity loads. Uplift loads due to wind may also generate tension forces. These axial forces must satisfy the criterion given in equation 16.

$$\sigma_{t/c,0,d} \leq f_{t/c,0,d} \quad (16)$$

Where, $\sigma_{t/c,0,d}$ is the design tension or compression stress, and $f_{t/c,0,d}$ is the design tension or compression strength. The applied axial stress for both tension and compression is assumed to be uniformly distributed through the cross section [5]. The design axial stress is determined from equation 17.

$$\sigma_{t/c,0,d} = \frac{F}{A} \quad (17)$$

The design axial strength is obtained from equation 18 for compression and equation 19 for tension.

$$f_{c,0,d} = \frac{k_{c,y} f_{c,0,k}}{\gamma_m} \quad (18)$$

$$f_{t,0,d} = \frac{k_h k_{sys} k_{mod} f_{t,0,k}}{\gamma_m} \quad (19)$$

2.4 Combination of Stresses

When a gridshell is formed into shape, the members are subjected to a combination of bending, shear and axial stresses. According to Eurocode 5, the limiting criteria for a combined bending and tension/compression stress condition are given in equations 20 and 21.

$$\frac{\sigma_{t/c,0,d}}{f_{t/c,0,d}} + \frac{\sigma_{m,x,d}}{f_{m,x,d}} + k_m \frac{\sigma_{m,y,d}}{f_{m,y,d}} \leq 1 \quad (20)$$

$$\frac{\sigma_{t/c,0,d}}{f_{t/c,0,d}} + k_m \frac{\sigma_{m,x,d}}{f_{m,x,d}} + \frac{\sigma_{m,y,d}}{f_{m,y,d}} \leq 1 \quad (21)$$

A limiting criterion for combined stress conditions for gridshells should include the shear stresses. Toussaint [9] presented a criterion for the combination of bending, shear and axial stresses (equation 22).

$$\left(\frac{\sigma_{m,d}}{f_{m,d}} \right)^2 + \left(\frac{\tau_{v,d}}{f_{v,d}} \right)^2 + \left(\frac{\sigma_{t/c,0,d}}{f_{t/c,0,d}} \right)^2 \leq 1 \quad (22)$$

Where:

$$\sigma_{m,d} = \sigma_{m,y,d} + \sigma_{m,z,d}$$

$$\tau_{v,d} = \tau_{x,d} + \tau_{y,d} + \tau_{tor,d}$$

Toussaint claims this is a conservative criterion in the absence of test data. Further investigation has to be carried out in order to establish a failure criterion for combined bending, shear and axial stresses.

2.5 Modification Factors

According to the equations for design strength presented in the previous section a number of modification factors are applied to the characteristic material strength values for each failure mode. The suitability of these modification factors for use in bending active gridshells is now discussed:

- γ_m is the material partial safety factor and is suitable in its current state in Eurocode 5.
- k_m is a factor to allow for the redistribution of bending stresses in a cross section. For rectangular sections, a value of 0.7 is used in Eurocode 5. The governing stress criterion presented in equation 22 is a limiting criterion for a combined stress condition. This formula is conservative given that no redistribution factors are accommodated. Along with k_m , further redistribution factors could be investigated for the other stresses.
- k_h is a modification factor based on section depth and is applied to the bending and tension strength values of solid timber, glulam and LVL. A value of 1.3 is used for sections with a thickness less than 40mm, which would be typical for gridshell structures. However if test data relevant to the gridshell members is available, this should be used instead.
- k_{sys} is a modification factor that affects all strength properties. It can be applied when several equally spaced, similar members, components or assemblies are connected in such a way that load can be transferred effectively between them. To apply this factor to gridshells would be unconservative and unsafe. This is because the analysis of gridshells fully accounts for all the connectivity of the system and there is no “hidden” load sharing mechanism to account for.
- k_{crit} is a modification factor that is applied to the bending strength of members subject to lateral torsional buckling. Given the typical aspect ratios for practical gridshell members, lateral torsional buckling is a remote possibility at most.
- k_{mod} is a strength modification factor for the effect of the duration of load and moisture content. The values quoted in Eurocode 5 are applicable to use here. The gridshell members are pre-stressed because of the forming process. The pre-stress is effectively a long-

term load while subsequent variable load is short term. Therefore, the pre-stress due to forming should be treated the same as the dead load.

k_c is an instability factor that is applied to nominally straight members in compression. This factor is not applicable to gridshell members, as these members are curved and their buckling behaviour must be accounted for in the computational model used.

k_{def} is a deformation factor for the effect of the duration of load and moisture content. The values quoted in Eurocode 5 are applicable to use here. The gridshell members are pre-stressed because of the forming process. Similar to k_{mod} , the pre-stress due to forming should be treated the same as the dead load.

3 JOINT DESIGN

This section makes proposals for the design of the gridshell joints. The crossover joint and the boundary joint are considered. The strength and stiffness of the joints will each need to be considered. The design strength of a joint can be established using the current standards and verified by experimental testing where test data is not provided. The design strength of joints in traditional timber structures are often governed by the spacing of the fasteners. Therefore, by increasing the design strength the design stiffness also tends to increase. The joint stiffness needs to be known to analyse the gridshell for design purposes. The joint stiffness can be determined experimentally.

The load-deformation behaviour of each joint can be described by six degrees of freedom in a three dimensional coordinate system. In a crossover joint, only four distinct stiffnesses occur (Figure 5). The moment-rotation properties about the x-axis are identical to those about the z-axis. The load-displacement properties in the direction of the x-axis are identical to those in the direction of the z-axis. The load-displacement properties in the direction of the y-axis are also required. However, during forming the moment rotation properties about the y-axis of the joint are assumed to behave as a pin. In the completed structure, it is assumed that no moment about the y-axis is transferred through the joint. In-plane shear forces are transferred through the bracing. During form finding, rotation about the y-axis is permitted (zero stiffness is assumed) and a cylindrical joint model is used during this stage to allow scissoring of the laths.

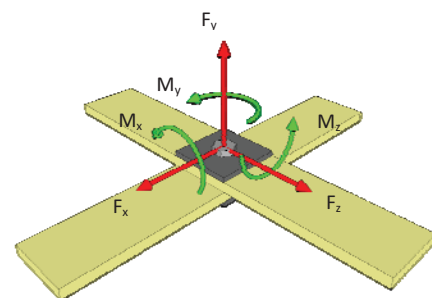


Figure 5: Crossover Joint

Boundary joints (supports) are assumed constrained against translation vertically (local y-axis). It has been established from modelling that only two of the other 5 degrees of freedom present at a boundary joint (support) significantly influence gridshell forces and deformations. These are the translation in the axial direction of the gridshell members (z-axis) and the rotation about the local x-axis (Figure 6). This conclusion would need to be verified for horizontal load cases.

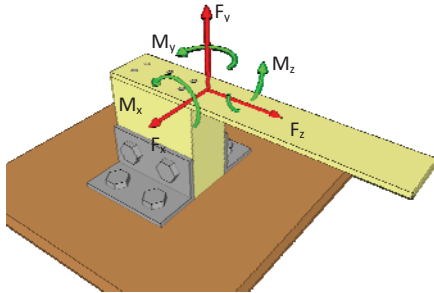


Figure 6: Boundary Joint

4 ANALYSIS AND DESIGN OF GRIDSHELLS

The analysis of bending active gridshells is focused on predicting the geometry and stress levels that a particular material will take when bent towards a given shape along with the analysis of stress and deformation under subsequent in-service loading. The dynamic relaxation technique was developed in 1965 by A.S. Day for the finite difference analysis of concrete pressure vessels. Day and Bunce [10] further developed this method for application to cable structures. The vector form of dynamic relaxation has become the most common. It is suited for non-linear structures such as gridshells. Brew and Brotton [11] developed this approach which separated the equations for equilibrium and motion and did not require the formulation of an overall stiffness matrix.

Dynamic Relaxation is a systematic method for tracing the motion of a structure from the time of loading to when it reaches a position of equilibrium due the effects of damping. The method of Dynamic Relaxation is utilised for static analysis as fictitious masses and moments of inertia are used to ensure stability and convergence [12]. A computational tool (MattGrid) for the analysis of bending active gridshells was developed by the authors using the dynamic relaxation method [13].

Just as the modelling and analysis process is split into two stages, stage 1 (form finding) and stage 2 (in-service loading), so should the design also be split into the same two stages as a limit state can occur during either stage. The form finding stage should be designed for ULS only, whereas the subsequent in-service loading stage (stage 2) should be designed for both ULS and SLS. SLS design would apply to the global deformation of the structure deflection limits for individual members might apply for various reasons.

During stage 1 the material and section stiffness will dictate the geometry, from which the curvatures and hence the

stresses are determined. The mean stiffness should be used for an accurate representation of the form and behaviour. Moreover, for a conservative design the design stresses should be determined using the 95th percentile stiffness. The 95th percentile values for stiffness are relevant to bending active gridshells, as a high stiffness will result in high stresses for a given curvature. For the design strength values, the characteristic (5th percentile) values should be used including the modification factors described in section 2.

Similarly, during stage 2 the 95th percentile stiffness should be used for ultimate limit state design. In Eurocode 5, it states that the design stiffness is the mean stiffness divided by the partial factor for material stiffness. It is suggested here that this design stiffness is used when examining the SLS design of stage 2.

5 PRACTICAL CONSIDERATIONS OF GRIDSHELLS

This section is based on lessons learnt from developing a computer model (MattGrid) to predict the form and behaviour of experimental gridshells. There are practical considerations that are relevant to the modelling and analysis of gridshells. Stresses induced during the forming process will depend on the process used. Therefore the form finding stage of the modelling process (stage 1) must reflect the forming process actually used. The initial orientation of the flat grid also influences the level of stress induced during forming. Therefore, both the erection sequence and initial flat grid orientation should be taken account of in the modelling process.

Continuous monitoring of the structure as it is being deformed is essential to ensure that the joints can freely rotate. Gridshell analysis tools typically model the joints with no eccentricities and do not account for locking of the joints due to friction. The measured coordinates of each joint must be continuously compared with its target location to ensure the structure is moving towards the target shape. In addition, a gradual uniform lifting process should be adopted.

When the gridshell members have been joined to the boundary supports, the geometry may be close to the target shape. However, the temporary supports must then be removed and any further change in geometry should be monitored and compared with the deformation predicted for the same step in MattGrid. The computer model developed by the authors has been proven to be sufficiently accurate for all stages [13].

In addition to constant monitoring, the design of the joint itself is another critical component. For double layer braced gridshells, up to five members need to be connected at the joints. Larger clearance holes and slots assist these connections but can diminish the strength of the sections. An accurate prediction of geometry can facilitate prefabrication of elements. Alternatively, the erection sequence can be altered to install the members individually and not drill the holes until the members are temporally clamped in their final position [14] and [15]. MattGrid could model this kind of sequence with some rearrangement of the code.

Due to the material, section and construction variations, members may not always arrive at the specified boundary joint locations. A method has been utilised that allows for the boundary locations to deviate from the designed location by the use of continuous perimeter beams [16] and [17]. This avoids forcing the ends towards an exact point, which could result in high local stresses (Figure 7).



Figure 7: Gridshell laths bolted to plywood perimeter

A lightweight structure and a loose assembly at the beginning of the forming are advantageous to the forming of the gridshells without the requirement for any mechanical lifting equipment. This type of structure is suited to a deployable structure whereby the structure itself as a whole can be reduced to linear foldup sections aiding to logistics. In this manner, large portions of a gridshell could be prefabricated off-site. A series of images in Figure 8 describes this concept.

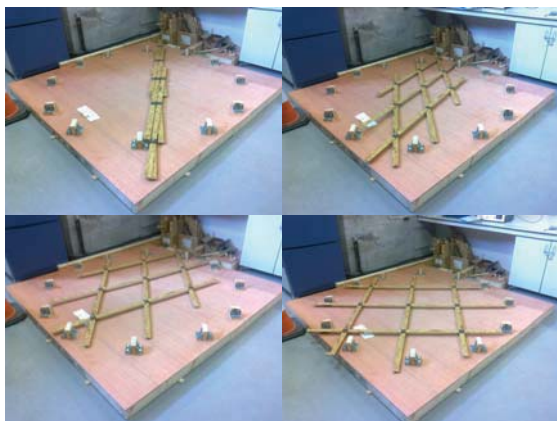


Figure 8: Deployability of gridshell sections

6 CONCLUSIONS

Gridshell members are subjected to a combination of stresses. A limiting criterion for combined stress conditions was presented. This limiting criterion is conservative as no redistribution modification factors have been included. A clear distinction has been made between the property requirements for modelling and design (both ULS and SLS). Additionally, the construction process has a significant role for the development of stresses in the structure. As a result, the exact construction sequence must be modelled and factored into the design for bending active gridshells.

ACKNOWLEDGMENTS

Funded by the Irish Research Council (IRC), EMBARK 2012.

REFERENCES

- [1] Lienhard J, Alpermann H, Gengnagel C, Knippers J. Active bending, a review on structures where bending is used as a self-formation process. *International Journal of Space Structures*. 2013;28(3-4):187-96.
- [2] Happold E, Liddell W. Timber lattice roof for the Mannheim Bundesgartenschau. *The Structural Engineer*. 1975;53(3):99-135.
- [3] Harris R, Romer J, Kelly O, Johnson S. Design and construction of the Downland Gridshell. *Building Research & Information*. 2003;31(6):427-54.
- [4] Harris R, Haskins S, Roynon J. The Savill Garden gridshell: design and construction. *The Structural Engineer*. 2008;28.
- [5] Blass HJ. *Timber Engineering STEP 1: Basis of Design, Material Properties, Structural Components and Joints*: Centrum Hout; 1995.
- [6] Roark RJ, Young WC, Budynas RG. *Roark's formulas for stress and strain*. New York: McGraw-Hill; 2002.
- [7] EN 1995-1-1:2004. Eurocode 5: Design of timber structures - Part 1-1: General - Common rules and rules for buildings. National Standards Authority of Ireland.
- [8] Möhler K, Hemmer K. Verformungs- und Festigkeitsverhalten von Nadelvoll- und Brettschichtholz bei Torsionsbeanspruchung. *Holz als Roh- und Werkstoff*. 1977;35(12):473-8.
- [9] Toussaint MH. A Design Tool for Timber Gridshells: The development of a Grid Generation Tool: Msc thesis Delft University of Technology, online http://homepage.tudelft.nl/p3r3s/MSc_projects/reportToussaint.pdf; 2007.
- [10] Day AS, Bunce JW. ANALYSIS OF CABLE NETWORKS. *Civ Eng Pub Works Rev*. 1970;65(765):383-6.
- [11] Brew J, Brotton D. Non-linear structural analysis by dynamic relaxation. *International Journal for Numerical Methods in Engineering*. 1971;3(4):463-83.
- [12] Adriaenssens SML. *Stressed spline structures*: University of Bath; 2000.
- [13] Collins M. A Computational and Experimental Study of Irish Orientated Strand Board in Bending Active Gridshells. Unpublished: University of Limerick; 2016.
- [14] Hara V, Puustinen A. Helsinki Zoo Lookout Tower. 2011.
- [15] Harris R, Roynon J, Happold B. The savill garden gridshell: Design and construction. *The Structural Engineer*. 2008;86:27-34.
- [16] Carpenter Oak & Woodland. Orangerie Gridshell. 2013.
- [17] Weald & Downland Open Air Museum. Downland Gridshell Construction Progress. 2002.

Probabilistic Climate Change Adaptation Analysis for Timber Power Pole Infrastructure

Paraic C. Ryan¹ & Mark G. Stewart²

¹Discipline of Civil Engineering, National University of Ireland, Galway

²Centre for Infrastructure Performance and Reliability, The University of Newcastle, Australia

Email: Paraic.Ryan@nuigalway.ie, Mark.Stewart@newcastle.edu.au

ABSTRACT: According to the most recent IPCC report, warming of the climate system is unequivocal, and this warming may lead to increased risk of breakdown of infrastructure networks due to extreme weather. A key means of reducing future risk exposure is implementation of effective climate change adaptation strategies for critical infrastructure assets. This however constitutes a significant engineering challenge, for a variety of reasons discussed herein. The work described in this paper examines the regional variability of climate change adaptation feasibility for timber power pole networks, an important critical infrastructure asset. This is achieved through development of a Monte-Carlo event-based sequential model, which incorporates structural reliability, deterioration, climatic effects and network maintenance. The hazards of interest are storm winds and timber decay - both of which may worsen due to a changing climate. A probabilistic life-cycle cost-benefit analysis is used to examine the appropriateness of a single climate adaptation strategy for a notional network of one million poles, for three Australian cities; Sydney, Melbourne and Canberra. The feasibility of the climate adaptation strategy, which incorporates both alterations to network maintenance procedures and implementation of performance based design, was found to vary significantly across the three regions. The analysis indicated that the adaptation strategy would have a substantially more positive cost-benefit outcome for Sydney than for the other two locations. This highlights the difficulties associated with implementation of a nationwide climate adaptation strategy for a power pole networks in Australia, and indeed for critical infrastructure in general.

KEY WORDS: Timber power poles, climate change adaptation, critical infrastructure, asset management.

1 INTRODUCTION

The latest assessment report from the International Panel on Climate Change (IPCC AR5) has stated that warming of the climate system is unequivocal (1). These observed changes in climate, and more importantly projected future changes, may lead to increased risk to human life and infrastructure (2). One of the key means of dealing with increased climate change related risk is implementation of effective climate change adaptation strategies e.g. Stewart and Deng (3). This can however be challenging given a) the considerable uncertainty associated with future climate change projections, and b) the regional variability of climate and climate change. The work presented in this paper is aimed at investigating the regional variation in climate change adaptation feasibility for critical infrastructure using a probabilistic approach. This probabilistic approach, which includes time-dependent structural reliability and probabilistic cost-benefit analysis, allows uncertainty and variability at various levels to be incorporated into the assessment. The analysis is conducted for three different regions of Australia. The critical infrastructure type examined is timber power pole networks.

To date very few studies have employed probabilistic methods to assess possible changes in timber power pole infrastructure performance due to climate change. Existing publications in this area are limited to the work of Bjarnadottir et al. (4) and Ryan et al. (5). Fewer studies still have examined the appropriateness of climate change adaptation strategies for power poles networks (6). This is somewhat surprising given the International scientific community's predictions about future climate (1), and the scale and value of timber power

pole networks worldwide. For instance, there are approximately two million timber power poles in Ireland, 120 million to 200 million in the United States (7) and over five million timber power poles in Australia, which have a net worth of over \$10 billion (8).

The work described herein builds on the existing literature through utilisation of probabilistic methods to investigate the regional variability of climate adaptation feasibility. Monte Carlo event-based sequential modelling is used to assess structural reliability of the power pole networks and conduct a probability based cost-benefit analysis of climate adaptation. This allows climate change uncertainty to be incorporated into the assessment, together with the other forms of uncertainty associated with time-dependent modelling of infrastructure networks. The following section of this paper presents the assessment methodology. Subsequently, details of the notional networks are given and results are presented for climate change impacts and the regional variability of climate change adaptation feasibility across the three Australian cities.

2 ASSESSMENT METHODOLOGY

The basis for the model used herein has been developed in detail in previous papers by the authors (5, 9). This section presents a brief description of the model, with a focus on how predicted climate change is incorporated into the assessment, and how adaptation is assessed using a probabilistic cost-benefit approach. The reader is referred to the previous papers for more detailed discussion on the model development and probabilistic model parameter selection (5, 9).

A structural reliability assessment requires consideration of structural resistance of the element being considered (R), and the load the element is subjected to (S), in order to calculate the probability of a given failure event. In the case of timber power distribution pole networks the load and resistance are time-dependent, especially when considering the possible effects of climate change over a period of 50 to 100 years. For this study the limit state failure event is defined as the bending failure of a power pole under wind loading, the most common failure mode for timber power poles (10). Consequently, the time-dependent resistance, ($R(t)$), will be the bending resistance of a power pole in a network at a given time t . The time-dependent load, ($S(t)$), will be the annual maximum wind load at year t .

2.1 Sequential Event-based Modelling

The sequential event-based modelling approach used herein allows power pole network performance over time to be assessed, considering both maintenance and climate change effects. The uncertainty and variability associated with a) climate change predictions, b) structural capacity, c) structural loading, and d) deterioration with time are incorporated in the analysis. The sequential aspect of the model relates to the fact that each Monte Carlo iteration runs on a year-by-year basis from the year 2015 to 2090. Each yearly step includes; calculation of $R(t)$ and $S(t)$, accounting for climate change effects on deterioration and wind load, in addition to simulation of network maintenance if appropriate. This time-dependent modelling approach simulates the actual stochastic behaviour of the system over time, thus creating “an artificial history” of infrastructure network performance. The event-based aspect of the probabilistic model refers to the fact that the occurrence of certain events over the monitoring period can influence the course of a given sequential Monte Carlo simulation. The two key events which can occur are a) violation of the limit state, whereby the annual wind load exceeds the deteriorated pole capacity and the pole fails, and b) the condemning of a pole as a result of the network inspections and maintenance programme. Upon occurrence of a wind failure or the condemning of a pole, the pole in question is replaced by a new pole in the Monte Carlo simulation. This pole is assigned new properties generated from the appropriate distributions i.e. pole diameter, pole bending strength, sapwood depth etc. The process of deterioration then restarts for this new pole, and the sequential Monte Carlo process continues for the iteration in question up to the year 2070. This sequential event-based approach means that, in effect, each Monte Carlo iteration represents one pole location in a network of poles, whereby if this pole fails at a given location it must be replaced to prevent a break in the power supply system.

2.2 Time Dependent Load and Resistance

The initial bending resistance ($R(0)$) of a timber power pole at time $t = 0$ can be represented based on established bending theory as follows;

(1)

$$R(0) = f_b \cdot \pi \cdot D^3 / 32$$

where f_b is the bending strength of the timber, and D is the ground line diameter of the distribution pole. It is noted however that this initial bending resistance ($R(0)$), will tell us little about the performance of timber power poles in service, which undergo significant deterioration over their service life. Thus, for timber power pole networks, as with any infrastructure network analysis, infrastructure element deterioration must be incorporated into the probabilistic model. Timber deterioration was incorporated herein based on the work of Wang et al. (11), who developed a timber decay model based on 35 years of field data for 77 timber species. The Wang et al. model represents decay progress as an idealised bilinear relationship, characterised by a decay lag time, t_{lag} (years), and a decay rate, r (mm/yr). These r and t_{lag} values can be calculated as;

$$r = k_{wood} \cdot k_{climate} \quad (2)$$

$$t_{lag} = 5.5r^{-0.95} \quad (3)$$

where k_{wood} is the wood parameter and $k_{climate}$ is the climate parameter. Wang et al. (11) provides formulas for k_{wood} for both hardwood and softwood timber which relate to the durability class of the timber and the section of the timber cross section being considered, in addition to providing adjustments for treated timbers. The uncertainty associated with the decay model is incorporated using a model error factor for decay, ME_{decay} (11). Of primary interest, however, in the context of the effects of climate change, is the $k_{climate}$ parameter. This parameter value is determined based on annual average temperature and yearly rainfall at the location considered. As shown by Wang and Wang (12) the influence of climate change predictions on this parameter can significantly affect the rate of timber deterioration. Predicted changes in temperature and rainfall to the year 2090 (13) were incorporated into the calculation of the $k_{climate}$ parameter herein. This allowed the effects of predicted climate change on deterioration, and the resulting time dependent resistance ($R(t)$), to be considered in the analysis.

2.3 Time Dependent Wind Loading

Possible changes in wind speed are an important consideration for power distribution infrastructure as increases or decreases in the annual maximum wind speed will reduce or increase the reliability performance of power pole infrastructure, respectively. The wind field for three locations examined in this paper (Sydney, Melbourne and Canberra) is dominated by non-cyclonic synoptic weather systems. These non-cyclonic gust wind speeds are modelled using the Gumbel distribution, with the annual maximum non-cyclonic peak gust speed as follows (14);

$$F(v) = e^{-A} \text{ where } A = e^{-\left(\frac{v-v_g}{\sigma_g}\right)} \quad (4)$$

where v_g and σ_g are the location and scale parameters for the Gumbel distribution. Values for these location and scale parameters for a range of locations in Australia have been developed by Wang et al. (14) based on data recorded from 1939 to 2007. Thus, this wind field does not account for the possible future reductions or increases in wind field magnitude due to climate change. A modification to Eqn. 4 has been suggested by Stewart (15) to allow climate change related effects to be incorporated into the Gumbel distribution. Eqn. 4 thus becomes;

$$F(v) = e^{-A} \quad (5)$$

$$A = e^{-\left(\frac{v}{1 + \frac{\gamma_{\text{mean}}(t)}{100}}\right)^{-v_g}} \quad \sigma_g$$

where $\gamma_{\text{mean}}(t)$ represents the time-dependent percentage change in gust wind speed for a given Monte Carlo simulation. The Wang et al. (14) statistical parameters for the Gumbel distribution are assumed to reflect pre-climate change wind speeds (i.e. 1990 levels). Having established an expression which probabilistically represents the time-dependent wind speed incorporating climate change, the work of Henderson and Ginger (16) was used to calculate the time-dependent wind load $S(t)$, as described in Ryan et al. (9). This model allowed uncertainty and variability to be incorporated into predictions for the wind load on the power poles, conductors etc. for a given wind speed v , at a given time t . Details of the statistical properties used for the model variables are provided in Table 2 in Section 3.

2.4 Climate change Projections

This study uses the latest IPCC Assessment Report (AR5) climate change predictions for Australia (13). In line with the large uncertainty and variability associated with long-term climate predictions, climatic changes were modelled probabilistically using Monte Carlo simulation. Wind speed, rainfall and temperature changes were considered for the no climate change scenario and the RCP 8.5 (severe case) emission scenario. The AR5 RCP 8.5 10th, 50th and 90th percentile predictions for Sydney, Melbourne and Canberra are presented in Table 1. In line with the framework set out by Stewart and Deng (3), and utilised in Ryan et al. (5, 17), truncated normal distributions were used to represent the uncertainty associated with climatic predictions provided by CSIRO (13).

Table 1. IPCC AR5 RCP 8.5 predicted climatic changes to year 2090

Parameter	10 th Percentile	50 th Percentile	90 th Percentile
Sydney			
Temperature (°C)	+ 2.9	+ 3.7	+ 4.6
Rainfall (%)	- 20	- 3	+ 16
Wind speed (%)	- 6.9	- 1.1	+ 4.2
Melbourne			
Temperature (°C)	+ 2.4	+ 3.0	+ 3.8
Rainfall (%)	- 27	- 9	+ 4
Wind speed (%)	- 5.9	- 1.7	+ 1.7
Canberra			
Temperature (°C)	+ 2.7	+ 3.8	+ 4.5
Rainfall (%)	- 27	- 5	+ 9
Wind speed (%)	- 5	- 0.6	+ 2.6

2.5 Probabilistic Cost-benefit Analysis

Stewart (18) proposed that the total life cycle cost (LCC) can be described as:

$$LCC(T) = C_D + C_C + C_{IN}(T) + E_{\text{damage}}(T) \quad (6)$$

where C_D is the design cost, C_C is the construction cost (materials and labour), $C_{IN}(T)$ is the cost of inspections during the service life T , and $E_{\text{damage}}(T)$ is the expected cost of repair or loss during service life T .

The expected cost of repair and loss can be described as a present value:

$$E_{\text{damage}}(T) = \sum_{i=1}^{DS} \sum_{j=1}^T P_{f,i} \frac{C_{\text{damage}}}{(1+r)^i} \quad (7)$$

where $P_{f,i}$ is the probability of damage in year i , C_{damage} is the cost of repair and loss, r is the discount rate and DS is the number of different damage states. In the present case there are two damage states, namely power pole condemnings and power pole wind failures. The probabilities used in the estimation of E_{damage} are calculated using Monte Carlo simulation techniques.

The aim of the current study is to examine the effectiveness of climate change adaptation on life cycle cost over the period 2015 to 2090 at three different locations. The initial design cost is assumed to be equal for all cases analysed. Thus, in accordance with Equation 1, the economic performance is determined by cost of initial pole construction, inspection costs, and the expected damage costs, all of which are impacted by the cost of adaptation strategy implementation, and the effectiveness of the adaptation strategy. The 'benefit' of an adaptation measure is the reduction in damage costs related to the adaptation strategy, and the 'cost' is the extra costs associated with implementation of the adaptation

strategy. The Net Present Value (NPV) of an adaptation strategy is;

$$NPV(t) = LCC_{BAU}(t) - LCC_{adaptation}(t) \quad (8)$$

where $LCC_{BAU}(t)$ and $LCC_{adaptation}(t)$ are the life-cycle costs for 'business as usual' (BAU, i.e. existing practice) and the adaptation measure, respectively, discounted to present value.

The Benefit-to-Cost Ratio (BCR) of the adaptation strategy is also examined herein whereby;

$$BCR = \frac{Benefit_{adaptation}}{Cost_{adaptation}} \quad (9)$$

The benefit is defined as the reduced losses due to reductions in pole condemnings, number of inspections, or pole wind failures, when compared to the BAU case. Similarly, the costs associated with implementation of an adaptation strategy can range from additional construction cost, to additional wind failure and condemning costs, to additional inspection costs, depending on the nature of the adaptation measure employed. A NPV greater than zero, and a BCR value greater than one, indicates that an adaptation measure is cost-effective. The study herein considered both direct and indirect costs and benefits. These costs were obtained from the power industry in Australia and from the international literature. The development of the costs for the study are discussed in detail in (6). A discount rate of 4% was used herein.

3 POWER POLE NETWORK DETAILS

A typical Australian power distribution pole layout, as detailed in Ryan et al. (9) was used for the illustrative example herein. Appropriate pole ground line diameters for this typical newly installed Australian pole set-up were obtained by carrying out detailed pole design in accordance with existing Australian standards for Sydney, Melbourne and Canberra (19, 20). Appropriate sizing grades were also utilised in line with those provided by pole suppliers in each region. The timber type used for the design was spotted gum, the most popular power pole timber species in South-East Australia. The pole was assumed to be CCA treated in line with current practice in the Australian power industry.

Inspection intervals were set at 5 years, with first inspection at 20 years (20). In accordance with common industry practice in Australia, inspection failure or pole condemning criteria was set at 50% of original pole capacity based on loss of section modulus (Z), meaning if inspection revealed that the pole moment capacity was less than 50% of the original pole moment capacity the pole failed the inspection and was condemned and replaced.

The climate change adaptation strategy investigated in this study was developed following consultation with industry and investigation into a range of proposed strategies at the Centre for Infrastructure Performance and Reliability at the University of Newcastle, Australia. It involved alterations to both the power pole design and maintenance procedures detailed above. The business as usual and adaptation strategy can be summarised as follows;

- Business as Usual (BAU): Pole diameter design in accordance with AS/NZS standards, inspection intervals set at 5 years, and pole condemning criteria set at 50% of original pole capacity
- Adaptation Strategy: Same as BAU with exceptions that both original poles and replacement poles are one size grade larger than required under the existing AS/NZS design procedure, and pole condemning criteria is reduced to 45% of original pole capacity.

The statistical details for the probabilistic parameters used herein are presented in Table 2. Due to space constraints the detailed discussion on the nature, definition, and source of each parameter is not provided herein, but can be found in Ryan et al. (5, 9). All results presented in this paper are based on one million Monte Carlo simulations, each of which ran from the year 2016 to 2090 in steps of one year.

Table 2. Statistical parameters for probabilistic model

Property	Units	Distribution	Mean	COV
Sydney and Canberra AS design pole GLD	mm	Uniform (242 - 294)	268	-
Melbourne AS design pole GLD	mm	Uniform (245 - 290)	268	-
Sapwood depth	mm	Uniform (25 - 50)	37.5	-
Corewood depth	Growth rings	Uniform (5-10)	7.5	-
f_b Spotted Gum	MPa	Normal	104.1	0.14
Conductor diameter	mm	Normal	13.5	0.06
Street lighting wire	mm	Normal	9.0	0.06
Pole height	m	Normal	10.7	0.03
High voltage wires	m	Normal	10.95	0.03
Low voltage cables	m	Normal	9.5	0.03
Communication wire height	m	Normal	8.1	0.03
Sydney annual max wind speed	m/s	Gumbel	29.29	0.09
Melbourne annual max wind speed	m/s	Gumbel	25.80	0.07
Canberra annual max wind speed	m/s	Gumbel	20.08	0.10
ME_w	-	Lognormal	1.00	0.05
ρ_{air}	kg/m ³	Lognormal	1.2	0.02
$M_{z,cat}$	-	Lognormal	0.95	0.10
$C_{d,pole}$	-	Lognormal	1.2	0.05
$C_{d,wires}$	-	Lognormal	1.0	0.05
G (poles)	-	Normal	0.96	0.11
G (wires)	-	Normal	0.81	0.11
ME_{decay}^a (durability class 2)	-	Lognormal	1.00	0.92

GLD = pole ground line diameter

4 RESULTS

4.1 Climate Change Impacts

The regional variability of climate change impacts can be seen in Table 3, which presents the predicted impact of climate

change for RCP 8.5 on power pole network performance for Sydney, Melbourne and Canberra. This impact is expressed in terms of percentage change in pole wind failure rates, % change in poles condemned, and increase in operating costs, over the 76 year monitoring period (2015 to 2090). As can be seen from the table there is considerable variation in climate change impact across the three regions. Sydney experiences the greatest impact with a predicted 6.8% increase in lifecycle operating costs, while Melbourne actually experiences a slightly positive predicted climate change impact, with a 0.1% reduction in operating costs.

It is noted that Canberra has a greater percentage increase in pole wind failures than Sydney. This is however due to the fact that Canberra has a far lower baseline pole failure rate than Sydney. The absolute increase in pole failures for Sydney is actually larger than that predicted for Canberra (3,500 for Sydney vs 237 for Canberra). An increase in pole wind failures of 3,500 is significant when considered in the context of the consequences of power pole wind failures, which range from loss of power to business and homes, to catastrophic wildfire events with significant loss of life and infrastructure.

Table 3. Impacts of IPCC AR5 RCP 8.5 emission scenario

Location	% Change in Pole Wind Failures	% Change in Poles Condemned	% Increase in Lifecycle Operating Cost
Sydney	+ 17.5	+ 10.7	+ 6.8
Melbourne	- 3.1	0.0	- 0.1
Canberra	+ 28.7	+ 3.7	+ 2.2

4.2 Cost-Benefit Analysis Results for Adaptation

In order to investigate the regional variability of climate change adaptation feasibility, a single adaptation strategy was employed across all three cities i.e. approach in line with a nationally implemented climate adaptation strategy. It is recognized that the climate change impact results in Table 3 indicate that the notional power pole network in Melbourne does not require increased structural resilience to compensate for climate change. It has been found, however, that carefully designed climate adaptation strategies can have a positive cost benefit outcome even if climate change does not occur i.e. adaptation results in improved asset management irrespective of climate change (6).

Table 4 shows the results of the probabilistic cost-benefit analysis investigating regional variability of climate change adaptation feasibility. These results were obtained through comparison of the climate adaptation strategy with the “business as usual” strategy over the 76 year life-cycle, under the RCP 8.5 climate emission scenario. The risk reduction value reflects the percentage reduction in operational costs of the power pole network, brought about by implementing the climate adaptation strategy. The NPV and BCR were calculated in accordance with Equations 8 and 9.

As can be seen from the table there is considerable variation in the feasibility of climate adaptation from region to region. The adaptation strategy has a positive cost benefit outcome for all three cities, however, the extent of this benefit varies

largely from city to city. For Canberra and Melbourne the risk reduction is modest at 3% to 4%, while the mean BCR values indicates that for every dollar invested in adaptation, the benefit will be approximately 1.1 dollars. This is a relatively small margin in the context of the inherent uncertainty in the system. Implementation of the adaptation strategy for Sydney is however far more feasible. It is predicted that the adaptation strategy NPV per pole is over \$300, while each dollar of investment in the adaptation strategy is predicted to return 1.7 dollars in direct and indirect benefit. Consequently, implementation of the adaptation strategy is an attractive proposition for Sydney under the RCP 8.5 emission scenario. This regional variation in climate adaptation effectiveness is driven by the condemning rates and failure rates in each of the cities. As shown in a detailed location analysis in Ryan et al. (5), for the no climate change condition, Canberra has the lowest pole condemning rates and the lowest wind failure rates. Melbourne also has low wind failure rates, and lower condemning rates than Sydney. These location specific rates are dictated by a range of factors (5). These reduced occurrences of pole condemnings and pole wind failures in Melbourne and Canberra reduces the benefit associated with implementation of the adaptation strategy adaptation strategy. The variation in climate adaptation feasibility across different Australian cities for the notional network of 1 million poles illustrates the difficulties associated with implementation of single climate adaptation strategies across Australia. Further research is currently being conducted at the University of Newcastle, Australia and The National University of Ireland, Galway to investigate different adaptation strategies under a variety of climate change conditions in Australia, Ireland and the UK.

Table 4. Climate adaptation cost-benefit analysis results under RCP 8.5 emission scenario for notional power pole networks

Location	Risk Reduction (%)	Mean NPV (\$/pole)	Mean BCR
Sydney	13.7	302	1.70
Melbourne	3.8	56	1.12
Canberra	3.0	43	1.09

5 CONCLUSIONS

A probabilistic event-based sequential model has been developed herein to facilitate investigation into the spatial variability of climate change adaptation feasibility for critical infrastructure. The critical infrastructure type examined is timber power pole networks. Climate change impacts and climate change adaptation feasibility were examined for a notional network of 1 million timber power poles for three Australian cities, namely Sydney, Melbourne and Canberra. Predicted climate change impacts were found to be largest for Sydney, with Melbourne actually experiencing a very slightly positive climate change impact. Examination of the appropriateness of a climate adaptation strategy showed significant spatial variation in cost-benefit outcomes across the three study locations. The adaptation strategy in question was found to perform significantly better for Sydney than for

Melbourne and Canberra, when considering both direct and indirect costs and benefits. This highlights the difficulties associated with implementation of nationwide climate change adaptation strategies for Australia.

6 ACKNOWLEDGEMENTS

The authors appreciate the financial support of the Commonwealth Scientific and Industrial Research Organisation (CSIRO) Flagship Cluster Fund through the project Climate Adaption Engineering for Extreme Events, in collaboration with the Sustainable Cities and Coasts Theme of the CSIRO Climate Adaption Flagship.

REFERENCES

1. IPCC. Summary for Policymakers. Cambridge, United Kingdom and New York, NY, USA 2013.
2. IPCC. Summary for Policymakers. Cambridge, United Kingdom and New York, NY, USA 2014.
3. Stewart M, Deng X. Climate Impact Risks and Climate Adaptation Engineering for Built Infrastructure. ASCE-ASME Journal of Risk and Uncertainty in Engineering Systems, Part A: Civil Engineering. 2015;1(1).
4. Bjarnadottir S, Li Y, Stewart MG. Hurricane Risk Assessment of Power Distribution Poles Considering Impacts of a Changing Climate. ASCE Journal of Infrastructure Systems. 2013;19(1):12-24.
5. Ryan PC, Stewart MG, Spencer N, Li Y. Probabilistic Analysis of Climate Change Impacts on Timber Power Pole Networks. International Journal of Electrical Power & Energy Systems. 2016;78(June 2016):513-23.
6. Ryan P, Stewart MG. Cost-benefit Analysis of Climate Change Adaptation for Power Pole Networks. Climatic Change. In Review.
7. Bolin CA, Smith ST. Life cycle assessment of pentachlorophenol-treated wooden utility poles with comparisons to steel and concrete utility poles. Renewable and Sustainable Energy Reviews. 2011;15(5):2475-86.
8. Crews KI, Horrigan A. Strength assessment of timber utility poles in Australia. New Zealand Timber Design Journal. 2000;9(2).
9. Ryan PC, Stewart MG, Spencer N, Li Y. Reliability assessment of power pole infrastructure incorporating deterioration and network maintenance. Reliability Engineering and System Safety. 2014;132(December 2014):261-73.
10. Winkler J, Duenas-Osorio L, Stein R, Subramanian D. Performance assessment of topologically diverse power systems subjected to hurricane events. Reliability Engineering and System Safety. 2010;95(4):323-36.
11. Wang C-h, Leicester RH, Nguyen M. Timber durability technical report. Manual No. 3 - Decay in ground contact. CRISO and FWPRDC, 2008.
12. Wang C-h, Wang X. Vulnerability of timber in ground contact to fungal decay under climate change. Climatic Change. 2012 2012/12/01;115(3-4):777-94. English.
13. Webb LB, Hennessy K. Climate Change in Australia - Projections for Selected Australian Cities. Commonwealth Scientific and Industrial Research Organisation (CSIRO) and Bureau of Meteorology, Australia, 2015.
14. Wang C-h, Wang X, Khoo YB. Extreme wind gust hazard in Australia and it's sensitivity to climate change. Natural Hazards. 2013;67:549-67.
15. Stewart M. Risk and economic viability of housing climate adaptation strategies for wind hazards in southeast Australia. Mitig Adapt Strateg Glob Change. 2015 2015/04/01;20(4):601-22. English.
16. Henderson DJ, Ginger JD. Vulnerability model of an Australian high-set house subjected to cyclonic wind loading. Wind Struct. 2007 May;10(3):269-85. PubMed PMID: WOS:000246935100004. English.
17. Ryan PC, Stewart MG, Spencer N. Cost-Effective Design and Maintenance of Timber Power Distribution Poles in a Changing Climate. 12th International Conference on Applications of Statistics and Probability in Civil Engineering, ICASP12; July 12-15 2015; Vancouver, Canada 2015.
18. Stewart MG. Spatial variability of damage and expected maintenance costs for deteriorating RC structures. Structure and Infrastructure Engineering. 2006 2006/06/01;2(2):79-90.
19. Standards Australia/New Zealand. AS/NZS 1170-2:2011 Structural design actions, Part 2: Wind actions. Sydney 2011.
20. Standards Australia/New Zealand. AS/NZS 7000-2010: Overhead line design - Detailed procedures. Sydney 2010.

An overview of the development of cement based batteries for the cathodic protection of embedded steel in concrete

Niall Holmes¹, Aimee Byrne¹ & Brian Norton²

¹School of Civil & Structural Engineering, Dublin Institute of Technology, Bolton Street, Dublin 1, Ireland

²Dublin Energy Laboratory, Dublin Institute of Technology, Bolton Street, Dublin 1, Ireland

Email: niall.holmes@dit.ie; aimee.byrne@dit.ie; president@dit.ie

ABSTRACT: This paper presents an overview of the cement-based batteries developed in DIT for use in the cathodic protection of embedded steel in reinforced concrete undergoing chloride-induced corrosion.

Cathodic protection delivers an external current (approximately 20mA per m² of embedded steel) which effectively polarises the internal current generated during corrosion. The batteries developed in DIT comprise of a cement-based electrolyte containing different additives including sand, aggregate, salts, carbon black and plasticiser with protruding anode and cathode metal plates. These batteries produced an initial electrical output of 1.5V and 23mA through a 10Ω resistor as measured using data acquisition units and a custom-built LabVIEW program. By enhancing the ionic conductivity and maintaining the internal moisture content in the cement pores, the batteries power and life span can be improved.

Following a concrete ponding regime to initiate corrosion of embedded steel in a concrete block sample, the power required to protect the reinforcement and arrest corrosion current was determined using a DC desktop supply. With the intention of replacing the desktop supply with a battery module ongoing work is focussing on increasing the life span of individual battery modules, improving their recharging capabilities and optimising for different shapes.

KEY WORDS: Cement-based batteries; cathodic protection; corrosion; electrolyte.

1 INTRODUCTION

The advancement of battery technology is one area that can reduce the reliance on fossil fuels. Current research is focusing on improving the lifespan, power storage and recharge capacity. The most efficient way of achieving all of these is by modifying the battery materials, specifically the electrolyte which is an ionic conductor [1]. Liquid electrolytes are preferred due to higher ion mobility and interface continuity between it and the electrodes. Solid electrolytes have lower ionic conductivities but are less likely to leak.

This paper presents a summary of the work undertaken at DIT into the utilisation of cement as a novel battery electrolyte. Results from a number of parametric studies to yield the optimum electrical current and longevity while establishing the relationships between the internal temperature and humidity with the electrical output shown. Application of the findings to protect embedded steel in concrete subject to corrosion using impressed current cathodic protection (ICCP) and a low-level external current are presented [2].

2 BACKGROUND

In any battery, ions and electrons move through the electrolyte and the circuit from the anode to the cathode respectively (Figure 1). Typical alkaline batteries use zinc as the anode, manganese dioxide as the cathode and a salt solution as the electrolyte. The electrolyte's ionic conductivity should be high with a low electrical resistance thereby allowing it to carry high current. Liquid electrolytes

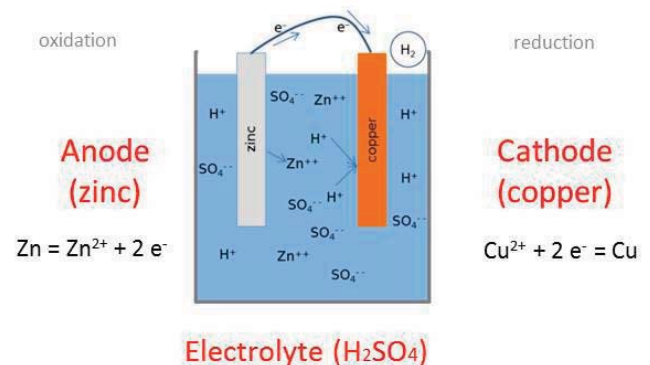


Figure 1. Conventional battery arrangement.

traditionally perform better due to the high mobility of ions. Doping solid electrolytes often improves ion movement.

The process of steel corrosion in concrete is an example of ionic flow through hardened concrete. Iron atoms removed from the steel surface by electrochemical reaction dissolve into the surrounding electrolyte solution. In concrete, this can only occur where pores exist at the steel anodic site. Electrons must therefore transfer from this anodic site to a cathodic area, which develops a surplus. The transfer of electrons occurs along the metal and creates a current between areas of differing potential (Figure 2). The ions from the reactions, such as the ferrous ion (Fe²⁺), pass into the solution trapped in the concrete pores and meet with hydroxyl ions (OH⁻) to form ferric hydroxide which reacts to form rust [3,4].

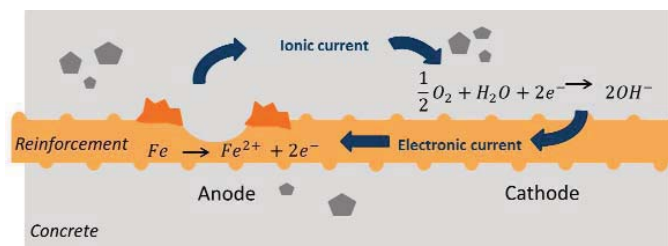


Figure 2. Corrosion process of steel in concrete [3,4].

3 LITERATURE REVIEW

Meng et al. [1] provided the initial proof of the concept that cement based batteries could provide an electrical output. Their design consisted of electrode cement layers with active additives separated by a basic cement electrolyte (Figure 3). The cathode layer was a mix of manganese dioxide particles and cement. The electrolyte consisted of cement and the anode contained cement and zinc particles. The advantage of this design over protruding electrode (non-cement-based) probes is the active phase in both anode (zinc) and cathode (manganese dioxide) are in direct contact with the electrolyte (pore solution in the cement paste) in the anodic and cathodic layers and not just at the interface with the electrolyte. The output from this type of battery design were very low with maximum open circuit voltages and currents of 0.72V and 120 μ A (current density 3.8 μ A/cm²) respectively. It also only produced current when saturated.

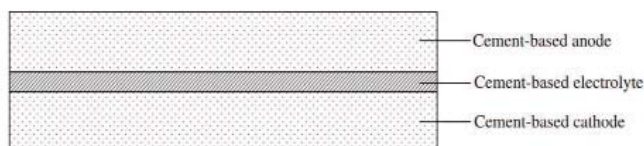


Figure 3. Layered cement-based battery [1]

Rampradheep et al. [5] used similar constituents in another layered design and produced maximum voltage of 0.6V. The current was undisclosed. Cement-batteries cast with carbon fibers and carbon nanotubes in the electrolyte layers [6] yielded maximum power outputs of 0.7V and 35.21 μ A/cm².

Ouellette & Todd [7] produced a battery incorporating a cement electrolyte between magnesium and carbon probes immersed in seawater as a corrosion-based energy harvester. Adding cement passively limited the amount of consumable oxygen rather than as a functioning electrolyte system. Attempts were made to use the battery to harvest the energy produced during corrosion and use it to power corrosion sensors [7,8]. Burstein et al. [9] developed a battery with a small current density, a steel cathode and an aluminum anode protruding from a concrete electrolyte.

The recommended design current density for (ICCP) is 20mA per m² of bar surface area [10] although many studies indicate that lower values are adequate [10-14]. Cathodic prevention, which is the provision of protective current before

any corrosion has taken place, requires a lower current density of 2-5mA/m² [14].

The following section presents the experimental work undertaken to determine the optimum cement-based battery to power cathodic protection in concrete taking into account environmental influences such as temperature and humidity.

4 EXPERIMENTAL WORK

Figure 4 shows the standard form of battery developed with different electrolyte and electrode combinations while limiting other characteristics such as size and shape. The size of the cell is irrelevant to its voltage, but does affect its internal resistance. However, it does affect the maximum current a cell can provide [3] as, with greater electrode/electrolyte contact area, there is less internal resistance and higher currents. Therefore, all batteries designed for comparison (except for the electrode ratio examinations) were of the same dimensions.

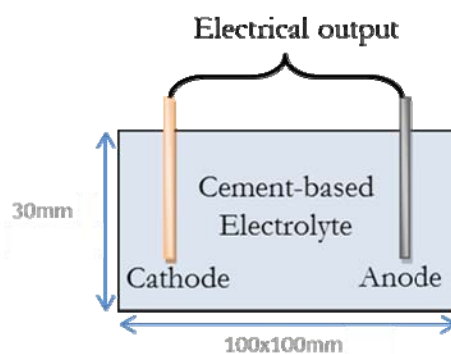


Figure 4. Basic schematic of the batteries developed

Using the highest purity non-toxic materials allowed their specific impact to be distinguished. Weighting and passing the electrolyte materials through a 200 μ m sieve removed any non-conforming lumps or bulk and achieved the desired powder format. The dry constituents were mixed well with deionised water and placed into 90 x 90 x 40mm plastic moulds (300 x 120 x 50mm were used for electrode ratio comparison tests) to create the electrolyte block. Sanding the electrode plates (60 x 30 x 0.5mm) and washing in a borax solution removed any impurities before inserting into the wet electrolyte. Each plate protruded by 5mm to facilitate the connection the resistor circuit. The fresh batteries were each placed on a vibration table for 30 seconds to remove any remaining air and allowed to set for 24 hours under a polythene sheet after which testing began.

The batteries consisted of cement and water paste to form the electrolyte, a copper plate cathode and an aluminium plate anode. The effect of different water/cement ratios, additives and electrode spacing on current, voltage and lifespan are shown in Table 1. As may be seen, the optimal electrical output and lifespans were obtained by using electrolytes with high w/c ratios, adding carbon black and salt [4].

Using these findings, an electrolyte was cast using the constituents shown in Table 2. This mix produced an average continuous current output of 0.02mA for more than a month through a 10 Ω resistor load [3].

Table 1 Electrolyte constituents refining battery design.

Additive	Current (under 10 Ω load)	Voltage (open circuit)	Lifespan
w/c ratio	↑	=	=
Sand & Aggregate	=	=	=
Silica fume	↑	=	↑
Carbon black	↑	↑	↑
Electrode volume	↑	=	=
Salt solution/crystals	↑	=	↑
Water-glass	=	=	=
Electrode spacing	=	=	=
Magnesium anode	↑	↑	↑

Table 2 Electrolyte constituents [3]

Constituent	Weight (g)	Description
Water	291	Mains supply tap water
Cement	595	CEM I (BS EN 197-1)
Alum Salt	47.3	>99% purity
Epson Salt	47.3	>99% purity
Carbon black	9.9	Average size 30nm
Plasticiser	9.9	Sika VistoCrete 30HE

4.1 Measurements

Measurement of current discharge was through a 10 Ω resistor using a National Instruments differential data acquisition unit (DAQ) NI 9205, as shown in Figure 5. Pilot testing using a multi-meter refined the frequency of readings and likely ranges of measured current and voltages. A suitable LabVIEW programme was calibrated using a DC power unit and voltmeter with logged files written into CSV (comma separated values) format and imported directly into MS Excel after testing was complete.

4.2 Influence of temperature and internal moisture

A k-type thermocouple was cast into the middle of ten batteries to investigate the effect of internal temperature and moisture. Five batteries were sealed using an acrylic based water and vapour proof varnish suitable for cement surfaces. The remaining five batteries were unsealed. Temperature readings were recorded using a NI 9211 DAQ unit (Figure 6).

Relative humidity probes were inserted into large blocks made of the same electrolyte mix (Figure 6) at depths of 40mm, 50mm and 65mm using Tramex CMEXPERT II Hygro I probes. The holes were drilled 24 hours after casting and cleaned and the moisture readings taken.

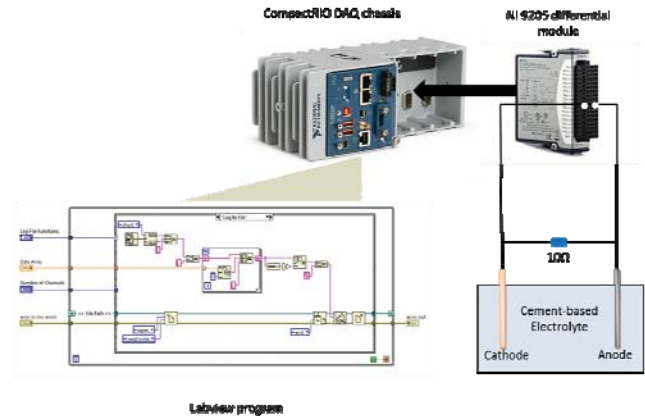


Figure 5. LabVIEW programme and DAQ used

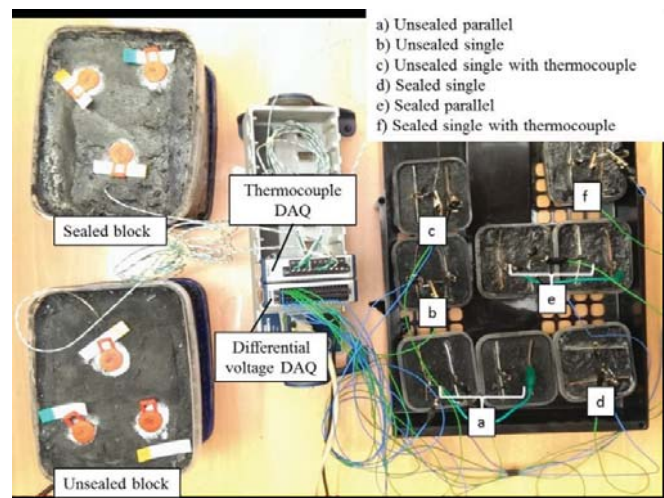


Figure 6. DAQ setup thermocouple recording.

4.3 Connecting batteries in parallel

A 10 Ω resistor was connected between the anode and cathode to act as a resistor load as shown in Figure 7a. The batteries were also connected in parallel and the resistor as shown in Figure 7b.

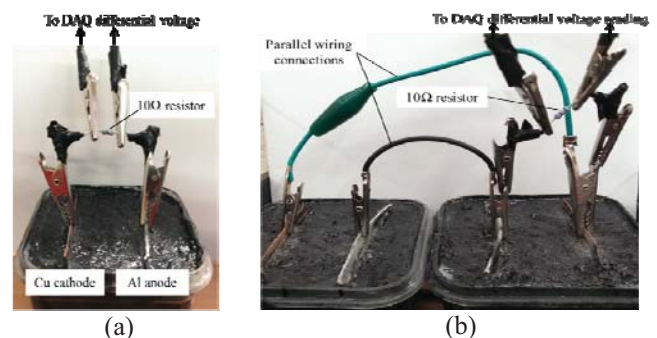


Figure 7. Differential voltage across a resistor for (a) a single cell and (b) multiple cells in parallel

5 EXPERIMENTAL RESULTS

5.1 Effect of internal temperature and humidity

The difference in current between the sealed and unsealed cells (Figure 8a) indicates that the former performs better in terms of electrical power output.

The sealed cells provided an improved resistor-loaded current (0.101mA) compared to the unsealed batteries (0.066 mA). The sealed block retained, on average, 1% higher relative humidity than the unsealed. For every 1% increase in relative humidity, the current increased by 0.01mA and 0.02mA for the unsealed and sealed cells respectively. Over time as the cells dry, the chemical reactions that create these currents will decrease and reaction products will build up on the electrodes.

Observed temperature fluctuations found that for every 1°C increase, the current increased by 0.015mA and 0.028mA for unsealed and sealed cells respectively (Figure 8b). Higher temperatures in batteries correlates with greater outputs as it enhances chemical reactions and improves electron / ion mobility thereby reducing the cell's internal impedance.

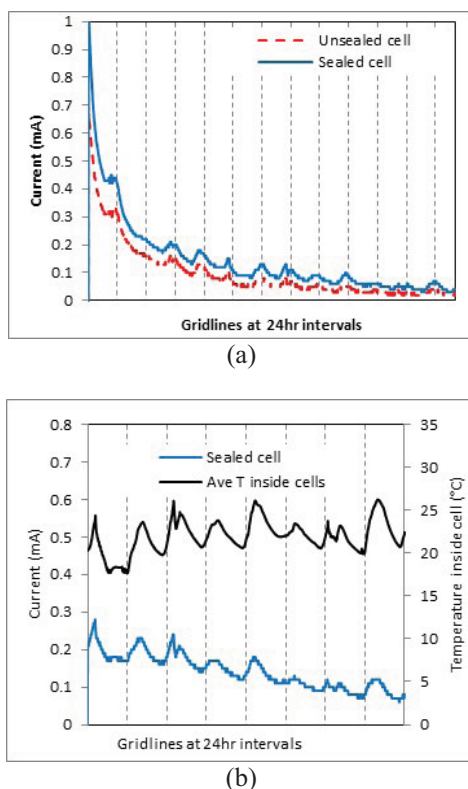


Figure 8. (a) Discharge current through a 10Ω resistor for a sealed and unsealed battery and (b) the relationship between temperature fluctuations within the cement electrolyte and resistor-loaded discharge current from the cells

5.2 Connecting cells in parallel

Connecting two cells in parallel increased the current output by 250% (to 0.16mA) and 360% (0.35mA) for the unsealed and sealed cells respectively (Figure 9). Parallel connections

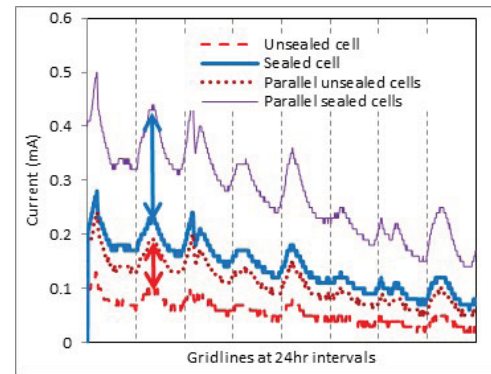


Figure 9. The resistor-loaded discharge current from single cells and two parallel-connected cells for the sealed and unsealed cases.

are commonly used to double the capacity while maintaining the same voltage.

5.3 Potential power source for cathodic protection

The amount of electrical power needed from the batteries developed above to power cathodic protection of reinforcement was determined using a measured macrocell electrochemical corrosion current. A reinforced concrete slab (245x245x110mm deep) was ponded with a 0.55M NaCl solution within a 10mm dyke in the laboratory. The top and bottom mild, and stainless steel bars respectively, were connected externally using a 10Ω resistor (Figure 10). An average corrosion current of 0.14mA was measured and peaked at 0.2mA.

A typical impressed current cathodic protection setup employed a titanium mesh anode coated in mixed-metal-oxide and cast into the ponding dyke with a cement/water mix.

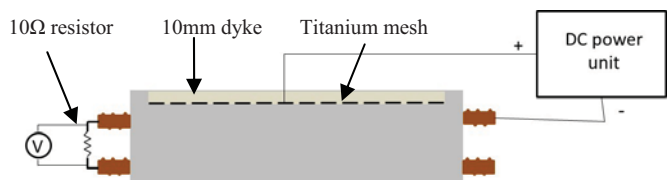


Figure 10. Experimental setup to measure the corrosion current

Figure 10 presents the results from the application of CP. As shown, there is a drop in macrocell current after application of CP. It was found that applying 0.2mA for 12 days reduced the corrosion current to zero indicating that corrosion had been arrested. Work is underway in DIT to attach a number of cement-based barriers in parallel to determine if they can mimic the results shown in Figure 11.

6 CONCLUSIONS

The results above demonstrate the potential for cement-based batteries to be used for the cathodic protection of embedded steel in concrete undergoing corrosion.

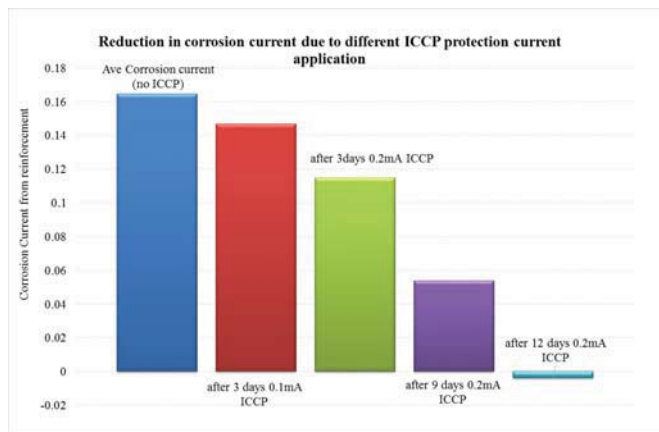


Figure 10. Change in macrocell current over time with CP application

The power output from the batteries have shown to be sufficient for CP albeit for a limited amount of time. Research is underway to further improve the ionic conductivity and maintaining the internal moisture. Work is also underway to recharge the batteries using photovoltaics thereby increasing the lifespan. Finally, research is planned for the assemblage of multiple batteries that when connected in parallel, will produce longer life spans with higher currents that are rechargeable using photovoltaics.

REFERENCES

- [1] Meng Q, Chung DDL (2010) Battery in the form of a cement-matrix composite, *Cement and Concrete Composites*, Vol. 32(10), pp. 829-39.
- [2] Polder RB (1998) Cathodic protection of reinforced concrete structures in the Netherlands – Experience and developments: Cathodic protection of concrete - 10 years' experience. *Heron*, Vol. 43(1), pp. 3-14.
- [3] Byrne, A., Holmes, N & Norton, B (2015) Cement based batteries and their potential for use in low-power operations, 2nd International Conference on innovative materials, structures and technologies, Riga Technical University, 30th September to 2nd October, Latvia.
- [4] Holmes, N., Byrne, A. and Norton, B. (2015) First steps in developing cement-based batteries to power cathodic protection of embedded steel in concrete, *Journal of Sustainable Design and Applied Research (SDAR)*, March 2015
- [5] Rampradheep GS, Sivaraja M, Nivedha K (2012) Electricity generation from cement matrix incorporated with self-curing agent, *Advances in Engineering, Science and Management (ICAESM)*, 2012 International Conference, 30-31 March, pp. 377-82.
- [6] Qiao G, Sun G, Li H, Ou J (2014) Heterogeneous tiny energy: An appealing opportunity to power wireless sensor motes in a corrosive environment, *Applied Energy*, Vol. 131(0), pp. 87-96.
- [7] Ouellette SA, Todd MD (2014) Cement Seawater Battery Energy Harvester for Marine Infrastructure Monitoring, *Sensors Journal*, Vol. 14(3), pp. 865-872.
- [8] Qiao G, Sun G, Hong Y, Qiu Y, Ou J (2011) Remote corrosion monitoring of the RC structures using the electrochemical wireless energy-harvesting sensors and networks, *NDT & E International*, Vol. 44(7), pp. 583-588.
- [9] Burstein G T, Speckert E I P 2008 Developing a battery using set concrete as electrolyte *ECS Transactions* 42 ed pp. 13-20
- [10] Glass GK, Hassanein AM, Buenfeld NR (2001) Cathodic protection afforded by an intermittent current applied to reinforced concrete, *Corrosion Science*, Vol. 43(6), pp. 1111-1131.
- [11] Glass GK, Chadwick JR (1994) An investigation into the mechanisms of protection afforded by a cathodic current and the implications for advances in the field of cathodic protection, *Corrosion Science*, Vol. 36(12), pp. 2193-2209.
- [12] Glass GK, Buenfeld NR (1995) On the current density required to protect steel in atmospherically exposed concrete structures, *Corrosion Science*, Vol. 37(10), pp. 1643-1646.
- [13] Koleva DA, Hu J, Fraaij ALA, Stroeve P, Boshkov N, van Breugel K (2006) Cathodic protection revisited: Impact on structural morphology sheds new light on its efficiency, *Cement and Concrete Composites*, Vol. 28(8), pp.696-706.
- [14] McArthur H, D'Arcy S, Barker J (1993) Cathodic protection by impressed DC currents for construction, maintenance and refurbishment in reinforced concrete, *Construction and Building Materials*, Vol. 7(2), pp. 85-93.

Strength assessment of in-situ concrete for the evaluation of structural capacity: State of the art

Md Shah Nur Alam Sourav¹, Dr. Salam Al-Sabah², Dr. Ciaran McNally³

¹Researcher, Arup, Ringsend Road, Dublin 4, Ireland

²Associate, Arup, Ringsend Road, Dublin 4, Ireland

³UCD School of Civil Engineering, University College Dublin, Belfield, Dublin 4, Ireland
email: sourav.2141@gmail.com, Salam.Al-Sabah@arup.com, ciaran.mcnelly@ucd.ie

ABSTRACT: With more emphasis on reusing and extending the life of structures, it often becomes necessary to assess the capacity of existing concrete structures. One major component of this assessment relates to the concrete strength. Most reliable results are obtained by taking cores. However, such assessment is ideally made with a combination of destructive and non-destructive testing to minimise damage to the structure. The currently available methods for assessing in-situ concrete strength of the existing structures can be broadly divided into two groups. One group of tests is completely non-destructive. The other group is partially destructive where limited damage to the surface is caused by the tests. For the strength evaluation of existing concrete, methods such as surface hardness test, ultrasonic pulse velocity test, penetration resistance test and maturity test fall under the non-destructive category. Partially destructive tests include pull out test, CAPO test, pull off test and break off test. This paper critically evaluates and analyses the applicability and limitations of the methods used for evaluating concrete strength in existing structures. Most methods for strength evaluation are found to measure a certain property such as elasticity, density, tensile strength or hardness of concrete and then relate the measured value to compressive strength. Studies on these methods show a wide variation in the correlations between estimated and predicted compressive strength. Partially destructive methods are noted to provide correlations with good consistency between estimated and predicted compressive strength.

KEY WORDS: Concrete; Compressive Strength; In-situ tests.

1 INTRODUCTION

Existing structures sometimes undergo structural modifications and changed loading condition with a view to reuse rather than demolishing and rebuilding. In these cases, assessment of the structure becomes necessary. Along with the information regarding the arrangement, orientation, dimension, and loading condition, properties of the materials used in the structures are required to be assessed for accurate evaluation of the existing structures.

Concrete is the most widely used construction material in the construction industry because of its ease of production, low cost, durability, and useful structural characteristics. Concrete is generally composed of aggregates, cement, and water. Properties of these constituting materials along with the mixing in different ratios affect the properties of concrete. Concrete properties are also affected by the variability of quality control in the production of concrete, its placement, consolidation, and curing. These result in the variation of concrete strength in the structure. Standard control samples prepared from the same concrete as in-situ may not reflect the strength of in-situ concrete. In-situ concrete strength is evaluated by destructive testing of cores collected from the structures. Core testing is time consuming and expensive and it may not be suitable in all cases because of difficult accessibility to the elements to be examined and risk of losing structural integrity. So, the number of cores that can be taken from the structures is limited. Several in-situ tests are used along with core test to minimize the number of cores to be undertaken and to reduce the uncertainty in compressive strength across a structure. In-situ tests have been developed based on the measurement of physical properties of concrete from which indirect measurement of concrete compressive strength can be inferred [1]. Among the in-situ tests, some are

completely non-destructive while others are partially destructive which cause little surface damage without having effects on the structural integrity. Ultrasonic pulse velocity (UPV) test, rebound hammer test, maturity test, resonance frequency test etc. can be considered as non-destructive test. Tests such as pull out test, cut and pull out (CAPO) test, pull off test, break off test, penetration resistance test are partially destructive. For the sake of simplicity, all these in-situ tests are considered as non-destructive tests.

Historically, in-situ testing for concrete strength evaluation started with the surface hardness test. In the beginning of the twentieth century, the Brinell hardness testing for metal based on the indentation technique was adopted for evaluation of in-situ concrete strength by several researchers [2]. Skramtjæw in 1938 reported 14 different techniques for the concrete strength estimation including pre-installed and post installed techniques [3]. Detailed historical evaluation of different in-situ tests can be found in the literature [2, 3, 5]. During recent years, much research has been devoted to the development and modification of the present in-situ tests, to gather information about the sensitivity of in-situ tests due to concrete variability, and to improve data processing technique for better strength assessment of concrete.

At present, standards and design manual and specifications suggests the requirement of calibration using core testing. The National Roads Authority in Ireland advises the use of in-situ tests after calibrating in-situ test results (usually by coring), as in-situ tests are not definitive and accuracy of in-situ test results is variable [5]. In-situ tests could be used to assist in determining the statistically most reliable results of core tests [6].

The paper addresses the in-situ tests that have been used for the strength estimation of concrete. The aim of the paper is to

present the development, application and limitation of the mentioned in-situ tests on basis of previous research.

2 IN-SITU TEST: STRENGTH ESTIMATION OF CONCRETE

Previously stated in-situ tests measure some physical properties of concrete and relate the measured properties with the compressive strength of concrete. So, all these tests estimate the concrete compressive strength indirectly which leads to the uncertainty in the measurement of strength estimation. In-situ tests are discussed in the following sections. They are divided into two major groups, one is non-destructive test and another is partially destructive test.

2.1 Non-destructive tests

2.1.1 Rebound hammer test

Schmidt in 1948 introduced spring impact device of concrete by rebound principle [2]. The technique provides an easy measurement of rebound of impact hammer and the operation is quite simple. During the operation, a hammer mass impacts the concrete with a fixed energy and rebounds from the surface of the concrete after the impact. Energy of the hammer is applied by tensioning of spring and it is independent of the operator. Loss of energy during the impact of the hammer with concrete depends on the strength and elastic modulus of concrete. Since the introduction of the test, extensive research has been carried out to explain the interaction of the hammer with the concrete and energy dissipation in concrete, to figure out the sensitivity of the hammer under different influencing factors related to concrete and rebound hammer [6–14]. Akashi and Amasaki [16] investigated that wave propagation behaviour would be different for concrete having different strengths and boundary conditions of the contact between the hammer and the concrete. A good number of empirical relationships having different mathematical models for strength estimation can be found [10, 16, 17]. Szilagyi and Borosnyoi [11] suggested the use of rebound hammer within the respective domain of each model for the strength evaluation. Malhotra [14] reported $\pm 15\text{--}20\%$ deviation in strength assessment for control specimens prepared in the laboratory. Brencich et al. [8] assessed many factors including moisture content, stress state and maturity. Liu et al. [13] designed a model with nine parameters for strength estimation using rebound hammer. Many researchers argued about the existence of universal relationship of strength and rebound value [18]. In recent years, two different mathematical approaches [15, 17] have been suggested considering some factors such as measurement error, uncontrolled factors and model error. Szilagyi et al. [19] proposed a model (SBZ model) considering the surface hardness as a time dependent material property affected by water-cement ratio, carbonation and time. With all the limitations, this test is the most widely used for the strength estimation as it is easy, simple and inexpensive. The test method, the statistical characteristics of test results, the implementation of in-situ testing and interpretation of test results are described in ACI 228.1R-03, ASTM C805/C805M-12, EN 12504- 2:2012 and ISO 1920-7:2004 [18–21].

Rebound hammer provides an impact measurement at the point of interaction. It produces high variability being affected by numerous factors. The test can be used to assess the

uniformity and quality of concrete in structure. The test should not be used for the basis of acceptance or rejection of concrete due to inherent uncertainty in concrete strength estimation.

2.1.2 Ultrasonic pulse velocity (UPV) test

Use of ultrasonic wave for defect detection in metal appeared in 1929. In 1940s, UPV test method was developed in Canada and England simultaneously [24]. The test method was developed on the basis of the propagation of mechanical wave through the material. For a homogeneous solid medium, the velocity of the ultrasonic wave depends on the elastic properties and density of the medium. The test method measures the time required for a wave to travel a particular distance from which velocity is measured. Several research and investigations were executed to understand the sensitivity of UPV test in concrete since the introduction of the test. In 1969, Jones and Facaoaru published the recommendation for testing concrete by UPV test [25]. Theoretical discussion can be found in details in [18, 20]. Kaplan [27] investigated the effect of age and water-cement ratio on the relationship of UPV and compressive strength of concrete. Ohdaira and Masuzawa [28] reported that high water content in the concrete results in higher velocity of the ultrasonic wave. Type and amount of aggregate significantly affect the UPV value in concrete [21, 26–28]. Ultrasonic pulse attenuation along with UPV was reported to be useful in estimation of concrete strength [32]. Bogas et al. [29] concluded that the relationship between UPV and compressive strength tends to be less affected by the aggregate volume in lightweight aggregate than normal weight aggregate. Solis-Carcano and Moreno [30] introduced a factor to define the aggregate property for better assessment of strength from UPV. Demirboga et al. [33] presented a general relationship of strength and UPV when assessing the effect of replacement of cement by different mineral admixtures. Type and amount of aggregate used for the research was constant. Presence of reinforcing bar in the concrete results in high error in UPV test as the velocity of wave is greater in steel than in concrete. Correction should be used if the reinforcement crosses the wave path. Turgut [34] suggested a universal relation between UPV and concrete strength. He considered laboratory specimens of different mix ratio and cores taken from the structures having different ages and unknown compositions. Popovics et al. discussed the difficulties of using UPV in concrete [35]. Komlos et al. [36] compared several standards of UPV test. He stated that the application of UPV test for strength estimation of concrete should be carried out with a suitable correlation curve.

Though with-in test variation has been found to be low [20], most reliable UPV test application is in concrete changes monitoring and mass uniformity checking [36]. The least recommended method of concrete strength estimation is the UPV test due to concrete inhomogeneity, material variability, and factors affecting the velocity of pulse.

2.1.3 Resonance frequency test

Resonance frequency method was first developed by Powers in 1938 and modified by Hornibrook in 1939 [37]. For a vibrating system of homogeneous, elastic and isotropic material, natural frequency of vibration is related to the

dynamic modulus of elasticity and density [37]. The test works on the principle of resonating concrete specimen by applying excitations either by vibrating the specimen or by impacting with a small hammer. Resonance frequency tests have been performed for over 50 years and it has been mostly confined to laboratory based work as opposed to in-situ testing [37]. The high cost of the instrument, difficulty in data processing and portability result in low popularity of the test. The test is influenced by properties of aggregate and their mixing proportions, curing condition, and specimen size. The test is usually used in detecting deterioration of concrete rather than estimating strength. The test is not included in ACI 228 for in-situ strength estimation of concrete [20]. ASTM C215 suggests the use of the test in detecting changes in dynamic modulus of elasticity of concrete undergoing harsh environment [38]. Resonance frequency test is not commonly used for strength estimation of concrete. The test provides the means of studying the deterioration of concrete specimen subjected to aggressive environment.

2.1.4 Maturity test

Maturity method is a technique for estimating strength gain of concrete based on temperature history. The strength of concrete can be expressed as a function of time and temperature history which is related to the hydration process of cement paste of concrete. The origin of the method can be traced to a series of research related to the accelerated curing methods conducted during the late 1940s and early 1950s [39]. In 1951, Saul [40] presented a theory in defining maturity as the product of time and temperature. He stated that concrete of the same mix at the same maturity has approximately the same strength whatever combination of time and temperature make up that maturity [41]. The proposed maturity function to estimate the concrete strength was based on the assumption of linearity of strength gain and temperature and was able to predict the strength for limited range of curing temperatures. Several mathematical expressions for the maturity function were suggested to estimate the concrete strength reliably [38, 41]. Carino and Lew [41] reported that there is no single maturity function that is applicable to all concrete mixes. Procedures for using the maturity method have been standardized in ASTM C1074 [43]. Temperature history of concrete is a must for the maturity method. This method is applicable to new construction and early age strength development. The method can be used to determine in-situ strength of concrete to allow removal of formwork or shoring, opening of roadways to traffic etc. This is typically carried out with the help of pre-established empirical relationship of time-temperature and strength development

2.2 Partially destructive tests

2.2.1 Probe penetration test

Probe penetration test, considered as a hardness test [41, 42], measures the depth of penetration of probe into the concrete which provides the measure of hardness or penetration resistance. This can be related to concrete strength. Though the method was first introduced by Voellmy in 1954, its origin can be traced back to one of the method suggested by Skramtajaw in 1938 [2]. In 1964, a device, known as Windsor

probe, was introduced in USA for the penetration testing of concrete to estimate the quality and strength. Later on Malhotra [46], Klotz [47], Arni [48] investigated the use of this test for compressive strength measurement. The test measures the compressibility of a localized area [44]. Aggregate hardness is taken to be the most influencing factor in the test results. The early age strength estimation of concrete has been reported to provide better accuracy compared to the rebound hammer test [49]. Manufacturer of the Windsor probe test system provides charts depending on the hardness of aggregate [44]. Several researchers indicated the correlations to be ineffective for strength estimation [cited in 22]. In 1980s, Windsor probe penetration test was modified to develop pin penetration test in which a smaller pin (in diameter and length) is forced into the concrete using a spring loaded device [44]. In recent years, nail penetration into the concrete by constant gas pressure has been studied [50]. Smaller sized nail with less energy than the Windsor probe penetration test is inserted into the concrete. Reliability of this nail penetration test has been reported to be higher than the rebound hammer, UPV and probe penetration test. The probe penetration test has been included in ASTM standard (ASTM C 803) in 1975 and the standard was modified to include the pin penetration test in 1990 [44].

Probe penetration test measures the compressibility of a small area. The test result produce high variability depending on the type of aggregates. Strength estimation is highly sensitive to the measured area. The test can be applicable to assess the uniformity of concrete.

2.2.2 Pull out test

Pull out test, also known as LOK test, measures the force required to extract an embedded metal insert from the concrete mass. The insert is pulled against a reaction force exerted on a concentric bearing ring placed around the insert. A conical shaped portion of concrete is extracted at the ultimate pull out load. Skramtajaw [3] first introduced the method which involved inserting a rod with a spherical end in the fresh concrete and then measuring the force needed to pull the rod from the hardened concrete. Later on in 1944, Tremper reported a non-linear relationship for the pull out force and compressive strength of concrete [51]. Both Skramtajaw and Tremper worked with the tensile strength of concrete because of the shape of the instrument they worked with. The present size and shape of the instrument is the result of the extensive study of Kierkegaard-Hansen carried out in the 1960s [51]. His work led to the introduction of bearing ring to fail the concrete along a predefined path. Many researchers studied the failure mechanism of concrete to explain the relationship between the pull out force and compressive strength [5, 48]. All these research concluded that pull out test subjects concrete to a non-uniform, three dimensional complex state of stress. Yener and Li [52] explained that relationship of concrete strength and pull out force could be attributed to the crushing of concrete. They performed plastic fracture finite element analysis to explain the failure mechanism. Krenchel and Shah [53] after the micro-cracking analysis, proposed with a two stage cracking process. A stable cracking begins at about 30% of peak load around the head of the insert inside the concrete and second stage that developed after the peak load defines the shape of

cone. Krenchel and Bickley [cited in 28] explained the failure mechanism based on the progression of micro-cracking. They stated that pull out load and uniaxial compressive strength both undergo similar micro-cracking before failure. Despite lack of agreement on the failure mechanism, pull out load has good correlation with the compressive strength of concrete [20]. Pull out instrument is to be inserted in the fresh concrete which limits the test applicability. To overcome this limitation and to use in existing structures, various types of post installed instruments were investigated in the 1970s [54]. A post installed method known as CAPO test having the same geometry as pull out test was developed by Petersen in 1976 [55]. The concrete is subjected to same type of loading as pull out test and the failure mechanism resembles the pull out test [51]. Petersen investigated several correlations proposed by researchers between pull out force and strength of concrete for both pull out and CAPO tests [55]. He reported identical correlation for the two tests. Petersen and Poulsen [56] suggested two general correlations for the strength estimation of normal concrete, one is for low strength region and another is for high strength region. For lightweight concrete, Krenchel and Nasser [cited in 32] suggested different correlations. Pull out test along with CAPO test as post installed pull out test has been included in different standards including ASTM C900 and EN 12504-part 3 [19,55]. In recent years, a new pull out technique (B15G insert) has been presented [57, 58]. Brencich [59] described the operation of the technique with respect to pull out/ CAPO test.

Pull out and CAPO test provide direct measurement of static loading subjected to concrete. Variability in strength estimation depends on the aggregate type. There exists a strong relationship between the compressive strength of concrete and pull out strength [20]. The application of the tests is in high reliable estimation of concrete compressive strength [60].

2.2.3 Break off test

Break off test was introduced by Johansen in 1976 in Norway. The test is based on the measurement of the flexural tensile strength parameter of concrete which can be indirectly related to compressive strength. The test measures the force required to break off a cylindrical core from a larger concrete mass. The test specimen can be prepared by inserting a tubular plastic sleeve during concrete casting or by drilling the hardened concrete at the time of testing. Load configuration is the same as the cantilever beam with circular cross section subjected to a concentrated load at its free end [61]. The test method creates a state of combination of bending and shear stress at the base of the cylindrical core [4]. A good number of research was carried out in the 1980s [61]. Nishikawa [62] reported impractical relationship between break off test result and compressive strength of concrete. Break off test was found to be sensitive to the water-cement ratio, age of concrete, curing and cement type. Naik et al. [63] found the influence of type of aggregate and specimen on the break off test results. Crushed aggregate resulted in higher test results than the rounded aggregate. However, while studying the performance of break off test in high strength concrete, Naik and Salameh [64] found the influence of type of aggregate and test specimen (preinstalled or post-installed) to be negligible. Size of aggregate has high influence on the variability of the test

results [20]. ASTM included the test in 1990 as ASTM C 1150 and withdrew the test in 2002 [61].

Break off test is not commonly used in recent years. The test provides an indirect estimation of compressive strength. The test results are highly variable. The test is suitable for near surface flexural tensile strength measurement of concrete.

2.2.4 Pull off test

Pull off test is based on the concept that the tensile force required to pull a metal disk, together with a layer of concrete from the surface to which it is attached is related to the compressive strength of concrete. The test was developed in 1970s in United Kingdom [65]. Similar test was developed in Austria (tear off test) and Denmark (007-Bond test) [2, 64]. The test is a direct tension test of concrete. With the pre-established correlation, compressive strength of a particular concrete is measured from the pull off test results. Aggregate type has high influence in the test results [65]. The test is included in ASTM C1583 [66]. BS 1881-207 reported 15% variation under laboratory condition in strength estimation [67]. ASTM C 1583 limits the use of the test for estimation of tensile strength of concrete surface and bond strength of overlay material [68].

Pull off test measures the compressive strength of concrete indirectly. The test is particularly suitable for testing near surface tensile strength of concrete. This test is not recommended for the estimation of concrete compressive strength.

2.3 Combination of in-situ tests

Combination of several in-situ tests has been reported in 1960s for the purpose of improving the reliability and precision in concrete strength estimation [69]. The concept behind the development of combining in-situ tests is that if two test methods are influenced in two different ways by the same factor, their combined use results in a cancelling effect which improves the strength estimation [2]. Among the various suggested combinations, use of combination of UPV and rebound hammer (known as SonReb method) is the most common practice. Different mathematical models have been proposed by researchers. Researchers reported better correlations while using the combined methods for strength estimation [62–68]. Many researchers proposed universal relations for the strength estimations [67, 69]. Qasrawi [75] proposed a nomograph where concrete strength was expressed as a function of two variables. Nomograph consisted of different contours of rebound hammer value having concrete strength along one axis, UPV test result along other axis. Arioglu [77] suggested similar nomograph having UPV test result as the contour line. Several other combinations of in-situ have been reported in recent years including the use of Windsor probe penetration test and resonance frequency test with SonReb method [64, 66]. Breyse [18] explained that combination may not always lead to better correlation. When one test provides much poorer results than the other, combination will not result in increased accuracy for strength estimation.

2.4 Comparative assessment

Several researchers reported comparative assessment of estimating concrete strength using different in-situ test

methods. Arni [48] compared the rebound hammer and probe penetration test for strength estimation. He concluded that neither of the tests should be used for strength estimation. For quality assessment, rebound hammer could be used ahead of probe penetration because of its low cost, less destructive nature, and ability to provide greater number of test data. Yun et al. [78] reported the comparison of several NDTs. The work of Qasrawi [75] indicated that UPV test showed more accuracy than rebound hammer in strength prediction. Shariati [76] found rebound hammer test to be more accurate than UPV test in strength prediction. Pascale et al. [79] showed limitation of probe penetration test in estimating strength of high strength concrete.

3 CONCLUSION

Several in-situ test methods have been reviewed in this paper based on previous research results. All in-situ tests are suggested to be used for strength estimation within their limitations. Correlation of strength and in-situ test result for the concrete to be investigated should be prepared beforehand. Rebound hammer and penetration resistance test provide information of surface properties. Break off test measures flexural property while pull off test provides tensile strength property of concrete. UPV and resonance frequency test provide inside properties of concrete. Pull out test and CAPO test provide strong relationship with the compressive strength. Efficiency and quality of strength estimation depend on the sensitivity of strength to the in-situ tests, measurement error and range of variation of in-situ test results as compared to the variation of strength. Combination of two or more in-situ tests can be helpful in that context.

ACKNOWLEDGMENTS

This project has received funding from the European Union's Horizon 2020 research and innovation programme under the Marie Skłodowska-Curie grant agreement No. 642453.

REFERENCES

- [1] V. M. Malhotra and Carino N. J., *Handbook on Non Destructive Testing of Concrete*, 2nd ed. Boca Raton, USA: CRC Press, 2004.
- [2] N. J. Carino, "Nondestructive Testing of Concrete - History and Challenges," in *Concrete Technology- Past, Present and Future*, 1994, pp. 623–678.
- [3] B. G. Skramtjæw, "Determining Concrete strength For Control Of Concrete In Structures," *Journal Proceedings*, vol. 34, no. 1, pp. 285–304, Jan. 1938.
- [4] N. J. Carino, "Nondestructive test methods," in *Concrete Construction Engineering Handbook*, 2nd ed., Edward G. Nawy, Ed. Boca Raton, USA: CRC press, 2008, pp. 1–74.
- [5] "NRA BA 86 Advice Notes on the Non-Destructive Testing of Road Structures," *National Roads Authority*, vol. 3, 2014.
- [6] L. Jacinto, L. O. Santos, and L. C. Neves, "Bayesian probabilistic assessment of in-situ concrete strength," *Large Structures and Infrastructures for Environmentally Constrained and Urbanised Areas*, pp. 228–229, 2010.
- [7] A. Basu and A. Aydin, "A method for normalization of Schmidt hammer rebound values," *International Journal of Rock Mechanics & Mining Sciences*, vol. 41, pp. 1211–1214, 2004.
- [8] A. Brencich, G. Cassini, D. Pera, and G. Riotto, "Calibration and Reliability of the Rebound (Schmidt) Hammer Test," *Civil Engineering and Architecture*, vol. 1, no. 3, pp. 66–78, 2013.
- [9] G. W. Greene, "Test Hammer Provides New Method of Evaluating Hardened Concrete," *Journal Proceedings*, vol. 51, no. 11, pp. 249–256, Nov. 1954.
- [10] S. Hannachi and M. N. Guetteche, "Review of the Rebound Hammer Method Estimating Concrete Compressive Strength on Site," in *International Conference on Architecture and Civil Engineering*, 2014, pp. 118–127.
- [11] K. Szilágyi and A. Borosnyói, "50 Years of Experience With the Schmidt," *Concrete Structures*, vol. 10, pp. 46–56, 2009.
- [12] E. Kolaiti and Z. Papadopoulos, "Evaluation of Schmidt Rebound Hammer Testing: a Critical Approach," *Bulletin of the International Association of Engineering Geology*, vol. 48, no. 1985, pp. 69–76, 1993.
- [13] J. C. Liu, M. L. Sue, and C. H. Kou, "Estimating the strength of concrete using surface rebound value and design parameters of concrete material," *Tamkang Journal of Science and Engineering*, vol. 12, no. 1, pp. 1–7, 2009.
- [14] V. M. Malhotra, "Surface Hardness Method," in *Handbook on Non Destructive Testing of Concrete*, 2nd ed., V. M. Malhotra and J. N. Carino, Eds. Boca Raton, USA: CRC Press, 2004, pp. 1–1–16.
- [15] K. Szilágyi, "Rebound surface hardness and related properties of concrete," Budapest University of Technology and Economics, 2013.
- [16] T. Akashi and S. Amasaki, "Study of the Stress Waves in the Plunger of a Rebound Hammer at the Time of Impact," *Special Publication, American Concrete Institute*, vol. 82, pp. 17–34, Sep. 1984.
- [17] D. Breyse and J. L. Martínez-Fernández, "Assessing concrete strength with rebound hammer: review of key issues and ideas for more reliable conclusions," *Materials and Structures*, vol. 47, no. 9, pp. 1589–1604, 2013.
- [18] D. Breyse, "Nondestructive evaluation of concrete strength: An historical review and a new perspective by combining NDT methods," *Construction and Building Materials*, vol. 33, pp. 139–163, 2012.
- [19] K. Szilágyi, A. Borosnyói, and I. Zsigovics, "Rebound surface hardness of concrete: Introduction of an empirical constitutive model," *Construction and Building Materials*, vol. 25, no. 5, pp. 2480–2487, 2011.
- [20] ACI Committee Report 228.1R, "In-Place Methods to Estimate Concrete Strength Reported," 2003.
- [21] ASTM C805 / C805M - 13a, "Standard Test Method for Rebound Number of Hardened Concrete," 2014.
- [22] EN 12504-2:2012, "Testing concrete in structures. Non-destructive testing. Determination of rebound number," 2013.
- [23] ISO 1920-7:2004, "Testing of concrete - Part 7: Non-destructive tests on hardened concrete," 2004.
- [24] T. R. Naik, V. M. Malhotra, and J. S. Popovics, "The Ultrasonic Pulse Velocity Method," in *Handbook on Nondestructive Testing of Concrete*, 2nd ed., no. Civil, V. M. Malhotra and N. J. Carino, Eds. Boca Raton, USA: CRC Press, 2004, pp. 8–1–8–19.
- [25] R. Jones and I. Façaoaru, "Recommendations for testing concrete by the ultrasonic pulse method," *Matériaux et Constructions*, vol. 2, no. 4, pp. 275–284, 1969.
- [26] J. H. Bungey, S. G. Millard, and M. G. Grantham, "The ultrasonic pulse velocity method," in *Testing of Concrete in Structures*, 4th ed., Abingdon, England: Taylor & Francis, 2006, pp. 51–81.
- [27] M. F. Kaplan, "The effects of age and water/cement ratio upon the relation between ultrasonic pulse velocity and compressive strength of concrete," *Magazine of Concrete Research*, vol. 11, no. 32, pp. 85–92, Jul. 1959.
- [28] E. Ohdaira and N. Masuzawa, "Water content and its effect on ultrasound propagation in concrete--the possibility of NDE," *Ultrasonics*, vol. 38, pp. 546–552, 2000.
- [29] J. A. Bogas, M. G. Gomes, and A. Gomes, "Compressive strength evaluation of structural lightweight concrete by non-destructive ultrasonic pulse velocity method," *Ultrasonics*, vol. 53, no. 5, pp. 962–972, 2013.
- [30] R. Solis-Carcano and E. I. Moreno, "Evaluation of concrete made with crushed limestone aggregate based on ultrasonic pulse velocity," *Construction and Building Materials*, vol. 22, no. 6, pp. 1225–1231, 2008.
- [31] H. Tanyidizi and A. Coskun, "Determination of the principal parameter of ultrasonic pulse velocity and compressive strength of lightweight concrete by using variance method," *Russian Journal of Nondestructive Testing*, vol. 44, no. 9, pp. 639–646, 2008.
- [32] M. T. Liang and J. Wu, "Theoretical elucidation on the empirical formulae for the ultrasonic testing method for concrete structures," *Cement and Concrete Research*, vol. 32, no. 11, pp. 1763–1769, 2002.

- [33] R. Demirboğa, I. Türkmen, and M. B. Karakoç, "Relationship between ultrasonic velocity and compressive strength for high-volume mineral-admixtured concrete," *Cement and Concrete Research*, vol. 34, no. 12, pp. 2329–2336, 2004.
- [34] P. Turgut, "Research into the correlation between concrete strength and UPV values," *NDT.net*, vol. 12, no. 12, pp. 1–9, 2004.
- [35] S. Popovics, J. L. Rose, and J. S. Popovics, "The behavior of ultrasonic pulses in concrete," *Cement and Concrete Research*, vol. 20, no. 2, p. Pages 259–270, 1990.
- [36] K. Komloš, S. Popovics, T. Nürnbergerová, B. Babál, and J. S. Popovics, "Ultrasonic pulse velocity test of concrete properties as specified in various standards," *Cement and Concrete Composites*, vol. 18, no. 5, pp. 357–364, 1996.
- [37] V. M. Malhotra and V. Sivasundaram, "Resonant Frequency Methods," in *Handbook on Non Destructive Testing of Concrete*, 2nd ed., Boca Raton, USA: CRC press, 2004, pp. 7–1–7–21.
- [38] ASTM C 215 - 14, "Standard Test Method for Fundamental Transverse, Longitudinal, and Torsional Resonant Frequencies of Concrete Specimens," 2014.
- [39] N. J. Carino, "The Maturity Method," in *Handbook on Non Destructive Testing of Concrete*, 2nd ed., V. M. Malhotra and N. J. Carino, Eds. Boca Raton, USA: CRC Press, 2004, pp. 5–1–5–47.
- [40] A. G. A. Saul, "Principles underlying the steam curing of concrete at atmospheric pressure," *Magazine of Concrete Research*, vol. 2, no. 6, pp. 127–140, Mar. 1951.
- [41] N. Carino and H. Lew, "The maturity method: from theory to application," *Structures Congress and Exposition 2001*, pp. 1–19, 2001.
- [42] T. Naik, "Maturity of concrete: Its applications and limitations," *Advances in Concrete Technology, CANMET, 1992, Canada*.
- [43] ASTM C1074-11, "Standard Practice for Estimating Concrete Strength by the Maturity Method," 2011.
- [44] V. M. Malhotra and Carette G.G., "Penetration Resistance Method," in *Handbook on Non Destructive Testing of Concrete*, 2nd ed., vol. 2, V. M. Malhotra and Carino N. J., Eds. Boca Raton, USA: CRC Press, 2004, pp. 2–1–2–18.
- [45] J. F. Lamond, *Significance of Tests and Properties of Concrete and Concrete-making Materials, Issue 169, Part 4*. ASTM International, 2006.
- [46] V. M. Malhotra, "Evaluation of the windsor probe test for estimating compressive strength of concrete," *RILEM Materials and Structures*, vol. 7, no. 37, pp. 3–15, 1974.
- [47] R. C. Klotz, "Field investigation of concrete quality using the windsor probe test system," *Highway Research Record*, no. 378, 1972.
- [48] H. T. Arni, "Impact and penetration tests of tests of portland cement concrete," *Highway Research Record*, no. 378, 1972.
- [49] G. G. Carette and V. M. Malhotra, "In Situ Tests: Variability and Strength Prediction of Concrete at Early Ages," *Special Publication*, vol. 82, pp. 111–142, Sep. 1984.
- [50] L. Selcuk, H. S. Gokce, K. Kayabali, and O. Simsek, "A Nondestructive Testing Technique: Nail Penetration Test," *ACI Structural Journal*, vol. 109, no. 2, pp. 245–252, 2012.
- [51] N. J. Caniro, "Pull out test," in *Handbook on Non Destructive Testing of Concrete*, 2nd ed., N. J. Malhotra, V. M. and Carino, Ed. Boca Raton, USA: CRC Press, 2004, pp. 3–1–3–40.
- [52] M. Yener and G. C. Li, "Progressive Finite Element Fracture Analysis of Pullout Concrete," *Journal of Structural Engineering*, vol. 117, no. 8, pp. 2351–2371, 1991.
- [53] H. Krenchel and S. P. Shah, "Fracture analysis of the pullout test," *Materials and Structures*, vol. 18, no. 6, pp. 439–446, Nov. 1985.
- [54] J. H. Bungey, S. G. Millard, and M. G. Grantham, *Testing of Concrete in Structures*, 4th ed. Abingdon, England: Taylor & Francis, 2006.
- [55] C. G. Petersen, "LOK-TEST and CAPO-TEST pullout testing, twenty years experience," in *Non-Destructive Testing in Civil Engineering Conference*, 1997.
- [56] C. G. Petersen and E. Poulsen, "Pullout testing by LOK-test and CAPO-test with particular reference to the in-place concrete of the Great Belt Link," Dansk Betoninstitut A/S, Virum, Denmark., 1992.
- [57] EN 12504-3:2005, "Testing concrete in structures. Determination of pull-out force," 2005.
- [58] F. L. Bovio, G. L. Bovio, A. Brencich, G. Cassini, D. Pera, and G. Riotto, "A New Pull-Out Technique for In-Place Estimation of Concrete Compressive Strength," *Advances in Materials Science and Engineering*, vol. 2014, p. 8, 2014.
- [59] A. Brencich, "A post-installed insert for pull-out tests on concrete up to 70MPa," *Construction and Building Materials*, vol. 95, pp. 788–801, 2015.
- [60] ASTM C 900 - 15, "Standard Test Method for Pullout Strength of Hardened Concrete," 2015.
- [61] T. R. Naik, "The Break-off Test Method," in *Handbook on Nondestructive Testing of Concrete*, 2nd ed., N. J. C. V. M. Malhotra, Ed. Boca Raton, USA: CRC Press, 2004, pp. 1–16.
- [62] A. S. Nishikawa, "A Nondestructive Testing Procedure for In-Place Evaluation of Flexural Strength of concrete: Informational Report. Joint Highway Research Project, Indiana Department of Transportation and Purdue University, Indiana," 1983.
- [63] T. Naik, Z. Salameh, and A. Hassaballah, "Evaluation of In-Place Strength of Concrete By The Break-Off Method," in *Proceedings of the NDT&E for Manufacturing and Construction Conference*, 1988, p. 54.
- [64] T. R. Naik and Z. Salameh, "Evaluation of high strength concrete by the break-off method," in *First Materails Engineering Congress*, 1990, vol. 2.
- [65] G. D. Henderson, P. A. M. Basheer, and A. E. Long, "Pull-off test and permeation tests," in *Handbook on non-destructive testing on concrete*, 2nd ed., V. M. Malhotra and N. J. Carino, Eds. Boca Raton, USA: CRC Press, 2004, pp. 6–1–6–12.
- [66] ASTM C1583 / C1583M - 13, "Standard Test Method for Tensile Strength of Concrete Surfaces and the Bond Strength or Tensile Strength of Concrete Repair and Overlay Materials by Direct Tension (Pull-off Method)," 2013.
- [67] BS 1881-207:1992, "Testing concrete. Recommendations for the assessment of concrete strength by near-to-surface tests," 1992.
- [68] ASTM C 1583/ C 1583M - 13, "Standard Test Method for Tensile Strength of Concrete Surfaces and the Bond Strength or Tensile Strength of Concrete Repair and Overlay Materials by Direct Tension (Pull-off Method)," 2013.
- [69] A. Samarin, "Combined Methods," in *Handbook on Non Destructive Testing of Concrete*, 2nd ed., V. M. Malhotra and N. J. Carino, Eds. Boca Raton, 2004, pp. 9–1–9–12.
- [70] M. Erdal, "Prediction of the Compressive Strength of Vacuum Processed Concretes Using Artificial Neural Network and Regression Techniques," *Scientific Research and Essays*, vol. 4, no. 10, pp. 1057–1065, 2009.
- [71] B. Hobbs and M. T. Kebir, "Non-destructive testing techniques for the forensic engineering investigation of reinforced concrete buildings," *Forensic Science International*, vol. 167, no. 2–3, pp. 167–172, 2007.
- [72] W. Martinez-Molina, A. A. Torres-Acosta, J. C. Jauregui, H. L. Chavez-Garcia, E. M. Alonso-Guzman, M. Graff, and J. C. Arteaga-Arcos, "Predicting concrete compressive strength and modulus of rupture using different NDT techniques," *Advances in Materials Science and Engineering*, vol. 2014, 2014.
- [73] L. Nobile, "Prediction of concrete compressive strength by combined non-destructive methods," *Meccanica*, vol. 50, no. 2, pp. 411–417, 2015.
- [74] R. Pucinotti, "The use of multiple combined non destructive testing in the concrete strength assessment," *HSNDT International 2007 on ndt.net*, pp. 1–7, 2007.
- [75] H. Y. Qasrawi, "Concrete strength by combined nondestructive methods simply and reliably predicted," *Cement and Concrete Research*, vol. 30, no. 5, pp. 739–746, 2000.
- [76] M. Shariati, N. H. Ramli-Sulong, M. M. Arabnejad, P. Shafigh, and H. Sinaei, "Assessing the strength of reinforced concrete structures through Ultrasonic Pulse Velocity and Schmidt Rebound Hammer tests," *Scientific Research and Essays*, vol. 6, no. 1, pp. 213–220, 2011.
- [77] E. Arioğlu, N. Ariolu, and C. Girgin, "A discussion of the paper 'concrete strength by combined nondestructive methods simply and reliably predicted' by H.Y. Qasrawi," *Cement and Concrete Research*, vol. 31, no. 8, pp. 1239–1240, 2001.
- [78] C. H. Yun, K. R. Choi, S. Y. Kim, and Y. C. Song, "Comparative Evaluation of Nondestructive Test Methods for in-Place Strength Determination," *Special Publication*, vol. 112, pp. 111–136, Jan. 1989.
- [79] G. Pascale, A. Di Leo, and V. Bonora, "Nondestructive Assessment of the Actual Compressive Strength of High-Strength Concrete," *Journal of Materials in Civil Engineering, ASCE*, vol. 15, no. 5, pp. 452–459, 2003.

Heat Activated Prestressing of $\text{Ni}_{48.46}\text{Ti}_{36.03}\text{Nb}_{15.42}$ Shape Memory Alloy for Active Confinement of Concrete Sections

R. Suhail¹, G. Amato², J.F. Chen³ and D. McCrum⁴

¹⁻⁴ School of Planning Architecture and Civil Engineering, Queen's University Belfast, Belfast, BT9 5AG, Northern Ireland

Email: rsuhail01@qub.ac.uk, j.chen@qub.ac.uk, g.amato@qub.ac.uk, d.mccrum@qub.ac.uk

ABSTRACT: This paper presents the results from the experimental investigation on *heat activated prestressing* of Shape Memory Alloy (SMA) wires for active confinement of concrete sections. Active confinement of concrete is found to be much more effective than passive confinement. Active confinement achieved using conventional prestressing techniques faces many obstacles due to practical limitations. A class of smart materials that has recently drawn attention in civil engineering is the shape memory alloy which has the ability to undergo reversible hysteretic shape change known as shape memory effect. The shape memory effect of SMAs can be utilized to develop a convenient prestressing technique for active confinement of concrete sections. In this study a series of experimental tests are conducted to study thermo-mechanical behaviour of $\text{Ni}_{48.46}\text{Ti}_{36.03}\text{Nb}_{15.42}$ (wt. %) SMA wires. Although, numerous studies on active confinement of concrete using NiTiNb SMA have been carried out in the past, no particular study on $\text{Ni}_{48.46}\text{Ti}_{36.03}\text{Nb}_{15.42}$ exists in the literature. A series of tests were conducted in this study to characterize the material properties of $\text{Ni}_{48.46}\text{Ti}_{36.03}\text{Nb}_{15.42}$ for active confinement of concrete sections. Parameters such as *heat activated prestress* (HAP), residual strain and the range of strain that can be used for effective active confinement after HAP were investigated in detail. The influence of pre-strain and temperature on HAP was also investigated. It was found that a significant amount of HAP can be developed in pre-strained $\text{Ni}_{48.46}\text{Ti}_{36.03}\text{Nb}_{15.42}$ upon heating, most of which is retained at room temperature. A substantial amount of strain recovery upon unloading and after heating was recorded in all tests. The range of strain available for effective active confinement was also found to be significant. The results from this study demonstrate that the chemical composition of NiTiNb along with level of pre-strain and the corresponding transformation temperature range significantly affects the HAP, which in turn can affect the efficacy of the retrofitting strategy in which NiTiNb is used as a means to apply active confinement.

KEY WORDS: Shape memory alloys, Heat activated prestressing, Active confinement of Concrete.

1 INTRODUCTION

Reinforced concrete (RC) buildings are probably the most popular choice of construction around the world for ease of construction and economic reasons. However, many RC buildings have exhibited poor performance during past earthquakes such as 1999 Kocaeli (Turkey) earthquake [1] and 2008 Wenchuan (China) earthquake [2]. One of the main reasons being most earthquake resistant design codes were only developed and implemented after the 1970's. Reinforced concrete buildings built prior to 1970's were designed to carry only gravity loads. These 'gravity load only' designed buildings possess many inherent deficiencies to withstand strong ground motions for example, inadequate shear strength and ductility of columns, inadequate shear strength of beam-column joint core, insufficient lap-splice length of rebars in plastic hinge zone and insufficient anchorage of beam rebars framing into the joint core. Without retrofitting, these deficiencies pose a significant fatality hazard and may lead to partial or complete collapse of buildings during strong earthquakes.

Over the past few decades, the importance of retrofitting these buildings has increased many folds. Many retrofitting strategies have been developed during the past few decades.

Most of them oriented to increase ductility of these buildings. The majority of these retrofitting strategies fundamentally involve confining structural elements. Traditionally, concrete or steel jacketing has been employed to confine concrete section at key locations. As an alternative to concrete and steel jacketing, fibre reinforced polymer (FRP) composite materials introduced in late 1980's also provide an easy to apply and light weight means to confine and reinforce RC sections. However, either of these techniques provide only passive confinement i.e., the confining pressure is developed only when the concrete starts to dilate upon loading. Conversely, if the confining pressure is applied before the application of the load, known as active confinement, the strength and ductility of the member can be further enhanced.

The concept of active confinement has been studied in the past by many researchers. Yamakawa et al. [3] investigated active confinement of concrete using prestressed aramid fiber belts and reported that active confinement of concrete contributes significantly to increasing the shear strength, axial load carrying capacity and restraint to circumferential strain of concrete. Moghaddam et al. [4] used prestressed metal strips to actively confine concrete prismatic and

cylindrical specimens. Their experimental work demonstrated a significant increase in strength and ductility of actively confined concrete sections. However, in spite of encouraging results from these works, applying these active confinement retrofitting techniques to the real structures using conventional mechanical pre-stressing methods faces many obstacles due to a number of practical limitations.

A class of smart materials that has recently drawn attention in active confinement strategies are the Shape Memory Alloys (SMAs). SMAs belong to a group of smart materials which have the ability to undergo large deformations with minimum residual strain, a behaviour known as *pseudoelasticity* or *superplasticity* (SE). SMAs also have the ability to undergo reversible hysteretic shape change known as *shape memory effect* (SME).

SMAs in general offer a wide range of possible application in civil engineering. This study focuses only on application of SMAs in active confinement of concrete sections. Several researchers [5-8] have studied active confinement of concrete using SMAs and reported a significant enhancement in the strength and ductility of retrofitted sections. A brief overview of the thermo-mechanical properties of SMAs is given in the next section.

2 THERMO-MECHANICAL FEATURES OF SMAs

SMAs have two distinct phases, each with different crystalline structure. The phases stable at low temperatures and high stresses is called *martensite* phase (M-phase) and the phase stable at high temperature and low stresses is called *austenite* phase (A-phase). The associated transformation from one phase to another results from reversible shear lattice distortion [9] and forms the basis of the unique behaviour of SMAs. A schematic explanation of phase transformation is given in the Figure 1.

The mechanical properties of SMAs are highly dependent on the temperature and the phase in which it is used. There are four characteristic temperatures associated with the phase transformation. SMAs in M-phase begin to transform into A-phase when the temperature is increased beyond *austenite start temperature* (A_s); complete transformation from M-phase to A-phase takes place only when temperature is increased beyond *austenite finish temperature* (A_f). Once in A-phase SMAs behaves as *pseudoelastic* material and recovers most of the deformation upon unloading, see Figure 1(c).

Similarly, if the temperature of A-phase SMAs is reduced below *martensite start temperature* (M_s), phase transformation from A-phase to M-phase starts to take place. A complete transformation from A-phase to M-phase takes place only when temperature is reduced below *martensite finish temperature* (M_f). In this phase, SMAs retain majority of the deformation upon unloading (See Figure 1(b)). A more elaborated explanation on this behaviour can be found elsewhere [9, 10].

If a sufficient mechanical load is applied to SMAs in the M-phase or the intermediate phase between M-phase and A-phase, a considerable amount of strain is retained upon unloading. A subsequent heating of the SMA results in a significant amount of strain recovery; leaving behind only a minimal residual strain. However, if the strain recovery is

restrained by anchoring the ends of SMAs a considerable amount of prestress can be generated in SMAs. This phenomenon can be conveniently utilised for actively confining concrete sections.

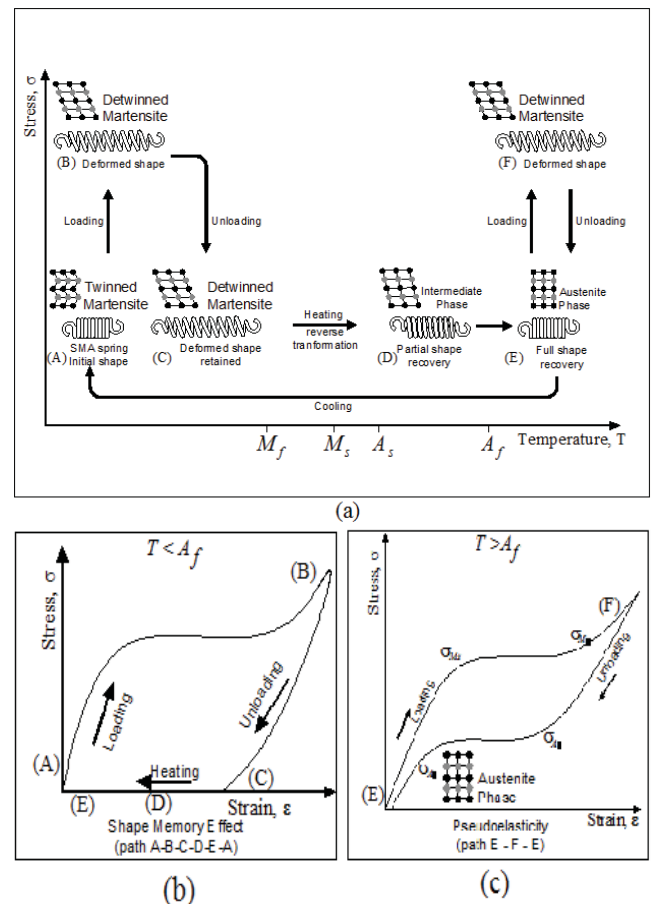


Figure 1. (a) Schematic of the one way shape memory effect (path A-B-C-D-E-A) and pseudoelasticity (path E-F-E) of an SMA spring; (b) stress-strain curve of SMA in M-phase; and (c) stress-strain curve of SMA in A-phase. Excerpts from [11].

3 EXPERIMENTAL PROGRAM

The behaviour of SMAs is complex and depends on a number of parameters. Depending upon the alloying elements, SMAs exhibit different behaviour in different conditions and are highly sensitive to variation in temperature, phase in which it is used, loading pattern and pre-strain conditions. Existing studies on active confinement of concrete sections using SMAs have shown that not all SMAs are suitable for this application. For active confinement, the phase transformation temperatures of SMAs needs to be such that the pre-strain required to cause reverse transformation is retained at room temperature. The transformation temperatures of SMAs depend not only on the alloying elements but also on the proportions in which they are combined. Among the existing group of SMAs, NiTiNb has been found to be the most suitable SMA for active confinement. Further, many different compositions of NiTiNb has been studied in the past. It has been found that different compositions of NiTiNb can have significantly different behaviour. In this project $\text{Ni}_{48.46}\text{Ti}_{36.03}\text{Nb}_{15.42}$ wires

are used as a material for active confinement of non-seismically designed reinforced concrete sub-assemblies. No detailed study on $\text{Ni}_{48.46}\text{Ti}_{36.03}\text{Nb}_{15.42}$ could be found in the literature. Therefore, a detailed thermo-mechanical characterization of NiTiNb was required before using it for the actual retrofitting.

This paper presents some results obtained from heat activated pre-stress tests conducted on $\text{Ni}_{48.46}\text{Ti}_{36.03}\text{Nb}_{15.42}$ wire specimen specimens.

4 HEAT ACTIVATED PRE-STRESS TESTS

4.1 Material Specifications

The chemical composition of NiTiNb used in this study was provided by the supplier and is given in Table 1.

Table 1. Chemical composition of SMAs used in this study (values given in % of weight)

Ti	Ni	Nb	C	N	H	O
36.03	48.46	15.42	0.039	0.004	0.001	0.042

The initial transformation temperatures of undeformed NiTiNb wire obtained from differential scanning calorimetry (DSC) tests were also provided by the supplier and are given in Table 2.

Table 2. Transformation temperature of $\text{Ni}_{48.46}\text{Ti}_{36.03}\text{Nb}_{15.42}$ used in this study ($^{\circ}\text{C}$)

M_f	M_s	A_s	A_f
-100	-78.79	-22.0	3.5

4.2 Test Setup

All $\text{Ni}_{48.46}\text{Ti}_{36.03}\text{Nb}_{15.42}$ (hereafter referred to as NiTiNb only unless the exact composition is necessary to mention) wire specimens used in this study were tested on a Zwick Roell universal testing machine. The machine was installed with a 100kN load cell having an accuracy of $\pm 0.02\%$ of the applied load between the range of 0-5kN. Several types of grips were tried to anchor the NiTiNb wires. Although direct slippage was prevented using wedge type grips, it was impossible to prevent minor slippage due to the embedment of the grip teeth in the wire specimen. Therefore, average strain measurement using crosshead travel data was discarded. Instead, strain was measured using noncontact single camera video extensometer or, in some cases, single Linear Variable Differential Transformer (LVDT) attached to the specimen. The details of the test setup are shown in Figure 2.

Two different techniques were used for heating the NiTiNb wire specimens. In the first instance, a 20 Amp DC current was passed through the wire specimen. However, due to heat loss through end grips and LVDT clamps attached to the wire, using this technique the temperature was raised only up to 100-120 $^{\circ}\text{C}$. Further increase in current to 40 Amp would have raised health and safety issue and therefore, this method was discarded. In the second approach the specimens were heated using fan heaters supplemented with a heat gun. This method was preferable as the heating process in the final application is also planned

to be carried out using heat gun. The temperature of the wire specimens was recorded using Type-T thermocouple attached directly to the surface of the specimens as shown in Figure 2.

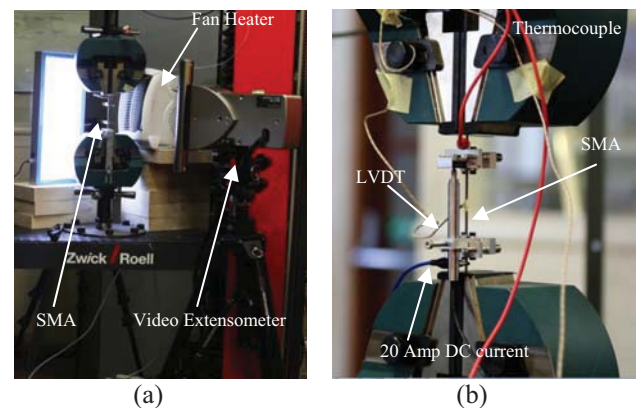


Figure 2. Test setup for thermo-mechanical tests of $\text{Ni}_{48.46}\text{Ti}_{36.03}\text{Nb}_{15.42}$ wire specimens. (a) Video extensometer used for measuring strain; heating carried out using fan heater and heat gun. (b) LVDT used for measuring strain; heating carried out using 20Amp DC current.

4.3 Test Plan

Results from three different types of tests viz. Test -1, Test-2 and Test -3 are presented in this paper. The tests were carried out to study parameters such as *heat activated prestress* (HAP), residual strain and the range of strain that can be used for effective active confinement after HAP. The influence of pre-strain and temperature on HAP was also investigated. $\text{Ni}_{48.46}\text{Ti}_{36.03}\text{Nb}_{15.42}$ wire of 2 mm diameter was used for all the tests. In the first test (Test-1), the wire specimen was pre-strained, heated above the austenite finish temperature and immediately unloaded after heating. In the second and the third tests (Test-2 and Test-3), specimens were loaded cyclically after heating. The cyclic loading of wire specimens after heating was carried out to determine the range of strain that could be used for active confinement.

NiTiNb specimens in Test-1 and Test-3 were pre-strained by 6% while in the Test-2 the specimen was pre-strained by 2.25%. NiTiNb wire used in the Test-2 was reused in Test-3 to investigate the behaviour of reused NiTiNb specimen.

4.4 Test Results

Test -1

In Test-1, the NiTiNb wire specimen was loaded to 6% strain (path A-B-C in Figure-3) and then unloaded to zero stress level (path C-D). Both loading and unloading were carried out in strain controlled manner at a strain rate of 0.003/sec. A gauge length of 50 mm was adopted in all the tests.

A yield stress equal to 638 MPa and a maximum stress of 733 MPa (Point C in Figure 3) were recorded before unloading. Once the specimen was unloaded to zero stress state (Point D in the Figure 3), heating was carried out in two stages keeping both ends of the specimen anchored throughout the heating process.

In the first stage of heating, the specimen was heated using two 2000 Watt fan heaters (up to point M in Figure 4)

up to 125°C. Since an increasing trend in HAP was observed, it was decided to keep increasing the temperature. A supplementary heating was provided using a 2000 watt heat gun. The wire heating was stopped at 230°C (Point E in Figure 4) after a plateau in the stress vs temperature plot (Figure 4) was observed. The wire was then allowed to cool down naturally to the room temperature.

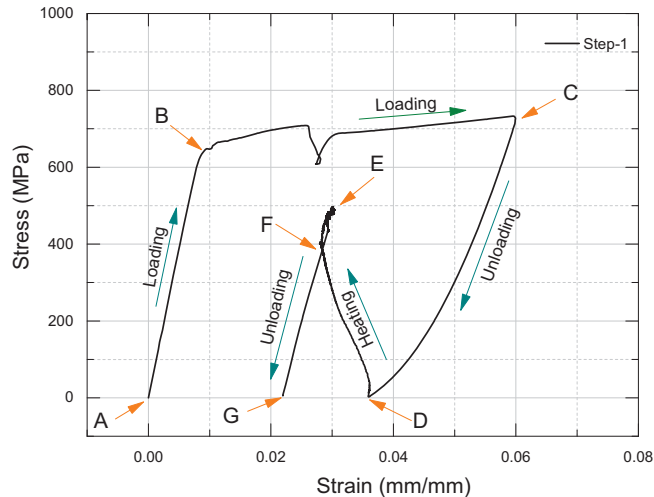


Figure 3. Stress vs strain obtained from Test-1

The max HAP achieved during the heating process was 498 MPa. On cooling to room temperature, a slight reduction in HAP was observed. HAP retained at room temperature was 438 MPa.

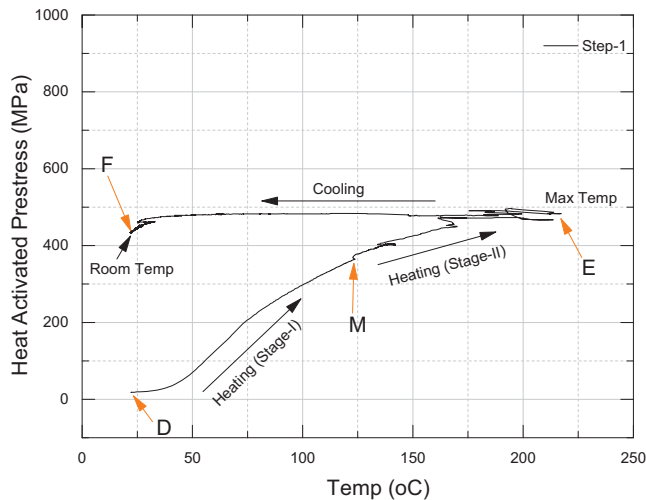


Figure 4. HAP vs temperature obtained from Test-1

Once the material cooled down to the room temperature (Point F in Figure 3 and Figure 4), the specimen was held in place for 1 hour to observe any HAP loss at room temperature. An insignificant HAP loss was observed during this time indicating HAP is only temperature dependent and no short term creep effect was observed. However, long term creep effect should be investigated separately. The specimen was then unloaded and a residual strain of 2.1% was recorded (Point G in the Figure 3). HAP recorded in the wire specimen during the heating and cooling process is plotted in Figure 3 (path D-E-F) and Figure 4 (path D-E-F).

Test-2

In Test-2 the SMA wire was pre-strained by 2.25% and then unloaded as shown in Figure 5 (path A-B-C-D). A yield stress equal to 608 MPa was measured and the specimen was unloaded at a stress of 638 MPa (point C in Figure 5).

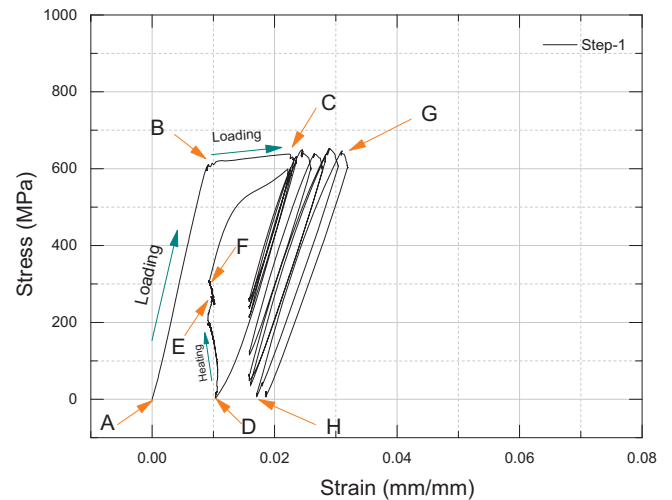


Figure 5. Stress vs strain obtained from Test-2

Once unloaded, the wire was heated in the same way as in Test-1. Upon heating, the HAP produced in the wire kept increasing until a temperature of 153°C was reached, it then decreased linearly until heating was stopped at 215°C as shown in Figure 6.

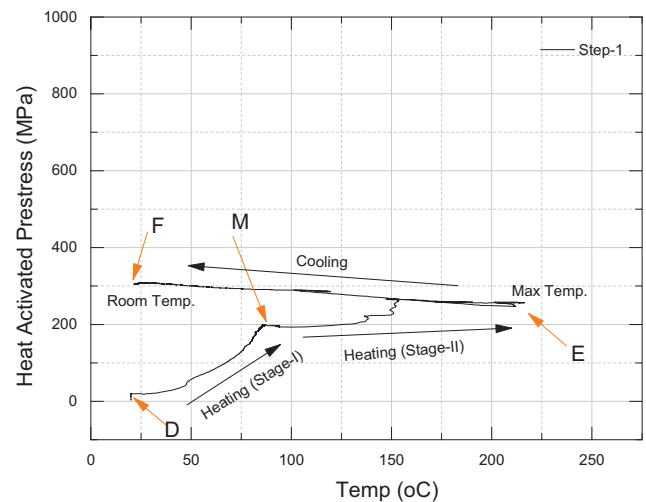


Figure 6. HAP vs temperature obtained from Test-2

The behaviour of NiTiNb wire shown in Figure 6 was found different from Test-1, in which the HAP gradually increased until a max value was achieved. Unlike in Test-1, on cooling, the wire specimen in Test-2 showed a gradual increase in HAP from 253 MPa at max temperature to 306 MPa at 25°C. After cooling, the wire was left undisturbed at room temperature for about 1 hour, no major change in HAP was observed during that time. The wire specimen was then cyclically loaded to study the response of prestressed NiTiNb wire under cyclic loading. The cyclic loading was carried out in such a way that unloading was always restricted to strain of 1.5% as shown in Figure 5. This was done to simulate a hypothetical situation in which

NiTiNb wire confining a concrete section would be restricted to contract beyond the actual cross-section of the concrete. The cyclic loading was ended when the stress level at unloading reached zero (corresponding to a strain value of about 1.66%), see point H in Figure 5. The difference in the strain between Point D and Point H in Figure 5 provides the range of strain for which HAP can be effectively used for active confinement. This range in Test-2 was 0.66%.

Test-3

Wire specimen used in Test-2 was reused in Test-3. The specimen was pre-strained by 6% (path A-B-C in Figure 7) and then unloaded to zero stress level (path C-D) in Figure 7.

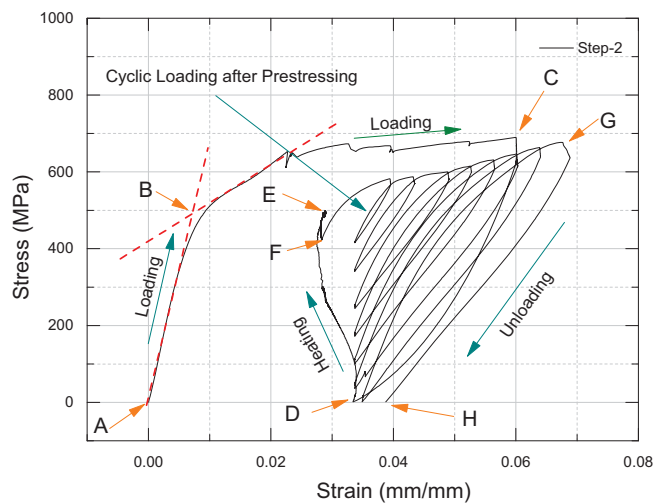


Figure 7. Stress vs strain obtained from Test-3

The yield stress of the specimen used for Test-3 was 491 MPa, see Figure 7. This reduction of yield stress was consistent with other tests performed afterwards. The yield stress was determined as shown in Figure 7 as the stress value of point B. It is worth noting that the stress vs strain plot shown in Figure 7 corresponds to loading in Test-3 only and does not include the residual strain equal to 1.82% measured at the end of Test-2.

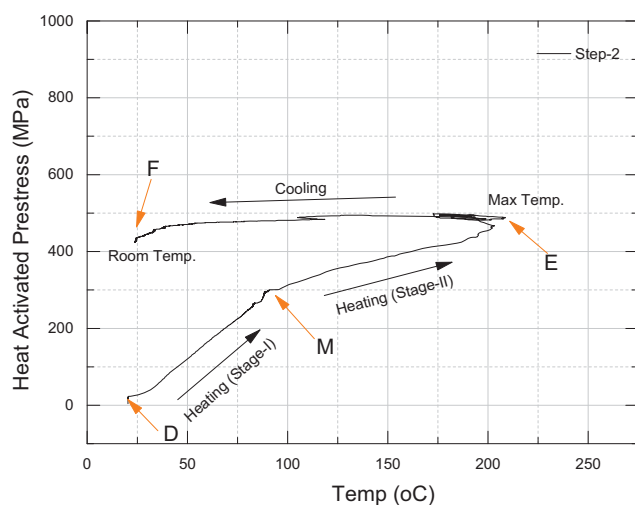


Figure 8. HAP vs temperature obtained from Test-3

Once the specimen was unloaded to zero stress state (Point D in the Figure 7), the specimen was heated in two stages in the same way as in Test-1 and Test-2. Heating was stopped at about 215°C. The max HAP achieved during heating process was recorded equal to 495 MPa at 200°C. On cooling the wire to room temperature, a slight reduction in HAP was observed. The HAP retained at room temperature was 427 MPa. HAP recorded in the wire specimen during heating and cooling process is plotted in Figure 7 (path D-E-F) and Figure 8 (path D-E-F).

After the heating and cooling process, the wire specimen was cyclically loaded as shown in Figure 7. Unloading in each cycle was restricted to strain value corresponding to Point D in Figure 7. The amplitude of each loading cycle was increased incrementally until HAP reduced to zero upon unloading. The range of strain between Point G and Point D in Figure 7 was recorded equal to 3%. This strain range can be effectively used to confine concrete actively. Beyond this strain range, the confinement will act as passive confinement.

5 DISCUSSION

With an austenite finish temperature (A_f) of 3.5°C, the Ni_{48.46}Ti_{36.03}Nb_{15.42} wire specimens were expected to behave *pseudoelastically* at room temperature which ranged between 17°C and 25°C. However, a significant amount of residual strain was retained after unloading the specimens from point C in all the tests; indicating the shift in the phase transformation temperatures. A similar behaviour in Ni_{47.45}Ti_{37.86}Nb_{14.69} was found by Choi et. al [7]. During the tests non-uniform reduction in cross-sectional area was observed in all the specimens' up to the strain of 6%, implying that *detwining* in Ni_{48.46}Ti_{36.03}Nb_{15.42} takes place in the bands of small lengths distributed non-uniformly along the length. When heated, these bands transform back to austenite phase and lead to strain recovery.

The maximum HAP recorded in Test-1 and Test-3 specimens, both pre-strained by 6%, was 498 MPa and 495 MPa respectively, while as HAP measured in Test-2 in which specimen was pre-strained by 2.25% was recorded only 308 MPa. HAP appears thus to be directly influenced by the amount of pre-strain. HAP measured in $\text{Ni}_{48.46}\text{Ti}_{36.03}\text{Nb}_{15}$ in this study was found to be substantially greater than HAP measured in $\text{Ni}_{47.45}\text{Ti}_{37.86}\text{Nb}_{14}$ [7].

The loss in the HAP on cooling was equal to 60 MPa (12%) in Test-1 and 68 MPa (13.7%) in Test-3. On the contrary, in the Test-2 the HAP increased by 53 MPa (20.9%) on cooling. Since the room temperature varied between tests, the HAP retained at 25°C in Test-1 and Test-3 both being pre-strained by same amount were compared to eliminate the influence of temperature. In Test-1 HAP at 25°C was 452 MPa while as in the Test-3 HAP of 436 MPa was recorded at 25°C. A difference of 16 MPa at 25°C can be found between the two tests.

In Test-1 the elastic strain recovered upon unloading was equal to 2.4% and the residual strain retained before the heating and cooling process was 3.6% (strain between Point A and D). In Test-3, the elastic strain recovered upon unloading was 2.67% and the residual strain retained was 3.33%. The slight increase in elastic strain recovery and a

slight decrease in residual strain recovery of the Test-3 specimen may be attributed to the influence of the loading history during Test-2. Loading history appears to affect not only the HAP but also the yield stress. A reduction of 119 MPa in the yield stress was observed when the NiTiNb was reused in Test-3.

A residual strain of 2.1% after HAP was recorded in Test-1. This strain may be regarded as permanent unrecoverable plastic strain in the specimen. During the heating process, some amount of strain was recovered (path D-E in Figure 3) within the gauge length. Similar trend was observed in Test-2 and Test 3 (path D-E in Figure 5 and 7). This strain recovery may be due to rearrangement at microscopic level. Since the grip to grip distance was kept fixed while heating, the strain recovery within the gauge length indicates non-uniform contraction and extension of individual hypothetical bands along the length of the specimens as discussed above.

The ability to develop HAP in NiTiNb can be conveniently used to actively confine concrete sections. As discussed above a significant portion of HAP produced in NiTiNb is retained at room temperature. In the practical applications, if the pre-strained NiTiNb wires are wrapped and anchored around the concrete section; with a simple heating procedure a significant amount of active confining pressure can be applied quite easily. In this study a 6% pre-strain is found to produce a significant amount of prestressing force however, depending upon the nature of applications different pre-strain levels can be tried. A detailed discussion on the influence of HAP and pre-strain level will be presented separately.

It is important to note that once a section that is actively confined with NiTiNb is cyclically loaded, depending on the level of strain imparted in the loading cycle, HAP is reduced upon unloading. Implying that HAP in NiTiNb for next loading cycle will be less than that in the previous cycle. The reduction in HAP with the increase in strain level in the loading cycle continues until it is completely lost. Beyond this point NiTiNb confinement will act as mere passive confinement. In order to determine the range of strain within which NiTiNb confinement will effectively apply active confining pressure, NiTiNb specimens in Test-2 and Test-3 were cyclically loaded and unloaded until the HAP became zero. The range of strain for which the HAP was found effective was about 3% in Test-3 corresponding to pre-strain value of 6%. A range of 3% can significantly contribute in enhancing ductility and strength of concrete sections.

6 CONCLUSIONS

Three different types of tests have been conducted on $\text{Ni}_{48.46}\text{Ti}_{36.03}\text{Nb}_{15}$ wire specimens to assess its suitability for active confinement of concrete members in engineering structures. The results presented in this paper show that:

- The chemical composition of SMA is an important aspect to consider while choosing the type of SMA for active confinement.
- Pre-strain can significantly influence the level of HAP achieved in SMAs.
- $\text{Ni}_{48.46}\text{Ti}_{36.03}\text{Nb}_{15}$ can be used in wide variety of applications in civil engineering. It offers a convenient option for applications involving pre-stressing. It can be

easily employed for effective active confinement of concrete members in engineering structures.

- HAP of about 500 MPa can be achieved in $\text{Ni}_{48.46}\text{Ti}_{36.03}\text{Nb}_{15}$ SMA when pre-strained by 6%. About 450 MPa of which is retained at 25°C. With this range of HAP, $\text{Ni}_{48.46}\text{Ti}_{36.03}\text{Nb}_{15}$ can be used to significantly increase the ductile and the strength of a poorly detail reinforced concrete member.
- A substantial amount of strain recovery is observed in $\text{Ni}_{48.46}\text{Ti}_{36.03}\text{Nb}_{15}$ wires. About 2.5% elastic strain recovery upon unloading from 6% strain level is observed. In the specimen pre-strained by 6%, a total of 4% strain is recovered when unloaded after heating.
- A 6% pre-strain in $\text{Ni}_{48.46}\text{Ti}_{36.03}\text{Nb}_{15}$ can avail a strain range of 3% for effective confinement after HAP. This range of strain can significantly enhance the ductility and strength

ACKNOWLEDGEMENTS

Financial support received from Queen's University Belfast in the form of a PhD studentship for the first author is gratefully acknowledged. The authors would also like to thank the technical support staff at Queen's University Belfast for their assistance.

REFERENCES

- [1] El-Amoury, T., and A. Ghobarah (2002). 'Seismic rehabilitation of beam-column joint using GFRP sheets' *Engineering Structures* 24.11, 1397-1407.
- [2] Zhao, B., Taucer, F. & Rossetto, T., (2009), 'Field investigation on the performance of building structures during the 12 May 2008 Wenchuan earthquake in China. *Engineering Structures*', 31(8), 1707-1723.
- [3] Yamakawa, T., Banazadeh, M., & Fujikawa, S. (2005), 'Emergency retrofit of shear damaged extremely short RC columns using pre-tensioned aramid fiber belts', *Journal of Advanced Concrete Technology*, 3(1), 95-106.
- [4] Moghaddam, H., Samadi, M., Pilakoutas, K., & Mohebbi, S. (2010), 'Axial compressive behavior of concrete actively confined by metal strips; part A: experimental study', *Materials and Structures*, 43(10), 1369-1381.
- [5] Andrawes, B., Shin, M., & Wierschem, N. (2009), 'Active confinement of reinforced concrete bridge columns using shape memory alloys', *Journal of Bridge Engineering*, 15(1), 81-89.
- [6] Park, J., Choi, E., Park, K., & Kim, H. T. (2011), 'Comparing the cyclic behavior of concrete cylinders confined by shape memory alloy wire or steel jackets', *Smart Materials and Structures*, 20(9), 094008.
- [7] Choi, E., Chung, Y. S., Kim, Y. W., & Kim, J. W. (2011), 'Monotonic and cyclic bond behavior of confined concrete using NiTiNb SMA wires', *Smart Materials and Structures*, 20(7), 075016.
- [8] Chen, Q., Shin, M., & Andrawes, B. (2014), 'Experimental study of non-circular concrete elements actively confined with shape memory alloy wires', *Construction and Building Materials*, 61, 303-311.
- [9] Lagoudas, D. C. (Ed.). (2008). Shape memory alloys: modeling and engineering applications', *Springer Science & Business Media*.
- [10] Otsuka, K. (Ed.) (1999) Shape Memory Materials, Cambridge University Press.
- [11] Suhail, R., Amato, G., Chen, J. F., and McCrum, D. (2015), 'Potential applications of shape memory alloys in seismic retrofitting of exterior RC beam-column joints. In *Proceedings for SECED 2015 Conference: Earthquake Risk and Engineering towards a Resilient World*. The Society for Earthquake and Civil Engineering Dynamics. Cambridge, United Kingdom, 9-10 July.
- [12] Takagi T, Sutou Y, Kainuma R, Yamauchi K, & Ishida K (2006), 'Effect of prestrain on martensitic transformation in a $\text{Ti}_{46.4}\text{Ni}_{47.6}\text{Nb}_{6.0}$ superelastic alloy and its application to medical stents', *Journal of Biomedical Materials Research. Part B, Applied Biomaterials*, 76(1): 179-83.

An Assessment of Reinforced Concrete Members in Tension Strengthened with Near Surface Mounted CFRP Strips

Andrew Meehan¹, Kieran Ruane^{1,2}

¹Department of Civil, Structural & Environmental Engineering, Cork Institute of Technology, Bishopstown, Cork, Ireland

²RPS Group Ltd., Innishmore, Ballincollig, Co. Cork, Ireland
email: andrew.meehan@mycit.ie, kieran.ruane@rpsgroup.com

ABSTRACT: The strengthening of structural elements by bonding Near Surface Mounted (NSM) Fibre Reinforced Polymer (FRP) strips and bars with epoxy resin into grooves cut in the concrete cover is an emerging technique which has recently attracted world-wide interest. FRP materials are well suited for applications in strengthening owing to their favourable properties such as their high stiffness and strength. However, existing knowledge on the technique is limited and this is reflected by the absence of relevant design guidance in existing international codes. In this regard there is a need for further research into the area. The experimental programme developed for this study involved the design and testing of six reinforced concrete beams in flexure that were strengthened using the NSM technique. The test beams were taken to failure under two monotonically increasing point loads. The section of the beam under the neutral axis, located between the two point loads was considered to be in tension. Three different sizes of Carbon Fibre Reinforced Polymer (CFRP) strip measuring 10 x 3mm; 15 x 2.5mm and 20 x 2.5mm were used for strengthening. Enhancement ratios of 2.3 times the moment capacity of an unstrengthened member were recorded for the study. The results further indicate that a doubly strengthened beam offers approximately one third extra capacity over a member that is strengthened using a single CFRP strip of similar dimensions. The 3D nonlinear finite element (FE) model developed from the experimental data can accurately simulate the structural behavioural responses of a CFRP-strengthened reinforced concrete member in flexure, under applied loading. It is concluded that strengthening reinforced concrete members with NSM CFRP strips significantly enhances the tensile and flexural capacities of the structural element.

KEY WORDS: NSM reinforcement; CFRP strips; Flexural strengthening; LUSAS; 3D nonlinear finite element analysis.

1 INTRODUCTION

The retro strengthening of structural members using externally bonded (EB) steel bars started circa 1949 in Sweden, where the method was used to strengthen bridge girders in flexure [3]. More recently the NSM technique of bonding FRP rods, bars and strips into grooves cut in the concrete cover has been introduced. This relatively new technique has many practical applications in the retro strengthening of ageing infrastructure and heritage structures. However, existing knowledge on the technique is limited and this is reflected by the absence of relevant design guidance in existing international codes [3].

Favourable properties of FRPs include their resistance to corrosion; easy and rapid installation; high fatigue resistance and the fact that there is minimal change in structural geometry when this type of strengthening system is used. Compared to the externally-bonded (EB) method, the NSM technique using CFRP strips has several advantages [1]; the CFRP/epoxy/concrete bond is enhanced by application of the epoxy to three surfaces in the groove, as opposed to one surface for the former method. The rectangular shape of the material and slot also help to improve the bond through the action of shear forces under applied loading [2]. Due to the fact that NSM FRP-composites are installed in grooves in the concrete cover of the structural member, they are more protected from damage by fire; accidental impact and vandalism than externally-bonded FRP strengthening systems. It is also easier to anchor NSM strengthening systems into adjacent structural members, in order to prevent problems arising due to debonding [1]. A comprehensive literature

review has been written by the author on the topic of NSM FRP [3].

In this paper the increase in capacity of reinforced concrete beams offered by strengthening the test specimens with CFRP strips using the NSM technique and subjected to flexure, is investigated. Three different sizes of carbon fibre reinforced polymer (CFRP) strip measuring 10 x 3mm, 15 x 2.5mm and 20 x 2.5mm were used. One type of concrete and one type of epoxy resin were tested. Laboratory tests were carried out up to failure under two monotonically increasing point loads. The tests focused on the increase in tensile capacity of the beams and failure mode of the test specimens. The section of the beam under the neutral axis, located between the two point loads was considered to be in direct tension at fibre level. The experimental results were compared with the results from nonlinear 3D Finite Element (FE) models of the test beams that were developed from the experimental results using LUSAS finite element analysis software.

2 EXPERIMENTAL PROGRAMME

2.1 Materials

A single type of strengthening strip was used: pultruded carbon fibre reinforced polymer (CFRP) with dimensions of 10 x 3 mm; 15 x 2.5 mm and 20 x 2.5 mm. The tensile strength and modulus of elasticity of the CFRP strips were obtained through laboratory testing and measured 1524 MPa and 156,000 MPa, respectively. One type of concrete was studied. 20 concrete test cubes (100 x 100 x 100 mm) were

cast from the same concrete as poured for the beams. The compressive strength, tensile strength and elastic modulus of the concrete were measured at 7 days; 14 days and on each of the 4 days of beam testing. The cubes were struck after 24 hours and stored in a curing tank that was kept at a constant temperature of 20° C, until needed for strength testing through crushing. One type of filling material, a two part epoxy resin, was used. Table 1 shows the tensile strength of the epoxy resin at 7 days and the mechanical properties of the concrete at various stages throughout testing. The tensile strength of the concrete was obtained from its compressive strength using standard Eurocode formulae [3].

Table 1. Mechanical properties of concrete and epoxy.

Material	Curing time (days)	Compressive strength (MPa)	Tensile strength (MPa)	Elastic modulus (GPa)
Epoxy	7	-	3.4	-
Concrete	7	29.7	2.9	32.8
Concrete	14	34.5	3.2	33.9
Concrete	32	35.7	3.3	34.2
Concrete	33	35.8	3.3	34.3
Concrete	34	36.7	3.3	34.5
Concrete	35	37.9	3.4	34.7

2.2 Test procedure and preparation

A total of seven 3m long steel reinforced concrete beams, with 150 x 280mm rectangular cross-section, were cast. All beams were air cured for a minimum of 28 days after striking the formwork. The area of tensile steel reinforcement provided in the test beams was marginally less than that required for a 'balanced' reinforcement ratio and as such, the beams may be described as being slightly 'under-reinforced'. The steel

reinforcement details for a single beam are shown in Table 2. The modulus of elasticity and yield strength of the reinforcing steel were determined through laboratory testing and measured 630 MPa and 210,000 MPa, respectively.

Table 2. Steel reinforcement details.

Bar type	Diameter (mm)	Number Of bars	Bar shape	Reinforcement designation
H12	12	2	straight	tension
H10	10	2	U-bar	compression
H8	8	12	Link	shear

The test beam configuration; dimensions; test setup; loading arrangement and steel reinforcement/CFRP strengthening details are shown schematically in Figure 1.

Installation of the CFRP strips was achieved by cutting grooves with specified dimensions into the concrete cover in the longitudinal direction, at the tension side of the beam. The grooves ran the full length of all of the strengthened beams. A wall chasing tool equipped with two diamond edged cutting blades was used to cut the grooves. The remaining concrete lugs were then removed using an angle grinder. The grooves were then cleaned using a power washer and a wire brush in order to remove any debris and fine particles to ensure proper bonding between the epoxy resin and the concrete. The grooves were filled to half way with the epoxy and the CFRP strips were then placed inside and pressed down. The groove was then filled with more epoxy and the surface was levelled off. The beams were left to cure for one week to ensure the filling material had reached adequate strength. Each beam was instrumented with a numerical displacement gauge to measure the mid-span deflection. Strain gauges were placed on the tension steel reinforcement; the CFRP strips and on the compression face of each beam; near to mid-span in all cases.

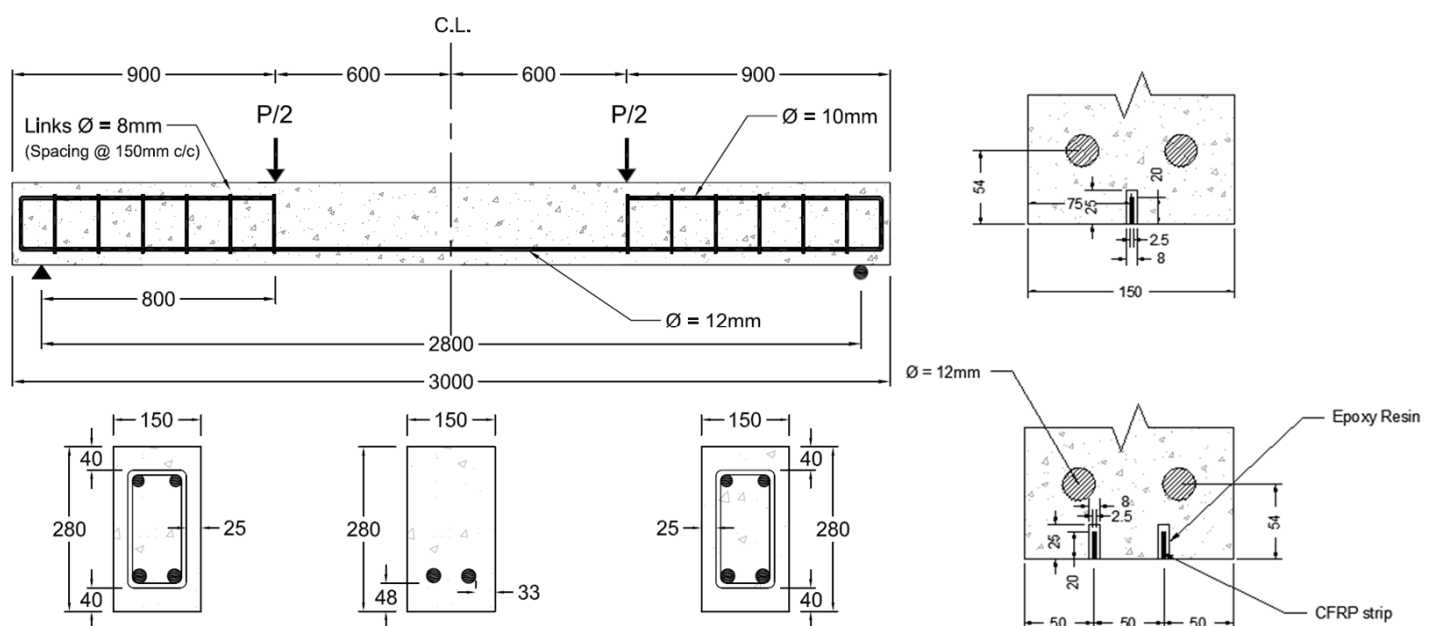


Figure 1. Test beam details and setup.

2.3 Beam strengthening details

Three of the test beams were strengthened by embedding a single CFRP strip in the epoxy resin. The three remaining doubly grooved beams were strengthened by installing two CFRP strips of similar dimensions (see Figure 2). The strips ran the full length of the beam in each case. Details of the beams tested are shown in Table 3. The laboratory test setup is shown in Figure 3.

Table 3. Matrix for the experimental programme.

Test Beam Details			
Beam I.D.	CFRP strip dims (mm)	No. of Strips	Groove dims (mm)
CB1	-	-	-
FRP10-1	10 x 3.0	1	8 x 15
FRP15-1	15 x 2.5	1	8 x 20
FRP20-1	20 x 2.5	1	8 x 25
FRP10-2	10 x 3.0	2	8 x 15
FRP15-2	15 x 2.5	2	8 x 20
FRP20-2	20 x 2.5	2	8 x 25



Figure 2. CFRP strips installed in the test beams.



Figure 3. Typical laboratory test setup.

3 EXPERIMENTAL RESULTS

The mode of failure for each of the tested beams was by concrete crushing in flexure. Figure 4 shows the load versus mid-span deflection for the six strengthened beams and the control beam.

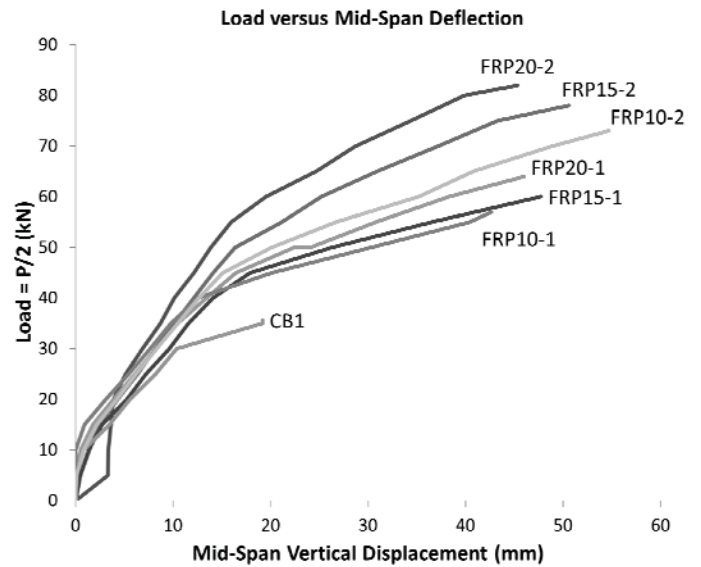


Figure 4. Load versus mid-span deflection for experiment.

3.1 Typical global behaviour

The load-deflection curve in Figure 5 illustrates the typical global behaviour of a beam strengthened with NSM CFRP strips, in flexure. As the positive bending moment increases under increasing monotonic loading, three distinct stages can be observed: 1) Elastic Stage (0-A); 2) Concrete Cracking to Steel yielding Stage (A-B); 3) Steel Yielding to Failure Stage (B-C) [1].

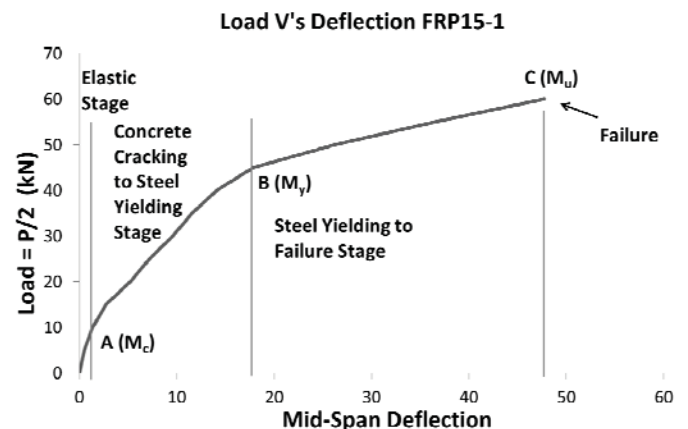


Figure 5. Typical global behaviour of strengthened beam.

3.2 Influence of size of CFRP strips

The moment capacity of the strengthened beams increased with the increase in area of CFRP used for strengthening.

Figure 6 shows the ultimate loads at failure for the test beams. The ultimate capacity of the doubly strengthened beam with the largest size of strip (FRP20-2) measured 2.3 times that of the unstrengthened control beam (CB1). The depth (i.e. I-value) of the strips also had an influence on the ultimate deflections of the strengthened beams. The study found that the difference in results for mid-span vertical displacement between singly and doubly strengthened beams using strips of similar dimensions, were not homogeneous. The differences in deflections were large for the smallest size of strips (10 x 3mm) while that for the largest size of strip (20 x 2.5mm) was negligible at just 1.4% (see Table 5).

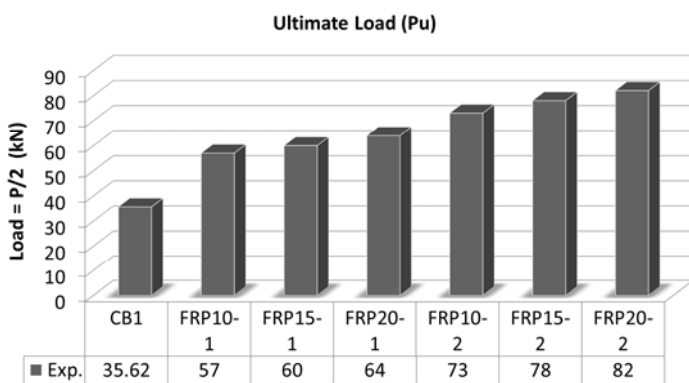


Figure 6. Ultimate loads at failure for test-beams.

3.3 Influence of number of CFRP strips

The influence of the number of CFRP strips used for strengthening was studied for all strengthened beams. The experimental results listed on Table 4 show that the moment capacities of the doubly strengthened beams were enhanced by approximately one third when compared to the beams that were strengthened with a single NSM CFRP strip, having the same anchorage length and strip dimensions.

Table 4. Increase in moment capacity for two CFRP strips.

CFRP Strip Dimensions (mm)	Ultimate Moment Capacity (M_u) (kNm)		Increase in Capacity (%)
	1 strip	2 strips	
10 x 3.0	45.6	58.4	+ 28
15 x 2.5	48.0	62.4	+ 30
20 x 2.5	51.2	65.6	+ 28

3.4 Influence of anchorage lengths

The epoxy/CFRP/concrete bond was enhanced by carrying the strengthening material over the location of the supports at the ends of the beams. The compressive forces in the shear zones acted to 'anchor' the strengthening system at the ends of the simply-supported beams, under applied loading. In this regard the likelihood of failure by debonding or through slippage of the CFRP strip was minimised. This enhanced the chances of the test specimens failing in flexure and thus utilising the full capacities of the CFRP strips. However, in practice it is not

always possible to anchor the strengthening system in this manner, owing to obstructions by structural elements such as columns.

4 FINITE ELEMENT MODELLING

4.1 FE Modelling Particulars

A programme of nonlinear finite element (FE) modelling using LUSAS version 15.0 FE analysis software was undertaken. A total of seven 3D models were developed based on the materials; dimensions and loading/support conditions of the experimental test specimens. A perfect bond was assumed between the steel reinforcing bars and the concrete; the epoxy resin and the concrete and the epoxy resin and the CFRP strips. Nonlinear concrete and steel properties were assigned to the model. The LUSAS 'Multi crack (model 94)' was used to simulate the plastic behaviour of the concrete. Linear properties were assigned to the CFRP material as it remains in the elastic range up to failure [3]. The modelling assumptions made agree with other work in the area [3].

4.2 Elements and meshing

HX20 hexahedral volume mesh with a quadratic interpolation order was used to model the concrete and the steel support plates. The HX20 volume elements have 20 nodes per element and 3 degrees of freedom at each node. The steel reinforcing bars and CFRP strips were modelled using 3D bar elements. These have 2 nodes per element and 3 degrees of freedom at each node. As the primary area of interest for beam analysis lies between the two point loads, a denser mesh was used in this area of the model. A convergence test was carried out to determine the optimum mesh density [3]. The finished 3D model comprised of approximately 1,300 elements.

4.3 3D FE model geometry

For economy of computer processing time, a quarter-sized 3D beam model was developed. Beam symmetry was modelled by applying supports in the x and z directions on the surface of the beam cross-section at mid-span. The model was also supported along the longitudinal surface in the z-direction to simulate symmetry along the width of the beam. Vertical support in the global Y-direction was then applied along the centre-line of the steel support plate, on the soffit of the beam. Figure 7 shows the deflected shape of the fully meshed 3D model under applied loading.

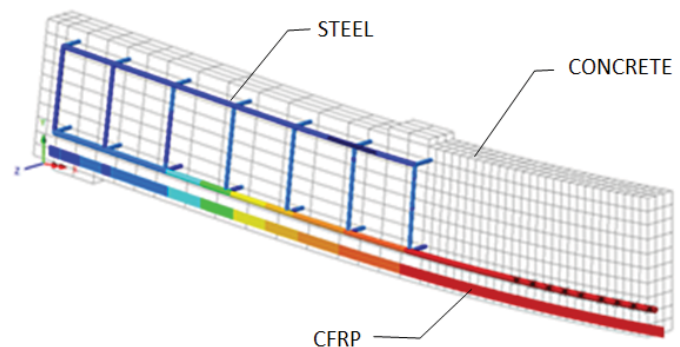


Figure 7. Deflected shape of the 3D LUSAS model.

Table 5. Comparison of significant experimental and numerical results.

Beam ID	M_c (kNm)		Diff. (%)	M_y (kNm)		Diff. (%)	M_u (kNm)		Diff. (%)	Δ (mm)		Diff. (%)	Overall Diff. (%)
	Exp.	FE		Exp.	FE		Exp.	FE		Exp.	FE		
CB1	5.20	4.80	- 7.7	26.40	27.60	+ 4.3	28.50	28.64	+ 0.5	19.80	17.40	- 12.1	12.1
FRP10-1	5.12	4.80	- 6.2	34.20	34.24	+ 0.1	45.60	48.00	+ 5.0	42.63	53.90	+ 20.9	20.9
FRP15-1	5.20	4.80	- 7.7	36.80	36.64	- 0.4	48.00	49.92	+ 3.8	47.73	46.00	- 3.6	7.7
FRP20-1	5.44	4.80	- 11.8	33.40	36.00	+ 7.2	51.20	52.64	+ 2.7	45.97	44.00	- 4.3	11.8
FRP10-2	5.44	4.80	- 11.8	40.80	42.40	+ 3.8	58.40	61.60	+ 5.2	54.68	49.00	- 10.4	11.8
FRP15-2	5.12	4.80	- 6.2	42.40	44.80	+ 5.3	62.40	62.40	0.0	50.59	42.00	- 17.0	17.0
FRP20-2	5.36	4.80	- 10.4	49.60	49.04	- 1.1	65.60	66.40	+ 1.2	45.31	37.00	- 18.3	18.3

Acronyms: M_c = Concrete cracking moment; M_y = Steel yielding moment; M_u = Ultimate moment at failure;
 Δ = Deflection at mid-span; Diff. = percentage difference between experimental and 3D FE results

4.4 Loading

A line load of 6.667×10^{-3} N/m in the negative y-direction, was applied along the centre-line of the loading plate, in order to simulate a load of $P/2 = 1$ N over the 150mm width of the beam. The load was applied at a distance of 600mm from mid-span. LUSAS 'nonlinear' loading was then applied to the model for analysis, with a starting factor of 5000N to simulate a 5kN load. This was followed by 500N increments (i.e. for $P/2$) until non-convergence of the model occurred and the beam was deemed to have failed.

5 FE RESULTS AND DISCUSSION

The results of numerical analysis for the 3D LUSAS FE models show good agreement with the results for the experimental beams. A comparison of the significant numerical and experimental results is presented in Table 5. As with the experimental specimens, each of the seven models failed by concrete crushing in flexure (see figure 9). The ultimate loads results (P_u) for the models were within 5.2% of the test-beam results (see Figure 10). As shown in Figure 8, the 3D FE results for deflection also showed good agreement with the experimental results. The difference between FRP10-2 and 3D FE deflections was just 2.7%. The FE results for concrete cracking moment (M_c), steel yielding moment (M_y) and ultimate moment (M_u) were within 11.8% of the experimental values. Overall, the deflection results from numerical analysis were within 20% of those for the experiment where, except for FRP10-1, the LUSAS models were slightly stiffer than their test beam counterparts.

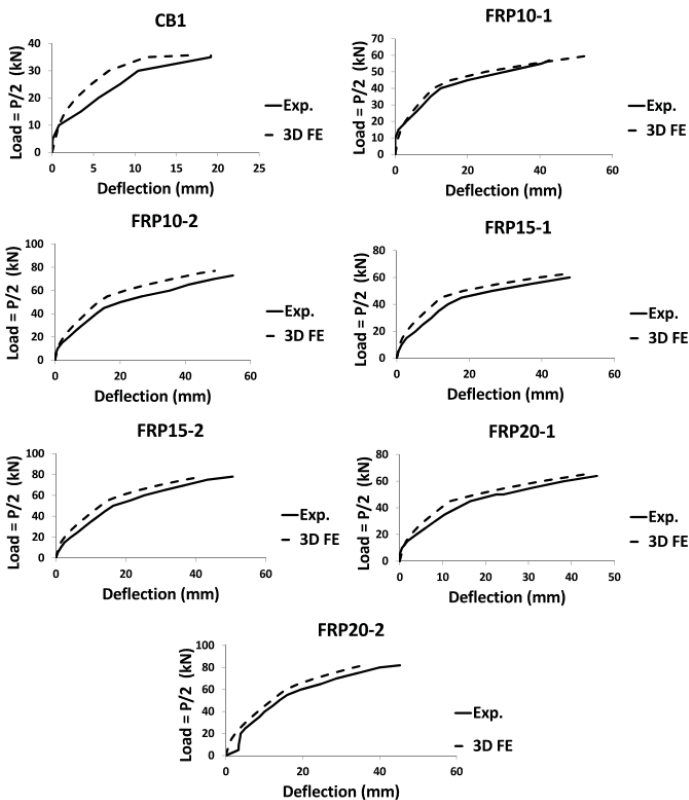


Figure 8. Load versus deflection curves for all beams.

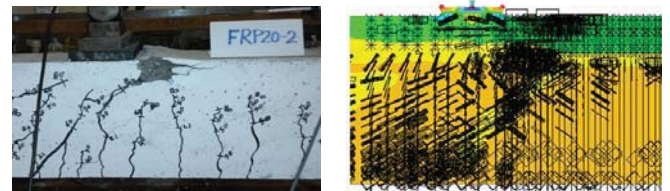


Figure 9. FRP20-2 and its numerical model at failure.

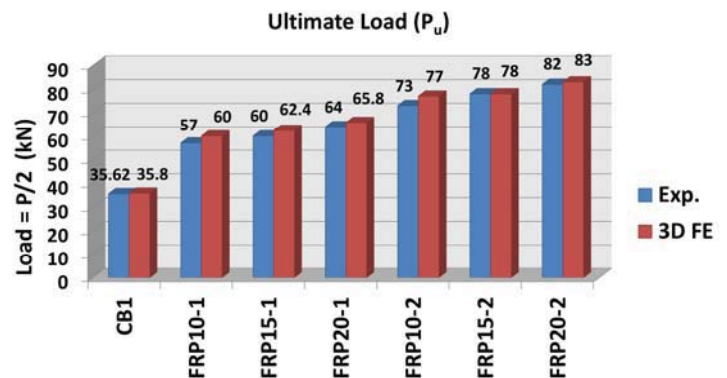


Figure 10. Ultimate loads results.

6 CONCLUSIONS

The experimental results indicate that strengthening reinforced concrete members with NSM CFRP strips significantly enhances the tensile capacity of the composite element. Enhancement ratios of 2.3 times the moment capacity of an unstrengthened member were recorded for the study. After the steel reinforcement has yielded, the NSM CFRP strips are still in the elastic range up to failure. As the loading is increased, the stiffer and well-bonded CFRP strips act as 'ties' which prevent the tensile and shear cracks from 'opening up'. This significantly enhances the tensile capacity of the member, while at the same time diminishing the vertical displacement and increasing the capacity of the beam in flexure.

A beam strengthened with two NSM CFRP strips benefits from approximately one third extra tensile and moment capacity than that recorded for a beam of the same size which is strengthened with a single NSM CFRP strip, having the same anchorage length and strip dimensions. The epoxy/CFRP/concrete bond is enhanced by carrying the strengthening material over the location of the supports at the ends of the beam. This is as a result of the compressive forces acting to 'anchor' the strengthening system in the shear areas of the simply-supported beam, under applied loading. In this regard the likelihood of failure by debonding or through slippage of the CFRP strip is minimised.

The deflection results for beams strengthened with one and two NSM CFRP strips of the same dimensions are not always homogeneous, as the width of the strip (i.e. I-value) has an influence on the outcome. The study found that the difference in results for deflection in this regard were large for the smallest size of strips (10 x 3mm); while the results were more agreeable for the intermediate-sized strips (15 x 2.5mm) and the difference between the deflection results for the singly and doubly strengthened beams with the largest width of strip (20 x 2.5mm) was negligible at just 1.4%. The results show that all of the strengthened beams deflected over twice as much as the unstrengthened beam, with FRP10-2 having the largest vertical deflection at 54.68mm. This value is 2.76 times that of the control beam (see Table 5).

The 3D LUSAS FE numerical model that was developed for the project is able to accurately track the tensile stresses and strains in the constituent materials of the composite beam which are in the tensile zone under the neutral axis, under applied monotonic loading. The model can also accurately predict the values for concrete cracking moments; steel yielding moments; ultimate moment capacities and beam deflections in flexure, up to failure. There is very good agreement between the 3D numerical and experimental results for the study, in all cases. The model also simulates the method of failure experienced by the experimental beams in flexure. In this regard it is a useful tool for carrying out further analysis and parametric studies on reinforced concrete beams strengthened with NSM CFRP strips.

The power regression equation that was produced on MS Excel from the experimental results (see Appendix A) may be used for parametric studies without the need to carry out additional laboratory testing.

ACKNOWLEDGMENTS

The authors would like to thank Mr Jim Morgan and Mr Liam Jones for their assistance with the laboratory testing, Mr Terry Broderick from SIKA, Ireland, for donating the CFRP materials and John A. Woods Ltd. for donating the concrete for the tests. The research reported in this paper was conducted as part of the taught MEng (Structural Engineering) programme at Cork Institute of Technology.

APPENDIX A

A.1. Enhancement ratio formula for parametric study

A trend line based on the experimental results was produced using MS Excel (see Figure 11). The equation for estimating the enhancement in flexural capacity of a NSM CFRP-strengthened 3m long beam with a cross-section of 150 x 280mm, that is reinforced in the tension-zone with two 12mm diameter steel bars is:

$$ER = ax^b \quad (1)$$

where:

ER = the enhancement ratio (i.e. Ultimate strengthened capacity / Ultimate unstrengthened capacity);

X = CFRP Area / Steel Area;

a = 0.68

b = 0.33

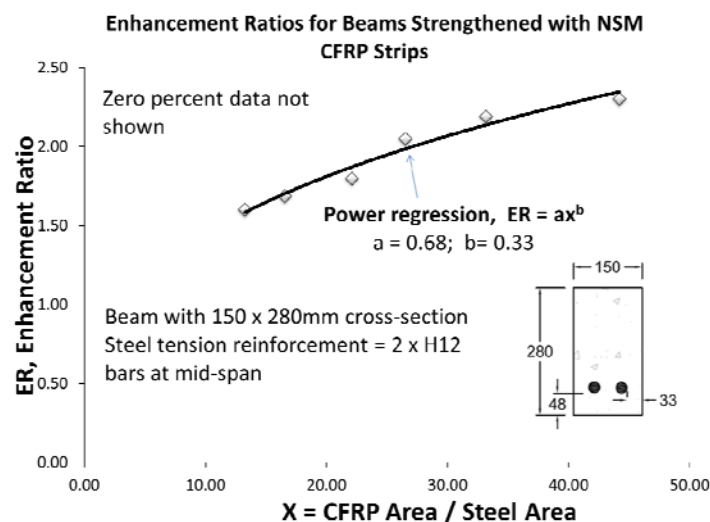


Figure 11. Enhancement ratio curve.

REFERENCES

- [1] Al-Mahmoud, F., Castel, A., François, R. and Tourneur, C. (2009) 'Strengthening of RC members with near-surface mounted CFRP rods', *Composite Structures*, vol. 91, no. 2, pp. 138–147 [Online] DOI: 10.1016/j.compstruct.2009.04.040.
- [2] Lorenzis, L. de and Teng, J. G. (2006) 'Near-surface mounted FRP reinforcement: An emerging technique for strengthening structures', *Composites: Part B*, vol. 38, pp. 119–143 [Online]. Available at www.elsevier.com/locate/compositesb (Accessed 20 April 2015).
- [3] Meehan, A. (2015). *An assessment of reinforced concrete members in tension strengthened with near-surface-mounted (NSM) carbon-fibre-reinforced polymer (CFRP) strips*, MEng thesis, Cork Institute of Technology, Ireland.

Horizontal Interface Shear Requirements for Precast Prestressed Concrete Bridge Beams with Slender Webs in Beam and Slab Bridge Constructions

Michael Slevin¹, Alan O'Connor²

¹Banagher Precast Concrete, Queen Street, Banagher, Offaly, Ireland

²Department of Civil, Structural and Environmental Engineering, Trinity College Dublin, College Green, Dublin 2, Ireland
email: michael.s@banconcrete.com, oconnoaj@tcd.ie

ABSTRACT: In Ireland and the United Kingdom precast prestressed concrete bridge beams are commonly used in small to medium sized highway and railway bridges, i.e. 20m-50m spans. Over the past ten years the majority of these bridges have been built using W-beams, a U shaped precast prestressed concrete bridge beam. When combined with a cast insitu deck slab they form a composite section that must be able to resist the horizontal shearing forces developed at the interface between the two elements. Interface shear requirements are generally more onerous than flexural shear when determining reinforcement ratios and this has become quite a contentious issue for bridge engineers in recent years with differing clauses in the design codes. This paper presents work which will form part of a PhD research project examining the performance of several full scale W1 beams statically and dynamically loaded using a four point loading test with varying loading and reinforcement ratios crossing the interface. The study will compare full scale beam testing to finite element analysis using midasFEA, a computer software package. The aim of the research is to propose a minimum interface shear reinforcement equation for incorporation into Eurocode 2 Part 1-1 [1]. It is recognised that a minimum percentage of reinforcement is required across the interface to prevent interfacial slip and brittle failure at loss of adhesion. Eurocode 2 Part 1-1 [1] does not presently include a minimum requirement.

KEY WORDS: Interface Shear; Prestress; Bridge Beam; Cyclic Loading; Minimum Interface Reinforcement.

1 INTRODUCTION

The research project examines the performance of sixteen 3.2m long reinforced concrete T-beams and several precast prestressed W1 bridge beams statically and cyclically loaded using a four point loading test with the loading and reinforcement crossing the interface the varying parameters. The interface roughness and concrete strength will not vary. The study will also investigate the appropriateness for setting the cohesion factor c equal to zero for fatigue and dynamic verifications as per clause 6.2.5(105) of Eurocode 2 Part 2 [2]. The reasoning behind which is to do with on-site issues such as dust, dirt and possibly laitance on the interface which is not cleaned off prior to the deck being cast. A more onerous reason behind setting the cohesion factor c equal to zero is the possibility of a breakdown of the interface over time as it is subjected to repeated loading and unloading during the lifetime of a bridge (120 years). The result of which amounts to an increase in interface shear reinforcement of approximately 20%. Since the introduction of the Eurocodes designers have been using the coefficient of cohesion based on clause 6.2.5 of Eurocode 2 Part 1-1 [1] and using their own views on clause 6.2.5(105) of Eurocode 2 Part 2 [2] as there is not enough information in the code specifically for precast prestressed bridge beams with cast on deck slabs. Section 6.8 of Eurocode 2 Part 2 [2] states that a fatigue verification is generally not necessary for prestressed steel in regions where under the frequent combinations of actions compressive stresses occur at the extreme concrete fibres. The national annex to Eurocode 2 Part 2 [2] also contains a clause that if the slab acts compositely with the supporting beams or webs then the structural element does not require a fatigue verification. For the majority of bridge structures this is the

case and thus can omit the designer from having to carry out a fatigue check.

The finish on the cast against concrete surface is a very important factor in calculating the interface shear strength. Eurocode 2 Part 1-1 [1] and the CEB-FIP Model Code [3] classify the different applicable types of finishes into four categories, very smooth (cast against a steel or timber form), smooth (left as cast), rough (exposing the aggregate or raking the concrete) and very rough (shear key or indented concrete surface). Depending on the finish of the cast against concrete the two parameters, friction (μ) and cohesion (c) are then calculated. For a typical twenty meter spanning W-beam used on a highway bridge the interface shear links when designed to Eurocode 2 Part 1-1 [1] can be at less than 100mm centres, the width of the interface can be as short as 250mm so placing concrete in and around these links is quite difficult (see figure 2) let alone trying to achieve a rough surface finish. The codes always specify a maximum stirrup spacing but a minimum stirrup spacing should also be considered. From industry experience 100mm is manageable anything less is extremely cumbersome in order to produce a high quality finished product.

2 RESEARCH OBJECTIVES

Three major objectives have been defined for this research study:

1. Carry out a literature review of the state of the art on interface shear, particularly regarding static and dynamic loading and a comparison with other recognised bridge design standards.

2. Propose a minimum interface shear reinforcement requirement for Eurocode 2 Part 1-1 [1] based on the testing undertaken. It is recognised that a minimum percentage of reinforcement is required across the interface to prevent interfacial slip and brittle failure at loss of adhesion. Eurocode 2 Part 1-1 [1] does not presently include a minimum requirement. The proposal will involve a review of the other design standards and the database of test results along with experimental testing as part of the project. Recent bridge projects in Ireland and the United Kingdom have used the CEB-FIP Model Code [3] recommendations for minimum interface shear reinforcement.
3. From the conclusions reached with the testing undertaken, to propose a set of values for the coefficient of cohesion based on the fatigue loading of a rough finished concrete interface.

3 PREVIOUS RESEARCH

3.1 Shear Friction Theory

The shear friction theory is used in all of the major bridge design codes, for example BS5400-4 [4], Eurocode 2 Part 1-1 [1], American Concrete Institution Building Code ACI 318 [5] and CEB-FIP Model Code [3] for designing the reinforcement required crossing the longitudinal interface between concrete members cast at different times. In this case a precast prestressed concrete bridge beam with a cast insitu top slab. Figure 1 shows a rectangular concrete block with a cracked interface which has also slipped, this is known as the saw-tooth model and was initially developed around 1960 to predict the longitudinal shear strength of concrete interfaces with the following four parameters considered:

1. Compressive strength of the weakest concrete
2. Normal stress at the interface
3. Shear reinforcement crossing the interface
4. Roughness of the interface substrate

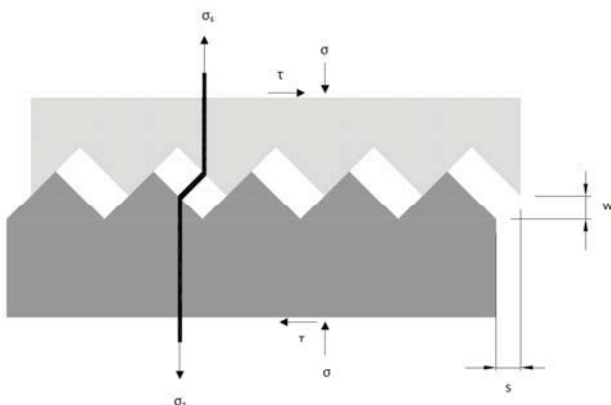


Figure 1. Saw Tooth Model representing the Shear Friction Theory (Source – Santos and Júlio [6])

Birkeland and Birkeland [7] stated that the external shearing loads tend to produce a slippage of the member along an axis, usually at an interface. This slippage is resisted by friction resulting from the external clamping force. If reinforcement is present along the interface this reinforcement will provide an external clamping force on the concrete. This reinforcement has to be anchored on both sides of the interface for it to be effective. The reinforcement then becomes stressed in tension as a direct result of the slippage of the concrete, known as dowel action, and this tension provides an external clamping force on the concrete resulting in compression across the interface, resulting in shear stresses to be transferred by shear friction.

The literature review identified several milestones of the shear friction theory from 1960 to the present date which are summarised in table 1.

Table 1. Shear Friction Theory Milestone Equations.

Author	Year	Equation	Note
Birkeland and Birkeland [7]	1966	$v_u = \mu \rho f_y$	Original equation
Mattock and Hawkins [8]	1972	$v_u = 1.38 + 0.8(\rho f_y + \sigma_n)$	Contribution of Cohesion
Loov [9]	1978	$\frac{v_u}{f_c} = k \sqrt{\frac{\rho f_y + \sigma_n}{f_c}}$	Concrete Strength Added
Walraven, Frenay [10]	1987	$v_u = C1(\rho f_y)^{0.2}$	Based on a Spherical Model
Randl [11]	1997	$v_u = c f_c^{1/3} + \mu(\rho k f_y + \sigma_n) + \alpha \rho \sqrt{f_y f_c}$	Cohesion, Friction and Dowel Action all considered

where; (in order of appearance in above calculations)

v_u = ultimate longitudinal shear stress at the interface

μ = coefficient of friction

ρ = the reinforcement ratio

f_y = reinforcement yield strength

f_c = concrete compressive strength

$k = 0.5$ for composite construction and 0.6 for monolithic construction Loov [9]

σ_n = normal stress acting on the interface due to external loading

$C1 = 0.822 f_c^{0.406}$

$C2 = 0.159 f_c^{0.303}$

c = coefficient of cohesion, 0.4 for rough surface and 0 for smooth surface - Randl [11]

$k = 0.5$ for rough surface and 0 for smooth surface -Randl [11]

$\alpha = 0.9$ for rough surface and 1.5 for smooth surface - Randl [11]

3.2 Minimum Interface Reinforcement

Currently Eurocode 2 Part 1-1 [1] does not have a minimum percentage of interface reinforcement requirement, it is recognised that a minimum percentage of reinforcement is required across the interface to prevent interfacial slip and brittle failure at loss of adhesion. BS5400-4 [4] and the CEB-FIP Model Code [3] have similar requirements for which the majority of bridge designers use in the present day. The push-off tests carried out by Hughes [12] resulted in differing minimum interface reinforcement compared to the 0.15% recommendation of BS5400-4 [4]. Simply the amount of minimum interface reinforcement should equate to 0.5 N/mm², 0.85 N/mm² and 1.5N/mm² for monolithic, roughened and rough as cast surfaces respectively. However BS5400-4 [4] deals with interfaces in beams and the push-off test specimens do not represent these beams accurately enough to increase the minimum percentage of interface reinforcement from 0.15% (0.72N/mm²) for the push-off test specimens. If reinforcement is required across the interface to satisfy the design shear stress then a minimum percentage of reinforcement is required along the remainder of the interface where the interface shear stress is less than the interface shear stress resistance without interface shear reinforcement. Randl [13] came up with an equation after performing extensive testing and was adopted in the 2010 version of the CEB-FIP Model Code [3].

Table 2. Minimum Interface Reinforcement Equations.

Author	Year	Equation	Note
Hughes [12]	1987	0.5N/mm ² 0.85N/mm ² 1.5N/mm ²	For Monolithic, Roughened and Rough as Cast
BS5400-4 [4]	1990	0.15%bh	
Eurocode 2 Part 1-1 [1]	2004	N/A	
CEB-FIP Model Code [3]	2010	$0.2 f_{ctm}/f_{yk} \geq 0.001$	
Randl [13]	2013	$0.2 f_{ctm}/f_{yk} \geq 0.001$	
American Concrete Institution Building Code ACI 318 [5]	2014	Max of (a) and (b) $0.062 \sqrt{f_c} \frac{b_w s}{f_y} \quad (a)$ $0.35 \frac{b_w s}{f_y} \quad (b)$	

3.3 Fatigue or Dynamic Verifications

The general consensus amongst bridge designers is that clause 6.2.5(105) of Eurocode 2 Part 2 [2] is not required to be used for short span highway and railway bridges. Reducing the coefficient of cohesion c to zero increases the amount of shear reinforcement crossing the interface to unmanageable levels. Figure 2 shows the end of a precast prestressed W beam with 12mm links at 100mm centres using a c value of 0.4 as per clause 6.2.5(2) of Eurocode 2 Part 1-1 [1]. This is a very high ratio of stirrups, reducing c to zero would mean 12mm links at

80mm centres, an increase of 20%. Reducing c to zero also results in the design shear resistance of the interface without stirrups being equal to zero when designing to Exp(6.25) of Eurocode 2 Part 1-1 [1] or Exp(7.3-50) of CEB-FIP Model Code [3], which basically says that the longitudinal shear stress capacity for concrete at the interface is neglected. According to Randl [13] the shear resistance of concrete interfaces subjected to fatigue loading has not been investigated in a comprehensive way. Randl [13] states that the most important thing to consider is will there be a crack along the interface. If the shear resistance of the interface is greater than the shear stress acting on it then the answer is unlikely and there is no requirement for shear reinforcement according to CEB-FIP Model Code [3] and Eurocode 2 Part 1-1 [1]. Chung and Chung [14] were one of the first to carry out dynamic testing in 1976. They concluded that fatigue failure of the interface joint is not probable if the repeated load is not more than 55% of the ultimate static load or if the horizontal shear stress at the interface does not exceed 2.75N/mm². That is an extremely high figure considering BS5400-4 [4] for a 40N/mm² concrete and type 1 interface surface is approximately 0.9MPa, Eurocode 2 Part 1-1 [1] for a similar concrete strength and rough interface is 0.56MPa and CEB-FIP Model Code [3] for a similar concrete strength and very rough interface is 0.7MPa. Therefore the decline in interface shear capacity without shear reinforcement from 1976 to present day has increased considerably, what is also shown is the variety of values between the three bridge codes used by Irish and UK bridge engineers for the past twenty years. Hughes [12] carried out small scale push off tests, small scale RC T-beams and large scale precast prestressed M-beams in 1987 using both static and cyclical loading. He concluded that service stresses in bridgeworks tended to be 2.0N/mm² and that the cracking stresses of 3.0 N/mm², 2.5 N/mm² and 2.0N/mm² for monolithic, roughened and rough as cast surfaces respectively proved that the interfaces would remain uncracked at service loads. Again much higher than the capacities of the three bridge codes and closer in fact to the 2.75N/mm² of Chung and Chung [14]. Loov and Patnaik [15] carried out tests on RC T-beams in 1994 the results of which proved that the stirrups are typically unstressed and ineffective until horizontal shear stress exceeded 1.5MPa to 2.0MPa. This indicates the strength of an interface without stirrups. They did confirm that the stirrups became relatively effective when the shear stress reaches about 3MPa.



Figure 2. Interface Reinforcement close to beam ends showing a Rough Surface Finish (Source - Banagher Precast Concrete).

4 EXPERIMENTAL PROGRAMME

4.1 Test Specimens – RC T-Beams

Sixteen reinforced concrete T-Beams have been manufactured and will be tested in Trinity College and Banagher Precast Concrete during the summer of 2016. These beams will be split into four series, with each series having a monolithically poured control beam that will be tested statically to failure in order to obtain the ultimate strength. The remaining three beams in each series will be loaded dynamically for 16,800 cycles or to failure whichever comes first. If after 16,800 cycles the beams have not failed they will be statically loaded to failure.

Test series 1 beams will have no reinforcement crossing the interface. Test series 2 beams will have 10mm stirrups at 150mm centres (0.5% bh) crossing the interface and test series 3 beams will have 10mm stirrups at 300mm centres (0.25% bh) crossing the interface and test series 4 beams will have 10mm stirrups at 500mm centres (0.15% bh) crossing the interface.

The varying parameters will be the level of load and the ratio of reinforcing stirrups crossing the interface. The beams will be poured with C57/70 concrete which is synonymous with precast prestressed bridge beams and the top slabs cast twenty eight days later with C40/50 concrete which is used as standard for on-site bridge deck construction. The beams will have a rough surface finish in accordance with Eurocode 2 Part 1-1 [1] Section 6.2.5 (2) and this will be tested using the sand patch procedure. It was felt that varying these parameters would not be of any great benefit.

Table 3. Test Specimen Parameters.

Test Specimen	Repeated Load		Reinforcing Stirrups			ISF
	Min.	Max.	No.	Size	c/c's	
TB1-1	To Failure		0	0	0	M
TB1-2	10%	70%	0	0	0	R
TB1-3	10%	70%	0	0	0	R
TB1-4	10%	70%	0	0	0	R
TB2-1	To Failure		2	10	150	M
TB2-2	10%	70%	2	10	150	R
TB2-3	10%	70%	2	10	150	R
TB2-4	10%	70%	2	10	150	R
TB3-1	To Failure		2	10	300	M
TB3-2	10%	70%	2	10	300	R
TB3-3	10%	70%	2	10	300	R
TB3-4	10%	70%	2	10	300	R
TB4-1	To Failure		2	10	500	M
TB4-2	10%	70%	2	10	500	R
TB4-3	10%	70%	2	10	500	R
TB4-4	10%	70%	2	10	500	R

Note: ISF = Interface Surface Finish, M = Monolithic, R = Rough

The monolithically poured specimens will be cast and left for twenty eight days to cure before the application of load. The beams will be cast and left to cure for twenty eight days, the deck slabs will then be cast making the specimen composite.

The composite beam will be left for a further twenty eight days to cure before the application of load.

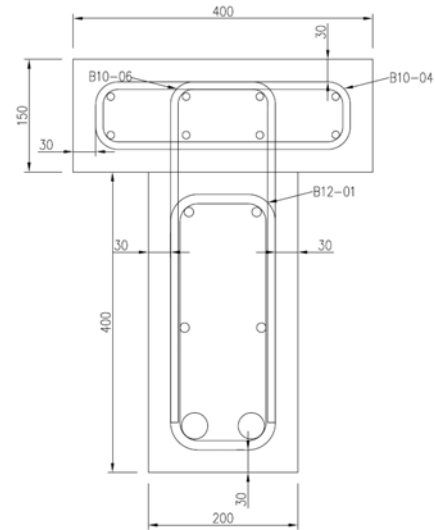


Figure 3. Section through TB2 and TB3 Test Specimens showing Reinforcement.

4.2 Test Specimens – W1-Beams

Precast prestressed concrete W1-beams will be manufactured and tested in Banagher Precast Concrete during the summer of 2017. The testing of these beams will depend on the findings of the small scale reinforced concrete T-beams. The S-N curves from the T-beam testing should provide adequate information in order to be able to test a small number of full scale W1 beams and obtain an interface failure. When these stress levels are obtained the testing frame and load cells will have to be examined to see if they have the capacity to reach these levels. Presently the variables will be load and interface reinforcement but this may change depending on the outcome of the T-beam testing.



Figure 4. Banagher Precast Concrete W Beam (Source - Banagher Precast Concrete).

4.3 Test Procedure

There will be four series of test beams with four beams per series. Each series will have a monolithically cast beam statically loaded to failure. The test will be stopped on the appearance of the first crack and the load recorded as the “cracking load”. Hughes (1987) defined the cracking load as the load which caused a 0.01mm crack of the interface. The remaining three beams per series will be cyclically loaded to 16,800 cycles or failure whichever comes first. If after 16,800 cycles the beams have not failed they will be loaded statically to failure. Chung (1976) defined fatigue failure as being a crack of 0.025mm of the interface. The beams will have an effective span of 3.0m and two point loads will be applied 500mm from each end support.



Figure 5. Beam Test Specimen prior to loading.

4.4 Cyclic Loading

The beams will be loaded with 16,800 cycles of load, the load itself will vary per beam depending on the ultimate strength of the monolithically tested control beam. The monolithically tested control beams ultimate strength will represent Load Model 1 (LM1) loading from Eurocode 1 Part 2 [16]. As per clause 4.6.2 of this code Fatigue Load Model 1 (FLM1) is equal to 70% of LM1. Therefore this will be represented in the testing and can be seen in table 3. The number of cycles is taken from Eurocode 1 Part 2 [16] and is shown Table 4. From this table it can be shown that two million commercial vehicles will cross the slow lane of a motorway bridge per year which equates to two hundred and forty million commercial vehicles during its lifespan. LM1 represents a vehicle weighing 600kN with four 150kN point loads dispersed through 400mm wide contact lengths. The test beams have 400mm wide top slabs and therefore can take half of a LM1 vehicle. From Table NA5 to IS EN 1991-2 the heaviest vehicle to use the bridge crosses it ten times per million crossings. The closest vehicle in weight to a LM1 vehicle crosses it seventy times per million crossings or 16,800 times during the life of a bridge. Based on a cycle taking 3 seconds 16,800 cycles should take approximately 14 hours.

Table 4. Indicative number of heavy goods vehicles expected per year and per lane in Ireland – (Source Table NA4 to IS EN 1991-2)

Traffic categories			Nobs per lane	
Type (see TD9/07 Table 4)	Carriageway Layout	No. of lanes per carriageway	Each slow lane	Each fast lane
Type 3 Dual	Dual	3	2,0 million/yr	1,5 million/yr

Clause 6.8.7 of Eurocode 2 Part 2 [2] states that Miners rule should be used to work out the number of cycles to be used. Using a minimum stress of 0.5MPa and a maximum stress of 4MPa the number of cycles is approximately 500,000 which is not practical for a laboratory test as it would take over 400 hours. However the finite element analysis models will be set up to run one million cycles.

4.5 Sand Patch Test

One of the major design parameters for estimating interface shear capacity is the roughness of the surface. To measure the roughness of the surface the sand patch test will be used, it is the simplest quantitative method to assess the roughness of a surface. The test itself involves spreading a known volume of fine sand (90-100% passing a 0.3mm BS Test Sieve and 0-15% passing a 0.15mm BS Test Sieve) on the surface that is being tested in a circular fashion. The sand is levelled and spread out until it is flush with the roughest part of the surface. This will result in a circular patch of sand with known diameter and volume. A simple calculation will give the mean thickness which has to be greater than 3mm to be a rough surface according to Eurocode 2 Part 1-1 [1].



Figure 6. Sand spread into circular fashion over rough surface. (Source - Banagher Precast Concrete).

5 FINITE ELEMENT ANALYSIS

Each specimen will be modelled and analysed using finite element analysis design software, midasFEA. The models will be three dimensional and will be able to predict reactions, displacements at the interface, element strains, element

stresses, reinforcement strains and reinforcement stresses (figure 8), and most importantly anticipated cracking patterns. The elements are modelled as solid mesh models split into 50mm segments. The reinforcement is modelled and also meshed. Finally the interface is modelled to represent a standalone meshed element with its own cohesion and friction properties to represent the rough surface of the composite beams and the monolithically cast beams. These properties can be altered to correctly align with the laboratory testing results. To date Eurocode 2 Part 1-1 [1] design calculations and midasFEA finite element models have been compared, see table 5 and figure 7.

Sensors have been placed on selected stirrups that cross the interface to monitor the strain in the reinforcement upon application of load, the finite element analysis has produced preliminary results which will be used as a guide whilst performing the laboratory testing. Best case the results will compare favourably without the need for any modifications to the model however this is difficult to predict at this stage and modifications to the finite element model will no doubt be required to align with the laboratory testing. Cyclic loading in the laboratory is a very time consuming process, 16,800 cycles of load is expected to take 24 hours to complete. One million cycles is a better representation of a fatigue lifetime and the only way to demonstrate this is with finite element technology. Therefore the models will need to correspond identically to the laboratory testing up to and including 16,800 cycles and supersede the laboratory testing for one million cycles.

Table 5. TB1-2 Design shear stresses as per Eurocode 2 Part 1-1 [1] compared to calculated actual shear stresses as per midasFEA

Applied Load (kN)	Shear Stress (MPa) Eurocode 2	Shear Stress (MPa) midasFEA
50	0.62	0.97
100	1.25	1.91
150	1.87	2.43
200	2.50	3.16
250	3.12	4.30

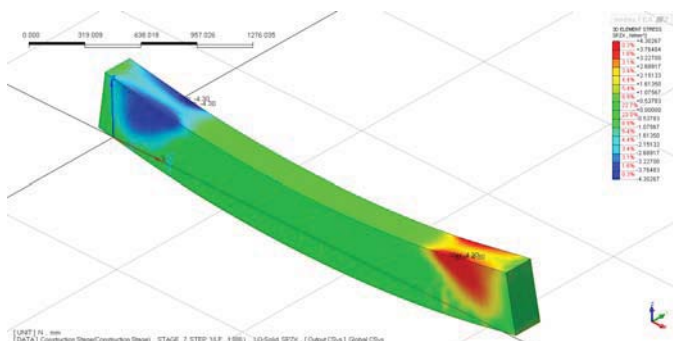


Figure 7. Output from midasFEA TB1-2 model showing the shear stress on the interface under 2No. 250kN point loads.



Figure 8. Output from midasFEA model displaying the stress in the reinforcement during the application of the 250kN loading for TB1-1.

6 CONCLUSION

At present no conclusions are available as the research has just commenced with testing due to start in summer 2016.

REFERENCES

1. Eurocode 2 Part 1-1, *Eurocode 2: Design of Concrete Structures: Part 1-1: General Rules and Rules for Buildings*. 2004: British Standards Institution.
2. Eurocode 2 Part 2, 2: *2005 Eurocode 2—design of concrete structures—Part 2: Concrete bridges—Design and detailing rules*, in *British Standard*. 2005.
3. CEB-FIP Model Code, *Model Code 2010—Final draft*, vol. 1, in *Fib Bulletin*. 2010.
4. BS5400-4, *BS5400 Part 4 Steel, concrete and composite bridges. Code of practice for design of concrete bridges*, London. British Standards Institution, 1990.
5. American Concrete Institution Building Code ACI 318, *Building code requirements for structural concrete (ACI 318-14) and commentary*. 2014. American Concrete Institute.
6. Santos, P.M. and E.N. Júlio, *Interface shear transfer on composite concrete members*. *ACI Structural Journal*, 2014. **111**(1).
7. Birkeland, P.W. and H.W. Birkeland. *Connections in precast concrete construction*. in *ACI Journal Proceedings*. 1966. ACI.
8. Mattock, A.H. and N.M. Hawkins, *Shear transfer in reinforced concrete—recent research*. PRECAST/PRESTRESSED CONCRETE INSTITUTE. JOURNAL, 1972. **17**(2).
9. Loov, R. *Design of precast connections*. in a seminar organized by Compa International Pte, Ltd. 1978.
10. Walraven, J., J. Frenay, and A. Pruijssers, *Influence of concrete strength and load history on the shear friction capacity of concrete members*. *PCI journal*, 1987. **32**(1): p. 66-84.
11. Randl, N., *Untersuchungen zur Kraftübertragung zwischen Alt- und Neubeton bei unterschiedlichen Fugenrauigkeiten*. 1997.
12. Hughes, G., *Longitudinal shear in composite concrete bridge beams*. Part, 1987. **2**: p. 97.
13. Randl, N., *Design recommendations for interface shear transfer in fib Model Code 2010*. *Structural Concrete*, 2013. **14**(3): p. 230-241.
14. Chung, H. and T. Chung. *Prestressed Concrete Composite Beams Under Repeated Loading*. in *ACI Journal Proceedings*. 1976. ACI.
15. Loov, R.E. and A.K. Patnaik, *Horizontal shear strength of composite concrete beams with a rough interface*. *PCI Journal*, 1994. **39**(1).
16. Eurocode 1 Part 2, *EN 1991-2: Eurocode 1: Actions on structures—Part 2: Traffic loads on bridges*. 2002: Brussels.

Behaviour of hybrid concrete lattice girder flat slab system using insitu structural health monitoring

Shane Newell^{1,5}, Jamie Goggins^{1,2,3,6}, Magdalena Hajdukiewicz^{1,2,3}, Dave Holleran⁴

¹ College of Engineering & Informatics, National University of Ireland, Galway, Ireland

² Ryan Institute, National University of Ireland, Galway, Ireland

³ Informatics Research Unit for Sustainable Engineering (IRUSE), National University of Ireland, Galway

⁴ Oran Pre-cast Ltd., Oranmore, Galway, Ireland

⁵ Galway-Mayo Institute of Technology, Galway, Ireland

⁶ Centre for Marine and Renewable Energy Ireland (MaREI), Galway, Ireland

email: s.newell2@nuigalway.ie

ABSTRACT: In recent decades, Structural Health Monitoring (SHM) has emerged as an increasingly important tool in Civil Engineering to understand how structures behave during construction and operation. Although SHM is not a new concept, it is only relatively recently that Civil Engineers have adopted SHM for the design, construction and management of civil engineering structures. One of the key benefits of SHM is the improved understanding of insitu structural behaviour.

This paper describes the SHM strategy implemented on a recently constructed building to monitor and record the behaviour of a hybrid concrete lattice girder flat slab floor system. Hybrid concrete construction (HCC) combines insitu and precast concrete to maximise the benefits of both forms of construction. HCC offers many advantages for both the designer and contractor and produces simple, buildable and economic structures which can result in faster, safer construction and reduced costs.

Sensors were embedded in both the precast and insitu components of the hybrid concrete floor system and are used to monitor various aspects of the behaviour of the floor during the manufacture, construction and operational phase of the building. The information from the real-time monitoring offers the opportunity to compare actual and predicted behaviour using structural codes, such as Eurocodes. The majority of the instrumentation is embedded within the structure so that long-term effects such as creep and shrinkage of concrete components can also be investigated.

KEY WORDS: Structural health monitoring; lattice girder flat slab, structural monitoring.

1 INTRODUCTION

This paper describes the implementation of a real-time structural health monitoring (SHM) scheme on a new building (Human Biology Building) under construction at the National University of Ireland, Galway (NUI Galway). This project is one of a number projects which forms part of a measurement framework strategy developed at NUI Galway to continuously monitor the structural and environmental performance of buildings during construction and operation [1, 2]. Although the building is currently under construction at the time of writing, some preliminary results from the project are presented in this paper.

A variety of sensors were embedded in the hybrid concrete floor structure of the building and are used to monitor various aspects of the behaviour of the floor during the manufacture, construction and operational phase of the building.

The overall objectives of this research project are:

- compare actual and predicted behaviour of the floor.
- analyse the long term behaviour of the floor.
- investigate construction and design parameters for potential optimisation of hybrid concrete floor system.
- develop and calibrate numerical models that predict the performance of the hybrid concrete floor system.

1.1 Structural Health Monitoring

SHM can be defined as ‘the use of *in-situ*, non-destructive sensing and analysis of structural characteristics, including the structural response, for purposes of estimating the severity of the damage and evaluating the consequences of the damage on

the structure in terms of response, capacity, and service-life [3]. Although the majority of SHM is related to civil infrastructure, in recent decades, it has emerged as an increasingly important tool in civil engineering for monitoring deterioration in concrete structures and predicting the future performance of structural components [4, 5]. It generally consists of continuous or periodic monitoring of a structure using sensors that are either embedded in it or attached to its exterior [6].

One of the key benefits of SHM is the improved understanding of insitu structural behaviour. The majority of design codes have been developed following research conducted in engineering laboratories where it can be very difficult to replicate the behaviour of real structures insitu. Consequently, testing and analysis is typically conducted on small-scale specimens which only partially represent the overall structure. SHM can be used to provide rich information on how real structures behave when subject to actual structural and environmental loads.

2 HUMAN BIOLOGY BUILDING

The Human Biology building (HBB) is a four storey building over basement and roof level plant enclosure with a gross floor area of 8200m² (Figure 1). This facility will encompass three schools; Anatomy, Physiology & Pharmacology and Therapeutics. The building will be a teaching and research facility with lecture theatres, laboratories, offices and meeting rooms. Construction commenced in January 2015 and the expected construction period is 19 months (July 2016). It is

anticipated that the building will achieve an A rating under the Commercial Energy Rating marking scheme and a BREEAM Excellent rating.



Figure 1. Human Biology Building (under construction)

The HBB is primarily constructed using precast concrete elements, including the building frame, twinwall system, hybrid concrete lattice girder slabs and hollowcore slabs, which were designed, manufactured and installed by Oran Pre-Cast Ltd.

2.1 Hybrid concrete lattice girder flat slab

Presently, the structural frame is substantially complete and external cladding and internal fit-out has commenced. The majority of the floor structure is 400mm thick and is constructed using a two-way spanning hybrid precast concrete lattice girder flat slab system. This consists of a 65mm thick precast lattice girder plank (Figure 2) and 335mm in-situ concrete topping. The lattice girder truss which protrudes from the plank provides stiffness in the temporary state and increases composite action with the in-situ structural concrete topping. The main bottom floor reinforcement is contained within the precast concrete plank and the top layer of reinforcement is placed on site along with a layer of stitching reinforcement across the joint between slabs, prior to pouring the insitu concrete topping. The precast planks are temporarily propped until the structural concrete topping has reached the required compressive strength.

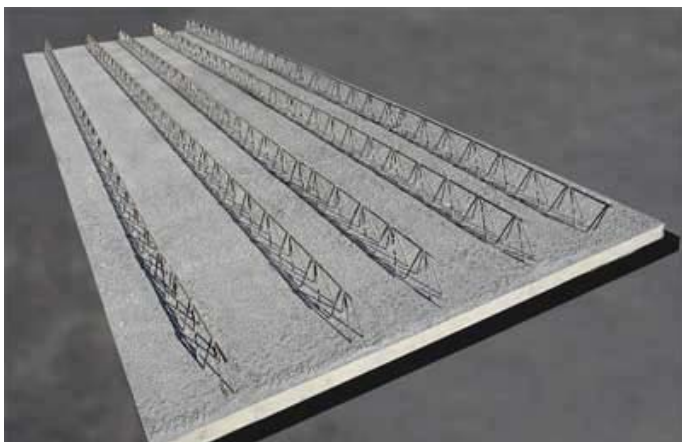


Figure 2. Precast Concrete Lattice Girder Plank(© Oran Pre-cast Ltd.)

Flat slabs are one of the most widely used forms of floor construction providing minimum structural depths, fast construction and uninterrupted service zones. Transportation and site handling limitations generally dictate the allowable sizes of the precast planks. The use of steel moulds results in a high-quality finish, which can be left exposed if required. The quality of the factory produced soffits also provides the opportunity to take advantage of the thermal mass properties of the concrete slab by exposing them. The main advantages of this floor system to the contractor are in terms of programme, reduction in steel fixing and formwork requirements on site.

The precast plank was manufactured using a C40/50 concrete mix with a CEM II A-V cement (370kg/m³ typically or 425kg/m³ if self-compacting concrete used). The mix design for the insitu concrete topping was C30/37 with 230kg/m³ of CEM I cement and 100kg/m³ of GGBS (i.e. 30%).

3 INSTRUMENTATION

3.1 Instrumentation

The SHM strategy implemented in the HBB used a number of sensors embedded in the floor structure to monitor the environmental and structural behaviour of the hybrid concrete lattice girder flat slab. Two zones in the second floor of the HBB were selected for instrumentation using a combination of vibrating-wire (VW) strain gauges, electrical resistance (ER) strain gauges and thermistors (Figure 3).

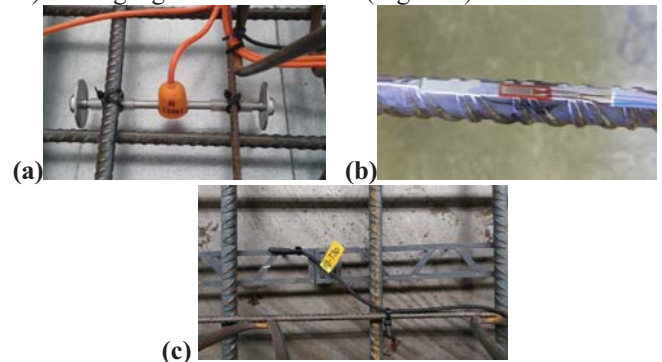


Figure 3. Sensors embedded in the buildings' structure: (a) VW Strain gauge in precast plank, (b) ER strain gauge on reinforcement, (c) Thermistor in precast plank

112 embedment VW strain gauges, manufactured by Gage Technique (Type TES/5.5/T), were installed in both the precast plank prior to manufacture and in the insitu concrete topping prior to pouring. The VW gauges measure both temperature and longitudinal strain in the concrete. These type of gauges were initially developed by the Transport and Road Research laboratory (TRRL) in the UK and are used extensively in bridge sections, tunnel linings and dam projects. They have a range of greater than 300 microstrain and resolution better than 1 microstrain. The temperature can be measured between -20°C and +80°C. These VW gauges are very robust and their stability makes them suitable for monitoring time dependent effects in concrete such as creep and shrinkage.

The VW gauges were positioned along a number of orthogonal grids in the floor structure at over 30 designated

locations so that two-way spanning behaviour of the floor structure could be monitored. At most locations, four VW gauges were positioned through the depth of the slab (1 in the precast plank and 3 in the insitu topping) so that the strain and temperature profile through the slab could be measured (Figure 4).

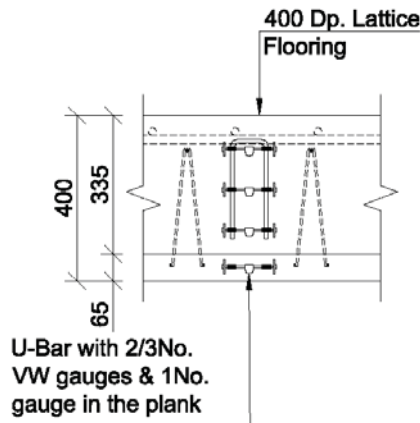


Figure 4. Typical section showing locations of vibrating wire gauge installed in the flat slab system.

To achieve two-way spanning behaviour in the floor structure, 'stitching' reinforcement bars are required across the joints between adjacent precast planks. The stitching bar is required to transfer the forces in the bottom transverse reinforcement bars across the joint and are positioned on site after the precast planks have been erected on site. Electrical resistance (ER) uniaxial strain gauges (Tokyo Sokki Kenkyujo model FLA-6-11-3LT, temperature compensating) were bonded to five stitching bars (H12 or H16) to measure the change in strain across the joint (Figure 5). Their gauge length is 6mm and they have a strain limit of 5%.

All ER gauges were protected using waterproof tape and sealant after bonding to the stitching bars to protect the gauges from the harsh environment (alkaline chemicals and pressurised water) when embedded in the concrete. Five individual ER gauges were bonded to each stitching bar so that the variation in strain along the stitching bar across the joint could be monitored.



Figure 5. ER strain gauges on stitching bar across joint in planks

In addition to the instrumentation embedded within the floor structure, the deformation of the plank soffit during the

construction phase was recorded at regular intervals using digital surveying. This will allow the measured strains using the embedded instrumentation to be related to the measured change in strain in the floor structure.

3.2 Data acquisition system

To collect data from the sensors, a data acquisition system containing CR1000 data loggers, AVW200 vibrating wire interface and AM16/32B multiplexers obtained from Campbell Scientific were employed. This system has been automatically logging data from the sensors embedded in the precast plank since manufacture and in the insitu concrete topping since their initial installation on site. During the construction phase, data is being stored on a flash memory card, which is manually downloaded onto a laptop weekly and backed-up on a server. However, data communication relay through the use of Campbell Scientific's NL116 Ethernet and Compact Flash Module will allow data to be collected over a local network after this is set up on commissioning of the building. This will allow the long term behaviour of the floor structure to be monitored during the operational phase of the HBB.

3.3 Material Testing

To accurately predict the behaviour of concrete elements, it is critical that the properties of the concrete are determined as they will change over time depending on the environment and loading. A comprehensive material testing programme was undertaken to measure the properties of the precast and insitu concrete used in the floor structure. Concrete cylinders, cubes and prisms specimens were made and cured in water and in air (to match the environmental conditions of the floor structure). Density, compressive strength, tensile strength and modulus of elasticity of the concrete in the precast plank and insitu topping were recorded during the construction phase of the project.

The information from the material testing is used to interpret the data from the instrumentation and can also be used for modelling of the behaviour of the floor structure.

3.4 Environmental Conditions

The environmental conditions around the floor structure will impact on the behaviour of the concrete slab, particularly at early stages of curing. Air temperature and relative humidity in the vicinity of the instrumented slab were measured using the weather data from the NUIG weather station (located approximately 1km from the site). When building was enclosed a sensor was positioned inside the building to record the air temperature and relative humidity.

4 PRELIMINARY RESULTS

4.1 Early-age thermal effects

Nine VW strain gauges were embedded in one of the 65mm thick precast planks prior to manufacture and data was recorded immediately after the plank was cast. Data was continuously recorded for this plank during curing, delivery and erection on site so that strain and temperature history of the precast plank can be analysed throughout the life cycle of the product from cradle to end of life. The instrumented plank

was cast during the Summer (June) and temperature curing was not used by the precast manufacturer in this case.

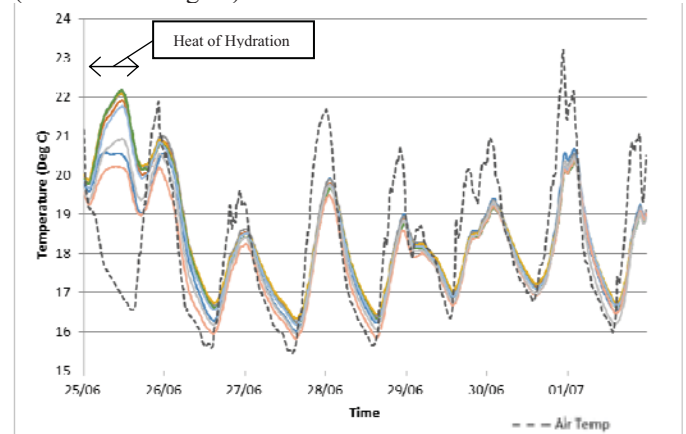
The concrete temperature for the nine VW gauges embedded in the plank and the air temperature (dashed line) are shown in Figure 6(a) for the 7 days after the plank is manufactured. In the first 24 hours after casting (25th June 2015), the peak in the concrete temperature due to the heat of hydration is noted and contrasts with the falling ambient air temperature during the night. The peak in the concrete temperature occurs 10 hours after casting and the max difference between the air temperature and the concrete temperature is approximately 5.5°C. It is noted that the peak temperature is slightly less for the three gauges located close to the perimeter of the plank (less than 300mm) as the plank cools more quickly along its external surfaces. However, because the concrete plank is relatively thin (65mm), after the first 24 hours the concrete temperature in the plank is relatively uniform for all nine VW gauges and they correlate with the ambient air temperature.

This contrasts markedly with the concrete temperature in the insitu topping in which the heat of hydration is more significant because of the thickness of the concrete (335mm thick), as well as the insulating properties of the precast biscuit resulting in only one surface of the insitu concrete being exposed. The concrete temperature in the insitu topping at one location in which three VW gauges are embedded to measure strain and temperature through the concrete (top, middle and bottom) are shown in Figure 6(b). The temperature for the VW gauge in the precast plank at this location is also shown. For the first 7 days after pouring, the temperature in the concrete exceeds the ambient air temperature and it is only after 7 days that the heat generated from the hydration process has fully dissipated. The effect of the diurnal temperature changes are clearly visible in the measured temperature in the concrete floor. Similar to the precast plank, the peak in concrete temperature occurs 10 hours after casting and at this point, the maximum temperature differential between the air and concrete temperature is approximately 13°C. As expected, the peak temperature is recorded for the VW gauge in the middle of the insitu topping as the internal section of the slab will be slowest to cool down. The effect of the heat of hydration from the insitu topping on the concrete in the precast plank can be noted almost immediately after pouring and results in a peak increase in temperature of 9°C.

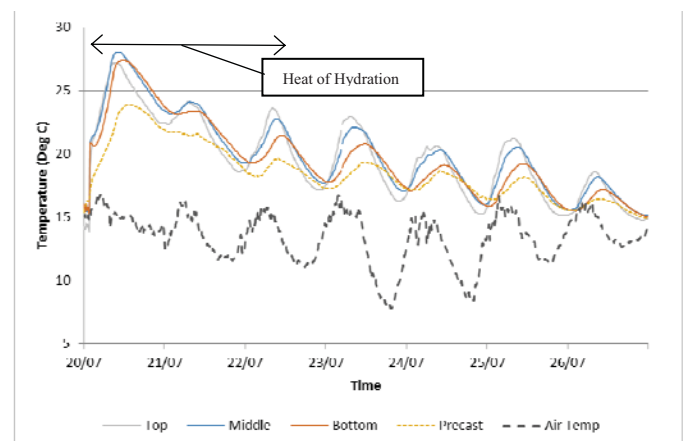
For 'thick' concrete sections (typically greater than 500mm), the temperature rise due to the heat of hydration can result in excessive thermal stresses and cracking generated by restraint to thermal movement. For the 335mm thick insitu topping in this project, the temperature differential through the slab is small (Figure 6(b)) because of the relatively thin section which allows the concrete to cool comparatively uniformly as the heat is readily lost to the environment. The temperature differential recorded by the VW gauges in top, middle and bottom of the insitu topping did not exceed 3°C and the maximum differential occurred during the cooling phase.

Predicting the potential for early-age thermal cracking is very difficult at the design stage because of numerous factors which affect the behaviour of the concrete and the limited

information on the concrete known at design stage. CIRIA Report C660 by Bamforth [7] gives guidance on predicting the early-age thermal behaviour of concrete sections based on a comprehensive testing programme undertaken at University Dundee [8]. However, the report recommends thermal modelling for reliable predictions which take account of the formwork and exposure conditions. Based on thermal modelling, it predicts that the maximum temperature differential in the insitu topping would be 13°C, but this figure is highly dependent on the thermal diffusivity of concrete, surface conditions and the environmental conditions (wind and solar gain).



(a) 65mm precast plank



(b) 335mm insitu concrete topping

Figure 6. Concrete temperature after pour (7 days)

As an upper bound, Fitzgibbon [9] estimated that the peak temperature rise under adiabatic conditions is 12°C/100kg per cubic metre of concrete, regardless of the type of cement used. Therefore, assuming a 100% CEM I cement for the insitu topping, it could be expected that the peak temperature be as much 40°C (total cement content of insitu topping was 330kg/m³). However, in this project 30% GGBS was used as a cement replacement in the concrete mix and this would help to reduce the heat of hydration generated during curing. The predicted peak temperature differential for the insitu topping using CIRIA Report C660 [7] is approximately 19°C, but other factors which can affect the peak temperature are the variation between cements, placing temperature and actual thermal conductivity of the precast plank. The measured peak

temperature of 13°C equates to a temperature rise of $4^{\circ}\text{C}/100\text{kg}$ per cubic metre of concrete. In terms of minimising cracks, the general rule of thumb used by designers is to limit temperature differentials to 20°C , although this figure is dependent on the type of aggregate used in the concrete mix. It can be seen from the above figures that the CIRIA report provides upper bounds for the peak temperature and temperature differentials for a specific concrete pour.

4.2 Strain and Temperature Profile

The strain and temperature profile in the precast planks and insitu topping is recorded using the embedded instrumentation so that the changes in strain during the manufacture of planks, delivery to site, pouring of insitu topping, during construction and operation phase can be analysed. The temperature profile for the nine VW gauges embedded in the same precast plank is shown in Figure 7 for the first 30 days after manufacture. As mentioned previously, following the cooling phase after manufacture, the temperature in the precast plank and air temperature are closely aligned and the diurnal temperature changes can be observed. When the precast plank was delivered to site on the 4th July 2015, the plank was exposed to direct sunlight and the ability of thin concrete plank to store and dissipate heat during the daily heating and cooling cycles is noted. In Figure 7, one can observe where the concrete temperature on some days in the precast plank prior to the pour is in excess of 12°C of the ambient air temperature during the day but returns to the ambient air temperature at night. These peaks in concrete temperature correlate with days of high solar irradiance as recorded by the NUIG weather station.

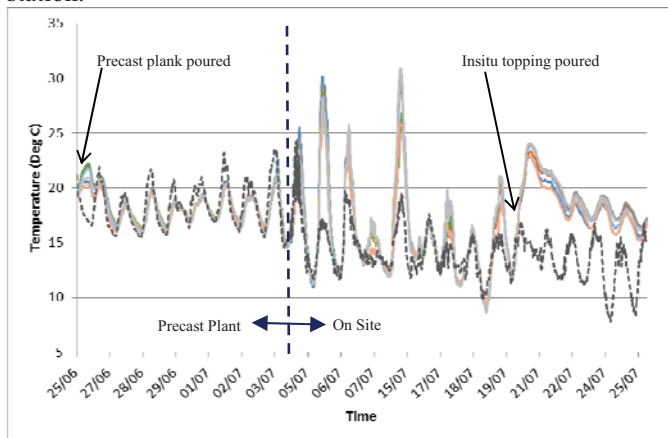


Figure 7. Temperature profile in precast plank (1 month)

The measured change in strain in the gauges in the precast plank when the insitu topping was poured on the 20th July 2015 was relatively small because the precast planks are propped (typically at 2.4m centres) during construction to limit deflection until the insitu topping has reached the required design strength.

The strain and temperature profile for three VW gauges through the depth of the insitu topping at one location is shown in Figure 8 for the first 7 days after pouring. After the dormant period of the hydration process, which lasted approximately 2 hours, there is a significant step change in tensile strain varying from $20\mu\epsilon$ near the bottom of the insitu

topping to $40\mu\epsilon$ at the top of the insitu topping due to the heating phase and the resulting expansive strains. Typically, the measured strains are greater for the gauges near the top of the insitu topping in comparison with the gauges near the bottom of the insitu topping which may be partially explained by the restraining effect of the precast plank. After the cooling phase of the heat of hydration is finished ($\sim 2\text{--}3$ days), thermal strains are significant and the concrete is subject to daily fluctuations in strains in response to the diurnal ambient air temperature. The daily changes in strain due to thermal effects can be estimated by multiplying the coefficient thermal expansion of concrete (α_c) and the measured temperature change in the concrete. It should be noted that whilst the floor structure is propped the measured strain is a combination of thermal, shrinkage (autogenous and drying) and creep and further analysis is required to determine the magnitude of the various strain components.

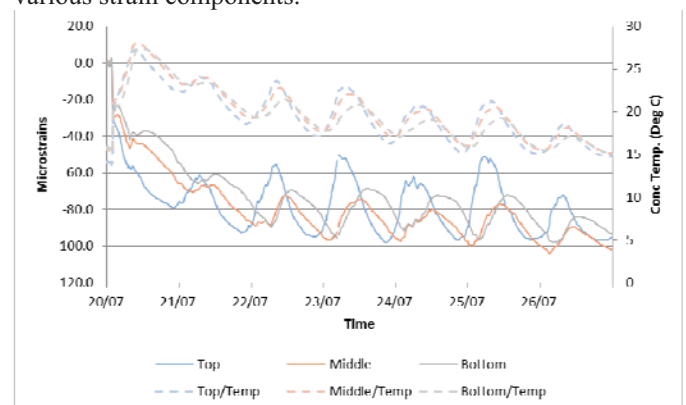


Figure 8. Strain and temperature profile in insitu topping (7 days)

4.3 Early-age cracking

During the early stages of curing, there is potential for cracking to occur if the tensile strain capacity of the concrete is exceeded. Some research has shown that microcracks can form even if 50% of the tensile strength of the concrete is exceeded [10]. The coefficient of thermal expansion of concrete (α_c) will determine the magnitude of thermal strain associated with a particular temperature change. Values for concrete vary from $8\text{--}13\mu\epsilon/^{\circ}\text{C}$ depending primarily on the aggregate used. EN 1992-1-1 [11] recommends a value of $10\mu\epsilon/^{\circ}\text{C}$ for normal weight concretes. However, a design value of $9\mu\epsilon/^{\circ}\text{C}$ may be used for limestone aggregates [12] which were used for the concrete on the HBB project. Using the measured peak recorded temperature of 13°C , this equates to thermal strains of approximately $117\mu\epsilon$ in the insitu topping. Observations have shown that early-age cracking is most likely to occur within three to six days [13].

The tensile strain capacity of concrete, ϵ_{ctm} , is the maximum strain that the concrete can withstand without the formation of a continuous crack. Tensile strain capacity is not dealt with in EN 1992-1-1, but can be derived from values of the tensile strength and elastic modulus of the concrete provided in EN 1992-1-1. Tensile strain capacity under short-term loading can be approximated as the ratio of the mean tensile strength of concrete f_{ctm} to its mean elastic modulus E_{cm} and this has been shown to represent lower bound values [7].

$$\varepsilon_{ctu} = f_{ctm} / E_{cm} \quad (1)$$

The values derived for tensile strain capacity are increased by 23% to take account of the relaxation of stress due to creep and reduction in tensile strength under a sustained load [7]. The aggregate type is of particular significance to the tensile strain capacity as aggregate comprises about 70% of the concrete volume.

The strain profile in the insitu topping at one location in the slab for the first seven days is compared in Figure 9 with the theoretical tensile strain capacity given in Equation 1. The graph indicates the measured strain is close to or exceeds the theoretical strain capacity during the first 3 days after the pour. No cracking was observed in the location of the slab in which strain gauges were embedded and the actual tensile strain capacity of the insitu topping is at least 20-30% greater than the theoretical tensile strain capacity based on material testing conducted on concrete samples at 3 Days and 7 Days, which were air cured to match the environmental conditions on site. This illustrates the difficulty of predicting early-age cracking without accurate knowledge of the environment or material properties.

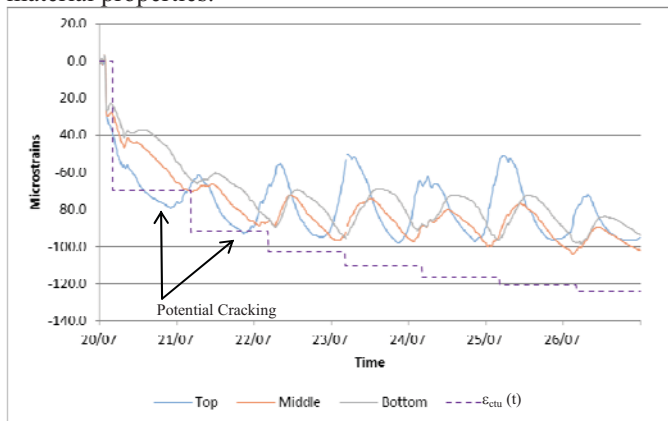


Figure 9. Comparison of measured strain and theoretical strain capacity (7 Days)

4.4 Construction stage behaviour

A hybrid concrete lattice girder flat slab structure was used to construct the ground to fourth floor of the HBB (the basement was constructed using insitu concrete). As mentioned previously, the precast planks are temporarily supported by props which are erected prior to installation of the planks. The precast planks acts as permanent formwork and contain the bottom reinforcement for the floor structure. As the concrete frame progressed upwards, the floors constructed below the floor under construction were used to support the self-weight of the next floor. A temporary works engineer was employed by the contractor to determine a back propping sequence for the floor structure at each level as construction progressed. The back propping sequence must ensure that the load from the wet concrete is transferred to a sufficient number of floors below so that no slabs are overloaded. When the compressive strength of the insitu topping had reached a specified strength, the supporting props were dropped and re-applied so that each slab was supporting its own self-weight.

During the construction phase of the HBB, the changes in strain when props were dropped, back-propped and removed

and floors were poured above second floor can be analysed. The deformation of the slab soffit during the construction phase was also recorded using a digital level. The change in strain along a gridline (GL H) in the second floor for a series of VW strain gauges in the top of the insitu topping at two loading events is shown Figure 10. The solid line is the change in strain when the third floor was poured (13th August 2015) and the dashed line is the change in strain when the props were dropped and re-propped 15 days later. The recorded strains shows that when the props were dropped from the third floor, so that it supports its own self-weight, that the imposed stresses on the second floor from the third floor pour are reversed.

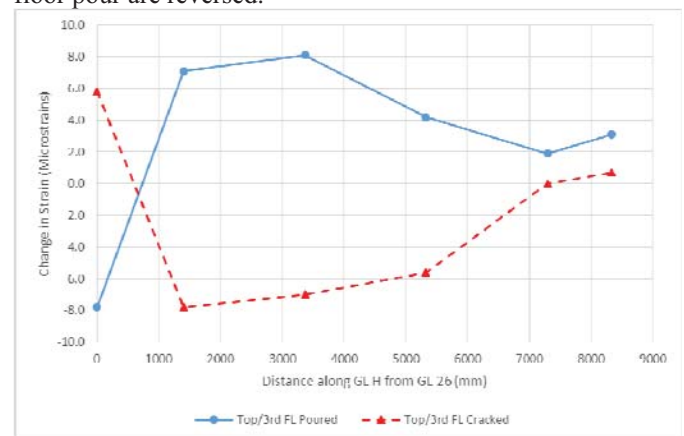


Figure 10. Measured change in strain along Gridline H

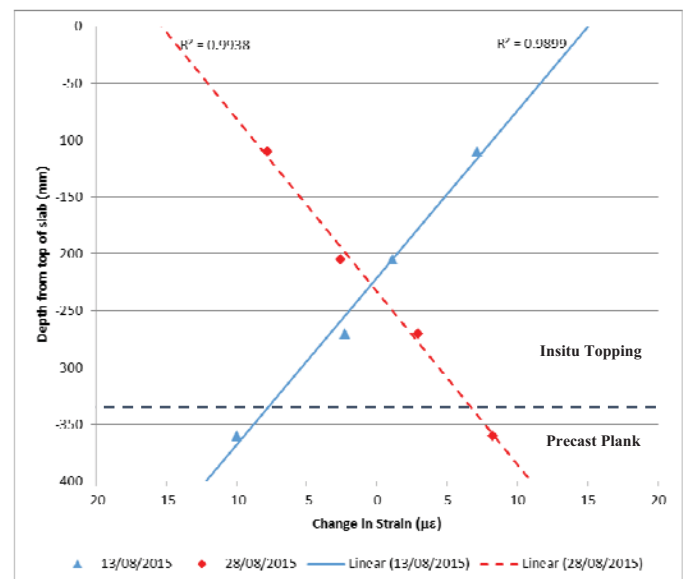


Figure 11. Strain profile through 400mm thick floor structure

The measured changes in strain through the 400mm thick floor structure at one location along gridline H is shown in Figure 11 when the third floor is poured (13th August 2015) and when the props supporting the third floor are dropped (28th August 2015). At this location, there are three VW gauges in the insitu topping and one VW gauge in the precast plank. The strain profile illustrates the composite nature of the hybrid concrete floor structure and also that the slab appears

to exhibit linear elastic behaviour at this stage of construction and could be considered ‘uncracked’.

5 CONCLUSIONS

This paper presents the motivation and implementation of a real-time structural health monitoring strategy for a hybrid concrete lattice girder flat slab floor system. The sensors installed allow many important aspects of the performance of the floor structure (structural, environmental etc.) to be monitored during the manufacture, construction and operational phase of the building. In combination with the material testing, weather monitoring station and laboratory testing, this SHM strategy provides rich information about the performance of the floor.

Design guidelines are typically approximations which simplify the behaviour of the structure so that it can be solved relatively quickly and simply. However, these approximations and simplifications have the potential to introduce errors or inaccuracies to the design process. The insitu instrumentation provides performance data on actual behaviour which can be used to verify design methods. Real-time monitoring offers potential benefits in relation to optimisation of structural components by understanding the actual behaviour of components in use and the possibility to develop and calibrate numerical models that predict structural performance.

The preliminary results presented in this paper are at an early stage and it is expected that the measured data will be used to compare actual behaviour with predicted behaviour using structural codes, such as the Eurocodes. Continuous monitoring of the data will allow long term effects in the structural performance of the slab to be monitored and compared with design guidelines.

ACKNOWLEDGMENTS

The authors would like to acknowledge the support of the European Commission Horizon 2020 project Built2Spec (637221). A great debt of gratitude is owed to all members of the project teams involved in the design and construction of the Human Biology Building who have facilitated our work throughout the project. A special mention is also owed to the technical staff at NUI Galway for their assistance during the instrumentation process. The support of Oran Pre-Cast Ltd. is gratefully acknowledged with respect to installation of sensors in the precast concrete elements. The second author would also like to acknowledge the support of Science Foundation Ireland through the Career Development Award programme (Grant No. 13/CDA/2200) and the National Centre for Marine and Renewable Energy Ireland (MaREI) (Grant no. 12/RC/2302).

REFERENCES

- [1] Goggins, J; Newell, S; King, D; Hajdukiewicz, M (2014) Real-time monitoring of a hybrid precast and in situ concrete flat slab system. *Proceedings of Civil Engineering Research in Ireland (CERI 2014)* Queens University Belfast, Northern Ireland, 321-326.
- [2] Hajdukiewicz, M., Byrne, D., Keane, M. M., & Goggins, J. (2015). Real-time monitoring framework to investigate the environmental and structural performance of buildings. *Building And Environment*, 86, 1-16.
- [3] Guan, H., Karbhari, V. M., & Sikorsky, C. S. (2006). Web-Based Structural Health Monitoring of an FRP Composite Bridge. *Computer-Aided Civil and Infrastructure Engineering*, 21(1), 39-56.
- [4] Habel, W. R. (2013). SHM systems supporting extension of the structures' service life. *Journal of Civil Structural Health Monitoring*, 3(4), 225-226.
- [5] Chang, P. C., Flatau, A., & Liu, S. C. (2003). Review paper: health monitoring of civil infrastructure. *Structural health monitoring*, 2(3), 257-267.
- [6] Bisby, L. A., & Briglio, M. B. (2004). ISIS Canada Educational Module No. 5: An Introduction to Structural Health Monitoring. *Prepared by ISIS Canada*, 3.
- [7] Bamforth, P. B. (2007). Early-age thermal crack control in concrete. CIRIA Report C660, London.
- [8] Dhir, R. K., Paine, K. A., & Zheng, L. (2004). Design Data for Use where Low Heat Cements are Used. *Concrete Technology Unit, Dundee*.
- [9] Fitzgibbon, M. E. (1976). Large pours for reinforced concrete structures. Current Practice Sheet 2P/15/1, No. 28 *Concrete*, 10(3), 41.
- [10] FIB (1999) Structural Concrete Textbook on behaviour, design and performance, Second edition: Basis of design. International Federation for Structural Concrete, 1999
- [11] CEN (1992), 'EN 1992-1-1, Eurocode 2: Design of concrete structures. General rules for buildings,' ed. Brussels, Belgium, 1992.
- [12] Bamforth, P., Chisholm, D., Gibbs, J., & Harrison, T. (2008). Properties of concrete for use in Eurocode 2. *The Concrete Centre, UK*.
- [13] ALEXANDER, S. J. (2006). Why does our concrete still crack and leak? *The Structural Engineer*, 84 (23/24) 2006, 40-43. London.

Sediment Transport Modelling on the River Bandon

Gamble, J.¹, Harrington, J.²

¹Department of Civil Structural & Environmental Engineering, Cork Institute of Technology, Bishopstown, Cork, Ireland

²School of Building and Civil Engineering, Cork Institute of Technology, Bishopstown, Cork, Ireland

email: john.gamble@mycit.ie ; joe.harrington@cit.ie

ABSTRACT: In November 2009 Ireland was subject to a severe weather event, causing widespread flooding nationwide. One of the worst effected towns was the town of Bandon in County Cork which regularly floods. The River Bandon is located in the South Western River District (SWRBD) with a catchment area of 608km². The River Bandon offers a positive environment for biodiversity, facilitating habitats for some endangered species. The River Bandon is planned to undergo significant river improvement works.

This paper presents the findings of an extensive sediment sampling, testing and analysis programme, including for suspended and bed sediments and sediment loadings. The HEC-RAS numerical model has been developed and applied to a 7.7 km river reach from Bandon town downstream. The model has been calibrated and validated with a preliminary application to predict sediment transport conditions.

KEY WORDS: Sediment Transport; HEC-RAS; Flooding.

1 INTRODUCTION

The River Bandon, located in County Cork, and its sediment behaviour is the subject of this paper. The town of Bandon is the largest urban settlement on the river and has a history of flooding. Stretches of the river in Bandon town and downstream are planned to undergo significant river improvement works in the summers of 2016 and 2017.

Sediment samples were taken at five locations along the river. The samples were analysed for suspended load and bed load characteristics. Turbidity sensor data was also gathered and analysed. Sediment loading rates were determined.

A numerical model was developed to predict sediment transport conditions on the river.

2 BANDON CATCHMENT

The River Bandon is located in the South Western River District (SWRBD), the largest of the eight river basin districts in Ireland. It is approximately 74km long with a catchment area of 608km² which is relatively large in an Irish context. The river rises in the Shehy Mountains and discharges to Kinsale Estuary. The river is tidal up to approximately 15km upstream of the Kinsale Estuary which is downstream of the town of Innishannon [1]. The catchment is primarily agricultural with three relatively large urban settlements along the river; Dunmanway, Bandon and Kinsale (see Figure 1). The catchment consists of two distinct areas; the upland Bandon/Caha area which is upstream of Dunmanway and comprises of mainly mountainous areas with poor soil conditions and downstream of Dunmanway which is generally low-lying agricultural land with good soil conditions.



Figure 1: River Bandon Catchment

3. RELEVANT LEGISLATION

Existing European Union (EU) legislation regarding sediments is quite limited [2]. Three of the most important EU directives relevant to the work are:

- Water Framework Directive
- Freshwater Fish Directive
- Habitats Directive

3.1 Water Framework Directive (2000/60/EU)

The Water Framework Directive (WFD) (2000/60/EU) was introduced in December 2000 with the aim of preventing the further deterioration of water quality and restoring all waters to good status by 2015 [3]. The WFD uses five water quality categories which are based on the biodiversity within the relevant aquatic system.

3.2 Freshwater Fish Directive (78/659/EU)

The Freshwater Fish Directive (FFD) (78/659/EU) was enacted to ensure that freshwater bodies are capable of

sustaining natural fish life. The FFD places limits on various parameters and limits the suspended sediment concentration to 25mg/l for salmonid waters [2]. This limit can be exceeded for short-term events, such as during flood and drought conditions. The FFD was repealed in 2013 (in the overall context of the WFD) leaving individual EU Member States to decide on how to assess impacts on fisheries [3].

3.3 Habitats Directive (92/43/EU)

The aim of the Habitats Directive (HD) (92/43/EU) is to conserve natural habitats of wild fauna and flora. The HD achieves this by creating Special Areas of Conservation (SAC), also referred to as European sites or Natura 2000 sites in Irish legislation; such sites are considered to be of exceptional importance for the protection of rare and endangered species.

4. RIVER BANDON – SITE CONDITIONS AND PROPOSED WORKS

4.1 River Ecology and Sediments

Sediment transport occurs naturally in rivers and is essential to maintaining habitats. Changes to land-use cause changes in the delivery of fine and coarse sediment and sediment transport can vary over space and time due to changing flows and catchment conditions. The ecological regime of a river can adapt to small changes in sediment transport over short time periods. However, excessively high levels of suspended sediment concentration can cause significant detrimental impacts, the effects on the ecosystem depend on the suspended sediment concentration level and duration of exposure. Four impact zones have been indicated with Zone 1 with suspended sediment concentration levels below 25mg/l has little or no impact on fish and their habitats. However, suspended sediment concentrations above 25mg/l have varying impacts depending on the duration of exposure. Zone 2 shows behavioural effects on fish causing population decline and/or increase in mortality rate. Zone 3 shows a physical effect on fish. In this zone fish gills and other tissue are damaged. The effect may not cause immediate death but increases the mortality rate and leads to a decline in the fish population. Zone 4 results in lethal effects on fish. With the majority killed immediately or suffer damaged tissue resulting in a large reduction in fish population and also damage to the capacity of the system to support a future fish population [4].

Bed load transport can create habitats, however, this transport also has the ability to remove and smother habitats. The movement of bed load has a greater impact on embryo and fry than on larger fish with deposition of bed load suffocating eggs and fry in spawning grounds. The build-up of sediment around fish eggs results in the water not being able to wash away the fish waste, leading to potential fish kill by poisoning [5].

The variation of habitats on the River Bandon offers a positive environment for biodiversity. Table 1 presents detail on important species on the River Bandon [6].

Table 1: Important Species on the River Bandon [6]

Species	Location	Comments
Atlantic salmon	Lower reach downstream of Innishannon	Salmon have been recorded upstream of Dunmanway
European Eels	Lower reach downstream of Innishannon	Eels have been found as far upstream as Bandon town
Lamprey	Lower reach up to Bandon town	Heavy density below Innishannon
Three-spined stickleback	Lower reach below Innishannon and upstream of Dunmanway	Recorded downstream of Innishannon

4.2 Proposed Works

The proposed river improvement works in Bandon Town and downstream are designed for a 1 in 100 year return period event [1]. Table 2 presents the proposed river improvement works with the improvement locations presented in Figure 2.

Table 2: Proposed Works [1]

Proposed Works	Area
Dredging	Bandon Weir to O'Driscoll's Bridge
Flood defence walls	Various locations in Bandon town, Bridewell river
Improvement to existing flood defences	Bridewell River, Bandon
Provision of removable flood barriers	Wastewater Treatment Plant
Provision of rock ramp and fisheries mitigation measures	Specific locations
Local drainage works	At Bandon weir
	Local drainage behind flood defences



Figure 2: Proposed Works

The proposed river improvement work includes the dredging of the River Bandon for 3.6km from the weir in Bandon town downstream to O'Driscoll's Bridge at a slope of 1/1000. The

dredging will cause a reduction of bed level at the weir of 1.9m, at Bandon Bridge of 1.7m, at the wastewater treatment plant of 1m and to bed level at O'Driscoll's Bridge as shown in Figure 3 [1]. Once dredging is complete, pools, riffles and a thalweg will become a feature of the improved river

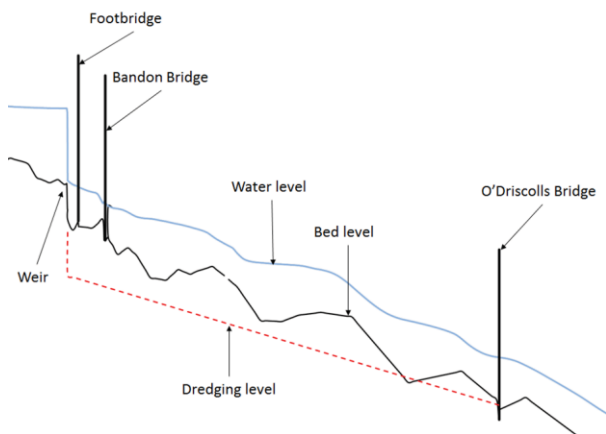


Figure 3: Proposed Dredging Levels

4.3 River Flow Analysis

The River Bandon has five hydrometric stations with two (Bandon town station and Curranure station) located within the modelled reach. An extreme flow analysis was undertaken for both stations using six different probability distribution functions. For the subsequent work the extreme flow rates determined for the Bandon station are used due to the longer term nature of the data record (see Figure 4). For this case the Generalised Logistic (GLO) probability distribution function was found to provide the best fit. Figure 4 also presents the 'outlier' 2009 flood condition.

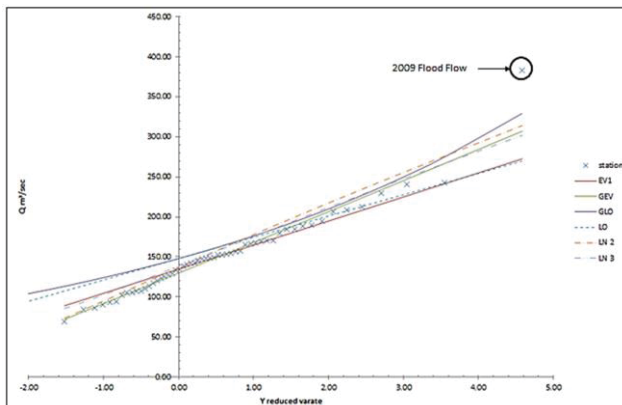


Figure 4: Bandon Station Flow Distributions

Figure 5 presents the top ten annual maximum flows recorded at the Bandon station, including the most recent 2015 event (in red). An L-moment extremal flow analysis was undertaken and the December 2015 event was found to correspond to a 1 in 35 year event, with the 2009 flood event, the highest event recorded, indicating a 1 in 100 year event.

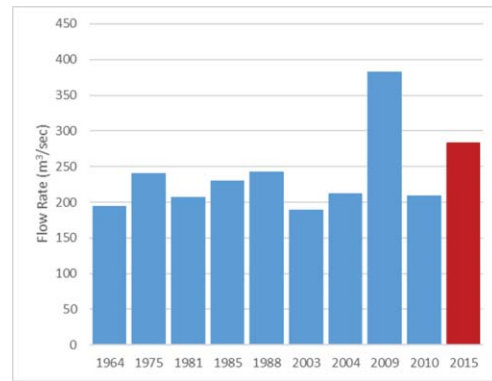


Figure 5: Top Ten Recorded Flood Events

Table 3 presents the extreme flood event analysis for both pre-2015 flows and for all flows.

Table 3: Variation in Return Period Flow Events

Return period	Pre-2015 Flow Rates (m ³ /sec)	All Flows Rates (m ³ /sec)	Variation (%)
2	148.0	148.0	0
5	188.6	188.3	0
10	217.3	219.8	1
25	257.8	268.1	4
30	266.5	279.0	4
50	292.0	312.1	6
100	330.0	364.4	9

4.4 Sediment Sampling and Analysis

A sediment sampling programme was undertaken at five locations along the river, as shown in Figure 6.



Figure 6: Sediment Sample Location

Suspended sediment samples were taken using both surface grab and depth integrating approaches. Water levels were recorded using the local staff gauge at each sampling location (if available) or downloaded from the OPW water level record website as necessary [7]. Water temperature was also recorded. Table 4 shows a summary of manually sampled suspended sediment concentration data. Figure 7 provides a longitudinal profile of measured values. These show suspended sediment concentration (SSC) values generally less than 10 mg/l reflecting the clear nature of the water flows observed along the river reach during the sampling work. It should be noted that suspended sediment concentrations can be elevated on high flow events.

Table 4: Summary of Suspended Sediment Concentration

Location	Suspended Sediment Concentration (mg/l)		
	Minimum	Maximum	Mean
Footbridge	0.2	11.84	2.57
Bandon Bridge	0.4	6.37	2.55
Bridewell	0.22	74.9	2.14
Millstream	1.98	9.99	3.66
O'Driscoll's Bridge	0.98	14.76	3.85

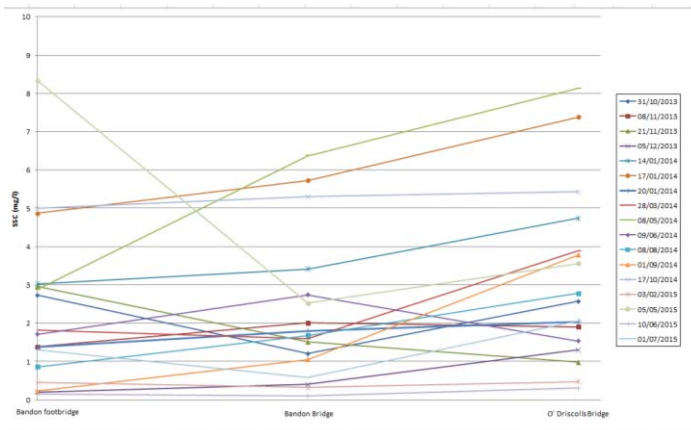


Figure 7: SSC on the River Bandon

Cork Institute of Technology installed a turbidity sensor at the Curranure Gauging Station in February, 2010. This sensor records turbidity on a continuous 15-minute basis. Previous analyses have shown that turbidity is a suitable surrogate for suspended sediment concentration at this location [8] and thus the continuous turbidity record allows conversion to a continuous suspended sediment concentration record.

The analysis has been based on applying the flow rate (Q) and turbidity as a surrogate for suspended sediment concentration (C) in the following equation (1).

$$SSL_s = \int_{t_1}^{t_2} Q_t C_t dt \quad (1)$$

Table 5 presents summary seasonal and annual suspended sediment loadings (in tonnes) for 2010, 2011 and 2014, for comparison purposes. These results indicate the highly variable and dynamic nature of suspended sediment behaviour and transport within the river system. The annual suspended sediment loading varies between approximately 2,000 and 3,000 tonnes; significant variation in the seasonal loadings estimated is also clearly evident.

Table 5: Annual and Seasonal Suspended Sediment Loadings

	2010	2011	2014
Spring Loading (March to May)	85.1	243.9	1072.2
Summer Loading (June to August)	296	107.9	239.5
Autumn Loading (September to November)	862	1406.1	268.6
Winter Loading (December to February)	708	1300	1205
Annual Loading	2148	3058	2785

Bedload samples were collected by entering the water body at each sampling location and were taken when conditions allowed, sampling within the context of Health & Safety requirements, generally using a grab sampler (an Ekman Grab Sampler) and in places using a piston type core sampler where bed conditions allowed. Table 6 presents summary results.

Table 6: Bed Sediment Size Summary

Location	D ₅₀ (mm)	
	Minimum	Maximum
Footbridge	10.4	29.6
Bandon Bridge	3.2	33.6
Bridewell	3.9	19.1
Millstream	28.5	> 50
O'Driscoll's Bridge	28.5	> 50

5. NUMERICAL MODELLING

5.1 Numerical Model – HEC-RAS

The U.S Army Corps of Engineers HEC-RAS model (a 1-Dimensional numerical model – Hydrologic Engineering Center's River Analysis System) has been applied to numerical modelling on the River Bandon [9]. It provides for both steady and quasi-steady flow conditions, the quasi-steady flow condition is required for the sediment transport aspect of the modelling.

Calibration of the model involves an analysis for both water level variation and sediment characteristics with comparison between field data and model outputs. The aim of the calibration process is to produce a best fit of model output to observed field data. Model validation involves additional model comparison with field data and is required to provide additional confidence in the numerical model to accurately simulate field conditions

Figure 7 shows the river reach modelled from the upstream model boundary located 0.7 miles upstream of the weir in the town of Bandon to the downstream boundary at Innishannon Bridge. Short reaches on the Bridewell, Millstream and River Brinny tributaries are also modelled. The upstream and downstream model boundaries are shown including the three tributary streams (the Bridewell, Mill Stream and the Brinny).

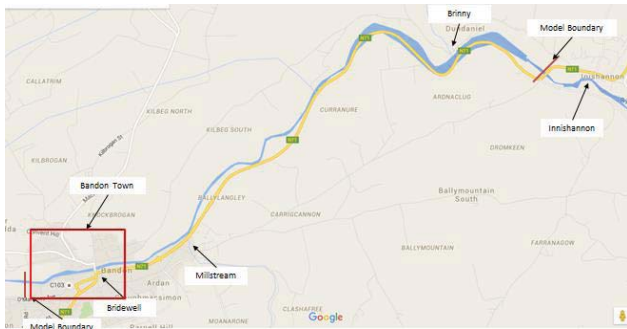


Figure 8: Numerical Model Boundary

5.2 Hydrodynamic Calibration

The hydrodynamics were calibrated at both Bandon town and Curranure hydrometric stations located within the model boundary. The calibration involves comparison of steady state water level predictions from the HEC-RAS model with water levels at gauging stations. This comparison was undertaken for a range of flow conditions for both in and out of bank flows, varying from 19 to 352m³/sec.

The analysis involves varying the Manning Roughness Coefficient 'n' to provide a best fit between model prediction and gauged field data. The best fit is determined using various statistical parameters: Root Mean Squared Error (RMSE) (Equation 2), Nash-Sutcliffe Coefficient of Efficiency (E) (Equation 3) and the Systematic Error (SE) (Equation 4).

$$RMSE = \sqrt{\frac{\sum_i^N (WS_{ob} - WS_{sim})^2}{N}} \quad (2)$$

$$E = \frac{\sum_i^N (WS_{ob} - WS_{sim})^2}{\sum_i^N (WS_{ob} - WS_{obavg})^2} \quad (3)$$

$$SE = \frac{\sum_i^N (WS_{sim} - WS_{ob})}{N} \quad (4)$$

where:

WS_{ob} = water surface level observed by the station

WS_{sim} = water surface level simulated by HEC-RAS

WS_{obavg} = is the average water surface level observed at the station

N = number of reference measurements (data points)

The results of the model calibration analysis are shown in Table 7 for both gauging station locations. The Manning 'n' values presented are typical for rivers similar to the River Bandon. The values found for each of the statistical parameters used are considered to be appropriate for model calibration purposes [10].

Table 7: Model Calibration Analysis Results

	Manning 'n' Coefficient	RMSE (m)	E	SE (m)
Bandon Bridge	0.0348	0.0808	0.993	-0.03
Curranure	0.0339	0.043	0.997	-0.024

The model was validated for flow rates over a 12 month period from 1/10/2009 to 30/9/2010; with flows ranging from 2.6 to 184.8m³/sec, with an average flow rate of 15.6m³/sec. Figure 8 presents the water levels at Bandon hydrometric

station. The validation of the model provided additional confidence in the calibrated model.

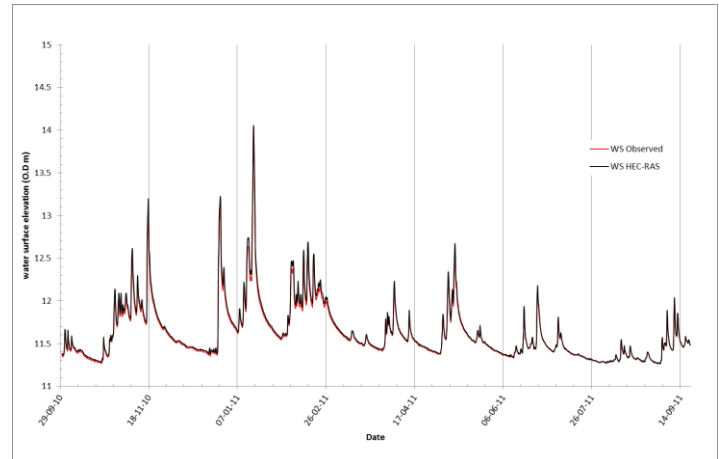


Figure 9: Model Validation for Water Level

5.3 Sediment Transport Calibration

Sediment transport data was collected over the period from 1st to 9th July 2015. Table 8 shows the measured bed load and suspended sediment load, which was estimated to have occurred over this time. This data suggests that the suspended sediment load is significantly higher than the bed load transport during this time period with the bed load accounting for approximately only 1.2% of the total load.

Table 8: Measured Sediment Transport for Calibration Period

	Sediment Load (tonnes)	
	Bed Load	Sediment Suspended Load
01-07-15 to 08-07-15	0.237	18.9

An extensive model calibration process was undertaken to determine key model parameter values. A summary of these key parameter values applied within the model and based on the model calibration and validation is given in Table 9.

Table 9: Sediment Transport Simulation - Model Parameters

Model Parameter	Value
Manning Roughness Coefficient - Bandon Station	0.0348
Manning Roughness Coefficient - Curranure Station	0.0339
Sediment Transport Function	Meyer Peter Muller
Total Rate Coefficient (C)	1.9
Power Function (P)	1.5
Critical Shear Stress τ^*	0.047
Time Step (Δt)	25 SECS

5.4 Model Simulation

The HEC-RAS model developed was applied to simulate flows over a 12 month period. Results from this simulation (for the year 2011) predicted five locations with identified erosion or deposition, as presented in Figure 9. These locations correspond to the actual river locations where sediment deposition has been observed.

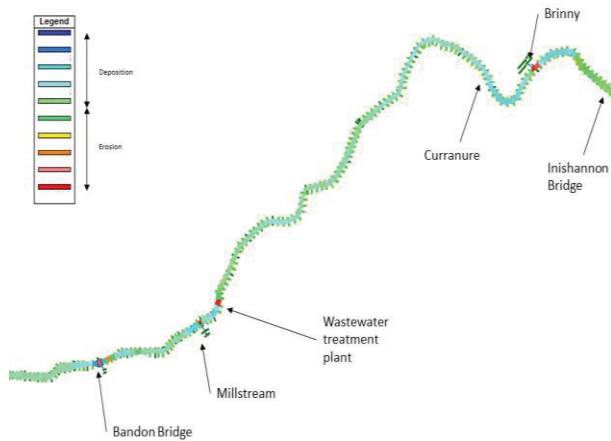


Figure 9: Identified Erosion and Deposition Locations

Total sediment transport rates at these locations were predicted from the HEC-RAS model with the results presented in Table 10.

Table 10: Predicted Annual Sediment Transport Rates

Location	Total sediment transport (tonnes/annum)	BL % of total load
Bandon Bridge	2866	7.8%
Bandon Station	2845	7.8%
Wastewater Treatment Plant	2957	7.6%
Brinny	3362	5.9%
Upstream of Innishannon Bridge	3395	5.6%

Model results indicate bed load transport at from 5.6 to 7.8% of the total load. These results are indicative in nature and a more extensive dataset for sediment calibration purposes would enhance confidence in model results.

6. CONCLUSIONS

A suspended and bed sediment manual sampling programme has been undertaken at five locations on the River Bandon and the sediment data has been presented and analysed. Manual suspended sediment data has been complemented by continuous turbidity data gathered at the Curranure Station using turbidity as a surrogate for suspended sediment concentration. The river is characterised by low suspended sediment concentrations (< 10mg/l) with peaks during high

flow events. Annual suspended sediment loadings vary from approximately 2,000 to over 3,000 tonnes.

An extremal flow rate analysis is presented for the Bandon station with the most recent December 2015 flood event estimated to be a 1 in 35 year event.

The HEC-RAS numerical model has been applied to a 7.7km stretch of the river system. Model inputs include geometric data based on a series of surveyed cross-sections, suspended sediment and bed sediment data and river flow rates.

The model has been satisfactorily calibrated for hydraulic conditions with a high level of confidence, it has also been satisfactorily validated for hydraulic conditions. The model has been calibrated on a preliminary basis for sediment transport. This calibration is based on available field data which is limited for the bed load. Additional model calibration and validation for bed sediment transport is required.

The HEC-RAS model has been applied to the river system with locations of erosion and deposition predicted. Sediment transport rates from the model have been estimated at from approximately 2800 to 3400 tonnes/annum with bed load transport estimated at from 5.6 to 7.8% of the total sediment load.

This paper presents new work on suspended and bed sediment behaviour and modelling for the River Bandon.

REFERENCES

- [1] JBA Consultants, *Bandon Flood Relief Scheme Final Hydrology Report*, Ireland, 2011.
- [2] Hickey, J., *Suspended Sediment and Nutrient Behaviour on the River Bandon*, MEng Thesis, Cork Institute of Technology, Ireland, 2014.
- [3] Collins, A., Jones, I., *Linking Agricultural Fine Sediment Pressure and Impacts on Aquatic Ecology for Informing Catchment Management across England and Wales*. SedNet Conference, p. 36, Poland, September, 2015.
- [4] Kemp, P.C., Collins, A., Jones, I., *The Impacts of Fine Sediment on Riverine Fish*. Hydrological Processes, 2011(11), pp. 1800-1821.
- [5] Ward, N., *The Problem of Sediment in Water for Fish*, in Technical Notes, N. Ontario Boreal Forest Management, Ministry of Natural Resources Ontario, 1992.
- [6] Ecofact Environmental Consultants, *App 5D Bandon EIA - Fish Stock Assessment*. 2011: Ecofact Environmental Consultants.
- [7] Office of Public Works. *Hydro-Data. Station Location: Bandon & Curranure*. Available from: <http://www.opw.ie/hydro/>, 2015.
- [8] Harrington, J., Harrington, S.T., *Sediment and Nutrient Behaviour on the River Bandon, Ireland*. River Basin Management VII, 2013: p. pp. 215 – 226.
- [9] US Army Corps of Engineers - USACOE, *HEC-RAS Hydraulic Reference Manual*, 2008.
- [9] Moriasi, D.N., Arnold, J.G., Van Liew, M.W., Bingner, R.L., Harmel, R.D., and Veith, T.L., *Model Evaluation Guidelines for Systematic Quantification of Accuracy in Watershed Simulations*, Transactions of the American Society of Agricultural and Biological Engineers, Vol. 50(3): 885-900, 2007.

Low Flow Analysis of Ungauged River Catchments in Ireland

Paul Forde¹, Leonard O'Driscoll²

¹ Postgraduate Student, Department of Civil, Structural and Environmental Engineering, Cork Institute of Technology, Cork, Ireland

² Department of Civil, Structural and Environmental Engineering, Cork Institute of Technology, Cork, Ireland

Email: paul.forde@mottmac.com, leonard.odriscoll@cit.ie

ABSTRACT: Low flows in rivers can present a significant amount of issues including problems in relation to the assimilation capacity of the river, the ecosystem within the river, as well as the availability of the catchment's water as a resource for water supply. The development of the OPW Flood Studies Update (FSU) web-portal has meant that catchment data for the entire country is now readily available. In addition, there is significant body of freely available flow data from river gauging stations in place around the country. As a result of this, the development of predictor equations for various low flow indices is now considered possible for individual ungauged catchments. These equations can be validated using existing river flow data. This paper presents the development of predictor equations for a 1 in 10 year low flow event for the 7-Day sustained low flow (7-Day SLF), the annual minimum mean daily flow (Amin) and the 7 day 10 year flow (7Q10) low flow indices. The method of stepwise regression is used to determine the most statistically significant catchment characteristics, of which twenty-one are considered. The final models developed for the 7-Day SLF and the 7Q10 indices contain five variables and have R squared values of 0.8248 and 0.7860 respectively. The Amin model contains six variables and has an R squared value of 0.7619. The final predictor equations for each index are shown below.

KEY WORDS: Low Flows, Hydrology, Catchment Descriptors, Prediction, River, Regression, Statistics

1 INTRODUCTION

In hydrology flooding is often considered the most significant problem, primarily due to the devastation that it can cause. However, low flows in rivers can also present many problems. Knowledge of low flows is crucial when considering water abstraction in projects such as water supply, hydro power schemes, or water resource projects. In addition, low flows can greatly reduce the assimilation capacity of a river, and therefore potentially increase water pollution. As well as this, the ecosystem of a river can be greatly affected during periods of lesser flows.

The definition of low flow, as given by the International Glossary of Hydrology (1), is the "flow of water in a stream during prolonged dry weather". This is not a very distinct definition as it doesn't clearly indicate the difference between low flows and droughts.

Low flow information is an important indicator for water resource planning and management, and is used for assessing the quality of river catchments. Low flows are a seasonal phenomenon as the lowest recorded flow each year will usually occur during the same season. Typically low flows occur during the summer periods, although in colder countries they may also occur during the winter period due to precipitation being stored as snow.

2 RELEVANCE OF THE RESEARCH

Over the past number of years, much more data has become available for the analysis of river catchments in Ireland. Additional data is also available due to the development of the Flood Studied Update (FSU) and the online Web Portal. The FSU presents data for thousands of catchments in Ireland, including flow and level data, available at gauging stations as

well as catchment descriptors for gauged and ungauged catchments.

However the FSU web portal only carries out analysis for high flows in rivers, and an online portal for low flow analysis is unavailable in Ireland. With the availability of data from the FSU Web Portal and the additional gauged data, low flows within river catchments may potentially be predicted more accurately.

There are various existing equations in hydrology which can be used to predict an estimate of different flow indices. However few models currently exist for the prediction of low flow indices in Ireland.

3 LOW FLOW INDICES

Three commonly used indices are considered as part of this study, which include the 7 day 10 year flow (7Q10), the 7 day sustained low flow (7-Day SLF), and the annual minimum mean daily flow.

These indices are similar to those used by the EPA for pollution control as well as assimilation capacity assessments of water bodies in Ireland. It is considered that the predictor equations created could be used similarly, as initial estimates of low flows.

The Annual minima is the lowest flow recorded for each year. The 7-Day SLF is the maximum value of the driest week recorded during the year (2). The Lowest 7-day average flow is the average value of the driest week recorded during the year. This value can be used to calculate the 7Q10 for the station when it is analysed. The 7Q10 is defined as "the average annual 7-day minimum flow that is expected to be exceeded on average in 9 out of every 10 years, which is

equivalent to the tenth percentile of the distribution of 7-day annual minimum streamflow” (3).

4 STATIONS

Gauging stations included as part of the FSU Web Portal which received an A1 rating classification, were initially considered as part of the study. This resulted in a total of 54 potential stations which may be used.

It was decided to follow the same approach as *Nasr and Bruen 2014* (4) and only use stations which had a total of ten or more years of data. A brief inspection of the data resulted in 40 stations (maintained by the OPW) which were considered useable and are included as part of this study.

A detailed inspection of the data available at the 40 stations was carried out. Five stations (-06025-), (-14004-), (-06026-), (-26020-) and (-36012-) had a significant amount of data missing and were discarded. This resulted in a total of 35 stations, 9 large catchments (>1000km²), 1 small catchment (<100km²) and 25 medium catchments (between 100km² and 1000km²), which have useful data.

This study considers the 25 medium sized catchments identified for the development of predictor equations, because it is believed that these would be most beneficial. The location of the gauging stations of these 25 catchments is shown in Figure 4-1.

Each year of data for every station was inspected in detail, and years which were considered unusable for low flow analysis, based on the quality codes assigned to the data, were identified. For many of the stations, the first year of data was not used as it typically didn't have recorded values for the full year.

The flow data for each year was examined and any significant (more than a week) gaps during periods of potential low flows were identified. Data with these gaps was not considered valid. None of the stations considered contained any recorded zero values.

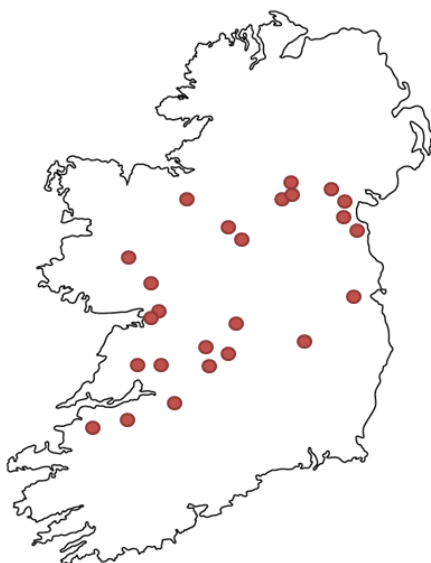


Figure 4-1 Location of stations included as part of the study

It was decided to only use data which had been derived from a rating curve which was deemed to be of good, fair or poor quality. Initially, poor quality data (code 46) was not

considered. However, there were large amounts of this data across a majority of the stations and if excluded would have resulted in little usable data. Consideration is therefore given to the potential impact on the models developed through the use of this information.

After all the data of each station was reviewed, 846 of the total 1,057 years of data were considered useable from the 25 medium sized catchment stations. This corresponds to an average of almost 34 years of useable data at each station.

5 STATION ANALYSIS

The Weibull distribution is the most favoured distribution for low flow analysis (5). This is because it has a lower bound. The Weibull distribution is shown below.

$$F(x) = 1 - \exp \left[- \left(\frac{x - \xi}{\alpha} \right)^\kappa \right] \quad \text{Equation [1]}$$

This distribution contains three different parameters; the location (ξ), the scale (α) and shape (κ) parameter. These parameters were estimated using the method of moments as outlined in the WMO Manual on Low Flow Estimation (6). The lower bound of the distribution is considered to be zero for most of the stations and therefore the location parameter (ξ) is equal to zero, resulting in a two parameter Weibull distribution (EV III).

Each station was analysed for three different sets of data, namely the annual minimum flow, the 7 day sustained low flow and the lowest 7 day average flow.

6 DEVELOPMENT OF LOW FLOW PREDICTOR MODELS

A total of 21 physical catchment descriptors (independent variables) were considered for the regression analysis. These are the same descriptors which were used in the FSU methodologies. A full list of these variables can be seen in Table 6-1.

To build the predictor equations for the various low flow indices considered, the method of stepwise regression was carried out. This is a step by step method which builds the model by adding (forward) or removing (backward) variables based on their statistical significance.

The addition or removal of the variables is based on a threshold which is decided by the user, known as F-to enter and F-to remove (where F is the t-statistic squared) (7). The typical F value used is 4, which corresponds to a t-statistic of 2. However this may potentially be set to a lesser value of 3 (t-statistic of 1.73) but it is not recommend to use a value less than this.

Various basin and climate characteristics most commonly associated with low flow indices, which were identified by *Smakhtin (2001)* (8), were noted prior to the analysis being carried out. These characteristics are the catchment area, annual rainfall, river slope, stream frequency, percentage area of lakes and forests, soil indices, and main stream length. Both forward and backward stepwise regression was carried out to determine any potential differences of the final R² values and predictor equations.

Table 6-1 Catchment descriptors (independent variables)

Variable	Definition
AREA (km ²)	Catchment area
CENTE (m)	Catchment centroid easting
CENTN (m)	Catchment centroid northing
SAAR (mm)	Standard annualised average rainfall
FARL (index)	Flood attenuation by reservoirs and lakes
URBEXT (Prop)	Proportion of urban extent
FOREST (Prop)	Proportion of forest extent
PEAT (Prop)	Proportion of peat extent
ALLUV (Prop)	Proportion of alluvium extent
FLATWET (index)	Mean value of FLATWET index
SAAPE (mm)	Standard average annual potential evapotranspiration
FAI (Prop)	Proportion of catchment occupied by FAI polygon
BFIsoil (index)	Base flow index
NETLEN (km)	Length of stream network
STMFRQ (no.)	Number of stream segments in river network
DRAIND (km/km ²)	NETLEN/ POLY_AREA
MSL (km)	Main-stream length
S1085 (m/km)	Slope of main stream channel excluding bottom 10% and top 15% of length
TAYSLO	Taylor-Schwarz channel slope
ARTDRAIN (Prop)	Proportion of catchment area benefiting from arterial drainage
ARTDRAIN2 (Prop)	Proportion of river network included in OPW arterial drainage schemes

7 7Q10 PREDICTOR MODEL

Both forward and backward regression was carried and the backward stepwise regression method resulted in a five variable model with the greatest R squared value of 0.7860.

A fit of the final model is shown in Figure 7-1 with the final predictor equation shown below.

$$7Q10 = -0.6546 + (0.0005 * AREA) + (1.0829 * PEAT) + (0.2171 * ARTDRAIN2) + (0.028 * S1085) + (0.5431 * FARL)$$

Equation [2]

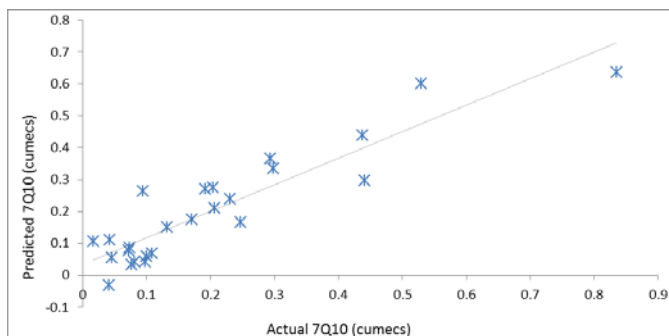


Figure 7-1 Fit of the final 7Q10 predictor model

8 7-DAY SLF PREDICTOR MODEL

As per the 7Q10 model both forward and backward regression was carried out. Both methods resulted in the same five variable model with an R squared value of 0.8248. A fit of the final model can be seen in Figure 8-1 with the final predictor equation shown in Equation [3].

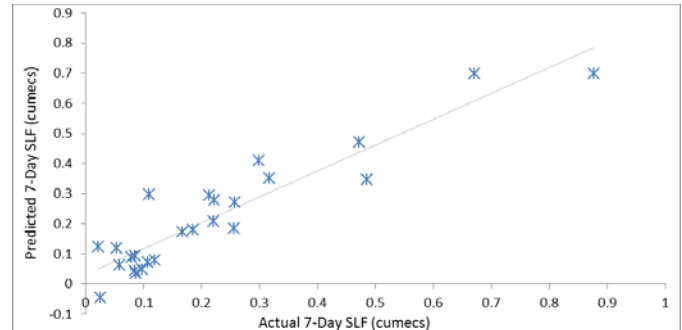


Figure 8-1 Fit of the final 7-Day SLF predictor model

$$7\text{-Day SLF} = -0.8164 + (0.0006 * AREA) + (1.2519 * PEAT) + (0.2005 * ARTDRAIN2) + (0.0335 * S1085) + (0.6849 * FARL)$$

Equation [3]

9 ANNUAL MINIMUM MEAN DAILY FLOW PREDICTOR MODEL

As before, both methods of regression were carried out. The backward stepwise regression method resulted in a potential six variable model (depending on the F- to enter threshold) with an R squared value of 0.7619.

It was considered that the t-statistic of the FARL variable (F value of 3.58) was significant enough to be part of the model and therefore the six variable model was considered to be the most accurate model achievable for the prediction of the annual minimum flow index. A fit of the final model can be seen in Figure 9-1 with the final six variable predictor equation outlined below.

$$\text{Annual Minimum Flow} = -0.6613 + (0.9561 * PEAT) + (0.0009 * AREA) + (0.1839 * ARTDRAIN2) + (0.0351 * S1085) - (0.0004 * STMFRQ) + (0.5195 * FARL)$$

Equation [4]

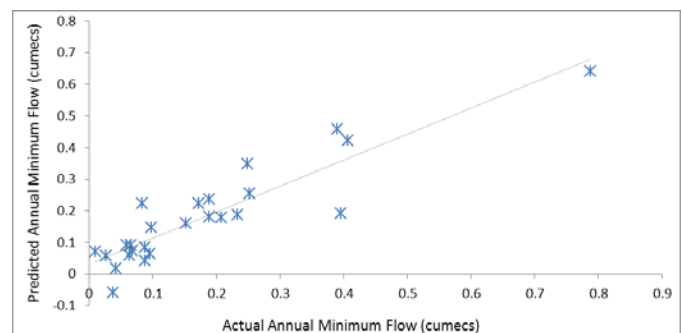


Figure 9-1 Fit of the final annual minimum flow predictor model

The predictor equation estimated one negative value (Ashfield station) of -0.0585m³/sec in contrast to the correct flow value

of $0.0374\text{m}^3/\text{sec}$. This is a significant error and it is recommended that any negative predictions are assumed to be incorrect and discarded.

10 RAPID MINER ANALYSIS

RapidMiner Studio was used to carry out multiple linear regression using all the 21 independent variables. Analysis was carried out in relation to the three different indices considered, to develop predictor models which could be compared to those obtained from the Excel analysis.

The model outputs for the three different indices contained an excessive number of variables and were far too complex. Therefore to compare any potential differences between the Excel and RapidMiner models, a regression analysis was carried out in RapidMiner using the same variables as outlined in the final predictor model of each index.

For all three low flow indices, the results of the RapidMiner regression analysis yielded coefficient values for each variable which were identical to those obtained from the five variable Excel analysis.

11 MODEL VALIDATION

The validity of the three different predictor models was assessed by analysing 6 different stations and applying the models to compare the predicted and analysed values.

The six stations used were (-07001-), (-07002-), (-15001-), (-16003-), (-25001-) and (-07006-). All catchment sizes are within the limits of the models. The location of the six validation stations is shown in Figure 11-1.

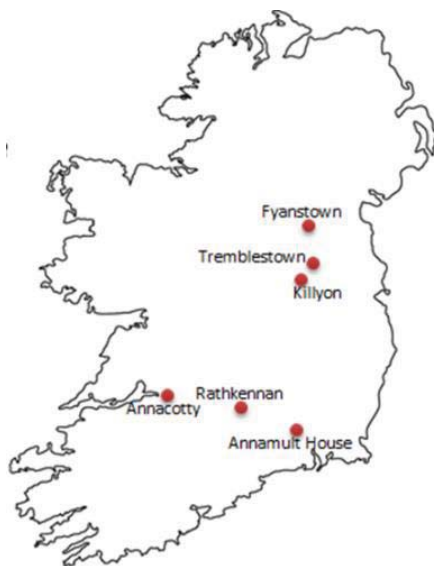


Figure 11-1 Location of validation stations

The results can be seen in Table 11-1. The percentage errors range from 69.41% to -79.88% which appears significant. However the percentages are representative of small flow values. The % error for the Tremblestown station is extremely small indicating a high degree of accuracy using the predictor equations.

Table 11-1 Predicted index flow values and corresponding % error of validation stations

Station Name	AMin (m^3/s)	% Error
Tremblestown	0.1663	1.7
Killyon	0.2199	-55.48
Annamult House	0.1625	-36.09
Rathkennan	0.1603	-32.40
Annacotty	0.2418	-79.88
Fyanstown	0.1379	69.41

Station Name	7-Day SLF (m^3/sec)	% Error
Tremblestown	0.1777	-12.37
Killyon	0.2469	-55.49
Annamult House	0.2592	-19.89
Rathkennan	0.2073	-32.28
Annacotty	0.4831	-65.70
Fyanstown	0.1526	37.47

Station Name	7Q10 (m^3/s)	% Error
Tremblestown	0.1820	-1.08
Killyon	0.2479	-54.68
Annamult House	0.2145	-25.20
Rathkennan	0.1718	-36.82
Annacotty	0.4058	-69.05
Fyanstown	0.145	44.13

11.1 Sensitivity Analysis

A sensitivity analysis was carried out on station 16003 to outline the effects on the results due to a small change. The station was originally analysed using only two parameters as the distribution fitted the data well when the location parameter (ζ) was equal to zero. Adjusting this parameter to become positive or negative will have a subsequent effect on the predicted index flow value.

The location parameter was adjusted from -0.02 to 0.07 in increments of 0.01. The 1-moment distribution fits the empirical data at the tail end for both values. However it appears to fit the overall shape of the distribution better when equal to -0.02

While both parameter values may be considered valid as part of the analysis due to their fit at the tail end, there is a potential for reducing the percentage error from 47.81% to 26.64%.

When analysing the stations used to develop the predictor models, the value of the location parameter was set equal to zero for majority of stations. This may have introduced an unwanted error when developing the various models.

11.2 Negative Predictions

It is considered to apply the three different predictor equations to all the FSU stations which are within the limits of the model. This will not indicate the accuracy of the predictor models. However it will provide an estimated flow value for the stations considered. This will highlight the potential of the models to predict negative flows depending on whether the predictions are positive or negative.

Of the 215 stations a total of 126 are within the catchment area limits of the model. When the regression equations were applied to these stations only six (-07004-), (-07011-), (-07033-), (-26018-), (-36012-) and (-36018-), indicated a negative estimated flow value for any of the three low flow indices. These were extremely small but they do indicate that there is a potential for the equations to estimate a negative flows.

11.3 BFIsoil and SAAR

There are two variables which surprisingly appear to have no statistically significant effect on low flows: - SAAR and BFIsoil. Although the BFIsoil variable is not included in any of the final predictor models, there are variables which have a significant influence on the base flow of a river, namely PEAT and FARL. Therefore the significance of these variables in the prediction of low flows is recognised.

A paper by Robert H.Flynn (9) developed regression equations to estimate seasonal low flows. The equations only contained rainfall basin characteristics for winter and summer 98% exceedance flows and not for similar spring and fall equations in New Hampshire streams. A total of 93 basin characteristics were considered.

That paper also outlined equations for the prediction of the seasonal 7Q2 and 7Q10 low flow indices. Precipitation characteristics were considered significant for the winter, spring and summer seasons, but not for the fall season.

Another paper by Rich Pyrcce (10) outlined existing regression equations which were developed to estimate the 7Q10 low flow index at various ungauged catchments in US states, and identifies some which are not influenced by rainfall characteristics.

The two papers discussed above indicate that there is a potential for low flow index predictor equations not be influenced by specific rainfall characteristics. Therefore with the evidence of these equations as well as the influence that the PEAT and FARL variables have on the base flow of a river, the absence of the BFIsoil and SAAR basin characteristics within the models developed is considered to be acceptable.

12 CONCLUSIONS

A total of 35 useable gauging stations were identified after a selection process, of which 25 had a catchment area of between 100km² and 1000km² and were considered as part of the study.

Each station was analysed to determine the 1 in 10 year event of three different low flow indices. These were the Amin, the 7-day SLF and the 7Q10. The method of moments was used to analyse the stations and a three parameter Weibull distribution proved to be a good fit for the empirical data at all stations. A general trend identified that the 1-moment distribution resulted in a much better fit than the p-moment.

A total of 21 physical catchment descriptors were considered as part of the regression analysis. A correlation analysis indicated that all three low flow indices showed the strongest relationship with the PEAT variable over any other.

A five variable model was developed using regression analysis, for the 7Q10 and 7-Day SLF indices, with R² values of 0.7860 and 0.8248 respectively. A 6 variable model was

developed for the annual minimum low flow index with an R² value of 0.7619. The final predictor equations for a 1 in 10 year event of each low flow index are shown below.

$$7Q10 = -0.6546 + (0.0005 * AREA) + (1.0829 * PEAT) + (0.2171 * ARTDRAIN2) + (0.028 * S1085) + (0.5431 * FARL)$$

Equation [5]

$$7\text{-Day SLF} = -0.8164 + (0.0006 * AREA) + (1.2519 * PEAT) + (0.2005 * ARTDRAIN2) + (0.0335 * S1085) + (0.6849 * FARL)$$

Equation [6]

$$\text{Annual Minimum Flow} = -0.6613 + (0.9561 * PEAT) + (0.0009 * AREA) + (0.1839 * ARTDRAIN2) + (0.0351 * S1085) - (0.0004 * STMFRQ) + (0.5195 * FARL)$$

Equation [7]

The lack of significance in which the BFIsoil and SAAR catchment characteristics appear to have on the prediction of low flows is surprising. However two research papers appear to agree that the prediction of low flow indices may not always be greatly influenced by rainfall.

A sensitivity analysis carried out on station 16003 indicated that there is a potential for significantly different final predictor equations to be developed as a result of small changes to the parameters, due to the size of the values analysed.

The predictor models overestimated flows at 43% of the stations considered and underestimated them at 57%. This indicates that there is no consistent miscalculated prediction associated with the three equations. However, with the evidence of negative predicted flow values it is recommended that the models be used with caution and only as an initial estimate of a low flow value at ungauged locations.

13 RECOMMENDATIONS

It is recommended that further research be carried out considering more stations than the 25 outlined in this study (over 200 available on the FSU), to determine any differences in the final predictor models developed. It is also recommended to consider the development of predictor equations for both small and large sized catchments.

A further recommendation would be to consider the development of seasonal predictor equations. This would involve the consideration of flows associated with each of the four seasons to develop their corresponding predictor models.

REFERENCES

1. WMO. International Glossary of Hydrology. Geneva: 1974.
2. MacCarthaigh M. A Statistical Analysis of River Flows. EPA, Water Resources Section: 1989.
3. Reilly CF, Kroll CN. Estimation of 7-day, 10-year Low-streamflow Statistics using Baseflow Correlation: 2003.
4. Bruen M, Nasr A. Statistical Analysis of River Low Flows in Support of Water Resources Management Planning in the Shannon International River Basin District: 2014.
5. L.M. Tallaksen. Streamflow drought frequency analysis: 2000.

6. WMO. Manual on Low Flow - Estimation and Prediction: 2008.
7. Nau R. Statistical forecasting: Notes on Regression and Time Series Analysis. [Online]: 2015 [cited 2015 July 23]. Available from: <http://people.duke.edu/~rnau/411home.htm>.
8. V.U. Smakhtin. Low Flow Hydrology: a review: 2001.
9. Flynn R.H. Development of Regression Equations to Estimate Flow Durations and Low-Flow-Frequency Statistics in New Hampshire Streams. New Hampshire Department of Environmental Services, U.S Geological Survey: 2003.
10. Pyrcie R. Hydrological Low Flow Indices and their Uses. Ontario: Trent University, Watershed Science Centre: 2004.

Tidal Stream Energy Resource Assessment of the Shannon Estuary, Ireland

Anna Phoenix^{1,2}, Stephen Nash^{1,2}

¹College of Engineering & Informatics, National University of Ireland, Galway, Ireland

²National Centre for Marine & Renewable Energy in Ireland (MaREI)

Email: a.phoenix2@nuigalway.ie, stephen.nash@nuigalway.ie

ABSTRACT: Tidal stream energy resource assessment is a fundamental step towards tidal power generation. Given that power is a function of tidal velocity cubed, assessments will be highly dependent on the precision of the velocity data employed. Traditional approaches to estimating the available tidal energy involve using either the peak or time-varying current velocities; in either case the total velocity vector is employed. At present, leading turbine technologies are horizontal axis designs with a fixed orientation, which restricts rotation of the turbine with changing current direction. A weakness of many published resource studies is that they ignore the directionality of tidal flows and therefore over predict the tidal potential for horizontal axis turbines. The primary aim of this research is to accurately quantify the potential tidal stream resource in an estuary. Tidal current ellipses are utilised to incorporate the prevailing direction of flow into available power calculations, resulting in a more accurate assessment. A secondary aim is to carry out a general resource assessment of the Shannon estuary, Ireland, and more detailed assessments at particular sites chosen as a result of the general assessment. It is shown that estimates of the available power can vary substantially depending on the assessment methodology that is employed and that omitting the effects of flow direction from an assessment leads to significant overestimation of the available resource.

KEY WORDS: Tidal stream energy; resource quantification; tidal ellipses; Shannon Estuary.

1 INTRODUCTION

Selection of a site suitable for tidal turbine deployment will be primarily dependant on the available tidal stream resource. Various approaches are used in the literature to estimate the power available from a tidal stream. (A review of these can be found in [1]). The main differences between approaches are the type of velocity data used and the means of calculation of available power. Early resource assessments utilised tidal velocity data from navigational charts (e.g.,[2]) but these are not very accurate. Long-term velocity measurements result in a more accurate assessment, however the assessment applies only to the measurement site and velocities, and thus available power, at a nearby location may differ substantially. High frequency radars can record flow fields at high resolution (e.g.,[3]) however, this method is very expensive. Numerical models are a more commonly used method of determining velocity data for tidal resource assessments as they simulate both temporal and spatial variations in velocities and therefore power (e.g., SEAI's study of Ireland's tidal stream resource [4]). Once accurate velocity data has been established there are a number of approaches to calculating the available tidal power, each varying in the accuracy of their energy estimates. For instance, the Fraenkel approach adopted by [4] limits the accuracy of its resource assessment as it fails to incorporate current flow direction.

The Shannon River and its estuary is one of the largest such systems in the British Isles. The tidal ranges at the mouth and head of the estuary are approximately 5m and 6.5m, respectively, during normal spring tides, inducing peak currents of up to 3m/s in water depths of 35m. The estuary has rightly been identified as a potential location for tidal energy extraction; however, little detailed analysis has been carried out to accurately determine its tidal energy potential. . The

primary aim of this research is to carry out a preliminary assessment of the estuary based on a relatively coarse model with the aim of identifying areas of high potential and comparing resource quantifications using different methods. The second phase of this study will involve utilising a nested model to produce a more detailed resource assessment for the sites of interest.

2 METHODOLOGY

2.1 Resource Availability

The power that can be extracted by a turbine placed in tidal flows can be calculated as:

$$P_{Available} = P_{Mean} A_t \epsilon \quad (1)$$

where P_{Mean} is the mean available power per m^2 of cross-sectional area of flow, A_t is the cross-sectional area of the turbine and ϵ is the turbine efficiency.

The Fraenkel formula is an accepted first step approach for estimating the mean available tidal power in an estuary. Assuming a spring-neap tidal cycle which is sinusoidal in nature, the mean available power is estimated as:

$$P_{Mean} = 0.5 \rho A_f K_s K_n V_{Peak}^3 \quad (2)$$

where ρ is water density, V_{Peak} is the maximum spring velocity at the area of interest, A_f is the cross-sectional area of the flow at the area of interest, K_s is the velocity shape factor, which accounts for the nature of the variation in velocities over a tidal cycle and K_n is the neap/spring factor which accounts for the nature of the difference in spring and neap peak velocities. It is typical to assume $K_s = 0.424$ for a sinusoidal flow and $K_n = 0.57$ for a 60% reduction in peak currents between spring and neap tides [5]; however, often current flow may not be sinusoidal in nature nor the ratio of

spring to neap tides equal to 60%, resulting in inaccuracies in power estimation using the Fraenkel formula.

In contrast to utilising peak velocities, time-varying velocity data can be used to provide a more accurate estimation of the mean power available for tidal energy extraction, calculated as:

$$P_{Mean} = \sum_{t=1}^{t_{max}} \frac{0.5 \rho V_t^3}{t_{max}} \quad (3)$$

where t_{max} is the number of timesteps and V_t is the magnitude of the current velocity at time t .

These traditional approaches to resource assessment employ the total velocity vector. Currently the most advanced tidal turbine designs are horizontal axis turbines. The nature of such devices prevents them from rotating into the tidal stream as it changes direction during different stages of the tide, as a result using the total velocity component in power calculations could lead to significant over predictions of the tidal energy potential.

The tidal resource assessment method presented here incorporates the primary direction of current flow. In this approach, 2D numerical modelling is employed along with tidal harmonic analysis and tidal ellipse theory to facilitate long-term forecasts of current velocities, enabling the mean available power at a location of interest to be determined in the following way:

$$P_{Mean} = \sum_{t=1}^{t_{max}} \frac{0.5 \rho V_p^3}{t_{max}} \quad (4)$$

where t_{max} is the number of timesteps and V_p is the time-varying velocity component aligned only with the primary direction of flow.

2.2 Hydrodynamic Numerical Model

Time-varying velocity data were produced using the numerical model DIVAST, a 2D finite difference, depth integrated, time-variant model, developed for shallow estuarine and coastal waters. The model consists of two main sections: a hydrodynamic module and a solute transport and water quality module. The hydrodynamic module is based on the depth integrated solution of the Navier-Stokes equations to determine values for the water surface elevations and the horizontal depth integrated velocities. The model solves the following governing equations:

Continuity Equation:

$$\frac{\partial y}{\partial t} = \frac{\partial q_x}{\partial x} + \frac{\partial q_y}{\partial y} = 0 \quad (5)$$

X-Direction Momentum Equation:

$$\begin{aligned} \frac{\partial q_x}{\partial t} + \beta \left[\frac{\partial U q_x}{\partial x} + \frac{\partial V q_y}{\partial y} \right] &= f q_y - g H \frac{\partial y}{\partial x} + \frac{\tau_{xw}}{\rho} + \frac{\tau_{xb}}{\rho} \\ &+ 2 \frac{\partial}{\partial x} \left[\varepsilon H \frac{\partial U}{\partial x} \right] + \frac{\partial}{\partial y} \left[\varepsilon H \left[\frac{\partial U}{\partial y} + \frac{\partial V}{\partial x} \right] \right] \end{aligned} \quad (6)$$

where ζ is the water elevation above or below datum, t is time, q_x and q_y are depth-integrated velocity flux components in the x and y directions, β is the momentum correction factor, U and V are depth averaged velocity components in the x and y direction, f is the Coriolis parameter, g is gravitation

acceleration, H is total water depth, τ_{xw} and τ_{xb} are the x -direction components of the surface wind stress and bed shear stress, ρ is the water density and ε is eddy viscosity.

The model utilizes an implicit finite difference scheme to solve these governing differential equations. An Alternating-Direction Implicit (ADI) scheme is incorporated, enabling the time step to be divided into two half time steps, allowing a two-dimensional scheme to be applied. Further details and explanations of the governing equations and the modules solution scheme can be found in [6].

2.3 Tidal Harmonic Analysis

Tidal harmonic analysis is based on the principle that tidal characteristics in a given location can be represented by a harmonic cosine curve which oscillates at a certain frequency determined by the astronomical tide generating forces. These forces are known as harmonic or tidal constituents [7]. The major constituents along with the astronomical phenomena causing them and the nature of the tide they produce are listed in Table 2-1.

Table 2-1: Major tidal harmonic constituents.

Tidal Harmonic Constituent		Tide
M2	Principal Lunar	Semi-diurnal
S2	Principal Solar	Semi-diurnal
N2	Larger Lunar Elliptic	Semi-diurnal
L2	Smaller Lunar Elliptic	Semi-diurnal
K1	Luni-solar Declinational	Diurnal
O1	Principal Lunar Declinational	Diurnal
P1	Principal Solar Declinational	Diurnal

Each individual constituent consists of a unique pair of amplitude and phase parameters, referred to as tidal constants [8]. The aim of any tidal harmonic analysis is to determine these constants at a given location for each individual tidal constituent, enabling the astronomical tide to be forecast. The resulting tidal height can be represented in the form:

$$h(t) = \sum_{i=1}^N A_i \cos[2\pi(\delta_i t - \theta_i)] \quad (7)$$

where $h(t)$ is the tidal height at a time t , N is the number of harmonic constituents selected for the analysis, i is the individual constituent, A_i and δ_i are the amplitudes and frequencies of the constituent respectively, and θ_i is the constituent phase, measured in radians.

In this research, tidal analysis was performed using the 'Flex Tidana tidal heights and current analysis and prediction software program'. The software was incorporated into the existing hydrodynamic DIVAST model of the Shannon estuary. The resulting water levels and velocities computed by the developed model were utilised as time series data in the harmonic analyses. Further details on the Flex Tidana software can be found in [9].

2.4 Tidal Current Ellipse Theory

In the case of tidal current analysis, the resulting tidal harmonics are determined in terms of tidal current ellipse parameters [10]. Currents, comprised of vector quantities, can be resolved into positive East and North direction components, U and V , which undergo separate tidal harmonic analysis. As a result each harmonic constituent included in the analysis will be represented by two amplitude and two phase parameters which are recombined to construct a tidal ellipse.

The basic parameters making up a tidal ellipse are illustrated in Figure 2-1.

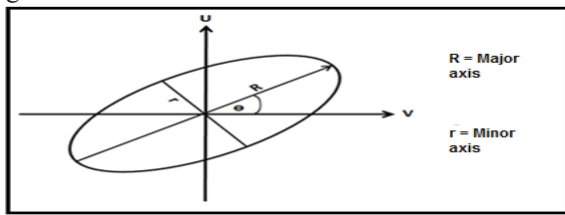


Figure 2-1: Basic parameters of a tidal ellipse.

Tidal current ellipses capture variations in tidal velocity. Each ellipse is defined by its major and minor axis, which represent maximum and minimum current speeds. The ratio of the minor and major axis of an ellipse describes variation in flow direction; low ratios (close to 0) indicate rectilinear flow whilst high ratios (close to 1) indicate rotary flows. This is of importance when determining suitable turbine deployment sites as energy extraction is most efficient in areas of rectilinear flow. The angle of inclination of an ellipse is also an important parameter for an accurate resource assessment and in determining device orientation as it indicates the primary direction of flow.

The dominant tidal constituent across the estuary was found to be M2 (see Table 2-1), hence it was considered the main contributor to the primary direction and speed of current flow and the analysis therefore takes the primary direction of flow to be equal to the angle of inclination of the relevant M2 ellipse.

3 MODEL APPLICATION

The Shannon estuary, located on the west coast of Ireland, is a highly dynamic system, possessing a large tidal range and strong peak currents. Due to its potential for tidal energy extraction it was chosen as a case study site for this research.

The existing numerical model was applied to the Shannon estuary and used to simulate its hydrodynamic regime. Bathymetry data of the estuary was obtained from admiralty charts and interpolated onto a finite difference grid to produce a domain with grid spacing of 189m and 507 x 217 computational cells. The model was run with a time step of 40 seconds and a bed roughness of 200mm for a simulation period of approximately 350 hours, equating to a full spring-neap tidal cycle. The western sea boundary is specified as a tidal elevation boundary. Boundary elevation data were specified using tidal constituent data obtained from analysis of measured tidal elevation data at Carrigaholt (shown in Figure 3-1) for a one-year period (2006). The northern and southern boundaries are specified as streamline flow boundaries.

The Shannon estuary model has been validated against measured tidal elevations at six locations (T1-T6) and tidal current velocities at two locations (C1& C2), shown in Figure 3-1. The performance of the model in relation to tidal elevations at locations T2 and T5 is illustrated in Figure 3-2. The accuracy of the model in relation to depth-averaged current velocities at location C2 is shown in Figure 3-3. Good correlation between measured and modelled velocities was achieved with correlation values of $R^2=0.97$ and 0.95 attained for spring and neap tides respectively.

Model values of water elevations, current velocities and ellipse parameters were computed. These data were then

utilised to calculate the available resource across the estuary using the three different approaches described in Section 2.1

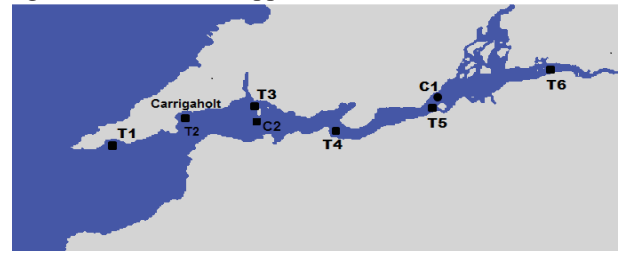


Figure 3-1 Extent of model domain and locations of measured data for tidal elevations (T1-T6) and current velocities (C2) used to validate the model.

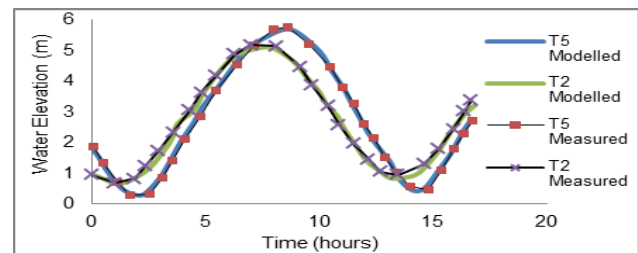


Figure 3-2 Comparison of measured water elevation data against the predicted model elevation data at T2 and T5.

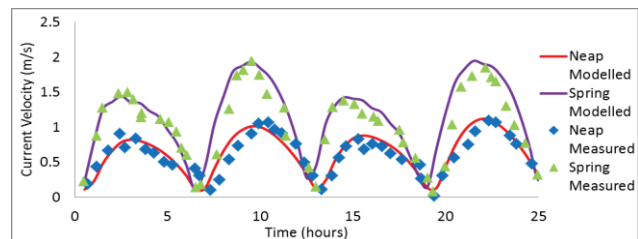


Figure 3-3 Comparison of measured current velocity data against the predicted model current data at C2.

4 RESULTS

4.1 Available Resource Assessments

The available power across the Shannon estuary, as calculated using the Fraenkel formula, the time-varying total velocity approach and the authors' developed time-varying primary direction of flow method, are presented in Figure 4-1 (a-c) respectively. All three assessments indicate greatest potential in three main areas (illustrated in red in Figure 4-1(a)), where the estuary narrows. Heightened tidal resource in these areas is due to the law of continuity; for mass flow to remain constant, when the area in which fluid flows is decreased, current velocities are forced to increase, resulting in greater power potential at that location.

Whilst a similar trend in tidal resource is indicated, there are substantial variations between the estimated powers. The Fraenkel approach is found to significantly over predict the tidal resource, estimating maximum powers of 2500W/m^2 , 33.3% greater than the 1875W/m^2 estimated using the time-varying approach and 100% greater than the 1250W/m^2 determined using the authors' primary flow approach. Whilst the time-varying total velocity method is more accurate than the Fraenkel approach it still over-estimates the tidal potential, with a reduction of approximately 33.3% noted between the

maximum powers estimated using the total and primary flow direction methods.

Overall the mean available power estimations across the estuary decrease with increasing accuracy of the methodology used. This accuracy is due to the fundamental nature of each method. For instance the Fraenkel formula is based on the assumption of sinusoidal flow with a neap/spring factor of 60%; however this may not always be the case. The time-varying total velocity approach contains inaccuracies as it fails to incorporate flow direction. The primary direction of flow approach considers the proportion of available energy that a fixed orientation horizontal axis turbine can extract from the flow by considering flow direction.

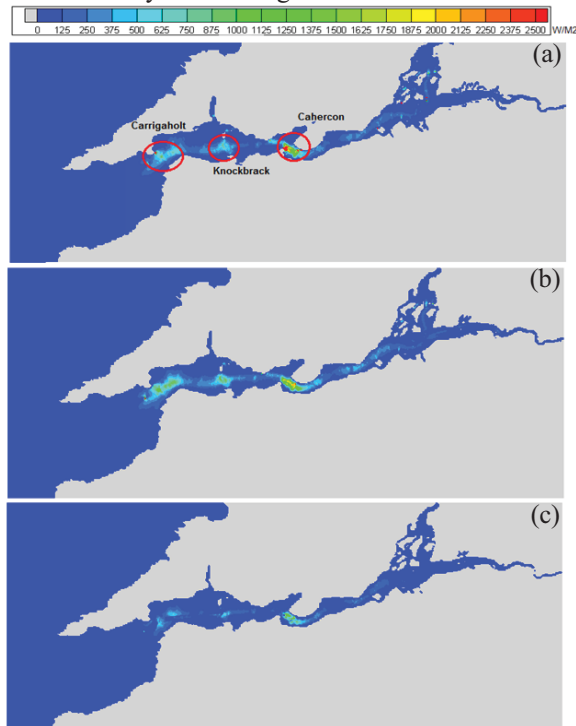


Figure 4-1 Mean available power (MW) across the Shannon estuary determined using (a) Fraenkel formula, (b) time-varying current velocities and (c) velocities aligned with the primary direction of flow, respectively.

4.2 Site Identification and Device Orientation

When selecting a suitable turbine deployment location both power availability and flow type must be considered. Tidal current ellipses were constructed for each grid cell in the model domain to assess variation in flow direction. The ellipses at four locations (A-D as illustrated in Figure 4-2) are presented in Figure 4-3. At all four locations, the M2 constituent was dominant. This was the case at all grid points and thus the properties of the M2 constituent were taken as being representative of the flow conditions.

The ideal location for fixed orientation, horizontal axis tidal turbines must have strong currents, and by extension large available power, combined with rectilinear flows. The ratio of M2 ellipse minor-to-major axes was used to indicate flow type with a low axis ratio confirming the presence of rectilinear flow.

Considering flow direction only, location A might be considered a suitable deployment site; however, most tidal

turbines require peak current velocities of 2.0-2.5m/s which are not reached at location A. Flow at location B was found to be both low in strength and multi-directional, meaning it is not a suitable turbine deployment site. The M2 ellipse at location C suggests flow is primarily rectilinear; however, the S2, MK3 and SK3 constituents, having relatively large major axes, which will also impact on flow direction at C, resulting in a multi-directional flow. Combined with the low ranging peak velocities of 1.0m/s experienced at the site it can be concluded it is not suitable for turbine siting. Analysis of the tidal ellipses at location D show strong rectilinear flow, and combined with strong peak currents in the range of 2.0m/s this is the most suitable of the four sites.



Figure 4-2 Locations A-D and potential berths (L1-L4).

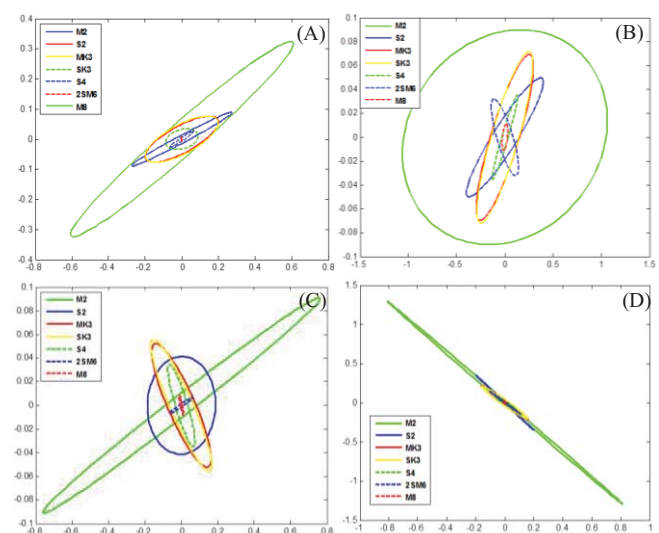


Figure 4-3 Tidal current ellipses for all constituents at locations A-D.

4.3 Frequency of Resource Availability

An accurate resource assessment of potential tidal energy extraction sites will depend on both flow speed and direction. Strong currents result in a high power potential, however, the proportion of available power a horizontal axis turbine can extract is dependent on the direction of current flow. Considering flow direction along with current speed will result in less over predictions of tidal power potential and improve accuracy of resource assessments.

Considering both the mean available power (see Figure 4-2) and the ratio of M2 ellipse minor-to-major axes, it is possible to identify the best locations for turbine deployment. Using this approach, three locations of interest within the estuary were chosen as potential sites for tidal energy extraction. The selected berths, (L1-L3) illustrated in Figure 4-2, are assessed in further detail, enabling validation of high tidal resource at these sites and allowing identification of the best deployment

locations. A fourth location, (L4) is also presented to demonstrate the benefits of incorporating flow directionality into the assessment. Further assessment of the potential resource at each selected site involved using both time-varying total velocity and the time-varying velocity vector aligned only with the primary direction of flow to determine the frequency of power availability. The resulting assessments based on both methodologies could then be compared and the most accurate results used to determine the most suitable tidal turbine to be deployed at a site. The current velocities utilised in each method and the resulting frequencies of power availability for each berth are presented in Figure 4-4 – 4-7.

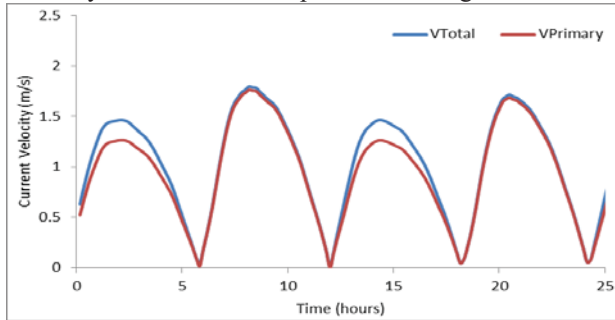


Figure 4-4 Comparisons of current velocities and power availability at location L1.

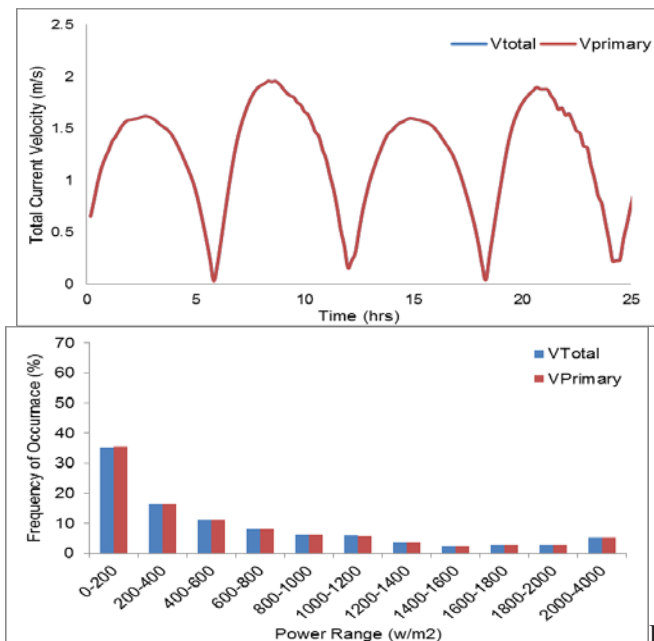


Figure 4-5 Comparisons of current velocities and power availability at location L2.

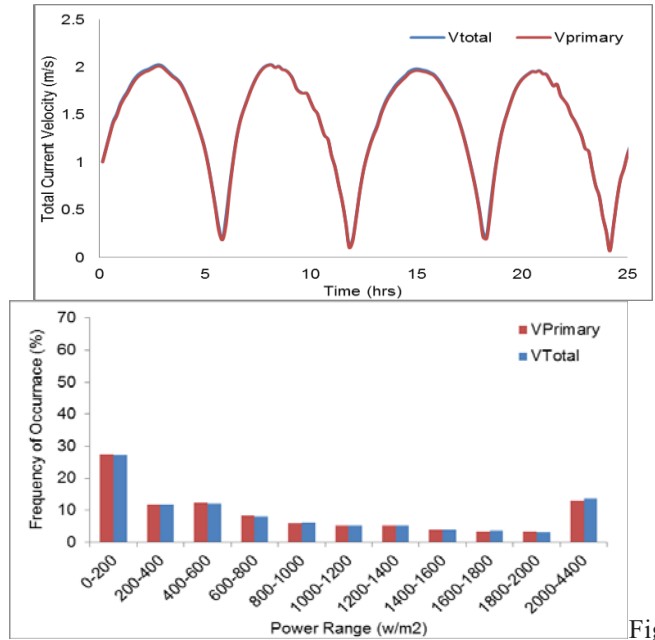


Figure 4-6 Comparisons of current velocities and power availability at location L3.

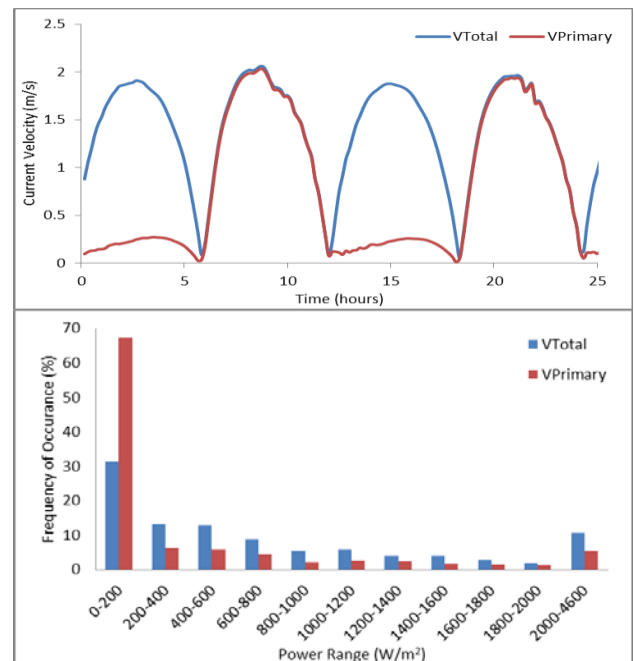


Figure 4-7 Comparison of current velocities and power availability at location L4.

Looking in more detail at the four selected locations it is noted that each varies in tidal nature. The impact of flow direction on resource assessments is demonstrated by drawing comparisons between the locations.

Tidal current ellipses indicated location L1 as a suitable turbine deployment location due to the strong currents and rectilinear flow present at the site. Further analysis (see Figure 4-4) strengthens this conclusion, indicating current velocities at L1 as relatively unchanged when the primary direction of flow is considered; this is a direct result of the rectilinear nature of the flow. Due to the high currents at location L1 high levels of power availability are expected. Results show maximum available powers of approximately 3000 W/m² and

2800W/m² determined using the total velocity and primary direction of flow methods respectively; however, these powers are available for extraction for less than 0.2% of the time in both cases.

Considering all four locations L2 and L3 are seen to have the highest current velocities, further assessment indicates rectilinear flow at both sites (see Figure 4-5-4-6). These results suggest they are highly suitable sites for tidal energy extraction. Maximum power estimates at location L2 reach 3800W/m² and 3400W/m² using the total velocity and primary flow approaches respectively. Location 3 possesses even greater maximum powers of over 4200W/m², determined using either method. The similarity of the results determined using both approaches is a result of the rectilinear nature of flow at these locations. As the powers decrease their extraction availability period is increased, this is a trend seen throughout assessment of all four locations, for example, in sites that stipulate rectilinear flow peak powers are available for extraction for a minimum proportion of time, whilst higher power ranges, for example, 400-600W/m² are available for over 10% of the full spring-neap tidal cycle.

Location L4 was initially noted as a potentially suitable site for turbine deployment, however, a closer look at current velocities indicates rotary flow, the effect of which is highlighted in the ebb tide, during which the magnitudes of primary and total flow velocities vary substantially. The rotary nature of the flow at this location has a significant impact on the resulting power availability, as illustrated in Figure 4 7.

Results emphasise the importance of incorporating flow directionality into resource assessments. Maximum powers at location L4 reach approximately 4500W/m²; however, these peak estimates are available for extraction for a minimal percentage of time. The difference in the frequency of power availabilities determined using both methods is substantial, for instance; resource estimates increase from 31% to 67% in the 0-100W/m² range and decrease from just 13% to around 6% in the 200-400W/m² range when the flow direction is considered. This is a direct result of the reduced currents during the ebb tide. The rotary nature of flow at this site emphasises the importance of incorporating flow direction in power estimations, however, it also suggests its unsuitability as a potential deployment site.

As a final comparison between the different assessment approaches, the annual power availability at the four initial locations of interest (L1-L4) was calculated using the mean powers determined by the three different approaches described in section 2.1.

Table 4.1 Annual available power at preferred berths using different assessment approaches

Average Available Power (kW/m ²) Over One Year			
Location	Fraenkel Formula	Time-Varying (Total) Velocity	Time Varying (primary) Velocity
L1	16.06	10.24	8.45
L2	24.82	15.37	15.31
L3	28.74	22.27	21.82
L4	12.36	6.73	2.62

5 CONCLUSIONS

Three methods for calculating the power that is available from tidal currents are presented. Traditional approaches employ the total velocity vector, using either the peak or time-varying velocities. The authors' approach employed velocity vector components aligned only with the primary direction of current flow.

Resource assessment analysis is carried out by applying these methodologies to the Shannon estuary. Results indicate three regions within the estuary that show potential for tidal energy extraction. Further detailed analysis on four specific locations determined the proportion of time that varying amounts of power are available for energy extraction over a full spring-neap tidal cycle.

It is shown that using the total velocity vector for power availability assessments can significantly over predict the tidal energy potential, whilst incorporating flow direction results in a more accurate assessment.

The over predictions involved when using the total velocity component in power calculations are due to the fact that horizontal axis tidal turbines cannot rotate into the tidal stream as it changes direction during different stages of the tide.

Results throughout this research have indicated that considering the primary direction of current flow is the most accurate approach to resource assessment and, hence, it is these results that should be used to determine the most suitable turbine to be deployed at a site.

This is a first stage tidal resource assessment of the Shannon estuary. The study has identified three areas of high resource availability that will be assessed in more detail using a high resolution nested model.

ACKNOWLEDGMENTS

The authors wish to thank the Irish Research Council and MaREI for funding this research.

REFERENCES

- [1] L. S. Blunden and a. S. Bahaj, "Tidal energy resource assessment for tidal stream generators," vol. 221, pp. 137–146, 2007.
- [2] M. Grabbe, E. Lalander, S. Lundin, and M. Leijon, "A review of the tidal current energy resource in Norway," *Renewable and Sustainable Energy Reviews*, vol. 13, no. 8, pp. 1898–1909, 2009.
- [3] N. Ren, Hartnett, "Assessment Methods of Data Assimilation in Oceanographic Model Forecasting," *E-proceedings fo 36th IAHR World Congr.*, 2015.
- [4] SEI (Sustainable Energy in Ireland), "Tidal & Current Energy Resources in Ireland," 2004.
- [5] L. Fraenkel, P., "Power from marine currents," *Proc. ImechE Part A J. Power Energy*, vol. 216, no. 1, pp. 1–14, 2002.
- [6] R. A. Falconer, *An introduction to nearly horizontal flows*, Coastal, E. E and F N Spoon Ltd, 1993.
- [7] E. Marone, F. Raicich, and R. Mosetti, "Harmonic tidal analysis methods on time and frequency domains: similarities and differences for the Gulf of Trieste, Italy and Paranagua Bay, Brazil," *Boll. di Geofis. Teor. ed Appl.*, vol. 54, no. 2, pp. 183–204, 2003.
- [8] VIMS (Virginia Institute of Marine Science), "Tidal analysis." [Online]. Available: http://web.vims.edu/physical/research/TCTutorial/tide_analysis.html. [Accessed: 15-Apr-2015].
- [9] M. G. G. Foreman and P. Bay, "Manual for Tidal Heights Analysis and Prediction," Sidney, B.C., Canada, 1996.
- [10] M. G. G. Foreman, J. Y. Cherniawsky, and V. a. Ballantyne, "Versatile harmonic tidal analysis: Improvements and applications," *J. Atmos. Ocean. Technol.*, vol. 26, no. 4, pp. 806–817, 2009.

Development of a 2D hydrodynamic model to assess the risk of flooding from wave overtopping and tidal inundation of a site in Co. Clare

K. Barry¹, D. Walsh¹, J. Reilly¹, S. Lizondo¹, J. Ascoop¹, S. Lahiffe², T. Tiernan²

¹Ove Arup & Partners, 50 Ringsend Road, Dublin 4

²Clare County Council, New Ennis Road, Ennis, Co. Clare

email: kevin.barry@arup.com, daniel.walsh@arup.com, joshua.reilly@arup.com, susana.lizondo@arup.com, julie.ascoop@arup.com, SJLahiffe@clarecoco.ie, ttiernan@clarecoco.ie.

ABSTRACT:

A very significant storm event in January 2014 resulted in severe coastal erosion and flooding to Cloughaninchy beach in Co. Clare. A coastal flood and erosion risk management feasibility study of the site was subsequently commissioned to understand the level of risk at the site and also to develop an engineering solution to mitigate the associated risks.

This paper details the construction, calibration and running of the 2D MIKE 21 hydrodynamic model that was developed as part of the study.

A 2km long embankment (natural and man-made) protects the site from tidal inundation but is vulnerable to overtopping by nearshore waves at a number of locations. The methodology used in estimating this risk was as follows: (1) Estimation of nearshore wave heights using a MIKE 21 SW model, (2) Estimation of wave overtopping discharges using the Eurotop manual. Given the significant length of embankment and its spatially varying crest level elevation, innovation in modelling was required to ensure the calculations were detailed and robust while not being overly burdensome, and (3) Inclusion of the wave overtopping discharges in the 2D model as source discharges points.

The results of the detailed modelling indicate that extensive areas of the site are at risk of flooding from wave overtopping. The results also suggest that a more simplified approach to estimating the wave overtopping flood risk at the site may not have been sufficient to highlight the risk.

KEY WORDS: flooding; wave overtopping; coastal modelling.

1 INTRODUCTION

1.1 Background

On Friday morning, 3 January 2014 a combination of high tide, substantial sea swell and onshore winds resulted in severe damage to the naturally occurring and man-made coastal protection infrastructure at Cloughaninchy Beach which is located approximately 2.5km from Quilty in Co Clare (Figure 1). The storm event also led to severe flooding of a number of residential properties in the vicinity of the beach which required the evacuation of residents. The primary source of flooding to the houses was wave overtopping. There were no human fatalities as a result of the event but a number of domestic animals drowned.



Figure 1 Site location

In January 2015 Arup was commissioned by Clare County Council (CCC) to develop a Coastal Flood and Erosion Risk Management Plan for Cloughaninchy. The plan was to assess the risk of flooding and coastal erosion to the site and to present engineering solutions to mitigate the associated risks.

A number of detailed numerical models were developed as part of the study. The models informed a detailed risk assessment, preliminary environmental assessment, options and feasibility assessment and multi-criteria analysis, which in turn informed the Coastal Erosion and Flood Risk Management Plan. A cost benefit analysis on the preferred engineering solution was also undertaken.

A two-dimensional hydrodynamic model of Cloughaninchy was developed as part of the study in order to simulate coastal flooding at the site. The model calculated the extent, depth and velocities for a range of return period events for the current, mid-range and high-end future scenario events. Output from the model was used to produce a suite of flood risk maps for the site which were used in the development of the Management Plan.

This paper details the development of the hydrodynamic model and presents model results.

1.2 The site

The site is approximately 2km long and reaches from Seafeld Pier in the North of the site to the White Cottage in the South of the site (Figure 2). There are a number of residential properties at the site as well as a pumping station and local roads. An embankment runs all along the Western boundary

of the site as indicated by the blue line in Figure 2. The embankment is characterised by a natural dune system in the northern section of the site (indicated by the top photograph in Figure 2) and a Clougher revetment in the southern section of the site (indicated by the bottom photograph in Figure 2).



Figure 2 Cloughaninchy

Four significant breaches occurred through the embankment during the January 2014 event. Clare County Council undertook emergency repair works on the breaches in the immediate aftermath of the event which prevented further damage to the site when an event similar to the 3 January event occurred again on 1 February (Figure 3).



Figure 3 Emergency repair work being undertaken on the coastal embankment (photo provided by Clare County Council)

2 DATA COLLECTION

A number of detailed high-resolution datasets were collected in order to construct the hydrodynamic model. These include: (1) LiDAR data, (2) topographic data, and (3) nearshore and offshore bathymetric data.

Additionally, design water levels from the Irish Coastal Protection Strategy Study (ICPSS), tide gauge data and flood event information were also collated.

2.1 LiDAR

A high resolution LiDAR survey of the site was undertaken in order to capture the spatially-varying floodplain elevations. The point density of the data is approximately 4 points per m² per flight line. The vertical accuracy is $\pm 12\text{cm}$ while the horizontal accuracy is $\pm 24\text{mm}$ on hard well defined areas. An image of the Cloughaninchy LiDAR dataset is presented in Figure 4.

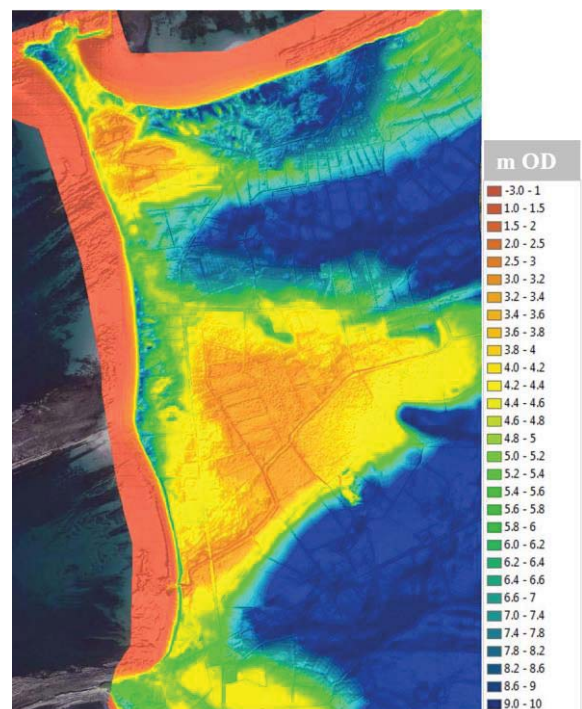


Figure 4 Lidar dataset

2.2 Topographic data

A topographic survey was undertaken to determine the ground elevations of the beach and nearshore areas as well as the crest level of the embankment.

The nearshore data was gathered during spring tides to ensure maximum coverage possible. Data was also recorded for the two rivers which discharge onto the beach. High water marks from the 2014 flood event indicated on post flood event photographs were also recorded as part of the survey.

2.3 Nearshore and offshore bathymetric datasets

The bathymetric survey was gathered using a single beam echo sounder survey undertaken with a CeeducerPro. The gathered data was combined with existing INFOMAR data from survey leg CB13_05 to provide an overall dataset of the

bathymetry adjacent to the site. The nearshore data was gathered during Spring tides to ensure maximum coverage possible. A number of INFOMAR datasets were also used in the development of a spectral wave model.

2.4 Tide gauge data

Tide gauge data was sourced from the Marine Institute, Shannon Foynes Port Company and ESBI for a number of gauges around the West coast of Ireland. The data was used to estimate the severity of the January 2014 event and to provide a tidal curve for the tidal boundary conditions of the site.

2.5 ICPSS Study

The Irish Coastal Protection Strategy Study (ICPSS) provides predictions of extreme sea levels for a number of return period events for various locations around the Irish coast. This data was used in the study to derive the design tidal water level (astronomical plus surge) boundary conditions at our site of interest. The ICPSS design water levels were also used to estimate the severity of the January 2014 event. The design water levels for the point closest to Cloughaninchy are presented in the table below.

Table 1. ICPSS design water levels for the site of interest

Return Period	Point SW52
2yr	2.66
5yr	2.79
10yr	2.88
20yr	2.97
50yr	3.08
100yr	3.17
200yr	3.26
1000yr	3.46

2.6 Previous flood events

Clare County Council provided Arup with photographs and video footage of the storm events of 2014. This information was used to understand the extent of the damage and flooding caused by the event.

3 DEVELOPMENT OF THE 2D HYDRODYNAMIC FLOOD MODEL

3.1 Software

The model has been developed using the flexible mesh (FM) version of MIKE 21 HD. MIKE 21 is developed by the Danish Hydraulic Institute (DHI) and is recognised internationally as being a leading edge software in the field of coastal modelling.

The model calculates the time varying water levels and current velocities on an irregular grid of nodes throughout the model domain.

3.2 Mathematical formulations

The model is based on the solution of the three-dimensional incompressible Reynolds averaged Navier-Stokes equations, subject to the assumption of Boussinesq and hydrostatic

pressure. Integration of the horizontal momentum equations and the continuity equation over depth yields the two-dimensional shallow water equations used by the model:

Continuity Equation:

$$\frac{\partial h}{\partial t} + \frac{\partial h\bar{u}}{\partial x} + \frac{\partial h\bar{v}}{\partial y} = hS \quad (1)$$

Horizontal momentum equation for the x – component (the y component follows a similar formulation):

$$\begin{aligned} \frac{\partial \bar{h}u}{\partial t} + \frac{\partial \bar{h}u^2}{\partial x} + \frac{\partial \bar{h}v\bar{u}}{\partial y} = f^{\bar{v}}h - gh \frac{\partial \eta}{\partial x} - \frac{h}{\rho_O} \frac{\partial p_a}{\partial x} - \\ \frac{gh^2}{2\rho_O} \frac{\partial \rho}{\partial x} + \frac{\tau_{sx}}{\rho_O} - \frac{\tau_{bx}}{\rho_O} - \frac{1}{\rho_O} \left(\frac{\partial s}{\partial x} \frac{\partial s}{\partial x} + \frac{\partial s}{\partial y} \frac{\partial s}{\partial y} \right) + \end{aligned} \quad (2)$$

Where:

t = time; x, y and z are the Cartesian co-ordinates; η = surface elevation; d = still water depth; h = $\eta + d$ is the total water depth; u, v and w are the velocity components in the x, y and z direction; f is the coriolis parameter; g = gravitational acceleration; ρ is the density of water; s_{xx} , s_{xy} , s_{yx} and s_{yy} are components of the radiation stress tensor; ν_t is the eddy viscosity; p_a is the atmospheric pressure; S is the point source discharge and (u_s, v_s) is the velocity by which water is discharged to the ambient water.

3.3 Model domain and grid resolution

The extent of the 2D model domain is presented in Figure 5.



Figure 5 Model domain

It can be seen from the figure that model covers a significant area of sea adjacent to the beach. The extent of the model on land is sufficient to ensure the full extent of the coastal floodplain is covered by the model.

The 2D model resolution is set by the size of the triangular mesh elements of the 2D model grid. As the model is a flexible mesh the resolution varies throughout the domain. Defining the model resolution involves a trade-off between utilising a high-resolution mesh to accurately resolve the flow and the computational run time of the model which increases with increasing mesh resolution. A close up view of the mesh is presented in Figure 6. It is noted that the areas used in the computational mesh (and presented on the figure) correspond to maximum values.



Figure 6 Close up view of the computational mesh of the model

Once the resolution was formalised the computational mesh was smoothed to optimise model performance and ensure a smooth transition between the areas of varying resolution.

3.4 Time step

An adaptive time step was used in the model with the maximum time step set as 5 seconds. The actual time step used by the model throughout the simulation was determined by the model computations based on the requirements of the mesh.

3.5 Model parameters

Appropriate Manning's n roughness values were selected for the model based on standard values in the literature [1]. Values were based on an analysis of land use, site visit observations and the model calibration.

3.6 Boundary conditions

A time varying water level time series has been applied all along the open sea tidal boundary of the model. The boundary condition (astronomical tide plus surge) was been derived from two separate datasets:

- The maximum water level of the tidal signal was taken from point 51 of the ICPSS dataset (Table 1);
- Data from the Ballyglass tide gauge (located approximately 100km from the site) was used to for the tidal curve of the boundary conditions.

Utilising data from an existing tide gauge to formulate the tidal curve was necessary given the absence of any tidal data from the site of interest. Ballyglass was selected as the most suitable tidal data to use based on its tidal amplitude and phase characteristics.

4 WAVE OVERTOPPING

4.1 Overtopping during the January 2014 event

Through a detailed assessment of the various datasets available on the January 2014 event and a close inspection of the LiDAR dataset coupled with site visits, it was determined that wave overtopping was the primary source of flooding during the January 2014 event. Significant volumes of water overtopped the embankment and flooded the site.

The overtopping was exacerbated by the formation of breaches through the embankment which succeeded in lowering the crest elevation which in turn lead to greater volumes of wave overtopping.

A detailed assessment of the risk of wave overtopping at the site was therefore undertaken as part of the study. Wave overtopping volumes were first estimated using a detailed methodology, and these were subsequently included in the 2D hydrodynamic model as multiple source discharge points.

4.2 Wave overtopping methodology

There were two key steps in the estimation of the wave overtopping volumes:

- **STEP 1** – Nearshore wave heights were calculated for a range of return period events. This was undertaken through detailed Spectral Wave modelling of the area adjacent to the site using MIKE 21 SW. It is noted that this work was also used to inform the engineering design of the solutions for the site;
- **STEP 2** – The empirical formulations in the Eurotop manual [2] and CIRIA Rock Manual [3] were used to calculate volumes of overtopping in litres per second per metre length of embankment. The nearshore wave heights, embankment geometry and various overtopping parameters were used in these calculations.

4.3 Defining the wave overtopping as source discharge points in the model

Once the overtopping volumes in l/s/m were calculated for a number of locations along the embankment, the total overtopping in m^3/s was estimated through consideration of the duration of a single overtopping wave, the time between successive overtopping waves and the water level threshold below which waves cannot overtop.

The overtopping flows were then defined in the model at 60 separate source discharge point along the full length of the embankment.

5 MODEL CALIBRATION

A post flood event photograph at one of the properties inundated by the January 2014 flood indicated the peak water level. This level was subsequently surveyed as part of the

topographic survey and the results of the model were compared against it.

The recorded flood depth at the property was 0.35m while the model water depth was 0.18m – a difference of 0.17m.

6 RESULTS OF THE MODEL

Six separate return periods were considered in the study for the current, MFRS and HEFS. In addition, three separate source scenarios were also considered:

- Tide only
- Tide + wave overtopping
- Tide + Wave Overtopping + Breach formation

Figure 7 and all subsequent figures present modelled maximum flood extents for various scenarios considered as part of the study. It can be seen from Figure 7 that the area behind the embankment on the North beach is at risk from tidal flooding for the 10%, 1% and 0.1% AEP event. The tide inundates this area of the beach through the culvert that allows the small stream discharge onto the beach.

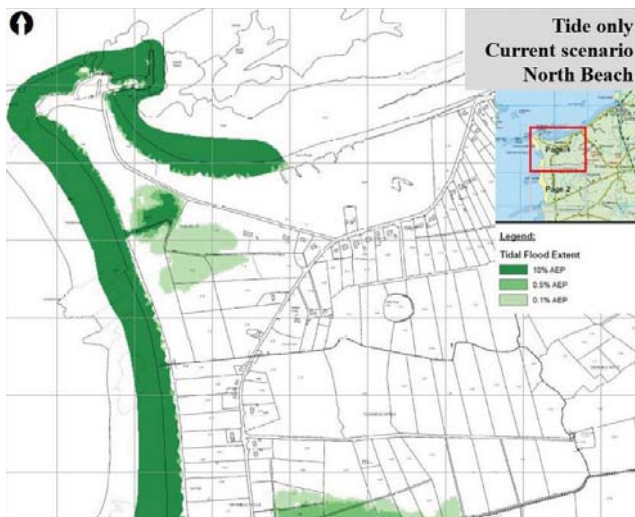


Figure 7 Flood extent map for the North Beach: Current Scenario, tide only

It can be seen from Figure 8 that when wave overtopping is considered along with the tidal inundation, a much greater extent of flooding is predicted by the model for the various return events. One of the key differences between the results is the flow path predicted by the model in the lower section for the tide + wave overtopping scenario. At this location the embankment is relatively low and is overtopped for the current scenario. If overtopped, the flood waters travel in south westerly direction and flood a number of houses due to local topography.

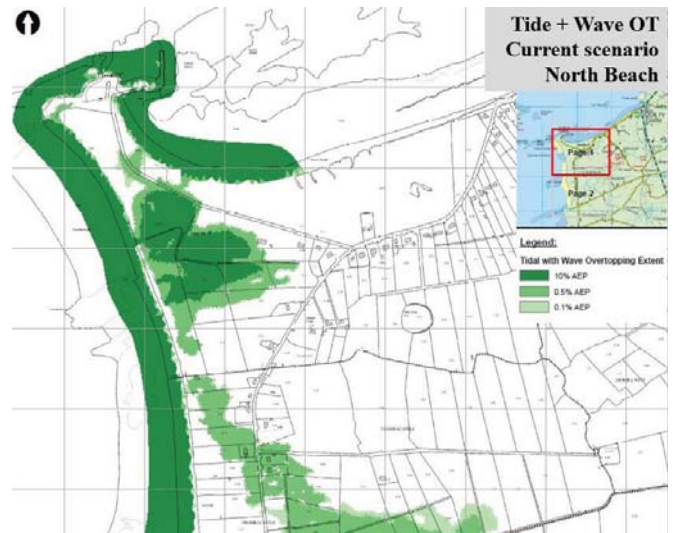


Figure 8 Flood extent map for the North Beach: Current Scenario, tide + wave overtopping

Figure 9 and Figure 10 present the flood extents for the South beach for the 10%, 1% and 0.1% AEP events for the current scenario. It can be seen from Figure 9 that while a large area of the site is at risk from tidal flooding, none of the houses are indicated as being at risk.

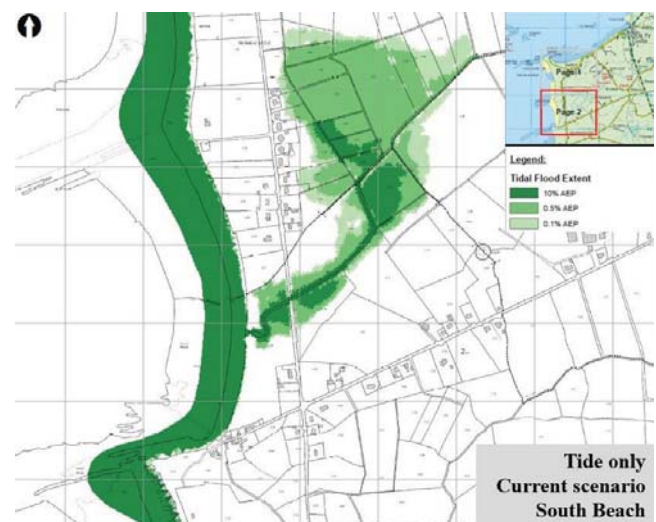


Figure 9 Flood extent map for the South Beach: Current Scenario, tide only

Figure 10 presents the extent for the tide + wave overtopping + breach scenario. It can be seen that a number of the houses are indicated as being at risk of flooding for this scenario. The location of the breaches in the model were selected based on a detailed inspection of the embankment which considered likely breach locations given the current state of the embankment.

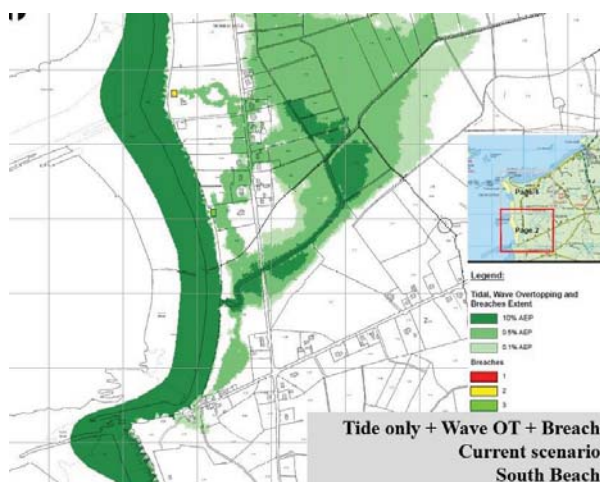


Figure 10 Flood extent map for the South Beach: Current Scenario, tide + wave overtopping + breach

It is noted that the breaches do not lead to tidal inundation of the site as the existing ground levels behind the embankment at the breach locations are elevated above the level of the return period events considered. The flooding that occurs through the breach is the result of wave overtopping volumes.

Figure 12 present the flood extents for the mid-range future scenario for the 10%, 1% and 0.1% AEP events for the tide + wave overtopping scenario for the South Beach. It can be seen from the figures that extensive areas of the site are at risk from flooding with all of the houses in the south beach indicated as being at risk.

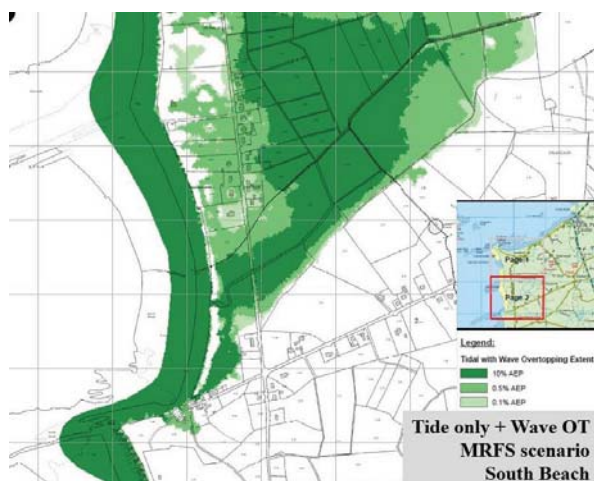


Figure 12 Flood extent map for the South Beach: MRFS, tide + wave overtopping

7 DISCUSSION

A detailed two-dimensional hydrodynamic model of Cloughaninchy Beach and the adjacent sea area was developed as part of the study. The model calculated the extent, depth and velocities for a range of return period events for the current, mid-range and high-end future scenario events. Output from the model was used to produce a suite of flood risk maps for the site which were used in the development of the Management Plan.

A number of detailed high-resolution datasets were collected in order to construct the hydrodynamic model which included LiDAR data, topographic data, and nearshore and offshore bathymetric data. Design water levels from the Irish Coastal Protection Strategy Study (ICPSS), tide gauge data and flood event information were also collated.

The model was used to simulate flooding from three separate sources: tidal inundation, wave overtopping the embankment at the site and wave overtopping through the breach formation.

A detailed methodology was developed to estimate the volume of wave overtopping. There were two key steps in the method: estimation of near shore wave heights using a spectral wave model and, calculation of wave overtopping volumes using the Eurotop manual and CIRIA Rock manual.

It was seen from the results that for the current scenario none of the houses at the site are at risk from the 200 year tidal flood event as they are elevated above the tidal floodplain. A number of the houses are however at risk of flooding due to wave overtopping. It was seen that waves can overtop a low point in the embankment in the northern section of the site and flood the area behind the embankment.

A number of breaches in the embankment formed during the 2014 event. When breaches of similar dimensions are included in the design runs of the model a greater number of properties are indicated as at risk from flooding. The breaches do not allow tidal ingress as the land elevation of the ground behind the breach is relatively high, but rather the breaches allow a greater volume of water from wave overtopping to flood the site.

The results indicate that extensive areas of the site are at risk from flooding for the MRFS with all of the houses in the south beach shown to be at risk from flooding.

While the houses are the key receptors at the site it is noted that extensive areas of agricultural land are at risk from both tidal and fluvial flooding.

The results illustrate the benefit of undertaking detailed high-resolution modelling in order to assess the risk of flooding. The results also demonstrate the benefit in undertaking a detailed assessment of the risk of wave overtopping. It was seen from the current scenario model results that a number of houses were at risk from flooding from overland flow arising from wave overtopping. Adopting a more simplified approach to assessing flood risk may not have highlighted this risk.

It is recommended that a similarly detailed modelling approach be adopted for all coastal flood risk management studies where wave overtopping is a known to be a significant source of flooding.

The results for the MRFS indicate extensive flood risk at the site highlighting the need for adequate engineering measures to address climate change for coastal communities at risk.

REFERENCES

- [1] Chow, V.T., Open Channel Hydraulics, McGraw-Hill, 1959;
- [2] EurOtop manual 2007. Overtopping manual; Wave overtopping of Sea Defences and Related Structures – Assessment Manual. UK: N.W.H. Allsop, T. Pullen, T. Bruce. NL: J.W. van derMeer. DE: H. Schüttrumpf, A. Kortenhaus. www.overtopping-manual.com.
- [3] CIRIA Rock Manual. The use of rock in hydraulic engineering (second edition) (C683). 1991. CIRIA, CUR, CETMEF.

Development of a high resolution wave model at AMETS using SWAN

Reduan Atan¹, Jamie Goggins², Stephen Nash³

College of Engineering and Informatics, National University of Ireland, Galway, Ireland

Centre for Marine and Renewable Energy Ireland (MaREI), Galway, Ireland

Ryan Institute for Environmental, Marine and Energy Research, Galway, Ireland

¹reduan.atan@nuigalway.ie, ²jamie.goggins@nuigalway.ie, ³stephen.nash@nuigalway.ie

ABSTRACT: The SWAN gridded wave model (version 41.01) is used in the development of a high resolution wave model at the Atlantic Marine Energy Test Site (AMETS), a full scale wave energy test site on the west coast of Ireland. A nesting methodology has been implemented in order to replicate wave conditions from oceanic scale to a local scale. The oceanic domain covers a large area of the north-eastern Atlantic Ocean at a coarse resolution of 0.05 degrees, while the AMETS domain is resolved at 0.0027 degrees (approximately 300m). The AMETS wave model is calibrated against two wave buoy stations at AMETS and a number of sensitivity tests were conducted for the period of December 2013. Model validation was conducted for the year of 2010-2013 and shows that the developed wave model performs well for longer periods. The results of the calibration/validation processes confirm that the model is accurate and can be reliably used for wave resource assessment at the site into the future.

KEY WORDS: AMETS, SWAN, wave energy test site, wave model.

1 INTRODUCTION

Ocean waves can be predicted with numerical modelling approaches which involve mathematical solutions solved by a computer program. Several developed numerical wave models such as Wave Modelling (WAM) wave model [1], Wave Watch III (WW3) wave model [2], MIKE21 spectral wave model [3] and Simulating Waves Nearshore (SWAN) wave model [4] are widely used in hindcasting and forecasting wave conditions.. Wave predictions at global or large ocean scales can be simulated with WAM, WW3 or SWAN models. However, SWAN is mostly used at regional scale, where the intention is for the transition from regional scales to local scales. Thus, the wave model used in the development of high resolution wave model at a local scale in this paper is SWAN, an open source numerical model developed by Delft University of Technology (TUDelft). SWAN wave models have been used widely in predicting wave conditions in oceanic and nearshore scale, such as in the Netherlands [5], the UK [6], Scotland [7], Portugal [8], Spain [9] and Ireland [10]. In Ireland, an oceanic scale forecast wave model using SWAN developed by Marine Institute covers an enormous extent of north-eastern Atlantic Ocean from -19.9875 E to 0.0125 E and 36.5125 N to 59.9875N, where the model resolution is 0.025 degrees (approximately 2.5km) gridded model. The model performance has been validated against offshore wave buoys within Irish waters and also generates a daily 6 day forecast for parameters such as significant wave height (Hs), zero-crossing wave period (Tz) and mean wave direction (MWD).

There is a major interest in wave energy resource and variability in Ireland [11][12]. For example, there are two existing test sites for wave energy convertors on Ireland's west coast [13] - the Galway Bay test site (GBTS) (-9.067E, 53.249N) and the Atlantic Marine Energy Test Site (AMETS) at Belmullet (-9.991E, 54.225N). A third site off the West

Coast of Ireland (off Killard in County Clare, near Doonbeg, -9.52E, 52.775N) is the focus of the Westwave demonstration project, which aims to deploy five wave energy devices by 2018 in a move towards commercialisation of wave power generation. The AMETS is located on the West coast of Ireland, where the coastline is exposed directly to the north-eastern Atlantic Ocean, as shown in Figure 1. The area is influenced by variable weather conditions for Ireland [14], as well as local geography and bathymetry [15]. The main objective of this paper is the development of high resolution wave model at the AMETS using SWAN (version 41.01), a nesting method was implemented from a coarse gridded wave model to a finer gridded wave model for at the AMETS. The boundary conditions for the finer grid are derived from the coarse grid computation [16]. A similar modelling approach has been conducted in [17] and [12] using SWAN. However, a detailed sensitivity tests on model calibration and a justification on model suitability for wave resource assessment were not presented in the aforementioned literature. Hence, in this paper, a detailed modelling approach with model calibration and model improvement is presented. Model accuracy is compared with the published values in "Guide of Wave Analysis and Forecasting" guidelines [18] and model suitability for wave resource assessment is also discussed. Moreover, the main purpose of developing the wave models is to conduct an assessment of wave characteristics and resource variability at the study area with a high resolution wave model for a 12 years period (2004 – 2015) in the future. A preliminary assessment of wave characteristics and resource assessment at the AMETS with the coarse wave model outputs is discussed in [19]. The models have been developed in the Centre for Marine and Renewable Energy (MaREI) at the National University of Ireland, Galway (NUI Galway), where the models were calibrated and validated against measured data. An overview

of the model development is presented in Section 2. Detailed model results improvement from a coarse to a fine model with model calibration and validation are presented in Sections 3. Finally, the conclusions from the model results analysis are presented in Section 4.

2 MODEL DEVELOPMENTS

SWAN is a third-generation wave model and the implemented equation used in the model is the action balance equation, where it takes consideration of wave-current interactions. The action balance equation used in SWAN model is

$$S(f, \theta) = S_{in}(f, \theta) + S_{nl3}(f, \theta) + S_{nl4}(f, \theta) + S_{wc}(f, \theta) + S_{bfr}(f, \theta) + S_{surf}(f, \theta) \quad (1)$$

where $S_{in}(f, \theta)$ term represents wave generation by the wind which can be activated with the third wave generation (GEN3) command, while the nonlinear wave-wave interactions represent by quadruplet wave-wave interactions ($S_{nl4}(f, \theta)$) and supplemented triad wave-wave interactions ($S_{nl3}(f, \theta)$). Furthermore, the dissipation source is represented by white-capping ($S_{wc}(f, \theta)$), bottom friction ($S_{bfr}(f, \theta)$) and depth-induced (surf) breaking ($S_{surf}(f, \theta)$). It is formulated in Cartesian coordinates, and optionally in spherical coordinates, to accommodate small and large scale computations based on the area of interest. The computational schemes to propagate the waves through geographical space use finite-difference schemes (two dimensional rectangular grid), which are simple, robust and economical for application in oceanic waters. A further detailed description on SWAN wave models can be found in “Waves in Oceanic and Coastal Waves, Chapter 9 The SWAN wave model” [20]. Two wave models have been developed in NUI Galway – the coarse Ireland (CI) wave model at 0.05 degrees resolution and the high resolution AMETS wave model at 0.0027 degrees resolution (approximately 300m). A detailed overview of each model is presented in the next section accordingly.

2.1 CI wave model

The CI wave model has been developed with a spherical coordinates setup to reproduce the development of swell waves in large open water including high wave events at regional scale before they reach Ireland coastlines. The CI model domain is illustrated in Figure 1. The model resolution is 0.05 degrees (gridded model) and covers a large area of the Atlantic Ocean to the extent of -20E to -3E and 50N to 59N. The main wind forcing supplied as surface boundary conditions is taken from the European Centre for Medium-Range Weather Forecast (ECMWF) Era-interim [21] at 0.5 degrees spatial resolution with 6 hourly time resolution. The wave data at the boundaries is extracted from a global WW3 wave model, a model developed by U.S. Navy Fleet Numerical Meteorology and Oceanography Centre (FNMOC) [22] at 6 hourly time resolution and bathymetry data was retrieved from ETOPO1 at 1 degrees resolution [23], [24]. Blue Kenue software [25] was used to interpolate processed bathymetry datasets in order to generate 0.05 degrees resolution gridded model domain. The recommended geographical propagation for large geographical domains for non-stationary mode in SWAN is Stelling and Leendertse

(S&L) scheme. Furthermore, a detailed methodology for the CI model development with number of sensitivity tests for model calibration to identify the best model setup is discussed in [26]. Thus, the best model setup used the third wave generation formulation (GEN3) of Janssen formulation with the coefficient of white capping dissipation rate (Cds) as 3×10^{-5} and delta (δ) of 1.5 for the CI wave model. The modelled outputs were compared to available measured data from wave buoys [27] located within Ireland waters (see Table 1, Figure 1 and Figure 2) for calibration (November 2013) and validation purpose (2010 to 2013). A comparative statistical analysis between measured and modelled data for significant wave height (H_s) and zero up-crossing wave period (T_z) was conducted in order to determine model accuracy based on root-mean square error (RMSE), coefficient of determination (R^2), Scatter Index (SI) and bias calculations. A detailed discussion on model performance is presented in Section 3.

Table 1 Summary of available measured data

Station	Point	Depth (m)	Available measured data	Measured Data resolution	Modelled data resolution
Berth A	-10.3E, 54.2N	100	Jan 2012 to date	30 min	30 min
Berth B	-10.12E, 54.23	50	Jan 2010 to date	30 min	30 min
M3	-10.6E, 51.2N	155	Jan 2007 to date	1 hour	30 min
M4	-9.9E, 54.9N	80	Jan 2008 to date	1 hour	30 min
M6	-15.9E, 53.0N	3280	Jan 2007 to date	1 hour	30 min

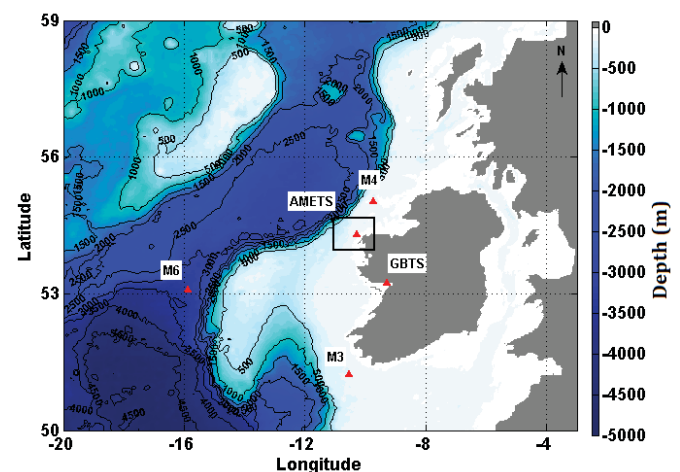


Figure 1 The CI model domain with wave buoy locations [19]

2.2 AMETS wave model

A nested local AMETS wave model at 0.0027 degrees resolution (approximately 300m) has been developed to reproduce the development of wind-generated waves in limited local fetch including high wave events at local scale with a nesting configuration from 0.05 degrees resolution to 300m resolution. Figure 2 shows an overview of the AMETS model domain, which covers -11.05E to -9.7E and 53.95N to 54.65N. The bathymetry data was obtained from INFOMAR datasets at 250m resolution [28] and the Blue Kenue software

was used to interpolate processed bathymetry datasets in order to generate 300m resolution gridded model domain. A high resolution wind forcing from ECMWF at 0.125 degrees spatial resolution with 6 hourly time resolution was used as surface boundary conditions, while the open boundary conditions were supplied from the nested spectral boundary outputs generated from the CI wave model at 30 minutes intervals. The orientation of the model is 0 degree clockwise in a spherical geometrical coordinate system to ensure all open boundaries are close to 90 degrees for all major in or outflow wave formations. The final model setup was achieved based on a number of sensitivity tests (see Section 3) conducted in the model calibration (December 2013) and validation process (2012 – 2013 at Berth A and 2010 to 2013 at Berth B). The best model setup used the GEN3 of Janssen formulation with the Cds as 2×10^{-5} and δ of 2 were found to be the best combination setup. Similar to the CI model, the performance of the AMETS model were analysed based on model calibration and validation parameters of RMSE, R^2 , SI and Bias for Hs and Tz. A detailed model performance analysis is discussed in the next section.

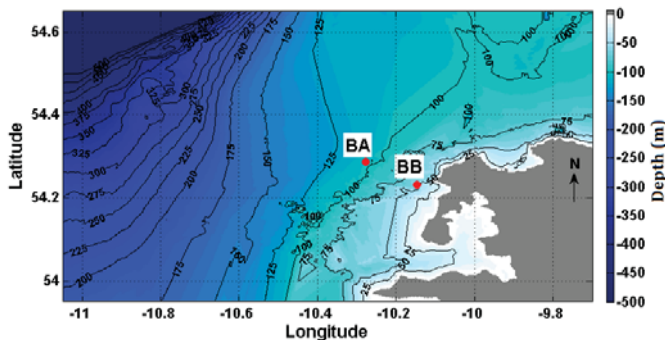


Figure 2 The AMETS model domain with wave buoy locations.

3 MODEL RESULTS

The model performance analysis was calculated based on validation parameters of RMSE, R^2 , SI and bias for the CI wave model and the AMETS wave model. Table 2 shows the summary of CI model validation, where the main stations selected for model validation are the offshore wave buoys at M3, M4 and M6 stations. Based on the values from Table 2, it is observed that the CI wave model managed to replicate similar wave conditions with the R^2 values above 0.9 for Hs and above 0.7 for Tz. It is also observed that the bias values were below 0.4m for Hs with RMSE below 0.7m, while the bias values for Tz were below 0.4s with RMSE values less than 1.8s at M3, M4 and M6 stations. The R^2 values for Hs and Tz at the offshore bouys (i.e. M3, M4 and M6 stations) are consistent with the published validation values of 0.94 and 0.88 in [29] with WW3 model. Moreover, the RMSE and bias values of wave height were within the range of the published statistical values (RMSE=0.4-0.7m, bias=0.05-0.2m) of the third wave generation model simulated by the ECMWF in the United Kingdom recorded in the “Guide of Wave Analysis and Forecasting” guidelines for wave height published by World Meteorological Organization (WMO) [18] for different part of the world oceans. Thus, it is evident that the CI wave model managed to reproduce wave conditions at an oceanic

scale following the WMO guidelines and sufficient to provide nested boundary conditions for the high resolution AMETS wave model. In addition, the CI model outputs were also compared with Berth A and Berth B stations at AMETS. Based on the values in Table 2, the model managed to replicate similar wave conditions at Berth A and Berth B stations, especially at Berth A, which is in deep water. However, it is cleared that the model was underestimated for Hs parameter based on bias values of -0.02m and -0.4m at Berth A and Berth B. Hence, it is crucial to develop a high resolution wave model at AMETS location in order to avoid underestimation of wave parameters especially when the model will be used for an assessment of wave characteristics and resource variability in the future. An overview of model comparison between measured data at M4 for available data in the year of 2013 is illustrated in Figure 3. Based on the figure, it is justified that the CI wave model compared well with the measured data including MWD where the dominant wave directions were coming from West, South-west, North-west and North direction with respect to the true North.

Table 2 Summary of CI model validation with measured mean values (2010-2013).

Station	Waves	Mean	R^2	RMSE	Bias	SI
Berth A	Hs (m)	3.01	0.95	0.55	-0.02	0.18
	Tz (s)	6.82	0.84	1.22	0.23	0.18
Berth B	Hs (m)	2.80	0.92	0.69	-0.40	0.24
	Tz (s)	6.98	0.77	1.74	0.23	0.25
M3	Hs (m)	2.87	0.95	0.48	0.14	0.17
	Tz (s)	6.85	0.86	1.16	0.39	0.17
M4	Hs (m)	2.67	0.95	0.54	0.01	0.20
	Tz (s)	6.69	0.87	1.01	-0.01	0.15
M6	Hs (m)	3.15	0.94	0.56	0.18	0.18
	Tz (s)	7.27	0.84	1.05	0.32	0.15

The calibration of the AMETS wave model was conducted based on a number of sensitivity tests, where the most important calibration parameter to be tuned was found to be the wave generation formulation, Cds and δ . Table 3 shows the key model settings in 6 model setups used in the AMETS wave model for model calibration with the GEN3 of Janssen formulation. The performance of each model setup was analysed based on RMSE, R^2 , SI and bias at Berth A and Berth B station for Hs and Tz parameter summarised in Table 4 and Table 5.

The selection of A5 (highlighted in Table 3) as the final model setup was based on RMSE, R^2 and bias values, especially for Tz parameter at both stations. For example, based on Table 4 and Table 5, A6 shows higher R^2 values with similar RMSE for Tz compared to A5, but the bias values for A5 are lower than A6. It is also observed that A1 shows similar R^2 and RMSE values compared to A5 for Hs and Tz. However, it is determined that the bias values for Tz are lower in A5 for both stations compared to A1. Thus, this condition eliminated A6 and A1 setups whereas a similar approach was applied to the other model setups. An overview of selected model setups comparison is shown in Figure 5 at Berth B station, where Hs shows a similar pattern, while Tz shows A6 was overestimated. On the other hand, set-up A4 was underestimated compared to A5 between modelled and measured data. The measured mean values for Hs and Tz at

Berth A were 5.6m and 8.4s with 4.9m for Hs and 8.1s for Tz at Berth B while in the mean values in Table 4 and Table 5 shows the modelled mean values for the calibration period of December 2013.

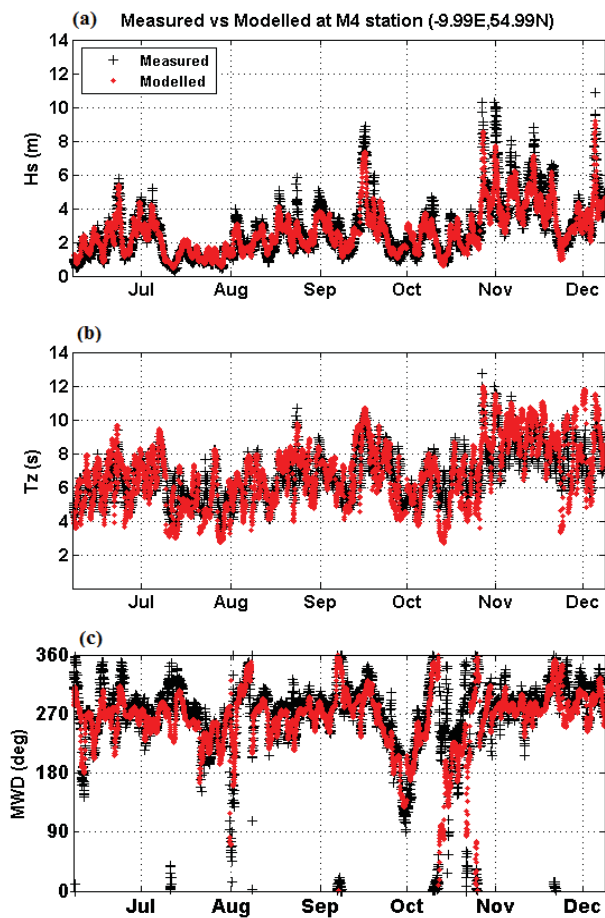


Figure 3 Comparison between measured and modelled data at M4 station for (a) significant wave height, Hs (m), (b) zero up-crossing wave period, Tz (s) and (c) mean wave direction, MWD (July- December 2013).

Table 3 Key model settings applied in calibration in AMETS model

Setup	Description		Setup	Description	
	GEN3 Janssen			GEN3 Janssen	
	Cds	δ		Cds	δ
A1	3	1.5	A4	2	1.5
A2	3	1	A5	2	2
A3	3	0.5	A6	3	2

A longer simulation has been computed for the year of 2010 to 2013 based on A5 setup to validate the AMETS wave model. Comparison plots between modelled and available measured data at Berth A and Berth B station for the year of 2013 are shown in Figure 5 and Figure 6, while the corresponding statistical measures of model performance are summarised in Table 6, where the R^2 values were above 0.9 with the RMSE values below 0.6m and the bias values were less than 0.2m for Hs at both stations. For Tz, the R^2 values

Table 4 Summary of model calibration analysis at Berth A station (December 2013).

Berth A	Waves	Mean	R^2	RMSE	Bias	SI
A1	Hs (m)	5.7	0.9	0.9	0.1	0.2
	Tz (s)	9.5	0.8	1.1	1.1	0.1
A2	Hs (m)	6.1	0.9	1.0	0.5	0.2
	Tz (s)	8.3	0.7	1.2	-0.1	0.1
A3	Hs (m)	6.8	0.9	1.0	1.1	0.2
	Tz (s)	7.2	0.7	1.0	-1.2	0.1
A4	Hs (m)	6.2	0.9	1.0	0.9	0.2
	Tz (s)	8.5	0.7	1.2	0.1	0.1
A5	Hs (m)	5.7	0.9	0.9	0.1	0.2
	Tz (s)	9.2	0.8	1.1	0.8	0.1
A6	Hs (m)	5.6	0.9	0.9	-0.1	0.2
	Tz (s)	10	0.9	0.9	1.6	0.1

Table 5 Summary of model calibration analysis at Berth A station (December 2013).

Berth B	Waves	Mean	R^2	RMSE	Bias	SI
A1	Hs (m)	5.2	0.9	0.9	0.3	0.2
	Tz (s)	8.6	0.8	1.3	0.5	0.2
A2	Hs (m)	5.6	0.9	1.0	0.7	0.2
	Tz (s)	7.7	0.7	1.1	-0.5	0.1
A3	Hs (m)	6.1	0.9	1.0	1.2	0.2
	Tz (s)	6.7	0.9	0.6	-1.5	0.1
A4	Hs (m)	5.6	0.8	1.0	0.8	0.2
	Tz (s)	7.7	0.7	1.1	-0.5	0.1
A5	Hs (m)	5.2	0.9	0.9	0.3	0.2
	Tz (s)	8.4	0.8	1.3	0.3	0.2
A6	Hs (m)	5.0	0.9	0.9	0.1	0.2
	Tz (s)	9.4	0.9	1.2	1.2	0.1

were above 0.8 with the bias values below 0.2s at Berth A and close to 0s at Berth B. The validation values were also compared with another published values in [17] and [12] with SWAN model and [29] with WW3 model at Berth B location. It is observed that the AMETS model managed to improve wave predictions based on validation values at Berth B station compared to in [17] and [12] with R^2 values above 0.9 for Hs and above 0.8 for Tz. It is also observed that the AMETS wave model produced lower bias values at Berth B especially for Tz parameter, which is close to 0s compared to 1.12s in [17] and -1.15s in [12]. Such low bias values are important for wave resource assessment in order to avoid overestimation of wave power level which is a function of wave height and wave period [30]. Moreover, the AMETS validation values are consistent with the published values in [29] (see Table 6). It is also observed that the RMSE and bias values for Hs were within the published values in the WMO guidelines. Hence, it is justified that the AMETS wave model satisfactorily replicates wave conditions at a local scale and is suitable to be used in a detailed wave assessment analysis for 12 years period in the future. Figure 5 and Figure 6 show that the AMETS wave model compared well with the measured data, including MWD, where the dominant wave directions were coming from West, South-west, North-west and North direction with respect to the true North at Berth A and Berth B for the year of 2013.

Table 6 Summary of AMETS model validation with measured mean values (2012 – 2013 at Berth A and 2010 to 2013 at Berth B). NA indicates non-available data.

Station	Waves	Mean	R^2	RMSE	Bias	SI
Berth A	Hs (m)	3.01	0.95	0.58	0.10	0.19
	Tz (s)	6.82	0.87	1.21	0.19	0.18
Berth B	Hs (m)	2.80	0.95	0.52	0.17	0.22
	Tz (s)	6.98	0.80	1.40	0.01	0.20
[17] at Berth B	Hs (m)	2.08	0.89	0.48	0.17	0.23
	Tz (s)	8.47	0.77	1.42	1.12	0.17
[12] at Berth B	Hs (m)	NA	0.84	0.73	-0.11	0.31
	Tz (s)	NA	0.52	1.82	-1.15	0.21
[29] at Berth B	Hs (m)	2.87	0.95	0.41	0.19	0.14
	Tz (s)	7.06	0.89	0.86	0.65	0.12

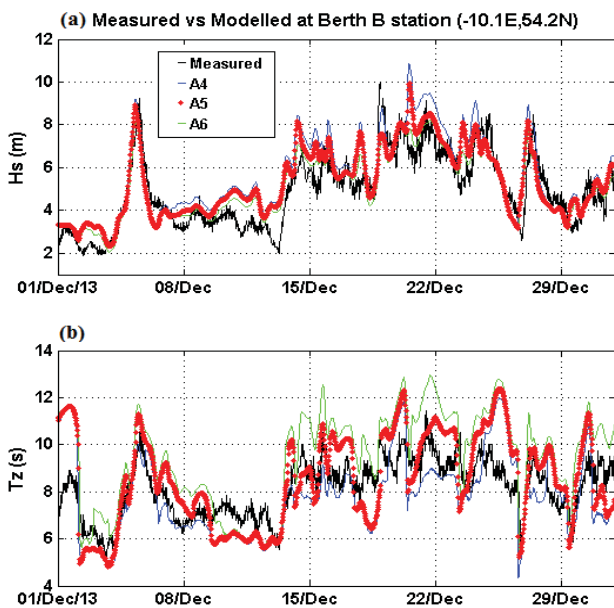


Figure 4 Comparison between measured and modelled data at Berth B station for sensitivity test (a) significant wave height, Hs (m), (b) zero up-crossing wave period, Tz (s).

4 CONCLUSION

A development of high resolution of AMETS wave model using SWAN has been presented where two separated wave models were developed, calibrated and validated at an oceanic scale to a local scale. The coarse Ireland (CI) wave model at oceanic scale (0.05 degrees resolution) was developed to supply nested boundary conditions for a local scale wave model, which is the AMETS wave model at 0.0027 degrees resolution (approximately 300m). Detailed model descriptions for both models have been presented, where the third wave generation (GEN3) of Janssen formulation with (i) the coefficient of white capping dissipation rate (Cds) of 3 and the delta (δ) of 1.5 for the CI wave model and (ii) the Cds value as 2 and the δ of 2 for the AMETS wave model were found to be the best combination setup for the study area based on a number of sensitivity tests in model calibration process conducted for the period of December 2013 (detailed in Section 2.2). The models were calibrated and validated against wave buoy stations within Irish water and the performance of the models was analysed based on RMSE, R^2 , SI and bias. Furthermore, the validation values from the

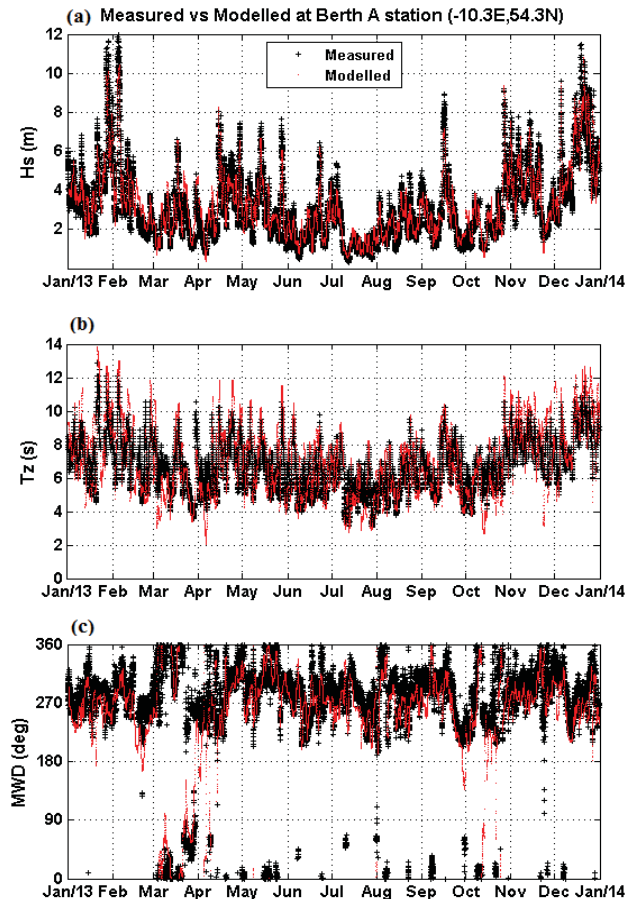


Figure 5 Comparison between measured and modelled data using preferred modelled set-up at Berth A station for (a) significant wave height, Hs (m), (b) zero up-crossing wave period, Tz (s) and (c) mean wave direction, MWD (2013).

AMETS wave model at Berth B station were also compared with other published values and it is evident that the model managed to satisfactorily replicate similar wave conditions at AMETS between measured and modelled data, improving on previously developed models (for example, [17] and [12]), as detailed in Table 6. In addition, it is also determined that the development of high resolution wave model from a coarse to a local scale area is extremely important in order to capture realistic wave propagations from offshore to nearshore areas at the study area. Ongoing work is developing the CI and AMETS wave model simulations for 12 years period (2004 - 2015) in order to deliver an assessment of wave characteristics and resource variability at wave energy test sites.

ACKNOWLEDGMENTS

This material is based upon works supported by the Science Foundation Ireland under Grant No. 12/RC/2302 through MaREL, the national centre for Marine and Renewable Energy in Ireland. The authors wish to acknowledge the DJEI/DES/SFI/HEA Irish Centre for High-End Computing (ICHEC) for the provision of computational facilities and support. The first author gratefully acknowledges the receipt of the College of Engineering & Informatics Fellowship. The second author would also like to acknowledge the support of Science Foundation Ireland through the Career Development Award programme (Grant No. 13/CDA/2200).

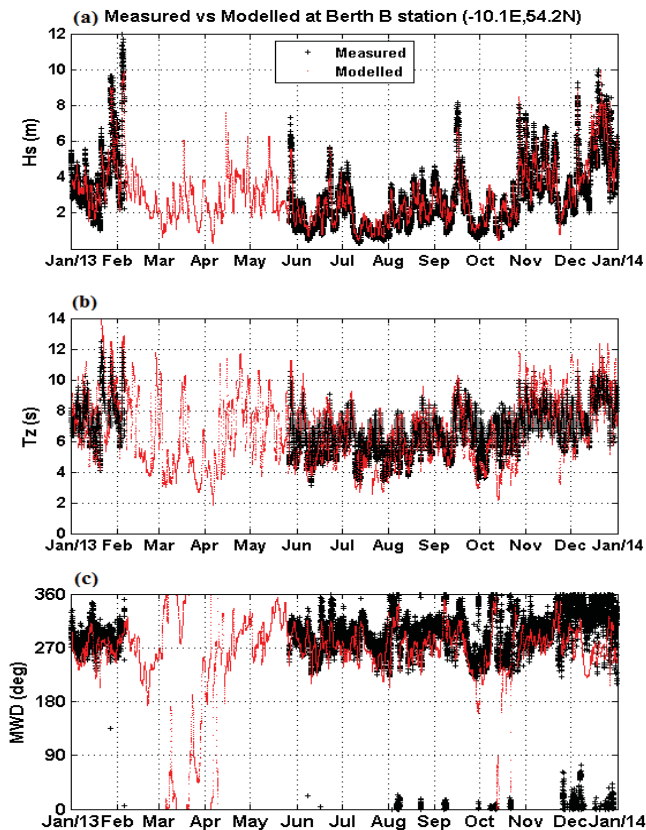


Figure 6 Comparison between measured and modelled data using preferred model set-up at Berth B station (a) significant wave height, H_s (m), (b) zero up-crossing wave period, T_z (s) and (c) mean wave direction, MWD (2013).

REFERENCES

- [1] WAMDI group, "The WAM model - a third generation ocean wave prediction model," *J. Phys. Oceanogr.*, vol. 18, pp. 1775–1810, 1988.
- [2] H. . Tolman, "Technical Note : User manual and system documentation of WAVEWATCH III version 4.18," College Park, MD, 2014.
- [3] DHI, "Mike 21 by DHI," 2012. [Online]. Available: <http://www.mikebydhi.com/products/mike-21/waves>. [Accessed: 03-Jul-2014].
- [4] TUDelft, "Hydraulic Engineering: SWAN," *Delft University of Technology*, 2015. [Online]. Available: <http://www.swan.tudelft.nl/>. [Accessed: 02-Feb-2014].
- [5] M. Zijlema, "Computation of wind-wave spectra in coastal waters with SWAN on unstructured grids," *Coast. Eng.*, vol. 57, no. 3, pp. 267–277, Mar. 2010.
- [6] J. Wolf, J. Hargreaves, and R. Flather, "Application of the SWAN Shallow water wave model to some U.K coastal sites," Prenton, Merseyside, UK, 2000.
- [7] P. Gleizon, F. J. Campuzano, P. C. García, B. Gomez, and A. Martinez, "Wave energy mapping along the European Atlantic coast," in *Proceeding of the 11th European Wave and Tidal Energy Conference (EWTEC)*, 2015.
- [8] L. Rusu and C. Guedes Soares, "Impact of assimilating altimeter data on wave predictions in the western Iberian coast," *Ocean Model.*, vol. 96, pp. 126–135, 2015.
- [9] G. Iglesias and R. Carballo, "Wave energy potential along the Death Coast (Spain)," *Energy*, vol. 34, no. 11, pp. 1963–1975, 2009.
- [10] Marine Institute, "Marine Institute : Wave Forecasts," *Marine Institute*, 2015. [Online]. Available: <http://www.marine.ie/Home/site-area/data-services/marine-forecasts/wave-forecasts>. [Accessed: 24-Feb-2015].
- [11] R. Atan, J. Goggins, M. Harnett, P. Agostinho, and S. Nash, "Assessment of wave characteristics and resource variability at a 1/4-scale wave energy test site in Galway Bay using Waverider and high frequency radar (CODAR) data," *Ocean Eng.*, vol. 117, pp. 272–291, 2016.
- [12] B. Cahill, "Characteristics of the Wave Energy Resource at the Atlantic Marine Energy Test Site," PhD Thesis, University College Cork, Ireland, 2013.
- [13] WestWave, "WestWave Converting Ireland's Wave Energy Potential : Location," *WestWave, ESB Ocean Energy, Dublin 2, Ireland*, 2010. [Online]. Available: <http://www.westwave.ie/location/>. [Accessed: 28-Nov-2013].
- [14] Met Éireann, "Met.ie, The Irish Meteorological Service Online, Download Historical Climate Data for our Synoptic Stations," *MET ÉIREANN, Glasnevin Hill, Dublin 9, Ireland*, 2015. [Online]. Available: <http://www.met.ie/climate-request/>. [Accessed: 27-Jan-2015].
- [15] S. K. Gulev and V. Grigorieva, "Variability of the Winter Wind Waves and Swell in the North Atlantic and North Pacific as Revealed by the Voluntary Observing Ship Data," *J. Clim.*, vol. 19, pp. 5667–5685, 2006.
- [16] TUDelft, "SWAN User Manual - Cycle III version 41.01A," *Delft University of Technology*, 2015. [Online]. Available: http://swanmodel.sourceforge.net/online_doc/swanuse/swanuse.html. [Accessed: 17-Jan-2014].
- [17] A. R. Bento, P. Martinho, R. Campos, and C. Guedes Soares, "Modelling Wave Energy Resources in the Irish West Coast," in *Proceedings of the ASME 2011 30th International Conference on Ocean, Offshore and Arctic Engineering OMAE2011*, 2011, pp. 945–953.
- [18] WMO, *Guide to Wave Analysis and Forecasting*, Second., no. 702. Geneva, Switzerland: Secretariat of the World Meteorological Organization (WMO), 1998.
- [19] R. Atan, J. Goggins, and S. Nash, "A preliminary assessment of the wave characteristics at the Atlantic Marine Energy Test Site (AMETS) using SWAN," in *Proceedings of the 11th European Wave and Tidal Energy Conference (EWTEC)*, 2015.
- [20] L. H. Holthuijsen, *Waves in Oceanic and Coastal Waters*, 2009th ed. New York, United State of America: Cambridge University Press, 2009.
- [21] D. P. Dee, S. M. Uppala, a. J. Simmons, P. Berrisford, P. Poli, S. Kobayashi, U. Andrae, M. a. Balmaseda, G. Balsamo, P. Bauer, P. Bechtold, a. C. M. Beljaars, L. van de Berg, J. Bidlot, N. Bormann, C. Delsol, R. Dragani, M. Fuentes, a. J. Geer, L. Haimberger, S. B. Healy, H. Hersbach, E. V. Hölm, L. Isaksen, P. Källberg, M. Köhler, M. Matricardi, a. P. McNally, B. M. Monge-Sanz, J.-J. Morcrette, B.-K. Park, C. Peubey, P. de Rosnay, C. Tavolato, J.-N. Thépaut, and F. Vitart, "The ERA-Interim reanalysis: configuration and performance of the data assimilation system," *Q. J. R. Meteorol. Soc.*, vol. 137, no. 656, pp. 553–597, Apr. 2011.
- [22] M. Meaux F, "U.S. Navy Fleet Numerical Meteorology and Oceanography Center (FNMOC)'s Wave Watch 3 (WW3)," 2009. [Online]. Available: http://gcmd.nasa.gov/records/GCMD_FNMOC_WaveWatchIII.html. [Accessed: 02-Oct-2014].
- [23] C. Amante and B. Eakins, "ETOPO1 1 Arc-Minute Global Relief Model: Procedures, Data Sources and Analysis. NOAA Technical Memorandum NESDIS NGDC-24," *National Geophysical Data Center, NOAA*. doi:10.7289/V5C8276M, 2009. [Online]. Available: <http://www.ngdc.noaa.gov/mgg/global/global.html>. [Accessed: 08-May-2014].
- [24] NOAA, "ETOPO1 Grid Extract," 2014. [Online]. Available: <http://maps.ngdc.noaa.gov/viewers/wcs-client/>. [Accessed: 08-May-2014].
- [25] NRC, "National Research Council Canada (NRC), Blue Kenue™: Software tool for hydraulic modellers," 2015. [Online]. Available: http://www.nrc-cnrc.gc.ca/eng/solutions/advisory/blue_kenue_index.html. [Accessed: 04-Feb-2014].
- [26] R. Atan, J. Goggins, and S. Nash, "Development of a Nested Local Scale Wave Model for a 1/4 Scale Wave Energy Test Site using SWAN," *Ocean Model.*, 2016.
- [27] Marine Institute, "Data.Marine.ie : Wave Buoy Network Real Time Data 30 Minute," *Marine Institute*, 2015. [Online]. Available: <http://data.marine.ie/Dataset/Details/20969#>. [Accessed: 20-Jan-2015].
- [28] GSI and MI, "INFOMAR : Data and Products - Data Processing and Interpretation," 2013. [Online]. Available: <http://www.infomar.ie/data/DataProcessing.php>. [Accessed: 05-Oct-2014].
- [29] S. Gallagher, E. Gleeson, R. Tiron, R. McGrath, and F. Dias, "Wave climate projections for Ireland for the end of the 21st century including analysis of EC-Earth winds over the North Atlantic Ocean," *Int. J. Climatol.*, vol. 5, p. n/a-n/a, 2016.
- [30] A. M. Cornett, "A global wave energy resource assessment," in *The Eighteen (2008) International Offshore and Polar Engineering Conference*, 2008, pp. 1–9.

Modelling the effects of Climate Change on historic maritime structures: Howth Harbour's East Pier (Ireland)

S. Lizondo¹, J. Reilly¹, J. Ascoop¹, G. Connolly², J. Campbell²

¹Department of Maritime Engineering, Arup, 50 Ringsend Road Dublin 4, D04 T6X0 Ireland,

² Department of Agriculture, Food and the Marine, Upper Main Street, Ballyshannon, Co Donegal,

email: susana.lizondo@arup.com,

Grainne.Connolly@agriculture.gov.ie

ABSTRACT: The effects of Climate Change present a number of challenges for historical maritime structures. A study was undertaken to assess the potential effects of Climate Change on the historical protected structure, Howth Harbour's East Pier, designed by John Rennie and constructed in 1813. The main stages of the study included; a statistical analysis of offshore wind and wave climate, numerical wave modelling, an overtopping assessment, an assessment of wave transmission through the structure and a structural stability analysis.

Wave modelling simulations were carried out for two scenarios: the present scenario and the future scenario which includes the potential effects of sea level rise and increase in the severity of storms. Specific consideration was given to overtopping which has become a hazard for pedestrians as well as a structural risk for the pier. A detailed overtopping assessment and a stability study of the existing revetment and pier structure was carried out for different sections of the pier for a number of different return periods for both the present day and the future scenario.

Based on the results of the study and the various assessments a number of different structural remedial solutions were proposed.

KEY WORDS: Climate Change; Maritime Structures; Overtopping; Wave Numerical Modelling.

1 INTRODUCTION

Historic maritime structures have been withstanding extreme wave conditions for centuries. Although there is much research into climate change effects, there has been less emphasis on the quantification and modelling of climate change effects on existing maritime structures.

This study assesses and quantifies the potential effects of Climate Change on the historical protected structure, Howth Harbour's East Pier, designed by John Rennie and constructed from 1807 to 1813. The location of this structure is shown in Figure 1.



Figure 1. Location of Howth Harbour's East Pier.

Howth Harbour is today one of six fishery harbour centres in Ireland, owned and managed by the Department of Agriculture, Food and the Marine. The East Pier provides the principal protection to the harbour which is an important fishing and leisure facility on the East Coast. It was included by Fingal County Council on its Record of Protected Structures under the Planning and Development Act 2000, making it a key historic maritime structure in their area while under the direct care of the Department.

2 METHODOLOGY

2.1 Main stages

The main stages of the study included:

1. Surveys: site investigation with recommendations, dive survey, topographic and bathymetric surveys.
2. Studies: statistical analysis of offshore wind and wave climate, numerical wave modelling, overtopping assessment, assessment of wave transmission through the structure and structural stability analysis.

2.2 Mechanisms of failure

The study identified various risks of damage or failure to the rubble mound breakwater due to the mechanisms identified in Figure 2 and assessed the structure for two scenarios: the current scenario and the future scenario (year 2100).

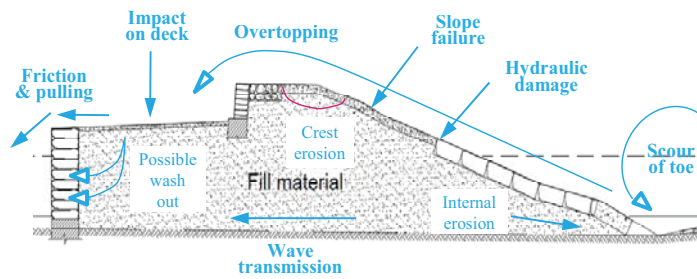


Figure 2. Mechanisms of failure/ damage for the East Pier structure (failure related to the breakwater structure only).

2.3 Modelling the influence of climate change on the risks

This assessment included the potential effects of sea level rise and increase in the severity of storms. Specific consideration was given to overtopping which has become a hazard for pedestrians as well as a structural risk for the pier.

Wave climate analysis and wave propagation analysis by computational modelling were required to investigate the forces which the East Pier structure at Howth Harbour must withstand and to establish the degree of overtopping. This was achieved with the use of MIKE 21 SW model from DHI (see Table 1 and Figure 3).

Table 1. Nearshore wave results for the future scenario and associated boundary conditions.

Return Period (years)	Input conditions for NNE direction			Tide level (m CD)	Nearshore wave height (m)
	Wave height (m)	Wave period (s)	Wind speed (m/s)		
1	2.2	6.5	13.4	MHWS	1.8
10	5.5	10.5	21.8	MHWS	4.2
100	7.8	13.2	27.7	MHWS	5
200	8.5	14.1	29.4	MHWS	5.1
200	8.5	14.1	29.4	MSL	4
200	8.5	14.1	29.4	MLWS	2

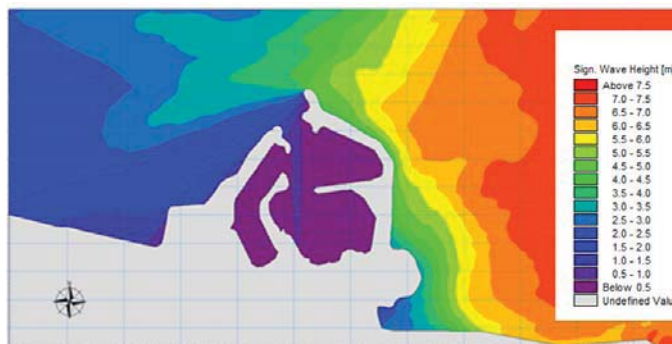


Figure 3. MIKE 21 SW modelling output showing nearshore significant wave heights at Howth Harbour (Tr = 200 years).

Offshore wave conditions were derived from Norwegian Meteorological Institute NORA10 hindcast model following a wave distribution and extreme value analysis. Tidal levels were derived from the United Kingdom Hydrographic Office Admiralty Charts and ranged from mean low water springs (MLWS) to mean high water springs (MHWS). Allowances were made for climate change in accordance with the draft

guidance by the OPW “Assessment of Potential Future Scenarios for Flood Risk Management” which derives two future scenarios, the Mid-Range Future Scenario (MRFS) and the High End Future Scenario (HEFS) corresponding to 500mm and 1000mm sea level rise respectively.

3 OVERVIEW OF THE RESULTS

3.1 Overtopping assessment

Overtopping discharge occurs because of waves running up the face of a seawall or revetment. If wave run-up levels are higher than the crest level of the structure, waves will reach and pass over the crest of the wall. This defines the ‘green water’ overtopping which is the case where a continuous sheet of water passes over the crest.

A different form of overtopping occurs when the splash is produced by waves breaking on the structure itself and is known as ‘white water’ overtopping. This effect can be exacerbated by strong local winds.

In the case of the East Pier, severe overtopping has been visually identified as occurring annually (see Figure 4). Overtopping is a hazard for pedestrians and it is also a risk for the structure due to the high loads that the impact of the water may cause on the upper and lower deck of the structure. In the case of cracks on the surface, this water discharge may also lead to wash out of the fill material.



Figure 4. Overtopping during an extreme event at Howth Harbour's East Pier.

A detailed overtopping assessment of the existing revetment and pier structure was carried out based on the Technical Report on Wave run up and wave overtopping at dikes by Van der Meer published by the Dutch Technical Advisory Committee on Flood Defence TAW, which is recommended for simple slopes in the EurOtop Manual [Ref 3]. The analysis was carried out for four sections (see Figure 5) for the present day and the future scenario taking account of expected sea level rise as described in the Future Structural Integrity of the East Pier report carried out by Arup in December 2013. The aim of this assessment was to determine the worst case present day and future overtopping rates. Section B1 (the elbow) was identified as producing the worst overtopping rates.

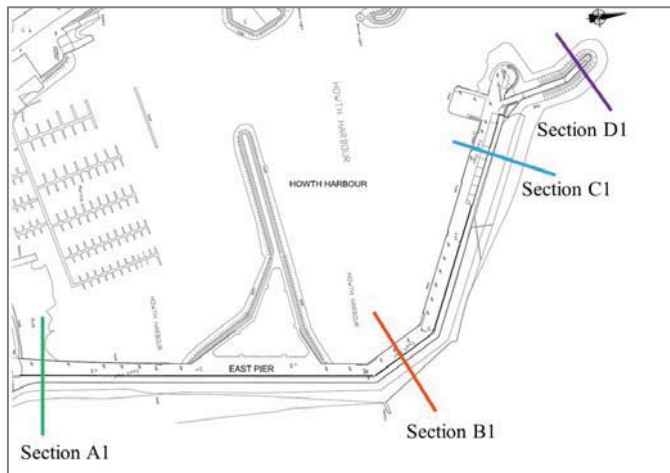


Figure 5. Sections assessed.

Resultant wave overtopping rates at section B1 were notably larger than the rates calculated at the other sections (See Table 2 and Figure 6). There was also a significant difference between the results for the present day and future scenario which considered sea level rise of 1m by 2100. The Coastal Engineering Manual derives the limit for damage on paved promenades fronted by revetments as 200 l/s/m i.e. if the overtopping rates exceed 200 l/s/m damage of the paved promenade will start to occur.

Table 2. Results of overtopping analysis for different sections

		Section A1		Section B1	
		Present	Future	Present	Future
Wave Return Period (yr)	Tidal Condition	Overtopping rate (l/s/m)		Overtopping rate (l/s/m)	
1	MHWS	0.05	0.41	1.36	6.28
10	MHWS	13	98	76	389
100	MHWS	83	392	170	709
200	MLWS	0.001	0.003	0.003	0.012
200	MSL	17	38	33	74
200	MHWS	122	484	224	820

From Table 2 the results show that for the future scenario damage will start to occur at section B1 when a 10 year return period wave is combined with MHWS whereas at Section A1 damage will start to occur when a 100 year return period wave is combined with MHWS. For the present day, damage will start to occur at section B1 when a 200 year wave is combined with MHWS.

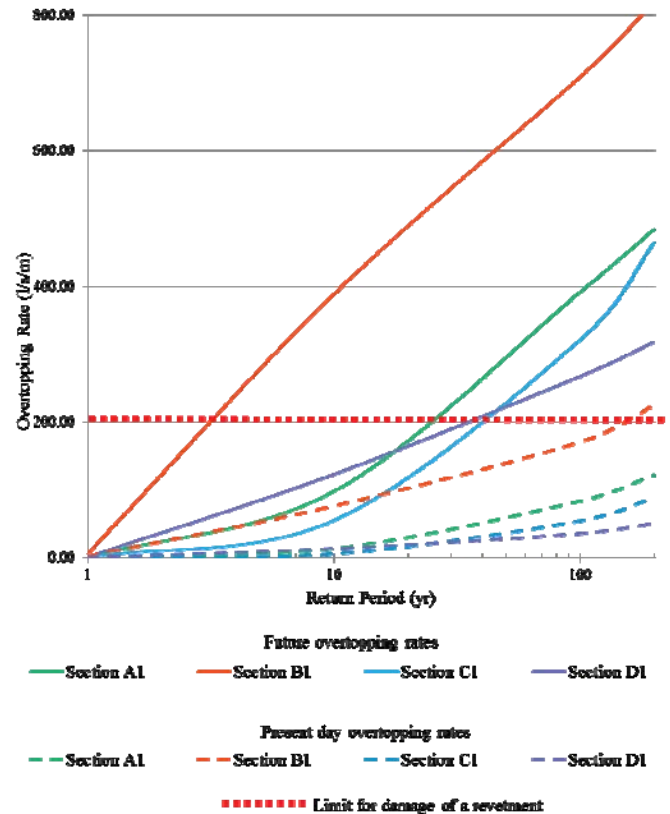


Figure 6. Overtopping rates vs return period.

3.2 Wave Transmission Analysis

A wave transmission assessment of the existing revetment and pier structure was carried out based on the Van der Meer formula presented in the CIRIA Rock Manual [Ref 2] for smooth low crested structures. The analysis was carried out for the four sections for a range of return periods, as described previously for the current and future scenarios. The aim of this assessment was to determine the proportion of the incident wave energy being transmitted through the pier structure. Transmission is related to both the mechanism of energy transmission through and over the structure.

Section B1 produced the highest transmission coefficients for all return periods and increased by roughly 10% from the current scenario to the future scenario for a 1 in 100 year return period.

3.3 Structural assessment

3.3.1 Wave pressures

Wave pressures were calculated using Goda's wave theory (1974) formulae and Tanimoto and Kimura's modification factors for wave loads on impermeable inclined walls (1985) (Ref 2 and 4) which accounts for the paved revetment slope of the East Pier structure. The H_{max} and corresponding period for a 100 year return period were used as the H_{design} in this scenario.

Table 3 Results of wave force calculations for the different sections.

		Section A1		Section B1	
		Present	Future	Present	Future
Pressure at water line (P1)	kN/m	65.2	76.0	62.3	73.0
Pressure at top (P2)	kN/m	34.3	52.6	32.8	50.5
Pressure at base (P3)	kN/m	63.9	73.8	61.0	70.8
Uplift Pressure at base (Pu)	kN/m	0.6	0.3	5.2	2.2

Table 3 shows the results for the wave pressure calculations for sections A1 and B1. P1, P2, and P3 refer to pressures at the waterline, top and bottom of the structure and Pu refers to the resultant uplift pressure due to the wave forces. From the table it can be seen that there is little difference between the pressures at different sections. The resultant pressures were then used for the analysis of sliding and overturning of the structure.

3.3.2 Overturning and sliding analysis

For the stability analysis of the East Pier, the resistance of the structure to sliding and overturning was assessed. The pier structure (lower deck and revetment) was considered as one joint mass.

This mode of failure is not typical for a rubble mound structure. However, calculations were carried out in order to get an estimation of the relationship between disturbing external forces and stability forces (weight of the structure).

In order to be able to assess the stability of the structure it was necessary to estimate a material density of the fill in the structure, which consists of granular material and different sized boulders. This was conservatively estimated as 1600kg/m^3 . The overturning and sliding forces acting on the pier included both the wave force and the uplift force as a result of wave pressure. The resisting forces solely consist of the self-weight of the structure. The results show that the pier structure considered only as a rubble mound breakwater is of sufficient size to resist the wave generated sliding and overturning forces with a high safety factor as was expected. This simplified analysis assumes that the wave forces are acting on an impermeable slope and as such no wave energy is penetrating through the structure.

3.3.3 Existing condition of the structure

A Site Investigation (SI) was undertaken in November 2013 with the aim of calibrating a previous Ground Penetration Radar (GPR) survey, which appeared to identify extensive areas with interconnected voiding primarily in the upper 1.2m of fill. The SI works comprised the excavation of 5 no. trial pits and the drilling of 20 no. shallow core holes to determine the presence of voids in the internal fabric of the pier structure as identified in the GPR survey. These works were carried out by IGSL Limited (IGSL) under the supervision of Arup, between 11 November 2013 and 22 November 2013.

According to the results of the SI, no significant voids were noted in the trial pits. Small “void” areas with an approximate size of 25 to 50mm were noted in the matrix material between the cobbles and boulders. Voids were also noted immediately beneath the slab in several of the core holes. The maximum observed void was 400mm in length with most ranging from 30mm to 270mm.

The voids immediately beneath the slab were assessed as being most likely due to settlement of the fill material in the pier (indicating poor compaction), but also possibly attributable to wash-out.

The minor voiding near the surface of the fill indicated that while the GPR results were informative, they likely over-estimated the extent of the voiding within the material. It is also likely that the regions identified in the GPR as voids were in fact changes in material type, moisture content or material compaction, or minor voids or loose finer matrix material contained between the boulders.

A dive survey was carried out in order to determine the conditions of the slope and toe on the seaward face of the East Pier breakwater. The seaward side of the structure presents different repairs that have been carried out over the years. The revetment is made up of masonry and has a smooth surface which allows for overtopping which also prevents the dissipation of wave energy. The survey which consisted of a visual and physical examination above and below the waterline was conducted by Collins Engineers on 11 November 2013. The results showed some significant voids in the revetment surface and significant undermining and voids at the toe of the structure (see figures 7 and 8).



Figure 7. Repairs in the revetment at Howth Harbour's East Pier.



Figure 8. Undermining at the toe of the structure.

The undermining of the toe which showed exposed fill material in some of the sections can lead to wash out of the fill material. Other key issues identified were:

1. Severe overtopping, particularly at the elbow section of the structure (section B). This can lead to:
 - a) Danger to the public: this is a very important factor, as the East Pier is frequently used by walkers.
 - b) Damage to the structure.
2. Wave transmission: this can lead to:
 - a) Wash out of the fill material. This is a risk to be considered in connection with the undermining of the toe.
 - b) High pressures on the slabs which may cause damage to the inside quay wall.

3.4 Possible solutions to increase the design life

3.4.1 Proposed Solutions

Undermining of the toe is a serious risk for the stability of the breakwater. Therefore, repair of the toe was recommended. This recommendation would be the starting point to further solutions which improve the existing condition of the structure and extend its design life.

In order to extend the design life of the structure, three solutions that could be implemented were proposed. The solutions were based on the findings of the structural assessment, wave modelling results, SI information, dive inspection and existing information on the East Pier. The proposed solutions and associated benefits with each solution were:

- 1) Additional revetment – Double layer of rock armour, which will result in:
 - a. Dissipation of wave energy and hence decrease of the forces that the existing revetment slope is exposed to.
 - b. Reduction of overtopping due to the increased roughness of the slope and the increased crest width.
- 2) Additional revetment – Single layer of concrete cube units, which will result in:
 - a. Dissipation of wave energy and hence decrease of the forces that the existing revetment slope is exposed to.
 - b. Reduction of overtopping due to the increased roughness of the slope and the increased crest width.
- 3) Additional rock armour toe, which will result in:
 - a. Preventing scour at the toe of the revetment due to the dissipation of energy of breaking waves.
 - b. Reduction of overtopping due to the reduced water depth at the toe of the structure.
- 4) New wave return wall, which will result in:
 - a. Reduction of overtopping due to the increased freeboard height.
 - b. Protection of the revetment crest due to the presence of the wave wall and concrete slab.

The proposed solutions were only recommended in the most exposed areas of the pier as some sections appear to be adequately protected. Figure 9 below shows the extent of the proposed solutions in plan.

More recently (in 2015) further site investigation was undertaken in order to gain more knowledge of the foundation type as well as the fill material of the structure.

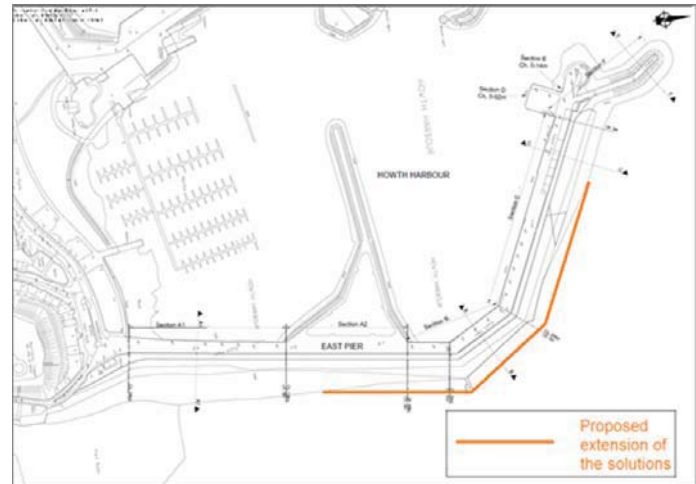


Figure 9. Extent of proposed solutions for Howth Harbour's East Pier.

4 CONCLUSIONS

Based on the results of the study and the various assessments a number of remedial solutions and different long term structural solutions were proposed. Each solution was assessed for the following:

- Dissipation of wave energy,
- Decrease of forces that the existing revetment slope is exposed to,
- Reduction of overtopping due to increased roughness of the slope and changes in crest width.

The methodology and proposed solutions employed in this project can be applied to maritime structures in different geographic locations however the definition of various climate change scenarios is a key issue to be considered.

The proposed solutions provide different levels of improvement to the existing structure and Arup recommended that the different solutions be assessed and valued in a further stage, taking into account DAFM interests and priorities.

Prior to any further assessment of the future integrity of the East Pier and the suitability of the options, it is vital that:

- a) The integrity of the existing structure is maintained;
- b) That further information about the structure is acquired

As such Arup recommended that further Site Investigation is carried out as well as emergency repairs to badly affected areas of the structure toe.

The Department has since completed the emergency repairs and the additional Site Investigations and has incorporated on-going monitoring into its annual maintenance programme

ACKNOWLEDGMENTS

The authors would like to thank the Marine Engineering Division of the Department of Agriculture, Food and the Marine for assistance with the existing information, site visits, queries, and comments that greatly improved this work.

REFERENCES

- [1] CIRIA, CUR, CETMEF, 2007, The Rock Manual: The use of rock in hydraulic engineering. (2nd Edition). C683, CIRIA, London, pp 519.

- [2] Goda, Y. 1974. "New Wave Pressure Formulae for Composite Breakwaters," Proceedings of the 14th International Coastal Engineering Conference, Vol 3, pp 1702-1720.
- [3] Pullen, T., Allsop, N.W.H., Bruce, T., Kortenhaus, A. et al., 2007, EurOtop Manual. Wave Overtopping of Sea Defences and Related Structures: Assessment Manual. Environmental Agency, UK, German Coastal Engineering Research Council (KFKI), Rijkswaterstaat, Netherlands, pp 80.
- [4] Tanimoto, K., and Kimura, K. 1985. "A Hydraulic Experimental Study on Trapezoidal Caisson Breakwaters," Technical Note No. 528, Port and Harbour Research Institute, Yokosuka, Japan (in Japanese).

Evaluation of UV disinfection technologies for water reuse and rainwater harvesting in the Irish dairy industry.

K. Fitzhenry¹, N. Rowan², W. Finnegan¹, E. Tarpey¹, J. Goggins^{1,3}, X. Zhan^{1,3}, E. Clifford^{1,3}

¹ College of Engineering and Informatics, NUI Galway; ²Bioscience Research Institute, Athlone Institute of Technology;

³Ryan Institute for Environment, Marine and Energy, NUI Galway.

Email: k.fitzhenry1@nuigalway.ie

ABSTRACT: With the abolition of quotas on milk production in early 2015, the Irish dairy sector is projected to expand by 50% by the year 2020. Legislation regarding the discharge limitations of dairy wastewater effluent is becoming increasingly stringent along with initiatives to conserve and reuse water within the industry. The use of tertiary treatment systems, specifically UV disinfection may play a dual role of acting as end-point effluent treatment systems as well as disinfection systems to restore dairy wastewater to reusable standards within dairy plants. This study will aim to investigate those themes by evaluating the potential of novel pulsed UV disinfection for dairy pathogen reduction in comparison to conventional low-pressure UV disinfection systems.

KEY WORDS: CERI 2016; Dairy Wastewater; UV Disinfection; Pathogen Removal.

1 INTRODUCTION

The Irish dairy sector processes approximately five billion litres of milk annually and is Ireland's largest growing indigenous industry with exports reaching a record €3 billion in 2013. Water consumption ratios within the sector are significant with approximately 2.5m³/m³ of milk processed and 14.9 m³/tonne product [1]. Aside from product manufacturing, water is used for other activities such as steam generation and cleaning of internal piping, floors and workplace areas thus vast quantities of liquid waste is produced. Fieldwork surveys at several Irish dairy plants have revealed that the majority of this liquid waste is not reused within the plant. While this water would not be recycled for purposes pertaining to the raw product, the potential for its reuse in heating/cooling systems, truck washes and cleaning external plant areas is a viable option [2]. In addition, legislation regarding the discharge limitations of dairy wastewater effluent is becoming increasingly stringent with survey feedback indicating the potential for an introduction of microbiological parameters in the near future. The use of tertiary treatment systems, in particular ultraviolet irradiation (UV) may play a dual role of acting as an end-point effluent treatment system as well as a disinfection system to restore dairy wastewater to reusable standards within dairy plants. This study attempts to address those themes by investigating a novel pulsed UV (PUV) system for enhanced germicidal properties in comparison to domestic continuous low-pressure UV (LPUV) systems. The impact of typical dairy wastewater parameters such as total suspended solids (TSS) and organic carbon on system efficiency will be evaluated. Furthermore, pathogenic bacterial strains of interest to the dairy sector will also be subjected to UV trials as well as highly resistant bacterial endospores to confirm the capacity of PUV disinfection. Finally, the potential for on-site rainwater harvesting at dairy plants will also be investigated.

2 DAIRY INDUSTRY LIASON

Preliminary work for this study began with site visits to dairy plants and wastewater treatment plants (WWTPs) to inform the research aspects of the project. Site surveys were carried out at six dairy plants (DP 1 - DP 6) nationwide (Figure 1). Information collected included annual water consumption and water reuse practices, tertiary disinfection systems in place and rainwater harvesting potential.



Figure 1. Sites of nationwide dairy plant survey

3 WASTEWATER CHARACTERISATION

An in-depth study was carried out at two of the dairy plants to determine the microbiological content of various water and wastewater streams and specifically to investigate whether any human pathogenic strains of interest were present. The following types of water/wastewater were analysed; process water (pre-treatment), condensate water, stormwater, WWTP influent and effluent.

4 UV SYSTEM ANALYSIS

Both the PUV and LPUV systems were fully optimised and set-up at laboratory scale. Laboratory analysis began with the investigation of the impact of TSS on optimum disinfection efficiency of the PUV via *E.coli* inactivation. Two types of TSS materials were evaluated; inert (bentonite and calcium carbonate; CaCO_3) and organic material (sludge). The impact of organic TSS on LPUV efficiency via *E.coli* inactivation is currently under investigation, preliminary results are presented in this paper.

5 MATERIALS AND METHODS

5.1 Wastewater characterization

Samples were collected from two dairy plants (dairy plant; DP-1 and DP-2) on three separate occasions;

1. Process water, WWTP influent and final effluent samples were collected from DP-1.
2. WWTP influent and effluent, stormwater, cooling water and condensate water samples were collected from DP-2.

100 μL of each sample was streaked onto non-selective nutrient agar and incubated at 37°C for 18-24 hours. Once cultured, all colonies that appeared morphologically different e.g. different colour, size, shape etc were isolated onto new nutrient agar plates and incubated under the same conditions. In total, 87 separate colonies were isolated and brought forward for further analysis. The following tests were performed on each of the 87 samples;

- Gram stain followed by microscopic analysis.
- Enzyme catalase test.
- IMViC test consisting of four separate tests; indole test, methyl-red test, Voges-Proskauer test and the Citrate test.

Results from the above tests determined which samples were to be cultured on specific agars for differentiation tests e.g. TBX agar was used for *E.coli* identification and Mannitol Salt agar for *Staphylococcus spp.* identification.

5.2 Laboratory scale UV trials

5.2.1 PUV system analysis

A bench-scale pulsed power source (PUV – 1, Samtech Ltd., Glasgow) (Figure 2) was used to power a low pressure (60 kPa) xenon-filled flashlamp (Heraeus Noblelight XAP type NL4006 series constructed from a clear UV transparent quartz tube) which produced a high intensity beam of polychromatic pulsed light. The lamp was placed 11 cm above a sterilised aluminium flow-through vessel which pumped water through the vessel at the desired flow rate corresponding to hydraulic residence time (HRT). The PUV system allows for the input voltage and the pulse rate to be varied between 300 and 1000 volts and 0.1 and 10 pulses per second (PPS). The PUV system when operating at 800 V and 2 PPS equated to a UV dose output of 1946 mJ/cm^2 at a HRT of 120 seconds. Batches of distilled water (2 – 2.5L) were spiked with a various concentrations of bentonite, CaCO_3 or IASBR sludge to give a series of TSS concentrations. In addition, 2mL of *E.coli* cultured in LB broth (at 37°C for approx. 16 hours on a rotary

shaker) was also spiked in to the distilled water to give a starting concentration of approximately 1×10^6 CFU/mL. Once complete, the water was pumped from the influent bucket to the aluminium vessel and the collected effluent was analysed for *E.coli* inactivation. One replicate of influent sample and three replicates of effluent sample were analysed per run. The range of TSS concentrations analysed during experimental analysis varied from 0 to 200 mg/L.

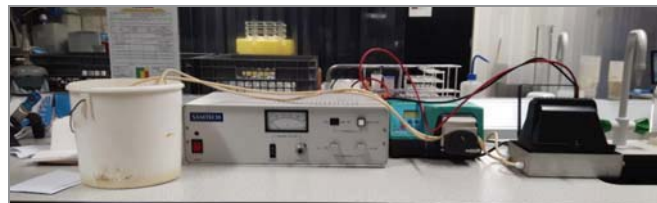


Figure 2. Bench-scale PUV system.

5.2.2 LPUV system analysis

Thirty litres of tap water was appropriately diluted with IASBR sludge and pumped through a domestic low pressure UV (LPUV) system (LCD 412 Plus, S.I.T.A., Halpin & Hayward Ltd.) at 27L/min to give a HRT of 0.4 seconds and UV dose of 11 mJ/cm^2 (Figure 3). The influent wastewater was spiked with vegetative *E.coli* to give a starting concentration of 1×10^6 CFU/mL. The LPUV system ran for 30 seconds before effluent was collected and analysed for *E.coli* inactivation. One replicate of influent sample and three replicates of effluent sample were analysed per run. The range of TSS concentrations analysed during experimental analysis varied from 0 to 130 mg/L.



Figure 3. Laboratory-scale LPUV system.

5.2.3 *E.coli* enumeration

Pre and post UV treated samples were transferred to sterile 60mL tubes. Appropriately diluted well-mixed samples (1mL) were analysed using the pour plate technique in triplicate with TBX agar pre-cooled to 45°C. Once solidified, plates were transferred to an incubator for 18-24 hours at 37°C after which distinct colonies were counted on plates between 25 and 250 and the results were expressed in CFU/mL.

5.2.4 Physical & chemical analysis of wastewater

A series of physical and chemical tests was performed on the organic wastewater to monitor other parameters which may impact on UV performance.

5.2.4.a Particle size analysis and suspended solids analysis

- Two segments of 1.2µm circular (47mm) filter paper were labelled and weighed before 60 mL samples were passed through each using a vacuum pump to give two replicates. The filter papers were then dried in a hot oven (105°C) for 24 h. Once dried, the filter papers were removed and re-weighed to determine suspended solids present. A mean of two measurements was taken for each sample tested.
- Particle size analysis was performed on IASBR sludge only. A glass fibre filter of 1.2µm pore and nylon filters of 60µm, 120µm and 180µm (two segments of each) were used to analyse particle size distribution. The filter papers were labelled and weighed before 10mL samples were passed through each using a vacuum pump to give two replicates. The filter papers were then dried in a hot oven (105°C) for 24 h. Once dried, the filter papers were removed and re-weighed to determine suspended solids present. A mean of two measurements was taken for each sample tested. Particle size distribution was determined by analysis of the percentage mass of suspended solids retained or passing at each pore size.

5.2.4.b Chemical analysis

- Total organic carbon (TOC) and total inorganic carbon (TIC) were measured using the Biotector TOC TN TP Analyser.
- The chemical oxygen demand (COD) was measured using Hach Lange test kits and a DR2010 spectrophotometer.

6 RESULTS & DISCUSSION

6.1 Dairy plant survey

The main findings of the survey highlight;

- Rainwater harvesting is not considered.
- Overall, water reuse practices do not appear to be widely implemented.
- Stricter legislation would result in microbial standards being applied to discharged effluents.

6.1.1 Water use within dairy plants

Findings from the dairy plant survey also highlighted the variation of water consumption between plants; survey results show variations of between 155,000m³ to 2.2million m³ annual water consumption (Figure 4).

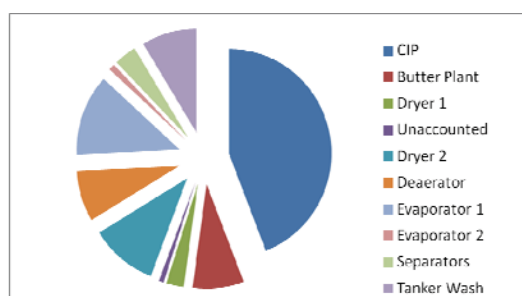


Figure 4. Typical water use breakdown of a butter & milk plant (DairyWater Project Survey, 2015).

6.2 Wastewater characterization

Two human pathogenic strains of interest were detected in both influent and effluent wastewaters;

- Bacillus cereus*
- Staphylococcus aureus*

Analysis of all of the samples (87 in total) is ongoing with colleagues at AIT analysing the data as well as colleagues at UCC who are testing some samples via molecular tests. It should be noted that tests performed were detection only and not enumeration.

6.3 Laboratory scale UV trials

6.3.1 Analysis of TSS on PUV efficiency

The impact of TSS concentrations on PUV efficiency in terms of *E.coli* inactivation was investigated using three different materials in distilled water; bentonite, calcium carbonate and IASBR sludge. The results are presented below.

6.3.1.a Bentonite investigation for TSS analysis

Two particle sizes of bentonite (<63µm and <100µm) were evaluated as a method of mimicking TSS in distilled water. A series of TSS concentrations ranging from 0 to 200 mg/L were analysed for impact on PUV efficiency. A TSS concentration of 30mg/L or above is thought to have a negative impact on the optimum performance of UV systems. It should also be noted UV doses were in line with recommendations given by EPA which states a UV dose of at least 8mJ/cm² is required for a 4 log reduction of *E.coli* [3]. Figure 5 illustrates the impact of bentonite on *E.coli* inactivation via PUV with the smaller particle size of <63µm. It is notable that when particles of less than 63 µm were investigated *E.coli* inactivation did not appear to be impacted by TSS concentration.

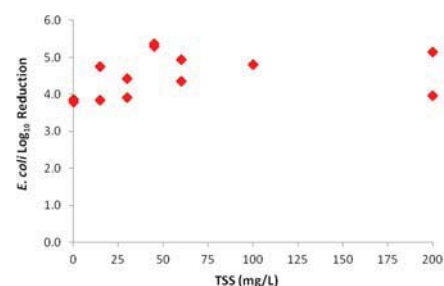


Figure 5. Relationship between TSS concentration (bentonite <63µm particle size) and *E.coli* inactivation via PUV treatment at UV dose output of 1946mJ/cm².

Figure 6 outlines impact of bentonite on *E.coli* inactivation via PUV with the larger particle size of <100µm. Analysis focused on TSS concentrations higher than 50mg/L to determine whether the particle size had any impact with increasing TSS concentration. The results in this figure also suggest that this particle size had no impact on *E.coli* log₁₀ reduction at any of the TSS concentrations.

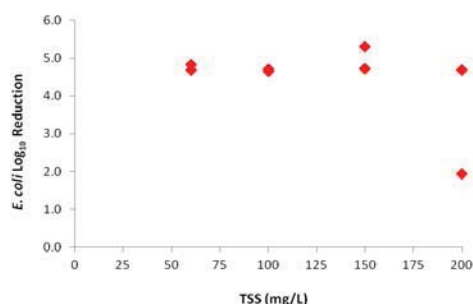


Figure 6. Relationship between TSS concentration (bentonite <100µm particle size) and *E. coli* inactivation via PUV treatment at UV dose output of 1946mJ/cm².

6.3.1.b CaCO₃ investigation for TSS analysis

CaCO₃ has a low specific gravity, close to that of water so it was trialled with the aim of it remaining fully suspended in the water thus mimicking TSS content. Two particle sizes (<10µm and <70µm) of CaCO₃ were sourced from a quarry and analysed at various concentrations similar to the PUV trials with bentonite. In addition to monitoring TSS content, turbidity readings of samples were recorded to ensure that the particles were remaining fully suspended. Figure 7 describes the relationship between TSS concentration and *E. coli* inactivation at five TSS concentrations; 0mg/L, 25mg/L, 50mg/L, 100mg/L and 200mg/L using the smallest particle size of <10 µm. The turbidity of the samples was also recorded and plotted on a second axis to illustrate that while the water was indeed turbid, there was no impact on PUV efficiency in terms of *E. coli* inactivation. Perhaps the particle size in this case was too small to shield the bacteria; *E. coli* is approx. 2 µm in length. Or perhaps the inert nature of this material does not impact on UV efficiency in the manner that organic material may impact UV treatment.

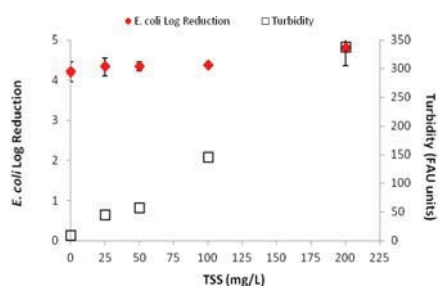


Figure 7. Impact of TSS (CaCO₃ <10µm particle size) on *E. coli* inactivation via PUV treatment at UV dose output of 1946mJ/cm².

The larger particle size of <75 µm of CaCO₃ was then analysed to determine whether the particle size of the material was having an impact on PUV efficiency. As this particle size was heavier than that of the <10µm size magnetic stirrers were added to both the influent bucket and aluminium vessel in an attempt to maintain particle suspension in the water. Figure 8 shows *E. coli* log₁₀ reduction via PUV at four TSS concentrations; 25mg/L, 50mg/L, 100mg/L and 200mg/L. Results indicate that there was no clear impact of increasing

TSS concentrations on PUV efficiency in terms of *E. coli* inactivation using this material & particle size. The turbidity values also indicate that the same level of turbidity was not achieved with the <75 µm particle size compared to the <10µm particle size. Notably, the *E. coli* log₁₀ reduction was lower overall (approx. 3 log₁₀ reduction) for these trials in comparison to the <10µm particle size trials. This may be attributed to the addition of the magnetic stirrers which increased turbulence in the water thus perhaps exposing more bacteria to UV irradiation in comparison to the water sitting static. However overall, there was no difference in *E. coli* inactivation at 25mg/L compared to the maximum 200mg/L.

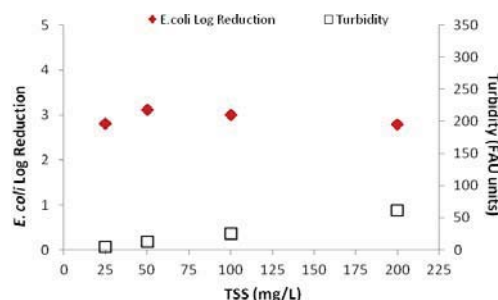


Figure 8. Impact of TSS (CaCO₃ <75µm particle size) on *E. coli* inactivation via PUV treatment at UV dose 1946mJ/cm².

6.3.1.c IASBR sludge investigation for TSS analysis

Typical dairy wastewater consists of both organic and inorganic suspended solids therefore it was decided to investigate the use of organic particles in evaluating the effect of TSS concentrations on PUV efficiency. Sludge from the lab-scale IASBR reactor at NUIG environmental labs was firstly sterilised (to remove any present pathogens) at 121°C for 15 minutes before a known quantity was spiked into distilled water to give TSS concentrations ranging from 0mg/L to 155mg/L. Figure 9 illustrates the impact of various TSS concentrations on PUV efficiency in terms of *E. coli* reduction via PUV. Results show a correlation between increasing TSS concentrations and decreasing *E. coli* log₁₀ reduction indicating that organic TSS material may have an impact on the efficiency of PUV systems.

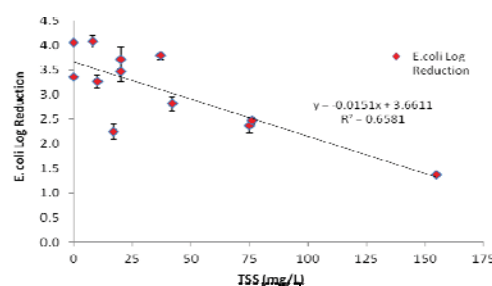


Figure 9. Relationship between TSS (IASBR sludge) and *E. coli* inactivation via PUV treatment at UV dose output of 1946mJ/cm².

Figure 10 shows total organic carbon concentrations in addition to the information presented in Figure 9. Results show a similar correlation with increasing TOC

concentrations and decreasing *E.coli* inactivation to that of the TSS readings for the same runs. Thus, it is important to consider other wastewater parameters when investigating such organic material.

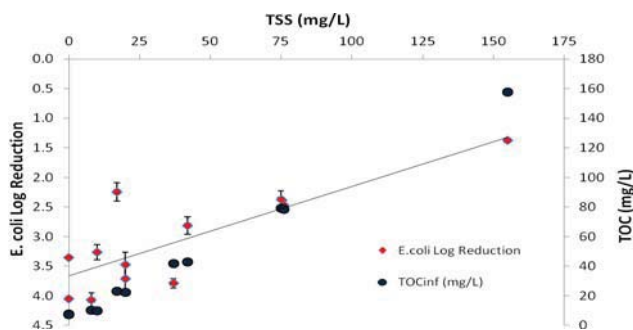


Figure 10. Relationship between TSS (IASBR sludge), TOC and *E.coli* inactivation via PUV treatment at UV dose output of 1946mJ/cm².

6.3.2 Analysis of TSS on LPUV efficiency

IASBR sludge was used to investigate TSS in wastewater with concentrations between 0mg/L and 130mg/L being investigated for LPUV runs to date. Figure 11 illustrates the impact of TSS on LPUV efficiency in terms of *E.coli* inactivation. Results show TSS concentrations of up to 85 mg/L to not have an impact on system efficiency with complete inactivation of *E.coli* being achieved up to this concentration. The higher TSS concentrations of 93mg/L and 126mg/L do appear to inhibit the efficacy of the LPUV with *E.coli* inactivation levels decreasing to between 4 and 5 log. It should be noted that the IASBR sludge used in this study is different to that used in the PUV study so comparison between systems was not possible in this case.

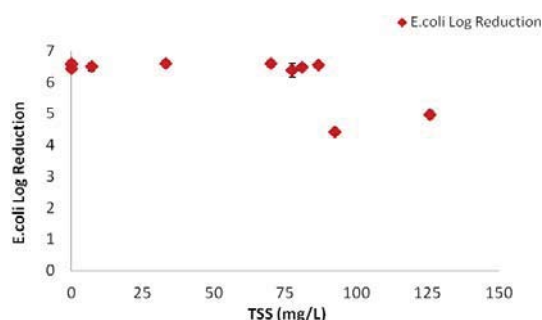


Figure 11. Relationship between TSS and *E.coli* inactivation via LPUV treatment at UV dose output of 11mJ/cm².

In contrast to the PUV analysis with IASBR sludge, the higher TSS concentrations do not appear to impact the LPUV system as much however other parameters of the wastewater should be taken into consideration such as particle size and organic carbon concentrations. Studies will continue with a direct comparison between PUV and LPUV systems using the same wastewater in addition to full physical and chemical analysis to ensure other factors besides that of TSS concentration are

being monitored. In addition, future work will include trialling actual wastewater from a dairy WWTP as opposed to synthetic wastewater as a means of investigating UV disinfection.

7 CONCLUSIONS

- Preliminary results from dairy wastewater characterization tests show the presence of human pathogenic bacteria in both influent and effluent of dairy WWTPs.
- Inert material mimicking TSS in wastewater does not appear to impact on PUV efficiency in comparison to organic material. This will be further investigated and compared to a 'cut-off' point of 30mg/L which is thought to impact negatively on UV disinfection according to the literature.
- Preliminary findings for LPUV trials in terms of *E.coli* inactivation show TSS concentrations of up to 85mg/L to not have an impact of system efficiency.

ACKNOWLEDGMENTS

The authors would like to acknowledge the funding provided by the Department of Agriculture, Food and the Marine for the DairyWater project (Ref.: 13-F-507), for additional details: www.dairywater.ie.

REFERENCES

- [1]Geraghty, R. (2011). *Benchmarking Resource Efficiency in Ireland's Dairy Processing Sector*. Dublin, Ireland.
- [2]Vourch, M., Balannec, B., Chaufer, B., & Dorange, G. (2008). Treatment of dairy industry wastewater by reverse osmosis for water reuse. *Desalination*, 219(1-3), 190–202. doi:10.1016/j.desal.2007.05.013
- [3] EPA. (2011). *Water Treatment Manual : Disinfection*. Johnstown Castle, Co. Wexford, Ireland.

Energy Benchmarking in Wastewater Collection and Treatment

Donald Cronin¹, Niamh Power²

¹ Cork County Council, County Hall, Cork, Ireland

² Department of Civil, Structural and Environmental Engineering, Cork Institute of Technology, Cork, Ireland
email: donalda.cronin@corkcoco.ie, niamh.power@cit.ie

ABSTRACT: This study develops a system of energy benchmarking that could be used to improve energy performance in Ireland. Using information available at local authorities, Irish Water, published EPA wastewater discharge license documentation and Census 2011 small area population statistics, a data sample of sewerage schemes was collated. The data sample comprised actual energy usage values and associated operation variable values related to energy usage, for both wastewater collection and treatment, for 59 independent Irish sewerage schemes. Using this data, a multiple linear regression analysis was carried out to determine two equations of significant predictor variables that would predict mean energy usage for wastewater collection and treatment. A five-variable linear regression model equation was used to predict the mean energy usage for each WwTP sample data point ($R^2 = 86.8$). This multi-variable equation was used to develop an energy benchmarking model that would provide an energy performance score between 0 (very poor) and 100 (excellent) based on the actual energy usage and the predicted mean energy usage. Using sensitivity analysis, the wastewater treatment benchmark model was found to be robust and logical. A three-variable regression model equation of wastewater collection system energy usage ($R^2 = 59.6$) was not as robust. Single variable energy benchmark models were also developed based on; actual energy usage, load treated, flow treated and treatment capacity utilised. The Irish data sample value of 45.9kWh/P.e./annum for the 15,000-30,000P.e. WwTP range is 48% greater than the German target of 31kWh/P.e./annum for the 10,000 to 30,000P.e..

KEY WORDS: Energy performance; Irish sewerage schemes; Multiple linear regression; Benchmark scoring.

1 INTRODUCTION

Many countries use formal systems of energy benchmarking to assess energy performance of sewerage schemes and these were often initiated based on studies or research projects such as were established in the U.K. in 2006 [1], Sweden in 2004 [2] and Austria in 1999 [3]. Implementation of formal benchmarking in Austria reduced energy usage cost by c.30% over 5 years [3]. Similar benchmarking in Ireland could reduce energy usage and its cost here. The Sustainable Energy Authority of Ireland (SEAI) has provided performance assessment tools for pumps and motors on its website and supports projects to reduce energy in wastewater treatment. However, there is no energy performance assessment tool for wastewater treatment and collection systems.

Wastewater services in Ireland consume approximately 0.5-1% of the total electrical energy consumed in Ireland [4]. This is significant and places pressure on these services to contribute to improvement in energy performance and also in terms of future sustainability of wastewater services in view of growing population and increased demand on wastewater services. Irish Water must consider not alone receiving water quality compliance in its capital investment but also energy performance and reduction of emissions.

Currently the main driver at EU level is the Energy Efficiency Directive (2012/27/EU) with the overall objective of an energy efficiency target saving of 20% of the Union's primary energy consumption by 2020 [5]. The public sector energy savings target was set by government at 33% in 2020 to demonstrate the leading role of the public sector in driving

the culture of energy efficiency and to showcase the benefits of energy efficiency improvements to the whole economy [6].

This paper shows how a benchmarking system could be developed and implemented to improve energy efficiency in wastewater treatment and meet the targets set out in the National Energy Efficiency Action Plan. Although this paper focuses on energy efficiency, the requirements of all other environmental legislation and policies for wastewater collection and treatment must be satisfied.

2 DATA AND METHODOLOGY

2.1 National Data Survey

There were many single variable performance indicators for wastewater treatment and collection. These were based on energy usage per unit productivity such as; kWh/P.e./annum or on %. Questions (categorical and numerical type) were formulated in a questionnaire seeking information on the energy usage, operating conditions of the wastewater treatment plants, collection systems and pumping stations. Generally the questions identified context, energy usage and operational variables.

Data was sought from each local authority for a single sewerage scheme for at least two of the reference years (2010, 2011 or 2012). The intention was to limit the effort required by wastewater personnel to participate and also to show variation in energy usage on a sewerage scheme during the reference years. A survey was implemented and a number of questionnaires were completed by wastewater personnel at local authorities. There were seven email responses to the survey; four partly completed questionnaires (four sewerage

schemes) and some responses with spreadsheets containing data that could be used to complete questionnaires.

Using the survey responses and other sources of data such as the Central Statistics Office Census 2011 small area population statistics [8] and the EPA wastewater discharge licensing documentation [9], a data sample was collated for analysis. The categorical survey questions were mostly yes/no options and the potential number of “yes” responses was 142. The actual number is labelled on the extract in Figure 1. The questions on Figure 1 are summarised from the survey.

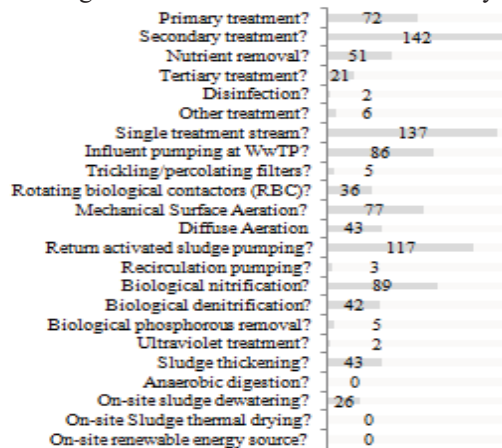


Figure 1: Dataset Extract (Survey Category Questions)

Figure 2 is also an extract to illustrate the compiled dataset where numerical answers were required. It shows the number of numerical data values compiled for each survey questions (summarised). Full sets of values (142) were collated in some instances. It was not possible within the project limits to consult further with local authorities on items of missing data.

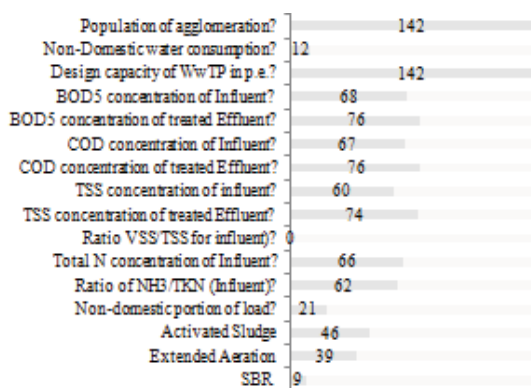


Figure 2: Dataset Extract (Numerical Questions)

2.2 Methodology of Data Analysis

Plausibility checks were developed for sample data values such as actual load treated in population equivalent. The data sample points were filtered to exclude data where flow per population equivalent values exceeded $1\text{m}^3/\text{P.e.}$ or were less than $0.1\text{m}^3/\text{P.e.}$. These were considered outliers and were re-checked or removed from the data sample. Also data sample points with energy usage values exceeding $300\text{kWh}/\text{P.e.}/\text{annum}$ were considered outliers. These were also rechecked or removed. Sample data points that were identified as non-compliant with the conditions of wastewater discharge licenses or certificates were removed.

Single variable linear regression analysis was carried out on the data sample to examine the relationship between each of the predictor variables and wastewater treatment plant (WwTPs) energy usage. Subsequently a multiple linear regression analysis was carried out to examine the most significant predictor variables for energy usage in wastewater treatment. A similar analysis was carried out for the wastewater collection system energy usage but this was less robust due to the limited dataset.

Linear regression model equations were formulated and performance scoring systems were developed using the resulting predicted energy values and actual energy values of the data sample points. Sensitivity analysis of the benchmark models was undertaken and the benchmark model was also tested on a new set of sample data points to examine how performance could be assessed and improved.

2.3 Data Sample Description

Ultimately after cleaning up and filtering, a database consisting of 142 data points was compiled for wastewater treatment and collection facilities. The data received was anonymised for use, the wastewater treatment plant data points were assigned alpha numeric identifiers (WwTP1 to WwTP142). The data points were based on a total of 59 independent sewerage schemes with multiple reference year data from some sewerage schemes. All 142 data points had data available for the wastewater treatment analysis but only 28 of these data points contained data that could be used for wastewater collection analysis.

Table 1 illustrates the scale of wastewater facilities that comprised the data sample. Table 1 describes the data sample in terms of the four WwTP groups identified based on the actual treatment population equivalent values. It illustrates a large number of smaller WwTPs and this would be representative of the Irish wastewater treatment context.

Table 1: Scale of wastewater treatment facilities.

WwTP Group	Actual P.e. Value Ranges	Portion by No. WwTPs	Portion by Actual Treated P.e.
1	0 -700	66.9%	9.9%
2	700 - 3,500	16.9%	11.4%
3	3,500 - 15,000	12.7%	42.6%
4	15,000 - 30,000	3.5%	36.1%

Figure 3 shows the distribution of WwTPs by energy usage and that there was a large number of WwTPs (64%) with annual energy consumption of 50MWh or less.

Table 2 further illustrates the sample data distribution of energy usage by WwTP size. It shows approximately 79% of WwTP data point actual energy usage values were below the $100\text{MWh}/\text{annum}$ threshold and comprised WwTPs with actual treated P.e. values less than 1,250P.e.. Table 2 also shows that the 30 large WwTPs consume approximately 79% of the total energy usage.

Table 3 lists the average and standard deviation values for the performance indicator ($\text{kWh}/\text{P.e.}/\text{annum}$) for each WwTP group identified. The average and standard deviation values reduce with increased actual treated P.e..

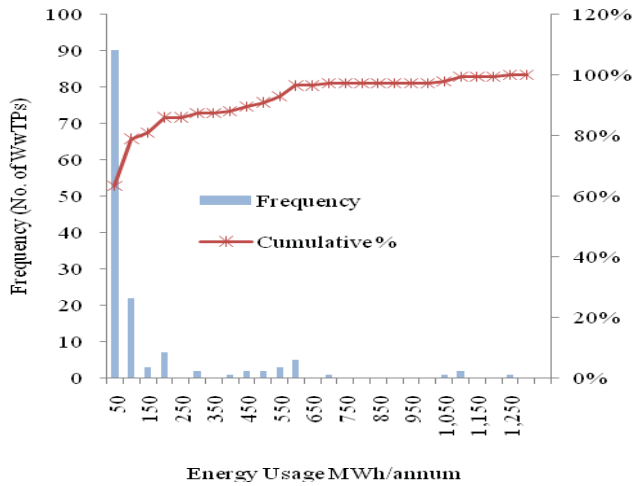


Figure 3: Energy usage WwTPs.

Table 2: Portion of WwTPs.

No. WwTP Data Points	Portion of WwTP Data Points	WwTP Energy Usage (MWh/a)	Total Energy (MWh/a)	Portion of Total Energy (%)	Actual Treated P.e.
30	21%	>100	13,771	79%	>1,250
112	79%	<100	3,722	21%	<1,250
142	100%		17,492	100%	

Table 3: Average energy usage for range of scales.

WwTP Group	Actual P.e. Value Range	Average kWh/P.e./a	Standard Deviation kWh/P.e./a
1	0 -700	99.4	57.7
2	700 - 3,500	66.8	37.1
3	3,500 - 15,000	60.9	26.1
4	15,000 - 30,000	45.9	6.9

3 MAIN WORK

The dependent WwTP energy usage variable data and the predictor variable data were used in both single and multiple regression analysis to develop predictive equations and subsequent benchmark scoring models.

3.1 Predictor Variable and Correlation

There were 23 category predictor variables with complete datasets (142 WwTP data point values) and 4 numerical predictor variables. The numerical predictor variable values were transformed to natural log values for convenience.

A Pearson correlation analysis was carried out to examine correlation between the WwTP energy usage dependent and predictor variables and also inter-correlation between predictor variables. High correlation values were noted prior to proceeding with the regression analysis. There was potential for high correlation among the predictor variables to skew/confound the outcome of the regression analysis.

Single variable regression analysis was carried out for each of the predictor variables and WwTP energy usage dependent variable. The results of the single variable regression analysis

showed the actual treated load predictor variable to be the most statistically significant.

3.2 Single Variable Regression Model

A single variable linear regression model was prepared using the $\ln(\text{ActualPe})$, actual treated load predictor variable and the dependent variable $\ln(\text{EnergyWwTP})$ for wastewater treatment energy usage. Figure 4 illustrates the strong positive linear relationship between these two variables. The R^2 value was 0.817; this model explained almost 82% of the variation in $\ln(\text{EnergyWwTP})$.

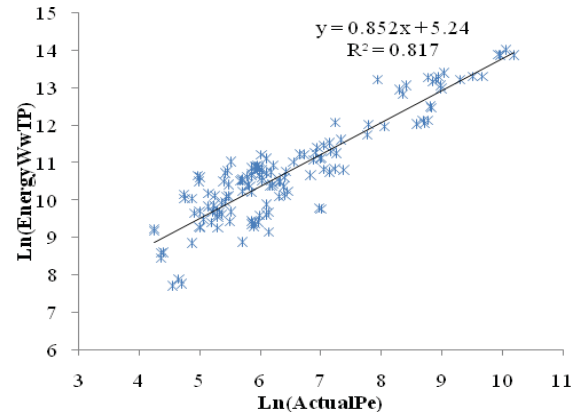


Figure 4: Linear regression of Actual Pe v Energy WwTP.

3.3 Multiple Linear Regression Analysis

The forward selection "Stepwise" statistical method was used to carry out a multiple linear regression analysis of the data sample [10]; where predictor variables are added in steps to examine their statistical significance. At each step, there was also elimination of variables that were not considered statistically significant including those for sludge processing. There was also some subjective input to the analysis and the decision to eliminate or retain variables was sometimes based on knowledge of the key factors.

3.4 Wastewater Treatment

The analysis resulted in formulation of a five-variable regression model equation that will predict the mean energy usage of a wastewater treatment plant. With an adjusted R^2 value of 86.6% the model explains much of the variation in WwTP energy usage. The equation uses natural log transformation:

$$\begin{aligned} \ln(\text{EnergyWwTP}) = & 3.9265 + 0.8373 * \ln(\text{ActualPe}) \\ & + 0.4328 * \ln(\text{DesignPe}) - 0.3789 * \ln(\text{Inflow}) \\ & + 0.3652 * \text{Class2RAS} + 0.1668 * \text{Class1InfPu} \end{aligned} \quad \text{Eqn 1}$$

Where:

$\ln(\text{EnergyWwTP})$ - natural log of the predicted energy usage WwTP;

$\ln(\text{ActualPe})$ - natural log of the actual treated load in P.e.;

$\ln(\text{DesignPe})$ - natural log of the design capacity in P.e.;

$\ln(\text{Inflow})$ - natural log of the average daily flow to treatment;

Class2RAS has a value of 1 if return activated sludge pumping is operated or 0, if not;

Class1InfPu has a value of 1 if influent or effluent pumping is operated or 0, if not.

The approach taken to develop the benchmark scoring system was similar to that by the U.S. EPA on its Energy Star analysis of building energy usage and that by Awwa Research Foundation on wastewater energy benchmarking [11]. The five-variable linear regression model equation was used to predict the energy usage for each WwTP sample data point based on the five predictor variable data values and intercept value. The calculated value for any given set of five variable data values was the predicted mean energy usage for all WwTPs with equivalent predictor variable values.

In order to generate a scoring system, the actual energy usage for all data points was divided by the corresponding predicted mean energy usage value. This gives a ratio of actual energy to predicted energy usage for each data point.

Actual Ln(EnergyWwTP)/ Predicted Ln(EnergyWwTP) Eqn 2

Each of the ratio values was then multiplied by 10.726 which was the overall predicted mean value of the model (average of all predicted mean energy values of data sample). This created a set of adjusted energy values for the sample data points. Figure 5 shows the plotted adjusted energy value distribution and a normal distribution fitted (blue). The percentile of a WwTP based on its adjusted energy value and using this normal distribution curve is its score in comparison to other plants with equivalent characteristics. The best performance scores 100 and the worst 0.

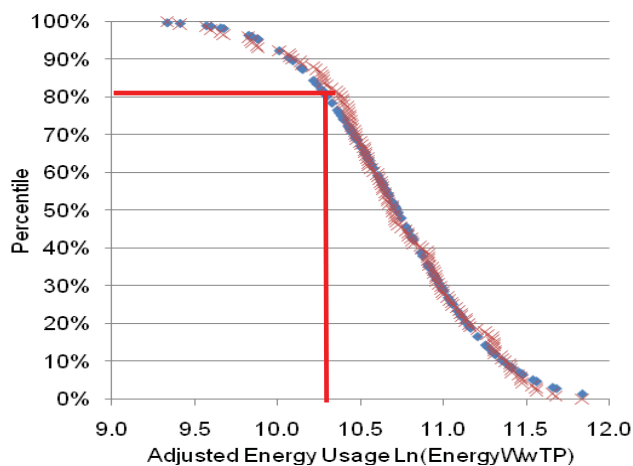


Figure 5: Benchmarking of WwTPs.

For example, using the five-variable equation the predicted energy for a wastewater treatment plant is calculated to be 13.6943 (natural log). The actual energy usage is 13.177 (natural log). The adjusted energy is calculated as follows:

$$(13.177/13.6943) * 10.726 = 10.3208$$

Using the adjusted energy value of 10.3208, the score for the wastewater treatment plant is shown on Figure 5 to be

approximately 81 and means that the performance is in the best 20% of performance.

The multiple linear regression model equation for wastewater treatment uses sensible predictor variables for the Irish context. It can exclude return activated sludge pumping for sequence batch reactors and also influent/effluent pumping. It adjusts for inflow variation using a negative coefficient to capture the difference between urban and rural context. It adjusts for design capacity P.e. variation and therefore captures capacity utilisation. The scoring system also compares each WwTP studied with other WwTPs that have equivalent characteristics.

3.5 Sensitivity Analysis and Range Limits

The sensitivity of the benchmark score was examined in relation to variation in regression equation predictor variable values. The predictor variable values of return activated sludge pumping and influent pumping were not typically subject to error. These variable values were confirmed in the wastewater discharge license documentation or on local authority spreadsheets. The predictor variables that were subject to error, were those calculated from the actual treated load, design capacity and the annual average daily flow values. These predictor variable values were based on estimated values in many cases. It was important to analyse how sensitive the energy benchmark score was to variation of these estimated values. Each variable value was varied by plus and minus 10, 20 and 50%. For WwTPs with either low or high scores the sensitivity was low but for WwTPs with scores closer to the average, there was increased sensitivity. This was expected due to the steepness of the normal distribution curve for score values (80 to 20); see Figure 5.

The multiple linear regression model equation and by extension the multi-variable energy benchmark model is not recommended for prediction of WwTP energy usage where the dependent/predictor variables values of the specific WwTP data point studied, fall outside the variable range limits of the data sample used and as shown in Table 4.

Table 4: Data range limitations.

Variable	Units	Minimum	Maximum
WwTP Energy Usage	kWh	2,235	1,207,416
Actual Treated P.e.	P.e.	70	26,680
Design P.e.	P.e.	125	31,500
Inflow	m ³ /day	15	7,746

3.6 Single Variable Benchmark Models

The relationship between WwTP energy usage and actual treated P.e. was shown previously in Figure 4 to be strong and positive with an R² value of approximately 82%. A single variable benchmark model was prepared using kWh/P.e./a; see Figure 6. The 10th, 50th and 90th percentile values for the data sample are shown.

A normal distribution curve was fitted (yellow) but would have lead to error. It was decided to use the curve distribution values as a simple means of scoring an individual WwTP against the sample data using its percentile; 100 being the best and 0 being the worst.

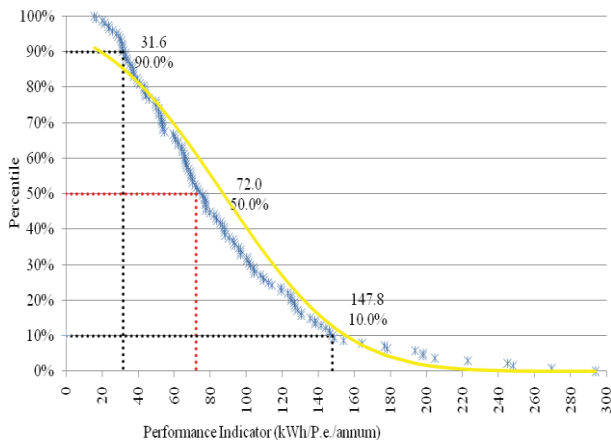


Figure 6: Single variable benchmark.

Use of curve distribution values results in some localised error. For example, a WwTP that scored 75 might actually have scored 76 or 77 on a best fit line but the level of error was considered low and unlikely to distort the perception of performance. Figure 7 illustrates the comparison of the Irish sample data values in kWh/P.e./annum to international values.

3.7 Verifying the Benchmarking Model

The regression model predictive accuracy is specific to the data sample used in its development. Its accuracy was examined by manually adjusting the predicted energy values for WwTPs and testing benchmark score sensitivity. For WwTPs with average performance, the benchmark score was more sensitive to adjustments.

Three new WwTP sample data points were collated and used to test the benchmark model. The benchmark scores assigned to the WwTPs and the subsequent examination of the WwTP operations data showed a robust and logical response. Table 5 shows the results of model testing. The operational data of the WwTPs was examined for potential energy usage reduction opportunities:

1. For WwTP A, the average aerator motor power required was estimated based on the actual treated load. It was found to be much lower than that installed and an estimate of the potential revised energy usage was made;
2. For WwTP B, there was potential to change from vertical surface aeration to diffuse aeration and an estimate of the potential revised energy usage was made;
3. For WwTP C, the aeration tank volume required was estimated based on standard organic loading for the rate of activated sludge and found to be much lower than that installed. An estimate of the potential revised energy usage was made based on the organic load.

Table 5: Verification of benchmarking model.

WwTP Data Point Ref		A	B	C
Initial Actual Energy Usage	kWh/a	239,000	528,301	119,193
Multi-variable Initial Score	%ile	6	79	23
Revised Energy Usage	kWh/a	148,122	380,905	105,235
Multi-variable Revised Score	%ile	35	91	31
Single Variable Benchmark				
Model Revised Actual Load PI	kWh/P.e./a	68.54	22.44	71.78
Single Variable Benchmark				
Model Revised Score	%ile	57	98	53

All of the potential improvements/estimates would require much more detailed examination. For example, the installation of diffuse aeration may not be technically feasible. It is worth noting that WwTP B had already taken energy efficient measures such as variable speed control of aerators and pumps which is reflected in the initial benchmark score of 79.

3.8 Comparison with Other Performance Indicators

With reference to Figure 7, the Irish data sample overall average value is 85.9kWh/P.e./annum. The Irish sample data average value for 700–3,500P.e. range of 66.8kWh/P.e./a is comparable to the German target of 41kWh/P.e./a for the 2,000–5,000P.e. range [7]; the Irish value being 63% higher.

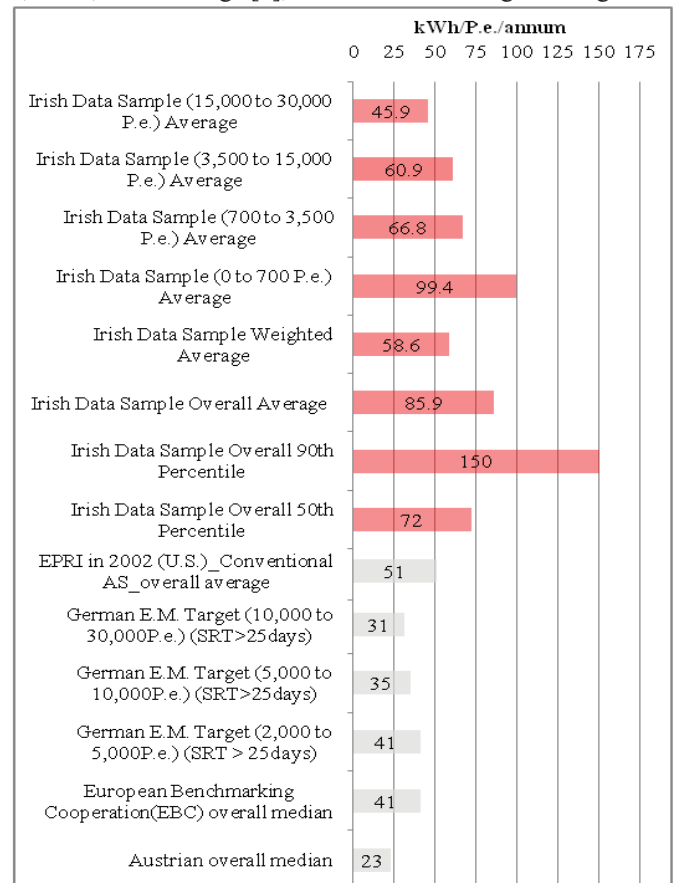


Figure 7: Comparison of Irish data to international targets [14][7] [13][12].

The Irish data sample value of 45.9kWh/P.e./a for the 15,000–30,000P.e. WwTP range is 48% greater than the German target of 31kWh/P.e./a for the 10,000 to 30,000P.e. (extended aeration) WwTP range. Based on German energy manual target values [7] there is potential for improved energy performance in Ireland. Use of energy benchmarking and energy manual targets has been ongoing in Germany and other European countries for many years.

3.9 Wastewater Collection

The data available for the wastewater collection systems was limited. There were 28 data points in total. Using this data, similar multiple linear regression analysis was undertaken for the wastewater collection system energy usage. The analysis resulted in a three-variable regression model equation for the prediction of energy usage for wastewater collection Eqn 3.

$$\begin{aligned} \ln(\text{EnergyColl}) = & 0.9189 * \ln(\text{EnergyWwTP}) \\ & + 0.8078 * \text{PSInCharge} - 0.5849 * \text{PSTotal} - 1.1365 \end{aligned} \quad \text{Eqn 3}$$

Where:

$\ln(\text{EnergyColl})$ - natural log of the predicted energy for wastewater collection;

$\ln(\text{EnergyWwTP})$ - natural log of the actual energy WwTP;

PSInCharge - number of pumping stations in the local authority's charge;

PSTotal - total number of pumping stations on the collection system.

The three-variable regression model equation explained c.59.6% of the total variation of wastewater collection system energy usage. It was not as robust as that for the WwTP analysis. A similar scoring system was developed as before. The overall predicted mean value of the model (average of all predicted energy values of data sample) is 10.314.

3.10 Fraction of Collection System Energy Usage

The fraction of total sewerage scheme energy used for the collection system is generally much smaller than the fraction for wastewater treatment as illustrated in Figure 8 so the associated error for an overall sewerage scheme analysis is low. Two thirds of the 28 WwTP data points analysed had collection system energy fraction values less than 20%.

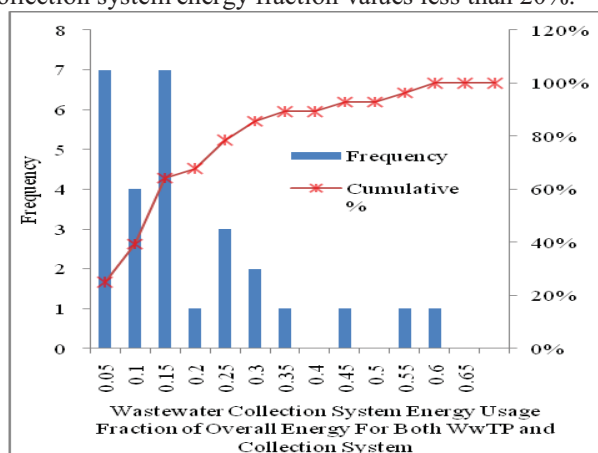


Figure 8: Fraction of collection system energy usage.

4 CONCLUSION

The single variable linear regression analysis showed a strong positive relationship between actual treated P.e. and WwTP energy usage with an R^2 value of almost 82%.

The collation of data and development of both multi-variable and single variable energy benchmark models demonstrates energy benchmarking in an Irish context. The model performed robustly during verification work using new data points (not included in its development).

The data sample was representative of the wastewater services in Ireland. While there were many smaller WwTPs included, there were also some medium and larger plants. As a result the benchmark model predictor variable range limits are such that it would be broadly applicable for the Irish context. The Irish data sample value of 45.9kWh/P.e./a for the

15,000-30,000P.e. WwTP range is 48% greater than the German target of 31kWh/P.e./a for the 10,000 to 30,000P.e. [7] which demonstrates that improvements can be made in an Irish context.

While the wastewater collection system multi-variable model is not as robust as that for WwTPs, the fraction of wastewater collection energy usage is low, so the associated error for overall sewerage scheme analysis is also low.

5 RECOMMENDATIONS

To have improved energy performance, one must have a system to measure it. A formal energy performance benchmarking system should be operated in Ireland. It is recommended that the multi-variable energy benchmarking model would be used so that the performance assessment is not distorted by different WwTP variable values such as whether or not there was influent or return activated sludge pumping. The multi-variable model should be used in combination with the more commonly used single variable models (particularly that based on kWh/P.e./annum).

The benchmarking system developed during this project should be further developed to use as a tool to assess performance on sewerage schemes and identify priority WwTPs or collection systems for more detailed examination.

ACKNOWLEDGMENTS

The Authors wish to acknowledge Irish Water and local authorities who provided access to data.

REFERENCES

- [1] Water Research Centre plc (WRc) established collaborative international research project, CP310, on energy benchmarking in 2006. Retrieve from <http://www.waterportfolio.com>.
- [2] Jonasson M., (2007), Energy Benchmark for Wastewater Treatment Processes – A Comparison between Sweden and Austria. MSc Thesis, Lund University.
- [3] Wett B., Buchauer K., Fimml C., (2007), 'Energy self-sufficiency as a feasible concept for wastewater treatment systems', IWA Leading Edge Technology Conference, Singapore, Asian Water, Sept. 2007.
- [4] SEAI, 2011. 'Water Services Overview Report', Sustainable Energy Authority of Ireland, Water Services Special Working Group, p.4.
- [5] Directive 2012/27/EU of the European Parliament and of the Council of 25 October 2012 on energy efficiency, amending Directives 2009/125/EC and 2010/30/EU and repealing Directives 2004/8/EC and 2006/32/EC.
- [6] Department of Communication Energy and Natural Resources (2012). 'Ireland's second National Energy Efficiency Action Plan to 2020' p. 24.
- [7] Ye Shi C. (2011). 'Mass Flow and Energy Efficiency of Municipal Wastewater Treatment Plants', IWA Publishing, London, ISBN 9781843393825
- [8] CSO. (2011). Census 2011 Results. Retrieved 2014, from Option 2 SAPS CSV DOWNLOADS: <http://www.cso.ie/en/census/census2011smallareapopulationstatisticsaps/>
- [9] EPA. (2014). Wastewater Discharge License Search. Retrieved from <http://www.epa.ie/terminalfour/wwda>
- [10] Devore, J. (2010). 'Probability and Statistics for Engineering and the Sciences'. Brooks/Cole, ISBN-10:0-538-73352-7, p. 582
- [11] AwwaRF. (2007). 'Energy Index Development for Benchmarking Water and Wastewater Utilities'. Available from www.nyserda.ny.gov.
- [12] Schaar. (2009). 'Water Days Presentation'. Retrieved from www.abwasserbenchmarking.at.
- [13] EBC, 2011. 'Learning From International Best Practice Water and Wastewater Benchmark', European Benchmarking Co-Operation.
- [14] EPRI, 2002. 'Water & Sustainability', Volume 4, Electric Power Research Institute.

Effect of aeration rate on laboratory-scale IASBRs treating synthetic dairy processing wastewater

Emma Tarpey^{1,2}, William Finnegan^{1,2}, Kelly Fitzhenry^{1,2}, Xinmin Zhan^{1,2}

¹Civil Engineering, College of Engineering and Informatics, National University of Ireland, Galway

²Ryan Institute, National University of Ireland, Galway

Email : e.tarpey1@nuigalway.ie

ABSTRACT: The dairy sector is a prominent industry in Ireland, accounting for over 30% of Ireland's agricultural products. However, its potential environmental impact is quite high, generating an average of 2.28 litres of wastewater per litre of milk processed. In Ireland, this sector is experiencing a period of growth due to the abolition of European milk quotas in 2015, with predicted increases of up to 50% in milk processed by 2020. This increase in production will lead to an increase in wastewater generation. The aim of this research is to investigate the efficiency of the intermittently aerated sequencing batch reactor (IASBR) technology in treatment of dairy processing wastewater. It has the potential to remove nutrients and organic matter from dairy processing wastewater with less energy usage and more cost effectiveness when compared to conventional technologies. Many dairy plants in Ireland currently remove phosphorus from wastewater using chemical precipitation techniques, which are very costly. The IASBR uses biological methods to remove phosphorus without the use of costly chemicals. Three laboratory-scale IASBR units were set up at the environmental engineering laboratory at NUI Galway to test the treatment efficiencies of the technology for synthetic dairy processing wastewater. In 200 days of testing, the nutrient removal efficiencies were investigated for five aeration phases, ranging from 2 litres per minute (LPM) to 0.4 LPM. The results show ortho-phosphate removal of up to 97% during the most efficient of these aeration phases, the 0.6 LPM phase. The average ortho-phosphate removal during this phase was 92%, 59% and 93% for Reactor 1, Reactor 2 and Reactor 3, respectively. The average ammonia nitrogen removal for each of the three reactors was 93%, 77% and 91%, respectively. The variation in results in the three reactors was due to operational differences early in the experiment, leading to different microbial ecology structures in the reactors.

KEY WORDS: Environmental engineering; dairy processing wastewater; intermittently aerated sequencing batch reactor; wastewater treatment; phosphorus removal; nitrogen removal

1 INTRODUCTION

1.1 Dairy Processing in Ireland

The dairy industry plays a large part in Ireland's economy. The industry accounts for over 30% of Ireland's agricultural products, and has an annual turnover of over three billion euros [1]. It is the 10th largest dairy industry in the world, and is expected to grow in future years [2].

While Irish dairy processors produce a wide variety of products (Figure 1), key products are infant formula and dairy ingredients. Ireland alone produces 10% of global exports of infant milk formula [2]. Following the abolition of European milk quotas in March 2015, the Irish dairy industry is experiencing a period of growth. An increase of up to 50% in milk processed from 2008/2009 levels is being predicted by 2020 [3].

The dairy industry is one of the most polluting industries globally in terms of wastewater generation. In Ireland, dairy processors use an average of 2.3 litres of water per litre of milk processed [4]. The water reuse rate is low so a large volume of wastewater is generated. The predicted increase in dairy processing will lead to an increase of wastewater generation.

Additional changes in legislation in Ireland, including the Water Framework Directive (WFD) and the Nitrates Directive are having an impact on wastewater treatment across all industries. The allowable discharge limits for contaminants are being reduced in wastewater treatment plants throughout the country, in an effort to improve the water quality of the nation, and that trend is set to continue. The Nitrates Directive has resulted in more stringent restrictions on land-spreading of waste. These factors combined with the predicted expansion

of the dairy industry contribute to the crucial need for more sustainable waste management.



Figure 1: Overview of Irish dairy sector [5]

1.2 Wastewater Treatment in the Dairy Industry

Dairy processing wastewater is generally characterised by high concentrations of organic matter, and consequently has high chemical oxygen demand (COD) concentrations, in comparison with municipal wastewater [6] [7]. Phosphorus levels in dairy wastewater are also significantly higher than municipal wastewater. In New Zealand phosphorus concentrations in dairy processing wastewaters are up to 125 mg/l [8] and on average 90% of total phosphorus is in the form of orthophosphate (PO_4^{3-}) [6]. Phosphorus most likely comes from cleaning agents used in the processing plants, such as phosphoric acid, as the majority of dairy wastewater is produced from cleaning activities in the plants [9].

There are a wide range of treatment systems used in the dairy processing industry. Visits to eight national dairy

processing plants were undertaken. The most common wastewater treatment system observed was a combination of aeration tanks, bio-towers, membrane filters and chemical phosphorus removal. Treatment systems such as these can be costly to run, and the operational costs will become higher as more stringent discharge limits are introduced.

1.3 Research Aims

NUI Galway are investigating the potential of the Intermittently Aerated Sequencing Batch Reactor (IASBR) technology for treatment of wastewater produced in dairy processing plants in a sustainable and cost efficient manner. The IASBR technology has previously been investigated for treatment of high strength slaughterhouse wastewater, as well as municipal wastewater [10]–[12]. The IASBR is a modification of the standard sequencing batch reactor (SBR) system. The cycle sequences of the conventional SBR and IASBR are given in Figure 2.

During the react phase, instead of continuous aeration, the system is aerated intermittently. The intermittent aeration strategy leads to alternating aerobic and anoxic conditions in the system. Nitrite and nitrate are produced during the aerobic phases via nitrification, and reduced during the anoxic phase via denitrification. Due to alternating periods of nitrification and denitrification, the alkalinity remains stable throughout the cycle, eliminating the need for addition of external alkalinity.



Figure 2: Operation of conventional SBR versus IASBR

Previous studies have indicated that the IASBR has excellent nitrogen (N) and phosphorus (P) removal efficiencies [10]–[13].

The aim of this research was to investigate nutrient removal efficiencies of the laboratory-scale IASBRs at various operating conditions. Synthetic wastewater with similar properties to dairy processing wastewater was used in the experiment.

2 METHODS AND MATERIALS

2.1 Laboratory Experiment

A laboratory-scale IASBR wastewater treatment system, shown in Figure 3, was set up at NUI Galway. The system had three Plexiglas reactors with a working volume of eight litres each. The system was controlled by a Siemens programmable logic controller (PLC). Three peristaltic pumps (Watson Marlow) were used for influent pumping, effluent withdrawal, and sludge wastage. The experiment was performed in triplicate, with all three reactors operating under identical

conditions. The treatment system was located in a temperature controlled environment where temperature was 11 °C.

The IASBR cycle was 12 hours in duration throughout the experiment. A more detailed explanation of the cycle is as follows:

- At the beginning of the cycle one litre of influent wastewater was pumped into each reactor.
- For the following 10 hours and 40 minutes, the reactors were stirred continuously to ensure complete mixing. The aeration pumps operated intermittently with 100-minute aeration periods followed by 60 min non-aeration periods (Figure 2).
- The settle phase lasted for 80 minutes with no mixing or aeration. The biomass settled to the bottom of the reactors.
- In the last 5 minutes of the cycle, one litre of treated wastewater (supernatant) was pumped out of the reactors into the effluent collection basin.
- 400 ml of mixed liquor was removed from each reactor once daily as sludge waste. This resulted in a sludge retention time (SRT) of 20 days.



Figure 3: Laboratory-scale system.

A number of dairy processing plants with on-site treatment facilities throughout the country were visited. These plants varied in size and products (Table 1). Influent of their wastewater treatment plants were sampled. These samples were tested to determine the levels of organic matter, nitrogen and phosphorus. The results of this characterisation experiment informed the design of the synthetic wastewater used in the laboratory-scale experiment. The average composition of the synthetic wastewater is given in Table 2.

Table 1: Dairy Processing Plant Visits

Plant	Milk Processed Annually (litres x10 ⁶)	Plant Products
1	244	Casein, whey powder, butter, milk powder,
2	50	Liquid milk, buttermilk, cream.

3	587	Butter, milk powder.
4	90	Casein, UHT milk, milk powder.
5	206	Butter, milk powder
6	486	Milk powder, butter, spreads, cheese, casein and whey derivatives.

Table 2: Average composition of synthetic wastewater

COD (mg/L)	3513
Soluble COD (mg/L)	3307
NO ₃ -N (mg/L)	0
NO ₂ -N (mg/L)	0
NH ₄ -N (mg/L)	48.9
Total N (mg/L)	122.2
PO ₄ -P (mg/L)	25.4
Total P (mg/L)	51.9
pH	7.9

2.2 Laboratory-scale IASBR Operation

The IASBR was operated in several distinct phases during the experiment, summarised in Table 3.

Phase 1 was the first seven days of operation. It had an aeration rate of 2 litres per minute (LPM) and a cycle length of 8 hours. This stabilisation phase allowed the growth of biomass in the reactors.

On day 8 of operation, the aeration rate was lowered to 1 LPM. Until day 38 the cycle length remained at 8 hours, resulting in three cycles per day. 1 litre of influent was pumped into the reactor at the beginning of each cycle. This was equivalent to a hydraulic residence time (HRT) of 2.7 days.

In the latter stage of this phase, the daily organic loading rate (OLR) was reduced by increasing the cycle length. The flow rate remained the same while the cycle length was extended to 12 hours. This resulted in a HRT of 4 days and a lower OLR. The aeration rate remained the same at 1 LPM.

In Phase 3, the aeration rate was reduced to 0.8 LPM. The cycle length remained at 12 hours. This phase lasted from days 60 to 75.

During Phase 4 the aeration rate was decreased to 0.6 LPM. This phase lasted from days 76 to 159.

The final phase (Phase 5) had an aeration rate of 0.4 LPM. It continued until the end of the experiment on day 201.

The solids retention time throughout the experiment remained constant at 20 days.

Table 3: Phases of laboratory-scale IASBR operation

Phase	1	2	3	4	5
Aeration Rate (LPM)	2	1	0.8	0.6	0.4
Days	1-7	8-38	60-75	76-159	159-201
Cycle Length (Hours)	8	8	12	12	12

2.3 Analysis

All samples were tested in the environmental engineering laboratory at NUI Galway.

Samples were filtered using 1.2 µm filter papers for testing suspended solids (SS) in accordance with the standard APHA Methods [14]. Samples used for testing soluble parameters were subsequently filtered using 0.45 µm membrane filters or syringe filters.

Chemical oxygen demand (COD) was tested using one of two methods. One method was to use Hach Lange kits and a DR2010 spectrophotometer according to the manufacturer's instructions. The other method was to use the COD reflux method in accordance with the standard APHA methods [14].

Total nitrogen (TN) and Total phosphorous (TP) were measured using the appropriate Hach Lange kits, or using a TOC TN TP Analyser (Biotector, Ireland).

A Thermo Clinical Systems Konelab nutrient analyser was used to detect NH₄-N, PO₄-P, TON and NO₂-N. This machine is based on the APHA standard method [14].

Dissolved oxygen was measured using a multi-meter WTW probe according to the manufacturer's instructions.

3 RESULTS AND DISCUSSION

3.1 Ortho-phosphate removal

The ortho-phosphate removal efficiency in the last three phases is given in Figure 4. The aeration rate and therefore the dissolved oxygen concentrations in the reactors had a substantial effect on the ortho-phosphate removal efficiency. During Phase 3, all three reactors had similar removal efficiencies for much of the time, although towards the end of the phase reactor 1 (R1) was performed significantly worse than reactor 2 (R2) and reactor 3 (R3).

In Phase 4, at 0.6 LPM, R1 and R3 out-performed R2. The difference was thought to have been caused by some mechanical problems which occurred in R2 in the early stages of operation, possibly leading to a different microbial population from the other two reactors. Samples of the biomass were taken throughout the duration of the experiment and this hypothesis will be tested using pyrosequencing. R1 and R3 performed best in Phase 4, and consistently removed more than 97% of the ortho-phosphate from wastewater.

When the aeration rate was reduced to 0.4 LPM the removal efficiency decreased significantly in all three reactors. R3, which had achieved the greatest removal rate in earlier phases was the least effected. After an initial decrease the removal efficiencies did recover somewhat, however they did not reach the efficiencies of Phase 4.

It should be noted that towards the end of this phase sludge bulking occurred in the reactors, resulting in biomass being lost through effluent withdrawal. The sludge bulking may

have impacted the results of this phase. While it is difficult to determine the cause of the sludge bulking event, possible causes include low DO levels, and the use of synthetic wastewater.

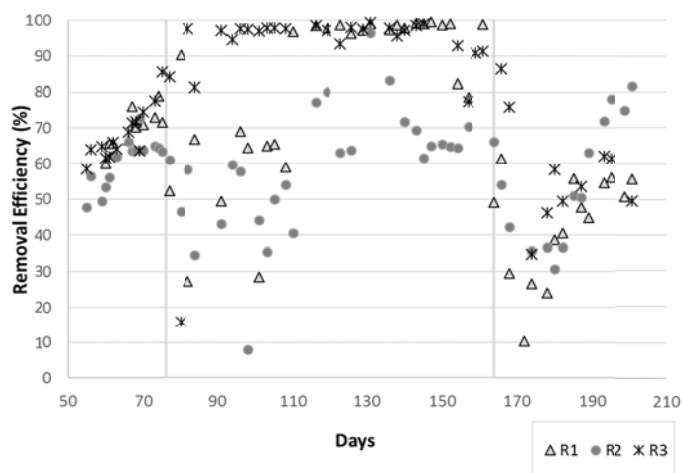


Figure 4: Ortho-phosphate removal from laboratory-scale reactors

3.2 Soluble COD removal

The majority of the COD in the influent wastewater came from soluble COD (approximately 91%). The soluble COD removal (Figure 5) remained constant throughout Phases 4 and 5, typically upwards of 97%. Once the aeration rate was reduced to 0.4 LPM however, the removal efficiency for both R1 and R2 dropped noticeably, while R3 remained unchanged. This most likely indicated that the microbial community in R3 had evolved differently to those in R1 and R2, and the reactor was more robust to change. Biomass samples were taken for pyrosequencing throughout the duration of the experiment, so this may be confirmed with future work.

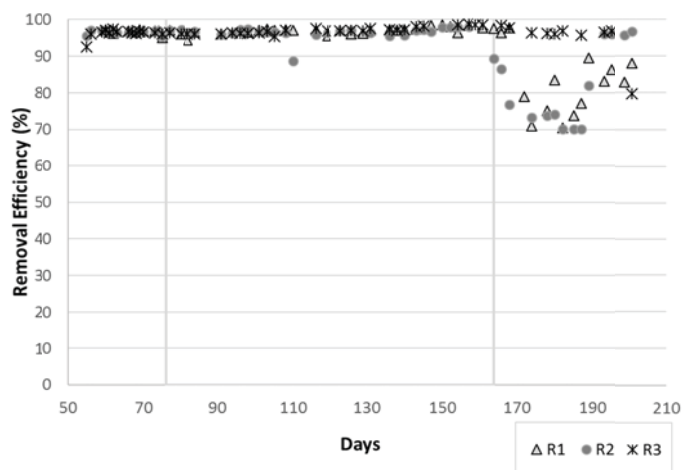


Figure 5: Dissolved COD removal from lab scale reactors.

3.3 Ammonia nitrogen and Filtered TN removal

The ammonia nitrogen removal efficiency is given in Figure 6. Its removal was slower than other parameters to recover from changes in the aeration rate. This trend can be seen especially in R2. Once the system stabilised, removal

efficiencies were consistently over 95% for R1 and R3, and over 90% for R2 in the first two phases. Once the aeration rate was reduced to 0.4 LPM however, ammonium removal efficiencies decreased in all reactors, and especially in R2. During this phase R2 was in an anaerobic condition, with the dissolved oxygen levels at almost zero even when the aeration was on.

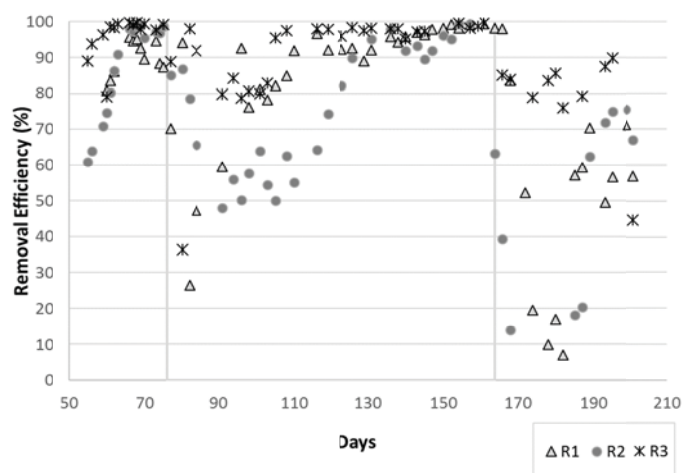


Figure 6: Ammonia removal from laboratory-scale reactors.

The overall trend in filtered TN removal (Figure 7) was similar to that of ammonium nitrogen removal but with a less significant impact visible when the aeration rates were adjusted. R2 again took the longest time to recover from the changes in the aeration rate, and performed the worst when the aeration rate was turned down to 0.4 LPM.

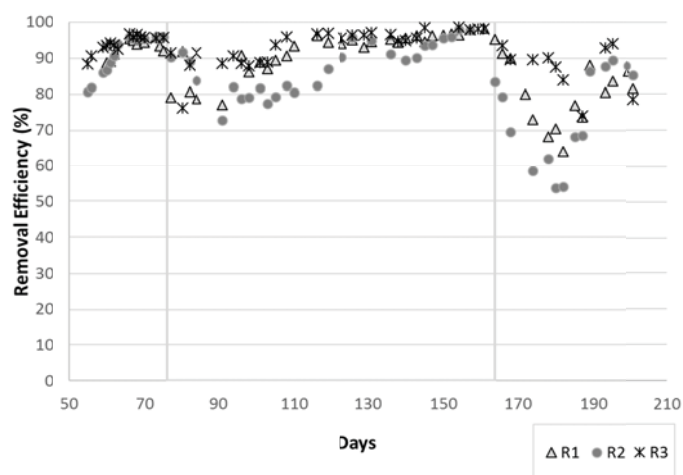


Figure 7: Filtered TN removal from laboratory-scale reactors

3.4 DO Profiles

The dissolved oxygen (DO) level is one of the most important parameters in the operation of an IASBR. The DO levels in the reactors were monitored using a WTW DO meter. The DO profiles shown in Figure 8 were from a 12-hour cycle, depicting the variation in the DO in one reactor throughout the cycle. The profiles typically consist of three spikes of DO in the reactors, each spike corresponding to an aeration period.

While there were four aeration periods in the 12-hour cycle, the first one generally was not registered by the DO meter, as

all the oxygen was consumed immediately for the degradation of organic carbon. It can be seen from Figure 8 that when the aeration rate was 0.4 LPM the second aeration period was also not detected by the DO meter.

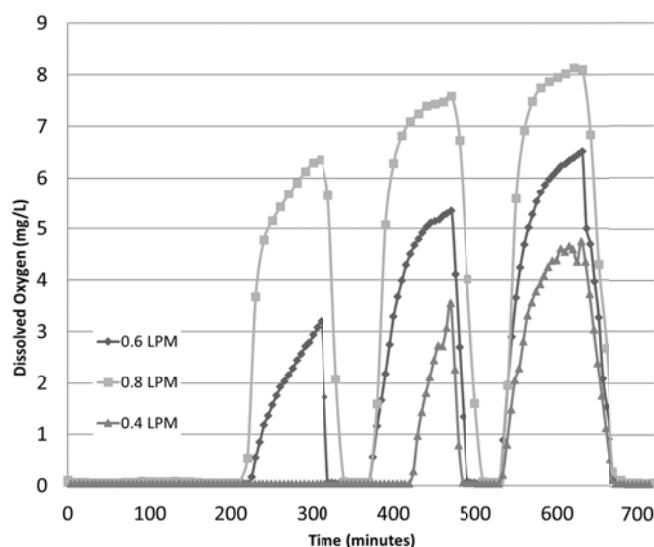


Figure 8: Typical DO Profile.

4 CONCLUSIONS

This study investigated the efficiency of a laboratory-scale IASBR system for treating dairy processing wastewater. The results indicate that the IASBR technology was the most effective in the treatment of dairy processing wastewater at an aeration rate of 0.6 LPM. At this aeration rate the IASBR was the most effective for phosphate and nitrogen removals, achieving removals of up to 98% for both. Soluble COD was removed by up to 97%.

The IASBR has the potential to provide a more energy efficient treatment system for dairy processing wastewater treatment than existing technologies, without the need for the addition of chemicals for phosphorus removal. With the introduction of legislation such as the WFD and more stringent licensing requirement, cost efficient treatment of wastewater is becoming more important.

Further studies are currently being carried out investigating the treatment of wastewater from one of the partner dairy processing plants. The next phase of the project will be to study the technology at a larger scale. A pilot-scale IASBR will be installed at a commercial dairy site and its performance will be monitored over a 12-month period. Additional planned future work will include a cost benefit analysis and mathematical modelling of the IASBR.

ACKNOWLEDGMENTS

The authors would like to acknowledge the funding provided by the Department of Agriculture, Food and the Marine for the DairyWater project (Ref.: 13-F-507). For additional details: www.dairywater.ie.

REFERENCES

[1] R. Geraghty, "Resource efficiency in Ireland's dairy processing

sector.," Dublin, Ireland., 2011.

- [2] Enterprise Ireland, "Dairy and Ingredients," 2015. [Online]. Available: <https://www.enterprise-ireland.com/en/Start-a-Business-in-Ireland/Food-Investment-from-Outside-Ireland/Key-Sectors/Dairy-and-Ingredients/>. [Accessed: 04-Jan-2016].
- [3] Department of Agriculture Fisheries and Food, "Food Harvest 2020: A Vision for Irish agri food and fisheries," Dublin, Ireland., 2010.
- [4] W. Finnegan, J. Goggins, E. Clifford, K. Fitzhenry, and X. Zhan, "Water consumption and direct energy use in the Irish dairy processing industry," in *World Water Congress*, 2015.
- [5] Bord Bia, "Dairy - Bord Bia Vantage," 2015. [Online]. Available: <http://www.bordbiavantage.ie/market-information/sector-overviews/dairy/>. [Accessed: 04-Jan-2016].
- [6] A. Broughton, S. Pratt, and A. Shilton, "Enhanced biological phosphorus removal for high-strength wastewater with a low rbCOD:P ratio.," *Bioresour. Technol.*, vol. 99, no. 5, pp. 1236–41, Mar. 2008.
- [7] M. Perle, S. Kimchie, and G. Shelef, "Some biochemical aspects of the anaerobic degradation of dairy wastewater," *Water Res.*, vol. 29, no. 6, pp. 1549–1554, Jun. 1995.
- [8] P. O. Bickers, R. Bhamidimarri, J. Shepherd, and J. Russell, "Biological phosphorus removal from a phosphorus-rich dairy processing wastewater," *Water Sci. Technol.*, vol. 48, no. 8, pp. 43–51, 2003.
- [9] T. J. Britz, C. van Schalkwyk, and Y.-T. Hung, "Treatment of Dairy Processing Wastewaters," in *Waste Treatment in the Food Processing Industry*, Taylor & Francis Group, 2006, p. 28.
- [10] L. Henry, L. Xiao, and X. Zhan, "Effect of aeration rate on domestic wastewater treatment using an intermittently aerated sequencing batch reactor (IASBR)," *Environ. Eng. Manag. J.*, vol. 12, no. 7, pp. 1329–1334, 2013.
- [11] M. PAN, T. CHEN, Z. HU, and X. ZHAN, "Assessment of nitrogen and phosphorus removal in an intermittently aerated sequencing batch reactor (IASBR) and a sequencing batch reactor (SBR)," *Water Sci. Technol.*, vol. 68, no. 2, pp. 400–405, 2013.
- [12] M. Zhang, P. G. Lawlor, G. Wu, B. Lynch, and X. Zhan, "Partial nitrification and nutrient removal in intermittently aerated sequencing batch reactors treating separated digestate liquid after anaerobic digestion of pig manure.," *Bioprocess Biosyst. Eng.*, vol. 34, no. 9, pp. 1049–56, Nov. 2011.
- [13] L. G. Henry, "Comparison of intermittently aerated sequencing batch reactors (IASBRs) and conventional sequencing batch reactors (cSBRs) in wastewater treatment," NUI Galway, 2014.
- [14] American Public Health Association (APHA), American Water Works Association, and Water Environment Federation, *Standard Methods for the Examination of Water and Wastewater 21st Edition*. Washington DC, 2005.

Numerical modelling of Cone Penetration Test in Clay using Coupled Eulerian Lagrangian Method

Sogol Fallah¹, Kenneth Gavin², Soroosh Jalilvand³

¹ Arup, 50 Ringsend Rd, Dublin 4, Ireland (Formerly UCD)

² Delft University of Technology, Department of Geoscience and Engineering, Delft, Zuid-Holland, Netherlands (Formerly UCD)

³ School of Civil Engineering, University College Dublin, Newstead, Belfield, Dublin 4, Ireland
email: sogol.fallah@arup.com, K.G.Gavin@tudelft.nl, soroosh.jalilvand@ucdconnect.ie

ABSTRACT: The Cone Penetration Test (CPT) has been extensively used in geotechnical engineering, to evaluate the properties of wide range of soils. Numerical simulations of CPT involves large deformations in the soil domain which causes numerical difficulties in traditional finite element analysis. Early numerical studies used simplifying assumptions such as wished-in-place condition and in-situ stress distribution as the initial stress state of the soil domain. Recent developments in finite element analysis allow large deformation analyses to be performed.

This paper presents the results of the continuous penetration of cone in single-layer and double-layer clay using the Coupled Eulerian Lagrangian (CEL) method. Performance of the CEL technique in modelling the cone penetration test was validated against the existing studies. Then, a parametric study was performed to develop a correlation between the cone bearing factor and rigidity index of the clay. The proposed correlation showed a very good agreement with the existing experimental and numerical correlations. The cone penetration test in double-layer clay was simulated. The results suggested that CEL analysis is a reliable technique in modelling large deformation problem of cone penetration test.

KEY WORDS: Large Deformation Finite Element Analysis; Cone Penetration Test; Eulerian Analysis.

1 INTRODUCTION

The Cone Penetration Test (CPT) is one of the most widely utilised in-situ tests used common to evaluate the properties of soil. It is widely used at both onshore and offshore sites due its applicability in a wide range of soil types. The cone tip end resistance, q_c profile obtained from the test is a good representative of engineering properties of the soil. The resistance provided by the cone tip can be represented by cone factor, $N_c = q_c/s_u$. Different studies have aimed to stimulate the cone resistance by developing correlations between N_c and soil properties [1]–[4].

Many researchers have used numerical analysis to investigate the mechanisms controlling the cone tip resistance during penetration [5]–[11]. Because of the numerical difficulties associated with performing large deformation analyses, early work on finite element analysis of cone penetration test assumed the cone to be wished-in-place with simplifying assumptions of original in-situ stress field around the cone.

This paper presents the results of an advanced technique in finite element analysis in modelling large deformation problems. Coupled Eulerian Lagrangian technique was used to simulate the continuous penetration of the cone in single-layer and double-layer clay. The results were compared with existing experimental and numerical studies and showed a very good agreement.

2 COUPLED EULERIAN LAGRANGIAN TECHNIQUE

When performing large deformation problems excessive mesh distortions may lead to difficulty with convergence or

inaccurate results during numerical modelling. To overcome these problems, different techniques have been introduced such as Arbitrary Lagrangian-Eulerian (ALE) and Coupled Eulerian Lagrangian (CEL) techniques. The ALE technique aims to reduce the distortions by remeshing the domain at a certain frequency. The field values are interpolated and transferred from the old mesh to a new improved mesh. In this method, the number of elements and the connectivity of the nodes do not change during the remeshing process. Instead the nodes are moved to find a new position in order to reduce the distortion of elements.

The Coupled Eulerian Lagrangian (CEL) method provides an environment in which both Lagrangian and Eulerian materials can be used. The difference between the Lagrangian and Eulerian approaches in finite element analysis is illustrated in Figure 1. In the traditional Lagrangian approach, shown in Figure 1 (a), the elements are filled with material and they deform as the material deforms. In the Eulerian approach, the elements are fixed and the material flows through the elements as shown in Figure 1 (b). As a result, there is no mesh distortion in the Eulerian approach. As shown in Figure 1 (b), multiple materials can exist in an Eulerian element.

This method of analysis avoids excessive mesh distortions although it has limitation on defining the material boundaries. Since the boundaries between the materials are approximate, the boundary surface may be discontinuous in this approach.

The reliability of CEL method in large deformation analysis has been addressed in recent researches on different types of geotechnical problems [12]–[17]. Qiu et al. (2011) investigated the capabilities of the CEL method by simulating pile installation and the effects of a ship running aground at an embankment [12]. The results showed good agreement with

classic finite element method and in-situ measurements. Tho et al. (2012, 2013) performed three dimensional Eulerian analyses to investigate the penetration of jack-up foundation, known as spudcan and assessed the effect of spudcan penetration on adjacent piles ([16], [17]). The results were compared to experimental data from a centrifuge test and a good agreement was obtained. The above studies suggest that the CEL technique is a reliable approach to solve large deformation problems such as spudcan installation. Consequently, the CEL method was adopted in this study.

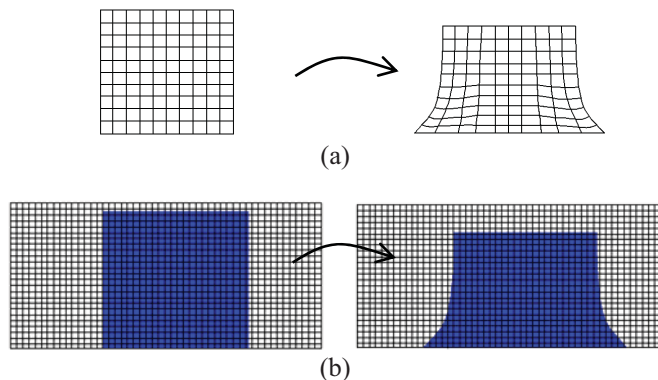


Figure 1. Lagrangian Vs Eulerian technique

The CEL method is implemented in Abaqus/Explicit [18]. In the explicit integration scheme the unknown solution for the next time step can be found directly from the solution of the previous time step, such that no iteration is required. Explicit calculations are not unconditionally stable. The numerical stability in the CEL analysis is guaranteed by introducing the critical time step size Δt_{crit} as following [18],

$$\Delta t_{crit} = \frac{L_e}{c_d} \quad (1)$$

Where L_e is the characteristic element length and Δt_{crit} is the critical time step.

2.1 Contact formulation in CEL technique

The implementation of Eulerian-Lagrangian contact is an extension of general contact in Abaqus/Explicit [18]. The contact interface is automatically identified between the Lagrangian structure and Eulerian elements so there is no need to generate a conforming mesh for the Eulerian domain. As the Lagrangian structure passes through Eulerian elements, the material is pushed out of the Eulerian elements. Similarly, the Eulerian material is prevented from flowing into the elements occupied by Lagrangian structure in order to ensure that two materials never occupy the same physical space. A layer of void Eulerian elements must be defined at the free surface to provide space for replaced Eulerian material that is driven out of the interior elements. This will be discussed in the following sections. In this study the tangential contact was considered to be frictionless.

3 CEL ANALYSIS OF CONE PENETRATION TEST

3.1 Validation

The accuracy of the present study was confirmed by comparing the results of analysis to existing numerical modelling. Zheng et al. (2013) presented the results of the analysis of cone penetration into a single-layer of weightless clay with a rigidity index, $I_R = G/s_u = 100$ [19]. The material had an undrained shear strength of 10 kPa and poison's ratio of 0.495.

The finite element model used for this analysis is shown in Figure 2. The domain was 7.5D wide and 7D in depth additional to penetration depth of 12D, where D is the diameter of the cone. The mesh was refined around the region where the cone was penetrating, whilst a coarser mesh was adopted remote from the cone in order to optimize computing resources for analyses. A total number of 2,604,960 elements were included in the domain. The time required for this analysis was about 78 hours using the Fionn supercomputer at the Irish Centre for High-End Computing (ICHEC) that provides 24 cores with 2.4GHz Intel processors. A penetration rate of (D/10) /s was selected to assure the quasi-static conditions during the analysis.

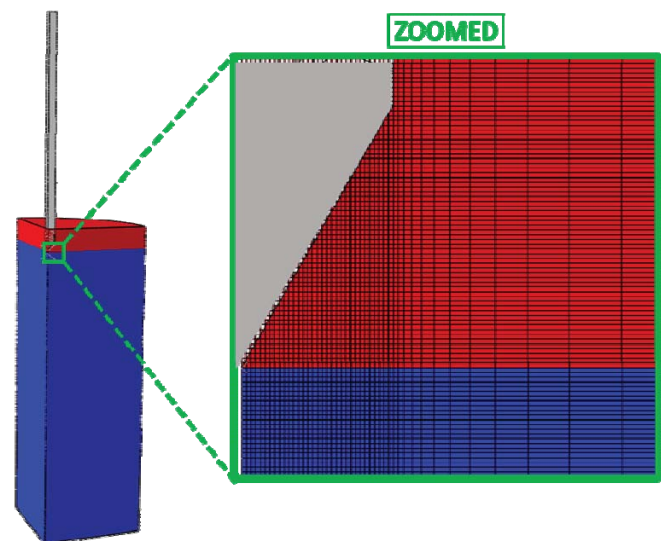


Figure 2. Finite element model of cone penetration analysis

Figure 3 shows the comparison of the results of cone penetration into the single-layer weightless soil from this study with the response predicted by Walker and Yu (2006) [20]. The vertical axis shows the normalised vertical displacement u/D . The displacement was considered zero when the maximum cross section of the cone entered the seabed. The load-penetration curves, the depth at which the cone reaches its steady state penetration resistance and the final penetration resistance were very well captured. The effect on the cone factor of the soils rigidity index will be discussed later in this paper and the results will be compared to the literature for further validation.

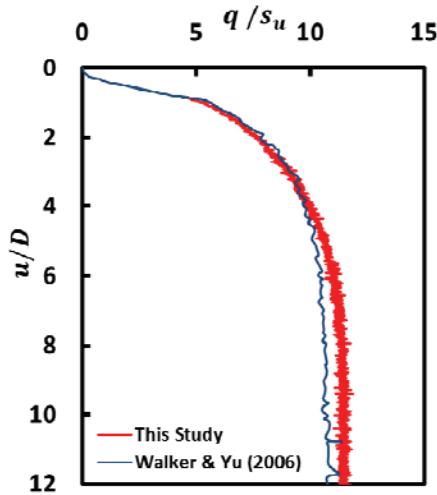


Figure 3. Comparison of penetration resistance in single-layer clay from this study and Walker and Yu (2006)

3.2 Effect of rigidity Index

The CEL analysis of a CPT with a standard cone angle of 60° was undertaken in clay with rigidity index in the range of 25 to 300. The soil was considered as weightless with uniform shear strength profile with depth. The maximum penetration depth considered was 14 times cone diameter (D_c) which allowed the cone resistance to reach the steady state that is the representative value for the cone factor.

The cone-soil interaction was considered frictionless and sliding is allowed at the soil-cone interface. Figure 4 shows the evolution of the cone resistance as the cone penetrometer was pushed into weightless uniform clay obeying the Tresca failure criterion. It can be concluded from Figure 4, that it is not necessary to continue the analyses beyond a penetration depth of 8 diameters as a steady state condition had been reached for all values of rigidity index.

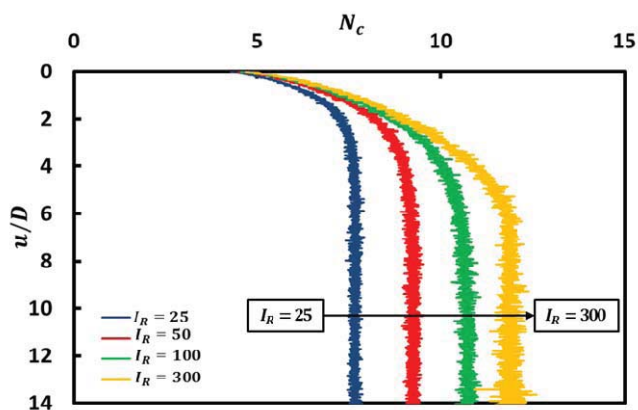


Figure 4. Variation of normalised bearing capacity with normalised depth for cone penetration in uniform clay with different rigidity index values

Figure 4 indicates that the required depth to achieve a steady state condition increased with rigidity index. These

results show that a steady state condition is achieved after a penetration depth of approximately 4 cone diameters in a Tresca material with $I_R = 25$, whilst a penetration depth of approximately 8 cone diameters is required for a material with $I_R = 300$.

The variation of steady state cone with rigidity index is plotted on a logarithmic scale and Figure 5. The equation shown is a numerical fit to the achieved data. This is validated against the existing correlation in literature as shown in Figure 6. It can be seen that the result obtained cone factors using the proposed correlation agrees well with the previous studies. Table 1 summarises the numerical values obtained.

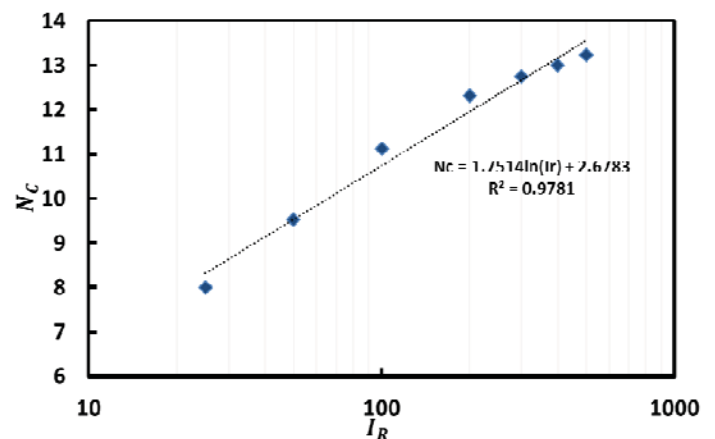


Figure 5. Variation of cone factor with rigidity index

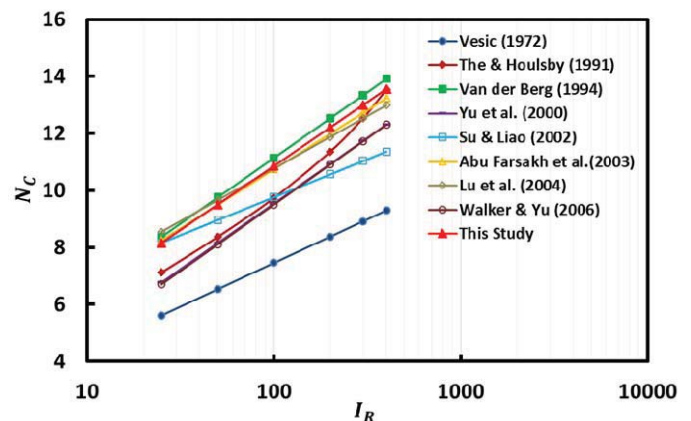


Figure 6. Comparison of cone factor from this study to literature

During deep penetration, the plastic zone is confined by elastically deforming soil. The extent of the plastic zone depends on the soil rigidity index. The results of the simulations were further verified by assessing of the plastic zone at different penetration depths. The distribution of the plastic zone at penetration depths of 1D, 3D, 5D, 7D, 9D, 11D, 13D and 15D are plotted and shown in Figure 7.

Table 1. Comparison of cone factor from this study to literature

I_R	25	50	100	300
Vesic (1972)	5.61	6.53	7.45	8.92
Teh and Houlsby (1991)	7.12	8.37	9.73	12.54
Van der Berg (1994)	8.37	9.75	11.14	13.34
Yu et al. (2000)	6.77	8.15	9.54	11.74
Su and Liao (2001)	8.16	8.96	9.76	11.03
Abu-Farsakh et al. (2003)	8.24	9.49	10.74	12.72
Lu et al. (2004)	8.55	9.66	10.77	12.53
Walker and Yu (2006)	6.70	8.10	9.50	11.72
This Study	7.94	9.12	10.29	12.16

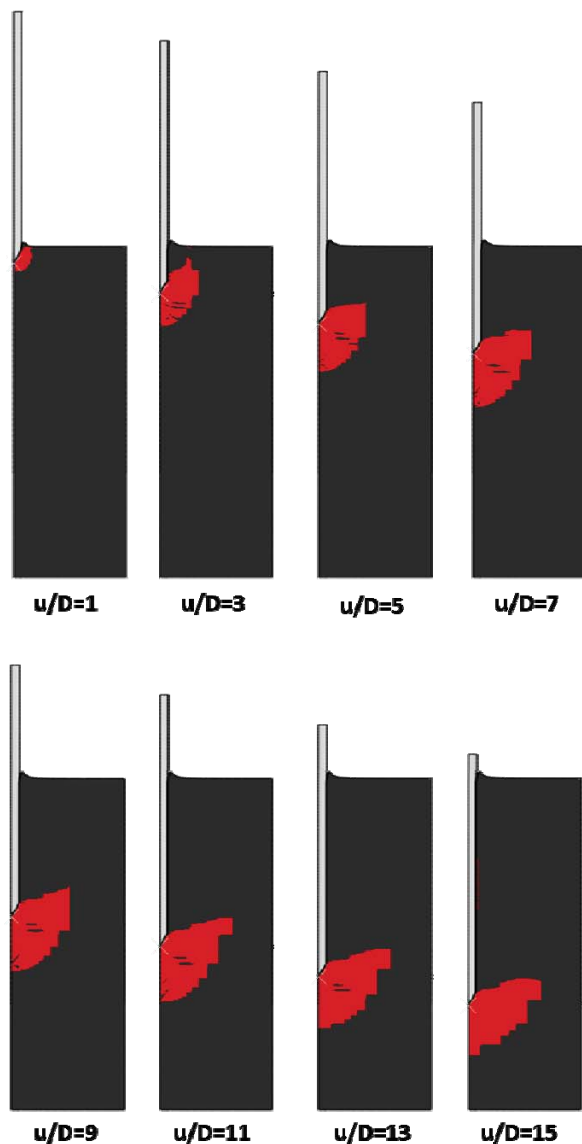


Figure 7. Plastic zone at different penetration depths

As seen in Figure 7 the border between the elastic and plastic zones is not smooth. This discontinuity occurs in the Eulerian mesh due to inaccuracies in defining the material interface for the Eulerian elements, as explained earlier. Since the mesh becomes coarser as the distance from the cone increases, the material discontinuity in the elements is more apparent for deeper penetrations. The discontinuity at the material interface definition did not affect the cone resistance profile. Figure 7 indicates that the size of plastic zone did not change after $u/D=7$, which shows the development of the local failure mechanism.

Teh and Houlsby (1991) reviewed previous studies on semi-analytical approaches to estimate cone resistance [22]. They concluded that the approaches used for the bearing capacity of shallow penetration are inappropriate for deep penetration. The shallow failure mechanism extends to the free surface while the deep failure mechanism is localized (confined) around the penetrating object. As the cone penetrates into the soil, the plastic zone that is surrounded by elastic soil moves deeper into the ground. This transition can occur at penetrations at a normalized depth of 2–3 diameters in homogeneous soil [26]. The results from this study illustrated in Figure 7 also shows that the plastic zone does not extend to the surface in cone penetration test and therefore the mechanism is different for shallow and deep penetration.

The size of the plastic region varies with the rigidity index of the soil, I_R . Lu et al. (2004) showed that the stress contours are formed around a centre, O, that is located at the distance equal to one radius of the penetrometer, R , below the maximum cross section of the penetrometer as illustrated in Figure 8 [9]. Variation of the radius of the plastic zone, R_p , and depth of the plastic zone Z_p with rigidity index of the soil is also shown in this figure. Figure 9 shows the plastic zone developed around the penetrometer tip for different values of rigidity index.

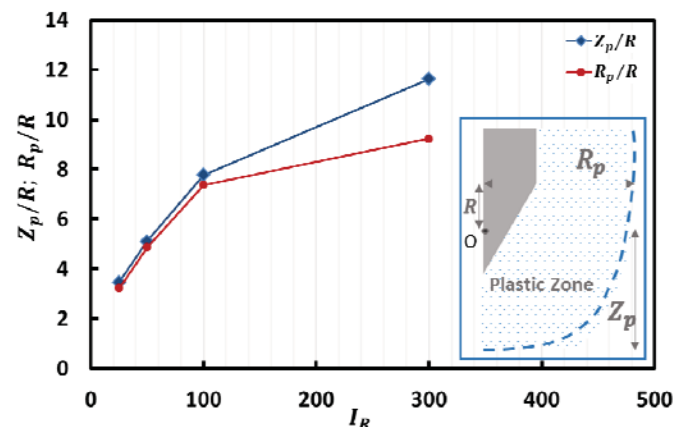


Figure 8. Variation of plastic zone extent with rigidity index of the soil

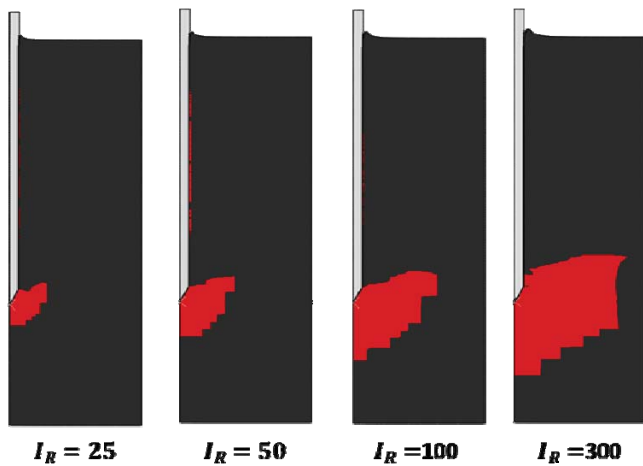


Figure 9. Plastic zones at steady state condition for different values of rigidity index of the soil

4 SIMULATION OF CONE PENETRATION IN DOUBLE-LAYER CLAY

Having validated the CEL technique in modelling cone penetration in a single layer clay, the performance of this method was assessed in simulating the cone penetration in a double-layer clay. A comparison was made between the results of this study and a numerical analysis previously conducted by Walker and Yu (2010) [11].

For the sake of consistency, the soil was modelled as a weightless undrained clay with elastic perfectly plastic behaviour. The shear modulus is selected as $G = 1 \text{ MPa}$ and the Poisson ratio is set to 0.49 for both the top and bottom layers. The rigidity index of the top and bottom layers are chosen as 100 and 300, respectively. Moreover, the top layer depth was taken as 8.4 times the diameter of the cone. The simulation continued until a penetration depth of 15 times the cone diameter was achieved. Walker and Yu (2010) modelled the soil using axisymmetry while a 3D model was employed in this study [11]. The use of 3D model is a constraint of the available implementation of Coupled Eulerian Lagrangian technique.

Figure 10 shows the result of the normalized bearing capacities (q/s_u) in terms of the normalized penetration depth (u/D) as obtained from this study (dots) and Walker and Yu (2010) [11] (solid lines). The results are reported for both single-layer (single value of rigidity index $I_R = 100$) and double-layer cases (rigidity indices of 100 and 300 for the top and bottom layers respectively). The single layer soil was treated as a double-layer soil with equal rigidity indices for the top and bottom layers [11]. The subset in Figure 10 shows the deformation of the bottom layer as the cone tip reaches the penetration depth of 8.4 times the cone diameter (the location of the bottom layer was equivalent to $u/D = 7.5$) in the double-layer case. The deformation in the bottom layer is exaggerated for the purpose of clarity. The interface of the top and bottom layers is demonstrated in Figure 10 with a horizontal line that passes through $u/D = 7.5$.

Comparison of the numerical results from CEL analysis in this study and the numerical results from ALE analysis by Walker and Yu (2010) [11] in Figure 10, suggests that the CEL technique provides smoother profile of bearing capacity, specifically at the interface of soft and stiff clay. This can be important when assessing the risk of punch-through problem in penetration of large offshore foundations such as spudcan.

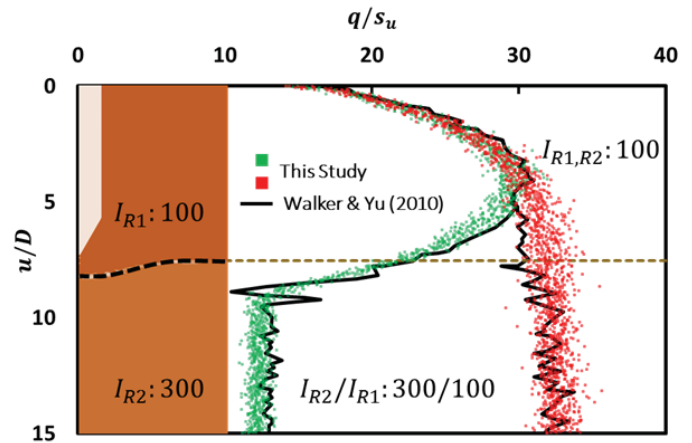


Figure 10. Comparison of the cone penetration results in double-layer clay to Walker and Yu (2010) [11].

5 SUMMARY AND CONCLUSION

This paper presented the results of large deformation analysis of cone penetration test in single-layer and double-layer clay. The coupled Lagrangian Eulerian technique was used for simulation of CPT in Abaqus/Explicit programme.

The cone resistance profile obtained from CEL analysis was validated against other numerical studies that were performed using the ALE technique. The results showed a very good agreement. A correlation was proposed to estimate the cone factor based on CEL analyses of CPT's in weightless soil with different values of rigidity index. The comparison of the proposed correlation with existing experimental and numerical correlations in the literature. The evolution plastic zone in the soil domain was also examined as the cone penetrated into the ground. The general pattern showed a good agreement with literature.

Finally, the cone penetration in double-layer clay was simulated and compared to other numerical studies. The results showed a very good agreement. The bearing capacity profiles from CEL analysis was found to be smoother than the ALE predictions and was deemed to be more realistic. This suggests that CEL can be a very good tool in predicting the potential of punch-through failure for example

REFERENCES

- [1] Abaqus 6.13-2, V. (2013). "Abaqus v6.13 documentation, 2013." Dassault Systèmes, Providence, RI, USA.
- [2] Abu-Farsakh, M., Tumay, M., and Voyiadjis, G. (2003). "Numerical Parametric Study of Piezocone Penetration Test in Clays." *International Journal of Geomechanics*, 1–12.
- [3] Ahmadi, M. M., Byrne, P. M., and Campanella, R. G. (2005). "Cone tip resistance in sand: modeling, verification, and applications." *Canadian*

- Geotechnical Journal*, NRC Research Press Ottawa, Canada, 42(4), 977–993.
- [4] Van der Berg, P. (1994). “Analysis of soil penetration.”
 - [5] Dutta, S., Hawlader, B., and Phillips, R. (2012). “Finite Element Modeling of Vertical Penetration of Offshore Pipelines using Coupled Eulerian Lagrangian Approach.” *Proceedings of the Twenty-second (2012) International Offshore and Polar Engineering Conference*.
 - [6] Hu, Y., Randolph, M. F., and Watson, P. G. (1999). “Bearing response of skirted foundation on nonhomogeneous soil.” *Journal of geotechnical and geoenvironmental engineering*, American Society of Civil Engineers, 125(11), 924–935.
 - [7] Liyanapathirana, D. S. (2009). “Arbitrary Lagrangian Eulerian based finite element analysis of cone penetration in soft clay.” *Computers and Geotechnics*, Elsevier Ltd, 36(5), 851–860.
 - [8] Lu, Q., Hu, Y., Randolph, M. F., and Bugarski, I. C. (2004). “A numerical study of cone penetration in clay.” *Géotechnique*, Thomas Telford, 54(4), 257–267.
 - [9] Mayne, P. W., and Rix, G. J. (1993). “Gmax-qc Relationships for Clays.” *Geotechnical Testing Journal*, GTJODJ, 16(1), 54–60.
 - [10] Pucker, T., and Grabe, J. (2012). “Numerical simulation of the installation process of full displacement piles.” *Computers and Geotechnics*, 45, 93–106.
 - [11] Qiu, G., and Henke, S. (2011). “Controlled installation of spudcan foundations on loose sand overlying weak clay.” *Marine Structures*, Elsevier Ltd, 24(4), 528–550.
 - [12] Qiu, G., Henke, S., and Grabe, J. (2011). “Application of a Coupled Eulerian–Lagrangian approach on geomechanical problems involving large deformations.” *Computers and Geotechnics*, Elsevier Ltd, 38(1), 30–39.
 - [13] Robertson, P. K. (1990). “Soil classification using the cone penetration test.” *Canadian Geotechnical Journal*, NRC Research Press, 27(1), 151–158.
 - [14] Robertson, P. K. (2009). “Interpretation of cone penetration tests—a unified approach.” *Canadian Geotechnical Journal*, NRC Research Press, 46(11), 1337–1355.
 - [15] Robertson, P. K., and Wride, C. E. (1998). “Evaluating cyclic liquefaction potential using the cone penetration test.” *Canadian Geotechnical Journal*, NRC Research Press, 35(3), 442–459.
 - [16] Su, S., and Liao, H. (2001). “Cavity expansion and cone penetration resistance in anisotropic clay.” *Journal of the Chinese Institute of Engineers*, (July 2012), 37–41.
 - [17] Teh, C., and Houlsby, G. (1991). “An analytical study of the cone penetration test in clay.” *Geotechnique*, (3), 529–532.
 - [18] Tho, K. K., Leung, C. F., Chow, Y. K., and Swaddiwudhipong, S. (2012). “Eulerian finite-element technique for analysis of jack-up spudcan penetration.” *International journal of geomechanics*, 12(February), 64–73.
 - [19] Tho, K. K., Leung, C. F., Chow, Y. K., and Swaddiwudhipong, S. (2013). “Eulerian finite element simulation of spudcan–pile interaction.” *Canadian Geotechnical Journal*, 50(6), 595–608.
 - [20] Tolooiyan, a., and Gavin, K. (2011). “Modelling the Cone Penetration Test in sand using Cavity Expansion and Arbitrary Lagrangian Eulerian Finite Element Methods.” *Computers and Geotechnics*, Elsevier Ltd, 38(4), 482–490.
 - [21] Vesic, A. (1972). “Expansion of cavities in infinite soil mass.” *Journal of Soil Mechanics & Foundations Div.*
 - [22] Walker, J., and Yu, H. (2010). “Analysis of the cone penetration test in layered clay.” *Géotechnique*.
 - [23] Walker, J., and Yu, H. S. (2006). “Adaptive finite element analysis of cone penetration in clay.” *Acta Geotechnica*, 1(1), 43–57.
 - [24] Yi, J., Goh, S., Lee, F., and Randolph, M. (2012). “A numerical study of cone penetration in fine-grained soils allowing for consolidation effects.” *Géotechnique*, (2012), 707–719.
 - [25] Yu, H. S., Herrmann, L. R., and Boulanger, R. W. (2000). “Analysis of Steady Cone Penetration in Clay.” *Journal of Geotechnical and Geoenvironmental Engineering*, American Society of Civil Engineers, 126(7), 594–605.
 - [26] Zheng, J., Hossain, M., and Wang, D. (2013). “3D large deformation FE analysis of spudcan and cone penetration on three-layer clays.” *Twenty-third (2013) International Offshore and Polar Engineering*, 9, 453–460.

The treatment of karst features encountered during road construction in County Galway.

Esther Madden¹, Deirdre O' Hara²

¹Arup Consulting Engineers, 50 Ringsend Road, Dublin 4, Ireland

²Halcrow Barry Ltd, Unit 9, N5 Business Park, Moneen Rd, Castlebar, Co. Mayo, Ireland
email: esther.madden@arup.com, dohara@jbbarry.ie

ABSTRACT: This paper addresses the identification and treatment of karst features during the construction of the M17/M18 Gort to Tuam motorway. Extensive karstification is known to occur in the limestones of the mid Galway region of Ireland. A karst risk assessment was carried out in advance of the geotechnical design of the earthworks and structural foundations which gave rise to a karst feature identification protocol and a “menu” of prescriptive treatment measures. Several karst features were identified and treated in this manner in a number of locations, however unusually extensive conduit karst features were found to be converging under the central pier of a bridge structure. Linear karst features were also encountered adjacent to this structure. The paper describes how these features were identified and how the surrounding completely weathered rock/clay infilled void was treated using a number of methods, dependent upon its depth, size and impact rating.

KEY WORDS: CERi 2016; Karst; Limestone, Galway, Treatment, Conduit., Void Cover Ratio

1 INTRODUCTION

The geology of east Galway is dominated by a karst landscape formed in the underlying limestone. While limestone provides high bearing capacity for founding structures it can be interspersed with karst features containing a combination of overburden deposits, water and air. Shallow karst features can cause a threat to the stability of road pavements and structural foundations. The design and construction of the M17/N18 Gort to Tuam motorway involved investigation and treatment of numerous karst features along the route. These karst features presented themselves in different forms and depending on the type of overburden present above the limestone bedrock, the risk that the karst feature posed to the road pavement, integrity of structural foundations and the groundwater schemes varied.

Careful treatment of each of these features was required to ensure that any existing drainage regimes were preserved and that drainage of the highway was managed to prevent future washing out of finer overburden material leading to sudden collapse and damage to the road pavement or structural foundations.

Appropriate foundation solutions were also required for the structures, which were constructed over karst features. To provide solutions, the quantity and magnitude of the features needed to be understood at design and construction stage. This was achieved through the use of GIS mapping to carry out desk studies and a karst risk assessment that analysed the risk of damage to the road pavement and each structure foundation from potential voids. A karst protocol was subsequently developed for the designers' site representative (DSR) to identify karst features and select appropriate standard solutions or to refer back to the office for bespoke designs. This approach allowed designers to predict the size, location and quantity of typical features expected in karst landscapes and to allow site personnel to identify the need for standard solutions or bespoke designs.

The bespoke foundation design for Ballinphuill Overbridge is presented as an example for future works in karst landscapes. The example details the various levels of investigation carried out and the usefulness of these methods in predicting the extent of the identified karst feature. Methodology by Waltham and Lu (2007) was used to assign a minimum thickness of competent rock between the top of an open void and the foundations. The attempted use of grouting as a solution beneath the central pier, its limitations and the geophysical surveys used to check the extent of grouting are also presented. The final design consisted of excavation to expose the feature and backfilling with a modified inverted filter. Based on the lessons learnt, this methodology of excavating to expose and treat the feature is recommended as best practice for dealing with karst features below structural foundations.

2 REVIEW OF EXISTING PRACTICE

The treatment of karst features on recent highways in Ireland has developed from case studies in other countries and from observing flooding and collapse of overburden associated with mismanaged blocking of drainage regimes. A case study published by Waltham, Bell and Culshaw (2005) depicts the treatment of a sinkhole in Pennsylvania where the treatment consisted of backfilling the sinkhole with a concrete slab, locally available fill and geogrid as per figure 1. Unfortunately, the bedrock had not been exposed and water actively infiltrating into the underlying limestone caused the material beneath the slab to erode and the void reopened at a later stage. Following this, the bedrock was exposed and the throat plugged with chunk rock to allow downward drainage of water while still providing stability to the overlying road pavement.

This approach and other existing practices of plugging the sinkhole and maintaining natural drainage regimes have been developed to create a series of standard design solutions for

smaller features along the route. Following on from detailed desk studies and specific scenarios encountered on site, various bespoke solutions were designed depending on the regional geology, hydrogeology and the size and complexity of features and the height of fill above the original ground level.

3 GEOLOGY AND KARSTIFICATION OF EAST GALWAY

The geology of east Galway comprises of a series of limestone formations with varying degrees of dissolution, overlain by glacial deposits in the form of silts, clays and sands. The evidence of this karstification has manifested at the ground surface in the form of Turloughs, depressions, channels in the buried bedrock and outcropping karst pavements.

According to the classification by Waltham and Fookes (2003), the overall karst morphology along the route can be identified as Glaciokarst, with overlying Fluviokarst features. Glaciokarst terrain is described as comprising of features resulting from glaciation in the form of outcropping limestone pavements and deep channels cut through the bedrock. Fluviokarst is described as the term used to describe the valleys, disappearing streams and underlying caves formed in the time periods close to or just after glaciation.

The Waltham and Fookes (2003) method detailing the engineering classification of karst shown in Table 1 was used to classify the levels of karst along the route of M17/N18. This was achieved using the knowledge that glacial deposits overlie the limestone and from information gathered about existing karst features some of which are shown in figures 2 to 5.

The karst landscape was identified as mostly falling into the juvenile and youthful karst classes with the presence of fissuring in the bedrock, small caves and depressions in the overburden at the surface. Some particular areas were further identified as being in the mature and extreme classes with more extensive fissuring and larger caves.

Table 1. Classification of karst after (Waltham and Fookes, 2003).

Karst	Class	Description
KI	Juvenile	Sinkholes, depressions and caves are rare. Minor fissuring of bedrock.
KII	Youthful	Small sinkholes, depressions and swallow holes. Widespread fissuring in top of bedrock. Small caves (< 3m wide).
KIII	Mature	Rockhead relief < 5m, with extensive fissuring. Extensive secondary opening of most fissures. Caves < 5m wide at multiple levels.
KIV	Complex	Rockhead relief < 20m, with extensive fissuring and pinnacles. Extensive large dissolution openings. Caves > 5m wide at multiple levels.
KV	Extreme	Rockhead relief \geq 20m, with extensive fissuring and pinnacles. Abundant and complex dissolution openings. Caves > 15m wide.

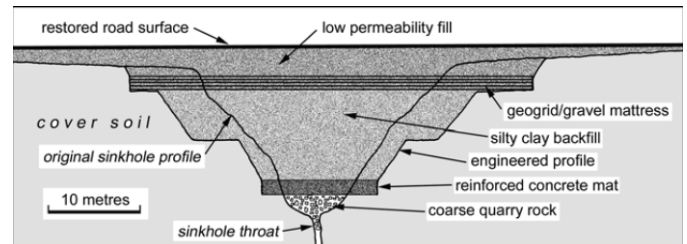


Figure 1. Sinkhole treatment in Pennsylvania after Waltham, Bell and Culshaw (2005)



Figure 2. Small cave.



Figure 3. Outcropping karst pavement.



Figure 4. Turlough.

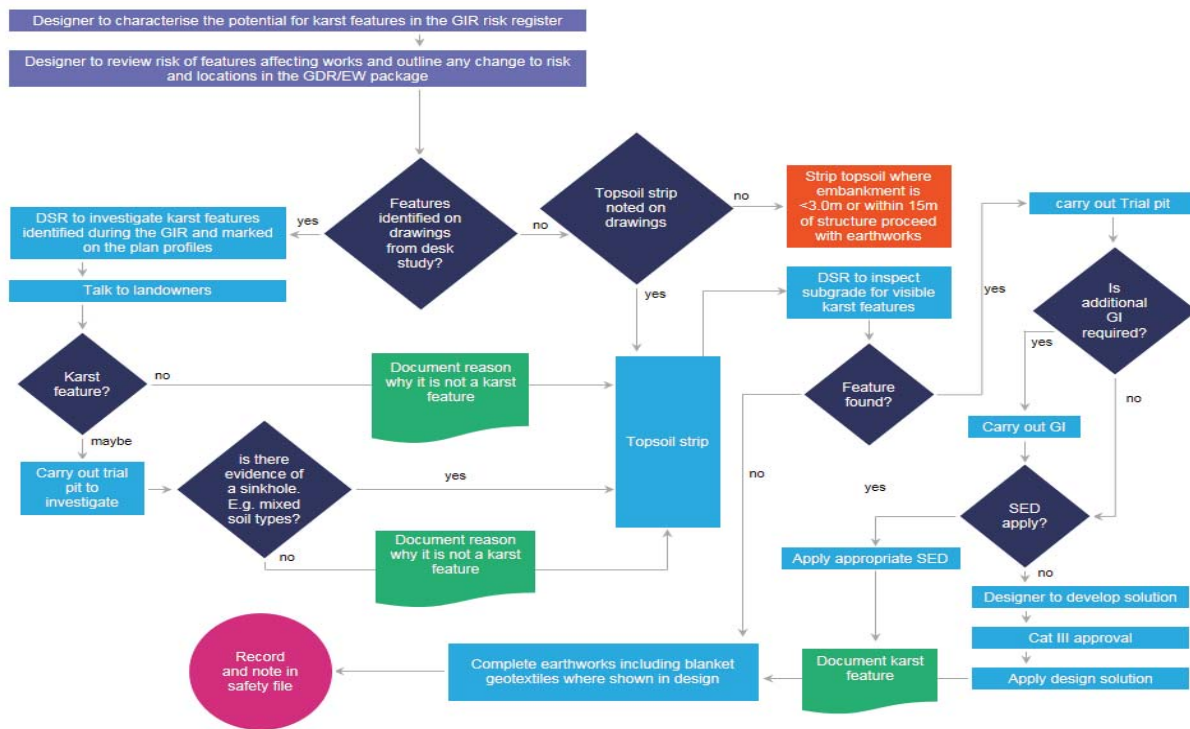


Figure 5. Karst protocol

4 ASSESSMENT OF SUBSIDENCE RISK TO THE ROAD PAVEMENT

Research by Waltham and Fookes (2003) has shown that natural events of rock collapse are not common and this hazard is considered to be of low risk however damage to foundations typically arise where there is between 2m and 10m of overburden between the underside of the foundation and the karst bedrock.

A detailed risk assessment was carried out along the route of the M17/N18 to identify areas where karst features could affect the stability of the structural foundations and the road pavement. While the risk assessment looks at the nature of the karst, the design solutions take the sensitivity of the design element into account. The solution for pavements has been designed to minimise the effects of ground failure on the pavement allowing time for investigation and remediation of the earthworks and pavement, while the solutions for the structures have been designed to limit the risk against collapse of the structure. The karst risk assessment methodology adopted for this project was based on assessments undertaken on a number of Design and Build road schemes in Ireland (Rutty and Jennings, 2012) and projects carried out by Arup (e.g. N22/N69 Tralee Bypass and Ballyadam in Carrigtohill).

The karst risk assessment methodology was modified where necessary to account for local conditions and available information. It was compiled by assessing geological attributes likely to give rise to karst hazards such as the presence of existing or known karst features as determined from site observations, exploratory holes, geophysical surveys and other information sources. The karst risk has been based on assessment of the following geological and evidence based risks:

- Underlying rock type
- Thickness of overburden cover / depth to bedrock
- Overburden cover type

- Proximity to known karst features
 - Logged feature in rotary core boreholes e.g. cavity, low/no TCR (Total Core Recovery), brecciated / broken zone of rock etc.
 - Anomalies noted in the geophysical survey (sharp changes in resistivity may indicate voids or in filled cavities)
 - Low blow counts in SPTs / Dynamic Probes (possibly indicative of highly weathered rocks or soft / loose cavity infill)
 - Buried topsoil / organic matter at depth in cable percussive boreholes or trial pits (possibly indicative of disturbed ground, in filled hollows or cavities).
- Figure 5 Karst Protocol

Rankings were assigned to each of the parameters and these have been multiplied together to form a karst risk assessment matrix, to which ratings of low, medium and high have been applied. The risk ratings adopted are as follows:

Low Risk: Significant karst development is unlikely and unstable ground and significant cavities are not anticipated. Mitigation measures are unlikely to be required.

Medium Risk: Some karst development is possible which may lead to unstable ground or cavities. Following inspection of formation levels, design mitigation measures may be required.

High Risk: Karst development is likely and active unstable ground and cavities already exist or may exist. Detailed assessment of the data, additional site investigation and geophysical surveying is recommended and mitigation is likely to be required.

5 KARST IDENTIFICATION PROTOCOL

The karst risk assessment identified over 50% of the route as being at risk of subsidence from underlying karst features. The risk level was highly sensitive to the quantity of features

in the area and it was agreed that a protocol was needed for the DSR to follow during construction.

This protocol as shown in figure 5 allowed the DSRs to examine the subgrade of the road for existing features and if necessary apply standard details to treat small features or to inform the design team of complex features requiring bespoke designs. Some of the features encountered during construction are shown on figures 6 and 7.



Figure 6. Fissured limestone.



Figure 7. Karst features in bedrock

6 TREATMENT OF KARST FEATURES

The approach outlined in Waltham, Bell and Culshaw, (2005) which plugs the throat of the sinkhole combined with the inverted filter solution by De Bruyn and Bell (2001) has been used to treat the karst features located beneath the proposed road pavement. A further measure of insurance has been employed in the form of a geotextile spanning beyond the footprint of the existing feature to provide a level of safety in the unlikely event that water infiltrates from another source and causes instability adjacent to the treated feature.

In some areas, a review of existing karst features, geology, watercourses and overlying overburden type has identified that there is a high risk that subsidence of the road pavement could be as a direct result of overburden collapsing into voids in the limestone. In these locations, large areas of geotextile have been placed between the existing ground and the pavement layers. In this scenario, the geotextile will span over the features and this will delay the subsidence of the pavement to allow for investigation and remediation of any such features.



Figure 8. Linear Karst Feature in rock

In following the karst protocol, a number of linear karst features were encountered at excavation level through some of the rock cuts. The original solution of backfilling with the inverted filter solution prescribed for the treatment of karst features in overburden was modified for use in rock cuts to minimise differential settlements and associated deterioration of the pavement. The modified solution incorporated a coarse rockfill to choke the feature while maintaining a groundwater flow through the feature. This was overlain by Class 6N2 Upfill with a geotextile layer profile as shown in figure 9.

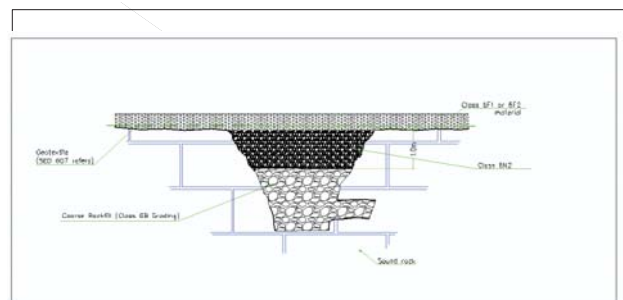


Figure 9. Backfill of karst features in rock

7 BALLINPHUIL OVERBRIDGE EAST AND WEST ABUTMENTS

The Ballinphuil Overbridge is a new overbridge located at chainage 17+070m on the new M17 carriageway and situated east of Corofin, Co. Galway. The proposed M17 mainline is situated in a cutting approximately 7.3m below the existing ground level at the structure location. Ground level near the overbridge is approximately 40.3m OD. The site is co-linear with the existing L-2130.

A karst risk assessment similar to the one outlined for the subsidence risk to the pavement was carried out for the structure, this risk assessment was based on the likelihood of impact against the magnitude of impact and it identified the risk of karstification as 'severe'. The assessment focussed on the collapse risk to the structure. Pre-construction stage site investigations comprised two trial pits, four rotary cored boreholes, geophysical ground conductivity profiling and four geophysical resistivity profiles. No televiewers were carried out in the boreholes. Pre and post-construction ground investigation results are appended to this paper. The geophysical results indicated that there were anomalies at the west abutment, additional boreholes were carried out in these targeted locations. A clay filled void was encountered in one rotary cored hole, however this was south of the west

abutment and rotary cored holes closer to the west abutment did not encounter any voids. Geophysics results were helpful in determining the presence of geophysical anomalies, however rotary coring was required to pin point actual karst locations.

During detailed design, analysis of the existing exploratory holes identified that the information available did not permit the complete assessment of the geotechnical risk from karst. It was decided that the east abutment and the central pier required additional site investigation and two additional rotary cores were carried out at each foundation. A 0.55m void was identified at the east abutment at 9.3m below ground level (approximately 30.6mOD), approximately 5.5m below the foundation.

Waltham and Lu (2007) indicate that there is a potential hazard in caves at shallow depth where the rock roof is thin in comparison to the underlying cave width. In construction over abandoned mine workings (CIRIA Special Publication 32, 1984), the maximum height of collapse is between 5 and 10 times the void height, however, this is considered to be contentious and may not be applicable to natural caves or karst features.

In an effort to establish guidelines for safe cover depths to engineering works over caves, Waltham and Lu (2007) numerically modelled the effects of loading over cave roofs in two dimensions, applying loads over caves of varying widths and cover thicknesses in order to assess cave roof stability in terms of the cover ratio (t/w , where t is the roof thickness and w is the cave width) that is appropriate for any limestone of given rock mass quality.

The Rock Mass Rating (RMR) system, described by Bieniawski (1989) and subsequently refined over the years, was used to describe the quality of the rock mass the caves were modelled within. The caves were modelled in rock masses with RMR values ranging from 20 to 50, which was considered to encompass the ground conditions in most types of cavernous karst in Limestones. The RMR system takes into account the uniaxial compressive strength of the rock material, the rock quality designation (RQD), the spacing, orientation and condition of discontinuities and the groundwater conditions in producing a rating score.

Waltham and Lu (2007) applied loads of 5 MN to define safe cave opening and cover depth conditions for wide range of RMRs. The safe conditions for the loading of a 1 MPa bearing pressure on a pad of 1m² with a factor of safety of 5 were modelled. If RMR is taken as between 30 and 40, a cover ratio of 1:0.5, where the roof thickness is at least half the cave width ($t=w/2$), appears to be adequate for most engineering practice. An RMR of 44 was assigned to the rock under the east abutment of the Ballinphuill Overbridge, assuming a cave width of less than or equal to three times the cave height, the cover ratio (t/w) was 5.5/1.65, it was determined that the east abutment could be constructed safely over the void.

8 BALLINPHUILL OVERBRIDGE CENTRAL PIER

Following analysis of the existing exploratory hole information, two boreholes were drilled at the central pier. A number of voids were encountered in both of these holes,

ranging in thickness from 0.25 to 1.5m and interspersed throughout the length.

As a safe depth of cover could not be provided to the voids, it was decided to drill and grout at the central pier location. An additional thirteen holes (Fifteen in total) were drilled to depths of 7m below ground level (approximately 24.0mOD). During drilling, it was noted that the exploratory holes were showing evidence of interconnection of voids, for example one of the probe holes produced venting at five previously drilled holes.

Drilling and grouting had been previously used, successfully, within the project at two other structure locations where voids were encountered. Following drilling and grouting at the two structure locations, the grouted ground underneath the footing was checked using Ground Penetrating Radar (GPR) to determine if all the void spaces had been filled. The GPR report identified a number of anomalies, so three further rotary cored holes were drilled at each location, six in total. One of the rotary cored holes identified a void which was backfilled using grout, while five rotary cored holes did not identify any voids. All rotary cored holes were subsequently backfilled using grout to the surface.

At the Ballinphuill Overbridge central pier, grouting operations were closely managed to determine the grout take in the holes. The calculated volume of grout required to fill the holes was exceeded, indicating that a void was present, however, it was identified that while seven of the fifteen holes were successfully grouted to the surface, the remaining eight holes were holding at approximately 3m bgl. It was decided to excavate to 3-4m bgl and find out why the grout was not backfilling to ground level.

Excavation discovered a large infilled karst feature at approximately 3.0 to 7.0m bgl (28.0-24.0mOD). The void was completely filled with pinnacles of rock and clay infill. Conduit karst features (0.5m diameter, running approximately north south (350°)) were found above 3.0m bgl (28.0mOD) shown in figures 10 and 11.



Figure 10. Conduit Karst Feature

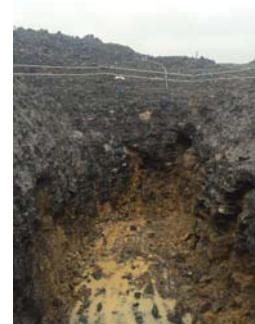


Figure 11. Karst Features at Central Pier

A bespoke solution was developed to detail the specific backfilling of this large karst feature. All clay was excavated and the feature thoroughly cleaned out. 3m of Class 6N2 upfill was placed to 27.8mOD for economy, a 200mm layer of concrete was placed above this to block the migration of water into the Class 6N2 upfill and thus mirror the previous ground conditions of an infilled karst feature. A 2m deep, 0.5m wide, “no fines” concrete surround was placed all around the outside of the excavation to allow the continuity of the potential water flow paths through the conduit karst features. Concrete was placed from 28.0mOD to the underside of formation to prevent excess differential settlement between the abutments and the central pier, shown in figure 12.

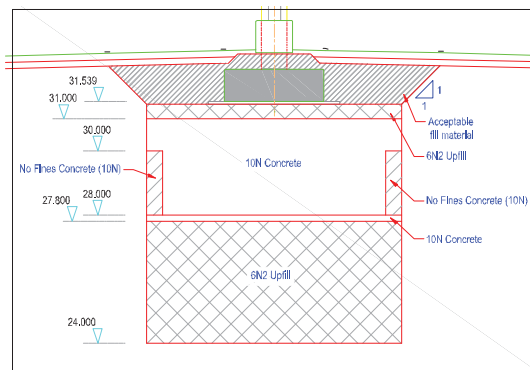


Figure 12. Backfill of Central Pier

The west abutment had no evidence of karstification under the structure, but following on from the excavation of the central pier at 25.0mOD, as a precaution an additional rotary percussive hole was drilled in line with a conduit karst feature which was trending towards the west abutment. No karst features were identified therein.

The Ballinphuil Overbridge provided a number of challenging geotechnical problems, in summary, bespoke treatment of each structural element was required, such as, application of Waltham and Lu's approach to the east abutment, excavate and replace at the central pier, following an abandoned drill and grout proposal, and confirmatory rotary cores at the west abutment.

While Waltham and Lu's paper provides clarity on the void cover ratio, it is not a catch all, similarly, in some cases, exploratory holes do not provide a full picture of the underlying ground conditions and drill and grouting does not solve all void problems, it is only through thorough assessment of each of these proposals in turn that a robust solution can be delivered.

CONCLUSION

Standard and bespoke solutions for identified karst features on the M17/N18 motorway were developed through the use of GIS mapping during the desk study, previous case studies, past design experience on other projects, and targeted ground investigations.

The classification system by Waltham and Fookes (2003) was used at desk study stage to identify the degree of karstification along the route. GIS mapping was used to gather

existing information on the topography, geology and mapped karst features along the route. The maps were updated with information from site surveys and used to identify gaps in information. Appropriate ground investigation was then employed to allow an assessment of the risk of subsidence in the pavement layers from collapse of overburden into underlying bedrock. Existing treatment solutions were developed to create standard earthworks details for small karst features and a karst protocol was established for use during investigation and construction to identify larger features and to gather information on their dimensions to allow design of bespoke treatments. It is recommended that all future road construction follows this approach detailed in the karst protocol.

Particularly challenging karst conditions were encountered at the Ballinphuil Overbridge. Following additional investigation, the Waltham and Lu (2007) approach to the safe cover ratio for engineering loading was adopted at the east abutment. This approach was considered as an economical and non-intrusive method of karst risk mitigation, avoiding expensive grouting or excavate and replace operations. As insufficient cover was present at the central pier, and due to the failure of a proposed grouting solution, large scale excavation and backfilling were required to mitigate the risk from karst at the central pier of the same structure. It is recommended that all karst features are exposed during construction and backfilled in a way that preserves the existing groundwater regime and provides support to the road pavement and structural foundations.

ACKNOWLEDGMENTS

H. Gibbons, C. Mac an tSearraigh, T. O' Brien, P. Casey, L. Brown, M. Fleming (Arup), P. Quigley, C. Reilly (GDG), J. Philbin, M. Ferry, D. Flanagan, S. Sorohan, (Lagan), N. Curtis (Sisk), P. McCarthy (Roadbridge), L. Prendiville, W. Lalor, J. McElhinney, J. Fallon, G. Barton, S. McGrath, C. Osbourne, B. Hastings, D. Treanor, A. Stewart (Halcrow Barry).

REFERENCES

- [1] J. Simpson and E. Weiner, Eds., *The Oxford English dictionary*, Clarendon Press, Oxford, UK, second edition, 1989.
- [2] Rutty, P. and Jennings, P. *Investigation, design and construction in karst*, GSI Roads Conference, 2012
- [3] Waltham, A.C, Fookes, P.G., *Engineering classification of karst ground conditions*, Quarterly Journal of Engineering Geology and Hydrogeology, 2003, vol 36, 101 – 118.
- [4] Waltham, T., Bell, F., Culshaw, M., *Sinkholes and Subsidence, Karst and Cavernous Rocks in Engineering and Construction*, Springer, ISBN 3-540-20725-2, 2005.
- [5] Waltham, T., & Lu, A., *Natural and anthropogenic rock collapse over open caves*, IN M. Parise & J. Gunn (eds) *Natural and anthropogenic hazards in karst areas: recognition, analysis and mitigation*. Geol. Soc. London, sp. Publ. 279: 13-21, 2007
- [6] Healy, P. R., & Head, J. M., *Construction over abandoned mine workings*. Construction Industry Research and Information Association (CIRIA), Special Publication, 32, 1984
- [7] Bieniawski, Z. T., *Engineering rock mass classification*. New York, Wiley, 1989
- [8] De Bruyn, I.A. and Bell, F.G., *The occurrence of sinkholes and subsidence depressions in the Far West Rand and Gauteng Province, South Africa and this engineering implications*, Environmental Engineering Geoscience, 7, 281-295, 2001

The Performance of Road Embankments on Glacial Deposits in Ireland

Fintan Buggy¹, Paul Kissane¹, Dominic Rush², Mike Long²

¹Roughan & O'Donovan, Sandyford, Dublin, Ireland

²University College Dublin, Belfield Campus, Dublin, Ireland

email: fintan.buggy@rod.ie, paul.kissane@rod.ie, dominic.rush@ucdconnect.ie, mike.long@ucd.ie

ABSTRACT: Glacial deposits are very common as foundation soils supporting road embankments in Ireland and are typically present in almost all road projects. Despite this there is limited research data linking the settlement performance of embankments to the compressibility and consolidation properties of such soils. This is largely due to the difficulties in obtaining representative, high quality undisturbed samples and laboratory testing of glacial deposits, which exhibit a large range of gradation particle sizes including gravels, cobbles and boulders.

The paper presents the results of several case histories of foundations and monitored road embankments supported on glacial deposits located throughout Ireland. In situ field compressibility and consolidation parameters are back calculated from field performance and correlated to standard index properties such as liquid limit, plasticity index, particle size gradations and SPT N values. Some general conclusions plus recommended ways to predict embankment performance from commonly obtained geotechnical test data are suggested. Identification of difficult glacial soil types requiring special investigation and treatment or improvement are suggested.

KEY WORDS: embankments, performance monitoring, case history, glacial till, compressibility, consolidation.

1 INTRODUCTION

Glacial deposits are very common as foundation soils supporting road embankments in Ireland and are typically present in almost all road projects. Despite this there is limited research data linking the settlement performance of embankments to the compressibility and consolidation properties of such soils. This is largely due to the difficulties in obtaining representative, high quality undisturbed samples and laboratory testing of glacial deposits, which exhibit a large range of gradation particle sizes including gravels, cobbles and boulders.

Attempts have been made to assess compressibility (either constrained modulus M' or coefficient of volume change m_v , where $M' = 1/m_v$) through oedometer testing of undisturbed and reconstituted samples e.g. Lehané and Simpson (2000). Hanrahan (1977) quotes a range of M' from 27 to 270 MPa for Irish glacial tills with moisture contents from 8% to 27% for low stress range from 27 to 54 kPa. As discussed by Trenter (1999) and Farrell (2010) laboratory testing tends to overestimate the true in situ soil compressibility in glacial soils due to exclusion of coarse fraction, changes in moisture content and destructuring of any cementation effects. Standard 75mm diameter by 20mm high laboratory oedometer tests on "undisturbed" samples are invariably performed on the more cohesive, fine grained portion of the till profile, tending to exclude those with significant stone content.

These measures all produce a significant bias in laboratory test data and in practice engineers have resorted to applying semi empirical correlations with in situ Standard Penetration Test data. The most widely used correlation in Ireland and UK (Eqn 1) is ascribed to Stroud and Butler (1975) who expanded earlier work by Stroud (1974) on similar correlations for insensitive clays and weak rocks:

$$m_v = 1 / f_2 N \quad (1)$$

where N = Standard Penetration Resistance (blows / 300 mm).

Stroud and Butler initially derived the correlation factor f_2 to laboratory measured values of m_v for stress increments of 100 kPa in excess of the in situ effective overburden stress, which can be approximated to a 5m high embankment fill load. Detailed correlation data was only obtained for 6 sites, mostly located in northern England with Plasticity Index (PI) ranging from 18 to 23% in boulder clays and 35 to 38% in laminated clays. A range of values for correlation factor f_2 to laboratory measured values of m_v from 440 to 600 kN/m² was reported for UK tills and 750 kN/m² was reported for one Canadian till site. The trend of increasing f_2 with reducing PI is shown in Figure 1.

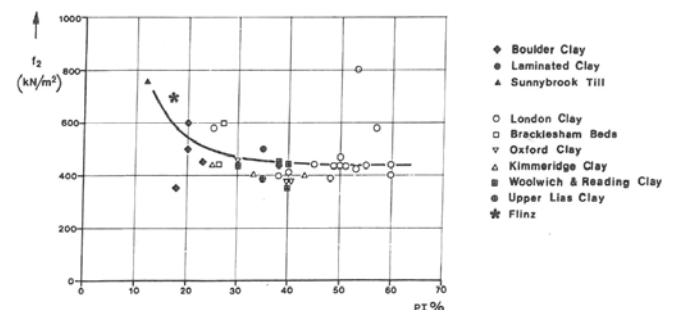


Figure 1 Variation of Correlation Factor f_2 (kN/m²) with Plasticity Index PI (Stroud & Butler, 1975)

Stroud & Butler (1975) further argued that the vertical drained secant elastic modulus E'_v is related to SPT N and E'_v / N should also be a constant for a material of given plasticity. They presented data for field measurements of foundation

settlements on four Canadian sites underlain by glacial till with a ratio of E'_v / N typically from 1,500 to over 2,000 kN/m², for tills with PI from 12% to 17%. This is at least double the correlation developed from laboratory measured values of m_v and is explored later in this paper. A range of secant shear modulus G (at shear strains up to 1%) from 10 to 20 MPa was reported by Trenter (1999) for UK tills derived from in situ 865mm diameter plate testing at three test sites. Where the constrained modulus $M' = 1 / m_v$ is derived from field settlement data from embankment filling over a wide area, E'_v has been derived from equation 2 (generally assuming $\nu = 0.25$ for stiff glacial tills giving $E'_v = 0.83M'$):

$$M' = E'_v \frac{(1 - \nu)}{(1 + \nu)(1 - 2\nu)} \quad \text{or} \quad E'_v = M' \frac{(1 + \nu)(1 - 2\nu)}{(1 - \nu)} \quad (2)$$

In contrast to compressibility modulus, there is even less documented guidance on relevant coefficient of consolidation c_v values for glacial till soils. Trenter (1999) reports a range of values generally between 1 and 3 m²/year for English tills and somewhat higher range of 2.5 to 8.5 m²/year in Scottish tills. Hanrahan (1977) reports a range of c_v from 7 to 270 m²/year, but at low stress ranges. Lehan and Simpson (2000) suggest values within the range of 20 to 60 m²/year for Dublin Boulder Clay.

2 SUMMARY OF CASE HISTORIES

2.1 Tallaght Town Square, Dublin, Farrell et al (1988), Lehan & Farrell (1997), Long & Menkiti (2007)

This data is derived from instrumented load tests on a 1.5m square trial footing maintained in stages at relatively very high pressures of 825 kPa and then 1013 kPa over incremental time period of 3 weeks and 3 months respectively. Test data collected at the end of both loading increments is considered to represent fully drained conditions as drainage columns were installed to locally accelerate drainage. Representative classification test and SPT N profiles are given in Figure 2.

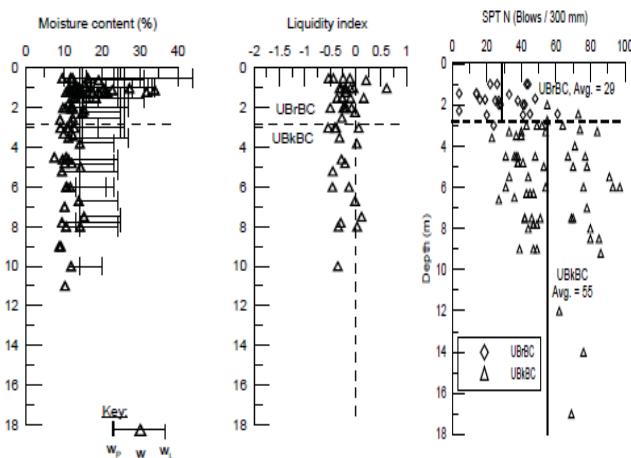


Figure 2 Index Data and SPT N for Tallaght Town Centre (Long & Menkiti 2007).

2.2 Dublin Port Tunnel, Menkiti & Long (2015).

Construction dewatering within a tunnel access shaft WA2 resulted in a significant drawdown of between 10m and 17m from an initial water table depth of 3m over a period of around two weeks. Average settlements of 6.3mm occurred quickly (mostly within a further month) within a 31m thick deposit of Dublin boulder clay.

2.3 M9 Motorway Service Area(MSA), Kilcullen, Co. Kildare

Earthworks including embankments up to 8.5m high for new slip roads, roundabouts and approach to an overbridge were constructed in 2014. The eastern side of the interchange contained a 2m to 3m thick layer of soft glacial melt water deposits with very low SPT N values from 3 to 7 blows / 300 mm beneath a firm - stiff cohesive till and underlain by gravels at depths of 5.5m to 7m. A ground improvement scheme consisting of prefabricated vertical drains installed at 1.3m c/c triangular spacing was constructed and performance monitored by settlement plates and piezometers.

Filling rates actually achieved were slower than originally planned and averaged only 0.5m / week for the first 4 weeks followed by a filling rate of 1 m/week giving a total filling duration of 8 to 10 weeks. Maximum settlements of 95mm and 49 mm were observed at SP6 and SP1 respectively. Both the settlement and piezometer records confirmed that drainage was rapid and consolidation was effectively complete within 4 to 5 weeks from the midpoint of loading.

2.4 M7 / M8 Motorway, Co. Laois

A 41 km motorway was constructed in the Irish midlands Co. Laois from 2007 to 2010 which included field settlement plate monitoring of several embankments. Settlements of embankments founded on glacial tills were in all cases less than 75mm and generally less than 40mm for embankment heights from 3m to 9m. Drainage was typically observed to be rapid upon loading and frequently had ceased within 3 to 6 months of final load application.

2.5 A2 Shore Road, Belfast

The A2 Shore Road involved a 4km length of a coastal route on the northern outskirts of Belfast. Earthworks on a side access road included the main embankment filling of up to 8.5m height on approach to an overbridge which was monitored by settlement plates and piezometers. The ground profile comprised on firm - stiff cohesive glacial till underlain by weathered Mercia Mudstone deposits at depths of between 4.0m to 7.2m. PI for this glacial deposit was high at 20 to 27%.

A ground improvement scheme local to the overbridge approaches was constructed with surcharge filling and a hold period of around 9 months. Embankment fill heights of between 5.2m and 8.7m. produced maximum settlements of between 30mm and 80 mm.

2.6 M6 Motorway Service Area, Athlone, Co. Westmeath

Earthworks including embankments up to 8.6m high for new slip roads, roundabouts and approach to an overbridge were constructed in 2014. The geomorphology of the site indicates varied glaciolacustrine and glacial meltwater deposits, with the MSA footprint to the northeast containing soft peat and

clay soils. The overbridge and approaches are sited over a local ridge of granular glacial soils.

Upon investigation the presence of pockets and linear channels of soft uniform intra-glacial deposits with high moisture contents and Plasticity Index (PI) > 20% was identified. A ground improvement scheme consisting of excavation and replacement of near-surface soft deposits coupled with hold periods (Westbound Roundabout & Diverge (WBD)) or surcharge loading (Service Area Link Road) over any underlying soft ground remaining in-situ was constructed. Note that in the absence of an SPT-N value at the specific level, a correlation to undrained shear strength $c_u = 5.N \text{ kN/m}^2$ as per Stroud & Butler (1975) has been assumed at the Westbound Roundabout.

Embankment performance was monitored by a combination of settlement plates and survey monuments. Filling rates actually achieved were slower than originally planned and averaged only 0.4m / week overall. Maximum settlements of 55mm to 65mm were observed. The settlement records yielded estimates for field c_v of between 5 and 11 m^2/year .

2.7 Limerick Tunnel Approach Roads, Limerick

A 10 km long bypass of Limerick City was constructed from 2006 – 2010 with about 3km of the route directly underlain by fill soils or glacial tills. Data for a location at the tie in of Clonmacken Link to the existing road network with 6m of glacial soils under a 5m high embankment is given in Table 1.

Site Location	<63 μm (%)	LL (%)	PI (%)	Nat. Moist (%)	Cohesiv e Till Thick. (m)	SPT N (blows / 300mm)	Load/ Fill Ht + Surcharge (kPa / m)	Settle ment (mm)	Field Modulus E'_v (MPa)	Field Consolid ation t_{95} (weeks)	Field c_v (m^2/year)
Tallaght, Dublin	39	24	10	10	3 ⁽¹⁾	55	1015 kPa	12.8	84	16	30
Dublin Port	40	28	13	10	31	55	100-170 kPa	6.3	553	6	
Tunnel											
M9 Kilcullen SP1	33	23	9	12	5.3	6	6m	49	10.8	5	16
M9 Kilcullen SP5&6	32	25	6	11	5.2	8	8.5m	95	7.7	4	20
M7/M8 Laois 20+090	42	25	9	17	3.7	30	7.3m	32	14.1	26	8
M7/M8 Laois 22+800 to 22+950	46	28	6	16	3.5	4	6m	27	13.3	12	15
M7/M8 Laois 23+200 to 23+600	45	24	9	15	10.8	22	5.9m	37	30.7	26	66
M7/M8 Laois 27+200 to 27+300	29	22	9	14	9.5	25	3.7m	35	16.6	33	40
M7/M8 Laois 27+770 to 27+870	29	20	8	14	10	20	8.9m	26	56	21	70
A2 Shore Road S Belfast		45	24	21	4.8	29	8.9m +1.25m	55	14.7	42	8
A2 Shore Road N Belfast	44	43	22	24	5.5	34	6.4m +2.9m	65	13.1	36	12
M6 Athlone WB Roundabout		36	14	22	2.2	12 ⁽²⁾	10.5m	65	5.9	14	5
M6 Athlone Link Rd	95	31	14	18	3.2	8	5.7m +1.0m	55	6.6	14	11
M6 Athlone WBD	21	25	8	14	3.5	19	7.4m	60	7.1	22	8
Limerick Tunnel Ch 1300 Clonmacken	36	34	14	18	6.2	13	3.0m +2.0m	78	6.9	39	14

Table 1: Summary of Glacial Till Classification and Field Test / Monitoring Results

1. Effective depth of loading from 1.5m square test area.
2. A correlation to undrained shear strength using $f_1 = 5$ as per Stroud & Butler (1975) has been assumed to derive SPT-N.

3 DISCUSSION

The field performance data base contains a total of seven sites and 14 monitored locations in Ireland as summarised in Table 1. The range of natural moisture content is from 4% to 38% with average values per location ranging from 10 to 25%. Average proportion of fine fraction (silt and clay) passing 63 micron sieve size per location is typically from 29% to 46%. The average range of plasticity index per location is from 6 to 24%. These values broadly compare well with ranges cited by Hanrahan (1977) for Irish lodgement, ablation, and englacial tills. Some sites at M7 / M8 in Laois and M6 Athlone exhibit fine contents in excess of 60% are likely to have been deposited from melt water.

The range of SPT N values is from 2 to 90 with average values per location varying from 4 to 55. Four locations have unusually low ranges of SPT N less than 12 which are less commonly observed in Irish till deposits. These include the M9 MSA Kilcullen, M7/M8 Co. Laois Ch 22+800 to 22+950m and the M6 Athlone site. The proportion of these soft till sites in part reflects a bias in relation to settlement monitoring being preferentially performed on sites with poor, compressible glacial till deposits. Settlements observed are typically less than 80mm with the one exception of 95mm occurring at M9 MSA site. For the road embankment sites, the constrained modulus M is first calculated directly from the observed settlement, embankment loading (total fill height \times fill density, γ assumed = 20 kN/m³) and till layer thickness. The secant drained elastic modulus E'_v has then been derived from equation 2 assuming $\nu = 0.25$ as discussed previously. For the plate load test site at Tallaght, the secant modulus is that reported at maximum load by Farrell et al (1988).

3.1 Correlations for Secant Drained Vertical Modulus E'_v

The secant drained vertical Young's Modulus E'_v derived from the field data is rarely less than 7 MPa in soft tills or higher than 80 MPa in very stiff deposits such as Dublin Boulder Clay. Modulus E'_v is broadly correlated to SPT N with ratios of E'_v / N varying between 0.5 and 1.5 MPa but some sites with low PI having E'_v / N around 3 MPa. The relationship between E'_v / N and PI for Irish till sites is plotted on Figure 3 and includes the suggested design line by Stroud & Butler (1975) but excludes four Canadian glacial till sites reported by them which exhibited E'_v / N ratios of between 1.5 and 2.2. There is some evidence for E'_v / N being correlated to PI, however the large scatter should be noted.

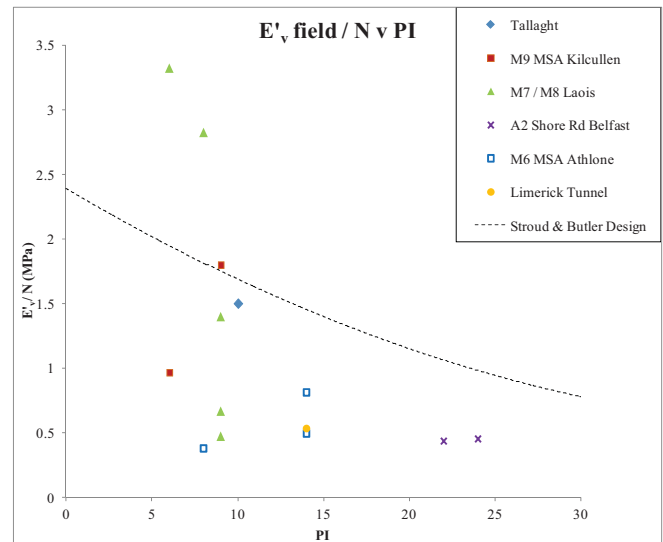


Figure 3 Variation of Field E'_v / N with Plasticity Index

A number of Irish sites with PI in the range of 10% to 25% exhibit E'_v / N ratios which are around half of the design line suggested by Stroud and Butler and which are closer to values derived from lab data. Laboratory data for coefficient of compressibility m_v are also consistently lower than the trend line previously reported by Stroud and Butler (1975) as shown in Figure 4. A comparison of constrained modulus M' derived from field measurements with those from laboratory tests for Irish glacial till sites found an average ratio of $M_{lab} / M_{field} = 0.81$. The ratio could be improved to 0.97 by correcting the M_{lab} for the proportion of gravel over 5mm in size using equation 3 such that:

$$M_{lab\ corr} = \frac{M_{lab}}{(1 - \text{Gravel fraction} > 5\text{mm})} \quad (3)$$

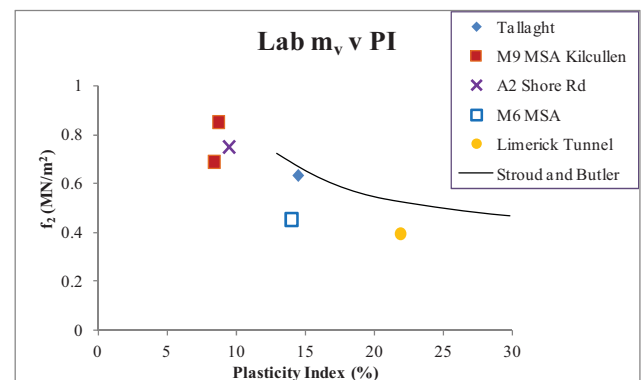


Figure 4 Variation of Laboratory m_v with Plasticity Index.

3.2 Variation of Secant Drained Vertical Modulus E'_v with Strain

The dependency of secant drained modulus magnitude with strain is well documented for many soils including glacial tills which exhibit highly non linear stress strain behaviour. Trenter (1999) reports large variations in secant shear modulus in laboratory triaxial tests and field plate load tests for Cowden Till in UK. Lehané & Farrell (1997) report similar laboratory drained triaxial test data for Dublin Boulder Clay suggesting a five fold decrease in secant modulus E'_v as strain increases from 0.01% to 0.1%. In the current study, an exceptionally high secant drained modulus was observed for the Dublin Port Tunnel which had a very deep till profile of over 30m. An effective stress loading due to dewatering resulted in an extremely high E'_v value of 553 MPa. The vertical strain level measured at the Dublin Port Tunnel site was around 0.02% which is between 10 and 100 times less than typical vertical strains of 0.25% to 3% in the other embankment and footing test case histories. The variation of average strain versus E'_v / N ratio is presented in Figure 5.

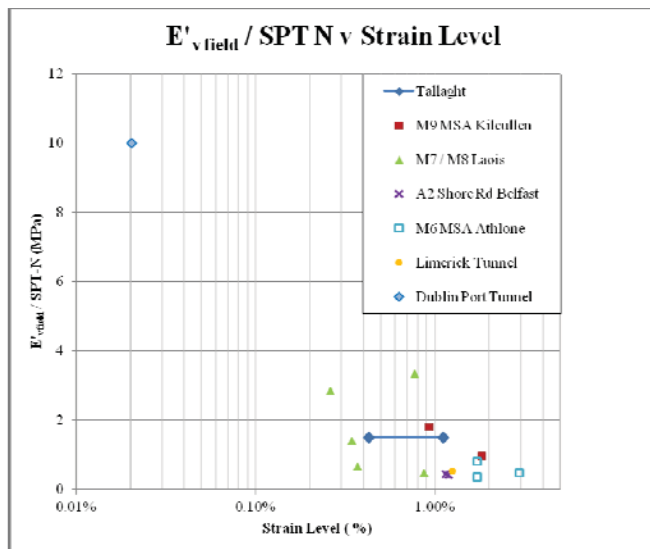


Figure 5 Variation of E'_v / N ratio with Strain.

For the embankments strain variation with depth is minimal due to the geometry of the loaded area and corresponding modest thickness and shallow depth of compressible glacial till foundation soil. The average strain is calculated simply as the settlement divided by compressible layer thickness. For the Tallaght site the loaded area is small compared to the total till thickness and thus the strain varies considerably with depth. A range of strain values are indicated representing average and maximum strain levels. There is a broad correlation apparent between strain level and E'_v / N ratio. This explains the very high modulus observed at the Dublin Port Tunnel site and reinforces that the field modulus of glacial soils is highly non linear and strain dependant.

3.3 Correlations for Coefficient of Consolidation c_v

The coefficient of consolidation c_v was derived from the field settlement – time history by assessing time for 95% consolidation to occur from the midpoint of loading and then back calculating the equivalent c_v parameter assuming double

drainage of the cohesive till layer thickness. In the case of M9 MSA Kilcullen site where vertical drains were installed the back calculation was made assuming Barron's (1948) equation. Field c_v values typically range from 10 to 40 m^2/year and compare well to values discussed earlier for Irish tills. c_v is broadly correlated to N / PI with ratios of $c_v(PI) / N$ varying between 4 and 15 m^2/year . The relationship between c_v and Liquid Limit (LL) for Irish till sites is plotted on Figure 6. This includes the correlation from NAVFAC (1982) for virgin compression which the trend line closely matches, but the scatter in data for LL below 25% is large.

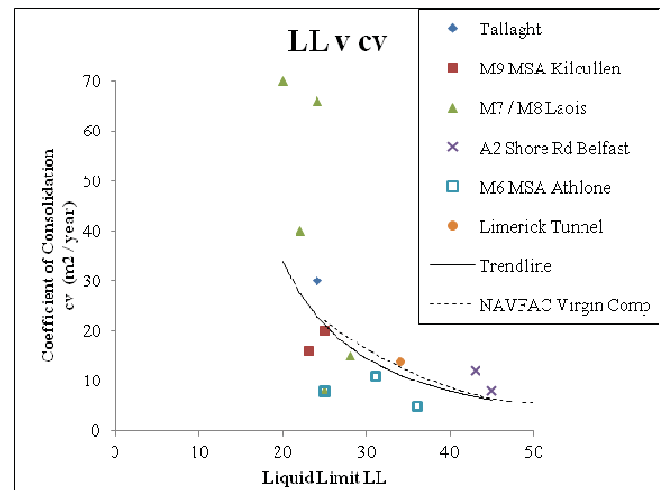


Figure 6 Variation of Field Coefficient of Consolidation with Liquid Limit

4 CONCLUSIONS

For embankment heights of up to 9m and cohesive till thicknesses of up to 10m, embankment settlements rarely exceed 60mm when constructed on Irish glacial till foundations soils. Exceptions can occur in untypical soft till sites with SPT N values of less than 12 or in higher plasticity tills ($PI > 20\%$) but even in these unusual cases, observed settlements did not exceed 100mm. Sites with these characteristics may require ground improvement by use of surcharge loading or possibly vertical drainage, dependent upon the construction programme constraints.

Irish glacial tills exhibit vertical secant drained modulus generally ranging from 7 to 80 MPa which is loosely correlated to SPT N and PI (refer to Figure 3). The ratio of E'_v / N generally varies between 0.5 and 1.5 MPa at strain levels from 0.3% to 3% and is highly strain dependent.

Consolidation appears to occur rapidly under most embankment loading scenarios, in practice rarely exceeding 6 to 9 months. Derivation of coefficient of consolidation c_v is not straight forward due to the influence and uncertainty of high permeability layers within cohesive till deposits. Based on the limited data obtained, values for c_v from 10 to 40 m^2/year seem typical for Irish tills and the correlation of c_v to Liquid Limit given in Figure 6 may have useful application for preliminary design.

ACKNOWLEDGEMENTS

The authors would like to acknowledge the National Roads Authority, Clonmel Enterprises Ltd., Celtic Roads Group Portlaoise, DirectRoute (Limerick) Limited, Graham Construction Limited and Colas-Roadbridge JV, for their kind permission to publish the data contained within this Paper. The views expressed in this paper are the sole views of the authors and do not represent the views of the organizations named above, Roughan & O'Donovan or UCD.

REFERENCES

- [1] Barron, R.A. (1948) "Consolidation of Fine Grained Soils by Drain Wells" Transactions ASCE, Vol 113.
- [2] Farrell, E.R., Bunni, N.G. and Mulligan J. (1988) "The bearing capacity of Dublin black boulder clay." Trans Inst Engineers Ireland, 112 1987/1988: pp 77 – 104.
- [3] Farrell, E.R. (2010) "Lessons Learnt – Problems to Solve", BCRI UCG / ITG Galway p 181 – 198.
- [4] Hanrahan, E.T. (1977) "Irish glacial till: origin and characteristics" An Foras Forbartha, Dublin. BC 164.
- [5] Lehane, B. and Simpson, B. (2000) "Modelling glacial till under triaxial conditions using a BRICK soil model" Can Geo Jnl., 37: pp 1078 – 1088.
- [6] Lehane, B.M. and Farrell, E.R. (1997). "Serviceability limit state design approach for footings"" Proc XIV Int. Conf. on Soil Mech. and Foundation Engineering, Hamburg, Germany , September 1997, Vol. 1, pp 359-362.
- [7] Long, M. & Menkiti, C.O. (2007) "Characterisation and engineering properties of Dublin Boulder clay" Proc. 2nd Int'l Workshop on Characterisation & Engineering Properties of Natural Soils, Singapore, Vol. 3, pp 2003 – 2045.
- [8] Menkiti, C.O. & Long, M (2015) "Consolidation settlements in Dublin boulder clay" Proc Eur Conf Soil Mech and Geotech Engng., Edinburgh. BGA. Pp 313 – 318.
- [9] NAVFAC DM-7.1 (1982) "Soil Mechanics Design Manual 7.1" US Dept of Navy, Alexandria, Va. p.7.1-144.
- [10] Stroud, M.A.. (1974) "The Standard Penetration Test in Insensitive Clays and Soft Rocks" European Symposium on Penetration Testing, Swedish Geotech Society, Stockholm.
- [11] Stroud, M.A. and Butler, F.G. (1975) "The standard penetration test and the engineering properties of glacial materials". Proc. of the Symposium on the engineering behaviour of glacial materials pp 117 - 128. University of Birmingham.
- [12] Trenter, N.A. (1999) "Engineering in glacial tills" CIRIA Report C504, London.

Energy Transfer Ratio for Hydraulic Pile Driving Hammers

Kevin N. Flynn¹, Bryan A. McCabe²

¹AGL Consulting, Sandyford, Dublin 18, Ireland

²College of Engineering & Informatics, National University of Ireland, Galway, Ireland

Email: kevin.flynn@agl.ie, bryan.mccabe@nuigalway.ie

ABSTRACT: The ability of hydraulic pile driving hammers to overcome energy losses during freefall enables a greater proportion of the impact energy to be transferred to the pile in comparison to diesel hammers. This percentage, termed the energy transfer ratio, is not routinely measured in practice however, and there is an element of uncertainty regarding appropriate energy transfer ratios to assume in driveability analyses. In light of such uncertainties, the energy transfer ratios of four- and five-tonne hydraulic hammers were assessed during installation of driven cast-in-situ piles at several sites in the United Kingdom. The piling rigs were fitted with instrumentation which enabled measurement of the hammer velocity (and hence kinetic energy) at impact for each blow during installation, with the corresponding magnitude of energy transferred to the closed-ended steel installation tube ascertained using a Pile Driving Analyser. The results of the study showed that energy transfer ratios were strongly dependent on the hammer drop height, with transfer ratios of 95% advocated by the pile hammer manufacturer only achievable when a drop height in excess of about 600 mm was used. As such, lower energy transfer ratios may need to be considered in driveability predictions for these pile types (i.e. steel or DCIS piles) if lower drop heights are used during driving. Further research is required to substantiate limited data suggesting that soil type may also be influential.

KEY WORDS: Foundations; Piling; Driving; Hydraulic; Hammer; Energy;

1 INTRODUCTION

The installation of a displacement pile to a required penetration typically necessitates the application of large forces to the pile head. For these pile types, impact driving remains the most common method of applying such forces, although vibratory [1] and jacking methods [2,3] are becoming increasingly popular, particularly in urban areas where noise and vibration tend to be restricted.

The principle of impact pile driving involves imparting a force on the pile head using a large mass, typically termed a ram, which falls vertically from a predetermined height. The potential energy of the hammer before freefall can be readily calculated. The magnitude of energy transferred to the pile during driving is routinely measured using a Pile Driving Analyser (PDA). These two quantities are commonly used by hammer manufacturers to classify hammer performance; the energy transferrable to the pile is expressed as a proportion of the energy corresponding to the maximum drop height, known as the rated energy. However, the 'intermediate' energy state at impact is less certain and is rarely, if ever, measured in practice. This is unfortunate given that it is the ratio of the energy at impact to the energy transmitted to the pile that is the more fundamental indicator of driveability.

In light of the paucity of such data, a systematic study of the energy transfer process relevant to the installation of a number of driven cast-in-situ (DCIS) piles using hydraulic hammers is presented in this paper. Examples of structures in Ireland that have been successfully supported on DCIS piles are the Sequence Batch Reactors (SBR) at Ringsend Wastewater Treatment Plant in Dublin [4]. All piles referred to in this paper were installed by Keller Foundations at sites in the United Kingdom. Unlike previous studies of energy transfer

ratio, the hammer velocity (and hence kinetic energy) at impact was measured for each blow during driving using instrumentation fitted to the piling rigs. The approach is analogous to that carried out for energy correction of the Standard Penetration Test [e.g. 5].

2 BACKGROUND

2.1 Hammer Efficiency

The ideology of pile driving involves impacting the pile head with a ram of mass m , which has fallen vertically from a predetermined drop height h . The potential energy of the ram immediately prior to release is given by:

$$E_{\text{potential}} = mgh \quad (1)$$

At impact, the hammer will be travelling at a velocity v_{impact} , with kinetic energy given by Equation 2:

$$E_{\text{impact}} = \frac{1}{2}mv_{\text{impact}}^2 \quad (2)$$

If no energy losses occur in the system during hammer freefall, the kinetic energy at impact would be equivalent to the potential energy, i.e. $v_{\text{impact}} = (2gh)^{0.5}$. However, losses invariably occur due to friction, ram misalignment and preadmission within the hammer, for example, resulting in a kinetic energy at impact which is lower than the potential energy prior to hammer release. The reduction in energy is typically quantified by the hammer efficiency according to Equation 3:

$$\eta_{\text{hammer}} = \frac{E_{\text{impact}}}{E_{\text{potential}}} \quad (3)$$

For hydraulic hammers, the additional acceleration of the ram during downfall (over and above that due to gravity) is exploited to overcome much of the energy losses outlined previously, rendering hydraulic hammers more efficient than traditional air, steam and diesel impact hammers in this regard. As a consequence, a value of $\eta_{\text{hammer}} = 0.95$ is typically assumed in driveability analysis programs [6].

The impact energy E_{impact} of the pile driving hammer was derived using the two timing signals technique in which the velocity of the hammer during freefall is measured using a pair of sensors located at the top of the hammer assembly. A Keller Foundations piling rig is shown in Figure 1 with the sensors circled on the photograph; these are mounted on a steel bracket placed ~50 mm vertically apart. During hammer freefall, the time taken for the hammer rod to transit this distance is measured by the sensors and the velocity at the bottom sensor location is computed. By accounting for the additional distance travelled between the bottom sensor and the level of impact, v_{impact} can be obtained using the equation of motion, and E_{impact} calculated in turn from Equation 2. The drop height is then back-figured using Equations 1 and 3. Further commentary on the rig instrumentation and its applications, as deployed by Keller Foundations, is given by Egan [7,8].



Figure 1. Pile hammer instrumentation for measuring hammer velocity prior to impact (courtesy of Keller Foundations, UK)

2.2 Transferred Energy

Dynamic pile testing is now routinely used for the verification of pile capacity as a complement to traditional static testing, with various proprietary software programs (e.g. GRLWEAP, TNOWAVE and PDPWAVE) available to provide predictions of pile resistance using signal matching techniques. Stress waves generated within a pile (or a pile tube in the case of DCIS piles) after each hammer blow are characterised using diametrically-opposite pairs of strain gauges and accelerometers attached within 1 m or 2 m of the pile head or top of the drive tube (see Figure 2).

The instrumentation and recording unit are collectively referred to as a Pile Driving Analyser or PDA. The energy transferred to the pile is then calculated using Equation 4 [e.g. 9]:

$$E(t) = \int F(t)V(t)dt \quad (4)$$

where $F(t)$ and $V(t)$ are the force and velocity magnitudes at time t after hammer impact respectively. The maximum energy generated in the pile during this time (corresponding to an individual blow) is referred to as EMX.

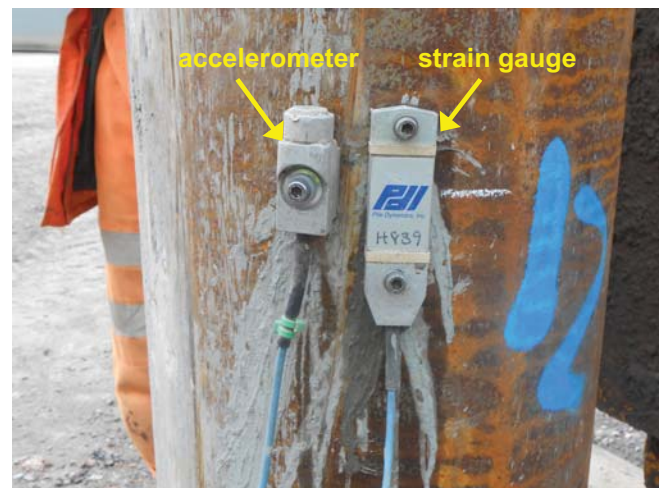


Figure 2. Pile Driving Analyser: an accelerometer and strain gauge pair for measuring transferred energy on a DCIS pile tube (top), data acquisition unit (bottom)

2.3 Energy Transfer Ratios

As alluded to in the introduction, the energy at impact E_{impact} is not routinely measured in practice. In this instance, driveability analyses typically assign the maximum potential energy of the hammer to the E_{impact} term, referred to as the rated energy E_{rated} . This leads to the definition of the rated energy transfer ratio (ETR_{rated}), calculated according to Equation 5:

$$ETR_{\text{rated}} = \frac{EMX}{E_{\text{rated}}} \quad (5)$$

However, as impact hammers tend to perform at drop heights considerably less than the maximum available, and hammers are not fully efficient (Section 2.1), it is worthwhile to assess the true energy transfer ratio (ETR) as a function of drop height. ETR falls below unity due to noise and heat generated at impact and is calculated as follows:

$$ETR = \frac{EMX}{E_{\text{impact}}} \quad (6)$$

The ETR ratio is a more fundamental indicator of pile driveability than ETR_{rated} . A driveability study by Hussein et al. [10] on prestressed concrete piles (with plywood hammer and pile-top cushions) is an example of a study that considered the effect of drop height on ETR_{rated} . The authors believe that the research reported here is unique as it allows determination of the actual ETR.

3 EXPERIMENTAL PROGRAMME

The energy transfer data herein pertain to five separate Keller Foundations DCIS sites in the United Kingdom, the locations of which are illustrated in Figure 3. The ground conditions at Shotton, reported by Flynn et al. [11], comprise uniform medium dense to dense marine sand to depths in excess of 10m. The stratigraphy at the remaining sites tended to be variable, typically comprising layers of soft clay overlying loose to very dense sands and gravels. Cone Penetration Test (CPT) profiles for the five sites are shown in Figure 4 from which it can be seen that a broad spectrum of driving conditions were encompassed by the study. Further details of the ground conditions at each site are provided in Flynn [12].



Figure 3. Test site locations

The energy transfer database is presented in Table 1, which summarises the locations of the sites, pile reference, length, diameter, average drop heights and total number of blows imparted. It can be seen that a wide range of drop heights are represented. While the database contains a total of 12 piles, 8

of these are from the Tilbury site, and therefore some bias of the results towards this site may be expected.

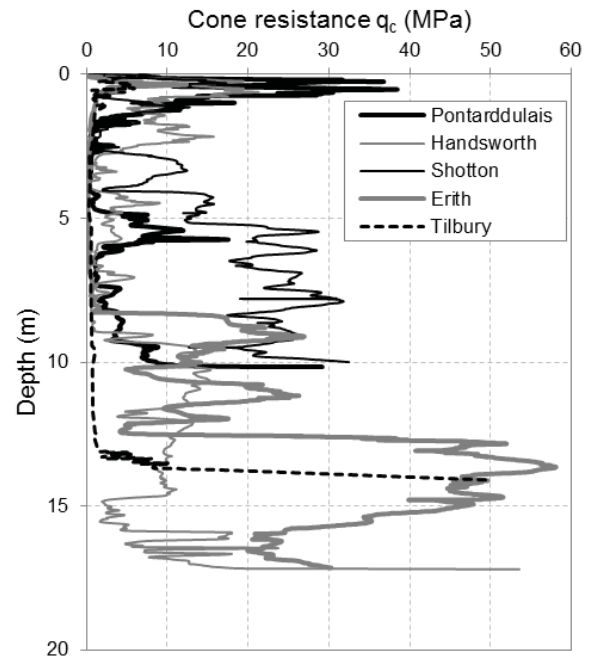


Figure 4. CPT profiles at test sites

All piles were installed using Junttan's HHK A-Series hydraulic hammers with a maximum drop height of 1.2 m. A four tonne HHK4A hammer was used to install the DCIS piles at Pontarddulais and Handsworth, with the five tonne HHK5AS hammer used at the remaining sites. Summary technical details of these two hammers are provided in Table 2 [13].

Table 1. Energy transfer ratio database

Site	Pile Ref.	Diameter (mm)	Length (m)	Average drop height (mm)	Hammer Blows
Pontarddulais	P1	320	8.50	240	95
Shotton	S1	320	5.75	450	157
Handsworth	H1	285	7.50	400	259
Erith	S594	320	12.10	370	223
Tilbury	C7	610	14.25	600, 820	1025
Tilbury	N21	610	14.25	580, 840	1087
Tilbury	N42	610	14.30	610, 840	1235
Tilbury	SE6	610	14.75	630, 820	1136
Tilbury	SE8	610	14.80	415, 550, 790	1221
Tilbury	SE16	610	14.75	624, 875	932
Tilbury	SE17	610	14.75	560, 805	1193
Tilbury	SE18	610	14.75	600, 820	1214

Table 2. Details of Junttan hammers used in this study [13]

Specification	HHK4A	HHK5AS
Ram mass (kg)	4000	5000
Total mass ¹ (kg)	7100	8400
Max. drop height (m)	1.2	1.2
Max. energy (kJ)	47	59
Blows per minute	40-100	40-100

¹ including A-Type drive cap for metal tubes

The installation process for a DCIS pile is described by Flynn and McCabe [14]; it is analogous to that for a closed-ended steel pile, comprising a 20 mm thick steel tube fitted with a sacrificial circular steel plate at the base to prevent ingress of soil and groundwater during the driving process. No pile cushions were used between the tube head and hammer assembly. The tube is subsequently filled with concrete before being withdrawn, although this stage is not relevant to the driveability study. Monitoring was undertaken on the majority of hammer blows during each pile drive, with the exception of Handsworth where PDA measurements were obtained for the final 50 blows only (of the 259 in total).

4 RESULTS

The variation in drop height is shown in Figure 5, back-figured by the rig instrumentation as described in Section 2.1, with blow number during the installation of each of the test pile in Table 1. Hammer drop heights at Pontarddulais, Shotton, Handsworth and Erith, ranged between 250 and 500 mm, and typically remained constant throughout each pile drive. At Tilbury, the driving sequence necessitated the use of two drop heights, comprising 400 to 600 mm for the initial 13 m, increased to between 750 and 900 mm below this depth during penetration in dense sandy gravel.

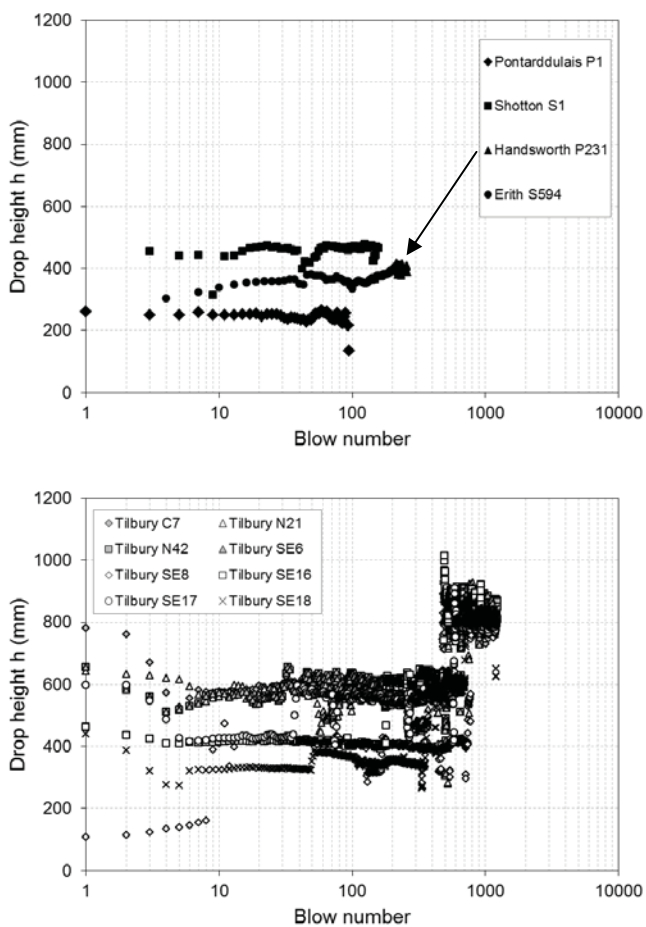


Figure 5. Variation of drop height with blow number for piles at (a) Pontarddulais, Shotton, Handsworth and Erith, and (b) Tilbury.

As mentioned in Section 3, each test pile was also monitored dynamically during driving using a PDA. All PDA testing reported in this paper was performed by the same pile testing company. Figure 6 shows an example of the energy data for Pile S594 at Erith. The impact energy and corresponding transferred energy (EMX) were assessed for each hammer blow of the pile drive.

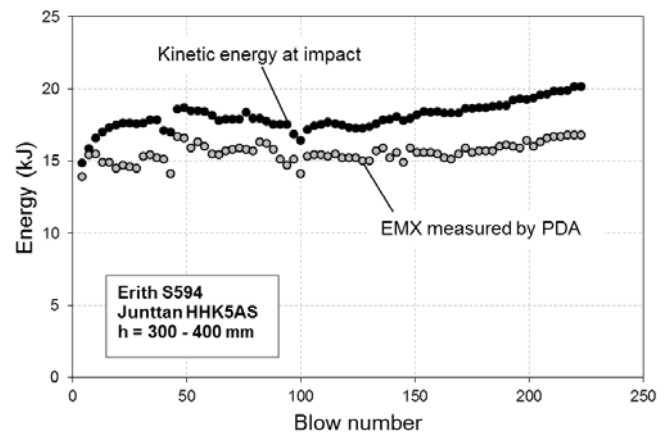


Figure 6. Comparison of impact and transferred energies during installation of Pile S594 at Erith

The variation in transferred pile energy EMX with the kinetic energy at impact is shown in Figure 7 for all 12 DCIS piles in the database. A linear trend is obtained, although the variability appears to increase with increasing drop heights (and hence impact energy).

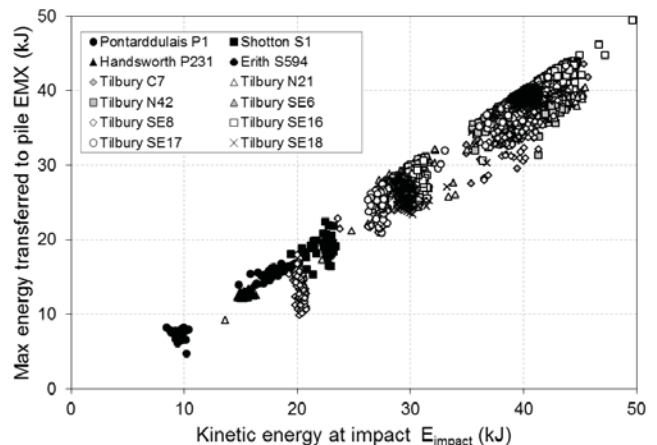


Figure 7. Relationship between kinetic energy at impact and energy transferred to pile

The energy transfer ratio (ETR) was calculated for each hammer blow using Equation 6. Due to inherent variability in the measured data, averaging was applied both to the drop heights and energy transfer ratios. The resulting variation in average energy transfer ratio ETR_{avg} with average drop height h_{avg} is shown in Figure 8. Note that the vertical range bars represent plus or minus one standard deviation about the average energy transfer ratio. It is apparent that:

- The average energy transfer ratio increases with drop height, ranging from ~75% at drop heights of 250 mm to over 90% when h is 600 mm or more.
- The variability in energy transfer ratio tends to reduce somewhat with increasing drop height.
- Pile SE8 at Tilbury had a considerably lower transfer ratio (~65%) in comparison to other piles at Shotton, Handsworth and Erith for a drop height of ~400 mm.

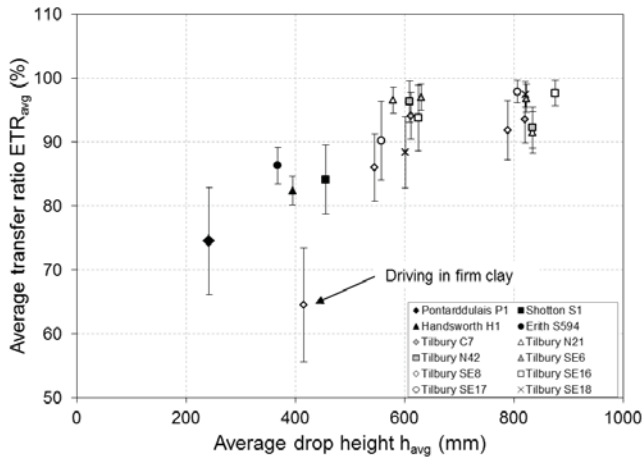


Figure 8. Variation in measured energy transfer ratio with drop height

Unlike the other piles at Tilbury, dynamic monitoring for Pile SE8 was initially carried out while the pile was penetrating a layer of firm clay above the sandy gravels and drop heights of about 400 mm were used within this stratum. It is therefore possible that the ground conditions may have a significant effect on the reduced energy ratio noted in this case. Further investigation of this effect is warranted, although the dearth of driveability data in firm clay in the database in Table 1 precludes such a study from being undertaken at present.

Hammer manufacturers advocate that energy transfer ratios of 95% are routinely achieved during driving of steel piles or casings without hammer cushions. Based on the data illustrated in Figure 8, it is apparent that such energy transfer ratios are only achievable for drop heights in excess of 600 mm. As such, lower energy transfer ratios may need to be adopted in driveability predictions for these pile types (i.e. steel or DCIS piles) if lower drop heights are used during driving.

As discussed previously, the energy at impact E_{impact} is not routinely measured in practice and driveability programs quote the energy transfer ratio as the transferred energy as a proportion of the maximum rated energy of the hammer. In order to facilitate comparison with the limited studies of energy transfer ratio in the literature, the transferred energies measured for each test pile in Table 1 have been normalised by the corresponding hammer rated energy (as given in Equation 6) and plotted against hammer drop height in Figure 9, with the vertical range bars representing plus or minus one standard deviation about $ETR_{\text{rated,avg}}$. A linear relationship is observed. In contrast, typical $ETR_{\text{rated,avg}}$ values of 30-40% were observed in the aforementioned study by Hussein et al. [10] which were relatively independent of drop heights in the

range 2 ft. (~610 mm) to 15 ft. (~4570 mm). This comparison highlights the dangers of applying $ETR_{\text{rated,avg}}$ values to piling scenarios other than those for which they were measured.

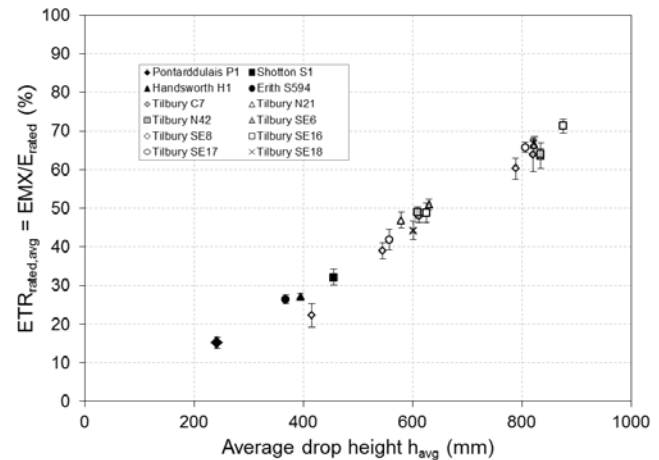


Figure 9. Variation in rated energy transfer ratio with drop height.

Finally, the magnitude of energy loss after hammer impact was determined as the difference between E_{impact} and EMX . As shown in Figure 10, energy losses ranged from 1 kJ to 6 kJ (and the vertical standard deviation bars indicating large variability) with no clear trend with drop height apparent. This suggests that the energy losses after impact may be independent of drop height. Furthermore, the magnitude of such losses represent a smaller proportion of the impact energy as the drop height increases, leading to the greater energy transfer ratios shown in Figure 8.

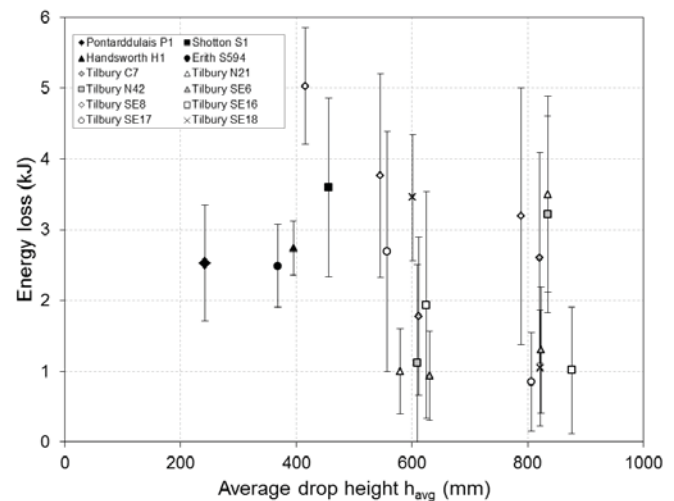


Figure 10. Variation in absolute energy loss with hammer drop height

5 CONCLUSIONS

This paper provides an assessment of the energy transfer ratio of hydraulic impact hammers during the installation of driven cast-in-situ piles at several sites in the United Kingdom. The impact energy was derived using the two timing signals technique, with a wide range of hammer drop heights analysed. The results of the study revealed the following:

- Energy transfer ratios (ETR) ranged from 65% and 95% during driving and were strongly dependent on hammer drop height.
- The ETR of 95% advocated by the pile hammer manufacturer was only achievable when a drop height in excess of about 600 mm was used. Increased variability in ETR occurred as drop height reduced.
- The ground conditions may have a significant effect on the energy ratio for a given drop height, with the ETR for pile in driven in firm clay ~20% lower than that observed for piles driven in sandy gravel.

As such, lower energy transfer ratios may need to be considered in driveability predictions for these pile types (i.e. steel or DCIS piles) if lower drop heights are deployed.

ACKNOWLEDGEMENTS

The authors wish to acknowledge Keller Foundations for sponsoring a comprehensive programme of DCIS pile testing, of which this driveability study is part. The first author was sponsored by the College of Engineering and Informatics Fellowship and University Foundation Bursary during his doctoral studies at NUI Galway.

REFERENCES

- [1] Rausche, F. and Beim, J. (2012), 'Analyzing and interpreting dynamic measurements taken during vibratory pile driving', *Proceedings from Testing and Design Methods for Deep Foundations/IS-Kanazawa*, Kanazawa, Japan, 123-131.
- [2] Lehane, B.M., Pennington, D. and Clarke, S. (2003), 'Jacked end-bearing piles in soft alluvial sediments of Perth', *Australian Geomechanics Journal*, Vol 38, Issue 3, 123-135.
- [3] White, D.J. and Deeks, A.D. (2007), 'Recent research into the behaviour of jacked foundation piles', *Advances in Deep Foundations*, Yokosuka, Japan, 3-26.
- [4] Suckling, T. (2003). 'Driven cast in situ piles, the CPT and the SPT – two case studies', *Ground Engineering*, Vol. 36, Issue 10, 28-32.
- [5] ASTM D4633-10 (2010) 'Standard Test Method for Energy Measurement of Dynamic Penetrometers', *ASTM International*, West Conshohocken, PA.
- [6] Rausche, F. and Klesney, A. (2007), 'Hammer Types, Efficiencies and Models in GRLWEAP', *PDCA 11th Annual International Conference and Exposition*, Nashville, USA, 97-118.
- [7] Egan, D. (2013), 'The load capacity of driven cast-in-situ piles derived from installation parameters', *Installation Effects in Geotechnical Engineering*, Rotterdam, The Netherlands, 99-103.
- [8] Egan, D. (2014), 'Real-time validation of driven cast-in-situ piles', *Proceedings of International Conference on Piling and Deep Foundations*, Stockholm, Sweden, 65-72.
- [9] Rausche, F. (2000), 'Pile driving equipment: Capabilities and properties', Keynote Lecture, *Proceedings of the 6th International Conference on the Application of Stress-Wave Theory to Piles*, Sao Paulo, Brazil.
- [10] Hussein, M.H., Rausche, F. and Likins, G.E. (1992), 'Dynamics of pile driving as a function of ram drop height', *Proceedings of the 4th International Conference on the Application of Stress-Wave Theory to Piles*, The Netherlands, 421-424.
- [11] Flynn, K.N., McCabe, B.A. and Egan, D. (2013), 'Axial load behaviour of a driven cast-in-situ pile in sand', *Proceedings of the 7th International Conference on Case Histories in Geotechnical Engineering*, Chicago, USA, 1-6.
- [12] Flynn, K.N. (2014), *Experimental investigations of driven cast-in-situ piles*, PhD Thesis, National University of Ireland, Galway, Ireland.
- [13] <http://www.junttan.com/products/hydraulic-impact-hammers/> accessed April 2016.
- [14] Flynn, K.N. and McCabe, B.A. (2016), 'Shaft resistance of driven cast-in-situ piles in sand', *Canadian Geotechnical Journal*, Vol 53, Issue 1, 49-59.

Sheet-pile corrosion rates within an existing outfall channel in Dublin Port

Brian G. Sexton¹, David R. Gill¹, Conor J. O'Donnell¹

¹AGL Consulting, Suite 2, The Avenue, Beacon Court, Sandyford, Dublin 18, Ireland
email: david.gill@agl.ie, brian.sexton@agl.ie, conor.odonnell@agl.ie

ABSTRACT: A new cooling water intake channel structure is being constructed as part of the Dublin Waste to Energy (DWtE) facility in Ringsend. This has required the extraction of old sheet-piles that had been in place for over 50 years. These sheet-piles formed part of an existing power station cooling water outfall channel. Extraction of the sheet-piles has allowed the loss in steel thickness to be measured over their full length and for average corrosion rates to be established. The age and type of the existing sheet-piles were determined by carrying out a detailed desk study. The average corrosion rates were found to give a good match with the general corrosion rates in the relevant Irish Standard (IS EN 1993-5:2007). The authors are not aware of any published data on corrosion rates for Irish coastal waters, so this case study provides useful data for the particular conditions present which include elevated water temperature and chlorine levels in the cooling water discharge. The effect of different flow conditions on corrosion rates could also be observed, with some sheet-piles being in the direct line of high velocity turbulent flow and other sheet-piles in more benign conditions. The Irish Standards and the relevant British Standard for Maritime Works, BS 6349-1-4:2013, differ in relation to their requirements for concentrated corrosion, sometimes referred to as Accelerated Low Water Corrosion (ALWC). In the absence of site-specific information, the rates of concentrated corrosion given in BS 6349-1-4:2013 are very onerous when compared to the general corrosion rates, and therefore the economic benefits of taking site measurements can be considerable.

KEY WORDS: General Corrosion; Concentrated Corrosion; Accelerated Low Water Corrosion (ALWC); Sheet-Pile Walls.

1 INTRODUCTION

The Dublin Waste to Energy Facility (DWtE) at Poolbeg, Ringsend has been designed to convert 600,000 tonnes of waste annually into electricity for 80,000 homes and district heating for 50,000 homes [1]. The site location for the Waste to Energy Facility is shown on Figure 1.



Figure 1. Site Location (Google Maps)

The WtE facility requires the construction of a cooling water intake channel and pump station to extract water from the tidal section of the River Liffey within Dublin Port. The cooling water intake channel is to be constructed within the existing outfall channel for the Synergen Dublin Bay Power Station. At its discharge point to the estuary, the outfall channel runs northwards and comprises two rows of sheet-piles as shown on Figure 2. The northern section of the sheet-

piles on the west wall of the channel had to be removed for a distance of approximately 80m where they obstructed the installation of the new DWtE structures. Their extraction has allowed corroded section measurements to be obtained over the full length of the sheet-piles. Measurements were taken at two locations in the channel approximately 35m apart, one set close to the weir, and another set approximately 40m back from the outfall discharge point at the middle of the wall, as shown on Figure 2. The age and type of the existing sheet-piles were determined from a detailed desk study and this has allowed average corrosion rates to be established for the piles.

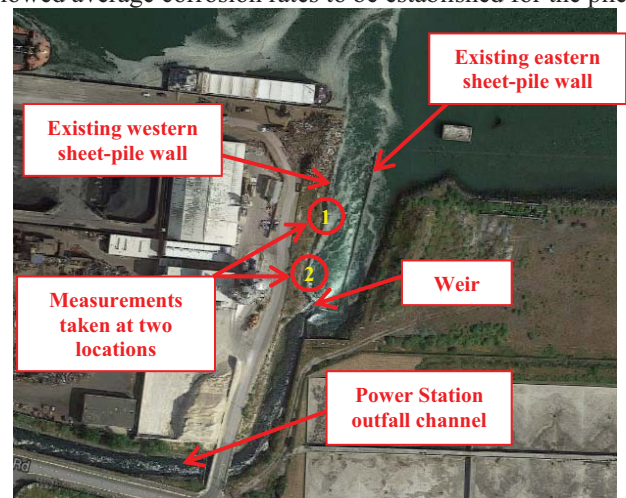


Figure 2. Aerial photograph showing outfall channel (Google Maps 2013)

The measured corrosion rates are compared with the recommended general corrosion rates in the Irish Standards, which are given in IS EN 1993-5:2007 *Design of steel structures - Part 5: Piling* [2]. It is noted that the general corrosion rates given in BS EN 1993-5:2007 *Design of steel structures - Part 5: Piling* [3] are identical to those in IS EN 1993-5:2007 [2].

However, the Irish Standards and the British Standards differ in relation to the requirement to consider concentrated corrosion. For maritime works, the relevant British Standard is BS 6349-1-4:2013 *Maritime works. General. Code of practice for materials* [4]. This requires consideration of concentrated corrosion, sometimes referred to as Accelerated Low Water Corrosion (ALWC). In the absence of site-specific information, concentrated corrosion rates can be very onerous when compared to the general corrosion rates given in IS EN 1993-5:2007 [2] and BS EN 1993-5:2007 [3]. This can have significant consequences for the design of steel structures in the low water zone.

2 CORROSION

2.1 Introduction

Typically, corrosion is accounted for in the design of sheet-piled wall structures by allowing for a reduction in thickness of the sheet-pile section during the lifetime of the structure. The reduction in thickness to be allowed for is dependent upon the relevant rate of corrosion at the proposed location, which depends on soil type, groundwater/seawater conditions, and the presence of oxygen/contaminants. In addition, corrosion will typically not be uniform over the whole length of the sheet-pile, with different corrosion rates applicable in different zones of the sheet-pile, as described in Section 2.2. Measures for prolonging the lifetime of a structure include using a thicker sheet-pile section, applying a protective organic coating (e.g. epoxy resin) and cathodic protection. Depending on the project-specific requirements, it may also be possible to adapt the design so that the maximum bending moment occurs in a zone with lower corrosion rates.

2.2 Corrosion Design - General

General corrosion rates are given in IS EN 1993-5:2007 [2]. The highest corrosion rates for seawater occur in the following zones, which are also shown on Figure 3:

- (i) Splash zone (Zone A): from Mean High Water (MHW, +1.6mOD) to Highest Astronomical Tide (HAT, +2.0mOD).
- (ii) Low water zone (Zone C): from Lowest Astronomical Tide (LAT, -2.6mOD) to Mean Low Water (MLW, -1.8mOD).

Note that the tide levels in Dublin Port are shown in brackets.

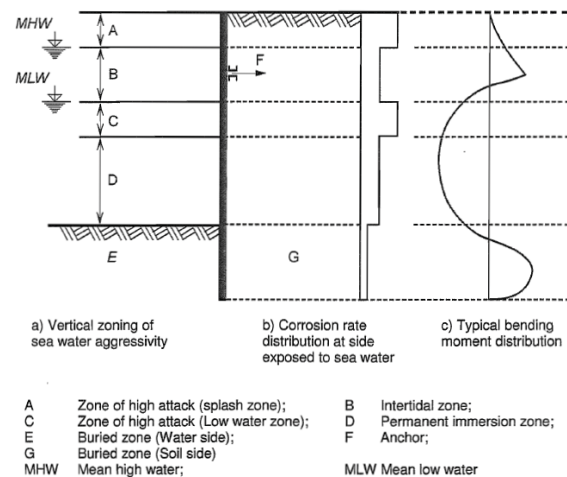


Figure 3. Example of corrosion rate distribution from IS EN 1993-5:2007 [2]

Lower corrosion rates are applicable in the intertidal zone (Zone B on Figure 3; from MLW to MHW) and in the permanent immersion zone (Zone D; from LAT to bed level). Typically, the maximum design bending moment in quay-side wall retaining structures occurs in the permanent immersion zone.

As per Table 4.1 of IS EN 1993-5:2007 [2], for sheet-piles in soils, with or without groundwater, and Table 4.2, for sheet-piles in fresh water or in sea water, the following allowance should be made for loss in steel thickness due to general corrosion for a design life of 50 years:

- Undisturbed natural soils: 0.012mm/year per exposed face.
- Low water and splash zones: 0.075mm/year per exposed face.
- Permanent immersion and inter tidal zones: 0.035mm/year per exposed face.

These rates have been extrapolated from measured data and are applicable to uniform/general corrosion.

Interestingly, the general corrosion rates specified by the EAU [5] for sheet-piles in the North Sea and Baltic Sea, which are presented in Figure 4, are marginally higher in the low water zone (LWz) at 0.078mm/year per exposed face for a design life of 50 years. The corresponding general corrosion rates specified by the EAU [5] are also marginally higher in the permanent immersion and inter tidal zones (UWz and WWz, 0.038mm/year per exposed face). However, in the splash zone (SPWz), the corresponding general corrosion rates are significantly lower (at 0.038mm/year per exposed face). EAU [5] therefore only considers the higher general corrosion rates to occur in the low water zone whereas IS EN 1993-5:2007 [2] considers both the low water and splash zones to be zones of "high attack". Note that it is not explicitly stated by the EAU [5] that the rates are per exposed face but it is assumed to be the case.

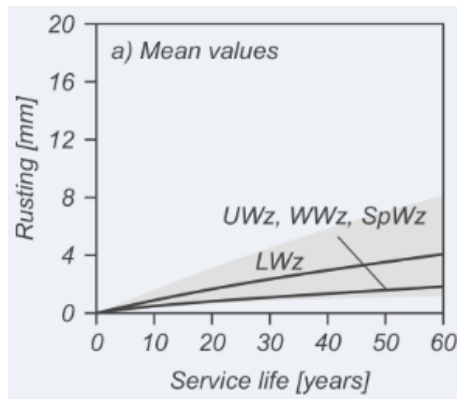


Figure 4. Sheet-pile thickness losses in seawater due to corrosion - mean values per exposed face - EAU [5]

2.3 Corrosion Design - Concentrated

BS 6349-1-4:2013 [4] requires localised higher concentrated corrosion rates to be considered "in situations where concentration corrosion is likely". BS 6349-1-4:2013 [4] has suggested that concentrated corrosion rates can be typically 0.5mm/side/year, with rates of 0.8mm/side/year recorded in UK coastal waters. The EAU [5] also specifies corresponding maximum corrosion rates for accelerated/pitting corrosion in the different zones as follows (see Figure 5):

- Low water zone: 0.318mm/year per exposed face.
- Splash zone: 0.160mm/year per exposed face.
- Permanent immersion and inter tidal zones: 0.116mm/year per exposed face.

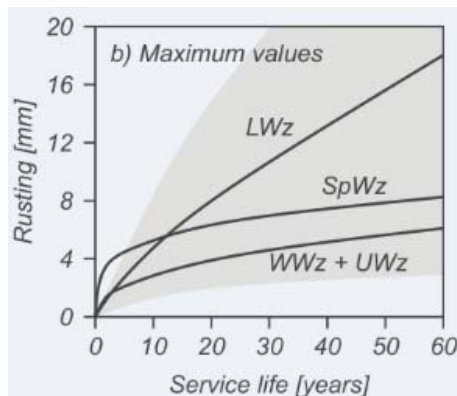


Figure 5. Sheet-pile thickness losses in seawater due to corrosion - maximum values per exposed face - EAU [5]

BS 6349-1-4:2013 [4] notes that concentrated corrosion to the point of perforation is "unlikely to cause catastrophic global failure of a sheet-piled structure". However, it could result in loss of retained material and collapse of adjacent surfacing or structures. Concentrated corrosion is sometimes referred to as Accelerated Low Water Corrosion (ALWC), and in some cases, can lead to extreme loss of section.

3 ACCELERATED LOW WATER CORROSION (ALWC)

3.1 Introduction

Accelerated Low Water Corrosion, or ALWC, is a rapid pitting form of microbially induced corrosion (MIC). As noted

by the International Navigation Association [6], the most common type of ALWC occurs as a horizontal band around low water, which can sometimes be found in patches and extend down to bed level. ALWC is recognizable as an orange/black hue over otherwise clean steel and an example of this is shown on Figure 6.

ALWC tends to occur in marine environments due to the presence of sulfates, which are converted by sulfate-reducing bacteria into hydrogen sulfide, resulting in direct anaerobic corrosion of steel surfaces [6]. In addition, the hydrogen sulfide serves as a food source for sulfide-oxidizing bacteria which convert the hydrogen sulfide to sulfuric acid.



Figure 6. Accelerated Low Water Corrosion, ALWC - International Navigation Association [6]

3.2 Studies on ALWC

According to the International Navigation Association [6], there is currently no known reliable basis for predicting the occurrence of ALWC at any given site although local incidence may give some indication. The International Navigation Association [6] have pointed to the results of two surveys:

- A survey by the European Commission in 1994 established, based on questionnaires, that at least 13% of ports in Europe were affected by ALWC.
- A 2001 UK survey found that ALWC was present in 10% of the sites polled.

The authors are not aware of any case studies or instances of ALWC in Dublin Port, although possible instances of it have been reported in four ports in Ireland, at Killybegs, Bangor, Belfast, and Cork [7, 8].

3.3 Effect of ALWC on Sheet-pile Section Type

The International Navigation Association [6] have distinguished between ALWC of Z-section and U-section sheet-piles as follows:

- Typically, Z-section sheet-piles are attacked mostly on the thinner web section(s), which results in holes forming quickly. However, these holes do not unduly affect section strength.

- U-section pile sheet-piles are attacked mostly on the protruding section of the outpan flange(s), which are the main stress-resisting section(s). In this instance, holes take longer to form, while the connecting clutches, which are the thickest parts of the sections, are rarely attacked.

4 OUTFALL CHANNEL SITE CONDITIONS

4.1 General

Prior to construction of the DWtE cooling water inlet, there were two rows of sheet-piles in the channel as shown in the most recent aerial photograph of the area in Figure 2. The western row of sheet-piles were removed where they obstructed the construction of new structures, thus making it possible to obtain corroded section measurements over the full length of the sheet-piles.

Considerable flow of cooling water exiting from the Synergen power station is clearly evident within the channel from the aerial photograph. Typical flow rates range from 6-8m³/s [9]. Elevated temperatures are reported to be on average 7° above the ambient water temperature in the estuary [10]. It is noted that higher water temperatures (up to approximately 40°C) are associated with faster corrosion rates, e.g. Zvivica [11].

In addition, chlorine is applied to the power station cooling water to prevent biofouling by mussels. This has also had an effect on the biological growth on the sheet-piles within the outfall channel, which are observed to be generally free of biological growth. Chlorination of seawater can increase corrosion rates of carbon steel [12] depending on the concentration but may also have the benefit of reducing the presence of sulfate-reducing bacteria (SRB) that can cause ALWC. Therefore the elevated water temperatures and chlorination are likely to increase the general corrosion rates but have the benefit of inhibiting the growth of the bacteria that can cause extremely high rates of concentrated corrosion in the low water zone.

The sheet-piles are observed to show varying degrees of corrosion depending on their position relative to the flow of cooling water from the power station. The eastern wall, which has water on both sides, and is directly subjected to high velocity, turbulent flow from the weir (see Figure 7) is heavily corroded with numerous holes having formed in the piles. As shown in Figure 8, water is now flowing through the wall. It can also be seen from Figure 8 that the webs of the Z-section sheet-piles have been corroded to perforation with the flanges more intact. This is probably due to their greater initial thickness of 11.7mm versus 8.9mm for the web (see Section 5.2). The western sheet-pile wall which is currently retaining ground on one side was corroded to a lesser extent and this is discussed in detail in Section 5.

4.2 Ground conditions

The ground conditions in the area typically comprise 3-6m of made ground over recent estuarine and alluvial deposits down to approximately -17mOD overlying stiff laminated clay (Port Clay) to -35mOD with limestone bedrock thereafter. The bedrock is at a significant depth in the Dublin Bay area due to the presence of a preglacial channel, first identified by Farrington [13].

The ground level behind the west wall is approximately +4.0mOD sloping to top of pile level at +0.3mOD. The channel bed level varies from -2.0mOD to -6.0mOD. Tide levels in Dublin Port range from a HAT = +2.0mOD to LAT = -2.6mOD.



Figure 7. High velocity turbulent water flow from the weir



Figure 8. Holes in existing eastern sheet-pile wall subjected to direct flow from weir

5 ESTABLISHING SITE-SPECIFIC CORROSION RATES

5.1 Measurement

Measurements of flange and web thicknesses of the existing sheet-piles were taken in September 2015 using a digital callipers accurate to 0.01mm. Measurements of the flange and web thicknesses of the extracted sheet-piles from the western wall were taken at two locations in the channel approximately 35m apart. At the western wall, the overall pile length was 10.6m, and the top of pile was +0.3mOD. The measurements were taken at 1m intervals along the length of the extracted piles. The exposure conditions at the south were found to be more severe due to their proximity to the weir and cooling water outflow, with turbulent water flow and more elevated temperatures. Photographs of extracted sheet-piles are shown in Figures 9, 10, and 11.



Figure 9. Sheet-pile extracted at south end of western wall (closer to weir)



Figure 10. Hole in web of sheet-pile extracted at south end of western wall (closer to weir)



Figure 11. Extracted sheet-pile - hole cut at -10.0mOD

5.2 Desk Study

The sheet-piles were constructed as part of the outfall channel for the old ESB Ringsend Power Station (operational from 1955 to 1982) and this outfall channel is now being used by the Synergen power station that now operates at the same site. A detailed desk study was carried out to establish the age of the sheet-piles (using both Ordnance Survey aerial photographs dating to the 1970's and historic ESB drawings) and in turn determine site-specific corrosion rates. The oldest available aerial photograph shows the sheet-piles to be present in 1973. Based on the desk study, the existing sheet-piles are considered to be between 50 and 60 years old and date to a period between 1955, when the power station was first operational, to 1965.

Aerial photographs show the western row of sheet-piles were exposed to corrosion from water on both sides of the piles (above bed level) for at least 30 years, with placement of fill to the western face taking place relatively recently. Both sets of sheet-piles have been exposed to the flow of cooling water in the channel from their installation until 1982 (i.e. 17 to 27 years for the operation of the old ESB station) and then from 2002 to 2015 (i.e. 13 years, for the operation of the new power station), which is a total of 30 or 40 years (depending on whether the piles are considered to be 50 or 60 years old).

5.3 Findings

Based on the measurements of the extracted sheet-piles from the western wall, the following was determined:

- Significant loss of thickness from corrosion was evident on some of the piles, depending on their location within

the channel, with greater corrosion closer to the weir. The piles close to the weir were perforated with holes and the section was so thin that they buckled easily during extraction with an excavator.

- The most heavily corroded zone was between mid-tide and about 0.5m below LAT.
- The lowest corrosion rates were below bed level and in particular at the level of a concrete slab that protected the bed from scour.
- The dimensions of the extracted sheet-piles didn't match modern sheet-pile sections, but, were found to correspond with the old British Steel Frodingham Z-section piles.
- The pile section that gave the closest match to the measurements taken was the 3N Normal Frodingham section, and this was subsequently confirmed from markings on extracted sheet-piles. The section properties are shown on Figure 12. The initial flange and web thicknesses were 11.7mm and 8.9mm respectively.

Dimensions and Properties

Section	b mm (nom)	h mm (nom)	d mm	t mm (nom)	t1 mm (nom)	t2 mm (nom)	Sectional Area sq. cm. per m of wall	Mass kg per linear metre	Moment of Inertia cm ⁴ per metre	Section Modulus cm ³ per metre	Section
1A*	400	146	6.9	6.9	83	131	113.0	35.6	89.1	4110	1A*
1B*	400	133	9.6	9.6	79	111	134.0	42.1	106.3	3737	1B*
1BXX	476	143	12.7	12.7	78	123	168.9	62.1	130.4	4919	1BXX
1N	483	170	8	8	106	137	126.0	47.8	99.1	6048	1N
2N	483	235	9.7	9.4	97	149	143.0	54.2	112.3	13513	2N
3N	483	283	11.7	8.9	89	146	175.0	66.2	137.1	22885	3N
Normal	483	283	11.2	9.5	86	140	175.0	66.3	137.3	22951	Normal
Modified	483	330	14.0	10.4	77	127	218.0	82.4	170.8	39831	Modified
4N	483	330	14.0	10.4	77	127	218.0	82.4	170.8	39831	4N
5	425	311	17.0	11.9	89	118	362.0	100.9	236.9	49202	5

Rolling margin is within 4 per cent over and 2.5 per cent under theoretical mass; 76 mm over and 90 mm under on length.
* It is advisable to check on the availability of these sections before specifying.

SPECIAL SECTIONS
Sections may be "rolled up" (Thickened) or "rolled down" (Thinned) by special arrangement to increase or decrease the thickness of both web and flange by a maximum of 0.8mm.

Frodingham Steel Sheet Piling

Figure 12. Frodingham Steel Sheet Piling - British Steel Corporation - BSC Sections - Piling Handbook [14]

5.4 Comparison of Measured and Recommended Corrosion Rates in Zone 1

The measurements taken at the middle of the western wall are presented in Figure 13. Also presented is the recommended loss in thickness given by IS EN 1993-5:2007 [2] for a design life of 50 and 60 years. This was determined for the exposure conditions on each pile face that was established by the desk study, as outlined in Section 5.2.

Examination of Figure 13 indicates that the general corrosion rates given in IS EN 1993-5:2007 [2] have not been exceeded and so are applicable at this particular part of the outfall channel (i.e. out of the direct flow from the weir). The lowest rates of corrosion were measured at the toe and at concrete slab, which was present at bed level. The maximum rate of corrosion occurred in the Low Water Zone, as would be expected. The piles did not extend into the Splash Zone, so no comparison can be made here. Relatively low corrosion rates were recorded in the Intertidal Zone and the Permanent Immersion Zone below LAT. As noted in Section 2.1, it is therefore beneficial for economic design when the maximum design bending moment for a quay wall can be designed to occur outside the zones of high attack and in particular the Low Water Zone.

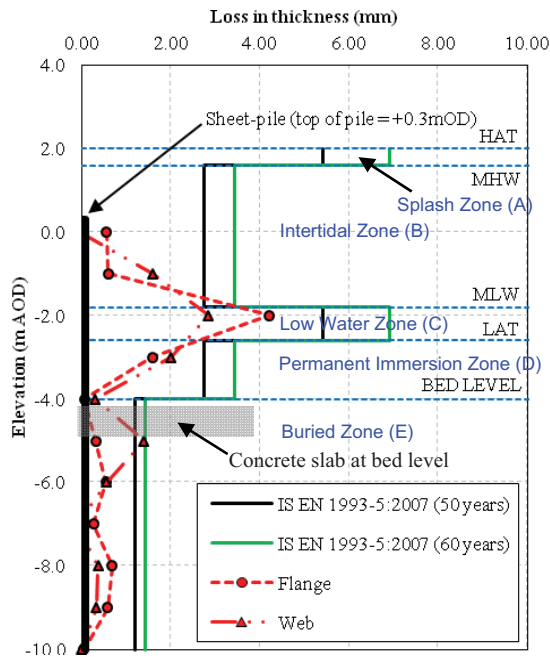


Figure 13. Comparison of measurements and recommended loss in thickness given by IS EN 1993-5:2007 [2]

5.5 Concentrated Corrosion Rates in Zone 2 (close to the weir)

The sheet-piles close to the weir on the west wall were corroded to the point of perforation, which was typically, but not always, within the web. The most heavily corroded zone occurred between mid-tide and about 0.5m below LAT (which is at -2.6mOD). The maximum rate of concentrated corrosion was estimated for these piles, as it is not known when perforation first occurred. Allowing for perforation to have occurred with the last 10 years gives corrosion rates in the range of 0.10-0.13 mm/year per exposed face. However, conservatively assuming the perforation to have occurred within the first 30 years gives a concentrated corrosion rate of 0.16mm/year per exposed face. These concentrated corrosion rates are significantly lower than the rates given in BS 6349-1-4:2013 [4] for ALWC of 0.5 to 0.8mm/side/year. The sheet-piles were observed to be free of the orange and black corrosion products associated with ALWC. Therefore, ALWC is not considered to have occurred for piles within the outfall channel. At this location, the concentrated corrosion is considered by the authors to be due to the turbulent, high-velocity oxygenated flow of cooling water which would lead to erosion and flaking/removal of rust which would have been exacerbated by the higher temperatures and chemical effects at this location.

6 CONCLUSIONS

The construction works for a new cooling water channel for Dublin Waste to Energy Facility (DWtE) in Poolbeg, Ringsend have presented a unique opportunity to establish long-term corrosion rates for sheet-piles over their full length in a range of exposure zones. The piles were within an existing cooling water outfall channel for more than 50 years. The corrosion rates were found to be consistent with the recommended general corrosion rates given in IS EN 1993-

5:2007 [2], despite the presence of elevated water temperatures and chlorination of the cooling water that would normally be expected to increase the rate of corrosion of carbon steel. At some locations within the channel, concentrated corrosion has resulted in perforation of sheet-piles which were in the direct line of the high-velocity, turbulent flow of cooling water from the Synergen power station. However conditions of Accelerated Low Water Corrosion, which is a particularly aggressive pitting form of microbially induced corrosion (MIC), is not considered to be present. The rate of concentrated corrosion of about 0.10-0.16mm/year per exposed face established at the western wall was also significantly lower than suggested values for ALWC which can be in the range 0.5 to 0.8mm/side/year. The relevant Irish Standard, IS EN 1993-5:2007 [2], does not require concentrated corrosion to be considered for the design of sheet-piles. However this is required by UK Standards (i.e. the National Annex to BS EN 1993-5:2007 [3] and BS 6349-1-4:2013 [4]), which refer to ALWC. Although ALWC does not affect every location, it can necessitate costly maintenance/repair works at an unexpected early stage in the design life of a structure when it does. There are reported cases of ALWC in Irish ports and therefore it should be considered in the design of new maritime structures in Ireland. Where possible by site measurement, there are significant economic advantages to establishing whether ALWC can be discounted as a risk at the locations of new maritime structures.

ACKNOWLEDGMENTS

The authors would like to thank BAM Civil and Covanta for permission to use the data presented in the paper.

REFERENCES

- [1] <http://dublinwastetoenergy.ie/the-project/> Accessed: 05/04/2016.
- [2] IS EN 1993-5:2007 (Eurocode 3: Design of Steel Structures - Part 5: Piling).
- [3] BS EN 1993-5:2007 (Eurocode 3: Design of Steel Structures - Part 5: Piling).
- [4] BS 6349-1-4: 2013 (Maritime works - Part 1-4: General. Code of practice for materials).
- [5] EAU (2004), 'Recommendations of the Committee for Waterfront Structures: Harbours and Waterways (EAU 2004)', Ernst & Sohn, Berlin, eight edition, 2004.
- [6] International Navigation Association (2005), 'Accelerated Low Water Corrosion', Report of Working Group 44 of the Maritime Navigation Commission.
- [7] http://www.portstrategy.com/news101/port-operations/marine-engineering/treating_your_piles Accessed 07/04/2016.
- [8] <http://www.irishtimes.com/news/metal-eating-bug-causes-concern-to-donegal-fishermen-1.181874> Accessed 07/04/2016.
- [9] Dublin Waste to Energy Project, Environmental Impact Statement, June 2006.
- [10] Dublin Bay Power Plant EPA Annual Environmental Report, IPCL no. P0486-01, Reporting period: 1 January to 31 December 2008
- [11] Zivica, V. (2002), 'Significance and influence of the ambient temperature as a rate factor of steel reinforcement corrosion', Bulletin of Materials Science, 25, 5, 375-379.
- [12] Franklin, M. J., Nivens, D. E., Vass, A. A., Mittelman, M. W., Jack, R. F., Dowling, N. J. E., and White, D. C. 'Effect of Chlorine and Chlorine/Bromine Biocide Treatments on the Number and Activity of Biofilm Bacteria and on Carbon Steel', Journal of Science and Engineering, Corrosion, 47, 2, 128-134.
- [13] Farrington, A. (1929), 'The pre-glacial topography of the Liffey basin', *Proceedings of the Royal Irish Academy*, 38(B): 148-170.
- [14] Piling Handbook. (1979), 'British Steel Corporation - BSC Sections', second edition.

Author Index

Al-Sabah, S.	527, 599	Callender, P.	243
Alawais, A.	347	Campbell, J.	661
Amato, G.	605	Campbell, N.	91
Andersson, A.	37	Cantero, D.	55
Antonopoulou, S.	189	Carey, C.	311
Archbold, P.	183, 271, 283	Casas, J. R.	67
Ascoop, J.	649, 661	Casey, P.	445
Atan, R.	655	Casey, T.	335
Attari, Y.	457	Cavalcante, M.	451
Barry, K.	649	Chen, J. F.	277, 605
Basheer, M.	91, 265	Clarke, J.	305
Basu, B.	421	Clifford, E.	141, 341, 667
Bhagat, D.	147	Coleman, D.	563
Bhalla, S.	147	Collery, D. D.	433
Blocken, B.	341	Collier, D.	159
Bond, S.	359	Collins, M.	575, 581
Bondar, D.	265	Connolly, G.	661
Bowe, C.	55, 73	Connolly, L.	73
Boyle, A.	329	Corbally, R.	79, 305
Bradshaw, A.	469	Cosgrove, T.	575, 581
Broderick, B.	421, 509	Costas De La Peña, L.	153
Buggy, F.	697	Cox, R.	413
Byrne, A.	165, 593	Cronin, D.	673
Byrne, B.	473	Crossett, P.	365
Byrne, G.	189	da Costa Santos, A. C.	271
Cahill, F.	79	Dal Lago, B.	365
Cahill, P.	37	Deakin, V.	433

Deegan, P.	171, 255, 365	Gehl, P.	305
Devaney, R.	521	Gendvilas, V.	551
Doherty, P.	463, 469	Ghosh, B.	383
Doyle, A.	195, 299	Gilbert, R. B.	469
Doyle, F.	299	Gill, D.	709
Dromey, L.	85	Gilmore, D.	243, 497
Décatoire, R.	61	Glavin, P.	563
Eadie, R.	427	Goggins, J.	97, 129, 141, 195, 289, 299, 377, 395, 401, 491, 503, 509, 515, 623, 655, 667
English, J.	503		
English, S.	277		
Ennos, J.	433	Gonzalez Merino, A.	153
Ettema, R.	249	González, A.	153
Fagan, E.	299, 491	Greaney, E.	329
Fallah, S.	445, 685	Griffin, C.	7
Farrelly, N.	557	Grogan, D.	195
Feerick, P.	299	Hajdukiewicz, M.	97, 341, 395, 401, 623
Feighan, K.	335	Hajializadeh, D.	311
Ferrara, L.	171, 365	Hamill, G.	249
Finnegan, W.	141, 289, 667, 679	Hanley, C.	237
Fitzgerald, P.	533	Harrington, J.	631
Fitzhenry, K.	667, 679	Harte, A.	21, 539, 545, 551, 557
Flanagan, M.	195, 299, 377	Hassan, M. S.	503
Flanagan, T.	299	Heitner, B.	61
Flynn, K.	703	Hester, D.	43, 201, 213, 231
Forde, P.	637	Hoey, C.	183
Frost, J. D.	31	Holleran, D.	623
Gamble, J.	631	Holmes, N.	359, 371, 593
Ganguly, T.	395	Hunt, A.	509
Gavin, K.	43, 457, 469, 479, 685	Hunt, P.	439

Ibáñez, J. L.	451	Magee, B.	293, 427
Jalilvand, S.	469, 685	Mannion, P.	341
Jose, D.	177	Martinez Otero, D.	49
Karoumi, R.	37	Martinez del Rincon, J.	201
Keane, L.	135	Martinez-Pastor, B.	123
Keane, M.	395, 401	Martinovic, K.	479
Kearney, J.	159	Mathewson, A.	37
Kearney, J.	497	Matos, J.	237
Keenahan, J.	117, 389	McCabe, B.	439, 451, 703
Kelliher, D.	237	McCarter, W. J.	15
Kelly, G.	171, 255	McCarthy, J.	321
Kenna, J.	283	McCloud, A.	433
Kennedy, C.	195	McCrum, D.	605
Kinnane, O.	353	McFarland, B.	159, 243, 497
Kissane, P.	697	McGetrick, P.	231
Krajnc, L.	557	McGranaghan, G.	421
Lahiffe, S.	649	McGrath, T.	91
Lam, J. C.	305	McHugh, K.	289
Lawther, S.	177	McIntosh, A.	177
Leahy, C.	61, 73, 207	McKenna, E.	159, 497
Leen, S.	195, 299, 491, 521	McKenna, T.	563
Lizondo, S.	649, 661	McKeon, E.	451
Long, M.	697	McNally, C.	189, 599
Loonam, A.	271	McPolin, D.	539, 545
Lydon, D.	201, 213	Mccormack, S.	353
Lydon, M.	201, 213	McGovern, P.	289
Mac Réamoinn, R.	117, 389	Meehan, A.	611
Macilwraith, A.	563, 569	Micu, E. A.	317
Madden, E.	691	Minehane, M.	219

Monaghan, R. F. D.	129	O'Rourke, B.	85
Moore, P.	225	O'Suilleabhain, C.	219
Moran, P.	97	OBrien, E.	49, 55, 61, 207, 311, 317, 533
Moughy, J.	67		
Mulheron, M.	283	O'Dwyer, D.	413
Mulry, B.	321, 335	Paduano, C.	117, 389
Murphy, J.	85	Pakrashi, V.	37, 237, 383
Nanukuttan, S.	91, 177, 265	Pattarini, A.	171, 255, 365
Nash, S.	643, 655	Pavia, S.	111
Newell, S.	377, 623	Phillips, B.	473
Niall, D.	353	Phoenix, A.	643
Nieuwenhuis, M.	551	Power, N.	135, 673
Nogal, M.	123, 485	Prendergast, L.	43, 457
Nolan, E.	165	Provis, J.	177
Norton, B.	359, 593	Purcell, P.	407
O'Byrne, M.	383	Quigley, P.	439
O'Callaghan, L.	359	Quirke, P.	55
O'Ceallaigh, C.	545	Reale, C.	479
O'Connell, A. M.	451	Reddy, J.	371
O'Connor, A.	73, 79, 123, 207, 485, 617	Reilly, C.	463
		Reilly, J.	649, 661
O'Donnell, C.	709	Rice, M.	427
O'Donoghue, P.	521	Robinson, D.	201, 213, 277
O'Driscoll, L.	637	Rodgers, M.	439
O'Flaherty, T.	259	Rowan, N.	667
O'Hara, D.	691	Royston, R.	473
O'Higgins, C.	243, 497	Ruane, K.	85, 219, 611
O'Neill, C.	539	Rugero, S.	463
O'Reilly, C.	551	Rush, D.	697

Russell, M.	183	Thompson, Douglas	265
Ryan, D.	249	Tiernan, T.	649
Ryan, P.	587	Torre, O. d. I.	377, 491
Ryan, T.	509	Tretsiakova-mcnally, S.	293
Salawdeh, S.	503, 509, 515	Tuinstra, D.	225
Schoefs, F.	61, 383	Vinayagamoothy, S.	469
Sevillano Bravo, E.	49, 317, 533	Walker, R.	111
Sexton, B.	451, 709	Walls, M.	195
Sheil, B.	473	Walsh, D.	649
Shiell, C.	105	West, R.	105, 147, 347, 353, 421
Sikora, K.	545	Whelton, M.	569
Simic, K.	551	Wilkinson, A.	293
Singlitico, A.	129	Wilson, W.	259
Siviero, E.	1	Woodward, D.	293
Slevin, M.	617	Yalamas, T.	61
Soban, D.	91	Zhan, X.	141, 667, 679
Solan, B.	249, 427	Zuhaib, S.	401
Sonebi, M.	171, 255, 365		
Sourav, S. N. A.	599		
Soutsos, M.	177, 265, 277		
Stewart, M. G.	587		
Suhail, R.	605		
Sweeney, P.	445		
Taalab, K.	305		
Tarpey, E.	667, 679		
Taylor, S.	171, 201, 213, 243, 255, 365, 539		
Teixeira, R.	485		
Thompson, David	371		

